

Twenty-First Symposium on NAVAL HYDRODYNAMICS

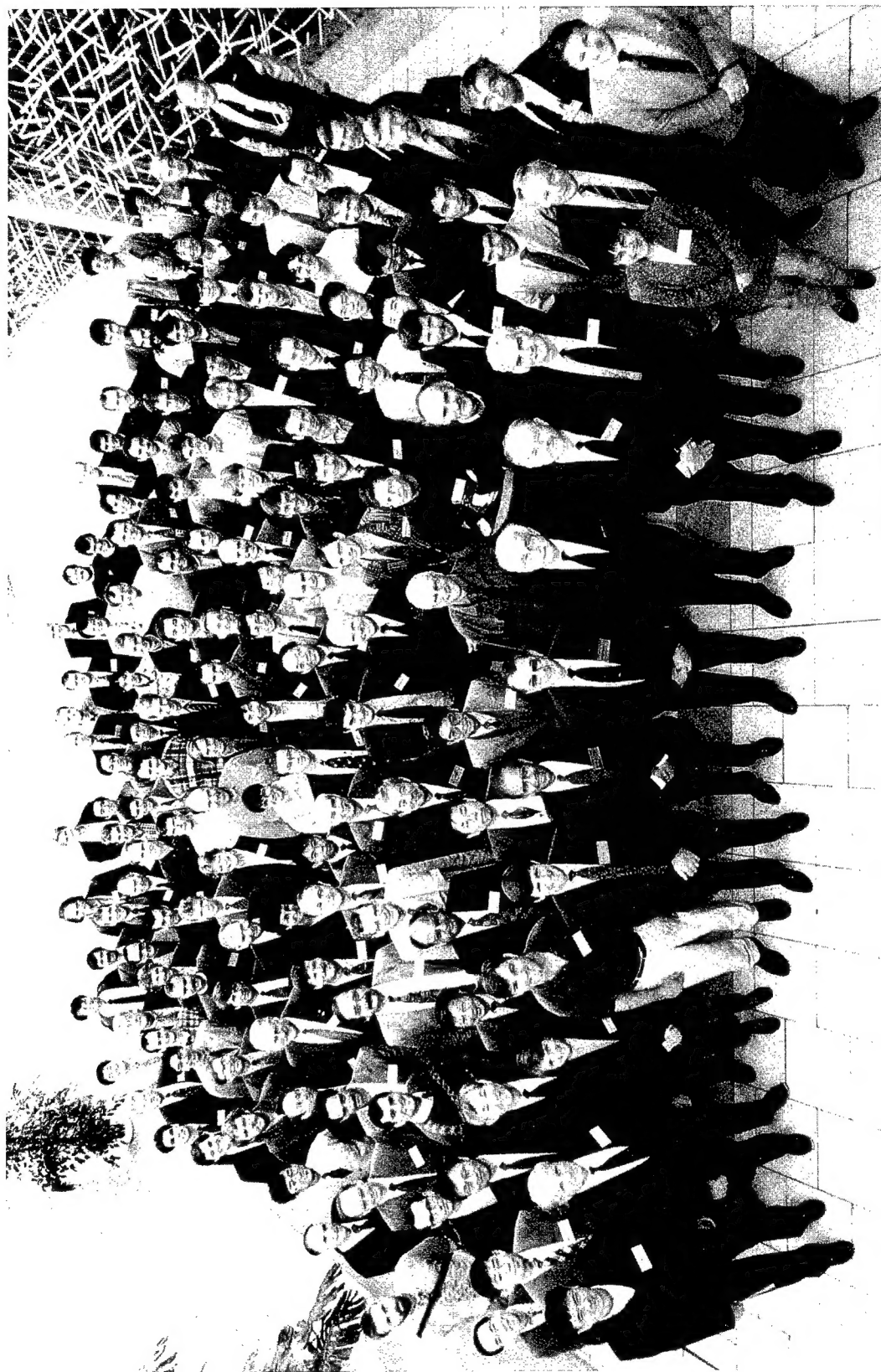
Wave-Induced Ship Motions and Loads
Frontier Experimental Techniques
Wake Dynamics
Viscous Ship Hydrodynamics
Water Entry
Wave Hydrodynamics/Stratified Flow
Bluff Body Hydrodynamics
Hydrodynamics in Ship Design
Shallow Water Hydrodynamics
Cavitation and Bubbly Flows
Propulsor Hydrodynamics/Hydroacoustics
Fluid Dynamics in the Naval Context
CFD Validation

DTIC QUALITY INSPECTED 4

DISTRIBUTION STATEMENT A

Approved for public release;
Distribution Unlimited

19970924 050



Attendees at the Twenty-First Symposium on Naval Hydrodynamics, Trondheim, Norway, June 24-28, 1996.

Twenty-First Symposium on NAVAL HYDRODYNAMICS

Wave-Induced Ship Motions and Loads
Frontier Experimental Techniques
Wake Dynamics
Viscous Ship Hydrodynamics
Water Entry
Wave Hydrodynamics/Stratified Flow
Bluff Body Hydrodynamics
Hydrodynamics in Ship Design
Shallow Water Hydrodynamics
Cavitation and Bubbly Flows
Propulsor Hydrodynamics/Hydroacoustics
Fluid Dynamics in the Naval Context
CFD Validation

Sponsored Jointly by

Office of Naval Research

Norwegian University of Science and Technology, Trondheim, Norway

Naval Studies Board

Commission on Physical Sciences, Mathematics,
and Applications

National Research Council

NATIONAL ACADEMY PRESS
Washington, D.C. 1997

The National Research Council serves as an independent advisor to the federal government on scientific and technical questions of national importance. Established in 1916 under the congressional charter of the private, nonprofit National Academy of Sciences, the Research Council brings the resources of the entire scientific and technical community to bear on national problems through its volunteer advisory committees. Today the Research Council stands as the principal operating agency of both the National Academy of Sciences and the National Academy of Engineering and is administered jointly by the two academies and the Institute of Medicine. The National Academy of Engineering and the Institute of Medicine were established in 1964 and 1970, respectively, under the charter of the National Academy of Sciences.

The National Research Council has numerous operating units. One of these is the Naval Studies Board, which is charged with conducting and reporting on surveys and studies in the field of scientific research and development applicable to the operation and function of the Navy.

A portion of the work done to prepare this document was performed under Department of Navy Contract N00014-95-1-1189 issued by the Office of Naval Research under contract authority NR 201-124. However, the content does not necessarily reflect the position or the policy of the Department of the Navy or the government, and no official endorsement should be inferred.

The United States Government has at least a royalty-free, nonexclusive, and irrevocable license throughout the world for government purposes to publish, translate, reproduce, deliver, perform, and dispose of all or any of this work, and to authorize others so to do.

Copyright 1997 by the National Academy of Sciences. All rights reserved.

Printed in the United States of America

NAVAL STUDIES BOARD

David R. Heebner, Science Applications International Corporation (retired), *Chair*
George M. Whitesides, Harvard University, *Vice Chair*
Albert J. Baciocco, Jr., The Baciocco Group, Inc.
Alan Berman, Applied Research Laboratory, Pennsylvania State University
Norman E. Betaque, Logistics Management Institute
Norval L. Broome, Mitre Corporation
Gerald A. Cann, Raytheon Company
Seymour J. Deitchman, Chevy Chase, Maryland, *Special Advisor*
Anthony J. DeMaria, DeMaria ElectroOptics Systems, Inc.
John F. Egan, Lockheed Martin Corporation
Robert Hummel, Hummel Enterprises, Inc.
David W. McCall, Far Hills, New Jersey
Robert J. Murray, Center for Naval Analyses
Robert B. Oakley, National Defense University
William J. Phillips, Northstar Associates, Inc.
Mara G. Prentiss, Jefferson Laboratory, Harvard University
Herbert Rabin, University of Maryland
Julie JCH Ryan, Booz, Allen and Hamilton
Harrison Shull, Monterey, California
Keith A. Smith, Vienna, Virginia
Robert C. Spindel, Applied Physics Laboratory, University of Washington
David L. Stanford, Science Applications International Corporation
H. Gregory Tornatore, Applied Physics Laboratory, Johns Hopkins University
J. Pace VanDevender, Prosperity Institute
Vincent Vitto, Lincoln Laboratory, Massachusetts Institute of Technology
Bruce Wald, Arlington Education Consultants

Navy Liaison Representatives

Paul G. Blatch, Office of the Chief of Naval Operations (N911T1)
Ronald N. Kostoff, Office of Naval Research

Ronald D. Taylor, Director

COMMISSION ON PHYSICAL SCIENCES, MATHEMATICS, AND APPLICATIONS

Robert J. Hermann, United Technologies Corporation, *Co-Chair*
W. Carl Lineberger, University of Colorado, *Co-Chair*
Peter M. Banks, Environmental Research Institute of Michigan
Lawrence D. Brown, University of Pennsylvania
Ronald G. Douglas, Texas A&M University
John E. Estes, University of California at Santa Barbara
L. Louis Hegedus, Elf Atochem North America, Inc.
John E. Hopcroft, Cornell University
Rhonda J. Hughes, Bryn Mawr College
Shirley A. Jackson, U.S. Nuclear Regulatory Commission
Kenneth H. Keller, University of Minnesota
Kenneth I. Kellermann, National Radio Astronomy Observatory
Margaret G. Kivelson, University of California at Los Angeles
Daniel Kleppner, Massachusetts Institute of Technology
John Kreick, Sanders, a Lockheed Martin Company
Marsha I. Lester, University of Pennsylvania
Thomas A. Prince, California Institute of Technology
Nicholas P. Samios, Brookhaven National Laboratory
L.E. Scriven, University of Minnesota
Shmuel Winograd, IBM T.J. Watson Research Center
Charles A. Zraket, Mitre Corporation (retired)

Norman Metzger, Executive Director

FOREWORD

The Twenty-First Symposium on Naval Hydrodynamics was held in Trondheim, Norway, from June 24 - 28, 1996. This international symposium was organized jointly by the Office of Naval Research (Mechanics and Energy Conversion S&T Division), the National Research Council (Naval Studies Board), and the Norwegian University of Science and Technology. This biennial symposium promotes the technical exchange of naval research developments of common interest to all the countries of the world. The forum encourages both formal and informal discussion of the presented papers, and the occasion provides an opportunity for direct communication between international peers.

More than 170 participants from 23 countries attended the symposium. The attendees represented a mixture of experience and expertise, as some attendees were newly graduated students and others were of established international repute. Seventy-two papers were presented in thirteen topical areas covered by the symposium, including wave-induced ship motions and loads, viscous ship hydrodynamics, wake dynamics, wave hydrodynamics, cavitation and bubbly flows, propulsor hydrodynamics/hydroacoustics, water entry, bluff body hydrodynamics, shallow water hydrodynamics, fluid dynamics in the naval context, CFD validation, frontier experimental techniques, and hydrodynamics in ship design. These topical areas were chosen for this particular meeting because of the recent advances made in them. Examples of the significant advances presented in the papers are the high-resolution numerical solution of bow waves for slender hull forms showing the origin of bow waves in the bow splash, the influence of cavitation nuclei on the cavitation bucket for full-scale predictions, the

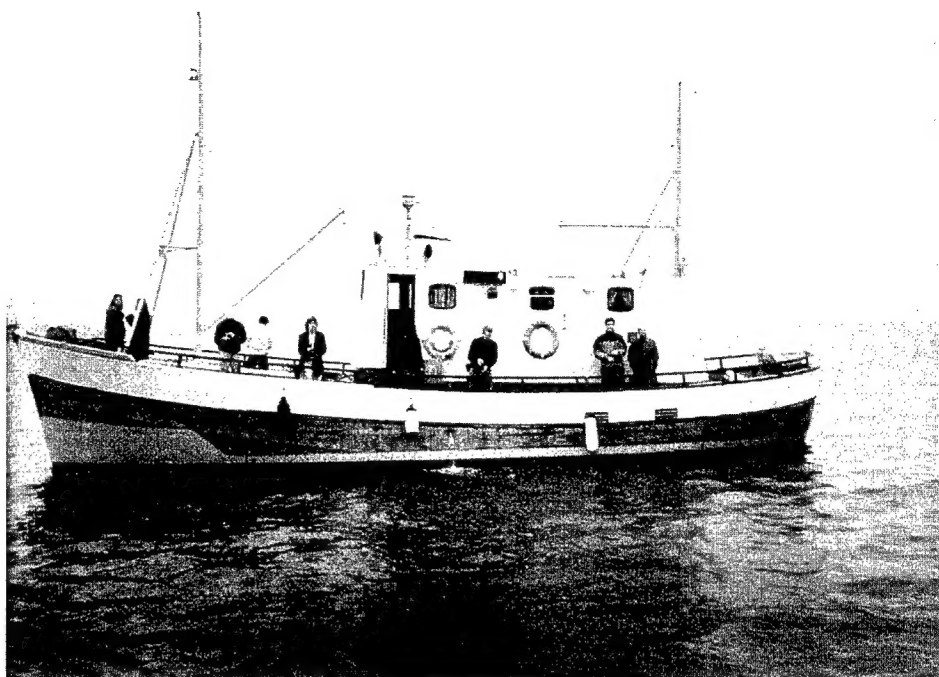
coupling of hydrodynamic impact and elastic response during slamming, and the development of a two-fluid turbulent flow computational method for surface ships. This brief list illustrates the quality and timeliness of the symposium for naval hydrodynamics.

The symposium featured invited lectures each morning. The lectures were presented by M. Longuet-Higgins, H. Miyata, P. Bearman, J. Milgram, and M. Sevik and covered topics from breaking waves to bluff body wakes to hydroacoustics, as well as CFD simulations and hydrodynamics in sailing. These lectures by prominent international experts set the pace for the sessions that followed.

The success of this symposium is the result of hard work on the part of many people. There was, of course, the Organizing and Paper Selection Committee consisting of myself, Dr. Patrick Purtell, and Mr. James Fein (Office of Naval Research), Dr. Ronald Taylor (National Research Council), Prof. Odd Faltinsen (Norwegian University of Science and Technology), Dr. William Morgan (David Taylor Model Basin), and Mr. John Dalzell (Journal of Ship Research). The contribution of this committee was certainly the cornerstone for the success of the symposium. However, the administrative preparation and execution, and the production of this archival volume, would not have been possible without the support of Mrs. Susan Campbell, Mrs. Dixie Gordon, and the staff of the Naval Studies Board of the National Research Council. Special appreciation is also extended to Ms. Emma Kenney, from my office, for handling the abstract collection and following through with the preparation of the discussion sections.

Edwin P. Rood
Office of Naval Research





CONTENTS

OPENING REMARKS

Dr. Fred E. Saalfeld	3
Deputy Chief of Naval Research/Technical Director	

TECHNICAL SESSIONS

Invited Lecture

<i>Progress Toward Understanding How Waves Break</i>	7
M. Longuet-Higgins (University of California at San Diego, USA)	

Wave-Induced Ship Motions and Loads

<i>Radiation and Diffraction Waves of a Ship at Forward Speed</i>	29
M. Ohkusu, G. Wen (Kyushu University, Japan)	
<i>Nonlinear Ship Motions and Wave-Induced Loads by a Rankine Method</i>	45
D. Kring, Y.-F. Huang, P. Sclavounos (Massachusetts Institute of Technology, USA), T. Vada, A. Braathen (Det Norske Veritas, Norway)	
<i>Nonlinear Water Wave Computations Using a Multipole Accelerated, Desingularized Method</i>	64
S. Scorpio, R. Beck (University of Michigan, USA), F. Korsmeyer (Massachusetts Institute of Technology, USA)	
<i>Computations of Wave Loads Using a B-Spline Panel Method</i>	75
C.-H. Lee, H. Maniar, J. Newman, X. Zhu (Massachusetts Institute of Technology, USA)	

Wave-Induced Motions and Loads

<i>Simulation of Strongly Nonlinear Wave Generation and Wave-Body Interactions Using a 3-D MEL Model</i>	93
P. Ferrant (SIREHNA, France)	
<i>Analysis of Interactions Between Nonlinear Waves and Bodies by Domain Decomposition</i>	110
G.-X. Wu, Q.-W. Ma (University College London, United Kingdom), R. Taylor (University of Oxford, United Kingdom)	
<i>Fourier-Kochin Theory of Free-Surface Flows</i>	120
F. Noblesse (David Taylor Model Basin, USA), X.-B. Chen (Bureau Veritas, France), C. Yang (George Mason University, USA)	

Frontier Experimental Techniques

<i>24-Inch Water Tunnel Flow Field Measurements During Propeller Crashback</i>	136
C.-W. Jiang, ¹ R. Dong, ² H.-L. Liu, ¹ M.-S. Chang ¹ (¹ David Taylor Model Basin, ² Johns Hopkins University, USA)	
<i>Accuracy of Wave Pattern Analysis Methods in Towing Tanks</i>	147
F.-X. Dumez, S. Cordier (Bassin d'Essais des Carènes, France)	
<i>Unsteady Three-Dimensional Cross-Flow Separation Measurements on a Prolate Spheroid Undergoing Time-Dependent Maneuvers</i>	161
T. Wetzel, R. Simpson (Virginia Polytechnic Institute and State University, USA)	

Wave-Induced Ship Motions and Loads

- Time-Domain Calculations of First- and Second-Order Forces on a Vessel Sailing in Waves* 177
L. Sier vogel, A. Hermans (Delft University of Technology, The Netherlands),
R. Huijsmans (Maritime Research Institute, The Netherlands)
- Third-Order Volterra Modeling of Ship Responses Based on Regular Wave Results* 189
L. Adegeest (Delft University of Technology, The Netherlands)
- Nonlinearly Interacting Responses of the Two Rotational Modes of Motion—Roll and Pitch Motions* 205
I.-G. Oh (Samsung Heavy Industries, Korea),
A. Nayfeh (Virginia Polytechnic Institute and State University, USA)
- Nonlinear Shallow-Water Flow on Deck Coupled with Ship Motion* 220
Z.-J. Huang, C.-C. Hsiung (Technical University of Nova Scotia, Canada)

Wake Dynamics

- Radar Backscatter of a V-like Ship Wake from a Sea Surface Covered by Surfactants* 235
G. Zilman, T. Miloh (Tel-Aviv University, Israel)
- Turbulent Free-Surface Flows: A Comparison Between Numerical Simulations and Experimental Measurements* 249
D. Dommermuth,¹ M. Gharib,² H. Huang,² G. Innis,¹ P. Maheo,² E. Novikov,³
J. Talcott,¹ D. Wyatt¹ (¹Science Applications International Corporation,
²California Institute of Technology, ³University of California at San Diego, USA)
- Conductivity Measurements in the Wake of Submerged Bodies in Density-Stratified Media* 266
T. Sarpkaya, T. Massidda (Naval Postgraduate School, USA)
- Macro Wake Measurements for a Range of Ships* 278
M. Hoekstra, A. Aalbers (Maritime Research Institute, The Netherlands)

Invited Lecture

- Time-Marching CFD Simulation for Moving Boundary Problems* 291
H. Miyata (University of Tokyo, Japan)

Viscous Ship Hydrodynamics

- Yaw Effects on Model-Scale Ship Flows* 312
J. Longo, F. Stern (University of Iowa, USA)
- A Multigrid Velocity-Pressure-Free Surface Elevation Fully Coupled Solver for Calculation of Turbulent Incompressible Flow Around a Hull* 328
B. Alessandrini, G. Delhommeau (Ecole Centrale de Nantes, France)
- The Shoulder Wave and Separation Generated by a Surface-Piercing Strut* 346
E. Pogozelski, J. Katz (Johns Hopkins University, USA),
T. Huang (David Taylor Model Basin, USA)
- Vorticity Fields due to Rolling Bodies in a Free Surface—Experiment and Theory* 359
R. Yeung, C. Cermelli, S.-W. Liao (University of California at Berkeley, USA)
- Numerical Calculations of Ship Stern Flows at Full-Scale Reynolds Numbers* 377
L. Eça (Instituto Superior Técnico, Portugal)
M. Hoekstra (Maritime Research Institute, The Netherlands)
- Near- and Far-Field CFD for a Naval Combatant Including Thermal-Stratification and Two-Fluid Modeling* 392
E. Paterson,¹ M. Hyman,² F. Stern,¹ P. Carrica,³ F. Bonetto,³ D. Drew,³ R. Lahey, Jr.³
(¹University of Iowa, ²Naval Surface Warfare Center [Panama City],
³Rensselaer Polytechnic Institute, USA)

Water Entry	
<i>Water Entry of Arbitrary Two-Dimensional Sections with and Without Flow Separation</i>	408
R. Zhao, ¹ O. Faltinsen, ² J. Aarsnes ¹ (¹ MARINTEK, ² Norwegian University of Science and Technology, Norway)	
<i>Coupled Hydrodynamic Impact and Elastic Response</i>	424
D.-J. Kim, ¹ W. Vorus, ² A. Troesch, ² R. Gollwitzer ³ (¹ University of Pusan, Korea; ² University of Michigan, USA; ³ Naval Surface Warfare Center [Panama City], USA)	
<i>A Practical Prediction of Wave-Induced Structural Responses in Ships with Large Amplitude Motion</i>	438
M.-K. Wu, J. Aarsnes, O. Hermundstad (MARINTEK, Norway), T. Moan (Norwegian University of Science and Technology, Norway)	
Viscous Ship Hydrodynamics	
<i>Evaluation of Eddy Viscosity and Second-Moment Turbulence Closures for Steady Flows Around Ships</i>	453
G. Deng, M. Visonneau (Ecole Centrale de Nantes, France)	
<i>On the Modeling of the Flow Past a Free-Surface-Piercing Flat Plate</i>	470
A. Di Mascio, M. Landrini, E. Campana (Istituto Nazionale per Studi ed Esperienze di Architettura Navale, Italy)	
<i>Self-Propelled Maneuvering Underwater Vehicles</i>	478
H. McDonald (Pennsylvania State University, USA), D. Whitfield (Mississippi State University, USA)	
<i>Spray Formation at the Free Surface of Turbulent Bow Sheets</i>	490
Z. Dai, L.-P. Hsiang, G. Faeth (University of Michigan, USA)	
Wave Hydrodynamics/Stratified Flow	
<i>Numerical Simulation of Three-Dimensional Breaking Waves About Ships</i>	506
A. Kanai, T. Kawamura, H. Miyata (University of Tokyo, Japan)	
<i>Generation Mechanisms and Sources of Vorticity Within a Spilling Breaking Wave</i>	520
D. Dabiri, M. Gharib (California Institute of Technology, USA)	
<i>The Flow Field in Steady Breaking Waves</i>	534
D. Coakley (David Taylor Model Basin, USA), J. Duncan (University of Maryland, USA)	
<i>Freak Waves—A Three-Dimensional Wave Simulation</i>	550
K. Trulsen, K. Dysthe (University of Bergen, Norway)	
Invited Lecture	
<i>Bluff Body Hydrodynamics</i>	561
P. Bearman (Imperial College of Science, Technology and Medicine, United Kingdom)	
Bluff Body Hydrodynamics	
<i>Large-Eddy Simulation of the Vortical Motion Resulting from Flow over Bluff Bodies</i>	580
S. Jordan (Naval Undersea Warfare Center, USA)	
<i>The Wake of a Bluff Body Moving Through Waves</i>	592
R. Arkell, J. Graham (Imperial College of Science, Technology and Medicine, United Kingdom)	
<i>Low-Dimensional Modeling of Flow-Induced Vibrations via Proper Orthogonal Decomposition</i>	605
D. Newman, G. Karniadakis (Brown University, USA)	

<i>Measurements of Hydrodynamic Damping of Bluff Bodies with Application to the Prediction of Viscous Damping of TLP Hulls</i>	622
P. Bearman, M. Russell (Imperial College of Science, Technology and Medicine, United Kingdom)	
Invited Lecture	
<i>Hydrodynamics in Advanced Sailing Design</i>	635
J. Milgram (Massachusetts Institute of Technology, USA)	
Hydrodynamics in Ship Design	
<i>Divergent Bow Waves</i>	661
M. Tulin, M. Wu (University of California at Santa Barbara, USA)	
<i>A Method for the Optimization of Ship Hulls from a Resistance Point of View</i>	680
C. Janson, L. Larsson (Chalmers University of Technology, Sweden)	
<i>Hydrodynamic Optimization of Fast-Displacement Catamarans</i>	697
A. Papanikolaou, P. Kaklis, C. Koskinas, D. Spanos (National Technical University of Athens, Greece)	
Shallow Water Hydrodynamics	
<i>On Ships at Supercritical Speeds</i>	715
X.-N. Chen (University of Stuttgart, Germany), S. Sharma (Mercator University, Germany)	
<i>The Influence of a Bottom Mud Layer on the Steady-State Hydrodynamics of Marine Vehicles</i>	727
L. Doctors (Australian Maritime Engineering Cooperative Research Center, Australia), G. Zilman, T. Miloh (Tel-Aviv University, Israel)	
<i>A Hybrid Approach to Capture Free-Surface and Viscous Effects for a Ship in a Channel</i>	743
V. Bertram (Institut für Schiffbau, Germany), S. Ishikawa (Mitsubishi Heavy Industries, Japan)	
Cavitation and Bubbly Flows	
<i>Shock Waves in Cloud Cavitation</i>	756
C. Brennen, G. Reisman, Y.-C. Wang (California Institute of Technology, USA)	
<i>Asymptotic Solution of the Flow Problem and Estimate of Delay of Cavitation Inception for a Hydrofoil with a Jet Flap</i>	772
K. Rozhdestvensky, I. Belousov (St. Petersburg State Marine Technical University, Russia)	
<i>Examination of the Flow Near the Leading Edge and Closure of Stable Attached Cavitation</i>	783
A. Leger, P.-W. Yu, K. Laberteaux, S. Ceccio (University of Michigan, USA)	
Wave Hydrodynamics/Stratified Flow	
<i>Numerical Investigation on the Turbulent and Vortical Flows Beneath the Free Surface Around Struts</i>	794
U.-C. Jeong, Y. Doi, K.-H. Mori (Hiroshima University, Japan)	
<i>Steep and Breaking Faraday Waves</i>	812
L. Jiang, M. Perlin, W. Schultz (University of Michigan, USA)	
<i>The Forces Exerted by Internal Waves on a Restrained Body Submerged in a Stratified Fluid</i>	827
N. Gavrilov, E. Ermanyuk, I. Sturova (Lavrentyev Institute of Hydrodynamics, Russia)	

Cavitation and Bubbly Flows

- Influence of the Cavitation Nuclei on the Cavitation Bucket when Predicting the Full-Scale Behavior of a Marine Propeller* 839
B. Gindroz (Bassin d'Essais des Carènes, France), G. Bailo (MARISPENAV, Italy),
F. Matera, M. Elefante (MARISTAT SPMM, Italy)
- Inception, Development, and Noise of a Tip Vortex Cavitation* 851
L. Briançon-Marjollet, L. Merle (Bassin d'Essais des Carènes, France)
- Velocity and Turbulence in the Near-Field Region of Tip Vortices from Elliptical Wings: Its Impact on Cavitation* 865
A. Pauchet (Ecole Nationale Supérieure de Techniques Avancées, France)
- Calculations of Pressure Fluctuations on the Ship Hull Induced by Intermittently Cavitating Propellers* 882
Y.-Z. Kehr, C.-Y. Hsin, Y.-C. Sun (National Taiwan Ocean University, Taiwan)

Invited Lecture

- Hydroacoustic Considerations in Marine Propulsor Design* 898
M. Sevik (David Taylor Model Basin, USA)

Propulsor Hydrodynamics/Hydroacoustics

- Prediction of Unsteady Performance of Marine Propellers with Cavitation Using Surface-Panel Method* 913
Y.-G. Kim (Samsung Heavy Industries Co., Ltd., Korea),
C.-S. Lee (Chungnam National University, Korea)
- A Comparative Study of Conventional and Tip-Fin Propeller Performance* 930
P. Anderson (Technical University of Denmark, Denmark)
- A New Way of Simulating Whale Tail Propulsion* 946
J. van Manen (Whale Tail Development, The Netherlands),
T. van Terwisga (Maritime Research Institute, The Netherlands)
- Effects of Tip-Clearance Flows* 959
Y.-T. Lee,¹ J. Feng,² C. Merkle,² M. Tse¹
(¹David Taylor Model Basin, ²Pennsylvania State University, USA)
- Experiments in the Swirling Wake of a Self-Propelled Axisymmetric Body* 973
A. Sirviente, V. Patel (University of Iowa, USA)
- Hydrodynamic Forces on a Surface-Piercing Plate in Steady Maneuvering Motion* 986
Z.-J. Zou (Wuhan Transportation University, China)

Fluid Dynamics in the Naval Context

- Advances in Panel Methods* 997
H. Söding (Institut für Schiffbau, Germany)
- Effect of Ship Motion on DD-963 Ship Airwake Simulated by Multizone Navier-Stokes Solution* 1007
T. Tai (David Taylor Model Basin, USA)
- Large-Eddy Simulation of Decaying Free-Surface Turbulence with Dynamic Mixed Subgrid-Scale Models* 1018
M. Salvetti (Università di Pisa, Italy), Y. Zang, R. Street (Stanford University, USA),
S. Banerjee (University of California at Santa Barbara, USA)

CFD Validation

Fully Nonlinear Hydrodynamic Calculations for Ship Design on Parallel Computing Platforms 1033
G. Cowles, L. Martinelli (Princeton University, USA)

Validation of Incompressible Flow Computation of Forces and Moments on Axisymmetric Bodies Undergoing Constant Radius Turning 1048

C.-H. Sung, T.-C. Fu, M. Griffin, T. Huang (David Taylor Model Basin, USA)

The Validation of CFD Predictions of Nominal Wake for the SUBOFF Fully Appended Geometry 1061
P. Bull (Defence Research Agency, United Kingdom)

APPENDIX—LIST OF PARTICIPANTS 1077

Twenty-First Symposium on
NAVAL HYDRODYNAMICS

Opening Remarks

Dr. Fred E. Saalfeld
Deputy Chief of Naval Research/Technical Director

Ladies and gentlemen, good morning and welcome to the Twenty-First Symposium on Naval Hydrodynamics. It is my pleasure to look out on this large number of participants from so many countries. This symposium reflects the widely recognized need for continual exchange of research information in the engineering sciences applicable to marine vehicle technology.

As technical director of the Office of Naval Research, I am responsible for science and technology supporting the U.S. Navy and Marine Corps. Naval hydrodynamics is an essential area of research, and I have a keen interest in encouraging advancement in this field. I am looking forward to hearing firsthand at this symposium the latest achievements in predicting and controlling hydrodynamics in an ocean environment. I have previewed the papers to be presented; clearly this symposium is the state of the art in naval hydrodynamics. As many of you know, the Office of Naval Research is celebrating its Fiftieth Anniversary this year. From its birth, ONR recognized the importance of international collaboration to the success of our endeavors. Right from our start, we had an office in Europe in appreciation of that desired collaboration.

The Office of Naval Research is a descendent of the World War II Office of Scientific Research and Development, which, during the war, forged a new partnership between the U.S. federal government and scientists. The success of the Office of Scientific Research and Development stimulated the Navy to establish its own permanent presence in Europe which would continue this partnership and ensure the technical evolution of the Navy beyond the war's end. Key to the establishment of ONR was Vannevar Bush's 1945 paper "Science, the Endless Frontier," in which he urged that the government support and participate in science. He also highlighted the need for international exchange of scientific information by stating, "increasing specialization of science will make it more important than ever that science in this country keep continually abreast of developments abroad." Shortly thereafter an act of Congress transformed the Office of Research and Inventions into the Office of Naval Research. The foundation of the ONR Europe (or as it was then known, ONR London) operations of the time were rooted in the thoughts of the 1947 Steelman report, which espoused that it is important for researchers to be aware of similar and overlapping interests

worldwide, at an early stage in the work, in order to make plans for cooperation or cross-checking results.

The Office of Naval Research supports hydrodynamics science and technology because there is a direct benefit to naval warfighting capabilities. As an intended ancillary product, the research also supports technological advances in the commercial arena. ONR provides the stable research infrastructure that scientific efforts require to produce beneficial results, even if the outcome cannot be foreseen at the beginning. It is in this spirit that ONR supports this symposium.

This symposium is unique. It is international in character, alternating in location between the United States and a host country other than the United States. This is the twenty-first meeting of the symposium since it began in 1956, 10 years after the creation of ONR. Thus, this is the Fortieth Anniversary year of this symposium. As always, the symposium is sponsored by the Office of Naval Research, the National Research Council, and a host institution, in this case, the Norwegian University of Science and Technology. Thank you, Professor Odd Faltinsen, for hosting this conference. The majesty of Norway is an appropriate setting for this auspicious meeting of the world's naval hydrodynamicists.

Many factors enter a nation's decision to design and construct ships. These factors include technological achievement, labor rates, government subsidy, and defense priority. However, the enabling factor is always technological achievement. For example, common to both naval and commercial interests is the need for fast, non-conventional transports. This requires basic understanding of, and a prediction capability for, complex turbulent flows and their effects on performance. An enabling technology would be the successful development of a useable computer prediction method to complement towing tank evaluations in the context of simulation-based design. Such a technology would use calibrated computational methods to interpret and expand the sparse database obtained from towing tank evaluations.

Computational ship hydrodynamics is a growing science and technology area. The naval hydrodynamics community has the option of managing this growth in such a manner that the product is affordable. We see then that the goal of affordable ships is both affordability in production as well as affordability in design evaluation. We have all heard the message that verification, validation,

and accreditation (words frequently attached to computational methods) are the next focus area.

The initial development of computational methods, or the evaluation in the towing tank of a physical model, is viewed with much greater relish by most researchers than the seemingly mundane task of validation. Yet such a task is with merit, requiring the best and the brightest of researchers, and is crucial to the successful implementation of computational ship hydrodynamics in the design environment. I can see the day, not too distant, that towing tank measurements and computational investigations occur simultaneously as the common database is filled and interrogated to achieve the designs for high-performance ships. Such a bold step is a major expense for any one nation to undertake. For this reason, and among other reasons in other fields, I have established the Naval International Cooperative Opportunities in Science and Technology Program (NICOP) under Dr. Craig Dorman, chief scientist and technical director of ONR Europe, who is attending this symposium.

This new program is designed to broaden, institutionalize, and improve coordination of ONR's

international efforts, and to improve the Navy's ability to access international science and technology opportunities in priority areas. NICOP provides for face-to-face exchange of technical expertise and perspectives between U.S. and international participants. The intent is to establish long-term collaborative relationships that match strength to strength and interest to interest. My staff, including the program officers leading the research efforts sponsored by ONR, agree with me that this program deserves special emphasis. I encourage all of you to consider, as you savor the international exchange of this symposium, an idea for international cooperation, and to present it to ONR as a candidate for NICOP.

Seventy-two papers from 18 countries will be presented and discussed at this symposium. These papers were selected from approximately 150 submitted papers, almost all of which were of sufficient quality to have been presented in this symposium. You can expect high-quality, state-of-the-art presentations. You are invited to vigorously participate in the paper discussions. Have a good meeting!

Twenty-First Symposium on
NAVAL HYDRODYNAMICS

Technical Sessions

Progress Toward Understanding How Waves Break

M.S. Longuet-Higgins (University of California at San Diego, USA)

Abstract. This paper reviews a number of investigations into the dynamics of breaking waves. The simplest time-dependent model of gravity-wave breaking is the lowest superharmonic instability of a steep Stokes wave. Recent calculations for both deep-water waves and for solitary waves in shallow water show that as the wave steepness increases, the region of instability is increasingly confined to the wave crest, and takes the limiting form of a "crest instability". The nonlinear development of the instability depends crucially on the sign of the initial disturbance. Positive perturbations lead to overturning of the crest, negative perturbations lead to a transition to a periodic wave of lower amplitude, then to a quasi-periodic recurrence.

At wavelengths up to 2m surface tension and viscous effects are found to be drastically important. An improved linear theory has been given for the generation of ripples ahead of the wave crest (parasitic capillaries). When these ripples become nonlinear, a "capillary jump" is sometimes formed, which can be described in terms of two half-solitary capillary waves. Shedding of mean vorticity by the highly-damped ripples leads to an unstable shear-flow, which may separate from the leading edge of the jump. Instabilities of the shear flow in the form of "vortex waves" may account for the "Type 2" capillary waves seen crestwards of the leading edge by Duncan et al. [1].

The onset of breaking in modulated groups of waves occurs at lower wave steepnesses than do crest instabilities. Some examples are discussed, but a satisfactory theory is still lacking.

1. Introduction

Since the early 1970's increasing attention has been given by oceanographers to the influence of breaking waves on the transfer of heat and momentum between atmosphere and ocean, the production of aerosols and spray, the generation of the underwater sound field, and the evolution of the wave spectrum itself. On the other hand, naval hydrodynamicists are interested especially with the action of breaking waves on moving or stationary structures – the influence of bow waves on wave resistance, turbulent wakes and noise production, wave loading on oil rigs and coastal defenses, not to mention the capsizing of ships in heavy seas.

My personal interest was rekindled recently by the striking photographs taken by Professor Duncan and his collaborators at the University of Maryland; see Duncan et al. (1994) [1]. These are illuminated cross-sections, taken at intervals of 0.01s, of gentle breaking produced by focussing wave energy with a controlled wavemaker – a technique for studying wave breaking demonstrated at an earlier Symposium on Naval Hydrodynamics (Longuet-Higgins 1974) [2]. The most remarkable feature is that the crest of the wave eventually collapses into turbulence without the surface ever having overturned on itself.

There are several problems raised by these photographs (see Figure 1):

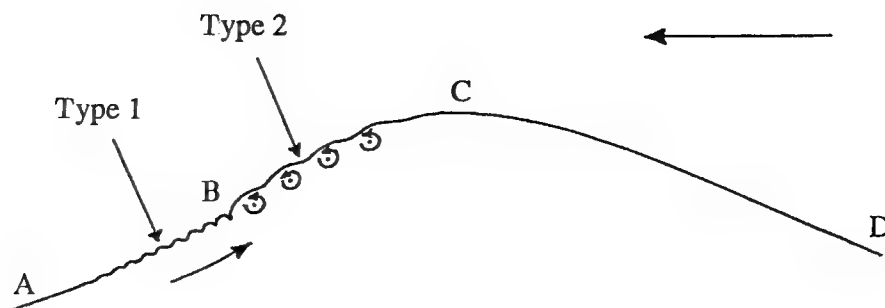


Figure 1. Schematic diagram of a gently breaking wave as observed by Duncan et al. [1].

1. Why does the wave crest become asymmetrical, with a bulge on the forward face?

2. Why do short (Type 1) capillary waves appear below the forward edge, or toe of the bulge?

3. Why do longer (Type 2) capillaries appear above the forward edge?

4. Why do the Type 2 capillaries grow and collapse?

5. How are these phenomena related to other types of wave breaking?

A few days after Jim Duncan made these observations in 1992, I happened to be visiting his laboratory and had with me a copy of a 1982 thesis by my student Philip Cleaver [3] which treated what we now call “crest instabilities”, that is the instabilities of the flow near the crest of an almost-highest Stokes wave. It appeared that these calculations might be relevant to the phenomena recorded by Duncan. As it turns out, the initial bulge in Duncan’s experiments cannot be interpreted directly as a crest instability. Nevertheless the incentive to carry out further investigations has led to a deeper understanding of how crest instabilities are related to other instabilities of steep waves, in both deep and shallow water. Furthermore, the presence of ripples, both Type 1 and Type 2, suggests that capillary, and also viscous, effects are in some ways important, even for gravity waves of length 1 m or more. Subsequent investigations have shown these suppositions to be correct, in a way that I hope to explain in this lecture.

One of the simplest approaches to wave breaking is to model the initial flow as an instability of a uniform train of steep, irrotational gravity waves. Here progress has recently been made by studying the basic *superharmonic* instabilities of a progressive wave, namely those having the same space periodicity as the unperturbed wave. Some recent numerical calculations extending to very steep waves are summarised in Section 4 below. It is found that these instabilities become localised near the wave crests. To interpret the results and to introduce a proper scaling, it is convenient first to summarise the theory of the “almost-highest wave,” which describes the asymptotic form of the flow in the crest of a steep Stokes wave of less than maximum steepness; see Section 2. The instabilities of this crest flow have been recalculated in three recent papers, as described in Section 3, and in Section 4 it is shown that these “crest instabilities” do indeed correspond to limiting forms of the superharmonic instabilities. Similar results for solitary waves in shallow water are described in Section 5.

To follow the development of the crest instabilities beyond the linear, infinitesimal stage, boundary-integral techniques can be used, as described in Section 6. This method reveals some surprising differences in the subsequent time-histories of the flow, depending upon the sign of the initial disturbance. The flow may either develop as a plunging breaker or make a recurrent transition to a wave of lower amplitude.

For waves up to 2m in length the effects of surface tension can be important. An improved linear theory for the production of parasitic capillary waves is described in Section 7. A descriptive theory is also given for the nonlinear features known as "capillary jumps;" see Section 8. The effect of surface tension on crest instabilities is described in Section 9. New work on viscous effects, including the generation of shearing currents and the production of turbulence, is described in Section 10. Lastly, in Section 11 we discuss one of the main unsolved problems to do with breaking waves: the incidence of breaking in modulated groups of waves. Section 12 is a brief summary of the conclusions.

As is customary in modelling the very rapid late stages of wave breaking, the direct action of the wind on the water surface will be ignored; the pressure there is assumed to be constant. For simplicity it is also assumed that the motion is essentially two-dimensional. Until the onset of the viscous effects discussed in Section 10, the flow is assumed to be irrotational.

Among many other investigations which it will not be possible to discuss in detail we may mention two: Jenkins' [4] calculation of a steady-state plunging wave crest – in this review we shall be concerned rather with the time-dependent problem of how such a flow comes into existence – and the dynamical theory by Shrira et al. [5] for the three-dimensional structures known as "horse-shoe" waves.

2. The near-limiting form of steep Stokes waves

When steady, irrotational gravity-waves (Stokes waves) approach their limiting steepness, conventional methods of calculation, e.g. by Fourier series or integral equations tend to lose accuracy. On the other hand the profile of the limiting wave in deep water, with a 120° rest angle, was determined many years ago by Michell (1893) [6]; a modern calculation by Williams (1981) [7] is accurate to at least 7 decimal places. So why not work downwards, from the steepest wave? In the wave of limiting steepness $(ak)_{\max} = 0.4432$ the radius of

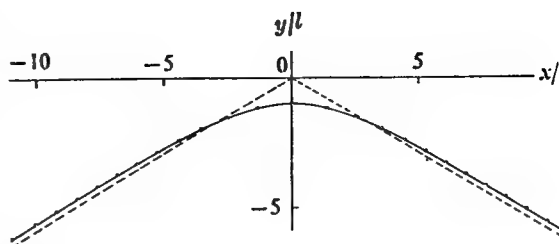


Figure 2. Form of the wave crest in a near-limiting progressive gravity wave. Full line: surface profile. Broken line: 30° asymptotes. From Longuet-Higgins and Fox [8].

curvature R at the crest is zero, and the particle velocity q at the crest vanishes, in a reference frame moving with the wave speed. Longuet-Higgins and Fox [8, 9] proposed that in general the flow near the crest be characterised by an inner length-scale

$$l = \frac{q^2}{2g} \quad (2.1)$$

where g denotes gravity (see Figure 2). As x/l and y/l go to infinity the flow tends asymptotically to the Stokes corner-flow. At the crest itself $(x/l, y/l) = (0, -1)$. The free surface is uniquely determined and the radius of curvature at the crest is found to be

$$R = 5.15l \quad (2.2)$$

see [8]. In deep water this crest-flow can be matched to the flow in the rest of the wave by defining a small parameter

$$\epsilon^2 = \frac{q^2}{2c_0^2} \quad (2.3)$$

where $c_0 = (g/k)^{1/2}$ denotes the speed of linear gravity waves of length $L = 2\pi/k$, and by identifying three regions of the wave as in Figure 3. In region I whose width is of order $\epsilon^2 L$, the flow is given by the asymptotic flow just described, to lowest order; and the length-scales are of order $\epsilon^2 L$. In region III the flow is that in the limiting Stokes wave to lowest order. Between these is a matching zone II, whose width is of order ϵL . The process of matching, described in [9], leads

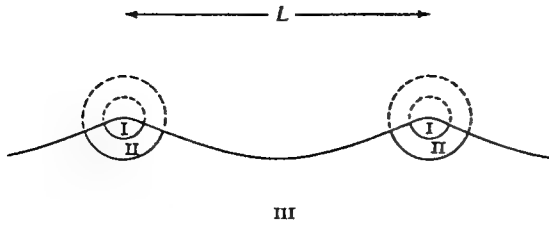


Figure 3. Sketch showing the three zones involved in the matching process. From Longuet-Higgins and Fox [9].

to the result that the parameter ϵ is related to the wave steepness ak by the simple formula

$$(ak)_{\max} - ak = \frac{1}{2}\epsilon^2 + O(\epsilon^3). \quad (2.4)$$

The lowest-order correction to the inner flow (that in Zone I) is of order $\epsilon^{3(\alpha-1)}$, where α is the lowest positive root of the transcendental equation

$$\frac{\pi\alpha}{2} \tan \frac{\pi\alpha}{2} = \frac{\pi}{2\sqrt{3}} \quad (2.5)$$

that is

$$\alpha = 1.8027. \quad (2.6)$$

In other words, the theory predicts that in near-limiting waves, quantities will typically differ from their limiting values by amounts of order $\epsilon^{2.4081}$, approximately.

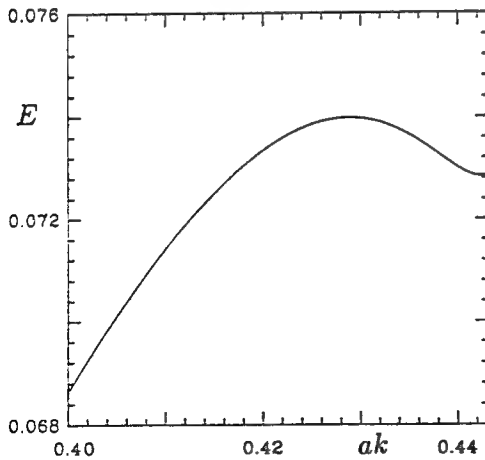


Figure 4. The energy density E in a steep progressive wave, as a function of the wave steepness ak .

A third prediction of the theory, relevant to what will follow, is that the energy density E of a steep Stokes wave of a given wavelength is not always an increasing function of the wave steepness ak , but goes through a sequence of maxima and minima before the maximum steepness ($ak = 0.4432$); see Figure 4. The first maximum in E occurs when $ak = 0.4292$.

3. Crest instabilities

The normal-mode instabilities of the crest flow, that is to say those growing initially like $e^{\beta t}$, where $\text{Re}(\beta) > 0$, have been investigated by Longuet-Higgins and Cleaver (1994) [10], Longuet-Higgins, Cleaver and Fox (1994) [11] and Longuet-Higgins and Dommermuth (1996) [12]. The form of the lowest mode is shown in Figure 5. It has a peak elevation on the forward face of the crest, and a peak depression on the rear face. Because the perturbations are linearised, the displacement is normalised so as to make the maximum elevation equal to unity.

How are these crest instabilities related to the known instabilities of a steep Stokes wave in deep water?

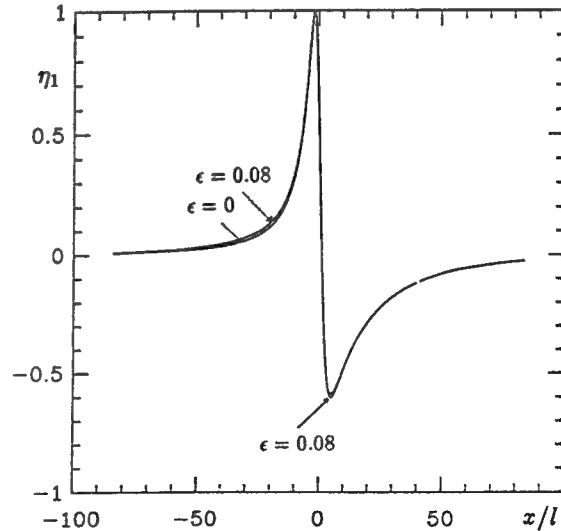


Figure 5. The lowest mode of instability of the crest flow in Figure 2; the eigenfunction η_1 . The wave travels to the left. From Longuet-Higgins and Dommermuth [12].

4. Superharmonic instabilities: deep water

Two kinds of normal-mode perturbations of steep Stokes waves can be distinguished, those that are superharmonic, having the same space periodicity as the initial wave train, and those that are subharmonic, i.e. with a longer space periodicity. We pay attention first to the simplest superharmonic perturbations. It was first shown numerically by Tanaka (1983) [13] and confirmed theoretically by Saffman (1985) [14] that the simplest superharmonic normal modes of a deep-water Stokes wave became unstable at a wave steepness ak corresponding to the first maximum of the energy density E (see Section 2). Thus the square of the eigenfrequency $\sigma = i\beta$ passes from positive to negative values at this value of the wave steepness ak . It was shown by Longuet-Higgins, Cleaver and Fox [11] that the values of β_1 for crest instabilities were asymptotic to the rates of growth calculated by Tanaka [13]. No data for the eigenfunctions were published by Tanaka, but the calculations have been carried to higher values of ak and the corresponding eigenfunctions computed in a more recent paper [15].

To verify the accuracy of the unperturbed surface profiles, we show in Figure 6 the radius of curvature R at the crest of steep waves. The length l being defined by equation (2.1), it will be seen that the values of R/l lie practically on a straight line,

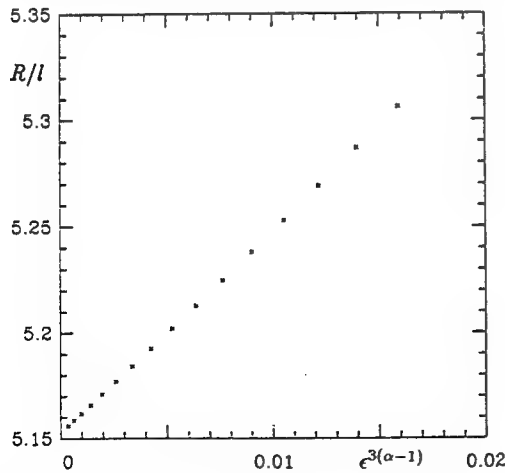


Figure 6. The scaled radius of curvature R of a steep Stokes wave, plotted against $\epsilon^{3(\alpha-1)}$. From Longuet-Higgins and Tanaka [15].

whose equation is

$$R/l = 5.1525 + 9.5 \epsilon^{3(\alpha-1)}. \quad (4.1)$$

In Figure 7a we see profiles of the lowest unstable mode at three different values of the parameter $\omega = 1 - q_c/q_t$, where q_c and q_t are the particle speeds at the crest and the trough respectively. The range of ω is from 0 to 1, with $\omega = 1$ corresponding to the steepest wave. (The three values $\omega = 0.84, 0.88$ and 0.92 correspond to $ak = 0.4331, 0.4375$ and 0.4405 respectively). As the wave steepness increases the perturbations become narrower. When, however, the profiles are plotted with the scaled coordinate x/ϵ^2 as in Figure 7b, they appear to converge to the same asymptotic form as shown in Figure 5. This earns them the name "crest instabilities."

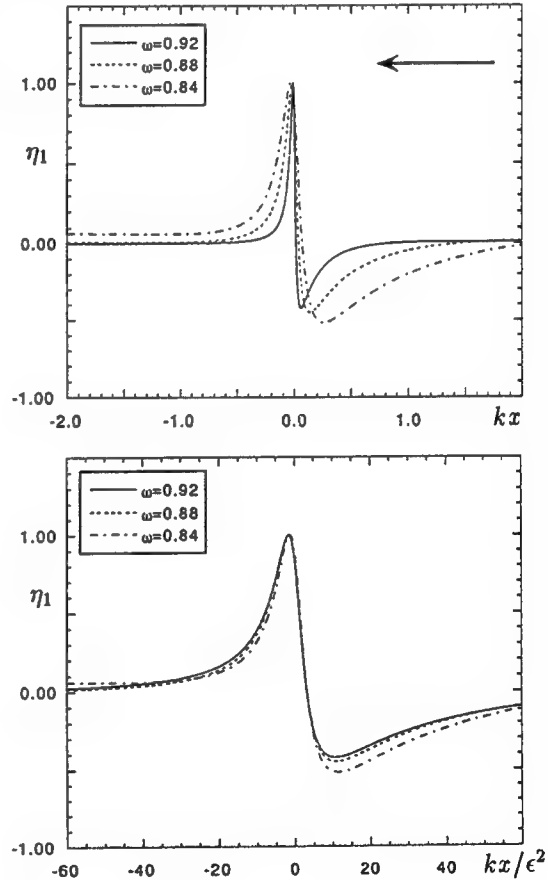


Figure 7. Profiles of the lowest superharmonic instability η_1 in a progressive deep-water wave at three wave steepness $ak = 0.4331, 0.4375$ and 0.4405 . (a) Unscaled, and (b) scaled horizontally by $l = q^2/g$. From Longuet-Higgins and Tanaka [15].

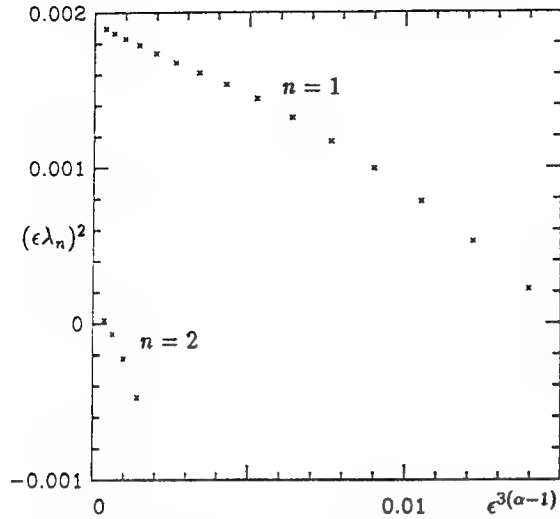


Figure 8. Squared rates of growth of the two lowest normal-mode instabilities of deep-water waves. From Longuet-Higgins and Tanaka [15].

The squared growth-rates λ_n^2 are shown in Figure 8, scaled by factor ϵ^2 . For the smallest values of ϵ , where the asymptotic theory applies, the squared frequencies do indeed depend linearly on $\epsilon^{3(\alpha-1)}$.

At larger values of ϵ the squared growth-rate diminishes, and passes through zero at the steepness ak corresponding to the first maximum of E . At this point the form of the perturbation tends towards a pure phase-shift; see Section 5.

5. Instabilities in solitary waves

Historically there has been some interplay between studies of solitary waves in shallow water and waves in deep water. Moreover, the corresponding calculations for solitary waves can often be carried to greater accuracy, yielding new or stronger conclusions.

Early calculations of the highest solitary wave have been summarised in a review paper by Miles (1980, Section 4) [16]. Probably the most accurate calculation was later performed by Williams [7] whose numerical results have been confirmed to at least five decimal places by Evans and Dorr [17].

The most interesting theoretical results, however, concern the behaviour of

solitary waves whose height is somewhat less than the maximum. In 1974 it was discovered that many integral properties of solitary waves, including their speed and total energy, attain maxima at heights less than the limiting wave height (Longuet-Higgins and Fenton) [18]. These authors used a series expansion with convergence accelerated by Padé approximants. Their conclusion was later confirmed by Byatt-Smith and Longuet-Higgins [19] using an integral equation method. The latter also gave a physical explanation. As with periodic waves in deep water, all the calculations experienced difficulties for waves approaching the maximum height.

An advance came with the introduction of a theory for the almost-highest wave [8, 9]. Besides the application to deep-water waves, Fox [20] in his Ph.D. thesis applied it also to solitary waves with similar results, namely that the speed c , height H , mass M , momentum (or impulse) I , and the potential and kinetic energies V and T , were all found to satisfy relations of the type

$$F = F_1 + A\epsilon'^3 \cos(2.143 \ln \epsilon' - B) + O(\epsilon'^4) \quad (5.1)$$

where a suffix 1 denotes the value for the highest wave and ϵ' is a small parameter defined by

$$\epsilon'^2 = gl/c_0^2, \quad l = q^2/2g, \quad (5.2)$$

similar to (2.3) except that here c_0 denotes the linear phase-speed $(gh)^{1/2}$ of waves in shallow water of depth h . Note that owing to the term $\ln \epsilon'$, which tends to $-\infty$ as the limiting wave is approached, the right-hand side of (5.1) is oscillatory in ϵ' . In fact, we can write

$$(F - F_1) = \epsilon'^3 A \cos(\theta - B) \quad (5.3)$$

where $\theta = 2.143 \ln \epsilon'$ and A and B are amplitude and phase constants. In Fox [20] the constants A and B were evaluated, in general, to only one significant figure, and the results were not published at that time. A more accurate computation of the integral quantities, described by Longuet-Higgins and Tanaka [15], has allowed the constant in (5.3) to be calculated to at least two significant figures (Longuet-Higgins and Fox) [21]. The results are summarised in Figure 9. Here the vectors are shown

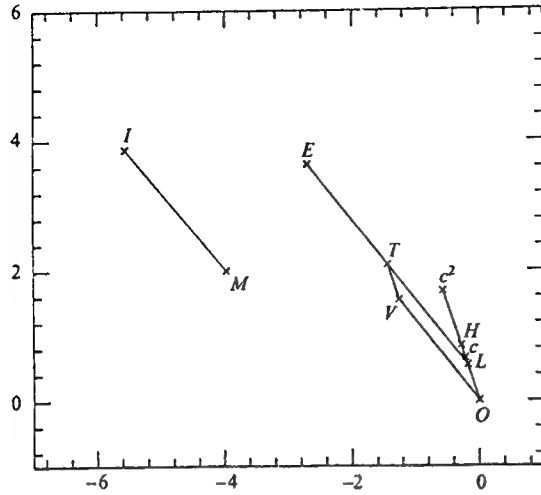


Figure 9. A plot of Δc , ΔH , ΔM , ΔI , ΔV , ΔT , ΔE and ΔL for a solitary wave (see equations (5.1) to (5.4)). From Longuet-Higgins and Fox [21].

$$\Delta F = A e^{iB} \quad (5.4)$$

graphically for each of the quantities $F = c, H, M, I, V$ and T ; also the total energy $E = V + T$ and the Lagrangian density $L = T - V$. It will be noticed that there are certain (exact) collineations. In particular L and H lie on the line Oc through the origin O . IM is not parallel to ET .

For many years it had been thought, on the basis of the approximate Korteweg-deVries equation, that all solitary waves were essentially stable to small perturbations. But Tanaka [22] showed numerically that the lowest-order perturbation of a solitary wave becomes unstable at the wave height for which the total energy E is a maximum – just as for waves in deep water. More recently (Longuet-Higgins and Tanaka [15]) the calculations have been carried to even steeper waves, and it has been shown that the second mode also becomes unstable at the next stationary value of E , the first positive minimum. The same is no doubt true of the higher modes. The eigenfunctions of the *two* lowest modes are also calculated accurately. Figure 10 shows the lowest mode plotted against the scaled coordinate x/ϵ'^2 at four successive wave heights approaching the limiting height. The profiles appear to be converging to the same

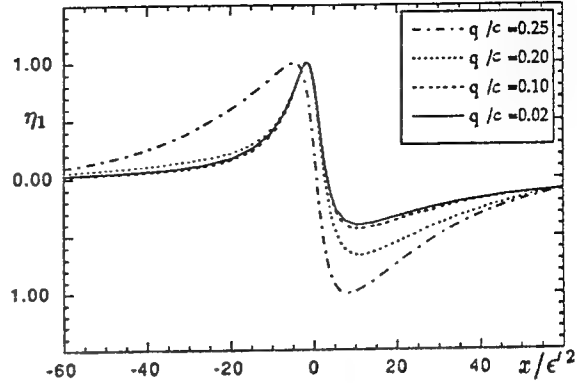


Figure 10. Scaled profiles of the lowest mode of instability η_1 of the solitary wave, at four different wave heights. From Longuet-Higgins and Tanaka [15].

limiting form as for the deep-water wave (Figure 6b).

When on the other hand $(\epsilon' \lambda_1)^2$ approaches zero, which is at the first stationary value of E , the eigenfunction tends to a pure phase-shift. This is illustrated by Figure 11 which shows the first mode η_1 when $q/c = 0.25$, corresponding to $\epsilon' = 0.2287$ or $H/d = 0.7842$, only marginally above the critical wave steepness. This is compared to a pure phase-shift of the same solitary wave (which is just proportional to the gradient of the surface profile).

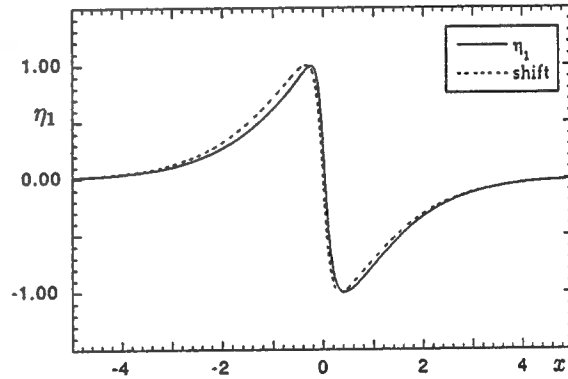


Figure 11. Comparison of the lowest mode of instability of the solitary wave at a wave height close to the first energy maximum, compared to a pure phase-shift. From Longuet-Higgins and Tanaka [15].

The form of the second mode is shown in Figure 12, scaled similarly. Here

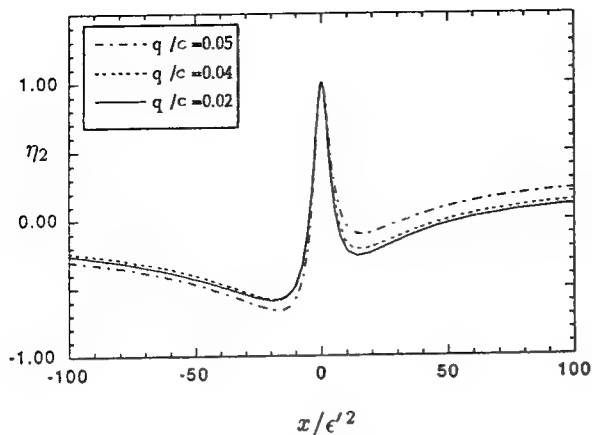


Figure 12. Scaled profiles of the second mode of instability η_2 for solitary waves at three different wave heights. From Longuet-Higgins and Tanaka [15].

also there appears to be convergence as $q/c \rightarrow 0$. Figure 13 shows the behaviour of the growth rates λ_1 and λ_2 . As predicted, when plotted against $\epsilon^{3(\alpha-1)}$ the scaled quantities $\epsilon'\lambda_1$ and $\epsilon'\lambda_2$, and their squares, behave linearly as $\epsilon' \rightarrow 0$. Further data and comparisons with deep water waves and with the asymptotic theory will be found in Longuet-Higgins and Tanaka [15].

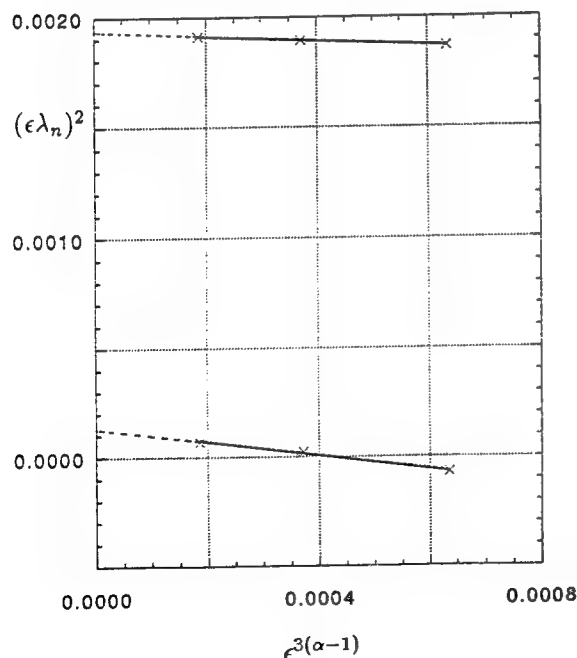


Figure 13. Squared growth-rates, scaled, for the two lowest instabilities of the solitary wave. From Longuet-Higgins and Tanaka [15].

6. Finite-amplitude development of crest instabilities

We have so far described only the initial, infinitesimal stage of a crest instability. Because of the rapid rate of growth of the lowest mode, this instability soon becomes nonlinear. The later stage of development can however be followed by a boundary-integral, time-stepping technique, as was first done for solitary waves by Tanaka et al. [23]. However, the nonlinear development was found to depend crucially on the *sign* of the initial disturbance. The same perturbation, if reversed in sign, led not to wave breaking but to a smooth transition of the original wave to a lower solitary wave having almost the same total energy. This is possible because of the energy maximum occurring at an intermediate wave height. The speed and momentum of the final wave were slightly different from their original values, the difference being made up by a slight disturbance trailing the main wave.

Similar calculations have been performed for deep-water waves by Longuet-Higgins and Dommermuth [12] following a less complete study by Jililians [24]. Here the initial perturbation was that given by the asymptotic theory of Section 3, which approximates the actual normal-mode instability. Figure 14 shows the growth of the lowest mode, for a "positive" initial perturbation, that is to say one with a maximum on the forward face, and Figure 15 shows overturning of the surface profile, as expected. The growth-rates of the "positive" and "negative" perturbations are compared with the linear theory in Figure 16.

The profile resulting from the "negative" initial disturbance developed as in Figure 17, with a transition to a wave of lower amplitude and almost the same total energy. Unlike the solitary wave, however, the wave profile then returned almost to its original form, in a kind of nonlinear recurrence; see Figure 18 where the crest-to-trough wave height is plotted as a function of the time t . One might say that this recurrence phenomenon resembles that displayed by the solitary wave, except that with the solitary wave the period of recurrence is infinite.

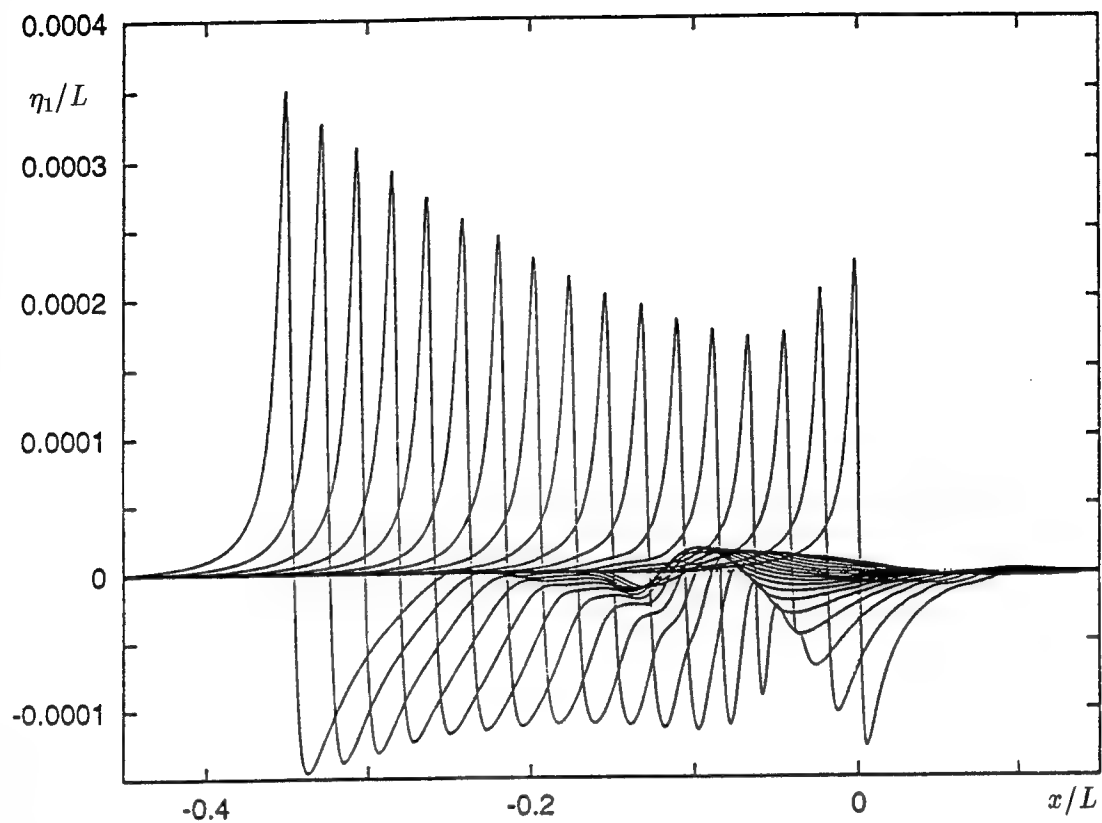


Figure 14. Nonlinear growth of the lowest superharmonic instability in a deep-water wave, at $ak = 0.4398$; positive perturbation. From Longuet-Higgins and Dommermuth [12].

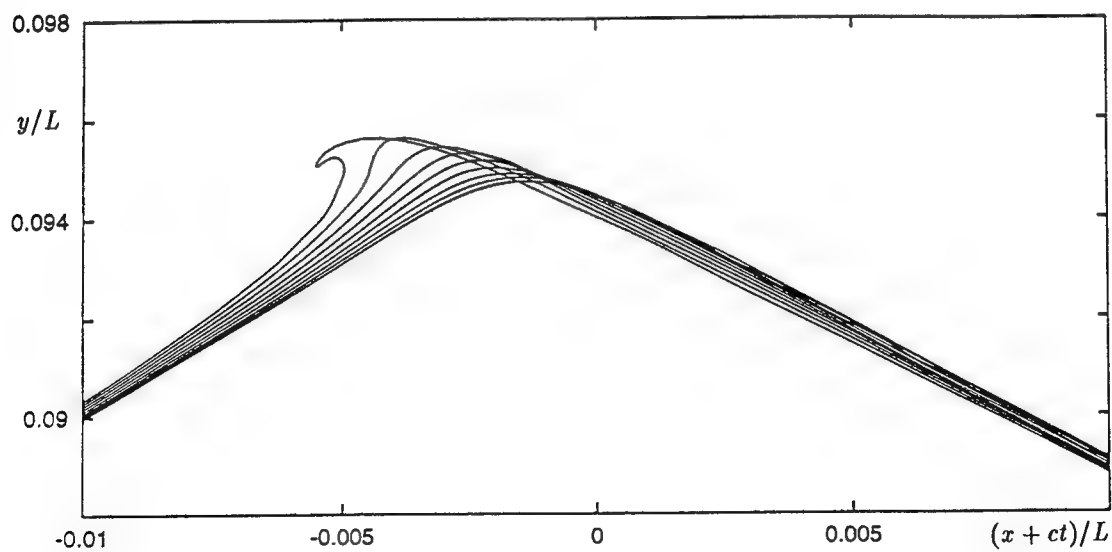


Figure 15. Nonlinear development of the surface profile corresponding to Figure 14. From Longuet-Higgins and Dommermuth [12].

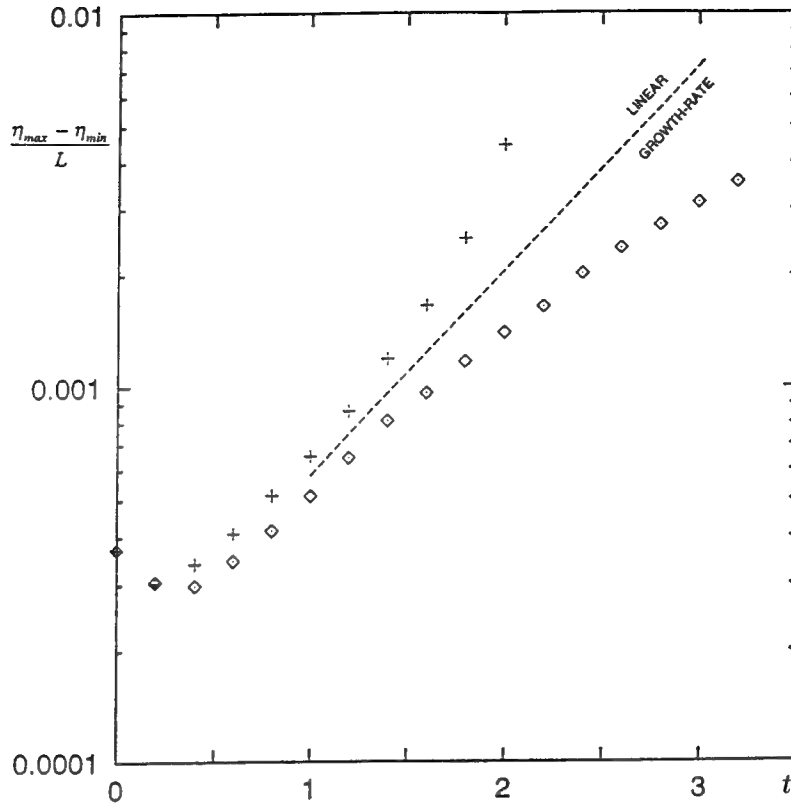


Figure 16. Growth of the lowest superharmonic instability in Figure 14 as a function of the time t . Crosses: positive perturbation. Square plots: negative perturbations. From Longuet-Higgins and Dommermuth [12].

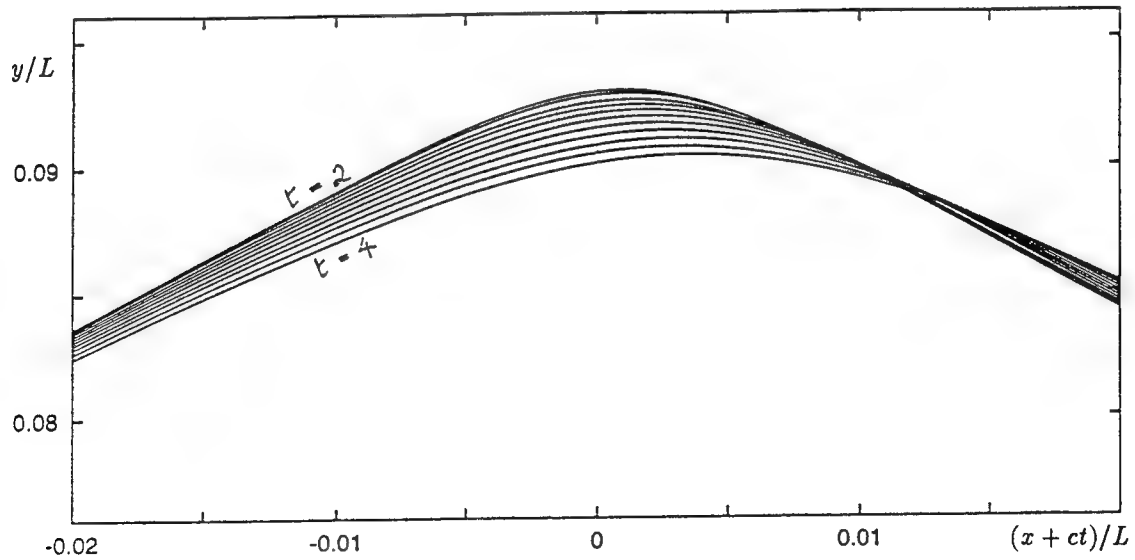


Figure 17. Nonlinear development of the surface profile resulting from a negative perturbation. From Longuet-Higgins and Dommermuth [12].

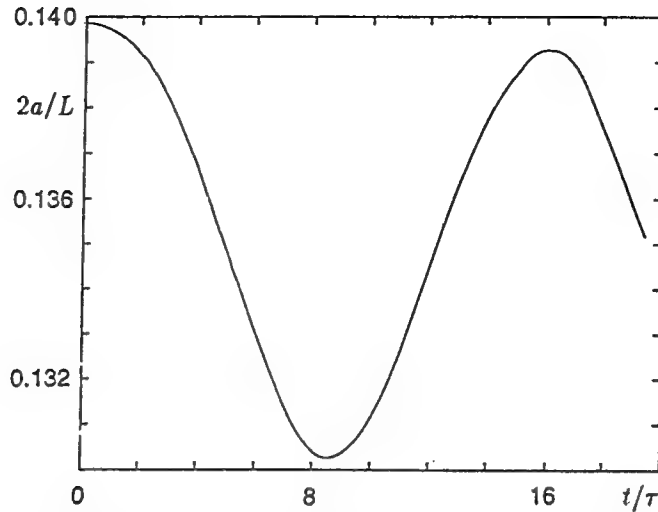


Figure 18. The crest to trough wave amplitude of a deep-water wave as a function of the time t following a negative perturbation. From Longuet-Higgins and Dommermuth [12].

7. Wave-generated ripples

We now discuss some of the unexpectedly important effects of surface tension on gravity waves having wavelengths even as great as 2m.

A typical photograph of short gravity waves (Figure 19a) shows a train of ripples riding just ahead of the wave crests. How are these "parasitic capillary waves" generated? An early theory [25] suggested that they were due to surface-tension forces

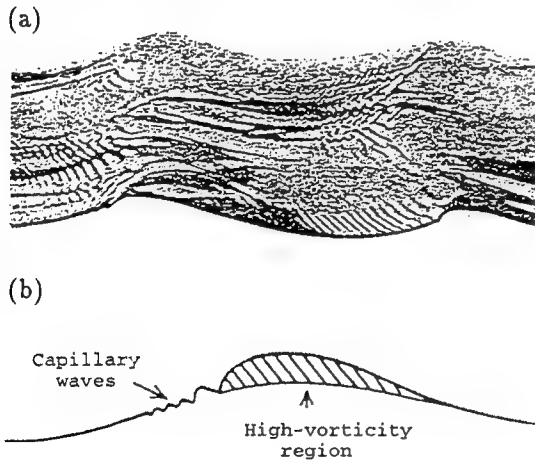


Figure 19. (a) Photograph of short gravity waves showing wave-generated ripples (b) sketch of turbulent zone beneath the wave crest. After Ebuchi et al. [26].

acting near the crest of a steep gravity wave, where the surface curvature is localised. As seen in a reference frame moving with the phase-speed c , the waves appear as a steady current in the opposite direction – the localised pressure near the crest then produces ripples upstream of the crest, that is on the forward face of the wave.

A modern form of the theory, which includes accurate calculations of the gravity-wave profile, has recently been given Longuet-Higgins [27]. Figure 20, from that paper, shows the curvature κ in steep Stokes wave as a function of the distance s from a wave crest, measured along the surface. Clearly κ is concentrated near the crests. In the troughs, κ is smaller and almost uniform; the profile is roughly a circular arc.

The influence of gravity on the ripples, which affects their speed, enters through the effective gravitational acceleration g^* . This includes not only the component of gravity normal to the surface but also the centrifugal acceleration arising from the speed q of the current and the curvature κ of the surface, that is

$$g^* = g \cos \theta - \kappa q^2 \quad (7.1)$$

where θ is the surface inclination. Figure 21 shows that g^* may vary from as little as $0.63g$ at the wave crests to $1.3g$ in the troughs. Ripples will be generated, accord-

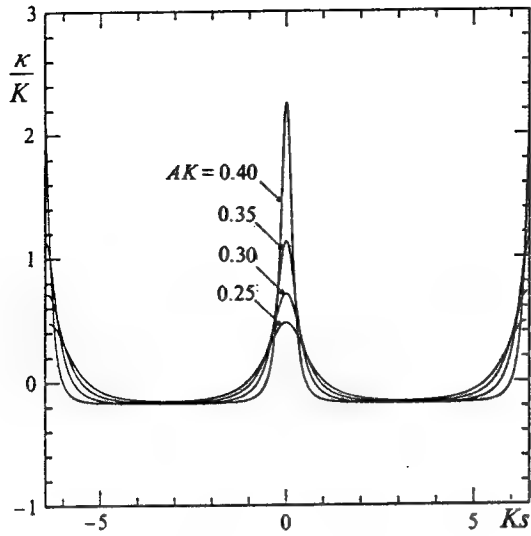


Figure 20. The surface curvature κ in steep gravity waves, as a function of the distance s from the wave crest, measured along the free surface. From [27].

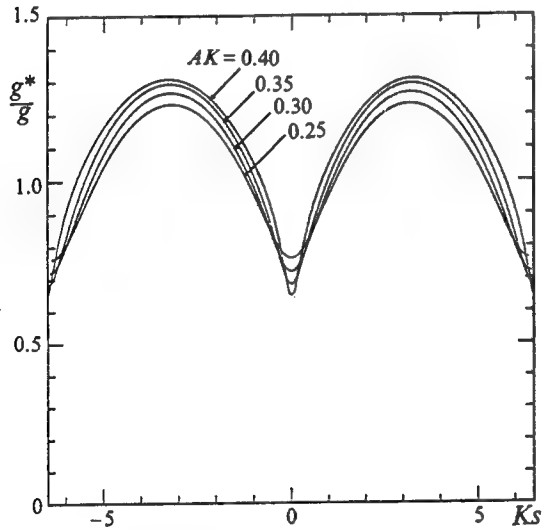


Figure 21. The effective gravity of g^* for a particle at the surface of a deep-water gravity wave, as a function of distance s along the profile. From [27].

ing to the linear theory, only when the local current-speed q exceeds the minimum phase-speed c_{\min} of capillary-gravity waves, given by

$$c_{\min} = (4g^*T)^{1/4} \quad (7.2)$$

where T denotes surface tension (the density being unity). For low (subcritical) gravity waves it is always true that $q > c_{\min}$, but for steep (supercritical) gravity waves there

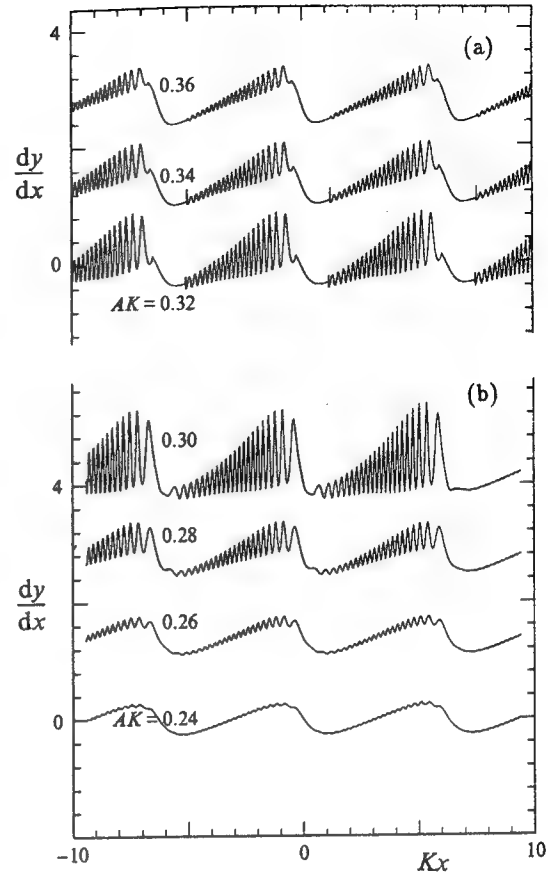


Figure 22. The calculated surface slope dy/dx in a wave of length 8.0 cm (a) Subcritical wave steepness, (b) supercritical. From [27].

is a region near the crest where $q < c_{\min}$. This part of the wave profile is non-resonant or "hard". It is bounded by two caustics, at which $q = c_{\min}$. The rest of the wave profile, where ripples can be generated is resonant or "soft". Figure 22 shows the calculated surface slope dy/dx of a typical wave of length $L = 8.0$ cm, at difference steepnesses AK of the gravity wave. The wave travels to the left and the crests are at $Kx = -2\pi, 0$ and 2π , where $K = 2\pi/L$. Viscous damping is included in the calculation. The ripples appear mainly on the forward face of the wave, as expected. The critical wave steepness is $AK = 0.32$. In Figure 22a, all the waves are subcritical, and the ripple steepness clearly increases with AK . In Figure 22b the gravity waves are supercritical and the ripple steepness diminishes with AK . Thus the ripple steepness is a maximum when $AK = (AK)_{\text{crit}}$.

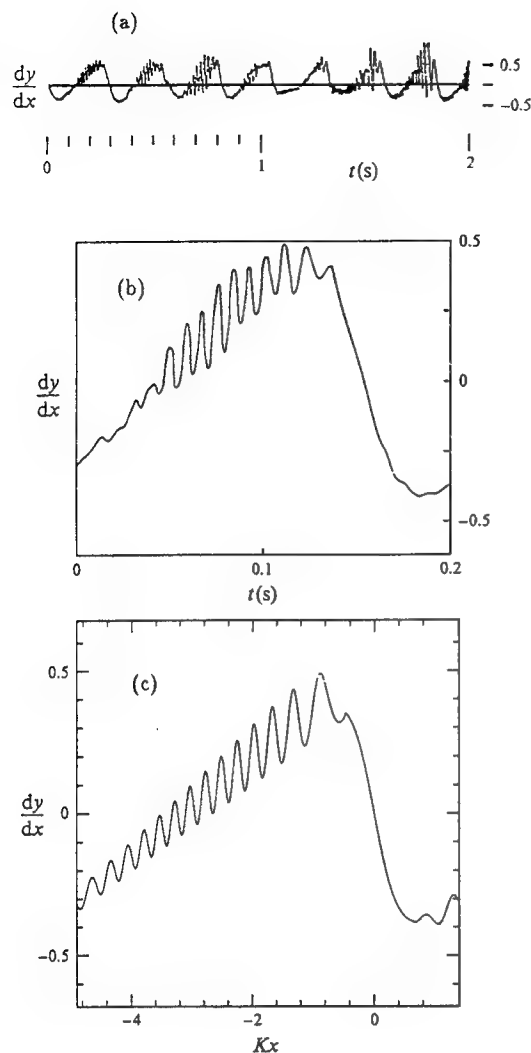


Figure 23. Surface slope dy/dx versus time t at a fixed point, in waves of length 6.5 cm. (a) Measurements by Cox [28]; (b) enlargement of one wave period of (a); (c) linearised theory. From [27].

Figure 23 shows a comparison between the calculated surface slopes in a gravity wave of period 0.20s (wavelength $L = 6.5$ cm) and the slopes measured by Cox [28] at a fixed point in his laboratory tank (without wind). There is generally good agreement. Some differences may be due to the fact that the waves were not perfectly steady, as can be seen from Figure 23a.

Figure 24 shows a similar calculation for the 10 cm waves in Figure 19. The waves are subcritical. The wavelengths of the ripples in the main train correspond very

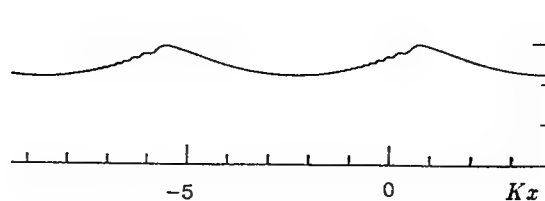


Figure 24. A theoretical calculation of the surface profile for waves of length 10 cm (c.f. Figure 19). From [27].

well. However, there is some discrepancy in the surface profiles immediately ahead of the crest, which is due to nonlinearity, as we shall now see.

8. Capillary jumps

The theory in Section 7 was based on the assumption that the parasitic capillaries were small perturbations superposed on nonlinear gravity waves, and that the slopes relative to the unperturbed gravity wave were small. Observations suggest that the assumption is not always justified. There is one feature near the crest, however, which may be understood in terms of a type of nonlinear capillary-gravity wave discovered recently, namely a solitary wave on deep water (Longuet-Higgins [29,30]; Vanden-Broeck and Dias [31]).

Figure 25 shows a one-parameter family of solitary waves each determined uniquely by its maximum surface slope α_{\max} or by the depth H of the central trough relative to the level at infinity. As H decreases towards zero the tails develop more oscillations, and the whole wave train resembles a packet of infinitesimal waves with phase and group velocity equal to c_{\min} ; see Longuet-Higgins [32]. Figure 26 shows that as H increases from zero the speed c of the solitary wave is a decreasing function of H , being generally less than c_{\min} .

Imagine then a non-uniform surface current U as in Figure 27, where U decreases towards the right. If U is everywhere slightly less than C_{\min} , it may be possible for a steady wave to be superposed on the current such that on the left it has the character of a solitary wave of speed $c_1 = |U_1|$, and on the right it is like a solitary wave

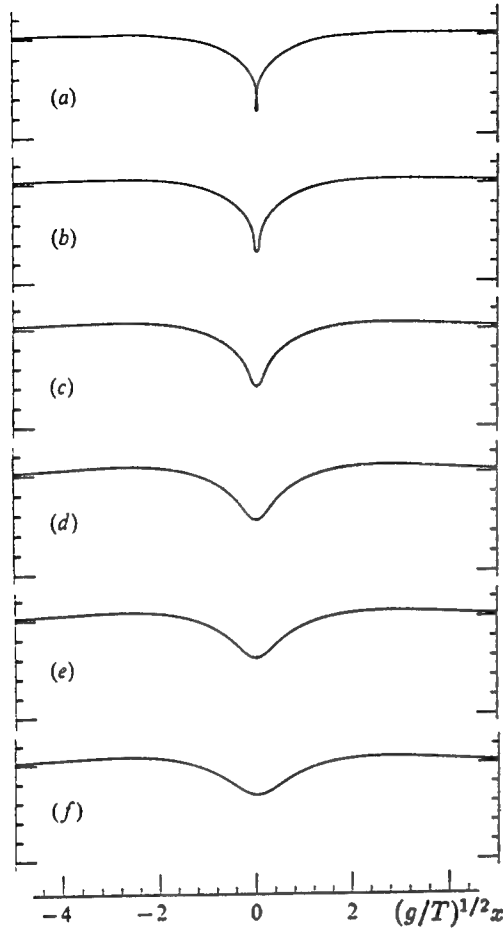


Figure 25. A family of capillary-gravity solitary waves. From Longuet-Higgins [28].

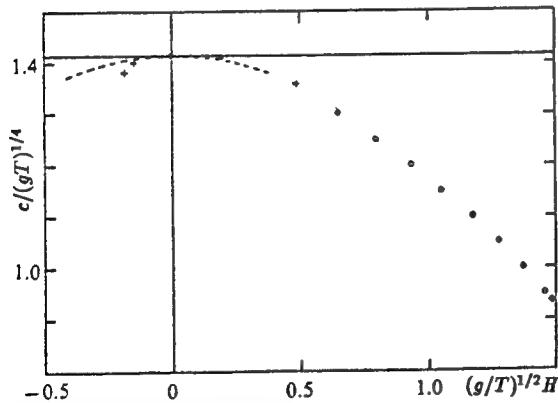


Figure 26. The phase-speed c of the capillary-gravity solitary waves in Figure 25 as a function of the maximum surface depression H . The broken curve represents a low-wave asymptote. After Longuet-Higgins [30].

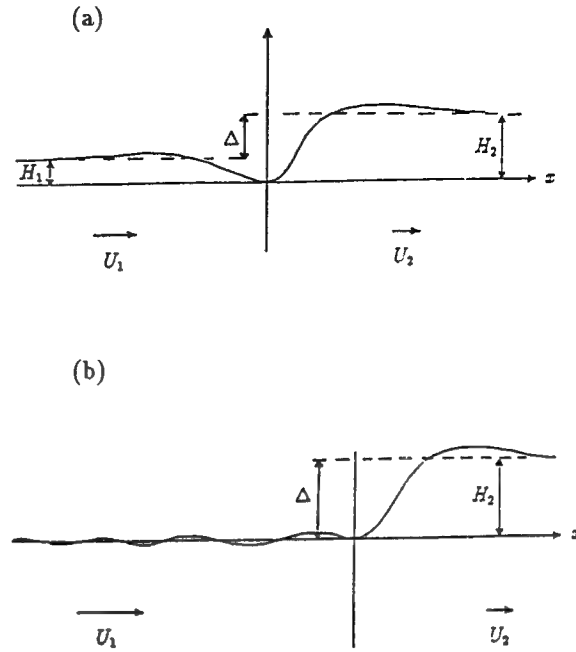


Figure 27. Sketch of a capillary jump on a non-uniform stream U (a) A trapping jump, (b) a leaky jump. From Longuet-Higgins [33].

of slower speed $c_2 = |U_2|$ and therefore of greater height H_2 . Assuming the two halves can be joined smoothly at the trough near $x = 0$, then the difference in level between the two sides at large distances from the origin will be

$$\Delta = H_2 - H_1. \quad (8.1)$$

In an extreme case the solitary wave on the right may have the limiting form shown in Figure 25a, and then

$$H_2 = 1.49 (T/g)^{1/2}. \quad (8.2)$$

This represents the maximum value of Δ . Provided the current-speed U_1 on the left is also less than c_{\min} , the energy will be trapped near $x = 0$ as in Figure 25c, giving a "trapping jump". If on the other hand $U_1 \leq c_{\min}$ we may expect an unlimited train of waves on the left, giving a "leaky jump". A common situation in which to find a velocity gradient such as described is on the forward face of a progressive gravity wave; see Figure 27c. For steep Stokes waves,

(c)

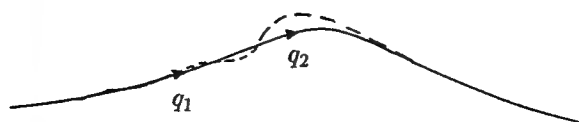


Figure 27c. Sketch of a capillary jump on a Stokes wave.

dq/ds is typically a minimum not far from the wave crest. Therefore we may expect to find a capillary jump in such a situation. Even though the wave is supercritical in the sense of Section 7 and the crest is "hard" to infinitesimal waves, nevertheless a half-solitary wave may occur which, in the case of a leaky jump, can produce a train of parasitic capillary waves.

9. Effect of surface tension on crest instabilities

We are now in a position to understand the influence of surface tension on the crest instabilities described in Sections 2 to 6.

If surface tension is applied artificially to the unstable wave in Figure 15 at time $t = 0$ and if the wavelength L is 132 cm, the wave develops not as in Figure 15 but as in Figure 28a. The crest does not overturn, but instead forms a capillary jump, with a few ripples or parasitic capillaries "upstream". Figure 28b shows a similar result when $L = 16.7$ cm. Surface tension dominates the motion. It makes little difference when the initial perturbation is absent altogether; in each case the capillary jump develops in a similar way, though at a somewhat lower rate.

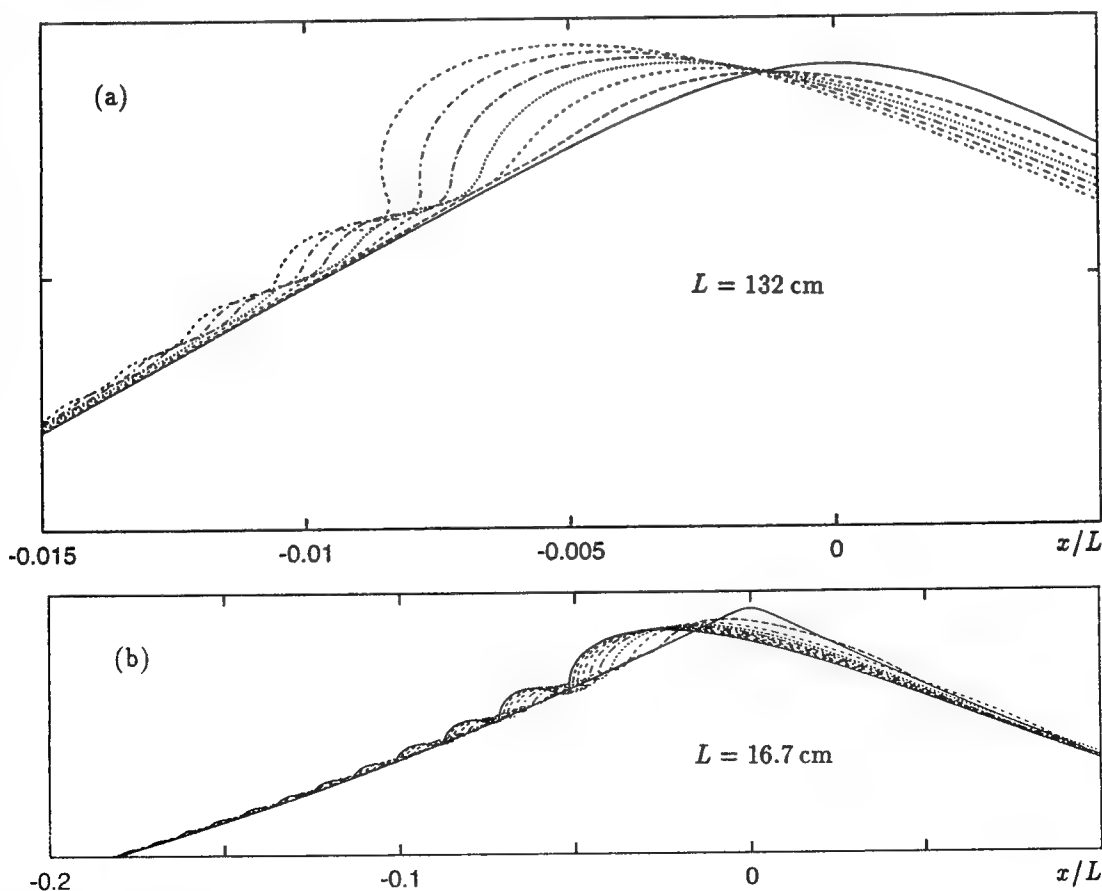


Figure 28. Effect of surface tension on the crest instability in Figure 15. (a) $L = 132$ cm, (b) $L = 16.7$ cm. From Longuet-Higgins and Dommermuth [34].

Our conclusion is that the crest instability is a comparatively weak instability, at these short gravity wavelengths. An example of surface tension acting on a fast-growing gravity-wave instability will be given in Section 11.

With the same time-stepping technique we are able to carry out a fully non-linear calculation of the growth of parasitic capillary waves on a regular, periodic train of Stokes waves. For example we show in Figure 29 the surface slope dy/dx corre-

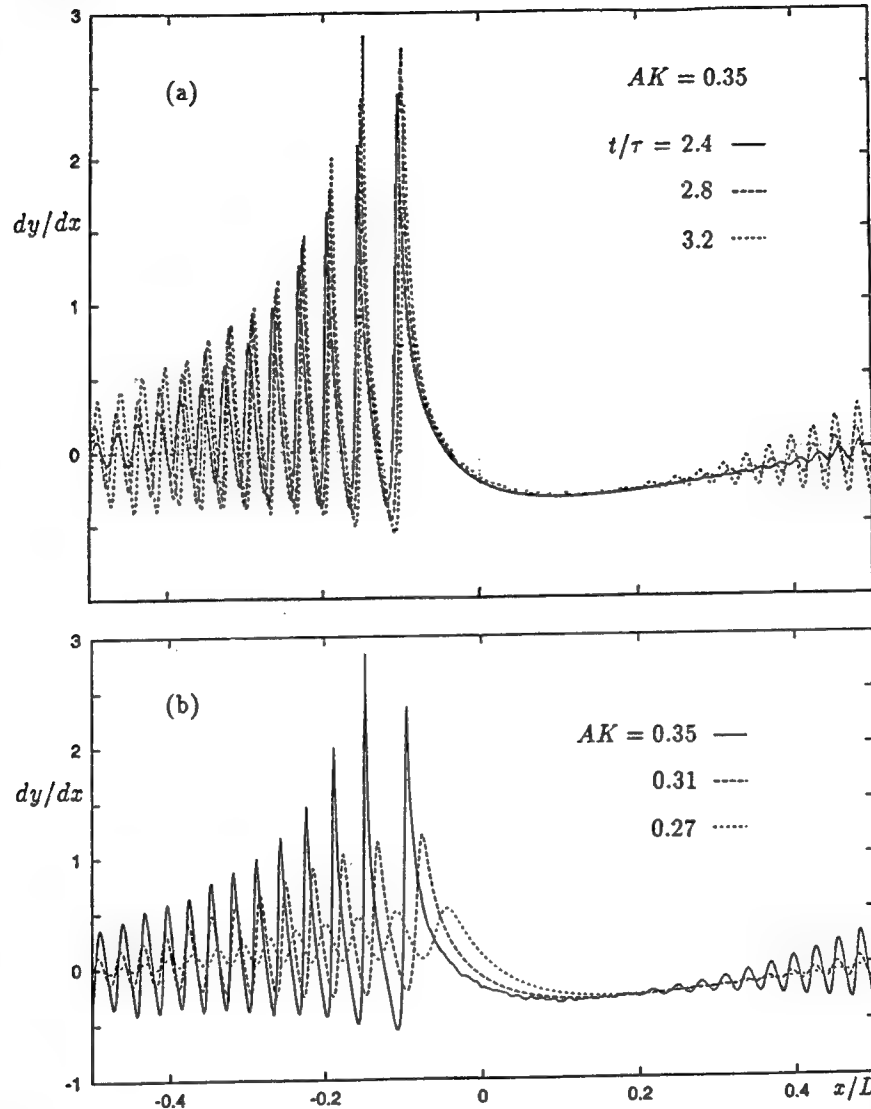


Figure 29. Computed surface slopes of an 8.0 cm gravity wave when surface tension is applied at time $t = 0$. (a) $AK = 0.35$, $t/\tau = 2.4, 2.8$ and 3.0 ($\tau =$ wave period); (b) $AK = 0.27, 0.31$ and 0.35 , $t/\tau = 3.2$. From Longuet-Higgins and Dommermuth [34].

sponding to a Stokes wave of length $L = 8.0$ cm, when surface tension is applied at time $t = 0$. Compare Figure 22. For the non-linear calculation there is no need to use a WKB approximation as in the linear theory. The two kinds of calculations are compared in Figure 30, where the maximum ripple

slope s has been plotted against the initial gravity-wave steepness ak . It can be seen that whereas in the linear theory s has a maximum at the critical value of ak , in the nonlinear theory s increases monotonically with ak throughout the whole range.

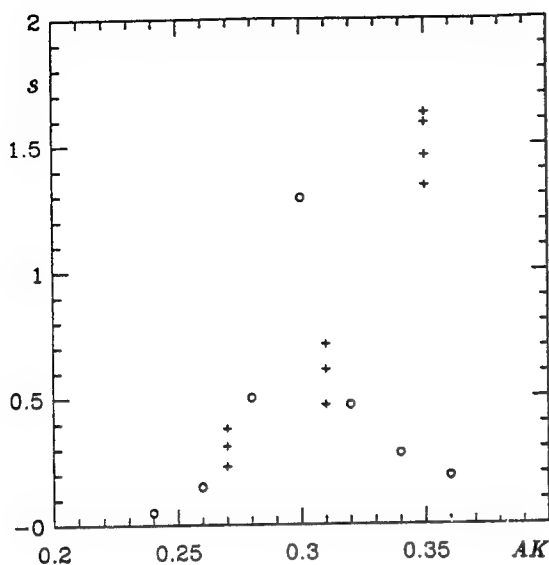


Figure 30. Maximum slope s of capillary waves on an 8.0 cm gravity wave as a function of ak . Comparison of linear theory (o) and nonlinear computation (+).

A numerical simulation of Duncan et al.'s experiment has been carried out by Yao et al. (1996) [45] using a boundary-integral technique embodied in their routine LONG-TANK. The initial conditions at the wave-maker are those of Duncan et al. [1]. Without surface tension, the focussed wave overturns and breaks, as in a plunging breaker. If a realistic value $T = 74$ dyne/cm is applied then the surface does not overturn but the profiles of Figures 1a and 1b of Duncan et al. [1] are accurately reproduced.

10. Viscous effects

Capillary waves will, because of their high rate of damping, produce a strong, rectified, shearing current at the free surface, as proved in Longuet-Higgins [35]. The vorticity in this shear will be convected back towards the crest, and the current so produced may become unstable (Longuet-Higgins 1994) [36]. Alternatively the flow can separate at the toe of the jump, producing a strong free shear layer which is unstable. This seems to be the explanation for the Type 2 ripples above the toe of the bulge in Figure 1 above. As shown in Longuet-Higgins [36] the ripples represent

"vortex waves," which soon break up into turbulence (c.f. Duncan et al. [1]). Thus the wave can effectively break without the free surface ever overturning. It is also possible that some spilling breakers may be initiated in this way.

In [36] only two-dimensional instabilities of a simple shear flow were considered. It is very likely that the surface current is unstable to three-dimensional disturbances also, and that these will eventually dominate. This would tend to explain the "streamwise vortices" that Ebuchi et al. [26] have observed in the crests of 10 cm waves.

On larger scales, vorticity may be injected by an overturning wave, simply as a result of the difference in horizontal velocity between the forwards jet and the forward face of the wave onto which it falls. This way of initiating a spilling breaker is qualitatively similar to that described above.

Lin and Rockwell [37] have carried out careful experiments on the evolution of breaking waves forced by a submerged aerofoil. They have found that, with one experimental configuration, the dominance of capillary wave effects which is exemplified in Duncan et al.'s photographs [1] may be limited to a certain range of Froude numbers (based on the chord of the aerofoil). Even within this range the surface profile and velocity field are extremely sensitive to small changes in the Froude number. It should be commented that the Weber number must also be highly relevant to the flow.

11. Breaking in modulated wave trains

On a scale larger than 2m, the capillary and viscous effects that were discussed in Section 7 to 8 become less important. The problem then is, how to give a rational account of breaking in a random field of gravity waves in an ideal fluid, and without the immediate influence of the wind.

In random seas there are two interesting limiting cases. The first is when the spectrum is broad, containing energetic short waves superposed on the dominant waves. In such a case the shorter waves can be shown theoretically [38] and experimen-

tally [39] to steepen and break on the crests of the dominant waves. A statistical model of whitecaps has been constructed on this basis [40, 41].

The second important limiting case is when the wave spectrum is sufficiently

narrow that the surface can be thought of as a more or less slowly modulated wave train. The best-known example, in two dimensions, is the subharmonic Benjamin-Feir instability, in which the modulation of the waves gradually increases and may lead

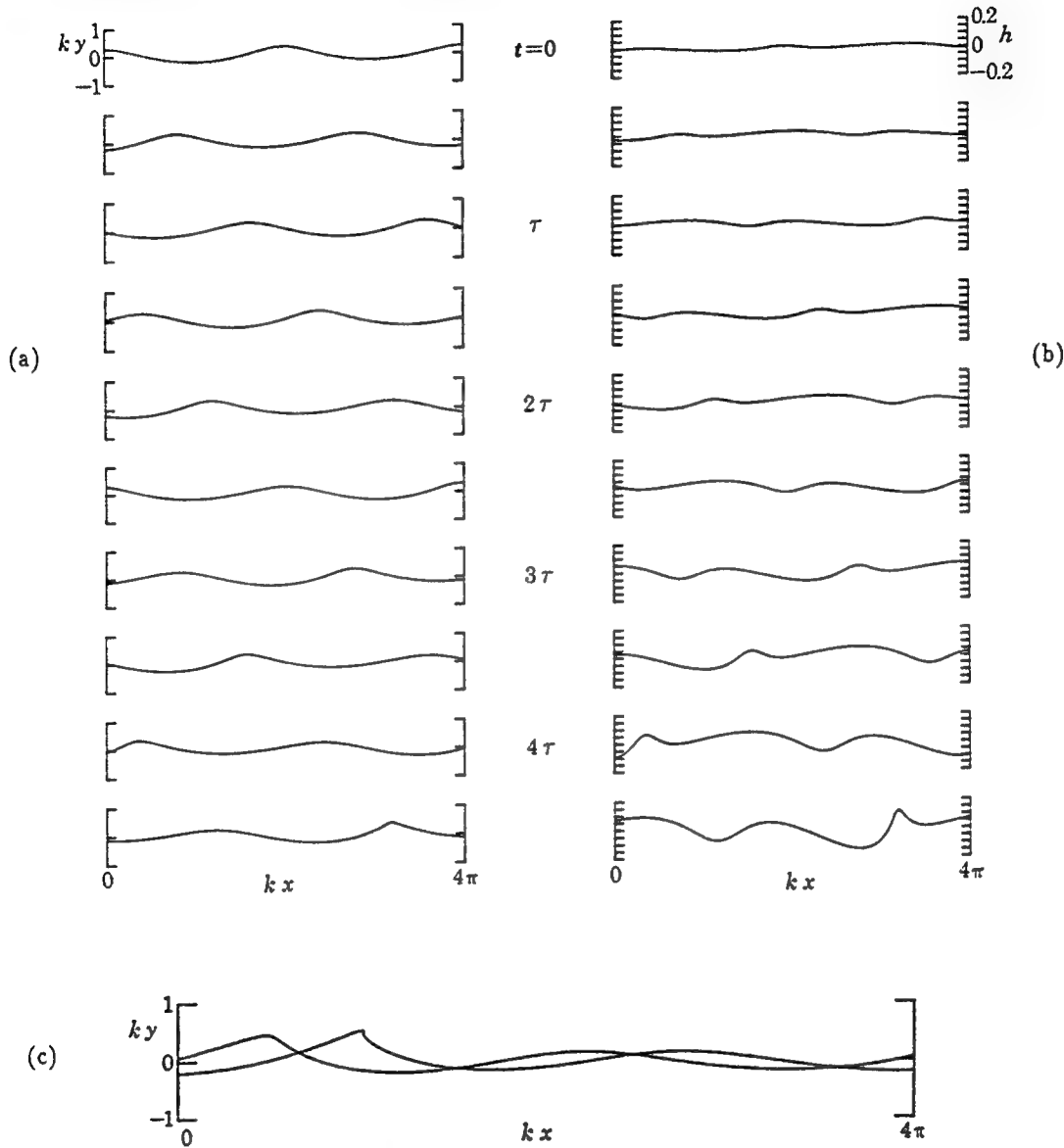


Figure 31. The nonlinear development of a subharmonic instability in a deep-water wave of initial steepness $ak = 0.25$. (a) Surface profiles, (b) the perturbation, enlarged $\times 20$, (c) final stage of wave breaking. From Longuet-Higgins and Cokelet (1978) [42].

to breaking. Figure 31 shows the nonlinear development of a wave group containing just two waves, studied numerically by Longuet-Higgins and Cokelet (1978) [42]. Starting with a nearly uniform wavetrain of steepness $ak = 0.25$, the modulation gradually grows

until after about 4.5 wave periods one of the waves suddenly develops a local instability, increases in height and overturns, all in about one-sixth of a wave period. The fluctuation in steepness of the individual waves is shown in Figure 32, as a function of time.

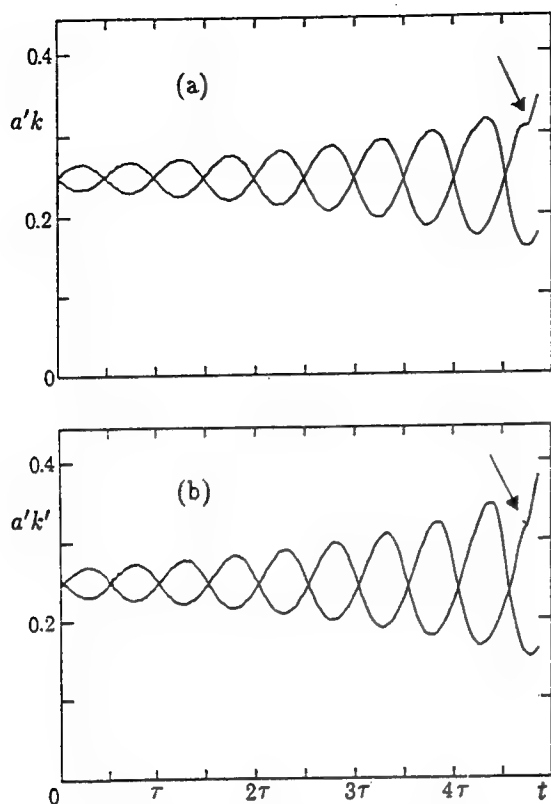


Figure 32. Time-dependence of the local wave amplitude a' and wave steepness $a'k'$ in Figure 31. From Longuet-Higgins and Cokelet (1978) [42].

It is important to distinguish between the initial wave steepness

$$(ak)_{IN} = 0.25, \quad (11.1)$$

the steepness at the onset of breaking

$$(ak)_{ON} = 0.32 \quad (11.2)$$

and the wave steepness at overturning

$$(ak)_{OV} = 0.38. \quad (11.3)$$

Similar results have been found in laboratory experiments by Bonmarin [43]. It is notable that the abrupt change in the character of the flow at the onset of breaking occurs at a much lower steepness than any of the superharmonic or crest instabilities discussed earlier which can occur only above the energy maximum at $ak = 0.429$. Nevertheless the shapes are very similar.

An interesting unsolved question is: what determines the onset of breaking?

Recently Yao et al. [44] have presented data on the inception of wave breaking in random seas, obtained with their numerical program LONGTANK. A summary is in Figure 5 of Yao et al. [45], which suggests that in water of arbitrary uniform depth breaking tends to begin when the horizontal particle velocity q is about equal to the local group-velocity c_g .

Here some caution must be exercised, since for nonlinear waves the concept of group-velocity is not well-defined. A discussion of various definitions is given by Peregrine and Thomas (1979) [46]. Their Figure 8 shows that when $ak > 0.3$ the various possibilities differ significantly from one another (and from the linear group-velocity) especially in deep water.

We may note that for solitary waves, where the group-velocity must presumably be defined as equal to the phase-speed c , the onset of crest instabilities actually occurs in waves of less than the limiting height (see Section 5). Hence the relation $q = c_g$ does not hold exactly.

It may also be noted that in order for the particle velocity in a deep-water wave to exceed one-half the phase-speed c , we find by calculation that the wave steepness ak must exceed 0.3490, not 0.32 as in Figure 32. This might be attributed to a nonlinear increase in the group velocity, if one adopted a suitable definition of c_g . However, we see from Figure 32 that the wave immediately preceding the wave that breaks does not itself break, although it attains a steepness of 0.343. Hence it seems that the apparent relation of the horizontal particle speed to the group velocity can be true only approximately, or else in a statistical sense. Nevertheless the question of how and why waves break in a modulated group remains one of the most important unsolved problems.

What is the effect of surface tension on the breaking of a modulated wave train? We can repeat the calculation by Longuet-Higgins and Cokelet [42] of a two-wave subharmonic instability but now including surface tension. If we assume a wavelength $L = 66$ cm, for example, (the horizontal periodicity being $2L$) then at an initial steepness $ak = 0.25$ capillarity has a negligible effect, at first. But in the final stage of overturning, seen in Figure 33, the form of the jet

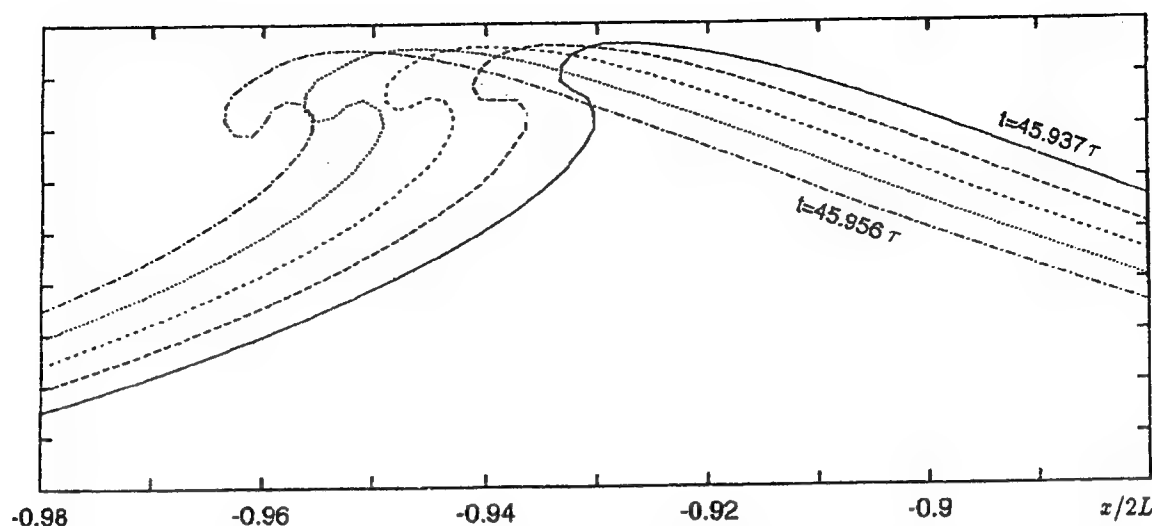


Figure 33. Consequence of applying surface tension to the subharmonic instability in Figure 31, starting at time $t = 0$. Final stages of overturning. From Longuet-Higgins and Dommermuth [34].

is considerably modified by surface tension. Unlike the crest instabilities and the gentle breaker seen in Duncan's experiments, here the jet is sufficiently energetic that capillarity is unable to prevent overturning of the surface, even when the wavelength L is smaller.

12. Conclusions

(1) The crests of steep periodic gravity waves conform accurately to the asymptotic theory for the almost-highest wave, having a radius of curvature R given by equation (2.7) with $l = q^2/2g$.

(2) The simplest superharmonic perturbations of Stokes waves, which become unstable at steepnesses ak corresponding to the first energy maximum, at first are simple phase-shifts of the whole wave. As ak increases the instabilities become more and more concentrated near the crest. Their length-scale is proportional to $q^2/2g$, and their form and rate of growth is in agreement with the lowest instability of the almost-highest wave. They may appropriately be called "crest instabilities".

(3) Similar results hold, with greater accuracy, for solitary waves in shallow water. Here the crest instabilities are the *only* normal-mode instabilities of the wave as a whole.

(4) The nonlinear development of a crest instability depends crucially upon the sign of the initial, infinitesimal disturbance. Positive perturbations lead to overturning and plunging breakers, negative perturbations lead to a transition to a lower wave of almost the same energy, then to a periodic recurrence – in deep-water. In shallow water the period of the recurrence is infinite.

(5) Surface tension has a drastic effect on steep gravity waves with lengths L up to 1.5m or more. Parasitic capillary waves appear on the forward face of the wave. A linear theory shows that the source of these ripples is the region of sharp curvature near the wave crest. For very steep (supercritical) gravity waves the waves are trapped between two caustics in the wave trough.

(6) A nonlinear theory for parasitic capillary waves shows that a "capillary jump" can occur near the crest of a steep gravity wave. This can be thought of as the joining of two deep-water solitary capillary-gravity waves, of different height. The jump may be either trapping or leaky.

(7) Viscous damping of the parasitic capillaries leads to the generation of a shearing current, which convects vorticity into the crest of the gravity wave, producing shear instability and turbulence. In short gravity waves this is called a "capillary roller". In the experiments of Duncan

et al., the Type 2 capillaries seen above the edge of the jump before turbulent collapse can be interpreted as shear instabilities, or "vortex waves".

(8) Breaking in modulated wave trains (wave groups) occurs generally at lower wave steepnesses than in a uniform wave train. In a periodic group containing two waves (Figure 31) the onset of breaking occurred in a wave for which $ak = 0.32$. Final overturning was at $ak = 0.38$. There is no unique relation between the group velocity and the horizontal particle velocity at the onset of breaking.

(9) Contrary to earlier conclusions, the initial crest bulge in the experiments of Duncan et al. is not a crest instability, since it occurs at a lower wave steepness, but resembles more the instability that occurs in a wave group. However the final form of a breaking wave is remarkably invariant, whether it arises from a crest instability or from a wave group. To find a rational theory for the onset of breaking waves in a group is a main unsolved problem.

Acknowledgements

The author's work has been supported by the Office of Naval Research under Contracts N00014-91-1582 and N00014-91-1-0008.

References

1. Duncan, J.H., Philomin, V., Qiao, H. and Kimmel, J. 1994 The formation of a spilling breaker. *Phys. Fluids* **6**, S2.
2. Longuet-Higgins, M.S. 1974 Breaking waves - in deep and shallow water. *Proc. 10th Symp. on Naval Hydrodynamics* (Cambridge, Mass.) U.S. Govt. Printing Off., pp. 597-605.
3. Cleaver, R.P. 1992 Instabilities of surface gravity waves. Ph.D. thesis, University of Cambridge, 224 pp.
4. Jenkins, A. D. 1994 A stationary potential-flow approximation for a breaking-wave crest. *J. Fluid Mech.* **280**, 335-347.
5. Shrira, V.I., Badulin, S.I. and Kharif, C. 1996 A model of water-wave "horseshoe" patterns. *J. Fluid Mech.* **318**, 375-405.
6. Michell, J.H. 1893 On the highest gravity waves on deep water. *Phil. Mag.* (5) **36**, 430.
7. Williams, J.M. 1981 Limiting gravity waves in water of finite depth. *Phil. Trans. R. Soc. Lond. A* **302**, 139-188.
8. Longuet-Higgins, M.S. and Fox, M.J.H. 1977 Theory of the almost-highest wave: The inner solution. *J. Fluid Mech.* **80**, 721-741.
9. Longuet-Higgins, M.S. and Fox, M.J.H. 1978 Theory of the almost-highest wave. II. Matching and analytic extension. *J. Fluid Mech.* **85**, 769-786.
10. Longuet-Higgins, M.S. and Cleaver, R.P. 1994 Crest instabilities of gravity waves. Part 1. The almost-highest wave. *J. Fluid Mech.* **258**, 115-129.
11. Longuet-Higgins, M.S., Cleaver, R.P. and Fox, M.J.H. 1994 Crest instabilities of gravity waves. Part 2. Matching and asymptotic analysis. *J. Fluid Mech.* **259**, 333-344.
12. Longuet-Higgins, M.S. and Dommermuth, D.G. 1996 Crest instabilities of gravity waves. Part 3. Nonlinear development and breaking. *J. Fluid Mech.* (in press).
13. Tanaka, M. 1983 The stability of steep gravity waves. *J. Phys. Soc. Japan* **52**, 3047-3055.
14. Saffman, P.G. 1985 The superharmonic instability of finite-amplitude water waves. *J. Fluid Mech.* **159**, 169-174.
15. Longuet-Higgins, M.S. and Tanaka, M. 1996 On the crest instabilities of steep surface waves. *J. Fluid Mech.* (in press).
16. Miles, J.W. 1980 Solitary waves. *Ann. Rev. Fluid Mech.* **13**, 11-43.
17. Evans, W.A.B. and Dörr, U. 1991 New minima in solitary water wave properties close to the maximum wave. Rep. Phys. Lab., Univ. of Kent, Canterbury, U.K., 22 pp.
18. Longuet-Higgins, M.S. and Fenton, J.D. 1974 On the mass, momentum, energy and circulation of a solitary wave. II. *Proc. R. Soc. Lond. A* **340**, 471-493.
19. Byatt-Smith, J.G.B. and Longuet-Higgins, M.S. 1976 On the speed and profile of steep solitary waves. *Proc. R. Soc. Lond. A* **305**, 175-189.

20. Fox, M.J.H. 1977 Nonlinear effects in surface gravity waves. Ph.D. thesis, Univ. of Cambridge, Sept. 1977, 90 pp.
21. Longuet-Higgins, M.S. and Fox, M.J.H. 1996 Asymptotic theory for the almost-highest wave. *J. Fluid Mech.* **317**, 1-19.
22. Tanaka, M. 1986 The stability of solitary waves. *Phys. Fluids* **29**, 650-655.
23. Tanaka, M., Dold, J.W., Lewy, M. and Peregrine, D.H. 1987 Instability and breaking of a solitary wave. *J. Fluid Mech.* **185** 235-248.
24. Jillians, W.J. 1989 The superharmonic instability of Stokes waves in deep water. *J. Fluid Mech.* **204**, 563-579.
25. Longuet-Higgins, M.S. 1963 The generation of capillary waves by steep gravity waves. *J. Fluid Mech.* **16**, 138-159.
26. Ebuchi, N., Kawamura, H. and Toba, Y. 1987 Fine structure of laboratory wind-wave surfaces using an optical method. *Boundary-Layer Met.* **39**, 133-151.
27. Longuet-Higgins, M.S. 1995 Parasitic capillary waves: a direct calculation. *J. Fluid Mech.* **301**, 79-107.
28. Cox, C.S. 1958 Measurements of slopes of high-frequency wind waves. *J. Mar. Res.* **16**, 199-225.
29. Longuet-Higgins, M.S. 1988 Limiting forms for capillary-gravity waves. *J. Fluid Mech.* **194**, 351-375.
30. Longuet-Higgins, M.S. 1989 Capillary-gravity waves of solitary type on deep water. *J. Fluid Mech.* **200**, 451-470.
31. Vanden-Broeck, J.-M. and Dias, F. 1992 Gravity-capillary solitary waves in water of infinite depth and related free-surface flows. *J. Fluid Mech.* **240**, 549-557.
32. Longuet-Higgins, M.S. 1993 Capillary-gravity waves of solitary type and envelope solitons on deep water. *J. Fluid Mech.* **252**, 703-711.
33. Longuet-Higgins, M.S. 1996 Capillary jumps on deep water. *J. Phys. Oceanogr.* (in press).
34. Longuet-Higgins, M.S. and Dommermuth, D.G. 1996 Effects of surface tension on breaking waves. (submitted).
35. Longuet-Higgins, M.S. 1992 Capillary rollers and bores. *J. Fluid Mech.* **240**, 659-679.
36. Longuet-Higgins, M.S. 1994 Shear instability in spilling breakers. *Proc. R. Soc. Lond. A* **446**, 399-409.
37. Lin, J.C., and Rockwell, D. 1995 Evolution of a quasi-steady breaking wave. *J. Fluid Mech.* **302**, 29-44.
38. Longuet-Higgins, M.S. 1987 The propagation of short surface waves on longer gravity waves. *J. Fluid Mech.* **177**, 293-306.
39. Longuet-Higgins, M.S. 1990 Mechanisms of wave breaking in deep water. pp. 1-30 in *Sea Surface Sound*, ed. B.R. Kerman. Dordrecht, D. Reidel Publ. Co., 639 pp.
40. Longuet-Higgins, M.S. 1987 A stochastic model for sea surface roughness. I. Wave crests. *Proc. R. Soc. Lond. A* **410**, 19-34.
41. Longuet-Higgins, M.S. 1991 A stochastic model of sea-surface roughness. II. *Proc. R. Soc. Lond. A* **435**, 405-422.
42. Longuet-Higgins, M.S. and Cokelet, E.D. 1978 The deformation of steep surface waves on water. II. Growth of normal-mode instabilities. *Proc. R. Soc. Lond. A* **364**, 1-28.
43. Bonmarin, P. 1989 Geometric properties of deep-water breaking waves. *J. Fluid Mech.* **209**, 405-433.
44. Yao, Y., Wang, P. and Tulin, M.P. 1994 Wave groups, wave-wave interaction and wave breaking: results of numerical experiments. *Proc. 20th Symp. on Naval Hydrodynamics* (Santa Barbara, Calif.) 16 pp.
45. Yao, Y., Wang, P. and Tulin, M.P. 1996 Surface tension effects on breaking waves - LONGTANK simulation. Univ. of Calif. Santa Barbara, Ocean Eng. Lab., Tech. Rep. 95-132.
46. Peregrine, D.H. and Thomas, G.P. 1979 Finite-amplitude deep-water waves on currents. *Phil. Trans. R. Soc. Lond. A* **292**, 371-409.

Radiation and Diffraction Waves of a Ship at Forward Speed

M. Ohkusu, G. Wen (Kyushu University, Japan)

Abstract

An improved method to measure diffraction and radiation waves around a ship model running in waves at forward speed is proposed. With this technique we are able to view the diffraction and/or radiation waves which are usually invisible in tank tests due to the existence of other effects such as incident waves and steady Kelvin waves. Measured wave pattern especially with blunt bow and shallow draft ships is used to investigate validity of an analytical method to predict the diffraction and radiation waves and added resistance of a ship.

1 Introduction

We are developing more and more sophisticated analytical method to understand and predict realistic nonlinear hydrodynamics of ships in waves. Validity of those methods is still tested, however, with traditional way of comparing the theoretically predicted and experimentally measured global hydrodynamic force on ships. The global force is an integrated effect and the implication of the test results is not always clear. The more sophisticated the analytical methods are, the more strict and direct experimental test such as the comparison of fluid pressure without any integration effect will be necessary to prove their advantage over traditional heuristic approaches. This kind of test is also plausible from practical point of view because ship designers do need analytical tool accurate enough to predict local sea loads as well as global sea loads.

The present author proposed (Ohkusu (1984)) to make careful observation of radiation and/or diffraction wave form generated by a ship running in waves and to compare them with the theoretically predicted ones. The purpose is to prove by more direct manner validity or invalidity of our current analytical methods to predict the flow and the pressure regarding the ships in waves. Measurement of the flow and the pressure themselves naturally serves better practically as well as academically this purpose. Reason

of the wave observation instead is that it undergoes less integration effect than the global force. Moreover the measurement is easier in terms of experimental instrumentation and its accuracy is much more reliable than that of the flow or pressure measurement.

Investigations based on this idea have already produced some successful results. A large discrepancy, for example, found between added resistance measured as a force and one directly derived from measured wave energy leads to an idea of breaking of the diffraction waves in front of the ship bow and new method has been developed to predict extra added resistance due to the breaking of the diffraction waves (Naitoh et al. (1987)). Yet we found recently that the difference is unusually large with hull forms of shallow draft or at ballast condition corresponding to the shallow draft (SR211(1993)). No theoretical explanation is available now for this large difference.

We have some to be improved in the original technique proposed by the present author to measure diffraction and radiation waves. It gave only wave distribution on a line parallel to the track of a ship model running in experimental tank. One can not construct two dimensional image of the wave pattern by those data alone. This was one reason to derive the amplitude function of the component wave composing the diffraction and radiation waves from the data and to reconstruct the global wave characteristics. This process is possible only when we can assume a mathematical expression of the waves, a linear superposition of component waves satisfying dispersive relation corresponding to its direction of propagation. Therefore some part of wave energy will not possibly be captured with this process. So it is plausible if we could measure two dimensional wave pattern and compare them without any processing with theoretical prediction. It is also desirable to separate the first and second order wave components to compare the former with the predicted by linear theories.

In this report we return to the present author's old approach of measuring waves but we attempt to improve it in order that we can obtain directly the global image of the diffraction and radiation waves at forward speed and separate them into the first and sec-

ond order parts. We investigate various information on the diffraction and radiation waves observed by the improved technique of wave measurement particularly for seeking any explanation of the discrepancy of added resistance of shallow draft ships.

We then propose a linear analytical approach to predict the fluid pressure on ships particularly due to the diffraction wave. This approach accounts effectively for nonuniform steady flow which is prominent in the vicinity of the blunt bow and is supposed to have large influence on accurate prediction of the wave pressure on the bow part.

We test the accuracy of our analytical approach by comparing the diffraction wave field predicted with the measured with our improved technique. We presume that if the prediction of the diffraction wave elevation around the bow is accurate, then the prediction of wave pressure on the bow part will be accurate and the added resistance, on which the wave loads at the bow is the most influential, will be predicted accurately.

2 Measurement of Radiation and Diffraction Waves

Neither radiation wave nor diffraction wave field generated by a ship advancing in waves is visible at tank test because of the coexistence of other waves such as steady wave generated by the forward speed of the ship on otherwise a calm water and incident waves. So we need a technique to separate each of those waves.

It is relatively simple to exclude the effect of the incident waves. We measure them upstream where they are not yet disturbed by a ship model and extrapolate them to near it. The extrapolated incident waves are subtracted from the measured wave.

Another problem is that instantaneous distribution of wave elevation around the model is not a full information of the radiation and the diffraction waves. One can obtain a complete picture of the radiation and the diffraction waves only when the distribution of the amplitude and the phase of the wave motion is measured.

Our method to overcome this at tank test is to place several wave probes on fixed positions to the water tank and on a line parallel to the track of the ship model with an equal spacing Δx . When the ship model advances in the tank, each wave probe comes to a location relative to the ship model at different time instant. In other words the wave probes record the wave elevation at every location on the line parallel to the ship model's track on several different time

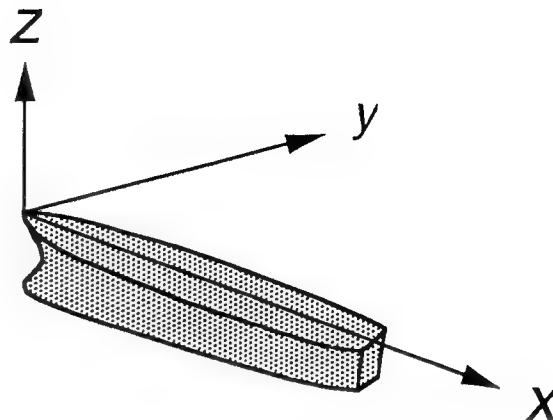


Figure 1: Coordinate System

instants whose interval is $\Delta x/U$. U is the speed of the ship model.

Temporal and spatial variation of the diffraction or radiation waves generated by the ship model running at forward speed in the monochromatic incident waves or sinusoidally oscillating is given to the second order by

$$\zeta(x, y, t) = \eta_0(x, y) + \eta_1(x, y)e^{i\omega t} + \eta_2(x, y)e^{i2\omega t} \quad (1)$$

where the coordinates fixed to the average position of the ship model are defined as a right-hand system shown in Fig.1.

The first term on the right of (1) is the steady wave elevation corresponding to the Kelvin wave pattern. Naturally it includes the second order steady component. The second term is the linear oscillatory part and the third the second order oscillatory component.

If the interval $\Delta x/U$ is small enough and the number of the wave probes is large enough, we fit measured wave elevation on several different time instants with equation (1) at every x of the line $y = \text{constant}$ to determine η_0 , η_1 and η_2 . Fig.2 is an example of the fitting of the wave motion in the vicinity of a ship model at midship; this example is the radiation waves of a Series 60 model of $C_B = 0.8$ at ballast condition forced to heave at relatively large amplitude (amplitude-to-draft-ratio is 0.9). We used

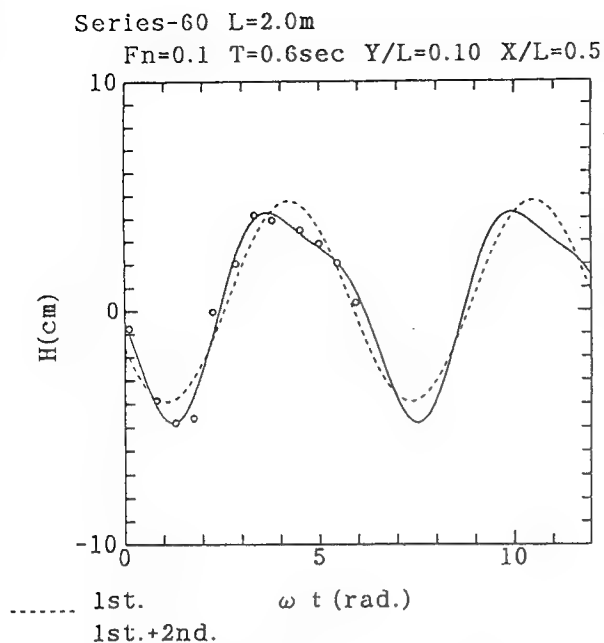


Figure 2: Time Series of Wave Elevation

twelve wave probes in this experiment and the number of the measured data represented by circles is naturally twelve. Introduction of the second harmonic terms in equation (1) is apparently appropriate and the η_1 determined is the complex amplitude distribution of linear radiation wave.

Replace the wave probes to another y and repeat the procedure described above, we have $\eta_{0,1,2}$ on various y values. With them we can compose the pattern of the radiation or diffraction waves as shown in Fig.3 and Fig.4.

Fig.3 is the diffraction wave $\eta_1(x, y)e^{i\omega t}$ and $\eta_2(x, y)e^{i2\omega t}$ at a time instant of $\omega t = 0$ for OHS hull form (a bulk carrier's hull form of $C_B = 0.80$, $L/B = 5.48$) at ballast condition. The relative position of the ship is drawn by a slender rectangle. Magnitude of η_2 to η_1 (about 20 %) in this example is found to be much larger than the second harmonic component of the incident waves (less than 5%) which is inevitably contained. We may conclude that the most part of η_2 is generated not by the second harmonic component of the incident waves but by some nonlinear interaction of waves and body.

Several features of the diffraction wave shown in Fig.3 and 4 are:

(1) Energy of other wave component than the component of the fundamental frequency is apparently very small. This means that added resistance due to the wave component other than the linear one may not be considerable.

(2) The second harmonic component is significant at the fore front of the diffraction wave pattern where naturally the wave steepness is the largest. Amplitude of the second harmonics is as large as 10 % of that of the incident waves. It might suggest the wave breaking at the front of the diffraction waves.

(3) No significant difference between the diffraction waves at full load and ballast conditions is observed.

Free wave component of $\eta_1(x, y)$ that is predominant away from the hull surface is expressed by

$$\eta_1(x, y) = \sum_{j=1}^2 \int_{-\pi}^{\pi} F_j(\theta) e^{-i(\lambda_j x + \mu_j y)} d\theta \quad (2)$$

where

$$\lambda_j(\theta) = \frac{K_0}{2 \cos \theta} (1 - 2\tau \cos \theta \pm \sqrt{1 - 4\tau \cos \theta}),$$

$$\mu_j(\theta) = \lambda_j(\theta) \tan \theta, \quad K_0 = \frac{g}{U^2}, \quad \tau = \frac{U\omega}{g}$$

The direction θ of the component wave for which real value of λ_j does not exist is to be excluded from the integral (2).

A technique is already established of obtaining experimentally the function $F_j(\theta)$ with a Fourier transform of the measured waves on a line of $y = \text{constant}$ (Ohkusu (1996)). Practically an extrapolation of the measured wave record to the location of x larger than some value is necessary since the record far behind the ship model is affected by the tank wall reflection and not to be used as the data for the transform. The expression (2) of the wave elevation is asymptotic one which is correct when $|x|$ is sufficiently large but $|y|$ is kept constant. Possible error in $F_j(\theta)$ due to a Fourier transform of the measured wave at a finite x was investigated by making use of theoretical wave elevation (Ohkusu and Iwashita (1986)). No considerable error was found especially for the dominant $F_2(\theta)$.

At higher Froude number the diverging wave part of diffraction and radiation waves will prevail; the diverging wave components propagate into the directions θ close to $\pi/2$ and their wave length $2\pi/\lambda_j$ in the x direction is very long. Naturally the x -wise Fourier transform of $\eta_1(x, y)$ will not give accurate amplitude $F_j(\theta)$ of those components. In such cases the y -wise transform of $\eta_1(x, y)$ is plausible. This transverse transform is possible when the measured wave data as shown in Fig.3 and 4 are available. The wave pattern in Fig.3 and 4 exemplifies that diffraction waves vanish rapidly as y become larger; the transverse transform is more convenient for one may terminate the transform at a finite y .

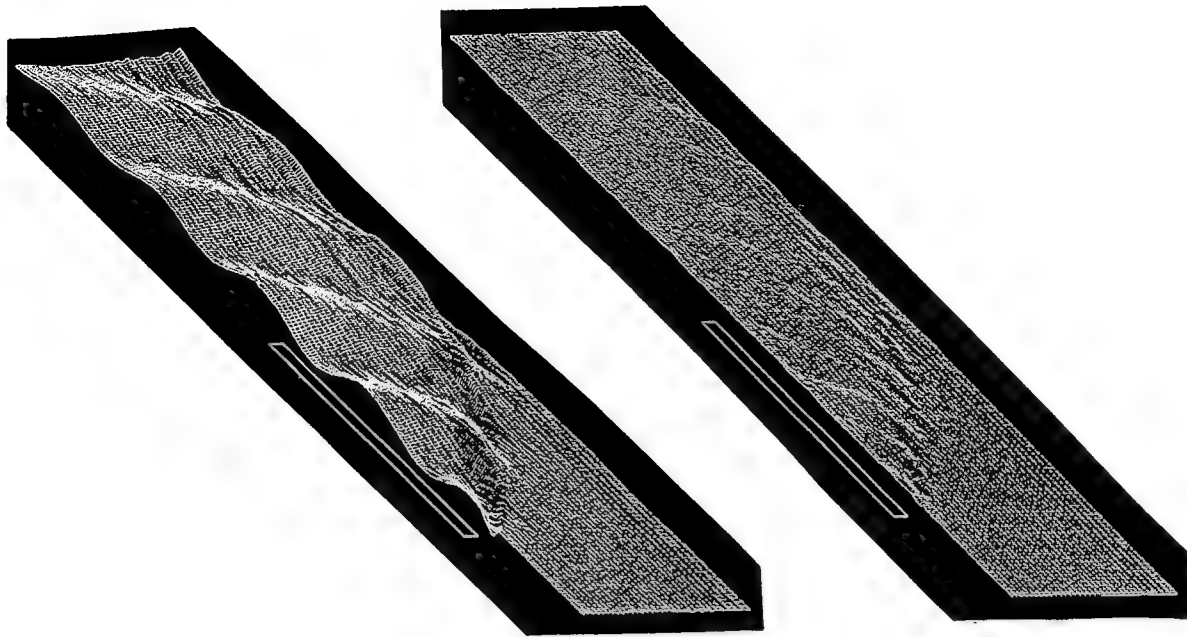


Figure 3: Diffraction Wave of OHS form at $\omega t = 0$, 1ω component (*left*) and 2ω component (*right*)
Ballast Condition, $F_n = 0.17$, $\lambda/L = 0.5$

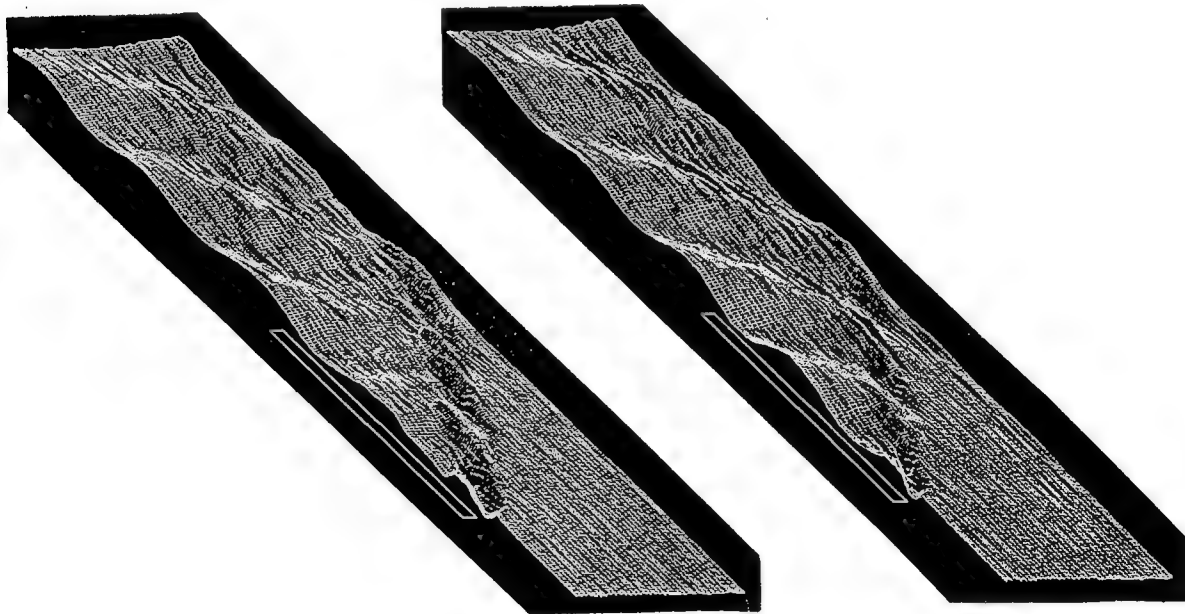


Figure 4: Diffraction Wave of a Series 60 ($C_B = 0.8$) at $\omega t = 0$, at Full Load(*left*) and Ballast (*right*)
 $F_n = 0.20$, $\lambda/L = 0.5$

Two wave components propagating into two different directions θ and θ^* have an identical wave number in the y direction:

$$\mu = \mu_1(\theta) = \mu_1(\theta^*)$$

$$\text{for } \mu > 4(\omega^2/g) \sin[\cos^{-1}(1/4\tau)]$$

$$\mu = \mu_1(\theta) = \mu_2(\theta^*)$$

$$\text{for } 0 < \mu < 4(\omega^2/g) \sin[\cos^{-1}(1/4\tau)]$$

Consequently the Fourier transform of η_1 into y direction provides a linear sum of $F_1(\theta)$ and $F_1(\theta^*)$ or $F_2(\theta^*)$ dependent on the value of μ as given in equation (3) and (4).

$$\begin{aligned} & \frac{1}{2\pi} \int_{-\infty}^{\infty} \eta_1(x, y) e^{i\mu y} dy \\ &= -\frac{F_1(\theta)}{f_1(\theta)} e^{i\lambda_1(\theta)x} - \frac{F_1(\theta^*)}{f_1(\theta^*)} e^{i\lambda_1(\theta^*)x} \\ & \text{for } \mu > 4(\omega^2/g) \sin[\cos^{-1}(1/4\tau)] \end{aligned} \quad (3)$$

$$\begin{aligned} &= \frac{F_2(\theta^*)}{f_2(\theta^*)} e^{i\lambda_2(\theta^*)x} - \frac{F_1(\theta)}{f_1(\theta)} e^{i\lambda_1(\theta)x} \\ & \text{for } 0 < \mu < 4(\omega^2/g) \sin[\cos^{-1}(1/4\tau)] \end{aligned} \quad (4)$$

where

$$f_j(\theta) = -\frac{\lambda_j(\theta)}{\cos^2 \theta} \left(1 \pm \frac{\sin^2 \theta}{\sqrt{1 - 4\tau \cos \theta}} \right) \quad (5)$$

In order to determine $F_1(\theta)$ and $F_2(\theta)$ we repeat the transform (3) and (4) for the data $\eta_1(x, y)$ at more than two different x . We compute the left hand side of equation (3) and (4) with $\eta_1(x_p, y)$ at several locations of $x_p (p = 1, 2, 3, \dots, M)$ that distribute at an equal spacing along the length $(2\pi/\lambda_2(\pi))$ from some distance behind the stern. We determine $F_j(\theta)$ such that equation (3) and (4) fit those values at different x_p with the least error. For μ , for example, in $0 < \mu < (\omega^2/g) \sin[\cos^{-1}(1/4\tau)]$, the following is a simultaneous equation to determine $F_1(\theta)$ and $F_2(\theta^*)$:

$$\begin{aligned} & \sum_{p=1}^M \frac{1}{2\pi} \int_{-\infty}^{\infty} \eta_1(x_p, y) e^{i\mu y} dy \cdot e^{-i\lambda_2(\theta^*)x_p} \\ &= \frac{F_2(\theta^*)}{f_2(\theta^*)} M - \frac{F_1(\theta)}{f_1(\theta)} \sum_{p=1}^M e^{i x_p (\lambda_1(\theta) - \lambda_2(\theta^*))} \end{aligned} \quad (6)$$

$$\begin{aligned} & \sum_{p=1}^M \frac{1}{2\pi} \int_{-\infty}^{\infty} \eta_1(x_p, y) e^{i\mu y} dy \cdot e^{-i\lambda_1(\theta)x_p} \\ &= \frac{F_2(\theta^*)}{f_2(\theta^*)} \sum_{p=1}^M e^{i x_p (\lambda_1(\theta) - \lambda_2(\theta^*))} - \frac{F_1(\theta)}{f_1(\theta)} M \end{aligned} \quad (7)$$

For $\mu > 4(\omega^2/g) \sin[\cos^{-1}(1/4\tau)]$, $F_1(\theta)$ and $F_1(\theta^*)$ will be determined in a similar manner with equation (4).

$F_j(\theta)$ that is determined by the transverse transform must be accurate for the component propagating into the direction $\theta \sim \pi/2$. It is, however, supposed to be less accurate for the components whose crest lines are parallel or almost parallel to the y axis. However this is improved in our method by using the data at several x_p covering the length $2\pi/\lambda_2(\pi)$, the wave length of the component with the crest line parallel to the y axis.

$F_j(\theta)$ determined by the y -wise transform will give the wave structure behind the ship model because it uses the measured wave behind the stern. On the other hand x -wise transform is on the waves measured close to the bow. We expect that comparison of $F_j(\theta)$ for the components propagating forward of the ship obtained by both transforms will possibly give some information on the difference of far and near field wave characteristics.

In Fig.5 and 6 we compare relative magnitude of $F_{1,2}(\theta)$ obtained by the x -wise and the y -wise transforms. They are of the diffraction waves due to a Series 60 model presented in the previous section. In those figures the abscissa β represents the angle of $\theta - \alpha_0$ where α_0 is the critical angle $\cos^{-1}(1/4\tau)$. $F_2(\theta)$ is plotted to the right direction from $\beta = 0$ but $F_1(\theta)$ to the left direction. $F_1(\theta)$ is negligibly small for larger angle θ . Naturally $F_1(\alpha_0) = F_2(\alpha_0)$ as known from $\mu_1(\alpha_0) = \mu_2(\alpha_0)$ and both curves are continuous at $\beta = 0$. Reason of the plotting $F_2(\beta)$ for relatively small range of β is that only this part prevails in the contribution to added resistance. It is seen clearly that $F_1(\theta)$ is very small compared with $F_2(\theta)$.

Agreement of $F_j(\theta)$ by the x -wise and y -wise transforms is considerable except that the latter seems to represent more details of it. This is not surprising since the latter is supposed to give more accurate $F_2(\theta)$ of the diverging waves ($\theta \sim \alpha_0 \sim \pi/2$). The agreement of regardless of the full load (Fig.5) or ballast condition (Fig.6). This agreement suggests that our linear model of the wave given by equation (2) is correct in describing diffraction waves around a ship.

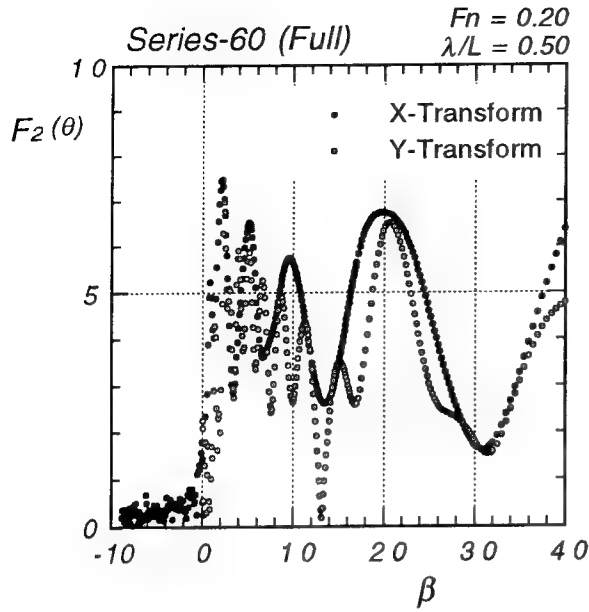


Figure 5: $F_j(\theta)$ of diffraction waves (full load)

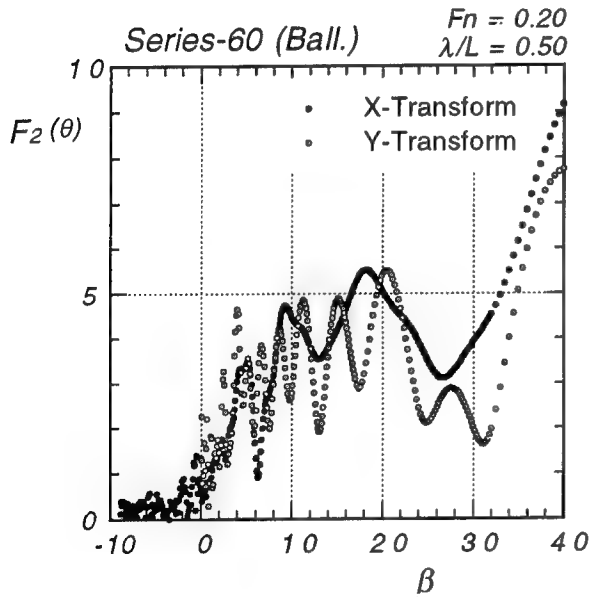


Figure 6: $F_j(\theta)$ of diffraction waves (ballast)

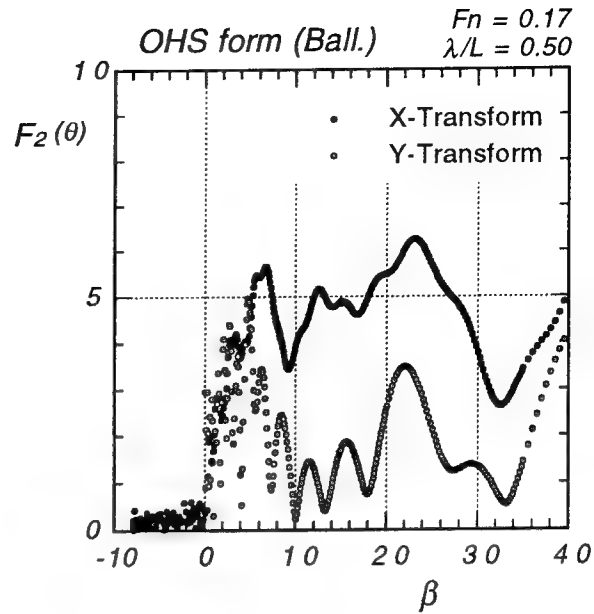


Figure 7: $F_j(\theta)$ of diffraction waves (ballast)

Fig.7 is a similar comparison with the diffraction waves of OHS form st ballast condition. The hull form has a big bulbous bow. Added resistance of this hull form particularly in head waves of short wave length and at ballast condition is unusually large as shown later. We see significant difference between $F_j(\theta)$ by the x and y -wise transforms. The disagreement suggests anomaly in the wave pattern of this hull form one can not describe by equation (2). However we can not find any considerable feature suggesting this anomaly of the wave in Fig.3. We may conjecture the the wave energy is dissipated during its propagation from near to behind the ship. But we can not conclude definitely so and we can not either say that this anomaly of the wave is the cause of unusually large added resistance of this ship.

3 Computation of Diffraction and Radiation Waves

Full nonlinear treatment of radiation or diffraction waves generated by a running ship is not straightforward. Even linear or quasi-linear theory is not so easy to be numerically implemented (Sclavounos (1996), Iwashita et al. (1994)). A panel method using 3D Green function satisfying a full linear free surface condition at forward speed, for example, needs formidable computer time and the results are some-

time ambiguous when we compute the fluid pressure close to the free surface or the wave elevation close to the hull surface. We should develop a theoretical method robust as well as rational in predicting the diffraction waves particularly close to the ship bow.

We give the first priority to accurate prediction of the diffraction wave, the divergent wave component in particular, close to the bow part. We suppose the diffraction wave at the bow almost determines the fluid pressure that decides added resistance of the ship in the incident waves of short wave length. Moreover the divergent waves propagating into the direction $\theta \sim \alpha_0$ to $\pi/2$ contribute much more to the added resistance than the transverse waves progressing into the direction $\theta \sim \pi$. The divergent wave prevails at the bow part and therefore is to be accurately predicted. We must consider interacting effect by nonuniform steady flow close to the bow of the ship.

Consider a ship running at forward speed U in incident regular waves on deep water. Let (x, y, z) be a right-handed coordinate system fixed to the mean position of the ship; the z is vertically upward through the fore end of the ship, $-x$ is in the direction of forward motion and the origin is in the plane of the undisturbed free surface. Here we restrict ourselves to diffraction waves for brevity of explanation.

The problem is formulated in terms of potential flow theory. The total velocity potential is expressed by

$$\Phi = Ux + \phi_S(x, y, z) + \phi_0(x, y, z)e^{i\omega t} + \phi(x, y, z)e^{i\omega t} \quad (9)$$

where ω is the circular frequency of encounter of the ship with the regular incident waves. ϕ_S is the velocity potential of the steady flow due to the ship forward velocity, $\phi_0 e^{i\omega t}$ the velocity potential of the incident waves and $\phi e^{i\omega t}$ the velocity potential of the first harmonics of the diffraction waves.

The boundary value problem for ϕ is simplified by introducing the slenderness parameter ε which represents the order of magnitude of the ratio of the beam or the draft to the ship length.

Faltinsen and Zhao (1991) gave a boundary value problem for the radiation wave ϕ derived from the assumptions $\partial f / \partial x = O(f\varepsilon^{-1/2})$, $\partial f / \partial y, z = O(f\varepsilon^{-1})$ in some region near the ship, where f is any flow variable caused by the ship. The first assumption is quite appropriate when we are concerned with the flow close to a relatively bluff bow, where the flow variation down the ship length is supposed to be not so small. The governing equation of ϕ near the ship is two dimensional Laplace equation:

$$\frac{\partial^2 \phi}{\partial y^2} + \frac{\partial^2 \phi}{\partial z^2} = 0 \quad (10)$$

Their free surface condition is complicated one and must be satisfied on the steady water surface displaced from $z = 0$. The relatively high steady wave elevation resulting from the first assumption for f does not admit the free surface condition of ϕ transferred onto $z = 0$. This free surface condition, though it is linear with respect to ϕ , apparently produces an intricate situation for the diffraction wave; the incident waves coming far upstream which is usually assumed linear will be diffracted on the displaced free surface and the ship surface. Numerical implementation of this formulation has not been successful for the diffraction waves.

Their formulation is yet attractive because it can deal with the bow flow rather correctly but by simpler way. It can account for the interaction effect of steady wave elevation considerable at the bow part on the diffraction wave. We introduce a rather inconsistent and simpler approach similar to it. Our simpler approach considers only weak interaction with the steady flow. Despite $\partial f / \partial x = O(f\varepsilon^{-1/2})$ we assume the steady wave elevation is not so high and the free surface condition for ϕ is transferred to $z = 0$. While we ignore $O(\phi_S^2)$ terms, we retain almost all other terms even if they are redundant. It yields the free surface condition when the ship is in head waves:

$$\begin{aligned} \left(U + \frac{\partial \phi_S}{\partial x} \right) \frac{\partial \phi}{\partial x} = & -i\omega\phi - g\zeta - \frac{\partial \phi_S}{\partial y} \frac{\partial \phi}{\partial y} - \frac{\partial \phi_S}{\partial z} \frac{\partial \phi}{\partial z} \\ & - \frac{\partial \phi_S}{\partial z} \frac{\partial \phi_0}{\partial z} - \frac{\partial \phi_S}{\partial x} \frac{\partial \phi_0}{\partial x} \\ & \text{on } z = 0 \end{aligned} \quad (11)$$

$$\begin{aligned} \left(U + \frac{\partial \phi_S}{\partial x} \right) \frac{\partial \zeta}{\partial x} = & -i\omega\zeta + \frac{\partial \phi}{\partial z} - \frac{\partial \zeta_S}{\partial y} \frac{\partial \phi}{\partial y} - \frac{\partial \zeta}{\partial y} \frac{\partial \phi_S}{\partial y} \\ & - \frac{\partial \zeta_0}{\partial x} \frac{\partial \phi_S}{\partial x} \\ & \text{on } z = 0 \end{aligned} \quad (12)$$

where $\zeta e^{i\omega t}$ represents the wave elevation due to $\phi e^{i\omega t}$, $\zeta_0 e^{i\omega t}$ the elevation of the incident wave and ζ_S the steady wave elevation by ϕ_S .

The difference of this free surface condition from usual linear free surface condition is the inclusion of the nonuniform steady flow and wave elevation represented by the terms of ϕ_S and ζ_S . They will represent partly the effect of the steady flow on the unsteady wave making. The terms including $\partial \phi_S / \partial x$

and $\partial\zeta_S/\partial x$ are all retained in our formulation because they are likely to be numerically of considerable magnitude, though they are the redundant terms of higher order of magnitude in the formalism of our perturbation scheme.

$\phi_0 = i\zeta_A g/(\omega - KU)\exp(Kz - iKx)$ (K : wave number) satisfies linear free surface conditions without the terms including ϕ_S and ζ_S :

$$U \frac{\partial \phi_0}{\partial x} = -i\omega \phi_0 - g\zeta_0 \quad \text{on } z = 0 \quad (13)$$

$$U \frac{\partial \zeta_0}{\partial x} = -i\omega \zeta_0 + \frac{\partial \phi_0}{\partial z} \quad \text{on } z = 0 \quad (14)$$

Nevertheless $\phi + \phi_0$ must satisfy the free surface condition retaining the nonuniform steady flow and wave elevation represented by ϕ_S and ζ_S . As a consequence the diffraction wave ϕ involves a part to correct the difference of the actual free surface condition from (13) and (14). This part might be called a diffraction of ϕ_0 by the nonuniform steady flow close to the ship. The last two terms of the right side of equation (11) and the last of equation (12) represent this effect. In other wave conditions than head seas some more terms appear to represent the effect.

The boundary value problem posed by equation (10), (11), (12) and the body boundary condition is solved starting from an appropriate condition at the bow to downstream. Equation (11) is used to forward the value of ϕ on $z = 0$ into x direction with the right hand side computed on the current x ; equation (12) updates the elevation ζ at new x value. The body boundary condition is imposed at the contour of a cross section at new x .

Condition imposed at $|y| = \infty$ is two dimensional flow due to a vertical dipole at the center of the cross section. This condition is derived by the behavior at $|y| = \infty$ with keeping x constant of a linear solution that satisfies the conditions (13) and (14) without the terms including ϕ_S and ζ_S . The linear solution is given in the form of impulsive source distribution on the cross sectional contour (Ohkusu and Faltinsen (1990)). The flow at $|y| = \infty$ and x constant due to an impulsive source is asymptotically the flow due to a vertical dipole (Stoker (1957)) and so is its distribution.

One implicit assumption of this approach is that the flow downstream does not affect that upstream. It is well recognized (Ogilvie (1977)) that the flow by this approach does not contain the transverse waves.

It does not, however, cause a trouble since our current concern is accurate prediction of divergent waves which are predominant in the vicinity of the bow; this method can account readily for the effect of the nonuniform steady flow which is also considerable close to the bow.

The steady flow ϕ_S and wave elevation ζ_S to be substituted in equation (11) and (12) are linear solutions of almost the identical boundary problem given by equation (10), (13), (14) and the body condition.

The initial condition for ϕ will be generally one weak point in this approach if we wish to account for the flow around the blunt bow. Presumably true nonlinear and three dimensional flow in the vicinity of the bow is required for it, because the three dimensionality and the nonlinearity are supposed to be the strongest there. Generally this flow is not available.

We tried two alternatives for the initial condition: one is the zero condition as for ϕ and ζ , and another is a three dimensional solution at $x = 0$ given by 3D panel method based on a linear free surface condition.

$$(i\omega + U \frac{\partial}{\partial x})^2 \phi + g \frac{\partial \phi}{\partial z} = 0 \quad \text{on } z = 0 \quad (15)$$

However the results are almost identical regardless of two alternatives.

On the fluid plane of each section we employ the method described by Faltinsen (1983) for numerically solving 2D flow; the Green's second identity was used to represent the velocity potential ϕ in the plane in terms of a distribution of fundamental 2D source and dipole over the closed surface consisting of the body surface, the free surface $z = 0$ and a control surface away from the body. Straight line segments were used to approximate all the control surface; constant value of the velocity potential and its normal derivatives were assumed over each segment. The contribution to the velocity potential from the control surface away from the body is zero because we assume no waves exist there. But the contribution from the free surface far away from the body is approximated by the flow due to a single vertical dipole at the center of the body section.

Data for numerical computation: For OHP form at the ballast condition, in which a large bulbous bow protrudes in front of the bow, the initial point of the calculation is its leading tip and the step Δx to forward the solution is 0.002 of the ship length L and the size of the free surface to the control surface is selected as large as 3.2 L . The free surface is divided into the segments of 0.007 L size at the least. We need not such fine mesh particularly for x of a Series 60 model which is less bluff at the bow. Actually

we found $\Delta x = 0.0033L$ gives sufficiently stable solutions.

Validity of our approach is tested by comparing the computed wave form with the measured as shown in Fig.3 and 4. Variation into y direction of ζ at $\omega t = 0$ and at $\omega t = \pi/2$ of the diffraction wave is plotted in Fig.8 to 15 at several positions down the ship length $x/L = 0.1, 0.2, 0.3$ and 0.4 . Fig.8 to Fig.11 for a Series 60 ($C_B = 0.8$) and in Fig.12 to 15 for OHS form. Both are at ballast condition. ζ_A is the amplitude of the incident waves.

Numerical results with uniform steady flow U with ignoring the terms of ϕ_S and ζ_S on the right side of equation (11) and (12) are compared. The results by 3D panel method based on the free surface condition (15) (Iwashita (1996) private communication) are plotted too. The present method is the best in terms of the correlation with the measured wave.

With closer look of the results we conclude:

(1) Our method considering the effect of nonuniform steady flow demonstrates better agreement closer to the bow.

(2) 3D panel method gives the better results than others when we come further down stream. This is natural because it account for the effect of the transverse wave correctly. However at the location very close to the hull surface 3D panel method does not always give good result. It might be due to the difficulty of numerical implementation of the method at the intersection of the free surface and the hull surface.

(3) The predicted wave elevation at $x/L = 0.1$ is much lower than the measured. The worse correlation at the place closer to the bow is of course due to our unappropriate initial condition ($\phi = \zeta = 0$). In order to obtain the better result at this location we need real three dimensional solution at $x = 0$ for the initial condition which is valid on nonuniform steady flow in front of the bow.

(4) $\partial\phi_S/\partial x$ affects the computational results considerably. It is due to its substantial magnitude at closer to the bow. Apparently inclusion of this term improves numerically the correlation with the measured. This is rather contradicting however because if the steady flow velocity in x direction is large enough to make $U + \partial\phi_S/\partial x$ small, then the diffraction wave propagates upstream and the present method assuming no effect from downstream to upstream is invalidated.

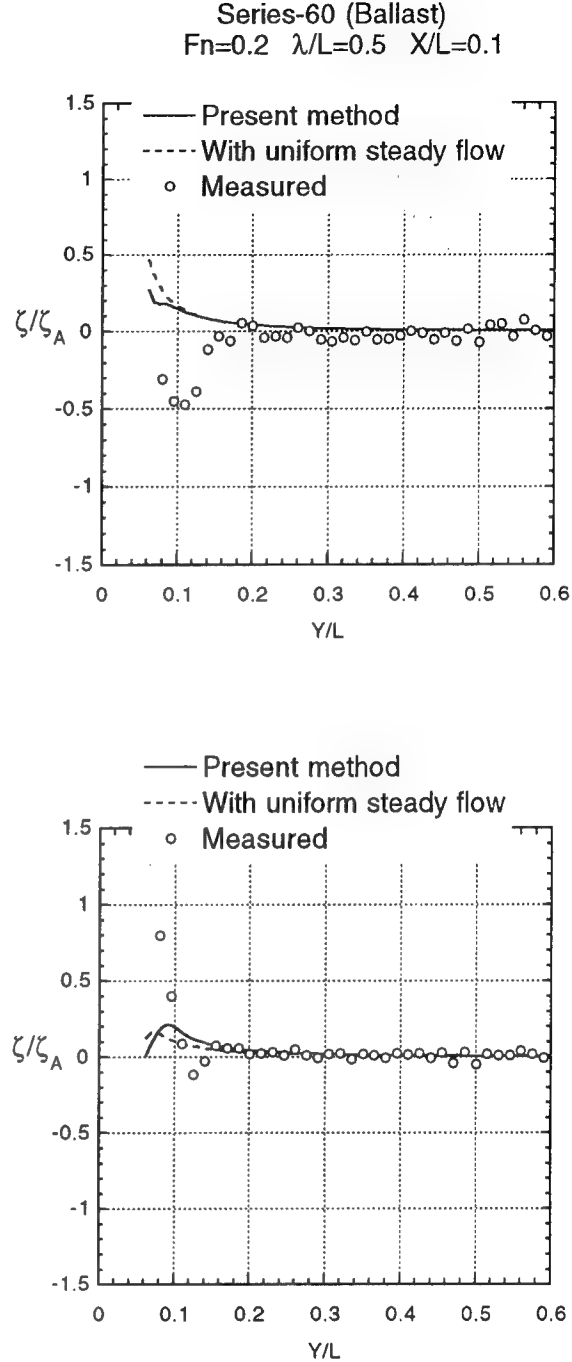


Figure 8: Wave Elevation at $\omega t = 0$ (upper) and $\omega t = \pi/2$ (lower)

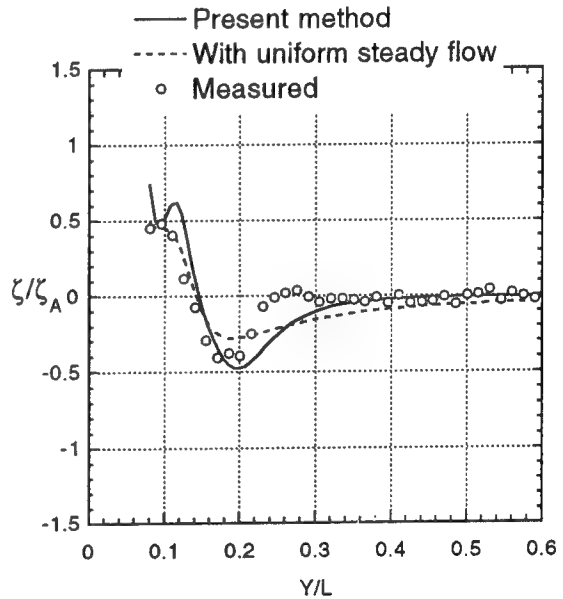
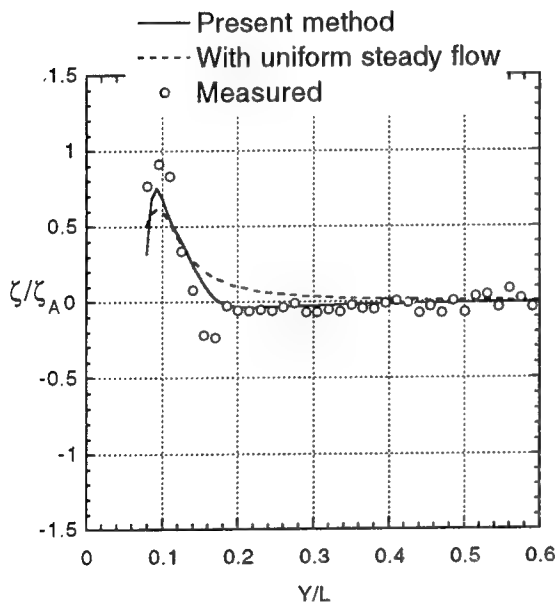
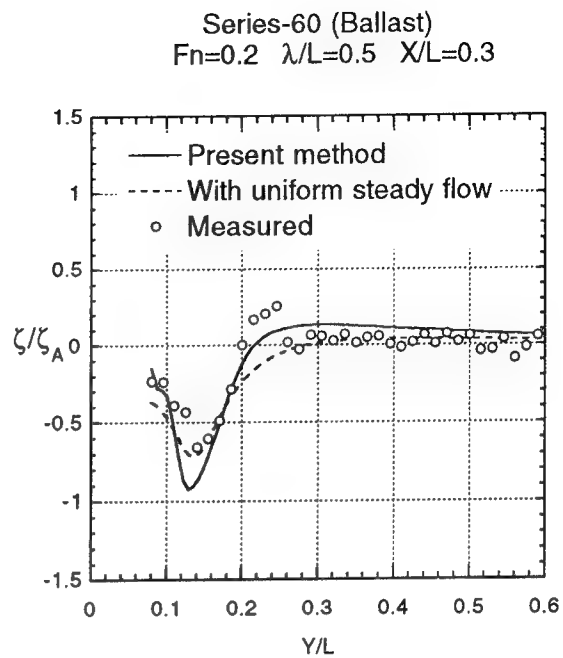
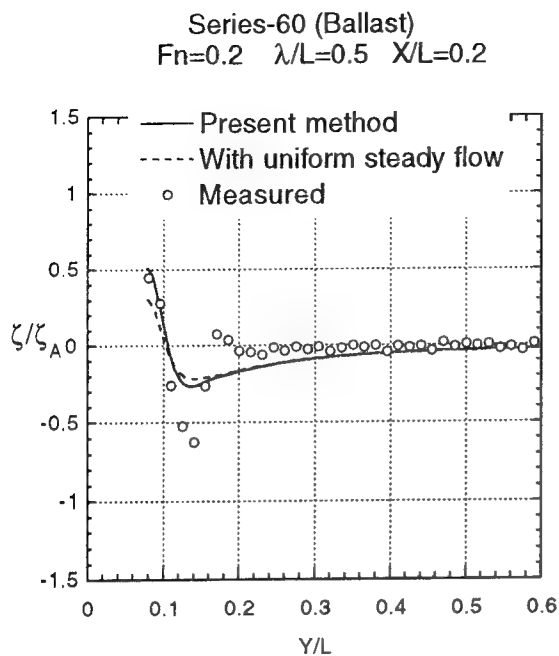


Figure 9: Wave Elevation at $\omega t = 0$ (*upper*) and $\omega t = \pi/2$ (*lower*)

Figure 10: Wave Elevation at $\omega t = 0$ (*upper*) and $\omega t = \pi/2$ (*lower*)

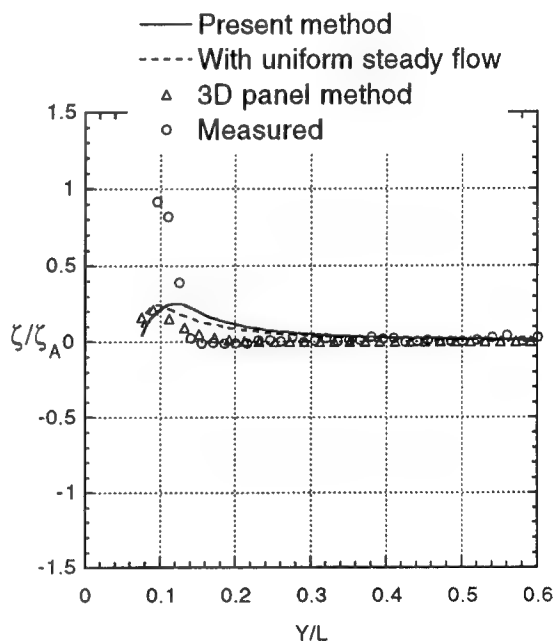
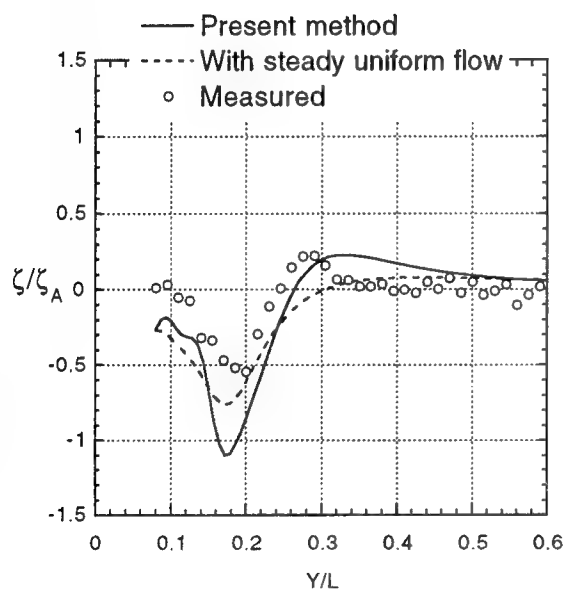
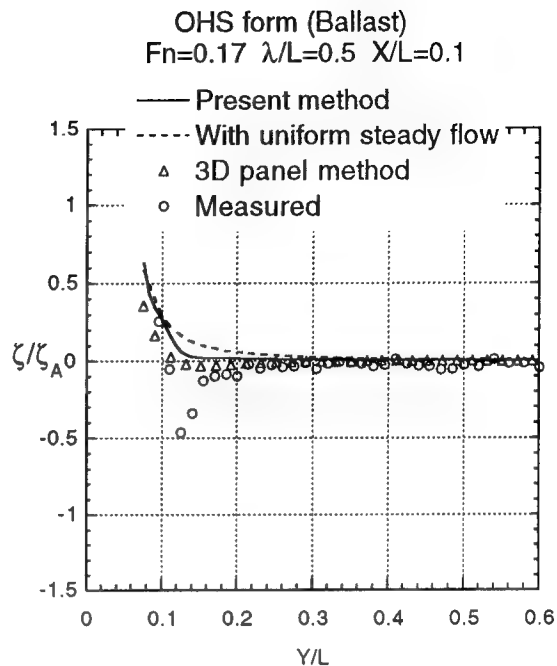
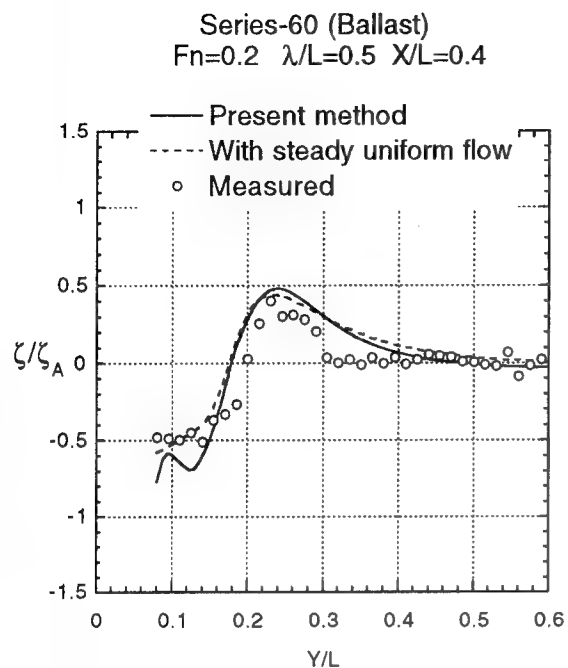


Figure 11: Wave Elevation at $\omega t = 0$ (*upper*) and $\omega t = \pi/2$ (*lower*)

Figure 12: Wave Elevation at $\omega t = 0$ (*upper*) and $\omega t = \pi/2$ (*lower*)

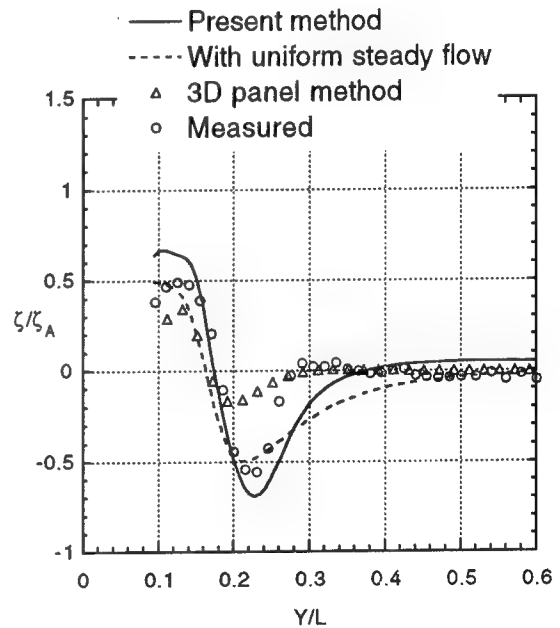
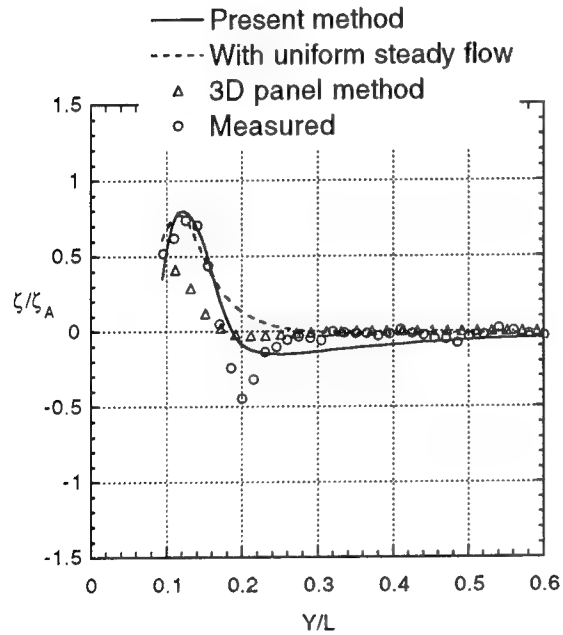
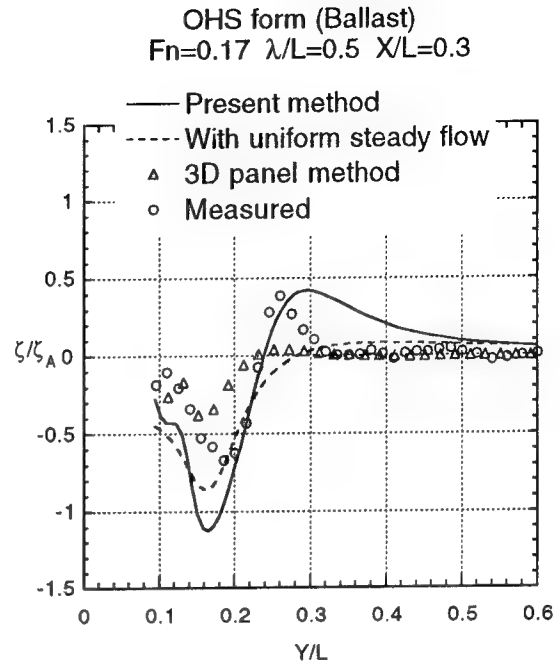
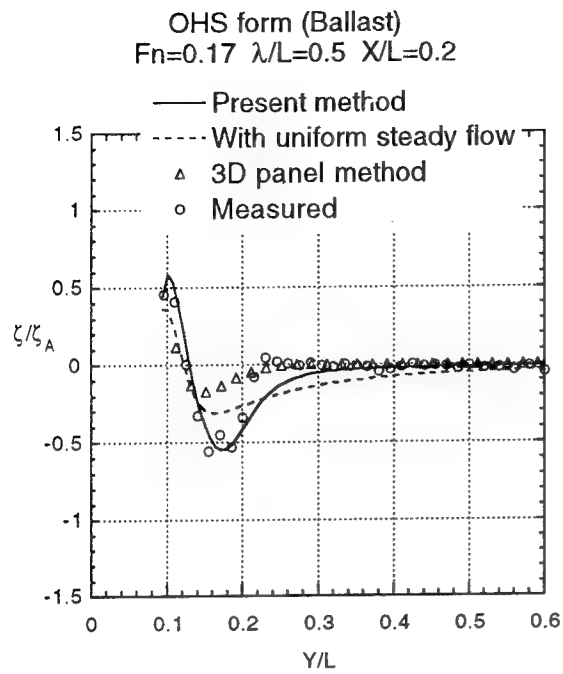


Figure 13: Wave Elevation at $\omega t = 0$ (upper) and $\omega t = \pi/2$ (lower)

Figure 14: Wave Elevation at $\omega t = 0$ (upper) and $\omega t = \pi/2$ (lower)

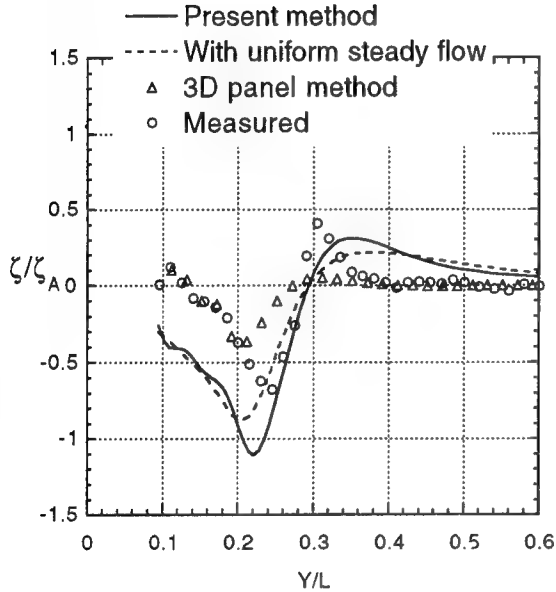
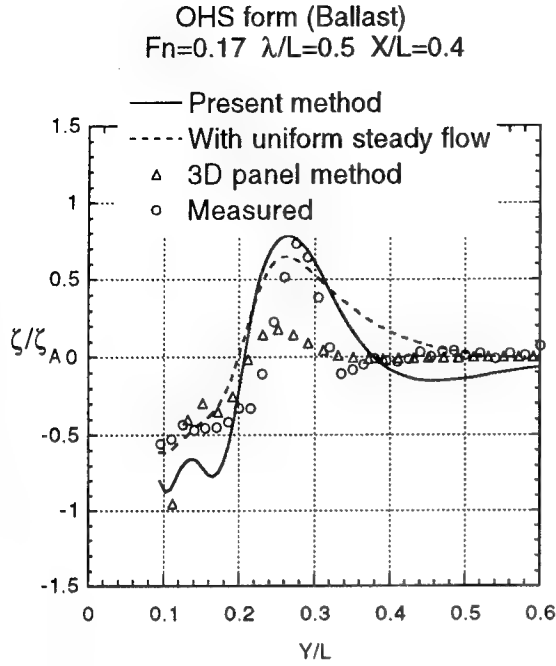


Figure 15: Wave Elevation at $\omega t = 0$ (upper) and $\omega t = \pi/2$ (lower)

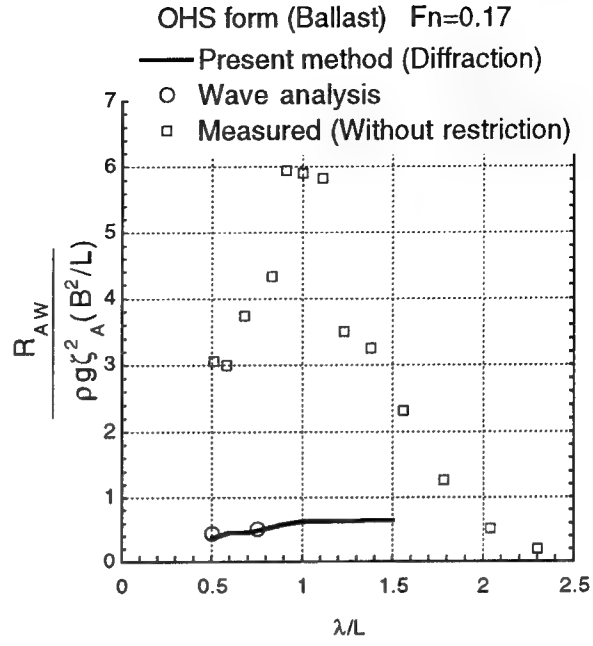


Figure 16: Added Resistance of OHS form

4 Added Resistance

One purpose of this study is an improvement of the accuracy of added resistance prediction. Very large added resistance of shallow draft and blunt bow ships at short wave length is reported (SR211(1993)).

In waves of small length the ship does not oscillate. Consequently one can ascribe the larger added resistance to the diffraction wave supposed to be larger for the blunt bow hull forms. If it is true, the present method which we confirmed is able to compute the diffraction waves more correctly than other approaches may possibly predict added resistance of those hull forms more correctly.

We integrate x component of fluid pressure given by the present theory on the hull surface correct to the second order $O(\phi^2)$ and take its time average to obtain added resistance ΔR due to the wave diffraction:

$$\Delta R = \frac{\rho}{4} \int_{S_0} |\nabla(\phi + \phi_0)|^2 n_x ds - \frac{\rho g}{4} \int_C |\zeta + \zeta_0|^2 n_x dl \quad (16)$$

The first integral is over the wetted surface of the ship S_0 below $z = 0$ and the second integral over the water line contour C . n_x is x component of the vector normal to the hull surface and directing into the fluid.

Other way to compute added resistance is to integrate $F_j(\theta)$ of the diffraction and radiation waves multiplied with a weighting function with respect to θ . Integration of the measured $F_j(\theta)$ will give added resistance directly derived from the measured wave energy. Added resistance, for example, in head seas is given by

$$\Delta R = \frac{\rho\pi g}{2} \left[\int_{-\frac{\pi}{2}}^{\frac{\pi}{2}} - \int_{\frac{\pi}{2}}^{\frac{3}{2}\pi} \right] |F_1(\theta)|^2 (\lambda_1(\theta) + K) \times \sqrt{1 - 4\tau \cos \theta} d\theta \\ + \frac{\rho\pi g}{2} \int_{-\pi}^{\pi} |F_2(\theta)|^2 (\lambda_2(\theta) + K) \sqrt{1 - 4\tau \cos \theta} d\theta \quad (17)$$

where K is the wave number of the incident waves. The range of $\alpha_0 < \theta < \alpha_0$ is to be excluded from the integration. In our numerical computation the integral on $F_1(\theta)$ was carried out only for $\alpha_0 < \theta < \pi/2$ and the contribution from other θ was ignored. Reason is that the measured $F_1(\theta)$ is generally very small and actually the contribution to the total added resistance is negligible. Moreover $F_1(\theta)$ is the amplitude of the wave component of so small length that any kind of experimental technique may not have enough resolution.

Added resistance plotted in Fig.16 by rectangles is the resistance measured as a force on the ship model (OHS form) in head waves and at ballast condition. Magnitude of added resistance of this hull form particularly in the range of small wave length is unusually large. It naturally includes the effect of heave and pitch in large wave length, say $\lambda/L > 0.75$. But in smaller wave length the ship does not move and the motions will have no effect on added resistance; at such wave length, for example at $\lambda/L = 0.5 \sim 0.6$, added resistance is supposed to be due to the diffraction wave alone.

Solid line represents added resistance due to the diffraction wave which was computed by substituting the velocity potential and wave elevation obtained by the present theory into equation (16). Two circles in this figure are the value obtained by equation (17) with the measured $F_j(\theta)$ of the diffraction wave.

Despite accurate prediction of the wave elevation and accurate correlation with the added resistance obtained from the measured wave elevation, the present theory cannot account for such a large added resistance value of OHS form at ballast condition. One thing which the present theory does not consider will be the wave generated in front of the bow. This weak-point was already guessed from the disagreement observed in the wave close to the bow part (Fig.8 and

12). Presumably the high wave in front of the bow will be steep and have higher harmonic component. Nevertheless we found its energy is not considerable.

5 Summary

We have presented an improved technique to measure the radiation and diffraction wave field generated by a ship running in waves at forward speed. Attempt was focussed on capturing complete energy of the waves without letting the energy of the second harmonics escape. We have succeeded in showing the whole picture of the radiation and diffraction wave based on the data obtained at tank test. It is usually invisible at tank test. With experiment by new technique we found the energy of the second harmonics of the diffraction wave is not considerable.

We proposed an analytical method, simple for numerical implementation but considering the interaction of the steady and unsteady flow prominent at the bow of the ship, to predict the elevation of radiation and diffraction wave and resulting fluid pressure. We tested the present analytical method on the comparison of the predicted wave elevation with the measured one by our new technique and confirmed its accuracy. However the present theory is not successful in predicting large added resistance of a shallow draft ship. More work on the wave formation in front of the bow will be required.

References

- Faltinsen, O. and Zhao, R.: "Numerical Predictions of Ship Motions at High Forward Speed", Trans. Royal Soc. London A. 1991
- Iwashita, H. and Ohkusu, M.: "The Green Function Method for Ship Motions at Forward Speed" *Ship Technology Research* 39(2) 1991
- Iwashita, H., Okada, T., Itoh, A., Ohkusu, M., Takaki, M. and Mizoguchi, S.: "Wave Forces Acting on a Blunt Ship with Forward Speed in Oblique Sea", *J. Society of Naval Architects Japan* vol.176 1994
- Naitoh, S., Nakamura, S. and Nishiguchi, A.: "Added Resistance in Regular Head Waves of a Ship with Blunt Bow", *Proc. 3rd Symp. on Practical Design of Ships and Mobil Units*, Trondheim, 1987
- Ohkusu, M.: "Added Resistance in Waves of Hull Forms With Blunt Bow" *Proc. of 15th Symp. on Naval Hydrodynamics* 1984
- Ohkusu, M. and Iwashita, H.: "Radiation and Diffraction Wave Pattern of Ships with Forward Speed", *Trans. West-Japan Society of Naval Architects* 73 1986

Ohkusu,M. and Faltinesen,O.:“Prediction of Radiation Forces on a Catamaran at High Froude Number”, *Proc. 18th Symp. on Naval Hydrodynamics* 1990

Ohkusu,M:“Hydrodynamics of Ships in Waves”, *Advances in Marine Hydrodynamics*, Computational Mechanics Publications 1996

Ogilvie,T.F.:“Singular Perturbation Problems in Ship Hydrodynamics”, *Advances in Applied Mechanics* 17 Academic Press 1977

Sclavounos,P.:“Computation of Wave Ship Interaction” *Advances in Marine Hydrodynamics*, Computational Mechanics Publication 1996

SR211:“Study on Improvement of Middle Size Bulk Carriers Performance”, *Report of Japan Ship Research Association* 1993

Stoker,J.J.: “ *Water Waves*”,Interscience Publishers 1957

DISCUSSION

C.M. Lee
Pohang Institute of Science and Technology, Korea

This paper presents one of the most fundamental aspects of the problems associated with the wave-excited ship motion. In the process of validating analytical methods, it is very important to check how accurately we are predicting the individual components of waves generated by a ship moving in waves. In this regard, this paper shows the proper direction in which we have to focus our investigations.

I would like to suggest that we should validate our panel codes by comparing with the results presented in this paper for each component of waves generated by a ship, i.e., the waves generated by the forward translation, diffracted waves, and radiated waves. We may then be able to find out where the deficiencies are with our panel codes.

AUTHOR'S REPLY

NONE RECEIVED

Nonlinear Ship Motions and Wave-Induced Loads by a Rankine Method

D. Kring, Y.-F. Huang, P. Sclavounos

(Massachusetts Institute of Technology, USA),

T. Vada, A. Braathen (Det Norske Veritas, Norway)

Abstract

This paper presents the computation, by a three-dimensional Rankine Panel Method, of nonlinear ship motions and structural loads induced by steep ambient waves. Founded upon a thoroughly validated model of the linear seakeeping problem for realistic ship hulls, the nonlinear extension presented in this study accounts for various nonlinear effects in the seakeeping problem. These include the variable wetness of the ship hull, the nonlinear hydrostatic effects and Froude Krylov exciting forces, and the treatment of the radiation and diffraction wave disturbances according to the "weak scatterer" hypothesis. Computations are presented of the vertical motions and structural loads for a Series 60 and the Snowdrift hull, and an assessment is carried out of the importance of nonlinear effects in the motion and load predictions.

1 Introduction

The simulation of steady and unsteady ship flows, wave induced motions, and structural loads by three-dimensional Rankine Panel Methods (RPM's) has enjoyed rapid growth and considerable success over the past ten years. Such CFD (Computational Fluid Dynamics) methods have evolved into valuable and trusted analysis and design tools which are today used routinely for the design and optimization of hull forms and the assessment of their safety in se-

vere sea states.

Since the mid-80's an RPM method known as SWAN (ShipWaveANalysis) has been under development at MIT. During the early stages of this research program the fundamental numerical properties of the method were studied and an algorithm was derived capable of accurately treating ship flows over a broad range of Froude numbers and wave frequencies. Early versions of SWAN treated the linear steady and seakeeping problems in the frequency domain [7],[12]. More recently the method was extended to solve the same problems in the time domain [6],[8], paving the way towards the treatment of the nonlinear seakeeping problem which is the focus of the present paper. The performance of the linear versions of SWAN for naval, commercial, twin-hull ships, and America's Cup sailing yachts is surveyed in [13].

The structural design of a ship requires the evaluation of its motions and wave induced pressure distributions over the hull in severe sea states. In order to estimate the importance of extreme events, a nonlinear seakeeping solution must simulate, with sufficient accuracy and efficiency, the seakeeping behavior of a ship in steep random wave trains that may be several hours long in duration. With this goal in mind, the development of the nonlinear extension of SWAN was initiated.

In order of importance, nonlinearities affecting the ship seakeeping problem are: a) the steepness of the ambient wave train; b) the nonlinear hydrostatic and Froude Krylov forces re-

sulting from the interaction of a steep wave train with the ship hull; c) roll damping mechanisms arising from viscous separation, viscous lift forces from appendages and transom sterns; d) slamming and e) nonlinearities in the radiated and diffracted wave disturbance. The simultaneous treatment of all these nonlinear effects, even by a potential flow computational method, leads to a prohibitively expensive seakeeping simulation of little use in ship design. The strategy was therefore adopted to treat the nonlinearities outlined above progressively and to assess their importance before proceeding towards a more complete treatment.

This paper treats the seakeeping problem in head waves, therefore only the surge, heave and pitch motions and wave loads are considered. The ambient wave train is modeled independently of the seakeeping problem using the techniques of perturbation theory to first, second, and, if necessary, higher orders, along the lines of [11] and [14]. This approach allows the efficient generation of long wave records designed to correspond to a given sea spectrum, independently of the computation of the wave ship interaction which represents the bulk of the seakeeping simulation.

The nonlinear hydrostatic and Froude Krylov effects are treated by introducing a time dependent panel mesh over the ship wetted surface defined by the intersection of the ambient wave profile with the ship hull. Upon integration of the hydrostatic and ambient wave hydrodynamic pressure over the ship hull, the nonlinear hydrostatic and Froude Krylov exciting forces are obtained. Efficient meshing algorithms have been developed which allow the discretization of realistic hull shapes with cruiser or transom sterns in ambient wave trains of high steepness.

The ship wave disturbance arising from its forward translation, the surge, heave, and pitch oscillatory motions, and the interaction with the ambient wave, are initially treated by linear theory. Heave and pitch motion simulations are carried out by combining the non-

linear treatment of the hydrostatic and Froude-Krylov effects and the linear solution of the surface wave disturbance. Comparisons with experimental measurements reveal that a significant portion of the nonlinearity is accounted for by these effects.

The nonlinear coupling of the ambient- and ship-wave disturbances is next treated according to the "weak scatterer" hypothesis. It is postulated that the ship wave disturbance is small compared to the ambient waves and therefore can be linearized about the ambient wave profile, an assumption justified by observations of seakeeping experiments in steep waves. Evidently the weak scatterer hypothesis is violated in the vicinity of the ship waterline where strong spray roots are often seen to form, caused by the ship forward motion or slamming. These effects and slamming in particular, are however not treated in the present study.

Boundary value problems have been derived for the ship wave disturbance and stated around the time-varying (but a priori known) ambient wave profile. The body boundary condition is stated exactly over the instantaneous position of ship hull, therefore the need to introduce the so-called m -terms of linear seakeeping theory is avoided. Assuming potential flow, integral equations are derived for the unknown velocity potential over the ship hull and the ambient wave profile, using the Rankine source as the Green function. The set-up and solution of the integral equation is carried out along lines similar to those in the linear time-domain problem discussed in [8]. The radiation condition is satisfied as in the linear problem via an absorbing beach located at some distance from the ship, and designed to dissipate the energy carried by the ship wave disturbance. An outline of the solution algorithm and a brief review of the linear problem are given in Section 2.1. The weak scatterer hypothesis and corresponding boundary value problem is presented in Section 2.3.

An important component of a nonlinear seakeeping simulation is the enforcement of the exact body boundary condition. In Section 2.3

computations are presented of the heave and pitch hydrodynamic coefficients by the body-nonlinear algorithm and comparisons are carried out of the same quantities computed by the linear method which makes use of the so-called m-terms. The agreement between these two methods is found to be very satisfactory for a Series 60 hull over a broad range of forced oscillation amplitudes, confirming the need for the presence of the m-terms in the linear problem and their absence when the exact body boundary condition is satisfied.

Heave and pitch motion simulations are presented in Section 2 in head regular waves of variable steepness of the Series 60 and the Snow-drift hull. Experimental measurements are compared to heave and pitch motion simulations obtained from; a) linear theory and b) nonlinear hydrostatic and Froude Krylov effects coupled with a linear computation of the ship wave disturbance. Consistent with the stated objectives of this study, the purpose of these comparisons is to assess the nature and importance of nonlinear effects in the prediction of the heave and pitch motions in head waves.

Computations of the vertical bending moment and shear force distributions along the ship length are presented in Section 3.1, along lines similar to the ship motion simulations presented in Section 2. Since wave induced structural loads are obtained by integration of the hydrodynamic pressure over a portion of the ship hull, end effects, and, therefore, nonlinearities play a more important role than in the prediction of the ship motions. This is also born out of experience with the measurement and computation of the midships peak hogging and sagging moments in steep waves which are often found to differ by as much as a factor of two, when linear theory predicts that they must be equal in a regular wave. The prediction of the structural loads by the linearized seakeeping method and its nonlinear extensions are compared to a nonlinear strip theory method and experiments in Section 3.1.

The paper concludes with a discussion

on how a nonlinear, time-domain, ship motion and structural load simulation might be used to determine the extreme value statistics needed in ship structural design. In order to detect a sufficient number of extreme events, a seakeeping simulation several hours long is necessary, a quite challenging task with a nonlinear seakeeping method. These issues are discussed in Section 3.2 where possible ways of coupling a linear with a nonlinear simulation method for the study of the extreme statistics are addressed.

2 Nonlinear Ship Motions

Consider a ship advancing with constant forward speed and a Cartesian coordinate system, \vec{x} , fixed to the mean, translating position of the ship with the origin on the calm free surface, x-axis pointing upstream and z-axis pointing upwards. A second Cartesian system, \vec{x}_s , fixed to the body is also introduced. The two coordinate systems coincide when the ship is in its equilibrium position and are related by translation and nonlinear rotation,

$$\vec{x}(t) = \vec{\xi}_T(t) + \mathbf{T}(t)\vec{x}_s, \quad (1)$$

where $\vec{\xi}_T$, are the translations (ξ_1, ξ_2, ξ_3) in surge, sway, and heave, and the matrix \mathbf{T} is a function of the Eulerian rotation angles (ξ_6, ξ_5, ξ_4) for yaw, pitch, and roll. The order of the Eulerian angles have been deliberately chosen in descending order.

Newton's Law expressed relative to the body-fixed frame lead to the following equation of motion for the six rigid body modes of motion, $\vec{\xi}(t)$,

$$\mathbf{M}\ddot{\vec{\xi}} = \vec{F}_D(\ddot{\vec{\xi}}, \dot{\vec{\xi}}, \vec{\xi}, t) + \vec{F}_S(\vec{\xi}), \quad (2)$$

where \vec{F}_D are the hydrodynamic forces, \vec{F}_S are the hydrostatic forces, and \mathbf{M} is the inertia matrix. It is important to note that, in this form, only the linear inertia terms are retained. Even

in realistic waves of large steepness, the effect of the nonlinear inertia terms is expected to be small when compared to the nonlinear hydrostatic, Froude-Krylov and hydrodynamic forces. These inertia terms will not be included in the present study.

In order to obtain the hydrodynamic wave forces, \vec{F}_D , for the freely floating body, a potential flow boundary-value problem is solved. In general, viscous forces do not contribute appreciably to ship motions and loads, especially in head seas. A possible exception occurs in the presence of a transom stern of large draft where unsteady flow separation may contribute appreciably to the heave and pitch damping. Also, viscous and lifting effects are known to be important for roll, sway, and yaw motion, therefore the present framework will be extended to incorporate these in the future.

The flow is assumed to be governed by a total velocity potential, $\Psi(\vec{x}, t)$, which satisfies the Laplace equation in the fluid domain and is subject to the kinematic and dynamic free surface conditions,

$$\left(\frac{d}{dt} + \nabla \Psi \cdot \nabla\right)[z - \zeta] = 0, \quad (3)$$

$$\frac{d\Psi}{dt} = -g\zeta - \frac{1}{2}\nabla \Psi \cdot \nabla \Psi, \quad (4)$$

imposed at the instantaneous position of the free surface, $\zeta(x, y, t)$.

On the wetted surface of the ship hull, a no-flux body boundary conditions states,

$$\frac{\partial \Psi}{\partial n} = \vec{V}_B \cdot \hat{n}, \quad (5)$$

where $\vec{V}_B \cdot \hat{n}$ is the component of the ship instantaneous velocity normal to the wetted surface of the hull. To close the exact problem, initial conditions are posed for $\frac{d}{dt}\Psi(\vec{x}, t)$, $\Psi(\vec{x}, t)$, and the body displacement and velocity. Also, the gradients of the disturbance potential must decay infinitely far from the ship for finite time.

2.1 Linear Foundation

The study of a linearized model for seakeeping simulation allows a better understanding of any proposed nonlinear model. A nonlinear method will only be successful if the underlying linear theory is well understood.

This paper presents two nonlinear extensions to the linear formulation and numerical implementation summarized in this section. Both the nonlinear restoring and Froude-Krylov effects and the Weak Scatterer hypothesis are direct extensions of this linear foundation.

2.1.1 Linear formulation

Assuming that the total velocity potential, Ψ , consists of a dominant double-body component, Φ , and a perturbation correction, φ , the linear form of the kinematic and dynamic free surface conditions reduce to the form,

$$\frac{\partial \zeta}{\partial t} - (\vec{W} - \nabla \Phi) \cdot \nabla \zeta = \frac{\partial^2 \Phi}{\partial z^2} \zeta + \frac{\partial \varphi}{\partial z} \quad (6)$$

$$\begin{aligned} \frac{\partial \varphi}{\partial t} - (\vec{W} - \nabla \Phi) \cdot \nabla \varphi = & -g\zeta \\ & + [\vec{W} \cdot \nabla \Phi - \frac{1}{2}\nabla \Phi \cdot \nabla \Phi] \end{aligned} \quad (7)$$

applied on $z = 0$, where \vec{W} is the mean translational velocity of the ship. A further decomposition of the perturbation potential into instantaneous and memory components is used to obtain a stable form for the integration of the equations of motions, as discussed in [6].

For an ambient wave steepness and ship motions that are sufficiently small, linear theory allows the decomposition of the incident, radiated and diffracted wave disturbances. The linear radiation body boundary conditions become,

$$\frac{\partial \varphi}{\partial n} = \sum_{j=1}^6 \left(\frac{d\xi_j}{dt} + \xi_j m_j \right) \quad (8)$$

applied on the mean wetted surface of the hull. Here, the m -terms, m_j , provide a coupling between the steady basis flow and unsteady ship motion. They have been shown in [7] to contribute appreciably to the hydrodynamic coefficients and therefore must be included in a linear formulation. The diffraction body boundary condition merely states that the normal velocity of the sum of the incident and diffraction velocity potentials vanishes over the hull mean position.

The Laplace equation is enforced in the fluid domain by a distribution of Rankine sources and dipoles over the free surface and wetted hull surface. Application of Green's second identity leads to a boundary integral formulation for the perturbation potential,

$$2\pi\varphi(\vec{x}) - \iint_{S_F \cup S_B} \frac{\partial\varphi(\vec{x}')}{\partial n} G(\vec{x}'; \vec{x}) dx' + \iint_{S_F \cup S_B} \varphi(\vec{x}') \frac{\partial G(\vec{x}'; \vec{x})}{\partial n} dx' = 0 \quad (9)$$

where $G(\vec{x}'; \vec{x}) = 1/|\vec{x} - \vec{x}'|$ is the Rankine source potential, S_F is the mean position of the free surface, and S_B is the mean position of the hull.

2.1.2 Numerical implementation

A full discussion of the linear formulation, numerical method, and applications can be found in [7], [10], and [12], for frequency domain solutions [5], [6], and [8], for time domain motion solutions, so the basic numerical algorithm for the linear problem is only summarized in this section. The algorithm for the nonlinear problem is a direct extension of this implementation.

The three unknowns in the formulation are the velocity potential, φ , the wave elevation, ζ , and the normal velocity, φ_n . To solve for these unknowns, the free surface conditions (6) and (7), which form a pair of evolution equations, and the integral equation (9) are satisfied numerically by a time-domain Rankine panel method.

The Rankine panel method discretizes the hull surface and a finite portion of the free surface lying near the ship. Each of the unknowns is approximated independently by a set of biquadratic spline functions that provide continuity of value and first derivative across panels.

The evolution equations employ an explicit Euler integration to satisfy the kinematic free surface condition and an implicit Euler integration to satisfy the dynamic free surface condition. This scheme is based on the numerical stability analysis for time-domain panel methods found in [16]. Higher order schemes are also considered.

This stability analysis quantifies the numerical solution in terms of ship speed, panel size and aspect ratio, and time-step size, allowing for an optimal choice for the parameters of the numerical algorithm. An important result of this analysis is the discrete dispersion relation. This relation demonstrates that, for wavelengths less than four panels long, the discrete group velocity contains significant errors. A low-pass, spatial filtering scheme removes these erroneous short waves without affecting the consistency and convergence of the method. The filter does have some effect on the local, non-radiating free surface disturbance, but this problem is minimized since the filter is not applied at every time-step. The local disturbance can recover its proper equilibrium position between consecutive applications of the filter.

A numerical, wave-absorbing beach has been designed to satisfy the radiation condition, since only a finite portion of the free surface is covered by the panel method. This beach, based on the studies of [1] and [2], is applied on an outer zone of free surface panels and has an effect that is similar to a Rayleigh viscosity in the equivalent frequency domain formulation. The particulars of this beach are discussed in [8]. A key feature of the beach is that it can treat the case of zero speed and the $\tau = \frac{1}{4}$ critical frequency problem.

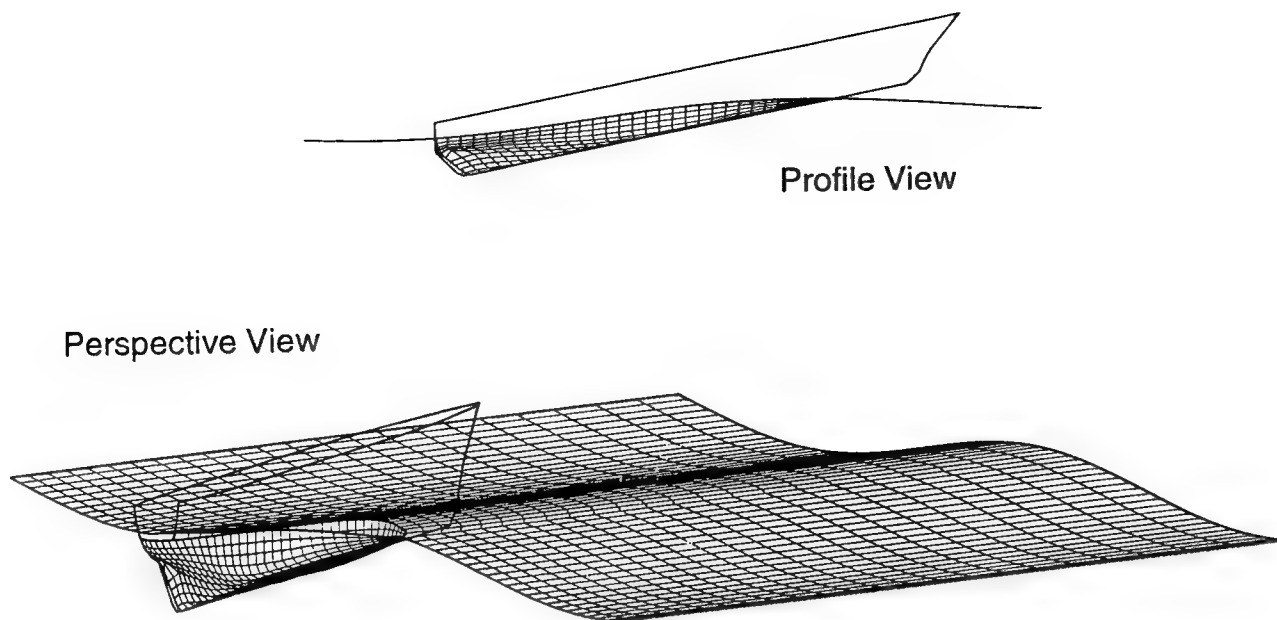


Figure 1: Snapshot of computational mesh for the Snowdrift hull at Froude number 0.325 in head seas.

The Rankine panel method produces a solution for the wave flow, but the equation of motion (2) for the ship must also be integrated at each time step in this simulation. This integration is delicate due to the presence of wave memory effects, but the numerical stability analysis of [6] provides an appropriate numerical integration scheme and time-step size.

2.2 Nonlinear Restoring and Froude-Krylov Forces

This first extension to the linear solution adds nonlinear restoring and Froude-Krylov forces to the equation of ship motion. These forces are considered to have a significant nonlinear contribution for ships with overhanging sterns or bows, or large degrees of flare.

This extension retains the linear results for radiation and diffraction forces, but replaces the linear restoring and Froude-Krylov forces. The hydrostatic and Froude-Krylov in-

cident wave pressures are integrated on the exact, wetted hull surface, to produce the nonlinear forces. At each time step, the intersection of the *a priori* known ambient wave profile and the ship hull defines this exact wetted surface. Figure 1 shows a snapshot of such a time-varying wetted surface for the Snowdrift hull.

In this study, motions and loads have been investigated for two ships, the Snowdrift and the Series 60, $C_b=0.7$. The Series 60 is a ship that is very nearly wall-sided at the design waterline so the motions are predicted well by linear theory. The Snowdrift, which was examined in its ballast condition, manifests important nonlinear effects in its motions because of an overhanging stern that is neglected by linear theory. Linear, nonlinear restoring and Froude-Krylov, and Weak Scatterer motion simulations will be compared with experiments for these two hulls in section 2.4.

2.3 Weak Scatterer Hypothesis

After establishing the validity and limitations of the time-domain Ranking Panel Method in the linear seakeeping problems and investigating the importance of the nonlinear hydrostatic and Froude-Krylov forces, a more exact formulation has been examined. In this study, the so-called weak scatterer hypothesis [9] is adopted. The Weak Scatterer approach relaxes two of the restrictions of linear theory. The incident wave and body motions are allowed to be large, but the ship wave disturbance due to its forward translation and its interaction with the ambient wave is considered to be small.

This relaxation is physically justifiable. The incident wave driven by the environmental conditions cannot be reasonably restricted in magnitude, but observation often shows ship-generated waves to be relatively small. This stems from the fact that most ships are designed to be slender and, hence, do not produce steep wave disturbances even for large wave motion. Those large disturbances that do exist, spray for instance, do not contribute significantly to global forces. Under this observation, the ship-generated disturbance can be formally linearized about a steep incident wave using an Eulerian formulation.

The advantage of this approach is that it offers a more exact solution, but one that is still simplified enough to retain computational efficiency and numerical control. The solution of the fully nonlinear potential solution could be undertaken by a Mixed Eulerian-Lagrangian (MEL) scheme, for instance, but this might be prohibitively expensive.

Under the weak scatterer assumptions, we introduce the total disturbance potential, Ψ , and the decomposition:

$$\Psi = \Phi + \phi + \varphi_0 + \varphi, \quad (10)$$

where Φ is a time-dependent basis flow, satisfying a no-flux condition on the instantaneous incident wave surface and wetted hull. The im-

pulsive flow, ϕ , governs the instantaneous impulse response of the ship to the surrounding fluid flows. Its introduction is motivated by the stability constraints [6] determined from the linear problem. φ_0 is the incident wave potential and φ is the disturbance potential excluding the impulsive part ϕ . The total wave elevation η is decomposed into the incident wave elevation ζ_0 and the disturbance wave elevation ζ .

The weak scatterer hypothesis assumes that the disturbance quantities φ and ζ are small, so only the first order terms are retained upon linearization about the ambient wave profile. Under this decomposition, the kinematic and dynamic conditions become,

$$\begin{aligned} & \left[\frac{\partial}{\partial t} - (\vec{W} - \nabla\Phi - \nabla\phi - \nabla\varphi_0) \cdot \nabla \right] \zeta = \\ & - \left[\frac{\partial}{\partial t} - (\vec{W} - \nabla\Phi - \nabla\phi - \nabla\varphi_0) \cdot \nabla \right] \zeta_0 \\ & + \frac{\partial\Phi}{\partial z} + \frac{\partial\phi}{\partial z} + \frac{\partial\varphi_0}{\partial z} + \frac{\partial\varphi}{\partial z} - \nabla\varphi \cdot \nabla\zeta_0 \\ & + \left[\frac{\partial^2\Phi}{\partial z^2} + \frac{\partial^2\phi}{\partial z^2} + \frac{\partial^2\varphi_0}{\partial z^2} \right. \\ & \quad \left. - \nabla \left(\frac{\partial\Phi}{\partial z} + \frac{\partial\phi}{\partial z} + \frac{\partial\varphi_0}{\partial z} \right) \cdot \nabla\zeta_0 \right] \zeta \\ & \text{on } z = \zeta_0(x, y, t), \end{aligned} \quad (11)$$

$$\begin{aligned} & \left[\frac{\partial}{\partial t} - (\vec{W} - \nabla\Phi - \nabla\phi - \nabla\varphi_0) \cdot \nabla \right] \varphi = \\ & - \left[\frac{\partial}{\partial t} - (\vec{W} - \nabla\Phi - \nabla\phi - \nabla\varphi_0) \cdot \nabla \right] \varphi_0 \\ & + \frac{1}{2} \nabla\varphi_0 \cdot \nabla\varphi_0 - g\zeta_0 \\ & - \left[\frac{\partial}{\partial t} - (\vec{W} - \nabla\Phi) \cdot \nabla \right] \Phi + \frac{1}{2} \nabla\Phi \cdot \nabla\Phi \\ & - \left[\frac{\partial}{\partial t} - (\vec{W} - \nabla\Phi - \nabla\phi) \cdot \nabla \right] \phi \\ & + \frac{1}{2} \nabla\phi \cdot \nabla\phi - g\zeta \\ & - \left[\frac{\partial}{\partial t} - (\vec{W} - \nabla\Phi - \nabla\phi - \nabla\varphi_0) \cdot \nabla \right] \frac{\partial\Phi}{\partial z} \zeta \\ & - \left[\frac{\partial}{\partial t} - (\vec{W} - \nabla\Phi - \nabla\phi - \nabla\varphi_0) \cdot \nabla \right] \frac{\partial\phi}{\partial z} \zeta \end{aligned}$$

$$-\left[\frac{\partial}{\partial t} - (\vec{W} - \nabla\Phi - \nabla\phi - \nabla\varphi_0) \cdot \nabla\right] \frac{\partial\varphi_0}{\partial z} \zeta$$

on $z = \zeta_0(x, y, t)$. (12)

A no-flux, body boundary condition is applied over the instantaneous nonlinear position of the ship wetted surface. The need to evaluate the so-called *m*-terms of linear theory is circumvented. To validate the consistency of the linearized and nonlinear enforcement of the body boundary conditions, the heave and pitch hydrodynamic coefficients were computed for the Series 60 $C_b=0.7$ hull using the linear and nonlinear methods. In the limit of small oscillation amplitudes the two methods are expected to agree, confirming the proper evaluation of the *m*-terms in the linear problem and of the correct enforcement of the exact body boundary condition in its nonlinear counterpart.

Figure 2 show the comparison among the linear, nonlinear, and experimental coefficients. For this relatively wall-sided ship and for sufficiently small oscillation amplitudes all results were expected to be in good agreement. The correlation is indeed very satisfactory, demonstrating that the *m*-terms resulting from the linearization of the body boundary conditions are accounted for by the present body nonlinear approach.

In the presence of a specified ambient wave profile, the boundary value problem obtained from the weak scatterer hypothesis is solved by discretizing the instantaneous position of the ship wetted surface and ambient free surface. The panel arrangement is illustrated in in Figure 1 which shows a typical snapshot of the computational mesh for the Snowdrift hull in free motion. As in the linear solution, a dissipative beach is included on an outer layer of panels in order to absorb the outgoing ship wave disturbance as in the linear problem.

Computations of the heave and pitch motions of the Series 60 hull predicted by the linear solution and the weak scatterer hypothesis are presented and discussed in Section 2.4.

An important step in the weak scatterer formulation, involves the evaluation of the Eulerian time derivative of the velocity potential which enters in the free surface condition and the evaluation of the hydrodynamic pressure over the ship hull. The direct approach of extracting the Eulerian time derivative from the Lagrangian derivative of the velocity potential, has been found to introduce numerical instability and to therefore lead to an excessive restriction of the time-step size.

Therefore, a more robust method has been devised. A boundary value problem may be posed for the Eulerian time derivative, $\partial\Psi/\partial t$, which is a harmonic function. Therefore, Green's theorem is directly applicable, as for the velocity potential, leading to the statement

$$2\pi\Psi_t + \iint_{S_F \cup S_B} \Psi_t(\vec{\xi}, t) \frac{\partial G(\vec{x}, \vec{\xi})}{\partial n_\xi} dS_\xi = \iint_{S_F \cup S_B} \frac{\partial \Psi_t(\vec{\xi}, t)}{\partial n_\xi} G(\vec{x}, \vec{\xi}) dS_\xi, \quad (13)$$

where the subscript *t* denotes the partial time derivative. A similar equation may be posed for the Eulerian derivative of the basis flow potential Φ . The numerical properties of this algorithm of evaluating the Eulerian time derivatives of the unknown potentials appear to be very promising and are under study. A similar treatment of the time derivative has been proposed by [17].

2.4 Linear and Nonlinear Motions

This section compares linear, nonlinear restoring and Froude-Krylov, and Weak Scattering motion simulations to experiments for two ships, the Series 60, $C_b=0.7$, and the Snowdrift.

Experiments for the Series 60 [3] are compared in Figure 3 with the results from the linear and Weak Scatterer nonlinear simulations. The nonlinear simulations were conducted in regular head seas of varying wave-

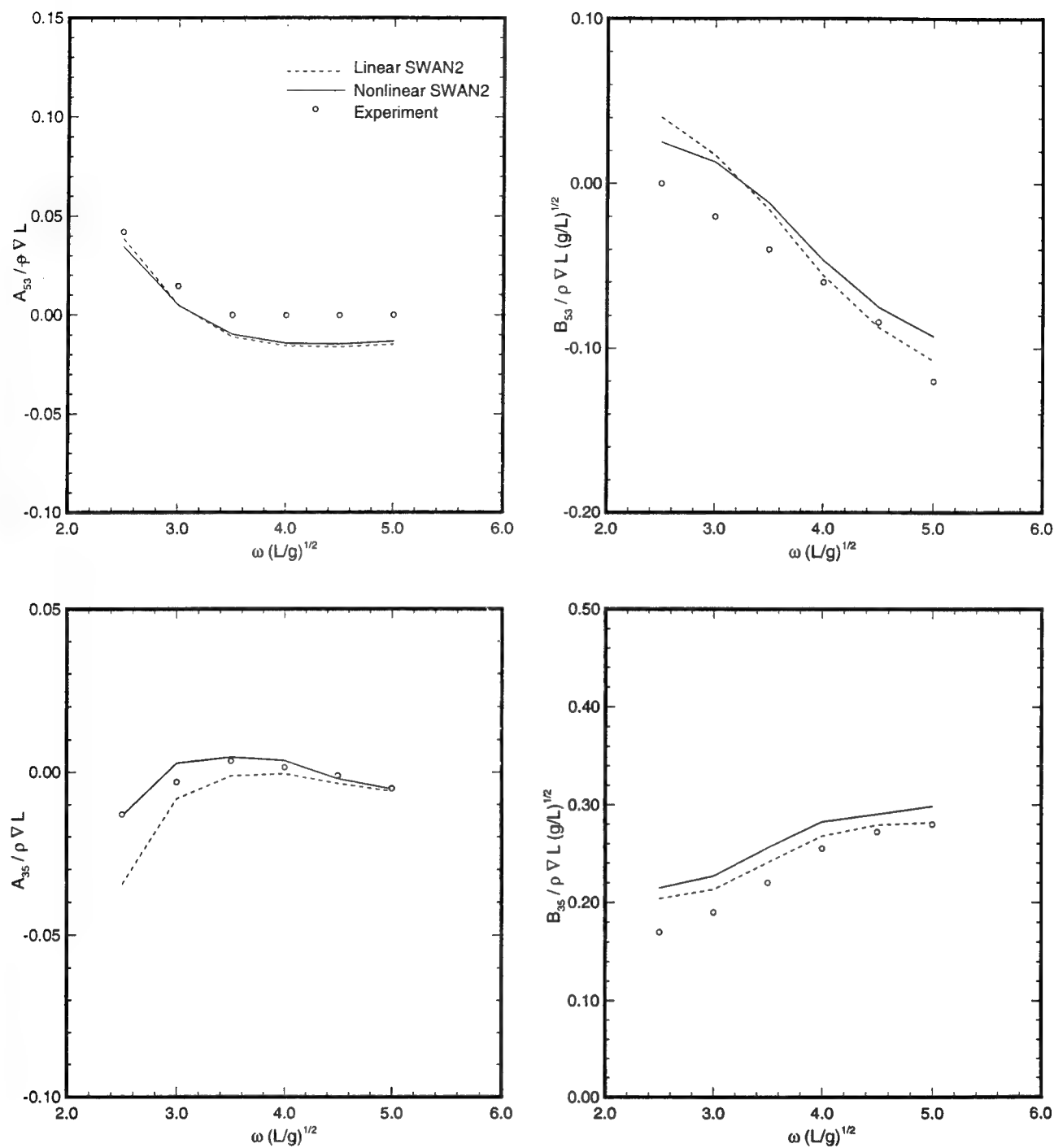


Figure 2: Cross-coupling added mass and damping coefficients for the Series 60 at Froude number 0.2.

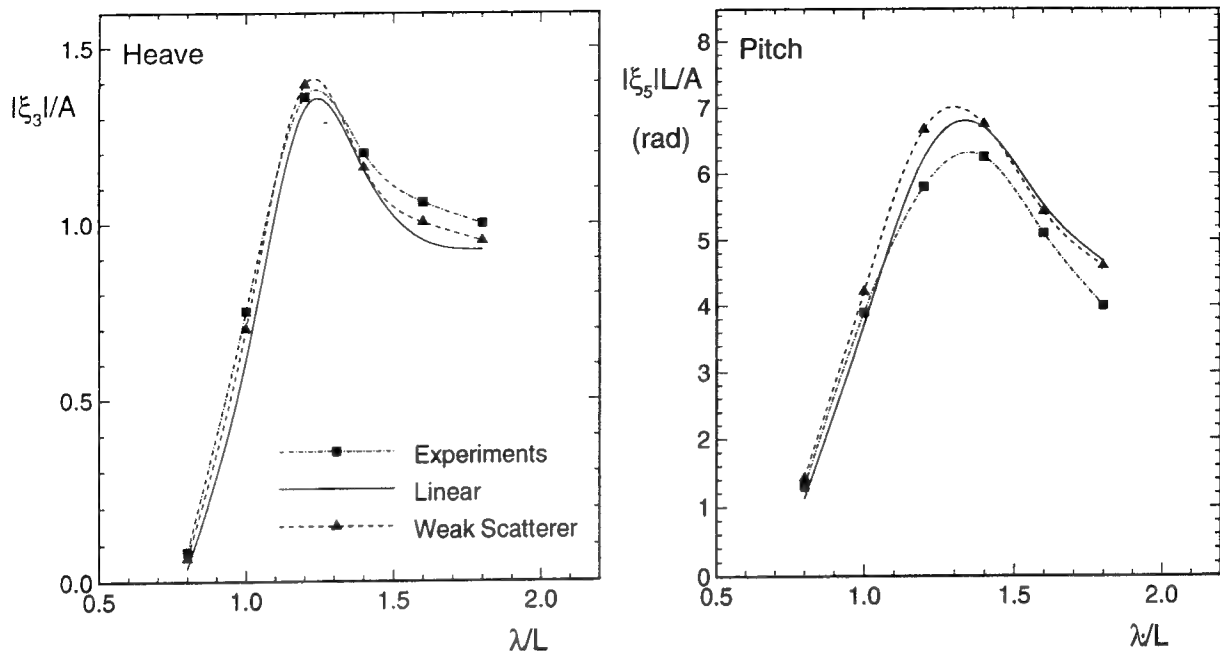


Figure 3: Heave and pitch motions for Series 60 at Froude number 0.2 in head seas.

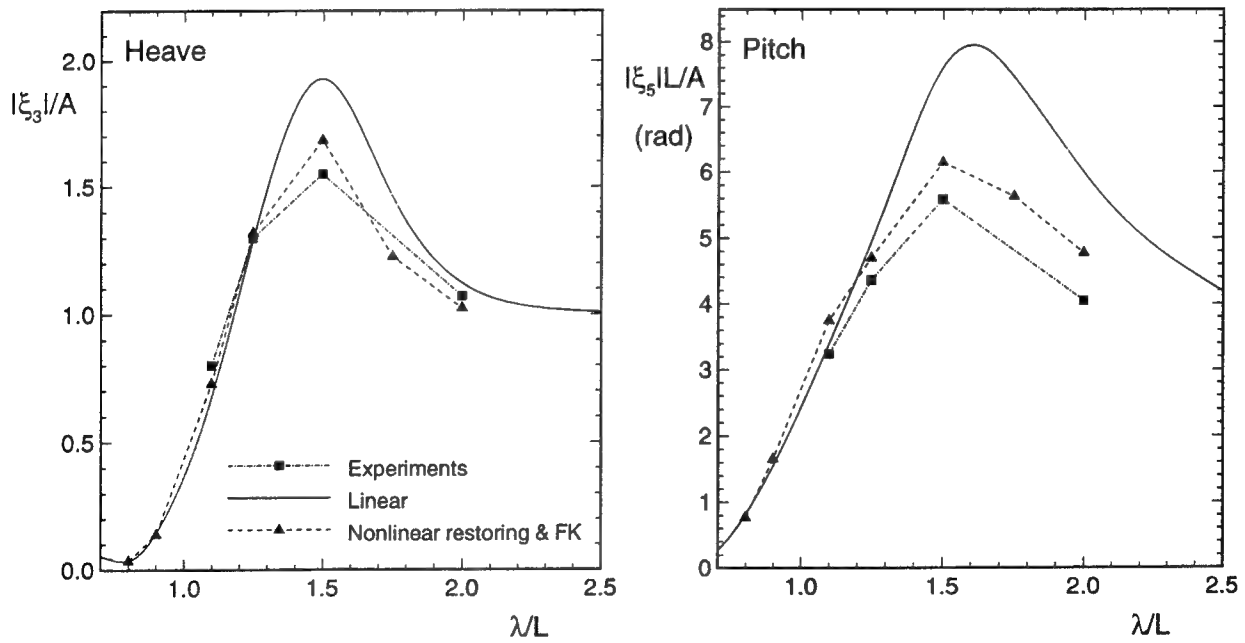


Figure 4: Heave and pitch motions for the Snowdrift hull ($T=8\text{m}$) at Froude number 0.325 in head seas.

length with a wave amplitude equal to one percent of the ship length. The reported motion amplitudes are half the difference between the maximum and minimum values for the nonlinear results. It is evident that the linear theory is in good agreement with the experiments, and that the nonlinear results from the Weak Scatterer simulation provide only a small correction. This was expected since the Series 60 is wall-sided at its design waterline.

A series of experiments in regular waves were carried out for the Snowdrift hull ($L=160\text{m}$) at a Froude number of 0.325 in head seas. These experiments were conducted as a cooperative program between the U.S. Navy and Det Norske Veritas. They include measurements of the ship motions, but also of the global loads which will be presented later.

In ballast condition ($T=8\text{m}$), there is an overhanging stern above the waterline that is neglected by linear theory but was observed to submerge in the tests. Experiments clearly demonstrated nonlinearity with increasing wave steepness.

Figure 4 compares the linear to the experimental results. Results for the nonlinear restoring and Froude-Krylov predictions in regular waves of 3.2 meter wave amplitude are also presented in this figure.

Figure 4 clearly demonstrates that nonlinear effects are significant for the Snowdrift hull and that the nonlinear restoring and Froude-Krylov extension provides a good prediction for the motions.

In all the simulations, both linear and nonlinear, for motions and loads, steady sinkage and trim effects were included. The choice of running condition has a significant effect on motions.

3 Global Loads

3.1 Global Loads in Regular Waves

This section presents results for the computation of global loads on the Snowdrift hull. The computations are carried out by linear theory and by linear theory with the non-linear hydrostatic and Froude-Krylov forces extension. Global load computations by the weak scatterer method have not yet been performed.

The computed results are compared with experimental data and with results from the computer program NV1418 which is a nonlinear strip theory program. Computations are carried out for the Snowdrift in both the ballast condition ($T=8\text{m}$) and a loaded condition ($T=11.4\text{m}$) in head seas. Results will be presented for the vertical shear force at $L/4$ (i.e. $1/4$ ship length aft of the fore perpendicular) and vertical bending moment at $L/2$ (i.e. mid-ship).

The global loads are computed by integration of forces from the bow to the section across which the load is computed.

Both the experimental data and the NV1418 time records are non-linear. The linear component of the signals can be extracted by numerical techniques. The method used is based on Volterra functional analysis, [4]. In Figures 5 and 6 these results are compared with results from the linear time domain code SWAN-2 and the corresponding frequency domain code, SWAN-1.

The results from non-linear strip theory is expected to be better for the low speed than for the high speed, and better for long waves than for short waves. For the shortest waves and the highest speed we are definitely outside the applicability region for the non-linear strip theory.

Results from SWAN-1 and SWAN-2 should be expected to agree well since they are obtained for very similar, although not identical, theories. The agreement is fairly good in most

cases, but the difference between the two types of simulation is significant in many cases. With the exception of the combinations where strip theory is not valid, and the high speed/ballast condition case, the general impression is, however, that all three simulations show reasonable agreement, but that the agreement with the experiments is not always good. For the ballast condition (i.e. 8m draft) and $Fr=0.325$ the codes differ dramatically around resonance with the experimental data lying between the SWAN and NV1418 results.

Figures 7 through 10 show a comparison between the experiments, non-linear strip theory and SWAN-2 with non-linear hydrostatic and Froude-Krylov forces. Positive values correspond to sag loads, negative values to hog loads. The sag and hog values are computed as deviations from the still water loads, which have been computed by SWAN-2 as well. The results clearly illustrate the expected result that the loads are much more non-linear than the motions.

With the sign conventions used in SWAN the hog situations will correspond to maxima on the curve for the shear force and minima on the curve for the bending moment. The wave amplitude is in both cases modest, but still the difference between the two results is large. For the full load condition (11.4m draft) the signal from the non-linear code looks quite harmonic, but the comparison still reveals strong non-linear effects with the results shown in Figures 7 through 10. In some cases SWAN is much closer to the experimental data than strip theory is, in other cases it is the other way around. At the 8m draft SWAN predicts larger sag bending moments than the experiments does. At the 11.4m draft the predicted hog loads for the high speed case are small compared to the experiments. In the latter case strip theory agrees very well with the experimental data.

The reasons for the deviations are yet unknown. The fact that non-linear strip theory is better in those cases where SWAN fails might

indicate that non-linear added mass effects may be important. In the weak scatterer version of SWAN this is included, since the radiation problem is always solved for the instantaneous wetted hull, so the results may improve.

3.2 Extreme Value Statistics

The prediction of extreme responses (loads and motions) is critical in the structural design of a ship. If the incoming waves have a Gaussian distribution then the response based on linear theory will also be Gaussian, and the response statistics can be calculated by well established methods. On the other hand, if nonlinear hydrodynamic effects are introduced, the response will be, in general, non-Gaussian which may require a simulation of considerable duration.

By extending the model for ship motions and global loads beyond linear theory, the physical accuracy of the simulation is reduced for a given deterministic input (i.e. reduced model uncertainty), but the computational requirements may become prohibitive. Even with the promise of "real time" simulation, the simulations may be too long to consider practically. So, this decrease in model uncertainty is offset by an increase in statistical uncertainty arising from the difficulty in producing sufficiently long records.

In order to overcome these problems, a method [15] which incorporates a well founded strategy for the selection of the inputs to the nonlinear simulations has to be used. The adoption of such a method will avoid impractical computational burdens by using the more exact physical model only when it is justified within time windows of extreme motion. A "critical wave episode" within a give sea-state will require initial conditions for the nonlinear simulation for this time window. A collection of these short duration episodes provides a basis for the estimation of the (short term) extreme value statistics. Statistical methods can then be applied to obtain an optimal choice for the necessary sea-state, the number of episodes, and the

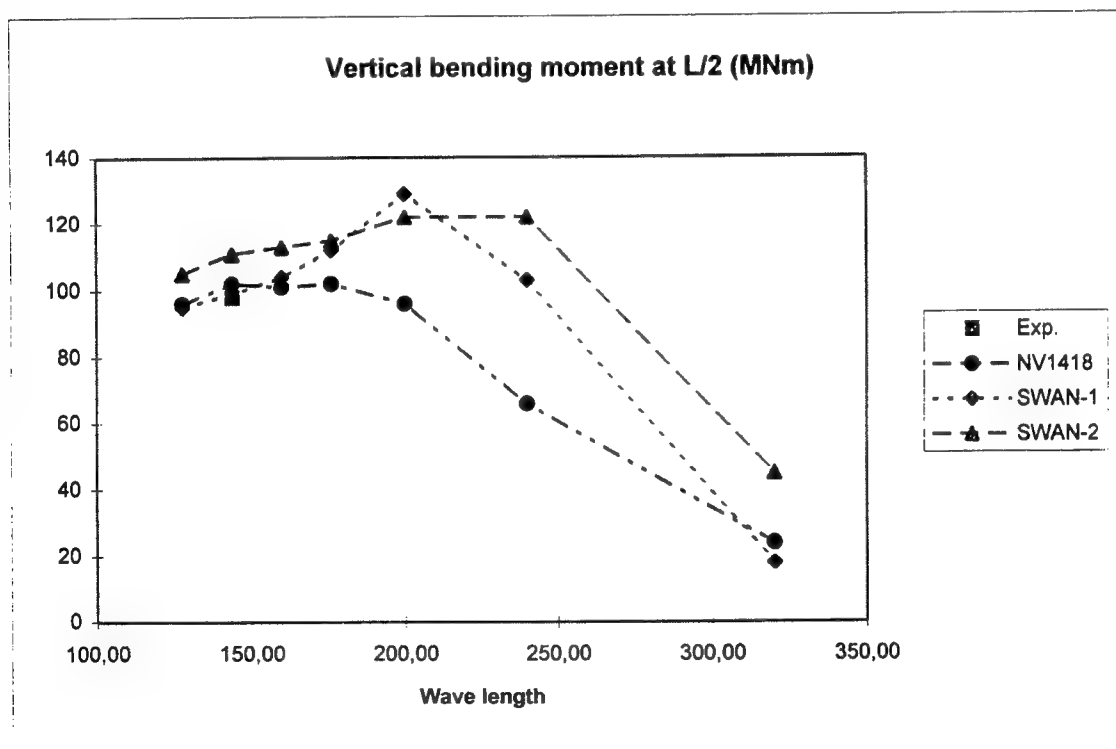
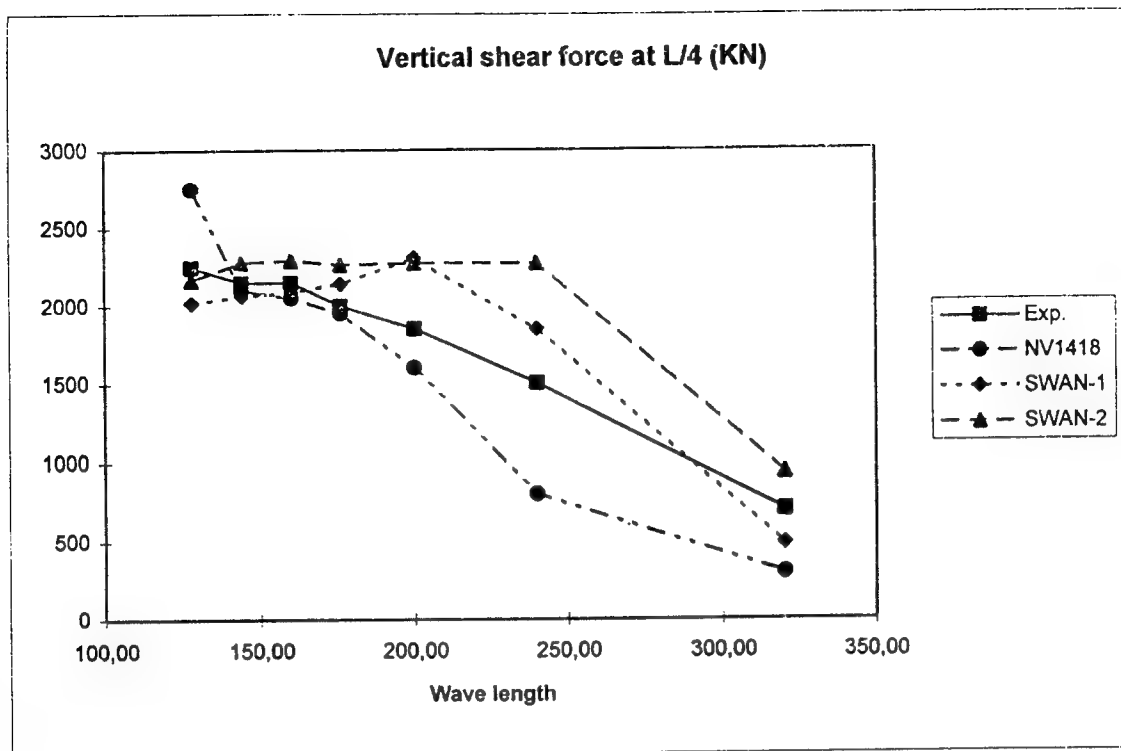


Figure 5: Linear transfer functions for the Snowdrift ($T=8m$) global loads at Froude number 0.325.

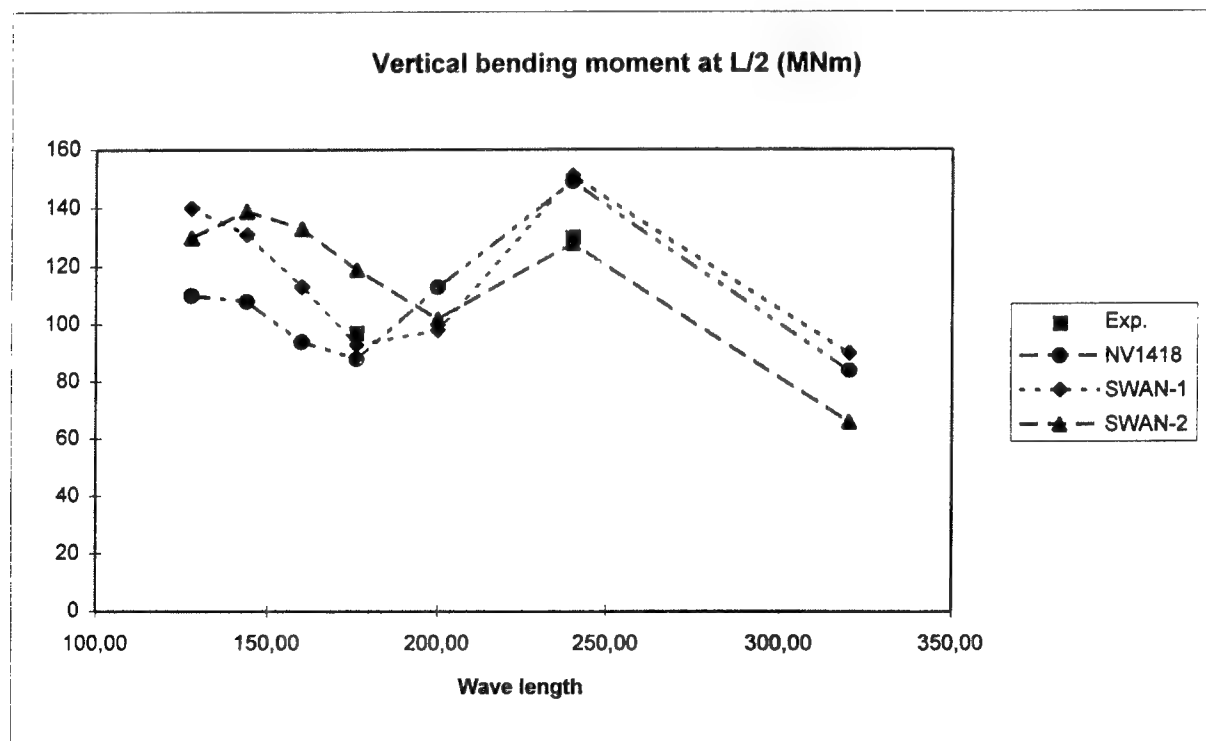
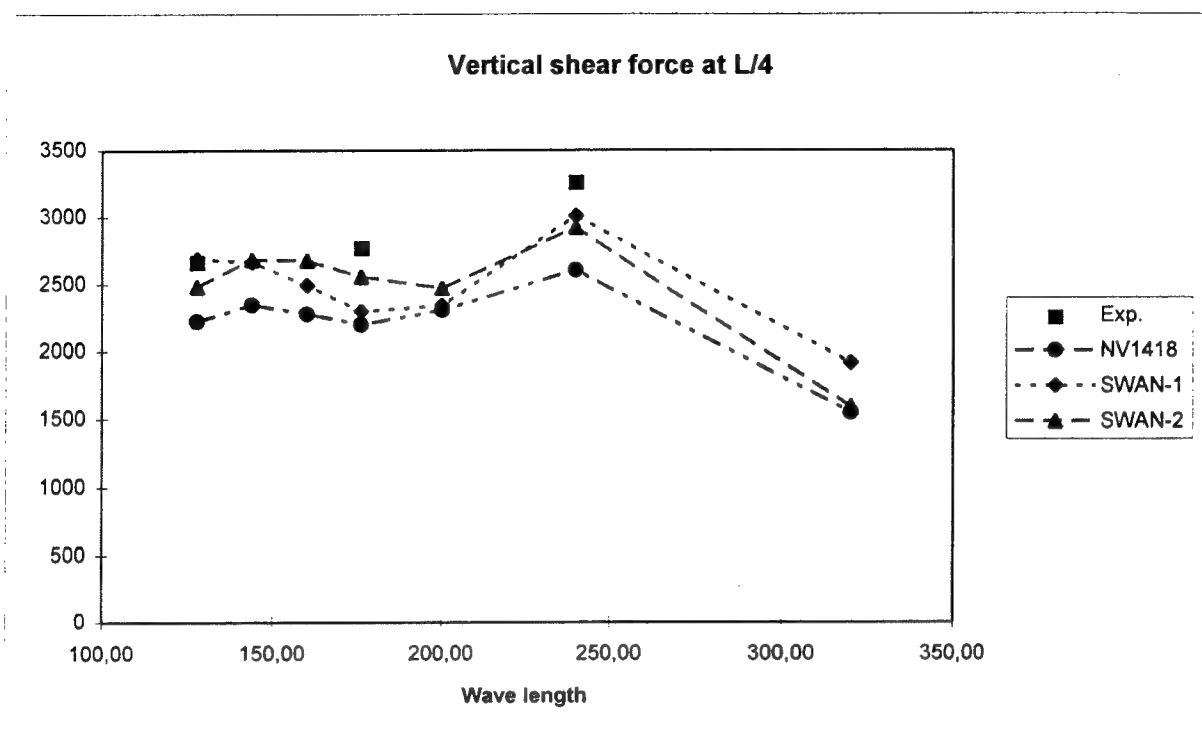


Figure 6: Linear transfer functions for the Snowdrift ($T=11.4\text{m}$) global loads at Froude number 0.325.

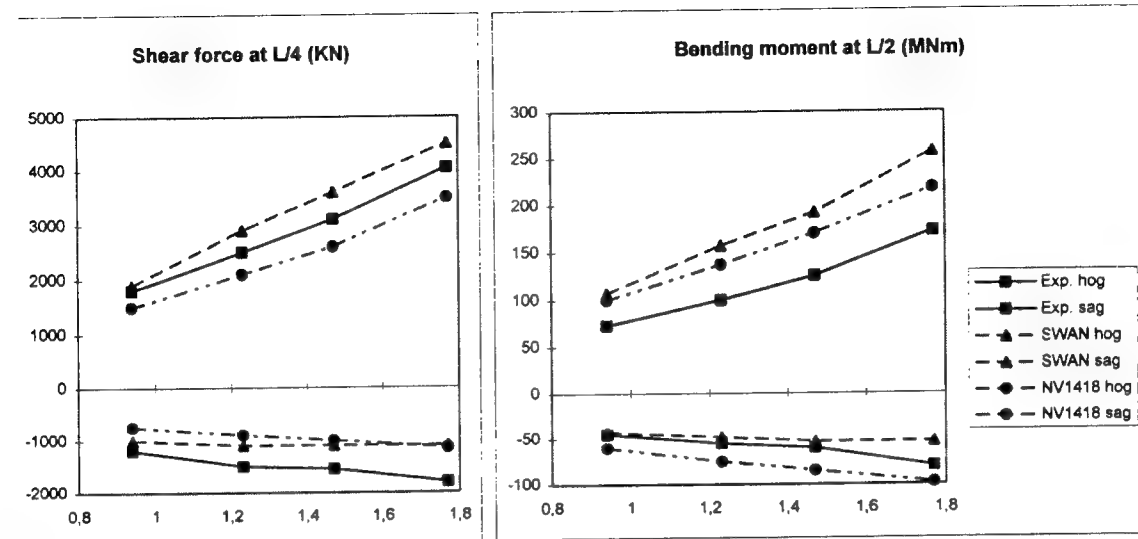


Figure 7: Sag (positive) and hog (negative) loads for Snowdrift ($T=8m$) at Froude number 0.145 and 160m wavelength as a function of wave amplitude(m).

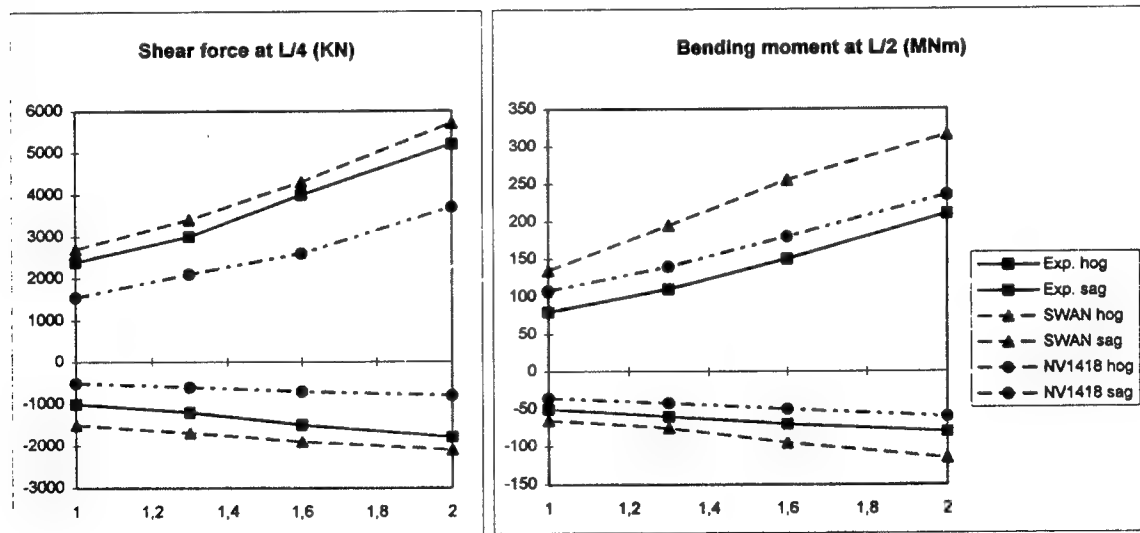


Figure 8: Sag (positive) and hog (negative) loads for Snowdrift ($T=8m$) at Froude number 0.325 and 240m wavelength as a function of wave amplitude(m).

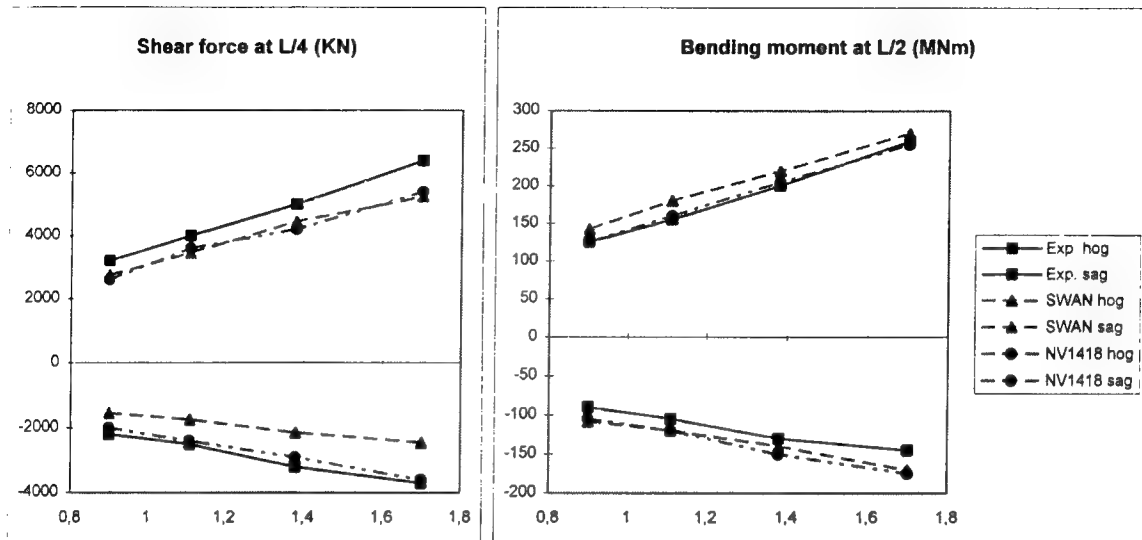


Figure 9: Sag (positive) and hog (negative) loads for Snowdrift ($T=11.4\text{m}$) at Froude number 0.145 and 160m wavelength as a function of wave amplitude(m).

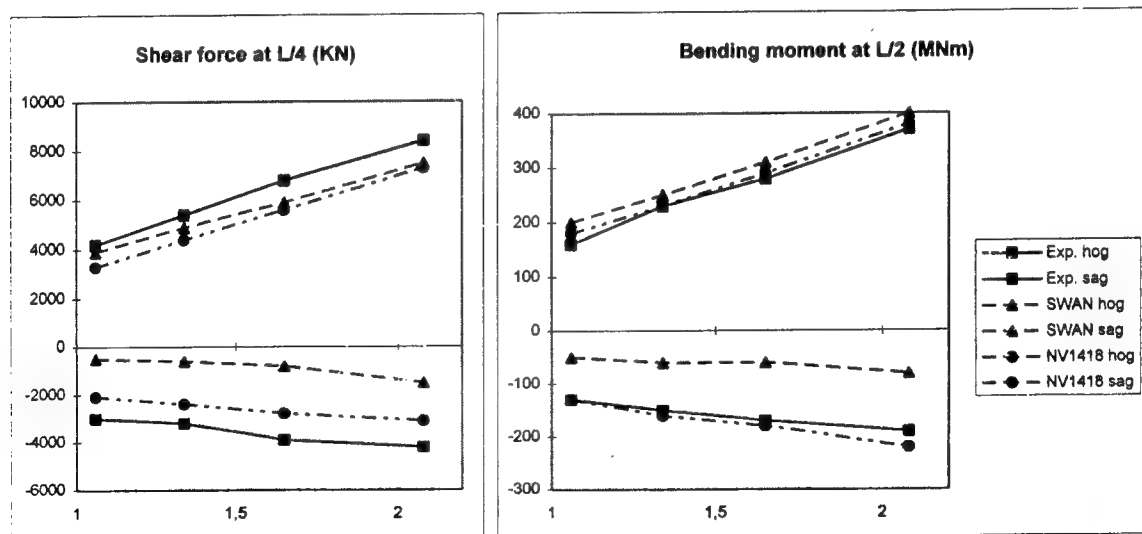


Figure 10: Sag (positive) and hog (negative) loads for Snowdrift ($T=11.4\text{m}$) at Froude number 0.325 and 240m wavelength as a function of wave amplitude(m).

number of repeated realizations of each of these episodes.

For the vertical bending moment of a container ship, for instance, an estimation of the extreme response with less than five percent statistical uncertainty can be based on simulations of only one percent of what would be needed for a direct time domain simulation.

4 Conclusions

A nonlinear seakeeping method has been presented for the simulation of the ship motions and wave induced loads in steep random waves. The method is based on a potential flow model which is treated by a Rankine Panel method based on the distribution of sources and dipoles over a mesh of panels placed on the instantaneous positions of the ship hull and the a priori known ambient wave profile. The computational method reflects an evolution of a host numerical algorithms developed for the solution of the linear seakeeping problems in the frequency and time domains, which have been developed from first principles and designed to be numerically stable, robust and efficient.

Computations of the hydrodynamic forces and motions of a wall-sided Series 60 hull and the flared Snowdrift hull in head regular waves of variable steepness, confirm the accuracy of linear theory for the Series 60 and the need for nonlinear corrections for the Snowdrift hull. In particular, accounting for nonlinear hydrostatic and Froude Krylov effects for the Snowdrift hull leads to a significant reduction of the heave and pitch motion amplitudes in head waves of moderate steepness, found to be in very good agreement with experiments.

Predictions of the bending moment and shear force distributions on the Snowdrift hull in head regular waves have been compared to experiments and a nonlinear strip theory method. The nonlinear loads reported in this study are based on the nonlinear computation of the hydrostatic and Froude Krylov effects and the lin-

earized ship wave disturbance. They have been found to be in satisfactory agreement with experiments and to reveal a clear sensitivity upon the ambient wave steepness, as expected. Discrepancies between the predictions and measurements of the global loads were identified and attributed to nonlinear effects which are presently not included in the method.

Future extensions of the method will incorporate missing nonlinear effects in the motion and global load computations, based upon the weak scatterer approximation. The extension of the method is also planned in oblique waves, where models for the roll, sway and yaw damping mechanisms will be developed for ships with appendages and transom sterns. Finally means to further improve the computational efficiency of the method will be investigated in order for the study of the ship motion and global load extreme statistics to become feasible.

5 Acknowledgements

The development of SWAN has been funded by the Office of Naval Research and Det Norske Veritas.

References

- [1] Baker, G.H., Meiron, D.I., and Orszag, S.A., "Application of a Generalized Vortex Method to Free Surface Flows", *3rd International Conference on Numerical Ship Hydrodynamics*, 1981.
- [2] Cointe, R., "Nonlinear Simulations of Transient Free Surface Flows", *5th International Conference on Numerical Ship Hydrodynamics*, 1989.
- [3] Gerritsma, J., Beukelman, W., and Glansdorff, C., "The Effects of Beam on the Hydrodynamics Characteristics of Ship Hulls", *10th Symposium on Naval Hydrodynamics*, 1974.

- [4] Korbijn, F.: "Analysis of the sag to hog regular wave model test results and comparison with results from available non-linear theory", DNV Rep. No. 91-0134, DNV Jan. 1991.
- [5] Kring, D.C. "Time Domain Ship Motions by a Three-Dimensional Rankine Panel Method", PhD Thesis, MIT, Cambridge, MA, 1994.
- [6] Kring, D.C., and Slavounos, P.D., "Numerical Stability Analysis for Time-Domain Ship Motion Simulations", *Journal of Ship Research*, Vol.39, No.4, Dec. 1995.
- [7] Nakos, D.E., and Slavounos, P.D., "Steady and Unsteady Ship Wave Patterns", *Journal of Fluid Mechanics*, Vol.215, 1990.
- [8] Nakos, D.E., Kring, D.C., and Slavounos, P.D. "Rankine Panel Methods for Transient Free Surface Flows", *Proceedings of the 6th International Conference on Numerical Ship Hydrodynamics*, Iowa City, Iowa, 1993.
- [9] Pawloski, J., "A Nonlinear Theory of Ship Motions in Waves", *Proceedings of 19th Symposium on Naval Hydrodynamics*, Seoul, Korea, 1992.
- [10] Slavounos, P.D., and Nakos, D.E., "Stability Analysis of Panel Methods for Free Surface Flows with Forward Speed", *17th Symposium on Naval Hydrodynamics*, The Hague, The Netherlands, 1988.
- [11] Slavounos, P.D., "On the Quadratic Effect of Random Gravity Waves on a Vertical Boundary", *Journal of Fluid Mechanics*, Vol.242, 1992.
- [12] Slavounos, P.D., Nakos, D.E., and Huang, Y., "Seakeeping and wave induced loads on ship with flare by a Rankine Panel Method" *Proceedings of the 6th International Conference on Numerical Ship Hydrodynamics*, Iowa City, Iowa, 1993.
- [13] Slavounos, P. D., "Computation of wave ship interactions" *Advances in Marine Hydrodynamics*, edited by M. Ohkusu, Computational Mechanics Publications, 1995.
- [14] Tick, L.J., "A Non-linear Random Model of Gravity Waves", *Journal of Maths Mech.*, Vol.8, 1959.
- [15] Torhaug, R., Braathen, A., and Winterstein, S., "Non-Linear Ship Loads: Stochastic Models for Extreme Response.", to be published.
- [16] Vada, T., and Nakos, D.E., "Time Marching Schemes for Ship Motion Simulations", *8th International Workshop on Water Waves and Floating Bodies*, 1993.
- [17] van Daalen, E.F.G. "Numerical and Theoretical Studies of Water Waves and Floating Bodies" PhD Thesis, University of Twente, Enschede, The Netherlands, 1993.

DISCUSSION

C.M. Lee

Pohang Institute of Science and Technology, Korea

This paper shows a definite improvement in predicting the motion and wave loads of ships. I would like to congratulate the authors for the excellent work presented here

My long-held assertion is that the validity of the methods in predicting ship motion in waves should be proved by checking the relative vertical motion of a ship with respect to waves, rather than checking the absolute motion alone with the corresponding experimental results. I would like to know how good the present theory is in this regard.

AUTHORS' REPLY

You are correct in that any method should be validated against as many experimental results as possible. However, due to the difficulty in obtaining relative wave elevations from experiments, few of these results can be found in the open literature. We have compared our relative wave elevation predictions to one set of experiments for the commercial design, TGC's FASTSHIP, and found a favorable comparison.

Also, for the purposes of global load predictions presented in this paper, the quantity of relative wave elevation is not directly relevant, since we have not examined slamming. When this quantity is evaluated there is also a question of physical significance. Exactly at the intersection of the wave and ship, the wave profile is difficult to measure due to localized effects such as jet formation and spray. In these loads, the relative wave elevation may be measured at some small distance away from this exact line of intersection. In this case a potential based method will perform well.

Nonlinear Water Wave Computations Using a Multipole Accelerated, Desingularized Method

S. Scorpio, R. Beck (University of Michigan, USA),
F. Korsmeyer (Massachusetts Institute of Technology, USA)

ABSTRACT

Nonlinear inviscid water wave computations are performed using an Euler-Lagrange approach to solve a boundary integral formulation. The integral equations are solved numerically at each time step using a desingularized method with multipole acceleration. Solutions obtained using multipole acceleration can require as little as $O(N)$ effort and $O(N)$ storage whereas conventional methods require $O(N^2)$ effort and storage. Multipole methods are applicable to a variety of physical simulation problems in astrophysics, plasma physics, molecular dynamics, electrostatics, and fluid dynamics. The application of multipole methods to the numerical solutions of these problems has the potential of significantly improving computational efficiency.

INTRODUCTION

The Euler-Lagrange method is due to Longuet-Higgins and Cokelet (1976) who present results for inviscid free surface wave problems in two-dimensions. The method requires at each time step: 1) The (Eulerian) solution of a linear boundary value problem and 2) the (Lagrangian) time integration of the nonlinear free surface boundary conditions. In the implementation of this method, it is important to have an accurate and stable time stepping procedure. However, it is the solution of the linear boundary value problem which requires most of the computational effort. Green's theorem is used to derive the indirect integral formulation of the problem. This equation is discretized by distributing fundamental singularities over a surface referred to as the "integration surface" and enforced at collocation points on the physical surface of the computational domain referred to as the "control surface." In conventional formulations, the integration and control surfaces coincide. This re-

sults in singular kernels which require special treatment by considering only their principal part. By moving the integration surface slightly off the control surface, the kernels are desingularized, hence the term "desingularized method." This method, probably first introduced in panel methods by Webster (1975), has several computational advantages over the singular formulation. Because of the nonsingular kernels, no special treatment is needed when evaluating the integrals so that simple numerical quadratures may be used. This removes the necessity of evaluating transcendental functions which appear in the singular formulation. In fact, the desingularized formulation becomes even simpler by replacing the singularity distribution with isolated singularities. These can be sources or higher order singularities such as dipoles. When desingularized isolated singularities are used, the necessity to evaluate surface integrals is eliminated and is replaced by simple summations. This leads to fast, stable free surface computations. Examples of desingularized, fully nonlinear free surface computations are given in Cao et al. (1991), Beck et al. (1993), and Beck et al. (1994).

The numerical approximation of the integral equations results in a linear system of equations. For free surface problems, the linear system consists of a matrix of coefficients (representing the influence of sources on control points in the desingularized method) multiplied by a vector of unknown source strengths. The matrix/vector product must equal a known boundary condition. Solution of this linear system by an iterative method will require $O(N^2)$ work and storage for the tasks of filling the matrix once and applying the matrix to a vector at each iteration. With large numbers of unknowns, as is required to discretize three-dimensional domains ($O(10^4)$), solutions by iterative solvers are too expensive for practical computations on workstations. However, the efficiency of an iterative solver can be im-

proved significantly when accelerated by a multipole algorithm.

Multipole expansions result when Laplace's equation is solved in spherical coordinates using the method of separation of variables. The multipole algorithm approximates the influence of groups of far field sources with expansions, thereby replacing the influence coefficient matrix. In a multipole-accelerated iterative solver, the matrix/vector product required at each iteration (normally $O(N^2)$ cost) is replaced by a multipole approximation ($O(N)$ cost). Greengard (1987) presents an efficient algorithm for the application of multipole expansions to potential problems. Nabors et al. (1994) presents a slightly different approach developed for electrostatics problems, and Korsmeyer et al. (1993) extend that approach to Laplace problems in general, particularly the Green's theorem formulation of free surface problems.

In the following sections, we present formulations for the boundary value problem for the fluid velocity potential, the desingularized integral equations for the perturbation potential, a domain decomposition solution technique, and the multipole algorithm. These are followed by numerical results. The efficiency of the multipole algorithm is evaluated by solving a fictitious boundary value problem for the Rankine source strength using an iterative solver with and without multipole acceleration. Next, a new method for including fully nonlinear incident waves in the forward speed problem is introduced. Finally, these methods are applied to a submerged submarine moving with constant forward speed under incident waves.

PROBLEM FORMULATION

Boundary Value Problem for the Fluid Motion

The fluid is assumed inviscid and incompressible. The problem is started from rest so that the flow remains irrotational. This implies that the fluid velocity field can be described by a scalar potential, Φ . Consider a vessel floating on a free surface and translating with speed $\vec{U}(t)$ with respect to a right handed space fixed coordinate system. The $z = 0$ plane defines the calm water level and the $x - z$ plane is coincident with the centerplane of the vessel. Since we are interested in ships, we want to concentrate on the "forward speed" case which is $\vec{U}(t) = (U(t), 0, 0)$ where $U(t)$ is in the negative x direction. The total velocity potential describing the fluid motion is then,

$$\Phi = U(t)x + \phi(\vec{x}, t) \quad (1)$$

where $\phi(\vec{x}, t)$ is the perturbation potential and $\vec{x} = (x, y, z)$. Both potentials Φ and ϕ satisfy Laplace's equation in the fluid domain.

$$\nabla^2 \Phi = 0 \quad (2)$$

In order to define a well posed problem, boundary conditions must be specified on all surfaces surrounding the fluid domain. Since the forward speed part of the potential is known, the boundary conditions can be set up in terms of the unknown perturbation potential with respect to the translating coordinate system in the centerplane of the vessel. On the body wetted surface (S_H) and on the bottom (S_B) the boundary conditions are,

$$\frac{\partial \phi}{\partial n} = -U(t)n_1 + V_H \cdot \vec{n} \quad \vec{x} \in S_H \quad (3)$$

and

$$\frac{\partial \phi}{\partial n} = -U(t)n_1 \quad \vec{x} \in S_B \quad (4)$$

where $\vec{n} = (n_1, n_2, n_3)$ is the unit normal out of the fluid. V_B is the velocity of the body surface. On the far field surface at infinity (S_∞) the boundary condition is,

$$\nabla \phi \rightarrow 0 \text{ as } |\vec{x}| \rightarrow \infty \quad (5)$$

Due to the fact that only a finite amount of the free surface can be modeled, this far field condition is usually treated by either an approximate radiation condition, an absorbing beach, walls, or, in some cases, it is ignored and the boundary is left open. If the far field surfaces are truncated with solid walls (S_W), the far field boundary condition is then,

$$\frac{\partial \phi}{\partial n} = -U(t)n_1 + V_W \cdot \vec{n} \quad \vec{x} \in S_W \quad (6)$$

There are two boundary conditions on the free surface (S_F), one kinematic and one dynamic. We use a special form of these conditions for following the temporal evolution of nodes on the free surface (see Beck et al. 1994). The kinematic condition is,

$$\frac{\partial \eta}{\partial t} = \frac{\partial \phi}{\partial z} - (\nabla \phi - \vec{v}) \cdot \nabla \eta - U(t) \frac{\partial \eta}{\partial x} \quad \vec{x} \in S_F \quad (7)$$

$$\frac{\delta}{\delta t} = \frac{\partial}{\partial t} + \vec{v} \cdot \nabla \quad (8)$$

where $z = \eta(x, y, t)$ is the free surface elevation. $\vec{v} = (u(t), v(t), \frac{\delta \eta}{\delta t})$ is the velocity of free surface nodes where $u(t)$ and $v(t)$ are prescribed horizontal velocities of the nodes. If $\vec{v} = \nabla \phi$ then the free surface nodes become material nodes and move with the fluid velocity. Prescribing the horizontal plane motions of the free surface nodes can prevent certain numerical problems such as the piling up of nodes at stagnation points. The disadvantage is that spatial derivatives on the free surface are required. These normally have to be computed using some type of numerical differentiation which is difficult to accomplish accurately. The dynamic free surface boundary condition is,

$$\frac{\delta \phi}{\delta t} = -g\eta - \frac{1}{2} \nabla \phi \cdot \nabla \phi + \mathbf{v} \cdot \nabla \phi - \frac{P_a}{\rho} - U(t) \frac{\partial \phi}{\partial x} \quad (9)$$

$\vec{x} \in S_F$

where ρ is the fluid density, g is the gravitational acceleration, and P_a is the atmospheric pressure.

Mixed Boundary Value Problem for the Perturbation Potential

The boundary value problem defined above has a linear field equation with nonlinear boundary conditions. The method used for the numerical solution of this problem is an Euler-Lagrange time stepping technique. A desingularized boundary integral method is used to solve the mixed boundary value problem for the perturbation potential at each time step. The kinematic and dynamic free surface boundary conditions are then integrated in time.

The mixed boundary value problem for the perturbation potential is determined by solving the Laplace equation in the fluid domain. At each time step ϕ is known on the free surface and $\partial \phi / \partial n$ is known on solid boundary surfaces. The boundary conditions are satisfied by distributing Rankine sources on an integration surface. The integration surface is offset a small distance from the problem boundary, i.e. above the free surface and inside the body. Rather than using Green's theorem (the direct method) to from integral equations for the unknown potential, we use an indirect formulation where the potential anywhere in the fluid volume is defined by,

$$\phi(\vec{x}) = \int_{\Omega} \sigma(\vec{\xi}) G(\vec{x}; \vec{\xi}) d\Omega \quad (10)$$

where $\vec{x} = (x, y, z)$ is a point in the fluid domain, $\vec{\xi} = (\xi, \eta, \zeta)$ is a point on the integration surface, $\sigma(\vec{\xi})$ is the

value of the source strength at $\vec{\xi}$, $G(\vec{x}; \vec{\xi})$ is the Rankine source Green function, and Ω is the integration surface. The Green function for three-dimensional problems is,

$$G(\vec{x}; \vec{\xi}) = \frac{1}{|\vec{x} - \vec{\xi}|} = \frac{1}{\sqrt{(x - \xi)^2 + (y - \eta)^2 + (z - \zeta)^2}} \quad (11)$$

In order to obtain the appropriate Dirichlet and Neumann boundary conditions, we simply enforce (10) on Dirichlet boundaries and multiply (10) by $\vec{n} \cdot \nabla$ to obtain a form suitable for Neumann boundaries.

$$\int_{\Omega} \sigma(\vec{\xi}) G(\vec{x}; \vec{\xi}) d\Omega = \phi_F(\vec{x}) \quad (12)$$

$\vec{x} \in S_F$

$$\int_{\Omega} \sigma(\vec{\xi}) \vec{n}(\vec{x}) \cdot \nabla_{\vec{x}} G(\vec{x}; \vec{\xi}) d\Omega = \vec{n}(\vec{x}) \cdot \nabla \phi_B(\vec{x}) \quad (13)$$

$\vec{x} \in S_B$

where,

ϕ_F	= given potential on the free surface at \vec{x}
S_F	= The free surface
$\vec{n}(\vec{x}) \cdot \nabla \phi_B(\vec{x})$	= given normal velocity on solid boundaries
S_B	= all solid boundary surfaces

After the integral equations are solved, the fluid velocities can be found without the need of numerical derivatives,

$$\nabla \Phi = U(t) \vec{i} + \nabla \phi \quad (14)$$

where,

$$\nabla \phi = \int_{\Omega} \sigma(\vec{\xi}) \nabla_{\vec{x}} G(\vec{x}; \vec{\xi}) d\Omega \quad (15)$$

SOLUTION TECHNIQUES

Domain Decomposition

When using desingularized Rankine sources, the integral equations 12 and 13 reduce to simple summations relating the influence of the source points ($\vec{\xi}$) on the node points (\vec{x}). In this case, the integral equations can be written as,

$$\mathbf{A} \cdot \Sigma = \mathbf{B} \quad (16)$$

Where A is the influence matrix, Σ is the source strength and B is the appropriate Dirichlet or Neumann boundary condition. The individual terms of the influence matrix A are,

$$A_{ij} = \frac{1}{|\vec{x}_i - \vec{\xi}_j|} \quad (17)$$

for nodes on the free surface. And,

$$A_{ij} = \frac{\partial}{\partial n_i} \left(\frac{1}{|\vec{x}_i - \vec{\xi}_j|} \right) \quad (18)$$

for nodes on the body.

We use a domain decomposition technique to solve the linear system for the source strength Σ . The linear system is written as,

$$\begin{bmatrix} A_{FF} & A_{FB} \\ A_{BF} & A_{BB} \end{bmatrix} \begin{pmatrix} \Sigma_F \\ \Sigma_B \end{pmatrix} = \begin{pmatrix} \phi_F \\ \frac{\partial \phi_B}{\partial n} \end{pmatrix} \quad (19)$$

Here, for example, A_{FB} would represent the influence of sources in the body (B) on nodes on the free surface (F). The decomposed linear system is solved by simply iterating between the solutions for the source strengths Σ_F and Σ_B .

$$\begin{aligned} A_{FF} \cdot \Sigma_F &= \phi_F - A_{FB} \cdot \Sigma_B \\ A_{BB} \cdot \Sigma_B &= \phi_B - A_{BF} \cdot \Sigma_F \end{aligned} \quad (20)$$

There are several advantages to using domain decomposition. The free surface and body may have different grid densities. This will result in poor conditioning of the total A matrix. Whereas the individual matrices A_{FF} and A_{BB} will have better conditioning because they have relatively constant grid densities. For most ship-wave problems, the majority of the nodes are used to discretize the free surface. The number of nodes on the body is often small enough to use an iterative method without multipole acceleration, or even direct factorization. The free surface domain is solved using a multipole algorithm. For the computations contained herein, the multipole algorithm is tailored for solving the free surface domain. This strategy is used to simplify the coding of the algorithm. For problems where the body geometry is complicated requiring large numbers of nodes to resolve the details, it will be necessary to extend the multipole algorithm for use on the body domain.

Multipole Expansions

Writing the Laplace equation in spherical coordinates yields,

$$\frac{1}{r^2} \frac{\partial}{\partial r} \left(r^2 \frac{\partial \Phi}{\partial r} \right) + \frac{1}{r^2 \sin \theta} \frac{\partial}{\partial \theta} \left(\sin \theta \frac{\partial \Phi}{\partial \theta} \right) + \frac{1}{r^2 \sin^2 \theta} \frac{\partial^2 \Phi}{\partial \phi^2} = 0 \quad (21)$$

The solution of this equation by separation of variables results in a series of spherical harmonic terms,

$$\Phi = \sum_{n=0}^{\infty} \sum_{m=-n}^n \left(L_n^m r^n + \frac{M_n^m}{r^{n+1}} \right) Y_n^m(\theta, \phi) \quad (22)$$

M_n^m and L_n^m are the moments of the expansion and $Y_n^m(\theta, \phi)$ are the spherical harmonics. Using the series solution to the Laplace equation, the far field potential due to a collection of near field sources can be expressed in a multipole expansion. Suppose there are k sources with coordinates $(\rho_i, \alpha_i, \beta_i)$, $i = 1, \dots, k$ and strengths σ_i . Consider a sphere of radius a containing the k sources. Let the center of a multipole expansion be defined as the center of this sphere. We can then express the potential due to the k sources at any point, $P(r, \theta, \phi)$, outside of the sphere,

$$\Phi(P) = \sum_{n=0}^{\infty} \sum_{m=-n}^n \frac{M_n^m}{r^{n+1}} Y_n^m(\theta, \phi) \quad (23)$$

where the coefficients of the expansion are given by,

$$M_n^m = \sum_{i=1}^k \sigma_i \rho_i^n Y_n^{-m}(\alpha_i, \beta_i) \quad (24)$$

Likewise, the near field potential due to a collection of far field sources can be expressed in a local expansion. Suppose the k sources now lay outside of the sphere of radius a centered at the origin. The center of a local expansion is defined by the center of the sphere inside which all of the evaluation points (P) lay. The potential due to these sources at any point, $P(r, \theta, \phi)$, inside of the sphere is given by,

$$\Phi(P) = \sum_{n=0}^{\infty} \sum_{m=-n}^n r^n L_n^m Y_n^m(\theta, \phi) \quad (25)$$

where the coefficients are given by,

$$L_n^m = \sum_{i=1}^k \frac{\sigma_i}{\rho_i^{n+1}} Y_n^{-m}(\alpha_i, \beta_i) \quad (26)$$

Several theorems are used in the multipole algorithm which involve shifting the origins of multipole and local expansions and the conversion of multipole expansions into local expansions. See Greengard (1987) for the development of these theorems and their error bounds.

Multipole Acceleration

There is a wide variety of $N \log N$ algorithms for accelerating the evaluation of N potentials due to N sources, typically these are based on some form of hierarchical panel clustering. The underlying idea is that the potential due to a cluster of panels may be evaluated at some distant point x_j by first accumulating the panel influences into a multipole expansion, and then evaluating the single expansion. It is the careful arrangement of the clusters of panels which leads to the $N \log N$ efficiency. The fast-multipole algorithm reduces the cost yet further, to order N , by a complementary arrangement of the evaluation points so that accumulated multipole expansions may be transformed to local expansions centered in the clusters of evaluation points, and these expansions are evaluated instead. More specifically, the use of multipole and local expansions is orchestrated by a tree-structured hierarchy of source clusters and evaluation point clusters; as shown in figure 1, multipole expansions for clusters of sources are accumulated from the *leaves* of the tree to the *root*, and local expansions are distributed from the root to the leaves for evaluation at collocation points. This is accomplished in order N operations while maintaining a uniform precision as shown by Greengard (1987).

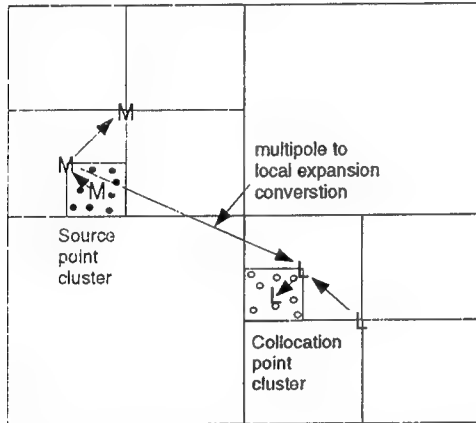


Figure 1: Multipole and local expansion manipulation

Local and multipole expansions must be carefully applied to insure that the potential is accurately approximated everywhere in the problem domain. The structure which makes this possible is the hierarchical partitioning of the domain. Consider the smallest cube which contains the entire domain, that is, all of the sources. We refer to this cube as the level 0 or root cube. This *parent* cube is subdivided into eight *child*

cubes, and the sources are divided among these level 1 child cubes. This process is repeated down to some *finest* level (the leaves), designated level L . The number of levels, L , is usually selected so that no finest level cube contains more than some fixed small number of sources. After setting up this hierarchical spatial decomposition, the fast multipole algorithm begins with the finest level, where each cube of sources is represented by a multipole expansion about the center of the cube. During an *upward pass* through the tree to the root, each child cube's multipole expansion is shifted to the child cube's parent's center, to generate a single expansion which represents all of the sources in the parent cube. In an *interaction phase*, at each level a local expansion is created for each cube by accumulating multipole expansions representing distant cubes at that level. In a *downward pass*, the local expansions in the parent cubes are shifted to the centers of their children. Finally, in an *evaluation phase*, the local expansions and direct contributions from nearby sources are evaluated at the points at which the potential is required: the collocation points.

For the computations herein, the multipole algorithm is applied only to the free surface domain. Since the free surface lies more or less in a plane with the elevations representing small deviations, the three-dimensional hierarchical tree structure can be collapsed into a two-dimensional "pancake". This simplifies some of the logic required in partitioning the domain.

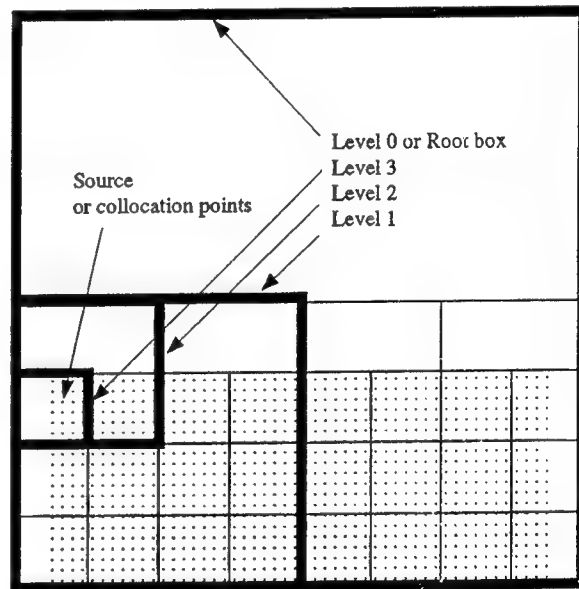


Figure 2: Typical hierarchical tree structure

Figure 2 shows a typical two-dimensional hierarchy. In the desingularized method, the source points are directly above (in the $+z$ direction) the collocation points. This guarantees that a source point and its collocation point will be in the same box. Therefore, the source clusters and evaluation (or collocation) point clusters will have the same hierarchy. The "pancake" hierarchy is oriented in the x - y plane and positioned at the calm water level ($z = 0$).

RESULTS

Multipole Efficiency

A sample problem is set up and solved for the purpose of studying the performance of multipole acceleration. A rectangular area is discretized with equally spaced nodes in the x - y plane. The z -coordinate of the nodes is given a small amplitude cosine distribution. Desingularized sources are placed a small distance (inversely proportional to the local node density) above the nodes. The potential at the nodes is prescribed with a cosine distribution. The source strengths for this fictitious problem are then solved using an iterative solver, GMRES.

For the *direct* solution, the linear system of equations (eqn. 16) is set up by assembling and storing the matrix of influence coefficients, A . With the right hand side ($B = \text{potential}$) given, the unknown source strength, Σ , is then solved using the GMRES solver. This solution procedure is an $O(N^2)$ method because the matrix, A , requires $O(N^2)$ storage on the computer and the linear system requires $O(N^2)$ computations to solve.

For the *multipole* solution, the "pancake" hierarchy is set up in the $z = 0$ plane. Each iterate of the GMRES solution is then computed using the multipole algorithm. This solution procedure results in an $O(N)$ method because the matrix A is no longer computed and stored and the multipole algorithm allows the linear system to be solved in $O(N)$ computations.

There is a third alternative to these two solution procedures that might be considered. The linear system can be solved using the direct method without storing the matrix of influence coefficients. Every time an influence coefficient is needed it is simply recomputed. This solution procedure requires $O(N)$ storage and $O(N^2)$ computational effort.

The following computations were performed on a DEC alphastation 600 5/266. Figure 3 shows the time required to arrive at the solution by the three methods versus the number of nodes (N) in the linear system. The direct method - no memory refers to the direct method without storing the influence matrix. This

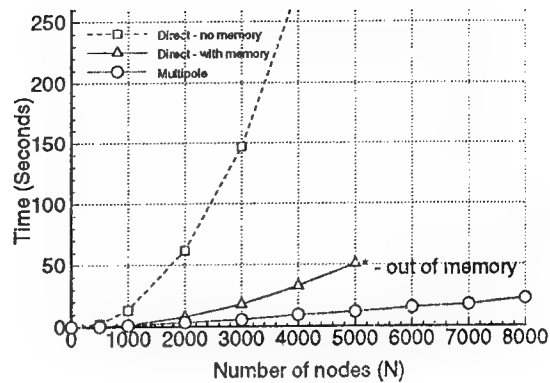


Figure 3: Time requirements

method has the advantage of using very little memory but the time requirements quickly become excessive. The direct method with memory is much faster but the memory requirements become larger than the available memory on the alphastation when N becomes greater than ~ 5000 . The multipole solution is more efficient than either option when $N > 1000$. Significant speed up is attained with multipole acceleration when N becomes very large ($O(10^4)$).

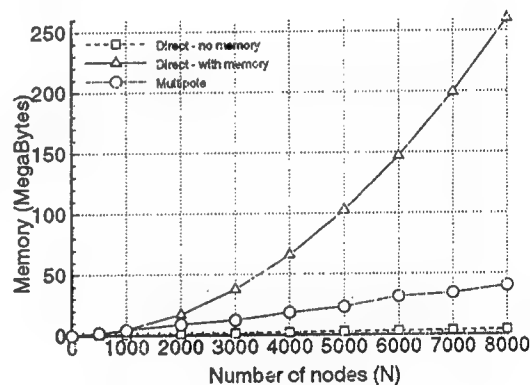


Figure 4: Memory requirements

Figure 4 shows the memory requirements of the three methods. The direct method - no memory requires very little memory but the time requirements (figure 3) are unreasonable. The direct method - with memory requires the most memory which quickly becomes excessive as N becomes large. The multipole method requires a moderate amount of memory which increases approx-

imately linearly with N .

These results clearly show the advantages of using a multipole solver. The $O(N^2)$ methods are severely limited by time and memory requirements with large N . The time and memory requirements for the multipole method increase linearly with N . This allows large problems to be analyzed without a significant computational penalty.

While we have shown that the fast-multipole algorithm is an effective means to accelerating the solution of nonlinear free-surface problems, it should be noted that an apparently more efficient algorithm has been developed recently which may be useful for these problems as well. This algorithm, referred to as the pre-corrected-FFT algorithm, was developed for application to electrostatics problems (Phillips 1994). Rather than using multipole expansions, this algorithm represents distant influences at evaluation points by replacing a cube's cluster of sources with a small number of weighted point singularities located at the corners and on the faces of the cube. The evaluation of the matrix/vector product then consists of the following four steps: The sources distributed on the integration surface are replaced by a uniform grid of sources; the value of the potential is computed on this uniform grid by FFT; this potential is computed at the evaluation points by interpolation; and the nearby interactions are computed directly including the correction for the fact that they have been included inaccurately in the previous two steps. A complexity analysis of this algorithm shows that it has a higher asymptotic cost than the fast-multipole algorithm demonstrated here (Phillips 1995), however in applications using up to order 10^5 degrees of freedom its actual cost is lower (Nabors et al. 1995). This is due in part to the fact that carefully tuned FFT routines are available for many architectures and distributed computing environments.

Nonlinear incident waves at forward speed

Because boundary conditions are required on all enclosing surfaces for any boundary integral method, the problem of producing fully nonlinear incident waves on a ship moving at forward speed is not trivial. The difficulty arises because computational limitations allow only a portion of the free surface to be modeled. Therefore, a method must be contrived to introduce waves into the computational domain. This is achieved by producing waves in a two-dimensional tank relative to a fixed reference frame X_o - Y_o . A small computational window, described in an x - y coordinate system moving relative to the fixed X_o - Y_o coordinates, can then be moved through

the waves by prescribing the upstream and downstream boundary conditions on the window.

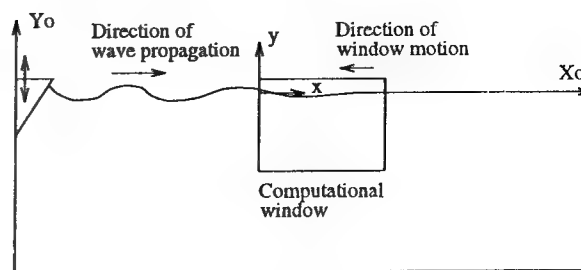


Figure 5: A two-dimensional wave making tank with a moving computational window

Figure 5 shows a two-dimensional tank with a plunger wave maker producing waves in the X_o - Y_o reference frame. The plunger wave maker has a 30 degree wedge angle and a prescribed sinusoidal motion in the Y_o direction. The computational window containing the ship is then moved through the incident wave field by prescribing $\partial\phi/\partial n$ on a vertical "wall" and ϕ and η on the free surface for both the upstream and downstream boundaries. However, for problems where a body is present in the window, the waves passing through the downstream boundary are unknown a priori. Therefore, the downstream boundary condition cannot be specified exactly. In this case, the downstream boundary can be left unspecified, an approximate radiation condition can be applied, or some type of numerical beach strategy may be used. For computations presented here, the boundary is unspecified.

Figure 6 shows the results of this method in two-dimensions with no ship form included. The computational window is moved at a constant speed through the wave tank by specifying the upstream boundary condition and leaving the downstream boundary condition unspecified. Four cases are studied for windows translating through the incident wave field at varying speeds. The incident waves have wavelength λ and the speed of the computational window is defined by a Froude number based on wavelength, $Fr = U_o/\sqrt{g\lambda}$. The wave elevations, η , in the moving window are compared with elevations in the stationary wave tank after the incident waves have been entering the moving window for some time. Because the downstream boundary condition is not applied in the moving window, the wave elevations do not agree exactly. They are, however, quite reasonable. If the downstream boundary had been specified, the waves in the window would agree with the waves in the tank to within graphical accuracy.

These results indicate that this method produces rea-

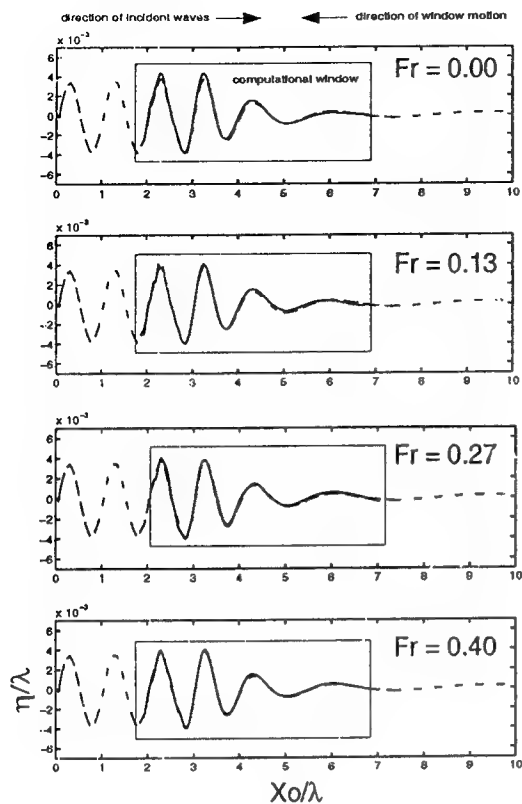


Figure 6: Incident waves in a moving computational window. Solid line - wave elevations in the computational window. Dashed line - wave elevations in the stationary wave tank

sonable waves inside a two-dimensional computational window with no body present. The question of whether the unspecified downstream boundary will produce acceptable results for a three-dimensional problem with a body present is the subject of the next section.

Wave forces on a submerged submarine with forward speed

Two-dimensional plane waves are introduced into a three-dimensional computational window via the method outlined in the previous section. The three-dimensional window is bounded by a vertical wall on the upstream boundary (on which the incident wave boundary conditions are applied), a vertical wall on the outer boundary, a plane of symmetry on $y = 0$, and the free surface. The downstream boundary is left open and the fluid is infinitely deep. A small distance below the free

surface an axisymmetric submarine hull form is translating with steady forward speed U_o .

The submarine hull form is described using the following formula from Jackson (1991). The local radius is defined as a function of position forward (r_f) and aft (r_a) of the parallel middle body.

$$r_f = R \left\{ 1 - \left(\frac{x_f}{L_f} \right)^2 \right\}^{\frac{1}{2}} \quad (27)$$

$$r_a = R \left\{ 1 - \left(\frac{x_a}{L_a} \right)^3 \right\}$$

Where R is the radius of the parallel middle body, L_f and L_a are the lengths of the forward and after bodies respectively and x_f and x_a are local coordinates which run from zero at the parallel middle body up to L_f and L_a . Given the total length of the submarine is L , then the parameters used to describe the submarine are: $L_f/L = 0.167$, $L_a/L = 0.389$, and $R/L = 0.046$.

The submarine is operating in infinitely deep water at a depth of submergence of $\text{Depth}/R = 2$. It is translating in the opposite direction of the incident waves (head seas). Preliminary results for forward speed cases of $Fr = 0.1$ and $Fr = 0.3$ are presented here. The incident waves have frequency $\omega_o^* = \omega_o \sqrt{L/g} = 3.31$. This wave frequency was selected because according to linear theory it produces the maximum mean second order diffraction moment about the center of buoyancy for the $Fr = 0.1$ case.

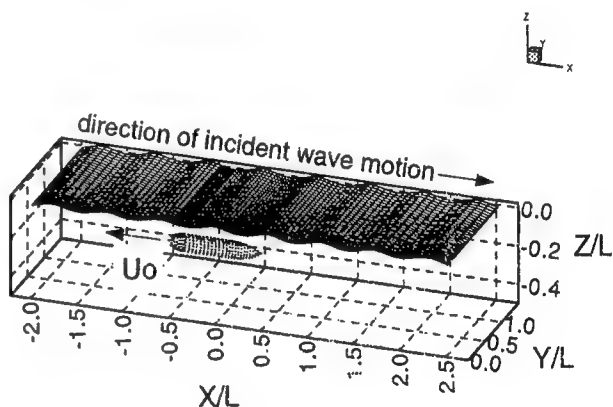


Figure 7: Incident waves with forward speed in a three-dimensional moving window

Figure 7 shows the three-dimensional computational domain. The submarine body is discretized with 251 nodes and the free surface with 2720 nodes. Not shown in the figure are the upstream and outer boundaries which are discretized with 320 and 500 nodes respectively resulting in a total of 3791 nodes. The non-dimensional time step for this problem is $\Delta t^* = \Delta t \sqrt{g/L} = 0.03$.

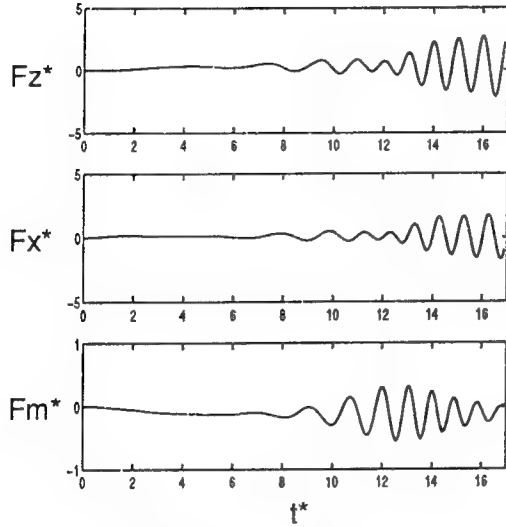


Figure 8: Exciting forces, $Fr = 0.1$, $\omega_o^* = 3.31$

Figure 8 shows the time histories of the exciting forces and moment for the $Fr = 0.1$ case. Here, the non-dimensional time, vertical force, horizontal force and pitch moment about the center of buoyancy are: $t^* = t \sqrt{g/L}$, $Fz^* = Fz/\rho g A^2 L$, $Fx^* = Fx/\rho g A^2 L$, and $Fm^* = Fm/\rho g A^2 L^2$. ρ and g are the density and gravitational acceleration and A is the incident wave amplitude. For this case, linear theory predicts a maximum second order mean shift of $Fm_{diffraction}^* = 0.005$ for the pitching moment due to wave diffraction. The mean shift for the total nonlinear pitching moment computed here is $Fm_{total}^* = -0.149$. The difference is due to the fact that in nonlinear computations, the diffraction force cannot be separated from the total force. Therefore, the total moment includes contributions from diffraction, incident waves and steady forward speed. This comparison gives an indication of the relative magnitudes of the total mean shift in the moment and the mean shift due only to diffraction.

The mean shift in the forces and moment due to steady forward speed in the absence of incident waves is

expected to be small due to the low Froude number. For this speed the ratio of wavelength in the Kelvin wake to body length is $\lambda/L \approx 1/16$. The free surface discretization shown in figure 7 is too coarse to resolve the waves accurately. The number of nodes required to adequately resolve the Kelvin wake would be very large. Since the forces resulting from steady forward speed are small relative to the Froude-Krylov forces due to incident waves, we used the coarse grid expecting a small error due to inadequate resolution of the Kelvin wake.

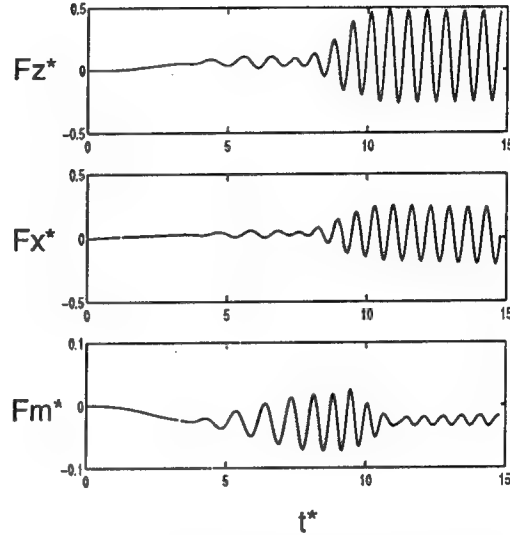


Figure 9: Exciting forces, $Fr = 0.3$, $\omega_o^* = 3.31$

Figure 9 shows the exciting forces and moment for the $Fr = 0.3$ case. Here we see that the increase in encounter frequency has resulted in a significant reduction in the exciting forces. This is expected since linear theory predicts a maximum at $Fr = 0.1$. Notice that the maximum pitching moment occurs before the moment reaches its steady state oscillation. This occurs when the submarine is passing under the wave front. The length of the incident waves in the front are longer due to dispersion. These longer waves are closer to the ship length and therefore create a larger exciting moment.

The results presented for this problem serve to indicate the validity of using the two-dimensional incident waves in the three-dimensional moving window. They do not constitute a complete set of results for the problem of exciting forces on a submerged submarine. The analysis of this problem was not completed by the preprint deadline. We expect to have a more thorough set of results available for presentation at con-

ference time.

CONCLUSIONS

The desingularized method is well suited for computing nonlinear wave-body problems. When combined with a multipole algorithm, solutions can be obtained with a reasonable amount of computational effort and storage on a workstation level computer. This significant improvement in efficiency will help in advancing nonlinear free surface computations from a research project to a usable design tool.

A new method has been presented for introducing nonlinear incident waves into problems with forward speed. This method can be used to produce waves inside both two- and three-dimensional computational windows. The wave exciting forces on a submerged submarine with forward speed results are incomplete. We expect to have a complete set of results for presentation by conference time.

ACKNOWLEDGMENTS

This research was funded by the Office of Naval Research Grant Numbers N00014-93-1-0629, N00014-94-1-0099 and N00014-95-1-0870 and the University of Michigan/Sea Grant/Industry Consortium on Offshore Engineering. Computations were made in part using a Cray Grant, University Research and Development Program at the San Diego Supercomputer Center.

REFERENCES

1. R.F. Beck, Y. Cao, and T.-H. Lee, "Fully nonlinear water wave computations using the desingularized method," In *Proceedings 6th International Conference on Naval Hydrodynamics*, University of Iowa, 1993.
2. R.F. Beck, Y. Cao, S.M. Scorpio, and W.W. Schultz, "Nonlinear ship motion computations using the desingularized method," In *20th Symposium on Naval Hydrodynamics*, Santa Barbara, California, 1994.
3. Y. Cao, W.W. Schultz, and R.F. Beck, "A three-dimensional desingularized boundary integral method for potential problems," *International Journal of Numerical Methods in Fluids*, 11:785-803, 1991.
4. L.F. Greengard, *The rapid evaluation of potential fields in particle systems*, The MIT Press, Cambridge, Massachusetts, 1987.
5. H.A. Jackson, *Submarine design trends*, MIT Department of Ocean Engineering, Cambridge, Massachusetts, 1991. Course Notes.
6. F.T. Korsmeyer, D.K.P. Yue, K. Nabors, and J. White, "Multipole-accelerated preconditioned iterative methods for three-dimensional potential problems," In *Proceedings of BEM*, volume 15, pages 517-527, Worcester, Massachusetts, 1993.
7. M.S. Longuet-Higgins and C.D. Cokelet, "The deformation of steep surface waves on water: I. a numerical method of computation," In *Proceedings of the Royal Society of London*, volume A350, pages 1-26, 1976.
8. K.S. Nabors, F.T. Korsmeyer, F.T. Leighton, and J. White, "Preconditioned, adaptive, multipole-accelerated iterative methods for three-dimensional first-kind integral equations of potential theory," *SIAM Journal of Scientific Computation*, 15(3):713-735, 1994.
9. K. Nabors, J. Phillips, F. T. Korsmeyer, and J. White, "Multipole and precorrected-FFT accelerated iterative methods for solving surface integral formulations of three-dimensional Laplace problems," *Domain-based Parallelism and Problem Decomposition Methods in Science and Engineering*, D. E. Keyes, Y. Saad, and D. G. Truhlar, eds., SIAM, Philadelphia, 1995.
10. J. Phillips and J. White, "A precorrected-FFT method for capacitance extraction of complicated 3-D structures," *Proceedings of the International Conference on Computer-Aided Design*, Santa Clara, California, 1994.
11. J. Phillips, "Error and complexity analysis for a collocation-grid-projection plus precorrected-FFT algorithm for solving potential integral equations with Laplace or Helmholtz kernels," *Colorado Conference on Multigrid Methods*, April, 1995.
12. W.C. Webster, "The flow about arbitrary, three-dimensional smooth bodies," *J. Ship Research*, 19:206-218, 1975.

DISCUSSION

C.M. Lee

Pohang Institute of Science and Technology, Korea

In the present morning session, we hear that the nonlinear ship motion theory cannot prescribe the radiation condition in the far field, and hence the numerical methods developed so far are based on the so-called "open boundary condition in the far field." For the 3-D potential theory, the physical condition dictates that the diffracted and radiated waves should decay in the far field. We unfortunately do not know how far the far field should be in the numerical solutions. I would like to see somebody perform a careful experiment to provide as a guideline how we should impose the far-field conditions in our numerical solutions for the nonlinear water waves.

AUTHORS' REPLY

In wave radiation and diffraction problems where the fluid domain is infinite, a radiation boundary condition is required in the computational domain in order to make the problem well-posed. No one has yet been able to find exact radiation boundary condition for fully nonlinear wave problems. This necessitates the use of approximate radiation boundary conditions. In our problem we have steady flow in a box which is perturbed by the

presence of a body or by the generation of incident waves. The box is unbounded below, bounded above the free surface and on the centerline by symmetry. The remaining boundaries upstream, downstream and side all require appropriate boundary conditions. The examples we have published here have all been for $\tau > 1/4$ so the upstream condition is defined by the steady flow or by incident waves. The side boundary is truncated with a vertical wall made with source and collocation points that extend down to a depth of one wavelength (defined by the incident wave or the boat speed). We have also tried absorbing beaches along the side boundary but they interfere with the propagation of the incident waves. Only the downstream boundary has the "open" boundary condition. In this case we justify its use because the waves are carried out of the problem domain by the natural downstream convection of the free surface nodes. This is an implied radiation boundary condition, not a rigidly defined boundary condition, and we provide no proof of its legitimacy. Our results indicate that the "open" boundary has little effect on the wave pattern of forces on the body relative to previously published experimental results. We agree with Dr. Lee that an experiment might be contrived to provide insight into this problem. We are still searching for the perfect far-field boundary.

Computations of Wave Loads Using a B-Spline Panel Method

C.-H. Lee, H. Maniar, J. Newman, X. Zhu
(Massachusetts Institute of Technology, USA)

Abstract

This paper describes the development of a higher-order panel method based on B-splines, and its application to problems involving linear and nonlinear wave interactions with floating or submerged bodies. The use of B-splines permits a very accurate representation of the body geometry, and a continuous representation of the velocity potential on the body surface. These features result in more efficient and robust solutions relative to the conventional low-order panel method.

Several applications are described to illustrate the computational advantages of this method. These include first-order solutions for a floating hemisphere, a tension-leg platform, and a long periodic array which is representative of very large platforms proposed for floating airports and cities. Also considered are second- and third-order wave loads, where fundamental difficulties exist in evaluating the free-surface forcing functions using the low-order method. This is particularly important at third order, where we present preliminary results from an investigation aimed at predicting the occurrence of ringing.

1. Introduction

Computations based on panel methods have achieved widespread use among practicing engineers and hydrodynamicists for external-flow potential problems. In applications concerning the wave loads and motions of offshore platforms, and other stationary vessels, the first-order analysis in the frequency domain is now routine (Korsmeyer *et al.* [10], Herfjord & Nielsen [6]). Panel methods can be used not only for single bodies but also for multiple interacting vessels, with important applications to marine operations. Success also

has been achieved in extending this method to the analysis of second-order wave effects (Molin & Chen [18]; Eatock Taylor & Chau [3]; Lee & Newman [12]). However, notwithstanding the popularity and success of this technique, there are various special problems where the computational burden is severe, or where quantities are required such as gradients of the velocity field, which cannot be computed robustly from the conventional 'low-order' panel method.

In low-order methods the submerged surface of the body is represented by a large number N of flat quadrilateral panels, and the velocity potential (or the source strength) is assumed piecewise constant on each panel. Only sources were used in the pioneering work of Hess & Smith [7], with the unknown source strength determined from an integral equation derived from the boundary condition on the body. In the complementary procedure where sources and normal dipoles are used, the potential is determined more directly from an integral equation based on Green's theorem. In either of these approaches, the integral equation is replaced by a system of linear equations, with the number of unknowns equal to N .

The use of flat panels simplifies the evaluation of the integrated singularity distribution on each panel, but a relatively large number of panels are required to achieve accurate representations of the geometry and the potential. A more fundamental restriction is that the potential derived from Green's theorem cannot be differentiated analytically to derive the fluid velocity on or near the body surface; this difficulty can be circumvented in a limited manner by using a distribution of sources only, but that method also fails if gradients of the velocity field are required.

Higher-order panel methods have been devel-

oped to overcome these difficulties. Most of the higher-order methods are based on piecewise polynomial approximations of the geometry and potential on each panel, usually restricted to linear or quadratic representations using local polynomials of first- or second-degree, respectively. In this paper we describe a different higher-order approach, where B-spline basis functions are used to represent the geometry and potential. This offers the possibility of a more continuous representation, with greater geometrical flexibility and numerical efficiency. Following a preliminary investigation of this technique in two dimensions (Hsin *et al.*, [8]), we have developed a three-dimensional panel program which will be referred to as 'HIPAN'. A more detailed description of the method is contained in the thesis of Maniar [16].

HIPAN was developed initially to solve linearized radiation-diffraction problems in the frequency domain. Thus the body is fixed, or performing small oscillatory motions about a fixed mean position, and plane progressive waves are incident from a prescribed direction. The fluid is either of constant finite depth, or infinitely deep. The body may be floating on the surface or submerged. For this case the free-surface Green function can be used effectively. The analogous low-order panel method WAMIT, which is described by Lee [11], can be used to test the accuracy and relative computational efficiency of HIPAN. The efficiency of HIPAN is most apparent for relatively complicated body shapes. This will be illustrated by considering a large array of floating cylinders similar to a floating bridge. In that particular problem we find not only that substantially larger arrays can be analyzed, but also that the results display very interesting features closely related to the occurrence of trapped waves in a channel.

In many applications important nonlinear effects must be analyzed, particularly the second-order sum- and difference-frequency loads which occur at relatively high and low frequencies compared to the first-order wave spectrum. High-frequency loads are important in cases where resonant structural response is encountered. Examples include hull deflections of long slender ships, bending of vertical monotowers, and vertical motions of tension-leg platforms. Conversely, low-frequency loads are important for rigid-body motions where the restoring forces are relatively weak. Examples include the horizontal oscillations of moored and towed vessels, and the vertical response of vessels with small waterplane ar-

reas. The analysis of these second-order loads can be performed using a low-order panel method, but the computational burden is quite large and much care is necessary to ensure robust results. The extension of HIPAN to include second-order loads is currently in progress, and we are not able to show complete computations, but preliminary results which have been obtained demonstrate the improvements that may be achieved using the B-spline methodology in the second-order analysis.

It should be noted that we refer to 'order' in two completely different contexts here, one specifying the numerical approximation of the geometry and velocity potential on the body surface, and the other referring to the order of the perturbation expansion in terms of the amplitude of the waves and body motions. Low-order and higher-order panel methods are distinguished by the type of numerical approximations used, whereas first- and higher-order wave loads are defined with respect to the corresponding powers of the wave amplitude.

Recent attention in the offshore community has been directed toward higher-order nonlinear loads which are thought to cause 'ringing', a hydrodynamic/structural resonance which has been observed for large platforms in extreme wave conditions. The relevant frequencies suggest that ringing may be caused by third-harmonic wave loads, and this has motivated two recent studies which are restricted to the simplest possible geometrical configuration, a vertical circular cylinder. In the work of Faltinsen *et al.* [4] a perturbation scheme is employed appropriate to the regime where the cylinder radius and wave amplitude are of comparable magnitude, and both are small compared to the wavelength. In the complementary work of Malenica & Molin [15], a conventional Stokes expansion is used with the wave amplitude assumed small compared to the cylinder radius and wavelength and without restricting the radius/wavelength ratio. Partly to clarify the differences between these two works, and also to develop a more general computational tool for analyzing practical bodies, we have extended HIPAN to include third-order loads. Here too our present results are incomplete, but they do indicate that the Stokes expansion may be more appropriate for contemporary platforms.

In Sections 2-3 we review the boundary-value problems to be addressed, and the formulation of the panel method for solving these problems based on B-splines. Solutions of several illus-

trative problems are described in Section 4. In the concluding Section 5 other possible applications and extensions of HIPAN are discussed. For simplicity we restrict our attention to diffraction problems where the body is fixed. Except where noted the fluid depth is assumed infinite.

2. The Boundary-Value Problem

Cartesian coordinates $\mathbf{x} = (x, y, z)$ are defined with $z = 0$ the plane of the undisturbed free surface and $z < 0$ the fluid domain. In accordance with the assumptions of potential theory, and a perturbation solution in terms of a small parameter ϵ (e.g. the incident-wave slope), the velocity potential is expanded in the form

$$\Phi(\mathbf{x}, t) = \epsilon \Phi^{(1)}(\mathbf{x}, t) + \epsilon^2 \Phi^{(2)}(\mathbf{x}, t) + \epsilon^3 \Phi^{(3)}(\mathbf{x}, t) + \dots, \quad (1)$$

where t denotes time.

Assuming a discrete spectrum with frequency components ω_n , the first-order potential can be expressed as

$$\Phi^{(1)}(\mathbf{x}, t) = \text{Re} \sum_n (\phi_n^{(1)} e^{i\omega_n t}), \quad (2)$$

where $\omega_n > 0$. The second- and third-order potentials, which result from quadratic and cubic interactions among first-order solutions, can be expressed as

$$\Phi^{(2)}(\mathbf{x}, t) = \text{Re} \sum_n \sum_m (\phi_{n,m}^{(2)} e^{i(\omega_n \pm \omega_m)t}), \quad (3)$$

$$\Phi^{(3)}(\mathbf{x}, t) = \text{Re} \sum_n \sum_m \sum_l (\phi_{n,m,l}^{(3)} e^{i(\omega_n \pm \omega_m \pm \omega_l)t}). \quad (4)$$

where Re denotes the real part of the complex quantity.

The complete higher-order solutions contain a variety of frequency components. For example, the second-order solution contains the second-harmonic, mean and sum- and difference-frequency components. The third-order solution contains more diverse combinations of frequency components. To simplify the discussion here we consider the case of monochromatic first-order incident waves. Specifically we consider the second-harmonic and mean components of the second-order solution and the third-harmonic component of the third-order solution.

The diffraction potentials can be decomposed into incident and scattering components. In general, it is convenient to solve for these potentials

separately, due to their different asymptotic behavior at the far-field. However in the case of monochromatic incident waves in infinite water depth, the second- and third-order incident wave potentials vanish and it is not necessary to distinguish between the diffraction and scattering components at these orders.

The diffraction potentials are subject to the free-surface condition

$$\phi_z^{(j)} - j^2 K \phi^{(j)} = Q_f^{(j)} \quad \text{on } z = 0, \quad (5)$$

where $j = 1, 2, 3$. The forcing functions at each order j are evaluated from the following equations, with $z = 0$:

$$\begin{aligned} Q_f^{(1)} &= 0, \\ Q_f^{(2)} &= -\frac{i\omega}{g} [\nabla \phi^{(1)} \cdot \nabla \phi^{(1)} + \frac{1}{2} \phi^{(1)} (K \phi_z^{(1)} - \phi_{zz}^{(1)})], \\ Q_f^{(3)} &= -\frac{1}{g} \left[K \phi^{(1)} (\nabla \phi^{(1)} \cdot \nabla \phi_z^{(1)}) \right. \\ &\quad + \frac{1}{8} \nabla \phi^{(1)} \cdot \nabla (\nabla \phi^{(1)} \cdot \nabla \phi^{(1)}) \\ &\quad + \frac{1}{4} (K \phi^{(1)} \phi_z^{(1)} + \frac{1}{2} \nabla \phi^{(1)} \cdot \nabla \phi^{(1)}) \\ &\quad \quad (K \phi_z^{(1)} - \phi_{zz}^{(1)}) \\ &\quad + \frac{K}{8} (\phi^{(1)})^2 (K \phi_{zz}^{(1)} - \phi_{zzz}^{(1)}) \left. \right] \\ &\quad + \frac{i\omega}{g} \left[-3 (\nabla \phi^{(2)} \cdot \nabla \phi^{(1)}) \right. \\ &\quad + \frac{1}{2} \phi^{(1)} (\phi_{zz}^{(2)} - 4K \phi_z^{(2)}) \\ &\quad \left. + \phi^{(2)} (\phi_{zz}^{(1)} - K \phi_z^{(1)}) \right]. \quad (6) \end{aligned}$$

Each of the diffraction potentials also satisfies the condition of zero normal velocity on the body surface, and vanishes at large depths. In addition, they are subject to appropriate radiation conditions in the far-field. The scattering part of the first-order potential satisfies a Sommerfeld radiation condition. The far-field behavior of the second- and third-order potentials include outgoing 'free' waves, which satisfy a Sommerfeld radiation condition, and 'locked' waves which are in phase with the $Q_f^{(j)}$ [15].

Integral equations suitable for evaluating the diffraction potentials are derived by applying Green's theorem to the volume of fluid in the domain which is bounded by S_b , S_f , and a closure surface which is in the far field and at large depths below the free surface. For this purpose we use

the wave source potential as the Green function (cf. [19], equation 7.9). The resulting equations are Fredholm integral equations for the unknown $\phi^{(j)}$ over the domain S_b . The first-order diffraction potential is obtained from

$$2\pi\phi^{(1)}(\mathbf{x}) + \iint_{S_b} \phi^{(1)}(\xi) \frac{\partial G(\mathbf{x}; \xi)}{\partial n_\xi} d\xi = 4\pi\phi_I^{(1)}(\mathbf{x}) \quad (7)$$

and the higher-order potentials from

$$\begin{aligned} 2\pi\phi^{(j)}(\mathbf{x}) + \iint_{S_b} \phi^{(j)}(\xi) \frac{\partial G(\mathbf{x}; \xi)}{\partial n_\xi} d\xi \\ = \iint_{S_f} Q_j^{(j)}(\xi) G(\mathbf{x}; \xi) d\xi. \end{aligned} \quad (8)$$

In the forcing function on the right-hand-side of the latter equation the integrals over S_b and the far-field closure vanish due to the boundary conditions of the diffraction potentials as stated above.

The principal difficulty in the computation of the higher-order potentials lies on the evaluation of the integral over the free surface. The integrands are oscillatory, and slowly decaying. Truncation at a finite distance from the body is generally not adequate. Instead, following Lee & Newman [12], S_f is divided into two regions separated by a circle which encloses the body, and is of sufficiently large radius so that the effect of the evanescent modes of the scattering waves is negligible outside the circle, compared to the propagating modes. In this infinite outer region, the Green function and the velocity potentials can be expanded in Fourier-Bessel series and the integrals can be reduced to the sums of one-dimensional integrals of the products of the corresponding Bessel functions. The latter integrals are nontrivial, but they can be evaluated numerically with appropriate algorithms. Direct numerical quadrature is used for the evaluation of the surface integral over the finite inner region. The details of this procedure, and the utilization of B-spline basis functions are discussed in Section 3.3.

The integrated wave loads or exciting forces are evaluated by integrating the pressure due to the diffraction potentials over the wetted surface of the body. The final expressions for the first-, second- and third-order forces are

$$\mathbf{F}^{(1)} = -\rho \iint_{S_b} \mathbf{n} \Phi_t^{(1)} dS, \quad (9)$$

$$\begin{aligned} \mathbf{F}^{(2)} = & -\rho \iint_{S_b} \mathbf{n} (\Phi_t^{(2)} + \frac{1}{2} \nabla \Phi^{(1)} \cdot \nabla \Phi^{(1)}) dS \\ & + \frac{1}{2} \frac{\rho}{g} \int_{C_w} \mathbf{n} (\Phi_t^{(1)})^2 dl, \end{aligned} \quad (10)$$

and

$$\begin{aligned} \mathbf{F}^{(3)} = & -\rho \iint_{S_b} \mathbf{n} (\Phi_t^{(3)} + \nabla \Phi^{(2)} \cdot \nabla \Phi^{(1)}) dS \\ & + \frac{\rho}{g} \int_{C_w} \mathbf{n} \Phi_t^{(1)} (\Phi_t^{(2)} + \nabla \Phi^{(1)} \cdot \nabla \Phi^{(1)}) \\ & - \frac{K}{2g} \Phi_t^{(1)} \Phi_t^{(1)} dl. \end{aligned} \quad (11)$$

Here ρ is the water density, C_w denotes the intersection of the body with the mean free surface, and \mathbf{n} is the normal vector to the body surface. For the corresponding moments \mathbf{n} is replaced by $(\mathbf{x} \times \mathbf{n})$.

3. The B-spline Methodology

We consider a three-dimensional body (or ensemble of separate bodies) where the submerged body surface consists of a finite set ($p = 1, \dots, P$) of continuous surfaces, referred to as *patches*. The Cartesian points $\mathbf{x} = (x, y, z)$ on each patch are mapped to a rectangular parametric domain (u, v) by a continuous mapping function, which is assumed here to be described by a B-spline tensor product expansion of the form

$$\mathbf{x}^p(u, v) = \sum_{i=1}^{I_p} \sum_{j=1}^{J_p} \mathbf{X}_{ij}^p \tilde{U}_i^p(u) \tilde{V}_j^p(v). \quad (12)$$

Here \tilde{U}_i^p and \tilde{V}_j^p are B-splines of order \tilde{k} (degree $\tilde{k} - 1$) in the parametric variables u and v respectively, and $\mathbf{X}_{ij}^p = [X_{ij}^p, Y_{ij}^p, Z_{ij}^p]$ are prescribed vertices or coefficients. The total number of \tilde{U}^p and \tilde{V}^p splines used for the approximation are \tilde{I}_p and \tilde{J}_p respectively.

For a detailed description of B-splines we refer to DeBoor [2]. It suffices here to note that B-splines are polynomial functions which are non-zero over a finite span (*support*), and that their shape and continuity are dependent on the order and on a monotonic increasing sequence of real numbers

$$\begin{aligned} [\tilde{u}_1^p, \tilde{u}_2^p, \dots, \tilde{u}_{I_p+k}^p] \\ [\tilde{v}_1^p, \tilde{v}_2^p, \dots, \tilde{v}_{J_p+k}^p] \end{aligned} \quad (13)$$

which are called *knots*. The rectangular parametric space which is mapped by (12) onto the physical surface is

$$[\tilde{u}_k^p, \tilde{u}_{I_p+1}^p] \times [\tilde{v}_k^p, \tilde{v}_{J_p+1}^p] \quad (14)$$

This is referred to as the *usable* space.

As an example, Figure 1 shows one quadrant of a tension-leg platform (TLP), represented by 35 patches. On the pontoons a total of 32 patches are used, and outlined separately in the figure. Three larger patches are used to represent the column, including one on the bottom circular disk, one on the side to represent the complete circular cylinder above the pontoons, and one on the lower outside surface of the cylinder between the pontoons. (While not relevant to the representation of the geometry, each of these larger patches is subdivided for hydrodynamic purposes into smaller *panels* which we define later. These panels are outlined in Figure 1.)

Utilizing the parametric space provided by each patch, we also approximate the potential by a B-spline tensor product expansion. Thus, the potential on patch p is represented in the form

$$\phi^p(u, v) = \sum_{i=1}^{I_p} \sum_{j=1}^{J_p} \phi_{ij}^p U_i^p(u) V_j^p(v) \quad (15)$$

Here U_i^p and V_j^p are B-splines of order k in the same parametric variables u and v , dependent on the knot vectors

$$[u_1^p, u_2^p, \dots, u_{I_p+k}^p] \quad (16)$$

$$[v_1^p, v_2^p, \dots, v_{J_p+k}^p],$$

and ϕ_{ij}^p are unknown complex coefficients to be solved for.

Since different B-splines may be used in (12) and (15) the method is not restricted to be isoparametric. To ensure that the usable parametric space implicit in (15) matches that of the geometry (12), we require that $u_k^p = \tilde{u}_k^p$, $u_{I_p+1}^p = \tilde{u}_{I_p+1}^p$, $v_k^p = \tilde{v}_k^p$ and $v_{J_p+1}^p = \tilde{v}_{J_p+1}^p$. Multiple knots may be used in (12-13) to represent special features of the patch geometry. Multiple knots are not allowed in the usable space for the potential splines. In the absence of multiple knots for potential splines, we define $M_p = I_p - k + 1$ and $N_p = J_p - k + 1$, which correspond to the total number of non-zero intervals between consecutive knots of the usable space in the u and v directions respectively.

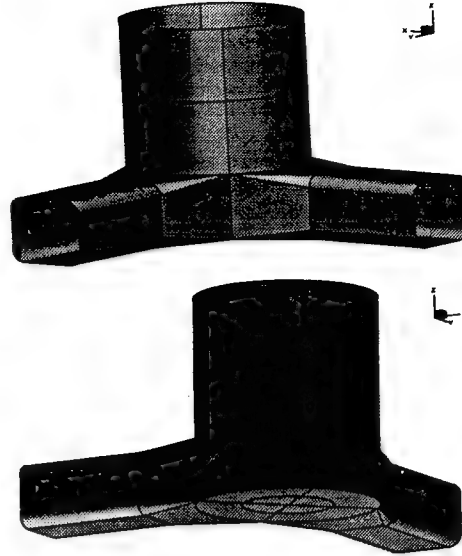


Figure 1: One quadrant of a TLP described by 35 B-spline patches. The lines on the surface are *panel* boundaries.

3.1 Features of the method

By allowing piecewise continuous bodies to be described in a patchwise fashion, one can represent a wide variety of complex structures with a very accurate geometric description of each patch.

While the potential is approximated in the same parametric variables as the surface, these two representations are otherwise independent. Consequently, increasingly accurate potential approximations can be sought without reconstructing the geometry.

The representations (12) and (15) are local approximants due to the finite support of the splines. Further, implicit in these equations is the possibility of a nonuniform distribution of the splines over the parametric space. Both of these features are desirable for approximating the solution in the vicinity of flow singularities (e.g., in the vicinity of body edges and the free surface).

An approximant based on B-splines of order k has $(k-2)$ degrees of continuity everywhere on a patch, unlike many higher-order methods where continuity is ensured only over a panel or element. Continuous descriptions of parametric derivatives of the potential can be obtained simply by analytic differentiation. Cartesian derivatives of the potential can also be derived analytically, using the parametric derivatives of the patch geometric description (see Bingham & Maniar [1]). Not only first- but also higher-order derivatives of the

potential can be derived, provided the order of the B-splines is appropriately selected.

No explicit conditions are imposed on the potential at the common boundaries of the patches. This absence of 'connectivity' between patches greatly simplifies the implementation of the method. No special considerations are required if a patch boundary coincides with a surface discontinuity where the potential is singular, as in the case of the corner at the lower edge of the TLP column in Figure 1.

3.2 The integral equation

The unknown coefficients which appear in (15) may be determined by imposing Green's theorem (7-8). For the sake of generality we define the forcing function which appears on the right side of this equation by \mathcal{F} , and also the residual r , by

$$r(u, v) = 2\pi\phi + \iint_S \phi \frac{\partial G}{\partial n} dS - \mathcal{F}, \quad (17)$$

i.e., the difference between the left- and right-hand sides of the integral equation. To obtain a linear system of equations for the complex coefficients, ϕ_{ij}^p , a Galerkin procedure is adopted. Specifically, we minimize the residual with respect to each of the (potential) B-spline tensor products directly over their support (Ω_{ij}^p) in the usable parametric space. Thus,

$$\iint_{\Omega_{ij}^p} r(u, v) U_i^p(u) V_j^p(v) du dv = 0, \quad (18)$$

for $i = 1, 2, \dots, I_p$; $j = 1, 2, \dots, J_p$; $p = 1, 2, \dots, P$. Each patch provides the same number of equations as the number of unknowns, resulting in a square complex dense system of equations of dimension $\mathcal{U} \times \mathcal{U}$ where

$$\mathcal{U} = \sum_{p=1}^P I_p \times J_p. \quad (19)$$

As a result of the Galerkin procedure, the influence coefficients in the linear system are double spatial integrals of $\partial G / \partial n$. These coefficients are evaluated by a semi-discrete Galerkin approach where the outer integral in (18) is replaced by a fixed order (N_g) product Gauss rule, applied to each of the intervals between the knots (Δ_{ij}^p) of the support of the (potential) splines in the usable space. For this purpose Gauss-Legendre

quadratures are efficient, and numerical experiments indicate that $N_g = 2$ and 3 suffice for linear and cubic B-splines, respectively. With this algorithm, the field points of the Green function in the inner integration are specified by the Gauss nodes in parametric space.

Special attention is required for the inner integrals, to account for the Rankine singularity of the Green function. When the field point lies within the domain of integration, the singularity is analytically removed and the resulting integrand expanded in a series with algebraic terms which are integrable in closed form. For other cases, and for the integrals of the non-singular part of the Green function, Gauss-Legendre quadratures are used. If the field point is near the integration domain, adaptive subdivision is used for the nearly-singular Rankine component to preserve the accuracy of the quadrature scheme. The contribution to the Green function from the free surface is evaluated using the algorithms described by Newman [19]. For further details see Maniar [16].

Similar procedures are used for the integrals of the forcing function, which are of the form

$$\iint_{\Omega_{ij}^p} \mathcal{F} U_i^p V_j^p du dv. \quad (20)$$

For the first-order diffraction potential, $\mathcal{F} = 4\pi\phi_I$, and (20) is straightforward to evaluate. In other cases the forcing function is of the form

$$\mathcal{F} = \iint f G dS$$

$$= \sum_{p=1}^P \sum_{i=0}^{M_p-1} \sum_{j=0}^{N_p-1} \iint_{\Delta_{ij}^p} f G dS, \quad (21)$$

where $f = \partial\phi / \partial n$ for first-order radiation problems and the integral is over the body surface, and $f = Q_f^{(j)}$ for second- or third-order diffraction problems with the integral over the free surface. In these cases f is approximated on each panel by a series expansion in the parametric variables, and it follows that

$$\iint_{\Delta_{ij}^p} f G dS \approx \sum_{m=0}^{N_i} \sum_{\mu=0}^m f_{\mu, m-\mu} \times$$

$$\iint_{\Delta_{ij}^p} (u - u_e)^\mu (v - v_e)^{m-\mu} G dS, \quad (22)$$

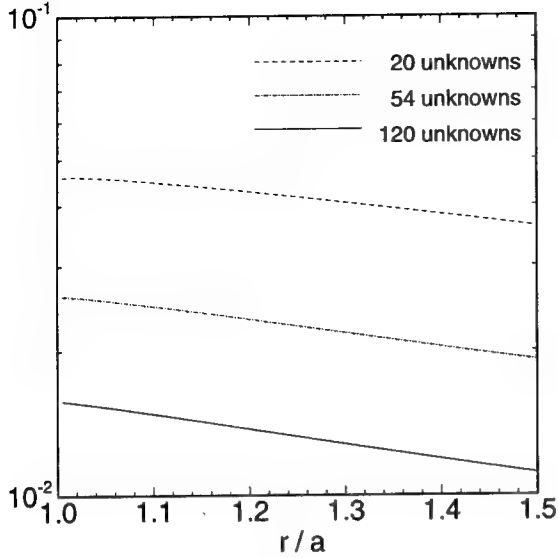


Figure 2: Relative error of $\phi^{(1)}$ on the free surface, evaluated by the low-order panel method. The geometry is a bottom-mounted cylinder (radius = a , draft $T = 0.5a$, wavenumber $\nu a = 1$) and the results are applicable along the radial line $\theta = \pi/4$ relative to the upwave direction. The number of unknowns shown is for one quadrant of the body. The total number of panels on one quadrant waterline is 5, 9 and 15 respectively.

where (u_e, v_e) is a central expansion point on the parametric space of the panel. The truncation index N_t is determined such that the first neglected term is of magnitude consistent with the other local errors.

3.3 Nonlinear methodology

When the integral equation (8) is used for the second- and third-order potentials, the principal modification is to evaluate the forcing function on the right-hand-side which involves integration over the free surface. As noted in §2, an appropriate procedure is to use numerical integration inside a circle of finite radius, and a semi-analytic analysis in the far field outside the same circle.

Since the inner integration is the most difficult computational task in the low-order panel method, we concentrate on it here and truncate the free surface at a specified partition radius r , and neglect the far field contribution in the forcing function. The resulting solutions are incomplete, but serve to demonstrate the advantages of HIPAN in solving the higher-order boundary-value problems. Another simplification which

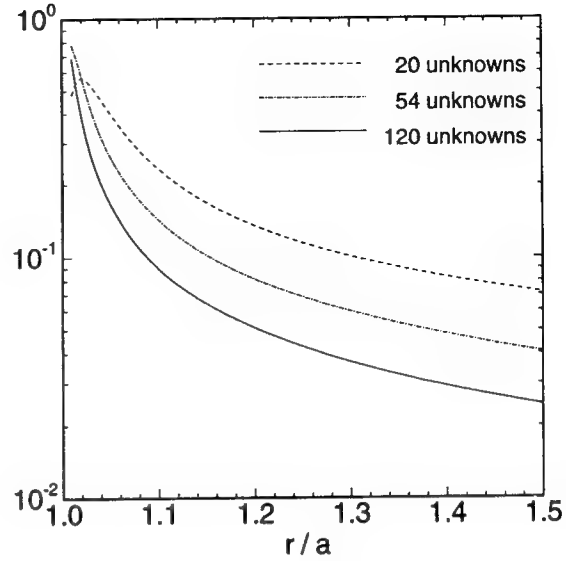


Figure 3: Relative error of $\phi_r^{(1)}$ on the free surface using the low-order panel method. See caption of Figure 2 for further details.

is made here is to neglect the contribution to the third-order forcing function from the second-order potential. This is motivated by the long-wavelength approximation of Faltinsen *et al.* [4]. Both of these simplifications can be overcome in a relatively straightforward manner, using the same procedures as in the second-order version of WAMIT.

After solving for the first-order diffraction potential using (7), the same equation is used (with the factor 4π in the first term) to evaluate $\phi^{(1)}$ at specified points on the free surface. A least-squares procedure is then used on an appropriate set of free-surface patches to approximate $\phi^{(1)}$ with B-spline expansions throughout the domain of the truncated free surface. The required first- and second- derivatives in the horizontal plane are then evaluated analytically. The required vertical derivatives are derived using the free-surface condition and Laplace's equation.

Since the above procedure results (locally) in a polynomial form for the functions $Q_f^{(j)}$, the integrals on the right-hand-side of equation (8) can be evaluated using the same algorithms described in Section 3.2. The subsequent procedure to solve (8) is essentially the same as for the first order potential.

A fundamental advantage of this procedure is that it is relatively robust in the vicinity of the body waterline, by comparison to the low-order

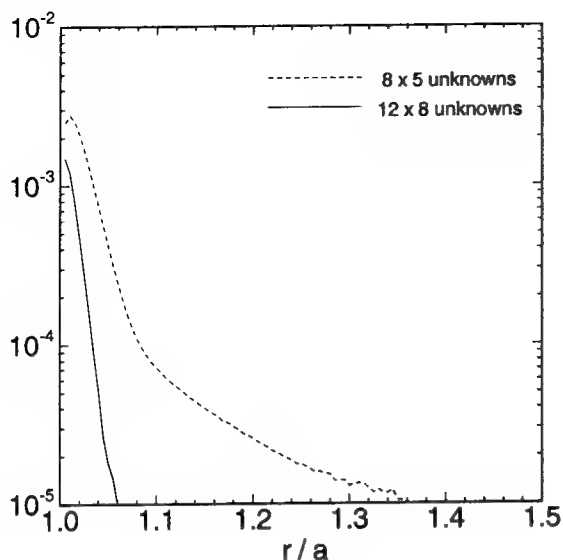


Figure 4: Relative error of $\phi^{(1)}$ on the free surface, evaluated by HIPAN. The geometry and wavenumber are the same as in Figure 2. The number of panels and unknowns shown are for one quadrant of the body.

panel method. To demonstrate this we first show results from WAMIT where the diffraction potential and its radial derivative are evaluated on the free surface, and compared with the analytical solution for a vertical circular cylinder. (These correspond more physically to the free-surface elevation and slope.)

The relative errors from the low-order computations are shown in Figures 2 & 3. In most cases the error is small, and can be reduced by increasing the number of panels, but close to the waterline intersection the derivative cannot be evaluated in a robust manner, as is true more generally near the body surface (Znao & Faltinsen [22]). (To achieve maximum accuracy from WAMIT the radial derivative is evaluated using the source formulation, and along the normal to the body boundary at the mid-point of waterline elements.) Clearly this procedure cannot be used to evaluate the second derivatives near the body. In the second-order solution this problem can be minimized by using Gauss' theorem [11], but this approach cannot be extended to third order. In Figures 4 & 5 we show the corresponding results from HIPAN. Using a similar number of unknowns as in WAMIT, the relative error of the potential is about one order smaller near the body and decays more rapidly in the radial direction. The relative error of the radial derivative is

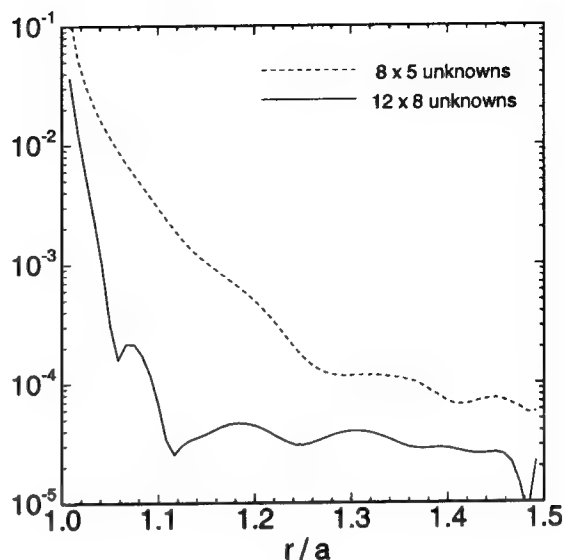


Figure 5: Relative error of $\phi_r^{(1)}$ on the free surface using HIPAN. See caption of Figure 4 for further details.

substantially smaller as well. Near the waterline intersection the error is larger than away from the waterline intersection, but the problem is far less serious than in the low order panel method. By increasing the number of panels or the order of the potential on the body, the error of the potential decreases. While a loss of accuracy is inherent in obtaining derivatives by analytic differentiation of the polynomial representation of $\phi^{(1)}$, it can be reduced with a suitable refinement of the B-spline characteristics on the body and on the free surface. The results shown in Figure 5 for $\phi_r^{(1)}$ use a B-spline representation where the potential is fit at 55×18 points on one quadrant of the free surface in the radial interval $1.0 < r/a < 1.5$. This sector is sub-divided into 12×4 panels and B-splines of order 4 are used. This representation is sufficiently accurate so that the errors shown in Figure 5 are associated only with the first-order potential representation on the body surface. Similar results have been confirmed for the second derivative of the potential.

The angular variation of the error using HIPAN is shown in Figure 6. It is interesting to note that the error is oscillatory, with maximum errors at the Gauss nodes and at the midpoints between these nodes. The error diminishes with increasing distance from the waterline intersection of the body, both radially and vertically. (Only the real part of the error is shown here since the imaginary component is relatively small.)

The free-surface Green function has a logarithmic singularity when the source and field points coincide on the free surface. This is presumed to be the dominant contribution to the errors discussed above. It is possible to treat this singularity in a semi-analytic manner, analogous to the technique described by Newman & Schlavounos [21]. This extension of HIPAN should further reduce the local error at the intersection.

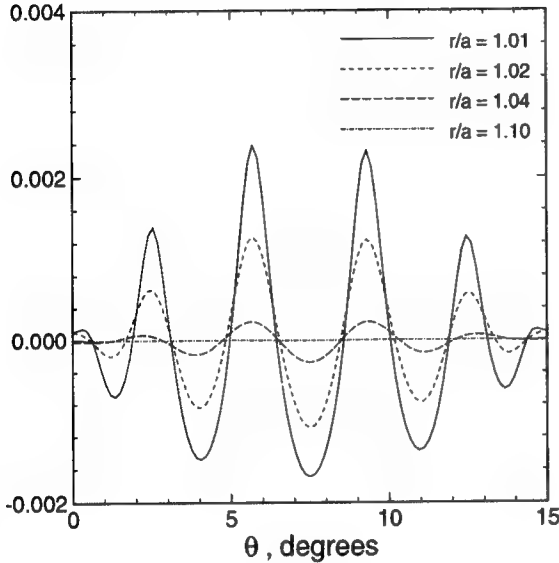


Figure 6: The error of the real part of $\phi^{(1)}$ on the free surface using HIPAN with the order of the inner Gauss-Legendre quadratures equal to six. The solution is obtained at points adjacent to the first waterline segment, at the radii r . The geometry and wavenumber are the same as in Figure 2. The number of panels is 6×2 for one quadrant of the body and the potential B-splines are cubic.

4. Results

A variety of examples are presented to demonstrate the robustness and efficiency of HIPAN. For the results presented, B-spline representation of patches are constructed by fitting points on the surface by a linear least-squares procedure. The geometric representations can be considered exact in relation to the approximation of the solutions for the velocity potentials. Generally we start with 'coarse' representations of the potential using the same knot vectors (13) as in the geometry representation. More accurate potential representations are obtained using knot vectors which subdivide the intervals between consecutive geometry knots. We define *panels* as the physical surface corresponding to the parametric

Notation	Quantity
A	wave amplitude
a	cylinder radius
d	half-distance between bodies
g	acceleration due to gravity
T	cylinder draft
λ	wavelength
ν	wavenumber
ρ	fluid density
ω	radian frequency

Table 1: Definition of commonly used symbols.

space between consecutive knots of the potential B-splines. Therefore, the number of panels refers to the product, $M_1 \times N_1$ for a body described by one patch, or the sum of products $\sum_p M_p \times N_p$ for a body described by several patches.

The most significant errors in this scheme are associated with the order (N_g) of the product Gauss-Legendre rule for the outer integration (Galerkin), and the limitations of the potential B-spline approximation (15). The latter is controlled by the total number of splines used, their degree, and their distribution over the region. Since these factors are independent, a simple but effective indicator of the approximating ability of (15) and the ensuing computational effort is the number of unknowns (19) involved. Secondary sources of error include the truncated normal derivative expansion, the amplification of errors in the solution due to an ill-conditioned linear system of equations, inaccuracies in the B-spline surface patches, and lack of continuity across patches.

Table 1 defines the notation used in presenting the results below.

4.1 First-order results

As the first example we evaluate the surge added-mass and damping coefficients for a floating hemisphere, where the benchmark results of Hulme [9] are available for comparison. One quadrant of the hemisphere is modelled as a patch ($\mathcal{P} = 1$). Symmetry is used to restrict the unknown solution to this patch, where the potential is represented by a cubic ($k = 4$) B-spline expansion. The expansion (22) for the normal derivative is truncated at degree $N_t = 4$. The outer integration is an $N_g \times N_g = 3 \times 3$ Gauss rule. Figure 7 compares the HIPAN results with those

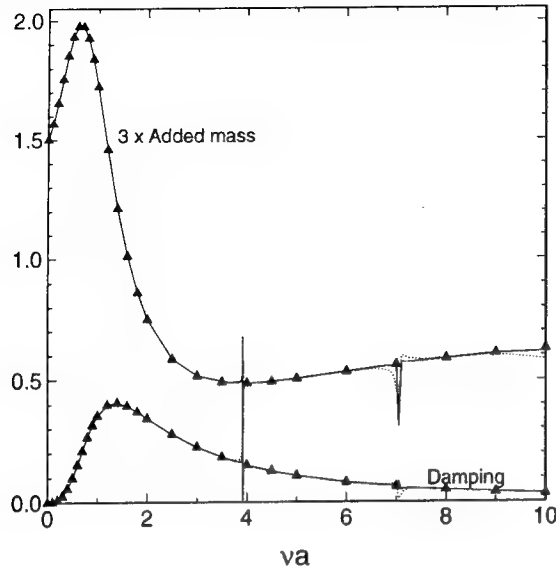


Figure 7: The surge added-mass and damping coefficients for a floating hemisphere, normalized by the factors $2\pi\rho a^3/3$ and $2\pi\omega\rho a^3/3$, respectively. The solid triangles are results from Hulme, and the dotted and solid lines correspond to computations with 2×2 and 3×3 panels per quadrant respectively.

of Hulme [9]. Two sets of results are plotted, corresponding to discretizations with $M_1 \times N_1 = 2 \times 2$ and 3×3 panels, corresponding to 5×5 and 6×6 unknowns. The corresponding curves are practically indistinguishable, except in the vicinity of the irregular frequencies. The bandwidth of the irregular frequencies is very narrow, particularly for the finer discretization.

To illustrate the application to a more complicated problem we next consider the surge exciting force on the Snorre TLP shown in Figure 1. Each quadrant of the TLP is represented by 35 patches. These computations are performed in a finite water depth (For the dimensions and depth see [12]). Two discretizations are used for the potential, labelled 'coarse' and 'fine'. The coarse discretization is shown in Figure 1, with panels as large as the entire pontoon side. The fine discretization corresponds to subdividing each panel of the coarse set into four smaller panels. Figure 8 compares the first-order surge exciting force on the TLP as computed by the present method and by the low-order panel method WAMIT. The graphical agreement with WAMIT is clear. The use of linear potential B-splines for the coarse case and cubic splines for the fine case, involve 164 and 989 unknowns per quadrant respectively.

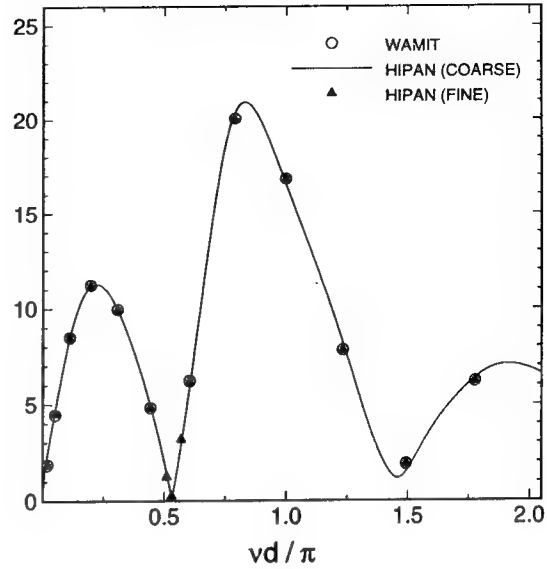


Figure 8: Surge exciting force on the Snorre TLP, normalized by $\rho g A a^2$.

We observe from Figure 8 that the maximum value of the surge exciting force occurs near $\nu d/\pi = 1$, where the wavelength λ is equal to the column spacing $2d$, and minimum values occur near the points where $\lambda/2d$ is equal to 0.5 and 1.5. These correspond respectively to the condition where the local phase of the incident waves is the same at both pairs of columns, and where the waves are out of phase. This simple explanation, which is well known, essentially follows from considering only the Froude-Krilov exciting force and neglecting the scattered pressure field. The importance of the latter, and the small shift of the maximum force to $\nu d/\pi \simeq 0.86$ corresponding to $\lambda/2d \simeq 1.16$, is illuminated by considering a long array of N circular cylinders in a single row, with equal spacing $2d$ between adjacent cylinders.

The first application of HIPAN to a long array was performed for the case of bottom-mounted circular cylinders in a finite water depth (Maniari & Newman [17]), to permit comparison with the semi-analytic interaction theory of Linton & Evans [13]. Computations were performed with up to 100 cylinders, revealing a singularly large surge exciting force (parallel to the array) acting locally on each cylinder, at the critical wavenumber where trapped waves occur for a single cylinder in a channel (Linton & Evans [14]). For $N = 100$ and $a/d = 0.5$ the local surge force on cylinders near the center of the array is about 35 times the magnitude of the force on a single isolated cylinder!

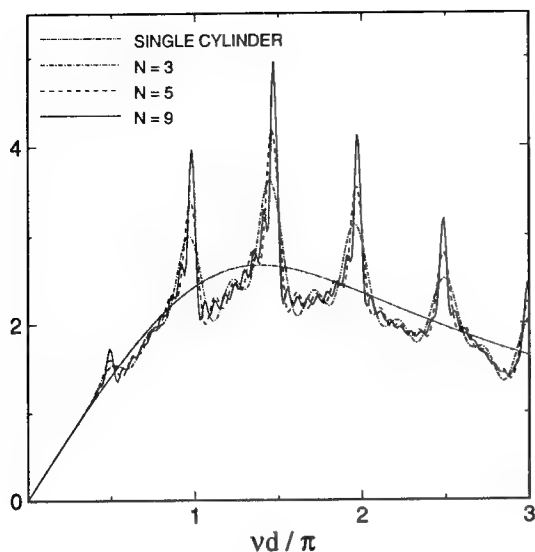


Figure 9: The magnitude of the exciting force in head seas on the first cylinder in an array of N truncated circular cylinders. The draft is equal to the radius a and the separation between adjacent cylinder centers is $2d = 10a$.

To further illustrate this phenomenon we consider the head-sea diffraction by a periodic array of N truncated circular cylinders, of radius a and draft $T = a$, with the centers separated by five diameters ($2d = 10a$). Figure 9 shows the magnitude of the exciting force on the first cylinder, for $N = 1, 3, 5, 9$. Sharp peaks are evident when $\nu d/\pi$ is equal to an integer or an integer plus one half. The peak values increase with increasing N , whereas the bandwidth decreases. Similar behavior has been observed with arrays of floating hemispheres and spheroids.

Figure 10 shows the magnitude of the exciting force on each cylinder in a long array with $N = 100$ elements, at the critical wavenumber near $\nu d/\pi = 1$. In this case the force increases along the first 20% of the array, and diminishes thereafter, with substantial sheltering only present near the leeward end. The maximum force is amplified by a factor of four times the force on a single cylinder, and total integrated force on the entire array is about two times the simple estimate based on one cylinder.

Computations of the free-surface elevation show that local 'sloshing modes' of large amplitude exist at the same wavenumbers where the exciting force on each cylinder is large. The first mode, near $\nu d/\pi = 1/2$, corresponds to the trapped mode for a single cylinder in a channel

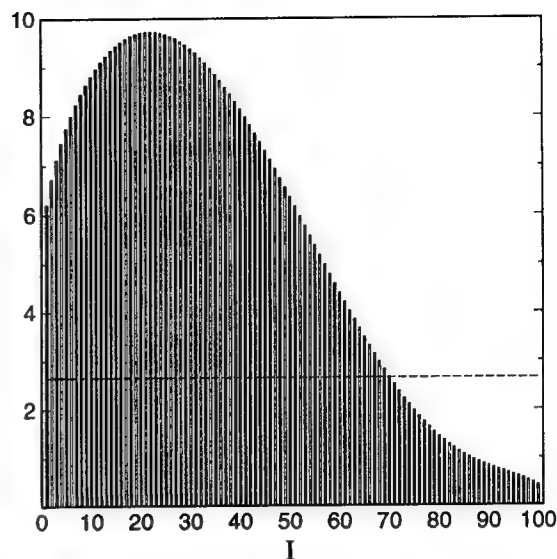


Figure 10: The distribution of the exciting force along an array of 100 truncated circular cylinders in head seas for $\nu d/\pi = 0.988$. The cylinder at the head of the array corresponds to $I = 1$. The horizontal dashed line indicates the magnitude of the exciting force on a single isolated cylinder.

with rigid walls; in this case the phase of the sloshing mode and local force differs by 180° between adjacent cylinders, and the total integrated force on the array is relatively small. The second mode, near $\nu d/\pi = 1$, appears to correspond to a trapped mode for a single cylinder in a channel with 'Dirichlet walls' where the potential is zero; here the motion at adjacent cylinders is in phase and the total integrated force is large. These trapped modes correspond to eigensolutions of the beam-sea diffraction problem in the limit $N \rightarrow \infty$. It appears that similar 'trapped' modes occur for the higher wavenumbers, corresponding to the successive peaks in Figure 9.

To address the issue of computational efficiency, Table 2 compares the number of unknowns required and execution time, for equivalent accuracy, using HIPAN and using the conventional low-order panel method. Two applications are included in this comparison, the heave exciting force on a single truncated circular cylinder and the vertical mean drift force on a submerged sphere. The times reported in the two cases are for a spectrum of 8 and 6 wavenumbers respectively. For a 1.0% – 0.1% relative error, the B-spline higher-order method is 10–200 times faster than the constant panel method. If greater accuracy is required, or for more complicated bodies,

	Relative Error	# of unknowns per quadrant	Time [seconds]
W	1%	512	44
H	1%	16 (48)	1 (3)
W	0.1%	2048	1140
H	0.1%	32 (72)	4 (17)

	Relative Error	# of unknowns	Time [seconds]
W	0.6 ~ 3%	800/quadrant	637
H	1%	- (49)/half-body	- (10)
W	0.05 ~ 1%	3081/quadrant	11428
H	0.1%	- (121)/half-body	- (108)

Table 2: Comparison of the number of unknowns and run times required to obtain equivalent accuracy, for HIPAN (H) and the low-order panel program WAMIT (W). The results in the upper table are for the surge exciting force on a truncated circular cylinder, and in the lower table for the vertical second-order drift force on a submerged sphere in finite depth. The figures in parenthesis are for cubic B-splines; the other HIPAN results are for linear B-splines. The last column shows the typical execution time, per wavenumber, on a DEC Alpha 3000/700 workstation.

the ratio of the computational effort between the two methods is even larger due to the faster rate of convergence of the higher-order method.

A comparison of the accuracy and convergence of the two programs is shown in Figure 11, for the surge exciting force on the Snorre TLP plotted in Figure 8. This example is intended to provide a more practical illustration of the computational efficiency of HIPAN, but it is somewhat difficult to study the very small errors involved in a systematic manner due to the complexity of the geometry and the difficulty of deriving benchmark values. For WAMIT the benchmarks are established by extrapolation of the computations shown. In the case of HIPAN the benchmark is a separate run with cubic B-splines and a greater number of unknowns. Uncertainties in the benchmark may be responsible for the inconsistent convergence rates shown. Nevertheless it is clear that the average errors experienced with HIPAN are 10 to 100 times smaller than with WAMIT, with similar numbers of unknowns.

The rate of convergence depends primarily on the order of the (potential) splines, their distri-

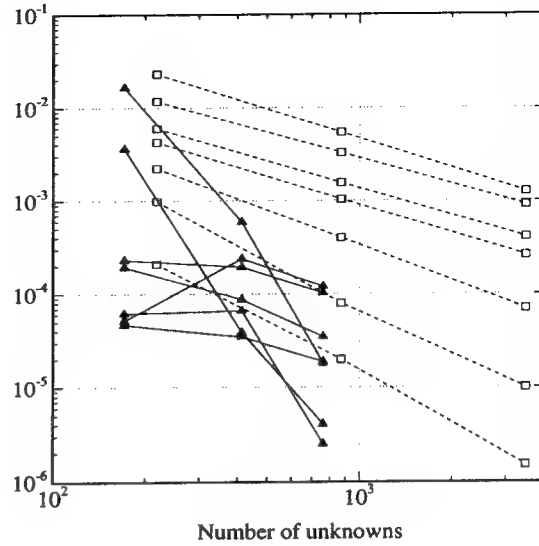


Figure 11: The computational error vs. the number of unknowns for the surge exciting force on the Snorre TLP. Each dashed line corresponds to WAMIT computations with (218, 872, 3488) unknowns. Each solid line corresponds to analogous computations from HIPAN using linear B-splines with (171, 413, 761) unknowns. Each line represents a discrete value of the wavenumber in the range shown in Figure 8.

bution on the body (governed by the use of uniform or nonuniform knot vectors) and the specific physical problem. Our experience to date indicates that for smooth bodies with uniform knots, the error in integrated quantities is proportional to $U^{-\alpha}$ where U is the total number of unknowns (19) and the exponent $\alpha \simeq 2k - 1$ (k = order of the splines). In the presence of flow singularities for bodies with corners, the use of higher-order splines based on uniformly distributed knots may result in linear convergence only. In such cases, the convergence rate is expected to improve with the use of nonuniform splines.

4.2 The second-order solution

Preliminary computations are presented here to verify the effectiveness of HIPAN in solving for the second-order potential. The problem considered is the second-order diffraction by a truncated circular cylinder with radius a and draft $T = 6a$. Cosine spacing is used to discretize the cylinder and a uniform discretization is used on the free surface. The free-surface integration in (8) is truncated at a finite radius $r = 6a$ to simplify the computations. The resulting potential

νa	$\Re\{F^{(2)}\}$ from HIPAN	
0.10	-0.07969	-0.07969
0.15	-0.32143	-0.32145
0.20	-0.47781	-0.47778
νa	$\Re\{F^{(2)}\}$ from WAMIT	
0.10	-0.0760	-0.0783
0.15	-0.3107	-0.3177
0.20	-0.4568	-0.4699
νa	$\Im\{F^{(2)}\}$ from HIPAN	
0.10	-0.05968	-0.05967
0.15	0.00932	0.00931
0.20	0.36915	0.36921
νa	$\Im\{F^{(2)}\}$ from WAMIT	
0.10	-0.0460	-0.0532
0.15	0.0321	0.0208
0.20	0.3946	0.3811

Table 3: The second-order horizontal force as computed by HIPAN and WAMIT. For the results in column 2, 96 + 86 panels are used on the body and the free surface for HIPAN and 2688 + 7680 panels for WAMIT. Finer discretizations are used in column 3, with 160 + 134 panels for HIPAN and 9984 + 30720 panels for WAMIT.

is incomplete, but since the integration over the truncated free-surface is the most computationally expensive task, we are able to evaluate the effectiveness of HIPAN without the additional effort associated with the far-field integration.

Table 3 shows the resulting second-order horizontal force, for three wavenumbers and two discretizations. Also shown are the corresponding results evaluated from the low-order panel program WAMIT. For the two B-spline discretizations the HIPAN results are converged to 4-5 decimals. The WAMIT results converge more slowly, although the number of panels is much larger.

4.3 The third-order solution

As noted in the Introduction, the problem of ‘ringing’ has focused attention on third-order wave loads, particularly the high-frequency components in a spectrum or the third-harmonic in a regular wave system. Two complementary studies of the third-harmonic force on a circular cylinder have been made by Faltinsen *et al.* [4] (‘FNV’) and by Malenica & Molin [15] (‘M&M’), using different assumptions and boundary conditions. While the magnitude of the third-harmonic force is similar in these two works, the phase is opposite

νa	FNV	$r/a = 6$	$r/a = 12$
0.025	-9.817E-04	-8.721E-04	-8.661E-04
0.05	-3.927E-03	-3.610E-03	-3.616E-03
0.10	-1.571E-02	-1.582E-02	-1.606E-02
0.15	-3.534E-02	-3.894E-02	-3.931E-02
0.20	-6.283E-02	-7.321E-02	-7.204E-02
0.025	0.00	4.017E-07	3.480E-07
0.05	0.00	7.600E-06	4.447E-06
0.10	0.00	1.101E-04	-6.292E-05
0.15	0.00	9.586E-05	-1.426E-03
0.20	0.00	-2.178E-03	-8.090E-03

Table 4: Real (top) and imaginary (bottom) parts of the third-harmonic force based on the long-wavelength approximation. The numerical solution is obtained by truncating the free surface at the radius r/a .

over the most important regime ($0.1 < \nu a < 0.4$).

We are using HIPAN to develop a more general solution of the third-order problem which is applicable to practical body shapes including the TLP. This computational approach can be developed following the boundary conditions and assumptions of either FNV or M&M, so that it is possible to develop independent results for comparison with their more analytical solutions. As a first step we simplify the solution of the third-order potential by neglecting both the far-field forcing on the free surface (as in the second-order results described above) and also the contribution to the third-order forcing function due to the second-order potential. Both of these simplifying assumptions are justified asymptotically in the long-wavelength regime, as shown by FNV.

The results presented here are for the truncated cylinder with draft $T = 6a$. This is considered to be sufficiently deep so that comparison can be made with the infinitely deep cylinder of FNV.

First, following the long-wavelength approximations of FNV, only the second term in the forcing function (6) is retained, and the Green function $G = 1/r + 1/r'$ is used to solve for the third-order potential. The resulting third-harmonic force is tabulated in Table 4 for two values of the truncation radius on the free surface, and compared with the corresponding force from the FNV analysis. The computations are relatively insensitive to the truncation radius, since the forcing is confined to the near field in the long-wavelength approximation. The agreement

νa	$r/a = 6$	$r/a = 9$	$r/a = 12$
0.025	-1.182E-03	-1.161E-03	-1.163E-03
0.05	-6.469E-03	-6.317E-03	-6.113E-03
0.10	1.013E-03	-3.141E-03	-3.354E-03
0.15	3.607E-02	4.447E-02	3.031E-02
0.20	7.451E-02	7.217E-02	9.383E-02
0.025	1.158E-04	7.391E-05	6.085E-05
0.05	3.701E-03	3.805E-03	3.668E-03
0.10	3.748E-02	3.410E-02	3.907E-02
0.15	5.654E-02	7.300E-02	6.284E-02
0.20	9.317E-02	6.980E-02	6.644E-02

Table 5: The real (top) and the imaginary (bottom) part of third-harmonic force based on the diffraction analysis.

with the FNV results is reasonable, considering the finite draft of the cylinder. The imaginary part of the force is zero in the FNV analysis, and relatively small in the computed results.

To correspond more closely with the diffraction analysis of M&M, the procedure described above has been extended by including all of the contributions from the first-order potential to the third-order forcing function (6), and by using the complete free-surface Green function. The results obtained in this manner are listed in Table 5. In this case the convergence with truncation radius is somewhat less satisfactory, except for the longest wavelength ($\nu a = 0.025$). Referring to the results for the largest radius, in the last column, and comparing these with the corresponding results in 4, it appears that the real component changes sign in the same manner as in the results of M&M, and the imaginary component is significant for all but the longest wavelength. These preliminary results appear to support the conclusion of M&M that diffraction effects are significant in the regime $\nu a > 0.1$.

5. Conclusions

The higher-order panel method described here makes use of B-splines to describe both the body geometry and the velocity potential on the body surface. The accuracy and efficiency of B-splines means that the description of the geometry can be practically exact, and the representations of the velocity potential and its derivatives are continuous. Thus wave radiation and diffraction problems can be analyzed more efficiently than with the low-order panel method, and it is possible

to develop second- and third-order solutions with a more robust evaluation of the inhomogeneous forcing function on the free surface.

A variety of examples have been used to illustrate the results of this method, based on the program HIPAN. For first-order wave loads comparisons of run time and accuracy are made with the low-order program WAMIT. One indication of accuracy is the very narrow bandwidth of the irregular frequencies in the results for a floating hemisphere. The computational efficiency of HIPAN is evident especially for applications where a relatively large number of panels are required. The long periodic array with up to 100 separate cylinders is used to illustrate the feasibility of analyzing a large complex structure which would be difficult or impractical with low-order programs.

The tests for long periodic arrays were originally intended to test the computational capabilities of HIPAN, but the results have given us a more complete understanding of the role of trapped wave modes. In particular, finite arrays of bodies are shown to experience relatively large wave loads at certain critical wavenumbers. These correspond to the existence of trapped modes, which have been associated in the past with wave diffraction by a single body in a channel of finite width.

The higher-order method is particularly advantageous in the analysis of second- and third-order wave loads. In these problems the computational cost is relatively high, and thus the efficiency of the B-spline technique is more significant. More fundamentally, the continuity of the resulting solution makes it possible to evaluate the free-surface forcing effects in a robust manner, particularly in the vicinity of the body/free-surface intersection. Another possible application where this feature may be useful is in the analysis of wave-drift damping [5].

One more possible advantage of the continuous B-spline representation is in applying the resulting wave loads to a structural-analysis code. In finite-element structural analysis it is necessary to use a refined discretization, for example with smaller elements in regions of stress concentration. This mismatch between appropriate discretizations for the hydrodynamic and structural analyses can be overcome easily if the wave loads are described continuously on the body surface.

The problems described here are based on perturbation expansions in the frequency domain,

and on the use of the special Green functions which satisfy the linearized free-surface boundary condition with harmonic time dependence. Similar higher-order techniques can be applied in the context of other applications of panel methods. One example is the solution of the double-body flow past a ship hull, where HIPAN has been used by Bingham & Maniar [1] to evaluate the so-called m -terms which involve second derivatives of the velocity potential. Another example is in the time-domain analysis of wave-body interactions, where parallel work is now underway using the transient free-surface Green function. Similar techniques may be applied also to linear and non-linear wave problems where Rankine Green functions are distributed on both the body and free surface.

An important practical consideration is the difficulty of using HIPAN. Unlike low-order panel methods where the geometry is described by a set of vertices, or points in Cartesian space situated on the body surface, HIPAN requires a set of B-spline control points which are relatively small in number, but more abstract to interpret. In practice, specialized pre-processor programs must be used in both cases, and we anticipate that suitable software will be developed so that B-splines can be used by practicing engineers with no more effort than is presently required to input the coordinates of panel vertices.

One feasible extension which offers substantial benefit in terms of 'user-friendliness' is to automate the process of testing for numerical convergence. In conventional panel methods there is no method for determining *a priori* if the panel representation of the body is sufficiently accurate in relation to the hydrodynamic parameters of interest; this question can only be answered by repeating the analysis with smaller panels and testing the results for convergence. Several examples of this procedure are described by Newman & Lee [20]. Assuming the B-spline description of a body surface is practically exact, it is relatively straightforward to automatically subdivide patches, or use B-splines of increasing order to represent the potential, and to test these results for convergence within the program. With such a procedure implemented it would be feasible for a user to specify the required precision of the hydrodynamic parameters of interest, and the program would then ensure that this precision is achieved without the need for the user to perform laborious convergence tests.

In the initial development of HIPAN we were attracted by the flexibility and elegance of B-splines. However they are but one of a large number of possible basis functions which might be used. An obvious extension is to consider rational B-splines with nonuniform knot-vectors (NURBS). In HIPAN the equivalence of B-splines to polynomials is exploited in the evaluation of the influence functions, but it appears that this restriction can be removed without substantial complication or loss of computational efficiency. It now seems feasible to develop a more general panel method where the description of the body surface is completely general, provided only that it is defined by a set of algorithms which correspond respectively to sub-regions or 'patches'. The only restriction is that the Cartesian coordinates of points on each patch can be transformed by a continuous mapping function onto a rectangular parametric coordinate space. The complete submerged surface of the body would then be described by the union of these patches. In this manner we envisage an extension of HIPAN which is applicable to any continuously-defined body shape, retaining the B-spline representation only for the solution on each patch and leaving it to the user to define the body geometry in whatever manner is most convenient and exact.

Acknowledgment

This work was conducted under a Joint Industry Project. The sponsors have included the Chevron Petroleum Technology Company, Conoco, David Taylor Research Center, Exxon Production Research, Mobil Oil Company, National Research Council of Canada, Norsk Hydro, Offshore Technology Research Center, Petrobrás, Saga Petroleum, Shell Development Company, Statoil, and Det Norske Veritas. Additional support was provided by the National Science Foundation, Grant 9416096-CTS.

References

- [1] Bingham, H. B. & Maniar, H., "Calculating the double body m -terms with a higher order B-spline based panel method", Eleventh International Workshop on Water Waves and Floating Bodies. Hamburg, 1996.
- [2] DeBoor, C., *A Practical Guide to Splines*, Applied Mathematical Sciences, 27, Springer-Verlag, 1978.
- [3] Eatock Taylor R. & Chau F. P. "Wave diffraction theory - some developments in linear and nonlinear theory," *J. of Offshore Mechanics and Arctic Engineering*, 114, 1992, pp. 185-194.
- [4] Faltinsen, O. M., Newman, J. N. & Vinje, T., "Nonlinear wave loads on a slender vertical cylinder." *J. Fluid Mech.*, 289, 1995, pp. 179-198.
- [5] Grue, J., & Palm, E., "The mean drift force and yaw moment on marine structures in waves and current." *J. Fluid Mech.*, 250, 1993, pp. 121-142.
- [6] Herfjord, K. & Nielsen, F. G., "A comparative study on computed motion response for floating production platforms: Discussion of practical procedures.", *Proc. 6th. International Conf. Behaviour of Offshore Structures (BOSS '92)*, Vol. 1, London, 1992.
- [7] Hess, J. L. & Smith, A. M. O., "Calculation of nonlifting potential flow about arbitrary three-dimensional bodies.", *J. Ship Research*, 8, 1964, pp. 22-44.
- [8] Hsin, C.-Y., Kerwin, J. E. & Newman, J.N., "A Higher-Order Panel Method Based on B-splines", Proceedings of the *Sixth International Conference on Numerical Ship Hydrodynamics*, Iowa City, 1993.
- [9] Hulme, A., "The wave forces acting on a floating hemisphere undergoing forced periodic oscillations.", *J. Fluid Mech.*, 121, 1982, pp. 443-463.
- [10] Korsmeyer, F. T., Lee, C.-H., Newman, J. N. & Sclavounos, P. D., "The analysis of wave interactions with Tension-Leg Platforms", *OMAE Conference*, Houston, 1988.
- [11] Lee, C.-H., *WAMIT Theory Manual*, Report No. 95-2, Dept. of Ocean Engg., Massachusetts Institute of Technology, 1995.
- [12] Lee, C.-H. & Newman, J. N., "Second-Order wave effects on offshore structures.", *Proc. 7th. International Conf. Behaviour of Offshore Structures (BOSS '94)*, Vol. 2, Pergamon, 1994.
- [13] Linton, C. M. & Evans, D. V., "The interaction of waves with arrays of vertical circular cylinders", *J. Fluid Mech.*, 215, 1990, pp. 549-569.
- [14] Linton, C. M. & Evans, D. V., "The radiation and scattering of surface waves by a vertical circular cylinder in a channel", *Phil. Trans. R. Soc. Lond. A*, 338, 1992, pp. 325-357.
- [15] Malenica, Š. & Molin, B., "Third-harmonic wave diffraction by a vertical cylinder." *J. Fluid Mech.*, 302, 1995, pp. 203-229.
- [16] Maniar, H., *A three dimensional higher order panel method based on B-splines*, Ph.D. thesis, Massachusetts Institute of Technology, 1995.
- [17] Maniar, H. & Newman, J. N., "Wave diffraction by a long array of circular cylinders", Eleventh International Workshop on Water Waves and Floating Bodies. Hamburg, 1996.
- [18] Molin B. & Chen X. B. 1990 *Vertical resonant motions of tension leg platforms*, Unpublished report, Institut Français du Pétrole, Paris.
- [19] Newman, J. N., "The approximation of free-surface Green functions", in *Wave Asymptotics*, P.A. Martin & G.R. Wickham, editors, Cambridge University Press, 1992, pp. 107-135.
- [20] Newman, J. N., & Lee, C.-H., "Sensitivity of wave loads to the discretization of bodies.", *Proc. 6th. Conf. on the Behaviour of Offshore Structures (BOSS '92)*, Vol. 1, London, 1992.
- [21] Newman, J. N., & Sclavounos, P. D., "The computation of wave loads on large offshore structures," *Proc. 5th. Conf. on the Behaviour of Offshore Structures (BOSS '88)*, Trondheim, 1988.
- [22] Zhao, R. & Faltinsen, O., "A discussion of the m -terms in the wave-body interaction problem", Fourth International Workshop on Water Waves and Floating Bodies. Øystese, 1989.

DISCUSSION

L.J. Doctors
University of New South Wales, Australia

I would like first to say how much I enjoyed the presentation of this work. I believe the careful analysis of the errors, such as that shown in Figures 2 through 6, is a most important and useful aspect of such research because it provides confidence in the method and the computer program.

Figure 7 shows the added-mass and damping coefficients for a floating hemisphere. The well-known problem of the misbehavior of the panel method in the neighborhood of the irregular frequencies is displayed there. Could the authors comment on how they eliminate this difficulty in practical applications of their work? In my own two-dimensional panel-method analysis of ship sections for a strip-theory ship-motion computer program, I have found the use of a "lid" on the internal free surface of a surface-piercing section to be both easy to program and very effective. Either a stationary or a moving lid seems to be equally good. This is detailed in the publication: Doctors, L.J., "Application of the Boundary-Element Method to Bodies Oscillating near a Free Surface," *Computational Fluid Dynamics, Proc. Intl Symposium on Computational Fluid Dynamics*, Sydney, Elsevier Science Publishers B.V., Amsterdam, pp. 377-386 (1988).

AUTHORS' REPLY

We thank Dr. Doctors kindly for his comments.

While the irregular frequencies are a set of isolated frequencies in the continuous problem, their effects in the discrete problem appear as erroneous solutions in the vicinity of those frequencies. The frequency bandwidth of the erroneous solution decreases as the discrete formulation of the problem is made more exact, either by increasing the number of panels in a low-order method or by using higher-order algorithms. The latter is illustrated by Figure 7, where the bandwidth is very narrow compared to typical results from low-order panel methods. Thus, the results in this Figure demonstrate the more accurate approximation to the continuous problem which can be achieved using the higher-order panel method.

There are several known techniques to eliminate the effects of irregular frequencies. Our own experience with the low-order panel method also suggested that putting a "lid" on the interior free surface is effective from the computational point of view. We have refined this technique and used it in the low-order panel code WAMIT to remove the irregular frequency effects from the first- and second-order nonlinear solution. This work was reported in Lee, Newman, and Zhu (1996). The same technique can be easily applied to the higher-order panel method but we have not done so, partly to illustrate the much narrower bandwidth that is present in the latter method.

ADDITIONAL REFERENCE

- [24] Lee, C.-H., Newman, J.N., and Zhu, X. "An extended boundary integral equation for the removal of the irregular frequency effect," *Int. J. for Numerical Methods in Fluids* (in print).

DISCUSSION

W.W. Shultz
University of Michigan, USA

1. Higher-order panels are known to be more susceptible to singularities. Have you noticed such problems at the corners? What constraints do you put on the patches?

2. The lines midway between cylinders look like appropriate locations to apply periodic boundary conditions if the wavenumber in the in-line cylinder direction is properly chosen. Then, couldn't waves come in many directions?

AUTHORS' REPLY

1. We do not place any constraints on the solution at the boundaries between contiguous patches. We find that the potential is practically continuous at these boundaries, even in cases where there is an external corner flow. Figure 12, reproduced from [16], illustrates this in the case of the streaming flow past a cube (without a free surface). The equipotential lines in this figure appear to be smooth and continuous within graphical accuracy, except for a small discontinuity which is evident near the corner where the three edges meet.

2. For a long array, the solution is nearly periodic along the array, with a constant phase shift between adjacent cylinders. Away from the resonant peaks, this phase shift is governed by the longitudinal component of the incident-wave wavenumber and by the cylinder spacing, as assumed by Linton & Evans [23]. However, at the resonant peaks, where the "sloshing modes" are dominant, the phase shift is either zero (Dirichlet modes), or 180° (Neumann modes), in accordance with the requirement that the sloshing modes be continuous between adjacent cylinders. In the latter case, the direction of the incident waves is irrelevant, as suggested by Professor Schultz.

ADDITIONAL REFERENCE

[23] Linton, C.M. & Evans, D.V., "The interaction of waves with a row of circular cylinders," *J. Fluid Mech.*, **251**, 1993, pp. 687-708.

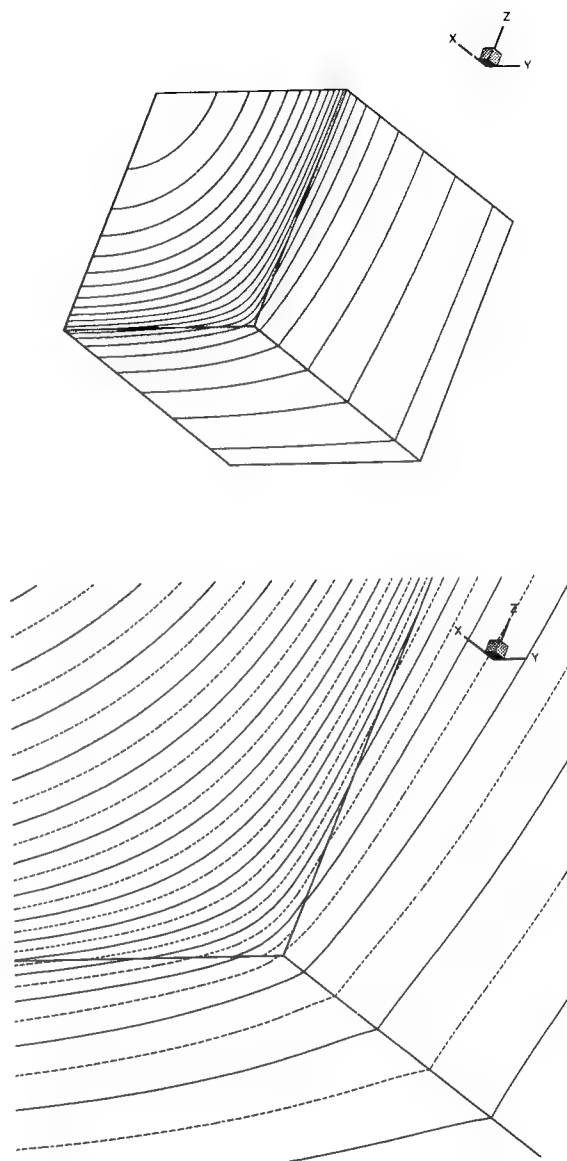


FIGURE 12: Equipotential contours on an octant of a translating cube. Each side of the octant is a patch and discretized by 8×8 panels/patch. The lower figure is a close-up of the corner showing continuity across patches.

Simulation of Strongly Nonlinear Wave Generation and Wave-Body Interactions Using a 3-D MEL Model

P. Ferrant (SIREHNA, France)

ABSTRACT

In this paper we give an overview of some of the possible applications of fully nonlinear wave simulation in three dimensions, through a report on our continuing research in this field. We describe the formulation, numerical implementation and practical applications of two different versions of the time domain Rankine panel code ANSWAVE.

The first one is based on a semi-Lagrangian formulation and is primarily applied to radiation and diffraction problems in waves of moderate steepness. The availability of an explicit model for the nonlinear incident wave allows the splitting of the total flow into incident and perturbation contributions. This "potential-splitting" formulation offers substantial savings of CPU time and memory. Applications presented hereafter include the nonlinear diffraction of long waves by a bottom-mounted vertical cylinder, the diffraction of a solitary wave by a three-dimensional obstacle, as well as the free motion of a floating body induced by a nonlinear regular wave.

In the second version, a fully Lagrangian description of the free surface is adopted, which allows the model to simulate the propagation of steep waves, possibly up to overturning, as well as their interaction with material boundaries. The behaviour of this model will be illustrated here by the simulation of large amplitude three dimensional standing waves in a rectangular tank.

INTRODUCTION

Among the different solution methods available for nonlinear free surface problems, in the frame of potential theory, the most popular is by far the mixed Euler-Lagrange method. This approach consists in a two-step procedure in which at a given time t a boundary-value problem is first solved for the normal velocities on the free surface S_f and the potential on material boundaries S_b , Φ on S_f and Φ_n on S_b being given. Then the kinematic and dynamic boundary conditions, treated as ODE's for Φ and $M(x,y,z,t)$ on S_f , are integrated in time to obtain the new positions and potential values of points on the free surface at $t+\Delta t$. The process may then be repeated to advance the solution in time.

The MEL approach was first applied in two dimensions to the simulation of steep and overturning waves by Longuet-Higgins & Cokelet (1976), and by Faltinsen (1977), who considered the interaction of waves with a floating body. Following these pioneering works, many research groups then implemented their own version of the 2D MEL method, including Vinje & Brevig (1981), and many others ([6], [7], [8], [9], [10], [18], [29]).

Its relatively moderate computational cost (compared to recent workstations power), and the easy implementation of sophisticated numerical schemes such as higher order boundary element methods, high accuracy Taylor series expansions for the time stepping, digital filtering, spline interpolations, etc..., give the 2D MEL method the

status of a mature and reliable model, which has been validated by cross-comparisons between different numerical codes (Nestegard 1994) or by comparison with experiments (Dommermuth *et al* 1988). In these conditions, it now offers a valuable power of insight into a wide variety of free surface problems, ranging from wave deformation and breaking (Dommermuth *et al*, 1988) to nonlinear wave body interactions (Cointe *et al*, 1990), coastal engineering (Grilli *et al*, 1993), long distance propagation of wave groups (Tulin *et al*, 1993), or computation of waves impacting on structures (Tanizawa & Yue 1992).

The implementation of the MEL method in three dimensions is much more difficult, and not only because of the larger number of unknowns. Of course, the typical size of the linear algebraic systems to be solved is one order of magnitude larger than in corresponding 2D applications, and the resulting memory and CPU requirements are a major issue, but other difficulties resulting from the three dimensionality of the domain must not be underestimated. This includes the accurate evaluation of the velocity components on moving surfaces, but also the implementation in three dimensions of numerical methods for the tracking of moving intersections lines between Dirichlet and Neumann boundaries, the possible regridding and/or smoothing techniques to be applied during the simulation and which are much more complicated than in two dimensions, where meshes are naturally structured and thus easy to manipulate.

These specific difficulties explain why, despite the continuous improvement of computer power and numerical methods, available results from three dimensional applications of the MEL method are still rare.

Some early publications directly tackled the problem of the diffraction of a nonlinear wave on a surface piercing body (Zhou & Gu 1990, Yang & Ertekin 1992, Chan & Calisal 1993). However, low order boundary element methods were used, with approximate treatment of free surface-body intersections and coarse discretizations, so that corresponding numerical results were merely qualitative.

At the same time, more refined numerical models were developed, based on higher order panel methods, and with special attention given to the specific difficulties of the three dimensional MEL scheme, such as the accurate computation of free

surface velocities and geometry, extrapolation techniques at the intersection lines, etc... In this category, first published results mainly concerned academic problems on simplified geometries. Kang & Gong (1990) computed waves produced by the forced motion of a submerged sphere, using a spline-based panel method with Adams-Bashforth-Moulton predictor-corrector scheme for the time stepping. Romate (1989), followed by Broeze (1993) developed a nonlinear simulation model for the propagation of waves explicitly given by a stream function theory. The interaction of these waves with bottom deformations was described in Broeze (1993). Their model is based on a second order panel method, with a fourth order Runge-Kutta scheme for the time stepping. The problem of the computation of overturning waves in three dimensions was successfully solved by Xü & Yue (1992). They used a boundary element method with bi-quadratic isoparametric curvilinear elements, under the assumption of double periodicity in horizontal directions, and without accounting for wave-body interactions, the overturning being induced by the imposition of non-zero pressure patches on parts of the free surface. More recently, Boo *et al* (1994) simulated the propagation of nonlinear irregular waves of moderate steepness, using an Eulerian scheme applied to a rectangular domain.

On the specific aspects of the three dimensional nonlinear radiation problem, recent advances have been reported by Beck *et al* (1993, 1994), using the so-called 'desingularized' method. A variety of applications were described, including the computation of added mass and damping on a modified Wigley hull at forward speed, and showed satisfactory agreement with experimental results. However, no incoming waves were accounted for in the computations.

In this paper, we describe some of the recent advances of our own approach of the solution of fully nonlinear wave-body interaction problems in three dimensions. This research started in Sirehna in 1989 and has since been mainly sponsored by the French Ministry of Defense (DRET), through successive research contracts. Unsteady linearized flows were first addressed, with the development and validation of a linearized numerical wave tank named *ANSWAVE*, including wave-body motion coupling and absorbing conditions, and based on a boundary element method (Ferrant 1991-1993). Nonlinear free

surface and body boundary conditions have then been introduced in the model, with applications related to radiation and diffraction problems for submerged bodies, using a fully Lagrangian description of the free surface (Ferrant 1994). A further step in the development of the nonlinear model was achieved with the treatment of surface-piercing bodies, involving bi-cubic spline interpolations at the free surface and extrapolation techniques at the waterline (Ferrant 1995).

We describe significant results of two versions of the code differing in the formulation of the free surface motion. The first version is based on a semi-Lagrangian formulation with an explicit treatment of the incident wave through a stream function model. This model is primarily dedicated to radiation and diffraction problems in waves of moderate steepness, without overturning. Two different applications of this version are presented. First we describe the nonlinear simulation of the diffraction of long waves by a surface-piercing vertical cylinder. Higher order loads and free surface motions are computed and compared with results from the third order frequency domain model of Malenica & Molin (1995). Thenafter, the simulation of the nonlinear free motion of a floating circular dock in a regular wave is presented.

The second version of the code uses a fully Lagrangian description of the free surface and material boundaries, which potentially allows the simulation of the generation of steep three dimensional waves up to overturning, as well as their interaction with material boundaries. It is applied here to the simulation of large amplitude standing waves in a three dimensional tank. This Lagrangian version is under development and we hope to be able to present results on the generation of steep three dimensional in a wave tank in a very near future.

FORMULATION OF THE PROBLEM

Boundary Value Problem

The fluid is heavy, inviscid and incompressible. The problem is started either from rest or from prescribed initial conditions so that the flow remains irrotational in the fluid domain D . The constant atmospheric pressure at the free surface S_f is taken as the pressure of reference. The fluid velocity derives from a scalar potential ϕ satisfying Laplace

equation in the fluid domain :

$$(1) \quad \vec{V}(M,t) = \nabla \phi(M,t) \quad \text{for } M \in D$$

$$(2) \quad \Delta \phi(M,t) = 0$$

An initial boundary value problem for ϕ is obtained by applying suitable boundary conditions on the surfaces limiting the fluid domain : the free surface S_f , the body surface S_b , and the external surface S_e which may include a bottom at finite but not necessarily constant depth.

On the body and bottom surfaces, Neumann conditions are applied :

$$(3) \quad \frac{\partial \phi}{\partial n} = \vec{V}_b \cdot \vec{n} \quad \text{on } S_b$$

$$(4) \quad \frac{\partial \phi}{\partial n} = 0 \quad \text{on the bottom}$$

where \vec{n} is the unit normal vector exterior to the fluid and \vec{V}_b is the local velocity of the body surface, relative to the fixed coordinate system $Oxyz$ with z pointing upwards and $z = 0$ on the calm water level. In the case of infinite depth, the bottom condition is replaced by :

$$(5) \quad \nabla \phi \rightarrow 0 \quad \text{for } z \rightarrow -\infty$$

Computations presented in this paper concern problems with a flat bottom at constant depth. The bottom condition is thus not explicitly satisfied, but is accounted for by an additional symmetry. The general case of a non uniform bottom may be treated without difficulty at the cost of additional unknowns.

On the free surface both kinematic and dynamic conditions must be satisfied. The kinematic condition states that the mass flux through the free surface is zero, and writes, in Lagrangian form :

$$(6) \quad \frac{D\vec{M}}{Dt} = \vec{\text{grad}} \phi \quad \text{on } (F)$$

Surface tension being ignored, the dynamic

condition accounts for the continuity of pressure across the free surface, and is obtained by applying Bernoulli's equation :

$$(7) \quad \frac{D\phi(M,t)}{Dt} = -z + \frac{1}{2} (\vec{\text{grad}} \phi)^2,$$

where D/Dt stands for the material derivative.

The formulation as described above supposes a fully Lagrangian description of the free surface, with free surface markers identified as material particles. In the present paper, this formulation will be used for the simulation of large amplitude standing waves.

In some situations, it is more convenient to prescribe the horizontal motion of markers at the free surface. In particular, the simulation of diffraction and diffraction-radiation problems described in this paper rely on a semi-Lagrangian formulation in which the horizontal motion of free surface markers is inhibited. In such a formulation, the free surface vertical coordinate becomes implicitly single-valued and may be written as :

$$(8) \quad z = \eta(x, y, t)$$

Introducing this notation in (6) and (7) and after some manipulations, we obtain new forms of the kinematic and dynamic free surface conditions, in which a fixed location of free surface markers in the x - y plane is implied :

$$(9) \quad \frac{d\eta}{dt} = -\vec{\text{grad}} \phi \cdot \vec{\text{grad}} \eta + \frac{d\phi}{dz}$$

$$(10) \quad \frac{d\phi}{dt} = -\eta - \frac{1}{2} (\vec{\text{grad}} \phi)^2$$

Compared to the fully Lagrangian formulation (6) - (7), there is an additional difficulty due to the necessary computation of the gradient of the free surface elevation in (9). A bi-cubic spline interpolation scheme, described in a following section, has been implemented for the accurate evaluation of this term together with the velocity potential and normal vectors at the free surface.

Applying Green's formula in the domain D to the velocity potential ϕ and the free space Green

function (Rankine source) :

$$(11) \quad G(M, M') = \frac{1}{4\pi MM'}$$

the following integral representation for the velocity potential is obtained, where W is the solid angle at point M :

$$(12) \quad \frac{\Omega(M)}{4\pi} \phi(M, t) = \int_s \left[\phi(M', t) \frac{\partial}{\partial n'} G(M, M') - G(M, M') \frac{\partial}{\partial n'} \phi(M', t) \right] dS_{M'}$$

In combination with the boundary conditions, the integral representation leads to a second kind Fredholm integral equation for points M on surfaces where a Neumann condition is applied and to a first kind integral equation for M on the free surface, where a Dirichlet condition is enforced.

The mixed Euler-Lagrange method consists in a time stepping procedure in which the boundary value problem is solved at each time step. At a given time t , the velocity potential on the free surface (Dirichlet condition) and its normal derivative on the other boundaries (Neumann conditions) are supposed to be given. With this mixed set of boundary conditions, the boundary value problem is solved for the normal velocity on the free surface and the potential on the other boundaries. This gives access to the right-hand sides of the free surface conditions. During a second step these equations are integrated numerically from t to $t + \Delta t$ to obtain the new position and velocity potential of markers at the free surface. In most cases, the normal velocity on other surfaces is prescribed and the process can be repeated to advance the solution in time. In the case of free body motions, the procedure is modified as described in the next section

Coupling with Body Motions

When dealing with free motions of a floating body, the main additional difficulty comes out from the necessity to solve simultaneously the dynamic equations of the body motion and the fluid problem. This requires the hydrodynamic force on the body to

be known at the current time step. The problem is with the time derivative of the potential which appear in the pressure. One solution would be to compute this term by backward differentiation from previous time steps, but it is known to lead to instabilities. Here we adopted a technique already applied for example by Vinje & Brevig (1981) or Cointe *et al* (1990), which consists in solving an auxiliary boundary value problem for Φ_t . Φ_t satisfies Laplace equation in the fluid domain, its current value on the free surface is easily deduced from Bernoulli's equation, and its normal derivative on the body surface may be expressed in terms of the velocity and acceleration of the body. Thus Φ_t is solution of an integral equation of the same form as the one that we solve for Φ . The kernel of the discretized problem is the same, the difference between the two problems lying in the right-hand sides. The acceleration terms in the Neumann condition for Φ_t on the body are factorized out in a manner similar to that exposed by Kang & Gong (1990) or Wu & Eatock-Taylor (1996), separating a memory term with an homogeneous Neumann condition on the body, and impulsive terms corresponding to unit accelerations on each of the degrees of freedom of the body. In the more general case of three dimensional motions, this results at each time step in the necessity to solve seven additional boundary value problems.

Accounting for Nonlinear Incoming Waves

The overall simulation strategy is the same as in the fully Lagrangian version (Ferrant 1994). The incident wave is given by the stream function theory of Rienecker & Fenton (1981). This steady wave solution is used to prescribe the initial conditions, as well as the time dependent boundary conditions on the outer surface of the computational domain. At time $t = 0$, the potential and wave elevation given by the incident wave model are imposed on the whole boundary of the computational domain. The Neumann condition on the body is then progressively introduced, with a ramp over half a wave period. During the simulation, Neumann conditions given by the wave model are maintained on the vertical outer boundary. On the free surface surrounding the body, the original conditions are applied, while on the other part, up to the outer Neumann boundary an absorbing layer is introduced,

in which the damping is applied only to the perturbation of the incident wave, resulting in the following modified free surface conditions :

$$(14) \quad \frac{d\eta}{dt} = -\vec{\text{grad}} \phi \cdot \vec{\text{grad}} \eta + \frac{d\phi}{dz} - v(R) (\eta - \eta_e)$$

$$(15) \quad \frac{d\phi}{dt} = -\eta + \frac{1}{2} (\text{grad } \phi)^2 - v(R) (\phi - \phi_e)$$

The coefficient v is zero except in the damping zone which is an annular portion of the free surface of radius $R = \lambda$.

In this zone, v is a cubic function varying from zero for $R = R_d - \lambda$ to its maximum value at the intersection with the vertical closing surface, for $R = R_d$. This allows a smooth transition between the numerical solution at the free surface and the incident wave model imposed on the outer boundary. This application of the absorbing layer method has some similarity with the approach of Cointe *et al* (1990) for the solution of 2D nonlinear diffraction-radiation problems.

Splitting the Incident Wave Contribution

When the incident wave is given by an explicit model, a further modification of equations (14) and (15) allows to derive a modified problem formulated in term of the perturbation induced to the incident flow by the influence of the body. A comparable procedure was exposed by Lalli *et al* (1995), and applied to the pure diffraction problem.

The perturbation (Φ_D, η_D) is defined by:

$$(16) \quad \Phi = \Phi_e + \Phi_D$$

$$(17) \quad \eta = \eta_e + \eta_D$$

where the subscript e indicates the potential or wave elevation of the incident wave, without perturbation. Plugging (16) and (17) into (14) and (15), we obtain the kinematic and dynamic free surface conditions for the perturbation flow:

$$(18) \quad \frac{d\eta_D}{dt} = -\frac{d\eta_e}{dt} - \vec{\text{grad}}(\phi_e + \phi_D) \cdot \vec{\text{grad}}(\eta_e + \eta_D) + \frac{d(\phi_e + \phi_D)}{dz}$$

$$(19) \quad \frac{d\phi_D}{dt} = -\eta_e - \eta_D - \frac{1}{2} \left[\vec{\text{grad}}(\phi_e + \phi_D) \right]^2 - \frac{d\phi_e}{dt}$$

where terms from the incident flow at the right-hand side can be evaluated exactly from the stream function wave model, without influence from time or space discretization. The problem being fully non linear, equations (18) and (19) must be satisfied on the instantaneous free surface position, and thus the incident potential may possibly be evaluated above the undisturbed incident wave. This is possible here because of the continuous prolongation of the incident potential above the incident wave. One of the advantages of this formulation is that the incident wave is treated explicitly, so that it is not altered during its travel from the external surface of the computational domain to the body. The free surface mesh only has to accommodate the perturbation flow, which is mainly composed of waves travelling in radial directions from the body. This allows us to adopt relatively coarse meshes meshes ar from the body, resulting in considerable savings of memory and CPU time, without noticeable loss of accuracy. Of course, the formulation described above is not universal and depends on the availability of an explicit model for the incident wave.

NUMERICAL METHODS

Boundary Element Method

A boundary element method is used for the solution of the boundary integral equation formulation of the problem. The method is based on isoparametric triangular elements distributed over the different boundaries. A piecewise linear, continuous variation of the solution over the boundary is thus assumed, and collocation points are placed at panel vertices. Meshes are made of an assembly of different patches, with the assumption of continuous normal on each of them. On intersection lines between two patches, two collocation points are kept at the same geometrical position, and the boundary conditions corresponding to the two surfaces are both satisfied. At the intersection between two solid patches, two Neumann conditions for the two different normals are enforced, whereas at

the intersection between solid boundaries and the free surface, both a Neumann (N) condition on the solid surface and a Dirichlet (D) condition on the free surface are satisfied. At corners of the domains, triple points and triple conditions, either of NNN or NND type. This discretization scheme reduces the integral formulation to a linear algebraic system to be solved for the normal velocity on Dirichlet boundaries (free surface) and the potential on Neumann boundaries. This system is made of the influence coefficients of linearly varying distribution of sources on boundary elements. Analytical formulas for the near field, and different approximate formulas for the intermediate and far field of the different panels are implemented. These coefficients are factorized with respect to sources or dipoles density at panel vertices, which are selected as control points. This scheme results in square systems of equations for the singularity distribution on the boundaries of the computational domain .

Solution of Linear Systems of Equations

For a moderate number of unknowns, the $O(N^2)$ task of evaluating the influence coefficients completely dominates CPU times, so that the majority of 2D mixed Euler-Lagrange formulations solve the linear system using direct $O(N^3)$ methods such as LU or Gauss elimination. Such a choice may also be convenient in linearized 3D formulations, where the time invariant kernel may be inverted once for all (Ferrant 1991, Nakos 1993).

However, in 3D nonlinear applications large systems of equations have to be solved at each time step, and any $O(N^3)$ solution algorithm must be rejected. In the present formulation, the linear systems to be solved are full and non-symmetric. Furthermore, due to mixed Dirichlet-Neumann conditions at the boundary, condition numbers are sensibly larger than for pure Neumann conditions.

Among the different existing iterative solution methods for nonsymmetric systems that have been implemented and tested in our boundary integral equation solver, we selected the GMRES scheme (Saad & Schultz 1983).

Applied to test cases with existing analytical solutions available for comparison, this scheme exhibited the better behaviour with a regular and monotonic convergence, and the lower overall CPU

cost for a given residual at convergence. The method is used with diagonal preconditioning, which reduces the necessary number of iterations by a factor of 2, at no additional cost. Further reductions of the number of iterations may be observed with more elaborate preconditioning techniques (Xü & Yue 1992), but the cost of such preconditionings applied to full matrices is no longer negligible and may annihilate the advantage of the lower iteration number. The monotonic convergence of GMRES also allows a further reduction of the necessary number of iterations, by exploiting an initial guess of the solution obtained by polynomial extrapolation from previous time steps.

Interpolations and Smoothing at the Free Surface

The quality of free surface geometry and velocity computations is essential to the stability and accuracy of mixed Euler-lagrange simulations. In two-dimensional applications of the method, free surface grids are naturally structured, which allows a straightforward implementation of higher order finite difference or interpolation schemes for the computation of normal vectors and velocities at the free surface, in terms of the location and potential values at free surface nodes. When necessary, smoothing procedures for the removal of saw-tooth instabilities are also easily introduced.

In three dimensions, the extensions of such numerical schemes requires the mapping of each part of the boundary by a set of two parameters. In Broeze (1993), each part of the domain boundary is transformed into a standard rectangular domain on which bivariate interpolation schemes are applied. In Xü & Yue (1992), the interpolation schemes are directly applied in the physical domain. In both cases, each subsurface is described by a bi-parameter array of grid points.

The discretization scheme used in the present method is based on unstructured triangulations of domain boundaries. This allows the representation of arbitrary surfaces but requires the implementation of special schemes for the computation of normal vectors and velocities at the free surface. In the general case, local polynomial fitting procedures are applied at each node of the free surface, based on the position and potential of the neighbouring nodes (Ferrant 1994).

In the applications based on the semi Lagrangian formulation, the projection of surface nodes on the x - y plane is invariant and axisymmetric, and the mesh is structured in the circumferential direction, that is nodes are distributed on circles surrounding the body, with a regular spacing on each circle. This situation has allowed us to implement a bi-cubic spline interpolation scheme for both the potential and the vertical coordinate at the free surface. These quantities are first interpolated at each radial station as functions of the azimuthal angle θ . Then, interpolating splines are computed in the radial direction, at each free surface node. At the end of the interpolation procedure, the C_1 representations for ϕ and η at the free surface allows an easily evaluation of the normal vector and velocity component, by direct differentiation of the interpolating splines. This procedure has been found to be more accurate than the local polynomial fitting. However, its extension to arbitrary geometries is not trivial.

In the Lagrangian simulations presented hereafter, the free surface is also bi-parameterized, but the potential and the three coordinates at free surface points are interpolated with respect to each parameter, directly using nodal values. This removes the restriction to a single-valued free surface

The particular structure of the mesh for the present applications also permits the implementation of smoothing formulas for the removal of possible saw-tooth instabilities at the free surface. In two dimensional MEL methods, smoothing formulas based on Chebyshev polynomials, given by Longuet-Higgins & Cokelet (1976) and revisited by Dold (1992) are most often used. Here we use five points formulas which are applied successively in each isoparametric directions.

Time Marching Scheme

After the solution of the boundary value problem and the computation of fluid velocities at the free surface, free surface conditions considered as ODE's for f and h are integrated in time, which is the second step for the MEL method. A fourth order Runge-Kutta method is used for that purpose, requiring four solutions of the boundary value problem per time step. A dynamic time step control is applied, based on a Courant condition :

$$(20) \quad \Delta t \leq C_n \left(\frac{\Delta l}{C} \right)_{\min} = \Delta t_c$$

where Δl is the minimum panel size and C the maximum fluid velocity, at the free surface. C_n is a predetermined Courant number, with $0 < C_n < 1$. In the present computations, a basic time step Δt_0 is chosen, and the time step is set to $\min(\Delta t_0, \Delta t_c)$ during the simulation, with $C_n = 0.6$.

Due to the very large CPU times required by 3D MEL simulations, some of the results presented in this paper were obtained using the Runge-Kutta scheme with "frozen" coefficients, that is the influence coefficients are updated only once per time step, while four solutions of the boundary value problem are performed.

NUMERICAL RESULTS

Nonlinear Diffraction of Long Waves by a Vertical Cylinder

A number of studies, experimental or numerical, have been recently undertaken in order to gain some understanding of the so-called "ringing" phenomenon. Ringing events observed during model tests or at sea occur in sea states with peak periods equal to 3 to 5 times the structure's resonance period, suggesting that highly nonlinear effects are involved.

If the phenomenon is to be modeled using a perturbation approach, it means that at least a third order expansion is required. Such a methodology has recently been adopted by Malenica & Molin (1995), who implemented a consistent perturbation scheme for the evaluation of third order-triple frequency loads on vertical bottom mounted cylinders submitted to regular Stokes waves. A third order time domain approach based on the code SWAN has also been undertaken by Sclavounos & Kim (1995), but up to our knowledge, no third order numerical results have yet been reported. Following a different approach, Faltinsen, Newman & Vinje (1995) developed a long wave theory in which both the radius of the cylinder and the wave amplitude are assumed to be small compared to the wavelength. The comparison of both methods gave rise to some controversy (see for example discussions at the 10th WWFEB in Oxford), as results from Malenica and

Molin seemed to restrict the validity of FNV theory to very low ka (under 0.025). However, in their conclusion, Malenica & Molin insisted on the lack of experimental validation of their results, while they suggested that fully nonlinear simulation codes were not mature enough for the accurate capture of such higher order diffraction effects.

In this section, we aim at partially answer this need for more validation, by reporting on nonlinear simulations of the diffraction of long waves on a vertical bottom-mounted cylinder. Full results including nonlinear time depending forces and runup on the cylinder as well as free surface maps in the vicinity of the cylinder are produced. Frequency domain coefficients for the forces and runups are then obtained by moving window Fourier analysis of the time series, and it is shown that with the adopted mesh density, stable results are obtained up to the fourth harmonics. However, the analysis is focused on triple frequency diffraction loads which tend to confirm M&M results in the long wave regime.

We use the semi-Lagrangian formulation with markers fixed horizontally. The incident nonlinear wave potential and elevation are given by a stream function model (Rienecker & Fenton 1981), and the problem is solved in terms of the perturbation flow, as described in a previous section.

A series of simulations have been undertaken with parameters corresponding to cases already treated by Malenica & Molin. The wavelength is set to a constant, $\lambda/H=0.785$, i.e. $kH=8$, where H is the water depth, while the radius a of the bottom-mounted cylinder is varied so that $0.05 \leq ka \leq 0.30$. The incident wave amplitude is $A/H = 0.0075$, except for the lowest wavenumber, $ka = 0.05$, for which the amplitude has been cut by half, because of stability problems in the simulations. For each different wavenumber (and cylinder radius), an adapted mesh is set up, with the free surface being discretised up to a radius equal to two wavelengths, and with a density of about 100 panels per wavelength in the vicinity of the cylinder, in order to be able to capture diffracted 3ω free waves. The mesh density becomes lower when the distance from the body increases, and the total number of panels on the half-domain is about 4000. Free surface conditions modified by damping terms acting on the perturbation potential and wave elevation are applied for radial distances over one incident wavelength.

Starting with initial conditions corresponding to

the undisturbed incident wave in the domain, the Neumann condition on the body is progressively introduced during the first wave period. Full time-depending nonlinear quantities such as wave patterns, runups and forces are available. Examples of time series are given here, for $ka=0.20$ (cylinder radius $a/H = 0.025$). Figure 1 is a plot of the horizontal force F_x on the cylinder. Figures 2 and 3 represent runups upwave and downwave, respectively. On each of these plots, the total wave elevation as well as the difference between the the total wave and the undisturbed wave, i.e. the perturbation, are given. For each of these signals, a periodic behaviour is reached within less than two periods. Nonlinearities are mostly apparent in the runups, especially at the upwave position. For comparison with frequency domain results, moving window Fourier analyses of these signals are then undercome. A window width equal to one wave period is applied. The resulting nondimensional force harmonics obtained for $ka = 0.20$ are given by figure 4, with results for the drift force F_0 up to the fourth harmonic F_4 . A zoomed graph excluding F_1 is given by figure 5. F_0 , F_1 and F_2 are very stable, some perturbations appearing for F_3 and more sensibly for F_4 , but without any drift, which is quite satisfying. F_0 and F_2 are scaled by $\rho g A^2 a$, F_1

by $\rho g A a^2$, F_3 by $\rho g A^3$ and F_4 by $\rho g A^4/a$, where A is the wave amplitude and a is the cylinder radius. The same analysis has been applied to runups upwave and downwave, see figures 6 and 7 respectively. Significant perturbations appear for the third harmonic in place of the fourth for the force. One can notice the stronger harmonic content of the runup upwave, which was already apparent on the time series.

These analyses have been repeated for values of ka ranging from 0.05 to 0.30, that is in the range for which ringing is observed. Figures 8 and 9 compare the real and imaginary parts of the triple frequency force F_3 obtained with ANSWAVE, with results from the frequency domain third order analysis of Malenica and Molin. The agreement is believed to be quite satisfactory, especially when one considers the very low absolute level of the 3ω force which is extracted from the force time series. For example, for $ka = 0.20$ and $2A/H = 0.015$, there is a scale of about 1 to 200 between F_1 and F_3 .

Globally, a quite satisfactory agreement has been found with previously published frequency domain results of Malenica & Molin on the triple frequency horizontal force. With the levels of time and space discretization adopted, nonlinear simulations using ANSWAVE produce stable results up to the fourth

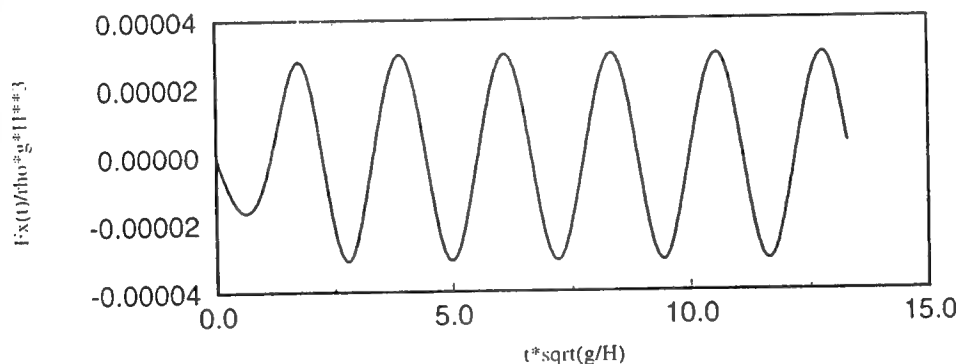


Figure 1 : Time series of the inline force F_x , $ka = 0.20$. $kH = 8$.

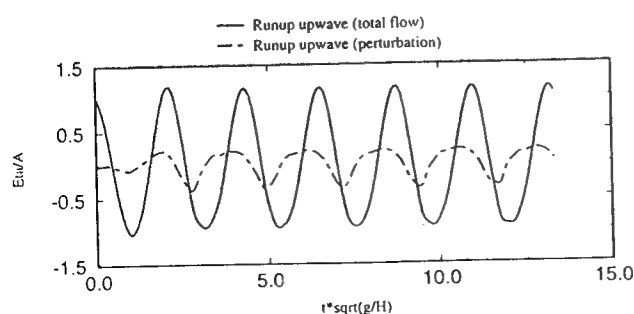


Figure 2: Runup upwave. $ka=0.2$ $kH=8$. $2A/H=0.015$

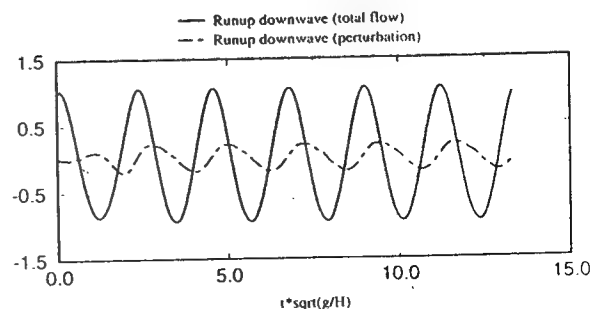
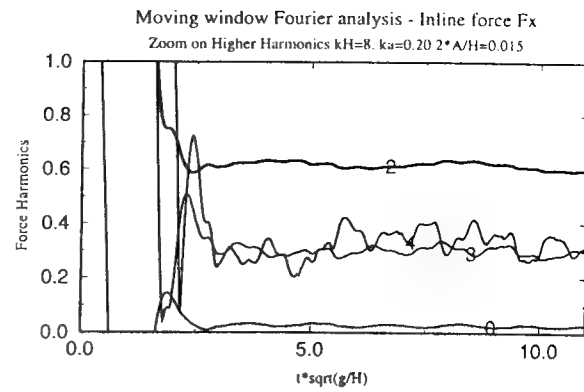
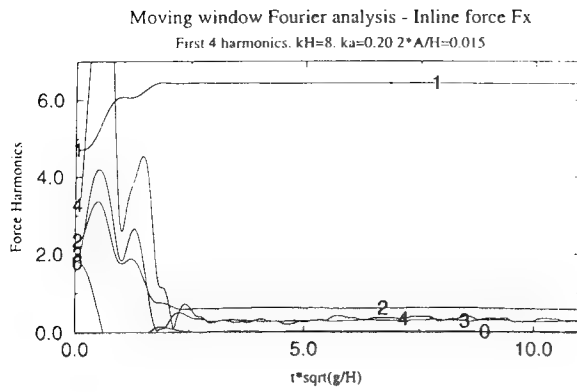
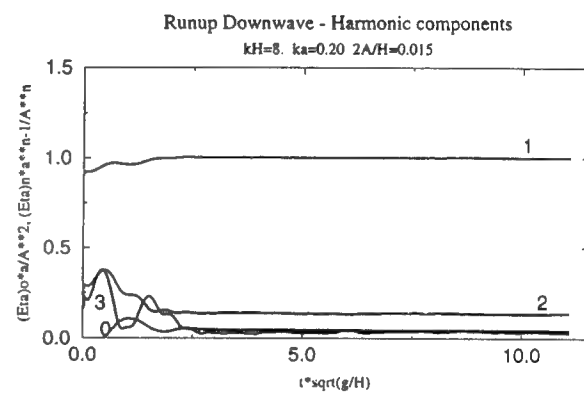
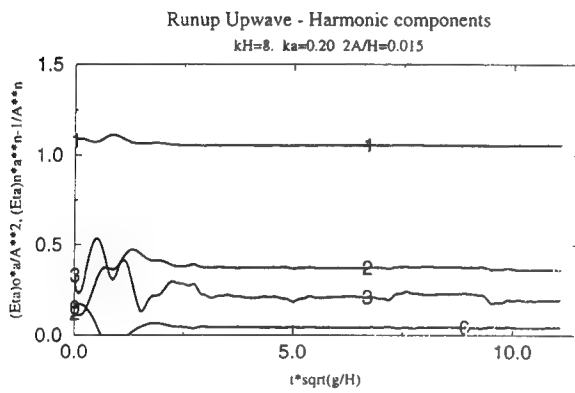


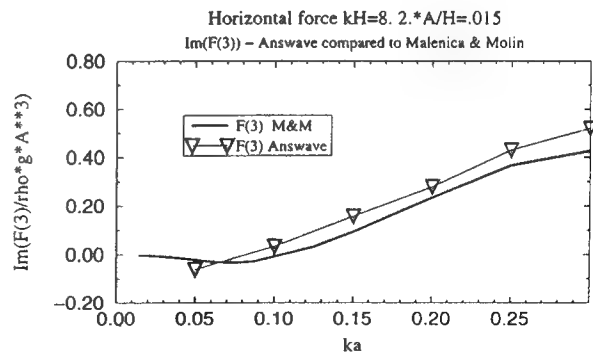
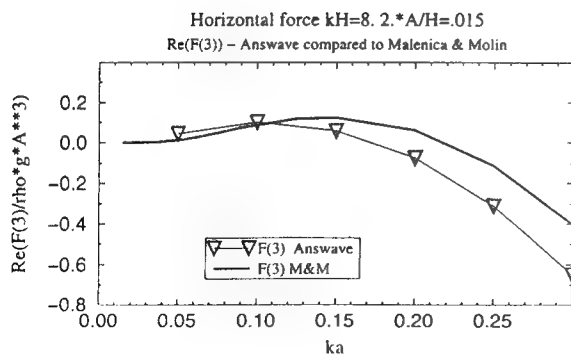
Figure 3: Runup downwave



Figures 4 and 5: Moving window Fourier analysis of the force. $ka=0.20$ $kH=8$. $2A/H=0.015$



Figures 6 and 7: Moving window Fourier analysis of the runups. $ka=0.20$ $kH=8$. $2A/H=0.015$



Figures 8 and 9: Components of the triple frequency force compared to M&M results.

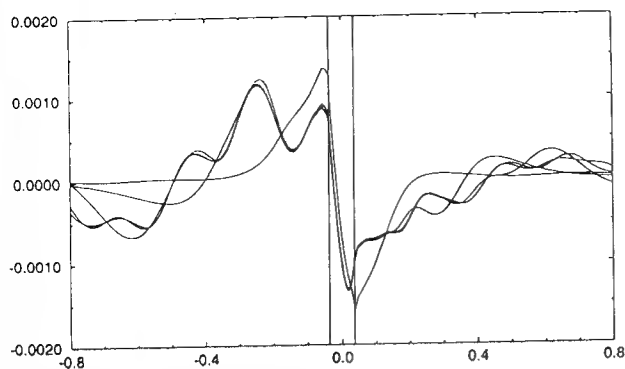


Figure 10: Perturbated wave in the symmetry plane
 $t/T=1.5, \dots, 4.5$. $ka=0.3$ $kH=0.8$ $2A/H=0.015$

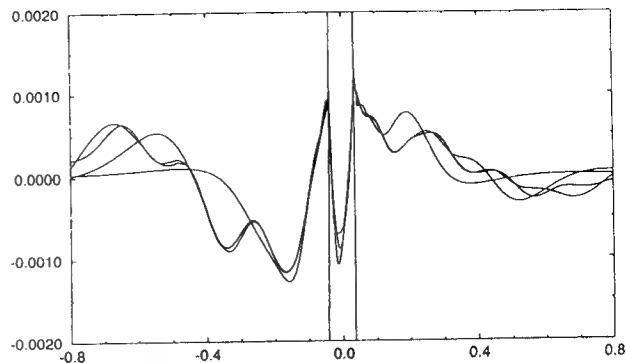


Figure 11: Perturbated wave in the symmetry plane
 $t/T=1.5, \dots, 4.5$. $ka=0.3$ $kH=0.8$ $2A/H=0.015$

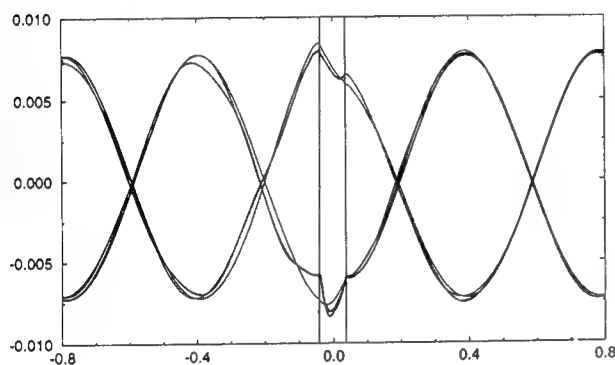


Figure 12: Total wave in the symmetry plane

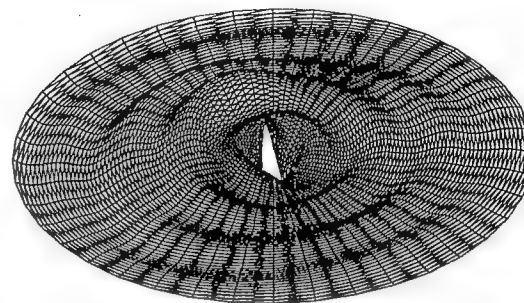


Figure 13: Perturbated wave elevation $t=5T$ $ka=0.3$

harmonic for the forces and to the third harmonic for the runups.

Some further results concerning the free surface deformation are presented in figures 10 to 13. These figures correspond to $ka=0.30$, $kH=8$, and $2A/H=0.015$. Figures 10 and 11 represent plots of the perturbation elevation in the vertical symmetry plane, respectively for integer values of the number of simulated periods for figure 10 ($t/T=1,2,3,4,5$) and for intermediate values for figure 11 ($t/T=1.5, 2.5, 3.5, 4.5$). Only a part of the computational domain of radius equal to one wavelength is considered. The perturbation wave field is mainly composed of a fundamental part of wavelength λ , plus 2ω waves of wavelength $\lambda/4$. One can notice the onset of a periodic steady state perturbation around the cylinder, and also the relatively steep trough on the side of the cylinder, which, if extrapolated to larger incoming waves, would certainly lead to a local breaking as observed in some experiments. Figure 12 represents the total wave in the symmetry plane, plotted every half of a period, while figure 13 is a three dimensional plot of the perturbation free surface in the disk of radius λ around the cylinder. In figures 10, 11 and 12, the incident waves comes from the left. In figure 13, the

incident waves propagates from the upper left of the plot to the opposite corner.

As a conclusion to this section, we first recognize that simulations with larger amplitudes are obviously desirable, in order to illustrate the anticipated divergence between fully nonlinear modelization and perturbation analysis. However we need first to improve the stability of the model. Another necessary comment is on the fact that the estimation of the higher harmonic components of the diffraction force in long waves from fully nonlinear simulations is very difficult, because of contradictory requirements. On one side, we must work with very low incoming wave amplitudes in order to respect the conditions of applicability of perturbation analysis. On the other side, the estimation of higher order harmonics from the time series becomes less and less accurate when their relative contribution to the signal goes to zero. In fact some further computations recently performed with varying amplitudes seem to indicate that the value of the amplitude chosen for comparison with perturbation analysis, $2A/H=0.015$, is not enough small to get stabilized values of the force coefficients. This probably explains the remaining small difference between coefficients obtained from

nonlinear simulation and those from perturbation analysis, illustrated by figure 8 and 9.

Cross comparison between existing three dimensional fully nonlinear simulation programs is also very desirable for quantities for which no reference results are available, such as higher order runups and 4ω forces (and over).

Nonlinear Motion of a Floating Dock in Regular Ambient Waves

In this section we present results of the simulation of the nonlinear motion of a floating body induced by regular incident waves. The formulation used is the same as for the application described in the previous section, except that here we simultaneously solve the dynamic equations of the body motion and the fluid flow problem. The floating body is a truncated vertical cylinder of radius $r/H = 1/3$ and of draft at equilibrium $d/H = 1/6$. Only vertical motions are allowed, the other degrees of freedom being inhibited. We consider a regular incoming wave of wavelength $\lambda/H = 6.064$, and of amplitude $A/H = 0.05$. The period is $T \cdot \sqrt{g/H} = 7.0$, that is twice the natural heaving period of the floating body. The radius of the computational domain is equal to two wavelengths, and the mesh is composed of 3560 panels on the half domain, that is 3160 on the free surface and 400 on the body. Figure 14 gives a plot of the mesh, after truncation at a radial distance of about half a wavelength. We used 50 constant time steps per period, and the simulation was run for 10 periods. The resulting time series of the vertical displacement, velocity and acceleration are given in figure 15. As expected, the motion contains a significant 2ω component, resulting from the resonant excitation of the natural heaving motion of the body by nonlinear terms in the hydrodynamic force. Figure 16 illustrate the

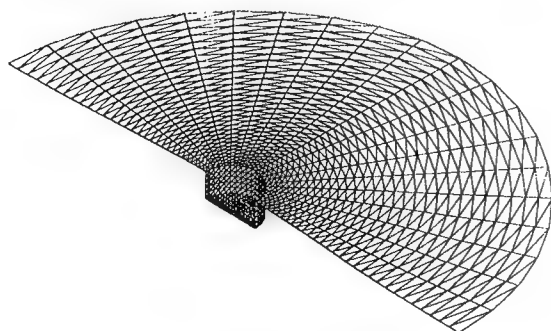


Figure 14: Partial view of the mesh

result of a moving window Fourier analysis of the vertical motion. Only the fundamental and second harmonics are significant. The amplitude of the fundamental component is close to the wave amplitude, which is consistent with the relatively low wave frequency. The amplitude of the 2ω component of the motion is about 20% of the fundamental one.

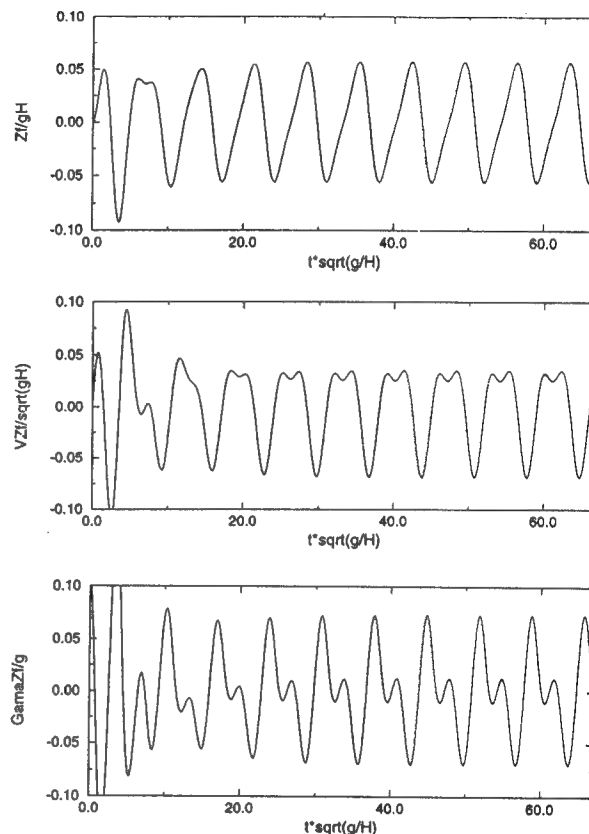


Figure 15: Vertical displacement, velocity and acceleration of a freely floating cylinder in regular incoming waves.

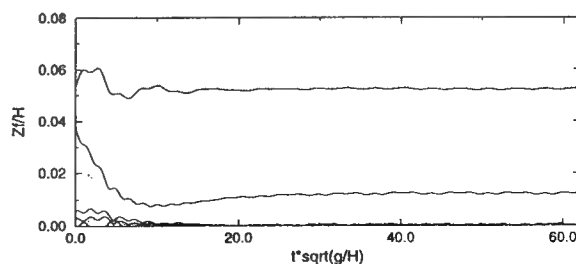


Figure 16: Moving window Fourier analysis of the vertical displacement

Large Amplitude Standing Waves in a Three Dimensional Tank

This last numerical application is dedicated to the demonstration of the behaviour of the fully Lagrangian version of the code. We compute the nonlinear fluid motion inside a three dimensional tank subject to an initial surface elevation. The tank dimensions are $(L_x, L_y, H) = (2, 4, 1)$, and the initial free surface elevation is $\eta_0 = A \cos(\pi X/2) \cos(\pi Y/2)$, with $A = 0.3$. The half domain is discretized by a total of 2450 panels. Figure 17 gives a view of the initial shape of the fluid domain. A constant time step $\Delta t \cdot \sqrt{g/H_0} = 0.025$ has been adopted, and the simu-

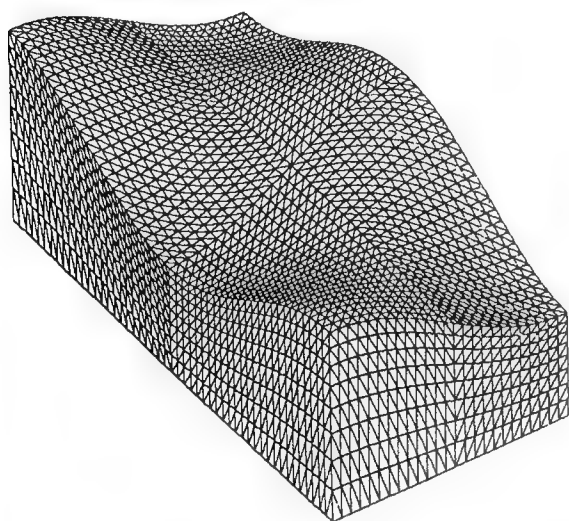


Figure 17: Initial free surface elevation in the tank.

lation was run for 1000 time steps. The fully Lagrangian formulation is used here, and we regrid the free surface at each time step with the constraint of keeping a constant difference in arc length between neighbouring nodes. Without regridding, we observed the concentration of nodes in certain regions of the free surface, leading to a necessary reduction of the time step and thus of the computing time. Walls are simply regridded in vertical directions at each time step, starting from the position of nodes on the intersection line with the free surface. The time marching is based here on the full Runge-Kutta scheme, with no "frozen coefficients" approximation. In these conditions, the total computing time was about 30 hours on a HP9000/J200 workstation.

Figure 18 gives the time series of the free surface elevations at two particular points: $(X, Y) = (0, 2)$ and $(X, Y) = (0, 0)$. We observe that, due to nonlinearities, there is no periodicity in the time series. Furthermore, large amplifications are observed, especially in the corner $(0, 0)$, where the elevation is above 0.5 for $t = 4.5$ and $t = 13.2$. We give in figures 19 to 24 plots of the computational domain at instants marked by vertical arrows in figure 18. Equal scales are adopted in horizontal and vertical directions. The free surface never recovers its initial shape, and there is no instant at which it is flat, as would be observed in a linearized computation.

The initial fluid volume is $V_0 = 8.0$. After 1000 time steps, the final value is $V_f = 7.99$, so that mass

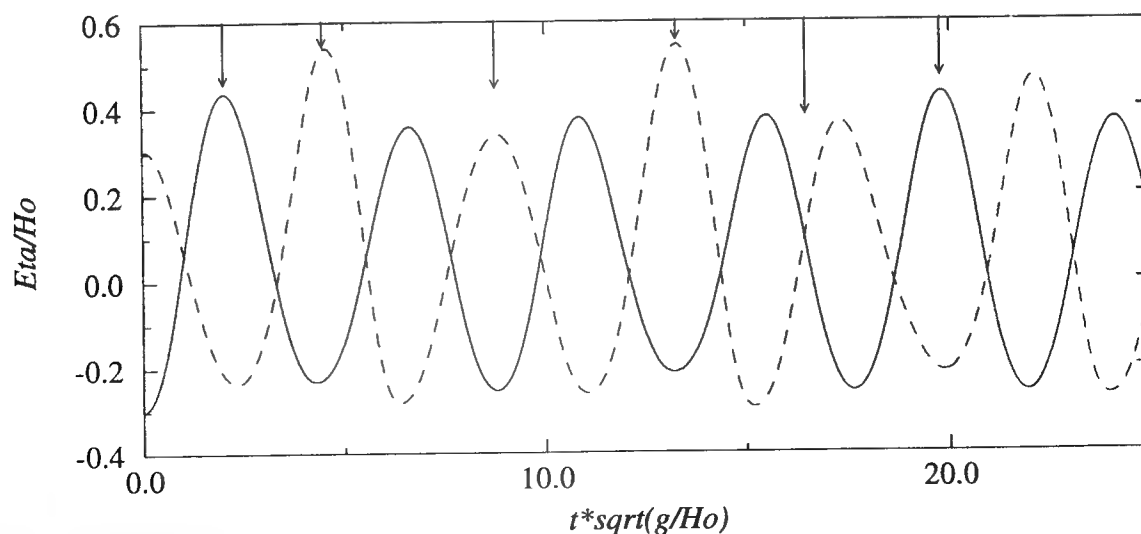


Figure 18: Free surface elevation at $(X, Y) = (0, 2)$ (solid line) and $(X, Y) = (0, 0)$ (dashed line)

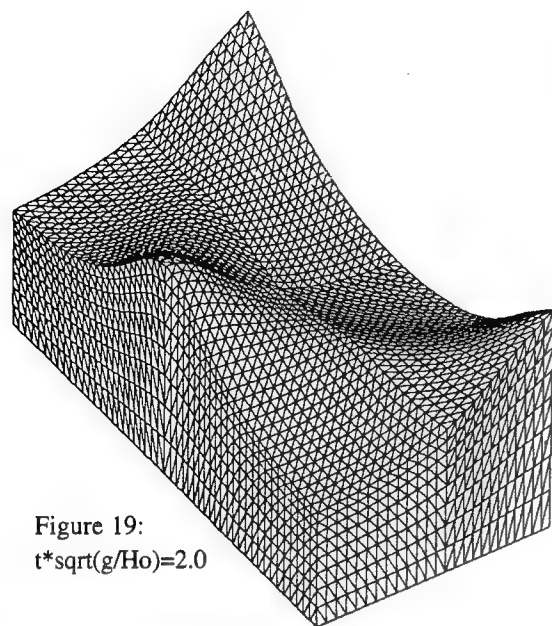


Figure 19:
 $t\sqrt{g/H_0}=2.0$

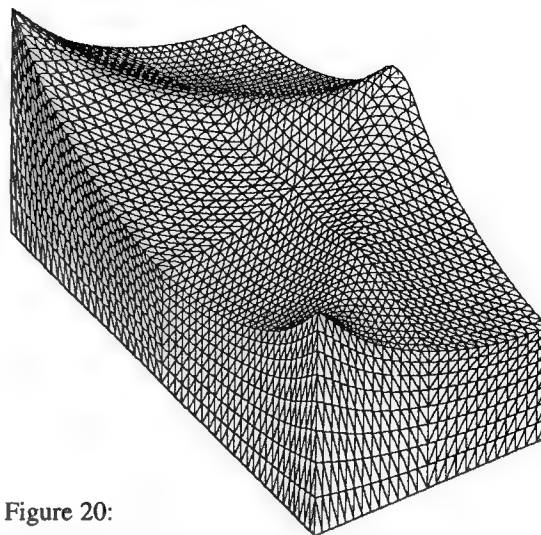


Figure 20:
 $t\sqrt{g/H_0}=4.5$

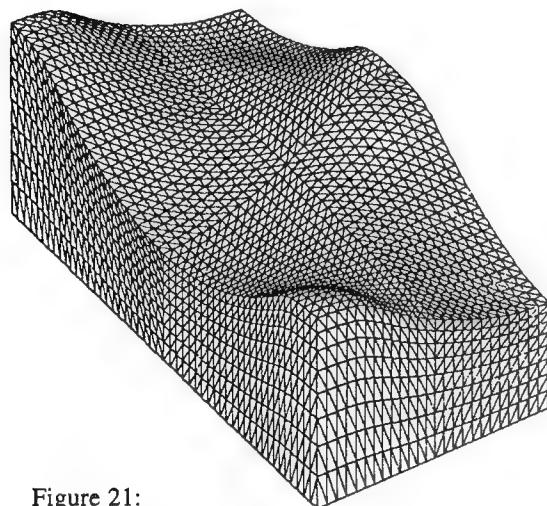


Figure 21:
 $t\sqrt{g/H_0}=8.75$

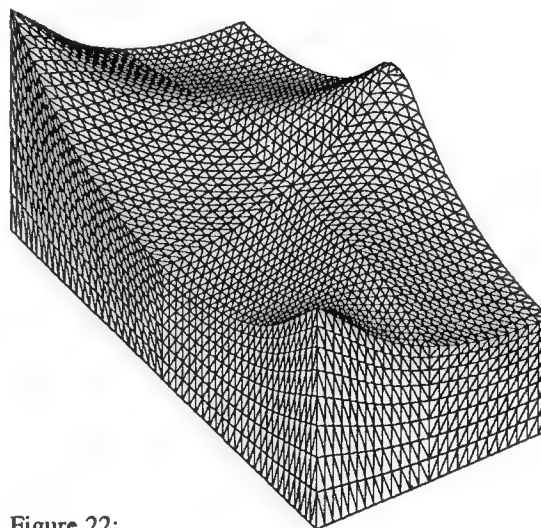


Figure 22:
 $t\sqrt{g/H_0}=13.2$

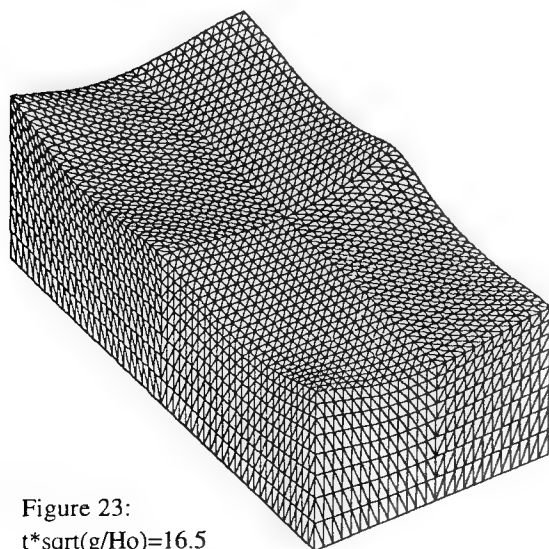


Figure 23:
 $t\sqrt{g/H_0}=16.5$

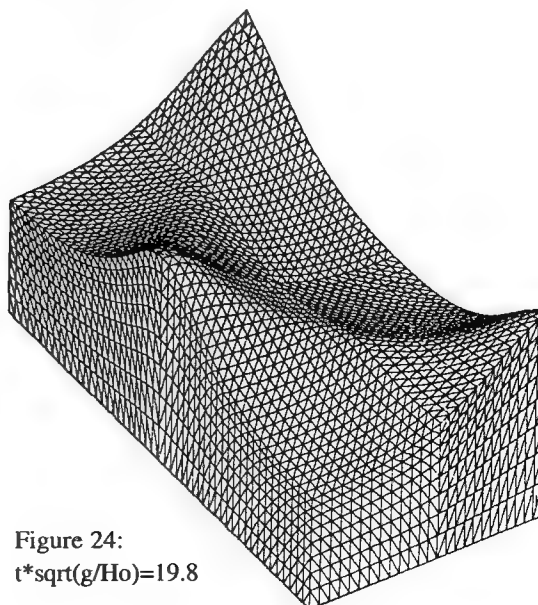


Figure 24:
 $t\sqrt{g/H_0}=19.8$

conservation is satisfied within an relative accuracy of about 10^{-3} . Similar figures are obtained regarding energy conservation.

CONCLUSION

Significant results of two different version of the three dimensional Rankine panel code ANSWAVE have been presented. Both version solve fully nonlinear free surface problems under the assumptions of potential flow.

The first version is based on a semi Lagrangian representation of free-surface motions, with markers fixed horizontally, and is formulated in terms of a perturbation flow defined as the difference between the incident and the total flow. This splitting is possible here with fully nonlinear free surface conditions because of the characteristics of the incident wave model based on a stream function theory. We first discuss with more details original results on the nonlinear diffraction of long waves by a bottom-mounted vertical cylinder, already presented at the 11th WWFEB in Hamburg (Ferrant 1996). The capacity of the model to capture stable higher order components of the diffracted flow is attested, although it seems to be difficult to find a common range of applicability of fully nonlinear simulation and of higher order perturbation analysis. This point will motivate further research in order to improve the accuracy of the model at low amplitudes, as well as its stability for larger ones. This first model has been extended to the problem of the free motions of a floating body in regular incoming waves. The behaviour of the model in such a configuration is illustrated by the stable simulation of the nonlinear vertical motion of a floating cylinder, over 10 wave periods.

The second version is based on a fully Lagrangian formulation. It is applied here to the computation of large amplitude standing waves in a three dimensional tank. Strongly nonlinear effects are observed, while the accuracy of the simulation is attested by mass and energy conservation. The Lagrangian representation of the free surface is potentially more adapted to the simulation of steep waves interfering with moving boundaries, a problem on which we concentrate our present research efforts.

Acknowledgments

The development of the code ANSWAVE was supported by the French Ministry of Defense, under contract DRET/SIREHNA 94/360. The application to nonlinear diffraction problems was part of a CLAROM project on "high frequency resonance of offshore structures", with BUREAU VERITAS, DORIS ENGINEERING, IFP, IFREMER, PRINCIPIA and SIREHNA as partners.

References

- [1] Beck R.F., Cao Y. & Lee T.H. (1993) 'Fully nonlinear waterwave computations using the desingularized method' - Proceedings 6th Conference on Numerical Ship Hydrodynamics, University of Iowa.
- [2] Beck R.F., Cao Y., Scorpio S.M. (1994) 'Nonlinear ship motion computations using the desingularized method' - Proceedings 20th Symposium on Naval Hydrodynamics, University of California, Santa Barbara.
- [3] Boo S.Y., Kim C.H., Kim M.H. (1994) 'A numerical wave tank for nonlinear irregular waves by 3D higher order boundary element method' - Int. Journal of Offshore and Polar Eng., Vol. 4, n° 4
- [4] Broeze J. (1993) 'Numerical modelling of nonlinear free surface waves with a panel method' - Ph. D. Thesis, University of Twente, Netherlands
- [5] Chan J.L.K. & Calisal S.M. (1993) 'A numerical procedure for time domain nonlinear surface waves calculations' - Ocean Engng., Vol. 20, n° 1, 19-32
- [6] Clément A., Mas S. (1995) 'Hydrodynamics forces induced by a solitary wave on a submerged circular cylinder' - ISOPE'95 Conference, The Hague, Netherlands
- [7] Cointe R., Geyer P. & Molin B. 'Nonlinear and linear motions of a rectangular barge in a perfect fluid' - Proc. 18th ONR Symp. on Naval Hydrodynamics, Ann Arbor, Michigan
- [8] Cooker M.J., Peregrine D.H., Vidal C. & Dold J.W. (1990) 'The interaction between a solitary wave and a submerged semicircular cylinder' - J.F.M., 215, 1-22
- [9] Dommermuth D.G., Yue D.K., Lin W.M., Rapp R.J., Chan E.S. & Melville N.K. (1988) 'Deep water plunging breakers : A comparison between potential theory and experiments' - J.F.M., Vol. 189, pp. 423-442

- [10] Dold J.W. (1992) 'An efficient surface-integral algorithm applied to unsteady gravity waves' - *Journal of Comp. Physics*, Vol. 103, PP 90-115
- [11] Faltinsen O.M. (1977) 'Numerical solution of transient free-surface motion outside or inside moving bodies' - *Proceedings 2nd Conf. on Num. Ship Hydro.*, U.C. Berkeley
- [12] Faltinsen, O.M., Newman, Vinje T. (1995), 'Nonlinear wave loads on a slender vertical cylinder', *J.F.M.* vol.289, pp 179-198
- [13] Ferrant P. (1991) 'Threedimensional unsteady wave-body interactions in a bounded domain' - 6th International Workshop on Water Waves and Floating Bodies, Woods Hole, Massachusetts
- [14] Ferrant P. (1993a) 'Computation of fully nonlinear free surface flows in three dimensions' - 8th International Workshop on Water Waves and Floating Bodies, St John's, Newfoundland
- [15] Ferrant P. (1993b) 'Threedimensional unsteady wave-body interactions by a boundary element method' - *Ship Technology Research*, Vol. 40 n° 4, 165-175
- [16] Ferrant P. (1994) 'Radiation and diffraction of nonlinear waves in three dimensions' - *Proceedings of the BOSS'94 Conference*, MIT, Cambridge
- [17] Ferrant P. (1996) "Computation of higher order diffraction effects using a fully nonlinear simulation method" 11th International Workshop on Water Waves and Floating bodies, Hamburg
- [18] Grilli S.T., Losada M.A., Martin F. (1993) 'Impact of breaking waves over emerged and submerged coastal structures' - 8th International Workshop on Water Waves and Floating Bodies, St John's, Newfoundland
- [19] Kang C.G. & Gong I.Y. (1990) 'A numerical solution for three dimensional nonlinear free surface problems' - 18th ONR Symposium on Naval Hydrodynamics, Ann Arbor, Michigan
- [20] Lalli F, Di Mascio, A. & Landrini M. (1995) 'Nonlinear diffraction effects around a surface-piercing structure', *Proceedings of the ISOPE'95 Conference*, The Hague
- [21] Longuet-Higgins M.S., Cokelet E.D. (1976) 'The deformation of steep water waves on water : I.A. numerical method of computation' - *Proc. R.Soc.Lond*, A350, pp. 1-26
- [22] Malenica S. , Molin B. (1995) 'Third harmonic wave diffraction by a vertical cylinder' *J.F.M.* vol 302, pp203-229.
- [23] Nakos D.E. (1993) 'Rankine panel methods for transient free surface flows' - 6th International Conference on Numerical Ship Hydrodynamics, Iowa City
- [24] Nestegard A. (1994) 'Comparative study of fully nonlinear wave simulation programs'. DNV Research report 94-2041.
- [25] Rienacker M.M. & Fenton J.D. (1981) 'A Fourier approximation method for steady water waves' - *J.F.M.*, 104, 119-137
- [26] Romate J.E. (1989) 'The numerical simulation of nonlinear gravity waves in three dimensions using a higher order panel method' - Ph.D. Thesis, University of Twente, Netherlands
- [27] Saad Y. & Schultz M.H. (1983) 'GMRES : A generalized minimal residual algorithm for solving nonsymmetric linear systems' - Research Report Yale University, RR-254
- [28] Sclavounos P.D., Kim, Y. (1995) 'Third-order diffraction of surface waves by a time-domain Rankine panel method', 10th Workshop on Water Waves and Floating Bodies, Oxford
- [29] Tanizawa K., Yue D.K.P. (1992) "Numerical computation of plunging wave impact loads on a vertical wall. Part2. The air pocket" 7th Workshop on Water Waves and Floating Bodies. Val de Reuil, France.
- [30] Wang P., Yao Y., Tulin M.P. (1993) 'Wave group evolution, wave deformation and breaking : Simulations using Longtank, a numerical wavetank' - Third ISOPE Conference, Singapore
- [31] Wu G.X., Eatock-Taylor R. (1996) "Transient motion of a floating body in steep water waves". 11th International Workshop on Water Waves and Floating bodies, Hamburg
- [32] Xü H. & Yue D. (1992) 'Computations of fully non linear three dimensional water waves' - 19th ONR Symposium on Naval Hydrodynamics, Seoul, Korea
- [33] Yang C. & Ertekin R.C. (1992) 'Numerical simulations of nonlinear wave diffraction by a vertical cylinder' - *J. Offshore Mech. and Artic Eng.*, Vol. 114, pp. 36-44
- [34] Zhou Z. & Gu M. (1990) 'Numerical research of nonlinear body-wave interactions' - 18th ONR Symposium on Naval Hydrodynamics, Ann Arbor, Michigan.

DISCUSSION

A.D. Papanikolaou
National Technical University of Athens, Greece

The author should be congratulated for a very interesting theoretical-numerical paper with various practical applications. The paper describes a fully nonlinear 3-D simulation method for the assessment of strong nonlinear effects in wave-body interaction problems. As an example of application and validation of the developed computer code, the results of Fig. 15 hold for an incident wave period equal to *twice the natural* heaving period of the studied floating body. For this particular case, the amplitude of the 2ω motion component appears to be quite significant, namely about 20% of the fundamental frequency component. Could the author explain how these results change, when the wave excitation period is equal to the *simple natural* heaving period of the floating cylinder? Do the higher-order motion components become relatively larger?

AUTHOR'S RESPONSE

Thank you for your kind comment. I ran the numerical model in the conditions you were interested in, i.e., for an incident wave period equal to the natural heaving frequency of the floating cylinder. The resulting vertical motion of the body is plotted in Figure A1. Contrary to the simulation presented in the paper, the present signal is almost purely monochromatic, with an amplification factor equal to about 1.7 with respect to the incident wave amplitude. Higher harmonics are negligible, but there is sensible negative vertical drift, as shown by Figure A2 representing the moving window Fourier analysis of the time series. The wave amplitude is $A/H=0.025$, the wave period is $T*\sqrt{g/H}=3.5$, and the wave length is $\lambda/H=1.956$.

In this resonant regime, body and free surface tend to move with opposite phases, and runs with larger wave amplitudes led to numerical breakdown, the bottom of the body getting very close to aerating. This problem could be solved by implementing a more refined remeshing procedure for the body, instead of the simple redistribution of nodes in the vertical direction used for the present simulations.

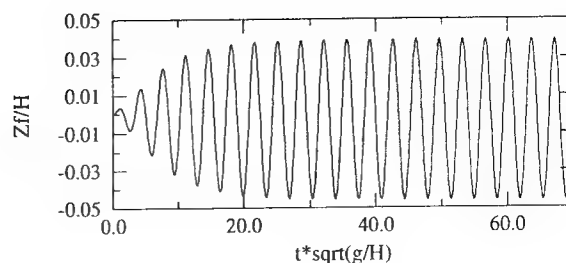


Fig. A1: Vertical motion of the body.
 $A/H=0.025$; $T*\sqrt{g/H}=3.5$

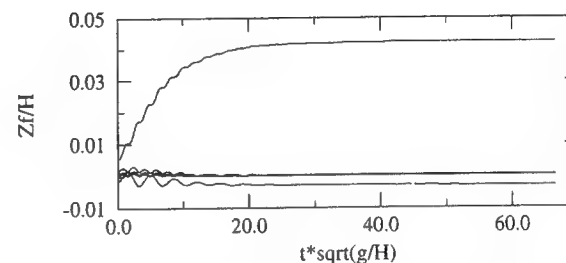


Fig. A2: Harmonic components of the motion

Analysis of Interactions Between Nonlinear Waves and Bodies by Domain Decomposition

G.-X. Wu, Q.-W. Ma (University College London, United Kingdom),

R. Taylor (University of Oxford, United Kingdom)

ABSTRACT

The paper extends to the three dimensions a previously described two dimensional finite element analysis of non-linear water waves interacting with bodies. The domain decomposition method is used to divide the computational domain into manageable regions, in each of which the computation is performed independently of the other regions. Results are given for standing waves in a rectangular container; waves generated by a wave maker in a rectangular tank; and the interaction between such waves and a vertical cylinder.

INTRODUCTION

Many problems in naval hydrodynamics are fully non-linear. Well known examples include motions in rough seas, slamming, ship capsize etc. The fully non-linear theory is usually solved by a time marching method. This assumes that the wave profile and the position of the structure are known at a particular instant. The problem can then be solved by numerical techniques. The Bernoulli equation enables us to find the force on the structure. If the structure is not fixed, Newton's law will give the new acceleration. The acceleration then gives a new velocity which further gives the new position of the structure. Similarly, the velocity obtained on the free surface will give a new free surface profile. All

these will enable the problem to be solved at the next time step. The procedure can be repeated for any desired number of time steps.

The solution of the velocity potential at each time step can be obtained by various numerical methods. The three dimensional boundary element method has been adopted in many publications (Liu & Yang [9], Zhou & Gu [10], Broeze & Zanbergen [11], Xu & Yue [12], Ferrant [13]). In this paper we shall adopt the finite element method. The method has been recently applied to the two dimensional problem by Wu & Eatock Taylor [5]. It has several distinct features. When triangular elements are used together with linear shape functions, the global matrix can be calculated explicitly. All it requires is the areas of the elements. This reduces CPU time dramatically. Also the global matrix is banded and symmetric. Experience with the two dimensional problem shows that in many cases the memory required by the finite element method is not much more or even far less than that required by the boundary element method which corresponds to a fully populated matrix. Our preliminary investigation suggests that the finite element method does have several advantages.

One of the difficulties in this problem is the radiation condition. Unlike the fully linearised problem, no explicit equation has been established for the condition when the problem is non-linear. In numerical calculation, various schemes have been proposed (e.g. [1], [4]). They

can absorb waves efficiently in some cases, but are not always effective in general. Even when they are effective, they have to be placed sufficiently far away from the body. This means that the computational domain is usually big, which will require a large number of elements. On the other hand, when the required memory exceeds the physical memory of the computer, only a small percentage of CPU will be used. This makes the calculation extremely inefficient. Wu and Eatock Taylor [5] therefore adopted domain decomposition. The required memory will then depend on the sizes of the subdomains which can always be subdivided if necessary. The continuity across the subdomain is achieved through iteration.

In this work, we shall use the three dimensional finite element method to consider the problem of a vertical cylinder in a wave tank. The methodology is first verified using the analytical solution for a two dimensional wave maker. The case may seem simple enough, but it is found that care is needed in dealing with cross waves. The computer code is also verified by the linearized analytical solution for three dimensional standing waves. The relative merits of various domain decomposition schemes are discussed. Results for the vertical cylinders in the tank are provided.

MATHEMATICAL FORMULATION AND NUMERICAL TECHNIQUE

We consider the problem of a vertical cylinder in a wave tank as shown in figure 1. (x,y,z) denotes a Cartesian co-ordinate system with x axis pointing in the longitudinal direction of the tank and z upwards. The origin of the

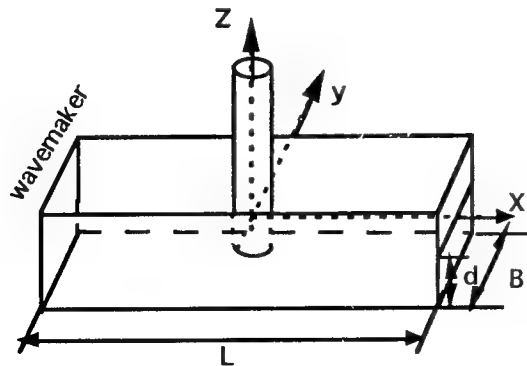


Fig. 1 The layout of the wave tank

system is located on the mean position of the free surface and the centre of the cylinder. B, L and d in the figure indicate the width, length and depth of the tank, respectively.

Based on the usual assumptions of ideal flow, the velocity potential ϕ satisfies Laplace's equation:

$$\nabla^2 \phi = 0 \quad (1)$$

in the fluid domain Ω . The condition on the piston wave maker can be written as

$$\frac{\partial \phi}{\partial x} = U(t) \quad (2)$$

where $U(t)$ is the velocity of the wave maker. On the fixed boundary the condition is:

$$\frac{\partial \phi}{\partial n} = 0 \quad (3)$$

where n is the normal of the surface pointing out of the fluid domain. On the free surface $z = \eta(x,y,t)$, the kinematic and dynamic conditions can be written as

$$\frac{Dx}{Dt} = \frac{\partial \phi}{\partial x} \quad \frac{Dy}{Dt} = \frac{\partial \phi}{\partial y} \quad \frac{Dz}{Dt} = \frac{\partial \phi}{\partial z} \quad (4)$$

$$\frac{D\phi}{Dt} = -gz + \frac{1}{2}(\nabla \phi)^2 \quad (5)$$

where g is the gravitational acceleration. These are then combined with the initial conditions which usually assume that the wave elevation and the potential on the free surface are zero.

When the wave generated by the wavemaker encounters the cylinder, it will be diffracted. The reflected wave will travel back towards the wave maker. The transmitted wave, on the other hand, will propagate towards the other end of the tank. As the time step increases, the waves reflected by the wavemaker and the far end of the tank will arrive at the cylinder. This will distort the wave loading on the cylinder. Several approaches have been proposed to absorb the reflected wave (e.g. [1]) and the transmitted wave (e.g. [4]). They are effective in some cases but they all have their limitations. Here we do not intend to investigate the effectiveness of various wave absorption schemes at the far end. Instead we simply use a relatively long tank and the computation is

terminated before the reflection at the far end has significant effects on the desired results.

At each time step, the above problem can be solved by a finite element method. The fluid domain will be discretised using finite elements and the velocity potential written in terms of the shape function $N_j(x, y, z)$:

$$\phi = \sum_{j=1}^N \phi_j N_j(x, y, z) \quad (6)$$

where N is total number of nodes and ϕ_j are the values of the potential at the nodes. Using the Galerkin method and Green's second identity, we have

$$\begin{aligned} 0 &= \iiint_{\Omega} \nabla^2 \phi N_i d\Omega \\ &= \iint_S N_i \frac{\partial \phi}{\partial n} dS - \iiint_{\Omega} \nabla \phi \cdot \nabla N_i d\Omega \end{aligned} \quad (7)$$

where S is the boundary surface of fluid domain. When the boundary conditions are imposed and equation (6) is used, equation (7) becomes

$$\begin{aligned} \iiint_{\Omega} \nabla N_i \sum_{\substack{j=1 \\ j \in S_f}}^N \phi_j \nabla N_j d\Omega &= \iint_{S_m} N_i U ds \\ - \iiint_{\Omega} \nabla N_i \sum_{\substack{j=1 \\ j \in S_f}}^N \phi_j \nabla N_j d\Omega & \quad I \notin S_f \end{aligned} \quad (8)$$

where S_f is the free surface and S_m is the wetted surface of the wave maker. If linear shape functions are used as in this paper, the integration in equation (8) can be obtained from the volumes of the elements. Once the solution is found, the force can be calculated using an equation similar to that in the paper of Wu & Ma [6].

DOMAIN DECOMPOSITION TECHNIQUE

It has been noted in the work of Wu & Eatock Taylor (5) on a two dimensional body, that the finite element method has some advantages over the boundary element method in terms of both CPU and memory requirement. The reason is that although the finite element method discretises the fluid domain rather than the boundary alone, the nodes influence each other only when they are physically connected.

As a result, the matrix is banded. In the boundary element method, on the other hand, each node will influence all other nodes through the Green function. This leads to a full matrix. Furthermore, the influence coefficients in the finite element method can be obtained from the volumes of the elements when linear shape functions are used, while in the boundary element method they are calculated from logarithmic and triangular functions, which requires more CPU.

The finite element method has been applied with some success in the two dimensional problem. For the three dimensional problem, however, the computational domain is increased dramatically. One hundred divisions in each direction will lead to over one million nodes. This is not helped by lack of a suitable radiation condition. The memory requirement is therefore usually beyond the limit of most computers. We therefore make use of the domain decomposition.

The domain decomposition technique has been used in many cases (see for example Glowinski et al. [2]). Wu & Eatock Taylor [5] have also adopted this method for the two-dimensional non-linear water wave problem. The essence of this technique is that it divides the computational domain into several subdomains, which may overlap. The computation is then performed in each subdomain. The continuity at the interface of the subdomains is achieved by iteration.

We consider an example shown in Fig. 2a in which two subdomains are used.

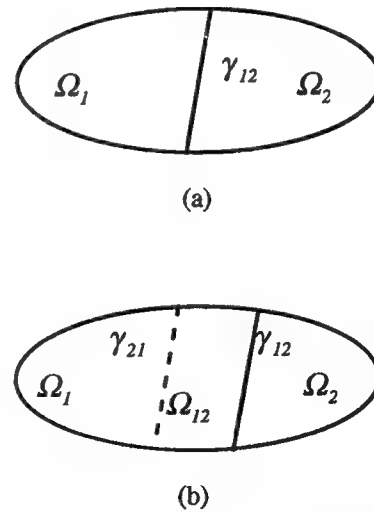


Fig. 2 Illustration of domain decomposition

γ_{12} in the figure is the interface of the two subdomains Ω_1 and Ω_2 , on which the following continuity conditions are imposed

$$\phi_1 = \phi_2; \quad \frac{\partial \phi_1}{\partial n} = -\frac{\partial \phi_2}{\partial n} \quad (9)$$

where ϕ_1 and ϕ_2 are the potentials in the corresponding subdomains. The problem is then solved in each subdomain and the continuity is achieved by the following iteration scheme

$$\frac{\partial \phi_1^{(n)}}{\partial n} = -\frac{\partial \phi_2^{(n)}}{\partial n} = \lambda^{(n)} \quad (10)$$

where

$$\lambda^{(n)} = \lambda^{(n-1)} + \rho(\phi_2^{(n-1)} - \phi_1^{(n-1)}) \quad (11)$$

and $\lambda^{(0)}$ can be taken from the normal derivative at the previous time step. It can be shown that if ρ is properly chosen the iteration will converge [2].

The case in Fig. 2b is similar to that in Fig. 2a, but there is an overlap between the two subdomains. Their common part is Ω_{12} . γ_{12} is the interface between Ω_2 and Ω_{12} ; γ_{21} is the interface between Ω_1 and Ω_{12} . Continuity is achieved by imposing the following condition

$$\phi_1 = \phi_2 \quad \text{in } \Omega_{12} \quad (12)$$

which can be found to be equivalent to:

$$\phi_1 = \phi_2 \quad \text{on } \gamma_{12} \text{ and } \gamma_{21} \quad (13)$$

as these functions satisfy the Laplace equation.

The solution starts by assuming ϕ_1 on γ_{12} to be known. This allows us to find ϕ_1 which gives its value on γ_{21} for ϕ_2 . The solution in Ω_2 can then be obtained which in turn gives a new boundary condition for ϕ_1 . This can be written as

$$\phi_1^{(i)}|_{\gamma_{12}} = \mu \lambda_1^{(i)} + (1-\mu) \lambda_1^{(i-1)} \quad i \geq 1 \quad (14)$$

$$\phi_2^{(i)}|_{\gamma_{21}} = \mu \lambda_2^{(i)} + (1-\mu) \lambda_2^{(i-1)} \quad i \geq 1 \quad (15)$$

where μ is the relaxation coefficient and

$$\lambda_1^{(i)} = \phi_2^{(i-1)}|_{\gamma_{12}} \quad \lambda_2^{(i)} = \phi_1^{(i)}|_{\gamma_{21}} \quad (16)$$

The initial condition is again taken from the solution at the previous time step.

RESULTS AND DISCUSSION

In the analysis below, the various parameters are nondimensionalized by redefining them as follows:

$$\phi \rightarrow d(gd)^{1/2} \phi \quad (x, y) \rightarrow d(x, y)$$

$$t \rightarrow (d/g)^{1/2} t \quad \omega \rightarrow (g/d)^{1/2} \omega$$

$$U \rightarrow U/\sqrt{gd}$$

where ω is a frequency.

The fluid domain is divided into many small hexahedra. Each hexahedron is then divided into six tetrahedra. A typical example is shown in Fig. 3.

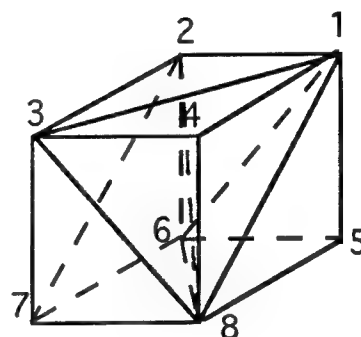
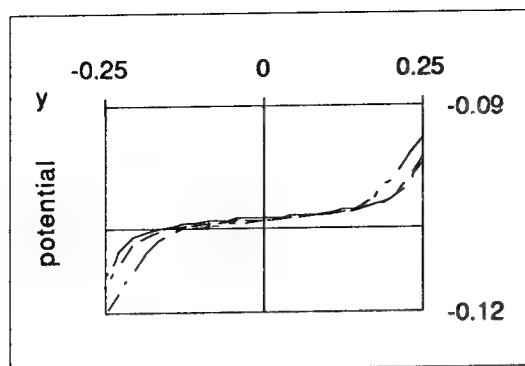
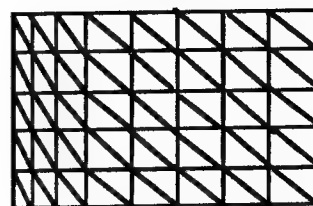


Fig 3. Division of hexahedron

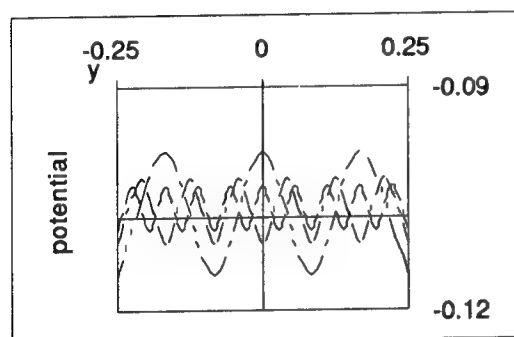
We first consider the problem of a wave maker which starts moving suddenly. The length of the tank is $L=5d$ and the width is $d/2$. The fluid domain is discretised by $J+1$ transverse planes, $M+1$ longitudinal planes and $N+1$ horizontal planes. This forms JMN hexahedra and $6JMN$ tetrahedra. The number of nodes is equal to $(J+1)*(M+1)*(N+1)$. Cosine spacing is used in the x direction and the z -coordinate of each node is determined from an exponential distribution as used by Wu and Eatock Taylor [5].



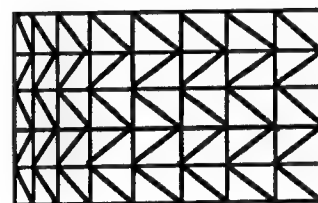
mesh 1



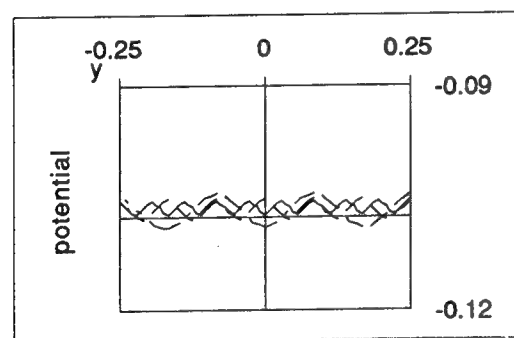
(a)



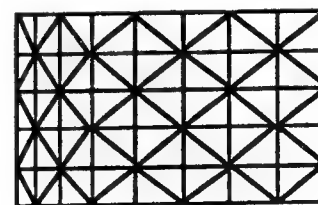
mesh 2



(b)



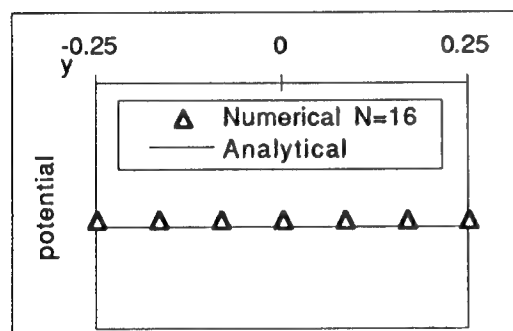
mesh 3



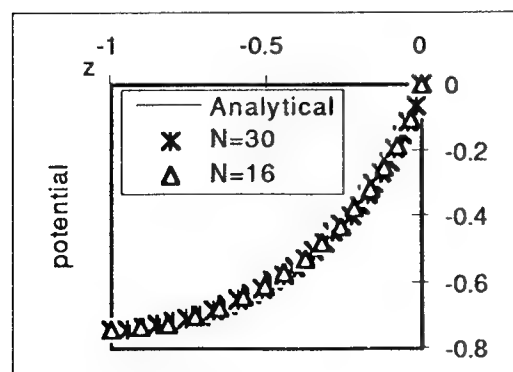
(c)

Fig. 4 The velocity potential on the wave maker at $z=-.0375$ with different meshes (— analytical — — — M=18
— · — M=12; — · · — M=6)

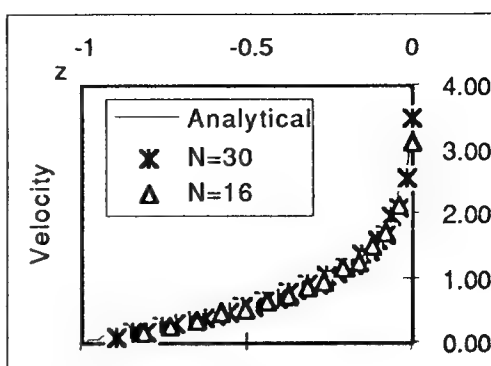
Physically, this problem is two-dimensional. The potential is not a function of y . In our analysis, however, it is found that the variation of the potential with y greatly depends on the mesh structure. Fig. 4 gives the velocity potentials at $z=-.0375$ on the wave maker obtained from different meshes. It shows that the variation of the potential with y decreases and the results tend to the analytical solution [8] when the number of elements increases, but the rate is quite slow. The difficulty here is that any error will cause a bigger error at the next time step. Before long, the accumulated error will cause instability. One way to solve this problem is to use a sufficient number of elements, but this would not be economical. Here we use the mesh in Fig.4c which has the least variation and combine this with a 5-point smoothing scheme [3] in the y direction. Fig. 5 gives the results after this treatment. Fig. 5a shows that there is no variation visible. Indeed it is found that the results are identical up to the fifth figure after the decimal point. They are also found to be in good agreement with the analytical solution [8]. Fig.5(b,c) give the results for the potential and the vertical velocity on the wave maker. They are in good agreement with the analytical solution.



(a)



(b)



(c)

Fig 5 The potential and vertical velocity on the wave maker at $t=0^+$ for the sudden motion with $U=1.0$ (mesh generated with $J=60$, $M=6$ and different N)

We next consider the problem of the wave maker undergoing the following oscillatory motion:

$$U(t) = a\omega \sin(\omega t) \quad (20)$$

where a is the nondimensionalised amplitude. The length of the tank is taken as $L=20d$ and width $B=d/2$. The calculation is made with $\omega = 1.5$ and $a = .016$. In this analysis, the fluid domain is divided by $J=200$, $M=6$ and $N=16$. Fig.6 gives the wave elevation history on the wave maker and at the centre of the tank. Some typical wave profiles in the tank at times $t=10, 15, 20$ and 25 are shown in Fig. 7.

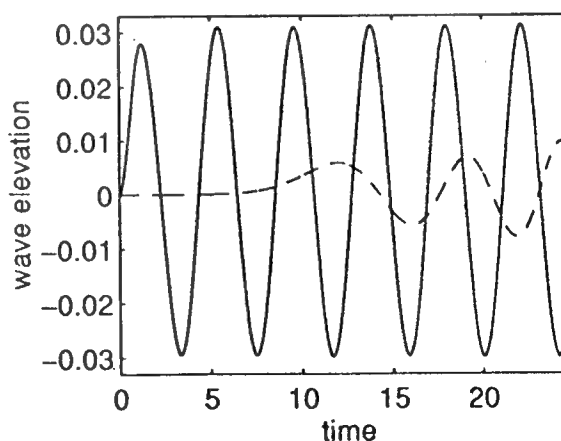


Fig 6. Wave elevation history (solid line: on the wave maker; dashed line: $x=0$)

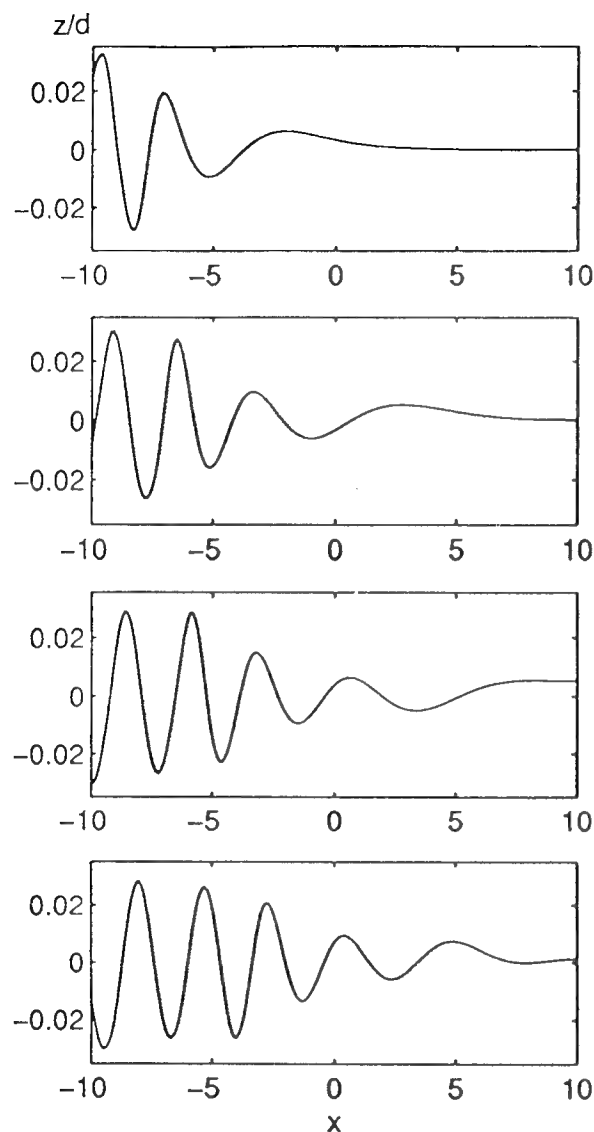


Fig 7 Wave profiles at different time steps

Next considered is the problem of a standing wave in a tank with $L=B=d$ which is discretised by $J=M=N=20$. The initial free surface elevation is given as:

$$\eta(x, y, 0) = -a \cos\left[\frac{\pi}{L}(x + L/2)\right] \times \cos\left[\frac{\pi}{B}(y + B/2)\right] \quad (21)$$

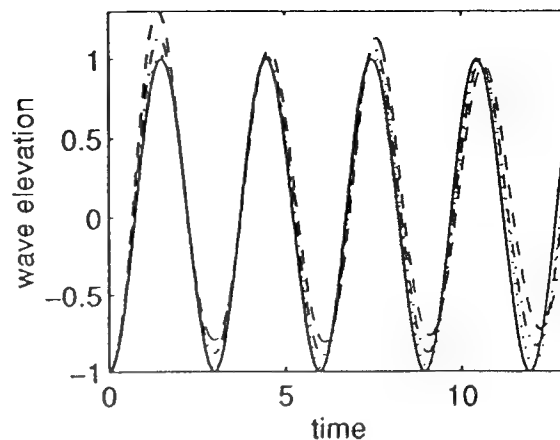


Fig 8 The standing wave elevation history at $x=L/2, y=B/2$ (— analytical ;
..... numerical for $a=0.01$;
—— numerical for $a=0.05$;
- - - numerical for $a=1$)

and the potential on the free surface is zero. The linearised solution can be found as

$$\eta = -a \cos\left[\frac{\pi}{L}(x + L/2)\right] \times \cos\left[\frac{\pi}{B}(y + B/2)\right] \cos(\omega t) \quad (22)$$

where

$$\omega^2 = \kappa \tanh(\kappa) \quad (23)$$

$$\kappa = \sqrt{\left(\frac{\pi}{L}\right)^2 + \left(\frac{\pi}{B}\right)^2}$$

Fig.8 gives the wave elevation (divided by a) at $x=L/2, y=B/2$ $a=0.01, a=0.05$ and $a=0.1$ respectively. The results have been compared with the linear analytical solution. It can be seen that the results agree well with the analytical solution when the amplitude is small. As the amplitude increases, nonlinear effects become more important.

We now consider the case of a vertical cylinder located at the centre of the tank as shown in Fig. 1. The radius of the cylinder is $R=0.05d$. The length and width of the tank are taken as $L=10.5d$ and $B=d/2$ (or $L=210R$ and $B=10R$), respectively. We shall use the domain decomposition to solve this problem. Before that

we shall first investigate the effectiveness of this technique by considering the case of the wave maker which starts moving suddenly. It is found that the scheme used by Wu and Eatock Taylor [5] without overlapping is less efficient than the one with overlapping. The latter is therefore adopted. It has also been found that the efficiency very much depends on the relaxation coefficient μ and the sizes of the overlapping zones.

Several tests have been conducted to find a suitable value for μ . In the calculation the whole fluid domain is divided into five subdomains: one enclosing the cylinder and two on each side. The details are shown in Fig.9, in which C_{ij} is the length of the overlapping zone. Fig.10 shows the number of iterations against μ with $C_{ij}=0.2d$. It can be seen from the figure that $\mu = 1.382$ is a suitable choice.

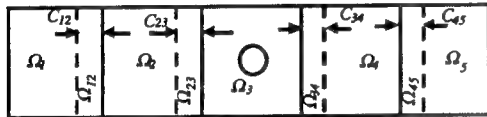


Fig 9 A typical configuration of subdomains

Further tests have been made for the sizes of the common domains (i.e. C_{ij}). The total CPU depends on the number of iterations and the CPU required for each subdomain. A bigger overlapping zone usually leads to a smaller number of iterations, which will reduce CPU. On the other hand, a bigger overlapping zone will lead to bigger subdomains, which will increase CPU. A proper balance is therefore needed. Fig. 11 gives some preliminary results which were obtained by taking the relaxation coefficient as $\mu = 1.382$ and all C_{ij} being the same. CPU for $C_{ij}=0.1d$ in the figure is taken as unity. It is seen that $C_{ij}=0.2d$ leads to least CPU.

It should be pointed out that the optimised values mentioned above may depend on other parameters such as the sizes of elements, the wave length and the number of the subdomains etc. Further investigation is needed to achieve a better understanding of the dependence of CPU on relaxation coefficient and the length of the overlapping zone.

We now give the results for the cylinder in the wave tank. The subdomains used are similar to those shown in Fig.9. The motion of the wave maker is similar to that given in equation (20) but

$$\omega = 2.0 \quad a = .008$$

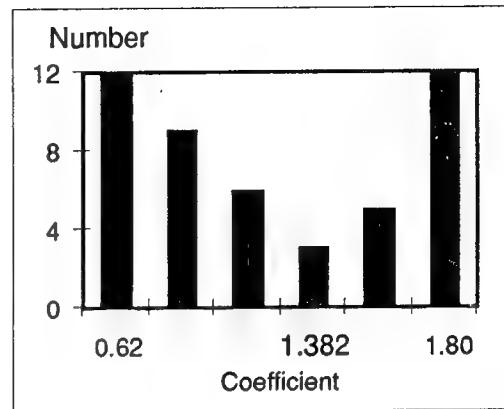


Fig. 10 The number of iterations against relaxation coefficients

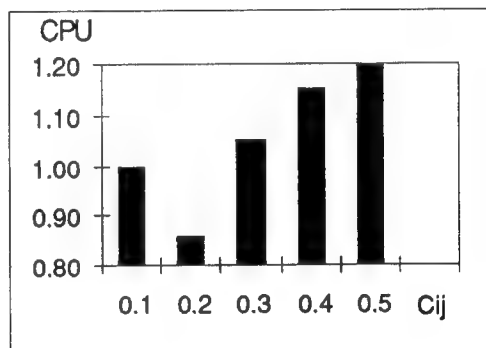


Fig. 11 CPU against C_{ij}

Fig. 12 gives wave runup on the surface of the cylinder at $t=15, 20$ and 25 , where θ represents the angle measured from x-axis. Fig 13 provides the horizontal force acting on the cylinder which has been nondimensionalised by $\rho g R^2 a$, (ρ is the density of water). The total number of elements used in this case is 203,520. The calculation takes about 193 hour CPU on a DECalpha 400 workstation for 1,000 time steps. Due to this extensive CPU demand, no systematical investigations using finer mesh and smaller time steps have been taken regarding the accuracy of the results shown. Further work is clearly needed.

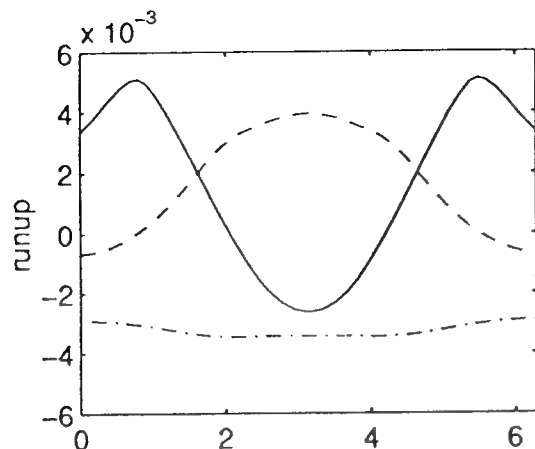


Fig 12 Runup on surface of the cylinder
(--- $t=15$; - · - $t=20$;
— $t=25$)

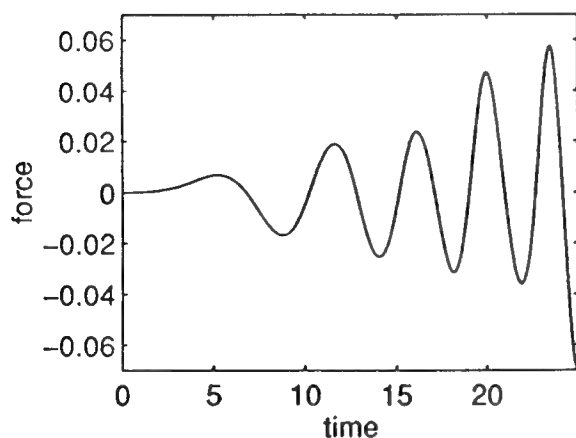


Fig 13 Horizontal force acting on cylinder

CONCLUSIONS

This paper has shown how the domain decomposition method may be extended to a three-dimensional finite element analysis of non-linear water waves interacting with bodies. A scheme of overlapping adjacent domains is found

to be more effective than an earlier scheme used by the authors for the two-dimensional problem, and a study has been conducted into the optimum amount of overlap and the optimum relaxation coefficient in the iterative scheme. Preliminary results have been obtained for the case of a vertical cylinder in a wave tank. The method requires extensive computer run times when implemented on a workstation, and further work is required to improve the methodology. This includes the development of a procedure for combining the domain decomposition method with wave absorbing techniques to allow the imposition of appropriate radiation conditions close to the body.

The results shown are for the case of a fixed cylinder. For a floating structure, body motions need to be taken into account, and it is intended to achieve this by using the method described by Wu and Eatock Taylor [7].

ACKNOWLEDGEMENT

This work forms part of the research programme "Uncertainties in Loads on Offshore Structures" sponsored by EPSRC through MTD Ltd and jointly funded with: Amoco (UK) Exploration Company, BP Exploration Operating Co Ltd, Brown & Root, Exxon Production Research Company, Health and Safety Executive, Norwegian Contractors a.s., Shell UK Exploration and Production, Den Norske Stats Oljeselskap a.s., Texaco Britain Ltd.

REFERENCES

1. Cointe, R., Geyer, P., King, B., Molin, B. and Tanoni, M., 1990, "Nonlinear and linear motions of a rectangle barge in a perfect fluid," 18th Symp. on naval hydrody., Univ. of Michigan, Ann Arbor, pp. 85-98.
2. Glowinski, R., Dinh, Q.V. & Periaux, J., 1984, "Domain decomposition for elliptic problems", in *Finite Element Methods*, John Wiley and Sons, Chichester, Vol. 5, pp. 45-106.
3. Longuet-Higgins, M.S. & Cokelet, E.D., 1976, "The deformation of steep surface waves on water: I. a numerical method of computation", *Proc. R. Soc. London, A* Vol.350, pp.1-26.
4. Romate, J.E., 1992, "Absorbing boundary conditions for free surface waves", *J. Comp. Physics*, Vol.99, pp.135-145.
5. Wu, G.X. and Eatock Taylor, R., 1995, "Time stepping solutions of the two dimensional

non-linear wave radiation problem," *Ocean Engng*, Vol. 22, No. 8, pp 785-798.

6. Wu, G.X. & Ma, Q.W., 1995, "Finite element analysis of nonlinear interactions transient waves with a cylinder", *OMAE'95*, Vol.1, part A, pp329-339.

7. Wu, G.X. & Eatock Taylor, R., 1996, "Transient motion of a floating body in steep waves", 11th international Workshop on Water Waves and Floating Bodies, Hamburg, Germany.

8. Peregrine, D.H., 1972, "Flow due to vertical plate moving in a channel", unpublished note, Department of Mathematics, University of Bristol.

9. Liu, Y.Z. and Yang, C, 1987, "Nonlinear radiation of an axisymmetric cylinder," *Adv. in Hydrodynamics (China)*, Vol.2

10. Zhou, Z. and Gu, M., 1990, "A numerical research of nonlinear body-wave interaction, *Proc. 18th Symp. on Naval Hydrodynamics*, Ann Arbor, Michigan, pp.103-117.

11. Broeze, L and Zandbergen, P.J., 1992, "The development of a three-dimensional panel method for nonlinear free surface waves, " 7th Intl. Workshop on Water Waves and Floating Bodies, Val de Reuil, France.

12. Xu, H and Yue, D.K.P , 1992, "Numerical study of three-dimensional overturning water waves," 7th Intl. Workshop on Water Waves and Floating Bodies, Val de Reuil, France.

13. Ferrant, P., 1994, "Radiation and diffraction of nonlinear waves in three dimensions, " *BOSS*, MIT, pp.507-524.

Fourier-Kochin Theory of Free-Surface Flows

F. Noblesse (David Taylor Model Basin, USA),

X.-B. Chen (Bureau Veritas, France), C. Yang (George Mason University, USA)

ABSTRACT

A recently-developed theoretical formulation of wave diffraction-radiation by a ship advancing in regular waves is summarized and extended. The basic results underlying the formulation, called the Fourier-Kochin theory because it is based on a Fourier representation of free-surface effects and an extension of Kochin's approach, are summarized. Two applications and extensions of the theory, to the coupling between an inner viscous flow and an outer potential flow and the representation of time-harmonic ship waves generated by an arbitrary singularity distribution, are also presented.

INTRODUCTION

For most practical purposes, the flow due to a ship advancing in waves is effectively potential and linear beyond a small distance from the ship hull, although viscous and nonlinear effects can be significant near the hull. Linear free-surface potential flows therefore are of fundamental importance in ship hydrodynamics.

A recently-developed theoretical formulation of wave diffraction-radiation by ships or offshore structures, motivated by the practical and theoretical importance of free-surface potential flows and the considerable complexities of existing calculation methods based on free-surface Green functions, is considered here. This formulation is called the Fourier-Kochin theory because it is based upon a Fourier representation of free-surface effects and an extension of the approach used by Kochin [1,2].

The basic results underlying the FK theory [3,4,5] are summarized. Two applications and extensions of the theory, to the coupling between viscous and potential flows and the representation of time-harmonic ship waves generated by an arbitrary singularity distribution, are also given.

BACKGROUND

We consider the potential flow due to a ship advancing at constant speed along a straight path through a train of regular waves in water of effectively infinite depth and lateral extent. The flow due to the ship is expressed in the usual way as the sum of the steady flow about the ship advancing in calm water and the time-harmonic flow associated with the incoming and diffracted-radiated waves. Thus, a frequency-domain analysis is considered. In addition, the steady ship waves and the time-harmonic diffracted-radiated waves are analyzed within the classical potential-flow theory.

Nondimensional coordinates $\vec{x} = (x, y, z)$, time t , velocity potential ϕ and related flow variables are defined with respect to the ship length L , the acceleration of gravity g , and the density of water ρ as basic reference units. The flow is observed from a moving system of coordinates (x, y, z) in steady translation with the mean forward speed U of the ship, and ω is the encounter frequency of the ambient waves. The nondimensional frequency and the Froude number are defined as $f = \omega \sqrt{L/g}$ and $F = U/\sqrt{gL}$. The x axis is along the path of the ship and points toward the bow. The z axis is vertical and points upward, and the undisturbed free surface is taken as the plane $z=0$.

The velocity potentials of the time-harmonic and steady ($f=0$) flow components are defined in terms of an exponential time-growth parameter ϵ as $\lim_{\epsilon \rightarrow +0} \Re [\phi(\vec{x}) \exp(\epsilon t - i f t)]$ and satisfy the linear free-surface boundary condition

$$[(f + i\epsilon - iF\partial_x)^2 - \partial_z] \phi = 0. \quad (1)$$

The Green function G associated with the boundary condition (1) may be expressed as

$$G = G^S + G^F \quad (2)$$

where G^S represents a local flow disturbance defined in terms of simple (Rankine) singularities as

$$4\pi G^S = -1/r + 1/r' \quad (3)$$

$$\text{with } \begin{cases} r = \sqrt{(x-\xi)^2 + (y-\eta)^2 + (z-\zeta)^2} \\ r' = \sqrt{(x-\xi)^2 + (y-\eta)^2 + (z+\zeta)^2} \end{cases}$$

and G^F accounts for free-surface effects. The free-surface component G^F is given by

$$4\pi^2 G^F = \lim_{\epsilon \rightarrow +0} \int_{-\infty}^{\infty} d\beta \int_{-\infty}^{\infty} d\alpha \mathcal{E} \mathcal{E}^* / D_{\epsilon} \quad (4)$$

$$\text{with } \begin{cases} \mathcal{E}(\alpha, \beta; \vec{x}) = \exp[\sqrt{\alpha^2 + \beta^2} z + i(\alpha x + \beta y)] \\ \mathcal{E}^*(\alpha, \beta; \vec{\xi}) = \exp[\sqrt{\alpha^2 + \beta^2} \zeta - i(\alpha \xi + \beta \eta)] \end{cases}$$

Here, $\vec{x} = (x, y, z \leq 0)$ and $\vec{\xi} = (\xi, \eta, \zeta \leq 0)$ respectively stand for the singularity and flow-observation points. Furthermore, D_{ϵ} is the *dispersion function*

$$D_{\epsilon} = (f + i\epsilon - F\alpha)^2 - k \quad (5a)$$

where $k = \sqrt{\alpha^2 + \beta^2}$ is the wavenumber. The function D_{ϵ} is equal to the real dispersion function D

$$D = (f - F\alpha)^2 - k \quad (5b)$$

in the limit $\epsilon = 0$.

The velocity potential $\phi(\vec{\xi})$ at a point $\vec{\xi}$ of the mean wetted surface of the ship (where the normal derivative $\partial\phi/\partial n$ is presumed known) is defined by the solution of an integral equation of the form

$$\phi/2 + \chi = \psi \quad (6a)$$

where the potentials ψ and χ respectively correspond to a-priori given and unknown distributions of sources and normal dipoles, with densities determined by the values of $\partial\phi/\partial n$ and ϕ , at the mean wetted hull H and the mean waterline W of the ship. The potential $\phi(\vec{\xi})$ at a point $\vec{\xi}$ in the mean flow domain outside H is given by

$$\phi = \psi - \chi. \quad (6b)$$

The source and dipole potentials ψ and χ in the integral equation (6a) and the flow representation (6b) can be expressed as

$$\psi = \psi^S + \psi^F \quad \chi = \chi^S + \chi^F \quad (7)$$

where the potentials ψ^S and χ^S correspond to the simple-singularity component G^S in expression (2) for the Green function, and the components ψ^F and χ^F correspond to the free-surface component G^F . Thus, the components ψ^S and χ^S and the components ψ^F and χ^F , defined by (16) and (17-18) in

[3], are expressed in terms of source and dipole distributions involving the simple singularity G^S and the free-surface term G^F , respectively.

FOURIER-KOCHIN FORMULATION

The free-surface potentials ψ^F and χ^F in (7) are now considered. In the usual *free-surface Green-function approach*, based on the Green function (2) associated with the free-surface condition (1), the Green function is evaluated and subsequently integrated over the ship hull and waterline to determine the source and dipole potentials ψ and χ . The well-known difficulties (stemming from the complex singularity of the free-surface component G^F for $x = \xi, y = \eta, z + \zeta = 0$) involved in this classical approach are partially circumvented in Kochin's formulation, in which the surface and line distributions of sources and dipoles over the ship hull and waterline defining the free-surface components ψ^F and χ^F are considered directly.

Within the Fourier-Kochin formulation, the potentials $\psi^F(\vec{\xi})$ and $\chi^F(\vec{\xi})$ are defined by (24) and (12) in [3] as

$$4\pi^2 \begin{Bmatrix} \psi^F \\ \chi^F \end{Bmatrix} = \lim_{\epsilon \rightarrow +0} \int_{-\infty}^{\infty} d\beta \int_{-\infty}^{\infty} d\alpha \begin{Bmatrix} N \\ \widehat{M} \end{Bmatrix} \frac{\mathcal{E}^*}{D_{\epsilon}} \quad (8)$$

where N and \widehat{M} are spectrum functions defined by distributions of the elementary wave function \mathcal{E} over the mean ship hull H and waterline W . The spectrum function \widehat{M} , associated with the potential χ in the integral equation (6a), is called the *kernel spectrum function*.

Two alternative mathematical representations, called the *potential representation* and the *velocity representation* because they respectively involve the potential ϕ and the velocity $\nabla\phi$, of the kernel spectrum function \widehat{M} are given in [3]. The potential representation follows from Kochin's formulation in a straightforward way. The velocity representation is obtained in [3] from the potential representation via an integration by parts based on Stokes' theorem. The velocity representation of the kernel spectrum function \widehat{M} is shown in [3] to provide a substantially more solid mathematical basis than the potential representation for the purpose of numerically evaluating influence coefficients. The velocity representation is also preferable for coupling viscous and potential flows, as is shown further on. Thus, only the velocity representation is considered here.

The velocity representation of the spectrum function \widehat{M} is defined by (65), with $\Delta = 0$, in [3]. A useful extension of this representation is obtained

if we use the identity $1+2Ff\hat{\alpha}-F^2\alpha\hat{\alpha}=(f^2-D)/k$, so that the spectrum function \hat{M} can be expressed as $\hat{M}=M-M_W^*D/k^2$. Here, D is the dispersion function (5b), the function M_W^* is defined as

$$M_W^* = i \int_W (\beta t_x - \alpha t_y) \phi \exp[i(\alpha x + \beta y)] d\mathcal{L} \quad (9)$$

and the function M is defined by (13b)-(13d) below. By using the relation $\hat{M}=M-M_W^*D/k^2$ in (8) we can express the potential $\hat{\chi}^F$ as

$$\hat{\chi}^F = \chi^F - \varphi^S. \quad (10)$$

The potential $\varphi^S(\xi)$ is defined by (8) as

$$4\pi^2 \varphi^S = \int_{-\infty}^{\infty} d\beta \int_{-\infty}^{\infty} d\alpha M_W^* \mathcal{E}^*/k^2 \quad (11)$$

where the spectrum function M_W^* is given by (9). Expression (11) does not involve the dispersion function D . The analysis given in [4] shows that the potential φ^S therefore corresponds to a nonoscillatory near-field disturbance. Indeed, the potential φ^S is expressed in terms of a distribution of simple singularities further on. By substituting (10) into (7) we obtain

$$\psi = \psi^S + \psi^F \quad \chi = (\chi^S - \varphi^S) + \chi^F. \quad (12)$$

The superscripts S and F identify simple-singularity and free-surface components, respectively. The representation $\chi = (\chi^S - \varphi^S) + \chi^F$ is a modification of the representation $\chi = \chi^S + \hat{\chi}^F$ given in [3]. Specifically, the simple-singularity component φ^S is extracted from the free-surface potential $\hat{\chi}^F$.

The free-surface potentials $\psi^F(\xi)$ and $\chi^F(\xi)$ are given by the Fourier representation

$$4\pi^2 \begin{Bmatrix} \psi^F \\ \chi^F \end{Bmatrix} = \lim_{\epsilon \rightarrow +0} \int_{-\infty}^{\infty} d\beta \int_{-\infty}^{\infty} d\alpha \begin{Bmatrix} N \\ M \end{Bmatrix} \frac{\mathcal{E}^*}{D_\epsilon} \quad (13a)$$

where the spectrum functions N and M are defined by (66)-(68)¹ in [3] as

$$\begin{aligned} N &= N_H + F^2 N_W \\ M &= M_H + F^2 M_W^F + 2Ff M_W^T + f^2 M_W^J. \end{aligned} \quad (13b)$$

The functions N_H and M_H and the functions N_W , M_W^F , M_W^T and M_W^J are given by

$$\begin{aligned} \begin{Bmatrix} N_H \\ M_H \end{Bmatrix} &= \int_H \begin{Bmatrix} A_H^N \\ A_H^M \end{Bmatrix} \exp[kz + i(\alpha x + \beta y)] dA \\ \begin{Bmatrix} N_W \\ M_W^F \\ M_W^T \\ M_W^J \end{Bmatrix} &= \int_W \begin{Bmatrix} A_W^N \\ A_W^F \\ A_W^T \\ A_W^J \end{Bmatrix} \exp[i(\alpha x + \beta y)] d\mathcal{L} \end{aligned} \quad (13c)$$

¹ where Δ is set equal to 0 and an integration by parts is performed in expression (66) for the function M_W^T

where dA and $d\mathcal{L}$ are the differential elements of area and arc length of H and W . The amplitude functions A_H^N , A_H^M , A_W^N , A_W^F , A_W^T , and A_W^J in (13c) are given by

$$\begin{aligned} A_H^N &= -\partial_n \phi \\ A_H^M &= i\sigma[(\beta t_x - \alpha t_y) \partial_s \phi - (\beta s_x - \alpha s_y) \partial_t \phi]/k \\ A_W^N &= n_x t_y \partial_n \phi \\ A_W^F &= -(t_x t_y + \alpha\beta/k^2) \partial_t \phi - \sigma t_y^2 n_z (\partial_s \phi - \mu \partial_t \phi) \\ A_W^T &= \beta \partial_t \phi / k^2 \\ A_W^J &= i(\beta t_x - \alpha t_y) \phi / k^2 \end{aligned} \quad (13d)$$

where $\sigma = 1/\sqrt{1-\mu^2}$ with $\mu = \vec{s} \cdot \vec{t}$. Furthermore, $(\partial_n \phi, \partial_s \phi, \partial_t \phi) = (\vec{n}, \vec{s}, \vec{t}) \cdot \nabla \phi$ where the unit vector $\vec{n} = (n_x, n_y, n_z)$ is normal to H and points into the ship, and the unit vectors $\vec{s} = (s_x, s_y, s_z)$ and $\vec{t} = (t_x, t_y, t_z)$ are tangent to H . The vector \vec{s} points downward, as is shown in Fig.1, and the vector \vec{t} is oriented so that $\vec{n} = \vec{s} \times \vec{t} / \|\vec{s} \times \vec{t}\|$. At the waterline, the unit vector $\vec{t} = (t_x, t_y, 0)$ is tangent to W , as is indicated in Fig.1.

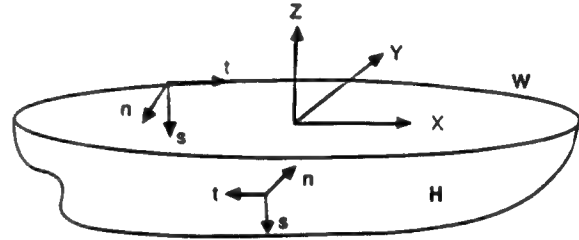


Fig.1 Definition sketch

The spectrum functions N_H , N_W , M_H , M_W^F , M_W^T and M_W^J defined by (13c) and (13d) are independent of the parameters F and f , which appear as coefficients in (13b). The formulation (13) partially circumvents the difficulties associated with the free-surface component (4) in the Green function by avoiding the direct calculation of G^F , which corresponds to a *point* source. Instead, the free-surface potentials (13a) due to surface and line *distributions* of sources and dipoles over the ship hull and waterline, or over hull patches and waterline arcs, are considered directly. A significant property of this approach is that the Fourier integrals (13a) are not singular because the spectrum functions N and M vanish in the large-wavenumber limit $k \rightarrow \infty$ for a singularity distribution, whereas (4) is singular for $\xi = x$, $\eta = y$, $\zeta + z = 0$. Thus, the difficulties associated with the numerical integration of the free-surface component G^F over a hull-panel or a waterline-segment in the vicinity of the singular point $\xi = x$, $\eta = y$, $\zeta + z = 0$ are

avoided. In fact, the *space integration* over hull-panels and waterline-segments, which consists in integrating the exponential function \mathcal{E} in (4), is an elementary task within the FK formulation.

The simple-singularity potentials $\psi^S(\xi)$ and $\chi^S(\xi)$ in (12) are defined by (16) in [3] as

$$\begin{cases} \psi^S \\ \chi^S \end{cases} = - \int_H \left\{ G^S(\vec{x}; \vec{\xi}) \nabla_x \phi(\vec{x}) \cdot \vec{n}(\vec{x}) \right\} d\mathcal{A}(\vec{x}) \quad (14)$$

where $\nabla_x = (\partial_x, \partial_y, \partial_z)$. By substituting (9) into (11) and exchanging the order in which the Fourier and space integrations are performed, we can express the potential $\varphi^S(\xi)$ as the waterline integral

$$2\pi\varphi^S = \int_W \Theta \vec{Z} \times (\vec{x} - \vec{\xi}) \cdot \vec{t}(\vec{x}) \phi(\vec{x}) d\mathcal{L}(\vec{x}) \quad (15a)$$

where $\vec{Z} = (0, 0, 1)$ is the unit vector along the z axis, Θ is the function

$$\Theta = \frac{1 + \zeta / \sqrt{(x - \xi)^2 + (y - \eta)^2 + \zeta^2}}{(x - \xi)^2 + (y - \eta)^2} \quad (15b)$$

and $\vec{t} = (t_x, t_y, 0)$ is the unit vector tangent to the waterline W as was already noted.

COUPLING OF VISCOUS AND POTENTIAL FLOWS

In the past few years, viscous-flow calculation methods accounting for viscous and nonlinear effects, and potential-flow calculation methods (based on Rankine singularities) accounting for nonlinear free-surface effects have been developed to compute steady ship waves. These calculation methods can be used to compute the velocity field (u, v, w) at a *control surface* Σ chosen at a sufficiently large distance from a ship, so that the flow may be regarded as effectively potential and linear outside Σ . A linear potential-flow representation can then be used to define the potential flow outside Σ in terms of a given nonlinear and/or viscous flow inside Σ , i.e. to extend a near-field flow (predicted via any calculation method) into the far field. This approach, a weak (one-way) inner nonlinear viscous flow \Rightarrow outer linear potential flow coupling, can be useful to determine far-field waves and wave drag (which can be evaluated more accurately via Havelock's formula for the energy radiated in the trailing wave pattern than by integration of the hull pressure), and to analyze the far-field influence (notably upon the wave pattern and the drag) of near-field viscous and nonlinear features. Hybrid calculation methods based on a strong (two-way) inner nonlinear viscous flow \Leftrightarrow

outer linear potential flow coupling have also been developed recently, e.g. [6,7], and will likely be used more widely.

This strong two-way coupling and the weak one-way coupling mentioned previously involve the basic task of determining the velocity field outside a control surface Σ enclosing a ship in terms of the velocity distribution $\vec{u} = (u, v, w)$ at Σ . This task is considered here for wave diffraction-radiation by a ship. Specifically, the flow in the region outside the control surface Σ is regarded as effectively potential and linear, i.e. the classical free-surface boundary condition (1) is assumed to hold outside Σ . In the special case of a body submerged deeply enough, a closed control surface Σ may be defined. Otherwise, the surface Σ intersects the mean free-surface plane $z=0$ along a curve Γ .

The outer potential flow under consideration can be defined explicitly, using a well-known Green identity, if both the normal velocity $\partial\phi/\partial n$ and the potential ϕ are known at the inner boundary surface Σ . However, this classical explicit representation of potential flows in terms of boundary values of ϕ and $\partial\phi/\partial n$ cannot be used for a viscous inner flow, for which the potential ϕ is not defined. The difficulty can be circumvented in a straightforward manner, employed in the matching procedure between a viscous inner flow and an outer potential flow developed in [6,7], since the potential ϕ at the surface Σ is defined in terms of the normal velocity $\partial\phi/\partial n$ at Σ via an integral equation.

A more direct and simpler alternative approach, which avoids the nontrivial task of solving an integral equation to determine the potential ϕ at Σ , to this matching procedure is expounded below. Specifically, the Fourier-Kochin formulation is used to obtain a mathematical representation of the velocity $\vec{u} \equiv \nabla\phi$ in the outer potential flow region (outside Σ) that defines $\nabla\phi$ explicitly in terms of a prescribed velocity distribution \vec{u} at Σ , i.e. that does not involve the potential ϕ at Σ (unlike the usual Green identity which defines ϕ within a flow domain in terms of boundary values of ϕ and $\partial\phi/\partial n$). Furthermore, $\nabla\phi$ is defined directly (not by numerical differentiation of ϕ).

By substituting (12) into (6b) we can express $\nabla_\xi \phi(\xi)$, where $\nabla_\xi = (\partial_\xi, \partial_\eta, \partial_\zeta)$, in the form

$$\nabla_\xi \phi = (\nabla_\xi \phi^S + \nabla_\xi \varphi^S) + \nabla_\xi \phi^F \quad (16)$$

with $\nabla_\xi \phi^S = \nabla_\xi(\psi^S - \chi^S)$ and $\nabla_\xi \phi^F = \nabla_\xi(\psi^F - \chi^F)$.

The component $\nabla_\xi \phi^F(\xi)$ is defined by (13a) as

$$4\pi^2 \nabla_\xi \phi^F = \lim_{\epsilon \rightarrow +0} \int_{-\infty}^{\infty} d\beta \int_{-\infty}^{\infty} d\alpha \left\{ \begin{matrix} -i\alpha \\ -i\beta \\ k \end{matrix} \right\} \frac{S\mathcal{E}^*}{D_\epsilon} \quad (17a)$$

with $S = N - M$. Expressions (13b)-(13d), where the ship hull H and waterline W become the control surface Σ and curve Γ , yield

$$S = \int_{\Sigma} A^{\Sigma} \exp[kz + i(\alpha x + \beta y)] dA + \int_{\Gamma} A^{\Gamma} \exp[i(\alpha x + \beta y)] d\mathcal{L} \quad (17b)$$

where the functions A^{Σ} and A^{Γ} are given by

$$A^{\Sigma} = i\sigma[(\beta s_x - \alpha s_y) \vec{u} \cdot \vec{t} - (\beta t_x - \alpha t_y) \vec{u} \cdot \vec{s}] / k - \vec{u} \cdot \vec{n} \quad (17c)$$

$$A^{\Gamma} = F^2[t_y^2 \vec{u} \cdot \vec{n} + (t_x t_y + \alpha\beta/k^2) \vec{u} \cdot \vec{t}] - 2Ff\beta \vec{u} \cdot \vec{t}/k^2 - if^2\phi(\beta t_x - \alpha t_y)/k^2. \quad (17d)$$

The identity $\nabla_x \phi = \vec{u}$ at Σ was used in (17c) and (17d) and the control surface Σ is assumed to intersect the free-surface plane $z=0$ orthogonally. The free-surface condition (1) yields

$$f^2\phi = w + 2iFfu + F^2\partial_x u. \quad (17e)$$

This relation can be used in (17d), so that expressions (17) define the free-surface component $\nabla_\xi \phi^F$ in terms of the velocity (u, v, w) at Σ .

The simple-singularity component $\nabla_\xi(\psi^S - \chi^S)$ is now considered. Expressions (14) readily yield

$$\nabla_\xi \psi^S = - \int_{\Sigma} \nabla_\xi G^S(\vec{x}; \vec{\xi}) \nabla_x \phi(\vec{x}) \cdot \vec{n}(\vec{x}) dA(\vec{x}) \quad (18a)$$

$$\nabla_\xi \chi^S = - \int_{\Sigma} \nabla_\xi \nabla_x G^S(\vec{x}; \vec{\xi}) \cdot \vec{n}(\vec{x}) \phi(\vec{x}) dA(\vec{x}) \quad (18b)$$

Expression (18a) defines the velocity field $\nabla_\xi \psi^S$ in terms of the velocity distribution $\nabla_x \phi$ at Σ . However, expression (18b) for the velocity field $\nabla_\xi \chi^S$ involves the potential ϕ at Σ (which is not known directly if the flow inside Σ is viscous). Furthermore, (18b) involves the second derivative $\nabla_\xi \nabla_x G^S(\vec{x}; \vec{\xi})$ of the simple-singularity component G^S of the Green function. This second derivative is highly singular for points $\vec{\xi}$ in the vicinity of Σ , so that (18b) is not well suited for numerical evaluation. A useful alternative expression for the velocity field $\nabla_\xi \chi^S$ is

$$\nabla_\xi \chi^S = \int_{\Sigma} \nabla_\xi G^S(\vec{x}; \vec{\xi}) \times [\nabla_x \phi(\vec{x}) \times \vec{n}(\vec{x})] dA(\vec{x}) \quad (18c)$$

This alternative expression defines the velocity field $\nabla_\xi \chi^S$ in terms of the velocity distribution $\nabla_x \phi$ at Σ and only involves the first derivative $\nabla_\xi G^S(\vec{x}; \vec{\xi})$. The simple-singularity component $\nabla_\xi \phi^S(\vec{\xi})$ in (16) is then defined by (18a) and (18c) as

$$\nabla_\xi \phi^S = - \int_{\Sigma} [\nabla_\xi G^S(\vec{u} \cdot \vec{n}) + \nabla_\xi G^S \times (\vec{u} \times \vec{n})] dA \quad (19a)$$

The simple-singularity component $\nabla_\xi \phi^S(\vec{\xi})$ can be expressed in the form

$$2\pi \nabla_\xi \phi^S = \int_{\Gamma} \Theta \vec{Z} \times (\vec{x} - \vec{\xi}) \vec{u} \cdot \vec{t} d\mathcal{L} \quad (19b)$$

with \vec{Z} and Θ given in (15). Expressions (19) define the simple-singularity component $\nabla_\xi(\phi^S + \varphi^S)$ in terms of the velocity \vec{u} at a control surface.

FOURIER REPRESENTATION OF GENERIC DISPERSIVE WAVES

The most difficult aspect of the Fourier-Kochin formulation, indeed of any approach based on a Green function satisfying the free-surface condition (1), resides in the free-surface components $\nabla_\xi \phi^F$, ψ^F and χ^F in the decompositions (16) and (12) into simple-singularity and free-surface components. These components are examined in [4,5], which are summarized and extended below. Expression (5a) yields $D_\epsilon \sim D + i\epsilon D_f$ as $\epsilon \rightarrow 0$ where D is given by (5b) and $D_f = \partial D / \partial f = 2(f - F\alpha)$. The dispersion function D_ϵ in the Fourier representations (17a) and (13a) of the free-surface components $\nabla_\xi \phi^F$, ψ^F and χ^F can then be replaced by $D + i\epsilon \text{sign}(D_f)$ with $\text{sign}(D_f) = \text{sign}(f - F\alpha)$. Thus, the Fourier representations (17a) and (13a) are of the form

$$\pi \varphi^F = \lim_{\epsilon \rightarrow +0} \int_{-\infty}^{\infty} d\beta \int_{-\infty}^{\infty} d\alpha \frac{\mathcal{S} \exp[k\xi - i(\alpha\xi + \beta\eta)]}{D + i\epsilon \text{sign}(D_f)} \quad (20)$$

where $\varphi^F/(4\pi)$ stands for ψ^F , χ^F , or $\nabla_\xi \phi^F$, and \mathcal{S} likewise stands for N , M , or $\vec{S} = (-i\alpha, -i\beta, k)S$.

In a typical numerical solution procedure, spectrum functions corresponding to distributions of sources and/or dipoles over flat or curved panels are defined. These spectrum functions are of the form $\mathcal{S} = A_p \exp[kz_p + i(\alpha x_p + \beta y_p)]$ where (x_p, y_p, z_p) define the centroids of the panels, and A_p is a slowly-varying function of α and β which vanishes as $\alpha^2 + \beta^2 \rightarrow \infty$. The contribution φ_p^F of a panel to the free-surface potential φ^F is then given by

$$\pi \varphi_p^F = \lim_{\epsilon \rightarrow +0} \int_{-\infty}^{\infty} d\beta \int_{-\infty}^{\infty} d\alpha \frac{A_p \exp[kZ - i(\alpha X + \beta Y)]}{D + i\epsilon \text{sign}(D_f)}$$

with $(X, Y, Z) = (\xi - x_p, \eta - y_p, \zeta + z_p)$. Expression (4) for the free-surface component G^F in the Green function corresponds to the special case $A_p = 1/(4\pi)$ and $(X, Y, Z) = (\xi - x, \eta - y, \zeta + z)$.

The Fourier representation of free-surface effects defined by (20) is considered in [4,5] for a generic spectrum function \mathcal{S} (assumed to be a slowly-varying function of α and β) and for a generic dispersion function D , so that the analysis and results given in [4,5], and below, are valid for an arbitrary distribution of singularities (sources and/or dipoles) and for a wide class of linear dispersive waves.

The Fourier integral (20) is expressed in [4] as

$$\varphi^F = \varphi^W + \varphi^N \quad (21)$$

where φ^W and φ^N respectively correspond to a wave component and a near-field component. The near-field component φ^N in the decomposition (21) is significant in the near field but is negligible in comparison to the wave component φ^W in the far field. The wave component φ^W is given by a single Fourier integral along the *dispersion curve(s)* defined in the Fourier plane by the dispersion relation $D=0$. Specifically, (31a,b) in [4] yield

$$i\varphi^W = \sum_{D=0} \int ds (\Sigma_1 + \Sigma_2) \frac{\mathcal{S} \exp[k\zeta - i(\xi\alpha + \eta\beta)]}{\|\nabla D\|} \quad (22)$$

where $\sum_{D=0}$ stands for summation over the dispersion curve(s), ds is the differential element of arc length of the dispersion curve(s), $\|\nabla D\|^2 = D_\alpha^2 + D_\beta^2$ with $(D_\alpha, D_\beta) = (\partial_\alpha D, \partial_\beta D)$, and Σ_1 and Σ_2 are the sign functions defined as

$$\Sigma_1 = \text{sign}(D_f) \quad (23)$$

and $\Sigma_2 = \text{sign}(\xi D_\alpha + \eta D_\beta)$. These sign functions are associated with the single and double integrals ϕ_1 and ϕ_2 in (16) of [4]. The single integral ϕ_1 is obtained in the limit $\varepsilon = +0$ of (20). The sign function Σ_2 stems from a far-field single-integral approximation of the double integral ϕ_2 . We have

$$\xi D_\alpha + \eta D_\beta = h \|\nabla D\| \cos(\theta - \gamma)$$

where $(\xi, \eta) = h(\cos\gamma, \sin\gamma)$ with $h = \sqrt{\xi^2 + \eta^2}$ and $(D_\alpha, D_\beta) = \|\nabla D\|(\cos\theta, \sin\theta)$. The sign function Σ_2 , given by

$$\Sigma_2 = \text{sign}(\xi D_\alpha + \eta D_\beta) = \text{sign}[\cos(\theta - \gamma)], \quad (24a)$$

is discontinuous at a point of a dispersion curve where $\theta = \gamma \pm \pi/2$.

The far-field waves contained in the wave component (22) stem from the point(s) of the dispersion curve(s) where the phase $\xi\alpha + \eta\beta$ is stationary, i.e. from the points defined by $\xi d\alpha/ds + \eta d\beta/ds = 0$. The unit vectors $(d\alpha/ds, d\beta/ds)$ and $(D_\alpha, D_\beta)/\|\nabla D\|$ are tangent and normal to a dispersion curve $D=0$, respectively, so that a stationary point is defined by $\xi D_\beta - \eta D_\alpha = 0$. We have

$$\xi D_\beta - \eta D_\alpha = h \|\nabla D\| \sin(\theta - \gamma),$$

so that the angle θ at a point of stationary phase is equal to γ or $\gamma + \pi$. The function Σ_2 defined by (24a) is equal to

$$\Sigma_2 = \text{sign}(\xi D_\alpha) = \text{sign}(\eta D_\beta) \quad (24b)$$

at a point of stationary phase. Expressions (24b) can be useful to represent far-field waves in regions centered around the axes $\eta=0$ and $\xi=0$, but are not convenient for far-field waves in the vicinity of the axes $\xi=0$ and $\eta=0$, respectively. The composite expression

$$\Sigma_2 = \frac{D_\alpha^2 \text{sign}\xi \text{sign}D_\alpha + D_\beta^2 \text{sign}\eta \text{sign}D_\beta}{\|\nabla D\|^2} \quad (24c)$$

generalizes (24b). The differences between the four wave components associated with expressions (24) for the term Σ_2 represent local flow disturbances since these expressions yield identical values of Σ_2 at a stationary point. Thus, the representations of the wave component φ^W associated with (24) correspond to alternative decompositions into wave and near-field components. The decomposition (21) indeed is nonunique.

A more general representation of the wave component φ^W (and related decomposition into wave and local components) can in fact be defined. In particular, the sign function Σ_2 may be taken as

$$\Sigma_2 = E_2 \text{sign}(\xi D_\alpha + \eta D_\beta) \quad (24d)$$

where E_2 is a real positive function that is equal to 1 at a stationary point. For instance, the function $E_2 = \exp[-\tan^2(\theta - \gamma)]$, where we have

$$\tan(\theta - \gamma) = (\xi D_\beta - \eta D_\alpha) / (\xi D_\alpha + \eta D_\beta),$$

is equal to 1 at a stationary point $\xi D_\beta - \eta D_\alpha = 0$ and vanishes at a point of discontinuity $\xi D_\alpha + \eta D_\beta = 0$. The integrand of the wave integral (22) may also be multiplied by a function E that is equal to 1 at a stationary point. Two such functions are

$$E = \exp\{-C [(\xi D_\beta - \eta D_\alpha) / (\xi D_\alpha + \eta D_\beta)]^{2N}\} \quad (25)$$

where $C \geq 0$ is a real constant and $N \geq 1$ is an integer, and

$$E = \exp\{-C[\mathcal{R}(\xi D_\beta - \eta D_\alpha)/(h \|\nabla D\|)]^{2N}\}$$

where \mathcal{R} is the radius of curvature of the dispersion curve at the stationary point. The latter function E is equal to 1 at a stationary point and decreases away from a stationary point at a rate independent of h and \mathcal{R} . The radius of curvature is given by

$$\mathcal{R} = \|\nabla D\|^3 / |D_\beta^2 D_{\alpha\alpha} - 2D_\alpha D_\beta D_{\alpha\beta} + D_\alpha^2 D_{\beta\beta}|$$

for a curve defined by the equation $D(\alpha, \beta) = 0$.

The method of stationary phase shows that the wave component (22) and the modified wave component

$$i\varphi^W = \sum_{D=0} \int ds E(\Sigma_1 + \Sigma_2) \frac{\text{Sexp}[k\zeta - i(\xi\alpha + \eta\beta)]}{\|\nabla D\|} \quad (26)$$

where any one of the four alternative expressions (24) may be used for Σ_2 , yield identical far-field waves. However, the near-field waves defined by (26) evidently depend on the functions E and Σ_2 .

The near-field component φ^N in the decomposition (21) is examined in [5]. The modified form of the Fourier representation (30) in [5] associated with the modified wave component (26) is

$$\pi\varphi^N \approx \int_{-\infty}^{\infty} d\beta \int_{-\infty}^{\infty} d\alpha (\Lambda^r + i\Lambda^i \{E\Sigma_2 - (1-E)\Sigma_1\}) \text{Sexp}[k\zeta - i(\xi\alpha + \eta\beta)] \quad (27)$$

where Λ^r and Λ^i are defined by (30b,c) in [5]. It is shown in [5] that the integrand of (27) is continuous (in fact varies smoothly) across a dispersion curve, and that the Fourier representation (27) is well suited for numerical evaluation.

The Fourier representation of the generic free-surface potential (20) defined by (21), (26) and (27) is a generalization of the representation given by (5) and (30) in [5], which is obtained if $E=1$ and (24a) is used for Σ_2 . Although the sum φ^F of the wave component φ^W and the near-field component φ^N is independent of the functions E and Σ_2 , each of the two components φ^W and φ^N depends on the functions E and Σ_2 . In the near field, the function E may simply be chosen equal to 1. However, the function Σ_2 can be chosen for the purpose of eliminating the discontinuity associated with (24a). Indeed, the term Σ_2 stems from a far-field approximation of the double integral ϕ_2 in (16) of [4], as was already mentioned. This far-field approximation is not relevant in the near field, so that

near-field modifications, e.g. of the form (24d), of the term Σ_2 are permitted.

The Fourier representation of (20) defined by (21), (26) and (27) is valid for generic dispersive waves and for arbitrary singularity distributions, including the special case of the Green function (i.e. a point source). Applications of this generic Fourier representation to wave diffraction-radiation by an offshore structure (without forward speed) and steady flows, and to the Green function of wave diffraction-radiation at small forward speed, are examined in [4,5]. Another application, to time-harmonic ship waves characterized by the dispersion function (5), is considered below. Only the wave component φ^W is considered here.

TIME-HARMONIC SHIP WAVES

The dispersion function (5b) is an even function of β , so that the dispersion curves are symmetric with respect to the axis $\beta=0$ and the integration in (26) can be restricted to the upper halves of the dispersion curves. In the upper half $\beta \geq 0$ of the Fourier plane, the dispersion curves are given by

$$\beta = \sqrt{(f-F\alpha)^4 - \alpha^2}. \quad (28a)$$

The dispersion function (5b) yields $D_\beta = -\beta/k$ and $D_\alpha = -\hat{\alpha}/k$ with

$$\hat{\alpha} = \alpha + 2(\tau - F^2\alpha)k = \alpha + 2F(f - F\alpha)^3, \quad (28b)$$

so that we have

$$\|\nabla D\|^2 = 1 + 4(\tau - F^2\alpha)\alpha/k + 4(\tau - F^2\alpha)^2. \quad (28c)$$

The term $\|\nabla D\|$ is an even function of β . The element of arc length $ds = \sqrt{1 + (d\beta/d\alpha)^2} d\alpha$ can be expressed as $ds = d\alpha \|\nabla D\| k/\beta$. The sign function Σ_1 defined by (23) becomes

$$\Sigma_1 = \text{sign}(f - F\alpha) \quad (29a)$$

and is an even function of β . Expression (24a) for the function Σ_2 yields

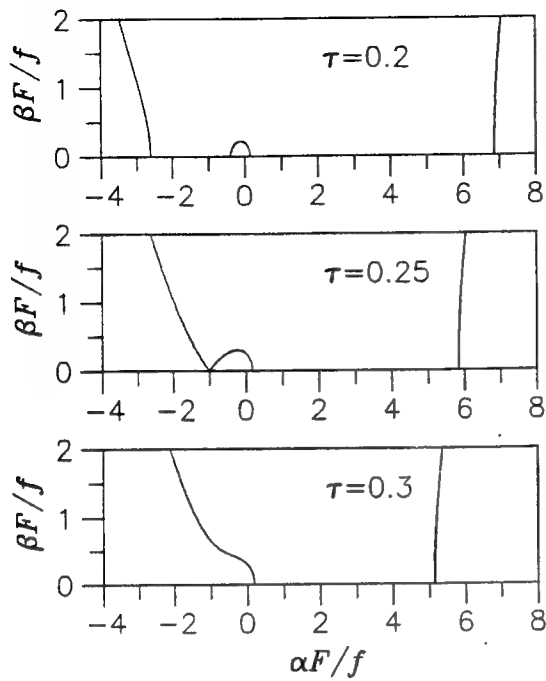
$$\Sigma_2^\pm = -\text{sign}(\xi\hat{\alpha} \pm \eta\beta) \quad (29b)$$

where $\Sigma_2^\pm = \Sigma_2(\alpha, \pm\beta)$ with $\beta \geq 0$. The function E defined by (25) becomes

$$E^\pm = \exp\{-C[(\eta\hat{\alpha} \mp \xi\beta)/(\xi\hat{\alpha} \pm \eta\beta)]^{2N}\} \quad (29c)$$

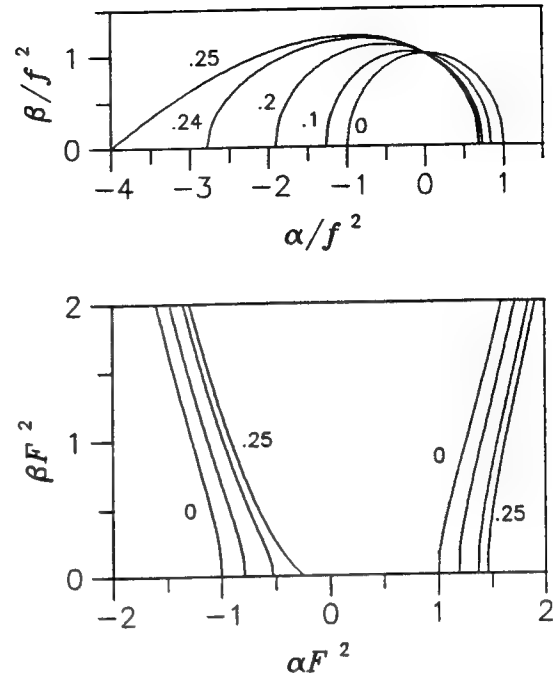
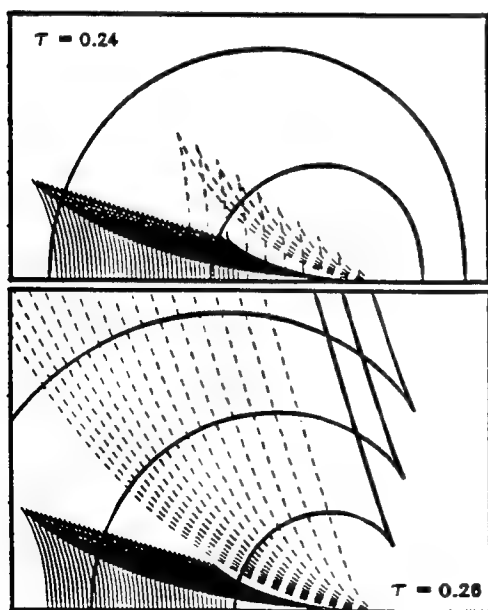
where $E^\pm = E(\alpha, \pm\beta)$ and $h = \sqrt{\xi^2 + \eta^2}$. The wave component (26) then becomes

$$i\varphi^W = \sum_{D=0} \int_{D=0} d\alpha \frac{k}{\beta} e^{k\zeta} [\Sigma^+ S^+ e^{-i(\xi\alpha + \eta\beta)} + \Sigma^- S^- e^{-i(\xi\alpha - \eta\beta)}] \quad (30)$$



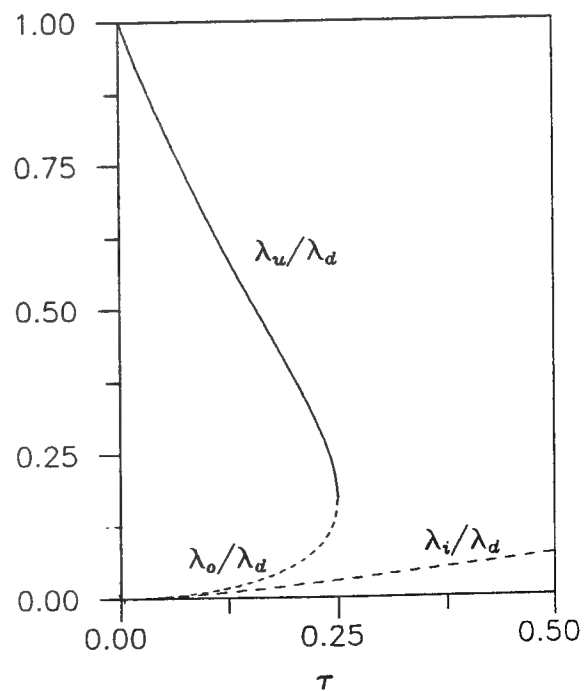
↑ Fig.2 Dispersion curves for $\tau = .2, .25, .3$ in the Fourier plane $(\alpha, \beta) F/f$

↓ Fig.4 Constant-phase curves for $\tau = .24$ and $.26$



↑ Fig.3 Dispersion curves in the Fourier planes $(\alpha, \beta)/f^2$ and $(\alpha, \beta) F^2$

↓ Fig.5 Comparison of wavelengths $\lambda_d, \lambda_u, \lambda_o, \lambda_i$



where $\Sigma^\pm = E^\pm(\Sigma_1 + \Sigma_2^\pm)$, $S^\pm = S(\alpha, \pm\beta)$ and the integration is restricted to the upper halves of the dispersion curves (in the upper half plane $\beta \geq 0$).

Dispersion curves

Expression (28a) defines several distinct dispersion curves and related distinct wave components, which include systems of inner and outer V waves, complete or partial ring waves and fan waves. The dispersion curves defined by (28a) are now analyzed. Equation (28a) can be expressed as

$$\beta F/f = \sqrt{\tau^2(1 - \alpha F/f)^4 - (\alpha F/f)^2} \quad (31)$$

where $\tau = fF = U\omega/g$ is the Strouhal number. We have two or three distinct dispersion curves if τ is larger or smaller than $1/4$, respectively.

If $\tau < 1/4$ the three dispersion curves intersect the axis $\beta = 0$ at four values of α , denoted α_o^\pm and α_i^\pm , which are given by

$$\begin{aligned} \alpha_o^\pm F/f &= \pm(1 + \sqrt{1 \pm 4\tau})^2/(4\tau) \\ \alpha_i^\pm F/f &= \pm(1 - \sqrt{1 \pm 4\tau})^2/(4\tau) \end{aligned} \quad (32a)$$

and satisfy the inequalities

$$\alpha_o^- < -f/F < \alpha_i^- < 0 < \alpha_i^+ < f/F < \alpha_o^+ \quad (32b)$$

These dispersion curves are located in the regions

$$-\infty \leq \alpha \leq \alpha_o^-, \alpha_i^- \leq \alpha \leq \alpha_i^+, \alpha_o^+ \leq \alpha \leq \infty \quad (32c)$$

if $\tau < 1/4$. We have $\alpha_o^- = \alpha_i^- = -f/F = -\omega L/U$ if $\tau = 1/4$ and the dispersion curves in the regions $-\infty \leq \alpha \leq \alpha_o^-$ and $\alpha_i^- \leq \alpha \leq \alpha_i^+$ are connected. The roots α_o^- and α_i^- are complex if $\tau > 1/4$. Thus, we have only two distinct dispersion curves located in the regions

$$-\infty \leq \alpha \leq \alpha_i^+, \alpha_o^+ \leq \alpha \leq \infty \quad (32d)$$

if $\tau > 1/4$. The dispersion curves defined by (31) are depicted in Fig. 2 for $\tau = 0.2, 0.25$ and 0.3 .

The inequalities (32b) show that the sign function Σ_1 defined by (29a) is equal to

$$\Sigma_1 = \begin{cases} -1 \\ 1 \end{cases} \text{ if } \begin{cases} \alpha_o^+ \leq \alpha \\ \text{otherwise} \end{cases} \quad (33)$$

so that Σ_1 in (30) is equal to 1 for all the dispersion curves except that in the region $\alpha_o^+ \leq \alpha \leq \infty$.

Expressions (32a) yield $\alpha_o^\pm F/f \sim \pm 1/\tau$ and $\alpha_i^\pm F/f \sim \pm \tau$ in the limit $\tau \rightarrow 0$, so that the values of the wavenumber k associated with the dispersion curve located in the inner region $\alpha_i^- \leq \alpha \leq \alpha_i^+$ are much smaller than those corresponding to the

dispersion curves in the outer regions $-\infty \leq \alpha \leq \alpha_o^-$ and $\alpha_o^+ \leq \alpha \leq \infty$. Indeed, (32a) yield

$$\alpha_o^\pm \approx \pm 1/F^2 \text{ and } \alpha_i^\pm \approx \pm f^2 \text{ as } \tau \rightarrow 0. \quad (34)$$

Thus, the *outer dispersion curves* correspond to values of the wavenumber k which are greater than $1/F^2$, whereas we have $k \approx f^2$ for the *inner dispersion curve*. The upper part of Fig. 3 depicts the inner dispersion curve, in the frequency-scaled Fourier plane $(\alpha/f^2, \beta/f^2)$, for $\tau = 0, 0.1, 0.2, 0.24$, and 0.25 ; and the lower part of Fig. 3 depicts the outer dispersion curves, in the Froude-scaled Fourier plane $(F^2\alpha, F^2\beta)$, for $\tau = 0, 0.1, 0.2$, and 0.25 . The dispersion function (5b) shows that the outer dispersion curves are symmetric with respect to the axis $\alpha = 0$ in the limit $\tau = 0$; (5b) also shows that the inner dispersion curve is given by $(\alpha/f^2 + 2\tau)^2 + (\beta/f^2)^2 = 1 + O(\tau^2)$ as $\tau \rightarrow 0$, so that the inner dispersion curve is approximately a circle of radius f^2 centered at $(\alpha, \beta) = (-2\tau f^2, 0)$.

Component wave systems

For $\tau < 1/4$ the wave component φ^W defined by (30) can be expressed as

$$\varphi^W = \varphi^R + \varphi^V \text{ with } \varphi^V = \varphi^{oV} + \varphi^{iV} \quad (35a)$$

where the components φ^R , φ^{oV} and φ^{iV} respectively correspond to the dispersion curves in the inner region $\alpha_i^- \leq \alpha \leq \alpha_i^+$ and the outer regions $-\infty \leq \alpha \leq \alpha_o^-$ and $\alpha_o^+ \leq \alpha \leq \infty$. The component φ^R represents a system of ring-like waves, identified hereafter as *ring waves*. The components φ^{oV} and φ^{iV} represent two systems of V waves contained within wedges and identified as *outer V waves* and *inner V waves*, respectively. Curves of constant phase corresponding to the ring waves (thick solid lines) and the outer (dashed lines) and inner (thin solid lines) V waves are depicted in Fig. 4 for $\tau = 0.24$. In the limit $\tau = 0$, the components φ^R and φ^V represent the ring waves generated by an offshore structure without forward speed ($F = 0$) and the Kelvin ship waves generated by a ship advancing in calm water ($f = 0$), respectively.

For $\tau > 1/4$ the wave component φ^W given by (30) can be expressed in the form

$$\varphi^W = \varphi^{RF} + \varphi^{iV} \quad (35b)$$

where the components φ^{RF} and φ^{iV} are respectively associated with the dispersion curves in the regions $-\infty \leq \alpha \leq \alpha_i^+$ and $\alpha_o^+ \leq \alpha \leq \infty$. The component φ^{iV} represents a system of *inner V waves*, qualitatively similar to the inner V waves φ^{iV} in (35a), contained within a wedge. The component φ^{RF} represents a system of *incomplete ring waves* and

fan waves, identified as *ring-fan waves*, that are also contained within a wedge. The system of ring-fan waves can be further divided into a system of inner fan waves and a system of partial ring and outer fan waves, which correspond to the portions $-\infty \leq \alpha \leq -f/F$ and $-f/F \leq \alpha \leq \alpha_i^+$ of the dispersion curve in the range $-\infty \leq \alpha \leq \alpha_i^+$. Constant-phase curves corresponding to the partial ring and outer fan waves (thick solid lines), the inner fan waves (dashed lines), and the inner V waves (thin solid lines) are depicted in Fig.4 for $\tau = 0.26$.

General features of component waves

For $\tau < 1/4$, Fig.4 shows that curves of constant phase for the outer V waves and the inner V waves are contained within wedges and are cusped at the wedge boundaries. Let θ_o and θ_i represent the wedge angles (i.e. the angles between the ship track and the cusp lines) for the outer and inner V waves, respectively. In the limit $\tau = 0$ the outer and inner wedge angles θ_o and θ_i are identical and equal to the Kelvin angle $19^\circ 28'$. The wedge angles θ_o and θ_i increase and decrease monotonically in the range $0 \leq \tau \leq 1/4$, respectively, and we have

$$19^\circ 28' \leq \theta_o \leq 54^\circ 44', \quad 19^\circ 28' \geq \theta_i \geq 15^\circ 48'$$

for $0 \leq \tau \leq 1/4$. The angle θ_o increases rapidly for values of τ in the vicinity of $1/4$.

For $\tau > 1/4$, Fig.4 shows that the ring-fan waves also have a cusp, at an angle with respect to the ship track denoted θ_r , and that the outer/inner fan waves are located outside/inside a wedge, at an angle denoted θ_f . Thus, Fig.4 shows that ring waves, outer fan waves, and inner fan waves exist within the regions $|\theta| \leq \theta_r$, $\theta_f \leq |\theta| \leq \theta_r$, $|\theta| \leq \theta_f$, respectively. The ring angle θ_r and the fan angle θ_f decrease monotonically for $\tau \geq 1/4$, with

$$125^\circ 16' \geq \theta_r \geq 0, \quad 90^\circ \geq \theta_f \geq 0$$

for $1/4 \leq \tau \leq \infty$. The angles θ_r and θ_f decrease rapidly for values of τ in the vicinity of $1/4$. The angle θ_r is equal to 90° for $\tau = \sqrt{2/27} \approx 0.27$. Thus, if $\tau > \sqrt{2/27}$ a ship only generates trailing waves, whereas waves are radiated both ahead and behind a ship if $0 \leq \tau < \sqrt{2/27}$. The upstream waves are ring waves if $0 \leq \tau < 1/4$ or incomplete ring waves and outer fan waves if $1/4 < \tau < \sqrt{2/27}$.

The systems of waves associated with the dispersion curves located in the regions defined by (32c) and (32d) involve waves of widely different length, as can be observed in Fig.4. The wavelengths of the *transverse* waves, i.e. the waves at the ship track $\eta = 0$, in the various component wave systems depicted in Fig.4 can easily be compared.

Specifically, (32b) shows that the wavenumber k of the waves at the ship track in Fig.4 is equal to α_o^+ for the inner V waves, $-\alpha_o^-$ for the outer V waves (if $\tau < 1/4$), $-\alpha_i^-$ for the upstream (forerunning) waves in the system of ring waves (if $\tau < 1/4$), and α_i^+ for the downstream (trailing) waves in the system of ring waves (if $\tau < 1/4$) or partial ring waves (if $\tau > 1/4$). Expressions (32a) then show that the corresponding values of the wavelength $\lambda = 2\pi/k$ are given by

$$\begin{aligned} \begin{Bmatrix} \lambda_i \\ \lambda_o \end{Bmatrix} &= 2\pi F^2 \begin{Bmatrix} 4/(\sqrt{1+4\tau}+1)^2 \\ 4/(1+\sqrt{1-4\tau})^2 \end{Bmatrix} \\ \begin{Bmatrix} \lambda_d \\ \lambda_u \end{Bmatrix} &= \frac{2\pi}{f^2} \begin{Bmatrix} 4\tau^2/(\sqrt{1+4\tau}-1)^2 \\ 4\tau^2/(1-\sqrt{1-4\tau})^2 \end{Bmatrix} \end{aligned} \quad (36)$$

where λ_i and λ_o are the wavelengths of the transverse waves in the systems of inner and outer V waves, and λ_d and λ_u correspond to the downstream and upstream ship-track waves in the systems of (complete or partial) ring waves.

Expressions (36) yield

$$\lambda_d = \lambda_u = 2\pi/f^2, \quad \lambda_i = \lambda_o = 2\pi F^2 \quad (37a)$$

for $\tau = 0$, in accordance with (34), and show that

$$\lambda_{d,u} = O(2\pi/f^2), \quad \lambda_{i,o} = O(2\pi F^2) \quad (37b)$$

for $0 \leq \tau \leq 1/4$. Furthermore, (36) show that the downstream/upstream waves in the system of ring waves and the outer/inner V waves become longer/shorter with increasing values of τ , i.e. with increasing forward speed. The wavelength λ_o of the outer V waves increases rapidly in the vicinity of $\tau = 1/4$. The wavelengths λ_u and λ_o are defined only if $\tau < 1/4$, whereas λ_d and λ_i are defined for all values of τ .

The wavelengths λ_i and λ_d can be scaled with respect to F^2 and $1/f^2$ as in (36), or with respect to F/f . Specifically, we have $\lambda_i f/F = \tau \lambda_i/F^2$ and $\lambda_d f/F = f^2 \lambda_d/\tau$. The functions $\lambda_d/(2\pi/f^2)$ and $\lambda_i/(2\pi F^2)$ are equal to 1 for $\tau = 0$ (as was already noted), whereas we have $\lambda_d f/F \sim 1/\tau$ and $\lambda_i f/F \sim \tau$ as $\tau \rightarrow 0$. Thus, for small values of τ the wavelengths λ_d and λ_i are more appropriately scaled with respect to $1/f^2$ and F^2 , in accordance with (37b), than with respect to F/f . However, λ_d and λ_i are most appropriately scaled with respect to F/f for values of $\tau > 1$. Indeed, expressions (36) yield $\lambda_{d,i} \sim 2\pi F/f$ as $\tau \rightarrow \infty$ and

$$\begin{aligned} \lambda_d &= O(2\pi/f^2) \text{ and } \lambda_i = O(2\pi F^2) \text{ for } \tau \leq 1 \\ \lambda_{d,i} &= O(2\pi F/f) \text{ for } \tau \geq 1. \end{aligned} \quad (38)$$

For typical values of f and F in the ranges $1 \leq f \leq 5$ and $0.1 \leq F \leq 0.5$, we have $0.1 \leq \tau \leq 2.5$, and

the wavelengths of the component wave systems may reasonably be scaled in accordance with (37b), although scaling in accordance with (38) is more appropriate for $\tau > 1$.

Figure 5 depicts the ratios λ_u/λ_d and λ_o/λ_d for $\tau \leq 1/4$ and the ratio λ_i/λ_d for $\tau \leq 1/2$. This figure and Fig. 4 show that the (complete or partial) ring waves are much longer than the V waves except for a fairly narrow range of values of τ in the vicinity of $\tau = 1/4$ (for which λ_o and λ_u are comparable), and for very large values of τ (for which λ_i and λ_d are comparable).

The wave components φ^{iV} , φ^{oV} , φ^{RF} and φ^R in (35) are now successively considered.

Fourier representations of wave components

The inner V wave component φ^{iV} exists for all values of τ and corresponds to the dispersion curve in the region $\alpha_o^+ \leq \alpha < \infty$ where α_o^+ is defined by (32a) as $\alpha_o^+ = (1 + \sqrt{1 + 4\tau})^2 / (4F^2)$. The Froude-scaled Fourier variables

$$F^2(\alpha, \beta, k) = (A, B, K) \quad (39)$$

are used to represent inner V waves. The dispersion curve associated with inner V waves is defined via a parametric representation. Specifically, we define the functions $K_0(\tau) \equiv F^2\alpha_o^+$, $K(\sigma; \tau)$, $A(\sigma; \tau)$, $B(\sigma; \tau)$ and $\hat{A}(\sigma; \tau) \equiv -F^2\hat{\alpha}$, where $0 \leq \sigma < \infty$, as

$$K_0 = (1 + \sqrt{1 + 4\tau})^2 / 4, \quad K = K_0 + (\sqrt{1 + 4\sigma^2} - 1) / 2$$

$$A = \tau + \sqrt{K}, \quad B = \sqrt{K^2 - A^2}, \quad \hat{A} = \sqrt{K}(2K - 1 - \tau/\sqrt{K}).$$

We have $d\alpha = (d\sigma/F^2)(\sigma/\sqrt{1 + 4\sigma^2})/\sqrt{K}$ and (33) yields $\Sigma_1 = -1$. It follows that (30) becomes

$$\varphi^{iV} = \frac{i}{F^2} \int_0^\infty d\sigma \Upsilon e^{K\zeta/F^2} [e^{-(1-\mu^-)} S^+ e^{-i(A\xi + B\eta)/F^2} + e^{+(1-\mu^+)} S^- e^{-i(A\xi - B\eta)/F^2}]$$

where the functions Υ and S^\pm are defined as

$$\Upsilon = \sigma\sqrt{K}/(B\sqrt{1 + 4\sigma^2}), \quad (40)$$

$$S^\pm = S(A/F^2, \pm B/F^2). \quad (41)$$

Furthermore, the functions $\mu^\pm \equiv \Sigma_2^\mp$ and $e^\pm \equiv E^\mp$ are defined by (29b) and (29c) with $(\alpha, \beta, k, \hat{\alpha}) = (A, B, K, -\hat{A})/F^2$. We thus have

$$\mu^\pm = \text{sign}(\xi\hat{A} \pm \eta B), \quad (42)$$

$$e^\pm = \exp\{-C[(\eta\hat{A} \mp \xi B)/(\xi\hat{A} \pm \eta B)]^{2N}\}. \quad (43)$$

We have $\Upsilon \sim 1/(2\sqrt{\sigma})$ as $\sigma \rightarrow \infty$ and

$\Upsilon \rightarrow [(1 + 1/\sqrt{1 + 4\tau})/2]^{1/2}$ as $\sigma \rightarrow 0$, so that Υ is continuous for $\sigma \geq 0$ and $\tau \geq 0$.

The outer V wave component φ^{oV} exists if $\tau < 1/4$ and corresponds to the dispersion curve in the region $-\infty < \alpha \leq \alpha_o^-$ where α_o^- is defined by (32a) as $\alpha_o^- = -(1 + \sqrt{1 - 4\tau})^2 / (4F^2)$. The Froude-scaled Fourier variables (39) are used to represent outer V waves. The dispersion curve associated with outer V waves is defined via a parametric representation. Specifically, we define the functions $K_0(\tau) \equiv -F^2\alpha_o^-$, $K(\sigma; \tau)$, $A(\sigma; \tau)$, $B(\sigma; \tau)$ and $\hat{A}(\sigma; \tau) \equiv F^2\hat{\alpha}$, where $0 \leq \sigma < \infty$, as

$$K_0 = (1 + \sqrt{1 - 4\tau})^2 / 4, \quad K = K_0 + (\sqrt{1 + 4\sigma^2} - 1) / 2$$

$$A = \tau - \sqrt{K}, \quad B = \sqrt{K^2 - A^2}, \quad \hat{A} = \sqrt{K}(2K - 1 + \tau/\sqrt{K}).$$

We have $d\alpha = -(d\sigma/F^2)(\sigma/\sqrt{1 + 4\sigma^2})/\sqrt{K}$ and (33) yields $\Sigma_1 = 1$. Thus, (30) becomes

$$\varphi^{oV} = \frac{-i}{F^2} \int_0^\infty d\sigma \Upsilon e^{K\zeta/F^2} [e^{+(1-\mu^+)} S^+ e^{-i(A\xi + B\eta)/F^2} + e^{-(1-\mu^-)} S^- e^{-i(A\xi - B\eta)/F^2}]$$

where the functions Υ and S^\pm are given by (40) and (41). Furthermore, the functions $\mu^\pm \equiv -\Sigma_2^\pm$ and $e^\pm \equiv E^\pm$, defined by (29b) and (29c) with $(\alpha, \beta, k, \hat{\alpha}) = (A, B, K, \hat{A})/F^2$, are given by (42) and (43). We have $\Upsilon \sim 1/(2\sqrt{\sigma})$ as $\sigma \rightarrow \infty$ and $\Upsilon \rightarrow [(1 + 1/\sqrt{1 - 4\tau})/2]^{1/2}$ as $\sigma \rightarrow 0$, so that Υ is continuous for $\sigma \geq 0$ and $\tau < 1/4$.

The wave component φ^V is defined by (35a) as the sum of the components φ^{iV} and φ^{oV} associated with inner and outer V waves. In the special case $\tau = 0$, corresponding to steady ship waves, now considered we have $K_0 = 1$, $K = (\sqrt{1 + 4\sigma^2} + 1)/2$, $B = \sigma$, $A = \pm\sqrt{K}$, and $\mp F^2\hat{\alpha} = \hat{A} = \sqrt{K}(1 + 4\sigma^2)$ for the inner/outer V waves. For steady flows the spectrum function $S(\alpha, \beta)$ satisfies the identity $S(-\alpha, -\beta) = \bar{S}(\alpha, \beta)$ where \bar{S} is the complex conjugate of S . It can then be shown that the V wave component is given by

$$\varphi^V = \frac{-2}{F^2} \int_0^\infty d\sigma \frac{\sqrt{K} e^{K\zeta/F^2}}{\sqrt{1 + 4\sigma^2}} [e^{-(1-\mu^-)} \Im m \mathcal{A}^+ + e^{+(1-\mu^+)} \Im m \mathcal{A}^-]$$

where $K = (\sqrt{1 + 4\sigma^2} + 1)/2$, μ^\pm and e^\pm are given by (42) and (43), and \mathcal{A}^\pm are defined as

$$\mathcal{A}^\pm = S(\sqrt{K}/F^2, \pm\sigma/F^2) \exp[-i(\sqrt{K}\xi \pm \sigma\eta)/F^2].$$

Thus, the sum of the components φ^{iV} and φ^{oV} , which contain real and imaginary parts, is real in the steady-flow limit $\tau = 0$.

The ring-fan wave component φ^{RF} exists if $\tau > 1/4$ and corresponds to the dispersion curve

in the region $-\infty < \alpha \leq \alpha_i^+$ where α_i^+ is defined by (32a) as $\alpha_i^+ = f^2(\sqrt{1+4\tau}-1)/(4\tau^2)$. The frequency-scaled Fourier variables

$$(\alpha, \beta, k)/f^2 = (A, B, K) \quad (44)$$

are used for the component φ^{RF} . The dispersion curve corresponding to ring-fan waves is defined via a parametric representation. Specifically, we define $K_0(\tau) \equiv \alpha_i^+/f^2$, $K(\sigma; \tau)$, $A(\sigma; \tau)$, $B(\sigma; \tau)$ and $\hat{A}(\sigma; \tau) \equiv \hat{\alpha}/f^2$, with $0 \leq \sigma < \infty$, as

$$K_0 = (\sqrt{1+4\tau}-1)/(4\tau^2), \quad K = K_0 + (\sqrt{1+4\sigma^2}-1)/2$$

$$A = (1-\sqrt{K})/\tau, \quad B = \sqrt{K^2-A^2}, \quad \hat{A} = A + 2\tau K^{3/2}.$$

We have $d\alpha = -(d\sigma f/F)(\sigma/\sqrt{1+4\sigma^2})/\sqrt{K}$ and (33) yields $\Sigma_1 = 1$. It follows that (30) becomes

$$\varphi^{RF} = -i \frac{f}{F} \int_0^\infty d\sigma \Upsilon e^{f^2 \zeta K} [e^+(1-\mu^+) S^+ e^{-if^2(\xi A + \eta B)} + e^-(1-\mu^-) S^- e^{-if^2(\xi A - \eta B)}]$$

where Υ is given by (40), the functions S^\pm are defined as

$$S^\pm = S(f^2 A, \pm f^2 B) \quad (45)$$

and the functions $\mu^\pm \equiv -\Sigma_2^\pm$ and $e^\pm \equiv E^\pm$, defined by (29b) and (29c) with $(\alpha, \beta, k, \hat{\alpha}) = f^2(A, B, K, \hat{A})$, are given by (42) and (43). We have $\Upsilon \sim 1/(2\sqrt{\sigma})$ as $\sigma \rightarrow \infty$ and

$$\Upsilon \rightarrow [(1-1/\sqrt{1+4\tau})/2]^{1/2} \text{ as } \sigma \rightarrow 0,$$

so that Υ is continuous for $\sigma \geq 0$ and $\tau > 1/4$.

The ring wave component φ^R exists if $\tau < 1/4$ and corresponds to the dispersion curve in the inner region $\alpha_i^- \leq \alpha \leq \alpha_i^+$ where α_i^\pm are defined by (32a) as $\alpha_i^\pm/f^2 = \pm(\sqrt{1\pm 4\tau}-1)/(4\tau^2)$. The frequency-scaled Fourier variables (44) are used for ring waves. The dispersion curve associated with ring waves is defined by a parametric representation in which A is expressed as $A = A_0 + K_0 \cos \theta$ with $f^2 A_0 = (\alpha_i^+ + \alpha_i^-)/2$, $f^2 K_0 = (\alpha_i^+ - \alpha_i^-)/2$ and $0 \leq \theta \leq \pi$, i.e.

$$A_0(\tau) = (\sqrt{1-4\tau} - \sqrt{1+4\tau} + 4\tau)/(4\tau^2)$$

$$K_0(\tau) = (2 - \sqrt{1+4\tau} - \sqrt{1-4\tau})/(4\tau^2).$$

Thus, we define the functions $A(\theta; \tau)$, $B(\theta; \tau)$, $K(\theta; \tau)$, and $\hat{A}(\sigma; \tau) \equiv \hat{\alpha}/f^2$ as

$$A = A_0 + K_0 \cos \theta, \quad K = (1 - \tau A)^2$$

$$B = \sqrt{K^2 - A^2}, \quad \hat{A} = A + 2\tau K^{3/2}.$$

We have $d\alpha = -f^2 d\theta K_0 \sin \theta$ and (30) becomes

$$\varphi^R = -if^2 K_0 \int_0^\pi d\theta \Upsilon e^{f^2 \zeta K} [e^+(1-\mu^+) S^+ e^{-if^2(\xi A + \eta B)} + e^-(1-\mu^-) S^- e^{-if^2(\xi A - \eta B)}]$$

where Υ is defined as $\Upsilon = (K/B) \sin \theta$ and S^\pm is given by (45). Furthermore, the terms $\mu^\pm \equiv -\Sigma_2^\pm$ and $e^\pm \equiv E^\pm$, defined by (29b) and (29c) with $(\alpha, \beta, k, \hat{\alpha}) = f^2(A, B, K, \hat{A})$, are given by (42) and (43). The function B vanishes for $\theta = 0$ and $\theta = \pi$, but we have

$$\Upsilon \rightarrow T \begin{cases} (1+4\tau)^{1/4} - 1/(1+4\tau)^{1/4} \\ 1/(1-4\tau)^{1/4} - (1-4\tau)^{1/4} \end{cases} \text{ as } \theta \rightarrow \begin{cases} 0 \\ \pi \end{cases}$$

with $T = 1/\sqrt{2 - \sqrt{1+4\tau} - \sqrt{1-4\tau}}$. Thus, the integrand of the Fourier integral defining the ring waves is continuous for $0 \leq \theta \leq \pi$ and $0 \leq \tau < 1/4$.

In the limit $\tau = 0$, i.e. for wave diffraction-radiation without forward speed, we have $A_0 = 0$, $K_0 = 1$, $(A, B, K) = (\cos \theta, \sin \theta, 1)$ and $\hat{A} = A$. The functions μ^\pm and e^\pm are then given by (42) and (43) with $\hat{A} = \cos \theta$ and $B = \sin \theta$. The ring-wave component becomes

$$\varphi^R = -2f^2 e^{f^2 \zeta} \int_0^{\pi/2} d\theta [e^+(\mu^+ \Im m \mathcal{A}^+ + i \Re e \mathcal{A}^+) + e^-(\mu^- \Im m \mathcal{A}^- + i \Re e \mathcal{A}^-)]$$

where the functions \mathcal{A}^\pm are defined as

$$\mathcal{A}^\pm = S(f^2 \cos \theta, \pm f^2 \sin \theta) \exp[-if^2(\xi \cos \theta \pm \eta \sin \theta)].$$

Here, the relation $S(-\alpha, -\beta) = \bar{S}(\alpha, \beta)$, which holds for time-harmonic flows without forward speed, was used.

Illustrative calculations

The foregoing Fourier representations of the wave components φ^{iV} , φ^{oV} , φ^{RF} and φ^R in (35) provide simple analytical representations of the wave components generated by an arbitrary (volume, surface, and/or line) distribution of singularities (e.g. sources and/or dipoles), characterized by the spectrum function \mathcal{S} . For purposes of illustration, the wave potential φ^W in (21) is now considered for a simple example spectrum function.

Specifically, a uniform distribution of sources with density $m/(4\pi)$ within a flat rectangular panel H_p of length $2h_p$ and depth d_p contained in a vertical plane making an angle γ_p with the x axis is considered. The source panel is centered at the point $(x_p, y_p, z_p \leq 0)$ and is defined by $x = x_p + u \cos \gamma_p$, $y = y_p + u \sin \gamma_p$, $z = z_p + v$ with $-h_p \leq u \leq h_p$ and $-d_p \leq v \leq 0$. The free-surface potential φ_p^F generated by this source distribution is integrated over a flat rectangular panel H_q of length $2h_q$ and depth d_q contained in a vertical plane making an angle γ_q with the x axis. Thus, we consider the free-surface component C_{pq}^F in the influence coefficient defined via a Galerkin integration (corresponding to domain collocation instead of point collocation)

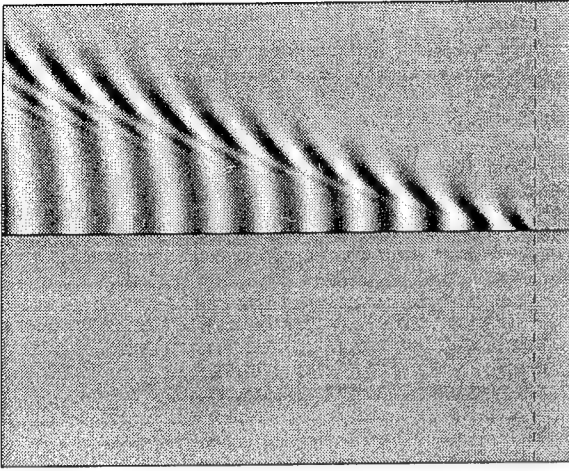


Fig.6a Inner and Outer V waves for $\tau = 0$ and $F = 0.245$
 $(-4.2 \leq \xi \leq 0.3, -1.8 \leq \eta \leq 0 \leq \eta \leq 1.8 \text{ and } \zeta = 0)$

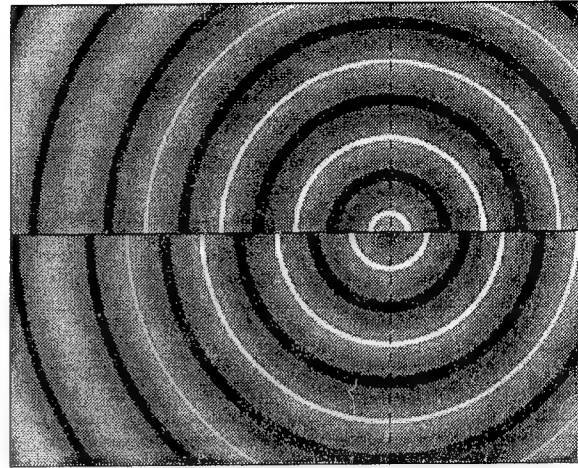


Fig.6b Ring waves for $\tau = 0$ and $f = 2$
 $(-8 \leq \xi \leq 4, -4.8 \leq \eta \leq 0 \leq \eta \leq 4.8 \text{ and } \zeta = 0)$

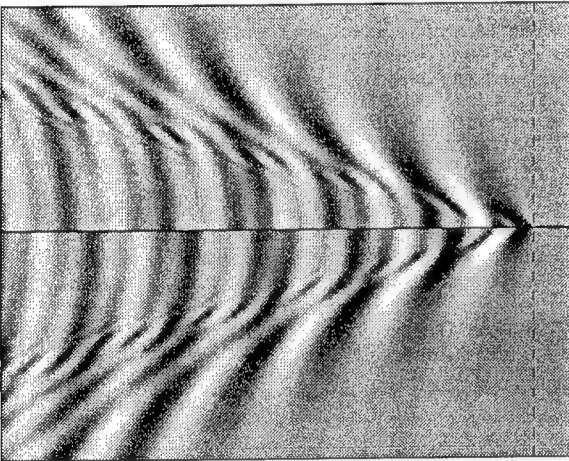


Fig.6c Inner and Outer V waves for $\tau = 0.2$ and $F = 0.245$
 $(-4.2 \leq \xi \leq 0.3, -1.8 \leq \eta \leq 0 \leq \eta \leq 1.8 \text{ and } \zeta = 0)$

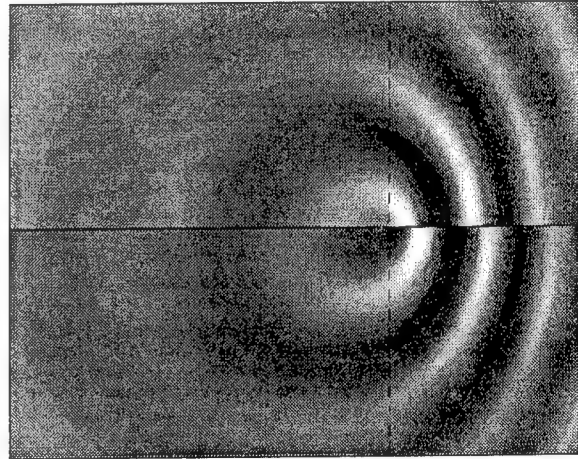


Fig.6d Ring waves for $\tau = 0.2$ and $f = 0.816$
 $(-30 \leq \xi \leq 15, -18 \leq \eta \leq 0 \leq \eta \leq 18 \text{ and } \zeta = 0)$

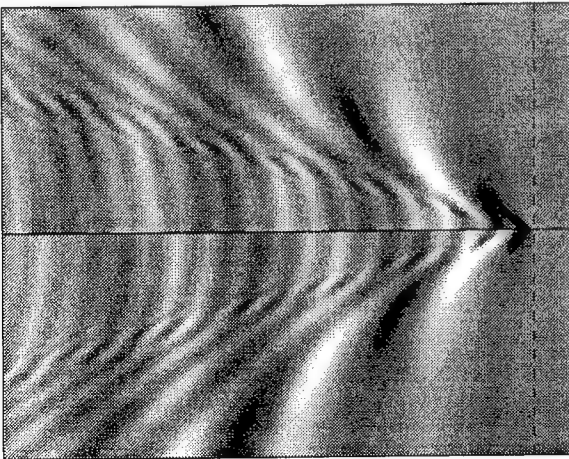


Fig.6e Inner and Outer V waves for $\tau = 0.245$ and $F = 0.245$
 $(-4.2 \leq \xi \leq 0.3, -1.8 \leq \eta \leq 0 \leq \eta \leq 1.8 \text{ and } \zeta = 0)$

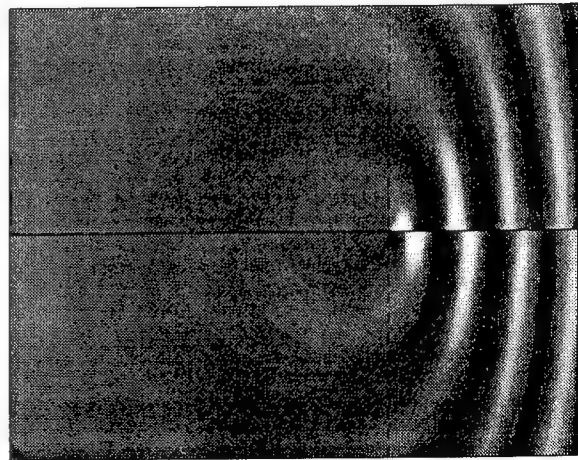


Fig.6f Ring waves for $\tau = 0.245$ and $f = 1$
 $(-15 \leq \xi \leq 7.5, -9 \leq \eta \leq 0 \leq \eta \leq 9 \text{ and } \zeta = 0)$

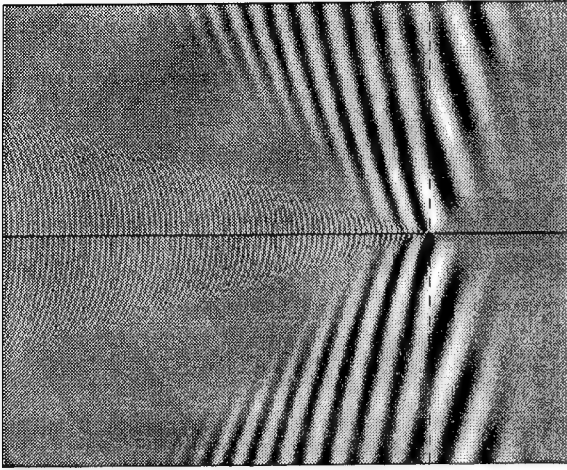


Fig.6g Ring-Fan and Inner V waves for $\tau = 0.255$ and $f = 1$
 $(-22.5 \leq \xi \leq 7.5, -12 \leq \eta \leq 0 \leq \eta \leq 12 \text{ and } \zeta = 0)$

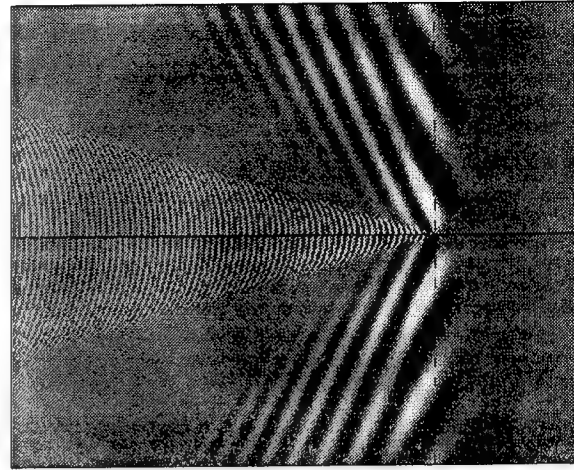


Fig.6h Ring-Fan and Inner V waves for $\tau = 0.272$ and $f = 1$
 $(-22.5 \leq \xi \leq 7.5, -12 \leq \eta \leq 0 \leq \eta \leq 12 \text{ and } \zeta = 0)$

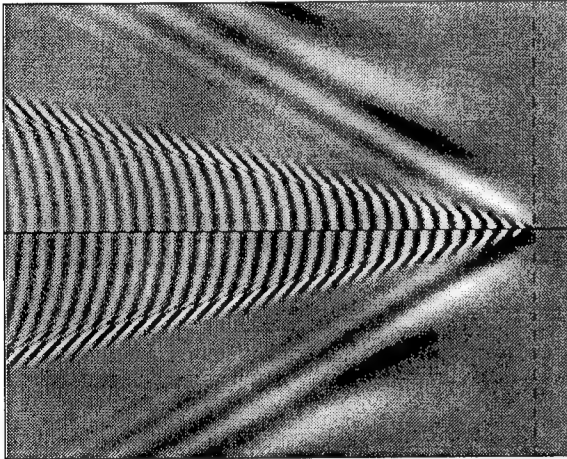


Fig.6i Ring-Fan and Inner V waves for $\tau = 0.5$ and $f = 1$
 $(-28 \leq \xi \leq 2, -12 \leq \eta \leq 0 \leq \eta \leq 12 \text{ and } \zeta = 0)$

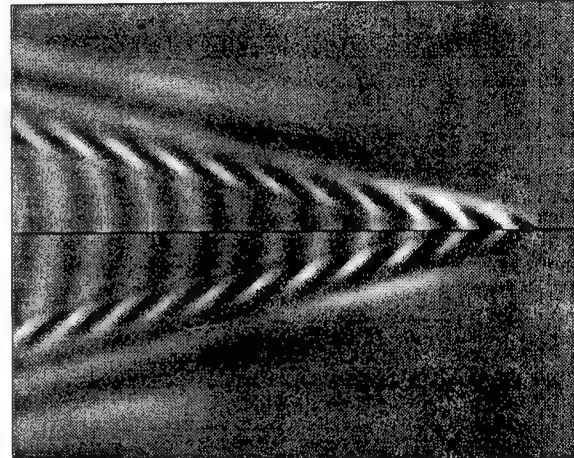


Fig.6j Ring-Fan and Inner V waves for $\tau = 1$ and $f = 1$
 $(-28 \leq \xi \leq 2, -12 \leq \eta \leq 0 \leq \eta \leq 12 \text{ and } \zeta = 0)$

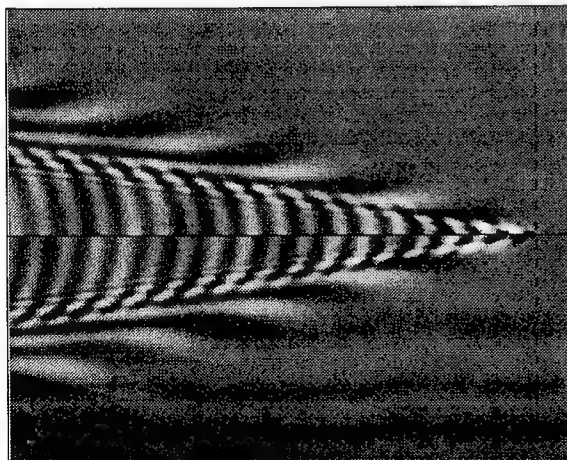


Fig.6k Ring-Fan and Inner V waves for $\tau = 2$ and $f = 2$
 $(-28 \leq \xi \leq 2, -12 \leq \eta \leq 0 \leq \eta \leq 12 \text{ and } \zeta = 0)$

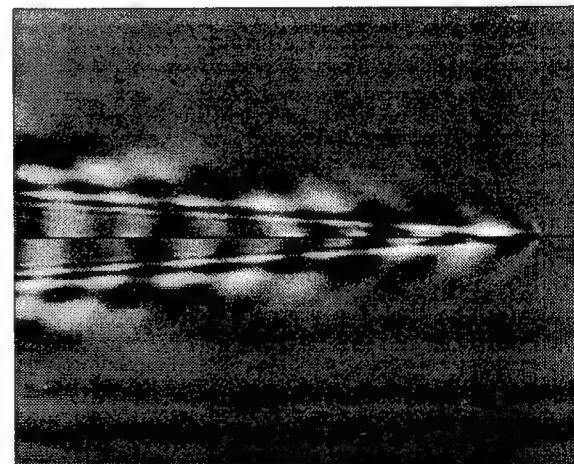


Fig.6l Ring-Fan and Inner V waves for $\tau = 4$ and $f = 2$
 $(-28 \leq \xi \leq 2, -12 \leq \eta \leq 0 \leq \eta \leq 12 \text{ and } \zeta = 0)$

of φ_p^F over the influenced panel H_q . This panel is centered at the point $(\xi_q, \eta_q, \zeta_q \leq 0)$ and is defined by $\xi = \xi_q + u \cos \gamma_q$, $\eta = \eta_q + u \sin \gamma_q$, $\zeta = \zeta_q + v$ with $-h_q \leq u \leq h_q$ and $-d_q \leq v \leq 0$. The influence coefficient C_{pq}^F can be expressed in the form $C_{pq}^F = M a_p a_q c^F$ where $M = m/(4\pi)$, $a_p = 2h_p d_p$ and $a_q = 2h_q d_q$ are the areas of the panels H_p and H_q , and c^F is given by (20) with

$$\varphi^F \rightarrow c^F, (\xi, \eta, \zeta) \rightarrow (\xi_q - x_p, \eta_q - y_p, \zeta_q + z_p), S \rightarrow A_p A_q;$$

the functions A_p and A_q are defined as

$$\begin{cases} A_p \\ A_q \end{cases} = \begin{cases} (\sin \varphi_p / \varphi_p) [1 - \exp(-k d_p)] / (k d_p) \\ (\sin \varphi_q / \varphi_q) [1 - \exp(-k d_q)] / (k d_q) \end{cases}$$

with $\begin{cases} \varphi_p = (\alpha \cos \gamma_p + \beta \sin \gamma_p) h_p \\ \varphi_q = (\alpha \cos \gamma_q + \beta \sin \gamma_q) h_q \end{cases}$.

The free-surface influence coefficient c^F can then be expressed as the sum of a wave component c^W and a near-field component c^N , as in (21). The wave component c^W is considered here for a source panel H_p and an influenced panel H_q of sizes $h_p = 0.025 = h_q$ and $d_p = 0.015 = d_q$. Furthermore, both the source panel and the influenced panel are at the free surface, so that we have $\zeta = \zeta_q + z_p = 0$ and the orientations of these panels with respect to the x axis are chosen as $\gamma_p = \pi/4$ and $\gamma_q = -\pi/4$.

Illustrative calculations of the real and imaginary parts of the V waves $\varphi^{iV} + \varphi^{oV}$, the ring waves φ^R , and the ring-fan and inner V waves $\varphi^{RF} + \varphi^{iV}$ associated with the foregoing spectrum function are depicted in the upper and lower halves of Figs 6a-l for $\zeta = 0$ at several values of the Strouhal number. Specifically, the inner and outer V waves and the ring waves are depicted in Figs 6a,c,e and Figs 6b,d,f for $\tau = 0, 0.2, 0.245$; and the ring-fan and inner V waves are depicted in Figs 6g-l for $\tau = 0.255, 0.272, 0.5, 1, 2, 4$.

CONCLUSION

Extensions of the Fourier-Kochin theory of wave diffraction-radiation by ships or offshore structures expounded in [3,4,5] have been presented. The main results given in the study are now briefly summarized.

The source and dipole potentials ψ and χ in the integral equation (6a) and the flow representation (6b) can be expressed in the form (12), i.e.

$$\psi = \psi^S + \psi^F \quad \chi = (\chi^S - \varphi^S) + \chi^F$$

where the superscripts S and F identify simple-singularity and free-surface components, respectively. The representation $\chi = (\chi^S - \varphi^S) + \chi^F$

is a modification of the representation $\chi = \chi^S + \hat{\chi}^F$ given in [3]. Specifically, the simple-singularity component φ^S is extracted from the free-surface potential $\hat{\chi}^F$. The free-surface potentials ψ^F and χ^F in (12) are given by the Fourier representation (13a) where D_ϵ is the dispersion function (5) associated with the linear free-surface boundary condition (1), and the spectrum functions N and M are defined in terms of distributions of elementary waves $\exp[kz + i(\alpha x + \beta y)]$ over the mean wetted hull H and waterline W of the ship. These distributions, defined by (13c) and (13d), are independent of the Froude number F and the nondimensional frequency f , which appear as coefficients in (13b). Expressions (13b)-(13d) for the spectrum functions N and M are shown in [3] to be well suited for the purpose of numerically evaluating influence coefficients, and are shown here to be useful also for coupling viscous and potential flows. The simple-singularity potentials ψ^S , χ^S and φ^S in (12) are defined by (14) and (15) in terms of distributions of simple singularities over H and W , respectively.

The Fourier-Kochin flow representation (12), (13), (14) and (15) is used to obtain a mathematical representation of the velocity $\nabla \phi$ defined explicitly in terms of a prescribed velocity distribution \vec{u} at a control surface Σ , i.e. that does not involve the potential ϕ at Σ (unlike the usual Green identity which defines ϕ within a flow domain in terms of boundary values of ϕ and $\partial \phi / \partial n$). Specifically, the velocity field $\nabla_\xi \phi(\vec{\xi})$, where $\nabla_\xi = (\partial_\xi, \partial_\eta, \partial_\zeta)$, is defined by (16) as

$$\nabla_\xi \phi = (\nabla_\xi \phi^S + \nabla_\xi \varphi^S) + \nabla_\xi \phi^F.$$

The free-surface component $\nabla_\xi \phi^F$ is given by the Fourier representation (17) where the spectrum function S is defined in terms of distributions of elementary waves over the control surface Σ and its intersection Γ with the mean free-surface plane $z = 0$. The simple-singularity components $\nabla_\xi \phi^S$ and $\nabla_\xi \varphi^S$ in (16) are defined by (19) in terms of distributions of simple singularities over Σ and Γ . The flow representation (16), (17) and (19) defines $\nabla \phi$ directly rather than by numerical differentiation of the potential ϕ . This potential flow representation can be used for coupling an inner viscous flow and an outer potential flow. Expressions (15), (18c) and (19b) for the simple-singularity components φ^S , $\nabla_\xi \chi^S$ and $\nabla_\xi \varphi^S$, given here without demonstration, will be established elsewhere.

The most difficult aspect of the Fourier-Kochin formulation, indeed of any approach based on a Green function satisfying the free-surface condition (1), resides in the free-surface components

$\nabla_{\xi}\phi^F$, ψ^F and χ^F in the decompositions (16) and (12) into simple-singularity and free-surface components. These components are examined in [4,5] and in this study. Specifically, the Fourier representation of free-surface effects defined by (20) is considered for a generic spectrum function S and a generic dispersion function D . The generic Fourier integral (20) is expressed in (21) as

$$\varphi^F = \varphi^W + \varphi^N$$

where φ^W and φ^N respectively correspond to a wave component and a near-field component. The wave component φ^W is given by (26), a single Fourier integral along the *dispersion curve(s)* defined in the Fourier plane by the dispersion relation $D = 0$. The Fourier representation (26) is a generalization of the representation given in [4], which is obtained if $E = 1$ and (24a) is used for Σ_2 . The near-field component φ^N in the decomposition (21) is significant in the near field but is negligible in comparison to the wave component φ^W in the far field. The component φ^N corresponding to the wave component (26) is defined by (27), which is a generalization of (30) in [5]. This expression for the near-field component φ^N is shown in [5] to be well suited for accurate numerical evaluation.

The Fourier representation of (20) defined by (21), (26) and (27) is valid for generic dispersive waves and for arbitrary singularity distributions, including the special case of the Green function (i.e. a point source). Applications of this generic Fourier representation to wave diffraction-radiation by an offshore structure (without forward speed) and steady flows, and to the Green function of wave diffraction-radiation at small forward speed, are presented in [4,5]. Another application, to time-harmonic ship waves characterized by the dispersion function (5), is examined here. Only the wave component φ^W is considered; a complementary detailed study of the near-field component φ^N will be reported elsewhere.

The wave component φ^W is defined by (35) as

$$\varphi^W = \begin{cases} \varphi^{iV} + \varphi^{oV} + \varphi^R \\ \varphi^{iV} + \varphi^{RF} \end{cases} \text{ if } \begin{cases} \tau < 1/4 \\ \tau > 1/4 \end{cases}$$

where φ^{iV} , φ^{oV} , φ^R and φ^{RF} represent distinct wave components, associated with the dispersion curves located within the regions of the Fourier plane defined by (32), which correspond to inner V waves, outer V waves, ring waves and ring-fan waves. Fourier representations of these wave components are given in the study. The spectrum function S , typically associated with a continuous

or discrete distribution of sources and/or dipoles over the hull of a ship, is arbitrary in these Fourier representations, which therefore provide simple explicit analytical representations of the wave components radiated by an arbitrary (volume, surface, and/or line) distribution of singularities (e.g. sources and/or dipoles), including the special case of a point source, i.e. the free-surface Green function. The integrands of the Fourier integrals defining the wave components φ^{iV} , φ^{oV} , φ^R and φ^{RF} are continuous, so that these expressions are well suited for numerical evaluation. For purposes of illustration, the wave potential φ^W in (21) is considered for a simple example spectrum function.

ACKNOWLEDGMENTS

The first and second authors were supported by DTMB's Independent Research program and a DRET research grant, respectively.

REFERENCES

- [1] Kochin, N.E. (1937) *On the wavemaking resistance and lift of bodies submerged in water*, translated in SNAME Tech. and Res. Bull. 1-8 (1951).
- [2] Kochin, N.E. (1940) *The theory of waves generated by oscillations of a body under the free surface of a heavy incompressible fluid*, translated in SNAME Tech. and Res. Bull. 1-10 (1952).
- [3] Noblesse, F. and Yang, C. (1995) *Fourier-Kochin formulation of wave-diffraction-radiation by ships or offshore structures*, Ship Technology Research, 42/3, 115-139.
- [4] Noblesse, F. and Chen, X.B. (1995) *Decomposition of free-surface effects into wave and near-field components*, Ship Technology Research, 42/4, 167-185.
- [5] Noblesse, F. and Yang, C. (1996) *Fourier representation of near-field free-surface flows*, Ship Technology Research, 43/1, 19-37.
- [6] Campana, E.; Di Mascio, A.; Esposito, P.G.; Lalli, F. (1993) *Domain decomposition in free surface viscous flows*, 6th Intl Conf. Numerical Ship Hydro.
- [7] Chen, H.C.; Lin, W.M.; Weems, K.M. (1993) *Interactive zonal approach for ship flow including viscous nonlinear and wave effects*, 6th Intl Conf. Numerical Ship Hydro.

24-Inch Water Tunnel Flow Field Measurements During Propeller Crashback

C.-W. Jiang,¹ R. Dong,² H.-L. Liu,¹ M.-S. Chang¹

(¹David Taylor Model Basin, ²Johns Hopkins University, USA)

ABSTRACT

Particle Displacement Velocimetry (PDV) is used for measuring the ring vortex flow field near a propeller tip during crashback. The experiment was conducted in the David Taylor Model Basin (DTMB) 24-inch Water Tunnel with Propeller 4381. The formulation and dispersion of the unsteady ring vortex are presented for two crashback conditions. This test demonstrated that the flow is unsteady even when the propeller is operated in the steady crashback condition. The propeller tip-region-flow velocity and vorticity are determined for several time instances at each different advance ratio. These results can be used to validate CFD predictions. The unsteady ring vortex movements are related to the frequency of propeller transverse forces. Several difficulties with the present system have been identified and recommendations are provided for future improvements.

INTRODUCTION

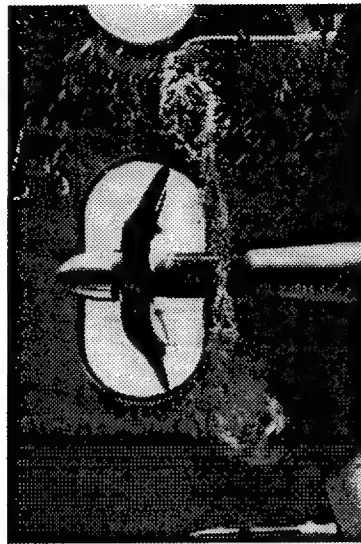
A most striking aspect of the propeller flow observed during crashback operation is the formation of an unsteady ring vortex. The existence of ring vortex was observed in the wind tunnel test by Lock [1] and the complete flow cycle of propeller operation was discussed by Durand [2]. The highly unsteady motion of the ring vortex was observed and visualized by towing tank [3] and water tunnel experiments at DTMB. Although some discrepancies are noted in measurements obtained from those different experiments, all data show following conclusions: First, the ring vortex is highly unsteady, and yet possesses a dominant frequency of movement and dispersion. This was observed using an air injection technique by which air bubbles were injected from upstream. These bubbles were trapped

inside the ring vortex to indicate the location and the existence of the ring vortex as shown in Fig. 1 for a generic skew propeller. These pictures were taken from the tunnel side window at 0.2 second intervals to show the continuous movements of the ring vortex during crashback operation. The formation of the ring vortices and its dynamic unsteady behavior are clearly demonstrated. The ring vortex oscillates vertically and horizontally as will be shown more clearly in the later section. Many times the vortex seems to start at the propeller tip and move away, only to return later and complete its cycle of motion. Also, the ring vortex would sometimes suddenly disperse into a mayhem of random cloudy air particles only to reform later into a moving ring vortex again. The trajectory and shape of the ring vortex are highly irregular and yet they are periodical. Second, the periods and the motions of the ring vortex are governed by the reversed mass flow through propeller disk. Third, the propeller exerts a large out-of-plane force rotates around the shaft with the same frequency of the ring vortex motion. Fig. 2 is a sample of the measured transverse force from shaft dynamometer during a crashback test. These force time histories are normalized by the mean thrust at the given test condition. It is seen that the force is unsteady with an unsteady peak to peak value of approximately one quarter of the steady thrust for the Propeller 4381. It is also seen that the force is periodical. The period of the force has been examined and it matches that of the moving ring vortex. In the past few years, researchers have been fascinated by those observations and consequently efforts were devoted towards the understanding and modeling of these unsteady phenomena.

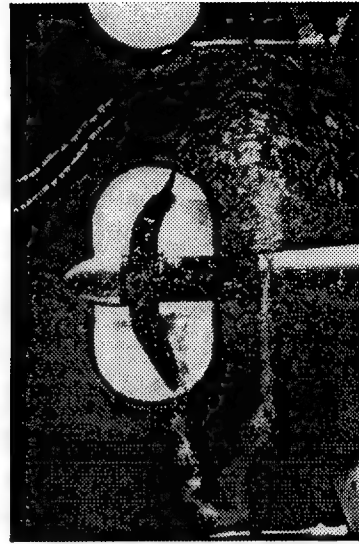
The flow around a propeller blade undergoes three different physical processes during crashback as shown in Fig. 3. (I) In the beginning of braking, a propeller turns in its normal direction and



1



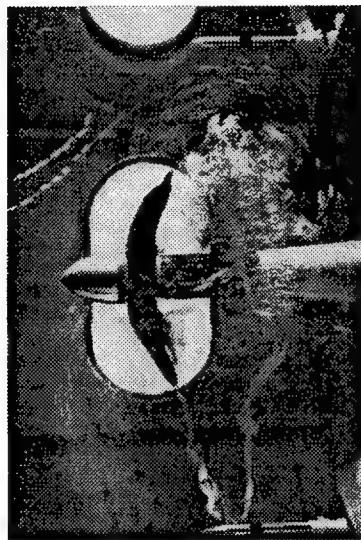
4



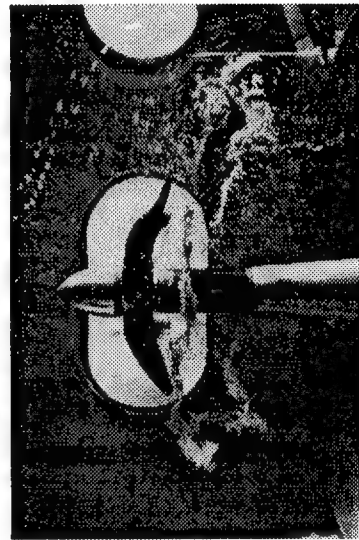
7



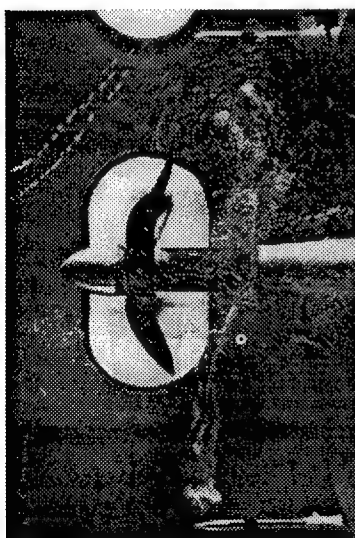
2



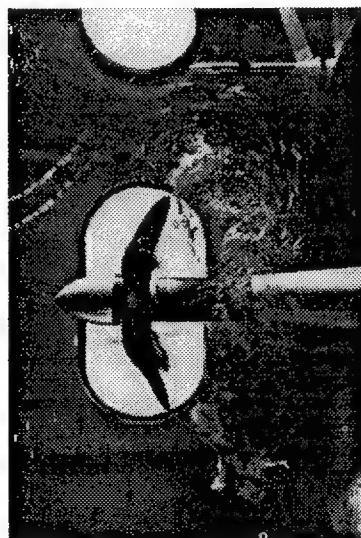
5



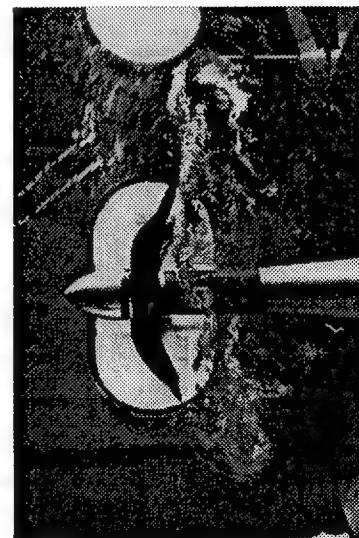
8



3



6



9

Figure 1. Photos of propeller ring vortex.
137

the flow around the blades is fully attached to the blade surfaces. The flow between the propeller blades moves towards the stern as designed. (II) As the braking procedure continues, the propeller begins to turn opposite to its normal direction and the flow around the propeller blades starts to separate. Also, the flow begins to reverse upstream toward the bow. (III) As the braking procedure continues even further, the flow may reattach to the blade surfaces. At this time, the reversed propeller flow should be well established and extend to a location far ahead of the propeller toward bow. Flow visualization has shown that unsteady ring vortices are present during the second stage of the crashback process; that is, (II) above, while the flow inside the propeller disk was reversed.

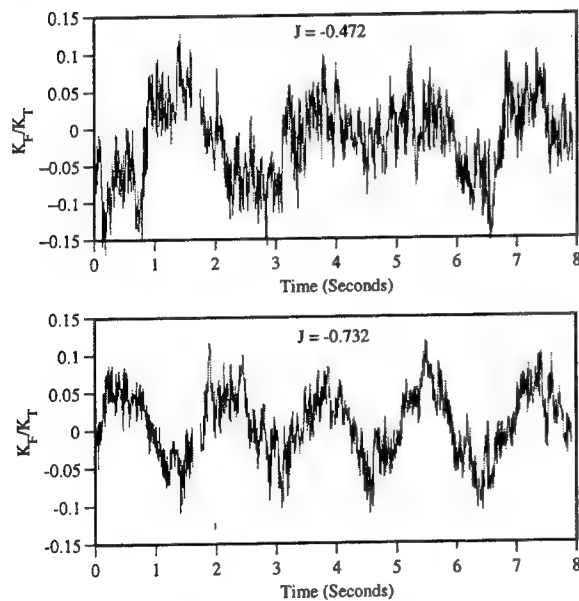


Figure 2. Time history of propeller unsteady side force.

Attempts were made towards the modeling of the unsteady flow field. For example, a two dimensional quasi-steady approach was investigated by the authors. In that approach, a two-dimensional RANS code was exercised and the propeller was replaced by a specified time-dependent body force obtained from propeller lifting surface code. The locations of the computed ring vortex were examined and the side forces were estimated. Fig. 4 presents a typical calculated result showing the formation of a vortical structure at $J = -0.5$. The advance ratio, J , is defined as V_0/nD , where V_0 is the ship (or tunnel) speed, n is the propeller revolution per second, and D is the propeller diameter. Although, those results show the observed features of a moving vortex field, it cannot explain the origin of unsteadiness. Detailed

quantitative measurements are needed for better understanding the phenomena and for advancing numerical modeling. The objective of the present research program was to measure the propeller induced flow field at the blade tip region. This paper presents the unsteady flow structures visualized by the use of laser sheet as well as the vortex velocity field measured by Particle Displacement Velocimetry.

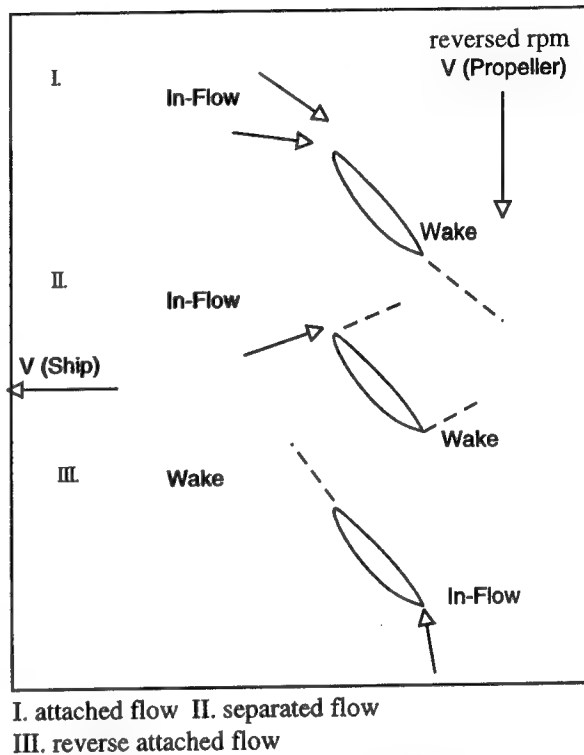


Figure 3. Flow field during propeller crashback.

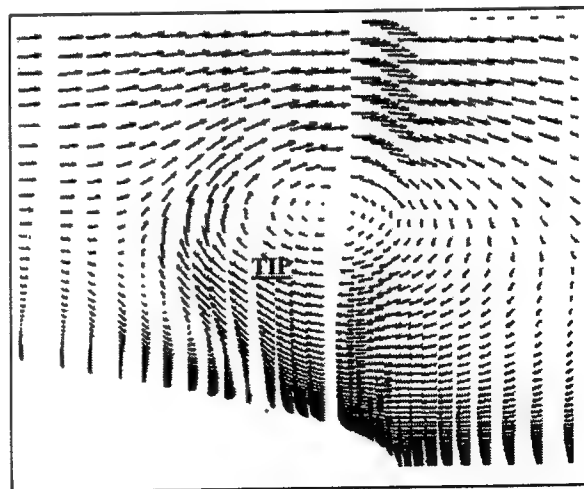


Figure 4. Numerically simulated velocity field at crashback, $J = -0.5$.

Particle Displacement Velocimetry (PDV or PIV), a quantitative flow visualization technique, has been used to measure flow separation and vortex structure in the DTMB towing tank [4,5] and in the DTMB rotating arm facility [6]. Although it is the same technology used to provide flow field information, the flow phenomenon in this case is more unsteady and complex than the previous ones. The present research program thus also serves to explore the capability of PDV in the water tunnel facility.

TEST FACILITY AND PDV SETUP

The DTMB 24-inch Variable Pressure Water Tunnel was used to conduct this test. This tunnel has a 24-in diameter open-jet test section. This test was conducted without a body and screen-generated wakes. The propeller was driven from the downstream shaft and the rotational direction was reversed to simulate crashback operation. In this test, only steady state braking was studied. Propeller RPM and tunnel velocity were varied to obtain different braking conditions. Propeller 4381 was chosen for this study. Geometric characteristics of this propeller are shown in Table 1.

Table 1. Geometric characteristics of Propeller 4381.

r/R	Pitch/D	Chord/D	Skew
0.20	1.265	0.1735	0.00
0.30	1.345	0.2283	0.00
0.40	1.358	0.2750	0.00
0.50	1.336	0.3125	0.00
0.60	1.280	0.3375	0.00
0.70	1.210	0.3475	0.00
0.80	1.137	0.3342	0.00
0.90	1.066	0.2808	0.00
0.95	1.033	0.2192	0.00
1.00	1.001	0.0000	0.00

Velocity measurements were performed using PDV with the experimental setup shown in Fig. 5. The light source was an air-cooled, 15W, continuously pulsed copper vapor laser (511 and 578 nm were the primary wavelengths). Timing for laser pulses was synchronized by a PC-based control system. The laser beam was expanded to a 6-mm thick light sheet by a combination of cylindrical and spherical lenses. This light sheet illuminated a desired section of the propeller flow field through a window on the bottom of the 24-inch WT test

section. Data was recorded by a 70-mm Hasselblad camera equipped with a 60-mm lens on TMAX 3200 film. This camera was located outside the test section. PDV images were taken at the lower part of the test section where the laser light was not in shadow. The data was recorded with three exposures per image with a delay between exposures at 800 to 960 μ sec. The tracer particles used were 40-60 μ m in diameter, neutrally buoyant, and fluorescent. The specific gravity of these particles varied between 0.95-1.05. The fluorescent dyes imbedded in these particles responded with green light excitation in the 550-560 nm range of the laser. The particles were seeded upstream from the test model during the image recording period.

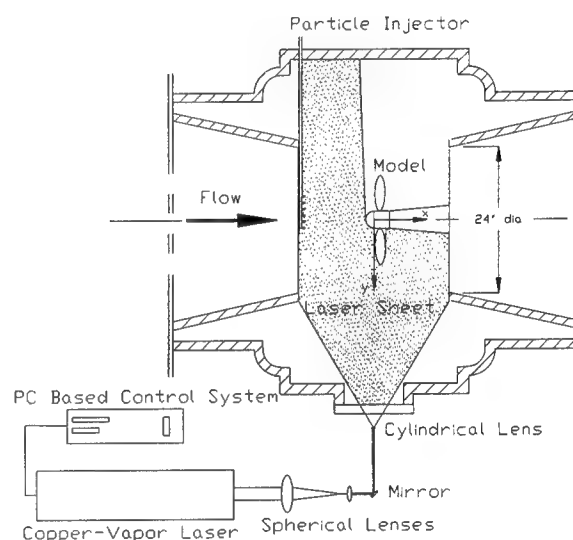
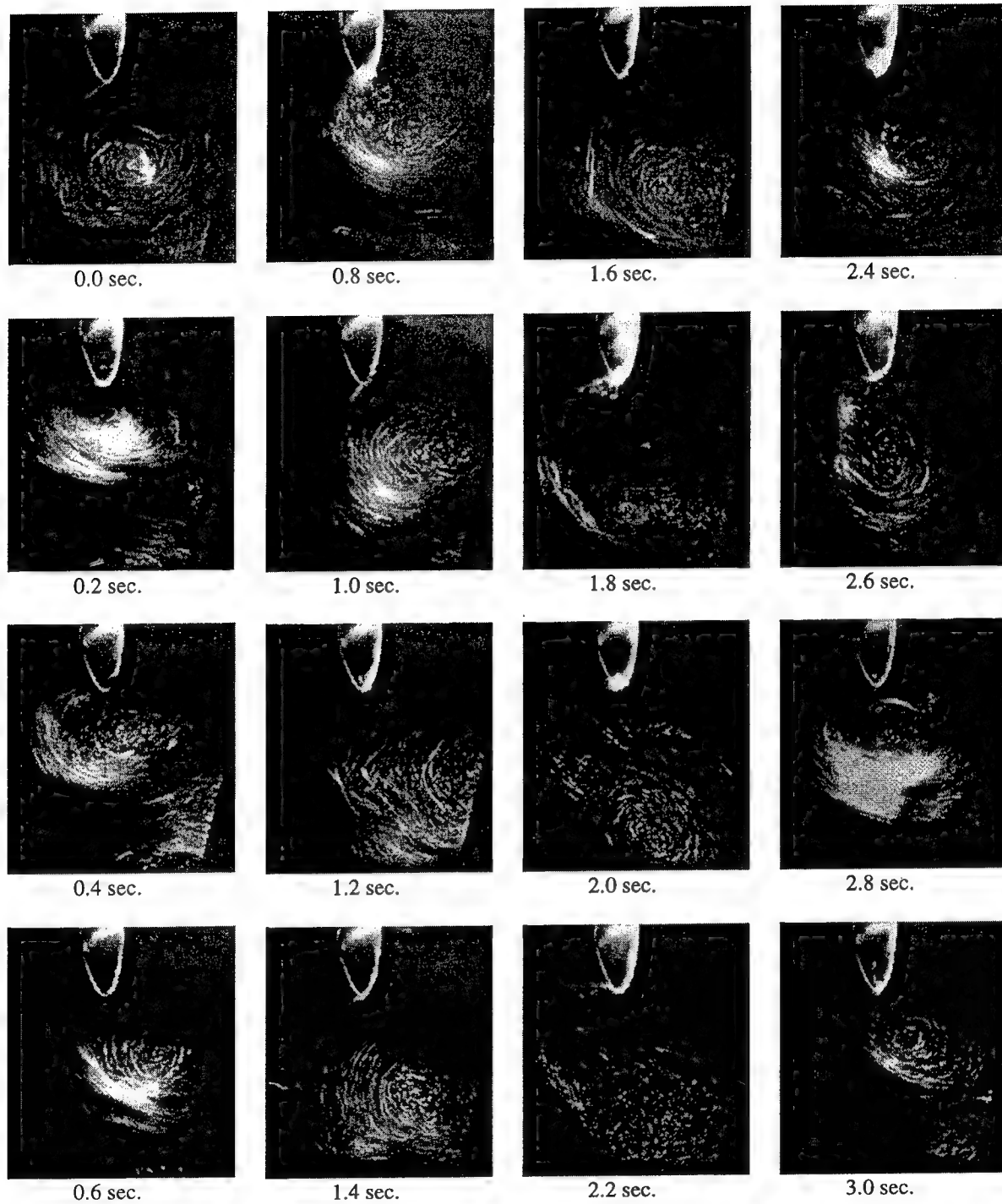


Figure 5. PDV experimental setup.

UNSTEADY FLOW BEHAVIOR

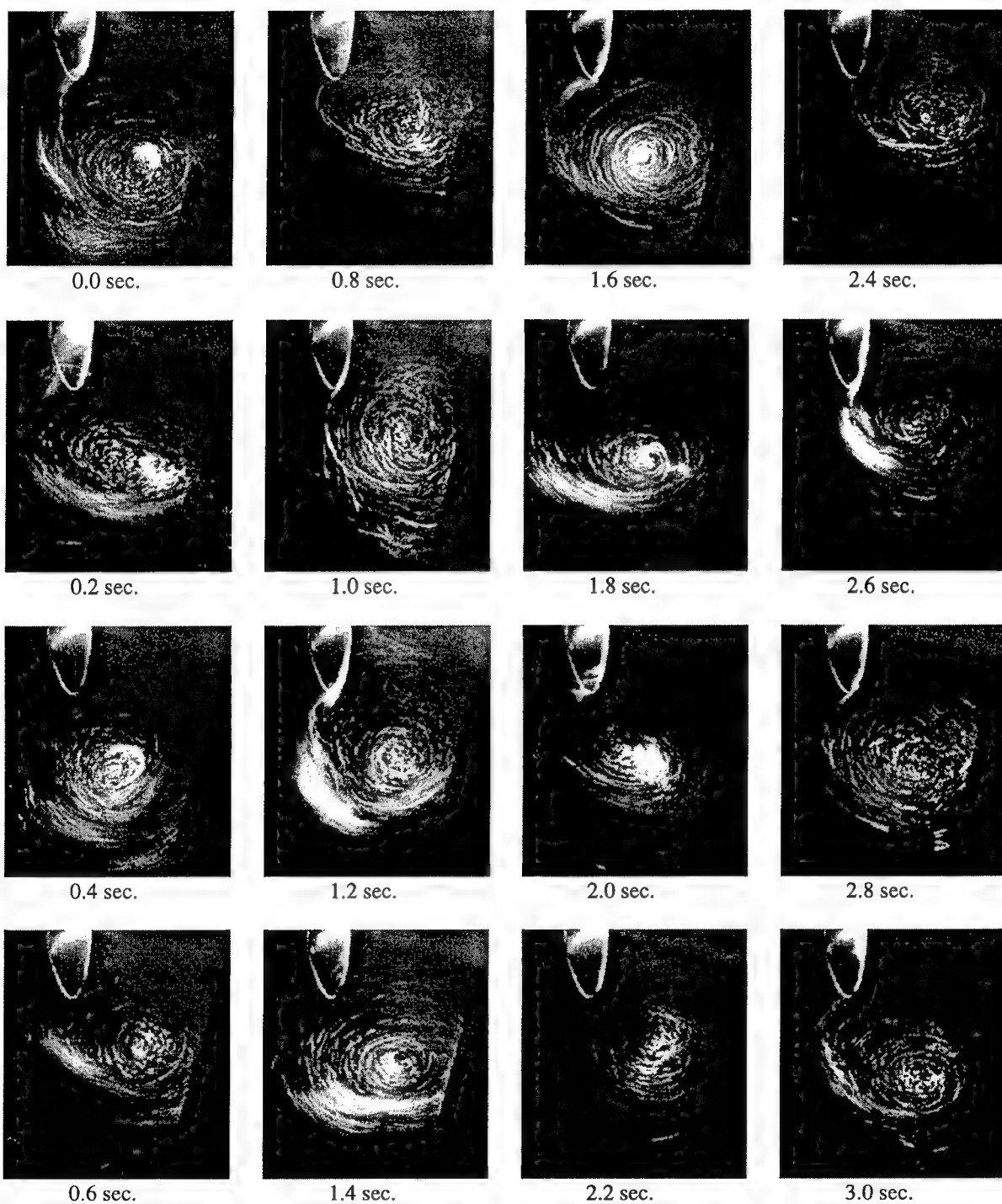
As shown in Fig. 1, dynamic behavior of the ring vortex is very unsteady. In order to better understand the generation and propagation mechanism of this unsteady ring vortex, a technique was designed to record the flow near the and at the propeller tip at different J values using laser sheet as a light source. A video recorder mounted outside the tunnel recorded the flow while the pressure inside the tunnel was lowered until the flow structures became clearly visible from the trajectories of the cavitation bubbles. Figs. 6 and 7 are samples of those recordings. The upstream tunnel is to the left in these pictures.

Fig. 6 presents the sequence of propeller ring vortex motion in the propeller tip region at $J=0.472$. The flow behaviors in these pictures are



$V_0 \Rightarrow$

Figure 6. Time sequence photos of Propeller 4381 at $J = -0.472$.



$V_0 \Rightarrow$

Figure 7. Time sequence photos of Propeller 4381 at $J = -0.732$.

typical for this J value. As shown in these pictures, a ring vortex is at the propeller tip at $t=0.2$ sec. and moves downstream and away from the tip. The ring vortex becomes more and more diffused as it moves away. At t approximately 2.0 sec., the vortex breaks into two due to the strong reversed axial flow near the tip. With further increase of the reversed flow at the tip, $t=2.2$ and 2.4 seconds, the original vortex starts to move back and the two vortices come close to each other. At $t=2.8$, one can again observe a single vortex at the propeller tip and the process repeats itself after that. The period of this process from those recordings is estimated at about 2.5 seconds. The period of the unsteady force obtained from spectral analyzed data for this same J is 2.1 seconds. They are in good agreement, in view of the randomness in the flow structures.

Fig. 7 is the ring vortex motion at $J=-0.732$. One sees basically the same flow motions as in Fig. 6 but quantitatively they are different. First, the period of the vortex motion is less at $J=-0.732$ and the movement of the vortex is less random; at $J=-0.732$ the flow is almost identical at $t=0.0$ and $t=1.6$ seconds. The spectral analyzed force obtains 1.6 sec. period also. Second, the movement of the vortex is less for $J=-0.732$ than $J=-0.472$. For the former ($J=-0.732$), it moves only from the 0.6 radius (propeller radius) to 0.9 radius at the flow direction and from 1.5 radius to 2.0 radius vertically. For the latter ($J=-0.472$), it moves from the propeller plane to 1.0 radius downstream and from propeller tip to 2.6 radius downward. Third, the shape of the cavitations at the propeller tip indicates the reversed axial flow is stronger at $J=-0.472$ than that at $J=-0.732$. These observations could support the conjecture that, for crashback operation, reversed flow is the main governing parameter.

In general, the frequency of the propeller unsteady force at crashback operation can be non-dimensionalized by the inflow velocity and propeller diameter. This non-dimensionalized number, $\omega D/V_\infty$, is about 0.5 at $-2 < 1/J < -1$ for the Propeller 4381.

PDV IMAGE PROCESS

The PDV images collected during the test were digitized and analyzed to obtain quantitative flow information including velocity vectors and vorticities. A review of the PDV technology can be found in Adrian's paper [7,8]. The fundamental principles on which the analysis is based are given in References 4 thru 6.

The images taken during the test were digitized by a Leaf Scanner to an array size of 1972×1747 pixels with resolution 250 pixels per

inch. Digitized images were enhanced locally, with 64×64 pixels interrogation area to deal with the variation of background non-uniformity. A typical triple exposure image is shown in Fig. 8 at $J=-0.732$ which corresponds to $t=0.0$ in Fig. 7. It is seen that the vortex structure is clearer in PDV image than that in cavitation image. The shaded area at the lower right corner is caused by tunnel blockage in which the light sheet is not transparent.

The PDV image velocity was analyzed from the images by an auto-correlation technique that determines the mean displacement of the particles within a given window area. The window area used in this paper is 64×64 pixels and is approximately 2.5×2.5 mm (0.1×0.1 inch) in the real physical space. Also, the distance between adjacent windows was 32 pixels (50% overlap). The window size selected was based on the displacement of the particles. Typically, window size is about three times particle displacement. During image analysis, a velocity vector was assigned to the center of the search area only if a satisfactory correlation pattern was found. Otherwise, the velocity of that area was left as null. The reason that a correlation was not obtained in certain regions could be either a lack of seeding or particle displacement too small to solve the mean displacement. It is very common that the velocities near the vortex center were unresolvable.

The uncertainty level of this auto-correlation technique was about 0.4 pixels. For a 20-pixel displacement with 8 pair particles within the window, it resulted in a characteristic error of 2% in velocity. The characteristic error rises in the vicinity of vortex center where displacement is smaller and at the areas where the particle density is lower. A detail uncertainty analysis was described in Dong et al.[9].

The particle tracing method calculates the displacement of single particle trace. The present analysis applied this analysis in the area where auto-correlation technique fails and the particle density is low. It is most useful in the vicinity of vortex center where directions of the velocities vary significantly.

VELOCITY AND VORTICITY DISTRIBUTIONS

After digitizing and calculating the image data, sample velocity and vorticity distributions are shown in Figs. 9 and 10 at $J=-0.472$ and -0.732 , respectively. Contours of the vorticity distribution for the data analyzed are presented at the right of the velocity vector map. The vorticity is normalized by the tunnel speed and propeller diameter. The solid line presents positive vorticity and the dotted line is negative vorticity. The increment between each contour is 10 with -10 and 10 labeled in the figures.

The length of the velocity vector is normalized by the inflow velocity which is plotted at the lower right corner of these figures. The velocity vector at every other grid points is presented in the figure for better quantitative presentation. The blade projection is shown as the solid line.



Figure 8. Typical flow image at $J = -0.732$.

Fig. 9 shows three instances of the analyzed image results at $J = -0.472$ corresponding to the time near 0.0, 1.8 and 2.6 seconds in Fig. 6. Three instances of flow at $J = -0.732$ are shown in Fig. 10 corresponding to the time at 0.0, 0.8 and 1.0 seconds in Fig. 7. These results provide instantaneous velocity and vorticity distribution along with the unsteady ring vortex structure. These results show that the flow field can be divided into three different regions: (I) velocity at the same direction as inflow, (II) velocity at the reverse direction as inflow and (III) ring vortex region. PDV analysis shows that the maximum velocities at region (I) are about to twice of the inflow speed for all cases, although their locations vary. The velocity fields in the reversed flow region show large variations and are influenced by the blade loading and the passage of the blade. The influence of blade passage is more clearly seen from the vorticity distributions. Higher vorticities near the blade tip are present in all three time instances for $J = -0.472$ while they are only weakly present for $J = -0.732$. This is because the blade is more loaded at $J = -0.472$. The influences of blade passage in the flow field are seen in $J = -0.732$. Nevertheless, we can not draw conclusions from those measured results because the laser control device didn't function during the test and consecutive flow images were not obtained. In the ring vortex

region, the vorticities are more uniform than one expected. The vorticity does not seem to vary significantly for different J values and for different locations of the vortex center. The feedback effect of the vortex ring on the blade unsteady loading is more likely from the variation of its location than from the intensity of the vorticity.

The flow field measurements collected in the present experiment are limited. It supplies a data base for CFD analysis. Future experiment should be designed to take consecutive images for detailed flow information.

CONCLUSIONS AND RECOMMENDATIONS

The 24-inch water tunnel experiment demonstrated that the shedding ring vortex associated with a braking propeller is related to the propeller reverse flow and that the unsteadiness is a speed-dependent phenomena. Typically, a low frequency of about 0.5 Hz is readily observed in the flow field photos and it matches the unsteady frequency of the propeller side forces at corresponding J 's. Therefore, the dynamic behavior of the ring vortex is directly related to the unsteady forces that the propeller experiences.

The flow field analysis from PDV images can provide quantitative measurements of the velocity and vorticity fields. The results shown in Figs. 6 thru 10 contribute not only a data base, but also provide some physical insights for future numerical simulation of this complex flow problem.

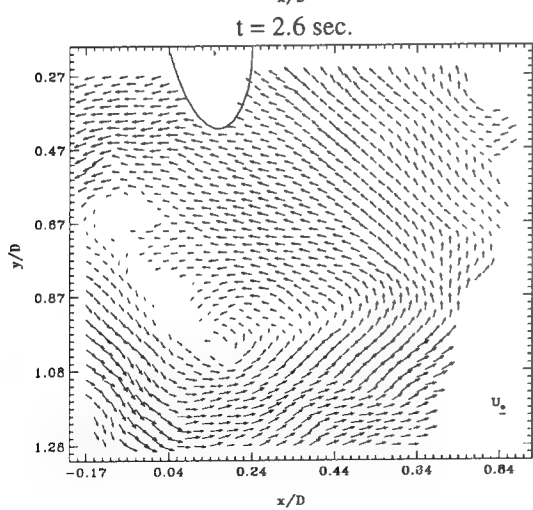
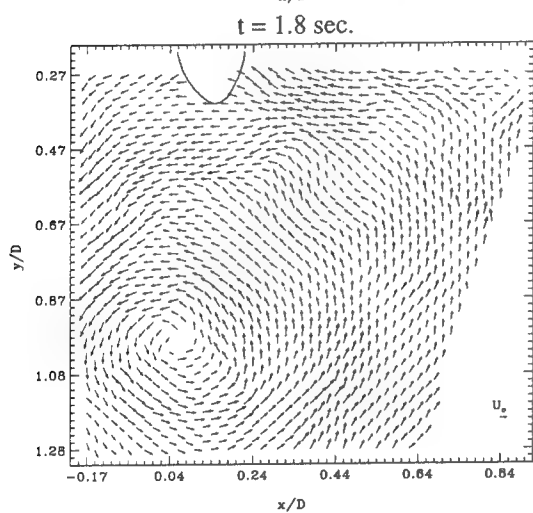
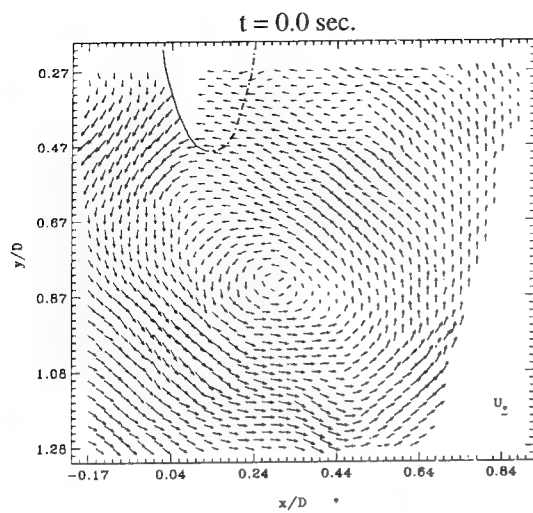
PDV technology was successfully extended to the DTMB 24-inch water tunnel, and it showed the capability of measuring an unsteady propeller flow field. It is most interesting to see that PDV can capture the blade-tip flow very well, Figs. 9 and 10. PDV technique may be used to improve blade-tip design.

Valuable lessons were learned in how to physically arrange the necessary hardware, such as lenses, cameras, laser light sheets and seeding injectors. Several areas can be improved for future experiments, e.g., the development of continuous picture and seed injection technique. Synchronized force and flow measurements and automated data recording could also be included.

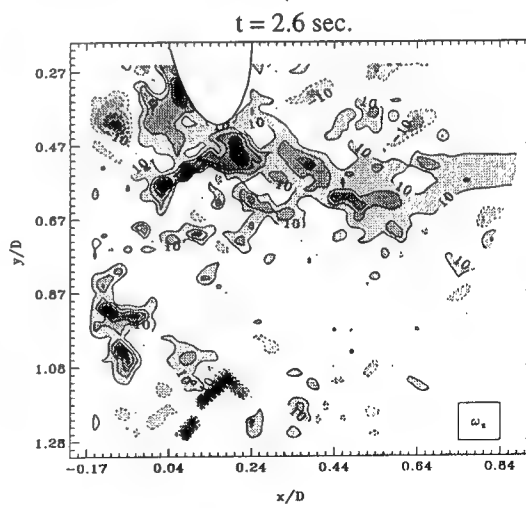
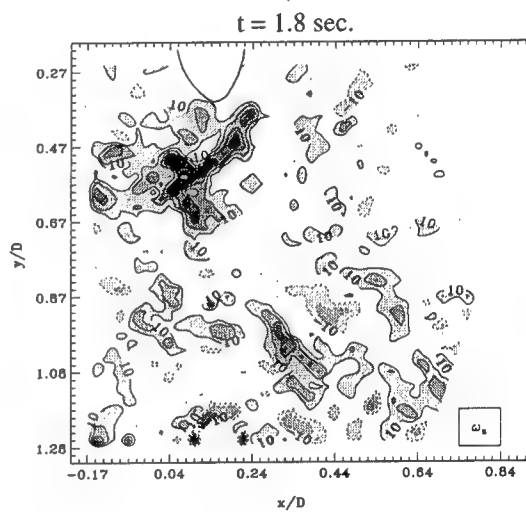
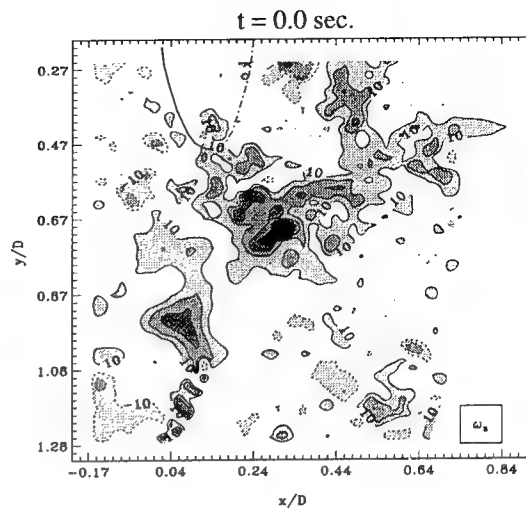
ACKNOWLEDGMENT

The work described herein was sponsored by the Office of Naval Research (ONR 334) and performed by the Carderock Division, Naval Surface Warfare Center.

The authors would like to thank Mr. David

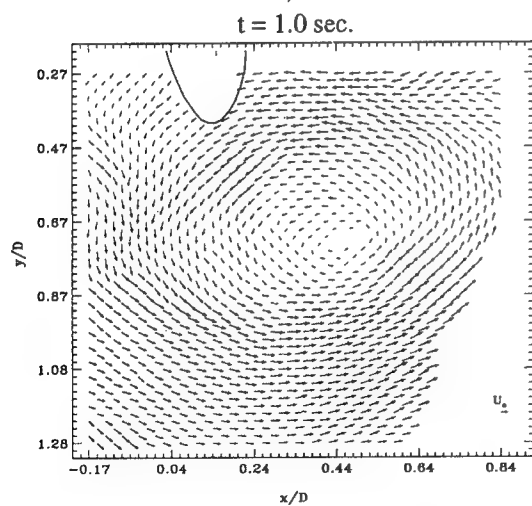
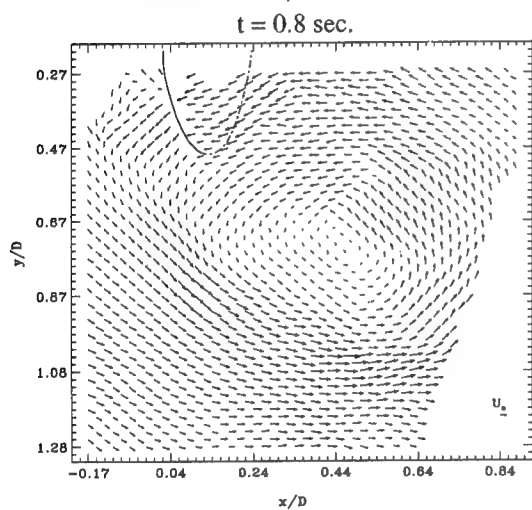
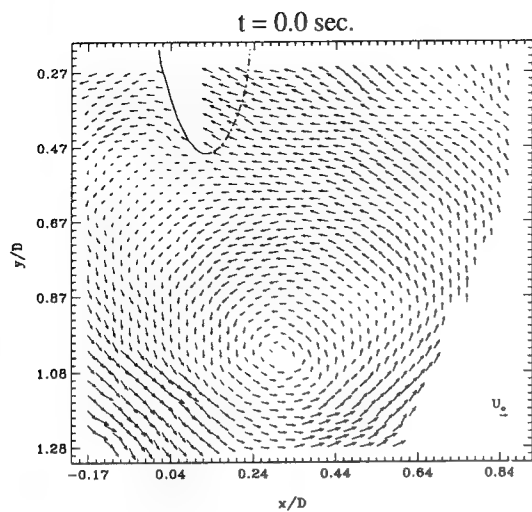


(a) velocity

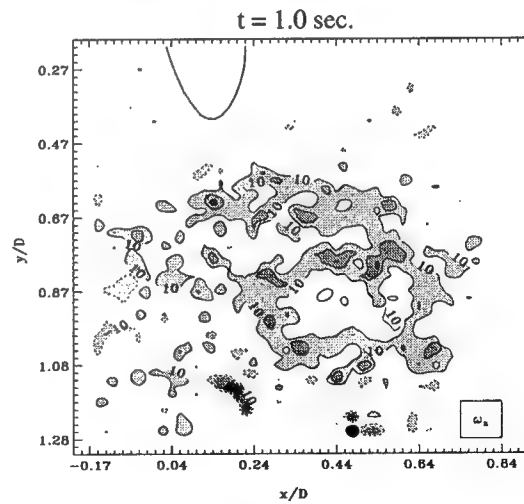
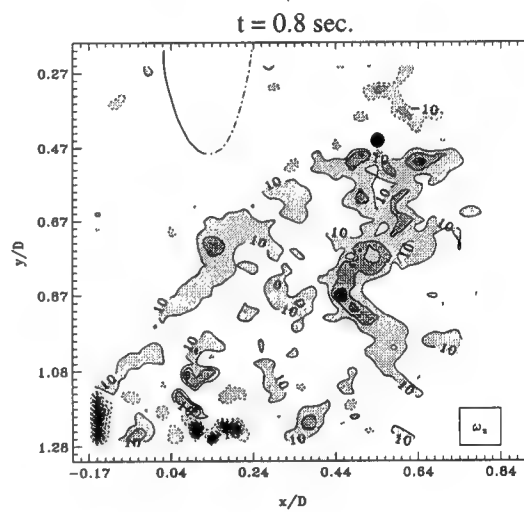
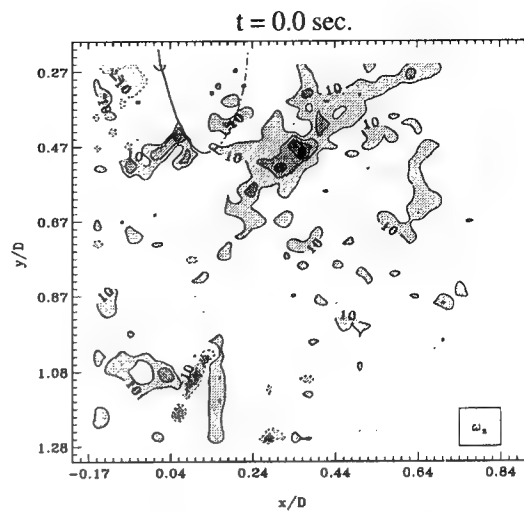


(b) non-dimensional vorticity
contour interval = 10

Figure 9. Vector map and vorticity distribution at $J = -0.472$.



(a) velocity



(b) non-dimensional vorticity
contour interval = 10

Figure 10. Vector map and vorticity distribution at $J = -0.732$.

Walden for his encouragement and support, Dr. Stuart Jessup for his technical discussions and support and James Diggs and Dave Fishpaw for their technical support in carrying out the experiment.

REFERENCES

1. Lock, C.N.H., "Photographs of Streamers Illustrating the Flow Around an Airscrew in the 'Vortex Ring State'," Br. ARC R&M 1167 (1928).
2. Durand, W.F. ed., Aerodynamic Theory, Vol. IV, Dover Publication, Inc., New York, (1963).
3. Hampton, G.A., "Open Water Force and Moment Characteristics on Three Propellers in a Crashback Condition," DTMB Report CRDKNSWC/HD-1126-01 (1995).
4. Liu, H.L. and M.S. Chang, "Sailplane Vortex Measured by Particle Displacement Velocimetry," Symp. on Laser Anemometry, ASME Fluid Engineering Division Summer Meeting, Lake Tahoe, NV (June 1994).
5. Fu, T.C., "Quantitative Visualization of Three-Dimensional Flow Separation and Vortex Structures by Particle Displacement Velocimetry," Ph.D. Dissertation, The Johns Hopkins University, Baltimore, Maryland (1993).
6. Liu, H.L. and T.C. Fu, "PDV Measurement of Vortical Structures in the DTMB Rotating Arm Facility," DTMB Report CRDKNSWC/HD-1416-02 (1994).
7. Adrain, R., "Particle-Imaging Techniques for Experimental Fluid Mechanics," Annu. Rev. Fluid Mech., Vol. 23, pp.261-304 (1991).
8. Landreth, C.C., R.J. Adrain, and C.S. Yao, "Double Pulsed Particle Image Velocimeter With Directional Resolution for Complex Flows," Experiments in Fluids, Vol. 6, pp.119-128 (1988).
9. Dong R., S. Chu, and J. Katz, "Quantitative Visualization of the Flow Structure Within the Volute of a Centrifugal Pump," J. Fluid Engineering, Vol. 114, pp.390-395 (1992).

Accuracy of Wave Pattern Analysis Methods in Towing Tanks

F.-X. Dumez, S. Cordier (Bassin d'Essais des Carènes, France)

INTRODUCTION

Wave pattern analysis methods enable the estimation of the wave resistance of a body in steady rectilinear motion using measured wave heights. The obvious advantage of applying these techniques in a towing tank is that the value of wave resistance which is extrapolated based on Froude number similarity is obtained directly and not by subtracting an empirical estimate of viscous drag from the total drag. These methods rely on conservation of momentum in a control volume attached to the body. The assumptions of potential flow, linearized free-surface conditions are essential in the development of these methods. Various wave pattern analysis methods have been developed in the sixties and seventies 1, 2 and three of them are considered in this paper:

The longitudinal-cut method (LCM) developed by Newman 3 and Sharma 1 is based on the analysis of wave height measurements along a semi-infinite line parallel to the model's axis assuming infinite depth, far field waves, and no reflection. In practice, the signal is cut before the reflected waves are measured and a correction has to be made for the lost momentum.

The discrete decomposition method (DDM) developed by Eggers 4, Landweber 5, and Hogben 6 is based on the use of one or several longitudinal cuts including reflections. These data are used to identify a wave field based on a decomposition in transverse wave numbers which correspond to the tank's transverse natural frequencies. Its use is not limited by wave reflection or finite depth. The linear system to be solved is usually over-determined which can add robustness to the result.

The singularity distribution identification method (SDIM) developed by Baba 7, Okhusu 8, Bessho 9, 10, and Ikehata 11 uses a distribution of singularities (sources or doublets, continuous or discrete) located in place of the model. The wave height measurements are used to identify a distribution of singularities whose wave field matches that which was measured. This method also yields an over-determined linear system for the singularity densities, which in turn give the wave resistance.

Recent work has been performed at the Bassin d'Essais des Carènes on the decomposition of resistance into different components for a Series 60 model and three geosims of the "Olive" planing hull, 12, 13, 14, 15. The accuracy required to conduct this work have led to a study of the limitations of the first two methods, and possible enhancements of the second method. As a consequence of this work, a third method was developed and implemented based on the SDIM method in order to obtain accurate and robust estimates of wave pattern resistance in a towing tank for wide ranging test conditions. The evaluation of the various methods was performed on the data base obtained during the Series 60 and "Olive" geosim tests.

It is important to note that limitations in computer resources at the time of their development prevented the application of these methods (particularly the last two). The increase in computational power and consequently in the size of linear systems which can be solved justifies the re-examination of these methods.

LONGITUDINAL CUT METHOD (LCM)

Description

The far field wave elevations $\eta_{ff}(x, y)$, generated by a body travelling at constant speed U with no confinement (walls or bottom) are given by, 1 and 3 :

$$\zeta_{ff}(x, y) = \text{Re} \left(\frac{1}{\pi} \int_1^\infty \bar{J}(\omega \sqrt{\omega^2 - 1}, \omega) \cdot \Gamma(\omega, y) d\omega \right) \quad (1)$$

$$\text{with } \Gamma(\omega, y) = \frac{\omega^2}{\sqrt{1 - \omega^2}} e^{i\omega(x + iy\sqrt{\omega^2 - 1})}$$

where $\bar{J}(\omega \sqrt{\omega^2 - 1}, \omega)$ is a degenerated form of the Kochin function. We also have:

$$K_0 = \frac{g}{U^2}; \omega = \frac{1}{\cos \theta}; u = \omega \tan \theta$$

θ is the angle between Ox and the direction of propagation of a given wave component and K_0 is the longitudinal wave number. The wave elevation $\eta_{ff}(x, y)$ can also be written as a function of u , $F(u)$ and $G(u)$:

$$\zeta_{ff}(x, y) = \frac{1}{4\pi} \int_{-\infty}^{+\infty} F(u) \sin(\omega(u) \cdot x + u \cdot y) + G(u) \cos(\omega(u) \cdot x + u \cdot y) du \quad (2)$$

$$G(u) + i \cdot F(u) = \frac{2(1 + \sqrt{1 + 4u^2})}{\sqrt{1 + 4u^2}} J(u, w(u)) \quad (3)$$

The functions $F(u)$ and $G(u)$ are the coefficients of the far field wave amplitude spectrum which, when integrated, yield the wave resistance:

$$C_w = \frac{1}{16 \cdot \pi} \int_{-\infty}^{+\infty} (F^2(u) + G^2(u)) \frac{\sqrt{1 + 4u^2}}{1 + \sqrt{1 + 4u^2}} du \quad (4)$$

These coefficients are obtained by a Fourier transform of the wave height measurements along a longitudinal cut which is required to extend to infinity downstream. In practice, the signal is truncated before the reflected waves are present in the signal (figure 1)

and the coefficients $F(u)$ and $G(u)$ would tend to 0 for small values of u . The missing part of the signal is treated by introducing a weighted Fourier transform with an analytical asymptotic expression for $\eta_{ff}(x, y)$ valid when $u \rightarrow 0$:

$$\zeta_{ff}(x) \approx \frac{c_1 \cos(x) + c_2 \sin(x)}{\sqrt{c_3 - x}} \quad (5)$$

However, the coefficients c_1 , c_2 , and c_3 can only be determined based on a regression on the signal before truncation. Hence, the amplitude coefficients of the transverse waves ($\theta < 35^\circ 16'$) are to a great extent determined by the truncation correction. Since, for moderate Froude numbers, the larger part of the wave resistance is generated by transverse waves, the point where the signal is cut, and the accuracy of the correction, play a large part in the accuracy of the computed wave resistance. For higher speed models the contribution of transverse waves to the resistance diminishes as shown in figure 2.

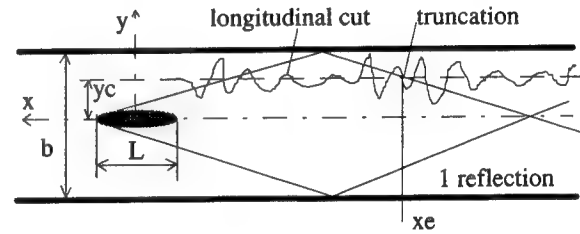


Figure 1: View of model in a towing tank.

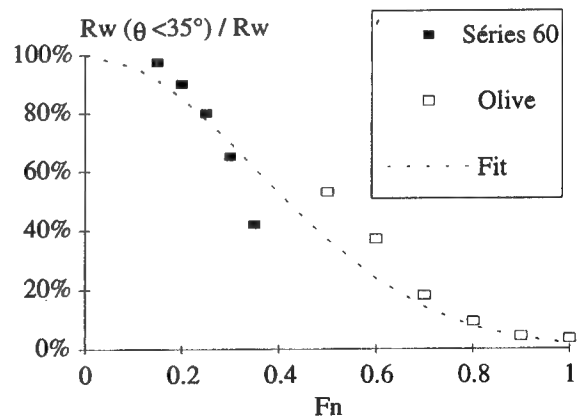


Figure 2: Fraction of the wave resistance generated by transverse waves for Series 60 and Olive model.

Transverse position

Since the transverse position of the cut (y_c) influences the length of the signal, it is important to know how close the probe can be to the model axis without introducing the influence of near field waves in the measurements. A value of $y_c/K_0 L = 0.5$ is usually taken as a minimum. A theoretical study by Ikehata (11, figure 5) shows that in order to achieve a 10% accuracy on wave resistance y_c should not be less than 40. Tests performed on the analysis of waves numerically generated by a polynomial source distributions show that a 1% accuracy on wave resistance can be achieved with y_c not less than 5.

Truncation

Once the minimal distance from the probe to the model axis has been selected, it is possible to study the influence of signal length on the computed resistance. The tests performed on the Series 60 model were used to evaluate this effect. Figure 3 shows the ratio of wave resistance to the average result of the 4 probes (respectively $y_c/K_0 L = 0.5, 0.53, 0.56, 0.59$) for the longest signal, as a function of signal length. The maximum signal length is slightly less than that calculated based on the Kelvin dihedral angle. The results are shown for three values of Fn and for 4 probe positions from position 1 to 4. The effect of Fn on signal length is clearly illustrated. It appears that Rw converges only at the lower Fn and for the closer probes. For the other Froude numbers, the trends for the three probes are very similar but convergence does not appear to be achieved. Hence, despite the rather large ratio of tank width to model length ($b/L = 2.67$), the wave resistance could not be determined accurately using the Longitudinal Cut Method (LCM).

Following this study, an analytical estimate of the error as a function of model size, tank width, and towing speed was sought. The relative importance of transverse waves in the wave pattern resistance as presented in figure 2 for the two models (series 60 and Olive) were fitted as follows:

$$\frac{Rw(\theta < 35^\circ)}{Rw} = e^{-4.Fn^2} \quad (6)$$

The difference in the contribution to Rw from the transverse waves between two consecutive truncation points is defined as follows:

$$e_i = \frac{Rw_{i+1} - Rw_i}{Rw_i \cdot (x_{i+1} - x_i)} \text{ with } i = 1; x_1 = 105; e_1 = 0 \quad (7)$$

Based on experimental data a fit of e_i is proposed:

$$e_i = e^{-3.45 - 0.028.x_i}$$

This error is plotted in figure 4 based on experimental data for the 4 probes. The trend toward a reduction in this difference as the signal length is increased before truncation is clearly shown. Hence, the total error E_i given by the transverse wave components can be expressed as a function of x in the following form:

$$E_i = \prod_{k=1}^i (e_k \cdot (x_{k+1} - x_k) + 1) \quad (8)$$

$$Rw_i = Rw_1 \cdot E_i$$

Based on experimental data a fit of $E(x)$ is proposed (figure 5):

$$E(x) = e^{1.02 - 0.048.x} \quad (9)$$

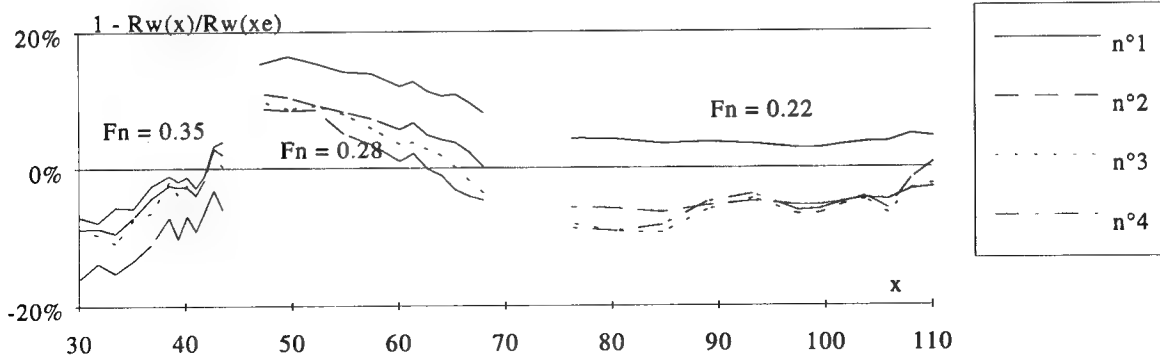


Figure 3: Effect of signal length on calculated wave resistance

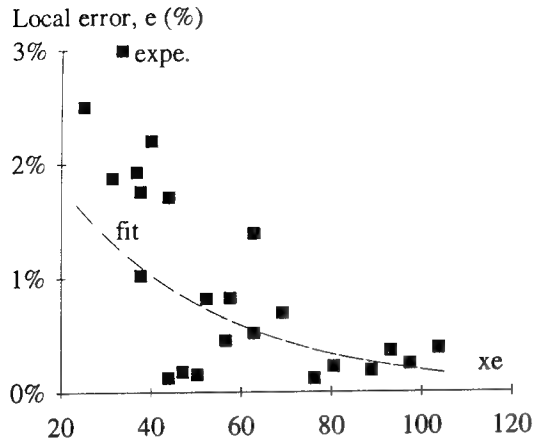


Figure 4: Convergence of wave resistance as a function of signal length

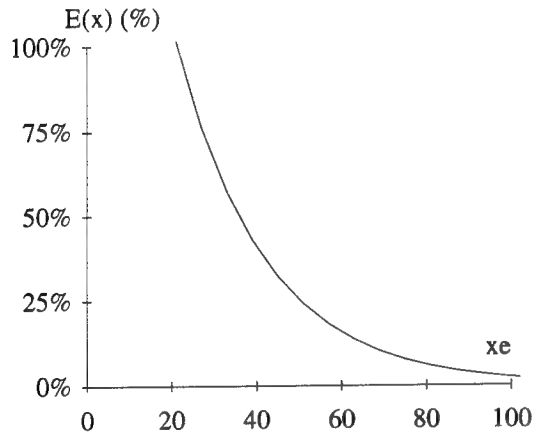


Figure 5: Estimated total error on transverse wave resistance ($\theta < 35^\circ$)

By multiplying equations (6) and (9) and assuming that the error on the diverging wave components is negligible, we obtain an estimate of the total error as a function of x_e . The useful signal length before truncation for a tank of width b and a gauge located at position y_c is given by:

$$x_e = \sqrt{8} (K_0 b - y_c) \quad \text{and} \quad \sqrt{8} = \frac{1}{\tan(19^\circ 28')} \quad (10)$$

In order to reduce errors introduced by the near field waves to less than 1% we take $y > 5$. Hence, the theoretical maximum signal length can be written:

$$x_e = \sqrt{8} \left(\frac{b}{Fn^2 \cdot L} - 5 \right) \quad (11)$$

The error is shown to depend only on Fn and b/L and the result is plotted in figure 6. These results show clearly that in order to obtain reasonably accurate (error $< 5\%$) wave pattern resistance estimates with the LCM, for displacement vessels with significant wave making component ($Fn < 0.4$), the required b/L is about 5. Hence, for typical large towing tanks ($b = 15$ m) the maximum model length is 3 m, much less than the size typically used in these facilities. Hence, this method is not sufficiently accurate for conventional towing tank use.

The limited accuracy of the LCM method, particularly for large, fast models was the principal reason for the development of a method which could analyse wave height measurements containing the waves reflected by the walls of the tank.

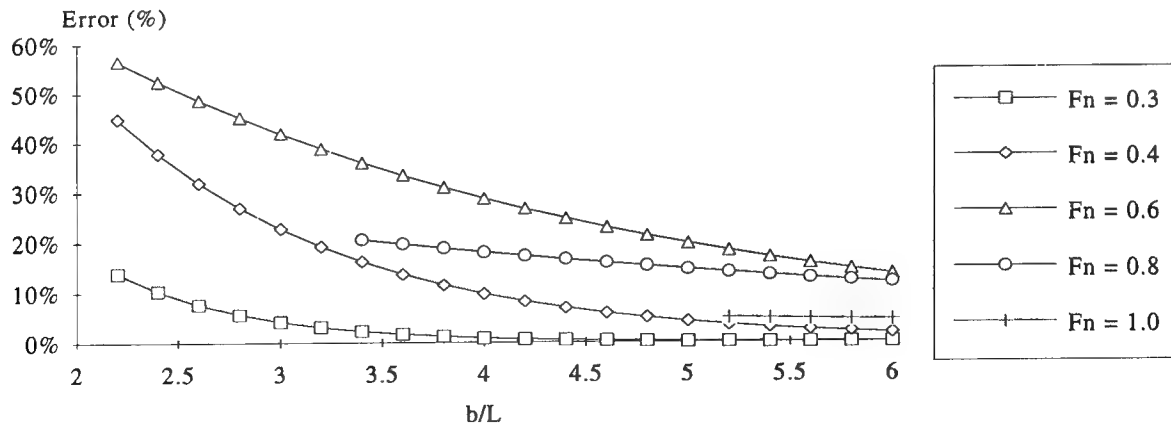


Figure 6: Estimated error inherent in the LCM method as a function of Fn and b/L

DISCRETE DECOMPOSITION METHOD (DDM)

Description

As opposed to the previous method, the DDM, 4, 5 and 6, assumes the spectrum to be composed of several discrete wave components. We consider the model to be in the middle of a tank of breadth b , the walls being located at $y = \pm b/2$. The expression for the far field wave elevation can be written as a discrete summation:

$$\zeta_{ff}(x, y) = \frac{1}{4\pi} \cdot \sum_{j=-\infty}^{j=+\infty} F(u_j) \sin(\omega(u_j) \cdot x + u_j y) + G(u_j) \cos(\omega(u_j) \cdot x + u_j y) \Delta u \quad (12)$$

with $\Delta u = \frac{2\pi}{K_0 \cdot b}$ and $u_j = j \cdot \Delta u$

For a model symmetric about the oxz plane, and considering the summation to be finite and limited to J_{max} components such that the amplitude spectrum coefficients for $j > J_{max}$ are negligible, we can write:

$$\zeta_{ff}(x, y) = \sum_{j=0}^{j=J_{max}} \gamma_j \cos(\omega_j x) + \sigma_j \sin(\omega_j x) \quad (13)$$

with $\gamma_j = G_j \cdot \cos(u_j \cdot y)$ and $\sigma_j = F_j \cdot \cos(u_j \cdot y)$

$$\text{and } \omega_j = \sqrt{\frac{1}{2} \left(1 + \sqrt{1 + 4u_j^2} \right)}$$

The solution to this problem consists in performing a Fourier decomposition along a segment of a longitudinal cut bounded by x_0 and x_t which includes a certain number of reflections (N_r). The unknowns γ_j and σ_j are identified based on the iterative resolution of a linear system where the right hand terms are given by:

$$\begin{aligned} H_i &= \int_{x_0}^{x_t} \zeta_{ff}(x, y) \cos(\omega_i x) dx \\ K_i &= \int_{x_0}^{x_t} \zeta_{ff}(x, y) \sin(\omega_i x) dx \end{aligned} \quad (14)$$

In order to improve the accuracy of the method and to limit numerical errors, the authors of

this method advise selecting transverse positions of the wave probes which correspond to anti-nodes of the transverse natural modes of the tank, and to use several probes such that the system is over determined. This choice leads effectively to a fit of the identified wave field over the measured data. These remarks proved to be well founded when the robustness of this method was tested.

Discussion of results

The results obtained by this method on the Series 60 and Olive models were in relatively good agreement with the results of the LCM method. Nonetheless, significant differences in R_w appeared as a function of the distance from the probe to the model's axis and number of reflections used in the analysis. Hence, a numerical study was performed to evaluate the robustness of this method based on computed longitudinal cuts at different distances y_c using near field and far field waves. The test case used for a similar study in 5 was modelled following thin ship theory: an infinitely long, thin strut, 2 m in chord, in a 13 m wide tank, at 1, 2 and 4 m/s. The strut was represented by a distribution of sources located in the plane of symmetry.

The analysis of the results obtained by using the DDM method on several longitudinal cuts, shows that the accuracy of the computed wave resistance depends directly on the number of modes (J_{max}) used, and on the length of the signal ($x_t - x_0$). The conditioning of the matrix used to solve the linear system is directly dependent on the length of the signal. A poorly conditioned system yields to large amplitudes at specific values of the transverse wave number. As signal length is reduced, this behaviour affects lower and lower frequencies until the solution "blows up". An alternative method based on the simultaneous resolution of several longitudinal cuts improves this problem but numerical errors in the solution still appear.

The wave amplitude spectrum calculated by this method for 4 longitudinal cuts measured in the wake of a Series 60 model at $Fn=0.35$ is shown on figure 7. The ordinate used does not represent the wave amplitude but has been transformed into the wave resistance per unit wave number. Hence, the integral of each curve in figure 7 yields the wave resistance. The longitudinal cuts contain 3 reflections. The 4 longitudinal cuts were also analysed simultaneously to yield an average labelled "fit".

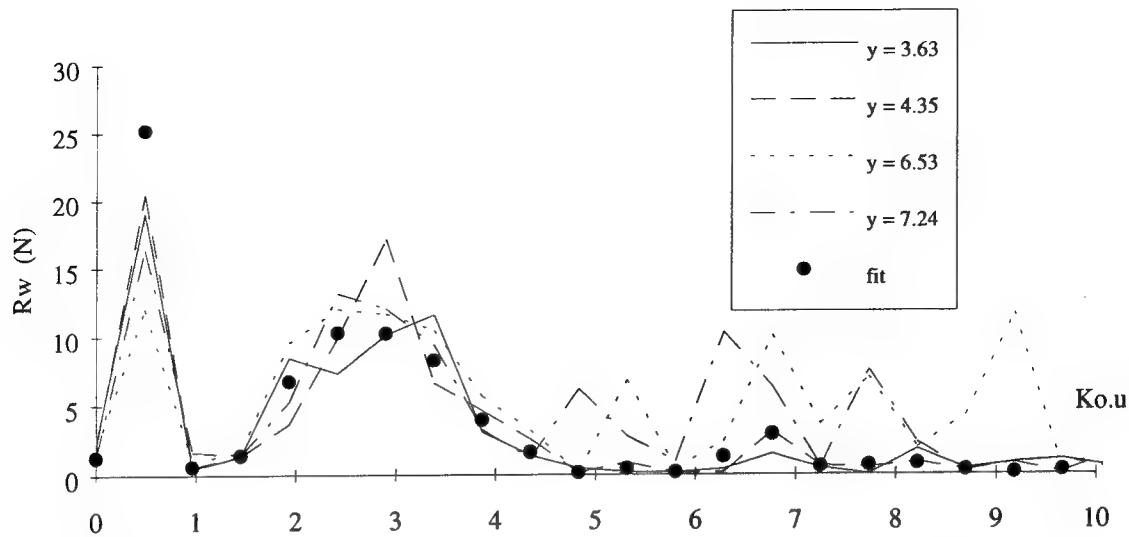


Figure 7: Wave amplitude spectrum for a Series 60 ($F_n=0.35$) using the DDM method.

It is clear on this graph that each longitudinal cut yields a significantly different spectrum and anomalous amplitudes appear in the high frequency range ($Ko.u > 5$). The advantage of using several cuts ("fit") is that these amplitudes are filtered through the regression process.

The most stable results and in best agreement with respect to the LCM method, are obtained for a very long signal ($N_r = 4$ or 5) and for a limited number of identified wave number components (J_{max}). However there is a systematic difference (10 to 20%) with respect to the LCM results. This discrepancy may be due to imperfection in the reflection and dissipation through the viscous wake.

Compared to the LCM method in which, through the Fourier transform, the wave amplitude components are solved independently, the DDM method solves for all components simultaneously through the resolution of a linear system. Hence, errors in the higher frequency, divergent wave components tend to introduce errors on the lower frequency, transverse wave components.

Also, as F_n is increased, and the energy shifts to the higher frequency components, the limitation in J_{max} can introduce significant errors as some of the divergent waves are neglected.

Hence, this method appears limited by the need for an extremely long signal and the relatively few wave numbers identifiable. These conclusions have led us to the study of a third method based on singularity distribution identification.

THE SINGULARITY DISTRIBUTION IDENTIFICATION METHOD (SDIM)

Description

This method is based on the use of an unknown distribution of singularities (sources or doublets, continuous or discrete) located on a line, in the centre plane or otherwise, advancing at the model speed U . The principle of the SDIM method, 7, 8, 9, 10 and 11, is to determine a distribution of singularities such that its far field waves match those measured. Several alternative approaches are then possible. The singularities may be located at the control points of a mesh, or they can be determined analytically based on an analytical expression. In our particular case, the reflections due to the walls of the tank are taken into account so that the whole wave field can be analysed, even where reflected waves are present.

For the sake of simplicity, we first consider a known continuous distribution of sources constant over a depth h and varying with the x direction. We later show that this formulation can be extended to sources which vary as a function of depth as well. Given $M(x')$ a source density distribution in the plane of symmetry located between $x'=-1$ and $x'=1$ and constant vertically between $z'=0$ and $z'=-h$, translating at speed U , along the centre line of a tank of breadth b , and of infinite depth. The wave elevation can be shown to be given by:

$$\zeta(x, y) = \frac{4}{2 \cdot U \cdot b \cdot K_0} \int_{x'=-l}^{x'=+l} (\zeta_{nf}(x, x', y) + \zeta_{ff}(x, x', y)) \cdot M(x') dx' \quad (15)$$

near field

$$\zeta_{nf}(x, x', y) = \sum_{j=-\infty}^{j=+\infty} \cos\left(\frac{2 \cdot \pi \cdot j \cdot y}{K_0 b}\right) \int_{\frac{2 \cdot \pi \cdot j}{K_0 b}}^{\infty} \frac{(\alpha_j \cdot \sin(h \cdot \alpha_j) - m^2 \cdot (1 - \cos(h \cdot \alpha_j)))}{\alpha_j \cdot (m^4 + \alpha_j^2)} \cdot e^{-m|x-x'|} \cdot m \cdot dm$$

far field

$$\zeta_{ff}(x, x', y) = \pi \cdot \Pi(x' - x) \sum_{j=-\infty}^{j=+\infty} \cos\left(\frac{2 \cdot \pi \cdot j \cdot y}{b \cdot K_0}\right) \frac{2}{k_j} \left(1 - e^{-\frac{h}{2}(1+k_j)}\right) \cos(\omega_j(x - x'))$$

In (15), $\Pi(x' - x)$ is the Heaviside function and:

$$\alpha_j = \sqrt{m^2 - \frac{4 \cdot \pi^2 \cdot j^2}{(K_0 b)^2}} \text{ and } k_j = \sqrt{1 + 4u_j^2}$$

The amplitude coefficients F_j and G_j are given by:

$$\begin{pmatrix} F_j \\ G_j \end{pmatrix} = \frac{16 \cdot \pi \cdot \varepsilon_j}{U \cdot b \cdot k_j \cdot K_0} \cdot \int_{x'=-l}^{x'=+l} \begin{pmatrix} \cos \omega_j x \\ \sin \omega_j x \end{pmatrix} \left(1 - e^{-\frac{h}{2}(1+k_j)}\right) M(x') dx' \quad (16)$$

where $\varepsilon_0 = \frac{1}{2}$ and $\varepsilon_j = 1$ when $j \neq 0$

If we assume that the source density distribution is represented by a 3rd degree polynomial, the unknowns of the problem are now the 4 polynomial coefficients of the expression:

$$M(x') = \sum_{k=0}^3 A_k \cdot (x')^k \quad (17)$$

If we consider the measurement of I_{max} wave heights at abscissa x_i along a line of constant y , the far field wave elevation at each position (x_i, y) can then be written as follows:

$$\zeta_{ff}(x_i, y) = \sum_{j=0}^{j=J_{max}} \cos\left(\frac{2 \cdot \pi \cdot j \cdot y}{b \cdot K_0}\right) \cdot (F_j \cos(\omega_j x_i) + G_j \sin(\omega_j x_i)) \quad (18)$$

The amplitude spectrum coefficients corresponding to the J_{max} number of wave numbers used in the decomposition can then be expressed as a function of the 4 polynomial coefficients A_k

$$\begin{pmatrix} F_j \\ G_j \end{pmatrix} = \begin{pmatrix} a_{kj} \\ b_{kj} \end{pmatrix} \left(1 - e^{-\frac{h}{2}(1+k_j)}\right) \frac{2 \cdot \varepsilon_j \cdot A_k}{U \cdot b \cdot k_j \cdot K_0} \quad (19)$$

$$\text{where } \begin{pmatrix} a_{kj} \\ b_{kj} \end{pmatrix} = \int_{x'=-l}^{x'=+l} (x')^k \cdot \begin{pmatrix} \cos(\omega_j \cdot x) \\ \sin(\omega_j \cdot x) \end{pmatrix} dx'$$

can be calculated analytically.

This formulation yields a linear system which is always over-determined since the number of measurement points (I_{max}) is usually much greater than the number of coefficients in the polynomial expression (4 in this case). Hence, the solution will be equivalent to a least square fit of the identified wave field over the measured wave field.

$$\zeta_{ff}(x_i, y) = E_{ik} \cdot A_k \text{ for } i = 1, I_{max} \text{ and } k = 0, 3$$

$$\text{with } E_{ik} = \sum_{j=0}^{J_{max}} \chi_j (a_{kj} \cdot \cos[\omega_j \cdot x_i] + b_{kj} \cdot \sin[\omega_j \cdot x_i]) \quad (20)$$

$$\text{and } \chi_j = \left(1 - e^{-\frac{h}{2}(1+k_j)}\right) \frac{2 \cdot \varepsilon_j}{U \cdot b \cdot k_j \cdot K_0}$$

The first polynomial distribution tested was given by a line of length $L = 2$ m, travelling at 2 m/s with the following polynomial coefficients: $A_0 = A_2 = 0$; $A_1 = -1.622 \text{ E-}03 \text{ m/s}$; $A_3 = 2.411 \text{ E-}03 \text{ m/s}$. The theoretical resistance of this "model" is 14.729 N. Eleven longitudinal cuts containing 5 reflections

($Nr=5$) were computed in a 13 m wide tank at transverse positions: $0.981 < y_c < 7.85$. The results obtained in terms of maximum difference compared to theoretical value using both DDM and SDIM methods are tabulated below:

Table 1: Error in % between calculated and theoretical wave resistance using DDM and SDIM methods

Method	DDM	SDIM
$Nr=5$	0.70 %	0.43 %
$Nr=0$	no solution	1.2 %

These early tests confirmed the potential of the SDIM method to obtain very accurate results, even with a limited signal length.

Near field wave correction

The knowledge of the singularity distribution enables the calculation of near field waves. It is then possible to use this information in the analysis of wave measurements which include a significant contribution from the near field. A method was devised and tested based on this observation.

The previous test case was used but at a speed of 4 m/s (the source distribution is multiplied by 2) and the theoretical resistance is then 32.68 N. The longitudinal cuts computed, with and without the near field (nf) wave contribution, at different transverse positions, were analysed and the results are presented in table 2.

Table 2: Error in % between calculated and theoretical wave resistance for different signal length and transverse positions

y_c	$Nr=5$		$Nr=0$	
	w/ nf	w/o nf	w/ nf	w/o nf
0.37	-0.848	0.138	-3.862	0.159
0.61	-0.315	0.135	-1.634	0.162
0.86	-0.101	0.129	-0.817	0.162

Hence, the near field waves, when present in the signal analysed, cause a significant increase in the error, particularly when the longitudinal cuts are close to the "model" and when the signal is short.

In order to take into account the near field waves, an iterative method was devised and programmed. The method is as follows:

- ① Analyse the measured longitudinal cut $\zeta_m(x_i, y_c)$ to obtain a distribution of sources:
- ② Compute the near field waves generated by these sources: $\zeta_{nf}(x_i, y_c)$

- ③ Compute a corrected far field longitudinal cut: $\zeta_{ff}(x_i, y_c) = \zeta_m(x_i, y_c) - \zeta_{nf}(x_i, y_c)$

This procedure is repeated using the corrected longitudinal cut, thereby replacing $\zeta_m(x_i, y_c)$ by $\zeta_{ff}(x_i, y_c)$. The differences with the theoretical wave resistance and the computed resistance at steps ① and ③ for the same test case and $Nr=5$ and $Nr=0$, are tabulated below:

Table 3: Error in % between calculated and theoretical wave resistance using near field correction

y	$Nr=5$		$Nr=0$	
	①	③	①	③
0.37	-0.848	-0.009	-3.862	-0.061
0.61	-0.315	0.003	-1.634	0.001
0.86	-0.101	0.003	-0.817	0.018

These results show that at the first iteration the accuracy of the method is significantly increased and the results are essentially exact (less than 1/1000) for all transverse positions and signal length. This result can be explained because the source distribution identified is very close to the actual source distribution so that the near field waves are indeed representative of the theoretical near field waves. The rapid convergence of the procedure can also be explained by the relatively small contribution of the near field waves in the analysed wave height data (a few percent on R_w). The fact that this procedure was shown to converge to the theoretical value of wave resistance gives us confidence in the programmed analysis method.

Discrete source distribution

This method was extended to a discrete distribution of sources at the centroid of panels located on the plane of symmetry of the model. A discrete representation was preferred over polynomial distributions because the numerical formulation is simpler and the choice of functions to be used would have required further tests.

The principle of the method is identical to that described above. A discrete distribution of sources is identified such that its wave field matches that measured. Again, the presence of the tank walls is taken into account by choosing a finite number of frequencies which correspond to natural transverse modes of the tank.

A numerical test of this method was performed on the Series 60 form at $Fn=0.35$ in an infinitely wide tank using the Neumann-Kelvin code POTFLO 16 configured in the slender ship approximation. The ship was discretised by 450 panels and the computed wave resistance based on the slender ship approximation is 596 KN. A signal of length $x = 75$ at a distance $y_c = 4.08$ was also calculated by the code.

This signal was analysed using SDIM assuming a 500 m wide tank, and a mesh of 9×3 panels in the centre plane of the ship and a wave resistance of 584 KN was obtained. Hence a 2% error on R_w between POTFLO and SDIM despite the small

number of singularities used. The amplitude spectrum calculated by POTFLO and identified by SDIM are shown in figure 8. The two spectra agree very well which supports the accuracy of the wave resistance result despite the limitations of the method. A further example of the global agreement between the slender ship model and the identified source distribution is the comparison between the wave elevations generated by POTFLO and by the equivalent source distribution (figure 9). The small differences between the two signals are due to the presence of near field waves close to the ship and to the oscillations due to the line integral term in POTFLO.

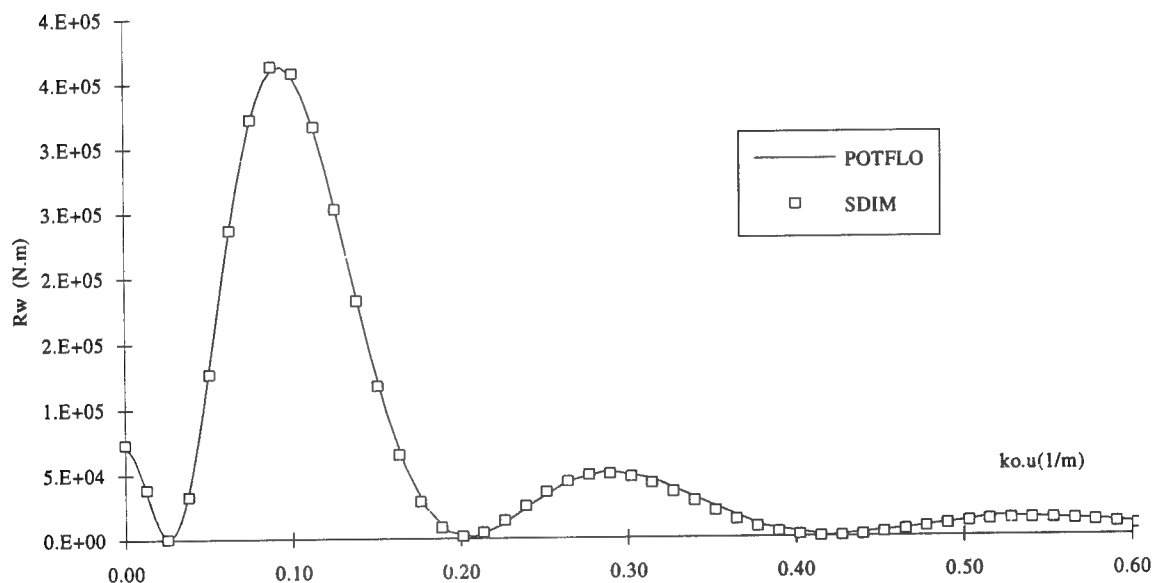


Figure 8: Amplitude spectra calculated by POTFLO and identified by SDIM

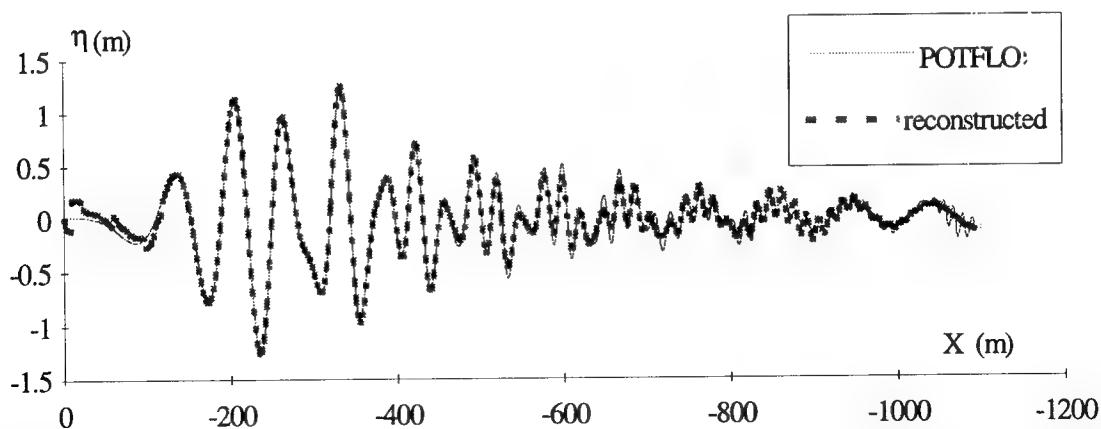


Figure 9: Wave elevations calculated by POTFLO and from the source distribution identified by the SDIM

Application to experimental data

Following the tests performed on the other method, the data used to evaluate the SDIM method are those performed in the Paris model basin (260 m x 13 m x 4.5 m). All the results obtained and analysed can not be presented here. The difference between the different methods are illustrated on a representative example: scale 1/25 Series 60 model at $Fn = 0.35$, $y_c = 3.63$. The mesh used for the SDIM method is as before: 9x3 panels in the centre plane.

It is important to note that the SDIM method converges as the number of transverse wave numbers (J_{max}) is increased, whereas the DDM method tended to diverge. In the present case, the SDIM method was run with $J_{max} = 300$ ($u_{max} = 145$) whereas the best compromise with the DDM method limited J_{max} to 50 ($u_{max} = 24.1$). The results presented with the DDM method correspond to the average of the results obtained with the 4 gages. The wave resistance results are presented in table 4.

Table 4: Comparison of calculated wave resistance using the three analysis methods

Method	LCM	DDM	SDIM	SDIM
Nr		Nr=3	Nr=0	Nr=5
Rw (N)	24.5	24.5	21.6	19.5

These results show significant differences but it is not possible to determine which of these estimates is the closest to the real wave resistance. In order to qualify these results, the amplitude spectra corresponding to each estimate are compared in figure 9. Besides the differences in the resolution in frequency, it is clear that the good agreement between LCM and DDM is fortuitous since there are significant differences in the two spectra. The agreement between SDIM and LCM spectra is good, except as u tends to 0, where the SDIM method shows

lower amplitudes, and hence explains the lower wave resistance value.

In order to further compare the three methods the experimental wave elevations are compared to the elevations calculated using the spectra obtained from the LCM method (figure 10) and the SDIM method (figure 11). The following comments can be made by the comparing the two figures at different axial positions:

$x > 5$ The SDIM method leads to a better agreement close to the model.

$-5 < x < -15$ The LCM method is more accurate in the region where the bow and stern waves interact.

$x < -15$ The SDIM method leads to a better identification of the amplitudes of the longitudinal waves.

Since the main differences between the SDIM and LCM spectra were at low frequencies (transverse waves), the agreement between measured and reconstructed SDIM wave elevations for $x < -15$, indicates that the wave resistance calculated by SDIM is closer to the real value.

Different tests performed on the parameters of the SDIM method did not succeed in obtaining a perfect agreement between measured and calculated wave elevations. Hence, there seems to be a limit as to the ability of this method to achieve an exact representation of the wave field. One possible explanation lies in the limited number of frequencies used in the analysis, particularly at low frequency.

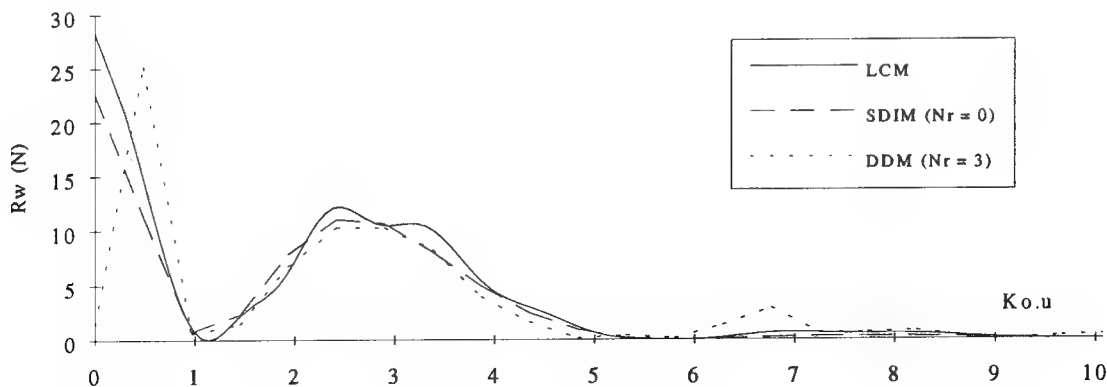


Figure 9: Comparison of the amplitude spectra obtained using the three analysis methods

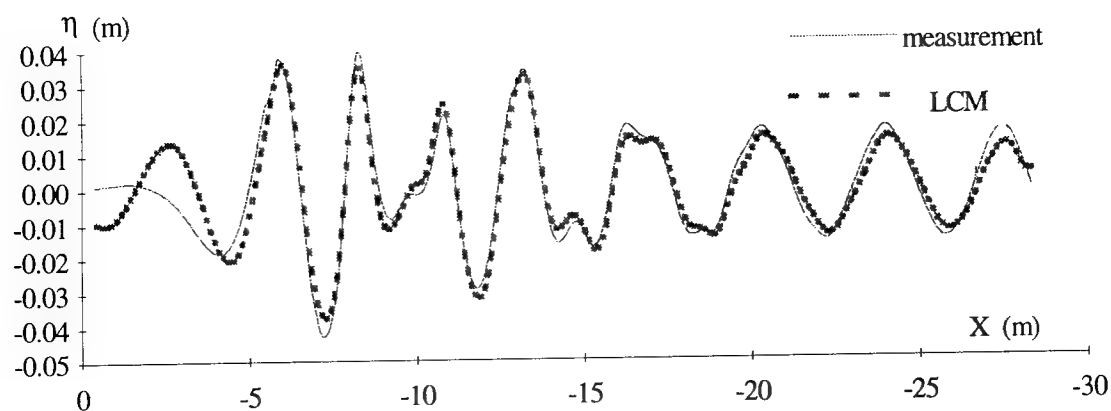


Figure 10: Comparison of measured and reconstructed (LCM) wave elevations

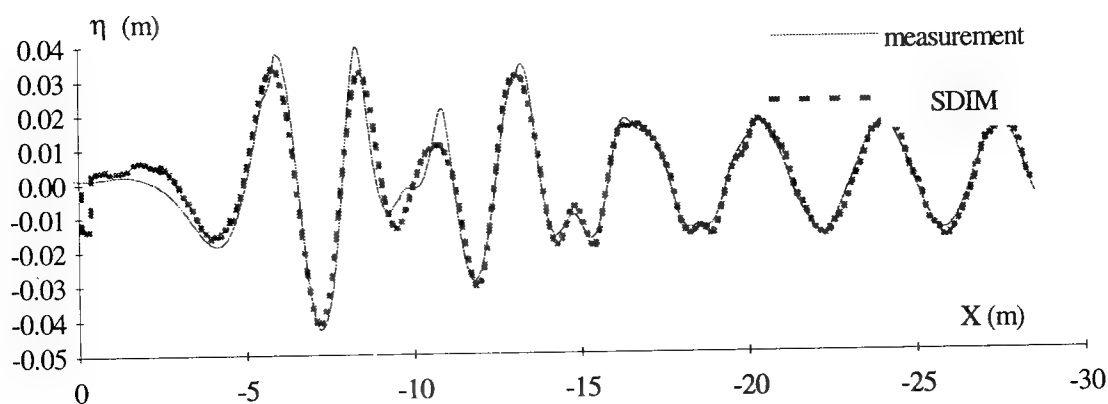


Figure 11: Comparison of measured and reconstructed (SDIM) wave elevations

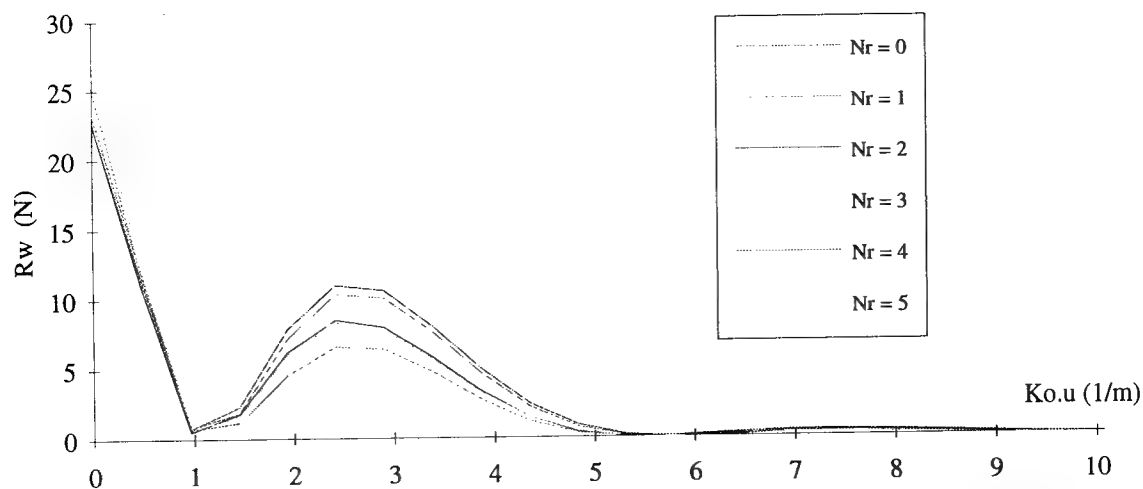


Figure 12: Wave spectra identified by SDIM for different signal lengths (or number of reflections)

Influence of signal length

Based on the same experimental data, tests were performed on the length of the signal which is characterized by the number of reflections included in the signal. The wave resistance calculated for 6 values of N_r are presented in table 5. The computed wave resistance decreases significantly as the number of reflections increases. Since previous numerical tests (table 2) showed that the method is independent of this parameter, there must be some physical phenomenon present in the experiment and which is not modelled. The fact that the reduction in computed resistance occurs every other 2 reflections, that is each time the reflected waves cross the viscous wake of the model, is an indication that the interaction of the waves and the wake might be responsible for the reduction in calculated wave resistance.

Table 5: R_w as a function of signal length

N_r	0	1	2	3	4	5
$R_w (N)$	21.7	20.8	17.8	18.3	15.8	15.8

Further tests were performed on the influence of signal axial position in order to verify these conclusions. The measured wave elevations were split in 3 zones as described in figure 13. The

signal corresponding to each zone was analysed and the resulting amplitude spectra are shown on figure 14. Again, the reduction in the amplitude spectra as the segment of signal used is taken further and further downstream is clear. These difference, lead to differences in wave resistances similar to those presented in table 5, and represent further evidence of the influence of the viscous wake on the energy present in the reflected waves. These tests further illustrate the robustness of the method which can analyse truncated parts of the wave elevations. This type of analysis is impossible with the LCM or DDM methods.

Probe transverse position

The influence of probe transverse position was again tested on the Series 60 test data measured at 4 different transverse probe position at $Fn=0.35$. The results of the SDIM analysis of these longitudinal cuts are presented in figure 15 in the form of amplitude spectra. This graph shows excellent agreement between the 4 cuts and should be compared to figure 7 in order to quantify the improvements gained by using the SDIM method over the DDM method where the scatter is much larger.

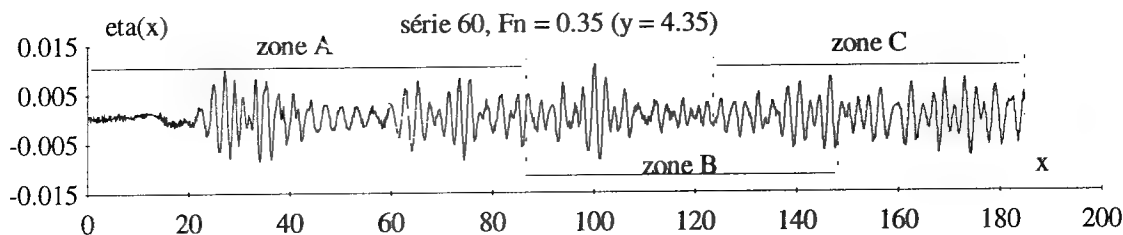


Figure 13: Measured wave elevations indicating the selected signal segments

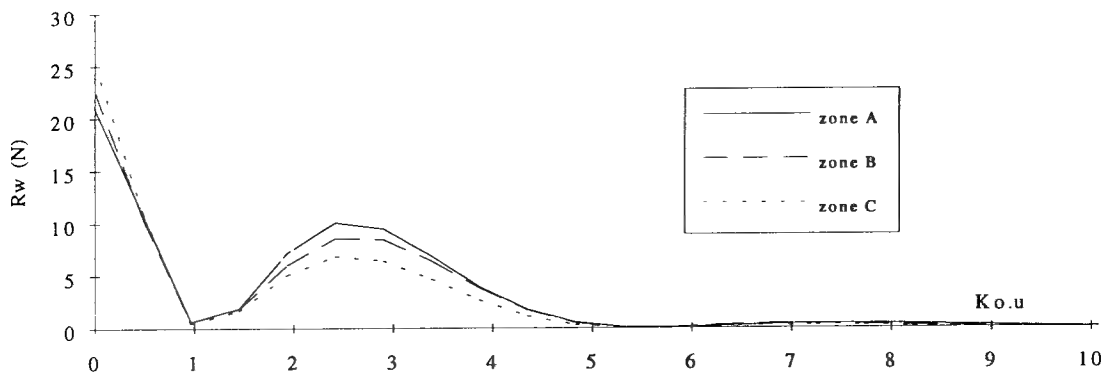


Figure 14: Wave amplitude spectra computed for each of the zone identified in figure 14 using SDIM

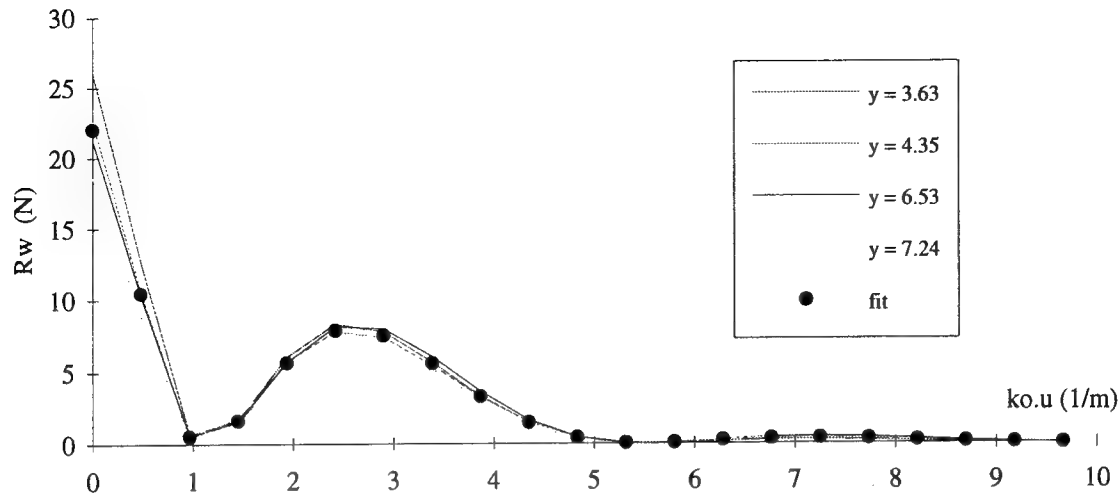


Figure 15: Wave amplitude spectra computed for 4 different longitudinal cuts using SDIM

CONCLUSIONS

The analysis of the two principal methods of wave pattern analysis from longitudinal cut measurements (LCM and DDM) has led to the identification of their respective inherent limitations.

The LCM method is very sensitive to errors in the truncation correction and neglects the influence of near field waves. The estimation of these errors has led to an analytical expression for the relative error on wave resistance as a function of the ratio of tank width to model length and Froude number.

In the DDM method, the presence of the near field is also neglected, and the numerical instabilities limit the length of the signal and the number of frequency components which can be taken into account.

These limitations have led us to develop a third method (SDIM) based on the identification of a singularity distribution in the centerplane of the model which takes into account the tank walls in the boundary conditions. Numerical tests have shown this method capable of taking into account the near field wave components through an iterative process, and of providing very accurate estimates of wave resistance independently of signal length (large number of reflections) and transverse position of the probe.

Tests performed on wave elevation data measured in the wake of a series 60 model have shown that this method is capable of calculating the wave resistance and of reconstituting the signal with an accuracy at least as good as the LCM method. These tests have as shown that the wave resistance could be computed for widely varying signal lengths without numerical problems (convergence, instabilities).

The tests on the experimental data indicate the presence of an interaction between the model wake and the reflected waves leading to a reduction in the wave resistance.

This work is to be continued in the following directions:

- o Implementation of the near field correction in the generalised version of this method.
- o Locate the sources on the hull surface (calculation of the line integral terms)
- o Investigate the possible advantages of extending this approach to an unbounded domain.

ACKNOWLEDGEMENTS

This work has been performed with the support of the Direction des Recherches et Etudes.

NOMENCLATURE

LCM	Longitudinal Cut Method.
DDM	Discrete Decomposition Method.
SDIM	Singularity Distribution Identification Method.

Symbol	Unit	Definition
b	(m)	Breadth of the tank.
e	(-)	Local error.
E	(-)	Global error.
$Fn = \frac{U}{\sqrt{g \cdot L}}$	(-)	Froude number.
F(u)+i G(u)	(-)	Components of Free-Wave spectrum.
h	(-)	Model depth.
$l = K_o \cdot L / 2$	(-)	Model half-length.
$K_o = \frac{g}{U^2}$	(1/m)	Speed-length number.
L	(m)	Model length.
Nr	(-)	Number of reflections.
Rw	(N)	Wave resistance.
$C_w = \frac{K_o^2 \cdot R_w}{\rho U^2}$	(-)	Wave resistance.
$u = \omega \tan \theta$	(-)	Transverse wave number.
U	(m/s)	Model velocity.
$x = X \cdot K_o$	(-)	Coordinate along Ox.
X	(m)	Coordinate along Ox.
x_e	(-)	Length of signal.
$y = Y \cdot K_o$	(-)	Coordinate along Oy.
Y	(m)	Coordinate along Oy.
y_c	(-)	Distance from model axis.
M(x')	(m/s)	Source density.
θ	(°)	Wave direction.
η	(m)	Wave elevation.
ζ	(-)	Wave elevation.
ζ_{nf}	(-)	Near field wave elevation.
ζ_{ff}	(-)	Far field wave elevation.
$\omega = \frac{1}{\cos \theta}$		

REFERENCES

- 1 Eggers K.W.H., Sharma S.D. and Ward L.W., "An assessment of some Experimental Methods for Determining the Wavemaking Characteristics of a Ship Form", Transactions SNAME, Vol 75.
- 2 Yokoo K. and Tanaka H. , " Application of Wave Analysis to Tank Experiments", Proceedings of the International Seminar on Wave Resistance, Tokyo, February 1976.

- 3 Newman J.N. , "The Determination of Wave Resistance from Wave Measurements along a Parallel Cut", Proceedings of the International Seminar on Theoretical Wave Resistance, Univ. of Michigan, 1963.
- 4 Eggers K.W.H. , "Wave Analysis, State of the Art", Universitat Hambourg, Germany.
- 5 Tsai C.E. and Landweber L. , "Further Development of Procedure for Determination of Wave Resistance from Longitudinal-Cut Surface Profile Measurements", Journal of Ship Research, vol 19, n° 2, June 1975.
- 6 Hogben N. "Automated recording and analysis of wave patterns behind towed models", Transactions of RINA, vol. n° 114, 1972.
- 7 Baba, E. "Study on Separation of Ship Resistance Components", MITSUBISHI Technical Bulletin N° 59, August 1969.
- 8 Okhusu, "Wave Analysis of Simple Hull Form", Journal of society Naval Architects of Japan, Vol. 126, 1969.
- 9 Bessho, "Wave Free Distribution and their Applications", Proceedings of the International Seminar on Theoretical Wave Resistance, Univ. of Michigan, 1963.
- 10 Bessho, "A Contribution of Wave Analysis of Ship Waves", Scientific and Engineering Reports of the Defence Academy, Vol. 7, n° 1, 1969.
- 11 Ikehata and Nozawa, "Determination of Wave Making Resistance of a Ship by the Method of Wave Analysis", 1st and 2nd Reports, Journal of the Society Naval Architects of Japan, Vol. 121, 1967 and Vol. 124, 1968.
- 12 Dumez F.X. and Cordier S. , "Scale Effects on the Resistance Components of a High-Speed Semi-Displacement Craft", FAST 93, Yokohama, December 1993.
- 13 Dumez F.X. "Décomposition de la Résistance à l'Avancement des Navires", Proceedings of the Quatrième Journées de l'Hydrodynamique, 1993, Nantes.
- 14 Cordier S. and Dumez F.X. , "Resistance Components of Displacement and Semi-Displacement Hull Forms" Proceedings of the 20th ITTC, Vol. II pp 75,77, 1993, San Francisco.
- 15 Tanaka H. and Nakatake K., "Cooperative Resistance Tests with Geosim Models of a High-Speed Semi-Displacement Craft" Journal of the society of Naval Architects of Japan, Vol. 169.
- 16 Hally D. "Implementation of a Free Surface in Calculations of the Flow into the Propeller Plane of a Ship", Proceedings of CADMO92, Madrid, 1992.

Unsteady Three-Dimensional Cross-Flow Separation Measurements on a Prolate Spheroid Undergoing Time-Dependent Maneuvers

T. Wetzel, R. Simpson

(Virginia Polytechnic Institute and State University, USA)

Abstract

The flow over a 6:1 prolate spheroid undergoing transient maneuvers is studied. The Dynamic Plunge-Pitch-Roll (DyPPiR) model mount provides the unique capability to simulate truly unsteady maneuvers in a wind tunnel. The DyPPiR is presented along with several transducer systems used to study specific aspects of the spheroid flow field. The types of unsteady measurements performed include hot-film surface skin friction measurements, surface pressure measurements, and force and moment measurements. Time-dependent separation locations are measured successfully for the first time, as are time-dependent force and moment measurements. Steady and unsteady data are presented for each of these systems for two maneuvers: a 0° to 30° , 0.33 second ($t'=11$) pure ramp pitchup about the model center (Pitchup Maneuver); and a 0° to 13.5° pure pitchup about the model center that simulates the time dependent sideslip angle of a submarine entering a turning maneuver (Submarine Maneuver). These data are compared with steady data sets from this work and other researchers. This flow field is characterized by complex, three-dimensional cross-flow separations that are highly non-linear and are expected to have very complex time dependencies in unsteady flows. It is shown that, especially at higher angles of attack, significant lags occur in the flowfield during the maneuvers compared to the steady cases. In particular, separation is delayed at all locations of the model at up to 10° higher angle of attack in the unsteady maneuvers compared to the steady data. Equivalently, the separation structure during the unsteady maneuvers lag the steady data by from 1.5 to 4.5 non-dimensional time units (t'). The range of these time constants and the fact they are constant for neither the entire model or a given sensor shows for the first time the complex nature of the time dependency of three-dimensional crossflow separation. In addition, the normal force and pitch moment lag by about one t' time unit.

Nomenclature

C_f skin friction coefficient, τ_w/q_∞

C_l	sectional lift coefficient, $(L/b)/2 q_\infty R$
C_M	pitch moment coefficient, $M/q_\infty \pi R^2 L$
C_p	pressure coefficient, $(p-p_s)/q_\infty$
C_z	normal force coefficient, $Z/q_\infty \pi R^2$
h	heat transfer film coefficient
k	thermal conductivity
l	effective gage length
L	model length
M	pitch moment
N	constant
p	model surface pressure
p_0	total pressure
p_s	free-stream static pressure, $p_0 - q_\infty$
\dot{q}	heat transfer
q_∞	dynamic pressure, $\frac{1}{2} \rho U_\infty^2$
Re	Reynolds number, $U_\infty L/\nu$
t	time
t'	non-dimensional time, $t U_\infty / L$
T_w	wall temperature
T_∞	reference temperature
U_∞	free-stream velocity
V	wall normal velocity
w	effective gage width
x	model longitudinal position from nose
y	wall normal coordinate
z	DyPPiR plunge ordinate
Z	normal force
α	DyPPiR pitch angle; or thermal diffusivity
δ	uncertainty
ρ	air density
τ_w	wall shear stress
ω_n	force and moment system natural frequency
ζ	force and moment system damping coefficient

1. Introduction

1.1 Unsteady Aerodynamics

With recent efforts to expand submarine, aircraft, and ordinance dynamic performance beyond conventional regimes, the need for studying the truly unsteady, high excursion, and high Reynolds number flows has increased. Standard stability derivative

techniques fail to capture the non-linearities in such flows and CFD techniques cannot accurately compute the highly complex, separated flow fields of full vehicle geometries in steady conditions, let alone unsteady ones. Such methods are deficient because they lack physical models on which to base their computations that accurately describe the complexities of a time-dependent, turbulent, separated flow field. These models can only be developed with suitable experimental flow field data from sufficiently realistic flows. A new apparatus at Virginia Tech, the Dynamic Plunge-Pitch-Roll (DyPPiR) model mount, provides for the first time the capability to model truly time-dependent, high-excursion, high Reynolds number flows in a laboratory setting (1,2).

"Dynamic" testing has been an important part of design and validation of various types of craft for decades. Typically these techniques are only "quasi-steady", relying on very small amplitude sinusoidal oscillations that can describe small-excursion maneuvers reasonably well (10). Even in these tests however, the measurements are usually limited to forces and moments. Seldom are flow field data taken in dynamic tests.

The DyPPiR is installed in Virginia Tech's 1.8m square Stability Wind Tunnel. The DyPPiR combines three 20.6 MPa hydraulic actuators to plunge a model through a 1.5m range vertically, pitch the model through a $\pm 45^\circ$ range, and roll the model through a $\pm 140^\circ$ range. Typical models are on the order of up to 2m long, and typical maneuvers last several tenths of a second. Even at Reynolds numbers of over 4 million the maneuvers are fast enough to exhibit significant unsteadiness. All degrees of freedom are digitally controlled by a personal computer, which allows the researcher to program not only sinusoidal trajectories, but more importantly, user-defined trajectories. Thus, the DyPPiR successfully fills the need of forcing a model to perform general, rapid, truly unsteady, high excursion, high Reynolds number maneuvers.

The DyPPiR has been used primarily to study submarine-like configurations. While some force and moment measurement capability has been developed for use with these configurations on the DyPPiR, the primary measurements made during DyPPiR tests are time-dependent surface pressure measurements and time-dependent, constant temperature surface hot-film measurements. The pressure measurements are useful in determining how unsteadiness affects the forces and moments and the structure of the vortical separations that form on the leeward side. The hot-film sensors are used to measure wall shear. Minima in the wall shear are interpreted as near separation locations. Thus, hot-film measurements provide the capability to study separation formation and migration during transient maneuvers.

To relate unsteady wind tunnel tests to real-time maneuvers, the time is non-dimensionalized by the time for flow to pass over a model, L/U_∞ (8):

$$t' = tU_\infty / L \quad (1)$$

Most parameters studied are related to the instantaneous angle of attack. The DyPPiR specifically sets a pitch actuator position during a maneuver. Since for all of the maneuvers studied the model is rotated about the model center, it can be stated that the DyPPiR pitch angle is equal to the instantaneous angle of attack of the model, referenced at the model center. Due to the rotational motion of the model, the instantaneous local angle of attack varies linearly from the nose to the tail of the model, with the nose being at a lower angle of attack than the model center and the tail being at a higher angle of attack than the model center. The magnitude of the local induced increment in angle of attack is a function of distance from the model center and rotational speed. In all cases studied here, these angle of attack increments, relative to the model center angle of attack, are less than 1.4° at the extreme nose and tail.

1.2 6:1 Prolate Spheroid

The prolate spheroid is an interesting geometry because although the body shape is very simple, the flow field is very complicated. In addition, the prolate spheroid flowfield carries over qualitatively to submarines, missiles, torpedoes, and to a certain extent aircraft fuselages. The prolate spheroid is a fairly well-documented flow. Other simple bodies that have been studied that are of interest are ellipsoid-cylinders and ogive cylinders. Until the present, all data taken on prolate spheroids has been steady. Wetzel (14) gives a brief overview of the steady prolate spheroid literature along with a detailed description of the steady flowfield. The prolate spheroid flowfield at angle of attack is characterized by massive crossflow separation that forms on the tail at low angles of attack and migrates windward and noseward at increasing angles of attack (2). The circumferential location of separation and even the separation topology are highly dependent on the state of the local boundary layer, that is, whether it is laminar, transitional, or turbulent. In all tests in this report, trip strips at $x/L=0.20$ guaranteed a relatively Reynolds number-insensitive separation over the rear 80% of the model. The separation on the nose, however, was governed by the laminar flow upstream of the trips. Here, at high angles of attack, the laminar flow will separate, undergo transition, reattach, and re-separate as a second, turbulent separation. These two separation lines merge downstream of the trip strips (14).

1.3 Overview of Present Research Program

The present work represents the first unsteady data taken on the DyPPiR at Virginia Tech. The focus up

through this report has been placed on making the DyPPiR fully operational and developing the measurement systems necessary to support DyPPiR experiments. These measurement systems include surface hot-film measurements, surface pressure measurements, and force and moment measurements.

With this present work as a basis, the DyPPiR is intended to provide a platform to study truly unsteady aerodynamics on a wide range of vehicles. The emphasis will be placed on high Reynolds number, high speed, high excursion maneuvers that are characterized by massive flow separations. The data obtained by DyPPiR experiments will provide data sets upon which to base unsteady models of the separation process in these flows. For example, by having the capability to measure separation location as a function of time, one can potentially develop a model describing that time dependency as a function of non-dimensional maneuver pitch rate. In addition to developing new models, the DyPPiR will be used to test existing models, particularly those for stability derivatives, and determine their applicability. As an example of this type of test, the DyPPiR can be used to determine all lateral and longitudinal stability derivatives for a given model. The DyPPiR can then be used to perform several general maneuvers, measuring the forces and moments during those maneuvers, and compare the measured forces and moments to those predicted by the stability derivatives. The DyPPiR represents a truly unique capability in its ability to perform these general time-dependent maneuvers.

2. Dynamic Plunge-Pitch-Roll Model Mount (DyPPiR)

2.1 Stability and Control Wind Tunnel

The DyPPiR is installed in the Virginia Tech 1.8mx1.8m Stability and Control Wind Tunnel. The Stability Tunnel is a closed return, closed test section, subsonic facility with a speed range of over 60 m/s. Turning vanes, screens, and a 9:1 contraction ratio inlet nozzle reduce the free-stream turbulence to less than 0.03% (6). The fan is powered by a 450 kW DC motor. For these tests, the tunnel speed, and thus non-dimensional time, was held constant at 45.7 m/s. Because the tunnel temperature is essentially ambient, the Reynolds number was thus allowed to vary as much as $\pm 5\%$.

2.2 DyPPiR Hardware Overview

The Dynamic Plunge-Pitch-Roll (DyPPiR) Model Mount (Figure 2) was designed to provide the unique capability of performing general, high-excursion, large-scale, high Reynolds number, truly unsteady maneuvers (1,2). The DyPPiR has three degrees of freedom: 1.5m

vertical plunge; $\pm 45^\circ$ pitch; and 280° roll. The DyPPiR is designed to carry models up to 2m or more in length and up to 45 kg of mass. Three 20.6 MPa actuators provide the power required to force 45 kg of model and over 250 kg of DyPPiR hardware at rates approaching 9 m/s in plunge and over $90^\circ/\text{s}$ in pitch. Most importantly, however, the DyPPiR is digitally controlled by a personal computer, so it is capable of performing *general*, pre-programmed maneuvers. It is not limited to sinusoids or fixed rate ramps. The nomenclature used for the three degrees of freedom, along with body nomenclature, are shown in Figure 3.

2.3 Maneuvers Tested

2.3.1 The 0.33s, 30° Ramp Pitchup

The Pitchup Maneuver, as it is referred to throughout this report, is a simple linear ramp from 0° to 30° in 0.33s. No specific acceleration or deceleration curves were programmed in. The objective is to get as abrupt a start and a stop as possible. The DyPPiR does, in any case, have a finite acceleration and deceleration capability. Figure 4 shows actual pitch angle position feedback taken during several hundred maneuver executions. The solid line is the mean over the ensemble, and the dotted lines delineate two-standard-deviation (2σ) boundaries. The model is pitched about the model center, so the carriage has to be plunged roughly 70 cm during the maneuver to prevent the model center from moving. Figure 5 shows the plunge position feedback data for the same maneuvers. While it is possible to keep the model center from moving vertically during a maneuver, it is inevitable that the model center will translate downstream during a maneuver. This downstream movement is deemed insignificant compared to the tunnel speed (typically 45 m/s).

2.3.2 The 0.25s Submarine Maneuver

The Submarine Maneuver is modeled after data taken on a real submarine during the initial transient portion of a turning maneuver by researchers at the David Taylor Model Basin. For the DyPPiR tests, the Submarine Maneuver models the time history of the sideslip angle from the actual submarine tests (Figure 6). This is characterized by a ramp up to 13.5° with a slight overshoot. Also, the motion simulated on the DyPPiR is roughly half the speed in non-dimensional time units than the DTRC data set.

2.4 Model Geometry

All models tested were 1.372 m long 6:1 prolate spheroids with circular cross section (Figure 3). The maximum radius was 114 mm. The rearmost 38 mm was removed to allow for sting entry.

3. Hot-Film Measurements

3.1 Theory of Operation

The surface skin-friction was measured with the hot film sensors designed and documented by Simpson et. al. (13). A detailed description of the sensors, their application to the model, and the instrumentation used to operate the sensors can be found in Wetzel (14). The sensors heat the near-wall fluid through forced convection. Due to the similarity between gradient transport of momentum and scalars (heat), the heat transfer into the fluid gives a measure of the wall shear. Simpson et. al. (13) show that the mean film coefficient \bar{h} is proportional to the cube root of the near-wall velocity gradient, which is thus proportional to the wall shear:

$$\bar{h} = \frac{\dot{q}}{lw(T_w - T_\infty)} = \frac{3}{2} Nk \frac{(\partial U / \partial y)_w^{1/3}}{(3\alpha l)^{1/3}} \quad (2)$$

$$\tau_w = \mu \frac{\partial U}{\partial y} \propto \bar{h}^3 \quad (3)$$

In this relation, \dot{q} is the time-mean heat transfer into the fluid, T_w is the wall (sensor) temperature, T_∞ is the free-stream temperature, N is a constant (1.12) from the mathematical analysis, k is the thermal conductivity, l and w describe the sensor size, α is the thermal diffusivity, and μ is the viscosity. Here, the main purpose of the sensors is not necessarily to measure the absolute magnitude of the wall shear or the skin friction coefficient, but to measure the relative shear distributions through measurements of the film coefficient to locate shear minima and thus separation locations. However, wall shear magnitudes are possible with adequate calibration.

In the same work, Simpson et. al. (13) show that the wall shear provides higher order information about the separation location than pressure by arguing that three-dimensional separations are characterized by high wall-normal velocity (V) components. By analyzing the continuity and momentum equations near the wall, Simpson et. al. (13) showed that

$$V = -\frac{1}{2\mu} (\nabla \cdot \bar{\tau}_w) y^2 + \frac{1}{6\mu} (\nabla^2 p) y^3 + \dots \quad (4)$$

To use this equation rigorously, the entire wall shear direction and magnitude fields would need to be known in order to perform the divergence operation to compute the wall-normal velocity at all points on the body and determine separation location. The sensors used in the present experiment are only magnitude sensitive, eliminating the possibility of using the last equation. Instead, it is found in practice that separations occur near wall shear minima. Bellhouse and Schultz (4) show

this phenomenon quite clearly in several circular cylinder flows. Wetzel (14) shows that in general the wall shear minima does not correspond *exactly* with separation location but instead typically lags separation by up to 10° circumferential position. The same work shows conclusively however that wall shear minima do in fact properly correlate separation location trends.

3.2 Experimental Apparatus And Uncertainties

For a detailed description of the apparatus and uncertainties, see Wetzel (14). Custom designed, directionally insensitive hot-film sensors were mounted at 12 locations along a lengthwise surface element: $x/L=0.118, 0.194, 0.220, 0.271, 0.347, 0.424, 0.500, 0.576, 0.653, 0.729, 0.831, \text{ and } 0.882$. The sensors were each connected to non-linearized Miller (11) anemometers. The DyPPIR roll actuator was used to position this strip at specific circumferential locations from $\phi=0^\circ$ to $\phi=180^\circ$ to map the circumferential skin friction distributions. A data acquisition board in a personal computer was used to read the sensor voltages. Tunnel temperature, total pressure, and dynamic pressure were all measured as well, as were DyPPIR positional outputs.

The relative uncertainty between two measurements made by a given sensor, and thus the relative uncertainty between any two measurements presented in a given circumferential distribution, is 5%. Due to calibration uncertainties, the uncertainty between any measurements made by two different sensors (and thus at two different axial model stations) is 20%. This latter uncertainty is unimportant, however, since circumferential distributions of skin friction are used to determine separation locations and are thus governed by the former 5% uncertainty. Due to low frequency response and large sensor size (5 mm), the sensors are insensitive to high frequency, small scale, turbulent fluctuations. The frequency response is high enough (200 Hz) for the sensors to accurately track temporal changes in the time-mean skin friction values.

3.3 Steady Results

Figure 7 shows typical results from both the constant temperature measurements and some measurements made with a different set of sensors connected to constant current anemometers. The agreement between the two data sets is excellent. In this case ($\alpha=10^\circ$, $x/L=0.77$) the minima, indicating a primary separation, occurs at $\phi=135^\circ$.

Figure 8 and Figure 9 show the constant temperature skin friction coefficients superimposed on top of secondary streamlines determined by Chesnakas and Simpson (5) from detailed laser Doppler anemometer measurements. It is important to note that the skin friction values are not in scale, but the streamline plots

are in scale. In fact, the secondary streamline plots represent data taken up to approximately 3 cm away from the wall and thus represents the near-wall flow field in these separated zones. The radial grid lines represent locations where the LDV data were actually taken, therefore separation uncertainties in this data set are limited by the 5° spacing of the profile locations. Each profile contains 17 points spaced logarithmically down to 0.007 cm from the wall, corresponding to y^+ values on the order of 7. In all cases, it is seen that the wall shear minimum qualitatively corresponds to the separation location. In fact, the wall shear minima seems to consistently lag the separation location by around 5° , although considering the positional uncertainties in both data sets, the true size of this lag is difficult to measure. Exactly where the separation is located in the streamline plots is subject to some subjectivity. In any case, the flow minima seems to consistently lag the visible flow separation streamline, and this fact is consistent with the findings of Chesnakas and Simpson (5).

Figure 10 shows circumferential skin friction distributions over the length of the model for $\alpha=15.2^\circ$. At the rearmost sensor ($x/L=0.882$), two minima are seen, indicating a primary and secondary separation. The secondary separation only extends up to $x/L=0.729$. Upstream the primary separation minima are located farther leeward and are weaker. The distribution at $x/L=0.220$ is very irregular due to the fact that this sensor was immediately downstream of the trip posts, where the flow had not completed transition.

Figure 11 shows how the circumferential skin friction distributions at one location ($x/L=0.729$) vary with angle of attack. At this location, a minimum indicating primary separation is first evident at $\alpha=12.2^\circ$. This minimum grows in strength and moves windward as angle of attack increases. A second minimum, indicating secondary separation, is fully developed by $\alpha=17.6^\circ$. It too grows in strength at increasing angle of attack but remains in roughly the same circumferential location.

The locus of the minima in these distributions for each axial station describes the separation topology. Figure 12 shows such a separation topology with the separation lines determined from both constant temperature and constant current data sets. At this angle of attack (20°), two separations are evident on the nose due to a laminar separation that undergoes transition, reattaches, and re-separates as a turbulent separation. Also, a strong secondary separation extends over the rear 40% of the model length. The agreement between the constant temperature and constant current datasets is excellent.

Figure 13 shows the primary separation locations as a function of angle of attack for each of the 12 constant

temperature measurement stations. In all cases except for the nose stations, the separation moves windward at increasing angles of attack, but eventually levels out at some windward-most circumferential location.

3.4 Unsteady Results

3.4.1 Pitchup Maneuver

Figure 14 shows the circumferential skin friction distributions for $x/L=0.729$ at discrete time steps during the pitchup maneuver. Time increases from bottom to top in these plots, and the range of time encompassed by a given plot column is indicated in the top of each column. The flow is essentially attached at the first time step ($t'=6.0$), but a primary separation is formed by the top of the first column ($t'=8.87$). Similarly, a secondary separation is formed by the top of the second column in Figure 14 ($t'=11.87$).

Again, the minima can be located for each time step and the separation location can be plotted versus time. Figure 15 shows an example of such a plot for $x/L=0.729$. The primary separations lag the steady data significantly, by as much as 1.5 to 4.5 t' units.

Figure 16 shows a comparison of separation lines at 17.6° for both the pitchup maneuver and the steady data. It is clear that the primary separation line in the pitchup maneuver lags the steady separation line by as much as 10° in circumferential position, and while the steady data show a strong, well-developed secondary separation line, no such secondary line exists in the unsteady data.

3.4.2 Submarine Maneuver

Figure 17 shows circumferential skin friction distributions for discrete time steps during the submarine maneuver, but this time at $x/L=0.831$. Again, there is no separation at the bottom of the left column in Figure 17 ($t'=6.0$), but a separation has formed by the top of that first column ($t'=8.87$). Variations produced by separation grow throughout the rest of Figure 17.

Figure 18 shows the time history of the separation location at $x/L=0.729$. This plot is not as informative as the equivalent plots in the pitchup maneuver due to the low number of steady data points for these low angles of attack, but a lag in separation formation is still evident.

Figure 19 to Figure 21 show direct comparisons between steady circumferential skin friction distributions and unsteady ones for $x/L=0.729$. Figure 19 shows data for both the pitchup and submarine maneuvers compared with steady data at an angle of attack of 12.2° . In the steady data, a clear primary separation exists at $\phi=135^\circ$, but no separation is seen in either the pitchup or submarine maneuver at the instant the model reaches this angle of attack. The data from the last recorded time taken during the submarine maneuver, which occurs $t'=20$ after the model has come to rest,

shows that the flow has essentially regained a steady-state condition. Figure 20 shows a comparison of the pitchup maneuver at 20° angle of attack with equivalent steady data. In this case, the steady data show both a primary and secondary separation, while the unsteady distribution shows only a primary separation which is more leeward than the steady primary separation. This shows that in unsteady flows the separation location topology itself can be very different than in an equivalent steady configuration. Figure 21 shows the pitchup maneuver at 29.9° and at the end of the time record ($t'=11$ time units after the model has come to rest). In this case, both the steady and unsteady data show primary and secondary separations, but the positions are more leeward by roughly 10°. Again, by the end of the time record, the flow has essentially reached steady state.

4. Pressure Measurements

4.1 Experimental Apparatus and Uncertainties

Model wall pressure taps were installed in the prolate spheroid model in a longitudinal row at 10 locations: $x/L=0.00, 0.11, 0.23, 0.31, 0.44, 0.56, 0.69, 0.77, 0.83,$ and 0.90 . A brass plug with a 0.74 mm diameter pinhole was mounted flush to the model surface at each location. Endevco 8510B-2 miniature pressure transducers were mounted in these plugs. A detailed description of the pressure transducer system is contained in Wetzel (14).

The model was rolled to various orientations in order to sweep the transducers from the windward to the leeward sides to map out the pressure distribution over the model surface. The flow was assumed to be symmetric in the ensemble mean, so data were only taken on one half of the model.

The unsteady data were sampled at 2000 Hz. Data were taken at every 10° roll on the windward side and every 5° on the leeward side. Fifty ensembles were taken at each roll angle.

The pressure differences measured by the transducers were non-dimensionalized by the free-stream dynamic pressure forming the standard definition of the pressure coefficient:

$$C_p = (p - p_\infty) / q_\infty \quad (5)$$

Pressure coefficient uncertainties are on the order of $\pm 13\%$ (14), and thus preclude accurate quantization of the differences between steady and unsteady data. For this reason, only steady data are presented.

4.2 Steady Results

Figure 22 shows typical steady circumferential pressure distributions for the model at $\alpha=14.9^\circ$. The data (solid lines) are compared to the potential solution (dotted lines) at the same angle of attack. While the

potential solution matches the data reasonably well on the nose, the data on the tail obviously don't match well due to the flow separation at this angle of attack.

Figure 23 shows the sectional lift coefficients C_l (as calculated using pressure data) for each of the nine stations as a function of angle of attack. The sectional lift coefficients were computed by integrating the circumferential pressure distributions at each station where surface pressure was measured (14). It is interesting to note that most of the lift is generated by the nose and not the separated tail. In fact, the tail region actually has a small but significant downforce. The highly accelerated fluid on the windward side near the tail provides a large amount of windward suction, while the separation region is stagnant enough as to produce no noticeable suction at all.

5. Forces and Moments

5.1 Introduction

Unsteady forces and moments will eventually become the staple measurement made on the DyPPiR, much as it is in steady wind tunnel testing, because the data describe a global effect of the aerodynamics on the model and as such provides much information in a small number of runs. This contrasts with surface parameters, such as pressure and skin friction, which require one or more orders of magnitude more runs in order to get enough data to map out the data over the entire surface, or flow field measurements that require another order of magnitude in order to piece together the topology of a three-dimensional space. Steady force and moment data are difficult enough to acquire with precision. Unsteady force and moment measurements are more difficult to make, especially compared to pressure and skin friction.

5.2 Two-point Balance and Light-weight Model

Several iterations of balance and model construction have been developed as the DyPPiR unsteady force and moment measurement methodology has matured. Details of the chronology of this development are contained in Wetzel (14). The first iteration utilized a standard sting-mounted bending beam strain gage balance. Inertial loads dominated the aerodynamic loads due to the mass of the 23 kg model, and the balance output consisted primarily of oscillatory response due to the relatively low dynamic stiffness of the balance geometry. It was eventually found that the common paradigm of a sturdy, heavy wind tunnel model coupled with a bending-beam type of balance must be abandoned for sensitive unsteady DyPPiR force and moment measurements.

The first change made was to replace the heavy fiberglass and aluminum model with a much lighter composite one. A composite sandwich construction was used consisting of a foam core surrounded by thin layers

of carbon fiber cloth (Figure 24). The model was left completely hollow except for the sting mounting hardware. The model was made in two symmetric top and bottom halves. The final weight was roughly 2.3 kg, a savings of an order of magnitude over the previous iteration. Many of the design details for the model structure can be found in Roback (12).

The solution to the balance problem rests on greatly increasing balance stiffness without decreasing sensitivity. The bending-beam type of balance system is completely incapable of meeting these requirements. A configuration more suitable is the type used at the David Taylor Research Center for very large scale, static and quasi-steady, sting-mount submarine hydrodynamic testing (3). In these tests, the models are mounted to the sting by two sets of load cells that are separated by a large distance, with one set of load cells in the forward half of the model and the second set in the aft model half. Strain-based load transducers in general have small deflections of displacements when under load. However, while bending beam sting-mounted balances used in many wind tunnel tests may bend by only a fraction of a degree, this translates into many millimeters at the model tips. If the transducers are placed at each model end, as they are in tests at DTRC, then each end can only move by a fraction of a millimeter, and overall system stiffness is greatly enhanced.

To test this concept on the DyPPIR, a two component system was constructed using Transducer Techniques MLP-50 200 N single component load cells (Figure 25). A key to the success of this system is that the load cells be mounted to the sting or model with low-friction pivots instead of rigid mounts. This prevents the sting or model structures from absorbing any of the moments acting on the model. These pinned mounts were provided by using hardened steel dowel rods fitted very closely in brass inserts. The pivots were mounted on a robust aluminum channel that was attached to the sting. Solid carbon fiber inserts 10 mm thick were molded into the model skin to provide a very stiff, light weight, and precise mounting surface for the load cells. This system proved to be very stiff in normal force and pitch moment.

However, the system was much less stiff in roll because the load cells were not designed to withstand moments. The model could vibrate slightly in roll, and the load cell is sensitive to such an out-of-plane load. Thus, while results are not free from corrupting oscillations, they provide insight into the fluid dynamics of the unsteady maneuvers, as well as point toward the next iteration. Data were again taken with both the wind off, as a tare, and the wind on. 50 ensembles of each the wind-on and wind-off cases were obtained and averaged for each maneuver. The results from these tests are presented below.

5.3 Steady Results

Figure 26 shows the steady normal force and pitch moment coefficients for the prolate spheroid at various angles of attack up to 35° . Details of the reduction and uncertainty determination are contained in Wetzel (14). The full-scale uncertainty of the normal force coefficient is less than $\pm 1.5\%$, or $\delta C_z = 0.015$, while the pitch moment coefficient is also accurate to less than $\pm 1.5\%$ full scale, or $\delta C_M = 0.0035$.

The data are compared with the data of Ahn (2), which are stated to have a $\pm 7.5\%$ uncertainty on the normal force and $\pm 15\%$ uncertainty on the pitch moment. The two data sets agree to within the stated uncertainties on Ahn's data. The data were primarily taken with increasing angles of attack. However, several data points were repeated going back down (these are on the plot), and these were found to be repeatable to within the stated uncertainty of 1.5% full scale. While the normal force coefficient increases at greater rates at the higher angles of attack, the pitch moment settles in at a relatively constant slope at around $\alpha = 10^\circ$.

5.4 Unsteady Results

The normal force and pitch moments for the pitchup maneuver are shown in Figure 27. The oscillations, while small, do make it difficult to discern the trends in the lower angles of attack of the ramp. However, there is a definite lag in both the unsteady normal force and pitch moment. The dynamic distortions seem to be due mainly to a low frequency (roughly 6 Hz damped sine wave) signal component that exists in the wind on and wind off data. These damped oscillations are caused by the inertial impulse imparted on the model-balance system by the DyPPIR as it accelerates the model from rest into a steady ramp, and again as the DyPPIR decelerates the model back to rest at the end of the maneuver. The natural frequency of the load cell in a normal load mode is 2500 Hz, which is well above this observed frequency. During the maneuvers the model exhibited roll oscillations. It was soon determined that the model/load-cell system was much less stiff in roll than in normal force/pitch moment. This is due to the fact that the load cells are not designed to withstand bending moments and the fact that the mounting area provided by the load cell consisted of only one bolt, which is adequate for a normal load but not adequate for a bending moment. Therefore, the low frequency oscillations are due to secondary roll oscillations of the model relative to the sting. The load cells are not designed to cancel out bending moments, so such loads imparted on the load cell corrupt the voltage output of the load cells.

In computing the aerodynamic loads, the wind-off force and moment time series is subtracted from the wind-on time series. The intent is that the undesired

inertial loads will be identical for both the wind-off and wind-on cases and thus subtract out exactly. Since these loads are the same order of magnitude as the aerodynamic loads, it can be expected that small errors in the repeatability of the inertial loads will corrupt the computed aerodynamic loads. The undesired loads, which includes mostly inertial loads imparted by the DyPPiR on the model but can also include the very small aerodynamic loads experienced during the wind-off tare runs, are actually slightly different from the wind-off case to the wind-on case. This is due to the small but significant loading effect of the aerodynamic forces and moments on the performance of the DyPPiR. It is important to stress that overall this effect should be small, at least as seen by the DyPPiR, since the DyPPiR force capacity is much much larger than the aerodynamic forces generated by the prolate spheroid model. However small these inertial loads are, it is also important to remember that they are *inputs* to a dynamical system, and that these small changes in the system inputs can have a more visible, amplified effect on the time series of the system output (7). As such, the low frequency oscillations that do corrupt the aerodynamic force and moment signals are relatively small. It is shown in the next section that the way to eliminate these distortions altogether is to design load cells that are very stiff in all modes of vibration (including roll), thus increasing the natural frequency of all modes to the point that damped sine oscillations no longer exist, and all that remains are actual measured loads, be they inertial or aerodynamic.

Several attempts were made to eliminate these distortions from the aerodynamic signals. The response of the load cells was modeled with second-order dynamic system impulse responses, but it was found that these did not come close to adequately modeling the oscillations for the precision required. The distortions in the final signals themselves were modeled as damped sine waves (outputs from a second order system given an impulsive input). These too did not faithfully eliminate the distortion, and required arbitrarily-selected parameters to come even close to matching the distortions. Finally, the wind-on and wind-off data were time-shifted relative to each other, but this also did not eliminate the distortions. The distortions can only be eliminated with properly designed hardware and *not* with any data post-processing.

Despite the presence of these dynamics, the lag in the unsteady forces and moments is due to unsteadiness in the flow. Wetzel (14) shows that the maximum time lag that can be attributed to the balance dynamics is $0.03 \tau'$. The lags in the plots are on the order of one time unit. Therefore, these lags cannot be due to system dynamics and must be due to actual lags in the flow field. This analysis is very important, as it establishes for the first

time a force and moment capability on the DyPPiR that adequately resolves flow-field lags from balance-induced dynamical effects.

It is also desirable to assess the potential impact of added mass forces and moments on the unsteady forces and moments during this maneuver. The force due to added mass is the product of any model acceleration relative to the freestream and some proportion of the mass (or inertia for rotational degrees of freedom) of the air displaced by the model (9). Details of the estimates of the added mass effects are contained in Wetzel (14). It was found that while added mass effects are small, they are at least the order of magnitude of the differences between the steady and unsteady forces and moments. There is an added mass component due to the impulsive accelerations at the beginning and end of the maneuvers. This added mass effect is present in both the wind on and wind off cases, but has a very limited temporal extent (21). The most significant added mass effect felt by the model is a relatively constant force due to the fact that the crossflow velocity is changing (going from zero to some finite value) while it is pitching; this added mass force is present only during the wind-on cases. This change in crossflow velocity is an acceleration and is expressed simply as:

$$\begin{aligned} V(t) &= U_{\infty} \sin(\alpha(t)) \\ V'(t) &= \frac{d\alpha}{dt} U_{\infty} \cos(\alpha(t)) \end{aligned} \quad (6)$$

This is due to a rotation of the free stream relative to the model and is thus present during the entire ramp portion of the maneuver. Since the ramp is at a constant angular rate, there is no similar angular flow acceleration during the maneuver. It is shown in Wetzel (14) that the magnitude of these added mass effects, in terms of non-dimensional normal force coefficients, is $\delta C_{Z, \text{ added mass}} = 0.047$. This is three times the stated uncertainty of 0.015. It is also shown in Wetzel (14) that this acceleration results in a higher normal force than the steady data. This is opposite the trend seen, that is, that the unsteady force is *smaller* than the steady force. Therefore, there are two opposing unsteady components: an added mass effect, which tends to increase the normal force (or equivalently a time lead), and a delayed separation process which tends to decrease the normal force (or introduce a time lag in the flow).

The added mass effect perhaps explains why the lags in the force and moment data are smaller than the lags in the separation location data. The added mass effect is such that a larger, not smaller, normal force should be generated. This is equivalent to the unsteady data leading the steady data, or the added mass resulting in a leading time constant. Using an estimated $\partial C_Z / \partial t'$ slope of 0.11 from Figure 27, a 0.047 positive shift in the

normal force is equivalent to a $0.4 t'$ lead. This may mean the effective force and moment lag of the flow field, minus added mass effects, is higher than the $1 t'$ time unit shown and may be as high as $1.4 t'$ time units. Wetzel (14) also shows that the pitch moment added mass effects are insignificant.

Figure 28 shows the normal force and pitch moment, respectively, for the submarine maneuver. The trends are much less clear in this maneuver than in the pitchup maneuver due to the lower relative aerodynamic forces and moments for this lower-excursion maneuver. Dynamic distortion is much lower at the start of this maneuver due to the lower accelerations imparted at the gentle initiation of this maneuver. However, the accelerations at the end of the maneuver are large and result in a significant stopping oscillation. The lags in the pitch moment are actually larger in this maneuver compared to the pitchup maneuver, but the normal force lags are smaller. However, such distinction in lag magnitude is hampered by the relative level of the force and moment uncertainties.

5.5 Future Improvements

Two main goals remain to be reached before a viable, robust force and moment measurement system is in place on the DyPPiR. The first is to improve signal fidelity. As demonstrated in section 5.2 this can be further improved by reducing the model weight, but will be most improved by increasing the balance stiffness. It was learned in the last generation balance that system stiffness is required in all possible degrees of freedom. In the case of the two-point balance system, a limiting condition was the fact that the load cells were not stiff in roll. During the summer of 1996 custom-designed load cells provided higher stiffness through better geometric design. Also, the strain gages were laid out in such a way as to minimize interactions from any off-axis loads. Wetzel (14) shows that such design changes will result in a load cell two orders-of-magnitude stiffer in all directions than the MLP-50.

As of August of 1996, a new set of load cells embracing these ideas was completed. The new load cells have demonstrated significantly higher roll stiffness through both a wider construction and a wider, 4-point mounting pad that replaces the weak, single-bolt mounting of the MLP-50 load cells. In addition, the low-friction pivots that mount the load cells to the sting were re-designed to be larger, stiffer, more precise, and carry even less friction. Data from this system will be included in Wetzel and Simpson (15).

The second major goal that still needs to be achieved is to obtain all six force and moment components instead of just two. To measure side force and yaw moment in addition to normal force and pitch moment requires twice as many gages, and, more importantly, a

two-degree-of-freedom gimbaled mount for each load cell pair. These are challenging to design on such a small scale, but are achievable. What is more difficult is measuring axial force and roll moment without compromising balance stiffness. The load cells are oriented longitudinally relative to the model, so all forces and moments measured perpendicular to the longitudinal axis are inherently stiff as shown in the DTRC system (3). The two components parallel to such an axis can not similarly benefit from the two-point configuration.

6. Discussion

The two maneuvers presented here represent non-dimensionally slow maneuvers, and thus the unsteadiness is subtle. In all cases the unsteady data lag the steady data. The separation locations lag both in formation and migration but do converge to the steady state case after the end of the maneuver (see Figure 15 and Figure 18). During the maneuver, the separations can lag the steady separations by as much as 15° . Perhaps more important is the associated time lag, which can range from 1.5 to 4.5 time units. These time lags are neither identical nor constant for each model location, thus pointing to the overwhelming complexity not only of a three dimensional separation but also of its time-dependent formation. Pending the development of a more robust, next-generation separation location system based on these findings, one could study in great detail the parametric effects of pitch rate, pitch range, pitch direction (up or down), Reynolds number, center of rotation, and even pitch maneuver shape (such as using the submarine maneuver or any imaginable maneuver) on the separation formation and migration. Such data could lead to dynamical models of unsteady separation on axisymmetric bodies.

The lagging separation locations implies lagging normal force and pitch moment. The force and moment data obtained with the two point balance supports these trends (Figure 27 and Figure 28). The force and moment lags are much smaller than the separation location lags in general. This may be due to the fact that the majority of the normal force and pitch moment is generated by the attached nose flow, which also exhibited the least amount of flow unsteadiness. So while the crossflow separation on the rear two-thirds of the model is significantly affected by the model motion, the delay in separation at the tail plays less of a role in lagging the forces and moments. Also, added mass effects contribute to lower time lags. Again, more robust systems will allow one to determine not only whether the unsteady aerodynamics lead or lag the steady data, but will also bring out more specific details about the processes involved and point to improved dynamical models.

7. Conclusions

Some features of steady and unsteady flow over a 6:1 prolate spheroid were measured experimentally. All tests were conducted at $Re = 4.2$ million. Trip strips were located on the model at $x/L=0.20$. The steady flowfield was established with surface pressure measurements, hot-film surface skin-friction measurements, and force and moment measurements. Hot-film and force and moment measurements were made on the model in two maneuvers. The hot-film data showed definite lags in the formation and migration of the separation line for the pitchup maneuver, but showed much weaker trends for the submarine maneuver due to the much weaker separations at the lower angles of attack. Separation formation occurred 1.5 to 4.5 time units later during the maneuvers compared to the steady data. An ultra-stiff, two point balance was successfully implemented for measuring unsteady force and moments, along with a very light-weight composite model. The force and moment data again shows definite lags at the higher angles of attack of the pitchup maneuver in both normal force and pitch moment, but shows only pitch moment lags during the submarine maneuver.

Acknowledgements

The authors are grateful for the years of encouragement and support by James A. Fein of the Office of Naval Research, and contracts N00014-87-K-0816, N00014-91-J-1732, and N00014-95-I-0101. We would also like to acknowledge Jon L. Fleming for his assistance in running the DyPPiR and the Wind Tunnel.

References

1. Ahn, S., Choi, K. Y., and Simpson, R. L., "The Design and Development of a Dynamic Plunge-Pitch-Roll Model Mount", AIAA-89-0048, AIAA 27th Aerospace Sciences Meeting, Reno, NV, 1989.
2. Ahn, S., *An Experimental Study of Flow Over a 6 to 1 Prolate Spheroid at Incidence*, Dissertation, Virginia Polytechnic Institute and State University Aerospace Engineering Department, 1992.
3. Bedel, J., David Taylor Research Center, Bethesda, MD, Private Discussion, 1996.
4. Bellhouse, B. J., and Schultz, D. L., "Determination of Mean and Dynamic Skin Friction Separation and Transition in Low-Speed Flow with a Thin-Film Heated Element", *Journal of Fluid Mechanics*, vol. 24, part 2, pp. 379-400, 1966.
5. Chesnakas, C. J., and Simpson, R. L., "A Detailed Investigation of the 3-D Separation about a 6:1 Prolate Spheroid at Angle of Attack", AIAA-96-0320, 34th Aerospace Sciences Meeting and Exhibit, Reno, NV., 1996.
6. Choi, K. and Simpson, R. L., *Some Mean Velocity, Turbulence, and Unsteadiness Characteristics of the VPI&SU Stability Wind Tunnel*, Virginia Polytechnic Institute and State University, Aerospace and Ocean Engineering Dept. Report VPI-AOE-161, 1987.
7. Doebelin, Ernest O., *Measurement Systems: Application and Design*, McGraw-Hill Publishing Company, New York, N.Y., 1990.
8. Etkin, B., *Dynamics of Atmospheric Flight*, John Wiley & Sons, New York, N.Y., 1972.
9. Lamb, H., *Hydrodynamics*, Dover Publications, New York, N.Y., p. 155, 1945.
10. McCroskey, W. J., "Some Current Research in Unsteady Fluid Dynamics", *Journal of Fluids Engineering*, Vol. 99, pp. 8-39, 1977.
11. Miller, James A., "A Simple Linearized Hot-Wire Anemometer", *Journal of Fluids Engineering*, December, 1976.
12. Roback, V. E., "Design and Development of a Graphite/Epoxy 6:1 Prolate Spheroid Wind Tunnel Model for Use in Time-Dependent Force and Moment Tests", 1995 AIAA Mid-Atlantic Student Conference, submitted to DTIC for distribution, 1995.
13. Simpson, R.L., Walker, D.A., and Shinpaugh, K.A., *Description of a 1000 Sensor Constant Current Anemometer System for Locating Three-Dimensional Turbulent Boundary Layer Separations*, Virginia Polytechnic Institute and State University, Aerospace and Ocean Engineering, Report VPI-AOE-185, 1991.
14. Wetzel, T. G., *Unsteady Flow Over a 6:1 Prolate Spheroid*, Dissertation, Virginia Polytechnic Institute and State University, Aerospace and Ocean Engineering, 1996.
15. Wetzel, T.G. and Simpson, R.L., "Unsteady Three-Dimensional Cross Flow Separation Measurements on a Prolate Spheroid Undergoing Time-Dependent Maneuvers", AIAA-97-0618, AIAA 35th Aerospace Sciences Meeting, Reno, NV, 1997.

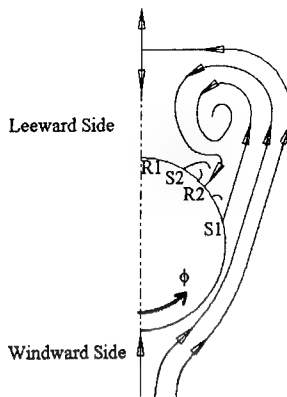


Figure 1. Simplified flow separation topology for the secondary streamlines in a plane normal to the major axis of an axisymmetric body. S1 and S2 refer to primary and secondary separation locations, respectively, and R1 and R2 refer to primary and secondary reattachment locations.

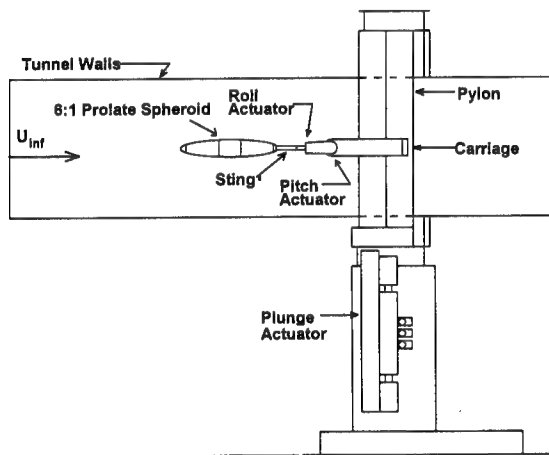


Figure 2. Dynamic Plunge-Pitch-Roll (DyPPiR) Model Mount installed in wind tunnel.

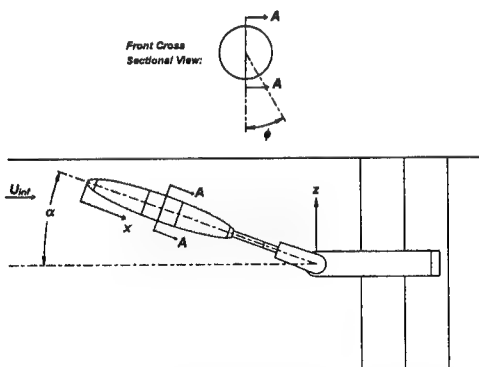


Figure 3. Coordinate Nomenclature. x is measured from the nose; ϕ is the circumferential location measured from the windward line of symmetry; z is the plunge ordinate; and α is the pitch angle and equivalently the model center angle of attack.

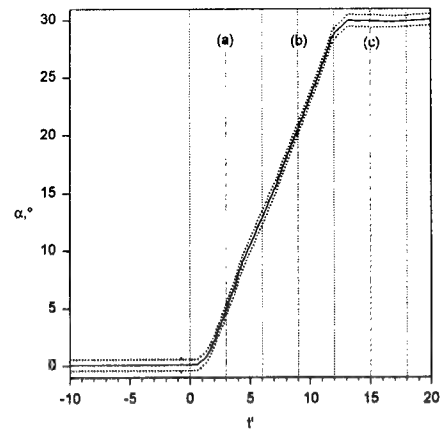


Figure 4. Pitch-up maneuver pitch angle position feedback. Dotted lines represent 20:1 odds positional repeatability.

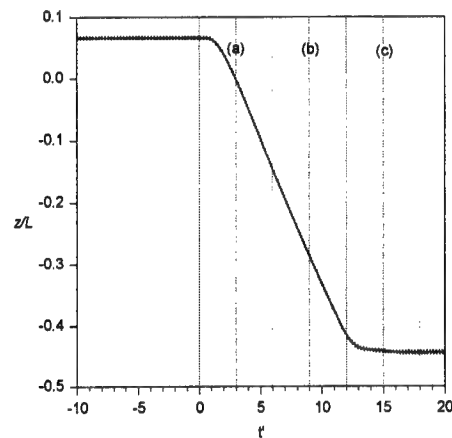


Figure 5. Pitch-up maneuver plunge position feedback. Dotted lines represent 20:1 odds positional repeatability.

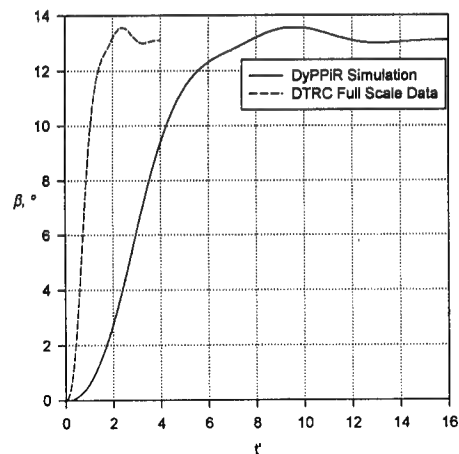


Figure 6. Submarine maneuver pitch angle command signal compared to data from DTMB sideslip data.

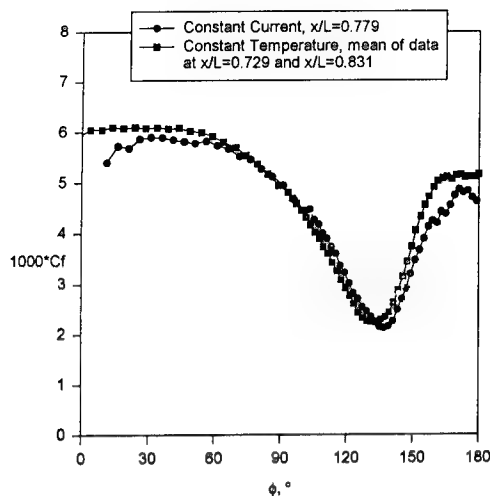


Figure 7. Comparison of steady flow skin friction magnitudes (both constant temperature and constant current) at $x/L=0.77$, $\alpha=10^\circ$, and $Re=4.2$ million.

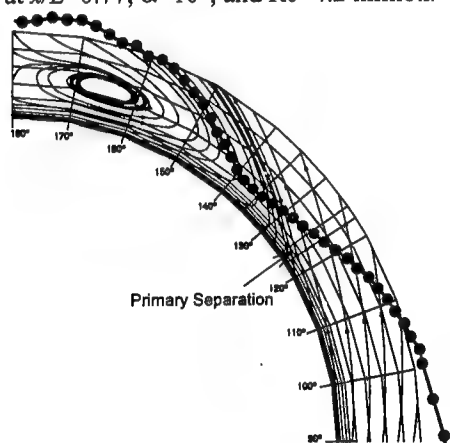


Figure 8. Steady flow skin friction values superimposed on secondary streamlines from Chesnakas and Simpson (5) at $x/L=0.77$ and $\alpha=10^\circ$.

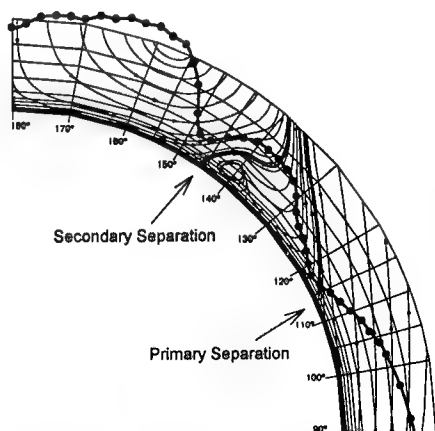


Figure 9. Steady flow skin friction values superimposed on secondary streamlines from Chesnakas and Simpson (5) at $x/L=0.77$ and $\alpha=20^\circ$.

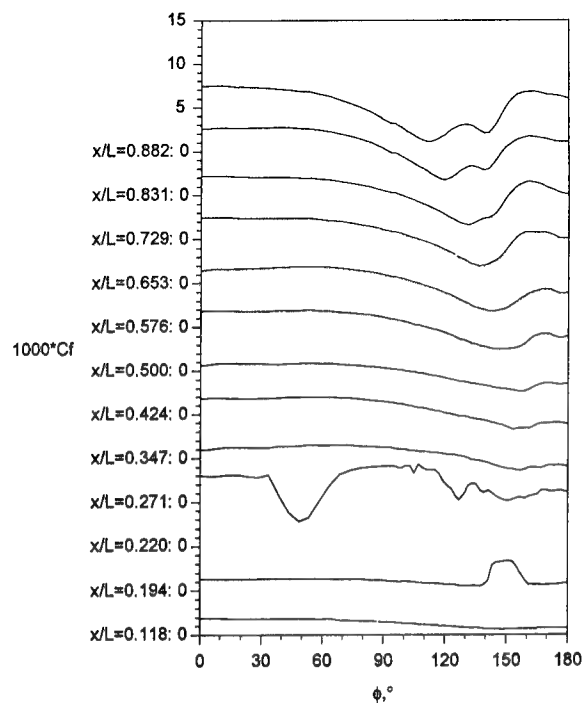


Figure 10. Steady flow Cf vs. ϕ for all x/L , $\alpha=15.2^\circ$.

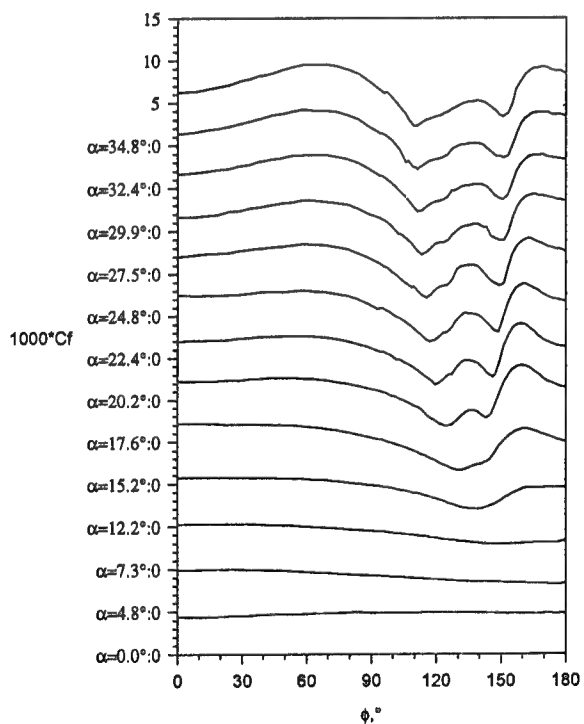


Figure 11. Steady flow Cf vs. ϕ for all α , $x/L=0.729$.

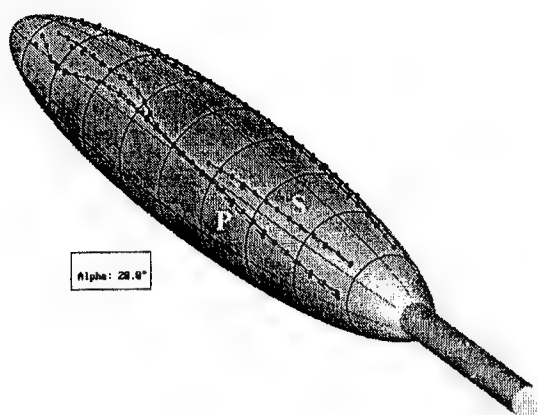


Figure 12. Comparison of constant current and constant temperature separation location topology on leeside for $\alpha=20^\circ$. Solid lines are steady constant current data. Dashed lines are steady constant temperature data. "P" indicates primary separation, while "S" indicates secondary separation.

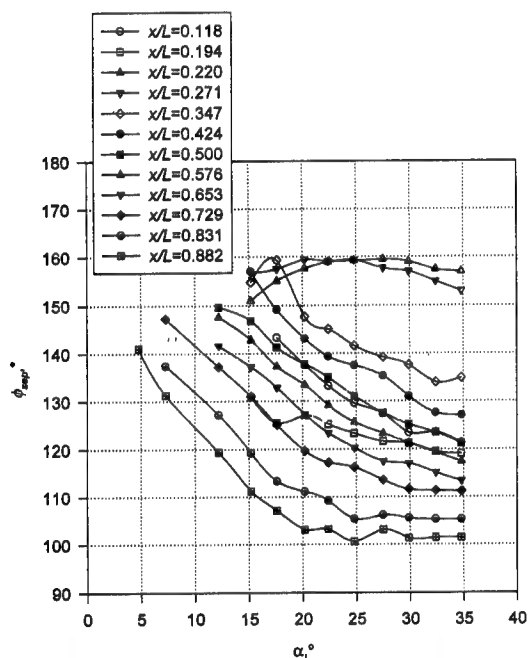


Figure 13. Constant temperature primary separation locations for various x/L stations sensors as a function of angle of attack for steady flow.

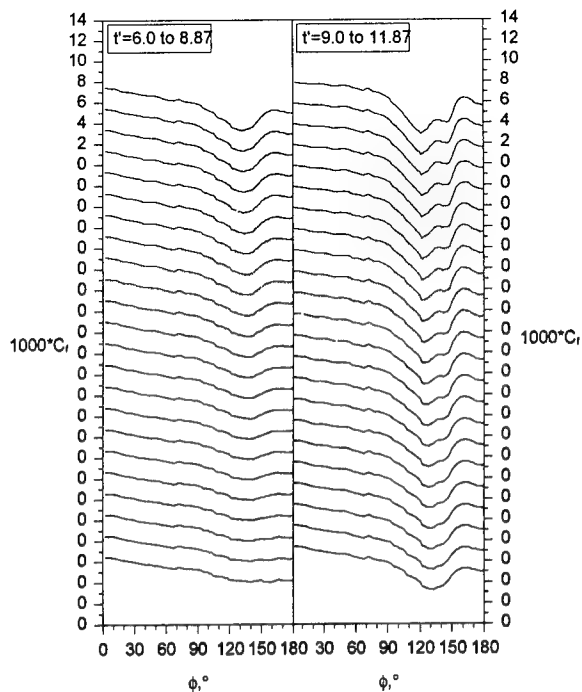


Figure 14. Pitch-up maneuver time development of C_f vs. ϕ for $x/L=0.729$. Times in columns delineated as section "b" in Figure 4 and Figure 5.

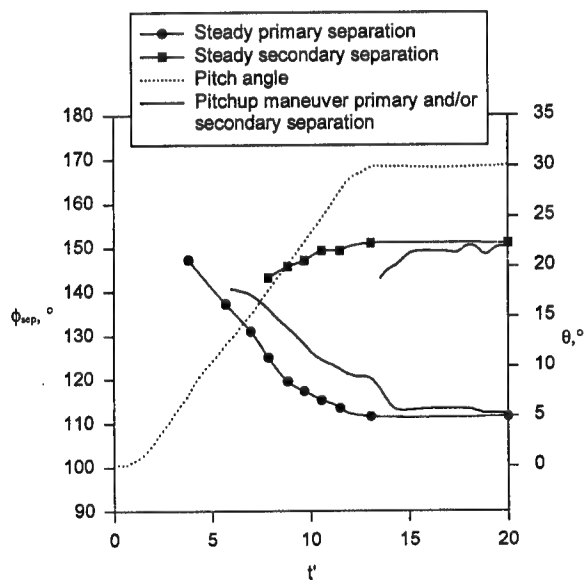


Figure 15. Separation position versus time for pitch-up maneuver at $x/L=0.729$ compared with quasi-steady separation positions.

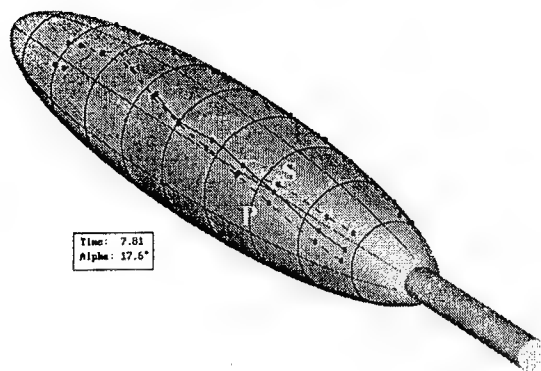


Figure 16. Comparison of steady and unsteady separation lines at $\alpha=17.6^\circ$. Dashed lines are equivalent steady separation lines, solid lines are instantaneous separation lines. "P" indicates primary separation, while "S" indicates secondary separation.

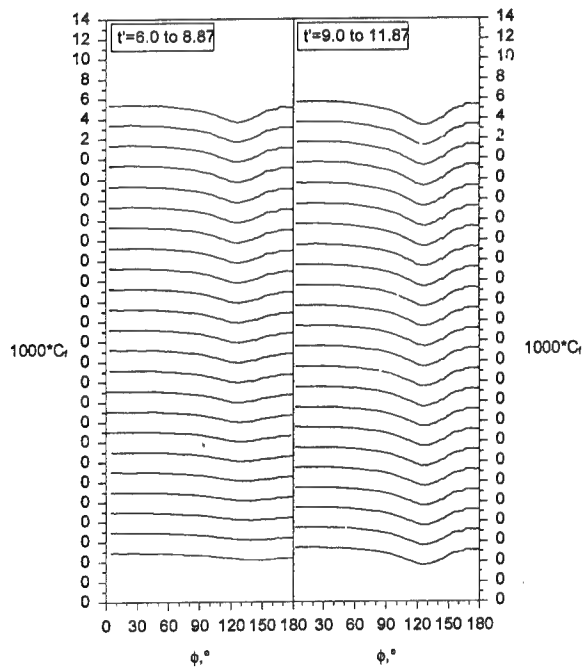


Figure 17. Submarine maneuver time development of C_f vs. ϕ for $x/L=0.831$.

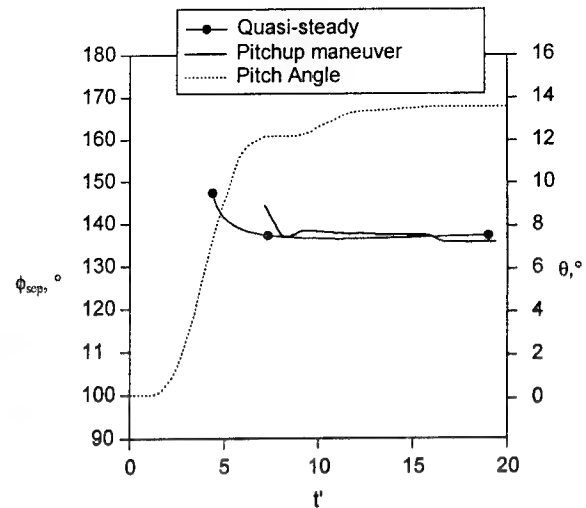


Figure 18. Separation position versus time for submarine maneuver at $x/L=0.729$ compared with quasi-steady separation positions.

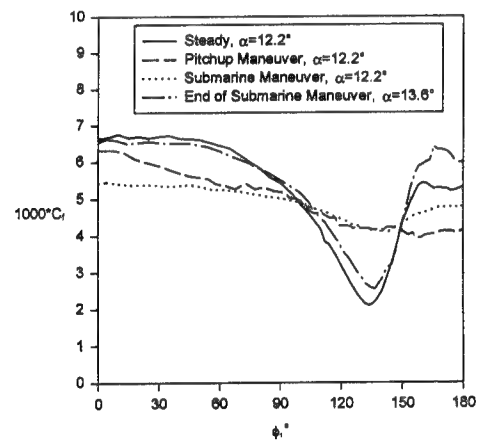


Figure 19. Comparison of wall shear distribution at $x/L=0.729$ for steady data, pitchup maneuver, and submarine maneuver at $\alpha=12.2^\circ$.

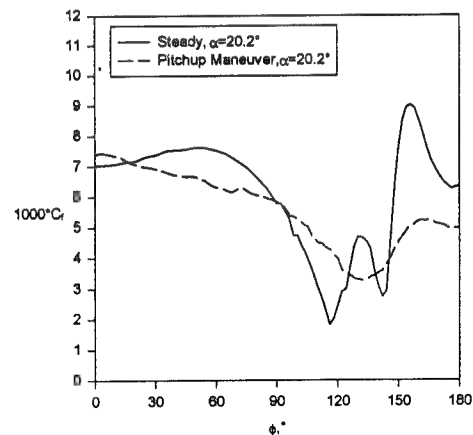


Figure 20. Comparison of wall shear distribution at $x/L=0.729$ for steady data and pitchup maneuver at $\alpha=20.2^\circ$.

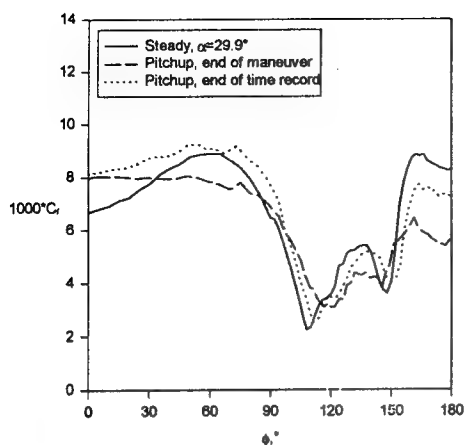


Figure 21. Comparison of wall shear distribution at $x/L=0.729$ for steady data and pitchup maneuver at $\alpha=29.9^\circ$.

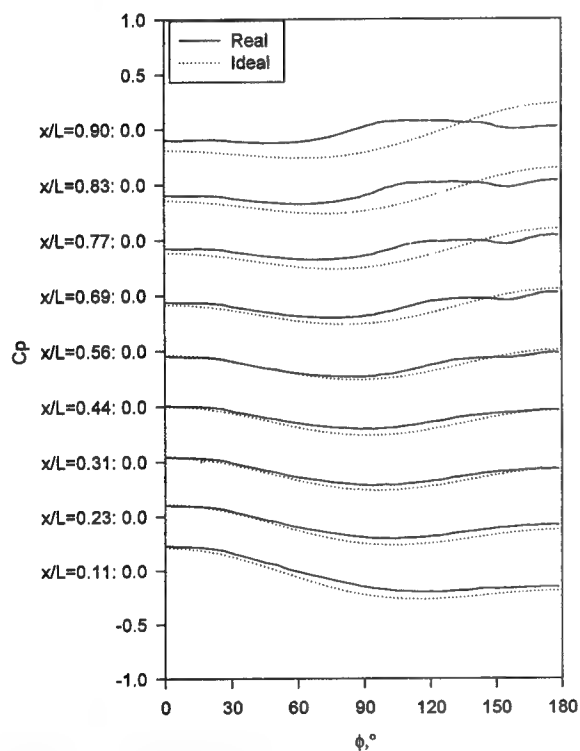


Figure 22. Steady C_p vs. ϕ for all x/L , $\alpha=14.9^\circ$. Solid lines are measurements, while dotted lines are potential flow results.

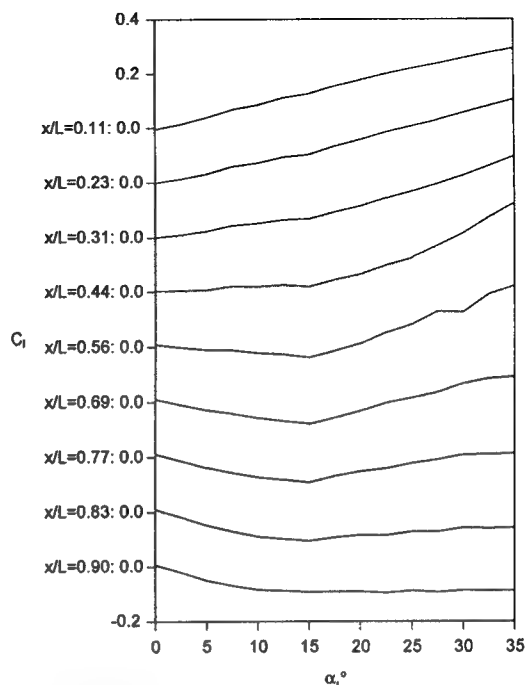


Figure 23. Steady sectional lift coefficients versus angle of attack for all x/L .

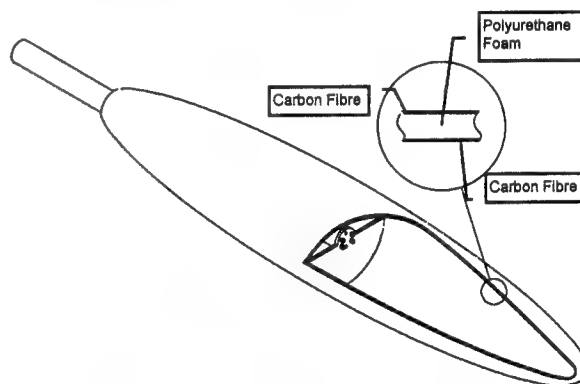


Figure 24. Lightweight model construction.

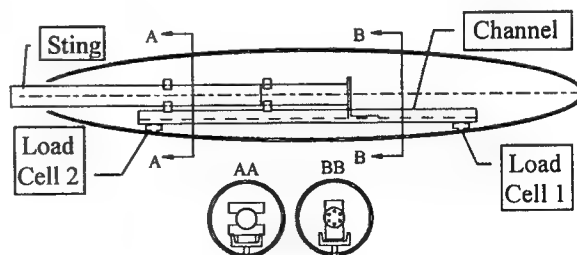


Figure 25. Two point balance.

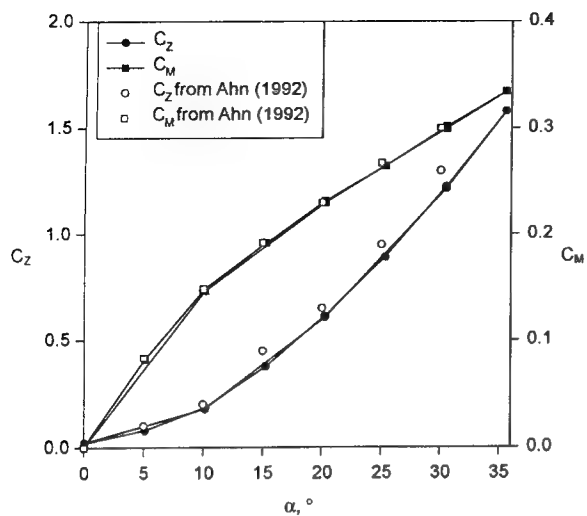


Figure 26. Steady normal force and pitch moment on prolate spheroid at $Re = 4.2$ million for various angles of attack. Compared with data from Ahn (1992).

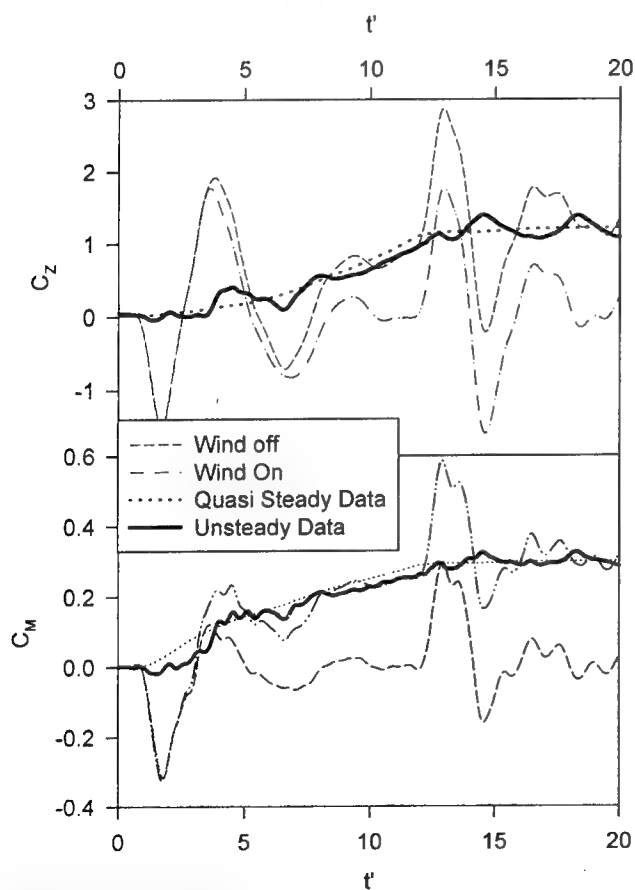


Figure 27. Unsteady normal force and pitch moment for pitchup maneuver.

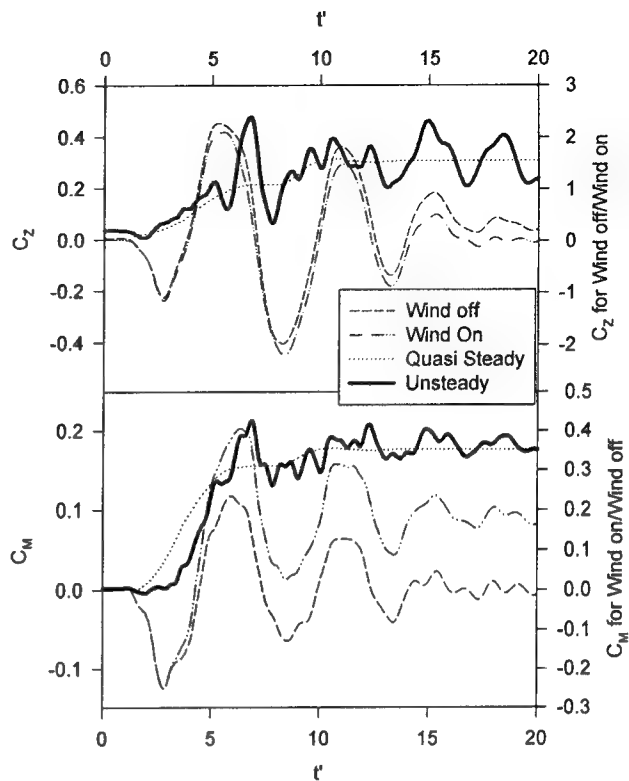


Figure 28. Unsteady normal force and pitch moment for submarine maneuver.

Time-Domain Calculations of First- and Second-Order Forces on a Vessel Sailing in Waves

L. Sierevogel, A. Hermans (Delft University of Technology, The Netherlands),
R. Huijsmans (Marine Research Institute, The Netherlands)

Abstract

In this paper we solve the time-dependent linear equations which describe the interaction between a LNG carrier at service speed and the waves. Our numerical algorithm is a time-domain model, solving the linear boundary conditions on the hull and the free surface, and the Laplace equation by using Green's theorem. As absorbing boundary condition we use a semi-discrete DtN-method. To compute the second-order wave drift forces or added resistance of the LNG carrier, we extend our algorithm to higher speed. Results of our computations are compared with measurements and strip theory results.

Nomenclature

A	added mass
B	damping
$\partial S, \partial \mathcal{D}$	boundary of interior, exterior
\vec{F}_1, \vec{F}_2	first- and second-order forces
Fn	Froude number
G	Green's function
g	gravitational acceleration
h	depth of the water
k	wave number
\vec{M}_1, \vec{M}_2	first- and second-order forces
n	normal
t	time
Δt	time step
U	uniform velocity of the current
\vec{x}, x, y, z	coordinate system

ζ_a	wave height due to incoming wave
ζ_r	linearized relative wave height
$\vec{\xi}, \xi, \eta, \zeta$	second coordinate system G
ρ	density of the fluid
Φ	total potential
ϕ	unsteady potential
$\bar{\phi}$	steady potential
ϕ_{inc}	potential due to incoming wave
ω	frequency of encounter
ω_0	frequency

Introduction

In recent years many studies have been carried out solving the unsteady ship motion problem. This problem is very important in predicting the behaviour of a ship in sea-keeping, which includes the interaction between waves and the velocity of a ship. Computing this interaction can be done by using the frequency domain or the physical time domain. The disadvantage of the studies in the frequency domain is their restriction to harmonic waves and their inability to use real time wave elevations for the calculation of the motion response. In the time domain we can also handle non-harmonic waves and it is not necessary to implement the conditions dependent on every frequency explicitly.

Prins [6] has developed a two- and three-dimensional time-domain algorithm to compute the behaviour of a cylinder, a sphere and a commercial tanker in current and waves. The results

were satisfactory. We have extended this method with, among other things, a frequency independent absorbing boundary condition [8].

In this paper we apply the method to a LNG carrier at service speed. The forward speed of the commercial tanker considered up to now is very low, the maximum Froude number is 0.018, i.e. 2 knots, while the usual speed of a 125,000m³ LNG carrier is about 20 knots (i.e. Froude number is 0.2). This fact causes some problems in our algorithm. We study increasing speed and the effect on our absorbing boundary condition. To remove the instabilities on the free-surface due to increasing forward speed, we introduce upwind discretization. Both cases were done in the two- and three-dimensional algorithm.

In the first section we give the main idea of the Prins' algorithm and our extension to a frequency independent boundary condition. In the second section we study increasing speed and the effect on our algorithm. In the third section results are presented for a 125,000m³ LNG carrier, at deep water. We will calculate the drift force or added resistance not only for low forward speed, but also the added resistance for higher forward speed has been studied. In order to check the method, we compare our results with measurements of Wichers [11] and with strip theory results [1, 2]. The last section we give the conclusions and ideas for further research.

1 Time-domain algorithm

The time-domain algorithm given below is based on the one given by Prins [7].

The physical fluid domain is an infinite (or large) domain. The computational domain cannot be infinite, so we have to introduce artificial boundaries and proper boundary conditions. In the literature several methods have been proposed to absorb free surface waves. On the basis of a literature search, Prins decided to use an extension of the Sommerfeld radiation condition for two families of waves. The disadvantage of this Sommerfeld condition is that it is dependent on the wave frequency, so it cannot handle non-harmonic waves, and on the forward velocity.

Keller and Givoli [3] introduce a semi-discrete DtN-method, using an artificial boundary, dividing the original domain into a computational and a residual domain (the interior and exterior). In our method we use a three-dimensional boundary condition independent of the wave frequency, using the idea of the Givoli's method with

Prins' algorithm. In the interior domain we use the same mathematical model as Prins [7] use but we do not implement a Sommerfeld radiation condition on the artificial boundary.

1.1 The interior problem

We consider a vessel sailing with an uniform velocity U in the negative x -direction, or an uniform current with velocity U is directed in the positive x -direction. Regular waves are travelling in the water-surface in a direction which makes an angle β with the positive x -direction, see figure 1. The coordinate system is chosen such that the undisturbed free surface coincides with the plane $z = 0$ and the centre of the gravity of the hull is on the z -axis, with z pointing upwards. The hull is free to move in all directions and to rotate around the main axes.

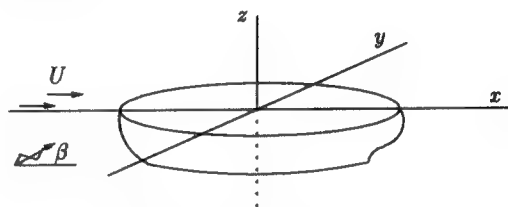


FIGURE 1: The geometry

We assume the following restrictions: there is no viscosity, the fluid is incompressible and homogeneous, and the flow is irrotational. We introduce the velocity potential Φ , which has to satisfy the Laplace equation

$$\nabla^2 \Phi = 0. \quad (1)$$

By using the dynamic and kinematic conditions and splitting the potential into a steady and an unsteady part, like

$$\Phi(\vec{x}, t) = \bar{\Phi}(\vec{x}) + \phi(\vec{x}, t),$$

we get the linearized free-surface condition on the undisturbed free surface

$$\phi_{tt} + g\phi_z + 2\vec{\nabla}\bar{\Phi} \cdot \vec{\nabla}\phi_t + (\bar{\Phi}_{xx} + \bar{\Phi}_{yy})\phi_t = 0 \quad \text{at } z = 0, \quad (2)$$

with subscripts denoting the partial derivative. In contrast with the two-dimensional algorithm, we do not include terms of $\mathcal{O}(U^2)$. Including them would cause us to calculate higher derivatives of the unsteady potential at the free surface. This would increase the computation time, because the need of the very fine mesh.

On the ship hull we have the linearized version of the body boundary condition

$$\frac{\partial \phi}{\partial n} = \frac{\partial \vec{\alpha}}{\partial t} \cdot \vec{n} - \vec{\alpha} \cdot \left(\vec{n} \cdot \vec{\nabla} \right) \vec{\nabla} \phi + \vec{n} \cdot \left(\vec{\nabla} \phi \cdot \vec{\nabla} \right) \vec{\alpha}$$

with $\vec{\alpha}$ the displacement vector of the ship, given by

$$\vec{\alpha} = \vec{X} + \vec{\Omega} \times \vec{x}$$

and \vec{n} the normal pointing out of the fluid domain, see Timman [9]. The bottom is a rigid wall, so we submit the potential on the bottom, ϕ , to the condition

$$\frac{\partial \phi}{\partial n} = 0. \quad (3)$$

The steady potential is represented by the double-body potential.

So far we can only say about the potential on the artificial boundary that it satisfies the Laplace equation and that it remains finite when we take the boundary at infinity.

To solve the interior problem, we introduce a Green's function, G , satisfying equations (1) and (3).

$$4\pi G(\vec{x}, \vec{\xi}) = -\frac{1}{|\vec{x} - \vec{\xi}|} - \frac{1}{|\vec{x} - \vec{\xi}'|} = -\frac{1}{r} - \frac{1}{r_2}, \quad (4)$$

where ξ' is the image of ξ with respect to the bottom. By using Green's second theorem it is possible to write the interior problem as

$$D\vec{\psi}(t) = E\vec{\psi}_n(t), \quad (5)$$

with D and E matrices built up by the Green's function and its derivative. And with $\vec{\psi}$ a vector $(\phi_f | \phi_H | \phi_B)$, containing the potential on the free surface, on the hull and on the artificial boundary. To solve this integral equation we discretize the boundaries by dividing these into panels. We assume that the potential has a constant value on such a panel. Prins' approach consists of two steps leading to a Fredholm integral equation of the second kind. Firstly, the free-surface condition(2) and the second-order Sommerfeld radiation condition are discretized with respect to t , where an implicit scheme is used for the time derivation. Secondly, ϕ_n is expressed in ϕ and its tangential derivative along the boundaries, while at the object ϕ_n is supposed to be known. Discretization of the integral equation leads to a matrix equation for the unknown vector $\vec{\psi}$

$$D_1 \vec{\psi}^{n+1} = D_2 \vec{\psi}^n + D_3 \vec{\psi}^{n-1} + \vec{f}^{n+1}, \quad (6)$$

with superscripts denoting the time level and \vec{f} a time-dependent vector. The matrices D_i are built up by the Green's function, its derivative and the surface conditions. In our approach we make use of the same algorithm as developed by Prins, except for the boundary B . Experience has taught that the implementation of the Sommerfeld condition on the outer boundary B is efficient if B is taken at a distance of about three wavelengths, while the coefficients for the two families of waves are dependent on the frequency. Hence, the matrix has to be updated for each frequency. Our purpose is to obtain a genuine time method, where the matrix is independent of the frequency.

1.2 The exterior problem

To solve the exterior problem in the three-dimensional case we developed a special Green's function, the same way as we did for two dimensions, see Sierrevogel [8]. The advantage of using our algorithm compared to using the conventional time-domain Green's function in the exterior, is that it will be easier to implement the effects of higher speed, because the boundaries of the exterior are already divided into panels.

In our first two-dimensional set up, we assumed the interior to be moving together with the object, while the exterior was fixed to the earth. To solve the problem in the interior as an overall matrix equation, we applied Green's theorem on the domain between the boundaries, see figure 2.

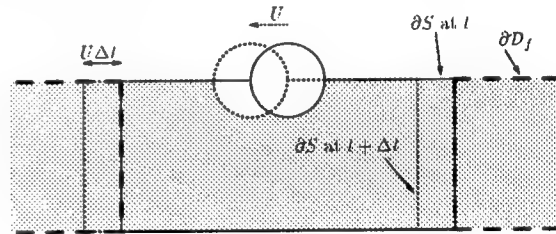


FIGURE 2: The 2-D geometry

In our new set up we assume the exterior also to be moving together with the object, because it is complicated to apply Green's theorem on the domain between the boundaries in the three-dimensional case and an advantage of the new algorithm is that it will be easy to implement the effects of the double-body potential. In the exterior we get the following linearized free surface condition

$$\phi_{tt} + g\phi_z + 2U\phi_{xt} = 0 \quad \text{at } z = 0. \quad (7)$$

Where $\phi(\vec{x}, t)$ is the unsteady potential and the steady potential is approximate by the undisturbed flow potential Ux . We use the following discretizations for the time derivatives

$$\begin{aligned}\phi_{tt}|^{n+1} &= \frac{2\phi^{n+1} - 5\phi^n + 4\phi^{n-1} - \phi^{n-2}}{(\Delta t)^2} \\ &+ \mathcal{O}((\Delta t)^2) \\ \phi_t|^{n+1} &= \frac{5\phi^n - 8\phi^{n-1} + 3\phi^{n-2}}{2\Delta t} \\ &+ \mathcal{O}((\Delta t)^2),\end{aligned}$$

with superscripts denoting the time level. Now we may write equation (7)

$$\begin{aligned}\phi_z^{n+1} + \mu\phi^{n+1} &= \frac{\mu}{2}(5\phi^n - 4\phi^{n-1} + \phi^{n-2}) - \\ &- \mu \frac{U\Delta t}{2}(5\phi_x^n - 8\phi_x^{n-1} + 3\phi_x^{n-2}),\end{aligned}\quad (8)$$

with $\mu = \frac{2}{g(\Delta t)^2}$. The last term between brackets is new compared to the old set up, the rest is exactly the same. If we also take into account the double-body potential the right-hand side will then also contain terms of that double-body potential. We use an upwind discretization scheme calculate the numerical differentiation of the potential (see section 2.1), and solve our problem by using Green's theorem, the same way we did in our first set up.

To use Green's theorem in the exterior problem, we introduce a Green's function, G , which satisfies

$$\begin{aligned}G_z + \mu G &= 0 & \text{at } z = 0 \\ \nabla^2 G &= 0 & \vec{x}, \vec{\xi} \in \mathcal{D} \\ G_z &= 0 & \text{at } z = -h \\ G = 0; \quad G_n &= 0 & \lim \vec{r} \rightarrow \infty.\end{aligned}\quad (9)$$

The last relation is the only physical radiation condition. Now we get for the potential in the exterior

$$\begin{aligned}\delta\phi^{n+1}(\vec{x}) &= \\ &\int_{\mathcal{B}} \left(\phi^{n+1}(\vec{\xi}) \frac{\partial G}{\partial n_{\xi}}(\vec{x}, \vec{\xi}) - G(\vec{x}, \vec{\xi}) \frac{\partial \phi^{n+1}}{\partial n_{\xi}}(\vec{\xi}) \right) dz_{\xi} \\ &- \mu \int_{\partial \mathcal{D}_f} G(\vec{x}, \vec{\xi}) \tilde{\phi}(\vec{\xi}) dx_{\xi},\end{aligned}\quad (10)$$

with

$$\delta = \begin{cases} 1 & \vec{x} \in \mathcal{D} \cup \partial \mathcal{D}_f \\ \frac{1}{2} & \vec{x} \in \partial \mathcal{B} \\ 0 & \text{elsewhere} \end{cases},$$

and

$$\begin{aligned}\tilde{\phi} &= \frac{5}{2}\phi^n - 2\phi^{n-1} + \frac{1}{2}\phi^{n-2} - \\ &- \frac{U\Delta t}{2}(5\phi_x^n - 8\phi_x^{n-1} + 3\phi_x^{n-2}),\end{aligned}$$

and $\partial \mathcal{D}_f$ the free surface of the exterior. We need to mention that the normal derivative on the boundary in the exterior is the negative of that of the interior. By analogy with Wehausen et al.[10] we derive a Green's function, which satisfies (9), for infinite deep water

$$4\pi G = -\frac{1}{r} - \int_0^\infty \frac{k - \mu}{k + \mu} e^{kz} J_0(kX) dk,$$

and for water with a finite depth

$$4\pi G = -\frac{1}{r} - \frac{1}{r_2} - \int_0^\infty F \cdot J_0(kX) dk,$$

with

$$F = \frac{2(k - \mu)e^{-kh} \cosh k(z + h) \cosh k(\zeta + h)}{k \sinh kh + \mu \cosh kh},$$

with X the horizontal distance and $Z = z + \zeta$. Here J_0 denotes the Bessel function of the first kind, order zero. These Green's functions can be rewritten to functions more friendly to computed numerically, the same way Noblesse [5] and Newman [4] rewrite their functions.

By using Green's theorem we have to integrate the Green's function with respect to the artificial boundary or the free surface of the exterior. We write Green's theorem like

$$\mathbf{D}_{\mathcal{D}} \vec{\psi}_{\mathcal{B}} = \mathbf{E}_{\mathcal{D}} \vec{\phi}, \quad (11)$$

with $\mathbf{D}_{\mathcal{D}}$ a matrix built up by the exterior Green's function and its derivative and with $\vec{\psi}_{\mathcal{B}}$ the vector $(\phi_{\mathcal{B}} | \phi_{\mathcal{B}_n})$ and $\mathbf{E}_{\mathcal{D}} \vec{\phi}$ is the last term of (10).

1.3 The total problem

Hence, combining equation(6) and (11), we are able to write the interior problem as an overall matrix equation, like equation(6),

$$\mathbf{D}_1 \vec{\psi}^{n+1} = \mathbf{D}_2 \vec{\psi}^n + \mathbf{D}_3 \vec{\psi}^{n-1} + \vec{f}^{n+1} + \mathbf{E}_{\mathcal{D}} \vec{\phi}, \quad (12)$$

with $\vec{\psi}$ a vector containing $(\phi_f | \phi_{\mathcal{H}} | \phi_{\mathcal{B}} | \phi_{\mathcal{B}_n})$.

We now derived an algorithm to compute the potential, knowing the potential due to the diffracted waves, we are able to compute the surface elevation, so we can look at the reflections. Also we are able to compute the hydrodynamic coefficients, like added mass, added damping and the first- and second-order forces.

The developed algorithm is tested on a two- and three dimensional test-problem, i.e. an cylinder of infinite length and a sphere. The results agreed well with known results from literature and the method turned out to be very efficient and accurate. The boundary condition absorbs the outgoing waves. The reflections due

to the artificial boundary are very small, less than $\frac{1}{2}\%$ of the total surface elevation, when the boundary is one wavelength away from the object. The method decreases computer time compared to the method using the Sommerfeld radiation condition, when computing the behaviour of an object in harmonic waves. Firstly the boundary will be closer to the object and secondly it is not necessary to implement the conditions dependent on every frequency explicitly. We are also able to use a step-response function to calculate the hydrodynamic coefficients and drift forces.

Also the calculations of the hydrodynamic coefficients and drift forces of a commercial tanker agreed well with measurements. The forward speed of the commercial tanker is very low, the maximum Froude number is 0.018, i.e. 2 knots. The service speed of the LNG-carrier causes some numerical problems in our algorithm. These are treated in the section 2.

1.4 Movement and forces

To compute the drift forces, we first have to compute the first-order forces and the movement of the ship.

Because the tanker is free to move in all six possible directions, both the force and the moment are needed to calculate the linear movement of the hull. This first-order force is given by

$$\vec{F}_1 = \rho \int_{\mathcal{H}} \left(\frac{\partial \phi}{\partial t} + \vec{\nabla} \phi \cdot \vec{\nabla} \bar{\phi} \right) \vec{n} ds$$

where ϕ is the potential due to the incoming and the diffracted wave, as the motion of the ship is yet unknown. For the moment we have

$$\vec{M}_1 = \rho \int_{\mathcal{H}} \left(\frac{\partial \phi}{\partial t} + \vec{\nabla} \phi \cdot \vec{\nabla} \bar{\phi} \right) \vec{x} \times \vec{n} ds$$

If we do not consider incoming waves but forced oscillation of the ship, we can calculate the added mass and damping coefficients by fitting the force and moment to the acceleration and the velocity:

$$F_{1i} = -A_{ij} \frac{\partial^2 \vec{x}_j}{\partial t^2} - B_{ij} \frac{\partial \vec{x}_j}{\partial t}$$

This expression gives the force in direction i due to a motion in direction j . Note that there is no summation over the index j . For the moment an equivalent formula holds.

The movement of the ship can then be calculated by solving the following set of differential equations:

$$\mathbf{M} \frac{\partial^2 \vec{Y}}{\partial t^2} + \mathbf{A} \frac{\partial \vec{Y}}{\partial t} + \mathbf{B} \vec{Y} + \mathbf{C} \vec{Y} = \mathcal{F}_{1i} \quad i = 1, \dots, 6 \quad (13)$$

with $\mathbf{Y}^T = (X_1, X_2, X_3, \Omega_1, \Omega_2, \Omega_3)$. The mass matrix \mathbf{M} is diagonal and consists of the mass and the relevant moments of inertia. \mathcal{F} is the force or the moment, whatever is appropriate. The non-zero elements of \mathbf{C} are

$$C_{33} = \rho g \int_D dA$$

$$C_{35} = C_{53} = -\rho g \int_D x dA$$

$$C_{44} = \rho g (z_b - z_g) V + \rho g \int_D y^2 dA$$

$$C_{55} = \rho g (z_b - z_g) V + \rho g \int_D x^2 dA$$

with D the deck of the hull.

Now that equation (13) enables us to calculate the movement of the ship, we can solve the equations for the total unsteady potential. Then the averaged second-order force and moment can be calculated by the formulas as derived in [6]:

$$\begin{aligned} \langle \vec{F}_2 \rangle &= \vec{\Omega} \times \left(\mathbf{M} \frac{\partial^2 \vec{X}}{\partial t^2} \right) - \begin{pmatrix} 0 \\ 0 \\ \Omega_1 \Omega_3 C_{35} \end{pmatrix} \\ &- \int_H \rho \vec{\alpha} \cdot \vec{\nabla} \left(\frac{\partial \phi}{\partial t} + \vec{\nabla} \bar{\phi} \cdot \vec{\nabla} \phi \right) \vec{n} dA \\ &- \int_H \frac{1}{2} \rho |\vec{\nabla} \phi| \vec{n} dA + \int_{wl} \frac{1}{2} \rho g \zeta_r^2 \vec{n} dl \quad (14) \end{aligned}$$

$$\begin{aligned} \langle \vec{M}_2 \rangle &= \vec{\Omega} \times \left(\mathbf{I} \frac{\partial^2 \vec{\Omega}}{\partial t^2} \right) - \begin{pmatrix} -\Omega_2 \Omega_3 C_{44} \\ \Omega_1 \Omega_3 C_{55} \\ 0 \end{pmatrix} \\ &- \int_H \rho \vec{\alpha} \cdot \vec{\nabla} \left(\frac{\partial \phi}{\partial t} + \vec{\nabla} \bar{\phi} \cdot \vec{\nabla} \phi \right) (\vec{x} \times \vec{n}) dA \\ &- \int_H \frac{1}{2} \rho |\vec{\nabla} \phi| (\vec{x} \times \vec{n}) dA \\ &+ \int_{wl} \frac{1}{2} \rho g \zeta_r^2 (\vec{x} \times \vec{n}) dl \quad (15) \end{aligned}$$

Here ζ_r is the linearized relative wave-height, which can be calculated by using Bernoulli's equation and the displacement of the hull. As incoming potential we use

$$\phi_{\text{inc}} = \frac{g\zeta_a}{\omega} \cos(\omega t - kx) \frac{\cosh(k(z+h))}{\cosh(kh)},$$

with

$$-\omega^2 + 2kU\omega + g \tanh(kh) = 0.$$

2 Increasing the speed

2.1 Upwind discretization

Increasing the speed, the potential is showing point-to-point oscillations. In this section we are first treating some tests we did with the two-dimensional problem. In figure 3 and 4 is shown that the potential shows local extremes, after one period of forced oscillation in the heave direction, if the Froude number $Fn = 0.5$. These numerical oscillations arise, when we use central discretization.

$$\phi_x|_i = \frac{\phi_{i+1} - \phi_{i-1}}{2\Delta x} + \mathcal{O}(\Delta x),$$

with subscripts denoting the element number of the clockwise numbered uniform mesh (like figure 2), with mesh size Δx . These oscillations, called wiggles, occur in the stationary convection-diffusion equation, when the Péclet number $Pe = UL/k$ is large and in the instationary convection-diffusion equation, when the Courant-Friedrichs-Lewy number $CFL = U\Delta t/\Delta x$ is large. To remove these numerical instabilities upwind discretization is used or artificial viscosity is added.

We noticed that in our case also the CFL -number plays an important role in the determination of stability of the scheme. For increasing values of the CFL -number the scheme becomes unstable. Therefore it seems to be that our problem will also be solvable by using upwind discretization and we replace the central discretization in our algorithm by

$$\phi_x|_i = \frac{\phi_i - \phi_{i-1}}{\Delta x} + \mathcal{O}(\Delta x).$$

This is called upwind discretization, because it is biased in upstream direction. Now the wiggles disappeared, see figure 5. To act more accurate it is possible to use a higher order three- or four-point scheme, or to use a combination of a two- and a three-point scheme, weighted such as to

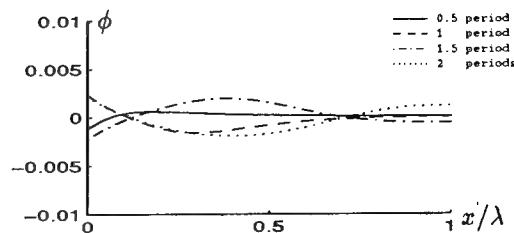


FIGURE 3: The potential, using central discretization, $Fn = 0.2$

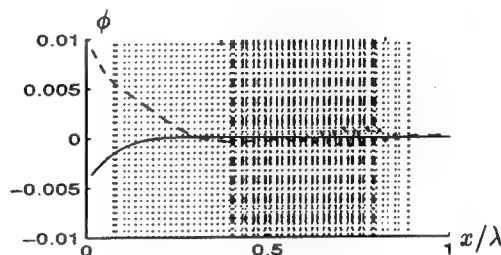


FIGURE 4: The potential, using central discretization, $Fn = 0.5$

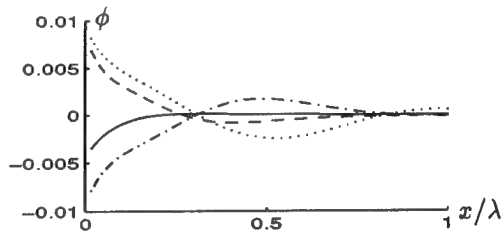


FIGURE 5: The potential, using upwind discretization, $Fn = 0.5$

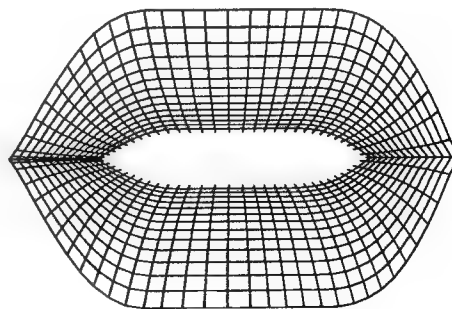


FIGURE 6: The free surface around the LNG carrier

reduce the numerical dispersion and damping to a higher order.

In the three-dimensional problem with the LNG carrier, wiggles also appear when we increase the speed. Implement upwind-discretization in this case is unfortunately not that easy as in two-dimensions. Firstly the mesh is not equidistant, so it is not possible to use the discretization schemes mentioned above. Secondly the mesh is designed to give a good representation of the waves, but not following the streamlines (See figure 6). By an accurate choice of the neighbour elements in upwind stream direction to give a good representation of the discretization, the wiggles disappear (See figure 7).

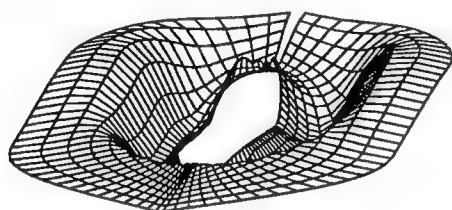


FIGURE 7: The free surface around the LNG carrier, upwind discretization is used. The speed is 20 knots and the carrier is forced to heave, the vertical scale is 5:1

3 Results

In this section we test our numerical algorithm, extended to increased forward speed, on a LNG carrier, whose particulars are given in table 1 and whose fine mesh of 1190 panels is given in figure 8. The first calculations were done with the coarse mesh of 384 panels.

TABLE 1: Particulars of the LNG carrier

Designation	Unit	
Length	m	273.90
Breadth	m	42.31
Draft	m	11.50
Displacement Δ	m ³	98,740
Centre of buoyancy above waterline	m	2.16
Centre of gravity above waterline	m	13.70
Longitudinal radius of gyration	m	62.52
Pitch period	s	8.8

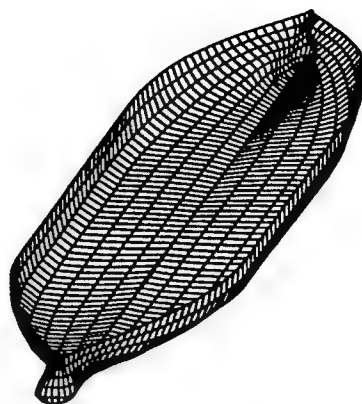


FIGURE 8: The mesh of the LNG carrier

The free surface was build up out of 14 non equidistant rings of 84 elements, the number of waterline elements on the hull. The artificial boundary was taken to be one wavelength away from the hull. The exterior was also taken one wavelength. Thus the wave will not be back at the hull during the 4 periods according to the frequency of encounter. On this time interval 200 time steps were taken. The equations of motion were integrated using the implicit method of Crank-Nicholson.

We calculated our results for the same speed, depth and wave frequencies as the measurements in Wichers [11], i.e. $F_n = 0$, $F_n = 0.14$, $F_n = 0.17$, $F_n = 0.20$ and the water depth is 175 m. At the Maritime Research Institute (MARIN) drift force calculations for zero and small forward speed were done, using the frequency domain diffraction program, extended to a small forward speed [12]. Calculations for the other velocities were done using strip theory [1, 2].

In figure 9 through 26 added mass and damping in surge, heave, and pitch motion are given. For small forward speed the coefficients are fairly independent of the speed, only the coupled coefficients seems depend on small speed. Increasing the speed gives more variation. We have no results to compare with. The reciprocity relations, which are shown by Timman and Newman [9], hold for small forward speed and $a_{35} - a_{53}$ and $b_{35} - b_{53}$.

Figure 27 shows the drift forces in head waves for zero speed. We compare our results computed for the fine mesh (1190 elements) and for a coarse mesh (384 elements), the results computed using the frequency domain diffraction program Diffac, and measurements. It is clear that it is important to use a fine mesh to calculate the

gradients in equation (14). Figure 28 shows the drift forces for small forward speed. In contrast with the Diffrac results, small speed has a small effect on the forces. In figure 29 we show the wave drift damping, which can be written as

$$B_x(\omega) = \frac{\partial F_{2x}}{\partial U} \bigg|_{U=0}.$$

Our results agree well with measurements.

In figures 30 and 31 respectively the heave and pitch response are shown for $Fn = .14, .17$ and $.20$. We compare the measurements with the strip theory calculations. In Figure 32 the drift forces or added resistance for higher speed are given. For the higher frequency strip theory doesn't agree very well with the measurements. Our first results, the small markers, look promising. For the lower frequencies the coarse mesh gives good results, but for the higher frequencies we need the finer mesh. At the presentation we will show more results. We have to make more calculation with the finer mesh, so the numerical differentiations on the hull, especially at the bow, will be more accurate.

4 Conclusions and further research

In this paper we show the extension of our method to higher speed. We have made a promising start. Our extended algorithm turns out to be efficient and reliable for low speed up to $Fn = .1$. Also the hydrodynamic coefficients for higher speed are calculated. Increasing the speed, we need a very accurate numerical differentiation of the gradient of the potential on the hull to compute the added resistance. After the implementation of a finer mesh we are able to tackle this problem as well. In the future we will also carry out the stability analysis.

Acknowledgements

Financial support for this work and the mesh of the ship-hull are given by the Maritime Research Institute Netherlands.

References

- [1] C. Flokstra. "The comparison of ship motion theories with experiments for a container vessel". *Int. Shipbuilding Progress*, Vol 21, no 238, 1974.
- [2] J. Gerritsma and W. Beukelman. "Analysis of the resistance increase in waves of a fast cargo ship". *Int. Shipbuilding Progress*, Vol 19, no 217, 1972.
- [3] J.B. Keller and D. Givoli. "Exact non-reflecting boundary conditions". *Journal of computational physics*, Vol 82, pp 172-192, 1989.
- [4] J.N. Newman. "Algorithms for the free surface green function". *Journal of Engineering Mathematics*, Vol 19, pp 57-67, 1985.
- [5] F. Noblesse. "The green function in the theory of radiation and diffraction of regular water waves by a body". *Journal of Engineering Mathematics*, Vol 16, pp 137-169, 1982.
- [6] H.J. Prins. Time-domain calculations of the drift forces and moments. PhD thesis, Delft University of Technology, The Netherlands, 1995.
- [7] H.J. Prins and A.J. Hermans. "Time-domain calculations of the second-order drift force on a tanker in current and waves". *Proceedings of the 20th symposium on naval hydrodynamics*, Santa Barbara, USA, 1994.
- [8] L.M. Sierrevogel and A.J. Hermans. "Absorbing boundary condition for floating two-dimensional objects in current and waves". *Journal of engineering mathematics* (to appear), 1996.
- [9] R. Timman and J.N. Newman. "The coupled damping coefficients of a symmetric ship". *Journal of ship research*, Vol 5, pp 1-7, 1962.
- [10] J.V. Wehausen and E.V. Laitone. "Surface waves". In *Handbuch der physik*. Springer-verlag, Berlin, Germany, 1960.
- [11] J.E.W. Wichers. Simulation model for a single moored tanker. PhD thesis, Delft University of Technology, The Netherlands, 1988.
- [12] J.E.W. Wichers and R.H.M. Huijsmans. "Wave drift current interaction on a tanker in oblique waves". *Hydrodynamics: computations, model tests and reality*, (Proceedings of Marin Workshops), Elsevier, Amsterdam, the Netherlands, pp 289-296, 1992.

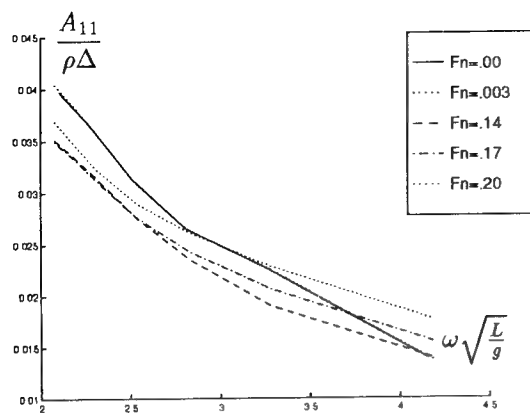


FIGURE 9: Added mass in surge

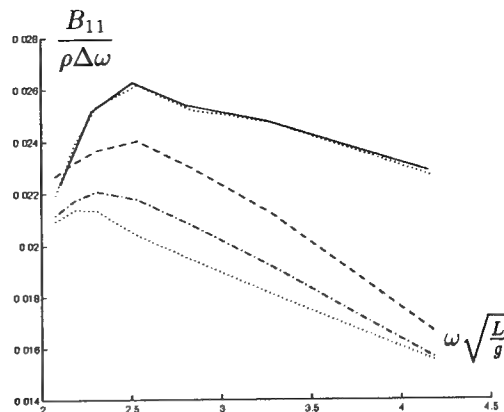


FIGURE 12: Added damping in surge

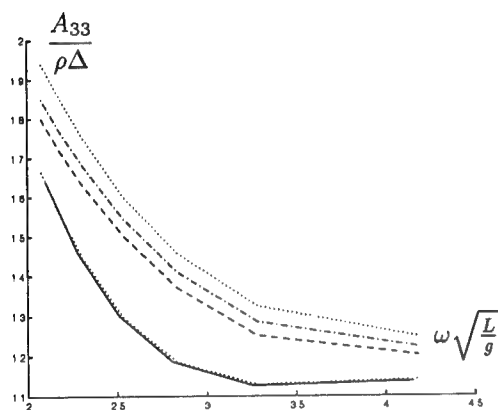


FIGURE 10: Added mass in heave

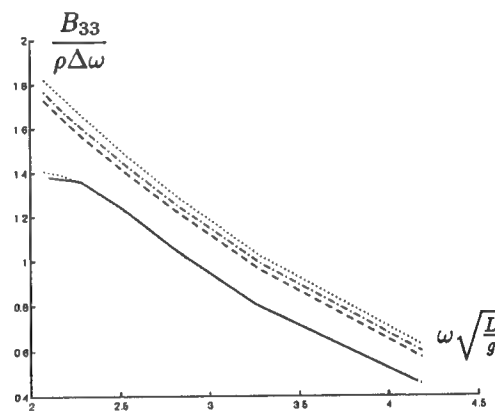


FIGURE 13: Added damping in heave

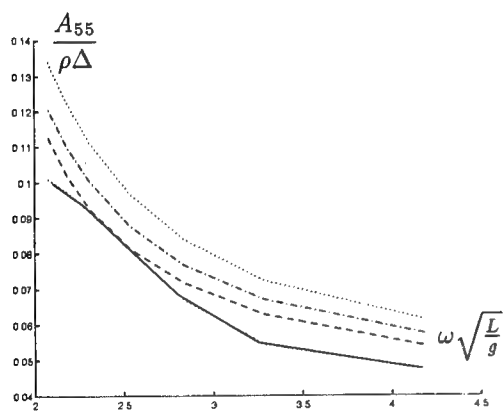


FIGURE 11: Added mass in pitch

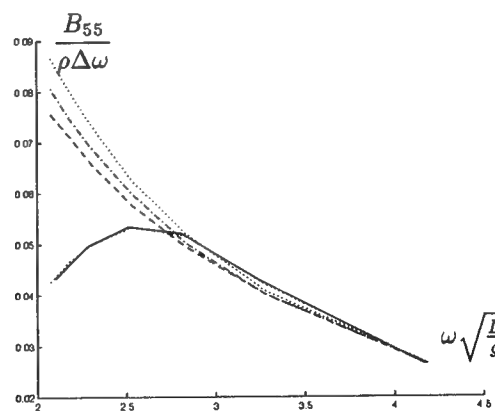


FIGURE 14: Added damping in pitch

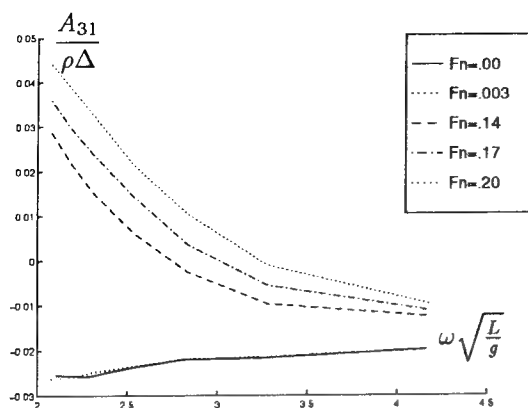


FIGURE 15: Coupled added mass from surge into heave

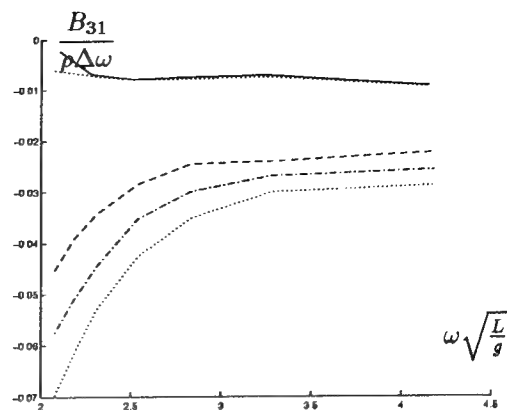


FIGURE 18: Coupled added damping from surge into heave

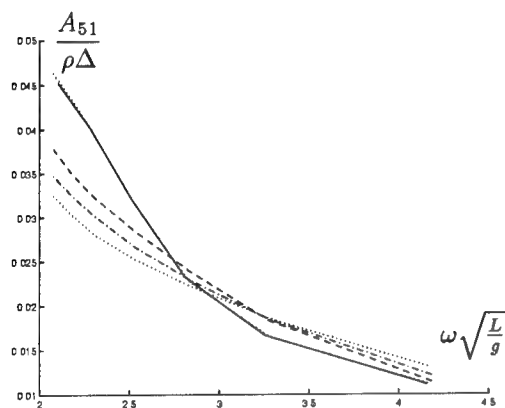


FIGURE 16: Coupled added mass from surge into pitch

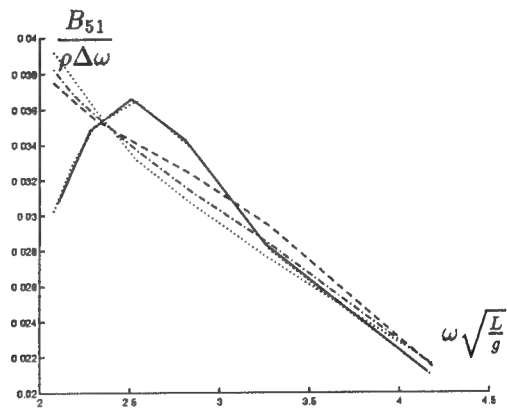


FIGURE 19: Coupled added damping from surge into pitch

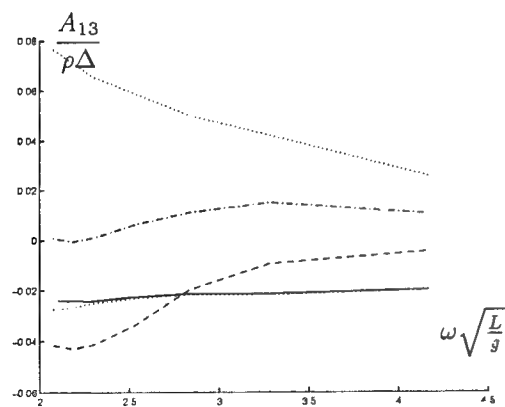


FIGURE 17: Coupled added mass from heave into surge

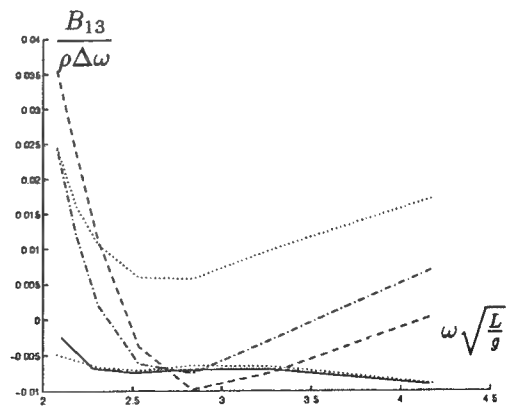


FIGURE 20: Coupled added damping from heave into surge

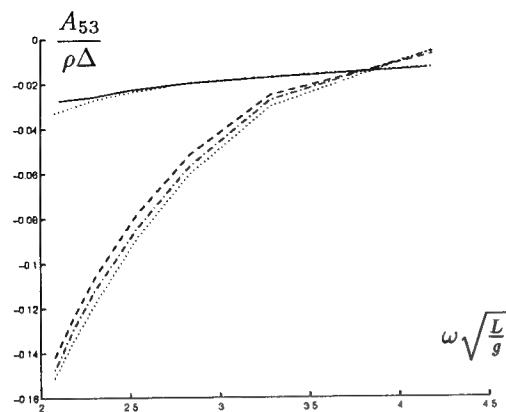


FIGURE 21: Coupled added mass from heave into pitch

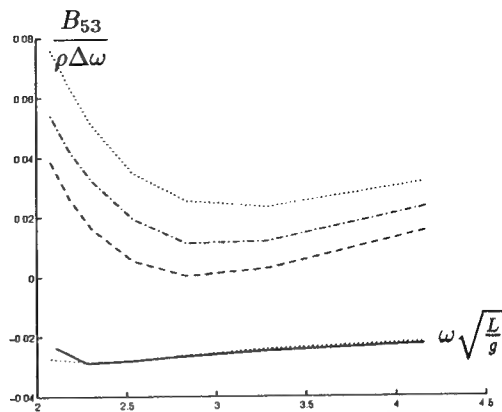


FIGURE 24: Coupled added damping from heave into pitch

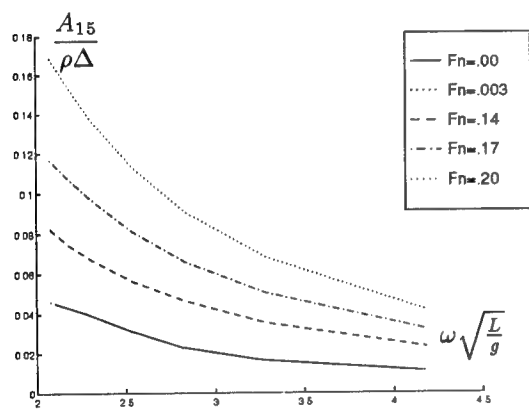


FIGURE 22: Coupled added mass from pitch into surge

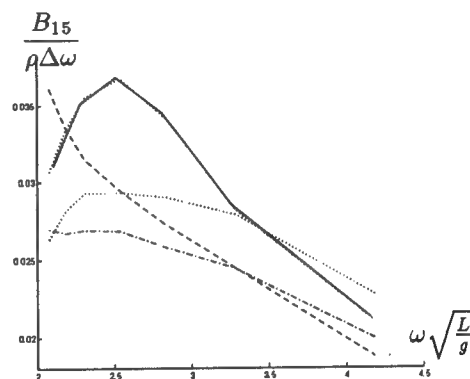


FIGURE 25: Coupled added damping from pitch into surge

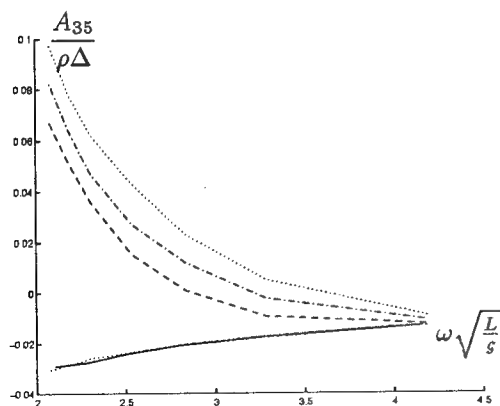


FIGURE 23: Coupled added mass from pitch into heave

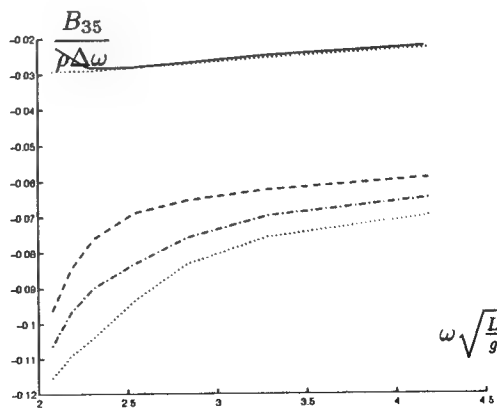


FIGURE 26: Coupled added damping from pitch into heave

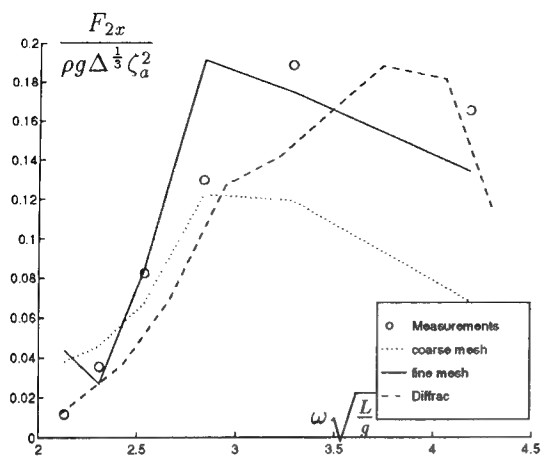


FIGURE 27: Horizontal drift force in head waves for zero speed.

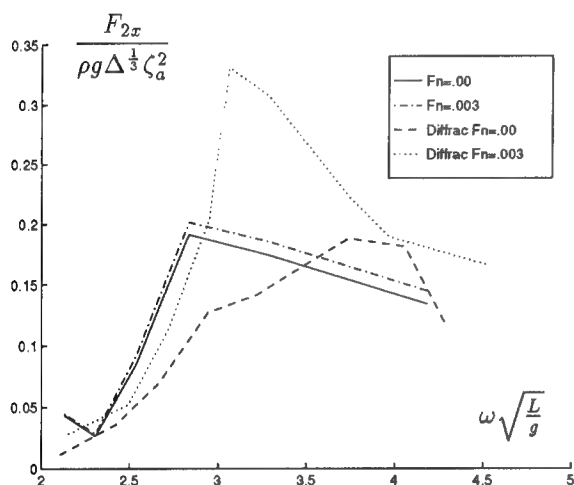


FIGURE 28: Horizontal drift force in head waves for small forward speed.

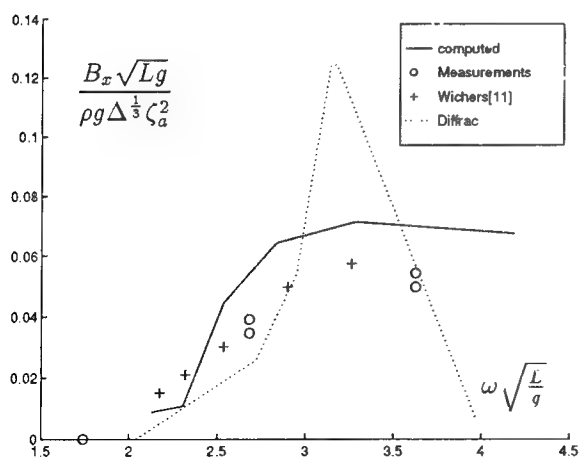


FIGURE 29: Wave drift damping

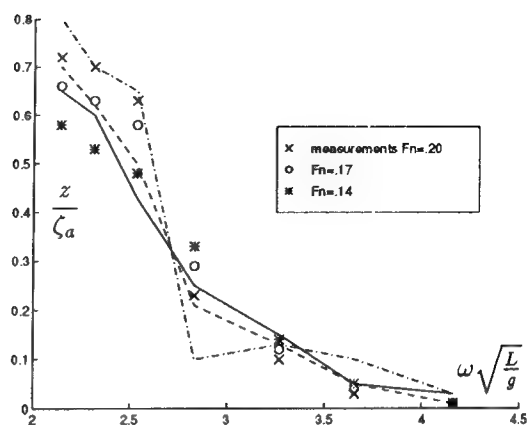


FIGURE 30: Heave response (legend as in Figure 30 and 31)

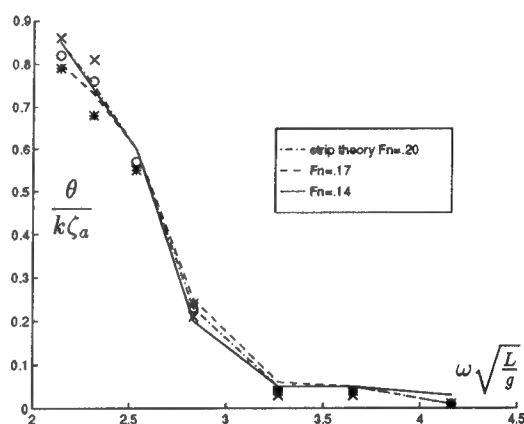


FIGURE 31: Pitch response (legend as in Figure 30 and 31)

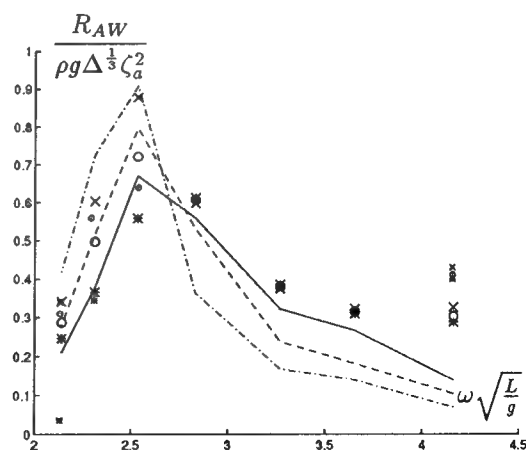


FIGURE 32: Added resistance (legend as in Figure 30 and 31). The small markers are our first results.

Third-Order Volterra Modeling of Ship Responses Based on Regular Wave Results

L. Adegeest (Delft University of Technology, The Netherlands)

Abstract

A third order Volterra modelling was used to calculate the nonlinear vertical hull girder loads in irregular head waves in two slender models with different degrees of bow flare. The first order and the required approximations of the second and third order frequency response functions were derived from systematical experiments in regular waves only. The comparison of time traces, power spectra and probability density functions with experiments in irregular waves showed a good agreement for both models. For the model with bow flare it was not possible to obtain the same degree of correspondence with the experiments using a linear or second order modelling.

1 Introduction

A practical and complete seakeeping theory should involve at least the following elements:

- A deterministic theory to relate ship's responses to the excitation by well-defined waves.
- A statistical model of the ship's response in irregular waves.
- A theory to describe the statistics of response maxima, minima and ranges as a function of the response statistics.

Since many years the validation of deterministic ship motion computer codes is based on the results obtained from towing tank experiments. Most of the experiments are performed in small amplitude waves to provide the necessary validation data for linear codes. Statistical techniques to analyse the linear seakeeping problem are widely available nowadays.

However, it is commonly known that the vertical hull girder loads can show a significant nonlinear behaviour when the relative motions at the bow are large compared with the draft or freeboard of the vessel.

Different solutions can be applied to nonlinear problems. Kac and Siegert [1] presented the mathematical fundamentals to calculate the probability density function of the second order problem. Some years later Wiener [2] introduced a method to analyse nonlinear electric circuits. The proposed method is based on a functional power series model, or a so-called Volterra series expansion. Hasselmann [3] suggested the use of a second order Volterra model to predict the linear and quadratic transfer functions from full scale measurements or model tests. This procedure was applied by many other researchers to analyse phenomena such as the added resistance of a ship in waves (Dalzell [4]), slowly varying drift forces (Pinkster [5]), sum and difference frequency loads on cylinders (Kim and Yue [6]) and vertical hull girder loads (Jensen and Pedersen [7]).

Based on the same principles, Longuet-Higgins [8] and Vinje and Skjördal [9] both showed that for slightly quadratic processes, the distribution of the extreme values can be derived analytically based on the nonlinear frequency response functions. The expressions are presented in the form of perturbation series expansions, called Edgeworth or Charlier series. Jensen and Pedersen [7] applied this method to predict extreme hull girder loads in ships. The fatigue damage inflicted on a construction by non-Gaussian wave-induced stresses was analysed by Jensen [10]. The results of these practical applications were obtained on the assumption of a weakly second order behaviour and a narrow band response spectrum.

The extension to a third order modelling of nonlinear ship motions was already suggested by Dalzell [11,12]. Formulations were derived for the probability density, the statistical moments and the distributions of extremes. Starting point was an assumed set of linear, quadratic and cubic frequency response functions. The results were compared with numerical results obtained for a particular nonlinear differential equation for which the linear, quadratic and cubic frequency response functions could be derived analytically. In principle, the statistics were

tical moments only (mean, variance, skew and kurtosis).

The similar assumption was made by Winterstein [13]. Using Hermite moment formulations approximate probability density functions, crossing rates and extreme values were derived solely based on the aforementioned statistical moments.

In summary, it was shown by different researchers that the statistics of weakly nonlinear stationary seakeeping problems are reasonably well defined by the first four statistical moments only. This paper shows the applicability of an approximate third-order Volterra modelling to analyze the statistics of the vertical hull girder loads in irregular waves. The numerical results are compared with extensive model tests in irregular waves. The comparisons comprise time traces, power spectra and spectral moments, statistical moments and probability density functions of the samples and of the peak-peak values. The required linear, quadratic and cubic frequency response functions were derived from the first three harmonic components measured in regular waves.

2 Experiments

The first results of systematical experiments, focussed on the nonlinear vertical hull girder loads, were presented by Dalzell [14,15] in 1964. Models of three variants of a Mariner ship, a tanker and a destroyer were subjected to a range of regular waves over a range of wave lengths and heights. The vertical bending moments were presented in hogging and sagging condition separately, not providing information about the harmonic components in the response signals. However, it was proved without a doubt that the sag/hog-ratio was not equal to unity, which should be the case for linear signals. Furthermore the experiments showed that the sag/hog-ratios tended to be larger for the slender destroyer model and the Mariner variants than for the full tanker model. Similar conclusions followed from two other model test series, reported by Murdey [16] and Nethercote [17].

O'Dea et al [18] reported the measurement of nonlinear heave and pitch responses for a S-175 model. The higher harmonic components were only a few percent in magnitude of the first harmonic response. This seems to be a negligible effect. It has to be realised, however, that the accelerations are more strongly nonlinear than the displacements when we compare them with the magnitude of their linear components. This can be illustrated on the assumption of a third order, zero mean periodic displacement, which is written in terms of the first three

harmonic components as

$$y(t) = y_1 e^{i\omega t + \epsilon_1} + y_2 e^{2i\omega t + \epsilon_2} + y_3 e^{3i\omega t + \epsilon_3} \quad (1)$$

Hence, the displacement, velocity and acceleration are given in matrix notation by

$$\begin{bmatrix} y(t) \\ \dot{y}(t) \\ \ddot{y}(t) \end{bmatrix} = \begin{bmatrix} 1 & 1 & 1 \\ i\omega & 2i\omega & 3i\omega \\ -\omega^2 & -4\omega^2 & -9\omega^2 \end{bmatrix} \begin{bmatrix} y_1(t) \\ y_2(t) \\ y_3(t) \end{bmatrix} \quad (2)$$

It can easily be seen that relative to the first harmonic component, the second harmonic acceleration is four times as large as the second harmonic displacement while the third harmonic component is even nine times larger. This much more pronounced nonlinear inertia effect directly influences the hull girder loads behaviour.

After a survey of literature it had to be concluded that the data sets presented were not sufficient to study the nonlinear hull girder loads in very much detail. Many of the experiments were performed in regular waves only. From those test results, too much information was lost due to the presentation of the results in terms of hog/sag-ratios or double amplitudes. No systematical results were presented showing the harmonic components of a response experienced in regular wave conditions in order to investigate the actual order of the process.

Therefore new extensive experiments were performed both in regular and irregular waves. The results were extensively reported and discussed by Adegeest [19,20,21]. The objective of the experiments was to collect motion and load data that can be studied and compared with numerical solutions in much more detail.

The experiments were conducted on a Wigley hull form with and without bow flare. The normalised beam y of the under water ship is described by a polynomial in the x - and z -coordinate according to

$$y = (1 - z^2)(1 - x^2)(1 + 0.2x^2) + z^2(1 - z^8)(1 - x^2)^4 \quad (3)$$

where $x \in [-1, 1]$ and $z \in [-1, 0]$. Table 1 shows the main characteristics of the Wigley geometries. The bow form variation is clearly illustrated in figure 1.

In regular waves both models were tested at two forward speeds, thirteen frequencies and at least four wave amplitudes. Fourier analyses of the results clearly showed the presence of pronounced higher harmonic components in the hull girder load

Length on waterline (L_{WL})	2.500	m
Beam (B)	0.357	m
Draught (T)	0.139	m
Displacement volume	0.0696	m ³
L/B	7.000	
L/T	18.000	
Block coefficient (C_B)	0.561	
Midship coefficient (C_M)	0.909	
Water plane coefficient	0.693	
k_{yy}/L	0.25	

Table 1: Main characteristics of the Wigley models

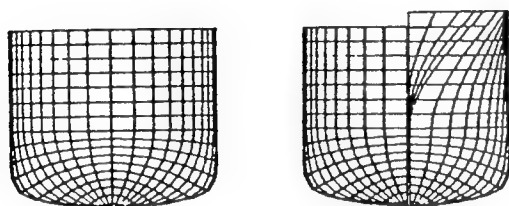


Figure 1: Plans of both Wigley variants

responses while the motion responses were hardly affected by nonlinear contributions, see for example figure 2.

In irregular waves about 50 runs were made for both models at one forward speed $Fn = 0.3$. This resulted in about 5000 wave encounters per model. The applied wave spectrum is shown in figure 3. In the same figure the Gaussianness of the waves was investigated by comparing the probability density with the theoretical normal distribution. It seems reasonable to assume a Gaussian distributed wave elevation. Figure 4 shows some examples of the measured response probability densities compared with their equivalent theoretical Gaussian probability density. The deviations from the Gaussian probability densities were an order larger than those observed in the excitation waves.

The equivalent first order RAOs were derived according to $|H(\omega)| = \sqrt{S_{yy}(\omega)/S_{\zeta\zeta}(\omega)}$ and successively compared with the measured first harmonic responses in regular waves (figure 5). For the original hull form in regular waves, only minor spreading was observed between the normalized first harmonics in different wave heights. This implied that third order effects hardly occurred. As expected, the RAOs from the irregular wave tests confirmed

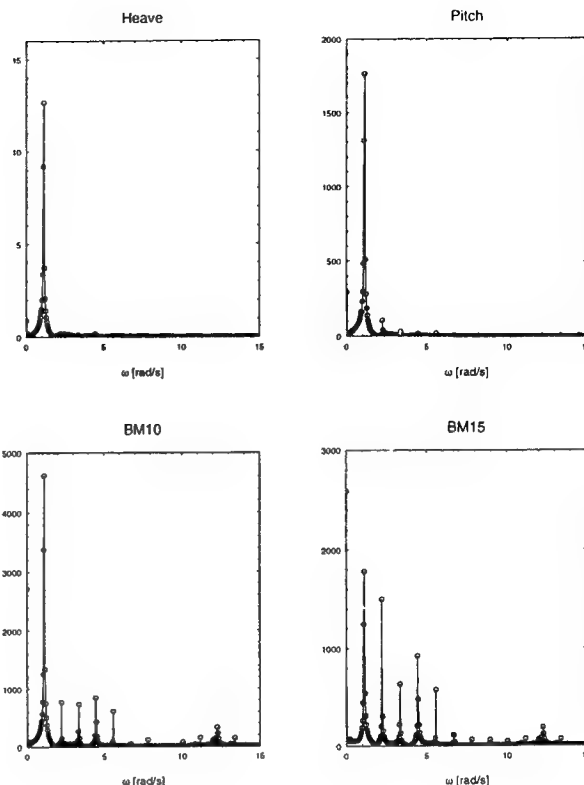


Figure 2: Fast Fourier Transforms of some measured responses of the Wigley with bow flare, $Fn = 0.3$, $\lambda/L = 1.36$, $H/\lambda \approx 1/75$

this result. For the Wigley with bow flare, significant spreading between the regular wave results was observed. Yet, the RAOs derived from the irregular wave tests approximate the regular wave results in the examined frequency range reasonably well. The result for the bending moment in the forward however immediately shows the presence of severe nonlinear effects.

The problem with the measured responses is the significant contribution to the total hull girder loads of not only second order but also of third order components. The low-frequency third order responses cause the response in the wave-frequency area to deviate from the linear predictions. The high-frequency higher order components cause the response spectra to become wider, which is another complication in extreme statistics.

In the following section a theory is outlined to derive approximations for the linear, quadratic and cubic frequency response functions using which it is possible to derive the response statistics in irregular waves for those nonlinear responses in which the first order term is still dominant.

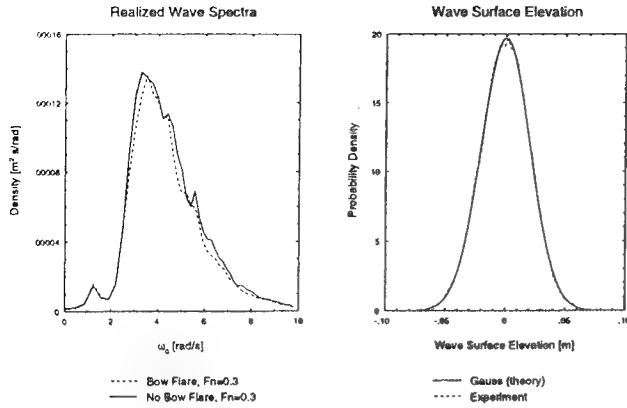


Figure 3: Realised wave spectra during experiments with both Wigley hull variants (left) and the probability density of the samples compared with the equivalent Gaussian probability density function (right)

3 The Third Order Volterra Model

The presented experimental results clearly identified the need for nonlinear computational methods in the statistical analysis of vertical hull girder loads, whether it concerns the prediction of the life time maximum wave-induced loads or a long-term distribution of load cycles for the purpose of fatigue analyses.

The general way to describe the nonlinear relation between an input- and output-signal as a Volterra series model is by means of a power series with memory. This memory effect is represented by a functional series which is, up to the third order, given by

$$y(t) = y_1(t) + y_2(t) + y_3(t) + n(t) \quad (4)$$

in which the total nonlinear system's output $y(t)$ is the sum of a linear or first order time-varying output $y_1(t)$, a bi-linear or second order time-varying output $y_2(t)$, a tri-linear or third order time-varying output $y_3(t)$ and, since no analytical model fits perfectly to a physical model, a zero mean term $n(t)$ representing higher order terms and measuring noise. This term is assumed not to be correlated with the other output components. From now on the component $n(t)$ will be assumed to be zero, which does not change the results derived below.

The Volterra functionals as defined in equation (4) are given by

$$y_1(t) = \int h_1(t_1)\zeta(t-t_1)dt_1 \quad (5)$$

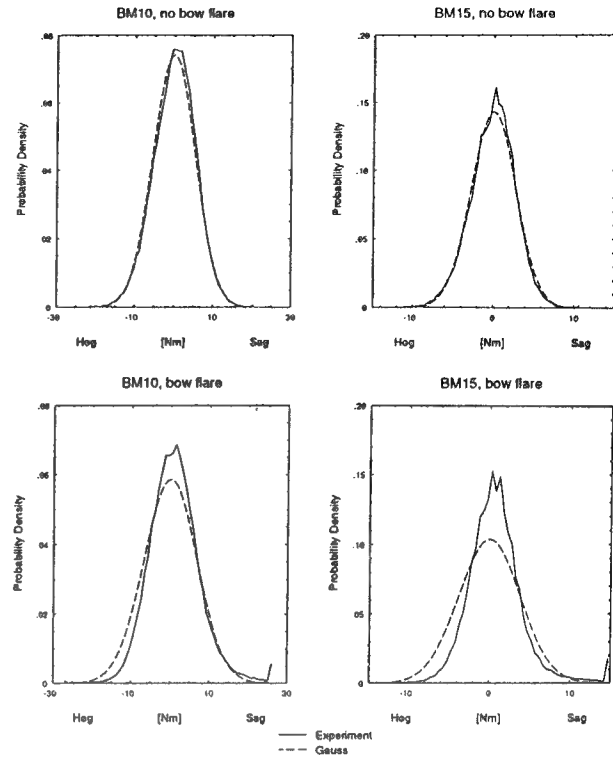


Figure 4: Probability density functions of the recorded bending moments in the original Wigley (upper) and in the Wigley with bow flare (lower) compared with the equivalent Gaussian probability density function

$$y_2(t) = \iint h_2(t_1, t_2)\zeta(t-t_1)\zeta(t-t_2)dt_1dt_2 \quad (6)$$

$$y_3(t) = \iiint h_3(t_1, t_2, t_3)\zeta(t-t_1)\zeta(t-t_2)\zeta(t-t_3)dt_1dt_2dt_3 \quad (7)$$

The functions $h_1(t_1)$, $h_2(t_1, t_2)$ and $h_3(t_1, t_2, t_3)$ are, respectively, the linear, quadratic and cubic time-domain Volterra kernels or weighting functions. In terms of impulse responses, these functions represent the system's memory effect in the time domain, affecting a linear response at time t due to an impulsive excitation at time $t-t_1$, a quadratic response due to two impulsive excitations at times $t-t_1$ and $t-t_2$ and a cubic response due to impulsive excitations at times $t-t_1$, $t-t_2$ and $t-t_3$. In physically realisable models, t_1 , t_2 and t_3 are positive quantities, which implies that only excitations in the past can result in a response. It can be derived that $h_2(t_1, t_2)$ and $h_3(t_1, t_2, t_3)$ are unique and symmetric with respect to their variables.

The frequency-domain kernels $H_1(\omega)$, $H_2(\omega_1, \omega_2)$ and $H_3(\omega_1, \omega_2, \omega_3)$, representing the lin-

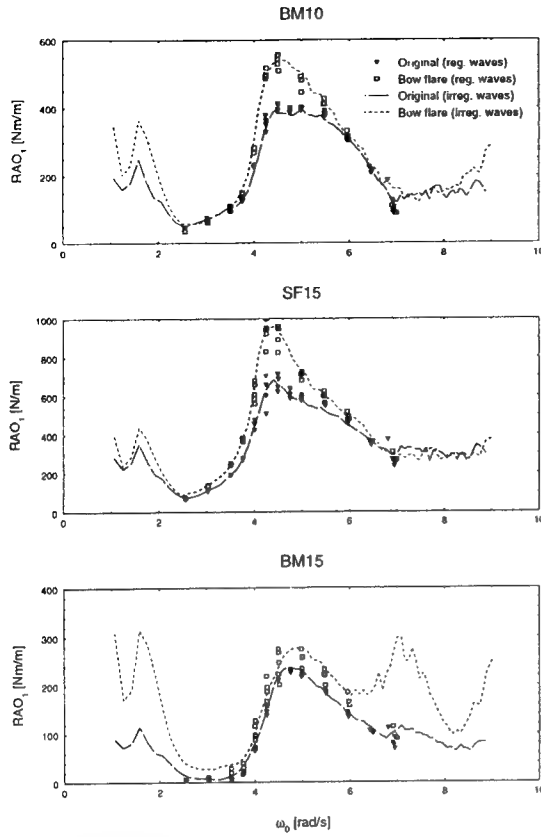


Figure 5: Equivalent RAO's derived from the irregular wave tests compared with the regular wave results

ear, quadratic and cubic frequency response functions respectively are given by the single, double and triple Fourier transform of the time-domain kernels and show the same symmetry relations with respect to the variables as the time-domain kernels.

By expressing the time domain kernels and the time-dependent wave surface elevation $\zeta(t)$ in terms of their equivalent frequency domain representation, it follows that

$$y_1(t) = \frac{1}{2\pi} \int H_1(\omega) Z(\omega) e^{i\omega t} d\omega \quad (8)$$

$$y_2(t) = \frac{1}{4\pi^2} \iint H_2(\omega_1, \omega - \omega_1) Z(\omega_1) Z(\omega - \omega_1) e^{i\omega t} d\omega_1 d\omega \quad (9)$$

$$y_3(t) = \frac{1}{8\pi^3} \iiint H_3(\omega_1, \omega_2 - \omega_1, \omega - \omega_2) Z(\omega_1) Z(\omega_2 - \omega_1) Z(\omega - \omega_2) e^{i\omega t} d\omega d\omega_1 d\omega_2 \quad (10)$$

in which, by means of a particular substitution of frequencies, the exponent occurring in all three equations is equal to $i\omega t$. This substitution is ad-

vantageous during the actual time history generation process, which can now be performed by a single inverse Fast Fourier Transformation. If the linear and nonlinear frequency response functions are known, the Volterra model offers the opportunity to perform simulations of realistic ship's responses in arbitrary random sea conditions very quickly. Generally this is an impossibility with direct nonlinear boundary value solutions in the time domain.

The general problem encountered when using the Volterra modelling is the determination of the full two- and three-dimensional nonlinear frequency response functions of the underlying system. A direct calculation in the frequency domain would be an enormous task. A second possibility is to derive these functions from existing time histories, provided that these are available. A major practical problem herein is the rapidly increasing amount of data required to make accurate predictions of the second but especially of the third order frequency response functions.

Bendat [22] presented two different types of third order system modellings which made it possible to make an estimation of the nonlinear frequency response functions purely based on regular wave results. For many types of responses it is hardly possible to predict the degree of fitting of their approximate modellings.

O'Dea et al [18] applied one of those modellings to analyse the nonlinear motion behaviour in head waves of a S-175 model. In regular waves, the same third order behaviour of the normalised first harmonic components was observed as discussed in the previous chapter. After substituting the frequency response function $H_2(\omega_1, \omega_2)$ by an additive frequency response function $A_2(\omega_1 + \omega_2)$ and the third order frequency response function $H_3(\omega_1, \omega_2, \omega_3)$ by $A_3(\omega_1 + \omega_2 + \omega_3)$, a polyspectral analysis of motion recordings in irregular waves confirmed the dominant role of third order effects in the wave frequency band.

It was shown by the author [23], however, that in case of the nonlinear hull girder loads, modelling of the nonlinear response as a linear frequency transfer operation followed by a zero-memory quadratic or cubic operation gave very good results. In that modelling, the frequency response functions as introduced in the equations (8)-(10) are redefined as frequency response functions of constant parameter linear systems:

$$H_1(\omega) = B_1(\omega) \quad (11)$$

$$H_2(\omega_1, \omega_2) = B_2(\omega_1) B_2(\omega_2) \quad (12)$$

$$H_3(\omega_1, \omega_2, \omega_3) = B_3(\omega_1) B_3(\omega_2) B_3(\omega_3) \quad (13)$$

Some typical results of this model are

$$H_2(\omega, \omega) = B_2^2(\omega) \quad (14)$$

$$H_3(\omega, \omega, \omega) = B_3^3(\omega) \quad (15)$$

$$H_2(\omega, -\omega) = B_2(\omega)B_2(-\omega) = |B_2(\omega)|^2 \quad (16)$$

$$H_3(\omega, \omega, -\omega) = B_3(\omega)|B_3(\omega)|^2 \quad (17)$$

From these equalities it follows that the required frequency response functions $B_1(\omega)$, $B_2(\omega)$ and $B_3(\omega)$ can be derived from the response in a regular wave train.

Assume that the degree of nonlinearity in the waves is negligible compared with the nonlinearities in the response. A regular monochromatic wave with frequency ω_0 is written as

$$\zeta(t) = A \cos \omega_0 t \quad (18)$$

or its Fourier transformation

$$Z(\omega) = \pi[A\delta(\omega_0 - |\omega|)] \quad (19)$$

Substitution of the frequency-domain representation of the wave surface elevation (19) into the equations describing the individual functionals of the complete third order Volterra model, given by equations (8)-(10), and making use of the symmetry of the frequency domain kernels, the following expressions are found for the first, second and third order response:

$$y_1(t) = A \operatorname{Re}[B_1(\omega_0)e^{i\omega_0 t}] \quad (20)$$

$$y_2(t) = A^2 \frac{1}{2} \operatorname{Re}[|B_2(\omega_0)|^2 + B_2^2(\omega_0)e^{2i\omega_0 t}] \quad (21)$$

$$y_3(t) = A^3 \operatorname{Re}\left[\frac{1}{4}B_3^3(\omega_0)e^{3i\omega_0 t} + \frac{3}{4}B_3(\omega_0)|B_3^2(\omega_0)|e^{i\omega_0 t}\right] \quad (22)$$

The response $y(t)$ in regular waves can also be written in the form:

$$y(t) = \operatorname{Re}[R_0 + R_1 e^{i\omega_0 t} + R_2 e^{2i\omega_0 t} + R_3 e^{3i\omega_0 t}] \quad (23)$$

in which the R_j 's are the complex amplitudes of the individual harmonic components. These amplitudes follow from a Fourier analysis of the response in regular waves.

The amplitude and phase of the frequency response function $B_2(\omega)$ are derived from the measured second harmonic component:

$$B_2^2(\omega_0) = \frac{2}{A^2} R_2 \quad (24)$$

The degree of fitting of the second order component of the proposed modelling to the underlying physical phenomenon is easily checked by comparing the measured mean value with the equivalent expression in terms of $B_2(\omega)$ as derived from the second harmonic. It was observed in the analysis of the regular wave results that the modulus of the experienced second harmonic and mean bending moment were generally of the same magnitude, especially for the Wigley with bow flare which shows the severest nonlinear behaviour [21].

The third and first order frequency response functions $B_3(\omega)$ and $B_1(\omega)$ are prescribed by

$$B_3^3(\omega_0) = \frac{4}{A^3} R_3 \quad (25)$$

$$B_1(\omega_0) = \frac{R_1}{A} - \frac{3}{4} A^2 B_3(\omega_0)|B_3(\omega_0)|^2 \quad (26)$$

Theoretically, the results obtained over a range of frequencies, each at just one wave amplitude, are sufficient to obtain a first estimate of $B_1(\omega_0)$, $B_2(\omega_0)$ and $B_3(\omega_0)$. It should be recognised that the first order frequency response function as predicted using equation (26) depends very much on the accuracy of the measured third harmonic responses, i.e. the high-frequency third order response.

In order to predict the first order results in a less sensitive way, use is made of the availability of regular wave results per frequency over a range of different wave amplitudes. From equation (26) it follows that $B_1(\omega_0)$ and $B_3(\omega_0)$ can be determined by a least square fitting of the results $R_{1,i}$ for $i = 1 \dots n$ different wave amplitudes A_i to a polynomial of the type

$$R_{1,i} = A_i B_1(\omega_0) + \frac{3}{4} A_i^3 B_3^{LF}(\omega_0)|B_3^{LF}(\omega_0)|^2 \quad (27)$$

where $B_3(\omega)$ has been replaced by $B_3^{LF}(\omega_0)$ to indicate that we are dealing with the low-frequency component of the third order response. The equivalent high-frequency third order component $B_3^{HF}(\omega_0)$ is determined from the third harmonic response:

$$B_3^{HF}(\omega_0) = \frac{1}{A} (4R_3)^{1/3} \quad (28)$$

The separation of the third order response into a low-frequency and a high-frequency contribution, accounted for by $B_3^{LF}(\omega_0)$ and $B_3^{HF}(\omega_0)$ respectively, allows the use of the maximum available information enclosed in regular wave results at the cost of a modification of the modelling given by definitions (11)-(13). Generally spoken $B_3^{LF}(\omega_0)$ and $B_3^{HF}(\omega_0)$ will not have the same value although this

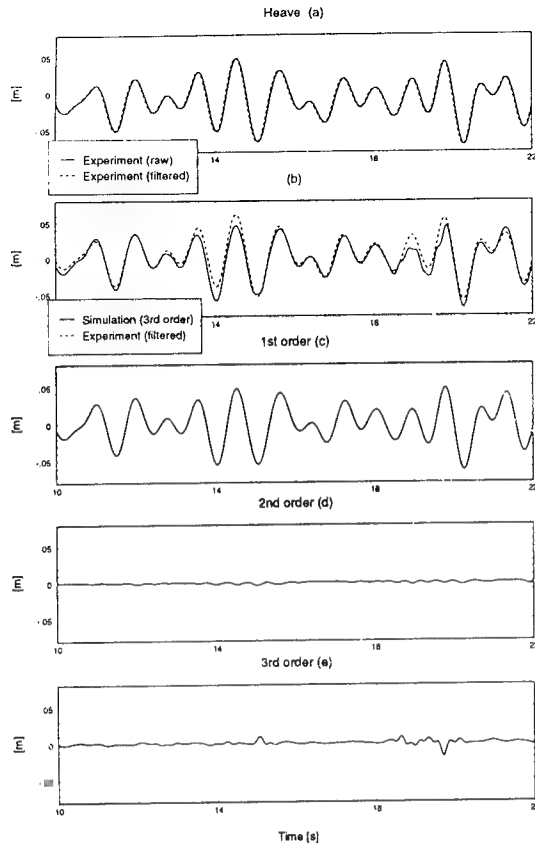


Figure 6: Measured and simulated heave motion of the Wigley with bow flare, $Fn = 0.3$

was implied by the proposed modelling. The virtue of this modification, however, is that the resulting first order results are less sensitive to variations or errors in the triple frequency response which in general is difficult to determine.

4 The Results

In this section, reconstructed time histories resulting from the first, second and third order Volterra modellings are analysed and compared in detail with experiments in irregular waves. The main purpose of these analyses is to investigate whether or not it is possible to make a proper prediction of the probability densities and of the statistics of the maxima, minima and ranges of the hull girder loads.

It should be realised that the presented simulations are purely transformations of a frequency domain formulation to time traces by adopting a specific wave spectrum. The benefit of analysing time traces is the applicability of ready-available techniques for determining response and extreme statistics. After validation of the applicability of the proposed modelling, direct frequency domain analyses are preferred.

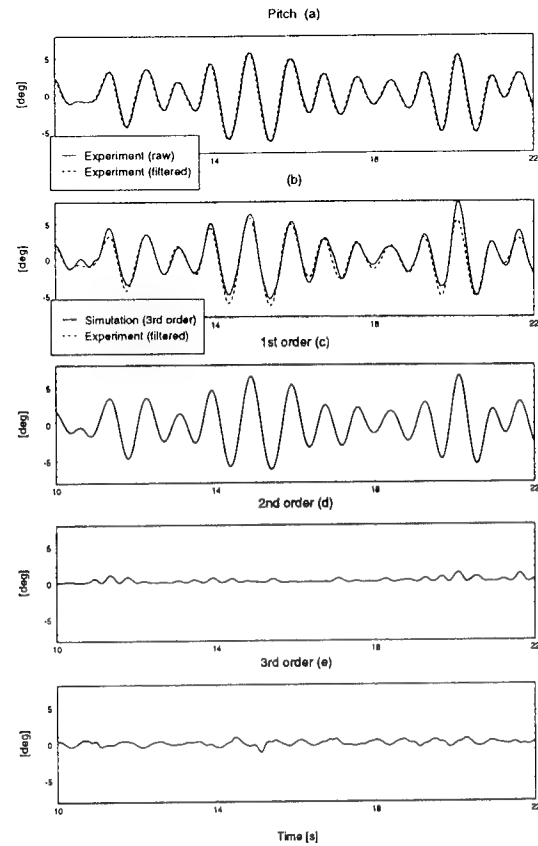


Figure 7: Measured and simulated pitch motion of the Wigley with bow flare, $Fn = 0.3$

4.1 Time Histories

In order to compare the statistical properties of the simulations with the experimental values, simulations were performed in exactly the same wave trains as realised during the experiments. When obtaining the wave surface elevation experienced during the irregular wave tests in the centre of gravity, use was made of the assumed linearity of the waves. This assumption was verified by the degree of fitting of the realised probability density to the theoretical Gaussian probability density function as shown in figure 3.

The amplitudes and phases of the wave components were calculated by Fourier transformation of the recorded wave signal in front of the model after which a phase correction per wave component was applied using the dispersion relation for shallow water.

After substituting the nonlinear frequency responses functions $B_1(\omega)$, $B_2(\omega)$ and $B_3(\omega)$ into the equations 8-10, time traces of the irregular responses were calculated using Fast Fourier Transform (FFT) routines. This method required the interpolation of 2^n frequency response function values at equal distances $\Delta\omega$. Use was made of the mea-

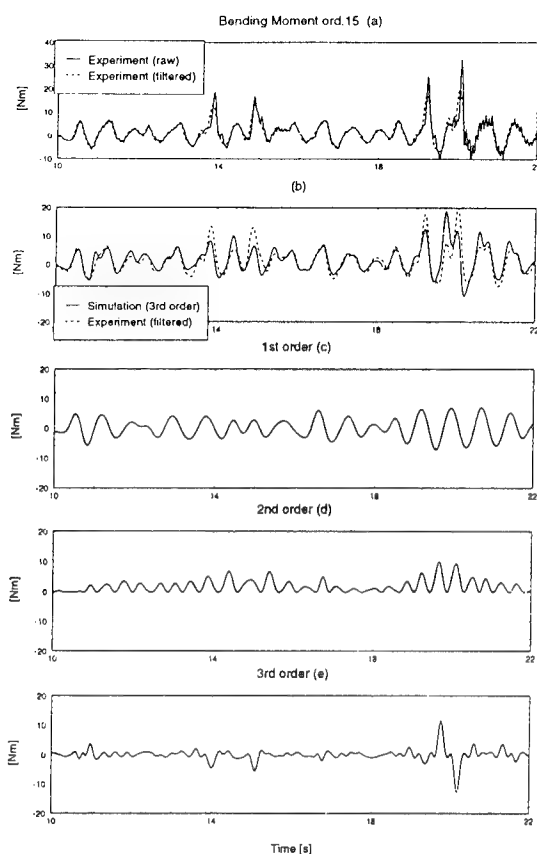


Figure 8: Measured and simulated vertical bending moment in the forward of the Wigley with bow flare, $F_n = 0.3$

sured first three harmonic components in regular waves. These responses were measured at incident wave frequencies in the range from $\omega_0 = 2.5 - 7.0$ rad/s. Outside this range proper estimates were made based on the known response at low and high frequency limits.

The reconstructed motion responses of the Wigley with bow flare are shown in figure 6 and 7. Figure 8 and 9 show some examples of the measured and numerically reconstructed vertical bending moments in the same Wigley model.

The upper graphs in these figures show the unfiltered signals resulting from the model test. Slamming events are noticed in the load recordings as sharp peaks in sagging condition, followed by a slowly decaying vibration. In order to remove the structure dependent springing loads and slam-induced whipping loads from the experimental results, all time recordings were filtered at 4 Hz. To allow an honest comparison, all simulated results were filtered at 4 Hz too.

It is clear that the motion responses are predicted well just by taking into account the first order contribution. The higher order components did

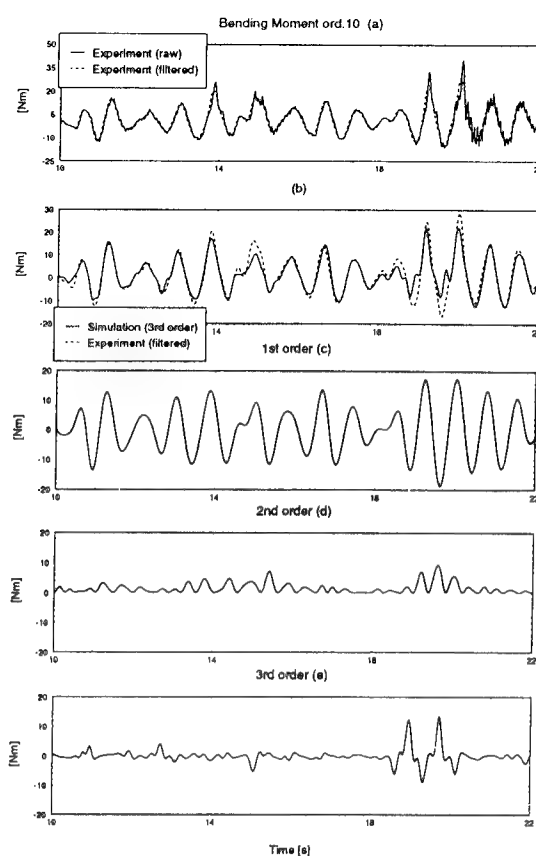


Figure 9: Measured and simulated vertical midship bending moment in the Wigley with bow flare, $F_n = 0.3$

not contribute significantly to the total motion response.

A satisfactory agreement was also found between the experimental load results and the third order simulations as can be seen from figures 8 (b) and 9 (b). Especially when it is realised that the wave had to be transformed to the centre of gravity and that hundreds of frequency response function values were interpolated linearly using only thirteen estimates. The individual first, second and third order contributions are presented in figures 8 and 9 (c), (d) and (e). It can be observed that at the instant of a slam, the second and third order contribution obtain similar magnitudes as the linear component of the simulation, especially in the forward. Furthermore it can be seen that the third order contribution is dominated by the low frequency component.

4.2 Response Spectra

The power spectra of the responses were calculated from the measured and simulated time histories. Each run was analysed separately after which the resulting spectra were averaged. Figure 10 shows

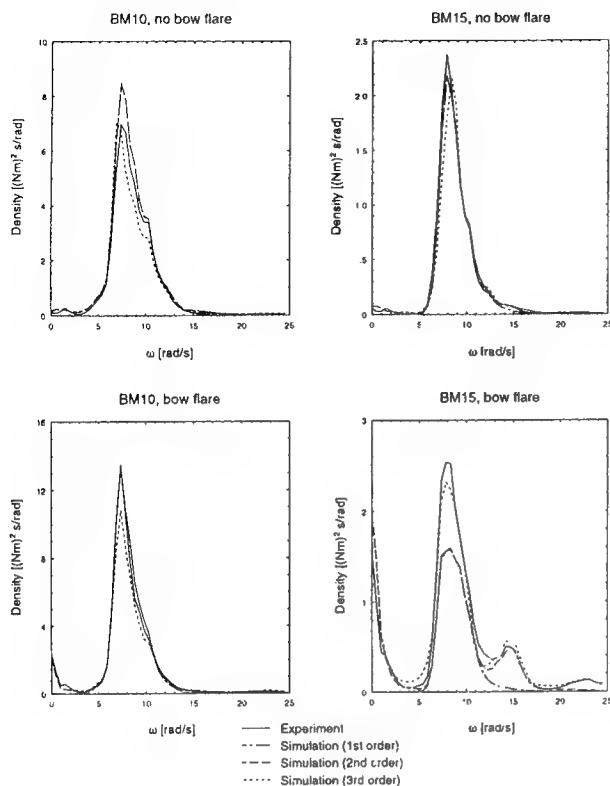


Figure 10: Measured and simulated auto-power spectra of the bending moments at $F_n = 0.3$, averaged over 50 runs of 50 seconds each

the power spectra of the bending moments amidships and at the bow for both the original Wigley and the Wigley with bow flare.

For the original Wigley hull form, no distinct higher order peaks can be observed in the power spectra of the experimental results nor in those of the simulated results. Generally a good correspondence with the experiments was obtained for all simulations. The main difference was found for the midship bending moment. For that case, the first and second order simulations overestimate the energy density in the wave frequency range. Using the third order simulations, the energy density is calculated more accurately.

For the Wigley with bow flare, a low frequency second order effect becomes visible in the bending moment response amidships. For this model, the use of the third order simulation model resulted in an energy density in the wave frequency range that was not high enough; i.e. the low frequency third order contribution is overestimated. The most interesting result, however, is found for the bending moment response in the forward. The experiments show a clear low frequency hump in the response

spectrum due to the low frequency second order response. Humps are also noticed at twice and three times the main peak frequency. Comparison of this experimental result with first, second and third order simulations respectively tells us that the first and second order simulation underestimate the peak in the wave frequency band of the power spectrum severely. Approximately 40% of the spectral energy is missed by the linear and second order prediction. This is the explanation for the large spreading in the normalised first harmonic responses in regular waves, which showed an increase of the normalised first harmonic response amplitude in the frequency response peak of more than 20 % over the range of tested wave amplitudes, see figure 5. The low frequency and double frequency peak are very well predicted by applying the second order Volterra modelling. But only by using the third order Volterra modelling the triple frequency peak and particularly the energy density in the wave frequency range are predicted well. This illustrates that the high peak in the wave frequency range is the net result of the linear response plus the low-frequency third order response.

The characteristics of the response spectra are determined by the spectral moments. The n th order moment is defined as

$$m_n = \int_0^{\infty} S_{yy}(\omega) \omega^n d\omega \quad (29)$$

The variance of the response $y(t)$, $E[y(t)^2]$, is found for $n = 0$. For linear responses, the mean square velocity $E[\dot{y}(t)^2]$ is given by m_2 and m_4 defines the mean square acceleration $E[\ddot{y}(t)^2]$. The spectral moments of the measured and simulated hull girder loads are presented in table 2.

In general, it can be observed that the spectral moments for the original Wigley are not very sensitive to the order of simulation. A good correspondence with the experiments is found for every order of simulation. Therefore, for this particular Wigley model, a first or second order simulation would satisfy to predict the spectral moments.

The spectral moments of the bending moment responses in the Wigley with bow flare, however, are very sensitive to the order of simulation. As expected, this is especially true for the higher order moments since these moments characterise the time derivatives of the responses. In the previous chapter, it was discussed already that the time derivatives of the responses are significantly more sensitive to nonlinearities than the responses themselves. This is confirmed by the higher order spectral moments. It can be concluded that the third order

Response:	No bow flare					Bow flare				
Shear Force st.15 [N]	m_0	m_1	m_2	m_3	m_4	m_0	m_1	m_2	m_3	m_4
Experiment	78.3	790	1.72e4	9.12e5	6.73e7	125	1.40e3	3.99e4	2.24e7	1.79e8
Experiment (4Hz)	75.9	632	6.04e3	6.81e4	1.10e6	119	955	8.43e3	8.82e4	1.52e6
1st order	88.4	705	6.16e3	5.97e3	8.47e5	129	1.00e3	8.26e3	7.59e4	1.13e6
2nd order	93.6	751	6.88e3	7.21e4	1.08e6	133	1.03e3	8.71e3	8.39e4	1.29e6
3rd order	78.1	635	6.18e3	7.26e4	1.20e6	113	883	7.64e3	7.84e4	1.29e6
Bending Moment st.15 [Nm]	m_0	m_1	m_2	m_3	m_4	m_0	m_1	m_2	m_3	m_4
Experiment	7.8	87.2	2.30e3	1.38e5	1.06e7	14.8	250	9.64e3	5.84e5	4.11e7
Experiment (4Hz)	7.5	65.3	631	6.88e3	1.02e5	12.3	115	1.33e3	1.85e4	3.36e5
1st order	6.7	57.3	526	5.20e3	6.98e4	6.1	54	500	4.98e3	6.62e4
2nd order	7.0	59.7	560	5.77e3	8.11e4	9.1	80	864	1.07e4	1.72e5
3rd order	6.9	59.9	588	6.54e3	9.97e4	12.4	116	1.36e3	1.92e4	3.52e5
Shear Force st.10 [N]	m_0	m_1	m_2	m_3	m_4	m_0	m_1	m_2	m_3	m_4
Experiment	48.6	458	5.91e3	1.73e5	1.17e7	35.3	337	5.73e3	1.69e5	8.94e6
Experiment (4Hz)	48.2	437	4.43e3	5.10e4	7.69e5	34.2	328	3.50e3	4.21e4	6.32e5
1st order	46.9	417	4.07e3	4.39e4	6.27e5	31.2	286	2.84e3	3.09e4	4.38e5
2nd order	49.5	439	4.40e3	4.95e4	7.34e5	35.4	323	3.38e3	3.96e4	6.13e5
3rd order	49.9	453	4.68e3	5.45e4	8.28e5	41.5	385	4.06e3	4.90e4	7.75e5
Bending Moment st.10 [Nm]	m_0	m_1	m_2	m_3	m_4	m_0	m_1	m_2	m_3	m_4
Experiment	28.9	330	9.53e3	6.02e5	4.70e7	46.2	662	2.57e4	1.70e6	1.27e8
Experiment (4Hz)	27.8	234	2.23e3	2.43e4	3.78e5	41.3	344	3.19e3	3.52e4	6.62e5
1st order	30.5	251	2.25e3	2.21e4	3.13e5	36.6	298	2.55e3	2.40e4	3.47e5
2nd order	32.0	265	2.67e3	2.58e4	3.81e5	38.7	316	2.81e3	2.84e4	4.36e5
3rd order	27.2	224	2.17e3	2.48e4	3.97e5	34.4	293	2.84e3	3.35e4	5.81e5

Table 2: Comparison of the measured and simulated spectral moments of the vertical hull girder loads in both Wigley variants, all simulations filtered at 4 Hz

simulations gave the best results for the higher order spectral moments.

These computations were performed in order to investigate the characteristics of the simulated results with those of the experiments. However, it is also possible to calculate the response spectra including first, second and third order contributions directly in the frequency domain. The suitable formulations were summarized in [21].

4.3 Sample Probability Densities

It was already shown in the qualitative analysis of the irregular wave experiments that the sample probability densities of the bending moments deviated strongly from the equivalent Gaussian probability density function. This was especially noticeable for the Wigley with bow flare.

Deviations from the Gaussian distribution can be expressed by the statistical moments such as there are the mean μ , skew κ_3 and kurtosis κ_4 , which should all be zero in case of Gaussian signals. The statistical moments presented in this section are defined by the following expressions:

$$\mu = \frac{1}{N} \sum_{j=1}^N y_j \quad (30)$$

$$\kappa_1 = \frac{1}{N} \sum_{j=1}^N |y_j - \mu| \quad (31)$$

$$\sigma^2 = \frac{1}{N-1} \sum_{j=1}^N (y_j - \mu)^2 \quad (32)$$

$$\kappa_3 = \frac{1}{N} \sum_{j=1}^N \left[\frac{y_j - \mu}{\sigma} \right]^3 \quad (33)$$

$$\kappa_4 = \frac{1}{N} \sum_{j=1}^N \left[\frac{y_j - \mu}{\sigma} \right]^4 - 3 \quad (34)$$

where N is the number of samples. The analyses and comparisons made in this section were performed by regarding the ensemble of runs as one set of data, in this case 100,000 samples with a total length of 2500 seconds. This was allowed since the input wave spectrum was stationary and ergodic.

Table 3 shows the statistical moments of the recorded loads before and after filtering as well as the statistical moments of the reconstructed signals by applying the first, second and third order

Response:	No bow flare					Bow flare				
Shear Force st.15 [N]	μ	κ_1	σ^2	κ_3	κ_4	μ	κ_1	σ^2	κ_3	κ_4
Experiment	-0.089	7.067	78.26	0.130	0.142	-0.951	8.753	125.4	-0.271	1.439
Experiment (4Hz)	-0.089	6.999	75.91	0.075	-0.180	-0.951	8.635	118.5	-0.197	0.172
1st order	0.007	7.476	88.42	0.016	0.047	-0.008	9.012	129.1	0.007	0.181
2nd order	-0.426	7.617	93.59	-0.217	0.402	-0.903	9.057	132.6	-0.325	0.535
3rd order	-0.426	7.020	78.13	-0.135	0.179	-0.901	8.440	113.4	-0.322	0.328
Bending Moment st.15 [Nm]	μ	κ_1	σ^2	κ_3	κ_4	μ	κ_1	σ^2	κ_3	κ_4
Experiment	-0.041	2.177	7.764	-0.097	1.420	0.826	2.522	14.76	2.575	28.57
Experiment (4Hz)	-0.041	2.157	7.509	-0.159	0.415	0.826	2.563	12.30	1.511	8.013
1st order	0.006	2.045	6.678	-0.015	0.184	-0.001	1.958	6.113	-0.005	0.308
2nd order	-0.175	2.084	6.964	-0.020	0.201	0.975	2.301	9.148	0.779	2.723
3rd order	-0.175	2.060	6.823	-0.024	0.268	0.975	2.465	12.39	1.391	14.35
Shear Force st.10 [N]	μ	κ_1	σ^2	κ_3	κ_4	μ	κ_1	σ^2	κ_3	κ_4
Experiment	-0.003	5.464	48.56	0.316	0.937	0.282	4.659	35.32	0.341	1.498
Experiment (4Hz)	-0.003	5.439	48.20	0.292	0.741	0.282	4.589	34.23	0.235	0.739
1st order	0.015	5.432	46.90	0.022	0.118	-0.008	4.425	31.21	0.008	0.246
2nd order	-0.233	5.566	49.50	-0.022	0.197	0.654	4.589	35.39	0.617	1.606
3rd order	-0.234	5.589	49.92	-0.041	0.251	0.655	4.756	41.51	1.008	5.207
Bending Moment st.10 [Nm]	μ	κ_1	σ^2	κ_3	κ_4	μ	κ_1	σ^2	κ_3	κ_4
Experiment	0.209	4.241	28.91	-0.072	0.905	1.161	5.049	46.25	0.949	6.322
Experiment (4Hz)	0.209	4.194	27.76	-0.060	0.034	1.162	4.927	41.34	0.685	1.821
1st order	-0.003	4.382	30.45	-0.016	0.089	0.004	4.792	36.59	-0.003	0.258
2nd order	0.202	4.449	31.97	0.240	0.419	1.133	4.840	38.71	0.677	1.225
3rd order	0.202	4.140	27.02	0.166	0.106	1.133	4.579	34.39	0.610	1.312

Table 3: Comparison of the measured and simulated statistical moments of the vertical hull girder loads in both Wigley variants, all simulations filtered at 4 Hz

Volterra modelling. It was shown that by filtering, the standard deviation, variance, skew and kurtosis were significantly reduced.

The presence of bow flare resulted in a skew and kurtosis for the bending moments which were an order larger than those resulting from the model without bow flare. The skew and kurtosis of the shear force responses were less sensitive to the degree of bow flare. Particularly noticeable in this context is the kurtosis of the bending moment in the forward of the original Wigley and the Wigley with bow flare of 0.4 and 8.0 respectively. The third order simulations predicted 0.3 and 14.3 respectively. In the previous section, an increase as a function of the order of the simulations could already be noticed for the variance of the bending moment in the flared bow. This is also shown in table 3. It was found that the variance resulting from the third order simulation was twice as high as the variance resulting from the first order simulation, 12.4 and 6.1 respectively. The measured variance was 12.3 which is remarkably close to the third order result.

The applied modelling also allowed the computation of the response moments directly in the frequency domain. Formulations for the moments of the responses were derived in [21] by expressing

the statistical moments in terms of auto-correlation functions.

For the most interesting response regarding the degree of nonlinearity, i.e. the bending moment in the forward of the Wigley with bow flare, the measured and, with different orders, simulated probability density functions are plotted in figure 11.

Two aspects are important to notice when looking at these curves; the shape of the curves and the predicted positive and negative extreme values. It is interesting to see how well the third order simulation was able to predict the probability density in sagging condition.

Up to the maximum plotted values with a probability of slightly more than 0.001, the experimental results are simulated very well. In the linear simulations, the loads did not even reach these values and the probability of these loads would already be less than 0.00001. A better overall correspondence was found with the second order modelling but the extreme sagging moments were slightly underestimated.

The bending moments in hogging condition seem to be predicted better by the second order simulations than by the third order simulations. Whereas the probability density of the sagging moments

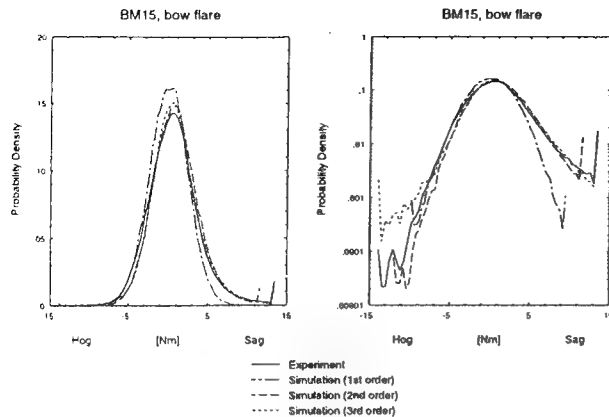


Figure 11: Measured and simulated probability density functions of the bending moment in the forward of the Wigley with bow flare at $F_n = 0.3$ on linear scale (left) and logarithmic scale (right) resulting from 100,000 samples

could not be predicted with a linear theory, it was possible to calculate the shape of the probability density of the bending moment in hogging condition quite well down to the 0.001 probability level. The calculated extreme linear hogging moment, however, was much smaller than observed in the experiments.

4.4 Peak-Peak Probability Densities

The final test for the proposed Volterra modelling was the comparison of the probability density of the peak-peak values. The time histories as well as the power spectra showed a wide band hull girder load response, which was not the result after the linear simulation, and was only partly estimated by the second order simulation. This implied that the number of extremes or cycles in the total simulated period varied for the different types of simulations. Values for the measured and calculated number of maxima are presented in table 4. From this table it can be read that the number of maxima in the motion responses was hardly affected by the order of the simulation. This was not the case for the hull girder loads. A maximum difference between the linear prediction and the third order prediction of 24 % was found, again for the bending moment in the forward of the Wigley with bow flare. For the original hull form, those differences were not as significant.

In order to compare the corresponding distributions of the response ranges properly, not the probability density functions $p_y(y)$ but the probability rates per unit of time were compared. Here, the

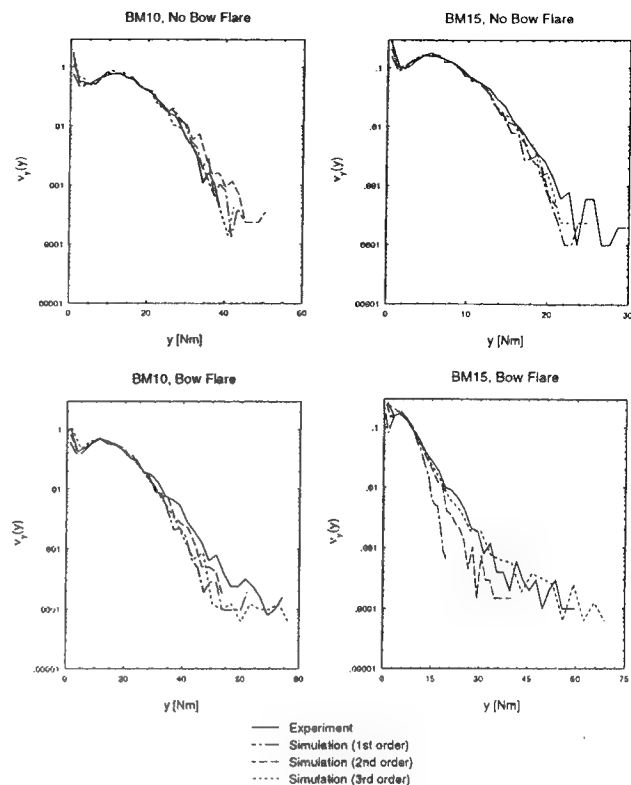


Figure 12: Probability density functions of the peak-peak values of the bending moments as measured and simulated for both Wigley models at $F_n = 0.3$

probability rate is defined as

$$\nu_y(y) = \frac{N}{T} p_y(y) \quad (35)$$

where N is the total number of cycles and T is the total length of all records together. Several counting methods, applied to stress records for fatigue damage analyses, were proposed in literature. In this report, the rain flow counting method is applied, which was proved to be superior to other counting methods by Wirsching and Moshen Shehata [24]. Using the rain flow counting method, high and low frequency cycles can be identified.

Figure 12 shows the probability density functions of the bending moments in terms of the probable number of events per second. The area under the curves from zero to the maximum observed value is a measure of the total number of events during a unity period. For the original Wigley, it was found that the different simulated curves and the experimental results were all within a rather narrow band. The predicted maxima were also of the same order.

For the Wigley with bow flare, the differences between the observed bending moment maxima in

Response (Original)	Experiment $N_E(100\%)$	1st order $N/N_E (\%)$	2nd order $N/N_E (\%)$	3rd order $N/N_E (\%)$
Wave	5050	100	100	100
Shear Force st.15	4286	86	94	103
Bending Moment st.15	4134	92	96	102
Shear Force st.10	4262	99	103	107
Bending Moment st.10	4075	91	96	104
Heave	2724	100	100	100
Pitch	2830	99	100	100

Response (Bow flare)	Experiment $N_E(100\%)$	1st order $N/N_E (\%)$	2nd order $N/N_E (\%)$	3rd order $N/N_E (\%)$
Wave	4953	100	100	100
Shear Force st.15	3872	90	93	97
Bending Moment st.15	4986	78	92	102
Shear Force st.10	4593	93	96	99
Bending Moment st 10	3952	90	95	103
Heave	2664	100	99	100
Pitch	2789	98	99	101

Table 4: Number of maxima N observed in the experiments and the first, second and third order simulations for the original Wigley (upper) and Wigley with bow flare (lower). All recordings filtered at 4 Hz, total length 2500 seconds

the forward resulting from the linear simulations and the third order simulations or experiments were about 300 %. The second order simulation only obtained values not more than about 60 % of the experimental maxima. It can also be seen that the third order simulated maximum bending moments in the forward were similar to the maximum bending moments amidships. This was confirmed by the experimental results.

5 Discussion and Conclusion

A third order Volterra modelling was developed for the calculation of the hull girder load responses in irregular waves. The fully nonlinear second and third order frequency response functions were estimated using the known nonlinear response in regular waves only. To validate the proposed modelling, the results from regular wave experiments were used as input of the modelling at this stage. This way, no assumptions had to be made concerning the physical origin of the different nonlinear effects in the response. The wave surface elevation itself was assumed to be Gaussian.

Using the proposed modelling, it was possible to make accurate predictions of the power-spectra of the most severe responses recorded. From the comparison of measured and simulated response spectra, it was concluded that including third order responses can be very important for two reasons.

The first reason is that the peak of the low

frequency third order response spectrum coincides with the peak of the energy spectrum of the first order response. This implies an additional third order response in the frequency band in which the responses are traditionally assumed to be linear and in which the wave energy density is generally high. The bending moments in the forward of the Wigley with bow flare were heavily affected by this contribution in particular.

The second reason is that due to the higher order contributions, the spectrum becomes wider. This is expressed by the higher order spectral moments, which were predicted better by the higher order simulations. This, in turn, also increases the number of cycles in a fixed period, which has its impact on the fatigue damage. The best prediction of the number of cycles were made using the third order modelling.

The probability density functions of the samples were calculated. For the severest nonlinear responses, it was shown that the first four statistical moments were predicted accurately. This could not be achieved with a lower order modelling.

The distribution functions of the peak-peak values showed that the maximum bending moments in the flared bow reached the same magnitudes as amidships. This could only be calculated using the third order simulation model.

Other researchers showed that the statistical characteristics of nonlinear responses are mainly determined by the first four statistical moments. Using the suggested modelling, these moments can be derived for realistic ship responses under severe non-

linear conditions, either directly in the frequency domain or indirectly by the analysis of long simulated time traces. Only the nonlinear response in regular waves is required to be known. In this paper, this information was deducted from the regular wave experiments but the results of a set of large amplitude ship motion simulations could be used as well.

Acknowledgements

The work reported herein was performed during the author's stay at the Laboratory of Ship Hydromechanics of the Delft University of Technology. The author is grateful to professor J.A. Pinkster and staff for inspiring discussions and for their assistance in model testing in particular. The research was financially supported by the Royal Netherlands Navy.

References

- [1] M. Kac and A. J. F. Siegert. On the theory of noise in radio receivers with square law detectors. *Journal of Applied Physics*, 18:383-397, 1947.
- [2] N. Wiener. *Nonlinear problems in random theory*. M. I. T. Press, Cambridge, Mass., 1958.
- [3] K. Hasselmann. On nonlinear ship motions in irregular waves. *Journal of Ship Research*, 10:64-68, 1966.
- [4] J. F. Dalzell. The applicability of the functional polynomial input-output model to ship resistance in waves. Technical Report SIT-DL-75-1794, Stevens Inst. of Technology, Hoboken, New Jersey, 1975.
- [5] J. A. Pinkster. *Low frequency second order wave exciting forces on floating structures*. PhD thesis, Techn. Univ. of Delft, 1980.
- [6] M. H. Kim and D. K. P. Yue. Sum- and difference-frequency wave loads on a body in unidirectional gaussian seas. *Journal of Ship Research*, 35(2):127-140, 1991.
- [7] J. J. Jensen and P. T. Pedersen. Bending moments and shear forces in ships sailing in irregular waves. *Journal of Ship Research*, 25:243-251, 1981.
- [8] M. S. Longuet-Higgins. The effect of nonlinearities on statistical distributions in the theory of sea waves. *Journal of Fluid Mechanics*, 17:459-480, 1963.
- [9] T. Vinje and S. O. Skjördal. On the calculation of the statistical distribution of maxima and minima of slightly non-linear, quadratic, stationary stochastic variables. *International Shipbuilding Progress*, 22:265-274, 1975.
- [10] J. J. Jensen. Fatigue analysis of ship hulls under non-gaussian wave loads. In *Marine Structures, Design, Construction and Safety*, pages 279-294. Elsevier Applied Science, 1991.
- [11] J. F. Dalzell. An investigation of the applicability of the third degree functional polynomial model of nonlinear ship motion problems. Technical Report SIT-DL-82-9-2275, Stevens Inst. of Technology, Hoboken, New Jersey, December 1982.
- [12] J. F. Dalzell. Approximations to the probability density of maxima and minima of the response of a nonlinear system. Technical Report EW-22-84, US Naval Academy, Annapolis, Maryland, 1984.
- [13] S. R. Winterstein. Nonlinear vibration models for extremes and fatigue. *Journal of Eng. Mech.*, ASCE, 114(10):1772-1790, 1988.
- [14] J. F. Dalzell. An investigation of midship bending moments experienced in extreme regular waves by a Mariner-type ship and three variants. Technical Report SSC-155, Ship Structure Committee, 1964.
- [15] J. F. Dalzell. An investigation of midship bending moments experienced in extreme regular waves by models of a tanker and a destroyer. Technical Report SSC-156, Ship Structure Committee, 1964.
- [16] D. C. Murdey. An analysis of longitudinal bending moments measured on models in head waves. *Transactions of Royal Institute of Naval Architects*, 114:221-240, 1972.
- [17] W. C. E. Nethercote. Motions and bending moments of a warship design. *Transactions of Royal Institute of Naval Architects*, 123:353-375, 1981.
- [18] J. F. O'Dea, E. Powers, and J. Zselecsky. Experimental determination of nonlinearities in vertical plane ship motions. In *Proc. of 19th Symp. on Naval Hydrodynamics*, pages 53-70, Seoul, Korea, 1992.

- [19] L. J. M. Adegeest. Experimental results of motion, shear force and bending moment measurements in large amplitude regular waves for a wigley model with bowflare. Technical Report 975, Delft University of Technology, Ship Hydromechanics Laboratory, 1993.
- [20] L. J. M. Adegeest. Experimental investigation of the influence of bow flare and forward speed on the nonlinear vertical motions, bending moments and shear forces in extreme regular waves. Technical Report 993 MEMT 32, Delft University of Technology, Ship Hydromechanics Laboratory, February 1994.
- [21] L. J. M. Adegeest. *Nonlinear Hull Girder Loads in Ships*. PhD thesis, Delft University of Technology, The Netherlands, 1995.
- [22] J. S. Bendat. *Nonlinear System Analysis & Identification from Random Data*. John Wiley and Sons, 1990.
- [23] L. J. M. Adegeest. Third-order volterra modeling of ship responses based on regular wave results. Technical Report 988 MEMT 30, Delft University of Technology, Ship Hydromechanics Laboratory, 1994.
- [24] P. H. Wirsching and A. Moshen Shehata. Fatigue under wide band random stresses using the rain-flow method. *Journal of Engineering Materials and Technology*, 99(3):205-211, 1977.

H	Wave height
$Z(\omega)$	Fourier transform wave surface elevation
$\delta(\cdot)$	Delta function
ε	Phase angle
$\zeta(t)$	Wave surface elevation
λ	Wave length
ω	Frequency of oscillation

Nomenclature

$h_1(t_1)$	First order time domain kernel
$h_2(t_1, t_2)$	Second order time domain kernel
$h_3(t_1, t_2, t_3)$	Third order time domain kernel
$n(t)$	Uncorrelated Gaussian noise
t	Time variable
$y_1(t)$	First order response
$y_2(t)$	Second order response
$y_3(t)$	Third order response
\bar{y}	Mean response
A	Wave amplitude
$B_1(\omega)$	First order frequency response function
$B_2(\omega)$	Second order frequency response function
$B_3(\omega)$	Third order frequency response function
$B_3^{LF}(\omega)$	Third order low-frequency component
$B_3^{HF}(\omega)$	Third order high-frequency component
$H_1(\omega_1)$	First order frequency response function
$H_2(\omega_1, \omega_2)$	Second order frequency response function
$H_3(\omega_1, \omega_2, \omega_3)$	Third order frequency response function

DISCUSSION

L.J. Doctors

University of New South Wales, Australia

The computed results seem to show that there is much more nonlinearity in the responses for the forces and moments than for the motions themselves. Is this simply due to the factor that the frequencies associated with the harmonics are higher and that the forces and moments depend on temporal derivatives of the motions?

AUTHOR'S REPLY

As mentioned by the discussor, the measured hull girder loads showed a much more pronounced nonlinear behavior than the motions did. To explain this phenomenon, it is necessary to explain the physical origin of the loads. In general, hull girder loads are defined as the forces and moments in a hull cross-section, i.e., the "internal loads," which make equilibrium with the net external forces and moments and the inertial reactions of the ship. The external loads are the net result of a pressure integration over the hull surface.

There are two reasons for the observation of much more pronounced nonlinearities in the hull-girder loads than in the motion responses. The first reason is the dominance of inertial effects in the hull girder loads. As illustrated by equation (2), the relative magnitudes of amplitudes of higher order effects in time-varying signals are increased simply by a time-derivation of the signal. It should be understood that the acceleration of the vessel is the net result of the global mass inertia characteristics of the vessel and of the overall excitation forces. The second reason is the sensitivity of hull girder loads to local external forces. Locally, the external forces acting on a part of the vessel can behave much more nonlinearly than the overall forces. This is because the local nonlinear force contributions are smoothed out over the whole surface. The internal loads are directly affected by these local nonlinearities in the bow and aft region of the vessel, especially in the case of bow flare in combination with large relative motions. Even then, it is possible that hardly any nonlinear behavior can be observed in the motion responses.

Nonlinearly Interacting Responses of the Two Rotational Modes of Motion—Roll and Pitch Motions

I.-G. Oh (Samsung Heavy Industries, Korea),

A. Nayfeh (Virginia Polytechnic Institute and State University, USA)

ABSTRACT

The nonlinear dynamic responses and stability of marine vehicles are investigated when they are excited by regular waves. When the vehicles are under the condition of a two-to-one internal or autoparametric resonance in which the natural frequency of the pitch mode is twice that of the roll mode, they may exhibit large-amplitude responses in an indirectly excited mode by the direct excitation of the other mode. Moreover, it is known that the damping in the roll mode is a highly viscous and thus a strongly nonlinear one while that in the pitch mode a linear one over a relatively wide range of motions.

The problem is modeled mathematically by a dissipative nonlinear two-degree-of-freedom system subject to harmonic external excitations in the presence of a two-to-one internal resonance. Also to take into account the damping effects, a linear-plus-quadratic damping model is introduced in the equation for the roll mode while a linear damping model is kept in the equation for the pitch mode. The method of multiple scales is used to determine the influence of the quadratic nonlinear roll damping on the periodic responses of both modes and their stability.

The cases when the encounter frequency is near the natural frequency of the pitch mode and when the encounter frequency is near the natural frequency of the roll mode are investigated to provide the force-response curves and frequency-response curves.

1. INTRODUCTION

The extent of the motion that a marine vehicle may experience has important consequences on its safety, operability, and economical aspects. So, one must understand the complicated dynamics of a

vessel moving in a general environment to design more comfortable and safe vessels.

Loss of stability due to excessive motions, such as heavy rolling, can happen through the energy transfer between the modes of motion if nonlinearities are present and various resonances of the internal, external, or parametric type occur. The present research is concerned with the dynamic stability and excessive motion of a vessel in the presence of two-to-one internal or autoparametric resonance in which the natural frequency in pitch is twice that in roll.

The significance of internal resonance has been recognized recently in many mechanical and elastic systems. To model the mechanism of nonlinear interactions between modes, one needs to model the system by two or more nonlinearly coupled oscillators. There are a number of references dealing with physical two-degree-of-freedom systems. Among others, Nayfeh and Mook (1) discussed problems involving the forced responses of robots, elastic pendulums, beams and plates under static loadings, composite plates, arches, shells, and the sloshing of liquid gasoline in the fuel container of an airplane. All of these problems can be modeled by coupled, inhomogeneous ordinary-differential equations with quadratic nonlinearities. When these systems possess internal (or autoparametric) resonances, which may occur if the natural frequencies of the system are commensurate, their responses may exhibit extraordinarily complicated behaviors, which cannot be explained by linear formulations.

Interestingly, two-to-one autoparametric or internal resonances may strongly influence the dynamic behavior and stability of vessels (1). A strong coupling of the involved modes of motion produced by internal or autoparametric resonance was first observed by Froude in 1863. He observed that a vessel whose linear undamped natural frequency in

pitch is twice that in roll (2) has undesirable seakeeping characteristics. This observation was a manifestation of the two-to-one internal resonance whose significance cannot be determined using linearized equations (3, 4, 5, 6, 7).

For a century after Froude, however, no further research on this phenomenon was pursued. In 1959, Paulling and Rosenberg (8) studied the coupled heave-roll motion of a vessel using a set of nonlinear ordinary-differential equations. They simplified the equations of motion and obtained a single roll equation having the form of a simple linear Mathieu equation which contains a time-varying coefficient due to a simple harmonic motion of the heave mode. In this model, the heave influences the roll but the roll does not influence the heave. Experimentally, they tested the case of unstable rolling motion excited by the heave mode only. This study has two principal shortcomings. First, due to the lack of consideration for damping and nonlinear coupling terms, the analytical model was not capable of yielding realistic results. Second, in the experimental setup, the heave mode was given a prescribed motion and hence the effect of roll motion and waves generated thereafter on the heave mode are not taken into account.

Kinney (9), Kerwin (10), Blocki (11), and Sanchez and Nayfeh (12) also studied the response of the roll to longitudinal waves. Except for Blocki's study, all other studies are theoretical ones. In his experiment, Blocki considered coupling of the heave and roll modes of a ship that possesses fore and aft symmetry, which is placed in beam waves. As in the study of Paulling and Rosenberg, he studied the case of parametrically excited roll motions in which energy is fed to the roll mode by a prescribed heave or pitch motion, or equivalently, wave motion. His equations reduce essentially to a one-degree-of-freedom model governing only the roll mode.

To explain Froude's observation, Nayfeh, Mook, and Marshall (13) and Mook, Marshall, and Nayfeh (14) modeled the ship motion by two nonlinearly coupled equations involving the pitch and roll modes; they included the dependence of the pitching moment on the roll orientation. Thus, the pitch (heave) motion is not prescribed but is coupled to the roll motion, and consequently, the pitch (heave) and roll orientations are determined simultaneously as functions of a prescribed excitation. They clearly showed the significance of the frequency ratio in causing undesirable roll behaviors, such as the "saturation" phenomenon. They offered an explanation of the observations of Froude.

Nayfeh (15) considered the nonlinearly coupled roll and pitch motions of a ship in regular

head waves in which the couplings are primarily in the hydrostatic terms when the pitch frequency is approximately twice the roll frequency and the encounter frequency is near either the pitch or roll natural frequency. He demonstrated the saturation phenomenon when the encounter frequency is near the pitch natural frequency.

In the present paper, we use a linear-plus-quadratic damping model for the roll motion and investigate the cases of primary resonances. The linear-plus-quadratic damping model has long been recognized by investigators to describe closely the dissipation of energy in the roll mode. However, it was not used so far because of some analytical difficulties. We obtain various complicated responses, which are common features of the nonlinear dynamics of many mechanical and elastic systems. These responses include supercritical and subcritical instabilities, periodic motions, and coexistence of multiple solutions and associated jumps. The quadratic damping eliminates the saturation phenomenon. Such phenomena can never be addressed by the linear approach because it is incapable of representing not only the strong nonlinear interaction between the two modes but also the effect of the viscous damping in the roll mode.

2. EQUATIONS OF MOTION

We consider the response of a ship that is restricted to pitch and roll to a regular wave. We assume that the ship is laterally symmetric. We use the right-handed coordinate systems: a body-fixed coordinate system $oxyz$ such that its origin o is at the center of mass, the x -axis is positive toward the bow, the y -axis is positive toward starboard, and the z -axis is positive downward. The orientation of the ship with respect to an inertial frame $OXYZ$ is defined by the Euler angles ϕ and θ as follows: θ is a pitch rotation about the original y -axis, and ϕ is a roll rotation about the new x -axis. The components p and q of the angular velocity about the x - and y -axes are related to $\phi, \theta, \dot{\phi}$, and $\dot{\theta}$ by

$$p = \dot{\phi} \quad \text{and} \quad q = \dot{\theta} \cos \phi \quad (1)$$

The equations of motion can be written as

$$I_{xx}\dot{p} - I_{xz}pq = K + K_o \cos \Omega t \quad (2)$$

$$I_{yy}\dot{q} + I_{xz}p^2 = M + M_o \cos(\Omega t + \tau) \quad (3)$$

where I_{xx} , I_{yy} , and I_{xz} are the moments and product of inertia, Ω is the encounter frequency, K_0 and M_0 are the amplitudes of the moments produced by the waves, and τ is a phase; they are assumed constants. We assume that the hydrodynamic moments K and M are analytic functions of ϕ and θ and their derivatives. Following Nayfeh (15) and Nayfeh, Mook, and Marshall (16) and including a quadratic damping term in the roll equation, we obtain

$$\ddot{\phi} + \omega_1^2 \phi = \varepsilon \left[-2\mu_1 \dot{\phi} - \mu_3 \dot{\phi} |\dot{\phi}| + \delta_1 \phi \theta + \delta_2 \phi \ddot{\theta} + \delta_3 \theta \ddot{\phi} + \delta_4 \dot{\phi} \dot{\theta} + F_1 \cos \Omega t \right] \quad (4)$$

$$\ddot{\theta} + \omega_2^2 \theta = \varepsilon \left[-2\mu_2 \dot{\theta} + \alpha_1 \phi^2 + \alpha_2 \phi \ddot{\phi} + \alpha_3 \theta^2 + \alpha_4 \theta \ddot{\theta} + \alpha_5 \dot{\phi}^2 + \alpha_6 \dot{\theta}^2 + F_2 \cos(\Omega t + \tau) \right] \quad (5)$$

where ε is a small dimensionless parameter that is introduced as a bookkeeping device in the perturbation analysis that follows.

3. ANALYSIS

We use the method of multiple scales (17,18) to determine a first-order approximation to the solutions of equations (4) and (5). We let

$$\phi(t; \varepsilon) = \phi_0(T_0, T_1) + \varepsilon \phi_1(T_0, T_1) + \dots \quad (6)$$

$$\theta(t; \varepsilon) = \theta_0(T_0, T_1) + \varepsilon \theta_1(T_0, T_1) + \dots \quad (7)$$

where $T_0 = t$ is a fast time scale, characterizing motions on the scales ω_1 and Ω ; and $T_1 = \varepsilon t$ is a slow time scale, characterizing the modulation of the amplitudes and phases of the motion. In terms of T_0 and T_1 , the time derivatives are transformed into

$$\begin{aligned} \frac{d}{dt} &= D_0 + \varepsilon D_1 + \dots \\ \text{and } \frac{d^2}{dt^2} &= D_0^2 + 2\varepsilon D_0 D_1 + \dots \end{aligned} \quad (8)$$

where $D_n = \partial / \partial T_n$.

Substituting equations (6)-(8) into equations (4) and (5) and equating coefficients of like powers of ε , we obtain

$O(\varepsilon^0)$:

$$D_0^2 \phi_0 + \omega_1^2 \phi_0 = 0 \quad (9)$$

$$D_0^2 \theta_0 + \omega_2^2 \theta_0 = 0 \quad (10)$$

$O(\varepsilon)$:

$$\begin{aligned} D_0^2 \phi_1 + \omega_1^2 \phi_1 &= -2D_0 D_1 \phi_0 - 2\mu_1 D_0 \phi_0 \\ &\quad - \mu_3 D_0 \phi_0 |D_0 \phi_0| + \delta_1 \phi_0 \theta_0 + \delta_2 \phi_0 D_0^2 \theta_0 \\ &\quad + \delta_3 \theta_0 D_0^2 \phi_0 + \delta_4 D_0 \phi_0 D_0 \theta_0 + F_1 \cos \Omega T_0 \end{aligned} \quad (11)$$

$$\begin{aligned} D_0^2 \theta_1 + \omega_2^2 \theta_1 &= -2D_0 D_1 \theta_0 - 2\mu_2 D_0 \theta_0 \\ &\quad + \alpha_1 \phi_0^2 + \alpha_2 \phi_0 D_0^2 \phi_0 + \alpha_3 \theta_0^2 + \alpha_4 \theta_0 D_0^2 \theta_0 \\ &\quad + \alpha_5 (D_0 \phi_0)^2 + \alpha_6 (D_0 \theta_0)^2 + F_2 \cos(\Omega T_0 + \tau) \end{aligned} \quad (12)$$

The solutions of equations (9) and (10) can be expressed as

$$\phi_0 = A_1(T_1) e^{i\omega_1 T_0} + \bar{A}_1(T_1) e^{-i\omega_1 T_0} \quad (13)$$

$$\theta_0 = A_2(T_1) e^{i\omega_2 T_0} + \bar{A}_2(T_1) e^{-i\omega_2 T_0} \quad (14)$$

where A_1 and A_2 are unknown functions at this level of approximation. They are determined by imposing the solvability conditions at the next level of approximation. Alternatively, the solutions of equations (13) and (14) can be expressed as

$$\phi_0 = a_1(T_1) \cos[\omega_1 T_0 + \beta_1(T_1)] \quad (15)$$

$$\theta_0 = a_2(T_1) \cos[\omega_2 T_0 + \beta_2(T_1)] \quad (16)$$

where the a_n and β_n are the amplitudes and phases of the roll and pitch modes. Comparing equations (13) and (14) with equations (15) and (16), we conclude that

$$A_n(T_1) = \frac{1}{2} a_n(T_1) e^{i\beta_n(T_1)} \quad (17)$$

Substituting equations (13) and (14) into equations (11) and (12) yields

$$\begin{aligned}
D_0^2 \phi_1 + \omega_1^2 \phi_1 &= -2i\omega_1 (A_1' + \mu_1 A_1) e^{i\omega_1 T_0} \\
&+ (\delta_1 - \omega_2^2 \delta_2 - \omega_1^2 \delta_3 - \omega_1 \omega_2 \delta_4) A_2 A_1 e^{i(\omega_2 + \omega_1) T_0} \\
&+ (\delta_1 - \omega_2^2 \delta_2 - \omega_1^2 \delta_3 + \omega_1 \omega_2 \delta_4) A_2 \bar{A}_1 e^{i(\omega_2 - \omega_1) T_0} \quad (18) \\
&+ \frac{1}{2} F_1 e^{i\Omega T_0} + cc + f [i\omega_1 A_1 e^{i\omega_1 T_0} - i\omega_1 \bar{A}_1 e^{-i\omega_1 T_0}]
\end{aligned}$$

$$\begin{aligned}
D_0^2 \theta_1 + \omega_2^2 \theta_1 &= -2i\omega_2 (A_2' + \mu_2 A_2) e^{i\omega_2 T_0} \\
&+ (\alpha_1 - \omega_1^2 \alpha_2 - \omega_1^2 \alpha_3) A_1^2 e^{2i\omega_1 T_0} \\
&+ (\alpha_3 - \omega_2^2 \alpha_4 - \omega_2^2 \alpha_5) A_2^2 e^{2i\omega_2 T_0} \quad (19) \\
&+ (\alpha_1 - \omega_1^2 \alpha_2 + \omega_1^2 \alpha_3) A_1 \bar{A}_1 \\
&+ (\alpha_3 - \omega_2^2 \alpha_4 + \omega_2^2 \alpha_5) A_2 \bar{A}_2 + \frac{1}{2} F_2 e^{i(\Omega T_0 + \tau)} + cc
\end{aligned}$$

where the prime indicates the derivative with respect to T_1 , \bar{A}_n is the complex conjugate of A_n , and the function f accounts for the term $-\mu_3 D_0 \phi_0 |D_0 \phi_0|$. Depending on the functions A_n , particular solutions of equations (18) and (19) contain terms proportional to $T_0 e^{\pm i\omega_n T_0}$ (i.e., secular terms). They also contain small-divisor terms if $\Omega \approx \omega_1$ or $\Omega \approx \omega_2$ (i.e., primary resonances of the pitch or roll mode) and/or if $\omega_2 \approx 2\omega_1$ (the frequency of pitch mode is approximately twice that of roll mode; i.e., two-to-one internal or autoparametric resonance).

To eliminate the secular and small-divisor terms, we first expand $f(D_0 \phi_0)$ in a Fourier series as

$$f = \sum_{n=-\infty}^{\infty} f_n(A_1, \bar{A}_1) e^{in\omega_1 T_0} \quad (20)$$

where

$$f_n(A_1, \bar{A}_1) = \frac{\omega_1}{2\pi} \int_0^{2\pi/\omega_1} f e^{-in\omega_1 T_0} dT_0 \quad (21)$$

Consequently, the component of f that produces a secular term is

$$\frac{\omega_1}{2\pi} \int_0^{2\pi/\omega_1} f e^{-i\omega_1 T_0} dT_0 \quad (22)$$

We analyze the case of primary resonance of the pitch mode in Section 4 and of primary resonance of the roll mode in Section 5.

4. PRIMARY RESONANCE OF THE PITCH MODE

4.1 Modulation Equations

To express the nearness of the resonances, we introduce two detuning parameters, σ_1 and σ_2 , defined as

$$\omega_2 = 2\omega_1 + \varepsilon \sigma_1 \quad \text{and} \quad \Omega = \omega_2 + \varepsilon \sigma_2 \quad (23a)$$

Hence,

$$\omega_2 T_0 = 2\omega_1 T_0 + \sigma_1 T_1 \quad \text{and} \quad \Omega T_0 = \omega_2 T_0 + \sigma_2 T_1 \quad (23b)$$

Using equations (23) and (22) and eliminating the terms that produce secular terms from equations (18) and (19), we obtain

$$\begin{aligned}
2i(A_1' + \mu_1 A_1) - 4\Lambda_1 A_2 \bar{A}_1 e^{i\sigma_1 T_1} \\
- \frac{1}{2\pi} \int_0^{2\pi/\omega_1} f e^{-i\omega_1 T_0} dT_0 = 0 \quad (24)
\end{aligned}$$

$$2i(A_2' + \mu_2 A_2) - 4\Lambda_2 A_1^2 e^{-i\sigma_1 T_1} - f_2 e^{i(\sigma_2 T_1 + \tau)} = 0 \quad (25)$$

where

$$4\omega_1 \Lambda_1 = \delta_1 - \omega_2^2 \delta_2 - \omega_1^2 \delta_3 + \omega_1 \omega_2 \delta_4 \quad (26)$$

$$4\omega_2 \Lambda_2 = \alpha_1 - \omega_1^2 (\alpha_2 + \alpha_3) \quad (27)$$

$$\omega_2 f_2 = \frac{1}{2} F_2 \quad (28)$$

Nayfeh (15) and Nayfeh, Mook, and Marshall (13) concluded that Λ_1 and Λ_2 have the same sign; otherwise, the unforced ship would be self-oscillating, which is unrealistic due to dissipation.

Substituting equation (17) into equations (24) and (25), rewriting equation (15) as

$$\phi_0 = a_1(T_1) \cos \chi_1, \quad \chi_1 = \omega_1 T_0 + \beta_1(T_1) \quad (29)$$

After separating real and imaginary parts of equations (24) and (25) and evaluating the terms corresponding to the last term in equation (24) by replacing the function f with $-\mu_3 D_0 \phi_0 |D_0 \phi_0|$, we obtain

$$-\frac{1}{2\pi\omega_1} \int_0^{2\pi} \sin \chi_1 (-\mu_3 D_0 \phi_0 |D_0 \phi_0|) d\chi_1 \quad (30)$$

$$= -\frac{4\mu_3\omega_1}{3\pi} a_1 |a_1|$$

$$-\frac{1}{2\pi\omega_1} \int_0^{2\pi} \cos \chi_1 (-\mu_3 D_0 \phi_0 |D_0 \phi_0|) d\chi_1 = 0 \quad (31)$$

Applying the appropriate transformation of variables, we obtain a generic system of equations as follows :

$$a_1' = -\mu_1 a_1 + a_1 a_2 \sin \gamma_1 - \frac{4\mu_3\omega_1}{3\pi} a_1 |a_1| \quad (32)$$

$$a_2' = -\mu_2 a_2 - a_1^2 \sin \gamma_1 + f_2 \sin \gamma_2 \quad (33)$$

$$a_1 \beta_1' = -a_1 a_2 \cos \gamma_1 \quad (34)$$

$$a_2 \beta_2' = -a_1^2 \cos \gamma_1 - f_2 \cos \gamma_2 \quad (35)$$

where

$$\gamma_1 = \sigma_1 T_1 + \beta_2 - 2\beta_1 \text{ and } \gamma_2 = \sigma_2 T_1 - \beta_2 + \tau \quad (36)$$

4.2 Fixed Points

We investigate the fixed points of the modulation equations (32)-(35), which correspond to periodic responses of the ship. They correspond to $a_1' = a_2' = 0$ and $\gamma_1' = \gamma_2' = 0$. It follows from equation (36) that

$$\beta_2' = \sigma_2 \text{ and } \beta_1' = \frac{1}{2}(\sigma_1 + \sigma_2) \quad (37)$$

Hence, the fixed points of equations (32)-(36) are given by

$$\mu_1 a_1 = a_1 a_2 \sin \gamma_1 - \frac{4\mu_3\omega_1}{3\pi} a_1 |a_1| \quad (38)$$

$$\mu_2 a_2 = -a_1^2 \sin \gamma_1 + f_2 \sin \gamma_2 \quad (39)$$

$$\frac{1}{2}(\sigma_1 + \sigma_2) a_1 = -a_1 a_2 \cos \gamma_1 \quad (40)$$

$$\sigma_2 a_2 = -a_1^2 \cos \gamma_1 - f_2 \cos \gamma_2 \quad (41)$$

There are two possible solutions for equations

(38)-(41). First,

$$a_1 = 0 \text{ and } a_2 = \frac{f_2}{\sqrt{\sigma_2^2 + \mu_2^2}} \quad (42)$$

and the response is given by

$$\phi = 0 \text{ and } \theta = a_2 \cos(\Omega t + \tau - \gamma_2) + \dots \quad (43)$$

which is essentially the linear solution. Second,

$$a_2 = \left[\frac{1}{4}(\sigma_1 + \sigma_2)^2 + \left(\mu_1 + \frac{4\mu_3\omega_1}{3\pi} a_1 \right)^2 \right]^{1/2} \quad (44)$$

and a_1 is given by the algebraic equation

$$a_1^4 + c_3 a_1^2 |a_1| + c_2 a_1^2 + c_1 |a_1| + c_0 = 0 \quad (45)$$

where c_i ($i = 0, 1, 2$, and 3) are constant coefficients determined from control parameters in use, such as $\sigma_1, \sigma_2, \mu_1, \mu_2, \mu_3, f_2$, and ω_1 ; they are given by

$$c_0 = (\mu_2^2 + \sigma_2^2) \left[\frac{1}{4}(\sigma_1 + \sigma_2)^2 + \mu_1^2 \right] - f_2^2 \quad (46)$$

$$c_1 = (\mu_2^2 + \sigma_2^2) \frac{8\mu_1\mu_3\omega_1}{3\pi} \quad (47)$$

$$c_2 = (\mu_2^2 + \sigma_2^2) \left(\frac{4\mu_3\omega_1}{3\pi} \right)^2 + 2\mu_1\mu_2 - \sigma_2(\sigma_1 + \sigma_2) \quad (48)$$

$$c_3 = \frac{8\mu_2\mu_3\omega_1}{3\pi} \quad (49)$$

The response in this case is given by

$$\phi = a_1 \cos\left(\frac{1}{2}\Omega t + \tau - \frac{1}{2}\gamma_1 - \frac{1}{2}\gamma_2\right) + \dots \quad (50)$$

$$\theta = a_2 \cos(\Omega t + \tau - \gamma_2) + \dots \quad (51)$$

We note from equations (44) and (45) that if $a_1 = 0$, then $c_0 = 0$ and thus this second solution reduces to the first solution (42); that is, the linear solution.

When $\mu_3 = 0$, but $a_1 \neq 0$, equation (44)

becomes

$$a_2 = \left[\frac{1}{4} (\sigma_1 + \sigma_2)^2 + \mu_1^2 \right]^{1/2} = a_2^* \quad (52)$$

which is independent of a_1 and f_2 . Moreover, $c_1 = c_3 = 0$, then we obtain

$$a_1 = \left[\Gamma_1 \pm (f_2^2 - \Gamma_2^2)^{1/2} \right]^{1/2} \quad (53)$$

where

$$\Gamma_1 = \frac{1}{2} \sigma_2 (\sigma_1 + \sigma_2) - \mu_1 \mu_2 \quad (54)$$

$$\Gamma_2 = \sigma_2 \mu_1 + \frac{1}{2} \mu_2 (\sigma_1 + \sigma_2) \quad (55)$$

The solution (52)-(55) is a special case of the second solution given by equations (44) and (45) and indicates the saturation phenomenon.

We note that the second solution (44)-(51) does not exhibit the saturation phenomenon unless $\mu_3 = 0$. Instead, the amplitude a_2 of the directly excited pitch mode as well as the amplitude a_1 of the roll mode vary as functions of f_2 . We have developed a computer code to solve equation (45) for a_1 . Then, a_2 is obtained from equation (44) and the corresponding γ_1 and γ_2 (β_1 and β_2 also) are obtained from equations (38)-(41).

4.3 Stability of Fixed Points

The stability of the fixed points and hence the stability of the periodic responses are determined in the following manner using the modulation equations (32)-(36).

The stability of a fixed point depends on the real parts of the eigenvalues of the Jacobian matrix A ; that is, the roots of

$$|A - \lambda I| = 0 \quad (56)$$

where

$$A = \nabla F(\tilde{p}_0) \quad (57)$$

is the Jacobian matrix evaluated at a given fixed point

\tilde{p}_0 and F is a real four-dimensional vector function of the four-dimensional vector $\tilde{p} = (a_1, a_2, \gamma_1, \gamma_2)^T$.

A given fixed point is asymptotically stable if and only if all the λ 's lie in the left half of the complex plane and is unstable if at least one eigenvalue lies in the right half of the complex plane. If the real part of a pair of complex-conjugate eigenvalues is positive, the modulation equations possess either periodically or chaotically modulated solutions.

A Hopf bifurcation point is defined as a critical value of a control parameter at which a pair of complex-conjugate eigenvalues of the Jacobian matrix cross the imaginary axis into the right half of the complex plane with nonzero speed. This type of loss of stability fits the Hopf bifurcation theorem, according to which the modulation equations possess limit-cycle solutions near the bifurcation points.

We note again that fixed points of the modulation equations correspond to periodic oscillations of the pitch and roll modes. Moreover, limit-cycle solutions of the modulation equations correspond to two-period quasiperiodic pitch and roll motions. Furthermore, chaotic solutions of the modulation equations correspond to chaotically modulated motions. Consequently, the response is an amplitude- and phase-modulated combined pitch and roll motion, with the energy being continuously exchanged between the two modes.

4.4 Numerical Results and Discussion

We implemented the computer simulations using an IBM 3090 digital supercomputer. The fixed-point solutions are verified by numerically integrating the autonomous amplitude- and phase-modulation equations (32)-(35) using a 5th- and 6th-order Runge-Kutta-Verner algorithm with double precision arithmetics. We examined bifurcations as we vary a bifurcation parameter, such as the detuning parameter σ_2 , the excitation amplitude f_2 , or the quadratic damping coefficient μ_3 while all the other parameters (i.e., σ_1 , μ_1 , μ_2) are kept constant.

We point out here that the existence of real solutions for a_1 and a_2 can be determined by examining equations (44) and (45). From equation (44), we can say that a_2 is real if a_1 is real, where a_1 is determined from equation (45). Because equation (45) is a fourth-order algebraic equation, an analytic solution for a_1 is not readily available. To determine the region where a_1 is real, we use

analytical continuations starting from $\mu_3 = 0$. Thus, we start by putting μ_3 equal to zero and obtain equations (52)-(55).

For simplicity in further discussion, we define the following two critical values of f_2 :

$$\zeta_1 = |\Gamma_2| \quad (58)$$

$$\zeta_2 = (\Gamma_1^2 + \Gamma_2^2)^{1/2} = a_2^* \sqrt{\sigma_2^2 + \mu_2^2} \quad (59)$$

It is clear that $\zeta_1 \leq \zeta_2$. It follows from equation (53), that f_2 must be greater than or equal to $|\Gamma_2|$ (i.e., $f_2 \geq |\Gamma_2| = \zeta_1$) for a_1 to be real. Then, there are two possibilities, depending on whether Γ_1 is positive or negative. When $\Gamma_1 < 0$, there is only one real root of equation (53) when $f_2 \geq (\Gamma_1^2 + \Gamma_2^2)^{1/2} = \zeta_2$. When $\Gamma_1 > 0$, equation (53) has two real roots when $|\Gamma_2| \leq f_2 \leq (\Gamma_1^2 + \Gamma_2^2)^{1/2}$ or $\zeta_1 \leq f_2 \leq \zeta_2$ and one real root when $f_2 \geq (\Gamma_1^2 + \Gamma_2^2)^{1/2}$ or $f_2 \geq \zeta_2$.

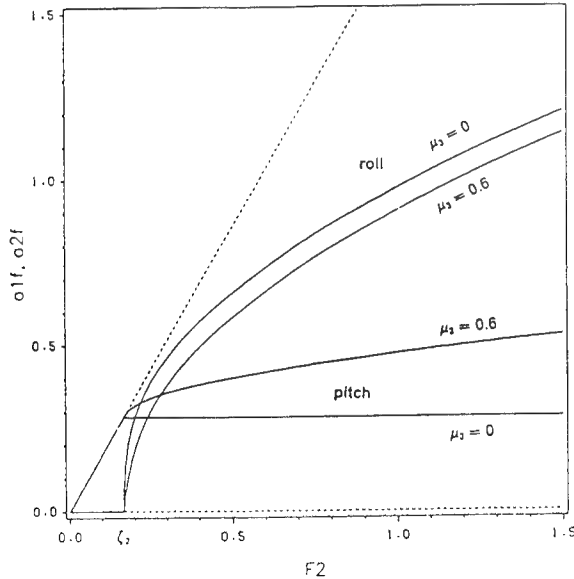


Fig. 1 (a) Force-Response Curves (Supercritical Type) : for $\mu_3 = 0$ and 0.6 ; stable(—), unstable(...)

4.4.1 Breaking of Saturation in Force-Response Curves

Figures 1 show the results for $\mu_3 = 0$ and $\mu_3 \neq 0$ when $\mu_1 = 0.2$, $\mu_2 = 0.5$, $\sigma_2 = 0.3$, $\sigma_1 = 0.1$, and thus $\Gamma_1 = -0.04$. Figure 1 (a) shows typical force-response curves of the supercritical-type in which a_1 and a_2 vary with f_2 for $\mu_3 = 0$ and

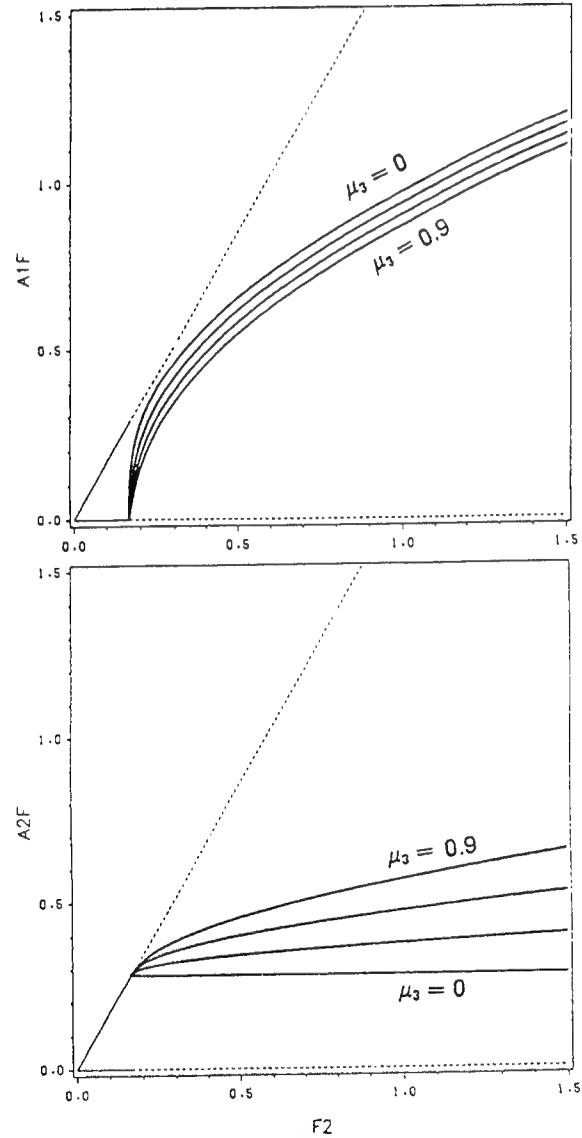


Fig. 1 (b)&(c) Force-Response Curves (Supercritical Type) : variation of (b) roll amplitude a_1 and (c) pitch amplitude a_2 , for different values of μ_3 ; stable(—), unstable(...)

$\mu_3 = 0.6$, a typical value of nonzero μ_3 . Since $\Gamma_1 < 0$ in this case, equation (53) has one stable real root for $f_2 \geq \zeta_2$ ($\zeta_2 \approx 0.1649$), irrespective of whether $\mu_3 = 0$ or $\mu_3 \neq 0$. When $f_2 \leq \zeta_2$, the responses are given by equation (43); their amplitudes are given by (42), which are independent of μ_3 . Thus, the response is linear in which the roll motion is not excited while the amplitude of the pitch mode is proportional to f_2 . When $f_2 > \zeta_2$, the responses are given by equations (50) and (51); their amplitudes are given by (52) and (53) for $\mu_3 = 0$ and by (44) and (45) for $\mu_3 \neq 0$. We note that when $\mu_3 \neq 0$ the amplitude a_2 of the pitch mode no longer exhibits the saturation phenomenon which exists for $\mu_3 = 0$. Thus, the quadratic damping μ_3 breaks the saturation. Instead, the amplitude a_2 of the pitch mode grows nonlinearly rather than staying at a constant value a_2^* as f_2 increases beyond ζ_2 . We note, however, that the slope of a_2 for $f_2 \geq \zeta_2$ is still much less than that corresponding to the linear case. With the introduction of the quadratic damping μ_3 , the rate of increase of the amplitude a_1 of the roll mode with f_2 is less than that in the case of $\mu_3 = 0$. Consequently, as f_2 increases beyond the bifurcation point ζ_2 , not all the extra energy input to the pitch mode is spilled over into the roll mode.

Figure 1 (b) shows variation of the amplitude a_1 of the roll mode with f_2 for different values of the quadratic roll damping coefficient μ_3 . We note that, for a given f_2 , a_1 decreases as μ_3 increases. While a ship is being operated in the ocean, the surface of the ship hull gets rougher and rougher due to peeling-off of paint or foul bottom. As a result, the magnitude of the quadratic damping coefficient will increase, producing a behavior as discussed here. Figure 1 (c) shows force-response curves for the pitch mode corresponding to Figure 1 (b). It is clear that the saturation phenomenon of the pitch mode no longer exists when μ_3 is different from zero. Moreover, for a given f_2 , the amplitude a_2 of the pitch mode increases with increasing quadratic roll damping coefficient μ_3 .

Figures 2 show typical force-response curves when $\Gamma_1 > 0$ ($\Gamma_1 = 0.2484$) when $\mu_1 = \mu_2 = 0.04$ and $\sigma_1 = \sigma_2 = 0.5$ for $\mu_3 = 0$ and $\mu_3 \neq 0$. Figure 2 (a) shows typical force-response curves of the subcritical-

instability type for $\mu_3 = 0$ and $\mu_3 = 0.6$. Since $\Gamma_1 > 0$ in this case, equation (53) has only one stable real root for $f_2 \geq \zeta_2$ ($\zeta_2 \approx 0.2517$) for $\mu_3 = 0$ and $\mu_3 \neq 0$; two real roots for $\zeta_1 \leq f_2 \leq \zeta_2$, where $\zeta_1 \approx 0.04$ when $\mu_3 = 0$ and $\zeta_1 \approx 0.1020$ when $\mu_3 = 0.6$. In the latter case, the larger root is stable whereas the smaller one is unstable. We note that the larger bifurcation value ζ_2 is independent of the value of μ_3 , whereas the smaller bifurcation value ζ_1 increases as μ_3 increases. When $f_2 \leq \zeta_1$, there exists only one stable response given by equation (43), which is linear and consists of only the pitch mode. When $\zeta_1 \leq f_2 \leq \zeta_2$, two stable solutions coexist with an unstable solution; one of the stable responses is given by equation (43), and the other stable solution is given by equations (50) and (51). The response of the ship in this region depends on the initial conditions. When $f_2 \geq \zeta_2$, there exists only one stable response given again by equations (50) and (51). We note that the response of the roll mode exhibits the coexistence of two stable motions and the associated jump phenomenon for both $\mu_3 = 0$ and $\mu_3 = 0.6$. The saturation phenomenon of the response of the pitch mode, which exists when $\mu_3 = 0$, does not exist

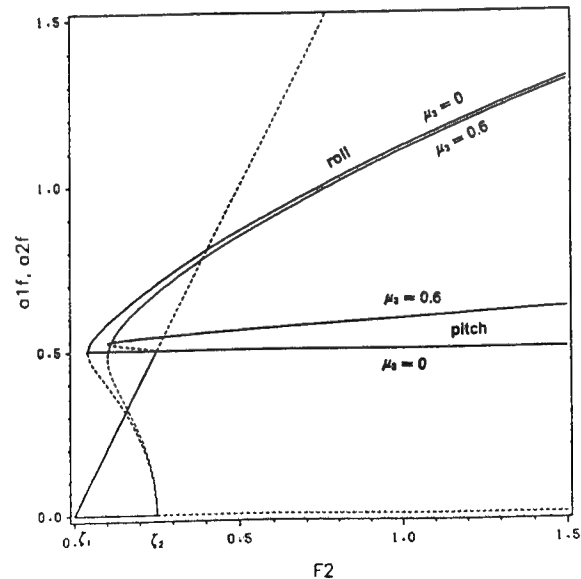


Fig. 2 (a) Force-Response Curves (Subcritical Type) : for $\mu_3 = 0$ and 0.6 ; stable(—), unstable(...)

when $\mu_3 = 0.6$. When $\mu_3 = 0.6$, the amplitude a_2 of the pitch mode grows rather than remains constant as f_2 increases beyond ζ_2 . We refer to this phenomenon as "breaking of saturation". We note, here again, that for a given $f_2 \geq \zeta_1$, a_2 increases as μ_3 increases. As in Figure 1 (a), for a given f_2 , a_1 decreases as μ_3 increases.

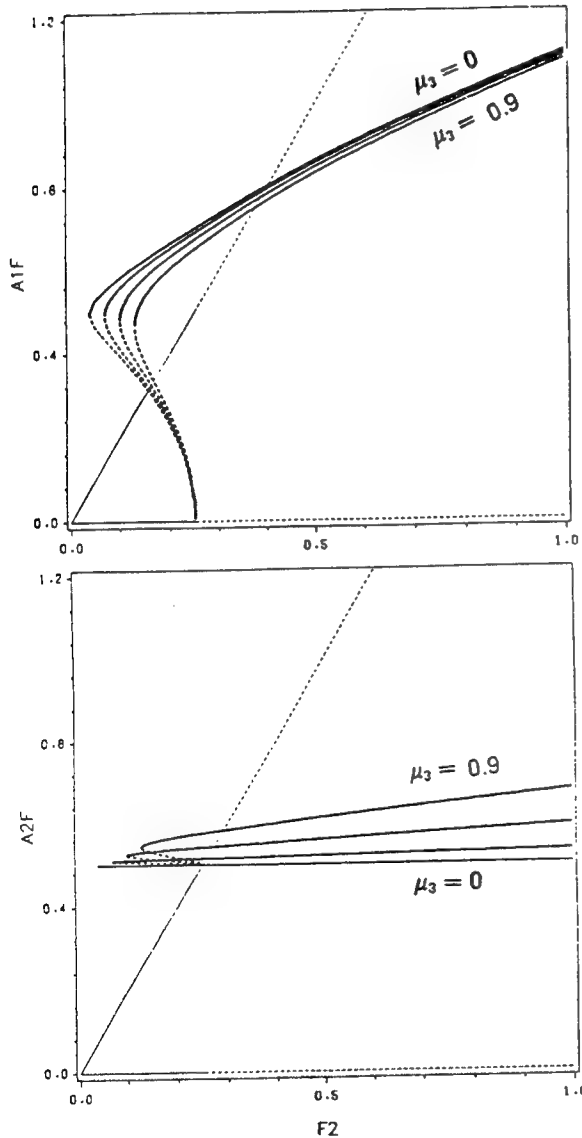


Fig. 2 (b)&(c) Force-Response Curves (Subcritical Type) : variation of (b) roll amplitude a_1 and (c) pitch amplitude a_2 , for different values of μ_3 ; stable(—), unstable(...)

Figure 2 (b) shows variation of the amplitude a_1 of the roll mode with f_2 for different values of the quadratic roll damping coefficient μ_3 . We note that a_1 decreases as μ_3 increases, as in Figure 1 (b). As μ_3 increases, the bifurcation value ζ_1 increases while ζ_2 does not change. For example, $\zeta_1 = 0.0715, 0.1020$, and 0.1313 when $\mu_3 = 0.3, 0.6$, and 0.9 , respectively. Hence, the overhang region between ζ_1 and ζ_2 decreases as μ_3 increases. This indicates that the bifurcation values ζ_1 and ζ_2 can coalesce as μ_3 increases, which results in the qualitative change of the responses from the subcritical type into the supercritical type. Then, when this happens, the response of the roll mode would no longer exhibit the coexistence of two stable motions and the subsequent jump phenomenon for large values of the quadratic roll damping coefficient μ_3 .

Figure 2 (c) shows the force-response curves of the pitch mode corresponding to Figure 2 (b). We note here again that the saturation phenomenon of the pitch mode no longer exists when μ_3 is different from zero. Moreover, the pitch amplitude a_2 increases as μ_3 increases.

We conclude from Figures 1 (a)-(c) and 2 (a)-(c) that the mechanism of energy transfer from the directly excited pitch mode to the indirectly excited roll mode becomes less effective as the quadratic damping coefficient μ_3 of the roll mode increases. When μ_3 is zero, all the extra energy into the pitch mode after saturation is transferred to the indirectly excited roll mode. When μ_3 is different from zero, only part of the energy input into the pitch mode is transferred to the roll mode.

4.4.2 Effect of Quadratic Roll Damping on Frequency-Response Curves

In Figures 3, we show frequency-response curves when $\mu_1 = \mu_2 = 0.02, \sigma_1 = 0.12$, and $f_2 = 0.1$ for $\mu_3 = 0$ and $\mu_3 \neq 0$. Figure 3 (a) shows typical frequency-response curves when $\mu_3 = 0$ and $\mu_3 = 0.6$. We note that the reversed pitchfork bifurcation points are independent of the value of μ_3 , whereas the saddle-node bifurcation points move closer to the reversed pitchfork bifurcation points as μ_3 increases. We also note that the jump phenomenon in the response of the roll mode exists for

both $\mu_3 = 0$ and $\mu_3 = 0.6$. The interval $-0.047 \leq \sigma_2 \leq -0.0127$ between the Hopf bifurcation points when $\mu_3 = 0$ disappears or becomes indiscernible when $\mu_3 = 0.6$. In this interval, the real part of a pair of complex-conjugate roots of equation (56) is positive, and hence the response is an amplitude- and phase-modulated combined pitch and roll motion. The frequency-response curves are shifted slightly leftward with respect to $\sigma_2 = 0$ because the detuning σ_1 is positive. They would be shifted to the right if σ_1 is negative, and they would be symmetric with respect to $\sigma_2 = 0$ if $\sigma_1 = 0$; that is, the case of perfect tuning. The qualitative behavior of the solutions in the three cases is the same.

Figure 3 (b) shows variation of the amplitude a_1 of the roll mode with σ_2 for different values of μ_3 . We note that, for a given σ_2 , a_1 decreases as μ_3 increases, except near $\sigma_2 = 0$, where a_1 is almost independent of μ_3 . Moreover, the reversed pitchfork bifurcation points are independent of μ_3 , but the saddle-node bifurcation points move closer to $\sigma_2 = 0$ as μ_3 increases. For example, the left saddle-node bifurcation points are -0.9367, -0.7091,

and -0.6066 whereas the right ones are 0.8729, 0.6442, and 0.5388 for $\mu_3 = 0.3, 0.6$, and 0.9 , respectively. The reversed pitchfork bifurcation values are -0.5050 and 0.3950 for all values of μ_3 .

In Figure 3 (c), we show the frequency-response curves for the pitch mode corresponding to Figure 3 (b). We note that, for a given σ_2 , a_2 increases as μ_3 increases.

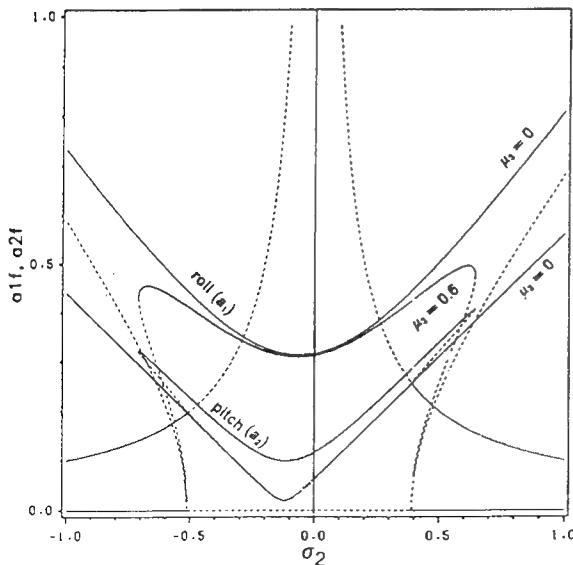


Fig. 3 (a) Frequency-Response Curves : for $\mu_3 = 0$ and 0.6 ; stable(—), unstable(...)

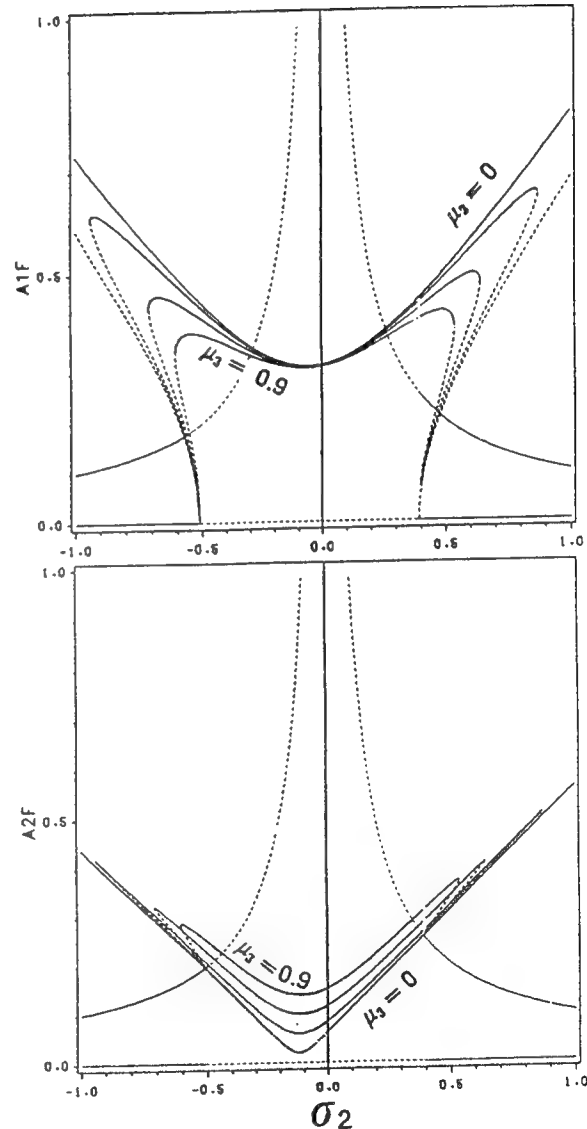


Fig. 3 (b)&(c) Frequency-Response Curves : variation of (b) roll amplitude a_1 and (c) pitch amplitude a_2 , for different values of μ_3 ; stable(—), unstable(...)

4.4.3 Hopf Bifurcation Region

Figure 4 shows the Hopf bifurcation curves in the parameter space $\sigma_2 - \sigma_1$ for different values of the quadratic roll damping parameter μ_3 when $\mu_1 = \mu_2 = 0.02$ and $f_2 = 0.1$. In the outer region, the fixed points of the modulation equations are asymptotically stable and hence correspond to periodic motions. On the transition curves, a complex conjugate pair of eigenvalues of the Jacobian matrix cross the imaginary axis into the right half of the complex plane with nonzero speed. The modulation equations possess limit-cycle solutions near the bifurcation curves. Between the two curves (i.e., in the inner region), oscillatory solutions, which may be either limit cycles or chaotic attractors, may be found.

Figure 4 shows that the Hopf bifurcation curves move upward and approach each other as the quadratic roll damping coefficient μ_3 increases. This implies that increasing μ_3 causes the disappearance of aperiodic responses.

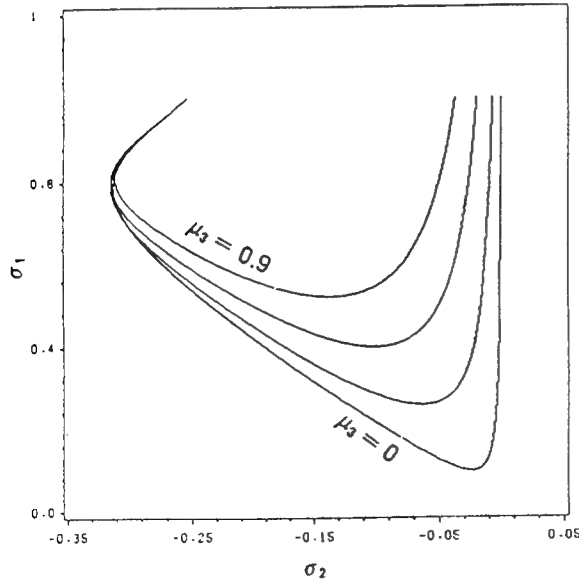


Fig. 4 Hopf Bifurcation Curves : for different values of μ_3

5. PRIMARY RESONANCE OF THE ROLL MODE

5.1 Modulation Equations

To express the nearness of the resonances, we let, $\Omega = \omega_1 + \varepsilon\sigma_2$ and $\omega_2 = 2\omega_1 + \varepsilon\sigma_1$. Then,

$$\Omega T_0 = \omega_1 T_0 + \sigma_2 T_1 \quad (60)$$

and

$$\omega_2 T_0 = 2\omega_1 T_0 + \sigma_1 T_1 \quad (61)$$

Using equations (60), (61), and (22) to eliminate the terms that produce secular terms from equations (18) and (19), we obtain

$$2i(A_1' + \mu_1 A_1) - 4\Lambda_1 A_2 \bar{A}_1 e^{i\sigma_1 T_1} - f_1 e^{i\sigma_2 T_1} - \frac{1}{2\pi} \int_0^{2\pi/\omega_1} f e^{-i\omega_1 T_0} dT_0 = 0 \quad (62)$$

$$2i(A_2' + \mu_2 A_2) - 4\Lambda_2 A_1^2 e^{-i\sigma_1 T_1} = 0 \quad (63)$$

where Λ_1 and Λ_2 are defined in equations (26) and (27) and

$$\omega_1 f_1 = \frac{1}{2} F_1 \quad (64)$$

Substituting equation (17) into equations (62) and (63), using equation (29), and separating real and imaginary parts of equations (62) and (63), we obtain, after applying the appropriate transformation of variables, a generic system of equations as follows :

$$a_1' = -\mu_1 a_1 + a_1 a_2 \sin \gamma_1 + f_1 \sin \gamma_2 - \frac{4\mu_3 \omega_1}{3\pi} a_1 |a_1| \quad (65)$$

$$a_2' = -\mu_2 a_2 - a_1^2 \sin \gamma_1 \quad (66)$$

$$a_1 \beta_1' = -a_1 a_2 \cos \gamma_1 - f_1 \cos \gamma_2 \quad (67)$$

$$a_2 \beta_2' = -a_1^2 \cos \gamma_1 \quad (68)$$

where

$$\gamma_1 = \sigma_1 T_1 + \beta_2 - 2\beta_1 \text{ and } \gamma_2 = \sigma_2 T_1 - \beta_1 \quad (69)$$

and the evaluated results given in equations (30) and (31), which are the terms corresponding to the last term of equation (62), have been used.

5.2 Fixed Points

Periodic solutions of (4) and (5) correspond to the fixed points of equations (65)-(69). They are obtained by setting $a'_1 = a'_2 = 0$ and $\gamma'_1 = \gamma'_2 = 0$. It follows from equation (69) that

$$\beta'_1 = \sigma_2 \text{ and } \beta'_2 = 2\sigma_2 - \sigma_1 \quad (70)$$

Hence, the fixed points of equations (65)-(69) are given by the solutions of the following set of coupled nonlinear algebraic equations:

$$\mu_1 a_1 = a_1 a_2 \sin \gamma_1 + f_1 \sin \gamma_2 - \frac{4\mu_3 \omega_1}{3\pi} a_1 |a_1| \quad (71)$$

$$\mu_2 a_2 = -a_1^2 \sin \gamma_1 \quad (72)$$

$$a_1 \sigma_2 = -a_1 a_2 \cos \gamma_1 - f_1 \cos \gamma_2 \quad (73)$$

$$(2\sigma_2 - \sigma_1) a_2 = -a_1^2 \cos \gamma_1 \quad (74)$$

Equations (71)-(74) can be manipulated to yield the following polynomial equation for a_1 :

$$a_1^6 + d_5 a_1^4 |a_1| + d_4 a_1^4 + d_3 a_1^2 |a_1| + d_2 a_1^2 + d_1 |a_1| + d_0 = 0 \quad (75)$$

where $D_i (i = 0, 1, \dots, 5)$ are constant coefficients determined from control parameters in use, such as $\sigma_1, \sigma_2, \mu_1, \mu_2, \mu_3, f_1$, and ω_1 ; they are given by

$$d_0 = -f_1^2 \Gamma_2^2, \quad (76)$$

$$d_1 = 0, \quad (77)$$

$$d_2 = \Gamma_1^2 \Gamma_2^2, \quad (78)$$

$$d_3 = 2\Gamma_2^2 \frac{4\omega_1}{3\pi} \mu_3 \mu_1, \quad (79)$$

$$d_4 = 2\mu_1 \mu_2 - 2\nu_1 \nu_2 + \Gamma_2^2 \left(\frac{4\omega_1}{3\pi} \mu_3 \right)^2, \quad (80)$$

$$d_5 = 2 \frac{4\omega_1}{3\pi} \mu_3 \mu_2, \quad (81)$$

$$\Gamma_n^2 = \mu_n^2 + \nu_n^2, \quad (82)$$

$$\nu_1 = \sigma_2, \quad (83)$$

$$\text{and } \nu_2 = 2\sigma_2 - \sigma_1. \quad (84)$$

We note that if $\mu_3 = 0$, then $d_3 = d_5 = 0$ and $d_4 = 2\mu_1 \mu_2 - 2\nu_1 \nu_2$. It follows from equations (71)-(74) that a_2 is given by

$$a_2 = a_1^2 / \Gamma_2 \quad (85)$$

The solutions of the sixth-order algebraic equation (75) are obtained numerically. Then, a_2 is calculated from equation (85). Finally, the corresponding phases γ_1 and γ_2 (β_1 and β_2 also) are obtained from equations (71)-(74).

5.3 Stability of Fixed Points

The stability of the fixed-point solutions are determined by the same procedure used in Section 4; that is, by investigating the eigenvalues of the Jacobian matrix of equations (65)-(69).

Again, a given fixed point is asymptotically stable if and only if all the λ 's lie in the left half of the complex plane and is unstable if at least one eigenvalue lies in the right half of the complex plane. If a pair of complex-conjugate eigenvalues crosses the imaginary axis with nonzero speed, then we have a Hopf bifurcation. Near these bifurcation points, the response is an amplitude- and phase-modulated combined pitch and roll motion, with the energy being continuously exchanged between the two modes.

5.4 Numerical Results and Discussion

In Figures 5, we show the frequency-response curves when $\mu_1 = \mu_2 = 0.08$, $\sigma_1 = 0$, and $f_1 = 0.08$ for different values of μ_3 . The unstable solutions are represented by broken lines and the stable solutions are marked by solid lines. Figures 5 (a) and (b) show variations of the roll amplitude a_1 and pitch amplitude a_2 with σ_2 for different values of μ_3 . As μ_3 increases from zero to 0.3, the reversed

pitchfork bifurcation points slightly change, whereas the saddle-node bifurcation points move towards $\sigma_2 = 0$. As μ_3 is increased further to 0.6 and 0.9, the saddle-node bifurcation points disappear and the frequency-response curves become single-valued. Consequently, the jump phenomenon and subcritical

instability disappear. Moreover, the Hopf bifurcation points approach each other as μ_3 increases. For example, the Hopf bifurcation interval $-0.09995 \leq \sigma_2 \leq 0.09995$ for $\mu_3 = 0$ shrinks gradually to $-0.055 \leq \sigma_2 \leq 0.055$ for $\mu_3 = 0.9$.

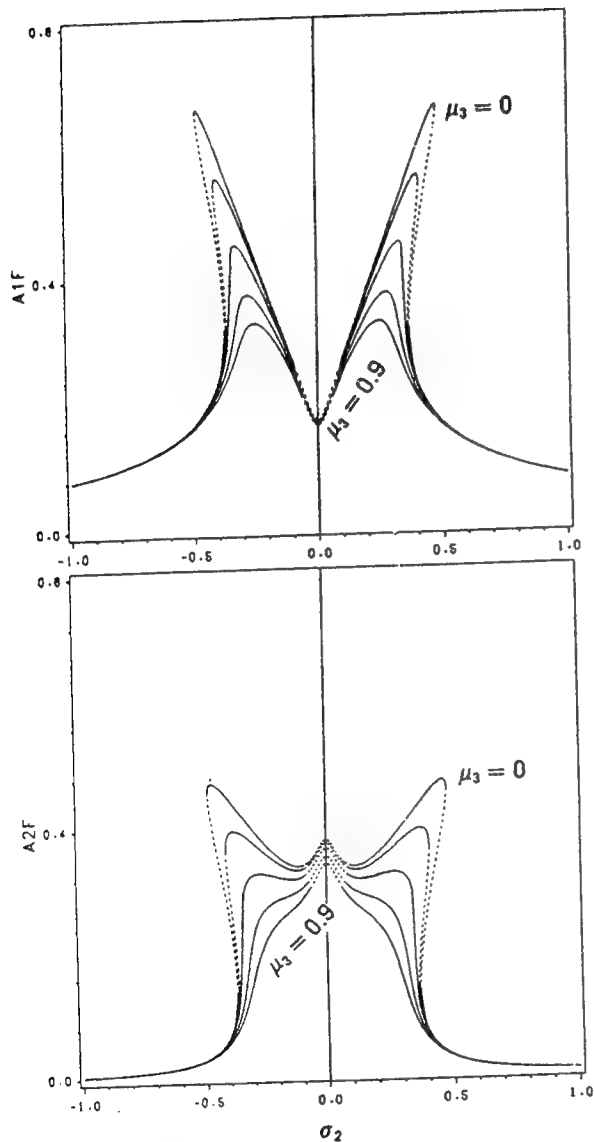


Fig. 5 (a) & (b) Frequency-Response Curves ($\sigma_1 = 0$) : variation of (a) roll amplitude a_1 and (b) pitch amplitude a_2 , for different values of μ_3 ; stable(—), unstable(...)

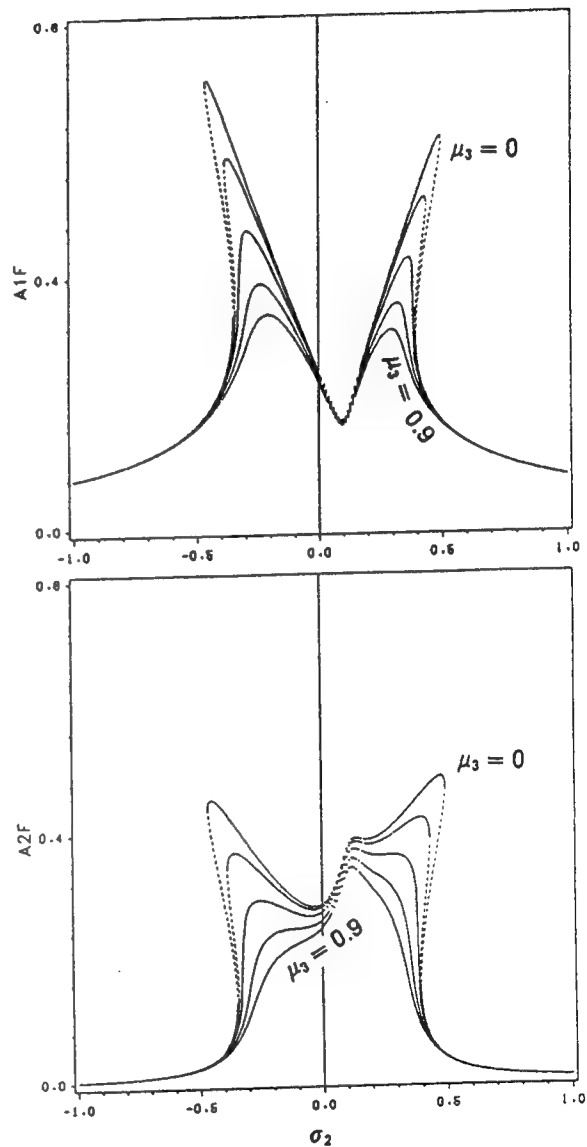


Fig. 6 (a) & (b) Frequency-Response Curves ($\sigma_1 = 0.2$) : variation of (a) roll amplitude a_1 and (b) pitch amplitude a_2 , for different values of μ_3 ; stable(—), unstable(...)

We note that for a fixed value of σ_2 , a_1 and a_2 decrease as μ_3 increases. The curves of unstable fixed points around the region of perfect tuning, $\sigma_2 \approx 0$, converge in both modes. The introduction of quadratic roll damping μ_3 , by say attaching antirolling devices like bilge keels, causes the region between the two Hopf bifurcation frequencies (close to perfect resonance) to shrink. However, it does not eliminate complicated motions completely in this region.

Figures 6 show the frequency-response curves for the case in which the values of all the parameters are the same as those in Figures 5 except that $\sigma_1 = 0.2$. In this case, the curves are shifted slightly to the right and the peak amplitudes of the right branches of the roll mode are smaller than those of the left branches. The opposite occurs in the response of the pitch mode. If σ_1 is chosen to be negative, the frequency-response curves would be shifted to the left. When $\sigma_1 = 0$, the case of perfect tuning, the curves would be symmetric with respect to $\sigma_2 = 0$. The qualitative behavior of the solutions in the three cases is the same.

6. SUMMARY AND CONCLUSIONS

To design more comfortable and safe vessels, one must understand the complicated dynamics of a vessel moving in a general environment. Included among the important dynamic parameters are the ratios of natural frequencies and the nonlinear interactions among the hydrostatic and hydrodynamic forces and moments. One of the objectives of the present work is to investigate the undesirable and potentially dangerous characteristics of the dynamics of a vessel.

It has been believed for a long time that the linear-plus-quadratic model could adequately describe the hydrodynamic damping of the roll motion. However, many investigators avoided using this model because of the difficulties in the analyses. In the present paper, a quadratic nonlinear damping model is introduced into the equation of the roll mode. We investigated the nonlinearly coupled pitch and roll response of a vessel in regular waves when the natural frequency in pitch is twice that of roll (a condition of a two-to-one internal or autoparametric resonance). The method of multiple scales was used to derive four first-order autonomous ordinary-differential equations for the modulation of the amplitudes and phases of the pitch and roll modes when either mode is excited.

The modulation equations were used to determine the influence of the quadratic nonlinear damping on the periodic responses and their stability.

When the encounter frequency is near the pitch natural frequency, the jump phenomenon exists for both zero and nonzero quadratic roll damping (μ_3 is the coefficient of the quadratic roll damping.). The saturation phenomenon is broken if a quadratic roll damping term is introduced. This implies that there is no critical value of the excitation amplitude beyond which all of the extra energy input to the pitch mode is spilled over into the roll mode. The amplitude of the roll mode decreases while that of the pitch mode increases as the magnitude of the quadratic roll damping μ_3 increases. In the subcritical case of force-response and frequency-response curves, the overhang regions narrow down as μ_3 increases. The fixed points of the modulation equations undergo a Hopf bifurcation as one of the control parameters is varied. Between the Hopf bifurcation points, the response is an amplitude- and phase-modulated motion consisting of both the pitch and roll modes.

When the encounter frequency is near the roll natural frequency, the amplitudes of both the roll mode and the pitch mode decrease as the magnitude of the quadratic roll damping coefficient μ_3 increases. Again, Hopf bifurcations occur as either the encounter frequency or excitation amplitude is varied.

REFERENCES

1. Nayfeh, A. H. and Mook, D. T., Nonlinear Oscillations, Wiley, New York, 1979.
2. Froude, W., "Remarks on Mr. Scott-Russell's Paper on Rolling," The papers of William Froude, published by the Institution of Naval Architects, 1995.
3. Evan-Iwanowski, R. M., Resonance Oscillations in Mechanical Systems, Elsevier Scientific Publishing Co., New York, 1976.
4. Haddow, A. G., Barr, A. D. S., and Mook, D. T., "Theoretical and Experimental Study of Modal Interaction in a Two-Degree-of-Freedom Structure," Journal of Sound and Vibration, Vol. 97, 1984, pp. 451.
5. Hatwal, H., Mallik, A. K., and Ghosh, A., "Nonlinear Vibrations of a Harmonically Excited Autoparametric System," Journal of Sound and Vibration, Vol. 81, 1982, pp. 153.
6. Nayfeh, A. H. and Zavodney, L. D., "The Response of Two-Degree-of-Freedom Systems with Quadratic Nonlinearities to a Combination

- Parametric Resonance," Journal of Sound and Vibration, Vol. 107, 1986, pp. 329.
7. Schmidt, G. and Tondl, A., Nonlinear Vibrations, Akademie-Verlag, Berlin, 1986.
 8. Paulling, J. R. and Rosenberg, R. M., "On Unstable Ship Motions Resulting from Nonlinear Coupling," Journal of Ship Research, Vol. 3, 1959, pp. 36.
 9. Kinney, W. D., "On the Unstable Rolling Motions of Ships Resulting from Nonlinear Coupling with Pitch Including the Effect of Damping in Roll," Series No. 173, Issue No. 3, 1961, Institute of Engineering Research, University of California, Berkeley.
 10. Kerwin, J. E., "Notes on Rolling in Longitudinal Waves," International Shipbuilding Progress, Vol. 2, 1955, pp. 597.
 11. Blocki, W., "Ship Safety in Connection with Parametric Resonance of the Roll," International Shipbuilding Progress, Vol. 27, 1980, pp. 36.
 12. Sanchez, N. E. and Nayfeh, A. H., "Nonlinear Rolling Motions of Ships in Longitudinal Waves," International Shipbuilding Progress, Vol. 37, 1990, pp. 247.
 13. Nayfeh, A. H. and Mook, D. T., and Marshall, L. R., "Nonlinear Coupling of Pitch and Roll Modes in Ship Motion," Journal of Hydronautics, Vol. 7, Oct. 1973, pp. 145.
 14. Mook, D. T., Marshall, L. R., and Nayfeh, A. H., "Subharmonic and Superharmonic Resonances in the Pitch and Roll Modes of Ship Motions," Journal of Hydronautics, Vol. 8, 1974, pp. 32.
 15. Nayfeh, A. H., "On the Undesirable Roll Characteristics of Ships in Regular Seas," Journal of Ship Research, Vol. 32, 1988, pp. 92.
 16. Nayfeh, A. H., Mook, D. T., and Marshall, L. R., "Perturbation-Energy Approach for the Development of the Nonlinear Equations of Ship Motion," Journal of Hydronautics, Vol. 8, 1974, p. 130.
 17. Nayfeh, A. H., Perturbation Methods, Wiley, New York, 1973.
 18. Nayfeh, A. H., Introduction to Perturbation Techniques, Wiley, New York, 1981.
 19. Oh, I. G., Theoretical and Experimental Nonlinear Dynamics of Floating Oscillatory System, Ph. D. Dissertation, Department of Engineering Science and Mechanics, Virginia Polytechnic Institute and State University, Blacksburg, Virginia, 1992.

Nonlinear Shallow-Water Flow on Deck Coupled with Ship Motion

Z.-J. Huang, C.-C. Hsiung (Technical University of Nova Scotia, Canada)

Abstract

Shallow water wave equations are employed to study the problem of nonlinear water flow on deck. The Flux-Difference Splitting method is devised to solve the nonlinear shallow water flow equations numerically. The finite difference scheme is a second-order Total Variation Diminishing scheme which is able to tackle discontinuities in the flow and gives satisfactory results. The nonlinear ship motions with considering water flow on deck are solved in the time domain. The flow patterns are validated against published model test data. Ship motions with water on deck are computed and discussed.

Introduction

The effect of water flow on deck on ship motion, especially for small vessels with open deck and RO-RO ferries, is very important for safe operations in waves (Caglayan and Storch, 1982; Grochowalski, 1989). Its effect on the roll motion of a ship has two folds. The first is the damping effect which will reduce or increase the roll motion depending on positive or negative damping (Van Den Bosch, 1966). The other is the change of GZ values in statical stability and consequently the resonant frequency of roll response is modified. In addition, the phase difference between water sloshing and roll motion is very important for the roll motion prediction. When the hydraulic jump or the bore is developed, its position affects the heeling moment exerted on the ship.

Dillingham (1981) initiated the numerical computation of the nonlinear shallow water flow on a two-dimensional deck using Random Choice method. In the numerical computation, the an-

alytical solution of a local Riemann problem in each spatial interval was first constructed. Then a random sampling procedure was applied to find an random abscissa in each interval. A piecewise constant numerical solution was found by substituting the abscissa into the local analytical solution. Pantazopoulos (1988) extended this method to a three-dimensional deck space. Huang and Hsiung (1994) introduced the Flux-Difference Splitting method to tackle the shallow water flow problem. The governing equations and the numerical method was first developed for the 2-D case (Huang and Hsiung, 1994), and later was extended to the 3-D case (Huang and Hsiung, 1995). This method was developed based on the same idea in the flux-vector splitting method which was originally introduced by Steger and Warming (1981) to compute the shock wave in a shock tube and later applied to hydraulics by others (e.g. Alcrudo et al., 1992). Based on this approach, the effect of water flow on deck on the motions of fishing vessels was investigated by Huang (1995).

Lee and Adey (1994) computed the motions of a cylinder in sway, roll and heave including the free water on deck. The equations of ship motion of the frequency domain were solved in the time domain in regular beam seas. The hydrodynamic forces on the hull were obtained from a 2-D strip theory in the frequency domain and the forces resulted from in the water flow on deck were obtained from the 2-D Random Choice method given by Dillingham (1981). Armenio et al. (1994) solved the equation of one degree roll motion in regular waves. The linear viscous damping was adopted and the frequency domain hydrodynamic forces were used in the equation of ship motion. The 2-D sloshing of water on deck was obtained from a Navier-Stokes solver.

The time domain Green function has been ap-

plied to the ship motion problem (e.g. King, et al., 1988). Lin and Yue (1994) extended this method to large amplitude ship motions. The exact hull surface boundary condition was satisfied on the instantaneous wetted surface under the incident wave profile. The local incident wave elevations were used to transform the hull geometry and the free surface into a computational domain so that the transient Green function method could be applied. Another approach was adopted by de Kat and Paulling (1989) and by Magee (1994), in which the Froude-Krylov force and restoring force were calculated based on the instantaneous wetted hull surface under the incident wave profile while linear radiated and diffracted wave forces were employed.

Typically, for the deck flow computation, the classical first order schemes have a strong dissipative effect on the numerical solution and the second order schemes produce numerical results with spurious oscillations near the discontinuity. In this paper, the governing equations of nonlinear shallow water flow on deck are derived in the flux vector form and are solved numerically by flux-Difference Splitting method. The Superbee flux limiter has been employed in the algorithm and the finite difference scheme is a second-order Total Variation Diminishing scheme which gives satisfactory results without non-physical spurious oscillations and is able to capture the hydraulic bore. The Fractional Step method is used so that solutions of the shallow water equation can be obtained by solving two sets of one-dimensional differential equations. The hydrodynamic forces caused by water flow on deck is considered in the time domain equation of ship motions. The time domain added mass, hydrodynamic damping and hydrodynamic restoring force coefficients are calculated using the impulse potential (King, et al., 1988). The equations of ship motion also include the nonlinear Froude-Krylov forces, nonlinear restoring forces and nonlinear viscous roll damping. However, the linear radiated and diffracted wave forces are used. Our approach can be summarized as follows:

- the time domain added mass, hydrodynamic restoring force and damping force coefficients are computed using the impulse potential function (linear);
- linear diffracted wave forces and retardation functions are computed based on the frequency domain diffracted wave forces and damping coefficients, respectively (linear);

- F-K forces and hydrostatic restoring forces are computed at the instantaneous position (nonlinear);
- forces due to water flow on deck, viscous damping, resistance, cross-flow drag, thrust, rudder and maneuvering forces are included (nonlinear); and
- nonlinear equations of ship motion solved in the time domain.

The present work has been applied to fishing vessels with shallow draft. Computations of water flow on deck and ship motions are compared with model test results.

Ship Motion in the Time Domain

Three coordinate systems are employed for the ship motion analysis as shown in Fig. 1.

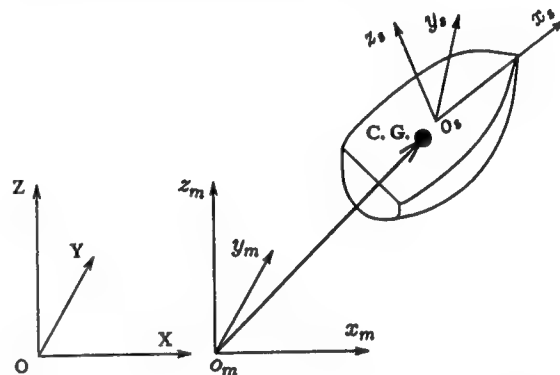


Fig. 1 Coordinate Systems for Ship Motions

$OXYZ$ is the space-fixed coordinate system with the OXY plane on the calm water surface and the OZ axis be positive upwards. The second coordinate system $O_m x_m y_m z_m$ is a moving system which moves with the same steady forward speed as the ship in OX direction. The $O_m x_m y_m$ plane always coincides with the OXY plane, the $O_m x_m$ axis is in the same direction as the OX axis and the $O_m z_m$ axis is positive upwards. The third coordinate system $O_s x_s y_s z_s$ is fixed on the ship with the $O_s x_s y_s$ plane coincident with the OXY plane when the ship is at its static equilibrium position, and the $O_s z_s$ axis is positive upwards.

The oscillatory ship motion are described in the $O_m x_m y_m z_m$ system. The ship motions are repre-

sented by $(\xi_1, \xi_2, \xi_3, e_1, e_2, e_3)$, in which, (ξ_1, ξ_2, ξ_3) are the displacements of the centre of gravity, and (e_1, e_2, e_3) are the Eulerian angles of the ship in space. The Eulerian angles are the measurements of the ship's rotation about the axes which pass through the centre of gravity of the ship. The instantaneous translational velocities of ship motion in the directions of o, x, o, y , and o, z , are u_1, u_2 and u_3 , respectively, and the rotational velocities about axes parallel to o, x, o, y , and o, z , and passing through the centre of gravity are u_4, u_5 and u_6 , respectively. The equations of ship motion are:

$$[m_{kj}] \begin{pmatrix} \dot{u}_1 \\ \dot{u}_2 \\ \dot{u}_3 \\ \dot{u}_4 \\ \dot{u}_5 \\ \dot{u}_6 \end{pmatrix} + \begin{pmatrix} m\vec{\Omega} \times \vec{u} \\ \vec{\Omega} \times ([I]\vec{\Omega}) \end{pmatrix} = \begin{pmatrix} F_1 \\ F_2 \\ F_3 \\ F_4 \\ F_5 \\ F_6 \end{pmatrix} \quad (1)$$

where $\vec{u} = (u_1, u_2, u_3)$, $\vec{\Omega} = (u_4, u_5, u_6)$, $[m_{kj}]$ is the generalized mass matrix:

$$[m_{kj}] = \begin{bmatrix} m & 0 & 0 & 0 & 0 & 0 \\ 0 & m & 0 & 0 & 0 & 0 \\ 0 & 0 & m & 0 & 0 & 0 \\ 0 & 0 & 0 & I_{11} & 0 & -I_{13} \\ 0 & 0 & 0 & 0 & I_{22} & 0 \\ 0 & 0 & 0 & -I_{13} & 0 & I_{33} \end{bmatrix} \quad (2)$$

and $[I]$ is the moment of inertia matrix

$$[I] = \begin{bmatrix} I_{11} & 0 & -I_{13} \\ 0 & I_{22} & 0 \\ -I_{13} & 0 & I_{33} \end{bmatrix} \quad (3)$$

in which m is the mass of the ship, I_{kk} ($k = 1, 2, 3$) denote the moments of inertia of the ship, and I_{kj} ($k \neq j$) are the products of inertia of the ship. The total external forces on the ship are

$$F_k(t) = F_k^{Rs}(t) + F_k^{FK}(t) + F_k^D(t) + F_k^{Ra}(t) + F_k^\nu(t) + F_k^{Dk}(t) + F_k^O(t) \quad (4)$$

for $k = 1, 2, \dots, 6$

where F_k^{Rs} are the restoring forces; F_k^{FK} are nonlinear Froude-Krylov forces; F_k^D the diffracted wave forces; F_k^R the radiated wave forces; F_k^ν the viscous damping forces; F_k^{Dk} the nonlinear forces due to water flow on deck; and the force component F_k^O may include the hydrodynamic maneuvering forces, the rudder force, propeller thrust, viscous resistance and cross-flow drag.

The ship translational displacements $(\xi_1, \xi_2, \xi_3)^T$ in the steady moving system and the Eulerian angles $(e_1, e_2, e_3)^T$ are solved from:

$$\begin{pmatrix} \dot{\xi}_1 \\ \dot{\xi}_2 \\ \dot{\xi}_3 \\ \dot{e}_1 \\ \dot{e}_2 \\ \dot{e}_3 \end{pmatrix} = \begin{bmatrix} [R] & 0 \\ 0 & [B] \end{bmatrix} \begin{pmatrix} u_1 \\ u_2 \\ u_3 \\ u_4 \\ u_5 \\ u_6 \end{pmatrix} \quad (5)$$

where matrices $[B]$ and $[R]$ are defined as follows:

$$[B] = \begin{bmatrix} 1 & s_1 t_2 & c_1 t_2 \\ 0 & c_1 & -s_1 \\ 0 & s_1/c_2 & c_1/c_2 \end{bmatrix} \quad (6)$$

$$[R] = \begin{pmatrix} c_2 c_3 & s_1 s_2 c_3 - c_1 s_3 & c_1 s_2 c_3 + s_1 s_2 \\ c_2 s_3 & s_1 s_2 s_3 + c_1 c_3 & s_1 s_2 s_3 - s_1 c_3 \\ -s_2 & s_1 c_2 & c_1 c_2 \end{pmatrix} \quad (7)$$

and $c_i = \cos e_i$, $s_i = \sin e_i$, and $t_i = \tan e_i$ for $i = 1, 2, 3$.

The ship motions in the time domain are solved simultaneously from twelve equations in both (1) and (5). At each time step, the motion velocities in the ship-fixed coordinate system are obtained by integrating (1) with the velocities at the previous time step as the initial conditions. The ship motion displacements are solved from (5) in the steady moving coordinate system.

Since the ship motion at a new time step, which is unknown, is required to compute the forces (e.g. the restoring force has to be calculated with the ship motion displacement), the linear prediction of stochastic theory is adopted to determine the ship motion for the force computation. With the predicted ship motion at $t = t_{n+1}$, the external forces are evaluated. Then, the ship motion is solved numerically from the first order ordinary differential equations (1) and (5) by the Extrapolation method (Magee, 1994).

Nonlinear Shallow Water Flow on Deck

Governing Equations

The flux difference splitting method has been developed for computing the shallow water flow in a three dimensional deck space (Huang and Hsiung, 1994,1995; Huang, 1995). The ship motions of six degrees of freedom has been considered in

the numerical scheme for the deck flow. The coordinate system $oxyz$ for water flow on the three dimensional deck is shown in Fig. 2.

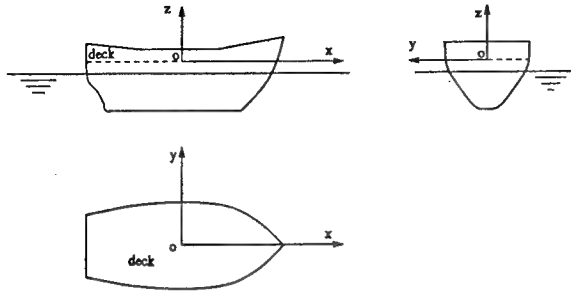


Fig. 2 Coordinate System for Deck Flow

It is fixed on the deck space with oxy attached on the deck bottom plane. The oz axis is positive upward and the origin o is at the centre of the deck bottom.

The continuity equation and Euler's equations of motion can be written as follows:

$$\frac{\partial u}{\partial x} + \frac{\partial v}{\partial y} + \frac{\partial w}{\partial z} = 0 \quad (8)$$

$$\frac{\partial \vec{u}}{\partial t} + (\vec{u} \cdot \nabla) \vec{u} = \vec{f} - \frac{1}{\rho} \nabla p - \vec{\Omega} \times \vec{r}_d - 2\vec{\Omega} \times \vec{u} - (\vec{\Omega} \cdot \vec{r}_d) \vec{\Omega} + (\vec{\Omega} \cdot \vec{\Omega}) \vec{r}_d \quad (9)$$

where $\vec{u} = (u, v, w)^T$, u , v and w are velocity components of the water particles in x -, y - and z - directions, respectively, measured at point in space from the field point of view; p is the pressure; and

$$\vec{f} = \begin{pmatrix} f_1 \\ f_2 \\ f_3 \end{pmatrix} = \begin{pmatrix} -g \sin(e_2) \\ -g \sin(e_1) \cos(e_2) \\ -g \cos(e_1) \cos(e_2) \end{pmatrix} \quad (10)$$

$\vec{r}_d = (x - x_g, y - y_g, z - z_g)^T$, and (x_g, y_g, z_g) is the coordinate of the centre of gravity of the ship in the $oxyz$ system.

On the free surface, the kinematic condition is:

$$w = \frac{\partial \zeta}{\partial t} + u \frac{\partial \zeta}{\partial x} + v \frac{\partial \zeta}{\partial y} \quad \text{on } z = \zeta \quad (11)$$

and the dynamic free surface condition is:

$$p = 0 \quad \text{on } z = \zeta \quad (12)$$

It is assumed that the deck bottom surface is flat and the wall of the deck is vertical. The boundary conditions are:

$$\vec{u} \cdot \vec{n} = 0 \quad \text{on the deck wall and bottom} \quad (13)$$

If the water depth is shallow compared with the horizontal dimension of the deck space, it can be assumed that w is a small quantity compared with u and v ; and the dependence of u and v on z may be ignored, i.e. $u = u(x, y, t)$ and $v = v(x, y, t)$. Let $q = g\zeta$, then the governing equations can be expressed in a vector form:

$$\frac{\partial \vec{W}}{\partial t} + \frac{\partial \vec{F}}{\partial x} + \frac{\partial \vec{G}}{\partial y} = [D] \frac{\partial \vec{H}}{\partial x} + [E] \frac{\partial \vec{L}}{\partial y} + \vec{f}_0 + \vec{g}_0 \quad (14)$$

in which,

$$\vec{W} = (q, uq, vq)^T, \quad \vec{F} = (uq, u^2q + \frac{1}{2}q^2, uvq)^T$$

$$\vec{G} = (vq, uvq, v^2q + \frac{1}{2}q^2)^T, \quad \vec{H} = (0, \frac{1}{2}q^2, 0)^T$$

$$\vec{L} = (0, 0, \frac{1}{2}q^2)^T, \quad \vec{f}_0 = (0, f_{02}, 0)^T$$

$$\vec{g}_0 = (0, 0, g_{03})^T$$

$$[D] = \begin{pmatrix} 0 & 0 & 0 \\ 0 & D_{22} & 0 \\ 0 & 0 & 0 \end{pmatrix}, \quad [E] = \begin{pmatrix} 0 & 0 & 0 \\ 0 & 0 & 0 \\ 0 & 0 & E_{33} \end{pmatrix}$$

where $D_{22} = 1 + q_2/g + qq_3/g^2$, $E_{33} = 1 + r_2/g + qr_3/g^2$, $f_{02} = qq_0 + q^2q_1/g$, and $g_{03} = qr_0 + q^2r_1/g$,

$$q_0 = -g \sin(e_2) - \dot{u}_1 + 2u_6v + (u_6^2 + u_5^2)(x - x_g) + (\dot{u}_6 - u_4u_5)(y - y_g) + (u_4u_6 - \dot{u}_5)z_g$$

$$q_1 = -u_4u_6$$

$$q_2 = -g \cos(e_1) \cos(e_2) - \dot{u}_3 - 2(u_4v - u_5u) - (u_4u_6 - \dot{u}_5)(x - x_g) - (u_5u_6 - \dot{u}_4)(y - y_g) - (u_4^2 + u_5^2)z_g$$

$$q_3 = u_4^2 + u_5^2$$

$$r_0 = -g \sin(e_1) \sin(e_2) - \dot{u}_2 - 2u_6u - (u_4u_5 + \dot{u}_6)(x - x_g) + (u_4^2 + u_5^2)(y - y_g) + (u_5u_6 - \dot{u}_4)z_g$$

$$r_1 = -u_5u_6, \quad r_2 = q_2, \quad r_3 = q_3$$

The derivatives of flux vectors \vec{F} , \vec{G} , \vec{H} and \vec{L} can be expressed in terms of the derivatives of vector \vec{W} as follows:

$$\frac{\partial \vec{F}}{\partial x} = [J_1] \frac{\partial \vec{W}}{\partial x}, \quad \frac{\partial \vec{G}}{\partial y} = [J_2] \frac{\partial \vec{W}}{\partial y},$$

$$\frac{\partial \vec{H}}{\partial x} = [J_3] \frac{\partial \vec{W}}{\partial x}, \quad \text{and} \quad \frac{\partial \vec{L}}{\partial y} = [J_4] \frac{\partial \vec{W}}{\partial y}$$

where $[J_i]$, $i = 1, 2, 3, 4$, are the Jacobian matrices. The eigenvalues of the Jacobian matrix $[J_1]$ are:

$$\lambda_1 = u + \sqrt{q}, \quad \lambda_2 = u - \sqrt{q} \quad \text{and} \quad \lambda_3 = u$$

and the eigenvectors:

$$\vec{e}_1 = (1, u + \sqrt{q}, v)^T, \quad \vec{e}_2 = (1, u - \sqrt{q}, v)^T \\ \vec{e}_3 = (0, 0, 1)^T$$

The eigenvalues of the Jacobian matrix $[J_2]$ are:

$$\lambda'_1 = v + \sqrt{q}, \quad \lambda'_2 = v \quad \text{and} \quad \lambda'_3 = v - \sqrt{q}$$

and the eigenvectors:

$$\vec{e}'_1 = (1, u, v + \sqrt{q})^T, \quad \vec{e}'_2 = (0, 1, 0)^T \\ \vec{e}'_3 = (1, u, v - \sqrt{q})^T$$

Finally, the governing equation is reconstructed into the following form:

$$\frac{\partial \vec{W}}{\partial t} + \frac{\partial \vec{F}}{\partial x} + \frac{\partial \vec{G}}{\partial y} = [D][J_3] \frac{\partial \vec{W}}{\partial x} + [E][J_4] \frac{\partial \vec{W}}{\partial y} \\ + \vec{f}_0 + \vec{g}_0 \quad (15)$$

In the numerical computation, the governing equation can be split into two equations using the Fractional Step method as given by Yanenko (1971) as:

$$\frac{\partial \vec{W}}{\partial t} + \frac{\partial \vec{F}}{\partial x} = [D][J_3] \frac{\partial \vec{W}}{\partial x} + \vec{f}_0 \quad (16)$$

and

$$\frac{\partial \vec{W}}{\partial t} + \frac{\partial \vec{G}}{\partial y} = [E][J_4] \frac{\partial \vec{W}}{\partial y} + \vec{g}_0 \quad (17)$$

and these two one-dimensional equations are solved for each time step.

The Flux Difference Splitting Scheme

The deck is divided into $m \times n$ nodes. The approximate Jacobian matrices $[\tilde{J}_1]$ and $[\tilde{J}_2]$ are so constructed that

$$\Delta \vec{F} = [\tilde{J}_1] \Delta \vec{W} \quad \text{and} \quad \Delta \vec{G} = [\tilde{J}_2] \Delta \vec{W}$$

In the present study, the differences of \vec{W} , \vec{F} and \vec{G} are approximated as follows:

$$\Delta \vec{W} = \sum_{k=1}^3 \alpha_k \vec{e}_k, \quad \Delta \vec{F} = \sum_{k=1}^3 \lambda_k \alpha_k \vec{e}_k$$

and

$$\Delta \vec{G} = \sum_{k=1}^3 \lambda'_k \alpha'_k \vec{e}'_k$$

Also, the vectors at the right hand sides of equations (16) and (17) are projected into the eigenvector space as follows:

$$[D][J_3] \frac{\partial \vec{W}}{\partial x} + \vec{f}_0 = -\frac{1}{\Delta x} \sum_{k=1}^3 \lambda_k \gamma_k \vec{e}_k$$

and

$$[E][J_4] \frac{\partial \vec{W}}{\partial y} + \vec{g}_0 = -\frac{1}{\Delta y} \sum_{k=1}^3 \lambda'_k \gamma'_k \vec{e}'_k$$

The finite difference equations can be derived as follows:

$$\vec{W}'_{i,j} = \vec{W}^n_{i,j} + \beta_1 \Delta \vec{F}^*_{i,j-\frac{1}{2}} - \beta_1 \Delta \vec{F}^*_{i+\frac{1}{2},j} \\ \text{for } j = 1, 2, \dots, n \quad (18)$$

and

$$\vec{W}^{n+1}_{i,j} = \vec{W}'_{i,j} + \beta_2 \Delta \vec{G}^*_{i,j-\frac{1}{2}} - \beta_2 \Delta \vec{G}^*_{i,j+\frac{1}{2}} \\ \text{for } i = 1, 2, \dots, m \quad (19)$$

where $\beta_1 = \frac{\Delta x}{\Delta t}$ and $\beta_2 = \frac{\Delta y}{\Delta t}$. With the Superbee limiter (Roe, 1985), $FL(r_{k,i-\frac{1}{2},j})$, it follows that

$$\Delta \vec{F}^*_{i-\frac{1}{2},j} = \frac{1}{2} (\vec{F}_{i,j} - \vec{F}_{i-1,j}) \\ + \frac{1}{2} \sum_{k=1}^3 \lambda_{k,i-\frac{1}{2},j} \gamma_{k,i-\frac{1}{2},j} \vec{e}_{k,i-\frac{1}{2},j} \\ + \frac{1}{2} \sum_{k=1}^3 (\alpha_{k,i-\frac{1}{2},j} + \gamma_{k,i-\frac{1}{2},j}) |\lambda_{k,i-\frac{1}{2},j}| \vec{e}_{k,i-\frac{1}{2},j} \\ + \frac{1}{2} \sum_{k=1}^3 FL(r_{k,i-\frac{1}{2},j}) (\alpha_{k,i-\frac{1}{2},j} + \gamma_{k,i-\frac{1}{2},j}) \\ |\lambda_{k,i-\frac{1}{2},j}| (1 - \beta_1 |\lambda_{k,i-\frac{1}{2},j}|) \vec{e}_{k,i-\frac{1}{2},j} \quad (20)$$

Similarly, $\Delta \vec{F}^*_{i+\frac{1}{2},j}$, $\Delta \vec{G}^*_{i,j-\frac{1}{2}}$ and $\Delta \vec{G}^*_{i,j+\frac{1}{2}}$ can be derived. The mathematical details are given by Huang (1995).

In the numerical computation, for each time step, equation (18) is first solved along the x -direction by assuming that $\vec{W}(x, y_j, t_n) = \vec{W}^n_{i,j}$ and $\vec{F}(x, y_j, t_n) = \vec{F}^n_{i,j}$; and they are constants for $x \in [x_i - \frac{1}{2}\Delta x, x_i + \frac{1}{2}\Delta x]$ and $y = y_j$, for $j = 1, 2, \dots, n$. Solutions at this stage, u' , v' and q' , are obtained, and $\vec{W}(x, y, t)$ and $\vec{G}(x, y, t)$

can be calculated. Furthermore, equation (19) is solved along the y -direction by assuming that $\bar{W}(x_i, y, t) = \bar{W}'_{ij}$ and $\bar{G}(x_i, y, t) = \bar{G}'_{ij}$; and they are constants for $y \in [y_j - \frac{1}{2}\Delta y, y_j + \frac{1}{2}\Delta y]$ and $x = x_i$, for $i = 1, 2, \dots, m$.

Computation of Forces

Forces Caused by Water Flow on Deck

As soon as the water depth and the water particle velocity are computed, the pressure on deck can be obtained as follows:

$$p(x, y, t) = \rho \{ \zeta [g \cos(e_1) \cos(e_2) + \dot{u}_3 + 2(u_4 v - u_5 u) + (u_4 u_6 - \dot{u}_5)(x - x_g) + (u_5 u_6 - \dot{u}_4)(y - y_g) + (u_4^2 + u_5^2)z_g] - \frac{1}{2}[(\zeta - z_g)^2 - z_g^2](u_4^2 + u_5^2) \} \quad (21)$$

Then forces and moments caused by water flow on deck are calculated by integrating the pressure over the deck area.

Nonlinear Froude-Krylov Forces

At each time instant, the ship motions ($\xi_1, \xi_2, \xi_3, e_1, e_2, e_3$) are solved from equations (1) and (5). Making use of the Eulerian angles (e_1, e_2, e_3), the ship-fixed coordinate system and the steady moving coordinate system can be related as:

$$\begin{pmatrix} x_m \\ y_m \\ z_m \end{pmatrix} = \begin{pmatrix} \xi_1 + x_{sg} \\ \xi_2 + y_{sg} \\ \xi_3 + z_{sg} \end{pmatrix} + [R] \begin{pmatrix} x_s - x_{sg} \\ y_s - y_{sg} \\ z_s - z_{sg} \end{pmatrix} \quad (22)$$

where (x_{sg}, y_{sg}, z_{sg}) are the coordinates of the centre of gravity of the ship in the ship-fixed coordinate system. Also, we have

$$X = Ut + x_m, \quad Y = y_m \quad \text{and} \quad Z = z_m \quad (23)$$

where U is the forward speed of the ship.

The wave profile $\zeta_0(X, Y, t)$ can be computed using equation (??). All the nodal points on the ship hull and deck are transformed into the $OXYZ$ coordinate system using equations (22) and (23). If a nodal point is below the free surface $\zeta_0(X, Y, t)$, then we compute the pressure at this point:

$$P(X, Y, Z, t) = P_s(X, Y, Z, t) + P_d(X, Y, Z, t) \quad (24)$$

where, the static pressure is:

$$P_s(X, Y, Z, t) = -\rho g[Z - \zeta_0(X, Y, t)] \quad (25)$$

and the dynamic pressure is:

$$P_d(X, Y, Z, t) = -\rho \frac{\partial \Phi_0}{\partial t} - \frac{1}{2} \rho |\nabla \Phi_0|^2 \quad (26)$$

In this work, quadrilateral panels are used to discretize the ship hull surface. It is assumed that at the instant t_n , there are $N(t_n)$ wetted panels on the hull surface and the deck space. The mean pressure on a panel is:

$$\bar{p} = \frac{1}{4} \sum_{j=1}^4 p_j(X, Y, Z, t) \quad (27)$$

where p_j is the pressure at a nodal point of the panel. The nonlinear restoring forces are computed as follows:

$$F_k^{R_s}(t) = -\rho g \sum_{j=1}^{N(t_n)} \bar{P}_{s,j} \Delta S_j n_{k,j} \quad k = 1, 2, \dots, 6 \quad (28)$$

where ΔS_j is the area of the j^{th} panel and $n_{k,j}$ is the k^{th} component of the unit normal on the j^{th} panel. The nonlinear Froude-Krylov forces are:

$$F_k^{FK}(t_n) = - \sum_{j=1}^{N(t_n)} \bar{P}_{d,j} \Delta S_j n_{k,j} \quad k = 1, 2, \dots, 6 \quad (29)$$

where the subscript "d" indicates the dynamic pressure.

The irregular waves are expressed in the space-fixed coordinate system, $OXYZ$. They are represented by superposition of finite number of regular sinusoidal waves. The incident wave potential of the irregular wave field is given as follows:

$$\Phi_0(X, Y, Z, t) = \sum_{j=1}^{N_w} \frac{a_j g}{\omega_j} e^{k_j Z} \cos(k_j X \cos \beta + k_j Y \sin \beta - \omega_j t + \delta_j) \quad (30)$$

where a_j is the amplitude of the j^{th} regular wave, ω_j is the frequency of the j^{th} regular wave, $k_j = \omega_j^2/g$ is the wave number and δ_j is the random phase lag of the j^{th} regular wave. The phase lag δ_j follows a uniform distribution over $[0, 2\pi]$. For practical computation, the number of wave components N_w is approximately 25. Wave spectra, such as Pierson-Moskowitz, JONSWAP, Bretschneider, Ochi-Hubble six parameter, or measured spectrum, can be used in generating irregular waves for the computer simulation.

Forces due to the Radiated and Diffracted Waves

The impulse response function method given by Cummins (1962) is used to describe the radiated wave forces on the ship hull. The radiated wave potential is caused not only by the oscillatory velocity but also by the oscillatory displacement which changes the position of the body in the steady flow field. The force due to radiated waves can be expressed as follows:

$$F_k^{Ra}(t) = \sum_{j=1}^6 F_{kj}(t) = -\bar{\mu}_{kj}\ddot{\eta}_j(t) - \bar{\lambda}_{kj}\dot{\eta}_j(t) - \bar{\gamma}_{kj}\eta_j(t) - \int_0^t K_{kj}(t-\tau)\dot{\eta}_j(\tau)d\tau$$

for $k = 1, 2, \dots, 6$ (31)

where $\bar{\mu}_{kj}$ is the time domain added mass of the ship, $\bar{\lambda}_{kj}$ is the time domain hydrodynamic damping, $\bar{\gamma}_{kj}$ is the coefficient of the time domain hydrodynamic restoring force. These coefficients are computed from the impulsive potentials (King, et al., 1988). $K_{kj}(t)$ is the retardation function which is obtained by:

$$K_{kj}(t) = \int_0^\infty (B_{kj}(\omega_e) - \bar{\lambda}_{kj})\cos(\omega_e t)d\omega_e \quad (32)$$

where $B_{ij}(\omega_e)$ is the damping coefficients in the frequency domain which is computed using the panel method (Hsiung and Huang, 1991).

In order to compute the hydrodynamic damping and hydrodynamic restoring coefficients, the m-terms have been calculated. To avoid the direct evaluation of the second derivatives, an integral equation method has been applied to the 2-D body by Wu (1991). Computations were carried for a 3-D body by Huang and Hsiung (1993) based on the double-body flow potential $\bar{\Phi}$. Applying the Green theorem, the following integral equation can be obtained for the m-terms:

$$\frac{\partial \bar{\Phi}(\vec{x}_m)}{\partial x_m} = \frac{1}{4\pi} \int_S [\bar{\Phi}_{\xi_m}(\vec{\xi}_m) \frac{\partial G}{\partial n} - G(\vec{x}_m, \vec{\xi}_m) m_1(\vec{\xi}_m)] dS \quad (33)$$

$$\frac{\partial \bar{\Phi}(\vec{x}_m)}{\partial y_m} = \frac{1}{4\pi} \int_S [\bar{\Phi}_{\eta_m}(\vec{\xi}_m) \frac{\partial G}{\partial n} - G(\vec{x}_m, \vec{\xi}_m) m_2(\vec{\xi}_m)] dS \quad (34)$$

and

$$\frac{\partial \bar{\Phi}(\vec{x}_m)}{\partial z_m} = \frac{1}{4\pi} \int_S [\bar{\Phi}_{\zeta_m}(\vec{\xi}_m) \frac{\partial \bar{G}}{\partial n} - \bar{G}(\vec{x}_m, \vec{\xi}_m) m_3(\vec{\xi}_m)] dS \quad (35)$$

where $G = \frac{1}{r} + \frac{1}{r_1}$, $\bar{G}(\vec{x}_m, \vec{\xi}_m) = \frac{1}{r} - \frac{1}{r_1}$, $r = |\vec{x}_m - \vec{\xi}_m|$, $r_1 = |\vec{x}_m - \vec{\xi}_m^*|$, $\vec{x}_m = (x_m, y_m, z_m)$ is the field point, $\vec{\xi}_m = (\xi_m, \eta_m, \zeta_m)$ is the source point, $\vec{\xi}_m^* = (\xi_m, \eta_m, -\zeta_m)$, and $\sigma(\xi_m)$ is the source strength. The m-terms: m_4 , m_5 and m_6 can be computed directly using m_1 , m_2 and m_3 (Newman, 1978).

The diffracted wave force in irregular waves may be obtained as:

$$F_k^D(t) = \sum_{j=1}^{N_w} a_j \bar{F}_{k,j}^d \cos(\omega_{e,j}t - \delta_j - \epsilon_{d,j})$$

for $k = 1, 2, \dots, 6$ (36)

where $\bar{F}_{k,j}^d$ is the amplitude and $\epsilon_{d,j}$ is the phase lag of the diffracted wave force, respectively. They are computed in the frequency domain using the panel method (Hsiung and Huang, 1991).

Viscous Roll Damping Moment

Various forms of formulation of the roll damping moment have been applied to the nonlinear roll motion, such as the linear plus quadratic model, the linear plus cubic model, etc (Haddara and Bass, 1990). Special attention should be paid on the choice of the form of damping coefficients for small vessels. Roll decay tests have been carried out for five inshore fishing vessels (Peng, et al., 1995). This type of fishing boat has a big skeg with flat bottom near the stern, as well as low L/B ratio and a shallow draught. Different forms of damping moment were applied to fit the roll decay curves based on the energy balance method. It has been realized that the evaluation of roll damping of this type of vessel is more difficult than conventional ships, such as cargo ships or frigates. In general, the roll damping coefficients are roll angle dependent and the following formulas are applied:

$$F_4^\nu(e_1) = 2(I_{11} + \bar{\mu}_{44})\omega_\phi(\alpha_1 + \alpha_2|e_1|)e_1 \quad (37)$$

or

$$F_4^\nu(e_1) = 2(I_{11} + \bar{\mu}_{44})\omega_\phi(\alpha_1 + \alpha_3 e_1^2)e_1 \quad (38)$$

where ω_ϕ is the natural frequency of the ship in roll.

Resistance, Cross-Flow Drag and Thrust

In this work, resistance model test results are used for inshore fishing vessels (Lacy, 1995). Models were also towed transversely in the tank in order to measure the cross-flow drag (Huang, 1995). Test results are used in the numerical simulation of the vessel motions.

If there is no test data available, empirical formulas, such as those given by Holtrop and Menen (1982), are used for resistance estimation. The cross-flow drag and moment can be calculated by:

$$F_2^v(t) = -\frac{1}{2}\rho \int_L C_d(x_s)T(x_s)v_2(x_s)|v_2(x_s)|dx_s \quad (39)$$

and

$$F_6^v(t) = -\frac{1}{2}\rho \int_L x_s C_d(x_s)T(x_s)v_2(x_s)|v_2(x_s)|dx_s \quad (40)$$

where $C_d(x_s)$ is the sectional cross-flow drag coefficient, $T(x_s)$ is the local draft of the ship and $v_2(x_s)$ is the transverse relative velocity between the hull and the water particle of the local cross-flow.

The thrust and torque of the propeller can be estimated from the available propeller charts as:

$$F_1^{Pr} = (1 - t_p)\rho n_p^2 D_p^4 K_T(J) \quad (41)$$

and

$$F_4^{Pr} = \rho n_p^2 D_p^5 K_Q(J) \quad (42)$$

where t_p is the thrust deduction fraction, n_p the revolution of the propeller per minute, D_p the propeller diameter, J the advancing coefficient, K_T the thrust coefficient and K_Q the torque coefficient.

Maneuvering Forces

The following nonlinear lateral force and turning moment are adopted in the seakeeping computation (Kijima et al., 1990):

$$F_2^L(t) = \frac{1}{2}\rho L d \tilde{U}^2 (Y_\beta \beta' + Y_r r' + Y_{\beta\beta} |\beta'| \beta' + Y_{rr} |r'| r' + (Y_{\beta\beta r} \beta' + Y_{\beta r r}) \beta' r' \quad (43)$$

and

$$F_6^L(t) = \frac{1}{2}\rho L^2 d \tilde{U}^2 (N_\beta \beta' + N_r r' + N_{\beta\beta} |\beta'| \beta' + N_{rr} |r'| r' + (N_{\beta\beta r} \beta' + N_{\beta r r}) \beta' r' \quad (44)$$

where L is ship length, d is ship draft, $\beta' = -u_2/\tilde{U}$ and $r' = \dot{e}_6 L/\tilde{U}$. In computation, \tilde{U} is the instantaneous relative velocity between the ship and the calm water in the x-direction, and u_2 the instantaneous sway velocity. The hydrodynamic derivatives Y 's and N 's are determined by empirical formulas or from test results.

Rudder Forces and Autopilot

It is defined that the rudder angle δ is positive when the rudder is turned to the port side. From

the paper by Kijima et al. (1990), the normal force acting on the rudder can be evaluated by:

$$F_N = -\frac{1}{2}\rho \frac{6.13\tilde{\lambda}}{\tilde{\lambda} + 2.25} A_r V_r^2 \sin \delta_e \quad (45)$$

where $\tilde{\lambda}$ is the aspect ratio of the rudder, A_r the rudder area of single side, V_r the relative velocity of the water particle to the rudder, and δ_e the effective rudder angle:

$$\delta_e = \delta + \tan^{-1} \frac{u_2 - l_x \dot{e}_6 + l_z \dot{e}_4}{\tilde{U} + u_1} \quad (46)$$

Suppose that the normal force acts on the pressure point C_{rud} on the rudder, the rudder force components can be obtained as follows:

$$F_1^{Rud} = -|F_N| \sin \delta \quad (47)$$

$$F_2^{Rud} = F_N \cos \delta \quad (48)$$

$$F_4^{Rud} = l_x F_N \cos \delta \quad (49)$$

and

$$F_6^{Rud} = -l_z F_N \cos \delta \quad (50)$$

where l_x and l_z are horizontal and vertical distances between the pressure point C_{rud} and the centre of gravity, respectively; U_{cx} and U_{cy} are the longitudinal and lateral components of current, respectively.

If the autopilot is considered, the following formula is recommended:

$$\delta(t) = \begin{cases} \alpha_1^r e_6(t) + \alpha_2^r \dot{e}_6, & \text{if } e_6 > \delta_0 \\ 0, & \text{if } e_6 \leq \delta_0 \end{cases} \quad (51)$$

where α_1^r is the yaw gain, α_2^r is the yaw rate gain, and δ_0 is the threshold value of yaw beyond which the rudder is activated.

Results and Discussion

First, we present the computed motion results of fishing vessel A. Motion tests of a free-running model of this vessel in a wave tank have been conducted. Heave acceleration, roll angle and pitch angle are measured; and wave slopes, $2\zeta_0/\lambda$, up to 0.09 are used, where λ is the incident wave length and ζ_0 is the incident wave amplitude. The principal dimensions of the model are given in Table 1 and the panelized hull up to waterline and bulwark are given in Fig. 3 and Fig. 4, respectively. It represents thousands of fishing vessels on the eastern seaboard of Canada. These vessels have very shallow draft, large skeg, flat bottom near the stern, as well as low length to beam ratio. The vessels are very stiff in waves, the typical full-scale natural period is only about 3 sec.

Table. 1 Characteristics of Fishing Vessel A

Length, Loa (m)	1.846
Maximum beam, B (m)	0.717
Mean draft, D (m)	0.187
Volume ∇ (m ³)	0.0663
Radius of gyration r_{xx} (m)	0.236
Radius of gyration r_{yy} (m)	0.430
L.C.G. (m) (from F. P.)	0.996
V.C.G. (m) (from baseline)	0.378
Natural roll period T_0 (sec)	1.150

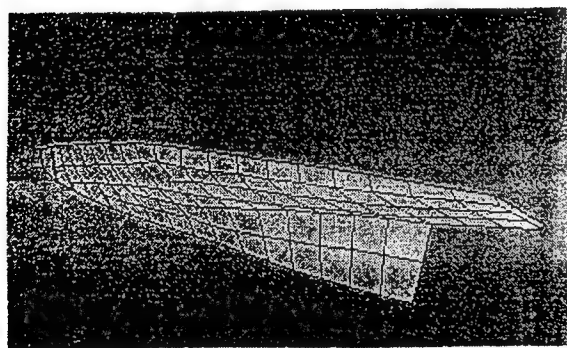


Fig. 3 Panelized Hull up to Waterline

At a nominal forward speed of 5 knots, comparison between computed results and the measurements are given in Fig. 5 and Fig. 6 for the double ampli-

tudes of heave acceleration and pitch motion. The double amplitude of heave acceleration is normalized by $2\omega_e^2\zeta_0$ and the double pitch amplitude by $2k\zeta_0$. The computed results agree well with the model test results.

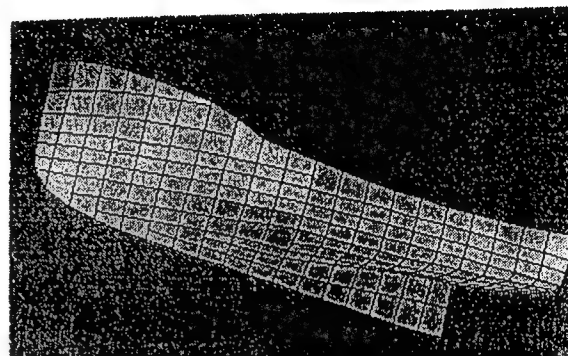


Fig. 4 Panelized Hull up to Bulwark

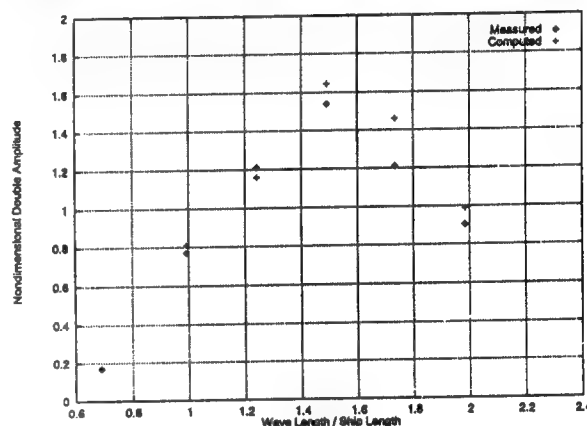


Fig. 5 Heave Acceleration in Head Seas

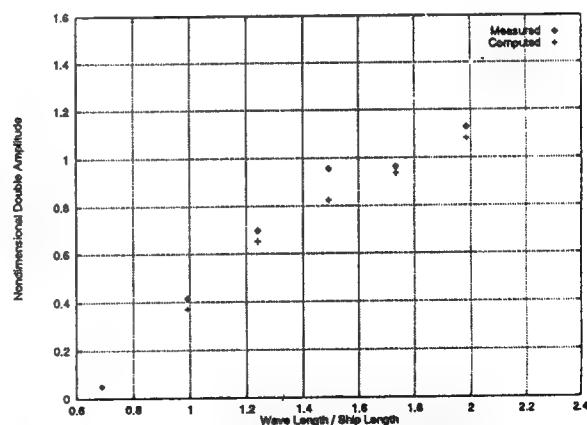


Fig. 6 Pitch Motion in Head Seas

The nondimensional double amplitude of roll in beam seas with a nominal forward speed of 5 kts is given in Fig. 7. Time histories of the measured and computed roll motions are shown in Fig. 8, in

which $\lambda/L = 1.5$ and wave height 0.62 m. Both computed and measured roll have a mean heel angle towards the incident waves.

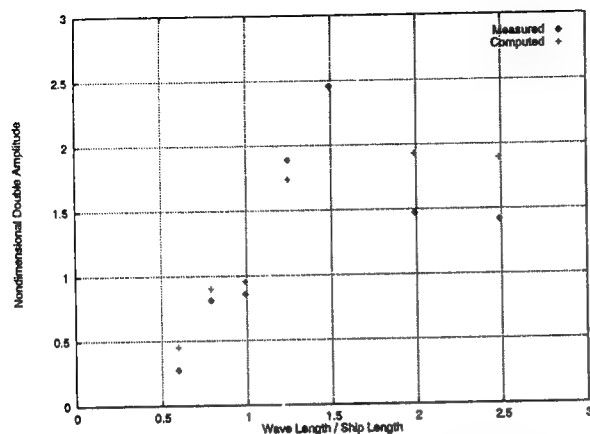


Fig. 7 Nondimensional Roll Motion in Beam Seas

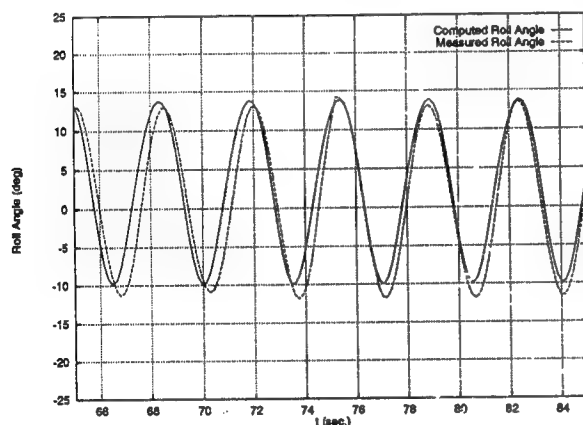


Fig. 8 Roll Time History in Beam Seas

Water flow on deck, which is subjected to roll excitation, is computed. The deck is 0.91 m wide. Numerical results are compared with experimental data given by Adey and Caglayan (1982). At the frequency 1.57 rad/sec which is close to one half of the first resonant frequency, roll amplitude 9.5 deg, water depth 7.62 cm, the computed and measured wave motions are shown in Fig. 9. For an amplitude 5.0 deg and a frequency 2.07 rad/sec, which is close to the primary resonant frequency, the wave profiles at $t=3.0$ sec is shown in Fig. 10 where the water depth is 5.08 cm. A bore can be clearly observed there. For the roll amplitude 7.5 deg and the exciting frequency 3.644 rad/sec,

which is one and a half of the primary resonant frequency, water depth 5.08 cm, the numerical results and measured data are shown in Fig. 11.

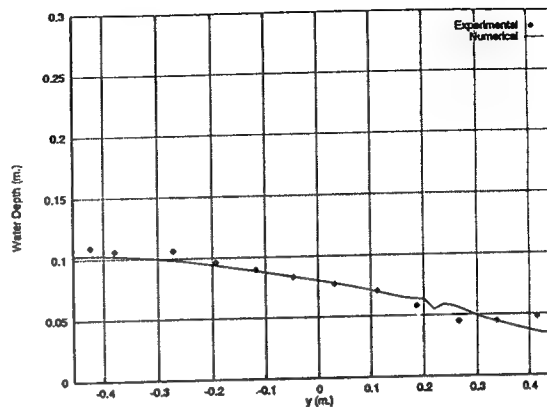


Fig. 9 Wave Profile, $a_4 = 9.5$ deg, $\omega = 1.57$ rad/sec, $t=2.0$ sec

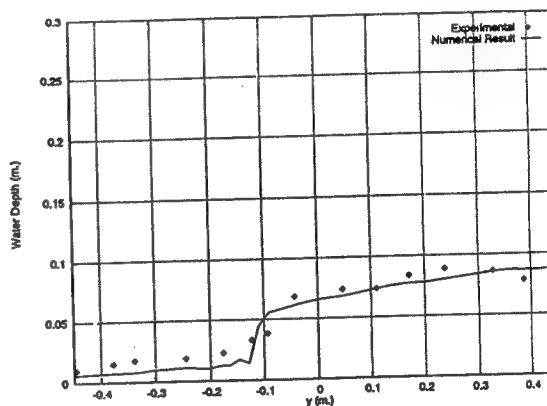


Fig. 10 Wave Profile, $a_4 = 5$ deg, $\omega = 2.07$ rad/sec, $t=3.0$ sec

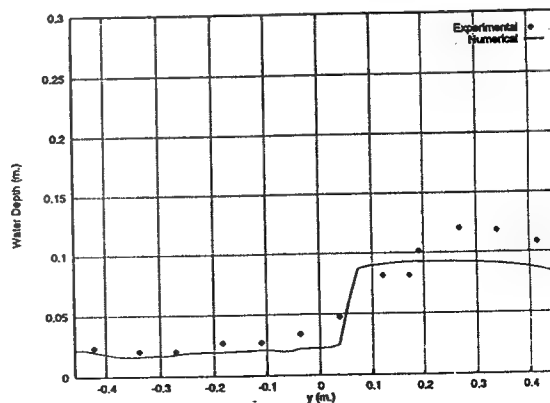


Fig. 11 Wave Profile, $a_4 = 7.5$ deg, $\omega = 3.644$ rad/sec, $t=2.0$ sec

For an amplitude 7.5 deg and a frequency 4.71 rad/sec, which is close to the second resonant frequency, the wave profiles at $t=3$ sec is given in Fig. 12. Two bore can be clearly observed in the computed results.

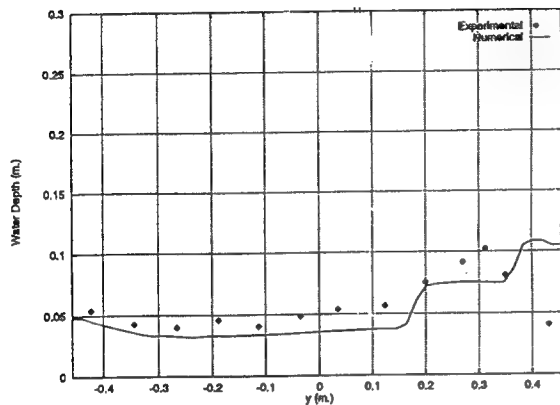


Fig. 12 Wave Profile, $a_4 = 7.5$ deg, $\omega = 4.712$ rad/sec, $t=3$ sec

The wave motion and the velocity distribution under the excitation of multi-degrees of freedom of ship motions are more complicated than those under the roll excitation only. Some characteristics of the wave motion can be found from numerical computations. Computed results are given below for a deck well of 1 m by 0.8 m with the water depth 10 cm. The rotation pivot is assumed to be located at the centre of the bottom surface. The primary resonant frequencies are $\omega_{0x} = 3.11$ rad/sec in the longitudinal direction and $\omega_{0y} = 3.89$ rad/sec in the transverse direction, respectively. Fig. 13 and Fig. 14 show the wave profile and the velocity distribution, respectively, under the coupled roll and pitch excitation. The roll and pitch amplitudes are 5 deg and frequencies 4.0 rad/sec which are close to the first resonant frequency. The time instant is 4.0 sec. In addition to the two bores which are caused by rolling and pitching, an oblique bore is produced by the interaction of two bores. The wave in the deeper water region travels faster than that in the shallower region. From Fig. 14, the particles near the oblique bore have greater speed than those in the other part of the deck.

As the frequency of deck oscillation is close to the second resonant frequency $2\omega_{0y}$, $\omega = 7.8$ rad/sec, the wave pattern at $t = 2$ sec is shown in Fig. 15.

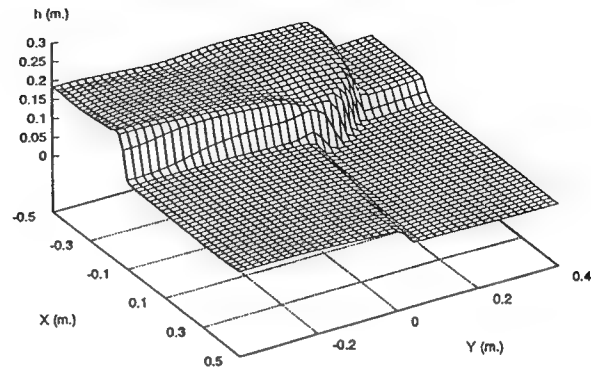


Fig. 13 Wave Pattern due to Roll and Pitch, $t=4.0$ sec, $\omega=4.0$ rad/sec

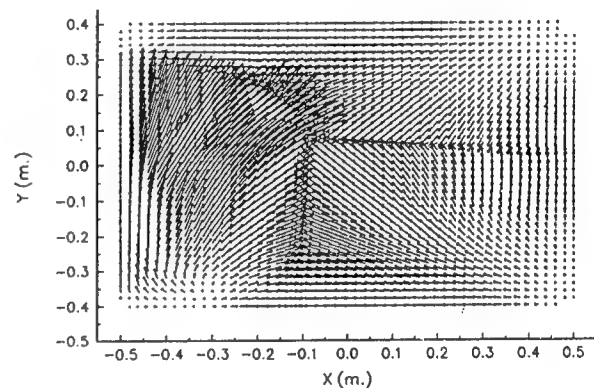


Fig. 14 Velocity Distribution due to Roll and Pitch, $t=4.0$ sec, $\omega=4.0$ rad/sec

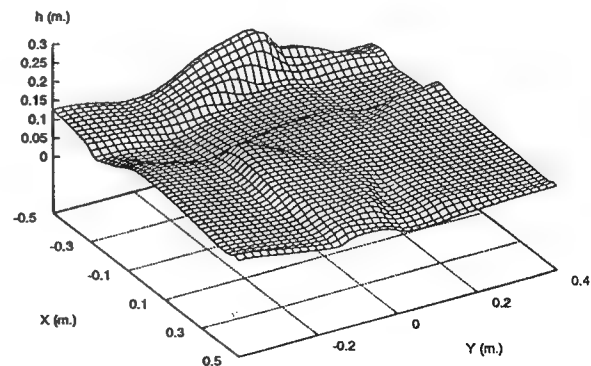


Fig. 15 Wave Pattern due to Roll and Pitch, $t=2.0$ sec, $\omega=7.8$ rad/sec

The wave motion due to the coupled surge and sway excitation is shown in Fig. 16. The surge

and sway amplitudes and frequencies are 2 cm and 6 rad/sec, respectively. Again, two bores can be clearly observed. However, the bores are not so steep as those caused by the roll and pitch motion near the first resonant frequency ω_{0y} .

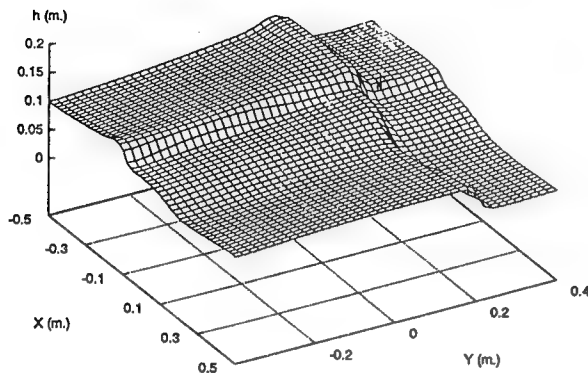


Fig. 16 Wave Pattern due to Surge and Sway, $t=1.5$ sec, $\omega=6.0$ rad/sec

In the computation of ship motion with water on deck, fishing vessel B, which is similar to fishing vessel A in hull geometry, is used in this paper. The boat is 12.5 m long, 4.2 m wide with a draft 1.47 m. Its displacement is 22.78 m^3 . The deck size is 4 m by 3 m. The amount of water trapped on deck is assumed to be $15\%V_0$ and $25\%V_0$, where V_0 is the intact vessel volume displacement. The corresponding water depths in the deck well are 0.285 m and 0.475 m, respectively.

Ship motions in six-degrees-of-freedom have been computed, all motions are coupled on another. The heave, roll and pitch motions with and without $15\%V_0$ water on deck are shown in Fig. 17, Fig. 18 and Fig. 19. It is assumed that the boat is in its upright position initially and has zero forward speed in beam seas. The wave length equals the boat length. With water on deck, the heave motion shown in Fig. 17 has a component of constant sinkage due to the water weight, and its amplitude and frequency are similar to those without water on deck. Small variations of the heave amplitude can be observed. From Fig. 18 and Fig. 19, the roll and pitch amplitudes are increased compared with those without water on deck. Nonlinear roll and pitch motions are observed in the predicted time history. It seems that the boat oscillates about a

bias heel angle towards the lee side or the weather side. But most time it is towards the lee side. No clear patterns of roll motion can be found.

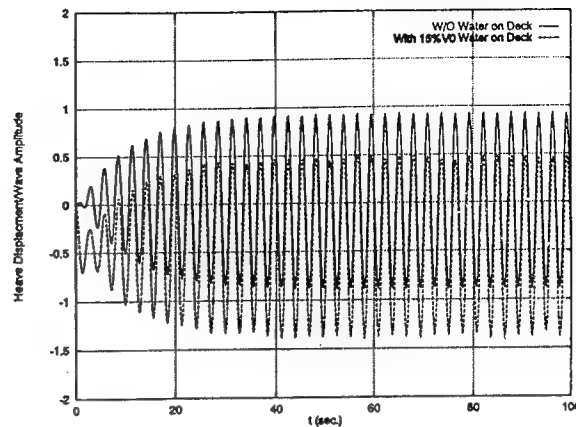


Fig. 17 Heave Motion, $\omega = 2.2$ rad/sec, $\beta = 90$ deg, $U = 0$ kts

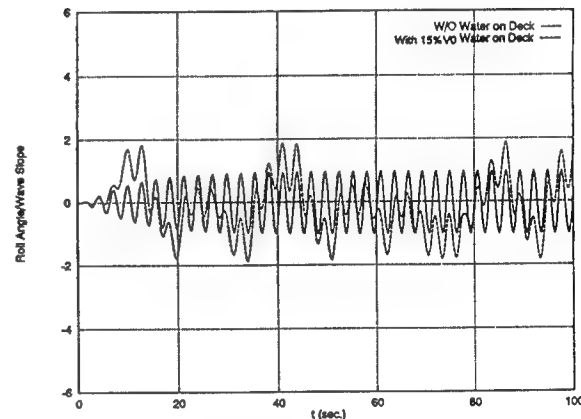


Fig. 18 Roll Motion, $\omega = 2.2$ rad/sec, $\beta = 90$ deg, $U = 0$ kts

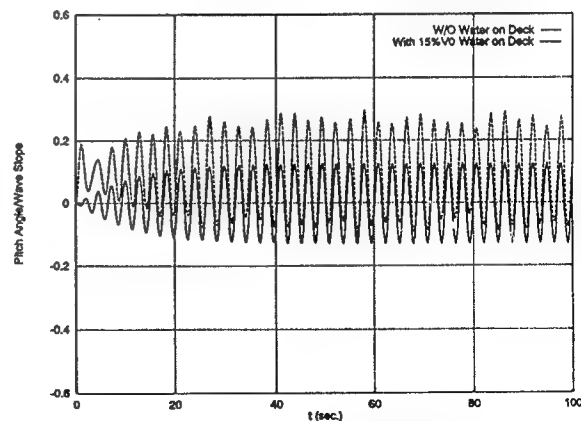


Fig. 19 Pitch Motion, $\omega = 2.2$ rad/sec, $\beta = 90$ deg, $U = 0$ kts

Keeping all other parameters the same as in the above case except increasing water on deck

$25\%V_0$, the predicted roll and pitch motions are given in Fig. 20, and Fig. 21, respectively. The roll motion in Fig. 20 shows a period-tripling oscillation caused by the water flow on deck. Also, the roll amplitude is enlarged. A mean trim exists in the pitch motion with water on deck as shown in Fig. 21. The pitch frequency is not changed compared with that of no water on deck. However, the nonlinear effects due to the water flow on deck and nonlinear coupling effect between roll and pitch (the nonlinear coupling effect is from the nonlinear equations of ship motion, the restoring force and the Froude-Krylov force) can be found in the pitch response time history. The pitch motion amplitude is increased.

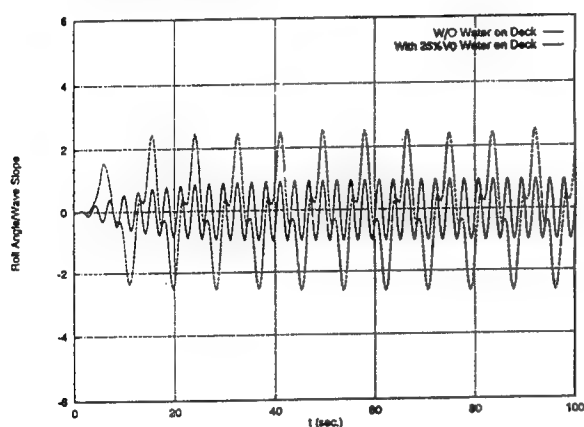


Fig. 20 Roll Motion, $\omega = 2.2$ rad/sec, $\beta = 90$ deg, $U = 0$ kts

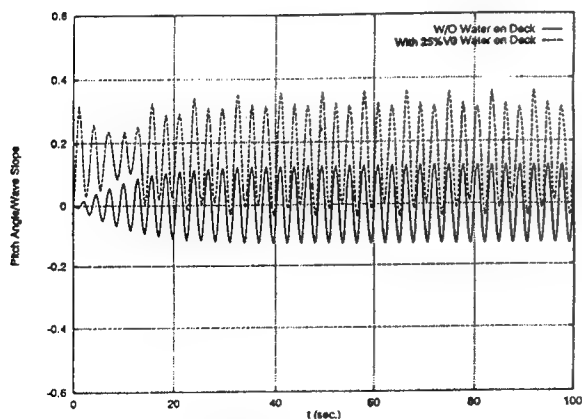


Fig. 21 Pitch Motion, $\omega = 2.2$ rad/sec, $\beta = 90$ deg, $U = 0$ kts

From above computations, it can be seen that the water flow on deck definitely affects the roll motion and that the pitch motion is not only affected by the water flow on deck but also coupled with roll

motion. Further computations were carried out for the boat at a forward speed of 5 knots with heading 45 deg and wave frequency 2.2 rad/sec. The roll and pitch motions with $25\%V_0$ water on deck are shown in Fig. 22 and Fig. 23, respectively. A steady trim and amplitude variations are found in the pitch motion, and there is no frequency shift. The roll motion is periodic, and the period three and a half of wave excitation period. The roll amplitude is magnified.

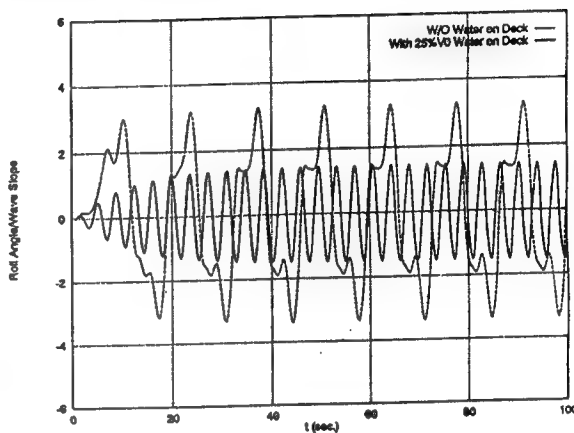


Fig. 22 Roll Motion, $\omega = 2.2$ rad/sec, $\beta = 45$ deg, $U = 5$ kts

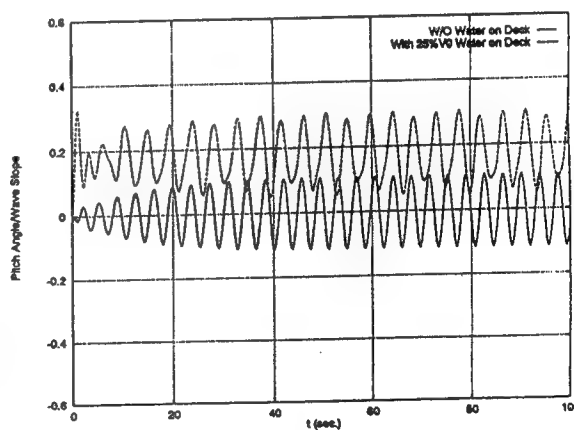


Fig. 23 Pitch Motion, $\omega = 2.2$ rad/sec, $\beta = 45$ deg, $U = 5$ kts

In this particular case, the resonant frequency of water sloshing inside the deck is much lower than the roll natural frequency, the water flow on deck may increase the roll motion amplitude and can alter the frequency of roll motion.

Conclusions

Equations of nonlinear ship motions are solved in the time domain. The linear radiated and diffracted wave forces are employed, however, other forces, such as nonlinear Froude-Krylov forces, deck flow forces and maneuvering forces are included in the equations. This method is applied to compute motions of fishing vessels of shallow draft. The computed results show good agreement with model test results.

The Flux-Difference Splitting method has been devised to study the shallow water flow on deck. It provides a tool to look into the hydrodynamic characteristics of the complicated deck flow phenomena and to investigate the effect of water depth and deck geometry. It can capture the steep wave front accurately. From the point of view of computing time required in simulation, it is faster than the Navier-Stokes solver. The nonlinear wave motion on deck is dominated by the water depth, deck width, position of rotation pivot, as well as the frequency and amplitude of excitation. When the exciting frequency is close to the primary resonant frequency, a single bore is generated and it travels back and forth in the deck well. Near the second resonant frequency, one or two bores can be observed.

For the small fishing vessels, the first resonant frequency of deck flow is within the frequency range of the major part of wave energy in irregular waves, therefore with water on deck a bore would occur. Nonlinear motion responses due to the water flow on deck have been observed. The vessels under investigation are "stiff" in roll, the first natural frequency of water sloshing inside the deck is much lower than the roll natural frequency. The water flow on deck actually increases the roll motion amplitude and the frequency of roll motion is also changed. The roll motion with multiple period of the incident waves has also been observed in the computation.

Acknowledgments

The authors are grateful for the research supports from Transport Canada, and Natural Sciences and Engineering Research Council of Canada.

References

- Adee, B. H. and Caglayan, I., "The Effects of Free Water on Deck on the Motions and Stability of Vessels", Proceedings of the Second International Conference on Stability of Ships and Ocean Vehicles, Tokyo, Japan, 1982.
- Alcrudo, F., Garcia-Navarro, P. and Saviron, J.-M., "Flux Difference Splitting for 1D Open Channel Flow Equations", International Journal for Numerical Methods in Fluids, Vol. 14, 1992.
- Armenio, V., Cardo, A. La Rocca, M., and Mele, P., "Numerical Prediction of Roll Motion of a Ship with Liquids on Board in Regular Waves from Different Directions", Proceedings of the Fifth International Conference on Stability of Ships and Ocean Vehicles, Melbourne, Florida, 1994.
- Caglayan, I. and Storch, R.L., "Stability of Fishing Vessels with Water on Deck: A Review", Journal of Ship Research, Vol. 26, No. 2, June 1982.
- Cummins, W. E., "The Impulse Response Function and Ship Motions," Schiffstechnik, Vol. 9, 1962.
- de Kat, Jan O. and Paulling, J.R., "The Simulation of Ship Motions and Capsizing in Severe Seas," Transactions, SNAME, Vol. 97, 1989.
- Dillingham, J., "Motion Studies of a Vessel with Water on Deck", Marine Technology, Vol. 18, No. 1, 1981.
- Grochowalski, S., "Investigation into the Physics of Ship Capsizing by combined Captive and Free Running Tests", Transactions, SNAME, 1989.
- Haddara, M. R. and D. W. Bass, "On the form of Roll Damping Moment for Small Fishing Vessels", Ocean Engineering, Vol. 17, No 6, 1990.
- Holtrop, J. and Mennen, G. G. J., "An Approximate Power Prediction Method", International Ship Building Progress, No. 335, Vol. 29, 1982.
- Hsiung, C.C. and Huang, Z.J., "Comparison of the Strip Theory and the Panel Method in Computing Ship Motion with Forward Speed", Proceedings of Symposium on Selected Topics of Marine Hydrodynamics, St. John's, Nfld, 1991.
- Huang, Z. J., Nonlinear Shallow Water Flow on Deck and Its Effect on Ship Motion, Ph. D. Thesis, Technical University of Nova Scotia, Halifax, Nova Scotia, 1995.
- Huang, Z. J. and Hsiung, C. C., "Nonlinear Shallow Water Flow on the Three-Dimensional Deck",

Proceedings of the Tenth International Workshop on Water Waves and Floating Bodies, Oxford, U. K., April 1995.

Huang, Z. J. and Hsiung, C. C., "Application of the Flux Difference Splitting Method to Compute Nonlinear Shallow Water Flow on Deck", Proceedings of the Fifth International Workshop on Water Waves and Floating Bodies, Kuju, Oita, Japan, April 1994.

Huang, Z. J. and Hsiung, C. C., "An Improved 3-D Panel Method to Compute n -Terms for Ship Motion", Proceedings of the Second Canadian Marine Dynamics Conference, Vancouver, B. C., August 1993.

Kijima, K., Katsuno, T., Nikiri, Y. and Furukawa, Y., "On the Maneuvering Performance of a Ship with the Parameter of Loading Condition", Journal of the Society of Naval Architects of Japan, Vol. 168, 1991.

King, B. K., Beck, R. F. and Magee, A. R., "Seakeeping Calculations with Forward Speed Using Time Domain Analysis", Proceedings of the Seventeenth Symposium on Naval Hydrodynamics, The Hague, Netherland, 1988.

Lacy, G., "Comparison of the Resistance Characteristics of Five Inshore Fishing Vessels", Proceedings of the Third Canadian Marine Hydrodynamics and Structures Conference, Halifax, Nova Scotia, August 1995.

Lee, K. and Adey, B., "Numerical Analysis of a Vessel's Dynamic Responses with Water Trapped on Deck", Proceedings of the Fifth International Conference on Stability of Ships and Ocean Vehicles, Melbourne, Florida, 1994.

Lin, W. M. and Yue, D. K., "Large Amplitude Motions and Wave Loads for Ship Design", Proceedings of the Twentieth Symposium on Naval Hydrodynamics, Santa Barbara, California, 1994.

Magee, A., "Seakeeping Applications Using a Time-Domain Method", Proceedings of the Twentieth Symposium on Naval Hydrodynamics, Santa Barbara, California, August, 1994.

Newman, J.N., "The Theory of Ship Motions", Advances in Applied Mechanics, Vol. 18, 1978.

Pantazopoulos, M. S., "Three-dimensional Sloshing of Water on Deck", Marine Technology, Vol. 25, 1988.

Peng, H., Lacy, G., Huang, Z. J. and Hsiung, C. C., "Nonlinear Roll Damping of Nova Scotia Inshore Fishing Boat", Proceedings of the Twenty-

Fourth American Towing Tank Conference, Texas A & M University, College Station, Texas, November 1995.

Press, W. H., Teukolsky, S. A., Vetterling, W. T. and Flannery, B. P., Numerical Recipes (Fortran), Cambridge University Press, 2nd Edition, 1992.

Roe, P. L., "Some Contributions to the Modelling of Discontinuous Flows", Lectures in Applied Mathematics, Vol. 22, American Mathematical Society, 1985.

Steger, J. and Warming, R. F., "Flux-Vector Splitting of the Inviscid Gas Dynamic Equations with Application to Finite-Difference Methods", Journal of Computational Physics, Vol. 40, 1981.

Van der Bosch, J. J. and Vugts, J. H., "On Roll Damping by Free-Surface Tanks", Transactions, RINA, Vol. 108, 1966.

Wu, G. X., "A Numerical Scheme for Calculating the m_j -terms in Wave-Current-Body Interaction Problem", Applied Ocean research, Vol. 13, No. 6, December 1991.

Yanenko, N. N., The Method of Fractional Steps, Springer-Verlag, New York, 1971.

Radar Backscatter of a V-like Ship Wake from a Sea Surface Covered by Surfactants

G. Zilman, T. Miloh (Tel-Aviv University, Israel)

ABSTRACT

In calm water synthetic aperture radar (SAR) ship wake images frequently form of a bright V with a narrow half angle of 2-3 deg. These images persist for many kilometers behind the ship and can be explained as a result of the Bragg scattering from ship-generated divergent waves (Milgram 1988). The present work is concerned with the generation of short divergent gravity waves and their radiation from the hull of a displacement ship moving on a free-surface covered by *surfactants*. Here it is shown that a contaminated free-surface significantly reduce the radar back scatter cross-section and drastically influence the V-wake detectability. Explicit formulas for the radar back scatter cross-section are obtained and numerical examples for their use are presented. The theoretical results are shown to be in a good qualitative and quantitative agreement with the experimental results of Shemdin (1990).

1 Introduction

Background. A moving ship generates a distinctive Kelvin free-surface waves system. It consists of two types of waves, transverse and divergent, which are located between two lines with a half angle of 19.5° . However, airborne synthetic aperture radar (SAR) images of the sea surface frequently display quite a different noticeable wave pattern in a form of a narrow V-like angle of 2° - 3° degrees (Munk, Scully-Power & Zachariassen 1986, Lyden et al. 1988, Shemdin 1990). Such wakes exhibit a central "dark area" and two "bright white arms" existing as far as 6-8

km behind surface ships.

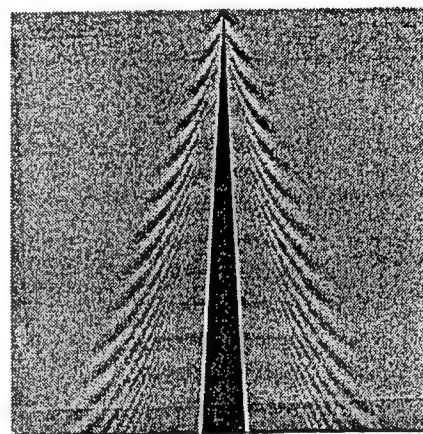


Figure 1: The wave pattern behind a displacement ship can be separated on:

1. Dark V-wake visible only in SAR images;
2. Two confining bright arms;
3. Optically visible Kelvin waves which are usually invisible in SAR images.

There is a belief that the bright arms of the V-wake stem from the radar back-scattering of short surface waves which are generated by the ship hull or its turbulent wake. Such a hypothesis is based on the Bragg scattering mechanism, which implies that a radar, roughly speaking, picks up a single wave number. The typical wavelength selected by L-band radars varies somewhat between 25-30 cm. Thus, it is plausible that such waves are presented in the ship wake.

To explain the V-wake phenomenon so far three alternative and somewhat mutually incompatible mechanisms have been invoked. They relate to:

1. Short divergent waves generated by a ship moving with a constant speed (Milgram 1988); in this approach the wave wake is a

result of wave interference between coherent sources replacing the hull of the vessel.

2. Short surface waves induced by the free-surface strain which is affected by ship-generated internal waves; the internal waves result from the interference of coherent sources replacing the hull (Keller & Munk 1970, Tulin & Miloh 1990, Miloh, Tulin & Zilman 1993).
3. Generation of short waves by incoherent point sources behind the ship (Munk et al. 1988); in the approach of Gu & Phillips (1995) incoherent sources simulate the oscillations of the edges of the turbulent wake.

In the present paper we investigate the attenuation of the short waves due to the presence of surfactant films compacted in the vicinity of the V-wake. Surfactants tend to concentrate at the free-surface and to alter the surface properties. In particular, this may result in a strong damping of ripples and short gravity waves (Levich 1962). It is common to interpret such a phenomenon as a *Marangoni* effect which is due to the gradient of the surface tension varying from point to point of the free-surface. The level of wave damping depends on many physical parameters of the water and the surfactants. The simplest mathematical model of the Marangoni phenomenon is based on the concept of a viscoelastic surface film and incorporates only three essential parameters: the water kinematic viscosity, ν , the surface tension coefficient, σ , and the elasticity of the surface film, ϵ , (Levich 1962). There exist strong experimental evidence that the elasticity of the surfactant film depends on the concentration of surfactants (Pelinovsky and Talipova 1990) and can be as high as 30 dyne/cm for natural surfactants of Black Sea.

The characteristics features of the radar return such as the brightness of the V-arms and their extent can be expressed in terms of the radar back scatter cross-section. As was indicated by Peltzer et al. (1991) these characteristics may depend on the density of the surfactant films covering the sea surface.

The basic mechanism of radar back-scattering. Herein we follow the work of Milgram (1988), where the radar back-scattering stems from the deformation of the initially flat free-surface by a system of ship generated divergent waves with the wave length about 20-30cm. This range is consistent with the L-band radar wave length and provides the Bragg resonance. However, as it was indicated in the work

of Munk, Scully-Power & Zachariansen (1986) the radar picks up not only the particular magnitude of a wave number, but also the direction of wave propagation, i.e., the direction for which the wave crests are normal to the look of sight of the radar. Thus, the brightness and the extent of the two bright arms can be different. If the direction of the radar look of sight α provides the maximal available signal for the, say, right V-arm, the left V-arm may be practically invisible on SAR images. For instance, the experimental database of Brown (1985) includes 49 SAR images of different ships; 24% percents of them have wakes with two arms, 41% show one arm, while 35% of the images do not exhibit any bright envelopes.¹ In all SAR images obtained by Shemdin (1990) the bright V-arms are visible only for those ships which travel in the same direction as the aircraft ($\alpha = 0$). Close scrutiny of SAR images presented in Shemdin (1990) shows that the extent, as well as the brightness of the arms are not the same. Moreover, in one of the reported images only one bright arm is visible.

The radar back scatter cross-section Θ depends on the wave elevation Z in the illuminated area, on the radar wave number k_r , the angle of incidence ψ , the length and width of the resolution cell $2l_c$ and $2b_c$ respectively and the complex back scatter coefficient, C , depending on the particular type of radar. For radars with a horizontal polarization the back scatter coefficient can be expressed approximately as $|C| \simeq \cos^2 \psi$.

According to the Bragg model the radar back scatter cross-section of a wavy surface per unit area is given by the following formula of Wright (1966, 1968):

$$\Theta = \frac{4k_r^4 |C|^2}{\pi b_c l_c} \left| \int_{-l_c}^{l_c} d\xi \int_{-b_c}^{b_c} Z(\xi, \eta) e^{2ik_r \sin \psi d\eta} \right|^2. \quad (1)$$

Here the coordinates (ξ, η) pertain to a local coordinate system of a rectangular resolution cell co-planar with the radar line of sight. Thus, if the wave elevation $Z(\xi, \eta)$ is known, the radar return also can be also computed.

Peculiarities of the ship wave-wake simulations. Simulation of the clean wave-wake of a ship is a classical problems of naval hydrodynamics and was considered by Kelvin (1891), Peters (1949), Ursell (1960, 1988), Wehausen & Laitone (1960), Sharma (1969), Newman (1970, 1971, 1987), Tuck, Collins & Wells (1971), Barnell

¹The authors are grateful to Dr. P.Wang for this information.

& Noblesse (1986), Barr & Price (1988), Noblesse, Hendrix & Barnell (1989), Nobless & Hendrix (1991), Ponizy et al. (1994), Nakos & Sclavounos (1994). The effect of viscosity on ship waves has been investigated, for example, by Wu & Mes-sick (1958), Cumberbatch (1965) and Kinoshita (1981). The effect of the surface tension on ship waves was investigated by Crapper (1964) and Sharma (1969). The unsteady Kelvin wake was investigated by Mei & Naqiri (1991), Eggers & Schultz (1992) and Cao, Schultz and Beck (1992).

The striking feature of the numerical simulations implemented by Noblesse and Hendrix (1991) is that they *..predict short divergent waves too steep to exist in reality within a significant sector in the vicinity of the ship track*". This difficulty was attributed by Milgram (1988) to a *collapse* of the divergent waves. In the framework of the present formulation such a pure theoretical obstacle can be lifted in a natural way since all short and non-realistic steep waves are *completely damped out by a surfactant film*.

The V-wake persist for many kilometers. Obviously, such a distance is much larger then the typical ship length. Thus, one can employ an asymptotic far field estimate for the wave elevations which greatly alleviate the consequent analysis. However, even a simplified expression for the wave elevation Z still makes the integration in the formula (1) not easy to perform. The relevant computations usually are time consuming and quite demanding of computer resources. The reason being that the expressions for the wave elevation Z are represented by integrals which hardly can be evaluated in an explicit form, and the numerical computation of (1) may involve millions of grid points.

It was noted by Milgram (1988), that in the far field the waves generated by a ship behaves almost as they came from a single location. In other words, far behind a ship the fine details of its shape may be inessential. It allows us to use a simplified description of the ship hull which takes into account only such gross geometrical parameters as ship length/beam ratio and the fullness coefficient of the waterline α_W . Such an approach provides an opportunity to select from the variety of ship forms only those which allows us to obtain an analytic representation of the wave elevation in the far field. Once such an analytic expression is known, one can try to find an asymptotic expression for the radar back scatter cross-section Θ .

The plan of the present work. Section 2

of this paper provides the mathematical outline for evaluating the wave elevations. It is based on linear water wave theory. In Section 3 we present the derivation of the Green function for a source moving below the free-surface covered by insoluble surfactant and an asymptotic expression for wave elevations. In this section we also discuss the damping effect of the surfactant film. An analytic expression for the radar back scatter cross-section is derived in Section 4. Starting from Section 5 the theoretical results are compared against the experimental data of Shemdin (1988). The particular numerical example involves a tanker *Bay Ridge* with the following characteristics:

Table 1. The particulars of the tanker *Bay Ridge*.

Length, m	334.9
Beam, m	43.7
Draft, m	21.4
Speed, m/s	7.5

The characteristics of the radar with received horizontal polarization which was used in the experiment of Shemdin are represented in Table 2:

Table 2. Aircraft L-Band SAR parameters.

Wavelength, m	0.246
Nominal resolution, m×m	11×11
Ground range resolution (at incident angle 30°),m	16×16
Ground range resolution (at incident angle 50°),m	10×10

2 Wave elevations induced by a moving ship.

Let us select the rectangular axes of the coordinate system attached to a moving ship in such a manner that the x and y -axes are situated on the undisturbed free-surface, and the z -axis is directed upward. We define the surface S of the hull by the function $y = \pm f(x, z)$. Our goal is to determine the free-surface profile $Z = Z(x, y)$ generated by a ship moving with constant velocity U in the direction of the positive x -axis. In the frameworks of the linear analysis we represent the resulting wave elevation $Z(x, y)$ induced by the ship as a sum of wave elevations due to sources of intensity $q_h(x, y, z)$ distributed over the surface S and wave elevations which stem from the sources $q_w(x, y)$ distributed over the contour of the waterline l_w (Brard 1972):

$$Z = Z_h + Z_w, \quad (2)$$

where

$$\mathcal{Z}_h(x, y) = \iint_S \zeta_h(M, N) q_h(N) dS(N), \quad (3)$$

and

$$\mathcal{Z}_w(x, y) = \oint_{l_w} \zeta_w(M, N) q_w(N) dl_w(N). \quad (4)$$

Here $N(x_0, y_0, z_0)$ is a point on the surface S and $M(x, y, z)$ is a field point. $\zeta_h = G(M, N)$ and $\zeta_w = \zeta_w(M, N)$ are two related *Green functions*. In general, for irrotational fluid motion the source density $q_h(x, y, z)$ can be found as the numerical solution of a corresponding boundary integral equation. The relation between the strength of the surface and the line source distribution is:

$$q_w(x, y) = \frac{U^2}{g} \frac{\partial f(x, 0)}{\partial l_w} \lim_{z \rightarrow -0} [n_x(x, y, z) q(x, y, z)], \quad (5)$$

where $n_x = \cos(n, x)$ is the projection of the normal to the ship surface on the x -axis, and g is the acceleration of gravity.

In the present work we consider a viscous fluid, but assume that the source density still can be calculated by invoking the potential theory. The combined effect of the fluid viscosity and the surfactant film elasticity will be included in the Green function. Such a heuristics approach has a real physical background. For the potential flow the source density distribution displays the form of the ship whereas the Green function manifests the physical properties of the fluid and the specific kinematic and dynamic boundary conditions to be applied on the free-surface. This approach can be partially improved by accounting for the thickness of ship boundary layer. Based on the work of Lavrentiev (1951) Kinoshita (1980) has been demonstrated that the Michell source distribution with the effect of the boundary layer displacement thickness is almost identical to the source distribution without a viscous effect, except a particular range near the stern. Havelock (1935) demonstrated many decades ago that the influence of the viscosity on the near stern flow can be accounted for by introducing a proper small "deformation" of the stern. It has been mentioned above that far behind a ship the fine details of its surface may be inessential. Thus, we assume that for estimating the far field wave wake the source density can be calculated on the basis of potential theory according to the formula:

$$q(x, y, z) = \frac{-1}{4\pi} \gamma(x, y, z) n_x, \quad (6)$$

where $\gamma(x, y, z)$ is a function which lamps the specific features of the shape of a ship. For a thin Michell type ship $\gamma(x, y, z) = 2$, and the integration in the formulas (3) and (4) can be performed at the ship the centerplane. For a ship of finite width γ varies from point to point of the ship surface, but it is bounded, i.e., $1 < \gamma < 1.5$ (Kostyukov 1968). In order to simplify the analysis and to obtain analytical results we employ the relation (6) with a constant coefficient $\gamma \simeq 1$, but perform the integration on both sides of the surface S . Such an approach has been previously justified by Milgram [20] who noted that "*comparative calculations of divergent waves and their scattering cross-section using thin ship source distribution (distributed on the actual ship shape-not the centerplane), and the source distribution obtained from its linear theory integral equation, show differences in details, but not in general form*".

3 The Green function of a moving surface disturbance.

3.1 Governing equations.

We consider a disturbance (a normal stress P_n) concentrated over a infinitesimally small area in the vicinity of the origin O of the coordinate system $Oxyz$. The disturbance moves rectilinearly with constant velocity U on the free-surface $\zeta_p = \zeta_p(x, y)$ of an incompressible viscous water covered by a surfactant film. A strong similarity between the wave elevation induced by a moving source and the wave elevation induced by a moving impulse of a normal stress applied to the free-surface is well known. For an inviscid fluid and irrotational fluid motion the wave elevation induced by a pressure impulse P_n moving over the free-surface is:

$$\zeta_p = \frac{1}{2\pi\rho U^2} \int_{-\pi}^{\pi} \int_0^{\infty} \frac{P_n k e^{ik(x \sin \theta + y \cos \theta)} dk d\theta}{g/U^2 - k \sin^2 \theta - i(+0)}.$$

Once the function ζ_p is defined, the functions $G_{h,w}$ can be reconstructed by using a formal substitution:

$$P_n = 2iU \sin \theta. \quad (7)$$

The linearized (Oseen) equation of fluid motion is expressed in the moving coordinate system as:

$$U \frac{\partial \mathbf{V}}{\partial x} - \frac{1}{\rho} \text{grad}(p + \rho g z) + \nu \nabla^2 \mathbf{V} = 0, \quad (8)$$

$$\text{div } \mathbf{V} = 0, \quad (9)$$

where \mathbf{V} is the vector of fluid velocity, p is the pressure in the fluid, ρ is the water density and ν is the kinematic viscosity. This equation can be splitted into potential and rotational parts

$$\mathbf{V} = \text{grad } \phi + \mathbf{V}_R(u, v, w),$$

such that

$$\nabla^2 \phi = 0, \quad (10)$$

and

$$U \frac{\partial \mathbf{V}_R}{\partial x} + \nu \nabla^2 \mathbf{V}_R = 0, \quad (11)$$

$$\text{div } \mathbf{V}_R = 0. \quad (12)$$

3.2 Boundary conditions.

The linearized kinematic condition on the free-surface is:

$$w + \frac{\partial \phi}{\partial z} = -U \frac{\partial \zeta_p}{\partial x} \quad \text{on } z = 0. \quad (13)$$

In the presence of surface tension the linearized normal stress dynamics boundary condition on the free-surface can be written as:

$$-p + 2\mu \left(\frac{\partial w}{\partial z} + \frac{\partial^2 \phi}{\partial z^2} \right) - \sigma \left(\frac{\partial^2 \zeta_p}{\partial x^2} + \frac{\partial^2 \zeta_p}{\partial y^2} \right) = P_n, \quad (14)$$

where μ is the water dynamic viscosity and σ is the surface tension coefficient. In general σ depends on the surfactant concentration Γ which, in turn, is a function of the coordinates (x, y) and thus, $\sigma = \sigma[\Gamma(x, y)]$. We assume that the concentration Γ of a surface-active agent is $\Gamma = \Gamma_0 + \Gamma'$, where Γ_0 is the constant concentration on the undeformed surface and $\Gamma' \ll \Gamma_0$. For slightly viscous fluid, low fluid velocity and small-amplitude waves it is common to assume that in equation (14) the surface tension coefficient is constant, $\sigma = \sigma(\Gamma_0)$. However, the gradient of the surface tension affects the tangential force

$$\mathbf{P}_t = -\frac{\partial \sigma}{\partial \Gamma} \text{grad } \Gamma,$$

and the tangential shear stress conditions on the free-surface become:

$$\mu \left(\frac{\partial u}{\partial z} + 2 \frac{\partial^2 \phi}{\partial x \partial z} + \frac{\partial w}{\partial x} \right) = p_{tx} \quad \text{on } z = 0, \quad (15)$$

$$\mu \left(\frac{\partial v}{\partial z} + 2 \frac{\partial^2 \phi}{\partial y \partial z} + \frac{\partial w}{\partial y} \right) = p_{ty} \quad \text{on } z = 0, \quad (16)$$

where p_{tx} and p_{ty} are the x and y -components of the shearing stress. Here the shearing stress vector can be expressed through the surfactant film concentration $\Gamma(x, y)$ and the concentration Γ_0 as (Levich 1962):

$$\mathbf{P}_t = -\epsilon \text{grad } \tilde{\Gamma} \quad \text{on } z = 0,$$

where ϵ is the elasticity of the surfactant film

$$\epsilon = \Gamma_0 \left. \frac{\partial \sigma}{\partial \Gamma} \right|_{\Gamma=\Gamma_0},$$

and $\tilde{\Gamma} = (\Gamma - \Gamma_0)/\Gamma_0$.

We assume that the insoluble surface-active agent is fully swept along with the liquid and that the influence of diffusion on the concentration distribution of the surface active agent may be disregarded. For low fluid velocity and small-amplitude waves the equation for the conservation of matter in the case of mass flow on an almost planar free-surface yields:

$$U \frac{\partial \tilde{\Gamma}}{\partial x} + \left(\frac{\partial^2 \phi}{\partial z^2} + \frac{\partial w}{\partial z} \right) = 0 \quad \text{on } z = 0. \quad (17)$$

3.3 Fourier transformation of the boundary-value problem

Let us denote the Fourier transform (FT) with respect to x and y as:

$$\hat{f}(k_x, k_y) = \frac{1}{2\pi} \iint_{-\infty}^{\infty} f(x, y) e^{-i(k_x x + k_y y)} dx dy. \quad (18)$$

The Fourier transform of (10) gives:

$$\hat{\phi} - k^2 \phi = 0 \quad (19)$$

with a solution

$$\hat{\phi} = A \exp(kz), \quad (20)$$

where $k = \sqrt{k_x^2 + k_y^2}$. The FT of (11) yields:

$$\frac{\partial \hat{V}_R}{\partial z} - (k^2 - i\omega/\nu) \frac{\partial \hat{V}_R}{\partial z} = 0$$

with a solution

$$\hat{V}_R(\hat{u}, \hat{v}, \hat{w}) = C(C_1, C_2, C_3) \exp(lz),$$

where

$$\omega = k_x U; \quad l = \sqrt{k^2 - i\omega/\nu} \quad (21)$$

and $\text{Re}(l) > 0$. Applying FT to (12) and (14) we have:

$$\hat{w} + \frac{\partial \hat{\phi}}{\partial z} = -i\omega \hat{\zeta}_p, \quad (22)$$

$$-i\omega \hat{\phi} + g \hat{\zeta}_p + 2\nu \left(\frac{\partial \hat{w}}{\partial z} + \frac{\partial^2 \hat{\phi}}{\partial z^2} \right) + Tk^2 \hat{\zeta}_p = \frac{\hat{P}_n}{\rho},$$

where $T = \sigma/\rho$. From (15) and (15) it follows:

$$\mu \left(\frac{\partial \hat{u}}{\partial z} + 2ik_x \frac{\partial \hat{\phi}}{\partial z} + ik_x \hat{w} \right) = -i\epsilon k_x \hat{\Gamma}, \quad (23)$$

$$\mu \left(\frac{\partial \hat{v}}{\partial z} + 2ik_y \frac{\partial \hat{\phi}}{\partial z} + ik_y \hat{w} \right) = -i\epsilon k_y \hat{\Gamma}. \quad (24)$$

Finally, equations (12) and (17) yield:

$$ik_x \hat{u} + ik_y \hat{v} + \frac{\partial \hat{w}}{\partial z} = 0, \quad (25)$$

$$i\omega \hat{\Gamma} + \left(\frac{\partial^2 \hat{\phi}}{\partial z^2} + \frac{\partial \hat{w}}{\partial z} \right) = 0. \quad (26)$$

The next step is to find the Fourier transform $\hat{\zeta}_p$ and its inverse ζ_p . This can be done by solving a system of linear algebraic equations with respect to unknown parameters A, C_1, C_2, C_3 . After some simple, but somewhat tedious calculations we obtain the following expression for $\hat{\zeta}_p$:

$$\hat{\zeta}_p = \frac{-\hat{P}_n}{\rho} \frac{(\omega^2 - \beta m k^2) k}{D},$$

where

$$D = -k(\omega^2 - \beta m k^2)(s - 2\nu i \omega l) + \omega(2\nu k m + i\omega)[2\nu \omega k^2 + i(\beta l k^2 - \omega^2)]$$

$\beta = \epsilon/\rho$, $m = l - k$, $\omega = U k_x$ and $s = g + Tk^2$. Performing the integration in the polar system of coordinates, taking into account (7), neglecting in

the numerator a small term incorporating $\beta \ll 1$ and small terms of order ν^2 in the denominator, we obtain the following expression for the regular part of the Green function:

$$\zeta_h = \zeta_h^+ + \zeta_h^-,$$

where

$$\zeta_h^\pm = \frac{-2iU^3}{\pi} \int_0^{\pi/2} d\theta \int_0^\infty k \frac{e^{ik\Omega^\pm + k(z+z_0)} \sin^3 \theta dk}{E(k, \theta)}, \quad (27)$$

$$\Omega^\pm = (x \sin \theta \pm y \cos \theta),$$

$$E(k, \theta) = (k\tau^2 - s)(\tau^2 - \beta l) + 2i\nu k \tau^2,$$

$$\tau = U \sin \theta,$$

and

$$l = \sqrt{k^2 - \frac{ik\tau}{\nu}}. \quad (28)$$

Here and in the sequel it is understood that in all complex expressions for the wave elevation similar to (27) have to be considered only the real part.

3.4 Poles of the integrand.

In the far field the asymptotic behavior of the Green function is determined through the poles of the integrand, or, in fact, by the roots of the equation:

$$E(k, \theta) = 0. \quad (29)$$

The effect of the inclusion of viscosity is to move the poles off the real axis, and viscous damping is thereby obtained. In the case of an inviscid fluid the two corresponding roots are real and can be found explicitly as:

$$k_0 = \frac{U^2}{2T} (\sin^2 \theta \pm \sqrt{\sin^4 \theta - 4gT/U^4}). \quad (30)$$

They corresponds to the capillary, capillary-gravity and gravity waves regions. The upper sign in this expression pertains to short capillary waves which are not important for our analysis for two reasons. First of all, they decay very fast with increasing distance from the disturbance and, secondly, they do not resonant with the radar wave length $\lambda_r \sim 20-30\text{cm}$. Thus, in the sequel we will

be concerned with short gravity-capillary waves which are defined by the lower sign of this relation. It is important to note that far downstream from the disturbance the integration in formula (27) is essential only for such values of θ which satisfies the inequality:

$$\theta \geq \frac{1}{U} \sqrt{4gT}. \quad (31)$$

For a viscous fluid with contaminated free-surface the roots of (30) become complex and the yielding poles can not be solved exactly. Only an approximate location of the poles can be obtained. To a good approximation the real part of the roots obeys the relation (30) while the imaginary part may depend on the elasticity of the surfactant film significantly. Thus, the complex roots may be written as follows:

$$k_c = k_0(\theta) - i\delta(\theta), \quad (32)$$

where $\delta > 0$ incorporates the damping effects of the water viscosity and the surfactant elasticity. If the initial value of the real root $k_0(\theta)$ is known, then the perturbation analysis of the of the dispersion relation (29) with respect to the small parameter $\delta/k_0 \ll 1$ yields an algebraic expression for the function $\delta = \delta[k_0(\theta), \theta, \nu, \epsilon]$. The additional complication for such an analysis arises from the branch points of the function E which are imposed by the relation (28). In order to avoid this mathematical difficulty we assume that

$$l = \sqrt{k^2 - \frac{ikU \sin \theta}{\nu}} \simeq (1-i) \sqrt{\frac{kU \sin \theta}{\nu}}.$$

Actually, since our interest resides in the range of wave numbers $k \sim 25 \text{ m}^{-1}$, ship velocity $U \sim 10 \text{ m/s}$, water kinematic viscosity $\nu = 10^{-6} \text{ m}^2/\text{s}$ and θ satisfying the inequality (31), it follows that $|k^2| \ll |ikU \sin \theta / \nu|$. In the limiting case of a viscous non-contaminated water the damping coefficient can be written as:

$$\delta^0 = -4g^2 \nu / U^5 \sin^5 \theta. \quad (33)$$

The ratio $\gamma = \delta/\delta_0$ characterizes the damping amplification factor which stems from the presence of surfactant film. It is plotted in Fig.2.

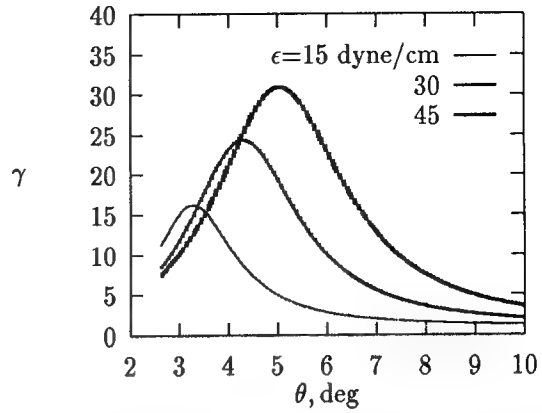


Figure 2: Relative viscous damping coefficient for different values of the surfactant film elasticity.

It can be seen clearly that the surfactant film greatly intensify the wave damping for small θ angles.

3.5 The Kochin function.

According to (3) and (4) the wave elevation induced by sources distribution over the hull surface S and the waterline contour l_w can be written as follows:

$$Z_h^\pm = \frac{-2iU^3}{\pi} \int_0^{\pi/2} \sin^3 \theta e^{k(z+z_0)+ik\Omega^\pm(x,y)} d\theta \times \int_0^\infty k \frac{H_h^\pm(k, \theta)}{E(k, \theta)} dk, \quad (34)$$

$$Z_w^\pm = \frac{-2iU^3}{\pi} \int_0^{\pi/2} \sin^3 \theta e^{kz+ik\Omega^\pm(x,y)} d\theta \times \int_0^\infty k \frac{H_w^\pm(k, \theta)}{E(k, \theta)} dk, \quad (35)$$

where

$$H_h^\pm = \iint_S q_h(x_0, y_0, z_0) e^{kz_0 - ik\Omega^\pm(x_0, y_0)} dS_0,$$

and

$$H_w^\pm = \oint_{l_w} q_w(x_0, y_0) e^{-ik\Omega^\pm(x_0, y_0)} dl_w \quad (36)$$

represent the Kochin functions. For short divergent waves with the wave length $\lambda_w \sim 20-30 \text{ cm}$ the hull integral H_h^\pm is significant only over a small depth of order λ_w . In this case $H_h(x, y, z) \simeq H_h(x, y, 0)$ and $q_h(x_0, y_0, z_0) \simeq q_h(x_0, y_0, -0)$. In

the vicinity of the waterline a ship has almost a vertical board and thus:

$$H_h^\pm = \int_{l_w} \kappa(k) q_h(x_0, y_0, -0) e^{-ik\Omega^\pm(x_0, y_0)} dl_w, \quad (37)$$

where

$$\kappa = \frac{1 - \exp(-k\lambda_w)}{k}.$$

It can be demonstrated that for short divergent waves the $|H_w^\pm| \gg |H_h^\pm|$ which implies that the contribution of the line integral is dominant in the final expression for the wave elevation.

3.6 Simplified waterline

As it was earlier mentioned, the fine details of hull shape are not really essential as far as the far wave field is concerned. Thus, we choose a particular polygonal contour of ship waterline as:

$$f_w(x) = \begin{cases} -a_F + b_F & \text{if } L_0/2 < x < L/2, \\ a_F + b_F & \text{if } -L/2 < x < L_0/2, \\ B/2 & \text{if } -L_0/2 < x < L_0/2, \end{cases}$$

where L is ship length, $(L_0/L) \sim 0.6 - 0.7$ and

$$a_F = \frac{-B}{(L - L_0)}, \quad b_F = \frac{BL}{(L - L_0)}.$$

Straightforward calculations give the following expression for the wave elevations:

$$\mathcal{Z} = \frac{-U^6}{\pi^2 g} a_F \int_0^{\pi/2} \sin^3 \theta d\theta \int_0^\infty \Lambda(k, \theta) \frac{A(k)}{E(k, \theta)} dk, \quad (38)$$

where

$$\Lambda = \sum_{n=1}^8 (-1)^{n+1} a_n [e^{-ikR_n \sin(\theta - \chi_n)} + e^{-ikR_n \sin(\theta + \chi_n)}],$$

$$R_n = \sqrt{x_n^2 + y_n^2},$$

$$x_n = -R_n \cos \chi_n,$$

$$y_n = R_n \cos \chi_n,$$

$$\tan \chi_n = y_n / (-x_n),$$

$$x_n = x + p_n,$$

$$y_n = y + q_n$$

$$p_{1,8} = -L/2, \quad p_{2,7} = -L_0/2,$$

$$p_{3,6} = L_0/2, \quad p_{4,5} = L/2,$$

$$q_{1,4,5,8} = 0, \quad q_{2,3} = -B/2, \quad q_{6,7} = B/2,$$

$$a_{1,2,7,8} = \frac{1}{(a_F \cos \theta - \sin \theta)},$$

$$a_{3,4,5,6} = \frac{1}{(a_F \cos \theta + \sin \theta)},$$

and

$$A(k) = -\frac{g}{U^2} \kappa(k) + \frac{a_F}{1 + a_F}.$$

3.7 Asymptotic expression for the wave elevation.

In order to determine the asymptotic behavior of (38) well downstream let us consider some n -component of the integrand tacitly omitting the subscript n :

$$\mathcal{Z}_n = \int_0^{\pi/2} \sin^3 \theta d\theta \int_0^\infty e^{-ikR \sin(\theta - \chi)} \frac{A(k) dk}{E(k, \theta)}. \quad (39)$$

Following Whitham (1974) let us represent the integral with respect to θ as a sum of two integrals:

$$\int_0^{\pi/2} = \int_\chi^{\pi/2} + \int_0^\chi.$$

In the first of them the function $\sin(\theta - \chi)$ is positive whereas in second one it is negative. We deform the contour of integration with respect to the complex variable k and represent the corresponding integral as a sum of three integrals: an integral along the real half-axis, an integral along the positive (negative) imaginary half-axis and a semi-circle of an infinitely large radius connecting the ends of the real and imaginary axes. The roots of the equation $E(k, \theta) = 0$ with respect to k are located in the lower half-plane. Thus, if $\sin(\theta - \chi) > 0$ the contour of integration is directed along the negative imaginary half-axis and the poles of the integrand give a contribution; if $\sin(\theta - \chi) < 0$ the contour of integration is directed along the positive imaginary half-axis and the poles of the integrand do not give a contribution. This also insures that the contour integral along the semi-circle vanishes. For the purpose of estimating the order of magnitude of the integrals along the imaginary axes their limiting values as $R \rightarrow \infty$ may be taken in the first approximation for a clean inviscid water without surface tension. It has been shown by Ursell (1960) that for $R \gg 1$ they are of the order of R^{-3} and thus can be neglected. We may conclude therefore that for large values of R formula (39) can be written as:

$$\mathcal{Z}_n = 2\pi i \int_\chi^{\pi/2} F(\theta) e^{-iR\Phi(\theta)} d\theta, \quad (40)$$

where

$$F(\theta) = \frac{A(k_0)\Delta(\theta)\sin\theta}{\sqrt{\sin^4\theta - 4gT/U^4}},$$

$$\Delta(\theta) = \exp[\delta R \sin(\theta - \chi)],$$

and

$$\Phi(\theta) = k_0(\theta) \sin(\theta - \chi).$$

Similar analysis can be performed for the integrand of (38) incorporating the terms $\sin(\theta + \chi)$. However, as it will be shown below, within the intended accuracy such integrals do not contribute to the final result.

Further calculations are based on the stationary phase method. For large values of R the integral (40) can be estimated as follows:

$$\mathcal{Z}_n = 2\pi i \sqrt{\frac{2\pi}{R|\Phi''(\theta_s)|}} e^{-i[R\Phi(\theta_s) + \frac{\pi}{4}\text{sign}\Phi''(\theta_s)]},$$

where θ_s denotes the root of the equation

$$\Phi'(\theta) = 0.$$

We intend to find an analytic expression for the wave elevation in the vicinity of a small angle χ which is comparable to the magnitude of the V -wake angle χ_V . Thus, it can be assumed that $\sin(\theta \pm \chi) \simeq \theta \pm \chi$. Furthermore, since $\chi_V \gg 4gT/U^4$, the root of (30) can be estimated as follows:

$$k_0 = \frac{U^2}{2T}(\sin^2\theta - \sqrt{\sin^4\theta - 4gT/U^4}) \simeq \frac{g}{U^2\theta^2}$$

which yields

$$\Phi = \frac{g}{U^2} \frac{\theta \pm \chi}{\theta^2}.$$

It is possible now to obtain simple expressions for the only point of the stationary phase θ_s ,

$$\theta_s = 2\chi,$$

which define the function $\Phi(\theta_s)$ and its second derivative $\Phi''(\theta_s)$:

$$\Phi(\theta_s) = \frac{g}{4U^2} \frac{1}{\chi}, \quad (41)$$

$$\Phi''(\theta_s) = -\frac{g}{8U^2} \frac{1}{\chi^3}.$$

Hence the final expression for the wave elevation can be written as:

$$\mathcal{Z} = \frac{4a_F U^3}{g} \sum_{n=1}^{n=8} (-1)^{n+1} a_n A(2\chi_n) \times \sqrt{\frac{\chi_n}{\pi g R_n}} \Delta(2\chi_n) \sin\left(\frac{g}{4U^2} \frac{R_n^2}{y_n} - \pi/4\right). \quad (42)$$

4 Asymptotic expression for the radar back scatter cross-section.

Consider an orthogonal local coordinate system $O_1\xi\eta$ with an origin located at the center of the resolution cell. The coordinates (ξ, η) are rotated by an angle α in the counter clockwise direction from (x, y) coordinates:

$$\begin{aligned} x &= -X + \xi \cos \alpha + \eta \sin \alpha, \\ y &= Y + \eta \cos \alpha - \xi \sin \alpha. \end{aligned}$$

Here $(-X < 0, Y > 0)$ are the coordinates of the center of the resolution cell in the coordinate system $Oxyz$. Substituting (42) into (1) we have:

$$\Theta = \frac{4k_r^4 |C|^2}{\pi b_c l_c} \left| \sum_{n=1}^{n=8} \int_{-l_c}^{l_c} d\xi \int_{-b_c}^{b_c} G_n(\xi, \eta) e^{i\Upsilon_n(\xi, \eta)} d\eta \right|^2, \quad (43)$$

where

$$\begin{aligned} G_n(R_n, \chi_n) &= (-1)^{n+1} \frac{4}{g} a_n a_F U^3 \times \\ &A(2\chi_n) \sqrt{\frac{\chi_n}{\pi g R_n}} \Delta(2\chi_n), \end{aligned} \quad (44)$$

$$\Upsilon_n = \frac{g}{4U^2} \frac{R_n^2}{y_n} + k_e \eta,$$

and $k_e = 2k_r \sin \psi$. The function $\Upsilon_n(R_n, \eta)$ for $R_n \gg 1$ has a distinctive extremum in some points η_n^0 . It allows us to employ the idea of the stationary phase method, but with some modification since the phase function by itself depends on a large parameter. We expand next the function Υ_n in Taylor series

$$\Upsilon_n = \sum_j \frac{1}{j!} \Upsilon_n^{(j)}(\eta_n^0) (\eta - \eta_n^0)^j \quad (45)$$

in the vicinity of some point $|\eta^0| \leq b_c$ such that $\Upsilon^{(1)}(\eta_n^0) = 0$. In order to simplify the final results we assume that $X \gg 1$, $\cos \alpha = 1$ and $\sin \alpha = \alpha$. After some tedious calculations the following expressions can be obtained:

$$\eta_n^0 = (\alpha - \frac{1}{m_e})\xi + \frac{X}{m_e} - Y - q_n - p_n/m_e, \quad (46)$$

$$\Upsilon_n^{(0)}(\eta_n^0) = K[(\alpha - \frac{2}{m_e})\xi + \frac{2X}{m_e} - Y - q_n - 2p_n/m_e], \quad (47)$$

$$\begin{aligned} \Upsilon_n^{(2)} &\simeq 2\sqrt{k_e F} \frac{m_e^2}{X}, \\ \Upsilon_n^{(3)} &\simeq 6\sqrt{k_e F} \frac{m_e^3}{X^2}, \\ \Upsilon_n^{(j)} &\sim \sqrt{k_e F} \frac{m_e^j}{X^{j-1}} \quad (j > 3), \end{aligned}$$

where

$$m_e = \sqrt{\frac{k_e}{F}} \gg 1 \text{ and } F = \frac{g}{4U^2} \ll 1.$$

For $U \sim 10\text{m/s}$, $k_r \approx 25\text{m}^{-1}$, $\sin \psi \sim 1/2$ and $X \sim 1,000\text{m}$ the numerical estimates of the derivatives show that $\Upsilon^{(2)} \sim 1$, $\Upsilon^{(3)} \ll 1$ and $\Upsilon^{(j)} \ll \Upsilon^{(3)}$ ($j > 3$). Thus, the higher derivatives in the expansion (45) can be disregarded but the second derivative should be kept.

In the expression (46) the coordinates of the resolution cell are the geometrical parameters of the problem which can be chosen in order to provide the maximal back scatter cross-section. Let us further assume that

$$\frac{X}{m_e} - Y = q_j + p_j/m_e,$$

where j is some particular integers ($i = 1, \dots, 8$). In this case the coordinates of the center of the resolution cell are situated on the line

$$\frac{Y}{X} = \frac{1}{m_e} - \frac{q_j + p_j/m_e}{X}, \quad (48)$$

where $(q_j + p_j/m_e)/X \ll m_e^{-1} \ll 1$. Thus, we can define the V -wake angle as:

$$\chi_V = \frac{Y}{X} = m_e^{-1} = \frac{1}{2U} \sqrt{\frac{g}{2k_r \sin \psi}}. \quad (49)$$

Consequently, the point of stationary phase is:

$$\eta_n^0 = (q_j - q_n) + \frac{p_j - p_n}{m} \quad (j, n = 1, \dots, 8).$$

The substitution of (48) into (47) gives the following expression of the phase function:

$$\Upsilon_n^{(0)}(\eta_n^0) = k_e[(\alpha - 2\chi_V)\xi + \frac{X}{m_e} + (q_j - q_n) + \frac{p_j - 2p_n}{m}].$$

Finally, the dependence of the function (44) on the coordinates of the local system is rather weak, and thus it can be estimated as:

$$G_n(R_n, \chi_n) \sim G_n(R_0, \chi_V),$$

where $R_0 = \sqrt{X^2 + Y^2}$.

Now the integration in the formula (43) can be performed analytically which yields the following expression for the radar back scatter cross-section:

$$\Theta = A_1 A_2 A_3 A_4 A_5, \quad (50)$$

where

$$A_1 = \frac{16k_r^3}{\pi \sin \psi} \frac{l_c}{b_c} |C|^2, \quad (51)$$

$$A_2 = \frac{(a_F U)^6}{g^3} \frac{\chi_V^2}{(1 + a_F^2)^2}, \quad (52)$$

$$A_3 = \frac{\sin^2[k_e(\alpha - 2\chi_V)l_c]}{[k_e(\alpha - 2\chi_V)l_c]^2}, \quad (53)$$

$$A_4 = \left| \sum_{n=1}^8 a_n [C_c(\rho_n) + iS_s(\rho_n)] \right|^2, \quad (54)$$

and

$$A_5 = \Delta^2(2\chi_V). \quad (55)$$

Here

$$C_c = \int_{\rho_n^-}^{\rho_n^+} \cos(\frac{\pi t^2}{2}) dt, \quad S_s = \int_{\rho_n^-}^{\rho_n^+} \sin(\frac{\pi t^2}{2}) dt$$

and

$$\rho_n^\pm = \frac{-\eta_n^0 \pm b_c}{U\chi_V} \sqrt{\frac{g}{2\pi X\chi_V}}. \quad (56)$$

Each factor in the product (50) allows a clear physical interpretation: A_1 reflects the characteristics of the radar, A_2 the parameters of the ship, A_3 the direction of propagation of the divergent waves and the radar look of sight, A_4 the interference between waves and their radiation decay and

A_5 the radar back scatter cross-section attenuation affected by the fluid viscosity and surfactant film elasticity. It is interesting to note that for a ship with a length, say, $L \sim 200\text{m}$ and width of a resolution cell about $2b_c \sim 10\text{m}$, at least one point of the stationary phase η_n^0 ($n = 1, \dots, 8$) is equal to zero whereas the rest of them are situated outside the resolution cell. Thus, the contribution from the rest of these points in the formula (54) is negligible. That leads to an additional simplification of (54):

$$A_4 = \frac{4}{(a_F \pm 2\chi_V)} [C^2(\rho_0) + S^2(\rho_0)], \quad (57)$$

where $C(\rho_0)$ and $S(\rho_0)$ are the Fresnel integrals and

$$\rho_0 = \frac{b_c}{\chi_V U} \sqrt{\frac{g}{2\pi\chi_V X}}. \quad (58)$$

It is seen now that for $\rho_0 \gg 1$ the asymptotic estimates of Fresnel integral gives: $C(\rho_0) = S(\rho_0) \sim 1/2$ which means that the brightness of the signal does not decay along the bright arms. In practice the value of ρ_0 is finite, but still can be large enough to provide a strong back-scattering signal. In fact, if $\rho_0 < 1.5$ the function A_4 behaves as $1/X$ whereas for larger values of ρ_0 it is an oscillatory function with a slowly decaying envelope.

5 Numerical simulation.

It is common to represent the radar cross-section in terms of its nondimensional rise above the background radar back scatter cross-section Θ_0 which depends on the sea state. The value Θ_0 can be estimated by a simple formula of Wright (1968). However, herein for the sake of consistency we prefer to invoke the experimental data of Shemdin (1990) which are represented in Table 3.

Table 3. Radar cross-section Θ_0 for different wind speed ($\psi = 30^\circ$).

Sea state	Wind speed, m/s	$\Theta_0(\text{dB})$
1	1-2	-30
2	2-4	-22
3	4-6	-17
4	6-8	-13

The dependence of the nondimensional rise of the radar back scatter cross-section above the background $\vartheta = \Theta/\Theta_0$ for Sea State 1 is shown in Fig. 3.

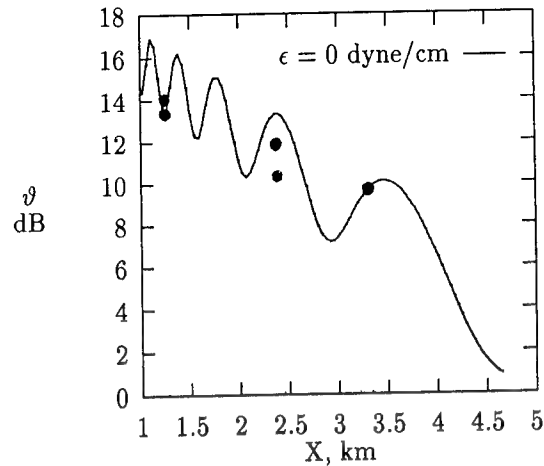


Figure 3: Rise of the radar cross-section above background versus distance aft of ship Bay Ridge. (Sea State 1) • —experimental data of Shemdin [35].

According to the experimental data of Shemdin the radar cross section decay along bright arms exhibits distinctive extrema, which, apparently, can not be explained by the noise of measurements. Moreover, the last significant maximum of the decaying curve occurs at the distance X about 3-4 km aft of the ship. According to the presented theory the various extrema result from the wave interference reflected by the relation (54). Noticeable, that according to the experimental data the length of the V-like bright arms varies between 5-6 km. It is reasonable to define the length of the bright arms L_V as a coordinate X_V where $|\Theta_0| < 1.0$ dB. Under such a definition the theoretical prediction gives the value of $L_V \sim 4.5-6.0$ km which is a good agreement with the experiment.

The bright V-wake arms appear in the SAR images only under the conditions of light wind and small wave height. The theoretical results presented in Fig. 4 are in a good agreement with these experimental observations.

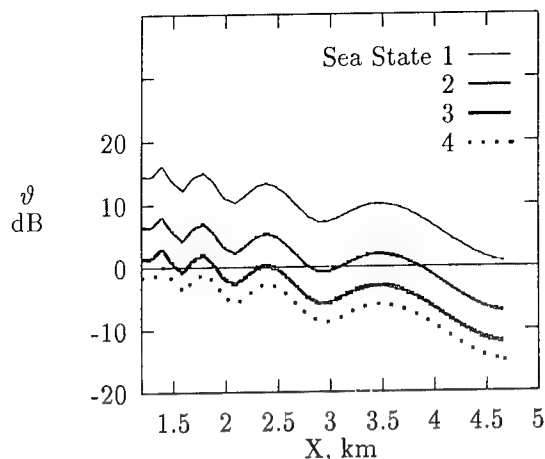


Figure 4: Rise of radar cross-section above background versus distance aft of ship Bay Ridge for different sea states.

It is seen that for Sea State 2 the visibility of the bright arms is actually much less than for the Sea State 1 but still noticeable. For Sea State 3 the visibility of the bright arms is doubtful. For Sea State 4 the magnitude of the radar cross-section is below the radar cross-section of the background level and thus can not be observed.

In Fig. 5 it is demonstrated the dependence of the radar cross-section on the elasticity of surfactant film.

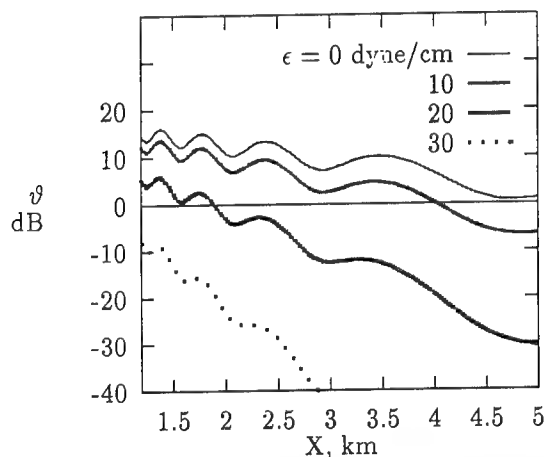


Figure 5: Radar cross-section versus distance aft of ship Bay Ridge for different surfactant film elasticity.

It is seen that even a relatively small surfactant elasticity (about 10 dyne/cm) significantly reduce the radar cross-section and the length of the V-wake. For relatively large but plausible values of surfactant elasticity about 25 dyne/cm the V-wake can not be anymore detected.

6 Summary.

An important progress has been achieved toward improving our general understanding of intriguing phenomenon of ship generated narrow V-wakes. The proposed analytic solution of the problem incorporates the important effect of sea surface contamination. It has been shown that the radar cross-section is a decaying oscillatory function along the bright V-arms. The asymptotic behavior of radar cross-section for a large distance X aft of a ship is governed by the asymptotic behavior of the Fresnel integrals $C(\rho_0)$, $S(\rho_0)$ where ρ_0 is defined by (58) and (49).

The theory predicts a slow decay of the radar cross-section with increasing distance X until the value of the parameter ρ_0 exceeds some threshold value $\rho_{thresh} \simeq 1.5$. When ρ_0 is below this critical value, the radar cross-section decays along the bright V-arms as $1/X$.

It has been demonstrated also that even a relatively small contamination of sea surface can change the radar back scatter cross-section drastically. According to the results of the present study the distance behind the ship for the surfactant film with elasticity $\epsilon \sim 20$ dyne/cm to diminish the radar back scatter cross-section by a factor e^{-1} can be only few hundreds meters.

In this context of the present research it has to be mentioned that the visibility of the dark turbulent wake in Sea States 1-4 presumably can be explained by the attenuation of wind-generated waves due to the contamination of sea surface within the V-wake (Peltzer et al. 1991). The physical mechanism of compacting surfactant films in the immediate vicinity of the V-wake is an important follow-up to this investigation.

7 Acknowledgment

The authors would like to express their gratitude to Dr. L. Shemer for many valuable advises. Dr. E. Kit made interesting comments influencing the research. Dr. E. Pelinovsky during his visit to Tel-Aviv University read the draft of the manuscript and his critical comments are appreciated by the authors.

The research was partially supported by the Israeli Ministry of Science.

References

- [1] Baar, J.J and Price, W.G. 1988 Evaluation of the wave-like disturbance in the Kelvin wave source potential. *J. Ship Research*, **32**, 1, pp. 44-53.
- [2] Barnell, A. and F. Noblesse. 1986 Far-field features of the Kelvin wake. *Proc. 16th Symposium on Naval Hydrodynamics*, University of California, Berkeley, pp. 18-36.
- [3] Brard, R. The representation of a given ship form by singularity distributions when the boundary condition on the free surface is linearized. *J. Ship Research*, **6**, pp. 79-92.
- [4] Brown, E.D. 1985 *Integrated Report on Mechanisms Responsible for Narrow Angle V-Wakes in the Georgia Strait Experiment*, Final Report, Science Applications International Corporation, La Jolla, CA.
- [5] Brown, E.D., Buchsbaum, S.B., Hall, R.E., Penhum, J.P., Schmitt, K.F., Watson, K.M. and Wyatt, D.C. 1989 Observation of a non-linear solitary wave packet in the Kelvin wake of a ship. *J. Fluid Mechanics*, **204**, pp. 263-293.
- [6] Cao, Y., W.W. Schultz and R.F. Beck. 1992 Inner-angle wavepackets in unsteady wake. *Proc. 19th Symposium on Naval Hydrodynamics*, Seoul, Korea.
- [7] Crapper, G.D. 1964 Surface waves generated by a travelling pressure point. *Proc. Royal Society*, ser. A, **282**, pp. 547.
- [8] Cumberbatch, E. 1965 Effect of viscosity on ship waves. *J. Fluid Mechanics*, **23**, pp. 471-479.
- [9] Eggers, K. and Schultz, W.W. 1992 Investigation on time-harmonic disturbances for inner-Kelvin-angle wave packets. *Seven International Workshop on Water Waves and Floating Bodies*, pp. 87-91.
- [10] Gu, D. and Phillips, O.M. On narrow V-like ship wakes *J. Fluid Mechanics*, **275**, pp. 301-321.
- [11] Havelock, T.H. 1935 Ship Waves: The relative Efficiency of Bow and Stern. *Proc. Royal Society London*, A, **149**, pp. 417-426.
- [12] Keller, J.B. and Munk, W.H. 1970 Internal wave wakes of a body in a stratified fluid. *Physics of Fluid*, **13**, pp. 1425-1431.
- [13] Kelvin 1887 On the waves produced by a single impulse in water of any depth or in a dispersive medium. *Proc. Royal Society London*, A, **42**, pp. 80-85.
- [14] Kinoshita, T. 1980 Viscous effect on waves of thin ship. *Proc. Thirteen Symp. on Naval Hydrodynamics*, Tokyo, pp. 793-703.
- [15] Kostyukov, A.A. 1968 The theory of ship waves and wave resistance. Effective Communication Inc., Iowa City, 1968.
- [16] Lavrentiev, V.M. 1951 The influence of the boundary layer on the wave resistance of a ship. *Doklady Akad. Nauk USSR*, **80**.
- [17] Levich, V.G. 1962 *Physicochemical Hydrodynamics*, Pretice-Hall, Elmsford Park, N.J.
- [18] Lyden, J.D., Hammond, R.R., Lyzenga, D.R. and Shuchman, R. 1988 Synthetic aperture radar imaging of surface ship wakes. *J. of Geophysical Research*, **93**, C10, pp. 12293-12303.
- [19] Mei, C.C and Naciri, M. 1991 Note on ship oscillations and wake solitons. *Proc. Royal Society London*, A, **432**, pp. 535-546.
- [20] Milgram, J.H. 1988 Theory of radar backscatter from short waves generated by ships, with application to radar (SAR) imagery. *J. Ship Research*, **32**, pp. 54-69.
- [21] Miloh, T., Tulin, M. and Zilman, G. 1993 Dead water effects of a ship moving in stratified seas. *J. of Offshore Mechanics and Arctic Engineering*, **115**, pp. 105-110.
- [22] Munk, W.H., Scully-Power, P. and Zachariasen, F. 1987 Ship from Space. *Proc. Royal Society London*, A **412**, pp. 231-254.
- [23] Nakos, D.E. and Sclavounos, P.D. 1994 Kelvin wakes and wave resistance of cruiser and transom-stern ships. *J. Ship Research*, **38**, pp. 9-29.
- [24] Newman, J.N. 1970 Recent Research on Ship Wakes. *Proc. 8th Symposium on Naval Hydrodynamics: Hydrodynamics in the Ocean Environment*, Arlington, Virginia, Office of Naval Research, Department of Navy, pp. 519-545.

- [25] Newman, J.N. 1971 Third order interaction in the Kelvin ship wave system. *J. Ship Research*, **15**, pp. 1-10.
- [26] Newman, J.N. 1987a Evaluation of the wave resistance Green function: part 1-the double integral. *J. Ship Research*, **31**, 2, pp. 79-90.
- [27] Newman, J.N. 1987b Evaluation of the wave-resistance Green function: part 2-single integral on the center-plane. *J. Ship Research*, **31**, 3, pp. 145-150.
- [28] Noblesse, F., Hendrix, D. and Barnell, A. 1989 The slender-ship approximation: comparison between experimental data and numerical prediction. *Journées de l'Hydrodynamique*, ENSM, Nantes, France, pp. 175-187.
- [29] Noblesse, F., and Hendrix, D. 1991 Near Field Nonlinearities and Short-Field ship Waves. *Proc. 18th Symposium on Naval Hydrodynamics*, Ann Arbor, Michigan, pp. 465-476.
- [30] Pelinovsky, E.H. and Talipova, T.G. 1990 *Films of surface active materials on the sea surface* (Russian). Preprint No. 219, Institute of Physics of Heat, Academy of Science USSR (Siberia Department).
- [31] Peltzer, R., J.H. Milgram, R. Skop, J. Kaiser, O. Griffin, W. Barger. 1991 Hydrodynamics of ship wake surfactant films. *Proc. 18th Symposium on Naval Hydrodynamics, National Academy Press*, Ann Arbor, Michigan, USA, pp. 533-552.
- [32] Peters, A.S. 1949 A new treatment of the ship wave problem. *Committee on Pure and Applied Mathematics*, **2**, pp. 123-148.
- [33] Ponizy, C.J., Noblesse, F., Ba, M., Guilband, M. 1994 Numerical evaluation of the free surface Green function. *J. Ship Research*, **38**, pp. 193-203.
- [34] Sharma, S.D. 1969 Some results concerning the wavemaking of a thin ship. *J. Ship Research*, **13**, 3, pp. 72-81.
- [35] Shemdin, O.H. 1990 Synthetic aperture radar imaging of ship wakes in the Gulf of Alaska. *J. of Geophysical Research*, **95**, C9, pp. 16319-16338.
- [36] Tuck, E.O., J.I. Collins and W.H. Wells. 1971 On ship wave patterns and their spectra. *J. Ship Research*, **15**, pp. 11-21.
- [37] Tulin, M.P. and Miloh, T. 1990 Ship internal waves in shallow thermocline: the supersonic case. *Proc. of the 18th Symposium on Naval Hydrodynamics*, Ann Arbor, Michigan, USA, pp. 567-584.
- [38] Ursell, F. 1960 On Kelvin's ship-wave pattern. *J. Fluid Mechanics*, **8**, pp. 418-431.
- [39] Ursell, F. 1988 On the theory of the Kelvin ship-wave source: asymptotic expansion of an integral. *Proc. Royal Society London, A* **418**, pp. 81-93.
- [40] Whitham, G.B. 1974 *Linear and nonlinear waves*. John Wiley & Sons, N.Y.
- [41] Wehausen, J.V. and Laitone, E.V. *Surface waves* in Encyclopedia of Physics, **9**, Springer-Verlag.
- [42] Wright, J.W. 1966 Backscattering from capillary waves with application to sea clutter. *IEEE Trans. Antennas and Propagation*, **14**, pp. 749-754.
- [43] Wright, J.W. 1968 A new model for sea clutter. *IEEE Trans. Antennas and Propagation*, **16**, pp. 217-223.
- [44] Wu, T.Y. and Messick, R.E. 1958 *Viscous effect on surface waves generated by steady disturbances*. Caltech. Rep. No. 85-8.

Turbulent Free-Surface Flows: A Comparison Between Numerical Simulations and Experimental Measurements

D. Dommermuth,¹ M. Gharib,² H. Huang,² G. Innis,¹

P. Maheo,² E. Novikov,³ J. Talcott,¹ D. Wyatt¹

(¹Science Applications International Corporation, ²California Institute of Technology, ³University of California at San Diego, USA)

Abstract

The results of large-eddy simulations (LES) are compared to measurements of a model-scale frigate wake. The measurements are compared to two types of large-eddy simulations: a nonlinear free-surface approach and a low Froude-number approximation. An unique procedure has been developed for initializing three-dimensional LES using two-dimensional measurements of the mean and fluctuating velocity fields of a cross section of the wake. The procedure also works well for extending Reynolds-averaged Navier-Stokes simulations of near-field flows into the far wake. The numerical results show that turbulent roughening of the ocean surface scales according to three-dimensional similarity theory. An extensive inertial range is established in the kinetic and potential energy spectras. There is no evidence of the effects of two-dimensional turbulence in the free-surface elevation. Based on analyses of energy spectra, third-order moments, and probability distributions, the performance of the Smagorinsky model is satisfactory in the inviscid limit. Preliminary results of some recent grid-stirred turbulence and splitter-plate experiments are discussed. The numerical predictions of the evolution of the wake agree well with towing-tank measurements.

1 INTRODUCTION

The results of towing-tank experiments are used to initialize and to validate large-eddy simulations (LES) of ship wakes. The towing-tank experiments were performed at the Maritime Research Institute, Netherlands (MARIN). The experiments were performed on a frigate. The model was propelled, and it was equipped with a rudder. Details of the experimental procedure are provided in Hoeskstra (1991).

Reed, et al (1990) and Hoeskstra (1991) review the physical attributes of ship wakes. In the turbulent portion of the wake, two pairs of vortices tend to form due to flow separation at the stern. A pair of bilge vortices forms due to the tapering of the parallel middle-body into the stern. A second pair of vortices forms near the free-surface due to the stern rising up to make room for the propeller. The bilge vortices can be entrained by propeller slipstreams and swirls. There can also be complex interactions with rudders. The free-surface vortices rise up into the drag wake of the hull and run parallel to the surface due to image vortex effects.

Both pairs of vortices are observed in the frigate experiments that had been performed at MARIN. The MARIN measurements are compared to two types of large-eddy simulations. The first type uses nonlinear free-surface boundary conditions and the second type uses a low Froude-number approximation to model free-surface roughness. The subgrid-scale (SGS) turbulence model uses the Smagorinsky model. Forcing at low wavenumbers is used to balance the dissipation at high wavenumbers to provide the proper dissipation rate based on experimental measurements. The free-surface code uses an adjustment scheme to prevent the generation of spurious high-frequency waves (see Dommermuth, 1994b). The free-surface code also implements a free-surface boundary-layer approximation that is valid for clean free surfaces (see Dommermuth, 1994a).

The LES codes are initialized using the experimental data. On a transverse cut all three velocity components are measured. The mean axial and transverse velocity components are used to assign the mean velocity in a cross section of fluid that is modeled using LES. LES is used to model the turbulent portion of the wake. The Kelvin wave disturbance is subtracted out of the measured data using linear wave-cut analysis. We superimpose on top of the mean velocity field a fluctuating velocity field that is based on the rms velocity fluctuations that are measured in the towing tank. The fluctuating velocity field is initialized using a realization of fully-developed turbulence with a $-5/3$ inertial range. We assume that the temporal behavior predicted in our numerical results is related to the spatial behavior measured in the laboratory experiments through a Galilean transformation. The numerical predictions of the evolution of the wake correlate well with towing-tank experiments.

2 MATHEMATICAL FORMULATIONS

2.1 Field Equations

Consider the unsteady incompressible flow of a Newtonian fluid under a free surface, and let $u_i(x, t) = (u, v, w)$ represent the three-dimensional velocity field as a function of time. Applying Helmholtz's decomposition gives

$$u_i = \frac{\partial \phi}{\partial x_i} + U_i, \quad (1)$$

where $\phi(x, y, z, t)$ is a velocity-potential which describes the irrotational flow and $U_i = (U, V, W)$ is a solenoidal-field which describes the vortical flow such that

$$\nabla^2 \phi = 0 \quad (2)$$

$$\frac{\partial U_i}{\partial x_i} = 0, \quad (3)$$

where ∇^2 is the Laplace operator. Since ϕ satisfies Laplace's equation and the divergence of the rotational field U is chosen zero, the total velocity field u conserves mass. The potential ϕ models the effects of waves, whereas the solenoidal velocity field U models the effects of shear currents and turbulence.

Based on this Helmholtz decomposition of the velocity field, the total-pressure Π is defined in terms of a vortical pressure P and an irrotational pressure, as follows:

$$\Pi = P - \frac{\partial \phi}{\partial t} - \frac{1}{2} \nabla \phi \cdot \nabla \phi - \frac{1}{F_r^2} z. \quad (4)$$

Here, the velocity and pressure terms are respectively normalized by u_c and ρu_c^2 , where u_c is the characteristic velocity and ρ is the density. $F_r^2 = u_c^2 / g \ell_c$ is the Froude number and ℓ_c is the characteristic length. The vertical coordinate z is positive upward, and the origin is located at the mean free surface. Substituting these decompositions (1 & 4) into the Navier-Stokes equations gives

$$\frac{\partial U_i}{\partial t} + u_j \frac{\partial U_i}{\partial x_j} + U_j \frac{\partial^2 \phi}{\partial x_i \partial x_j} =$$

$$-\frac{\partial P}{\partial x_i} + \frac{1}{R_e} \nabla^2 U_i + \frac{\partial \mathcal{M}_{ij}}{\partial x_j} + \alpha S_i, \quad (5)$$

where $R_e = u_c \ell_c / \nu$ is the Reynolds number and ν is the kinematic viscosity. \mathcal{M}_{ij} is a subgrid-scale model and S_i is a stirring force. The stirring term, which is a linear operator, is required to impose the correct dissipation rate for LES of wakes. The stirring coefficient α is calculated to provide a prescribed turbulent dissipation rate ϵ :

$$\alpha = \frac{\left(\epsilon - \frac{1}{R_e} \int_V U_i \nabla^2 U_i - \int_V U_i \frac{\partial \mathcal{M}_{ij}}{\partial x_j} \right)}{\int_V U_i S_i}, \quad (6)$$

where V is the volume of fluid.

The divergence of the momentum equations (5) used in combination with the mass-conservation equations (2 & 3) can be used to derive a Poisson equation for the vortical pressure:

$$\begin{aligned} \frac{\partial^2 P}{\partial x_i^2} = & -\frac{\partial U_j}{\partial x_i} \frac{\partial U_i}{\partial x_j} - 2 \frac{\partial U_j}{\partial x_i} \frac{\partial^2 \phi}{\partial x_i \partial x_j} \\ & + \frac{\partial^2 \mathcal{M}_{ij}}{\partial x_i \partial x_j} + \alpha \frac{\partial S_i}{\partial x_i}. \end{aligned} \quad (7)$$

As shown by Dommermuth (1993), the vortical pressure is also subject to a solvability condition due to the imposition of Neumann boundary conditions.

2.2 Free-Surface Boundary Conditions

The Helmholtz decomposition of the velocity field requires that an additional boundary condition be imposed on the free surface. An expedient boundary condition that can be specified is that the normal component of the rotational velocity is zero on the free surface:

$$U_i \cdot n_i = \frac{-U \eta_x - V \eta_y + W}{\sqrt{\eta_x^2 + \eta_y^2 + 1}} = 0, \quad (8)$$

where $z = \eta(x, y, t)$ is the free-surface elevation and n_i is the unit-normal on the free surface. The preceding constraint imposed on the rotational velocity field means that the evolution of

the free-surface elevation is entirely prescribed in terms of the free-surface elevation itself and the velocity potential, as follows:

$$\frac{\partial \eta}{\partial t} + \eta_x \phi_x + \eta_y \phi_y - \phi_z = 0, \quad (9)$$

where everything is evaluated on the exact position of the free surface, $z = \eta$.

The normal stress on the free surface must balance with the atmospheric pressure and the surface tension:

$$\begin{aligned} \frac{d\phi}{dt} + \frac{1}{2}(\phi_x^2 + \phi_y^2 - \phi_z^2) + (\eta_x \phi_x + \eta_y \phi_y) \phi_z \\ + \frac{1}{F_r^2} \eta = -\frac{1}{W_e} \frac{\partial n_i}{\partial x_i} + P - P_a \\ - \frac{n_i n_j}{R_e} \left(\frac{\partial u_i}{\partial x_j} + \frac{\partial u_j}{\partial x_i} \right), \end{aligned} \quad (10)$$

where P_a is the atmospheric pressure due to wind forcing, $W_e = \rho u_c^2 \ell_c / \sigma$ is the Weber number, and σ is the surface tension. $d/dt = \partial/\partial t + \eta_t \partial/\partial z$ is a substantial derivative. In addition to the normal-stress condition there are also two tangential-stress conditions that are provided in Dommermuth (1993).

The normal stress condition (10) and the corresponding tangential stress conditions are appropriate only if the free-surface boundary-layer is sufficiently resolved. Since it is difficult to resolve the boundary-layer at full-scale Reynolds numbers, a boundary-layer approximation is required.

Longuet-Higgins (1991), Lundgren (1989), and Dommermuth (1994a) provide examples of free-surface boundary-layer formulations. For a clean free surface, the boundary-layer approximation of the normal stress condition is

$$\begin{aligned} \frac{d\phi}{dt} + \frac{1}{2}(\phi_x^2 + \phi_y^2 - \phi_z^2) + (\eta_x \phi_x + \eta_y \phi_y) \phi_z \\ + \frac{1}{F_r^2} \eta = -\frac{1}{W_e} \frac{\partial n_i}{\partial x_i} + P - P_a \\ - \frac{4n_i n_j}{R_e} \frac{\partial^2 \phi}{\partial x_i \partial x_j}. \end{aligned} \quad (11)$$

This equation correctly predicts the laminar dissipation for small amplitude waves. The two

tangential stress conditions are not required in this boundary-layer approximation. Excluding the boundary-layer correction, the same free-surface boundary conditions are also used for the Euler equations. This approximation is valid when the temporal and spatial scales of the turbulence are longer than the scales of the waves.

The boundary-layer approximation models the dominate effects of refraction, radiation, scattering, and dissipation of waves by shear currents and turbulence through the combination of the kinematic condition for the rotational velocity (Equation 8) and the vortical pressure term (P) in the normal stress condition (Equation 11). The generation of vorticity by spatial and temporal changes in the free-surface elevation is not modeled, but the boundary-layer approximation does model the dissipation of waves due to the direct action of viscosity.

If the Froude number is sufficiently low, Dommermuth (1994b) shows that the free-surface elevation is hydrostatically balanced with the portion of the pressure that is induced by the vortical flow:

$$\eta = F_r^2 P . \quad (12)$$

For a clean free surface, Dommermuth, et al (1994) show that the corresponding boundary conditions for the solenoidal velocity field are as follows:

$$\frac{\partial U}{\partial z} = \frac{\partial V}{\partial z} = W = 0 . \quad (13)$$

These boundary conditions are satisfied on the plane $z = 0$. At this level of approximation, the velocity potential, which represents dispersive wave behavior, is zero.

Based on the nonlinear free-surface conditions (8-11) and the low-Froude number approximation (12 & 13), two LES approaches have been developed. Aside from the treatment of the free surface, both numerical schemes are the same.

2.3 Sub-Grid Scale Modeling

The performance of several subgrid scale (SGS) models was discussed by Dommermuth & Novikov (1993). As pointed out by them, a major advantage of the Helmholtz decomposition is that SGS models for the turbulent portion of the flow can be developed independently of the potential portion of the flow. As a result, waves will not be excessively attenuated, and the potential flow will not adversely affect the turbulence model. A Smagorinsky SGS model is used here:

$$\mathcal{M}_{ij} = C_s \Delta^2 |S| S_{ij} + C_i \Delta^2 |S|^2 \delta_{ij} , \quad (14)$$

where C_s is the Smagorinsky coefficient, C_i is the coefficient of the isotropic turbulence model, Δ is the grid scale, δ_{ij} is the Kronecker delta function, and S_{ij} is the rate-of-strain tensor:

$$S_{ij} = \frac{1}{2} \left(\frac{\partial U_i}{\partial x_j} + \frac{\partial U_j}{\partial x_i} \right) . \quad (15)$$

$|S| = (S_{ij} S_{ij})^{1/2}$ is the magnitude of the strain tensor. Most LES absorb the isotropic SGS stresses into the pressure-gradient term in the Navier-Stokes equations, but in free-surface flows this term is required to predict turbulent roughening of the free surface (see Dommermuth & Novikov, 1993).

Germano, et al's (1991) test filter approach in combination with Lilly's (1991) least-squares procedure is used to predict the Smagorinsky coefficient and the coefficient of the isotropic turbulence model. Details of the procedure are provided in Dommermuth & Novikov (1993).

The SGS terms associated with wavy portion of the velocity field and the cross-coupling between the wavy and vortical portions of the velocity field are not modeled. At low Froude numbers, the effects of these terms are not expected to be large because wave generation is minimal.

2.4 Stirring

A stirring force is applied to maintain the proper dissipation rate (6). The stirring term forces the lowest wavenumbers, whereupon the energy cascades to higher wavenumbers. In wavenumber space, the stirring operator (\tilde{s}) is given by:

$$\tilde{s}(\kappa) = ((20 + 30 \cos(\kappa) + 12 \cos(2\kappa) + 2 \cos(3\kappa))/64)^4, \quad (16)$$

where κ is a nondimensional wavenumber based on grid spacing and $0 \leq \kappa \leq \pi$. This filter is applied to the velocities along the three coordinate axes. For example, let \tilde{s}_x , \tilde{s}_y , and \tilde{s}_z represent low-wavenumber filtering along the x , y , and z axes, respectively. Let \tilde{U}_i denote the three-dimensional Fourier transform of the Solenoidal velocity field, and let \tilde{S}_i denote the Fourier transform of the stirring force, then

$$\tilde{S}_i = \tilde{s}_x \tilde{s}_y \tilde{s}_z \tilde{U}_i. \quad (17)$$

Similar filters are described in Dommermuth & Novikov (1993).

2.5 Initialization

A Galilean approximation is used to relate the spatial evolution of a ship wake to the temporal evolution of a LES:

$$x = U_o t, \quad (18)$$

where x is the longitudinal distance downstream in the wake and t is the corresponding time in the LES. U_o is the ship speed.

Based on this Galilean approximation, we further assume that

$$\overline{F(x = X_o)} = \frac{1}{T} \int_0^T dt F(t, x = X_o) \Leftrightarrow \frac{1}{L} \int_0^L dx F(x) = \langle F(t = T_o) \rangle, \quad (19)$$

where F is a physical quantity, an overbar denotes time averaging, brackets denote spatial averaging, L is the length of the LES, and T is the duration of a large-scale event in the

wake. X_o and T_o are positions in space and time where the ship wake and LES correspond.

For LES of ship wakes, we assume that the potential and solenoidal velocity fields can be decomposed as follows:

$$\begin{aligned} \phi &= U_o x + \phi_w + \phi_u \\ U_i &= \mathcal{U}_i + v_i, \end{aligned} \quad (20)$$

where ϕ_w is the wave disturbance due to Kelvin waves, ϕ_u is the wave disturbance due to turbulence, \mathcal{U}_i is a mean disturbance due to turbulence, and v_i is a fluctuating disturbance due to turbulence. We assume that the Kelvin waves do not interact strongly with the turbulent wake.

If the mean temporal velocities and the Reynolds stresses are provided on a transverse cut of the wake, the assumptions (18-20) can be used to initialize a LES. A cross section of the wake is modeled using LES. The first step in the procedure is to use linearized wave-cut analysis to represent the Kelvin wave disturbance in the wake:

$$\begin{aligned} \phi_w &= Re \int_{-\pi/2}^{\pi/2} d\theta \Phi(\theta) \\ &\exp \left(-i \frac{g}{U_o^2 \cos^2 \theta} (x \cos \theta + y \sin \theta) \right), \end{aligned} \quad (21)$$

where x and y are respectively the longitudinal and transverse positions in the wake. The angular dependence $\Phi(\theta)$ is calculated using Neumann-Kelvin theory or wave-cut data. The water-particle velocity due to the Kelvin waves is calculated using $\mathbf{U}_w = \nabla \phi_w$.

LES is used to simulate the vortical portion of the flow and the free-surface waves that are induced by the turbulence. The disturbance due to Kelvin waves is subtracted from the total velocity field. The remaining disturbance is primarily due to the effects of vortical flow. The vortical portion of the flow can be initialized using the results of RANS, experiments, or empirical data.

In the case of experimental data, the mean temporal disturbance due to the vortical flow is projected onto a solenoidal field using a

vorticity-stream function formulation. Let $\bar{\mathbf{u}}$ denote the mean vector velocity with respect to time on a transverse cut of a wake, and let $\langle \mathbf{u} \rangle$ denote the mean velocity with respect to the streamwise direction in the LES. In general, $\bar{\mathbf{u}}$ is not solenoidal, nor does $\bar{\mathbf{u}}$ satisfy the proper boundary conditions. To impose solenoidality and to enforce boundary conditions, we first calculate the vorticity (Ω):

$$\Omega = \nabla \times \bar{\mathbf{u}} . \quad (22)$$

This vorticity is used to calculate a vector stream function (Ψ):

$$\nabla^2 \Psi = -\Omega , \quad (23)$$

where free-slip boundary conditions are initially imposed on the free surface and the bottom, and periodic boundary conditions are imposed in the horizontal plane. The mean velocity in the LES is calculated by definition:

$$\langle \mathbf{u} \rangle = \nabla \times \Psi , \quad (24)$$

which is solenoidal and satisfies the boundary conditions.

To complete the initial conditions, a fluctuating velocity field (v_i) is superimposed over the mean velocity field in the LES. Let \tilde{v}_i denote a fully-developed realization of homogeneous anisotropic turbulence with zero mean, $\langle \tilde{v}_i \rangle = 0$. We project \tilde{v}_i onto v_i using a deformation tensor:

$$v_i = C_d \left(\frac{\partial B_i}{\partial x_k} \tilde{v}_k - B_k \frac{\partial \tilde{v}_i}{\partial x_k} \right) , \quad (25)$$

where B_i is a solenoidal deformation tensor and C_d is a deformation constant.

Let \hat{v} denote the fluctuating velocity field as modeled by RANS or measured during experiments. Let $\frac{1}{2} \overline{\hat{v}_k \hat{v}_k}$ denote the turbulent kinetic energy on a transverse plane of the wake, and let $\frac{1}{2} \langle v_k v_k \rangle$ represent the LES counterpart. These two turbulent kinetic energies are fitted together using a least-squares and averaging procedure to determine the deformation constant:

$$\frac{\partial}{\partial C_d} \int_S dS \left(\frac{1}{2} \overline{\hat{v}_i \hat{v}_i} - \frac{1}{2} \langle v_i v_i \rangle \right)^2 = 0 , \quad (26)$$

where the surface integral is over a transverse cut of the wake S .

A natural choice for B_i , the deformation tensor, is the mean velocity field:

$$B_i = \langle u_i \rangle . \quad (27)$$

This choice of B_i is solenoidal, as required, and it leads to a fluctuating velocity field that satisfies the free-surface boundary conditions in the low-Froude number limit. Since this choice of B_i assigns a relationship between the large-scale features of the flow and the small-scale fluctuations, it could also potentially be used in RANS to provide closures for the Reynolds stresses.

Another choice for B_i is the measured rms velocity distribution:

$$B_1 = \sqrt{\frac{1}{3} \overline{\hat{v}_k \hat{v}_k}} , \quad B_2 = B_3 = 0 . \quad (28)$$

By construction, this B_i is also solenoidal. If the condition $\partial B_1 / \partial z = 0$ on $z = 0$ is imposed, then the free-surface boundary conditions will be satisfied by the fluctuating velocity field in the low Froude-number limit. The advantage of this approach is that it correlates well with the experimental input.

In summary, the mean and rms velocities on a transverse cut of a wake are used to seed a three-dimensional LES. The initial data can be provided by either experiments or RANS. A Galilean transformation is used to relate the duration of the simulation to the distance downstream in the experiments. Spatial averaging in the LES corresponds to temporal averaging in the experiments. First, the Kelvin wave disturbance is subtracted from the experiments, and then the mean velocities are projected onto a solenoidal field. Finally, a realization of fully-developed turbulence is fitted to the measured turbulent kinetic energy distribution on a transverse cut of the wake to construct the three-dimensional fluctuating velocity field in the LES.

3 NUMERICAL FORMULATION

The Navier-Stokes equations, and the boundary and initial conditions are discretized using 2nd-order finite differences. A fully-staggered grid is used in the numerical simulations. The momentum equations (5), kinematic condition (9), and the normal stress condition (11) are integrated with respect to time using a third-order Runge-Kutta scheme. The convective terms in the momentum equations (5) are expressed in conservation-law form. Each stage of the Runge-Kutta scheme is formulated to inhibit the accumulation of errors in the divergence of the rotational flow field. The rotational pressure is used to project the rotational velocity onto a solenoidal field (3 & 7) with zero normal velocity on the free surface (8). Laplace's equation for the potential (2) and Poisson's equation for the rotational pressure (7) are solved at each stage of the Runge-Kutta scheme, and a solvability condition is enforced for the rotational pressure. A multigrid solution scheme is used to solve the three-dimensional elliptic equations (see Dommermuth, 1994a). The z -coordinate is mapped onto a flat plane (see Dommermuth, 1994b). This mapping is applied to Laplace's equation (2), the Poisson equation for the pressure (7), the momentum equations (5), and all the boundary conditions. Periodic boundary conditions are used on the sides of the domain and free-slip boundary conditions are used on the bottom. For the low Froude-number approximation, free-slip boundary conditions are also used on the top (13). The numerical algorithms have been implemented on CM-5 parallel computers. The results of several validation studies are provided in Dommermuth & Novikov (1993).

4 LABORATORY EXPERIMENTS

Grid-stirred turbulence experiments are being performed in an open water tunnel with a width of 45.7cm and a water depth of 41cm. The free-stream velocity is $U_c = 28.36\text{cm/s}$. Turbulence is generated by a mesh grid. The wire diameter is $D_o = 1.5\text{mm}$ and the spacing between wires is $D_w = 8.3\text{mm}$. Based on mesh spacing, the Reynolds number is $Re_m = U_c D_w / \nu = 2350$.

The wake of a vertical flat plate is being studied in a splitter-plate facility. The cross-section of the flow channel is 101.6cm wide and 53.65cm deep. The splitter plate is $D_p = 7.6\text{cm}$ wide in its thickest section, and it tapers to zero at its end. The speed of the stream is $U_c = 40\text{cm/s}$. Based on plate thickness, the Reynolds number is $Re_p = U_c D_p / \nu = 30,400$.

Velocity measurements are performed using Digital Particle Image Velocimetry (DPIV). DPIV provides instantaneous 2-D velocity fields in a plane (see Willert & Gharib, 1991). For the grid-stirred turbulence experiments, three planes have been measured: one vertical plane in the center of the water tunnel and two horizontal planes, 3mm and 110mm below the free surface. The area of each image plane is about 180mm \times 130mm and the leading edge is about 235mm downstream of the wire mesh. 1000 images, which corresponds to 66.7 seconds of measurement, has been acquired in each plane to enable statistical analyses. Analysis of the rms velocity shows that averaging over 1000 samples gives relative errors less than one percent.

5 NUMERICAL RESULTS

Towing-tank experiments were performed at MARIN using a model-scale frigate. The frigate was propelled, and it was equipped with a rudder (see Hoeskstra, 1991). Based on the towing speed ($U_c = 2\text{m/s}$) and the length of the beam ($\ell_c = 0.758\text{m}$), which are used

to normalize the LES results, the Reynolds, Froude, and Weber numbers are respectively $Re = 1.52 \times 10^6$, $F_r^2 = 0.538$, and $We = 4.10 \times 10^4$.

Data was measured at five transverse planes using laser doppler velocimetry. Longitudinal and transverse wave cuts were also performed. The velocity measurements were performed at about 200 points on each transverse plane. The sampling density was about 6 points across the draft and about 16 points across the beam. The sampling density was highest near the free surface and behind the stern and became coarser near the edges of the wake.

The experimental data has been interpolated onto a computational domain that is four beams wide and one beam deep. The length of the computational domain is one beam. Details of the two-dimensional interpolation procedure, the Kelvin-wave removal, and the noise reduction are provided in Innis (1993).

A fully-developed realization of homogeneous anisotropic turbulence is required to initialize LES of ship wakes. The resulting dataset is projected onto a transverse cut of the wake as discussed in Section 2.5. Once the LES has been initialized, it is advanced in time to simulate the spatial development of a ship wake. In the next two sections, we discuss LES of grid-stirred turbulence and ship wakes. The grid-stirred turbulence results, which are discussed in the first section, are used to initialize a ship wake study, which is discussed in the second section.

5.1 Grid-Stirred Turbulence

Numerical simulations of grid-stirred turbulence have been performed using the low Froude-number approximation. Figure 1 shows energy and surface-pressure spectra. The surface-pressure is the pressure on the plane $z = 0$, where the free-surface approximation is made. Results are shown for 128^3 and 256^3 grid points. Stirring at low wavenumbers is used to maintain a constant kinetic energy with a rms velocity equal to one. The sides of the compu-

tational domain are one unit long. The kinematic viscosity is zero for these simulations. In this infinite Reynolds number limit, the only sink of energy is provided by the SGS model.

An energy cascade is established as indicated by the $-5/3$ and $-7/3$ slopes in the inertial ranges of the velocity and the surface-pressure spectra, respectively. The Kolmogorov constant for these simulations ($K_o \approx 2$) agrees with other LES and DNS numerical simulations (see Chasnov's review, 1991, Vincent & Meneguzzi, 1991), but it is higher than most experimentally observed values, which typically are about 1.5. Since the surface pressure can be directly related to the surface elevation through the relation provided in Equation (12), the $-7/3$ power-law behavior in the pressure spectra shows that the effects of two-dimensional turbulence are not likely to be observed in the far wake of a ship where the turbulence is well-stirred and the Froude number is low.

Table 1 summarizes the power-law dependency of the energy spectra that are shown in figure 1. The following power-law formula

$$E(\kappa) = K_o \epsilon^{2/3} \kappa^\beta \quad (29)$$

is fitted using a least-squares technique. For the 128^3 simulation the fitting is performed for $20 \leq \kappa \leq 400$, and for the 256^3 simulation, $20 \leq \kappa \leq 800$.

Resolution	K_o	β
128^3	2.1	-1.687
256^3	2.0	-1.667

Table 1. *Power-law behavior of energy spectra.*

The results of other researchers seem to suggest that a free surface is capable of supporting a reverse energy cascade, which is a property of two-dimensional turbulence (see Sarpkaya's review, 1995). Observations of two-dimensional turbulence may be based on low-Reynolds-number flows that are not well-stirred. If the flow is well-stirred and the Reynolds number is sufficiently high, the present numerical results

indicate that the free surface does not support a reverse energy cascade.

Figure 2 shows two energy spectra measured in the grid-stirred turbulence experiments. One spectrum is based on data measured close to the free surface ($z = -3mm$) and the other is based on data measured in the bulk of the flow ($z = -110mm$). The data has been normalized by the free-stream velocity and the mesh spacing. For wavenumbers greater than the wavenumber at which turbulence is injected, $k_i > 2.5$, both spectra are close to a Kolmogorov $-5/3$ power-law. The presence of the free surface does not appear to influence the shape of spectra, which is consistent with the LES results. Due to limitations of the spatial resolution of DPIV in the present study, the energy spectra at very small scales, $k > 25$ have not yet been resolved. A DPIV study that is zoomed in on the flow is currently underway.

Higher-order moments associated with the velocity increments are also useful measures of how well a turbulence model is performing. Following Novikov (1992), the velocity increment is defined as

$$\delta u_i(\mathbf{r}, \mathbf{x}) = u_i(\mathbf{x}') - u_i(\mathbf{x}) , \quad (30)$$

where \mathbf{x} is a vector position, \mathbf{r} is a vector offset, and $\mathbf{x}' = \mathbf{x} + \mathbf{r}$. The radial component of the velocity increment $\delta u_i(\mathbf{r}, \mathbf{x})$ is given by

$$u_r = \delta u_i n_i ,$$

where $n_i = r_i r^{-1}$, r_i are the components of the offset, and r is the magnitude of the offset. This leads to Kolmogorov's formula for third-order moment, which is valid in the inertial range:

$$[u_r^3] = -\frac{4}{5}\epsilon r$$

where the brackets denote volume averaging and ϵ is the dissipation rate.

Figure 3 shows the third-order moment normalized by its expected behavior in the inertial range. The normalized third-order moment

asymptotically approaches one for small radial distances. The curve should be one throughout the inertial range. The Smagorinsky turbulence model appears to perform well for local disturbances, but its performance for long-range disturbances requires improvement. We note that the establishment of an extensive inertial range is adequate for remote-sensing applications, which only require good prediction of second-order moments. Applications include wave roughening, wave scattering, and turbulent wave dissipation. In order to predict intermittent turbulence effects, third and higher-order moments are required.

Figure 4 shows the probability distributions of the velocity increments for three radial offsets. The velocity increments have been normalized such that their rms value is one. A Gaussian distribution is also included along with results from the field and laboratory experiments of Praskovsky & Oncley, 1994. The probability distributions are shown for various radial offsets. The radial offsets for the experiments are normalized by the Kolmogorov length-scale (η_k). The radial offsets in the LES are not normalized by η_k because dissipation scales are not readily available in LES.

The experimental results are strongly non-Gaussian, much more so than the numerics. However, the experiments do show a tendency to become more Gaussian as the radial offset increases. We note that the probability distribution can never become completely Gaussian because the third-order moment is non-zero in the inertial range. LES, with zero kinematic viscosity, corresponds to the limit $r/\eta_k \rightarrow \infty$. In this context, the LES results represent a limiting value to the experiments, which is supported somewhat by the results illustrated in Figure 4 as r/η_k increases. The DNS results of Vincent & Meneguzzi (1991) show similar behavior. In the dissipation range, their DNS results are strongly non-Gaussian, but when the radial offset is outside the dissipation range and inside the inertial range, their results are more Gaussian.

5.2 A Model-Scale Frigate

The data from the MARIN experiments (see configuration 81, Hoekstra, 1991) measured at $x = 4.62$ beams astern is used to initialize a LES using the procedure described in Section 2.5. The duration $t = 3.95$ of the LES is long enough to advance the data to the next set of measurements at $x = 8.57$. Based on the difference in kinetic energies between the two stations, a constant dissipation rate is assigned. This dissipation rate is maintained using stirring as described in Section 2.4. A more complex temporal behavior for the dissipation rate could be assigned, perhaps based on self-similarity arguments, but since the simulation is short, a constant dissipation rate is sufficient.

Table 2 provides the correlation coefficients for two different cases and several physical quantities. The two cases correspond to the two techniques for initializing the fluctuating portion of the velocity field. Case 1 uses the mean velocity field (see Equation 27), and Case 2 uses the rms velocity field (see Equation 28). In both cases, a low Froude-number approximation is used to model the wake.

	Case 1		Case 2	
	$t = 0$	$t = 3.95$	$t = 0$	$t = 3.95$
$\langle \Omega_1 \rangle$	0.90	0.52	0.90	0.39
$\frac{1}{2} \langle v_k v_k \rangle$	0.80	0.92	0.94	0.89
$\langle U_1 \rangle$	0.99	0.95	0.99	0.95

Table 2. *Correlation Coefficients.*

Initially, the correlation coefficients are very high for all physical quantities, especially for the mean axial velocity ($\langle U_1 \rangle$) and the mean axial vorticity ($\langle \Omega_1 \rangle$). For the initial conditions, these quantities just undergo a minor correction to ensure that the initial velocity field is solenoidal and to enforce the boundary conditions.

The correlation coefficient for the turbulent kinetic energy ($\frac{1}{2} \langle v_k v_k \rangle$) is also very high initially. The correlation coefficient for Case 1 is initially lower than for Case 2 for the turbulent kinetic energy. The mean velocity field

that is used in Case 1 tends to emphasize regions where the magnitude of the velocity is high. However, most turbulence production occurs in regions where the gradients of the mean velocity field are high. There are gradients of the mean velocity in the fitting procedure (see Equation 25), but these terms tend to be dominated by the terms containing gradients of the grid-stirred turbulence field. Case 2, which uses the rms velocity as a fit, tends to do better in the high-gradient regions. These issues are more evident in the color Figures 5 and 6, which will be discussed later. A combination of mean velocity and mean vorticity may be used to provide a better fit to the turbulent kinetic energy field.

At the next station, at time $t = 3.95$, the correlation coefficients for the mean axial velocity and the turbulent kinetic energy are high, whereas the coefficient for the mean axial vorticity is low. The low correlation coefficient in the vorticity field is due to the breakup of a pair of bilge vortices.

Case 1 has also been run using the nonlinear free-surface code. Comparisons to the low Froude-number approximation indicate that wave generation is not very strong. The correlation coefficients between the hydrostatic approximation (see Equation 12) and the nonlinear free-surface elevation vary from 0.8 near the middle of the simulation to 0.5 at the end of the simulation. The low-Froude approximation appears to be reasonable four beams astern, and further back in the wake, where the turbulence is weaker, it would get even better.

We had earlier hypothesized that when the mean velocity is used as a deformation tensor, Equations 25 and 27 could be used in RANS to provide closures for the Reynolds stresses. To test this hypothesis, we fitted a fluctuating velocity field to the stations at $x = 4.62$ and $x = 8.57$ in the MARIN experiments. The deformation constant (C_d) changed by less than 15% between the two stations. This provides some evidence that the initialization procedure could also be used as a RANS closure.

Figures 5 and 6 compare the experimental

measurements and the numerical predictions for the two cases. Figure 5 is at $t = 0$ and Figure 6 is at $t = 3.95$. The mean turbulent kinetic energy, mean streamwise velocity, and mean axial vorticity are respectively shown in the (a) top, (b) middle, and (c) bottom plots.

For the mean axial velocity, the drag wake of the hull (blue) is located near the surface, and the thrust wake of the propeller (red) is concentrated below the free surface. Some spreading of the wake is observed between times $t = 0$ and $t = 3.95$. In both cases, LES predicts the evolution of the axial velocity very well.

The plots of mean axial vorticity show that the free-surface vortices are concentrated in a thin layer near the free surface. They spread laterally outward. The pair of bilge vortices have been entrained in the slipstream of the propeller and split by the rudder. The experimental data is ragged at $t = 0$ because there are only a few sample points across the wake. Between time $t = 0$ and $t = 3.95$, the bilge vortices break up and the free-surface vortices grow weaker. The free-surface vorticity also spreads out laterally. The spreading of the wake is more evident in the free-surface elevation, which is not shown. The two numerical cases appear to perform equally well.

As illustrated in the plots of turbulent kinetic energy (tke), high concentrations of tke are initially located in the region between the drag and thrust wakes of the experiments. The numerics do not seem to capture this high concentration very well. As discussed earlier, it may partially be attributed to the gradients of the fluctuating velocity field dominating the gradients of the mean quantities that are used in the fitting procedure. The effect of using different realizations of turbulence to initialize the flow should also be investigated.

6 CONCLUSIONS

A new procedure for initializing LES and simulating wakes has been developed. The procedure provides a framework for testing SGS

models. Based on this procedure, two types of LES capabilities have been developed: a nonlinear free-surface capability and a low Froude-number approximation. These capabilities have been used to simulate grid-stirred turbulence and the wake of a model-scale frigate.

Neither the results of LES or preliminary grid-stirred turbulence experiments shows evidence of a reverse energy cascade. For well-stirred flows at sufficiently high Reynolds numbers, the numerically-predicted and experimentally-measured energy spectra scale according to three-dimensional similarity theory, both in the bulk of the flow and near the free surface. The roughening of the free surface also scales according to three-dimensional similarity theory.

Comparisons between LES predictions and towing-tank measurements are very good. As predicted by LES, the attenuation of the mean axial-velocity field and the turbulent kinetic energy, and the breakup of the axial vorticity field agrees with measurements. The enhanced spreading of the wake near the free surface is also predicted well by LES. Additional validation studies are currently underway using the results of grid-stirred turbulence and splitter-plate experiments.

ACKNOWLEDGEMENTS

DGD, GEI, JCT, and DCW are supported by ONR under contract number N00014-93-C-0046. MG, HTH, and PM are supported by ONR under contract number ONR-N00014-92-J-1610. EAN is supported under contract numbers ONR-N00014-92-J-1610 and ONR-14-94-1-0040. Dr. Edwin P. Rood is the program manager. This work is also supported in part by the Army Research Office contract number DAALO3-89-C0038 with the University of Minnesota Army High Performance Computing Research Center (AHPARC) and the DoD Shared Resource Center at the AHPARC. The numerical simulations have been performed on the CM-5 computers at Naval Research Laboratory and the AHPARC.

REFERENCES

- [1] Chasnov, J.R. (1991) Simulation of the Kolmogorov inertial subrange using an improved subgrid model. *Phys. of Fluids*, **3**(1), 188-200.
- [2] Dommermuth, D.G. (1993) The Laminar Interactions of a Pair of Vortex Tubes with a Free Surface. *J. of Fluid Mech.*, **246**, 91-115.
- [3] Dommermuth, D.G. (1994a) Efficient simulation of short- and long-wave interactions with applications to capillary waves. *J. Fluids Eng.*, **116**, 77-82.
- [4] Dommermuth, D.G. (1994b) The initialization of vortical free-surface flows. *J. Fluids Eng.*, **116**, 95-102.
- [5] Dommermuth, D.G., Novikov, E.A., & Mui, R.C.Y. (1994) The interaction of surface waves with turbulence. In *Proc. of the ASME Symp. on Free-Surface Turbulence, Lake Tahoe*.
- [6] Dommermuth, D.G. & Novikov, E.A. (1993) Direct-numerical and large-eddy simulations of turbulent free-surface flows. In *Sixth Inter. Conf. on Numer. Ship Hydro.*, Iowa City, 239-270.
- [7] Germano, M., Piomelli, U., Moin, P., & Cabot, W.H. (1991) A dynamic subgrid-scale eddy viscosity model. *Phys. Fluids*, **A 3**(7), 1760-1765.
- [8] Hoekstra, M. (1991) Macro wake features of a range of ships. *Maritime Research Institute, Netherlands*, MARIN Report No. 410461-1-PV.
- [9] Innis, G.E. (1993) Computations of full-scale wakes from model-scale data. *Science Applications International Corporation*, SAIC Report No. SAIC-93/1139.
- [10] Lilly, D.K. (1991) A proposed modification of the Germano subgrid-scale closure method. *Phys. Fluids*, **A 4**(3), 633-635.
- [11] Longuet-Higgins, M.S. (1991) Theory of weakly damped Stokes waves: a new formulation and its physical interpretation. *J. Fluid Mech.*, preprint.
- [12] Lundgren, T.S. (1989) A free-surface vortex method with weak viscous effects. In *Mathematical Aspects of Vortex Dynamics*, ed. by R.E. Caflisch, SIAM, 68-79.
- [13] Monin, A.S. & Yaglom, A.M. (1975) Statistical Fluid Mechanics II. *The MIT Press, Cambridge, MA*
- [14] Mui, R.C.Y. & Dommermuth, D.G. (1995) The vortical structure of a near-breaking gravity-capillary wave. *J. Fluids Eng.*, **117**, 355-361.
- [15] Novikov, E.A. (1992) Probability distribution for three-dimensional vectors of velocity increments in turbulent flow. *Phys. Rev. A*, **46**(10), 6147-6149.
- [16] Praskovsky, A. & Oncley, S. (1994) Probability density distribution of velocity differences at very high Reynolds numbers. *Phys. Rev. Lett.*, **73**(25), 3399-3402.
- [17] Reed, A.M., Beck, R.F., Griffin, O.M., & Peltzer, R.D. (1990) Hydrodynamics of remotely sensed surface ship wakes. In *SNAME Trans.*, **98**, 319-363.
- [18] Sarpkaya, T. (1995) Vorticity, free surface, and surfactants. *Ann. Rev. of Fluid Mech.*, **28**, 83-128.
- [19] Smagorinsky, J. (1963) General circulation experiments with the primitive equations. *Mon. Weather Rev.*, **91**, 91-164.
- [20] Vincent, A. & Meneguzzi, M. (1991) The spatial structure and statistical properties of homogeneous turbulence. *J. Fluid Mech.*, **225**, 1-20.
- [21] Willert, C. & Gharib, M. (1991) Digital particle image velocimetry. *Exp. in Fluids*, **10**, 181-183.

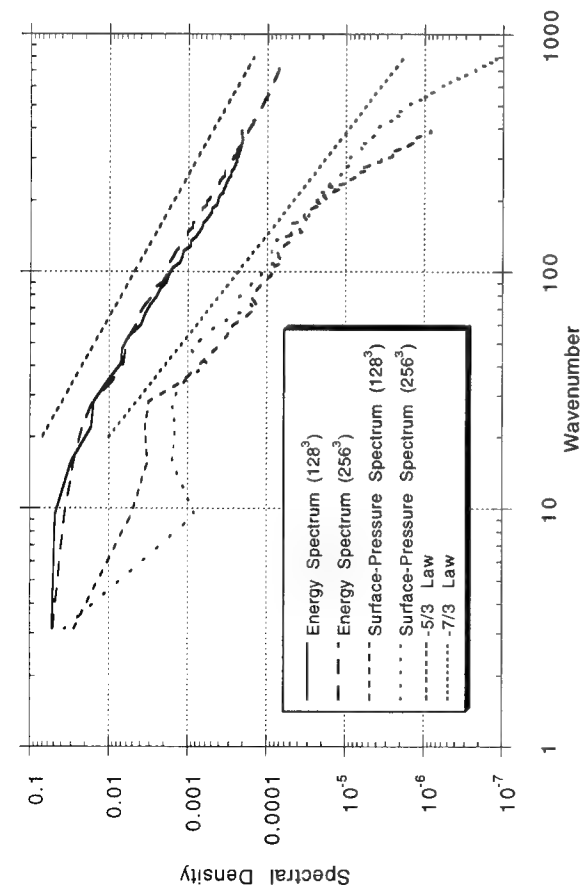


Figure 1. Grid-stirred LES of free-surface flow.

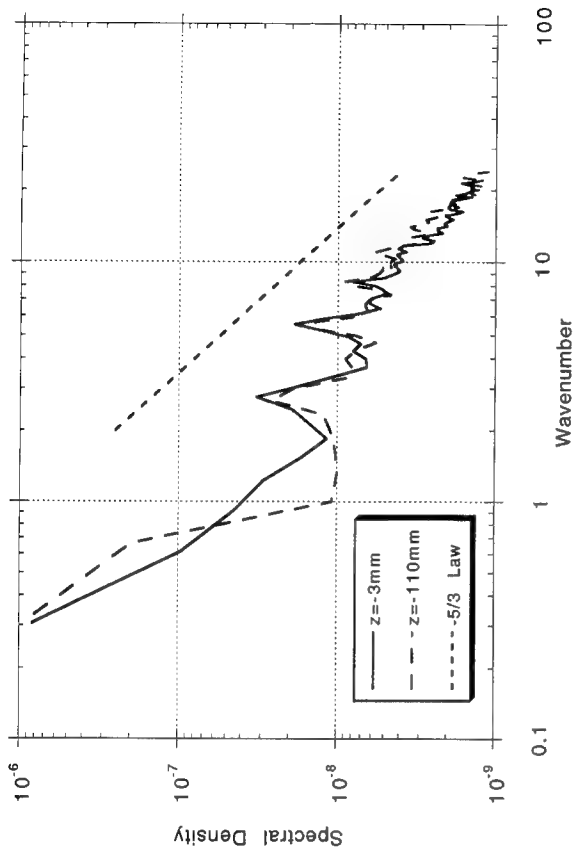


Figure 2. Grid-stirred turbulence energy spectra.

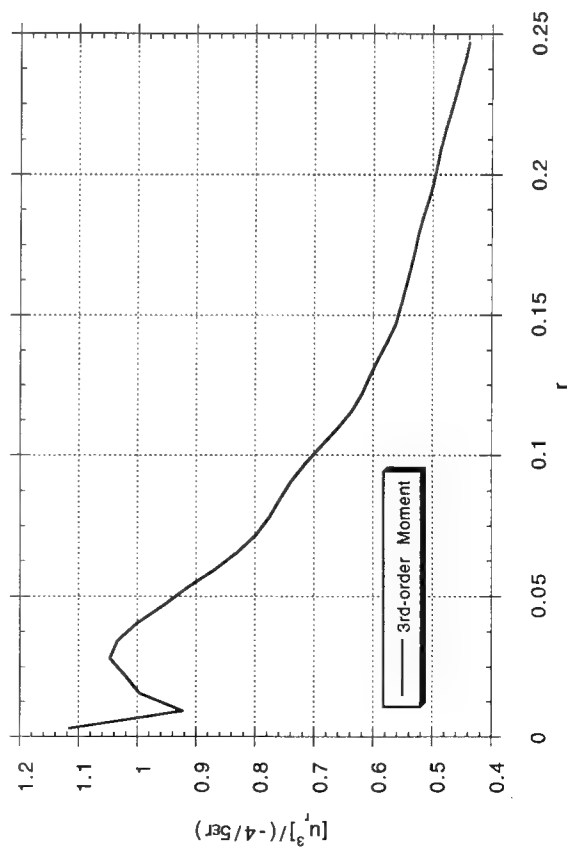


Figure 3. Normalized third-order moment.

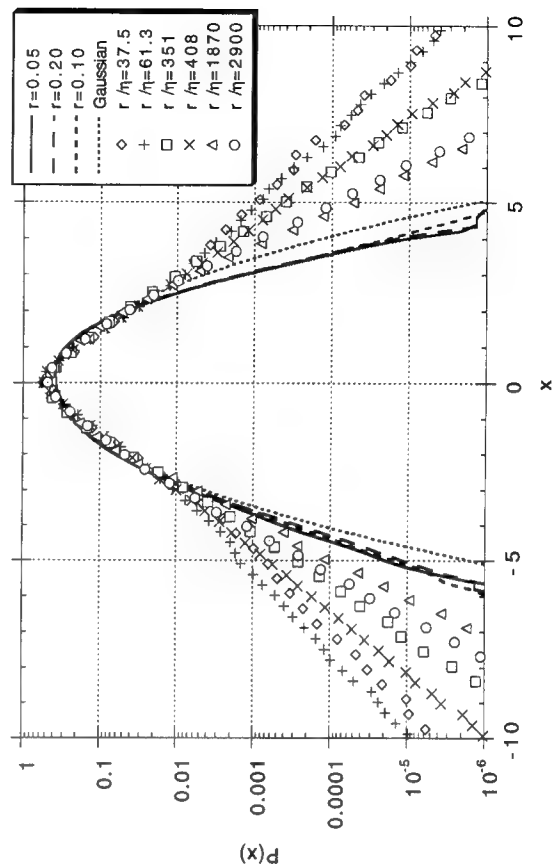


Figure 4. Probability distribution of velocity increments.

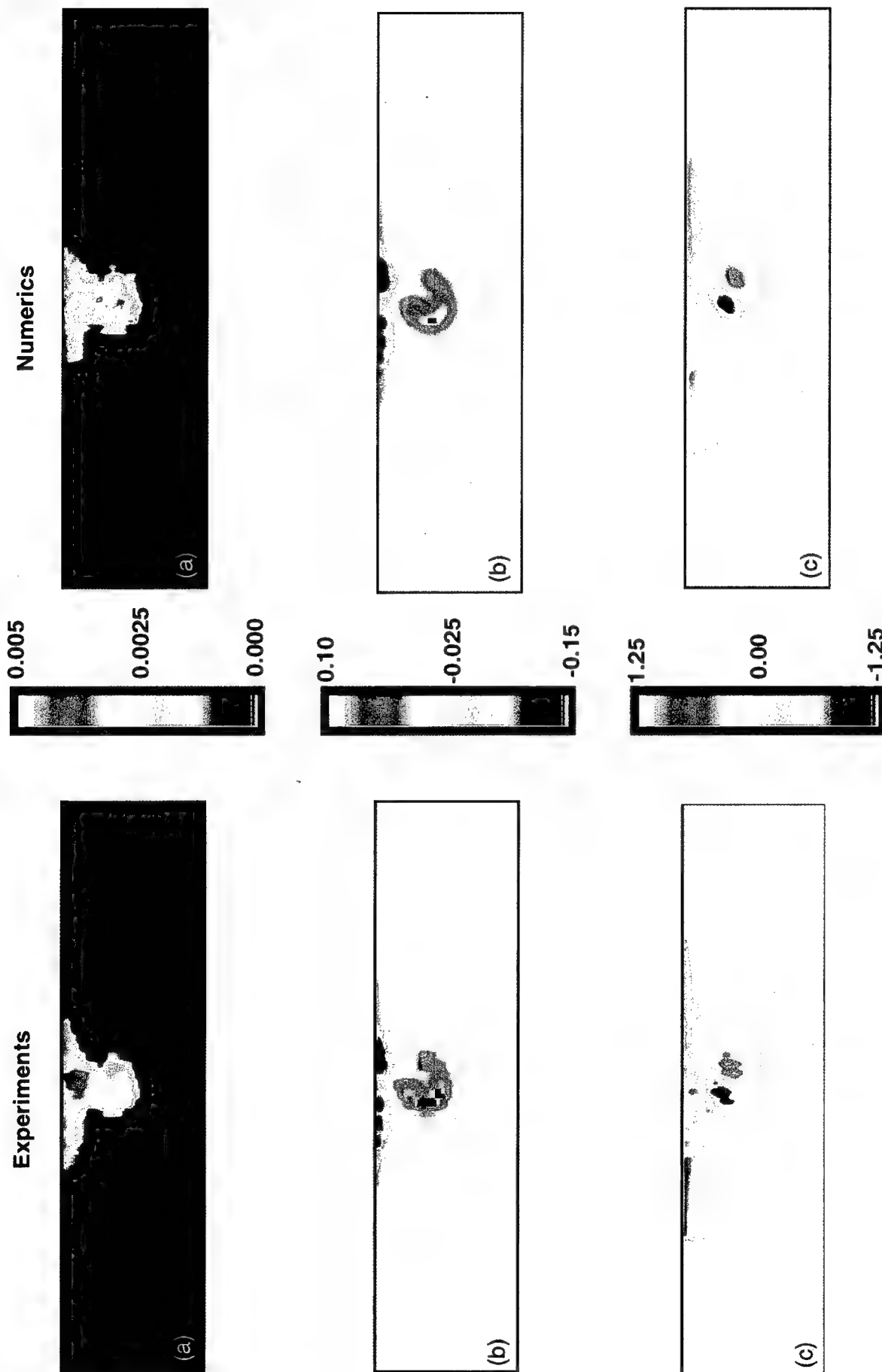


Figure 5. Case 2. Model-scale wake experiment at $t=0$. (a) Mean turbulent kinetic energy. (b) Mean streamwise velocity. (c) Mean axial vorticity. Experiments shown on left, numerics shown on right.

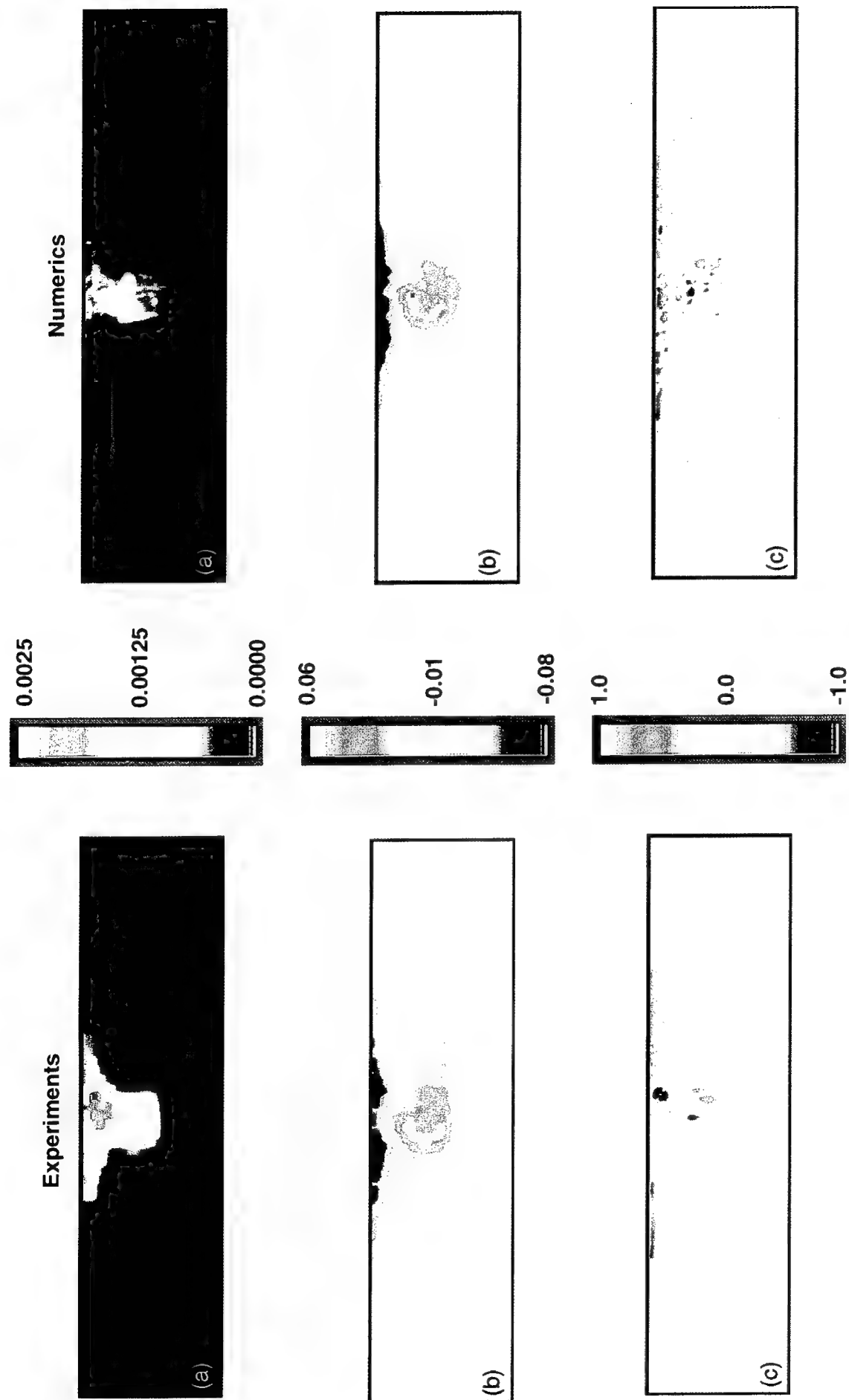


Figure 6. Case 1. Model-scale wake experiment at $t=3.95$. (a) Mean turbulent kinetic energy. (b) Mean streamwise velocity. (c) Mean axial vorticity. Experiments shown on left, numerics shown on right.

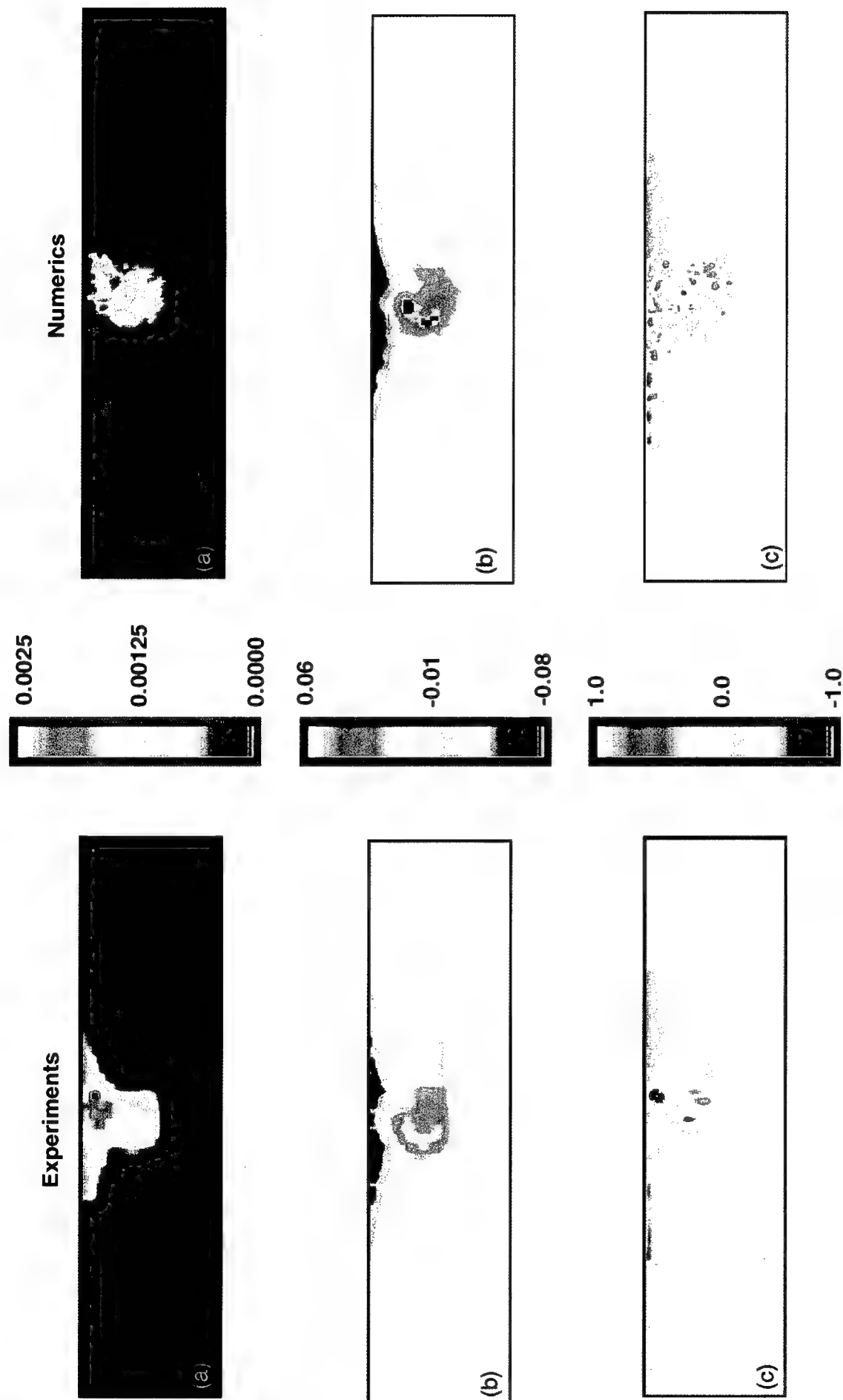


Figure 6. Case 2. Model-scale wake experiment at $t=3.95$. (a) Mean turbulent kinetic energy. (b) Mean streamwise velocity. (c) Mean axial vorticity. Experiments shown on left, numerics shown on right.

Conductivity Measurements in the Wake of Submerged Bodies in Density-Stratified Media

T. Sarpkaya, T. Massidda (Naval Postgraduate School, USA)

ABSTRACT

The variations of the relative conductivity in the wake of self-propelled, single-screw, submarine-shaped bodies in a continuously (linearly) stratified fluid were measured. The internal Froude-number scaling ($Fr = U_0/ND$) was used between the model and the prototype to select the buoyancy (Brunt-Väisälä) frequency $N (= [g\Delta\rho/\rho_0 H]^{1/2})$ with ρ_0 as the mean density at mid-depth, the model diameter (D) and speed (U_0) for representative environmental conditions. The model Froude number ranged from about 50 to 200 and the Reynolds number ($U_0 D/\nu$), from about 3×10^4 to 6×10^4 . The boundary layer along the body was tripped to be turbulent. Furthermore, the size of the propeller was scaled with respect to the size of the wake and not the size of the body, by scaling wake diameter on the basis of Reynolds number, in a manner to that described by Schetz and Jakubowski [1]. Nevertheless, the scale effects (due to widely different model and prototype Reynolds numbers) cannot be assessed and have been left to prototype tests and some scientific speculation. The wake collapse (at a distance of about 400 diameters downstream) gave rise to large conductivity changes and to many modes of short internal waves of mean length D . The upstream conductivity field anticipated the arrival of the body (the upstream effect or blocking), for only impulsive starts and stops, to and from moderate speeds.

INTRODUCTION

Density stratification occurs naturally in many fluids, particularly in the ocean environment. The stratification can be due to thermal effects or results from salt or other impurities in the fluid. The study of the effects of various types of stratifications is important because even a mild stratification can

radically alter the dynamic behavior of the interaction between the fluid and a body passing through it. In an homogeneous fluid, all portions of the wake are subjected to the same gravitational forces. This is not true for the wake of a body in a density stratified fluid because the turbulent mixing causes a disruption in the equilibrium density configuration resulting in gravity induced pressure gradients. These gradients generate secondary motions in the fluid that are not present in a homogeneous wake. The changes that occur in the flow due to these secondary motions (physical as well as turbulent collapse in the wake, internal waves) are important to the understanding of the interaction between a submerged body and its environment.

Examples of hydrodynamic phenomena, most likely to be encountered in various parts of a submerged body, include flow about the bow planes; three-dimensional flow at the body/bow-plane junction; three-dimensional, unsteady and severely-separated flow in the vicinity of torpedo-tube-ports; interaction of flow with devices and unconventional aft-body shapes (applied in recent times to bodies to improve the overall efficiency of the propulsion); interference of tip and junction vortices with the existing boundary layers and with the propulsor; and numerous other fluid-structure interactions. These phenomena give rise to complex wake structures, even for a relatively simple linear body motion in an homogeneous medium. The unsteady motions such as impulsive starts and stops, changes in course or depth give rise to additional wake widening in both the homogeneous and stratified media.

Hydrodynamic models, utilizing recently developed numerical techniques, attempt to predict the behavior of unsteady flow fields in the wakes of submerged bodies. However, the results are highly dependent on the turbulence model used and on the previous measurements for overall model verification.

Unfortunately, there are not any detailed measurements of the flow field resulting from the motion of a submarine-like body in a stratified medium. Most of the existing and relatively meager experiments do not deal with wake conductivity measurements at Froude numbers of practical significance. Also, the causes of the wake turbulence are seldom similar.

It is a well-known fact that electric currents generated in a fluid contribute to the total electromagnetic field, but in the absence of fluid motion these modifications of the applied field remain at a steady state. If a hydrodynamic disturbance, such as a wake in a stratified medium, sets part or all of the conducting fluid into motion, an additional electric field is generated in the fluid which is moving across the geomagnetic field. The change in current density then produces a magnetic anomaly which may be observable and thus important for stealthing purposes.

Wakes caused by bodies traveling in homogeneous fluids have been subjected to a large number of studies. A summary for the axisymmetric or circular wake is presented in Schlichting [2]. In this case, the wake width in a homogenous fluid increases as $x^{1/3}$ vice $x^{1/2}$ for the two-dimensional case. This relationship can be used for the initial wake growth in a stratified fluid because the effect of the turbulent mixing dominates the wake in that region. As a result, the wake expands in all directions in the same manner as the wake in a homogenous fluid. As the distance behind the body increases, the gravitational effects on the displaced fluid become more dominant. This results in a vertical collapse and a horizontal growth in the wake region. The horizontal spreading causes the vertical collapse to occur at a greater rate relative to the two-dimensional case. This is the source of the major difference between the two- and three-dimensional wakes.

The vertical collapse and the subsequent horizontal spreading also cause a horizontal displacement of the fluid surrounding the mixed region. This fluid then converges above and below the level at which the spreading is taking place resulting in the generation of random internal gravity waves in the bulk fluid. These waves then continue to travel away from the body at the level where the mixed fluid finds density equilibrium with the surrounding fluid. Most of these effects have been documented thirty years ago by Stockhausen, et al. [3] for a circular disk mounted on a self propelled body. Surveys on stratified flows may be found in the papers by Torobin and Gauvin [4], Lin and Pao [5], and Fernando [6]. Laboratory measurements of the evolution of wakes behind a sphere and a right circular cylinder, moving in a linearly stratified fluid at relatively low Froude and Reynolds numbers, were carried out, among others, by

Lin et al. [7] and Xu et al. [8]. In both cases, the wake formation was primarily due to the shedding of vortices from the separation points.

In the present investigation, the conductivity measurements were made in the wake of self-propelled bodies (with momentumless wakes) through the use of numerous, temperature-compensated, high accuracy, microscale, conductivity probes [9]. Under normal conditions, i.e., for a submarine-like body in steady rectilinear motion, the characteristics of the wake are dictated primarily by the propeller and, to a lesser extent, by the necklace and sail-plane vortices. However, in transient motions (body undergoing time-dependent maneuvers), nonlinear waves, the unsteady three-dimensional cross-flow separations and body vortices play significant roles. Also, it must be emphasized that there are fundamental differences in the wakes of towed or dragged bodies and the self-propelled bodies. The wake of a towed body represents typical elementary shear flow profiles, where the velocity deficit spreads outward and decreases on the centerline as the flow proceeds downstream. The wake of a momentumless body exhibits a velocity-defect region near the axis and a velocity-excess region in the neighborhood of $r/R_0 = 0.8$, before leveling off beyond $r/R_0 = 1.2$ (here r is the radial distance and $R_0 = D/2$, the maximum radius of models).

MODELS, FACILITIES, AND TECHNIQUES

Scaling of the Model

The parameters used in the current study were taken from the design specifications for a typical attack submarine. They provide an accurate representation of the conditions that would be encountered under normal operating conditions. Of special importance is the relative conductivity which we define here as the ratio of the time change in conductivity at a given point to that which existed prior to the motion of the body at the same point, i.e., $RC(x,y,z) = (\Delta C/C)_{xyz}$. The effect of the conductivity perturbations on the distortion of the prevailing magnetic field is of special importance and directly related to the ultimate purpose of the investigation.

A standard dimensional analysis shows that the relative conductivity depends on the internal Froude number $Fr = U_0/ND$ (or its inverse ND/U_0 , known as the stratification parameter), the Reynolds number $Re = U_0D/\nu$, and U_0t/D or Nt (here N is measured in rad/s, not in Hz). The foregoing is predicated on the assumptions that (i) the Schmidt number (ν/κ) is not important since the timescales for the salt diffusion are considerably larger than those for the occurrence of fluid-dynamical events of interest, (ii) the geometrical

confinement effects are negligible, i.e., the relative width W/D , length L/D , and depth H/D of the test tank are sufficiently large, (iii) the Boussinesq number ($U_0 N/g$ or U_0^2/gD) is sufficiently small (here in the order of 10^{-3} , amply justifying the Boussinesq approximation for deeply-submerged submarine wakes), and (iv) the turbulence parameter $(\epsilon D)^{1/3}/U_0$, with ϵ as the dissipation rate of turbulent kinetic energy, is negligible since the flow environment prior to the experiments was kept essentially free from disturbances (whenever a particular fill was used twice, it was done so only after a sufficiently long rest period, about 2-3 hours). Additional discussion of the various governing parameters for similar situations are discussed in Sarpkaya [10] and Sarpkaya and Daly [11].

The internal Froude-number ($Fr = U_0/ND$) was used to establish the model/prototype relationship. This resulted in model speeds from 0.3 m/s to 1.5 m/s and model stratifications from 0.05 to 0.20 rad/s. The model speed is intended to cover the prototype speed range from 1/3 bell to a full bell. The range provided by the stratification system represents from a weak stratification ($N = 0.005$ rad/s) to a strong stratification ($N = 0.02$ rad/s) that would be expected under normal operational conditions. The stratification profile can be changed at will, however, the current runs were limited to linear profiles in order to gain a further understanding of the effects of the most dominant parameters in this highly complex, multi-parameter, phenomenon. No attempt has been made to assess the scale effects due to the mismatch of the model and prototype Reynolds numbers. This is left to judiciously conducted prototype tests.

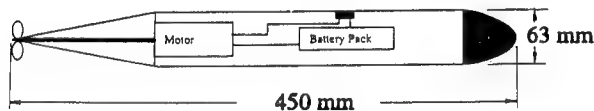


Fig. 1 Schematic of the test model

Three similar models were used in the experiments (see Fig. 1). The selection of the model size was driven partly by the model-to-prototype scaling factor and partly by the width of the tank. The basic model was constructed from plexiglas tubing with removable sections to allow for future modifications. It had a base length of 0.45 m and a main body diameter of 63 mm. It provided a large enough interior space to allow for the installation of a four-bladed propeller shaft, propeller motor, and batteries and was small enough to minimize the potential interference with tank walls. The second

model was identical to the first except that it had a sail and two adjustable sail planes.

The motion of the self-propelled model was guided by two extremely thin and taut wires going through the body. Both models were made slightly buoyant to compensate for the small sag of the cables and capable of speeds up to 1 m/s. The propeller system consisted of a variable speed motor and a set of Ni-Cd batteries, all embedded inside the model. The propulsion system was controlled remotely.

Test Tank

It is 15 m long, 1.2 m wide, and 1.8 m deep and contained linearly stratified salt water to a depth of 1.65 m. Its interior is coated with marine epoxy to minimize corrosion. The entire front wall is fitted with one inch thick Plexiglas windows to allow for flow visualization. The fill system and the inlet piping are located at the bottom of the tank under a turbulence management system. The latter consists of one inch thick polyurethane foam sandwiched between two perforated aluminum plates.

Stratification System

It had two constant head tanks (one for fresh water, one for brine) and a large reservoir. The brine was prepared in the reservoir, four to five days prior to the day of experiment, before being pumped into the brine head tank. The purpose of this was to assure that the fluid was suitably degassed. The two head tanks supplied a three way mixing valve, driven by a direct current motor. The strength of the stratification is determined by the amount of salt premixed in the reservoir. Effluent from the two head tanks is gravity fed to the inlet of the three way mixing valve. It is this mixing action that ensures a smooth stratification profile in the tank. The mixing valve is constructed from two one-inch PVC ball valves that are mounted 90 degrees out of phase. The handles of these valves are attached to a motorized drive system that consists of a set of four reduction gears driven by a 3/4 Hp direct current motor.

The valves are cycled starting with full-open fresh water valve and fully-shut brine valve, and ending with full-open brine valve and fully-shut fresh water valve. This provided a linear stratification profile as the tank was filled from the bottom. The inlet to the tank consisted of a set of 50-mm diameter PVC pipes, perforated along their entire length with 1.5-mm diameter holes. This relatively simple but novel system provided a consistent linear stratification in about five hours. The density gradients were verified twice. First, during the fill process using a profile conductivity probe, mounted near the bottom of the

tank. The output of the probe was continuously recorded for viewing and verification during the entire filling period. Second, the density profile was measured before each run through the use of two vertically traversing conductivity probes.

Conductivity Measurements

They were made through the use of numerous, temperature-compensated, high accuracy, microscale, conductivity probes [9], manufactured by the Precision Measurement Engineering. They were calibrated before and after each run. They had an output voltage of ± 5 volts, a linear conductivity range of $5\text{E-}3$ to $800\text{E-}3$ mSiemens/cm, a time response of -3db at 800 Hz, a spatial response of -3db at 4 cycle/cm, and a noise level less than 1 mV rms in the range of 10 Hz to 1 kHz. In addition to the initial calibration, each probe is checked during the tank fill and prior to the data acquisition. This is critical as each tank fill takes about five hours. In addition to the conductivity data, the speed of the model is monitored with a Linear-Variable-Velocity transducer and the output signal is fed to the data acquisition system.

The probes were mounted along the tank centerline at regular intervals ($x/D = 20$) and along the width of the tank at strategic locations in a horizontal plane that is located at $r/R_0 = 1.1$. The vertical separation distance between the top of the model and the tip of the probe was $0.10R_0$. Output from these probes was sent to a preamplifier, a low gain DC amplifier, and, finally, to a computer. The input signals are managed by a Data Acquisition Control Unit with a 40 channel digital multiplexer and a high speed voltmeter. The program allowed data rates from 5 to 200 Hz. The data rates are based on the observed frequency content of the early test runs and the duration of an experiment is based on the rate of decay observed in the mean conductivity change long after the passage of the model. Finally, the conductivity data and the speed of the model (obtained from the velocity transducer) are provided to the computer for further analysis.

Test Procedures

Each experiment required about three days to accomplish and was repeated at different weeks. This was due to setup operations, long tank fill times, and clean up procedures to minimize corrosion. After the fill was completed, the tank was allowed to settle for at least an hour to ensure that the stratification profile was smooth and linear. This was verified prior to each run by recording the output of a slowly submerging conductivity probe. Experience has shown that at least two tests could be done with the same tank fill without significant deviations from the initial

stratification profile if sufficient time is allowed between the two runs (2-3 hours).

In contrast to its preparation, the actual test was indeed rather short. First, the computer system was initialized for the run to be made. This required input of the probes to be recorded, data rate, and data run duration. The model was either (i) started impulsively to a given speed and stopped smoothly at the end of the run, or (ii) accelerated smoothly to a desired speed over a reasonable distance and allowed to run along the tank, until it was stopped smoothly by decelerating it first, or (iii) started smoothly to a constant velocity and then stopped suddenly, or (iv) subjected to a series of impulsive starts and stops along the tank. Impulsive starts and stops were accomplished smoothly with the help of a spring activated launcher and an arresting cable. For the impulsive start, the Froude number was defined as $Fr = U_0/ND = \Delta U/ND$. For the case of smooth acceleration, Fr is based on the steady velocity U_0 . The effect of the variations of $D(dU/dt)_0/U_0^2$ and $(D^2/\nu)(1/U_0)(dU/dt)_0$ (or $U_0 D/\nu$) has not been investigated. In any case, the maximum initial acceleration $(dU/dt)_0$ in the experiments did not exceed 1.5 ft/s^2 .

PRESENTATION OF RESULTS

Impulsive Start and Wake Collapse

Examples of the ensemble-averaged relative conductivity records for the central probes, for an impulsively-started clean body (no sails), are presented in Figs. 2 and 3 as a function of the normalized time Nt (the upper limit depends on the particular run and may be smaller or greater than 30).

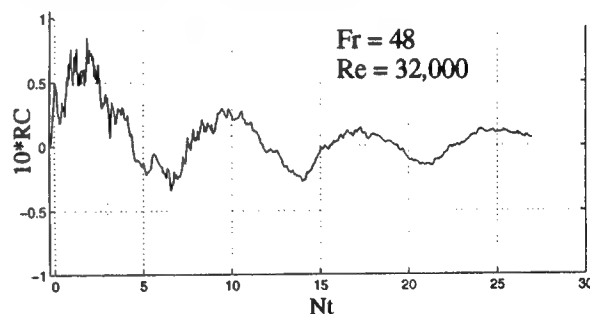


Fig. 2 Relative conductivity versus Nt for an impulsively-started clean model ($N = 0.15 \text{ rad/s}$, $U = 0.46 \text{ m/s}$)

Normally, the time is measured from the start of the experiment, but during the post-processing of the data the clock times for each probe are reset to perform ensemble averaging for several reasons. First, it removes random anomalies, if any, from the record of

any one probe. Second, it enables one to compare the ensemble-averaged data with those of each of the contributing probes, and it increases the credibility of conclusions based on a broader spectrum of the data.

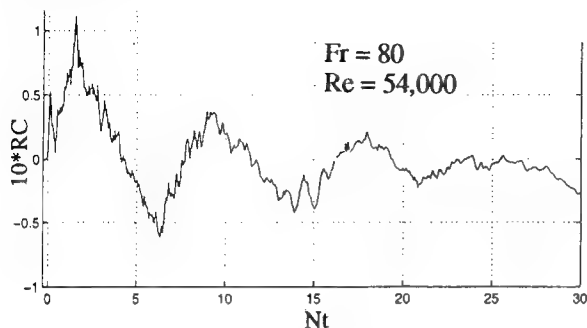


Fig. 3 Relative conductivity versus Nt for an impulsively-started clean model ($N = 0.15$ rad/s, $U = 0.76$ m/s)

In Figs. 2 and 3, and in all other plots belonging to the same family, the relative conductivity (henceforth referred to as RC) is multiplied by 10 in order to deal with relative conductivity values near unity. Thus, a value of 1.0 on the vertical scale corresponds to a 10% change in conductivity. Figures 2 and 3 show that the overall character of the relative conductivity is like that of a damped harmonic wave. Noting that $Nt = 0$ is slightly to the right of the coordinate origin and that $Nt = 0$ corresponds to the instant at which the nose of the model arrives at the probe, it is clear that a probe anticipates the arrival of the body or "sees" it before it is actually seen (the first sharp rise in the figures). This phenomenon is referred to as the "upstream effect" and will be discussed in more detail later.

As the model continues to move, RC decreases at first (when the probe is over the axisymmetric cylindrical part of the body) and then increases again sharply when the probe enters the wake and reaches a maximum at about $Nt = 2$ ($\Delta Nt = 1$ corresponds to $\Delta t = 6.67$ s or to about 50 body diameters for this particular case). Immediately afterwards, the wake begins to collapse. The wake collapse is virtually complete at about $Nt = 7$, i.e., after about 47 s or about 340 body diameters. At later times ($Nt > 7$), RC rises and falls at an ever decreasing amplitude due to internal waves generated by the wake collapse. In other words, the mixing of the fluid in the wake is never complete and the collapse as well as the recovery of the wake occurs with an ever decreasing overshoot in either direction towards the equilibrium. Thus, the events associated with the collapse follow the model at a certain speed. For the conditions of Figs. 2 and 3, the wave period is about $\Delta Nt = 7$ or $T = 47$ s. To be sure, there are additional oscillations in

the wake-conductivity due to smaller eddy motions and internal waves, but the wake collapse is the phenomenon most likely to give rise to measurable periodic waves and geomagnetic perturbations. It must also be emphasized that the intensity of the wake collapse depends on the Froude number and the configuration of the body. Large density gradients increase the stability of the density profiles and the collapse takes place much sooner. A streamlined body (as in the present case) is likely to generate a less severe wake collapse than the one undergoing maneuvers or sharp velocity changes, i.e., the bluffer the body and larger the density gradient, the faster the collapse. Inversely, the more streamlined the body and milder the density gradient, slower is the occurrence of the collapse, as in the foregoing example. The wake phenomena associated with unsteady maneuvers (turns, dives, and porpoising, etc.) were not part of the present investigation.

An equally important feature of Figs. 2 and 3 is the magnitude of RC. At its peak, RC reaches values from about 8% to 12%, at a distance of about 100 body diameters (at $t = 13$ s). The subsequent two peaks occur at distances $x/D = 480$ ($Nt = 10$, $t = 67$ s), and $x/D = 815$ ($Nt = 17$, $t = 113$ s), after the passage of the body. Figure 4 is an expanded version of the earlier times of Fig. 2 for clarification of the various regions. Similar conductivity changes across the three-dimensional momentumless wake of a self-propelled body are seen in the isochlor maps of Stockhausen et al. [3].

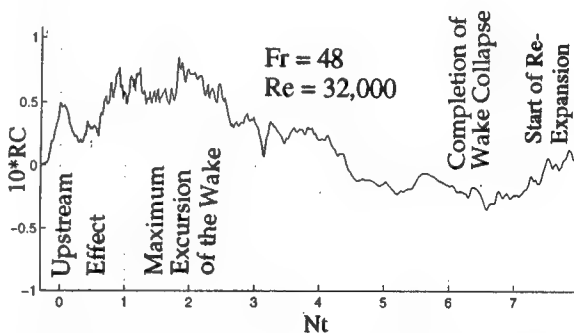


Fig. 4 An expanded version of the earlier times of Fig. 2 ($N = 0.15$ rad/s, $U = 0.76$ m/s)

Figure 5 shows the output of three probes, situated in the lateral direction near the mid-length of the tank. The probe C is directly above the axis of the model at $r/R_0 = 1.1$. Probes B and A are, respectively, at 75 mm and 375 mm to the left of the axis of the 63 mm model (all three probes are at the same level). It is clear that the signals B and C are significantly larger than A, as expected. Figure 5 and many others like it have conclusively shown that the wall interference on the response of the central probe is indeed

negligible. The probes on the other side of the axis yielded nearly identical outputs except that the traces were somewhat smoother. This was due to the direction of the rotation of the propeller.

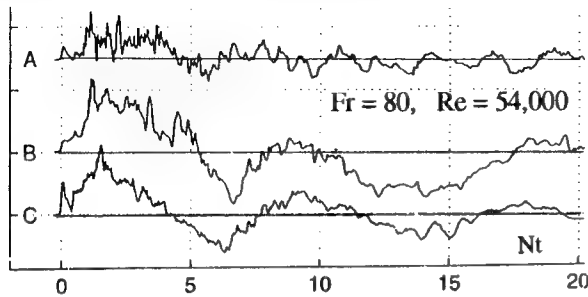


Fig. 5 Spanwise variation of RC
($N = 0.15$ rad/s, $U = 0.76$ m/s)

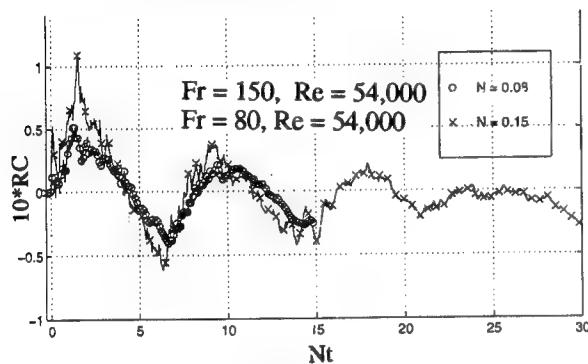


Fig. 6 Relative conductivity versus Nt for an impulsively-started clean model (\circ , $N = 0.08$ rad/s; \times , $N = 0.15$ rad/s), $U = 0.76$ m/s for both

The effect of halving N (from 0.15 to 0.08 rad/s) is shown in Fig. 6 for $U = 0.76$ m/s. It seems that only the very early stages of the motion and the maximum value of RC are affected by the change in N . The remainder of the data, such as the period of oscillation and its decay, remain largely unaffected. Comparisons at other velocities yielded similar results.

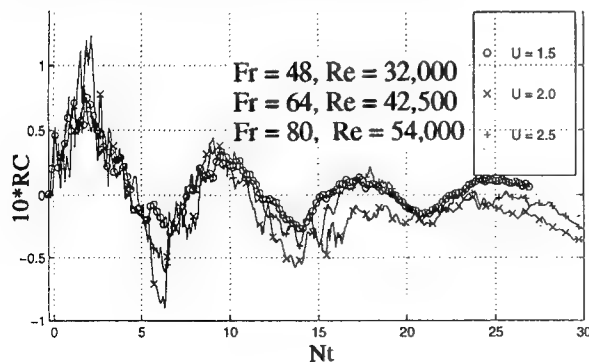


Fig. 7 RC versus Nt for various U ($N = 0.15$ rad/s)

Figure 7 shows the effect of the variation of U from 0.46 m/s to 0.76 m/s for $N = 0.15$, again for an impulsively-started clean body (no sails). Within the range of velocities encountered, the variation of RC is practically independent of the velocity. Only the amplitude of RC during the period of wake growth and collapse seems to be affected.

Non-Impulsive Start and Wake Collapse

Examples of the ensemble-averaged relative conductivity records for the central probes, for a clean body (no sails) smoothly-accelerated to a constant velocity, are presented in Figs. 8 and 9 as a function of the normalized time Nt . They are similar to Figs. 2 and 3 with two exceptions: (i) the extrema of the output are slightly shifted to the right (see also Fig. 10), as would be expected; and (ii) the initial sharp rise in RC near $Nt = 0$ is essentially absent. Figure 9 also shows that at higher speeds (nearly 1 m/s), the signal is somewhat noisier. Figure 11 shows a comparison of the RC values for two N values for $U = 0.6$ m/s. As expected on the basis of earlier observations, the larger the N , the higher the output and sooner the collapse.

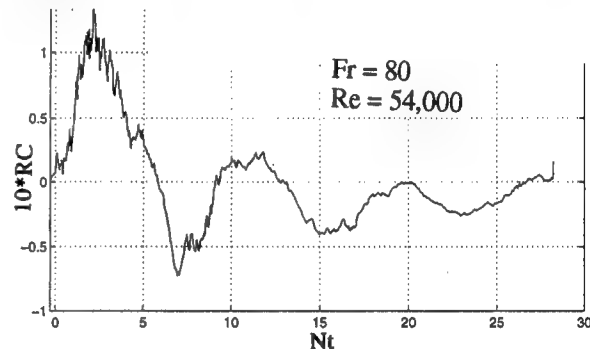


Fig. 8 RC versus Nt for $N = 0.15$ rad/s and $U = 0.76$ m/s (non-impulsive start of a clean model)

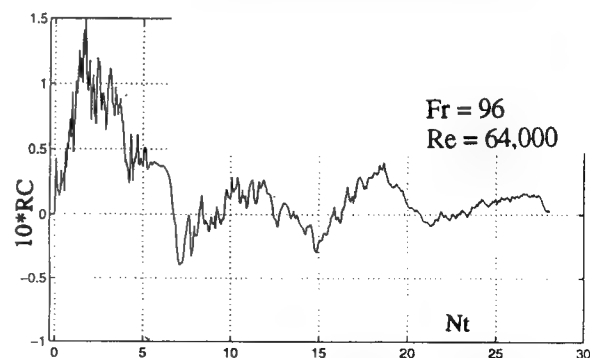


Fig. 9 RC versus Nt for $N = 0.15$ rad/s and $U = 0.92$ m/s (non-impulsive start of a clean model)

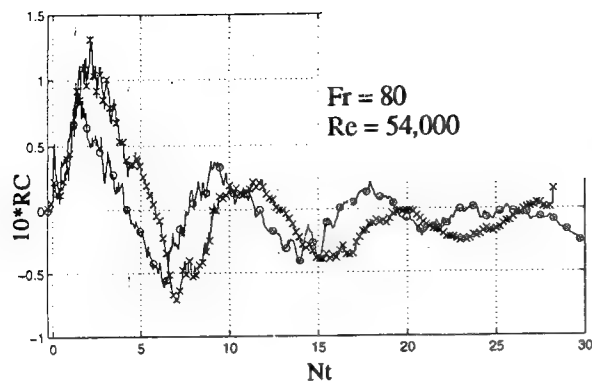


Fig. 10 Comparison of the impulsive (o) and non-impulsive (x) starts ($N = 0.15$ Rad/s, $U = 0.76$ m/s)

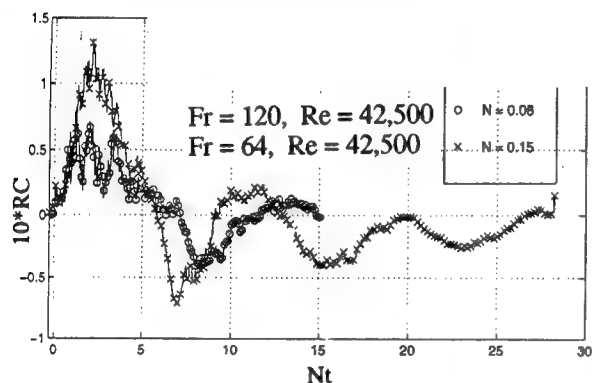


Fig. 11 Comparison of the RC values for non-impulsive starts for two N values ($U = 0.6$ m/s)

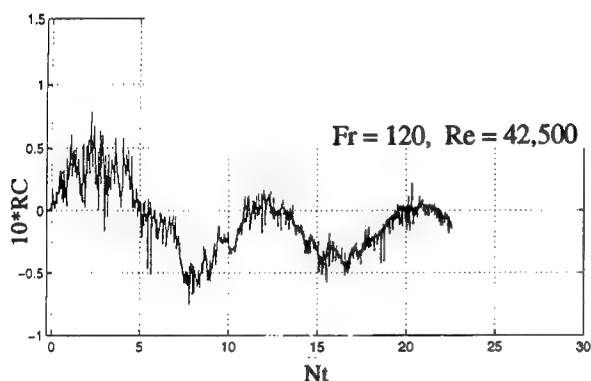


Fig. 12 RC for a non-impulsively-started model with sail and sail planes ($N = 0.08$ rad/s, $U = 0.6$ m/s)

Figure 12 shows a sample output of a probe for a non-impulsively-started model with sail and sail planes. Aside from its noisy character, the signal cannot be directly compared with the non-impulsively-started clean-body case because the probe had to be placed at a suitable point ($r/R_0 = 1.1$, $\theta = 60$ deg. to avoid the sail planes. Nevertheless, the collapse and

recovery times and the fundamental period of oscillations are essentially the same as the smooth-body case. Figure 13 shows the output of three different runs for $N = 0.08$. It seems that the increase of velocity from 0.6 m/s to 0.92 m/s does not materially affect either the form or the magnitude of the relative conductivity. The noisy nature of the signals is obviously due to the trailing and necklace vortices emanating from the sail planes and the sail/body juncture.

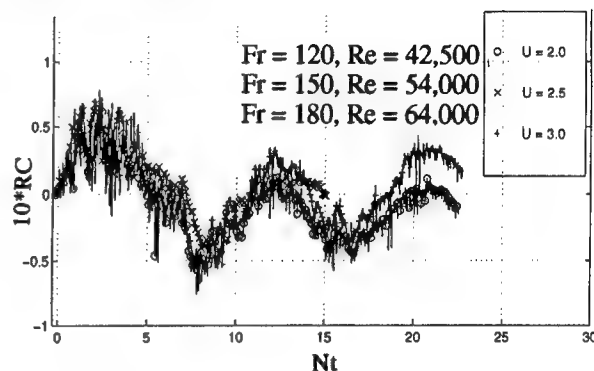


Fig. 13 RC values for a non-impulsively-started model with sail and sail planes at three different velocities ($N = 0.08$ rad/s)

Upstream Effect

The "blocking" phenomenon or the "upstream effect" is quite well known for two-dimensional bodies and has been studied extensively (see, e.g., Lin and Pao [5]). Whenever the buoyant force is not sufficient to overcome the inertial force, the fluid particles are trapped in the upstream side of the body and this gives rise to an upstream wake. For an axisymmetric body, however, the question is far more complex since the fluid is free to move around the body in all directions rather than being forced to move only from the top and bottom, as in the case of a cylinder moving parallel to its axis between two walls. Nevertheless, the question is not whether there are upstream effects for axisymmetric bodies, but rather how does some measure of the magnitude of this effect vary with distance upstream from the body and whether this magnitude is of potential technological importance. The fact that there is an upstream effect for all bodies in all fluids, stratified or unstratified, is clear from the fact that a body generated by a suitable combination of hydrodynamic singularities (sources, sinks, doublets) and uniform flow gives rise to upstream effects, albeit small, at relatively short distances. Thus, a more appropriate question is whether there are stratification-excited mechanisms (solitons, non-linear waves) which lead to significantly larger signals at significantly larger distances, i.e., to larger signal-amplitude to

upstream-distance ratio above the threshold noise level. One may consider linear internal waves as a possible cause of upstream effect but quickly realize that they travel at speeds slower than the prototype. According to Miles [12], internal waves generated by a horizontally moving source appear only in the lee of the source. However, unsteady motions, including impulsive starts and stops, can give rise to unsteady internal waves which propagate upstream of the generating body. Graham [13] investigated theoretically transient internal waves produced by a moving body in a stratified fluid and presented examples showing how well or how poorly the quasi-steady state is defined relative to the magnitude of fluctuations. Graham did not, however, consider the effect of a collapsing wake.

Rehm and Radt [14] calculated the internal-wave system excited by a translating and periodically heaving body in a constant Brunt-Väisälä frequency fluid. They have shown that the surfaces of constant phase change character as the ratio ω/N varies through unity. Along preferred directions, the amplitude of the internal waves decay inversely with distance to the 5/6 power, whereas, for uniform translation, the amplitude of the internal waves falls off inversely with distance from the body. The conditions corresponding to $\omega/N = 1$ are not of prototypical importance for the stratification range ($N = 0.005$ rad/s to $N = 0.02$ rad/s) in the ocean environment, even if the stratification was horizontally coherent. However, this does not imply that other types of unsteady motions such as practical maneuvers, including sudden starts and stops, are not capable of giving rise to measurable conductivity changes far upstream of a submarine-like body.

It is against this background and much unsubstantiated speculation that a series of sudden-start-stop experiments were undertaken with the clear understanding that the demonstration of an upstream effect under laboratory conditions does not necessarily imply that it will be equally observable in the ocean environment. It is quite probable that the highest speed of nonlinear internal waves or solitons, though exceeding the model speed, may fall far short of the prototype speeds even under ideal conditions.

Figure 14 shows the initial instants of the variation of conductivity at a sample probe due to a slowly- or non-impulsively-started model ($N = 0.15$ rad/s, $U = 0.46$ m/s). Noting that the time for each probe is measured from the time the stagnation point of the model arrives at the particular probe, it is clear that there is no notable upstream effect. Figure 15 shows similar data for three different velocities. Again, the presence of the model is felt only when the model arrives at the probe, not before.

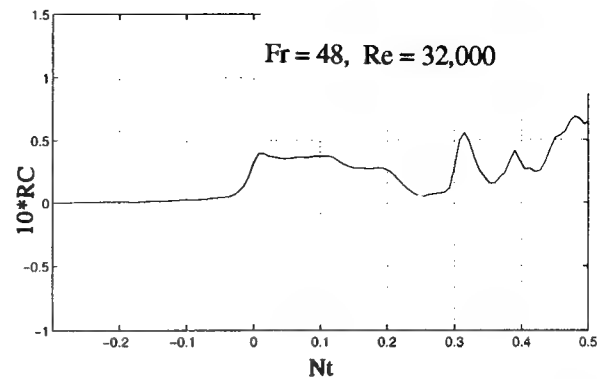


Fig. 14 RC versus Nt during the initial stages of a non-impulsively-started motion ($N = 0.15$ rad/s, $U = 0.46$ m/s)

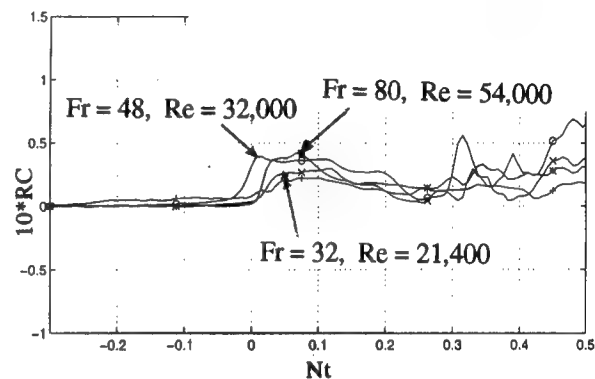


Fig. 15 Same as Fig. 14 for three different velocities

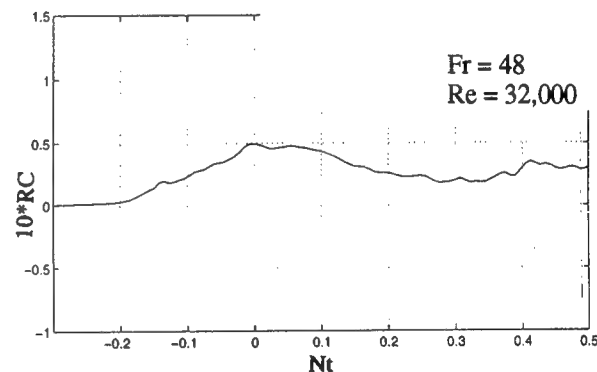


Fig. 16 RC versus Nt during the initial stages of an impulsively-started motion ($N = 0.15$ rad/s, $U = 0.46$ m/s)

Figure 16, obtained with an impulsively-started model ($N = 0.15$ rad/s, $U = 0.46$ m/s) shows that the probe anticipates the arrival of the model by about $\Delta Nt = 0.2$ (or by about 1.35 s or 1.35 body lengths). However, the larger the speed the shorter is the time of anticipation. For example, for $U = 0.76$

m/s, ΔNt from the start of the model to its arrival at the probe was reduced to 0.05. For $U = 0.90$ m/s, there was no noticeable upstream effect. Apparently, the nonlinear waves generated by the model are traveling at speeds larger than 0.46 m/s but not much larger than about 0.90 m/s. Figure 17 shows a comparison of the impulsively and non-impulsively started runs. It must be emphasized that experiments with impulsive starts have been repeated a number of times at different initial accelerations with different mechanisms and with or without a small uniform current in order to ascertain that the observed upstream effect was not due to some anomalous phenomenon. The addition of sail planes did not materially affect the results. The individual probe data differed very little from the ensemble averaged data and the upstream effect decreased at higher speeds. These are clear indications of the fact that the observed upstream effect is a genuine hydrodynamic phenomenon, at least, in model tests. As noted earlier, however, its prototypical significance remains unclear and should be the subject of a number of judiciously conducted large scale experiments.

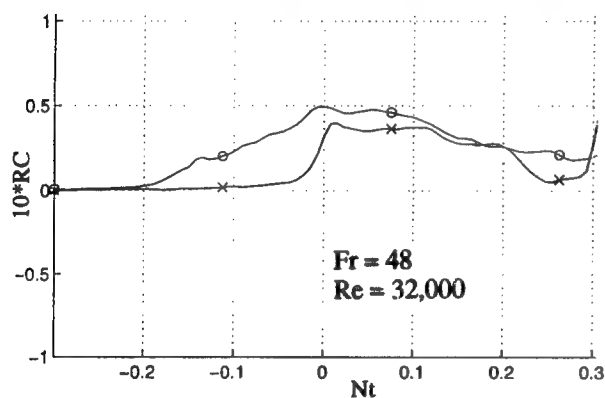


Fig. 17 Comparison of the upstream effects of impulsively (o) and non-impulsively (x) started models ($N = 0.15$ rad/s, $U = 0.46$ m/s)

CONCLUSIONS

Variations of the relative conductivity in the wake of self-propelled, single-screw, submarine-shaped bodies in a linearly stratified fluid were measured. The model Froude number ranged from about 50 to 200 and the Reynolds number, from about 3×10^4 to 6×10^4 .

The results have shown that the wake collapse (at a distance of about 400 diameters downstream) gives rise to large conductivity changes and to many modes of short internal waves [15]. The relative conductivity is sufficiently large to cause measurable changes in the geomagnetic field. The

conductivity field ahead of the body anticipates the arrival of the body for relatively short distances and then only for impulsively-started or impulsively-stopped motions at relatively moderate speeds.

As in the case of many other studies in stratified fluids, the range of the governing parameters is dictated not by technological needs but by what is achievable under the laboratory conditions. Even though the Froude numbers encountered in this investigation are the largest we have ever seen, and certainly closest to the prototypical conditions, the scale effects (due to widely different model and prototype Reynolds numbers) cannot be assessed and must be evaluated through prototype tests. As noted earlier, trip wires were used to render the boundary layer turbulent and, furthermore, the size of the propeller was scaled with respect to the size of the wake, and not the size of the body, by scaling wake diameter on the basis of Reynolds number. The validity of such common practices in laboratory experiments needs to be assessed through sea tests, particularly when the Reynolds numbers of the model and prototype differ by several orders of magnitude.

ACKNOWLEDGMENTS

Support for this investigation was provided by Naval Research Program Office. The authors would like to thank Mr. Thomas H. McCord and Mr. Charles E. Crow for their assistance with the construction and smooth operation of the test facilities.

REFERENCES

1. Schetz, J. A., and Jakubowski, A. K., "Experimental Studies of the Turbulent Wake behind Self-Propelled Slender Bodies," *American Institute of Aeronautics and Astronautics Journal*, Vol. 13, 1975, pp. 1568-1575.
2. Schlichting, H., *Boundary-Layer Theory*, 7th ed., McGraw-Hill, New York, 1987, pp. 729-755.
3. Stockhausen, P. J., Clark, C. B., and Kennedy, J. F., "Three-Dimensional Momentumless Wakes in Density Stratified Fluids," Massachusetts Institute of Technology Hydrodynamics Laboratory Report Number 93, 1966, Massachusetts Institute of Technology, Cambridge, Mass.
4. Torobin, L. B., and Gauvin, W. H., "Fundamental Aspects of Solids-Gas Flow. Part 1: Introductory Concepts and Idealized Sphere Motion in

Viscous Regime," Canadian Journal of Chemical Engineering, Vol. 37, 1959, pp. 224-236.

5. Lin, J. T., and Pau, Y. H., "Wakes in Stratified Fluids," Annual Review of Fluid Mechanics, Vol. 11, 1979, pp. 317-338.

6. Fernando, J. S. H., "Turbulent Mixing in Stratified Fluids," Annual Reviews of Fluid Mechanics, Vol. 23, 1991, pp. 455-491.

7. Lin, Q., Lindberg, W. R., Boyer, D. L., and Fernando, H. J. S., "Stratified Flow Past a Sphere," Journal of Fluid Mechanics, Vol. 240, 1992, pp. 315-354.

8. Xu, Y., Fernando, H. J. S., and Boyer, D. L., "Turbulent Wakes of Stratified Flow Past a Cylinder," Physics of Fluids, Vol. 7(9), 1995, pp. 2243-2255.

9. Head, M. J., "The Use of Miniature Four-Electrode Conductivity Probes for High Resolution Measurement of Turbulent Density or Temperature Variations in Salt-Stratified Water Flows," Ph. D. Thesis, University of California, San Diego, CA, 1983.

DISCUSSION

H.J.S. Fernando
Arizona State University, USA

This is an interesting study dealing with conductivity fluctuations in a stratified media generated by traveling disturbances. The aim is to study whether internal waves and turbulence generated by underwater vehicles, such as submarines, can be detected by using Magnetic Anomaly Detection (MAD) devices that sense changes in background magnetic induction. Using models of attack submarines, both with and without sail planes, it is shown that the variation of average RC can be as high as 12%. Also, it is argued that the upstream influence can be pronounced for impulsively started and stopped bodies at moderate speeds, but the upstream influence is notably absent for non-impulsively started bodies indicating the possible role played by "unsteady" external parameters such as $D(dV/dt)_0 / U_0^2$, in addition to conventionally used RE and Fr.

10. Sarpkaya, T., "Trailing Vortices in Homogeneous and Density Stratified Media," Journal of Fluid Mechanics, Vol. 136, 1983, pp. 85-109.

11. Sarpkaya, T., and Daly, J. J., "Effect of Ambient Turbulence on Trailing Vortices," Journal of Aircraft, Vol. 24, No. 6, 1987, pp. 399-404.

12. Miles, J. W., "Internal Waves Generated by a Horizontally Moving Source," Geophysical Fluid Dynamics, Vol. 2, 1971, pp. 63-87.

13. Graham, E. W., "Transient Internal Waves Produced by a Moving Body in a Tank of Density-Stratified Fluid," Journal of Fluid Mechanics, Vol. 61, 1973, pp. 465-480.

14. Rehm, R. G., and Radt, H. S., "Internal Waves Generated by a Translating Oscillating Body," Journal of Fluid Mechanics, Vol. 68, 1975, pp. 235-258.

15. Gilreath, H. E., and Brandt, A., "Experiments on the Generation of Internal Waves in a Stratified Fluid," American Institute of Aeronautics and Astronautics Journal, Vol. 23, No. 5, 1985, pp. 693-700.

Inspection of conductivity records presented indicate that large amplitude variations of RC can be attributed to the isopycnal displacements around the body, rather than to wake signatures as proposed. In the far field, however, the conductivity variations are due to the wake, but the signal at this stage is in a decaying state and is weak. Above a certain height of the body, known as the level of the dividing streamline, the flow passes over rather than flowing around the body, and, at large Fr, the dividing streamline height becomes independent of FR (Lin et al. [7]). If the conductivity changes are due to a kindred isopycnal displacements, it is possible to expect the maximum conductivity change to be $\Delta C \propto N^2 D$, which is corroborated by the observation that RC is independent of U (Figure 7). This scaling may provide a better normalization for RC, and the authors may want to check whether $RC/N^2 D$ performs better in their plots. The above estimates, however, were made by assuming that the body-generated disturbances are dominant over the propeller-generated disturbances, and scrutiny of this assumption is also in order.

Another question is whether the observed increase of conductivity before the arrival of the body is really due to the upstream influence or due to the finite amplitude perturbations of isopycnals in a limited area around the body. In a classical sense, the upstream influence is defined as the initiation of upstream motions due to the pushing forward of a slug of fluid ahead of the body at the neutrally buoyant level of the slug. At slow obstacle speeds and large stratifications, the fluid particles do not have enough kinetic energy to rise and flow over/under the body, and as a result a column of fluid upstream will be pushed ahead. This influence is markedly weak for three-dimensional bodies, as the fluid particles can shunt around (rather than over) the body. Because the upstream influence is pronounced only at small FR and only for two-dimensional bodies, it is appropriate to re-evaluate the authors' claim of upstream influence in large Fr experiments. Another important aspect that warrants attention is the generation of upstream-propagating shear waves (or zero-frequency internal waves) and their reflection from the end walls. These waves can also influence conductivity variations (Manins[16]).

It seems appropriate to define the term "collapse of the wake." The wakes can have two types of collapse, physical and turbulent. In addition, the wakes can oscillate thus leading to sharp conductivity changes behind the body. The authors state that the wakes collapse at $Nt \sim 7$, which is coincident with the lowest point of RC. This minimum, however, can also be interpreted as a consequence of the dipping of isopycnals behind the body.

Most of the plots presented by the authors are ensemble averaged over several runs, concurrent with the standard practice of analyzing random signals. For practical purposes, however, it is also instructive to devise methods to recognize signals using single realizations. After all, in submarine detection, one has to work with a single record rather than an ensemble average! To this end, it would be worthwhile to define the variable $(\Delta C)_{\max}/n^2D$, where $(\Delta C)_{\max}$ is the maximum conductivity of a given realization, and investigate how it varies among identical runs and how its r.m.s. value varies with external governing parameters.

ADDITIONAL REFERENCE

16. Manins, P.C. "Intrusion into a Stratified Fluid," *J. Fluid Mech.*, Vol. 74, 1976, pp. 547-560.

AUTHORS' REPLY

The discussor has attempted to interpret our results in light of his experiments with right circular cylinders and spheres dragged in a linearly-stratified fluid at Reynolds and Froude numbers of little or no practical significance. There are fundamental differences in the wakes of towed and self-propelled bodies as clearly noted in the paper. The topology of the wakes of towed bodies of special geometries used by the discussor does not generalize to slender self-propelled body shapes. Our experiments with slender self-propelled bodies at realistic Froude numbers are the first ever reported in the literature.

As far as the effect of isopycnal displacements are concerned, the model completes its passage under a probe in about 0.13 seconds or $Nt = 0.02$ for $N = 0.15$ during which the largest isopycnal displacements occur. This, however, is a very small fraction of the time that the probes respond to the changes in the wake created by the body and the propeller. Our experiments have confirmed from plunging conductivity probes at $Nt = 0.1$ ($x/D = 5$), $Nt = 0.2$ ($x/D = 10$), $Nt = 0.4$ ($x/D = 20$), and $Nt = 1$ ($x/D = 50$) through the use of Thorpe reordering that the wake was well mixed, i.e., the propeller has provided excellent molecular mixing. The fact that the passage of a slender self-propelled body causes large conductivity changes in an otherwise undisturbed region of a stratified medium and that these changes have a decaying harmonic character is all that is needed for the understanding and interpretation of the corresponding geomagnetic anomalies. This has not been demonstrated before. As to the normalization of the relative conductivity RC by N^2D , as suggested by the discussor, it is easy to see that RC/N^2D does not provide a better correlation because for a constant D (as in our experiments), RC does not vary with N^2 as evidenced from Fig. 6 for two different N values. If the discussor's suggestion were to be adopted, the two conductivity traces in Fig. 6 would have yielded amplitudes differing by a magnitude of 3.5, i.e., according to Fig. 6, RC is independent of N for a given Re. Contrary to the discussor's assumption, Fig. 7 shows that RC varies with U (even in the small range of U values) with U for a given N . These two facts show that the conductivity changes are not primarily due to "kindred isopycnal displacements" and that the propeller-generated

disturbances are dominant (as in model as well as prototype scales) over the body-generated disturbances.

The definition of the upstream effect does not need repetition. It is a well-known fact that there are stratification-excited mechanisms (solitons, nonlinear waves), which lead to significantly larger signal-amplitude to up-stream-distance ratios above the threshold noise level. The end-wall reflections have nothing to do with the issue because the upstream effect under unsteady circumstances (impulsive starts, turns, dives, porpoising, etc.) manifests itself almost immediately after the passage of the bow and certainly long before the waves reach the end wall and return to the probe.

The discussor has incorrectly stated that the wakes collapse at $Nt = 7$. What we have written is this, "As the model continues to move, RC decreases at first (when the probe is over the axisymmetric cylindrical part of the body) and then increases again sharply when the probe enters the wake and reaches a maximum at about $Nt = 2$ ($\Delta Nt = 1$ corresponds to $\Delta t = 6.67s$ or to about 50 body diameter for this particular case)." Immediately afterwards, the wake begins to collapse. The wake collapse is virtually complete at about $Nt = 7$, i.e., after about 47s or about 340 body diameters."

As to the nature of the plots, the discussor did not read the paper carefully. They are not "ensemble averaged over several runs. . . ." The plots are ensemble averages of the data obtained simultaneously *during a single run* with numerous probes positioned along the axis of the body. No two runs have ever been ensemble averaged. Our data have shown that the ensemble-average of n-number of probe signals resulting from a single run is indistinguishable from the individual probe data for that same run. As noted earlier $(\Delta C)_{\max}/N^2D$ is not a meaningful parameter.

In summary, it appears that the discussor read the paper rather hastily. The topology of the wakes of towed bodies of such special geometries as right circular cylinders and spheres does not generalize to slender self-propelled bodies and to more general problems of the evolution of isolated turbulent patches in stratified fluids. Our work presents, for the first time, body geometries and measurements on both fundamental and applied levels. It is hoped that future studies in stratified flows will move toward high Re and F experiments with slender self-propelled bodies. After all,

spheres and right circular cylinders do not make good submarines at any speed.

The comments of the discussor gave us the opportunity to expand on several topics of scientific and practical interest and are appreciated.

Macro Wake Measurements for a Range of Ships

M. Hoekstra, A. Aalbers (Marine Research Institute, The Netherlands)

Abstract

An extensive experimental investigation has been carried out to measure the global structure of the wake, including possibly-related free surface elevations, of various ship models. While wake measurements on ships are usually restricted to the propeller disc region, here the wake structure was recorded in several transverse planes, and in each plane over an area of several propeller diameters wide and extending well below the keel plane of the ship. Moreover, several longitudinal and transverse wave cuts were made. No less than 8 ship models were involved in the project, and some of them in more than one operational condition. The measurements comprised:

- the three components of the velocity vector
- the six components of the Reynolds stress tensor
- longitudinal and transverse wave profiles

The measurement equipment, a three-component LDV system and two types of wave probes, is described. An error analysis is included to provide an estimate of the accuracy of the data.

The huge amount of data gathered does not permit a complete presentation of all results. Instead, the paper will address the most relevant and most unexpected results. Emphasis is placed on the differences in the wake structure between propelled and towed hulls, on the remarkable effect of the rudder, and on the influence of the trim/loading condition, the beam-draft ratio and the bulb.

The data sets are available as validation material for computational methods.

1. Introduction

Synthetic Aperture Radar (SAR) has successfully been operating from a NASA scientific satellite called SEASAT to record images of ships and their wakes. When environmental conditions were not disturbing, most of these images revealed fairly consistent wake features as well as some indicators as to the potential military or commercial use of the images for detection and recognition of ships. Naturally questions arose about the interpretation of the images and whether the wake scar left by a passing ship could be minimised under a given set of environmental conditions. It turned out soon that these questions are more easily posed than answered. Information on how the wake of a ship - or more precisely the manifestation of the wake at the free surface - is affected by operational and hull geometric aspects is scarce, scattered and incomplete. Since factors in hydrodynamic ship design that could influence the wake might also lead to reduced fuel consumption or power required, the exploration of the structure of ship wakes has a wider relevance than just radar image interpretation, and might well yield benefits in other areas than remote sensing.

The above was the incentive to start an extensive model-scale experimental investigation on ship wakes, carried out in the period from 1987 to 1990 at the Maritime Research Institute Netherlands on behalf of the United States Navy. The investigation was the second part of the project on 'Advanced Fluid Dynamic Experimentation and Analysis for Signature Reduction' (AFDEASR). The primary goal of the investigation was to set up a data base

TABLE I
Overview of Data Sets

Data set no.	Cb	L/B	B/Ta	Prop.	Bulb	Loading	Speed m/s
Tankers							
11	0.84	6.4	2.5	single	yes	full	1.3
12	0.79	6.4	4.7	single	yes	ballast	1.3
21	0.78	5.7	4.2	single	yes	full	1.3
22	0.76	5.7	5.1	single	yes	ballast	1.3
31	0.82	5.0	4.0	twin, inw.	yes	full	1.3
32	0.82	5.0	4.0	twin, outw.	yes	full	1.3
34	0.75	5.0	5.8	twin, outw.	yes	ballast	1.3
Containerships							
41	0.69	7.1	2.8	single	yes	full	2.0
51	0.61	6.1	3.6	single	yes	full	2.0
61	0.62	5.4	3.7	twin, inw.	yes	trimmed	2.0
62	0.62	5.4	3.7	twin, outw.	yes	trimmed	2.0
64	0.62	5.4	3.7	twin, outw.	no	trimmed	2.0
Frigates *)							
71	0.50	8.0	4.0	twin, inw.	no	full	2.0
81	0.44	7.3	3.2	single	no	full	2.0

*) A third frigate data set was obtained at DTRC in the U.S.A. [2]

of 'macro wake' measurements for a wide range of ships, wide enough to cover a large part of the world's ship population.

With the term 'macro wake' we follow the terminology of [1] and it is used here with the intention to convey two things: i) that the measurements have not been restricted to the propeller disc area, as is the common practice in ship model testing, and ii) that the emphasis is on the detection of large scale features in the wake.

This paper starts with an overview of the scope of the investigation, i.e. the main characteristics of the ship models used, the kind and the extent of the measurements, etc. The description of the measuring devices and an error analysis follows in section 3. Subsequently, a summary is given of the main findings, extracted from a careful examination of the collected experimental data, in section 4. Closing remarks in section 5 complete the paper.

2. Scope of investigation

Wake data were acquired for 8 ship models: 3

tankers, 3 container or auxiliary vessels and 2 frigates (complementary data for a third frigate were collected at DTRC [2]). The bodyplans of the hulls are shown in Fig. 1. Each data set has an identification number of two digits of which the first refers to the hull geometry and the second to an operating condition. A change of operating condition is either a draft variation or a reversal of the direction of rotation of the propellers; in one case however a local bow form change is involved. Table I gives a summary. It is noted that each data set includes results with and without operating propeller(s). Moreover, additional measurements were carried out under data set 21 for the propelled hull in absence of the rudder.

The measurements comprised:

- the three components of the velocity vector;
- the six components of the Reynolds stress tensor;
- longitudinal and transverse wave profiles.

The velocity and Reynolds stress measurements were made in several transverse planes. An overview of the number of planes and their position for each data set is given in Appendix I.

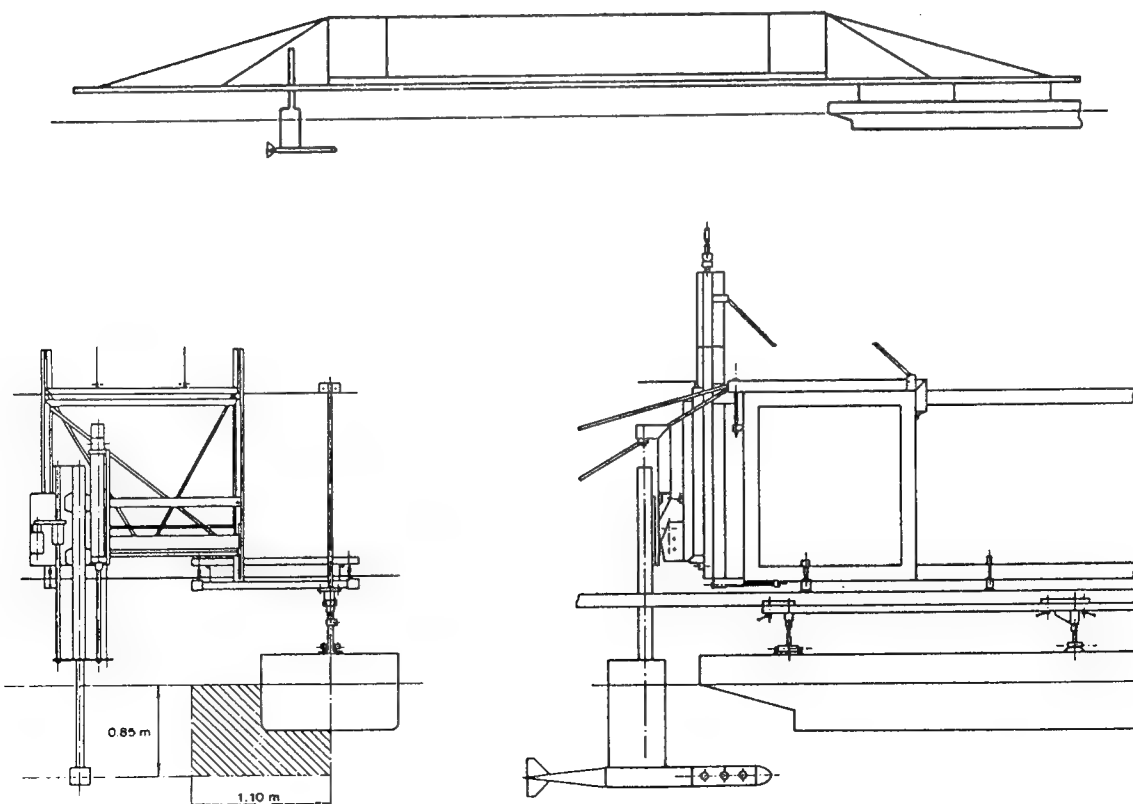
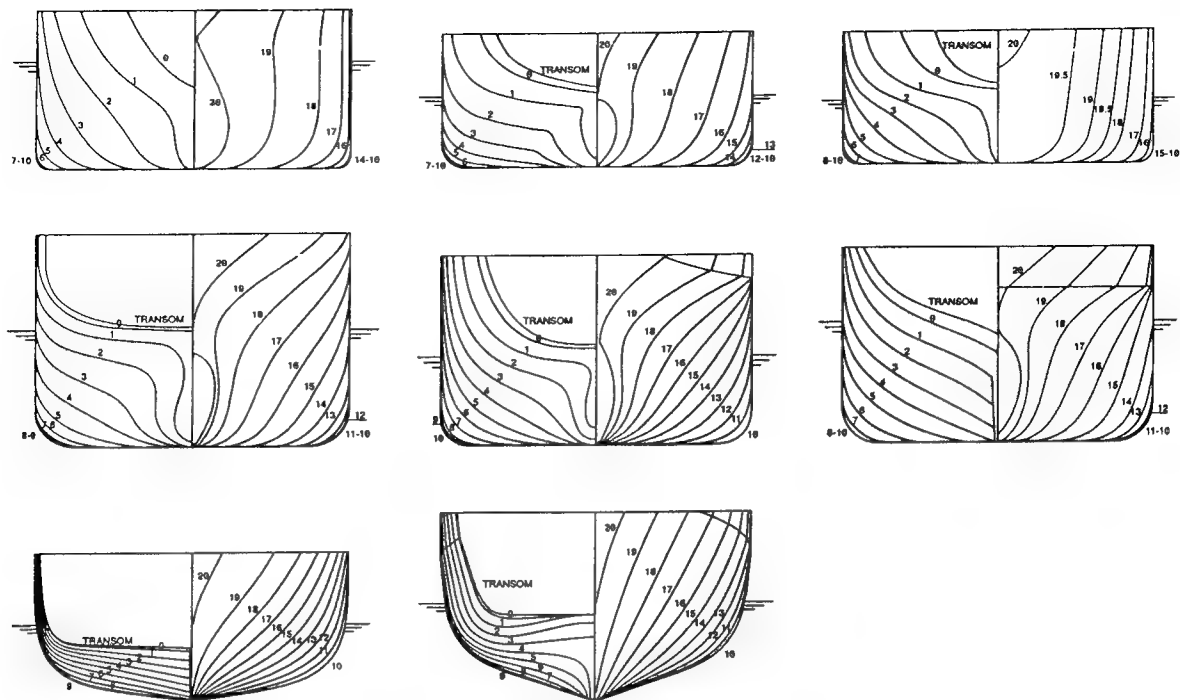


Fig. 2. Test setup for flow speed measurement

3. Measurement equipment

The measurement equipment comprised the following elements:

- A DANTEC three-component LDV system for the mean velocity, turbulence intensity and the Reynolds stresses;
- A laser-based wave profile measuring device for longitudinal wave cuts and wave slope/direction;
- A needle type wave probe for the measurement of free surface elevation on transverse wave cuts.

In addition, standard electronic equipment was used for the measurement of tow speed, ship model position and coordinates of traversing systems for the optical head of the LDV and the needle wave probe.

3.1. Setup

Because measurements had to be made as far as two ship lengths behind the stern, a 25 m longitudinal girder was rigidly fixed to the towing carriage. The LDV equipment was installed at the rear end of the carriage, while the ship model was connected to the girder at various positions to obtain the required distances. Fig. 2 gives an impression of the test setup.

The laser-Doppler velocimeter used is a two-colour backscatter system for the simultaneous measurement of the three velocity components [3]. The laser light source is a 4 Watt argon laser, mounted on the towing carriage. The laser light is transmitted via a mono-mode fiber to the optical head, the assembly of all optical components in a waterproof housing. In the optical head the laser light is split into two blue beams ($\lambda=488.0$ nm) and three green beams ($\lambda=514.5$ nm). These five beams are directed so as to intersect at a common point in the flow, the measurement location, which is at a distance of 815 mm from the optical head. The probe volume measures $1.3 \times 0.4 \times 0.4$ mm. The scattered light is received by the optical head and fed into three burst spectrum analysers (BSA's), which derive the three velocity components [4]. The location of the probe volume is fixed with respect to the optical head. Its location with respect to the ship model is adjusted by traversing the optical head. The traversing system has two degrees of freedom with a reach of 1.15 m in one direction and 0.85 in the other.

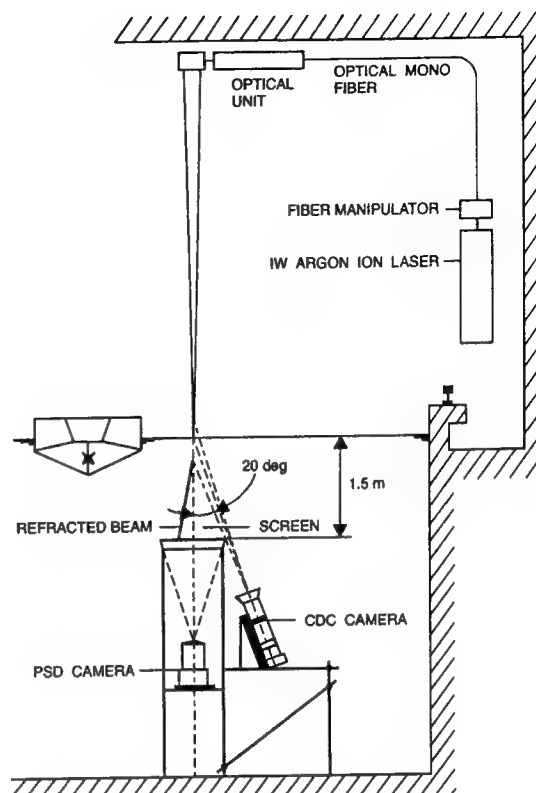


Fig. 3. Test setup for longitudinal wave cuts

The wave profile measurement system, using a 1 Watt argon laser, was mounted at a fixed position in the basin and data recording took place while the model passed by. The setup in the basin is shown in Fig. 3. The system uses two types of position-sensitive camera's to measure wave elevation and wave direction and slope respectively.

The needle wave probe measurement system was mounted on a traversing system with servo motors for moving the two sub-carriages in x and y direction respectively. The traversing system was mounted on the towing carriage.

The measurement grid for the needle probe partly overlapped the longitudinal wave laser cuts, allowing a comparison as shown in Fig. 4. It illustrates that the consistency of the wave profile measurements is quite good.

3.2. Accuracy

An elaborate accuracy evaluation was carried out. The results are summarised in the following subsections.

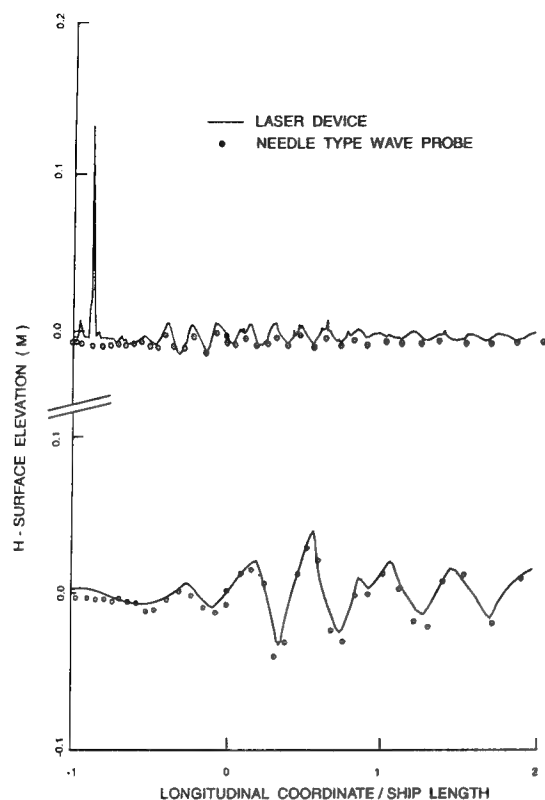


Fig. 4. Comparison of wave height recordings by two different methods

3.2.1. LDV measurements of macro wake

The accuracy evaluation concerns two aspects: the LDV measurement of flow speed and the position in the grid with respect to the ship. Typical values for the speed are:

LDV flow velocity: 0.002m/s
Carriage speed: 0.45%

When the LDV measurements are non-dimensionalised with tow speed, the inaccuracy of the carriage speed is introduced. This applies to the longitudinal velocity component only.

For the grid point location with respect to the ship also two aspects can be distinguished: the location of the grid plane with respect to the ship's aft perpendicular and the location of the grid points in the plane. Typical values are:

x-coordinate of grid plane: 0.0035 m
y- & z-coord. of grid plane: 0.028 m
y- & z-coord. of grid point: 0.0025 m

Note that the accuracy of the y and z-coordinate of the grid plane is with respect to the ship centre line and specified draft. The larger error is caused by

the 0.1 degree uncertainty in the alignment of the longitudinal girder to which the model was connected. The reference was at the grid plane just aft of the aft perpendicular, so that for that plane the y and z-coordinate accuracy is as good as 0.0035 m.

The data rate of the LDV was not always fully under control. Sometimes it was good enough to allow the recording of turbulence frequencies up to about 100 Hz, but at other instances it dropped substantially with a consequent reduction of the accuracy of the Reynolds stresses.

3.2.2. Wave profile measurements

The needle type wave probe scans can be analysed as to the wave elevation error and the error in the reference of the traversing system. The following values apply:

Wave elevation: 0.0018 m
Vertical reference: 0.003 m
x-coord. of plane: 0.0035 m
y-coord. of plane: 0.028 m

The value for the vertical reference can be related to the bias in the comparison of the two wave scanning systems in Fig. 4. The errors in the x and y coordinates are similar to those for the LDV grid planes since the same model tow arrangement was used.

For the laser type wave cuts the following accuracy limits apply:

Wave elevation: 0.0015 m
Wave slope: 3% in amplitude
0.1 degr. bias
x-coordinate: 0.01 m
y-coordinate: 0.004 m

3.2.3. LDV near-free-surface measurements

The LDV equipment was also used to measure the flow as close as possible to the free surface. The velocities measured follow the accuracy analysis of the normal LDV signals given in 3.2.1, but for the vertical position the local position of the free surface was used as a reference. The LDV laser beams were used to determine the location of the water surface, whereupon the grid point was defined as 0.002 m below the water surface.

The vertical position accuracy was 0.00025 m if the water surface was smooth. For the near-surface

points right behind the ship the water surface was turbulent and the positioning accuracy dropped to some 0.001 m

3.3. Conclusion

The accuracy of the LDV measurements was sufficient to have the flow patterns in the far field reliably measured. The accuracy margins are defined as "standard deviations with respect to the truth in the model basin". Hence, possible scale effects are ignored. With respect to the inaccuracy in the model reference position of the grid planes and wave cuts, our evaluation of the results suggests that the achieved accuracy for the bulk of the measurements is better than the theoretical values, because for the evaluation conservative values were applied.

4. Presentation and discussion of results

Limits on the size of this paper do not permit a presentation of all the data collected in the AFDEASR project. Instead, the most relevant and most unexpected results will be discussed. Emphasis is placed on the differences in the wake structure between propelled and towed hulls, on the effect of the rudder, and on the influence of the trim/loading condition, the beam-draft ratio and the bulb. The description is phenomenological, here and there illustrated with specific examples. For details the data base should be consulted, which is available for that purpose as well as for validation of computational methods. Requests for data release should be directed to DTRC.

In the presentation of the data a right hand coordinate system x, y, z is used with the origin at the intersection of the aftperpendicular and the undisturbed free surface. The x -coordinate is positive in the direction from bow to stern; y is positive to starboard and z in upward direction.

4.1. Mean flow and vortex systems

4.1.1. Wake of unpropelled hulls

We start with a brief account of the structure of the nominal wakes, i.e. the wakes behind the unpropelled hulls, without rudder (on the twin-screw models skegs, shafts and brackets were present).

For most of the hulls the vector plots of the

transverse velocity components revealed patterns which indicate the presence of longitudinal vortices. That ship hulls can generate such vortices is well-known from ordinary wake measurements in the propeller plane. In general two pairs of counter-rotating vortices are observed; an example is given in Fig. 5. One pair, created close to the stern in the bilge region - and therefore often referred to as the 'bilge vortex' pair - usually passes through the propeller disc area. These vortices, one on either side of the symmetry plane, are close to each other and the path they follow on being carried downstream is visibly influenced by their mutual induction: they both tend to move slowly

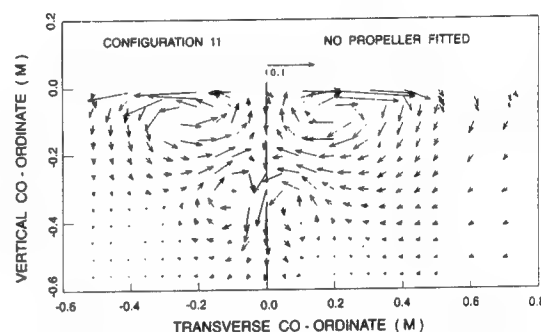


Fig. 5. Example of transverse flow at $x/L=0.240$

downward. The other pair, generated near the waterline and here for convenience called 'side vortex' pair, is often outside the influence region of the propulsion device. These vortices are far apart, whence they show little interaction. It should be noted however that with regard to vortex kinematics the free surface behaves almost as a free-slip symmetry plane. Therefore an imaginary vortex system above the free surface can be added to account for the effect of the free surface on the vortex motion. So each vortex has a nearby imaginary companion and, again by mutual induction, the core position of the side vortices tends to move away from the longitudinal symmetry plane of the ship with increasing distance to the stern.

Not all ships produce two clearly identifiable vortex pairs; a dependency on the stern shape is evident. With a (hypothetical) axisymmetric body shape no longitudinal vortices would be generated. It is the need to install a propeller with shafting and machinery and the need to increase the waterline length as much as possible to minimize wave formation which give ship hulls the typical shape that produces longitudinal vortices. Not only the

presence, but also the strength of a vortex - and hence its identifiability - depends on the hull lines. Sometimes only a single vortex pair is observed, either the bilge or the side vortex pair.

The pattern of the iso-lines of the mean longitudinal velocity in the nominal wake of a ship looks usually like an upside-down rimmed hat (see Fig. 6 for an example). One can observe a central lobe at or below the keel level and two side lobes close to the free surface. To some extent the pattern reflects the frame shape of the afterbody, but it is also clearly correlated with the structure of the transverse flow field: often the longitudinal velocity component exhibits a local minimum near the core of a longitudinal vortex.

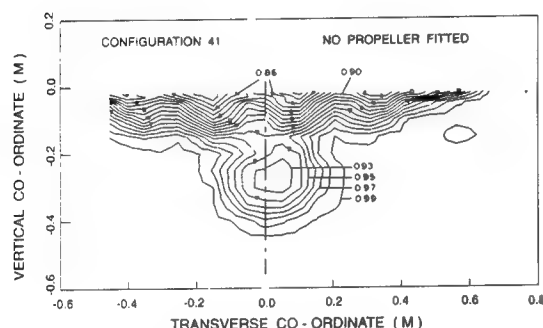


Fig. 6. Example contourplot of longitudinal velocity at $x/L=0.594$

The smallest axial velocity is usually found in the symmetry plane of the wake near the free surface. But there are exceptions. When strong side vortices are produced, the minima occur near their cores, again at or directly below the free surface.

Outside the main-wake region there may be small momentum-deficit areas near the free surface which are attributed to wave breaking.

4.1.2. Wake of propelled hulls

The wake of a ship with running propeller(s) is quite different from the wake of a towed hull (nominal wake). The differences are not only related to the diminished momentum deficit - because all wake measurements on propelled hulls were carried out under the condition of the so-called self-propulsion-point-of-ship a small deficit remains - but also to the interaction between the propeller-induced flow and the hull wake.

A propeller in a uniform onset flow tends to accelerate the flow ahead as well as in the jet behind, and to weakly decelerate the flow outside these regions. Moreover, the propeller jet aft of the propeller disc rotates in the same sense as the propeller itself. Ahead of the propeller and outside the jet there is no propeller-induced rotation.

For a qualitative analysis of the interaction of the propeller-induced flow and the nominal wake, let us first recall that vorticity, once generated, is carried with the flow and is spread by diffusion like heat, on the understanding that at a high Reynolds number the convection dominates the diffusion. Now imagine a stream tube, encompassing all the flow going through the propeller disc. Due to the acceleration of the flow by the propeller, this streamtube is contracting. When a hull-generated vortex happens to be inside the streamtube - which is usually the case for the bilge vortices - the vortex is subjected to this contraction as well; as a result, the vorticity is concentrated. This process is often referred to as vortex stretching.

The streamlines in the aforementioned stream tube start to swirl around the centreline of the propeller jet as soon as they have passed the propeller disc. This must hold for an embedded longitudinal vortex as well. In the case of a single-screw ship, both the port and the starboard bilge vortex are captured in the screw race and start swirling. Moreover, due to the strong mixing in the propeller jet, the bilge vortices soon lose their identity, i.e. they are not recognizable as vortices in a graphical representation of the transverse velocity field. Only the rotation in the propeller jet remains. A swirling vortex pair does not generate the downwash effect found in nominal wakes. But usually a rudder is fitted behind the propeller which causes that the downwash is maintained, albeit in an oblique direction, as we shall see later.

In the case of a twin-screw vessel each propeller jet will capture one bilge vortex, if present. Usually the bilge vortex and the propeller jet are nearly co-axial. If, in addition, they are co-rotating an accumulation effect will occur. On the other hand, for outward rotating propellers the jet rotation is opposite to the bilge vortex rotation; the amount of swirl found in the wake will therefore be smaller than for inward rotating propellers. Hence a better propulsive efficiency is to be expected under such circumstances for outward rotating propellers (a fact

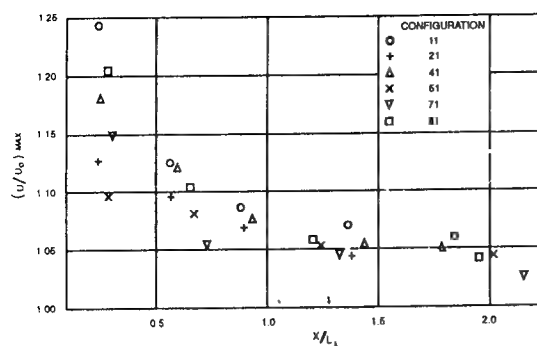


Fig. 7. Development of maximum flow speed in the propeller jet as a function of x/L

that has found ample corroboration in model tank propulsion tests).

The presence of a propulsion unit has a strong influence on the axial velocity distribution also. Of course the propeller jet appears as a dominant feature, but there are strong additional effects caused by the interaction between the propeller-induced flow and the longitudinal hull-vortices. It would be wrong to suppose that the wake of a propelled hull can be obtained by a simple superposition of the nominal wake and the propeller-induced flow.

Where in most towed-hull wakes the smallest axial velocity occurs in the symmetry plane, this is seldom the case in the propelled-hull wake; two minima away from the symmetry plane but at or near the free surface are commonly observed. The implication is a more-than-average acceleration of the flow in the symmetry plane near the free surface. While this flow is clearly outside the propeller jet which is at a much lower position, we suppose that this is accomplished primarily by the bilge vortices which are very effective in transporting momentum from the propeller jet or the outer flow to that location.

In ideal-flow propeller models (actuator disk, lifting line or lifting surface models) the axial velocity in the propeller jet is greater far downstream than at the location of the propeller. In the present experimental data, however, the maximum axial velocity decreases steadily, at least from a position $x/L_{pp}=0.25$ on (see Fig. 7). Apparently the viscous diffusion effects are so strong as to more than neutralize the acceleration effect. This may not be true, though, for the region between the propeller and $x/L_{pp} = 0.25$.

4.1.3. Effect of rudder

The presence of a rudder can have an appreciable influence on the structure of the macro wake. If a rudder is fitted directly behind the propeller so as to cut the propeller jet in two halves as it were, it effectively eliminates the jet rotation. It does not

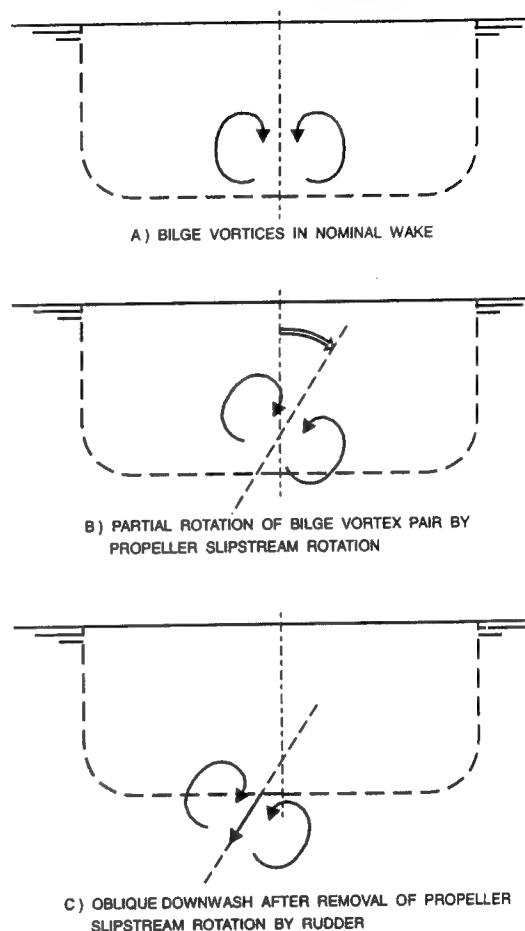


Fig. 8. Oblique downwash with rudder behind propeller

necessarily take all the axial vorticity out of the propeller jet but what remains is not identifiable as a single-vortex flow structure.

The bilge vortices can pass the rudder without encountering significant obstruction and are not much affected. The same holds of course for the propeller jet if the rudder is not placed in it, such as in the case of a twin-screw ship with a single central rudder.

The elimination of the propeller jet rotation by the rudder has important consequences for the behaviour of the bilge vortices of single-screw ships

(Fig. 8^A). Recall that these vortices, except for diffusion effects, follow the streamlines. Therefore, as soon as these vortices have passed the propeller disk, they start to swirl around the propeller axis: behind a right-hand propeller the starboard bilge vortex core moves downward, the port vortex core upward. Upon reaching the rudder, the swirling motion is interrupted and the bilge vortices maintain the orientation they have at that stage (Fig. 8^B). That orientation obviously depends on the non-dimensional advance ratio formed by the axial flow speed, divided by the rotation rate of the propeller and the distance between propeller and rudder.

The path followed by the bilge vortices after they have passed the rudder is again influenced by the self-induced downwash. The downwash is not in the vertical direction, however, but in an oblique direction perpendicular to the line connecting the two vortex cores (Fig. 8^C). In the far wake therefore we see a strong asymmetry: the jet of the propeller, flanked by the two hull vortices, is found on

port side (right-hand propeller; see Fig. 9 for an example) or on starboard (left-hand propeller). The downwash is stronger than in the nominal wake because the vortices have been stretched by propeller induction.

The enhancement of the vortex strength by stretching effects is also responsible for the acceleration of the flow in the central region near the free surface, to which has been alluded in section 4.2. As bilge vortices in a nominal wake are effective in reducing the wake peak in the top sector of the propeller disk, the stronger vortices in the propelled-hull wake have a proportional effect on the flow in the central region near the free surface.

4.2. Wave pattern

In the wave profile measurements several features of the well-known Kelvin pattern due to a point disturbance, with its characteristic combination of transverse and diverging wave crests, were confirmed. In the longitudinal wave cuts in the symmetry plane of the ship the fundamental wave length $\lambda = 2\pi V_s^2/g$ clearly appeared. Recording of this wave length is one of the means to determine the speed of a ship. The longitudinal wave cuts away from the symmetry plane revealed the change in the direction of propagation of the waves. For the initial part of the wave record consists of contributions of the diverging wave components, the end of the record of transverse waves.

In closer proximity of the hull the complexity of the wave system is greater but it is of minor importance for the macro wake as long as wave breaking does not occur. When a wave crest breaks - be it a wave generated at the bow, a shoulder or the stern - , wave energy is converted into turbulence kinetic energy, and a clearly identifiable trace is left behind in the wake. The associated peak value of the turbulence kinetic energy decreases with increasing distance to the hull. At the same time the location of the peak moves gradually away from the longitudinal symmetry plane. The turbulence activity is accompanied with a slight but noticeable reduction of the longitudinal velocity component.

The occurrence and the intensity of wave breaking depend not only on the hull shape but also on the speed of the vessel. Unlike many other aspects of the wake, the traces of wave breaking will therefore

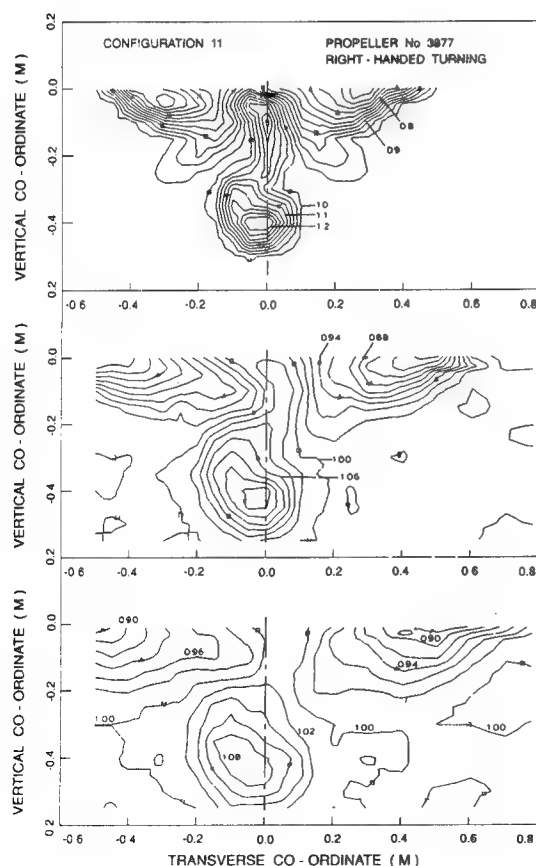


Fig. 9. Migration of propeller jet to port by oblique downwash (top: $x/L=0.24$; middle: $x/L=0.56$; bottom: $x/L=0.88$)

even after proper nondimensionalisation change with the Froude number. This makes it impossible to give typical values for the turbulence intensity as a result of wave breaking.

Some influence of the propeller on the wave profiles could be detected if the propeller is close to the free surface (e.g. tankers in ballast condition). Even then the effect is usually weak, however. Our measurements have confirmed that the propeller has no noticeable influence on wave breaking.

4.3. Near-free-surface flow

With a view to the possibilities of remote wake sensing, free surface phenomena are of greater interest than the flow behaviour at large depths. It is important, therefore, to consider which flow features are visible or detectable at the free surface. The formation of gravity waves, possibly breaking, as discussed in the previous section 4.2, is of course such a feature. But the sub-surface LDV measurements have intentionally been extended to very near the free surface to detect disturbances which might be connected with satellite-observable phenomena. This section is devoted to this "near-free-surface flow".

The near-free-surface velocities measured abreast of the ship models clearly revealed the orbital motion in the waves. If the advance speed of the ship model was subtracted, the velocity vectors in a wave crest and a wave trough respectively were pointing in opposite direction.

Although not in all cases flow information has been obtained on port as well as on starboard, the available data seem to indicate that the wake of unpropelled ships is practically symmetric in the near-free-surface flow. But once the propeller is operating, considerable asymmetries can occur, which is exemplified by Fig. 10, showing velocity vectors in an earth-fixed reference frame.

The occurrence of such asymmetries is directly related to the flow behaviour at greater depth. It has been outlined in section 4.1.3 how the combination of bilge vortices, propeller and rudder can produce strong asymmetry. The typical result for a right-hand single propeller is that the bilge vortex pair migrates to port, causing the apparent symmetry line for the near-free-surface flow to be displaced to starboard.

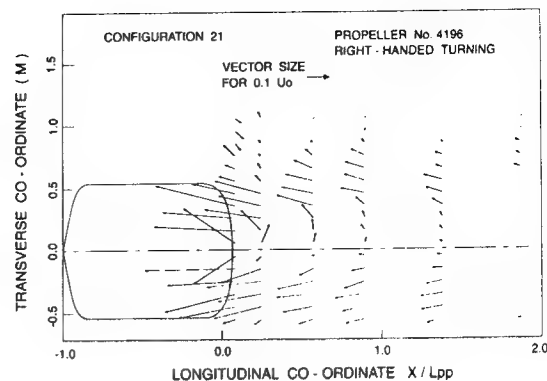


Fig. 10. Asymmetry in near-free-surface flow behind a propelled hull

Not all propeller-hull wakes are asymmetric near the free surface, however. For example in our data configuration 11 has the propeller so deeply submerged that the asymmetry does not extend to the free surface. Also twin-screw ships have a symmetric wake.

In section 4.1.2 it was pointed out that the distribution of the primary velocity component u in the wake of a propelled hull usually exhibits two minima, one on either side of the vertical symmetry plane. These minima are found very close to the air-water interface and are still identifiable at two ship lengths behind the stern. Fig. 11 shows that the local minimum velocity is there about 5 per cent below the undisturbed flow speed; or, in an earth-fixed reference frame, that there is a fluid motion in the advance direction of the ship with a speed of $0.05 V_s$ at $x/L_{pp} = 2.0$. The figure also shows the rate of change.

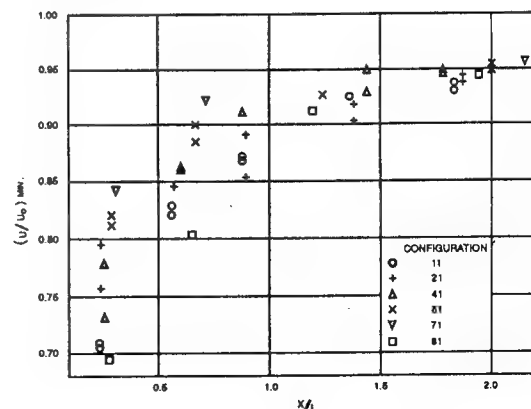


Fig. 11. Development of local minimum longitudinal velocity in propelled-hull wakes

4.4. Turbulence

The results of the Reynolds stress measurements reveal the shear-layer character of the flow. By the composition of the shear stresses $\overline{\rho u'v'}$ and $\overline{\rho u'w'}$, the resulting vectors appear to be roughly perpendicular to the iso-lines of the axial velocity field, to point in the direction of decreasing u , and to attain their greatest length in regions of high gradients in the u -field. These characteristics are typical for thin shear layers.

Turbulence activity near the free surface is important for wake signature because it shows up as "white water" behind ocean vessels. The turbulence kinetic energy is a good and convenient measure of turbulence activity. This scalar quantity typically exhibits peaks in the three lobes of the axial velocity field. A breaking bow wave may cause an additional pair of trails of high turbulence kinetic energy. Being isolated from the main wake region, these trails retain their identity well into the far wake.

The level of turbulence kinetic energy is remarkably insensitive to the type of ship. For the root-mean-square value of the velocity fluctuations as a fraction of the ship speed (which equals the square root of twice the turbulence kinetic energy) we find in the towed-hull wakes maxima of:

$$0.106 \pm 0.02 \text{ at } x/L_{pp} = 0.25$$

$$0.067 \pm 0.01 \text{ at } x/L_{pp} = 0.60$$

$$0.047 \pm 0.01 \text{ at } x/L_{pp} = 1.00$$

without a clear differentiation with respect to ship types: For the propelled-hull wakes a similar conclusion can be drawn. The decay of the maximum value of the turbulence kinetic energy in

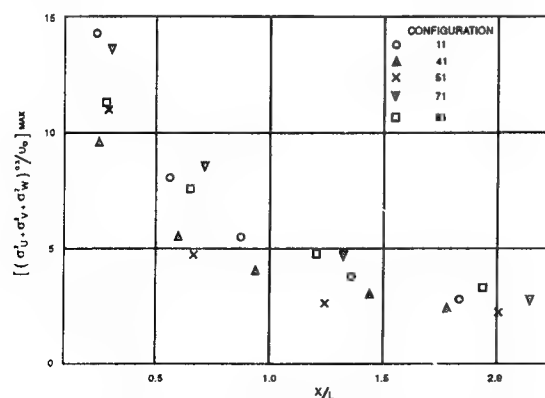


Fig. 12. Decay of maximum value of turbulence kinetic energy in propeller jet

the propeller jet is plotted in Fig. 12 for several hull/propeller combinations. All data stay within a narrow band.

We did consider to fit the decay rate into a simple power law, but this turned out to be unjustified. The measurements do not extend far enough to have a region of sufficient length where self-similarity of the flow has been established. A least-squares approximation would certainly yield a misleading figure for the exponent in the power law.

4.5. Effects of ship features

4.5.1. Propulsion configuration

The data base allows us to study the differences between the wakes of single and twin-screw propeller configurations. In addition, for twin-screw propeller units the influence of the direction of rotation of the propellers can be examined.

Since all hull forms of the data base have port-starboard symmetry, the only source of asymmetry in the time-averaged velocity field behind single-screw ships is the propeller (assuming ideal test conditions). Serious port-starboard asymmetries are therefore basically introduced by the propeller, although bilge vortices and rudder can considerably enhance them (cf. section 4.1.3). Twin-screw configurations, on the other hand, maintain the port-starboard symmetry.

The direction of rotation of twin-screw propellers proves to be relevant for the secondary flow pattern found behind the hull. Particularly, when the hull in front of the propellers generates bilge vortices roughly co-axial with the propeller axes, either a cancelling or an amplification effect of the secondary motion occurs, depending on the sense of rotation of the propellers.

4.5.2. Beam-draft ratio

There seems to be a strong correlation between the beam-draft ratio and the significance of the side vortices: for low B/T pronounced side vortices are found, while they are virtually absent for high B/T . As a consequence of the presence of strong side vortices with their rapid outboard motion due to the induction effects of the virtual image vortex system, the initial rate of spreading near the free surface is comparatively high for ships with low B/T .

4.5.3. Trim/Loading condition

Tankers operate usually at two distinct drafts, associated with the fully loaded and the ballast condition respectively. The two loading conditions imply different beam-draft ratio's, the effects of which have been reviewed above. Another aspect, however, is the trim. When a tanker operates in ballast condition, it is usually trimmed by the stern. It means that the keel plane is slightly inclined with respect to the direction of the onset flow. Consequently some extra lift production is expected, which is revealed by the increased strength of the bilge vortices. This argument is confirmed by the results of two tankers in the data base. The results for one of them are shown in Fig. 13. Unfortunately, the third (31) seems to indicate an opposite effect so that there is no full corroboration.

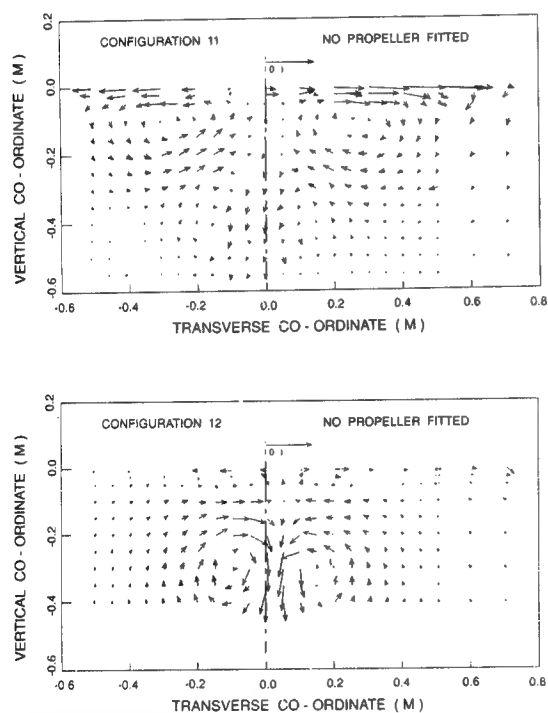


Fig. 13. Comparison of secondary flow behind tanker in full load (top) and ballast (bottom) condition ($x/L=0.559$)

5. Closing remarks

The main aim of the present investigation was the establishment of a data base of macro wake measurements for a broad range of ships. Data have been collected for eight hull forms, a supplementing ninth data set being already available. Although macro wake measurements are not new, the scope

of the AFDEASR project went beyond that of all previous ones. A rich source of information has therefore been established.

An analysis has been made of the data and the main results have been collected in this paper. Plausible explanations have been found for some initially puzzling results. In this regard the wide scope of the investigation proved to be helpful: conjectures about the explanation of one data set could be corroborated by another.

The results have also provided clues for the deliberate modification of a wake structure. Hull shaping, rudder positioning, propeller turning direction, to name a few, have proved to be means which can affect the global structure of a wake considerably.

The analyses presented in this paper are not exhaustive. The data can be used for further analyses and for correlations with either satellite observations or numerical simulations.

References

1. Reed, A.M., Beck, R.F., Griffin, O.M. & Peltzer, R.D. : "Hydrodynamics of Remotely Sensed Surface Ship Wakes", SNAME Transactions, Vol. 98, 1990, pp. 319-363.
2. Lindenmuth, W.T. & Frye, D. : "Viscous Macro-wake Behind a Twin-screw High Speed Surface Ship", DTRC/SHD-1273-01 (1987).
3. Buchhave, P. : "Three-Component LDA Measurements", DISA Information, No. 29 (1984).
4. Tropea, C., Dimaczek, G., Kristensen, J., Caspersen, Chr. : "Evaluation of the Burst Spectrum Analyser LDA Signal Processor", Fourth International Symposium on Applications of Laser Anemometry to Fluid Mechanics, Lisbon (1988).

APPENDIX I : Lengthwise position of measurement planes

Plane positions are indicated per data set as a fraction of the ship's length, the positive direction being from bow to stern with the origin at the aft perpendicular.

nom. = wake of unpropelled hull

prop. = wake of propelled hull

11		12		21		22		31		32		34	
nom.	prop.	nom.	prop.	nom.	prop.	nom.	prop.	nom.	prop.	nom.	prop.	nom.	prop.
-.719		-.719		-.732		-.732		-.770				-.770	
-.479		-.479		-.488		-.488		-.514				-.514	
-.160		-.160		-.163		-.163		-.171				-.171	
.000	.080	.000	.080	.000	.081	.000	.081	.000	.086		.086	.000	.086
.240	.240	.240	.240	.244	.244	.244	.244	.257	.257		.257	.257	.257
.559	.559	.559	.559	.569	.569	.569	.569	.599	.599		.599	.599	.599
.879	.879	.879	.879	.894	.894	.894	.894	.941	.941		.941	.941	.941
	1.358		1.358		1.382		1.382		1.455		1.455		1.455
	1.838		1.838		1.870		1.870		1.969		1.969		1.969

41		51		61		62		64		71		81	
nom.	prop.	nom.	prop.	nom.	prop.	nom.	prop.	nom.	prop.	nom.	prop.	nom.	prop.
-.678		-.667		-.664				-.664		-.713		-.648	
-.509		-.381		-.379				-.379		-.408		-.370	
-.170		-.190		-.190				-.190		-.204		-.278	
.000	.085	.000	.095	.000	.095		.095	.000	.095	.000	.102	-.185	
.254	.254	.286	.286	.284	.284		.284	.284	.284	.306	.306	.000	.093
.594	.594	.667	.667	.664	.664		.664	.664	.664	.713	.713	.278	.278
.933	.933	1.238	1.238	1.233	1.233		1.233			1.325	1.325	.648	.648
	1.441		2.000		1.991		1.991				2.140	1.203	1.203
	1.781												1.943

Time-Marching CFD Simulation for Moving Boundary Problems

H. Miyata (University of Tokyo, Japan)

Abstract

The state of the art of the CFD application to the ship hydrodynamics and ocean engineering is overviewed. The solution procedure for the unsteady fluid flow phenomena is briefly explained and the substantial techniques to treat moving boundaries are reviewed as well as the appropriate choice of the grid system. Simulation results are summarized from the research works of the author's laboratory for the problems of free-surface shock wave, wave resistance, ship maneuvering, sailing mechanism, ocean wave and bubble flow.

1 INTRODUCTION

How can we make progress in ship hydrodynamics? How the technology for hydrodynamical design of ships has been advanced? We may have three important factors of substantial importance for the progress of technology, they are science, analysis and synthesis. Scientific finding provides sound understanding of the nature of the fluid motion and this can directly contribute to the improvement of hull form in an intuitive manner or through reasoning based on theoretical analysis. The theoretical and computational analyses give us clear understanding of the structure and mechanism of fluid flow and these lead to the ideas of controlling the fluid flow aiming at the optimization of the ship. Synthetic works are substantially important for the conceptual development of the new hull-form, new devices or new system of transportation.

It is often the case that the research works are focused on analysis although we well realize that the innovation of technology is mostly achieved either by scientific findings or by synthetic ideas. However, in our field of naval architecture, the scientific finding and synthesis have not greatly contributed to the progress in comparison with other field of engineering. Analysis is usually very useful for the improvement of industrial products and it reinforces the design procedure. Design is performed with good help of analysis. It may be safe to

say that the most important part of the progress of ship technology in the past half century is made by the development of production technique and analysis technique. The enlargement of ship size, the improvement of hydrodynamical performance and many others are attributable to these techniques.

Computational fluid dynamics (CFD), to which research efforts have been focused in the past 15 years in our field, is one of the most effective techniques of analysis. The flow-field and resultant forces and moments are estimated by computer simulations. Since the Navier-Stokes equation is solved, they can cope with a variety of nonlinear flow, such as turbulent flow, shock wave and breaking wave. Considerable part of tank test can be taken place by the CFD simulation on the computers. Almost all fluid motions are unsteady. Almost steady flow also contains unsteady aspects, especially when the Reynolds number is high and turbulence occurs. Therefore the time-marching CFD technique is essentially suitable to fluid dynamics.

Recently the advance of CFD technique enables us to simulate moving body or body in deformation by some special technique. On the other hand the technique of treating the moving free-surface is established long ago in the 1960's. Therefore we can simulate moving or deformed body in the fluid domain with moving free-surface. This means that we can simulate a sailing ship in arbitrary motions. Considering that tank experiments are usually performed by restricting the freedom of model ship, the CFD simulation is now going to surpass tank test in some respects. The purpose of the present review paper is to summarize the state of art of such CFD technology used for the design of ships and related researches. A large number of examples are collected from the simulation results at the author's laboratory.

2 TIME-MARCHING SOLUTION METHOD AND GRID SYSTEM

2.1 Solution algorithm

The development of CFD code was started at the author's laboratory in 1979 when the author noticed the existence of the nonlinear ship wave called free-surface shock wave [1]. The typical codes developed in the past 17 years are listed in Table 1. The series of TUMMAC code is based on the finite-difference method in the rectangular grids and those of WISDAM code is based on the finite-volume method in the curvilinear, boundary-fitted grids [2], but they all follow the same solution algorithm of the MAC-type [3]. The MAC-type solution algorithm is based on the LU decomposition and explicit time-differencing and it is most suitable to the time-marching solution.

The velocity and pressure field are separately solved in the time-marching process. The velocity field is updated by the following Navier-Stokes equation modified by the explicit time-differencing.

$$\begin{aligned} u_{i+1/2,k}^{n+1} &= \xi_{i+1/2,k} - \frac{\Delta}{\Delta x} (\phi_{i+1,k} - \phi_{i,k}) \\ w_{i,k+1/2}^{n+1} &= \zeta_{i,k+1/2} - \frac{\Delta}{\Delta z} (\phi_{i,k+1} - \phi_{i,k}) \end{aligned} \quad (1)$$

Here, two-dimensional equation is used and the terms ξ and ζ contain previous velocity, convection terms and diffusion terms. Pressure divided by the density of fluid is denoted ϕ . The pressure field is determined by the following Poisson equation of which implementation means conservation of mass.

$$\left. \begin{aligned} \phi_{i,k} &= \frac{1}{2(1/\Delta x^2 + 1/\Delta z^2)} \\ &\times \left(\frac{\phi_{i+1,k} + \phi_{i-1,k}}{\Delta x^2} + \frac{\phi_{i,k+1} - \phi_{i,k-1}}{\Delta z^2} - R_{i,k} \right) \\ R_{i,k} &= \frac{\xi_{i+1/2,k} - \xi_{i-1/2,k}}{\Delta t \cdot \Delta x} + \frac{\zeta_{i,k+1/2} - \zeta_{i,k-1/2}}{\Delta t \cdot \Delta z} \end{aligned} \right\} \quad (2)$$

With these two equations the flow-field is sequentially updated in the time-marching procedure under the boundary conditions on the body-surface, free-surface and open boundary.

The block-diagram is shown in Fig.1 for the case of two-layer flow solution making use of the density-function for the implementation of the free-surface conditions. From the velocity field and their boundary conditions the source term for the Poisson equation of the pressure is given. Then the pressure fields of the two layers are solved with the source term under appropriate boundary conditions. The updated pressure gives new velocity field through the relation of the Navier-Stokes equation. This is

repeated with the time-dependent boundary configuration and conditions imposed on it. In the open flow problems the disturbance of the flow takes place by the interaction between fluid and body and the disturbance may be artificially given by the generation of the waves at the inflow boundary or by the movement of the body.

2.2 Grid System

In the past 30 years the technique of solving the Navier-Stokes equation has made remarkable progress and the gradient of improvement has recently been decreased. The CFD technology is now putting more stress on customizing, for which the grid generation technique plays an important role. Since we have reliable solution method for the Navier-Stokes equation, the success of the CFD simulation rely on the grid generation to a larger extent than before. Actually a large part of the efforts is devoted to the grid generation when a three-dimensional body of complex geometry is deal with. Although the gridless technique is continuously investigated, it still has some substantial difficulties, such as poor implementation of the conservation laws. Presently we must work within the framework of the method with grid system.

Since the unstructured grids like those for the finite element method (FEM) still have difficulties in developing into three-dimensional (3D) cases, we can choose either the rectangular grids of the boundary-fitted, curvilinear grids (structured grids). When we employ the rectangular grids both the body-boundary and the free-surface cannot be fitted to the grid lines, while the body-boundary-fitted grids can be either fitted to the free-surface or not. In general the structured grids find difficulties in the representation of the boundary of extreme complexity, such as the automobile shape or free-surface shape of breaking wave. In this context the choice and design of the grid system is of significant importance for the appropriateness, convergence, robustness and accuracy of the CFD simulation.

The cross-sectional grids of the TUMMAC-IV[4][5] and WISDAM-V [9][10] methods are shown in Fig.2. Apparently the degree of accuracy for the implementation of the body-boundary condition is deteriorated in the TUMMAC-IV method. However the purpose of the TUMMAC-IV method is to simulate free-surface waves and the advantage of the shorter CPU time due to the larger spacing and of the needless efforts of grid generation made this code very popular. The boundary-fitted grids are

designed so that the delicate fluid motions both on the body surface and free-surface are well resolved and the degree of accuracy is raised as far as possible within the limited number of grid points. However the small spacing and the singularity give rise to the problem of convergence and robustness. A grid system for a tanker is shown in Fig.3 in which it is well noted that the grid spacing abruptly varies in all directions.

3 MOVING BOUNDARY TREATMENT

3.1 Moving body-boundary conditions

In case the rectangular grids are used for a body of arbitrary configuration, the body-boundary condition is very approximately implemented. In the typical 2D case of Fig.4 either no-slip or free-slip condition can be satisfied even if the divergence free condition is fulfilled in the cell together with the no penetrating condition on the boundary. However, it is almost impossible to realize the velocity profile of turbulent boundary layer with such grid system.

In case the boundary-fitted grids are used we can put one or two grid points within the thickness of viscous sublayer. However, we still find it difficult to realize the turbulent boundary layer with sufficient degree of accuracy. In the 3D case the number of grid points increases 8 times when the spacing is reduced to half length, which means the number of grid points are always insufficient in spite of the rapid advance of the semiconductor technology. The cell on the body surface is usually disproportionate, i.e. the length and width is more than 100 times larger than the thickness. Therefore the present turbulence models do not work well, and we often impose an empirical formula of wall function as shown in Fig.5.

For the numerical simulation of moving boundary problems the grid system must be accordingly deformed as shown in Fig.6 for the case of a fish in propulsive motion at a low Reynolds number. Since the variables and all related quantities are defined by the underlying grid coordinates, their movement is supposed to cause serious difficulties in the solution procedure. Actually when we tried to solve both viscous flow on the body surface and waves on the free-surface simultaneously in a structured grid system[9], the formulation resulted in a very complicated form, almost all terms containing the velocity of grid movement in the framework of the

finite-difference method. However the finite-volume method appeared to have sufficient degree of robustness and the ALE method improved to implement the conservation laws in the boundary cells as shown in Fig.8 [12][13].

In the case of Fig.6 the grid points on the body surface remains at the fixed position and the surrounding grids are regenerated. However, such treatment is not suitable to the rolling motion of a boat in Fig.7, because the intersection of the body on the free-surface moves in time and the wetted surface, on which grid points are located, significantly changes. For such motions with large amplitude the grid regeneration is performed in two steps as shown in Fig.7. The velocity of rotation is separated and this is not used for the deformation of the grids, but it is assumed to be the given fluid velocity on the body surface. This technique enables us to solve the problem of a boat moving with arbitrary degrees of freedom [14].

3.2 Free-surface conditions

There are a number of technique of implementing the free-surface conditions; i.e., the Eulerian method, the Lagrangian method, the ALE method, the VOF method and the marker-density method. The free-surface conditions are composed of the dynamic and kinematic conditions each comes from the conservation laws of momentum and mass, respectively. When the fluid motion above the free-surface can be ignored and the viscous stress as well as the surface tension on the free-surface can be neglected, the dynamic condition is simplified to be a condition of giving the atmospheric pressure on the free-surface. When the small-scale free-surface motions can be assumed out of the scope of the research, the free-surface conditions can be well implemented both in the boundary-fitted grids and in the rectangular grids.

In most of the methods using free-surface-fitted grids the Eulerian method is employed and the Lagrangian method, following the original MAC method, is often used in the framework of the rectangular grids, see Fig.10. The difference of the two methods is not so substantial, since the boundary-fitted grids is transformed into the rectangular grids as shown in Fig.9. The difference consists in the way of determining the free-surface location by satisfying the kinematic condition. It is usually difficult to exactly fulfill the conservation law of mass, but by use of the ALE method the degree of accuracy in the implementation of the mass conservation law is remarkably raised.

The VOF (volume of fluid) and the density-function method [11] implement the mass-conservation law by the transport of the fluid volume or fluid flux instead of the tangential movement of the fluid on the free-surface. This treatment of the mass conservation law enables us to model the free-surface configuration of complexity such as that of overturning wave as shown in Fig.11.

4 SHIP FLOW SIMULATION

4.1 Bow wave simulation

After the author clearly noticed the inadequacy of the wave resistance theories during the practical work of hull form design at a shipbuilding company, the experimental work to investigate into the non-linearity of bow wave was started in 1977. When some of the important features of the nonlinear bow waves called free-surface shock wave (FSSW) were elucidated, we started CFD works for nonlinear bow waves in 1979 when the author first discussed FSSW with Prof. Wehausen and when the workshop on wave resistance computation was organized by Dr. Bai at DTNSRDC. The MAC method developed at Los Alamos scientific laboratory seemed us most suitable to nonlinear ship waves, since it was already demonstrated that this numerical technique can deal with nonlinear waves including breaking wave.

The development of the TUMMAC method had been continued with the multi-purpose mainframe computer of the University of Tokyo and the TUMMAC-IV method for ship waves was completed in 1983 [4][5][16] when the first supercomputer from HITACHI was introduced and the second workshop on wave resistance computation was organized by Dr. Noblesse at DTNSRDC. In the subsequent 10 years the TUMMAC-IV method has been widely employed as a reliable tool to optimize the fore-part of the hull-form in Japan and later in Korea. The TUMMAC-IV method cannot estimate the wave resistance value of the whole ship but it can simulate the wave system and resultant pressure distribution on the hull with sufficient degree of accuracy. Its reliability mostly consists in the property of accuracy in discriminating the better hull-form from others.

For the TUMMAC-IV method the rectangular grid system shown in Fig.12 is employed and the marker is used to implement the kinematic free-surface condition. The dynamic condition for the pressure is satisfied on the exact location of the free-surface. A large part of the difficulties consists in

the technique of implementing the free-slip body-boundary conditions in the irregularly distributed boundary cells denoted B in Fig.12. The treatment at the singular points such as the bow-end or the intersection of the free-surface with the body surface necessitates special techniques.

Simulation results for bow waves of bulk carriers are shown in Figs.13 and 14 comparing with the measured wave contours. The hull form M55FO has a conventional bow-bulb and M55F1 has a thin, long-protrudent bulb which is designed from the knowledge of the characteristics of FSSW. The hull-form design of a bulk carrier "USUKI PIONEER" based on the lines of M55F1 and the verification of the computation was performed in 1983 and since then both the TUMMAC-IV method and the thin-long protrudent bulb have been widely employed for low-speed and middle-speed merchant ships. Although the difference of the waves between two hull-forms seems to be gentle, the value of wave resistance has meaningful difference. Since the nonlinearity of the bow wave is mostly governed by the Froude number based on draft, waves show non-linearity more strongly on the ballast condition, in which the agreement is deteriorated due to the occurrence of wave breaking. However the accuracy in relative magnitude is usually correct probably because the steep waves before breaking are well simulated.

4.2 Diffraction waves at a bow

Since the TUMMAC-IV method is a finite-difference time-accurate simulation, it can be applied to a wave diffraction problem [6]. The experimental results are shown in Fig.15 for the most simple case of a fixed wedge model advancing steadily against incoming regular periodic waves with their crests normal to the direction of model advancement. It is clearly noted that shock-like waves are generated and they show different formation, normal, oblique and mixed type depending on the phase of the incident waves.

The simulation for this problem gives rise to the difficulty of the location of the wave-maker. In a towing tank where the experiments shown in Fig.15 are performed the wave-maker is set at a fixed location and the wedge model is towed reducing the distance to the wave-maker. However in the numerical simulation the coordinates are fixed to the wedge model and the computational domain is limited within the area surrounding the model. The incident waves need to be generated at the inflow boundary of the computational domain. Therefore

the distance between the numerical wave-maker and the wedge-model is invariant, and the numerical wave generation is performed by considering the encounter frequency. However the generated waves are slightly different from the physical experiments.

The comparison is made in Figs.16 and 17 between computed and measured wave contours at five phase angles. Due to the above-mentioned condition as well as the fact that the breaking phenomenon is not interpreted in this code the agreement is beyond satisfaction. However the typical features of varying wave formation are well simulated.

4.3 Free-surface shock wave

The 3D wave breaking can be simulated by the TUMMAC-VIII method which makes use of the density-function technique. The physical stages of FSSW is (1) steep wave generation, (2) breaking and (3) dissipation. The TUMMAC-IV method can simulate (1) and the TUMMAC-VIII (2), but the wave dissipation into momentum loss cannot be well simulated caused by the numerical dissipation of comparable magnitude by the coarse grid spacing.

As shown in Fig.18 the typical wave breaking features are simulated for a wedge model at three Froude numbers [15]. Detailed analysis of the computed results shows that the shock condition of the horizontal velocity vector is almost completely fulfilled on the layer near the free-surface and that the shock phenomenon is limited within the thin-layer of which depth is grossly 20% of the ship draft.

4.4 Stern wave of fast ship

The wave from the transom stern of high-speed vessels is one of the difficult problem for theoretical fluid dynamics, since the cornered end is a singular point for the fluid flow. Some special treatment is introduced here in the previous attempts. However, by use of the density-function technique for the kinematic free-surface condition the flow and waves about the transom corner can be simulated without any additional assumptions as shown in Figs.19 and 20, which are results of the WISDAM-VI method in the framework of curvilinear coordinates fitted to the body surface but not to the free-surface.

4.5 Maneuvering motion

Because of the facts that the tank test to predict the maneuvering properties requires a lot of time and efforts and that some of the maneuvering motions

cannot be well realized in the experimental facilities, the realization of the maneuvering simulation in the computer is of significant importance.

In case the motion is steady such as oblique towing or steady circling motion, the movement of the ship is represented by the body-force term added to the Navier-Stokes equation, and in case the motion is unsteady the moving grid technique becomes useful. In the past 5 years the maneuvering simulation has been studied within the framework of the WISDAM-V method for which boundary-fitted grid system is employed. We still find some difficulties in realizing the Z-test motion mostly due to the wide variation of the heading angle. However, the oblique tow test, steady circling test and PMM test have been achieved [19]. An example of steady circling test is shown in Figs.21 and 22. It is demonstrated that the advantage of CFD simulation is that instantaneous pressure distribution and flow features can be clearly explained. The degree of accuracy in the magnitude of forces and moments is almost of the satisfactory level for low speed ships. For instance, the effect of the difference of the framelines of the after-part is explained as a difference of longitudinal distribution of lateral force in the circling motion.

5 SAILING BOAT SIMULATION

5.1 Steady motion

In comparison with large-scale merchant ships the dynamics of sailing boat is much more complicated. They have absolutely larger freedom of motion in 6 degrees. When a sailing boat moves in the upwind direction the VMG speed is more important than the boat speed, which means that not only the resistance but also the balance of forces and moments are important to achieve high performance. This situation is similar to airplanes or hydrofoil crafts. A sailing boat obtains propulsion force from wind through the work of sails. This implied that the actual sailing condition is very difficult to realize in the model tests. Sailing boat simulation by the combination of the CFD simulation with the solution of the equations of motion seems to be substantially useful for its design when sufficient degree of accuracy is attained.

The development of the WISDAM-VII code for sailing boat was started in the middle of 1993 when the author was assigned to be a general coordinator for the technical team supporting the Nippon

Challenge for the America's Cup 1995. It was evident that this development cannot contribute to the challenger's series started in the beginning of 1995 and actually other codes TUMMAC-IV and WISDAM-V were used for the development of new hulls.

Considering the six degrees of freedom of motion for sailing boats, the 0-0 type grids shown in Fig.23 are employed. Since the Froude number based on the boat length exceeds 0.3, free-surface waves must be taken into account. Therefore, the grids are clustered to the free-surface and body-surface. The finite-volume method is employed and the moving grid technique is fully utilized including the hull-surface slipping technique for the rolling motion.

Exerting forces are illustrated in Fig.24 for the vertical section of a boat on the upwind sailing condition. Sails and appendages would better be simulated in the same way with the hull. But at present they are treated as simple lifting surfaces and generated forces are incorporated into the equation of motion.

This simulation method for sailing boat composed of the WISDAM-VII method and the solution of the equations of motion is also connected to the CAD system. Thus, the difference of performance by the modification of hull-form can be studied in a straightforward manner in the computer simulation. The results of the study of beam-length series are shown in Figs.25 to 27. The forces and moments by the sails and appendages are set at constant and the sailing boats are set to be free to trim, heave and heel. Then the fluid-dynamical properties are compared as shown in Figs.26 and 27. When the advance speed is set at constant the forces and values determining the sailing performance are all provided and compared.

5.2 Unsteady motion

By changing the freedom of the boat and introducing the control of rudder and other moving surfaces into the equation of motion arbitrary sailing behavior can be simulated. The case of course changing by 4 degrees during upwind sailing is shown in Fig.28 with two variation of gains of the automatic control system for the rudder. The results of the simulation of this maneuver are shown in Figs.29 and 30. It is understood that the time-variation of rudder angle and the components of lateral forces depends on the helmsman's technique although steering is automatically made in this simulation. Unfortunately such simulation requires almost 1000 times longer time in an engineering work-

station than the actual maneuvering time of a sailing boat. Therefore this technique cannot be used as a real-time sailing simulator for the purposes of the training of helmsman and the development of boats of better performance. However, it may be safe to say that it is a most advanced design tool for sailing boats of high performance.

6 OCEAN WAVE SIMULATION

6.1 2D breaking wave

More than 10 years ago 2D breaking simulation was first completed by use of the movement of free-surface segment within the framework of rectangular grid system [7][16]. A typical result of a 2D bow wave in front of an advancing floating body is shown in Fig.31. Due to the robustness of the method with equal spacing and staggered arrangement of variables the overturning motion together with the impingement of the breaking wave front is well simulated. As seen in Fig.31, the successive overturning motion of the type of plunging breaker is realistically solved.

However this technique cannot be extended to the 3D problem since the complicated free-surface configuration may not be represented by the succession of segments or something similar. The free-surface may intersect the rectangular cells in a variety of manner. The free-surface-fitted curvilinear grids may resolve the fluid motion on the breaking free-surface with sufficient degree of accuracy. However such grids find serious difficulties in making the configuration of overturning wave front. Furthermore the 3D impinging motion cannot be imagined to be dealt with by such a technique.

6.2 3D breaking wave

For the numerical representation of the extremely complicated configuration of the 3D breaking free-surface the density-function method is developed. The density is a scalar value to determine the fluid fraction in a rectangular cell, i.e., porosity of fluid in a cell. The free-surface location is approximately represented by this value and the slope of the free-surface by the combination of these values in the neighboring cells.

The first idea was to solve both gas and liquid regions continuously. However it turned out to be unsuccessful firstly because the density was 1000 times different between water and air and small difference of water pressure gave rise to very large difference

of air velocity and secondly because the equation of density-function showed excessive diffusive effect. Therefore it is used only for the determination of the interface location and the fluid flow is separately solved as shown in the block diagram in Fig.1 [8].

A grid system for the simulation of a wave flow about a part of semisubmersible is shown in Fig.32. In order to compensate the low degree of accuracy inherent to the density-function method the variable grid system is employed in the vertical direction.

The results of time-marching simulation of wave diffraction with semisubmersible are shown in Fig.33. Since steep regular waves of large wavelength interact with a lowerhull and a number of vertical pillars, which is realized by the symmetric condition on the side boundaries, a peculiar wave is formed behind the pillar [20].

The case of extremely nonlinear waves about a vertical pillar in a uniform stream of air and water is shown in Fig.34 to 36. Since the Froude number based on the horizontal length is 1.25 the bow wave shows breaking phenomenon and almost vertical free-surface configuration appears on the sides and behind the cylinder. Spray and air-entrainment are also observed in the vicinity of the cylinder, although their reality is not well guaranteed.

This simulation technique is easily applied to another two-layer flow, i.e., water flow above liquefied sand layer by simply changing the density value of the fluid. One feature of scoring sand layer by the water flow interaction with the pillar is shown in Fig.37. First the sand in front of the pillar is suppressed by the stagnation pressure and secondly the horseshoe vortex here accelerates the scoring and thirdly the scoring intensifies the horseshoe vortex until the scored region reaches a certain upstream point. This process is simulated by the time-marching simulation started from the rest condition. Although the degree of accuracy is not high, the TUMMAC-VIII method with the density-function technique can be applied to a variety of two-layer flow with strongly interacting interface.

7 MULTI-PHASE FLOW SIMULATION

7.1 Bubble flow simulation

The technique of treating the free-surface can be applied to other fluid phenomenon with interface. The density-function method has good versatile properties for the resolution of the interface. A lot of

fluid phenomena associated with environmental engineering or production process engineering seem to be simulated by the CFD techniques slightly modified from those described in this article and the simulation results will contribute to the improvement of technology. The single experience of the author is the simulation of continuous casting for steel plate production for which modified TUMMAC-IV method is useful.

Quite recently two CFD research works for bubble flow are executed at the author's laboratory. One is the method using an overlapping grid system fitted both to the wall boundary and bubble surface, and the other is that of TUMMAC-VIII, i.e., the combination of rectangular grid system with the density-function technique for the bubble surface. The surface tension is incorporated into the bubble surface conditions.

The results of a bubble freely rising in a still water region are presented in Figs.38 and 39. The Weber number is 4.8 and the Reynolds number is 1440 [21]. The bubble makes a spiral trajectory after the vortex shedding downward reaches the periodically steady state. It is interesting to note that the successive shedding of horseshoe vortices shown in Fig.39 is common to many other vortex shedding from blunt bodies such as a sphere and an automobile.

8 CONCLUSION

It is described in this article that the time-marching CFD technique for moving or deforming problems provides us wide possibility to improve the understanding of unsteady fluid phenomenon and the design of moving objects. In the field of naval architecture one symbolic goal is to complete simulation technique for a ship in slamming motion at rough sea. However it must be also noted that such technique can contribute to a lot of problems in the fields of process engineering, environmental engineering and so on.

One of the serious problem is that a great deal of efforts by able CFD researchers must be devoted for the customizing the software. Since the progress of computer technology remarkably reduced the problem of hardware investment, almost all the computations have been executed by workstations at the author's laboratory in the past seven years. Therefore all the results in this article, except those of Figs.13, 14 and 16, are provided by workstations.

References

- [1] Miyata, H. and Inui, T., "Nonlinear ship waves," *Advances in Applied Mechanics*, Vol. 24, 1984, pp. 215-288.
- [2] Miyata, H., "Free-surface flow simulations by finite-difference techniques," *Computational Fluid Dynamics '94*, Sept. 1994, pp. 61-71. ECOMAS Computational Fluid Dynamics Conference, Stuttgart.
- [3] Welch, J. E., Harlow, F. H., Shannon, J. P. and Daly, B. J., "The MAC method," Los Alamos Scientific Lab. Report, LA-3425, Univ. California, 1966, Los Alamos, New Mexico.
- [4] Miyata, H. and Nishimura, S., "Finite-difference simulation of nonlinear ship waves," *Journal of Fluid Mechanics*, Vol. 157, Aug. 1985, pp. 327-357.
- [5] Miyata, H., Nishimura, S. and Masuko, A., "Finite difference simulation of nonlinear waves generated by ships of arbitrary three-dimensional configuration," *Journal of Computational Physics*, Vol. 60, No. 3, 1985, pp. 391-436.
- [6] Miyata, H., Kanai, M., Yoshiyasu, N. and Furuno, Y., "Diffraction waves about an advancing wedge model in deep water," *Journal of Ship Research*, 34-2, June 1990, pp. 105-122.
- [7] Miyata, H., "Finite-difference simulation of breaking waves," *Journal of Computational Physics*, Vol. 65, No. 1, 1986, pp. 179-214.
- [8] Miyata, H., Katsumata, M., Lee, Y. G. and Kajitani, H., "A finite-difference simulation method for strongly interacting two-layer flow," *Journal of the Society of Naval Architects of Japan*, Vol. 163, 1988, pp. 1-16.
- [9] Miyata, H., Sato, T. and Baba, N., "Difference solution of a viscous flow with free-surface wave about an advancing ship," *Journal of Computational Physics*, 72-2, Oct. 1987, pp. 393-421.
- [10] Miyata, H., Zhu, M. and Watanabe, O., "Numerical study on a viscous flow with free-surface waves about a ship in steady straight course by a finite-volume method," *Journal of Ship Research*, Vol. 36, No. 4, 1992, pp. 332-345.
- [11] Park, J. C., Zhu, M. and Miyata, H., "On the accuracy of numerical wave making techniques," *Journal of the Society of Naval Architects of Japan*, Vol. 173, 1993, pp. 35-44.
- [12] Roseneld, M. and Kwak, D., "Time-dependent solution of viscous incompressible flows in moving coordinates," *Intern. Journal for Numerical Methods in Fluids*, Vol. 13, 1991, pp. 1311-1328.
- [13] Akimoto, H. and Miyata, H., "Finite-volume simulation of a flow about a moving body with deformation," *Proceedings of the 5th Intern. Symposium on Computational Fluid Dynamics*, Vol. 1, Aug. 1993, pp. 13-18. Sendai.
- [14] Akimoto, H., "Development and application of CFD simulation technique for a hull in 3D motions," Ph. D thesis, University of Tokyo, 1996.
- [15] Kanai, A. and Miyata, H., "Elucidation of the structure of free surface shock waves about a wedge model by finite-difference method," *Journal of the Society of Naval Architects of Japan*, Vol. 177, 1995, pp. 147-159 (in Japanese).
- [16] Miyata, H., Nishimura, S. and Kajitani, H., "Finite difference simulation of non-breaking 3-D bow waves and breaking 2-D bow waves," *Proceedings of the Intern. Conference on Numerical Ship Hydrodynamics*, Sept. 1985, pp. 259-292. Washington. D. C.
- [17] Kawamura, T. and Miyata, H., "Simulation of nonlinear ship flows by density-function method," *Journal of the Society of Naval Architects of Japan*, Vol. 176, 1994, pp. 1-10.
- [18] Kawamura, T. and Miyata, H., "Simulation of nonlinear ship flows by density-function method. (Second report)," *Journal of the Society of Naval Architects of Japan*, Vol. 178, December. 1995, pp. 1-7.
- [19] Omori, T., Miyata, H., Fujino, M., Usami, S. and Eguti, S., "A study of flow field around full ship forms in maneuvering motion (second report: Hydrodynamic forces and pressure distribution on ship's hull in steady turning condition)," *Journal of the Society of Naval Architects of Japan*, Vol. 177, May. 1995, pp. 13-28.
- [20] Park, J. C. and Miyata, H., "Numerical simulation of 3D breaking wave motions about an off-shore structure under a severe sea condition,"

Journal of the Society of Naval Architects of Japan, Vol. 176, December. 1994, pp. 31-42.

- [21] Kanai, A. and Miyata, H., "Numerical simulation of a bubble flow by modified density function method," Journal of the Society of Naval Architects of Japan, (to appear).

Body boundary fitted grid	Free surface fitted grid	Wave breaking consideration	Moving coordinate	Code name	Application
×	×	×	×	TUMMAC-IV	Ship wave
		○	×	TUMMAC-VIII	breaking ocean wave beach wave, bubble flow
○	×	○	×	WISDAM-VI	breaking ship wave
			○2D	WISDAM-V	ship viscous flow ship maneuvering
			○3D	WISDAM-VII	sailing boat simulation

Table 1: Characteristics of finite-difference and finite-volume methods developed at the University of Tokyo.

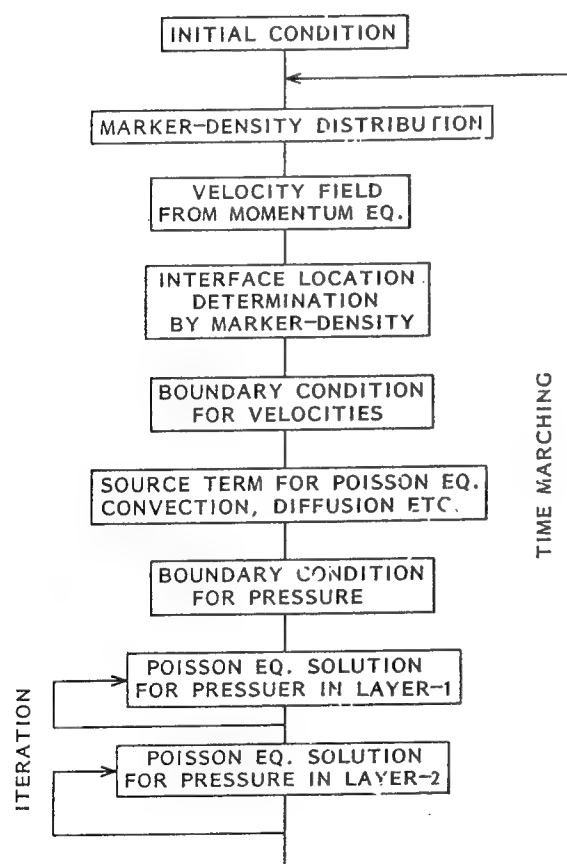


Figure 1: Block diagram of the MAC-type solution procedure for two-layer flow.

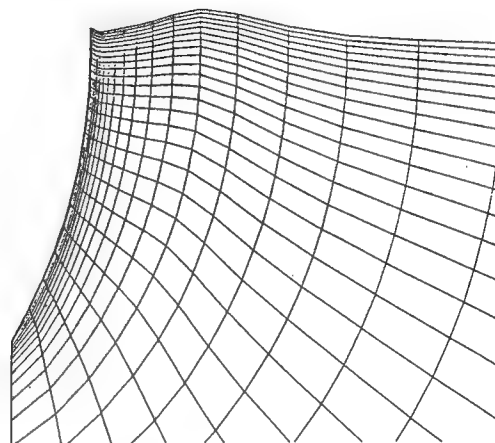
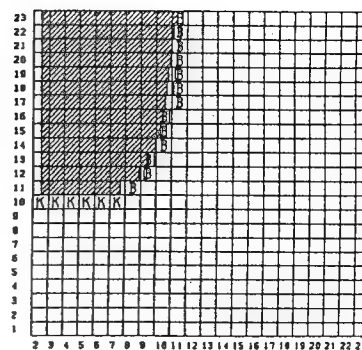


Figure 2: Rectangular and curvilinear grid system.

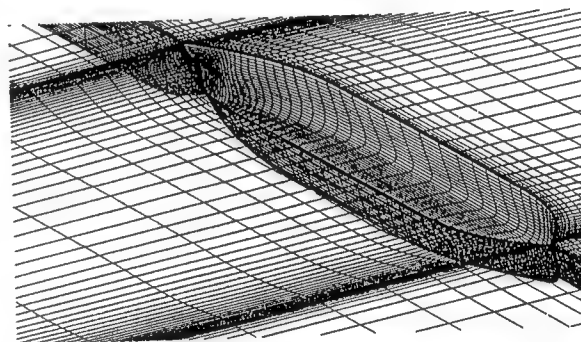


Figure 3: Boundary-fitted coordinate system for a tanker hull.

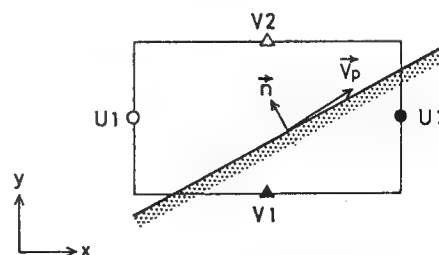


Figure 4: Schematic sketch for the body boundary condition in the rectangular grid system.

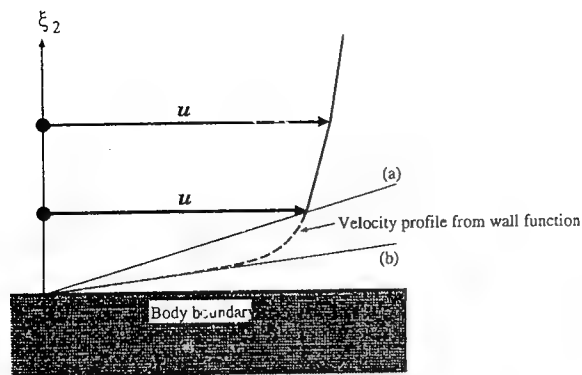


Figure 5: Schematic sketch for the body boundary condition in the boundary-fitted grid system.

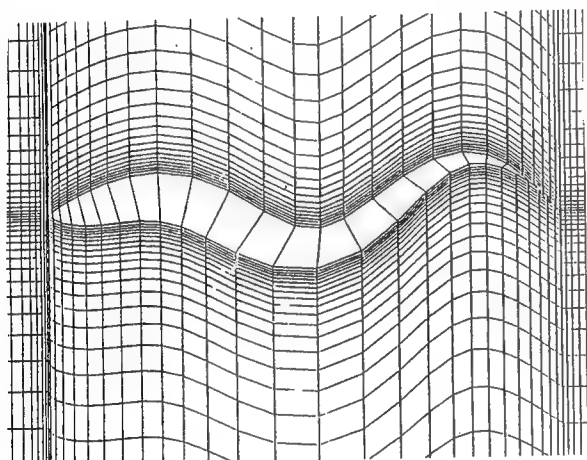
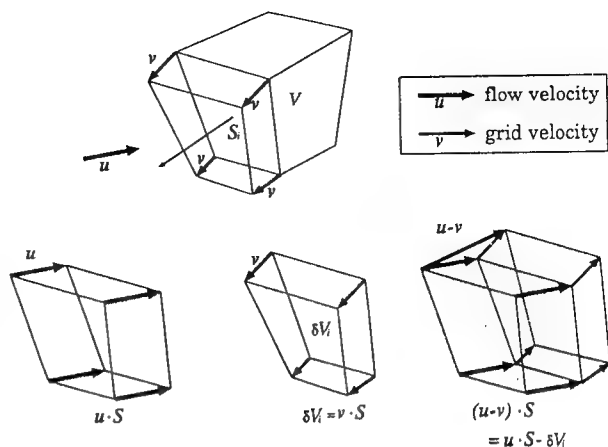


Figure 6: Moving grid system for a 2D case.

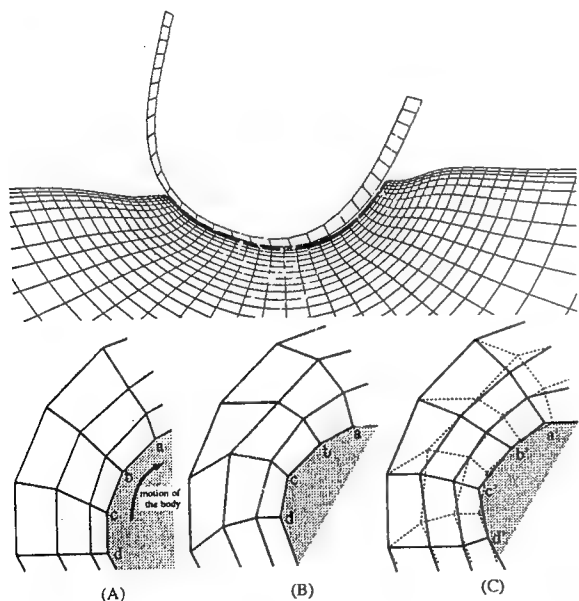


Figure 7: Moving grid system for a rolling ship.

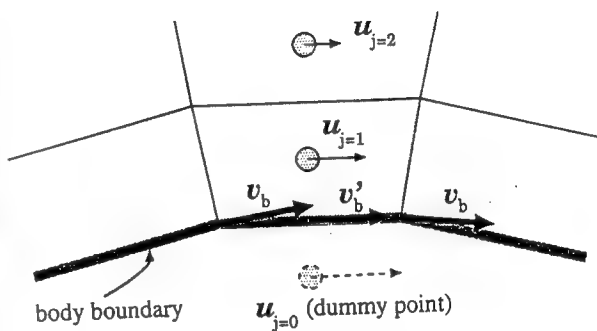


Figure 8: Schematic sketch for the treatment of the moving velocities on the body boundary.

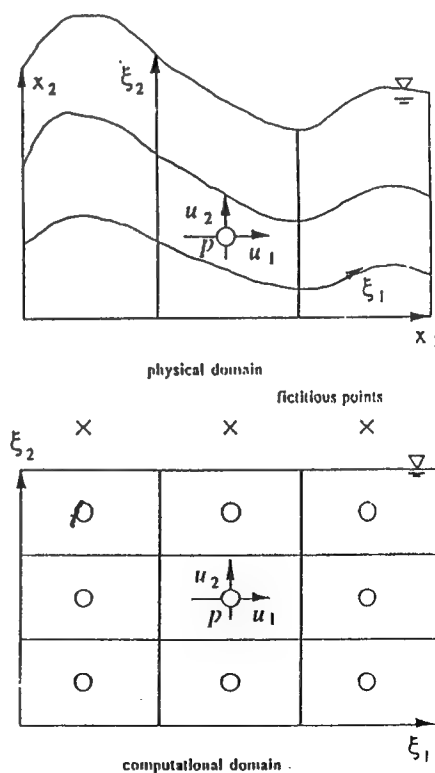


Figure 9: Velocity and pressure points of the grid system fitted to the free-surface.

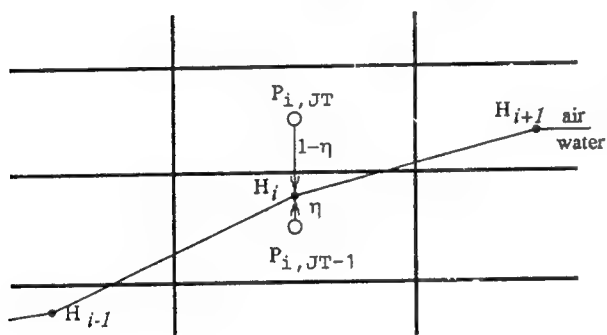
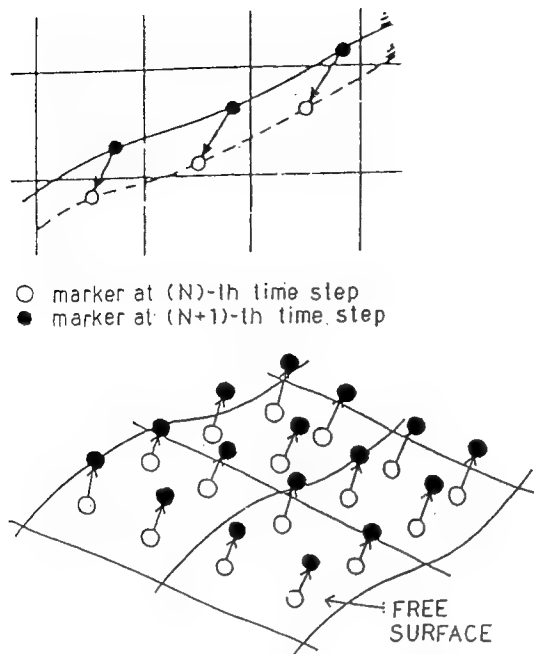


Figure 10: Schematic sketch for the fulfillment of the kinematic and dynamic conditions on the free-surface in the rectangular grid system.

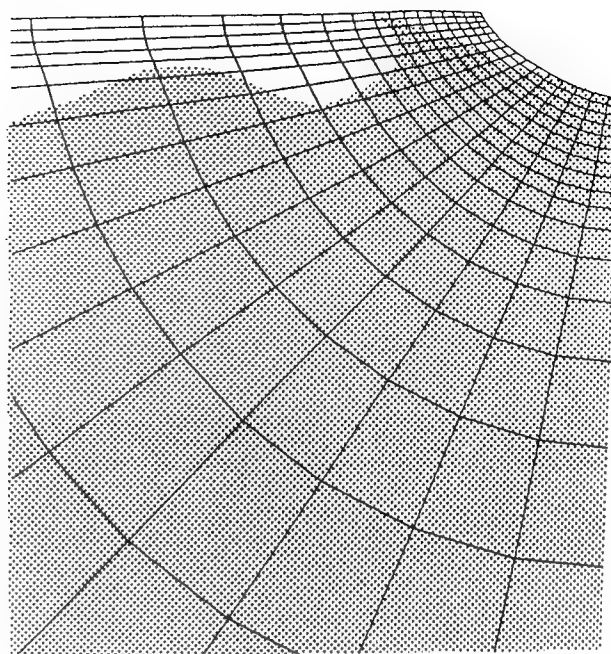


Figure 11: Schematic sketch for the determination of the free-surface location by the density-function method used in the body-boundary-fitted grid system.

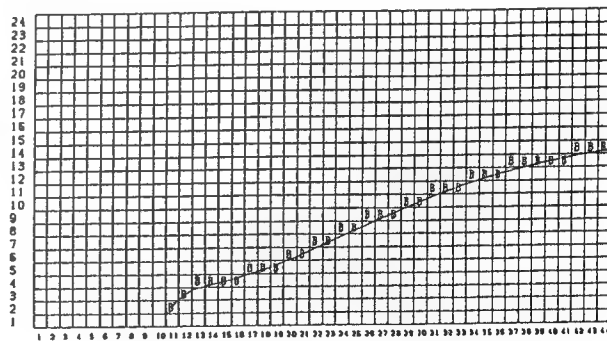


Figure 12: The horizontal grid arrangement and body-boundary cells of the TUMMAC-IV code for ship waves.

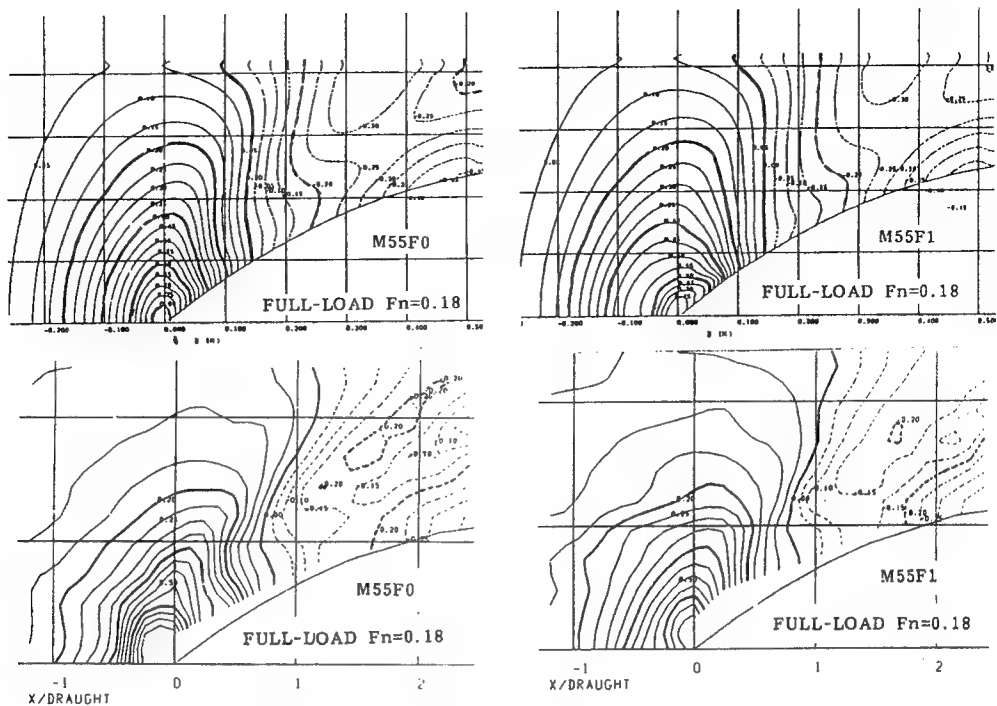


Figure 13: Comparison of computed and measured wave contours of two hull-forms of a 26000 DWT bulk carriers M55 F0 and M55 F1 at $Fn=0.18$.

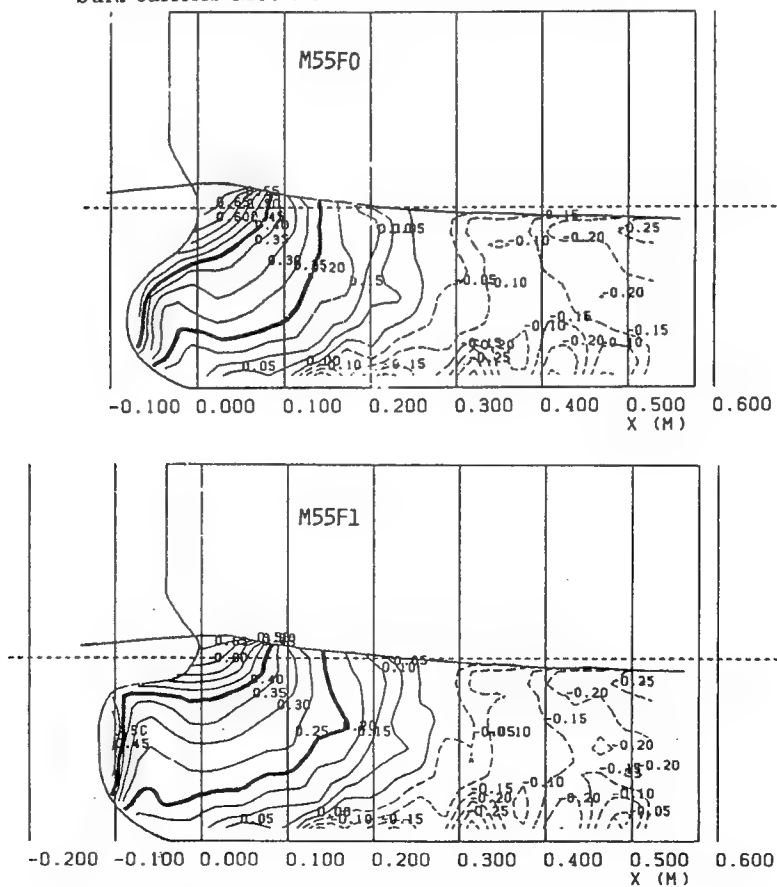


Figure 14: Comparison of pressure distribution on the hull of the two ships of Fig.13.

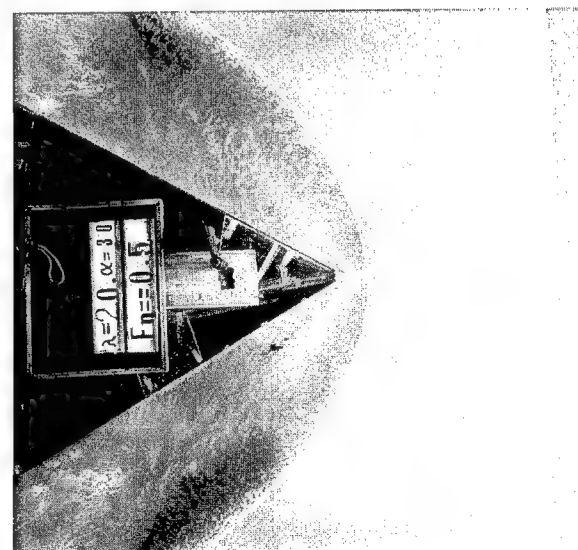
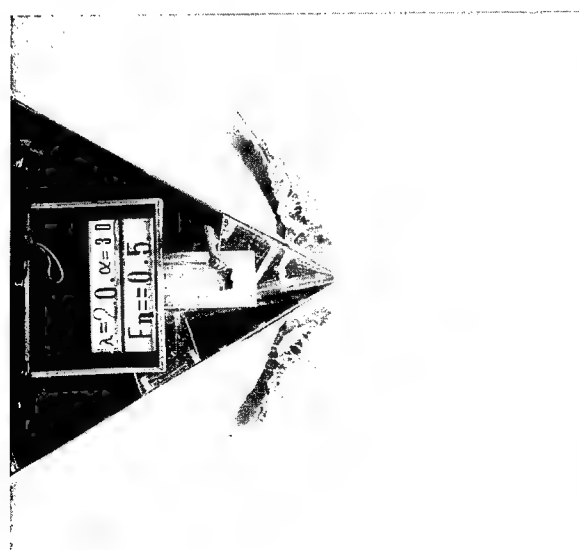
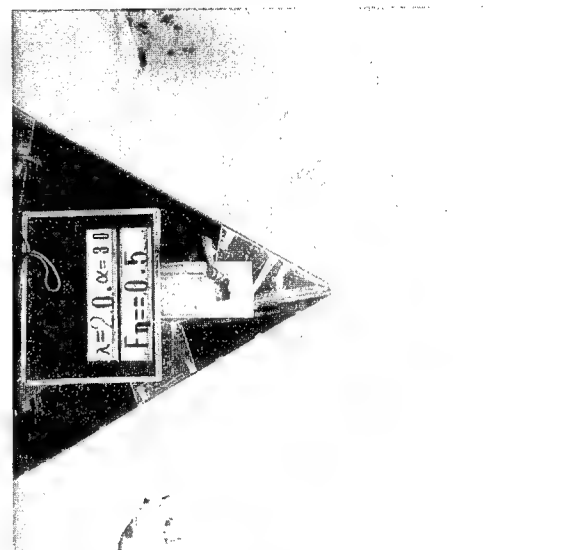
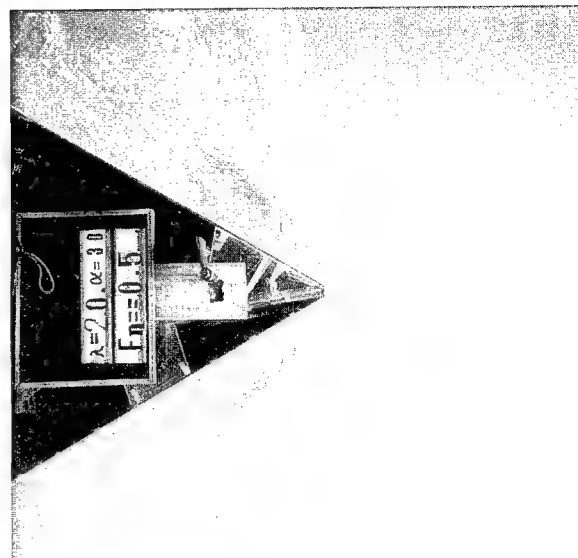


Figure 15: Time-variation of nonlinear diffraction waves about a wedge model placed in regular incident waves, $F_n=0.5, \lambda=2.0\text{m}, \alpha=30^\circ$

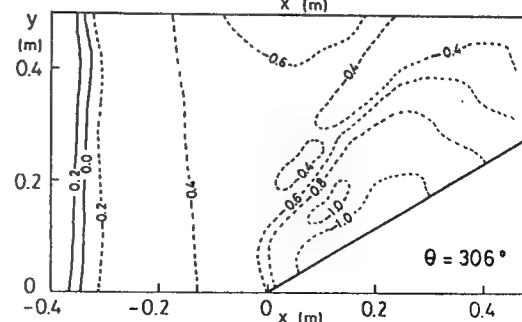
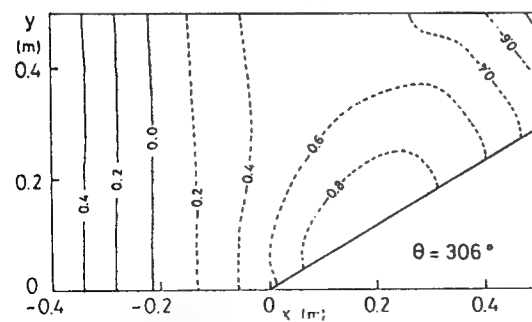
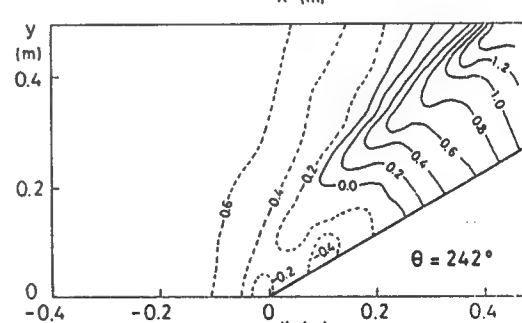
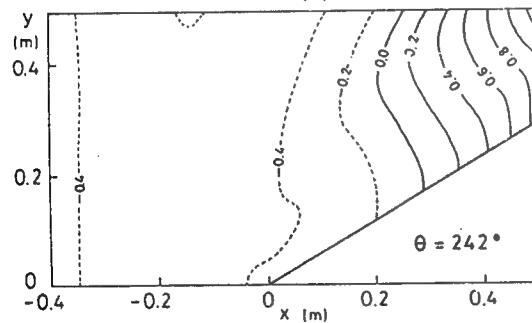
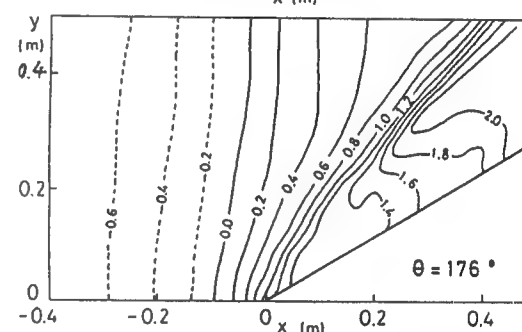
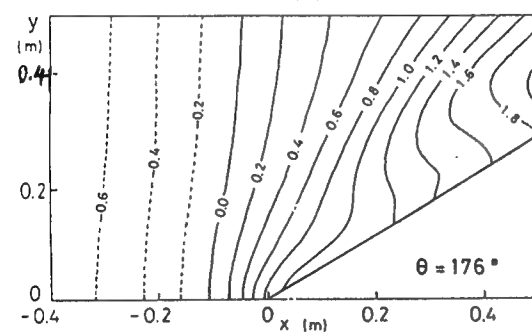
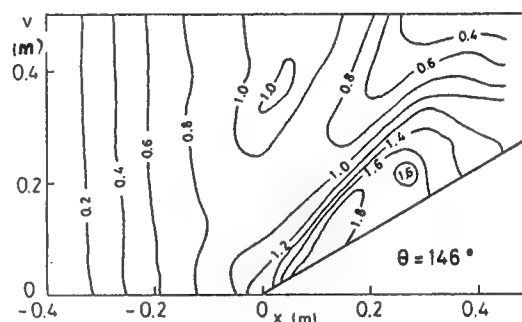
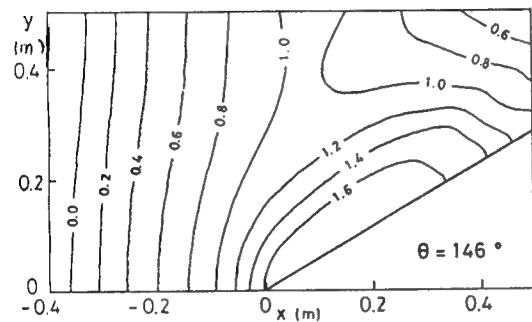
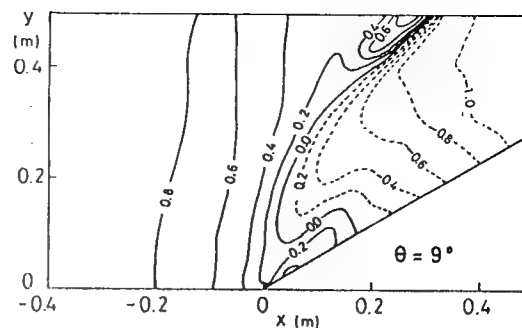
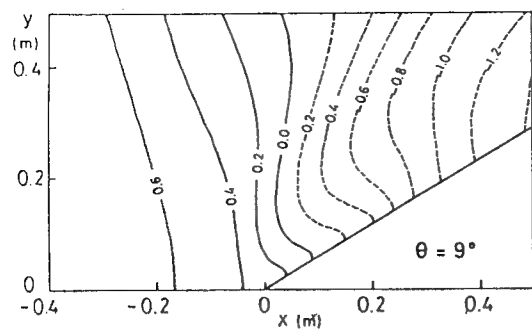


Figure 16: Simulated wave contours at five phases of the incident wave on the condition in Fig.15.

Figure 17: Measured wave contours for the comparison with Fig.16.

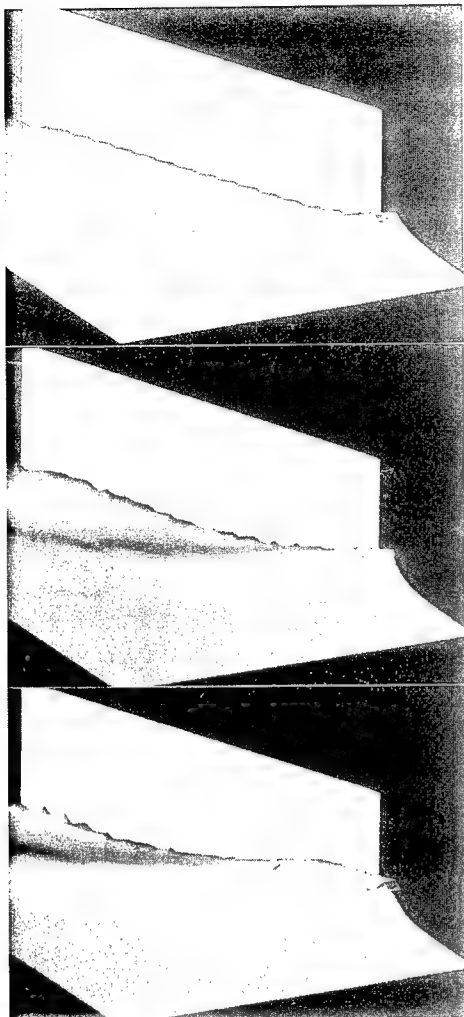


Figure 18: Perspective view of the computed bow waves about a 20° wedge model at three Froude numbers, $Fd=0.8$, 1.1 and 1.4 from above.

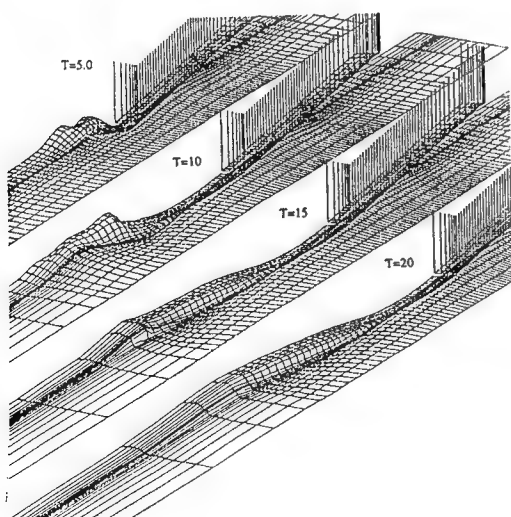


Figure 19: Perspective view of the computed stern wave emanating from a high-speed vessel.

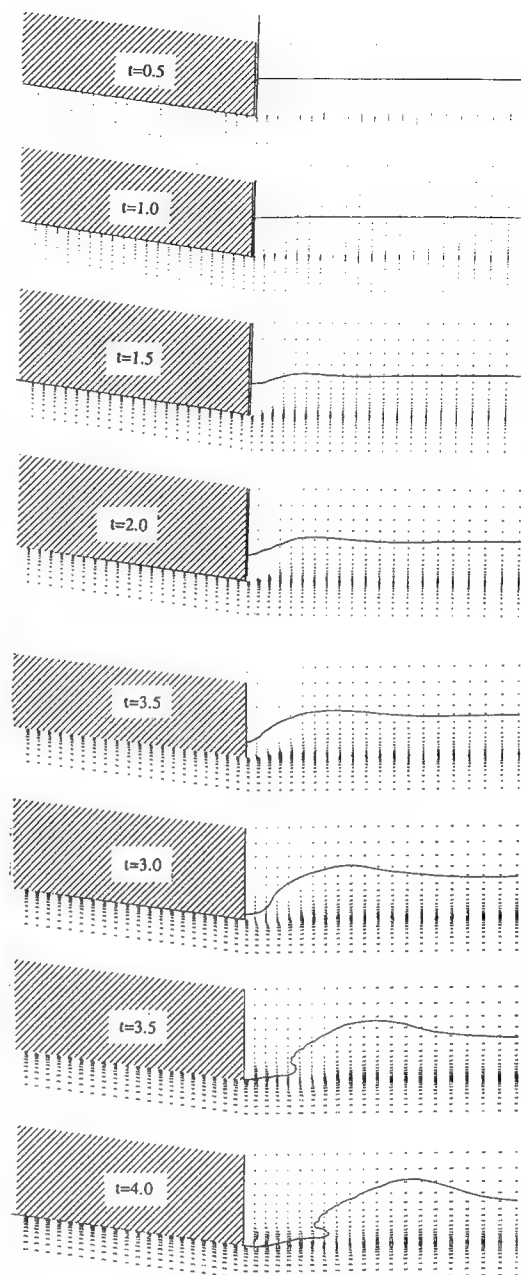


Figure 20: Time-sequence of the evolution of the stern wave at a high Froude number.

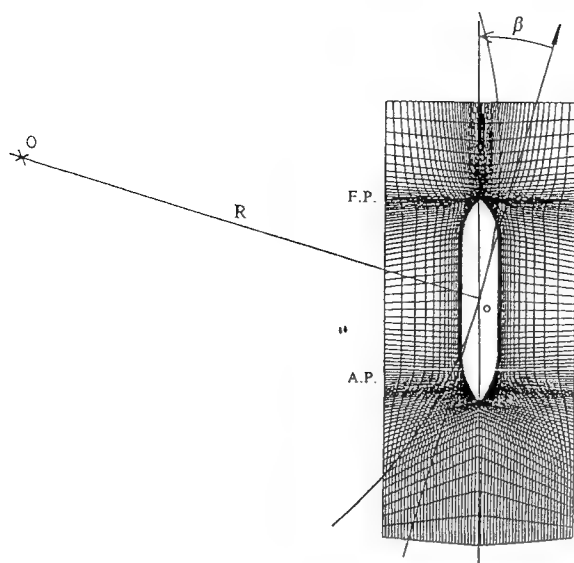


Figure 21: Grid system for a ship in steady turning motion.

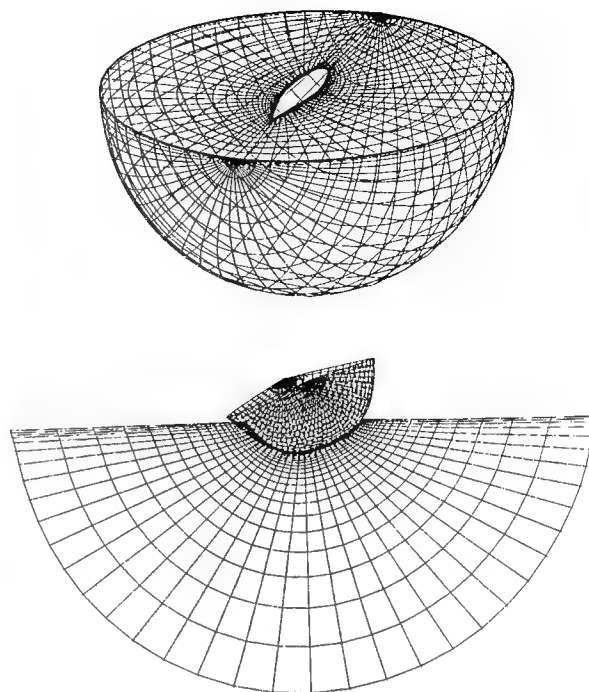


Figure 23: Grid system for the hull of a sailing boat.

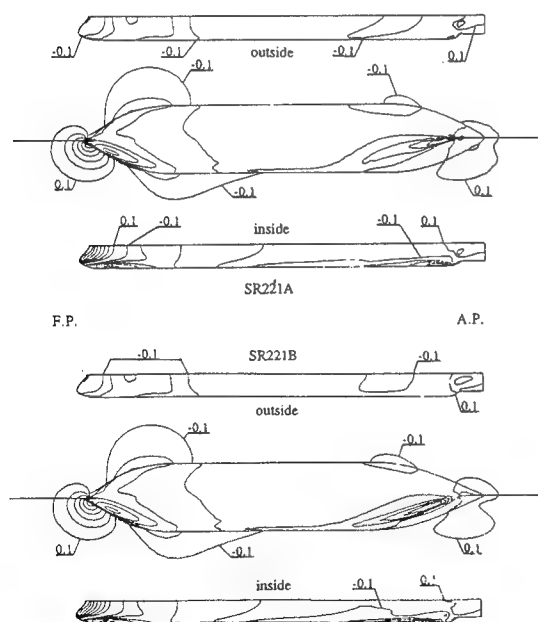


Figure 22: Distribution of pressure coefficient on the hull surface and water surface of two tanker hulls SR221A and SR221B in steady turning motion, $r'=0.4$, $\beta=0^\circ$, contour interval is 0.1.

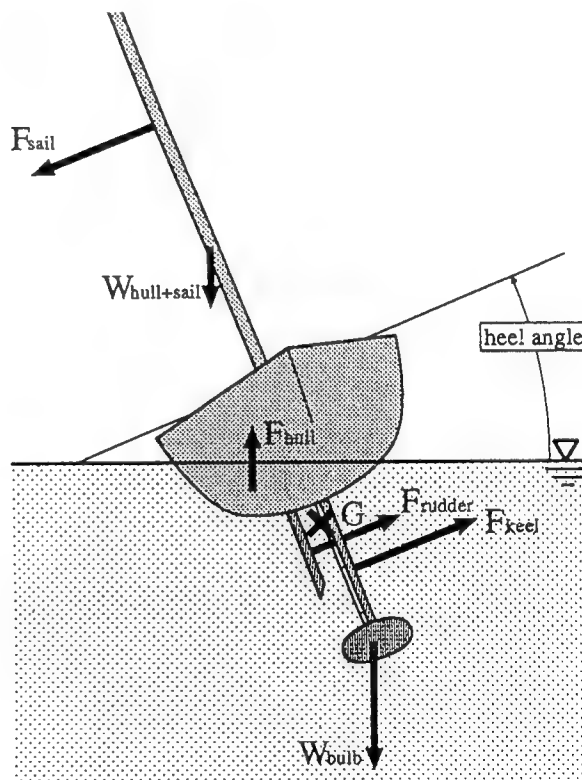


Figure 24: Forces exerted on a sailing boat in a upwind course.

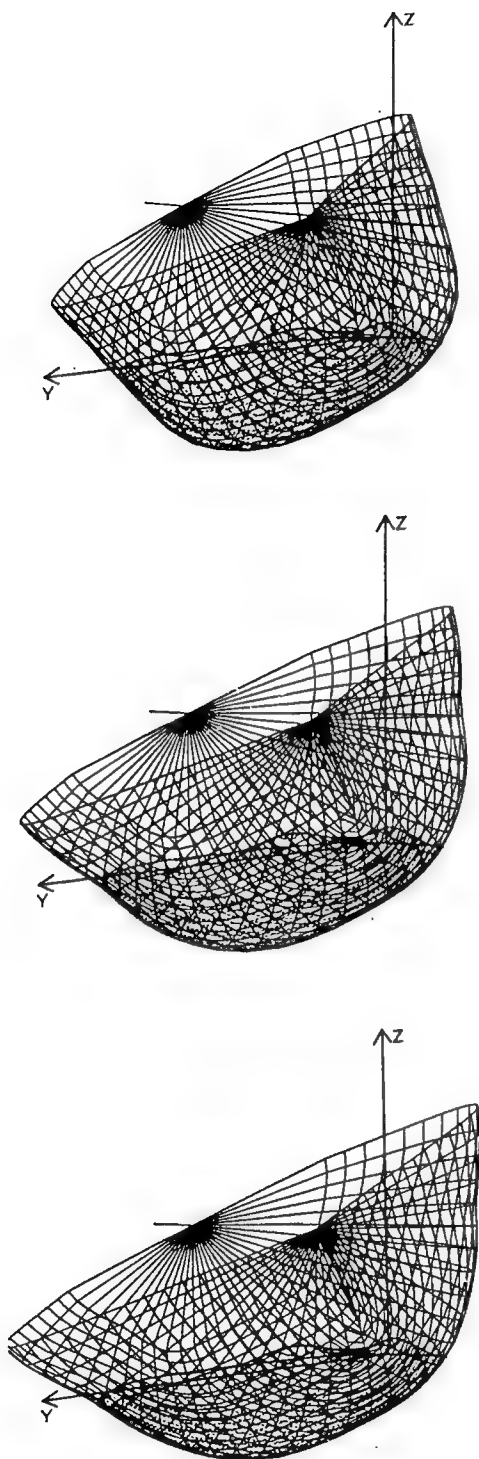


Figure 25: Body and free-surface configuration of sailing boats with different framelines on a upwind sailing condition.

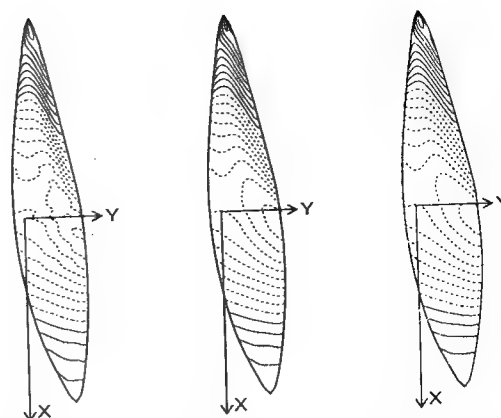


Figure 26: Comparison of pressure distribution of the three boats in Fig.25.

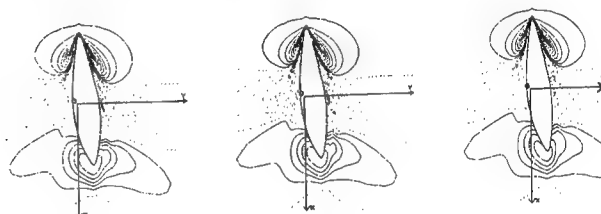


Figure 27: Wave contours of the three boats in Fig.25.

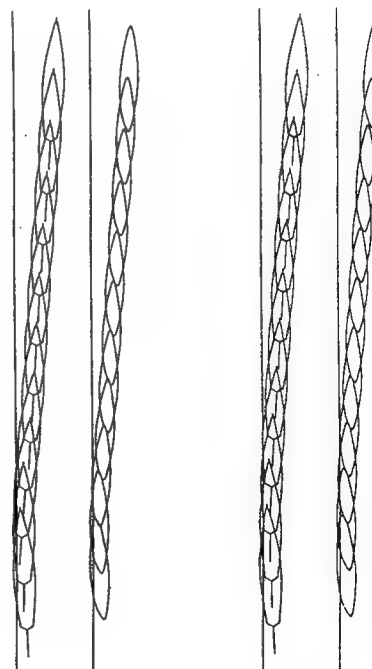


Figure 28: Time-sequential variation of the location, sheerline configuration and waterline configuration of a sailing boat in course changing maneuver during upwind sailing, case 1 (left) and case 2 (right).

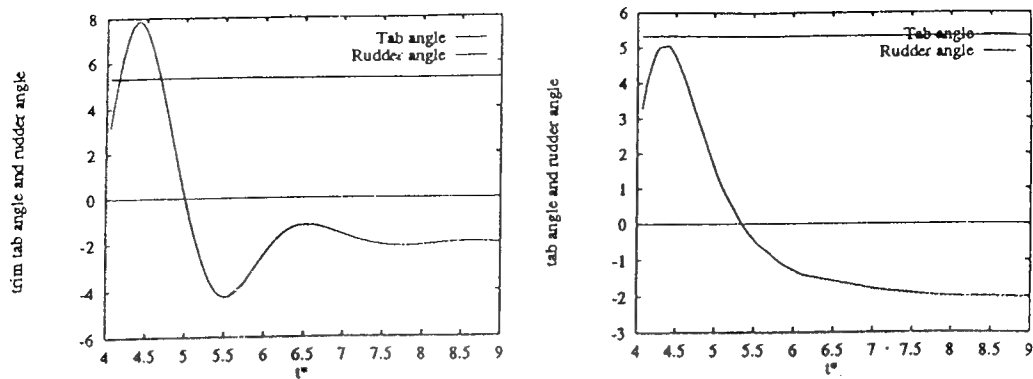


Figure 29: Time-sequence of rudder angle in the course of maneuvering in Fig.28, case 1 (left) and case 2 (right).

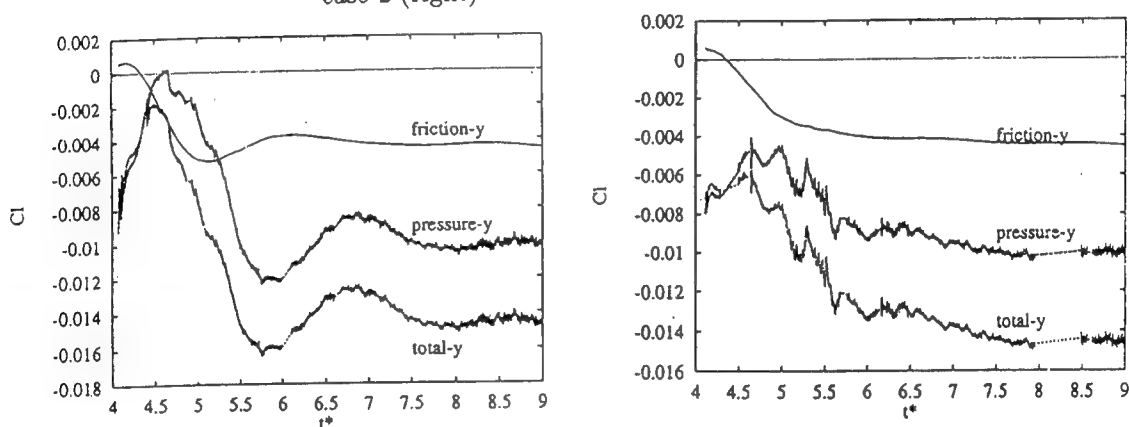


Figure 30: Time-history of the longitudinal and transverse forces in the course of maneuvering in Fig.28, case 1 (left) and case 2 (right).

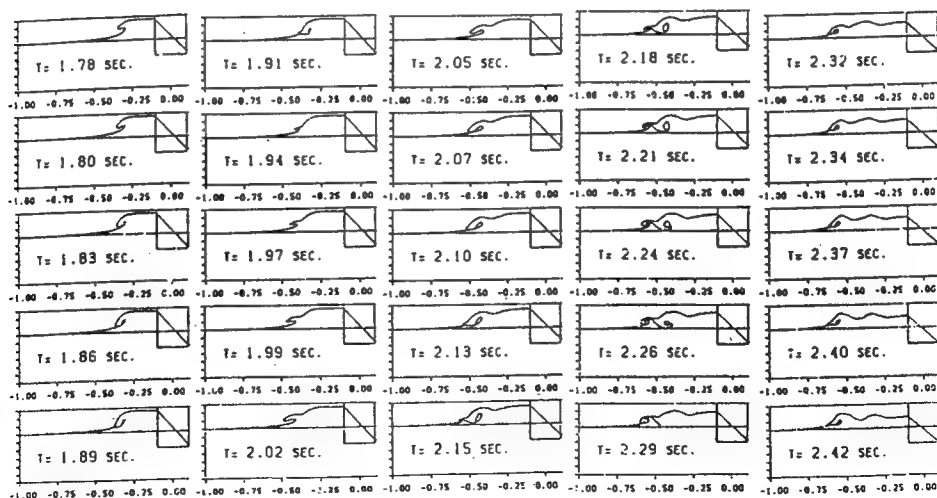


Figure 31: Evolution of breaking bow wave in a 2D case.

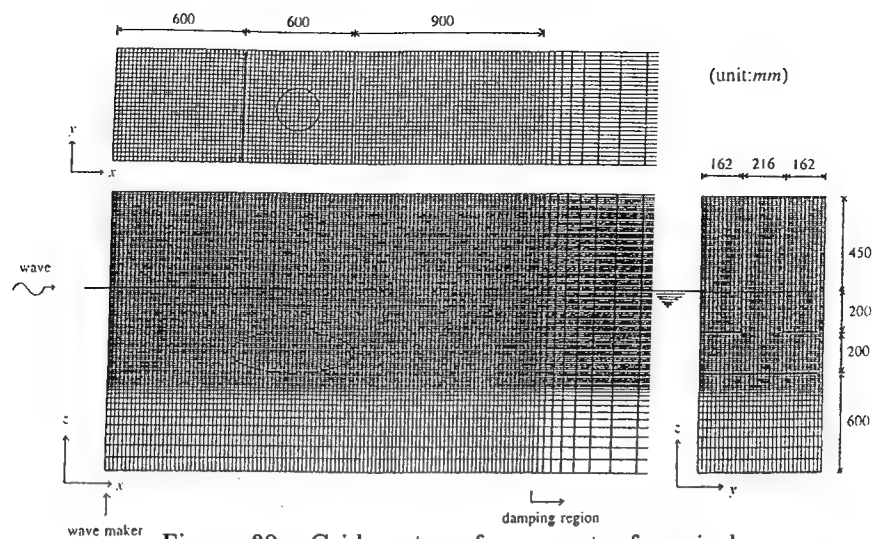


Figure 32: Grid system for a part of semisubmersible for the simulation by TUMMAC-VIII code.

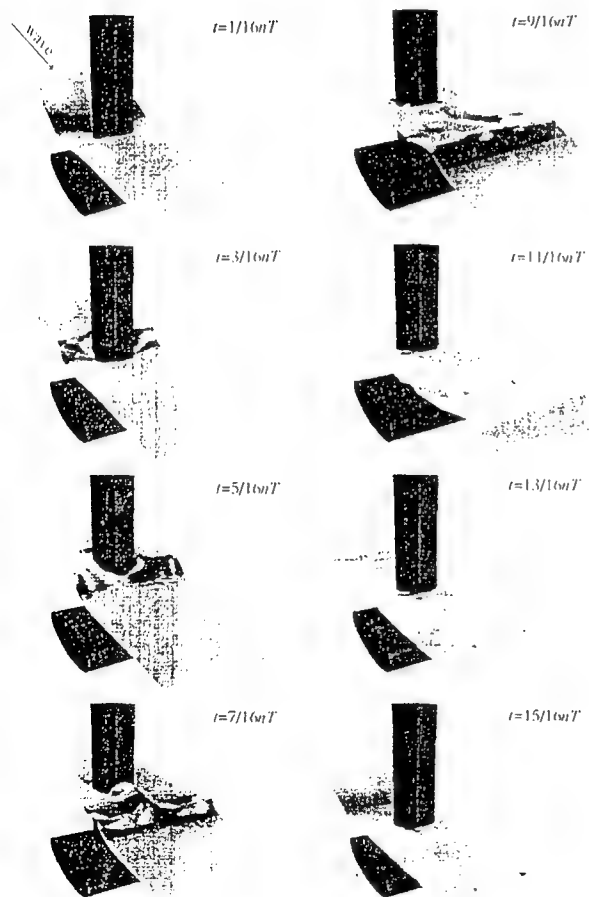


Figure 33: Time-sequence of wave diffraction about a semisubmersible placed in regular steep waves.

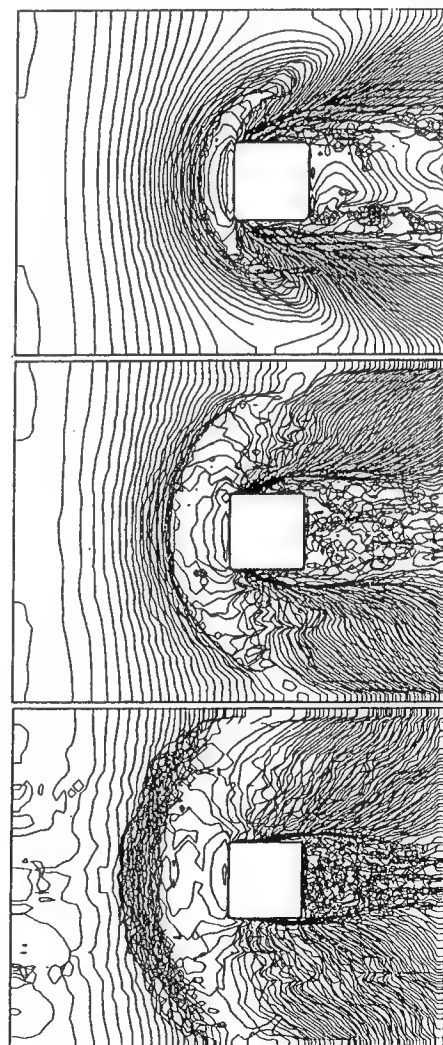


Figure 34: Evolution of breaking wave about a vertical cylinder.

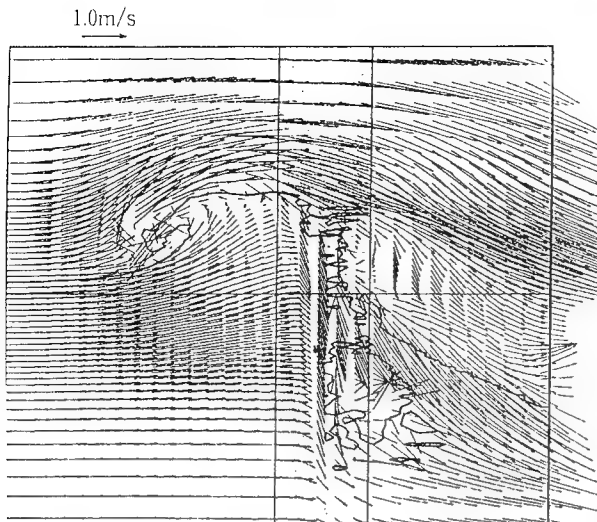


Figure 35: Wave profile and velocity vectors on a vertical plane including the side-surface of a vertical cylinder.

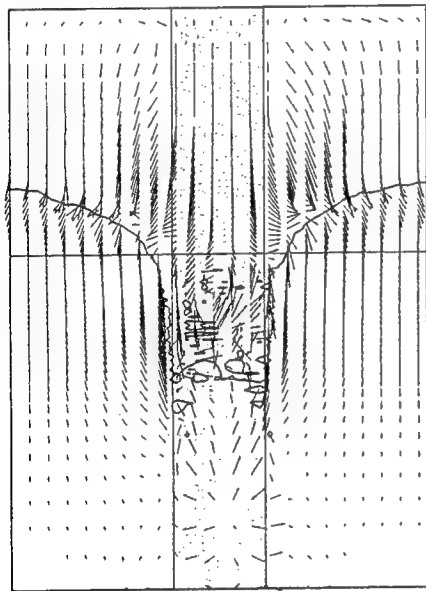


Figure 36: Same as Fig.35, on the vertical plane including the back-surface of a vertical cylinder.

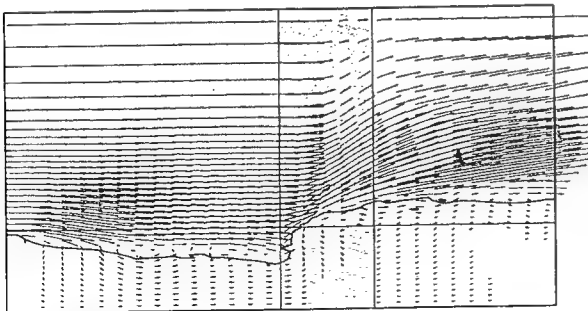


Figure 37: Interface configuration and velocity vectors of the simulation of sand-scoring by water current interacting with a vertical cylinder.

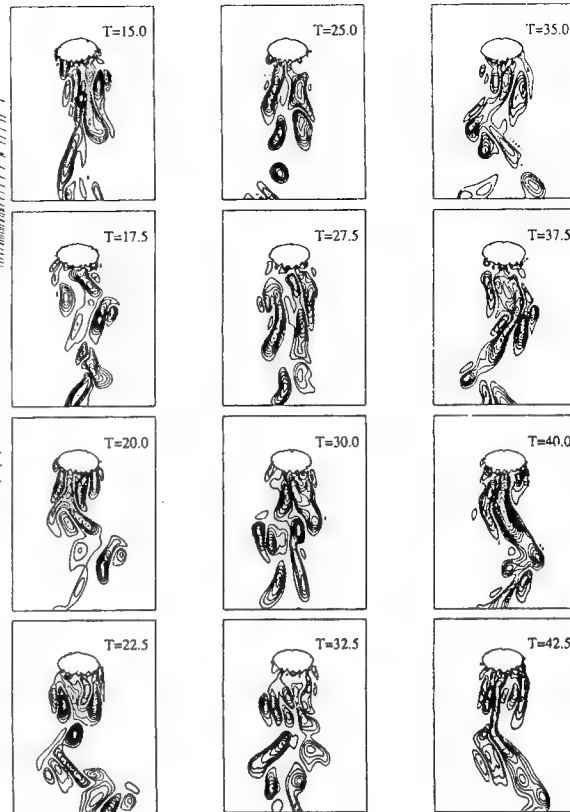


Figure 38: Time-evolution of longitudinal vortices behind a rising bubble, contours of vorticity about a vertical axis.

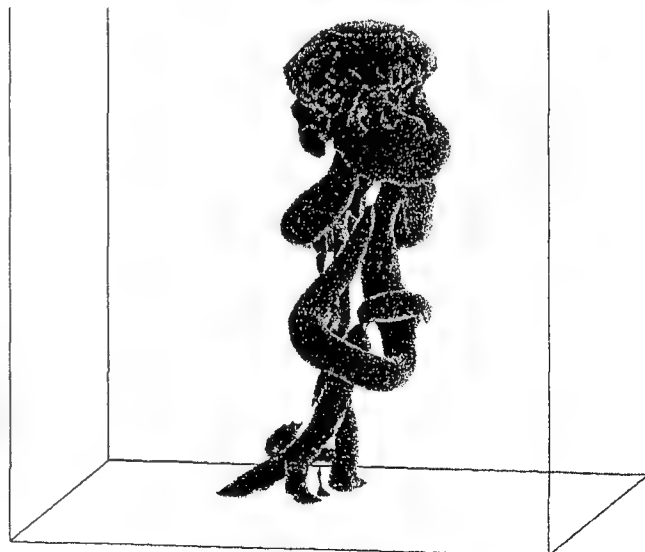


Figure 39: Iso-surface of the second-derivative of pressure in the flow-field about a rising bubble.

Yaw Effects on Model-Scale Ship Flows

J. Longo, F. Stern (University of Iowa, USA)

ABSTRACT

Yaw effects on model-scale ship flow is documented through towing-tank experiments for a 3.048 m Series 60 $C_B=0.6$ model ship. The data includes: photographs and video; resistance, side force, and yaw moment; sinkage, trim, and heel angle; wave profiles along the hull and wave elevations; and mean-velocity and pressure fields for numerous crossplanes from the bow to the near wake. Detailed descriptions are provided of the experimental equipment, procedures, and uncertainty analysis. Comparison of results for low (0.16) and high (0.316) Froude number with those from an earlier study for the without-yaw condition enables identification of the salient yaw- and wave-induced effects. The forces, yaw moment, and displacements increase significantly with increasing yaw angle. The wave pattern is asymmetric with increased/decreased Kelvin angle, wave lengths, and amplitudes on the windward/leeward sides, respectively. Close to the hull, the differences are confined to the bow, whereas away from the hull the differences are throughout the measurement region, i.e., nearfield. The mean-velocity and pressure fields are dominated by strong crossflow effects, including forebody and afterbody keel and bilge vortices. The results should be useful for computational fluid dynamics validation and are available along with the geometry and conditions.

NOMENCLATURE

α_K, β, η	Kelvin (wave envelope), yaw, heel angle
AP, FP	After and forward perpendicular
B	Ship model beam
C_B	Block coefficient $[= \nabla / (L_{PP}BT)]$
C_M	Moment coefficient
C_S	Sideforce coefficient
C_T	Total-resistance coefficient
δ	Boundary-layer thickness
$d_{FP, m, AP}$	Displacements at FP, midship, and AP
Fr	Froude number $(= U_o / \sqrt{gL_{PP}})$

$F_{x, y}$	Resistance and sideforce, respectively
g	Gravitational constant
H	Total head
L_{PP}	Model length between perpendiculars
λ_t, λ_d	Transverse and diverging wavelengths
M_z	Yaw moment
ν	Kinematic viscosity
p	Mean pressure
θ	Diverging-wave angle
ρ	Density
Re	Reynolds number $(= U_o L_{PP} / \nu)$
S	Hull surface area
σ, τ	Sinkage and trim, respectively
T	Ship model draft
u, v, w	Mean velocities in ship coordinate system
U_o	Carriage speed
ω_x	Axial vorticity
ζ, ζ_x	Wave elevation and axial wave slope
∇	Ship model displacement

INTRODUCTION

Ship-flow patterns depend on hull geometry and operating conditions such as speed, maneuvering, and ambient seas. Ships that operate in the straight-ahead condition in calm water generate symmetric flow patterns with respect to the hull centerplane. This is the design condition. For slender, medium-speed ships, these patterns have limited wave breaking and wave- and body-induced vortices and are well documented, but only partially documented for other hull forms that have some of the above features. Furthermore, high-speed and full-form ships in the design condition can exhibit features such as wave breaking and wave- and body-induced vortices that are observed in what are called off-design conditions for a ship. Other examples of off-design features that occur for design conditions include flow over an asymmetric stern, a yacht that requires a sideforce to counteract the load on the sails, or the straight-ahead motion of a SWATH or catamaran where

interaction of the hulls creates lifting effects. There are limited data that document off-design characteristics, and lack of understanding as to the underlying physics of the flow features. Off-design conditions frequently occur such as when ships maneuver or advance through a cross current. These situations produce the off-design features defined above and spray and bubble entrainment, which are also not well documented. A summary of documented surface-ship studies is provided in (1), including an evaluation of their usefulness for computational fluid dynamics validation.

Herein, the straight-ahead condition is defined as the zero-yaw, i.e., $\beta=0^\circ$ condition. The other cases, such as maneuvering, cross current, or lift cases (yacht, SWATH, or catamaran), are defined as yaw or $\beta \neq 0^\circ$ conditions. It is shown that even for a slender ship, the yaw condition displays many flow features that are common in off-design ship flows. Admittedly, the yaw case is an approximation to the off-design condition, i.e., nominal-wake measurements in the propeller plane of a high-speed FF 1052 combatant (2) display significant differences between zero-yaw tests in a straight basin, yaw tests in a straight basin, and yaw tests in a maneuvering basin (rotating arm). Some of these differences, i.e., axial-velocity contours, were unexpected. Nonetheless, the yaw case has many features of interest that are shared by both design and off-design conditions, it can be performed in a towing tank, and it builds on previous experimental work. This paper is concerned with documentation of the yaw case.

The goals for the present work are to (i) explore and identify the important flow features associated with a yawed body and (ii) document the flow features in sufficient detail for validation of RANS CFD codes. The emphasis is on 'explore' because the range of yaw-induced changes to the flow field was unknown.

The yaw project is part of an Iowa Institute of Hydraulic Research (IIHR) study concerning free-surface effects on boundary-layer and wake flow. The research and discussions of wave-boundary layer and wake interactions herein, rely upon and compliment previous fundamental studies with flat plates, (3)-(6) and previous work at the IIHR for the 3.048 m Series 60 $C_B=0.6$ in the zero-yaw condition, (7) and (8), which is precursory for the present study. Also of relevance is the recent Series 60 $C_B=0.6$ bow study (9). The yaw study is related to the basic topics of three-dimensional separation (10), wave breaking (11), and vortex-free surface interaction (12) each of which represents a major field of study. Other related work with application to ship flows are provided in (13).

In this study, model-scale experiments are performed in a towing tank with a 3.048 m Series 60

$C_B=0.6$ ship hull. Visualization of the flow is performed with photographs and video for a range of Froude number (Fr) and β . Resistance, sideforce, yaw moment, sinkage, trim, and heel angle are measured for a range of Fr and β . Additionally, wave profiles along the hull and wave elevations are measured for a range of yaw angles and high (0.316) and low (0.16) Fr . For $\beta=10^\circ$, detailed mean-velocity and pressure fields are measured at ten axial stations for $Fr=0.16$ and 0.316 and at several stations in the wake of a breaking wave for $Fr=0.316$. Finally, and in accordance with established standards and guidelines, an uncertainty analysis is performed for each experiment.

The organization of this paper is as follows. First, a brief description of the experimental facilities and equipment, procedures and conditions, and uncertainty analysis is given. Then, the results are presented with regard to the essential yaw- and wave-induced effects observed in the experiments. This paper is based on Ph.D. thesis research and the results are extensive. Many discussions are abbreviated, however, the complete results are provided in (13). Finally, conclusions from this study are given with recommendations for future work.

OVERVIEW OF THE EXPERIMENTS

Facilities and equipment

A cartesian-coordinate system (Figures 1 and 2) is used that is fixed to the model. The x-axis is coincident with the model centerline, and the y- and z-axes are directed toward the starboard side of the model and upward, respectively, with the origin at the intersection of the waterplane and the FP. Yaw angle is the angle between the model centerline and the tank centerline. For the orientation shown in Figures 1 and 2, the port side is the windward side and the starboard side is the leeward side. Alternately, if the yaw condition approximates a turning ship, the port and starboard sides correspond to the outboard and inboard sides of the turn, respectively.

Towing tank

The IIHR towing tank is 100 m long and 3.05 m wide and deep. Wave dampers near the free surface on the sidewalls allow for twelve-minute intervals between carriage runs. The carriage is cable driven by a 15-horsepower motor. On board the carriage, a cabinet holds the computer and other instrumentation.

Ship model and geometry

The ship model for the experiments is a 1:40 scale 3.048 m Series 60 $C_B=0.6$ (Figure 1). The Series 60 $C_B=0.6$ is a single-propeller merchant-type ship, a standard for ship-hydrodynamic research, and in particular, was chosen with three other hull types as a representative hull form for the CEP (14). The lines of

the present model conform to the standard offsets. The stern geometry is based on the original methodical series (15). The model is constructed of fiber-reinforced Plexiglas and epoxy resin. It is equipped with a stern tube aperture and propeller hub, however, all experiments are for the without-propeller condition. A set of grids is applied to the model for the wave-profile measurements and replaced with station lines from the FP to the AP every $0.1 \times L_{pp}$ for the mean-flow measurements. To initiate transition to turbulent flow, a row of cylindrical studs of 1.6 mm height and 3.2 mm diameter are fixed with 9.5 mm spacing on the model at $x=0.05$. The size and spacing of the studs is in accordance with standard practices, however, for the yaw cases, there is some question about the effectiveness of the port-side studs because the boundary layer (δ) is very thin on that side.

Instrumentation

A three-channel (two force and one moment) load cell is fixed at the midpoint of the model to measure the total resistance, sideforce, and yaw moment. The towing height is above the waterline, $z/T=0.24$. Dedicated signal conditioners are used at each channel for filtering and amplifying the output from the load cell. Sinkage, trim, and heel angle are determined from measurements of the linear displacements at the FP, midship, and AP with rectilinear potentiometers. The range of each potentiometer is 10 cm. Global-wave elevations are measured with two capacitance-wire probes that have digital interfaces developed at the IIHR for high-resolution, low-noise, wave-elevation measurements (16). The local-wave elevations are measured with four manual point gauges. These devices have a measurement range of about 20 cm. Mean-velocity and pressure measurements are taken with two five-hole pitot probes and a static-pressure tube. Each probe orifice is ported via vinyl tubing to a differential pressure transducer with a 0.32 psi range. The transducers are electrically connected to individual signal conditioners equipped with 1-Hz low-pass filters. A Modulynx precision-positioning system is used in the local-wave and mean-velocity and pressure measurements for movement of the traverses in the yz-plane. The Modulynx communicates through the computer serial port by a RS-232 cable.

Data-acquisition systems

Data is sampled with an IBM PC-XT compatible microcomputer and a multi-channel analog-digital translation board. An eight-channel board is used for the forces, yaw moment, displacements, and global-wave elevation tests. A sixteen-channel board is used for the mean-velocity and pressure measurements. All data is sampled through a low-pass filter in order to remove the effect of carriage vibration noise.

Calibration procedures

The load cell is statically calibrated with weights and a moment arm. The potentiometers are calibrated by placing the unit horizontal and extracting the core to its midpoint. Then, the core is moved in increments throughout the measurement range using a ruler as a reference for the changes in position. The capacitance-wire probes are statically calibrated. Initially, the probes are submerged at their midpoints and then manually moved up and down throughout the measurement range. The ten differential pressure transducers are statically calibrated with two water tanks. One is moved up and down with an automated traverse while the other is fixed. The calibration setup and procedures for the five-hole probes are very similar to those used in (7). The details of the calibrations are reported in (13).

Procedures and conditions

Three types of measurements are made: (i) forces, yaw moment, and displacements, (ii) wave profiles and elevations, and (iii) mean-velocity and pressure fields. All tests are done with the static model at its design waterline. For the forces, yaw moment, and displacements, the model is in the free condition, i.e., it is allowed to heave, pitch, and roll. For all other measurements, the model is fixed to the carriage, i.e., restrained from moving in any direction relative to the carriage. A summary of the type (ii) and (iii) experiments is shown in Figure 3.

Forces, yaw moment, and displacements

Resistance, sideforce, yaw moment, sinkage, trim, and heel angle are measured for five yaw angles, $\beta=0^\circ, 2.5^\circ, 5^\circ, 7.5^\circ$, and 10° and a range of Fr, $Fr=0.1-0.35$ ($U_0=0.55-1.91$ m/s). The carriage is started and after the initial acceleration and necessary delay for steady-flow conditions, data are acquired on four channels (speed, total resistance, sideforce, and yaw moment; or speed, FP, midship, and AP displacements) at a rate of 100 Hz and 200 samples per channel. The total sampling period is eight seconds per carriage run.

Wave profiles

Wave profiles on the hull are recorded for two Fr, $Fr=0.16$ and 0.316 (0.87 and 1.73 m/s, respectively) at three yaw angles, $\beta=0^\circ, 5^\circ$, and 10° . For each combination of Fr and yaw angle, twenty-nine measurements are made on port and starboard sides of the model except for $\beta=0^\circ$ where symmetry of the flow allows measurements on one side, only. The measurements are made by marking the top of the wave profile at every axial station with a fine-tipped wax pencil. The position of the mark is converted to a wave height with the grid on the hull surface. The wave

profiles are recorded after the carriage achieves a steady speed and the wave pattern is steady state.

Wave elevations

Global wave elevations are measured for high and low Fr and two yaw angles, $\beta=5^\circ$ and 10° . Wave-elevation data are taken with a capacitance-wire system situated 55 m upstream of the carriage and model. A capacitance-wire probe on the port and starboard side are fixed to wall-mounted traverses and electrically connected to an IBM-compatible computer via a digital interface developed for processing wave-height data. The carriage attains a steady speed 25 m prior to reaching the traverses, and after contacting a switch that is fixed to the tank wall, the sampling period is initiated. A sampling frequency of 100 Hz over 8 seconds is used for each wave cut. The initial wave cuts are taken very near the model (within 2 cm) and subsequent cuts are taken at 5 cm intervals in the $\pm y$ -direction up to the tank sidewalls. In the x -direction, data is taken 1 m upstream of the FP to 1 ship length and 3 ship lengths downstream of the AP for low and high Fr, respectively. Wave reflection from the tank sidewalls limits the axial amount of useful data in the wake. Roughly sixteen cuts on each side of the model are recorded at every Fr and yaw angle.

Local regions at the bow, stern, and near wake on port and starboard sides of the model could not be measured with the wire probes. These areas are measured with a set of point gauges. The gauges are fixed to the automated traverses and positioned relative to the model. After reaching a steady speed and allowing the wave field to reach steady state, the gauges are adjusted to rest on the free surface. In areas of high free-surface turbulence such as the near wake and at the crest of the port bow wave for $Fr=0.316$ and $\beta=10^\circ$, the probes are adjusted to a level of average wave elevation¹. Several runs are made at each x -station in order to measure the gaps between the model and the global wave field.

Mean-velocity and pressure field

Mean-velocity and pressure fields are measured for high and low Fr ($Re=5.3e06$ and $2.7e06$, respectively) at one yaw angle, $\beta=10^\circ$ and on both the port and starboard sides of the model. Before every carriage run, a 'zero-point' file is taken for the zero-velocity condition, i.e., the voltage output from the speed circuit and ten pressure transducers is measured while the carriage is at rest, thus, creating a speed and

pressure reference for the pending measurements. The carriage is started and the data acquisition is manually initiated at a designated point at which the model speed is steady and the wave pattern is steady state. Two or four measurements per probe are taken per carriage run for high and low Fr, respectively. A delay of 3.5-4 seconds is used between each measurement position to allow for probe movements and transducer responsiveness. Following each carriage run, the velocity components, pressure coefficients, and total head are plotted. Data is acquired at a rate of 750 Hz and 600 samples are collected per channel giving a sampling period of about 0.9 second per channel. At every station and high and low Fr, approximately 800-1500 points are measured in the yz -plane. The yz -measurement positions are determined from the zero-yaw experiment (7), however, several additional points are measured further from the model where the effects of yaw angle are evident but absent in the zero-yaw experiment.

Uncertainty analysis

The uncertainty analysis is carried out according to the standards and guidelines of the American Society of Mechanical Engineers (17). The detailed methodology and procedures are provided in (18). The error sources are divided into three categories: calibration, data acquisition, and data reduction. The measurement systems are those for the model geometry, data locations, carriage speed, and the various (loadcell, marker/grid, capacitance wire, five-hole probe) data-acquisition systems. Each measurement system has associated variables that are measured and contain bias (fixed) and precision (random) errors. The bias errors for the measurement systems are estimated and the precision errors are determined through a program of repeated measurements. Often, several measured variables are used to derive an experimental result, and the errors from each variable propagate into the final result. Propagation of errors are addressed with data-reduction equations in order to derive final values of bias and precision errors for each result. The bias and precision errors are combined with a root-sum-square method to derive an uncertainty for each result with a 95% confidence level. The uncertainties are listed in Table 1 and are considered reasonable for a towing tank experiment. There tends to be more scatter of the data for low Fr which explains the Fr dependence of the uncertainties. Values for the resistance and flow are comparable to the uncertainties listed in (1).

RESULTS AND DISCUSSION

Discussion of the results follow with regard to yaw- and wave-induced effects and the features of the flow for both high and low Fr. Initially, an overview

¹ Average wave elevation is defined as a point where the probe tip appears to make contact with the free surface approximately 50 % of the carriage-run duration.

of ship-wave patterns and definitions of certain parameters are provided. Then, photographs of the wave field at the port bow and the stern and wake for $\beta=0^\circ$, 5° , and 10° provide qualitative descriptions of yaw effects. Subsequent discussion of the detailed quantitative results begin with resistance, sideforce, yaw moment, sinkage, trim and heel angle. Next, the wave profiles along the hull and the wave patterns are discussed. Finally, the mean velocity and pressure field results are presented for $Fr=0.316$.

General observations

The Kelvin wave pattern (Figure 4c) can be used to explain the features of full- and model-scale (Figure 4a-b) wave patterns. A Kelvin wave pattern results from a point source moving at a speed, U_s , across a free surface with gravity waves, which is a potential-flow solution for an infinite fluid with linearized free-surface boundary conditions. The resulting Kelvin wave pattern is enclosed in a delta-shaped envelope with a semiangle (wave-envelope angle) of $\alpha_K=19^\circ28'$. The pattern consists of transverse waves that travel along the line of motion and diverging waves that radiate at an angle, $\theta=35^\circ$ (diverging wave angle), from the symmetry plane. The transverse waves move at the speed of the disturbance ($U_t=U_s$) and have wavelength:

$$\lambda_t = 2\pi Fr^2 \quad (1)$$

The diverging waves move at a reduced speed ($U_d=U_s \cos\theta$) and have wavelength:

$$\lambda_d = 2\pi Fr^2 \cos^2\theta = \lambda_t \cos^2\theta \quad (2)$$

The diverging wave amplitudes are larger and more conspicuous than the transverse wave amplitudes.

In the far field, a ship hull can be approximated as a single point source because the global wave pattern exhibits many characteristics that are illustrated in Figure 4c. The near field is considerably more complex as it includes interactions of many point sources, i.e., every point along the hull acts as a source. However, the wave pattern can still be characterized by the same parameters (α_K , θ , λ_t , λ_d) and some additional flow features. Table 2 summarizes the Kelvin and present (for $\beta=0^\circ$, 5° , and 10°) values of these parameters for $Fr=0.316$.

The present study focuses on the near field, which is conveniently referred to by regions. The local region is close to the hull (Figure 4a) and the global region is further from the hull (Figure 4b). The local region is characterized by steep waves that overturn and break and create significant white water and bubbles. The important features of the local wave pattern include the bow and stern waves which initiate as crests and the shoulder waves which initiate as troughs. In the global

region, the wave pattern is complex due to the interactions of the divergent and transverse wave systems.

At the bow, the incident flow creates a stagnant region (decelerated flow) near the bow stem. At the FP of a wedge-shaped bow, a thin film develops aft of the free surface-bow stem juncture and transitions into a bow wave. The thin film can be a site where bow vortices are generated. The hull-free surface contact line is the juncture line between the hull surface and the free surface. Typically, the contact line is a localized region of high free-surface turbulence. Free-surface turbulence is characterized by random or unsteady fluctuations of the free surface and also occurs in the wake and when wave breaking is present. Wave breaking is characterized by white water and free-surface turbulence along a wave front that becomes unstable (this is also observed in the yaw study). Waves that curl, overturn, and entrap air pockets are called plunging breakers. Spilling breakers occur when the crestline of a wave becomes unstable and slides down the wave front. When a wave breaks and impinges on the free surface, air can be entrained into the flow field (bubbles) and vorticity can be introduced into the flow, (wave-induced vorticity). Clearly, at model-scale, there is a comparative absence of wave breaking and white water near the hull and in the wake which is largely not understood. The wake regions of ships or models are characterized by significant free-surface turbulence and unsteady flow.

Photographs of the port-side bow and wake are shown in Figure 5 for $\beta=0^\circ$, 5° , and 10° . At $\beta=0^\circ$, the wave pattern is typical of a slender hull form and follows the general pattern described above, i.e., the wave pattern is enveloped in a Kelvin wedge that sweeps back from the bow. In the figures, the local regions show the bow and fore-shoulder waves and the stern wave system. The global regions show interactions of the bow and fore-shoulder wave and interaction of the wave systems at the stern. The stern flow and wake are symmetric. Although not apparent from the photo, measurements indicate that the flow gradually rises for $-0.05 \leq x \leq -0.0027$ followed by a sharp increase of a thin film at the bow-stem/free-surface juncture. Similarly, at $x=0$, measurements of the wave elevation indicate a gradual rise for $0.03 \leq y \leq 0.002$ followed by a sharp increase of a thin film up to the hull surface. Beads of fluid originate at the bow stem and FP and form along the top of the thin film and appear vortical. Initially, they are steady and laminar. They are carried downstream and transition to unsteady and turbulent and merge with the downstream flow. The flow at the bow has the appearance of an attached spray sheet and bow vortices. Observations of the FP

at $Fr=0.16$ show that the incident flow initiates on the bow similarly as $Fr=0.316$ with a thin film and attached spray sheet but on a much smaller scale. In the photograph, the bow wave grows in amplitude and fullness with increasing x but does not break. There is very little free-surface turbulence in the wave pattern except along the hull-free surface contact line downstream of the bow wave and at the stern and wake where there is moderate unsteadiness.

At $\beta=5^\circ$, the wave field is altered. On the port side, the Kelvin wedge appears to be displaced further from the hull centerplane, [i.e., $\alpha_K(5^\circ) > \alpha_K(0^\circ)$]. At the stern and wake, the wave field is noticeably asymmetric with respect to the hull centerplane due to the diverging stern wave which is roughly aligned with the models longitudinal axis, i.e., the x -axis in Figure 1. Locally at the bow, the wave amplitude and steepness is increased. In the global regions, interaction of the wave systems give the wave pattern an asymmetric appearance. The flow initiates on the FP similarly as for $\beta=0^\circ$ with an attached spray sheet and bow vortices, although, the amplitude and thickness of the thin film is increased. Again, observation at the low speed confirms a similar flow pattern at the FP but on a smaller scale. In the photograph, wave breaking appears to be imminent which is verified by the free-surface turbulence at the crestline along the wave front. Free-surface turbulence also appears in the wake of the bow wave, along the hull-free surface contact line near the midbody, and in the wake. Observation shows no air entrainment into the flow but increased unsteadiness at the bow and in the wake.

At $\beta=10^\circ$, the wave field is altered in extreme. On the port side, further displacement of the Kelvin wedge from the model is displayed, [i.e., $\alpha_K(10^\circ) > \alpha_K(5^\circ) > \alpha_K(0^\circ)$]. In the wake, the diverging stern wave is roughly aligned with the models longitudinal axis. Locally at the port bow, the bow and fore-shoulder wave systems appear to merge. In the global regions, interaction of the wave systems increase the asymmetry of the wave pattern. The flow upstream of the FP initiates on the bow similarly as $\beta=0^\circ$ and 5° , however, observation shows that the thin film rises more steeply than for the previous cases and is thicker. Observations of the flow over the bow at $Fr=0.16$ are consistent with those for $\beta=0^\circ$ and 5° . In the photograph, the bow wave increases in size and rises steeply on the upstream side with increasing x and then falls away from the hull. At the crest, the spray sheet becomes detached and evolves into a plunging-type breaker close to the hull and then a spilling-type breaker as the wave is further displaced from the hull. The overhead side view shows large disturbances including white water, bubbles, and air entrainment into the flow

field similarly as is evident in Figure 4b but clearly less than at full-scale in Figure 4a. The wake is characterized by significant free-surface turbulence. At the hull-free surface contact line, the level of turbulence is consistent with $\beta=0^\circ$ and 5° . The unsteadiness of the wave pattern is increased especially in the wake of the port bow wave and at the stern.

Forces, yaw moment, and displacements

Resistance, sideforce, yaw moment, sinkage, trim and heel angle results are presented in Figure 6 and the equations are provided below.

$$C_T = F_x / (0.5\rho U_o^2 S) \quad (3)$$

$$C_S = F_y / (0.5\rho U_o^2 S) \quad (4)$$

$$C_M = M_z / (0.5\rho U_o^2 L_{PP}^3) \quad (5)$$

$$\sigma = \frac{2}{Fr^2} \frac{\Delta d_{FP} + \Delta d_{AP}}{2L_{PP}} \quad (6)$$

$$\tau = \frac{2}{Fr^2} \frac{\Delta d_{AP} - \Delta d_{FP}}{L_{PP}} \quad (7)$$

$$\eta = \tan^{-1} \frac{2\Delta d_m - (\Delta d_{FP} + \Delta d_{AP})}{B} \quad (8)$$

Resistance and sideforce are the drag and lift, respectively, in the ship coordinate system, and yaw moment is the counter-clockwise moment (top view, Figure 2) in the xy -plane resulting from the yawed orientation. Sinkage quantifies the upward or downward deflection (heave) of the hull and is positive for downward deflection. Trim quantifies the relative deflections of the FP and AP (pitch) about the midbody and is negative for the bow-down orientation. Heel quantifies the motion of the hull about its longitudinal axis (roll) and is positive for counterclockwise rotation as seen by looking upstream.

At $\beta=0^\circ$, results for resistance are compared with those in (7). For the same model and towing conditions, the quantitative and qualitative character of the results are very similar. At low Fr ($0.1 \leq Fr \leq 0.2$), C_T is low, small oscillations are present, and the resistance decreases. Wave making is minimal and the resistance is mainly viscous. For medium Fr ($0.2 \leq Fr \leq 0.3$), C_T sharply increases due to increased wave resistance. At high Fr ($Fr > 0.3$), the resistance plateaus and then increases again at $Fr=0.34$. Through the Fr range, the wave pattern continuously changes especially at higher Fr . The interference of the diverging and transverse wave systems accounts for the Fr dependence of C_T . These are the 'humps and hollows' in the resistance curve. As expected, results for sideforce and yaw moment are zero when $\beta=0^\circ$. The

Fr for the detailed measurements are determined from the resistance curve where for $Fr=0.16$, the resistance is low, and the effects of wavemaking are small, while at $Fr=0.316$, the resistance has passed through a sharp peak and reached a plateau where the effects of wavemaking are comparatively large.

For $\beta>0^\circ$, resistance curves increase but are qualitatively similar versus Fr for each β . For fixed Fr, ΔC_T is relatively constant for increasing β . The side-force curves are linear in Fr for low and medium Fr and all β . The slope increases with β . For high Fr, nonlinearity in Fr is indicated with increasing nonlinearity for increasing β . Also, for $\beta=10^\circ$, the curve displays wavy characteristics. For fixed Fr, ΔC_S increases with increasing β . The yaw-moment curves appear to be roughly linear through the Fr range for $\beta=2.5^\circ$ and 5° and then nonlinear for increasing β .

Resistance increases with increasing β are probably a result of increased viscous and wave-making effects. It will be shown in the following sections that wave breaking and wave- and body-induced vortices are dominant flow features for the yaw case and surely play a role in the towing resistance of the model. Likewise, the wave patterns for the yaw cases will be shown to have greater area and larger amplitudes, and thus, larger components of wave-making resistance. Interestingly, interactions of the separate wave systems in the global regions of the wave pattern for $\beta>0^\circ$ are probably similar to those for $\beta=0^\circ$ because the positions of the humps and hollows for increasing β are constant.

In the free condition, the changing shear stress and pressure distributions with Fr are responsible for adjusting the models sinkage and trim. Additionally, yaw angle induces a heeling angle toward the windward side. At low Fr small deflection of the hull (sinkage) and downward deflection of the FP in relation to the AP (trim) occurs (19). As Fr increases the bow-down movement is reduced, and at about $Fr=0.32$, the bow rises upward, the stern sinks downward, and the attitude of the hull is appreciably different than for low Fr. Significant sinkage, trim, and heel are associated with increases in wave resistance and wave elevations. At $\beta=0^\circ$, the sinkage is roughly linear in Fr but with oscillations, and σ increases with increasing Fr. The trim decreases slightly for low and medium Fr and then increases sharply in $0.25 \leq Fr \leq 0.35$. Interestingly, τ looks very similar to C_T through the Fr range with corresponding sharp increases where the wave resistance grows. As expected, the heel is uniformly zero for $\beta=0^\circ$.

For $\beta>0^\circ$ and similarly as the forces and yaw moment, σ , τ , and η increase in magnitude. As per C_T , the sinkage curves maintain consistent shape and slope through the range of yaw angles, however, $\Delta\sigma$ increases

with β . Similarly with σ , trim curves retain consistent shape and slope for all β , and $\Delta\tau$ increases with β . The trim becomes more negative with β which means that increases in yaw angle cause increases in the downward and upward pitch of the bow and stern, respectively. The heel angle is roughly linear in Fr for $\beta=2.5^\circ$ and then increasingly nonlinear in Fr for the higher yaw angles. Note that for $\beta=10^\circ$, $Fr=0.32$ was the maximum Fr at which the breaking bow wave did not swamp the model.

Wave profiles

Wave profiles on the hull are measured for high and low Fr and $\beta=0^\circ$, 5° , and 10° and are shown in Figure 7. The results are normalized by the velocity head, $U_0^2/2g$. Several points along the wake centerplane are interpolated from the wave patterns in order to extend the wave profiles downstream of the AP.

For $\beta=0^\circ$ and $Fr=0.316$, the wave profiles (marker/grid) are in close agreement with those in (7) (35 mm photography). The data in (7) compare favorably with data in the CEP (14). The wave profile along the hull defines the local wave system and the transverse wavelength, λ_t . The bow and stern waves initiate as crests and the forebody- and afterbody-shoulder waves initiate as troughs. The initial bow crest and forebody trough are larger than the stern crest and afterbody trough, probably due to the relative effects of the expansion and contraction of the hull at the forebody and afterbody, respectively, and the associated pressure field and viscous damping with increasing x. Two transverse wavelengths are apparent on the hull. The first, $\lambda_t=0.55$, is fairly close to the value for a Kelvin source at the same speed, $\lambda_{t0.316}=0.63$, and the second, $\lambda_t=0.425$, is somewhat shorter. The data on the centerplane upstream of the FP show the sharp rise in elevation at the free-surface bow-stem juncture.

For $\beta=0^\circ$ and $Fr=0.16$, the zero-yaw wave profile is in fair agreement with (7). The bow and stern wave crests are apparent between which there is a broad region along the hull where the profile is negative. The fore- and aft-shoulder wave troughs are very shallow. The initial bow crest and forebody trough rapidly diminish in amplitude with increasing x probably due mainly to viscous damping with increasing x. One transverse wavelength is apparent on the hull, $\lambda_t=0.13$, and is shorter than for the high Fr, $\lambda_t=0.55$, and also shorter than for the Kelvin source at $Fr=0.16$, $\lambda_{t0.16}=0.16$. The bow wave amplitude exceeds that for the high-Fr case when nondimensionalized by the velocity head.

For $\beta=5^\circ$ and 10° , and $Fr=0.316$, most resulting changes to the profiles occur upstream of $x=0.25$. For $x<0.25$, and the port side, the profiles shift upward significantly with increases in β . The

largest increases in the profiles occur where $\zeta_x=0$. On the starboard side, the profiles decrease significantly with increases in β . Again, the largest $\Delta\zeta$ occur where $\zeta_x=0$. For $x>0.25$, the influence of β is fairly small except for decreases and increases in the fore and aft shoulder-wave troughs. On the wake centerplane, ζ increases with increasing yaw angle. On both sides, two transverse wavelengths are apparent on the hull. On the port side, the initial λ_t increases to 0.6 for $\beta=5^\circ$ and 10° . On the starboard side, the initial λ_t decreases to 0.53 and 0.5 for $\beta=5^\circ$ and 10° , respectively. The subsequent transverse wavelengths are similar as per $\beta=0^\circ$.

For $\beta=5^\circ$ and 10° and $Fr=0.16$, again most yaw-induced changes to the profiles occur upstream of $x=0.25$. For $x<0.25$ on the port side, ζ shifts upward with increases in β . On the starboard side, oscillations are apparent such that the crests and troughs have increased amplitudes. For $x>0.25$, the influence of β is minimal except for $\beta=10^\circ$ on the port side which shows reduced crests and troughs and the starboard side which shows increased troughs on the forebody. On the wake centerplane, ζ decreases with increases in yaw angle. On both sides, two transverse wavelengths are apparent on the hull. On the port side, λ_t is invariant with increasing β . On the starboard side, λ_t decreases from 0.13 ($\beta=0^\circ$) to 0.1 ($\beta=5^\circ$ and 10°). Similarly with $\beta=0^\circ$, the bow wave amplitudes exceed those for the high- Fr case when nondimensionalized by the velocity head.

Wave elevations

Next, contours of the wave elevations and axial wave slopes are discussed for $Fr=0.316$ and $\beta=0^\circ, 5^\circ$, and 10° (Figure 8). Figures for $\beta=5^\circ$ are not shown. The low- Fr data is not discussed because the elevations and gradients are comparatively negligible with those at $Fr=0.316$. The measurements are made in the tank coordinate (x, y, z) system, but, are presented in the ship coordinate (x, y, z) system by rotating the wave field by the amount of yaw (Figure 3). The axial gradients in the wave patterns are obtained by numerically differentiating ζ . The wave-pattern parameters, α_K , θ , and λ_d are determined from the ζ_x contours with line drawings as per Figure 4c and presented in Table 2.

For $\beta=0^\circ$ and $Fr=0.316$, the contours display the overall features of the wave pattern. The diverging systems in ζ_x give the pattern a wedge-shaped appearance. The wave-envelope angle is 22° , which is close to the Kelvin-source value, and the apex of the wedge is upstream of the FP. The diverging wave angle, $\theta=53^\circ$, is considerably larger than the Kelvin-source value such that $\lambda_t/\lambda_d=2.75$, i.e., $\lambda_d=0.2$, which is less than half the Kelvin-source value. Note that the largest difference among the Kelvin parameters is

$\lambda_d < \lambda_t|_{\text{Kelvin}}$. Clearly, there are many different amplitudes in the wave field with the highest values at the bow wave crest and fore-shoulder wave trough. The local region characteristics are similar to those of the wave profiles. In the global region, the complex interaction of the wave systems is apparent. The rapid rise of the free surface at the FP and the thin film of fluid in that region is indicated by a dense clustering of contours. Free-surface turbulence and general unsteadiness of the wave pattern is suggested by the irregularity of the contours at the afterbody and stern. ζ_x is in phase with the elevations and has similar patterns.

For $\beta=5^\circ$ and 10° and $Fr=0.316$, the wave patterns become asymmetrical, i.e., for $\beta=5^\circ$ on the port and starboard sides $\alpha_K=25^\circ$ and $\alpha_K=22^\circ$, respectively, and for $\beta=10^\circ$ on the port and starboard sides $\alpha_K=30^\circ$ and $\alpha_K=21.5^\circ$, respectively. Note that α_K increases on the port side and remains nearly constant on the starboard side with increasing β . Also, the total wave-envelope angle (α_T) increases in comparison to that for $\beta=0^\circ$ by about β . On the port side, θ decreases with increasing β and λ_d increases with β , i.e., $\lambda_d=0.31$ and 0.34 for $\beta=5^\circ$ and 10° , respectively, such that λ_t/λ_d continuously decreases. On the starboard side, θ decreases at $\beta=5^\circ$ and then increases for $\beta=10^\circ$. Also, λ_d increases and then decreases with increasing β , i.e., $\lambda_d=0.35$ and 0.18 for $\beta=5^\circ$ and 10° , respectively, such that λ_t/λ_d decreases and then increases. The wave amplitudes clearly increase on the port side and decrease on the starboard side of the model with increasing β . In particular, note the increases and reductions of the bow wave on port and starboard sides, respectively, when β is increased from 0° to 10° . Observation of ζ_x indicates that the port bow-wave crestline curves back toward the model with increasing x . As per the wave profiles, the local regions are affected only for $x<0.25$, whereas in the global regions, the wave patterns are significantly changed with increasing β from bow to stern. Dense clustering of contours at the bow on the port side confirms the sharp increase of the bow wave at the FP and the existence of an attached thin film. For $\beta=5^\circ$ and 10° , the wave breaking in the patterns is difficult to distinguish in the contours because of the unsteadiness of this phenomenon. Free-surface turbulence and unsteadiness are mainly evident along the crestline of the port bow wave and at the stern and near wake as per $\beta=0^\circ$. However, at the stern for the yaw cases, the merging of the port and starboard systems is a source of increased unsteadiness. These results are consistent with the photographs (Figure 5). Similarly with $\beta=0^\circ$, ζ_x is in phase with ζ and has similar patterns, but the magnitudes are significantly increased and decreased globally on the port and starboard sides, respectively.

Mean-velocity and pressure field

Results for the mean-velocity and pressure field are presented next in Figures 9a-f. Contours of ω_x , H , p , u , and v and w are shown at all crossplanes for high Fr only, although, the discussions for the low- Fr tests are retained. The overall trends are similar between the high- and low- Fr flow fields, although significant free-surface effects are also exhibited for the former. Equations for the total head and axial vorticity are:

$$H = \sqrt{u^2 + v^2 + w^2} + p \quad (9)$$

$$\omega_x = \left(\frac{\partial w}{\partial y} - \frac{\partial v}{\partial z} \right) \quad (10)$$

TECPLOT was used to numerically differentiate the mean crossplane velocities to obtain ω_x . Results are presented at $x=0, 0.1, 0.2, 0.4, 0.6, 0.8, 0.9, 1, 1.1$, and 1.2 , and the discussions begin with the forebody and proceed to the afterbody and wake. Also, discussions in (13) provide details of each crossplane and the wave-induced vortex.

Most of the flow features in the yawed condition are significantly different than for the zero-yaw case. In many respects, the flow is completely altered. The boundary-layer and wake development is dominated by strong crossflow effects and vortices as opposed to p_x and weak crossflow effects observed in the $\beta=0^\circ$ case. The wave-induced effects at $Fr=0.316$ are explainable similarly as for $\beta=0^\circ$, i.e., the Fr -related differences in the velocity and pressure correlate with the wave field, which, however, is significantly more complex for $\beta=10^\circ$ than for $\beta=0^\circ$ creating a more complex boundary-layer and wake response. Also, a wave-induced vortex is identified due to the breaking bow wave on the port side of the hull which significantly affects the boundary layer and wake.

In Figure 9a, the extensive vorticity (ω_x) in the flow field is evident. On the forebody at $Fr=0.316$, keel and bilge vortices are visible beginning at $x=0.1$. The keel vortex is relatively weak and not evident beyond $x=0.4$. The bilge vortex is relatively strong. The vortex core is off the body and moves further from the centerplane with increasing x . On the afterbody, the forebody-bilge vortex weakens, but is distinct with a trajectory off of the body toward the free surface at an angle of about 5.7° to the centerplane. An afterbody-bilge vortex develops as per $\beta=0^\circ$. The vorticity has a core region that is off of the body and toward the free surface with a tail that extends toward the centerplane. There appears to be a weak interaction with the forebody-bilge vortex. At $x=1$ (AP), a counter rotating keel vortex is evident. In the wake, the forebody-bilge vortex dissipates and diffuses with trajectory towards the

free surface. The afterbody-bilge vortex becomes oval shaped and dissipates and diffuses with a trajectory off the body towards the free surface at an angle of about 2.1° to the centerplane. The vorticity pattern appears to rotate counterclockwise and reorganizes its structure with increasing x , i.e., at $x=1$, the long axis is parallel with the stern stem and subsequently parallel with the free surface at $x=1.2$. The afterbody-keel vortex dissipates relatively fast with a trajectory as per the afterbody-bilge vortex but at an angle of about 2.6° to the centerplane. There is limited interaction between fore- and afterbody-bilge vortices. A wave-induced vortex is evident on the port-side forebody which initiates between $0.2 < x < 0.4$ underneath the breaking bow wave and follows a trajectory near the free surface along the side of the hull. The vorticity in the breaking wave wake is also visible at $x=0.4$ near the free surface. At the afterbody and wake, the wave-induced vortex dissipates, diffuses, and mixes with the hull boundary layer and wake such that the overall wake pattern is largely increased on the port side. At $Fr=0.16$, the overall flow pattern is very similar to that of $Fr=0.316$ but with two important differences. First, the bilge and keel vortices appear weaker, and the trajectories are altered somewhat, i.e., the forebody-bilge vortex is at an angle of 5° to the centerplane (outward) and does not intersect the free surface at $x=1.2$ in contrast to $Fr=0.316$; the afterbody-bilge vortex is at an angle of 2° (outward); and the afterbody-keel vortex is at an angle of 2.8° to the centerplane (inward). Secondly, and due to the reduced wavefield, there is no wave-induced vorticity in the flowfield.

In Figure 9b, the viscous regions (H) on the hull and in the wake are evident. At $Fr=0.316$, the patterns correlate with ω_x and the boundary layer and wake losses but with stronger interactions between the loss regions of the keel and bilge vortices on the afterbody creating a somewhat more complex pattern. H displays similar Fr differences as per ω_x for the wave-induced vortex. For $Fr=0.16$ and in contrast with ω_x which decreased in magnitude with decreasing Fr , H is somewhat increased in magnitude which is a Reynolds number effect, i.e., the viscous regions are thicker for the lower Fr .

In Figure 9c, the pressure (p) field around the hull is displayed. At the forebody for $Fr=0.316$, p correlates with u such that the trends are the same but the magnitudes are reversed especially in the bow and stern regions and at the midbody where the flow accelerates and the pressure is low. An asymmetric stagnation-type flow is exhibited at the FP. In general, high and low pressure regions exist on the port and starboard sides, respectively. The lowest pressures are in regions of high ω_x with minimums in the core

regions. The bow wave stagnation effects are evident as increased pressures at $x=0$ and 0.1 . The pressure differences (Δp) between port and starboard sides are reduced near the midbody at $x=0.4$. At the afterbody, there is a continued reduction in Δp up to $x=0.9$ when Δp increases with the lowest p in regions of high ω_x and minimums in the core regions, i.e., for the forebody-bilge vortex and afterbody-bilge vortex. In the wake, the pressure recovery is evident. Lastly, apparently, most of the sideforce is generated at the bow and somewhat from the stern where Δp is largest. For $Fr=0.16$, the general patterns are similar except for some diminished features due to Fr and viscous effects. The pressure at the bow and stern is lower due to the reduced port-side bow wave system and wave effects at the AP and wake, respectively. The pressure field is higher over the midbody and stern especially in the regions of the vortex cores.

In Figure 9d, for $Fr=0.316$ and 0.16 , the axial velocity (u) contours are similar to H but also exhibit inviscid effects such as the stagnation flow at the FP and the acceleration around the midbody. For $Fr=0.316$, wave-induced effects are especially apparent at the bow on the port side and also at $x=0.4$ in association with the wave-induced vortex. By cross-referencing Figure 9d with Figure 9c, one can observe the correlation between u and p particularly at the bow and midbody and moderately at the stern.

In Figures 9e and 9f, the combination of transverse (v) and vertical (w) components of velocity show the nature of the crossflow that is induced by the keel, bilge, and wave-induced vortices. w is particularly useful for observing wave effects near the free surface and charting the dissipation and diffusion of vortices in the flow field. Differences in v and w due to Fr are evident at every x -station and confirm increased wave effects and vorticity for $Fr=0.316$.

CONCLUSIONS

Yaw effects on model-scale ship flow is documented through towing-tank experiments for a 3.048 m Series 60 $C_B=0.6$ model ship. The data includes: photographs and video; resistance, side force, and yaw moment; sinkage, trim, and heel angle; wave profiles along the hull and wave elevations; and mean-velocity and pressure fields for numerous crossplanes from the bow to the near wake. Detailed descriptions are provided of the experimental equipment, procedures, and uncertainty analysis. Comparison of results for low and high Fr with those from an earlier study for the without-yaw condition enables identification of the salient yaw- and wave-induced effects. When β increases, the forces, yaw moment, and displacements increase significantly. Increases in β produce

asymmetric wave profiles and elevations with large changes in ζ locally at the bow and globally everywhere. In contrast to the zero-yaw case, the yaw condition is dominated by strong crossflow effects that drive the flow from the port to the starboard side and asymmetric vorticity development at the forebody bilge, forebody keel, afterbody bilge, and afterbody keel. The distinct vorticity in the flow field originates from strong yaw-induced crossflow and large crossplane pressure gradients. Most of the wave-induced effects on the boundary layer and wake are explained as per $\beta=0^\circ$, by correlating the wave elevations and slopes of the free surface with the velocities and pressures in the underlying flow for both values of Fr .

Some unresolved issues for the Series 60 $C_B=0.6$ in yaw are hull surface-pressure distributions, turbulence measurements, unsteady flow, and wave breaking. These data would compliment the present study.

With regard to future work and recommendations, a new modern combatant hull form (DTMB model 5415) shown in Figure 4b has been adopted for study by the US Navy in support of rapid advancements in CFD. Some of the crucial unresolved issues in experimental ship hydrodynamics and model testing are turbulence measurements, unsteady problems such as a ship in waves, bubble entrainment into the flow field, wave breaking, bow flow, effects of appendages, and rigorous uncertainty analysis. Currently, efforts are underway at the IIHR to equip the towing tank with PIV instrumentation and a wavemaker for unsteady experiments with model 5415.

ACKNOWLEDGMENTS

This research was sponsored by the Office of Naval Research under Contract N00014-92-J-1092 under the administration of Dr. E.P. Rood whose support is greatly appreciated. The first author is indebted to The Department of Mechanical Engineering of The University of Iowa who provided partial financial support over the course of this study.

REFERENCES

1. Longo, J. and Stern, F., (1995), "Evaluation of surface-ship resistance and propulsion model-scale database for CFD validation," *J. Ship Research*, Vol. 40, No. 2, pp. 112-116.
2. Day, W.G. and Hurwitz, R.B., (1980), "Propeller-disk wake survey data for model 4989 representing the FF 1052-class ship in a turn and with a bass dynamometer boat," Report no. SPD-0011-21, David Taylor Naval Research and Development Center, Bethesda, MD.

3. Stern, F., Hwang, W.S., and Jaw, S.Y., (1989), "Effects of waves on the boundary layer of a surface-piercing flat plate: experiment and theory," J. Ship Research, Vol. 33, No. 1, pp. 63-80.
4. Stern, F., Choi, J.E., and Hwang, W.S., (1993), "Effects of waves on the wake of a surface-piercing flat plate: experiment and theory," J. Ship Research, Vol. 37, No. 2, pp. 102-118.
5. Stern, F., Parthasarathy, R.N., Huang, H.P., and Longo, J., (1994), "Effects of waves and free surface on turbulence in the boundary layer of a surface-piercing flat plate," ASME Symposium on Free-Surface Turbulence, Invited Speaker, Lake Tahoe, NV., pp. 37-51.
6. Longo, J., and Huang, H.P., and Stern, F., (1996), "Solid/free-surface juncture boundary layer and wake," Physics of Fluids, (in review).
7. Toda, Y., Stern, F., and Longo, J., (1992), "Mean-flow measurements in the boundary layer and wake and wave field of a Series 60 $C_B=0.6$ ship model-part 1: Froude numbers 0.16 and 0.316," J. Ship Research, Vol. 36, No. 4, pp. 360-377.
8. Longo, J., Stern, F., and Toda, Y., (1993), "Mean-flow measurements in the boundary layer and wake and wave field of a Series 60 $C_B=0.6$ ship model-part 2: scale effects on near-field wave patterns and comparisons with inviscid theory," J. Ship Research, Vol. 37, No. 1, pp. 16-24.
9. Stern, F., Longo, J., Zhang, Z.J., and Subramani, A., (1996), "Detailed bow-flow data and CFD for a Series 60 $C_B=0.6$ ship model for Froude number 0.316," J. Ship Research, Vol. 40, No. 3, pp. 61-67.
10. Tobak, M. and Peak, D.J., (1982), "Topology of three-dimensional separated flows," Annual Review of Fluid Mechanics, Vol. 14, pp. 61-85.
11. Cointe, R. and Tulin, M.P., (1994), "A theory of steady breakers," J. of Fluid Mechanics, Vol. 276, pp. 1-20.
12. Rood, E.P. and Katz, J., (1994), ASME symposium on free-surface turbulence, FED-Vol. 181, 169 pp.
13. Longo, J., (1996), "Yaw effects on model-scale ship flows," Ph.D. Thesis, The Department of Mechanical Engineering, The University of Iowa, Iowa City, IA., 275pp.
14. ITTC, (1987), "Report of the resistance and flow committee," 18th International Towing Tank Conference, Kobe, Japan, pp. 47-92.
15. Todd, F.H., (1963), "Series 60 methodical experiments with models of single-screw merchant ships," David Taylor Model Basin Report 1712.
16. Houser, D., Toda, Y., and Stern, F., (1989), "High-resolution, low noise, capacitance-wire wave-height interface," Proc. IAHR Workshop on

Instrumentation for Hydraulics Laboratories, Burlington, Canada.

17. Rood, E.P. and Telionis, D.P., (1991), "J. of fluids engineering policy on reporting uncertainties in experimental measurements and results," ASME J. Fluids Eng., Vol. 113, pp. 313-314.
18. Coleman, H.W. and Steele, W.G., (1989), "Experimentation and uncertainty analysis for engineers," John Wiley & Sons, New York.
19. Todd, F.H., (1967), "Resistance and propulsion," Principles of Naval Architecture, The Society of Naval Architects and Marine Engineers, New York, New York, pp. 288-447.
20. Toda, Y., Stern, F., Tanaka, I., and Patel, V.C., (1988), "Mean-flow measurements in the boundary layer and wake of a Series 60 $C_B=0.6$ model ship with and without propeller," J. Ship Research, Vol. 34, No. 4, pp. 225-252.
21. Newman, J.N., (1977), "Marine hydrodynamics," MIT Press, Cambridge, MA., 401 pp.

Table 1. Uncertainties for the yaw experiments

Result	0.316	0.16
Total resistance (C_T)	0.6 %	6.0 %
Sideforce (C_S)	0.1 %	1.8 %
Yaw moment (C_M)	0.1 %	4.1 %
Sinkage, trim, heel (σ, τ, η)	0.3 %	1.8 %
Wave profiles (ζ)	1.3 %	2.6 %
Global elevations (ζ)	1.1 %	2.2 %
Local elevations (ζ)	1.3 %	5.0 %
Mean velocities (u, v, w)	1.5 %	1.5 %
Mean pressure (p)	3.0 %	3.0 %
Vector direction (α, ϕ)	1.3 %	1.3 %

Table 2. Wave-pattern parameters ($Fr=0.316$)

† Kelvin		Port/Starboard		
		0°	5°	10°
α_K	19°28'	22°/22°	25°/22°	30°/21.5°
θ	35°16'	53°/53°	44°/36°	41.5°/53.5°
$\lambda_t \ddagger$	0.63	0.55/0.55	0.6/0.53	0.6/0.5
$\lambda_d \ddagger$	0.42	0.2/0.2	0.31/0.35	0.34/0.18

† : Kelvin wave pattern illustrated in Figure 4c

‡ : nondimensionalized by ship length

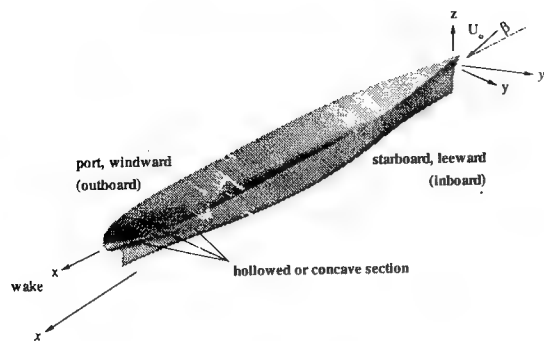


Figure 1. Experimental coordinate system

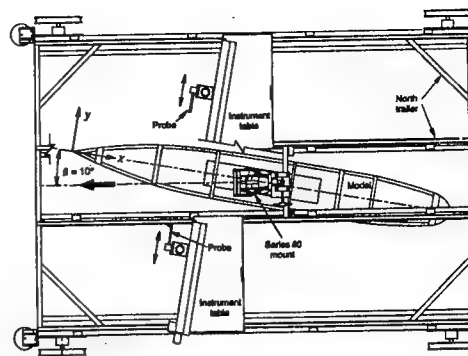


Figure 2. Carriage with Series 60 $C_B=0.6$ at yaw

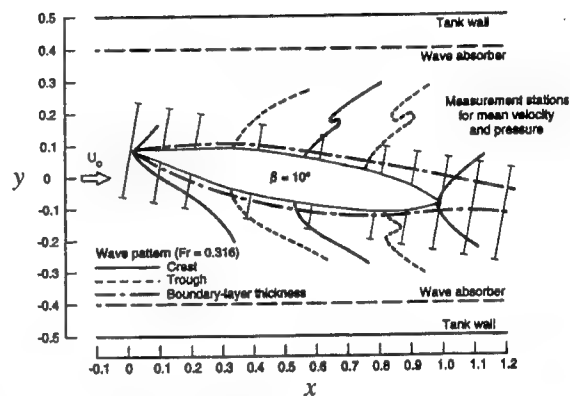
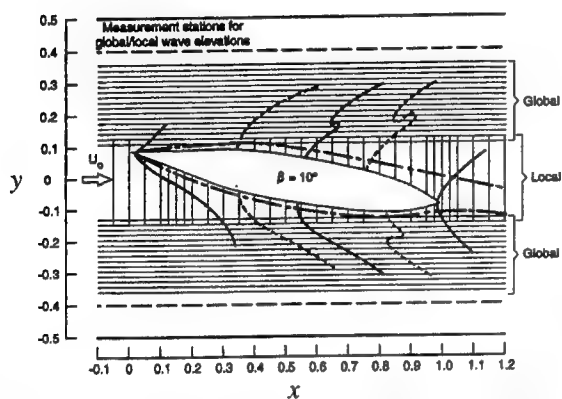
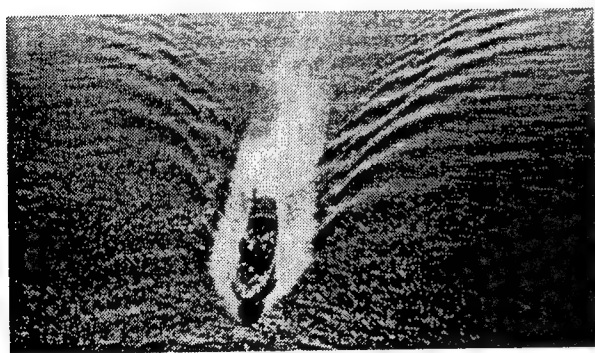


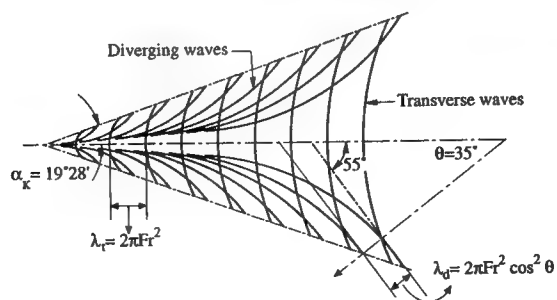
Figure 3. Summary of experimental measurements



(a) Transverse and diverging waves of a full-scale ship



(b) Wave pattern of the 5.5 m 5415 combatant ($Fr=0.41$)



(c) Transverse and diverging waves from a Kelvin point source

Figure 4. Kelvin ship-wave patterns

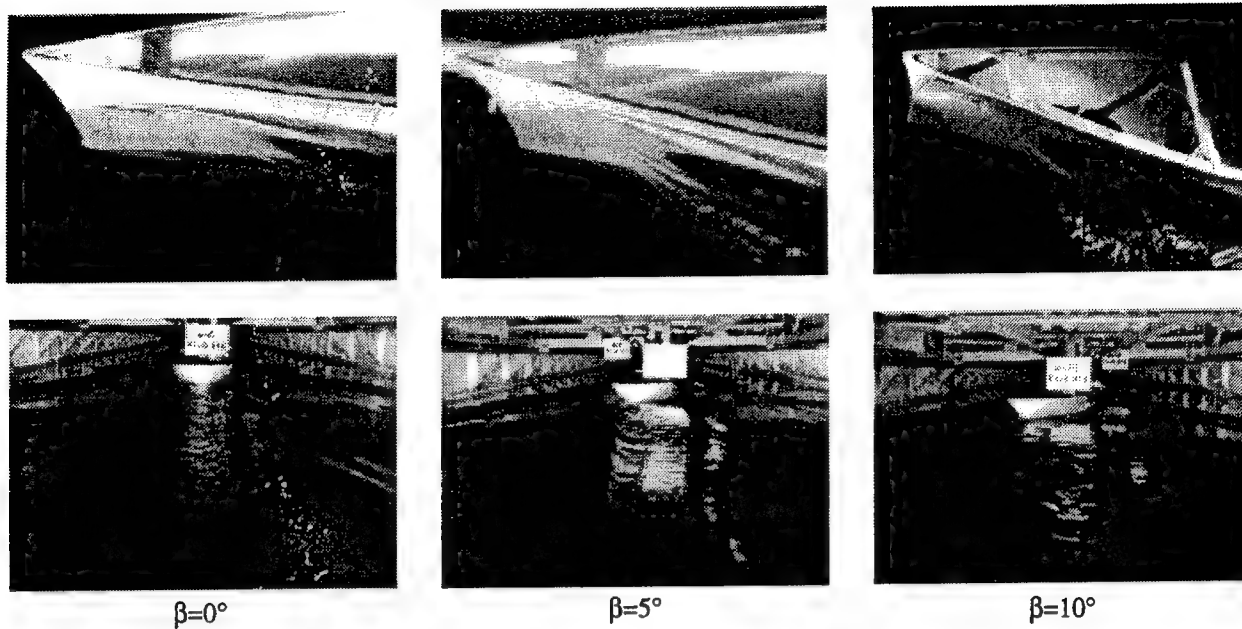


Figure 5. Photographs of the wave field at $Fr=0.316$

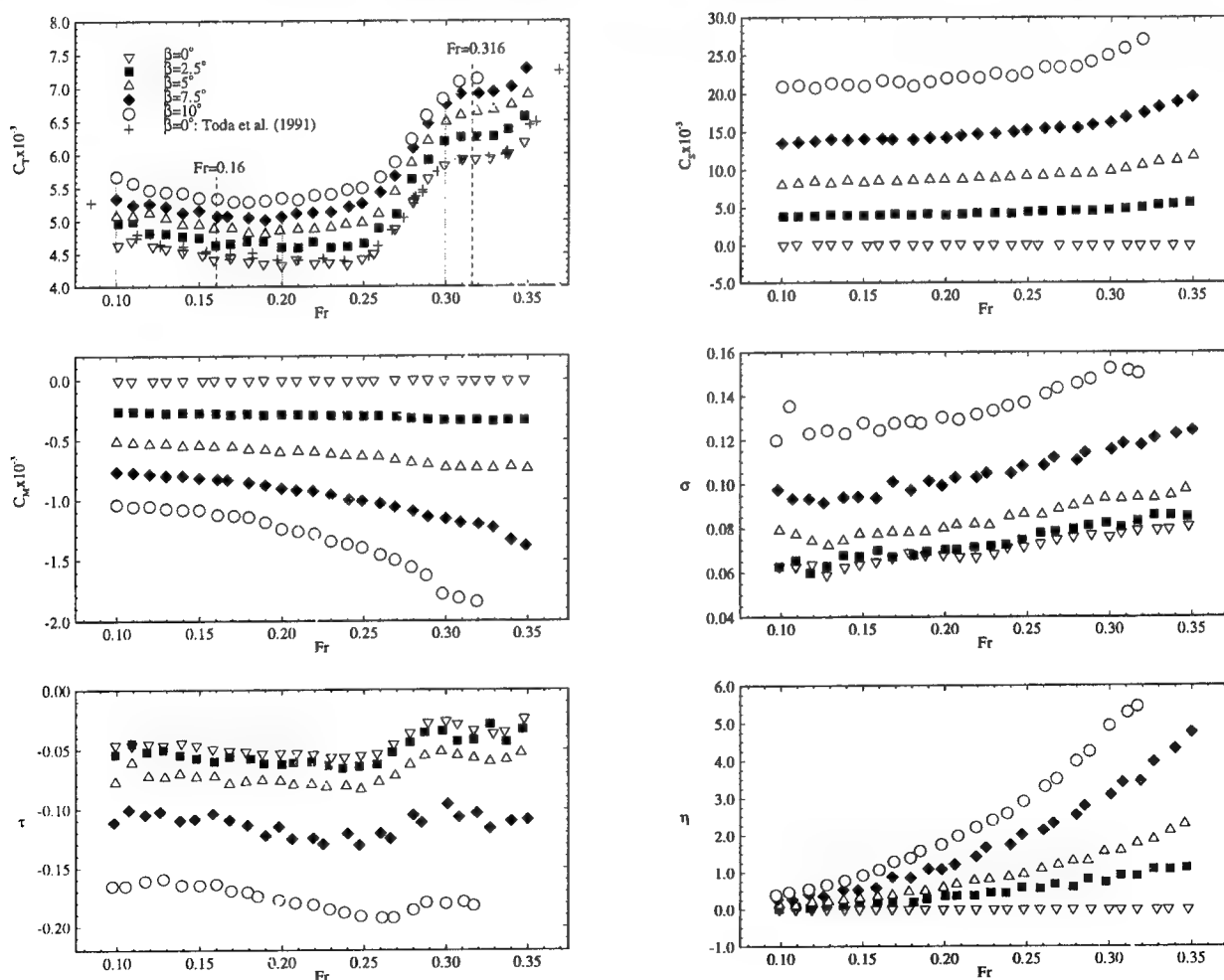


Figure 6. Forces, moment, and displacements

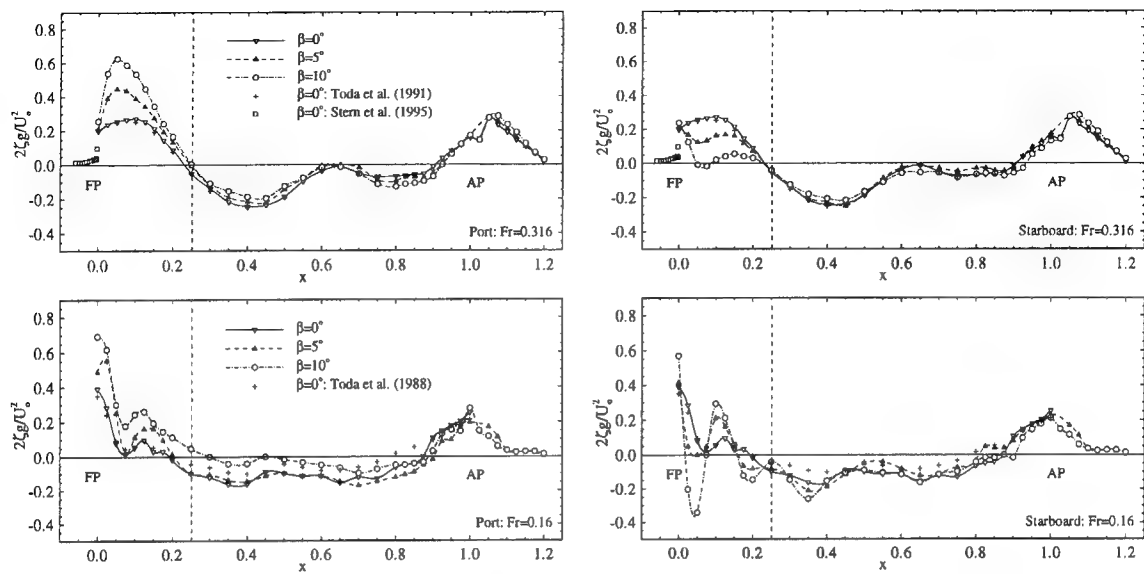


Figure 7. Wave profiles

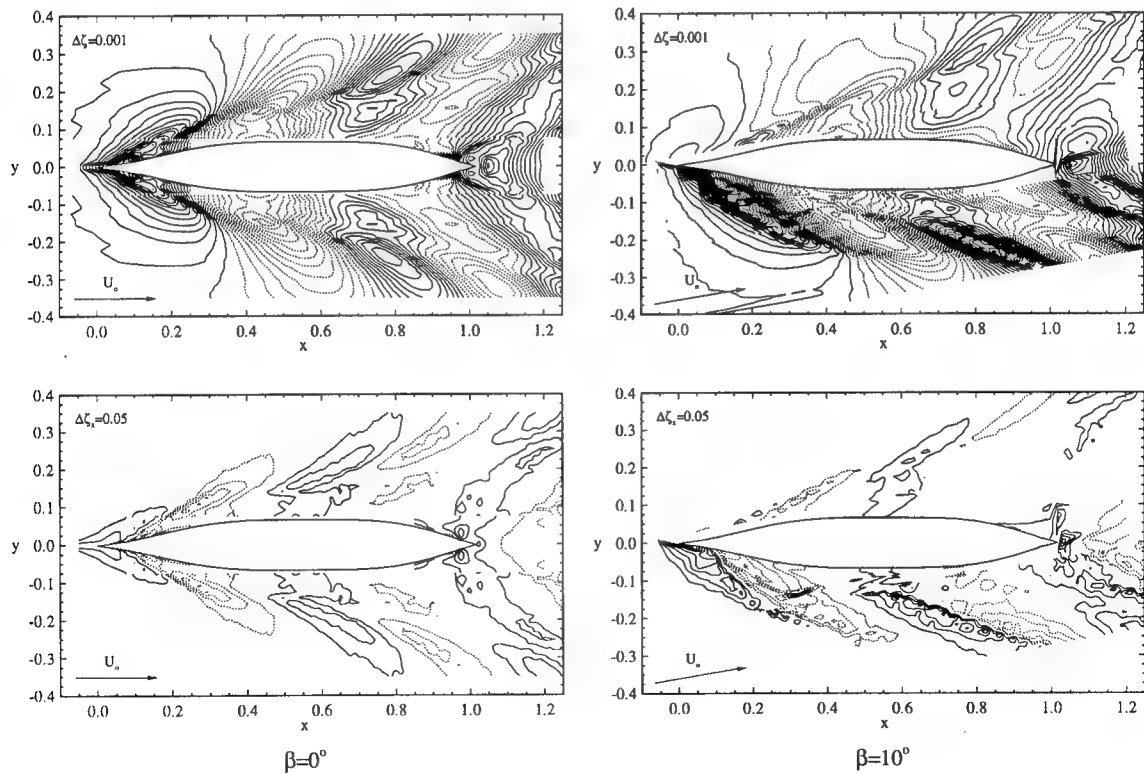
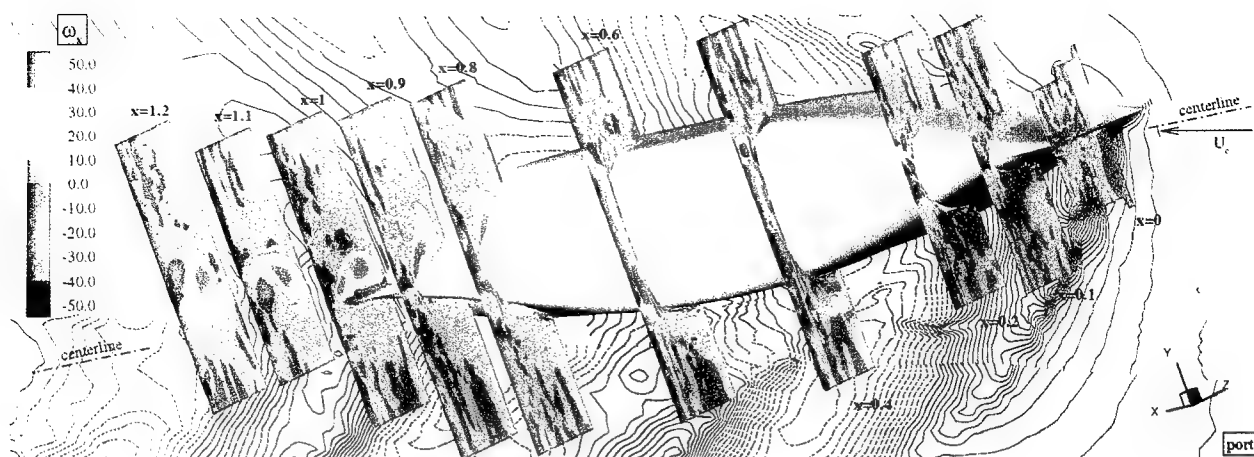
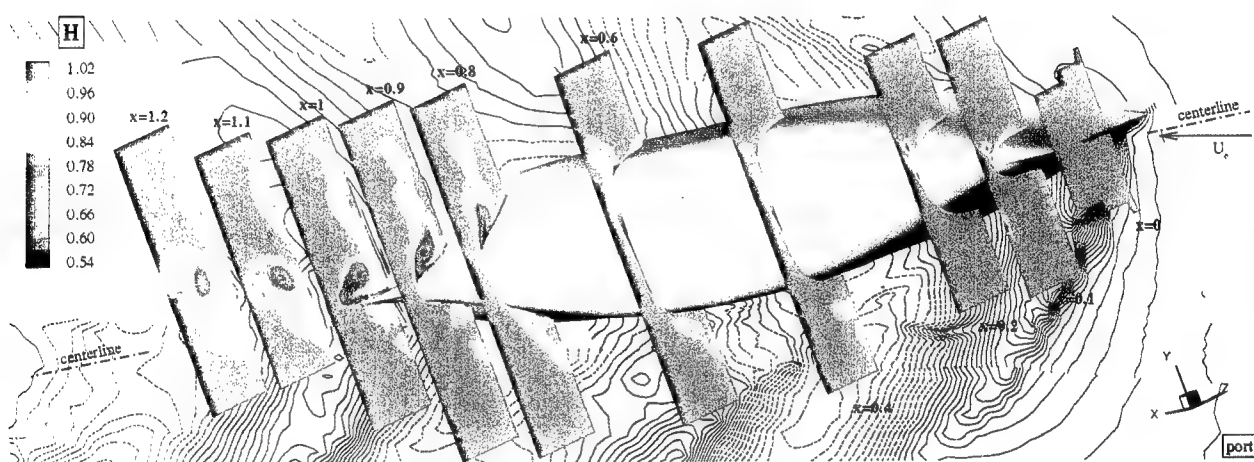


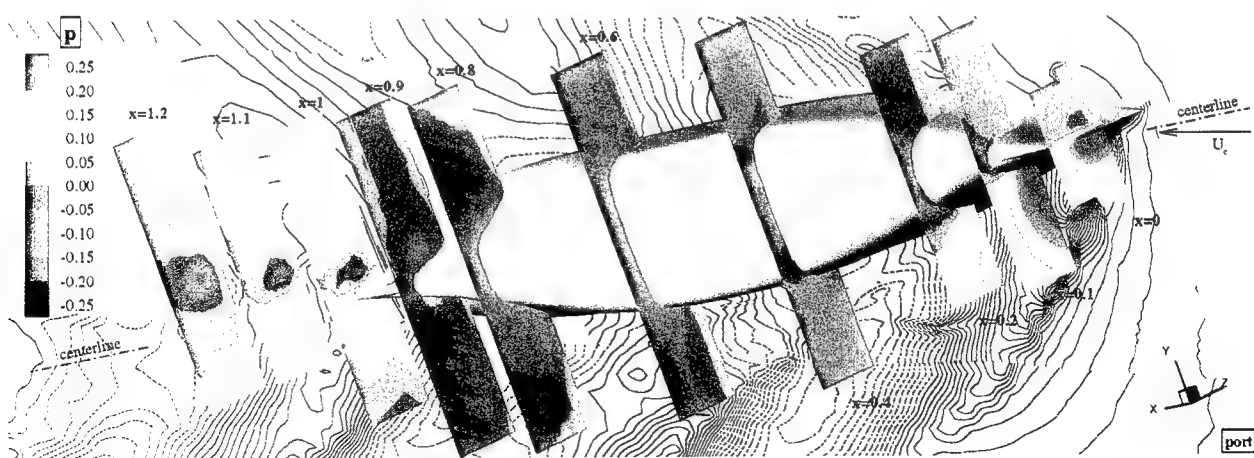
Figure 8. Wave elevations



(a) axial vorticity

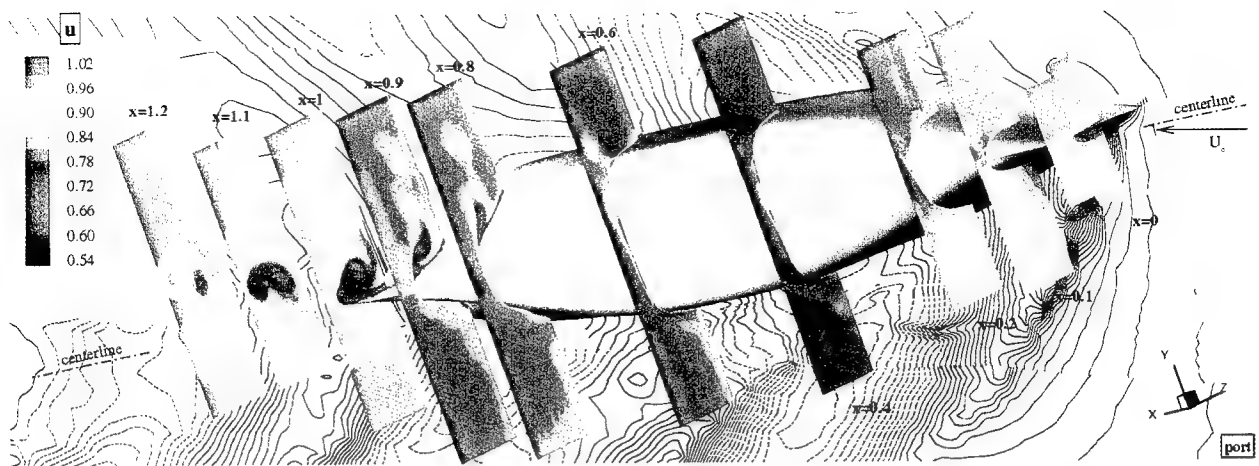


(b) total head

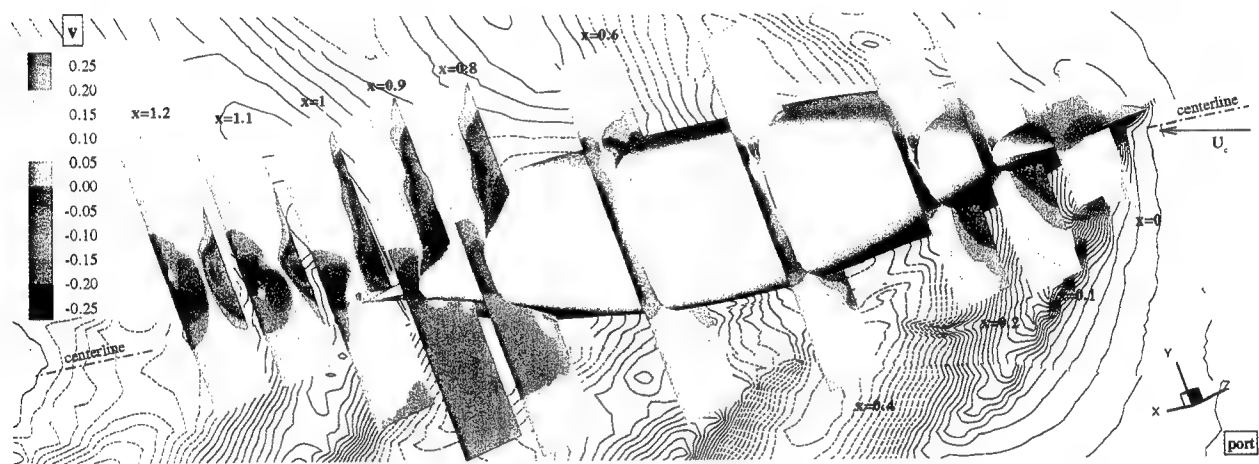


(c) pressure

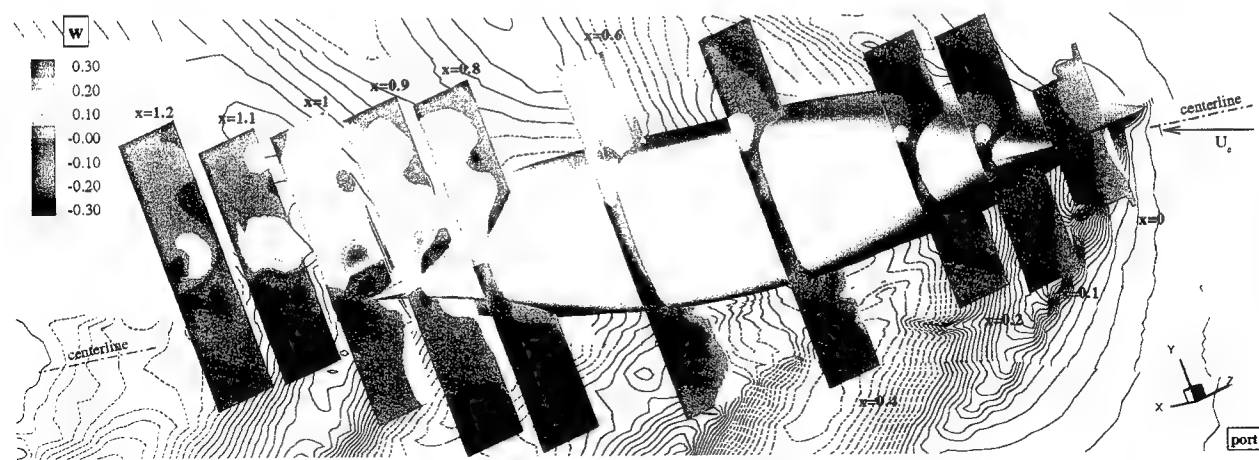
Figure 9. Mean-flow measurements for the Series 60 $C_B=0.6$ at yaw: $\beta=10^\circ$, $Fr=0.316$



(d) axial velocity



(e) transverse velocity



(f) vertical velocity

Figure 9. continued

A Multigrid Velocity-Pressure-Free Surface Elevation Fully Coupled Solver for Calculation of Turbulent Incompressible Flow Around a Hull

B. Alessandrini, G. Delhommeau (Ecole Centrale de Nantes, France)

1. ABSTRACT

This paper deals with the calculation of free surface flow of viscous incompressible fluid around the hull of a boat moving with rectilinear motion. An original method to avoid a large part of the theoretical problems connected with free surface boundary conditions in three-dimensional Navier-Stokes-Reynolds equations is proposed here.

The linearised system of convective equations for velocities, pressure and free surface elevation unknowns is discretised by finite differences and two methods to invert the resulting matrix are presented here.

A $k-\epsilon$ model solving two transport equations is used for the calculation of turbulent viscosity.

Numerical results are presented on the Series 60 CB = 0.60 ship model.

2. INTRODUCTION

Today most of the computing codes solving Navier-Stokes equations, including free surface effects, take their numerical algorithms in double model theory [1] [2] [3] [4]. The method is based on uncoupling of velocity and pressure unknowns on one side and free surface elevation calculated using kinematic condition on the other side. This evolution of hydrodynamic softwares seems reasonable but free surface boundary conditions reveal some unpredictable difficulties.

The use of kinematic equation for free surface height calculation when velocity field is known necessarily involves adding of non physical boundary conditions which do not allow neither resolution of tangential dynamic conditions nor introduction of viscosity or surface tension effects. This phenomenon takes of course more consequences when the discrete free surface elevation is located on nodes of the grid, setting unknowns on the singularity of kinematic condition at free surface and hull intersection. Moreover, in this case, pressure Dirichlet condition and continuity equation under free surface cannot be satisfied together. This formulation leads at last to a software inefficient in taking into account the complete free surface boundary conditions particularly near the hull and unable to verify the global conservation of mass.

Theoretical and numerical resolution of these problems seems essential and constitutes the present objective of this study. We propose to solve the Three Dimensional Navier-Stokes Reynolds equations, with Newtonian closure, written in the convective form in a curvilinear computational space, fitted at each time to the hull and the free surface.

A $k-\epsilon$ model solving two transport equations for kinetic energy and turbulence dissipation is used. Near the hull a Jones-Launder low Reynolds formulation [5] has been developed. The main boundary conditions are the no-slip condition on the hull and the fully non-linear free surface conditions written on the real position of the surface.

A dual unknown location on the volumic grid associated to the Rhie & Chow interpolation technique is used for the construction of pressure equation. The three components of velocity are located on the nodes of the grid, pressure at the centre of elementary volumes and free surface elevation at the centre of free surface interfaces.

Transport equations are written on the nodes of the mesh, the pressure equation is solved at the centre of elementary volumes and normal dynamic free surface condition at the centre of the free surface interfaces. The two tangential dynamic conditions and the kinematic condition form the set of velocity boundary conditions on the free surface.

The fully linear system obtained by second order finite difference schemes for the velocity components, the pressure and the free surface unknowns is solved at each iteration using a multigrid method with three levels of grid. A generalised Rhie & Chow technique is used to ensure the invertibility of the pressure block.

Numerical results concerning the free surface, the velocity and the pressure field around a Series 60 CB = 0.60 ($Rn = 4.5.10^6$, $Fn = 0.316$) show a good agreement with experiments. The problem of singularity of kinematic condition on the hull is well solved and we can calculate the formation of unsteady meniscus near the wall in the whole boundary layer.

Efficiency of k-ε model, in spite of free surface conditions, waves, pressure and velocity fields are presented here, for the steady state and also during the unsteady phase.

3. EQUATIONS

Navier-Stokes-Reynolds equations are written under a convective form for a three-dimensionnal turbulent flow in a Newtonian incompressible fluid. The 3 components of velocity (u^i), pressure (p) including the gravitational effects ($\rho g x^3$) and turbulent kinetic energy ($2/3 \rho k$) are the dependant unknowns. Independent unknowns are the 3 directions of curvilinear co-ordinates (ξ^i) and the time (t), (x^i) is the Cartesian basis and Ua the forward velocity. the curvilinear system is chosen to

simplify boundary conditions on the hull and on the free surface. $\xi^2 = 0$ et $\xi^3 = 0$ are the equation of wetted part of the hull and of the free surface respectively at each time.

A partial four-dimensionnal transformation of the Cartesian space moving with time in a curvilinear computation space is then applied. The metric of this transformation uses covariant basis (a_i) and contravariant basis (a^i), contravariant metric tensor (g^{ij}), control grid functions (f^i) and deformation velocities of the computational domain (u_g^i). Transport equations in the frame moving with the hull are written :

$$u_{,i}^\alpha + \left(a_i^j (u^i - u_g^i) - v_{eff} f^j - a_k^i v_{t,i} a_k^j \right) u_{,j}^\alpha + \frac{1}{\rho} a_\alpha^k p_{,k} - v_{eff} g^{ij} u_{,ij}^\alpha - a_k^i v_{t,i} a_j^\alpha u_{,j}^k + \delta_{1\alpha} U a_{,1} = 0 \quad (1)$$

and the continuity equation :

$$a_i^j u_{,j}^i = 0 \quad (2)$$

A classical k-ε model is given for completely developed turbulent flow and does not allow to describe parietal flow where the turbulent viscosity is negligible versus molecular viscosity. The Jones and Launder's model [7] allows to integrate transport equations up to the wall. It gives the damping function, describing attenuation of turbulence, as a function of turbulent Reynolds number $Rt = k^2 / (v \bar{\epsilon})$. In the curvilinear space (ξ^i, t) the two transport equations for k and $\bar{\epsilon}$ are :

$$k_{,i} + \left(a_i^j (u^i - u_g^i) - \left(v + \frac{v_t}{h_k} \right) f^j - a_k^i \frac{v_{t,i}}{h_k} a_k^j \right) k_{,j} - \left(v + \frac{v_t}{h_k} \right) g^{ij} k_{,ij} - P_r + \bar{\epsilon} - E_k = 0 \quad (3)$$

$$\bar{\epsilon}_{,i} + \left(a_i^j (u^i - u_g^i) - \left(v + \frac{v_t}{h_\epsilon} \right) f^j - a_k^i \frac{v_{t,i}}{h_\epsilon} a_k^j \right) \bar{\epsilon}_{,j} - \left(v + \frac{v_t}{h_\epsilon} \right) g^{ij} \bar{\epsilon}_{,ij} - C_{\epsilon 1} f_1 \frac{\bar{\epsilon}}{k} P_r + C_{\epsilon 2} f_2 \frac{\bar{\epsilon}^2}{k} - E_\epsilon = 0 \quad (4)$$

Turbulent viscosity is given by :

$$\nu_t = C_\mu f_\mu \frac{k^2}{\tilde{\epsilon}} \quad (5)$$

f_1 , f_2 and f_μ are given as functions of turbulent Reynolds number :

$$\begin{aligned} f_1 &= 1, \quad f_2 = 1 - 0.3 \exp(-Rt^2) \\ f_\mu &= \exp(-2.5 / (1 + Rt / 50)) \end{aligned} \quad (6)$$

The production term and the two other source terms are given by the following expression, n being the normal at the hull and Vt the tangential velocity :

$$\begin{aligned} P_r &= \nu_t a_{jk}^k u_i^i (a_{jl}^l u_i^i + a_{il}^l u_j^j), \quad E_k = -2 \nu \left((\sqrt{k})_{,n} \right)^2 \\ E_\epsilon &= 2 \nu Vt (Vt_{,nn})^2 \end{aligned} \quad (7)$$

Numerical values of constants are :

$$\begin{aligned} C_\mu &= 0.09, \quad C_{\epsilon 1} = 1.44, \quad C_{\epsilon 2} = 1.92 \\ h_k &= 1, \quad h_\epsilon = 1.3 \end{aligned} \quad (8)$$

4. BOUNDARY CONDITIONS

The previous formulation implies to have boundary conditions for the velocity field, the kinetic energy and the turbulence dissipation. But no other equation is needed to give pressure or free surface elevation on the boundaries. Particularly, there is no algebraic interpolation in the vicinity of the wall. We note Γ_c the hull, Γ_e the external boundary, Γ_a the symmetry plane and Γ_s the free surface.

We use on k and $\tilde{\epsilon}$ the following boundary conditions :

$$\begin{aligned} k &= k_{\min} \quad \text{and} \quad \tilde{\epsilon} = \tilde{\epsilon}_{\min} \quad \text{on} \quad \Gamma_e \cup \Gamma_c \cup \Gamma_s \\ \frac{\partial k}{\partial x^2} &= \frac{\partial \tilde{\epsilon}}{\partial x^2} = 0 \quad \text{on} \quad \Gamma_a \end{aligned} \quad (9)$$

It is known by experiments [3] that the turbulent viscosity is greatly damped on the free surface. This fact justifies the boundary conditions given by (9).

However, the decrease is very local and its influence on the results presented in this paper is weak.

Boundary conditions for the velocity field on other boundaries than Γ_s are given by:

$$\begin{aligned} u^i &= 0 \quad \text{on} \quad \Gamma_c, \quad u^1 = Ua, \quad u^2 = u^3 = 0 \quad \text{on} \quad \Gamma_e \\ u^2 &= 0, \quad \frac{\partial u^1}{\partial x^2} = \frac{\partial u^3}{\partial x^2} = 0 \quad \text{on} \quad \Gamma_a \end{aligned} \quad (10)$$

Boundary conditions on Γ_s are one kinematic condition, two dynamic tangential conditions and one normal dynamic condition. The kinematic condition, coming from the continuity hypothesis, expresses that the fluid particles of free surface stay on it. To write this condition in a curvilinear frame, we must remark that h is only a function of two independent variables on the surface. Noting (b^i) the contravariant basis of the metric bidimensionnal transformation, we have :

$$h_{,i} + \left(b_i^j (u^i - u_g^i) h_{,j} \right)_{(i,j) \in \{1,2\}} - u^3 = 0 \quad \text{on} \quad \Gamma_s \quad (11)$$

Numerical difficulties at the intersection of the hull with free surface come from this equation. We have to satisfy both no-slip condition and free surface condition on the intersection. If we put directly no-slip condition into free surface equation without care, one can deduce that $\partial h / \partial t = 0$. This conclusion is not verified by experiment and shows the singular numerical behaviour of kinematic condition on the intersection. Mathematically, the only way for the free surface to move is to become tangential to the hull. In this case, the value of the Jacobian of the transformation is zero and kinematic condition cannot be used on the hull.

Dynamic conditions are given by the continuity of strains at the free surface. If we suppose that pressure is constant above the free surface, normal dynamic condition is :

$$p - \rho gh - 2 \frac{\rho \nu_{eff}}{|a^3|^2} a_i^3 a_j^3 a_{jk}^k u_i^i - \frac{\gamma}{r} = 0 \quad \text{on} \quad \Gamma_s \quad (12)$$

where γ is the superficial tension coefficient and r the free surface medium curvature radius. The tangential dynamic conditions are simply given by a linear combination of first velocities derivatives :

$$a_{\alpha i} g^{j3} u_{,j}^i = 0 \quad (13)$$

5. DISCRETISATION OF EQUATIONS

The discrete components of velocity (U_i^α), kinetic energy (K_i) and turbulence dissipation (E_i) are located along the curvilinear co-ordinates lines defining the volumic grid (Ω), which allows to write easily the boundary conditions on ($\partial\Omega$). Pressure unknowns (P_k) are located at the centre of elementary volumes (Ω_v) to ensure mass conservation without special treatment at the boundaries. Free surface elevation (H_k) is located at the centre of free surface interfaces ($\partial\Omega_{si}$) avoiding the singularity of kinematic free surface condition. $\partial\Omega_s$ are the points of Ω belonging to the free surface only and $\partial\Omega_b$ is the complementary of $\partial\Omega_s$ in $\partial\Omega$.

All numerical schemes used in the remaining part of this chapter are second order schemes.

5.1 Discretisation of transport equations

This discretisation needs a linearisation of equations : convection velocities and a part of turbulence terms are computed at the previous time step. Convection terms are computed with an upward second-order scheme and need a 13 points grid. Diffusion terms need a 7 points grid and the cross second derivatives are in the source terms. Pressure gradient is computed on the nodes with a 8 points grid. So we have at node i :

$$U_i^\alpha + (\chi u)_{ij} U_{j \neq i}^\alpha + (\chi p)_{ik}^\alpha P_k = f u_i^\alpha \quad \text{on } \Omega \setminus \partial\Omega \quad (14)$$

5.2 Discretisation of transport equations for kinetic energy and turbulence dissipation

Transport equations for k and ε have the same form after the linearisation as the convection-

diffusion equations, the fundamental difference coming from the linear coupling between k and ε . The terms in factor of $C_{\varepsilon 1}$ and $C_{\varepsilon 2}$ are not in the source terms, but are implicit when ε is introduced in the convection terms. Discretisation with second-order scheme gives :

$$\begin{cases} (\chi k)_{ij} K_j + \gamma_i E_i = f k_i & \text{on } \Omega \setminus \partial\Omega \\ (\chi \varepsilon)_{ij} E_j = f \varepsilon_i & \text{on } \Omega \setminus \partial\Omega \end{cases} \quad (15)$$

5.3 Discretisation of free surface conditions

Uncoupled methods use classically kinematic equation to compute free surface elevation and dynamic normal condition, without viscous terms, as a Dirichlet condition on the pressure. The problem of these methods has been described, so we use here a completely different algorithm. The two tangential dynamic conditions associated with kinematic condition give the 3 boundary conditions on the velocity at the free surface and normal dynamic condition allows to compute the free surface elevation.

With this formulation, we linearise the kinematic condition as a implicit relation between the 3 velocity components and the free surface elevation :

$$h_{,i} + A^1 u^1 + A^2 u^2 - u^3 = A^1 u_g^1 + A^2 u_g^2 \quad (16)$$

Spatial derivatives of free surface elevation in the terms A^i are expressed with second-order centred schemes on a 4 points grid. Unsteady term is computed by a 3 points non-centred scheme. \tilde{H} is the free surface elevation on the nodes of free surface given by interpolation of H , so the discrete expression of kinematic condition is :

$$\begin{aligned} \lambda_i^{1,1} U_i^1 + \lambda_i^{1,2} U_i^2 + \lambda_i^{1,3} U_i^3 \\ + \eta_i^{1,4} \tilde{H}_i = f c c_i \quad \text{on } \partial\Omega_s \end{aligned} \quad (17)$$

Discretisation of the two tangential dynamic conditions on a 6 points grid can be written :

$$\begin{cases} \lambda_i^{2,1}U_i^1 + \lambda_i^{2,2}U_i^2 + \lambda_i^{2,3}U_i^3 \\ + (\eta_{ij}^{2,1}U_j^1 + \eta_{ij}^{2,2}U_j^2 + \eta_{ij}^{2,3}U_j^3)_{j \neq i} = 0 \\ \lambda_i^{3,1}U_i^1 + \lambda_i^{3,2}U_i^2 + \lambda_i^{3,3}U_i^3 \\ + (\eta_{ij}^{3,1}U_j^1 + \eta_{ij}^{3,2}U_j^2 + \eta_{ij}^{3,3}U_j^3)_{j \neq i} = 0 \end{cases} \text{ on } \partial\Omega_s \quad (18)$$

The three equations (17) and (18) are free surface velocity field boundary conditions.

To obtain a well-conditioned system, we solve analytically, on each node, the linear system of 3 equations (17) and (18) for the unknowns U^i . The boundary conditions are solved together and become :

$$U_i^\alpha + (\chi su)_{ij}^\alpha U_{j \neq i}^\alpha + (\chi sh)_i^\alpha \tilde{H}_i = fs_i^\alpha \text{ on } \partial\Omega_s \quad (19)$$

It must be noted that a better conditioning of equation (19) is obtained by avoiding to centre the derivatives of the tangential dynamic conditions in the way to maximise the absolute value of coefficients λ^{ii} .

Discretisation of normal dynamic condition gives no problem. Viscous terms are explicit in the RHS. The only point to note is that the pressure is known at the centre of control volumes and the free surface at the centre of free surface interfaces. Pressure at free surface is linearly extrapolated with 2 points.

$$H_k + (\chi sp)_{kj} P_j = fh_k \text{ on } \partial\Omega_{si} \quad (20)$$

5.4 Discretisation of continuity equation, use of a generalised Rhie and Chow method to obtain pressure equation

The Rhie and Chow method is commonly used to obtain, from continuity equation, a pressure equation without spurious modes. This method gives for the double model an infinity of solutions differing by a constant and numerical solution needs the compatibility of RHS. In the case of free surface problem, the new boundary conditions ensure invertibility of linear coupled system and unicity of

the solution. Unfortunately, due to the pressure block, numerical convergence is poor. A method giving an invertible and well conditioned pressure block is used. All free surface conditions are explicitly introduced into the continuity equation for calculation of the divergence. The symbols with a ~ or a line above are respectively interpolated on the nodes of the mesh or at the centre of free surface interfaces.

Free surface elevation is eliminated of equation (19) using normal dynamic condition (20) :

$$U_i^\alpha + (\chi su)_{ij}^\alpha U_{j \neq i}^\alpha - (\chi sh)_i^\alpha (\tilde{\chi sp})_{ii} \tilde{P}_i = fs_i^\alpha - (\chi sh)_i^\alpha \tilde{f}h_i \text{ on } \partial\Omega_s \quad (21)$$

If we introduce the secondary unknowns $(U_i^{*\alpha})$, the 3 transport equations and 3 free surface conditions can be expressed at the centre of each interface (Ω_i) under the following form :

$$\begin{aligned} \bar{U}_n^\alpha - \bar{U}_n^{*\alpha} + \sigma_v (\bar{\chi p})_{nk}^\alpha P_k \\ - \sigma_s (\bar{\chi sh})_n^\alpha (\chi sp)_{nj} P_j = 0 \text{ on } \Omega_i \end{aligned} \quad (22)$$

with :

$$\begin{cases} U_i^{*\alpha} + \sigma_v ((\chi u)_{ij} U_{j \neq i}^\alpha - fu_i^\alpha) \\ + \sigma_s \left((\chi su)_{ij} U_{j \neq i}^\alpha - fs_i^\alpha + (\chi sh)_i^\alpha \tilde{f}h_i \right) = 0 \text{ on } \Omega \\ \sigma_v = 1 \text{ on } (\Omega \cup \Omega_i) \setminus (\partial\Omega \cup \partial\Omega_i) \\ \sigma_v = 0 \text{ on } \partial\Omega \cup \partial\Omega_i \\ \sigma_s = 0 \text{ on } (\Omega \cup \Omega_i) \setminus (\partial\Omega_s \cup \partial\Omega_{si}) \\ \sigma_s = 1 \text{ on } \partial\Omega_s \cup \partial\Omega_{si} \end{cases} \quad (23)$$

Pressure equation is obtained by cancellation of the divergence on the control volumes. The case $\sigma_s = 0$ is the classical Rhie and Chow method and gives an ill-conditioned system. Introduction of boundary conditions for the divergence calculation under free surface ($\sigma_s \neq 0$) corrects the previous equation and

gives a system easy to solve numerically. Pressure equation becomes :

$$(\chi_{mp})_{kl} P_l + (\chi_d)_{ki}^{\alpha} U_i^{*\alpha} = 0 \text{ on } \Omega_v \quad (24)$$

6. COUPLED SOLUTION

The coupled linear system matrix is :

ld			$-ld$		χ_p	$U/(\Omega \setminus \partial\Omega)$	
	ld		$-ld$		χ_{shp}	$U/\partial\Omega_s$	
χ_{cl}	χ_{cl}	χ_{cl}				$U/\partial\Omega_b$	f_{cl}
χ_u	χ_u	χ_u	ld			$U^*/(\Omega \setminus \partial\Omega)$	f_u
χ_{su}	χ_{su}	χ_{su}		ld		$U^*/\partial\Omega_s$	f_{ssh}
		$-ld$		ld		$U^*/\partial\Omega_b$	
			χ_d	χ_d	χ_d	P/Ω_v	
					χ_{mp}	$H/\partial\Omega_{si}$	f_h
					χ_{sp}	ld	

$$= X$$

The linear system allowing to obtain kinetic energy and the dissipation of turbulence is solved independently. So it is necessary to summarize the equations at each step to obtain the velocity, the pressure and the free surface elevation. The transport equation is written on $\Omega \setminus \partial\Omega$ (14), the relation between the main and secondary unknowns on $\Omega \setminus \partial\Omega$ (23), the kinematic and tangential dynamic conditions on $\partial\Omega_s$ (21), the implicit definition of secondary unknowns compatible with the values taken by σ_v and σ_s on $\partial\Omega_s$ (23), boundary conditions on velocities and the implicit relations for secondary velocity unknowns on $\partial\Omega$, the normal dynamic condition on $\partial\Omega_{si}$ and the pressure equation on Ω_v (24). It is important to note that no condition on pressure or free surface elevation is needed.

The main interest of the discretisation of the present method is that the velocities-pressure block is uncoupled with the free surface in the linear system. The solution for velocities and pressure can be obtained independently from free surface elevation, which can be computed at the end of each time step by the normal dynamic condition.

Figure 1 presents the general resolution algorithm of unsteady Navier-Stokes equation. The most expensive step concerns the resolution of linear

systems for k-ε solver on one side and for velocities, pressure and free surface unknowns on other side.

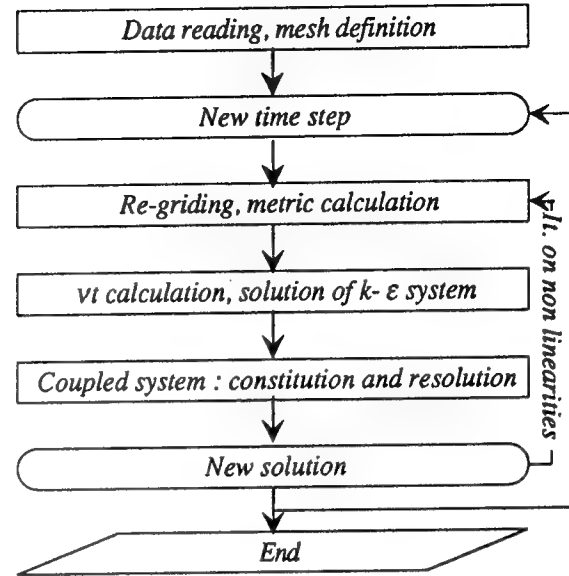


Figure 1, General resolution algorithm

7. SOLUTION OF LINEAR SYSTEM

Linear system for turbulence kinetic energy and turbulence dissipation issued from k-ε model is first solved.

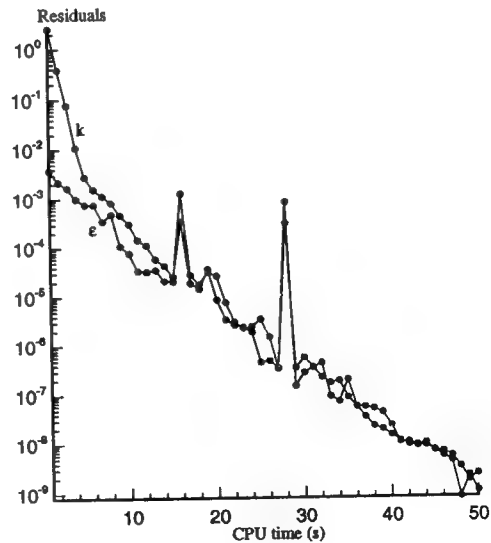


Figure 2, Convergence of k-ε system

This system is well conditioned and easily invertible by a classical CGSTAB (accelerated and stabilised bi-conjugate gradient) without any preconditionning.

Unfortunately the fully coupled linear system for the velocities, pressure and free surface elevation unknowns is very ill-conditioned, particularly the χ_{mp} block concerning the incompressible pressure equation, that means the mass conservation. So classical iterative methods are not available to solve this very large system. Two up to date iterative methods have been tested in this paper.

First method consists on the amelioration of CGSTAB algorithm using matrix preconditionning. The second method is based on linear multigrid algorithms.

7.1 Preconditionning of CGSTAB algorithm

Preconditionning CGSTAB algorithm consists in multiplying the system matrix A and the right side of discrete equations f by the same matrix M in order to decrease the conditioning number of the resulting matrix. The system becomes :

$$Ax = f \Leftrightarrow (MA)x = (Mf) \quad (25)$$

If $M = Id$ (identity matrix), it is clear that there is no preconditioning. $M = A^{-1}$ is the more effective theoretical preconditioning, but in this case A^{-1} is still to be computed. A classical way to calculate the preconditioning matrix M is to express it under an approximation form of A^{-1} by an incomplete LU decomposition [1]. This decomposition is very easy to perform on a multi-diagonal matrix but here the matrix structure is much more complicated. Moreover a large part of sub-system is well-conditioned. The pressure equation (χ_{mp} block) only is ill-conditioned and gives the divergence of single CGSTAB algorithm. So incomplete LU decomposition on the full matrix is not very suitable because of the algorithm complexity and the excessive cpu time increase. The solution proposed here is to perform an incomplete LU decomposition

on the multi-diagonal pressure block only. The conditioning matrix becomes :

Id							
	Id						
		Id					
			Id				
				Id			
					Id		
						LU_p	
							Id

where LU_p is the incomplete LU decomposition of χ_{mp} block. The figure 3 present the performance of this iterative method to solve the fully linear system during a current iteration of flow calculation around a Series 60 CB = 0.60.

7.2 The Full Multi-Grid algorithm

In order to improve the cpu time a second fully coupled system solver has been tested : the linear multi-grid method and its improvement, the Full Multi-Grid algorithm.

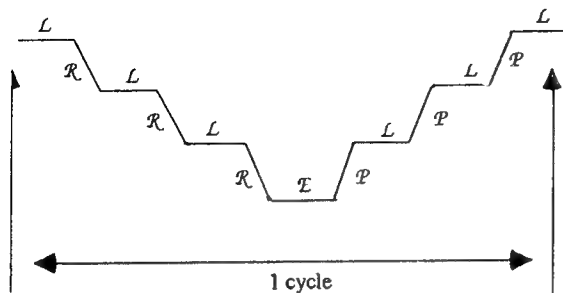
Iterative relaxation methods (Jacobi, Gauss-Seidel, SLOR) to solve linear system work very well in smoothing high spatial frequencies of the error but fail in smoothing low frequencies. So the principle of bi-grid method is :

- (i) to smooth the high frequencies of the error on the fine grid using iterations of relaxation method (L)
- (ii) to restrain the residuals (essentially low frequencies on the fine grid) on a coarse grid (\mathcal{R}) and compute the error system exact solution to eliminate low frequencies (\mathcal{E}).
- (iii) to prolong the error system in order to correct the solution on the fine grid (\mathcal{P}).

Multi-grid algorithms are defined recursively using multi-grid algorithm to solve the linear system on the coarse grid (step (ii)). So linear multi-grid method are entirely given by :

- The smoothing method on the fine grid
- The restriction operator of residuals on the coarse grid
- The linear solver on the coarser grid

- A classical cycle of multi-grid algorithm (4 grids) can be presented like this :

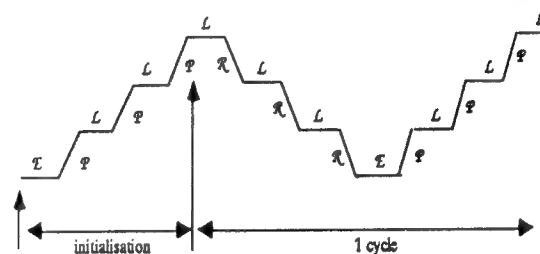


The restriction operators allow to calculate the coarse grid residuals with the fine grid residuals. The classical injection is used for the unknowns located on the nodes of the grid (velocities). Concerning the unknowns located at the centre of each elementary volume an algebraic interpolation with the height adjacent nodes on the fine grid is necessary.

There are two classical ways to obtain the linear operator on the coarse grids. First way is the construction of operator using prolongation and restriction operations (Galerkin method) and second way is to apply a new discretisation on the coarse grid. Galerkin method is very effective when the linear system is basic but in the present calculation fully coupled matrix is very complicated and

The exact solution on the coarser grid is obtained using CGSTAB + ILU process described in the previous paragraph.

Full Multi-Grid algorithm (FMG) is a very efficient way to initialize multigrid algorithm. Initial solution on the fine grid is computed by successive prolongation and smoothing of the exact solution calculated on the coarser grid. This method is very easy to apply when prolongation and smoothing operators are coded. FMG algorithm can be presented like this :



The convergence of FMG and CGSTAB + ILU algorithm are compared on the figure 3 for velocity residuals.

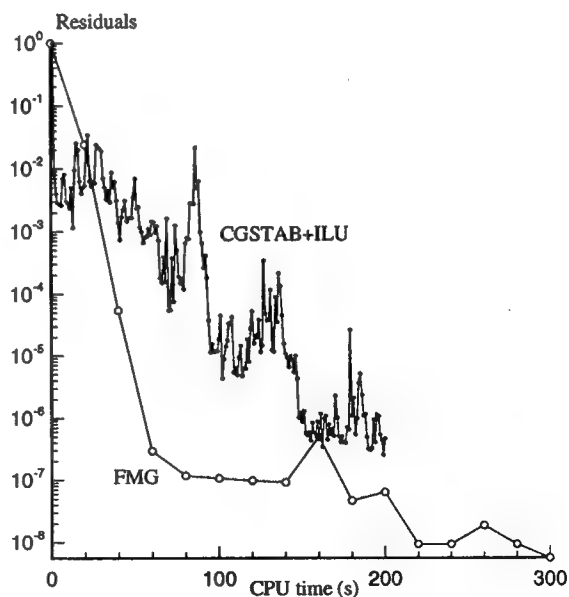


Figure 3, velocity residuals with FMG and CGSTAB+ILU

First FMG cycles (white symbols) are very efficient and the residuals decrease very quickly but after 5 or 6 cycles the convergence slows down due to saturation of smoothing process. I think Galerkin method could improve this situation and should be a new research orientation.

8. NUMERICAL RESULTS

Numerical results of this method are presented here. The calculations are performed on a Series 60 $CB = 0.6$ hull for a Reynolds number $Rn = Ua.l / \nu = 4.5.10^6$, a Froude number $Fn = Ua / \sqrt{gl} = 0.316$ and a Bond number $Bn = \rho g l^2 / \gamma = 1.33.10^6$. Two O-O topology grids are compared : a coarse grid with 190 905 nodes ($89 \times 65 \times 33$) and a fine grid with 314 265 nodes ($105 \times 73 \times 41$).

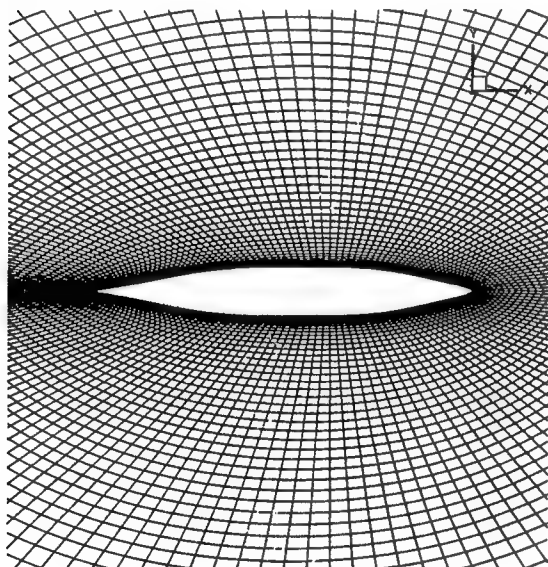


Figure 4, free surface view of the volumic mesh

Figures 4 and 5 show two different views of the coarse volumic mesh around the Series 60 hull. Three zones are considered on the grids. The first one, which first calculation point is located at 1.10^{-5} of the hull is stretched on the whole boundary layer to take into account no-slip condition without wall function, a second zone without stretching with a non-dimensional radius $R = 1$ well to compute the gravitational effects (waves propagation) and a third

zone with a non-dimensional radius $R' = 15$ very stretched to damp the waves up to the external boundary

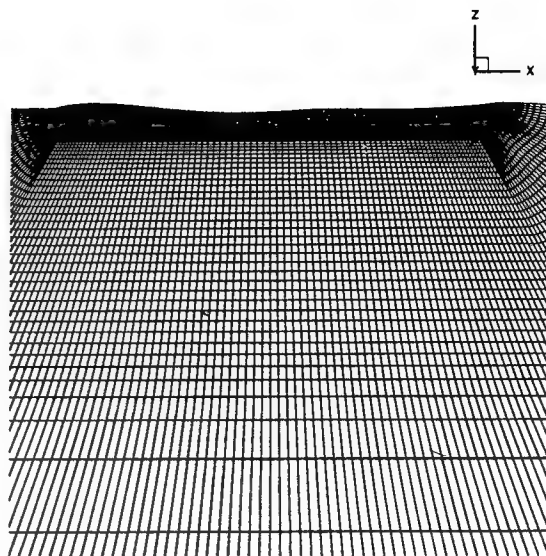


Figure 5, lateral view of the volumic mesh

To obtain a steady state 300 time iterations are necessary. A non dimensional time step $\tau = 0.020$, corresponding to a non-dimensional final duration $T = 6$, are necessary. The CPU time is about 30 hours in a HP-J200 workstation.

Starting calculation with the final boat speed is physically the same as suddenly introducing a hull in a water-circulating channel. A shock is created on the free surface and this requires an important sub-relaxation of the velocity field and free surface elevation to converge. In order to avoid this problem the calculation simulates an uniform acceleration to reach the final speed. The unsteady boat speed is computed according to the figure below.

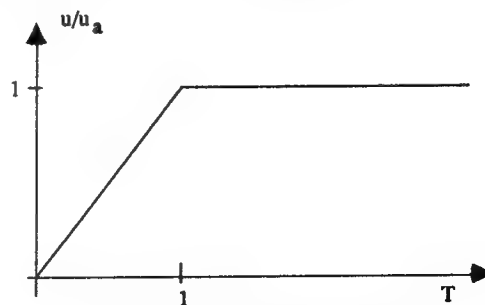


Figure 6, unsteady boat speed

8.1 Turbulence model

It has been shown in a previous paper [2] that Baldwin-Lomax model is efficient for non free surface flows but very unstable combined with free surface boundary conditions. The calculation of y_{max} parameter presents important instabilities which reflect on the turbulent viscosity calculation. So general iterative process converges with a lot of difficulties. Moreover, the vorticity increase on the crests and on the hollows of free surface induces an increase of turbulent viscosity not in accordance with experimental values. So this model has been given up in favor of two transport equation of $k-\epsilon$ model.

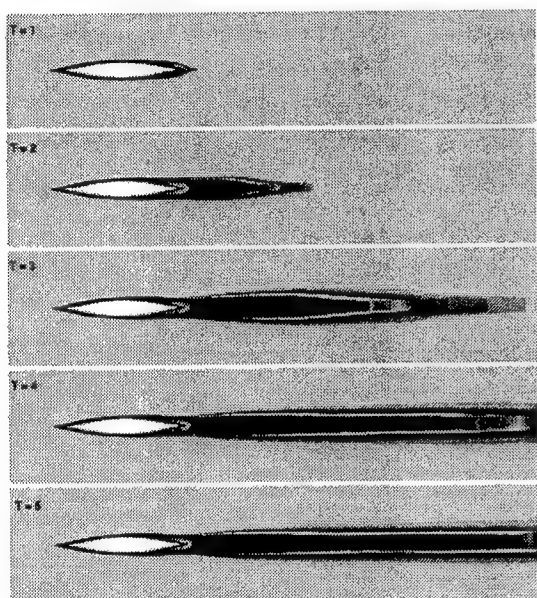


Figure 7, turbulent viscosity during the simulation

This last turbulence formulation allows to avoid all the numerical problems which appear with the Baldwin-Lomax model. The evolution of turbulent viscosity in space and in time is very smooth and does not produce divergence in the general process.

Figure 7 presents turbulent viscosity just under the free surface for various time steps during the simulation on the fine grid and figure 8 shows the same scalar in the $x/l = 0.4$ section. We can see the high regularity of turbulent viscosity which comes from $k-\epsilon$ model. Of course this argumentation is not complete and turbulent values have to be compared

with experiments. Unfortunately it seems that this experiments does not exist on the Series 60 $CB = 0.60$. So, efficiency of turbulence model has to be evaluated through comparison on velocity profiles.

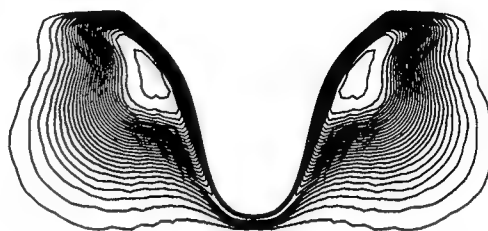


Figure 8, turbulent viscosity on the $x/l = 0.4$ section

8.2 Free surface field

The originality of the method is its ability to take into account the exact free surface conditions in the whole space and particularly near the hull. Additional non physical boundary conditions, like Neumann conditions, are not required and the kinematic condition is solved, without smoothing, up to the first free surface elevation control point next to the body. Of course interpolation are necessary to compute free surface elevation on the nodes of the mesh and the contact line elevation requires an extrapolation but this is only for re-gridding operation and the coupling with unknowns of the problem is very weak.

Figure 9 shows computed free surface field around the Series 60 hull for the two meshes. We can see good accordance between the two calculations. However a weak damping is noticeable on the coarse mesh and it seems that the convergence relative to the mesh is not yet obtained. Our opinion is that calculation on finer grid (around 500 000 nodes) is necessary to have a good grid convergence (that is to say independency of solution with the grid for the present Froude and Reynolds numbers).

The same conclusion can be made on figure 10 which presents free surface elevation along the hull located between $x/l = -0.5$ (bow) and $x/l = +0.5$ (stern). Numerical calculations on the two grids are

compared with experimental results. We can observe a good accordance between computed and experimental values. The free surface crests on the bow and on the stern are well predicted but a light damping (of course more important on the coarse grid) can be noticed.

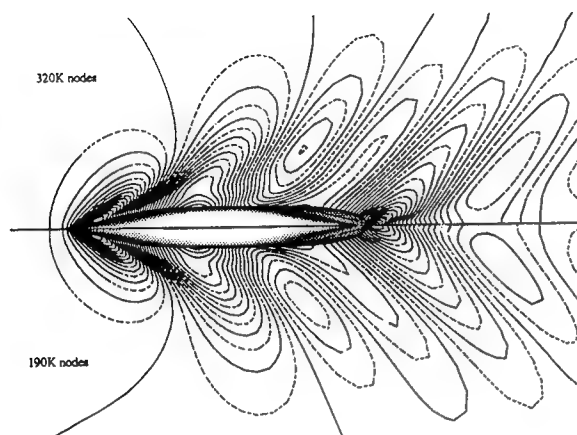


Figure 9, free surface field calculations on two grids

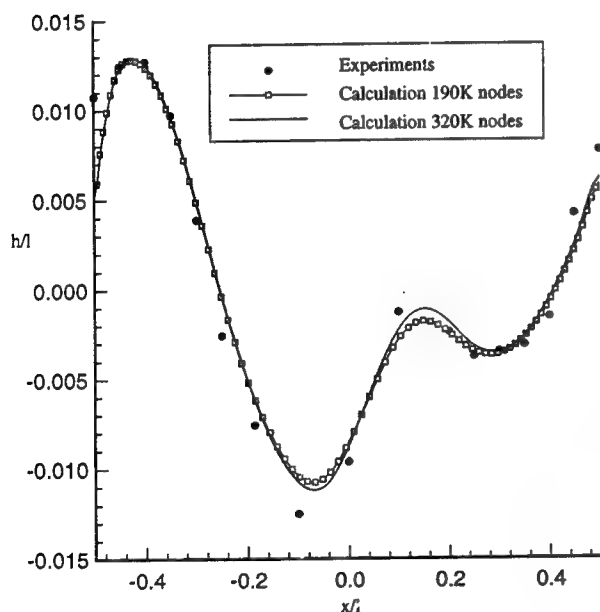


Figure 10, free surface elevation along the hull

Figure 11 present a comparison between measured and computed free surface field on the fine grid. Exploitation of this figure is quite difficult

because of the noise in measurements. However experiment and calculation are in quite good agreement. Kelvin dihedron is more perceptible on the experimental values due to numerical damping of the calculation.

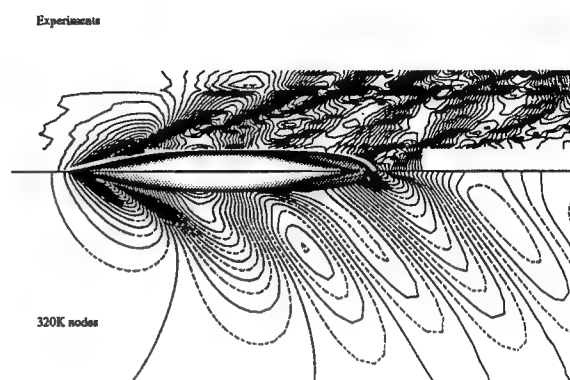


Figure 11, Comparison between measured and computed free surface field

8.4 velocity field

Figure 12 shows the calculated pressure fitted on the wet part of the hull. We can see the difference between initial mesh and final mesh which defines fluid domain only. Wall streamlines are presented also in this picture. They correspond to the limit of velocity direction when the distance to the hull decreases to zero.

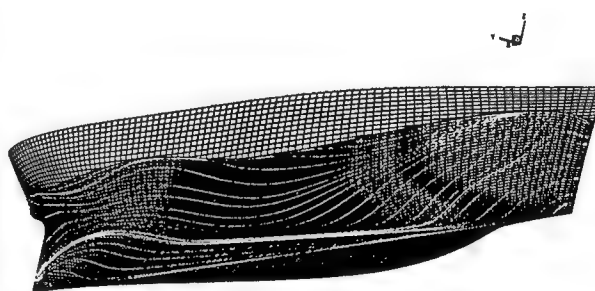


Figure 12, pressure and wall streamlines on the hull

The topology of wall streamlines shows accumulation lines near the keel on the stern which is very common on this kind of hull and traduces open

separation when the flow crosses the bilge. An accumulation is also present on the first crest on the bow and explains important difficulties to calculate the solution at this place.

It has been shown that the influence of grid size on free surface elevation is light despite a small damping of oscillations for the coarse grid. On the contrary the grid size is very important to compute well the velocity profiles connected to a good calculation of turbulent values in the boundary layer. The figure 13, 14 and 15 presents isolines of longitudinal velocity for the coarse grid (on the left) and the fine grid (on the right). In a section located at the bow (figure 13) numerical results are very similar but for the sections located at the stern, where viscous effects are more important, (figure 14 and 15) differences are very important. The influence of open separation on the accumulation line is much more noticeable with coarse grid calculation and the boundary layer is much more thick. Fortunately, Comparisons with experiment given below (figure 19 and 20), show that best results are obtained with finest grid calculation. Moreover the turbulent kinetic energy, the turbulent dissipation and, of course, the turbulent viscosity are very different in the two calculation.

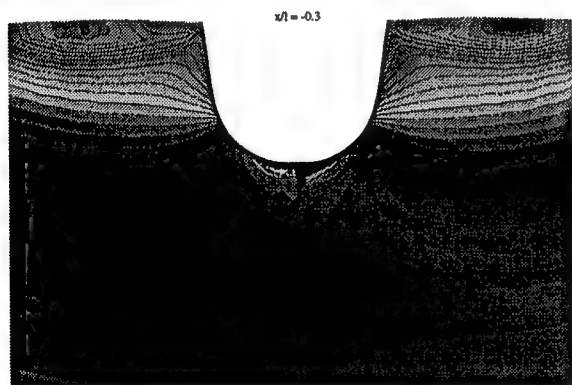


Figure 13, longitudinal velocity in $x/l = -0.3$ section for the coarse grid (left) and the fine grid (right)

Our opinion is that good calculation of turbulent quantities with a $k-\epsilon$ model and law Reynolds formulation and furthermore velocity components requires a lot of nodes in the boundary layer. In fact,

regarding to turbulence phenomena finest grid is still too coarse.

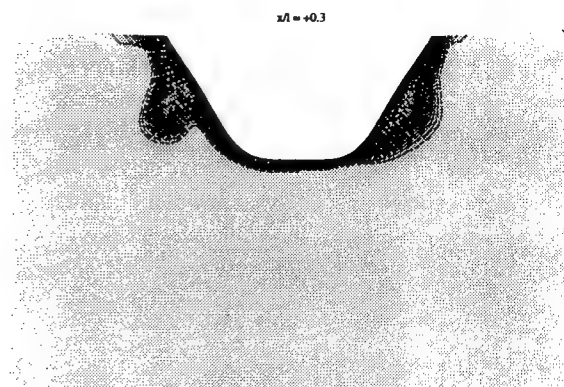


Figure 14, longitudinal velocity in $x/l = +0.3$ section for the coarse grid (left) and the fine grid (right)

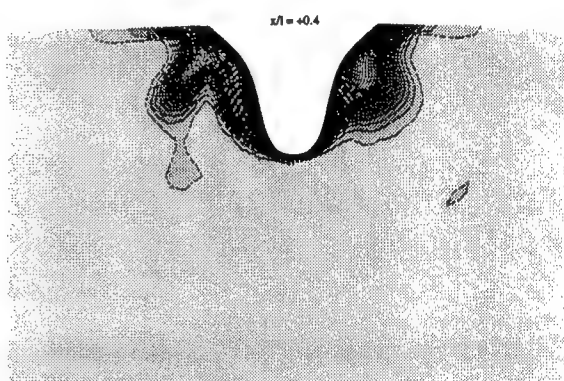


Figure 15, longitudinal velocity in $x/l = +0.4$ section for the coarse grid (left) and the fine grid (right)

Figures 16 to 21 show the 3 cartesian components of velocity field in various fluid domain sections at the bow of Series 60 hull ($x/l = -0.5, -0.4$ and -0.3) and at the stern ($x/l = +0.3, +0.4$ and $+0.5$). The calculations on the fine grid are on the right of each picture and experimental data on the left. Agreement is very good for the three components particularly on the bow.

Stern numerical results are good too in spite of a light boundary layer thickness overestimate (figure 19, 20 and 21 at the top) and a vertical component underestimate (figure 20 at the bottom).

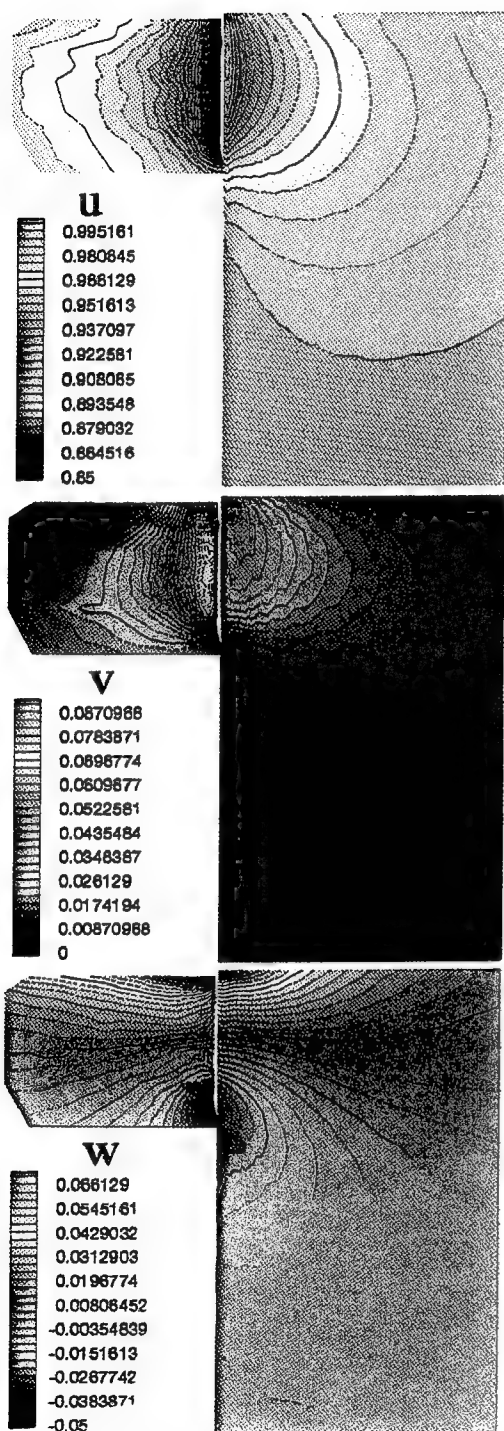


Figure 16 Computed (right) and measured (left) velocity field at $x/l = -0.5$ section

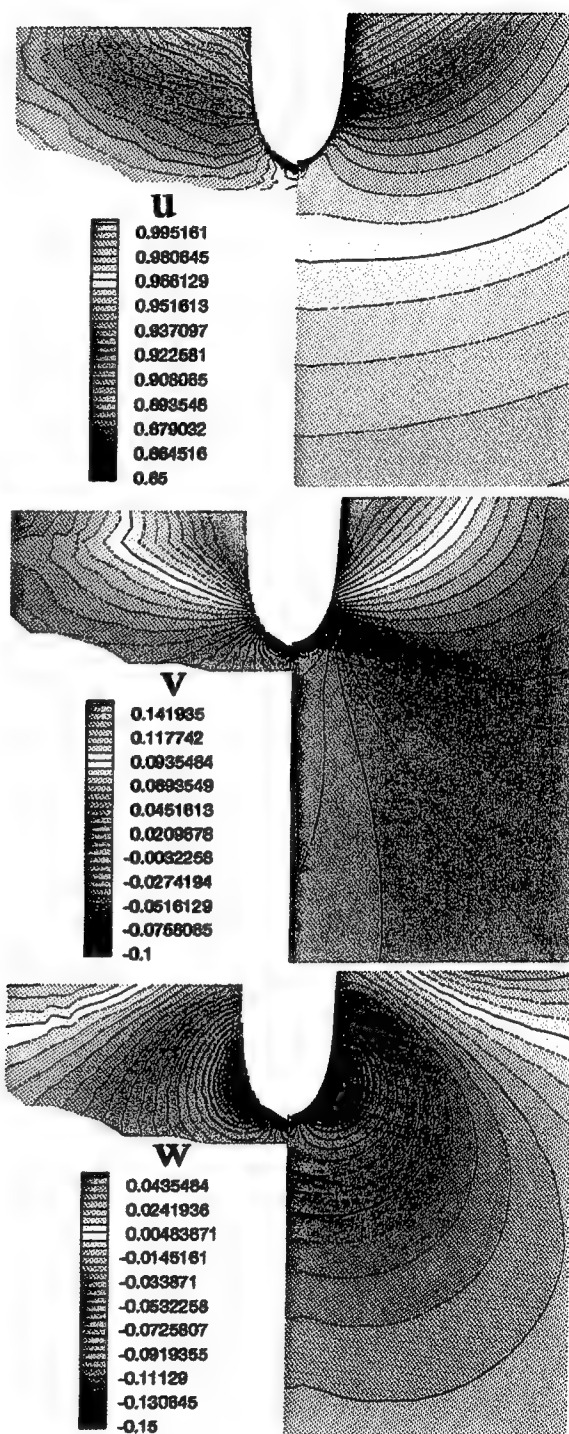


Figure 17 Computed (right) and measured (left) velocity field at $x/l = -0.4$ section

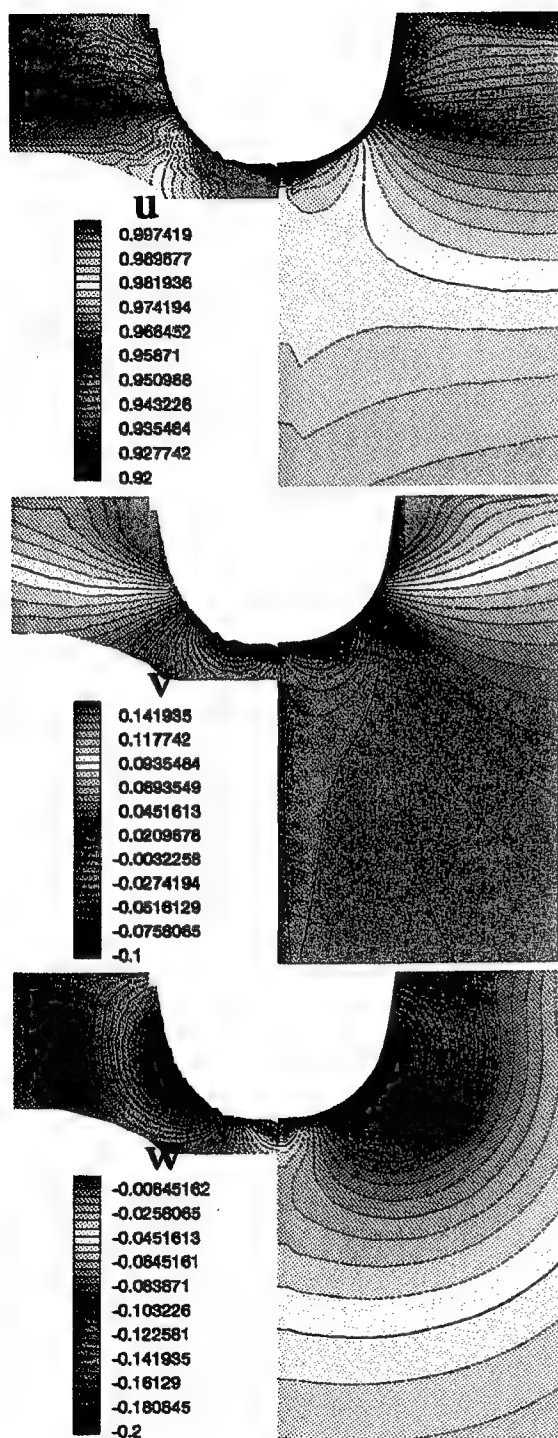


Figure 18 Computed (right) and measured (left) velocity field at $x/l = -0.3$ section

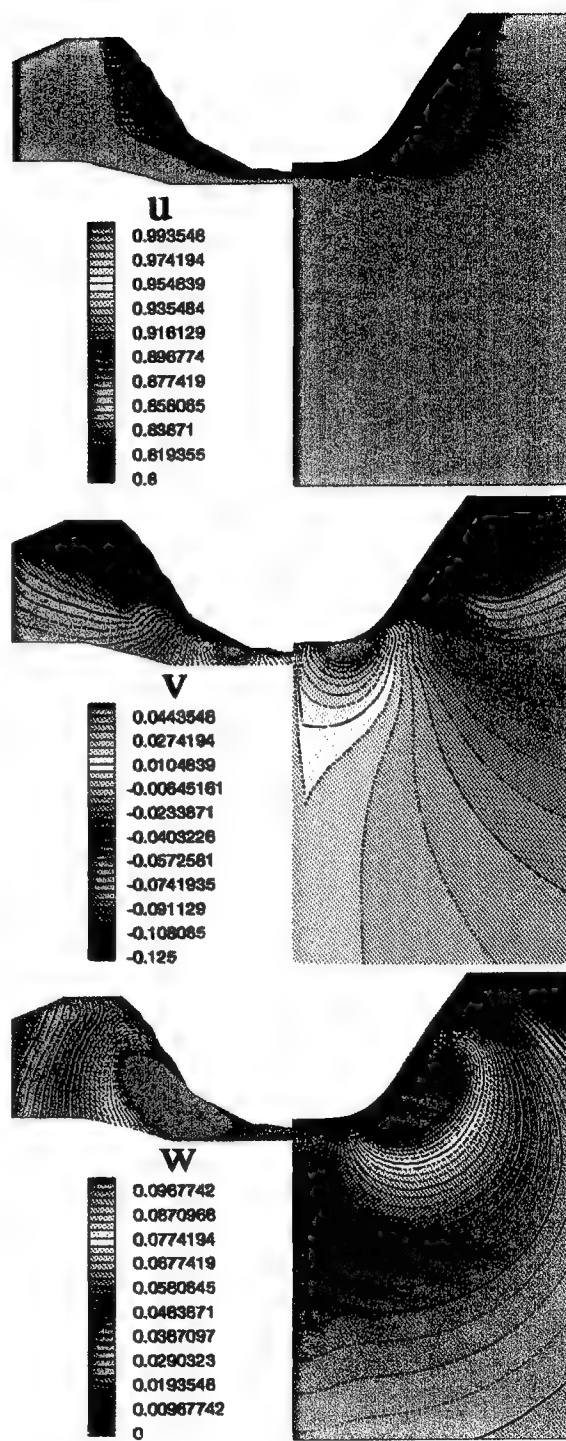


Figure 19 Computed (right) and measured (left) velocity field at $x/l = +0.3$ section

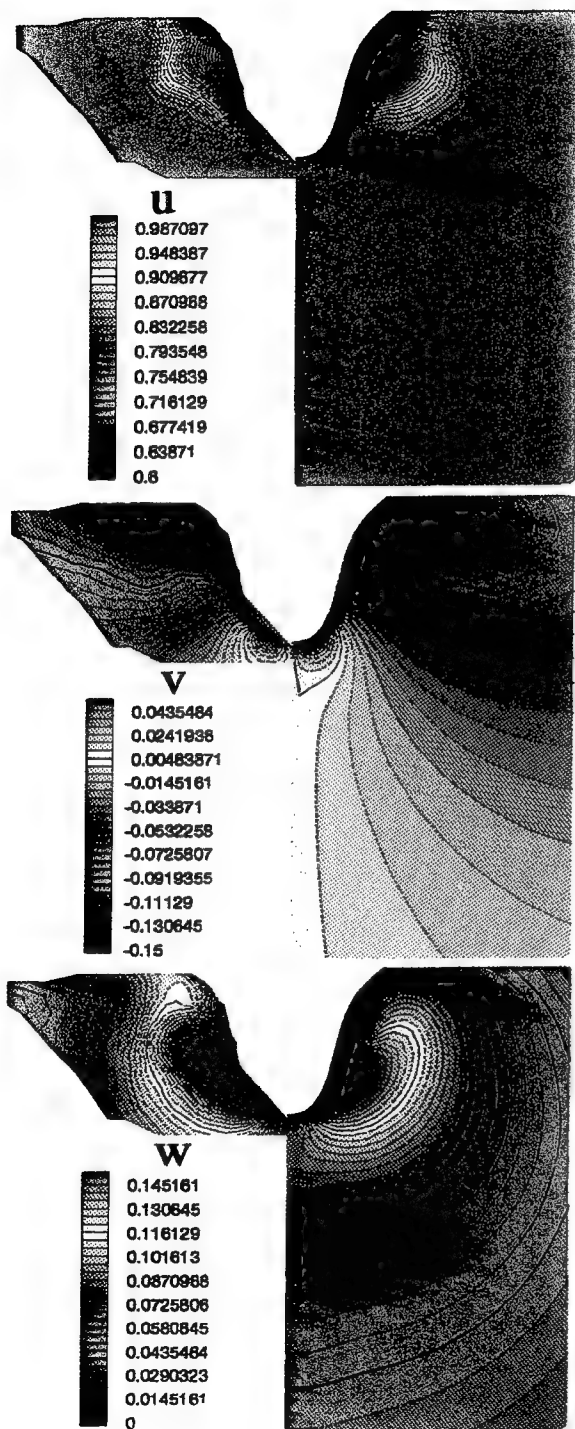


Figure 20 Computed (right) and measured (left) velocity field at $x/l = +0.4$ section

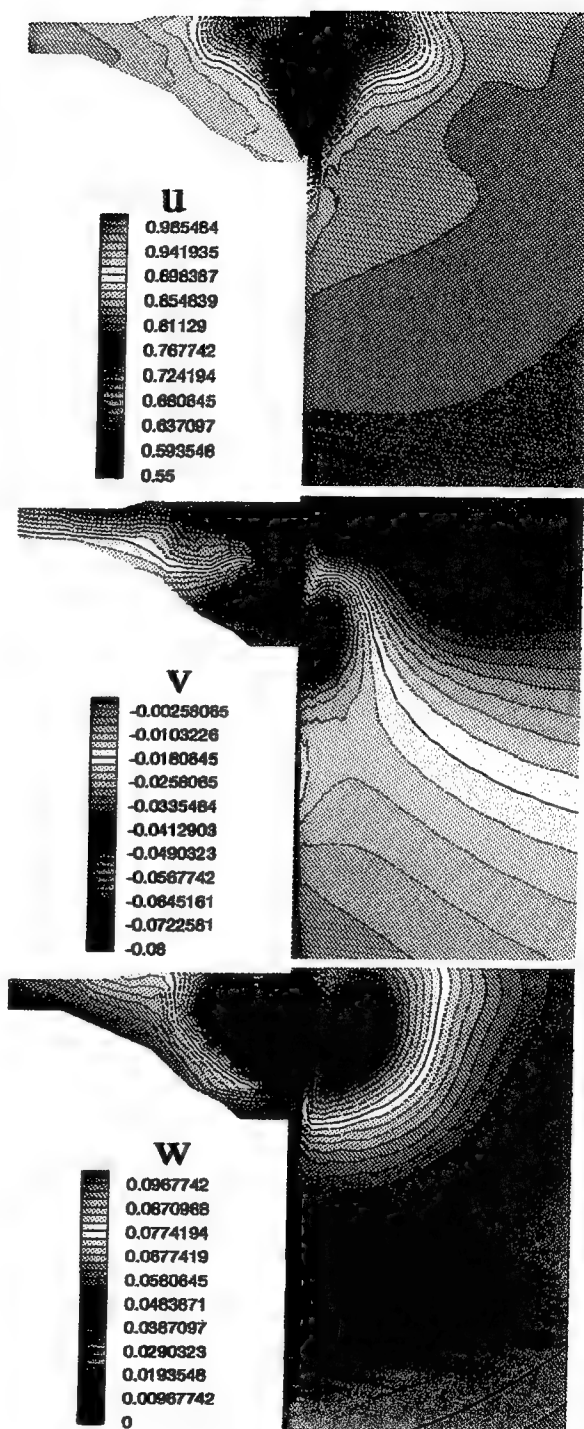


Figure 21 Computed (right) and measured (left) velocity field at $x/l = +0.5$ section

9. CONCLUSION

The results presented here show the ability of fully coupled method to take into account the exact free surface conditions and to solve the kinematic condition near the hull in spite of the singularity of equations at free surface and hull intersection. However the finest grid size seems too coarse to compute well free surface elevation, pressure velocity field and especially turbulent quantities.

The continuation of this work will consist in perform calculation with finer mesh to obtain grid independency results (perhaps around 500 000 or 600 000 nodes). After this step it will be possible to consider the problem of turbulence modelisation and the influence of various schemes.

Short-dated study will concern comparisons between $k-\epsilon$ and $k-\omega$ turbulence model. Calculations on yawed hull and turning hull will be the long-dated work.

10. ACKNOWLEDGMENTS

The authors express their thanks to the french *Direction des Recherches et Etudes Techniques* (DRET) of the *Délégation Générale pour l'Armement* (DGA) and the *Institut du Développement et des Ressources en Informatiques Scientifique* (IDRIS) of the CNRS which are supporting this work.

11. REFERENCES

1. B. ALESSANDRINI, G. DELHOMMEAU, "Simulation of three-dimensional unsteady viscous free surface flow around a ship model", International Journal for Numerical Methods in Fluids, vol 19, August 1994.
2. B. ALESSANDRINI, G. DELHOMMEAU, "Numerical calculation of three-dimensional viscous free surface flow around a Series 60 CB = 0.6 ship model", CFD WORKSHOP, Tokyo, March 1994.
3. I. CELIK, W. RODI, M.S. HOSSAIN, "Modelling of free surface proximity effects on turbulence", Proc. Refined Modelling of Flows, Paris, 1982.
4. H. C. CHEN, W. L. LIN, K. M. WEEMS, "Interactive zonal approach for ship flows including viscous and nonlinear wave effects", 6th international Conference on Numerical Ship Hydrodynamics, Iowa City, August 1993.
5. E. B. DUSSAN V, "On the spreading of liquids on solids surfaces: static and dynamic contact lines", Ann. Rev. Fluid Mech., vol 11, 1979.
6. J. FARMER, L. MARTINELLI, A. JAMESON "Multigrid solutions of the Euler and Navier-Stokes equations for a series 60 $C_b = 0,6$ ship hull for Froude numbers 0,160, 0,220 and 0,316", CFD Workshop, Tokyo, March 1994.
7. W.P. JONES, B.E. LAUNDER, "The prediction of low Reynolds number phenomena with a two equation model of turbulence", International Journal of Heat Mass Transfer, vol 16, 1972.
8. E. E. MARKOVITCH, "Effect of free surface tension on the free outflow of a wetting fluid from a horizontal tube", Traduction of Mekhanika Zhidkosti i Gaza, No 2, March-April 1988.
9. Y. TAHARA, F. STERN, "A large domain approach for calculating ship boundary layers and wakes for nonzero Froude number", CFD Workshop, Tokyo, March 1994.
10. Y. TODA, F. STERN, J. LONGO, "Mean-flow measurements in the boundary layer and wake and wave field of a Series 60 $C_b = 0,6$ ship model for Froude numbers 0,16 and 0,316", IIHR report No 352, August 1991.
11. Y. TODA, F. STERN, I. TANAKA, V.C. PATEL, "Mean-flow measurements in the boundary layer and wake and wave field of a Series 60 $C_b = 0,6$ ship model with and without propeller", Journal of Ship Research, Vol 34, December 1990.
12. H. A. VORST, "Bi-CGSTAB : a fast and smoothly converging variant of Bi-CG for the solution of nonsymmetric linear systems", J. Sci. Stat. Comp. vol 13, 1992.

DISCUSSION

M. Peric

University of Hamburg, Germany

This is an interesting and certainly original approach to solving fluid flow problems with free surface. Both the solution method and the obtained results are worth reporting in the conference proceedings.

The use of finite difference (FD) method and structured grids limits the applicability of the method to geometries which are not too complicated; otherwise, highly distorted grids would result (e.g., for ships with more complicated bow and stern shapes than in the case of the Series 60 hull). This is where the method has disadvantages compared to finite volume (FV) methods, which can use block-structured and unstructured grids with cell-wise local refinement. Especially the local refinement capability is essential if a high accuracy is to be achieved in calculating flows around ship hulls, since very fine grid is needed close to the hull and in the wake while much coarser grid can be used elsewhere.

The strong point of the algorithm presented by the authors is the coupled solution for velocity and pressure. Only after the second reading I recognized that the explicit calculation of the free surface elevation at the end of each time step is not a drawback, since the dependence of velocities on H has been taken into account implicitly by combining Eqs. (20) and (19).

The authors are solving linear systems for κ - ϵ , and ϵ velocity-pressure coupling sequentially and are iterating within each time step to account for nonlinearities and coupling of the two systems (velocities depend on κ and ϵ through v , and κ and ϵ depend on the velocity field through the production rate and the convective terms). However, they seem to be solving these two systems to a tight tolerance for each "outer" iteration, as indicated in Figs. 2 and 3. I doubt that is really necessary, since the residuals increase each time the matrix and source terms are updated; the reduction of residual levels for a fixed matrix and right-hand side by one to two orders of magnitude should normally suffice. No information was given about the required number of iterations on nonlinearities and the criterion used to control them (usually, the residual norm calculated after the matrix and source terms are updated is used as a measure of convergence). Also, no information is given about

the decision on when the steady state is reached (usually, if the residuals do not increase above certain level when the matrices and source terms at the new time level are calculated, the changes in the time can be considered negligible).

The full multigrid method is applied only to the linear velocity-pressure system. The efficient sequential solution methods use multigrid to accelerate also (or only) the outer iterations, so I would expect that it would be beneficial to do so in this case too. This would mean performing iterations on non-linearities on each grid level using a non-linear (full approximation) multigrid scheme. It is difficult to predict what reduction of computing time would result in the case of free surface flows, but for a fixed free surface shape this is certainly the most efficient way to calculate steady flows. The comment that the multigrid method "saturates" after few V-cycles is not appropriate; a properly implemented multigrid method is supposed to converge at a constant rate up to machine accuracy.

A few words about the presented solutions: The grid refinement from 190,000 to 320,000 nodes is not a substantial refinement in 3 dimensions, less than 20% more nodes in each direction. To assess the discretization errors reliably, a systematic refinement is most appropriate (halving mesh spacing in all directions, at least in the regions where large errors are expected, e.g., near ship hull and in the wake). One can then use Richardson extrapolation to estimate the "grid-independent" solution.

The contours of Ω in Figs. 13, 16, 18, and 21 show high gradients normal to the symmetry plane; this should not happen, as the symmetry plane must have zero gradient in the normal direction (zero shear stress). Either the boundary conditions are not properly implemented in the code, or the grid is severely distorted in this region. Otherwise, the results seem to agree well with experimental data. However, it would be necessary to quantify the discretization errors as noted above in order to be able to judge the performance of the turbulence model, since the model errors and discretization errors tend to sometimes partially cancel out.

AUTHORS' REPLY

Figures 2 and 3 show the convergence of various iterative algorithms to solve linear problems with the zero machine accuracy. For practical calculations we reduce the linear residuals by two orders.

In the present paper only steady state is compared with experiments so only one non-linear iteration is made at each time step. Concerning the obtaining of steady state, free surface flow problem is much more complicated than zero Froude number problem. Because of the propagation of wave field, convergence on the whole calculation domain takes a long time. In fact we test only the convergence on a sphere near the full ($R/1 = 1$) and we reduce the non-linear residuals by two order of magnitude (non-linear residuals are obtained after the matrix and source terms are updated).

The multigrid algorithm converges up to the machine accuracy at a constant rate on elementary case but in 3-D for the fully coupled system the convergence depends strongly of prolongation and restriction operators and of smoothing operator. A bad smoothing leads to the divergence. Here the small wave lengths of the error induced by prolongation procedure are very difficult to smooth under the saturation level.

The grid refinement is not a "substantial refinement" but the solutions on the two grids are very different (figure 14). The conclusion is that small variation of grid size can induce strong differences on the solution due certainly to turbulence behavior.

DISCUSSION

W.W. Schultz
University of Michigan, USA

The rolling motion (tangency condition) you require at the free surface singularity makes matters worse for the second fluid (air in this case). It has been shown that the singularity has to be relieved in a different way. E.B. Dussan [(1979) *Ann. Rev. Fluid Mech.*] shows that slip is observed and material on the surface is mapped into the interior! Ting & Perlin [(1995) *J. Fluid Mech.*] shows similar behavior for high Reynolds number, oscillatory flow.

AUTHORS' REPLY

The purpose of our work is to propose a numerical formulation to solve Navier-Stokes equations coupled with classical boundary conditions (no-slip conditions on the wall, kinematic and dynamic conditions on the free surface). It is well known that the wetting problem cannot be solved by these macroscopic equations. The physics does not follow the continuity hypothesis, and particularly the kinematic condition seems to be unverified. The problem is not to predict the meniscus and the dynamic contact angle at a very small scale, but to ensure the contact line progression with classical boundary conditions. In this case, mathematically, free surface has to be tangent to the wall.

DISCUSSION

H. Raven
Maritime Research Institute, The Netherlands

Your figures 10 and 11 compare calculated and measured wave patterns. The bow wave at the hull is well predicted, the wave profile is fair, but the diverging bow wave system is completely absent. Using a nonlinear free surface condition and a paneling like shown in figure 4, a panel method would probably give a better result for the waves. Does the use of Navier-Stokes equations have a greater amount of numerical damping than a panel method and does it therefore require a finer free surface discretization? Or are there other effects leading to this difference.

AUTHORS' REPLY

We have compared Navier-Stokes formulation with Rankine panel method for the same grid refinement (except in the boundary layer zone). It appears clearly that Navier-Stokes formulation has a greater amount of numerical damping. In fact to obtain similar results we have to use more or less a two times finer grid in each direction in the Navier-Stokes formulation. The explanation is that in the panel method a part of the solution (the mass conservation, that is to say the continuity equation) is mathematically exact and does not proceed from a discretization as in the Navier-Stokes formulation.

The Shoulder Wave and Separation Generated by a Surface-Piercing Strut

E. Pogozielski, J. Katz (Johns Hopkins University, USA)

T. Huang (David Taylor Model Basin, USA)

ABSTRACT

The flow near a surface piercing, symmetric body with a long draft is examined, focusing in particular on the structure of the shoulder wave and the separated region behind it. The experiments are performed in a towing tank at $Fr_L=0.25$, and include velocity measurements using PIV as well as video and film photography above and below the free surface. At $Fr_L \geq 0.15$, formation of the shoulder wave is preceded by impingement of the flow on the model, a process associated with the bow wave, which generates a turbulent, bubbly wake. Consequently, the origin of the shoulder wave consists of several powerful counter-rotating vortices which entrain bubbles from the free surface. The wave crest becomes milder and eventually irrotational with increasing distance from the model. Behind the shoulder wave, at $x/L=0.7$, boundary layer separation begins, but only near the free surface. The separated zone contains several large scale streamwise vortices that detach from the model; the first one from the intersection with the free surface, and later ones from below the free surface. At $Fr_L=0.25$, there is no reverse flow within the separated region, but at $Fr_L > 0.30$, flow reversal does occur. The entire process involves considerable energy dissipation.

INTRODUCTION

The flow around a surface piercing body is a very complex phenomenon, involving both viscous effects near the surface of the body, and free surface phenomena, including waves of various forms, formation of liquid sheets, bubble entrainment and three dimensional flow separation. For bodies with a long draft, where the model length is the only significant length scale, data is particularly scarce and includes mostly surface wave mapping. Most of the available data related to surface piercing bodies

involves flows around ships, i.e., shallow bodies. Velocity measurements are scarce, even for ships.

A comprehensive review of flow structures and wave patterns around ships is provided by Miata and Inui (1), who observe strong dependence on Froude number and bow shape. Using Pitot tubes, they show that flow moving across the wave crest involves significant energy loss and an abrupt change in flow direction. The velocity component normal to the wave decreases significantly, but the parallel component remains largely unchanged. This observation naturally leads to an analogy between these bow waves and oblique shock waves. Miata and Inui (1) also discovered that the dominating length scale for ships is the draft, which for the present study is very large. Their studies do not include velocity measurements in the immediate vicinity of the wall. Some LDV measurements near a ship, performed by Fry and Kim (2), indicate that this three dimensional flow involves interaction of the boundary layer with the non-linear bow waves and the formation of large scale vortices. Combined mean velocity, pressure, and wave height measurements around a ship were performed also by Toda et al (3) and Longo et al.(4). These studies provide data on the distribution of mean axial velocity and energy loss around the model. PIV measurements within the bow wave and near the body were performed by Dong et al. (5), focusing on the vorticity distribution within the wave and the liquid sheet attached to the model.

Averaged measurements and computations performed by Stern et al. (6) around a surface piercing flat plate with a horizontal submerged foil, demonstrate that the presence of surface waves alter the pressure distribution around the body and cause massive flow separation. There was qualitative agreement in overall wave shape and trends between the measurements and computations, but the

quantitative results differ substantially. A recent paper dealing with the flow around a surface piercing blunt body by Zhang and Stern (7) contains mostly results of a numerical analysis, but also some surface elevation measurements at the intersection with the model. They predict that separation with reverse flow occurs at virtually all Froude numbers, and that the separation is limited to a region near the free surface for $Fr_L \leq 0.55$. Some of their trends will be compared later to the present results. To the best of our knowledge, there isn't any other source that provides data on the velocity distribution and vorticity structure around a surface piercing blunt body with a long draft. Due to the occurrence of flow separation and the formation of a bubbly wake at the trough of the bow wave (even in full scale models, such as catamarans and SWATH), they represent a unique problem. The present paper deals with such a flow.

EXPERIMENTAL PROCEDURES

The experiments were performed in the 140 ft towing tank located at the David Taylor Model Basin. The facility is 152 cm deep, 305 cm wide, and 4270 cm long. The experimental setup and model are shown in Figure 1. The model draft is 1.37 m. Experiments are performed at 0° incidence, at Froude numbers based on model length, Fr_L , ranging between 0.051 and 0.51. The corresponding range of Reynolds numbers is 1.39×10^5 to 1.39×10^6 , respectively.

PIV measurements are conducted with three orientations of the laser sheet: a vertical plane inclined 115° to the streamwise direction (Figure 1c), a sheet inclined 59° to the streamwise direction and tilted 9° to the vertical (Figure 1b), accounting for the majority of presented data, as well as a sheet inclined 34° and tilted 9° to the vertical. The slight vertical tilt facilitates observations of the wave crest by avoiding any blockage caused by the wave trough. As shown in Figure 1, the primed coordinates (x' , y' , z') refer to the plane of a given image. Note that the axial position, x/L , varies across any given image. The reference to a specific x/L for an image indicates the position of the origin of the (x, y, z) frame on the center line of the model.

The 6 mm thick laser sheet is generated by a 15W, air cooled, copper vapor laser. The optical setup is sketched in Figure 1b. Data is recorded using a 35 mm film camera, equipped with a 90 mm lens, that has a maximum recording rate of 65 frames per second. The actual rate is approximately 10 frames per second, in order to allow adequate time delays between laser pulses while recording a single photograph. Each image consists of three exposures, with delays ranging from 3 to 15 ms. The images are

recorded on Kodak TMAX ASA 3200 B&W film. The acrylic particle tracers are 40 to 60 μm diameter, neutrally buoyant (specific gravity ranging from 0.95 to 1.05), and fluorescing (they respond in the 550 to 560 nm range when subjected to green excitation), as described by Dong, et al. (9). The water is seeded with particles prior to each run. Fine aluminum powder is added to the free surface before some of the runs to improve the visualization of the free surface. Comparison of data with and without the aluminum powder confirms that the presence of the powder has an insignificant impact on the flow. A band-pass filter is inserted in front of the camera to reduce glare caused by the reflection of the light sheet from the model, free surface, and large entrained bubbles. It partially eliminates the green reflections without significantly affecting the fluorescence from the particles. A sample image is shown in Figure 2.

Photographic images are digitized using a Nikon LS3500 slide scanner, at magnifications ranging between 8 - 22 pixels/mm of fluid, as needed. The digitized images are enhanced and particularly bright objects, such as the model and the free surface, are removed. Velocities are computed using in-house auto-correlation software, as described by Dong et al. (8), and Roth et al. (9). The interrogation window size is 64×64 pixels, and the distance between adjacent windows is 32 pixels (i.e., 50% overlap). The typical uncertainty level is about 0.4 pixels, which for a typical 20 pixel displacement yields a characteristic uncertainty of 2%. The free surface contour for each vector map is measured directly from the digitized image. Video images, recorded with a submerged camera are also used for mapping the free surface elevation and for qualitative observations on the flow structure.

RESULTS

Sample photographs of the free surface at different Froude numbers are presented in Figure 3. They clearly show the increase in elevation of the bow wave with Froude number and the generation of bubbles (splashing) within the trough behind the bow wave. This splashing occurs at $Fr_L \geq 0.15$ and curiously, it begins near $x/L = 0.41$, regardless of Froude number. At $Fr_L = 0.205$ (Figure 3a) it is possible to identify several additional waves behind the bubbly trough. At $Fr_L = 0.255$ the second shoulder wave crest is pushed further downstream, and at $Fr_L = 0.36$ the flow becomes extremely unsteady, violent, and turbulent, without any additional steady crests. However, the front of the bubbly region involves an abrupt change in surface elevation, much like a hydraulic jump. For all $Fr_L \geq 0.25$, the shoulder

wave and the separated region behind it are extremely dissipative (data and discussions follow), and seem to overcome the system of Kelvin's waves. The majority of the data presented in this paper is at $Fr_L=0.255$. This condition is selected since there is already considerable bubble generation, significant changes in surface elevation, and the appearance of turbulence in the flow, as seen in Figure 3d. Additionally, unlike higher Froude numbers, at this condition the number of entrained bubbles is still small enough that we can still measure the velocity distribution accurately all the way to the free surface.

At $Fr_L=0.255$, the bow wave still contains several clear capillary waves near its crest (Figure 3d). However, the PIV data clearly indicates that there is already considerable vorticity entrainment, both at the toe, similar to the two dimensional waves demonstrated by Lin & Rockwell (10,11), and along the wave crest. This can be seen in Figure 4. Downstream of the bow wave crest, the free surface is bumpy, which as Dong et al. (5) and Sarpkaya (12) show, is indicative of subsurface vortices. At higher Froude numbers the organized capillary waves disappear and wave breaking as well as transition to turbulence at the toe of the bow wave become clearly evident. There is no bubble entrainment in the bow wave at $Fr_L \leq 0.255$.

The shoulder wave, whose crest is located behind the splashing region (see Figure 3b), is obviously turbulent from its onset, as Figure 3d shows. The splashing is caused by energy dissipation in the bow wave. Further downstream, where the bow wave is milder, the resulting discrepancy in total head causes an inrush of fluid towards the body that impacts on the surface and causes the splashing, as discussed in Pogożelski et al. (13). This lateral flow can be seen also on a ship model (Dong, et al. (5), for example), but does not impact on the body due to the formation of the shoulder wave, which diverts the flow away from the model.

A contour map of the wave profile near the model, measured by video photography, is shown in the bottom side of Figure 4. The maximum wave height measured upstream of the model, $z/L=0.33$, is within 2% of the total head of the incoming flow, $z=U_0^2/2g$, or $z/L=0.324$ for $Fr_L=0.255$. The difference is consistent with our estimated measurement error. The experimental data is compared to results of numerical predictions using a free surface potential flow paneling program developed by Hendrix and Noblesse (14). This program involves several simplifying assumptions, including a slender body and linearized free surface conditions. There is some agreement in general trends, especially in the forward

side. The discrepancy is mostly evident when energy dissipation due to bow wave breaking, splashing, shoulder wave breaking and flow separation are significant.

For example, the peak elevation in the experimental bow wave is located upstream of the model and not on its side, due to bow wave breaking and the associated dissipation. Note that in ship flows, where the Froude number based on draft is super-critical, the origin and crest of the bow wave are located on the side of the model (Miata and Inui (1), for example). Another discrepancy is that the experimental trough is deeper and longer, and occurs at $x/L=0.4$ instead of the theoretical $x/L=0.3$. The Kelvin wave structure, which is evident in the potential flow solution, disappears close to the model due to the impingement, splashing and flow separation that occurs at $x/L>0.6$ (detailed data follows). However, remnants of the Kelvin wake structure are still evident in the experimental data away from the model, but with a phase shift that starts in the longer trough.

When the instantaneous velocity distribution is available in more than one light sheet orientation, one can determine all three velocity components along the intersection lines of the sheets. Uncertainties in the sheet angle and in the measured velocities result in an error of approximately 0.7 pixels in v_x and v_y , but only 0.4 pixels in v_z . (v is the velocity and the subscript denotes the direction). The latter is more accurate since one of the sheets is vertical, so that v_z is calculated from a single sheet. Using the measured free surface elevation and the three velocity components along the intersection line, it is possible to estimate the total head of the fluid. Sample results of such an analysis are presented in Figure 5, along with the local values of v_x and v_y . It can be seen that the total head decreases to about $0.9U_0^2/2g$ across the bow wave, except very near the body where ~50% of the energy is lost. Even at a very mild slope of the bow wave, there is already considerable entrainment of vorticity, as seen in Figure 6. A second sudden decrease occurs across the shoulder wave, where the total head is reduced to values ranging between 0.64 - 0.77. Near the body the levels remain near 50%. Thus, the shoulder wave and the separated region behind it are dissipating one third to one half of the total energy along the free surface. The velocities behind the shoulder wave are also slower, ranging between 0.5 - 0.75 U_0 . Away from the model, near the thickest part of the body, the near surface velocity is 1.4 U_0 .

Velocity and vorticity distributions demonstrating the development of the shoulder wave

during a single experiment are shown in Figure 7. Due to the impingement that occurs just upstream of the wave, the flow at the origin of the shoulder wave (Figure 7a and b) is already unsteady, turbulent and bubbly. In this particular case, most of the vorticity is negative, much like the two dimensional spilling breaker of Lin and Rockwell (10,11), but there is positive vorticity at the crest. Further downstream, however (Figure 7d), the wave contains several distinct vorticity structures of both signs. To illustrate the unsteady nature of this flow, Figure 8 contains several velocity and vorticity maps at the same location, $x/L=0.6$, and flow conditions, recorded during different runs. There are common phenomena, but the flow is clearly unsteady and contains several large scale vorticity structures of alternating signs. Their existence contributes substantially to the entrainment of bubbles both by convecting them away from the surface and by trapping them. Video images (see a sample in Figure 10c) of this flow show some bubbles trapped in the vortex cores. However, the regions containing bubbles, which are marked on each map, also vary substantially in shape and correspond to the large eddies only in some of the cases. The common phenomena include negative vorticity entrainment at the toe of the wave, and in all but one case the vorticity near the wall is positive. Further downstream, at $x/L=0.7$ (Figure 7e & f), the surface elevation is higher, the free surface is more wavy, and the near surface flow still consists of several counter-rotating vortices, most of which are located away from the model. The dominant phenomenon seems to be an upward flow (upwelling) that splits near the surface at $y'/L=0.21$ to create a pair of counter rotating eddies. In this plane the presence of bubbles far from the surface is clearly associated with the large eddies. With increasing distance from the model (Figures 7g-j) the wave becomes milder in size, slope and extent of vorticity production. Residuals of vortices that are generated in upstream planes are still distributed along the free surface, but they eventually disappear. The large structures that appear near the model are associated with flow separation rather than the shoulder wave, and will be discussed shortly.

A series of velocity and vorticity distributions from a single run (Figure 9) focuses on the flow near the model between $x/L=0.73$ and $x/L=0.91$. Sample video images of the same flow, as seen using the optical setup of Figure 1c, is provided in Figure 10. It is clearly evident that boundary layer separation occurs near the free surface. The separated region increases in width and depth between $x/L=0.73$ and 0.82, and in depth only between 0.82 and 0.91.

This region contains several large scale vortices with peak vorticities of about $80U_0/L$ - 4 to 10 times higher than the vorticity peaks within the breaking waves upstream. The magnitudes of the velocity in these planes reach levels of approximately $0.5U_0$. Although their exact shapes and sizes vary, the existence of these vortices is consistent and repeatable. Bubble entrainment and trapping in the vortex cores also occurs consistently. A sample video image of an entrained bubble is shown in Figure 10c. Using the quantitative data and the video images, we attempted to construct an overall sketch of the flow structure within the separated region, as shown in Figure 11a-d. Data from two inclined planes was used to determine all three components of the velocity along the intersection lines. The arrows shown in Figure 11d are actually quantitative data with a reference velocity provided on the same figure. There is no reverse flow in the entire separated region at this Froude number. This trend contradicts the conclusions of a computational study performed by Zhang and Stern (7). However, in agreement with their conclusions, reverse flow near the present body has been observed at Froude numbers exceeding 0.30, using video cameras above the surface.

Note that in the bottom parts of Figures 9c-e that there is a change in flow direction near the model. This effect is caused by the boundary layer on the model, as seen in the inclined light sheet. The projection of the model speed onto the plane of the laser sheet (Figure 1b) points to the right, and as a result, the fluid within the boundary layer has a velocity component in that direction. The outer flow is affected only by the narrowing of the body, moving to the left, which causes the observed effect. The characteristic thickness of this layer, $.01L$ at $x/L=0.82$ and $.025L$ at $x/L=0.91$, is consistent with the expected width of a laminar boundary layer.

Repeated examination of the video records has shown that the origin of the separated zone at $Fr=0.255$ is at the intersection of the model with the free surface, at the trough behind the shoulder wave. The vortex with positive vorticity, which appears at $y'/L=0.21$ and $z'/L=-0.035$ in Figure 9a and $y'/L=0.195$, $z'/L=-0.04$ in Figure 9c, originates in this corner. The negative vortex located near it ($y'/L=0.19$ and $z'/L=-0.045$ in Figure 9a) is originated on the model, below the free surface a short distance downstream. Only the positive vortex remains at $x/L=0.91$ (Figure 9e). A second pair of counter-rotating vortices is generated on the model in the same sequence, well below the free surface and further downstream. The positive vortex is already visible near the model, at $z'/L=-0.06$ and -0.08 in Figures 9a

and c, respectively; however, its negative partner appears only at $x/L=0.91$ (Figure 9e). Figure 10 shows the second pair (but in a different run) moving away from the surface, shortly after the negative vortex is generated. These images are recorded with a video camera using the setup of Figure 1c. As noted before, one of the vortices in Figure 9e traps a bubble. Figure 11c attempts to illustrate the sequence of vortex generation on the model. The entire process has some resemblance to three dimensional, open separation in the lee side of inclined bodies of revolution. However, considerably more data analysis, which is still in progress, is required before we are able to construct the complete flow topology. In addition to the repeatable vortices that develop near on the model, the flow near the free surface contains numerous vortices with alternating signs. Their locations and spatial distributions are unsteady and they regularly entrap bubbles.

CONCLUSIONS

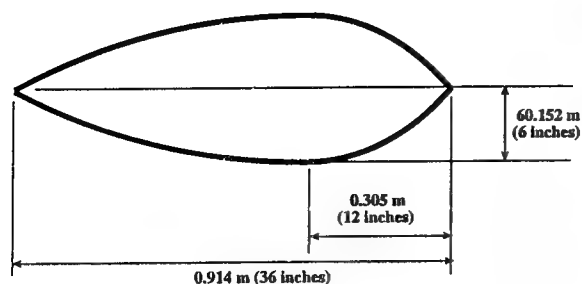
For the present surface piercing model with a long draft a bubbly wake is generated at the trough between the bow and the shoulder wave. This phenomenon occurs at $x/L=0.41$ and $Fr_L \geq 0.153$ due to impingement of the flow on the model, a process associated with energy dissipation in the bow wave. Consequently, the origin of the shoulder wave consists of several powerful counter-rotating vortices which entrain bubbles from the free surface. The wave crest becomes milder and eventually irrotational with increasing distance from the model. Behind the shoulder wave, at $x/L=0.7$, boundary layer separation begins, but only near the free surface. The flow within the separated region consists of two pairs of counter rotating vortices that detach from the boundary layer on the model. The first vortex is generated at the intersection of the body with the free surface, but the following ones are originated below the free surface. At $Fr_L=0.255$ there is no reverse flow within the separated region, but flow reversal seems to occur at $Fr_L \geq 0.307$. The flow structure is turbulent and involves considerable dissipation.

ACKNOWLEDGMENTS

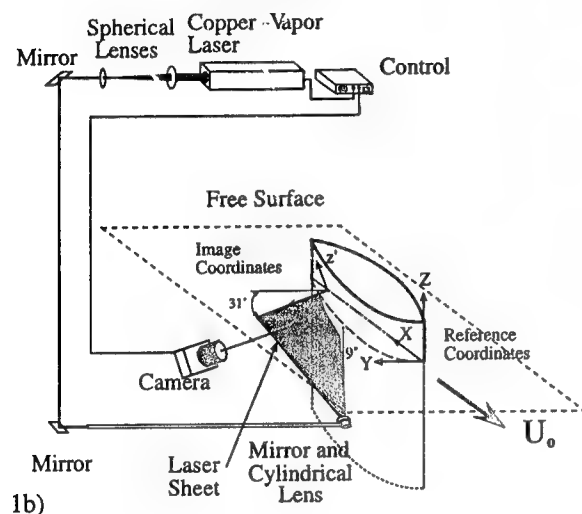
This project is sponsored by the Office of Naval Research under grant number N00014-93-1-0204, under the management of Dr. Edwin Rood. Thanks are also due to R. Dong for his assistance.

REFERENCES

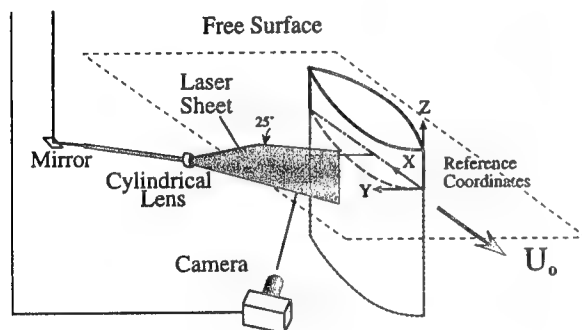
1. Miata, H., Inui, T., "Nonlinear Ship Waves," Advances in Applied Mechanics, Vol. 24, 1984, pp. 215-288.
2. Fry, D.J., and Kim, Y.H., "Bow Flow of Surface Ships," Proc. of the 15th Symp. on Naval Hydrodynamics, Hamburg, Germany, pp. 319-346.
3. Toda, Y., Stern, F., and Longo, J., "Mean-Flow Measurements in the Boundary Layer and Wake and Wave Field of a series 60 $C_B=0.6$ Ship Model - Part 1 : Froude Numbers 0.16 and 0.316," J. of Ship Res., Vol. 36, No. 4, 1992, pp. 360-377.
4. Longo, J., Stern, F., and Toda, Y., "Mean-Flow Measurements in the Boundary Layer and Wake and Wave Field of a series 60 $C_B=0.6$ Ship Model - Part 2 : Scale Effects on Near-Field Wave Patterns and Comparisons with Inviscid Theory," J. of Ship Res., Vol. 37, No. 1, 1993, pp. 16-24.
5. Dong, R.R., Katz, J., and Huang, T.T., "PIV Measurements of the Flow Structure Around a Ship Model," ASME/EALA Sixth International Symp. on Laser Anemometry, 1995, pp. 425-434.
6. Stern, F., Hwang, W.S., Jaw, S.Y., "Effects of Waves on the Boundary Layer of a Surface-Piercing Flat Plate: Experiments and Theory," J. Ship Res., Vol. 33, No. 1, 1989, pp. 63-80.
7. Zhang, Z.J., and Stern, F., "Wave-Induced Separation," Forum on Advances in Numerical Modeling of Free Surface and Interface Fluid Dynamics, 1995, ASME IMECE, San Francisco, CA.
8. Dong, R., Chu, S., and Katz, J., (1992), "Quantitative Visualization of The Flow Structure Within The Volute of a Centrifugal Pump, Part A: Technique," J. Fluids Eng., Vol. 114, No. 3, 1992, pp. 390-395.
9. Roth, G., Hart, D., and Katz, J., "Feasibility of Using the L64720 Video Motion Estimation Processor (MEP) to Increase Efficiency of Velocity Map Generation for PIV," ASME/EALA 6th International Symp. on Laser Anemometry, August 1995, pp. 387-394.
10. Lin, J.C., and Rockwell, D., "Instantaneous Structure of a Breaking Wave," Physics of Fluids, Vol. 6, No. 9, 1994, pp. 2877-2879.
11. Lin, J.C., and Rockwell, D., "Evolution of a Quasi-Steady Breaking Wave," Journal of Fluid Mech., vol. 302, 1995, pp. 29-44.
12. Sarpkaya, T., "Vorticity, Free Surface, and Surfactants," Ann. Rev. Fluid. Mech., Vol. 28, 1996, pp. 83-128.
13. Pogozielski, E., Katz, J., and Huang, T., "Flow Structure Around a Surface-Piercing Blunt Body," Proc. 20th ONR Symposium on Naval Hydrodynamics, August 1994.
14. Hendrix, D., and Noblesse, F., "Recipes for Computing the Free-Surface Flow Due to a Source Distribution," Journal of Ship Research, vol. 36, No. 4, Dec. 1992, pp. 346-359.



1a)



1b)



1c)

Figure 1: Schematic description of the model and the experimental setup; a) cross section of the model, b) primary orientation of the underwater camera and the light sheet, and c) orientation of the camera and light sheet during observations from upstream. In b), the origin of the $x'-y'-z'$ coordinate system is on the centerline of the model at the intersection of the light sheet and the undisturbed free surface.

Figure 2 (next column): Three-exposure image at $x/L=0.27$ and $Fr_L=0.255$, viewed with the setup shown in figure 1b. A 64×64 pixel correlation window is shown magnified. The model is on the left and the free surface is on top.

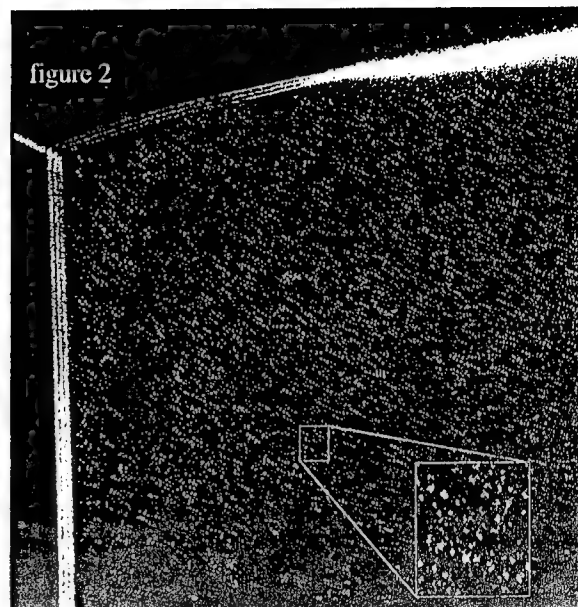


figure 2

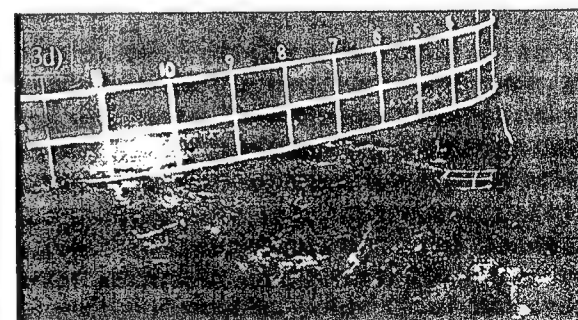
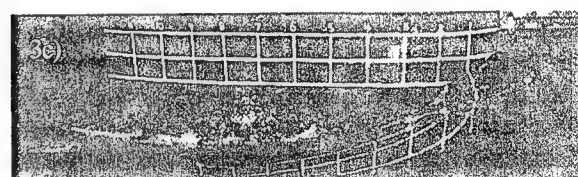
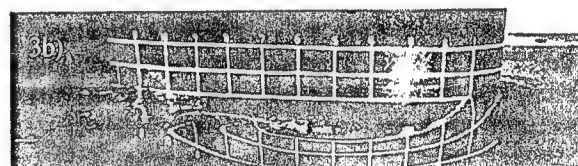
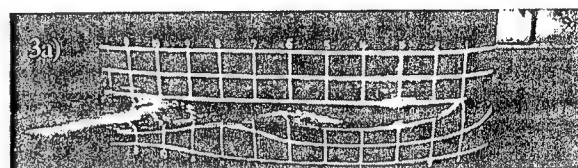


Figure 3: Starboard views at a) $Fr_L=0.204$, b) $Fr_L=0.255$, c) $Fr_L=0.357$; d) back-starboard view at $Fr_L=0.255$. The painted rectangles on the model are 3 inches long ($L/12$) and 2 inches high. The lowest line indicates the position of the undisturbed free surface.

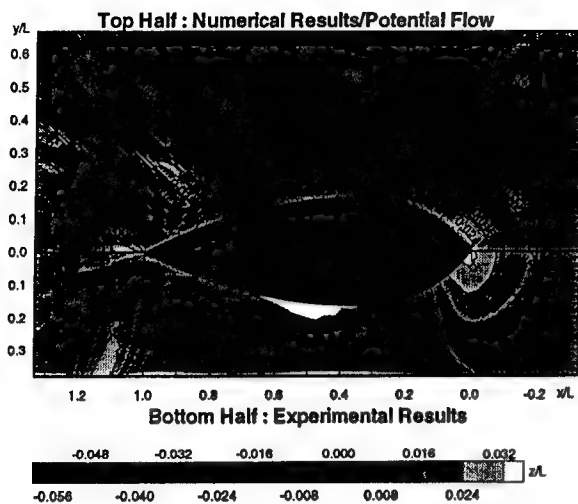


Figure 4: Elevation contours of the free surface at $Fr_L=0.255$. The blank area near the center of the model is due to the presence of bubbles, which make it difficult to accurately establish the position of the free surface.

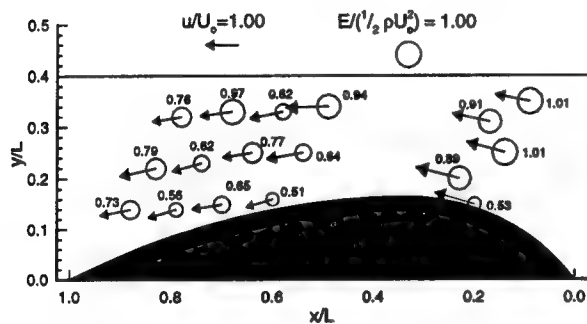


Figure 5: Total energy ($E = \frac{1}{2} \rho u^2 + \rho gh$) and velocity on the free surface at $Fr_L=0.255$. Data is provided at the intersection of light sheets.

Figure 7 (next column and following pages): Velocity and vorticity ($\omega L/U_0$) distributions of the shoulder wave at $Fr_L=0.255$, viewed as shown in figure 1b. a,b) $x/L=0.49$; c,d) $x/L=0.58$; e,f) $x/L=0.69$; g,h) $x/L=0.78$; i,j) $x/L=0.88$. The contour interval is 4; shaded areas indicate negative vorticity, and dashed lines indicate the boundaries of the bubbly region. In figures 6g-j, the model has moved out of the picture.

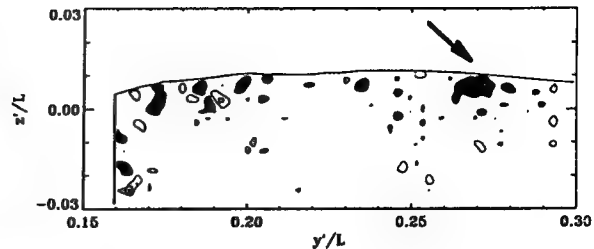
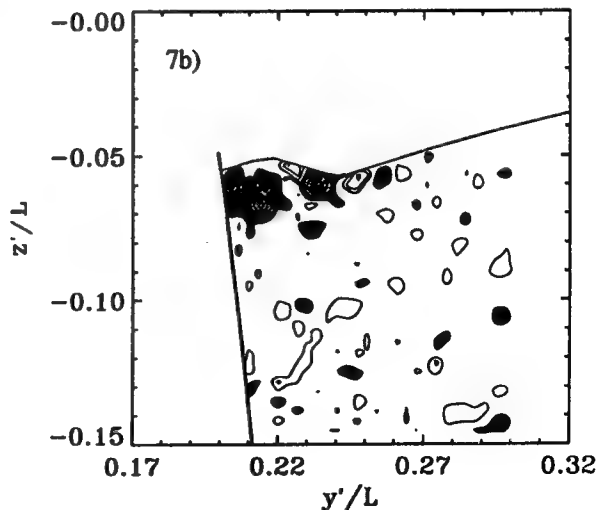
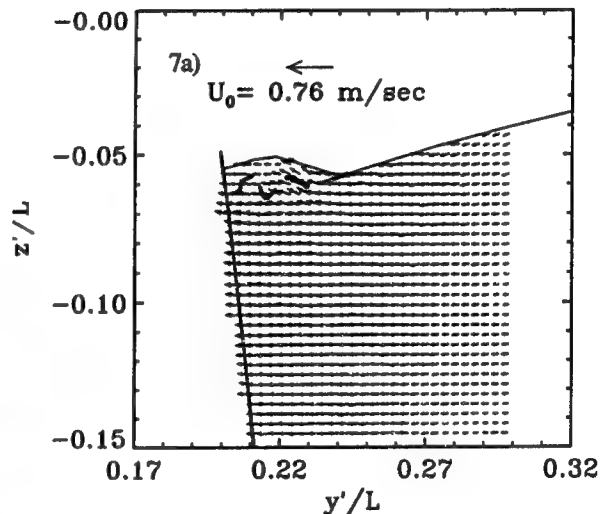
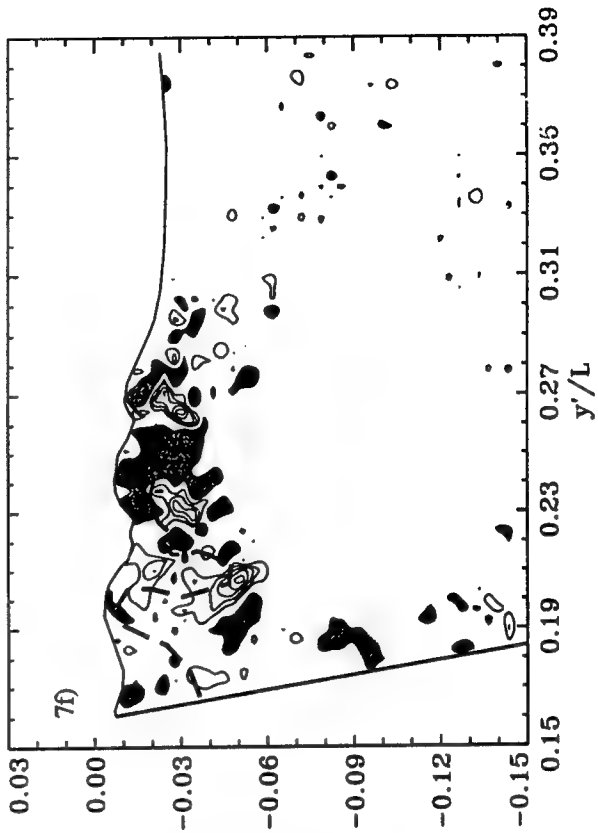
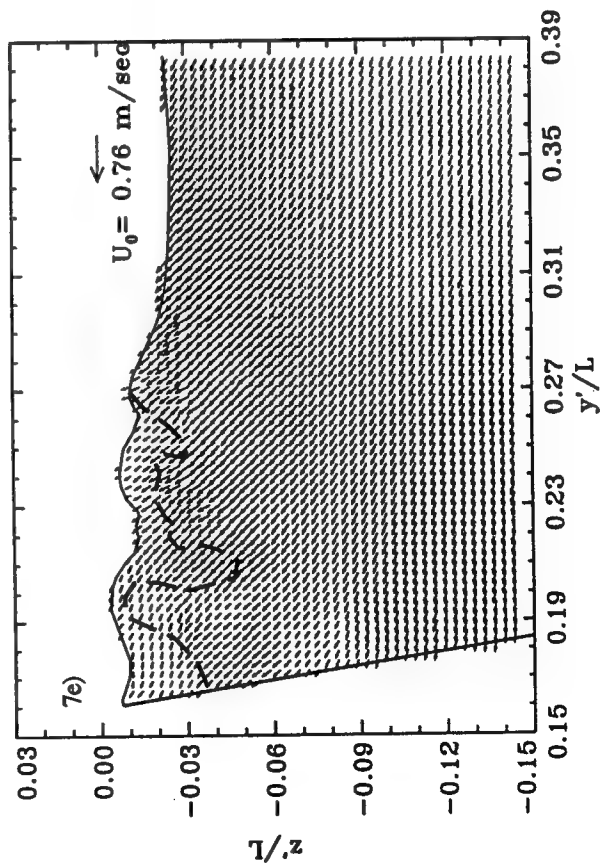
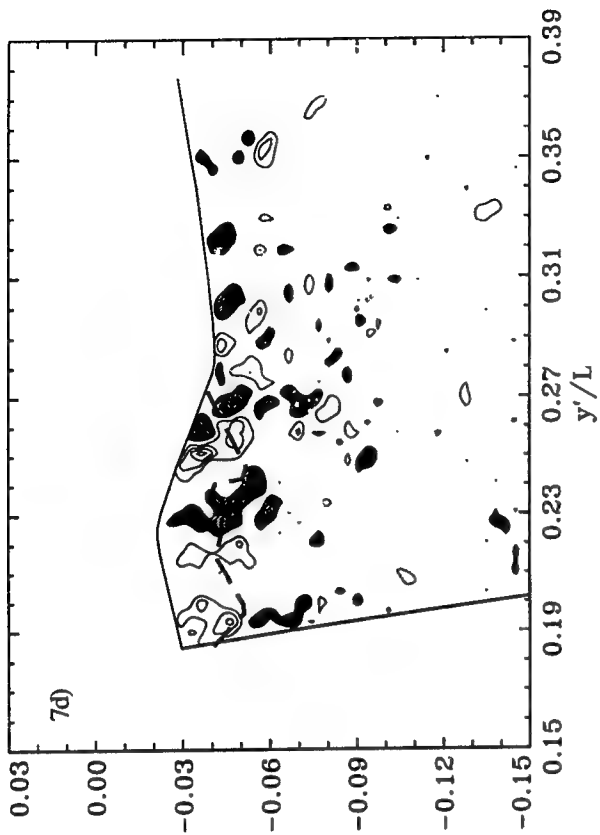
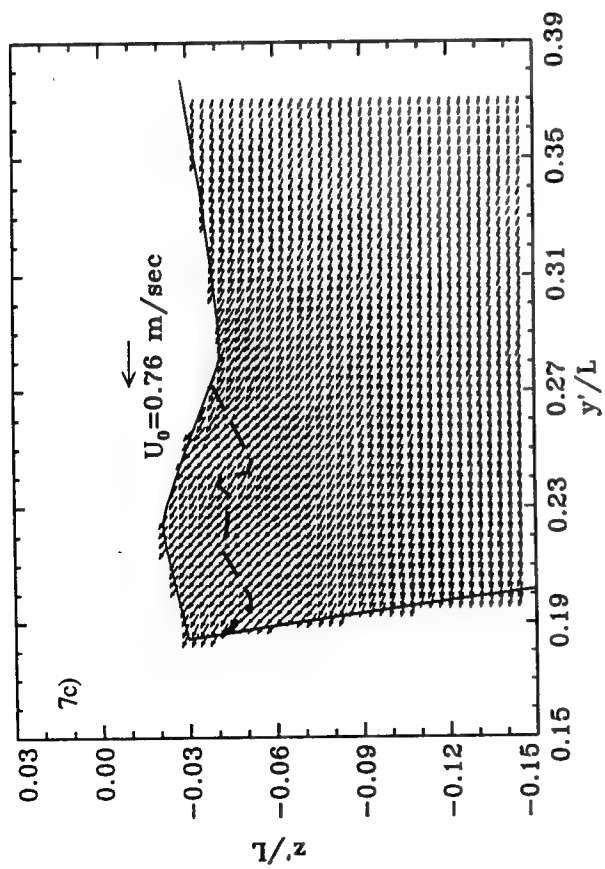
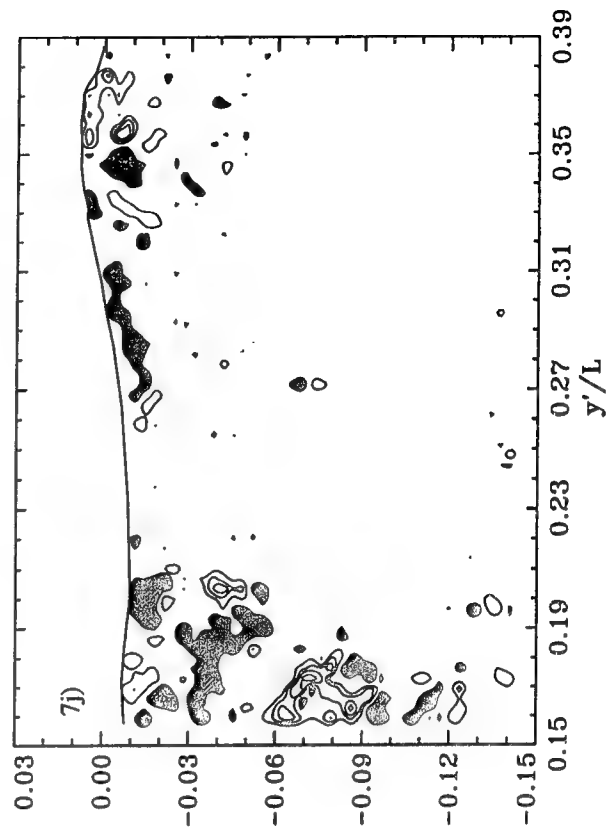
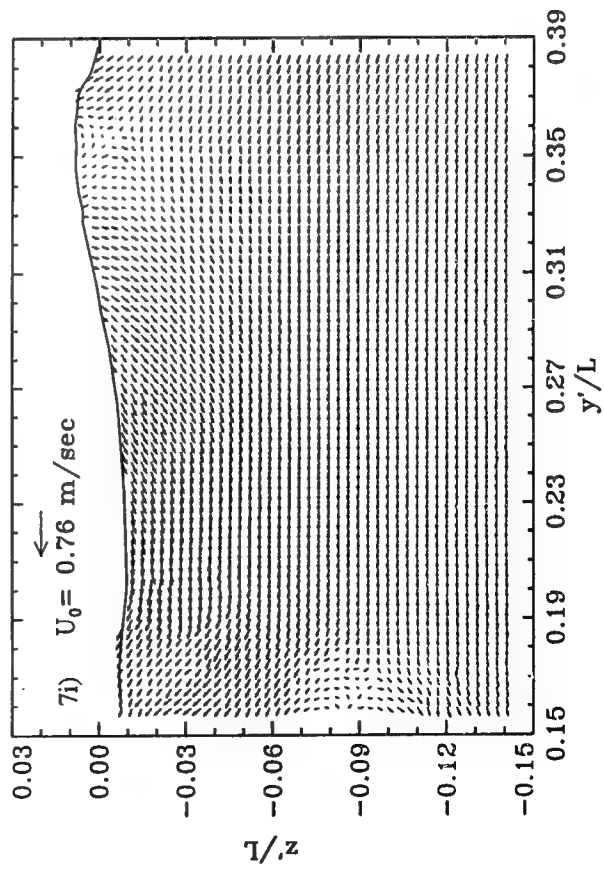
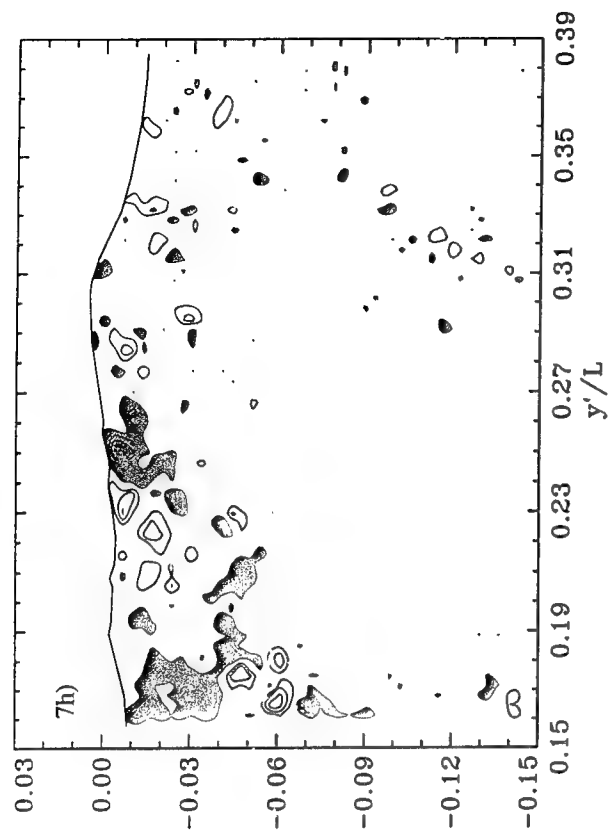
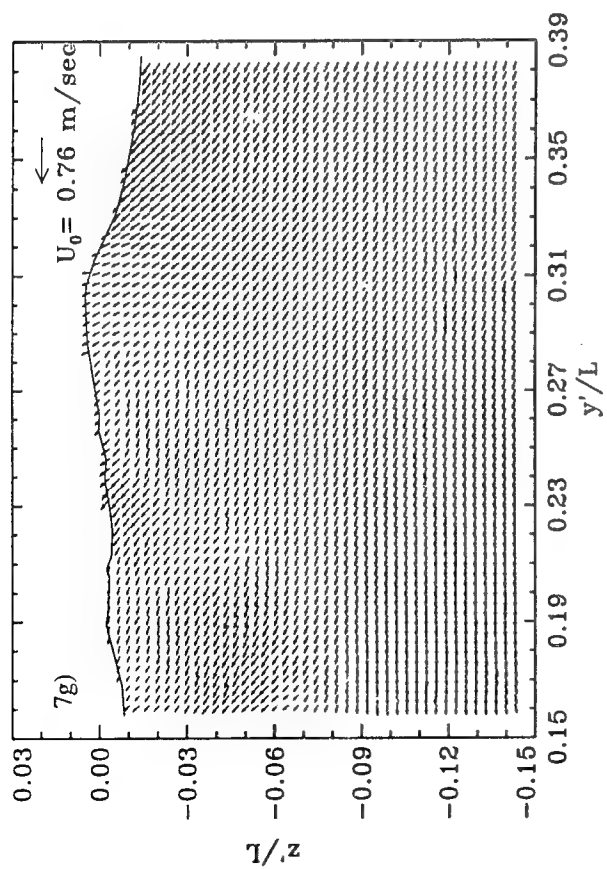


Figure 6: Vorticity ($\omega L/U_0$) distribution within the bow wave at $x/L = 0.22$ and $Fr_L=0.255$, as seen from behind (at 34°). The contour interval is 8; shaded areas indicate negative vorticity. The vertical line on the left side of the figure is the model.







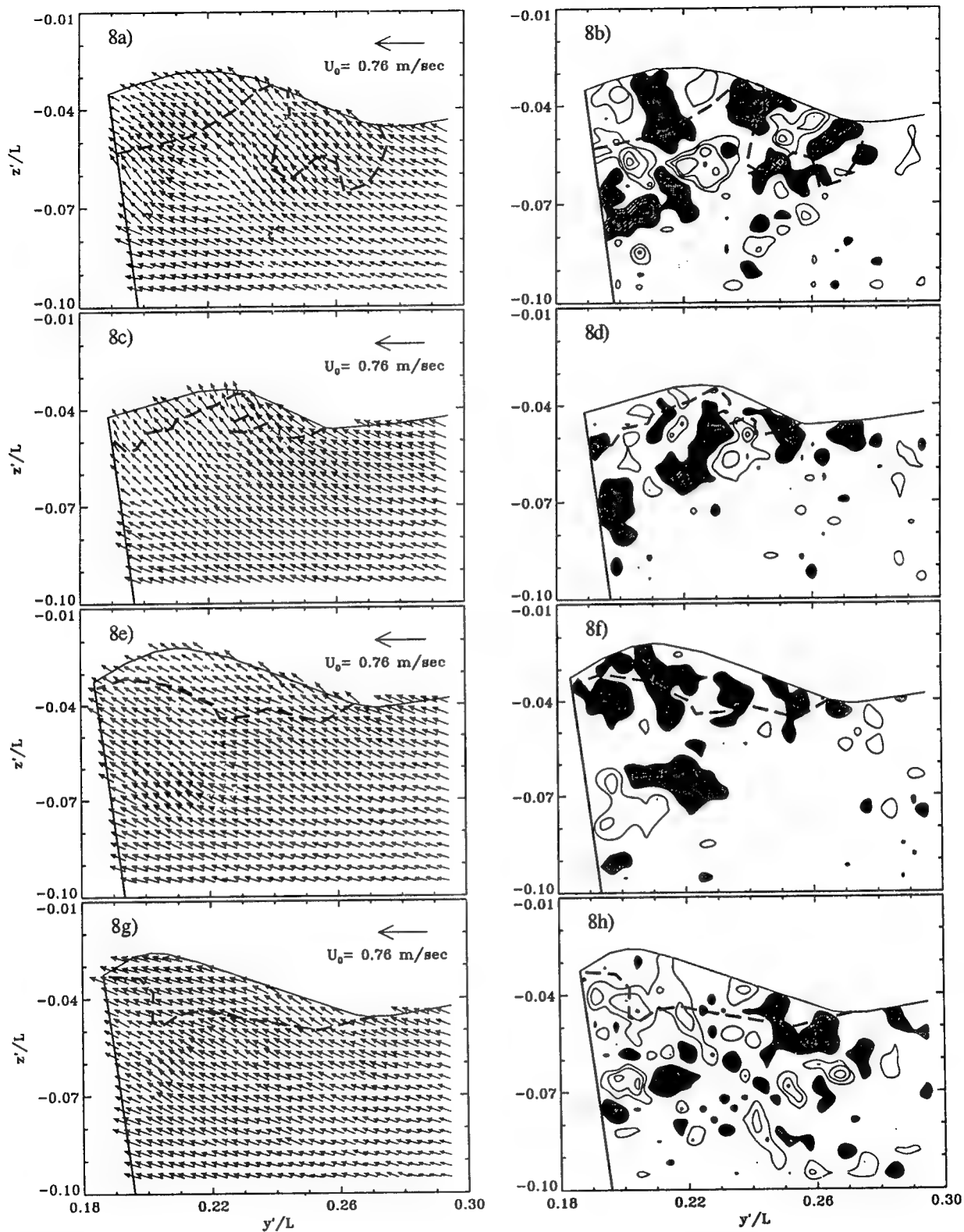


Figure 8: Velocities and vorticity contours ($\omega L/U_0$) at $Fr_L=0.255$, viewed with the figure 1b setup. a,b) $x/L=0.58$; c,d) $x/L=0.59$; e,f,g,h) $x/L=0.60$. The vorticity contour interval is 4; shaded areas indicate negative vorticity, and dashed lines indicate the presence of bubbles.

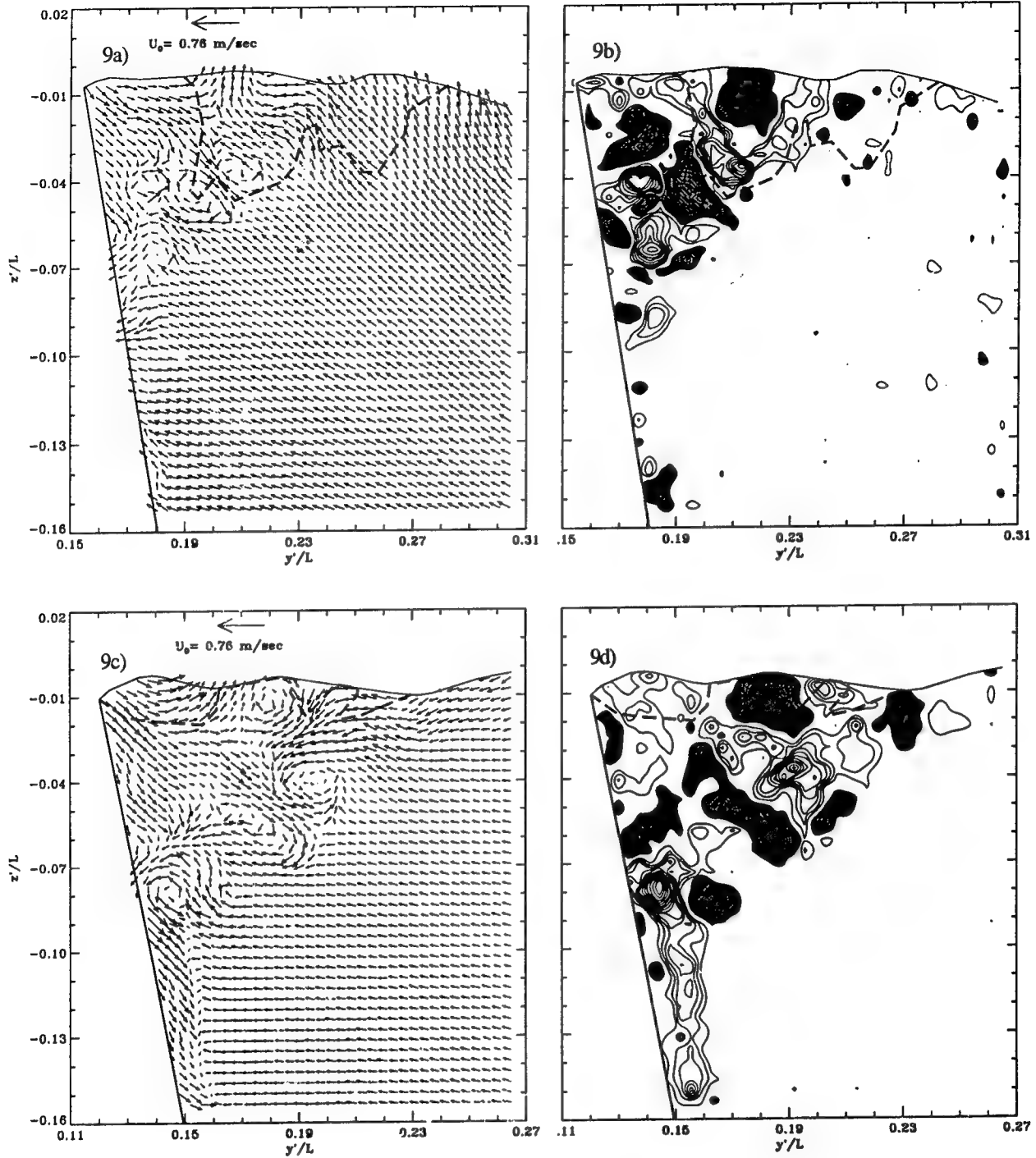


Figure 9 : Velocity and vorticity ($\omega L / U_0$) plots at $Fr_L=0.255$, at a,b) $x/L = 0.73$, c,d) $x/L = 0.82$, e,f) $x/L=0.91$. The contour interval is 8; shaded areas indicate negative vorticity and dashed lines indicate the boundaries of the bubbly region.

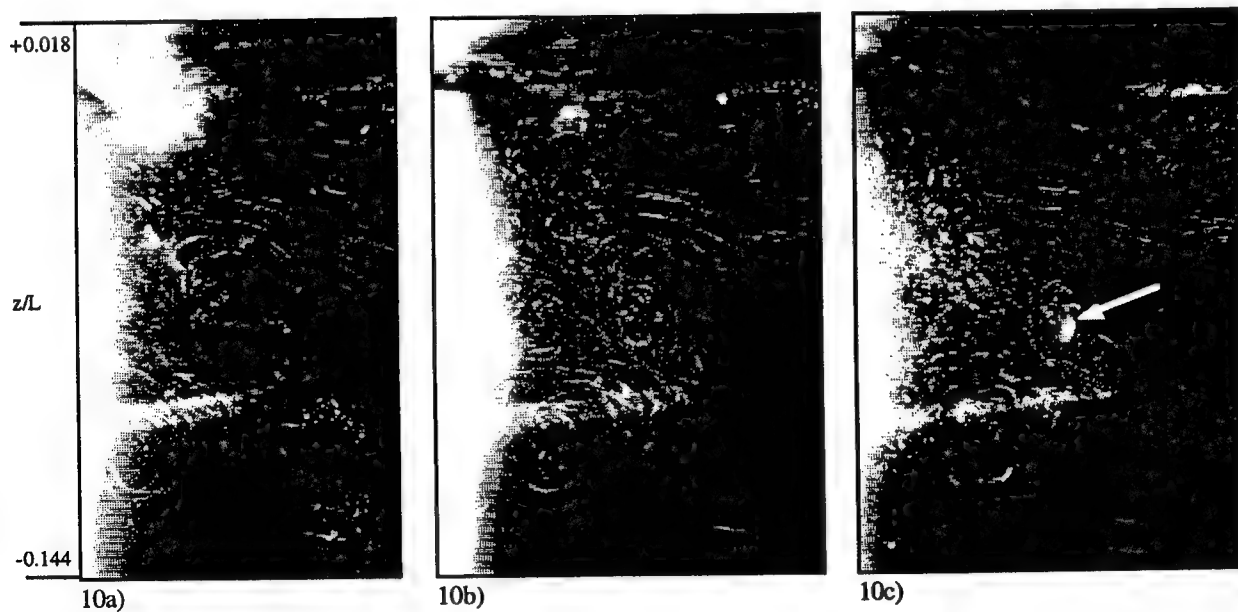
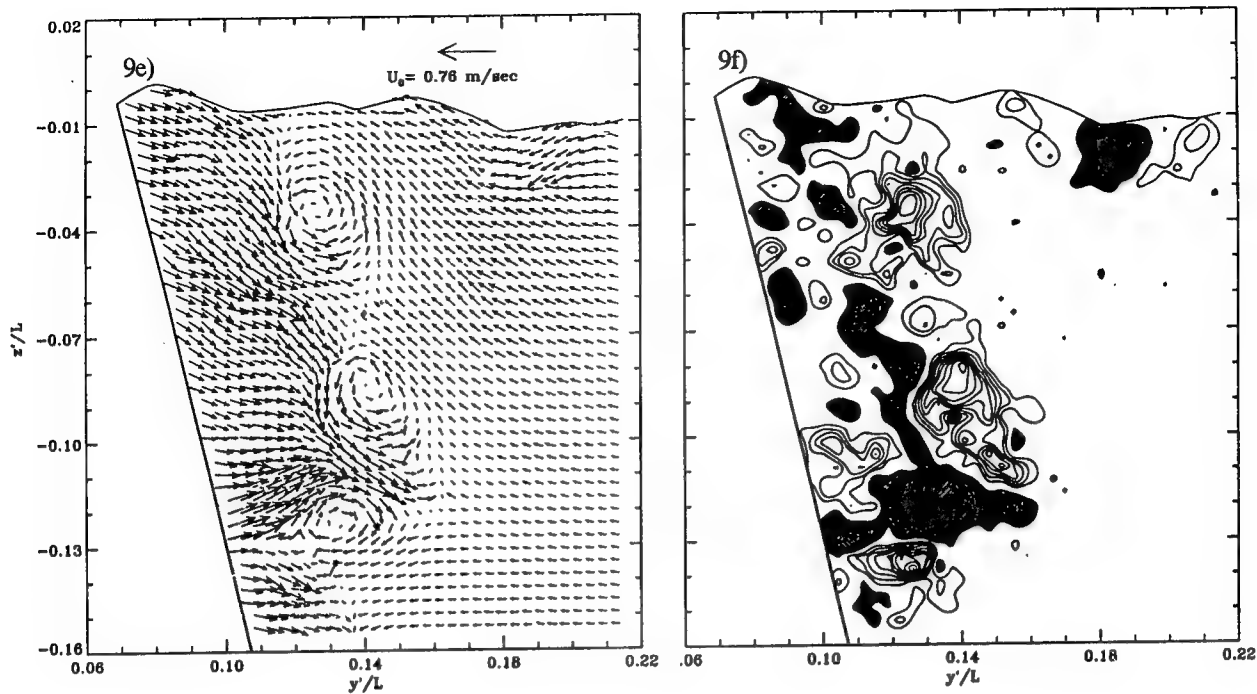
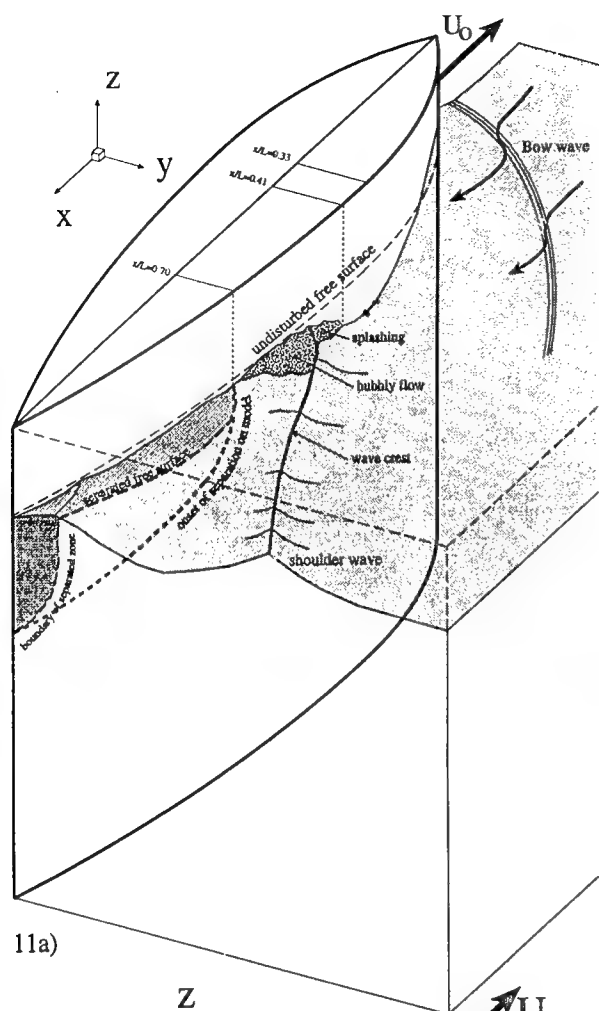
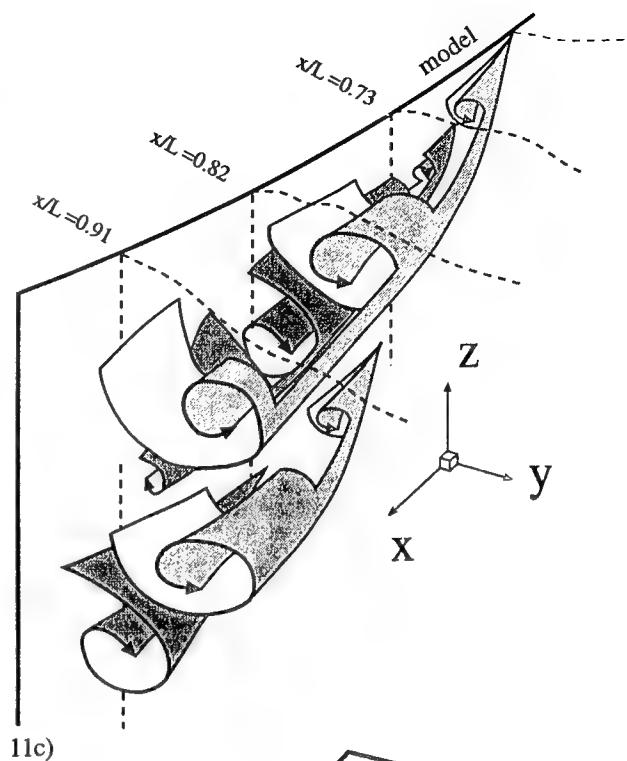


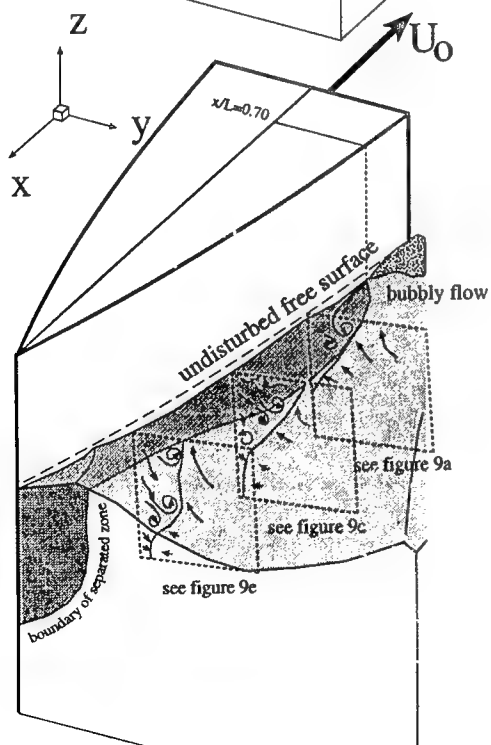
Figure 10: Video images from a single run at $Fr_L=0.255$, at a) $x/L=0.83$, b) $x/L=0.88$, and c) $x/L=0.89$, viewed as shown in Figure 1c. The arrow indicates an entrained bubble.



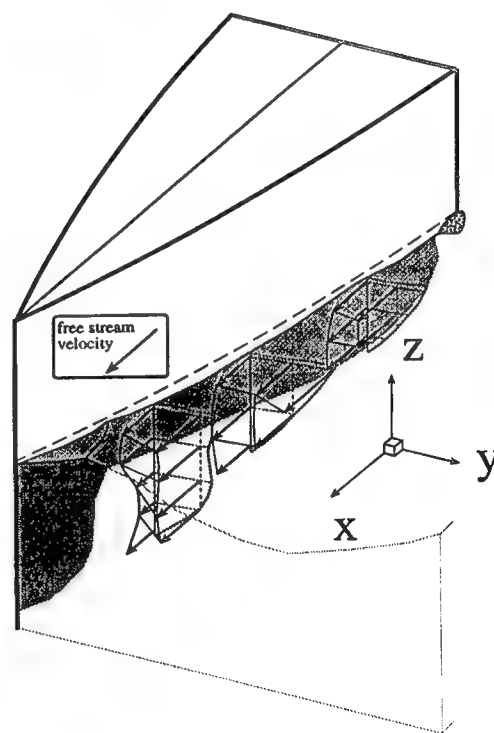
11a)



11c)



11b)



11d)

Figure 11 : Sketches of the flow structure at $Fr_L=0.255$: a) overall view, b) view of the separated zone data included in Figure 9, c) schematic of vortex growth in the separated region, d) quantitative axial velocity components in the separated region, in the model's frame of reference.

Vorticity Fields due to Rolling Bodies in a Free Surface— Experiment and Theory

R. Yeung, C. Cermelli, S.-W. Liao (University of California at Berkeley, USA)

ABSTRACT

Viscous effects are known to have significant influence on hydrodynamic forces on bluff-shape bodies. Ocean structures in long waves and roll-damping arising from bilges of a ship hull are important examples. Some recent efforts to understand and model such real-fluid effects in the presence of surface waves are described. As a canonical problem for studying ship roll, a surface-piercing plate is oscillated sinusoidally in the free surface. A Digital Particle Image Velocimetry system (DPIV) was developed at the UC Berkeley Ship-Model Facility to map out the flow details. In one regime, the flow exhibits an asymmetrical vortex shedding pattern. This steady-state pattern is observed to be systematically dependent on the initial conditions. DPIV and other experimental results were used to validate the predictive capabilities of the Free-Surface Random-Vortex Method (Yeung & Vaidhyanathan, 1994). This grid-free Lagrangian method is briefly described. With some calibrations, the method reproduces very well the observed vortical structures, the measured forces and moments, and the wave-generation characteristics. Application of the methodology to a rolling rectangular section with sharp bilges is also considered. The limitations and promise of the method are discussed.

1 INTRODUCTION

To be successful in predicting the motion of marine vehicles, particularly motion in the horizontal plane, sway, roll and yaw, one needs to be able to model viscous effects in a reasonably accurate way. In the last decade, much strides have taken place in the development of solution based on potential-flow theory that includes the effects of free surface (Yeung, 1982, Korsmeyer et al., 1988,

Newman, 1992). While heave and pitch motions are generally considered to be well predicted, successful predictions of roll motion still rely on empirical estimation of roll damping, often on a trial-and-error basis (e.g. Schmitke, 1978, Brown et al., 1983).

Progress in this area has been slow since the proper modeling of viscous effects would involve the solution of the Navies-Stokes equations with a capability of modeling massive separation arising from the bilge corners or bilge keels. Further, one may also need to account for coupling coming from the free-surface.

A closely related problem involving flow-separation effects occurs in offshore engineering where the bluff shapes of the structures lead to substantial "drag" and "inertia" forces in waves. Here, separation effects are commonly characterized by the "Keulegan-Carpenter Number" $KC = U_m T/D$, where U_m is a characteristic velocity, T the time period of the flow, and D the body dimension. When KC is of $O(10)$ or higher, real-fluid effects are known to be significant, (Sussbielles & Bratu, 1981, Sarpkaya & Isaacson, 1981). Typical applications have KC values ranging from $O(10)$ to $O(10^2)$.

The objective of the present paper is to report our recent efforts in developing a model for such separated-flow phenomena, particularly in the presence of surface waves. When a marine vehicle undergoes extreme roll motion, separation from the bilge corners, or from bilge keels are the dominant contribution to damping, whose magnitude critically determines the severity of motion, especially in conditions close to resonance. Thus any theoretical or computational model should be properly validated. This requires careful complementary experimental work which is also described in this paper.

It is worthy to mention that there are existing semi-empirical methods for roll-damping estimation due to the hull surface and bilge keels (Himeno, 1981, Ikeda, 1977, Tanaka, 1960). Of course, one component of damping is surface-wave generation, which is normally well predicted by potential-flow theory. There have been efforts also to predict viscous damping without relying on empiricism, (Fink and Soh 1974, Brown and Patel 1985, Braathen and Faltinsen 1988, Cozens 1987, Downie et al. 1990). None has yet been able to model the interaction of hull geometry, vorticity generation and free-surface simultaneously.

Recently, Yeung & Vaidhyanathan (1994) have developed a Free-Surface Random-Vortex Method (FSRVM) to model near-surface flows for body geometry that may or may not have sharp edges. Their earlier works involved several important improvements (Yeung et al., 1993) over the Random Vortex Method (RVM) proposed originally by Chorin (1973). An efficient numerical scheme was devised to compute the mutual induction of discrete vortex elements. A boundary-integral formulation was used to handle arbitrary body geometry. These new developments were extended to take into account of free-surface effects. The essence of this method is briefly described in Section 4. FSRVM does not require any prior knowledge of the location of the separation point. Since the method is grid-free, it can represent vortex structures of a rather wide range of scales. Accurate predictions at high Reynolds number is also possible, as illustrated in Section 5 by some direct comparisons of the numerical predictions with experimental results.

Although forces and moments are usually the primary quantities of interest, it is not always appropriate to establish the validity of a mathematical model on forces or moments *alone*. A more rigorous validation should involve comparing flow patterns also. At the University of California Ship-Model Testing Facility, a Digital Image Particle Velocimetry (DPIV) was developed and implemented to provide quantitative results on the velocity and vorticity fields generated by a body moving in a free surface (Cermelli, 1995). Some of the major findings of such an investigation are reported in Section 3.

Because of the complexity of vortex patterns generated by a realistic hull model, a simplified "canonical" problem was introduced to study the roll motion of a ship section. The canonical problem chosen is that of a surface-piercing plate rolling periodically about the free surface. The flow

is primarily two dimensional so that comparison with applicable theoretical results is immediately possible. For the typical frequency range of interest, this rolling plate is designed so that surface-wave generation and vorticity generation are important. Naturally, besides providing a validation on our theoretical model, this canonical experiment is closely relevant to the understanding of the performance of bilge keels, the prevalent passive device for reducing roll motion. In the last section of the paper, we present predictions of added inertia and "equivalent" linear damping for a rectangular hull section and compare them with some existing data.

2 THE ROLLING-PLATE EXPERIMENT

2.1 Design of experiment

A special model was designed and fabricated to study the vortical structures generated by a plate undergoing rolling motion in a free surface. This experiment was carried out at the Ship-Model Testing Facility of the University of California at Berkeley. The towing tank is 61m(L) x 2.44m(W) x 1.52m(D). The plate is oscillated by a hydraulic piston. Flow visualization can be conducted through four observation windows along tank walls.

The plate was built out of one-inch thick acrylic and stiffened longitudinally. It has a natural frequency of 4 Hz, while the range of forced-motion frequency being investigated is less than 0.6 Hz. The clearance between the plate vertical edges and the tank walls was kept to a minimum (0.64cm) to reduce end effects. The plate was hinged at the free surface. Its draft was primarily set to 30.48cm (12 in). Flow visualizations were conducted also with a 15.24cm (6 in) draft.

A plate with a tip that was rectangular in section was found to yield force and moment measurements that were not repeatable, primarily as a result of chaotic vortex shedding from the bottom edges of the plate. The tip of the plate was then modified by the addition of a half circle rod at the bottom of the plate (see Fig. 1). This greatly improved the consistency and repeatability of force records.

Plate rotation was achieved by applying horizontal motion to a rod which was hinged to the plate on one side and to (a random motion) hydraulic piston on the other side (Fig. 1). A software controller was developed to ensure speedy

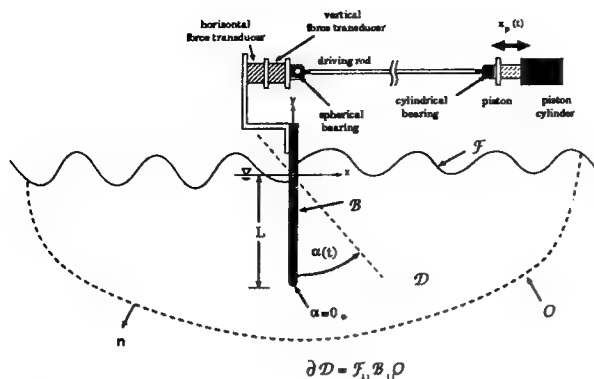


Figure 1: Definitions of flow domain and roll-motion driving mechanism

response of the piston to any prescribed function of time. The software controls the plate angle $\alpha(t)$ according to the following prescribed time function:

$$\alpha(t) = \alpha_0 \tanh\left(\frac{t}{sT}\right) \sin(\omega t) \quad (1)$$

where $\omega = 2\pi/T$ is the angular frequency of the prescribed oscillation and α_0 the roll amplitude. α_0 can be either positive or negative, depending on whether the plate starts with a right or left swing. The "smoothness parameter", s , determines the number of periods needed to reach a sinusoidal steady state of $\alpha(t)$. The plate motion always starts with the vertical position, $\alpha = 0$.

For later purposes, it is helpful to introduce a *phase angle* Φ to define the plate position. Φ equals to 0° is defined to be when the plate is vertical ($\alpha = 0$) and the plate tip is moving toward the right (i.e., increasing α). $\Phi = 90^\circ$ when the plate reaches its maximum angle of swing ($\alpha = |\alpha_0|$). $\Phi = 180^\circ$ represents the instant of $\alpha = 0$ when the plate tip is swinging toward the left (decreasing α). Thus, $\Phi = 270^\circ$ corresponds to the plate at its minimum angle position ($\alpha = -|\alpha_0|$).

Force transducers were installed at the two side hinges holding the plate and at the hinge connected to the driving rod to measure the moment and the horizontal and vertical forces. The equations of motion of the plate were developed. The desired hydrodynamic forces and moment can be obtained by deducting contributions of the hydrostatic component (computed from the plate roll angle) and of the inertia components from the measured values. Output from the force transducers and from a wave gage were digitized at 50 Hz and recorded on a 486-PC. In addition,

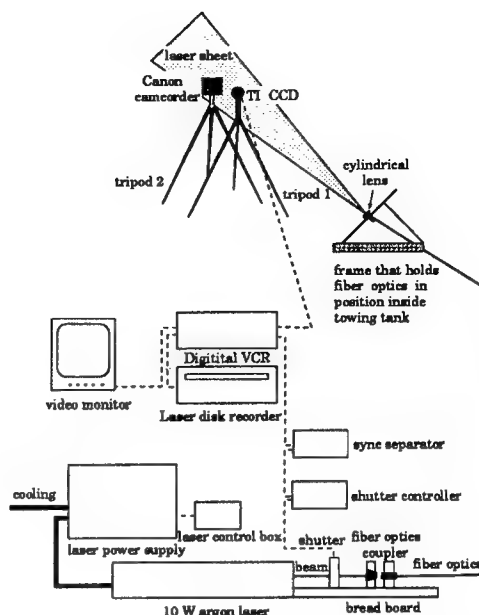


Figure 2: Image acquisition system and optical set-up

the piston-location feed-back signal and the wave elevations at two points were recorded.

2.2 Flow-Image Capturing and Analysis

The Digital Particle Image Velocimetry (DPIV) System set up for this experiment is shown in Fig. 2. The light source consists of a 10-W argon laser generates a 570 nm wavelength (green) beam of approximately 2 mm in diameter. To avoid light refraction at the free surface, fiberoptics are used to direct the laser light into the tank. The beam emerges into a cylindrical lens to form a divergent light sheet shining on the rolling plate from the underside.

Two video systems are used to record successive images of the flow. One is composed of a black-and-white CCD camera with RS170 output, and a Sony laser disk video recorder. The second system is a Hi8 Canon Camcorder that records images on a video tape with high fidelity. A specially-designed electro-mechanical shutter is installed between the laser head and the fiberoptic coupler to control the exposure time of the cameras.

For flow-field seeding, low-cost Pliolite particles of the Goodyear Company are used. It has a specific gravity of 1.05. Pliolite granules were grind down to particles of size about $300 \mu\text{m}$. With some pre-soaking, they are less buoyant, and their reflective properties make them quite

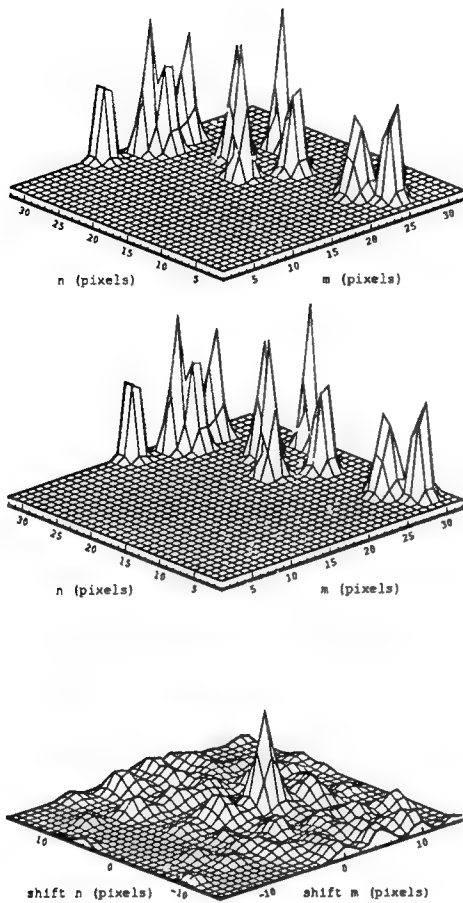


Figure 3: DPIV algorithm, (top): $F_1(m, n)$, (middle): $F_2(m, n)$, (bottom): $\phi(m, n)$

suitable for DPIV.

A three-step procedure was developed to compute the velocity and vorticity fields from pairs of successive digitized images at 1/30-sec apart. In the first step, a well-known cross-correlation algorithm of Willert and Gharib (1991) is implemented to yield a good estimate of the flow field. In the second step, spurious vectors are discarded or replaced by re-interpolated neighboring values. In a third step, suggested by Fabris (1994), a modified version of the cross-correlation algorithm is performed to obtain a more accurate representation of the flow field. In theory, these last two steps can be iterated until a converged velocity field is obtained. In practice, results were found to be satisfactory after only one iteration.

The algorithm implemented in the first step consists of the following:

- Select an interrogation window ($F_1(m, n)$ in digital form) on the first image where m

and n are pixel indices in the horizontal and vertical directions and $F_1(m, n)$ is the grey scale value at (m, n) .

- Select an interrogation window ($F_2(m, n)$ in digital form) on the second image taken a time Δt later. The two interrogation windows ($F_1(m, n)$ and $F_2(m, n)$) correspond to the same location on each image.
- Compute $\mathcal{F}_1(u, v)$ and $\mathcal{F}_2(u, v)$, Fourier transforms of $F_1(m, n)$ and $F_2(m, n)$ respectively, using FFT.
- Multiply $\mathcal{F}_1(u, v)$ by $\mathcal{F}_2^*(u, v)$ (complex conjugate of $\mathcal{F}_2(u, v)$) to obtain the function $\Phi(u, v)$ and compute its inverse Fourier transform. Illustrative representations of the pixel functions $F_1(m, n)$, $F_2(m, n)$ and $\phi(m, n)$ are shown in Fig. 3.
- The exact location of the highest peak of ($\phi(m, n)$) is obtained with sub-pixel accuracy by fitting a parabola around the maximum of ($\phi(m, n)$). The shift in horizontal and vertical direction (d_x, d_y) is the distance from the peak to the origin. Horizontal and vertical velocity are obtained by dividing (d_x and d_y) by the time step between the two frames.

The process above is repeated after shifting the location of the interrogation window horizontally or vertically by a small amount (16 pixels). One vector corresponding to the velocity at the center of each interrogation window is obtained every 16 pixels. Because of the large size of the interrogation window (64×64 pixels), the velocity is usually strongly smoothed out. The advantage of using a large interrogation window is that higher velocities can be resolved better. In high velocity gradient regions, spurious vectors are sometimes obtained; they are removed in the second step described next.

In high velocity regions (near the vortex cores), spurious data is removed manually and velocity is estimated based on the streak length (usually 5 to 10 pixels). Accuracy of the results is not critical at this stage. Only a "reasonable" estimate of the velocity field is required since "fine tuning" is carried out in the third step. A graphic interface showing simultaneously the digitized images and corresponding velocity field was helpful in speeding up this "manual" process. Different algorithms based on statistical removal and re-interpolation of spurious data were not satisfac-

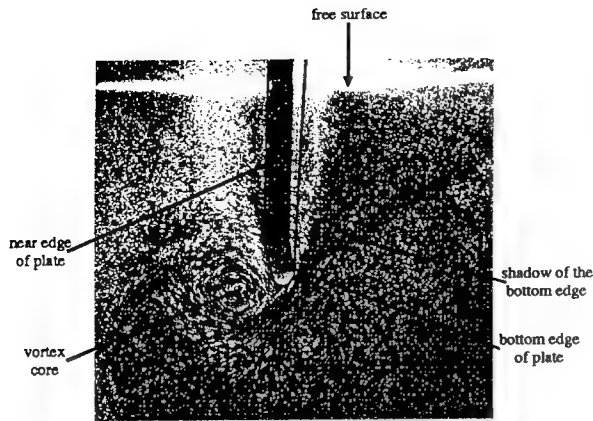


Figure 4: A sample digitized image as captured.

tory due to the high density of erroneous data in some regions.

In the third step, smaller interrogation windows (16×16 pixels) are used and the interrogation window on the second image is shifted by an amount corresponding to the shift (d_x, d_y) determined by the previous steps. Cross-correlation of the two interrogation windows is then carried out using a FFT based algorithm similar to that followed in step 1. This technique allows high velocities be resolved without sacrificing spatial resolution.

A thorough error analysis (Cermelli, 1995) has shown that peak vorticity may be in error up to 20 % near the vortex core and less than 10 % in other flow regions. Figure 4 shows a digitized image of a typical data frame.

3 VORTICITY STRUCTURES - EXPERIMENTAL RESULTS

For the specific set-up described in Section 2, the "Rolling Plate Experiment" can be characterized by the three dimensionless parameters. Let L be the draft of the plate. An appropriate Reynolds number is based on the maximum tip velocity of the plate and the distance traveled by the plate tip:

$$Re = \frac{2|\alpha_0|\omega L^2}{\nu} \quad (2)$$

where ν is kinematic viscosity.

The Keulegan-Carpenter number (KC), a traditional parameter in the study can be defined based on the plate thickness t_P :

$$KC = \frac{2\pi\alpha_0 L}{t_P} \quad (3)$$

The third parameter is the non-dimensional frequency, which is defined by:

$$\tilde{\omega} = \omega \sqrt{\frac{L}{g}} \quad (4)$$

Limited by the capacity of the force transducers, the range of $\tilde{\omega}$ is confined to $[.28, .63]$ for the experiment. Even so, this is a range that is quite close to typical roll-resonance of ships.

For most runs, L was set at 31.75cm (12.5 in) and the following parameters were varied: the roll amplitude, α_0 , (from 5° to 15°), the roll period, T , (from 1.8 to 4 seconds), the number of periods for the plate angle to reach full stroke s and the direction of the first swing of the plate, sign of α_0 . Additional runs were made with L set at 16.51cm (6.5 in) and with the same motion parameters. Flow visualizations were carried out also at different stations across the tank to study the wall influence. The flow is partially turbulent in all runs, and many small three-dimensional vortical structures interact in an intricate manner. However, after several periods of oscillation, a harmonic steady state can be observed for the main vortical structures.

3.1 Asymmetrical flow regime

A significant flow-feature that was uncovered during the experiment is somewhat counter-intuitive and will be referred to henceforth as the "asymmetrical flow regime". Figure 5 shows results that correspond to the case of $KC = 20.6$ ($L = 31.75\text{cm}$), with a starting swing to the left. In this and other subsequent plots, the following conventions are adopted. The x and y scales represent linear dimensions in mm. A vector of 20 mm length in this scale represents a velocity magnitude of 170 mm/sec. Vorticity contours are shown at increment of 3 vorticity units (3 sec^{-1}), with solid lines taken as counterclockwise and dashed lines as clockwise.

Referring to Fig. 5, we note that during the first half of a typical period when the plate tip moves toward the left, with α decreasing, a counterclockwise vortex rolls up in the wake of the plate (Fig. 5a, $\Phi = 158^\circ$), which is to be expected. When the plate stops at the minimum roll angle ($-\alpha_0$), a small jet is created between the backside of the plate and the existing vortex, generating as a consequence a clockwise vortex (Fig. 5b, $\Phi = 280^\circ$). When the back swing takes place (α increasing), the strength of the second vortex increases quickly. When the two vortices

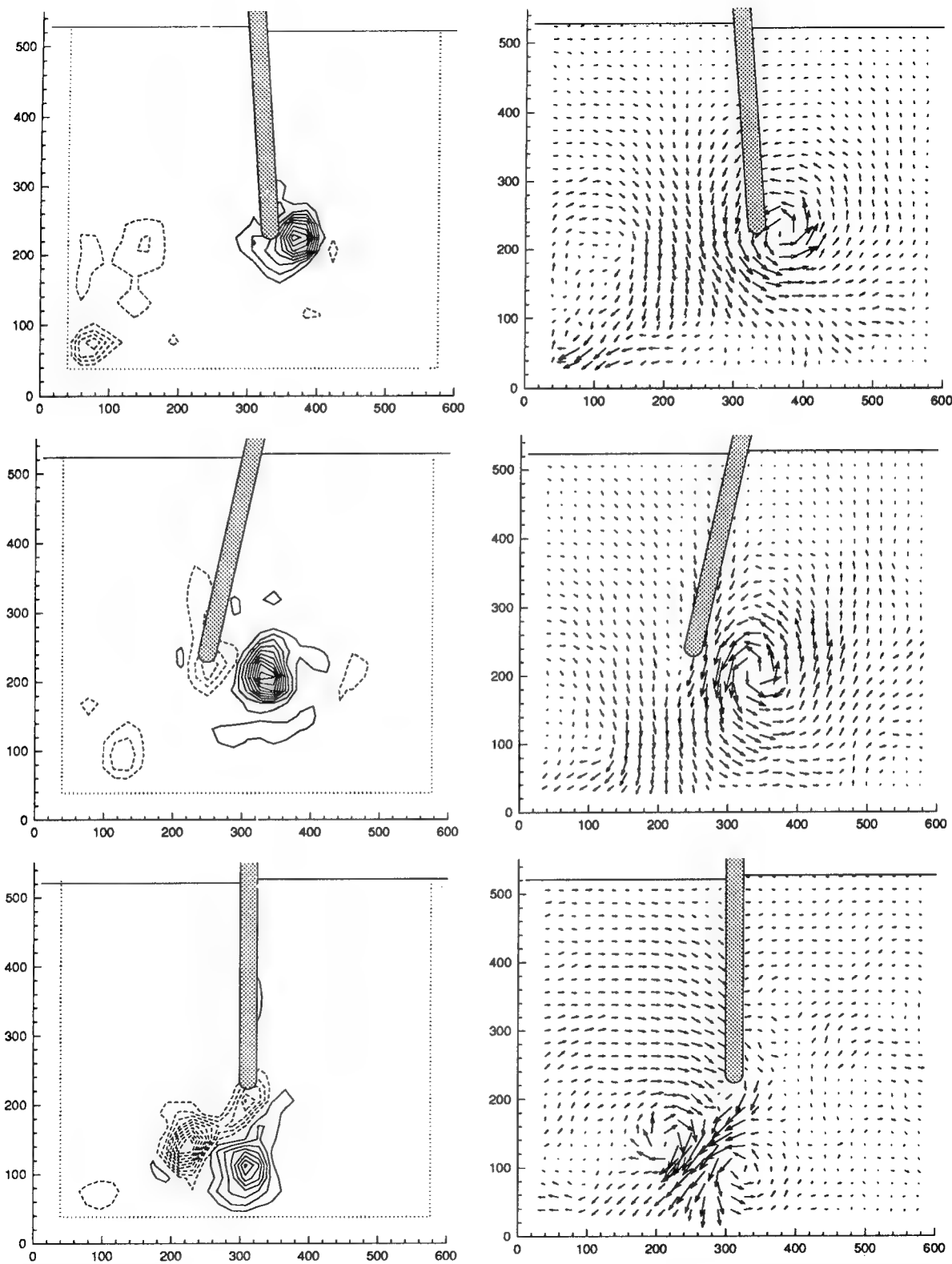


Figure 5: DPIV results for $R_e=28,900$, $KC=20.6$, $\tilde{\omega}=0.377$, $s=0.7$, $\alpha_0=-15^\circ$ for 3 instants of t : (a) – (c), top to bottom. *Left*: vorticity contours, *right*: velocity field; (a) $t=4.94T$ ($\Phi=150^\circ$); (b) $t=5.28T$ ($\Phi=28^\circ$); (c) $t=5.5T$ ($\Phi=360^\circ$).

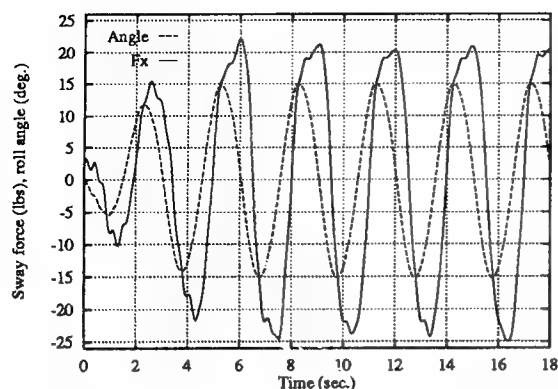


Figure 6: Sway force, $R_e = 28,900$, $KC = 20.6$, $\tilde{\omega} = .377$, $s = 0.7$, $\alpha_0 = -15^\circ$.

are of similar strengths, they move away from the plate as a vortex pair at about 45° angle with respect to the vertical (Fig. 5c, $\Phi = 360^\circ$). As the vortex pair moves away, it breaks down into turbulent motion and the vorticity intensity in the light sheet plane decreases rapidly. The vortex movement of the return half cycle is thus distinctively different from that associated with the forward half cycle. Because of this asymmetry, the magnitude of positive and negative peaks of the moment and horizontal force are noticeably different, as illustrated by Fig. 6. In this figure, the sway force time history F_x is shown together with $\alpha(t)$. The periodic asymmetric behavior is evident. This asymmetrical flow regime was observed for KC in the range $[13.7, 20.6]$ and R_e in the range $[9,600, 28,900]$. They correspond to all runs with $L = 31.75\text{cm}$ and $|\alpha_0|$ equals to 10° or 15° and to values of $\tilde{\omega}$ between .28 and .63.

For flows without a free surface, a somewhat similar phenomenon was reported by Singh (1979) and more recently by Sarpkaya and O'Keefe (1995). In the present work, it was possible to identify the factor that determines the direction toward which the vortex pairs are shed. It was found that it depends almost entirely on the direction of the *first* swing. Out of 32 runs resulting in vortex pairs moving toward the left, 31 started with a left stroke. Out of 14 runs resulting in vortex pairs moving toward the right, 13 started with a right stroke. This excellent correlation between direction of shedding and direction of the first stroke is related to the use of a rounded bottom edge (with a rectangular edge, the direction of shedding was random). One may surmise that a plate edge with a triangular tip would behave similar to the rounded-bottom case.

Vorticity-contour plots of the transient state have shown that a vorticity imbalance originating during the first few strokes of the plate is responsible for determining the direction toward which the vortex pairs move after establishment of a steady state. In some cases, this can take as many as ten periods of motion. We have observed a very nonlinear phenomenon, in which the long-time behavior of the system depends on very small perturbations generated during the first few periods of motion - a characteristics of "bifurcation".

In most runs, the light sheet was located at the tank centerplane (half way between the walls). Several experimental runs were made with the light sheet located at different transverse stations across the tank. Figure 7 shows the flow two feet from the tank wall for a run with $T = 2$ seconds and $\alpha_0 = 10^\circ$. The flow observed is similar to the flow at the tank centerplane. A vortex pair is shed toward one side of the plate. The direction of shedding also corresponds to the direction in which the plate tip moves at the first stroke. Flow visualization taken at a distance of six inches from the tank wall do show strong "end-wall effects". The wall inhibits the vortex-pair from moving away. Instead, they hover around the tip of the plate.

3.2 Symmetrical flow regime

For smaller roll amplitude ($\alpha_0 = 5^\circ$) and for all the runs with a 16.51cm draft, a different flow regime is obtained. It is more consistent with one's intuitive expectation (see Yeung & Cermelli, 1996).

In a typical scenario, a vortex is generated on the plate back side (say the right side as the plate tip moves toward the left). This vortex remains attached to the plate and as the plate reverses direction, a smaller vortex of opposite sign is generated on the left side of the plate. The resulting vortex pair is not strong enough to move away from the plate, and the growing vortex eventually absorbs the earlier one as the plate's backswing continues.

In all, the flow patterns corresponding to motion of the plate in one direction are mirror images (about the vertical axis) of those corresponding to motion of the plate in the other direction. In terms of the nondimensional parameters, this "symmetrical flow regime" corresponds to KC between 6.9 and 10.0 and R_e between 3,200 and 9,600, with $\tilde{\omega}$ varying from .28 to .58.

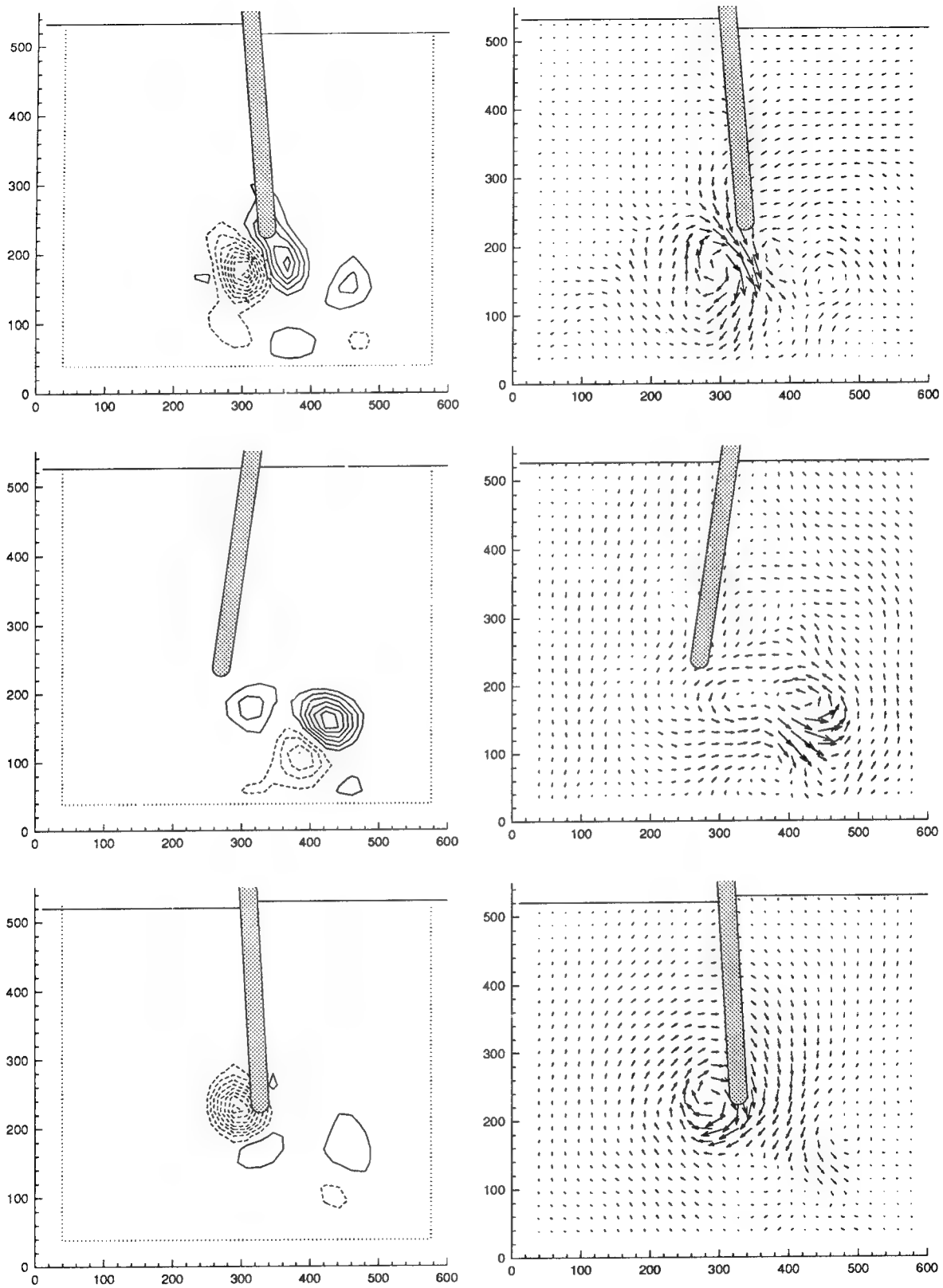


Figure 7: DPIV results for $Re=19, 200$, $KC=13.7$, $\tilde{\omega}=0.565$, $s=0.7$, $\alpha_0=10^\circ$ for 3 instants of t : (a) – (c), top to bottom. *Left*: vorticity contours, *right*: velocity field; (a) $t=9.4T$, $\alpha = 5.8^\circ$ ($\Phi=144^\circ$); (b) $t=9.73T$, $\alpha = -9.9^\circ$ ($\Phi=262.8^\circ$); (c) $t=10.1T$, $\alpha = 4.1^\circ$ ($\Phi=36^\circ$). Light sheet is 2 feet from tank wall.

4 THEORETICAL MODEL

A very powerful method for modeling viscous flow in the presence of surface waves is the Free-Surface Random-Vortex Method (FSRVM), developed recently by Yeung and Vaidhyanathan (1994). The RVM is a grid-free formulation which can capture vortex scales of a wide range. Validation on this model has been carried out for a number of unbounded fluid problems (Yeung et al., 1993). The experimental results of the last section provide an excellent opportunity to validate and calibrate the theoretical model. Towards this goal, the FSRVM code was improved and adapted to solve the rolling plate problem. The original formulation of this method can treat bodies of arbitrary shapes and three degrees of freedom of motions of an arbitrary type. Hence, the theoretical development outlined below is applicable to problems of body-free-surface interaction of a general nature.

4.1 Viscous flows with a free surface

The fluid domain in question \mathcal{D} is defined in Fig. 1, with the boundary ($\partial\mathcal{D}$) consisting of the free surface (\mathcal{F}), the body surface (\mathcal{B}) and the open boundary (\mathcal{O}), the latter being an artificial boundary introduced to truncate the computational domain. The Random Vortex method solves the Navier-Stokes equations using a vorticity-stream function formulation. Thus for an incompressible Newtonian fluid, the governing equation for the vorticity vector $\xi\mathbf{k} = \nabla \times \mathbf{u}$ is the vorticity transport equation:

$$\frac{D\xi}{Dt} = \nu \nabla^2 \xi, \quad (5)$$

where D/Dt is the material derivative. The stream function satisfy the Poisson equation:

$$\nabla^2 \psi = -\xi. \quad (6)$$

For material points on the free surface \mathcal{F} , the kinematic free-surface boundary condition can be written in the following form:

$$\frac{D\mathbf{x}}{Dt} = \mathbf{u}, \quad (7)$$

where \mathbf{x} is the location of a material point and \mathbf{u} is the velocity at that point. The dynamic boundary condition states that the stress should vanish at the interface (see Wehausen & Laitone, 1960). However our previous experiences with full

Navier-Stokes solution in the presence a free surface (Yeung & Ananthakrishnan, 1992a,b) indicate that the shear layer due to the full-stress condition on the free surface is normally of secondary importance (compared with body-generated vorticity). Thus an effective dynamic boundary condition is simply an inviscid one:

$$p = 0, \quad (8)$$

which states that the gauge pressure vanishes.

On the body the no leakage and no slip boundary conditions apply:

$$\mathbf{u} = \mathbf{v}_b, \quad (9)$$

where \mathbf{v}_b is the velocity at a boundary point \mathbf{x} on \mathcal{B} . At any parametric point s along the body contour, \mathbf{v}_b is given by:

$$\mathbf{v}_b(s) = \mathbf{U}_b + \Omega \mathbf{k} \times (\mathbf{x}(s) - \mathbf{x}_0(s)), \quad (10)$$

where \mathbf{U}_b represents translation of a reference point $(x_0(t), y_0(t))$ on the body and $\Omega(t)$ is the angular velocity about \mathbf{x}_0 .

At the open boundary \mathcal{O} , at a sufficiently large distance from the body, the fluid motion is assumed to be minimal. Hence the pressure can be taken as hydrostatic,

$$p = -\rho g y. \quad (11)$$

4.2 Vorticity representation by blobs

The two-dimensional vorticity field of Section 4.1 is represented by a collection of regions of concentrated vorticity called "blobs", i.e.

$$\xi(\mathbf{x}, t) = \sum_{i=1}^{N(t)} \Gamma_i G(\mathbf{x} - \mathbf{x}_i(t)), \quad (12)$$

$$\psi_v = \sum_{i=1}^{N(t)} \Gamma_i F(\mathbf{x} - \mathbf{x}_i(t)). \quad (13)$$

Here \mathbf{x} is an Eulerian field point in the fluid domain \mathcal{D} , or on the boundary $\partial\mathcal{D}$, at time t . Γ_i is the circulation associated with each vortex blob (of which there are N) centered at \mathbf{x}_i . The function G describes the distribution of vorticity within each blob whereas F is related to G by integration. The 'Chorin blob', which consists of a step distribution of vorticity in a finite core radius, was successfully employed in our earlier works (Yeung et al., 1993). Outside of the blob core, the flow is irrotational.

To obtain the complete velocity field, we let ψ in \mathcal{D} be decomposed into two components:

$$\psi = \psi_v + \psi_h, \quad (14)$$

It follows from the Poisson equation (6) that

$$\nabla^2 \psi_v = -\xi, \quad (15)$$

$$\nabla^2 \psi_h = 0. \quad (16)$$

ψ_v , the rotational component, is given by (Eqn. 13), which is known everywhere once the blob strengths Γ_i are known. On the other hand, the irrotational component ψ_h has to be solved to satisfy Laplace's equation, subject to the various boundary conditions on $\partial\mathcal{D}$. This non-trivial hydrodynamic problem is discussed in Section 4.4.

4.3 Vorticity diffusion and convection

Per Chorin's (1973) original algorithm, the vorticity transport equation Eqn. (5) can be split into two equations, each more tractable by itself than the combined equation. This is a fractional step method. At the first and second half of each time step, the convection part and the diffusion part of the equation

$$\frac{\partial \xi}{\partial t} = -(\mathbf{u} \cdot \nabla) \xi, \quad (17)$$

$$\frac{\partial \xi}{\partial t} = \nu \nabla^2 \xi, \quad (18)$$

are solved successively.

Eqn. (17) corresponds to the convection equation of an *inviscid* fluid, with the blobs taken as material (lagrangian) points, i.e.,

$$\dot{\mathbf{x}}_i = \mathbf{u}(\mathbf{x}_i, t), \quad i = 1, \dots, N \quad (19)$$

where the velocity field \mathbf{u} has contributions coming from both the free-surface and the body motion. The free surface effects can be included in this convection step.

The diffusion equation (Eqn. 18) can be simulated by the random walk algorithm (Chorin, 1973 and Einstein, 1956). In this algorithm, each of the blobs is given an independent random walk in both the x and y directions with standard deviation $\sqrt{2\nu\Delta t}$, Δt being the time step over which Eqn. (18) is integrated. The numerical implementation of this 'integration' is simply:

$$\mathbf{x}_i(t + \Delta t) = \mathbf{x}_i(t) + (\eta_x, \eta_y), \quad (20)$$

where η_x, η_y are chosen from a set of random numbers with Gaussian distribution whose mean

is zero and standard deviation $\sqrt{2\nu\Delta t}$. The errors introduced by this method are statistical in nature and decrease with increasing number of blobs. The effect of the free surface is neglected in this diffusion model.

In many such computations, long-time solutions are often necessary in order to capture the flow features of interest. Equation (19) represents the heaviest computational burden since by the Biot-Savart law, each time step would involve N^2 interactive computations among the blobs. As N increases, the solution process slows down very quickly. Fortunately, by using the fast multipole method of Carrier et al. (1988), we were able to implement an $O(N)$ interactive algorithm which greatly enhanced computation efficiency (see Yeung & Vaidhyanathan, 1993).

4.4 Solution of the stream function ψ_h

ψ_h satisfies the Laplace equation, which is most conveniently solved by a boundary-integral equation technique. For free surface flow problems, the following complex-variable formulation following the works of Vinje and Brevig (1980) and Grosenbaugh and Yeung (1989) is especially attractive. Introducing the conjugate function of ψ , i.e., a velocity potential ϕ , we can write the time-dependent complex potential β as:

$$\begin{aligned} \beta(\mathbf{x}, t) &= \beta_h + \beta_v = (\phi_h + \phi_v) + i(\psi_h + \psi_v) \\ &= \beta_h - \sum_{i=1}^{N(t)} \frac{i\Gamma_i}{2\pi} \ln(\mathbf{z} - \mathbf{z}_i(t)). \end{aligned} \quad (21)$$

Here \mathbf{z}_i and $\Gamma_i, i = 1, \dots, N$, are the complex coordinates and circulations of the N vortex blobs present in the fluid domain. For any field point outside of each individual blob core, the complex velocity can be written similarly as:

$$\begin{aligned} \mathbf{w} &= \frac{d\beta}{dz} = u - iv = \mathbf{w}_h + \mathbf{w}_v \\ &= \mathbf{w}_h - \sum_{i=1}^N \frac{i\Gamma_i}{2\pi} \frac{1}{\mathbf{z} - \mathbf{z}_i}. \end{aligned} \quad (22)$$

At any given time t , the location of the body boundary is prescribed while the location of the free surface boundary is determined from its previous location by using the kinematic boundary condition (Eqn. 7). β_h is sought as an analytic function of \mathbf{z} , subject to the inviscid free-surface condition Eqn.(8). In terms of ϕ , this condition can be written as:

$$\frac{D\phi_h}{Dt} = -\frac{D\phi_v}{Dt} + \frac{\rho}{2} |\nabla\phi|^2 - \rho g y. \quad (23)$$

The first term on the right hand side may be derived from Eqn. (21):

$$\frac{D\phi_v}{Dt} = \Re \frac{D\beta_v}{Dt} = \Re \left\{ \sum_{i=1}^N \frac{-i\Gamma_i}{2\pi(z - z_i)} (\dot{z} - \dot{z}_i) \right\}, \quad (24)$$

where, \Re denotes the real part of the expression. In Eqn. (24), \dot{z} is the complex velocity at a Lagrangian point z located at the free surface and $\dot{z}_i = \dot{x}_i + i\dot{y}_i$ is the complex velocity of the i -th vortex. Thus, Eqn. (24) can be used to compute the value of ϕ_h at the new location of the free surface, which is determined by a time integration of Eqn. (7). A Dirichlet condition for ϕ_h is therefore available at every discrete time instant on \mathcal{F} .

On the open boundary, we approximate Eqn. (11) by

$$\frac{\partial\phi}{\partial t} = 0, \quad (25)$$

which can be expanded as:

$$\frac{\partial\phi_h}{\partial t} = -\frac{\partial\phi_v}{\partial t} = \Re \sum_{i=1}^N \frac{i\Gamma_i \dot{z}_i}{2\pi(z - z_i)}. \quad (26)$$

Using fixed (Eulerian) node points on the open boundary, we can integrate Eqn. (26) to obtain a Dirichlet condition for ϕ_h .

Finally, the normal-component of the boundary condition on the body (Eqn. 9) can be implemented as a specification of ψ_h on \mathcal{B} . By (10), it is simple to show that:

$$\psi_h = -\psi_v + U_b(y - y_0) - V_b(x - x_0) - \frac{1}{2}\Omega R_0^2 + K(t), \quad (27)$$

where $K(t)$ is an arbitrary time-dependent constant and $R_0 = |\mathbf{x} - \mathbf{x}_0|$. Note that the value of ψ_v on the body can be evaluated from Eqn. (13).

In summary, we have obtained a boundary value problem for β_h , where ϕ_h is specified on a portion of the boundary contour $\partial\mathcal{D}$, while ψ_h is specified on the remaining portion. This allows us to solve for either ψ_h or ϕ_h on all the boundary points using a boundary integral-equation method based on Cauchy's integral formula:

$$\beta_h(z) = \frac{1}{\pi i} \oint_{\partial\mathcal{D}} \frac{\beta_h(\zeta)}{(\zeta - z)} d\zeta \quad \text{for } z \in \partial\mathcal{D}. \quad (28)$$

Details on the treatment of such an integral equation can be found in (Grosenbaugh & Yeung,

1989). Once β_h is determined on the boundary, the velocity \mathbf{w}_h at any interior point can be computed by using the following Cauchy's integral:

$$\mathbf{w}_h(z) = \frac{d\beta_h}{dz} = \frac{1}{2\pi i} \oint_{\partial\mathcal{D}} \frac{\beta_h(\zeta)}{(\zeta - z)^2} d\zeta. \quad (29)$$

So far, we have mentioned that the vorticity field is represented by blobs, without explaining how they are generated. In the RVM, the blobs are introduced to the flow domain through the no-slip boundary condition. At the end of every convection step (i.e., the integration of Eqn. (5)), the Poisson equation (6) is solved, and then the fluid velocity is computed along the body surface \mathcal{B} . The tangential component of this velocity will not satisfy the no-slip boundary condition (Eqn. 9). The boundary condition can be satisfied by generating vortex blobs of appropriate strength (circulation) and radius at the body panels (Chorin, 1973). It is then released into the flow during the solution of the diffusion equation (18).

4.5 Hydrodynamic pressure and forces

When the vorticity field is approximated by point vortices, inviscid-flow results can be used to compute the forces and moment on the body (Yeung et al., 1993). In terms of the complex velocity potential, the pressure on the body is given by:

$$\frac{p}{\rho} = -\Re \frac{\partial\beta_h}{\partial t} - \Re \frac{\partial\beta_v}{\partial t} - \frac{1}{2} \mathbf{w} \mathbf{w}^* - g y, \quad (30)$$

where $\partial\phi_v/\partial t$ is given by the last equality of Eqn. (26). An integral equation similar to Eqn. (28) is used to solve for $\partial\phi_h/\partial t$ (Vaidhyanathan, 1993). Forces and moments on the body can then be obtained by direct integrations of the pressure. This model does not compute the tangential stress on the body surface, which are typically insignificant if the flow has substantial separation.

5 THEORY VS. EXPERIMENT - COMPARISON OF RESULTS

The fully nonlinear FSRVM algorithms in the last section was implemented with two modifications. First, it was found that a linearized, instead of the fully nonlinear, free-surface condition was adequate for the range of parameters covered during the experiment. Specifically, Eqn. (7) and Eqn. (23) are now replaced by

$$\frac{\partial^2\phi_h}{\partial t^2} + g \frac{\partial\phi_h}{\partial y} = 0, \quad \text{on } y = 0. \quad (31)$$

For long-time simulations, this reduced computational time to about one half of that for the nonlinear case.

Second, a decaying model for the blob strengths was implemented so as to bound the number of blobs to $O(10^5)$. The evolution in time of blob strength was chosen to be the following function:

$$\Gamma_i(\tau) = \Gamma_i(0)[1 - \tanh(3\tau - 6)]/2, \quad (32)$$

where $\tau = t/T$ is the time (in number of periods) after the introduction into the flow of blob i with intensity $\Gamma_i(0)$. If the ratio $\Gamma_i(\tau)/\Gamma_i(0)$ is less than 10^{-3} , the blob is removed from the flow. With this decaying function, the strength of each blob remains almost unchanged for 1.5 period and then decays rapidly during the following period. Implementation of a decaying model results in substantial savings in computational efforts. Typically, 6 to 8 periods of motion are needed to obtain a periodic steady state. Further, this model can reflect in part the decay of vorticity due to turbulent break-up. The decaying function was calibrated by observing visually that vortices typically break down on the average of about 2 periods. Note that this model is not meant to be a turbulence model.

Several runs were made with all parameters set to those of the actual experiment. Flow structures obtained numerically turned out to behave somewhat differently from those observed experimentally. A downward adjustment of the Reynolds number greatly improved the match between numerical and experimental results.

Two hypothesis may explain this discrepancy. First, the number of blobs could be insufficient. This limitation arises from computer resources. A finer spatial and time discretization increases the number of blobs in the flow field. Flow configurations based on a larger number of blobs and the actual Reynolds number corresponding to the experiment showed much improved match. However because of staggering computational demand, simulations could not be run long enough to achieve a steady state.

The second hypothesis is that turbulence, which is not taken into account by the two-dimensional FSRVM model, accounts for discrepancy between prediction and observed flow features. Eddy viscosity, in the actual experiment, may contribute to an increase in the "apparent" viscosity of the fluid. A quantitative estimate of the relative influence of each of these factors is difficult to obtain. Some ongoing research aimed at implementing turbulence models on parallel computers may

yield a better understanding.

A comparison of the experimental and numerical vorticity fields is shown in Fig. 8 for the asymmetrical flow regime. This corresponds to case of $R_e = 19,200$, $KC = 13.7$, $\alpha_0 = 10^\circ$, $\tilde{\omega} = 0.565$, with the numerical method run at $R_e = 6,400$. Evidently, very good agreement is observed, reproducing all interesting features of the flow discussed in Section 3.

Force and moment comparisons for this run are shown in Fig. 9. The top figure of Fig. 9 shows that the vertical (heave) force exhibits a double harmonic behavior. This peculiar behavior was first observed in some earlier computations by FSRVM and was later confirmed by experiment. The behavior is attributable to the nonlinear body boundary conditions, i.e., Eqn. (9) is satisfied at the instantaneous position. If the fluid were unbounded, it can be shown that the horizontal and vertical hydrodynamic force (F_1 , F_2) and the hydrodynamic roll moment M_6 are given "exactly" by

$$F_1 = -\dot{\Omega}\mu_{16}, \quad F_2 = \Omega^2\mu_{16}, \quad M_3 = -\dot{\Omega}\mu_{66} \quad (33)$$

where the μ_{ij} 's are the hydrodynamic added masses of the plate. Since the coupling hydrodynamic coefficient μ_{16} does not vanish for a plate hinged at the end, the double-frequency behavior of F_2 is dominant. This behavior could not be predicted within the context of linearized motion theory which would include only linear terms in velocity and acceleration.

Figure 9 also shows the hydrodynamic roll moment for the same case. The agreement is very encouraging, representing an important improvement over potential-flow results. The wave elevation obtained at two locations, $x = \pm 355$ mm, are compared with the predicted results in Fig. 10. Excellent agreement is observed. Since the wave amplitude is directly related to wave damping, it provides a validation that the theoretical model can capture both viscous and wave effects well.

Figure 11 displays the details of the vortical structures generated under the free surface by the plate and the free-surface elevation for the case of $\alpha_0 = -10^\circ$. Each dot represents a blob from the FSRVM solution. These six "snap-shots" bracket about one cycle of oscillation.

A limitation of the FSRVM code is that the symmetric and attached vortical-flow features in the regime described by Section 3.2 could not be reproduced, even though the force and moment predictions were in good agreement with measured values.

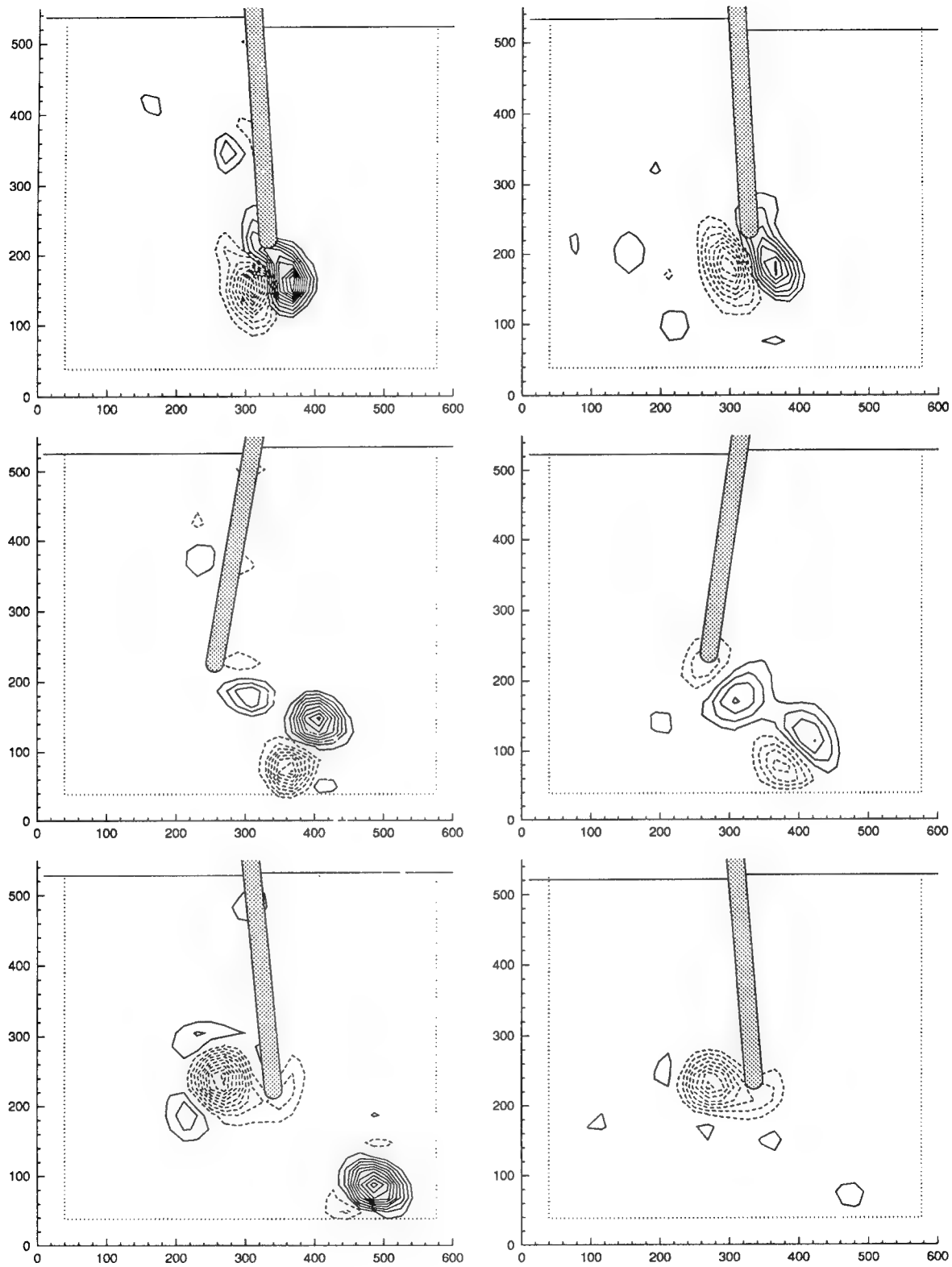


Figure 8: Vorticity contours, comparison between results of FSRVM (left) and DPIV (right) for $R_e=19,200$, $KC=13.7$, $\tilde{\omega}=0.565$, $s=0.7$, $\alpha_0=10^\circ$ for 3 instants of t : (a) – (c), top to bottom. (a) $t=4.4T$ ($\Phi=150^\circ$, FSRVM), $t=9.43T$ (DPIV); (b) $t=4.7T$ ($\Phi=270^\circ$, FSRVM), $t=9.76T$ (DPIV); (c) $t=5.1T$ ($\Phi=36^\circ$, FSRVM), $t=10.1T$ (DPIV).

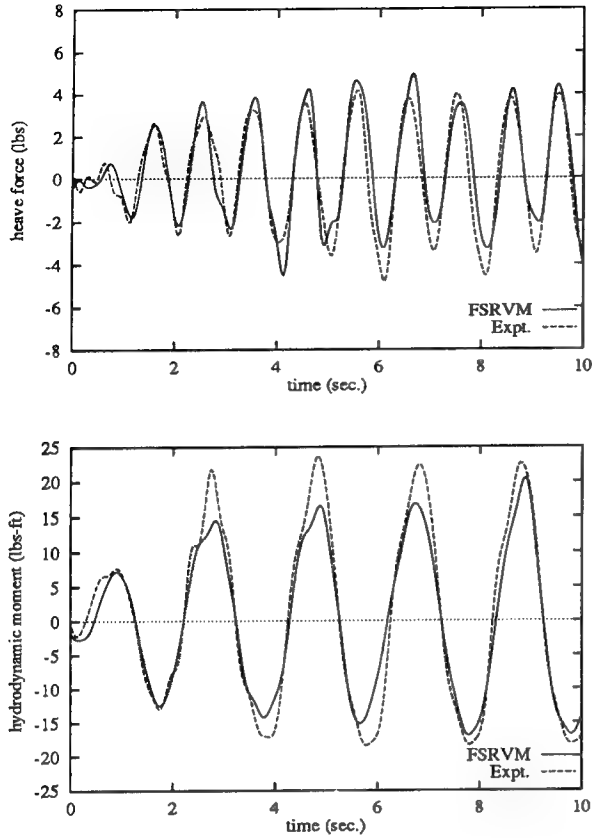


Figure 9: Heave (restraining) force and hydrodynamic roll moment for $Re = 19,200$, $KC = 13.7$, $\tilde{\omega} = .565$, $s = 0.7$, $\alpha_0 = 10^\circ$.

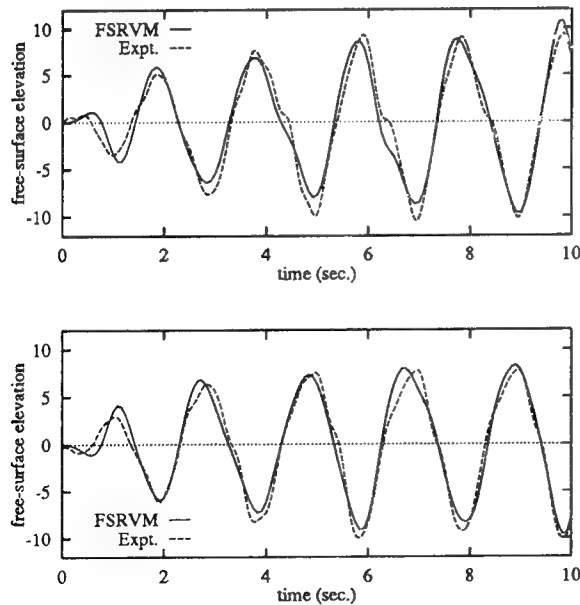


Figure 10: Free-surface elevations for $Re = 19,200$, $KC = 13.7$, $\tilde{\omega} = .565$, $s = 0.7$, $\alpha_0 = 10^\circ$; top : at $x=355$ mm, bottom : at $x=-355$ mm.

6 HYDRODYNAMIC COEFFICIENTS OF ROLLING CYLINDERS

As an illustration of the application of the theoretical model to study ship sections of a general shape, we consider the problem of a rectangular section with relatively sharp bilges which undergoes prescribed rolling motion of the form:

$$\alpha(t) = \alpha_0 \sin(\omega t) \quad (34)$$

The specific geometry has a beam-to-draft ratio B/D of 2.0. This shape was used in the experiments of Vugts (1968) which has a physical beam of 0.4m and a rounded bilge radius of 2.5mm. The frequency parameter $\tilde{\omega} = \omega \sqrt{D/g}$ is defined as before (Eqn. 4). The experimental Re number is 49,000. Guided by the rolling plate results, we adjust Re downwards to 25,000 in the numerical simulation.

The solution of this nonlinear problem at $t/T = 5.75$ for $\tilde{\omega} = 0.5$ is shown in Fig. 12. The complexity of vortex array shed from the corners after only several periods is evident from this plot. The solution method is sufficiently robust that as many as eight periods of motion have been successfully run to allow one to examine the "steady-state" behavior. Figure 13 shows the time history of the heave force and roll moment due to this prescribed $\alpha(t)$. Also shown is the roll angle itself. Note the double-harmonic behavior of the force as in the case of the rolling plate. There exists also a net "set-down" to pull the section downwards. The continuous shedding of vortices and interaction with existing vortices produce a roll moment signature that is quite complex. Even so, the overall pattern is still reasonably periodic.

If one adopts an equivalent linearized characterization of the roll moment as Vugts,

$$M_3 = -\mu_{66}\ddot{\alpha} - \lambda_{66}\dot{\alpha} \quad (35)$$

where μ_{66} is the added moment of inertia, λ_{66} is the total damping, a Fourier analysis of the moment signature will yield the μ_{66} and λ_{66} . The "moving window" analysis based on a window of one period yields rather steady values of added inertia and damping coefficients (see Fig. 14). It is possible to separate the "equivalent" damping to linear and quadratic components (Yeung & Cermelli, 1996), but this would not be pursued here.

Simulations were carried out for this particular hull section so that the equivalent added inertia and damping could be extracted over a frequency range. The roll amplitude α_0 is taken to be a

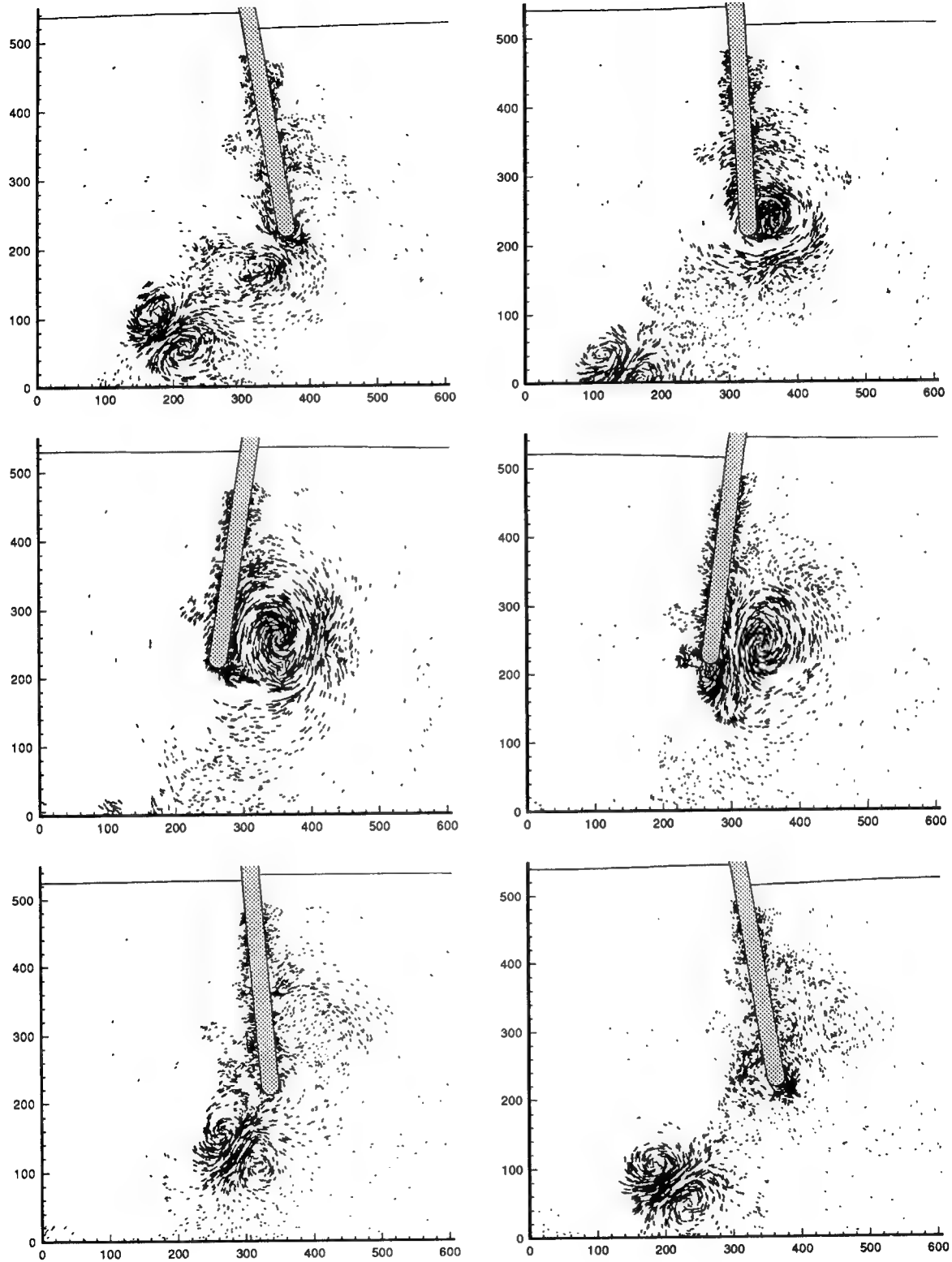


Figure 11: Vortex blob distribution from FSRVM (corresponding to same case as Figs. 11-12). $R_e = 19,200$, $KC = 13.7$, $\bar{\omega} = .565$, $s = 0.7$, $\alpha_0 = -10^\circ$ for 6 instants of t : (a) – (f), left to right, top to bottom. (a) $t = 3.75T$ ($\Phi = 90^\circ$); (b) $t = 3.96T$ ($\Phi = 165.6^\circ$); (c) $t = 4.17T$ ($\Phi = 241.2^\circ$); (d) $t = 4.38T$ ($\Phi = 316.8^\circ$); (e) $t = 4.58T$ ($\Phi = 28.8^\circ$); (f) $t = 4.79T$ ($\Phi = 104.4^\circ$).

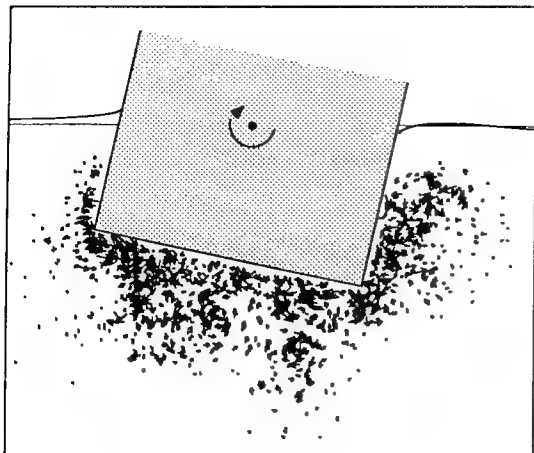


Figure 12: Rectangular hull section in roll motion - vorticity-blobs plot at $t=5.75T$, $\tilde{\omega}=0.5$ and $\alpha_o = 11.5^\circ$.

relatively small value of 0.05 radians (2.86 degrees). The range of $\tilde{\omega}$ considered was $[0.6, 1.25]$. The nondimensional added moment of inertia and damping are shown in Figs. 15 and 16 respectively. In these figures, $\tilde{\mu}_{66}$ and $\tilde{\lambda}_{66}$ are nondimensionalized according to $\tilde{\mu}_{66} = \mu_{66}/(\rho \nabla B^2)$ and $\tilde{\lambda}_{66} = \lambda_{66}/\rho \nabla B^2 \sqrt{B/2g}$, where ∇ denotes the sectional area of the hull.

A comparison of these results with existing data of Vugts shows that the inertia coefficients are over-predicted. However, the inertia coefficients are consistent with inviscid theory. In unbounded flow, our experience indicates that added masses are not strongly affected by flow separation. The experimental results of Vugts suggest otherwise. More extensive experimentations are needed to resolve this issue. The all-important quantities of wave and viscous damping are well predicted. In particular, the deficiency of inviscid theory is evident. The theoretical model thus holds much promise.

7 CONCLUSIONS

The flow generated by a body undergoing periodic rolling motion was studied experimentally and theoretically. A "rolling plate in a free surface" is taken as the canonical problem. A Digital Particle Image Velocimetry (DPIV) system was developed and used to obtain accurate velocity and vorticity maps. For the range of parameters studied, when KC is larger than 13, it was found that an asymmetrical periodic steady state is reached. In this state, a vortex pair is shed toward a "preferred side" of the plate in one half

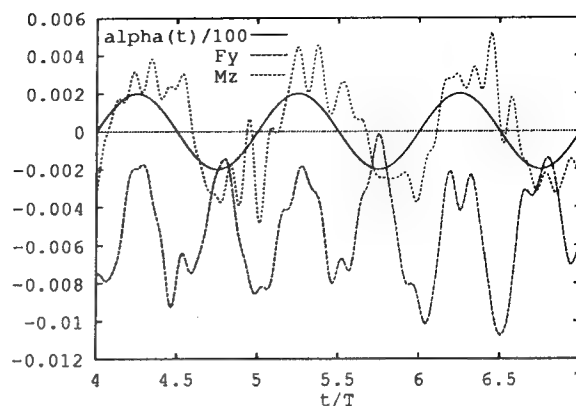


Figure 13: Time history of vertical force and roll moment. $\tilde{\omega}=0.5$ and $\alpha_o = 11.5^\circ$.

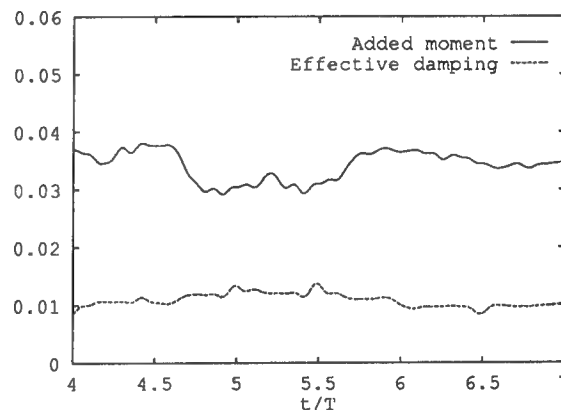


Figure 14: Added moment of inertia and effective damping using Fourier analysis.

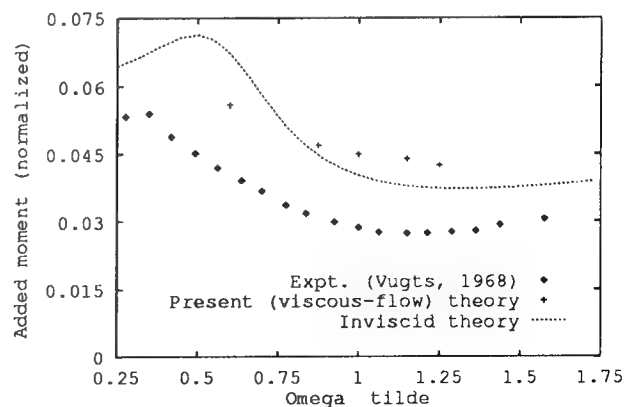


Figure 15: Added roll moment of inertia coefficient, $\tilde{\mu}_{66}$, as a function of $\tilde{\omega}$.

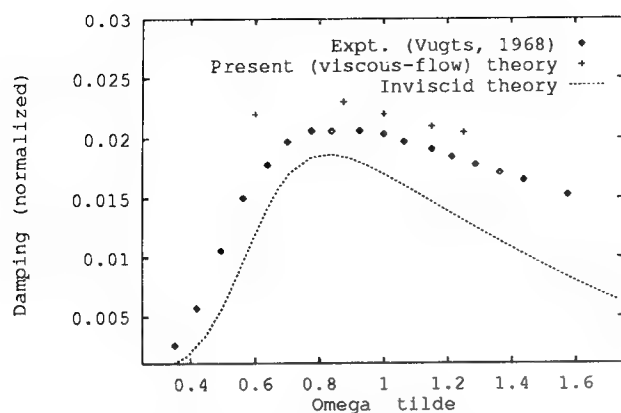


Figure 16: Damping coefficient in roll, $\tilde{\lambda}_{66}$, as a function of $\tilde{\omega}$.

of each period of swing. This directional preference was identified to correlate with the initial direction of the swing and could be caused by the gradual increase of motion amplitude at the start of the swing. This graduality generates vortex pairs of unequal strengths. For smaller KC number, the flow patterns exhibit features that are symmetrical with respect to the vertical axis during successive half periods, a more intuitive result.

The theoretical model used is one based on solving the Navier-Stokes equations with an inviscid free-surface condition. The Free-Surface Random-Vortex Method (FSRVM, Yeung & Vaidhyanathan, 1994) uses a grid-free Eulerian-Lagrangian formulation. It is capable of capturing vortical structures of a wide range of scales. The method is not particularly effective in predicting features observed in the symmetrical flow regime. For the asymmetrical flow regime, i.e., large KC -number flow, the FSRVM provides accurate predictions. Even so, in order to obtain excellent matching, the Reynolds number used in FSRVM simulations had to be adjusted downwards. It is surmised that this was due either to an insufficient number of blobs in the calculations or to a lack of turbulence modeling in the method. Neither represent obstacles that are insurmountable to overcome in the future. The FSRVM method also yields satisfactory force and moment predictions. In particular, a demonstration is made to compute the viscous damping of a rectangular hull section in roll. The predicted damping agree well with some existing laboratory-scale results, a considerably improvement over computations based on inviscid-fluid theory.

It is also worthy to note that the heave restraining force generally appears as a double harmonic of the roll-motion frequency, a consequence of the nonlinear body boundary condition, not viscous effects. This characteristic is quite prominent in larger angles of roll, experiment and theory.

The extensive experimental and numerical works reported here have been complementary to each other. A continuing understanding of this subject will require such parallel efforts.

Acknowledgements

We are pleased to acknowledge the support of the Office of Naval Research under Grant N00014-91-J1614 & N00014-95-1-0980, with Jim Fein as the program officer. Partial support from grants of the University of California, the Lawrence Livermore Laboratory, and the Shell Foundation are also gratefully acknowledged. Thanks also go to Dr. M. Vaidhyanathan (3Es), Prof. P. Ananthakrishnan (FAU), Profs. O. Savaş and D. Liepmann (UCB), who had assisted in many valuable ways during the course of this research.

References

- [1] Brown, D. T. Eatock-Taylor, R. & Patel, M. H. (1983). "Barge motion in random seas - a comparison of theory and experiment", *J. Fluid Mech.*, **129**, pp. 385-407.
- [2] Brown, D. T. and Patel, M. H. (1985). "A theory for vortex shedding from the keels of marine vehicles", *J. Engng. Math.*, **19**, pp. 265-295.
- [3] Braathen, A. and Faltinsen O. M. (1988). "Application of a vortex tracking method to roll damping", *Advances in Underwater Technology, Ocean Science and Offshore Engineering*, **15**, Society of Underwater Technology. pp. 177-193.
- [4] Carrier, J.; Greengard, L. and Rokhlin, V. (1988). "A fast adaptive multipole algorithm for particle simulations", *SIAM J. Sci. Stat. Comput.*, **9**, pp. 669-686.
- [5] Cermelli, C. A.. (1995)., "Vortical flows generated by a plate rolling in a free surface", Ph.D. dissertation, Dept. of Naval Arch. and Offshore Engrg., Univ. of Calif., Berkeley.
- [6] Chorin, A. J. (1973). "Numerical study of slightly viscous flow", *J. Fluid Mech.*, **57**, pp. 785-796.
- [7] Cozens, P. D. (1987). "Numerical modelling of the roll damping of ships due to vortex shedding", Ph.D. dissertation, Dept. of Aeronautics, Univ. of London, UK.

- [8] Downie, M.; Graham, J. and Zheng, X. (1990). "Effect of viscous damping on the response of floating bodies," *Proc. 18th Symp. on Naval Hydrodyn.*, Ann Arbor, Michigan, pp. 149-155.
- [9] Einstein, A. (1956). *Investigation on the theory of Brownian movement*, Dover, New York.
- [10] Fabris, D. (1994). *Private communications*.
- [11] Fink, P. T. and Soh, W. K. (1974). "Calculation of vortex sheets in unsteady flow and applications in ship hydrodynamics," *Proc. 10th Symp. on Naval Hydrodyn.*, Cambridge, MA, pp. 463-491.
- [12] Grosenbaugh, M. A. and Yeung, R. W. (1989). "Nonlinear free-surface flow at a two-dimensional bow", *J. Fluid Mech.*, **209**, pp. 57-75.
- [13] Himeno, Y. (1981). "Prediction of ship roll damping - state of the art" Dept. Naval Arch. & Mar. Engrg., Univ. of Michigan, Rep. no 239.
- [14] Ikeda, Y., Himeno, Y., and Tanaka, N. (1977). "On eddy-making component of roll damping force", *J. Soc. Naval Arch. Japan*, **142**, pp. 54-64 (in Japanese).
- [15] Korsmeyer, F. T., Lee, C. H., Nemwan, J. N., & Slavounos, P. D., (1988) "The analysis of wave effects on tension-leg platforms" *Proc. 7th Int'l. Conf. of Offshore Mechanics & Arctic Engineering (OMAE)*, Houston, TX.
- [16] Newman, J. N. (1992). "Panel methods in marine hydrodynamics", *Proc. 11th Aust. Fluid Mech. Conf.*, Tasmania, Australia.
- [17] Sarpkaya, T. and Isaacson, M. (1981). *Mechanics of wave forces on offshore structures*, van Nostrand Reinhold Company.
- [18] Sarpkaya, T. and O'Keefe J. L. (1995) "Oscillating flow about two- and three dimensional bilge keels", *Proc. 14th Int'l. Conf. of Offshore Mechanics & Arctic Engineering (OMAE)*, Copenhagen, Denmark.
- [19] Schmitke, R. T. (1978) "Ship sway, roll, and yaw motions in oblique seas", *Trans. SNAME*, **86**, pp. 26-46.
- [20] Singh, S. (1979). "Forces on bodies in oscillatory flow", Ph.D. dissertation, Univ. of London, UK.
- [21] Susbielles, G. and Bratu, C. (1981). *vagues et ouvrages pétroliers en mer*, Publications of The Institute of Petroleum of France, Editions Technip, Paris, France.
- [22] Tanaka, N. (1960). "A study on the bilge keels. Part 4. On the eddymaking resistance to the rolling of a ship hull", *J. Soc. Naval Arch. Japan*, **109**.
- [23] Vaidhyanathan, M. (1993)., "Separated flows near a free surface", Ph.D. dissertation, Dept. of Naval Arch. and Offshore Engrg., Univ. of Calif., Berkeley.
- [24] Vinje, T. and Brevig, P. (1980). "Nonlinear, two-dimensional ship motions" Tech. Rept., The Norwegian Inst. of Tech., Trondheim.
- [25] Vugts, J. H. (1968). "The hydrodynamic coefficients for swaying, heaving and rolling cylinders in a free surface", Rept. No. 194, Laboratorium voor Scheepsboukunde, Technische Hogeschool Delft, The Netherlands.
- [26] Wehausen, J. V. and Laitone, E. V. (1960). "Surface Waves", in *Handbuch der Physik*, **9**, Springer-Verlag.
- [27] Willert, C. E. and Gharib, M. (1991). "Digital particle image velocimetry", *Experiments in Fluids*, **10**, pp. 181-193.
- [28] Yeung, R. W. (1982). "Numerical methods for free-surface flows", *Ann. Rev. Fluid Mech.*, **14**, pp. 395-442.
- [29] Yeung, R. W. and Ananthakrishnan, P. (1992a). "Oscillation of a floating body in a viscous fluid", *J. Engrg. Math.*, **26**, pp. 211-230.
- [30] Yeung, R. W. and Ananthakrishnan, P. (1992b). "Vortical flows with and without a surface-piercing body", *Proc. 19th Symp. on Naval Hydrodyn.*, Seoul, Korea.
- [31] Yeung, R. W., and Cermelli, C. A. (1996), "Vortical Flow Generated by A Plate Rolling in a Free Surface", *Chapter in Advances in Fluid Mechanics*, Computational Mechanics Publisher.
- [32] Yeung, R. W., Sphaier, S. H., and Vaidhyanathan, M. (1993). "Unsteady flow about bluff cylinders", *Int'l. J. Offshore and Polar Engrg.*, **3**, pp. 81-92.
- [33] Yeung, R. W. and Vaidhyanathan, M. (1993). "Flow past oscillating cylinders", *ASME J. Offshore Mech. and Arctic Engrg.*, **115**, pp. 197-205.
- [34] Yeung, R. W. and Vaidhyanathan, M. (1994). "Highly separated flows near a free surface", *Proc. Int'l. Conference on Hydrodynamics*, Wuxi, China.

Numerical Calculations of Ship Stern Flows at Full-Scale Reynolds Numbers

L. Eça (Instituto Superior Técnico, Portugal)

M. Hoekstra (Maritime Research Institute, The Netherlands)

Abstract

This paper investigates the numerical calculation of ship stern flows at full scale Reynolds numbers, avoiding the use of wall-functions for the description of the near-wall flow behaviour. The calculation method is based on the Reduced Navier-Stokes equations, which allow the use of large numbers of grid nodes even with modest computer resources. The grid dependency studies show that it is possible to obtain grid independent solutions in the flow around the HSVA tanker. The comparison of the solutions at model scale and full scale Reynolds numbers for the flows around the HSVA tanker and the Mystery tanker show a strong dependence of the flowfield on the Reynolds number.

Nomenclature

\bar{a}^i	- Contravariant base vectors.
C_p	- Pressure coefficient, $\left(\frac{p-p_\infty}{\frac{1}{2}\rho U_\infty^2}\right)$.
g_{ij}	- Covariant metric tensor.
g^{ij}	- Contravariant metric tensor.
\sqrt{g}	- Jacobian of the coordinate transformation.
L	- Ship length.
n_i	- Number of grid nodes in i direction.
p	- Pressure.
Re	- Reynolds number, $(Re = \frac{U_\infty L}{\nu})$.
u_τ	- Skin friction velocity, $(u_\tau = \sqrt{\frac{\tau_w}{\rho}})$.
U_∞	- Free-stream velocity.
U^i	- Cartesian velocity components.
$V(i)$	- Grid-aligned physical components of the velocity vector.
x, y, z	- Cartesian coordinates.
y^+	- Non-dimensional distance to the wall, $(y^+ = \frac{u_\tau y}{\nu})$.
ξ, η, ζ	- Curvilinear coordinates.
μ	- Fluid effective viscosity.
ν	- Fluid kinematic viscosity.

ρ	- Fluid mass density.
τ^{ij}	- Stress tensor.
ω^i	- Cartesian vorticity components.

1 Introduction

One of the most challenging tasks of numerical Ship Hydrodynamics is the calculation of ship stern flows. The quality assessment of the hull form and the design of the propeller will benefit from such calculations if they have sufficient predictive capability. The major part of the work on numerical stern flow prediction has been focused on the flow at model scale Reynolds numbers, $10^6 < Re < 10^7$. The results of the Workshops of Göteborg, [1], and Tokyo, [2], give a good impression of the achievements.

Attempts to predict a stern flow at full scale Reynolds number have undoubtedly been made by several of those having successfully completed a similar calculation at model scale; but only a few have been reported. Three participants of the Göteborg Workshop of 1990, [1], and one participant of the Tokyo 1994 Workshop, [2], presented results of full scale Reynolds numbers calculations. One of the major difficulties of these calculations is to maintain stability of the numerical solution in the near-wall region. Resolution requirements impose a highly stretched grid, implying extreme grid cell aspect ratios. As a result the performance of a numerical method can deteriorate dramatically.

Ju and Patel in [3] used a two-point wall function approach to avoid the direct solution of the flow in the sublayer and buffer regions. Understandably, this alleviates the numerical difficulties considerably. However, the performance of the wall-function approach was evaluated by them on the flow around an axisymmetric body. In a complicated three-dimensional flow like a ship stern flow the restrictions of the wall function descrip-

tion are much more severe and in our opinion unacceptable in the end.

The present work investigates therefore the feasibility of performing full scale Reynolds number calculations without the use of wall functions. The numerical method is the present version of the computer code PARNASSOS, [4] to [7], which has been originally developed at MARIN and more recently extended and improved in cooperation with IST, [8]. The method is based on the reduced form of the Reynolds-averaged Navier Stokes, (RANS) equations, [9]. An eddy-viscosity algebraic turbulence model based on the formulation of Cebeci and Smith, [10], completes the mathematical model. The reduced form of the RANS equations allows the use of large numbers of grid nodes even with modest computer resources, both in memory and c.p.u.

The direct application of the no-slip condition at the wall and the use of the reduced form of the RANS equations make grid generation one of the major difficulties of full scale Reynolds number calculations. The present grid generation procedure combines elliptic and algebraic grid generation techniques. A large number of grid nodes is required in the hull-normal direction. It is important to investigate the sensitivity of the solution to the grid and to verify the grid requirements in the near-wall region.

The present paper presents the main features of the numerical method in section 2. The grid generation methodology is described in section 3. The grid dependency studies and an investigation of the influence of the distance of the first grid node to the wall in the direct application of the no-slip condition follow in section 4. Also included in section 4 is a comparison between numerical predictions at full scale and model scale Reynolds numbers for the two test cases of the Tokyo Workshop, [2]: the HSVA tanker and the Mystery tanker. The conclusions of the paper are summarized in section 5.

2 Computational Method

2.1 Mathematical Formulation

The Reynolds-averaged Navier-Stokes equations for steady flow of an incompressible fluid consist of equations expressing mass and momentum conservation, supplemented with a turbulence model. The conservation equations are written here for a general curvilinear coordinate

system ξ^i (alternatively denoted as the ξ, η, ζ system) in contravariant form with the cartesian velocity components, U^i , as the dependent variables:

$$\vec{a}^i \cdot \frac{\partial \vec{U}}{\partial \xi^i} = 0, \quad (1)$$

$$\rho \left(\vec{a}^j \cdot \vec{U} \right) \left(\vec{a}^i \cdot \frac{\partial \vec{U}}{\partial \xi^j} \right) + g^{ij} \frac{\partial p}{\partial \xi^j} - \left(\frac{\partial \tau^{ij}}{\partial \xi^j} \right)^* = 0, \quad (2)$$

with

$$\tau^{ij} = \mu \left[g^{im} \left(\vec{a}^j \cdot \frac{\partial \vec{U}}{\partial \xi^m} \right) + g^{jm} \left(\vec{a}^i \cdot \frac{\partial \vec{U}}{\partial \xi^m} \right) \right], \quad (3)$$

$$\begin{aligned} \left(\frac{\partial \tau^{ij}}{\partial \xi^j} \right)^* &= g^{im} \left(\vec{a}^j \cdot \frac{\partial}{\partial \xi^j} \left(\mu \frac{\partial \vec{U}}{\partial \xi^m} \right) \right) \\ &+ g^{jm} \left(\vec{a}^i \cdot \frac{\partial}{\partial \xi^j} \left(\mu \frac{\partial \vec{U}}{\partial \xi^m} \right) \right) + A, \end{aligned} \quad (4)$$

and

$$\begin{aligned} A &= \left(\vec{a}^i \cdot \frac{\partial \vec{a}^m}{\partial \xi^j} \right) \left(\vec{a}^j \cdot \mu \frac{\partial \vec{U}}{\partial \xi^m} \right) \\ &+ \left(\vec{a}^j \cdot \frac{\partial \vec{a}^m}{\partial \xi^j} \right) \left(\vec{a}^i \cdot \mu \frac{\partial \vec{U}}{\partial \xi^m} \right). \end{aligned} \quad (5)$$

The tensorial summation convention applies; \vec{a}^i are the contravariant base vectors:

$$\vec{a}^i = \left(\frac{\partial \xi^i}{\partial x}, \frac{\partial \xi^i}{\partial y}, \frac{\partial \xi^i}{\partial z} \right),$$

p is the pressure, ρ the fluid mass density, μ the fluid effective viscosity, \sqrt{g} is the Jacobian of the transformation between the two systems and g^{ij} is the contravariant metric tensor. A partial parabolisation is obtained by choosing ξ^1 as the mainstream direction and by neglecting diffusion in that direction, i. e. the terms with $j = 1$ in the viscous terms of momentum equations (2). The elliptic character of the equations is retained in the pressure field. All diffusion terms are dropped in the momentum equation in the normal direction. The present set of equations is classified by Rubin *et al.* in [9] as the Reduced Navier-Stokes (RNS) equations.

The fluid effective viscosity, μ , is obtained with an isotropic eddy-viscosity algebraic turbulence model, [10].

The use of the RNS equations implies that a physical meaning is attached to the grid, since diffusion is neglected in the streamwise direction, while that direction is determined by the grid. To take advantage of the roughly flow-conforming

coordinate system ξ, η, ζ , the grid-aligned physical components of the velocity vector, $V(i)$, are chosen as the velocity dependent variables. These are defined by

$$V(i) = (a^i \cdot \vec{U}) \sqrt{g_{ii}}, \quad (6)$$

where

$$g_{ii} = \left(\frac{\partial x}{\partial \xi^i} \right)^2 + \left(\frac{\partial y}{\partial \xi^i} \right)^2 + \left(\frac{\partial z}{\partial \xi^i} \right)^2. \quad (7)$$

The fourth dependent variable is the pressure, used without geometrical scaling.

The conversion from the cartesian to the grid-aligned physical velocity components is achieved with the following relations :

$$U^i = \frac{\partial x^i}{\partial \xi} \frac{V(1)}{\sqrt{g_{11}}} + \frac{\partial x^i}{\partial \eta} \frac{V(2)}{\sqrt{g_{22}}} + \frac{\partial x^i}{\partial \zeta} \frac{V(3)}{\sqrt{g_{33}}}. \quad (8)$$

But the form of the equations as written in (2) is maintained as the basis for the discretization. This procedure ensures that the discrete equations can reproduce a uniform flow exactly, [11].

The flow solution is obtained by solving the continuity and momentum equations with the appropriate boundary conditions. In matrix notation the velocity component in the normal direction, $V(2)$, is associated with the continuity equation and the pressure with the ξ^2 momentum equation. This is an alternative for the replacement of the continuity equation by a Poisson equation for the pressure or for the introduction of artificial compressibility. The coupling of the equations is maintained in the solution process.

2.1.1 Boundary Conditions

The flow around a ship hull has six boundaries. The inlet station, the outlet station, the free-surface, the symmetry plane of the ship, the ship surface and the external boundary. In the present calculations, the three velocity components at the inlet station were prescribed with standard boundary layer profiles, based on given momentum thickness and wall friction coefficient [12]. The streamwise pressure gradient was set equal to zero at the outlet boundary. Symmetry boundary conditions are applied at the symmetry plane of the ship but also at the free-surface. The latter means that the formation of gravity waves is left out of account. On the ship surface the three velocity components are set equal to zero and the flow is calculated down to the surface,

without wall-functions. At the external boundary the tangential components of the velocity and the pressure are prescribed by a potential flow calculation, [13].

2.1.2 Grid Singularities

At a grid singularity, ($\sqrt{g} = 0$ or $\sqrt{g} = \infty$), the metric relations of the coordinate transformation are not applicable. This means that the solution at grid singularities cannot be obtained with the same procedure as used for non-singular points. In the present approach, grid singularities are dealt with explicitly. The cartesian velocity components and the pressure at a grid singularity are calculated with a different system of equations and substituted in the discretized equations as known values. The cartesian velocity components and the pressure at the singular node are obtained by a weighted¹ mean of the surrounding nodes in a previous iteration².

2.2 Numerical Solution

2.2.1 Discretization

The continuity and contravariant momentum equations, (1) and (2), after replacement of the cartesian velocity components by the grid-aligned physical velocity components with the relations (8), are discretized in a single-block regular grid by a finite-difference approximation. The discretization procedure is the same as the one used in the original code PARNASSOS, [4] to [7]. The main characteristics of this procedure are summarized below :

- All the variables are defined on the grid nodes, (i, j, k) ³ ; grid staggering is not used.
- Newton linearization is applied to the convective terms.
- The streamwise convective terms are dropped at points where the streamwise velocity is negative.
- The momentum equation in the ξ and ζ directions are discretized at the nodal points (i, j, k) .

¹The weights are calculated from the distance to the singularity of the nodes involved.

²The solution procedure has to be iterative due to the non-linearity of the equations.

³The indices refer to the ξ, η and ζ direction, respectively.

- The momentum equation in the normal direction, η , is discretized at $(i, j + \frac{1}{2}, k)$.
- The continuity equation is discretized at $(i, j - \frac{1}{2}, k)$.

A detailed description of the implementation of the finite-difference approximations can be found in [8].

2.2.2 Iterative Procedure

The solution is obtained iteratively by a space-marching process. Two iteration cycles can be distinguished: the local and the global iteration process.

The local iteration process refers to the solution of the flow at a streamwise station where all the grid nodes have the same main-stream coordinate ξ . The solution is obtained simultaneously for all the variables with a Coupled Strongly Implicit Procedure (CSIP) [14]. The non-linearity of the differential equations and the incomplete factorization of the CSIP require an iterative solution.

The discretized equations at a streamwise station where all the grid nodes have the same main-stream coordinate ξ , include the pressure field at the downstream station. This implies that in order to obtain the solution by a space-marching process in the main-stream direction, the pressure field at the downstream stations has to be taken from a previous sweep. The downstream marching process has to be repeated until the changes in the pressure field between consecutive sweeps are negligible. Thus the global iteration process involves the evaluation of the solution in repeated sweeps from the inlet to the outlet boundary of the computational domain. To increase the convergence rate of this process each downstream sweep is followed by an upstream sweep to update the pressure field. The two sweeps form a predictor-corrector method for the pressure, which is constructed by adding a quasi-time derivative to the momentum equations, [7].

2.2.3 Grid Sequencing

Streamwise Direction

To improve the pressure field convergence a multiple stepsize is used in the initial global iteration sweeps to allow a rapid approach of the correct pressure level, [6]. In the initial sweep

only every 8th grid node⁴ of each ξ line is used. The multiple stepsize is subsequently reduced to 4, 2 and finally 1. The changes in the multiple stepsize are controlled by the maximum pressure coefficient difference between consecutive sweeps, $(\Delta Cp)_{max}$, with

$$\Delta Cp = Cp^n - Cp^{n-1}, \quad (9)$$

where the superscript n indicates the number of the sweep of the global iteration process and

$$Cp = \frac{p - p_\infty}{\frac{1}{2}\rho U_\infty^2}. \quad (10)$$

Girthwise Direction

The technique used for the girthwise direction is similar to the one used in the streamwise direction and has the same purpose. The use of a grid sequencing technique in the girthwise direction also increases the convergence rate of the CSIP in the initial global iteration sweeps, when the initial approximation at each streamwise station is still too far from the final solution. The reduction of the stepsize in girthwise and streamwise directions is simultaneous.

Normal Direction

The grid sequencing technique applied in the streamwise and transverse directions is related to the global iteration process. A different grid sequencing technique is applied in the normal direction. Grid sequencing in the normal direction is mainly required by the clustering of grid lines close to the symmetry plane of the wake, imposed by the application of the no-slip condition at the ship surface. Therefore, the grid sequencing technique in the normal direction is related to the local iteration process.

The CSIP is applied at a streamwise station where all the grid nodes have the same ξ -coordinate. The boundary conditions at the ζ -line $\eta = 0$ ($j = 1$) may include the following situations:

1. Wake station. The nodes are all on the symmetry plane of the wake and symmetry conditions apply to all the nodes.
2. Ship station. The nodes are all on the ship surface and the no-slip condition applies to all the nodes.

⁴This implies that the total number of nodes in the streamwise direction has to be a multiple of 8 plus 1.

3. Mixed station. The no-slip condition applies to part of the nodes and symmetry conditions apply to the others.

In a wake station, the essential parameter to control the convergence rate of the CSIP close to the symmetry plane of the wake is the distance between the grid nodes. In this case, the use of a multiple stepsize is not a good option. For it would mean that the multiple stepsize required for grid distance enlargement close to the symmetry plane yields an unacceptably large distance between grid nodes close to the outer boundary.

The present approach is to perform an initial calculation of the CSIP in a coarser grid where the distance between grid nodes in a given η line is larger than a specified distance. When the calculation process proceeds to the fine grid, the initial approximation for the solution on the fine grid is obtained by linear interpolation of the solution on the coarse grid. There are no restrictions on the number of grid nodes to be used in the normal direction with this grid sequencing technique.

In the ship stations grid sequencing is not applied because a solution on a coarse grid does not yield a good initial approximation for the solution on the fine grid, due to the no-slip boundary condition.

A compromise has to be made at a streamwise station where the ship surface and the wake symmetry plane coexist. Grid sequencing is required by the wake boundary condition but it is undesirable at η lines where the no-slip boundary condition applies. In these mixed stations, we apply a grid sequencing technique as for wake stations. However, the specified minimum distance between grid nodes is chosen one order of magnitude smaller than in the wake stations. Furthermore, we do not apply grid sequencing in the global iteration sweeps performed with multiple stepsize factors 8 and 4.

3 Grid Generation

If the RNS equations are chosen as the basis for a numerical simulation of ship stern flows the computational grid must be roughly flow conforming. For a simulation at full scale Reynolds numbers the distance between grid lines close to the ship surface may be of the order of 10^{-9} of the ship length L . Furthermore, the grid lines should be nearly orthogonal to the ship surface in the near-wall region, which may be troublesome in ship

stern cross-sections including both concave and convex regions. All these requirements together mean that grid generation in such a numerical calculation is a complex problem, but at the same time a crucial factor for its success.

In order to be able to deal with all the requirements of an acceptable grid, the present grids are generated in two steps :

1. Generate a basis grid using a 3D elliptic grid generator.
2. Apply grid line stretching along the normal, η , grid lines with an algebraic technique.

The present 3D grid generator, [15], is based on the elliptic generating system incorporated in the EAGLE code, [16]. The method allows the specification of the coordinates of all the boundary nodes and the grid line pattern is defined by the so-called control functions, which are calculated iteratively to obtain the following properties :

- Orthogonality at the boundaries.
- A specified distance of the first grid node to the boundary.
- An interior grid line spacing that reflects the boundary point distribution.

The present elliptic generating system follows Thompson's description, [17], of the so-called GRAPE approach, [18].

The non-linear terms of the control function that guarantee grid line orthogonality at the boundaries are inversely proportional to the grid line spacing. This means that it is extremely difficult, if not impossible, to compute an acceptable grid if the desired near-wall grid line distance is imposed directly on the 3D elliptic grid generator. Therefore, we generate a basis grid using moderate grid line stretching in the normal direction.

The final grids are obtained by carrying out step 2: stretching of the basis grid with an algebraic interpolation technique. The interpolation is performed along the η lines using three cubic splines, one for each cartesian coordinate of the grid nodes involved. The stretching functions proposed by Vinokur in [19] are used. For all η lines in a grid plane $\xi = \text{constant}$ the same stretching is applied so that the deviations from orthogonality of the final grid are similar to the ones of the basis grid. It has been found that the number of grid nodes of the basis grid in the vicinity of the boundaries $\eta = 0$ and $\eta = 1$ must be sufficient to avoid oscillations in the spline representation of the η grid lines.

4 Results

4.1 General

The flow around the sterns of the HSVA tanker and of the Mystery tanker were selected for the present studies. These two sterns are the test cases of the Göteborg and Tokyo Workshops, [1] and [2]. The calculations were performed at full scale Reynolds number, 2.0×10^9 , and at model scale Reynolds number, 5.0×10^6 . The Reynolds number is defined by

$$Re = \frac{U_\infty L}{\nu},$$

where U_∞ is the undisturbed flow velocity, L is the ship length, and ν is the kinematic viscosity of the fluid.

A cartesian coordinate system is introduced with the x axis along the undisturbed stream, the z axis vertical positive pointing upwards and y completing a right-hand system. The origin of the coordinate system is located on the foreword perpendicular at the ship symmetry plane on the free surface. All the variables presented in the results are made non-dimensional using U_∞ and L as the velocity and length reference scales.

The convergence criterion used in the global iteration process of all the calculations performed was a minimum pressure coefficient difference, $(\Delta C_p)_{max}$, between consecutive sweeps of 5.0×10^{-3} . In the local iteration process, CSIP, the convergence criteria was a maximum difference between physical components of the contravariant velocity components of $1.0 \times 10^{-4} U_\infty$ and a maximum C_p difference between iterations of 2.0×10^{-5} . The maximum number of iterations allowed for the CSIP at each streamwise station was 51.

In the present calculations the boundaries of the computational domain are located as follows :

- The inlet boundary is a $x = \text{constant}$ plane at $x = 0.65$.
- The outlet boundary is a $x = \text{constant}$ plane at $x = 1.20$.
- The external boundary is an elliptic surface with y and z axis of approximately 0.19 and 0.15.
- The remaining boundaries are the free surface, plane $z = 0$, the symmetry plane of the ship, plane $y = 0$, and the ship surface.

The results of the present calculations are plotted at $x = \text{constant}$ planes and on the ship surface. The local values of all the variables at the x constant planes, which do not coincide with grid nodes, are calculated by linear interpolation along the streamwise grid lines. The limiting streamlines are obtained by a predictor-corrector integration of the wall shear-stress.

All the calculations were performed on a DEC Alpha 7620 with 64 bytes precision. The program requires 65 Mbytes of RAM and with the present convergence criteria the c.p.u. time is approximately 0.05 seconds per grid node.

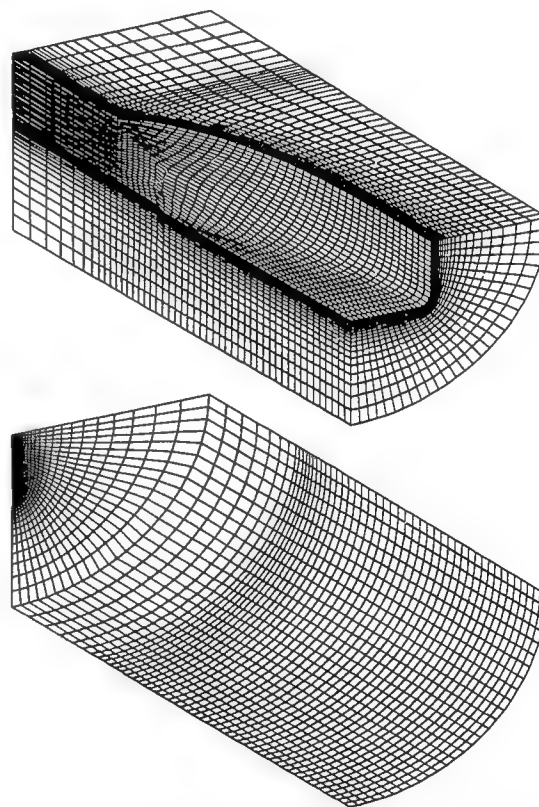


Figure 1: Illustration of the grid for the calculation of the flow around the HSVA tanker.

4.2 Grid Dependency Studies

A limited number of grid dependency studies was performed for the flow around the HSVA tanker. A reference grid was adopted which has $97 \times 149 \times 57$ grid nodes. The streamwise step size in the stern region is approximately equal to $0.005L$. In the wake region the streamwise step size is increased up to $0.014L$. The grid has an

equally spaced boundary point distribution in the girthwise direction.

The near-wall grid density is monitored by the maximum y^+ distance of the first grid node to the wall,

$$y_2^+ = \frac{u_\tau y_2}{\nu},$$

where u_τ is the skin friction velocity. The y_2^+ can not be known a priori, because it depends on the flow solution. This means that the stretching required to obtain a given value of y_2^+ is estimated from a previous calculation. The reference grid has $y_2^+ \simeq 0.5$, which corresponds to a minimum grid node distance of 10^{-9} L.

The grid boundary point distribution of the reference grid is illustrated in figure 1, where only half of the grid nodes in each direction are plotted.

The grid dependency studies concerned variations of the number of grid nodes in the normal direction. On the one hand this number was changed, keeping approximately the same near-wall spacing; on the other hand, the near-wall grid node density was systematically changed, keeping the discretization in the outer region equal.

4.2.1 Outer region grid refinement

Calculations were performed with three different numbers of grid nodes in the normal direction, n_η , 105, 125, and 149, keeping approximately the same value of y_2^+ in all the grids.

The surface pressure distribution and the limiting streamlines of the three calculations are plotted in figure 2. The surface isobars and limiting streamlines are graphically almost coincident. Only the solution with $n_\eta = 105$ grid nodes shows some small deviations at the end of the stern.

Figure 3 presents the comparison of the isolines of axial velocity, U^1 , pressure coefficient, C_p , and axial vorticity, ω^1 , at $x = 0.976$ and $x = 1.005$. The isolines of axial velocity of the three calculations are almost undistinguishable; there are insignificant differences between the solutions in the outer region only. The differences between the three solutions are better visible in the isobars, where in particular the solution obtained with $n_\eta = 105$ deviates; the differences between the solutions with $n_\eta = 125$ and $n_\eta = 149$ are small. The axial vorticity isolines of the three calculations are almost identical. Bearing in mind that the axial vorticity is computed by numerical differentiation in grids with different grid nodes location, the differences between the axial vorticity

isolines are not significant. The transverse velocity fields of the three calculations at these two planes are identical and the maximum transverse velocities of the three calculations differ less than 0.1% of U_∞ .

It should be mentioned that the performance of the CSIP is getting worse with the increase of the number of grid nodes per streamwise station. This deterioration becomes rather serious for discretizations finer than a critical value. A test run made with $n_\eta = 175$ showed that 51 iterations of the CSIP are not sufficient to satisfy the present convergence criteria, which means that a larger number of iterations must be used in the CSIP to obtain the same precision. Therefore, the c.p.u. per grid node with $n_\eta = 175$ is much larger than the one obtained for $n_\eta = 105$, $n_\eta = 125$ and $n_\eta = 149$. However, the present results suggest that there is no need to increase the number of grid nodes in the normal direction beyond 149.

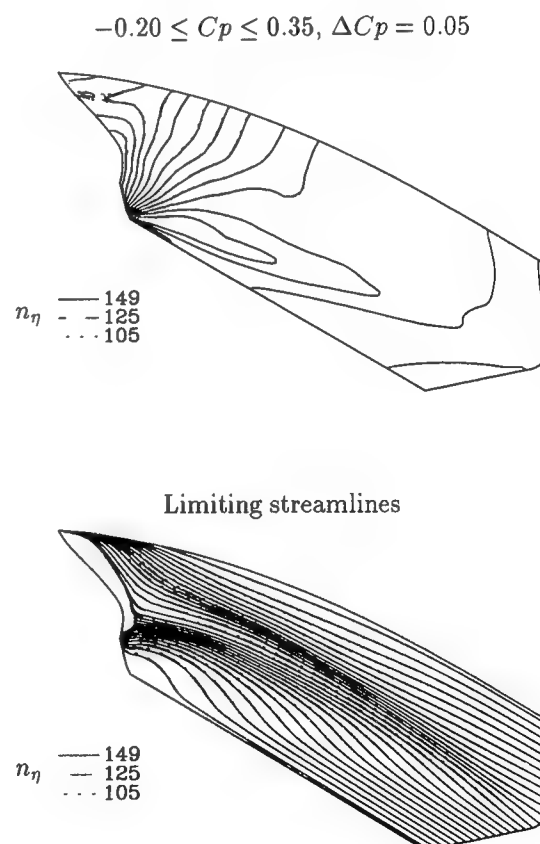


Figure 2: HSVA tanker, $Re = 2.0 \times 10^9$. Comparison of surface pressure distribution and limiting streamlines obtained with different numbers of grid nodes in the normal direction.

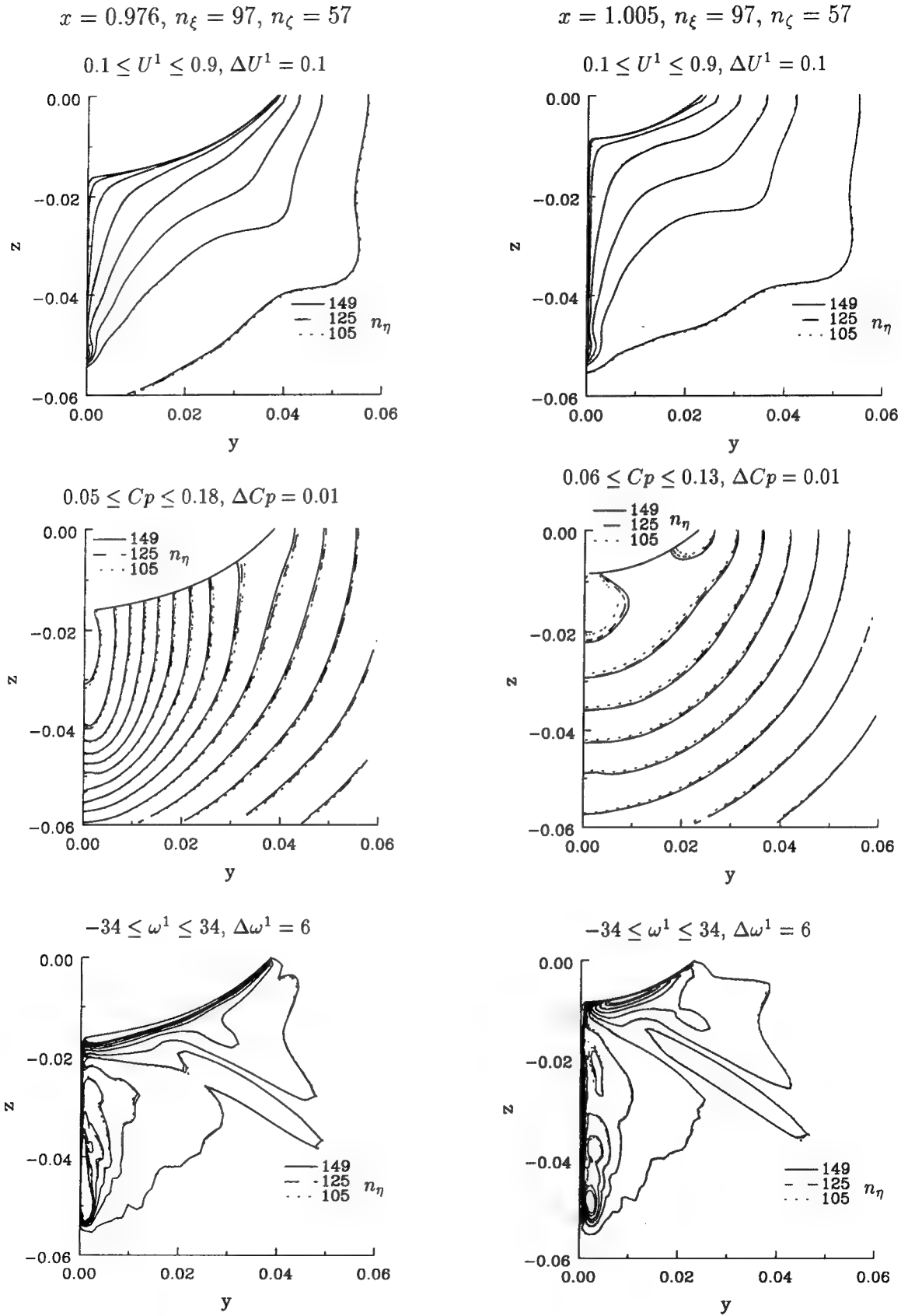


Figure 3: HSVA tanker, $Re = 2.0 \times 10^9$. Comparison of calculations performed with different numbers of grid nodes in the normal direction.

4.2.2 Near-Wall Discretization

The required grid node density in the near-wall region to obtain a grid independent solution was investigated keeping an approximately constant grid node density in the outer region. Three calculations were performed with the following grids: $n_\eta = 139$ and $y_2^+ \simeq 1.0$, $n_\eta = 149$ and $y_2^+ \simeq 0.5$ and $n_\eta = 159$ and $y_2^+ \simeq 0.1$.

The surface pressure distribution and the limiting streamlines of the three calculations are plotted in figure 4. The surface isobars and limiting streamlines are graphically coincident.

Figure 5 presents the comparison of the isolines of axial velocity, U^1 , pressure coefficient, C_p , and axial vorticity, ω^1 , at $x = 0.976$ and $x = 1.005$. The three solutions are graphically coincident. Only the axial vorticity isolines show some very small differences, which are not significant. The transverse velocity fields of the three calculations at these two planes are also identical and the maximum transverse velocities of the three calculations differ less than 0.05% of U_∞ , which is of the order of magnitude of the present convergence criteria.

These results suggests that it is possible to obtain a grid independent solution of the near-wall region in a ship stern flow at full scale Reynolds number.

4.3 Comparison of Solutions at Full Scale and Model Scale Reynolds Numbers

The flow around the HSVA tanker and the Mystery tanker were calculated at full scale and model scale Reynolds numbers, 2.0×10^9 and 5.0×10^6 , respectively. The calculations at $Re = 2.0 \times 10^9$ were performed on grids with $97 \times 149 \times 57$ grid nodes. The grids of the model scale calculations have $97 \times 105 \times 57$ grid nodes.

4.3.1 HSVA tanker

The isolines of U^1 , C_p and ω^1 of the two calculations are plotted in figure 6. Not surprisingly, the isolines of axial velocity show a strong reduction of the thickness of the boundary layer region when the Reynolds number is increased. In the present calculation the typical 'hook' shape of the U^1 contours is not reproduced, which was to be expected with the present turbulence model.

The maximum pressure at the stern increases with Reynolds number and so does the axial vorticity.

Figure 7 presents the transverse velocity fields at $x = 0.976$ and $x = 1.005$. The core position of the bilge vortex moves to the symmetry plane with increasing Re . The cross-stream velocities at $Re = 2.0 \times 10^9$ are larger than at $Re = 5.0 \times 10^6$.

The surface pressure distribution of the two flows is compared in figure 8. In general the pressure distribution becomes less smooth with higher Re ; peaks are higher, troughs deeper. Figure 9 presents the limiting streamlines of the two calculations. Most striking are the difference in the location where a confluence of limiting streamlines occurs, that is the location from which the bilge vortex originates. It has been found from additional calculations at intermediate Reynolds numbers that this upward shift of the line of confluence is systematic. There is also a slight delay of streamwise flow separation at high Re .

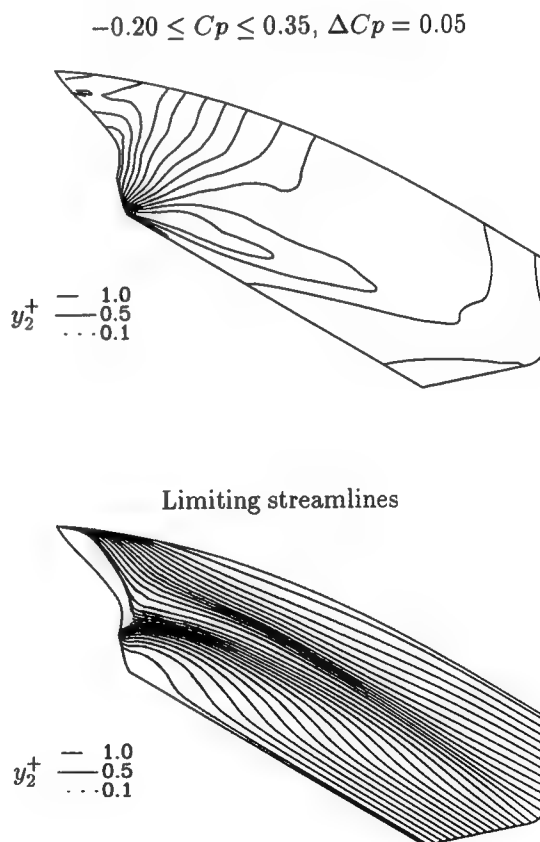


Figure 4: HSVA tanker, $Re = 2.0 \times 10^9$. Comparison of surface pressure distribution and limiting streamlines obtained with different near-wall grid nodes density.

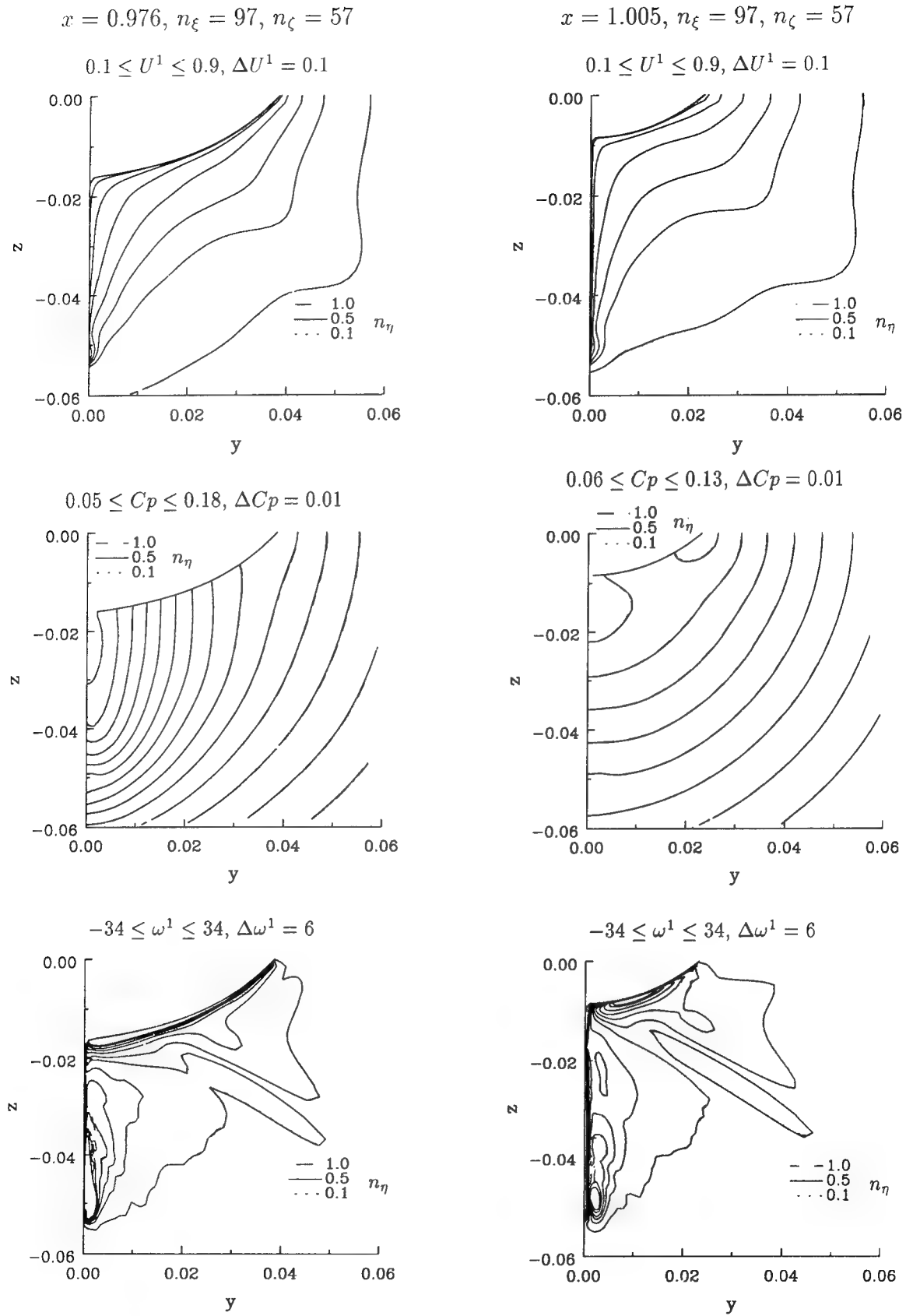


Figure 5: HSVA tanker, $Re = 2.0 \times 10^9$. Comparison of calculations performed with different near-wall grid nodes density.

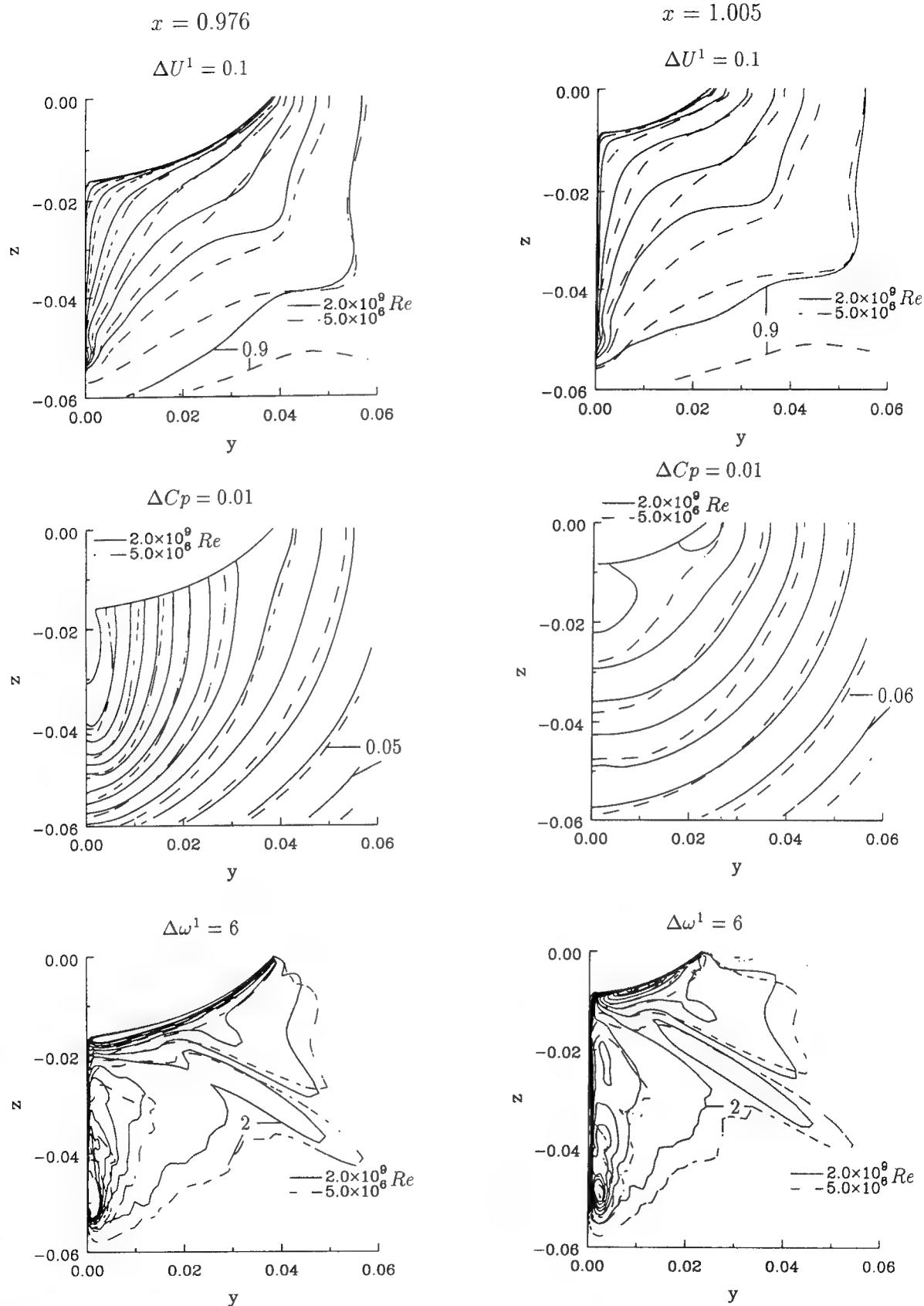


Figure 6: HSVA tanker. Comparison of calculations performed at full scale and model scale Reynolds numbers.

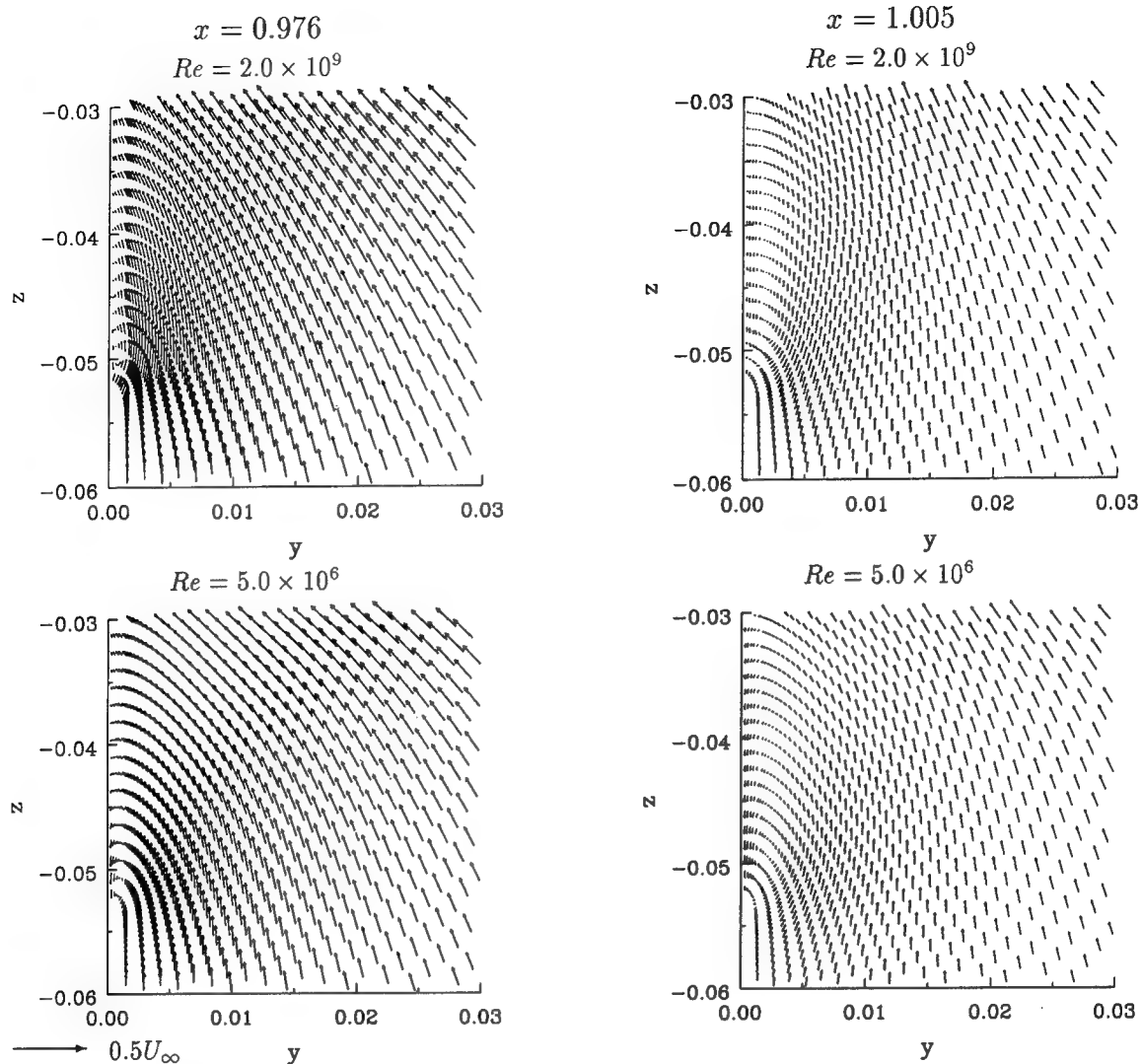


Figure 7: HSVA tanker. Transverse velocity fields of calculations performed at full scale and model scale Reynolds numbers.

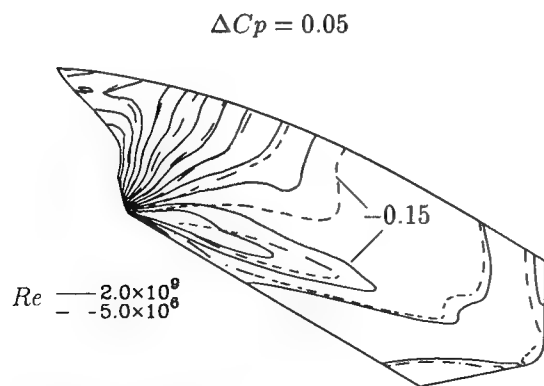


Figure 8: HSVA tanker. Comparison of surface pressure distribution for calculations performed at full scale and model scale Reynolds numbers.

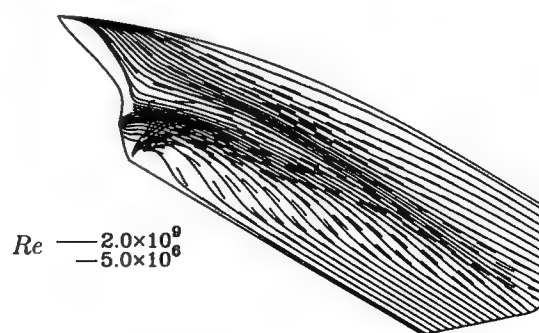


Figure 9: HSVA tanker, $Re = 2.0 \times 10^9$. Comparison of limiting streamlines for calculations performed at full scale and model scale Reynolds numbers.

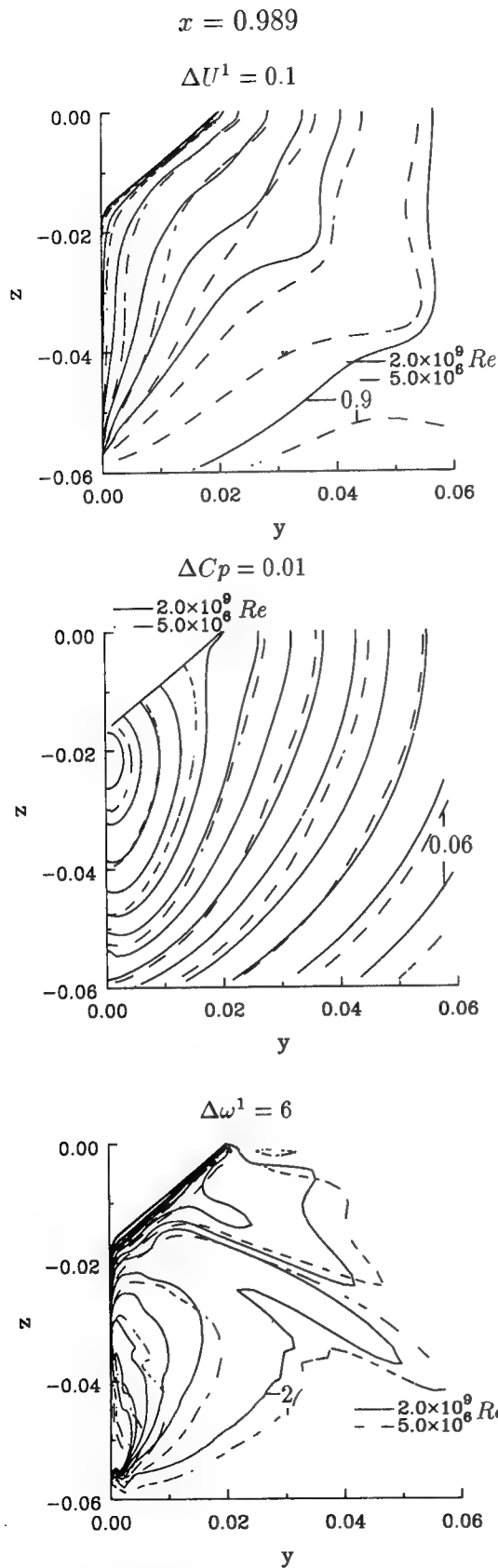


Figure 10: Mystery tanker. Comparison of calculations performed at full scale and model scale Reynolds numbers.

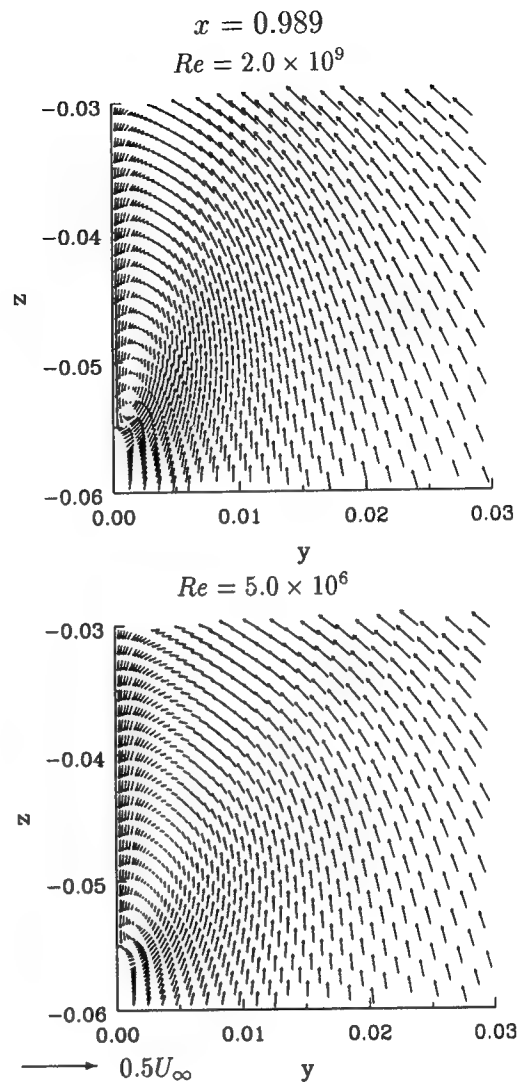


Figure 11: Mystery tanker. Transverse velocity fields of calculations performed at full scale and model scale Reynolds numbers.

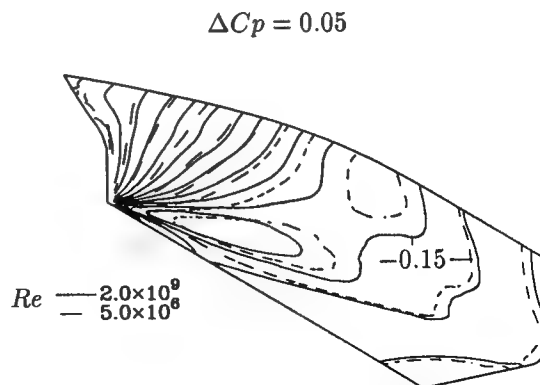


Figure 12: Mystery tanker. Comparison of surface pressure distribution for calculations performed at full scale and model scale Reynolds numbers.

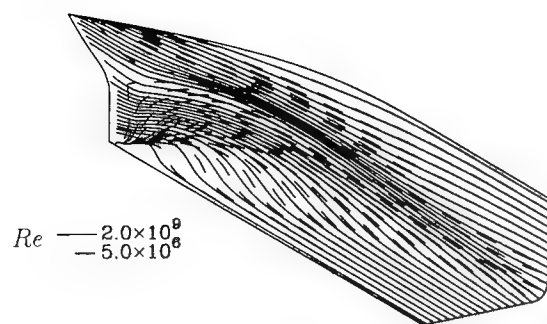


Figure 13: Mystery tanker, $Re = 2.0 \times 10^9$. Comparison of limiting streamlines for calculations performed at full scale and model scale Reynolds numbers.

4.3.2 Mystery tanker

The comparison between results at model scale and full scale Reynolds numbers is presented in figures 10 to 13. In general, the comparison of results at model and full scale Reynolds numbers is similar to the one obtained for the HSVA tanker.

The isolines of U^1 , C_p and ω^1 are plotted in figure 10, where the decrease of the boundary layer thickness with the increase of Reynolds number is clear. The transverse velocity fields at $x = 0.989$ are presented in figure 11. The bilge vortex location of the two calculations is not equal and the cross-stream velocities are larger at $Re = 2.0 \times 10^9$ than at 5.0×10^6 . The isobars on the ship surface of the two calculations are compared in figure 12. The effect of the Reynolds number in the surface pressure distribution is evident.

The limiting streamlines of the two calculations are plotted in figure 13. There is a significant difference between the two flows. At model scale, a small streamwise flow separation region is predicted at the end of the stern close to the free surface. No streamwise flow separation is predicted at full scale Reynolds number.

5 Conclusions

The feasibility of the calculation of ship stern flows at full scale Reynolds numbers with direct application of the no-slip condition at the hull surface has been proven. The numerical method with which this result has been obtained is based on the Reduced form of Reynolds averaged Navier-Stokes equations, which allows the use of large

numbers of grid nodes, required by the calculation of the near-wall region, at acceptable computing time.

The grid dependency studies performed for the flow around the HSVA tanker suggest that it is possible to obtain a grid-independent solution without the use of wall-functions. The number of grid nodes required in the normal direction is within the acceptable limits of the present method. This is fortunate because further increase of the number of grid nodes per streamwise station may require a more robust – but also more expensive – solver.

In the present calculations for the HSVA tanker, it was found that the solution was independent of the near-wall grid density for distances of the first grid node to the wall smaller than $y_2^+ \approx 1$.

The comparison of full scale and model scale Reynolds numbers calculations for the HSVA tanker and the Mystery tanker confirmed a strong dependence of the flow field at the end of the stern on the Reynolds number. The limiting streamlines showed a systematic change in position of the confluence of limiting streamlines with increasing Reynolds number. On the two test ships streamwise flow separation was delayed at high Re .

References

- [1] Larsson L., Patel V.C., Dyne G. (eds.) - *Ship Viscous Flow*. - Proceedings of 1990 SSPA-CTH-IIHR Workshop, Flowtech International AB, Research Report N° 2, Gothenburg, June 1991.
- [2] Proceedings of CFD Workshop Tokyo 1994, Ship Research Institute Tokyo, March 1994.
- [3] Ju S., Patel V.C. - *Stern Flows at Full-Scale Reynolds Numbers*. - Journal of Ship Research, Vol. 35, N° 2, June 1991, pp. 101-103.
- [4] Raven H.C., Hoekstra M. - *A Parabolised Navier-Stokes Solution Method for Ship Stern Flow Calculations*. - 2th International Symposium on Ship Viscous Resistance, Göteborg Sweden, March 1985.
- [5] Hoekstra M., Raven H.C. - *Application of a Parabolised Navier-Stokes Solution System to Ship Stern Flow Computation*. - Osaka International Colloquium on Ship Viscous Flow, Osaka Japan, October 1985.

- [6] Hoekstra M., Raven H.C. - *Ship Boundary Layer and Wake Calculation with a Parabolised Navier-Stokes Solution System*. - 4th International Conference on Numerical Ship Hydrodynamics", Washington D.C., 1985.
- [7] Hoekstra M. - *Recent Developments in a Ship Stern Flow Prediction Code*. - 5th International Conference on Numerical Ship Hydrodynamics, Hiroshima, September 1989.
- [8] Eça L. - *Numerical Solution of the Parabolised Navier-Stokes Equations for Incompressible Tip Vortex Flows*. - PhD Thesis, Instituto Superior Técnico, Lisbon, March 1993.
- [9] Rubin S.G., Tannehill J.C. - *Parabolized/Reduced Navier-Stokes Computational Techniques*. - Annual Review of Fluid Mechanics, Vol. 24, 1992, pp. 117-144.
- [10] Cebeci T., Smith A.M.O. - *Analysis of Turbulent Boundary Layers*. - Academic Press, November 1984.
- [11] Eça L, Hoekstra M. - *Discretization of the Parabolised Navier-Stokes Equations*. - First European Computational Fluid Dynamics Conference, Brussels, September 1992.
- [12] Hoekstra M. - *Generation of Initial Velocity Profiles for Boundary Layer Calculations* - Marin Report N° 50028-1-SR, March 1980.
- [13] Raven H.C. - *Berekening van de potentiaalstroming rond draagvlakken met het programma DAWSON* - Marin Report N° 50501-1-RD, May 1985.
- [14] Rubin S.G. - *Incompressible Navier-Stokes and Parabolised Navier-Stokes Formulations and Computational Techniques*. - Computational Methods in Viscous Flow, Vol. 3 in the series Recent Advances in Numerical Methods in Fluids (ed. Habashi) Pineridge Press, 1984.
- [15] Eça L. - *Grid Generation with Systems of Partial Differential Equations* (in Portuguese), IV National Meeting of Computational Mechanics, Lisbon, April 1995.
- [16] Thompson J.F. - *Composite Grid Generation Code for General 3-D Regions - the EAGLE code* - AIAA Journal, Vol. 26, March 1988, pp. 271-272.
- [17] Thompson J.F. - *A General Three-Dimensional Elliptic Grid Generation System on a Composite Block Structure*. - Computer Methods in Applied Mechanics and Engineering, Vol. 64, 1987, pp. 377-411.
- [18] Sörenson R.L. - *Grid Generation by Elliptic Partial Differential Equations for a Tri-Element Augmentor-Wing Airfoil* - Numerical Grid Generation, ed. Thompson J.F., North-Holland, 1982.
- [19] Vinokur M. - *On One-Dimensional Stretching Functions for Finite-Difference Calculations*. - Journal of Computational Physics, Vol. 50, 1983, pp. 215-234.

Near- and Far-Field CFD for a Naval Combatant Including Thermal-Stratification and Two-Fluid Modeling

E. Paterson,¹ M. Hyman,² F. Stern¹

P. Carrica,³ F. Bonetto,³ D. Drew,³ R. Lahey, Jr.³

(¹University of Iowa, ²Naval Surface Warfare Center [Panama City],
³Rensselaer Polytechnic Institute, USA)

ABSTRACT

A computational fluid dynamics approach for simulating the near and far field of a Naval combatant in a thermally-stratified two-phase flow is presented. The approach is based upon, for the near field, coupling a single-phase Reynolds-averaged Navier-Stokes method with both the energy equation, to account for transport of thermal energy and creation of buoyancy forces, and a two-fluid model, to account for the transport of monodisperse microbubbles and their interaction with the liquid phase. Far-field solution is based upon parabolic Reynolds-averaged Navier-Stokes equations with the initial data plane prescribed by the near-field solution. An extensive number of conditions are simulated: model-scale Re ; medium and high speeds; with and without thermal stratification; with and without propeller; and two-fluid calculations over a range of bubble sizes. The two-fluid near-field results, however, are preliminary in that they are for zero Fr and are not coupled to the far-field. For the single-phase, unstratified, and unpropelled case, a detailed uncertainty analysis following ASME guidelines is performed. The results show that both global and detailed features of Naval combatant flows can be accurately predicted and, despite many uncertainties and lack of validation data, the prognosis with regard to predicting two-phase surface-ship wake signatures is optimistic.

1 INTRODUCTION

Knowledge of surface-ship flow fields is useful in many aspects of ship design and in the evaluation of their performance. Applications of such knowledge range from powering, structural loading, and noise production to far-field signature estimation. These phenomena are dependent on both Froude (Fr) and Reynolds (Re) number and so require testing or simulation at full scale to be adequately determined. The cost and uncertainty of full-scale measurements provides strong motivation to utilize scale model testing and scaling relationships to obtain full-scale estimates. In many cases, scaling relationships are

not known or are based upon very limited data. This is particularly true in the design of new hulls. As a result, there is a pressing need to develop computational tools to either help with scaling model data or to enable the calculation of full-scale flows.

The flow in question is quite complex. It involves a deforming surface which undergoes breaking in certain regions, an extensive three dimensional boundary layer, air entrainment in the form of bubbles at the surface, and a strong momentum source at the propeller plane. There are additional influences including ambient density stratification due to thermal and salinity variations, sea state and other environmental effects, and particulates and surfactants suspended in the fluid which have a poorly understood effect, if any, on the flow. It is clear that bubbles, in particular, can become sufficiently numerous to locally interact with the flow, but that density stratification influences generally take place over a long time scale and so are important primarily in the wake.

While direct simulation of these flows is many years away, a considerable amount of very useful information can be extracted from ensemble-average modeling. Over the past several years, a number of ensemble-average models have reached a level of maturity that allows them to be applied to some of these problems. In this paper we will focus on modeling the near and far wakes for the purpose of signature estimation but the modeling capability is general and likely to be equally applicable to other problems of concern.

As noted, the near ship flow responds to a no-slip boundary, a strong local momentum source, and a free surface. Reynolds-averaged Navier-Stokes (RANS) solvers have evolved to the point where they can be applied to model-scale Reynolds number, full-scale Froude number ship flow simulation with propulsion effects and non-linear free surface boundary conditions. The algorithm discussed in (1,2) in particular has demonstrated the ability to accurately calculate the viscous-flow and wave fields, resistance,

and propeller-hull interaction. While most applications of the algorithm have been to generic hull forms such as the Wigley hull and to research forms such as the Series 60, accurate simulation of the flow around these hulls suggest that it is capable of general application and represents a good starting point for complex forms such as combatants with transom sterns and bulbous bows.

At full scale, this flow is not uniformly single phase. Air bubbles from boundary-layer entrainment, propeller ventilation and/or cavitation, and breaking waves serve to inject bubbles into the flow. In most regions the void fraction is small and does not influence the flow, but in others it can become large enough to play a significant role on flow dynamics. Even though the degree of complexity of the problem increases considerably when the bubbles are taken into account, two phase flow modeling of (3,4,5) can be used to determine the spatial distribution of moderately high concentration (i.e., α less than 10%), monodisperse air bubble populations and the associated fluid coupling in turbulent flows. While the mechanisms and degree of air entrainment at the free surface remain unresolved, considerable insight can be achieved by introducing air void at likely injection locations and calculating its evolution.

More or less simultaneously, considerable effort has been devoted toward developing computational models of surface ship wakes. The effort has been motivated by a desire to estimate micro-bubble populations in the far wake as well as predict the radar scattering characteristics of the free surface. The work in (6,7,8) detail application of far-wake modeling to micro-bubble evolution. In general, the strategy has been to model the hydrodynamic and relevant scalar fields via a parabolic subset of the RANS equations. Scalar fields such as temperature, micro-bubble populations, salinity and surface contaminants have been included because of their influence on the flow field and because they are of interest in their own right.

The ability to predict the near and far fields of naval surface ships requires that these models be extended to include realistic hull geometries and operating environments and coupled together. The work presented in this paper discusses some of the extensions necessary to use these tools to simulate the flow fields associated with naval combatants operating in commonly encountered conditions. They are illustrated via a set of simulations on a U.S. Navy FF-1052 (figure 1). This ship represents most of the geometric complexities found in modern combatant forms; a transom stern and bulbous bow. The near- and far-field flow is computed for both the unpropelled and propelled hull operating in a thermally-stratified environment. The transport of a monodisperse microbubble population introduced in

the near-bow region is also computed for the unpropelled hull at zero Froude number.

This paper is arranged in the following manner. The problem formulation is described in section 2. In section 3 the computational methods are briefly discussed. The conditions and grids are presented in section 4 and the uncertainty analysis in section 5. Results for both the FF-1052 near and far field are presented in section 6. Finally, concluding remarks and discussion of future work are provided in section 7.

2 PROBLEM FORMULATION

To predict surface-ship bubbly wakes, separate, but coupled, CFD methods are used for the near and far fields. Formulation of the problem is based upon coupling the RANS method (1), which has been extended for combatant geometries (9) [i.e., multi-block to handle transom stern and propeller-hull interaction using (2)] and thermal stratification, and an Eulerian two-fluid ensemble-averaged model (4) for the near field and a parabolic method (6) for the far field with its initial data plane (IDP) prescribed by the near-field solution. It should also be noted that (9) provides detailed documentation, user instructions, and discussion of and implementation recommendations for uncertainty analysis. Figure 2 provides a schematic of the relationship between near- and far-field domains.

2.1 Near Field

The unsteady three-dimensional continuity and RANS equations for a gas-liquid two-phase flow are written for each phase separately and derived assuming: negligible bubble inertia (i.e., $\rho_g \ll \rho_l$); small void fraction and void-fraction gradients; spherical bubbles; and constant liquid density. Using Cartesian tensor notation and in non-dimensional form, the liquid-phase equations are

$$\frac{\partial(1-\alpha)}{\partial t} + \frac{\partial(1-\alpha)U_{t,i}}{\partial x_i} = 0 \quad (1)$$

$$\begin{aligned} & \frac{D_t U_{t,i}}{Dt} + \frac{\partial \hat{p}}{\partial x_i} - \frac{1}{Re} \frac{\partial^2 U_{t,i}}{\partial x_j \partial x_j} + \frac{\partial}{\partial x_j} (\overline{u_{t,i} u_{t,j}}) \\ & - f_{b,i} + \frac{1}{Fr^2} \left(\frac{\rho_a - \rho}{\rho} \right) \delta_{i3} \\ & + \frac{\alpha}{(1-\alpha)} \left\{ C_{vm} \alpha \left(\frac{D_g U_{g,i}}{Dt} - \frac{D_t U_{t,i}}{Dt} \right) \right. \\ & + C_L \epsilon_{ijk} \epsilon_{klm} U_{r,i} \frac{\partial U_{t,l}}{\partial x_m} + \frac{3}{8} \frac{C_D}{r_b} U_{r,i} |U_{r,i}| \\ & \left. + \frac{1}{\alpha} C_{TD} k_t \frac{\partial \alpha}{\partial x_i} \right\} = 0 \end{aligned} \quad (2)$$

and the gas-phase equations are

$$\frac{\partial(\rho_g \alpha)}{\partial t} + \frac{\partial(\rho_g \alpha U_{g,i})}{\partial x_i} = 0 \quad (3)$$

$$C_{vm} \left(\frac{D_g U_{g,i}}{Dt} - \frac{D_l U_{l,i}}{Dt} \right) + C_L \varepsilon_{ijk} \varepsilon_{klm} U_{r,i} \frac{\partial U_{l,j}}{\partial x_m} - \frac{3}{8} \frac{C_D}{r_b} U_{r,i} |U_{r,i}| + \frac{1}{\alpha} C_{TD} k_t \frac{\partial \alpha}{\partial x_i} + \frac{\partial p}{\partial x_i} - \frac{\delta_{i3}}{Fr_b^2} = 0 \quad (4)$$

where the subscripts ℓ and g indicate liquid and gas, $x_i = (X, Y, Z)$ are the Cartesian coordinates, $\frac{D_g}{Dt}$, $\frac{D_l}{Dt}$ are the substantial derivatives with respect to each phase, $U_{\ell,i} = (U_{\ell}, V_{\ell}, W_{\ell})$ and $U_{g,i} = (U_g, V_g, W_g)$ are the liquid and gas mean-velocity components, $U_{r,i}$ is the relative velocity between phases ($U_{\ell,i} - U_{g,i}$), $\overline{u_{\ell,i} u_{\ell,j}}$ are the Reynolds stresses, \hat{p} is the piezometric pressure ($p + Z/Fr^2$), ν is the kinematic viscosity, f_{b_i} are the body-force terms which represent the effects of the propeller, $Re = U_o L / \nu$, $Fr = U_o / \sqrt{gL}$, and α is the gas-phase volume fraction. Coupling between the liquid- and gas-phase momentum equations is accomplished through the continuity equation (1) and the last- and first-four terms of (2) and (4), respectively, which represent interfacial momentum transfer due to virtual mass (i.e., acceleration of the liquid caused by the bubbles), lift, drag, and turbulent dispersion effects. Derivations and model constants for each term are provided in (3,4). The sixth term of (2) represents buoyancy due to thermal stratification, where ρ_a represents the ambient density of sea water prescribed by an equation of state, and is used only for single-phase simulations. The equations are normalized by ship speed U_o and length L , and liquid density ρ_l . Note that for $\alpha=0$, (2) reduces to the single-phase RANS equations.

The temperature field is obtained from the energy equation which is written for an incompressible fluid as

$$\frac{\partial T}{\partial \tau} + U_{\ell,j} \frac{\partial T}{\partial x_j} = \kappa \frac{\partial^2 T}{\partial x_j \partial x_j} - \frac{\partial}{\partial x_j} (\overline{u_{\ell,j} t}) \quad (5)$$

where κ is the non-dimensional thermal diffusivity and T and t are the ensemble-averaged and fluctuating temperatures, respectively. The velocity and temperature fields interact through the previously mentioned buoyancy term in the Z -momentum equation, the energy equation (5), and the equation of state.

The Reynolds stresses and turbulent transport of thermal energy are modeled using a Boussinesq assumption, i.e., linear relationship with mean rate-of-strain and temperature gradient, respectively, and an isotropic eddy viscosity ν_t

$$-\overline{u_{\ell,i} u_{\ell,j}} = \nu_t \left(\frac{\partial U_{\ell,i}}{\partial x_j} + \frac{\partial U_{\ell,j}}{\partial x_i} \right) - \frac{2}{3} \delta_{ij} k_t \quad (6)$$

$$-\overline{u_{\ell,i} t} = \nu_t \frac{\partial T}{\partial x_i} \quad (7)$$

Although higher-order models (i.e., both linear and non-linear $k-\omega-\varepsilon$) have/will be used, the Baldwin-Lomax algebraic turbulence model is used here to determine ν_t because of its simplicity, efficiency, and stability. Bubble-induced turbulence, which is expected to be important in the near wall region, contributes to both the total effective viscosity and the turbulent kinetic energy

$$\nu_{eff} = \nu + \nu_t + \nu_b \quad (8)$$

$$k = k_t + k_b$$

where k_t is determined using ν_t and the mixing length, and ν_b and k_b are determined from model equations (10).

Referring to figure 3, the specified boundaries of the solution domain are the body surface S_b ($\eta = 1$), the inlet plane S_i ($\xi = 1$), the exit plane S_e ($\xi = imax$), the symmetry plane S_k ($\zeta = 1$ and parts of $\eta = 1$), the outer boundary S_o ($\eta = jmax$), the multi-block interfaces S_{mb} , and the free-surface S_ζ ($\zeta = kmax$ and, for full-domain simulation, $\zeta = 1$). Note that for zero Fr , S_ζ becomes the waterplane S_w .

For the liquid phase and zero Fr the boundary conditions are as follows: on S_b

$$U_\ell = V_\ell = W_\ell = \partial p / \partial n = \partial T / \partial n = 0 \quad (9)$$

where n is normal to the body; on S_i , free-stream values are imposed

$$U_\ell = U_o, \quad V_\ell = W_\ell = p = 0$$

$$T = \begin{cases} 20 & Z > -0.02 \\ 20 + 10(Z + 0.02) & -0.5 \leq Z \leq -0.02 \\ 15.2 & Z < -0.5 \end{cases} \quad (10)$$

on S_e , a zero gradient condition is used

$$\partial(U_\ell, V_\ell, W_\ell, p, T) / \partial X = 0 \quad (11)$$

on S_k

$$\partial(U_\ell, W_\ell, p, T)/\partial Y = V_\ell = 0 \quad (12)$$

on S_w

$$\partial(U_\ell, V_\ell, p, T)/\partial Z = W_\ell = 0 \quad (13)$$

on S_Q

$$U_\ell = U_o, \quad V_\ell = \partial p / \partial r = 0 \quad (14)$$

and W_ℓ is extrapolated; and, on S_{mb} , a parametrically-mapped bilinear-interpolation scheme (9) is used to interpolate all dependent variables between overlapping planes in each block.

For the liquid phase and nonzero Fr , the boundary conditions are similar, except: p is replaced by \hat{p} and on S_{ζ} , exact nonlinear kinematic free-surface conditions

$$\frac{\partial \zeta}{\partial t} + U_\ell \frac{\partial \zeta}{\partial x} + V_\ell \frac{\partial \zeta}{\partial y} - W_\ell = 0 \quad (15)$$

and approximate dynamic free-surface conditions

$$\begin{aligned} \hat{p} &= \frac{\zeta}{Fr^2} \\ \frac{\partial(U_\ell, V_\ell)}{\partial Z} &= 0 \\ \frac{\partial(1-\alpha)W_\ell}{\partial Z} &= -\frac{\partial(1-\alpha)V_\ell}{\partial Y} - \frac{\partial(1-\alpha)U_\ell}{\partial X} \end{aligned} \quad (16)$$

are applied on the actual free-surface, which is determined as part of the solution.

The determination of the boundary conditions for the complete two-fluid model is not a simple problem. Bubble sources and entrainment mechanisms are not well understood. Possible sources include: wave breaking; bow, contact-line, and stern flows; propulsor aeration and cavitation; and ambient sea state. Properly stated boundary conditions must provide the gas flux through the generating surfaces including the gas-volume fraction, bubble-size distribution, and net bubble velocity. Herein, bubbles are introduced on the free surface near the bow modeling breaking-wave sources.

Since a finite-volume method is used for the gas phase, the boundary conditions are formulated in terms of fluxes. The boundary conditions are as follows: on S_b , a zero-flux condition is used; on S_i , the gas velocity equals the liquid velocity and the void fraction is zero; on S_e , a free gas-flow condition is used in which the flux at the boundary is set to the value at the center of the control volume; on S_k , a

zero-flux condition is used; on S_w , free gas-flow condition is used except at the inlet where the flux and void fraction are specified; on S_Q , free gas-flow condition is used; and on S_{mb} , the multi-block interpolation scheme in (9) is used.

2.2 Far Field

Simulation of the far-field consists of modeling the flow, temperature, and micro-bubble fields. The parabolized RANS (PRANS) equations, i.e., (1) and (2) with $\alpha=0$ and $\partial^2 U_{\ell,i} / \partial X^2 = 0$, and $k-\epsilon$ turbulence-model, with modifications to account for production of turbulence due to buoyancy and interaction with the free surface, are solved for the velocity and turbulence fields. Temperature is determined by solving a parabolic version of (5). Given the temperature, ρ is determined from an equation of state. A transport equation for the evolution of the micro-bubble field is derived assuming that the bubbles are sufficiently numerous such that they can be treated as a continuum and that they neither coalesce nor divide.

The specified boundaries of the solution domain are the IDP S_{IDP} , the top boundary S_T , the bottom boundary S_B , the right boundary S_R , and the left boundary S_L . The boundary conditions are as follows: on S_{IDP} , all variables are provided by the near-field solution; on S_R and S_L , k, ϵ are fixed to free-stream values, zero-gradient conditions are used for U, W, p, T, S ; and V is determined from continuity, on S_B , U, k, ϵ, T, S are fixed to free-stream values and zero-gradient conditions are used for V, W, p ; and on S_T , zero-gradient conditions are used for U, V, k, ϵ, T, S , and $W=p=0$.

3 COMPUTATIONAL METHODS

3.1 Near Field

The liquid-phase continuity (1), momentum (2), and energy (5) equations are transformed into nonorthogonal curvilinear coordinates such that the computational domain forms a simple rectangular parallelepiped with equal grid spacing. The transformation is a partial one since it involves the coordinates only and not the velocity components $U_{\ell,i}$. The transformation is accomplished through use of the expression for the divergence and "chain-rule" definitions of the gradient and Laplacian operators which relate the Cartesian coordinates x_i to the nonorthogonal coordinates (ξ, η, ζ) . The equations are reduced to algebraic form through the use of the 12-point finite-analytic method. The pressure equation is derived using the generalized continuity equation in discrete form and a staggered-grid control volume. Herein, prescribed body forces are used in lieu of an interactive solution and are based upon

known thrust and torque coefficients (\tilde{C}_T and K_Q) speed of advance J , and an assumed circulation distribution (9). The overall solution algorithm is based on the pressure-implicit split-operator (PISO) algorithm where the velocity and pressure fields are coupled through a two-step iterative procedure. In the first step, the momentum equations are solved implicitly using a tridiagonal algorithm and the method of lines and the pressure from the previous time step for an intermediate velocity field. The second step consists of sub-iterations. First, the pressure equation is solved implicitly using a tridiagonal algorithm and the method of lines for an intermediate pressure. Second, the momentum equation is solved explicitly using the intermediate pressure for the momentum correction which is then used to update the pressure. For steady flow, convergence of the second step is not required; therefore, only several sub-iterations are used. For stratified flows, the energy equation is solved implicitly using a tridiagonal algorithm and the method of lines and the buoyancy term in the Z-momentum equation is updated each time step. Convergence is determined using the L_2 norms (residuals) of U, V, W, \hat{p}, T , when appropriate, and ζ between time steps (n) and ($n-1$) and should ideally display 3 or 4 orders of magnitude drop for a converged solution.

The gas-phase continuity (3) and momentum (4) equations are solved on the same grid as the liquid-phase equations, and as such, are transformed into the computational domain using the relations outlined above. The equations are reduced to algebraic form using a second-order control-volume upwind approach for the spatial derivatives and a first-order finite difference for the temporal derivative. Due to the homogeneous nature of the continuity equation, the superbee TVD flux limiter, although computationally expensive to evaluate, is used to reduce non-physical oscillations through the prescription of an optimal artificial viscosity. In contrast, the momentum equations are dominated by the source terms due to the interfacial momentum transfer. This effectively eliminates the need for the flux limiter. To maintain diagonal dominance, the source term is partitioned into parts that can/cannot be included into the implicit operator acting on the variable being solved. Both equations are solved implicitly using a tridiagonal algorithm and the method of lines.

The overall solution procedure for a two-phase solution is as follows. First, several hundred iterations of the liquid equations with zero void fraction are performed to establish the liquid flow field. Next, the gas and liquid equations are solved iteratively to establish coupling between the phases. Finally, because the effect of the gas phase in the liquid phase is weak, as was assumed in the derivation

of the two-fluid model, final convergence is achieved through several hundred iterations of the gas equations.

3.2 Far Field

Because the far-field grid is nonuniform in the cross planes and stretched in the axial direction, the PRANS equations are also transformed and solved in the computational domain. The momentum equations are discretized using second-order central differences for the cross-stream directions and Crank-Nicholson differencing with Newton linearization in the axial direction. The algebraic equations form a large sparse matrix which is iteratively solved with a modified conjugate-gradient minimization method. This procedure explicitly couples the pressure into the momentum equation and simultaneously satisfies mass conservation. The $k-\epsilon$ equations are discretized using second-order central differences and solved using an alternating direction implicit (ADI) scheme with under-relaxation and Newton linearization. The micro-bubble transport equation is discretized using second-order finite-volume approach and the QUICK algorithm and solved using an ADI scheme. Finally, the free-surface elevation is determined using a linearized implementation of (15).

4 CONDITIONS AND GRIDS

The computational conditions are for two $Fr = (0.29, 0.39)$ corresponding to medium and high speeds. At full scale, $L=415.3$ ft and $(U_0, Re) = (20 \text{ knots}, 1.3 \times 10^9)$ and $(27 \text{ knots}, 1.7 \times 10^9)$. At model scale, $L=21.28$ ft. (i.e., scale ratio=19.5) and $(U_0, Re) = (4.53 \text{ knots}, 1.49 \times 10^7)$ and $(6.11 \text{ knots}, 2.01 \times 10^7)$. However, note that the two-phase simulations were performed at $Fr=0$ and liquid $Re=4.3 \times 10^6$ and gas $Re=1.7 \times 10^9$. Also, available experimental fluid dynamics (EFD) validation data (11,12,13) is for the free condition, i.e., the model was free to sink and trim where for $Fr=0.29$ $\sigma=0.0264$ and $\tau=-0.0450$ and for $Fr=0.39$ $\sigma=0.0405$ and $\tau=-0.0120$, and for nominal-wake data, includes appendages. The CFD, on the other hand, is for the bare hull in the fixed condition (i.e., $\sigma=0$ and $\tau=0$). For the propelled calculations, the thrust and torque coefficients and speed of advance are based upon balancing the thrust with the model-scale values of resistance. Using the experimental C_T , wake fraction, thrust deduction, and the open-water curves, $\tilde{C}_T=0.610$, $K_Q=0.031$, and $J=0.797$.

4.1 Near-Field

The near-field grid has its inlet, exit, and outer boundaries located at $X=(-.4, 2.0)$ and $R=1$. For the unpropelled cases, the flow is symmetric about the centerplane which allows a half-domain grid to be used. Four such grids were generated: $110 \times 31 \times 22$ (very coarse=75,020); $207 \times 60 \times 40$ (coarse=496,800);

252x60x45 (medium=680,400); and 302x60x50 (fine=906,000). The first grid is used for the $Fr=0$ two-phase simulations and the latter three for single-phase simulations. Since the FF1052 has a single propeller, the propelled cases are asymmetric about the centerplane and, as such, require a full-domain grid (i.e., the unpropelled grid is doubled in the ζ -direction). Propelled calculations were made only on the doubled coarse grid 207x60x79=981,180. For each grid, the first point off the body surface is located in the range $Y^+ < 2$, and the number of points over the bow/dome, afterbody, and wake are (10, 74, 26), (30, 95, 50), (40, 110, 65), and (50, 120, 80), respectively. An overview of the RANS grids is shown in figure 3. The free-surface boundary conditions grid is 460x100 and fixed for all cases.

The time step is 0.1 and the under-relaxation factors for velocity and pressure are 0.2 and 0.02, respectively. On a CRAY C90, CPU-time and memory requirements were 25 hours and 32 megawords, respectively, for the single-phase simulations on the coarse grid.

The two-phase flow cases were run with a gas entrance near the bow simulating a breaking wave. The entrance region is rectangular and extended from $Y/L=3.95 \times 10^{-3}$ to 7.9×10^{-3} and from $X/L=0$ to 2.13×10^{-2} . The gas and liquid velocity were assumed to have a vertical component of -2.7 m/s at the entrance and the gas volume fraction was set to 10%. The bubble radius at the gas entrance was varied in different runs from $R_b=25$ to 200 μm . The lift coefficient C_L was set to 0.1, based on the experience in high-shear flows. The virtual mass coefficient C_{vm} was set to 0.5, its theoretical value for spheres. The turbulent dispersion coefficient is nominally set to $C_{TD}=0.1$ which is taken from experiments in pipe flows with medium size particles. Since small bubbles are of interest here, sensitivity to C_{TD} is investigated through a calculation for $C_{TD}=1.0$ and a single bubble radius $R_b=150\text{mm}$.

4.2 Far-Field

The far-field grid has its inlet, exit, side, and bottom boundaries located at $X=1.75$ and 20.75, $Y=\pm 0.5$, and $Z=-0.5$, respectively. The grid is 200x161x51 (1,642,200), stretched in the axial direction, and regular and rectangular in the cross-stream directions. Data on the upstream boundary is obtained by interpolating mean velocity, turbulent viscosity, temperature, and surface elevation from the RANS solution onto the PRANS grid. Turbulent kinetic energy and dissipation rate, which are required for the far-wake simulation, are computed from the viscosity by assuming a length scale of $\ell_t = 0.01$ and that the kinetic energy is given by:

$$k = \left(\frac{v_t}{C_\mu \ell_t} \right)^{1/2}$$

$$\varepsilon = k^{1/2} \ell_t$$

5 Uncertainty Analysis

Uncertainty analysis follows the ASME guidelines and implementation recommendations provided in (9). Grid design was based on user experience and the Series 60 $C_B=0.6$ zero and non-zero Fr results of (1). Preliminary calculations aided in determining grid-clustering in the bow and sonar dome regions. Due to the flow features associated with the sonar dome, skeg and transom stern, grid number in both ξ (axial) and ζ (girthwise) directions were varied. Minimum Y^+ , η -direction variation, and leading- and trailing-edge clusterings are constant and their effect upon uncertainty was not studied.

Using the residuals, each solution displays iterative convergence by displaying 3 orders-of-magnitude drop and a magnitude less than 10^{-4} . Grid convergence is evaluated for the single-phase unstratified solutions using both integral and pointwise quantities. Detailed grid studies have not yet been performed for the near-field solutions with propeller, stratification, or two-fluid modeling or for the far-field solutions. Integral grid convergence is shown in Table 1 for C_T , C_F , and C_P . The relative change between grids, as indicated by the grid convergence parameter ε , decreases with increasing grid resolution and, in general, the changes in C_T , C_F , and C_P are less than 2% between grids. Pointwise grid convergence, which is shown and discussed in (9), unfortunately is not as conclusive in that it shows that the wall-shear stress on the fine grid contains oscillations and is not fully converged.

Assessment of overall uncertainty is difficult with a limited analysis. Experience has shown that continued iteration beyond what has normally been considered converged (i.e., as described above) leads to a 2% iterative-convergence uncertainty in C_T due to oscillations which are not damped with further iterations. Since calculations for the FF1052 were not extended past 6000 iterations, the Series 60 $C_B=0.6$ value of 2%, which was determined from a 20,000 iteration run, will be assumed valid. Grid convergence, however, is good and shows a 2% uncertainty for a grid-refinement ratio of 1.25 between the medium and fine grids. Summing these components into an overall uncertainty for C_T gives a total of 4%. Note, however, that basing overall uncertainty on integral parameters is very optimistic.

Finally, order-of-accuracy was not calculated and validation, which involves detailed comparisons with EFD validation data, is discussed where appropriate in the following and in detail in (9).

6 RESULTS

6.1 Near Field

In the following, near-field results are first discussed for the baseline flow, i.e., single phase, unstratified, and without propeller. For brevity, however, discussion focuses solely on $Fr=0.39$ results. Discussion of medium-speed single-phase solutions and effects of Fr are provided in (9). Then, modifications to this flow are discussed: stratification, with propeller, and two-phase flow, the latter of which is somewhat preliminary in that it is for $Fr=0$ and has not yet been coupled to the far-wake bubble-transport CFD.

6.1.1 Single phase, unstratified flow, without propeller

Table 1 shows the wetted surface area S , breakdown of resistance, and comparison of C_T to data and C_F to the ITTC friction line. In the table, the wetted surface area below both the DWL and the wave are shown. As discussed in detail in (9), the difference for the below-DWL (or static) area between the different grids and data indicates geometry uncertainty. This creates an imbalance of the axial hydrostatic force of magnitude 1% of C_T . However, the accuracy of the data area is unknown. With the wave, S decreases in comparison to the static area indicating that the area between the wave troughs and DWL is larger than the area between the wave crests and DWL. In comparison to data, C_T is within 10%. This is in contrast to the Series 60 $C_B=0.6$ results which showed negligible geometry error and 2% difference with the data. The total resistance is 48% C_F and 52% C_P . In comparison to the ITTC friction line, C_F ranges from 90% to 105% of C_{F0} , and as such, indicates small and, in some cases, negative form-related frictional resistance. Current research on full-scale Re flows indicates that a new CFD-generated friction line is more appropriate and, if used, results in positive form factors for all cases. The force due to pressure is split into piezometric and hydrostatic components to show their relative magnitude. This shows that the hydrostatic force due to waves, which is created primarily at the bow due to the bow-wave height and axial-projected area, is significant, i.e., 27% of the piezometric component, and effectively reduces C_P magnitude.

Ship wave systems are complex and comprised of divergent and transverse wave systems formed at the bow, shoulder, and stern. The global ship-wave pattern is due to interactions between these systems and can be characterized using parameters based upon the Kelvin-source solution: the angle α_k of the Kelvin boundary ($=19.5^\circ$); the angle θ of the wave crests at the Kelvin boundary ($=55^\circ$); the transverse $\lambda_t (=2\pi Fr^2)$ and divergent $\lambda_d (= \lambda_t \cos \theta)$

wavelengths, wave amplitude A , and velocity of the transverse $U_t (=U_0)$ and divergent $U_d (=U_0 \cos \theta)$ waves. Although useful for providing a gross far-field description, the Kelvin solution is obviously an over simplification for real ships, especially in the near field. Combatant geometries display many local complexities (e.g., spray, breaking and spilling waves, free-surface turbulence, transom flow and "rooster tail") which interact to create a wave pattern which is markedly different from the Kelvin model. Further complicating prediction are the differences between full- and model-scale flows. Full-scale flows display, in comparison to model scale, increased breaking, air entrainment, spray formation, and free-surface turbulence. Also, there are additional full-scale complexities such as sea state, density stratification, and suspended particulates and surfactants.

Figure 4 shows a comparison of the wave profile to data. As previously mentioned, the model was free to sink and trim whereas the simulation was performed in the fixed condition. The effects of sinkage and trim are significant, therefore, to compare to data, the solutions were corrected by translating and rotating the free surface by the amount of sinkage and trim in the experiments. After making the corrections, the level of agreement is similar to the Series 60 $C_B=0.6$ and, in general, the solutions show both correct amplitude and phase¹. Despite agreement with the data, some details are lacking: the location of the bow crest is slightly displaced aftward; the wave height is under predicted at the stern; and similar to the Series 60 $C_B=0.6$, the wave height upstream of the bow-wave crest is under predicted.

Figures 5(a) and (b) show wave-elevation contours which display patterns described earlier: divergent and transverse wave systems and a rapid rise from the transom to a "rooster tail", which in this case happens to be double-humped at $X/L=1.09$. Using the axial wave slopes, (α_k, θ) are graphically estimated to be 14° and 15° . These values are greater than and less than the Kelvin values, respectively, and indicate that the diverging waves travel nearly in the direction of the ship. With θ , the diverging wavelength may be estimated from $\lambda_d = \lambda_t \cos^2 \theta$. Given the small θ , λ_d is nearly the same as λ_t . Finally, data for combatant model 5415 confirms the results for the FF1052, particularly the transom flow, however, the FF1052 solution does not resolve the wave breaking and free-surface turbulence shown in the data.

Figure 6 shows details of the flow field through axial velocity (U) contours, cross-plane (V - W) vectors, piezometric pressure (\hat{p}) contours, and

¹ Note that for the Series 60 $C_B=0.6$, both EFD and CFD were conducted for zero sinkage and trim.

temperature (T) contours for both unstratified (left side) and stratified (right side) flow at $X=0.05, 0.40, 0.95$ (propeller plane), and 1.75 (IDP). For the unstratified flow, since the temperature and velocity fields are uncoupled, the T contours simply are an indication of the ambient stratification. At $X=0.05$, the U contours show a reduced magnitude near the hull/free-surface juncture due to the bow wave. The flow accelerates around the sonar dome indicating increased magnitude and is insensitive to wave effects. The boundary layer over the hull and sonar dome is thin. The vectors show the displacement effects of the hull and the upward flow near the free surface due to the bow wave. The \hat{p} contours correlate with the wave elevation and dome flow, i.e., high and low pressures, respectively. At $X=0.4$, the U contours show a thickening of the boundary layer which interacts with the large sonar-dome wake. The vectors clearly show a downward flow, an enlarged and outwardly displaced sonar-dome vortex, and reduced free-surface effects. The \hat{p} contours indicate small magnitudes with the largest variations near wave troughs between $0.05 < Y < 0.10$ on the free surface. At $X=0.95$, which corresponds to the propeller plane, the U contours show a hull boundary layer with a minimum/maximum boundary layer thickness of $\delta=0.015/0.022$ where the former occurs near the free surface and the latter at mid-girth. For comparison, the thickness of a flat plate boundary layer at the corresponding Re_τ is $\delta=0.013$. The larger hull δ is consistent with U_τ at this location: it is smaller than the zero pressure-gradient flat-plate value. Also, U contours show a reduced sonar-dome wake with a deficit of approximately 0.1, and the appearance of the skeg wake along the centerplane. Since the sonar-dome wake is large and, therefore, will have significant influence upon the propeller inflow, the wake rate-of-recovery is qualitatively checked through comparison to an axisymmetric body. It is known that beyond 5 body lengths downstream for a 6:1 prolate spheroid that the wake achieves similarity and the wake-deficit recovery follows the well-known 2/3-power law relationship, wake deficit $\propto x^{-2/3}$. At $6.5L$ downstream, which corresponds to the distance between the dome trailing edge and the propeller plane, the spheroid wake deficit is 0.1, which is the same as the sonar-dome wake deficit. Although the 2/3-power law proportionality constants are a function of geometry (i.e., the dome length/diameter is closer to 4:1), this provides an estimate of the recovery. The vectors indicate a general upward flow as the body contracts and the pressure contours indicate very small waves and gradients in this region. Finally, at $X=1.75$, which corresponds to the far-wake IDP the axial-velocity contours show the overall wake recovery and the persistence of the dome wake. The vectors indicate

small cross-plane flow towards the centerplane and the pressure contours show correspondingly small pressure-gradient and wave magnitudes.

Comparisons are made to the nominal-wake data which was obtained for a hull including appendages, i.e., propeller shaft and struts, whereas, as previously mentioned, the CFD was for the bare hull. Figure 6(d), which was discussed above, showed the details of the flow at the propeller plane. Figure 8 shows the axial-, tangential-, and radial-velocity components in a local propeller coordinate system [i.e., the propeller is centered at $(X_0, Y_0, Z_0) = (0.9488, 0.0, -0.035516)$, has a radius $R_p=0.01806$, and is mounted on a shaft with an angle of 4.3° downward from the X -axis] at three different radii in the propeller disk including comparisons to data. For each radii, it can be seen that the axial component has small circumferential variation and, on average, is equal to 0.9 and 1.0 for the CFD and data, respectively. In addition, there are other differences in comparison to the data. The CFD shows a large skeg wake (i.e., at $\theta=0$ and 2π ,) which is not in the data, and, as expected, the data shows the strut wakes (i.e., at $\theta=\pi/4$ and $7\pi/8$). In contrast to the axial component, the tangential and radial components show a nearly pure first-harmonic response and good agreement with the data for both amplitude and phase at all three radii.

6.1.2 Stratification

Calculations of the near field when thermal stratification is included were performed for the temperature profile (10) which consists of a layer of warm, uniform temperature fluid over an increasingly cold mass. The result is a stable thermal structure with the ambient gradient just under the ship keel. The right-hand side of the plots in Figure 6 show the near-field stratified solution and indicate that the velocity and pressure fields are relatively unaffected by the presence of stratification. This is not a surprising result since the time scale of the stratified field ($t'=28$, where $t'=TU_0/L$ and T is the Brunt-Vaisalla period) is considerably longer than the ship passage time scale ($=1$). This point is further strengthened by noting that the differences between the resistance, wave field, and nominal wake for the stratified vs. unstratified solutions are very small.

On the other hand, the thermal field is strongly altered by the passage of the ship and can be seen in the temperature contours shown in Figure 6. The influence takes the form of a strong upwelling in the near wake in which deep colder water is brought to the surface in a plume at the centerline. Because it is dependent on details of the cross flow in the wake, this feature will vary considerably with ship geometry and propulsor type and operating conditions. While not presented, far wake calculation show that the plume subsides, creating internal waves propagating

within the thermal gradient. In doing so, it creates a set of vortices on either side of the wake center which serve to amplify the lobed appearance.

6.1.3 With Propeller

The prescribed body forces used herein are axisymmetric distributions which are simple functions of \tilde{C}_T , K_Q , and J . As discussed, the parameters are based upon matching \tilde{C}_T to the EFD C_T and, as such, does not correspond to a self-propelled condition for the CFD. It should be noted that even the simplified approach used herein, as opposed to the more rigorous approach in (2), is amenable to interactive calculations. By setting thrust equal to the CFD resistance and calculating speed of advance from the Taylor-wake fraction, "updated" values of \tilde{C}_T , K_Q and J can then be determined from the open-water curves.

Table 1 shows that the total resistance coefficient C_T increases from 5.15×10^{-3} to 5.25×10^{-3} . If thrust is assumed to be equal to C_T , the thrust deduction factor is 0.02. This is significantly smaller than data values of 0.07 to 0.105. Using the nominal-wake analysis to determine speed of advance V_A , the thrust coefficient when nondimensionalized in the same fashion as the resistance coefficients is 4.36×10^{-3} . This is only 85% of the bare-hull resistance and indicates an under-propelled condition.

Figure 4 also shows the wave profiles on both sides of the hull for the propelled solution. The difference between starboard and port sides is very small. The difference between the unpropelled and propelled solutions is also very small up to about the propeller plane. Fore and aft of this point, the low and high pressure associated with the propeller slightly decreases and increases the wave-profile slope, respectively.

Figure 5(c) shows a detailed view of the wave-elevation contours in the stern region and shows that the propeller has a large effect aft of the propeller and in the transom wake, and in general, affects the overall stern wave pattern. The contours between $X/L=0.95$ and 1.0 indicate the increased wave-profile slope, and in the wake, the close contour spacing indicates a single-hump rooster tail with a dramatically increased wave steepness and peak magnitude.

Figure 7 shows details of the flow field. The effect of the propeller is limited to about one propeller diameter upstream. At the propeller plane $X/L=0.95$, the propeller slipstream and swirl is clearly shown in the U and P contours and cross-plane vectors. The temperature field at this point, however, is essentially unchanged from that shown in Figure 6(d). At $X/L=1.1$, which corresponds to the location of maximum wave elevation in the wake, it is most interesting to note the high-pressure region between

the center of propeller swirl and the free surface and the corresponding increase, in comparison to the unpropelled case, in wave height. At $X/L=1.75$, the propeller wake is still clearly seen and, interestingly the perturbation of the thermal field is smaller than in the unpropelled case in which colder water reaches the surface and the thermal scar is broader. This is due to the propeller swirl which effectively mixes and transports the thermal energy away from the surface. Obviously, this result will depend on temperature profile, its relationship to the propeller location, and overall propulsor geometry.

Finally, Figure 8 shows the axial-, radial-, and tangential-components of the total wake in the propeller disk. The axial velocity shows the accelerated flow associated with the slipstream and the radial velocity remains essentially unchanged from the nominal wake distribution. Interestingly, the tangential distribution has exactly the same distribution as the nominal wake but is simply offset by an amount equal to the swirl induced by the propeller.

6.1.4 Two-Phase Flow

Bubble size plays a major role in the volume-fraction distribution. This is expected since the drag-related term of (4) is directly related to the inverse of the bubble radius and also to the bubble Re through the drag coefficient. Figure 9 shows the streamwise evolution of the bubble field. Void-fraction contours for bubble radius $R_b=25\mu\text{m}$ (left) and $150\mu\text{m}$ (right) show that the larger the bubble radius the larger the peak in volume fraction at the hull of the ship. This is due to two effects which attract the bubbles towards the hull, gravity and lift, the latter of which acts towards the hull over the entire boundary layer. Also, from the shape of the contours, it is clear that in the wake, the larger bubbles get transported more easily to the surface.

Figure 10 shows the void fraction at $X/L=0.95$ for a range of bubble radii along a line which cuts perpendicular to the hull and passes through the maximum value. The bubble accumulation below the hull is largest for large bubbles and decreases for small bubbles.

As previously mentioned, the validity of using the turbulent dispersion coefficient $C_{TD}=0.1$, which was taken from pipe flows with medium-sized particles, is unknown given the application to small bubbles. Figure 10 shows that by increasing C_{TD} to 1.0, the peak at the wall disappears and the gradient is reduced resulting in a more uniform distribution. Therefore, it appears that correct determination of C_{TD} is important because the void-fraction distribution is sensitive to its magnitude and because it is the only term in (4) that avoids unphysical accumulation of gas and the situation of gas-phase streamlines ending at the hull surface. Also, the validity of neglecting

important forces in high void-fraction or void-fraction-gradient regions such as bubble-bubble collisions, induced shear stress, and non-uniform bubble distribution, appears to be dependent upon the value of C_{TD} which is used.

6.2 Far Field

Far-field simulations were performed using both the unstratified and stratified propelled RANS solutions to prescribe the IDP. However, in the following, the discussion is only for the stratified results. Figure 11 shows axial-velocity (U), axial-vorticity (ω_x), and temperature contours (T) at the $X/L=1.75, 5.44$ and 11.15 cross planes. These show the gradual decay of both velocity and vorticity with distance. However, both the sonar-dome wake and propeller swirl remain visible at 11.15 and, in fact, they do so all the way to the exit plane. A small secondary vortex forms on the other side of the centerline from the principal swirl structure which has migrated a small distance. One feature that is missing (as compared to qualitative observations of full scale data) is a strong near surface outward velocity component. One of the goals of applying RANS solvers to upstream condition estimation was to determine if this feature is due to bulk flow phenomena or to turbulence/free-surface interaction. It is likely to be due to the latter. The strong, though compact, propeller swirl causes the axial velocity and turbulent energy fields to form two maxima at the surface. This agrees qualitatively with aerial photographs of the far wake. The deep axial velocity contours seen in the figure are remnants of the decaying surface wave induced axial velocities. They are present, but not too small to be discernible in the cross flow velocity plots. One may note that the wake has net momentum defect. This is due, as previously mentioned, to using \tilde{C}_T , K_Q , and J , which correspond to an under-propelled condition. Use of interactively-obtained propulsion parameters is expected to produce stronger axial and swirling velocities. The thermal field evolves such that a persistent cold water region near the centerline at the surface remains through 10 ship lengths and in fact considerably further. At 10 ship lengths, internal waves begin to form from the displaced cold water. Outer boundary conditions on temperature in the model are imperfect wave absorbers and so there is some solution contamination. The error however remains local to the boundaries for the time scales of our interest. Finally, comparison with the semi-empirical IDP generation method used previously shows that the RANS computed momentum defect wake is narrower and shallower and therefore the defect axial velocities are larger. The general ratios between wake width and depth however, are very similar between the two estimates. Since the semi-empirical method is based on satisfying global

constraints, such as axial and circumferential momentum, the RANS propeller effects are weaker than expected for the reasons noted above. This also means that turbulent kinetic energy in the propeller jet is smaller than estimated by the semi-empirical method.

7 CONCLUDING REMARKS

A CFD approach for simulating the near and far field of a Naval combatant in a thermally-stratified two-phase flow has been presented. This approach is based upon, for the near field, coupling a single-phase RANS method with both the energy equation, to account for transport of thermal energy and creation of buoyancy forces, and a two-fluid model, to account for the transport of monodisperse microbubbles and their interaction with the liquid phase. Far-field solution is based upon PRANS equations with the IDP prescribed by the near-field solution.

An extensive number of conditions were simulated: model-scale Re ; medium and high speeds; with and without thermal stratification; with and without propeller; and two-fluid calculations over a range of bubble sizes. The two-fluid near-field results, however, are more preliminary in that they are only for zero Fr and have not been coupled to the far-field through the IDP. For the single-phase, unstratified, and unpropelled case, a detailed uncertainty analysis following ASME guidelines was performed.

The single-phase results show that both global and detailed features of Naval combatant flows can be accurately predicted, particularly the total resistance, wave profiles, and nominal wake. With regard to interaction with the ambient temperature field, the ship flow field transports cold water to the surface creating a thermal scar, which is an excellent tracer. However, the thermal field has small influence on the flow. The effect of the propeller is qualitative shown by the slipstream, swirl, and increased wave height in the near wake. Also, it is shown that the propeller moderately affects the thermal field, such that the scar on the free surface is reduced in comparison to the unpropelled calculation. The two-phase results show that void-fraction introduced near the bow, as a model of breaking-wave entrained bubbles, accumulates in the boundary layer and creates large void-fraction gradients near the wall, where the velocity gradients are large and is strongly influenced by bubble size. In the wake, the bubbles are transported as two streaks, which in general, qualitatively agree with observations of wake white water. The far-field simulations successfully used the near-field results as the IDP and showed that the dome wake, propeller swirl, and cold-water region near the centerline persist 10 ship lengths downstream.

In conclusion, the prognosis of the approach is optimistic, however, there are many uncertainties

which must be addressed. By using systematic verification analysis, numerical uncertainties can be made relatively small. However, improvement in numerics is required, particularly, efficiency and accuracy. Modeling uncertainties are daunting and their estimation requires EFD validation data which, unfortunately, is very difficult to obtain. For single-phase flow, modeling uncertainty is due to geometry, turbulence, wave-breaking, and free-surface boundary conditions. In contrast, there are many areas of concern for two-phase flow. The accumulation of bubbles in the boundary layer suggests that other possible mechanisms of interfacial momentum and mass transfer may be important in this region, such as bubble-bubble collision and interfacial pressure, Einstein forces, dissolution, and breakup. Some of these models will require incorporation of an approach to handle polydisperse bubble populations: a formidable computational challenge.

To accurately predict bubbly-wake signatures, much future work remains. For the near-field RANS, further improvements in both numerics and models will be made in conjunction with work on more complex single-phase flows, e.g., unsteady flow. Also, capability to resolve appendages, calculate sinkage and trim, and employ more sophisticated propeller-hull interaction methods must be incorporated. The lack of strong thermal-hydrodynamic interaction suggests that a variety of common and in-situ temperature profiles be studied. In certain environments, salinity fields may need to be included in the transport and density calculations. Finally, work on two-fluid modeling will focus on extending the method for nonzero Fr , development of a coupled multigroup scheme to calculate bubble-size distribution, including bubble breakup and dissolution, and inclusion of propulsor effects on the bubble size distribution.

ACKNOWLEDGMENTS

This research was sponsored by Office of Naval Research Grants N00014-93-1-0052 (Iowa), N00014-96-AF00002 (NSWC CSS), and N00014-91-J-1271 (RPI) under the administration of Dr. E.P. Rood. The computations were performed on the Naval Oceanographic Office, NASA Numerical Aerodynamic Simulation Program, and San Diego Supercomputer Center supercomputers. The assistance of Dr. Rood and Ms. Margo Frommeyer is especially acknowledged.

REFERENCES

1. Tahara, Y. and Stern, F., "A Large-Domain Approach for Calculating Ship Boundary Layers and Wakes for Nonzero Froude Number", Proc. of the CFD Workshop, Tokyo, March, 1994; also, to appear Journal of Computational Physics.
2. Stern, F., Kim, H., Zhang, Z., Toda, Y., Kerwin, J. and Jessup, S., "Computation of Viscous Flow around Propeller-Body Configurations: Series 60 $C_B=0.6$ Ship Model, Journal of Ship Research, Vol. 38, No. 2, June, 1994
3. Bonetto, F., Drew, D., and Lahey, R.T., "A Numerical Simulation of a Turbulent Two-Phase Jet Using a Multidimensional Two-Fluid Model," in review, International Journal of Numerical Methods in Fluids.
4. Carrica, P., Bonetto, F., Drew, D., and Lahey, R.T., "Gas-Liquid Two-Phase Flow Around a Ship," in preparation, International Journal of Multiphase Flow.
5. Lahey, R.T., and Drew, D.A., "The Current State-of-the-Art in Modeling of Vapor/Liquid Two-Phase Flows," ASME paper 90-WA/HT-13, 1990.
6. Smith, R.W., and Hyman, M., "Convective-Diffusive Bubble Transport in Ship Wakes," NCSCTN 857-87, 1987.
7. Hyman, M., "Modeling Ship Microbubble Wakes," CSS/TR-94/39, 1994.
8. Hyman, M., Influence of Temperature Stratification On The Development of Surface Ship Micro-Bubble Wakes," NCSCTN 1017-90, 1990.
9. Stern, F., Paterson, E., and Tahara, Y., "CFDSHIP-IOWA: Computational Fluid Dynamics Method for Surface-Ship Boundary Layers, Wakes, and Wave Fields," IIHR Report 666, Iowa City, Iowa, February 1996.
10. Lopez de Bertodano, M., "Turbulent Bubbly Two-Phase Flow in a Triangular Duct," Ph.D. Thesis, Rensselaer Polytechnic Institute, Troy, NY, 1992.
11. West, E.E., "Reisittance Characteristics and Appendage Orientation Data for DE 1052 Represented by Model 4989," DTNSRDC/SPD-C-011_H01, Unclassified 3/13/81, September 1964.
12. Day, W.G.Jr. and Hurwitz, R.B., "Propeller-Disk Wake Survey Data for Model 4989 Representing the FF 1052-Class Ship in a Turn and with a Bass Dynamometer Boat," DTNSRDC/SPD-0011-21, December 1980.
13. Ratcliffe, T., and Lindenmuth, W.T., "Kelvin-Wake Measurements Obtained on Five Surface Ship Models," DTRC-89/038, 1990.

Conditions	Fr=0.29 Re=14,900,000		Fr=0.39 Re=20,100,000			Fr=0.39 w/ prop
Grid	207x60x40	302x60x50	207x60x40	252x60x45	302x60x50	207x60x40
Surface Area (S/L*L)						
calculation	0.117909	0.117304	0.117313	0.117413	0.117540	0.116420
calc. (DWL)	0.117609	0.117706	0.117609	0.117695	0.117706	0.117609
data (DWL)	0.118166	0.118166	0.118166	0.118166	0.118166	0.118166
% diff	-0.47%	-0.39%	-0.47%	-0.40%	-0.39%	-0.47%
Total Resistance (CTx1000)						
calculation	4.57	4.59	5.15	5.10	5.07	5.25
ε	-0.5%		0.9%	0.6%		
data	4.27	4.27	4.61	4.61	4.61	
% diff	7.0%	7.5%	11.6%	10.6%	10.0%	
Frictional Resistance (CFx1000)						
calculation	2.95	2.83	2.55	2.46	2.41	2.7
ε	4%		4%	2%		
ITTC line	2.80	2.80	2.67	2.67	2.67	2.67
% diff	5%	1%	-4%	-8%	-10%	1%
Pressure Resistance (CPx1000)						
calculation	1.62	1.76	2.60	2.64	2.66	2.56
piezometric (p hat)	2.22	2.40	3.27	3.35	3.42	3.17
hydrostatic (z/Fr*Fr)	-0.60	-0.64	-0.678	-0.71	-0.759	-0.617
ε	-8%		-2%	-1%		

Table 1. Resistance and grid convergence

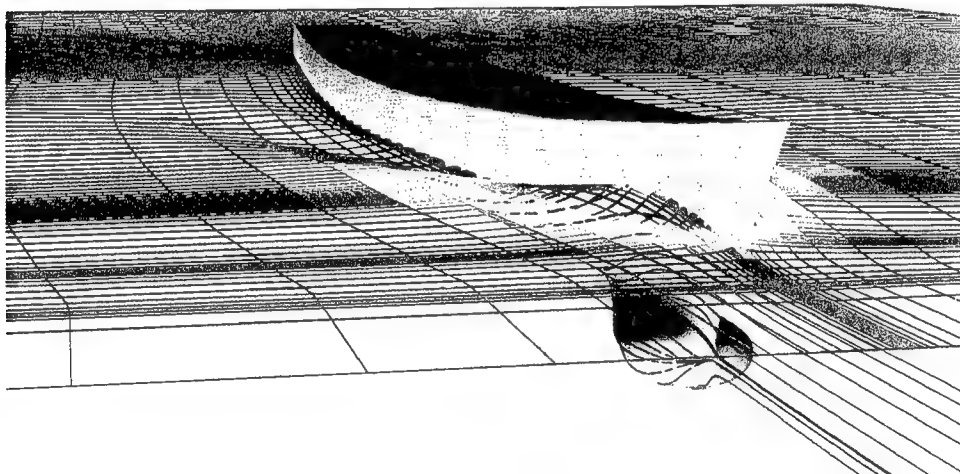


Figure 1. Naval combatant FF1052: free-surface conforming grid colored by wave elevation and surface streamlines

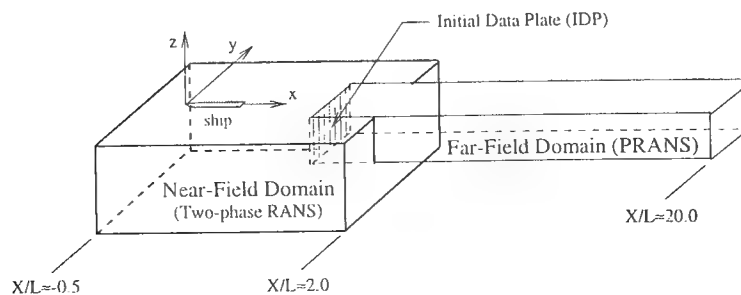
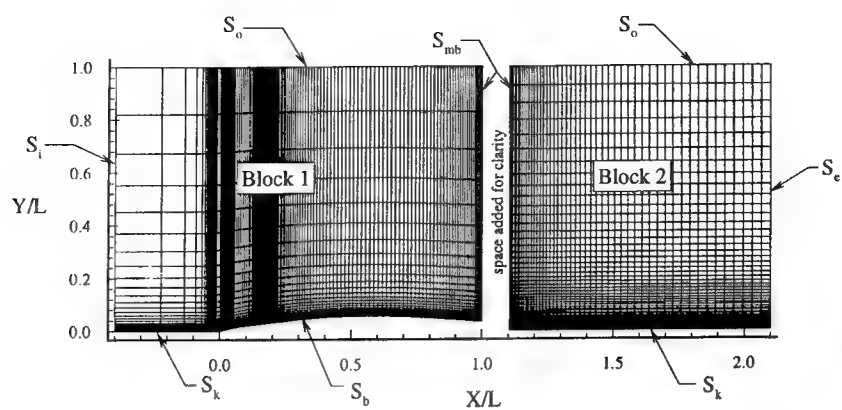
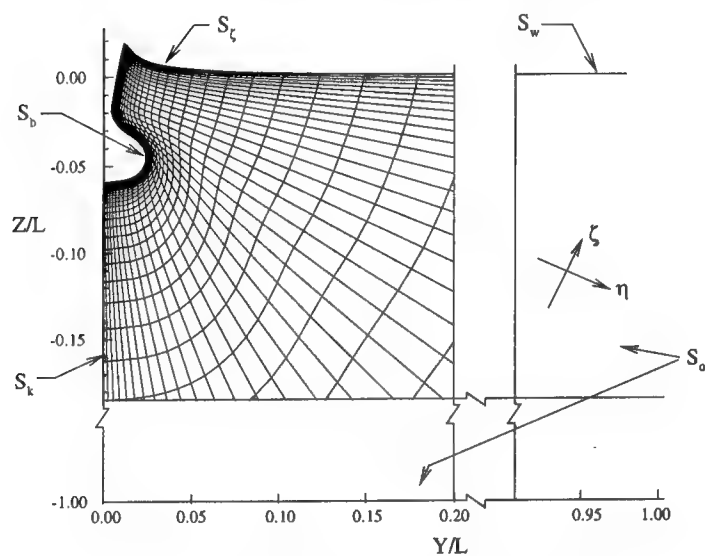


Figure 2. Relationship between near- and far-field domains.



(a) longitudinal free-surface plane



(b) block 1 crossplane at $x/L = 0.05$

Figure 3. Near-field multi-block RANS grid system.

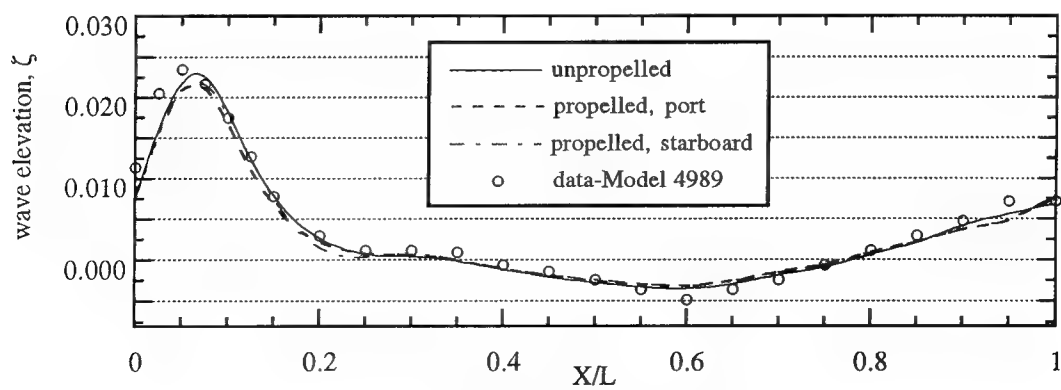


Figure 4. Wave profiles.

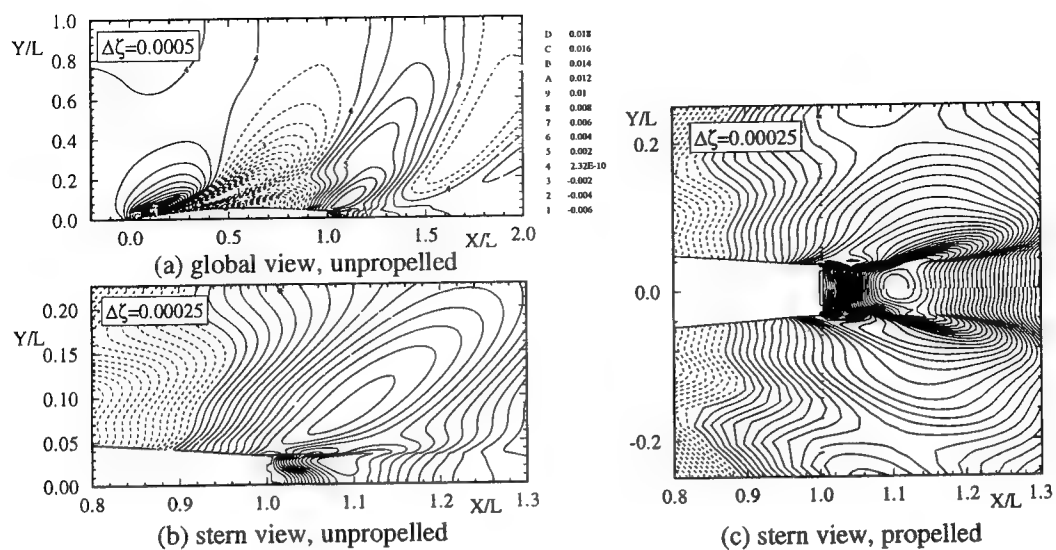


Figure 5. Wave-elevation contours.

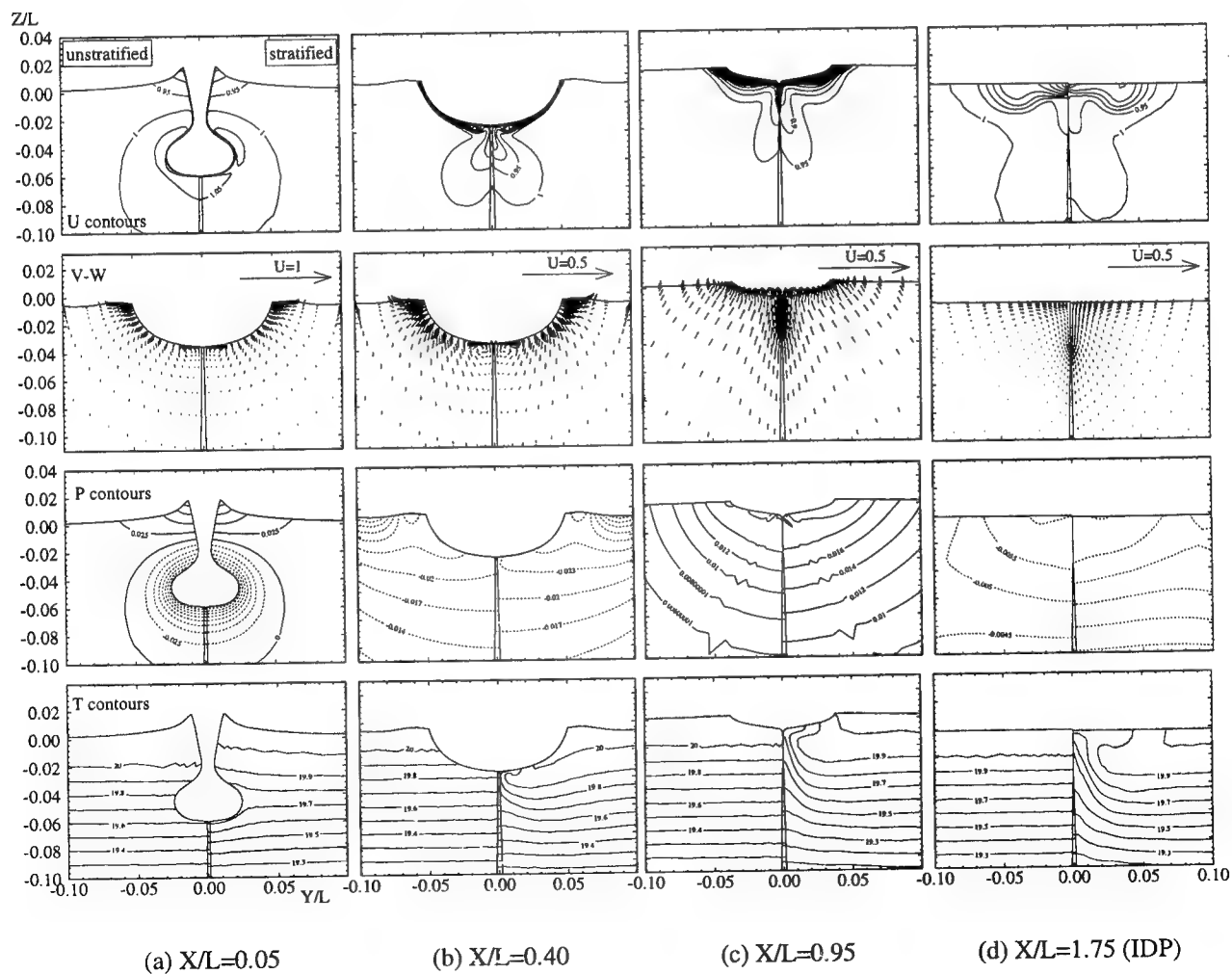


Figure 6. Axial velocity, cross-plane flow, pressure, and temperature for unstratified (left) and stratified (right) flows.

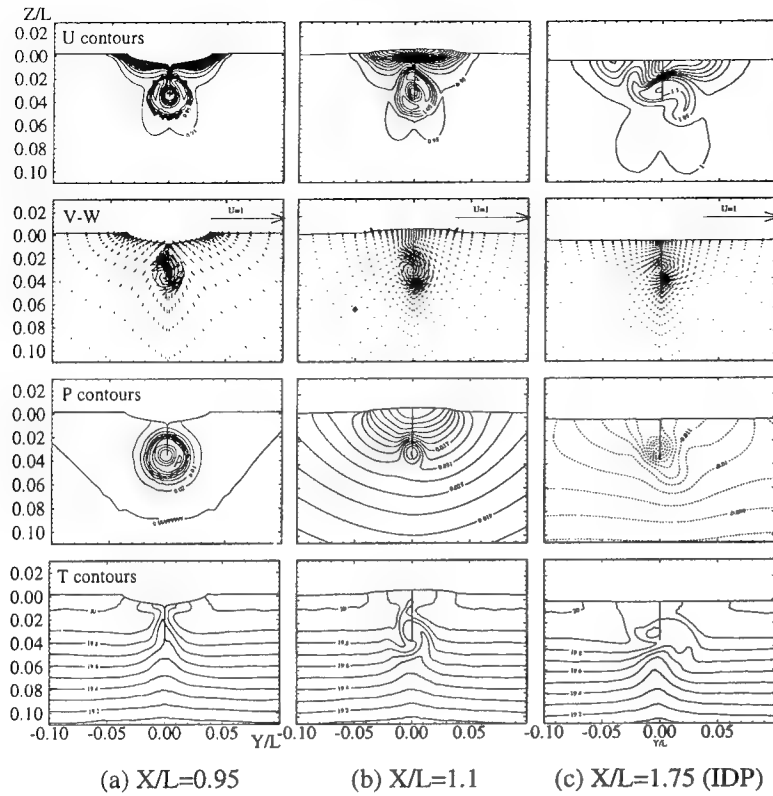


Figure 7. Axial velocity, cross-plane flow, pressure, and temperature with body-force propeller.

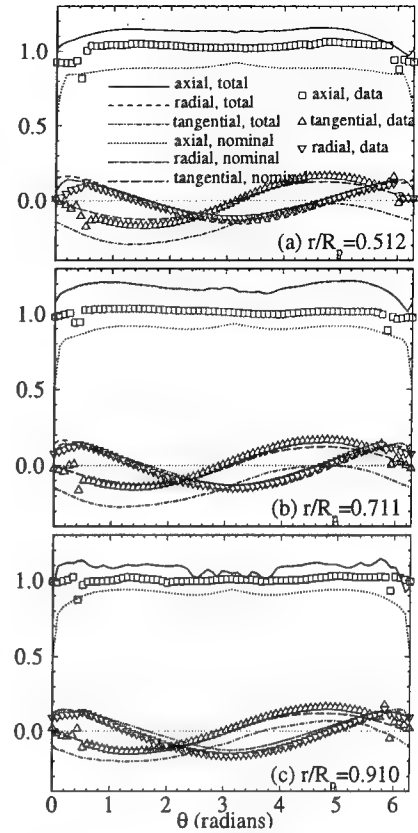


Figure 8. Nominal- and total-wake velocity profiles.

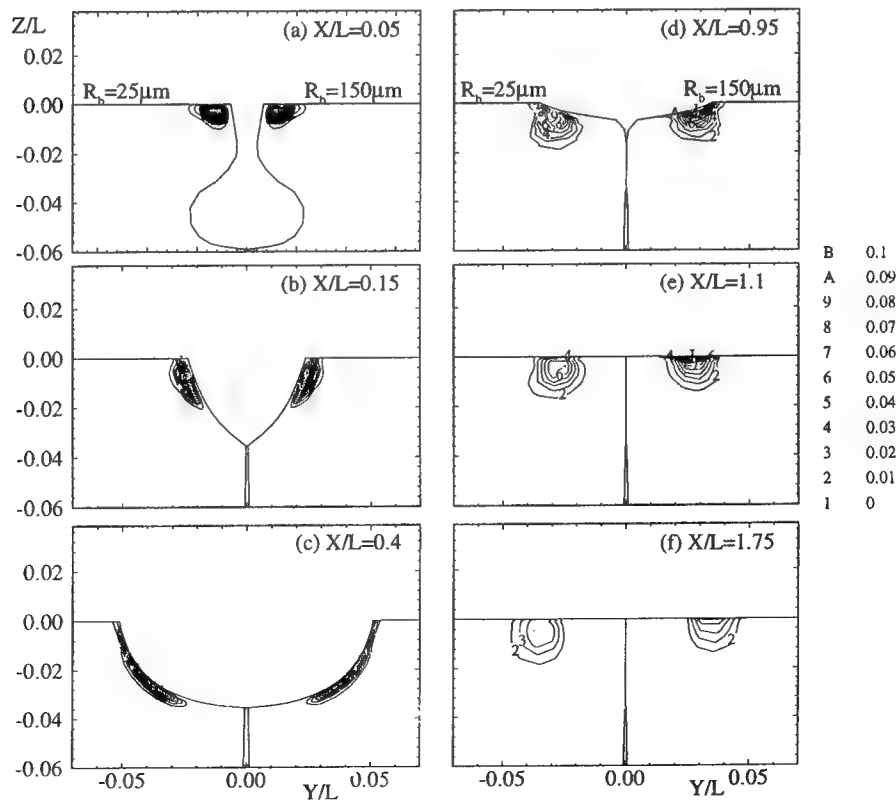


Figure 9. Void-fraction contours.

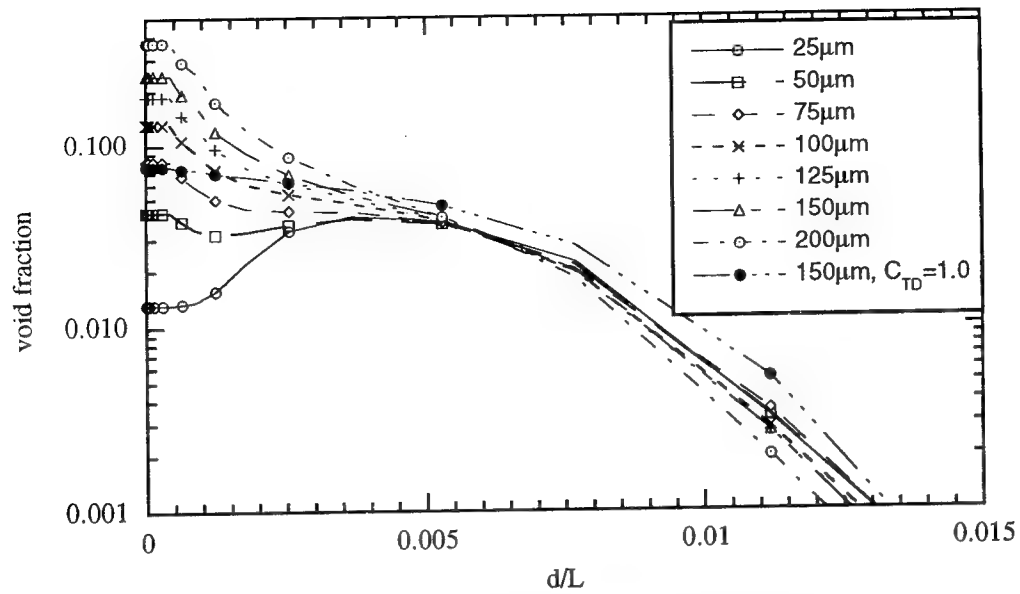


Figure 10. Void fraction as a function of bubble radius vs. distance perpendicular to hull at $X/L=0.95$.

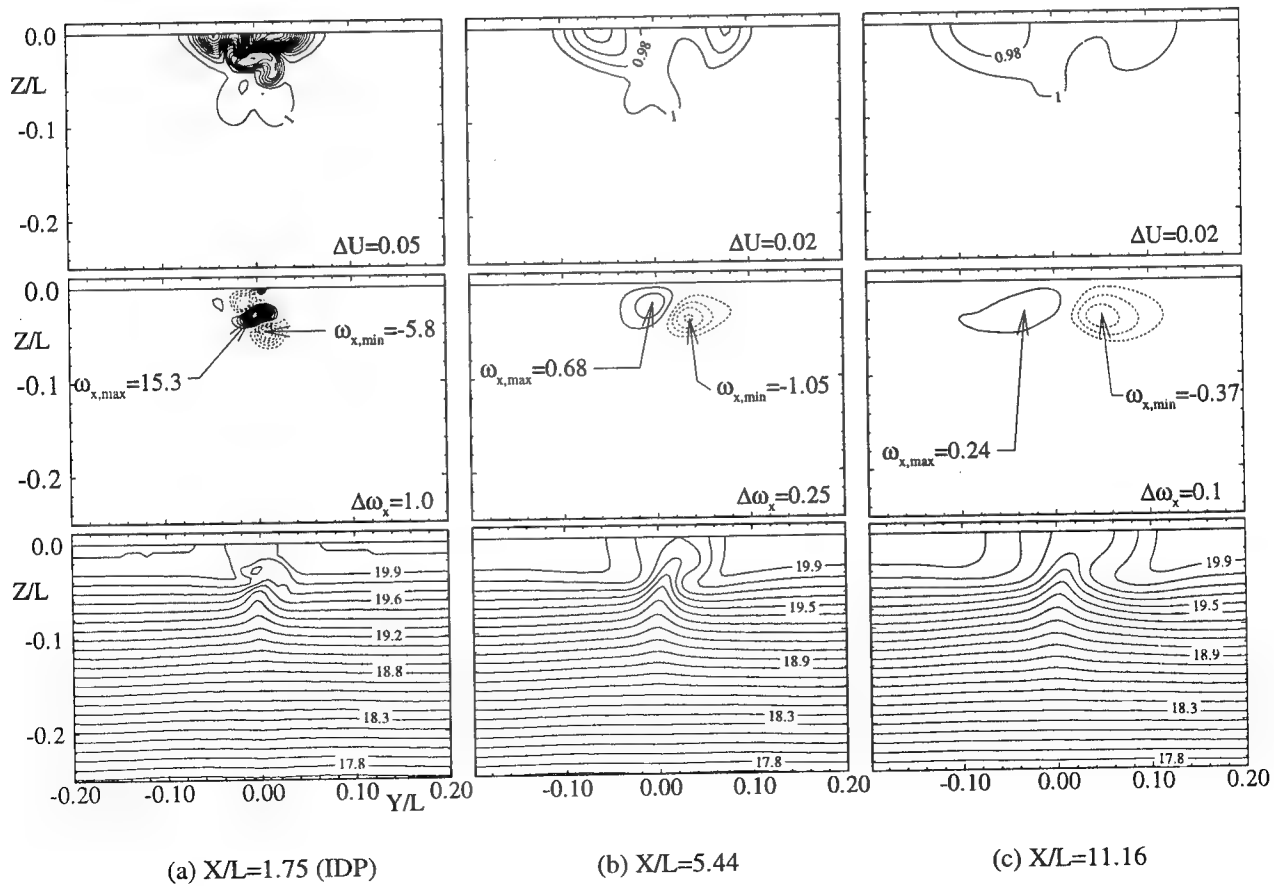


Figure 11. Far-wake contours of axial velocity, vorticity, and temperature: propelled and stratified.

Water Entry of Arbitrary Two-Dimensional Sections with and Without Flow Separation

R. Zhao,¹ O. Faltinsen,² J. Aarsnes¹

(¹MARINTEK, ²Norwegian University of Science and Technology, Norway)

1 ABSTRACT

Two different theoretical methods for predicting slamming loads on two-dimensional sections have been developed. One of the methods is a fully nonlinear numerical simulation, that includes flow separation from knuckles or fixed separation points of a body with continuously curved surface. The other method is an extension of Wagner's solution(1932). It is an approximate solution and does not include flow separation. The numerical methods are validated by comparing with new experimental results from drop tests of ship cross-sections.

2 INTRODUCTION

Many experimental, analytical and numerical studies of slamming loads have been reported since the pioneering works by von Karman(1929) and Wagner(1932). A strip theory approach is common to use in the analyses of slamming loads on ship hull sections. This is also implicitly assumed in this paper. Three-dimensional flow effects are present in reality. However the many challenging physical and numerical problems are obviously easier to study properly by a two-dimensional method. This will also give guidance on how to treat the three-dimensional flow properly during water entry. Two different two-dimensional methods are presented together with new experimental results. One of the methods represents a fully nonlinear solution. This is a further development of the work by Zhao and Faltinsen(1993). They studied slamming loads on two-dimensional symmetrical sections without the effect of flow separation. The problem was solved as an initial value problem. The exact body boundary condition and fully nonlinear free-surface conditions without gravity were used in the numerical analysis. A local jet flow was introduced near the intersections between the body and

the free-surface. The method was verified by Zhao and Faltinsen(1993) by comparing with analytical and asymptotic solutions for water entry of symmetrical wedges with deadrise angles from 4° to 81° . Faltinsen(1993) applied the method with good results for a bow flare section. The numerical method of Zhao and Faltinsen(1993) is in this paper extended to general asymmetric bodies. Flow separation from knuckles and bodies with continuously curved surfaces has been included. When separation occurs from a continuously curved surface, the separation points are determined empirically. The separation mechanism has to be better understood in this case. Viscous boundary layer effects are not believed to be important. Some insight can be gained by studying solutions for steady cavity flow past cylinders.

An approximate solution based on a generalization of Wagner's solution(1932) is also presented. The effect of flow separation is not included. The problem is solved numerically in the time domain by using Green's second identity for each time step. The body boundary condition is satisfied exactly. The piled-up water around the intersection between the free surface and the body surface is calculated by a similar approach as Wagner(1932) used. The dynamic free-surface condition is zero velocity potential on horizontal lines that go through the intersection points between the free surface and body surface. The approximate solution has been compared with the similarity solution for wedges and the fully nonlinear numerical solution. Satisfactory prediction of the maximum pressure and total slamming loads are documented. This approximate solution is fast to calculate and more easy to use for non-experienced users than the complete nonlinear numerical solution.

The numerical methods are validated by comparing with new drop test experiments of a wedge and a bow flare sec-

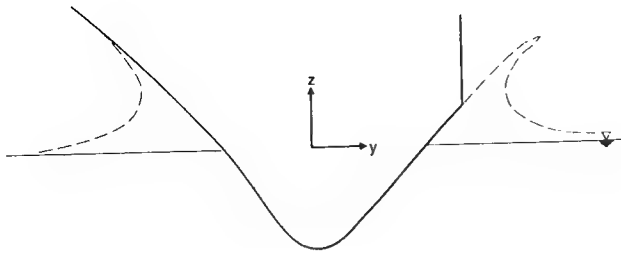


Figure 1: The (y,z) coordinate system, and the water entry of a body with flow separation on the right side and no separation on the left side.

tion. Each section has knuckles. The pressure and the total slamming forces are measured for the whole period of water entry. Systematic comparisons between the numerical and experimental results have been carried out. The three-dimensional flow effects in the drop tests have been theoretically estimated. The maximum estimated three-dimensional effect represents a 20% reduction of the two-dimensional results. This method of estimating three-dimensional flow effects can in a qualitative way be used to analyze an error source in strip theory predictions of bow flare slamming. It is shown that the common method of estimating bow flare impact forces based on fluid momentum conservation and infinite frequency added mass coefficients as a function of submergence relative to undisturbed free surface, gives too low maximum force and wrong time history of the force.

3 FULLY NONLINEAR SOLUTION

A general two-dimensional asymmetric body with time dependent vertical downwards velocity, is forced through initially calm water. The problem is solved as an initial value problem. Since viscous effects are neglected, the problem can be solved by potential theory. The effects of compressibility of the water and air cushions between the water and the structure are neglected. Gravity is not included in the analysis. This has a negligible effect in the initial phase of water entry of a blunt body, but will be more important at a later stage after flow separation has occurred. Hydroelastic effects are disregarded. This can be significant when the slamming loads are large, like for wetdeck slamming (Faltinsen(1996), Kvålsvold et al.(1995)). Cavitation and ventilation can also occur in the latter case.

The reference coordinate system yz is fixed in space. The origin of the coordinate system is in the plane of the undisturbed water surface. The z-axis is positive upwards (see figure 1). The velocity potential ϕ satisfies the Laplace

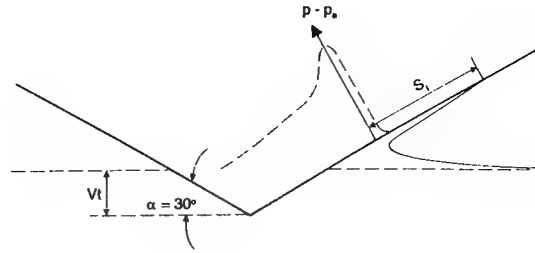


Figure 2: The free-surface elevation and pressure(p) distribution on the body surface during water entry of a symmetric wedge with constant velocity V. Deadrise angle $\alpha = 30^\circ$. p_a is atmospheric pressure. The results are based on a similarity solution (Zhao and Faltinsen(1993)).

equation

$$\frac{\partial^2 \phi}{\partial y^2} + \frac{\partial^2 \phi}{\partial z^2} = 0 \quad (1)$$

in the fluid domain. The dynamic free-surface condition on the exact free surface can be written as

$$\frac{D\phi}{Dt} = \frac{1}{2} \left[\left(\frac{\partial \phi}{\partial y} \right)^2 + \left(\frac{\partial \phi}{\partial z} \right)^2 \right] \quad (2)$$

D/Dt means the substantial derivative and t is the time variable. The kinematic free-surface condition is that a fluid particle remains on the free surface. Hence the free surface can be found by convecting particles on the free surface with the local fluid velocity. The body boundary condition on the wetted body surface is satisfied on the instantaneous body surface. It can be written as

$$\frac{\partial \phi}{\partial n} = V_n \quad (3)$$

where V_n is the body velocity in the normal direction \vec{n} on the body surface. Positive direction of \vec{n} is into the fluid domain. The initial conditions are zero velocity potential and free-surface elevation.

The problem without flow separation will be studied first. A jet flow is created at the intersection between the free surface and the body surface. A similarity solution can be found for a symmetrical wedge with constant vertical impact velocity (Dobrovolskaya(1969), Zhao and Faltinsen(1993)). Figure 2 shows the similarity solution for the free-surface elevation and pressure distribution during water entry of a symmetrical wedge with deadrise angle 30° . Figure 2 illustrates that the thin jet will not contribute much to the total force on the body. The part of the jet, where the pressure is close to atmospheric pressure, can therefore be neglected. This makes it unnecessary to find the intersection point between the body

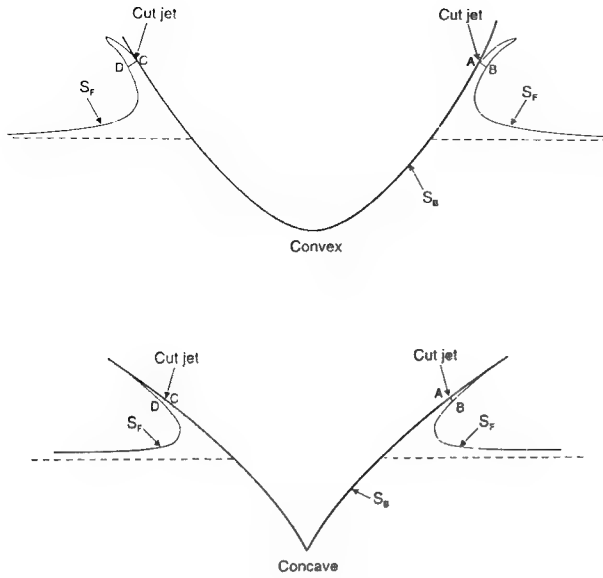


Figure 3: The water entry of bodies with convex and concave shapes. The jets are cut at AB and CD in the numerical simulations. S_F is the free surface.

and free surface. This angle is very small for bodies with small deadrise angles and will cause numerical problems (Greenhow (1987)). The geometry of the body may be either convex or concave around the spray root of the jet flow (see figure 3). Part of the jet will leave the body for a convex shape. This can be observed from experimental tests (see for instance Faltinsen (1990)). One should cut the jet before it leaves the body in the numerical simulations (see figure 3). The thin jet will follow the body surface for a body with concave shape (see figure 3), but it will give a small force on the body surface. Therefore one may cut the most part of the jet.

An instantaneous fluid domain Ω that does not contain the whole jet flow, is defined. The jet flow is cut at AB and CD (see figure 3). The velocity potential ϕ for the flow inside the fluid domain is represented by Green's second identity, i.e.

$$2\pi\phi(y, z, t) = \int_S \left[\log r \frac{\partial \phi(\eta, \zeta, t)}{\partial n} - \phi(\eta, \zeta, t) \frac{\partial \log r}{\partial n} \right] dS(\eta, \zeta, t) \quad (4)$$

where $r = [(y - \eta)^2 + (z - \zeta)^2]^{0.5}$. $\frac{\partial}{\partial n}$ means derivative in the normal direction of S . Positive direction is into the fluid domain. The surface S consists of AB, CD, S_B , S_F and S_C . Here S_B is the instantaneous wetted body surface below A and C, S_F is the instantaneous free sur-

face outside B and D, S_C is a control surface infinitely far away from the body. The contribution from integrating over S_C in equation (4) is zero. The contribution from the free surface far away from the body can be rewritten. The velocity potential ϕ for $|y| > b(t)$, where $b(t)$ is large relative to the cross-dimensions of the hull, can be expressed as a vertical dipole (symmetrical part) and a multipole (asymmetrical part) in infinite fluid. The reason is that the free surface condition is $\phi = 0$ on $z=0$ from a far-field point of view. ϕ can then be written as

$$\phi = C_1(t) \frac{z}{y^2 + z^2} + C_2(t) \frac{yz}{(y^2 + z^2)^2} \quad (5)$$

where $C_1(t)$ and $C_2(t)$ are unknowns that are found as a part of the solution. Using equation (5) in equation (4) makes it possible to analytically express the integrals from b to ∞ and from $-\infty$ to $-b$. The angle between the body surface and AB(CD) is 90° , while the angle between the free surface and AB(CD) is close to 90° (see figure 3). The line AB(CD) is in the area where the jet starts and where the pressure can be approximated by atmospheric pressure.

An integral equation based on equation (4) is set up by letting (y, z) approach points on S for each time step. The free surface S_F inside $|y| = b(t)$, and the body surface S_B , are divided into a number of straight line segments in the numerical evaluation of this integral equation. One straight line element is used to represent AB and CD. ϕ and $\partial\phi/\partial n$ are set constant on each element, except on AB and CD, where ϕ has a linear variation over the element. For each element on the free surface inside $|y| = b(t)$, and on AB and CD, ϕ is known and $\partial\phi/\partial n$ is unknown. The instantaneous position of these elements and the values of ϕ follow from the free-surface conditions. Special care is necessary in describing the motion of the free surface in order to satisfy conservation of fluid mass. A second order description of the free surface is used in areas with large curvature. On the body surface ϕ is unknown and $\partial\phi/\partial n$ is known. In addition there are two unknowns which come from the representation of the far field solution, namely $C_1(t)$ and $C_2(t)$. The total number of unknowns is $N_B + N_F + 2$, where N_B is number of elements on the body surface and N_F is number of elements on the free surface and on AB and CD. The integral equation resulting from equation (4) is satisfied at the midpoint of each element on S_B , S_F , AB, CD and at two control points in the fluid domain with $|y|$ -value larger than $b(t)$. One obtains then a system of linear equations with the same number of equations as the number of unknowns. The linear equations are solved by a standard procedure. AB and CD (see figure 3) are not used in the initial phase. When the free surface at the intersection with the body is

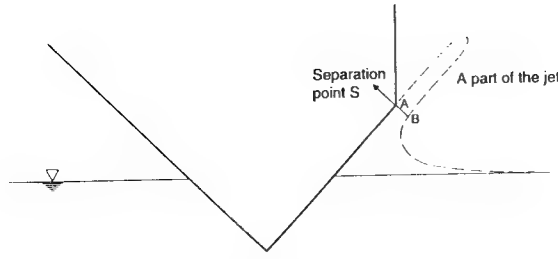


Figure 4: The water entry of a body with flow separation at the knuckles. When the spray root of the jet reaches the separation point S, a part of the jet is introduced in the numerical simulation.

close to the slope of the body surface, AB and CD are introduced.

It will now be described how to solve the problem when the flow separates from a knuckle (or a fixed separation point). When AB (or CD) reaches the separation point S, a part of the previously neglected jet is introduced. The computational domain will then include a larger part of the jet (see figure 4). The reason for doing this is to avoid numerical difficulties. The thin jet, which has been introduced here, is assumed to have the same thickness and constant velocities in the y and z-direction for the whole jet. The length of the introduced jet part is about 6 times the length of AB. In reality the thickness will not be the same. For instance the angle at the intersection between the water and the body surface is about 1.8° during water entry with constant velocity of a wedge with deadrise angle 30° (see figure 2). The length of the total jet is almost the same as the length of the wetted body surface when the wetted surface is defined as the distance from the keel to the spray root of the jet. The introduced jet part is therefore a small portion of the whole jet. It is a good approximation to assume constant jet thickness in this part of the jet. The numerical results are not sensitive to the length of the introduced jet part. A hemisphere is used at the end of the jet. This is advantageous in the time stepping of the solution.

A Kutta condition is applied at the separation point S. This implies that the flow leaves tangentially at the knuckle and the velocities at point S are finite. In a small region near the knuckle the behaviour of the velocities can be studied by a local analysis.

Here a local polar coordinate system (r, θ) and a local Cartesian coordinate system (s, n) is used (see figure 5). A local solution of the velocity potential ϕ_{loc} , that satisfies the body boundary condition, can be written as

$$\phi_{loc} = A_0(t) + U(t)s + \sum_{n \geq 1} A_n(t)r^n \cos n\theta \quad (6)$$

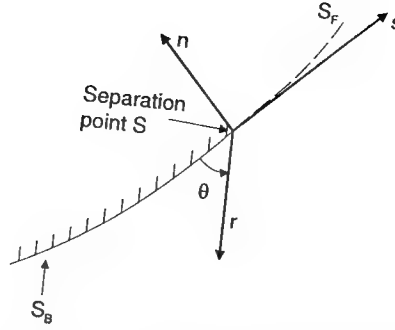


Figure 5: The local polar coordinate system (r, θ) and the local Cartesian coordinate system (s, n) . S is the separation point, S_B the body surface and S_F the free surface. The s-coordinate coincides with the tangent of the body surface at the separation point S.

The velocity potential ϕ_{loc} satisfies the free-surface condition

$$\frac{\partial \phi_{loc}}{\partial t} + \frac{1}{2} \left[\left(\frac{\partial \phi_{loc}}{\partial s} \right)^2 + \left(\frac{\partial \phi_{loc}}{\partial n} \right)^2 \right] = 0 \quad \text{on } \theta = \pi \quad (7)$$

This leads to the following approximation for small r

$$\frac{\partial A_0}{\partial t} + \frac{\partial U}{\partial t}s + \frac{1}{2} [U^2 + 2U A_n n r^{n-1} \cos n\theta + A_n^2 r^{2(n-1)} n^2 \cos^2 n\theta + A_n^2 n^2 r^{2(n-1)} n^2 \sin^2 n\theta]_{\theta=\pi} = 0 \quad (8)$$

The lowest order term in equation (8) is

$$\frac{\partial A_0}{\partial t} + \frac{1}{2} U^2 = 0 \quad (9)$$

This equation says simply that the pressure is atmospheric at the separation point. This is automatically satisfied as a part of the solution. The next term in equation (8) gives

$$2U A_n n r^{n-1} \cos n\pi = 0 \quad (10)$$

Possible values of n are $\frac{1}{2}, \frac{3}{2}, \dots$. $n = \frac{1}{2}$ cannot be a solution since it leads to a singular velocity. Choosing $n = \frac{3}{2}$ is consistent with that $r^{2(n-1)}$ should be a smaller term than r^{n-1} . This means that the solution in the vicinity of the separation point can be written as

$$\phi_{loc} = A_0(t) + U(t)s + A_{\frac{3}{2}}(t)r^{3/2} \cos\left(\frac{3}{2}\theta\right) \quad (11)$$

Equation (11) implies that the tangential velocity at the free surface is $U(t)$. Close to the separation point, the tangential velocity at the body surface can be written as

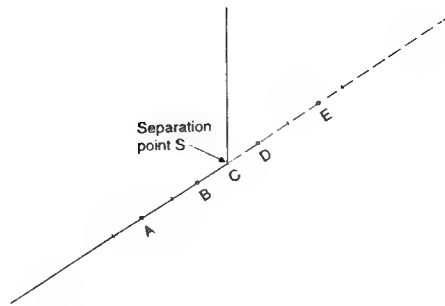


Figure 6: Element distribution and midpoints A, B, D, and E of the elements near the separation point S.

$$u(s) = U(t) - \frac{3}{2} A_{\frac{3}{2}}(t) r^{\frac{1}{2}} \quad (12)$$

The free surface near the separation point can be found by equation (11). It can be shown that the flow leaves the knuckle tangentially. Very small elements are used near the knuckle in the numerical calculations. The length of the segments used near the knuckle on the body and free surface is about 0.3% of the length of the wetted body surface for the wedge with deadrise angle 30° . Therefore the tangential velocity for the segments closest to the knuckle on the body can be approximated by the particle velocity on the free surface closest to the knuckle. This means that the last term in equation (12) is neglected. The numerical details of the implementation of the conditions at a separation point are described below.

Figure 6 shows the element distribution around a knuckle. Based on the velocity potentials at points A, B and D, the tangential velocity at point B can be estimated. Based on the velocity potentials at points B, D and E the tangential velocity at point D can be estimated. These two velocities are set equal. This gives a linear relationship between unknown velocity potential values on the body surface and known potential values of the free surface near the separation point. In addition the normal derivative $\frac{\partial \phi}{\partial n}$ of the potential near the knuckle is set equal on the body and the free surface. These two relationships implies that two equations in the linear equation system that follows from the integral equation based on equation (4) must be excluded. This is done by not satisfying the integral equation at the closest segments to the knuckle on the body and free surface. The same procedure can be used for flow separation from the other side of the body.

When the solution is stepped from time t_i to t_{i+1} , the free surface location and velocity potential on the free surface for t_{i+1} are obtained by using the kinematic and the dynamic free-surface conditions. Because the velocities on

the body and free surface for the elements closest the separation point are the same, the element closest to the separation point on the free surface will always be located on the tangential continuation of the body surface from the separation point.

The front part of the jet has larger velocities than the rest of the fluid in the beginning of flow separation from the knuckle. Number of elements to represent the jet must therefore be increased as time goes. It is also found that the free surface can be unstable at the front part of the jet. This problem can be suppressed for a long time by cutting the front part of the jet. It has been checked that this does not affect the pressure on the body surface. The particle velocities near the original jet flow will be strongly reduced at a late stage. This means that it is not really a jet flow anymore. It should also be noted that the acceleration of fluid particles will not be much larger than the gravitational acceleration at a late stage of the flow. The effect of gravitation should therefore be included in the numerical simulation at this stage. This has not yet been studied.

The pressure p on the body surface is calculated by Bernoulli's equation, which can be written as

$$p - p_a = -\rho \frac{\partial \phi}{\partial t} - \frac{1}{2} \rho \left[\left(\frac{\partial \phi}{\partial y} \right)^2 + \left(\frac{\partial \phi}{\partial z} \right)^2 \right] \quad (13)$$

Here the hydrostatic pressure is neglected. p_a is atmospheric pressure and ρ is the mass density of the fluid. The term $\frac{\partial \phi}{\partial t}$ is found by generalizing the concept of substantial derivative. One introduces

$$\frac{D' \phi}{D' t} = \frac{\partial \phi}{\partial t} + \vec{U} \cdot \nabla \phi \quad (14)$$

where $\frac{D' \phi}{D' t}$ is the change in ϕ when one follows the midpoint of a segment, that moves with velocity \vec{U} .

The numerical results have been checked by changing number of elements and time step and by checking conservation of mass, momentum and energy. The expressions can be found in Zhao and Faltinsen(1993) and are valid both with and without flow separation.

4 SIMPLIFIED SOLUTION

Wagner(1932) developed an asymptotic solution for water entry of two-dimensional bodies with small local deadrise angles. The flow was studied in two fluid domains. The inner flow domain contains a jet flow at the intersection between the body and the free surface. In the outer flow domain the body boundary condition and the dynamic free-surface condition $\phi = 0$ were transformed to a horizontal

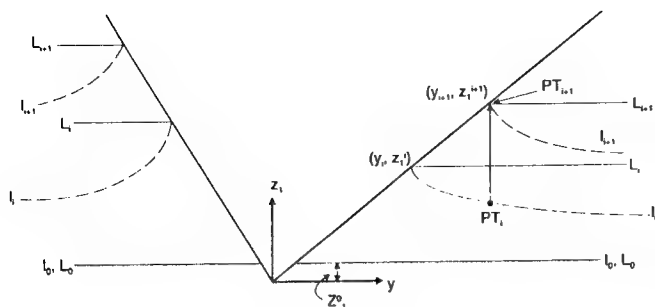


Figure 7: The coordinate system (y, z_1) , the real free surface l and the horizontal lines L used in the numerical simulation for time steps t_0 , t_i and t_{i+1} in the simplified solution.

line. The kinematic free-surface condition was used to determine the intersection between the free surface and the body in the outer flow domain. Zhao and Faltinsen (1993) presented a composite solution for the pressure distribution in the outer and inner flow domain and showed satisfactory agreement with similarity solutions for wedges with deadrise angles smaller than 20° .

A generalization of Wagner's solution to larger local deadrise angles is presented in the following text. Only the outer flow domain solution is analyzed. A main difference from the Wagner theory is that the exact body boundary condition is satisfied at each time instant. The wetted body surface is found by integrating in time the vertical velocities of fluid particles on the free surface and finding when the particles intersect the body surface. Wagner did also that, but he could use analytical solutions because of the simplified body boundary condition. The dynamic free-surface condition will be the same as Wagner used. The pressure is calculated by the complete Bernoulli's equation without gravity. It has not been possible to find an inner flow solution near the spray roots that matches the outer flow solution. This would have made it possible to exclude in a rational way the large negative pressures that occur at the intersection points in our outer flow solution. The procedure is now simply to neglect the negative pressure.

The problem is solved as an initial value problem. The velocity potential satisfies two-dimensional Laplace equation in the fluid domain. A boundary value problem is solved by using equation (4) for each time step. The numerical procedure is similar as the fully nonlinear problem. A coordinate system y, z_1 which follows the vertical motion of the body is used (see figure 7). The dynamic free surface condition $\phi = 0$ is satisfied on horizontal lines that starts at the intersection points between the body and the free surface on each side of the body (see figure 7). The dy-

namic free surface condition implies that fluid particles on the free surface have only vertical velocities. The instantaneous z_1 -coordinate of the intersection points on the two sides of the body are different for water entry of an asymmetrical body.

The numerical simulation starts at time t_0 . The submergence of the body is z_1^0 at t_0 (see figure 7). The effect of free-surface elevation is neglected initially, so the free surface l_0 is horizontal. In the numerical computation, t_0 is set equal to $0.15t_{pout}$, where t_{pout} is the time instance when one needs the pressure distribution and slamming forces as output. This procedure has been tested against the Wagner solution for a water entry of a circle at an early stage and water entry of a wedge with small deadrise angles. Satisfactory predictions of the pressure distribution and the slamming forces were obtained.

Figure 7 illustrates the free surface l_i and l_{i+1} at two time instances t_i and t_{i+1} . The free-surface conditions are satisfied on the horizontal lines L_i and L_{i+1} at t_i and t_{i+1} . An integral equation following from equation (4) is used at each time step t_i to find the velocity potential on the body surface and the vertical velocities at L_i . It is assumed that the vertical velocity on L_i for a given y -value is the same as the vertical velocity on l_i . The solution can be stepped from $t = t_i$ to $t = t_{i+1}$ in the following way. The procedure is first to decide the intersection point (y_{i+1}, z_{i+1}^{i+1}) for positive y -values at time t_{i+1} and then find what $\Delta t = t_{i+1} - t_i$ must be. By knowing Δt , the intersection point for negative y -values at t_{i+1} is determined afterwards. Δt is found in details as follows. One can write

$$\Delta P = \int_{t_i}^{t_{i+1}} W(c(t), y_{i+1}) dt \quad (15)$$

where $\Delta P = PT_{i+1} - PT_i$ (see figure 7) and W is the relative vertical velocity of a point between PT_i and PT_{i+1} with y -coordinate y_{i+1} . W depends on $c(t)$ which is the y -coordinate of the intersection point between the free surface and the body surface at time t . Equation (15) can be written

$$\Delta P = \int_{y_i}^{y_{i+1}} W(c(t), y_{i+1}) \frac{dt}{dc} dc \quad (16)$$

This is evaluated numerically by using an average value $(\frac{dt}{dc})_m$ for $\frac{dt}{dc}$. W is expressed in terms of a local solution. Here a local polar coordinate system (r_2, θ_2) is used (see figure 8). W can be written as

$$W = -\frac{D}{2 - \frac{\theta}{\pi}} r_2^{\frac{1}{2 - \frac{\theta}{\pi}} - 1} \quad (17)$$

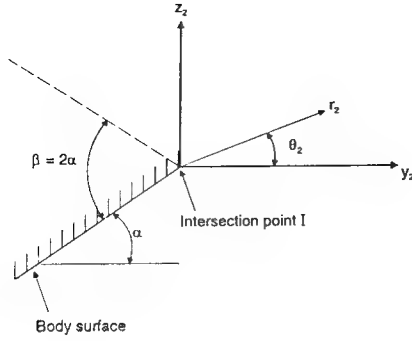


Figure 8: Local polar coordinate system (r_2, θ_2) and local Cartesian coordinate system (y_2, z_2) . I is the intersection point between the body and the free surface. The local deadrise angle is α . The free surface condition is satisfied on the y_2 -axis in the numerical simulation of the simplified method.

Here r_2 is $(y_{i+1} - c(t))$. β is defined in figure 8 and is assumed constant from t_i to t_{i+1} . D is found from the global solution and an average value is used from t_i to t_{i+1} . This is found for a symmetric body by solving the global problem for t_i and t_{i+1} , and use an average value D_m for D at these two time instances. The procedure for an asymmetric body will be explained later. Equation(16) can now be written as

$$\Delta P = -\left(\frac{dt}{dc}\right)_m \frac{D_m}{2 - \frac{\beta}{\pi}} \int_{y_i}^{y_{i+1}} (y_{i+1} - c(t))^{-\frac{1}{2 - \frac{\beta}{\pi}} - 1} dc$$

$$= -\left(\frac{dt}{dc}\right)_m D_m (y_{i+1} - y_i)^{-\frac{1}{2 - \frac{\beta}{\pi}}} \quad (18)$$

This means that

$$\left(\frac{dt}{dc}\right)_m = -\frac{\Delta P}{D_m (y_{i+1} - y_i)^{-\frac{1}{2 - \frac{\beta}{\pi}}}} \quad (19)$$

Δt is now determined as

$$\Delta t = \left(\frac{dt}{dc}\right)_m (y_{i+1} - y_i) \quad (20)$$

If the body is asymmetric, D_m is determined as follows. An estimate of the horizontal line L_{i+1} on the left hand side of the body(see figure 7) is based on the rate of change with time of the intersection point from the previous time step. D_m is then again determined as the average value at t_i and t_{i+1} . Δt can then be determined by equation (20) and equation (19).

Knowing Δt , the intersection point on the left hand side of the body can be determined by linear interpolation. This

has been done by using similar equations, as used for the right hand side of the body, to calculate the times it takes for points on the left hand free surface to move up to the body surface. Then one can determine the y -coordinate of the intersection point by linear interpolation.

After the velocity potential on the body surface has been determined, the pressure distribution on the body can be found from equation (13). Special care is shown near the intersection between the body and the free surface. Since the velocity is infinite there, the last term in equation (13) will be negative infinite. It can be shown that the first term is positive infinite at the intersection point, and that the last term is more singular than the first term. Therefore the total pressure is negative infinite. But this is an integrable singularity. Let us define the integrated vertical force for the part with negative pressure as F_N , and from the part with positive pressure as F_P . It can be shown that F_N/F_P goes to zero when the deadrise angle goes to zero. For small deadrise angles, the maximum pressure(positive) is obtained near the intersection point. The maximum pressure obtained from the outer solution is the same as the maximum pressure from the composite solution based on Wagner's solution(Zhao and Faltinsen(1993)) when the deadrise angle goes to zero.

5 VERIFICATION OF THE SIMPLIFIED METHOD

Figure (9) compares predicted pressure distributions by the simplified solution and the similarity solution. Wedges with deadrise angles 10° , 30° , 45° , 60° and 81° are analyzed. The negative pressures in the simplified solution have been omitted. The maximum pressure occurs near the spray root for small deadrise angles. When the deadrise angle is larger than approximately 40° , the maximum pressure is located at the keel of the wedge. For small deadrise angles there are good agreement between the simplified and similarity solution in the region near the spray root of the jet. The agreement is less satisfactory near the spray root for large deadrise angles. But from a design point of view this has no consequence for the total slamming loads and the maximum pressure, because the pressure is relatively low compared with the average pressure on the body surface.

Numerically predicted total slamming force and maximum pressures on a wedge with different deadrise angles are presented in figure 10. There are good agreement between the simplified and the similarity solution. The results from Wagner's solution and von Karman's solutions are also presented in figure 10a. A von Karman solution means that the local up-rise of the water is not accounted for. The dynamic free-surface condition is the same as in

Wagner's solution. Two different von Karman solutions are presented in figure 10a. One is based on a flat plate solution, similar as Wagner did. The other von Karman solution is obtained by using the exact body boundary condition and the principle of conservation of momentum. The vertical force is expressed by

$$\frac{d}{dt}(A_{33}V) \quad (21)$$

where A_{33} is the infinite frequency added mass in heave as a function of submergence. V is the drop velocity. This is referred to as the von Karman-momentum solution. Figure 10a shows that the Wagner solution clearly over-predicts the slamming loads for larger deadrise angles. The von Karman solution based on the flat plate solution clearly under-predicts slamming loads for relatively small deadrise angles. The von Karman-momentum solution with exact body boundary condition clearly under-predicts slamming loads. The latter approach is common to use in practical nonlinear ship motion and sea load computations during water entry of a bow flare section. The results in figure 10 illustrate unsatisfactory predictions based on this method.

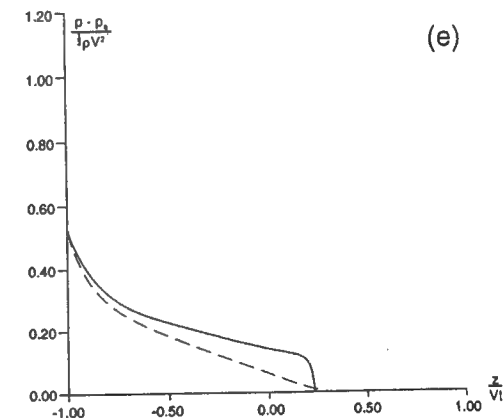
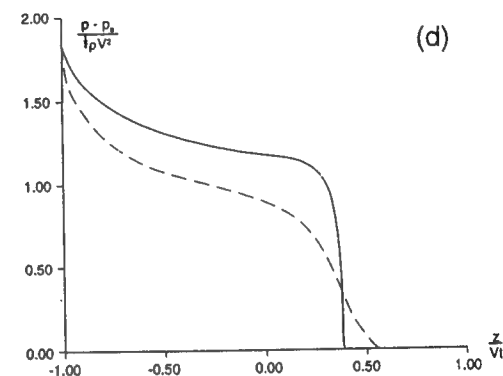
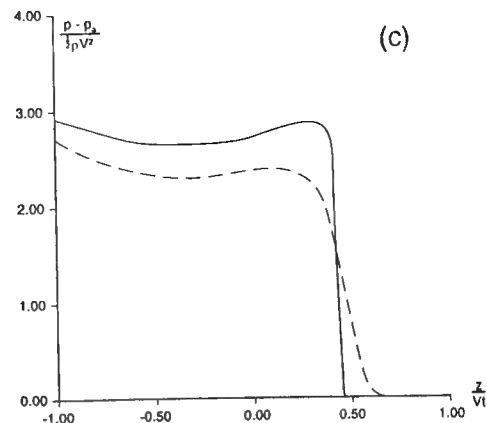
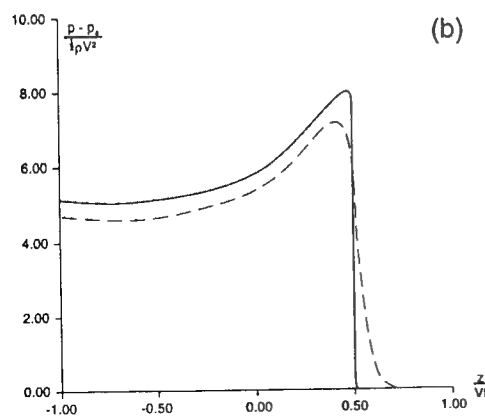
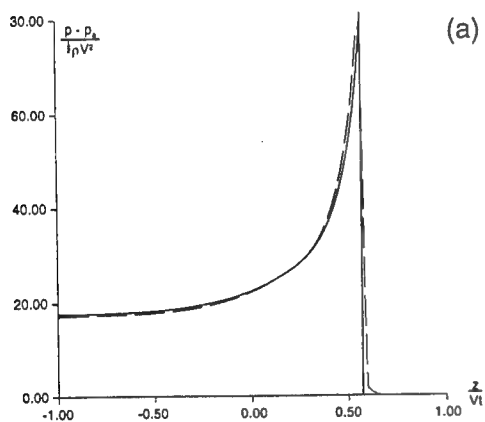


Figure 9: Pressure(p) distribution on symmetric wedges during water entry with constant vertical velocity V . —, simplified solution; ---, similarity solution. p_a is atmospheric pressure, α is deadrise angle, ρ is mass density of the fluid, z is vertical coordinate, t is time variable and Vt is the instantaneous draft relative to calm water. (a) $\alpha = 10^\circ$; (b) $\alpha = 30^\circ$; (c) $\alpha = 45^\circ$; (d) $\alpha = 60^\circ$; and (e) $\alpha = 81^\circ$.

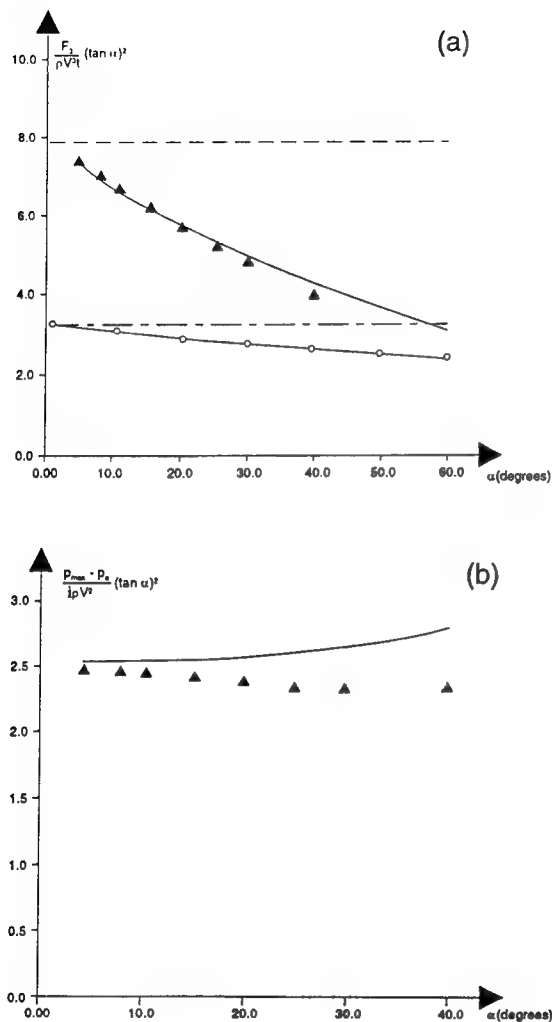


Figure 10: The vertical slamming force F_3 and maximum pressure p_{max} on symmetric wedges during water entry with constant vertical drop velocity V . p_a is atmospheric pressure, α is deadrise angle, ρ is mass density of the fluid, t is time variable and Vt is the instantaneous draft relative to calm water.

(a) the vertical slamming force, —, simplified solution; $\triangle \triangle \triangle$, similarity solution; ----, Wagner solution; - · -, von Karman; $o - o - o$, von Karman-momentum.

(b) the maximum pressure, —, simplified solution; $\triangle \triangle \triangle$, similarity solution.

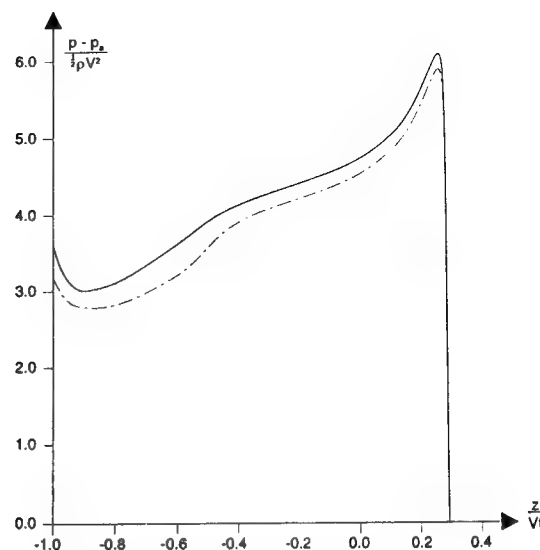


Figure 11: Numerically predicted pressure(p) distribution during water entry of a bow flare section. The vertical velocity V is constant. p_a is atmospheric pressure and ρ is mass density of the fluid. The geometry of the body is shown in figure 13b. The numerical results are presented for the time instance just before the spray roots of the jets reach the knuckles. z is vertical coordinate on the body surface, t is time variable and Vt is the instantaneous draft relative to calm water. —, simplified solution; --, fully nonlinear solution.

The simplified and the fully nonlinear solution have been compared for different ship sections. Figure 11 shows the predicted pressure distribution for the bow flare section, which was used during the drop tests(see figure 13b). The vertical velocity of the section is constant. The time instance is just before the spray roots of the jets reach the knuckles. The comparison between the theories and the experimental results will be shown in section 7. Figure 11 shows satisfactory agreement between the two different methods.

The general conclusion is that the simplified theory represents a reasonable approximation of the total slamming force and the local slamming loads.

6 DESCRIPTION OF DROP TESTS

6.1 THE MODEL

Drop tests have been carried out at MARINTEK. The objective was to validate the theoretical methods. A sketch of the free-falling rig used in the tests is shown in figure 12. The rig consists of four different parts; the vertical guide rails, the trolley, a rotatable horizontal beam and the test

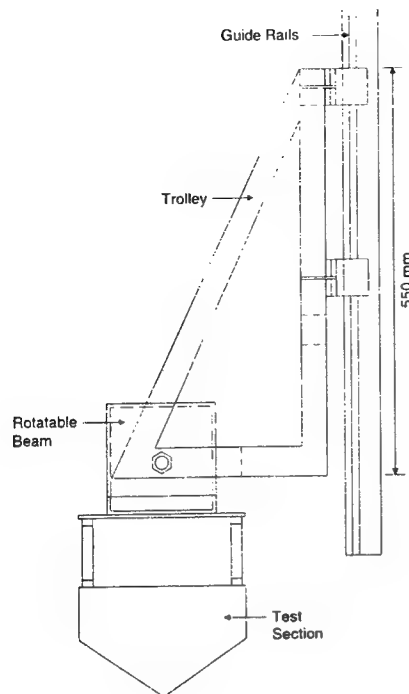


Figure 12: The free-falling rig used in the drop tests.

sections. The rotatable beam is connected to the trolley using one bolt at each end of the beam. The beam can be rotated in intervals from zero to a maximum roll angle of 28 degrees. Only results for non-rotated sections will be presented. The ballast weights are located within the rotatable beam. The trolley is engaged with the vertical guide rails. The test sections are mounted directly to the horizontal, rotatable beam. The test sections are connected to the trolley during the entire drop. Any rotation of the test sections are in this way suppressed during the impact. The total length of the test sections are $L = 1.0$ m. The breadth B of the test sections can vary from 0.25 to 0.60 m. The maximum drop height for this rig is about 2.0 m. The trolley is raised using a winch fitted with a quick-release hook. The hook is connected to an automatic release mechanism. After the test section has hit the water surface, the trolley is stopped using two elastic ropes.

Both a V-shaped section with 30 degrees deadrise angle and a typical ship bow section were tested. The shape of the two different sections are shown in figure 13. The total test section was divided into three parts, one measuring section with a dummy section on each side (see figure 13). No vertical end plates were used. The measuring section was connected to the rig using two force transducers. The main data for the test setup for the two different sections can be summarized as follow:

	V shape	bow flare
Breadth of section	0.50 m	0.32 m
Vertical distance from keel to knuckles	0.29 m	0.203 m
Length of measuring sections	0.20 m	0.10 m
Length of each dummy sections	0.40 m	0.45 m
Total length	1.00 m	1.00 m
Weight drop rig (without ballast)	141 kg	161 kg
Ballast weight	100 kg	100 kg
Total weight of drop rig	241 kg	261 kg
Weight of measuring section	14.5 kg	6.9 kg

Table 1. The main data of the test sections.

The total weight of the measuring section represents the total weight of the section connected underneath the vertical force transducers.

6.2 INSTRUMENTATION

The instrumentation in the tests is shown in figure 13 and the following parameters were measured:

*Pressures in 4-5 points using pressure cells of piezoresistive type with resonance frequency of 500 kHz. The cell diameter is 4 mm. The positions of the pressure cells are shown in figure 13.

*The vertical force using two force transducers connected to the ends of the measuring section.

*Wetted surface measurements using wave gauges tape.

*Vertical acceleration of the drop rig using an accelerometer.

*The vertical drop velocity was measured using an optical sensor. The time development of the drop velocity was obtained by using this value in combination with the measured vertical acceleration of the drop rig.

The sections were dropped against calm water. At least two drops were performed for each test condition.

7 COMPARISONS BETWEEN THEORY AND EXPERIMENTS

Only the fully nonlinear method can be used to predict the pressure distribution on bodies after flow separation occurs. An example with water entry of a wedge with deadrise angle 30° and with knuckles is presented in figure 14. The vertical velocity is constant. The pressure distribution and free surface elevation for different time instances after the spray roots separate from the knuckles are presented. Figure 14a shows that the maximum pressure is located near the spray root of the jet before separation occurs. After the flow separates, the maximum pressure near the separation point drops fast and the maximum pressure moves to the keel of the wedge. Figure

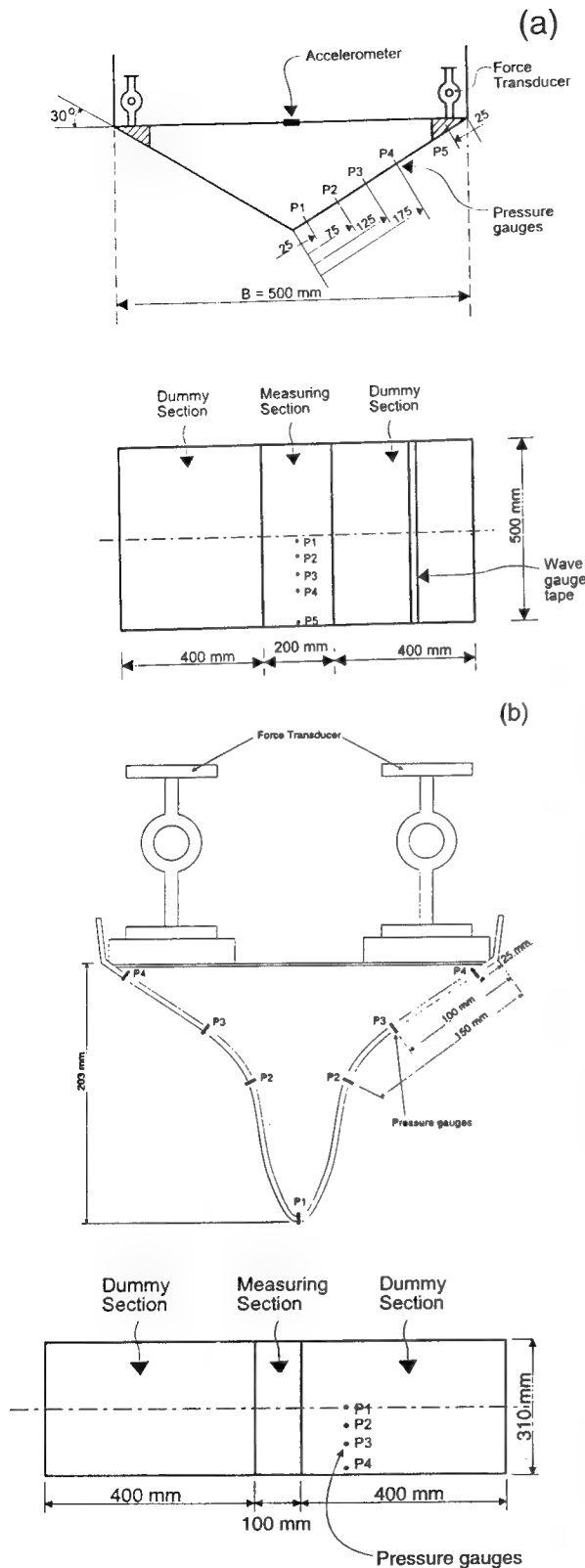


Figure 13: The geometry of the test section and the locations P_i of the pressure gauges.
(a) the wedge section; (b) the bow flare section.

14b shows the free-surface elevation after the flow separation. Greenhow and Lin(1983) studied experimentally water entry of a wedge with deadrise angle 30°. One of the pictures showed the water elevation after flow separation. Figure 14c shows both experimental and theoretical predictions of the free-surface elevation. The agreement seems satisfactory. However information on the variation of the experimental drop velocity was not available. Deceleration of the test section will effect the free-surface elevation.

Fig.15a compares numerical and experimental time histories of the vertical hydrodynamic force on the symmetrical wedge with deadrise angle 30° described in figure 13. The fully nonlinear method is used. The measured vertical drop velocity of the body during water entry is presented in figure 15b. The same velocity has been used in the numerical simulations. There is good agreement between numerical and experimental results initially. The differences are larger at a later stage. A main reason is three-dimensional flow effects.

The three-dimensional effects can approximately be explained by combining Meyerhoff's(1970) calculations of added masses of thin rectangular plates with a generalization of Wagner's theory to three-dimensional flow. This implies that at each time step, the cross-flow around a flat plate of local beam $2B$ and length $2L$ in infinite fluid is solved. The coordinates B and $-B$ represents an approximation of the local intersection between the instantaneous free surface and the exact body surface. This has to be find by an integral equation in a similar way as Wagner(1932) did for two-dimensional flow. However by applying Meyerhoff's(1970) results, we are assuming the same wetted surface at each cross-section. This procedure can only be applied up to the time instant when the spray roots are in the vicinity of the knuckles.

The vertical force per unit length on the measurement section can then be written as

$$F_3 = \frac{d}{dt}(0.5\rho\pi B^2(t)Vf(\frac{B}{L})) \quad (22)$$

where $f(\frac{B}{L})$ accounts for three-dimensional flow effects. The value of $f(\frac{B}{L})$ for different values of $\frac{B}{L}$ can be found by using Meyerhoff's(1970) results. The three-dimensional effect $f_{3D} = F_3/F_3^{2D}$ have been estimated for $\frac{B}{L}=0.25, 0.4$ and 0.5 . It is found that $f_{3D}(0.25) = 0.95$, $f_{3D}(0.40) = 0.87$ and $f_{3D}(0.5) = 0.80$. Here F_3^{2D} is the two-dimensional vertical force valid when B/L goes to zero. $B/L = 0.5$ represents the situation when the spray roots are at the knuckles. It means that three-dimensional effects cause a 20 % reduction in the vertical force at the stage when the spray roots reach the knuckles. Including these three-dimensional effects clearly improve the numerical predictions relative to the experiments(see

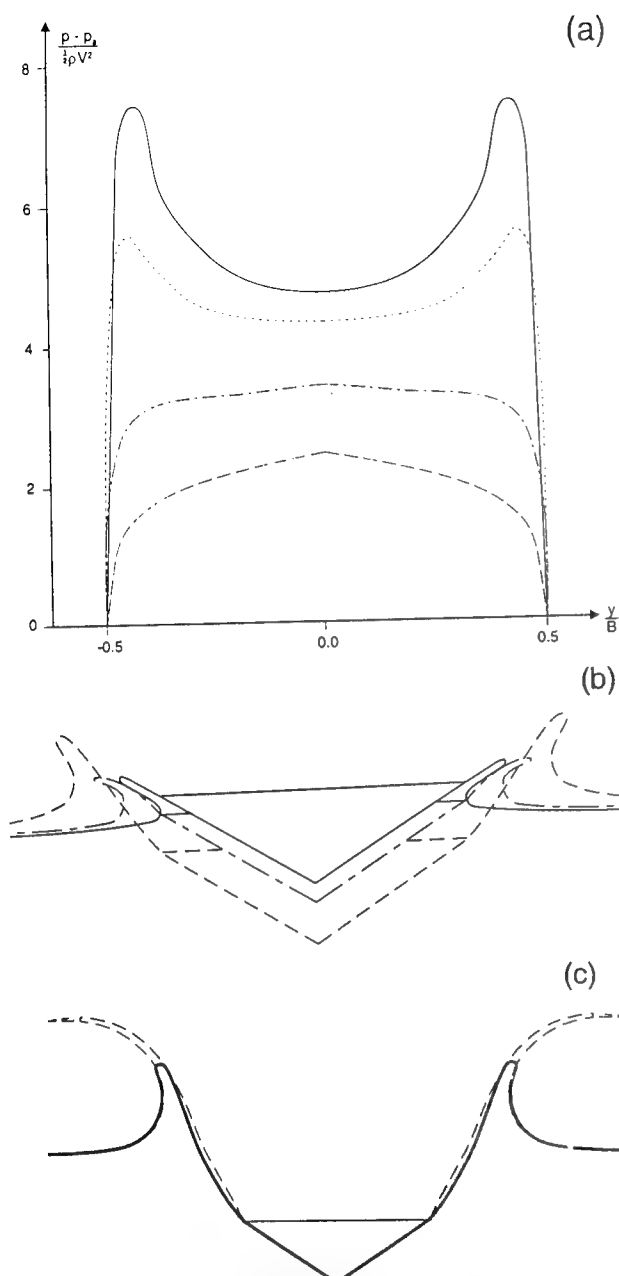


Figure 14: The pressure(p) distribution and free-surface elevation during the water entry of a wedge with deadrise angle 30° and knuckles. Calculated by the fully nonlinear solution. V is constant drop velocity, p_a is atmospheric pressure, ρ is mass density of the fluid and B is breadth of the wedge. y is horizontal coordinate on the body surface. t_0 is the time instance when the spray roots of the jets reach the separation points.

(a) pressure distribution, —, $t = t_0$; ···, $t = 1.1t_0$; - · -, $t = 1.3t_0$; ---, $t = 2.0t_0$.
 (b) free-surface elevation, —, $t = t_0$; ···, $t = 1.1t_0$; - · -, $t = 1.3t_0$; ---, $t = 2.0t_0$.
 (c) comparison of free-surface elevation between theory and experiments, $t = 2.9t_0$ (Greenhow and Lin (1983)). —, theory; ---, experiment.

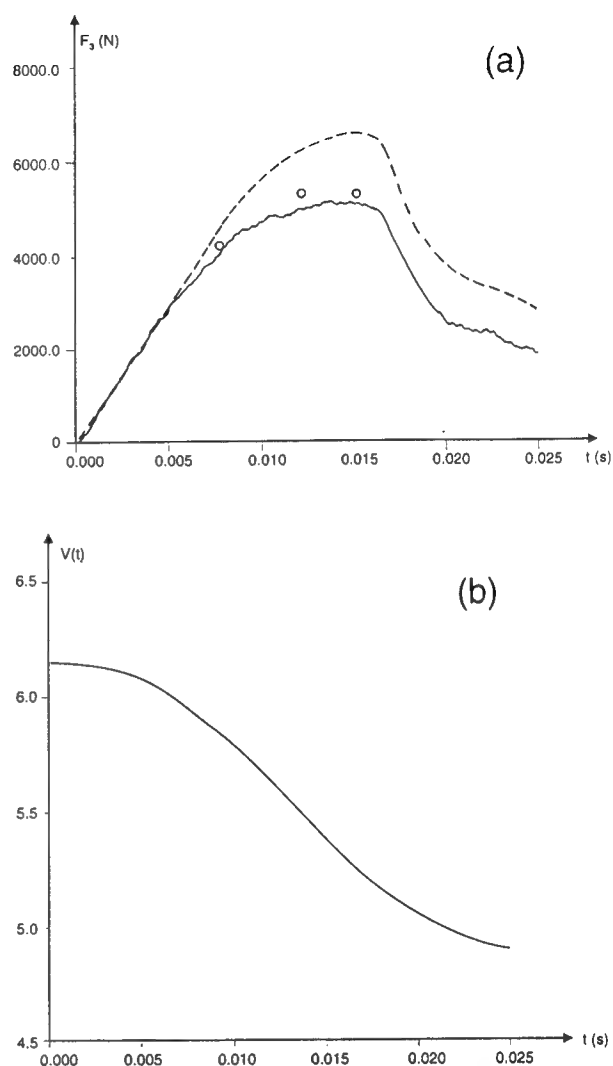


Figure 15: The vertical slamming force F_3 on a wedge with deadrise angle 30° and knuckles (see figure 13a) during water entry. t is time variable and $V(t)$ is measured vertical drop velocity of the wedge. (a) the vertical slamming force —, experimental results; ---, fully nonlinear solution with three-dimensional corrections; (b) experimental drop velocity.

figure 15a). When there is a drop in the vertical force and later on, Wagner's procedure does not apply. However the body is also non-slender during this stage of the flow. It is therefore qualitatively speaking believed that three-dimensional effects are at least as important as when $B/L=0.5$. Figure 15a shows that the slamming force reduces quickly in the beginning after flow separation, then decay more slowly. If equation (21) is used to predict the vertical hydrodynamic force, V is assumed constant and infinite frequency added mass values are calculated for different submergences, it follows that the force is zero after separation. If the deceleration of model is accounted for, the vertical force based on equation (21) will be negative after flow separation. Since the maximum force (see figure 10) and the time rate of change of the wetted area in a von Karman type of solution will be clearly lower than in our predictions, the time history of the force will also be quite different before flow separation.

At a late stage of the water entry, it is of interest to compare the numerical results of vertical force with theoretical drag coefficients for steady symmetric cavity flow past a wedge. These values are a function of the cavitation number. Knapp et al. (1970) defines the cavitation number as

$$K = \frac{p_0 - p_B}{0.5\rho V^2} \quad (23)$$

for water entry. Here V is the velocity of the body, p_0 is pressure in undisturbed fluid at the depth of the nose of the entering body, p_B is the cavity pressure. The cavity pressure is the same as atmospheric pressure in our case. According to Knapp et al. (1970), $C_D = 0.745$ for two-dimensional symmetric steady supercavitating flow ($K=0$) past a wedge with interior angle 120° at the nose. C_D is defined as $C_D = F/(0.5\rho V^2 B)$. Here F is the total force and B is the maximum breadth of the section.

Since gravity is neglected in the numerical computations, the water entry force on the wedge should approach the results for supercavitating flow when the submergence goes to infinity and the drop velocity is constant. The different force components are plotted in figure 16a as a function of Vt/B , where B is breadth of the body and Vt is the submergence of the keel relative to calm water. The force term associated with the pressure term $D'\phi/D't$ in equation (14) should go to zero and the sum of the rest of the terms should approach 0.745 when the submergence goes to infinity. The results show that the $D'\phi/D't$ -term of the force reduces slowly after a rapid decrease just after flow separation from the knuckles. The results are plotted as a function of $b/(Vt)$ in figure 16b. This makes it easier to estimate asymptotic values when Vt goes to infinity. Figure 16b indicates that the computed C_D -value approaches an asymptotic value close to 0.745 when Vt goes to infinity.

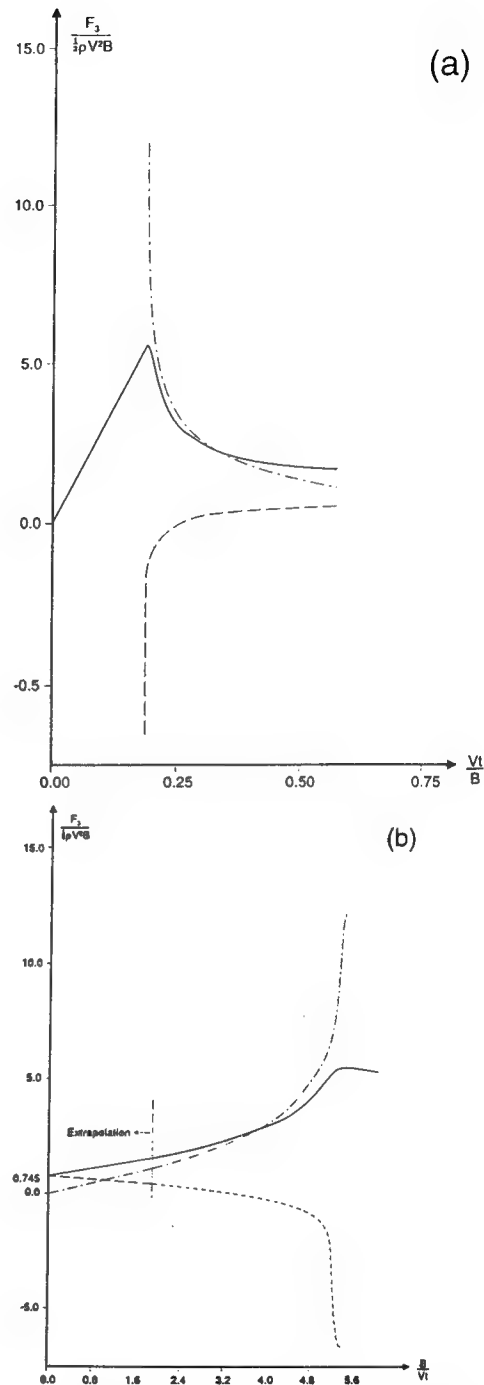


Figure 16: Different components of the numerical predicted slamming force F_3 on a symmetric wedge with deadrise angle 30° and knuckles during water entry. Fully nonlinear method is used. V is constant vertical drop velocity, ρ is mass density of the fluid, t is time variable, Vt is the instantaneous draft relative to calm water and B is breadth of the body. —, total slamming force; ---, force due to $-\frac{1}{2}\rho[(\frac{\partial\phi}{\partial y})^2 + (\frac{\partial\phi}{\partial z})^2] + \rho\vec{U} \cdot \nabla\phi$; - · -, force due to $-\rho\frac{D'\phi}{D't}$. (a) the horizontal axis is Vt/B , (b) the horizontal axis is $B/(Vt)$.

The numerical simulations should ideally have been continued for larger submergences, but numerical difficulties were encountered. Our computations indicate that the cavity becomes infinitely long when Vt goes to infinity. It is expected that the cavity will be finite if gravity is included. The deceleration of the section will also affect the solution.

The numerical and experimental pressure distribution for three time instances are plotted in figure 17. Good agreement between theory and experiments are documented at an early stage of the water entry. The differences are larger at a later stage, but this is mainly due to three-dimensional effects in the experiments. Figure 17c corresponds to a time instant after the spray roots have separated from the knuckles. The pressure level is then low and spatially uniform over the body surface. The vertical force found by integrating the measured pressure are in good agreement with the measured vertical force presented in figure 15.

Figure 18 shows a comparison of numerical and experimental values of slamming loads on the bow flare section. The measured vertical velocity of the body during water entry is presented in figure 18b. The fully nonlinear solution is used. Good agreement between the numerical results and the experiments are obtained. The ratio B/L is 0.31 when the spray roots reach the knuckles in this case. The previous simplified analysis shows that three-dimensional effect causes 8% reduction of the force relative to the two-dimensional force when the spray roots of the jets reached the knuckles.

The pressure distributions for the bow flare section are plotted for three time instances in figure 19. A comparison is made between the fully nonlinear solution and the experimental results. There are quite good agreement between the results. Generally speaking, the experimental results give lower values than the numerical results. By comparing the measured pressures with measured force presented in figure 18, it appears that the measured force is somewhat higher than the force obtained by pressure integration. This indicates measurement errors.

8 CONCLUSIONS

A fully nonlinear numerical method that predicts slamming loads on a general two-dimensional body is presented. Two-dimensional Laplace equation is solved by a boundary element method. The jet flows at the intersection between the body surface and the free surface are approximated. The fully nonlinear free-surface conditions without gravity and the exact body boundary condition are satisfied. The effect of flow separation is incorporated by a Kutta condition. The numerical method is validated by comparing with new experimental results from drop tests of a wedge and a bow flare section. Both sections have knuckles. Satisfactory agreement is documented for the

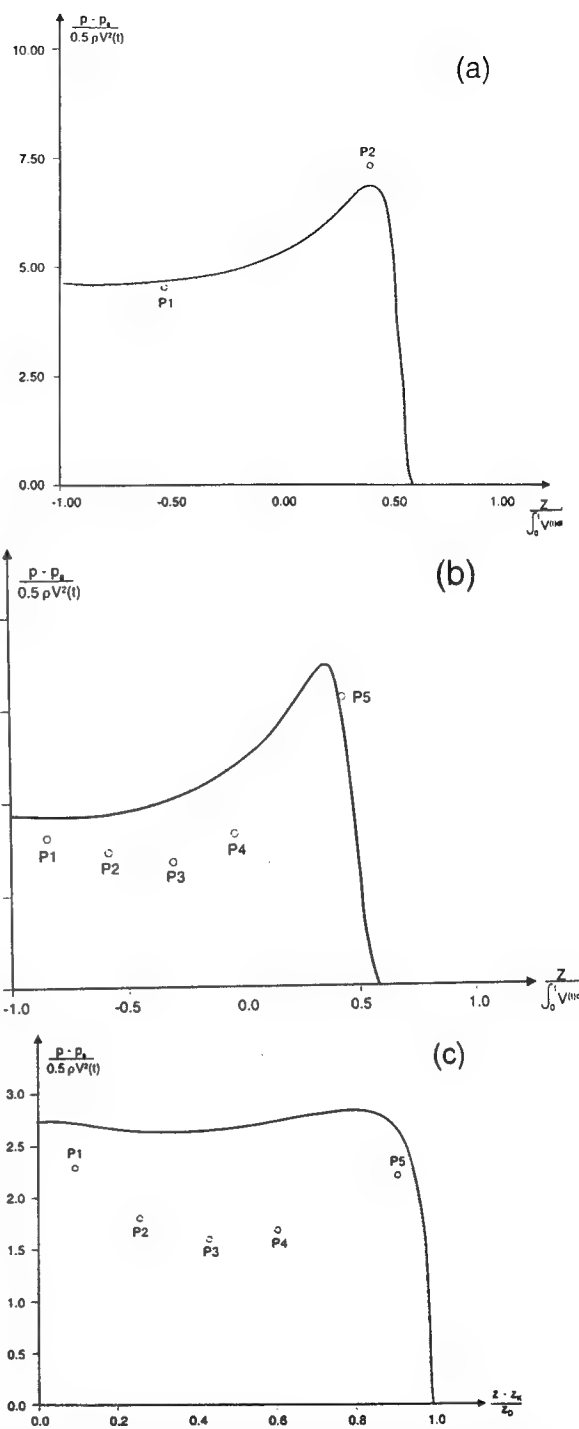


Figure 17: The pressure distribution(p) at three time instances during water entry of a wedge with deadrise angle 30° and knuckles(see figure 13a). $V(t)$ is the drop velocity, which is shown in figure 15b, p_a is atmospheric pressure, ρ is mass density of the fluid, t is time variable, $t=0$ corresponds to that the keel touches the water surface, z is vertical coordinate on the body surface, z_k is vertical coordinate of the keel and z_D is the draft of the body. \circ , experimental results; —, fully nonlinear solution. (a) $t=0.00435$ s; (b) $t=0.0158$ s; (c) $t=0.0202$ s.

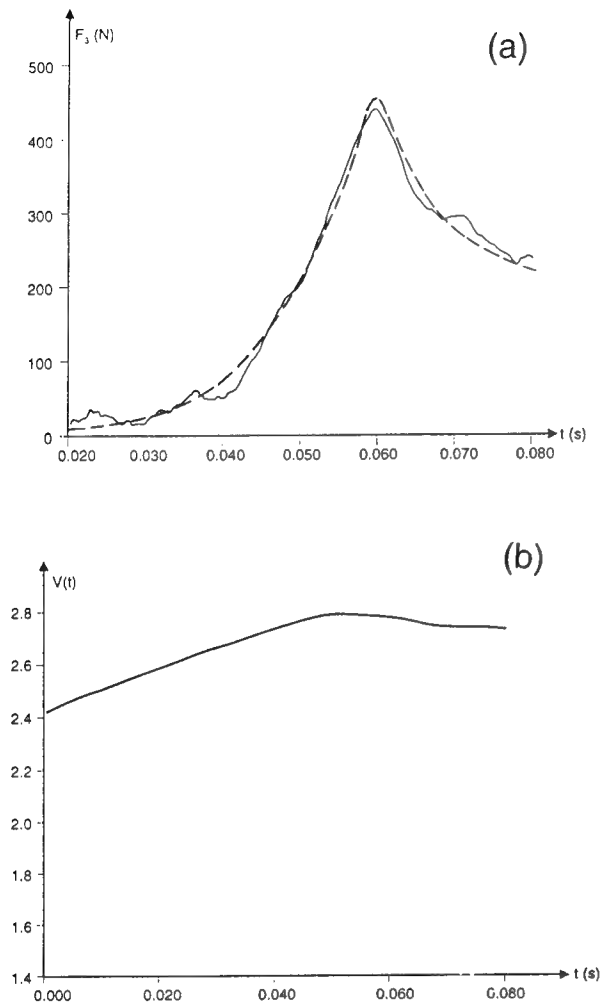


Figure 18: The vertical slamming force F_3 on a bow flare section with knuckles(see figure 13b) during water entry. t is time variable. $t=0$ corresponds to that the keel touches the water surface. $V(t)$ is measured vertical drop velocity. (a) the vertical slamming force ———, experimental results; - - - -, fully nonlinear solution. (b) experimental drop velocity

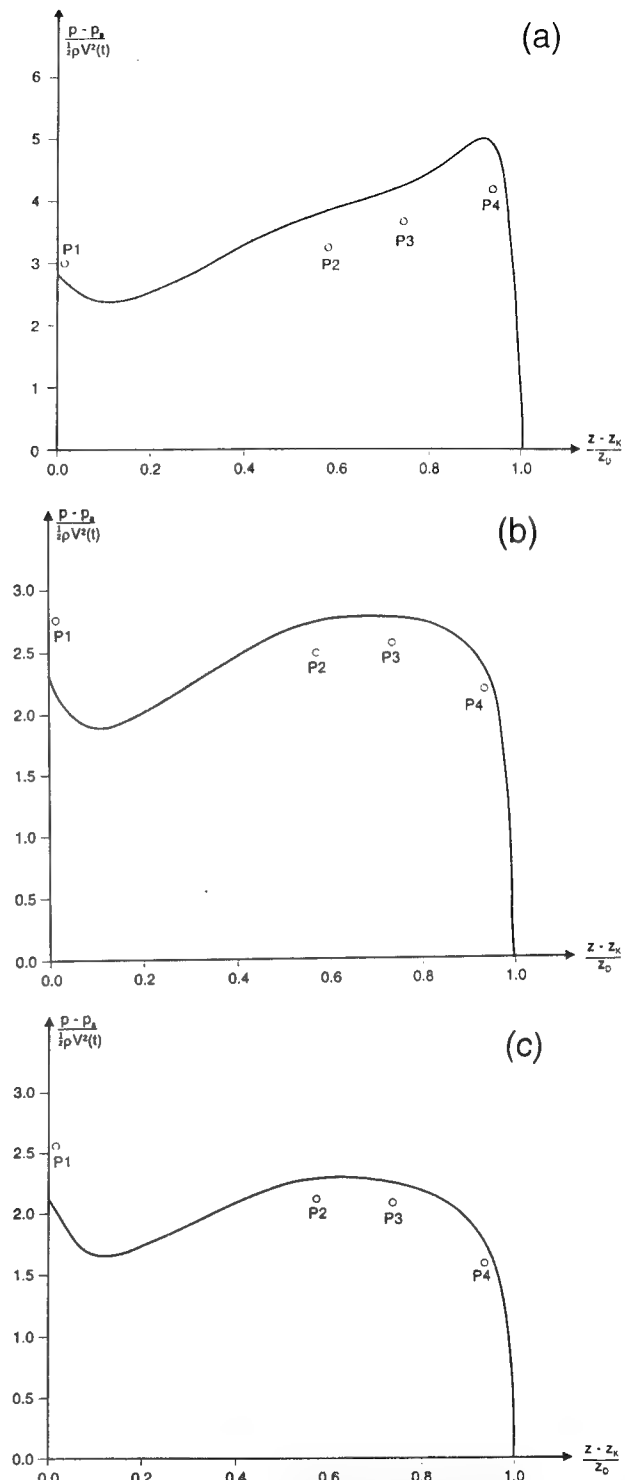


Figure 19: The pressure distribution(p) at three time instances during water entry of a bow flare section with knuckles(see figure 13b). $V(t)$ is the measured drop velocity(see figure 18b), p_a is atmospheric pressure, ρ is mass density of the fluid, t is time variable, $t=0$ corresponds to that the keel touches the water surface, z is vertical coordinate on the body surface, z_k is vertical coordinate of the keel and z_D is the draft of the body. o, experimental results; ———, fully nonlinear solution. (a) $t=0.06$ s; (b) $t=0.07$ s; (c) $t=0.08$ s.

whole period of water entry including when separation from the knuckles occurs. Three-dimensional flow effects in the experiments are theoretically estimated. A simplified method to predict slamming load is also presented. This is based on a generalization of the Wagner(1932) approach. The exact body boundary condition is satisfied. No flow separation is accounted for. It is demonstrated that the simplified solution gives reasonable results. The commonly used method to calculate forces on bow flare sections based on von Karman method and conservation of momentum gives too low maximum force and a wrong time history of the force.

9 ACKNOWLEDGEMENT

This work is carried out as a part of the DYNAMIC ANALYSIS SUPPORT SYSTEM PROJECT, DASS-Project. The project is a 5-years cooperative project between The Royal Norwegian Navy and The US Naval Sea System Command, Norwegian and US research institutes and universities, and the Norwegian industry.

10 REFERENCES

Dobrovolskaya, Z.N. "On some problems of similarity flow of fluid with a free surface," J.Fluid Mech. Vol.36, pp.805-829, 1969

Faltinsen, O.M. "Sea loads on ships and offshore structures," Cambridge University Press, 1990.

Faltinsen, O.M. "On seakeeping of conventional and high-speed vessels," 15th Georg Weinblum Lecture, Journal of Ship Research, Vol.37, no.2, June 1993.

Faltinsen, O.M. "The effect of hydroelasticity on ship slamming," to be published in Phil. Trans. R. Soc. Lond., 1996.

Greenhow, M. and Lin, W.M. "Nonlinear free surface effects: experiments and theory," Department of Ocean Engineering, MIT, report no.83-19, 1983.

Greenhow, M. "Wedge entry into initially calm water," Appl. Ocean Res., Vol.9, pp.214-223, 1987.

Knapp, R., Daily, J.W., Hammitt, H.F.G. "Cavitation," McGraw-Hill Book Company, 1970.

Kvålsvold, J., Faltinsen, O.M., Aarsnes, J.V. "Effect of structural elasticity on slamming against multihull vessels," In Proc. 6th. Int. Symp. on the Practical Design of Ships and Offshore Mobile Units (PRADS), pp.1684-1699, Seoul, 1995.

Meyerhoff, W.K., "Added masses of thin rectangular plates calculated from potential theory," Journal of Ship Research, pp.100-111, June 1970.

von Karman, T., "The impact of seaplane floats during landing," N.A.C.A. TN321, Washington, 1929.

Wagner, H., "Über stoss- und Gleitvorgänge an der Oberfläche von Flüssigkeiten," Zeitschr. f. Angew. Math. und Mech., Vol.12, No.4, pp.193-235, 1932.

Zhao, R., Faltinsen, O.M., "Water entry of two-dimensional bodies," J.Fluid Mech., Vol.246, pp.593-612, 1993.

Coupled Hydrodynamic Impact and Elastic Response

D.-J. Kim,¹ W. Vorus,² A. Troesch,² R. Gollwitzer³

(¹University of Pusan, Korea; ²University of Michigan, USA;

³Naval Surface Warfare Center [Panama City], USA)

ABSTRACT

A theoretical model for hydrodynamic impact of hulls with hard chines is described. Two distinct conditions are considered: one in the initial stages of impact where the jet-head travels along the hull towards the chine and one in the later stages of impact where the jet-head leaves the body at the chine and outwardly travels across the water surface. Numerical calculations of the hull impact force and acceleration are given and compared with experimental drop test results. The model is then extended to include an internal body, supported by springs and dashpots. The mass of the impacting hull and the mass of the internal body form a two body system subject to the external force of the fluid. The motion of the masses are coupled through the hydrodynamic boundary value problem to form a time dependent hydroelastic impact model. Results applicable to shock mitigation and shock isolation studies are given.

INTRODUCTION

The hydroelastic behavior of high speed craft in a seaway is becoming an important design consideration as hull scantlings are made lighter in a never-ending search for weight reduction. This optimization of hull strength is occurring at the same time vessel speeds are increased due to extended performance demands. In addition to structural considerations, the high speed and resulting high acceleration environment affect human performance and comfort. Severe shock loads certainly cause a reduction in operating personnel effectiveness and can result in potentially severe injury.

The accurate prediction of hull loads and responses during impact, though, requires the

solution of coupled external hydrodynamic and internal elasto-dynamic problems. In previous impact loading calculations (e.g. Yamamoto et al., 1980, Meyerhoff and Schlachter, 1980, and Belik et al, 1988), either the hydrodynamic force was decoupled from structural response by assuming constant-velocity water entry, or simplistically coupled hydroelastic models were used where the hydrodynamic load was treated as quasi-steady. Recent works by Kvålsvold and Faltinsen (1993) and Kvålsvold et al (1995) have shown that the impact-initiated dynamic response of an elastic structure can be an important factor in changing local pressures and thus hull girder loads. The coupling between the hydrodynamics and an internal structural response has also been investigated in shock mitigation studies where biodynamic human response was a primary consideration (e.g. Gollwitzer and Peterson, 1995, 1996). These more recent efforts demonstrate the importance of a validated, general time-dependent, impact theory to which hull structural response can be coupled.

Starting with von Karman (1929) and Wagner (1932, 1933), the hydrodynamic impact problem has been investigated in various forms for years. However, the different theories are approximations and forced compromises reflecting the inherent difficulty of the problem. Traditionally, the analysis has either been conducted in two dimensions using a nonlinear free surface boundary condition without gravity, or in three dimensions using a simplified pressure release condition, i.e. $\phi = 0$ on $z = 0$. Some recent representative examples of these two different approaches are Cointe (1991), Zhao and Faltinsen (1992, 1993) and Vorus (1992, 1996) for the two dimensional solutions and Troesch and Kang (1986 and 1988) for the simplified three dimensional

solution. These papers did not couple the elastic response of the hull with the hydrodynamic problem.

The following sections will present the theory of transient impact, experimental validation, and numerical calculations of coupled wedge impact with elastic hull response. A time-dependent free surface impact boundary value problem (Vorus 1992, 1996) will be used to estimate the impact load acting on a rigid, constant deadrise section. The paper will discuss the significant difficulties associated with solving the fully nonlinear boundary value problem when time dependent spray sheets are present and assumptions based upon similarity flows are no longer valid. In addition, the impact problem for a finite wedge where the wedge surface becomes vertical at a hard chine will be briefly reviewed (Vorus, 1996). Comparisons between theory and experiments will also be presented. The experiments involve the drop testing of nearly prismatic sections of typical planing hulls. The analysis is then extended to include the coupling of a discrete mass attached to the rigid hull by springs and dashpots. This model has direct application to the shock problem associated with high speed planing vessel impact in waves. Numerical studies are presented which show the effect of different parameter values in system mass ratio, stiffness, and damping on maximum acceleration response.

THEORETICAL MODELING OF IMPACT

The characteristics of the flow during impact, which include the hull pressure distribution, jet velocity, and free surface deformation, change dramatically as the jet head passes over severe hull geometric variations. When the jet head reaches a location on the hull's surface where the surface curvature exceeds that which would normally occur in an unrestrained jet, such as at a chine, the pressure drops significantly. See Figure 1 for a schematic defining the "chines dry" and "chines wet" stages of impact. A variation of the model described in the following paragraphs (Vorus, 1992, 1996) has been compared extensively with steady planing pressure distributions (Lai and Troesch, 1995) which include the essential characteristics of impact hydrodynamics. A summary of the impact model is reviewed here briefly for completeness. Details can be found in Vorus (1996).

The theoretical formulation of Vorus (1992, 1996) can be viewed as a solution to the complete two dimensional nonlinear impact initial-boundary value problem in all respects except that the nonlinear boundary conditions are satisfied on the horizontal axis. This is argued to be consistent to lowest order in the flatness limit. Physically, as the cylinder

flattens toward coincidence with the horizontal axis, the boundary conditions more and more accurately apply on the axis, implying a limit of geometric linearity. However, with increasing flatness, the transverse flow velocity tends toward infinity over the entire material contour (except with a singular zero at the plane of symmetry for symmetric impact). This implies the limiting condition of uniform hydrodynamic nonlinearity. The theory is therefore mixed: It is *geometrically linear* in that the boundary conditions are satisfied on the horizontal axis, but it is *hydrodynamically nonlinear* in that the large transverse perturbation velocity is fully retained in the axis boundary conditions.

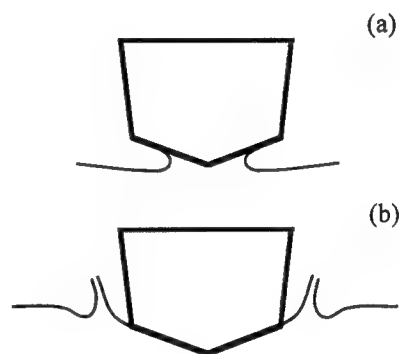


Figure 1: Definition of "chines dry" (a) and "chines wet" (b) impact phases

The mathematics problem is defined with the aid of Figure 2. Although depicted on Figure 2 as a semi-infinite wedge, the cylinder contour is of arbitrary shape and can include a hard chine where separation is forced to occur. The impact velocity $V(t)$ is also arbitrary and can include, for example, forced deceleration which also produces contour flow separation, as is demonstrated in Vorus (1996).

Referring to Figure 2, the principal solution unknowns are the zero pressure point offset $z_c(t)$, the jet head offset $z_b(t)$ and the jet velocity distribution, $V_s(z,t)$, between $z_c(t)$ and $z_b(t)$. A multi-layered nonlinear iteration is required in computing these unknowns starting from an initial condition corresponding to the self-similar semi-infinite wedge at the initial impact velocity $V(0)$. The solution equations that must be iterated derive from the nonlinear boundary conditions satisfied on the axis segments indicated in Figure 2 b.

The *dynamic boundary condition* of zero pressure on the jet head free vortex sheet leads to a one-dimensional Burger's equation in terms of the $V_s(z,t)$ and $z_c(t)$ unknowns:

$$(V_s - z_c \tau) \frac{\partial V_s}{\partial \zeta} + z_c \frac{dV_s}{d\tau} = 0 \quad 1 \leq \zeta \leq b(\tau) \quad (1)$$

Here $\zeta = z/z_c$, τ is nondimensional time, and $b = z_b/z_c$. As shown in Vorus (1996), Eq. (1) can be solved analytically by Galaen transformation to express $V_s = V_s(\zeta, \tau; z_c(\tau))$ on the free sheet. The solution to Eq. (1) assures that the pressure is constant on $1 \leq \zeta \leq b(\tau)$. The condition that the value of the constant be zero is assured by:

$$z_{b\tau} = \frac{V_s^2(b, \tau) + V_n^2(\tau) - V^2(\tau)}{2V_s(b, \tau)} \quad (2)$$

In Eq. (2), the free sheet normal velocity V_n is taken as 0 or 1 depending on whether at τ the chine is unwetted or wetted, respectively.

Equation (2) and the solution to Eq. (1) provide two conditions on the unknowns $z_c(t)$, $z_b(t)$, and $V_s(z, t)$ in $z_c < z \leq z_b$. $V_s(z_c, t)$, the velocity entering the jet head, is the boundary condition in Eq. (1) and must be considered to be a fourth unknown.

The integral equation formed from the cylinder *kinematic boundary condition* is of the Carleman type, which is inverted analytically to produce the contour vortex strength, $\gamma_c = -2V_s$ in $0 \leq z \leq z_c(\tau)$ in terms of the principal unknowns as:

$$\gamma_c(\zeta, \tau) = -\frac{2 \cos \bar{\beta}(\zeta, \tau) \zeta \kappa(\zeta, \tau)}{\sqrt{1 - \zeta^2}} \left[V(\tau) + \frac{1}{\pi} \int_{s=1}^{b(\tau)} \frac{\gamma_s(s, \tau) ds}{\kappa(s, \tau) \sqrt{(s^2 - 1)}} + \frac{\zeta^2 - 1}{\pi} \int_{s=1}^{b(\tau)} \frac{\gamma_s(s, \tau) ds}{\kappa(s, \tau) \sqrt{(s^2 - 1)(s^2 - \zeta^2)}} \right] \quad (3)$$

The two new terms in (3) are both unknown functions at time τ :

$$\bar{\beta} = \bar{\beta}(\zeta, \tau) \equiv \tan^{-1}[\sin \beta(\zeta, \tau)], \text{ where } \beta(\zeta, \tau) \text{ is the spatially variable contour deadrise angle at } \tau \text{ in } 0 \leq \zeta \leq 1.$$

$$\kappa(\zeta, \tau) \equiv \prod_{k=1}^K \left| \frac{\zeta^2 - \zeta_{k+1}^{*2}}{\zeta^2 - \zeta_k^{*2}} \right|^{\frac{\bar{\beta}_k^{*}(\tau)}{\pi}} \text{ is from a}$$

K-element piecewise linear discretization of the cylinder contour at τ in $0 \leq \zeta \leq 1$ with the ζ_k^* and $\bar{\beta}_k^*$ being the element end-point offsets and angles, respectively, as developed in Vorus (1996).

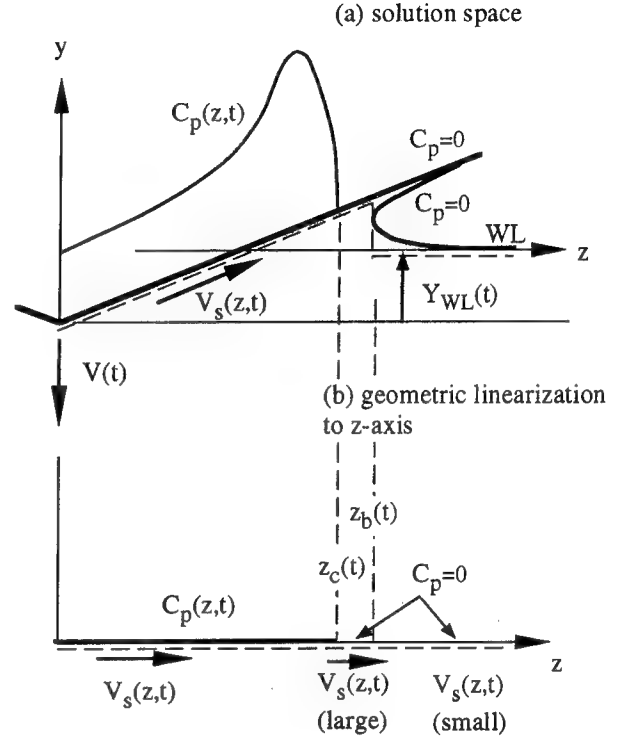


Figure 2: Solution space and unknowns

Equation (3) is singular at $z = z_c(\zeta = 1)$. Removal of the singularity requires that the first two terms in the bracket be collectively zero:

$$V(\tau) + \frac{1}{\pi} \int_{s=1}^b \frac{\gamma_s(s, \tau) ds}{\kappa(s, \tau) \sqrt{(s^2 - 1)}} = 0 \quad (4)$$

Equation (4) is a *velocity continuity condition*, in the sense of a "Kutta Condition," providing with Eqns. (1) and (2) a third relationship among the four unknowns.

For the chine-wetted penetration phase of the cylinder immersion, with $z_c(\tau)$ known and equal to the chine offset Z_{ch} the formulation is theoretically complete with Eq. (4). Equations (1), (2), and (4) determine the remaining principal unknowns $\gamma_s(\zeta, \tau)$, $\gamma_s(1, \tau)$, and $z_b(\tau)$ uniquely, given the values at the time of chine-wetting. For the initial chine-unwetted flow however, $z_c(\tau)$ is an additional independent unknown, and an additional condition is required.

By Figure 2a, the velocity of the jet head, $z_b(t)$, is jump discontinuous from a large value on the cylinder contour to a small (higher order) value on the free-surface at the jet-head. However, the cylinder and free-surface contours must be continuous at $z_b(t)$ for the chine unwetted flow $z_c(t) \leq Z_{ch}$. The *displacement continuity condition* is obtained by integrating the kinematic boundary condition in time and solving the resulting Carleman integral equation for a displacement vortex strength:

$$\gamma_c^*(\xi, \tau) = -\frac{2\xi \cos \bar{\beta}(\xi, \tau) \left(\frac{1-\xi^2}{\xi^2} \right) \pi}{\sqrt{1-\xi^2}} \left[Y_{wl}(\tau) - \frac{2}{\pi} \int_{s=0}^1 \frac{\cos \bar{\beta}(s, \tau) h_c(s, \tau) ds}{\kappa(s, \tau) \sqrt{1-s^2}} + \frac{2}{\pi} (1-\xi^2) \int_{s=0}^1 \frac{\cos \bar{\beta}(s, \tau) h_c(s, \tau) ds}{\kappa(s, \tau) \sqrt{1-s^2} (s^2 - \xi^2)} \right] \quad (5)$$

As with Eq. (3), the singularity in the first two bracketed terms of this solution must be removed to achieve the required displacement continuity. There results the fourth and final condition on the unknowns:

$$Y_{wl}(\tau) = \frac{2}{\pi} \int_{s=0}^1 \frac{\cos \bar{\beta}(s, \tau) h_c(s, \tau) ds}{\kappa(s, \tau) \sqrt{1-s^2}} \quad (6)$$

where $h_c(s, \tau)$ in Eq. (6) is the cylinder contour elevation above the baseline from the plane of symmetry to the jet head, $s = 1$. $Y_{wl}(\tau)$ is the distance above the baseline to the undisturbed water surface and is just the integral of $V(\tau)$ in time. Both $h_c(s, \tau)$ and $Y_{wl}(\tau)$ are known functions at time τ .

The four generally unknown functions $z_c(t)$, $z_b(t)$, $V_s(z_c, t)$ in $z_c < z < z_b$, and $V_s(z_c, t)$ are iterated forward in time using Eqns. (1), (2), (4), and (6). Since all integral equation inversions have been performed analytically and the spatial integrations have been performed semi-analytically in terms of special functions, the numerical computations required with this highly nonlinear problem are stable and well behaved even with relatively coarse discretization. The numerical analysis employed to date is outlined in Vorus (1996); all the numerical results exhibited there were executed on a 16 mHz desk-top computer.

Once the four solution variables have been determined for any time, back substitution into Eq. (3) (with the singular terms removed) gives the cylinder contour vortex strength:

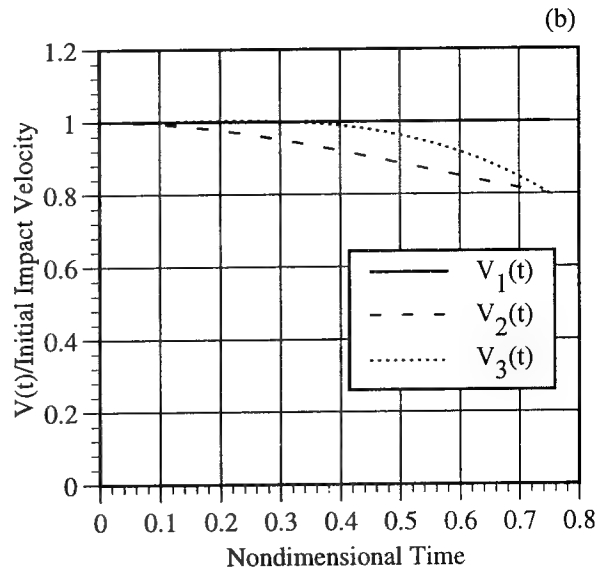
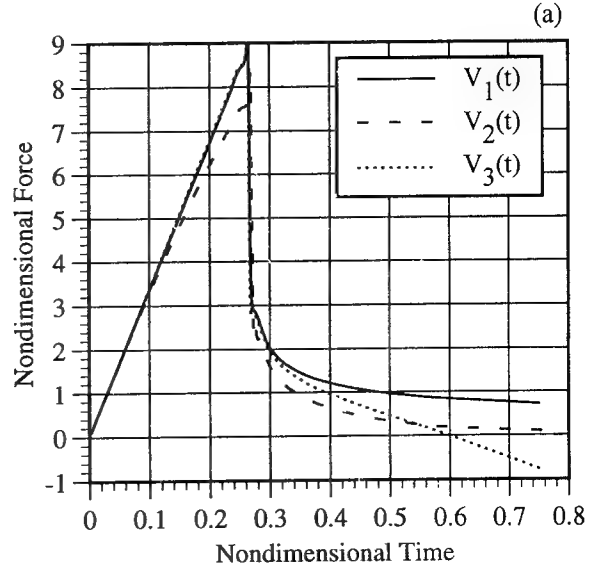


Figure 3: Impact force (\bar{F}) vs time (τ) for prescribed time varying impact velocities (a) \bar{F} vs τ . (b) Prescribed $V(t)$ vs τ . Deadrise = 20 degrees

$$\gamma_c(\zeta, \tau) = -\frac{2 \cos \bar{\beta}(\zeta, \tau) \zeta \kappa(\zeta, \tau)}{\sqrt{1 - \zeta^2}} \left[\frac{\zeta^2 - 1}{\pi} \int_{s=1}^{b(\tau)} \frac{\gamma_s(s, \tau) ds}{\kappa(s, \tau) \sqrt{(s^2 - 1)(s^2 - \zeta^2)}} \right] \quad (7)$$

In a standard manner, the contour vortex strength, Eq. (7), is applied with the unsteady Bernoulli equation to produce the cylinder pressure distributions and the impact forces of primary interest.

Typical results for impact forces on a twenty degree wedge with non-constant impact velocity are presented in Figures 3 and 4. The nondimensional form of the impact force, \bar{F} , and time, τ , are defined below as follows:

$$\bar{F} = \frac{F}{\rho V_0^2 B/2} \quad (8)$$

$$\tau = \frac{V_0 t}{B/2}$$

where $B (=2 Z_{ch})$ is the hull beam at the chine and the initial impact velocity is V_0 . Four different prescribed velocities were used to calculate the impact forces. These prescribed velocities possess attributes of velocities shown in the coming sections where rigid body equations of motion are coupled with impact hydrodynamics. Three of the less severe velocity changes (characteristic of heavily loaded hulls during drop tests) are shown in Figure 3. The first velocity, V_1 , is constant for reference. The other two velocities, $V_2(t)$ and $V_3(t)$, are reduced 20%, one gradually (i.e. V_2) and one quickly (i.e. V_3). The large drop in impact force at an approximate value of $\tau = 0.265$ is due to the transition from chines dry to chines wet flow as the jet head passes the chine. The solution becomes square root singular at that instant, but of course integrable. The different accelerations produce significantly different impact forces, with the sharpest deceleration leading to negative impact loads.

In Figure 4, the velocity, $V_4(t)$, is reduced quickly to 30% of the initial value. This would be characteristic of lightly loaded hulls during drop tests. The large reduction in velocity produces a significantly smaller maximum impact force (but not necessarily lower accelerations, as will be demonstrated later) which occurs not at the instant of chines wetting, but rather at some time before. Of particular interest is the negative impact force during

the chines-wetted phase of the impact. This "suction force" is due to the reduced momentum of the jet and downward momentum of the surrounding fluid. The velocity of the jet, $V_{jet}(t) (=V_s(Z_{ch}, t))$, is also shown in Figure 4 b. During the initial stages of impact, the jet velocity for a twenty degree deadrise hull is approximately eight times the impact velocity. Once the jet head clears the chine, $V_{jet}(t)$ decreases significantly, actually becoming less than the magnitude of the downward velocity of the hull.

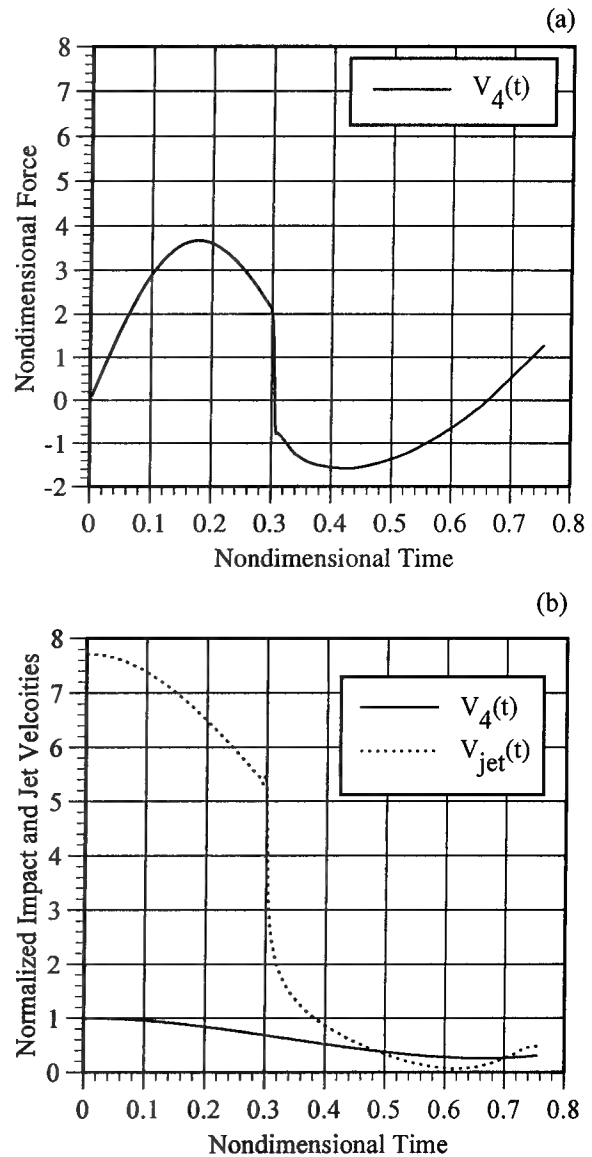


Figure 4: Impact force (\bar{F}) and jet head velocity for a prescribed time varying impact velocity (a) \bar{F} vs τ . (b) Prescribed $V(t)$ and $V_{jet}(t)$ vs τ . Deadrise = 20 degrees

EXPERIMENTAL VALIDATION PROGRAM

Objectives and Application

Drop tests were conducted at the Coastal Systems Station (CSS), Dahlgren Division, Panama City, Florida. These types of tests have been shown to be vital to the ongoing CSS shock mitigation program, and are expected to be useful in conjunction with future shock mitigation investigations. Within the CSS program, the data have been used for initial, qualitative evaluation and identification of shock mitigation concepts, for calibrating and validating the 2-D vertical water-entry model, and for validating evolving 2-D cylinder impact theories. The application to qualitative evaluation and identification of shock mitigation concepts is justified in part by the observed similarity between at-sea measurements of high-speed-vessel acceleration time histories, and those of boat-segment drop tests for approximately similar hull geometries and vertical entrance velocities. The most important and relatively long term application of drop test data, however, is calibration and validation of the 2-D components within evolving wave-to-wave planing boat theories.

Facility, Model Description, and Procedures

All test drops were conducted in the above ground test pool in Building 319 at CSS. The test tank is a fresh water pool that measures 40.0 ft (12.2 m) long by 15.0 ft (4.6 m) wide by 16.5 ft (5.0 m) deep. The water depth was reduced to 11.25 ft (3.43 m) to minimize the amount of water splashing out of the pool during water impact. The test models were lifted above the water surface by an overhead crane, and dropped into the center of the water surface. The temperature of the water varied slightly as the ambient temperature in the building varied. The average temperature for all drops was within 70 degrees $F \pm 5$ degrees F . Water density differences were insignificant and consequently no corrections for density were made in the data.

Drops were made of prismatic and non-prismatic hull segments and aluminum and fiber reinforced plastic hull segments. Also two full-length scale model hulls were dropped: a baseline hull and a hull with a shock mitigation system installed. This paper will presents results of the aluminum full-scale prismatic hull segments. A more detailed discussion of all drops is given by Gollwitzer and Peterson (1996).

The aluminum hull segments represent longitudinal segments of a full scale hard-chine hull about 40 ft (12.2 m) long overall. The baseline test

segment was a prismatic 23 deg deadrise segment without strakes, 3.4 ft (1.04 m) long as measured longitudinally along the keel, with a chine beam of 5.0 ft (1.52 m). A variation of the baseline segment with strakes added parallel to the keel was also tested.

A test fixture served as the central hardware interface for the testing. The test hull bottom, the drop sling arrangement, and the accelerometers were mounted to the test fixture to form the complete hull segment which weighed 916 lb (4.07 kN). The drop test fixture and hull bottom were essentially structures assembled from plates of aluminum. Longitudinal and transverse plates were welded into the drop test fixture for stiffening, reducing the contribution of structural elastic effects to the total measured accelerations during water-entry impact.

A four-leg sling was used to connect the test segment to an overhead crane. One leg of the sling was secured to each of the four corners of the test fixture. For each drop, the four legs were fitted into a quick-release mechanism attached to the overhead crane hook. The segment was hoisted by the crane to the desired drop height. The data collection process was initiated, a verbal countdown was made, and the fixture was dropped by opening the quick-release hook.

Other impact tests have used vertical rails to ensure the vertical drop orientation of the test fixture (e.g. Chuang, 1970). Mechanical guides were not used here after three-axis accelerometer measurements confirmed that the free drops were indeed vertical. The models were dropped from heights of 2, 4, 6, and 8 ft (0.61, 1.22, 1.83 and 2.44 m) above the water surface. Other varied parameters were the mass and the trim angle of the models.

Instrumentation

Hull mounted accelerometers were used in the experimental part of this shock and vibration study, primarily to enable comparisons between laboratory measurements and previously acquired at-sea data. The signals in both sets of tests were digitally recorded.

Both piezoelectric and piezoresistive accelerometers were used for this investigation to measure the full range of accelerations and the full frequency response of interest. Hermetically sealed accelerometers were chosen to reduce the harmful effects of the test environment. The piezoresistive accelerometers were Entran Inc. semiconductor Wheatstone bridge instruments, Model EGA3 series. Their nominal sensitivity was 0.5 mV/g with a range of ± 500 g's and a nominal resonant frequency of 3000

Hz. Low frequency resolution is effectively unlimited. The piezoelectric accelerometers were Dytran Instruments Inc. low impedance quartz crystal and seismic mass transducers, Model 3100 series. Their nominal sensitivity was 50 mV/g with a range of $\pm 100 \text{ g's}$. Low frequency response was $1 \text{ Hz} \pm 10\%$ at 5% down.

All accelerometers used for these tests measured 0 g when at rest. All reported accelerations are referenced to 0 g for the test segment floating in static equilibrium.

The accelerometers were secured in the longitudinal, transverse, and vertical directions to a solid mounting block. The mounting block was placed at the top center of the drop test fixture, which was the location of the longitudinal and transverse centers of gravity of the test segment. The analog voltage signals from the accelerometers were transmitted by hard wire to Ectron Model 562 analog amplifiers. The amplifiers provided wideband frequency response to 80 kHz and supply voltage to the accelerometers of $10.00 \text{ V} \pm 0.002 \text{ V}$. Data were sampled at a 200 microsecond sample rate and recorded by a Nicolet Model 310 Digital Oscilloscope and a TEAC digital tape recorder, Model RD-200T, with a 200 kHz low pass anti-aliasing filter. A desktop personal computer was used to process the collected data using in-house software. A more detailed discussion of the instrumentation is included in Gollwitzer and Peterson (1996).

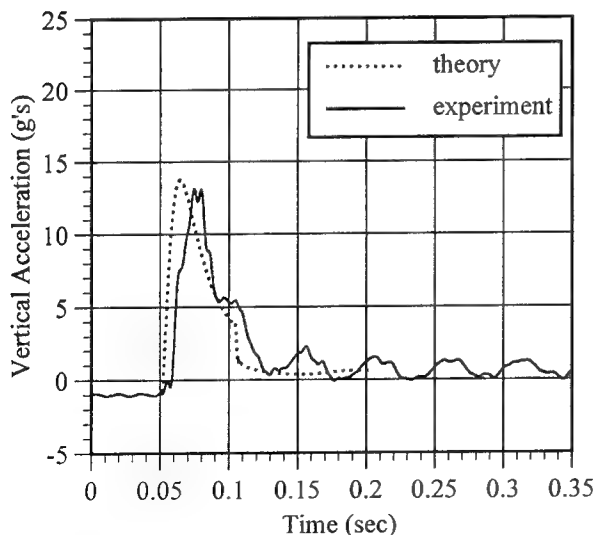


Figure 5: Experimental (solid line) and theoretical (dashed line) impact accelerations in g's for a twenty three degree deadrise (nominal) hull section. No strakes attached. Drop height = 8.0 ft (2.438 m)

Discussion of the Experimental Results

Two typical acceleration time histories are presented here, one for the constant deadrise section without strakes, Figure 5, and one for a similar section with strakes, Figure 6. Numerical results based upon the theory of Eqns. (1)-(7), where $V(\tau)$ is determined from $F = m\dot{V}$, are also plotted for comparison.

In Figure 5, the results for the constant deadrise section without strakes are shown. The vertical axis is the acceleration in g's and the horizontal axis is the elapsed time in seconds. The solid line represents the filtered (cutoff frequency = 200 Hz) experimental acceleration and the dashed line represents the theoretical equivalent.

Generally, the unfiltered data of the constant deadrise section without strakes indicates mechanical frequency components at about 20 Hz and 60 Hz superimposed on the basic hydrodynamic shock record. An impulse test of the model indicated the fundamental frequency of the test fixture to be 63 Hz . For reference, a human is susceptible to motion sickness at frequencies between about 0.2 Hz and 1 Hz (ISO 2631 Part 3). The spine of the seated human is susceptible to discomfort and injury at frequencies from about 4 Hz to 8 Hz , and the lower extremities of a standing human are susceptible to discomfort and

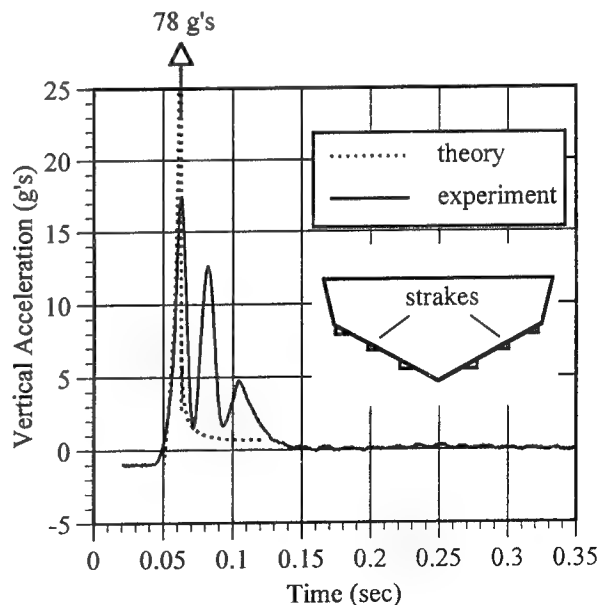


Figure 6: Experimental (solid line) and theoretical (dashed line) impact accelerations in g's for a twenty eight degree deadrise (nominal) hull section. With strakes attached. Drop height = 8.0 ft (2.438 m)

injury at frequencies as high as 30 to 40 Hz (ISO 2631 Part 1). The model scale time histories shown in Figures 5 and 6 were digitally filtered at 200 Hz. This filtering frequency captures the relevant human body discomfort and injury dynamics while eliminating contaminating high frequency noise effects.

In Figure 6, the results for the constant deadrise section with strakes are shown. A significant characteristic of the experimental curve is the large drop in acceleration when the jet head reaches the first strake and the flow effectively becomes chines-wet-type-flow until reattachment. The cycle is repeated as the jet head advances toward the next strake. At present, the theoretical model is only valid up to the first strake. The model assumed that the flow became chines wet after the first strake and remain separated which is clearly not the case. The time to reach the first strake edge is approximately predicted, but the maximum acceleration is severely over-predicted due to the high rate of change of locally decreasing deadrise. This is an area of ongoing research.

For the constant deadrise section without strakes, the distinct phases of the individual shock event can be seen in the Figure 5. The water re-entry shock pulse is shown in the time histories by the rapid rise from -1 g up to the peak amplitude and the subsequent fall back towards 0 g. The rise time is approximately 20 msec, and the fall time is approximately 50 msec, producing a total pulse duration of about 70 msec. The submergence/emergence phase occurs for about 500 msec after the water re-entry shock phase.

The impact of the hull segment with strakes as shown in Figure 6 is significantly different from the time history shown in Figure 5. An examination of the geometry of the strakes and the boat velocities at water entry indicates that multiple peaks in the acceleration time histories are caused by the strakes entering the water. The drop tests indicate that strakes shorten the duration but increase the amplitudes of the shocks. Care must be taken in the positioning of the strakes so as to not excite hull or human resonant frequencies during impact.

Based upon the above comparisons between theory and experiment, we conclude that the theory predicts hydrodynamic impact characteristics for constant deadrise shapes, both up to and beyond the point where the jet head reaches the chine. The magnitude of the maximum acceleration is slightly over predicted and the rise time is slightly offset. The elastic response of the test section certainly plays a role in defining the impact characteristics, but without an extensive structural analysis, this role is

difficult to quantify. For sections with strakes, there are discernible differences between theory and experiment. More work is clearly needed to describe the impact of sections with locally large slope changes leading to separation and then re-attachment.

IMPACT OF A MULTI-DEGREE-OF-FREEDOM BODY

This part of the paper examines the effect of variable impact velocity on multi-degree of freedom bodies experiencing slam conditions. An obvious application of this analysis is the design of shock mitigating devices for occupants of high speed vessels. A simplified lumped-mass model for the hull structure is assumed. The time-dependent free surface impact boundary value problem (Vorus 1992, 1996) described in the first sections of this paper has been used to estimate the impact load acting on an externally rigid, finite beam, constant deadrise section.

The system equations of motion can include a finite number of discrete masses attached to the rigid hull by springs and dashpots. The mass of the impacting hull and the mass of the internal body form a time dependent hydroelastic impact model. See Figure 7 for a schematic of the two degree model considered here. Since the solution is presented as the time integration of the equations of motion, the internal stiffness and damping can be nonlinear functions of the relative displacement and velocity. In this work, the system damping and stiffness are linearized as shown in Eq. (9).

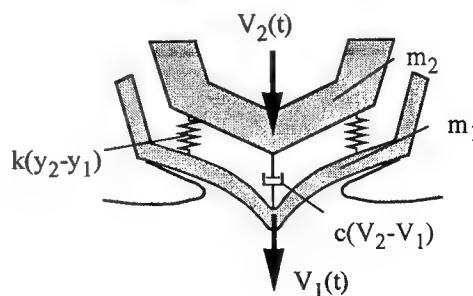


Figure 7: Schematic of coupled hydroelastic impact model with variable impact velocity.

$$\begin{aligned}
m_1 \ddot{y}_1 = & -m_1 g - k(y_1 - y_2) - c(\dot{y}_1 - \dot{y}_2) + \\
& + F_y(\ddot{y}_1, \dot{y}_1, y_1, t) m_2 \ddot{y}_2 = -m_2 g - \\
& - k(y_2 - y_1) - c(\dot{y}_2 - \dot{y}_1)
\end{aligned} \quad (9)$$

where the hydrodynamic impact force, $F_y(\ddot{y}_1, \dot{y}_1, y_1, t)$, is determined from the theory governed by Eqns. (1 - 7). This dynamic multi-body model has been incorporated into the hydrodynamic impact simulator forming a coupled hydroelastic analysis program. The time dependent impact velocity is not prescribed, but rather the solution of Eq. (9).

A characteristic beam loading parameter, $\alpha = (m_1 + m_2) / (\rho B^2)$, is defined, where m_1 is the mass per unit length of the impacting hull bottom and m_2 is the mass per unit length of the suspended interior mass. The impact velocity is represented by the parameter H/B , where B is the beam of the section and H is the drop height. The initial impact velocity, V_0 , then is given by $V_0 = \sqrt{2gH}$.

Time dependent, single degree-of-freedom impact

Before the dynamic effect of an interior oscillating mass is examined, the infinite spring constant case is investigated first. This will provide a basis for describing the effects of mass and stiffness parameter variations on the maximum acceleration, the maximum impact force, and the times to maximum impact force and chines wetting.

In Figure 8, a plot of the nondimensional maximum acceleration of the section and the beam loading parameter, α , is given for two values of the H/B parameter, 1.0 and 1.6 respectively. There is a slight drop height dependence in the results due to the relative contribution of the buoyancy term to the velocity squared term in Bernoulli's equation, depending upon the immersion of the section. Since the connecting spring constant is infinite, large values of α represent the limit of constant velocity impact, a typical assumption of classic impact analysis. The acceleration (deceleration) is in the nondimensional form \ddot{y} , where

$$\ddot{y} = \frac{\ddot{y}}{4g} \frac{B}{H}$$

For small values of α , there is a large increase in maximum acceleration (i.e. maximum deceleration) for decreasing α and for values of $\alpha > 2$, the relative change rapidly decreases, asymptoting

to $-g$ as $\alpha \rightarrow \infty$. Generally, the maximum acceleration occurs prior to chine wetting for small values of α , and corresponds to when the jet head reaches the chine for large values of α (see Figures 3 and 4). From this figure, we can conclude that when the mass is relatively small the acceleration, or deceleration, is large.

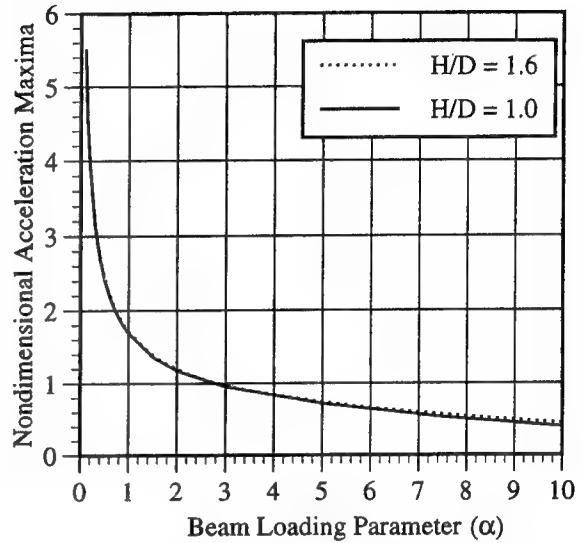


Figure 8: Maximum impact accelerations (\ddot{y}_{\max}) as a function of the beam loading parameter, α , and drop heights. $H/B = 1.0$ (solid line), 1.6 (dashed line). Infinite spring constant. Deadrise = 23 deg.

In Fig. 9, representative nondimensional dynamic force coefficient time histories for two different mass parameters are shown. The nondimensional form of the impact force, \bar{F} , and time, τ , are defined above in Eqns. (8). Even though the maximum deceleration for $\alpha = 0.1$, as shown in Fig. 8, is approximately ten times the maximum deceleration for $\alpha = 10.0$, the relative impact force for the lighter hull is an order of magnitude smaller. This suggests that light craft may experience accelerations that are potentially damaging to humans while heavier, better riding craft experience large local structural loads. Chine wetting for $\alpha = 0.1$ occurs at approximately $\tau = 1.41$ and for $\alpha = 10.0$ occurs at approximately $\tau = 0.314$. Generally, when the mass parameter is larger, it follows that the deceleration is relatively smaller, the value of the force coefficient is relatively greater, and the effect of chine wetting is more pronounced.

The nondimensional time of the maximum acceleration, τ_{\max} , and the nondimensional time of the chine wetting, τ_{wet} , are plotted together in Fig. 10. When the mass parameter α , is small the chine

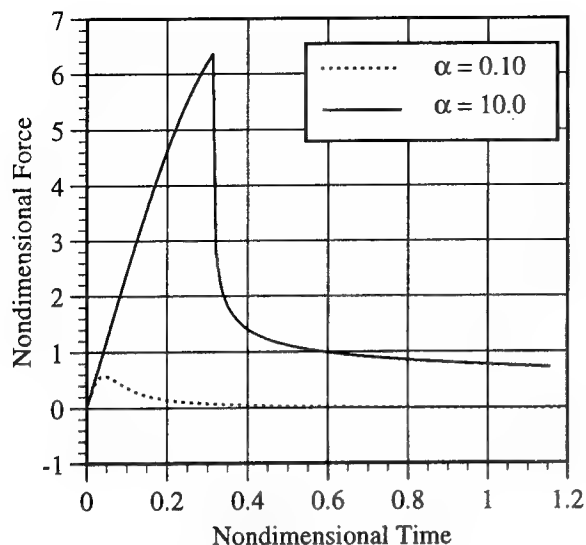


Figure 9: Impact force time histories (\bar{F} vs. τ) for two values of the beam loading parameter, $\alpha = 0.1$ (dashed line) and 10.0 (solid line). $H/B = 1.0$. Infinite spring constant. Deadrise = 23 deg.

wetting time occurs after the time of maximum acceleration. As α approaches zero, which would be the case for lightly loaded hulls, chine wetting does not occur. When α is large, the maximum acceleration coincides with the time of chine wetting. This is analogous to heavily loaded hulls where the assumption of constant velocity impact is most nearly valid.

Time dependent, two degree-of-freedom impact

Based upon these results, two mass parameter values are chosen as $\alpha = 0.3$ and $\alpha = 2.5$ for the finite spring constant case. (The experimental test hull had a value of $\alpha = 0.587$.) From Figure 10, the nondimensional chine wetting times for the infinite spring constant case with these two values of α are approximately 0.66 and 0.37 respectively. Three representative values of the spring constant are calculated so that one of the system natural periods (i.e. $T_n = 2\pi\sqrt{m_1/k}$) are 0.1 (relatively very stiff), 1 (relatively moderately stiff), and 5 (relatively soft), times the chine wetting time, t_{wet} . The damping coefficient is selected such that the damping ratio is 0.01. Here the damping ratio is defined as $\zeta = c/2\sqrt{km_1}$. (An investigation into the influence

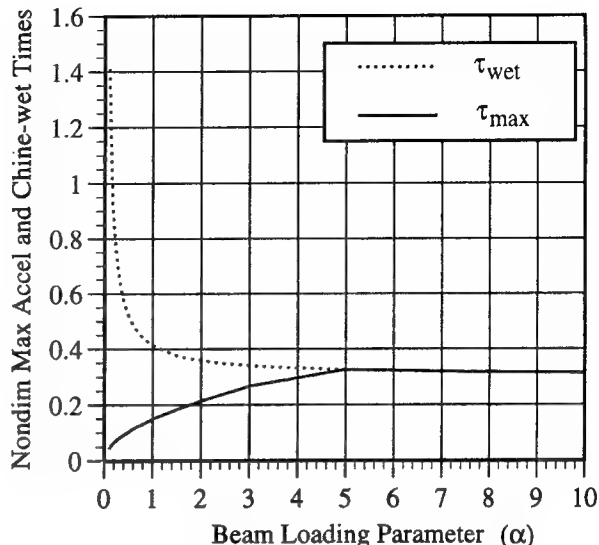


Figure 10: Time of maximum acceleration (solid line) and time of chine wetting (dashed line) as a function of the beam loading parameter, α . $H/B = 1.0$. Infinite spring constant. Deadrise = 23 deg.

of damping was carried out. As expected, for light damping the actual value of the damping ratio had little effect on the maximum values and general character of the responses.) To find the effect of mass distribution on acceleration of coupled body motion, another parameter, the mass distribution ratio (m_2/m_1), is defined.

In Figure 11 acceleration time histories of the coupled body for a constant mass distribution ratio of $m_2/m_1 = 1.0$ are given. Three different system stiffness' corresponding to values of $T_n/t_{wet} = 0.1, 1$, and 5 are shown. The value of the mass parameter is $\alpha = 2.5$. In the large spring constant case ($T_n/t_{wet} = 0.1$) there seems to be little phase shift in the two accelerations of m_1 and m_2 until chine wet conditions are reached. After chine wetting, the time histories exhibit typical lightly damped free vibration behavior where the masses then oscillate 180 degrees out of phase. In the intermediate stiffness case ($T_n/t_{wet} = 1.0$), the interior sprung mass experiences a dynamic overshoot of approximately 80%. In the soft system case ($T_n/t_{wet} = 5.0$), the sprung mass experiences the lowest acceleration on a much expanded time scale. The time history also suggests that the largest

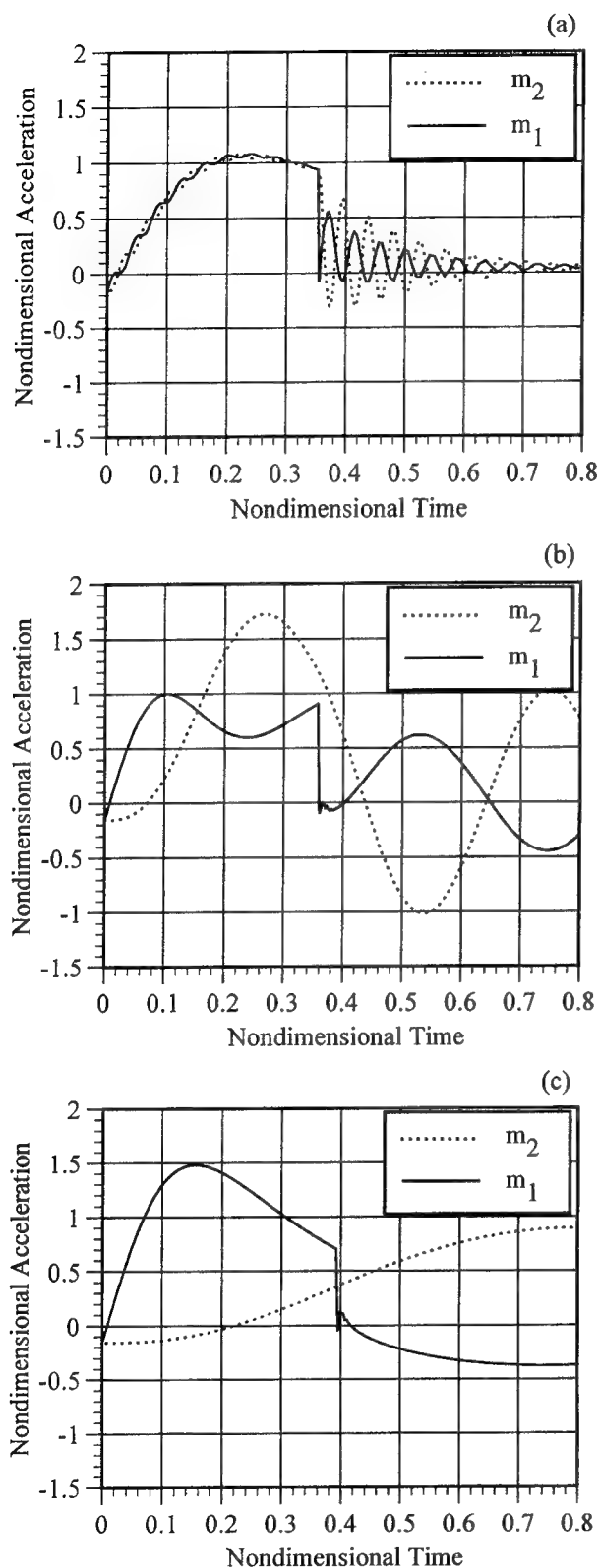


Figure 11: Impact acceleration time histories (\ddot{y} vs. τ) for three spring constants. Deadrise = 23 deg. (a) $T_n/t_{wet} = 0.1$. (b) $T_n/t_{wet} = 1.0$. (c) $T_n/t_{wet} = 5.0$. $H/B = 1.6$. $m_2/m_1 = 1.0$. $\alpha = 2.5$.

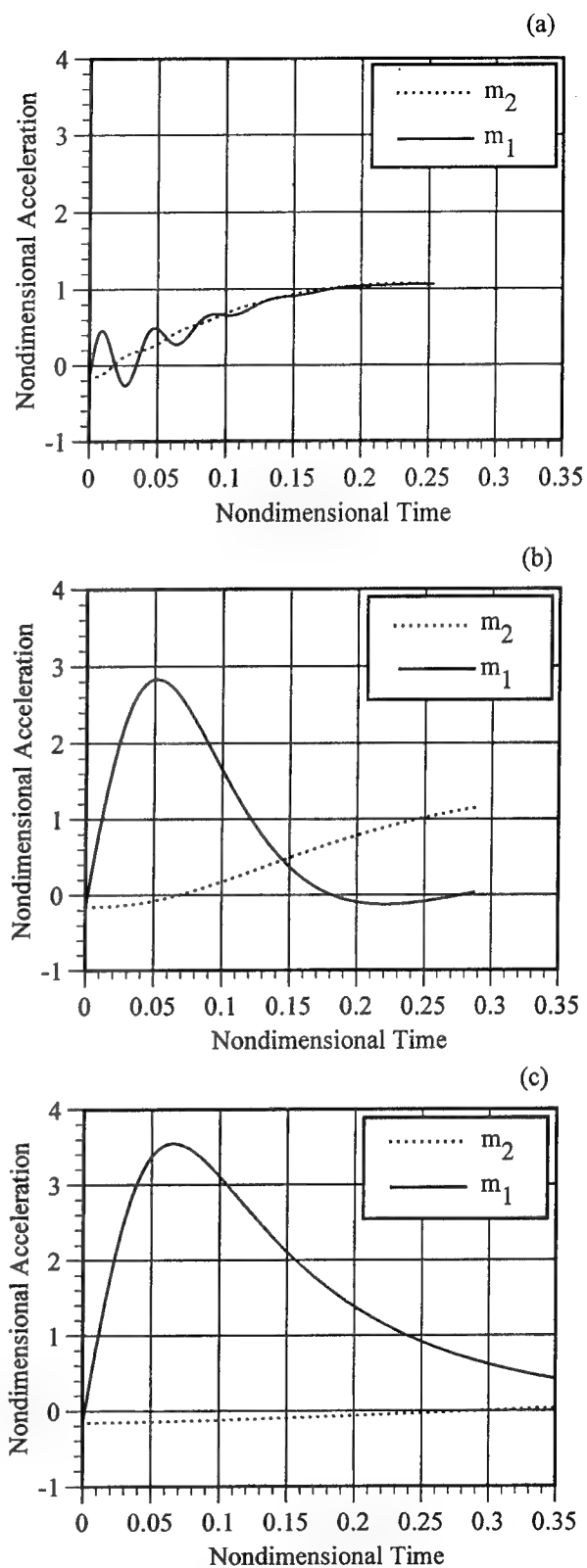


Figure 12: Impact acceleration time histories for three spring constants. (a) $T_n/t_{wet} = 0.1$. (b) $T_n/t_{wet} = 1.0$. (c) $T_n/t_{wet} = 5.0$. $H/B = 1.6$. $m_2/m_1 = 10$. $\alpha = 2.5$. Deadrise = 23 deg.

relative displacement occurs during the soft system impact. For all three cases, increased damping would be particularly effective in reducing the acceleration. In general, for a given drop height which is equivalent to specified loading condition, the acceleration can be decreased by selection of a proper mass/stiffness distribution of the two bodies.

Acceleration time histories are shown in Figure 12 for a mass distribution ratio of $m_2/m_1 = 10.0$. Here the time histories for the two stiffer systems are stopped at chine wetting due to numerical convergence difficulties in the time integration routines. Generally, the results have similarities to the results shown in Figure 11 with the exception that the interior mass experiences a significant reduction in acceleration. A possible shock mitigation device suggested by the plots would be a heavy inner hull attached by springs to a much lighter outer skin.

In Figures 13 and 14, the acceleration time history results for a mass parameter of $\alpha = 0.3$ are shown. The mass distribution ratios, m_1/m_2 , are 1.0 and 10.0 respectively. These time histories are typical of lightly loaded craft impacting the water surface. The trends are the same as the previous results of Figures 11 and 12 but the magnitude of accelerations, particularly the impacting mass m_1 , is greater by approximately a factor of three.

SUMMARY AND CONCLUSIONS

The paper has shown results of variable speed impact and hydroelastic impact for systems such as that illustrated in Figure 7. Both experimental and theoretical results are presented. The theory, strictly valid in the limit of flat hulls, is based upon a geometrically linear but hydrodynamically nonlinear model. Important factors in the determining the severity of impact accelerations are hull geometry, hull weight, initial impact velocity, and ratios of internal/external masses and system internal stiffness. Generally, light craft experience high accelerations, but low impact forces and heavier, better riding craft experience large local structural loads but low accelerations. Shock mitigation, or the study of shock mitigation devices, involves the solution of coupled hydrodynamic and elastic problems. Results given here have demonstrated the potential for reducing impact accelerations through proper choice of mass distributions and system natural frequencies.

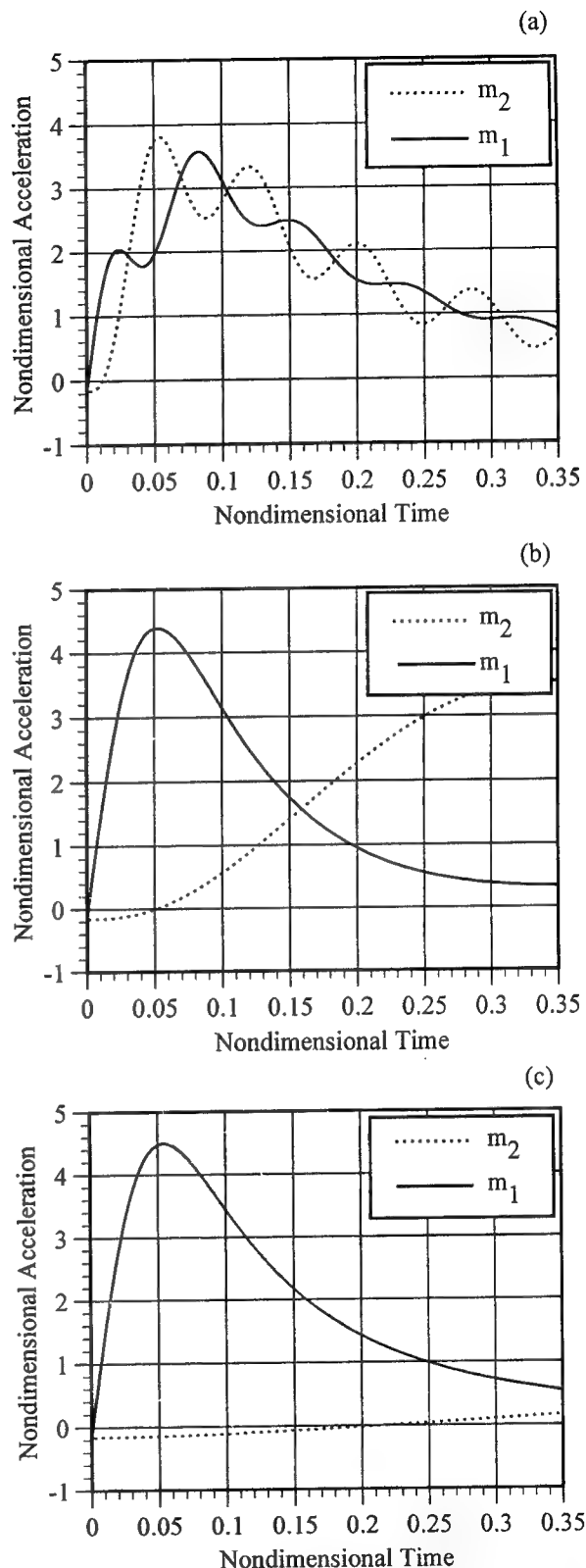


Figure 13: Impact acceleration time histories for three spring constants. (a) $T_n/t_{wet} = 0.1$. (b) $T_n/t_{wet} = 1.0$. (c) $T_n/t_{wet} = 5.0$. $H/B = 1.6$. $m_2/m_1 = 1.0$. $\alpha = 0.3$. Deadrise = 23 deg.

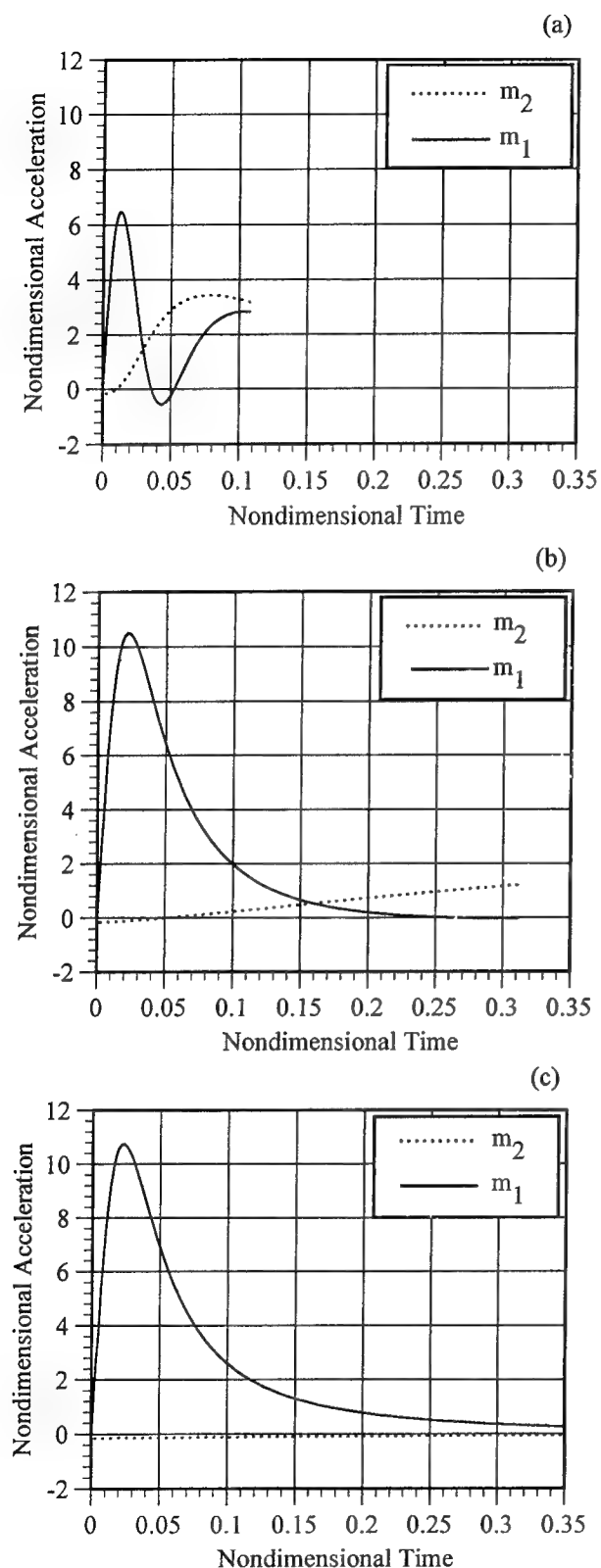


Figure 14: Impact acceleration time histories for three spring constants. (a) $T_n/t_{wet} = 0.1$. (b) $T_n/t_{wet} = 1.0$. (c) $T_n/t_{wet} = 5.0$. $H/B = 1.6$. $m_2/m_1 = 10.0$. $\alpha = 0.3$. Deadrise = 23 deg.

ACKNOWLEDGMENTS

This work has been supported by the Korea Science and Engineering Foundation, the Office of Naval Research under Contracts DOG-G-N00014-94-1-0652 and DOD-G-N0014-95-1-1124 with program managers Dr. Peter Majumdar, Dr. Edwin Rood and Dr. Thomas Swean, respectively, the Michigan Sea Grant College Program, projects R/T-27, R/T-30 under grant number NA89AA-D-SG083, NOAA, U.S. Dept. of Commerce, and the University of Michigan, Office of the Vice President for Research Program to Promote International Partnerships.

REFERENCES

1. Belik, O., Bishop, R.E.D., and Price, W.G., "Influence of Bottom and Flare Slamming on Structural Responses," *Trans. RINA*, Vol. 130, 1988.
2. Chuang, S.-L., "Investigation of Impact of Rigid and Elastic Bodies with Water," DTNSRDC Report No. 3248, 1970.
3. Cointe, R., "Free Surface Flows Close to a Surface Piercing Body," *Math. Approaches in Hydrodynamics*, Soc. Ind. Appl. Maths., 1991, pp. 319-334.
4. Gollwitzer, R.M. and Peterson, R.S., "Repeated Water-Entry Shock Mitigation for High Speed Planing Boats," *Proceedings, 66th Shock and Vibration Symposium*, Oct. 30 - Nov. 1, 1995, Biloxi, MS.
5. Gollwitzer, R. M. and Peterson, R. S., "Drop Tests and Planing Boat Modeling," *Proceedings, Small Craft Symposium*, May 15-17, 1996, University of Michigan, Ann Arbor, MI.
6. Kvålsvold, J. and Faltinsen, O.M., "Hydroelastic Modeling of Slamming Against the Wetdeck of a Catamaran," *Proc., FAST '93*, Yokohama, Japan, Vol. 1, December 1993, pp 681-697.
7. Kvålsvold, J., Faltinsen, O.M., and Aarsnes, J., "Effect of Structural Elasticity on Slamming Against Wetdecks of Multihull Vessels." *Proc., PRADS '95*, Seoul, Korea, Vol. 1, September 1995, pp 684-699.
8. Lai, C. and Troesch, A.W., "Modeling Issues Related to the Hydrodynamics of Three Dimensional Steady Planing." *Jour. of Ship Research*, Vol. 39, No. 1, 1995, pp. 1-24.

9. Meyerhoff, M. and Schlachter, G., "An Approach for the Determination of Hull Girder Loads in a Seaway Including Hydrodynamic Impacts," Ocean Engineering, Vol. 7, 1980.

10. Troesch, A.W. and Kang, C.-G., "Hydrodynamic Impact Loads on Three-Dimensional Bodies." 16th Symposium on Naval Hydrodynamics, University of California, Berkeley, 1986.

11. Troesch, A.W. and Kang, C.-G., "Evaluation of Impact Loads Associated with Flare Slamming," SNAME STAR Symposium, Pittsburgh, 1988.

12. von Karman, T. "The Impact on Seaplane Floats During Landing." NACA TN 321, 1929.

13. Vorus, W. S., "An Extended Slender Body Model for Planing Hull Hydrodynamics," presented at the SNAME Great Lakes and Great Rivers Section Meeting, Cleveland, January 23, 1992.

14. Vorus, W. S., "A Flat Cylinder Theory for Vessel Impact and Steady Planing Resistance," June, Journal of Ship Research, 1996.

15. Wagner, H., "Über Stoss- und Gleitvorgänge an der Oberflächen von Flüssigkeiten." Z. Angew. Math. Mech. **12**, 1932.

16. Wagner, H. "Planing of Watercraft," NACA TN 622, 1933.

17. Yamamoto, Y., Fujino, M., and Fukasawa, T., "Motion and Longitudinal Strength of a Ship in Head Sea and the Effects of Nonlinearities," Naval Architecture and Ocean Engineering, Society of Naval Architects of Japan, Vol. 18, 1980.

18. Zhao, R. and Faltinsen, O., "Water Entry of Two-Dimensional Bodies," Seventh International Workshop on Water Waves and Floating Bodies, Val de Reuil, France, May 24-27, 1992.

19. Zhao, R. and Faltinsen, O., "Water Entry of Two-Dimensional Bodies," Journ. Fluid Mech., 246, 1993, pp. 593-612.

A Practical Prediction of Wave-Induced Structural Responses in Ships with Large Amplitude Motion

M.-K. Wu, J. Aarsnes, O. Hermundstad (MARINTEK, Norway),
T. Moan (Norwegian University of Science and Technology, Norway)

Abstract

A practical nonlinear time-domain simulation method for predicting structural responses in ships at head or following sea is presented. The total response is decomposed into linear and nonlinear parts. The linear part is evaluated by using appropriate linear potential flow theory. The nonlinear part comes from the convolution of the impulse response function of the ship-fluid system and the nonlinear modification in hydrodynamic forces. The method is applied to a high-speed catamaran model running in regular head waves. The calculated structural responses are compared with those from model tests. Although the comparison is rather limited, the satisfactory agreement between numerical and experimental results is quite encouraging.

1. Introduction

In the traditional ship design the wave-induced ship motions, hydrodynamic forces and structural responses are evaluated directly or indirectly by applying the linear potential flow theory, especially the strip theory. With the growing interest in fast monohulls and catamarans, this design method has been challenged to a greater extent. The linearity assumption of small ship motions relative to the wave surface is violated at the fore quarter of most fast ships even in moderate sea states. This violation, together with the V-

shaped cross section of the ship hull in that region, will introduce significant nonlinear effects in the hydrodynamic forces, though the heave and pitch may be predicted quite well by linear theory. An increase of sagging moment in both magnitude and frequency is one of the consequences. It might cause severe structural damage such as the buckling of the main deck, and it will also reduce the fatigue life of bottom structures. Therefore, the prediction of nonlinear hydrodynamic forces and structural responses is extremely important to the safety of ship structures.

For the past two decades, significant research efforts have been devoted to the nonlinear hydrodynamic analysis. The most recent developments can be found in Maskew(1991), Pawlowski and Bass(1991), and Lin *et al*(1994) among others. Three-dimensional time-domain potential flow theory is used. Both incident waves and ship motions are assumed to be large. The free surface condition is satisfied on the exact wave surface or the incident wave surface. The body boundary condition is satisfied on the exact wetted surface or the wetted surface below the incident wave profile. However, it does not enjoy the universal success as linear strip theory did in ship hydrodynamics. It is partly because of the difficulties involved in the theory and implementation such as the treatment of transom stern effects and the numerical stability and accuracy in the computational methods. Mainly it is due to the requirement of tremendous computer power. Therefore, it may only serve as validation

tools of less sophisticated methods at present and in the near future.

On the other hand, driven by the need of ship design some simplified approaches emerged at the expense of accuracy, see e.g. Meyerhoff and Schlachter(1980), Yamamoto *et al*(1978-1979), Jensen and Pedersen(1979,1981), Schlachter(1989) and Xia *et al*(1995). Almost all of them use the combination of the conventional strip theory and nonlinear modifications of some kind. As a new effort in this direction, Wu and Moan(1996) presented a nonlinear hydroelastic simulation method for the prediction of wave-induced structural responses in ships with large amplitude motion in head or following sea. The total response is decomposed into linear and nonlinear parts. The linear part is evaluated by using appropriate linear potential flow theory. The nonlinear part comes from the convolution of the impulse response function of the ship-fluid system and the nonlinear hydrodynamic force caused by slamming and nonlinear modifications of added mass, damping, restoring and wave forces. Unlike the previous ones, it can be used with high-speed strip theory or three-dimensional flow theory and the frequency dependence of added mass and damping has been taken care of, to some extent. However, it has not yet been verified by experiments.

In this paper, we will apply the method to a high-speed catamaran model in regular head waves. We will compare the calculated structural responses with those from model tests which were conducted at MARINTEK. The main purpose of the model tests is to verify the linear hydroelastic formulation of high-speed strip theory (Wu *et al* 1993, Hermundstad *et al* 1995, Hermundstad 1995). However, strong nonlinear effects are observed at some frequencies of regular waves. It offers an opportunity for verifying the proposed formulation which is outlined in the next section. Although the comparison is rather limited, the satisfactory agreement between numerical and experimental results is quite encouraging.

2. Theoretical Background

Consider a flexible ship moving in the long-crested head waves on deep water. Let (x,y,z) be a right-handed coordinate system with the positive z -direction vertically upwards. The ship has a forward speed U in the negative x -direction. Only the global

structural responses are investigated here and the hydrodynamic forces are understood in this sense. We assume that

- (1) the nonlinearity comes from the large ship motions in heave and pitch while the structural deformation remains small,
- (2) the incident waves can be described sufficiently by linear wave theory,
- (3) the influence of ship motions on the incident wave elevation is not significant,
- (4) the hydrodynamic interaction among the multiple hulls of high speed vessels(Froude number $Fn>0.4$) is negligible.

In addition, the radiation and diffraction velocity potentials are assumed to be zero on the free surface which means there is no free surface memory effect. The memory effect of free surface will be introduced later and therefore this assumption is actually removed, to a great extent. The dynamic vertical force per unit length exerted by the fluid on each hull of the ship at position x may be expressed as(e.g. Faltinsen 1990)

$$F(x,t) = -\frac{D}{Dt}[m(x,t)\frac{D\xi(x,t)}{Dt}] + f(x,t), \quad (1)$$

where $m(x,t)$ is the high-frequency added mass of the submerged cross section. $f(x,t)$ consists of the Froude-Krylov force and hydrostatic restoring force per unit length on the instantaneous wetted surface. D/Dt represents the total derivative with respect to time t ,

$$\frac{D}{Dt} = \frac{\partial}{\partial t} + \frac{\partial}{\partial x} \frac{\partial x}{\partial t} = \frac{\partial}{\partial t} + U \frac{\partial}{\partial x}. \quad (2)$$

$\xi(x,t)$ is the vertical displacement of the ship hull relative to the wave surface,

$$\xi(x,t) = w(x,t) - \zeta(x,t). \quad (3)$$

The vertical displacement of the ship hull $w(x,t)$ is approximated by the s lowest symmetric dry eigenmodes, $w_k(x)$, including heave and pitch which are the dominant part,

$$w(x,t) = \sum_{k=1}^s w_k(x)p_k(t). \quad (4)$$

Here $p(t)=[p_1(t), p_2(t), \dots, p_s(t)]^T$ is the vector of generalized coordinates. Multiplying Eq.(1) by $w_k(x)$ and integrating over the length of hulls, we get the k th generalized, or modal hydrodynamic force

$$F_k(t) = N \int_L w_k(x) F(x,t) dx, \quad (5)$$

where N is the number of hulls.

The governing equation of the nonlinear ship-fluid system can be written as

$$(M+A_0)\ddot{p}(t) + (C+B_0)\dot{p}(t) + (K+R_0)p(t) = F_0(t) + F(t), \quad (6)$$

in which M , C and K are the generalized structural mass, damping and stiffness matrices. A_0 , B_0 and R_0 represent the generalized linear fluid added mass, damping and restoring coefficient matrices. $F_0(t)$ is the generalized linear wave force vector. They come from the hydrodynamic pressure over the mean wetted surface. All the nonlinear effects have been put into the generalized force vector $F(t)$. The elements of $F(t)$ are

$$F_k(t) = F_{1k}(t) + F_{2k}(t) + F_{3k}(t) + F_{4k}(t), \quad (7)$$

$k=1,2,\dots,S$

where

$$F_{1k}(t) = -N \int_L w_k(x) \frac{\partial m(x,t)}{\partial t} \frac{D\xi(x,t)}{Dt} dx \quad (8)$$

is the slamming force.

$$F_{2k}(t) = -N \int_L w_k(x) [m(x,t) - m_0(x)] \frac{D^2 \xi(x,t)}{Dt^2} dx \quad (9)$$

and

$$F_{3k}(t) = -NU \int_L w_k(x) \frac{\partial [m(x,t) - m_0(x)]}{\partial x} \frac{D\xi(x,t)}{Dt} dx \quad (10)$$

are the hydrodynamic forces due to the nonlinear modifications of the two-dimensional added mass and its derivative with respect to x . They reflect, to some extent, the nonlinear effects in the fluid added mass, damping, hydrodynamic restoring force and diffraction force. $F_{4k}(t)$ is the nonlinear modification of the Froude-Krylov force and hydrostatic restoring force,

$$F_{4k}(t) = N \rho g \int w_k(x) [Q(x,t) - Q_0(x) + b_0(x) \xi(x,t)] dx \quad (11)$$

$m_0(x)$ represents the high-frequency added mass of the mean submerged cross section. $Q(x,t)$ and $Q_0(x)$ are the areas of instantaneous and mean submerged cross section, respectively. $b_0(x)$ denotes the beam at mean draft.

If we decompose the total generalized response $p(t)$ into its linear and nonlinear parts,

$$p(t) = p_l(t) + p_n(t), \quad (12)$$

then (6) can be rearranged as

$$(M+A_0)\ddot{p}_l(t) + (C+B_0)\dot{p}_l(t) + (K+R_0)p_l(t) = F_0(t), \quad (13)$$

$$(M+A_0)\ddot{p}_n(t) + (C+B_0)\dot{p}_n(t) + (K+R_0)p_n(t) = F(t). \quad (14)$$

In order to take into account the memory effect of the free surface, we respectively replace A_0 , B_0 , R_0 and F_0 with frequency dependent added mass A , damping B , restoring coefficient matrix R , and Froude-Krylov and diffraction force $F^f + F^d$ derived in linear theory, see e.g. the high-speed strip theory (Wu *et al* 1993, 1996), the three-dimensional flow theory (Wu 1984, Bishop *et al* 1986) or the conventional strip theory (Bishop and Price 1979). Eq.(13) and Eq.(14) now have the form

$$(M+A)\ddot{p}_l(t) + (C+B)\dot{p}_l(t) + (K+R)p_l(t) = F^f(t) + F^d(t), \quad (15)$$

$$(M+A)\ddot{p}_n(t) + (C+B)\dot{p}_n(t) + (K+R)p_n(t) = F(t). \quad (16)$$

The linear and nonlinear responses are found by applying convolution integrations,

$$p_l(t) = \int_{-\infty}^t h(t-\tau) [F^f(\tau) + F^d(\tau)] d\tau, \quad (17)$$

$$p_n(t) = \int_{-\infty}^t h(t-\tau) F(\tau) d\tau, \quad (18)$$

where

$$h(t) = \int_{-\infty}^{\infty} [-\omega_e^2(M+A) + i\omega_e(C+B) + (K+R)]^{-1} e^{-i\omega_e t} d\omega_e \quad (19)$$

is the impulse response function matrix. In the time-

domain simulation, the linear response $p_l(t)$ may be obtained by superposing the frequency-domain solutions instead of using Eq.(17).

The way we deal with the nonlinear hydrodynamic force implies that although large amplitude relative motion is introduced, the memory effect of the free surface is still treated in a linear manner. The slamming force in Eq.(8) always acts upwards regardless of the direction of relative motion. This feature implies that the momentum of the fluid will be transferred back to the ship hull during a fast reduction of the submerged cross section. However, it is not supported by experiments (Greenhow 1988). There is a general agreement that the slamming force should be neglected during water-exit and this is done in the present analysis. More discussion on the formulation can be found in Wu and Moan(1996).

3. Numerical Procedures

In the calculation of nonlinear responses, each hull is divided into r segments along the longitudinal direction. The number of segments is normally in the range of 20-40. The vertical displacements of those segments relative to the wave surface as well as their first and second total derivatives can be written in vector form,

$$\Xi(t) = [\xi(x_1, t), \xi(x_2, t), \dots, \xi(x_r, t)]^T \quad (20)$$

$$= W(\dot{p}_l + \dot{p}_n) - \dot{Z}$$

$$\frac{D\Xi(t)}{Dt} = \left[\frac{D\xi(x_1, t)}{Dt}, \frac{D\xi(x_2, t)}{Dt}, \dots, \frac{D\xi(x_r, t)}{Dt} \right]^T$$

$$= W(\ddot{p}_l + \ddot{p}_n) - \ddot{Z} + U[W'(\dot{p}_l + \dot{p}_n) - \dot{Z}'], \quad (21)$$

$$\frac{D^2\Xi(t)}{Dt^2} = \left[\frac{D^2\xi(x_1, t)}{Dt^2}, \frac{D^2\xi(x_2, t)}{Dt^2}, \dots, \frac{D^2\xi(x_r, t)}{Dt^2} \right]^T$$

$$= W(\ddot{p}_l + \ddot{p}_n) - \ddot{Z} + 2U[W'(\ddot{p}_l + \ddot{p}_n) - \ddot{Z}'] + U^2[W''(\dot{p}_l + \dot{p}_n) - \dot{Z}''], \quad (22)$$

where x_i , $i=1,2,\dots,r$, is the x -coordinate of the i th segment. Z denotes the wave elevation vector,

$$Z(t) = [\zeta(x_1, t), \zeta(x_2, t), \dots, \zeta(x_r, t)]^T. \quad (23)$$

W is the eigenvector matrix,

$$W = [w_1, w_2, \dots, w_s],$$

$$w_k = [w_k(x_1), w_k(x_2), \dots, w_k(x_r)]^T, \quad (24)$$

$$k=1,2,\dots,s.$$

Overdot and prime represent the differentiation with respect to time t and x -coordinate, respectively. In the same manner, the nonlinear generalized force vector is written as

$$F(t) = F_1(t) + F_2(t) + F_3(t) + F_4(t), \quad (25)$$

$$F_1(t) = -NW^T m_l L \{ W(\dot{p}_l + \dot{p}_n) - \dot{Z} + U[W'(\dot{p}_l + \dot{p}_n) - \dot{Z}'] \}, \quad (26)$$

$$F_2(t) = F_{21}(t) + F_{22}(t),$$

$$F_{21}(t) = -NW^T m_l L W \ddot{p}_n,$$

$$F_{22}(t) = -NW^T m_l L \{ W \ddot{p}_l - \ddot{Z} + 2U[W'(\ddot{p}_l + \ddot{p}_n) - \ddot{Z}'] + U^2[W''(\dot{p}_l + \dot{p}_n) - \dot{Z}'] \}, \quad (27a,b,c)$$

$$F_3(t) = -NUW^T m_x L \{ W(\dot{p}_l + \dot{p}_n) - \dot{Z} + U[W'(\dot{p}_l + \dot{p}_n) - \dot{Z}'] \}, \quad (28)$$

$$F_4 = N\rho g W^T L \{ Q - Q_0 + b_0 [W(\dot{p}_l + \dot{p}_n) - \dot{Z}] \}, \quad (29)$$

in which

$$Q = [Q(x_1, t), Q(x_2, t), \dots, Q(x_r, t)]^T, \quad (30)$$

$$Q_0 = [Q_0(x_1), Q_0(x_2), \dots, Q_0(x_r)]^T. \quad (31)$$

The matrices m , m_l , m_x , L and b_0 are diagonal. The k th diagonal elements of m , m_l and m_x are $m(x_k, t) - m_0(x_k)$, $\partial m(x_k, t)/\partial t$ and $\partial [m(x_k, t) - m_0(x_k)]/\partial x$, respectively. The k th diagonal elements of L and b_0 are the length and beam at mean draft of the k th hull segment.

The problem is solved numerically in the time-domain. The nonlinear generalized displacement, velocity and acceleration are evaluated through discrete convolutions,

$$p_n(t) = T \sum_{k=1}^{\infty} \tilde{h}(kT) F(t-kT), \quad (32)$$

$$\dot{\mathbf{p}}_n(t) = T \sum_{k=1}^{\infty} \tilde{\mathbf{h}}_v(kT) F(t-kT), \quad (33)$$

$$\begin{aligned} \ddot{\mathbf{p}}_n(t) = & T \tilde{\mathbf{h}}_a(0) F(t) \\ & + T \sum_{k=1}^{\infty} \tilde{\mathbf{h}}_a(kT) F(t-kT). \end{aligned} \quad (34)$$

Here T is the time step. $\tilde{\mathbf{h}}(t)$, $\tilde{\mathbf{h}}_v(t)$ and $\tilde{\mathbf{h}}_a(t)$ are the discrete impulse response function matrices of displacement, velocity and acceleration, respectively.

The continuous versions of $\tilde{\mathbf{h}}_v(t)$ and $\tilde{\mathbf{h}}_a(t)$ take the form

$$\begin{aligned} \mathbf{h}_v(t) = & \int_{-\infty}^{\infty} [-\omega_e^2(\mathbf{M}+\mathbf{A}) + i\omega_e(\mathbf{C}+\mathbf{B}) \\ & + (\mathbf{K}+\mathbf{R})]^{-1} i\omega_e e^{-i\omega_e t} d\omega_e \end{aligned} \quad (19)$$

$$\begin{aligned} \mathbf{h}_a(t) = & \int_{-\infty}^{\infty} [-\omega_e^2(\mathbf{M}+\mathbf{A}) + i\omega_e(\mathbf{C}+\mathbf{B}) \\ & + (\mathbf{K}+\mathbf{R})]^{-1} \omega_e^2 e^{-i\omega_e t} d\omega_e \end{aligned} \quad (19)$$

Unlike $\mathbf{p}_n(t)$ and $\dot{\mathbf{p}}_n(t)$, $\ddot{\mathbf{p}}_n(t)$ depends partly on $F(t)$. Therefore, $\ddot{\mathbf{p}}_n(t)$ and $F(t)$ should be solved simultaneously. Substituting Eq.(34) and Eq.(27) into Eq.(25) and rearranging it, we get

$$\begin{aligned} \mathbf{F}(t) = & [\mathbf{I} + \mathbf{NTW}^T \mathbf{m} \mathbf{L} \mathbf{W} \tilde{\mathbf{h}}_a(0)]^{-1} \\ & [\mathbf{F}_1(t) + \mathbf{F}_{22}(t) + \mathbf{F}_3(t) + \mathbf{F}_4(t) \\ & - \mathbf{NTW}^T \mathbf{m} \mathbf{L} \mathbf{W} \sum_{k=1}^{\infty} \tilde{\mathbf{h}}_a(kT) F(t-kT)] \end{aligned} \quad (37)$$

with \mathbf{I} being an identity matrix. In this way, the present nonlinear forces and responses are determined by the past nonlinear forces and the present linear responses. No iteration is needed because the present linear responses can be calculated separately using linear theory.

In order to save computer time, \mathbf{m} , \mathbf{m}_p , \mathbf{m}_x and \mathbf{Q} are evaluated beforehand for a given number of drafts from bottom to deck and stored for interpolation during the simulation. Furthermore, we can truncate the impulse response functions without significant loss of accuracy since $\tilde{\mathbf{h}}(kT)$, $\tilde{\mathbf{h}}_v(kT)$ and $\tilde{\mathbf{h}}_a(kT)$ decay rapidly as k increases due to the damping.

4. Application to a High-Speed Catamaran Model

4.1 Description of Model Tests

As mentioned in the introduction, the main purpose of the model tests is to verify the linear hydroelastic formulation of high-speed strip theory and therefore a very flexible catamaran model is adopted. The main particulars and the body plan of the model are given in Tab. 1 and Fig. 1, respectively. Each hull consists of three separate rigid segments. They are made of Divinycell foam/GRP in which stiff aluminum beams are mounted in order to make them rigid. Two longitudinal elastic hinges made of slender steel beams are used to connect the hull segments. Rubber bands are introduced to cover the gap between the segments and make it watertight. Another three transverse elastic hinges are also used as connectors of the two hulls, see Fig. 2. Since wetdeck slamming is a part of the experiment, the model is equipped with three wetdeck plates. Each plate is connected to the hull segments at four points via two stiff aluminum beams. A pinned joint is adopted to transfer only vertical forces due to wetdeck slamming without taking up the bending moments or shear forces between the two hulls. In this way, the influence of the wetdeck plates on the global stiffness of the catamaran model is minimized.

The model is first tested in air to determine the dry natural frequencies, vibration shapes and structural damping. It is suspended from six springs, one at the midpoint of each segment. The natural frequencies of the springs are much lower than those of the model and hence their influence is negligible. Different modes can be vibrated by giving the model an impulse excitation at different places. The model is also tested statically in order to make sure that the wetdeck plates contribute as little as possible to the global stiffness.

The wave tests are performed in the Ocean Basin at MARINTEK. A free running model is used. It is self propelled and can be directed arbitrarily to the incident waves. The model direction is kept stable by an auto-pilot system which controls the rudder angle. The Ocean Basin is equipped with a high speed carriage system. It has the capacity of following free running models at speeds from zero to 6 m/s. The tests include regular, irregular and impulse waves. Wave heading 0°(head

Table 1 Main particulars of the catamaran model. Values refer to zero speed condition

Description	Unit	Value
Length over all	m	4.1
length between perpendiculars	m	3.78
Total beam at waterline amidships	m	1.02
Beam of each hull at waterline amidships	m	0.267
Distance between center of hulls	m	0.753
Draft at aft perpendicular	m	0.197
Draft at fore perpendicular	m	0.207
Total mass	kg	203
Block coefficient	m	0.54
Vertical center of gravity (above keel)	m	0.352
Longitudinal center of gravity (from AP)	m	1.65
Roll radius of gyration	m	0.38
Pitch radius of gyration	m	1.03
Yaw radius of gyration	m	1.09

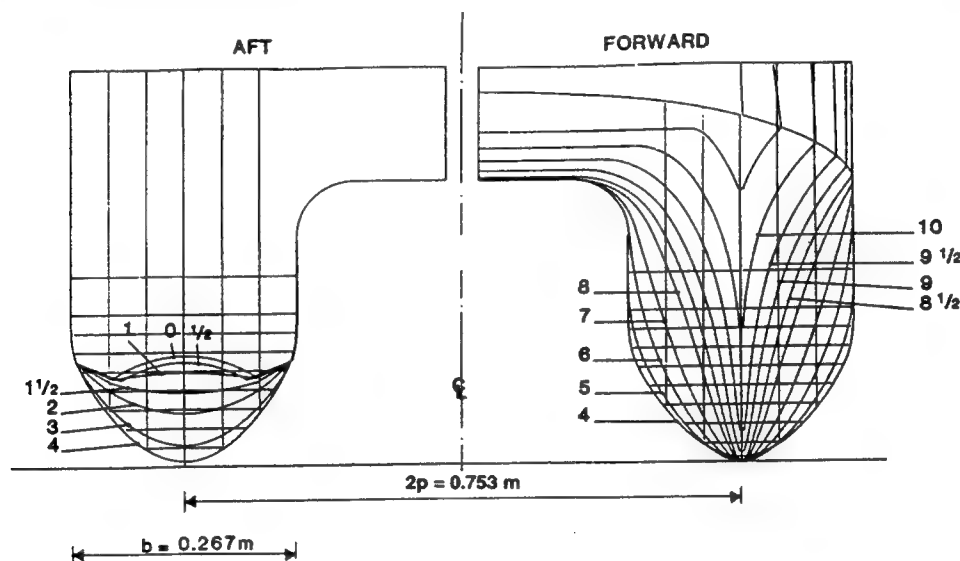


Fig. 1 Body plan of the catamaran model

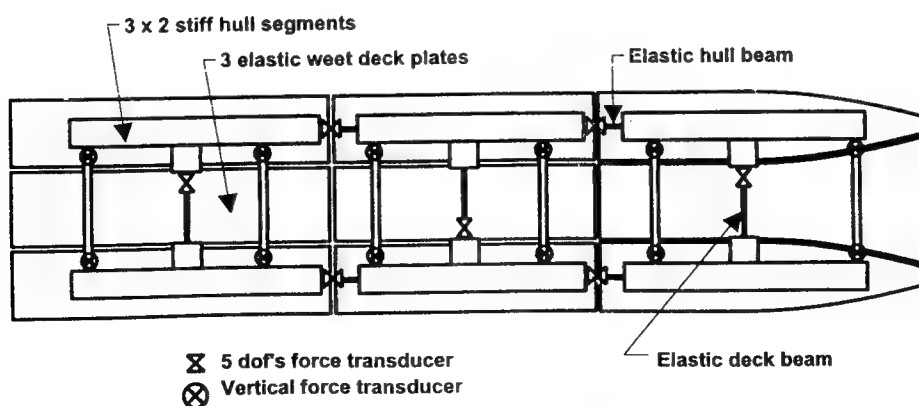


Fig. 2 Top view of the catamaran model

sea), 30° (bow sea) and 90°(beam sea) are covered. Two different speeds, 3m/s and 4m/s, are used. Based on the length overall, they correspond to Froude number 0.47 and 0.63, respectively.

During the tests a comprehensive measuring program is carried out. Among other things, the vertical and horizontal bending moments and shear forces as well as the torsional moment in each elastic hinge are measured by using a 5 d.o.f. strain gauge transducer which is located at one end of the hinge, see Fig. 2. The time histories of those moments and forces are recorded digitally at a sampling rate of 100 Hz. To avoid noise and Nyquist phenomena, all the signals are lowpass filtered before digitalization. The cut-off frequency is 40 Hz.

4.2 Numerical and Experimental Results

In order to evaluate the dry eigenmodes of the catamaran, a finite element model of 2112 degrees of freedom has been made, see Fig. 3. Hull surfaces are represented by triangular shell elements. Two-node beam elements are used for the backbone frame, the elastic hinges (slender steel beams), the force transducers and other beam-like structural parts. Wetdeck plates are also modelled by two-node beam elements with equivalent mass distribution. Lumped masses are employed for the motors and other objects. The modelling details are given in Hermundstad(1995). Table 2 shows the measured natural frequencies and modal damping in air together with the calculated dry natural frequencies of the first four symmetric flexible modes using a finite element program PUSFEA (Wu 1994). Fig. 4 depicts the calculated vibration shapes. 1.7% is adopted as the structural damping for the first mode and 2.6% will be used for the remaining flexible modes throughout the calculation.

Based on the theory and numerical process described in the previous sections, a computer program has been developed. The linear part of response $p_f(t)$ and the frequency dependent added mass A , damping B and restoring coefficient matrix R are evaluated by applying high-speed strip theory (Faltinsen and Zhao, 1991a,b). The detailed linear hydroelastic formulation of this theory can be found in Wu *et al*(1993,1996). The ship hull is divided into 80 segments on account of the relatively small wave lengths in the high frequency range which is needed for the evaluation of impulse response function matrices. The calculation is carried out at

200 equally spaced wave frequencies. The solution is obtained by solving a two-dimensional Laplace equation in each cross-sectional plane. But as opposed to the conventional strip theory, a three-dimensional free surface condition is used so that the divergent wave system generated by high-speed vessels is properly incorporated.

Table 2 Calculated and measured dry natural frequencies(Hz) together with measured modal damping

mode no.	calculated freq.	measured freq.	measured damp.
1	4.24	4.2	1.7%
2	4.98	5.1	2.6%
3	10.64	10.5	-
4	12.94	-	-

The discrete impulse response function matrices $\tilde{h}(t)$, $\tilde{h}_v(t)$ and $\tilde{h}_a(t)$ play an important role in the calculation of nonlinear responses. In order to verify those matrices, we use the generalized linear wave force caused by irregular waves as the external force vector and calculate the generalized linear displacement $p_f(t)$, velocity $\dot{p}_f(t)$ and acceleration $\ddot{p}_f(t)$ in time-domain by discrete convolution and in frequency-domain by superposition, respectively. The results of the two approaches are shown in Fig. 5 for the first flexible mode. The general agreement between the two approaches is excellent.

By investigating the measured bending moments and shear forces in the seven slender steel beams of the catamaran at two different forward speeds and three different regular wave headings, we find that most of them display a linear behaviour for most wave periods. However, severe nonlinear effects are found in the vertical shear force of the fore longitudinal elastic hinges when the ship model is running at forward speed 4 m/sec. in regular head waves of period 2.2 sec., 2.0 sec. and 1.8 sec., respectively. Further observation shows that wetdeck slamming occurs at wave period 1.8 sec. The numerical prediction of structural responses due to wetdeck slamming is beyond the scope of the present paper.

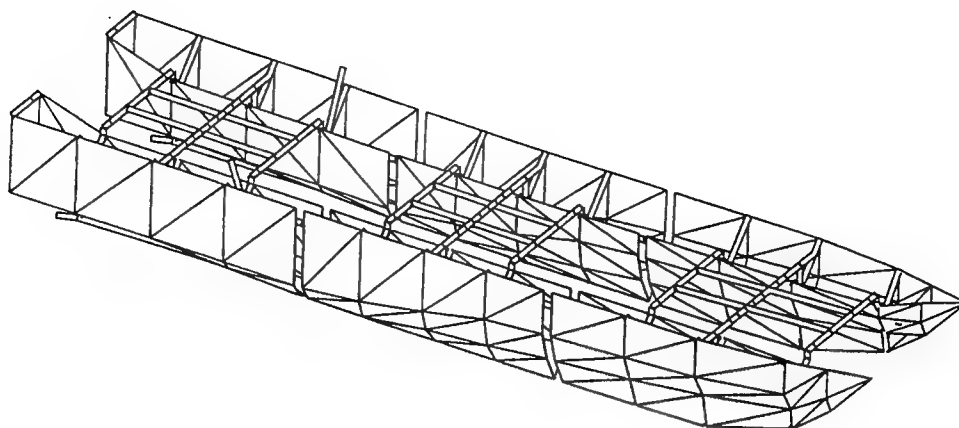
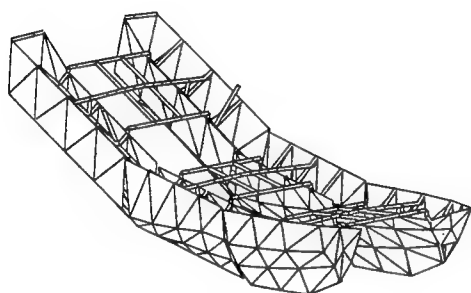
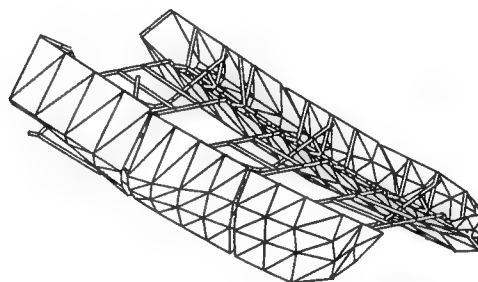


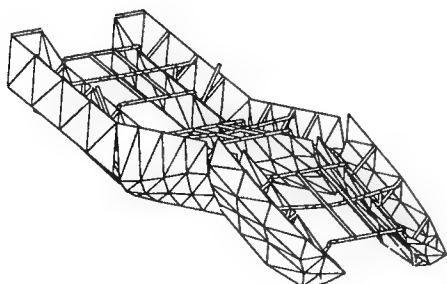
Fig. 3 The finite element model used in the numerical analysis.



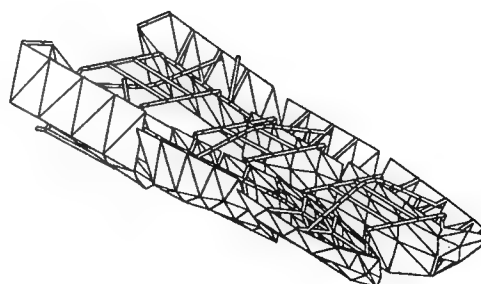
(1) 2-node longitudinal bending



(2) prying/transverse bending



(3) 3-node longitudinal bending



(4) prying/squeezing

Fig. 4 Calculated vibration shapes of the first four symmetrical flexible modes. The deformation has been exaggerated for presentation.

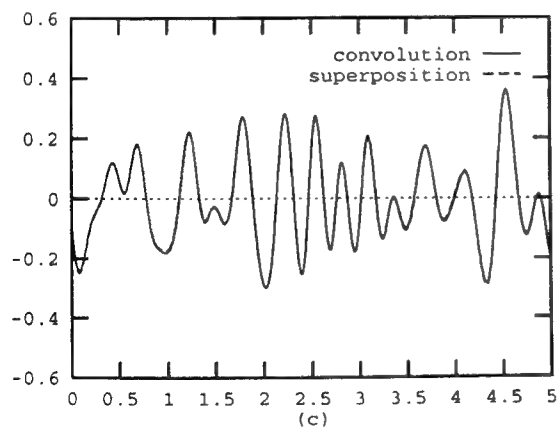
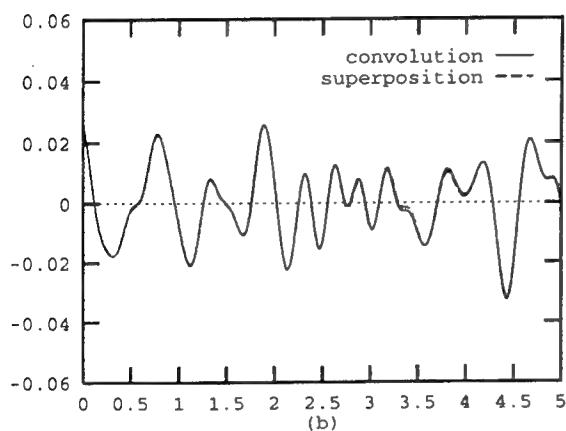
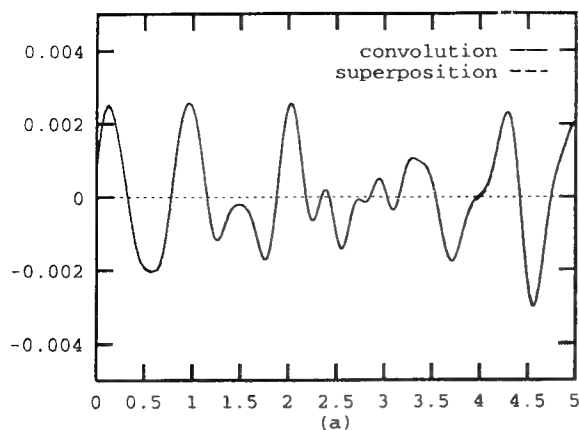


Fig. 5 Time history of the first flexible modal response. abscissa: sec. (a) displacement. (b) velocity. ordinate: 1/sec. (c) acceleration. ordinate: 1/sec.².

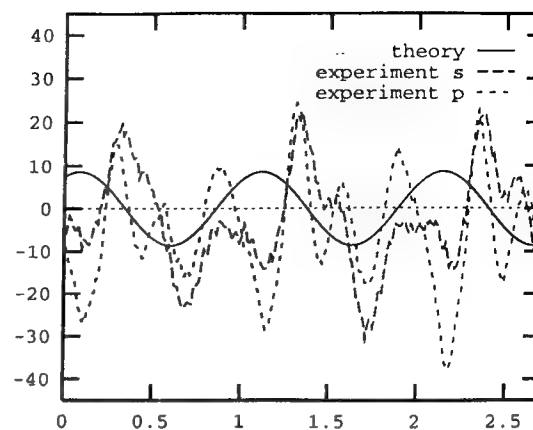


Fig. 6 Calculated linear vertical shear force and the measurements in the fore longitudinal elastic hinges. s and p stand for starboard and port hull, respectively. abscissa: sec. ordinate: N. Ship forward speed = 4 m/sec. Wave period = 2.2 sec. Wave height = 0.087 m.

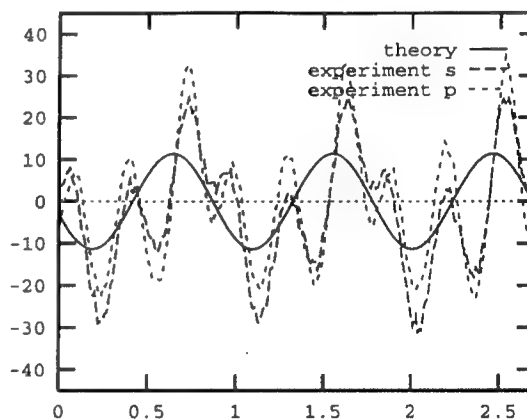


Fig. 7 Calculated linear vertical shear force and the measurements in the fore longitudinal elastic hinges. s and p stand for starboard and port hull, respectively. abscissa: sec. ordinate: N. Ship forward speed = 4 m/sec. Wave period = 2.0 sec. Wave height = 0.052 m.

The calculated linear vertical shear forces in the fore longitudinal elastic hinges as well as the measured time histories at wave periods 2.2 sec., 2.0 sec. and 1.4 sec. are depicted in Fig. 6 through Fig. 8. Large discrepancies between the linear prediction and the measurement can be clearly observed in Fig. 6 and 7. If we introduce the nonlinear force components described in Eqs.(8-11), the discrepancies are reduced remarkably, see Fig.

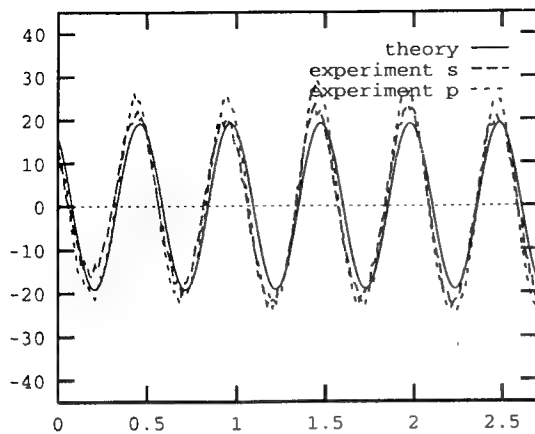


Fig. 8 Calculated linear vertical shear force and the measurements in the fore longitudinal elastic hinges. s and p stand for starboard and port hull, respectively. abscissa: sec. ordinate: N. Ship forward speed = 4 m/sec. Wave period = 1.4 sec. Wave height = 0.042 m.

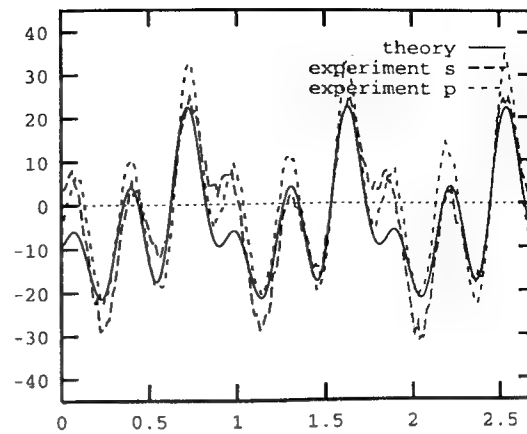


Fig. 10 Calculated total vertical shear force and the measurements in the fore longitudinal elastic hinges. s and p stand for starboard and port hull, respectively. abscissa: sec. ordinate: N. Ship forward speed = 4 m/sec. Wave period = 2.0 sec. Wave height = 0.052 m.

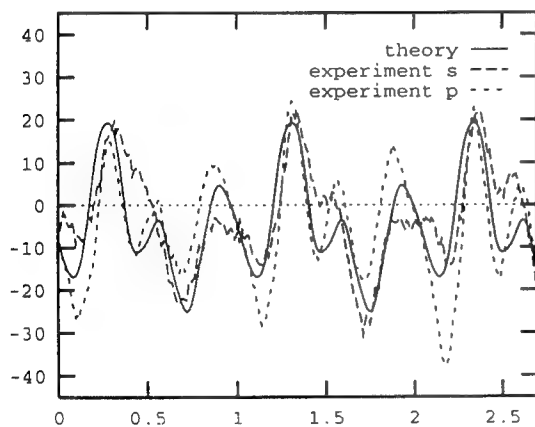


Fig. 9 Calculated total vertical shear force and the measurements in the fore longitudinal elastic hinges. s and p stand for starboard and port hull, respectively. abscissa: sec. ordinate: N. Ship forward speed = 4 m/sec. Wave period = 2.2 sec. Wave height = 0.087 m.

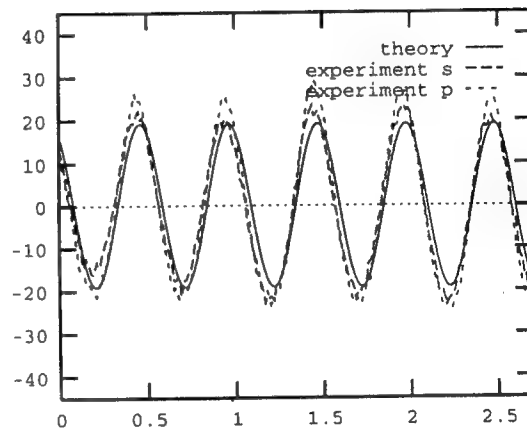


Fig. 11 Calculated total vertical shear force and the measurements in the fore longitudinal elastic hinges. s and p stand for starboard and port hull, respectively. abscissa: sec. ordinate: N. Ship forward speed = 4 m/sec. Wave period = 1.4 sec. Wave height = 0.042 m.

9 and 10. However, as shown in Fig. 8 and 11 the nonlinear effect at wave period 1.4 sec. is insignificant because the ship motion is relatively small, see Fig. 12. Further, the responses obtained by only including the nonlinear modification of Froude-Krylov and hydrostatic restoring force Eq.(11), the slamming force Eq.(8) or the combination of Eq.(11) and Eq.(8) are also depicted in Fig. 13 through Fig. 18 for comparison.

In the integral-differential method presented by Xia(1994) and Xia *et al*(1995), only the nonlinear modification of Froude-Krylov and hydrostatic restoring force, and the slamming force are taken into consideration. Therefore, their method is a special case of our more general approach, Fig 17 and 18.

In the above nonlinear analysis, time step $T=0.002$ sec., segment number $r=30$ and the first six

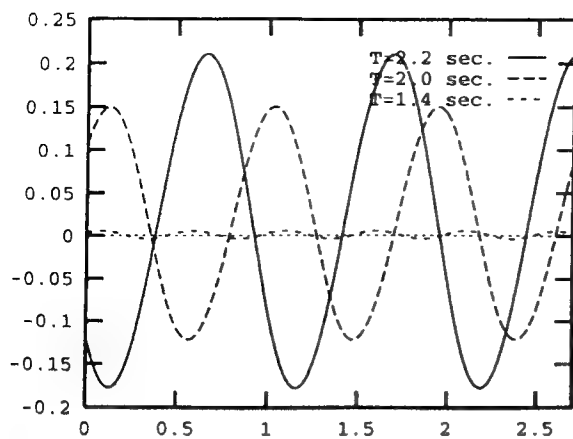


Fig. 12 Calculated ship bow displacements at three different wave periods 2.2 sec., 2.0 sec and 1.4 sec. The corresponding wave heights are 0.087 m, 0.052 m and 0.042 m, respectively. Ship forward speed = 4 m/sec. abscissa: sec. ordinate: m.

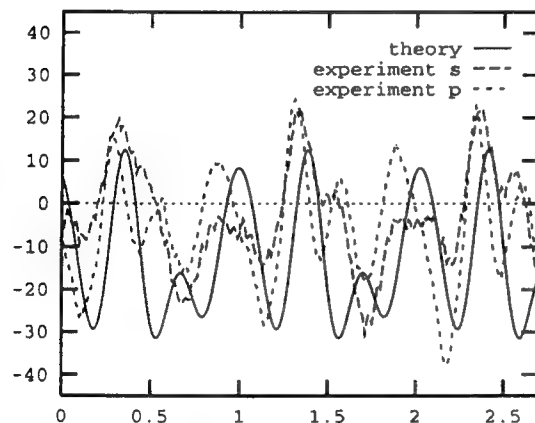


Fig. 13 Calculated vertical shear force. Only part of the nonlinear forces, namely Eq.(11), is included. abscissa: sec. ordinate: N. Ship forward speed = 4 m/sec. Wave period = 2.2 sec. Wave height = 0.087 m.

flexible modes are used. The influence of more global modes and segments, and smaller time step to the total responses is not significant. The steady sinkage and trim caused by high forward speed have been taken care of in the calculation. But other effects of the steady wave are neglected both in linear and nonlinear analysis. For the high speed vessels the steady wave elevation may not be very small and therefore it seems reasonable to use the

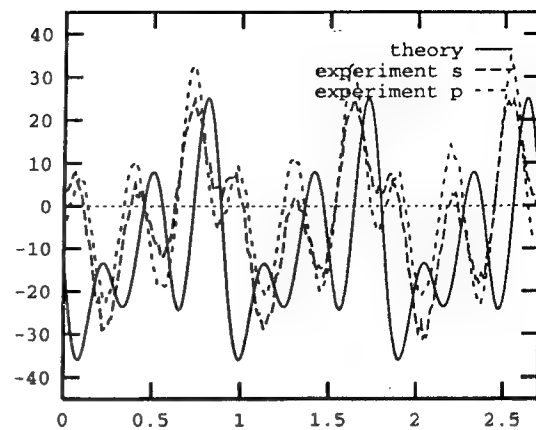


Fig. 14 Calculated vertical shear force. Only part of the nonlinear forces, namely Eq.(11), is included. abscissa: sec. ordinate: N. Ship forward speed = 4 m/sec. Wave period = 2.0 sec. Wave height = 0.052 m.

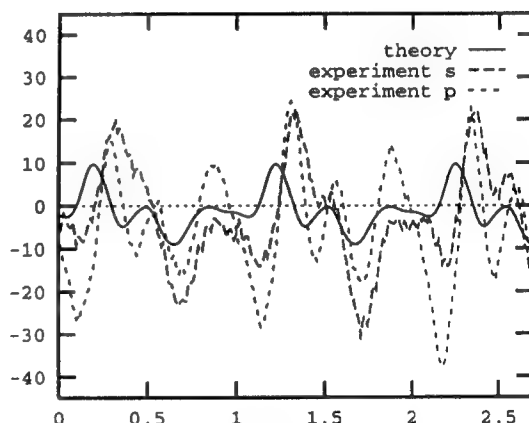


Fig. 15 Calculated vertical shear force. Only part of the nonlinear forces, namely Eq.(8), is included. abscissa: sec. ordinate: N. Ship forward speed = 4 m/sec. Wave period = 2.2 sec. Wave height = 0.087 m.

wetted surface under the steady wave profile instead of that under the calm water as the mean wetted surface if it is available.

From Fig. 9 we can see some discrepancy in the measurements around time 1.0 and 2.0 between port hull and starboard hull. The same phenomenon is also found in Fig. 10. It is probably due to the fact that the configuration of the transverse elastic hinges and transducers is not symmetric about the

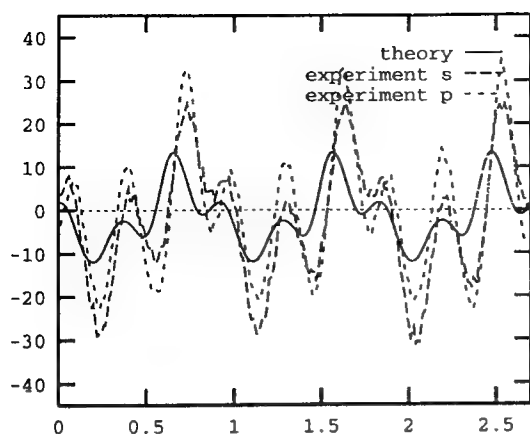


Fig. 16 Calculated vertical shear force. Only part of the nonlinear forces, namely Eq.(8), is included. abscissa: sec. ordinate: N. Ship forward speed = 4 m/sec. Wave period = 2.0 sec. Wave height = 0.052 m.

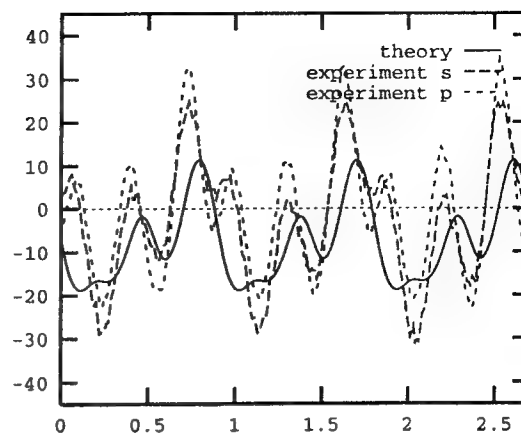


Fig. 18 Calculated vertical shear force. Only part of the nonlinear forces, namely Eq.(8) and Eq.(11), is included. abscissa: sec. ordinate: N. Ship forward speed = 4 m/sec. Wave period = 2.0 sec. Wave height = 0.052 m.

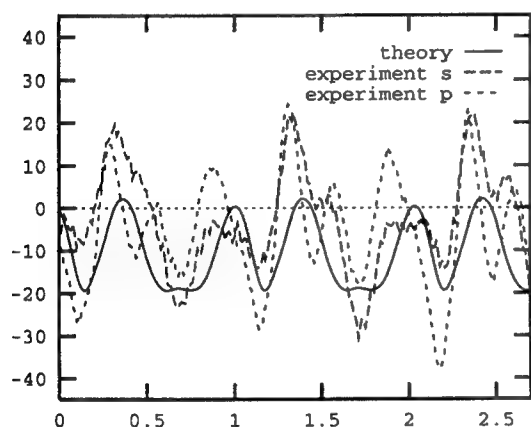


Fig. 17 Calculated vertical shear force. Only part of the nonlinear forces, namely Eq.(8) and Eq.(11), is included. abscissa: sec. ordinate: N. Ship forward speed = 4 m/sec. Wave period = 2.2 sec. Wave height = 0.087 m.

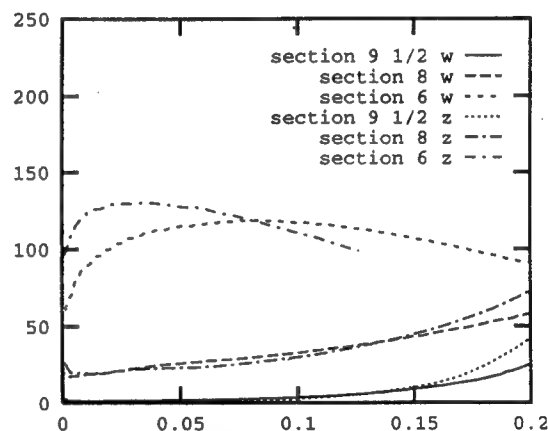


Fig. 19 Comparison of 2-dimensional slamming force. w denotes the results by using the present method. z denotes the results from a more sophisticated approach(Zhao *et al* 1996). Dropping speed = 1.0 m/s. abscissa: sec. ordinate: N/m.

catamaran's centerplane, see Fig. 2. This results from practical considerations during the fabrication process. However, it has been made symmetric in the FEM model so that the added mass A , damping B , Froude-Krylov and diffraction force $F^f + F^d$ can be evaluated more quickly and efficiently. Small deviations in the catamaran's heading will also trigger the excitation of antisymmetric modes, like the one-node torsion mode.

At the beginning of section 2 we assume that the influence of ship motion on the wave elevation is negligible and then use (8) to calculate the slamming force. This is a von Karman type of solution where the pile-up water around the intersection between the free surface and the ship hull is not accounted for. In order to investigate the influence of the pile-up water upon the 2-dimensional slamming force, we have compared our

calculations with those from a more sophisticated method (Zhao *et al* 1996), which is a generalization of Wagner's solution to the water entry problem. In that method the jet flow occurring in the vicinity of the intersection when the ship hull impacts the water is handled properly and the slamming force is obtained by integrating the pressure distribution at each time step.

The results of the comparison are shown in Fig. 19 for cross section no. 6, 8 and 9½ at a constant dropping speed of 1 m/s. The agreement is quite good for the early part of the impact at cross section no. 8 and 9½ and for the later part at cross section no. 6. They correspond to regions where the local deadrise angle (angle between hull section and water surface) is large, see Fig. 1, and therefore little pile-up water exists. When the local deadrise angle gets smaller due to the increased flare or near the bottom of full cross sections, the present method will underpredict the slamming force. However, the three-dimensional effect could cancel, to some extent, the extra slamming force caused by the pile-up water. Therefore, our simplified evaluation of slamming force is acceptable from a practical point of view. Further, slamming is only one source of nonlinear forces. The overall influence of any underprediction of slamming force on the structural responses is believed to be less significant than it is shown in Fig. 19.

5. Concluding Remarks

A simplified method for the prediction of wave-induced structural responses in ships with large amplitude motion at head or following sea is presented. The total response is decomposed into linear and nonlinear parts. The linear part is calculated by using appropriate linear potential flow theory, such as high speed strip theory or conventional strip theory. The nonlinear part comes from the convolution of the impulse response function of ship-fluid system and the nonlinear modification in hydrodynamic forces. The method is then applied to a high-speed catamaran model running in regular head waves. The calculated structural responses are compared with those from model tests. The satisfactory agreement between numerical and experimental results shows that the present method is able to capture the nonlinear effects with reasonable accuracy in this specific

case. However, more verification work should be carried out through both experiment and more sophisticated numerical methods before any general conclusions can be reached.

Acknowledgements

This work has been partly financed by the Hydroelasticity Project of NTNU and the Dynamic Analysis Support System Project of MARINTEK AS. Both of them are sincerely acknowledged.

References

- Bishop, R.E.D. and Price, W.G. (1979), *Hydroelasticity of Ships*, Cambridge University Press, Cambridge.
- Bishop, R.E.D., Price, W.G. and Wu, Y. (1986), A General Linear Hydroelasticity Theory of Floating Structures Moving in Seaway, *Phil. Trans. Soc. Lond.*, A 316, pp. 375-426.
- Faltinsen, O. (1990), *Sea Loads on Ships and Offshore Structures*, Cambridge University Press.
- Faltinsen, O. and R. Zhao (1991a), Numerical Prediction of Ship Motions at High Forward Speed, *Phil. Trans. R. Soc. Lond.*, A 334, pp. 241-252.
- Faltinsen, O. and R. Zhao (1991b), Flow Predictions Around High-speed Ships in Waves, *Mathematical Approaches in Hydrodynamics*, SIAM, pp. 265-288.
- Greenhow, M. (1988), Water-Entry and -Exit of a Horizontal Circular Cylinder, *Applied Ocean Research*, Vol. 10, No. 4.
- Hermundstad, O.A., Aarsnes, J.V. and Moan, T. (1995), Hydroelastic Analysis of a Flexible Catamaran and Comparison with Experiments, *Proc. Third Int. Conf. on Fast Sea Transportation FAST'95*, Germany, pp. 487-500.
- Hermundstad, O.A. (1995), *Theoretical and Experimental Hydroelastic Analysis of High Speed Vessels*, Ph.D. Thesis, Dept. of Marine Structures, The Norwegian Institute of Technology.
- Jensen, J.J. and Pedersen, P.T. (1979), Wave-induced Bending Moments in Ships - A Quadratic Theory, *Trans. RINA*, Vol. 121, pp. 151-165.
- Jensen, J.J. and Pedersen, P.T. (1981), Bending Moments and Shear Forces in Ships Sailing in

- Irregular Waves, *Journal of Ship Research*, Vol. 24, No. 4, pp. 243-251.
- Lin, W.M., Meinhold, M.J., Salvesen, N. and Yue, D.K.P. (1994), Large-Amplitude Motions and Wave Loads for Ship Design, *Twentieth Symposium on Naval Hydrodynamics*, August, University of California, Santa Barbara, California, USA.
- Maskew, B. (1991), A Nonlinear Numerical Method for Transient Wave/Hull Problems on Arbitrary Vessels, *Trans. SNAME*, Vol. 99, pp. 299-318.
- Meyerhoff, M.K. and Schlachter, G. (1980), An Approach for the Determination of Hull-Girder Loads in a Seaway Including Hydrodynamic Impacts, *Ocean Engng.*, Vol. 7, pp. 305-326.
- Pawlowski, J.S. and Bass D.W. (1991), A Theoretical and Numerical Model of Ship Motions in Heavy Seas, *Trans. SNAME*, Vol. 99, pp. 319-352.
- Schlachter, G. (1989), Hull Girder Loads in a Seaway Including Nonlinear Effects, *Schiffstechnik*, 36, pp. 169-189.
- Wu, M.K., Hermundstad, O.A. and Moan, T. (1993), Hydroelastic Analysis of Ship Hulls at High Forward Speed, *Proc. Sec. Int. Conf. on Fast Sea Transportation FAST'93*, Yokohama, Japan, pp. 699-710.
- Wu, M.K. (1994), *How to Use PUSFEA - A Complete Manual*, Dept. of Marine Structures, Norwegian Institute of Technology, Trondheim.
- Wu, M.K. and Moan, T. (1996), Linear and Nonlinear Hydroelastic Analysis of High Speed Vessels, to appear in *Journal of Ship Research*.
- Wu, Y. (1984), *Hydroelasticity of Floating Bodies*, Ph.D. Thesis, Dept. Mech. Engng., Brunel University, U.K.
- Xia, J. (1994), *Hydroelasticity Theories of Slender Floating Structures*, Ph.D. Thesis(in Chinese), China Ship Scientific Research Center, Wuxi, China, 204 pp.
- Xia, J., Wang, Z., Gu, X., Shen, J. and Wu, Y. (1995), Numerical Simulation of the Wave-induced Non-linear Bending Moment of Ships, *OMAE'95*.
- Yamamoto, Y., Fujino, M. and Fukasawa, T. (1978-1979), Motion and Longitudinal Strength of a Ship in Head Sea and Effects of Nonlinearities, *Journal Soc. Nav. Arch. of Japan*, Vol. 143-145.
- Zhao, R., Faltinsen, O. and Aarsnes, J.V. (1996), Water Entry of Arbitrary Two-dimensional Sections with and without Flow Separation, *21st Symposium on Naval Hydrodynamics*, June, Trondheim, Norway.

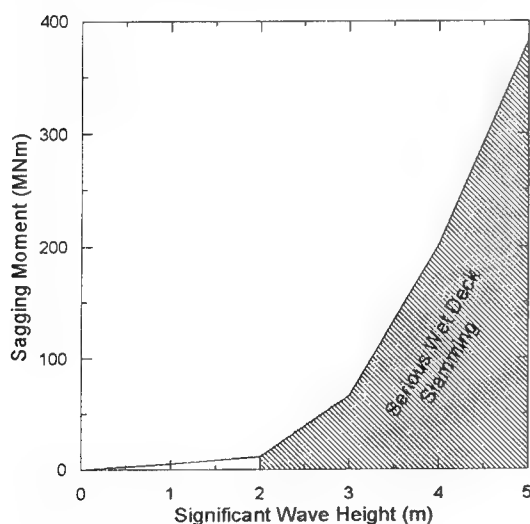
DISCUSSION

G. Schlachter
MTG, Germany

The authors should be thanked for their effective contribution to more reliable design loads on ships in a seaway. Different from the approach of Meyerhoff/Schlachter (1980), the present method contains a clear separation of linear and nonlinear loads neglecting the frequency influence only with impact, i.e., slamming effects. The approach of Schlachter (1989) is different because it is based on frequency-independent hydrodynamic coefficients. All three methods calculate the elastic response of the hull girder by superposition of eigenmodes. However, the present approach is based on "dry" modes, whereas the other two mentioned use "wet" modes assuming that orthogonality is still given.

In order to make the present method even more attractive for practical use, the future development of it should aim at the solution of the following problems:

- Wet-deck slamming: The figure below shows how wet-deck slamming dominates the hull girder loads of a 700 t SES in higher sea states (from calculations verified by tank tests).



- Deformation of incoming waves by the ship: It can have a considerable impact on local pressures on the shell.

Furthermore, a statistical evaluation should be part of the computer program which enables the user to extrapolate extreme, i.e., design loads.

AUTHORS' REPLY

Thank you for your kind comments. The purpose of the current paper was to verify our nonlinear simulation method which did not take into account the wet-deck slamming. We agree that the whipping response due to wet-deck slamming might be significant as you suggested in your figure and therefore deserves a thorough investigation on its own. We have been working on this problem for some time. Parts of the results will be published in the near future.

Also, statistical analysis of extreme responses is beyond the scope of the current paper. This issue was, however, touched upon in an accompanying paper (Wu and Moan, 1996). But the activity in this area will be emphasized in order to establish results for probability-based design of advanced vessels.

We totally agree with you that the pile-up water should be taken into consideration as far as local pressure and local structure are concerned.

Evaluation of Eddy Viscosity and Second-Moment Turbulence Closures for Steady Flows Around Ships

G. Deng, M. Visonneau (Ecole Centrale de Nantes, France)

1 Introduction

The flow around the so-called HSVA Tanker hull, experimentally studied by Dr. J. Kux [1] at the Institute of Shipbuilding in Hamburg, is considered by the hydrodynamical community as one of the best documented testcases among all the available experimental ship flow databases. Despite the relative geometric simplicity of the body, the flowfield around this hull is the result of many complicated features involving convergence and divergence of streamlines, a strong thickening of the boundary layer due to rapid changes in cross-sectional shape leading to the development of an intense longitudinal vortex which is slowly relaxed in the wake at large distances downstream from the ship. A more accurate understanding of the flow is provided by the analysis of the limiting streamlines (Figure 1 from [1]). This figure indicates the existence of two lines of convergence located in the aftpart of the hull. The first S-shaped line delimits a vertical wall flow region and a limited zone of flow reversal. The second line of convergence is almost rectilinear and situated slightly above the keel plane of symmetry. It indicates the existence of a region characterized by a large normal velocity which, in that case, is correlated with the development of an intense longitudinal vortex. Figure 2 from [1] shows the axial velocity contours at $x/L=0.978$. It enables a complementary interpretation of the print provided by the previous figure. The longitudinal velocity contours are characterised by a "hook" shape in the central part of the wake illustrating the interaction between the velocity and vorticity fields, the longitudinal isovels being significantly distorted by the longitudinal vorticity.

Considering the complexity of this physical configuration, the simulation of such a flow is a considerable challenge for the numerical methods. The availability of a remarkable experimental data base gives us a formidable opportunity to assess the rel-



Figure 1: HSVA Tanker - $Re = 5.0 \cdot 10^6$.
Experimentally observed wall flow.

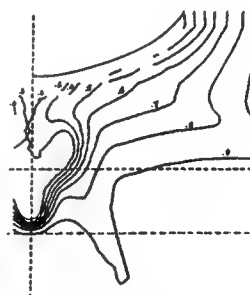


Figure 2: HSVA Tanker - $Re = 5.0 \cdot 10^6$.
Experimental isowake contours at $x/L=0.978$

ative influences and respective merits of discretisation algorithms and turbulence models. It is why this database was chosen as one of the two test cases of the 1990 SSPA-CTH-IIHR Workshop on Viscous Flow held at Goteborg [2], and again selected for the 1994 CFD Workshop held at Tokyo [3].

The results obtained during the first workshop held at Goteborg [2], indicated that most of the methods based on Reynolds Averaged Navier-Stokes Equations were able to simulate the gross features of the flowfield and predicted the shape and location of the wake. However, neither the central region of the wake (the now famous "hook" shaped contours) nor the details of the wall flow were simulated by the methods used at that time. Actually, most of compared methods produced essentially the same too diffusive flow, particularly in the near wake region. Insufficient grid resolution, especially on such complex three-dimensional configurations, spatial discretisation errors, limited convergence on non-linearities are the usual reasons put forward to justify the bad performances of a numerical simulation. Even if these reasons are to be considered, and this paper will draw attention to another one (the influence of inlet conditions), the authors noticed [4] that the turbulence models used at that time were mainly responsible for the bad representation of longitudinal vortex. A systematic comparison of the respective influences of various discretisation schemes and grids was conducted and used to quantify the consequences of ad-hoc modifications of the turbulent viscosity in the central region of the wake. This systematic analysis established that the modifications of eddy-viscosity distribution were the only ones responsible of dramatic improvements of the iso-velocity contours. The aim of this previous study [4] was obviously not to promote such a-posteriori alterations, but rather to underline the likely weaknesses of an eddy-viscosity based turbulence closure for such a complex flow in order to stimulate the validation and assessments of more complex turbulence models in the context of complex geometries.

One year later, during the 1994 CFD Workshop held at Tokyo [3], a session was again devoted to the same test cases, namely the HSVA and Dyne Tankers. Although many contributors employed again algebraic zero equation models (Cebeci-Smith or Baldwin-Lomax models), the results were significantly improved since the "hook-shape" behaviour was often captured, at least to some extent, by an increased number of participants. Those results are somewhat difficult to understand since the same

Baldwin-Lomax turbulence models used in 1990 and 1994 did not provide the same results. An analysis of eddy-viscosity contours in the near wake conducted by Sotiropoulos and Patel suggests that "the apparent success of methods using the Baldwin-Lomax model is mainly due to the arbitrary restriction of the computed eddy-viscosity level in the central part of the wake". Therefore, this unexpected and undesirable consequence of [4] can be considered as a not-always-confessed illustration of the major role played by the turbulence closure in the representation of such complicated afterbody flows.

During this last workshop and for the first time in the context of naval hydrodynamics, two research teams tried to use second-moment turbulence closures ([5], [6]). Sotiropoulos & Patel [5] employed the near-wall second-moment transport closure of Shima [7]. Comparisons with results obtained with the two-layer $k - \epsilon$ turbulence model of Chen & Patel [8] revealed that the second-moment closure was able of reproducing most of the features observed in the measurements and particularly the S-like structure of the isovels in the central part of the wake. However, a closer examination of their results revealed that the longitudinal vorticity in the near wake was noticeably overestimated, the computed rate of decay of secondary motion in the wake being also slower than its measured counterpart. Chen et al. [6] employed a second-moment closure based on the pressure-strain correlations of Speziale, Sarkar and Gatski [9] in the fully turbulent flow regions whereas the low Re near-wall closure of Shima [10] was used to provide the necessary viscous damping in the laminar sublayer and buffer layer. Here again, their results clearly established the superiority of second-moment closures over simpler isotropic eddy viscosity models for this kind of applications, even if, on the contrary of the previous contributors, the longitudinal vorticity appeared to be slightly underestimated.

The objectives of the present study are twofold:

- The analysis in the first part will be conducted under the general context of isotropic eddy viscosity turbulence closures. New turbulence closures based on the $k - \omega$ model and its recent variants developed in the aerodynamical context will be examined. The influence of inlet conditions will be examined in order to determine if full-body computations provide mechanisms for generating longitudinal vorticity that would be absent or underestimated when computations start at mid-body.

- The second part will be devoted to the assessment of a second-moment closure with near-wall low-Re formulation [7] which was successfully employed by Sotiropoulos and Patel. Numerical implementation of this new approach in the difficult context of implicit pressure Poisson equations will be described. Comparisons between this promising second-moment closure and the more robust and validated eddy-viscosity models will conclude this paper.

2 The Numerical Method

Our CFD Group has developed a code (HORUS) which is used for the validations presented in this paper. This code is based on a partial transformation, for which the curvilinear space coordinates are used as independent variables and the cartesian components of velocity and pressure are retained as dependent variables. Many turbulence models are already implemented ranging from eddy-viscosity based models (one equation: Baldwin & Barth's model [11]; two equations: $k - \varepsilon$ models (Chen & Patel [8], Nagano & Tagawa [12], Deng & Piquet [13]), $k - \omega$ models (Wilcox, Menter BSL and SST modified versions [14], [15])) to models requiring the solution of Reynolds Stress Transport Equations (Shima's model [7], Craft & Launder's model presently in test [16]). To avoid any wall-function boundary conditions which turn out to be unacceptable when three-dimensional flows are considered, near-wall low-Reynolds number treatments are systematically implemented in the aforementioned turbulence models.

A structured cell-centered layout is used in which the pressure, turbulence and velocity unknowns share the same location. The momentum and continuity equations are coupled through the PISO procedure with the help of the Rhie & Chow flux interpolation procedure and several implicit second order accurate schemes are implemented for the space and time discretisations.

Preconditioned conjugate gradient solvers (CGS, CGSTAB) are used to solve the linear systems.

This code can be used with almost any kind of mathematical boundary conditions and additional no-slip condition can be added inside the computational domain to enable the computation of configurations of intermediate complexity (afterbody + nozzle, for instance) without having recourse to a multiblock approach. However, a multiblock extension, currently based on point-to-point coincident blocks, has been developed and is under validation before

the more promising "Chimera approach", based on overlapping grids, which is now under development.

This code is included into a modelisation chain comprising a multiblock mesh generator (ICEM-CFD) able to read CAO formats, a X-MOTIF interface facilitating the use of RANSE solver and a three-dimensional interactive graphic post-processor.

3 The Isotropic Eddy Viscosity Closures

3.1 The $k - \omega$ Models

Among the two-equation models, the $k - \varepsilon$ models are by far the most validated today in the hydrodynamical domain. However, even if they are relatively robust, they are known for their lack of sensitivity to adverse pressure-gradients. The models tend to underpredict the separation region or to delay its development. Moreover, if low-Reynolds number $k - \varepsilon$ formulations are employed, the additional non-linearities introduced by the damping functions often deteriorate the overall convergence of the algorithm. The $k - \omega$ model of Wilcox [14], [17] employs one equation for the turbulent kinetic energy k and a second equation for a specific turbulence frequency ω . This model is known to perform better than the $k - \varepsilon$ models under adverse pressure-gradient conditions and, moreover, since its formulation does not employ damping functions in the viscous sublayer, it is characterised by an increased numerical robustness. However, the results of this model depend strongly on the freestream values ω_f that are prescribed outside the shear-layer [18]. In order to remove this unacceptable sensitivity, Menter [15] proposed two variants, the BSL and SST formulations, which result from a blending between the original $k - \omega$ model in the inner region of a boundary layer and a transformed version of the $k - \varepsilon$ model in the outer wake region.

3.1.1 The Original $k - \omega$ Model

The eddy-viscosity is defined by;

$$\nu_t = \frac{\mu_t}{\rho} = \frac{k}{\omega} \quad (1)$$

and the turbulence transport equations are defined by:

$$\begin{aligned} \frac{Dk}{Dt} &= \tau_{ij} \frac{\partial U_i}{\partial x_j} - \beta^* \omega k \\ &+ \frac{\partial}{\partial x_j} \left[(\nu + \sigma_k \nu_t) \frac{\partial k}{\partial x_j} \right] \end{aligned} \quad (2)$$

$$\begin{aligned} \frac{D\omega}{Dt} &= \frac{\gamma}{\rho\nu_t} \tau_{ij} \frac{\partial U_i}{\partial x_j} - \beta \omega^2 \\ &+ \frac{\partial}{\partial x_j} \left[(\nu + \sigma_\omega \nu_t) \frac{\partial \omega}{\partial x_j} \right] \end{aligned} \quad (3)$$

with:

$$-\overline{u_i u_j} = \nu_t \left(\frac{\partial U_i}{\partial x_j} + \frac{\partial U_j}{\partial x_i} \right) - \frac{2}{3} \delta_{ij} k \quad (4)$$

The various constants are defined by:

$$\begin{aligned} \beta^* &= 0.09 \quad \sigma_k = 0.5 \\ \gamma &= \frac{\beta}{\beta^*} - \frac{\sigma_\omega \kappa^2}{\sqrt{\beta^*}} = \frac{5}{9} \\ \gamma^* &= 1.0 \quad \sigma_\omega = 0.5 \\ \beta &= \frac{3}{40} \quad \kappa = 0.41 \end{aligned} \quad (5)$$

• ϕ_1 (Wilcox):

$$\begin{aligned} \sigma_{k1} &= 0.5 \quad \sigma_{\omega 1} = 0.500 \\ \beta_1 &= 0.0750 \\ \gamma_1 &= \frac{\beta_1}{\beta^*} - \sigma_{\omega 1} \frac{\kappa^2}{\sqrt{\beta^*}} \end{aligned} \quad (9)$$

• ϕ_2 ($k - \varepsilon$):

$$\begin{aligned} \sigma_{k2} &= 1.0 \quad \sigma_{\omega 2} = 0.856 \\ \beta_2 &= 0.0828 \\ \gamma_1 &= \frac{\beta_2}{\beta^*} - \sigma_{\omega 2} \frac{\kappa^2}{\sqrt{\beta^*}} \end{aligned} \quad (10)$$

and:

$$\kappa = 0.41 \quad \text{et} \quad \beta^* = 0.09 \quad (11)$$

The boundary conditions for ω , [14], are given by:

1. No-slip wall boundary conditions:

$$\left| \begin{array}{l} k = 0 \\ \omega \xrightarrow{y \rightarrow 0} \frac{6\nu}{\beta y^2} \end{array} \right.$$

2. Freestream boundary conditions:

$$\left| \begin{array}{l} k_\infty = \nu_{t\infty} \omega_\infty \\ \omega_\infty = (1 \rightarrow 10) \frac{U_0}{L_0} \\ \nu_{t\infty} = 10^{-3} \nu \end{array} \right.$$

The blending function F_1 is built to be one in the near-wall region and zero away from the body. It is defined by:

$$F_1 = \tanh(\zeta_1^4) \quad (12)$$

with

$$\zeta_1 = \min \left[\max \left(\frac{\sqrt{k}}{0.09 \omega y}, \frac{500 \nu}{y^2 \omega} \right), \frac{4 \rho \sigma_{\omega 2} k}{C D_{k\omega} y^2} \right] \quad (13)$$

where:

$$C D_{k\omega} = \max \left(2 \rho \sigma_{\omega 2} \frac{1}{\omega} \frac{\partial k}{\partial x_j} \frac{\partial \omega}{\partial x_j}, 10^{-20} \right) \quad (14)$$

3.1.2 BSL variant from Menter

$$\begin{aligned} \frac{Dk}{Dt} &= \tau_{ij} \frac{\partial U_i}{\partial x_j} - \beta^* \omega k \\ &+ \frac{\partial}{\partial x_j} \left[(\nu + \sigma_k \nu_t) \frac{\partial k}{\partial x_j} \right] \end{aligned} \quad (6)$$

$$\begin{aligned} \frac{D\omega}{Dt} &= \frac{\gamma}{\rho\nu_t} \tau_{ij} \frac{\partial U_i}{\partial x_j} - \beta \omega^2 \\ &+ \frac{\partial}{\partial x_j} \left[(\nu + \sigma_\omega \nu_t) \frac{\partial \omega}{\partial x_j} \right] \\ &+ 2(1 - F_1) \sigma_{\omega 2} \frac{1}{\omega} \frac{\partial k}{\partial x_j} \frac{\partial \omega}{\partial x_j} \end{aligned} \quad (7)$$

ϕ_1 represents the constant relative to the original model (σ_{k1}, \dots), ϕ_2 the corresponding constant in the transformed $k - \varepsilon$ model (σ_{k2}, \dots) and ϕ the constant associated to the new $k - \omega$ BSL model (σ_k, \dots). The relation between these constants is given by:

$$\phi = F_1 \phi_1 + (1 - F_1) \phi_2 \quad (8)$$

with the following two sets of constants:

4 The Second Moment Closures

Difficulties encountered by eddy-viscosity models in modelling complex flows are most often related to models' inability to account for the selective amplification or attenuation of different Reynolds stresses by curvature-related strain components. These limitations are principally rooted in the fact that the eddy-viscosity models have been designed to provide the correct level of shear stress in flows in which only this stress is influential. The eddy-viscosity models are not able to modelize separately the normal

turbulent stresses, since only the kinetic turbulent energy is taken into consideration. Therefore, the essential inability of eddy-viscosity closures to simulate anisotropic turbulence can explain their bad performances on flows containing recirculating regions or intense vortices, since the turbulence anisotropy strongly influences the magnitude of longitudinal vorticity ([19]). With the need to resolve anisotropy taken for granted, the main choice is between non-linear eddy-viscosity models and second-moment closures. The non-linear eddy-viscosity models are very attractive because they can be seen as the natural and painless evolution from linear eddy-viscosity models. It is now difficult to evaluate the potentialities of such models in complex three-dimensional flows. However, we believe that they will perform better than linear eddy-viscosity models only on a limited range of flows characterised by a weak turbulent anisotropy. On complex three-dimensional flows, second-moment closures will be probably superior because of the exact representation of stress production which enables realistic interactions between normal stress anisotropy and shear-stress components.

Here and there, very promising computational studies employing second-moment closures on highly complex three-dimensional flows are emerging ([5], [6], [20], [21]). In the same time, new proposals of low-Reynolds number near-wall second-moment closures make it possible the eviction of wall-function boundary conditions, what is for us a prerequisite for validating them on three-dimensional flows.

4.1 The Shima Model

This model [7] is defined by the following transport equations:

$$\begin{aligned} \frac{Dr_{ij}}{Dt} = & P_{ij} - \frac{2}{3}\varepsilon\delta_{ij} + \phi_{ij}^{(1)} \\ & + \phi_{ij}^{(2)} + \phi_{ij}^{(w1)} + \phi_{ij}^{(w2)} \\ & - \frac{\partial}{\partial x_k} \left(J_{ijk} - \nu \frac{\partial r_{ij}}{\partial x_k} \right) \end{aligned} \quad (15)$$

where the source terms corresponding to production, dissipation, transfer and diffusion are modelled by by:

$$P_{ij} = - \left(r_{jk} \frac{\partial U_i}{\partial x_k} + r_{ik} \frac{\partial U_j}{\partial x_k} \right) \quad (16)$$

$$\phi_{ij}^{(1)} = -C_1 \frac{\varepsilon}{k} \left(r_{ij} - \frac{2}{3}\delta_{ij}k \right) \quad (17)$$

$$\phi_{ij}^{(2)} = -C_2 \left(P_{ij} - \frac{2}{3}\delta_{ij}P \right) \quad (18)$$

where:

$$P = -r_{kl} \frac{\partial U_k}{\partial x_l} \quad (19)$$

$$\begin{aligned} \phi_{ij}^{(w1)} = & C_{w1} \frac{\varepsilon}{k} \left(r_{km} n_k n_m \delta_{ij} \right. \\ & - \frac{3}{2} r_{ki} n_k n_j \\ & \left. - \frac{3}{2} r_{kj} n_k n_i \right) \frac{k^{\frac{3}{2}}}{C_l \varepsilon d} \end{aligned} \quad (20)$$

$$\begin{aligned} \phi_{ij}^{(w2)} = & C_{w2} \left(\phi_{km}^{(2)} n_k n_m \delta_{ij} \right. \\ & - \frac{3}{2} \phi_{ki}^{(2)} n_k n_j \\ & \left. - \frac{3}{2} \phi_{kj}^{(2)} n_k n_i \right) \frac{k^{\frac{3}{2}}}{C_l \varepsilon d} \end{aligned} \quad (21)$$

$$J_{ijk} = -C_s \frac{\varepsilon}{k} r_{kl} \frac{\partial r_{ij}}{\partial x_l} \quad (22)$$

with $C_s = 0.22$ and $C_l = 2.5$.

The coefficients are given by:

$$\begin{aligned} C_1 = & 1 + 2.58 A A_2^{1/4} \\ & [1 - \exp[-(0.0067 R_T)^2]] \\ C_2 = & 0.75 A^{1/2} \\ C_{w1} = & -C_1/3 + 1.67 \\ C_{w2} = & \max[2(C_2 - 1)/3 \\ & + 0.5, 0]/C_2 \end{aligned} \quad (23)$$

where:

$$A = 1 - \frac{9}{8} A_2 + \frac{9}{8} A_3 \quad (24)$$

$$A_2 = a_{ij} a_{ij} \quad (25)$$

$$A_3 = a_{ij} a_{jk} a_{ki} \quad (26)$$

$$a_{ij} = \frac{r_{ij}}{k} - \frac{2}{3} \delta_{ij} \quad (27)$$

$$R_T = \frac{k^2}{\nu \varepsilon} \quad (28)$$

where d is the distance to the wall.

A transport equation for ε must also be solved:

$$\begin{aligned} \frac{\partial \varepsilon}{\partial t} + U_k \frac{\partial \varepsilon}{\partial x_k} = & (C_{\varepsilon 1} + \psi_1 + \psi_2) \frac{\varepsilon}{k} P \\ & - C_{\varepsilon 2} \frac{\varepsilon \bar{\varepsilon}}{k} \\ & + \frac{\partial}{\partial x_k} \left(C_{\varepsilon} \frac{k}{\varepsilon} r_{kl} \frac{\partial \varepsilon}{\partial x_l} + \nu \frac{\partial \varepsilon}{\partial x_k} \right) \end{aligned} \quad (29)$$

with:

$$\bar{\varepsilon} = \varepsilon - 2\nu \left(\frac{\partial k^{1/2}}{\partial x_l} \right)^2 \quad (30)$$

$$\psi_1 = 1.5 A (P/\varepsilon - 1) \quad (31)$$

$$\psi_2 = \frac{0.35(1 - 0.3A_2)}{\exp[-(0.002R_T)^{1/2}]} \quad (32)$$

The additional constants take their usual values: $C_{\epsilon 1} = 1.45$, $C_{\epsilon 2} = 1.9$ and $C_{\epsilon} = 0.18$.

4.2 Numerical Implementation

Second-moment closures are particularly difficult to include into a time-implicit RANSE solver because of:

- the absence of the numerically stabilising eddy viscosity,
- the strong coupling between anyone stress and strains other than the ones linked to that stress via the Boussinesq relations,
- the predominant influence in the momentum transport equations of equilibrium between several strong and opposite source terms, namely, the pressure and Reynolds-stress gradients,
- the complexity of second-moment transport equations through added non linearities introduced by the actual low-Reynolds near-wall formulations. In particular, the practical impossibility of obtaining theoretically or numerically realisable turbulence in complex configurations makes it difficult to reach a safe numerically converged state.

Moreover, the incorporation of second-moment closures into solvers designed for flows around complex geometries is considerably complicated by the mandatory use of colocated variable arrangement. Different numerical strategies have been designed to enhance stability in this context. Some authors, [20], enforce stability by extracting apparent turbulent viscosity from the source terms of second-moment transport equations. On the other hand, [22] developed a fully coupled implicit resolution of momentum and second-moment transport equations to avoid velocity-turbulence decoupling. More recently, several authors, [5], [21], have employed explicit time-marching procedures, often based on a four stage Runge-Kutta scheme for the mean flow equations, without reporting any severe stability problem.

Actually, if one wants to include a second-moment closure into an existing time-implicit solver based on the resolution of a Poisson equation for the pressure, many problems of stability may be expected. In the momentum equations, the predominant role played by the source terms in absence of turbulent

viscosity makes it necessary deep modifications of the original numerical algorithm. When the Reynolds stress is treated implicitly in the momentum equations when using eddy-viscosity models, it appears explicitly when second-moment closures are used. This situation is particularly difficult for the normal velocity component when it is integrated down to the wall. In fact, in the wall region, due to the rapid growth of normal Reynolds stress, its gradient becomes a predominant term which is balanced only by the normal pressure gradient, both appearing explicitly in the momentum source term. It is why the main idea behind the present proposed modifications of the original algorithm is the obligation of treating the turbulent and pressure gradients in the same way if we want to maintain the regularity of small magnitude velocity components. We think that the main source of irregularity is not necessarily the absence of turbulent viscosity but the discrete disequilibrium between several strong and opposite gradients which would provide, if perfect balance was achieved, a regular solution of small magnitude. To enforce this discrete equilibrium is not a trivial task because of the numerous source terms interpolations which are carried out if the popular Rhie & Chow interpolation practice is used to build the mass fluxes in the general context of a pressure equation method on non-staggered variable arrangement. The only physical tool able to restore this equilibrium is the pressure and it is why it is perhaps more justified to speak of a pressure-turbulence-velocity coupling instead of the conventional pressure-velocity coupling.

In a pressure equation RANS solver, the three fundamental steps are the prediction step, the solution of pressure equation and the correction step. Each step must be somewhat revised in order to maintain a strict discrete equilibrium between the dominant source terms, namely, the pressure and turbulent correlations gradients. These generalisations which are designed to enforce the regularity of discrete fields and consequently the stability of the numerical algorithm, are now described on a 2D curvilinear example.

4.2.1 A pressure-turbulence equation

The RANS equations are defined by:

$$\frac{Du_i}{Dt} + \frac{\partial p}{\partial x_i} + \frac{\partial r_{ij}}{\partial x_j} = \frac{1}{Re} \left(\frac{\partial^2 u_i}{\partial x_i^2} \right) \quad (33)$$

where $r_{ij} = \overline{u'_i u'_j}$. Once discretised, the momentum equations can be written as:

$$u_1(c) = \sum_{nb} C_{nb} u_1(nb) - C_p \left[S_{u1} + \frac{\partial p}{\partial x} + \frac{\partial r_{11}}{\partial x} + \frac{\partial r_{12}}{\partial y} \right]_c \quad (34)$$

$$u_2(c) = \sum_{nb} C_{nb} u_2(nb) - C_p \left[S_{u2} + \frac{\partial p}{\partial y} + \frac{\partial r_{12}}{\partial x} + \frac{\partial r_{22}}{\partial y} \right]_c \quad (35)$$

where C_{nb} and C_p are the usual influence coefficients.

Once expressed with the curvilinear coordinates, the momentum equations become:

$$u_1(c) = \hat{u}_1(c) - \frac{C_p}{J} \left(b_1^1 \frac{\partial p}{\partial \xi} + b_1^2 \frac{\partial p}{\partial \eta} \right) - \frac{C_p}{J} \left(b_1^1 \frac{\partial r_{11}}{\partial \xi} + b_1^2 \frac{\partial r_{11}}{\partial \eta} \right) - \frac{C_p}{J} \left(b_2^1 \frac{\partial r_{12}}{\partial \xi} + b_2^2 \frac{\partial r_{12}}{\partial \eta} \right) \quad (36)$$

$$u_2(c) = \hat{u}_2(c) - \frac{C_p}{J} \left(b_2^1 \frac{\partial p}{\partial \xi} + b_2^2 \frac{\partial p}{\partial \eta} \right) - \frac{C_p}{J} \left(b_1^1 \frac{\partial r_{12}}{\partial \xi} + b_1^2 \frac{\partial r_{12}}{\partial \eta} \right) - \frac{C_p}{J} \left(b_2^1 \frac{\partial r_{22}}{\partial \xi} + b_2^2 \frac{\partial r_{22}}{\partial \eta} \right) \quad (37)$$

where J is the jacobian of the transformation and b_j^k are the usual j components of $\mathbf{b}^k = \frac{\partial \mathbf{r}}{\partial \xi^i} \times \frac{\partial \mathbf{r}}{\partial \xi^j}$.

The contributions of neighboring points and source term (except the pressure and turbulent stress gradients) are incorporated into the pseudo-velocity \hat{u}_i :

$$\hat{u}_1(c) = \sum_{nb} C_{nb} u_1(nb) - C_p S_{u1} \quad (38)$$

$$\hat{u}_2(c) = \sum_{nb} C_{nb} u_2(nb) - C_p S_{u2} \quad (39)$$

To build a pressure equation, the continuity equation is written under its fully conservative form on the mass control volume:

$$[JU^1]_d - [JU^1]_u + [JU^2]_n - [JU^2]_s = 0 \quad (40)$$

with $JU^i = b_i^j u_j$. The contravariant velocity components $JU^i = b_i^j u_j$ have now to be rebuilt at the interfaces and this reconstruction must avoid checkerboard pressure oscillations and maintain the discrete link between pressure and turbulent gradients. The mass flux at the interface d is rebuilt through the

following interpolation of velocity components:

$$u_1(d) = \bar{u}_1(d) - \frac{\bar{C}_p(d)}{J} \frac{b_1^j}{\partial \xi^j} \frac{\partial p}{\partial \xi^j}(d) - \frac{\bar{C}_p(d)}{J} \frac{b_1^j}{\partial \xi^j} \frac{\partial r_{11}}{\partial \xi^j}(d) - \frac{\bar{C}_p(d)}{J} \frac{b_2^j}{\partial \xi^j} \frac{\partial r_{12}}{\partial \xi^j}(d) \quad (41)$$

$$u_2(d) = \bar{u}_2(d) - \frac{\bar{C}_p(d)}{J} \frac{b_2^j}{\partial \xi^j} \frac{\partial p}{\partial \xi^j}(d) - \frac{\bar{C}_p(d)}{J} \frac{b_1^j}{\partial \xi^j} \frac{\partial r_{12}}{\partial \xi^j}(d) - \frac{\bar{C}_p(d)}{J} \frac{b_2^j}{\partial \xi^j} \frac{\partial r_{22}}{\partial \xi^j}(d) \quad (42)$$

where the overlined quantities are linearly interpolated in the computational domain, the pressure and turbulent stress gradients being rediscritised at the interface. Once the contravariant components are expressed with the help of the previous interpolations, a pressure equation is obtained which is somewhat different because the contributions of turbulent stresses are explicit instead of being accumulated (and linearly interpolated) in the source terms.

$$\frac{\partial \hat{U}^i}{\partial \xi^i} = \frac{\partial}{\partial \xi^i} \left(\frac{C_p}{J} \left[b_i^j b_j^k \frac{\partial p}{\partial \xi^k} \right] \right) + \frac{\partial}{\partial \xi^i} \left(\frac{C_p}{J} \left[b_i^j b_j^k \frac{\partial r_{lk}}{\partial \xi^m} \right] \right) \quad (43)$$

where:

$$\hat{U}^i = J b_j^i \hat{u}_j \quad (44)$$

With this special treatment of turbulent stresses gradients in the pressure equation source term, the discrete link between pressure and turbulence gradients is enforced, and a first source of numerical oscillations is avoided when pressure and turbulent correlations gradients compete in the momentum equations.

4.2.2 The correction step

Since the source terms of momentum equations do not contain any turbulent contribution, it is necessary to devise a slightly modified correction step:

$$u_1(c) = \hat{u}_1(c) - \frac{C_p}{J} \left(b_1^1 \frac{\partial p}{\partial \xi^1} + b_1^2 \frac{\partial p}{\partial \xi^2} \right) - \frac{C_p}{J} \left(b_1^1 \frac{\partial r_{11}}{\partial \xi^1} + b_1^2 \frac{\partial r_{11}}{\partial \xi^2} \right) - \frac{C_p}{J} \left(b_2^1 \frac{\partial r_{12}}{\partial \xi^1} + b_2^2 \frac{\partial r_{12}}{\partial \xi^2} \right) \quad (45)$$

$$\begin{aligned}
u_2(c) &= \hat{u}_2(c) \\
&- \frac{C_p}{J} \left(b_2^1 \frac{\partial p}{\partial \xi^1} + b_2^2 \frac{\partial p}{\partial \xi^2} \right) \\
&- \frac{C_p}{J} \left(b_1^1 \frac{\partial r_{12}}{\partial \xi^1} + b_1^2 \frac{\partial r_{12}}{\partial \xi^2} \right) \\
&- \frac{C_p}{J} \left(b_2^1 \frac{\partial r_{22}}{\partial \xi^1} + b_2^2 \frac{\partial r_{22}}{\partial \xi^2} \right)
\end{aligned} \quad (46)$$

where the turbulent stresses gradients are explicitly computed and combined with the new pressure gradients. Here, it is important to point out the role of pressure relaxation factor for maintaining the discrete balance between pressure and turbulence. If the pressure is under-relaxed after solving the pressure equation as:

$$p^{corr.} = \alpha_p p^{sol} + (1 - \alpha_p) p^{(n-1)} \quad (47)$$

where $p^{corr.}$, p^{sol} and $p^{(n-1)}$ stand for, respectively, the under-relaxed pressure used in the correction step, the current solution of pressure equation and the previous pressure field, it is necessary to under-relax similarly the turbulent correlations before adding their contributions in the correction step as:

$$r_{ij}^{corr.} = \alpha_p r_{ij}^{(n)} + (1 - \alpha_p) r_{ij}^{(n-1)} \quad (48)$$

This joint under-relaxation of pressure and turbulent stresses will maintain the discrete equilibrium for which the pressure is designed in the modified pressure equation.

4.2.3 The overall coupling algorithm

Since the pressure is the only variable which is able to account for the turbulent gradients to promote numerical regularity, the conventional organisation of the coupling algorithm must be modified.

Conventional coupling algorithm Non-linear iteration 1

Solve momentum equations:

$$u_i^{(1)} = M.E. \left(p^{(0)}, r_{ij}^{(0)} \right) \quad (49)$$

Solve the pressure equation:

$$p^{(1)} = P.E. \left(u^{(1)}, r_{ij}^{(0)} \right) \quad (50)$$

Correction step:

$$u_i^{(2)} = C.S. \left(p^{(1)}, r_{ij}^{(0)} \right) \quad (51)$$

Solve the second-moment transport equations:

$$r_{ij}^{(1)} = \left(u_i^{(2)}, \dots \right) \quad (52)$$

Non-linear iteration 2

Solve momentum equations:

$$u_i^{(3)} = M.E. \left(u_i^{(2)}, p^{(1)}, r_{ij}^{(2)} \right) \quad (53)$$

where M.E., P.E., C.S. and T.E. stand for momentum equations, pressure equation, correction step and turbulence equations.

It is clear that the pressure $p^{(1)}$ which was devised to maintain regularity with respect to $r_{ij}^{(0)}$ can not cope with the new turbulent field $r_{ij}^{(1)}$. That is a strong source of oscillations because the discrete equilibrium is broken.

It is the reason why the overall algorithm must be modified in order to restore the link between turbulence and pressure:

Modified coupling algorithm Non-linear iteration 1

Solve momentum equations:

$$u_i^{(1)} = M.E. \left(p^{(0)}, r_{ij}^{(0)} \right) \quad (54)$$

Solve the second-moment transport equations:

$$r_{ij}^{(1)} = \left(u_i^{(1)}, \dots \right) \quad (55)$$

Solve the pressure equation:

$$p^{(1)} = P.E. \left(u^{(1)}, r_{ij}^{(1)} \right) \quad (56)$$

Correction step:

$$u_i^{(2)} = C.S. \left(p^{(1)}, r_{ij}^{(1)} \right) \quad (57)$$

Non-linear iteration 2

Solve momentum equations:

$$u_i^{(3)} = M.E. \left(u_i^{(2)}, p^{(1)}, r_{ij}^{(1)} \right) \quad (58)$$

4.2.4 An appropriate pressure boundary condition

In the same order of idea, we have devised a special wall boundary condition for the pressure which links pressure and turbulence in the immediate vicinity of the walls. Let us suppose that the wall is located

at $\eta = \text{cste}$. The transport equation for the normal contravariant component $V = b_1^2 u + b_2^2 v$ is given by:

$$\begin{aligned} V = \hat{V} - b_1^2 & \left[\frac{C_p}{J} (b_1^1 p_\xi + b_1^2 p_\eta \right. \\ & + b_1^1 r_{11\xi} + b_1^2 r_{11\eta} + b_2^1 r_{12\xi} + b_2^2 r_{12\eta}) \\ & - b_2^2 \left[\frac{C_p}{J} (b_2^1 p_\xi + b_2^2 p_\eta \right. \\ & + b_1^1 r_{12\xi} + b_1^2 r_{12\eta} + b_2^1 r_{22\xi} + b_2^2 r_{22\eta}) \end{aligned} \quad (59)$$

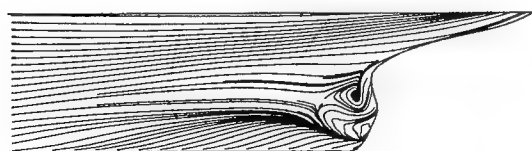
The η derivatives are the only prominent terms near the wall, leading to the equilibrium:

$$\begin{aligned} b_1^2 b_1^2 p_\eta + b_1^2 b_1^2 r_{11\eta} + b_1^2 b_2^2 r_{22\eta} \\ + b_2^2 b_2^2 p_\eta + b_2^2 b_1^2 r_{12\eta} + b_2^2 b_2^2 r_{22\eta} = 0 \end{aligned} \quad (60)$$

which is used as generalised wall boundary condition for the pressure.

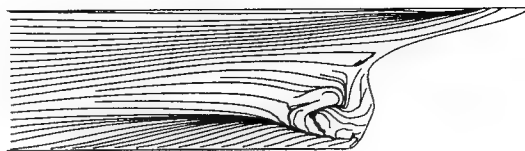
5 Results

The first part of this section is devoted to the comparison of the aforementioned turbulence closures, all the others characteristics (grid, numerical schemes, level of convergence) being kept unchanged. These computations have been carried out on an O-O grid topology. The flow domain is defined by $0.5 < x/L < 5.0$ and $r_s < r/L < 4.0$ (L being the length between perpendiculars and r_s the radius of the hull's surface). This domain is covered by $65 \times 81 \times 34$ nodes in the streamwise, radial and girthwise directions respectively. The first coordinate surface is situated at $y^+ \approx 1.0$. Each eddy-viscosity solution necessitated about 5000 non-linear iterations and the $R_{ij} - \epsilon$ solution, which was initialised by several hundred non-linear iterations using eddy-viscosity models, needed 1000 additional non-linear iterations to reach a not enough converged state.



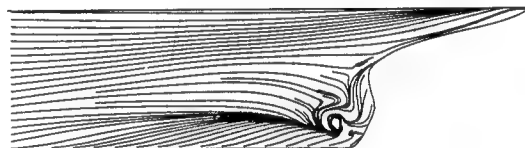
K-Epsilon(Chen-Patel)

Figure 3: Chen & Patel $k - \epsilon$ model - Computed wall flow



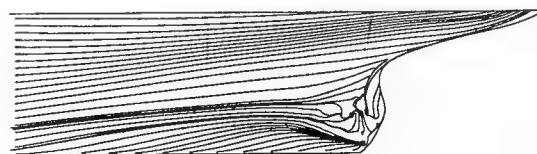
K-Omega (Wilcox)

Figure 4: Wilcox $k - \omega$ model - Computed wall flow



K-Omega BSL(Menter)

Figure 5: BSL $k - \omega$ model - Computed wall flow



Rij-Epsilon(Shima)

Figure 6: Shima $R_{ij} - \epsilon$ model - Computed wall flow

Figures 3, 4, 5 and 6 show the limiting streamlines on the hull with the various turbulence closures. The

limiting streamlines are found to be very sensitive to turbulence model. Previous comparisons [4] with Chen & Patel $k-\epsilon$ model underestimated the separation region compared with the present results shown in figure 3. We believe that it is due to numerical stiffness. In the present computations, convergence is ensured by checking the convergence of wall shear stress which is quite slow to establish in the separation region. Several thousands iterations were found to be necessary to achieve convergence. The $k-\epsilon$ and BSL $k-\omega$ models (at a lesser degree) provide a too diffusive flow even if the limiting streamlines exhibit the main characteristics indicated by the experiments. For the $k-\epsilon$ models, the behaviour of computed wall flow has been found independent from near-wall low-Reynolds number treatments which are present in our code ([12], [13], [8]). This analysis is confirmed by the isovels at $x/L = 0.978$ (Figs. 7, 9) although the BSL model performs slightly better than the Chen & Patel closure. The $k-\omega$ and $R_{ij}-\epsilon$ models simulate a very accurate location of the first rectilinear convergence line near the keel, behaviour which is confirmed by the isovels (Figs. 8, 10) which indicate that the flow in the near-wake is more rotational. Moreover, the $k-\omega$ predicts a weak longitudinal vortex near the waterplane, which is not the case with other closures. However, Figure 10 show that the simulated longitudinal vorticity is now too intense. These results exaggerate the tendencies already present in the previous computations of [5] obtained with a totally different numerical methodology. It is important to notice that the iso-velocity contours are regular, which confirms the efficiency of the proposed modifications, except near the symmetry plane where computational grid is not fine and regular enough to capture rapid changes of flow field due to the longitudinal vortex.

These conclusions are illustrated more convincingly by Figures 11, 12, 13, 14, 15 and 16 which show the axial and vertical velocity profiles at different longitudinal stations and depths. The $R_{ij}-\epsilon$ model overpredicts the secondary motion and its rate of decay is slower than indicated by the measurements. These results are also in accordance with [5].

The second part of the results is devoted to the influence of inlet condition. To determine if a significant amount of longitudinal vorticity is created at the fore part of the ship, complementary computations using a full body domain have been carried out. The flow domain is defined by $-3.0 < x/L < 5.0$ and $r_s < r/L < 4.0$. This domain is covered by $120 \times 81 \times 34$ nodes in the streamwise, radial and

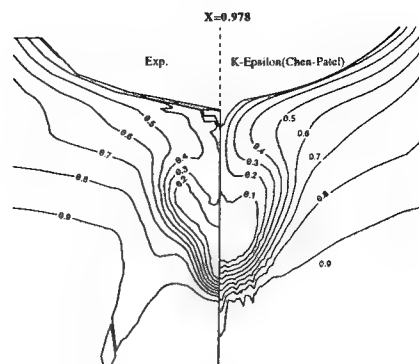


Figure 7: Chen & Patel $k-\epsilon$ model - Comparison between experimental and computed isowakes at $x/L = 0.978$

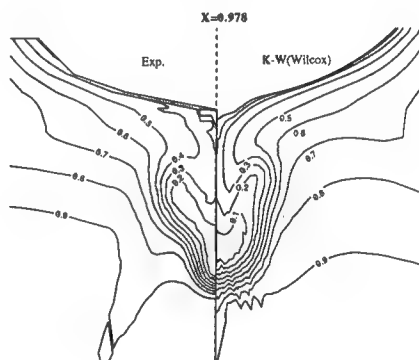


Figure 8: $k-\omega$ model - Comparison between experimental and computed isowakes at $x/L = 0.978$

girthwise directions respectively. The after part of this grid ($i > 55$) is identical to the above grid, so that uncertainty related to grid resolution can be excluded in the following comparisons. Computations were started with $U = 1$ as initial conditions everywhere (except at the wall) which were different from above computations where prescribed inlet conditions were used as initial conditions. No special transition treatment was employed except that the production of turbulent kinetic energy is bounded by 20 times the dissipation as proposed by [15], that is $P_k = \min(P_k, 20\epsilon)$.

Figures 17, 18, 19, 20, 21 and 22 show the longitudinal and vertical velocity profiles at several stations and depths for the original $k-\omega$ model and its BSL variant. It is clear that we can not exclude the

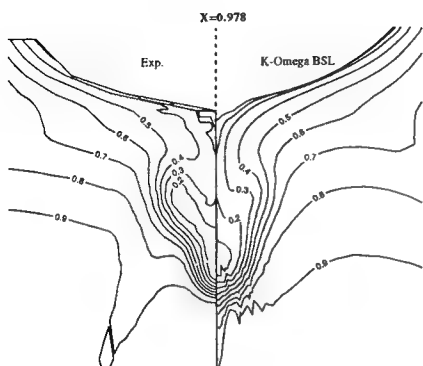


Figure 9: BSL $k - \omega$ model - Comparison between experimental and computed isowakes at $x/L = 0.978$

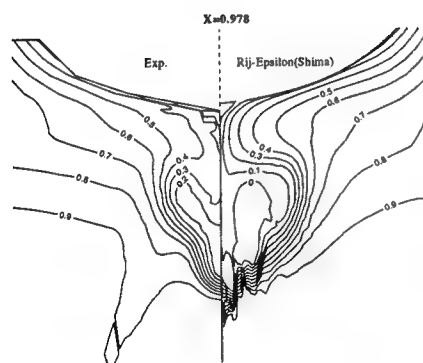


Figure 10: Shima $R_{ij} - \epsilon$ model - Comparison between experimental and computed isowakes at $x/L = 0.978$

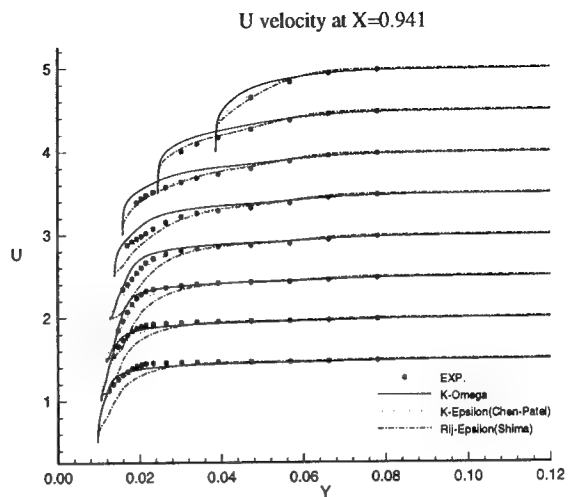


Figure 11: Half-body - Axial velocity profiles at $x/L = 0.941$ as functions of y for several depths: symbols are from measurements

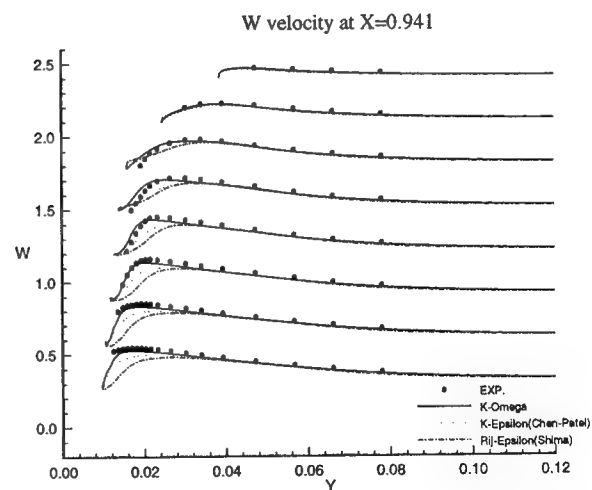


Figure 12: Half-body - Vertical velocity profiles at $x/L = 0.941$ as functions of y for several depths: symbols are from measurements

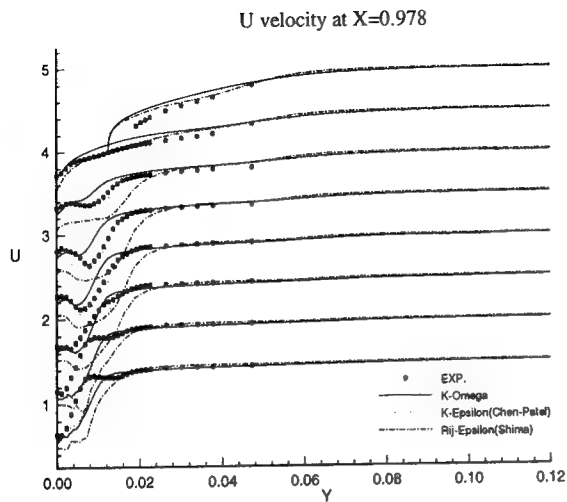


Figure 13: Half-body - Axial velocity profiles at $x/L = 0.978$ as functions of y for several depths: symbols are from measurements

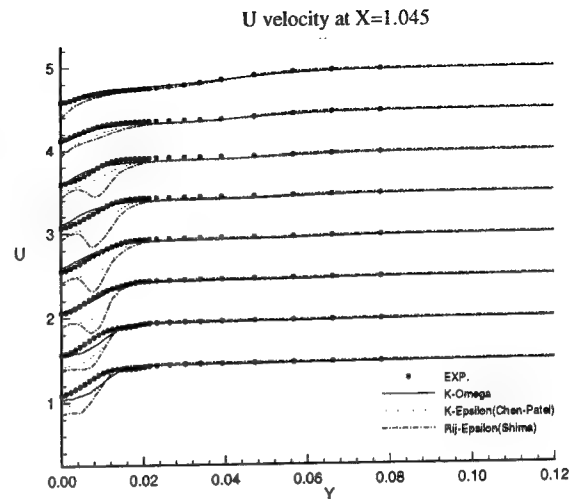


Figure 15: Half-body - Axial velocity profiles at $x/L = 1.045$ as functions of y for several depths: symbols are from measurements

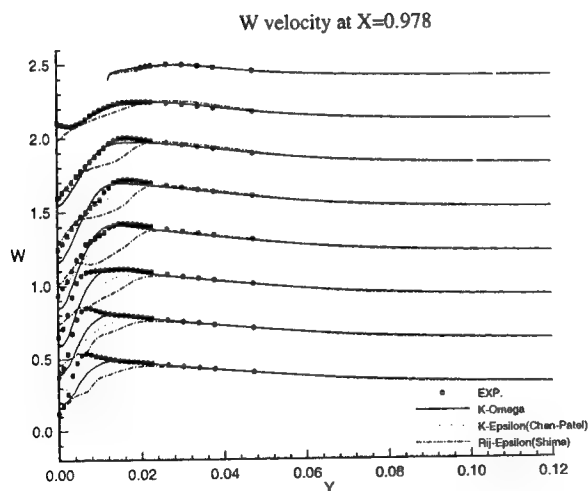


Figure 14: Half-body - Vertical velocity profiles at $x/L = 0.978$ as functions of y for several depths: symbols are from measurements

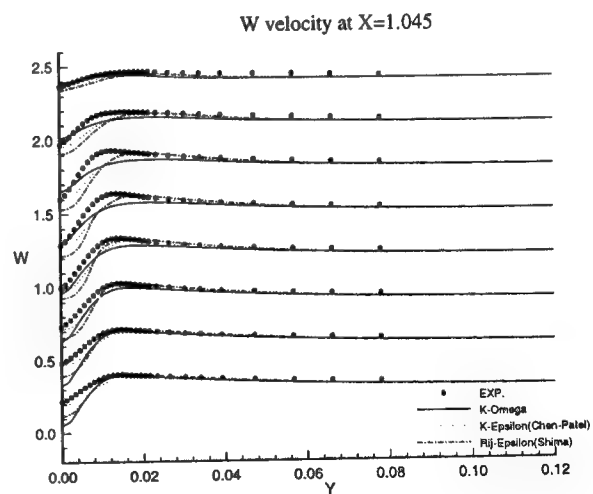


Figure 16: Half-body - Vertical velocity profiles at $x/L = 1.045$ as functions of y for several depths: symbols are from measurements

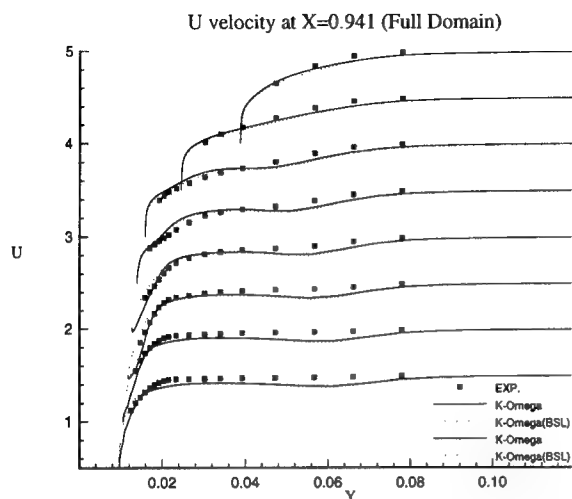


Figure 17: Full-body - Axial velocity profiles at $x/L = 0.941$ as functions of y for several depths: symbols are from measurements

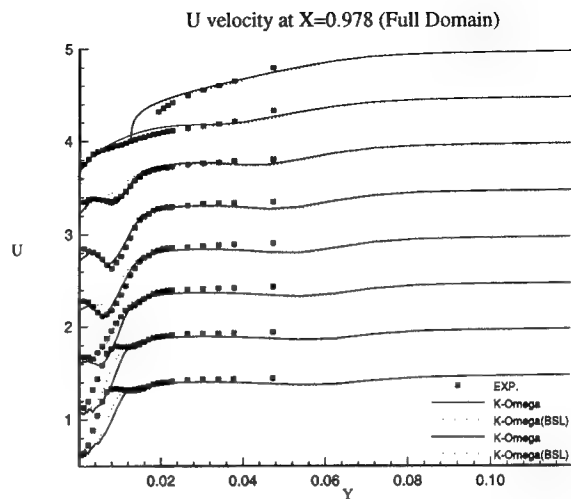


Figure 19: Full-Body - Axial velocity profiles at $x/L = 0.978$ as functions of y for several depths: symbols are from measurements

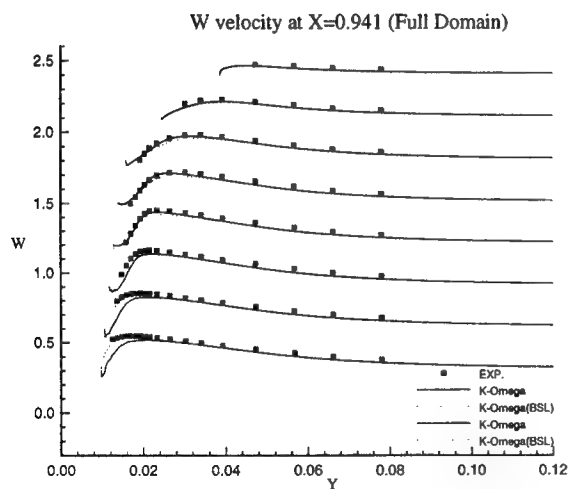


Figure 18: Full-body - Vertical velocity profiles at $x/L = 0.941$ as functions of y for several depths: symbols are from measurements

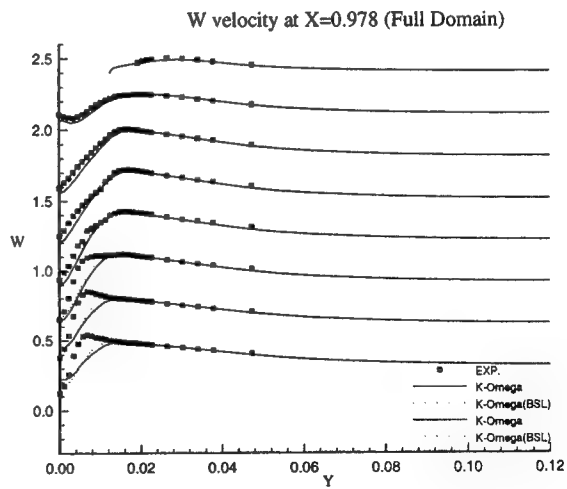


Figure 20: Full-Body - Vertical velocity profiles at $x/L = 0.978$ as functions of y for several depths: symbols are from measurements

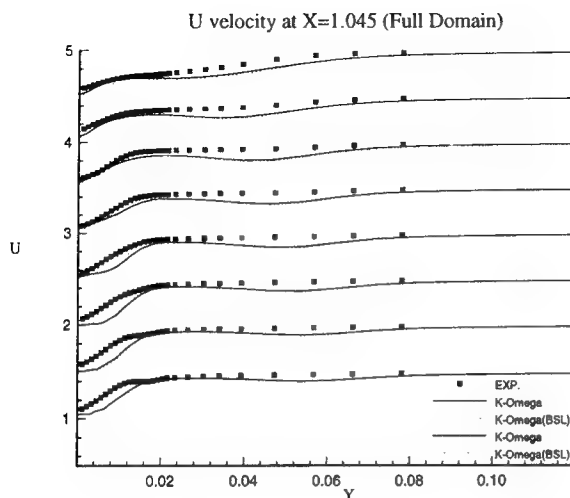


Figure 21: Full-Body - Axial velocity profiles at $x/L = 1.045$ as functions of y for several depths: symbols are from measurements

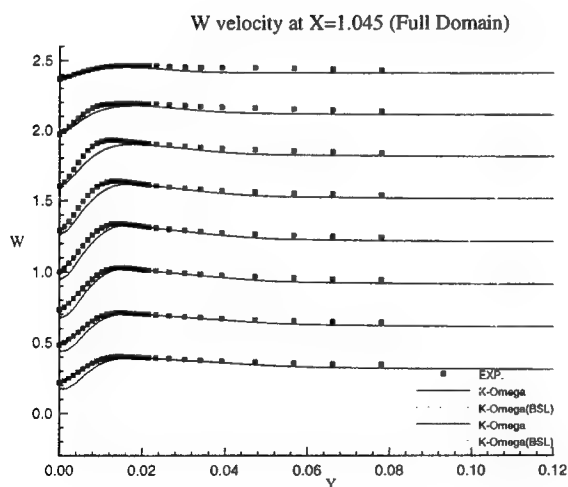


Figure 22: Full-Body - Vertical velocity profiles at $x/L = 1.045$ as functions of y for several depths: symbols are from measurements

influence of inlet conditions since the full-ship computations provide a better simulation of the velocity profiles at the experimental stations even if the boundary conditions on turbulent quantities at the inlet plane (half-domain) are Neumann conditions. The superiority of $k-\omega$ model over $k-\varepsilon$ closure can be observed not only the separation region, but also in the attached boundary layer under adverse pressure gradient. At the section $x/L = 0.941$ where no separation occurs, $k-\omega$ model yields a better prediction, especially on the vertical velocity component (fig.18). Although longitudinal velocity component is somewhat overpredicted near the waterline with half-domain computations (fig. 11) in this section, it is equally well predicted with full-domain computations (fig. 17). Sensitivity to free stream values of ω is not observed in this configuration, but influence of inlet conditions seems to be important for $k-\omega$ model when we compare U velocity component given at $x/L = 0.978$ (figs 13 and 19). For the sake of brevity, no comparisons are presented with the $k-\varepsilon$ model but additional computations have not indicated such a sensitivity to inlet conditions for this closure.

6 Concluding Remarks

Several eddy-viscosity models and a second-moment closure have been employed to calculate the flow around the HSVA Tanker. Deep modifications of the original algorithm have been designed to maintain the discrete equilibrium between the various source terms involved in the momentum equations. These modifications made it possible to implement a second-moment closure into a Poisson pressure RANSE solver without introducing any apparent turbulent viscosity. The results obtained for this complex geometry, illustrate the potentialities of this approach. The Shima $R_{ij} - \varepsilon$ closure is very promising but yields a too intense secondary flow in the near wake. However, in that case, it is still necessary to improve the robustness of second-moment closures when strong variations of physical quantities are present in the flow field. Actually, we consider that the $k-\omega$ models offer, till now, the best compromise for this particular class of flows since the best simulation of the flow around the HSVA Tanker is provided by the original Wilcox model with a full-domain computation.

7 Acknowledgments

Thanks are due to the Scientific Committee of IDRIS and the DS/SPI for attributions of Cpu on the Cray C98.

References

- [1] K. Wieghardt and J. Kux. Nomineller nachstrom auf grund von windkanal versuchen. *Jahrb. der Schiffbau Technischen Gesellschaft (STG)*, 1980.
- [2] In L.Larsson, V.C. Patel, and G. Dyne, editors, *Proc. of 1990 SSPA-CTH-IIHR Workshop on Ship Viscous Flow*. Flowtech Int. Report 2, 1990.
- [3] In Ship Research Institute, editor, *Proc. CFD Workshop for Improvement of Hull Form Designs - Tokyo*, 1994.
- [4] G.B. Deng, P. Queutey, and M. Visonneau. Navier-stokes computations of ship stern flows: A detailed comparative study of turbulence models and discretisation schemes. In V.C. Patel and F. Stern, editors, *Proc. 6th Int. Conf. on Numerical Ship Hydrodynamics*, pages 367-386. National Academy Press, 1993.
- [5] F. Sotiropoulos and V.C. Patel. Second moment modelling for ship-stern and wake flows. In Ship Research Institute, editor, *Proc. CFD Workshop for Improvement of Hull Form Designs - Tokyo*, pages 187-198, 1994.
- [6] H.C. Chen, W.M. Lin, and K.M. Weems. Second moment rans calculations of viscous flows around ship hulls. In Ship Research Institute, editor, *Proc. CFD Workshop for Improvement of Hull Form Designs - Tokyo*, pages 275-284, 1994.
- [7] N. Shima. Prediction of turbulent boundary layers with a second moment closure. *Journal of Fluids Engineering*, 115:1-27, 1993.
- [8] H.C. Chen and V.C. Patel. Practical near-wall turbulence models for complex flows including separation. *AIAA-87-1300*, 1987.
- [9] C.G. Speziale, S. Sarkar, and T.B. Gatski. Modeling the pressure-strain correlation of turbulence: An invariant dynamical systems approach. *Journal of Fluid Mechanics*, 227:245-272, 1991.
- [10] N. Shima. A reynolds-stress model for near-wall and low-reynolds-number regions. *Journal of Fluids Engineering*, 110:38-44, 1988.
- [11] B.S. Baldwin and T.J. Barth. A one equation turbulence transport model for high reynolds number wall-bounded flows. In *AIAA 29th Aerospace Sciences Meeting*, AIAA Paper 91-0610, 1991.
- [12] Y. Nagano and M. Tagawa. An improved $k - \epsilon$ model for boundary layers flows. *Journal of Fluids Engineering*, 100:33-39, 1990.
- [13] G.B. Deng and J. Piquet. $k - \epsilon$ turbulence model for low-reynolds number wall-bounded shear flow. In *Proc. 8th Turbulent Shear Flows*, 26-2, 1991.
- [14] D.C. Wilcox. Reassessment of the scale-determining equation for advanced turbulence models. *AIAA Journal*, 26:1299-1310, 1988.
- [15] F.R. Menter. Zonal two-equations $k - \omega$ turbulence models for aerodynamic flows. In *AIAA 24th Fluid Dynamics Conf.*, AIAA Paper 93-2906, 1993.
- [16] T.J. Craft and B.E. Launder. Improvments in near-wall reynolds stress modelling for complex flow geometries. In *Proc. 10th Turbulent Shear Flows*, 20-25, 1995.
- [17] D.C. Wilcox. *Turbulence Modeling for CFD*. DCW Industries, 1993.
- [18] F.R. Menter. Influence of freestream values on $k - \omega$ turbulence model prediction. *AIAA Journal*, 30-6, 1992.
- [19] C.G. Speziale. On turbulent secondary flows in pipes of non circular sections. *Int. J. Eng. Sci.*, 20:863-872, 1982.
- [20] F.S. Lien and M.A. Leschziner. Computational modelling of multiple vortical separation from streamlined body at high incidence. In *Proc. 10th Turbulent Shear Flows*, 4-19, 1995.
- [21] L. Davidson. Reynolds stress transport modelling of shock-induced separated flow. *Computers & Fluids*, 24-3:253-268, 1995.
- [22] S. Sebag, V. Maupu, and D. Laurence. Non-orthogonal calculation procedures using second moment closure. In *Proc. 8th Turbulent Shear Flows*, 20-3, 1991.

DISCUSSION

F. Sotiropoulos
Georgia Institute of Technology, USA

This is a very careful and useful numerical study in line with the authors previous significant contributions in the area of viscous ship hydrodynamics. It is very encouraging that they were able to successfully employ a full, near-wall, Reynolds-stress transport closure and essentially reproduce previous results for the same case obtained with an entirely different numerical methodology (Sotiropoulos and Patel, 1995). Their work underscores the significance of the turbulence length-scale equation and demonstrates the potential of ω -based closures for modeling flows of practical interest. Studies like this, which carefully eliminate grid-related and other numerical uncertainties, are essential for meaningful assessment of advanced turbulence closures and should continue.

I have two comments/questions:

1. The propeller-plane isowakes obtained with the Reynolds-stress closure of Shima are very similar to the results reported by Sotiropoulos and Patel (1995) who employed the same turbulence model on a somewhat coarser computational mesh. The corresponding limiting streamline patterns (Figure 6), however, are markedly different than those obtained by Sotiropoulos and Patel. On the other hand, the limiting streamline patterns produced by the two-layer κ - ϵ model, shown in Figure 3, are essentially identical to the Reynolds-stress results of Sotiropoulos and Patel. I suspect that two figures were switched by mistake, that is the Shima predictions are actually those shown in Figure 3 while the κ - ϵ predictions are shown in Figure 6.

2. Sotiropoulos and Patel (1995) showed that the Launder-Shima model resolves with remarkable accuracy several velocity harmonics at the propeller plane of the modified HSVA tanker. Have the authors compared their various predictions in terms of velocity harmonics? Such a comparison would be very interesting, particularly in light of the very encouraging results obtained with the standard κ - ϵ model.

REFERENCE

Sotiropoulos, F., and Patel, V.C. (1995) "Application of Reynolds-Stress Transport Models to Stern and Wake Flows," *J. Ship Research*, Vol. 39, No. 4, pp. 263-283.

AUTHORS' REPLY

1. Actually, the figures 3 & 6 are put in correct order. Shima's model does not yield satisfactory results for this particular flow configuration. A marked tendency towards relaminarization has been observed here as on several other geometries previously tested by the authors. This incorrect behavior is mainly due to the near-wall modeling of the transport equation for turbulent dissipation through: (i) the use of $O(\epsilon;\leq)$ to damp the destruction term which is numerically dangerous on complex geometries and highly-stretched non-orthogonal grids, (ii) the introduction of Ψ_1 which can take strong negative values in some regions of the flow.

2. We have not compared our simulation in terms of velocity harmonics. However, this is a very useful suggestion and we will give in the future this element of comparison which is a good indicator for possible computations of propeller-hull interactions.

DISCUSSION

L. Larsson
Chalmers University of Technology, Sweden

The authors have again presented a paper which could become a milestone in the development of CFD for stern flows (the first one was in 1993). A quite interesting and surprising outcome of their investigation is the fact that an isotropic eddy viscosity model (the κ - ω model) seems to be superior to the much more advanced Reynolds stress model. The authors correctly stress in the introduction that an isotropic model is not likely to work well in a vortical flow since the turbulence anisotropy influences the longitudinal not vorticity. Still the isotropic model is the best. Any explanation for this?

AUTHORS' REPLY

The modelization of Reynolds Stress Transport equations requires the development of closures for several complicated turbulent correlations (pressure-strain, diffusion, and dissipation correlations) mainly based on a local turbulence homogeneity hypothesis. Moreover, near-wall low Reynolds number closures are still under development and not yet enough validated. In our opinion, the Reynolds Stress closures are probably the missing link between the classical

and robust isotropic eddy-viscosity based turbulence models and the future Large Eddy Simulations, as long as high Reynolds number flows on complex geometries are considered. But, it is still difficult to evaluate their actual potentialities because of a lack of counter-validations on flows in realistic configurations.

On the Modeling of the Flow Past a Free-Surface-Piercing Flat Plate

A. Di Mascio, M. Landrini, E. Campana

(Istituto Nazionale per Studi ed Esperienze di Architettura Navale, Italy)

Abstract

Some numerical simulations and experiments for the analysis of the free surface flow past a flat plate in drift motion have been carried out. Two mathematical models were used in the simulation: the first one is a linear inviscid model with a vortex layer shed from the trailing edge and from the tip of the plate; the second one is described by the Navier-Stokes equations with the algebraic Baldwin-Lomax turbulence model. The computed forces acting on the plate are compared with the data measured in the towing tank at INSEAN and with those found in the literature. Though the accuracy of both models is satisfactory in the low Froude number range (below $Fr = 0.5$ for the aspect ratios considered), the inviscid model overestimates the forces acting on the plate when increasing the velocity and/or the angle of incidence. This deviation seems to be related to the absence of nonlinear effects in the inviscid model, that cannot be neglected when a "jump" in the free surface height appears at the trailing edge.

1 Introduction

The prediction of the maneuverability performances of a ship can be gained by simple models based on the knowledge of possibly few coefficients that summarize the dynamical behaviour of the vessel. Actually, these parameters are obtained by means of extensive experimental tests in towing tanks. Such predictive tools accurately depict the maneuvering capability in most cases. Nevertheless, experimental observations [6] reveal that slight geometrical differences sometimes have a great influence on the maneuvering performances. With this regard, the availability of a numerical tool for the prediction of the ship behaviour can be helpful to reduce the design costs.

If the main features of the flow are retained, a

reasonable description of the flow can be obtained with relatively simple models. The rotational inviscid model, in which a vortex sheet mimics the formation and evolution of the wake in the real flow, gives satisfactory information about the hydrodynamic coefficients in most cases.

The complete description of the flow field requires, however, additional information regarding the separation lines from which the wake is shed, and the mechanism for its evolution. These information can be gained by both experiments and Navier-Stokes numerical simulations.

In order to grasp a deeper insight of the phenomenon we have decided to study a model problem that allows to guess the configuration of the separation lines in advance, the study of their correct location being postponed to the future research. The flow past a flat plate in a steady drifting motion is the simplest prototype, in that the separation lines can be assumed to coincide with the tip and the trailing edge.

In spite of its geometrical simplicity, this flow embodies very interesting features. Indeed, previous experimental observations [10] detect the existence of two distinct sub- and supercritical flow regimes, the latter being characterized by the appearance of a free-surface jump, localized at the intersection between the free surface and the trailing edge.

It will be shown in the following that, when the jump at the trailing edge appears, the inviscid flow model overestimates the side force, whereas the Navier-Stokes model with nonlinear boundary conditions on the free-surface, used in the present work, succeeds in dealing with the flow in both subcritical and supercritical regime.

At present, the reasons of the inaccurate prediction obtained by the inviscid flow model are not clear. In fact, it seems not to be related to the geometrical nonlinearity of the boundary condition at the free-surface, because a Navier-Stokes computation with a "frozen" free surface yields almost the same answer

as the fully nonlinear simulation. Moreover, the discrepancy has probably nothing to do with the separation bubble at the leading edge. This can be inferred from the zero-Froude number results, for which the inviscid model gives an excellent prediction of the hydrodynamic coefficients, in spite of the recirculation.

The present paper is organized as follows: the mathematical models used in the simulation are briefly described in Sec.1, while in Sec.2 the experimental apparatus is illustrated. Then, numerical results with both the inviscid model and the Navier-Stokes model will be reported in Sec.3, and they will be discussed in comparison with the experiments.

2 Mathematical Models

In this section, the mathematical models used in the simulation of the flow past a flat plate are described. The first one is the inviscid flow model with a vortex sheet. The second one is the more complex Navier-Stokes model, with an algebraic turbulence model.

2.1 Inviscid Model

In this model viscous effects are supposed to be confined close to the rigid boundary, where the fluid viscosity determines the generation of vorticity. The vorticity evolution and shedding are described by means of the inviscid fluid mechanics, that is viscous effects are completely neglected and rotational zones are modelled as vorticity layers, emerging from known separation lines (the lower tip and the trailing edge).

The fluid is supposed to fill a domain Ω of infinite depth, bounded by the free surface \mathcal{F} , by the plate surface $\partial\mathcal{B}$ and by a zero thickness wake \mathcal{W} emanating from the tip and the trailing edge.

The total fluid velocity $\mathbf{U} = (U, V, W)^T$, with respect to a reference frame fixed with the plate, is written in the form $\mathbf{U} = \mathbf{U}_\infty + \mathbf{u}$, \mathbf{U}_∞ being the undisturbed flow velocity. The flowfield is supposed to be solenoidal, i.e.

$$\nabla \cdot \mathbf{u} = 0 \quad \text{in } \Omega \quad (1)$$

and irrotational, that is

$$\nabla \times \mathbf{u} = 0 \quad \text{in } \Omega \quad (2)$$

The perturbation velocity \mathbf{u} satisfies the impermeability constraint on the body surface $\partial\mathcal{B}$

$$(\mathbf{U}_\infty + \mathbf{u}) \cdot \mathbf{n} = 0 \quad \text{on } \partial\mathcal{B} \quad (3)$$

A kinematic condition in terms of the wave height h is enforced on the free surface \mathcal{F}

$$U \frac{\partial h}{\partial x} + V \frac{\partial h}{\partial y} = W \quad \text{on } \mathcal{F} \quad (4)$$

together with a dynamic boundary condition, that fix the pressure p , computed from the Bernoulli theorem, to the atmospheric pressure (set to zero)

$$p = \frac{1}{2}(U_\infty - \mathbf{U} \cdot \mathbf{U}) - \frac{h}{Fr^2} = 0 \quad \text{on } \mathcal{F} \quad (5)$$

Continuity of pressure and normal velocity are required through the wake \mathcal{W}

$$p^+ = p^- \quad \mathbf{u} \cdot \mathbf{n}^+ = \mathbf{u} \cdot \mathbf{n}^- \quad \text{at } \mathcal{W} \quad (6)$$

Finally, the Kutta condition is enforced along the separation lines and the radiation condition is required far from the body.

In the general case, the free surface and the wake shapes are unknown and therefore are to be determined as a part of the solution.

It may be shown that, under quite general assumptions [2], the field $\mathbf{u}(\mathbf{Q})$ may be expressed by the integral form of the Helmholtz decomposition (Poincaré Formula [5]), that specializes, when dealing with zero-thickness bodies, in

$$\begin{aligned} \mathbf{u}(\mathbf{Q}) = & \nabla_{\mathbf{Q}} \int_{\mathcal{F}} \sigma G dS_P \\ & - \nabla_{\mathbf{Q}} \times \int_{\partial\mathcal{B}} \gamma G dS_P \\ & - \nabla_{\mathbf{Q}} \times \int_{\mathcal{W}} \gamma_{\mathcal{W}} G dS_P \end{aligned} \quad (7)$$

where the source distribution σ accounts for the free surface effects, γ is the bound vorticity and $\gamma_{\mathcal{W}}$ represents the vorticity confined in the wake. It is relevant to recall that, by virtue of the Helmholtz theorem applied to a vortex layer, both the bound vorticity and the trailing vorticity satisfy the continuity relation $\nabla_{\Sigma} \cdot \gamma = 0$.

The unknown source and vortex distributions are computed by enforcing the boundary conditions. The problem is strongly nonlinear and, consequently, very CPU time consuming. In order to make the computation as cheap as possible, the problem is simplified on both the free surface and the wake: free surface boundary conditions are linearized by using the double model flow as basis flow, while the dynamics of the wake is simplified by constraining the wake "particles" to move only in the horizontal plane, thus preventing the wake roll-up (see [8, 9] for details).

In the numerical solution, the source and the vorticity distribution are supposed to be piecewise constant. The enforcement of the boundary condition at control points yields a set of algebraic equations to be used in the computation of the unknown discrete values of σ , γ and $\gamma_{\mathcal{W}}$.

Some examples of numerical simulation are reported in figures 1 and 2, where the wave pattern is depicted for two values of the Froude number and

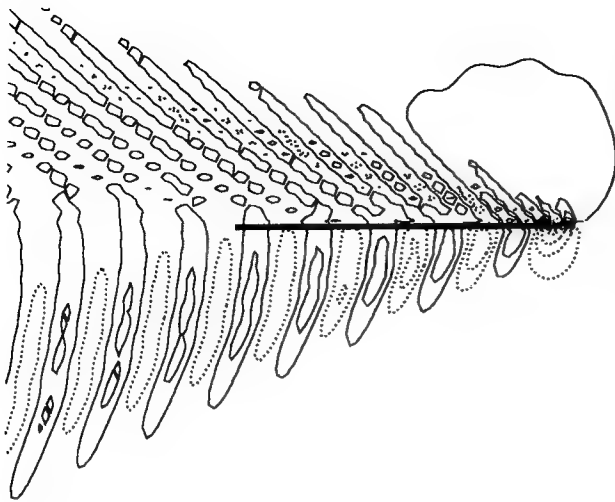


Figure 1: Wave system generated by a yawed flat plate in straight motion [8, 9] ($Ar = 0.5$, $\alpha = 9^\circ$, $Fr = 0.17$); contour levels: $-0.0200, -0.0175, \dots, 0.0200$.

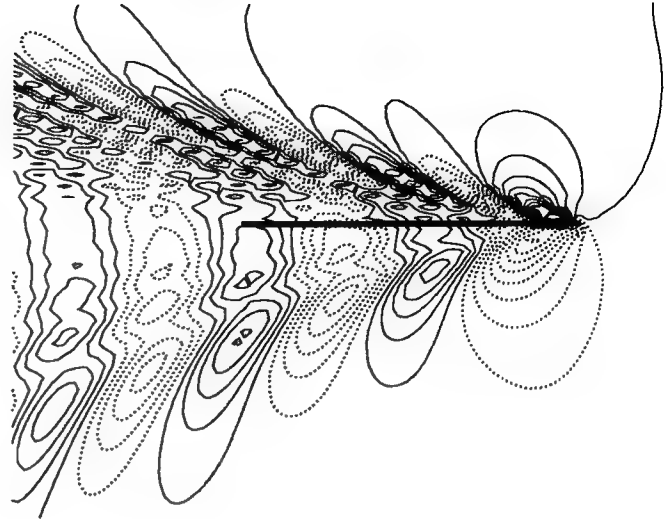


Figure 2: Wave system generated by a yawed flat plate in straight motion [8, 9] ($Ar = 0.5$, $\alpha = 9^\circ$, $Fr = 0.29$); contour levels: $-0.0200, -0.0175, \dots, 0.0200$.

incidence $\alpha = 9^\circ$. In fig.3 the computed forces are compared with experiments. Whilst the prediction is excellent when the Froude number is low, an increasing deviation is noticed when the forward speed grows. This effect is more pronounced for the larger aspect ratio ($Ar = \text{draught} / \text{chord length}$)

2.2 Viscous Model

Also a more complex Navier-Stokes model was used in the computations reported in the following. The fluid is again supposed to fill all the space below the free surface around the flat plate. In this case, the velocity $\mathbf{u} = (u_1, u_2, u_3)^T = (u, v, w)^T$ and the pressure p are the solution of the system of partial differential equations

$$\begin{aligned} \frac{\partial u_i}{\partial x_i} &= 0 \\ \frac{\partial}{\partial x_j} [u_j u_i + p \delta_{ij} - \tau_{ij}] &= 0 \end{aligned} \quad (8)$$

where the first equation is the mass conservation equation, while the second one represent the momentum equation parallel to the x_i -axis, $i = 1, 2, 3$ and

$$\tau_{ij} = (\nu_T + \nu) (u_{i,j} + u_{j,i}) \quad (9)$$

ν being the kinematic viscosity, ν_T the eddy viscosity computed with the algebraic Baldwin-Lomax model

[1]. δ_{ij} is the Kronecker symbol.

The no-slip condition is enforced on the body surface

$$\mathbf{u} = 0 \quad \text{on } B, \quad (10)$$

On the free surface, if the action of the wind and the surface tension are neglected, the dynamic boundary conditions to be satisfied are

$$(-p \delta_{ij} + \tau_{ij}) n_j = 0 \quad \text{on } \mathcal{F} \quad (11)$$

while the kinematic boundary condition reads

$$u \frac{\partial h}{\partial x} + v \frac{\partial h}{\partial y} = w \quad \text{on } \mathcal{F} \quad (12)$$

In the numerical solution, these equations are discretized by means of a standard finite volume technique on a curvilinear grid, that moves to fit the actual free surface shape. All the derivative are expressed by centered differentiation, and the variables at cell interfaces are evaluated by simple averaging from the neighbouring points. A fourth order artificial dissipation term is added to stabilize the calculation.

With regard to the boundary conditions, there is no particular problem to enforce the no-slip condition on the wall of the plate and the kinematic boundary condition at the free surface. On the contrary,

the dynamic boundary condition (11) is simplified to $p = 0$. Moreover, the velocity vector at the free surface is extrapolated from the first inner point. This simplified boundary condition are a common practice when computing free surface viscous flows, because in general the grid near the water-air interface is too coarse to resolve the boundary layer.

The nonlinear algebraic equation system, that stems from the discretization process, is solved by a Collective S.O.R. algorithm, whose speed of convergence is increased by a Full Approximation Storage-Full Multigrid (FAS-FMG) algorithm (see [4] for details).

Two kind of grids were used in the computation: a two-block grid with H-H topology (fig.4), each block being a cartesian grid $80 \times 32 \times 32$, and a two-block grid with O-O topology shown in fig.5, with $40 \times 24 \times 16$ cells each. In both cases, the cells were clustered near the wall, in order to have the proper resolution of the boundary layer.

3 Experimental set-up

The numerical study of the flow past a flat plate was integrated by some experiments carried out in the towing tank at INSEAN. The aluminum flat plate used in the tests has chord length 50 cm, height 100 cm and thickness 0.6cm. Both the trailing edge and the leading edge were rounded. The plate was fixed to carriage by means of a mechanism able to position it with any draught and angle of incidence.

The experiments were carried out in the smaller

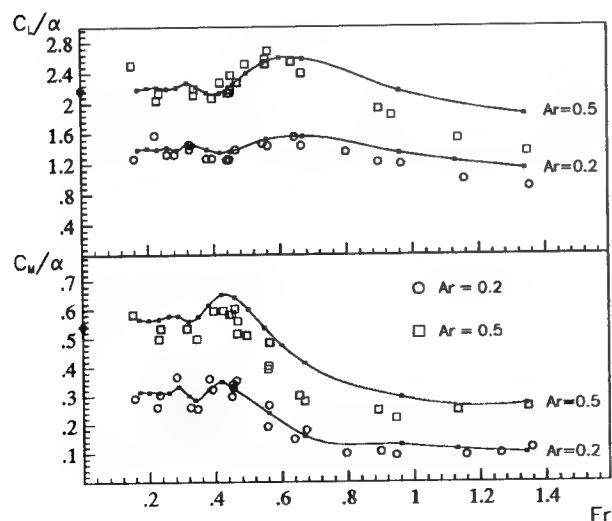


Figure 3: Hydrodynamic forces on a flat plate in drift motion ($\alpha = 9^\circ$). Inviscid computation (solid lines) [8, 9] and experiments (symbols) [12].

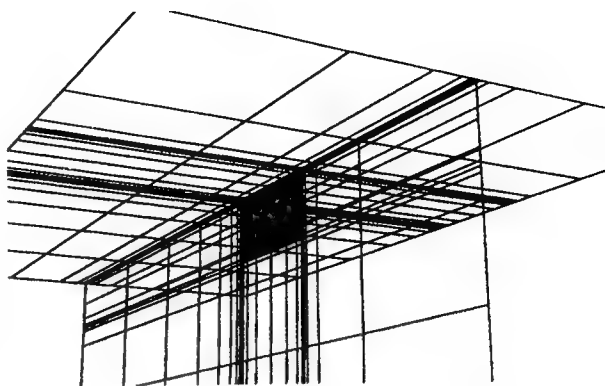


Figure 4: Sample grid. H-H topology

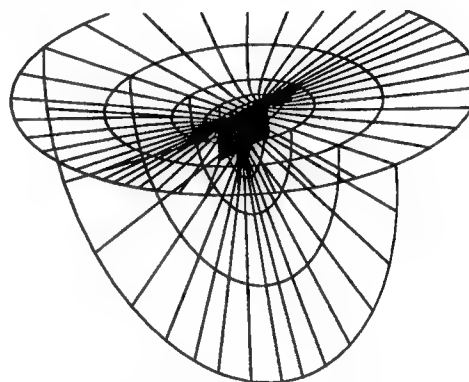


Figure 5: Sample grid. O-O topology

tank at INSEAN. The tank is 220 meters long, 9 meters wide and 3.6 meters deep.

The forces acting on the plate were measured by a six-component balance Kempf & Remmers. Analogic force-tension transducer were used in the measures. A/D conversion was done with sampling frequency equal to 240 Hz. The equipment was calibrated in the measured force range with assigned weights, resulting in a deviation of 1.4 per cent at most.

The wave elevation on the wetted surface was evaluated by photographic observations on the two sides of the plate. A regular grid with 1 cm spacing was drawn on the body surface to facilitate observations.

A picture of the plate during the test is shown in fig. 6

4 Discussion of Results

First of all, the inviscid model with vortex layer and the Navier-Stokes model were tested in the zero-Froude number case. Fig. 7 reports the computations for a flat plate with unit aspect ratio and Reynolds number (for the RANSE calculation) $Re = 1 \times 10^5$. The grid for the inviscid calculation was 32×32 on the plate, while a two-block $80 \times 32 \times 32$

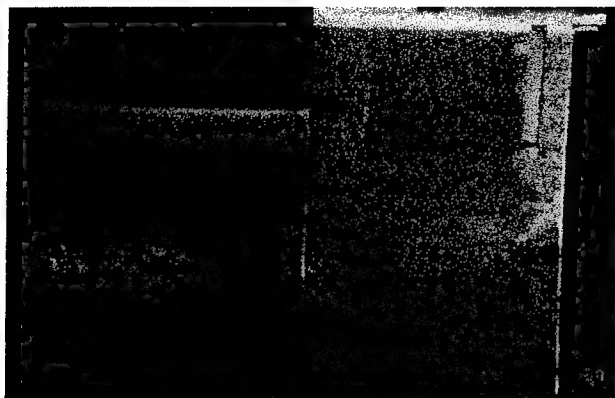


Figure 6: Experimental set-up

grid was used in the RANSE calculation, with 32×16 cell faces on each side of the flat plate.

It can be seen that the prediction of lift C_L , drag C_D and moment C_N coefficients is very accurate for both models when compared with experiments, in spite of the fact that the inviscid model does not take into account the separation bubble predicted by the Navier-Stokes computation. This flow separation is caused by the sharp leading edge, and it grows when the angle of incidence increases. Nevertheless, the prediction of the hydrodynamic coefficients is very good also at 20 degrees of angle of attack.

On the contrary, the numerical prediction of the lateral force coefficient C_Y , gained by the inviscid model, departs from both the Navier-Stokes calculation

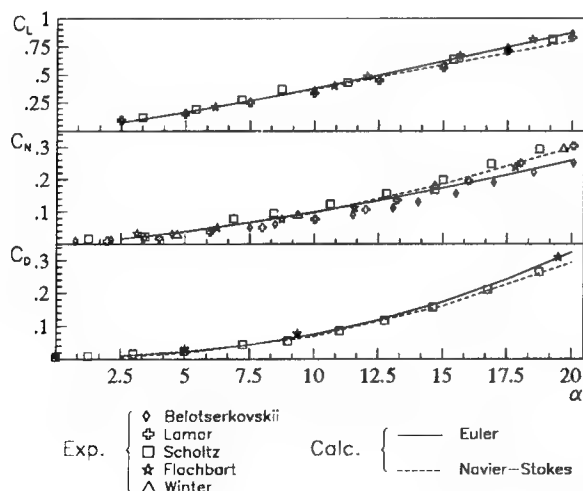


Figure 7: Hydrodynamic coefficients for a flat plate, $AR = 1$, for a zero-Froude number flow. Comparison of the inviscid calculation, viscous calculation and experiments

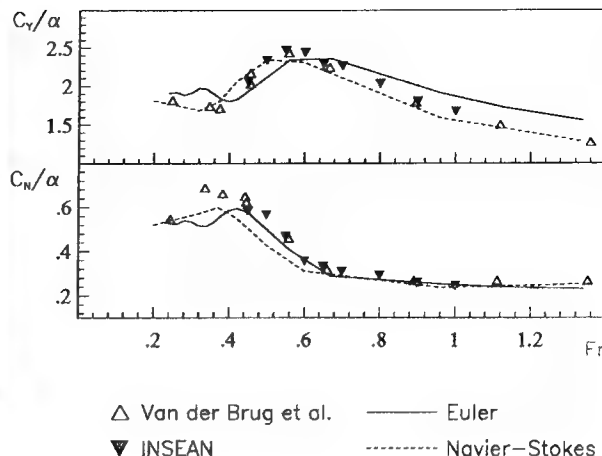


Figure 8: Ratio of the force normal to the plate (top) or the yaw moment (bottom) to the incidence as function of the Froude number. Comparison of the inviscid calculation, the Navier-Stokes simulation and experimental data measured at INSEAN and by van den Brug et al. [12]. Incidence 4.5 degrees.

tions and experimental data when computing free-surface flows beyond certain values of the Froude number and angle of attack. Fig.8 and 9 show the hydrodynamic coefficients as functions of the Froude number, with 4.5 and 9 degrees of incidence and aspect ratio equal to 0.5. In the same figures, the data measured in the experiments carried out at INSEAN and those obtained by van den Brug et al. [12] are also reported.

The dependence of the Navier-Stokes solution on the grid was checked by repeating the computation with the O-O grid shown in fig.5. It can be inferred from figure 10, that, in spite of the different size and topology of the grids, the two predictions are reasonably similar to each other.

The first thing to be noticed is that both our measures and Navier-Stokes predictions mirror exactly the data reported in [12], and this seems to confirm the reliability of the viscous model predictions and the experimental equipments. Moreover, although the numerical predictions with the inviscid model are good up to $Fn=0.60$, they depart from experimental data when the velocity increases, for both values of incidence.

It is interesting to stress that the prediction with the inviscid model begin to depart from the experiments and from the Navier-Stokes computation when, in addition to the separation bubble at the leading edge, another interesting phenomenon appears at the trailing edge. In fig. 11 and 12 the wave elevation along the plate are reported for 4.5 and 9

degrees of angle of attack, as computed by means of the Navier-Stokes model. It can be seen that, as the Froude number increases, a "jump" in the wave height is clearly observed.

The occurrence of this phenomenon is not new. Maniar et al. [10] observed a similar behaviour in their experiments in a water tunnel, and reported the measured wave height. To the purpose of comparison, we repeated the experiments in the INSEAN towing tank and the numerical simulation with the two models for the same conditions (6 degrees of incidence and unit aspect ratio). A perspective view of the free surface is shown in fig.13 for $Fr=0.63$ and $Fr=0.74$, whereas Fig.14 reports the numerical calculation together with the experimental wave profiles on both sides of the plate. In particular, it can be seen that the Euler prediction (dashed lines) oscillates around the experimental data (symbols), while the Navier-Stokes computation (solid lines) correctly mirrors the measurements of the INSEAN experiment. It can be also seen that, for the higher Froude number flow, our data significantly differ from those by Maniar et al. The reason of this discrepancy is currently under analysis.

The increasing inaccuracy of the inviscid model in the high Froude number range is not well understood. In fact, it seems not to be caused by the separation at the leading edge: the same happens in the double model flow and, nevertheless, the prediction is still very good. Moreover, it seems not to be related to the geometrical nonlinearities of the free

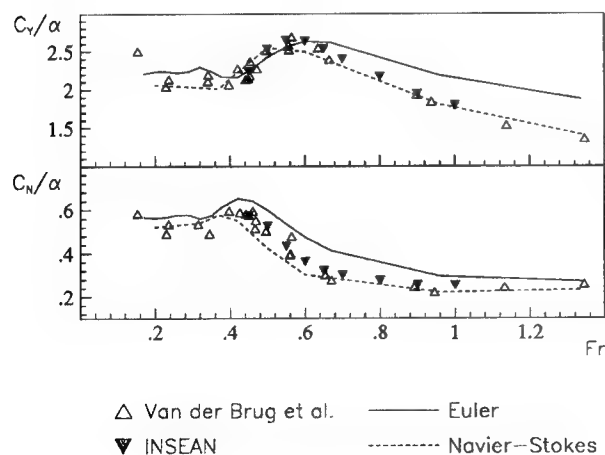


Figure 9: Ratio of the force normal to the plate (top) or the yaw moment (bottom) to the incidence as function of the Froude number. Comparison of the inviscid calculation, the Navier-Stokes simulation and experimental data measured at INSEAN and by van den Brug et al. [12]. Incidence 9.0 degrees.

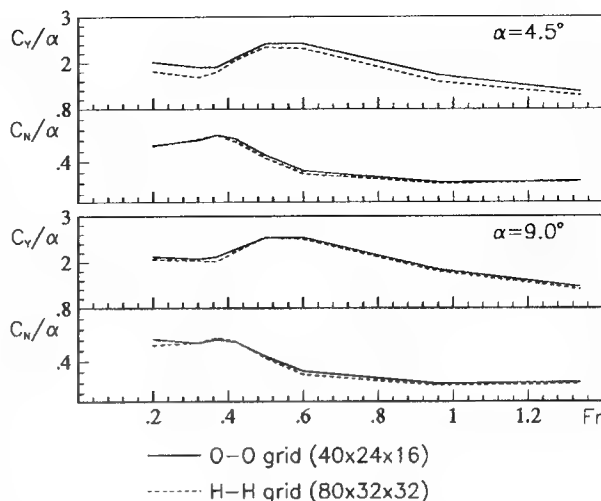


Figure 10: Ratio of the force normal to the plate and the yaw moment to the incidence as function of the Froude number. Comparison of two the Navier-Stokes simulations. Incidence 4.5 degrees (top) and 9.0 degrees (bottom).

surface. The role of the actual wave displacement was in fact analysed with the Navier-Stokes model, retaining the usual form of the free surface boundary conditions, but preventing the motion of the boundary, and therefore enforcing them on the undisturbed water plane $z = 0$. As shown in fig. 15, the effect on the hydrodynamic coefficients is very small, also in the supercritical regime.

5 Conclusion and Perspectives

This work is the first stage on a more general program concerning the prediction of the hydrodynamic coefficients of maneuvering ships. In particular, the capabilities of simple inviscid rotational models was considered for free surface flows. The very simple case of a flat plate in drift motion was analysed and the results were compared with a Navier-Stokes computation and with experimental data. The geometry of the problem was chosen so simple because we wanted to postpone the location of vortex sheet separation lines to further research, and to concentrate on global force prediction.

In spite of the simple shape, some interesting features were detected. In fact, the prediction of the hydrodynamic coefficients is rather inaccurate when the velocity and/or the angle of incidence is increased beyond certain values. This happens in conjunction with the appearance of a jump in the free surface elevation at the trailing edge, which is likely to be somehow in connection with the poor prediction.

The reason of the discrepancy of the prediction by

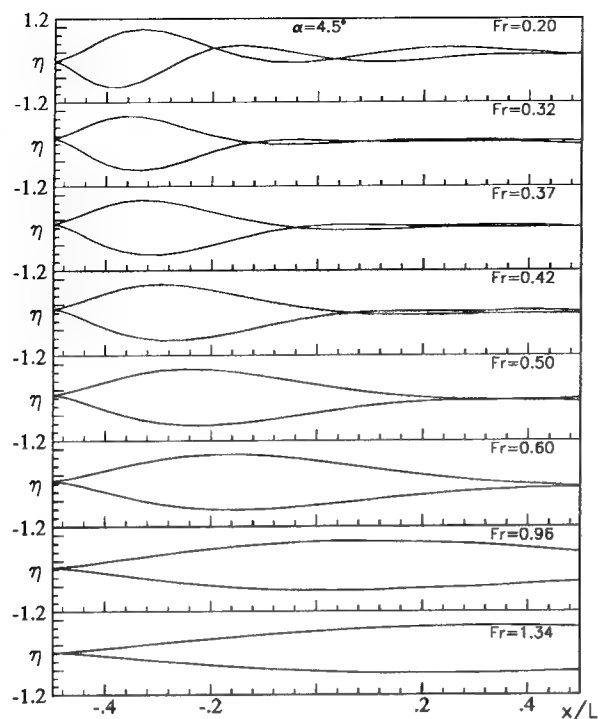


Figure 11: Wave profile along the plate for increasing Froude number (top to bottom). Normalized wave height $\eta = h/(\alpha Fr)$, $\alpha = 4.5^\circ$. Navier-Stokes simulation: two-block O-O grid $40 \times 24 \times 16$.

means of the inviscid model with respect to the experiments and to the Navier-Stokes calculation is not clear at the present stage. In more details, the gap between the two predictions seems not to be due to the separation bubble at the leading edge, otherwise the same problem would be observed when computing double model flows. Moreover, it is unlikely to be caused by geometrical linearization of the free surface, because the same condition has very little effects on the forces when applied to the Navier-Stokes calculation.

Therefore, a possible reason of such a behaviour must be sought in the nonlinear terms in the free surface boundary conditions, neglected in our inviscid computations. Another possible cause could be related to the Kutta condition imposed at the trailing edge. In fact, this condition implies continuity of the total pressure, and therefore it does not allow a free surface jump across the vortex layer. Future investigations will try to clarify the question.

References

- [1] Baldwin, B.S., Lomax, H. "Thin Layer Approximation and Algebraic Model for Separated Turbulent Flows", *AIAA Paper* 78-257, 1978.

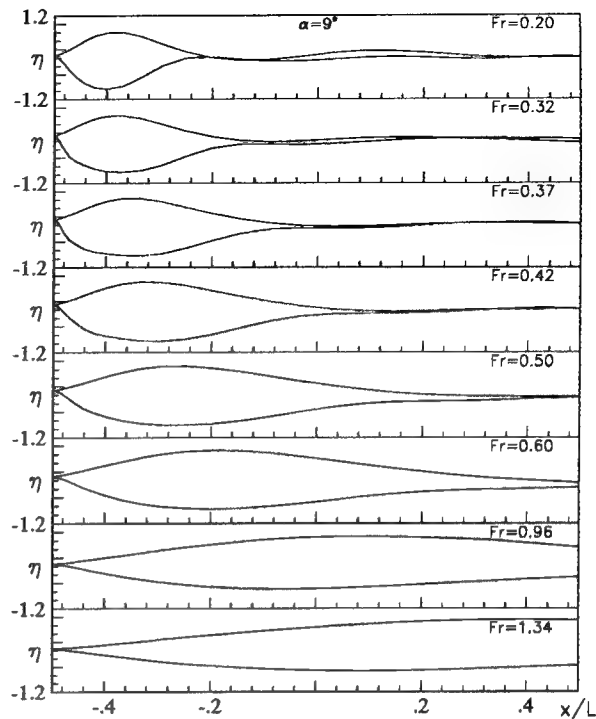


Figure 12: Wave profile along the plate for increasing Froude number (top to bottom). Normalized wave height $\eta = h/(\alpha Fr)$, $\alpha = 9.0^\circ$. Navier-Stokes simulation: two-block O-O grid $40 \times 24 \times 16$.

- [2] Bassanini P., Casciola C., Lancia M. R., Piva R., "A Boundary Integral Formulation for the Kinetic Field in Aerodynamics", *Eur. J. Mech., B / Fluids*, vol 10, 605-627, 1991; vol 11, 69-92, 1992.
- [3] Belotserkovskii, S.M. (1969). "Calculation of the flow around wings of arbitrary planforms in a wide range of angles of attack". NASA TT F-12.
- [4] Brandt A., "Multigrid Techniques: 1984 Guide with Application to Fluid Dynamics", The Weizmann Institute of Science, Rehovot (Israel), 1984.
- [5] Brard R., "A Vortex theories for bodies moving in water", *9th Symp. on Naval Hydrodynamics*, R. Brard and A. Castera Eds, Washington, U. S. Gov. Printing Office, 1187-1284.
- [6] Burcher R.K., "The prediction of the manoeuvring characteristics of vessels" *Phil. Trans. R. Soc. Lond., A*, 334, 265-279, 1991.
- [7] Lamar, J. E. (1974). "Extension of leading-edge suction analogy to wings with separated flow around the side edges at subsonic speeds". NASA TR R-428.

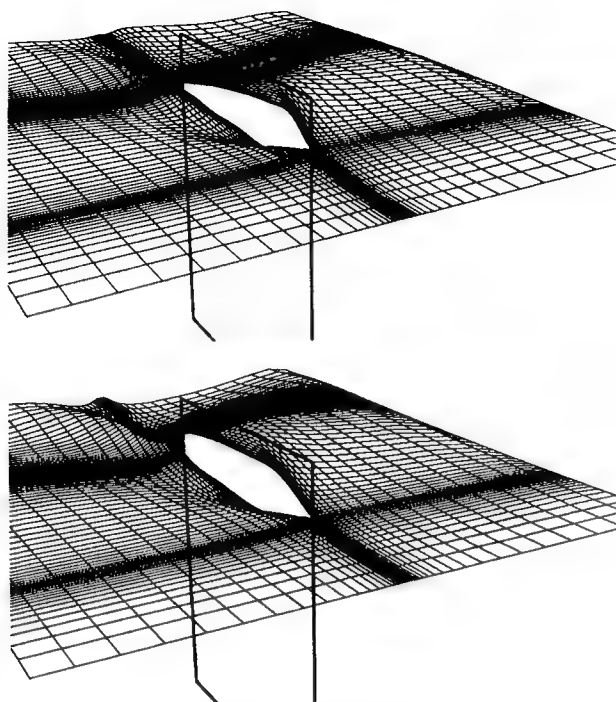


Figure 13: Numerical viscous simulation in subcritical (top, $Fr=0.63$) and supercritical (bottom, $Fr=0.74$) flow regime. $Ar = 1.0, \alpha = 6.0^\circ$

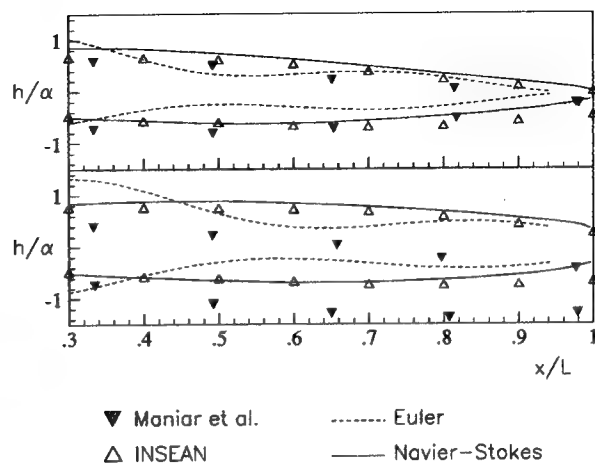


Figure 14: Wave profile along the plate at $Fr=0.63$ (top) and $Fr=0.74$ (bottom) for $Ar = 1.0$ and $\alpha = 6.0^\circ$. Wave height is normalized by the incidence α .

- [8] Landrini M., Campana E., "Wave and Forces about a Turning Flat Plate", 10th Inter. Workshop on Water Waves and Floating Bodies, Oxford, UK, April 1995.
- [9] Landrini M., Campana E., "Steady Waves and Forces about a Yawing Flat Plate", INSEAN Tech. Report, Progr. Ricerca 1991-1993, area 3, July 1995. Also submitted to J. Ship Res.
- [10] Maniar H., Newman J.N., Xü H., "Free surface effects on a yawed surface-piercing plate", 18th Symp. on Naval Hydro., Ann Arbor, Michigan, 1990.
- [11] Scholz, N. (1949) "Kraft und Druckverteilungsmessungen an Tragflächen Kleiner Steckung". Forsch. Ingenieurwes, Vol. 16, 3.
- [12] van den Brug J.B., Beukelman W., Prins G.J., "Hydrodynamic forces on a surface piercing flat plate", Rep. 325, Shipbuilding laboratory, Delft Univ. of Tech., 1971.
- [13] Winter, H. "Flow phenomena on plates and airfoils of short span". NACA Tech. Mem. No 798 (1936).

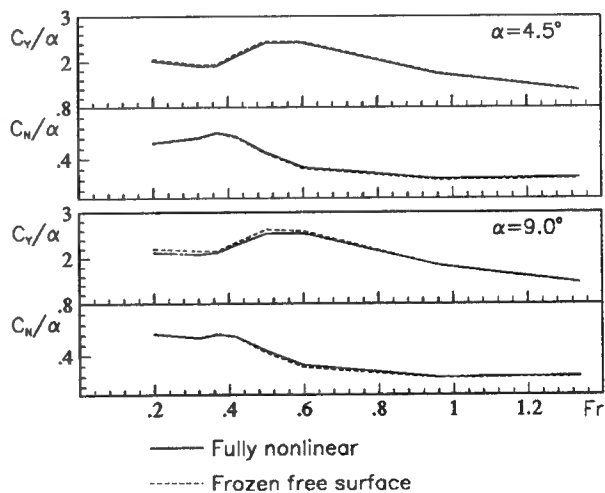


Figure 15: Ratio of the force normal to the plate and the yaw moment to the incidence as function of the Froude number. Comparison of two the Navier-Stokes simulations, one with standard free surface condition and with "frozen" free surface. Incidence 4.5° (top) and 9.0° (bottom).

Self-Propelled Maneuvering Underwater Vehicles

H. McDonald (Pennsylvania State University, USA),

D. Whitfield (Mississippi State University, USA)

ABSTRACT

A physics-based computational method is presented for the trajectory prediction of fully appended self-propelled underwater vehicles, including a rotating propeller. The approach is to interactively couple the numerical solution of the three-dimensional unsteady incompressible turbulent Navier-Stokes equations with a six-degree-of-freedom (6-DOF) computational method. The Navier-Stokes equations are solved using a multiblock multigrid scheme with relative motion structured subblocks for handling the rotating propellers. The computational methods, including the Navier-Stokes/6-DOF coupled code, has been validated using numerous examples. Two fully appended configurations that include sail, sail plane, and four stern appendages are presented, one with a body force propulsor and the other with an actual rotating propulsor.

1.0 INTRODUCTION

Maneuvering characteristics of undersea vehicles are determined from, or at least based on, results from large scale model tests. Experimental information from these tests are used to investigate maneuverability directly, or the information is used to develop correlations that in turn are used in dynamic motion codes to perform semi-empirical maneuvering predictions. This experimental-based approach is a necessary, but expensive, method of determining maneuvering characteristics of sea-going vehicles. Also, this approach frequently has to be used outside the regime corresponding to the experimental data on which it is based, such as the particular flow conditions, geometric configuration, and propulsor device. It might be that the experimental configuration used may have even lacked a suitable propulsor. This experimental-

NOTE: This research was sponsored by the Office of Naval Research (ONR) with James A. Fein as the first technical monitor, and Dr. Pat Purtell as the present technical monitor. This support is gratefully acknowledged.

based approach also has the disadvantage that the Reynolds number of an actual submarine, for example, is much larger than can be simulated in experimental test facilities. Therefore, the Office of Naval Research (ONR) initiated a research program that had as its objective the development of a physics-based method for the maneuvering prediction of self-propelled underwater vehicles.

In conjunction with the development of this physics-based maneuvering prediction method the experimental-based maneuvering results will be of major importance with regard to validation of the physics-based approach. The idea would be to use the strengths of each approach to supplement the other, and thereby, produce a physics-based computational approach that can be used for various flow conditions, geometric configurations, and propulsor devices that can be used outside the regime of available experimental data and yet has been validated to the extent possible. The approach to developing this physics-based maneuvering prediction of self-propelled underwater vehicles is to solve the three-dimensional time-dependent incompressible turbulent Navier-Stokes equations and interactively couple these numerical results with a six-degree-of-freedom (6-DOF) computational code.

This work on maneuverability has been a team effort between the Computational Fluid Dynamics Laboratory of Mississippi State University and the Applied Research Laboratory of Penn State University. Close contact among the researchers at each Laboratory was maintained at all times during the development of these computational tools. The researchers included faculty members, research engineers, post docs, graduate students, and undergraduate students.

This paper is organized as follows. The numerical approach used to solve the three-dimensional time-dependent Navier-Stokes equations is discussed in Section 2. Two propulsor treatments are available, a body force propulsor and an actual rotating propulsor, and these two propulsor treatments are described in Section 3. The 6-DOF computational approach is discussed in Section 4, turbulence modeling in Section 5, and results and concluding remarks are given in Sections 6 and 7.

2.0 NUMERICAL APPROACH

The approach of this physics-based research aimed at maneuvering predictions of self-propelled underwater vehicles is to solve the three-dimensional time-dependent incompressible turbulent Navier-Stokes equations. Because of the magnitude of the problem size with regard to resolving full configurations that include sail, sail planes (or bow planes), stern appendages, and rotating propulsor, the numerical solution of the Navier-Stokes equations is carried out on dynamic relative motion multiblock structured grids. The Reynolds numbers of these flows are extremely large and the viscous regions are resolved to y^+ values of near one. This places severe demands on the numerical solution scheme in terms of stability and accuracy. Moreover, the flow is both three dimensional and unsteady in the sense of the Reynolds averaged mean flow. To make the computation of these high Reynolds number unsteady flow problems practical in terms of the total CPU time required, the time step needs to be restricted by the physics of the problem being solved and not the numerics of the scheme used to solve the equations. The equations, numerical flux formulation, and the solution algorithm used to solve the equations and achieve the physics-based time restriction is discussed in this section.

2.1 Navier-Stokes Equations

The three-dimensional time-dependent Navier-Stokes equations are first transformed to a time-dependent curvilinear coordinate system. The artificial compressibility idea of Chorin [1] is then introduced [2, 3, and 4]. The use of artificial compressibility permits the experience gained in the numerical solution of compressible flow problems to be exploited in the numerical solution of incompressible flow problems [5]. The artificial compressibility form of the three-dimensional time-dependent Navier-Stokes equation in general curvilinear coordinates is

$$\frac{\partial Q}{\partial \tau} + \frac{\partial F}{\partial \xi} + \frac{\partial G}{\partial \eta} + \frac{\partial H}{\partial \zeta} = 0 \quad (1)$$

where

$$Q = J \begin{bmatrix} p \\ u \\ v \\ w \end{bmatrix}$$

$$K = J \begin{bmatrix} \beta(\theta_k - k_i) \\ u \theta_k + k_x p - T_{k_x} \\ v \theta_k + k_y p - T_{k_y} \\ w \theta_k + k_z p - T_{k_z} \end{bmatrix}$$

and

$$\theta_k = k_i + k_x u + k_y v + k_z w$$

$$K = F, \quad \theta_k = U \quad \text{for } k = \xi$$

$$K = G, \quad \theta_k = V \quad \text{for } k = \eta$$

$$K = H, \quad \theta_k = W \quad \text{for } k = \zeta$$

In these equations, β is the artificial compressibility coefficient, with a typical value of 5~10; p is static pressure; u , v , and w are the velocity components in Cartesian coordinates x , y , and z . U , V , and W are the contravariant velocity components in curvilinear coordinate directions ξ , η , and ζ , respectively. Terms $T_{k_x}, T_{k_y}, T_{k_z}$, where $k = \xi, \eta$, and ζ , are the viscous flux components in curvilinear coordinates. J is the Jacobian of the inverse transformation, and k_x, k_y, k_z , and k_i with $k = \xi, \eta$, and ζ are the transformation metric quantities [4], where a subscript denotes differentiation.

In this work, the thin-layer approximation is introduced to simplify the full Navier-Stokes equations, an algebraic turbulence model [6], a k - ϵ model and a nonlinear k - ϵ model [7] were implemented within the code and used for the turbulent flow computations. The details of treating the viscous terms is explained in the work of Gatlin [8]. In addition, improvements have been made by Chen [9] with regard to the computation of the wall shear stress by improving the computation of the tangential velocity derivatives normal to a solid surface. This improvement is simple to implement and works extremely well on grids that may be highly skewed [9].

2.2 Numerical Flux Vector

Equation (1) is discretized into a cell-centered finite-volume form which for one-dimensional flow, for example, can be written as

$$\frac{Q_i^{n+1} - Q_i^n}{\Delta \tau} + (\bar{F}_{i+1/2}^{n+1} - \bar{F}_{i-1/2}^{n+1}) = 0 \quad (2)$$

where the index i corresponds to a cell center and indices $i \pm 1/2$ correspond to cell faces. In this expression, the dependent variable vector Q is considered to be constant throughout the cell whereas the flux \bar{F} is assumed to be uniform over each surface of the cell. A flux vector is therefore needed at each cell face.

There are numerous ways of developing this flux vector, and the formulation used early on [4] in this maneuvering underwater vehicle research was the flux difference split scheme of Roe [10] for the first-order contribution and a hybrid numerical flux vector for the higher-order contribution that was patterned after the flux vector developed for compressible flow [11]. An advantage of this hybrid flux is that the formulation leads more or less naturally to the limiting of characteristic variables which is important for compressible flows

with discontinuities. However, perhaps because two of the eigenvalues never change sign in this artificial compressibility formulation [12], limiting the characteristic variables for these incompressible flow computations has not been required. Therefore, some considerable time after the first version of this incompressible code was written it was determined to investigate the sort of results that could be obtained for second and third-order flux vectors by the more classical van Leer MUSCL-type of numerical flux vector formulation [13]. The nonlimited form of the dependent variable extrapolation method of Anderson, Thomas, and van Leer [14] was found to work rather well for this incompressible formulation and the numerical results were found to be extremely close to the results provided by the hybrid numerical flux vector [12]. The numerical flux currently used [12] is based on Roe's approximate Riemann solver [10], which in the interest of reduced floating point operation count is written for this one-dimensional example (Eq. (2)) in the form [11]

$$\bar{F}_{i+\frac{1}{2}} = \left[F(Q_{i+\frac{1}{2}}^L) \right]_{i+\frac{1}{2}} + \bar{A}^- \left(Q_{i+\frac{1}{2}}^L, Q_{i+\frac{1}{2}}^R \right) (Q_{i+\frac{1}{2}}^R - Q_{i+\frac{1}{2}}^L) \quad (3)$$

where \bar{A}^- is the Roe matrix given by

$$\bar{A}^- = R_{\xi} \Lambda_{\xi}^- R_{\xi}^{-1} \quad (4)$$

The eigenvalue matrix, Λ_{ξ}^- , contains only the nonpositive eigenvalues of \bar{A} and the similarity matrix, R_{ξ} , has the right eigenvectors of \bar{A} as columns. The matrix \bar{A} consists of the Roe averaged variables [12], and all metric quantities occurring in Eq. (3) are evaluated at cell face $i + 1/2$.

The numerical scheme is made higher order by using the MUSCL approach of van Leer [13]. Anderson, Thomas, and van Leer [14] used a MUSCL-type approach in flux vector split schemes. Following [14], the dependent variables just to the right of the cell face, Q^R , located at $i + 1/2$ and just to the left of the same cell face, Q^L , are written as

$$Q_{i+\frac{1}{2}}^R = Q_{i+1} - \frac{\phi}{4} [(1-\kappa)(Q_{i+2} - Q_{i+1}) + (1+\kappa)(Q_{i+1} - Q_i)] \quad (5a)$$

$$Q_{i+\frac{1}{2}}^L = Q_i + \frac{\phi}{4} [(1-\kappa)(Q_i - Q_{i-1}) + (1+\kappa)(Q_{i+1} - Q_i)] \quad (5b)$$

For $\phi = 0$ in Eqs. (5) the numerical scheme would be first-order in space. For higher order schemes set $\phi = 1$. With $\kappa = -1$ only points to the right of the cell face are used for Q^R and only points to the left of the cell face are used for Q^L , and a second-order scheme results. With $\kappa = 1/3$ two points to the right and one point to the left of the cell face are used for Q^R , and two points to the left and one point to the right of the cell face are used for Q^L . The resulting scheme is referred to as third-order upwind-biased [14]. Note that the third-order upwind-biased scheme depends on information from the same number of points as the second-order scheme. All numerical results presented here were obtained with $\kappa = 1/3$.

2.3 Solution Algorithm

The normal procedure for the solution of Eq. (2) would be to linearize the spatial difference terms, move the terms not containing ΔQ^n to the right-hand-side of the equations, and solve for ΔQ^n . This is particularly true for problems expected to have steady state solutions because the sum of the spatial difference operator terms as well as ΔQ^n would both go to zero. However, for unsteady flow, the ideal situation would be to find Q^{n+1} such that Eq. (2) is satisfied. That is, find Q^{n+1} such that [15]

$$\mathcal{F}(Q^{n+1}) = \frac{\Delta Q_i^n}{\Delta \tau} + \delta_i \bar{F}(Q^{n+1}) = 0 \quad (6)$$

One way of attempting to solve this problem is to use Newton's method. Newton's method [16] for the function $\mathcal{F}(x)$ would be

$$\mathcal{F}'(Q^{n+1,m})(Q^{n+1,m+1} - Q^{n+1,m}) = -\mathcal{F}(Q^{n+1,m}) \quad (7)$$

where $m = 1, 2, 3, \dots$ and $\mathcal{F}'(x)$ is the Jacobian matrix of the vector $\mathcal{F}(x)$. In principle the generated sequence $Q^{n+1,m+1}$ converges to Q^{n+1} and, hence, Eq. (6) is satisfied. For the one-dimensional example

$$\begin{aligned} & -\bar{F}'_{i-\frac{1}{2},i-1} \Delta Q_{i-1}^{n+1,m} \\ & + \left(\frac{1}{\Delta \tau} + \bar{F}'_{i+\frac{1}{2},i} - \bar{F}'_{i-\frac{1}{2},i} \right) \Delta Q_i^{n+1,m} \\ & + \bar{F}'_{i+\frac{1}{2},i+1} \Delta Q_{i+1}^{n+1,m} = \\ & - \left[I_a \frac{Q_i^{n+1,m} - Q_i^n}{\Delta \tau} + \left(\bar{F}_{i+\frac{1}{2}}(Q^{n+1,m}) - \bar{F}_{i-\frac{1}{2}}(Q^{n+1,m}) \right) \right] \end{aligned} \quad (8)$$

In this expression, \bar{F}' is the Jacobian of the numerical flux vector, with the first subscript representing the position of the cell face of the numerical flux vector and the second subscript representing the position of the dependent variable vector that the numerical flux vector is differentiated with respect to. I_a is an identity matrix, except the first diagonal element is zero in order to satisfy the true incompressible continuity equation.

A linear system of equations must be solved at each iteration of Newton's method. For three-dimensional problems a direct solution seems to be impractical [17] and in this work symmetric Gauss-Seidel relaxation is used. Because the flux Jacobian of the flux vector based on Roe's formulation is difficult to obtain analytically in three dimensions, and also in the interest of simplicity, the flux Jacobian is obtained numerically [18]. The solution scheme is referred to as discretized Newton-relaxation [16], or the DNR scheme [17]. Multigrid is used to accelerate the numerical solutions [19]. This multigrid scheme has been extended to multiblock [20] and unsteady flow [21]. The solution process is, therefore, a multigrid scheme for three-dimensional unsteady viscous flow on dynamic relative motion multiblock grids.

3.0 PROPULSOR TREATMENTS

From the beginning of the program it was determined that there needed to be two methods of handling the propulsor. One was to be a simulation of the propulsor using a relatively simple model that was computationally efficient, and the other was to incorporate the capability of handling the actual rotating propulsor. Both methods were developed, have been included in the code, and are discussed below.

3.1 Body Force Propulsor

The model selected that satisfies the conditions of simplicity and efficiency was one that has been used for a number of years for similar simulations such as open propellers [22] and ducted fans [23]. The basic approach is explained in [22] and consists of including body forces in Eq. (1) which operate on the fluid in a manner similar to the way an actual propulsor operates on the fluid. All three components of the body force vector were taken into account and consequently thrust, swirl, and their radial distributions can be included in the computations. In any given situation this force data may be obtained from conventional propulsor design tools or data bases. Here this information is based on thrust and torque coefficient data which were obtained from an actual marine propulsor. A description of the experiment and the measured results are reported in [24]. This

coefficient information was used to determine the components of the body force vector and then distribute these components to the center of the cells in this cell-centered finite volume scheme in the region where the propulsor was located.

3.2 Actual Rotating Propulsor

The method used to include an actual rotating propulsor is one that has been continually developed and also used for a number of years, primarily for compressible flows [25-31]. The approach is to use relative motion blocks with structured grids, whereby the blocks that include the rotating blades move relative to adjacent blocks with a region of the blocks near the relative motion interface being treated using the localized grid distortion technique introduced by Janus [31]. This method of handling relative motion blocks insures the continuity of grid lines (although they do change partners periodically, or "click") and restricts the maximum distortion of the grid to be of the order of the distance between grid points which for viscous grids is, of course, small. This approach eliminates the need to interpolate the solution vector from one grid to another. The cell volumes do change in time, however, and the geometric conservation law must be satisfied [31].

4.0 DYNAMIC MOTION OF THE VEHICLE

The trajectory of the body at any instant of time is described by its linear velocities u, v, w , and by its angular velocities p, q, r , in the body fixed frame of reference and its position and orientation in an inertial frame of reference. The governing six-degree-of-freedom (6-DOF) Equations Of Motion (EOM) can be written as:

Axial Force

$$m[\dot{u} - vr + wq - x_G(q^2 + r^2) + y_G(pq - \dot{r}) + z_G(pr + \dot{q})] = F_{x_H} + F_{x_{GB}}$$

Lateral Force

$$m[\dot{v} - wp + ur - y_G(r^2 + p^2) + z_G(qr - \dot{p}) + x_G(qp + \dot{r})] = F_{y_H} + F_{y_{GB}}$$

Normal Force

$$m[\dot{w} - uq + vp - z_G(p^2 + q^2) + x_G(rp - \dot{q}) + y_G(rq + \dot{p})] = F_{z_H} + F_{z_{GB}}$$

Rolling Moment

$$I_x \dot{p} + (I_z - I_y) qr - (\dot{r} + pq) I_{xz} + (r^2 - q^2) I_{yz} \\ + (pr - \dot{q}) I_{xy} + m [y_G (\dot{w} - uq + vp) \\ - z_G (\dot{v} - wp + ur)] = M_{x_H} + M_{x_{GB}}$$

Pitching Moment

$$I_y \dot{q} + (I_x - I_z) rp - (\dot{p} + qr) I_{xy} + (p^2 - r^2) I_{zx} \\ + (qp - \dot{r}) I_{yz} + m [z_G (\dot{u} - vr + wq) \\ - x_G (\dot{w} - uq + vp)] = M_{y_H} + M_{y_{GB}}$$

Yawing Moment

$$I_z \dot{r} + (I_y - I_x) pq - (\dot{q} + rp) I_{yz} + (q^2 - p^2) I_{xy} \\ + (rq - \dot{p}) I_{xz} + m [x_G (\dot{v} - wp + ur) \\ - y_G (\dot{u} - vr + wq)] = M_{z_H} + M_{z_{GB}}$$

where

$$\begin{aligned} F_{x_{GB}} &= -(W - B) \sin \theta \\ F_{y_{GB}} &= (W - B) \cos \theta \sin \phi \\ F_{z_{GB}} &= (W - B) \cos \theta \cos \phi \\ M_{x_{GB}} &= (y_g W - y_B B) \cos \theta \cos \phi \\ &\quad - (z_g W - x_B B) \cos \theta \sin \phi \\ M_{y_{GB}} &= -(x_g W - x_B B) \cos \theta \cos \phi \\ &\quad - (z_g W - z_B B) \sin \theta \\ M_{z_{GB}} &= (x_g W - x_B B) \cos \theta \sin \phi \\ &\quad + (y_g W - y_B B) \sin \theta \end{aligned}$$

and

$W = \text{vehicle weight}$

$B = \text{vehicle buoyancy}$

$x_g, y_g, z_g = \text{position of the cg in the body-axis system}$

$x_B, y_B, z_B = \text{position of the cb in the body-axis system}$

$\phi, \theta = \text{vehicle roll and pitch Euler angles with respect to an inertially fixed reference frame, here taken to be Earth-fixed}$

The hydrodynamic forces $F_{x_H}, F_{y_H}, F_{z_H}$, and moments $M_{x_H}, M_{y_H}, M_{z_H}$, are determined by integrating the pressure field and viscous stresses, obtained from the Navier-Stokes solver, over the body.

Since the frame of reference adopted for the equations of motion is fixed to the body, and moves with it, the position and orientation of the body cannot be described relative to it. Seven more equations are needed to describe the vehicle's orientation and position in an inertial reference frame. This frame of reference is taken to be fixed on the surface of the Earth (neglecting the Earth's rotation), with X-axis pointing to North, Y-axis

pointing East and Z-axis pointing towards the center of the Earth. The orientation of the vehicle with respect to this frame is defined by four quaternions e_0, e_1, e_2, e_3 , as follows:

$$\frac{de}{dt} = \Omega e$$

where

$$e = [e_0, e_1, e_2, e_3]^T$$

$$\Omega = \frac{1}{2} \begin{bmatrix} 0 & -p & -q & -r \\ p & 0 & r & -q \\ q & -r & 0 & p \\ r & q & -p & 0 \end{bmatrix}$$

The Euler angles (ϕ, θ, ψ) are related to e as follows:

$$\tan \phi = \frac{2(e_0 e_1 + e_2 e_3)}{(e_0^2 - e_1^2 - e_2^2 + e_3^2)}$$

$$\tan \psi = \frac{2(e_1 e_2 + e_0 e_3)}{(e_0^2 + e_1^2 - e_2^2 - e_3^2)}$$

$$\tan \theta = (2(e_0 e_2 + e_1 e_3)) / (2 \sin \phi (e_0 e_1 + e_2 e_3) \\ + \cos \phi (e_0^2 - e_1^2 - e_2^2 + e_3^2))$$

Finally, the position of the vehicle in the inertial frame of reference is derived from:

$$\frac{dx}{dt} = u[(e_0^2 + e_1^2) - (e_2^2 + e_3^2)] + v[2(e_1 e_2 - e_0 e_3)] \\ + w[2(e_1 e_3 - e_0 e_2)]$$

$$\frac{dy}{dt} = u[2(e_1 e_2 + e_0 e_3)] + v[(e_0^2 + e_2^2) - (e_1^2 + e_3^2)] \\ + w[2(e_2 e_3 - e_0 e_1)]$$

$$\frac{dz}{dt} = u[2(e_1 e_3 - e_0 e_2)] + v[2(e_0 e_1 + e_2 e_3)] \\ + w[(e_0^2 + e_3^2) - (e_2^2 + e_1^2)]$$

The final result is a set of 13 O.D.E.'s in 13 unknowns. These are:

(I) - Six strongly coupled, highly nonlinear O.D.E.'s for the motion in the body-fixed frame of reference. Solution of these equations yields the linear velocities of the vehicle u, v, w and the angular velocities of the vehicle p, q, r in the body fixed frame of reference.

(II) - Four strongly coupled, nonlinear O.D.E.'s for the body orientation in the inertial frame of reference. Solution of these equations yields the four quaternions e_0, e_1, e_2, e_3 , from which Euler angles can be derived.

(III) – Three linear (not coupled) O.D.E.'s for the body position in the inertial frame of reference whose solution yields the position of the body in the inertial frame of reference.

The above 13 vehicle dynamics O.D.E.'s are numerically integrated using a fourth-order accurate Runge–Kutta technique. The assembly and solution of the vehicle dynamics equations was implemented directly from the vehicle simulation code TRJv [32].

The coupled Navier–Stokes flow solver and the 6-DOF equations of motion solver was successfully used to simulate a free falling sphere ($Re = 1000$) and a 6:1 ellipsoid ($Re = 7500$) prior to the SUBOFF calculation presented later in this paper.

5.0 TURBULENCE MODEL

Turbulence models used in this work include the Baldwin–Lomax mixing length model [6] the Launder–Sharma Low–Reynolds number k – ϵ model and a Low–Reynolds number nonlinear k – ϵ model based on the work of Nisizima and Yoshizawa, Speziale, and Myong and Kasagi [7].

The bulk of the initial work was done with the algebraic mixing length model typified by the eddy viscosity

$$\mu_T = \rho l_{mix}^2 |\omega|$$

Here, a representative length scale is determined empirically, and it is combined with vorticity, ω , to provide a representative velocity scale.

A more general model uses two transport equations to find the representative length and velocity scales of the flow. In this work, the Launder–Sharma model was used to find the turbulent kinetic energy, k , and the turbulent energy dissipation rate, ϵ . The resulting velocity scale is $k^{1/2}$ while the length scale is provided by $k^{3/2}/\epsilon$, so that the turbulent viscosity is given by

$$\mu_T = C_\mu \rho k^2 / \epsilon$$

Damping functions, including one for the eddy viscosity, are used to allow integration of the flow directly to the wall. Both of the above models rely on the Boussinesq approximation, which provides for an isotropic eddy viscosity and so fails to capture important anisotropic effects. For this reason, the k – ϵ model was extended by a nonlinear Reynolds stress assumption of the form

$$\begin{aligned} -\rho \overline{u_i u_j} = & -\frac{2}{3} \rho k \delta_{ij} + 2\mu_T S_{ij} \\ & - (S_{ik} S_{kj} - \frac{1}{3} \delta_{ij} S_{mn} S_{mn}) (C_1 \rho k^3 / \epsilon^2) \\ & + (S_{ik} \Omega_{kj} + S_{jk} \Omega_{ki}) (C_2 \rho k^3 / \epsilon^2) \end{aligned}$$

where S_{ij} and Ω_{ij} represent the mean strain and rotation tensors, respectively, and k and ϵ continue to be determined by the Launder–Sharma Low–Reynolds number k – ϵ model. The standard model is recovered when C_1 and C_2 are set to zero. However, the nonlinear effects provided by this new Reynolds stress assumption prove to be dramatic. Calculation in a three-dimensional square duct, shown in Fig. 1, demonstrates secondary flow which is absent when a standard two-equation model is used. Additionally, it has been shown that the model greatly improves the prediction of the normal Reynolds stresses in highly three-dimensional flows, such as the flow over a 6:1 prolate spheroid at 10° angle of attack. Results, compared to the experimental data of Reference [33], are shown in Figs. 2–5.

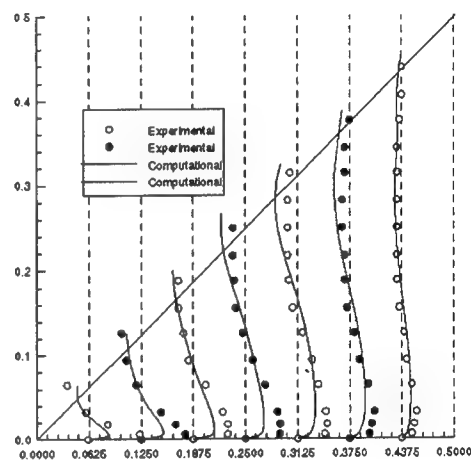


Fig. 1 W/U_r Profiles in the Square Duct.

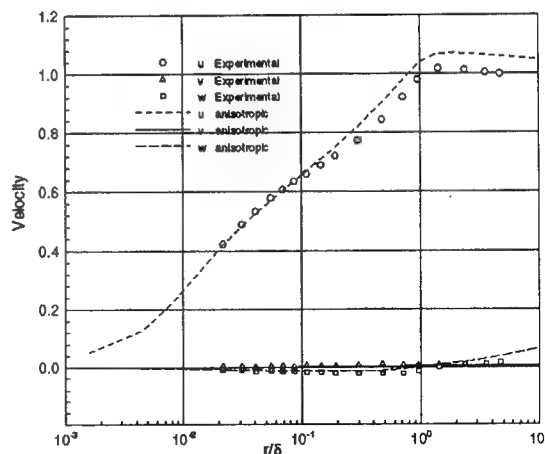


Fig. 2 Boundary Layer Velocity Profile, $x/L = 0.4$, $\Phi = 100^\circ$, Anisotropic Model, $Re = 4.2 \times 10^6$, $\alpha = 10^\circ$.

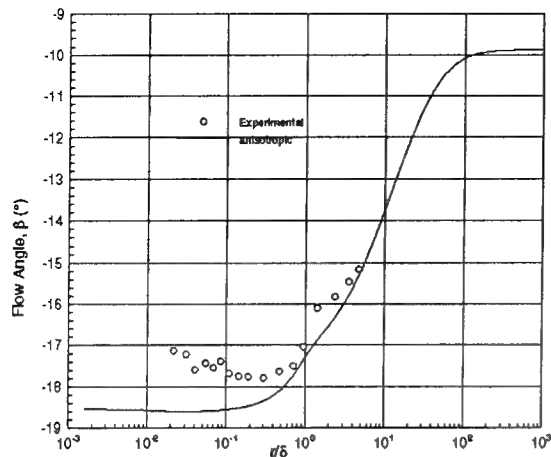


Fig. 3 Flow Angle $\beta = \tan^{-1}(W/U)$, Anisotropic Model, $Re = 4.2 \times 10^6$, $\alpha = 10^\circ$.

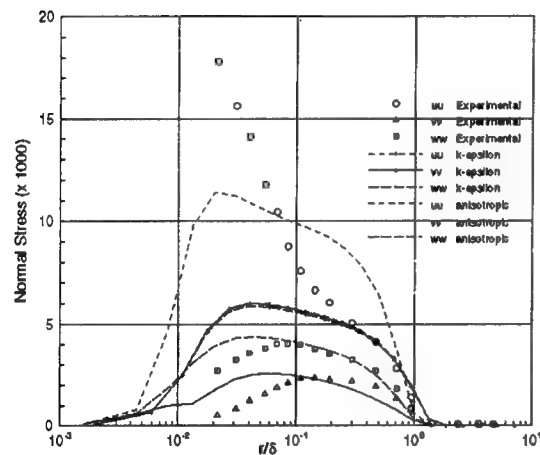


Fig. 4 Boundary Layer Normal Stress Profiles, $x/L = 0.4$, $\Phi = 100^\circ$, Anisotropic Model, $Re = 4.2 \times 10^6$, $\alpha = 10^\circ$.

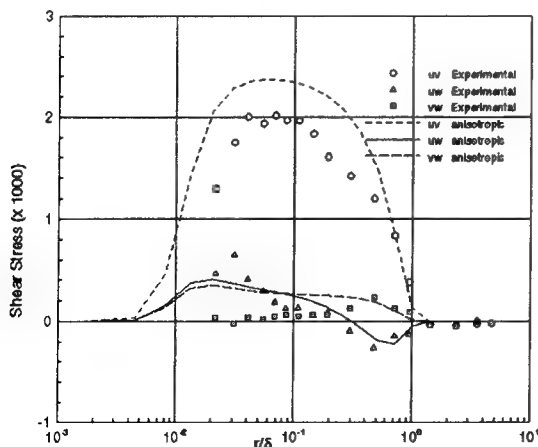


Fig. 5 Boundary Layer Shear Stress Profiles, $x/L = 0.4$, $\Phi = 100^\circ$, Anisotropic Model, $Re = 4.2 \times 10^6$, $\alpha = 10^\circ$.

6.0 RESULTS

Throughout this research effort, computations were carried out in order to validate the code as each additional computational capability and improvement was added. These test cases have ranged from steady state laminar flow over a flat plate to unsteady turbulent flow about a fully appended submarine configuration that included sail, sail plane, four stern appendages, and an actual rotating propeller; and, the coupling of this unsteady flow computation to the 6-DOF computation in order to predict the trajectory of the submarine. The computations performed between these two extremes were cases where analytical solutions or experimental data were available for comparison whenever possible. The solutions were carried out on multiblock grids with structured subgrids, and nearly all of these grids were built using EAGLEView [34]. Moreover, all of the grids were tight with y^+ values near surfaces of order one.

6.1 Validation Computations

The ultimate objective of this work, which was the prediction of the trajectory of fully appended self-propelled maneuvering vehicles, involved more complicated flow fields and configurations than those corresponding to the experiments for which measured data were available. Nevertheless, the approach taken, whenever data and time permitted, was to perform rather critical comparisons with the experimental data that were available. For steady state flows, comparisons have been made between numerical results and experimental data that include one or more of the measurements of pressure, skin friction, and/or boundary-layer velocity profiles for geometric configurations that include SUBOFF [35], inflected stern [36], 6:1 prolate spheroid [37], and wing-body junction [38]. These numerical and experimental comparisons are included in [4, 18, 19, 20, 39, and 40]. For unsteady flows, comparisons with experimental pressure and velocity measurements have been made with the so-called flapping foil experiment [41], the 6:1 prolate spheroid in pitch, plunge, and roll maneuvers [42 and 43], an impulsively started cylinder [44], and isolated rotating propellers [45 and 46]. These numerical and experimental comparisons are included in [21, 39, 47, 48, and 49]. The quality of agreement for all of the steady and unsteady flow comparisons have been considered reasonable to excellent.

The computations mentioned above that have been carried out for comparisons with experimental data have involved an enormous number of calculations and essentially all of these calculations were performed on workstations that included SGI 75 MHz R8000 processors and IBM RS/6000 Model 560 and 590 processors. Examples of processing speed are given in [20] and include an example of the computation of a

submarine configuration that was gridded using 12 blocks with a total of 2.5 million points and was carried to a steady state solution in 200 multigrid cycles in 45 hours on an IBM Model 590 using 512 MB of memory. Versions of the UNCLE code have now been parallelized by Pankajakshan and Briley [50] and are just beginning to be used for routine calculations. However, the computations mentioned above and the results presented below have been obtained on workstations in serial mode.

The validation comparisons cited in the references above have involved, primarily, comparisons with pressure and flow field velocity data and to a lesser extent skin friction and velocity profile experimental data. Since the trajectory of a vehicle depends on the forces and moments produced by the flow on the vehicle, these comparisons do not indicate the accuracy to which the resulting forces and moments can be computed. Roddy [51] has reported experiments that include measurements of forces and moments of the SUBOFF bare hull with and without appendages. These data were used in what might be considered component form, that is, with the various appendage combinations, to determine how accurately the forces and moments on the body with these isolated appendages could be predicted. As has been the case in times past, it was found that excellent agreement between the computations and the experimental data could be obtained by "tuning" the turbulence model for each data point. This, however, does not seem to be appropriate for the problem in general. Therefore, computations are being carried out where the turbulence model is frozen in the sense that computations for the various appendage combinations have the same turbulence model. An example of these results for the SUBOFF bare hull with four stern appendages is given in Fig. 6. Numerical and experimental comparisons are presented in Fig. 6 for various angles of drift and the results indicate that the computed forces and moments are essentially within the error bars of the experimental data. Of course this is a simplified configuration compared to the fully appended configuration with a rotating propulsor, but it is an example of the type of validation computations that have been, and are being, performed.

6.2 Maneuvering Predictions

Maneuvering predictions of two self-propelled vehicles are presented. The vehicles are fully appended with sail, sail plane, four stern appendages, and propulsor. The vehicles differ only in that their propulsor units differ. One vehicle has a body force propulsor and the other an actual rotating propulsor. The hull, sail, and four stern appendages were taken from the standard SUBOFF configuration. The sail plane was constructed from viewing various published pictures of

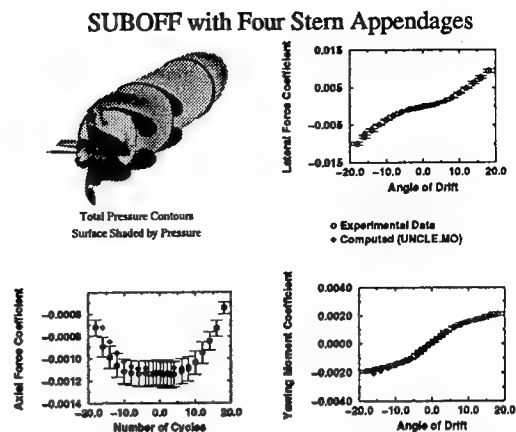


Fig. 6 Comparison of Computed and Experimental Force and Moment Coefficients for SUBOFF with Four Stern Appendages.

submarines and although it was not designed by marine designers it is thought to be representative of a typical sail plane. The body force propulsor was located at 98.7% of the body length. The actual rotating propulsor was located in the same region and was scaled for the SUBOFF geometry by ARL personnel who have experience in marine propeller design.

The computed trajectory of the body force propelled vehicle was carried out by first computing the steady state flow field about the vehicle at zero degrees angle of attack and drift. The ballast tanks were then blown and the Navier-Stokes/6-DOF computation was initiated. The resulting trajectory is presented in Fig. 7. At first the vehicle rises and then this motion is followed by the pitching moment causing a nose down attitude which causes the propelled vehicle to descend at a rather steep angle as shown in Fig. 7. The trajectory calculation was carried out for five body lengths. These computations were performed on an IBM Model 590 workstation with 512 MB of RAM and took 100 hours of CPU time. The grid consisted of a total of 1.4 million points and 36 blocks.

The computation of the trajectory of the fully appended vehicle with an actual rotating propulsor was carried out in the same fashion as the trajectory calculation for the body force propelled vehicle, except in this case a complete steady state solution does not exist due to the rotating propulsor. Rather, a periodic solution at zero angle of attack and drift is first obtained and then the Navier-Stokes/6-DOF computation was initiated. An example of the multiblock grid used for this calculation is given in Fig. 8. The grid consists of a total of 1.6 million points and 51 blocks. It turns out that the rotation of the propeller was such that the vehicle initially had more drag than thrust and consequently the rotation rate of the propeller was increased to compensate for this imbalance of axial force. With this adjustment, the drag and thrust were much more in

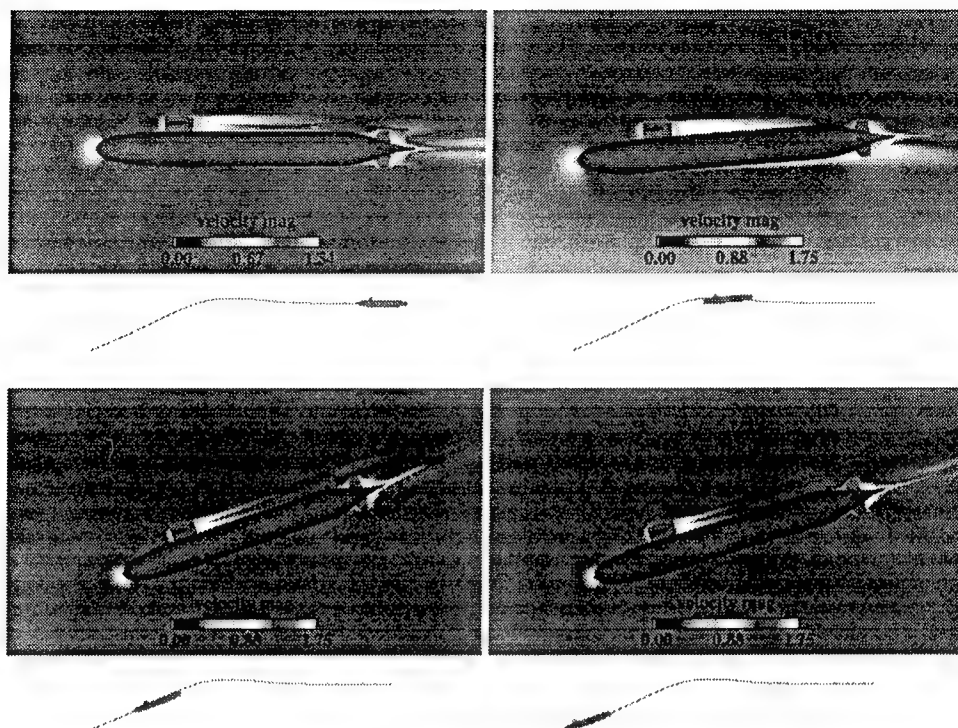


Fig. 7 Trajectory and Flow Field about SUBOFF Configuration with Sail, Sail Planes, and Stern Appendages with Body-Force Propulsor.

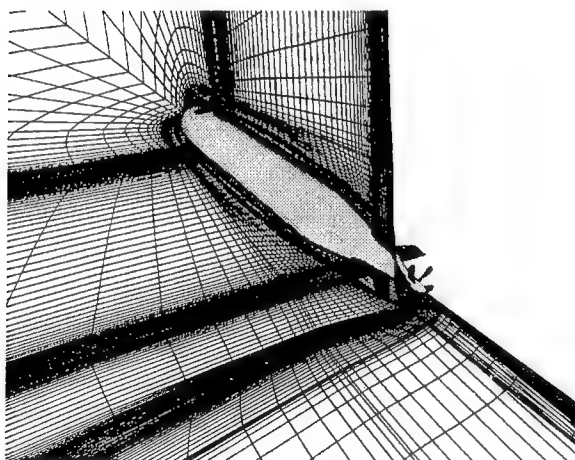


Fig. 8 Multiblock Grid for SUBOFF Configuration with Sail, Sail Planes, Stern Appendages, and Propeller.

balance and the rapid deceleration of the vehicle was eliminated. This trajectory computation continues to be carried out but the additional CPU time required for the rotating propulsor computation limits the number of body lengths that can be computed in a reasonable amount of computer time. It is estimated that 1000 CPU hours on the IBM Model 590 is required to complete five body lengths of travel. Whereas, this is a large amount of computer time, it is anticipated that a five body length

computation can be carried out overnight using the parallel version of the code. The parallel computation of this trajectory calculation is just now being initiated. The vehicle trajectory that has been computed thus far is shown in Fig. 9.

All of the above calculations were performed using an algebraic turbulence model and are currently being repeated using $k-\epsilon$ and nonlinear $k-\epsilon$ turbulence models.

7.0 CONCLUDING REMARKS

A physics-based method was presented for the maneuvering prediction of self-propelled underwater vehicles. The method is based on coupling the numerical solution of the three-dimensional time-dependent incompressible turbulent Navier-Stokes equations with the numerical solution of the equations of motion of the vehicle. The computational methods were previously verified independently on numerous test cases, and also verified in the coupled mode. The Navier-Stokes/6-DOF coupled code was applied to the trajectory calculation of two fully appended submarine configurations that differed only in their propulsor units. One had a body force propulsor and the other had an actual rotating propeller.

This research effort was of three and one-half years duration and was sponsored by the Office of Naval

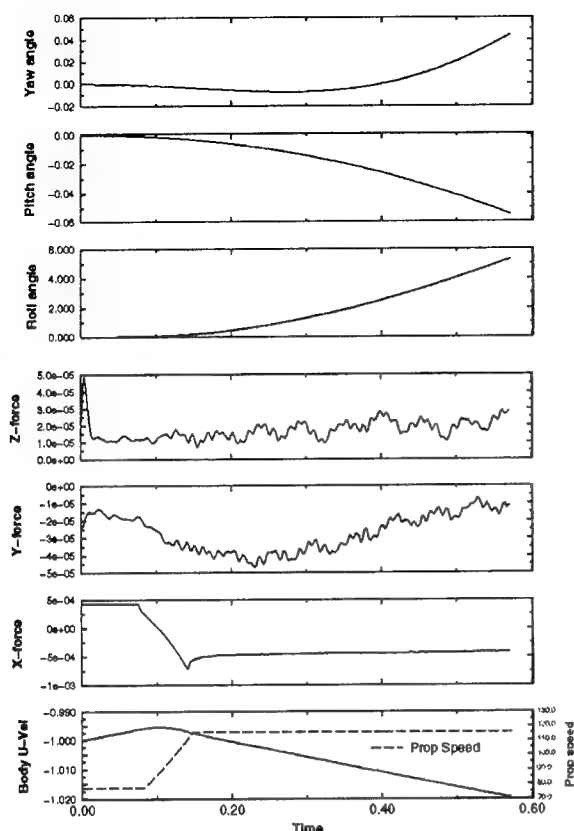


Fig. 9 Forces on the Body, Angles of the Body, Streamwise Velocity, and Propeller Speed for the SUBOFF Configuration with Sail, Sail Planes, Stern Appendages, and Rotating Propeller.

Research (ONR). The work involved a team of rather significant size that was composed of researchers at both the Applied Research Laboratory at Penn State University and the Computational Fluid Dynamics Laboratory at Mississippi State University. Close contact among the researchers was maintained throughout the effort. Credit for all involved in this research program would involve a list of more than twenty people. The two authors of this paper are not to be considered the leaders of this effort, rather servants to the faculty, research engineers, post-docs, graduate students, and undergraduate students who so admirably carried out the real work involved in putting ONR's idea of a physics-based maneuvering prediction method on a firm foundation.

ACKNOWLEDGEMENTS

The authors are indebted to their colleagues at the Engineering Research Center, Mississippi State University and the Applied Research Laboratory, Pennsylvania State University for their contribution to this project. Special thanks are due to Mr. James Fein of the

Office of Naval Research for his ideas, advocacy, and support.

REFERENCES

1. Chorin, A. J., "A Numerical Method for Solving Incompressible Viscous Flow Problems," *Journal of Computational Physics*, Vol. 2, 1967, pp. 12-26.
2. Pan, D. and Chakravarthy, S., "Unified Formulation for Incompressible Flows", AIAA Paper No. 89-0122, January 1989.
3. Rogers, S. E. and Kwak, D., "Upwind Differencing for the Time-Accurate Incompressible Navier-Stokes Equations", *AIAA Journal*, Vol. 28, No. 2, 1990, pp. 253-262.
4. Taylor, L. K., "Unsteady Three-Dimensional Incompressible Algorithm Based on Artificial Compressibility," Ph.D. Dissertation, Mississippi State University, May 1991.
5. Whitfield, D. L., "Perspective on Applied CFD," AIAA Paper No. 95-0349, AIAA 33rd Aerospace Sciences Meeting and Exhibit, Reno, NV, January 9-12, 1995.
6. Baldwin, B.S. and Lomax, H., "Thin-Layer Approximation and Algebraic Model for Separated Turbulent Flows," AIAA Paper No. 78-0257, January 1978.
7. Boger, D. A., and McDonald, H., "Observations on Non-linear $k-\epsilon$ Models of Turbulent Transport," 1996, to appear.
8. Gatlin, B., "An Implicit, Upwind Method for Obtaining Symbiotic Solutions to the Thin-Layer Navier-Stokes Equations," PhD Dissertation, Mississippi State University, August 1987.
9. Chen, J. P., "Unsteady Three-Dimensional Thin-Layer Navier-Stokes Solutions for Turbomachinery in Transonic Flow," PhD Dissertation, Mississippi State University, December 1991.
10. Roe, P. L., "Approximate Riemann Solvers, Parameter Vector, and Difference Schemes," *Journal of Computational Physics*, Vol. 43, 1981, pp. 357-372.
11. Whitfield, D. L., Janus, J. M., and Simpson, L. B., "Implicit Finite Volume High Resolution Wave-Split Scheme for Solving the Unsteady Three-Dimensional Euler and Navier-Stokes Equations on Stationary or Dynamic Grids," Engineering and Industrial Research Station Report MSSU-EIRS-ASE-88-2, Mississippi State University, Mississippi State, MS, February 1988.
12. Whitfield, D. L., and Taylor, L. K., "Numerical Solution of the Two-Dimensional Time-Dependent Incompressible Euler Equations," MSSU-EIRS-ERC-93-14, April 1994.

13. van Leer, B., "Towards the Ultimate Conservative Difference Scheme. V. A Second Order Sequel to Godunov's Method," Journal of Computational Physics, Vol. 32, 1979, pp. 101-136.
14. Anderson, W. K., Thomas, J. L., and van Leer, B., "Comparison of Finite Volume Flux Vector Splittings for the Euler Equations," AIAA Journal, Vol. 24, No. 9, September 1986, pp. 1453-1460.
15. Whitfield, D. L., "Newton-Relaxation Schemes for Nonlinear Hyperbolic Systems," Engineering and Industrial Research Station Report MSSU-EIRS-ASE-90-3, Mississippi State University, Mississippi State, MS, October 1990.
16. Ortega, J. M. and Rheinboldt, W. C., Iterative Solution of Nonlinear Equations in Several Variables. Academic Press, Inc., New York, 1970.
17. Vanden, K. J., and Whitfield, D. L., "Direct and Iterative Algorithms for the Three-Dimensional Euler Equations," AIAA Journal, Vol. 33, No. 5, May 1995, pp. 851-858.
18. Whitfield, D. L. and Taylor, L. K., "Discretized Newton-Relaxation Solution of High Resolution Flux-Difference Split Schemes," AIAA Paper No. 91-1539, June 1991.
19. Sheng, C., Taylor, L. K., and Whitfield, D. L., "Multigrid Algorithm for Three-Dimensional Incompressible High-Reynolds Number Turbulent Flows," AIAA Journal, Vol. 33, No. 11, November 1995, pp. 2073-2079.
20. Sheng, C., Taylor, L. K., and Whitfield, D. L., "Multiblock Multigrid Solution of Three-Dimensional Incompressible Turbulent Flow About Appended Submarine Configurations," AIAA Paper No. 95-0203, AIAA 33rd Aerospace Sciences Meeting and Exhibit, Reno, NV, January 9-12, 1995.
21. Sheng, C., Taylor, L. K., and Whitfield, D. L., "A Multigrid Algorithm for Unsteady Incompressible Euler and Navier-Stokes Flow Computations," Sixth International Symposium on Computational Fluid Dynamics, September 4-8, 1995, Lake Tahoe, Nevada, USA.
22. Whitfield, D. L. and Jameson, A., "Euler Equation Simulation of Propeller-Wing Interaction in Transonic Flow," Journal of Aircraft, Vol. 21, No. 11, November 1984, pp. 835-839.
23. Pankajakshan, R., Arabshahi, A., and Whitfield, D. L., "Turbofan Flowfield Simulation Using Euler Equations with Body Forces," AIAA Paper No. 93-1978, AIAA/SAE/ASME/ASEE 29th Joint Propulsion Conference and Exhibit, Monterey, CA, June 28-30, 1993.
24. Yang, C. I., Hartwich, P. M., and Sundaram, P., "A Navier-Stokes Solution of Hull-Ring Wing-Thruster Interaction," Eighteenth Naval Hydrodynamics Symposium, University of Michigan, Ann Arbor, MI, August 1990.
25. Whitfield, D. L., Swafford, T. W., Janus, J. M., Mulac, R. A., and Belk, D. M., "Three-Dimensional Unsteady Euler Solutions for Propfans and Counter-Rotating Propfans in Transonic Flow," AIAA Paper No. 87-1197, June 1987.
26. Janus, J. M. and Whitfield, D. L., "A Simple Time-Accurate Turbomachinery Algorithm with Numerical Solutions of an Uneven Blade Count Configuration," AIAA Paper No. 89-0206, January 1989.
27. Janus, J. M., Whitfield, D. L., Horstman, H., and Mansfield, F., "Computation of the Unsteady Flowfield About a Counter Rotating Propfan Cruise Missile," AIAA Paper No. 90-3093, August 1990.
28. Janus, J. M., Horstman, H. Z., and Whitfield, D. L., "Unsteady Flowfield Simulation of Ducted Prop-Fan Configurations," AIAA Paper No. 92-0521, January 1992.
29. Chen, J. P. and Whitfield, D. L., "Navier-Stokes Calculations for the Unsteady Flow Field of Turbomachinery," AIAA Paper No. 93-0676, 31st AIAA Aerospace Sciences Meeting and Exhibit, Reno, Nevada, January 1993.
30. Webster, R. S., Chen, J. P., and Whitfield, D. L., "Numerical Simulation of a Helicopter Rotor in Hover and Forward Flight," AIAA Paper No. 95-0193, AIAA 33rd Aerospace Sciences Meeting and Exhibit, Reno, NV, January 9-12, 1995.
31. Janus, J. M., "Advanced 3-D CFD Algorithm for Turbomachinery," PhD Dissertation, Mississippi State University, May 1989.
32. Smith, N. S. and Watkinson, K. W., "A Six-Degree-Of-Freedom Simulation Program For Underwater Vehicles With Significant Vortical Flow Effects," V.C.T. Report No. 3; User's Manual for TRJv, Vehicle Control Technologies, Inc., August 1994.
33. Chesnakas, C. J., Simpson, R. L., and Madden, M. M., "Three-Dimensional Velocity Measurements on a 6:1 Prolate Spheroid at 10° Angle of Attack," Department of Aerospace and Ocean Engineering, Virginia Polytechnic Institute and State University, Report VPI-AOE-202, January 1994.
34. Jiang, M. Y., Remotigue, M. G., Stokes, M. L., and Thompson, J. F., "EAGLEView: Grid Enhancement and Applications," AIAA Paper No. 94-0316, January 1994.
35. Huang, T. T., Liu, H.-L., Groves, N. C., Forlini, T. J., Blanton, J. N., and Gowing, S., "Measurement of Flows Over an Axisymmetric Body with Various Appendages," Nineteenth Symposium on Naval Hydrodynamics, Seoul, Korea, August 24-28, 1992.

36. Huang, T. T., Groves, N. C. and Belt, G., "Boundary-Layer Flow on An Axisymmetric Body with An Inflected Stern," David W. Taylor Naval Ship Research and Development Center, Report No. DTNSRDC-80/064, August 1980.
37. Ahn, S., "An Experimental Study of Flow Over a 6 to 1 Prolate Spheroid at Incidence," Ph.D. Dissertation, Aerospace and Ocean Engineering Department, Virginia Polytechnic Institute and State University, October 1992.
38. Devenport, W.J. and Simpson, R.L., "An Experimental Investigation of the Flow Past an Idealized Wing-Body Junction: Final Report," Department of Aerospace and Ocean Engineering, Virginia Polytechnic Institute and State University, Report VPI-AOE-172, July 1990.
39. Taylor, L. K. and Whitfield, D. L., "Unsteady Three-Dimensional Incompressible Euler and Navier-Stokes Solver for Stationary and Dynamic Grids," AIAA Paper No. 91-1650, June 1991.
40. Sheng, C., Taylor, L. K., and Whitfield, D. L., "An Efficient Multigrid Acceleration for Solving the 3-D Incompressible Navier-Stokes Equations in Generalized Curvilinear Coordinates," AIAA Paper No. 94-2335, *25th AIAA Fluid Dynamics Conference*, Colorado Springs, CO, June 1994.
41. Kerwin, J., Keenan, D., Mazel, C., Horwich, E., and Knapp, M., "MIT/ONR Flapping Foil Experiment, Unsteady Phase," unpublished data.
42. Hoang, N. T., Wetzel, T. G., and Simpson, R. L., "Unsteady Measurements Over a 6:1 Prolate Spheroid Undergoing a Pitch-Up Maneuver," AIAA Paper No. 94-0197, January 1994.
43. Hoang, N. T., Wetzel, T. G., and Simpson, R. L., "Surface Pressure Measurements Over a 6:1 Prolate Spheroid Undergoing Time-Dependent Maneuvers," AIAA Paper No. 94-1908, June 1994.
44. Bouard, R. and Coutanceau, M., "The Early Stage of Development of the Wake Behind an Impulsively Started Cylinder for $40 < Re < 10^4$," *Journal of Fluid Mechanics*, Vol. 101, Part 3, 1980, pp. 583-607.
45. Bushnell, P., "Measurement of the Steady Surface Pressure Distribution on A Single Rotation Large Scale Advanced Prop-Fan Blade at Mach Numbers from 0.03 to 0.78," NASA Contract Report 182124, July 1988.
46. Jessup, S. D., "An Experimental Investigation of Viscous Aspects of Propeller Blade Flow," Ph.D. Dissertation, The Catholic University of America, 1989.
47. Taylor, L. K., Busby, J. A., Jiang, M. Y., Arabshahi, A., Sreenivas, K., and Whitfield, D. L., "Time Accurate Incompressible Navier-Stokes Simulation of the Flapping Foil Experiment," *The Proceedings Sixth International Conference on Numerical Ship Hydrodynamics*, Iowa City, Iowa, August 2-5, 1993, pp. 721-738.
48. Taylor, L. K., Arabshahi, A., and Whitfield, D. L., "Unsteady Three-Dimensional Incompressible Navier-Stokes Computations for a 6:1 Prolate Spheroid Undergoing Time-Dependent Maneuvers," AIAA Paper No. 95-0313, *AIAA 33rd Aerospace Sciences Meeting and Exhibit*, Reno, NV, January 9-12, 1995.
49. Arabshahi, A., Taylor, L. K., and Whitfield, D. L., "UNCLE: Toward a Comprehensive Time-Accurate Incompressible Navier-Stokes Flow Solver," AIAA Paper No. 95-0050, *AIAA 33rd Aerospace Sciences Meeting and Exhibit*, Reno, NV, January 9-12, 1995.
50. Pankajakshan, R. and Briley, W. R., "Parallel Solution of Viscous Incompressible Flow on Multi-Block Structured Grids Using MPI." *Accepted for Parallel Computational Fluid Dynamics - Implementations and Results Using Parallel Computers*, Edited by S. Taylor, A. Ecer, J. Periaux, and N. Satofuca, Elsevier Science, B. V. Amsterdam, 1995.
51. Roddy, R. F., "Investigation of the Stability and Control Characteristics of Several Configurations of the DARPA SUBOFF Model (DTRC Model 5470) from Captive-Model Experiments," David Taylor Research Center Report DTRC/SHD-1298-08, September 1990.

Spray Formation at the Free Surface of Turbulent Bow Sheets

Z. Dai, L.-P. Hsiang, G. Faeth (University of Michigan, USA)

ABSTRACT

An experimental study of transitions at the free surface of turbulent liquid wall jets in still air at normal temperature and pressure is described. Measurements involved initially nonturbulent annular wall jets with the growth of a turbulent boundary layer along the wall initiated by a trip wire. Pulsed photography, shadowgraphy and holography were used to observe the location of the onset of roughened liquid surfaces, the location of the onset of turbulent primary breakup, and drop sizes at the onset of turbulent primary breakup, along the free surface of the liquid wall jets. Test conditions included several liquids (water, ethyl alcohol and various glycerol mixtures), liquid gas density ratios of 680-980, wall jet Reynolds numbers of 10,000-600,000 and Weber numbers of 4,000-53,000, at conditions where direct effects of liquid viscosity on turbulent primary breakup were small. It was found that transitions to roughened liquid surfaces and turbulent primary breakup were caused by turbulence originating in the liquid phase, while direct effects of aerodynamic forces at the liquid surface were small. Transition to a roughened liquid surface could be correlated by associating the thickness of the growing turbulent boundary layer along the wall with the thickness of the wall jet. Drop sizes at the onset of turbulent primary breakup could be correlated by equating the surface energy required to form a drop to the kinetic energy of an eddy of corresponding size. Finally, the location of the onset of turbulent primary breakup could be correlated in terms of the distance convected at the mean velocity of the wall jet for a time needed to initiate the Rayleigh breakup of the ligaments protruding from the liquid surface that produce drops at the onset of turbulent primary breakup.

NOMENCLATURE

b	annulus width
C_r	empirical constant for roughened liquid surface
C_{si}	empirical constant for SMD at onset of breakup
d	round jet diameter
d_{rod}	diameter of center rod of annulus
D	hydraulic diameter of wall jet, $4b(1+b/d_{rod})$
e_p	volume-averaged ellipticity
k	trip wire height
ℓ	characteristic eddy size
ℓ_K	Kolmogorov length scale
L	passage length, Rayleigh breakup length
Oh_D	Ohnesorge number, $\mu_f/(\rho_f D \sigma)^{1/2}$
Re_D	wall jet Reynolds number, $u_o D/\nu_f$
Re_x	boundary layer Reynolds number, $u_o x/\nu_f$
SMD	Sauter mean diameter
u	streamwise velocity
u^*	friction velocity, $(\tau_w/\rho_f)^{1/2}$
v	radial velocity
v_ℓ	radial velocity associated with eddy of size ℓ
We_{ta}	Weber number, $\rho_f u_o \Lambda/\sigma$
x	streamwise distance
δ	boundary layer thickness
Λ	radial integral length scale
μ	molecular viscosity
ν	kinematic viscosity
σ	surface tension
τ_i	characteristic drop formation time
τ_w	wall shear stress
Subscripts	
f	liquid-phase property
g	gas-phase property
i	at point of breakup initiation
k	at the location of trip wire
r	at the point of rough surface initiation

- t transition from laminar to turbulent boundary layer
 w wall condition
 o jet exit condition
 Superscripts
 () time-averaged mean property
 ()' time-averaged rms fluctuating property

INTRODUCTION

An experimental investigation concerning aspects of the generation of sprays by the bow waves (or bow sheets) of ships is described. This flow is important as a representative spray formation process of the marine environment, which contributes to the structure of ship-generated waves and the electromagnetic scattering properties (e.g., the photographic and radar signatures) of vessels. The overall objectives of the investigation were to make new measurements of several properties associated with the sprays produced by bow sheets, emphasizing transitions at the free surface of attached turbulent bow sheets (or turbulent wall jets). This work included measurements of the onset location of roughened liquid surfaces, and the properties (drop sizes and location) of the onset of primary drop breakup (turbulent primary breakup) along the liquid surface. Finally, the new measurements were interpreted and correlated using phenomenological theories.

Bow sheet/spray flows are complex and involve a number of turbulence/surface interactions and spray formation mechanisms. This complexity has prevented complete understanding of bow sheet/spray flows; nevertheless, there is general agreement about the qualitative features and spray forming mechanisms of bow sheets (1-3). In particular, flows associated with chutes, spillways, plunge pools, hydraulic jumps, open water waves and jets exhibit similar features of spray formation. In general, the mechanism appears to involve the propagation of vorticity (especially turbulence) to the liquid surface, or its development along the surface, with the subsequent appearance of a turbulence-wrinkled interface between the liquid and gas and eventually the

formation of drops due to turbulent primary breakup at the liquid surface.

An important issue concerning the transitions of turbulent bow sheets is the origin of the turbulence near the liquid surface, e.g., whether this turbulence mainly is caused by motion along the bow surface or whether it mainly results from aerodynamic forces at the liquid surface. This issue was partly addressed during the present study by observing round water jets injected into still air at normal temperature and pressure (NTP), with large jet Reynolds numbers ($Re_D > 120,000$) and a variety of passage configurations. In all cases, a large contraction (roughly 100:1 and shaped according to Smith and Wang (4)) followed by boundary layer removal, was used to generate a uniform nonturbulent flow. This flow then entered round constant diameter passages having various lengths in order to study the effect of turbulence developed in the passage on liquid jet properties. Some typical pulsed shadowgraphs of the flow near the jet exit for short and long passages are illustrated in Fig. 1. For the short passage, $L/d = 0.15$, the flow remains essentially uniform and nonturbulent at the jet exit; this



Fig. 1. Pulsed shadowgraphs of round nonturbulent and turbulent liquid jets in still air.

yields a liquid jet that has a smooth surface with no tendency to break up into drops over the range of jet lengths that could be observed. In contrast, for $L/d = 41$, the passage is sufficiently long to obtain fully-developed turbulent pipe flow at the exit (5,6); this immediately yields a liquid jet that has a roughened liquid surface. These results provide rather strong evidence that turbulence generated by motion along solid surfaces, rather than by relative motion at the gas/liquid interface, causes liquid surface roughness and primary breakup with drops at liquid surfaces in air at NTP when the liquid has similar relative velocities with respect to both the solid surface and the air.

Based on the notion that turbulence causing liquid surface roughness and primary breakup along liquid surfaces in bow sheets originates from liquid motion along the bow surface, the resulting spray formation processes typical of most bow sheets are sketched in Fig. 2. The reference frame used in this figure involves an observer on the ship so that the bow sheet moves over the surface as a plane wall jet before detaching at some point into a plane free jet. Notably, the air adjacent to the liquid surface generally is moving at nearly the same velocity as the liquid, which further reduces the potential for significant aerodynamic effects at the liquid surface, compared to the conditions illustrated in Fig. 1. The liquid flow along the surface then involves a relatively inconsequential laminar boundary layer, followed by a growing turbulent boundary layer. The onset of liquid surface roughness

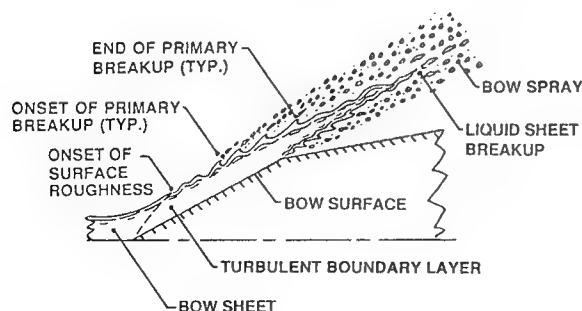


Fig. 2. Sketch of bow-sheet and bow-spray transitions.

is thought to correspond to conditions where the outer boundary of the turbulent boundary layer reaches the liquid surface, however, existing studies (1-3) have not yet quantified this condition in terms of boundary layer properties. Subsequently, primary breakup can begin along the surface of the turbulent liquid and can continue in the free jet region, ultimately causing the bow sheet to break up as a whole. Past work treating such turbulent primary breakup processes will be considered next.

The existence of turbulent primary breakup has been recognized for some time (1-3). Round turbulent liquid jets injected into still gases, or liquid free jets, generally have been used to study turbulent primary breakup. The early studies of DeJuhasz et al. (7) and Lee and Spencer (8,9) showed that liquid turbulence properties at the jet exit affected the atomization, breakup and mixing properties of liquid jets in still gases at NTP. Next, Grant and Middleman (10), Phinney (11) and McCarthy and Malloy (12) observed that jet stability and the onset of breakup were affected by turbulence at the jet exit as well. Finally, in a series of experiments involving coflowing and counterflowing gas/liquid round jets at NTP, Hoyt and Taylor (13-15) provided substantial evidence that aerodynamic effects did not have a large influence on turbulent primary breakup, as discussed in connection with Fig. 1.

Several recent studies of the properties of turbulent primary breakup were completed in this laboratory, based on observations of round liquid jets injected into still gases with fully-developed turbulent pipe flow at the jet exit (16-25). These studies involved pulsed shadowgraphy and holography to find the properties of turbulent primary breakup. The results showed that drop properties were related to the properties of the turbulence near the liquid surface and yielded correlations based on phenomenological theories for the onset and end of drop formation along the liquid surface, the evolution of drop size and velocity distributions with distance along the surface and the conditions required for breakup of the liquid column as a whole. It was also found

that aerodynamic effects did not influence the properties of turbulent primary breakup for liquid/gas density ratios greater than 500, providing a substantial data base confirming the negligible role of aerodynamic effects for water/air breakup processes at NTP discussed in connection with Fig. 1.

Although the earlier studies of round free turbulent jets have been helpful, a round free turbulent jet where the turbulence decays with increasing streamwise distance is fundamentally different from the attached portion of the turbulent bow sheet illustrated in Fig. 1 where the turbulence approximates a stationary wall jet (issues of round as opposed to plane geometry differences aside). Thus, the present investigation was undertaken to consider the properties of transitions for turbulent wall jets and to compare these findings with the earlier findings for turbulent free jets. The present measurements considered the onset conditions for a roughened liquid surface, the location of the onset of turbulent primary breakup along the surface, and the drop sizes produced at the onset of turbulent primary breakup. The experiments involved various liquids injected as wall jets into still air at NTP, with the flows observed using pulsed photography, shadowgraphy and holography. Phenomenological analysis was used to help correlate and interpret the measurements.

EXPERIMENTAL METHODS

Apparatus

The turbulent wall jet apparatus is illustrated in Fig. 3. The test liquid was placed within a test chamber that has a round, sharp-edged nozzle at its bottom. Combined with a rod passing down the axis of the test chamber and the nozzle, this configuration provided an initially nonturbulent annular wall jet flow along the rod. Premature liquid outflow was prevented by placing an annular cork in the nozzle exit. The liquid was then forced through the nozzle, ejecting the cork down the rod at the start of the flow, by admitting high-pressure air to the top of the test chamber through a solenoid-actuated

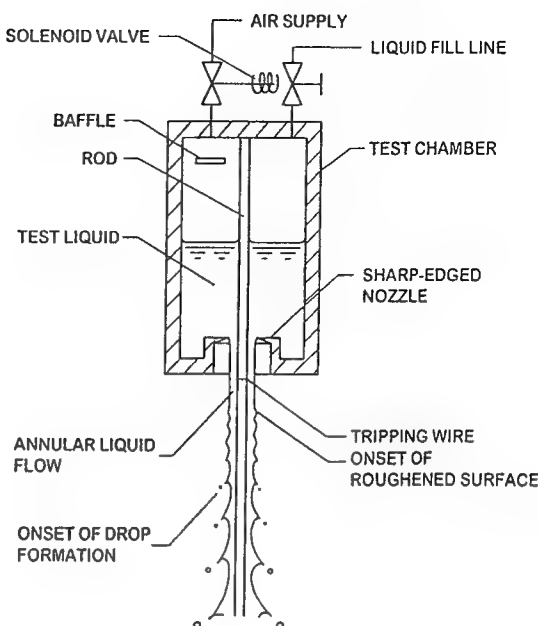


Fig. 3. Sketch of bow-sheet test apparatus.

valve. A baffle near the air inlet to the test chamber reduced mixing between the air and the test liquid. The solenoid was closed at the end of liquid delivery, allowing the test chamber to vent to the ambient pressure. The annular cork was then replaced in the nozzle exit so that the system could be resupplied with liquid through the liquid fill-vent line for the next test.

The high-pressure air was obtained from the laboratory air supply system (dew point < 240 K) and stored in an air accumulator at the upstream side of the solenoid valve. The air accumulator had a volume of 0.25 m^3 and provided air at pressures up to 1.3 MPa . The test chamber had an inside diameter of 50 mm and a length of 195 mm while the rod diameter was 6.4 mm . Two different nozzle diameters were used to provide annulus heights of 2.3 and 4.3 mm . Injection was vertically downward with the liquid captured in a baffled tub. Instrumentation was mounted rigidly; therefore, various positions in the flow were observed by moving the entire test chamber assembly using vertical and horizontal traversing systems.

Tripping wires were positioned near the exit of the nozzle in order to initiate growth of a turbulent boundary layer along the rod at a well-defined location. The tripping wires had diameters in the range 0.1-0.4 mm and were designed so that $k/b < 15\%$, and with the laminar boundary layer thickness at the location of the tripping wire less than 15% of the annulus thickness, in order to avoid separation of the annular flow from the rod due to the presence of the tripping wire. It was also necessary to provide large enough values of u^*k/v_f to insure that transition actually occurred at the tripping wire; this issue will be discussed in more detail later.

Total times of injection were 250-1250 ms. These relatively short times were not a problem, however, because flow development times were short for the present wall jets, roughly 10-80 ms. Additionally, measurements were made using pulsed photography, shadowgraphy and holography, which required times less than 100 μ s for triggering and data accumulation. Jet velocities were calibrated in terms of the test chamber pressure and liquid type using a short center rod (extending only to the underside of the test chamber) in conjunction with an impact plate.

Instrumentation

Instrumentation consisted of pulsed photography, shadowgraphy and holography, using arrangements and methods similar to (16-25). Pulsed direct photography was used for flow visualization based on a flashlamp (Xenon Corp. Micropulse, Model 457A) depositing 50 mJ in roughly 5 μ s. The flow was observed using roughly a 100×125 mm film format at a magnification of 1.1, focused at the median plane of the annular wall jet. These photographs were obtained with an opened camera shutter under darkroom conditions with the flash duration controlling the exposure time.

Pulsed shadowgraph photography was used to measure turbulent primary breakup properties near the onset of breakup as well as the streamwise location of the

onset of breakup. The holocamera was used for this purpose with the reference beam blocked to yield a shadowgraph rather than a hologram. The light source was a Spectra Physics GCR-130 pulsed YAG laser, depositing up to 200 mJ of optical energy in roughly 7 ns. This laser beam was expanded to a 46 mm diameter collimated beam for the purpose of flash photography. The shadowgraph image was obtained using the same camera system as the flash photography, with magnifications of 2.0 and 4.5. Data was found by observing the photographs using the same optical arrangement as the hologram construction system. The photographs were mounted on a computer controlled x-y traversing system (having 1 μ m resolution) and observed with an MTI Model 65 video camera with optics to provide fields of view of roughly 1.0×1.2 mm and 2.5×3.0 mm that could be traversed in the z direction (with 5 μ m resolution). The video image was analyzed using Image-Pro Plus software.

Drops and more-or-less ellipsoidal-shaped objects were sized from the shadowgraphs by measuring their maximum and minimum diameters through the centroid of the image. Then assuming that the liquid element was ellipsoidal, its diameter was taken to be the diameter of a sphere having the same volume. This approach is not adequate for elongated objects which were analyzed by measuring the perimeter and cross-sectional area of the image and then defining the size of the object as before, based on an ellipsoid having the same properties.

The holocamera was similar to past work (17-25) except that the YAG laser mentioned earlier was used instead of a ruby laser. An off-axis holographic arrangement was used. The optical penetration properties of the holocamera were improved for use in dense sprays by reducing the diameter of the object beam through the flow and subsequently expanding it (3:1) back to the same size as the reference beam (85 mm) when the two beams were optically mixed to form a hologram. The high power and short duration of the laser pulse allowed the motion

of even small drops to be stopped so that drops as small as $2\text{ }\mu\text{m}$ in diameter could be observed and drops as small as $5\text{ }\mu\text{m}$ in diameter could be measured. The holograms were reconstructed using a 15 mW HeNe laser with the laser beam collimated at a 60 mm diameter and passed through the hologram to provide a real image of the spray in front of the hologram. Analysis of the reconstructed images was the same as the shadowgraphs with x and y traversing of the hologram and z traversing of the video camera.

Experimental uncertainties (95% confidence) of the location of the onset of breakup were less than 30%, similar to past work (21-25), which is relatively large due to the angular variation of ligaments protruding from the surface, the randomness of drop separation from the tips of ligaments and the fact that only one measurement of onset location was made for each test which limited statistics. Measurements of drop properties consisted of the Sauter mean diameter (SMD) by summing over roughly 50 objects at each condition to obtain experimental uncertainties (95% confidence) less than 20%, mainly dominated by sampling limitations.

Test Conditions

Test liquids included water, ethyl alcohol and various glycerol mixtures (21, 42 and 63% glycerol), annulus widths of 2.3 and 4.3 mm, and mean annulus velocities of 15-38 m/s. These conditions yield ranges of experimental parameters, as follows: $\rho_f/\rho_g = 680-980$, $Re_D = 10,000-600,000$, $We_{fa} = 4,000-53,000$ and $Oh_D = 0.0008-0.0121$.

RESULTS AND DISCUSSION

Flow Visualization

Flash photographs of annular wall jet flow, with growth of a turbulent boundary layer initiated by a tripping wire, appear in Fig. 4. This experiment involved water flow with an annulus height of 2.3 mm and mean liquid velocity of 31.1 m/s. The tripping wire can be seen near the top of the left-most photograph, with progressively increasing

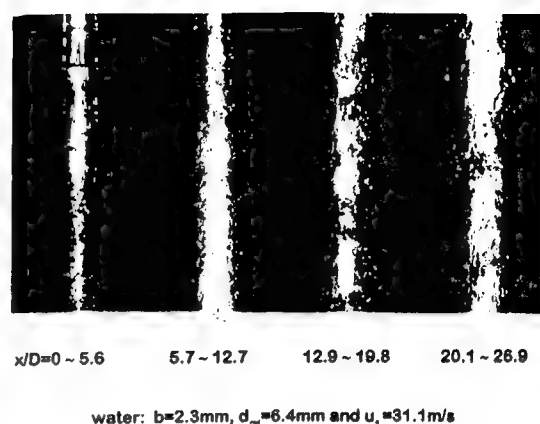


Fig. 4. Pulsed photographs of a bow-sheet of water.

distance from the tripping wire proceeding from top to bottom and left-to-right. The capability of the sharp-edged nozzle to generate a turbulence-free initial flow is evident from the smooth surface of the flow prior to reaching the tripping wire. For these conditions, the boundary layer along the wall is laminar prior to reaching the tripping wire as well, with growth of a turbulent boundary layer beginning along the wall at the location of the tripping wire.

Both transitions of interest during the present investigation — onset of a roughened liquid surface and onset of turbulent primary breakup — can be seen in the flash photographs of Fig. 4. The surface of the wall jet remains smooth for some distance past the tripping wire. Once surface roughness begins, both the degree of surface roughness and the size of surface roughness elements increase with increasing distance from the tripping wire. The roughness elements become surprisingly long as ligaments protruding from the samples, and eventually begin to form drops by breakup of these tips at the onset of turbulent primary breakup.

It is of interest to compare present visualizations of wall jets with earlier visualizations of round turbulent free jets (13-15,16-25). First of all, there is no counterpart to the onset of a roughened

surface seen in the present wall jets with a comparable transition in the turbulent free jets. In particular, turbulence penetrates very rapidly to the liquid surface after the exit of the turbulent free jet from the passage and the distance of this transition has not been resolved during previous work (16-25). The process leading to the onset of turbulent primary breakup, however, is rather similar for both flows: the scale of surface distortion and the length of ligaments protruding from the surface both progressively increase, until turbulent primary breakup begins by drop formation at the tips of the ligaments. These similarities will be exploited later to develop correlations for the properties of the onset of turbulent primary breakup for wall jets.

The qualitative behavior of the onset of a roughened liquid surface, the subsequent development of liquid surface distortions, and the properties of the onset of turbulent primary breakup, can be seen rather clearly from pulsed shadowgraph photographs — particularly for the glycerol mixtures. A typical example, for a 62% glycerol mixture with an annulus height of 2.3 mm and a mean liquid velocity of 17.3 m/s, appears in Fig. 5. In this case, the tripping wire was located slightly above the top of the left-most shadowgraph, with progressively increasing distance from the tripping wire proceeding from top-to-bottom and left-to-right. Similar to the wall jet illustrated in Fig. 4, the initial flow is nonturbulent and the wall boundary layer remains laminar up to the tripping wire, while a turbulent boundary layer begins to develop along the wall beginning at the location of the tripping wire.

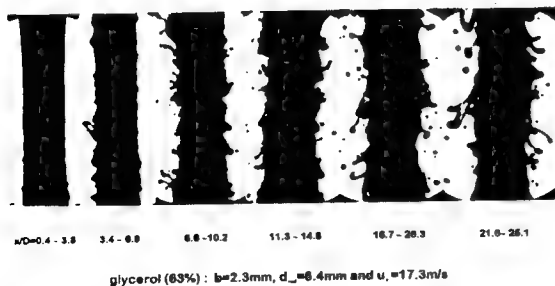


Fig. 5. Pulsed shadowgraphs of a bow-sheet of 63% glycerol.

Analogous to the discussion in connection with Fig. 2, the shadowgraphs of Fig. 5 show that the liquid surface remains smooth for a time as distance increases past the location of the tripping wire. The onset of surface roughness is finally observed, however, toward the bottom of the left-most shadowgraph. Subsequent increases of distance are accompanied by progressively increasing surface roughness and size of roughness elements. The ligaments projecting from the liquid surface become long with increasing distance as well, and eventually break up at their tips, causing the onset of turbulent primary breakup. Further increases of distance into the turbulent primary breakup region yields progressively increasing ligament diameters, ligament lengths, and drop sizes after primary breakup. Taken together, these trends are very similar to past observations of turbulent primary breakup in instances where aerodynamic effects are small (22-25).

Onset of a Roughened Surface

As discussed in connection with Fig. 2, the onset of surface roughness is thought to occur when the growing boundary layer along the surface attains a thickness comparable to the thickness of the wall jet. This hypothesis will be explored in the following, considering three cases: (1) untripped laminar boundary layer reaches the surface first, (2) untripped laminar boundary layer makes the transition to a turbulent boundary layer which subsequently reaches the surface, and (3) tripped turbulent boundary layer reaches the surface first. Boundary layer development within the wall layer will be simplified considerably for present analysis of this problem, as follows: effects of the free surface on boundary layer growth will be ignored; variation of wall jet mean velocity and thickness will be ignored because values of x/b are modest for both present test conditions and most practical bow sheets ($x/b < 100$); aerodynamic effects will be ignored as discussed earlier; the wall surface will be assumed to be smooth; and liquid properties will be assumed to be constant.

Consider the interaction between the laminar boundary layer and the surface first. Under the present assumptions, the well-known expression for the variation of the thickness of a laminar boundary layer developing along the wall is (4):

$$\delta/x = 5.0/Re_x^{1/2} \quad (1)$$

where x is the streamwise distance from the onset of boundary layer growth and δ represents the distance normal to the wall where the streamwise velocity reaches 99% of \bar{u}_0 . Then, the condition where the outer edge of the laminar boundary layer begins to interact with the surface of the wall jet (although whether this would lead to a roughened surface for a laminar boundary layer is debatable) is given by $b = C_r \delta$ at $x = x_r$, where C_r is an empirical constant. Then, introducing the hydraulic diameter of the wall jet for present experimental conditions:

$$D/b = 4(1 + b/d_{rod}) \quad (2)$$

the expression for x_r becomes:

$$x_r/D = (b/(5C_r D))^2 Re_D \quad (3)$$

This untripped laminar regime will continue until the boundary layer becomes turbulent before its outer edge reaches the surface, which will be defined in the following as the condition where $Re_{x_t} = 3.2 \times 10^5$, see (4).

Turbulent boundary layer growth must be considered when $Re_x > Re_{x_t}$. The following discussion of this regime is based on Schlichting (4) assuming a 1/7th power law velocity distribution, which is reasonable for the present Reynolds number range, and considering the same definition of boundary layer thickness, δ , as before. Then the expression for the streamwise distance where the turbulent boundary layer begins to interact with the surface becomes:

$$(x_r - x_t)/D = 3.46[(C_r b/D)^{5/4} - (\delta_t/D)^{5/4}] Re_D^{1/4} \quad (4)$$

where C_r is an empirical constant appropriate

for turbulent boundary layer conditions.

The third situation involves a tripped boundary layer at $x=0$ so that $x_t = \delta_t = 0$ in equation (4). As a result, the distance to onset of a roughened liquid surface for a tripped turbulent boundary layer becomes:

$$x_r/D = 3.46(C_r b/D)^{5/4} Re_D^{1/4} \quad (5)$$

where C_r is an empirical constant and b/D is given by equation (2).

Experimental evaluation of the ideas expressed by equations (1)-(5) proceeded in two stages, involving consideration of the variation of x_r with Re_D , and evaluation of the variation of x_r with tripping wire properties. The latter considerations showed that the onset of liquid surface roughness due to a turbulent boundary layer along the wall was not significantly affected by tripping wire properties as long as $u^*k/v_f > 50$ so that the disturbance due to the wire was sufficiently strong. Thus, effects of Re_D will be considered first for this strong tripping wire disturbance limit.

Present measurements of x_r are plotted as suggested by equation (5) in Fig. 6, considering results for various test liquids over the present range of test conditions. Results shown on the figure include the measurements using the tripped turbulent boundary layer expression of equation (5), and three so-called theoretical results based on equation (3) for an untripped turbulent boundary layer/surface interaction, on equation (4) for an untripped turbulent boundary layer/surface interaction, and on equation (5) for a the tripped turbulent boundary layer/surface interaction. For these "theoretical" results, the plane wall layer approximation has been made, i.e., $D/b = 4$ from equation (2), and $C_r = 1$; these selections are not critical because the results that follow are mainly for illustrative purposes.

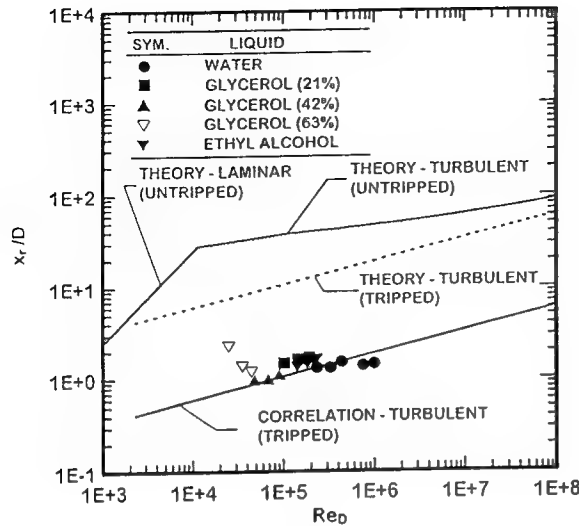


Fig. 6 Influence of Reynolds number on the onset of a roughened surface for bow sheets.

The untripped laminar and turbulent boundary layer predictions meet where $Re_x = Re_{xt}$. For the same criteria, the tripped turbulent boundary layer predictions yield generally smaller values of x_t/D than the untripped predictions, due to the faster mixing rates of the turbulent boundary layer. Except for low values of Re_D , where poorly developed turbulence in the boundary layer probably retards the appearance of a wrinkled liquid surface (24), a correlation based on tripped turbulent boundary layer predictions of equation (5) is seen to provide an excellent fit of the data, as follows:

$$x_t/D = 0.061 Re_D^{1/4}, Re_D > 30,000 \quad (6)$$

where the criterion $Re_D > 30,000$ for onset of effects associated with turbulent wall jets is very similar to the analogous criterion found by Wu et al. (24) for turbulent free jets. Based on equation (5), the coefficient obtained from the fit of equation (6) implies $C_t = 0.2$, which is a reasonable value in view of the present rather arbitrary, and conservative, estimate of boundary layer thickness.

The height of the tripping wire influenced the onset of a roughened liquid surface. This effect was correlated in terms

of a Reynolds number based on the wire diameter and the friction velocity, where (4):

$$u_k^* = (\tau_{wk} / \rho_f)^{1/2} \quad (7)$$

and

$$\tau_{wk} / (\rho_f \bar{u}_o^2) = 0.332 / Re_{xk}^{1/2} \quad (8)$$

where x_k denotes the streamwise position of the tripping wire measured from the nozzle.

Present measurements of the effect of tripping wire Reynolds number on x_t are plotted in Fig. 7. The coordinates of this plot have been selected based on equation (6), where $x_t/(D Re_D^{1/4})$ should be a constant based on the growth of a tripped turbulent boundary layer developing along the wall of the turbulent wall jet; this correlation from equation (6) also is illustrated on the figure.

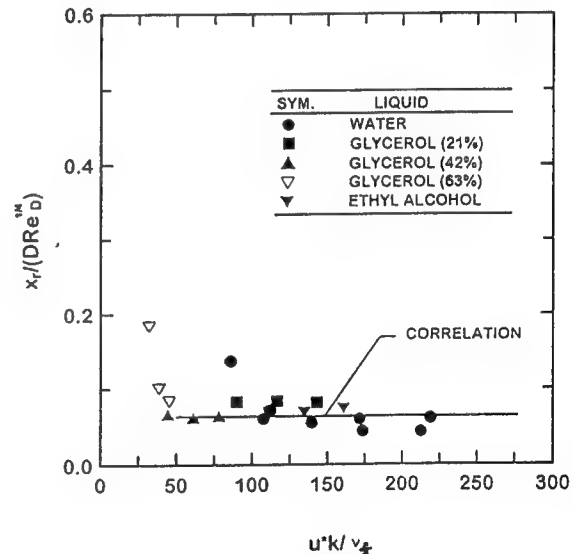


Fig. 7. Influence of tripping wire properties on the onset of a roughened surface for bow sheets.

Aside from a possible outlier for a water wall jet at the lowest tripping wire Reynolds number considered for this liquid, the results show little effect of tripping wire properties for $u_k^* k / \nu_f > 50$. Below these limits, x_t progressively increases with decreasing

$u_k^* k/v_f$. This behavior follows because the tripping wire disturbance is too weak to initiate a fully turbulent wall boundary layer for these conditions. In this weak tripping wire regime, behavior tends toward delayed onset of a roughened liquid surface, analogous to the differences between the untripped and tripped "theoretical" estimates of x/D illustrated in Fig. 6.

Onset of Primary Breakup

Approximate analysis to find properties at the onset of turbulent primary breakup was carried out for the turbulent wall jets, using methods analogous to earlier considerations of properties at the onset of turbulent primary breakup for round free turbulent jets (22). This analysis is based on the flow configuration illustrated in Fig. 8. The process involves the formation of a drop from a turbulent eddy having a characteristic size, ℓ , and a characteristic cross-stream velocity relative to the surrounding liquid of v_ℓ . The eddy, is shown with a somewhat elongated shape because length scales in the streamwise direction are generally larger than in the cross-stream direction for typical jet-like flows, e.g., values of the ellipticity, e_p , up to roughly 2 have been observed for turbulent primary breakup of round free turbulent jets (22). Onset of turbulent primary breakup occurs after the onset of a

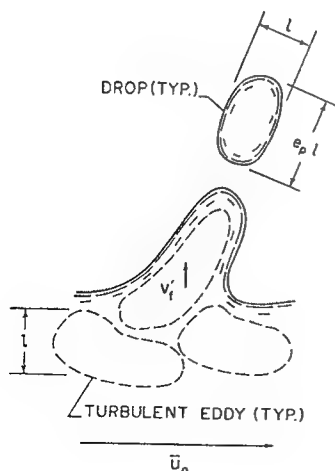


Fig. 8. Sketch of turbulent primary breakup at the liquid surface.

wrinkled liquid surface. This suggested that the wall jet is reasonably turbulent at the onset of turbulent primary breakup so that the turbulence properties of the wall jet can be taken to be the same as a fully-developed turbulent pipe flow for the same hydraulic diameter Re_D (5,6). Other assumptions were the same as analysis of the onset of a wrinkled liquid surface: values of the mean velocity and the thickness of the wall jet were assumed to be constant at \bar{u}_0 and b , other physical properties were assumed to be constant, and aerodynamic effects were assumed to be small. Thus, the eddy was assumed to convect in the streamwise direction at the local mean velocity, u_0 , while the drop formed by the eddy was assumed to have a diameter comparable to ℓ .

Based on both shadowgraph observations and time scale considerations, the drops at the onset of turbulent primary breakup are the smallest drops that can be formed by this mechanism. For turbulence, however, the the smallest drops that can be formed are either comparable to the smallest scale of the turbulence, the Kolmogorov microscale, or to the smallest eddy that has sufficient kinetic energy relative to its immediate surroundings to provide the surface energy needed to form a drop, whichever is larger. For fully-developed turbulent pipe flow, the Kolmogorov length scale can be estimated as follows (26):

$$\ell_K = 4\Lambda/(4\Lambda \bar{u}_0'/v_f)^{3/4} \quad (9)$$

where the streamwise integral length scale has been taken to be equal to 4Λ based on Laufer's measurements for fully-developed turbulent pipe flow (6). For present conditions, values of ℓ_K are less than $10 \mu\text{m}$, which is much smaller than the smallest drop size observed experimentally at the onset of turbulent primary breakup for the present conditions; therefore, only energy requirements will be considered to find drop properties at the onset of turbulent primary breakup in the following.

The energy criterion for the smallest drop that can be formed is found by equating the kinetic energy of an eddy of characteristic

size ℓ_i , relative to its surroundings, to the surface energy required to form a drop, as follows:

$$\pi \rho_f \ell_i^3 v_{\ell_i}^2 \sim \pi \ell_i^2 \sigma \quad (10)$$

where only crude proportionality is implied, due to effects of ellipticity, nonuniform velocities within the eddy and the efficiency of the conversion of kinetic energy into surface energy. The largest eddy length scales are comparable to Λ while $\ell_k < \ell_i$ as just discussed. Then it is reasonable to assume that ℓ_i is within the inertial range of the turbulence spectrum, where ℓ_i and v_{ℓ_i} are related as follows (26):

$$v_{\ell_i} \sim \bar{v}_o' (\ell_i/\Lambda)^{1/3} \quad (11)$$

while variations of turbulence properties within the liquid have been ignored, similar to earlier considerations of turbulent primary breakup for round turbulent free jets (22). Combining equations (10) and (11), setting $SMD_i \sim \ell_i$ and assuming that turbulence properties within the liquid can be approximated by the properties of fully-developed turbulent pipe flow for a velocity, diameter and Reynolds number of u_o , D and Re_D , the expression for SMD_i becomes:

$$SMD_i/\Lambda = C_{si} (\bar{u}_o/\bar{v}_o')^{6/5} We_{f\Lambda}^{-3/5} \quad (12)$$

where C_{si} is an empirical constant involving the various proportionality constants. For fully-developed turbulent pipe flow, \bar{v}_o'/\bar{u}_o is a constant (5,6); therefore, SMD_i/Λ should only be a function of $We_{f\Lambda}$ for present test conditions. Finally, analogous to the earlier studies of turbulent primary breakup for round turbulent free jets (22,23), the radial integral length scale was taken to be $D/8$, based on the measurements of Laufer for fully-developed turbulent pipe flow (6).

The present measurements for SMD_i for turbulent wall jets are plotted in terms of the variables of equation (12) in Fig. 9, along with the earlier correlation found by Wu et al. (22) for round turbulent free jets. The

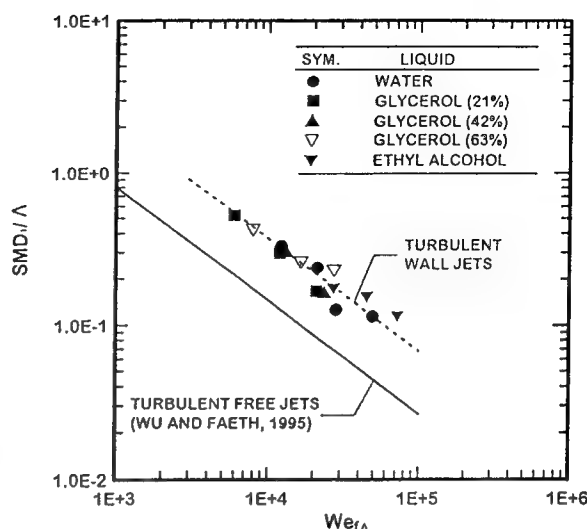


Fig. 9. SMD at the onset of turbulent primary breakup as a function of bow sheet Weber number.

correlation of the present measurements in these coordinates is similar to the earlier free jet result and is well within the scatter anticipated based on experimental uncertainties. The power of $We_{f\Lambda}$ for the correlation of present measurements is not $-3/5$, as suggested by equation (12); instead, the power was not statistically different from the earlier round jet results. Thus, the present correlation of SMD_i for the turbulent wall jets adopts the same power as the round turbulent free jets, yielding the following empirical fit that is shown on the plot:

$$SMD_i/\Lambda = 340 We_{f\Lambda}^{-0.74} \quad (13)$$

The standard deviations of the coefficient and power of equation (13) are 10 and 8%, respectively, while the correlation coefficient of the fit is 0.96; these parameters are similar to the round jet results (22). The reduction of the power from $-3/5$ in equation (12) to -0.74 in equation (13) is statistically significant but is not large in view of the crude approximations of the present phenomenological analysis. The coefficient of equation (13) is relatively large but this can be anticipated from equation (12) because $(\bar{u}_o/\bar{v}_o')^{6/5}$ is relatively large; thus, C_{si} is of order unity as anticipated for an empirical

parameter of this type. The present correlation for turbulent wall jets gives values of SMD_i that are somewhat larger than the earlier results for turbulent free jets at the same value of $We_{f\Lambda}$, e.g., the constants on the right-hand sides (RHS) of the two correlations are 340 and 133, respectively. This difference is not large in view of the crudeness of the present analysis. In particular, differences of this magnitude might be anticipated when concepts of hydraulic diameter are used to estimate the integral scales of turbulence and to compare findings for turbulent round free jets and wall jets.

Similar to past studies of turbulent round free jets (22,23), it is assumed that the eddy initially forming drops at the onset of turbulent primary breakup convects along the liquid surface with a streamwise velocity u_0 for the time τ_i required for an eddy having characteristic size ℓ_i to form a drop. There are several characteristic breakup times that can be used to estimate τ_i , discussed by Wu and coworkers (22,23); based on these considerations, the Rayleigh breakup time was chosen for the present analysis. Thus ignoring effects of liquid viscosity on the Rayleigh breakup time, discussed by Weber (27), the expression for τ_i becomes (22):

$$\tau_i \sim (\rho_f \ell_i^3 / \sigma)^{1/2} \quad (14)$$

which is independent of $v_{\ell i}$. The distance required for the onset of turbulent primary breakup is then obtained relative to the first appearance of significant effects of turbulence at the liquid surface, as follows:

$$x_i - x_r \sim \bar{u}_0 \tau_i \quad (15)$$

An expression for $x_i - x_r$ is subsequently found by substituting equation (14) into equation (15) and letting $SMD_i \sim \ell_i$, as before:

$$(x_i - x_r) / \Lambda \sim (SMD_i / \Lambda)^{3/2} We_{f\Lambda}^{1/2} \quad (16)$$

Finally, eliminating SMD_i from equation (16), using equation (12), yields the following expression for the location of the onset of turbulent primary breakup for wall

jets:

$$(x_i - x_r) / \Lambda = C_{xi} (\bar{u}_0 / \bar{v}_0')^{9/5} We_{f\Lambda}^{-0.4} \quad (17)$$

where C_{xi} is a constant of proportionality and \bar{v}_0' / \bar{u}_0 is a constant for a fully-developed turbulent wall jets.

Present measurements of $x_i - x_r$ are plotted in terms of the variables of equation (17) in Fig. 10, along with the earlier correlation for x_i / Λ found by Wu et al. (22)

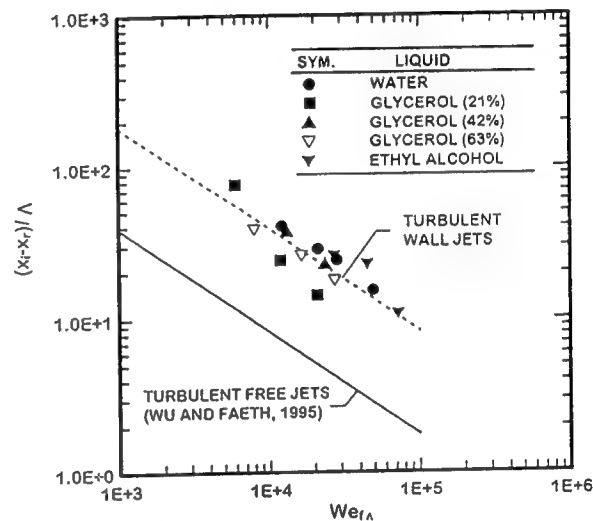


Fig. 10. Length to initiate turbulent primary breakup as a function of bow sheet Weber number.

for round turbulent free jets. The correlation of the present measurements in these coordinates is similar to the earlier free jet results and is well within the scatter anticipated based on experimental uncertainties. As before, however, the power of $We_{f\Lambda}$ for the present data correlation is not -0.4, as suggested by equation (17), but can be represented better by the following empirical fit that is shown on the plot:

$$(x_i - x_r) / \Lambda = 18800 We_{f\Lambda}^{-0.67} \quad (18)$$

where the present power of $We_{f\Lambda}$ was not statistically different from the findings for round turbulent free jets and has been taken to be the same to simplify comparisons

between turbulent round free and wall jet results. The standard deviations of the coefficient and power of equation (18) are 12 and 14%, respectively, and the correlation coefficient of the fit is 0.92. The large value of the coefficient on the RHS of equation (18) can be anticipated from equation (12) because $(\bar{u}_0/\bar{v}_0')^{9/5}$ is quite large for typical turbulent pipe or channel flow. The correlation for the turbulent wall jets is above the correlation for the round turbulent free jets, which is consistent with the relative positions of the SMD_i for these two flows seen in Fig. 9, and the fact that larger distances to the onset of breakup are required when drop sizes at the onset of breakup becomes large. Finally, the differences between the constants on the RHS of correlations for turbulent wall jets and for round turbulent free jets, 18,800 and 3980, respectively, are reasonable in view of the limitations of estimates of scales from hydraulic diameters, as discussed earlier.

CONCLUSIONS

Properties of transitions for the onset of roughened liquid surfaces and turbulent primary breakup for turbulent bow sheets were studied for liquid wall jets in still air at normal temperature and pressure. Experimental conditions involved water, ethyl alcohol and various glycerol mixtures as test liquids, with $\rho_f/\rho_g = 680-980$, $Re_{mD} = 10,000-600,000$, $We_{tA} = 4,000-53,000$ and $Oh_D = 0.008-0.0121$. The major conclusions of the study are as follows:

1. Roughness of the liquid surface, and primary breakup into drops along the liquid surface were caused by turbulence due to liquid motion past the wall surface, while direct effects of aerodynamic forces at the liquid surface were small, for present conditions
2. Transition to a roughened liquid surface occurred when the developing turbulent boundary layer along the wall surface reached a thickness that was comparable to the thickness of the wall jet itself. For present conditions, where turbulent boundary layer growth was initiated by a

trip wire, distances to the onset of a roughened liquid surface could be correlated based on a turbulent boundary layer thickness expression, see equation (6).

3. Drop sizes at the onset of turbulent primary breakup along the liquid surface could be correlated by equating the surface energy required to form a drop to the kinetic energy of an eddy of corresponding size within the inertial region of the turbulence spectrum, see equation (13). This finding highlights the close correspondence between liquid turbulence properties and turbulent primary breakup properties for turbulent wall jets in still gases, yielding behavior that is similar to turbulent primary breakup of round turbulent free jets in still gases (19,20).
4. The onset of turbulent primary breakup occurs at some distance from the point of onset of liquid surface roughness, but tends to approach this position at We_{tA} increases. The distance required for the onset of turbulent primary breakup along the surface could be correlated by considering the distance convected at the mean velocity of the wall jet for the residence time needed to initiate the Rayleigh breakup of ligaments protruding from the liquid surface that are associated with onset-sized drops, see equation (18).

Present results are limited to moderate Ohnesorge number conditions, where the SMD at the onset of turbulent primary breakup corresponds to eddy sizes in the inertial range of the turbulence, and where the relative velocities between the liquid and gas are comparable to the relative velocities between the liquid and the wall surface. Consideration of the Rayleigh breakup of ligaments protruding from the liquid surface, and past findings for round turbulent free jets (18-22), suggest potential effects of liquid viscosity at larger Ohnesorge numbers, difficulties with the present description of turbulent primary breakup as the limits of the inertial turbulent subrange are approached,

and potential aerodynamic effects due to enhancement of ligament motion and merging of turbulent primary and secondary breakup when $\rho_l/\rho_g < 500$. Until these effects are better understood, the correlations reported here should not be used outside the present test range. In addition, the streamwise evolution of drop sizes and velocities produced by turbulent primary breakup, and the rate of liquid removal from the wall jet due to turbulent primary breakup, are issues that merit attention in the future.

ACKNOWLEDGMENTS

This research was sponsored by the Office of Naval Research Grant No. N00014-95-1-0234 under the technical management of E. P. Rood. Initial development of research facilities for this study was carried out under Air Force Office of Scientific Research Grant Nos. AFOSR F49620-92-J-0399 and F49620-95-1-0364 under the technical management of J. M. Tishkoff.

REFERENCES

1. Gad-el-Hak, M., "Measurements of Turbulence and Wave Statistics in Wind-Waves," *International Symposium on Hydrodynamics in Ocean Engineering*, The Norwegian Institute of Technology, Oslo, Norway, 1981, pp. 403-417.
2. Townson, J.M., *Free-Surface Hydraulics*, 1st ed., Unwin Hyman, London, 1988, Chapt. 6.
3. Irvine, D.A., and Falvey, H.T., "Behavior of Turbulent Water Jets in the Atmosphere and in Plunge Pools," *Proc. Inst. Civ. Eng.*, Pt. 2, Vol. 83, Mar. 1987, pp. 295-314.
4. Smith, R.M., and Wang, C.-T., "Contracting Cones Giving Uniform Throat Speeds," *Journal of Aeronautical Sciences*, Vol. 11, 1944, pp. 356-360.
5. Schlichting, H., *Boundary Layer Theory*, 7th ed., McGraw-Hill, New York, 1979, p. 599.
6. Hinze, J.O., *Turbulence*, 2nd ed., McGraw-Hill, New York, 1975, p. 427 and pp. 724-742.
7. De Juhasz, K.J., Zahm, O.F., Jr., and Schweitzer, P.H., "On the Formation and Dispersion of Oil Sprays," Bulletin No. 40, Engineering Experiment Station, Pennsylvania State University, University Park, PA, 1932, pp. 63-68.
8. Lee, D.W., and Spencer, R.C., "Preliminary Photomicrographic Studies of Fuel Sprays," NACA Technical Note 424, Washington, D.C., 1933.
9. Lee, D.W., and Spencer, R.C., "Photomicrographic Studies of Fuel Sprays," NACA Tech. Note 454, Washington, D.C., 1933.
10. Grant, R.P., and Middleman, S., "Newtonian Jet Stability," *AIChE Journal*, Vol. 12, No. 4, 1966, pp. 669-678.
11. Phinney, R.E., "The Breakup of a Turbulent Jet in a Gaseous Atmosphere," *Journal of Fluid Mechanics*, Vol. 60, Pt. 4, 1973, pp. 689-701.
12. McCarthy, M.J., and Malloy, N.A., "Review of Stability of Liquid Jets and the Influence of Nozzle Design," *Chemical Engineering Journal*, Vol. 7, No. 1, 1974, pp. 1-20.
13. Hoyt, J.W., and Taylor, J.J., "Waves on Water Jets," *Journal of Fluid Mechanics*, Vol. 88, Pt. 1, 1977, pp. 119-123.
14. Hoyt, J.W., and Taylor, J.J., "Turbulence Structure in a Water Jet Discharging in Air," *Physics of Fluids*, Vol. 20, Pt. II, No. 10, 1977, pp. S253-S257.
15. Hoyt, J.W., and Taylor, J.J., "Effect of Nozzle Boundary Layer on Water Jets Discharging in Air," *Jets and Cavities* (J.H. Kim, O. Furuya and B.R. Parkin, ed.) ASME-FED, Vol. 31, American Society of Mechanical Engineers, New York, 1985, pp. 93-100.

16. Ruff, G.A., Sagar, A.D., and Faeth, G.M., "Structure of the Near-Injector Region of Pressure-Atomized Sprays," AIAA Journal, Vol. 27, No. 7, 1989, pp. 901-908.
17. Ruff, G.A., Bernal, L.P., and Faeth, G.M., "Structure of the Near-Injector Region of Non-Evaporating Pressure-Atomized Sprays," Journal of Propulsion and Power, Vol. 7, No. 2, 1991, pp. 221-230.
18. Ruff, G.A., Wu, P.-K., Bernal, L. P., and Faeth, G.M., "Continuous- and Dispersed-Phase Structure of Dense Non-Evaporating Pressure-Atomized Sprays," Journal of Propulsion and Power, Vol. 8, No. 2, 1992, pp. 280-289.
19. Tseng, L.-K., Ruff, G.A., and Faeth, G.M., "Effects of Gas Density on the Structure of Liquid Jets in Still Gases," AIAA Journal, Vol. 30, No. 6, 1992, pp. 1537-1544.
20. Tseng, L.-K., Wu, P.-K., and Faeth, G.M., "Dispersed-Phase Structure of Pressure-Atomized Sprays at Various Gas Densities," Journal of Propulsion and Power, Vol. 8, No. 6, 1992, pp. 1157-1166.
21. Wu, P.-K., Ruff, G.A., and Faeth, G.M., "Primary Breakup in Liquid/Gas Mixing Layers for Turbulent Liquids," Atomization and Sprays, Vol. 1, No. 4, 1991, pp. 421-440.
22. Wu, P.-K., Tseng, L.-K., and Faeth, G.M., "Primary Breakup in Gas/Liquid Mixing Layers for Turbulent Liquids," Atomization and Sprays, Vol. 2, No. 3, 1992, pp. 295-317.
23. Wu, P.-K., and Faeth, G.M., "Aerodynamic Effects in Primary Breakup of Turbulent Liquids," Atomization and Sprays, Vol. 3, No. 3, 1993, pp. 265-289.
24. Wu, P.-K., Miranda, R.F., and Faeth, G.M., "Effects of Initial Flow Conditions on Primary Breakup of Nonturbulent and Turbulent Round Liquid Jets," Atomization and Sprays, Vol. 5, No. 2, 1995, pp. 175-196.
25. Wu, P.-K., and Faeth, G.M., "Onset and End of Drop Formation Along the Surface of Turbulent Liquid Jets in Still Gases," Physics of Fluids A, Vol. 7, No. 11, 1995, pp. 2915-2917.
26. Tennekes, H., and Lumley, J.L., *A First Course in Turbulence*, MIT Press, Cambridge, MA, 1972, pp. 248-286.
27. Weber, C., "Zum Zerfall eines Flüssigkeitsstrahles," Z. Angewesen. Math. Mech., Vol. 2, 1931, pp. 136-141.

DISCUSSION

D. Liepmann

University of California at Berkeley, USA

1. The results shown in Figure 9 and 10 and discussed in the text of the article indicate that both spray generation and initiation length for both turbulent free jets and turbulent wall jets have the same dependence on the Weber Number with just the constant of proportionality differing between the two cases. What is the physical significance of this? Does this imply that in your experiments the presence of a boundary layer has little fundamental effect on the spray dynamics?

2. In the analysis linking turbulent eddy size to droplet generation, an implicit assumption was made that the flow is homogeneous and isotropic. In our experiments at Berkeley (at much lower Reynolds numbers) we find that the droplet size is strongly influenced by instabilities that develop due to the flow geometry. In your paper there is some indication that "the roughness elements become surprisingly long as ligaments protruding from the samples." Do you see any indication of this comparing droplet sizes from experiments with different sizes or locations of trip wires or, possibly, between the two geometries?

3. In the paper empirical models are presented for droplet generation at extremely high Reynolds Number, which are reasonable for full scale ships. What do the authors think are the next steps needed to (a) understand the fundamental physics of the flow and (b) provide input to numerical simulations or numerical design tools?

AUTHORS' REPLY

Our replies are numbered to correspond to Professor Liepmann's discussion:

1. The presence of a developing turbulent boundary layer along the surface of the wall jets is fundamentally important because the surface only becomes roughened (which is a prerequisite for turbulent primary breakup) when the outer edge of this boundary layer reaches the surface. Beyond this, however, properties at the onset of turbulent primary drop breakup are similar for both free and wall jets because they only depend on properties of turbulence spectra that are the same for both flows. Greater differences between the two flows are possible for the variation of drop properties after turbulent primary drop breakup as a function of

distance along the surface but this remains to be seen.

2. The only assumptions made about the properties of the turbulence were that breakup was caused by eddies in the inertial range of the spectrum and that eddy sizes and velocities are related by equation (11); this does not entail an implicit assumption of homogeneous and isotropic turbulence. Without considering the details of Professor Liepmann's experiments, it is difficult to comment about his observations of drops sizes after primary breakup except to note that smaller inertial ranges of the turbulence spectrum at low Reynolds numbers would make large-scale features more important and that initial disturbances of wall jets can dominate the turbulent wall boundary layer phenomena emphasized during the present paper for some experimental configurations. Finally, effects of trip wire and flow properties on drop sizes for the present experiments were explained reasonably well by the phenomenological theories discussed here.

3. There are a number of issues that should be better understood in order to provide the technology base needed to address these flows, including the evolution of drop size/velocity distributions and the rate of production of dispersed liquid due to turbulent primary breakup as a function of distance along the surface. The mean and turbulent structure of the liquid wall jet, the drag and ligament properties at the gas/liquid interface and the structure of the dispersed multiphase flow region adjacent to the liquid wall jet, among others.

Numerical Simulation of Three-Dimensional Breaking Waves About Ships

A. Kanai, T. Kawamura, H. Miyata (University of Tokyo, Japan)

Abstract

Two types of numerical methods are developed for the simulation of three-dimensional breaking waves. One is a finite-difference-method approach (TUMMAC-VIII) for solving the incompressible Navier-Stokes equation employing orthogonal staggered grid system which is not fitted to the body surface. Body boundaries are treated by a porosity technique. The other is a finite-volume-method approach (WISDAM-VI) with the body-fitted curvilinear coordinate system to cope with viscous flows on the body boundary. Both methods employ density-function method for implementing free surface boundary conditions.

The finite-difference method can deal with arbitrary complicated bodies due to its simplicity of the grid system. Using this method simulations of bow waves around a wedge model and a simple parabolic-waterline model WM2 are conducted and the three-dimensional breaking wave is successfully simulated. Also the numerical results clarify the detail structure of the Free Surface Shock Wave (FSSW) generated around the bow and show good agreement with experiments.

The viscous effects are very important for the stern flow around a ship. The WISDAM-VI method is developed to simulate bow wave breaking and viscous stern flow simultaneously. Two cases of simulations are carried out for flows around a bulk carrier model and a tanker model. The computed wave patterns show good agreement with experiments, and it is noted that the loss due to wave-breaking is distributed near the free surface and that it effects on the formation of the wake.

INTRODUCTION

Wave breaking is one of the most nonlinear phenomena in fluid dynamics. It gives various significant influences on fluid flows and obstacles in many hydrodynamical problems. In the ship wave problem waves generated by an advancing ship are usu-

ally very steep ones called free surface shock wave (FSSW)[1][2][3], which gives great contribution to ship resistance. Hence the clarification of the breaking wave phenomenon is of essential importance for the progress in both marine structural dynamics and ship hydrodynamics represented by hull form design.

Some numerical simulations for the strongly nonlinear waves have been carried out by many researchers. In two-dimensional cases the boundary element method of irrotational free surface flows following the work by Longuet-Higgins & Cokelet (1976)[4] can explain the plunging wave breaker. However, it has difficulty in the explanation of wave motion after the stage of overturning which is only the beginning of the nonlinear behaviour of wave breaking. The finite-difference approach with the VOF method by Hirt & Nichols (1981)[5] and Ng & Kot (1992)[6] can be applicable to the bore or two-layer flows. Another finite-difference method by Miyata (1986)[7] and Miyata & Lee (1990)[8] have succeeded in the simulation of breaking waves including the impinging and the vortex generation processes. Since all above methods seem to be incapable of treating three-dimensional wave-breaking motions. A 3D finite-difference method for breaking is developed by Miyata et al. (1988)[9]. It employs the density-function method to cope with two-layer flows involving strongly interacting interface. The technique is very useful not only for the treatment of wave breaking but also for various engineering problems concerning interface of multi-phase or multi-layer flows. Some similar methods using the concept of the density-function method have been developed recently by Xiao & Yabe (1993)[10] and Brackbill, Kothe & Zemach (1992)[11].

In this paper two types of approach for 3D wave-breaking simulations are shown. One is the finite-difference method called TUMMAC-VIII[12] in the framework of a rectangular coordinate system that enables us to express complicated geometries without elaborate efforts of grid generation. And the other is the finite-volume method, WISDAM-

VI[13], employing a boundary-fitted curvilinear coordinate system that is advantageous for resolving viscous flows near body boundaries. Both methods use the density-function method to implement the nonlinear kinematic free surface condition. Some applications of those methods to ship wave problems are explained.

NUMERICAL METHOD

Finite-difference Method

The modified marker-and-cell method called TUMMAC-VIII[12] is constructed by combining the free surface treatment of the TUMMAC-VI[9] method for a two-layer flow and the no-slip body boundary treatment and the porosity expression for geometries of the TUMMAC-VII method[14]. A rectangular grid system with variable spacing is employed and the velocity and pressure points are defined in a staggered manner.

The governing equations for the two-layer flow are the following incompressible Navier-Stokes equations and the continuity equation.

$$\frac{\partial \mathbf{u}}{\partial t} + (\mathbf{u} \cdot \nabla) \mathbf{u} = -\frac{1}{\rho^{(1)}} \nabla p + \mathbf{a}^{(1)} \quad (1a)$$

$$\frac{\partial \mathbf{u}}{\partial t} + (\mathbf{u} \cdot \nabla) \mathbf{u} = -\frac{1}{\rho^{(2)}} \nabla p + \mathbf{a}^{(2)} \quad (1b)$$

$$\nabla \cdot \mathbf{u} = 0 \quad (2)$$

where,

$$\mathbf{a} = \nu \nabla^2 \mathbf{u} + \mathbf{f} \quad (3)$$

Here, the subscripts (1) and (2) denote the fluids below and above the interface respectively. In the present study (1) corresponds to the water region and (2) the air region. \mathbf{u} is the velocity, p is the pressure, t is the time, ν is the kinematic viscosity and \mathbf{f} is the external force including the gravitational acceleration. The surface tension is ignored here since its effect can be considered to be very small in the problems described in this paper.

The above equations for each layer are quite separately solved at each time step of time-marching following the MAC-type algorithm. Firstly the pressure field in the air region is obtained by solving the Poisson equation and secondly in the water region. The Richardson's method is used for the solution of the Poisson equation. The configuration of the interface is determined by the free surface condition described in the subsequent section.

For the time derivative of velocity forward differencing is used and second-order centered differencing is for the space derivatives excluding the convective terms for which third-order upwind differencing is used.

Finite-volume method

The WISDAM-VI method employs the coordinate system that is fitted to the body boundary but not to the free surface, so that the boundary layer around the body of arbitrary form and large free-surface deformation is simultaneously simulated. Since the numerical schemes of the WISDAM-VI method are based on the WISDAM-V method[15] except for the free-surface treatment, the computational method is briefly explained here.

The governing equations are the Navier-Stokes equation and the continuity equation in conservative form.

$$\frac{\partial \mathbf{u}}{\partial t} + \text{div} \{ \phi \mathbf{I} + \mathbf{T} \} = 0 \quad (4)$$

where,

$$\mathbf{T} = \mathbf{u}\mathbf{u} - \frac{1}{Re} \{ \text{grad } \mathbf{u} + (\text{grad } \mathbf{u})^T \} \quad (5)$$

Here \mathbf{I} and Re is the unit matrix and Reynolds number respectively and ϕ is the normalized pressure without hydrostatic component defined as

$$\phi = p + \frac{x^3}{Fn^2} \quad (6)$$

where Fn is the Froude number. The continuity equation for incompressible fluid is written as

$$\text{div } \mathbf{u} = 0. \quad (7)$$

Third order upwind-biased flux interpolation scheme for the convective term and second-order central interpolation scheme for the other terms is used for the finite-volume discretization of Eq.(4) and Eq.(7).

Since the MAC type solution algorithm is employed, the pressure term is separated from the other terms and thus, the velocity field of the (n+1) time level is written as

$$\mathbf{u}^{n+1} = \mathbf{u}^n + \Delta t \cdot \text{div } \mathbf{T} - \Delta t \cdot \nabla \phi, \quad (8)$$

where, the superscript n denotes the time level. Taking the divergence of Eq.(8), following Poisson equation for ϕ is obtained.

$$\nabla^2 \phi^{n+1} = \frac{\nabla \cdot \{ \mathbf{u}^n + \Delta t \cdot (\text{div } \mathbf{T}) \}}{\Delta t} \quad (9)$$

Eq.(9) is solved iteratively by use of the SOR method.

FREE SURFACE CONDITION

Density-function method

The density-function method is employed for the fulfilment of the kinematic free surface condition. The density-function plays the role of conserving mass and the determination of the interface location. Assuming that both viscous stresses and the surface tension on the free surface can be ignored, the dynamic free surface condition becomes the condition of pressure continuity between the two layers. Then the kinematic and dynamic free surface conditions are approximately implemented by the following equations.

$$\frac{\partial M}{\partial t} + u \frac{\partial M}{\partial x} + v \frac{\partial M}{\partial y} + w \frac{\partial M}{\partial z} = 0 \quad (10)$$

$$p^{(1)} = p^{(2)} \quad (11)$$

Here, M is the density-function, u, v, w are the velocity components in the x, y, z directions which represent the longitudinal, lateral and vertical coordinates, respectively, and $p^{(1)}$ and $p^{(2)}$ are the pressures of the water and air on the interface. For the time differencing in Eq.(10) the Adams-Bashforth method is used and the third-order MUSCL-type upwind scheme for the space differencing. Eqs.(1a) and (1b) are solved with constant value of density-for respective fluid and the location of interface is defined to be the surface on which the value of the density-function takes the value of $(M^{(1)} + M^{(2)})/2$, where $M^{(1)}$ and $M^{(2)}$ are the density-function values initially set for the water and air regions, respectively. Due to the inherent numerical diffusion in the solution of Eq.(10) the sharpness of interface can be lost as calculation proceeds. However, it is demonstrated in the subsequent section that the degree of accuracy can be raised to a sufficient level in case a higher-order differencing scheme such as third-order upwind scheme used here is employed in a fine grid system.

After determining the interface location the dynamic free surface condition is implemented by the so-called "irregular star" technique[16] in the solution process of the Poisson equation. The length of leg in the irregular star technique is calculated using the density-function. The pressure on the interface is determined by extrapolating the pressure in the air region, in which the pressure is extrapolated with zero gradient in the horizontal direction while in the vertical direction the pressure difference due to the gravitation is considered. Since the velocity must be continuous between the two layers, the extrapolation of velocity from the water region to the

air region is conducted by approximately satisfying zero normal gradient to the interface.

Accuracy examination

As described in the previous section the numerical diffusion takes place in the computation of the free-surface location and this should be solved to keep sufficient degree of accuracy. For the numerical test, regular periodic waves of finite-amplitude based on the linear theory is generated by the finite-difference method with density-function method and the accuracy of the generated waves is compared with the records of physically generated waves by a flap-type wave generator[17].

For the space derivative terms of the Eq.(10), a variety of schemes are tested. Three of them are represented as follows only for the first term for simplicity.

(1) 1st-order upwind differencing

$$u \frac{\partial M}{\partial x} = \begin{cases} u_0 \frac{M_i - M_{i-1}}{\Delta_{i-\frac{1}{2}}} & (u_0 \geq 0) \\ u_0 \frac{M_{i+1} - M_i}{\Delta_{i+\frac{1}{2}}} & (otherwise) \end{cases} \quad (12)$$

where,

$$u_0 = \frac{u_{i-\frac{1}{2}} + u_{i+\frac{1}{2}}}{2} \quad (13)$$

Δ is the grid spacing in the x -direction and the subscript i is used for the x location.

(2) 2nd-order centered differencing + filtering

$$u \frac{\partial M}{\partial x} = u_0 \frac{M_{i+1} - M_{i-1}}{\Delta_{i+\frac{1}{2}} + \Delta_{i-\frac{1}{2}}} \quad (14)$$

The filtering is used only in the vertical direction as follows.

$$\frac{-M_{i+2} + 4M_{i+1} + 10M_i + 4M_{i-1} - M_{i-2}}{16} \quad (15)$$

(3) 3rd-order upwind differencing

$$u \frac{\partial M}{\partial x} = u_0 \frac{M_{i+\frac{3}{2}} - M_{i-\frac{3}{2}}}{\Delta_i} \quad (16)$$

where,

$$M_{i+\frac{3}{2}} = \begin{cases} M_{i+\frac{3}{2}}^L & (u_{i+\frac{3}{2}} \geq 0) \\ M_{i+\frac{3}{2}}^R & (otherwise) \end{cases} \quad (17)$$

In the case of variable grid spacings, the values of $M_{i+\frac{1}{2}}^L$ and $M_{i+\frac{1}{2}}^R$ are determined as follows.

$$M_{i+\frac{1}{2}}^L = M_i + \Delta_{L1} (M_i - M_{i-1}) + \Delta_{L2} (M_{i+1} - M_i) \quad (18a)$$

$$M_{i+\frac{1}{2}}^R = M_i + (1 - \Delta_{R1}) (M_{i+1} - M_i) - \Delta_{R2} (M_{i+2} - M_{i+1}) \quad (18b)$$

where,

$$\begin{cases} \Delta_{L1} = \frac{\Delta_i \Delta_{i+1}}{(\Delta_{i-1} + \Delta_i + \Delta_{i+1})(\Delta_{i-1} + \Delta_i)} \\ \Delta_{L2} = \frac{\Delta_i(\Delta_{i-1} + \Delta_i)}{(\Delta_{i-1} + \Delta_i + \Delta_{i+1})(\Delta_i + \Delta_{i+1})} \\ \Delta_{R1} = \frac{\Delta_{i+1}(\Delta_{i+1} + \Delta_{i+2})}{(\Delta_i + \Delta_{i+1} + \Delta_{i+2})(\Delta_i + \Delta_{i+1})} \\ \Delta_{R2} = \frac{\Delta_i \Delta_{i+1}}{(\Delta_i + \Delta_{i+1} + \Delta_{i+2})(\Delta_{i+1} + \Delta_{i+2})} \end{cases} \quad (19)$$

The schemes above are compared for the period of ten times of wave period (T) of the case of T=1.5sec, and the results are shown for the vertical variation of the density-function in Fig.1. It is obviously noted that the higher the order of derivative of the differencing error is, the less the density-function is diffused in the vertical direction. The smaller time increment (DT) is also very effective for suppressing the numerical diffusion. As shown in Fig.2 the discontinuity of the density-function disappears and a very sharp interface is obtained when the time increment is reduced to the half value of the original one for the third order upwind scheme. Therefore, the third order upwind scheme is employed hereafter.

The simulated waves for three cases of wave period, T=0.9, 1.2 and 1.5sec, are presented in Figs.3 and 4, which indicate respectively the wave profile with a sine curve for each case and the time variation of wave height with measurements. It is demonstrated that at least ten waves are generated with sufficient degree of accuracy and the magnitude of the error due to the numerical modelling is of the same order with that of experiments. Therefore it may be safe to say that the density-function method employed here can have sufficient accuracy for simulating waves without special treatments for suppressing the numerical diffusion when it uses sufficiently fine grid spacing and small time increment.

FREE SURFACE SHOCK WAVE ABOUT A WEDGE MODEL

The nonlinear features of ship waves in the near field had been noticed in the 1970s and the detailed structure and mechanism of nonlinear bow waves are experimentally investigated by Miyata et

al.[1][2][3]. It is elucidated that the nonlinear bow wave had a lot of common properties with supersonic shock waves and the nonlinear bow waves involving these properties are called free surface shock wave (FSSW). The typical properties of FSSW are (1) steepness of the wave slope, (2) discontinuity of velocities satisfying the shock wave condition, (3) free surface turbulence on and behind the wave front, (4) systematic change of the wave-front-angle depending on the Froude number (Fd) and the ship configuration and (5) dissipation of wave energy into momentum loss far behind the ship. Also the FSSW is limited in the thin layer near the free surface.

Although the above properties are recognized by experiments, the details of the FSSW structure had to be investigated by numerical simulations. However, due to the property of (1), wave breaking occurs at the wave-crest point, which makes the numerical simulation of FSSW significantly difficult. The finite-difference method mentioned in 2.1 with density-function method is applied to this problem and a wedge model of which half entrance angle is 20deg and draft is 0.1m is chosen for the simulation[20]. The simulations are carried out at three Froude numbers based on the draft, 0.8, 1.1 and 1.4, with normal grid spacing. The case of Fd=1.4 is also simulated with fine grid spacing of which minimum spacing is 1/4 of that for the former case. See the Ref.[20] for other details for computational conditions.

The systematic change of the wave-front-angle depending on the Froude number is realized showing good agreement with the experimental results and other properties of FSSW including 3D wave breaking phenomenon are recognized in the simulations by the finite-difference method. In this paper only the result of the case of Fd=1.4 with fine grid spacing is shown. The time-sequential overviews of the wave at Fd=1.4 are presented in Fig.5 The uniform flow is accelerated until dimensional time (T) reaches 1.77sec. Spilling breaker appears at T=1.564sec before the flow acceleration is ceased and the wave crest overturns at around T=1.932sec. The plunging wave front breaks at T=2.024sec and the wave again develops. The breaking wave front is laterally extended after T=2.208sec and the above process of breaking is periodically repeated. The secondary wave also shows breaking features in the vicinity of the body surface, however the accuracy is supposed to be inferior to the foremost wave due to the influence of the momentum deficient motions of the foremost wave.

A typical plane vertical and parallel to the di-

rection of uniform stream is chosen and the time-sequential development of the wave profile is shown as well as the contours of Lamb vector and helicity respectively in Figs.6 and 7. The Lamb vector indicates the magnitude of the tangential component of vortical motion and the helicity the longitudinal component. The vorticity that appears on the wave front is intensified when the breaking motion occurs, which shows the periodical generation of its own due to the periodical property of the wave breaking motion. It is, however, noted that the vortical layer is limited within the thin layer near the free surface.

BREAKING WAVES AROUND PRACTICAL HULLS

In the preceding section, it is shown that the TUMMAC-VIII method can simulate highly nonlinear free-surface wave by use of the density-function method. However, since the TUMMAC-VIII method employs the rectangular grid system, it can not accurately simulate the viscous phenomena such as growth and separation of the boundary layer, which contributes to the most significant part of resistance of a ship of practical hull forms. In a practical sense, the simultaneous simulation of nonlinear wave system and viscous flow around ships would give very useful information to hull form designers. Therefore, the WISDAM-VI method is developed in the framework of the curvilinear body fitted coordinate system. The treatment of the free surface condition is as described for rectangular coordinate system in the preceding section. However, since the WISDAM-VI method is based on the finite volume method Eq.(10) is written in conservative form as follows:

$$\frac{\partial M}{\partial t} + \text{div}(Mu) = 0. \quad (20)$$

In this section the WISDAM-VI method is applied to the flow around a VLCC model SR196C and a bulk carrier model M55F0A0 in ballast condition. The number of the control volumes used in the simulation is about 85,000, and the Reynolds number is set at 1.0×10^6 . The Froude number is set at 0.16 for the VLCC model and 0.18 for the bulk carrier model. The grid system is shown for the VLCC model in Fig.8.

Perspective view of computed waves are shown for both models in Fig.9, and computed wave contour maps are compared in Figs.10, 11 and 12. As shown in these figures, the bow waves observed in the experiments show the feature of the FSSW. The

computed wave patterns agree well with the experiments in the near field, however because of the large grid spacing in the far field of the ship, dispersive wave system of low wave height observed in the experiments are dissipated in the computation. In Fig.12, the present computational result is compared with the experimental result and with a result of another computational method TUMMAC-IV[18]. The number of grid points in the two calculations are comparable, but it is clear that the present calculation shows much better agreement with the experiment.

As Miyata and Inui[1] pointed out, dissipation of energy is one of the most important characteristics of FSSW. Baba[19] found that energy deficit due to bow wave breaking is observed in the wake far behind the ship. In order to discuss the energy loss due to bow wave breaking, distribution of total head H is shown at five transverse sections in Fig.13. The total head is defined as follows:

$$H = (u_1^2 + u_2^2 + u_3^2) + \frac{x^3}{Fn^2}. \quad (21)$$

The energy deficit generated near the bow is convected downstream and distributed near the free surface. At the aft-part of the ship, the loss due to wave breaking is mingled with the loss due to viscous effect, and apparently has influence on the formation of the wake. However the above discussion remains qualitative, and further validation of accuracy is necessary for the qualitative discussion.

CONCLUDING REMARKS

The free-surface flow is of significant importance in a variety of fields, and some of the problems include high degree of nonlinearity. By use of the density-function method, numerical simulations of such highly nonlinear free-surface flow including three-dimensional breaking waves has been achieved. The new treatment of the free surface condition is introduced both into the two simulation techniques based on either the rectangular or curvilinear grid systems. Each type of the grid system has the advantages and the disadvantage, and the choice depends on the true nature of the problem.

On the whole the numerical results shown in this study demonstrate that we can accomplish qualitatively realistic reproduction of highly nonlinear free surface phenomena, but there are still greater demands for the improvement of qualitative accuracy. Breaking waves are dissipating in their nature, however, we still do not have clear understanding and modelling of free surface turbulence and we do not

have the free-surface condition that can cope with the turbulent free-surface. Further researches must be focused on the development of novel modelling of nonlinear free-surface motions.

References

- [1] Miyata, H. and Inui, T., "Nonlinear ship waves," *Advances in Applied Mechanics*, Vol. 24, 1984, pp. 215-288.
- [2] Miyata, H., Inui, T. and Kajitani, H., "Free surface shock waves around ships and their effects on ship resistance," *Journal of The Society of Naval Architects of Japan*, Vol. 147, 1981, pp. 1-9.
- [3] Takahashi, M., Kajitani, H., Miyata, H. and Kanai, M., "Characteristics of free surface shock waves around wedge models," *Journal of The Society of Naval Architects of Japan*, Vol. 148, 1980, pp. 1-9.
- [4] Longuet-Higgins, M. S. and Cokelet, D., "The deformation of steep surface waves on water, I. A numerical method of computation," *Proceedings of the Royal Society of London*, A.350, 1976, pp. 1-26.
- [5] Hirt, C. W. and Nichols, B. D., "Volume of fluid (VOF) method for the dynamics of free boundaries," *Journal of Computational Physics*, Vol. 39, 1981, pp. 201-225.
- [6] Ng, C. O. and Kot, S. C., "Computations of water impact on a two-dimensional flat-bottomed body with a volume-of fluid method," *Ocean Engineering*, Vol. 19, No.4, 1992, pp. 377-393.
- [7] Miyata, H., "Finite-difference simulation of breaking waves," *Journal of Computational Physics*, Vol. 65, No.1, 1986, pp. 179-214.
- [8] Miyata, H. and Lee, Y. G., "Vortex motions about a horizontal cylinder in waves," *Ocean Engineering*, Vol. 17, No.3, 1990, pp. 279-305.
- [9] Miyata, H., Katsumata, M., Lee, Y. G. and Kajitani, H., "A finite-difference simulation method for strongly interacting two-layer flow," *Journal of The Society of Naval Architects of Japan*, Vol. 163, 1988, pp. 1-16.
- [10] Xiao, F. and Yabe, T., "A method to trace sharp interface of two fluids by one grid with density function," *Proceedings of the 5th International Symposium on Computational Fluid Dynamics*, Vol. 3, 1993, pp. 337-342.
- [11] Brackbill, J. U., Kothe, D. B. and Zemach, C., "A continuum method for modeling surface tension," *Journal of Computational Physics*, Vol. 100, 1992, pp. 335-354.
- [12] Park, J.C. and Miyata, H., "Numerical simulation of the nonlinear free-surface flow caused by breaking waves," *ASME, FED-Vol. 181, Free-Surface Turbulence*, 1994, pp. 155-168.
- [13] Kawamura, T. and Miyata, H., "Simulation of nonlinear shipflows by density-function method," *Journal of The Society of Naval Architects of Japan*, Vol. 176, 1994, pp. 1-10.
- [14] Miyata, H. and Yamada, Y., "A finite difference method for 3D flows about bodies of complex geometry in rectangular co-ordinate systems," *International Journal of Numerical Methods in Fluids*, Vol. 14, 1992, pp. 1261-1287.
- [15] Miyata, H., Zhu, M. and Watanabe, O., "Numerical study on a viscous flow with free-surface waves about a ship in steady straight course by a finite-volume method," *Journal of Ship Research*, Vol. 36, No.4, 1992, pp. 332-345.
- [16] Chan, R. O. C. and Street, R. L., "A computer study of finite amplitude water waves," *Journal of Computational Physics*, Vol. 6, 1970, pp. 68-94.
- [17] Park, J.C., Zhu, M. and Miyata, H., "On the accuracy of numerical wave making techniques," *Journal of The Society of Naval Architects of Japan*, Vol. 173, 1993, pp. 35-44.
- [18] Miyata, H., Nishimura, S. and Masuko, A., "Finite difference simulation of nonlinear waves generated by ships of arbitrary three-dimensional configuration," *Journal of Computational Physics*, Vol. 60, No.3, 1985, pp. 391-436.
- [19] Baba, E., "A new component of viscous resistance," *Journal of The Society of Naval Architects of Japan*, Vol. 125, 1969, pp. 23-34.
- [20] Kanai, A. and Miyata, H., "Elucidation of the structure of free surface shock waves about a wedge model by finite-difference method," *Journal of The Society of Naval Architects of Japan*, Vol. 177, 1995, pp. 147-159(in Japanese).

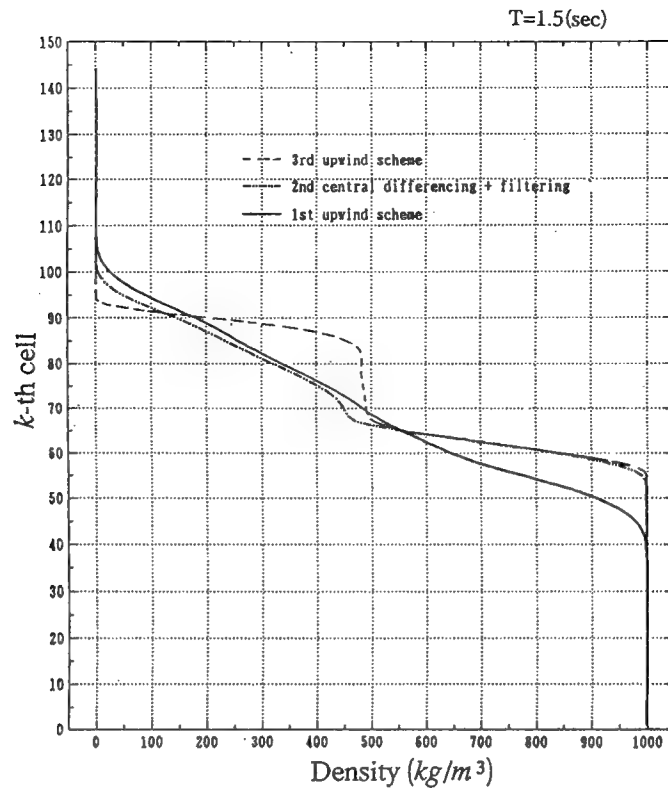


Figure 1: Comparison of the vertical distributions of density function by three differencing schemes at $t=10T$.

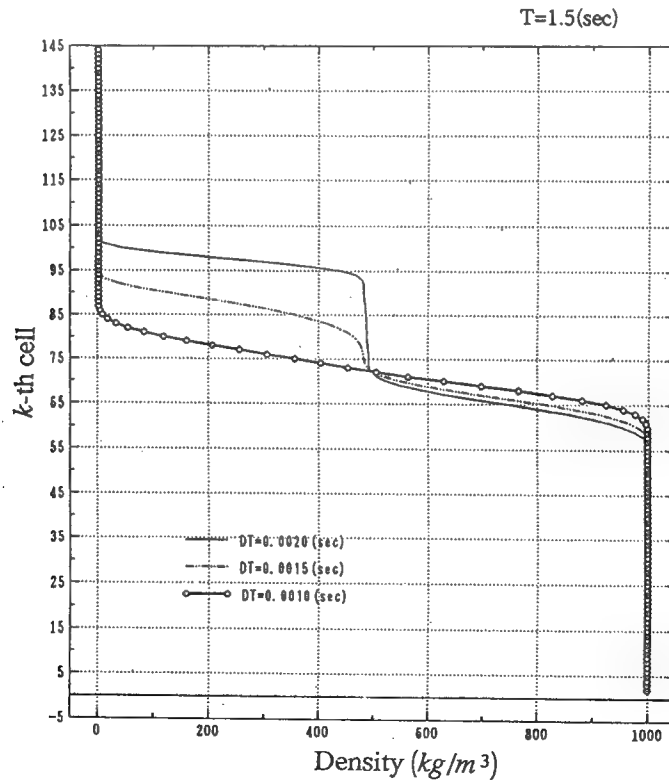


Figure 2: Difference of the vertical distributions of density function due to the time increment in case of 3rd order upwind scheme.

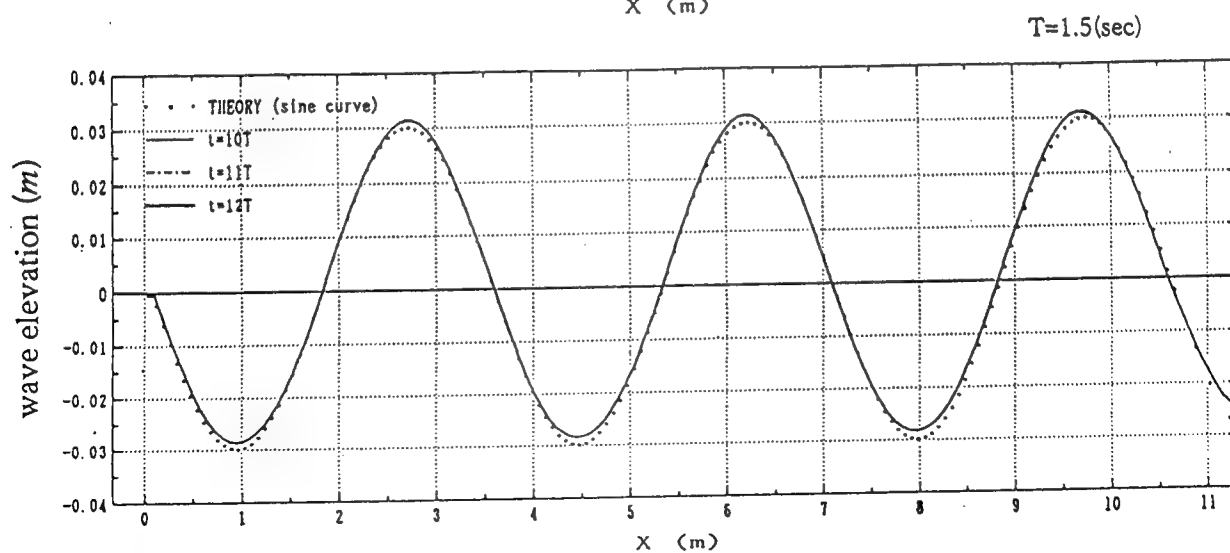
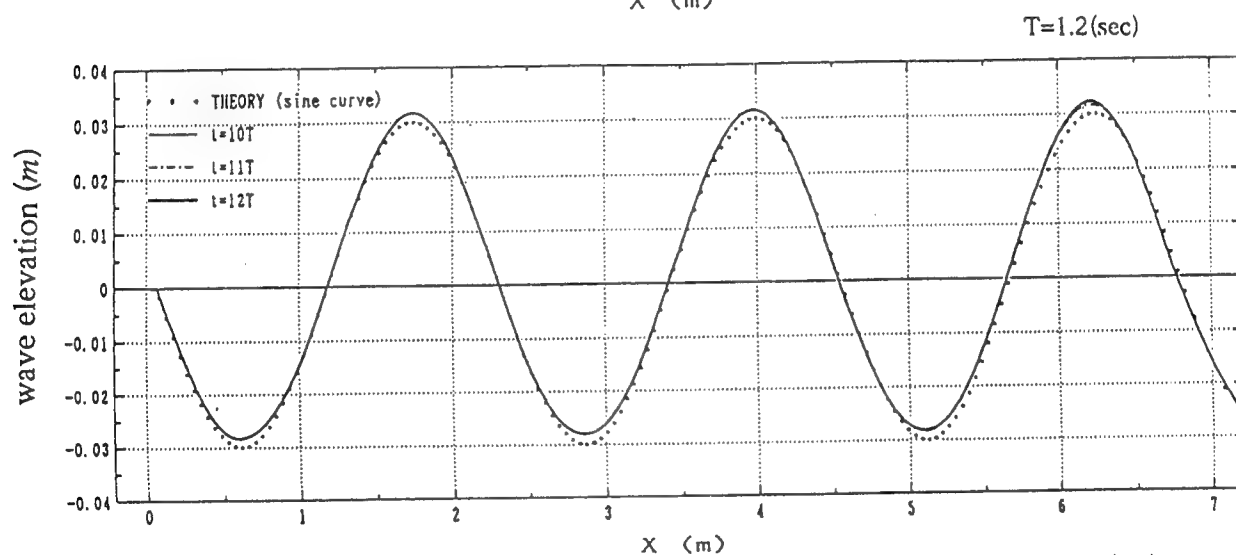
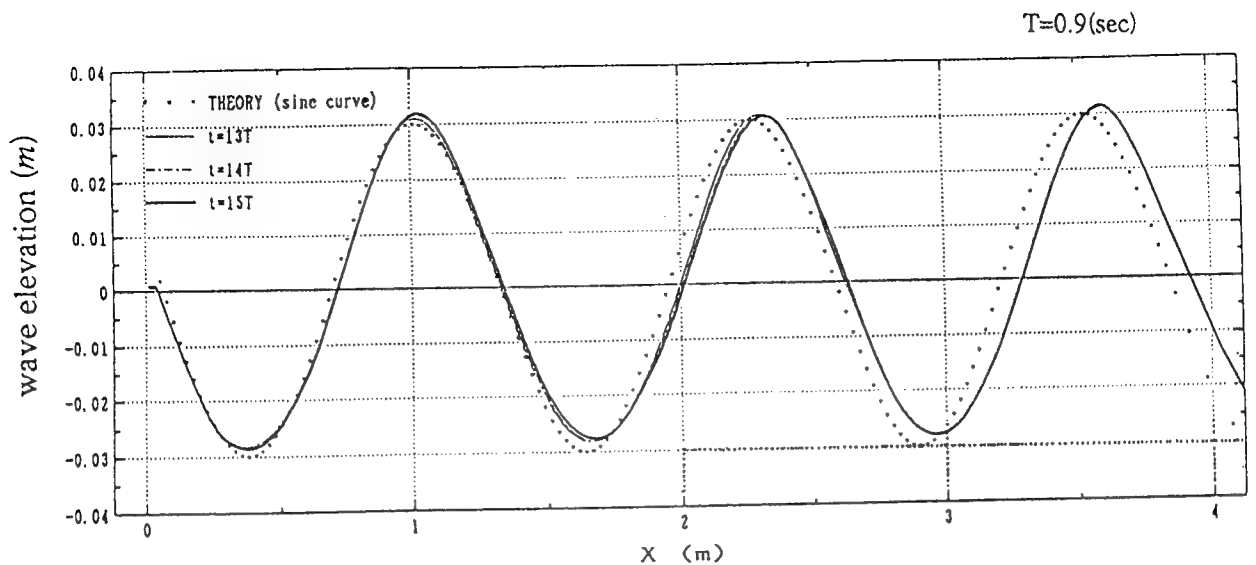


Figure 3: Wave profiles by calculations in the wave-proceeding direction for three wave periods, $T=0.9$, 1.2 and 1.5sec. The theoretical curve (sine curve) is also presented.

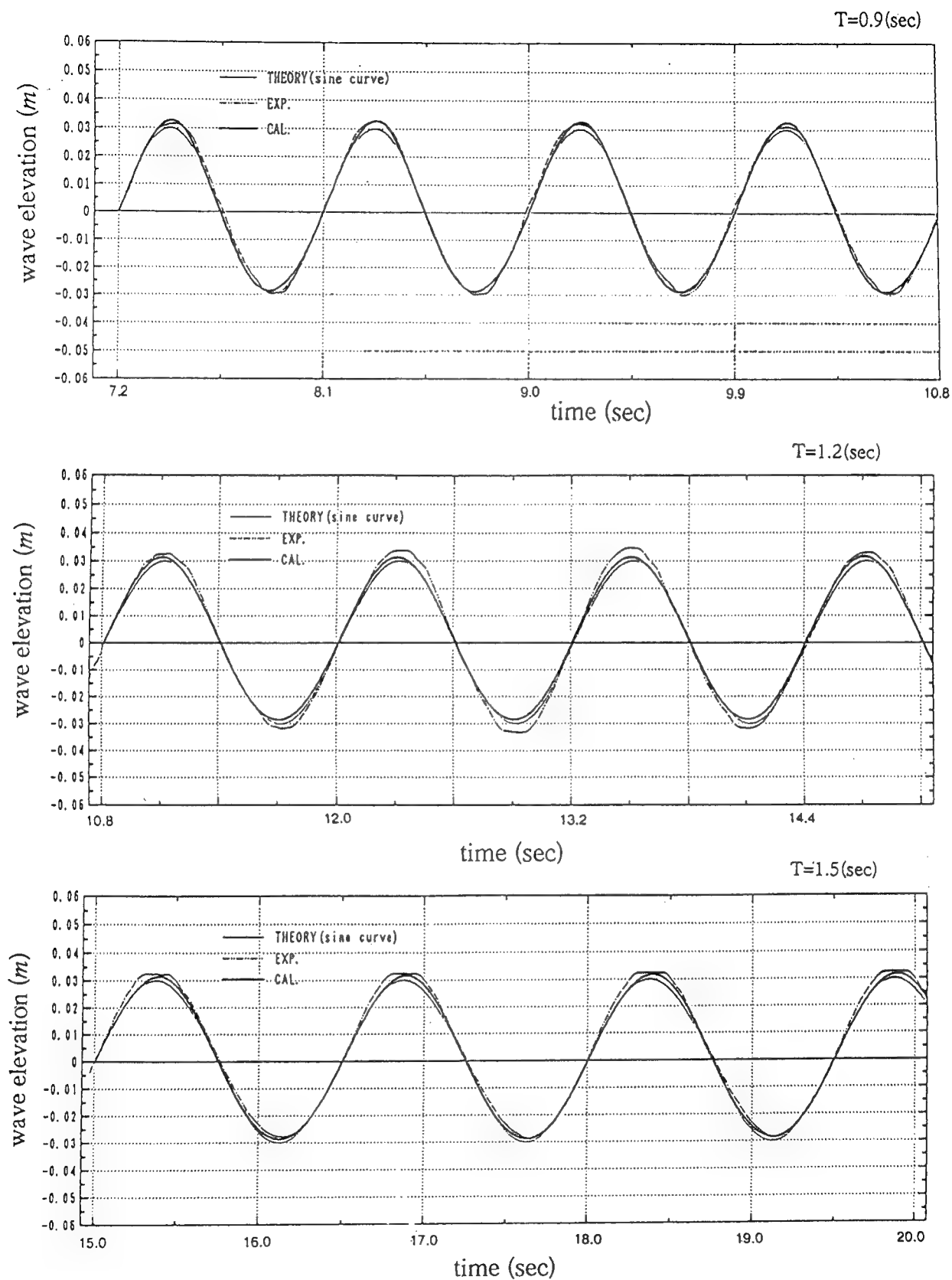
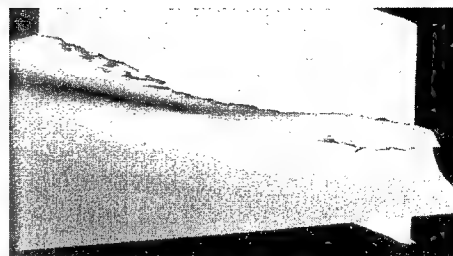


Figure 4: Time variations of the wave elevation by calculations and experiments for three wave periods, $T=0.9$, 1.2 and 1.5 sec. The theoretical curve (sine curve) is also presented.



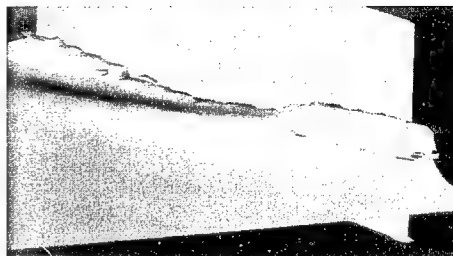
$T=1.472(\text{sec})$



1.932



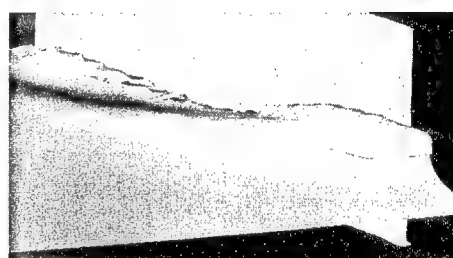
1.564



2.024



1.656



2.116



1.748



2.208



1.840



2.3

Figure 5: Time sequential wave pattern around a wedge model of which entrance angle is 20deg at $Fd=1.4$. The flow field is accelerated up to $T=1.77\text{sec}$.

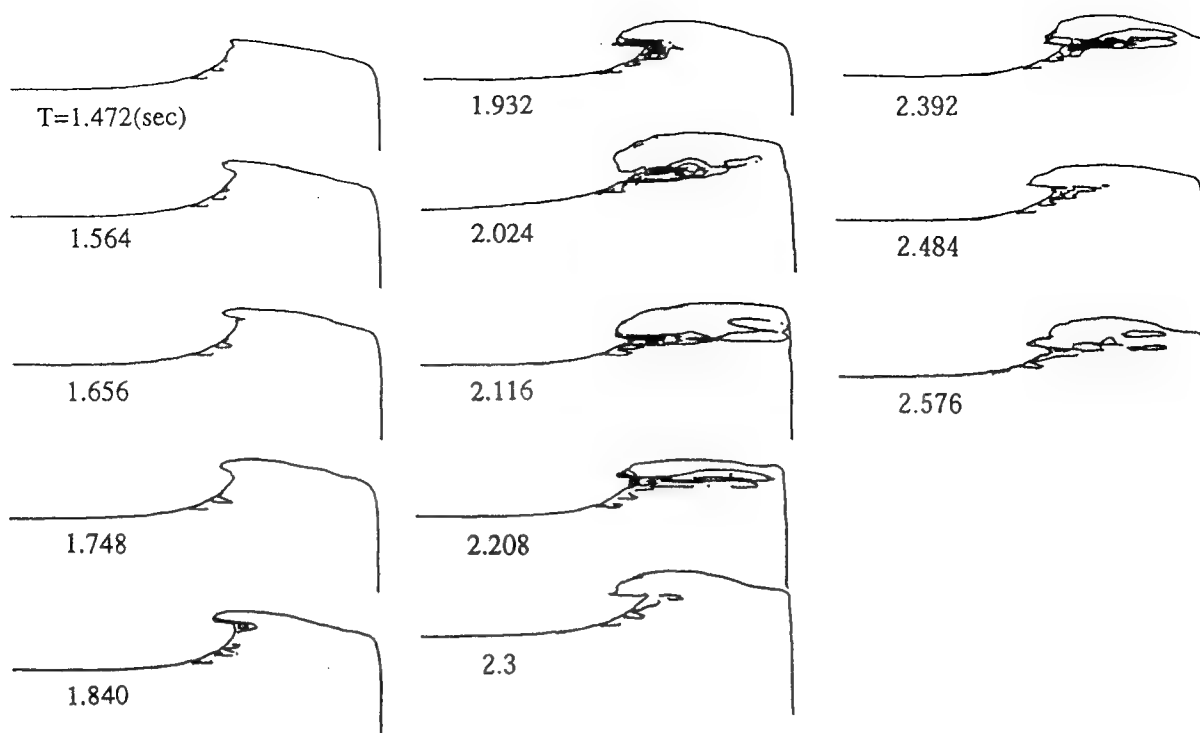


Figure 6: Time-sequential contour of the magnitude of Lamb Vector on the plane vertical and parallel to the direction of uniform stream. The distance from the center line to the plane is 0.0525m. The contour interval is 5. ($T=1.472$ 2.576sec, $Fd=1.4$, fine grid)

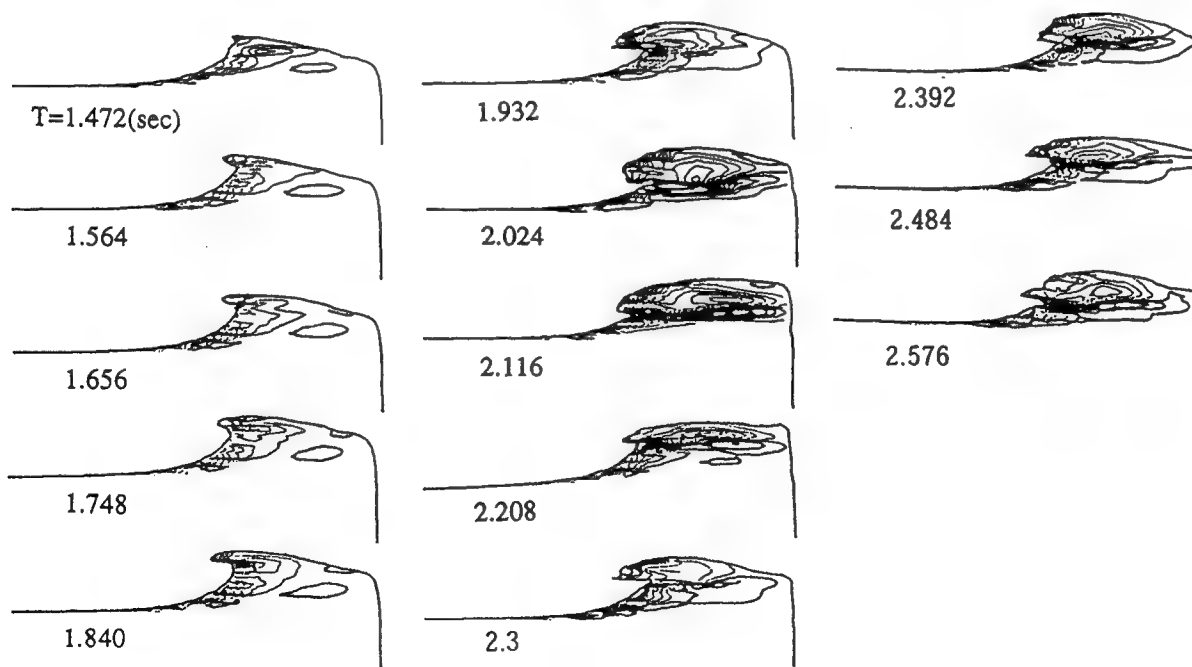


Figure 7: Time-sequential contour of helicity on the plane vertical and parallel to the direction of uniform stream. The distance from the center line to the plane is 0.0525m. The contour interval is 10. ($T=1.472$ 2.576sec, $Fd=1.4$, fine grid)

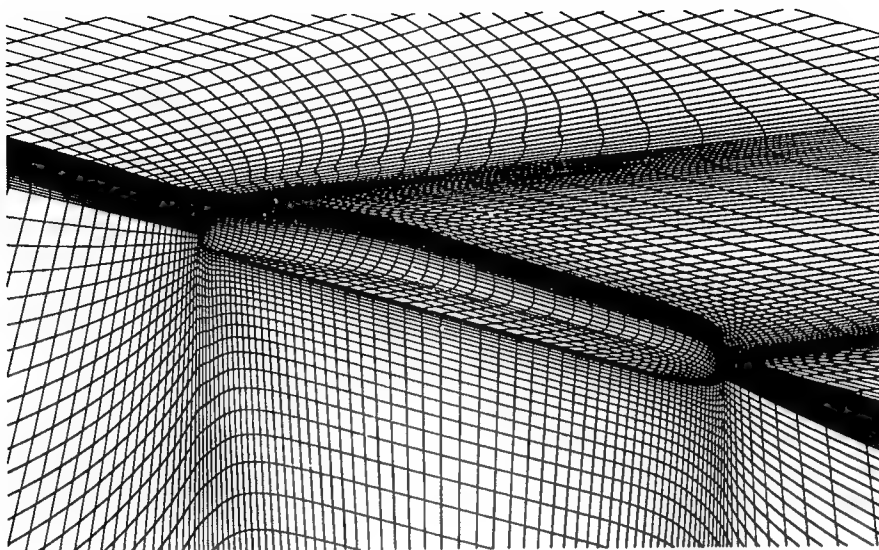
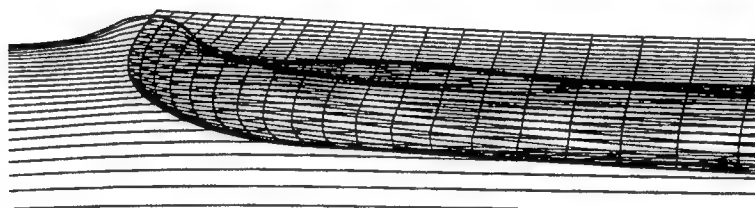
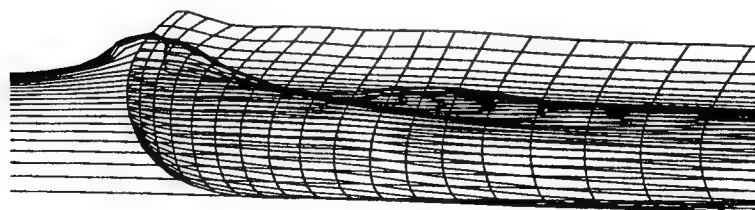


Figure 8: Grid system for the VLCC model: SR196C



VLCC model: SR196C ($Fn = 0.16$)



Bulk carrier model: M55F0A0 ($Fn = 0.18$)

Figure 9: Perspective view of computed waves

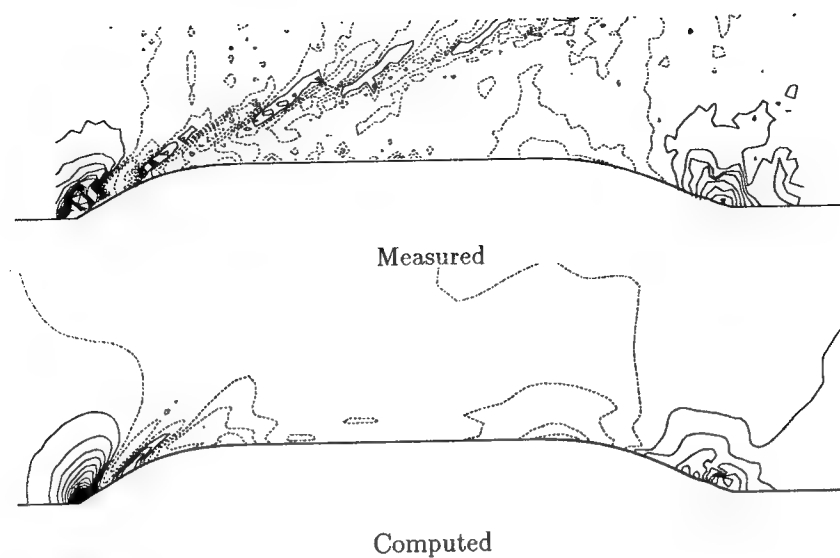


Figure 10: Comparison of the wave contour map for the VLCC model (SR196C $Fn = 0.16$)

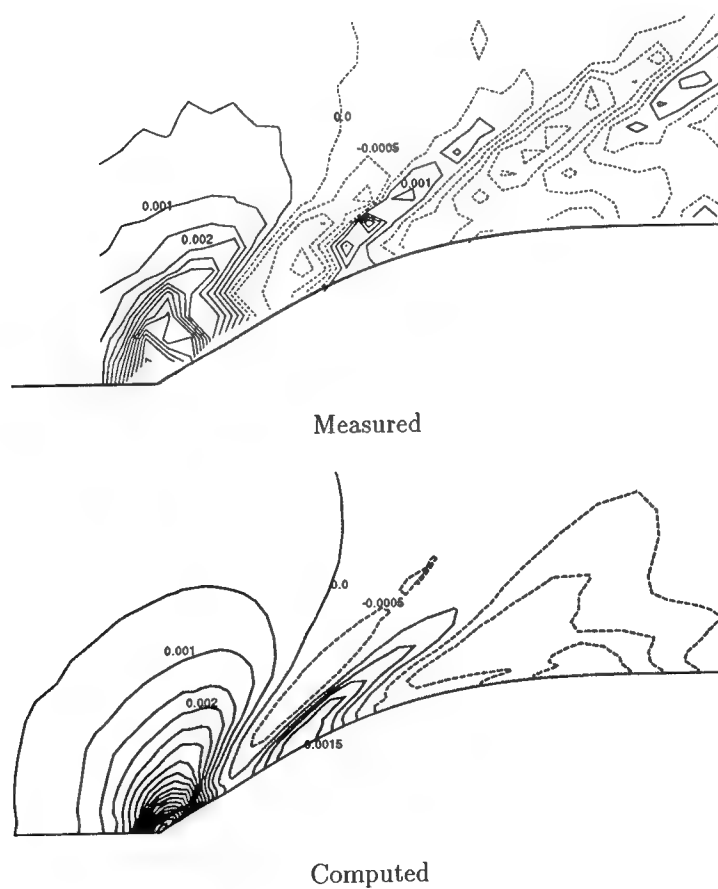


Figure 11: Comparison of the bow wave contour map for the VLCC model SR196C (Contour interval is 5×10^{-4} , $Fn = 0.16$)

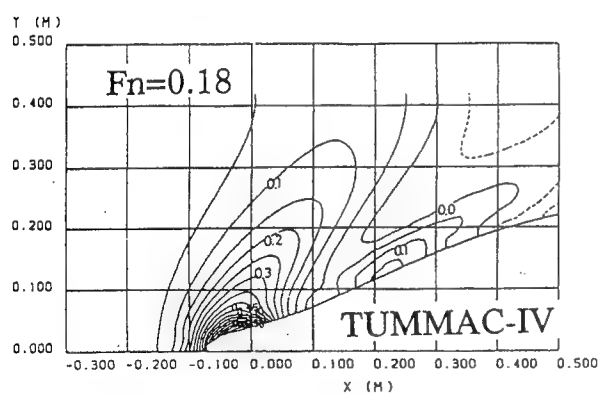


Figure 12: Comparison of the bow wave contour map for the bulk carrier model M55F0A0 (Wave height is nondimensionalized by the head of uniform flow, $Fn = 0.18$)

Figure 13: Distribution of total head loss (contour interval is 5% of total head of the uniform flow, SR196C $F_n = 0.16$)

Generation Mechanisms and Sources of Vorticity Within a Spilling Breaking Wave

D. Dabiri, M. Gharib (California Institute of Technology, USA)

ABSTRACT

Sources of vorticity are examined for a spilling breaking wave. Through the use of a honeycomb/screen section, spilling breaking waves are generated and examined. Two cases were studied. For the first case, based on the breaker height, the Reynolds and Froude numbers were 7370 and 2.04, respectively. The breaker is preceded by 1 mm wavelength capillary waves, with the largest amplitude to wavelength ratio equal to 0.18. For this case, it is found that the dominant source of vorticity flux is a viscous process, and is due to the deceleration of a thin layer of the surface fluid. Furthermore, a thin free surface fluid layer is found to precede wave breaking that moves at a faster speed with respect to the fluid directly beneath it and to the fluid bulk. For the second case, also based on the wave height, the Reynolds and Froude numbers were 1500 and 1.35, respectively. No breaking is observed for this case; rather a capillary-gravity wave is observed with 4 mm wavelength capillaries preceding the gravity wave. The largest amplitude to wavelength ratio of these capillary is 0.28. This case shows that capillary waves do not contribute to the vorticity flux, rather the only dominant source of the vorticity flux into the flow is the free surface fluid deceleration. Lastly, similar to case 1, a thin free-surface fluid layer, which moves faster than the fluid beneath it and to the fluid bulk is found preceding the capillary-gravity wave.

1. INTRODUCTION

Breaking waves are a phenomena quite common in nature. Historically, breakers have been categorized as either spilling breakers, where the water spills down the front face of the wave, and plunging breakers, where a jet emanating through the water crest falls into the base of the wave. The most commonly occurring breakers are spilling breaking waves which occur mostly in deep ocean waters. These spilling breakers, known as white caps, are responsible for the most of the air/sea interactions, and consequently the air entrainment which is important for the life under the sea (1). Likewise, one can easily observe the wave breaking phenomena in shallow water hydraulic jumps or bow and stern waves of boats. One important aspect of wave breaking is the subsequent spray formation and air entrainment in the form of bubbles which can be important in terms of ship wake signatures.

It is not clear whether the breaking process or bubble entrainment has any connection to the near surface turbulence or vorticity field. However, it is

known that the onset of spilling is connected to the near surface vorticity field as well as the dynamic characteristics of the near surface shear layers (2, 3). In this respect, studies of near surface shear layers or vorticity fields and their sources is important to the understanding of the breaking process.

Several investigators have contributed to our basic understanding of spilling breaking waves. Elementary models showed breaking as laminar flow suddenly erupting into a breaker, where the breaker was initially modeled as a roller residing over the front face of a wave. However, Banner and Phillips (2), being the first to experimentally study the spilling breaking wave, showed that there exists a turbulent wake beneath the spilling breaker which extended downstream beyond the breaker, even though the flow remains highly laminar and steady prior to breaking. Peregrine and Svendsen (4), after a series of experiments, suggested that it may be best to model the whole region beneath the spilling breaking wave as a turbulent region, rather than a roller residing over a wave. Battjes and Sakai (5) used a hydrofoil to induce spilling breakers, and obtained velocity profiles at various stations downstream of the hydrofoil. They determined that the turbulent wake downstream of the separation at the surface is self-preserving, indicating the possible existence of a shear layer. Tulin and Cointe (3, 6), present a detailed and comprehensive theory of steady wave breaking. Their model also presents the breaker as a stagnant eddy held in place over the front face of the wave. These and further results were then compared with experimental work performed by Duncan (7, 8) and found to agree quite well. In their most recent work, Duncan and Philomin (9) show some of the features associated with the development of spilling breaking waves. Finally, using the Particle Image Velocimetry (PIV) technique, Lin and Rockwell (10) were able to map the flow field directly beneath the spilling breaker, and were therefore able to show the existence of a shear layer beneath the breaking wave. Through further study, they were also able to characterize the evolution of wave breaking (11).

Thus, once organized vorticity was observed within the breaker, the question arose, where does this vorticity come from? Banner and Phillips suggest that "incipient breaking in a steady wave train is characterized by the occurrence of stagnation points at wave crests, but not necessarily by discontinuities in slope". Longuet-Higgins (12) predicts that parasitic capillaries seen on the forward slope of gravity waves contribute significantly to

the vorticity seen in the crest roller. After a series of analyses, he shows that due to surface curvature, there exists a Stokes layer $\delta = (2\nu/\gamma)^2$, where ν is the kinematic viscosity, and γ is the radian frequency of the wave, within which vorticity is generated, and beyond which vorticity escapes and is $\omega \approx 2(a\kappa)^2\gamma$, where a is the wave amplitude, κ is the wave number, and $a\kappa$ describes the wave steepness. After detailed observations, Lin and Rockwell (10, 11) conclude that the sharp surface curvature serves as a source of vorticity, thereby giving rise to a separated mixing layer. They also observe that the region between the free surface and the mixing layer contains vorticity levels which are small compared with the mixing layer itself. Lastly, Hornung, et. al. (13) suggest that the substantial vorticity seen downstream of a hydraulic jump is due to the entrainment of bubbles during breaking. This was further explained by suggesting that the circulation around a loop, drawn directly beneath the free surface on oneside and stretching into the fluid bulk on all other sides such that the loop incorporates a bubble, is non-zero. Furthermore, they also suggest that the entrainment of vorticity is also connected to how the circulation loop is drawn.

It is therefore the purpose of this paper to shed some light on the origins of the source of vorticity seen within a spilling breaking wave. Specifically, the questions that will be answered are a) What is the source of the vorticity seen beneath and downstream of the breaker? b) Do capillary waves contribute to the vorticity? c) Do we need large breaking and therefore air entrainment in order to generate vorticity?

2. EXPERIMENTAL SET-UP

2.1 The test facility

In order to answer these questions, a series of spilling wave breaking experiments were performed in a closed-loop water tunnel facility at CALTECH. The water tunnel has a contraction ratio of 4:1, with a $15.2 \times 15.2 \times 61 \text{ cm}^3$ test section. Previous approaches for generating spilling breaking waves have been to situate a hydrofoil located at some distance below the water level in a water tunnel. This caused the fluid above the

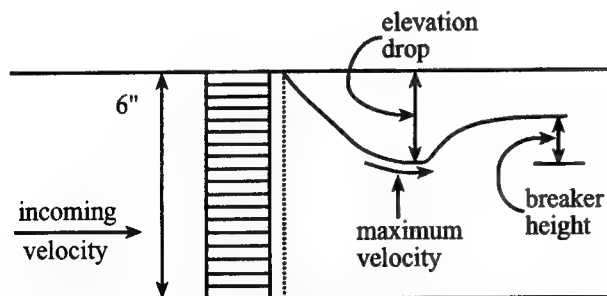


Figure 1. Wave breaking experimental set-up (not to scale).

hydrofoil to accelerate, and therefore generate spilling breaking waves. For the present experiments, an original

technique was devised to generate spilling breaking waves. A $15.2 \times 15.2 \times 2.54 \text{ cm}^3$ honeycomb section with a screen is placed at the beginning of the test section, where the honeycomb straws are 2.3 mm in diameter, and the wire screen is 50 mesh/inch stainless steel (see figure 1). Due to the pressure drop across the honeycomb/screen section, the fluid is accelerated to a maximum velocity, while dropping in height, and thereby generating spilling breaking waves.

2.2 The DPIV set-up and acquisition system

Figure 2 shows a schematic for the experimental setup for data acquisition. The flow is seeded with 14 ± 5 micrometer silver-coated hollow glass spheres with a specific gravity of 1.4 g/cm^3 . Through a series of optics and mirrors, a laser light sheet with a maximum thickness of 1 millimeter is generated. This light sheet is then set parallel to the flow direction allowing the wave to be viewed before, during, and after breaking. The Dantec Flowgrabber DPIV system is used to record images onto a laser disk, which are subsequently digitized onto the hard disk. The Dantec Flowgrabber DPIV system is based on the cross-correlation technique. Therefore, images are exposed only once and are recorded at 30 frames per second. For analysis, a small

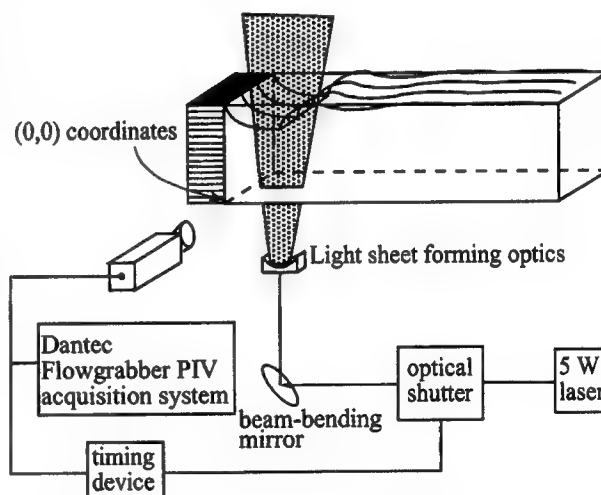


Figure 2. Image acquisition set-up.

interrogation window uniformly steps through the same locations within sequential pairs of images, performing a cross-correlation analysis at each location. Finally, a gaussian curve-fit is used to obtain sub-pixel accuracy of the cross-correlation peak. Once this is done at all locations within the image pairs, a displacement field in pixel values is obtained. By calibrating the pixels to spatial values, and knowing the time difference between exposures, the velocity field can be obtained. A more detailed description of the cross-correlation technique used here can be found in Willert and Gharib (14). Unfortunately, previous cross-correlating hardware limited the technique to slow flows, since each image

could only be exposed at the same location within the frame, as shown in the second timing diagram of figure 3. Therefore, the pulse separation, Δt , was always limited to 1/30 second, limiting this approach to maximum velocities of ~ 10 cm/s for typical applications. However, the present modified system used for the present experiments is capable of exposing full-frame pulsed images at any point within the frame.

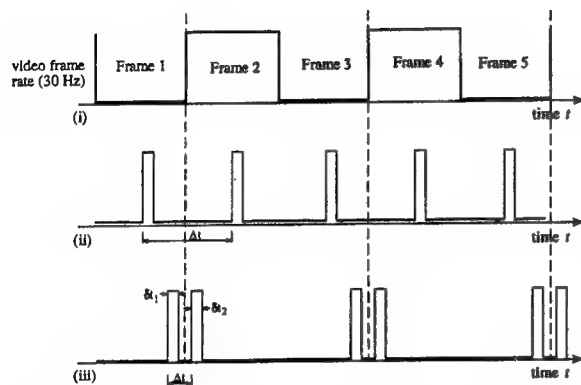


Figure 3. High speed cross-correlation DPIV timing diagram in relation to conventional cross-correlation DPIV timing diagram. (i) shows the frame rate of the video camera, (ii) shows the pulsed exposure of CCD camera for typical cameras, (iii) shows the pulsed exposure capability of the Dantec Flowgrabber camera.

Therefore, it is possible to expose the first image of the cross-correlating pairs towards its very end, while exposing the second image of the cross-correlating pairs towards its very beginning, as shown in (iii) of figure 3. Consequently, this allows for very short pulse separations between two image pairs, denoted by Δt in (iii) of figure 3, thereby making cross-correlation DPIV measurements possible at high-speeds. For the present experiment, $\delta t_1 = \delta t_2 = 150$ microseconds, and $\Delta t = 200$ microseconds. The typical field of view is 2.5×1.8 cm². This area is digitized at 768×480 pixels², and processed with an interrogating window size of 32×32 pixels² with a step size of 16×16 pixels² (50% window overlap). Particles images are 28.8 ± 0.5 micrometers. The uncertainties are 1.4% in the velocities and 3.9% in the vorticities.

2.3 Free surface treatment of the DPIV images

The acquired images have reflections over the free surface that may affect the DPIV processing and result in erroneous velocity results. It is therefore imperative to treat the image area above the free surface. First, the image area above and including the free surface is replaced with a constant value equal to the image background of the fluid beneath the free surface. Then DPIV is performed on these images. Since the area

above the free surface has no particles, the cross-correlation produces a zero shift. Interrogation windows which incorporate part of the image above the free surface and part below the free surface will therefore produce cross-correlation peaks that are due only to particles below the free surface. For these windows, results are only considered valid when the windows' center is either at or below the free surface. If the vorticity were to be calculated from these vector fields, an artificial shear layer would be generated at the free surface. Therefore, in order to minimize this effect, the no-shear boundary condition is applied at the free surface. All vectors above the last valid vector within a column are replaced by that vector for each column within the velocity field. Then vorticity is calculated. Since there are only velocity gradients in the x-direction above the free surface, only artificial vertical contours will be generated above the free surface in the vorticity plots, while accurate vorticity contours will be generated below the surface. Details concerning this approach will be published in a separate paper.

3. RESULTS & DISCUSSION

Two sets of experiments were done in order to answer the questions posed in the Introduction. The first set was done at higher Reynolds and Froude numbers.

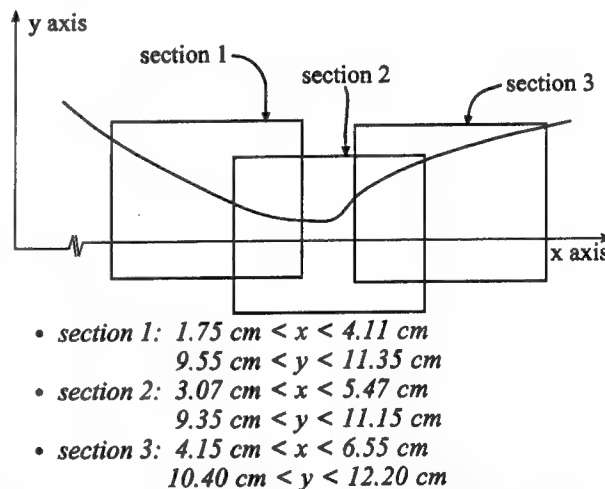


Figure 4. Imaged areas within higher Froude number spilling wave (not to scale).

Though very informative, this set of results produced capillary waves which were too, and therefore, were unable to ascertain the role of capillary waves in the flux of vorticity. Therefore a second set of experiments were done at lower Reynolds and Froude numbers to produce larger capillary waves, in order to determine their role in the vorticity flux.

3.1 Case 1: Higher Froude & Reynolds numbers

For this case, the incoming velocity into the grid is 24.6 cm/s. Due to the pressure drop across the honeycomb/screen section, the fluid accelerates to a

maximum velocity of 67 cm/s, while dropping in height by 4.2 cm (figure 1). Breaking occurs at the point when the fluid elevation sharply rises. The breaker rises to a maximum height of 1.1 cm (figure 1). Based on the velocity at the point immediately prior to breaking and the breaker height, the Reynolds and Froude numbers are 7370 and 2.04, respectively. For this case, three regions shown in figure 4 are interrogated. Section 1 interrogates the wave region such that breaking occurs at the far right of the imaged area. Section 2 interrogates the wave such that breaking occurs at the middle of the imaged area. Lastly, section 3 interrogates the wave such that breaking occurs at the left of the imaged area.

3.1.1 Velocity and vorticity fields

The velocity and vorticity fields for case 1 are plotted in figures 5, 6, and 8 through 13. The vectors within the velocity fields show the magnitude and direction of the velocity vectors throughout each of the three sections. For the vorticity plots, positive vorticity are shown by solid lines while negative vorticity are shown by dashed lines. The capillaries preceding spilling wave breaking are ≤ 1 mm in wavelength, and were too small to produce results that clearly determine the role of the capillaries in vorticity production. Yet, the raw images do show that the amplitude (crest-to-trough height) to wavelength ratio is ~ 18 . These capillaries correspond to a calculated phase speed of 68.7 cm/s. It therefore becomes obvious that the phase speed has matched the velocity just prior to wave breaking, thus exciting these capillaries (15, 16).

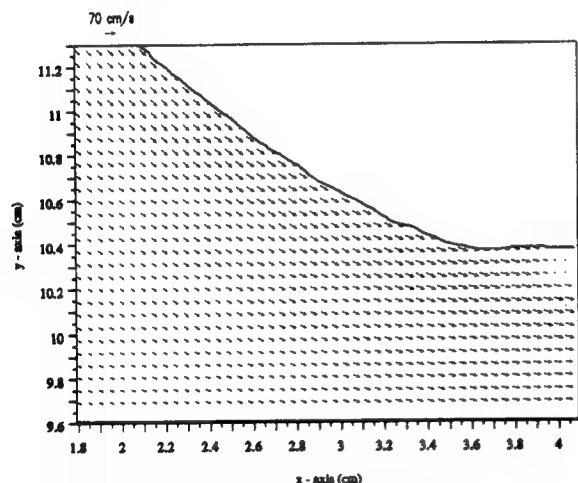


Figure 5. Vector field of section 1 of case 1.

Figures 5, 6 show the velocity and vorticity field at section 1. The velocity field shows high velocities, except for a small region just beneath the free surface at 3.9 cm downstream from the grid, where the velocities are almost negligible. The vorticity field shows that the fluid mostly contains negative vorticity except for a

small region just below the surface between 3.7 and 4.0 cm downstream from the grid which contains positive vorticity. Note that upstream from this positive

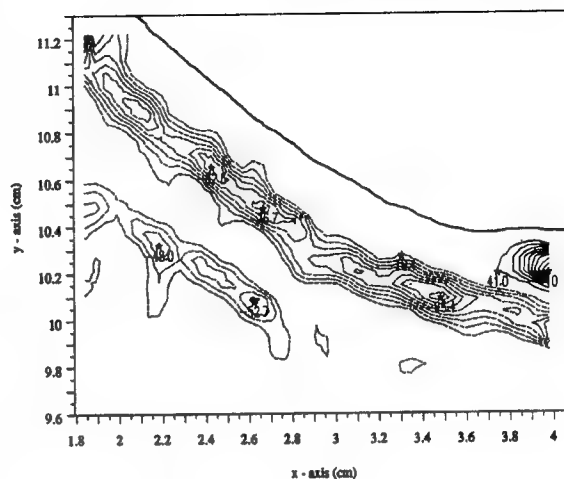


Figure 6. Vorticity field of section 1 of case 1. The negative contours (dashed lines) are in increments of 10 1/s while the positive contours (solid lines) are in increments of 40 1/s.

vorticity, the fluid directly beneath the free surface for a depth of 0.2 cm is almost vorticity-free. Furthermore, the vorticity field also shows the existence of a negative vorticity layer located 0.3 cm below the free surface, which exists directly below the vorticity-free layer, and has a thickness of ~ 0.3 cm. The negative vorticity layer starts upstream, extends downstream up to the positive vorticity region located at 3.68 cm, and continues further downstream, but below the positive vorticity layer.

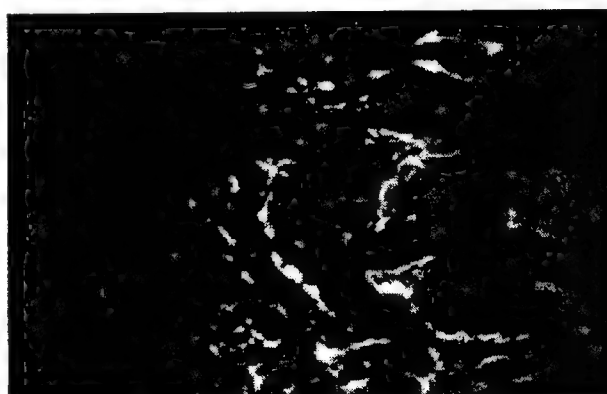


Figure 7. Shadowgraph for case 1. Flow is from left to right. "a" shows the capillaries, while "b" shows the boundary at which wave breaking initiates

The shadowgraph for section 2 is shown in figure 7, where the flow is from left to right. The capillary waves preceding wave breaking are clearly seen and are shown by "a". The beginning of breaking is

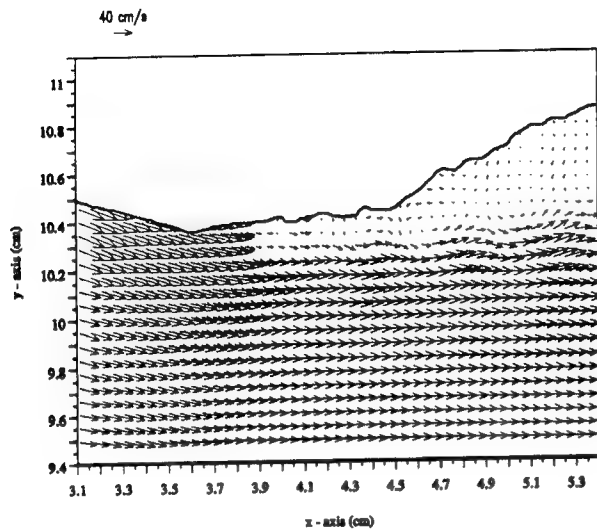


Figure 8. Vector field of section 2 of case 1.

shown by the line labeled "b", and finally spilling breaking is seen to the right of "b". The shadowgraph shows that the breaker free surface is deformed

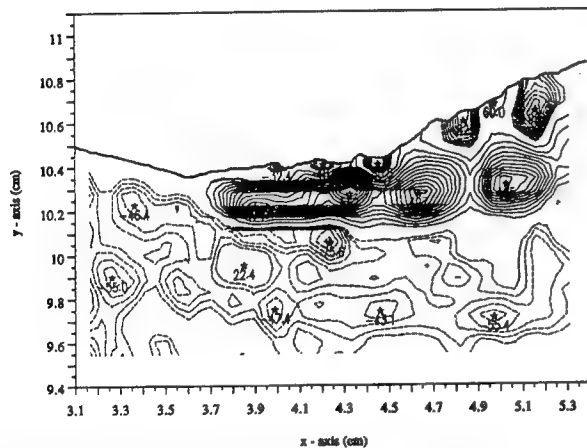


Figure 9. Vorticity field of section 2 of case 1. The negative contours (dashed lines) are in increments of 10 1/s while the positive contours (solid lines) are in increments of 40 1/s.

non-uniformly. This is due to the turbulent zone directly beneath the breaker, the existence of which will be shown below. Figures 8 through 11 show the velocity and vorticity fields at section 2 for two different times,

with a time difference of .267 seconds. The vector plots show that directly beneath the breaker the velocities are quite small with respect to the rest of the flow. This is due to the spilling on its front surface, thus, creating the spilling breaker, and thus a turbulent region beneath the breaker. Furthermore, note that for both these cases, the higher-velocity free surface layers directly beneath the free

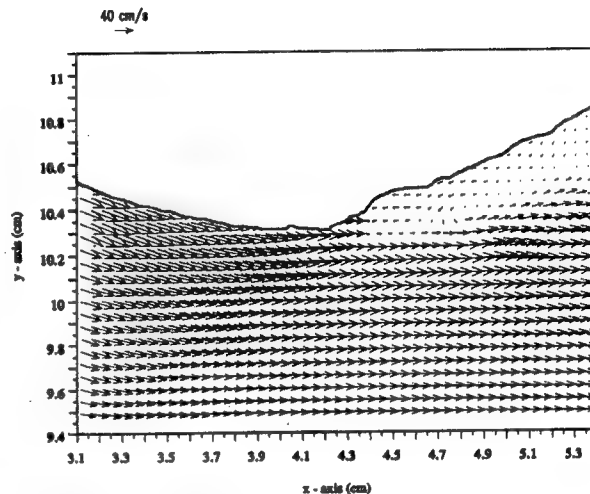


Figure 10. Vector field of section 2 of case 1 at .267 seconds after figure 5.

surface and upstream of the positive vorticity layer are also evident. Also, the negative vorticity layer which was shown to exist beneath the free surface higher-velocity layer in section 1 still continues further downstream beneath the positive vorticity layer. Also,

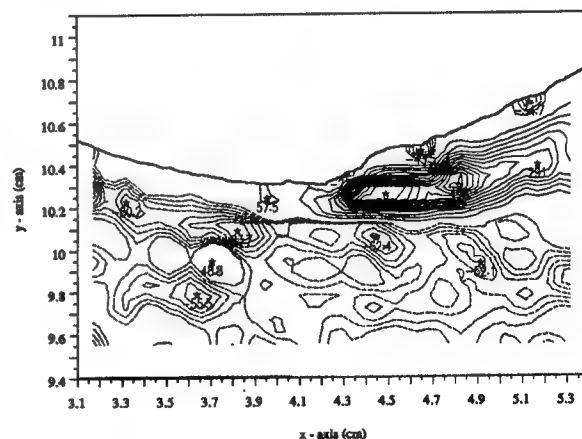


Figure 11. Vorticity field of section 2 of case 1 at .267 seconds after figure 9. The negative contours (dashed lines) are in increments of 10 1/s while the positive contours (solid lines) are in increments of 40 1/s.

the fully developed positive vorticity layer which was initially seen in section 1 is captured in figures 9 and 11, and seen to convect downstream. This positive vorticity layer, however, does not separate into a shear layer until the free surface sharply curves upwards. Note that there are also areas of negative vorticity at the free surface that are not as strong in magnitude as those in the mixing

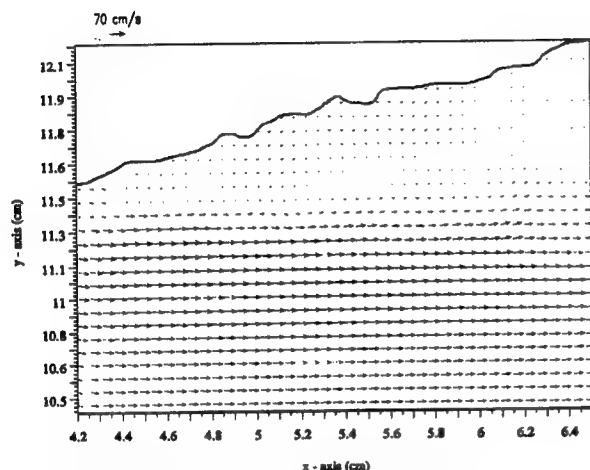


Figure 12. Vector field of section 3 of case 1.

layer. Upon comparison of the flow of figures 9 and 11, it is seen that the positive vorticity shear layer origin has been displaced by 0.5 cm in the x-direction. In fact, after examining several minutes of the flow in detail, it became evident that this "breathing" effect is quite persistent yet erratic in amplitude, with an oscillation

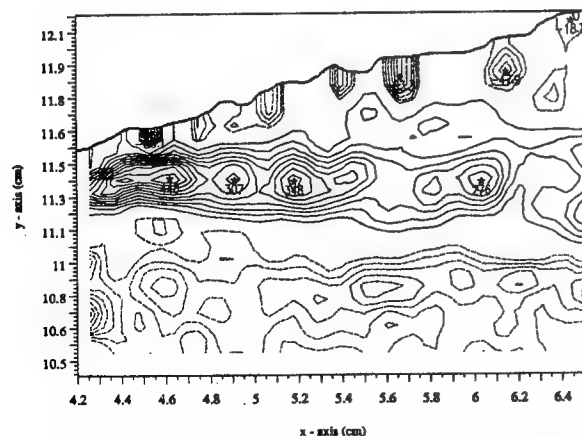


Figure 13. Vorticity field of section 3 of case 1. The negative contours (dashed lines) are in increments of 10 1/s while the positive contours (solid lines) are in increments of 40 1/s.

frequency of ~ 3.75 Hz. It was initially believed that this frequency might be the shedding frequency. Figure 9 shows the necessary parameters to determine this frequency. The convective velocity of the rollers in the shear layer is about the average of the velocity across the shear layer, or ~ 33.5 cm/s. The average spacing between the rollers is .35 cm, resulting in a shedding frequency of $(33.5 \text{ (cm/s)} / .35 \text{ cm}) \sim 96$ Hz. Finally, figures 12, 13 show the velocity and vorticity field associated with section 3. The vorticity field shows the persistence of the shear layer beneath the breaker. It is also interesting to note that even though the flow between the shear layer and the free surface is turbulent, its vorticity field is quite weak with respect to the vorticity within the shear layer. This is in fact consistent with the observations of Lin and Rockwell.

3.1.2 Sources of Vorticity

As has been seen by the previously mentioned investigators and shown in the present velocity and vorticity fields, almost irrotational flow, immediately after breaking, becomes highly rotational.

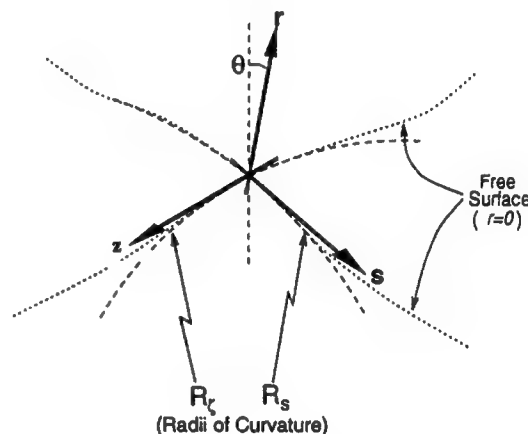


Figure 14. The natural curvilinear orthogonal coordinates. r is the unit vector perpendicular to the free surface, s is the unit vector parallel to the free surface, and perpendicular to r , and z is the unit vector parallel to the free surface and perpendicular to s and r .

In order to understand the origin of this vorticity, one must first look at the terms which contribute to sources of vorticity. The vorticity flux of surface-parallel vorticity through the surface given in natural curvilinear orthogonal coordinates is (17, 18, 19):

$$\nu \left(\frac{\partial \omega_z}{\partial r} \right)_{r=0} = -\frac{\partial u_s}{\partial t} - \frac{1}{\rho} \frac{\partial p}{\partial s} - g \cos \theta - \frac{1}{2} \frac{\partial u_s^2}{\partial s} \quad (1)$$

where ν is the kinematic viscosity, ω_z is the surface-parallel vorticity, u_s is the velocity parallel to the free surface, u_r is the velocity normal to the free surface, ρ is the fluid density, P is the pressure, and θ is the angle of the surface with respect to the gravity vector. Figure 9 shows the system of coordinates used for the equation shown above. For the steady breaker,

$$u_s|_{r=0} \cong \text{const} \tan t \quad (2)$$

through time. Therefore

$$\frac{\partial u_s}{\partial t} \cong 0 \quad (3)$$

Likewise, the pressure along the free surface is constant. Therefore,

$$\frac{\partial P}{\partial s} \cong 0 \quad (4)$$

Furthermore,

$$|g \cos \theta| \leq |g| = 981 \text{ cm/s}^2 \quad (5)$$

Therefore, the dominant terms contributing to the vorticity flux are the gravity term and the deceleration term. Equation (1) thus reduces to:

$$\nu \left(\frac{\partial \omega_z}{\partial r} \right)_{r=0} \approx -g \cos \theta - u_s \frac{\partial u_s}{\partial s}, \quad (6)$$

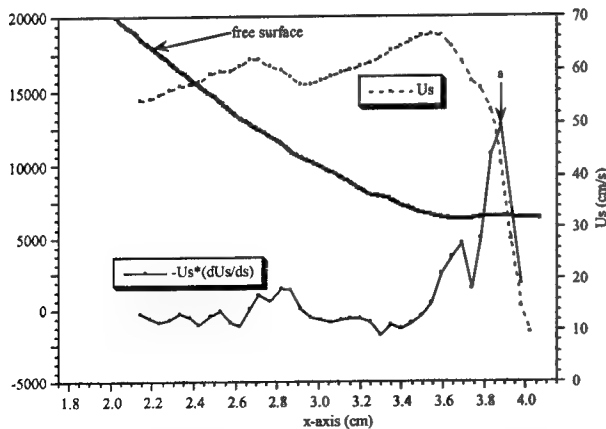


Figure 15. The free surface velocity and deceleration for section 1 of the higher Froude number case. The vorticity flux is shown on the left axis, while the velocity scale is shown on the right axis. Marker "a" at 3.84 cm shows the position of the maximum

deceleration, and therefore flux of vorticity into the flow.

3.1.3 Experimental observations of the sources of vorticity

As shown in the previous section, in order to understand the behavior of the vorticity flux, one must first examine the behavior of the deceleration and the gravity term. Figure 15 shows the deceleration and the surface velocity for section 1. The deceleration shows a strong peak at 3.84 cm from origin. This coincides with the strong generation of positive vorticity seen in figure 6. The velocity curve shows that the velocity rapidly decreases after 3.5 cm from the origin. However, the fluid does not approach the stagnation point until at least 0.15 cm farther downstream from the peak. Figure 16 shows the deceleration and the surface velocity for section 2. The deceleration reaches a peak at 3.75 cm from the origin, shown by marker "a". This coincides with the strong generation of positive vorticity seen in figure 9. The free-surface velocity curve shows that the fluid reaches a stagnation point at 4.58 cm shown by marker "b", 0.83 cm downstream from the vorticity flux peak. Consequently, it is important to realize that the generation of vorticity does not coincide with the stagnation point. Furthermore, the initiation of wave breaking does not contribute to the positive vorticity generation.

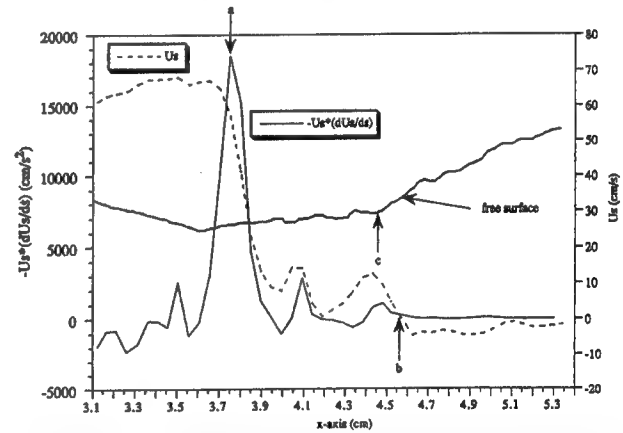


Figure 16. The free surface velocity and deceleration for section 2 of the higher Froude number case. The vorticity flux is shown on the left axis, while the velocity scale is shown on the right axis. Marker "a" at 3.75 cm shows the position of the maximum deceleration, and therefore flux of vorticity into the flow. Marker "b" at 4.58 cm shows the stagnation point of the free surface fluid, and marker "c" at 4.47 cm shows initiation of wave breaking observed visually.

This can be seen by observing that the vorticity is generated 3.75 cm from the honeycomb/screen section, while visually observed breaking occurs at 4.47 cm, shown by marker "c". Figure 17 shows the deceleration and the surface velocity for section 2 at 0.267 seconds

later with respect to figure 16. The deceleration reaches its peak at 4.25 cm from the origin, shown by marker "a", while the fluid stagnates at 4.4 cm, shown by marker "b". Therefore, as in the previous figure, the strong generation of vorticity represented by the deceleration of the free-surface fluid coincides with the appearance of strong positive vorticity. Curiously, figure 17 seems to indicate that the source of vorticity might be the sharp curvature of the free surface due to breaking, shown by marker "c" at 4.35, since vorticity generation and the sharp free surface curvature coincide. However, this coincidence is due solely to the "breathing" effect mentioned earlier where the positive vorticity layer oscillates at a lower frequency to and from the sharp free surface curvature. Once again, it should be emphasized that figure 16 clearly shows that the source of vorticity is not due to the free surface's sharp curvature, but due to the deceleration term shown in equation 6. It should be pointed out, however, that perhaps the best indication of breaking is the occurrence of the stagnation points shown by markers "b" in figures 13 and 17.

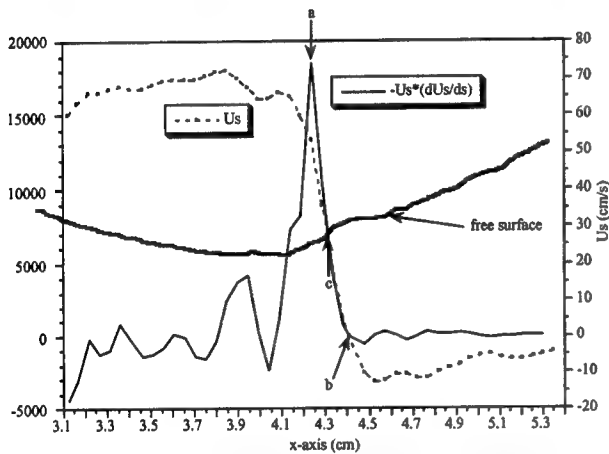


Figure 17. The free surface velocity and deceleration for section 2 at 0.267 seconds after that shown in figure 16. The vorticity flux is shown on the left axis, while the velocity scale is shown on the right axis. Marker "a" at 4.25 cm shows the position of the maximum deceleration, and therefore flux of vorticity into the flow. Marker "b" at 4.4 cm shows the stagnation point of the free surface fluid, and marker "c" at 4.35 cm shows initiation of wave breaking observed visually.

For both these cases, even though the vorticity flux peaks fluctuate back and forth with respect to breaking, the stagnation points are consistently within 0.1 cm of breaking, thus verifying the observations of Banner and Phillips. Finally, figure 18 shows the deceleration and the velocity profiles shown for section 3. This plot does not show any strong peaks as in the previous figures,

since vorticity is not generated, rather convected downstream. Thus, the important point to realize in figures 15 through 17 is that given equation 6, the dominant contributing term to the vorticity flux is the deceleration term, which is of the order of 20,000 cm/s², while the gravity term, which can be no greater than 981 cm/s², is negligible with respect to the deceleration term.

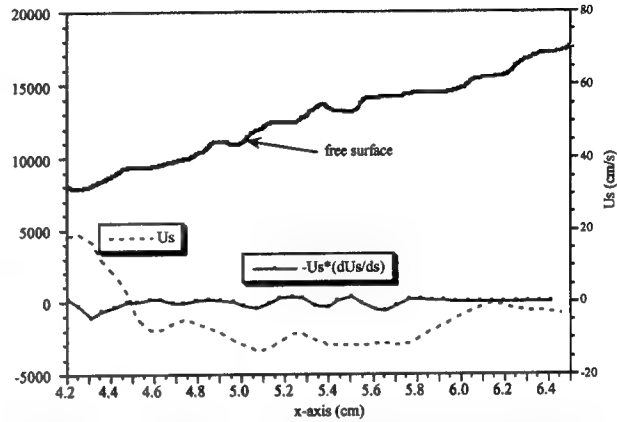


Figure 18. The free surface velocity and deceleration for section 3 for the higher Froude number case. The vorticity flux is shown on the left axis, while the velocity scale is shown on the right axis. Note that in this case, there are no outstanding peaks, since there are no fluxes of vorticity at this section.

Up to present, it has been shown that the flux of vorticity into the flow is due primarily to viscous effects. However, it can be argued that perhaps the vorticity flux is due to the velocity difference across the shear layer, thus making the vorticity flux an inviscid effect. Further reflection, however, can resolve this issue. The reduced vorticity flux equation derived earlier is shown below for convenience:

$$v \left(\frac{\partial \omega_z}{\partial r} \right)_{r=0} \approx -g \cos \theta - u_s \frac{\partial u_s}{\partial s}. \quad (7)$$

This equation, evaluated at the free surface, specifically shows that the source of vorticity is from the free surface, and that its flux from the free surface to the fluid, although equal to the free surface fluid deceleration, is entirely a viscous process. However, the free surface fluid not only decelerates with respect to the free surface fluid upstream of itself, but also with respect to fluid directly beneath it, thus creating a sharp velocity gradient, or "slip velocity".

Figure 19 shows several velocity profiles which are perpendicular to the free surface at section 2 of case 1, corresponding figures 8, and 9. These velocity profiles are from various x-locations about x=3.7 cm, illustrating the large velocity gradient, or "slip velocity" directly

beneath the free surface. It is this "slip velocity" which is the origin of the shear layer evident in figures 9, 11, and

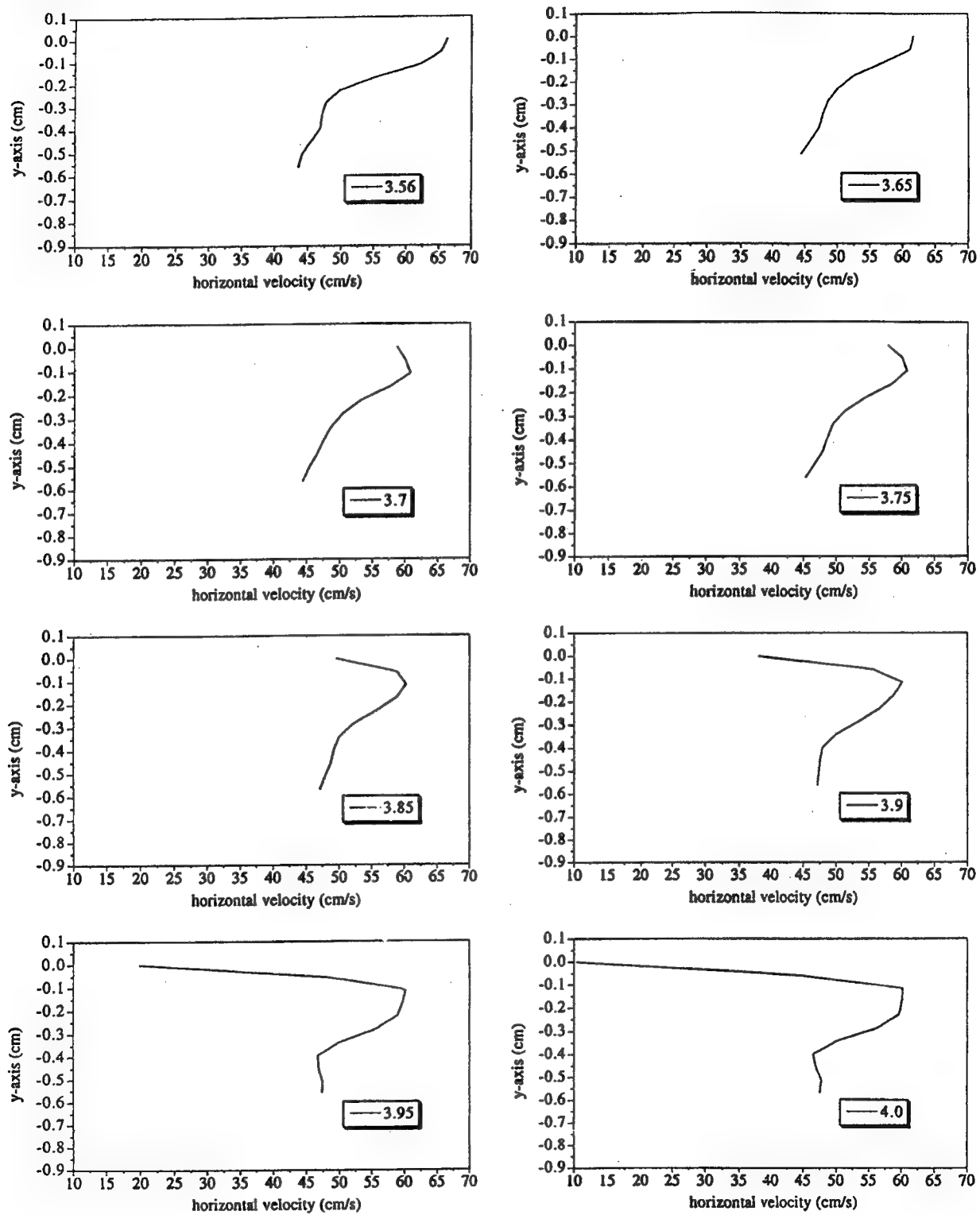


Figure 19. Velocity profiles taken from section 1 for case 1 at different x-locations. The profiles are perpendicular to the free surface, and the stated x-locations are x-locations of the free surface. The origin on the y-axis indicates the free surface.

13. It can therefore be concluded that the free surface deceleration not only

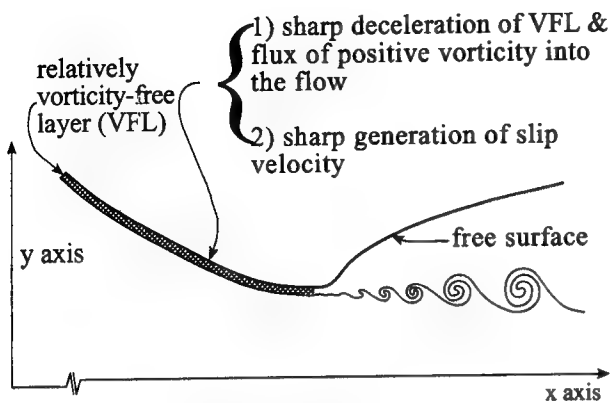


Figure 20. Diagram demonstrating the process of flux of vorticity into the flow.. The vorticity free layer decelerates sharply, introducing a high flux of vorticity into the flow, and simultaneously producing a sharp slip velocity which then grows into the shear layer seen beneath spilling breaker waves. (Drawing not to scale)

produces a vorticity flux into the flow through a diffusive process, but in doing so, simultaneously generates a sharp slip velocity which grows into a shear layer, convecting the vorticity downstream which has been fluxed into the fluid from the free surface (see figure 20).

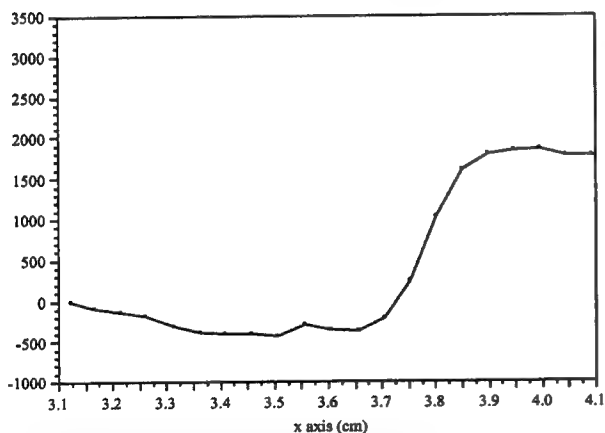


Figure 21. The running integral of the viscous vorticity flux of section 2.

This can also be seen by realizing that the free surface fluid decelerates to a stagnation point. Therefore, the vorticity must be fluxed deeper into the fluid, beyond the stagnation region, so that it can be convected downstream through the shear layer. A good check of the above analysis is to first calculate the net vorticity flux from

the free surface into the fluid bulk by integrating the fluid deceleration at the free surface; second, calculate the convected vorticity flux by integrating the vorticity flux in the y-direction for each x-location; and finally show that the vorticity fluxed into the flow is equal to the vorticity being convected through the flow.

Figure 21 shows the integrated viscous vorticity for section 2, corresponding to figures 8, 9 and figure 16. Note that there is a sharp jump at 3.65 cm indicating a large injection of vorticity into the flow. The total jump is $\sim 2250 \text{ cm}^2/\text{s}^2$. Beyond this injection, the level of integrated vorticity flux remains constant, indicating that there is no more vorticity flux from the free surface into the fluid, rather convection of the existing vorticity downstream.

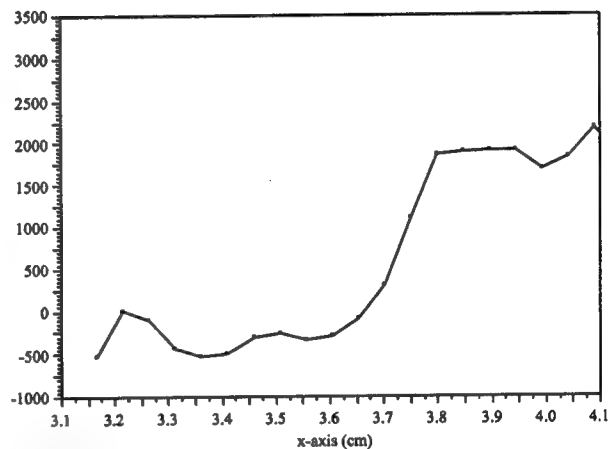


Figure 22. The integrated convective vorticity flux for section 2.

Figure 22 shows the integrated convected vorticity flux for section 2 corresponding to figures 8, 9 and figure 16. Also seen is a sharp jump of vorticity flux at 3.6 cm indicating a large injection of vorticity into the flow. The total jump is also $\sim 2250 \text{ cm}^2/\text{s}^2$. Thus, the integral convective flux value is almost identical to the jump value found for the viscous flux integration. This clearly confirms that the vorticity is fluxed into the flow from the free surface, and is convected downstream by the shear layer, without the need to break, or entrain air into the fluid.

3.2 Case 2: Lower Froude & Reynolds numbers

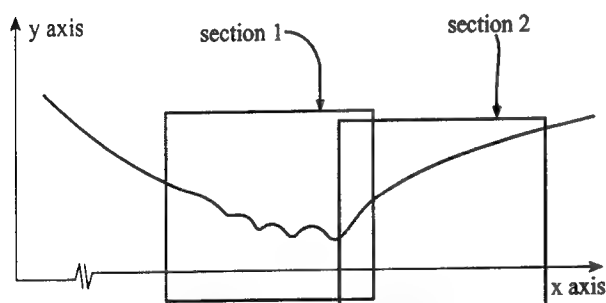
For the second case, the incoming velocity into the grid is 17 cm/s. Due to the pressure drop across the honeycomb/screen section, the fluid accelerates to a maximum velocity of 30 cm/s. For this case, instead of the occurrence of breaking, a capillary-gravity wave is seen. The shadowgraph for this case is shown in figure 23, where the flow is from left to right. The capillary waves preceding wave breaking are shown by "a", and the gravity wave begins and continues after "b". The

shadowgraph clearly shows the last capillary wave, as in case 1, thus indicating that breaking has not occurred.



Figure 23. Shadowgraph for case 2. The flow is left to right. "a" shows the capillaries, while "b" shows the boundary at which the gravity wave initiates.

This will be further discussed below. Based on the velocity at the point immediately after the last capillary wave and the final fluid elevation after the last capillary wave, the Reynolds and Froude number are 1500 and 1.35, respectively. For this case, two regions are interrogated (figure 24). Section 1 interrogates the wave region such that capillaries are seen within the imaged area, while section 2 interrogates the wave such that the portion of the wave after the capillaries is seen in the imaged area. The physical dimensions of these sections are given in figure 24. The origin of these coordinates is the bottom right corner of the honeycomb/screen section.



- section 1: $0.27 \text{ cm} < x < 2.27 \text{ cm}$
 $10.40 \text{ cm} < y < 13.03 \text{ cm}$
- section 2: $1.31 \text{ cm} < x < 3.21 \text{ cm}$
 $10.40 \text{ cm} < y < 13.03 \text{ cm}$

Figure 24. Imaged areas within higher Froude number spilling wave (not to scale).

3.2.1 Velocity and vorticity fields

The velocity and vorticity fields for this case are plotted in figures 25 through 28. The vectors within the velocity fields show the magnitude and direction of the velocity vectors throughout each of the three sections.

For the vorticity plots, positive vorticity are shown by solid lines while negative vorticity are shown by dashed lines. The capillaries preceding the gravity wave are 4 mm in wavelength, and therefore large enough to extract related velocity, vorticity, and flux information. The raw images further show that the amplitude (crest-to-trough height) to wavelength ratio is ~ 0.28 . These capillaries correspond to a phase speed of 35 cm/s since the maximum speed of the flow prior to the gravity wave is 30 cm/s. It is therefore evident that the phase speed has matched the velocity just prior to wave breaking, thus exciting the capillaries. Figures 25, 26 show the velocity and positive vorticity fields at section 1. The velocity field through the capillaries is fully attached despite the high curvature, thus resembling flow through a series of converging and diverging sections.

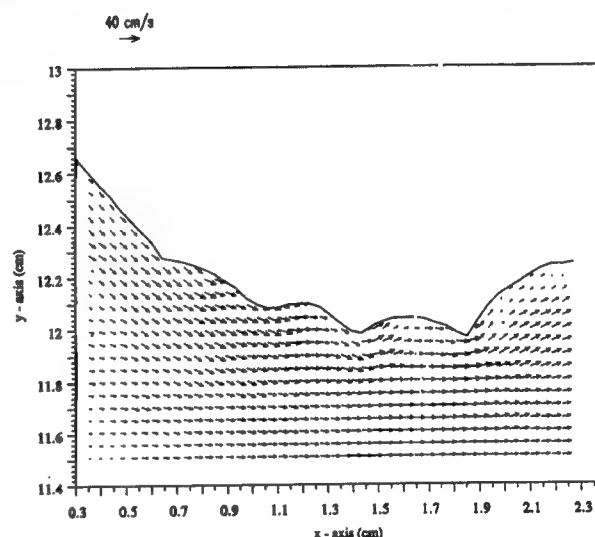


Figure 25. Vector field of section 1 of case 2.

Therefore, the turning of the flow through the capillaries generates a series of quasi-stationary negative and positive regions of vorticity that exists solely due to the curvature of the free surface (20). The velocity fields show that there are no separation of the flow from the free surface, or recirculation zones. Likewise, the vorticity plots show no separation of a shear layer as seen in the higher Froude number case, rather a positive shear layer is seen that bends upwards, following the contour of the gravity wave. This thus confirms that breaking has not occurred, as was shown in the shadowgraph for this case (figure 23). This positive vorticity layer is seen to be connected to the last positive vorticity situated under the last capillary trough just prior to the gravity wave. Lastly, a small region of negative vorticity is seen on the gravity wave, below the surface, and above the positive shear layer at $x = 1.95 \text{ cm}$,

indicating the existence of a stagnation point at that location.

this vorticity seems to be connected to the positive vorticity located beneath the trough of

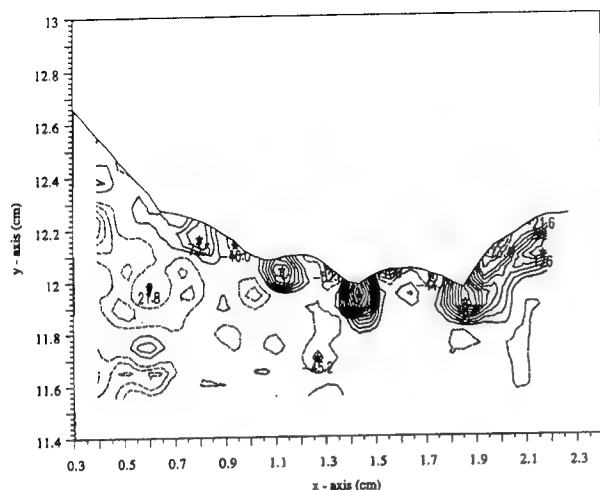


Figure 26. Vorticity field of section 1 of case 2. The negative contours (dashed lines) are in increments of 20 1/s while the positive contours (solid lines) are in increments of 20 1/s.

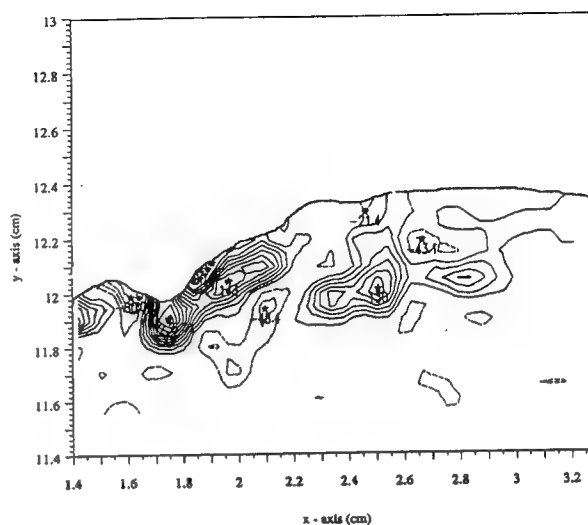


Figure 28. Vorticity field of section 2 of case 2. The negative contours (dashed lines) are in increments of 20 1/s while the positive contours (solid lines) are in increments of 20 1/s.

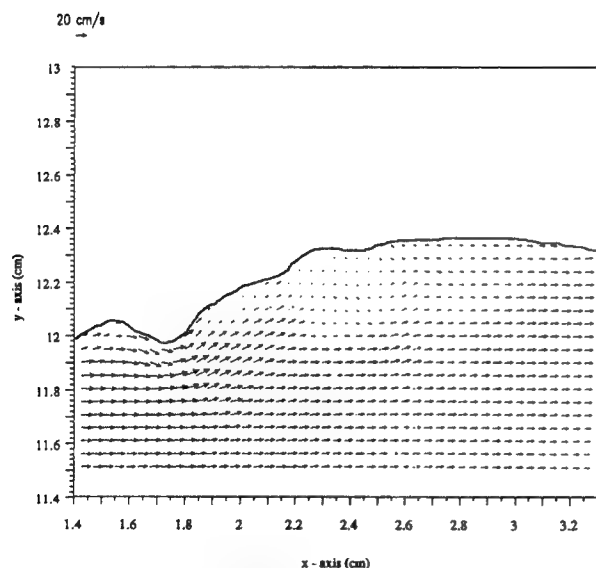


Figure 27. Vector field of section 2 of case 2.

Figures 27, and 28 show the velocity and positive vorticity field at section 2. The vorticity field from this section confirms that the positive shear layer seen within the gravity wave does not separate from the free surface, but follows its contour. Also, it is seen that

that last capillary prior to wave breaking. Lastly, the small region of negative vorticity, though very small is also present, and is located beneath the free surface and above the positive shear layer at $x = 1.85$ cm.

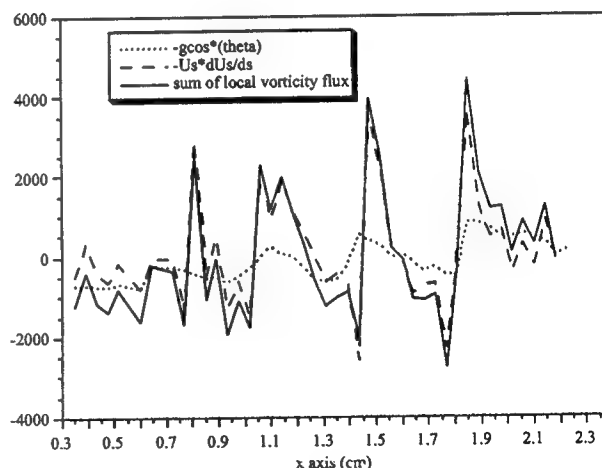


Figure 29. Contributing terms to the vorticity flux. The kinematic deceleration is shown by the dashed line, the gravity term by the dotted line, and their sum is shown by the solid line.

3.2.2 Experimental observations of the sources of vorticity

Since the flow is slower in this case, the capillaries are larger, and can therefore be resolved, thus determining the importance of the gravity term in equation 7. Figure 29 shows the deceleration, the gravity term, and their sum for section 1, and how these terms vary as the fluid flows through the capillaries. It is seen that the contribution to the vorticity flux is due mostly to the deceleration term and not the gravity term.

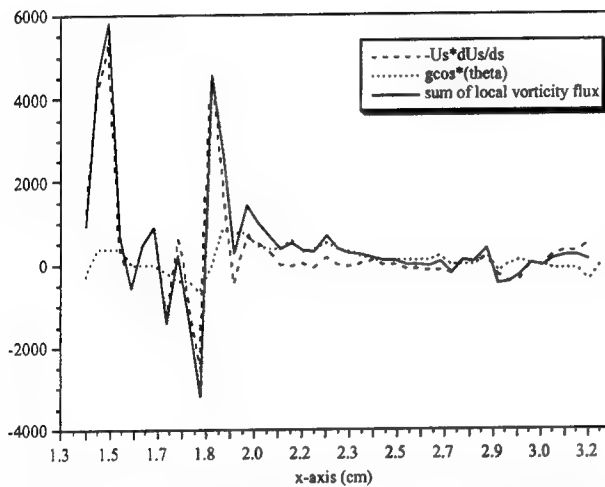


Figure 30. Contributing terms to the vorticity flux. The kinematic deceleration is shown by the dashed line, the gravity term by the dotted line and their sum is shown by the solid line.

Figure 30 shows the deceleration, the gravity term, and their sum for section 2. Likewise, the variations of these terms are seen with the passing of the fluid through the capillaries. Similarly, the contribution to the local vorticity flux is due mostly to the deceleration term and not the gravity term. Furthermore, note that the vorticity flux goes to zero after the last capillary, indicating that there is no flux of vorticity from the free surface beyond the capillaries. Also, the integrated vorticity flux due to the free surface acceleration, the gravity term, and their sum for section 1, corresponding to figure 25, is plotted starting from the first capillary and is shown in figure 31. The integrated viscous vorticity flux shows that after the last trough, the final value achieved is $\sim 200 \text{ cm}^2/\text{s}^2$ at $x=2.2 \text{ cm}$, while that achieved by the integrated vorticity flux due to the gravity term at that point is $\sim 0 \text{ cm}^2/\text{s}^2$. Thus, the capillaries do not contribute to the generation of positive vorticity. The sum of these vorticity fluxes show that the total flux of positive vorticity is $\sim 200 \text{ cm}^2/\text{s}^2$. Clearly, capillary waves are not major sources of positive vorticity generation, rather the dominant source of positive vorticity flux is the deceleration of the free surface.

Aside from the visual observations that breaking does not occur for this case, the mild injection of positive vorticity, of $\sim 200 \text{ cm}^2/\text{s}^2$, into the flow is further indication that breaking has not occurred, and that the phenomena seen is a capillary-gravity wave.

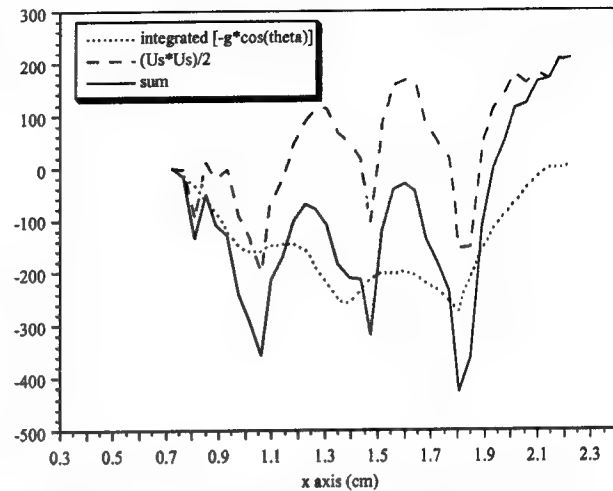


Figure 31. The integrated viscous vorticity flux for section 2 corresponding to figures 25, 26. Integration is begun at the first capillary.

4. CONCLUSION

The sources of vorticity flux are examined for the spilling wave. For the steady spilling breaker, the vorticity flux equation shows contributions from two terms: the fluid deceleration term, and the gravity term. Furthermore, the present results reveal the underlying structure within a spilling breaker responsible for the vorticity flux into the flow. A thin higher-velocity free surface fluid layer decelerates, thus injecting a large amount of vorticity into the fluid bulk, entirely through a viscous process. Moreover, the vorticity injection due to the free surface deceleration is seen to dominate over the gravity-generated vorticity flux. As suggested by Banner and Phillips (2), the higher Froude number data presented indicates that the breaking of the steady spilling wave is characterized by the occurrence of the stagnation point rather than by the discontinuities of the slope due to the breaker. However, further study shows that the source of the viscous vorticity flux for a steady spilling wave is due to the deceleration of the surface fluid, rather than the free surface stagnation point or its sharp curvature, as Lin and Rockwell (10, 11) have suggested. Their setup shows that the transformation to a breaker is particularly abrupt, and the severe changes in the velocity field suggest that the region of deceleration, onset of wave breaking, and stagnation point location are extremely close together. This lead them to the conclusion that the process of flow separation, which is due to the sharp free surface curvature, is the apparent source of vorticity. Our setup, which allows for the clear

distinction between these regions, shows that the surface discontinuous point does not serve as a source of vorticity, but rather as point from which the vorticity separates into a shear layer.

Case 2, the lower Reynolds and Froude number case, shows that the capillary curvature provides a negligible contribution of the gravity term to the vorticity flux, and that the contribution is dominated by the deceleration term as the flow passes through the capillaries. The net flux of vorticity into the flow is shown to be one order of magnitude smaller than that seen in case 1, which would also serve as an indication of the separating shear layer in case 2. Also, the vorticity seen beneath the capillaries is due to the free surface curvature, and while remaining at the free surface, does not flux into the flow from the free surface. The vorticity is thus confined to a region within a thickness of the order of the capillary amplitude.

ACKNOWLEDGMENTS

This work is supported by URI research grant number N00014-92-J-1618 by the office of Naval Research. We gratefully acknowledge the insightful discussions with Dr. Longuet-Higgins, Dr. Doug Dommermuth, and Dr. Edwin Rood that lead to our insight into this topic.

REFERENCES

1. Banner, M.L. & Peregrine, D.H., "Wave Breaking in Deep Water," Annu. Rev. fluid Mech., Vol. 25, 1993, pp. 373-397
2. Banner, M.L. & Phillips, O.M., "On the Incipient Breaking of Small Scale Waves," J. Fluid Mech., Vol. 65, 1974, pp. 647-656.
3. Tulin, M.P. & Cointe, R., "A Theory of Spilling Breakers," Proc. 16th Symp. Naval Hydrodynamics, Berkeley, pp. 93-105. National Academy Press, Washington D.C., 1986
4. Peregrine, D.H. & Svendsen, I.A., "Spilling breakers, bores and hydraulic jumps," Proc. 16th Coastal Engng. Conf. ASCE, Hamburg, Germany, 1978, pp. 540-550.
5. Battjes, J.A., & Sakai, T., "Velocity Field in a Steady Breaker," J. Fluid Mech., Vol. 111, 1981, pp. 421-437.
6. Cointe, R. & Tulin, M., "A Theory of Steady Breakers," J. Fluid Mech., Vol. 276, 1994, pp. 1-20.
7. Duncan, J.H. "An Experimental Investigation of Breaking Waves Produced by a Towed Hydrofoil," Proc. R. Soc. Lond. A, Vol. 377, 1981, pp. 331-348.
8. Duncan, J.H., "The Breaking and Non-breaking Wave Resistance of Two-Dimensional Hydrofoil," J. Fluid Mech., Vol. 126, 1983, pp. 507-520.
9. Duncan, J.H. & Philomin, V., "The Formation of Spilling Breaking Water Waves," Phys. Fluids 6, Vol. 8, 1994, pp. 2558-2560.
10. Lin, J.C. & Rockwell, D., "Instantaneous Structure of a Breaking Wave," Phys. Fluids, Vol. 6, 1994, pp. 2877-2879.
11. Lin, J.C. & Rockwell, D., "Evolution of a Quasi-Steady Breaking Wave," J. Fluid Mech., Vol. 302, 1995, pp. 29-44.
12. Longuet-Higgins, M.S., "Capillary Rollers and Bores," J. Fluid Mech., Vol. 240, 1992, pp. 659-679.
13. Hornung, H.G.; Willert C.E. & Turner, S., "The Flow Field Downstream of a Hydraulic Jump," J. Fluid Mech., Vol. 287, 1995, pp. 299-316.
14. Willert, C.E.; & Gharib, M., "Digital Particle Image Velocimetry," Exp. Fluids, Vol. 10, 1991, pp. 181-193.
15. Cox, C.S., "Measurements of Slopes of High-Frequency Wind Waves," J. Marine Res., Vol. 16, 1958, pp. 199-225.
16. Longuet-Higgins, M.S., "The Generation of Capillary Waves by Steep Gravity Waves," J. Fluid Mech., Vol. 16, 1963, pp. 138-159.
17. Rood, E.P., "Interpreting Vortex Interactions with a Free Surface," Trans. ASME J. Fluid Engng., Vol. 116, No. 1, 1994a, pp. 91-94.
18. Rood, E.P., "Free Surface Vorticity," chapter 17 in Fluid Vortices, S. Green (ed.), Kluwer Academic Publishing, Norwell, MA 1993, in review.
19. Gharib, M. & Weigand, A., "Experimental Studies of Vortex Disconnection and Connection at a Free Surface," Submitted to J. Fluid Mech., 1995
20. Longuet-Higgins, M.S., "Shear Instability in Spilling Breakers," Proc. R. Soc. Lond. A, Vol. 446, 1994, pp. 399-409.

The Flow Field in Steady Breaking Waves

D. Coakley (David Taylor Model Basin, USA),

J. Duncan (University of Maryland, USA)

Abstract

An experimental investigation of steady breaking waves produced by towing fully submerged two-dimensional hydrofoils at constant depth (d), speed (U) and angle of attack is presented. Measurements include the temporal evolution of streamwise and cross-stream profiles of the breakers and flow fields, obtained by particle image velocimetry, in the turbulent zone that rides on the forward face of the wave. (This zone is called the breaking region.) Disturbances on the streamwise profiles propagate downstream at a speed of roughly 0.65 times the speed of the breaker, while disturbances on the cross-stream profiles do not appear to propagate. The wavenumbers, frequencies, phase speeds and amplitudes of the dominant disturbances in the cross-stream profiles increase as the breaker strength is increased (by decreasing the depth of the foil below the free surface). In order to explore the effect of scale on the above results, experiments are performed with three foils with chords of 15, 20 and 30 cm at the same values of Froude number (U/\sqrt{gc} , where g is the acceleration of gravity) and d/c . When the results are nondimensionalized using the time scale $2\pi U/g$ and the length scale $2\pi U^2/g$, it is found that as the scale is increased the frequencies and wavenumbers decrease and the disturbance amplitude increases. The phase speed of these disturbances nondimensionalized by the foil speed does not change with scale. One instantaneous flow field and one mean flow field obtained by averaging 10 instantaneous flow fields are presented for a breaker generated by the 15-cm foil. The development of a shear layer between the nearly stagnant fluid in the breaking region and the fast-moving underlying fluid is clearly seen in the average flow field. This shear layer grows in thickness with distance from the leading edge of the breaking region and significant downstream flow appears at the free surface upstream of the wave crest.

1 Introduction

A number of authors have investigated steady two-dimensional breaking waves produced by hydrofoils moving at constant depth, speed and angle of attack. Battjes and Sakai [1] performed LDV measurements of the flow fields of two such breakers. They found the wake to behave like the momentum-deficient wake of a two-dimensional body in an infinite fluid. Duncan [2, 3, 4] measured the mean breaker shape and the mean flow field in the wake for a number of experimental conditions. The turbulent region of fluid riding on the forward face of the wave was defined as the breaking region. It was found that the drag associated with the breaking process correlated with the downslope component of the weight of the breaking region. The magnitude of the drag due to breaking was found to range from about 1.0 to 3.0 times the maximum drag that could be associated with a nonbreaking wavetrain. Cointe and Tulin [5] performed a theoretical analysis of these waves. The theory was based on a mixing-zone model of the breaker and used some of the experimental data of Duncan to determine the constants of the model. The results were consistent with Duncan's data and explained a number of dynamical effects. The first flow field measurements in the breaking region of these waves was presented by Lin and Rockwell [6, 7]. From analysis of several instantaneous flow fields obtained by particle image velocimetry, they were able to verify that the flow in the breaking region was nearly stagnant as was assumed by other investigators.

Surface ripples generated by these breaking waves have also been investigated previously. Banner and Fooks [8] used two wire-type wave-height gauges to obtain two-point statistics both upstream and downstream of the wave crests. Two breaking waves were studied (wavelengths of 0.2m and 0.33m). Radar returns from these waves were also obtained. It was found that the frequency spec-

tra at all spatial locations showed the same peak frequency in a given wave and that this frequency decreased with the wavelength of the breaker. The wavelength of these fluctuations increased with the wavelength of the breaker. These disturbances were found to propagate downstream. More recently, Walker, Lyzenga, Ericson and Lund [9] studied surface ripples on waves generated with a submerged hydrofoil in a recirculating water channel. They used a single flow speed of 108 cm/sec and studied three waves of different breaking strengths by varying the angle of attack of the foil. Surface shape measurements in the breaking region and in the wake were made photographically with a laser light sheet (aligned with the flow direction) and a video camera. The temporal sampling rate of this system was 30 images per second. Radar returns from these breakers were also measured. It was found that the variance in surface height fluctuations was largest at the breaking region and decreased rapidly with distance behind the breaking wave crest. The temporal frequency of these fluctuations was low at the toe of the breaker and about 8 Hz further back on the breaker. This frequency remained constant with distance downstream in the wake. The variation of these frequencies with breaker strength was not reported, presumably because of the rather low temporal sampling frequency used in this work. It was also found that the wavenumber of the ripples decreased with distance downstream. The fact that the frequency was constant with distance downstream while the amplitude and wavenumber decreased lead the authors to speculate that the ripples were behaving like surface waves propagating on a spatially varying current, which has speeds of 0 at the breaking region and 108 cm/sec in the far wake.

In the present work, both the surface ripples and flow fields in steady, hydrofoil-produced breaking waves are investigated. The waves are generated by three NACA 0012 hydrofoils with chords (c) of 15, 20 and 30 cm. Waves were generated with with one towing speed (U) and three depths of submergence (d) for each foil. The conditions were chosen with a single Froude number U/\sqrt{gc} and three values of d/c that were used for all the experiments. In this way, the effect of experimental scale was investigated. The surface ripple measurements were taken from high-speed movies of the breakers. Both streamwise and cross-stream profiles were taken. The flow field in the breaking region was measured with particle image velocimetry for the weaker breaking conditions. Unlike the studies of Lin and Rockwell [6, 7] many realizations

of the flow field were measured in order to obtain average statistics of the flow fields. In addition, the flow field in the wake of the breakers was also measured to obtain the drag due to breaking. At the time of this writing the analysis of the data is incomplete. In the following the data presented is primarily from the experiments with the 15- and 20-cm foils and is centered on results from stream-wise profiles. Some data from cross-stream profiles and limited PIV measurements in the breaking region is also presented.

In the following the details of the experimental methods are presented in Section 2. This is followed in Section 3 by the results and discussion. Finally, the conclusions are given Section 4.

2 Experimental Details

2.1 Tank and hydrofoils

The experiments were performed in a tank that is 15 m long, 1 m deep, and 1.2 m wide, see Fig. 1. For visualization purposes, the side walls of the tank are composed of tempered glass. The tank includes an underwater towing system for the hydrofoils and an above-surface instrument carriage that moves with the breaking wave. The tracks for the subsurface towing system are 14 meters long and are made of 3.8 cm stainless steel angle. These tracks are positioned at a nominal distance of 48 cm from the tank bottom. Measurements showed that the rail depth variation did not exceed ± 0.75 mm in the center 8 m of the tank where the wave measurements were taken. The force for moving the foil through the water is supplied by a cable and pulley towing system that is powered by an electric motor and gear box located below the tank at one end (see Figure 1). The foil can be towed at speeds up to 1.2 m/s. The same motor that tows the hydrofoils also tows the above-surface instrument carriage. The carriage travels on two precision tracks, one on each side of the tank, and is supported by hydrostatic oil-film bearings. These bearings result in a very low vibration level for the carriage which serves as a platform for the camera and optical equipment. Reproducibility checks on the towing speed speed, made by timing the foil and carriage over a 4-m distance, showed less than 1% error in speed from run to run.

Three hydrofoils were used in the present study. Each hydrofoil has a NACA 0012 shape and is made of anodized aluminum. This foil shape is symmetric

about the chord (c) with the maximum thickness ($0.12c$) occurring at $0.3c$ from the nose. The three hydrofoils have chords of 15.0, 20.0 and 30 cm. All foils have a span of 1.191 m (a little smaller than the width of the tank). The hydrofoils ride on the stainless steel tracks described above via two delrin guides. The guides are attached to the hydrofoils via thin extension plates which are aligned with the flow and are located 2.87 cm from each end of the foil. The breaking waves produced by these hydrofoils appeared to be two-dimensional in the center 0.6 m of the tank. Thus, all measurements were conducted in this region.

2.2 Measurement techniques

The measurements reported herein include surface profile histories of the breaking waves, water surface height versus time at a fixed location in the tank as the wave passes by, and velocity field measurements in the breaking region. The above measurement techniques are described in the following sections.

2.2.1 Surface profile measurements

The breaker surface profile measurement apparatus is shown in Figure 2. The measurement technique is photographic and uses a 5-W Argon-Ion laser mounted at one end of the tank for a light source. The laser beam was collimated by two spherical lenses mounted near the laser. This collimated beam was directed along the center of the tank, at a distance of 0.8 m above the water surface. Upon reaching the instrument carriage, a 12-facet mirror rotating at 25,000 rpm reflected the beam downward and spread it into a light sheet exceeding 50 cm in width. The thickness of the light sheet was adjusted by a pair of cylindrical lenses also mounted on the carriage. The thickness was set to 1 mm for all the experiments. Fluorescein dye was mixed with the water at a concentration of 2 ppm. Thus, the water illuminated by the laser light sheet emitted greenish-yellow light. A 16-mm high-speed camera mounted on top of the carriage, and set to 400 frames per second viewed the measurement area with the aid of two front-surface mirrors. A high-pass optical filter was placed in front of the camera lens to block out any light coming directly from the laser due to specular reflections from the water surface. Lenses and object distances were chosen so that the field of view was nominally equal to the chord of the foil. To minimize regions where

the intersection of the light sheet and the water surface was hidden by local peaks of the water surface between the camera and the light sheet (called dropouts) while allowing reasonably height sensitivity, a look-down angle of nominally 40 degrees was used. The above system produced high-speed movies of the intersection of the light sheet with the water surface. Profile histories were taken with the light sheet and camera oriented as shown in Figure 2 to obtain streamwise profiles of the breaker and with the camera and light sheet turned 90 degrees about a vertical axis to obtain cross-stream profiles with the camera looking downstream.

In order to obtain the surface profile history from the high-speed movies, each frame was digitized with a resolution of 130 pixels/mm and the surface profiles were obtained using a numerical technique with a threshold-based edge finder. To provide reference points in each frame, light-emitting diodes were mounted on the carriage in a manner such that they appeared in the upper left and right corners of all images. Calibration of this system was achieved by photographing several stationary targets including a flat water surface at various heights. Thin lens theory rectification equations including perspective distortion according to Rosenfeld and Kak [10] were implemented. The difference between the actual positions and the predicted positions was minimized using the Powell optimization routine [11] by allowing the lookdown angle to vary. Using this method gives an error of 0.12 cm or less at ± 95 uncertainty for any point in any wave profile. It is estimated that the precision accuracy of this measurement system is 1% for length measurements. (Unless otherwise specified, all precision errors will be based on the student t test to the 95 percent level [12].) The bias error of the data is estimated at 3.0% for length measurements.

Profiles of surface height versus time as the waves passed by a fixed location in the tank were also measured. These measurements were made for both nonbreaking (for calibration purposes) and breaking waves in order to obtain the profile of the entire surface deformation pattern. For these measurements, the instrument carriage was disconnected from the towing cables and held at a fixed position in the tank. The high-speed movie camera was replaced by a ccd line-scan camera (EG&G Reticon) with a 105-210 mm lens. The single line of 2048 light sensitive elements in the camera was oriented vertically so that the top pixels imaged the air where the illumination was low and the bottom pixels imaged the water which was bright due to

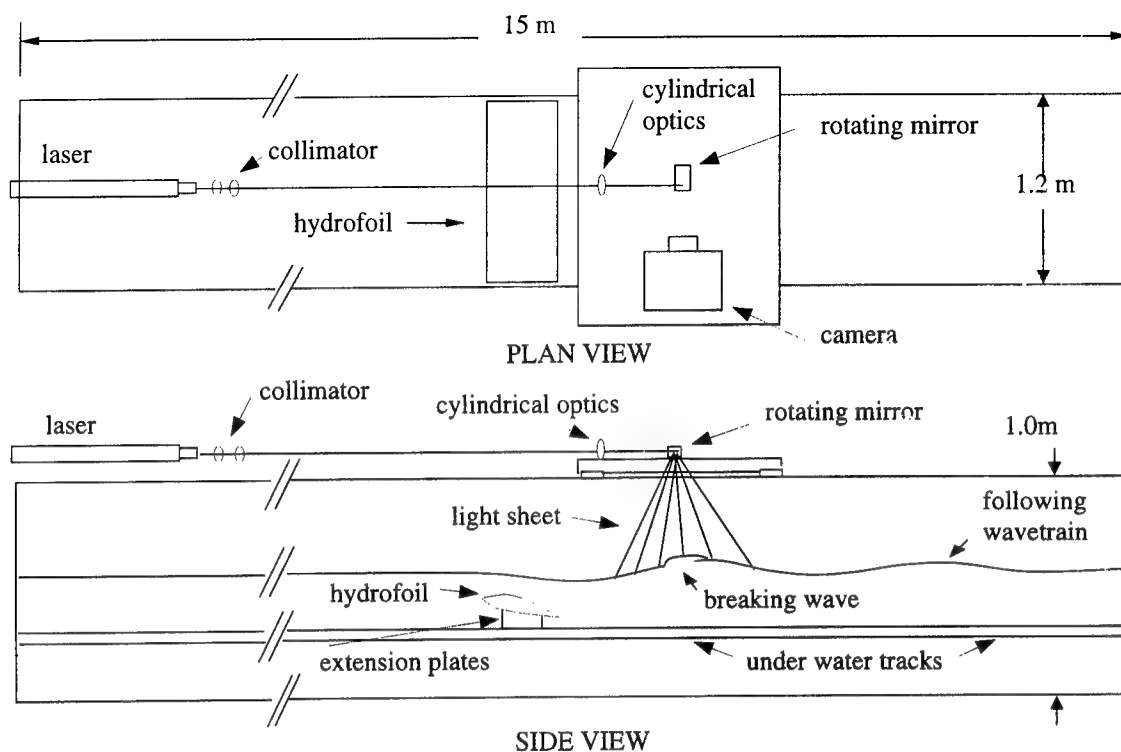


Figure 1: Schematic showing plan and side views of the towing tank with the instrument carriage and hydrofoil.

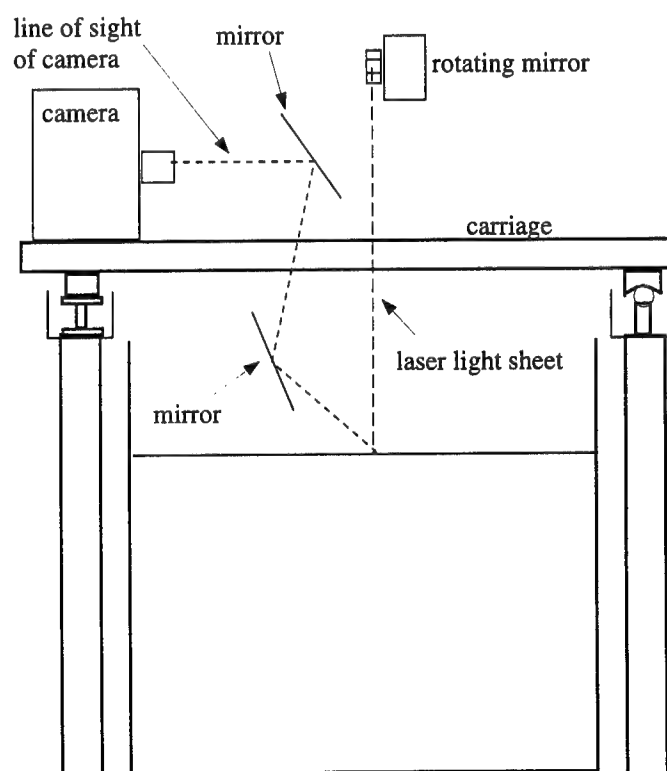


Figure 2: Schematic showing end view of tank with setup for profile measurements.

the fluorescing dye illuminated by the laser. The surface height was taken as the boundary between the dark and light pixels. The sampling frequency of the camera was set to 200 Hz. To increase the light available to the camera, the wide light sheet generated with the rotating prism was replaced by a narrow light sheet generated with two cylindrical lenses.

2.2.2 Particle image velocimetry

The flow field was measured in the breaking region of the wave with particle image velocimetry (PIV). The light source for these measurements was a dual NdYAG laser system. The laser system provided two sequential light pulses at up to 200 mJ in energy and 10 ns duration at precise time separations. In all cases reported here, the time separation between pulses was 0.5 ms or shorter, and was measured by two calibrated oscilloscopes to be within 1% of its set value. The two laser beams were collimated into a single beam which then formed a light sheet as it passed through a set of cylindrical lenses before entering the side of the tank with a horizontal trajectory, see Figure 3. An underwater mirror arrangement deflected the spreading light sheet so that it was vertical and aligned with the direction of wave travel. The light sheet thickness was focused near the still water surface. The light sheet thickness was chosen to be either 1 mm, 2 mm or 4 mm depending on the measurement condition.

The flow was seeded with either 12-micron silver-coated hollow glass spheres or 1.4-micron Titanium-Dioxide particles. The light sheet thickness and particle density were such that about 12 particles were present per square millimeter of measurement area. The images of the particles were captured with a Nikon F3 35-mm camera and a 200-mm, f/2.8, fixed-focal-length lens and recorded on Kodak Tmax ASA 400 black-and-white film. A rotating mirror was placed in the optical path of the camera to provide a bias velocity to the images of the particles. The camera and rotating mirror were mounted in a sturdy housing which maintained the close geometrical alignment needed for the experiments, see Figure 3. The camera pointed in a direction parallel to the length of the tank. The mount also allowed rotation of the camera and mirror about the centerline of the camera lens so that the camera could look up toward the water surface with an angle of up to 20 degrees from the horizontal. The in-air optical distance from film plane to the measurement volume was approximately 0.9

m resulting in a field of view of about 12 cm at the light sheet. The bias velocities provided by the rotating mirror were typically equivalent to, but sometimes faster than, twice the wave phase speed and in the direction opposite to the wave propagation.

Timing of the lasers, camera and mirror rotation was accomplished with a specially constructed timing circuit. Between experimental runs, the timing circuit fired the laser system continuously with a 30 Hz repetition rate. During each run, upon the closing of a stationary limit switch actuated by the passing of a spindle attached to the tow cables, the timing box interrupted the laser firing cycle so that the lasers fired a known time later, triggered the camera whose shutter remained open for 1/30 of a second, and started the mirror rotation. The relative position of the foil and the camera at the time the lasers fired was repeatable to less than 1 mm with this system. The magnitude of this error was governed by the interaction of the spindle with the limit switch.

In the breaking region, the turbulence intensity is high, the local velocities range approximately from 0 up to the wave phase speed, and the free surface is very rough. Therefore, a look-up angle of 17 degrees was used for the camera and a second camera was used to view the water surface from above with a 30 degree look-down angle, see Figure 3. The combination of the two camera views allowed the surface to be located with an accuracy of about 1 mm in most regions of the images despite the large local peaks and valleys of the surface. To achieve adequate quality of the images of the particles in the underwater images, the lens aperture was set to f/16 or f/22 and the camera was modified by the inclusion of a wedge-shaped lens mount which tilted the film plane with respect to the centerline of the lens. This tilting was such that it shortened the optical path for particles in the top of image and increased it for particles in the bottom of the image, thus offsetting the difference in optical path caused by the large look-up angle.

The PIV images were digitized with a Nikon 3510AF, eight-bit film scanner at a spatial resolution of 125 pixels per millimeter (4000 by 2500 pixels per negative). Images with no flow (stationary hydrofoil) were analyzed to obtain the bias velocity induced by the mirror. Velocities were obtained using two-dimensional correlation techniques. The correlation functions were computed directly and with Fourier transform methods using window sizes

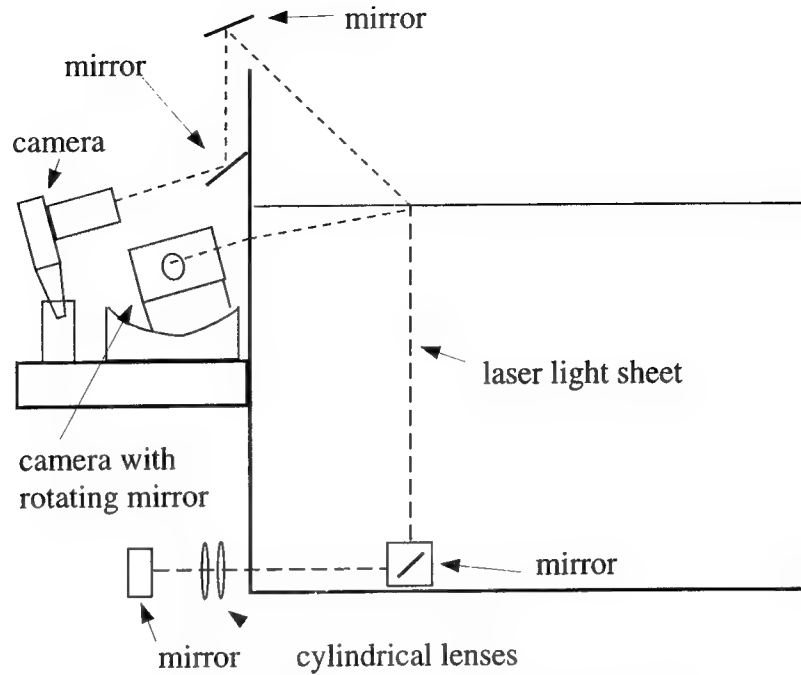


Figure 3: Schematic showing end view of PIV setup.

of 80 by 80 pixels. The resulting velocities are accurate to better than 5% of the 11 pixel displacement corresponding to the wave phase velocity. (Based on laboratory-scale velocity, with velocities of almost twice the phase velocity, the accuracy is 3%). The correlation techniques give obviously bad results in areas of high shear. Techniques to deal with this problem are presently under investigation. In the present, preliminary results, bad vectors (a bad vector being defined as a vector exceeding a threshold standard deviation from its nearest neighbors), were replaced by the average of their nearest neighbors. Since the PIV results are used only for descriptive purposes in the present paper, the above techniques are considered adequate.

2.3 Experimental conditions

A set of Froude-scaled experimental conditions was chosen in order to aid in scaling the laboratory results up to full scale. The largest towing speed practical in the present tank, 100cm/s, was chosen for the largest foil. At the present time, preliminary results are available only for the two smaller foils and the corresponding experimental conditions are given in Table 1 ($Fr = U/\sqrt{gc}$).

$c(\text{cm})$	$U(\text{cm/s})$	$d(\text{cm})$	d/c	Fr
15	69.28	12.0	0.8	0.571
15	69.28	15.3	1.02	0.571
15	69.28	16.5	1.10	0.571
20	80.0	16.0	0.8	0.571
20	80.0	20.4	1.02	0.571
20	80.0	22.0	1.10	0.571
30	97.98	24.0	0.8	0.571

Table 1: Experimental conditions.

3 Results and Discussion

In the following, the data is presented nondimensionally with lengths and times scaled with the wavelengths (λ_0) and periods (T_0) obtained from the deepwater dispersion relation:

$$\lambda_0 = 2\pi \frac{U^2}{g} \quad (1)$$

and

$$T_0 = \frac{1}{f_0} = \frac{2\pi U}{g} \quad (2)$$

When mass units are required the value of the density of fresh water at 20C, 0.9982 gm/cm³ is used. For the cases considered in this paper, $\lambda_0 = 30.77$, 41.02 and 61.55 cm and $f_0 = 2.25$, 1.95 and 1.59 Hz

for the breakers produced by the 15-cm, 20-cm and 30-cm foils, respectively. Throughout this paper, the breakers will be referred to by the speed which produced them, e.g. the 69-cm/s breaker refers to the breaker produced by the 15-cm foil.

3.1 Surface profile measurements

The parts of the surface profiles upstream of the breaker, where the flow is laminar and the surface curvatures are small, should not be affected significantly by surface tension and viscous effects. Thus, if the flow conditions are successfully Froude scaled, surface profiles upstream of the breaker for tests with the two hydrofoils and the same values of d/c should be identical when nondimensionalized by λ_0 . The surface profiles were measured with the optical wave-height gauge placed at a fixed position in the tank. Figure 4 shows the results of averaging a small number of runs (between 3 and 8) of each of the 6 cases (the 15 and 20-cm foils with $d = 0.8c$, $1.02c$, and $1.1c$). An important measure contained in these figures is the vertical distance from the mean water level to the trough immediately behind the foil. This height was found not to vary by more than 3% between the two foil scales for a given value of d/c . It is believed that this variation is due to a slight change in angle of attack between the two foils. This inaccuracy in angle of attack is estimated at 0.24 degrees and is considered unavoidable with the present experimental setup.

Surface profile histories of the breaking regions were obtained from the high-speed movies (taken at 400 frames/s) as described in the previous section. Every other frame of each movie (a sampling rate of 200 Hz) was digitized and the surface profiles were obtained with a threshold-based edge detector that allowed multi-valued surface heights at any streamwise position. This process typically resulted in about 400 profiles from a single experimental run. In order to perform the spectral analysis described in the following, the surface profiles were then conditioned to remove the multi-valued surfaces, taking the highest value in such cases. The data was then averaged and the average was subtracted from each of the conditioned profiles. The resulting data from both streamwise and cross-stream profiles for both hydrofoils and $d/c = 1.02$ is given in Figure 5. All profiles are plotted in non-dimensional coordinates. The streamwise profiles show an area near the leading edge of the breaking region where the surface fluctuations oscillate upstream and down-

stream. However, over most of the breaking region it is apparent that the surface height fluctuations propagate downstream and that the wavelength of these fluctuations increases with downstream distance. Similar results for a single flow speed and several depths of submergence were reported by Walker et al. (1996) with a sampling frequency of 30 Hz. In the cross-stream profiles, the surface height fluctuations do not appear to propagate. It is evident from the comparison of the streamwise and cross-stream profile histories that there is a strong two-dimensional component to the surface ripples which is aligned parallel to the wave crest. Since the distances and times in Figure 5 are scaled with λ_0 and T_0 , respectively, the profile histories would be identical in a statistical sense if surface tension and viscosity did not play a role. The difference between the sets of profiles from the larger and smaller scale experiments is primarily that there is more small-scale structure in the larger scale experiment.

Further examination of the differences between the surface-height fluctuations at the two experimental scales was performed through spectral analysis of data like that shown in Figure 5. Figure 6 shows the resulting spectra for the streamwise profile histories and Table 2 contains the nondimensional frequencies (f/f_0) and wavenumber (k/k_0) of the spectral peaks. The dimensionless phase speed, c/c_0 where $c = \omega/k$ and $c_0 = \omega_0/k_0$, is also given in the table. All three dimensionless quantities decrease as the breaker becomes more intense (smaller d/c) for both hydrofoils. The dimensionless frequencies and wavenumbers decrease as the scale is increased from the 69-cm/s breaker to the 80-cm/s breaker while the phase speeds remain nearly the same. The smallest changes in frequency and wavenumber with scale occur for the cases with $d/c = 1.02$. It is expected that processing additional experimental runs will give more consistent results between the different experimental conditions.

Wavenumber-frequency spectra calculated from the cross-stream surface profile histories for $d/c = 1.02$ are shown in Figure 7. The corresponding wavenumber-frequency spectra calculated from the streamwise surface profile histories were presented in the center row of Figure 6. Cross-stream profiles for the other experimental conditions ($d/c = 0.8$ and 1.10) are currently being reduced. The cross-stream spectra are dominated by energy at zero wavenumber. This result can be anticipated from the profile history data in Figure 5 in that the data is dominated by two-dimensional structure

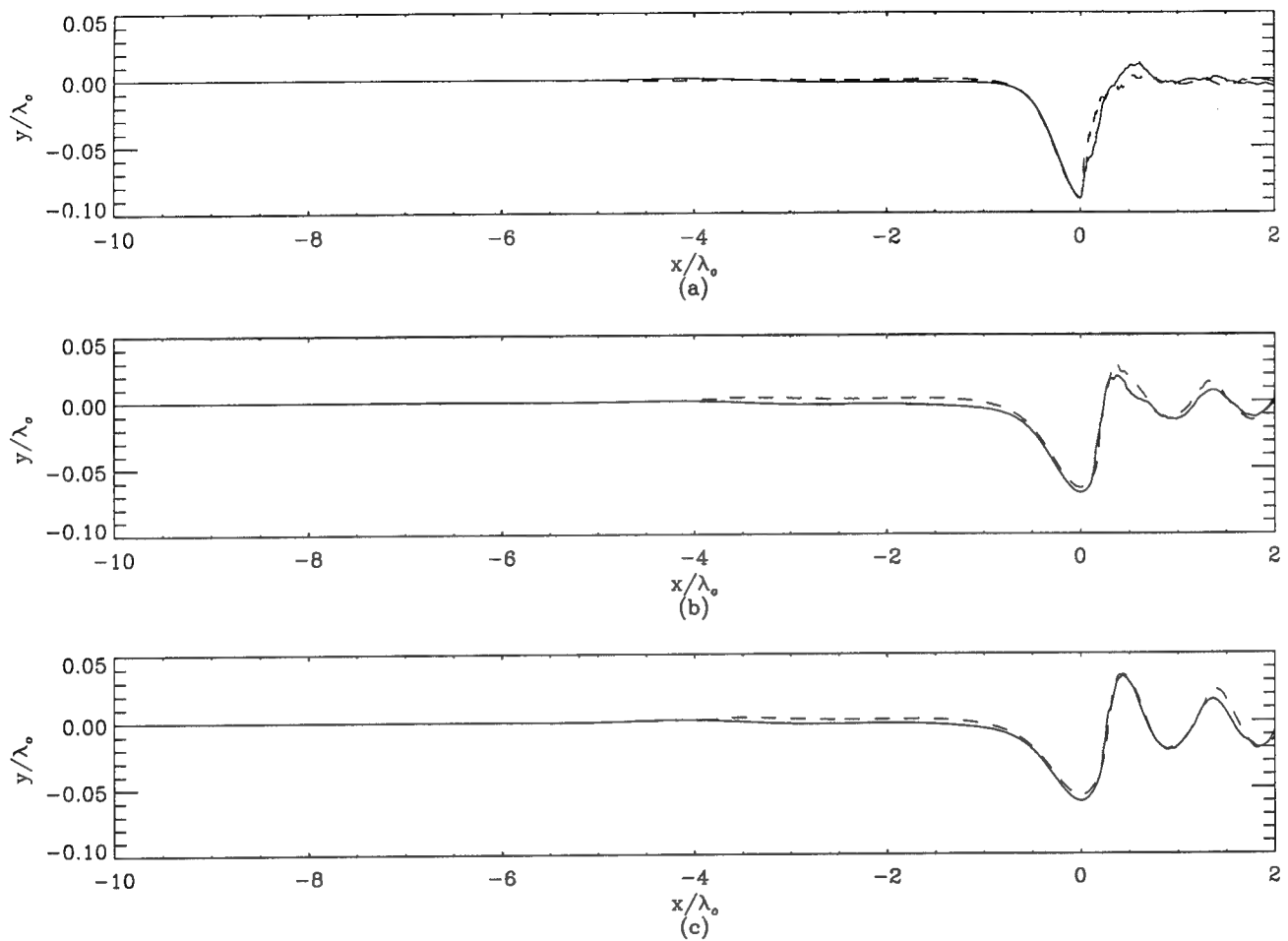


Figure 4: Comparison of the nondimensional average wave profiles for the 15-cm and 20-cm hydrofoils. This data was taken with the stationary optical wave-height gauge. (a) 0.8c depth; (b) 1.02c depth; (c) 1.10c depth. The solid lines are the 15-cm foil cases, and the dashed lines are the 20 cm foil cases.

	69-cm/s wave				80-cm/s wave			
d/c	k/k_0	f/f_0	c/c_0	$\eta'^2/\lambda_0^2 \times 10^5$	k/k_0	f/f_0	c/c_0	$\eta'^2/\lambda_0^2 \times 10^5$
0.8	6.7	4.0	0.60	6.91	5.4	3.2	0.59	10.7
1.02	7.2	5.0	0.69	3.72	6.8	4.9	0.72	5.69
1.10	8.8	6.6	0.75	1.47	7.6	6.0	0.79	2.12

Table 2: Spectral peaks, dominant disturbance, presented as reciprocal wavenumber (length/cycle) nondimensionalized by the wavelength, frequency, nondimensionalized by the deep water wave frequency, and characteristic velocity.

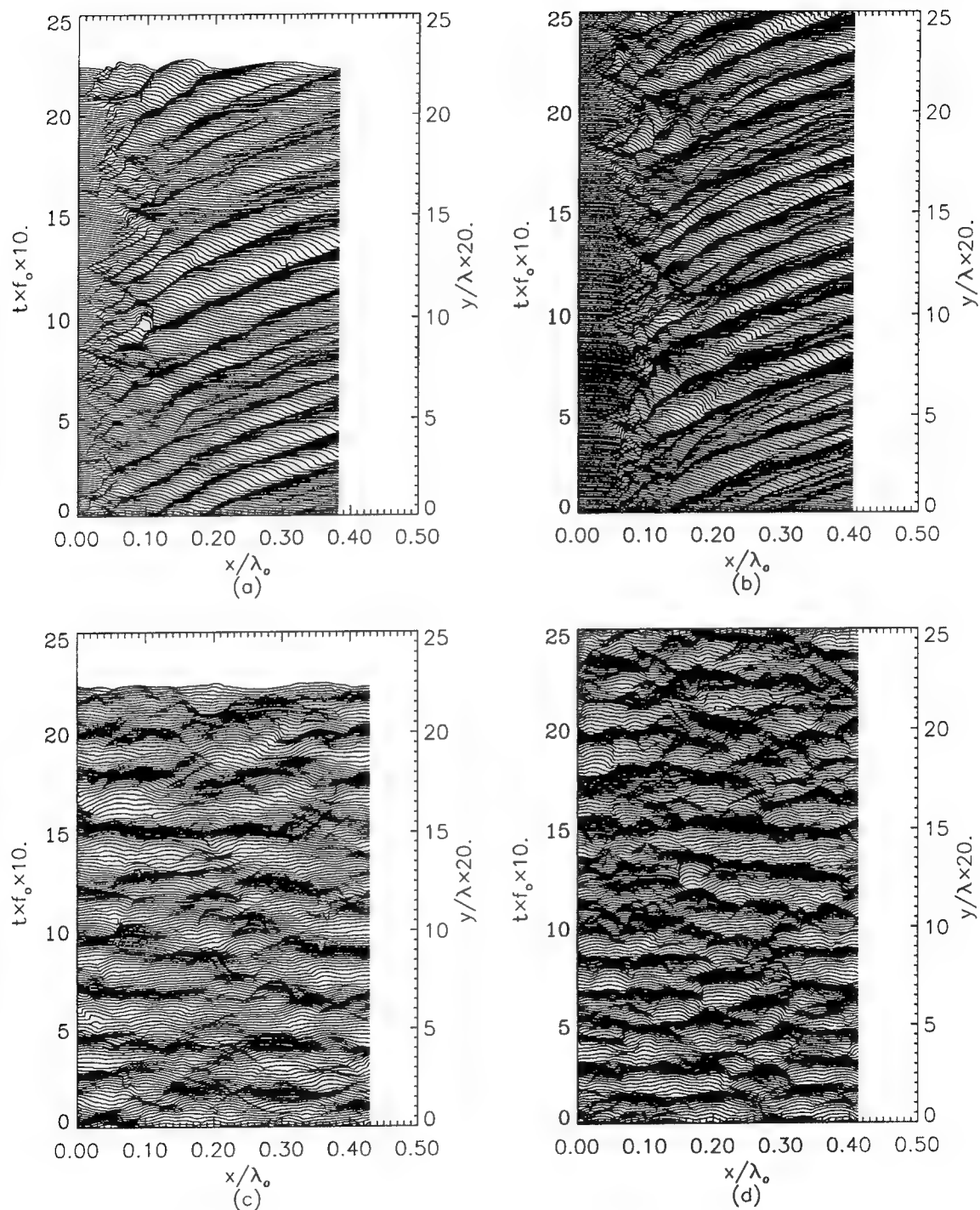


Figure 5: Breaking region profile histories for $d/c = 1.02$. Each curve is a profile of dimensionless surface height versus dimensionless horizontal distance. The profiles at successive times are displaced vertically upward in the plots for clarity of the presentation. (a) 15-cm foil, streamwise profiles; (b) 20-cm foil streamwise profiles; (c) 15-cm cross-stream profiles; (d) 20-cm foil cross-stream profiles.

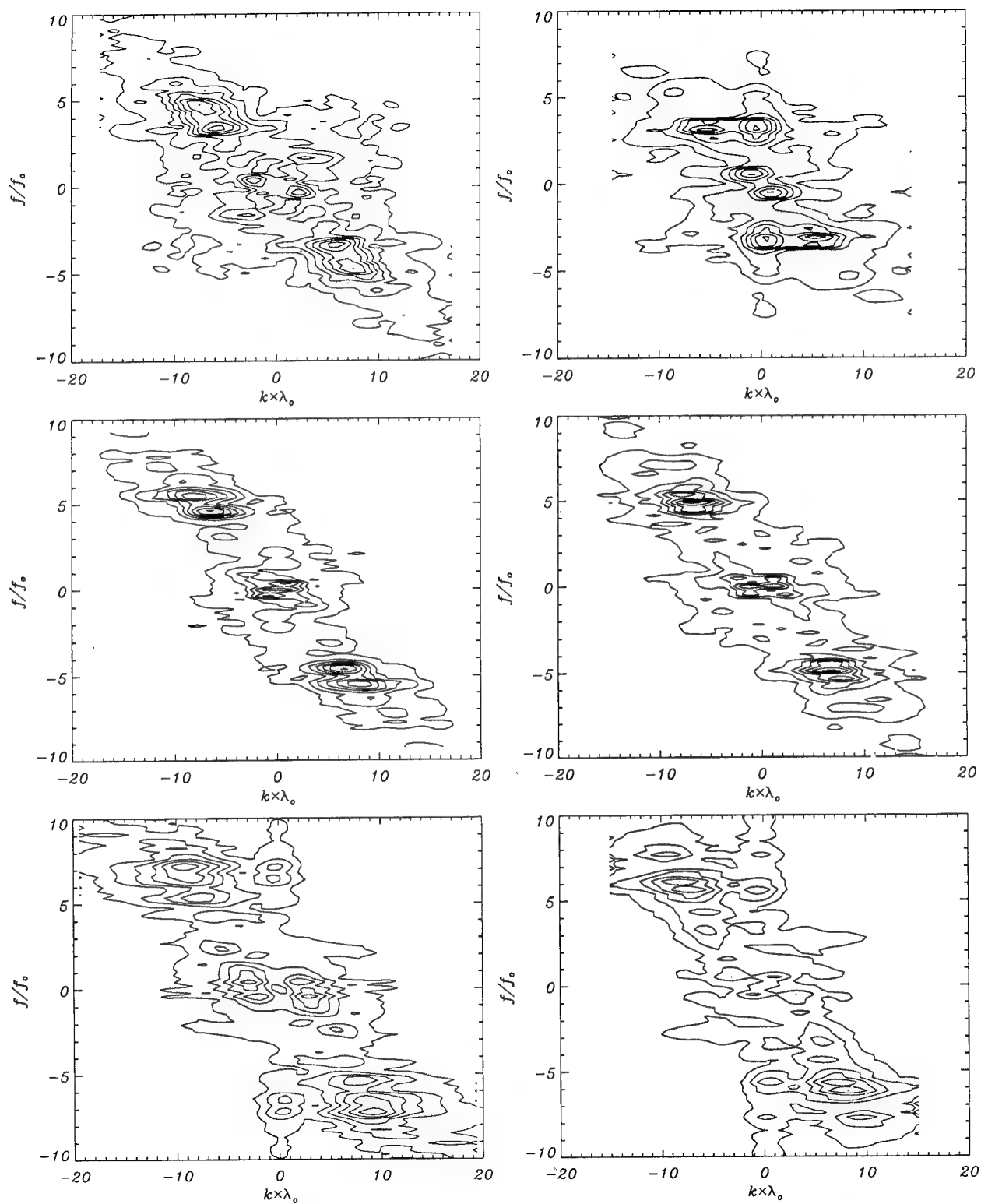


Figure 6: Wavenumber-frequency spectra from streamwise profile histories for the six Froude-scaled conditions. The three left-hand graphs are the 69-cm/s cases, and the right-hand graphs are the 80-cm/s cases. In both columns, the depths of submergence are 0.8c (top), 1.02c (middle) and 1.10c (bottom).

that is aligned cross-stream and propagates downstream. Thus, the cross-stream profiles show high-frequency structure that rides on a mean level that moves up and down as the two-dimensional structures move through the measuring station.

Another interesting parameter describing the surface-height fluctuations is the variance. The variances were calculated from the streamwise profile histories for each of the six experimental conditions and are given in Table 2 nondimensionalized by λ_0^2 . As can be seen from the data, the variance increases with both breaker intensity and wave scale. The difference in variance between the breakers produced by the two foils appear to increase with the intensity of the breaker. The change in variance between the 69-cm/s breakers and the 80-cm/s breakers is approximately a factor of 1.2 for the weakest breakers and 1.5 for the strongest breakers.

The above results indicate a significant departure from Froude scaling for the wavenumbers, frequencies and amplitudes of the surface ripple statistics. Duncan and Dimas [13] compared experimental ripple measurements to the results of an inviscid, linear, free-surface shear-flow instability model without surface tension. It was found that the dominant frequencies and wavenumbers of the surface-height fluctuations correspond to the most unstable waves on a shear layer that is produced between the flow in the breaking region, which was assumed to be a weak recirculation region, and the fast-moving underlying flow. Using this model of ripple generation one can think of two causes for the lack of Froude scaling of the present surface ripple data. First, at the two experimental scales, the scaled shear layer maybe significantly different and this would then affect the most unstable wavenumbers and frequencies. Second, if the shear layers do Froude scale, the most unstable waves might be changed because of the varying influence of surface tension and viscosity. The flow field measurements presented in the following section are aimed at exploring these effects. Only preliminary results for one experimental condition are available at the present time.

3.2 Flow field measurements

To gain a measure of understanding of the flow field beneath the breakers, particle image velocimetry (PIV) was conducted for three of the nine cases studied as part of this work. Approximately 400 images have been taken but, to date only data

from 10 images taken of the 69-cm/s breakers with $d/c = 1.02$ have been partially analyzed. Figure 8 shows a single realization of flow field of this breaking wave and an average flow field obtained 10 similar instantaneous flow fields. The reference frame chosen is that of the breaking wave crest. The instantaneous flow field shows a nearly stagnant region on the forward face of the wave with a thin shear layer separating it from the underlying flow. This is similar to the findings of Lin and Rockwell (1995 and 1996). Downstream of $x = 65$ mm the flow in the breaking region is slow but primarily downstream while upstream of this point the flow close to the free surface is directed upstream. The average flow field shows some spatial fluctuations that indicate that a larger number of samples is needed to obtain a good average. However, it does begin to show the characteristics of a mixing-layer flow. The mean shear layer is thin at the toe of the breaking region and increases in thickness with distance downstream. Upstream of about $x = 75$ mm the flow at the surface is nearly stagnant as can be seen by the small magnitude and nearly random orientation of the velocity vectors. Downstream of $x = 75$ mm the shear layer has grown significantly in thickness and the flow at the surface is consistently downstream. A mixing layer model with a stagnation point at the crest was used in the work of Cointe and Tulin [5].

3.3 Jet formation

Drops are sometimes formed from the surface of the breaking region. This process can be initiated by jets which emerge from the surface due to strong turbulent motions which overcome gravitational and surface tension forces. A sequence of streamwise wave profiles showing the formation of two jets is presented in Figure 9. This sequence is from an experimental run with the 30-cm foil at $d/c = 0.8$. The sequence on the left shows 0.86 seconds of data, with the time between profiles of 0.025 s. The two jets are formed near the toe of the breaker during this sequence, one at a time of 0.2 s and one at 0.55 s. Both jets have at least some forward component of velocity over their entire lifetime. The center plot in Figure 9 shows the first jet in more detail. The underside of the jet is somewhat ragged and changes from frame to frame because of the image digitization. The second jet, shown in the right-hand plot, appears after the remnants of the first jet are overtaken by a forward moving disturbance which falls ahead of the toe. As this second disturbance is overtaken by the

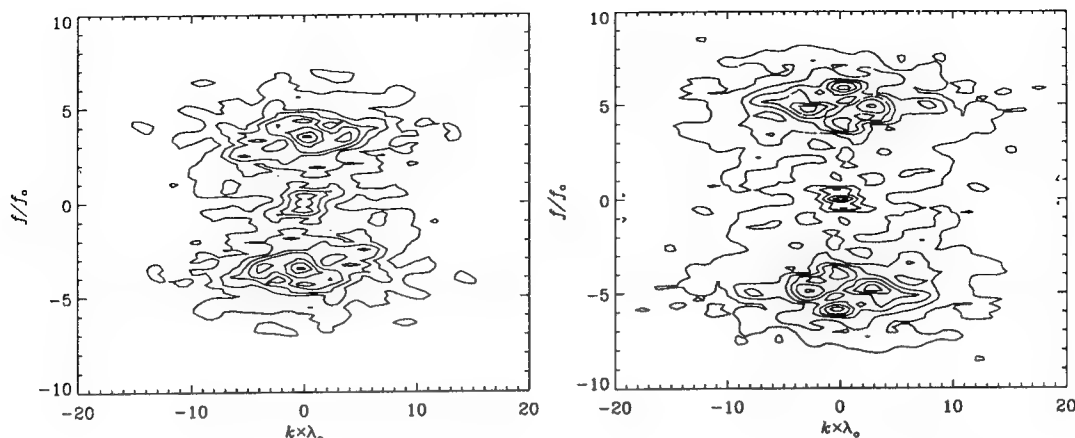


Figure 7: Wavenumber-frequency spectra from cross-stream profile histories for two Froude-scaled conditions with $d/c = 1.02$. The left-hand graph is for $U = 69$ cm/s, and the right-hand graph is for $U = 80$ cm/s.

rest of the wave, a third forward moving disturbance interacts with it, producing the jet. The jet characteristic speed is on the order of 100 cm/s, the characteristic acceleration is 10 m/s^2 , and the length of the jet is about 1 cm. The high-speed movies indicate that drops are formed after the jet falls into the water surface. These are not picked up by the surface following algorithm and are therefore not visible in the figure.

3.4 Full-scale observations

The present experiments cover a range of flow speeds from about 70 to 100 cm/s. Full scale ship speeds might be as high as 1500 cm/s, but because it is primarily the divergent waves that are breaking and the crest angle of these waves is at about 19° from the ship's path, the actual phase speed of these waves is at most about $1500 \cos(90 - 19^\circ) \approx 500$ cm/s. This indicates that the wave phase speed at full scale can be as much as 5 times the wave phase speeds in the present experiments. Thus, it is relevant to ask whether the surface disturbances found in the laboratory will be seen in the breakers around full-scale ships. To this end, Figure 10 is presented which shows two photographs of the stern waves generated by the Brittany, a 60-ft long personnel transport vessel / work boat. Both photographs were taken in the summer of 1995, off Eleuthera Island, Bahamas. The top photograph shows the diverging transom wave at a steady speed of 11 knots. The camera was pointed in a direction slightly starboard of astern. The field of view is 8 to 10 m at the center of the photograph. The wave crest is shown as a dashed line. The local peaks ahead of the crest appear similar to the ones

in the present experiments as shown in the streamwise profiles in Figure 5. The bottom photograph shows a diverging transom wave at a steady speed of 8 knots. The camera is pointed in a direction slightly aft of midway between the starboard and stern quarters. The wave crest is shown as a dashed line. The dotted line is the peak of a dominant disturbance which is in the process of traveling up and to the left (towards the wave crest). This disturbance is so large that it might be mistaken for the wave crest itself. Six to 8 m of the crest is visible. Many of the approximately 150 photographs taken during the voyage display similar large disturbances. These disturbances are thought to be large-scale versions of the disturbances observed in the laboratory. It is also interesting to note that in the bottom photograph many droplets can be seen as well as many jet-like projections from the surface. These projections are similar to those shown in Figure 9. Many of the droplets appear to be formed from the jet-like projections

4 Conclusion

Surface profile and flow field measurements from a Froude-scaled steady breaking wave experiment have been presented. The streamwise profile measurements show significant effects of scale with the dimensionless wavenumber and frequency of the surface disturbances decreasing, the dimensionless phase speed remaining nearly constant and the dimensionless amplitude increasing with scale. At the larger scales, the formation of surface jets that tend to eject droplets into the air are observed. Preliminary particle-image-velocimetry measurements

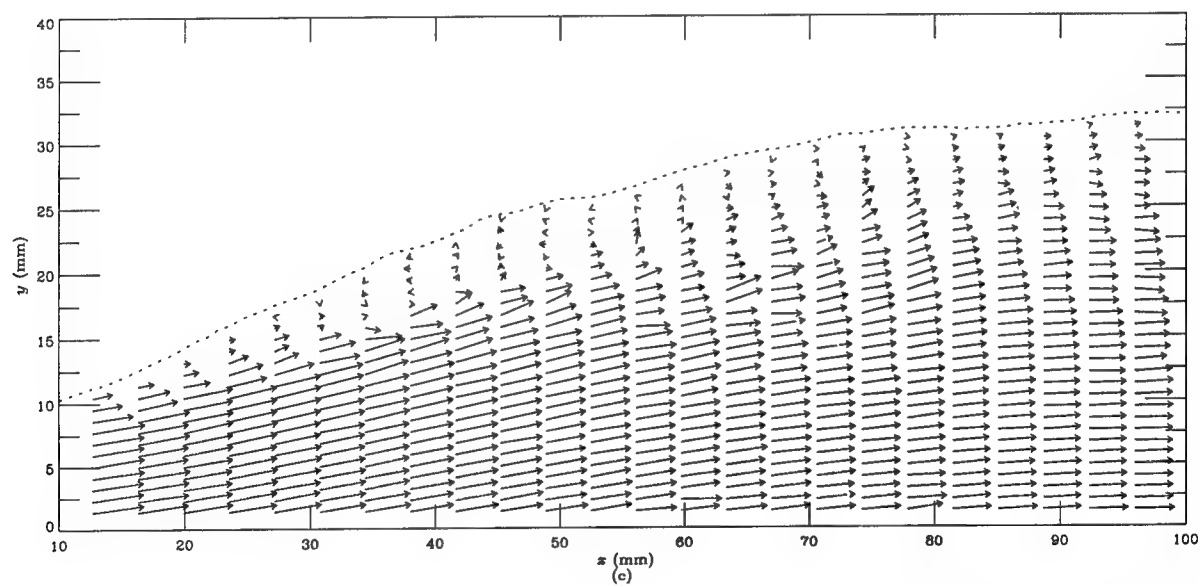
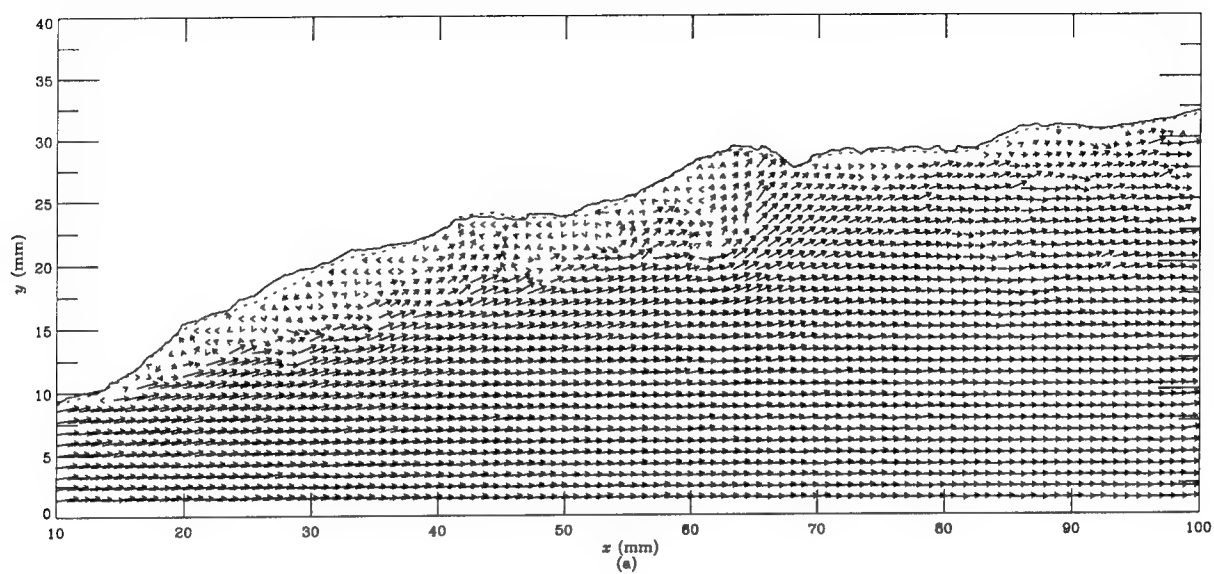


Figure 8: Particle image velocimetry results, 15-cm foil, $d/c = 1.02$. Top: instantaneous velocity field. Bottom: average of ten velocity fields. Solid lines are the surface obtained from the top camera, dotted lines are the surface obtained from the bottom camera.

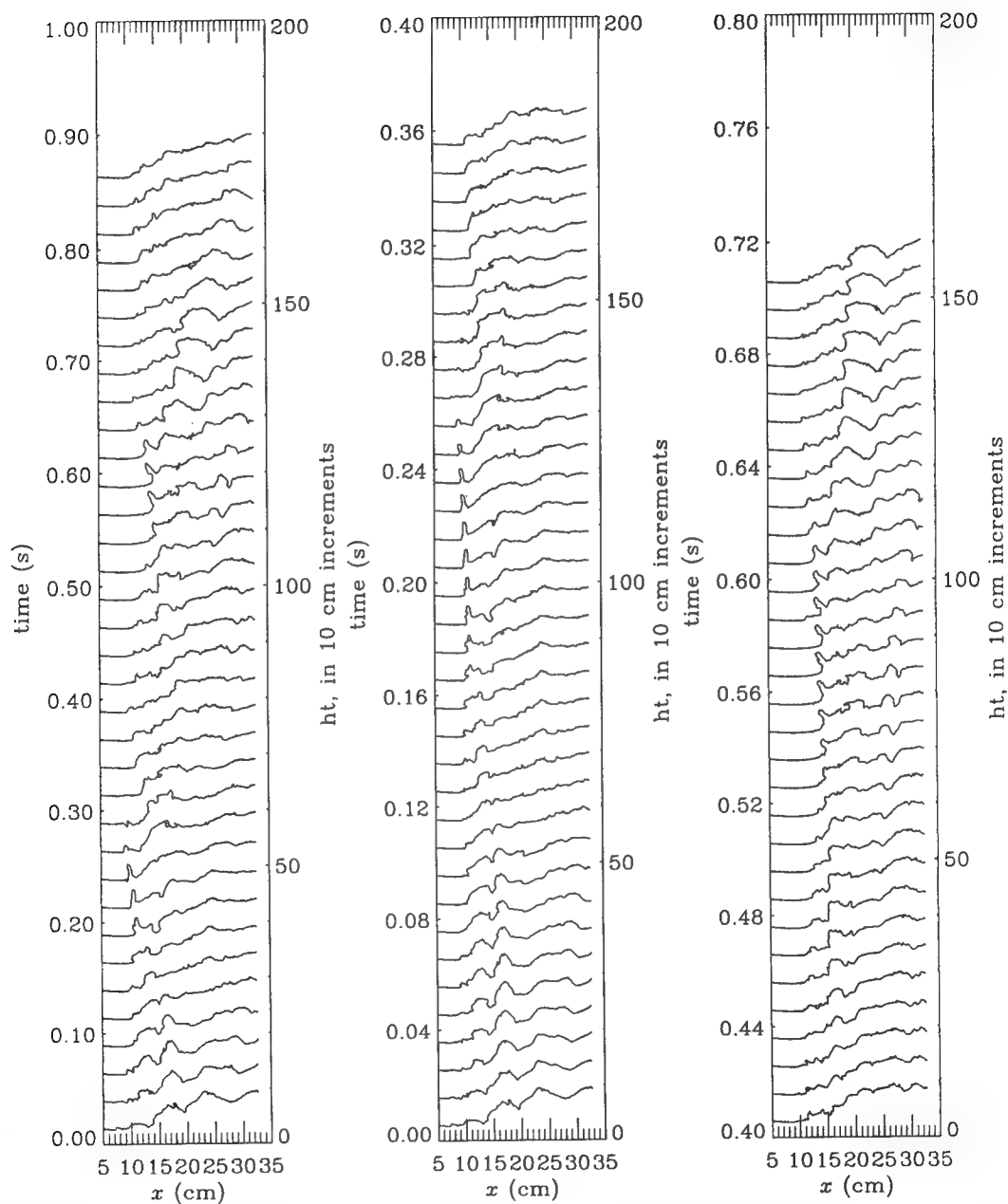


Figure 9: Sequence of jet formation, 30-cm foil, $d/c = 0.8$: (left) 1-second time sequence with 0.025 seconds between frames; (center) closeup of first jet formation in the left sequence, 0.01 seconds between frames; (right) closeup of second jet formation in the left sequence, 0.01 seconds between frames.



Figure 10: Waves produced by the work boat Brittany.

in the breaking region were presented. A flow field obtained by averaging 10 instantaneous flow fields clearly shows the evolution of a shear layer between the nearly stagnant fluid in the breaking region and the fast-moving underlying flow. From this preliminary data, it appears that the flow at the free surface near the crest is directed downstream.

Acknowledgments

This work was supported by the Office of Naval Research under contract N00014-90-J-1977 and the David Taylor Model Basin (DTMB). The authors acknowledge a number of helpful discussions with D. Rockwell and J. Katz on PIV techniques. Haibing Qiao assisted in the data acquisition of the breaker region PIV experiments, construction of the PIV equipment, and in writing some of the PIV analysis software. John Hamilton of DTMB engineered and built a timing device that was used in the PIV measurements. Alexandra Wenz developed most of the high-speed films used during these experiments. Arno Miessner and Sebastian Muncher helped to analyze some of the early high-speed movie films. Sven Eisen helped to construct some of the tank apparatus. Bruce Webster of DTMB is gratefully acknowledged for his patience in allowing a flexible work schedule for Mr. Coakley.

References

- [1] Battjes, J. A. and Sakai, T. 1981 Velocity field in a steady breaker. *J. Fluid Mech.* **111**, 421-437.
- [2] Duncan, J. H. 1981 An experimental investigation of breaking waves generated by a towed hydrofoil. *Proc. R. Soc. Lond. A* **377**, 331-348.
- [3] Duncan, J. H. 1983a The breaking and non-breaking wave resistance of a two-dimensional hydrofoil. *J. Fluid Mech.* **126**, 507-520.
- [4] Duncan, J. H. 1983b A note on the evaluation of the wave resistance of two-dimensional bodies from measurements of the downstream profile. *J. Ship Res.* **27**, No. 2, 90-92.
- [5] Cointe, R. and Tulin, M. P. 1994 A Theory of Steady Breakers. *J. Fluid Mech.* **276**, 1-20.
- [6] Lin, J.-C. and Rockwell, D. 1994 Instantaneous Structure of a Breaking Wave. *Physics of Fluids* **6**, 2877-2879.
- [7] Lin, J.-C. and Rockwell, D. 1996 Evolution of a Quasi-Steady Breaking Wave. *J. Fluid Mech.* (in press).
- [8] Banner, M. L. and Fooks, E.H. 1985. On the microwave reflectivity of small-scale breaking water waves. *Proc. R. Soc. London Ser. A* **399**, 93-109.
- [9] Walker, D. T., Lyzenga, D. R., Ericson, E. A. and Lund, D. E. 1996 Radar Backscatter and Surface Roughness Measurements for Stationary Breaking Waves. *Proc. R. Soc. Lond. A* (in press).
- [10] Rosenfeld, A. and Kak, A. 1982 *Digital Picture Processing*, Academic Press.
- [11] Press, W., Flannery, B., Teukolsky, S. and Vetterling, W. 1986 *Numerical Recipes*, Cambridge University Press, Cambridge, U.K.
- [12] Coleman, H.W. and Steele, W.G. 1989 *Experimentation and Uncertainty Analysis for Engineers*, John Wiley and Sons, New York.
- [13] Duncan, J. H. and Dimas, A. A. 1996 Ripples Generated by Steady Breaking Waves, submitted to the *J. Fluid Mech.*

Freak Waves—A Three-Dimensional Wave Simulation

K. Trulsen, K. Dysthe (University of Bergen, Norway)

Abstract

We seek to understand the occurrence of so-called freak waves, extremely large and steep ocean surface waves. Our basic assumption is that these waves can be produced by nonlinear self modulation of a slowly modulated wave train. A field experimental record of a freak wave event is presented, and is shown to comply with a description as a weakly nonlinear band-limited process. However, existing models for weakly nonlinear, slowly modulated surface gravity waves, i.e. the third order nonlinear Schrödinger equation and the fourth order modified nonlinear Schrödinger equation, do not have sufficient resolution in bandwidth. We thus extend the modified nonlinear Schrödinger equation by relaxing the narrow bandwidth constraint to make it more suitable for application to a realistic ocean wave spectrum. A split-step Fourier collocation method is discussed for the numerical solution of the new equation.

1 Introduction

The sudden occurrence of extremely large and steep ocean waves imposes a hazard to fishing boats, ships and off-shore oil activities. It is therefore important to understand the mechanisms that can give rise to such waves.

The term "freak wave" was apparently introduced by Draper (1965). It has been used to denote single waves that are extremely "unlikely" as judged by a Rayleigh distribution of waveheights (Dean 1990). In practical terms, a waveheight H exceeding the significant waveheight $H_{1/3}$ by a factor 2.2 has been applied as a criterion. Extreme waves occurring in laboratory generated irregular wavetrains have been found to possess a significant crest-to-trough asym-

metry (Stansberg 1990). A ratio between the maximum crest height and the associated peak-to-trough height H in the range 0.6–0.65 is not unusual.

One can often explain frequent events of extreme waves at certain geographical locations by the presence of ocean currents or bottom topography that can cause wave energy to focus in a small area due to refraction, reflection (caustics) and wave trapping. A well known locality with frequent reports of dangerous waves is the area off the east coast of South Africa, where the Agulhas current runs southwest along the coast and meets swells from storms farther south. Many ships have been lost due to unusually high waves in this area (Mallory 1974). These mechanisms are well understood, and can essentially be explained by linear theory.

It is, however, not well understood why exceptionally large waves can occur in the open ocean, away from non-uniform currents or bathymetry.

Field measurements of such an event are presented in figures 1 and 2. Figure 1 shows a time series of the water surface elevation at one particular point. The measurements were taken by a downward pointing radar at 16/11-E in the Norwegian sector of the North Sea on January 1, 1995. We see a high wave occurring approximately four and a half minutes after the beginning of the time series. From these data we compute the significant waveheight (crest-to-trough) to be 10.8 m, while the maximum waveheight is 25.6 m (we have defined crests/troughs as the maxima/minima of the time series between zero crossings, sometimes referred to as z-crests and z-troughs). With the ratio 2.36 between the maximum height and the significant height, this wave qualifies as a freak wave according to the above definitions. The corresponding power spectrum is shown in figure 2. Unfortunately, no measurements on the direc-

tional spread of the wave spectrum is available at the same location for this event.

The field measurements presented in figures 1 and 2 can be used to get a rough quantitative idea of the magnitudes of some relevant parameters characterizing these waves. We will describe the wavetrain as a slow modulation around a central wave (with wave vector k_0) of the energy spectrum. The central frequency can be estimated from figure 2 to be $f_0 \approx 0.074$ Hz. The depth at 16/11-E is $h \approx 70$ m, and the bottom is virtually horizontal in a large neighborhood of this site. The dispersion relation for gravity waves on finite depth is

$$\omega^2 = gk \tanh kh, \quad (1)$$

where $\omega = 2\pi f$ and $g = 9.8$ m/s². The central wavenumber can be estimated as $k_0 \approx 0.024$ m⁻¹, and the normalized inverse depth is $(k_0 h)^{-1} \approx 0.60$. The wave amplitude is seen to be about $a \approx 5$ m, and the central wave steepness is therefore of the order $k_0 a \approx 0.12$.

The deviation in frequency (half the width of the "top" of the spectrum) associated with the slow modulation can be estimated to be $\Delta f \approx 0.018$ Hz. As an estimate for frequency bandwidth we therefore have $\Delta f/f_0 \approx 0.24$. An estimate of the wavenumber bandwidth in the direction of the central wave vector can then be obtained by substituting

$$\omega = \omega_0 \pm \Delta\omega \quad \text{and} \quad k = k_0 \pm \Delta k_{\parallel} \quad (2)$$

into the dispersion relation (1). To linear order in the bandwidths one has

$$\frac{\Delta k_{\parallel}}{k_0} \approx \frac{2}{1 + 2k_0 h \operatorname{csch} 2k_0 h} \frac{\Delta\omega}{\omega_0}. \quad (3)$$

The factor multiplying the frequency bandwidth is 2 for deep water and decreases to unity for decreasing depth. In our case (3) provides the estimate for the wavenumber bandwidth along the direction of the central wave vector $\Delta k_{\parallel}/k_0 \approx 0.40$.

The time series in figure 1 cannot give information on the directional spread in the two horizontal dimensions. However, these wind-driven wave systems typically have angular deviations between 20° and 30°. This gives $\Delta k_{\perp}/k_0 \sim (0.36 - 0.58)$.

We seek to explain the occurrence of freak waves in the absence of ocean currents or non-uniform bottom topography by nonlinear self modulation of a wave train. Even though the wind is essential to produce the wave spectrum, it can be neglected over the relatively short scales characteristic for a freak wave event. The directional spread of the spectrum is assumed to be important and a three-dimensional model must therefore be employed.

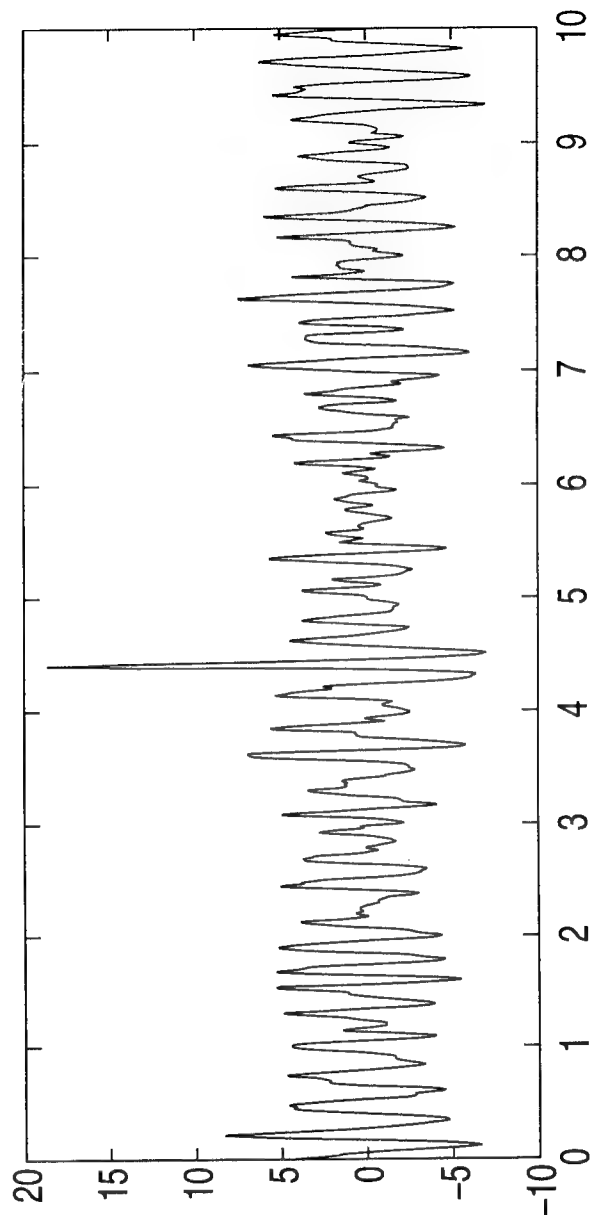


Figure 1: Ten minute wave elevation time series measured by a downward pointing radar at 16/11-E in the Norwegian sector of the North Sea. First axis is time in minutes, second axis is elevation in meters. Data courtesy of J. I. Dalane and O. T. Gudmestad of Statoil.

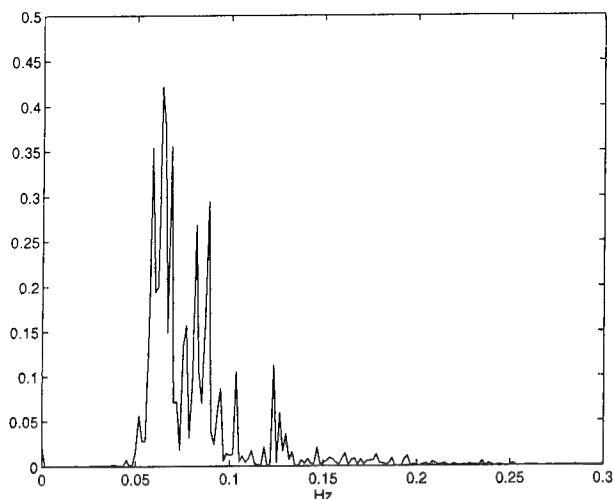


Figure 2: Power spectrum for the time series in figure 1. The frequency is given in Hertz. Data courtesy of J. I. Dalane and O. T. Gudmestad of Statoil.

Theoretical models describing the slow space and time evolution of weakly nonlinear surface gravity waves are generally based on the two assumptions: that the steepness is small $k_0 a \ll 1$, and that the bandwidth is narrow $|\Delta k|/k_0 \ll 1$. Typically, one assumes that the steepness and the bandwidth are of the same order of magnitude $\mathcal{O}(\epsilon)$, such that the leading nonlinear and dispersive effects balance at the third order $\mathcal{O}(\epsilon^3)$. The resulting amplitude modulation equation is known as the nonlinear Schrödinger equation (NLS). This equation was pioneered by Benney & Newell (1967) for nonlinear dispersive waves in general, by Zakharov (1968), Hasimoto & Ono (1972) and Davey (1972) for gravity waves on deep water, and by Benney & Roskes (1969) for gravity waves on finite depth. A modification of the nonlinear Schrödinger equation to fourth-order accuracy $\mathcal{O}(\epsilon^4)$, which we shall denote the MNLS equation, was derived by Dysthe (1979) for gravity waves on infinite depth, with minor modifications for gravity waves on deep water by Lo & Mei (1985), and by Brinch-Nielsen & Jonsson (1986) for gravity waves on finite depth. We here define finite depth, deep water and infinite depth as $(k_0 h)^{-1}$ being $\mathcal{O}(1)$, $\mathcal{O}(\epsilon)$ and 0, respectively.

The MNLS equation has successfully been used to model several aspects of the long-time evolution of weakly nonlinear narrow-banded water waves. It predicts the asymmetric growth of upper and lower sidebands, accompanied by the forward steepening of initially symmetric wave-groups as reported in the experiment of Feir (1967). Enhanced with a highly

simplified model for wave damping due to breaking, it was shown by Trulsen & Dysthe (1990) that the MNLS equation can predict the permanent downshift of the carrier wave frequency, which was observed experimentally by Lake *et al.* (1977). Furthermore, with the additional enhancement of a model for wind growth due to Plant (1982) and damping by wave breaking, it was shown by Trulsen & Dysthe (1992) that the MNLS equation can also predict that a strong wind can stabilize Stokes waves such that modulational instability and frequency downshift are suppressed. This was observed experimentally by Bliven *et al.* (1986). The MNLS equation was employed by Hara & Mei (1991) to predict downshift of the carrier wave frequency for waves forced by a weak wind and damped by eddy viscosity. There has also been recent work further investigating the downshift by the addition of damping terms to the MNLS equation (e.g. Uchiyama & Kawahara 1994; Kato & Oikawa 1995). These applications all consider evolution in one horizontal dimension.

For application of the MNLS equation to describe the situation in figures 1 and 2, we observe that the central wave steepness is within the domain of validity of the MNLS equation, but the bandwidth is not. Therefore, an improved model is called for that can describe broader bandwidth wave trains. To this end the Zakharov integral equation (Zakharov 1968; Crawford, Saffman & Yuen 1980; Stiassnie & Shemer 1984) has been developed to avoid the limitation in bandwidth altogether. This additional generality has the price of making the Zakharov equation unnecessarily expensive to solve numerically for the present problem. In order to maintain the relative simplicity of the MNLS equation, it is desirable to look for ways to relax the bandwidth constraint, while keeping the same accuracy in nonlinearity.

Even though the waves in figure 1 are not on deep water, we limit the present discussion to waves on deep water. In section 2 we first review the NLS and MNLS equations, and then summarize a new modified nonlinear Schrödinger equation for broader bandwidths by requiring $|\Delta k|/k = \mathcal{O}(\epsilon^{1/2})$ while keeping the same accuracy in nonlinearity (Trulsen & Dysthe 1996). The new equation will be denoted the BMNLS equation. The resolution in bandwidth can be assessed by comparison between predicted and exact stability results for Stokes waves, and the new equation has been found to be in good conformance with the resolution required by the above order-of-magnitude analysis. An extension to finite depth has been derived by us, and will be reported in the future.

The BMNLS equation can be solved numerically with periodic boundary conditions in two hor-

horizontal dimensions by a split-step Fourier collocation method. This method has been successfully used to solve the MNLS equation in one horizontal dimension by Lo & Mei (1985) and Trulsen & Dysthe (1990, 1992), and in two horizontal dimensions by Lo & Mei (1987). The NLS equation has been found to be unsuitable for computations of the evolution of a Stokes wave in two horizontal dimensions (Martin & Yuen 1980) because the unboundedness of the region of instability of Stokes waves in the Δk plane can cause energy to be leaked to high spectral components. Lo & Mei (1987) found that this energy leakage was suppressed by the higher-order corrections of the MNLS equation. In section 4 we review the numerical method for application to the BMNLS equation.

Experiments (Stansberg 1990) have shown that extreme waves ($H \leq 2H_{1/3}$) may also occur for essentially two-dimensional waves. Yasuda *et al.* (1992) have made two-dimensional simulations based on a method of Dommermuth & Yue (1987). They claim to see freak events that are similar to those observed in nature. Further two-dimensional computations have been carried out by Baldock & Swan (1994) and Taylor & Haagsma (1994) based on Fourier expansion of the potential flow equations.

We believe that three-dimensional wave modulation is important and plan to use the BMNLS equation to carry out fully three-dimensional computations of a spectrum that is statistically stationary and homogeneous, similar to the energetic part of a realistic ocean wave spectrum. Our interests include the occurrence, parametric dependence and dynamics of freak waves. This work is underway and will be reported in the future. Preliminary numerical results are briefly discussed in section 5, revealing that evolution in two and three dimensions are qualitatively different.

2 Evolution equations for narrow-banded irregular waves on deep water

We start with the equations for the velocity potential $\phi(t, \mathbf{x}, z)$ and surface displacement $\zeta(t, \mathbf{x})$ of an incompressible fluid with uniform depth h ,

$$\nabla^2 \phi = 0 \quad \text{for} \quad -h < z < \zeta, \quad (4)$$

with the surface conditions at $z = \zeta$

$$\frac{\partial^2 \phi}{\partial t^2} + g \frac{\partial \phi}{\partial z} + \frac{\partial}{\partial t} (\nabla \phi)^2 + \frac{1}{2} \nabla \phi \cdot \nabla (\nabla \phi)^2 = 0, \quad (5)$$

$$\frac{\partial \zeta}{\partial t} + \nabla \phi \cdot \nabla \zeta = \frac{\partial \phi}{\partial z}, \quad (6)$$

and the bottom condition

$$\frac{\partial \phi}{\partial z} = 0 \quad \text{at} \quad z = -h. \quad (7)$$

The horizontal position vector is $\mathbf{x} = (x, y)$, the vertical coordinate is z , and $\nabla = (\frac{\partial}{\partial x}, \frac{\partial}{\partial y}, \frac{\partial}{\partial z})$.

Subject to the assumptions

$$\left. \begin{aligned} k_0 a &= \mathcal{O}(\epsilon), \\ |\Delta k|/k_0 &= \mathcal{O}(\epsilon), \\ (k_0 h)^{-1} &= \mathcal{O}(\epsilon), \end{aligned} \right\} \quad (8)$$

we employ the harmonic expansions of the velocity potential and surface displacement,

$$\phi = \bar{\phi} + \frac{1}{2} \left(A e^{i\theta + k_0 z} + A_2 e^{2(i\theta + k_0 z)} + \dots + \text{c.c.} \right), \quad (9)$$

$$\zeta = \bar{\zeta} + \frac{1}{2} \left(B e^{i\theta} + B_2 e^{2i\theta} + \dots + \text{c.c.} \right), \quad (10)$$

where c.c. denotes the complex conjugate, and the phase is $\theta = k_0 x - \omega_0 t$ for a wave with central wave vector in the x -direction. The slow drift $\bar{\phi}$ and set-down $\bar{\zeta}$ as well as the harmonic amplitudes $A, A_2, \dots, B, B_2, \dots$ are functions of the slow modulation variables $\epsilon \mathbf{x}$ and ϵt . Additionally, $\bar{\phi}$ depends on the slow vertical variable ϵz , while A, A_2, \dots depend on the basic vertical coordinate z .

The leading-order perturbation problem for the first harmonic simply requires that the dispersion relation for deep-water gravity waves must be satisfied

$$\omega_0^2 = g k_0. \quad (11)$$

In the following, results have been made dimensionless by the substitutions

$$\left. \begin{aligned} \omega_0 t &\rightarrow t, \\ k_0(\mathbf{x}, z) &\rightarrow (\mathbf{x}, z), \\ k_0(B, B_n, \bar{\zeta}) &\rightarrow (B, B_n, \bar{\zeta}), \\ k_0^2 \omega_0^{-1}(A, A_n, \bar{\phi}) &\rightarrow (A, A_n, \bar{\phi}). \end{aligned} \right\} \quad (12)$$

Hence, the ordering parameter ϵ is implied in the variables, but does not appear explicitly.

At the third order $\mathcal{O}(\epsilon^3)$, the celebrated nonlinear Schrödinger equation is obtained for the slow evolution of A

$$\frac{\partial A}{\partial t} + \frac{1}{2} \frac{\partial A}{\partial x} + \frac{i}{8} \frac{\partial^2 A}{\partial x^2} - \frac{i}{4} \frac{\partial^2 A}{\partial y^2} + \frac{i}{2} |A|^2 A = 0. \quad (13)$$

At the fourth order $\mathcal{O}(\epsilon^4)$, we get the coupled evolution equations for A and $\bar{\phi}$ known as the modified nonlinear Schrödinger equation,

$$\frac{\partial A}{\partial t} + \frac{1}{2} \frac{\partial A}{\partial x} + \frac{i}{8} \frac{\partial^2 A}{\partial x^2} - \frac{i}{4} \frac{\partial^2 A}{\partial y^2} + \frac{i}{2} |A|^2 A$$

$$-\frac{1}{16}\frac{\partial^3 A}{\partial x^3} + \frac{3}{8}\frac{\partial^3 A}{\partial x\partial y^2} + \frac{3}{2}|A|^2\frac{\partial A}{\partial x} - \frac{1}{4}A^2\frac{\partial A^*}{\partial x} + iA\frac{\partial\bar{\phi}}{\partial x} = 0 \quad \text{at } z=0 \quad (14)$$

$$\nabla^2\bar{\phi} = 0 \quad \text{for } -h < z < 0 \quad (15)$$

$$\frac{\partial\bar{\phi}}{\partial z} = \frac{1}{2}\frac{\partial}{\partial x}|A|^2 \quad \text{at } z=0 \quad (16)$$

$$\frac{\partial\bar{\phi}}{\partial z} = 0 \quad \text{at } z=-h \quad (17)$$

In order to improve the resolution in bandwidth, we employ the new assumptions on the dimensional variables

$$\left. \begin{aligned} k_0 a &= \mathcal{O}(\epsilon), \\ |\Delta k|/k_0 &= \mathcal{O}(\epsilon^{\frac{1}{2}}), \\ (k_0 h)^{-1} &= \mathcal{O}(\epsilon^{\frac{1}{2}}). \end{aligned} \right\} \quad (18)$$

The previous harmonic expansions of the velocity potential (9) and surface displacement (10) can still be used, but now $\bar{\phi}, \bar{\zeta}, A, A_2, \dots, B, B_2, \dots$ are functions of the new slightly faster modulation variables $\epsilon^{\frac{1}{2}}x$ and $\epsilon^{\frac{1}{2}}t$. Additionally, $\bar{\phi}$ now depends on the new slightly faster vertical variable $\epsilon^{\frac{1}{2}}z$.

We insist on keeping the same accuracy in nonlinearity as in the MNLS equation. Since none of the fourth-order contributions here are fourth-order nonlinear, it suffices to consider the new equation only up to order $\mathcal{O}(\epsilon^{3.5})$. Carrying the perturbation analysis through in a similar fashion, the coupled evolution equations for A and $\bar{\phi}$ now become

$$\begin{aligned} \frac{\partial A}{\partial t} + \frac{1}{2}\frac{\partial A}{\partial x} + \frac{i}{8}\frac{\partial^2 A}{\partial x^2} - \frac{i}{4}\frac{\partial^2 A}{\partial y^2} - \frac{1}{16}\frac{\partial^3 A}{\partial x^3} + \frac{3}{8}\frac{\partial^3 A}{\partial x\partial y^2} \\ - \frac{5i}{128}\frac{\partial^4 A}{\partial x^4} + \frac{15i}{32}\frac{\partial^4 A}{\partial x^2\partial y^2} - \frac{3i}{32}\frac{\partial^4 A}{\partial y^4} + \frac{i}{2}|A|^2A + \frac{7}{256}\frac{\partial^5 A}{\partial x^5} \\ - \frac{35}{64}\frac{\partial^5 A}{\partial x^3\partial y^2} + \frac{21}{64}\frac{\partial^5 A}{\partial x\partial y^4} + \frac{3}{2}|A|^2\frac{\partial A}{\partial x} - \frac{1}{4}A^2\frac{\partial A^*}{\partial x} \\ + i\frac{\partial\bar{\phi}}{\partial x}A = 0 \quad \text{at } z=0 \end{aligned} \quad (19)$$

$$\nabla^2\bar{\phi} = 0 \quad \text{for } -h < z < 0 \quad (20)$$

$$\frac{\partial\bar{\phi}}{\partial z} = \frac{1}{2}\frac{\partial}{\partial x}|A|^2 \quad \text{at } z=0 \quad (21)$$

$$\frac{\partial\bar{\phi}}{\partial z} = 0 \quad \text{at } z=-h \quad (22)$$

The surface displacement is expressed by (10), where

$$\bar{\zeta} = -\frac{\partial\bar{\phi}}{\partial t} - \frac{1}{16}\frac{\partial^2}{\partial x^2}|A|^2 - \frac{1}{8}\frac{\partial^2}{\partial y^2}|A|^2, \quad (23)$$

$$\begin{aligned} B = iA + \frac{1}{2}\frac{\partial A}{\partial x} + \frac{i}{8}\frac{\partial^2 A}{\partial x^2} - \frac{i}{4}\frac{\partial^2 A}{\partial y^2} - \frac{1}{16}\frac{\partial^3 A}{\partial x^3} + \frac{3}{8}\frac{\partial^3 A}{\partial x\partial y^2} \\ - \frac{5i}{128}\frac{\partial^4 A}{\partial x^4} + \frac{15i}{32}\frac{\partial^4 A}{\partial x^2\partial y^2} - \frac{3i}{32}\frac{\partial^4 A}{\partial y^4} + \frac{i}{8}|A|^2A, \end{aligned} \quad (24)$$

$$\begin{aligned} B_2 = -\frac{1}{2}A^2 + iA\frac{\partial A}{\partial x} + \frac{1}{8}A\frac{\partial^2 A}{\partial x^2} + \frac{3}{8}\left(\frac{\partial A}{\partial x}\right)^2 \\ - \frac{1}{4}A\frac{\partial^2 A}{\partial y^2} + \frac{3}{4}\left(\frac{\partial A}{\partial y}\right)^2, \end{aligned} \quad (25)$$

and

$$B_3 = -\frac{3i}{8}A^3. \quad (26)$$

For numerical solution of the governing equations it is convenient to transform into a moving coordinate system to eliminate the leading order advection with the group velocity of the central wavenumber $c_g = \frac{1}{2}$. Hence we may introduce the transformations

$$x - c_g t = \xi \quad \text{and} \quad t = \tau, \quad (27)$$

where τ is a slow evolution time coordinate.

It has been found advantageous to use the different moving transformation (Lo & Mei 1985)

$$x/c_g - t = \xi \quad \text{and} \quad x = \eta, \quad (28)$$

where η is a slow evolution space coordinate measuring the fetch. The faster coordinate ξ is now the negative time seen by a stationary observer.

3 Stability of Stokes waves

The three evolution equations presented herein (NLS, MNLS and BMNLS) all have the uniform Stokes wave as an exact solution. It is given by

$$A = A_0 e^{-\frac{1}{2}|A_0|^2 t} \quad \text{and} \quad \bar{\phi} = 0. \quad (29)$$

The surface displacement can then be expressed as

$$\begin{aligned} \zeta = \frac{1}{2} \left\{ i \left(A_0 + \frac{1}{8}A_0^3 \right) e^{-\frac{1}{2}|A_0|^2 t + \theta} - \frac{1}{2}A_0^2 e^{-i|A_0|^2 t + 2\theta} \right. \\ \left. - \frac{3i}{8}A_0^3 e^{-\frac{3}{2}|A_0|^2 t + 3\theta} + \text{c.c.} \right\}. \end{aligned} \quad (30)$$

Upon making the substitutions $B_0 = i(A_0 + \frac{1}{8}A_0^3)$ and $\bar{\theta} = \theta - \frac{1}{2}|A_0|^2 t$, we recover the familiar form of the Stokes wave expansion accurate to the third order

$$\zeta = B_0 \cos \bar{\theta} + \frac{1}{2}B_0^2 \cos 2\bar{\theta} + \frac{3}{8}B_0^3 \cos 3\bar{\theta}. \quad (31)$$

The stability of the Stokes wave can be investigated by assuming small perturbations in amplitude and phase of the form

$$A = A_0(1 + a' + i\theta')e^{-\frac{1}{2}A_0^2 t}, \quad (32)$$

now with A_0 real, having the plane wave solution

$$\begin{pmatrix} a' \\ \theta' \\ \phi' \end{pmatrix} = \begin{pmatrix} \hat{a} \\ \hat{\theta} \\ \hat{\phi} \end{pmatrix} e^{i(\lambda x + \mu y - \Omega t)} + \text{c.c.} \quad (33)$$

The linear dispersion relation for this perturbation for the NLS equation is given by

$$\Omega = \frac{\lambda}{2} \pm \sqrt{\left(\frac{\lambda^2}{8} - \frac{\mu^2}{4}\right) \left(\frac{\lambda^2}{8} - \frac{\mu^2}{4} - A_0^2\right)}, \quad (34)$$

while for the MNLS and BMNLS equations we have

$$\Omega = P \pm \sqrt{Q \left(Q - A_0^2 + A_0^2 \frac{\lambda^2}{K} \coth(Kh) \right) + \frac{1}{16} A_0^4 \lambda^2} \quad (35)$$

where

$$P = P_{\text{MNLS}} = \frac{1}{2} \lambda + \frac{1}{16} \lambda^3 - \frac{3}{8} \lambda \mu^2 + \frac{3}{2} A_0^2 \lambda, \quad (36)$$

$$Q = Q_{\text{MNLS}} = \frac{1}{8} \lambda^2 - \frac{1}{4} \mu^2, \quad (37)$$

for the MNLS equation, while

$$\begin{aligned} P &= P_{\text{BMNLS}} = \frac{1}{2} \lambda + \frac{1}{16} \lambda^3 - \frac{3}{8} \lambda \mu^2 \\ &+ \frac{7}{256} \lambda^5 - \frac{35}{64} \lambda^3 \mu^2 + \frac{21}{64} \lambda \mu^4 + \frac{3}{2} A_0^2 \lambda, \quad (38) \\ Q &= Q_{\text{BMNLS}} = \frac{1}{8} \lambda^2 - \frac{1}{4} \mu^2 \\ &+ \frac{5}{128} \lambda^4 - \frac{15}{32} \lambda^2 \mu^2 + \frac{3}{32} \mu^4, \quad (39) \end{aligned}$$

for the BMNLS equation, and where

$$K = \sqrt{\lambda^2 + \mu^2}. \quad (40)$$

Stokes waves are not representative of realistic ocean waves like those shown in figure 1. However, the enhanced resolution in bandwidth of the BMNLS equation can conveniently be assessed by comparing the predicted instability of Stokes waves with exact results. Such detailed comparisons are presented in Trulsen & Dysthe (1996). The new equation has been found to have good resolution in bandwidth for the characteristic steepness and bandwidths discussed in the introduction.

In figure 3 we show the characteristic shapes of the unstable domains in the (λ, μ) plane for the three evolution equations when $A_0 = 0.12$. The NLS equation has an unbounded instability region with most unstable perturbations continuously distributed along the hyperbola $\lambda^2/4 - \mu^2/2 = A_0^2$. The higher-order modified nonlinear Schrödinger equations have

primary instability regions that are bounded, and they have the most unstable perturbations located at isolated points near the origin. The BMNLS equation confines the instability region even better than the MNLS equation. This confinement of the instability region resolves the problem of energy leakage reported by Marin & Yuen (1980) for numerical computations with the NLS equation.

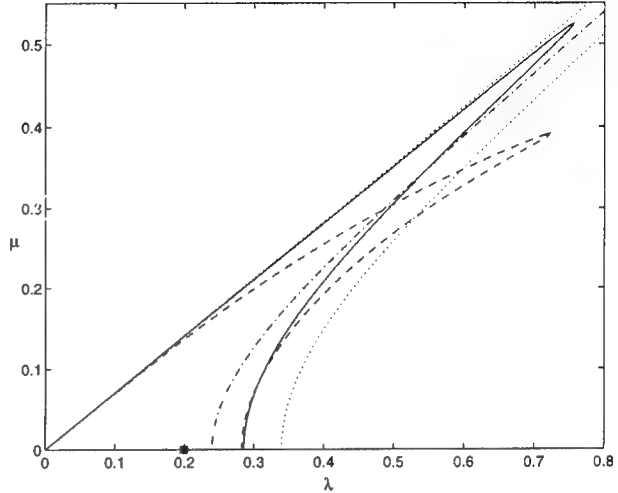


Figure 3: Instability regions for $A_0 = 0.12$: - · -, BMNLS; —, MNLS; · · ·, NLS. Most unstable perturbation: *, BMNLS; o, MNLS; - · -, NLS.

4 Numerical method

The split-step Fourier collocation method previously used by Lo & Mei (1985, 1987) and Trulsen & Dysthe (1990, 1992) for the MNLS equation has been implemented for the BMNLS equation. The method is briefly reviewed here.

The governing equations for A (subject to the transformation (27)) can be written in the form

$$\frac{\partial A}{\partial \tau} = LA + N(A) \quad (41)$$

where L is a linear spatial differential operator and N is a nonlinear function of A .

The solution is assumed to be periodic in ξ and y . If we let both periods be 2π , the discrete Fourier transform of A is defined as

$$\hat{A}_{k,l} = \frac{1}{MN} \sum_{m=0}^{M-1} \sum_{n=0}^{N-1} A(\xi_m, y_n) e^{-i(k\xi_m + ly_n)} \quad (42)$$

where $\xi_m = 2\pi m/M$ and $y_n = 2\pi n/N$.

The linear part LA is characterized by high-order spatial derivatives, which normally suggests that the time-step must be small to maintain numerical stability. The linear differential equation

$$\frac{\partial A}{\partial \tau} = LA \quad (43)$$

can be solved exactly and efficiently in Fourier space by multiplication of each Fourier mode by a constant,

$$\frac{\partial \hat{A}_{m,n}}{\partial \tau} = S_{m,n} \hat{A}_{m,n}. \quad (44)$$

The nonlinear part $N(A)$ contains no higher than first derivatives, and the nonlinear equation

$$\frac{\partial A}{\partial \tau} = N(A) \quad (45)$$

can be solved by an explicit one-step scheme in physical space. A numerical solution for (41) can therefore be obtained by a split-step method where the linear and nonlinear parts are alternately solved in Fourier and physical space. The order of accuracy of this scheme is limited by the fact that the linear and nonlinear operators do not commute. Thus with the iteration $\dots NL \dots$ the method is first order accurate provided the integration scheme for (45) is at least first order accurate. With the iteration $\dots NLLN \dots$ the method is second order accurate provided the integration scheme for (45) is at least second order accurate.

5 Preliminary numerical results

We here briefly mention some preliminary results on the evolution of a wave spectrum in two and three dimensions.

It is well known that the two-dimensional conservative evolution of a Stokes wave according to the NLS, MNLS and Zakharov integral equations exhibit cyclical modulation and demodulation (recurrence) provided the Stokes wave has been perturbed on few of its unstable sidebands. If the Stokes wave has been perturbed on several unstable sidebands, the simple cyclical behavior disappears, and the evolution becomes more complicated. The peak frequency in the wave spectrum can be temporarily upshifted and downshifted, but there is no tendency of a permanent shift. It is generally assumed that the frequency downshift observed in long wave tanks (Lake *et al.* 1977) is due to dissipation and wave breaking (Trulsen & Dysthe 1990; Tulin 1996).

The three-dimensional evolution of waves has so far not been extensively studied. It is worthwhile

to notice that in the experiment of Lake *et al.* (1977) where the downshift was first reported, the wave tank was three times wider than the central wavelength. Other experiments reporting downshift have also used wide tanks. Narrow-banded oblique sideband modulation is therefore possible, and can be investigated with the BMNLS equation. From our numerical computations, we find that the conservative evolution in three dimensions is qualitatively different from that in two dimensions: The peak frequency in the wave spectrum can be permanently downshifted (for the duration of the numerical computation). We intend to publish these results elsewhere.

6 Conclusion

We seek to understand the occurrence of freak waves by nonlinear self modulation of a slowly modulated weakly nonlinear wave train, for which ocean currents or non-uniform bottom topography can be neglected. Field observations have been presented, suggesting that the wave conditions leading to freak waves can be described as a narrow-banded weakly nonlinear wave train. However, the required bandwidth is wider than the constraints imposed by the existing fourth order modified nonlinear Schrödinger equation of Dysthe (1979).

We have derived a new modified nonlinear Schrödinger equation valid for broader bandwidths, which is more appropriate for a realistic ocean wave spectrum. This paper is limited to a discussion of the new broader bandwidth equation for deep water, and a description of a numerical method for its solution.

Preliminary numerical results indicate that the evolution of a wave spectrum in two and three dimensions are qualitatively different.

Extension of the modified nonlinear Schrödinger equation for finite depth to broader bandwidth is necessary to properly deal with the field measurements presented above.

Stimulating discussions with Dr. Anne Karin Magnusson of The Norwegian Meteorological Institute (DNMI/Bergen) are gratefully acknowledged. We thank J. I. Dalane and O. T. Gudmestad of Statoil for providing the field experimental data. This research has been supported by the Norwegian Research Council through a post doctoral fellowship (NFR 109328/410) and a grant for computing time (Programme for Supercomputing).

References

- [1] Baldock, T. E. & Swan, C. (1994). Numerical calculations of large transient water waves. *Appl. Ocean Res.*, **16**, 101–112.
- [2] Benney, D. J. & Newell, A. C. (1967). The propagation of nonlinear wave envelopes. *J. Math. Phys.*, **46**, 133–139.
- [3] Benney, D. J. & Roskes, G. J. (1969). Wave instabilities. *Studies Appl. Math.*, **48**, 377–385.
- [4] Bliven, L. F., Huang, N. E., & Long, S. R. (1986). Experimental study of the influence of wind on Benjamin-Feir sideband instability. *J. Fluid Mech.*, **162**, 273–260.
- [5] Brinch-Nielsen, U. & Jonsson, I. G. (1986). Fourth order evolution equations and stability analysis for Stokes waves on arbitrary water depth. *Wave Motion*, **8**, 455–472.
- [6] Crawford, D. R., Saffman, P. G., & Yuen, H. C. (1980). Evolution of a random inhomogeneous field of nonlinear deep-water gravity waves. *Wave Motion*, **2**, 1–16.
- [7] Davey, A. (1972). The propagation of a weak nonlinear wave. *J. Fluid Mech.*, **53**, 769–781.
- [8] Dean, R. G. (1990). Freak waves: A possible explanation. In A. Tørum & O. T. Gudmestad (Eds.), *Water Wave Kinematics* (pp. 609–612): Kluwer.
- [9] Dommermuth, D. G. & Yue, D. K. P. (1987). A high-order spectral method for the study of nonlinear gravity waves. *J. Fluid Mech.*, **184**, 267–288.
- [10] Draper, L. (1965). 'Freak' ocean waves. *Marine Observer*, **35**, 193–195.
- [11] Dysthe, K. B. (1979). Note on a modification to the nonlinear Schrödinger equation for application to deep water waves. *Proc. R. Soc. Lond. A*, **369**, 105–114.
- [12] Feir, J. E. (1967). Discussion: some results from wave pulse experiments. *Proc. R. Soc. Lond. A*, **299**, 54–58.
- [13] Hara, T. & Mei, C. C. (1991). Frequency downshift in narrowbanded surface waves under the influence of wind. *J. Fluid Mech.*, **230**, 429–477.
- [14] Hasimoto, H. & Ono, H. (1972). Nonlinear modulation of gravity waves. *J. Phys. Soc. Japan*, **33**, 805–811.
- [15] Kato, Y. & Oikawa, M. (1995). Wave number downshift in modulated wavetrain through a nonlinear damping effect. *J. Phys. Soc. Japan*, **64**, 4660–4669.
- [16] Lake, B. M., Yuen, H. C., Rungaldier, H., & Ferguson, W. E. (1977). Nonlinear deep-water waves: theory and experiment. Part 2: Evolution of a continuous wave train. *J. Fluid Mech.*, **83**, 49–74.
- [17] Lo, E. & Mei, C. C. (1985). A numerical study of water-wave modulation based on a higher-order nonlinear Schrödinger equation. *J. Fluid Mech.*, **150**, 395–416.
- [18] Lo, E. Y. & Mei, C. C. (1987). Slow evolution of nonlinear deep water waves in two horizontal directions: A numerical study. *Wave Motion*, **9**, 245–259.
- [19] Mallory, J. K. (1974). Abnormal waves on the south east coast of South Africa. *Int. Hydrog. Rev.*, **51**, 99–129.
- [20] Martin, D. U. & Yuen, H. C. (1980). Quasi-recurring energy leakage in the two-space-dimensional nonlinear Schrödinger equation. *Phys. Fluids*, **23**, 881–883.
- [21] Plant, W. J. (1982). A relationship between wind stress and wave slope. *J. Geophys. Res.*, **87**, 1961–1967.
- [22] Stansberg, C. T. (1990). Extreme waves in laboratory generated irregular wave trains. In A. Tørum & O. T. Gudmestad (Eds.), *Water Wave Kinematics* (pp. 573–589): Kluwer.
- [23] Stiassnie, M. & Shemer, L. (1984). On modifications of the Zakharov equation for surface gravity waves. *J. Fluid Mech.*, **143**, 47–67.
- [24] Taylor, P. H. & Haagsma, I. J. (1994). Focussing of steep wave groups on deep water. In *Waves — Physical and Numerical Modelling*.
- [25] Trulsen, K. & Dysthe, K. B. (1990). Frequency down-shift through self modulation and breaking. In A. Tørum & O. T. Gudmestad (Eds.), *Water Wave Kinematics* (pp. 561–572): Kluwer.
- [26] Trulsen, K. & Dysthe, K. B. (1992). Action of windstress and breaking on the evolution of a wave-train. In M. L. Banner & R. H. J. Grimshaw (Eds.), *Breaking Waves* (pp. 243–249): Springer.
- [27] Trulsen, K. & Dysthe, K. B. (In press 1996). A modified nonlinear Schrödinger equation for

broader bandwidth gravity waves on deep water.
Wave Motion.

- [28] Tulin, M. P. (1996). Breaking of ocean waves and downshifting. In J. Grue, B. Gjevik, & J. E. Weber (Eds.), *Waves and Nonlinear Processes in Hydrodynamics* (pp. 177–190): Kluwer.
- [29] Uchiyama, Y. & Kawahara, T. (1994). A possible mechanism for frequency down-shift in nonlinear wave modulation. *Wave Motion*, **20**, 99–110.
- [30] Yasuda, T., Mori, N., & Ito, K. (1992). Freak waves in unidirectional wave trains and their properties. In *Proc. 23rd Int. Conf. on Coastal Engineering*.
- [31] Zakharov, V. E. (1968). Stability of periodic waves of finite amplitude on the surface of a deep fluid. *J. Appl. Mech. Tech. Phys.*, **9**, 190–194.

DISCUSSION

C.T. Stansberg
Norwegian Marine Technology Research Institute,
Norway

The paper presents an interesting approach for extending the Modified Nonlinear Schrodinger Equation (MNLS), previously developed for weakly nonlinear, narrow-banded deep-water waves, to more broad-banded spectral conditions. The principles and procedures of the approach are described, while final numerical simulations have not yet been carried out. In the future, further development including finite water depths and multidirectional waves are also planned. By this, the authors seek to explain the occurrence of extraordinarily large ("freak") wave events observed in the real ocean. The work is based on previous works by the same authors, demonstrating the performance of the existing MNLS model for slowly varying envelope waves. This model is believed to work quite well for such waves, in fact recent experiments on bichromatic deep-water unidirectional waves in a long channel (Stansberg 1995) have further confirmed its validity.

The question is whether the same model is capable of explaining extreme waves occurring in the full-scale conditions presented in Figures 1 & 2. It will therefore be quite interesting to see the forthcoming results from the simulations. I have some comments to this problem, based on recent experimental results:

1. One has reason to believe that increased spectral bandwidth as well as multidirectionality will reduce the growth of nonlinear self-modulations. This has, for example, been experimentally demonstrated in Stansberg (1994), where these effects have been systematically investigated. It may possibly be explained by the reduced "lifetime" of wave groups. Other recent experiments (not yet published) also indicate that self-modulation instabilities are less pronounced in finite water conditions, which may be due to change of the dispersion relation as well as the increasing presence of other bottom-induced processes. As a result, we can raise the following questions:

2. How dominating will the self-modulation instability effects be relative to other physical processes in the full scale wave condition presented in the paper? And if the extreme event in Figure 1 is due to such self-modulation effects,

what is its statistical significance?

Although the complete answering of these questions is probably far ahead, the forthcoming simulation work announced in the paper will be valuable contributions on the subject, and are being looked forward to.

REFERENCES

Stansberg, C.T. (1994), "Effects from Directionality and Spectral Bandwidth on Non-Linear Spatial Modulations of Deep-Water Surface Gravity Waves", in Proceedings, Vol. 1. the 24th International Conference on Coastal Engineering (Ed.: B. Edge), held in Kobe, Japan, October 1994 (Proceedings published by ASCE in 1995), pp. 579-593.

Stansberg, C.T. (1995), "Spatially Developing Instabilities Observed in Experimental Bichromatic Wave Trains", in Proceedings, Vol. 3, the 26th IAHR Congress (HYDRA 2000), London, September 1995, pp. 180-185.

DISCUSSION

O.T. Gudmestad
STATOIL, Norway

The development of the fourth order modified nonlinear Schrodinger equation for narrow banded deep water waves [Dysthe, 1979] represented an important contribution to the understanding of non-linear waves. This paper has been much referred to in the literature. The present modification for a relaxed narrow bandwidth constraint is very much welcome and contributes to further understanding of non-linear wave processes in deep waters.

The offshore industry is at present very interested in obtaining detailed knowledge about wave processes in steep waves as these contribute to transient higher order loading of slender structures (Stansberg and Gudmestad, 1996). Given a more exact description of the velocity potential as obtained by Trulsen and Dysthe, it will be possible to obtain more exact values for velocity and acceleration terms whereby the loading can be estimated with higher accuracy also in steep waves. The industry is looking forward to the continuation of this promising research.

REFERENCES

Dysthe, K.B. (1979). "Note on a modification of the nonlinear Schrodinger equation for application to deep water wave," *Proc. R. Soc. London A*, 369, 105-114.

Stansberg, C.T. and Gudmestad, O.T. (1996). "Nonlinear random wave kinematics models verified against measurements in steep waves," *Proc. OMAE 96*, Firenze, June 1996.

AUTHORS' REPLY

According to the theoretical work of Alber (1978), the self-modulational instability disappears when the spectral bandwidth (σ) exceeds a critical value that is proportional to the mean square slope $k_0^2 \overline{\zeta^2}$. His stability criterion seems to be satisfied in most sea conditions. The absence of the self-modulation instability does not mean that nonlinear interactions are unimportant.

In the spectral regime, they are at least partly responsible for the downshift of the spectral peak. That is a slow statistical effect described by the Hasselman type interaction integral. Only when the spectral bandwidth is small (subcritical in Alber's sense) can a rapid downshift take place, as demonstrated by us.

In the spatial regime, the nonlinear interaction may have unexpected effects yet to be explored.

REFERENCE

Alber, I.E. (1978). "The effects of randomness on the stability of two-dimensional surface wave-trains," *Proc. R. Soc. Lond. A*, 363, pp. 525-546.

Bluff Body Hydrodynamics

P. Bearman

(Imperial College of Science, Technology and Medicine, United Kingdom)

SUMMARY

This paper presents some issues related to the fluid dynamics of bluff bodies in steady currents and in oscillatory flows. The importance of vortex shedding and its three-dimensional structure, even from two-dimensional geometries, is discussed. Vortex shedding patterns from a circular cylinder in oscillatory flow are reviewed. The potential for applying CFD in bluff body hydrodynamics is discussed and results are presented for the forces on a fixed cylinder and for the response of a flexible cylinder.

INTRODUCTION

Bluff body hydrodynamics is a general term that may be used in the naval field to describe the study of hydrodynamics of floating and fixed structures that generate significant regions of separated flow. Clearly bluff body aerodynamics and bluff body hydrodynamics are closely related but in the naval context the presence of an air/water interface and surface waves introduce additional phenomena that are absent in aerodynamic flows. A common feature of bluff body flows is that they are complex and often difficult to predict. In practical naval bluff body flows, Reynolds numbers are usually high and in a range where disturbances are massively amplified through instability mechanisms. This leads to both turbulence, i.e. multi-scale, random, three-dimensional motion, and the generation and shedding of large coherent vortex structures. Both types of motion may have a profound effect on the fluid loading of marine structures.

A bluff body can be defined as a body that, as a result of its shape, has separated flow over a substantial part of its surface. An important feature of a bluff body flow is that there is a very strong interaction between the viscous and inviscid regions. If we consider that at the moment of starting the flow is attached, then the adverse pressure gradients that this flow imposes on the boundary layer will be too great to sustain the attachment. Separation may occur either from sharp edges or from a continuous surface. Prediction of separation position from a continuous surface is particularly difficult because it depends on both the characteristics of the upstream boundary layer and on the structure of the near wake region. Also the separation position may move in response to pressure gradients imposed by unsteady flow features in the wake. Usually bluff bodies induce flow separation at positions where the velocity at the edge of the boundary layer is higher than the free stream velocity. This leads to a high rate of shedding of circulation which in turn leads to a high drag. Also due to the generation and shedding of coherent vortices, large unsteady forces may develop, particularly in a direction transverse to the flow direction.

Ships are usually designed to avoid large areas of flow separation in forward motion, although in practice there may be some separation at the stern. However, when moored or when manoeuvring at low speeds the relative flow velocity due to currents, waves and perhaps large roll motion may induce substantial separations. For example, to help minimise the response of moored vessels used by the oil industry for floating production and storage offshore (FPSOs), it is important to have reliable systems in place to control the heading. However, the traditional types of floating and fixed offshore structure used for oil recovery can expect waves and

currents from any direction and they are designed using bluff cross sections, such as the circle and the square. Hence the offshore structure designer needs to have some knowledge of bluff body hydrodynamics.

Within the field of naval architecture ideal flow theory has been used very successfully to estimate wave-induced motions and loads on large floating structures. However, it cannot be used to model realistically phenomena resulting from the viscous nature of water such as boundary layers, flow separation and vortex generation and shedding. Bluff body hydrodynamics is concerned with real fluids and with understanding the effects of flow separation. Traditionally bluff body flows have been studied experimentally with relatively simple models developed to provide ways of correlating data. As computer power has increased more and more CFD studies of bluff body flows are becoming available, based on numerical simulations of the unsteady Navier Stokes equations. In some applications, such as predicting the slow drift response of moored structures, predictions from ideal flow theory are being combined with results from bluff body research. The drag arising from viscous

effects is treated as a form of hydrodynamic damping which is considered as independent of the primary loading which is developed by waves. This is an attractive approach but there is a need to validate how successfully flows can be superposed in this way.

Circular cross-section members are a common form used in offshore structures and hence it is fortunate that the circular cylinder is also the most studied bluff body shape. It has geometric simplicity enabling models to be easily manufactured for basic experimental research. Its simple form also makes it attractive as a representative bluff body for CFD investigations. Much of this paper will be concerned with the circular cylinder but such a great deal of research has been carried out using this shape that it is impossible to provide a comprehensive review within the confines of a single paper. Basic questions that will be addressed include: does a bluff body with a two-dimensional geometry placed in a uniform stream generate a two-dimensional flow, what new phenomena appear when a bluff body is placed in waves and how successfully can CFD be used to predict loading and response of bluff bodies?

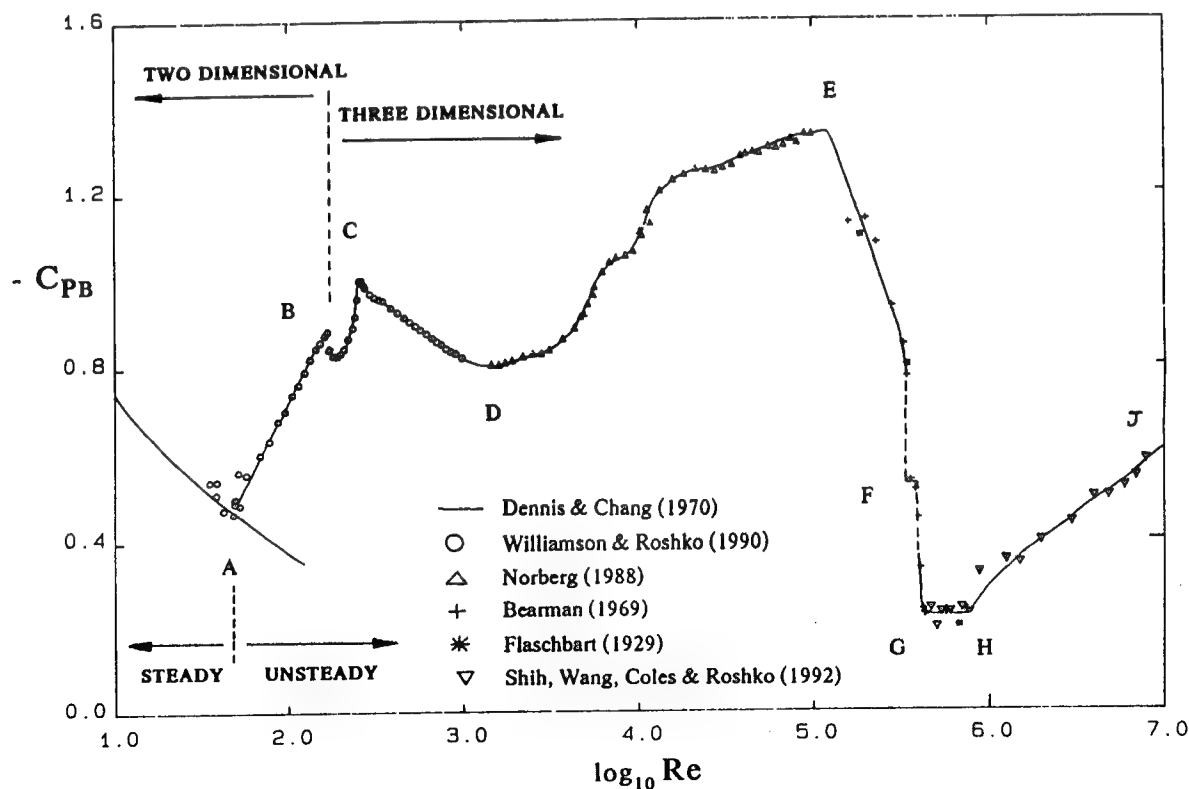


Figure 1 Base Pressure Coefficient versus Reynolds Number for a Circular Cylinder (Roshko (1))

BLUFF BODIES IN A CURRENT

The sensitivity of circular cylinder flow to varying the Reynolds number, Re , where $Re = UD/\nu$ and U is current velocity, D cylinder diameter and ν kinematic viscosity is well illustrated in figure 1 from Roshko(1). Here the pressure in the separated region, or the base pressure, is plotted as a pressure coefficient, C_{pb} , for a wide range of Reynolds numbers. The variations in C_{pb} with increasing Re are linked to the growth of disturbances occurring in different regions of the flow; first in the near wake, then in the free shear layers and finally in the boundary layer. Disturbances introduced externally, say by turbulence in the approaching flow or by surface roughness, may modify the shape of figure 1. In an ocean environment roughness, in the form of various species of marine life, may attach itself to a cylinder and substantially change the fluid loading. This often leads to increased drag and stronger vortex shedding. In this paper it will not be possible to discuss these aspects in detail and bluff body surfaces will be assumed smooth and approaching currents will have minimal levels of turbulence.

The vortex shedding frequency, n , is normally presented in non-dimensional form as a Strouhal number, S , where $S = nD/U$. The value of the Strouhal number varies from one bluff body to another and, as in the case of a circular cylinder, it may change with changing Re . In general, the bluffer the body then the lower the value of S . A number of researchers have proposed that if Strouhal number is based on appropriate wake parameters then it should take a universal value, regardless of body shape. The best known universal Strouhal number, S^* , is that due to Roshko(2). He proposed that rather than use the free stream velocity, the velocity just outside the shear layer at separation, U_b , should appear in S^* . This velocity is related to the base pressure by the expression $U_b = U(1 - C_{pb})^{1/2}$. Also he argued that the length scale in the universal Strouhal number should be related to the distance between the free shear layers as they roll up to form vortices. He obtained this length theoretically using a notched hodograph method (Roshko(3)). Later other workers, most notably Griffin (4), carried out experiments to measure this distance for a large range of bluff body shapes. A compilation of results for a variety of bluff bodies, gathered together by Griffin, is plotted in figure 2 where it can be seen that a roughly constant value of S^* is obtained. The scatter in this data arises most likely from two causes:

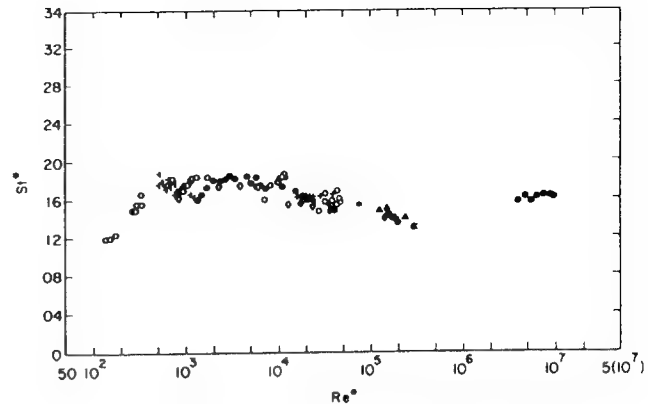


Figure 2 Universal Strouhal No versus Reynolds No for a variety of bluff body shapes (Griffin (4))

experimental error and physical processes of secondary importance which have only a weak effect on the shedding frequency.

Above a Reynolds number of about 150 to 200, vortex shedding from nominally two-dimensional bluff bodies exhibits certain three-dimensional characteristics, irrespective of how carefully the experiment is carried out. A simple way of quantifying this three-dimensionality is to measure the spanwise correlation length of some property related to vortex shedding, such as fluctuating pressure on the body surface, fluctuating velocity in the wake or local fluctuating lift. For many shapes of bluff body the correlation length at moderate and high Reynolds numbers is equal to just a few body diameters. This length cannot be predicted theoretically and the mechanisms responsible for limiting spanwise correlation are not fully understood. A number of authors have presented measurements of the spanwise correlation length for flows with regular vortex shedding. For example, Szepessy (5) has investigated the correlation of vortex shedding from a circular cylinder at a high subcritical Reynolds number. While on average vortices are shed parallel to the cylinder axis, he shows that instantaneously there are substantial variations in the phase of vortex shedding over relatively short spanwise distances.

Gerrard (6) was one of the first to study in detail the three-dimensionality of cylinder wakes. He identified three important ways in which vortex shedding may deviate from a two-dimensional form: oblique shedding in which vortices are shed at a small angle to the cylinder axis, the splitting or dislocation of vortices of similar sign and the

looping of vortices across to the other side of the wake. Vortex looping is a particularly strong form of three-dimensionality in which a vortex joins with one or more vortices of opposite sign on the other side of the wake. Examples of where it might occur are at a free end or where a bluff body meets a wall. Experiments by Williamson (7), Eisenlohr and Eckelmann (8) and Hammache and Gharib (9) on a circular cylinder at Reynolds numbers up to about 150, have all shown that two-dimensional vortex shedding may only be obtained if the cylinder end conditions are very carefully controlled. At higher Reynolds numbers it is still possible to influence the flow by adjusting the end conditions but it is no longer possible to preserve the instantaneous flow in a two dimensional state. A vortex dislocation, or split, has been shown by Eisenlohr and Eckelmann (8) to occur when there is a spanwise variation in the frequency of vortex shedding and it is a means by which vortices of similar sign can connect with each other at a boundary between cells with different shedding frequencies.

The types of three-dimensional vortex motion most often found in the wakes of nominally two-dimensional bluff bodies are oblique shedding and vortex dislocation. Bearman and Tombazis (10) visualised the flow in the wake of a two-dimensional blunt-trailing-edge model fitted with end plates and mounted in a water tunnel. The Reynolds number of their experiment, based on trailing-edge thickness, was 2,500 and they found that departures from two-dimensional vortex shedding appear to occur at random points along the span and at irregular time intervals. Both oblique shedding and vortex dislocations were observed. At this higher Reynolds number there is three-dimensional motion related to spanwise instabilities of the Karman vortices (Triantafyllou (11)), smaller scale three-dimensionality due to shear layer instability (Wei and Smith (12)) and three-dimensional motion associated with turbulence generated in the flow past the bluff body. To what extent these motions interact is unknown.

Since the primary instability mode in the wake of a two-dimensional bluff body is itself two-dimensional, as discussed by Monkewitz and Nguyen (13), it is reasonable to suppose that two-dimensional numerical simulation schemes should be able to successfully predict bluff body flows. However, Szepessy and Bearman (14) measured the fluctuating lift on a thin section of a large aspect ratio circular cylinder and found that two-

dimensional simulation schemes generally overestimate the root mean square value of fluctuating lift, in some cases by substantial amounts. This observation has been substantiated by Graham (15) who gathered together numerical predictions for circular cylinder flow and compared them with experimental results. He found that above a Reynolds number of 150 the mean and fluctuating forces were generally over predicted, with the largest differences occurring in the fluctuating lift. It should also be noted that measured time histories of fluctuating lift show a pronounced amplitude modulation whereas simulated time histories mostly display a constant amplitude, once the flow has settled. While some of the differences between measurement and prediction may be due to problems in modelling turbulence it seems likely that the three-dimensional features of vortex shedding should also be modelled. It is interesting to note that several researchers have developed three-dimensional simulation programs to predict nominally two-dimensional bluff body flow. Generally the results from this approach show a closer agreement with experiment.

Key three-dimensional features of the wake of a nominally two-dimensional body appear apparently randomly in time and space. Using a blunt-trailing-edge model, Bearman and Tombazis (10) decided to try to control locations along the span by applying a mild geometric disturbance in the form of a wavy trailing edge. It is not immediately apparent that applying a spanwise wave to the trailing edge of a constant thickness blunt-trailing-edge model will affect the vortex shedding frequency selection process. Two interesting possibilities present themselves: if the vortex formation length is constant along the span then the vortices themselves will be wavy or, if the vortices are two-dimensional, then the base pressure is likely to vary along the span since the vortex formation length varies.

It is well known, for example Bearman (16), that the phase of vortex shedding along the span of a bluff body can be synchronised by oscillating the body or the flow at the shedding frequency. Such a situation arises when a flexible bluff body is excited into oscillation by vortex shedding. A certain threshold amplitude has to be exceeded before extensive regions of correlated vortex shedding are achieved. During these oscillations, which occur over a range of flow speed, the vortex shedding frequency becomes locked to the body oscillation frequency. Under these

circumstances the flow is highly two-dimensional and it is likely that a two-dimensional, direct numerical simulation code will provide accurate predictions.

INFLUENCE OF A THREE-DIMENSIONAL DISTURBANCE

In order to study three dimensional aspects of bluff body wakes, Bearman and Tombazis (10) deliberately introduced three-dimensionality by modifying the base of a bluff body. Wind tunnel and water flume experiments were carried out on a number of bluff body models, each with a nose in the shape of a half ellipse and with a blunt trailing edge

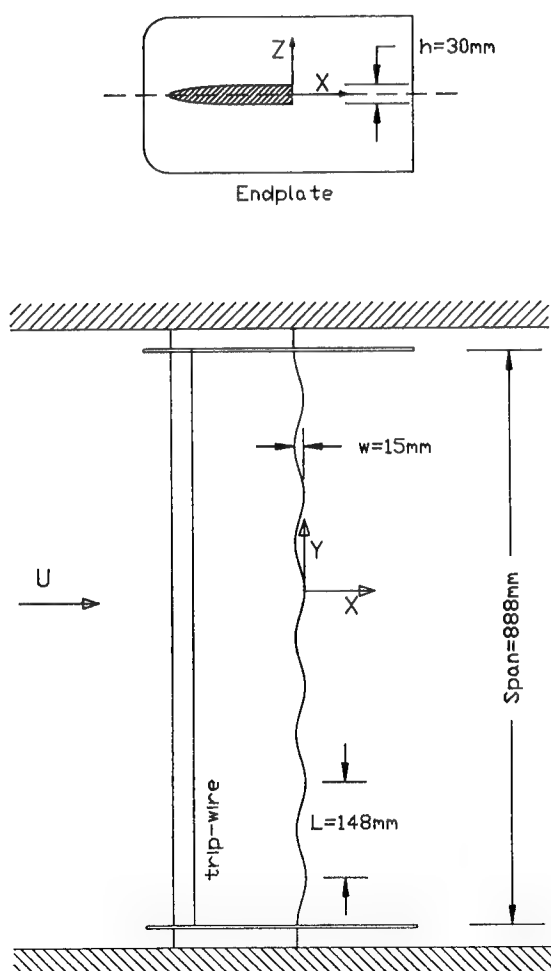


Figure 3 Model with a Sinusoidal Trailing Edge

which was either straight or in the form of a sinusoidal wave. In the wind tunnel experiments the mean chord of the models along their spans was 190 mm and the semi-major axis of the nose section was 120 mm and the semi-minor axis was 15 mm. The remainder of each model was parallel sided giving a base height of 30 mm. Eight models were constructed in order to be able to study the effect on the flow of both base wavelength, L , and base peak-to-peak wave height, w . A diagram of a typical model is shown in figure 3. The Reynolds number range, using model base height as the reference length, was from 20,000 to 60,000. Flow visualisation was performed at a Reynolds number of 2,500 in a water flume. As an initial comparison between the various models, the spanwise distribution of mean base pressure was measured. For the straight trailing-edge model a constant value of C_{pb} was found in a spanwise region of $10h$ around the mid-span. The value obtained of -0.585 is in good agreement with previous measurements of Bearman (17).

Tanner (18), working with models having a similar cross-sectional shape to the ones studied here, found that by "breaking" the separation line along the span he could achieve significant drag reduction. In accordance with his results, the wavy models have higher (less negative) values of C_{pb} . The distributions of base pressure coefficient along a half wavelength of the various wavy models (all with a wave height w of 15 mm) are shown in figure 4. Measurements on all the wavy models showed distributions of base pressure values that repeated themselves over the spanwise waves between the end plates. A notable feature in figure 4 is that the steeper the wave, where steepness $= w/L$, the larger the drag reduction. Compared to the straight-edge model, the drag reduction for the models with $w/L = 0.09, 0.10, 0.11, 0.13$ and 0.14 is about 10%, 16%, 24%, 25% and 34% respectively.

A further important feature of figure 4 is the significant difference between the measured values of C_{pb} at a peak and a valley. All wavy models show a similar trend, with a peak exhibiting less negative values of C_{pb} than a valley. For the model with $L = 148$ mm and $w/L = 0.1$, the value at the valley is about -0.48 , with C_{pb} smoothly increasing to a maximum of -0.44 at the peak. It should be noted that from $y/L = 0.2$ to $y/L = 0.5$ (a valley) the base pressure remains quite constant, the main variations being observed for $y/L < 0.2$, i.e. close to the peak.

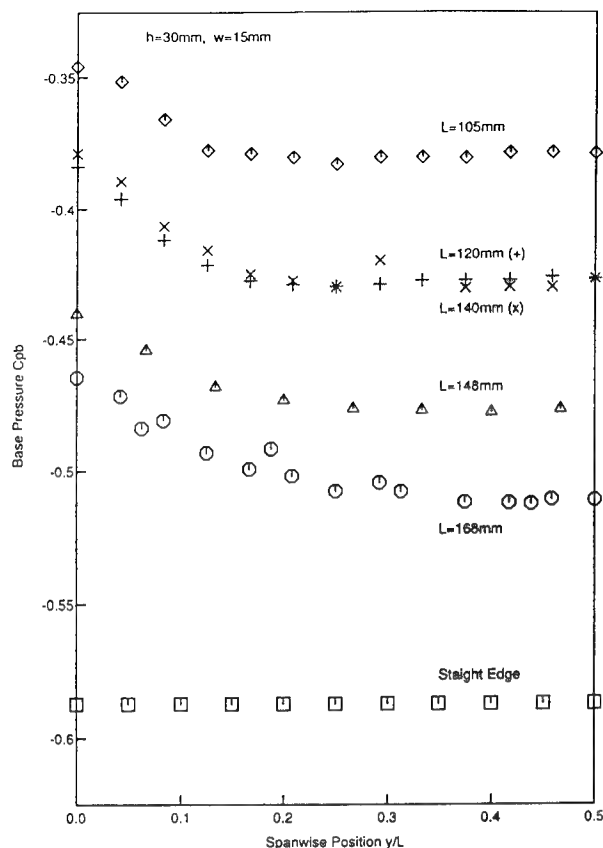


Figure 4 Variation of Base Pressure Coefficient for models with different wavelengths, L ; $y/L = 0$ corresponds to a peak in the base.

Power spectra of the velocity records obtained from hot-wire probes were calculated in order to determine the characteristic frequencies of the wakes of the various models. For the straight-edge model the Strouhal number, obtained using the frequency for the dominant peak in a power spectrum, was 0.24 and this is in agreement with the value obtained by Bearman (17).

Figure 5 shows velocity spectra for the wavy model with $w/L=0.1$, measured at different spanwise distances, y , from the peak in a wave. The main characteristic is the presence of two shedding frequencies with one at a Strouhal number of $S=0.24$, referred to later as f_1 , and the other at $S=0.29$, referred to as f_2 . At a peak in the base the lower of the two frequencies is the stronger, but as we move towards a valley it weakens (becoming almost undetectable at $y/L=0.333$) and the high frequency component becomes increasingly strong. The presence of the two frequencies suggests that, at

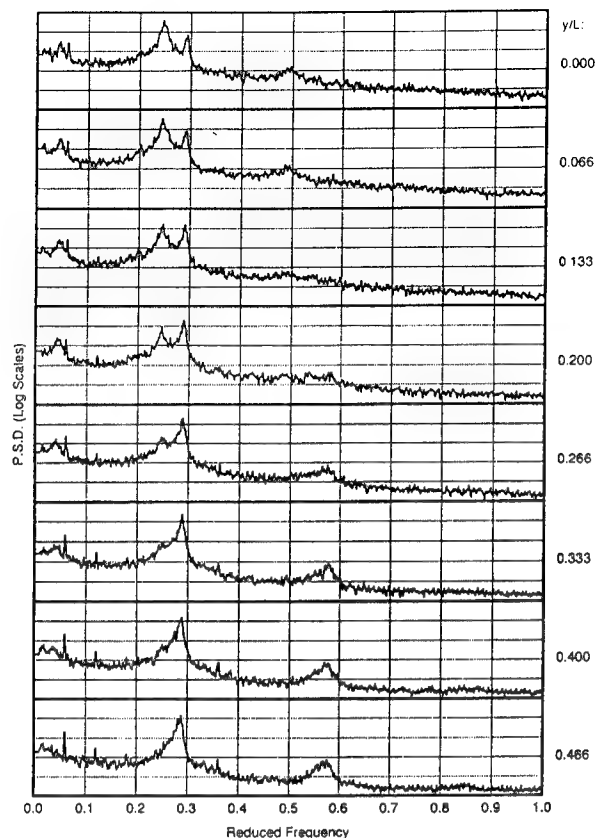


Figure 5 Velocity spectra for a model with $w/L = 0.1$, at different spanwise positions

least at some times, we have two cells within this spanwise region, corresponding to a half-wavelength of the trailing edge, shedding at different frequencies. Further, it follows that it is highly likely that there is some form of vortex splitting occurring at the boundary between the cells. The velocity spectra for all wavy models follow a similar pattern. Figure 6 shows spectra measured at the peaks of the various wavy models together with the spectrum for the straight trailing-edge model. As the wave steepness, w/L , increases so the higher of the two shedding frequencies become more and more distinct.

The existence of a dual frequency characteristic has been demonstrated by measuring power spectra of fluctuating velocity but what does this mean from a physical point of view? We cannot be sure that both of the main peaks in a power spectrum of velocity necessarily reflect the frequency of vortex shedding (at some time instants, at least) at that spanwise position. Does the dual frequency indicate a simultaneous presence of two frequencies,

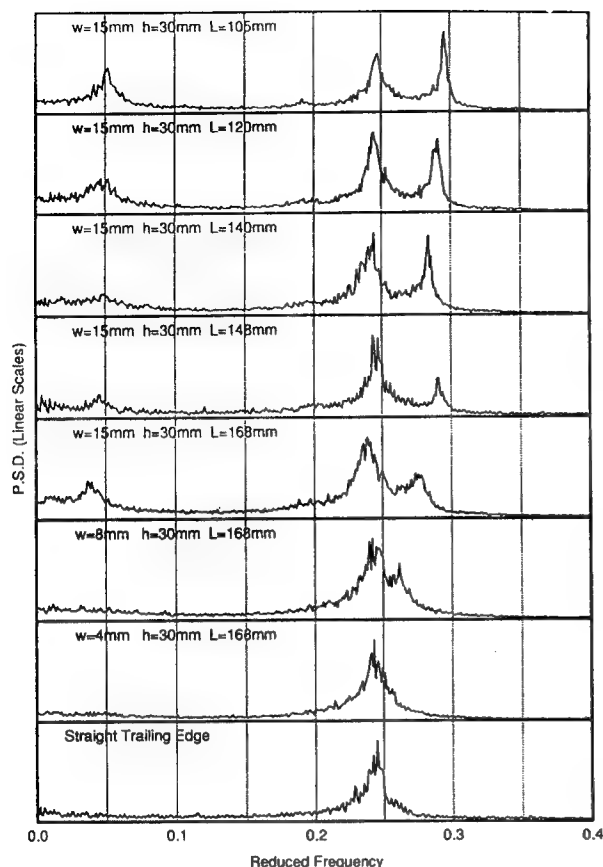


Figure 6 Velocity spectra measured at the peaks of models with various wave steepnesses, w/L

e.g. a signal like $C_1 \sin(2\pi f_1 t) + C_2 \sin(2\pi f_2 t)$, or does it represent an interval of $C_1 \sin(2\pi f_1 t)$, followed by an interval at $C_2 \sin(2\pi f_2 t)$? In the main it appears that at a particular spanwise position the vortices shed for a while at one frequency and then switch to the other frequency.

Flow visualisation performed in the water flume confirmed the cellular nature of the wake of the sinusoidal trailing-edge model. Figure 7 shows a sequence which indicates the low-frequency periodicity of vortex splitting. The images were extracted from a video tape, with the shots being roughly one shedding cycle apart. From (a) there is little to indicate the complicated three-dimensional nature of the flow. One shedding cycle later, at (b), the cell at the peak has delayed its vortex shedding by a small amount. The vortices from the two neighbouring valleys bow backwards to accommodate this delay. At (c), another cycle later, a further delay at the peak seems to have brought the two cells out of phase. The vortices from the valleys

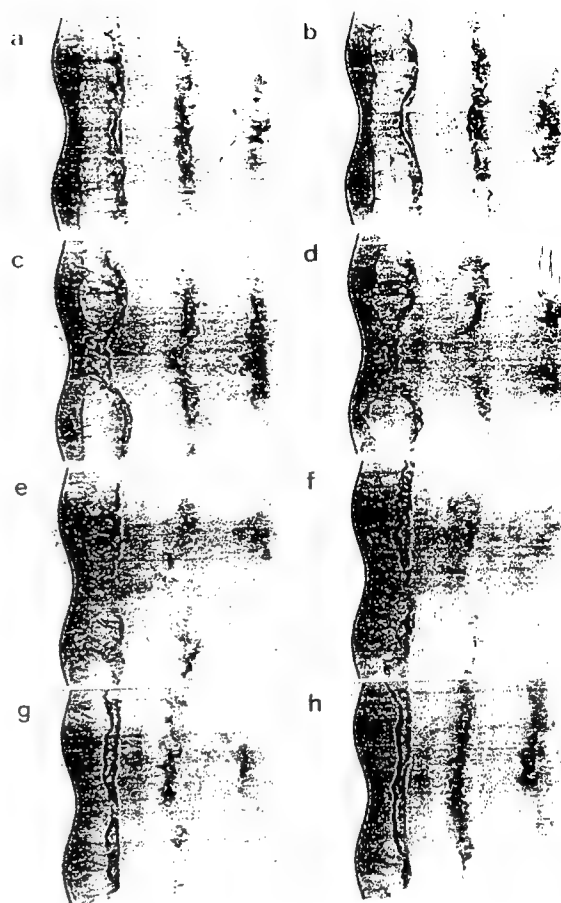


Figure 7 Visualisation in the wake of a model with $w/L = 0.1$, showing successive shedding cycles in the symmetric mode

have bent further back. It appears that when this bowing angle becomes too large then vortex splitting occurs and the vortex from the peak links up with two vortices from each adjacent valley. Eisenlohr and Eckelmann (8) also identified the large oblique bowing angle as one of the characteristics of vortex splitting. Image (d) follows a similar pattern with vortex splitting once again being very pronounced, while from (e) to (h) the phase difference between the two cells reduces and the vortex filaments then become straight again.

An interesting feature of this flow is the persistent way each cell stays at its selected frequency, acting like an oscillator operating at its own characteristic frequency. Even in figures 7 (a) and (b), where the vortices appear to be fairly straight and undisturbed, the cell at the peak is shedding vortices at a slower rate than that at the

adjacent valleys. So that even though the flow may at certain instants seem two-dimensional, the underlying physical mechanisms are always three-dimensional.

In the sequence of pictures in figure 7 the flow is symmetric with respect to the peak. Flow visualisation revealed a total of four modes, here termed symmetric, antisymmetric (two types) and oblique. The oblique mode can be seen in (a)-(d) of figure 8. From these pictures one can see that there is no preferred positive or negative oblique shedding angle, i.e. the oblique mode is not due to an imperfection in the alignment of the model.

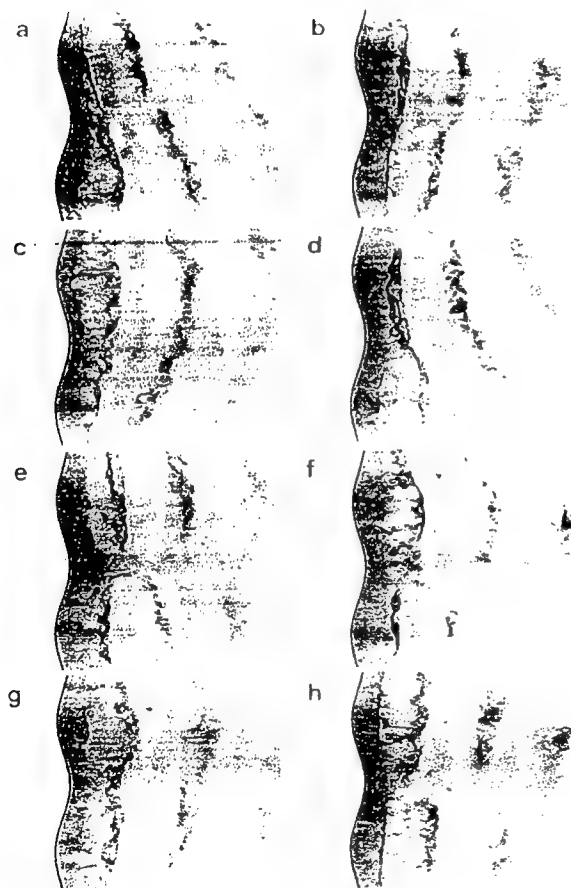


Figure 8 Visualisation in the wake of a model with $w/L = 0.1$: (a) to (d) oblique vortex shedding mode and (e) to (h) antisymmetric vortex shedding mode

In the antisymmetric mode, shown in figure 8 (e) to (h), the vortex shedding in the valleys either side of the peak are in anti-phase. It is unclear in this mode exactly what is happening in the region of the peak. One possibility is that there are two cells, each

associated with a valley and shedding at f_2 , that extend up to the peak and link up in that region. Another possibility is that there are three cells with shedding frequencies f_2 at one valley, f_1 at the peak and f_2 again at the other valley. The dislocations would then follow a pattern similar to that for the symmetric mode described earlier. It was found that for transition to occur between the symmetric and the oblique modes, both kinds (two-cell and three-cell) of antisymmetric mode must exist.

The flow alternates at seemingly irregular intervals from one mode to another. The transition between the modes does not, as a rule, occur

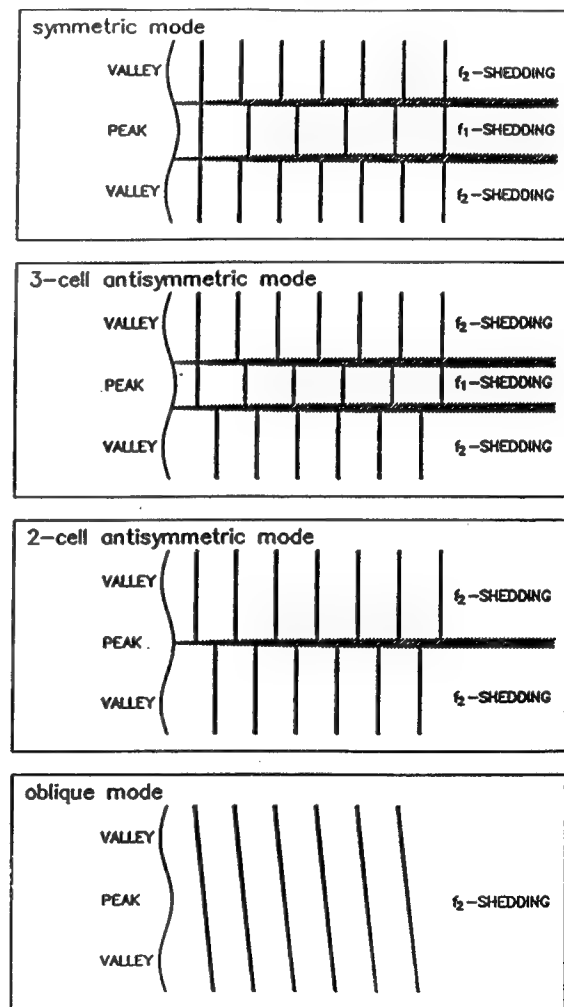


Figure 9 Schematic representation of the various shedding modes: shaded areas represent positions where dislocations occur

instantaneously, but is gradual. Thus, in order to understand the flow we have to identify possible intermediate states that may accompany the transition from one mode to another. It is unlikely, for example, that the flow will change directly from a symmetric to an oblique mode because so many features of the wake would have to change instantaneously. Figure 9 provides paths, derived from detailed study of flow visualisation, for the transitions between modes. The modes are ordered in such a way that each one is above or below the other modes which it most closely resembles. It is suggested that when a mode changes it can only "jump" between two consecutive boxes of figure 9, either upwards or downwards.

It was mentioned earlier that the flow would switch between modes at seemingly random intervals. Although a number of mode-transition procedures were proposed above, the actual *mechanism* of transition is unclear. Obviously a number of questions regarding mode-transition arise. We do not know if the four proposed modes are genuinely "self-contained" modes. They could each conceal a low level instability that gradually forces a change of mode. On the other hand, each of the observed modes could be a stable mode, in the sense that, in the absence of external de-stabilising factors, it could continue ad infinitum. In that case the transitions could be triggered by some irregularities in the flow. However, one thing is clear: all modes would occur, irrespective of initial conditions and after sufficient time had been allowed for the flow to settle.

The general conclusion reached from studies such as the one outlined above is that at high Reynolds numbers three-dimensionality is a very important feature of bluff body wakes, even for wakes generated from nominally two-dimensional geometries. From direct numerical simulation studies at relatively low Reynolds numbers it appears that three-dimensionality has a particularly strong influence on the level of fluctuating transverse force at a local section. Three-dimensional flow mechanisms also control another important aspect of bluff body wakes, the spanwise correlation length of vortex shedding and presently there is no reliable method, apart from experiment, to predict this quantity. It would appear likely that vortex dislocations are present across a wide range of Reynolds numbers. Further research is needed into the three-dimensionality of bluff body wakes particularly for the prediction of loads and responses

of cables and riser pipes in uniform and sheared currents.

BLUFF BODIES IN OSCILLATORY FLOW

The ocean flow environment is extremely complex and naval structures are exposed to random wave fields, with directional spreading and possibly a superimposed current. This complexity poses a severe problem for an engineer wishing to calculate the fluid loading on a bluff marine structure. Small scale model tests might be carried out in a wave basin but the results would need careful interpretation because of the sensitivity of viscous flows to scale effects. CFD offers the possibility of an attractive solution but substantial improvements in computational resources are required before this can become a reality. However, researchers are beginning to make the first steps towards numerically simulating the flow about a bluff body in waves and this is likely to be an important growth area.

Much has been achieved by conducting experiments on elementary bluff body shapes in waves and planar oscillatory flow to improve physical understanding and to test empirical models for predicting fluid loading. The object has been to try to uncover the main underlying flow processes and this is often best achieved by carefully restricting the range of variables examined. For example, a wave field may be idealised as a regular train of unidirectional waves or, carrying the idealisation a stage further, the ambient flow may be replaced by a planar, harmonic, oscillatory flow. The latter simplification is the equivalent of using a strip theory approach to predict the loading on a vertical, surface-piercing, circular cylinder in waves. While it does not model the orbiting flow which is characteristic of waves it does reproduce what appears to be the most important feature of a bluff body in waves, i.e. the re encounter with the wake generated in a previous half cycle. The return of a wake containing coherent vortices has a significant influence on future flow development and subsequent vortex shedding. In a random wave field the influence of wake re encounter appears to make the prediction of loading even more complex as it may depend as much on the present wave as on say the influence of previous waves which will have different characteristics.

In a planar, harmonic, oscillatory flow with kinematic viscosity ν and velocity $U = \hat{U} \sin(2\pi t/T)$, where \hat{U} is the peak velocity and T is time period, the loading on a cylindrical section of diameter D depends on the following non-dimensional parameters: $\hat{U}T/D$, $\hat{U}D/\nu$ and t/T . $\hat{U}T/D$ is known as the Keulegan Carpenter number, KC , and is often rewritten as $2\pi A/D$, where A is the amplitude of the oscillatory motion. Many authors prefer to replace the Reynolds number, $\hat{U}D/\nu$, by an alternative viscous parameter, $D^2/\nu T$, which is known as either the Stokes number or the β parameter. KC can be interpreted as being related to the ratio of the distance particles convect during a flow cycle to the cylinder diameter and β can be explained as being related to the ratio of the time it takes for viscosity to diffuse particles a distance equal to the cylinder diameter to the flow time period. For a vertical cylinder in waves KC is a maximum at the surface and decreases with depth but β remains constant over the depth of the cylinder. In a laboratory experiment it is relatively easy to match full scale KC values but β may be up to two or even three orders of magnitude too small. Reynolds number is the product of β and KC and at full scale its peak value is often in a range that in steady current flow would be described as post-critical. Most laboratory experiments have Reynolds numbers firmly in the sub-critical range. However, it may be dangerous to use directly concepts derived for steady flow to describe phenomena observed in oscillatory flow. As KC becomes very large it may be permissible to consider the flow as quasi-steady but at most KC values observed in practice the flow is strongly influenced by unsteady effects. These will affect boundary layer stability, transition and separation. Hence a whole new set of loading coefficients has had to be derived for cylinders in oscillatory flow (see, for example, Sarpkaya and Isaacson (18)).

A number of authors, including Bearman et al. (19), Bearman (20), Williamson (21) and Obasaju et al. (22), have studied vortex shedding patterns developed by a circular cylinder in oscillatory flow. For KC values of order unity or less, depending on the value of β , the flow remains attached during a flow cycle and strictly the cylinder should not be described as bluff. As KC increases above this threshold value the flow separates during a flow cycle and at first a pair of weak vortices are formed during each half cycle. At the end of a half cycle these vortices are convected back on to the cylinder and may be destroyed by mixing with opposite sign

vorticity or, as KC increases, they may survive to influence the vortex activity in the next half cycle. With increasing KC more circulation is generated and shed from the separation points during a half cycle and hence the vortices become stronger. Associated with this strengthening, the vortices become disturbed from their pattern of symmetry and unsteady transverse forces are developed. The root mean square transverse force coefficient reaches a maximum at a KC value of around 10 to 12 where presumably the vortices are at their strongest. With further increases in KC a vortex is shed before the end of the half cycle and a third vortex begins to form. During the wake re encounter process, under the influence of the other vortices, this new vortex passes around the cylinder and acts as the nucleus for the first vortex forming in the next half cycle from the diametrically opposite point from which it was formed. As KC is increased further this third vortex gains more circulation before the end of the half cycle. When it approaches the strength of a fully formed vortex it convects back over the cylinder on the same side on which it was initially formed. It now acts as a free vortex and accelerates the development and shedding of an opposite sign vortex from the other side of the cylinder and together they convect away under the influence of their mutual velocity fields. For KC values where the third vortex is about half fully formed at the end of a half cycle it may pass either under or over the cylinder causing apparently random changes to the transverse force time history. This general pattern of behaviour is repeated as KC is increased with the next partly formed vortex influencing the flow.

It is clear from the above description that there will be some KC values where the vortex flow pattern is stable and intermediate values where it exhibits an apparently chaotic behaviour. If for a moment we neglect the influence of flow history and assume that during a half cycle the flow behaves in a quasi-steady manner then we can estimate the number of vortices that will be formed. The number of vortices shed per second from one shear layer of a bluff body in a steady flow U is given by SU/D . If we assume that S remains constant in an oscillatory flow then the instantaneous shedding frequency is given by $S\hat{U} \sin(2\pi t/T)/D$. Integrating this over half a flow cycle shows that a fully formed vortex will be generated each time KC increases by $\pi/2S$. Assuming S to be 0.2 then the predicted KC increment is just under 8. This agrees quite well with flow visualisation studies and suggests, for example,

that if two fully formed vortices are formed during a half cycle at $KC = 12$, then three full vortices will be formed at $KC = 20$. At $KC = 16$ the vortex shedding pattern is likely to be unstable. This acute sensitivity to changing KC number makes the flow around a circular cylinder in oscillatory flow particularly difficult to predict.

No review of bluff bodies in oscillatory flow or waves would be complete without some discussion of the applicability of Morison's equation. This is an empirical equation, devised by Morison et al (23), to represent in-line loading on bodies in waves and was formulated in advance of much of the research that has been carried out into the flow around cylinders in oscillatory flow. The load per unit length, $F(t)$, is given by:

$$F(t) = \frac{1}{2}\rho U |U| DC_D + \frac{1}{4}\rho \pi D^2 C_M dU/dt,$$

where C_D and C_M are the drag and inertia coefficients respectively. It was envisaged by Morison et al that these coefficients would be derived from experiment but it is now possible, under certain limited conditions, also to calculate them using CFD. The two terms in the above equation are interpreted as the drag contribution and the inertia contribution because of their relation to the flow velocity and acceleration respectively. For a bluff body in a viscous oscillatory flow the generation and shedding of vortices develops forces which are not necessarily in phase with velocity and so, in addition to generating a drag force, vortices affect the value of the inertia coefficient. At low KC values where we know vortex shedding is weak or even non-existent the inertia coefficient for a circular cylinder is found to be close its inviscid value of 2. When vortex shedding is thought to be at its strongest, around $KC=10$, the added mass contribution to the inertia coefficient is small and at some β values may even be negative. Physically this is perfectly acceptable and simply reflects the fact that vortices do not necessarily induce an in-line force that is in phase with flow velocity.

In general the comparison between measured in-line force time histories and those predicted using Morison's equation is remarkably good. A number of attempts have been made to improve on Morison but none have been sufficiently successful to permit them to find their way into the design process. The agreement between Morison and measurements is, perhaps as is to be expected, worst

at around $KC = 10$ where there is very strong vortex activity. In addition to contributing to the in-line force, vortices also generate transverse forces and while there are equivalent model equations to predict transverse forces in planar oscillatory flow (see, for example, Verley (24) and Bearman et al. (25)), it is not clear how best these should be applied to a vertical cylinder in waves where KC is varying with depth. From the earlier discussion on vortex shedding patterns it is clear that this KC variation will result in differences in the frequency of the transverse force with depth. Also if the KC is such that there is not a stable vortex pattern established then it is possible that the phase of the transverse force may vary by about 180° over quite short axial lengths of the cylinder. Hence in design transverse forces are often ignored on the argument that they are likely to be poorly correlated over a long length of cylinder. How best to predict the correlation length remains an open question.

NUMERICAL SIMULATION OF OSCILLATORY FLOW PAST A CIRCULAR CYLINDER

Several numerical solutions of the unsteady, two dimensional Navier Stokes equations for flow around a circular cylinder at low KC and relatively low β parameter have been reported in the literature. A version of the discrete vortex method has been used by Smith and Stansby (26) to calculate forces for KC values up to 4. A finite difference method, based on the stream function-vorticity formulation, was used by Justesen (27) and Zhang and Zhang (28) employed a finite volume method with primitive variables. Lin et al (29) have carried out simulations up to a KC of 36, for a relatively a low value of the β parameter, using the so called hybrid discrete vortex method due to Graham (30). Following the development of the discrete vortex method by Chorin (31), (32) it has been used in a wide variety of applications, as discussed by Sarpkaya (33). The method uses point vortices to represent regions of vorticity in the flow and a two step algorithm is employed to calculate separately convection and diffusion of these vortices. In the code used by Lin et al convection is accomplished by a Lagrangian scheme based on the cloud-in-cell method, while diffusion is carried out with a finite difference method, using the cloud-in-cell mesh. This hybrid Lagrangian/Eulerian approach has been applied by Cozens (34) to study roll damping of ships due to vortex formation and shedding, and by Arkell et al (35) to investigate the wake of a circular cylinder in

a combined wave and current flow. More recently, Meneghini and Bearman (36) used the same method to study the flow about a circular cylinder forced to oscillate transversely to a steady current.

Numerical simulation methods that can achieve an acceptable level of accuracy are presently limited to low values of β because of the difficulties of resolving thin boundary layers and other small scale motions. All the methods mentioned above are restricted to two-dimensional flow although there are already some three dimensional simulations emerging for very low KC values. The development of numerical simulation poses new challenges for experimentalists. In the design problem data is required at as high a value of β as possible whereas to validate numerical solutions very low β results are needed. In practice loading data in oscillatory flow is often obtained by mounting a cylinder in a U tube

apparatus driven at its natural period. Low β can be achieved by making D small but then the loading also becomes small and difficult to measure accurately. By increasing the length of the water column in the U tube, which often is not a practical possibility, T can be increased but again the actual loading will be small. At Imperial College a new set of experimental measurements of drag and inertia coefficients for a range of KC and for a low β parameter of 70 has recently been obtained by Kuhtz (37). She replaced the water in the Imperial College U tube with a high viscosity water glycol mixture which enabled her to use a sufficiently large cylinder diameter to give accurate force measurements. Vortex shedding patterns at low values of β have been observed by Tatsuno and Bearman (38) using flow visualisation and these are also available for comparison with numerical simulations.

Table 6 Force coefficients calculated cycle by cycle

KC	2.0		10.0		24.	
Cycle	C _M	C _D	C _M	C _D	C _M	C _D
2	2.2218	1.7335	1.8404	1.5549	1.4105	2.0128
3	2.2225	1.7436	2.0377	1.5036	1.6975	1.4868
4	2.2234	1.7438	2.0180	1.5212	0.8748	1.4908
5	2.2248	1.7375	1.7519	1.9222	1.6503	1.6236
6	2.2251	1.7229	1.6364	1.9383	0.8474	1.2015
7	2.2265	1.7356	1.4232	1.6836	3.2107	1.3909
8	2.2253	1.7305	2.1087	1.4305	1.6183	2.0592
9	2.2263	1.7226	1.8800	1.4875	0.8591	1.5127
10	2.2258	1.7212	1.7260	1.6388	0.7449	1.5481
11	2.2269	1.7207	1.9686	1.3787	0.5359	0.6681
12	2.2265	1.7234	1.6678	1.4558	1.5706	1.6501
13	2.2257	1.7164	1.6107	1.7831	0.5893	2.0629
14	2.2262	1.7175	1.1891	1.6347	1.3549	1.5429
15	2.2260	1.7203	2.0274	1.8365	1.3036	1.9965
16	2.2264	1.7189	0.9485	2.5663	1.7632	1.4651
17	2.2261	1.7181	1.3007	1.6059	1.1826	1.7758
18	2.2265	1.7167	1.9486	1.3374	2.0329	1.4744
19	2.2271	1.7121	1.7526	1.9175	1.7615	1.9998
20	2.2261	1.7139	1.2197	2.0437	1.2437	1.5261
21	2.2268	1.7136	1.0763	1.9665	1.6612	2.1811
22	2.2266	1.7139	0.9362	2.2909	0.5750	1.7843
23	2.2269	1.7157	1.2732	1.8460	0.6186	2.5953
24	-	-	0.9296	2.2094	2.6571	1.4261

Details of the computations to be described here for $\beta = 70$ can be found in the paper by Lin et al (29); only a small selection of the results will be presented. C_M and C_D are obtained from Morison's equation on a flow cycle by flow cycle basis by applying a standard Fourier averaging process to computed time histories of the in-line force. Then mean values of the coefficients are found over a number of cycles. At small KC values the variation of the force coefficients from cycle to cycle is small but at larger KC , where there is shedding of strong vortices, the variations can become large. Hence the values of the Morison force coefficients will depend to some extent on the number of flow cycles computed. Typically 24 flow cycles were simulated and the force coefficients were averaged over the last 18 flow cycles. To illustrate the cycle by cycle variations results are presented in Table 1 for $KC = 2, 10$ and 24 . It can be seen that the variations become much larger as KC increases. Similar variations are observed in experiment even though the U tube is operating at a constant frequency. Once again this illustrates the influence of wake re encounter which introduces a random factor into the flow.

C_M and C_D averaged over 18 cycles are shown plotted in Figures 10 and 11 respectively (note that Wu's method and the dp/dr method, which are fully explained in Lin et al, refer to two ways of calculating pressure forces). Also shown in figures 10 and 11 are drag and inertia coefficients measured by Kuhtz (37) for $\beta = 70$. The numerical predictions do not reproduce the rapid rise of C_D and decrease of C_M at KC values around 8, although the predictions of C_M are generally closer to the experimental data than those of C_D . In particular, the peak in C_D measured at around $KC = 10$ is missing from the predictions. The reason for this is rather puzzling and may be related to three-dimensional flow features which cannot be reproduced by a two-dimensional simulation. However, it is interesting to note from figure 12, where measured and computed root mean square in-line force coefficients are plotted, that the predicted r.m.s force coefficients agree well with the experimental results throughout the KC range examined. At larger KC (16 - 30), the computed C_D values appear to agree quite well with those from the experiments. At KC above 30 the values of C_M predicted by the two methods used to calculate forces deviate significantly from each other. At these KC s the inertia component represents a small proportion

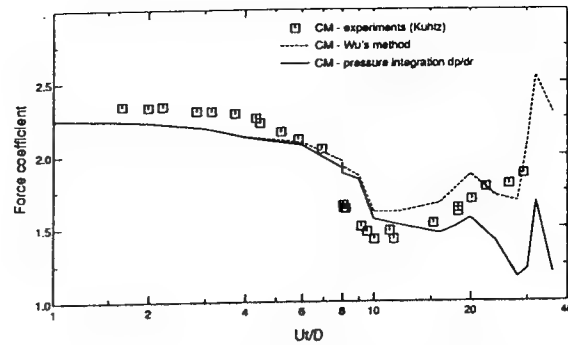


Figure 10 Computed and measured inertia coefficients for $\beta = 70$

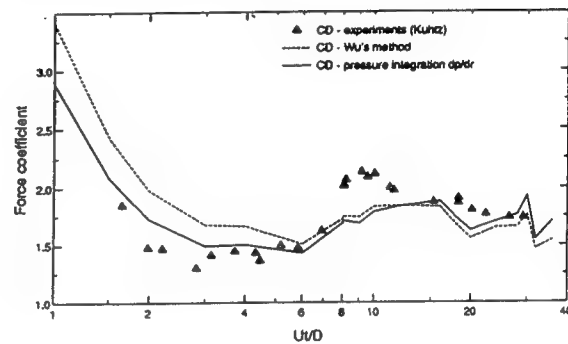


Figure 11 Computed and measured drag coefficients for $\beta = 70$

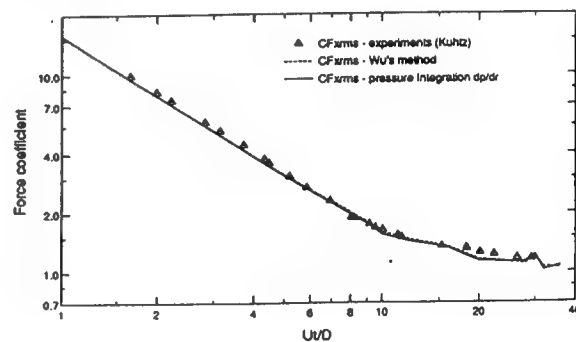


Figure 12 Computed and measured r.m.s. force coefficients for $\beta = 70$

of the total force and in terms of overall loading these differences are insignificant. Nevertheless it is important to try to understand why these variations occur and it seems likely that there may be a slight phase difference in the total force computed by the two methods. A thorough study of time step, mesh resolution etc. would be needed to resolve this question.

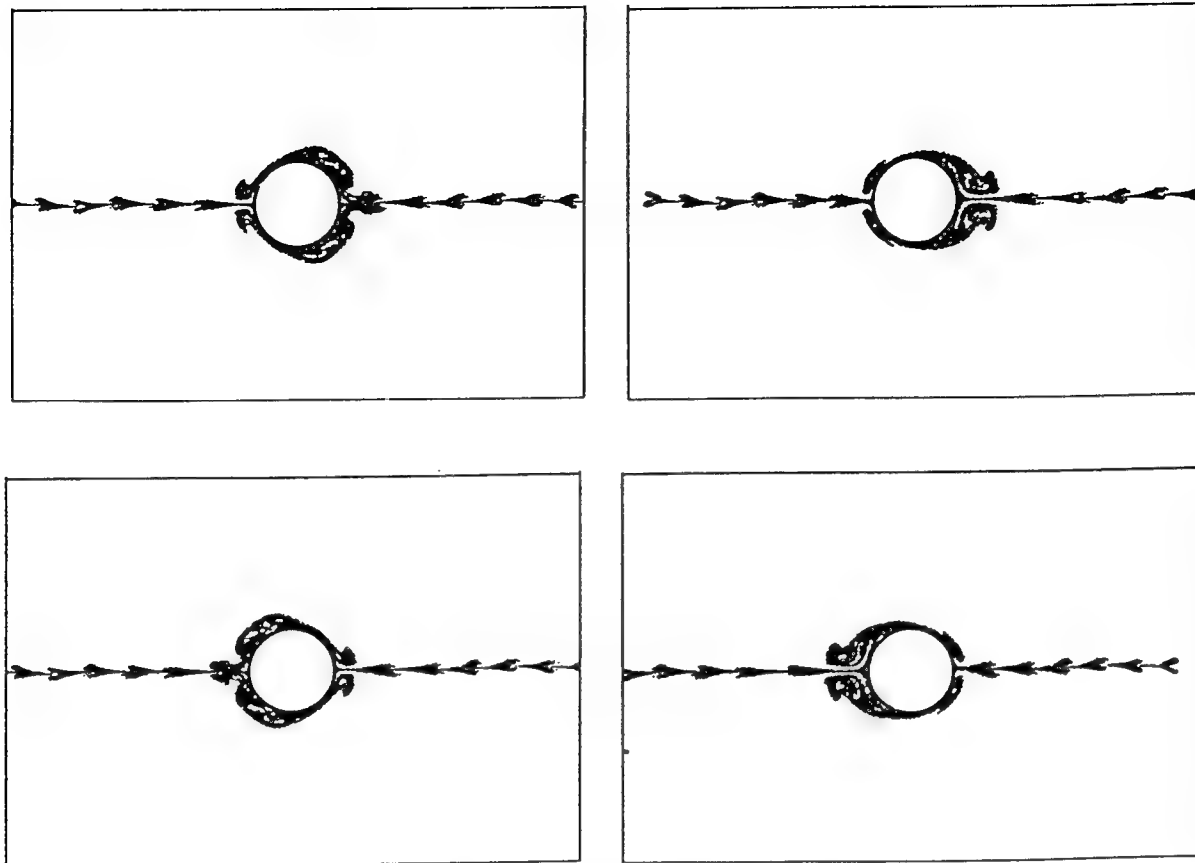


Figure 13 Numerical flow visualisation for $KC = 3$ and $\beta = 70$

During the course of the numerical study a considerable amount of data was generated relating to the velocity field about a circular cylinder in an oscillatory flow. In order to be able to view the data it was presented in the form of computed flow visualisations. These can then be compared with actual flow visualisations performed in water, such as those by Tatsuno and Bearman (38). With the discrete vortex method, recording the positions of the point vortices provides a relatively simple method of visualising the flow. However, in a flow visualisation experiment it is particles that are observed rather than point vortices and the resulting flow patterns may appear quite different. Tatsuno and Bearman (38) employed an electrolytic precipitation method in which fine white particles are released from the surface of the cylinder and initially they mark the vorticity generated at the surface. However, these particles are passive markers and will not retain their original vorticity. In order to provide a direct comparison between physical and computed

visualisations, passive particles were introduced near the cylinder surface in the computations and their subsequent motion followed.

Two sample computed visualisations will be presented. Figure 13 shows the flow in the symmetric vortex regime at $KC=3$ and at various stages during a flow cycle. The particles concentrate into blobs and convect away to either side of the cylinder. These plots closely resemble the photograph presented in figure 4 of Tatsuno and Bearman (38). Figure 14 shows a visualisation for $KC=10$, with the flow oscillating from left to right. In this regime the majority of the vortex activity occurs either above or below the cylinder. In the example shown the main vortex activity is above the cylinder. It is at this KC value that the drag coefficient and the transverse force coefficient take their maximum values.



Figure 14 Numerical flow visualisation for $KC = 10$ and $\beta = 70$

THE RESPONSE OF FLEXIBLE CYLINDERS IN OSCILLATORY FLOW

A flexible circular cylinder mounted normal to a steady current flow is susceptible to flow induced vibration, depending on the level of damping and the non-dimensional mass ratio $M/\rho D^2$, where M is the mass per unit length of the cylinder and ρ is the density of the fluid. Large transverse oscillations may occur when the frequency of vortex shedding coincides with the natural frequency of the cylinder. If the mass and damping are sufficiently small, in line oscillations may also be excited; although they will be of a much lower amplitude. In a relatively dense fluid such as water vortex excited oscillations can pose a serious problem. Much has been written about this phenomenon and readers are referred elsewhere for a detailed account.

In a planar oscillatory flow or in waves a flexible cylinder can also be excited into vibration, both in-line and transverse to the flow. Measurements of the response of a circular cylinder in oscillatory flow have been presented by Bearman et al. (39). At most values of KC the general form of the response in the in-line direction can be estimated quite successfully by using as input the unsteady force predicted by Morison's equation. In this application of the equation the force coefficients used are those appropriate to a fixed cylinder and the velocity and acceleration are relative to the responding cylinder. This is the so called "relative motion form" of Morison's equation. Figure 15 shows an example of the response and the associated prediction for a frequency ratio of around 2. The frequency ratio is defined as the ratio of the cylinder frequency measured in still water to the flow

oscillation frequency. Measuring the cylinder frequency in still water is easy to do but it is not clear that this is the most appropriate frequency. Other frequencies that might be used are the frequency in air and the frequency in oscillating water.

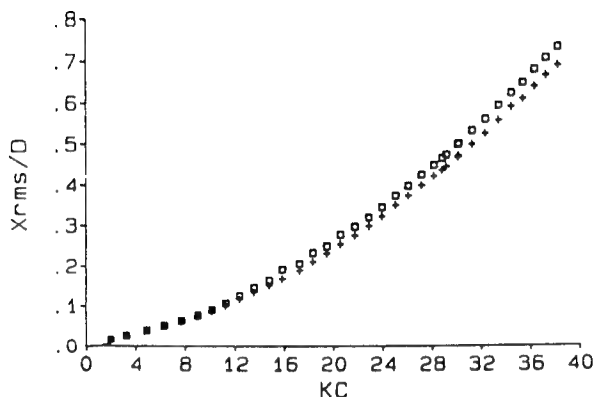


Figure 15 In-line response versus KC for a frequency ratio of 2; \square , measured, $+$, predicted using Morison

When the frequency ratio is near 3 application of Morison's equation seriously under estimates the response over a KC band from about 8 to 25, as can be seen from figure 16. The frequency ratio as defined above for this case is 2.85 but the cylinder is observed to respond at precisely three times the flow frequency. There is clearly more excitation at three times the flow frequency than that which arises from the drag term in Morison's equation. The extra response is thought to be due to the influence of vortex shedding. Using the numerical simulation procedure outlined above we have predicted the response for a flexible cylinder over a broad range of KC . However, to date we have been unable to reproduce the responses shown in figure 16 for KC values between about 8 and 25. We have carried out various checks on the experimental data and believe it to be correct and hence are unable to explain the discrepancy.

Bearman and Mackwood (40) have presented measurements of the transverse response of a flexible cylinder in oscillatory flow and some sample results are shown in figure 17 for a variety of frequency ratios. In these cases we know that the response is due directly to vortex shedding and it will be noted that the KC value for maximum response increases with increasing frequency ratio. It

has been pointed out earlier that the number of vortices shed per half cycle increases by one every time KC is increased by about 8. Hence we can expect vortex-excited response over a range of KC for each frequency ratio and for the KC at the centre of that range to increase with increasing frequency ratio. In the transverse direction the cylinder is forced to oscillate at an integer multiple of the flow frequency since the vortex shedding force is also at a multiple of the flow frequency.

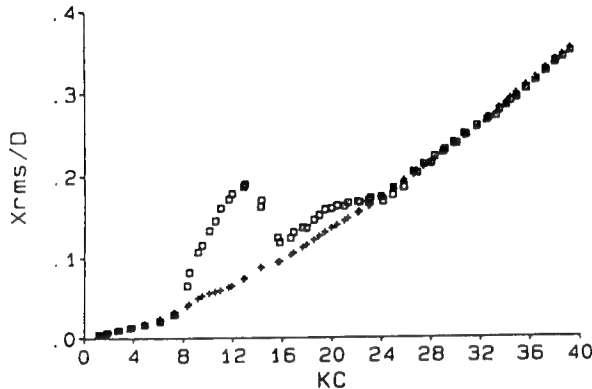


Figure 16 In-line response versus KC for a frequency ratio of 2.85; \square , measured, $+$, predicted using Morison

Computations to predict the transverse response of a flexible cylinder have been reported by Bearman et al. (41), using the discrete vortex method described by Lin et al (29). The most marked difference between the experimental and computational flow environments is that one is three dimensional while the other is two dimensional. However, in experiments the motion of the cylinder is expected to force much of the flow into predominantly two-dimensional motion and hence it is believed that the flow code should give realistic predictions of cylinder response. Figure 18 shows a comparison between computed and measured root mean square response amplitudes for a range of KC values. The agreement is remarkably good and it would appear that the computational method has successfully captured the physics of the complex fluid structure interaction that takes place. The onset of oscillation and the sharp rise in amplitude for KC values in the range 3 to 4 are well predicted.

CONCLUSIONS

Bluff body hydrodynamics is important in a number of naval applications and is particularly important in

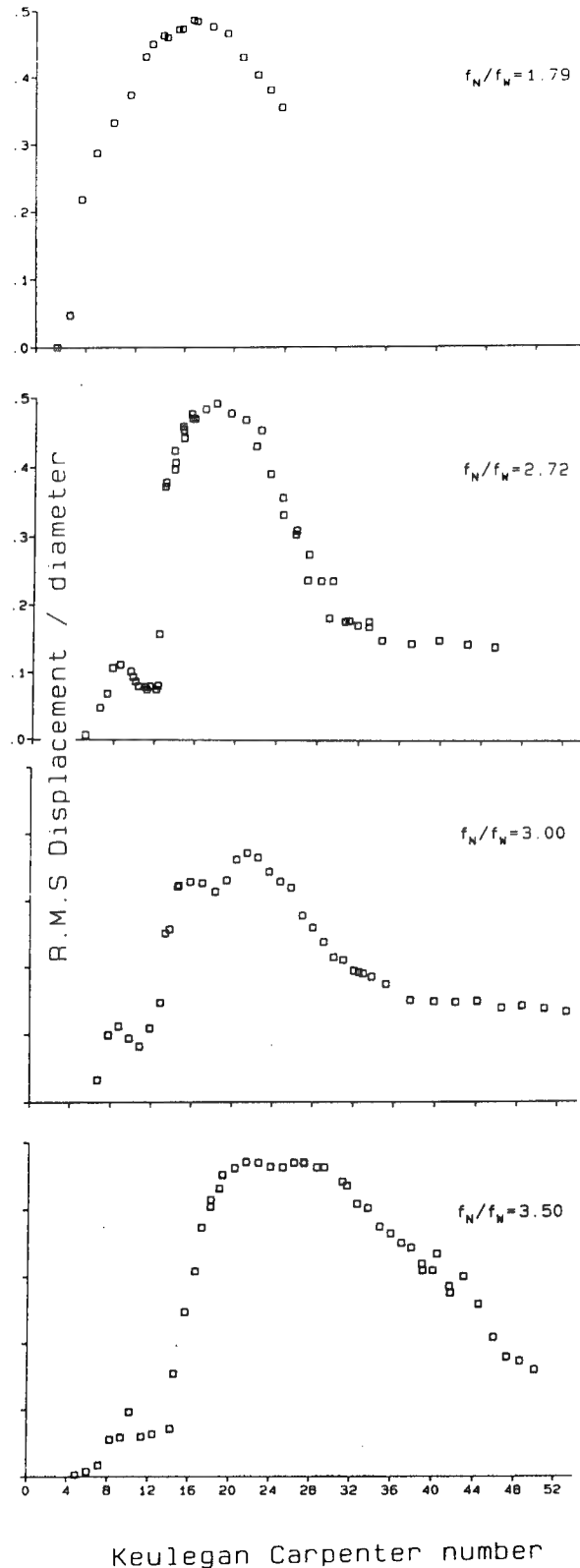


Figure 17 Transverse response versus KC for various ratios of the frequency of the model to the flow frequency

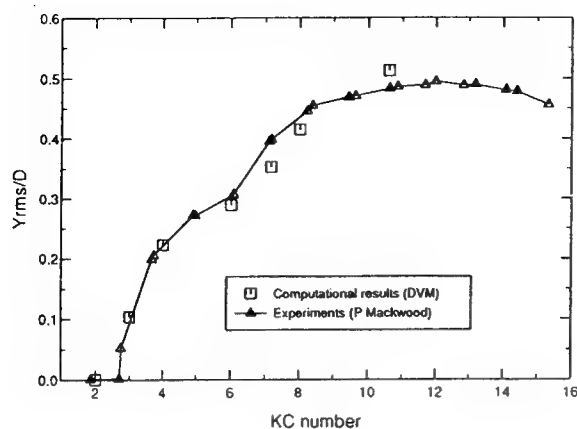


Figure 18 Transverse response versus KC; comparison of computed and experimental results for a frequency ratio of 1.81

certain aspects of the design of offshore structures. While much research has been directed towards the study of two-dimensional bluff bodies the instantaneous flows generated by such bodies can be far from two dimensional. The correlation length associated with vortex shedding from a rigid bluff body is a critical flow quantity but presently it cannot be predicted. In oscillatory flow and waves the return of vortices already shed play a significant role in the flow development. There are some values of Keulegan Carpenter number where shedding patterns are quite stable while at others, when perhaps a half formed vortex is left at the end of a cycle, there are substantial cycle to cycle variations. For a flexible circular cylinder in an oscillatory flow both in-line and transverse oscillations can be excited. In the in-line direction the response can be well predicted by applying the relative motion form of Morison's equation, except when the cylinder frequency is near to three times the flow frequency. In this case substantially larger responses are recorded which presumably are related to vortex shedding. Vortex shedding is directly responsible for vibrations in the transverse direction and as the cylinder frequency ratio increases so the Keulegan Carpenter number for maximum response increases. CFD is being increasingly used to study circular cylinders in oscillatory flow and in order to validate these codes more experimental data is required, particularly at low values of β .

ACKNOWLEDGEMENTS

The author would like to acknowledge the support of the US Office of Naval Research for work into three-dimensional aspects of bluff body flow and the EPSRC and the offshore industry, through MTD Ltd, for support of research into oscillatory flow past bluff bodies.

REFERENCES

1. Roshko A., "Perspectives on Bluff Body Aerodynamics," *J. Wind Eng. & Ind. Aero.*, Vol. 49, 1993, pp. 79-100.
2. Roshko A., "On the Wake and Drag of Bluff Bodies," *J. Aero. Sci.*, Vol. 124, 1995, pp 124-132.
3. Roshko A., "A New Hodograph for Free Streamline Theory," *NACA Tech Note 3168*, 1954.
4. Griffin O.M., "Universal Similarity in the Wakes of Stationary and Vibrating Bluff Structures," *ASME J. of Fluids Eng.*, Vol. 103, No. 1, 1981, pp 52-58.
5. Szepessy S., "On the Spanwise Correlation of Vortex Shedding from a Circular Cylinder at High Reynolds Number," *Phys. Fluids*, Vol. 6, No. 7, 1994, pp 2406-2416.
6. Gerrard J.H., "The Three-dimensional Structure of the Wake of a Circular Cylinder," *J. Fluid Mech.*, Vol. 25, 1966, pp 143-164.
7. Williamson C.H.K., "Oblique and Parallel Modes of Vortex Shedding of a Circular Cylinder," *J. Fluid Mech.*, Vol. 206, 1989, pp 579-627.
8. Eisenlohr H. and Eckelmann H., "Vortex Splitting and its Consequences in the Vortex Street Wake of Cylinders at Low Reynolds Numbers," *Phys. Fluid.*, A1, 1989, pp 189-192.
9. Hammache M. and Gharib M., "An Experimental Study of the Parallel and Oblique Shedding from Circular Cylinders," *J. Fluid Mech.*, Vol. 232, 1991, pp 567-590.
10. Bearman P.W. and Tombazis N., "The Effects of Three-dimensional Imposed Disturbances on Bluff Body Near Wake Flows," *J. Wind Eng. & Ind. Aero.*, Vol. 49, 1993, pp 339-350.
11. Triantafyllou G.S., "Three-dimensional Flow Patterns in Two-dimensional Wakes," *ASME Symp. on Non-Steady Fluid Dynamics*, FED Vol 92, 1990, pp 395-402.

12. Wei T. & Smith C.R., "Secondary Vortices in the Wake of a Circular Cylinder," J.Fluid Mech., Vol. 169, 1986, pp 513-533.
13. Monkewitz P.A. & Nguyen L.N., "Absolute Instability in the Near-wake of Two-dimensional Bluff Bodies," J.Fluids & Struct., Vol. 1, 1987, pp 165-184.
14. Szepešsy S. & Bearman P.W., "Aspect Ratio and End Plate Effects on Vortex Shedding from a Circular Cylinder," J.Fluid Mech., Vol. 234, 1992, pp 191-218.
15. Graham J.M.R., "Comparing Computation of Flow Past Circular Cylinders with Experimental Data," Bluff Body Wakes, Dynamics and Instabilities, Springer Verlag, Berlin, 1993, pp 317-324.
16. Bearman P.W., "Vortex Shedding from Oscillating Bluff Bodies," Ann. Rev. Fluid Mech., Vol. 16, 1984, pp 195-222.
17. Bearman P.W., "Investigation of the Flow behind a Two-dimensional Model with a Blunt Trailing Edge and Fitted with Splitter Plates," J.Fluid Mech., Vol. 21, 1965, pp 241-255.
18. Sarpkaya T. and Isaacson M., Mechanics of Wave Forces on Offshore Structures, Van Nostrand Reinhold, New York, 1981.
19. Bearman P.W., Graham J.M.R., Naylor P. and Obasaju E.D., "The Role of Vortices in Oscillatory Flow about Bluff Cylinders," Proc. Intl. Symp. on Hydrodynamics in Ocean Eng., Trondheim, Norway, August, 1981, pp 621-635.
20. Bearman P.W., "Vortex Trajectories in Oscillatory Flow," Proc. Intl. Symp. on Separated Flow around Marine Structures, Trondheim, Norway, June, 1985, pp 133-153.
21. Williamson C.H.K., "Sinusoidal Flow Relative to Circular Cylinders," J.Fluid Mech., Vol. 155, 1985, pp 141-174.
22. Obasaju E.D., Bearman P.W. and Graham, J.M.R., "A Study of Forces, Circulation and Vortex Patterns around a Circular Cylinder in Oscillating Flow," J. Fluid Mech., Vol. 196, 1988, pp 467-494.
23. Morison J.R., O'Brien M.P., Johnson J.W. and Schaaf S.A., "The Force Exerted by Surface Waves on Piles," Petroleum Transactions, Vol. 189, 1950, pp 149-157.
24. Verley R.L.P., "A Simple Model of Vortex-Induced Forces in Waves and Oscillating Currents," Appl. Ocean Res., Vol. 4, 1982, pp 117-120.
25. Bearman P.W., Graham J.M.R. and Obasaju E.D., "A Model Equation for the Transverse Forces on Cylinders in Oscillatory Flows," Appl. Ocean Res., Vol.6, 1984, pp 166-172.
26. Smith P.A. and Stansby P.K., "Viscous Oscillatory Flows around Cylindrical Bodies at Low Keulegan-Carpenter Numbers Using the Vortex method," J. Fluid and Structures, Vol. 51, 1991, pp 339-361.
27. Justesen P., "A Numerical Study of Oscillating Flow around a Circular Cylinder," J. Fluid Mech., Vol. 222, 1991, pp 157-196.
28. Zhang H.L. and Zhang X., "Flow Structure Analysis around an Oscillating Circular Cylinder at Low KC Number: a Numerical Study," To be Published, 1996.
29. Lin X.W., Bearman P.W. and Graham J.M.R., "A Numerical Study of Oscillatory Flow about a Circular Cylinder for Low Values of Beta Parameter," J.Fluid and Structures, Accepted for Publication, 1996.
30. Graham J.M.R., "Computation of Viscous Separated Flow Using a Particle Method," Numerical Methods in Fluid Mechanics, Vol. 3, 1988, pp 310-317.
31. Chorin A.J., "Numerical Study of Slightly Viscous Flow," J.Fluid Mech., Vol. 57, 1973, pp 785-796.
32. Chorin A.J. "Vortex Sheet Approximation of Boundary Layers," J. Comput. Phys., Vol. 27, 1978, pp 428-442.
33. Sarpkaya T. "Computational Methods with Vortices - The 1988 Freeman Scholar Lecture," J. of Fluids Engineering, Vol. 111, 1989, pp 5-52.
34. Cozens P.D., Numerical Modelling of the Roll Damping of Ships due to Vortex Shedding, PhD Thesis, University of London, 1987.
35. Arkell R.H., Graham J.M.R. and Zhou C.Y., "The Effects of Waves and Mean Flow on the Hydrodynamic Forces on Circular Cylinders," Proc. of the 6th Int. BOSS Conf., London, UK, July, 1992, pp 445-455.
36. Meneghini J.R. and Bearman P.W., "Numerical Simulation of High Amplitude Oscillatory Flow about a Circular Cylinder," J. of Fluids and Structures, Vol. 9, 1995, pp 435-455.
37. Kuhtz S., "Experimental Investigation of Oscillatory Flow around Circular Cylinders at Low β Numbers," PhD Thesis in Preparation, University of London, 1996.
38. Tatsuno M. and Bearman P.W. "A Visual Study of the Flow around an Oscillating Circular cylinder at Low Keulegan Carpenter Numbers and Low Stokes numbers," J. Fluid Mech., Vol. 211, 1990, pp 157-182.

39. Bearman P.W., Lin X.W. and Mackwood P.R., "Measurement and Prediction of Response of Circular Cylinders in Oscillating Flow," Proc. of the 6th Int. BOSS Conf., London, UK, July, 1992, pp 297-307.

40. Bearman P.W. and Mackwood P.R., "Non-linear Vibration Characteristics of a Cylinder in an Oscillating Water Flow," 5th Int. Conf. on Flow Induced Vibrations, I Mech E, 1991-6, 1991, pp 21-32.

41. Bearman P.W., Graham J.M.R., Lin X.W. and Mackwood P.R., "Modelling the Cross-flow Resonse of Cylinders in Oscillatory Flow," Proc. of the 7th Int. BOSS Conf., MIT, Boston, USA, Pergamon, 1994, pp 827-844.

Large-Eddy Simulation of the Vortical Motion Resulting from Flow over Bluff Bodies

S. Jordan (Naval Undersea Warfare Center [Newport], USA)

ABSTRACT

The focus of the present investigation is resolution of the vortical motion within the near wake of two example bluff bodies. Specifically, the mixing of the secondary eddies and primary Strouhal vortex frequencies in the separated shear layer of a circular cylinder and the subsequent vortical motion in the near wake are numerically investigated using the large-eddy simulation (LES). These LES investigations were performed at Reynolds numbers (Re) of 5600 and 8000. Preliminary results of a NACA 0018 hydrofoil is also presented. The vortical flow of the hydrofoil was simulated at $Re = 25000$ and an angle-of-attack of 7.5 degrees. The governing LES equations were formulated in curvilinear coordinates to accommodate the non-orthogonal grids. A corresponding generalized dynamic model is developed for the sub-grid scale turbulence. At the cylinder sub-critical Reynolds number of 8000, the LES results showed that laminar separation is quickly succeeded by Tollmien-Schlichting instabilities, secondary eddies and finally the formation of the primary Strouhal vortex. Through the separated shear layer, the LES results showed a range of transition wave frequencies that dominated the high-frequency components of the pressure spectrum compared to the low frequency component of the Strouhal vortex. The results also showed several modes of mixed transition and Strouhal frequencies. At $Re = 5600$, the LES results showed good comparisons to the published experimental data in terms of the time-averaged pressure distribution along the cylinder periphery, the shedding frequency, the vortex detection frequency, and the overall characteristics of the

Strouhal vortices in the near wake. The results also showed streamwise filaments that connect subsequent Strouhal vortices. The time-averaged Reynolds stress results of the formation region reveal symmetric characteristics similar to published experimental data at the sub-critical Reynolds number of 140,000. The LES results of the hydrofoil showed laminar separation of the upstream upper boundary layer followed by transition to turbulence and reattachment near the beginning of the trailing edge.

INTRODUCTION

Many engineering problems within the Navy involve very complicated flow behaviors that cannot be accurately simulated using simple computational methods. In addition, the physical geometries are generally quite arbitrary and require special attention when attempting to predict the associated flow. In most problems, the flow is unsteady, incompressible and very turbulent. Traditionally, numerical simulations of these flows are performed using the Reynolds-averaged Navier-Stokes (RANS) equations with a general purpose phenomenological model to fully represent the turbulence. The available turbulence models vary extensively in complexity; in particular, from simple algebraic eddy viscosity relationships to complex formulations involving several additional differential equations. In each model, values for the empirical constants are supplied from turbulent flows that are usually fundamentally simpler than the complexity of the problem at hand. Consequently, a RANS simulation can not be expected to give accurate predictions of the fine-scale turbulent physics using these general purpose models.

A viable alternative for numerical simulation of complex turbulent flows is the large-eddy simulation (LES). This approach is gaining popularity over the traditional RANS simulation. The LES success rests primarily on the rapid advancements in supercomputer technology as well as the recent developments in the methodology itself. Unlike the full-scale modeling inherent in a RANS technique, the LES method requires resolution of the dominate energy-bearing scales of the turbulent field while modeling only the remaining finer eddies which tend toward homogeneous and isotropic characteristics. Demarcation between the resolved and modeled scales is formally instituted by spatially filtering the basic governing equations of the fluid motion. In most computations however, this filter is actually treated implicitly through the spatial resolution of the implemented grid. Those physics lying beneath the grid resolution embody the subgrid scales (SGS) of the turbulent field and usually encompass most of the equilibrium range of the kinetic energy. Under this premise of an energy balance, today's SGS models are much simpler in form and better delineate the turbulent physics of their assigned scales as opposed to the typical full-turbulence models used in the RANS computations.

Studies of the turbulent vortical formation behind bluff bodies and the subsequent transport of the vorticity downstream has many important and practical Naval implications. Resolution of the turbulent vortical characteristics within the bluff body wake poses an excellent challenge for the large-eddy simulation. Except for only minor dispersion, the large scale motion usually remains strongly coherent for many characteristic lengths downstream of the bluff body. Since the impetus of LES is full resolution of the large scale motion, the results can provide specific information regarding the cyclic formation and downstream transport of the vortical motion including the local turbulent physics.

The formation and the downstream transport of the Strouhal vortices in the near wake of a circular cylinder is an excellent example of a difficult bluff body flow. The vortices themselves derive most of their large-scale vorticity from the separated shear layers and they organize downstream to form the well-known Karman vortex street. The upper and lower separated shear layers constitute the transverse outer regions of the formation regime. Both layers lie between the point of separation and the initial formation of the shed Strouhal vortices.

Besides these shear layers, the fluctuating base pressure near the downstream stagnation location contributes to the Strouhal vortex formation as well. A sketch illustrating these features is depicted in Figure 1.

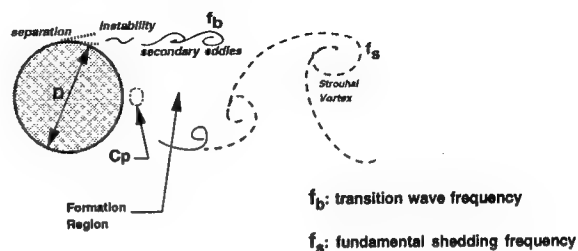


Figure 1: Sketch of the Primary Strouhal Vortex and Secondary Eddies in the Cylinder Wake Formation Region.

Our understanding of the cylinder shear layer physics improved significantly due to the experimental investigation by Bloor (1), Unal and Rockwell (2) and Wei and Smith (3). Bloor hypothesized that transition from laminar separation to turbulent vortex formation occurs within the separated boundary layer. This process occurs in two phases. Soon after separation, two-dimensional small-scale instabilities arise within the separated layer that amplify into Tollmien-Schlichting waves and eventually lead to turbulence. Due to the three-dimensional nature of the flow, these instabilities experience substantial spanwise distortion which also contribute to the transition mechanism. Unal and Rockwell also found high-frequency instabilities to exist, but for only $Re \geq 1900$ with pronounced amplification at specific Reynolds numbers of $Re = 3400$ and $Re = 5040$. At the latter Re in particular, they showed the spectral amplitudes to vary significantly across the shear layer at the predominant frequencies of the small-scale instabilities as well as the frequencies of the much larger scale Strouhal vortex.

Through flow visualization testing, Wei and Smith proposed a different phenomena for the separated shear layer physics. They observed creation of small-scale secondary vortices between separation and the initial large-scale Strouhal vortex formation. These secondary structures evolve from the same two-dimensional instabilities described by Bloor. The Strouhal vortices receive the majority of their vorticity from the secondary structures which

in-turn originate further upstream from the vorticity contained in the separated boundary layer. One primary difference between the Strouhal and shear layer structures is the minor influence of the rear base pressure on the secondary vortex formations. In the spanwise direction, the secondary vortices distort to periodic cellular structures that align themselves streamwise. Wei and Smith attributed the alignment to some feedback mechanism delivered from the downstream to upstream structures. At the higher Reynolds numbers within the intermediate range, the cellular structures become less pronounced and highly irregular.

The phenomena occurring in the separated shear layers just described as well as the organized vortex formation and subsequent downstream motion in the near wake is the subject of the present LES investigation. Only a few LES investigations have been previously reported of the cylinder separated shear layers and near wake flow. The first was a two-dimensional study by Song and Yuan (4) at a high Reynolds number. Since vortex stretching strongly dominates the turbulent production in the near wake (5), their simulation appears quite inadequate for capturing the important scales of the turbulent physics. Braza et al. (6,7) reported mixing layer eddies and pressure-frequency spectra of the cylinder shear layers, but their computations were also two-dimensional. Besides obviously ignoring important three-dimensional contributions to the streamwise maturity of the secondary eddies, pressure predictions near rear stagnation are always overpredicted thereby lengthening the formation region of the primary vortices. Another study was reported by Kato et al. (8) who concentrated on predicting the aerodynamic noise in the near wake using the finite element method. Their LES results served as input into the Lighthill-Curle equation for predicting the radiated far field acoustic pressures. However, due to their simple subgrid-scale turbulence model and their relatively coarse mesh of the wake region, agreement with the experimental data in terms of the spectral physics was obtained only at the low frequency levels.

In the following work, results from large-eddy simulations will be presented at a Reynolds number of 8000 to investigate the mixing of frequencies in the formation region due to the primary Strouhal vortex and the separated shear-layer secondary eddies. Results from a simulation at $Re = 5600$ will also be presented of the organized

vortex motion in the near wake of the circular cylinder with special emphasis placed on the turbulent statistics of the formation region. These Reynolds numbers are based on the cylinder diameter (D) and the uniform freestream velocity (U_∞) and are both sub-critical, meaning that the boundary layer at separation is strictly laminar. At these Reynolds numbers, the shedding of the primary shed vortices occurs at a dimensionless frequency (Strouhal number, S_f) of approximately 0.21; $S_f = f D / U_\infty$. Experimental measurements of the near wake turbulent statistics at a Reynolds number of 5600 were published by Zhou and Antonia (9). They reported the near wake as being fully turbulent over a downstream distance (x) ranging from 10 to 60 diameters referenced to the cylinder center. Over that range, their data showed little variation in the cross-sectional area of the primary vortices.

Finally, the preliminary results of the fine-scale turbulent motion resulting from trailing edge separation of the boundary layer of a hydrofoil will close the presentation and discussion of this paper. To adequately resolve the near wake flow of these geometries, non-orthogonal grid topologies were implemented. The corresponding equations were therefore solved in a curvilinear coordinate framework. Additionally, the dynamic subgrid scale turbulence model of Germano et al. (10) was reformulated for application in the curvilinear space. Since non-orthogonal topologies are often necessary to properly resolve the flow characteristics in many complex domains like the cylinder and hydrofoil wake, this LES formulation with the dynamic model has extensive applicability.

FORMULATION

Extension of the LES strategy to non-orthogonal grids was presented in detail by Jordan (11). For brevity, an abbreviated version will be described. Transformation of the Navier-Stokes equations to curvilinear coordinates where the Cartesian velocity components are the primary dependent variable has the form

$$\frac{\partial U^k}{\partial \xi^k} = 0 \quad (1)$$

$$\frac{\partial \sqrt{g} u_i}{\partial t} + \frac{\partial U^k u_i}{\partial \xi^k} = \frac{\partial \sqrt{g} \xi_{x_i}^k p}{\partial \xi^k} + \frac{1}{Re} \frac{\partial}{\partial \xi^k} \left[\sqrt{g} g^{kk'} \frac{\partial u_i}{\partial \xi^{k'}} \right] \quad (2)$$

The contravariant velocity components (U^k) are defined here as $U^k = \sqrt{g} \xi_{x_i}^k u_i$. The Jacobian \sqrt{g} of

the transformation appears in the formulation to place it in strong conservation-law form (12). To derive the corresponding LES equations, each term in equation (1) must be filtered (designated by an overbar). Except for convection, these terms commute with the filtering process to yield an analog set of equations in curvilinear coordinates that appear as

$$\frac{\partial \bar{U}^k}{\partial \xi^k} = 0 \quad (3)$$

$$\frac{\partial \sqrt{g} \bar{u}_i}{\partial t} + \frac{\partial \bar{U}^k \bar{u}_i}{\partial \xi^k} = \frac{\partial \sqrt{g} \xi_{x_i}^k \bar{p}}{\partial \xi^k} + \frac{\partial \sigma_i^k}{\partial \xi^k} + \frac{1}{\text{Re}} \frac{\partial}{\partial \xi^k} \left[\sqrt{g} g^{kl} \frac{\partial \bar{u}_i}{\partial \xi^l} \right] \quad (4)$$

The subgrid scale (SGS) stress tensor σ_i^k is defined in terms of the Cartesian and contravariant velocity components as $\sigma_i^k = \bar{u}_i \bar{u}^k - \bar{u}_i \bar{u}^k$.

For the cylinder and hydrofoil formation regions, the LES system of equations in (3 and 4) was time-advanced according to a variant of the fractional-step method (13). The convective terms were spatially discretized by third-order upwind-biased finite differences while the diffusive terms were differenced by second-order central differences. All terms in pressure-Poisson's equation were central differenced to the second order. Strong coupling between the pressure and velocity components was maintained through a fourth-order accurate compact differencing scheme for the pressure gradient in the velocity update equation. Details of the solution methodology, along with several test cases, were reported by Jordan and Ragab (14). The method is second-order accurate in both space and time.

DYNAMIC SUBGRID SCALE MODEL

To generalize the dynamic model by Germano et al. (10) for the cylinder application, the model was mathematically transformed to the computational space. This transformation was first reported by Jordan and Ragab (14). The SGS stress tensor in terms of the Cartesian velocity components is defined as

$$\sigma_i^k = \bar{u}_i \sqrt{g} \xi_{x_i}^k \bar{u}_j - \bar{u}_i \sqrt{g} \xi_{x_j}^k \bar{u}_j \quad (5)$$

Removal of the metrics from the filtering process provides a definition for σ_i^k as

$$\sigma_i^k = \sqrt{g} \xi_{x_i}^k (\bar{u}_i \bar{u}_j - \bar{u}_i \bar{u}_j) \quad (6)$$

which in terms of its Cartesian counterpart τ_{ij} is defined by $\sigma_i^k = \sqrt{g} \xi_{x_i}^k \tau_{ij}$. Using this expression, a generalized dynamic model (GDM) for the SGS stress tensor was defined as

$$\sigma_i^k - 1/3 \zeta_i^k \tau_{\ell\ell} = 2C\bar{\Delta}^2 |\bar{S}| \bar{S}_i^k \quad (7)$$

where C is Smagorinsky's constant. The turbulent eddy viscosity is defined as $\nu_T = C\bar{\Delta}^2 |\bar{S}|$ where $|\bar{S}| = \sqrt{2 \bar{S}_{ij} \bar{S}_{ij}}$, and the strain-rate tensor \bar{S}_{ij} in the computational space is computed according to

$$\bar{S}_{ij} = \frac{1}{2} \left(\frac{\partial \bar{u}_i}{\partial x_j} + \frac{\partial \bar{u}_j}{\partial x_i} \right) = \frac{1}{2} \left(\xi_{x_j}^k \frac{\partial \bar{u}_i}{\partial \xi^k} + \xi_{x_i}^k \frac{\partial \bar{u}_j}{\partial \xi^k} \right) \quad (8)$$

The resolvable strain-rate field \bar{S}_i^k in the computational space is $\bar{S}_i^k = \sqrt{g} \xi_{x_i}^k \bar{S}_{ij}$. By combining this transformation with equation (8), the complete definition for \bar{S}_i^k is

$$\bar{S}_i^k = \frac{1}{2} \left(\sqrt{g} g^{kl} \frac{\partial \bar{u}_i}{\partial \xi^l} + \bar{U}_i^k \right) \quad (9)$$

where $g^{kl} = \xi_{x_i}^k \xi_{x_i}^l$,

$$\bar{U}_i^k = \xi_{x_j}^k \frac{\partial \sqrt{g} \xi_{x_i}^l \bar{u}_j}{\partial \xi^l}$$

The procedures of Germano et al. (10) and Lilly (15) were used by Jordan and Ragab (14) to derive an expression for Smagorinsky's coefficient in the GDM. To implement their procedures directly the metrics were kept as part of the filtering process. An expression for Smagorinsky's coefficient in the computational space was obtained by filtering the governing LES equations in curvilinear coordinates a second time (by the test filter) to produce terms similar to those obtained by Germano et al. in the Cartesian coordinate system. In the computational space however, two new resolvable stress tensors arose. These two tensors are the: Reynolds stress tensor τ_i^k where

$$\tau_i^k = \bar{u}_i \bar{u}^k - \bar{u}_i \bar{u}^k \quad (10)$$

and a Leonard tensor \mathcal{L}_i^k defined as

$$\mathcal{L}_i^k = \bar{u}_i \bar{u}^k - \bar{u}_i \bar{u}^k \quad (11)$$

Consistent with the model scaling law for σ_i^k , the stress tensor τ_i^k was modeled as

$$\tau_i^k - 1/3 \zeta_i^k \tau_{\ell\ell} = 2C \overline{\Delta}^2 \overline{|\mathcal{S}|} \mathcal{S}_i^k \quad (12)$$

Using the identity $\mathcal{L}_i^k = \tau_i^k - \overline{\sigma}_i^k$, the resolvable tensor \mathcal{L}_i^k in the computational space became

$$\mathcal{L}_i^k - 1/3 \zeta_i^k \mathcal{L}_{\ell\ell} = 2C \overline{\Delta}^2 \mathcal{M}_i^k \quad (13a)$$

$$\mathcal{M}_i^k = \alpha^2 \overline{|\mathcal{S}|} \mathcal{S}_i^k - \overline{|\mathcal{S}|} \mathcal{S}_i^k \quad (13b)$$

Following the least-squares minimization procedure of Lilly (15), the GDM coefficient in equation (7) appeared as

$$C = - \frac{\mathcal{L}_i^k \mathcal{M}_i^k}{2 \overline{\Delta}^2 \mathcal{M}_i^k \mathcal{M}_i^k} \quad (14)$$

where the tensorial components in \mathcal{L}_i^k and \mathcal{M}_i^k are given in equations (11) and (13b), respectively. For the present computations, the tensors \mathcal{L}_i^k and \mathcal{M}_i^k were determined through application of a box filter. Negative values of the coefficient were truncated to zero, therefore all backscatter effects were eliminated.

RESULTS AND DISCUSSION

Simulation of the cylinder flow was focused specifically on resolving the separated shear layer physics and the formation and transport of the Strouhal vortices. To establish sufficient grid resolution near the cylinder surface, comparisons were made to the experimental results reported by Bouard and Coutanceau (16) of the early wake formation. According to Bouard and Coutanceau, the structural characteristics of the early wake formation behind the circular cylinder are similar for $1000 < Re < 10000$. Specifically, they visualized the early time evolving profiles of the exterior wake boundary and measured the horizontal velocity along the downstream centerline axis. LES computations were compared to those experimental measurements to help estimate the grid resolution that is required adjacent to the cylinder surface for the present study at the lower Reynolds numbers.

If a 2D simulation is performed of the cylinder wake flow at these sub-critical Reynolds numbers, one will grossly over-predict both the minimum and the base pressure coefficients along the cylinder surface. The base pressure coefficient $(C_p)_b$ in this case refers to the local region directly behind the

cylinder. In view of the experimental data, this parameter strongly correlates with the formation length, strength and Strouhal number of the primary shed vortices. Typically, a 2D simulation under-predicts the vortex formation length while over-predicting the strength and the shedding frequency of the vortices. Resolving the correct base pressure is therefore a minimum prerequisite of the field spacing. In our simulations, we found 16 points in the spanwise direction sufficient to satisfy this requirement at the lowest possible computational cost. Moreover, our results will show that this spanwise resolution was also adequate to capture the large-scale three-dimensionality of the near wake flow.

The final grid was $241 \times 241 \times 16$ (x,y,z directions). Along the cylinder surface, the distribution of points was $\Delta s \approx 0.011\pi$ within the upstream laminar boundary layer and $\Delta s \approx 0.007\pi$ within the turbulent wake. Normal to the cylinder surface, the spacing in wall units was $\langle \Delta y^+ \rangle = \pm 4$. In the spanwise direction, the grid point spacing was uniform at $\Delta z \approx 0.04\pi$.

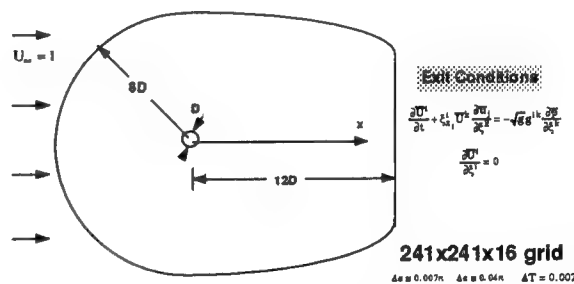


Figure 2: Grid and Flow Conditions for the LES Simulation of the Circular Cylinder.

The flow was impulsively started with unit velocity, zero reference pressure and a fixed non-dimensional time step of $\Delta T = 0.0005$; $T = tU_\infty / D$. After the initial transients ($T = 0.05$), new velocity and pressure conditions were imposed at exit. Specifically, a zero tangential pressure gradient condition was enforced along the downstream grid boundary while a combination of the continuity and Euler equations were found satisfactory to exit the shed vortices with minimum distortion. The inner boundary which is the cylinder surface was always no-slip and the upstream centerline axis was a branch cut. The spanwise boundaries were periodic.

These above conditions are illustrated in Figure 2. It should be noted that unlike some previous works, vortex shedding was not artificially initiated by numerically inducing a slight twist to the cylinder. For the present simulation, shedding of the Strouhal vortices was allowed to occur naturally through time evolution of an unstable wake.

A comparison of the experimental measurements (16) and the present numerical results at the span's mid-plane is shown in Figure 3 for $Re = 3000$ and a non-dimensional time $T = 2.5$. Their agreement is acceptable for the horizontal velocity profile. The computation under-predicted the minimum horizontal velocity component by 6 percent, but the overall error is just under 5 percent. This error is due principally to the rapid growth of the main eddies just prior to this instance in time that demands a very fine grid resolution to sufficiently resolve the associated gradients.

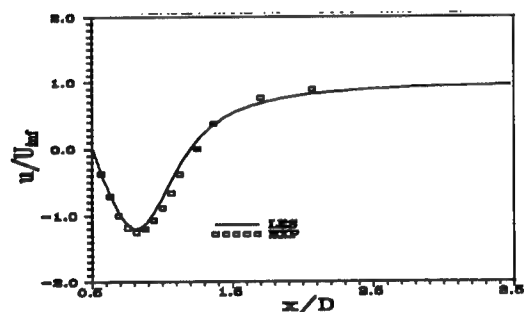


Figure 3: Comparison of LES Results and Experimental Data (16) of the Circular Cylinder. Profiles Depict Downstream Horizontal Velocity at $T = 2.5$.

A useful quantity for visualizing the large-scale three-dimensional structures of the near wake is the helicity ($\vec{v} \cdot \vec{\omega}$). A typical snapshot is shown in Figure 4 which depicts isosurfaces of this parameter taken from the LES results at $Re = 5600$. The snapshot clearly shows elongated large-scale streamwise structures connecting the alternating shed vortices. Gerrard (17) regularly observed these filaments in his flow visualization experiments and termed them as "fingers". These intermediate structures persist downstream and possess a high degree of streamwise vorticity, but low streamwise velocity. In terms of the helicity quantity, they are apparently on the same local scale as the adjacent Strouhal vortices which by comparison contain a high degree of spanwise vorticity, but low spanwise

velocity. The fingers themselves comprise pairs of counter-rotating vortices which is a circumferential plane of the cylinder.



Figure 4: Typical Snapshot of the Three-Dimensionality of the Cylinder Wake.

As mentioned earlier, the experimental measurements of Zhou and Antonia (9) detected an exponentially downstream decay of the peak vorticity of the Strouhal vortices. A two-dimensional snapshot of these vortices is shown in Figure 5 and represents spanwise averages of the z -component of the vorticity vector. Their time-averaged decay (23 cycles) is plotted in Figure 7 along with the streamwise variation reported by Zhou and Antonia. Using both the numerical and experimental results, the peak vorticity (ω_p) decays according to $\omega_p = 6 \exp(-0.056x)$ over the wake region $5 \leq x \leq 60$.

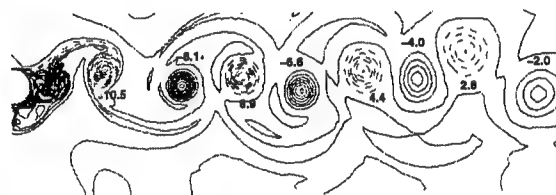


Figure 5: Typical Snapshot of the Vorticity in the Near Wake at $Re=5600$.

In contrast to their relative size, the detection frequency of the Strouhal vortices displayed considerable variability. Figure 6 is a good illustration of this characteristic where a non-uniform streamwise and relative transverse spacing can easily be seen between subsequent vortices. This distribution was typical throughout the wake region and provides an explanation for detecting the large

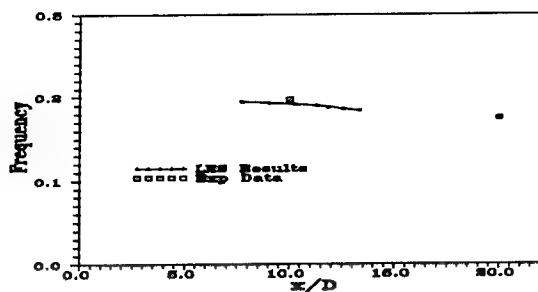


Figure 6: Time Averaged Downstream Decay of the Vortex Detection Frequency.

disparity in the relative frequency. However, time-averaging (23 cycles) this frequency reveals a near linear downstream decay as shown in Figure 6 over the entire wake region of interest ($8 \leq x \leq 60$) when the current results are combined with the experimental data (9).

Time traces of the lift and the drag force coefficient over approximately 23 shedding cycles along with their corresponding spectral components are shown in Figure 8. The dominate peak in the lift spectra occurs at the fundamental frequency which identifies the Strouhal frequency (f_s) of the oscillation. The value of $f_s = 0.21$ shown in the spectra is close to the measurement of 0.205 as reported by Zhou and Antonia (9), and it characterizes one complete shedding cycle (actually two vortices). The other peaks in the lift frequency spectra are of minor consequence which echoes the modulating appearance of the respective time trace. Conversely, the time signal of the drag force coefficient displays periods of intermittency and bursting phenomena which can largely be attributed to the numerous mixed modes occurring in the separated shear layers (2). The corresponding frequency spectra reflect these characteristics by indicating dominate peaks at several frequencies and over broader bandwidths. Inasmuch as the periodicity of the drag coefficient should be ideally equal to one-half that of the lift, its fundamental frequency is expected to be near $2f_s$ (or ≈ 0.42) with modes $(m/n)f_s$ ($n, m = 1, 2, 3 \dots$) signifying various harmonics and subharmonics. In Figure 8c, the predominate modes of the drag frequency spectra follow this criteria approximately with the strongest peak occurring at $2f_s$. The existence of this peak supports the conclusion drawn by Karniadakis and Triantafyllou (18), that the absolute instability which accounts for the low-frequency shedding of the large-scale vortices persists and dominates those disturb-

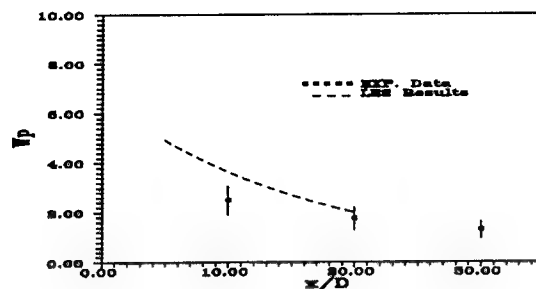


Figure 7: Time Average Decay of Peak Vorticity Within Strouhal Vortices.

ances associated with the transitional and the full turbulent regimes of the near wake.

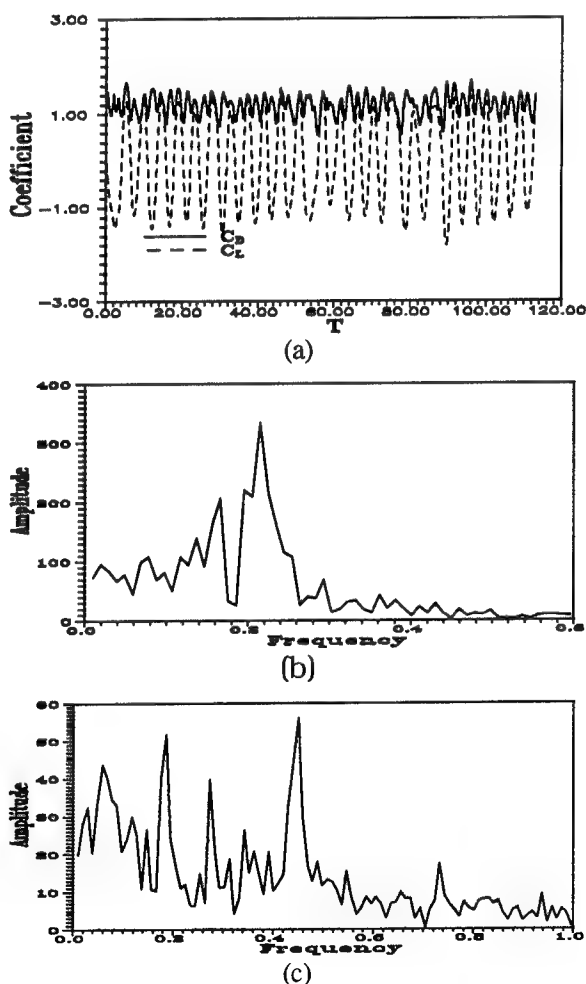


Figure 8: Lift and Drag Force Profiles and Corresponding Amplitudes Over 23 Shedding Cycles; (a) Time Traces, (b) Lift Force Amplitudes and (c) Drag Force Amplitudes

Along the cylinder surface, the local mean and root-mean-square (rms) pressure results are compared in Figure 9 to the time-averaged experimental data published by Norberg (19). As previously discussed, the spatial resolution in the spanwise direction was governed principally by achieving good agreement with the experimental data in terms of the base (and minimum) pressure coefficients. Although the maximum rms magnitudes are slightly over-predicted, the overall results are also in good qualitative agreement with the experimental data. The corresponding mean drag force coefficient is 1.18 which is the same value obtained after time-averaging the trace data shown in Figure 8a.

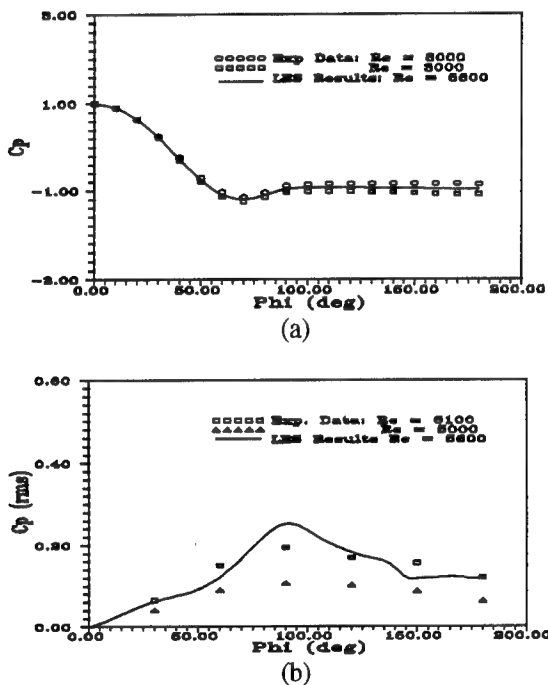


Figure 9: Comparisons of (a) Mean and (b) RMS Pressure Distributions Along the Cylinder Surface to Experimental Measurements (19)

As discussed earlier, past experimental observations and measurements conclude that the most fundamental physics of Strouhal vortices originate from the region immediately behind the cylinder. Consequently, by verifying our LES predictions of these basic physics, we can now investigate the mean turbulent energy production $\langle -P \rangle$ in the formation region where no conclusive data currently exists; $\langle -P \rangle = \langle \tau_{ij} \rangle \partial \langle u_i \rangle / \partial x_j$.

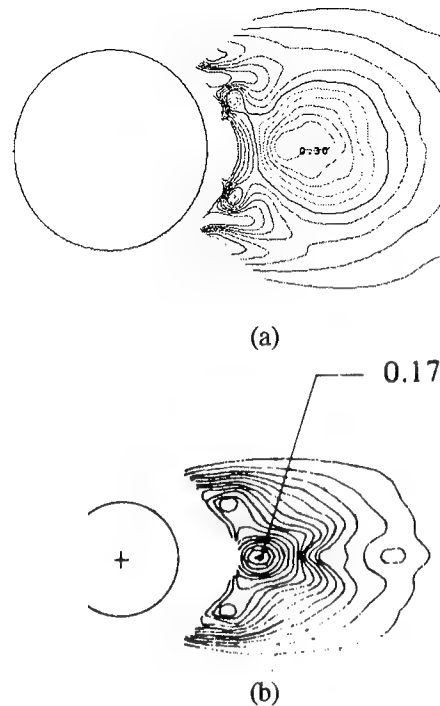


Figure 10: Contours of Turbulent Production in the Formation Region; (a) LES Results at $Re = 5600$ and (b) Experimental Data (5) at $Re = 140,000$.

Figure 10 shows the computed contours of production in the formation region along with the corresponding globally averaged experimental data of Cantwell and Coles (5) at $Re = 140,000$. The qualitative agreement between the two figures further suggests that both of these sub-critical Reynolds numbers do indeed share similar turbulent physics within the formation region. Each figure indicates negligible production levels beyond 2-3 diameters downstream. The highest production levels for the $Re = 5600$ simulation occur along the horizontal centerline axis approximately 1.11 diameters downstream compared to 1.17 diameters at $Re = 140,000$. Two additional peak levels of lesser magnitude are also shown that are symmetric about the formation region centerline. At $Re = 140,000$, these lower levels arise at an angle approximately 60 degrees (origin at the highest peak location and measured from the centerline axis) compared to an angle of 50 degrees for the present $Re = 5600$ results.

Presentation of the LES results at $Re = 8000$ begins with a typical snapshot of the vorticity contours inside the formation region as shown in Figure 11 where the dashed contours denote negative

vorticity. The contours appear to verify the three progressive phenomena of the separated shear layer as described by Wei and Smith (3) that lead to formation of the turbulent vortex; namely, laminar separation, T-S instability waves and secondary eddy formation. Moreover, the contours also show the turbulent vortex deriving the majority of its vorticity from the secondary eddies.

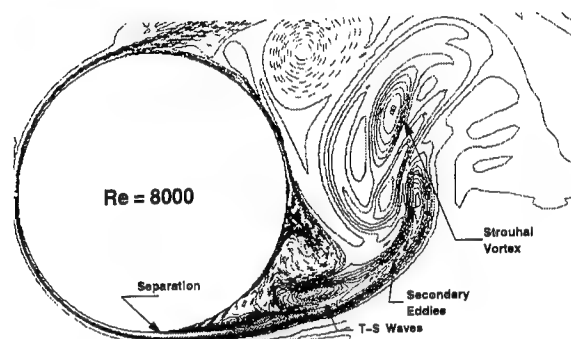


Figure 11: Snapshot of the Vorticity Contours Inside the Cylinder Formation Region ($Re=8000$).

According to the experimental relationships (1,3), a range for the transition wave frequency at $Re = 8000$ is $2.52 \leq f_b \leq 2.93$. By scanning the pressure-frequency spectra for peak amplitudes over this range, one should be able to discern a region within the shear layer where transition initiates. Shown in Figure 12 is the distribution of the peak amplitudes found in the spectra over the range of f_b given. The figure clearly suggests a zone of laminar flow as depicted by the low level and widely distributed contours of the peak amplitudes. Construction of an imaginary radial line with $\theta = 125^\circ$ (measured from upstream stagnation) is possible that delineates the limit of laminar flow or the initiation of transition. This line is drawn as dashed in the figure. If a data point is selected to the left of this line, the predominant subharmonics of the Strouhal frequency f_s should be identifiable with little mixing of f_b . In Figure 13a, the pressure spectrum at coordinates (8.34, 8.45) in fact shows these subharmonics (nf_s) with $f_s = 0.112$.

Although Figure 12 indicates two areas of highest peak amplitude in the formation region, only one can be perceived as within the separated shear layer. This maximum occurs at coordinates (8.61, 8.45). The mixing of secondary and Strouhal frequencies can be studied along development of the

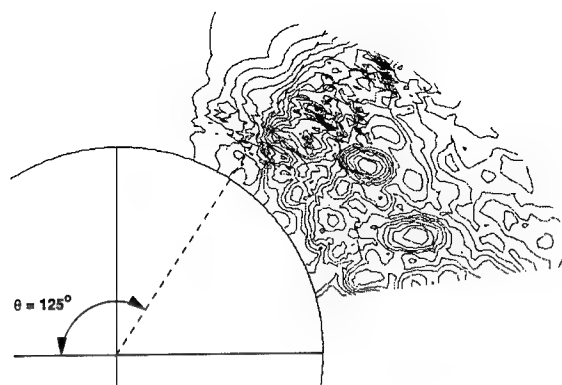


Figure 12: Distributions of the Maximum Peak Amplitude of the Secondary Eddies in the Formation Region.

separated shear layer by simply examining specific data points along a horizontal line through this peak. We begin in the laminar flow zone at point (8.34, 8.45) which is adjacent to the cylinder surface. The pressure spectrum in Figure 13a at this point is clearly indicative of deterministic physics. Further downstream at point (8.40, 8.45) which is still within the shear layer, the transition wave frequency appears and some minor mixing with the Strouhal frequency ($f_b - 2f_s$ for example in Figure 13b). This point lies slightly to the right of the radial line in Figure 12. The ratio f_b/f_s is 11.57 which falls within the range $10.12 \leq f_b/f_s \leq 11.78$ as determined from Bloor (1) and Wei and Smith (3), respectively. At the highest peak amplitude in the shear layer (8.61, 8.45), the mixing of f_b and f_s become more salient as indicated in Figure 13c by the significant amplitudes in the pressure spectrum at predominant modes of $nf_s \pm mf_b$. Notice that subharmonics of f_b in both samples are not indicated which agrees with experimental measurements (2). Much further downstream within the shear layer where the flow has fully transitioned to turbulent, the mixing of frequencies is much less discernible as expected. As shown in Figure 13d at sample point (9.00, 8.45), the amplitudes have diminished and the frequency bandwidths have widen significantly at the predominant modes shown further upstream. These series of sample points show good agreement with the shear layer physics hypothesized by Bloor (1) and Wei and Smith (2).

Investigations of the turbulent vortical motion resulting from trailing edge separation of the hydrofoil were performed at $Re = 25,000$. A C-grid

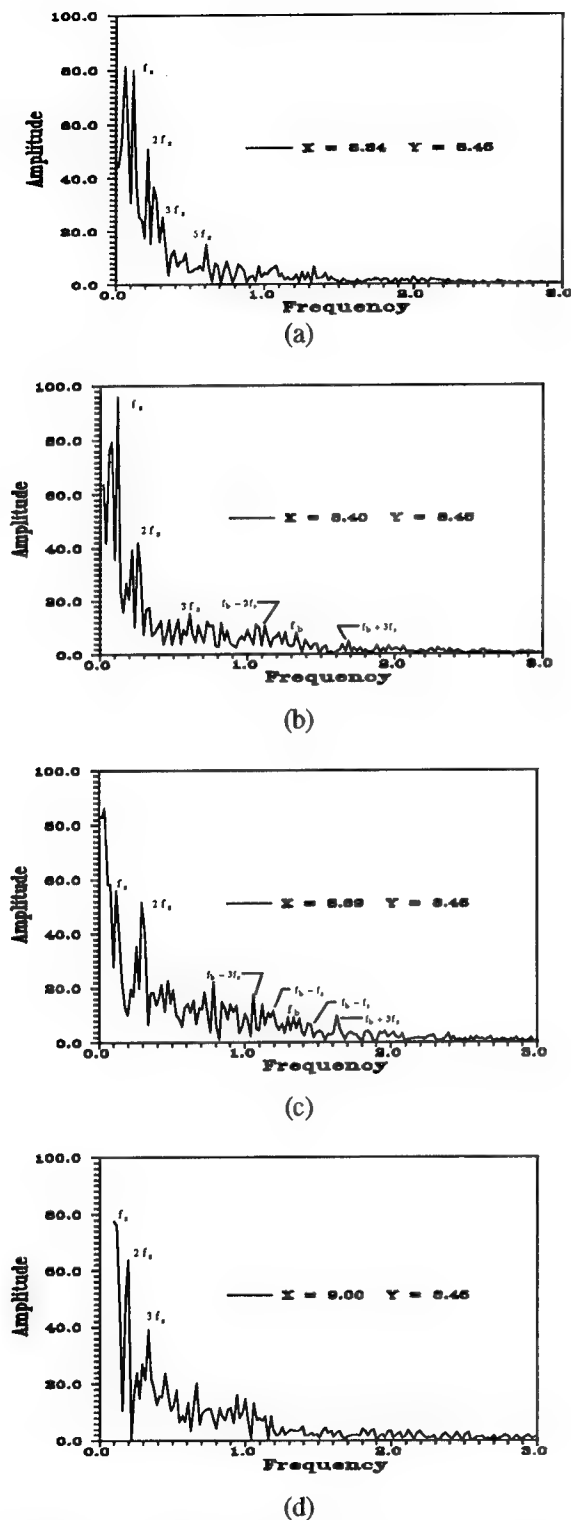


Figure 13: Pressure-Frequency Spectra at Various Grid Points Within the Separated Shear Layer; (a) $x=8.34, y=8.45$, (b) $x=8.40, y=8.45$, (c) $x=8.61, y=8.45$ and (d) $x=9.00, y=8.45$.

389x89x16 which had line clustering along the hydrofoil surface provided the best discretization strategy. The spanwise boundaries were assumed to be periodic. Expect for the downstream boundary and the hydrofoil surface (no-slip), unit velocity and potential flow conditions were applied along the other external grid boundaries. Conservation of energy across the downstream branch-cut was verified by examining the spectral energy content of the turbulent fluctuating quantities. The turbulent vortices exited without loss of peak vorticity through transformation of Euler's equation combined with continuity.

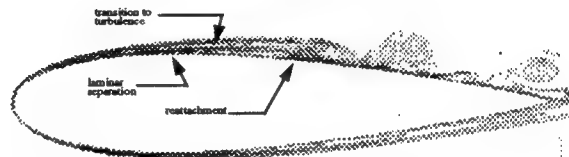


Figure 14: Flow Characteristics on Upper Surface of a NACA 0018 Hydrofoil at $Re=25,000$ and Angle-of-Attack of 7.5 degrees.

The hydrofoil was subjected to a 0° and a 7.5° angle-of-attack (AOA). Both upstream conditions produced trailing edge separation, but of different physical character. At $AOA = 0^\circ$, both of the upper and lower laminar boundary layers separated along the trailing edges and then quickly transitioned to the generation of turbulent vortices. The interplay between the separated regions produced asymmetric oscillatory separation points on the hydrofoil surfaces. At $AOA = 7.5^\circ$ (Figure 14), a separation bubble was produced through laminar separation along the upper surface followed by reattachment due to an abrupt transition to turbulence of the separated free-shear layer. However, the now turbulent boundary layer separated further downstream along the trailing edge. These physics have been verified qualitatively through corresponding experimental flow visualization testing. Qualitative verification of these LES computations to previously published data is currently underway.

CONCLUDING REMARKS

The impetus of the present large-eddy simulation (LES) was to investigate the turbulent physics of the near wake behind a circular cylinder and a NACA hydrofoil. The governing LES equations and subgrid-scale (SGS) turbulence model were formulated in curvilinear coordinates where both the Cartesian and the contravariant velocity components were utilized to dynamically evaluate the model coefficient. Initially, we computed the early evolution of the near wake at a Reynolds number of 3000. Based on this study, the following concluding remarks are offered:

1. The primary Strouhal vortices were shed at a non-dimensional frequency of 0.21. Their time-averaged peak vorticity (ω_p) exponentially decayed with downstream distance with a near linear decline of their local detection frequency over the near wake region of interest $5 \leq x \leq 60$; specifically, $\omega_p = 6 \exp(-0.056 x)$.

2. Between subsequent shed vortices are pairs of connecting intermediate structures (or "fingers").

3. The root-mean-square (rms) pressure results along the cylinder surface compared reasonably well with the experimental data (9), although the maximum rms magnitude which occurred at an angle near 90° from upstream stagnation was slightly over-predicted.

4. The distribution of the turbulent production within the formation region was symmetric and maximum levels occurred along the centerline axis. The distributions compared qualitatively well with the published experimental data (5) at a much higher sub-critical Reynolds number of 140,000. This agreement indicates that each wake flow share similar structural dynamics.

5. The transition waves in the shear layer dominated the high-frequency component (f_b) of the pressure spectrum whereas the Strouhal vortex comparatively occurred at low frequencies (f_s).

6. Simulation results in the form of pressure time traces and the corresponding spectra at specific points through the shear layer showed amplified peaks in the spectra easily distinguishable at modes of mixed frequencies $mf_s \pm mf_b$. No subharmonics of f_b were detected.

7. The ratio of f_b/f_s through the shear layer was found to be approximately 11.57. This value falls within the range of the relationships based on the published experimental evidence (3).

8. Preliminary LES results of a NACA 0018 hydrofoil showed laminar separation of the upstream upper boundary layer followed by transition to turbulence in the separated shear layer and finally reattachment near the beginning of the trailing edge.

ACKNOWLEDGMENTS

The author gratefully acknowledges the support of the Office of Naval Research (Dr. L. P. Purtell, Scientific Officer) and the Independent Research Program (Dr. S. Dickinson Coordinator) at the Naval Undersea Warfare Center Division Newport.

REFERENCES

1. Bloor, M.S., 1964, "The Transition to Turbulence in the Wake of a Circular Cylinder," Journal of Fluid Mechanics, Vol. 19, pp. 290.
2. Unal, M.F. and Rockwell, D., 1988, "On Vortex Formation from a Cylinder. Part 1. The Initial Stability," Journal of Fluid Mechanics, Vol. 190, pp. 491-512.
3. Wei, T. and Smith, C.R., 1986, "Secondary Vortices in the Wake of Circular Cylinders," Journal of Fluid Mechanics, Vol. 169, pp. 513-533.
4. Song, C.C.S. and Yuan, M., 1990, "Simulation of Vortex-Shedding flow About a Circular Cylinder at High Reynolds Number," Journal of Fluids Engineering, Vol. 112, pp. 155-163.
5. Cantwell, B. and Coles, D., 1983, "An Experimental Study of Entrainment and Transport in the Turbulent Near Wake of a Circular Cylinder," Journal of Fluid Mechanics, Vol. 136, pp. 321-374.
6. Braza, M., Chassaing, P. and Minh, H., 1990, "Prediction of Large-Scale Transition Features in the Wake of a Circular Cylinder," Physics of Fluids, A. 2, pp. 1461-1470.
7. Braza, M., Persillon, H. and Sers, F., 1993, "Prediction of Certain transition Characteristics in the Wake of a Circular Cylinder in Free and Forced Flow," IUTAM Symposium on Bluff-Body Wakes, Dynamics and Instabilities, ed. Eckelmann et al., Springer-Verlag, pp. 279-284.
8. Kato, C., Iida, A., Takano, Y. Fujita, H. and Ikegawa, M., 1993, "Numerical Prediction of Aero-dynamic Noise Radiated from Low Mach Number Turbulent Wake," AIAA 93-0145.

9. Zhou Y. and Antonia, R.A., 1993, "A Study of Turbulent Vortices in the Near Wake of a Cylinder," Journal of Fluid Mechanics, Vol. 253, pp. 643-661.
10. Germano, M., Piomelli, U., Moin, P., and Cabot W.H., 1991, "A Dynamic Subgrid-Scale Eddy Viscosity Model," Physics of Fluids, A. 3, pp. 1760-1765.
11. Jordan, S.A., 1994, "The Large-Eddy Simulation of Incompressible Flows in Simple and Complex Geometries," Ph.D. Dissertation, Virginia Polytechnic Institute and State University.
12. Vinokur, M. 1974, "Conservative Form of Gas Dynamics Equations," La Recherche Aerospatiale, No. 1974-1, pp. 65-68.
13. Kim, J. and Moin, P., 1985, "Application of a Fractional-Step Method to Incompressible Navier-Stokes Equations," Journal of Computational Physics, Vol. 59, pp. 308-310.
14. Jordan, S. A. and Ragab, S. A., 1994, "An Efficient Fractional-Step Technique for Unsteady Three-Dimensional Flows," Journal of Computational Physics, (accepted).
15. Lilly, D.K., 1992, "A Proposed Modification of the Germano Subgrid-Scale Closure Method," Physics of Fluids, A. 4, pp. 633-635.
16. Bouard, R. and Coutanceau, M., 1980, "The Early Stage of Development of the Wake Behind an Impulsively Started Cylinder for $40 < Re < 10^4$," Journal of Fluid Mechanics, Vol. 101, pp. 583-607.
17. Gerrard, J.H., "The Wakes of Cylindrical Bluff Bodies at Low Reynolds Number," Phil. Transactions Royal Society of London, Vol. 288, pp. 351-382.
18. Karniadakis, G.E. and Triantafyllou, G.S., 1992, "Three-Dimensional Dynamics and Transition to Turbulence in the Wake of Bluff Bodies," Journal of Fluid Mechanics, Vol. 238, pp. 1-30.
19. Norberg, C., 1992, "Pressure Forces on a Circular Cylinder in Cross Flow," IUTAM Symposium on Bluff-Body Wakes, Dynamics and Instabilities, ed. Eckelmann et al., Springer-Verlag, pp. 275-278.

The Wake of a Bluff Body Moving Through Waves

R. Arkell, J. Graham (Imperial College, United Kingdom)

Abstract

This paper describes a numerical simulation of the development of a vortex street wake behind a bluff body when subject to a disturbance field induced by free surface waves. The geometry studied in the present case is of a long vertical surface piercing circular cylinder moving steadily parallel to the direction of propagation of the waves.

In the first part of the study, the flow field is simulated at low Reynolds numbers and assuming locally two dimensional flow. The numerical simulation is based on a vortex (particle) method which includes the effect of viscous diffusion and accurately simulates the time dependent Navier-Stokes equations, which are solved in stream function-vorticity form to compute the velocity and diffusion fields. Comparisons are presented between the numerical simulations and flow visualisations at similar Reynolds numbers and wave-cylinder conditions obtained in towed cylinder experiments in a wave tank using dye.

In the second part, three-dimensional numerical flow simulations are carried out using an unsteady Navier-Stokes code based on convection of vortons. Results for a vertical cylinder translating through waves and a tapered cylinder in uniform translation are presented.

1 Introduction

The fundamental problem of the persistence of the wake of a moving body is an interesting one: wakes of ships are observed to persist for tens of kilometers on the surface of the sea under the right conditions. Frictional forces

within the fluid tend to reduce the velocity defect in the wake rapidly, and diffuse vorticity causing the wake to spread in a lateral sense (where gradients of vorticity are largest). The effects on the wake decay of parameters which include body shape, local Reynolds number, free surface conditions, and background turbulence are not yet fully understood.

The work reported here is an investigation into the effect of free surface waves on the vortex shedding and subsequent development of the wake of a vertical cylinder translating steadily under conditions such that the forward speed exceeds that of the particle orbital speed of the wave-induced local velocity field. A reversing incident flow relative to the cylinder is therefore not normally present, and the wave field represents a perturbation to the uniform incident flow. The vast majority of bluff body studies have focused on the effects of either a steady incident flow or of oscillatory incident flow on circular cylinders. Some have included the combined effects of oscillation and current. The study of many oscillatory flow problems arises due to the fact that most marine platform type structures are fixed or at most undergo limited motions, and are subject to the oscillatory velocity component induced by passing waves. In these cases the current is normally of smaller amplitude than the important wave induced velocities. Some common ground is to be found between these problems and the work presented here when the current, or forward speed, and the wave are of near equal strengths.

The present investigation is carried out at various levels of idealisation of the physical problem. The problem differs from the undisturbed (i.e. von Kármán) wake problem by the appearance of essentially two new mechanisms: (a) the fact that the local velocity at the cylinder surface is a combination

of a mean component and a smaller wave induced component varying in time, and thus the strengths of the shed vortices vary with time, resulting in a (weak) periodic spatial variation of vortex strengths away from the body, (b) that the vortices in the far wake are subject to a 'concertina-like' effect in which the wave-induced velocities cause a periodic dilation and extension of the vortex spacing in a sense parallel to the wave direction. The former mechanism (a) is dependent on the wave amplitude and frequency and is approximately independent of the wavelength of the wave, whilst the wavelength is important in the latter mechanism (b). The waves considered in this work have wavelengths many times that of the body size (as is generally the case of towed bodies in the open sea), and thus are not subject to significant diffraction effects around the body.

It is a well known that the idealisation of a vortex street to an infinite system of point vortices is only neutrally stable - that is to say, an infinitesimal disturbance introduced into the system will grow infinitely slowly (Lamb (1932)), and moreover there is only a single configuration of horizontal to vertical vortex spacing for which this neutrally stable configuration holds; all other spacing ratios are unstable. For an assumed two-dimensional flow and an infinite periodic point vortex model, the imposition of an additional two-dimensional approximation to simulate the effect of the wave motion on the point vortices as described by mechanisms (a) and (b) leads to a degeneration or breaking-up of the wake structure (Graham and Arkell (1992)), characterised by a process of vortex pair dissolution, in which vortex pairs are seen to eject from the central wake.

In reality a surface gravity wave induces orbital velocities which decay exponentially with depth in deep water, but are in phase in the plane normal to the wave propagation direction. Therefore a towed vertical cylinder in waves experiences a spanwise variation in velocity which consists of both horizontal and vertical components and leads to three-dimensional vortex shedding, vortex stretching, and inevitably a much more complicated velocity field.

2 Computational Method

Two flow simulation codes were used in the present work. A two-dimensional viscous vortex-in-cell code was developed using a Finite Volume approach. The method uses a streamfunction-vorticity formulation, in which vorticity is convected on moving particles (vortices) and diffusion is carried out on the mesh (see Graham and Arkell (1992)). A three-dimensional vortex code (FEMVOR) has also been developed in order specifically to investigate some of the three-dimensional effects. FEMVOR, as in the two-dimensional code, employs a particle representation of the vorticity field, in this case using vortons:

$$\vec{\omega}(\vec{x}, t) = \sum_{\alpha} \kappa_{\alpha}(t) \delta(\vec{x} - \vec{x}_{\alpha}) \quad (1)$$

where κ_{α} is the strength of the α^{th} vorton, and δ the Dirac delta function. In the present method the velocity field is calculated on a fixed mesh by projecting the volume-integrated vorticity (vortonicity) carried by the moving vortons onto that mesh. Integration of the field equations is performed over fully unstructured tetrahedral-element meshes using a piecewise linear Galerkin Finite Element method; this allows for compact coding and efficient spatial representation. The mesh generator was the FELISA system (Peraire, Morgan and Peiro (1990)), which is an Advancing Front type and is highly efficient for complex geometries and allows the user to modify mesh densities through application of point, line and triangular source distributions.

Vortonicity is interpolated from the particles onto the mesh nodes, and division of this quantity by the node control volume yields values of vorticity on the mesh. Changes to the vorticity field which arise through diffusion and stretching are re-interpolated back onto the particles at the end of a time step. New particles are created at mesh nodes if the vorticity magnitude there is finite at the end of a time step and no particles originally contributed to that node. New particles therefore materialise at a diffusion front. The method developed here is a hybrid one - similar to the two-dimensional code - in which only the convection is done by tracking particles, all other processes being implemented

on the mesh. Clearly, this reintroduces a certain amount of mesh dependency, but the unstructured tetrahedral-element mesh affords a great deal of flexibility in the distribution of elements. The solution to the field equations on the mesh is obtained using a preconditioned Conjugate Gradient method. The Lagrangian convection step of the current method using particles introduces minimal numerical diffusion, and is appropriate for modelling the complex vortical structures of separated flows. A detailed description of the method appears in Graham and Arkell (1995).

3 Two-dimensional viscous flow computations

A series of numerical experiments are carried out to study the results of adding a progressive wave to the steady incident flow past a circular cylinder. The characteristics of the flow field are presented in the form of instantaneous plots of point vortices; these demonstrate the dynamics of the vortices in the wake and the overall changing structure of the wake. We start by considering the far field free stream velocity to which the cylinder is subjected:

$$\begin{aligned} u(\vec{x}, t) &= U_c + u_w \sin(\omega_w t - k_w x) \\ v(\vec{x}, t) &= 0 \end{aligned} \quad (2)$$

where U_c is the translational velocity of the cylinder, u_w is the particle orbital speed induced by the wave, ω_w is the angular frequency of the wave, and k_w the wavenumber of the wave. Equation (2) is the velocity field of a progressive wave of wavelength $\lambda_w = \frac{2\pi}{k_w}$ travelling in the positive x -direction with a celerity $c = f_w \lambda_w = \frac{\omega_w \lambda_w}{2\pi}$. The three-dimensional free surface wave problem also has components of velocity in the direction normal to the free surface (i.e. along the cylinder in this case) such that the divergence of this potential velocity field is identically zero. Since the vertical motions are not accounted for in this two-dimensional analysis, mass is not conserved exactly in the two-dimensional potential field. The solution adopted is to split the temporal and spatial components of the phase of the wave so that the potential velocity field applied at the centroids of the computational el-

ements consists of a steady free stream component plus a planar oscillatory component, whilst the velocity applied to the point vortices also includes the spatial component. The potential velocity field around a cylinder of diameter $D = 2$ is therefore given by:

$$\begin{aligned} u_p(\vec{x}, t) &= (U_c + u_w \sin \omega_w t) A_x \\ v_p(\vec{x}, t) &= -(U_c + u_w \sin \omega_w t) A_y \\ A_x &= 1 - \frac{x^2 - y^2}{(x^2 + y^2)^2} \\ A_y &= \frac{2xy}{(x^2 + y^2)^2}. \end{aligned} \quad (3)$$

This velocity field satisfies continuity, i.e. $\nabla \cdot \vec{u}_p = 0$. The positions of the vortices are updated using the following velocity field:

$$\begin{aligned} u_v &= u_p + u_r + u_w (\sin(\omega_w t - k_w x_v) - \sin \omega_w t) A_x \\ v_v &= v_p + v_r - u_w (\sin(\omega_w t - k_w x_v) - \sin \omega_w t) A_y \end{aligned} \quad (4)$$

where subscript p refers to the potential solution, r refers to the rotational or vortical solution, and v refers to the point vortex with integer identifier v .

There are two parameters associated with a wave of height h , which are:

$$\hat{\lambda} = \frac{\lambda_w}{D} ; \quad \hat{h} = \frac{h}{D}. \quad (5)$$

Once the cylinder is in motion, with speed U_c , a third parameter may be inferred for the relative time scales. A natural choice for this third parameter in this case is the ratio of the frequency of the wave to the natural vortex shedding frequency in the absence of the wave, i.e. $\hat{f} = \frac{f_w}{f_n}$, where $f_n = SU_c/D$, and S is the Strouhal number. In the cases presented here, the Reynolds number is equal to 150. This is near the upper limit of the two-dimensional vortex shedding regime for steady incident flow, and within the known 'working range' of the two-dimensional code. The particular case of steady incident flow is presented first so that the effects of waves on the wake structure may be compared with a 'standard' result. Details of the vortex structures in the near-wake are shown in the point vortex plot for this steady incident flow case (figure

1). The Strouhal number for the steady incident flow case at this Reynolds number of 150 was found to be 0.182, through measuring the zero-crossings over many periods in the time trace of the transverse velocity field close to the cylinder.



Point vortices. $Re = 150$. No waves.

Figure 1

Figure 2 is a table of the various wave cases studied here. Note that $\hat{u} = \frac{u}{U_c}$.

Case #	λ	f	\hat{h}	\hat{u}
1	30	2.265	0.077	0.2
2	30	2.265	0.193	0.5
3	30	2.000	0.087	0.2
4	30	2.000	0.219	0.5
5	30	1.825	0.096	0.2
6	30	1.825	0.240	0.5
7	60	1.565	0.112	0.2
8	60	1.565	0.279	0.5
9	60	1.295	0.135	0.2
10	60	1.295	0.338	0.5
11	100	1.200	0.146	0.2
12	100	1.200	0.364	0.5
13	100	1.000	0.175	0.2
14	100	1.000	0.437	0.5
15	200	0.690	0.253	0.2
16	200	0.690	0.634	0.5

Summary of wave cases.

Figure 2

The range of \hat{f} is quite large, and spans the two central values at which lock-in occurs for in-line oscillations ($\hat{f} = 2.0$) and transverse oscillations ($\hat{f} = 1.0$). Assuming that, as far as the near wake is concerned, the hydrodynamic effects of in-line oscillations and progressive wave-trains are correlated, the data from Griffin and Ramberg (1976), who conducted experiments on in-line oscillations of a circular cylinder in a steady free stream, indicate that not all the wave cases presented here lie within the lock-in region. Their experiments were carried out at $Re = 190$, which is

close to that of the present data. The wave cases are basically divided into two categories of weak ($\hat{u} = 0.2$) and strong ($\hat{u} = 0.5$) waves, each being studied over a range of frequencies (\hat{f}) and amplitudes (\hat{h}). Weak wave case numbers are odd, and strong wave case numbers even. Figures 3 to 10 are plots of point vortices for all weak wave cases presented here, and show the vortex structures of the near-wake. The wakes are shown to a downstream distance of about 30 diameters. The flow is from left to right, and the waves propagate from left to right.



Point vortices. $Re = 150$. Case 1.

Figure 3



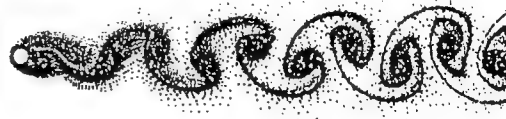
Point vortices. $Re = 150$. Case 3.

Figure 4



Point vortices. $Re = 150$. Case 5.

Figure 5



Point vortices. $Re = 150$. Case 7.

Figure 6



Point vortices. $Re = 150$. Case 9.

Figure 7



Point vortices. $Re = 150$. Case 11.

Figure 8



Point vortices. $Re = 150$. Case 13.

Figure 9



Point vortices. $Re = 150$. Case 15.

Figure 10

The characteristics of the wakes in the weak and strong wave cases are quite different. For weak wave cases for which $1.565 \leq \hat{f} \leq 2.0$ (cases 3,5,7), the wake is regular and closely resembles that of the steady incident flow case, in which alternate signed vortices are shed to form a staggered street. This is true even at very large distances downstream. It seems that for waves of this amplitude and within this frequency band, the stability of the resultant street is similar to the steady incident flow case. Case 3 most resembles the steady incident flow case, but as the frequency of the wave decreases, and the amplitude increases,

the staggered structure of the wake is lost. At frequencies outside this range, the alternate pattern is disrupted fairly close to the cylinder. In the near-wake, the inter-vortex spacing is no longer regular, and the formation of vortex pairs is apparent (see figure 10). The irregularity of the inter-vortex spacing is generally small; the formation of a definite vortex pair is slow, and takes place several diameters downstream of the cylinder. Often, the vortex pair results from the interaction of three closely spaced vortices; such a vortex triplet may be seen at $x/D \approx 24$ in figure 8. In weak wave cases the vortex pairs are not able to travel too far in the transverse sense due to the small differences in vortex strengths and inter-vortex spacings. The result is that the shape of the wake is mildly jagged (figure 11), and not particularly broad far downstream of the cylinder, by which time of course, the vortex strengths have been greatly diminished by diffusion and vorticity cancellation. The far wakes of these cases are sometimes characterised by the presence of large vortex structures, which arise through the coalescence of like-signed vortices. In general, the vortices in these cases are not so compactly arranged, and once the staggered configuration has been interrupted close to the cylinder, the vortices tend to spread out in the longitudinal sense, with the lengthscale of the vortex structures increasing with distance downstream.



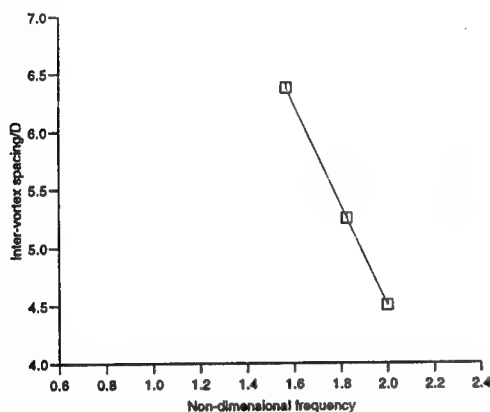
Vorticity contours. $Re = 150$. Case 9.

Figure 11

If the transverse velocity field is sampled close to the cylinder ($x/D = 2.5$, $y/D = 1.5$), it is observed that in cases (3,5,7) the period of the fluctuation in velocity is equal to twice the wave period. The vortex shedding has become synchronised with the wave. This synchronisation phenomenon, in which the wave is of sufficient amplitude and appropriate period to dictate the formation and shedding processes is similar to cases of oscillation of a cylinder in a uniform flow. This has been studied for the

case of cylinders and cables vibrating in-line (e.g. Griffin and Ramberg (1976)) and transversely (e.g. Meneghini (1993)). Time traces of the transverse velocity in the near wake indicate that for cases 3, 5 and 7, the vortex shedding is locked on to twice the wave frequency.

From the corresponding point vortex plots of these cases (i.e. figures 3 to 10), it is possible to measure the longitudinal inter-vortex spacing (a). Figure 13 is a plot of the values of the non-dimensional longitudinal inter-vortex spacing (a/D) versus non-dimensional frequency (\hat{f}). This plot applies to the synchronised cases only (3, 5, 7), although the special case of the $\hat{f} = 1.0$ (case 13) is also included (filled circle). The longitudinal inter-vortex spacing in this case is the same as the steady incident flow case.



Variation of vortex spacing with frequency.
Figure 13

The three co-linear data points in figure 13 lie on a line of equation:

$$\frac{a}{D} = -4.25\hat{f} + 13. \quad (6)$$

Figure 13 shows that for cases with non-dimensional frequency less than about 2.0 the longitudinal inter-vortex spacing is greater than the steady incident flow case, whilst for cases in which the non-dimensional frequency is greater than about 2.0, the longitudinal inter-vortex spacing is smaller.

The strong wave cases ($0.192 \leq \hat{h} \leq 0.633$) generally have broader wakes, and demonstrate a rich variety of vortex configurations. Figures 14 to 21 are point vortex plots

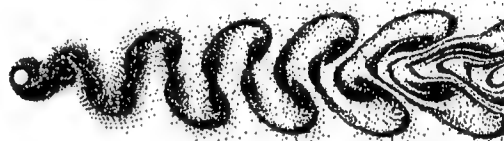
for these cases. These plots are arranged in an order of descending frequency, increasing amplitude. The flow is from left to right, and the waves are propagating from left to right.



Point vortices. $Re = 150$. Case 2.
Figure 14



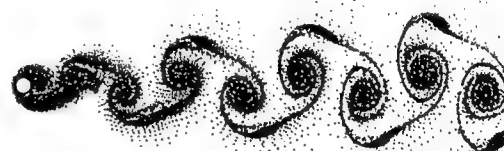
Point vortices. $Re = 150$. Case 4.
Figure 15



Point vortices. $Re = 150$. Case 6.
Figure 16



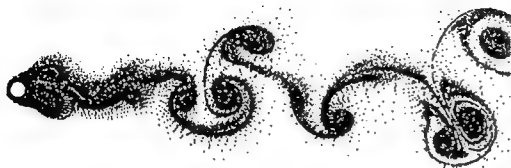
Point vortices. $Re = 150$. Case 8.
Figure 17



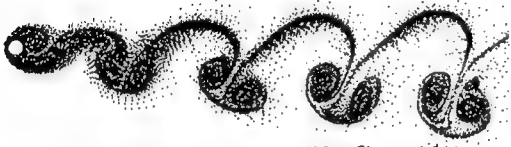
Point vortices. $Re = 150$. Case 10.
Figure 18



Point vortices. $Re = 150$. Case 12.
Figure 19



Point vortices. $Re = 150$. Case 14.
Figure 20



Point vortices. $Re = 150$. Case 16.
Figure 21

Case 2 (figure 14) is quite similar to its weaker counterpart (case 1, figure 8). The inter-vortex spacing is not regular, and there is some evidence of vortices 'bunching' in the near wake. The far wake becomes broad, whilst the longitudinal inter-vortex spacing increases with distance downstream. Figure 22 is a vorticity contour plot of this case.



Vorticity contours. $Re = 150$. Case 2.
Figure 22

Case 4 is the special case of $\hat{f} = 2$, i.e. the wave frequency is exactly twice the natural shedding frequency. The wake structure consists of alternately shed vortices of opposite sign; however, the transverse inter-vortex spacing is large and has a value of $2.75D$ in the near wake. This compares with $1.5D$ for the steady

incident flow case. The longitudinal inter-vortex spacing has the same value of $4.75D$. Figure 23 shows that the wake undergoes a sudden transition at a downstream distance of approximately $70D$, after which the vortex structures become larger and the longitudinal inter-vortex spacing increases; meanwhile, the wake undergoes very little broadening, even far from the cylinder.



Vorticity contours. $Re = 150$. Case 4.
Figure 23

If the wave frequency is lowered, a change in the mode of vortex shedding is seen to occur. Figure 16 is a plot of the point vortices in case 6 ($\hat{f} = 1.825$). In the near wake it may be seen that a symmetric mode occurs over the region $7.5D \leq x \leq 16D$. Further downstream, vortices of like-sign merge, and an anti-symmetric street is realised. At $\hat{f} = 1.565$ (figure 17), the transverse distance between vortices increases so that no merging of vortices occurs, and a double vortex street is established. This configuration persists far downstream, and is seen to exist up to the edge of the computational domain ($x = 115D$). The configuration observed in case 8 is very similar to the flow visualisation data presented by Detemple and Eckelmann (1989), in which the steady flow past a cylinder is acoustically disturbed by in-line waves at a non-dimensional frequency of $\hat{f} = 1.5625$. The structures observed in the wake are termed "Sea-horses".

At still lower non-dimensional frequencies, the wake structure undergoes further change. Case 10 (figure 18) shows that the wake is mainly comprised of alternately shed vortices, for which the transverse spacing is quite small. One particularly interesting aspect of both this case and the very similar case 12, is that the vortex rows have become interchanged compared with the classical von Kármán vortex street, i.e. vortices with -ve circulation form the top row, whilst vortices with +ve circulation form the lower row. This

is characteristic of a typical wake configuration of a body generating thrust. The longitudinal inter-vortex spacing is approximately double that of the von Kármán value. Plots of contours of vorticity for a larger portion of the wake indicate that broadening of these wakes is rapid, and occurs as a result of a vortex pair dissolution process (see figure 24).



Vorticity contours. $Re = 150$. Case 10.

Figure 24

At $\hat{f} = 1.0$ (case 14), the near wake consists of pairs of primary vortices which have formed from vortex triplets; in between these three vortices are weaker vortices. This particular case demonstrates the most rapid broadening of the wake (see figure 25), and the differences between this case and the weak wave counterpart (case 13) are marked.



Vorticity contours. $Re = 150$. Case 14.

Figure 25

At wave frequencies below the natural shedding frequency the wake is seen to consist of a regular line of closely formed vortex pairs, which move in a transverse flow sense under their mutually induced velocity field (figure 21). Samples of transverse velocity at $x/D = 2.5, y/D = 1.5$ show that the shedding is locked-in, and has a period equal to the wave period. This case indicates that there is a second lock-in region in the (\hat{h}, \hat{f}) parameter space for $\hat{f} < 1$. Detemple and Eckelmann (1989) report lock-in for the range $0.53 < \hat{f} < 2.46$. For $0.77 < \hat{f} < 1.16$, they report that the vortex shedding experiences lock-in at the driving frequency, and over

$0.53 < \hat{f} < 2.46$ the vortex shedding experiences lock-in at half the driving frequency. In the overlapping range, the mode of lock-in is unpredictable, and sometimes may not occur.

4 Three-dimensional Aspects

The work presented in this paper has so far examined the modifications which take place in the wake as a result of a two-dimensional progressive wave train, which models the presence of a surface gravity wave. However, it has long been recognised (e.g. Williamson (1995)) that even in the case of a two-dimensional incident flow past a nominally two-dimensional body, the rôle of three-dimensional instabilities in the development of the wake is of crucial importance to the structure of the wake. On this basis, the case of a circular cylinder translating into surface gravity waves, for which the incident flow is highly three-dimensional, merits an investigation into the three-dimensional aspects of the wake. Unfortunately, the number of degrees of freedom that exist in the three-dimensional numerical problem is very large, even for the relatively low Reynolds numbers under consideration here. Thus there exist quite severe restrictions on the numerical computations in terms of the length of wake which might be modelled and the spatial accuracy of the solutions.

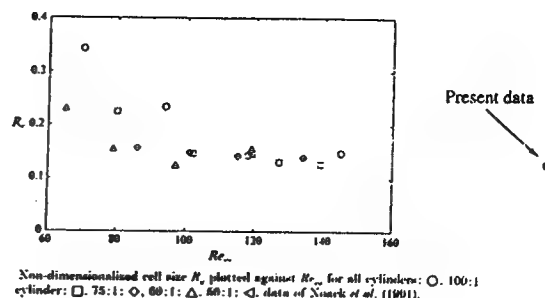
As a prelude to studying surface wave effects on the vortex wake of a circular cylinder, the flow past a mildly tapered cylinder with diameters D_1 and D_2 at sections H apart is analysed. This flow was initially studied experimentally by Gaster (1969), and has been shown to demonstrate three-dimensional Y-type structures in the wake, which arise through cellular shedding vortex patterns. The taper ratio (T_r) is defined as $T_r = H/(D_1 - D_2)$, and for the case under consideration here has the value of $T_r = 40$. The Reynolds number is 200, based on the mid-span diameter, and the aspect ratio is 8. Figure 26 is a plot of the vortons in the flow field after several shedding cycles have taken place. It quite clearly shows the existence of Y-type vortices. In this plot the larger end is at the top. The boundary conditions for the two end

planes are symmetry conditions which support no in-plane components of vorticity; thus, the vortices meet these planes orthogonally.



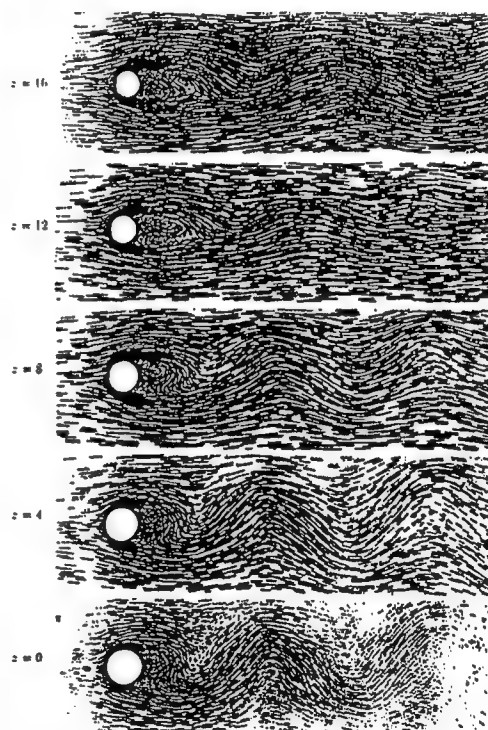
Vorton plot. Tapered cylinder. $T_r = 40$
Figure 26

Piccirillo and Van Atta (1993) found that the non-dimensionalised cell size became a constant value for a range of taper ratios at Reynolds number greater than about 100. Figure 27 is a reproduction of their figure for the non-dimensional cell size versus the Reynolds number at the centre of the cell. Included on this figure is the data for the case run here; only the larger cell is plotted, which agrees reasonably well with their data. The cylinders used by Piccirillo and Van Atta are of an aspect ratio roughly 5 to 6 times greater than the cylinder tested here, and so the possible number of cells generated is higher. Their data indicate that the cell sizes decrease slowly in the direction of the smaller end. The second cell in the present data (i.e. that nearer the smaller end) has become shortened, because the cylinder length cannot accommodate a full cell. Roughly speaking, a cylinder of aspect ratio of at least 12 at this taper ratio is required for two complete cells.



From Piccirillo and Van Atta (1993)
Figure 27

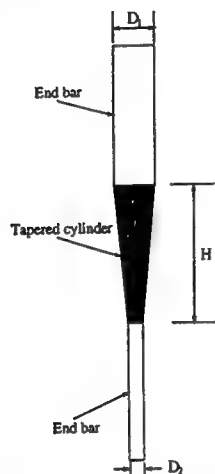
Figure 28 is a velocity vector plot at various spanwise locations for the case computed here. It shows the lack of correlation in the spanwise sense, and indicates that the shedding phase is dictated by the larger end over the majority of the cylinder length.



Velocity vectors at various spanwise locations
Figure 28

An experimental visualisation of this flow is performed for an identical tapered cylinder geometry. The method used is an electrolytic precipitation technique, as detailed in Honji, Taneda and Tatsuno (1980). The experiments

are carried out in the water flume in the hydraulics laboratory of the Department of Aeronautics at Imperial College. The working section is 0.6m wide and 0.65m deep. Non-tapered cylinders are connected at either end of the tapered cylinder. The larger end protrudes through the water surface, whilst at the lower end a 15cm circular end plate is attached. A schematic of the tapered cylinder is shown in figure 29.



Schematic of tapered cylinder
Figure 29

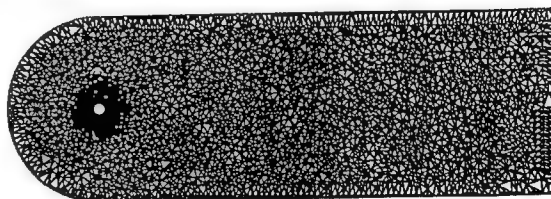
The Reynolds number of the flow is 200 based on the mid-span diameter. A very thin strip of rolled solder the length of the cylinder is attached to the front of the cylinder and is connected to the anode of a low voltage d.c. supply. The cathode is connected to a large steel plate placed many body lengths from the cylinder; when the current is switched on, a whitish precipitate forms at the anode and is drawn into the shear layers, marking the flow patterns. A 5 watt argon ion laser is used to illuminate a thin vertical plane of the wake. Figure 30 is a digitised frame from the video recording of this flow. It shows that the wake is characterised by bi-cellular shedding. The two ends of the cylinder have two different shedding frequencies and a linear variation in diameter implies a linear variation in Strouhal number along each cell. Since the vortex lines formed by the rolled up shear layer must be continuous from the top of the cylinder to the bottom, the disparity in shedding frequency across the cells results in a dislocation or splitting of the vortex.



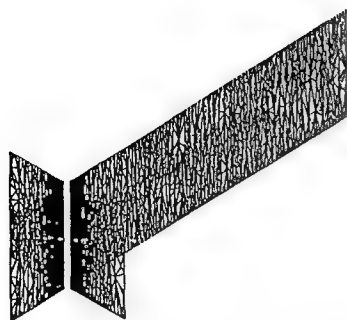
Precipitate in the wake of a tapered cylinder
Bi-cellular shedding
Figure 30

A three-dimensional numerical simulation of the towed cylinder in waves has also been carried out. The free surface is approximated by the usual linearised wave boundary condition. A transformation is applied to the computational mesh which is exactly equal and opposite to the vertical w -component of the basic potential velocity.

An unstructured mesh with 400,000 tetrahedra is used for the computation. Figure 31 is an $x - y$ plane through the mesh, and figure 32 shows both an $x - y$ and a $y - z$ plane. The mesh is first generated over the interval $0 \leq z \leq 1.0$, and then stretched in the z -direction, so that the aspect ratio of the cylinder is 16.

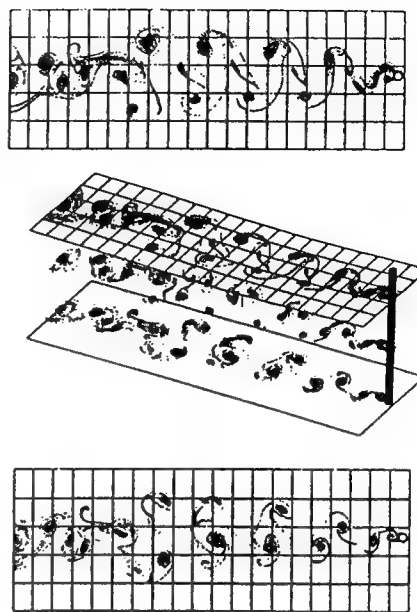


$x - y$ plane in the mesh
Figure 31



$x - y$ and $y - z$ planes in the mesh
Figure 32

A case is run for $Re = 150$; $\hat{\lambda} = 60$; $\hat{f} = 1.8$; $\hat{u} = 0.5$. Figure 33 shows the vortons at a non-dimensional time of $t^* = 68.4$. The top plot is a plan view on to the free surface; the middle plot is a three-dimensional perspective of the flow field, and the bottom plot is a plan view of the flow at $z = -H$. The middle plot shows only three slices of the vorton field, otherwise the image would be too complicated to interpret. At this point in the computation there are just over 2×10^6 vortons in the field. Here, the free surface is shown as a grid. The cylinder is travelling from left to right, the waves from right to left, and the viewer is looking down on the cylinder; a small length of cylinder is drawn protruding through the free surface. The length of the cylinder is approximately equal to $\lambda_w/4$, meaning that the u -component of the wave velocity field spans the approximate range: $\hat{u} : 0.2 \rightarrow 0.5$ between the bottom ($z = -H$), and the free surface ($z = 0$). Figure 33 shows that near to the free surface the vortex shedding is almost symmetric. In the bottom plane the near-wake resembles the von Kármán vortex street. The middle plane near-wake flow is quite similar to the two-dimensional result of Case 6, and the correlation between this plane and the free surface is high over this region. It is difficult to visualise what is happening to the vortices in the wake in a three-dimensional sense; the flow behind the tapered cylinder has been shown to be structurally quite simple, but what form of vortex connection is taking place here is hard to say. More insight may be gained by forming iso-vorticity surfaces from the data, and examining the way in which these 'structures' behave in the wake.



Vorton plot. $Re = 150$; $\hat{\lambda} = 60$; $\hat{f} = 1.8$; $\hat{u} = 0.5$.
Figure 33

A series of flow visualisation experiments are carried out in the 20m wave flume in the Department of Aeronautics, Imperial College to examine the free surface vortices of the wake of a vertical cylinder translating steadily into waves. The working section of this flume is 0.6m wide, 3 metres long, and typically has a depth of about 0.8m. The twin-paddles which create the waves may be driven over the frequency range of $0.5 \rightarrow 2.5 Hz$, giving a range of wavelengths of between 6.25m and 0.25m. A signal generator is used with a sinusoidal output signal.

The cylinder penetrates the free surface, and has minimum clearance at the bottom of the flume. The Reynolds number of the experiments is 600. Visualisation is achieved by bleeding a solution of potassium permanganate on to the front part of the cylinder. This is done through a hypodermic needle to help maintain an even, minimal flow rate whilst avoiding the formation of droplets of dye. Two 1000 Watt tungsten lights either side of the working section provide illumination. Fairly high speed (400 ASA) black and white film is used in a camera mounted above the water surface and fixed relative to the flume. Figure 34 demonstrates the formation of the classical von Kármán vortex street which re-

mains stable up to about $30D$ downstream; thereafter structure in the flow patterns becomes much less distinct and there is a small but fairly abrupt change in the wake width. There is a slight bias in concentration of dye, which makes the vortices on the lower row appear a little darker.

twice the transverse distance when compared with the no wave result. The parameters in this case are very close to case 14 of the two-dimensional viscous analysis, and there are similarities in the data. Figure 37 is a plot of the numerical data for approximately the same length of wake as in the experimental photograph.



Free surface flow visualisation
Cylinder in steady translation
Figure 34

Figure 35 demonstrates the effects of adding a wave of $\hat{\lambda} = 60$, $\hat{f} = 1.31$, $\hat{u} = 0.5$. The vortex patterns that emerge in the wake are similar to the "Sea-horses" of Detemple and Eckelmann (1989). The parameters of this case lie in between those of case 8 and case 10 of the two-dimensional viscous analysis data (figures 17 and 18 respectively). The structure of the near wake in the experiment most closely resembles that of case 8, although the inter-vortex spacing is not quite as small as that of the numerical simulation. At a streamwise distance of about $20D$ from the cylinder, this double street pattern is replaced by a different configuration which consists of a single vortex in the lower row and a complex arrangement in the upper row, whilst the flow field in the upper row has become quite complex. The vorticity contour plot for case 10 (figure 24) shows a similar behaviour at around a downstream distance of 35 diameters.

For longer wavelength, lower frequency waves, a different flow pattern emerges. Figure 36 is a photograph for the case $\hat{\lambda} = 100$, $\hat{f} = 1.03$, $\hat{u} = 0.5$. The wake is characterised by the presence of large vortex pairs in the upper half plane, and a single vortex in the lower half plane. The vortex pairs apparently convect quite rapidly in a transverse sense, so that at a streamwise distance of about $30D$ from the cylinder, the wake is very broad; dye has spread over approximately



Free surface flow visualisation
 $\hat{\lambda} = 60$, $\hat{f} = 1.31$, $\hat{u} = 0.5$
Figure 35

Figure 37 is fairly close to being a mirror image of the experimental data; the vortex pairs in this case are in the lower half plane, and the single vortex is almost directly above the corresponding pair. Notice also that in between the single vortex and the next downstream vortex pair there exists a smaller vortex in the connecting free shear layer. This is just observable in the experimental data of figure 36 between the two vortex pairs closest to the cylinder. Further downstream there is no evidence of a formed vortex at this location (also true of the numerical data), which may be related to the local strain field exerted by the rapid transverse motion of the next downstream vortex pair. The formation of the first vortex pair in the numerical data occurs further from the cylinder than in the experimental data; indeed, the entire wake pattern is more stretched in the longitudinal sense, and the vortex pairs themselves travel a smaller distance in the transverse sense. This may be a result of the difference in Reynolds number between the two sets of data.



Free surface flow visualisation
 $\hat{\lambda} = 100$, $\hat{f} = 1.03$, $\hat{u} = 0.5$
 Figure 36



Point vortices. $Re = 150$. Case 14
 Figure 37

5 Conclusions

Results have been presented of both 2-D and 3-D computations of the vortex wake behind a cylinder towed through waves. The computations are at a Reynolds number of 150. A survey of the changing wake patterns as a function of the wave parameters is presented. These data are in good qualitative agreement with both data in the literature on vertical cylinders in steady flow undergoing in-line oscillations, and surface flow visualisation data conducted in the Department of Aeronautics wave flume. A 3-D computation proved computationally expensive, but demonstrated reasonable agreement with the 2-D computations, and provides useful experience for future research in this direction. A 3-D computation of flow past a linearly tapered cylinder in a steady current is also presented. The data show the spanwise cell formation observed in flow visualisation experiments carried out by the authors on an identical geometry.

6 Acknowledgements

This work was supported by the Office of Naval Research under contract No. N00014-90-J-4122.

7 References

- E.Detemple-Laake and H.Eckelmann. Phenomenology of Kármán vortex streets in oscillatory flow. *Exp. Fluids*, 7:217-27, 1989.
- M.Gaster. Vortex shedding from slender cones at low Reynolds numbers. *J. Fluid Mech.*, 38:565-76, 1969.
- J.M.R.Graham and R.H.Arkell. End of contract reports to ONR. Contract No.N00014-90-J-4122. 1992 and 1995.
- O.M.Griffin and S.E.Ramberg. Vortex shedding from a cylinder vibrating in line with an incident uniform flow. *J. Fluid Mech.*, 75:257-71, 1976.
- H.Honji, S.Taneda and M.Tatsuno. Some practical details of the electrolytic precipitation method of flow visualization. Technical Report 89, Research Institute for Applied Mechanics, Kyushu University, 1980.
- H.Lamb. *Hydrodynamics*. Cambridge Univ. Press, 1932.
- J.Meneghini. *Numerical Simulation of bluff body flow control using a discrete vortex method*. PhD Thesis, Imperial College, London, 1993.
- J.Peiro, J.Peraire and K.Morgan. *FELISA System, Reference Manual* 1994.
- P.S.Piccirillo and C.W.Van Atta. An experimental study of vortex shedding behind a linearly tapered cylinder at low Reynolds number. *J. Fluid Mech.*, 246:163-95, 1993.
- C.H.K.Williamson. Three-dimensional vortex dynamics in the wake of a cylinder. In *Fluid vortices*, ed. S.I.Green. Dordrecht: Kluwer Academic, 1995.

Low-Dimensional Modeling of Flow-Induced Vibrations via Proper Orthogonal Decomposition

D. Newman, G. Karniadakis (Brown University, USA)

ABSTRACT: We investigate the use of proper orthogonal decomposition analysis on direct numerical simulations of flow over vibrating cylinders and cables. We first simulate the 2-d and 3-d wakes behind vibrating cylinders and cables, and then use the method of snapshots to compute the most energetic eigenmodes of these wakes. We examine the eigenmode energy decay versus mode number, and discuss the possibility of constructing low-dimensional dynamic models to simulate and predict the behavior of these systems.

1 Introduction

Fluid flows over flexible cables arise in many engineering situations, such as marine cables towing instruments, flexible risers used in petroleum production and mooring lines [1], [2], [3], [4], [5]. It is therefore important to understand and be able to predict the hydrodynamic forces and motion of cables caused by flow-induced vibration. Direct numerical simulations provide a means of computing these flows; however, as the problem size increases and as the Reynolds number increases, the computational requirements grow rapidly. One alternative method for simulating these flows is to use databases of existing computations to construct low-dimensional dynamical models to efficiently simulate the system at other operating conditions. In this paper we examine the use of proper orthogonal decomposition analysis to model the complex dynamics in the wake of vibrating cylinders and cables.

This paper is organized as follows: First, we describe the fluid/structure interaction problem, outline the solution method and describe the proper or-

thogonal decomposition procedure of computing the most energetic eigenmodes. Next we present results of 2-d simulations of flow over a vibrating cylinder, and compute the 2-d eigenmodes. Finally we consider 3-d simulations of flow-induced vibrations of flexible cables, and we compute the 3-d eigenmodes for these wakes, and discuss the construction of low-dimensional dynamic models.

2 Formulation

2.1 Governing Equations

We consider the interaction of an incompressible fluid flowing past a long flexible cable under tension. The equations that describe this problem are the coupled system of fluid equations and cable equations. The fluid equations are given by the Navier-Stokes equations and the continuity equation. In a stationary, Cartesian coordinate system (x', y', z') these equations are:

$$\begin{aligned}\frac{\partial \mathbf{u}'}{\partial t} + (\mathbf{u}' \cdot \nabla) \mathbf{u}' &= -\nabla p + \nu \nabla^2 \mathbf{u}', \\ \nabla \cdot \mathbf{u}' &= 0.\end{aligned}$$

For forced cable vibration, the motion of the cable is prescribed, usually in the form of a standing wave (for simplicity, constrained to move only in the cross-flow direction) with an amplitude A , wavelength L , and frequency ω_f :

$$\zeta(z, t) = A \cos \omega_f t \cos 2\pi z/L.$$

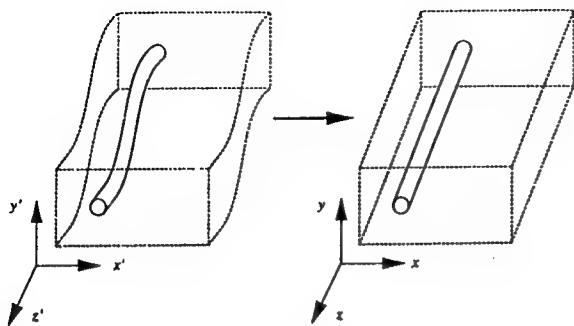


Figure 1: The coordinate system is attached to the moving cable, producing an undeformed, stationary computational domain.

In the case of flow-induced vibration, the equation of motion of the cable for its two directions of motion (i.e. in the x and y -directions) is given by a slightly modified forced wave equation:

$$\frac{\partial^2 \xi}{\partial t^2} = c^2 \frac{\partial^2 \xi}{\partial z^2} - \omega_n^2 \xi + \frac{1}{m} F(z, t),$$

where $\xi(z, t) = (\zeta(z, t), \eta(z, t))$ gives the cable displacement in the streamwise and crossflow directions and $c = \sqrt{T/m}$ gives the phase speed of waves in the cable. The cable has mass per unit length m and tension T . To maintain a mean displacement, the cable is lightly elastically supported by linear springs with spring constant k , giving a natural frequency of $\omega_n = \sqrt{k/m}$. The spring constant is selected sufficiently small to have negligible effect on the cable response. The fluid force on the cable is denoted by $F(z, t)$. The components of $F(z, t)$ in the streamwise and crossflow directions are the drag and lift force on the cable. Internal damping is neglected here as it does not significantly influence the response.

To simplify the solution of the fluid equations we use a coordinate system attached to the cable. This maps the time-dependent and deforming problem domain to a stationary and non-deforming one as shown in Figure 1. This mapping is described by the following transformation:

$$\begin{aligned} x &= x' - \zeta(z', t'), \\ y &= y' - \eta(z', t'), \\ z &= z'. \end{aligned}$$

Accordingly, the velocity components and pressure are transformed as follows:

$$u = u' - \frac{\partial \zeta}{\partial t} - w' \frac{\partial \zeta}{\partial z},$$

$$\begin{aligned} v &= v' - \frac{\partial \eta}{\partial t} - w' \frac{\partial \eta}{\partial z}, \\ w &= w', \\ p &= p'. \end{aligned}$$

The Navier-Stokes equation and continuity equation are transformed to

$$\begin{aligned} \frac{\partial \mathbf{u}}{\partial t} + (\mathbf{u} \cdot \nabla) \mathbf{u} &= -\nabla p + \nu \nabla^2 \mathbf{u} + \mathbf{A}(\mathbf{u}, p, \xi), \\ \nabla \cdot \mathbf{u} &= 0, \end{aligned}$$

where the forcing term $\mathbf{A}(\mathbf{u}, p, \xi)$ is the extra acceleration introduced by the transformation, consisting of both inviscid and viscous contributions.

2.2 Numerical Method

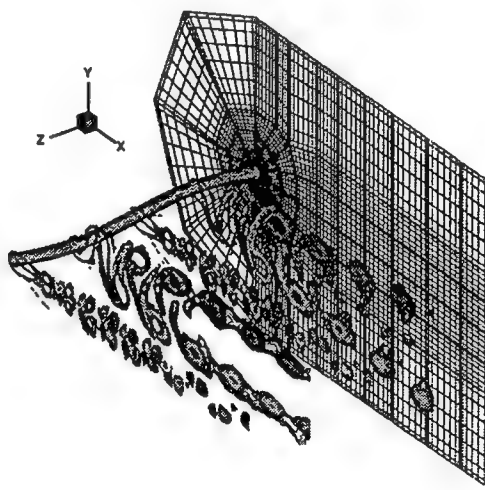


Figure 2: View of cable showing "slices" of spanwise vorticity and spectral element mesh.

To solve the three-dimensional Navier-Stokes equations, we use a parallel spectral element/Fourier method [6]. Spectral elements are used to discretize the x - y planes, while a Fourier expansion is used in the z -direction (i.e. along the cable). Consequently, all flow and cable variables are assumed to be periodic in the spanwise direction. The computational domain extends $35d$ (cable diameters) downstream, and $15d$ above and below the cable. The "cable span", i.e. wavelength of vibrations in the cable was $L/d = 12.6$ for the 3-d simulations. Each x - y plane is discretized by a 110 element mesh, with each element

having 81 collocation points. Typically 32 x -planes (16 Fourier modes) are used giving a total of 225,000 mesh points (see Figure 2). A non-dimensional time step of $\Delta t U/d = 0.002$ is used giving over 3,000 time steps per shedding cycle. For each simulation, the cable initial position and velocity are set and the simulations are run for at least 20 shedding cycles, or until the statistics are relatively stationary.

2.3 POD Analysis

To get a more general indication of the structure of a particular wake, we use proper orthogonal decomposition. Proper orthogonal decomposition (POD) is a methodology that first identifies the most energetic "modes" in an evolving system, and second provides a means of obtaining a low dimensional description of the system's dynamics. POD was applied to turbulence problems by Sirovich [7], while Dean et al. [8] generated low-order models for incompressible flows in complex geometries. Once the POD model has been generated, we can use it to predict behavior outside the parameter range used to compute the modes, e.g. predict the dynamics of a particular incompressible flow at different Reynolds numbers. Here we apply POD to examine the structure of the 2-d and 3-d wakes behind vibrating cylinders and cables.

The POD method starts by expressing the evolution of a field $u(x, t)$, by a sum of functions of time, $a_j(t)$, multiplied by spatial eigenmodes, $\phi_j(x)$,

$$u(x, t) = \sum_{j=1}^J a_j(t) \phi_j(x).$$

In this paper we will use POD to just compute eigenmodes $\phi_j(x)$ of the wakes in order to study their structure. The procedure to compute the eigenmodes ϕ_j can be described in a general form. Consider the time varying field $u(x, t)$. Let us define the instantaneous energy as

$$e(t) = \frac{1}{2} \int u^2(x, t) dx,$$

and the discrete approximation of $u(x, t)$ be given by vector $u(t)$, where the dimension of $u(t)$ is n . This dimension n would correspond to the total number of mesh points used to discretize $u(x, t)$. Let us consider $u(t)$ at discrete time intervals $t = i\Delta t$, and denote $u_i = u(i\Delta t)$. Then the discrete version of the energy integral becomes

$$e_{ii} = \frac{1}{2} u_i^T W u_i$$

where W would be a positive definite matrix (typically diagonal) of discrete integration weights from quadrature. Now we introduce the method of snapshots, where we examine a series of snapshots of $u(x, t)$ taken at m time intervals, $t = i\Delta t$, $i = 1, \dots, m$. Let us construct a matrix U of these snapshots u_i , so $U = \{u_1, \dots, u_m\}$ and the dimension of U is $n \times m$. We compute the covariance matrix E by taking the weighted inner product of each snapshot u_i with every other snapshot u_j :

$$E = \frac{1}{2} U^T W U$$

Note that the i^{th} diagonal entry of E is e_{ii} , the energy of snapshot u_i . The dimension of E is $m \times m$, and typically $m \ll n$, i.e. the number of snapshots is much lower than the number of spatial degrees of freedom (e.g. for our applications $O(m) = 100$ and $O(n) = 10^4 - 10^6$). The eigenmodes ϕ_j are computed by first computing the E 's eigenvalues and eigenvectors: $Eq = \lambda q$ or $EQ = \Lambda Q$, where λ is the eigenvalue, q is the eigenvector, Λ is a diagonal matrix of all the eigenvalues, and Q is the corresponding matrix of eigenvectors. Note that E is symmetric positive definite (if $U > 0$), and consequently (after normalization) the eigenvectors are orthonormal, with $Q^{-1} = Q^T$. Proceeding, we now define our set of eigenmodes Φ as

$$\Phi = UQ$$

Orthogonality of the eigenmodes is automatically guaranteed by their construction. Furthermore, the eigenvalues measure the energy of each eigenmode. Writing out the components of $\Phi = \{\phi_1, \dots, \phi_m\}$ and the diagonal entries of $\Lambda = \{\lambda_1, \dots, \lambda_m\}$, we have the energy of eigenmode ϕ_i is λ_i . One important quantity we will measure is how quickly the eigenmode energy λ_i decreases (i.e. convergence rate), as this will indicate an appropriate point to truncate the collection of eigenmodes.

At this point we have the m eigenmodes ϕ_i and corresponding mode energies λ_i . If we wish to reconstruct a snapshot u using J out of the m eigenmodes, we simply project the snapshot u onto the eigenmode basis to get the J coefficients. Let the projected (or reconstructed) snapshot be \hat{u} . Then

$$\begin{aligned} \hat{u} &= \sum_{j=1}^J a_j \phi_j, & \text{where} \\ a_j &= \frac{1}{2\lambda_j} u^T W \phi_j. \end{aligned}$$

3 2-D DNS Results

In this section we will examine the effect of cylinder oscillation on the 2-d wake. Experimental cross-flow vibration studies were first performed by Koopmann [9]. Ongoren and Rockwell [10] studied vortex pairing in the wake of an oscillating cylinder also at low Reynolds numbers. Williamson and Roshko [11] did an extensive study classifying the wake modes as a function of the forcing frequency and amplitude. We will concentrate on vibration frequencies and amplitudes that are close to those observed in flow-induced vibration cases. The forced cylinder oscillation cases are parameterized by the non-dimensional vibration amplitude A and frequency ω_f . We will refer to the forcing frequency ratio ω_f/ω_0 , which is defined as the ratio of forcing frequency ω_f to the frequency of vortex shedding of the fixed cylinder, ω_0 .

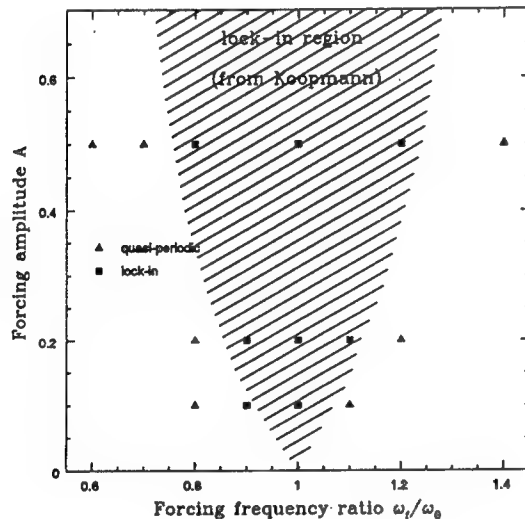


Figure 3: Forced vibration frequency-amplitude plot showing lock-in region from Koopmann, and Re=100 simulation results.

Koopmann [9] conducted a series of experiments at several Reynolds numbers measuring the flow behind cylinders oscillating in the crossflow direction. He considered crossflow vibration amplitudes from $\eta/d = 0.05$ to $\eta/d = 1$, and he varied the vibration frequency above and below the vortex shedding frequency of the fixed cylinder at that Reynolds number. We conducted 2-d simulations for several frequency-amplitude pairs, and the results are plotted in Figure 3. The points show the simulation results, while the shaded region is from Koopmann's data at Re=100. Here we illustrate the wake

“lock-in” phenomenon, where the frequency of vortex shedding in the wake matches the frequency of cylinder vibration. The shaded region delineates the frequency-amplitude envelope where we observe a locked-in wake. We see that the simulation results agree with the lock-in region measured by Koopmann.

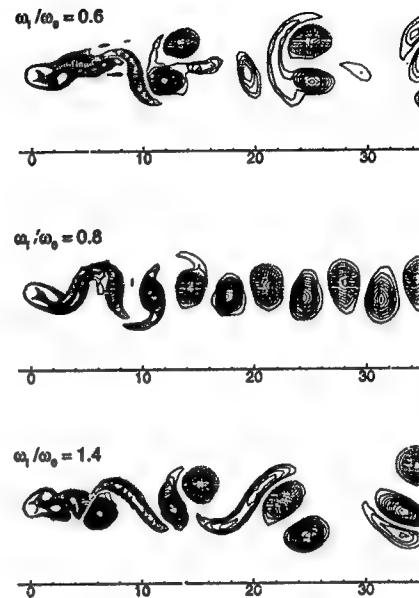


Figure 4: Forced vibration wakes at Re=100: vorticity for frequency ratios $\omega_f/\omega_0 = 0.6, 0.8$ and 1.4 and amplitude $\eta/d = 0.5$.

To more closely examine this lock-in/no lock-in behavior, we concentrate on the Re=100 results for non-dimensional crossflow amplitude $\eta/d = 0.5$, and frequency ratios $\omega_f/\omega_0 = 0.6, 0.8, 1.0, 1.2$ and 1.4 (i.e. synchronous, and 20% and 40% above and below synchronous). These simulations were run for 120 time units (20 shedding cycles for the fixed cylinder case). To illustrate the different wake patterns, we highlight three cases: sub-lock-in $\omega_f/\omega_0 = 0.6$, lock-in (but sub-synchronous) $\omega_f/\omega_0 = 0.8$, and super-lock-in $\omega_f/\omega_0 = 1.4$. Contour plots of vorticity for these frequency ratios of 0.6, 0.8 and 1.4 are shown in Figure 4. We immediately see from the picture of the wake vorticity that when $\omega_f/\omega_0 = 0.8$ (middle plot) a regular wake structure is displayed, and classed as locked-in, but when $\omega_f/\omega_0 = 0.6$ and

1.4, the wakes are not classed as locked-in. Note that although the wake in case $\omega_f/\omega_0 = 0.8$ looks similar to that of the fixed cylinder, it is in fact different due to the lower frequency of vortex shedding, producing vortices with streamwise spacing of $6.8d$ compared to $5.4d$ for the fixed cylinder, commensurate with the ratio of 0.8. Although the wake patterns in cases $\omega_f/\omega_0 = 0.6$ and 1.4 do not resemble the usual Karman vortex street, we do observe some regularity and pattern to the wake, with vortex pairing observed when $\omega_f/\omega_0 = 0.6$ and vortex merging occurring when $\omega_f/\omega_0 = 1.4$.

3.1 2-D POD Eigenmodes

Here we compute the eigenmodes for the 2-d simulations. Note that although the POD procedure was described for some scalar field u , and energy function $e = \frac{1}{2} \int u^2 dx$, we simply apply the procedure to the 2-d flow problem by concatenating the u and v velocities, giving the consistent energy function $e = \frac{1}{2} \iint (u^2 + v^2) dx dy$, (and similarly for the 3-d flows). We computed the eigenmodes for the fixed cylinder flow as well as the five forced vibration cases $\omega_f/\omega_0 = 0.6, 0.8, 1.0, 1.2$ and 1.4. In each case we took 300 snapshots ($m = 300$) over $tU/d = 60$ time units (on average, about 10 shedding cycles), giving the interval between snapshots of $\Delta t U/d = 0.2$. We examine the results for the fixed cylinder and the three forced vibration cases $\omega_f/\omega_0 = 0.6, 0.8$ and 1.4. We compute the vorticity eigenmode directly from the computed velocity eigenmodes, i.e. $\phi_\omega = \nabla \times (\phi_u, \phi_v)$. Note that this gives the desired answer, rather than computing the eigenmodes from snapshots of vorticity, which would be based on enstrophy $e = \frac{1}{2} \int \omega^2 dx$. We also mention here two points: first, we are computing the eigenmodes based on the fluctuations from the mean flow, and second, the eigenmodes are computed in the reference frame of the cylinder, i.e. in the transformed coordinate system where the cylinder (or cable) appears stationary and straight. Figures 5, 6, 7 and 8 show the six most energetic eigenmodes for the fixed cylinder and forced vibration cases $\omega_f/\omega_0 = 0.6$, $\omega_f/\omega_0 = 0.8$, and $\omega_f/\omega_0 = 1.4$ respectively.

First looking at the fixed cylinder case, where the wake is the most regular, we see that the eigenmodes occur in "conjugate pairs", i.e. ϕ_2 is 90° out of phase with ϕ_1 . This phase relationship is the same for the eigenmode pairs (ϕ_3, ϕ_4) and (ϕ_5, ϕ_6) . The size of the structures in the first pair (ϕ_1, ϕ_2) match the vortex spacing in the snapshots, and these eigenmodes are symmetric about the x-axis. We classify the patterns in these 2 eigenmodes as (1,1), i.e. structures with a scale of 1 vortex in the x-

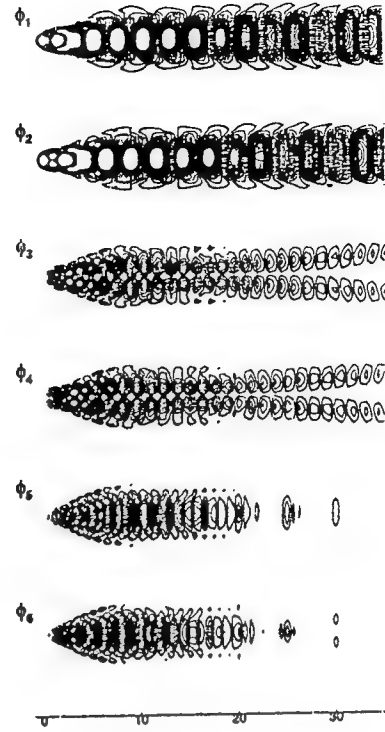


Figure 5: Eigenmodes 1-6 for the fixed cylinder.

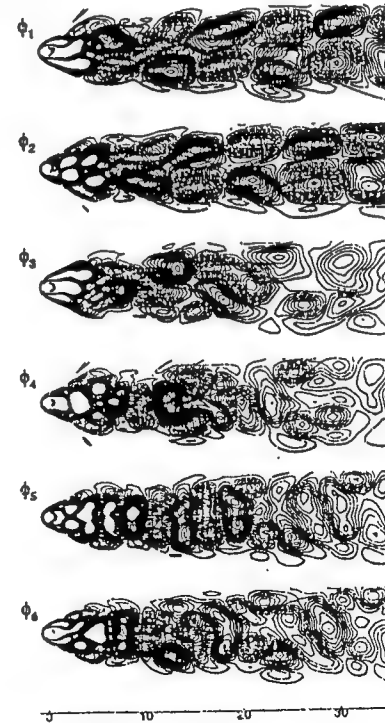


Figure 6: Eigenmodes 1-6 for forced vibration $\omega_f/\omega_0 = 0.6$.

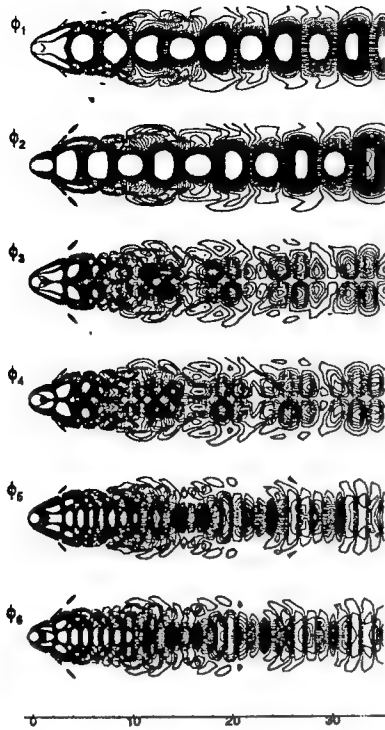


Figure 7: Eigenmodes 1-6 for forced vibration $\omega_f/\omega_0 = 0.8$.

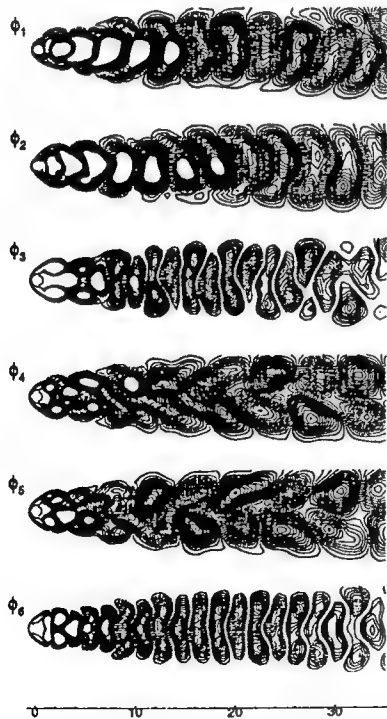


Figure 8: Eigenmodes 1-6 for forced vibration $\omega_f/\omega_0 = 1.4$.

Mode	Fixed	0.6	0.8	1.4
1	49.1	18.9	48.4	19.6
2	48.1	17.8	42.8	18.0
3	0.9	10.8	3.1	12.1
4	0.9	9.4	2.3	11.6
5	0.4	7.9	1.4	10.9
6	0.4	7.2	1.2	6.0

Table 1: Modal energy percentages of eigenmodes 1-6 for 2-d cases: fixed cylinder, and forced vibration cases $\omega_f/\omega_0 = 0.6, 0.8$ and 1.4 , $Re=100$.

direction, and 1 vortex in the y-direction. The next pair would then be classified as (2,2), since the size of the structures is half in both the x and y-directions. These eigenmodes are anti-symmetric about the x-axis. The third pair is classified as (3,1), again symmetric about the x-axis. Each subsequent pair of eigenmodes introduces successively finer scales into the structure of the wake.

How do the energies of these modes decrease with increasing mode? Since the same contour levels are used in all the plots, we get some indication of the amount of energy in each mode. The values are given in Table 1 for the four cases, showing the percentage of the total energy that that eigenmode contains. The pairing of the eigenmodes is clearly indicated by the energies, for the fixed cylinder case. The eigenmode energy rapidly decreases with increasing mode number (the first 2 modes contain 97.2% of the energy, while the first 6 modes contain 99.8% of the energy). This is also an indication of how unimodal time periodic the flow is.

Now looking at the sub-locked-in eigenmodes for $\omega_f/\omega_0 = 0.6$ (Figure 6), we see quite a different set of patterns compared to the fixed cylinder case. Again, the first pair of eigenmodes show some regularity, this time with anti-symmetry about the x-axis, but again, approximately 90° out of phase with one another. Modes 3-6 are more difficult to classify specifically, but we do see the finer structures emerging with increasing mode number. Looking at the Table 1 in this case shows that the first 2 eigenmodes only contain 36.7% of the total energy. The decay rate of eigenmode energy is relatively low – the first 6 eigenmodes contain just 72% of the total energy. Furthermore, the total energy in this forced case is 3.2 times larger than that in the fixed case.

The locked-in case $\omega_f/\omega_0 = 0.8$ (Figure 7) eigenmodes closely resemble those for the fixed cylinder (taking into account the $1/0.8$ expansion of the length scales). The classification of the eigenmode pairs follow that of the fixed cylinder, however in this forced case the energy of each eigenmode is substan-

tially larger (comparing the numbers in the table) – and the total energy in this forced case is more than four times larger than that in the fixed case.

Finally in the super-lock-in case $\omega_f/\omega_0 = 1.4$ (Figure 8), we see a reasonably regular first pair of modes. Here we point out that the $\omega_f/\omega_0 = 0.6$ flow case was the one where the first pair of eigenmodes did not have approximate symmetry about the x -axis. Furthermore, it looks like modes ϕ_3 and ϕ_6 are a conjugate pair, and modes ϕ_4 and ϕ_5 are a conjugate pair. This splitting of the conjugate pairs is possibly due to time sampling resolution. We see a similar decay rate of mode energy to the sub-lock-in case – 37.6% of the energy is contained in the first 2 modes, and just 78.2% of the energy is contained in the first 6 modes. The total energy in this case was the largest, at 4.4 times that of the fixed cylinder.

We demonstrate how the eigenmodes are used to reconstruct a snapshot. This gives us a qualitative indication of how a low-order dynamical model would reproduce the dynamics of a particular wake. Let us review the reconstruction procedure. We seek an approximation \hat{u} to a snapshot u using the first J of m eigenmodes, i.e. $\hat{u} = \sum_{j=1}^J a_j \phi_j$. Of course when we use all the eigenmodes $J = m$, we get a perfect reproduction, $\hat{u} = u$, so for $J < m$, \hat{u} approximates u . The coefficients a_j are simply computed by projection.

The three forced vibration cases were used to demonstrate the reconstruction procedure. In each case we reconstruct using (the highest) 2, 4, 8, 16 and 32 eigenmodes (the total number of eigenmodes available is equal to the number of snapshots, $m = 300$). The results are shown in Figures 9, 10 and 11.

We see that when $\omega_f/\omega_0 = 0.6$, the coarse structure of the wake is captured using 2-4 modes, however it requires at least 32 modes to get a reasonable qualitative match with the original snapshot. Note that this is still just using approximately one tenth of all the eigenmodes (32 out of 300). The locked-in case, ($\omega_f/\omega_0 = 0.8$, Figure 10) requires far fewer modes to get a qualitative match – here just 8 eigenmodes capture the details of the wake structure reasonably well. Finally, the super-lock-in case ($\omega_f/\omega_0 = 1.4$, Figure 11) shows a similar trend as for $\omega_f/\omega_0 = 0.6$, i.e. 32 modes are required to obtain a reasonably accurate reconstruction.

The point at which we choose to truncate the collection of eigenmodes can be selected by examining the eigenmode energy spectrum. This is plotted for our fixed cylinder and forced vibration cases in Figure 12. Here we plot the eigenmode energy (as a proportion of the total energy for that case), λ_j/λ_{tot}

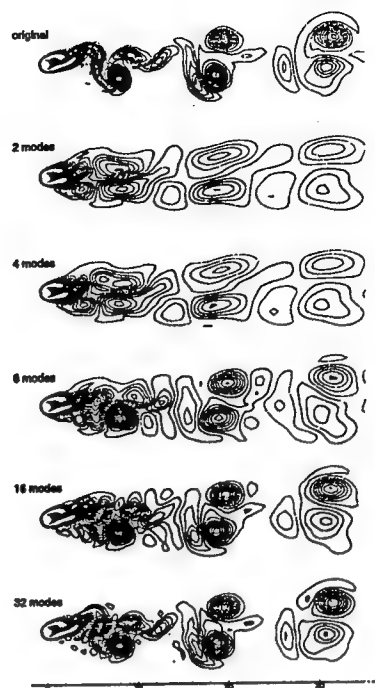


Figure 9: Reconstruction of vorticity field using 2 to 32 modes: forced vibration $\omega_f/\omega_0 = 0.6$

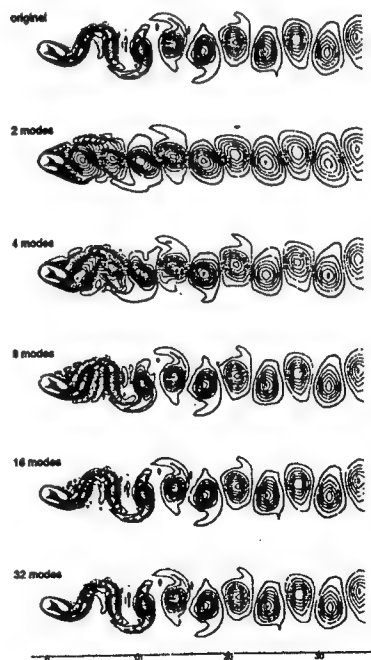


Figure 10: Reconstruction of vorticity field using 2 to 32 modes: forced vibration $\omega_f/\omega_0 = 0.8$

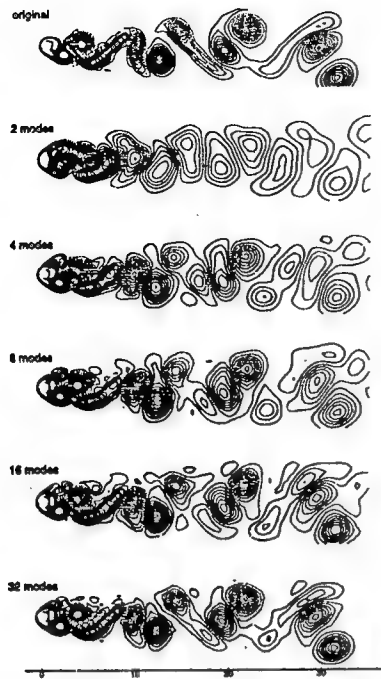


Figure 11: Reconstruction of vorticity field using 2 to 32 modes: forced vibration $\omega_f/\omega_0 = 1.4$

versus mode number j . The curves show quantitatively what we see qualitatively in the eigenmode and reconstruction plots – in the fixed cylinder and locked-in cases ($\omega_f/\omega_0 = 0.8$ and 1.0), the curves have a steep gradient (note the log axis), while in the non-locked-in cases ($\omega_f/\omega_0 = 0.6, 1.2$ and 1.4), the mode energy decreases at a much slower rate. These curves provide a systematic means of deciding where to truncate the series for low-order dynamical models. For example, let us assume that we wish to retain 99.9% of the total energy, we would need to keep approximately 10 modes for the locked-in cases, and approximately 30 modes for the non-locked in cases (i.e. where the curves intersect $\epsilon = 0.001$).

4 3-D DNS Results

We first wish to simulate flow-induced vibrations of a flexible cable, then compute the POD eigenmodes for these flows. The authors have been conducting an ongoing investigation of direct numerical simulations of flow over flexible cables – results for flow-induced vibrations are reported in [12], and a comparison of forced and flow-induced vibrations is given in [13]. For this paper, we concentrate on three flow-induced vibration cases: standing wave

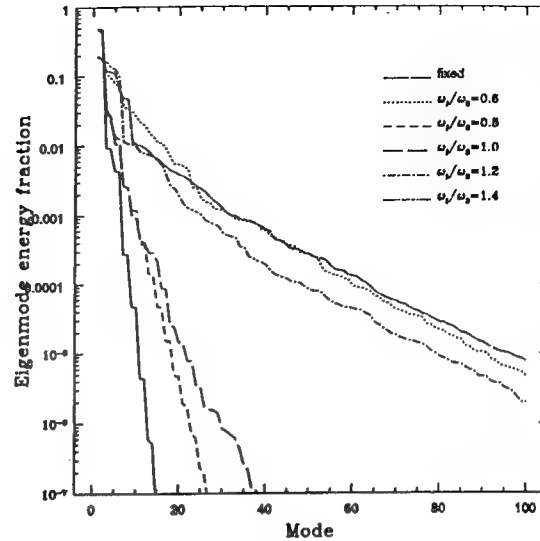


Figure 12: Eigenmode energy fraction versus mode number for fixed cylinder and 2-d forced vibration cases, $Re=100$.

and traveling wave responses at $Re=100$, and the flow-induced vibration response at $Re=200$. For each of these simulations, we assume spanwise periodicity with a length of $L/d = 12.6$. The standing wave and traveling wave flow-induced vibration responses were generated by placing the initial cable position in the form of a standing wave and traveling wave, and then running the simulation for several shedding cycles, at which point a time-periodic state was reached. The cable tension was selected so that vibrations of wavelength $L/d = 12.6$ would respond to the forcing frequency (estimated from the fixed cylinder Strouhal number, i.e. $St = 0.17$ at $Re=100$). The $Re=200$ flow-induced vibration case was started from the $Re=100$ simulations. For this case, neither the cable nor the flow reached a strictly time-periodic state, indicating the turbulent nature of the wake at this Reynolds number (here, the simulation was run for more than forty shedding cycles).

At $Re=100$, flow over a cylinder is 2-d, and we see parallel vortex shedding. If we take a slice of the flow field perpendicular to the cylinder, we see the well-known von Karman vortex street pattern of staggered vortices with alternating signs. A top view of this (looking in the negative y -direction) would show parallel rolls of alternating sign vorticity being shed and convecting downstream. Starting with the familiarity of the wake structure in this simple case, we now look at iso-contours of spanwise vorticity in the wake of the flow-induced standing wave, and

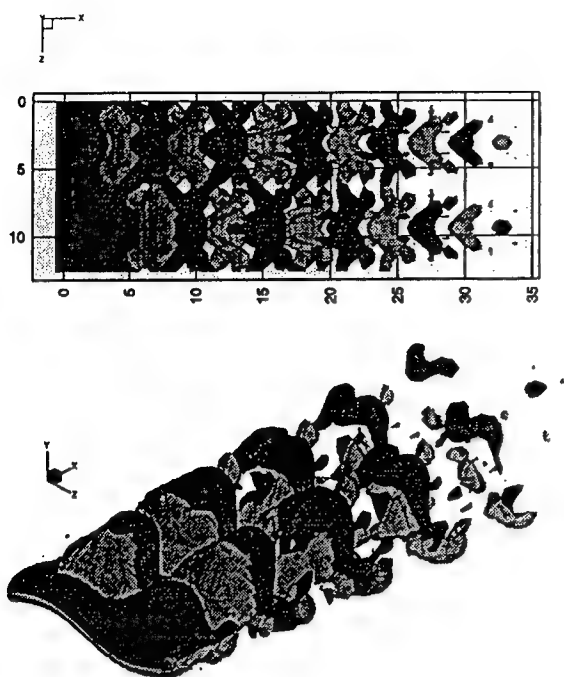


Figure 13: Top and perspective view of spanwise vorticity for standing wave cable response, $Re=100$. Contour level set at $\omega = 0.2$.

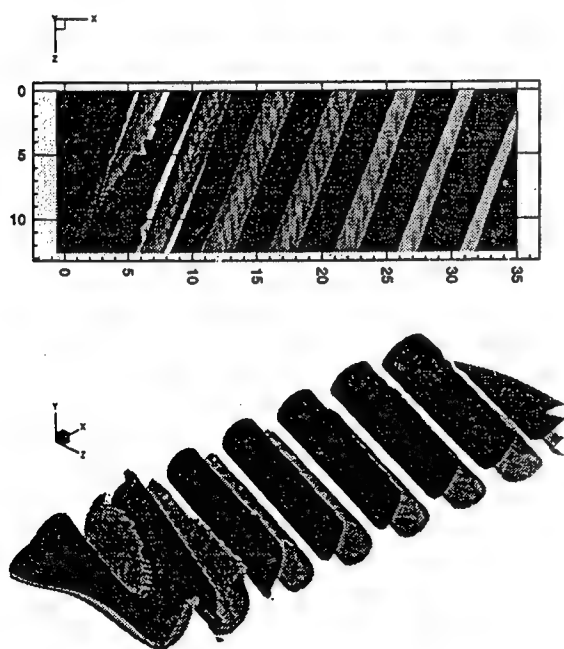


Figure 14: Top and perspective view of spanwise vorticity for traveling wave cable response, $Re=100$. Contour level set at $\omega = 0.2$.

flow-induced traveling wave. Figures 13 and 14 show a top view and perspective view of equal and opposite levels of spanwise vorticity ($\omega_x = \pm 0.2$) for the standing wave cable wake and traveling wave cable wake respectively (for $L/d = 12.6$ wavelength vibration case). The darker shade shows negative spanwise vorticity, while the lighter shade shows positive spanwise vorticity. The flow is from left to right, and the cable is located at $x = 0$. We see a remarkably different structure to the flow in the wake depending on the flow-induced cable response. The standing wave cable response produces an interlocked lace-like structure to the spanwise vorticity. In contrast, the traveling wave cable response produced oblique shedding of spanwise vorticity, i.e. much like the shedding in the fixed cylinder case, but at an angle to the spanwise direction. Oblique shedding has been observed in flows over fixed cylinders under certain experimental conditions [14] [15]. The nodes of the cable's standing wave are located at the two ends and middle of the cable in the figure. In the case of the traveling wave, the "nodes" (point of zero displacement) move in the negative x -direction with the phase velocity c . The streamwise spacing of vortices is about six diameters in the standing wave case, and about five diameters in the traveling wave case.

One obvious difference between the wake in both the standing and traveling wave flow-induced vibration cases with the wake of a fixed cylinder (all at $Re=100$) is that the former wakes are intrinsically three-dimensional, while the wake behind the fixed cylinder is two-dimensional. Consequently, the streamwise and normal vorticities (ω_x and ω_y) will be non-zero in the 3-d case. Figure 15 shows a top view of the three vorticity components for the standing wave (top plots) and traveling wave (bottom plots) wakes. The two shades are again, equal and opposite levels of the vorticity, and the same contour levels are used in all the plots to allow easy comparison. Looking first at the standing wave wake, we see that the cable vibration introduces significant streamwise vorticity; in fact further downstream the streamwise vorticity is the largest vorticity component. This is in direct contrast to the 2-d flows where we only see spanwise vorticity. The magnitude of this streamwise vorticity will be somewhat related to the cable vibration amplitude to wavelength ratio (since this is a direct means of introducing streamwise rotation into the flow), which is relatively large in this case. Note that the streamwise and normal vorticities are zero in the planes of the anti-nodes. Again, we see the staggered pattern of spanwise vorticity. Now looking at the top view of the three vorticity components for the traveling wave wake, we

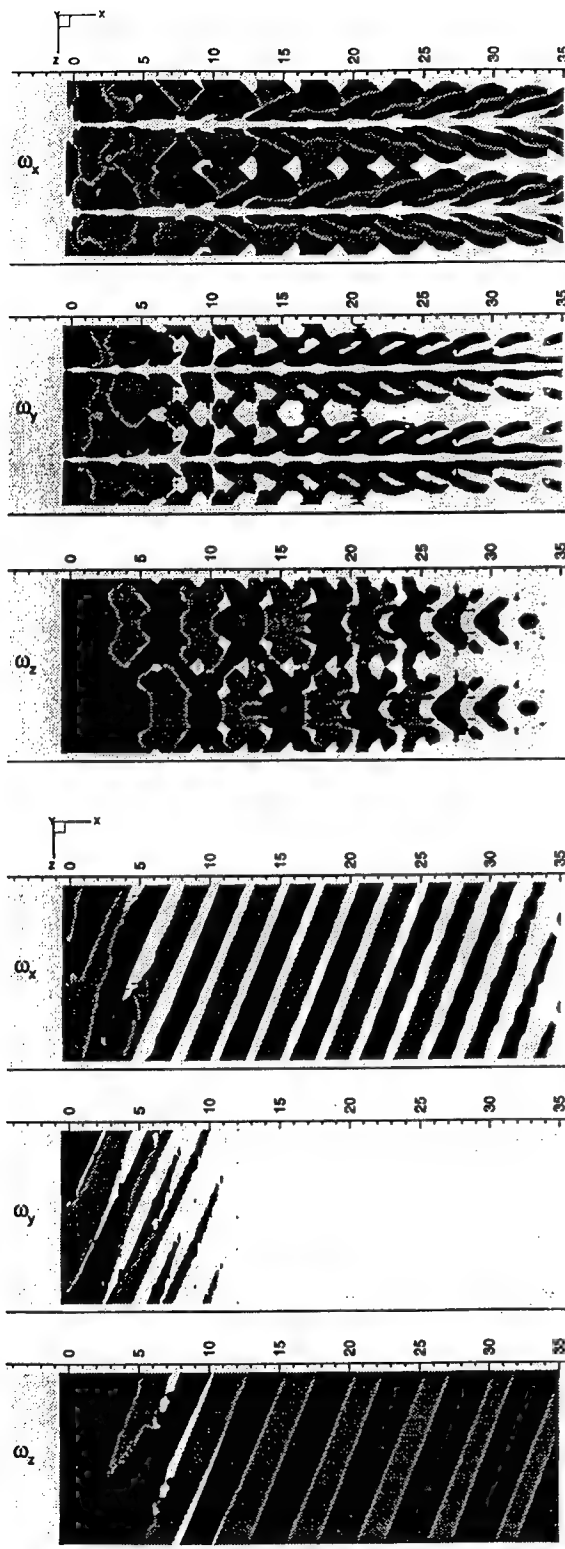


Figure 15: Top view of three vorticity components for wake behind standing wave (top) and traveling wave (bottom), $Re=100$. Contour level set at $\omega = 0.2$.

see a similar picture for the three components. Note that in this traveling wave case, further downstream, the largest vorticity component is spanwise vorticity. Approximately, in this case, given a vorticity magnitude of ω , the streamwise and spanwise vorticity components will be $\omega_x = \omega \sin \theta$ and $\omega_z = \omega \cos \theta$ respectively, where θ is the shedding angle. The normal vorticity ω_y in this case decreases rapidly with downstream distance.

All the $Re=100$ flow-induced vibration simulations resulted in time-periodic cable and flow responses after the transients died out. The question naturally arises as to what happens at higher Reynolds numbers. We conducted simulations examining the case of unconstrained flow-induced vibrations at $Re=200$ for the $L/d = 12.6$ spanwise wavelength case. We started the $Re=200$ simulation from the $Re=100$ unconstrained flow-induced vibration simulation. The simulation was run for more than 100 shedding cycles at which point the transients due to the change in Reynolds number had died out, and the cable and wake response had reached statistical stationarity. The top view and perspective view of equal and opposite levels of spanwise vorticity ($\omega_z = \pm 0.2$) for the $Re=200$ flow-induced vibration wake is shown in Figure 16. These plots can be directly compared with those in Figures 13 and 14. Furthermore, Figure 17 shows a top view of the three vorticity components for the wake behind the cable undergoing flow-induced vibrations at $Re=200$. Note the highly three-dimensional nature of this flow.

4.1 3-D POD Eigenmodes

We computed the eigenmodes for the three 3-d simulations: standing wave at $Re=100$, traveling wave at $Re=100$ and the flow-induced vibration response at $Re=200$. In this case, we took 300 snapshots ($m = 300$) over $tU/d = 15$ time units (about 3 shedding cycles), giving the interval between snapshots of $\Delta tU/d = 0.05$. Let us first show the eigenmode energy fraction decay rate in Figure 18. Not surprisingly, we see that the modal energy for the two $Re=100$ cases decays at more than twice the (exponential) rate of the $Re=200$ decay. The modal energy fraction for the traveling wave case is only slightly lower than that for the standing wave case. It is interesting to compare these with the 2-d modal energy fraction plots (Figure 12). The curves suggest that the 3-d $Re=200$ case has similar complexity/dimensionality to the 2-d non-lock-in cases.

Next we plot the three vorticity components computed from the eigenmodes from the 3-d simulations. In each case we plot a top view (looking in

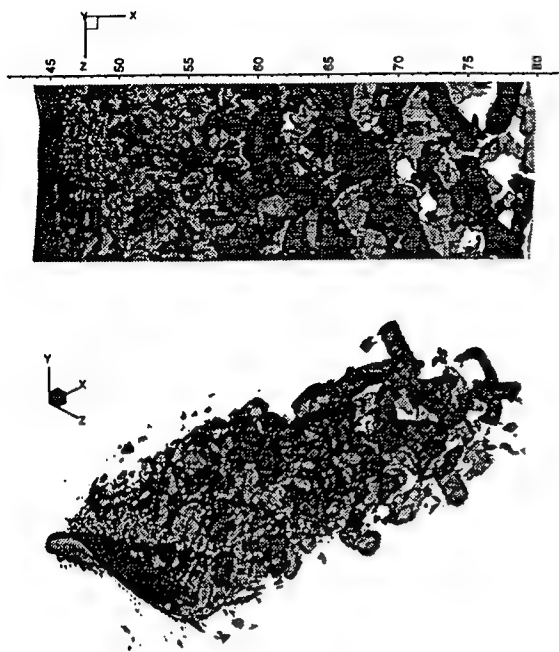


Figure 16: Top and perspective view of spanwise vorticity for $Re=200$ flow-induced vibration response. Contour level set at $\omega = 0.2$.

the negative- y direction) of equal and opposite signs of ω_x , ω_y and ω_z (the same levels are used for all plots, all $\omega = 0.2$), with the flow going left to right, and the cable positioned at $z = 0$. For the $Re=100$ simulations we plot just the odd eigenmodes (eigenmodes 1, 3, 5 and 7) because the eigenmodes occur in conjugate pairs, and consequently the set of even eigenmodes are very similar (i.e. just differing by approximately 90°). Because of the slower eigenmode energy decay rate at $Re=200$, we plot eigenmodes 1, 4, 8 and 16.

Starting with the standing wave wake at $Re=100$, the vorticity for eigenmodes 1, 3, 5 and 7 are plotted in Figures 19, 20, 21 and 22. We see that for all the eigenmodes, the symmetry of each vorticity component matches that of the original standing wave vorticity snapshots shown in Figure 15 (top). Furthermore, we see an indication of the decay of eigenmode energy by the decreasing volume of iso-surface. We observe an increasing amount of detail as we increase mode number – in fact going from mode 1 to mode 3, we see structures with half the length scale in both the x and z -directions (in the z -direction, this is seen as increasing number of planes of symmetries going from mode 1 to mode 3). Note again, that the largest vorticity component for all the standing wave eigenmodes is the streamwise vorticity.

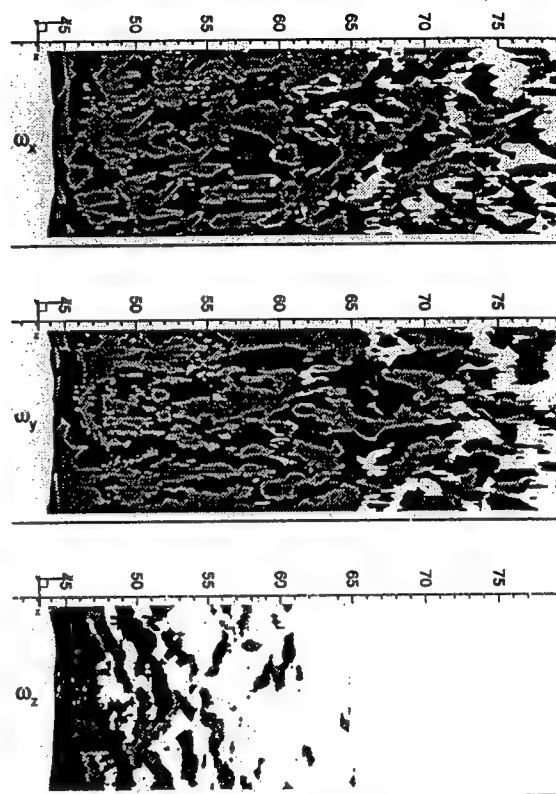


Figure 17: Top view of three vorticity components for wake behind cable flow-induced vibrations, $Re=200$. Contour level set at $\omega = 0.2$.

Mode	Stand.	Trav.	Re=200
1	44.4	45.1	21.2
2	39.7	44.9	20.9
3	6.4	3.6	12.0
4	5.7	3.6	10.7
5	1.4	1.0	6.9
6	1.3	1.0	4.3

Table 2: Modal energy percentages of eigenmodes 1-6 for 3-d cases: standing wave (Re=100), traveling wave (Re=100) and traveling wave (Re=200) flow-induced vibrations.

Now moving on to the traveling wave wake at Re=100, the vorticity for eigenmodes 1, 3, 5 and 7 are plotted in Figures 23, 24, 25 and 26. Again, we can compare these plots with the original traveling wave vorticity snapshots shown in Figure 15 (bottom). Here we see spanwise wavelengths of L , $L/2$, $L/3$ and $L/4$ in the structure of the vorticities for eigenmodes 1, 3, 5 and 7 respectively. It is interesting to observe that in the standing wave case we only saw even fractions of the spanwise wavelength (in contrast to the $L/3$ scale observed in the traveling wave mode 5 plot). Comparing each mode of the standing wave plots and the traveling wave plots indicates that the traveling wave vorticity eigenmodes exhibit approximately the same energy levels as the standing wave vorticity eigenmodes. This is consistent with the corresponding eigenspectra shown in Figure 18.

Finally the flow-induced vibration wake at Re=200 (which was not time-periodic) eigenmodes 1, 4, 8 and 16 are plotted in Figures 27, 28, 29 and 30. Compare these plots with the original traveling wave vorticity snapshots shown in Figure 17. The relatively large (absolute) energy of these eigenmodes is illustrated by the large volume enclosed by the iso-surfaces. At this Reynolds number, we do not observe much scale difference between the structures in eigenmodes 1 and 4. However, we do start to see some finer structure emerging in eigenmodes 8 and 16. The traveling wave nature of the wake response is somewhat observed in the ω_z vorticity eigenmodes.

Table 2 lists the modal energy percentages of eigenmodes 1-6 for the three 3-d cases: standing wave (Re=100), traveling wave (Re=100) and Re=200 flow-induced vibrations. Again we see the pairing of the eigenmodes, and the rapid decay for the Re=100 cases – here after six modes we have captured 98.9% and 99.2% of the flow's energy compared with only 76% for the Re=200 flow-induced vibration wake.

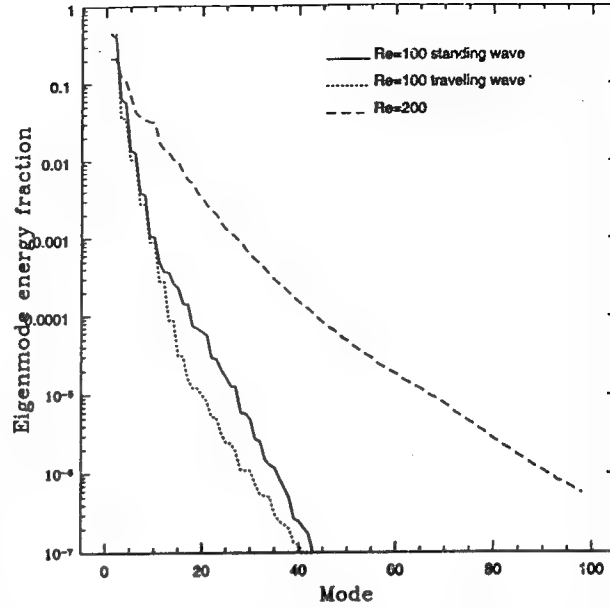


Figure 18: Eigenmode energy fraction versus mode number for 3-d flow-induced vibrations, Re=100 and Re=200.

5 Discussion

In this paper we conducted direct numerical simulations of 2-d and 3-d flows over oscillating cylinders and flexible cables, and then performed proper orthogonal decomposition analyses on the wakes. Table 3 gives a summary of the cases run. In the 2-d forced vibration cases, we see a big difference in the eigenmode energy spectrum depending on whether the wake is locked-in or not. When the wake is locked-in, the eigenmodes look similar to the case of a fixed cylinder, except for a length

Dim.	Re	Case
2-d	100	Fixed
	100	$\omega_f/\omega_0 = 0.6$
	100	$\omega_f/\omega_0 = 0.8$
	100	$\omega_f/\omega_0 = 1.0$
	100	$\omega_f/\omega_0 = 1.2$
	100	$\omega_f/\omega_0 = 1.4$
3-d	100	Standing
	100	Traveling
	200	Traveling

Table 3: Summary of POD cases analyzed. The 2-d simulations were fixed and forced vibration cases, while all the 3-d simulations were flow-induced vibration cases.

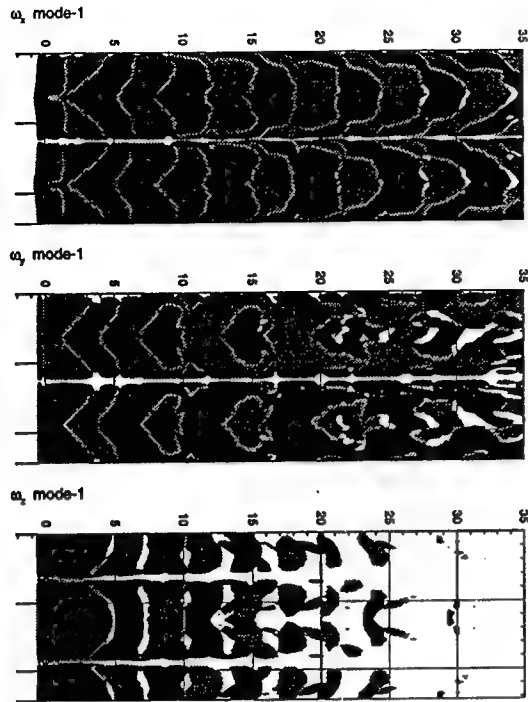


Figure 19: Eigenmode 1 for $Re=100$ standing wave.

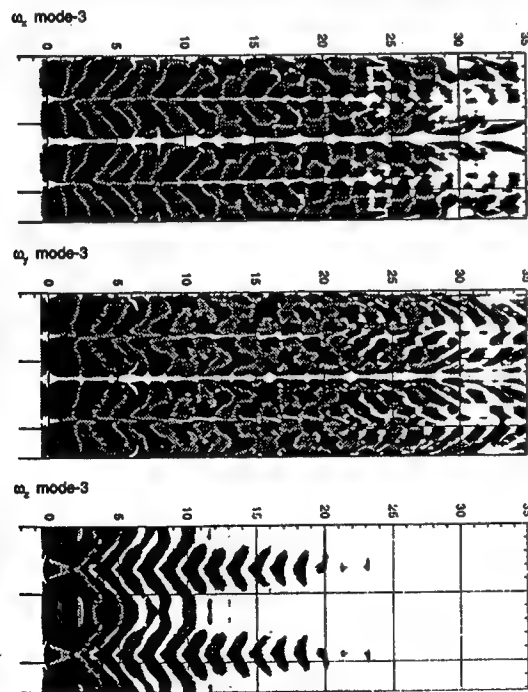


Figure 20: Eigenmode 3 for $Re=100$ standing wave.

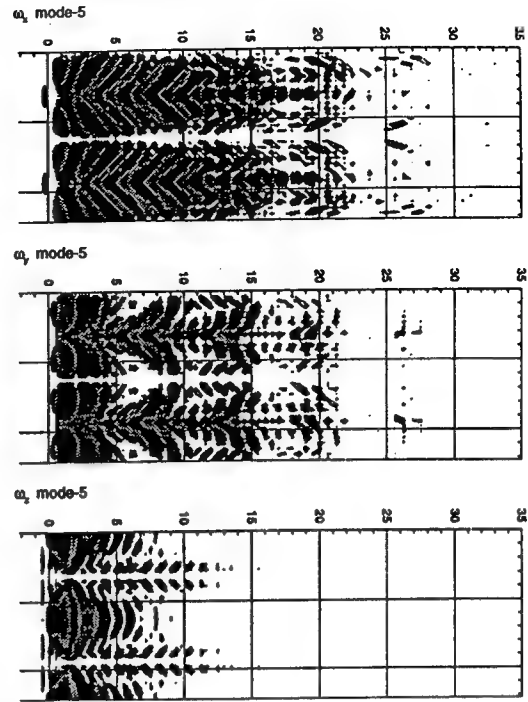


Figure 21: Eigenmode 5 for $Re=100$ standing wave.

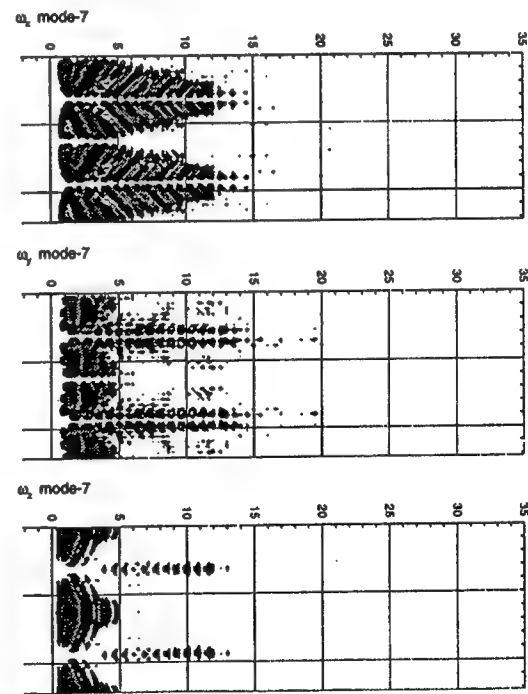


Figure 22: Eigenmode 7 for $Re=100$ standing wave.

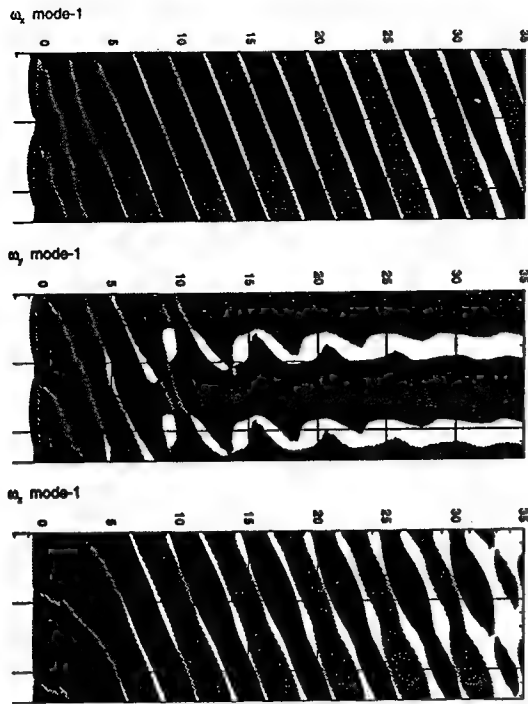


Figure 23: Eigenmode 1 for $Re=100$ traveling wave.

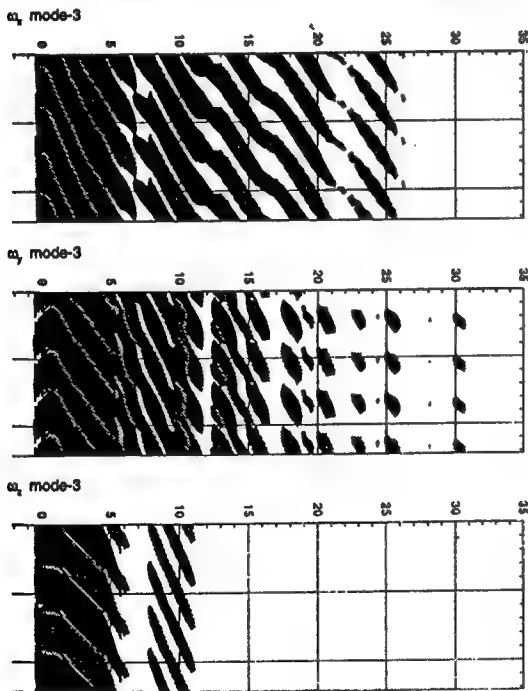


Figure 24: Eigenmode 3 for $Re=100$ traveling wave.

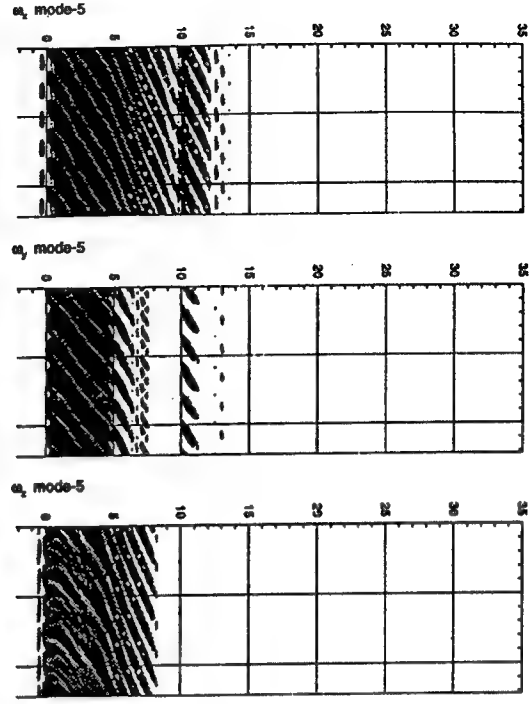


Figure 25: Eigenmode 5 for $Re=100$ traveling wave.

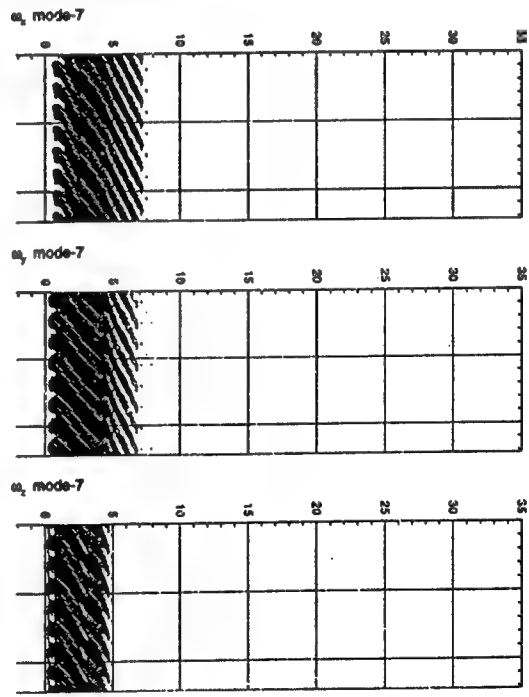


Figure 26: Eigenmode 7 for $Re=100$ traveling wave.

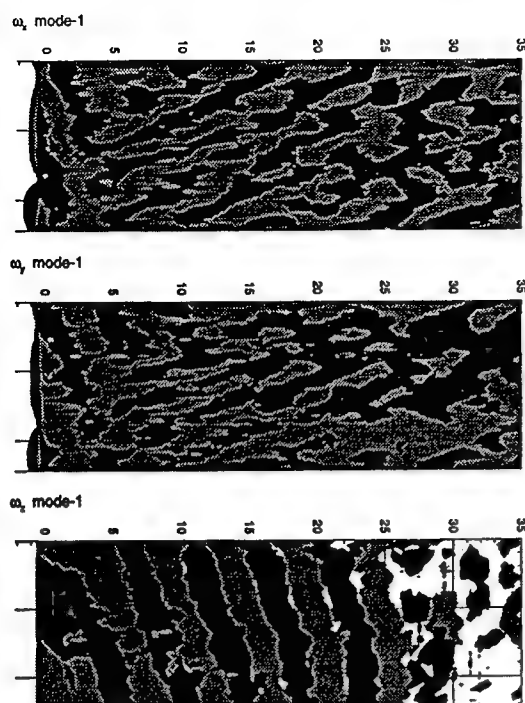


Figure 27: Eigenmode 1 for Re=200 flow induced vibration wake.

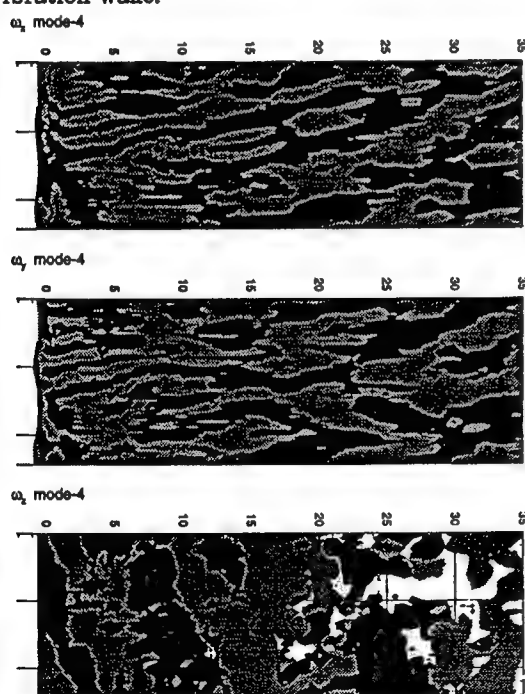


Figure 28: Eigenmode 4 for Re=200 flow induced vibration wake.

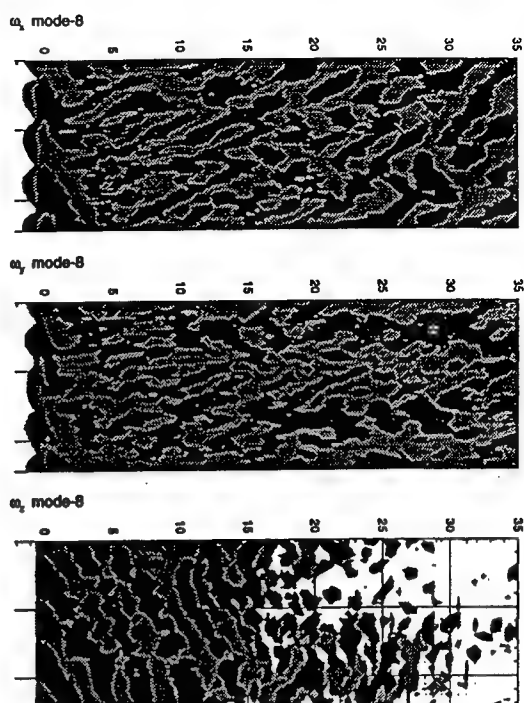


Figure 29: Eigenmode 8 for Re=200 flow induced vibration wake.

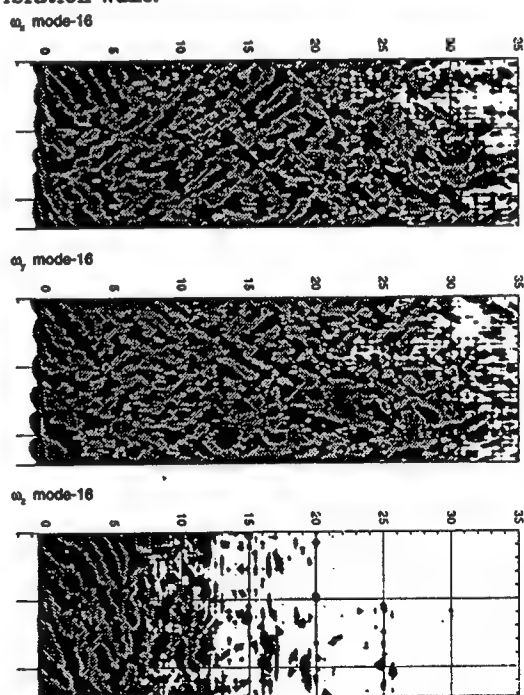


Figure 30: Eigenmode 16 for Re=200 flow induced vibration wake.

scaling that is proportional to the frequency ratio ω_f/ω_0 . When the wake is not locked-in, the eigenmodes for the sub-lock-in case are quite different to the eigenmodes for the super-lock-in case. In the non-lock in cases, we need to retain three to four times as many modes to get the same accuracy as the locked-in cases. For example, to retain 99.9% of the flow energy, we would need about 10 eigenmodes to model a locked-in wake, and about 30 eigenmodes to model a non-locked-in wake. We see a similar effect with Reynolds number in the 3-d cases – for the $Re=200$ case we need to retain two to three times as many modes to get the same accuracy as the $Re=100$ cases. Here, to retain 99.9% of the flow energy, we would again need about 10 eigenmodes to model the $Re=100$ cases, and about 30 eigenmodes to model the $Re=200$ flow-induced vibration case.

6 Acknowledgements

This work was supported by the Office of Naval Research, under the supervision of Dr. T. F. Swean. Computations were performed on the IBM-SP2s at the Cornell Theory Center and the Center for Fluid Mechanics at Brown University.

References

- [1] R. D. Blevins. *Flow Induced Vibration*. Van Nostrand Reinhold Company, New York, New York, 1977.
- [2] J. K. Vandiver. Dimensionless parameters important to the prediction of vortex-induced vibrations of long, flexible cylinders in ocean currents. *MIT Sea Grant Report, MITSG 91-93*, 1991.
- [3] S. E. Ramberg and O. M. Griffin. The effects of vortex coherence, spacing, and circulation on the flow-induced forces on vibrating cables and bluff structures. *Naval Research Laboratory Report 7945*, 1976.
- [4] F. S. Hover, M. A. Grosenbaugh, and M. S. Triantafyllou. Calculation of dynamic motions and tensions in towed underwater cables. *IEEE J. Oceanic Engineering*, 19:449, 1994.
- [5] D. R. Yoerger, M. A. Grosenbaugh, M. S. Triantafyllou, and J. J. Burgess. Drag forces and flow-induced vibrations of a long vertical tow cable – part 1: Steady-state towing conditions. *J. Offshore Mechanics and Arctic Engineering*, 113:117, 1991.
- [6] R. D. Henderson and G. E. Karniadakis. Unstructured spectral element methods for simulation of turbulent flows. *J. Computational Physics*, 122:191, 1995.
- [7] K.S. Ball, L. Sirovich, and L.R. Keefe. Dynamical eigenfunction decomposition of turbulent channel flow. *Intl. J. Num. Meth. Fluids*, 12:585, 1991.
- [8] A. E. Deane, I. G. Kevrekidis, G. E. Karniadakis, and S. A. Orszag. Low-dimensional models for complex geometry flows: Application to grooved channels and circular cylinders. *Physics of Fluids*, 3(10):2337, 1991.
- [9] G. H. Koopmann. The vortex wakes of vibrating cylinders at low reynolds numbers. *J. Fluid Mechanics*, 28:501–512, 1967.
- [10] A. Ongoren and D. Rockwell. Flow structure from an oscillating cylinder – part 1: Mechanisms of phase shift and recovery in the near wake. *J. Fluid Mechanics*, 191:197–223, 1988.
- [11] C. H. K. Williamson and A. Roshko. Vortex formation in the wake of an oscillating cylinder. *J. Fluids and Structures*, 2:355–381, 1988.
- [12] D.J. Newman and G.E. Karniadakis. Simulations of flow past a freely vibrating cable. *J. Fluid Mechanics*, 1996. Submitted.
- [13] D.J. Newman and G.E. Karniadakis. Simulations of flow over a flexible cable: A comparison of forced and flow-induced vibration. *J. Fluids and Structures*, 1996. Submitted.
- [14] M. Hammache and M. Gharib. An experimental study of the parallel and oblique vortex shedding from circular cylinders. *J. Fluid Mechanics*, 232:567–590, 1991.
- [15] C. H. K. Williamson. Oblique and parallel modes of vortex shedding in the wake of a circular cylinder at low Reynolds numbers. *Journal of Fluid Mechanics*, 206:579–627, 1989.

DISCUSSION

J.M.R. Graham
Imperial College, United Kingdom

The three-dimensional simulations have produced some very interesting results. In the case of the traveling wave, locking-on of vortex shedding should be similar to locking of two-dimensional vortex shedding by oscillation of the cylinder, with constant amplitude and phase along the span. In the case of the standing waves there are two opposite effects. The oscillation tends to control and possibly strengthen non-oblique vortex shedding, when locked on, but the three-dimensional effect of the phase variation limits this to finite length spanwise cells of alternating sign which might be expected to weaken the vortex shedding. Can any observations be made from your three-dimensional results about the lock-in boundaries (oscillation amplitude vs. frequency ratio) for these two cases (traveling and standing wave), as a function of spanwise wavelength?

AUTHORS' REPLY

The current paper deals with the question of modeling the coupled motions of cable and wake using low-dimensional constructs. It does not deal directly with the lock-in boundaries that Professor Graham addresses. From ongoing work, however, we have concluded that the same dynamics encountered in simply dynamical systems and in the two-dimensional case is also present in the cable system. We have not yet determined the exact boundaries of the lock-in for the standing and traveling wave response on which we will report in a future publication.

Measurements of Hydrodynamic Damping of Bluff Bodies with Application to the Prediction of Viscous Damping of TLP Hulls

P. Bearman, M. Russell

(Imperial College of Science, Technology and Medicine, United Kingdom)

SUMMARY

A static water tank to test oscillating cylinders and scale models of offshore structures has been constructed. The main purpose of the tank, which is approximately a cube of side 2.4m, is to provide a facility to measure the viscous contribution to the hydrodynamic damping of models. Models are mounted from a pendulum suspension system and the damping is measured following the deflection and release of the pendulum. Circular cylinders with diameters of 150mm and 312mm have been tested and the damping measured up to values of the viscous scale parameter β of about 6×10^4 . The processed data is presented as a variation of drag coefficient with Keulegan Carpenter number for different values of β . The KC range studied is from about 0.003 to 3. Measurements have also been made using a square cross-section cylinder of side 300mm. Some preliminary results are presented for an approximately 1/100 scale model of a TLP hull. The form of the experimental results is explained by considering the drag to be composed of a boundary layer and a vortex component.

INTRODUCTION

Wind, waves and currents induce loading on tethered floating structures and this loading can lead to both a mean displacement and an oscillatory response. In the case of waves the resulting response may be at the main wave frequency and at

frequencies substantially higher and lower than the wave frequency. For a tension leg platform (TLP) the high frequency loading can lead to the phenomenon known as springing and the low frequency loading is responsible for the slow drift oscillations of floating systems. Accurate estimation of the responses in these frequency ranges depends on many factors but it is particularly important to have a reliable evaluation of the hydrodynamic loading and precise knowledge of damping levels. The hydrodynamic damping arises from a number of sources and includes wave-drift damping of the hull which is related to wave radiation and diffraction and can be predicted using irrotational flow theory. Other forms of damping include mooring line damping, damping from the riser array, tether damping in the case of TLPs and additional damping from the hull arising as a consequence of the viscous nature of water.

In this paper the term "hydrodynamic damping" refers to the viscous contribution to the damping arising from flow around the hull of a TLP which typically may be constructed from circular and rectangular cross-section members. In the design process the hydrodynamic loading due to waves is usually considered separately from the damping and for large structures the loading is derived from ideal flow theory. In the case of large volume structures, viscosity is likely to have only a small effect on the total hydrodynamic loading. This implies that the loading on the structure is inertia dominated and that the influence of boundary layers, flow separation and vortices are all very small. However, for a compliant

structure the magnitude of the response depends critically on the damping level and viscous effects may make a significant contribution to this damping. Estimates of damping coefficients are required to predict both surge and heave motions. Here we will present some direct measurements of the viscous damping of components of TLP hulls obtained by displacing them and recording their decay in still water. By appropriately combining these it should be possible to approximate the damping of a complete hull. It is intended to check the accuracy of this procedure by also measuring the damping of a model of a TLP hull.

In reality, of course, the fluid is always viscous and the damping is just that part of the total loading that happens to be in phase with the structure velocity. When a structure is excited into oscillation by wave forces is it permissible to predict the response using damping levels obtained in still water? Sarpkaya (1) has expressed a similar concern about this approach and states "damping is used to lump into one parameter our inability to solve the fluid-structure interaction problem". However, until we are able to solve satisfactorily this interaction problem designers will need estimates of damping. Hence damping values, expressed in terms of drag coefficients, will be presented in this paper.

When considering the damping of TLP hulls in real seas the relative motion between the water and the structure is considerably more complex than the harmonic motion considered in simple decay tests. The relative flow has three components which in the general case are not collinear. These motions are due to waves, currents and the response of the structure. The wave motion may excite response of the structure in three distinct frequency ranges appropriate to slow drift response, wave response and springing response. There is evidence available to suggest that damping due to a current and waves, together with response in surge, can be dealt with by the relative motion form of Morison's equation, provided there is no resonance with vortex shedding. The heave response in the springing mode is characterised by relatively high frequencies and very small motions and it may not be appropriate to lump this motion together with the others into Morison's equation. One possibility is that it may act independently within a much slower varying velocity field. It is clear that there are many outstanding questions surrounding the concept of hydrodynamic damping. However, the study of viscous effects for small amplitude oscillatory motion

is in itself an interesting subject and some new results, and perhaps some fresh understanding, may result from our experiments.

Assuming that the fluid loading on an oscillating body can be described by Morison's equation then the hydrodynamic damping is related to the drag term in this equation. It can be shown, see for example Bearman and Mackwood (2), that the logarithmic decrement of damping, δ , is related to the drag coefficient of a body, C_D , through the relationship:

$$\delta = 2\rho D^2 KC C_D / 3\pi m. \quad (1)$$

In this expression ρ is water density, D a length scale used in C_D (in the case of a circular cylinder it would normally be the diameter), KC is Keulegan Carpenter number and m is the effective mass per unit length of the body. KC is defined as UT/D , where U is the maximum velocity of the body relative to the water during a cycle and T is the period of oscillation. For harmonic motion KC can be defined as $2\pi A/D$, where A is the amplitude of oscillation.

The viscous drag coefficient is composed of a skin friction component and a component related to the pressure force on the body. For circular cylinders, at KC values of order unity or less the contributions from pressure and skin friction are of a similar magnitude. However, at higher KC numbers separation occurs and the drag coefficient, and hence damping, is then dominated by the pressure component. Mooring lines, tethers and risers experience large motions relative to their diameters and hence their KC numbers are also large and in a range where there is considerable data available on drag coefficients. Apart from large amplitude slow drift oscillations, the flow around hulls is characterised by small KC numbers and is in a regime where there is sparse information on C_D values that can be applied with confidence to full scale structures.

In the case of TLP hulls viscous damping arises from flow about the vertical columns and from the pontoon. The columns are usually circular whereas the pontoon may be constructed from square or rectangular section with various degrees of corner rounding. The damping level is dependent on characteristics of the boundary layer flow and on whether separation occurs from the circular members

and from the corners of the pontoon. In addition to KC, an important parameter in determining the damping level is the β parameter, where $\beta = D^2/\nu T$. In the case of slow drift oscillations of full scale structures C_D values are required that are appropriate for the resulting high values of β .

At low KC the oscillatory flow around a circular cylinder develops a three-dimensional instability, known as the Honji (3) instability. This takes the form of a regular array of vortex structures along the cylinder span, the wavelength of which reduces with increasing β . This instability appears to be part of the transition process whereby the boundary layer flow changes from a laminar to a turbulent state. Experiments show the instability to be present over a wide range of β and it is known to exist up to β values of at least 5×10^4 . The generation of the vortex structures extracts energy from the flow and the damping levels are higher than those given by the analytical solution for laminar attached flow. The transitional nature of the flow at low KC makes it particularly difficult to predict.

Much of the previous work on viscous damping has been carried out for circular cylinders. Bearman and Mackwood (2) mounted circular cylinders on a pendulum suspension system and measured damping by recording the amplitude of decaying oscillations. The results are presented in the form of C_D versus KC and typically the KC numbers range from 0.1 to 3 and β values are up to 3×10^4 . A similar technique has been used by Otter (4), (5) and he presents two sets of C_D values for KC up to around 2 and for $\beta = 5.47 \times 10^4$. There is substantial disagreement between the two sets which he ascribed to sloshing in his tank. Sarpkaya (6) has made direct measurements of C_D at low KC in a U tube for values of β up to 1.1×10^4 . Direct measurement of C_D at very low KC is extremely difficult because the fluid loading is dominated by the inertia component. For example, at KC = 1 and for $\beta = 3 \times 10^4$ the maximum drag load in a cycle is only about 2% of the maximum inertia load. At KC = 0.1 it drops to about 1%. One of the main reasons why viscous damping at low KC remains so uncertain is because it is caused by such a small fraction of the total hydrodynamic loading.

The values of KC and β to be modelled depend on the mode of response being considered and the dimensions of the structure. A diagram of a TLP hull is shown in figure 1 and it has circular

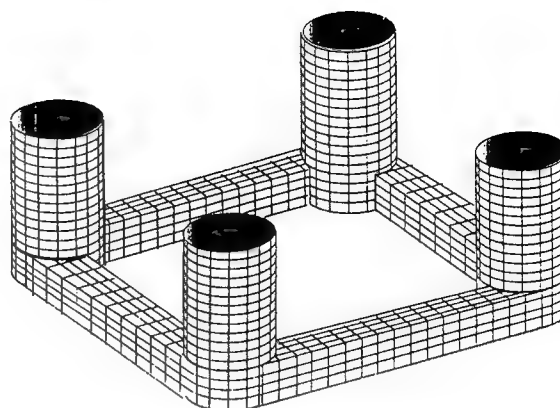


Figure 1 A typical TLP hull below the still water level

columns and the pontoon is constructed using a square cross section. Data appropriate to such a structure is used to estimate typical values of the flow parameters. Basing parameters on the length of a side of the cross section of the square pontoons, 8.5m; in surge β may be up to about 1.5×10^6 and KC up to 15 or 20. On the other hand, for the high frequency springing motion in heave β is likely to be about 2.5×10^7 and KC only around 0.004. For large values of KC and β , drag coefficients can be estimated from existing data for circular cylinders and, because of the relatively smaller amount of data, perhaps less reliably for square sections. Bearman et al (7) have measured the C_D for KC numbers down to about 1.5, of square-section cylinders with various degrees of corner rounding. However, the highest β value in these experiments is limited to 432. Little or no information seems to exist on the viscous damping contribution due to free ends or that due to intersections between members, such as occurs for TLPs between the columns and the pontoon.

The present investigation is aimed at providing the viscous contribution to the hydrodynamic damping for small amplitude motions, i.e. KCs of order unity and less. In order to be able to generate data that will be applicable to design, drag coefficients at as large a value of β as possible are required. β can be increased by increasing D, reducing T and using a fluid with a smaller kinematic viscosity. Using as large a linear scale as possible requires as big a tank as possible in order to keep the blockage of the model to a reasonable limit. For the present study a new tank 2.4m x 2.4m and 2.4m deep was constructed. There is no cheap, safe and easily available fluid that has a substantially

lower kinematic viscosity than water and so water was chosen for this investigation. By mounting models from a pendulum arrangement and then increasing the stiffness by the addition of springs the time period can be reduced. A number of bluff sections have been tested. These include circular cylinders with diameters of 150mm and 312mm and a square section with sides of 300mm. In the case of the square cylinder, damping has been measured for a range of angles of incidence to the ambient relative flow. Using models with widths of about 300mm, β values up to 6×10^4 could be obtained. The KC range is then from around 0.001 to 2 or 3.

EXPERIMENTAL ARRANGEMENT

A water tank was constructed using prefabricated GRP panels supplied by BTR Hydroglas, that are available in sizes of 1.22m x 1.22m and 0.61m x 1.22m. The panels are bolted together using a bitumastic sealant between the flanges to provide a water-tight joint. Ten large and twenty small panels were purchased to permit a cube of side length 2.4m to be constructed. Visual access to the tank was required to allow flow visualisation techniques to be used and four of the large panels were converted into window panels. This was achieved by cutting out a section of the panels, (dimensions 0.91m x 0.91m) and bolting a sheet of clear acrylic (1.22m x 1.22m by 15mm thick) to the inside, using a bitumastic sealant to provide a water tight joint. When not in use the windows were covered to prevent light affecting the water. To support the tank an external steel corsetry was constructed from rectangular box sections. Steel channel was attached to the flanges of the uppermost panels, which then supported a steel framework spanning the tank. The steel framework in turn supported a decking of marine quality plywood panels which almost completely covered the tank, preventing light and dust particles from entering the water. It also provides a working platform on top of the tank.

An acrylic cover was installed to prevent free surface waves from developing and affecting the damping measurements when models were oscillating. The cover was suspended from the sides of the tank, 5cms below the water level. A section was removable to allow models to be inserted and within this piece a further removable section was fabricated to fit around the model support system to complete the cover.

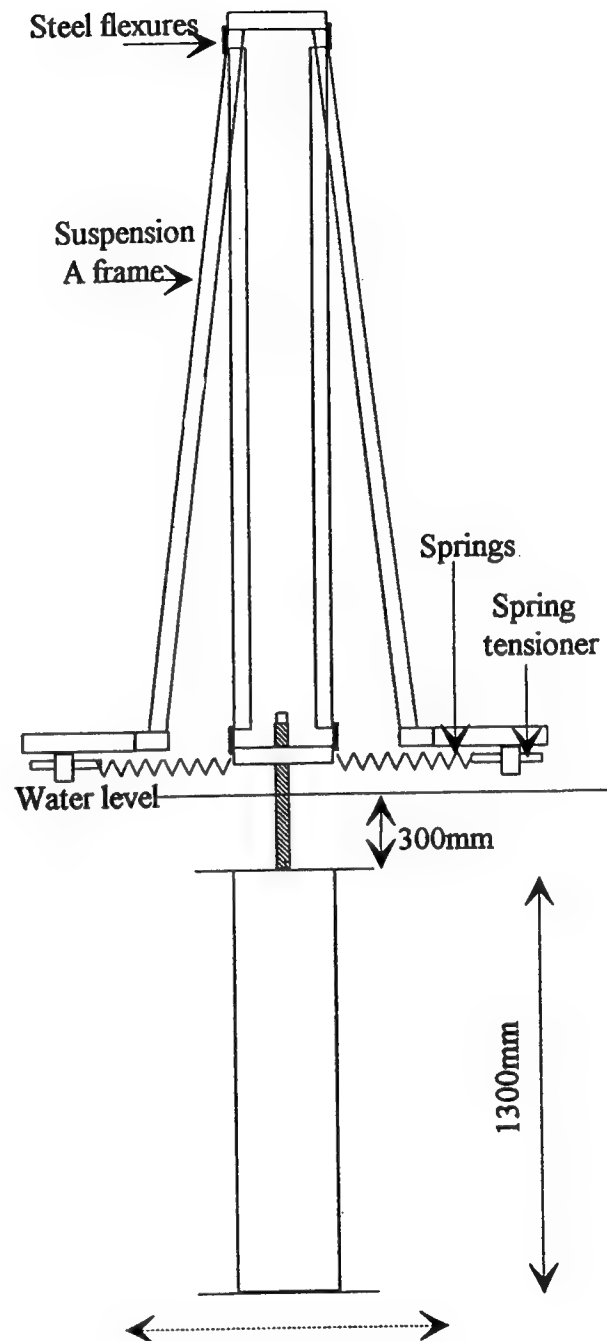


Figure 2 Cylinder and pendulum support system

In order to support the models a larger version of the pendulum arrangement used by Bearman and Mackwood (2) was constructed. It is shown in figure 2 and consists of an 'A frame' structure secured to the steel uprights of the tank. The arms of the pendulum were constructed from

aluminium lengths of 2m x 50mm x 50mm which are held by the steel frame at their top end. At the bottom end they support a second steel frame to which models are attached. As shown in figure 2, the attachment of these arms is by spring steel flexures. Models are supported from the lower frame via a streamlined, stainless steel strut. Springs of different stiffness are attached to the lower frame of the pendulum to increase the natural frequency of oscillation of the pendulum.

Bearman and Mackwood (20) had tested models in the horizontal plane, supported by a streamlined strut at each end. By now mounting the cylinders vertically only a single strut is required and the correction to the data needed to take account of the additional damping caused by the support arrangement should be less. The streamlined strut supported models at a depth of 300mm below the water level. A steel plate was welded to the lower end of the strut and steel rods then bolted to it. These rods passed through the models and were attached to a plate at the bottom of the models. This then held the hollow cylinders in compression and transferred the loading through the model and through the strut to the pendulum. The models were made water tight by using a silicon sealant on all the joints. A diagram of a model is shown in figure 3. To ensure the models were almost neutrally buoyant lead weights were bolted to steel plates inside the models. Various length models could be accommodated, by the use of different length rods, and various diameter models, by the addition of different fittings to the plate attached to the strut. Various length circular cross-section models with diameters of 150mm and 312mm, along with a square cross-section model of 300mm across the flats, were constructed and tested.

Two methods were employed to sense the amplitude of the pendulum. In the first method used, strain gauges were attached to the flexures. However, the signal became noisy as the amplitude of oscillation became small and hence the results for low KC were unreliable. In order to obtain accurate decay data at very low KC, a non-contacting displacement transducer was used which could be placed so as to pick up the displacement at various distances along the pendulum arms. Both methods had to be carefully calibrated in order to calculate KC and to be able to obtain accurate C_D results from decay records. Data acquisition and analysis was carried out using a PC-based system. The system was programmed to provide a sampling frequency of 50Hz for the analogue to digital conversion of the

signals from the displacement gauges. In addition, the PC provides a digital to analogue signal to trigger the release of the models. A pair of electromagnets hold the pendulum, at a known displacement, prior to its release by the signal from the PC.

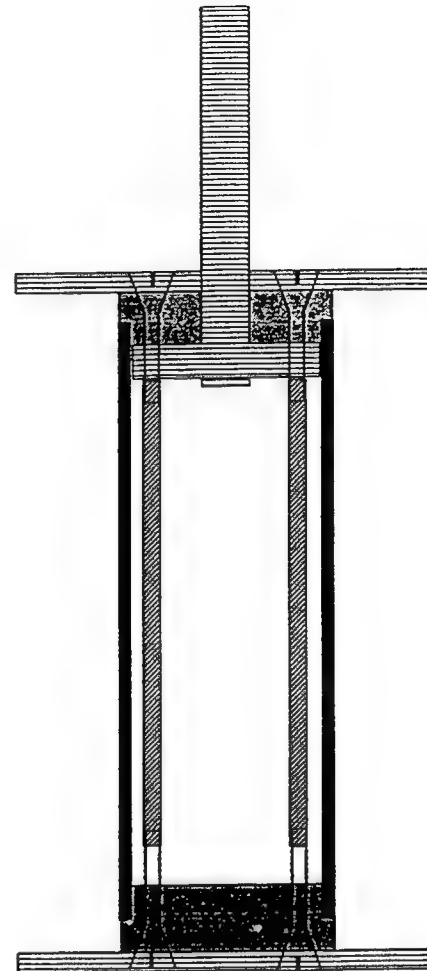


Figure 3 Details of model construction

EXPERIMENTAL METHOD

While the experimental method is basically very simple, accurate results can only be obtained by carrying out the various stages as carefully as possible. The main difficulty is separating the viscous damping of the model from other sources of damping such as the structural damping of the pendulum, the viscous damping of the support strut and the contribution from end conditions, such as end plates. Tests carried out without a model and strut, but with mass added to the pendulum to

represent the mass of the model, showed the structural damping to be extremely small and much smaller than any contribution arising from hydrodynamic effects.

Two techniques were used to correct data for the effects of the additional damping that arises from end plates and from the way models were mounted. In the first method the additional components of damping are measured in a separate experiment with the model removed but with first the strut and then the strut and an end plate in place. Mass is added to the pendulum in order to ensure that the frequency of oscillation is the same, so that the value of β will be maintained. This method is referred to as the plate subtraction technique. The second method involves testing two lengths of model at the same value of β . Provided the tests are conducted at the same frequency, then the structural damping of the pendulum and the viscous damping due to the end plates and strut should be identical for similar KC numbers. Therefore subtracting the product of the drag coefficient and the length for the short model from that for the long model and by dividing this result by the difference between the two lengths provides the drag coefficient for the cylinder. This method is referred to as long-short.

Once the log decrement due to just the hydrodynamic damping of the model is known as a function of amplitude then the corresponding drag coefficient can be calculated as a function of Keulegan Carpenter number, using equation (1). In order to obtain C_D the effective mass of the model and suspension system, including the added mass of the water, has to be known. This is determined by displacing the model a known distance and measuring the force required to hold the model in place. Once the stiffness and frequency of oscillation of the system are known, the effective mass can be determined. This experiment also enables the calibration of the strain gauges to be verified.

EXPERIMENTAL RESULTS AND DISCUSSION

When using a pendulum suspension system the model experiences a small change in its vertical position as it oscillates back and forth. This small vertical displacement may have some influence on the flow and the effect may be different if a cylinder is mounted vertically rather than horizontally. In order to determine if this has a significant effect on the results experiments were carried out on a 150mm

diameter circular cylinder. A model of length 586mm, fitted with 234mm diameter end plates, was tested horizontally using a double strut system and vertically employing a single strut. In separate experiments, the damping due to the struts, end plates and the structural damping was measured, for the two orientations, at similar β values. Obtaining drag coefficients by subtracting the end plate, strut and structural damping from each set of data indicated a good degree of agreement between the two orientations. Figure 4 shows drag coefficient versus KC for $\beta = 16,538$ and it can be seen that there is reasonable agreement between the results for the horizontal and vertical cylinder. The figure also shows the large scatter obtained at low KC due to noise from the strain gauges.

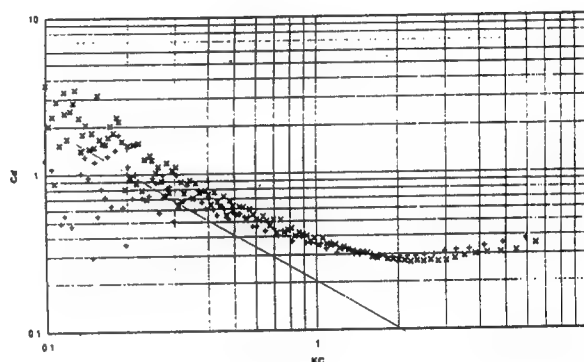


Figure 4 C_D versus KC for a circular cylinder with $\beta = 16,538$. x, vertical model; +, horizontal cylinder; —, Wang.

The straight line in figures 4 represents results from a theoretical analysis due originally to Stokes (8), and which was extended later by Wang (9). These theoretical results, which will be referred to here as the Wang results, apply to two-dimensional, laminar attached flow about an oscillating circular cylinder. The theory gives rise to the following expression for the drag coefficient:

$$C_D = 3 \pi^3 / 2 KC (\pi\beta)^{1/2}. \quad (2)$$

Alternatively, this can be written as:

$$C_D KC \beta^{1/2} = 26.24. \quad (3)$$

As KC is increased from very small values the above theory will break down due to two reasons: firstly the flow may separate and additional drag will be

created by the generation of vortices and secondly the flow may become three-dimensional due to the onset of instabilities. When the flow becomes three-dimensional, even though it may remain attached, the drag coefficient rises above the Wang value, as shown by Sarpkaya (6). This is assumed to be due to the generation of Honji (3) vortices. Hall (10) studied the stability of oscillating cylinder flow and found that there is a critical KC value, KC^* , above which three-dimensional instabilities are amplified. For high β values this KC is given approximately by:

$$KC^* = 5.778 / \beta^{1/4}. \quad (4)$$

Over the β range studied in this investigation, KC^* varies between 0.58 and 0.37. The results plotted in figure 4 are typical of all the ones we obtained and show that drag coefficient values are generally greater than those predicted using equation (2), even for KC values below the critical values given by equation (4). It is not clear why this difference occurs below KC^* but perhaps, with decaying motion, three dimensional boundary layer flow established at a higher KC value remains to influence the flow as KC falls. However, it is apparent that at low KC the drag coefficient and KC number are related by the expression:

$$C_D KC = A \quad (5)$$

where A depends on β .

The experiments with the 150mm model established that the orientation of the cylinder had little effect on the results and that drag coefficient values similar to those reported by Bearman and Mackwood (2) could be obtained. Hence it was decided to move on to a 312mm diameter circular cylinder model. Using this larger diameter model, tests were first carried out to determine if the amplitude of release has any effect on the subsequent decay data. A model of length 1214mm and diameter 312mm, with 392mm diameter end plates, was tested at various β values. The tests consisted of releasing the model from different amplitudes and comparing the variation of drag coefficient with KC number, where the drag coefficient has been calculated without any correction for the drag of the strut and end plates. Results are shown plotted in figures 5 for $\beta = 61022$ and indicate that the drag coefficients are higher than those obtained from continuous decay tests for the first few cycles after release. Drag coefficients gathered from the first three or four

oscillation cycles are generally neglected from further presentations of results..

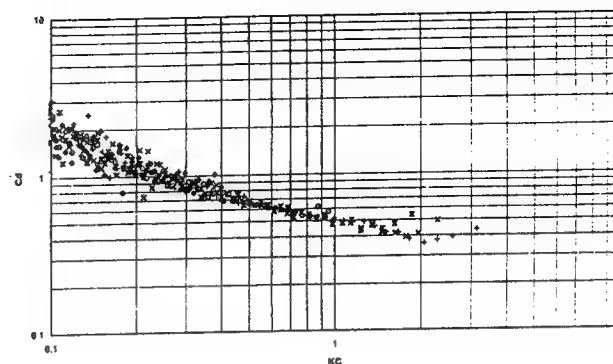


Figure 5 C_D versus KC for a circular cylinder with $\beta = 61,022$; effect of release Keulegan Carpenter number with release from $KC = 0.44$ to 3.4.

Circular cylinder models of diameter 312mm and lengths of 1214mm and 620mm, with 392mm end plates, were tested vertically using a single strut for a range of β values between 18,000 and 61,000. The drag coefficients were first obtained from these tests by subtracting the difference in the damping between the long and the short models. Next the drag component arising from the strut, end plates and the structural damping of the pendulum was determined separately. This was achieved by testing a single 392mm diameter plate, suspended from a wooden strut with similar dimensions to those of the stainless steel strut used for supporting the models. The tests were carried out at similar β values to those of the main experiments. The resulting drag coefficients, which are referred to as the tare drag coefficients, were then subtracted from those obtained for the long and short models individually. Results for $\beta = 61,022$ are shown in figure 6. The figure shows the original long and short cylinder drag coefficients, the drag coefficients obtained by subtracting the long and short cylinder data and the drag coefficients for the long and short cylinders obtained by subtracting the tare drag. The Wang prediction of drag coefficient is also plotted. By comparing the three different estimates of drag coefficient obtained from the experiments it is clear that there are differences. In each case the C_D for the short cylinder is larger than the C_D for the long cylinder, which in turn is larger than the C_D obtained by subtracting the long and short cylinder data. This suggests that a larger tare drag should

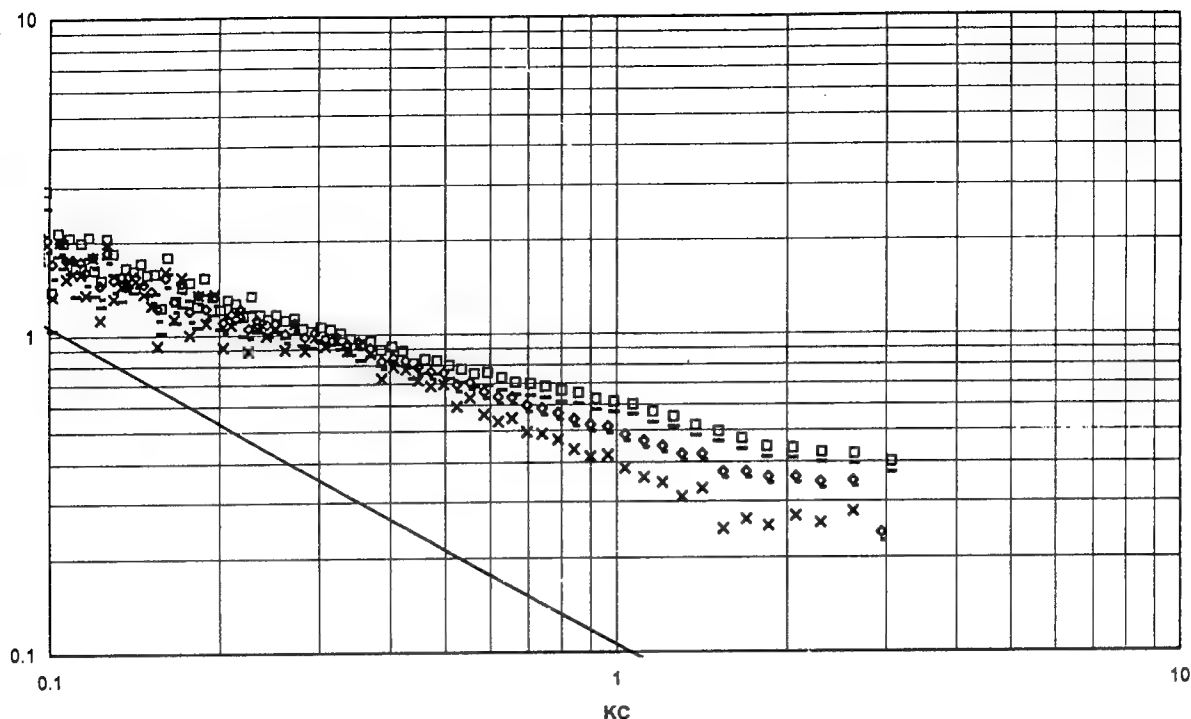


Figure 6 C_D versus KC for a 312mm diameter circular cylinder with $\beta = 61,022$ and with 392mm end plates. \diamond , long cylinder; \square , short cylinder; \times , long minus short; $-$ long minus plate; $—$, short minus plate

have been subtracted from the total drag and that the effect of the ends is greater than assumed.

In order to try to identify where the extra component of drag might be coming from some flow visualisation was carried out using the electrolytic precipitation method. Fine white particles are emitted from the model surface into the flow. By observing the flow near one end of the cylinder it became evident that pairs of vortices were being shed from the edge of the end plate. Also close to the end plate there was a region of three dimensional flow on the cylinder as a vortex formed in the corner between the end plate and the cylinder. This vortex appeared to be spilling out past the end plate and causing the shedding of the vortex pairs. The diameter of the end plates was now increased to 700mm and the visualisation repeated. The shedding of vortex pairs no longer occurred and the flow appeared much more nearly two dimensional near an end plate. Encouraged by these findings it was decided to repeat the earlier measurements using the larger end plates.

The two different length 312mm diameter models were tested again with the larger end plates (700mm) for a range of β values from 20,000 to

58,000. A 700mm end plate was also tested at similar β values to those of the cylinder measurements. A comparison of drag coefficients

obtained by the plate subtraction and long - short methods is shown in figure 7 for $\beta = 20,526$. Although there are still some differences between the three sets of data, the spread is substantially reduced compared to that obtained with the smaller end plates. The results with the smaller end plates show that end conditions are important, even for a cylinder in oscillatory flow at low KC .

It is apparent for all the circular cylinder data, when plotted in a log log form, that as KC reduces so the drag coefficient follows a line parallel to the theoretical values of Wang. This confirms that at low KC , for a particular β value, the product of drag coefficient and Keulegan Carpenter number tends to a constant. Also the ratio of the measured drag coefficient to the Wang drag coefficient, C_D/C_{DW} , is greater than unity. Typically this ratio seems to take a value between about 1.5 and 2.5. A further feature to observe from the circular cylinder C_D plots is that above a KC value of about 0.5 the data deviates from the straight line form given by equation (5). Perhaps this marks the first appearance

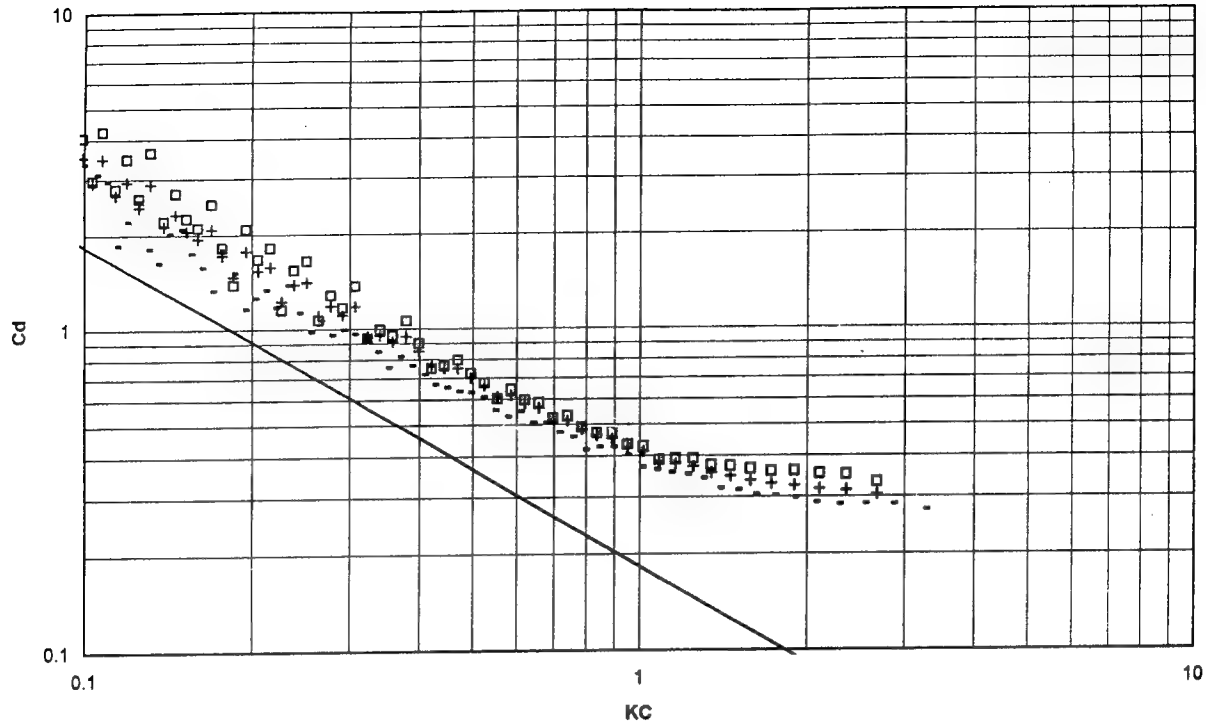


Figure 7 C_D versus KC for a 312mm diameter circular cylinder with $\beta = 20,526$ and with 700mm end plates. +, long minus plate; x, long minus latex, \square , long minus short; —, Wang.

of separation which, as KC increases further, leads to vortex shedding and a rising drag coefficient. The minimum C_D in our experiments seems to occur for KC values between about 2 and 3.

Bearman et al (11) have suggested that the drag of a bluff body in oscillatory flow can be considered as the sum of a boundary layer component and a vortex component. Further it is argued that at low KC the vortex drag coefficient for a circular cylinder should increase linearly with KC . Figure 8, taken from Bearman et al (11), shows the vortex drag component, C_{DV} , versus KC for low values of β of about 1000. Also plotted on the same figure is an estimate of C_{DV} obtained from large scale oscillatory flow and wave experiments carried out at SSPA and DHL respectively, for β of order 100,000. This gives

$$C_{DV} = 0.08 KC. \quad (6)$$

The boundary layer contribution, C_{DBL} , takes the form predicted by Wang but our experiments show that approximately,

$$C_{DBL} = 2 C_{DW}. \quad (7)$$

Hence we can express the variation of C_D with KC as follows:

$$C_D = 52.48/(KC \beta^{1/2}) + 0.08 KC. \quad (8)$$

The prediction obtained using equation (8) is plotted in figure 9 for $\beta = 34,946$ and shows good agreement with the experimental results.

C_D values for the square section cylinder model, with sides of length 300mm, are shown plotted in figure 10 against KC for $\beta = 8, 14, 28, 39$ and 48×10^3 . These results have been obtained using the plate subtraction method. Compared to the circular cylinder drag coefficient results there is considerably less scatter at very low KC . However, this is not related to the flow but is due to the fact that the displacement transducer was used for amplitudes corresponding to KC values less than about 0.1.

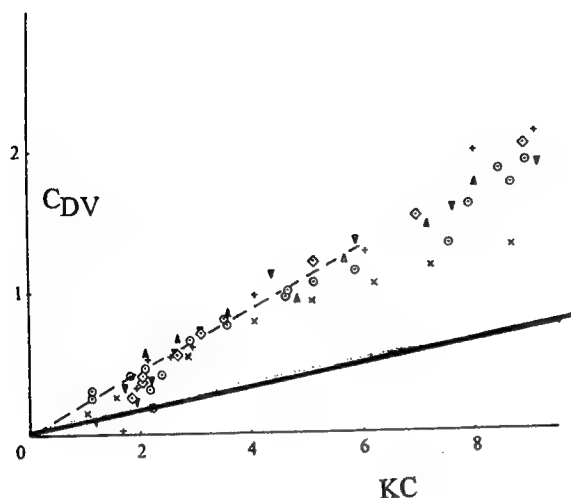


Figure 8 Circular cylinder vortex drag coefficient. Symbols for $\beta = (O)$ 1,000; —, $\beta = (O)$ 100,000.

Using an analysis similar to that of Wang (9), Bearman et al (11) showed that the drag coefficient for attached laminar flow on a square cylinder is given by

$$C_D KC \beta^{1/2} = 38.18. \quad (9)$$

The predictions obtained using equation (9) are plotted in figure 10 and they reproduce the correct form of the β dependence but, just as in the case of the circular cylinder, the C_D is under estimated. In this case the measurements are 50% to 60% higher and for the square section the equivalent of equation (7) is roughly

$$C_D KC \beta^{1/2} = 60. \quad (10)$$

Bearman et al (11) also estimate the vortex-related drag for a square section cylinder using a simplified isolated edge, vortex analysis. This predicts a C_D which is independent of KC and β , and takes the value 5.88. Inspection of figure 10 shows that as KC approaches unity the C_D values do lose their β dependence, as predicted, but the asymptotic value of C_D is nearer 2.5 than 5.88. The vortex analysis assumes that each edge of the square behaves independently and this may well be too idealised and lead to an excessively high prediction of drag. To obtain a more accurate result a full interactive flow

field calculation would need to be carried out. Bearman et al (11) found that the isolated edge analysis also overestimated their drag coefficient measurements for $\beta = 231$.

Following the method used to describe the circular cylinder drag coefficient variation with KC and β , an equivalent expression for the square section is given by:

$$C_D = 60/(KC \beta^{1/2}) + 2.5 \quad (11)$$

Equation (11) is plotted in figure 11 and is seen to provide a good representation of the data. The drag of a square section is dominated by the generation of vortices from its sharp corners at all but extremely low KC values. At low enough KC the separated flow regions will be so localised near the edges that the drag contribution from vortices will be small and viscous damping will be due mainly to boundary layer drag arising from the regions of attached flow over the body.

The TLP hull shown in figure 1 was constructed to a scale of 1:113. The design allows the hull to be tested only in surge but the model can be oriented in various directions to the relative flow, in a similar manner to the square model. Preliminary drag coefficient results are shown plotted in figure 12 versus KC , for 0° and 45° orientations and for $\beta = 19,000$. In this case β and KC are based on the diameter of the TLP columns. The results have not been corrected for the effect of tare drag and it should be noted that the area used in the drag coefficient is the same for both orientations. At very low KC the inverse relationship between C_D and KC is similar to that observed for the circle and square measured separately. Near $KC = 1$ the vortex drag of the square section pontoon seems to dominate the drag coefficient. It is interesting to note that the damping of the TLP seems to be unaffected by its orientation. However, these are preliminary results and they need to be carefully checked.

CONCLUSIONS

Experiments have been carried out to determine the viscous damping of a circular and a square cross section cylinder by mounting the sections on a pendulum and observing the decay of oscillations. Circular cylinders with diameters of 150mm and 312mm have been tested as well as a square section of side 300mm. The data is presented

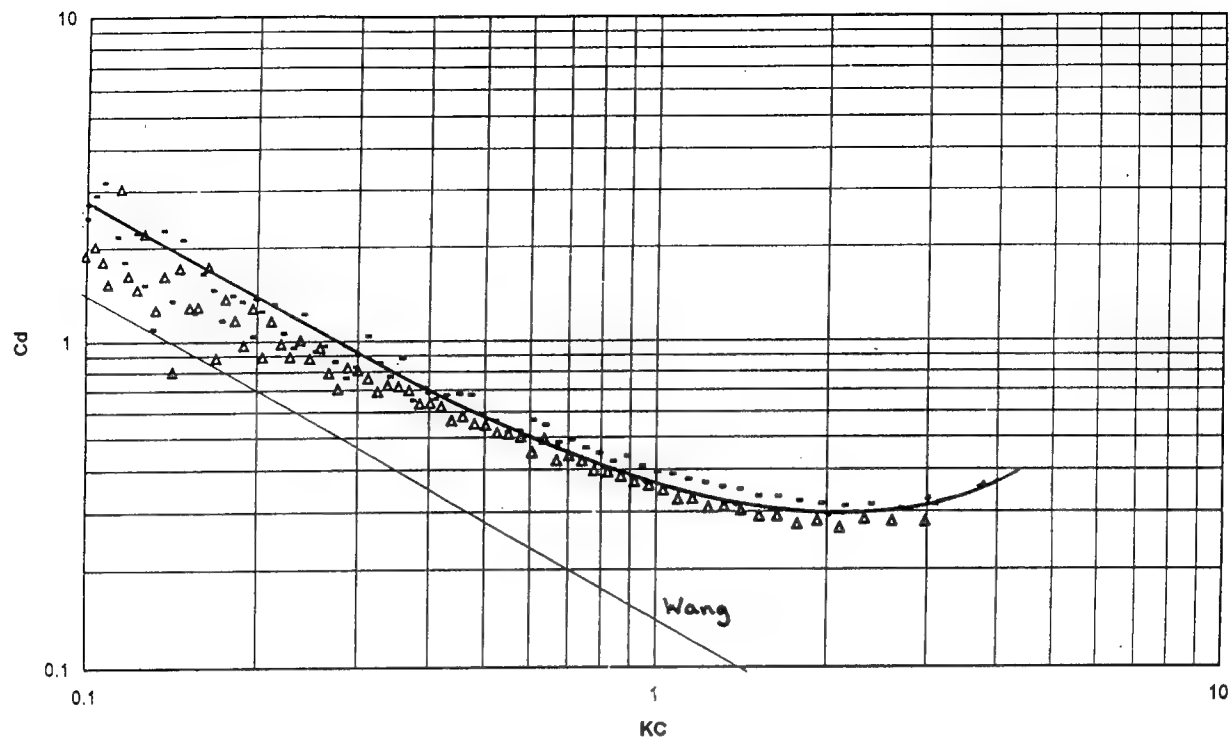


Figure 9 C_D versus KC for a circular cylinder with $\beta = 34,946$; —, prediction using equation (8).

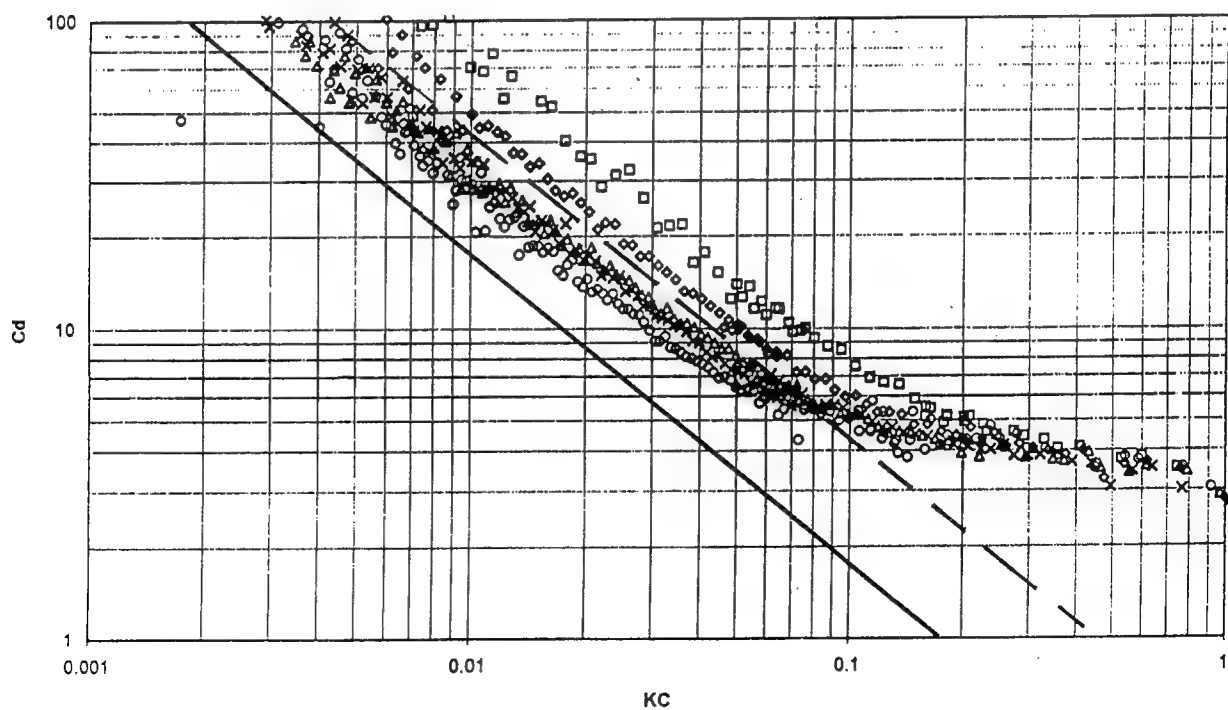


Figure 10 C_D versus KC for a square section cylinder; o, $\beta = 40,000$; Δ , 39,000; x, 28,000; \diamond , 14,000; \square , 8,000; —, prediction using equation (9) with $\beta = 48,000$; ----, prediction using equation (9) with $\beta = 8,000$.

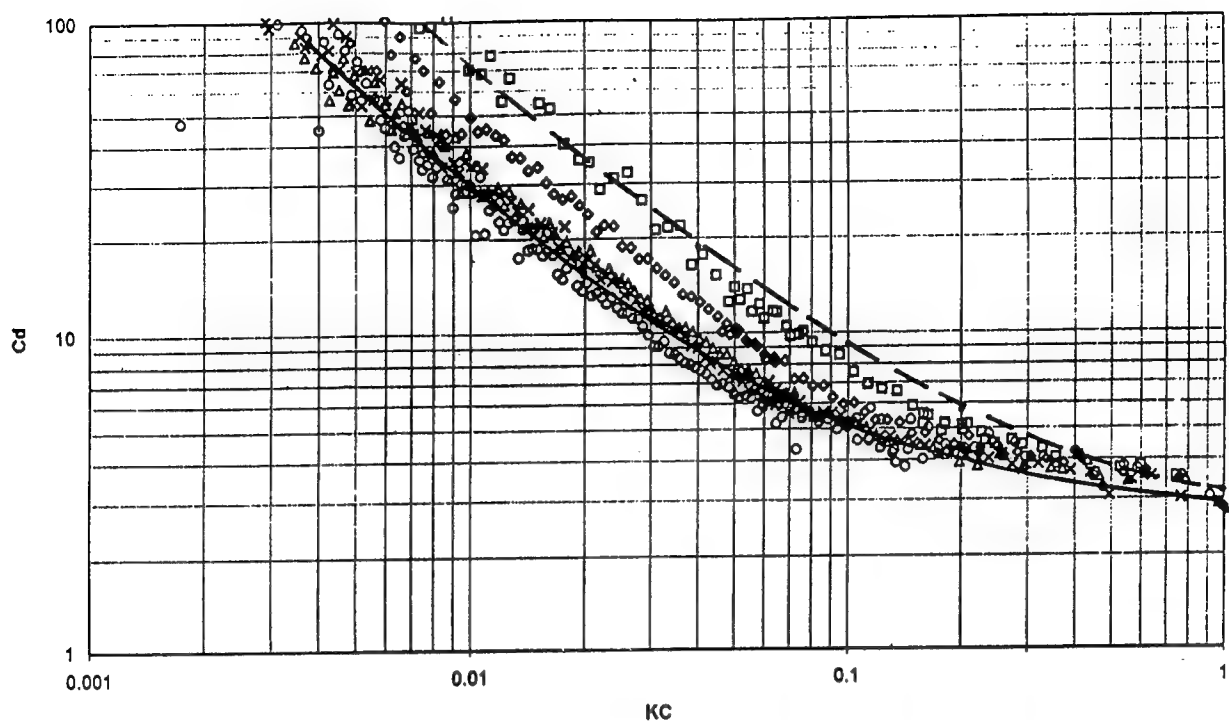


Figure 11 C_D versus KC for a square section cylinder; \circ , $\beta = 40,000$; Δ , $39,000$; \times , $28,000$; \diamond , $14,000$; \square , $8,000$; —, prediction using equation (11) with $\beta = 48,000$; ----, prediction using equation (11) with $\beta = 8,000$.

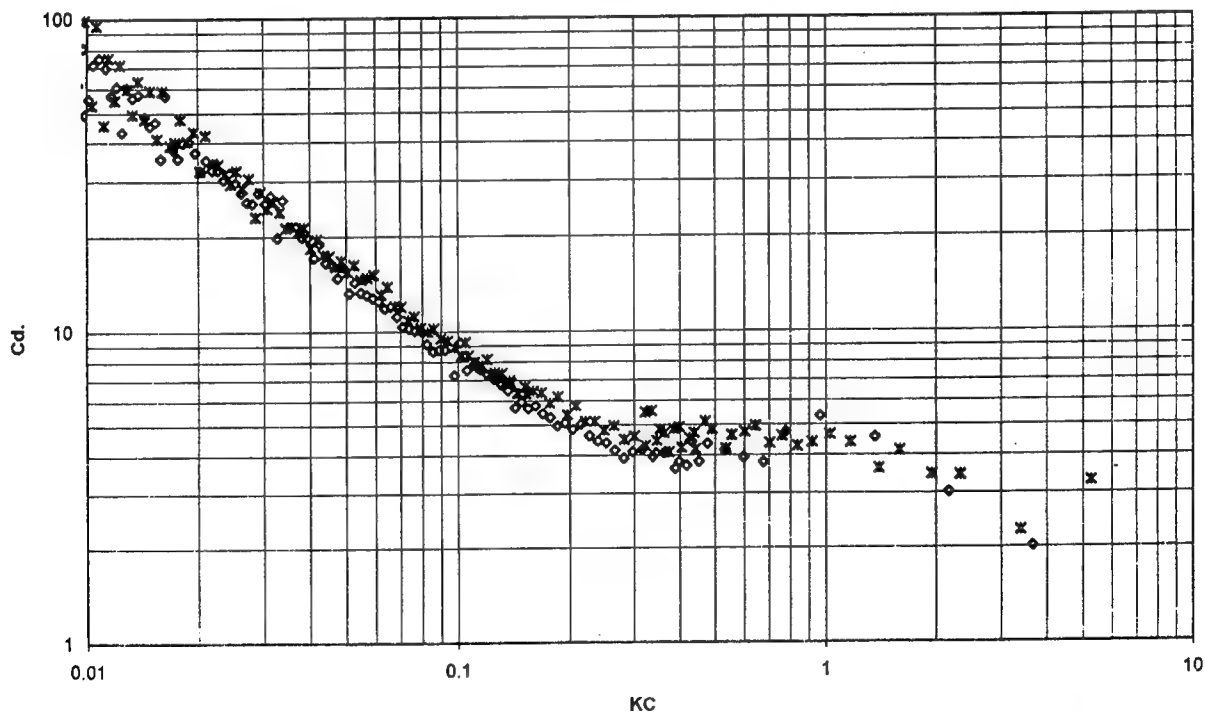


Figure 12 Uncorrected drag coefficient versus KC for TLP model with $\beta = 19,000$; KC and β based on column diameter. \times , zero degrees; \diamond , 45 degrees.

as a variation of drag coefficient with Keulegan Carpenter number for different β values. The KC range tested was from about 0.003 to 3 and the maximum β was about 60,000. Two methods have been used to correct the results for the effect of tare drag. It is found that end conditions are important at low KC and large diameter end plates were required to give approximately two dimensional flow. Some preliminary results have been presented for a model of a TLP hull.

At low KC all results indicate that the product of C_D and KC tends to a constant, as predicted by laminar flow theory. However, the level of C_D is higher than that predicted by the theory at all KC values. By considering the drag to be composed of a boundary layer and a vortex component, relationships are proposed for the variation of C_D with KC and β . These are shown to give a reasonable fit to the experimental data for the complete KC range examined. It remains for these relationships to be applied to predict the damping of the complete TLP hull. The TLP results show the same inverse relationship between C_D and KC at low KC and C_D appears to be dominated by the drag of the square section pontoon at higher KC values. The damping levels measured for the TLP at 0° and 45° incidence are similar.

ACKNOWLEDGEMENT

This research is sponsored by the Marine Technology Directorate Ltd and is funded by EPSRC and the Offshore Industry. It forms part of a managed programme of research entitled Uncertainties in Loads of Offshore Structures.

REFERENCES

1. Sarpkaya T., "Hydrodynamic Damping , "Flow-Induced Oscillations and Biharmonic Response," J. of Offshore Mech. and Arctic Eng., Vol. 117, 1995, pp 232 -238.
2. Bearman P.W. and Mackwood P.R., "Measurements of the Hydrodynamic Damping of Oscillating Cylinders," Proc. of the 6th Int. BOSS Conf., London, UK. July, 1992, pp 405 - 414.
3. Honji H., "Streaked Flow around an Oscillating Circular Cylinder," J.Fluid Mech., Vol. 107, 1981, pp 509 -520.
4. Otter A., "Damping Forces on a Circular Cylinder Oscillating in a Viscous Fluid," Applied Ocean Research, Vol. 12, 1990.
5. Otter A., "Forces on an Oscillating Cylinder and Related Fluid Flow Phenomena," Doctoral Thesis, University of Twente, 1992.
6. Sarpkaya T., "Force on a Circular Cylinder in Viscous Oscillatory Flow at Low Keulegan-Carpenter Numbers," J.Fluid Mech., Vol. 165, 1986, pp 61 - 71.
7. Bearman P.W., Graham J.M.R., Obasaju E.D. and Drossopoulos G.M., "The Influence of Corner Radius on the Forces Experienced by Cylindrical Bluff Bodies in Oscillatory Flow," Applied Ocean Research, Vol. 6, 1984.
8. Stokes G.G., "On the Effect of the Internal Friction of Fluids on the Motion of Pendulums," Trans. Camb. Phil. Soc., Vol. 9, 1851, pp 8-106.
9. Wang C.-Y., "On High-Frequency Oscillating Viscous Flows," J. Fluid Mech., Vol. 32, 1968, pp 55-68.
10. Hall P., "On the Stability of Unsteady Boundary Layer on a Circular Cylinder Oscillating Transversely in a Viscous Fluid," J. Fluid Mech., Vol. 146, 1984, pp 347-367.
11. Bearman P.W., Downie M.J., Graham J.M.R. and Obasaju E.D., "Forces on Cylinders in Viscous Oscillatory Flow at Low Keulegan-Carpenter Numbers," J. Fluid Mech., Vol. 154, 1985, pp 337-356.

Hydrodynamics in Advanced Sailing Design

J. Milgram (Massachusetts Institute of Technology, USA)

Abstract

A review of up-to-date methods for incorporating the results of hydrodynamic studies in the sailing vessel design process is given. It is shown that a requirement for design evaluation is a Velocity Prediction Program (VPP) which simultaneously accounts for all the effects of design features and their variations. The need for experimental data, both for sails and hulls, as starting points in the design process is emphasized. Such data includes interactions which cannot be fully evaluated by numerical hydrodynamics. Much emphasis is given to the use of numerical hydrodynamics for refining design variations. Existing procedures in areas including wave resistance, lift and induced drag of appendages, and resistance due to sea waves are reviewed, and their roles in the design process are evaluated. New procedures and results in the areas of viscous flow over appendages, thrust due to unsteady motions and sail aerodynamics with influence of the hull beneath the sails are given.

1 Introduction

Development of sailing vessels began as a full scale trial and error process and still is, to a large extent. The first "research" done in a different way was scale model testing. Although ship model testing has been conducted for over 500 years, the process was not put onto the firm scientific basis of dimensional analysis until the work of William Froude beginning in 1868. The science and art of ship model testing has advanced considerably in the last 128 years. However, during most of this time the commercial and naval ships being developed were driven by propellers, not by sails. Therefore matters involving heel, side force and leeway have not been in the mainstream of devel-

opments in model testing. Instead, these specialties have been developed by those naval architects and ship hydrodynamicists involved with advancing the state of the art of sailing yachts.

Another aspect of hydrodynamic development for waterborne vessels is numerical hydrodynamics. Similar to model testing, the mainstream in numerical ship hydrodynamics relates to ships whose mean operating condition does not involve substantial side forces, heel angles or leeway angles. Again, these specialties have occupied the efforts of people involved with sailing yachts.

Almost all the experimental and numerical hydrodynamics used for ships driven by propellers has application to sailing vessels. Although the application of propeller hydrodynamics may seem remote when viewed superficially; there are, in fact, many similarities between them and numerical sail aerodynamics. The addition of the unique hydrodynamics of sailing vessels to the those that apply to all ships results in the complex aero/hydrodynamical system that is our subject here.

The development of numerical and experimental methods for advanced sailing vessel hydrodynamics has been stimulated almost entirely by the design of sailing craft for participating in some sort of speed contest. Although much of the development of such vessels is done by the usual trial and error process, the advantages of very small increments in speed have brought all resources to bear on the design of these craft. The most common type of contest is a yacht race whose distance can vary from several hundred meters to a circumnavigation of the globe. Most of these races are for monohulled craft, although a number of them involve multihulled craft. A less common contest is a time trial where the goal is to set a speed record. Long distance time trials involve vessels that are similar to those used in yacht races whereas short distance time trials involve a broader

range of craft geometries. In fact, in recent times the world sailing speed record has been held by a sailboard for which a significant component of the sail force is vertically upward.

The focus here is on the aero/hydrodynamics used in support of the design of monohulled yachts. However, several of the approaches have application to the less common sailing craft mentioned above.

The history of aero/hydrodynamic research related to sailing vessels can be divided into two categories. The first is the set of individual research programs of varying intensity and longevity whose modern history covers more than 50 years. The second category is the applied hydrodynamic research on sailing vessels stimulated by competition in the America's Cup yacht races. These events, typically held once every 3 to 5 years, have attracted extraordinary and unique international interest and intense competition. As a result, very substantial resources have been applied to every known way to increase the sailing speed of vessels which meet the specified requirements for the competition. Applied aero/hydrodynamic research is one of them. Most of the material to be presented herein is drawn from this category.

2 Evaluation of Designs and Design Ideas

Since a sailing vessel is a complex interconnected "system", most design changes influence more than one kind of fluid force. For example, suppose one wishes to reduce the frictional resistance of the hull by reducing its wetted surface. For most hull shapes, if length is maintained, the reduction in hull wetted surface requires a reduction in beam. This in turn reduces the heeling stability which, for prescribed sail shapes, leads to an increase in heel angle. The change in heel angle not only changes the hull shape, but also changes the sail forces. How does one determine whether the sum of all these effects is advantageous or disadvantageous? More importantly, how can one evaluate the effects if the sail shapes are simultaneously changed to optimize them for the altered hull? Short of complete full scale sailing experiments, answering these questions must be done with a numerical method of predicting performance. A computer program that does this is called a *Velocity Prediction Program* (VPP). One can think of a VPP as "sailing a boat in the computer".

2.1 Fundamental Principles for a Velocity Prediction Program

The primary purpose of a velocity prediction program is to predict the boat speed for any prescribed wind conditions and sailing angle, β_T , between the wind direction and the course of the boat. This is achieved in a computational model by balancing counteracting aerodynamic and hydromechanic forces and moments. The course of the vessel differs from the heading of its centerline by the yaw (leeway) angle, λ .

A few preliminary definitions and descriptions are needed before proceeding further. The true wind speed varies with the distance, z , above the water. Here, we will consider logarithmic wind velocity profiles described by:

$$v(z) = V_{10} \frac{\ln z - \ln z_o}{\ln 10 - \ln z_o}, \quad (1)$$

where V_{10} is the wind speed at a height of 10 meters and z_o is the roughness height which is taken here as 0.001 meters (1 mm). Hence the wind velocity profile $v(z)$ is described by the single parameter V_{10} .

The *deck plane* is defined as a plane perpendicular to the centerplane of a vessel. Figure 1 shows the aerodynamic and hydromechanic force and moment components in the deck plane. Those involved in the VPP force and moment balance are:

F_{af} , the aerodynamic forward force in the course direction,

F_{ah} , the aerodynamic heel force which is perpendicular to the forward force and the parallel to the deck plane. The aerodynamic force is presumed to be parallel to the deck plane. Thus the aerodynamic forces perpendicular to the deck plane are neglected in our model for evaluating performance here,

M_{ah} , the aerodynamic heeling moment whose vector is along the centerline of the yacht,

F_{wr} , the resistance of the yacht in the direction opposite to the course direction,

F_{wh} , the hydromechanical force component which is perpendicular to the course and parallel to the deck plane, F_{wh} is exclusive of components of that part of the buoyancy force which balances the weight of the yacht.

M_{wh} , the righting moment of the water on the yacht. Its vector is in the direction of the yacht centerline. It includes both hydrostatic and hydrodynamic components.

For any equilibrium sailing condition there are three "balance equations" involving these forces and mo-

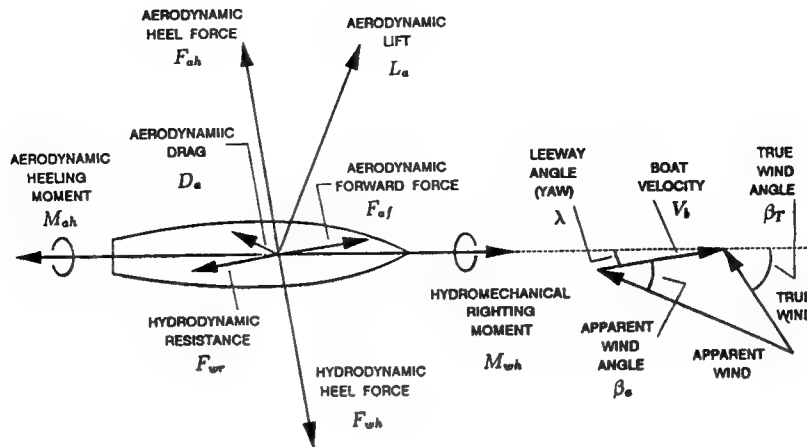


Figure 1: Forces and moments in the Deck Plane.

ments:

$$\begin{aligned} F_{wr}(V_b, \phi, \lambda) &= F_{af}(V_b, \phi, \lambda), \\ M_{wh}(V_b, \phi, \lambda) &= M_{ah}(V_b, \phi, \lambda), \\ F_{wh}(V_b, \phi, \lambda) &= F_{ah}(V_b, \phi, \lambda), \end{aligned} \quad (2)$$

where V_b is the boat speed in the direction of the course, ϕ is the heel angle and λ is the leeway (yaw) angle.

For prescribed values of the wind speed, V_{10} , and the sailing angle β_T , all six terms in equations 2 depend on the boat speed, the heel angle and the leeway angle. There are three equations for these three unknowns. The VPP solves the three equations for the three unknowns. Figure 2 is a block diagram of the VPP model.

Although solving the balance equations 2 is computationally intensive because the equations are non-linear and the solution variables are intrinsic to the expressions, each related numerical step is precise and any desired level of numerical accuracy can be achieved. On the other hand, modeling all the forces involved is an approximate and imperfect science. Hydrodynamics, as we do it in terms of theory, experiment and numerical computation, makes its greatest contribution to this field by predicting forces and teaching us how to model them.

In addition to the basic force models, two additional VPP features, which involve feedback, are shown in Figure 2:

The Sail Shape Optimizer adjusts the sail shapes, and therefore their aerodynamic characteristics, so as to maximize the boat speed for the prescribed wind speed and direction.

The Direction Optimizer is activated for sailing upwind or downwind. Then, the best speed made good (VMG) occurs when sailing in a direction different from the direct path between end points. Tacking or gybing is done so as to achieve the net desired course with all the sailing done at the optimum wind angle.

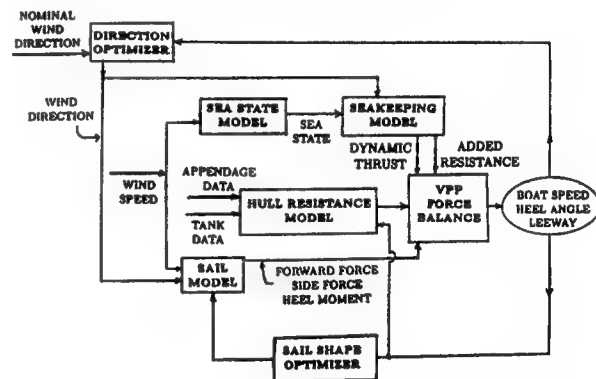


Figure 2: A Block Diagram of the VPP. This emphasizes the fact that solving the force balance equations is the minor and more ordinary part of the process. The modeling of the forces is necessarily imperfect and requires most of the effort in developing a faithful VPP.

2.2 An Example of Use of A Velocity Prediction Program

As an example of using a VPP, Figure 3 shows the effect of a 1% change in total resistance of an International America's Cup Class (IACC) yacht on time required to sail a course of 17.2 km upwind and 17.2 km downwind.

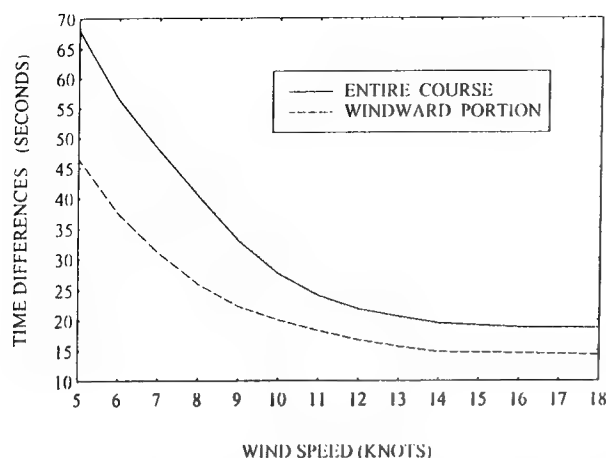


Figure 3: Time Differentials in Sailing a 34.3 km Course Due to a 1% Change in Resistance.

This example has been chosen not only to show one capability of a VPP, but also to demonstrate that requirements for performance prediction accuracy are extraordinary when optimizing the designs of racing yachts. A 1% change in resistance corresponds to a change in race course sailing time of 25 to 45 seconds depending on the wind speed. These times themselves relate to substantial margins of victory or defeat. When the tactical advantages of the faster boat are considered as well, the influences of the speed differences are even greater.

The time differentials shown in Figure 3 correspond to about 0.3% in the sailing time and in the average speed. In ordinary applications of naval architecture speed variations of 0.3% are negligible. If a new ship on trials deviates from her design speed by 0.3% (for example, 15.95 instead of 16 knots) it makes little difference. However, for racing vessels 0.3% is more than the difference between a true winner and an "also ran." Even smaller speed differences can be meaningful so differences of very small magnitude need to be considered not only in designs, but also in methods of evaluating designs.

It is not possible to predict absolute boat speeds for a prescribed design to within 0.3% of the actual sailing speed, let alone the even smaller variations that are significant. However, this extreme accuracy is not required on an absolute basis. It is required on a relative basis and this can be achieved, to a greater or lesser degree depending on the design area under consideration, if the technology is pushed to its limit.

3 The Design Process

The design of a specific vessel needs initial data on what is always an incomplete relationship between performance and design parameters for similar vessels. Often, this comes from qualitative or semi-quantitative information from racing performance in competitions in which vessels of varying designs compete. Although it is the most common information source, such data suffers from being in a form which makes it impossible to separate hull hydrodynamics, sail aerodynamics and sailing ability of the crew.

At its best, initial data on the relation between hull geometry and the hydrodynamic aspects of performance come from towing tank model tests, supplemented by numerical results on the added resistance in sea waves as it is very difficult to determine this experimentally with sufficient accuracy. Ideally, initial tank tests results include a series of models with systematic variations of design parameters. Although systematic data is most helpful to hydrodynamicists in developing improved designs, projects which acquire model test data are almost always under pressure to conduct tests on all the latest design ideas or one designer's "breakthrough brainstorm." It takes unusual discipline and substantial resources in a design effort to acquire initial data on systematic parametric variations.

No matter how the initial data is obtained or the form it takes, the next step is to try to achieve design improvements. In addition to the "artistic" approaches used by many naval architects and yacht designers, this is the stage where quantitative theoretical, numerical and experimental hydrodynamics can make significant contributions. It is especially helpful to have systematic model test data at this stage since it provides a basis for comparison with the results of numerical hydrodynamics. If the later is verified by comparison with experiments, it can be used with more confidence in exploring new designs.

A significant technical management effort is required to integrate the initial data, the artistry of the traditionalists and the findings obtained by hydrodynamics. The goal is to achieve one or more improved designs. If the time has come to build a new design and if one of the new designs is an improvement over the starting designs, the best one can be chosen. However, if the development process is to continue further, it is best to conduct model tests on systematic variations of the new best design and repeat the process.

4 Decomposition of the Force Components

A vessel under sail with non-zero heel and yaw angles is a complex interrelated system. The exact situation is one in which the water flow around the hull is not symmetric, port and starboard, due to the heel and yaw; and the air and water flows influence each other. It is necessary to make simplifying approximations; not only to be able to apply the present state-of-the-art in hydrodynamics, but also to be able to achieve a practical design process.

The first simplifying approximation is that the air and water flows do not influence each other. In other words, the coupling between air forces and water forces is approximated as being wholly mechanical (the rig and the hull are structurally connected) and not hydrodynamical. This is not to say that the optimum aerodynamic design is independent of the optimum hydrodynamic design. In fact, since different hulls require different sails for optimum performance, these optima are closely coupled. Rather, it is to say that for any prescribed geometry and sailing conditions the aerodynamic and hydrodynamic flows are determined independently.

4.1 Hydrodynamic Resistance

The essential goal in modeling hydrodynamic resistance is determination of the function $F_{wr}(V_b, \phi, \lambda)$, or alternatively $F_{wr}(V_b, \phi, F_{wh})$, for any prescribed hull form in prescribed sea conditions. A useful approach is to use an additive resistance model of the following form:

$$F_{wr} = D_{hf} + D_r + D_{af} + D_{hi} + D_w - T_u \quad (3)$$

where:

F_{wr} is the total hydrodynamic resistance (drag),

D_{hf} is the frictional drag of the hull,

D_r is upright residuary resistance of the entire vessel,

D_{af} is the friction and interference drag of the appendages,

D_{hi} is the drag due to heel and yaw (leeway), or equivalently, due to heel and heel force production,

D_w is the resistance due to sea waves (added resistance), and

T_u is the mean *dynamic thrust* due interactions of appendages with the unsteady flow resulting from vessel seakeeping motions and sea wave orbital velocities.

Usually, non-dimensional force coefficients, C ,

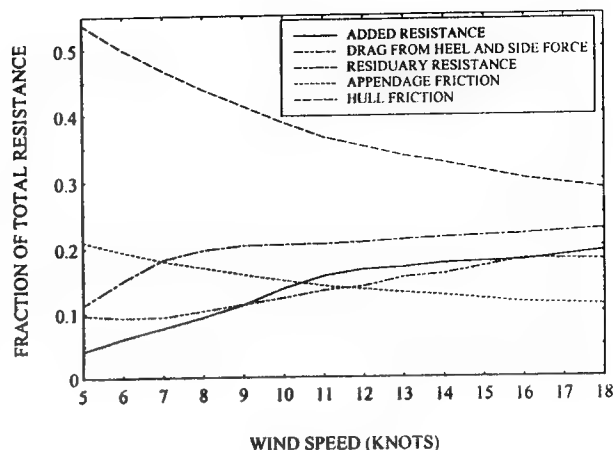


Figure 4: Fractions of Total Resistance for Each Component for Upwind Sailing

are obtained by dividing corresponding forces by $\frac{1}{2}\rho_w V_b^2 S_h$, where ρ_w is the density of the water, V_b is the boat speed and S_h is the wetted surface. It is sometimes useful, particularly in wind tunnel model testing, consider "force areas", A , obtained by dividing corresponding forces by $\frac{1}{2}\rho V^2$, where ρ is the density of the test fluid and V is the relative inflow velocity.

Figure 4 shows the fraction of resistance contributed by each component, exclusive of T_d , vs. wind speed from VPP computations for an IACC yacht using tank test data and measured sea spectra in San Diego California as inputs. Figure 5 shows the fractions for sailing downwind. Tacking angles for optimum speed made good are used both upwind and downwind.

The hull friction is always the largest component for upwind sailing and it is largest for downwind sailing in wind speeds less than 12 knots. For higher wind speeds in downwind sailing the residuary resistance becomes the largest because of the high boat speeds in these conditions. The effects of resistance due to heel, side force, and added resistance are negligible in downwind sailing and are neglected in Figure 5. The reader needs to be aware that the relative merits of two boats sailing downwind in large seas are also influenced by the relative surfing ability, and that is not included in the computations. For upwind sailing, in the mid-range of wind speeds, all the other resistance components are comparable to each other. At very low wind speeds the appendage friction is largest component after hull friction. The boat speed is low enough in these conditions for the residuary resistance to be considerably smaller than the appendage friction, and the sea waves are small enough for the added resistance to be small as well. On the other hand, at high wind speeds the combi-

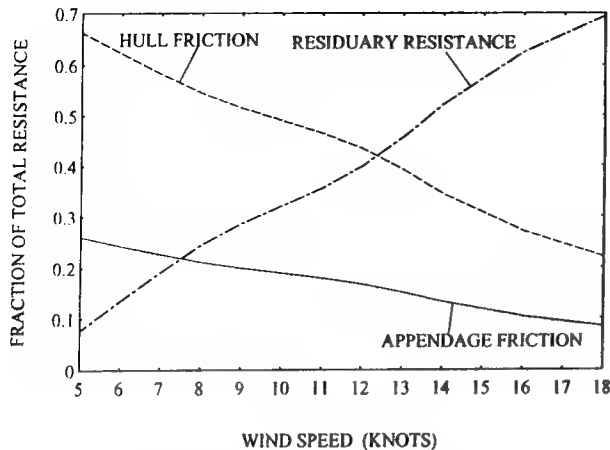


Figure 5: Fractions of Total Resistance for Each Component for Downwind Sailing.

nation of boat speed, sail side force, and sea waves makes the residuary resistance, resistance due to heel and side force, and added resistance similar and large enough for the fraction due to appendage friction to be somewhat less. This exercise is one demonstration of the requirement for using velocity prediction programs. The increase in fraction of residuary resistance with increasing wind speed is due to the increase in boat speed with wind speed. However, the ratio of sail side force to the square of the boat speed increases and this is why the fraction of resistance due to induced drag increases as well.

Strictly speaking, the terms in equation 3 are not independent of each other. For example, the viscosity, which is mainly responsible for friction drag, causes boundary layers whose displacement thickness influences the residuary wavemaking resistance. Similarly, the ship-generated waves cause pressure gradients along the hull which influence the boundary layers and the associated friction drag. If each term in equation 3 is determined or estimated independently of the others, the interactions between terms are not accounted for. However, if scale model tests are conducted the interactions are captured if the model scale is not too small. They get mixed into the various terms in the decomposition. For example if the upright residuary resistance is defined as the measured resistance minus the presumed frictional resistance, the sum of these two resistances automatically includes the interactions. The work of Kirkman and Pedrick (1974) suggests that scale model waterline lengths need to be 5 meters or more for there to be a reasonable assurance of reliable results in the experimental process and expansion of its data to full scale.

Once a set of resistance components which includes

their interactions are determined by model testing, it is often quite useful to use numerical methods to estimate the difference in one of the resistance components between two designs. Although this may not capture differences in the interactions, it often provides a good approximation to the differences that are the most significant. Some of the numerical methods in use will be considered in the sequel here.

4.2 Aerodynamic Forces

The forward and heeling aerodynamic forces, F_{af} and F_{ah} , are given in terms of the aerodynamic lift and drag forces, L_a and D_a , and the apparent wind angle, β_a , as:

$$F_{af} = L_a \sin \beta_a - D_a \cos \beta_a \quad (4)$$

$$F_{ah} = L_a \cos \beta_a + D_a \sin \beta_a \quad (5)$$

Similarly, the aerodynamic heeling moment, M_{ah} , is determined from these forces and the heights of their centers.

On a moving vessel, the apparent wind speed and angle depend on height since the components due to true wind speed depend on height and the component due to vessel speed is independent of height. Some height must be chosen for a reference apparent wind speed, V_a , and a reference apparent wind angle, β_a . Here the reference height will be taken as 10 meters above the water.

The lift force, L_a , can be quite accurately determined from lifting surface theory (c.f. Greeley et al., 1989 and Milgram, 1968) for upwind and close reach sailing where the local sail cambers and incidence angles are modest. For offwind sailing, flow separation is almost always large enough to materially influence the lift so that experimental data are required to "construct" a mathematical model for it.

The aerodynamic drag force includes the induced drag of the sails as well as the frictional and parasitic drag on the sails, mast, rigging and hull. For windward and close reach sailing, the induced drag data can come from the same computational implementation of lifting surface theory that provides the lift. However, all the drag for offwind sailing and the friction and parasitic drag for upwind sailing must come from experiments or empirical estimates.

Aerodynamic lift and drag coefficients, C_{L_a} and C_{D_a} , are taken as:

$$C_{L_a} = \frac{L_a}{\frac{1}{2}\rho_a V_a^2 S_a} \quad C_{D_a} = \frac{D_a}{\frac{1}{2}\rho_a V_a^2 S_a} \quad (6)$$

where ρ_a is the air density and S_a is the actual sail area.

Each sailing condition has a different lift and drag coefficient for optimum performance. The usual modeling approach is to determine a maximum allowed lift coefficient as a function of apparent wind angle, $C_{L_{max}}(\beta_a)$. For each apparent wind angle and operating lift coefficient, which can be any positive value less than or equal to $C_{L_{max}}(\beta_a)$, there is an associated drag coefficient. The VPP also needs to choose the amount of sail area to set, up to a maximum allowed amount, for optimum performance. To complete the specification, the drag coefficient needs to be "modeled" as a function of C_L and β_a .

The author has had success in modeling the drag coefficient as:

$$C_D(C_L, \beta_a) = C_{D_o}(\beta_a) + C_L^2 C_i(\beta_a) + C_L^2 C_{D_p}(\beta_a) \quad (7)$$

where:

$C_{D_o}(\beta_a)$ includes the friction drag of the sails and the profile drag coefficient of the hull, mast and rigging,

$C_i(\beta_a)$ is a coefficient of induced drag, and

C_{D_p} is a coefficient of lift-dependent profile drag.

The last two terms in equation 7 are proportional to the square of the lift coefficient so one might ask why they are not combined into one. The reason is that for a given lift coefficient the induced drag is particularly sensitive to aspect ratio and vertical distribution of lift, whereas the profile drag is less sensitive. Therefore, by keeping the terms separate, a model for one sailplan can be adjusted for a change in vertical lift distribution (Euerle and Greeley, 1993) or used to model a different sailplan by altering C_i in ways that can be well approximated theoretically.

Two approaches can be taken for estimating $C_{D_o}(\beta_a)$ and $C_{D_p}(\beta_a)$. One is to add estimates of the drags from hull, mast, rigging and sails, with each determined as well as possible from existing data. As examples, rigging drag can be based on published drag coefficients for cylinders and sail parasitic drag can be based on section data (Milgram, 1971). The other approach is to measure the drag and subtract the induced drag computed from lifting surface theory for the sail shapes in use to obtain the other drag components. This has been done by the author (Milgram, 1993) by using an instrumented sailing vessel for measuring aerodynamic forces.

5 Towing Tank Testing

A complete consideration of the towing tank testing of model scale sailing vessels will not be presented here as it is well covered in the literature (c.f. Van Oosannen, 1993 and Milgram, 1993). Rather, the process is outlined and some special problems are described.

When data are obtained by model testing, the frictional terms, D_{hf} and D_{af} , are subject to Reynolds scaling whereas the other terms, D_r , D_{hi} and D_w , are considered to be subject to Froude scaling. The upright quantities, hull friction, appendage friction and residuary resistance are determined in the same way in ordinary resistance tests of vessels that are not powered by sails. Appendage friction is estimated on the basis of appendage geometry and the hull friction coefficient is taken as:

$$C_{hf}(Re) = (1 + k)C_f(Re) \quad (8)$$

where :

Re is the Reynolds number based on length,

k is the form factor evaluated from the tank data by the method of Prohaska (1966), and

$C_f(Re)$ is the "flat plate" frictional resistance.

The difference between the measured resistance and the estimated frictional resistance is taken as the residuary resistance, D_r .

In addition to straight ahead tests with the vessel upright, a sailing vessel model needs to be tested with non-zero heel and yaw (leeway) angles with both resistance and side force measured. This greatly increases the number of tank runs required for a sailing vessel as compared to an engine-propelled vessel. In the author's experience, about 135 test combinations of speed, heel and leeway are required to fully quantify the hydrodynamic forces on a sailing vessel.

In conducting tank tests of vessels to be used for racing, accuracy and repeatability are of paramount importance. Section 2.2 describes the sensitivity of racing performance to small changes in resistance. Since total accuracy is impossible, a reasonable approach is to strive to limit measurement errors or lack of repeatability to 1% or less and to take special measures when one has to choose between designs whose predicted performances differ by less than the amount associated with a 1% change in resistance. For example, the scale model of each design can be tank tested at four separate times and the results then averaged together. This reduces the erroneous data variability by a factor of 2.

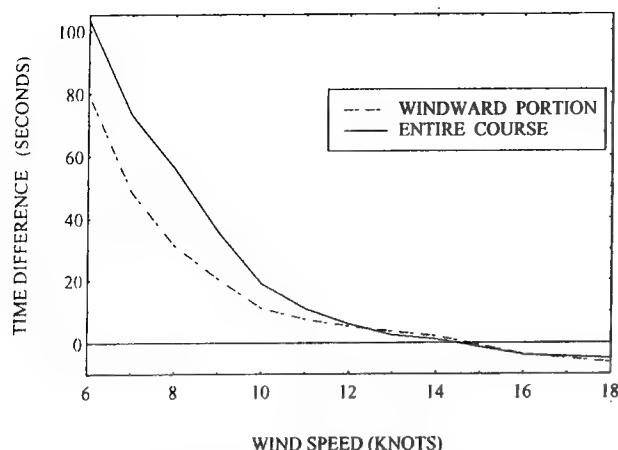


Figure 6: Performance Prediction Comparison Based on Two Test Sequences on the Same Yacht Model.

It is not easy to obtain this 1% level of accuracy and repeatability. Although state-of-the-art instrumentation can measure the forces, model orientations and speeds with the desired accuracy, variable fluid motions due to thermal stratification and from circulation patterns in many towing tanks can lead to errors larger than the set limit. It is common to "stir" tanks with several high speed runs generating breaking ship waves and then to wait until surface currents measured by small floats are sufficiently small before conducting a test sequence. Then, to make comparative results between similar designs as accurate as possible, the exact same test run sequence with the same timing of runs is used for all models. Nevertheless, the errors are still sometimes excessive. Figure 6 shows the difference in performance prediction from two separate model test sequences done several weeks apart on the same IACC yacht model in the same facility, using the aforementioned precautions and carefully calibrating all measurement instruments before the sequence and checking to be sure the calibrations are unchanged at the end of the sequence. The model waterline length is about 6 m, which is thought to be large enough. Yet, for this case errors in excess of the desired limit exist. Dr. Bruce Parsons (Private communications, 1995 and 1996) has told the author that the 1% repeatability error limit on forces is met by tests he conducts in a different facility. As yet, we do not know why a difference in repeatability of measured data exists in the different facilities.

6 Individual Components of Resistance

This section focuses on the components of resistance individually, with emphasis on numerical methods for estimating some of them. As was previously described, existing numerical methods are not physically complete enough for the sum of the resistance components to yield speed predictions which are precise on an absolute basis. However, numerical methods for some of the resistance components are useful for comparing design differences.

6.1 Hull Friction

Although hull friction is often the largest of the resistance components, it is the one that is least amenable to numerical hydrodynamics. Similarly, systematic experimental studies of the relationship between sailing vessel hull parameters and the friction drag coefficient have not been done, at least to this author's knowledge.

At the present state-of-the-art, a meaningful experimental program would be extensive and difficult. The essential difficulty in conducting experiments to relate hull friction drag to hull form parameters is determination of the friction drag in the experiments. It could be based either on flow measurements or force measurements.

The approach using flow measurements would be to examine the momentum flux in the central portion of the wake. A complication is that some of this momentum flux is associated with the ship waves and this needs to be subtracted from the total measured momentum flux. One possibility is to determine the wave field in the wake by a "wake cut analysis." Another is to compute the wave field numerically. This computation would not be precise because of limitations in the state-of-the-art for such computations and because the influence of the boundary layers on the ship-generated wave field is not known precisely. However, they might be good enough for this purpose. It is a possibility worth considering.

A similar problem exists if the friction drag is to be determined from force measurement. The wave-making drag would have to be subtracted from the measured drag. The aforementioned statements about determining the wavemaking drag from "wake cut height measurements" and from using numerical computation apply here too.

Without either a robust numerical tool or an experimental "data base" for friction drag, towing tank

experiments with the friction drag estimated by Prohaska's method is the state-of-the-art. This cannot estimate the friction drag precisely since it yields a coefficient that depends only on the Reynolds number whereas there are Froude number effects on the friction drag. Thus the error in the estimate gets mixed into the other resistance components which are all subject to Froude scaling, except for the appendage friction. This is one reason why tank test models must be large.

Development of numerical methods for calculating hull friction is currently being pursued as an area of research. Some RANS codes show promise and extension to free surface flows of the integral boundary layer equation method described subsequently for appendages is an exciting possibility.

6.2 Computation of Viscous Drag on Appendages

Appendages on a fin keeled sailing vessel include the keel fin and the rudder. There may also be a ballast bulb and the keel or the rudder, or both, might have winglets. One underwater profile showing such appendages is shown subsequently in Figure 15. The rudder and keel fin and optional winglets are typically high aspect ratio lifting surfaces so there is reason to examine their friction drag from the basis of two-dimensional section analysis. This will be discussed here, first for clean water. Then brief speculations about the influences of particulate matter and small gas bubbles in the ocean will be given.

The goal for numerical hydrodynamics of airfoil sections is prediction of lift, drag and moment coefficients for a prescribed angle of incidence and Reynolds number, which is based on the chord length for the sections. The problem involves a largely inviscid outer flow away from the immediate vicinity of the airfoil and boundary layers adjacent to it. For many years people tried to iterate between the inviscid and boundary layer solutions. The idea was to compute an inviscid flow, use its pressure gradients in solving the integral boundary layer equations, re-solve for the inviscid flow with the airfoil "thickened" by the displacement thickness of the boundary layer, including the viscous wake, re-solve the boundary layer equations, etc. This approach failed when the boundary layer thickened rapidly, even for very small amounts of flow separation close to the trailing edge.

Over the past several years, ingenious schemes for solving for the outer flow and the boundary layer

flow simultaneously and with tight coupling have been developed. They have been extraordinarily successful in providing predictions in close agreement with experiment. Examples are the developments of Eppler and Somers (1980) and Drela and Giles (1987) (see also Drela, 1989). These schemes contain a mix of mathematically precise panel methods and integral boundary layer equations, and empirical or semi-empirical relations that relate various boundary layer parameters.

An outline of a method similar to that of Drela (1989) is presented here. The only significant difference is that Drela cast the outer inviscid flow in terms of its stream function and the presentation here is the form used by W. Milewski (1996) in terms of the velocity potential continued onto the airfoil surface, ϕ , which is represented as:

$$\pi\phi = \int_{s_b} \left(G \frac{\partial\phi}{\partial n} - \phi \frac{\partial G}{\partial n} \right) ds - \int_{s_w} \Delta\phi_w \frac{\partial G}{\partial n} ds + \int_{(s_b+s_w)} \sigma G ds \quad (9)$$

where:

G is the two-dimensional Green Function, $\log r$,
 n is the normal into the airfoil surface,
 s_b is the path around the airfoil,
 s_w is the path along the centerline of the wake,
 $\Delta\phi_w$ is the jump in potential across the wake from top to bottom. It is constant along the entire wake, and

σ is a fictitious "transpiration" source strength distribution along the airfoil surface and wake that has to be determined so as to make the outer flow the same as the real boundary layer would cause.

The left hand side and first two integrals on the right hand side of equation 9 comprise the ordinary application of Green's theorem for inviscid lifting flows and the last integral simulates the effect of the boundary layer displacement thickness on the outer flow. The discretized form of equation 9 with the usual summation convention is:

$$\pi\phi_i = B_{ij} \left(\frac{\partial\phi}{\partial n} \right)_j - \phi_j A_{ij} - C_i \phi_N + C_i \phi_1 + B_{ij} \sigma_j \quad (10)$$

Here, the panels on the airfoil start with number 1 at the trailing edge on the bottom, go around the foil and end with number N at the trailing edge at the top. The C_i coefficients include the integral of $\frac{\partial G}{\partial n}$ over the entire wake. In this form, equation 10 is strictly valid only if the vector between control points 1 and N is orthogonal to the incident velocity

vector. Otherwise, $C_i \vec{U}_\infty \cdot \vec{r}_{tc}$ is subtracted from the left hand side since it contributes to $\Delta\phi_w$ (c.f. J. T. Lee, 1987).

The left hand side can be combined with the second, third and fourth terms on the right hand side to obtain:

$$A_{ij}\phi_j = B_{ij} \left(\frac{\partial\phi}{\partial n} \right)_j + B_{ij}\sigma_j \quad (11)$$

where:

$$A_{ij} = \pi\delta_{ij} + A_{ij} + (\delta_{jN} - \delta_{j1})C_i \quad (12)$$

and

$$\delta_{ij} = \begin{cases} 1 & \text{if } i = j \\ 0 & \text{otherwise.} \end{cases} \quad (13)$$

Multiplying all terms by A_{ij}^{-1} gives:

$$\phi_i = A_{ik}^{-1} B_{kj} \left(\frac{\partial\phi}{\partial n} \right)_j + A_{ik}^{-1} B_{kj}\sigma_j \quad (14)$$

The first term on the right hand side is the perturbation velocity potential for the inviscid flow around the airfoil, which will be called ϕ^{inv} . The second term is the contribution to the outer flow potential from the existence of the boundary layer as represented by the transpiration sources. Equation 14 is then written as:

$$\phi_i = \phi_i^{\text{inv}} + Q_{ij}\sigma_j \quad \text{where: } Q_{ij} \equiv A_{ik}^{-1} B_{kj} \quad (15)$$

The total potential, Φ , is the sum of the perturbation potential and the free stream potential, ϕ^{inf} ,

$$\Phi_i = \phi_i^{\text{inf}} + \phi_i^{\text{inv}} + Q_{ij}\sigma_j \quad (16)$$

The surface velocity, which corresponds to the tangential velocity at the outer edge of the boundary layer is called U^e , and is obtained as the derivative of the total potential with respect to the tangential coordinate, s .

$$U_i^e = U_i^{\text{inv}} + Q'_{ij}\sigma_j \quad (17)$$

$$\text{where: } Q' \equiv \frac{\partial Q}{\partial s} \quad \text{and} \quad U^{\text{inv}} \equiv \frac{\partial(\phi^{\text{inv}} + \phi^{\text{inf}})}{\partial s} \quad (18)$$

The mass defect in the boundary layer, M , is related to the displacement thickness, $\delta^* = \int (1 - u/U^e) d\eta$ (η is the coordinate normal to the surface) and the transpiration source strength by:

$$M = U_e \delta^* \quad \text{and} \quad \sigma = \frac{dM}{ds} \quad (19)$$

$$\text{In discretized form: } \sigma_j = \frac{M_{j+1} - M_j}{s_{j+1} - s_j} \quad (20)$$

By substituting equation 20 into equation 17 and collecting terms that multiply each element of mass defect, M_j , equations of the following form are obtained:

$$U_i^e = U_i^{\text{inv}} + D_{ij} M_j \quad (21)$$

$$\frac{dU_i^e}{dM_j} = D_{ij} \quad (22)$$

D is a known matrix. The objective is to find a solution for M and the other boundary layer parameters that satisfy the integral boundary layer equations:

$$\frac{d\theta}{ds} + (2 + H) \frac{\theta}{U^e} \frac{dU^e}{ds} - \frac{C_f}{2} = 0 \quad (23)$$

$$\theta \frac{dH^*}{ds} + H^*(1 - H) + H \frac{\theta}{U^e} \frac{dU^e}{ds} - 2C_D + H^* \frac{C_f}{2} = 0 \quad (24)$$

where:

$\theta \equiv \int (u/U^e)(1 - u/U^e) d\eta$ is the momentum thickness,

$H \equiv \delta^*/\theta$ is the shape parameter,

$C_f \equiv 2\tau_{\text{wall}}/[\rho(U^e)^2]$ is the skin friction coefficient,

$\theta^* \equiv \int (u/U^e)([1 - (u/U^e)^2] d\eta)$ is the kinetic energy thickness,

$H^* \equiv \theta^*/\theta$ is the kinetic energy shape parameter,

$C_D \equiv \int \tau(du/d\eta) d\eta/[\rho(U^e)^3]$, and

τ is the shear stress and u is the local velocity in the boundary layer.

In addition to equations (23, 24) a third equation is used. The third equation is an empirical one, based on correlations with boundary layer measurements, and is different for laminar and turbulent boundary layers. For the laminar case, the ratio of the amplitude of the most unstable Tolmein-Schlichting wave at any chordwise location to its ratio at the leading edge is expressed as $e^{\tilde{n}}$. The empirical equation is:

$$\frac{d\tilde{n}}{ds} - f_1(H, \theta) = 0 \quad (25)$$

where f_1 is an empirically determined function of H and θ . The user must specify either the location of the point of transition from laminar to turbulent flow or the value of n for which this occurs. In flows of clean fluids, the transition value of \tilde{n} depends on the turbulence level of the incoming stream. Mack (1977) gives this value as:

$$n = -(8.43 + 2.4 \log T_f) \quad (26)$$

where T_f is the ratio of the rms turbulence speed to the free stream speed.

For a turbulent boundary layer, an empirical equation for the spatial derivative of the maximum shear

stress coefficient, C_τ , in the following form is used:

$$\frac{d \log C_\tau}{ds} - f_2(c_\tau, H, H^*, \theta) = 0 \quad (27)$$

For any location on the airfoil, specification of θ , M , and U^e provides all the other boundary layer parameters in laminar flow through empirical and semi-empirical relations which can be found in Drela and Giles (1987). For a turbulent boundary layer, values of θ , M , C_τ and U^e are required to obtain all the other parameters (θ^* , δ , C_f , C_D).

The approach for a prescribed distribution of U^e , which is taken as the inviscid solution for a starting point, is to iteratively determine values for the "independent parameters", θ , M and C_τ (when needed), that solve equations 23, 24 and 27. Until the correct values for these quantities are obtained, the sum of the terms on the left hand sides of these equations will not equal zero. Newton's Method is used to iterate on the independent parameters. The crucial feature, that makes the whole scheme work, is that at each iteration the distribution of U^e along the entire airfoil is changed according to the iterative changes in the M_j 's and equation 22. Hence, as the boundary layer is altered toward correctness, iteration by iteration, the outer flow which generates the pressure distribution that drives the boundary layer is simultaneously altered toward correctness.

Figure 7 shows drag coefficient vs. lift coefficient for an airfoil section as calculated by this method using the program XFOIL (Drela, 1989) and as measured in the M.I.T. water tunnel. For the calculation, \tilde{n} was set to 3.5, which corresponds to the turbulence level of 0.7% which exists in the tunnel. Experimental forces were based on velocities around a large rectangle surrounding the section, measured with a laser doppler velocimeter, and applying the Bernoulli equation outside the wake and momentum conservation principles to the flow.

Figure 8 shows the airfoil section characteristics calculated by this method for two section shapes that could be used for the keel fin of a sailing vessel. One section has a thickness fraction of 0.13 and the other has a thickness fraction of 0.17. The calculation is done for $\tilde{n} = 9$ which corresponds to an incident stream with negligible turbulence. The figure indicates that for lift coefficients in excess of 0.33 the thicker section has less friction drag. The reason for this is that the thicker section is predicted to have more laminar flow.

Design experience runs counter to this result. A boat goes faster with a keel thickness fraction of 0.13 than with a thickness fraction of 0.17. If one reduces \tilde{n} to

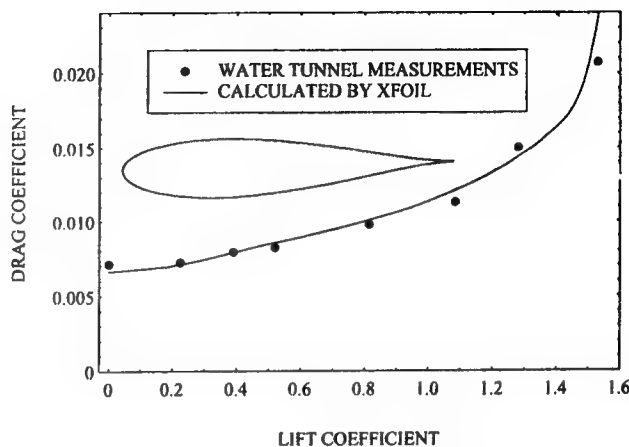


Figure 7: Calculated (line) and Measured Section Drag vs Lift Coefficients.

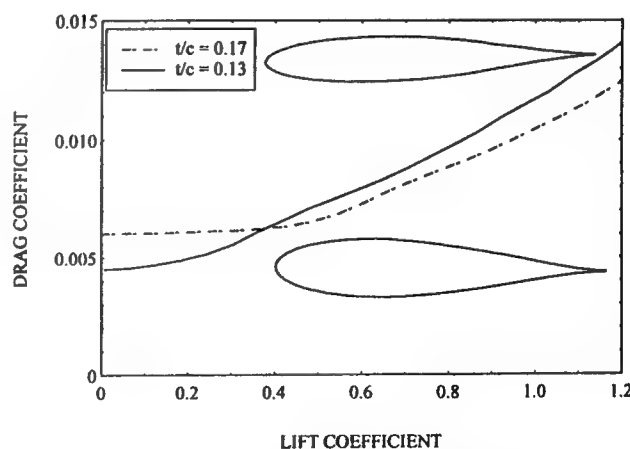


Figure 8: Section Characteristics for Two Airfoil Sections with a Clean, Low-Turbulence Inflow.

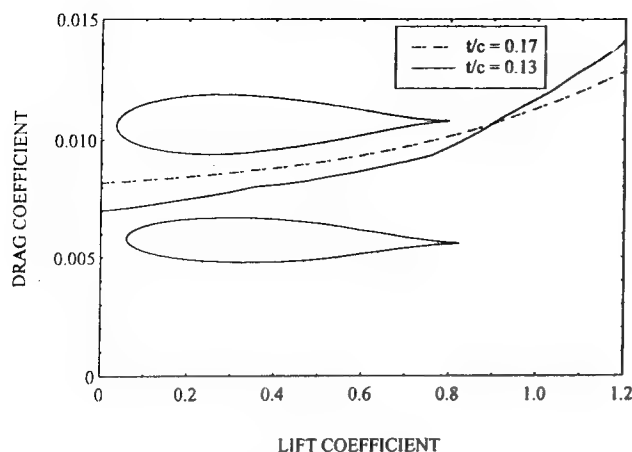


Figure 9: Section Characteristics for Two Airfoil Sections with Forced Suction Side Transition at 5% of the Chord.

3.5 which corresponds to a turbulence level of 0.7% (incoming rms turbulence of 3.5 cm/s with a boat speed of 5 m/s), the drag "crossover" occurs at a lift coefficient of 0.6, but we know that for a boat with a keel fin operating at this lift coefficient the thinner keel is still better.

The reason for the disparity between the computed results and sailing experience could be that the combination of free stream turbulence, particulate matter and small gas bubbles in ocean water near the surface cause transition near the leading edge on the suction side – no matter what the section shape (c.f. Lauchle and Gurney, 1984).

Figure 9 shows the airfoil characteristics with suction side transition set at a maximum downstream location of 5% of the chord. For this forced transition condition, the thinner section has less drag up to a lift coefficient of 0.88. This is consistent with design experience as operating lift coefficients are designed somewhat lower than 0.88. The combined effects of free stream turbulence and particulate matter in the flow is an area in need of further study.

Milewski (1996) has extended the approach of coupling the integral boundary layer equations to inviscid panel methods, as described above, to three dimensional problems. The method provides the tangential friction drag and the normal pressure drag individually. Figure 10 shows these drag coefficients (based on surface area) vs. Reynolds number, as calculated by Milewski, for a form that might be used as the ballast bulb on a sailing vessel, with forced transition at 5% of the bulb length. It is an NACA 0020 section rotated to form a body of revolution. Coincidentally, the friction drag coefficients are remarkably close to the ITTC friction "line".

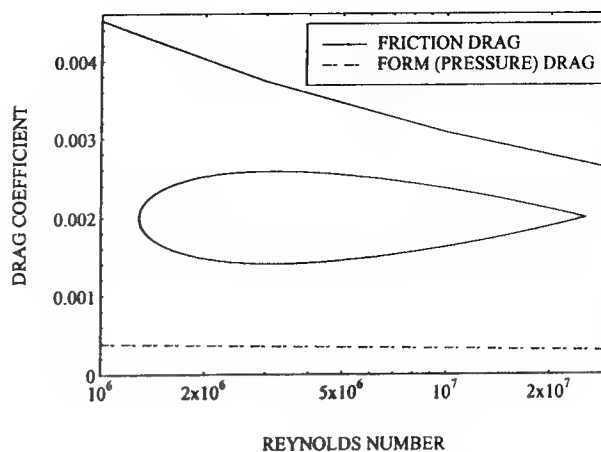


Figure 10: Drag Coefficient, Based on Bulb Area, for an Axisymmetric Ballast Bulb.

6.3 Residuary Resistance

The residuary resistance is the sum of the wavemaking resistance, interactions between resistance components that are not explicitly modeled, and errors in the presumed frictional resistance that get included in the residuary resistance by the resistance decomposition process. To the extent that these resistance components are influenced by the Reynolds number, errors in predicting full scale resistance from towing tank measurements are minimized by using large models. For example, with a one-third scale model of a 20 meter long vessel, if the frictional resistance is in error by 4% due to an error in estimated form factor, the full scale predicted resistance is in error by less than 1% at typical sailing speeds.

6.3.1 Numerical Methods

The most attractive possibility for the use of numerical hydrodynamics in minimizing residuary resistance is computation of the wavemaking resistance for differing hull geometries. As will be shown here, the state-of-the-art is not yet good enough to do this effectively in a design development program. However, it is getting better, and the routes to further improvements can be planned.

Although formal theoretical procedures for estimating wave resistance began almost 100 years ago with the thin ship theory of Michell (1898) and continued in several directions, including the slender ship theory of Tuck (1961), their level of accuracy did not approach one that could be considered for use in design until development of the method of Dawson (1977). . Whereas all the prior methods linearized the mathematical problem about the flat free sur-

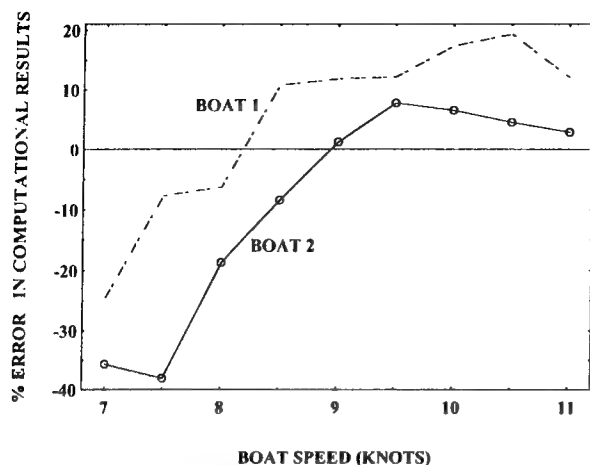


Figure 11: Percentage Error in the Wave Making Resistance Computed by Rosen et al.

face with a uniform stream, Dawson linearized the ship wave problem about the double-body flow which corresponds to the submerged portion of the ship beneath a rigid free surface. This basis flow contains many of the influences of the flow around the displacement form of the ship. Only the surface waves are left out and these are approximated as a linear perturbation on the double body flow. Both the basis double body flow and the perturbation wave flow are determined by a source or source and dipole based panel method using the Rankine source Green function.

Two notable extensions and applications of Dawson's method to sailing vessel hulls are those of Rosen et al. (1993) ; and of Nakos, Kring and Sclavounos (1993) (also described by Sclavounos, 1995). These approaches and their associated computer codes are the best we have today, but it will now be shown that they are not accurate enough to meet design requirements.

Figure 11 shows the percentage error in the numerical predictions of wave resistance in the upright condition for two different IACC hulls having identical appendages as measured from the figures in Rosen et al. (1993). The percentage error, $E\%$, is defined as:

$$E\% \equiv \frac{\text{computed wave res.} - \text{measured wave res.}}{\text{measured wave resistance}} \quad (28)$$

The difficulties in using numerical results in support of design are both absolute and relative. Absolute errors in wave resistance on the order $\pm 20\%$ correspond to time differences in sailing a 34.3 km windward-leeward course of ± 2 minutes, a huge amount in match racing terms.

Figure 11 shows a difference in wave resistance er-

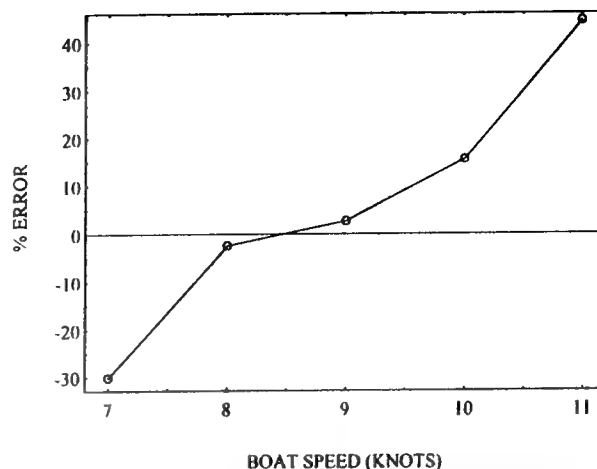


Figure 12: Percentage Error in the Wave Making Resistance of an IACC Yacht Computed by Sclavounos.

ror for the two designs of as much as 25%. Two caveats concerning these data need to be mentioned. The measured data were obtained by subtracting $(1 - k)C_{ITTC}$ from the measured total resistance coefficient, where C_{ITTC} is the ITTC friction coefficient. An error in estimating the form factor, k , could cause an overall vertical shift in each curve. That notwithstanding, the data cannot provide design-level confidence since correction by a constant shift of one curve still leave excessive error differences over the important speed range.

The second issue is that demands of their sponsoring organizations required that Rosen et al. omit scale numbers on the axes of their graphs for the case shown by dashed lines in Figure 11. This does not compromise the percentage errors since they are ratios. However, the location of each point on the abscissa is not precisely known. This author has assigned an abscissa scale on the basis of the wave resistance vs. speed characteristics for the type of vessel in question. It could be slightly in error, necessitating a slight shift or dilation in the abscissa location for the points on the dashed curve. However, this does not alter the conclusions about the results.

Figure 12 shows percentage wave resistance error vs boat speed for an IACC yacht as computed and presented by Sclavounos (1995). Again, the data here are scaled from a figure presented by Sclavounos and equation 28 is used.

Although the form and magnitude of the error is similar to the cases of Rosen, et al. there are a number of minor differences and one major one in the numerical methods which could be of importance when it comes to improving them. The approach of Sclavounos and his colleagues solves the initial value problem

in which the vessel is brought to speed from rest and the time domain computation is continued until the wave resistance becomes nearly steady. In this process, the surface elevation is computed at each time step. Due to the shallow slope profiles of the vessels under consideration, the wetted length changes throughout the computation. An artifice that is used is to stretch the vessel longitudinally at various time steps so the still water length matches the computed wetted length, followed by re-computing the double body basis flow. This was found to reduce the error between computation and measurements at the higher speed. Another artifice used by Sclavounos is to alter the boundary condition on some of the near-centerline free surface panels that border on the separation line of the stern underbody profile. Instead of using the usual kinematic free surface boundary condition on these panels, the condition of tangent separation was used inasmuch as this is what is observed on real vessels.

In spite of these special features in the numerical methods, they show considerable over-prediction of the wave resistance at high speed. Part of this in the Sclavounos method may be related to the fact that displacement is not preserved in the mathematical hull stretching process. It is well known to naval architects that wave resistance increases rapidly with displacement at high Froude numbers. Another potential source of the high speed error is the fact that the real flow and its forces are not a linear perturbation about the double body flow as is presumed in the computations.

6.3.2 Realities About the Resistance of Sailing Vessels

The progression of IACC sailing yachts whose design involved this author included those designated as USA 9 and USA 23. In nearly all conditions, the latter could sail a course of about 34 km two or more minutes faster than the former. Figure 13 shows the upright resistance drag areas determined by expanding towing tank test data to full scale. For all boat speeds less than 11.5 knots, the slower USA 9 is shown to have slightly less resistance. The total upright resistances predicted from model scale towing tank test data are very nearly equal for these two designs whose actual performances are quite different. The reasons for the difference in performance involve some smaller factors and one larger one. In this instance, the smaller ones include differences in heel stability and in the added resistance from sea waves. However, the largest difference involves the

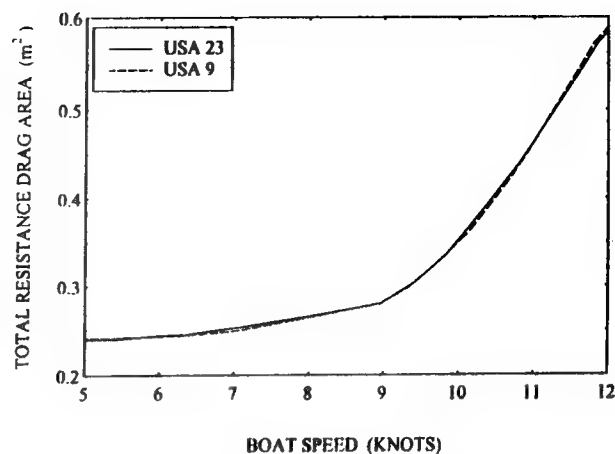


Figure 13: Total Upright Resistance Drag Areas for two IACC Yachts Predicted from Towing Tank Model Test Data.

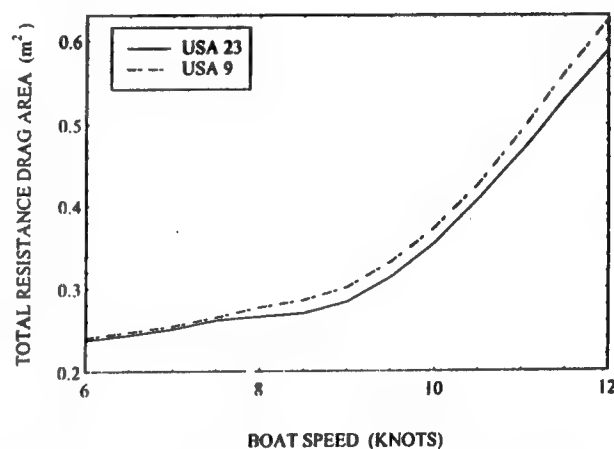


Figure 14: Total Resistance Drag Areas for Two IACC Yachts with a Heel Angle of 20 Degrees as Predicted from Towing Tank Model Test Data.

relative calm water resistances when the vessels are heeled. Figure 14 shows the drag areas vs speed, as determined from the tank tests, for the same two designs at a heel angle of 20 degrees and zero side force. Differences in resistance up to 4% are seen and the design with superior performance is the one with lower resistance. Of course, in actual sailing there would be non-zero side forces when the heel angle is 20 degrees, but the zero side force cases are shown here to show the effects of heel most clearly.

It is not at all uncommon for sailing vessels of differing performance potential to have similar upright resistances, but significantly different resistances when heeled. This fact is well appreciated by many yacht designers, but is often given insufficient consideration by marine hydrodynamicists and those naval architects that do not work with vessels that oper-

ate in the heeled condition. For example, most of the numerical predictions which have been made for sailing vessels are for the upright condition.

6.3.3 The Future for Numerical Evaluation of Residuary Resistance in Support of Design

Results from both towing tank and numerical experiments indicate a route that may lead to numerical methods for residuary resistance that can have greatly increased utility in the design process. First of all, present methods must be extended to the case of heeled vessels. This is a straightforward extension.

It is known that the increase in wetted length with increasing speed for sailing vessel forms with shallow slope overhangs must be accounted for. As described above, present day computations are done by solving the startup problem and waiting for a steady state to occur, with artificial adjustments to the hull shape at each time step. The natural extension is to do the startup problem for the fully nonlinear case, although there are complications. For example, the free surface panels will no longer lie in the still water plane and their locations will be time-dependent. At each time step, the computed wetted shape would be used instead of the artificial stretching. Thus, programs will be more complicated and require more computer resources. Convergence studies will necessarily be more complicated. However, there does not appear to be any major roadblock that would stop extension of the time domain panel methods for wave resistance to the nonlinear case.

Section 6.2 describes the ongoing work related to coupling inviscid panel methods with the integral boundary layer equations for determining forces on three-dimensional objects in the absence of a free surface. This method might be able to be coupled with future wave resistance calculations so as to get the frictional resistance and frictional-wavemaking interactions at the same time.

6.4 Induced Drag of the Hull and its Appendages

The form of resistance decomposition shown in equation 3 is chosen, in part, for convenience. The first three terms provide the calm water resistance in the upright condition, the fourth is the change due to the vessel operating at non-zero heel and leeway (yaw) angles and the fifth adds the resistance increase due to the presence of sea waves. The focus of this section

is the use of theoretical and numerical methods for estimating a portion of the differences in the fourth term, the resistance increase due to heel and leeway, for different designs.

The portion under consideration here is the induced drag associated with the production of side or heel force. The induced drag occurs because the circulation around all side force-producing portions of the hull and appendages induces changes in the flow direction everywhere and the local lift is perpendicular to the induced flow direction. The induced flow is in exact analogy to the downwash of an airplane which is responsible for its induced drag.

The sailing vessel designer has a great deal of control over the induced drag because it is influenced in a minor way by variations in hull shape, and in major ways by variations in the appendages. These include keel fins, rudders, keel ballast bulbs and transverse winglets on keels, rudders or both.

In theory, the induced drag of a lift (heel force) producing object is very nearly proportional to the square of the lift for flows in the absence of a free surface. However, towing tank tests show that the actual induced drag vs. lift² function of a sailing vessel differs from the theoretical one based on no free surface, both in its mean slope and in its linearity. Examples can be found in Greeley and Cross-Whiter (1989). The disparity is certainly related to free surface effects, although it is likely that some nonlinearity is due to the leeway-dependent location of the aft stagnation zone on the heeled hull.

Completely numerical determination of induced drag for use in speed prediction at the required level of accuracy for racing vessels is beyond the state-of-the-art. It awaits development of robust numerical methods that accurately solve for the heeled and yawed entire vessel, including both the boundary layers and the largely inviscid outer flow. However, there is good reason to believe that presently available numerical hydrodynamics can evaluate the difference in induced drag between identical canoe-body hulls with different appendages. The approach used is to solve for the inviscid flow about the heeled and yawed wetted portions beneath a rigid free surface. In practice, this is done by solving for the double body flow in an infinite fluid. Reasons justifying this approach include:

- The free surface effects on the side force and induced drag are strongest on the canoe body. With the same canoe body used in comparisons, the *difference* in these effects due to appendage variations should be small.

- Most of the hull-induced flow variations on the appendages are due to the hull displacement effects, which are captured in the rigid free surface problem. The ship wave flow effects on the appendages, which are not included in the rigid free surface problem, are very nearly the same when only the appendages are varied so that they have little effect on the *differences* between appendage forces.

Two effective methods are in general use for calculating the heel force (lift) and induced drag for double body problem: the Boundary Integral Equation Method (BIEM), often called a potential panel method, and the vortex lattice method.

The Boundary Integral Equation Method is based on the usual application of Green's theorem leading to the integral equation:

$$\begin{aligned}
 -2\pi\phi(\mathbf{x}) = & \int \int_{S_b} \left(\phi(\mathbf{x}') \frac{\partial G(\mathbf{x}, \mathbf{x}')}{\partial n'} + G(\mathbf{x}, \mathbf{x}') \vec{V} \cdot \vec{n}' \right) dS' \\
 & + \int \int_{S_w} \Delta\phi(\mathbf{x}') \frac{\partial G(\mathbf{x}, \mathbf{x}')}{\partial n'} dS'
 \end{aligned} \quad (29)$$

where:

ϕ is the disturbance velocity potential caused by the body,

S is the surface of the body and its vortex (equivalently dipole) wake,

\vec{V} is an onset flow velocity vector,

\mathbf{x} and \mathbf{x}' represent 3-d locations of field and source points, respectively, and all points lie on the body or on the wake,

G is the Rankine source Green function, $1/|\mathbf{x} - \mathbf{x}'|$, subscript S_b refers to an integral over the body with normal into the body, and

subscript S_w refers to an integral over the wake on which the potential jump from side 1 to side 2 is $\Delta\phi$, and the normal to the wake is in the direction from side 2 to side 1.

Discretization of the integral equation 29 leads to the set of linear algebraic equations that is the panel method. In formulating it, the jump in velocity potential across any vortex/dipole wake streamline has to be set equal to the jump in velocity potential at the position on the trailing edge of the body from which the streamline originates (c.f. Lee, 1987). Initially, the position of the wake sheet is unknown, and needs to be determined for maximum accuracy. This is done by iteratively solving the integral equation

and tracing wake streamlines.

The vortex lattice method, as originally developed by Greeley and Cross-Whiter (1989), is a simplification of the panel method. It requires simpler program input data and provides much faster computation. Its origins actually stem from the lifting body panel method first developed by Hess (1972). That approach was to use both surface source and surface dipole panels, as indicated in equation 29, on lifting surfaces such as aircraft wings and tails, but only source panels on fuselages, which are boat canoe bodies and keel bulbs here. To properly model the circulation at the lifting surface roots it was carried into the fuselage to the centerline. If the sum of the body-entering circulations was not zero, the difference was modeled as a centerline vortex that exited the trailing tip of the fuselage.

The simplified vortex lattice method starts with the Hess model, but represents the lifting surfaces as their centerplane distributions of sources and vortex lattices (or, equivalently, dipole panels). In the development of Greeley and Cross-Whiter, hull canoe bodies and keel bulbs have surface source distributions, whereas rudders, keel fins and winglets have centerplane distributions of sources and vortex lattices, with the root circulations of the latter extended into hulls and bulbs as necessary.

Both Greeley and Cross-Whiter (1989) and Ramsey (1996) have done extensive comparisons between the results of panel methods and vortex lattice methods. The only difference in computed forces is that the vortex lattice method gives slightly less lift because the increase in lift slope of a wing due to its thickness is not included in the vortex lattice method. However, the ratio of the induced drag coefficient to the square of the lift coefficient is the same for both methods and that is the quantity which measures the induced drag efficiency of a lift-producing three-dimensional object.

Now, two examples of the use of the vortex lattice code in support of design are given. Figure 15 is a drawing of the submerged portion of an IACC yacht at a heel angle of 20 degrees. It is customary to adjust the fore and aft location of the rig (sails) such that the rudder carries about 20% of the heel force exerted by the sails. This corresponds to rudder angles of about 1 degree in light winds and 3 degrees in strong winds. This amount of rudder loading, sometimes called "pressure", is common on many kinds of sailing vessels. Since rudders are designed to be underbalanced about their stocks, if there is "helm pressure" the boat turns to windward when the helmsman eases off on his steering force. Sailors

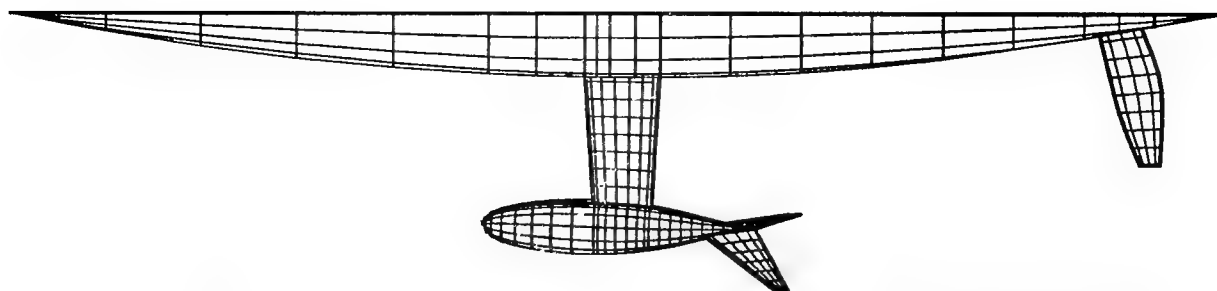


Figure 15: Submerged Portion of an IACC Racing Yacht. It is shown at a heel angle of 20 degrees.

have come to like and expect this behavior. The particular vessel geometry under consideration here is significantly more efficient at generating heel (side) force on the keel fin than on the rudder. Because the keel is not only deeper, but also has winglets, less induced drag occurs when a prescribed side force is generated on the keel than on the rudder. In fact, use of a vortex lattice code has shown that minimum induced drag occurs when the rudder side force is very nearly zero. For typical sailing conditions, the numerical computation predicts the induced drag to be reduced by 8% when the rudder side force is reduced from 20% of the total to zero and the keel side force increased accordingly. Figure 16 shows the time gained vs. wind speed when sailing a 34.4 km windward leeward course due to an 8% reduction in induced drag as determined by a VPP. All of these gains, except for a fraction of a second, occur on the 17.2 km windward portion of the course. These time gains correspond to distance gains of about 7 boat lengths in light wind and 4 boat lengths in strong wind. By top level racing standards, it is substantial. There are further design considerations in this result. In particular, the rudder design needs to be considerably different if the crew learns to sail the boat with minimum rudder force than if the crew chooses a heavily loaded rudder. In the former case, the rudder needs to be as small as possible, even to the extent of requiring dynamic sail trim variations to help steer the boat. The unloaded small rudder simultaneously minimizes the induced drag and the frictional drag of the rudder. On the other hand, if the rudder is heavily loaded there is incentive to make it as deep as possible so as to minimize the extra induced drag. However, to achieve an acceptably low rudder wetted surface with a deep rudder, it must have short chords which leads to small thickness for acceptable thickness fractions. This inevitably results in structural considerations dictating how deep and narrow the rudder can be. It must have sufficient strength and it must be stiff enough to prevent excessive bending, particularly when dy-

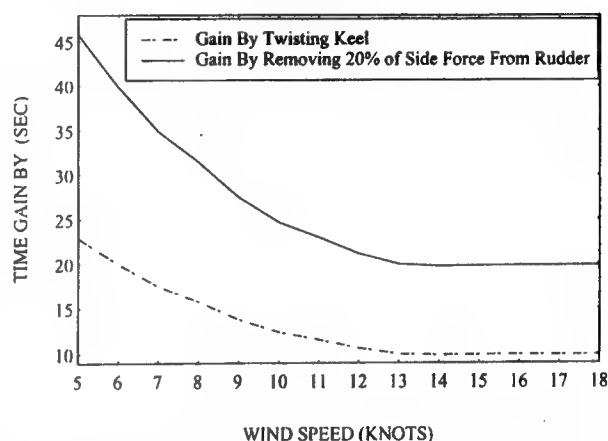


Figure 16: Time Gained when Sailing a 34.4 km to Windward - Leeward Course. Solid line is for moving 20% of the total force off the rudder. Dashed line is for 3 degrees of keel fin twist.

namic wave forces result in substantial time-varying changes in rudder forces.

As a second example, the effect of a 3 degree twist of the keel fin is considered. The twist direction has the trailing edge moving to leeward and the leading edge to windward. The twist varies linearly with depth such that it is zero at the root and 3 degrees at the lower tip. Such a twist can be accomplished either by mechanical control or by arranging the center of gravity of the ballast bulb aft of the structural shear center of the keel fin. The reason why such a twist may be beneficial is that for a keel configuration with winglets as shown, the vertical circulation distribution on the fin for minimum induced drag is nearly uniform. However, a structurally sound keel fin can be substantially smaller at the tip (bottom) than at the root (top) since the bending moment with the boat heeled is much smaller at the bottom. Making the keel small at the bottom, to the extent permitted by structural considerations, minimizes the friction drag due to reduced wetted surface, but increases the induced drag unless some other means is used

to increase circulation at the bottom. Twist accomplishes this.

Use of a vortex lattice computer code has shown that the twisted configuration has 96% of the induced drag of the untwisted configuration. The reduction in time to sail the 34.4 km course with this reduction in induced drag is shown in Figure 16.

6.5 Added Resistance Due to Sea Waves

Speed reduction of ships by sea waves from ahead is hydrodynamically very complicated, involving all the nonlinearities related to breaking waves, ship slamming, large relative motions between the ship and the water, and more. The present state-of-the-art for applying numerical hydrodynamics to this problem does not account for these large motion and wave breaking effects. Rather, the numerical method for added resistance is at the lowest contributing order in wave amplitude. This is order two with the added resistance due to a wave being proportional to the square of its amplitude. The approach used is to determine the added resistance for sinusoidal waves individually and to combine the contributions from all the waves. In spite of the low order of the numerical approximation, it provides helpful results which must be included in the total resistance for predicted boat speeds to be in reasonable correspondence with actual sailing speeds. Although the detailed accuracy is not as good as we would like, the difficulty and high cost of meaningful added resistance experiments more or less forces one to take the numerical approach and do it as well as possible.

The *added resistance operator*, $\mathcal{A}(\omega, \psi)$ is the ratio of the added resistance to the square of the amplitude of a wave of circular frequency ω and angle ψ . ψ is 0 for stern seas and 180 degrees for head seas. For a long crested (two-dimensional) sea approximation, the mean added resistance, D_w for a sea wave spectrum $S(\omega)$ with wave angle ψ is:

$$D_w = 2 \int_0^\infty \mathcal{A}(\omega, \psi) S(\omega) d\omega, \quad (30)$$

The role of numerical hydrodynamics is the determination of $\mathcal{A}(\omega, \psi)$. Until quite recently, the procedure of Gerritsma and Beukelman (1972) gave the best agreement between computation and experiment. This procedure uses "strip theory" to estimate the added resistance from the rate of energy imparted to radiated waves caused by relative vertical motions between the ship and the water. Part of

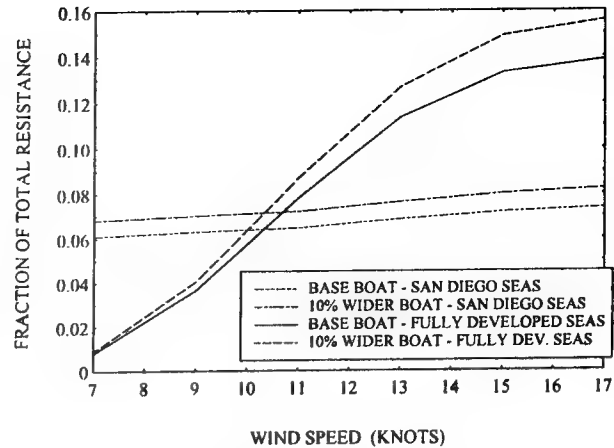


Figure 17: Added Resistances of two IACC Designs in Two Sets of Sea Conditions.

the contribution to added resistance from sea wave diffraction by the ship is neglected in the procedure.

Recent advances have led to the calculation of the added resistance with panel methods, as exemplified in the works of Sclavounos and Nakos (1993) and Sclavounos (1995). As in the aforementioned wave resistance computations by the same people, the linearized free surface problem about the double body basis flow is determined. This is a more accurate approach than earlier procedures and provides a more representative treatment of the effects of diffracted waves. It is, however, still limited to the second order effects. Sclavounos has reported (private communication) that theoretical results were brought into improved agreement with model scale measurements when the vessel length was "stretched" to the wetted length associated with the steady flow.

Figure 17 shows the added resistance computed by the panel methods and equation 30 for two IACC yachts. One is a "base boat" and the other has the waterline beams increased by 10% and the canoe body depth decreased by 10% so as to maintain displacement. This pair of shapes is chosen for demonstration here because for fixed displacement and length, beam is the dominant parameter for variations in numerically-determined added resistance. In the figure, the added resistance is shown as a fraction of the total resistance of the base boat sailing to windward as determined through a velocity prediction program.

Computational results are provided in Figure 17 for two sets of wave spectra. The fully developed seas are for Pierson Moskowitz Spectra, S_{PM} , at the indicated wind speeds. The San Diego Seas have spectra S_{SD} which are empirical curve fits to spectra that were measured over the wind speed range in waters

off San Diego, California in 1991. These spectra are given by:

$$S_{PM}(\omega) = 0.081 \frac{g^2}{\omega^5} \exp \left[-0.74 \left(\frac{g}{U_w \omega} \right)^4 \right] \quad (31)$$

$$S_{SD}(\omega) = 0.0563 \frac{U_w}{g} / [1 + (1.59\omega - 1.8)^2] \quad (32)$$

where: g is the acceleration of gravity, U_w is the wind speed at a height of 10 meters and the numerical value of the circular frequency ω is used in the last factor of the curve fit equation 32.

Several important conclusions can be drawn from the information in the figure. They are:

1. The added resistance in typical sea conditions is large enough that it must be included in speed prediction procedures if they are to be accurate.
2. Using the correct sea spectrum is important in estimating added resistance. The San Diego spectra differ from fully developed spectra in two ways. First, in light winds the waves are larger than the winds would indicate because waves propagate into the region from other areas. Second, in the heavier winds the seas are generally smaller than fully developed seas because the heavy winds do not last long enough for the seas to become fully developed.
3. Except for the fully developed seas in heavier winds, the difference in computed added resistance is less than observed performance differences in disparate designs. Experience shows that the wider boat suffers in waves by considerably more than the 1% of total resistance indicated in the figure. The author believes this disagreement is mainly due to lack of incorporation of nonlinear effects in present numerical methods.

6.6 Mean Forward Thrust Due to Unsteady Motions

An intriguing subject is the potential for dynamic thrust, which is a mean forward thrust due to the flow on appendages associated with unsteady vessel motions and sea waves. On traditional vessels this thrust is very small, and therefore it has not received much attention in the history of sailing vessel hydrodynamics. However, the dynamic thrust can be larger on the nearly horizontal keel and rudder

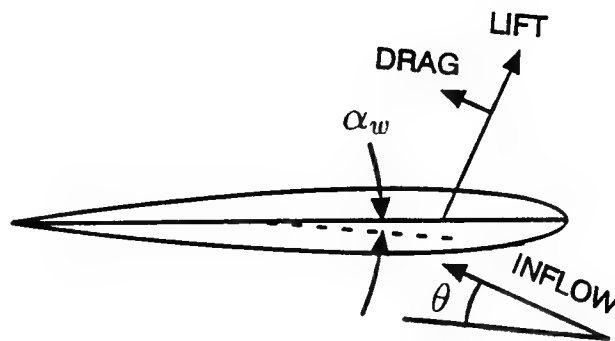


Figure 18: Forces on a Wing Section at an angle of Attack.

winglets which have been used recently on some vessels. Before explaining a mathematical method for relating dynamic thrust to design parameters, a general description of its origins is provided.

As is sketched in Figure 18, the lift on an air or hydrofoil is perpendicular to the incident flow and the drag is parallel to it. For explanatory purposes here, foils with symmetrical thickness forms are considered. Lift occurs when the inflow has an angle of attack, $\alpha_w + \theta$, with respect to the nose-tail line of the foil and a component of this lift force is forward when $\alpha_w \neq 0$. The inflow angle of attack on horizontal appendages occurs when there is a relative vertical velocity due to vessel motions or vertical components of the "orbital velocities" of the sea waves. As shown in the figure, there is a net forward force if $\text{Lift} \times \sin(|\alpha_w|) > \text{Drag} \times \cos(\alpha_w)$. Importantly, this net forward force occurs if α_w is either positive or negative. As the vessel undergoes unsteady motions in waves, the inflow angle to a horizontal appendage oscillates between upward and downward. The lift vector direction can be mainly up or down, but it almost always has a forward component. If the average of this forward component exceeds the average of the aft component of the drag, positive average thrust occurs. Otherwise, there is net drag.

The dynamic thrust can be quantitatively estimated by the use of lifting line theory, largely because horizontal appendages that are efficient at its generation necessarily have large aspect ratios. For relative motions of frequency f_e with boat speed V_b and appendage dimensions of order ℓ , the thrust-producing effects have reduced frequencies, $f_e \ell / V_b$, which are low enough for quasi-steady lifting line or lifting surface theory to be accurate. Ship hydrodynamicists came to this conclusion on the general bases of unsteady hydrodynamics and dimensional analysis over six years ago, and more recently Dr. Spiros Kinnas (private communication) has shown this to be the

case in a computation using fully unsteady lifting surface theory. The quasi-steady lifting line analysis is used here.

In this approximate analysis, the yaw motions of the vessel are neglected since they are strongly influenced, and often minimized, by the way the vessel is steered. In addition, the dynamic thrust on generally vertical appendages, such as a keel fin or a rudder are not considered. Just the dynamic thrust on horizontal appendages such as a rudder wing or keel winglets is analyzed. The effects of spanwise flow are neglected.

The relative angle of incidence on the wing is $\alpha_w + \theta \cos \varphi$, where θ is the pitch angle of the boat and φ is the, presumed steady, heel angle. The lift coefficient, C_L , is given by:

$$C_L = 2\pi\kappa(\alpha_w + \theta \cos \varphi) \quad (33)$$

Ignoring a small increase due to thickness of the wing, the lift slope factor, κ (c.f. Glauert, 1959 and Thwaites, 1960), is given by:

$$\kappa = \frac{R_A \cos \chi}{2 + R_A} \quad (34)$$

where R_A is the aspect ratio and χ is the sweep angle of the wing.

Using the approximation of an elliptical spanwise circulation distribution, the induced drag coefficient, C_{Di} , is:

$$C_{Di} = \frac{1}{\pi R_A} C_L^2 \quad (35)$$

Thus, the forward thrust, T , to lowest order in α_w and temporarily neglecting viscous effects, is:

$$T = \frac{1}{2} \rho V_b^2 A_p \cdot [2\pi\kappa\alpha_w(\alpha_w + \theta \cos \varphi) - \kappa^2 \pi \beta (\alpha_w + \theta \cos \varphi)^2] \quad (36)$$

where A_p is the planform area of the wing and $\beta \equiv 4/R_A$.

The angle of incidence, to lowest order, is given by:

$$\alpha_w = \frac{w}{V_b} \cos \varphi \quad (37)$$

where w is the relative vertical velocity at the fore and aft location of the wing. It is the difference between the vertical component of the sea wave orbital velocity and the heave velocity of the boat at the wing location. Since the boat is both heaving and pitching, w depends not only on time, but also on the fore and aft location of the wing. Denoting statistical (or time) averages by overbars, taking the average of

equation 36 and using equation 37 provides the fundamental equation for the dynamic thrust, T_d .

$$T_d = \frac{\pi}{2} \rho V_b^2 A_p \kappa \cos^2 \varphi \cdot \left(\frac{2 - \kappa\beta}{V_b^2} \overline{w^2} + \frac{2 - 2\kappa\beta}{V_b^2} \overline{w\theta} - \kappa\beta \overline{\theta^2} \right) \quad (38)$$

The ship motions are approximated as being linearly dependent on the sea state with complex transfer functions (frequency responses) from sea wave elevation to heave of $H_{\zeta w}(\omega_e)$ and to pitch of $H_{\zeta \theta}(\omega_e)$. In practice, these transfer functions are determined numerically from strip theory (c.f. Salvesen et al., 1970) or from a panel method (c.f. Nakos and Sclavounos, 1990). Then, for a one sided sea wave encounter frequency spectrum $S(\omega_e)$:

$$\overline{w^2} = \int_0^\infty |H_{\zeta w}(\omega_e)|^2 S(\omega_e) d\omega_e \quad (39)$$

$$\overline{\theta^2} = \int_0^\infty |H_{\zeta \theta}(\omega_e)|^2 S(\omega_e) d\omega_e \quad (40)$$

$$\overline{w\theta} = \int_0^\infty \text{Re}[H_{\zeta w}^*(\omega_e) H_{\zeta \theta}(\omega_e)] S(\omega_e) d\omega_e \quad (41)$$

Equation 38 is the fundamental equation for dynamic thrust and can be used when the viscous and parasitic drag of the thrust-producing wing are accounted for in the appendage friction drag. This procedure is appropriate for performance prediction of a design with keel winglets whose principal purpose is reduction of induced drag, but which can also produce dynamic thrust.

For force comparisons of various designs of wings whose principal purpose is to generate dynamic thrust, or to decide whether to use such a wing at all, it is useful to consider the difference of the dynamic thrust and the friction and parasitic drags of the wing.

Here, an example is provided for a rudder wing located at a depth of 3 meters and 8 meters aft of midship on an IACC yacht. The wing area is 1 square meter. It has an aspect ratio of 9, a taper ratio (tip chord / root chord) of 1/2 and a sweep angle of 25 degrees. The wing has an NACA 0012 section and its friction drag coefficient is approximated from XFOIL (Drela, 1989) results at a Reynolds number of 1.5 million as $0.008 + 0.164 \alpha^2$, where the relative angle of incidence, α , has units of radians. The angle of incidence used in the friction drag calculation is the rms relative incidence angle which is determined

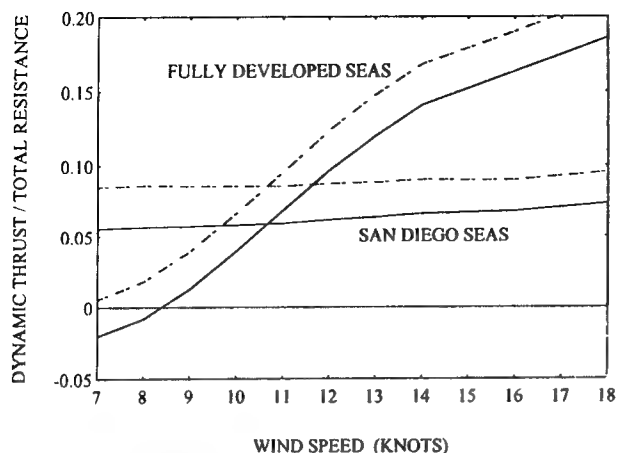


Figure 19: Dynamic Thrust from a Rudder Wing for Windward Sailing. The dynamic thrusts are shown by dashed lines and the dynamic thrusts minus the friction and interference drags are shown by solid lines.

in terms of the quantities used in this section as:

$$\overline{\alpha^2} = \left(\frac{1}{V_b^2} \overline{w^2} + \frac{2}{V_b} \overline{w\theta} + \overline{\theta^2} \right) \cos^2 \varphi \quad (42)$$

The interference drag area, A_I , between the wing and the rudder is taken as that given by Hoerner (1965) for strut junctions:

$$A_I = t^2 \left[17 \left(\frac{t}{c} \right)^2 - 0.05 \right] \quad (43)$$

where t is the thickness and c is the chord length at the root intersection.

Figure 19 shows both the dynamic thrust and the difference between the dynamic thrust and the sum of the friction and interference drags for upwind sailing in fully developed seas with spectra given by equation 31, and for San Diego seas with spectra given by equation 32. The angle between the seas and the course of the boat is taken as 142 degrees (38 degrees from ahead) for the calculations.

The dynamic thrust is greatly diminished by reducing the wing aspect ratio. Figure 20 shows the dynamic thrust less the friction and interference drags in fully developed seas for a wind speed of 9 knots, both upwind and downwind, as functions of aspect ratio. All other quantities are the same as in the preceding example except the taper ratios are 2/3 and the wave angle for the downwind case is taken as 30 degrees from astern.

Findings from numerical studies of a broad range of wing parameters include:

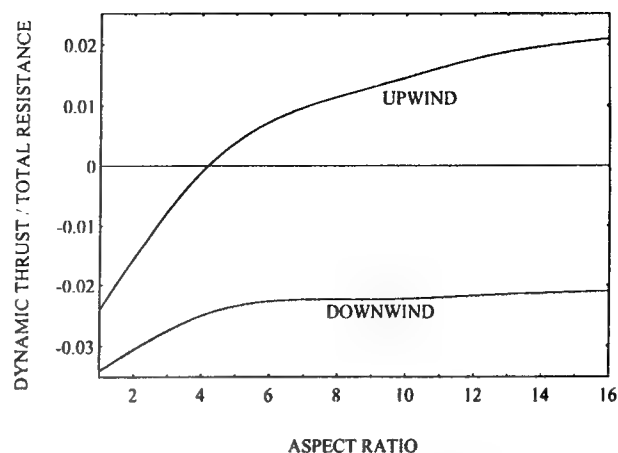


Figure 20: Dynamic Thrusts, Upwind and Downwind, in Fully Developed Seas for a Wind Speed of 9 Knots as Functions of Wing Aspect Ratio.

1. Dynamic thrust, exclusive of friction and interference drag, is positive and significant for upwind sailing, and is generally so small as to be insignificant for downwind sailing.
2. Dynamic thrust less the friction and interference drag of a wing is negative for downwind and upwind sailing in light winds. As the wind strength and the corresponding seas increase, the net thrust becomes positive for upwind sailing in medium winds if the aspect ratio is high, roughly 7 or higher. The net downwind thrust is positive only in strong winds and then of small magnitude.
3. Both the upwind and the downwind net thrusts increase as the wing is moved further aft as a result of the relative phases between heave and pitch. The effect is nearly insignificant for downwind sailing, but can be quite influential for upwind sailing.

The foregoing information refers to numerical calculations according to the method described. Actual sailing experience is somewhat different. In particular, the predicted upwind advantage and the predicted downwind disadvantage of wings are not realized. Rather, the upwind speed gain is generally less than predicted and the downwind speed loss is often much less than predicted. The reasons for this are not well understood at this time. It is an area of interest for further study.

7 Computation of Lift and Induced Drag of Sails

Numerical methods for calculating the lift and induced drag of sails have similarities with the vortex lattice method used for the induced drag and heel force of hull appendage combinations that is described in section 6.4. The essential differences are:

- The sails are thin, unsymmetrical lifting surfaces. This makes their representation by dipole or vortex sheets complete for the inviscid problem.
- The inflow speed varies with height in the atmospheric boundary layer. Although the height varying inflow is used in older methods as well as the one used here, all of these methods neglect the influence of spanwise flow on the inflow velocities. Both calculations and measurements show that most of the spanwise flow has speeds that are small in comparison to the inflow speeds so that the error is similarly small due to the mild gradient of the wind speed over most of the sailplan.

The application of lifting surface theory to sails began with the author's work 28 years ago (Milgram, 1968). The sails were represented by vortex lattices and the wakes were flat. The lower boundary beneath the sails was approximated as a flat plane by numerical use of image sails beneath the plane. The plane was at a user-specified location between locations of the water surface and the deck. The procedure was aimed at the design problem for which the pressure distributions were specified and the shapes needed to attain them were computed. For the next 20 years, a number of proprietary programs were developed for the sailmaking industry. It is thought they use the same principles, but also include the analysis problem for which the shapes are specified and the resulting pressure distributions and integrated lift and induced drag forces are computed.

The next significant advancement in the fluid dynamics was the work of Greeley, et al. (1989). They solved the analysis problem iteratively with the vortex wakes of the sails convected along the horizontal components of streamlines at each step. In addition, the sails and their images were heeled with respect to the image plane. The resulting computer program has been broadly used to evaluate lift and induced drag of sail shapes.

Optimized sail design requires use of both design and analysis programs. When the sails are a mainsail and

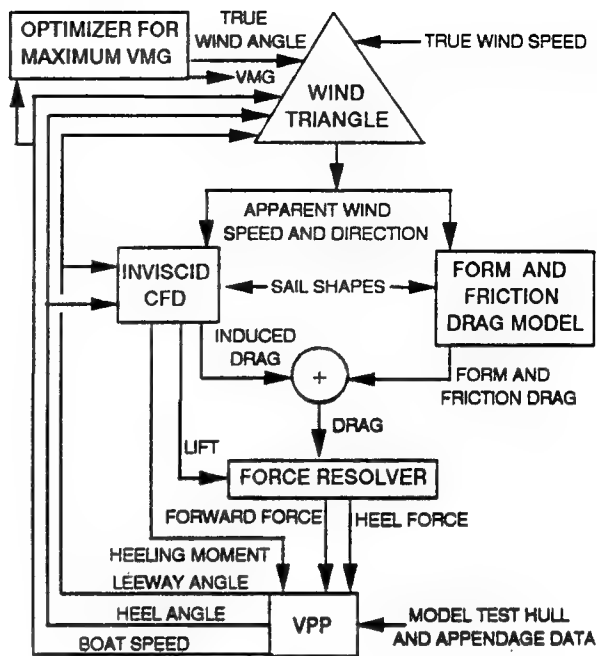


Figure 21: Method of Evaluation of Sail Shape on Performance.

a jib which does not go the full height of the mainsail, computed shapes for ideal pressure distributions are ones which cannot be built. The induced flow on the mainsail due to the jib and its wake is to windward below the top of the jib and to leeward above it. The shape of a mainsail that can accommodate this jib-induced flow variation and also have an ideal pressure distribution is generally complex and cannot be achieved with sail fabric that cannot support compression. Hence, results of the design programs can be used to guide the shapes of sails, but generally their designed shapes cannot be attained exactly. The analysis program can then be used to evaluate lift and induced drag on "the designer's approaches" toward the ideal shapes.

The best use of an inviscid sail analysis program is for comparing performance of candidate designs. In order to do that, the form and friction drag of the sails must be included and the resulting total sail forces used in a VPP. For windward sailing, which is the condition for which the process is most useful, the operational true wind angle, ψ , must be optimized in the VPP such that the speed made good to windward, $VMG = V_b \cos \psi$, is maximized. Since the sail forces depend on ψ , or more precisely on the apparent wind angle, the process is necessarily iterative. Figure 21 is a block diagram of this process as developed by Mr. Jack Kleene and the author and which has been found to be effective in practice.

Ramsey (1996) has taken the next step in development of numerical hydrodynamics of sails: he has added the above water portion of the hull. The sails are represented as vortex lattices with convected wake geometries determined by iteration. The hull can be represented by source panels as in the appendage numerical method of section 6.4, or as vortex quadrilaterals around the periphery of each hull panel. The two methods give total forces within 1% of each other. If a sail is sealed to the deck of the hull, its root circulation is carried on a continuation of the sail through the deck down to the reflection plane. Figure 7 shows the hull, sails and panelization for which we have done computations. The sailing conditions are for a 4.52 m/s wind speed at a height of 10 meters, a boat speed of 4.51 m/s, a heel angle of 20 degrees, and a true wind angle of 40 degrees from ahead. The true wind velocity has a logarithmic profile with a roughness height of 0.001 m for heights greater than 0.5 m. Below 0.5 m, where the wind speed is 3.05 m/s, it is reduced linearly to 1.53 m/s at the sea surface. The rapid decrease of the real wind speed with decreasing height to zero at the surface is avoided as it would make the computations singular. The camber and twist distributions are chosen to be consistent with good sails in practice. At the mast, the hull freeboard is 1.3 meters before heeling. For these computations, an image plane is located at the water surface. Computations have been carried out for the sails without a hull, for the sails and the hull together with spaces between the bottoms of the sails and the deck, and for the sails and hull with the bottom of the jib sealed to the deck. Table 1 shows the results for the forward and side forces. Computed results for the effect of the hull on the total forces, which include aerodynamic pressures on the hull, are new and of particular interest. The existence of the hull adds significantly to the forces, particularly on the jib which is closest to it, and improves (decreases) the ratio of induced drag coefficient to the square of the lift coefficient. This is particularly true when the bottom of the jib is sealed to the deck. Figure 23 shows the vertical circulation distributions on the sails for each of these cases. It demonstrates the influence on the mainsail of the jib which is of lesser span.

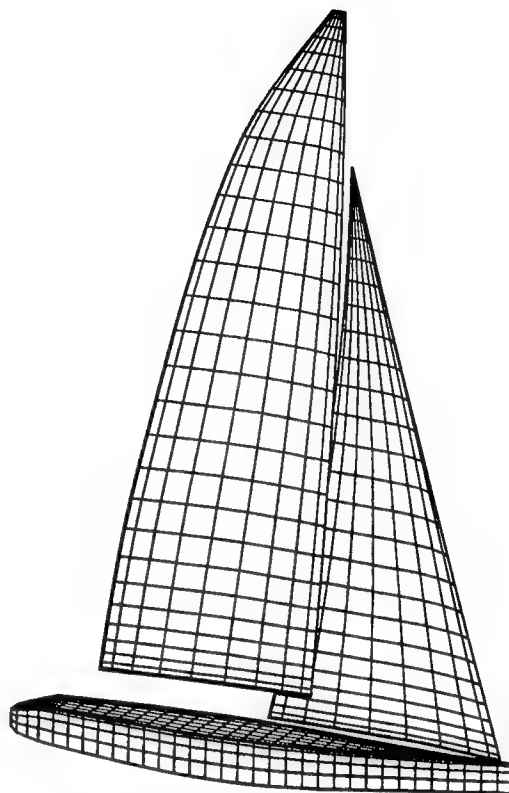


Figure 22: Geometry and Panelization for Example Sail Computations. The view shown is from the leeward side with the boat heeled 20 degrees, with the viewpoint elevated and forward of the midship.

	NO HULL	HULL NO JIB SEAL	HULL WITH JIB SEAL
FORWARD FORCE			
HULL		58	85
JIB	2376	2505	3083
MAIN	1544	1571	1588
TOTAL	3920	4133	4756
HEEL FORCE			
HULL		516	525
JIB	6901	7212	8173
MAIN	8529	8600	8614
TOTAL	15430	16329	17312

Table 1: Sail Forces. Units are Newtons.

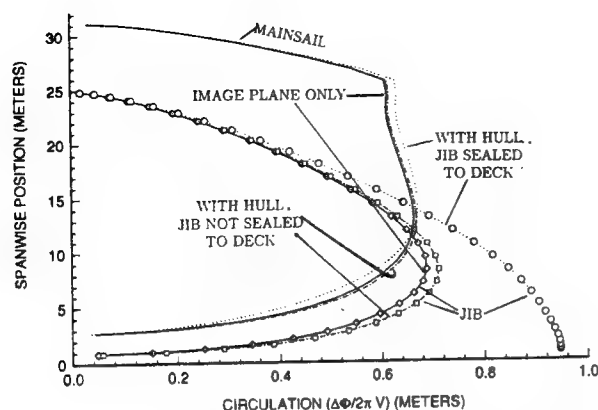


Figure 23: Circulation Distributions on the Sails

References

- [1] M. Drela. Xfoil: An analysis and design system for low reynolds number airfoils. In *Lecture Notes in Engineering*, volume 54, Low Reynolds Number Aerodynamics. Springer-Verlag, New York, 1989.
- [2] M. Drela and M.B. Giles. Viscous-inviscid analysis of transonic and low reynolds number airfoils. *AIAA Journal*, 25(10), October 1987.
- [3] R. Eppler and D. Somers. A computer program for the design and analysis of low speed airfoils. Technical Memorandum TM-81862, NASA, 1980.
- [4] S.E. Euerle and Greeley D.S. Towards a rational upwind sail force model for vpps. In *Proceedings of Eleventh Chesapeake Sailing Symposium*. Society of Naval Architects and Marine Engineers, 1993.
- [5] J. Gerritsma and W. Beuleman. Analysis of the resistance increase in waves of a fast cargo ship. *International Shipbuilding Progress*, 19, 1972.
- [6] H. Glauert. *Airfoil and Airscrew Theory*. Cambridge University Press, London, 1959.
- [7] D.S. Greeley and J.H. Cross-Whiter. Design and performance of sailboat keels. *Marine Technology*, 26(4):260-281, 1989.
- [8] D.S. Greeley, K.L. Kirkman, A.L. Drew, and J.H. Cross-Whiter. Scientific sail shape design. In *Proceedings of Ninth Chesapeake Sailing Symposium*. Society of Naval Architects and Marine Engineers, 1989.
- [9] J.L. Hess. Calculation of potential flow about arbitrary three-dimensional lifting bodies. Technical Report MDC J5679-01, Douglass Aircraft Company, 1972.
- [10] S.F. Hoerner. *Fluid Dynamic Drag*. S. F. Hoerner, Midland Park, New Jersey, 1965.
- [11] K.L. Kirkman and D.R. Pedrick. Scale effects in sailing yacht hydrodynamic testing. *Transactions of the Society of Naval Architects and Marine Engineers*, 1974.
- [12] G.C. Lauchle and G.B. Gurney. Laminar boundary-layer transition on a heated underwater body. *Journal of Fluid Mechanics*, 144:79-101, 1984.
- [13] J.T. Lee. *A Potential Based Panel Method For the Analysis of Marine Propellers*. PhD thesis, Department of Ocean Engineering, Massachusetts Institute of Technology, Cambridge, MA 02139, 1987.
- [14] L.M. Mack. Transition prediction and linear stability theory. In *Laminar-Turbulent Transition*, pages 1-1 — 1-22, 1977. AGARD-CP-224.
- [15] J.H. Michell. The wave resistance of a ship. *Philosophical Magazine*, pages 106-123, 1898.
- [16] W. Milewski. *Coupled Potential Flow and Boundary Layer Equations for Three Dimensional Objects*. PhD thesis, Department of Ocean Engineering, Massachusetts Institute of Technology, Cambridge, MA 02139, 1996. In Preparation.
- [17] J. H. Milgram. Section data for thin, highly cambered airfoils in incompressible flow. Contractor Report CR-1767, NASA, 1971.
- [18] J. H. Milgram. Naval architecture technology used in winning the 1992 america's cup match. *Transactions of the Society of Naval Architects and Marine Engineers*, 101:399-436, 1993.
- [19] J.H. Milgram. The aerodynamics of sails. In *Proceedings of 7th Symposium on Naval Hydrodynamics*. Office of Naval Research, 1968. Held in Rome, Italy.
- [20] J.H. Milgram. The analytical design of yacht sails. *Transactions of the Society of Naval Architects and Marine Engineers*, 1968.
- [21] D.E. Nakos, D. Kring, and P.D. Sclavounos. Rankine panel methods for transient free surface flows. In *Proceedings, Sixth International*

Conference on Numerical Ship Hydrodynamics. University of Iowa, 1993.

- [22] D.E. Nakos and P.D. Slavounos. Ship motions by a three dimensional rankine panel method. In *Proceedings of 18'th Symposium on Naval Hydrodynamics*. Office of Naval Research, 1990. Held at University of Michigan, Ann Arbor, August 20-23, 1990.
- [23] C. W. Prohaska. A simple method for the evaluation of the form factor and the low speed wave resistance. In *Proceedings of 11'th ITTC*. International Towing Tank Conference, 1966.
- [24] W. Ramsey. *Numerical Methods for Flows Around Lifting Bodies with Vortex Wake Rollup*. PhD thesis, Department of Ocean Engineering, Massachusetts Institute of Technology, Cambridge, MA 02139, 1996. In Preparation.
- [25] B.S. Rosen, J.P. Laiosa, W.H. Davis, and D. Stavetski. Splash free-surface code methodology for hydrodynamic design and analysis of iacc yachts. In *Proceedings of Eleventh Chesapeake Sailing Symposium*. Society of Naval Architects and Marine Engineers, 1993.
- [26] N. Salvesen, E. O. Tuck, and O. Faltinsen. Ship motions and sea loads. *Transactions of the Society of Naval Architects and Marine Engineers*, 78, 1970.
- [27] P.D. Slavounos. A practical computer method for solving ship-wave problems. In *Proceedings, Second International Conference on Numerical Ship Hydrodynamics*. University of California at Berkeley, September 1977.
- [28] P.D. Slavounos. *Computation of Ship Wave Interactions*, chapter 4, pages 177-231. Computational Mechanics Publications, 1995.
- [29] P.D. Slavounos and Nakos D.E. Seakeeping and added resistance of iacc yachts by a three-dimensional panel method. In *Proceedings of Eleventh Chesapeake Sailing Symposium*. Society of Naval Architects and Marine Engineers, 1993.
- [30] B. Thwaites. *Incompressible Aerodynamics*. Oxford University Press, Oxford, 1960.
- [31] E.O. Tuck. *The Steady Motion of a Slender Ship*. PhD thesis, University of Cambridge, Cambridge, England, 1963.

- [32] P. Van Oossanen. Predicting the speed of sailing yachts. *Transactions of the Society of Naval Architects and Marine Engineers*, 101:339-397, 1993.

Acknowledgements

The author is appreciative of the technical information provided by America³ Foundation (A³) and by the Partnership for America's Cup Technologies (PACT). It has made this a more informative paper than would otherwise be the case. Five organizations which engaged in extensive technical efforts in support of their designs of IACC yachts were contacted and only A³ and PACT provided information and permission to use it. This is why much of the technical information provided herein is attributed to people associated with these organizations.

Hydrodynamics in Advanced Sailing Vessel Design

Errata

Equation (18) contains a typographical error. The corrected equation is:

$$\text{where: } Q' \equiv \frac{\partial Q}{\partial s} \text{ and } U^{\text{inv}} \equiv \frac{\partial(\phi^{\text{inf}} + \phi^{\text{inv}})}{\partial s} \quad (18)$$

Equation (24) contains a typographical error. The corrected equation is:

$$\theta \frac{dH^*}{ds} + H^*(1 - H) \frac{\theta}{U^e} \frac{dU^e}{ds} - 2C_D + H^* \frac{C_f}{2} = 0 \quad (24)$$

The rightmost data point in Figure 12 is in error. The corrected figure follows:

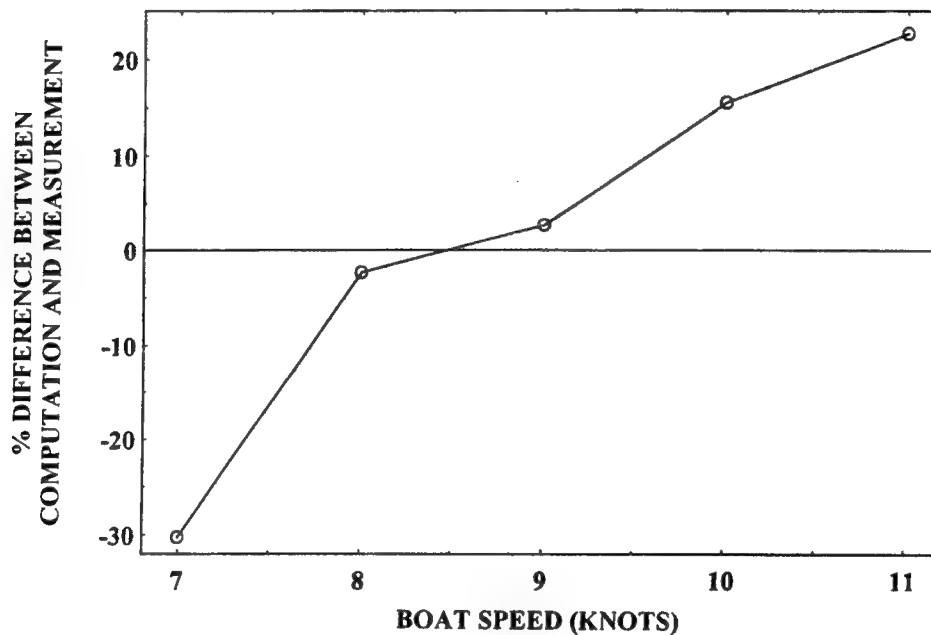


Figure 12: Error in the Wave Making Resistance of an IACC Yacht Computed by Slavounos.

The labeling and orientation in Figure 18 are not correct. The corrected figure follows:

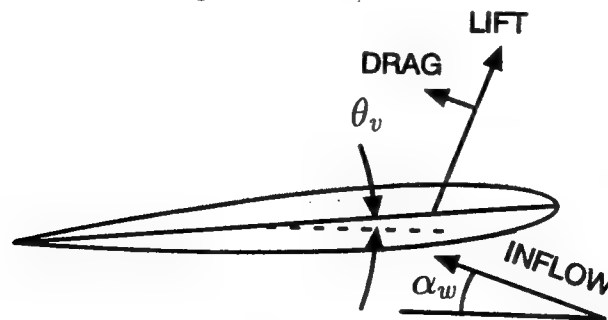


Figure 18: Forces on a wing section at an angle of attack.

In the second paragraph below the figure change $\alpha_w + \theta$ to $\alpha_w + \theta_v$.

Divergent Bow Waves

M. Tulin, M. Wu (University of California at Santa Barbara, USA)

Abstract

Divergent waves are studied utilizing a high resolution $2D+T$ simulation. The effects of changes in speed, beam, and draft are studied and discussed for Wigley-like hulls. A satisfactory comparison is made with fully non-linear 3-D calculations by Hoyte Raven with RAPID. The present simulations confirm the non-linear characteristics of the bow waves, earlier observed by W. Froude, Inui, and Miyata. An explanation is offered here for these observations in terms of the narrow wave spectra arising from interference between the two sides of the hull at the location of the splash peak. For normal ship slenderness ($B/L=0.1-0.2$) the divergent bow wave crests tend to be straight due to the narrow spectrum, and the wave crests are very steep, resembling Stokes limiting waves, and/or breaking. Strong breaking has a similarity to the breaking of two dimensional progressive waves: an energetic plunging jet forms. Further simulations and measurements are recommended.

1. Introduction

The flow at the bow of ships takes a variety of forms, depending mainly on the shape of the bow. For sufficiently blunt shapes, breaking occurs ahead of the bow. For sufficiently fine bows, a thin splash is created on the side of the hull which rises and eventually falls, and oblique waves appear moving away on either side. For a long time the study of both of these bow flows had been neglected. Finally, however, the blunt bow came under scrutiny through: experimental studies of full tankers, Baba(1969); suggestions about the morphology of the free surface before blunt bodies, Tulin(1970); an analysis of the inviscid free surface stability before the bow, and detailed two-dimensional calculations at

both low(smooth) and high(jet) Froude numbers, Dagan and Tulin(1973); exact two-dimensional calculations of the "smooth" flow before the bow, vanden Broeck and Tuck(1977); an asymptotic analytical theory of blunt bow flow before three dimensional shallow water ships, Fernandez(1981); studies of the necklace vortex and of viscous free surface stability, Mori(1985); exact unsteady free surface calculations of evolving bow waves, Grosenbough and Yeung(1989), Yeung(1991); and through exact analytical modeling of jet flows at the bow, Dias and vanden Broeck(1993); and others.

The flow is decelerated in front of the blunt bow and the free surface rises a distance which scales with the square of the draft Froude number, F_d . In this process, the free surface is seen to be disrupted for small draft Froude numbers, $F_d=O(1)$. It is not yet known whether a smooth undisrupted rise is possible even for very small F_d , while for larger speeds, a jet sheet runs up at the bow before falling over forward. The earliest schematic guess as to these flow regimes is shown as Figure 1 (a)-(c) from Tulin(1970). To these we should add Figure 1 (d), showing a low speed turbulent eddy sitting on the dividing stream line; the later is our present view as to what happens for $F_d=O(1)$; this situation is somewhat similar to a breaker above a hydrofoil, Cointe and Tulin (1994).

Between blunt and fine ships, a sequence of events may occur in the transition between bow breaking and divergent wave systems. We do not know very much about this transition, but it certainly deserves to be explored systematically.

For fine ships with a sharp stem, the free surface flow is not much decelerated before the stem, but upon reaching it, is diverted sharply upwards and then rises on the hull at a constant upward velocity first, but then in almost ballistic trajectory, eventually to level off and fall down.

An entire thin sheet is formed in this process and appears as a splash or spray on either side of the hull, Figure 2. This spray as viewed in successive vertical sections aft of the stem, resembles the rise or jet formation which occurs during two dimensional water entry; indeed the mechanism of water entry and of the fine bow flow are closely related.

In Michell's thin ship theory, this splash appears as a result of the calculation so that it is not entirely of nonlinear origin. Following the splash, an oblique wave then appears on each side of the hull, often followed by others. These waves were observed by Froude, who called them "divergent" waves, Figure 3, and described them in the context of the entire wave system, including the broad crested transverse waves. Subsequently, Lord Kelvin, who knew about Froude's observations deduced the wave pattern behind an infinitesimal disturbance. A set of nested divergent waves appeared, Figure 4. Since that time, actual divergent bow waves have with little exception been linked with the Kelvin wave pattern, and simply considered part of it. In fact, the waves drawn by Froude, Figure 3, differ substantially and in a basic way from Kelvin's picture, Figure 4; we will account for this difference later. We owe to Inui(1970) and his colleagues in Tokyo, Inui, et al(1979), Miyata(1981), the earliest attention to little understood aspects of divergent bow waves. Miyata claimed, following experimental studies that these waves were non-dispersive and non-linear; he called them "surface shock waves". After their work, the subject rested until now, perhaps because for conventional Froude numbers the divergent waves do not contribute in a major way to the wave resistance. Of course, at higher speeds, they are important and eventually merge with spray. Recently, there has arisen an interest in the very long narrow wake behind ships which can be observed remotely. For naval combatant ships, photographs show substantial wakes created abeam the ship by the extensive breaking of divergent bow and stern waves; the same can be observed in early photographs in the Tokyo tank using aluminum powder on the surface, see Figure 5. This has created an interest in divergent waves for their own sake.

How to predict these waves? The numerical computation of ship wave resistance and patterns has evolved through Michell, Guilloton, Neuman-Kelvin, and Dawson techniques to fully

non-linear codes [Daube, Raven(1993)]. No doubt, the best of these latter codes can provide useful information on the divergent waves, provided they can resolve the thin bow splash and steep waves which sometimes appear. Very often bow waves are seen to break, sometimes strongly, and the 3-dimensional codes may then have trouble. For sufficiently fine ships, we know that the divergent wave pattern, both at the bow and stern, emerges from numerical calculations made on the basis of nonlinear slender body theory, Tulin and Wu(1994). The calculation is carried out in two dimensions, vertical and transverse, and successively in time ($2D+T$). It has the advantage of high resolution, sufficient to define breaking, and even to trace out overturning jets. At the same time, it neglects certain three dimensional effects which become increasingly important as the ship becomes full. For instance, it does not allow upstream influence, so it can not predict breaking before the bow. However, it has much to recommend it for fine ships like combatants, and especially for the higher Froude numbers where massive breaking of divergent waves is observed. Furthermore, the theory can be applied to divergent stern waves, about which we know little.

There is much to understand about divergent waves, both bow and stern: their source or origin; the shapes they take and the patterns they make; the influence of the beam, draft, and the speed on their strength and propagation, the onset and type of breaking, and even their post breaking behavior.

Our principal purpose here is to report and comment on the calculations of some nonlinear $2D+T$ numerical studies of divergent waves and to illuminate their basic mechanics. We begin with a discussion of some past ideas.

2. The inadequacy of ray theory; the splash as a high speed inner flow

For fine ships without sharp corners except at the bow and stern, at normal Froude numbers, the Michell theory shows that the ship's wave pattern is equivalent to two Kelvin patterns originating at the bow and stern. The ray theory according to Keller(1974,1979) also concludes that all the rays must originate at discontinuities in the waterline shape, which normally occur only at the bow and stern.

After originating at the bow (and stern), the trajectory of the rays depends upon and may be calculated in terms of the "displacement" flow about the hull. The deformation by the displacement flow of the ray propagating waves, with amplitudes calculated according to linear theory, was studied by Inui and Kajitani(1977) and later, in the same spirit, by Yim(1981). Subsequently, Tulin(1985) produced a general ray analysis of the generation and propagation of waves around a ship of finite beam.

In Keller ray theory it was proposed to base the displacement flow on a naive Froude number expansion. Tulin showed that the calculation of the amplitude of waves propagating on rays is dependent on the pressure gradient at the stagnation point in the low Froude number flow, and the theory gives rise to unbounded amplitudes for wedge bows. Then he raised the question, "is the naive Froude number expansion even applicable (uniformly convergent) in the neighborhood of the point of the bow?" He continued, "there exists a good chance that it is not. I say that because in nature it is normal on wedge models, see Standing (1974), to find the highest point on the free surface at some distance aft of the point of the bow (as Michell's theory predicts!); is it possible that this behavior is reflected at all Froude numbers on a scale near the bow which increases with speed, perhaps as U^2 , creating an inner flow at the point of bow for which the naive Froude number expansion is an outer flow."

The simulation results presented here clearly show that the side splash on the hull is crucial for the generation of divergent waves. Furthermore, we shall show that it scales exactly as the "high speed" inner flow suggested by Tulin. Our calculations indicate that the relaxation of the splash is the prime source of divergent waves. One of the consequences of this discovery is that conventional ray theory, which is conceived as asymptotic to zero Froude number, cannot predict the generation of divergent waves. Whether it is relevant to wave propagation is another question.

Eventually we conclude that neither ray theory nor linear theory is relevant to the understanding of bow divergent waves. The key to their understanding lies in the spectral wave number content in the splash, which for typical ships is governed by the ship's beam. This is a

non-linear effect. Furthermore the waves are typically very steep and sometimes breaking.

3.The wedge flow

The free surface flow about the inclined wedge, for which a length scale is absent, offers an important opportunity for understanding the morphology of bow waves produced by fine ships. Its consideration leads immediately to understanding of the inner flow (side splash) and to essential scaling relations. These, in turn, allow us to understand some of the effects of speed on the divergent waves, particularly, their spatial pattern.

For an inclined wedge (wedge angle α , stem angle β) at speed U , the wave height η , at any longitudinal location \bar{x} , measured from the wedge-still water intersection, must on dimensional grounds obey the scaling law:

$$\kappa\eta = f(\kappa\bar{x}; \alpha, \beta): \text{ where } \kappa = g/U^2 \quad (1)$$

This means that the flow speed U simply serves(through κ) as a factor scaling both η and the actual position \bar{x} , on the free surface where certain flow features appear. Therefore high speed features such as the origination of splash, appear closer and closer to the bow as the speed decreases; equivalently low speed features (like disappearance of waves) will always appear if we look far enough behind the wedge. And in between the splash at the bow and the wave free field to the rear, we can expect to find observable waves. These are the divergent waves. A chronology of events near the bow can be constructed, based on the scaling of eq. (1) and using other results, see Figure 6.

The flow near the bow begins as a spatially self similar spray, just as in gravity-free water entry, and every line originating at $\bar{x}=0$ and lying on the free surface is a straight line, since in the absence of κ ,

$$\eta / \bar{x} = f(\alpha, \beta) \quad (2)$$

This is confirmed in the 2D+T calculations, which then show that for sufficiently large values of $\kappa\bar{x}$ along the wedge, the spray sheet is maintained at high levels by the continually expanding wedge, and does not fall. However, divergent waves do originate in the sheet and propagate outwards, Figure 7. We note that the

area in a vertical cross section of any wedge, $A(x)$, increases as the square of the distance aft ($A \sim x^2$) and this growth seems sufficient to maintain the splash and prevent its fall. Meanwhile, the water displaced by the growing wedge is partially carried off in the transversely propagating wave. In the case of a ship like the Wigley hull, the vertical section area grows at first like $A \sim x$, and the splash is then not maintained, but reaches a peak and falls; the growth after the bow region actually decreases and eventually falls to zero midships. This slow growth no doubt accounts for the difference between the wedge and conventional hulls. Another major difference is that the hull has a characteristic length, the beam B , while the wedge does not.

Wedge Bow Resistance The wedge flow possibly sheds light on the wave resistance originating at the bow. From dimensional considerations, it must be that the wedge resistance, R_b , is:

$$R_b \sim C_D \cdot \rho U^6 / g^2 \quad (3)$$

where C_D is a non-dimensional number depending only on α , β . Since we have neglected the transverse waves in our considerations, this can be regarded as the wedge wave resistance arising from the inner flow at the bow, and which we associate with the divergent wave system.

The Water Entry and Wavemaker Analysis. The wedge flow corresponds to the vertical water entry of a two dimensional wedge in a vertical cross section. In the $2D+T$ view, the fine bow corresponds to an expanding section in the vertical plane, more like a wavemaker action. In each successive section the underwater area of the wedge or ship increases and the water displacement appears generally above the mean water line. This is the basic reason for the appearance of the splash. In this process, the water acquires potential and kinematic energy which must correspond to work done by the downward moving wedge or by the expanding hull. In the case of the ship, this splash relaxes, and its energy is transformed into a wave propagating to each side. This wave lies mainly above the mean water level.

For typical F_L , the splash collapses before midship; there may be additional water rise further along the hull, however, to accumulate additional displaced water due to the growth in ship sectional area.

In accord with the scaling of eq.(1), as the speed and/or beam increases, the splash height, area and energy grow. The area and energy do not grow as the same way, as area is linear with increase in height, and energy is quadratic. This seems to lead to divergent waves which for typical ships are strongly non-linear in their $2D+T$ simulations.

Very little is understood about these non-linear positive waves, which are, furthermore, propagating in the presence of the hull. Our simulations show them often to be very sharp and/or breaking. One of our main purposes here is to learn more about them in their $2D+T$ simulation.

4. The $2D+T$ approximation

Linear slender body theory has, of course, been applied to the ship wave problem, and is known to lead to results similar to Michell's theory. It is, however, restricted to small wave elevation and cannot predict non-linear wave behavior. We will show later, that divergent waves for typical ship slenderness, behave very differently than predicted by Michell theory.

The theory we will use here is a so called non-linear cross flow theory. It was first developed at the OEL of UCSB by H. Maruo (1990) (see also Song and Maruo(1993), Maruo and Song (1994)) for the prediction of ship deck wetness, and therefore allows for the motion of ships in oncoming waves. The application here to steady ship motion is a special and simple case. The great advantage of this theory is that it allows free surface elevations around the hull of the same order as the ship draft. The theory does this by reducing the 3-D problem to a continuous sequence of unsteady 2-D problems in vertical sections. Since the 2-D free surface problem can be solved with high resolution by the BEM, it is possible to compute the shape of the free surface with high resolution, including overturning jets. This is another advantage of the method.

The $2D+T$ approximation was introduced into aerodynamics by M. Munk for the prediction of loads on inclined slender bodies of revolution and low aspect ratio wings. It has

been extended to compressible flow and is known to be very useful for bodies of beam/length of $O(10^{-1})$ or smaller. These aerodynamic cases correspond, in a certain way, to the flow about ships at sufficiently high $F_L(O(1)$ or greater), and the $2D+T$ method has been used for the analysis of the performance of high speed, low aspect ratio planing boats, Tulin(1956), and for the study of the resistance of high speed, slender displacement hulls, Tulin and Hsu(1986); in both cases, gravity is completely neglected.

All $2D+T$ methods are asymptotic to the regime: $(B/L)^2 \ll 1$. As a result, the continuity equation, $\nabla^2 \Phi = 0$, is approximated by:

$$\nabla^2 \Phi = \Phi_{yy} + \Phi_{zz} = 0 \quad (4)$$

where x, y, z are the streamwise, transverse, and vertical coordinates respectively; B, d, L are beam, draft, and ship length. This approximation fails, even for slender bodies, in the vicinity of hull stagnation points and other corners, where the flow is highly accelerated in the streamwise direction. The method would not apply, for example, to blunt bows, even for small (B/L) . For fine bows, however, the stagnation point is weak, and does not exist on the free surface.

As a consequence of (4), the flow is two dimensional and each section is unaware of the hull in any downstream section. The absence of upstream influence has the consequence that the water rises abruptly at the stem of the ship; actual observations are in accord with this for fine ships, where the rise is observed to begin only a small distance, see Figure 8, ahead of the stem.

In the small slenderness regime, $(B/L)^2 \ll 1$, the free surface condition is also approximated by,

$$U\Phi_x + \frac{1}{2}[(\Phi_y)^2 + (\Phi_z)^2] + g\eta = 0 \quad (5)$$

and is satisfied on the actual free surface; the motion is steady in ship co-ordinates. In fixed co-ordinates, the motion becomes unsteady and,

$$U \partial / \partial x = \partial / \partial t \quad (6)$$

so that on the free surface, (5) becomes the exact two dimensional condition in a fixed vertical section through which the ship moves,

$$\Phi_t + \frac{1}{2}[(\Phi_y)^2 + (\Phi_z)^2] + g\eta = 0 \quad (7)$$

I II III

As the water first encounters the ship bow, η has not had time to grow very much, and I and II dominate. This is the region described by eq.(2) in the case of the wedge. When η is fully developed and of $O(d)$, I and III are of the same order, and, $II/III = O(F_d^2)$. For typical ship speeds, $F_d = O(1)$, so all of the terms in (7) are important for normal speeds in the vicinity of the bow.

Away from the hull, the divergent crest lines are fairly straight and steep, see Figure 3; eq.(7) is capable of dealing with propagating divergent waves of very high steepness because of the inclusion of II . Although eq.(7) is also capable of describing transverse waves, eq.(4) can not. Therefore transverse waves do not arise in this approximation. This is, it seems, the principal deficiency of the $2D+T$ approximation. However, the transverse waves may be adequately described by other methods, and, it seems possible to marry the two systems. This possibility is, however, beyond the present scope.

The Computations. The general scheme of the BEM computation has been described in Song and Maruo (1993). In the present calculations, time steps and grid size were chosen to provide convergence. Most of the calculations were made with $\Delta t \cdot U/L = 0.0007$ and $\Delta y/L = 0.0017$, and were carried out on supercomputer CRAY C90. For a typical computation, one hour CPU time is required for one ship length.

5. Wave patterns for the Wigley like hulls

For ease of computation and in order to do parametric studies, the Wigley hull was used as a basis. The stem was slightly raked (5° usually), as required by the program. Many calculations have been made and only a sampling can be presented here.

The calculation of splash requires very high resolution in both time step and free surface. In Figure 8 we show a prediction compared with measurements from Tokyo. The effect of the rise before the hull has been captured by moving the calculation forward by a small distance; then the comparison is excellent.

Adequate measurements of Wigley wave patterns away from the hull are not available for a general comparison with calculations. We are, however, able to compare a specific calculation with the 3-D fully non-linear calculation made at MARIN by Hoyte Raven using RAPID. The comparison of the wave pattern for our parent ship ($L/B=L/d=10$) is shown as Figure 9. The same individual divergent waves, bow and stern, can be seen in each calculation, and their origins and extent match well. Notice the prominent "rooster trail" behind the stern and the resulting diverging waves. There are differences. The $2D+T$ waves are sharper and less dispersive, and transverse waves are absent. Much remains for the future in terms of understanding the roles of differences in the two methods: transverse waves; grid sizes, etc. It is hoped that in future we may also make comparison with experiments of other hull shapes (Series 60, for example). Meanwhile the present comparison with Raven's calculation gives some confidence in the general patterns predicted in our calculations.

Speed Effects. The effect of speed is shown in a series of calculations for the parent ship for $F_L=0.23-0.90$, Figure 10. The forward wave, (A), is always the steepest and most prominent and it seems to originate from the center of the bow splash. Its crest is very sharp over extensive regions for the F_L shown up to 0.46, but it doesn't quite break. The splash becomes higher, and moves aft with increase in speed. For the highest speed, the splash is dominant and is beginning roughly to resemble the spray thrown off by planing craft; wave (A) in this case seems weaker than at lower speeds, perhaps due to the reduction in hull cross sectional area past midships. In all cases the crest lines are much straighter than Kelvin's pattern suggests, and their angle to the flow decreases with increasing speed, as noted by Miyata.

Bottom Effects What is the effect of the ship bottom on these divergent waves? This is illustrated in Figure 11 (top) where the draft is systematically varied. Most striking, for the largest draft, $L/d=1$, the crest lines are not straight, but are continuously concave, as in the Kelvin pattern. On the other hand, for the shallowest draft, $L/d=20$, the wave crests are straight and sharper (close to breaking) and even show a slightly convex tendency where they are

strongest. The bottom is therefore playing an important role.

Beam Effects and Breaking The marked effect of beam is shown in Figure 11 (bottom). A decrease in beam provides dispersive-type bow waves, but as might be expected, an increase in beam leads to breaking. This takes the form of an overturning jet, as shown in Figure 12. To continue the calculations aft, the jets are cut and the calculation resumed. This accounts for the sawtooth appearance of the jet locus in Figure 11 (bottom right). As can be seen, the breaking can be very prolonged. In nature the plunging jets will impact the water and in plunging into undisturbed water throw up a splash of its own. This kind of behavior can be observed in pictures of strongly breaking ship waves, Figure 2, and plunging waves in tanks and the ocean. The calculation of these effects is beyond our scope, although hope exists for inviscid modeling. The details of the initiation and development of a strong wave (A) at the bow is shown in figure12. Notice particularly that the outgoing wave originates in the collapse of the splash. Its propagation is similar in many ways to waves breaking in wave groups: in the rise of the crest, the steepening of the front, and in the jet's formation and growth.

Overturning Splash For other hull shapes than Wigley, the hull splash itself may overturn and merge with a breaking wave, (A). A comparison is made here of a portion of the bow splash for a naval frigate (calculated) and a similar ship under way (photo), see Figure 13. The comparison is striking, and gives confidence to the $2D+T$ modeling. This example serves to demonstrate that the shape of the bow is essential for the details of the splash formation; perhaps the bow flare has accentuated the breakdown of the splash. Since we believe that divergent bow waves are produced, at least in part, by the bow splash, it could be a test of 3-D codes to reproduce the flow at the bow of this frigate in reasonable detail.

Non-linear Effects vs. Michell Theory We have computed the divergent wave field for the hulls based on Michell theory and applied it by offsetting transversely the center line in the Michell theory to the edge of the hull for each distance aft; a somewhat distorted Kelvin-like pattern appears, which is not at all surprising.

For the parent hull, this Kelvin pattern has hardly any resemblance to the calculation. Moreover, when the beam is reduced by half, to $L/B=20$, maintaining the draft at $L/d=10$, a resemblance begins to emerge, see Figure 14. We may therefore conclude that the slenderness of the hull, B/L , is a dominant factor in determining not only the steepness, but also the wave patterns of divergent waves. In particular, an increase in B/L to about 0.1 produces waves (A) and (B) with straight or almost straight crest lines. This is an indication of a narrow spectrum for the divergent waves with a concentration of energy at a particular wave number corresponding to the speed of the waves with straight crests. This is a different situation than predicted by Michell theory, where the spectrum is continuous.

6. The narrow divergent wave spectrum

Since the bow divergent waves seem to arise from the relaxation of the bow splash, the spectral wave number content of the free waves in the divergent system must be found in a transverse cut through the splash at its maximum. It is crucial, however, to consider both sides of the hull, since the opposing sides can communicate under the hull for normal drafts; this results in interference between the two sides. Then it can be seen that the transverse spacing, B' , between the two splashes is the dominant length in the spectrum, at least when this distance is much larger than the width of the splash itself. This spacing, B' , scales with the beam, B , and may be roughly approximated as B . However, for the lowest speeds, $B' < B$, since the splash moves forward and the hull narrows, and at the highest speed where the splash has moved in the vicinity of the maximum beam, $B' > B$, since the effective transverse spacing, B' , must also include the actual width of the splash.

As a consequence of this narrow spectrum around wave length B , the normal spacing between successive straight divergent waves, when they occur, will be close to B . This is the case for the parent hull at $F_L=0.30$.

The key to understanding the bow wave system is Figure 3, the Froude sketch. The individual straight and parallel waves require for their existence a narrow wave spectrum. The normal spacing between the crests seems close to the beam, confirming that the dominant spectral length is B . The angle through the groups

(dashed) is about half of the inclination of the separate wave crests to the ship direction. This confirms the propagation of the wave energy at the group velocity, $C_g=C/2$. And this proves that the bow system is thoroughly dispersive, despite the straightness of the crests, whose explanation, given above, lies in the narrow wave spectrum. The disappearance of the crests outside (roughly) the Kelvin angle may also be observed and requires a dispersive mechanism; in fact, it is due to destructive interference with other waves. Shock waves created at the bow of airfoils, it may be noted, would propagate long distances without such effects.

This explanation of the narrow spectrum, that it is due to the dominance of the transverse separation of the two side splashes on either side of the hull, is completely consistent with the reported effect of the draft and beam on the crest lines. When the draft is abnormally large, as the case $L/d=1$, the water on opposite sides of the hull cannot effectively communicate, and the splash acts if it is on a single deep wall. In this case, the distributed spectral content in a single splash by itself will result in a dispersive type bow wave. This effect was illustrated in figure 11 (top). The same effect occurs as the beam is decreased, as shown in Figure 11 (bottom). However, a reduction in draft from the parent form, $L/d=10$ to $L/d=20$, results, as might be expected, in even straighter crests. All of these remarks apply to wave (A), and sometimes to (B), although the speeds of the latter are sometimes slightly lower.

The Wave Angles According to the ideas just put forth, the velocity of the divergent wave normal to itself, C_N , is approximated by the linear dispersion relationship in the form:

$$C_N^2 = g / \kappa \approx gB / 2\pi \quad (8)$$

The inclination, δ , of the straight crests is:

$$\delta = \sin^{-1} C_N / U \quad (9)$$

or, using (8):

$$\delta = \sin^{-1} [1 / F_L \cdot (B / 2\pi L)^{1/2}] \quad (10)$$

In Figure 15, comparisons are made between the inclination of bow wave (A) and: our $2D+T$

calculations for various Wigley hulls; NSRDC measurement; Tokyo measurements; and equation (10). The comparison between present estimates and the NSRDC measurement, Ratcliffe and Lindenmuth(1990), are excellent. The Tokyo measurements are high at low speeds, and this may be due to the presence of surface tension effects. The approximation, eq. (10), is surprisingly good, considering its simplicity. Certainly the correlation with calculations is sufficient to justify the ideas behind it: that the width of the hull, $B' \approx B$, in the neighborhood of the splash determines the location of the energy in the divergent wave spectrum, and that the length and speed of the divergent wave (A) is closely related to B' .

7. The steepness of divergent waves; the Stokes limiting wave

The divergent bow waves for typical ship parameters are steep. This is illustrated in Figure 16 where we show the shape of a divergent, non-breaking bow wave in a vertical cross section at $X/L=0.206$ for the parent hull at $F_L=0.3$. the crest is almost, but not quite pointed and the included angle is only 10% larger than for Stokes limiting wave. The height of the wave in the transverse plane is also somewhat larger than that of the Stokes limiting wave ($k = g / C^2$):

$$kH \approx 0.826; \quad kH = 0.943 \quad (11)$$

Stokes Divergent Waves

This is clearly quantitative evidence as to the non-linearity of the wave. The calculation of waves of this steepness may pose a difficult challenge for 3-D computation methods.

Eventually as the waves propagate outward, in every case the waves lose height and at the same time the crest broadens and the wave form rapidly subsides. This seems to occur rapidly, and is no doubt due to destructive interference effects, as in the Kelvin kinematical theory.

8. Summary and conclusion

1. New understanding of the divergent waves produced by normal fine ship bows is reached, based largely on high resolution numerical simulations in $2D+T$.

2. The $2D+T$ simulations have been carried out from the bow into the region behind the

ships and reproduce the bow splash waves, the rooster tail, and stern waves.

3. These simulations have the advantage of high resolution, sufficient to define both breaking and post breaking. The evolution and growth of plunging breakers (jets) has been calculated.

4. A comparison has been made for a typical Wigley hull ($B/L=d/L=0.1$; $F_L=0.3$) with the exact fully non-linear 3-D calculation of Raven at MARIN, Figure 9. The general appearance of the multi-wave system is identical in each simulation (splash, three bow divergent waves, rooster tail, two stern divergent waves on each side of the hull). The origins of each feature and general extent are closely similar. However, the crests of the $2D+T$ waves are much sharper.

5. For typical fine ship slenderness ($B/L=0.1$), the crests of the divergent bow waves tend to be straight and their inclination decreases with increasing Froude number.

6. The divergent bow waves have their origin in the bow splash which appears on either side of the bow and the spectral content of the waves originates in the spectral content in the splash cross section taken where the splash reaches its maximum height.

7. For ships of normal beam and draft, the wave spectral content is dominated by the width of the bow at the maximum of the splash due to interference between the two sides. When this width is approximated by B , a good estimate of the wave inclination and its variation with speed can be made.

8. For a slender ($B/L=0.1$) Wigley hull, the steepness of the divergent bow wave is close to that of a Stokes limiting wave. When the beam is increased to $B/L=0.2$, massive breaking (plunging) of the divergent waves occurs.

9. The deformation of a breaking bow wave when observed in a vertical cross section has strong similarities to that of breaking two dimensional progressive waves.

10. There remains much yet to learn about divergent waves and the $2D+T$ method seems a highly useful tool. Although it fails to produce transverse waves, it offers the high resolution necessary to study very steep and breaking waves.

11. Some subjects for future $2D+T$ simulation studies are: other ship hulls (Series 60; naval frigate); bow modifications to reduce breaking;

transom flows; the rooster tail; stern wave breaking and its reduction.

12. It is strongly recommended that a data base be provided of detailed measurements and photographs of divergent waves and stern flows for a suitably broad family of hulls.

Acknowledgement

The authors are grateful for the support from the Office of Naval Research, Computational Ship Hydrodynamics Program, directed by Dr. Edwin P. Rood; and to Hoyte Raven for providing RAPID calculations for comparison purposes.

References

- Baba, E. 1969 A study on free surface flow around bow of slowly moving hull forms. *J. Soc. Naval Arch. Japan* **137**.
- Cointe, R. and Tulin, M. P. 1994 A theory of steady breakers. *J. Fluid Mech.* **276**.
- Dagan, G. and Tulin, M. P. 1972 Two dimensional free surface past blunt bodies. *J. Fluid Mech.* **51**.
- Dias, F. and vanden Broeck, J.-M. 1993 Nonlinear bow flows with spray. *J. Fluid Mech.* **255**.
- Fernandez, G. 1981 Nonlinearity of the three-dimensional flow past a flat blunt ship. *J. Fluid Mech.* **108**.
- Grosenbough, M. A. and Yeung, R. W. 1989 Nonlinear free-surface flow at a two dimensional bow. *J. Fluid Mech.* **209**.
- Inui, T. 1970 Wave patterns and hull forms of ships. JUBILEE Memorial, NSMB.
- Inui, T. and Kajitani, 1977 H. A study on local nonlinear free surface effects in ship waves and wave resistance. *Schiffstechnik*, Band 24 Heft 118.
- Inui, T., Kajitani, H and Miyata, H. 1979 Experimental investigation of the wave making in the near field of ships. *J. Soc. Naval Arch. Japan* **173**.
- Keller, J. B. 1974 Wave patterns of non-thin or full-bodied ships. *Proc. 10th Symp. Naval Hydrodynamics*, Cambridge, MA.
- Keller, J. B. 1979 The ray theory of ship waves and the class of streamlined ships. *J. Fluid Mech.* **91**.
- Maruo, H. 1990 Prediction of deck wetness: A theoretical development. Technical Report 90-53, OEL, UCSB.
- Miyata, H. 1980 Characteristics of nonlinear waves in the near field of ships and their effects on resistance. *Proc. 13th Symp. Naval Hydrodynamics*, Tokyo, Japan.
- Mori, K. 1985 Necklace vortex and bow wave around blunt bodies. *Proc. of 15th Symp. Naval Hydrodynamics*, Hamburg, Germany.
- Ratcliffe, T. J., Lindenmuth, W. T. 1990 Kelvin wake measurements obtained on five surface ship models. DTRC-89/038.
- Raven, H. 1993 Nonlinear ship wave calculations using the RAPID method. *Proc. 6th Int. Conf. on Num. Ship Hydrodynamics*. Iowa City, USA.
- Song, W and Maruo, H. 1993 Bow impact and deck wetness: simulations based on nonlinear slender body theory. *Proc. ISOPE*, Singapore.
- Standing, R. 1974 Phase and amplitude discrepancies in the surface wave due to a wedge-ended hull form. *J. Fluid Mech.* **62**.
- Tulin, M. P. 1956 Theory of slender surface planing at high speeds. *Schiffstechnik*, **14**.
- Tulin, M. P. 1970 Cavity flows and breaking waves. JUBILEE Memorial, NSMB.
- Tulin, M. P. 1985 Surface waves from the ray point of view. *Proc. of 15th Symp. Naval Hydrodynamics*, Hamburg, Germany.
- Tulin, M. P. and Hsu, C. C. 1986 Theory of high speed displacement ships with transom sterns. *J. S. R.*, **21-1**.
- Tulin, M. P. and Wu, M 1994 Bow waves on fine ships - nonlinear numerical studies. In *Proc. 9th Int. Workshop on Water Waves and Floating Structures*. Kyushu, Japan.
- vanden Broeck, J.-M. and Tuck, E. O. 1977 *Proc. 2nd Int. Conf. Num. Ship Hydrodynamics*, Berkeley.
- Yeung, R. W. 1991 Nonlinear bow and stern waves-inviscid and viscous solutions. *Mathematical Approaches in Hydrodynamics*, SIAM press.
- Yim, B. 1981 A ray theory for nonlinear ship waves and wave resistance. *Proc. 3rd Int. Conf. on Num. Ship Hydrodynamics*, Paris.

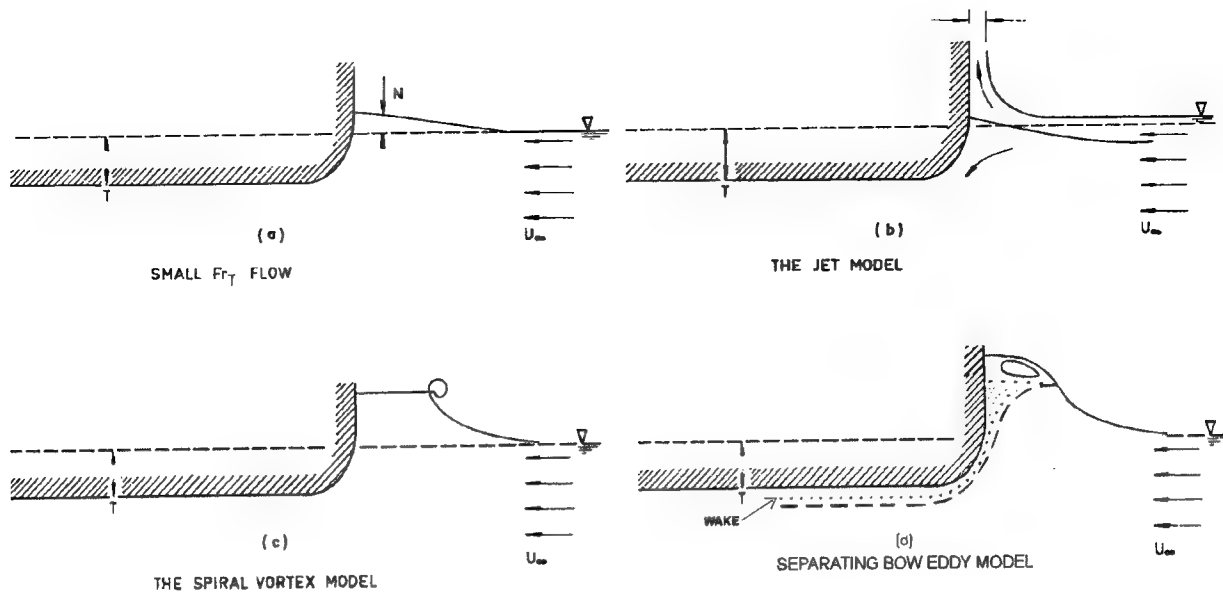


Figure 1: Models of Blunt Bow Flow(Tulin)



Figure 2: The Bow Splash

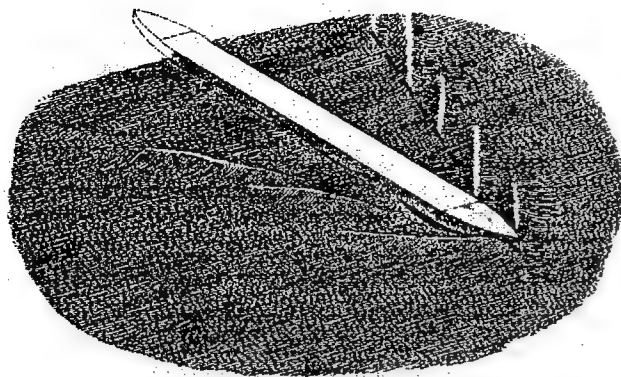


Figure 3: Divergent Bow Waves, As Observed and Drawn by W. Froude (Long Parallel Mid-Body)

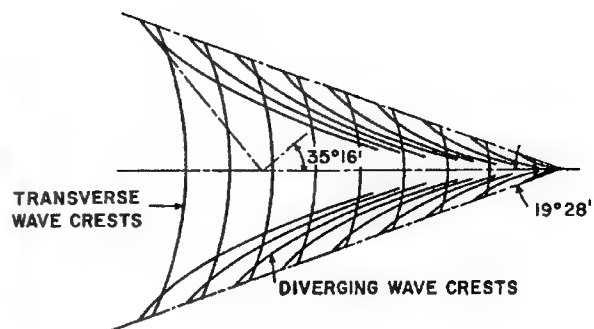


Figure 4: Kelvin Kinematical Wave Pattern

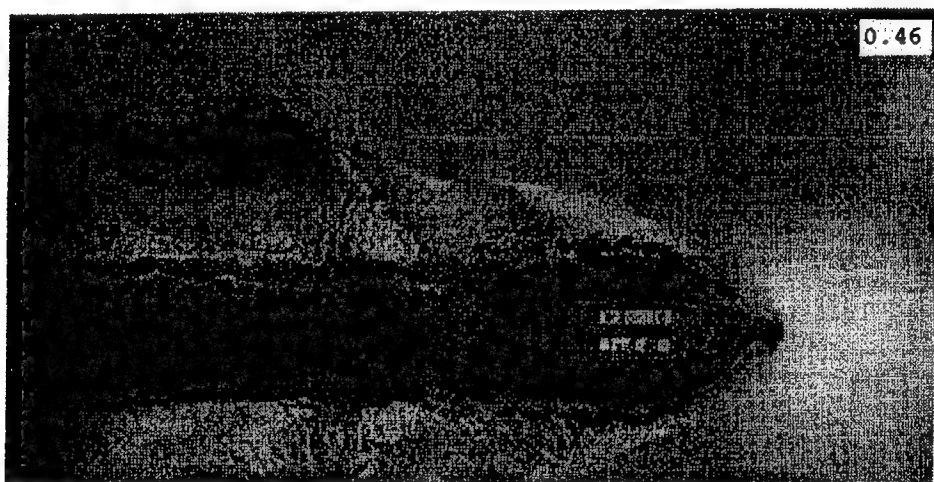


Figure 5: Large Wake (Black) Originating in Breaking Divergent Waves
Alluminum Powder Visualizaton, From Inui(1980)

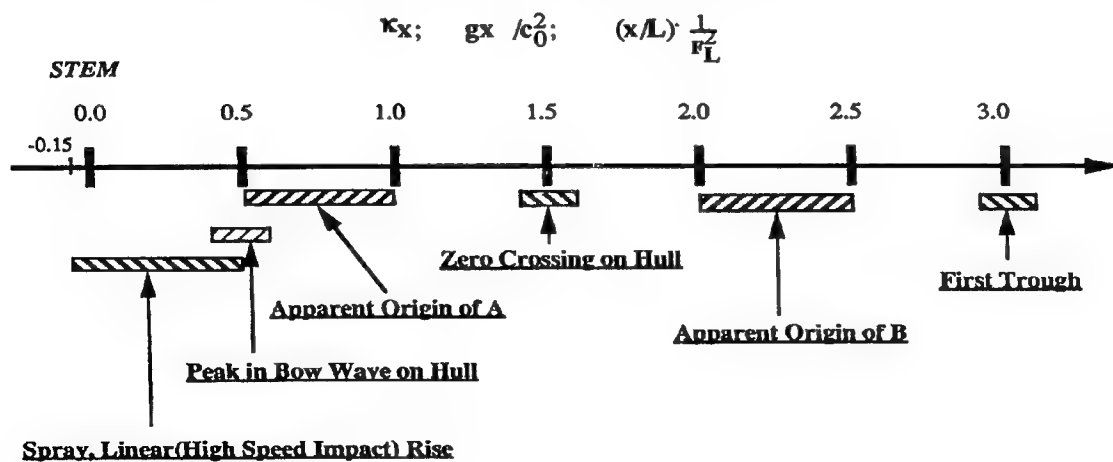


Figure 6: Chronology of Events in The Bow Region

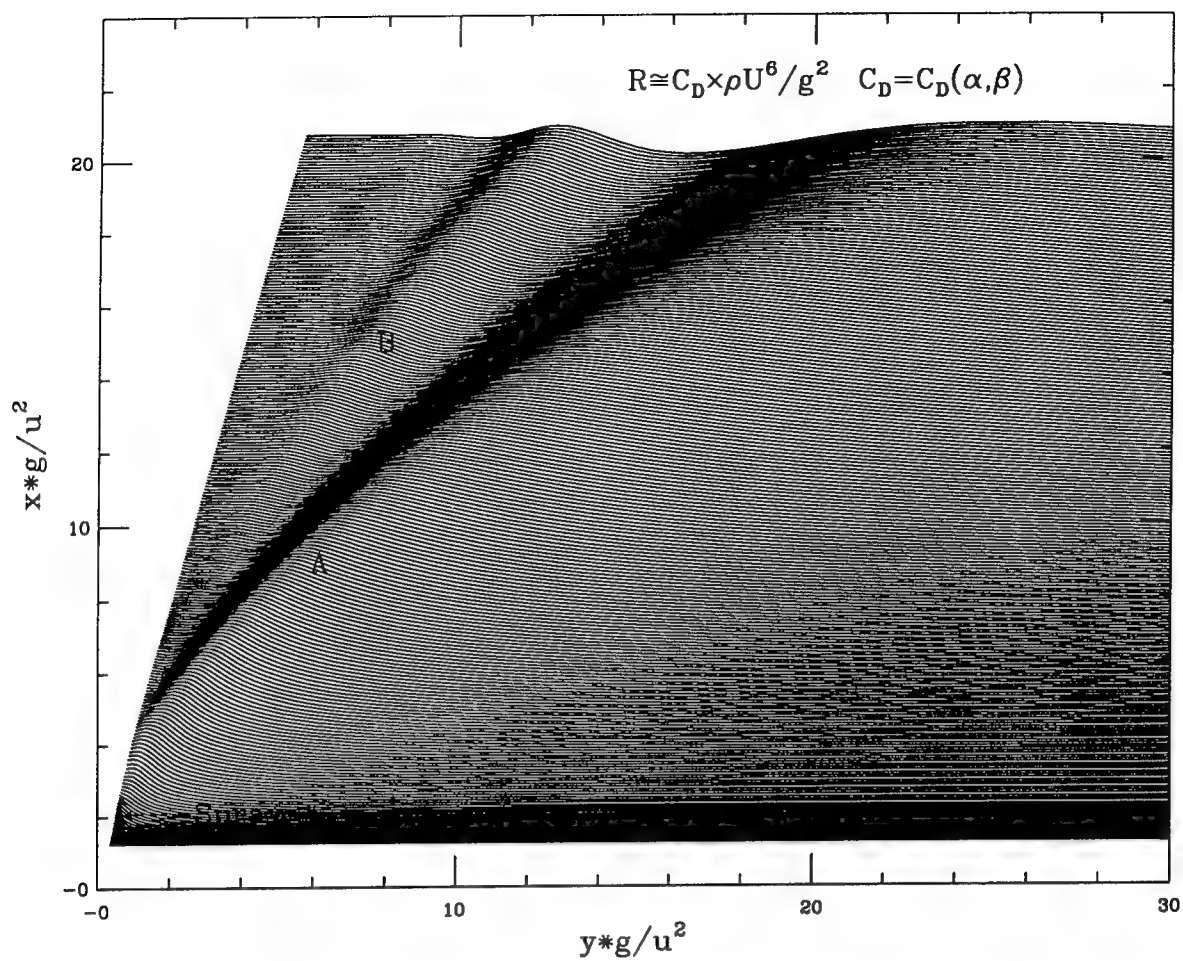


Figure 7: The Wave Field Produced By a Wedge of Angle 18° , Stem Angle 45° , at Speed U

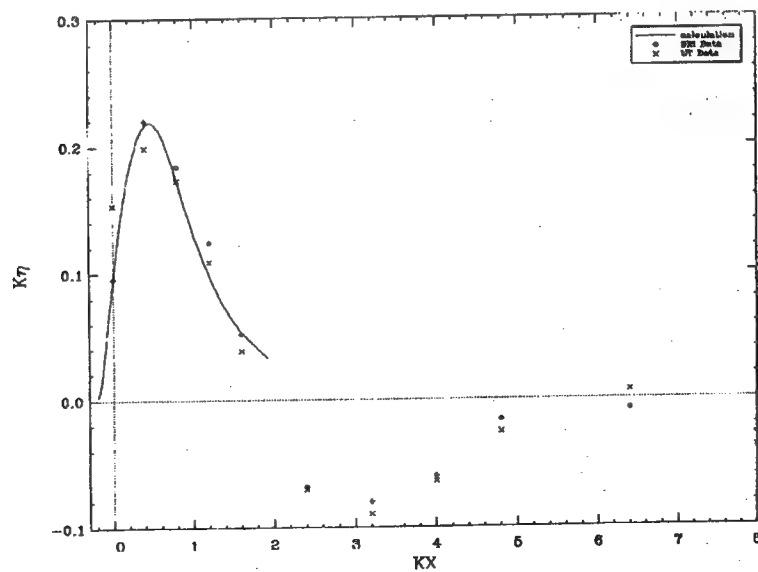
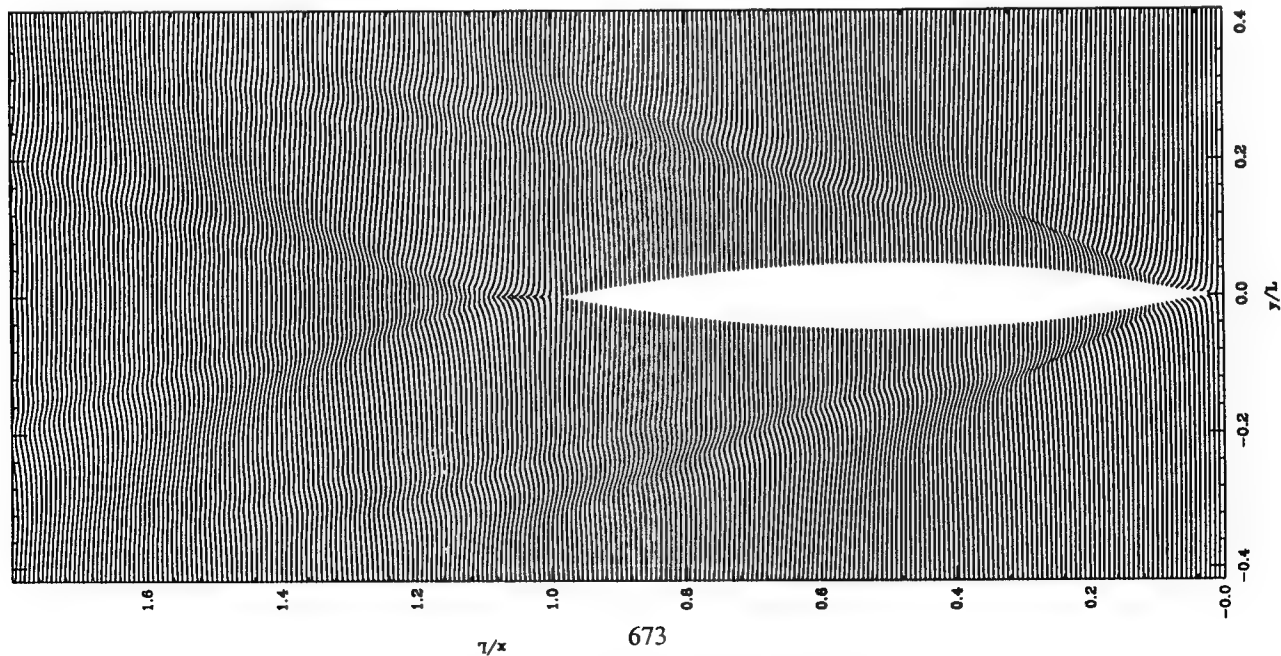
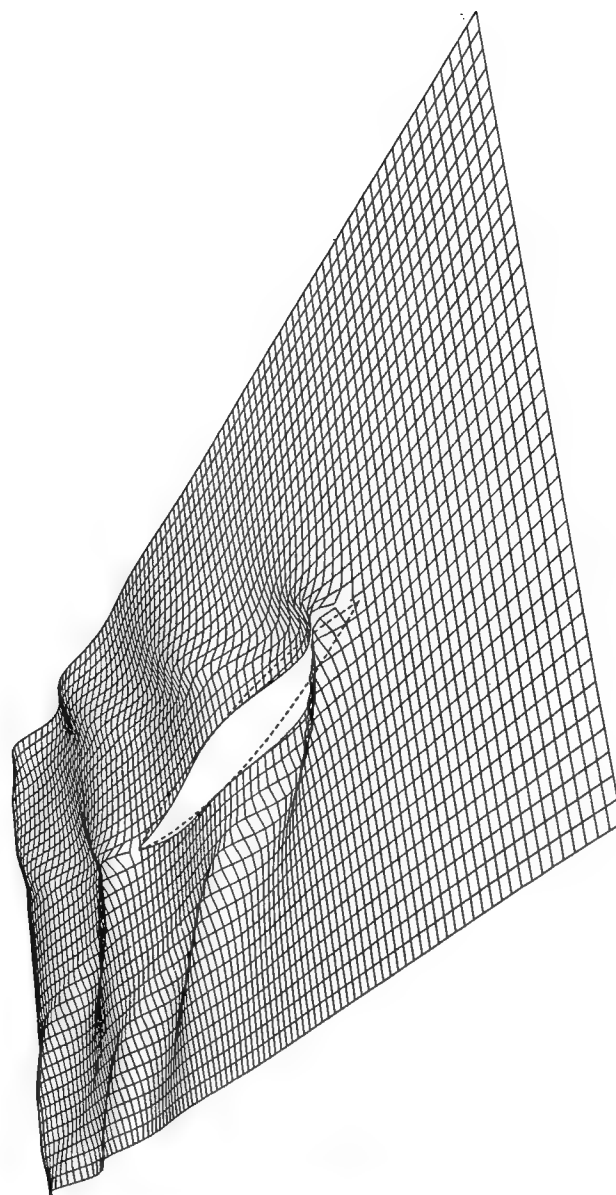


Figure 8: Wave Profile on Wigley Hull, $F_t=0.25$ (Simulation Shifted by $Kx=0.18$)
 $B/L=0.11$; $d/L=0.072$



$L/B=10, L/D=10, F_L=0.30$

Figure 9: A Comparison Between 2D+T(left) and Exact Non-Linear(RAPID) Wave Prediction
The RAPID Calculation is by Dr. Hoyte Raven of MARIN



EXACT: SAME HULL

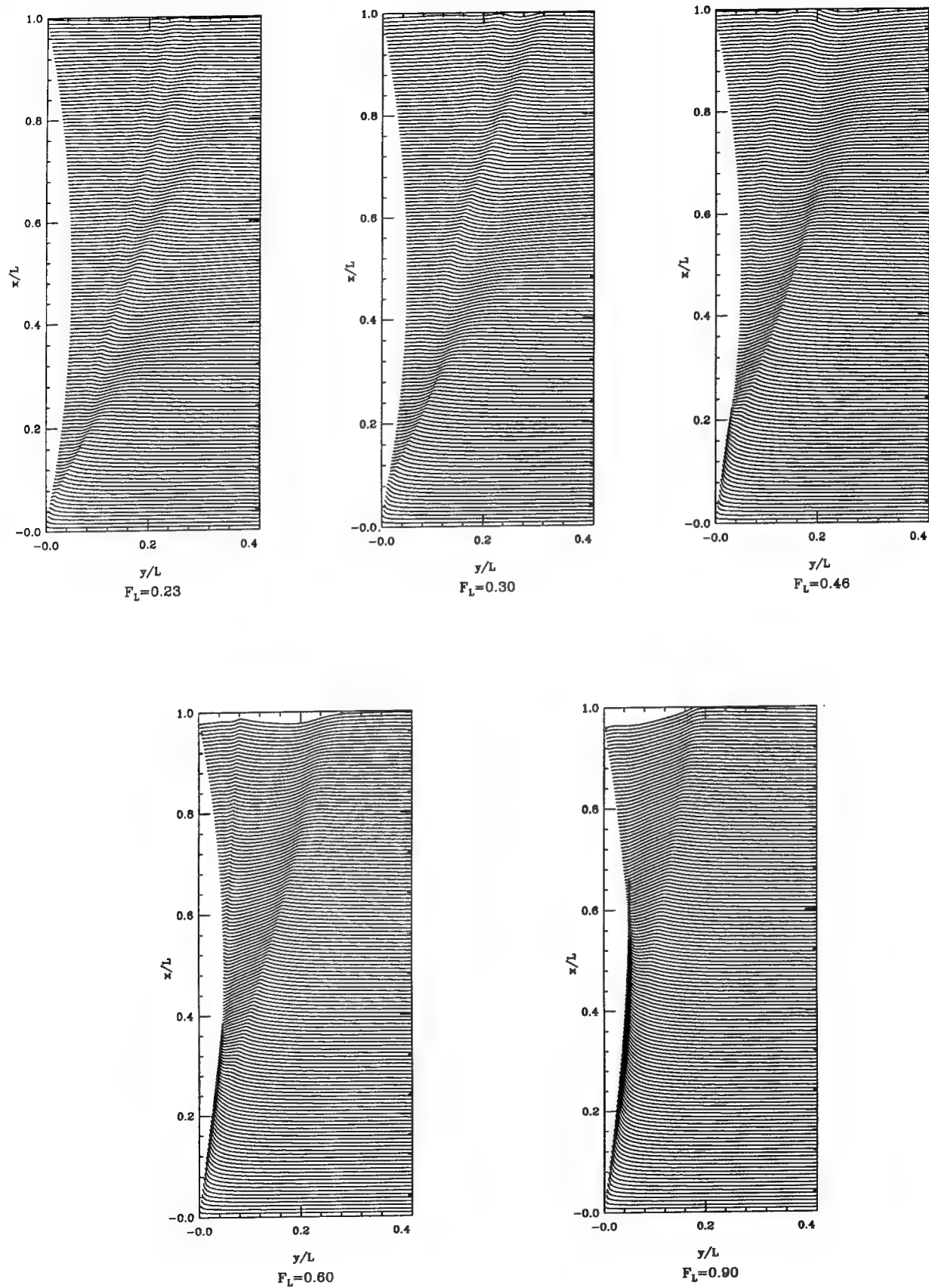


Figure 10: Wave Pattern of Parent Wigley Hull at different F_L ; $L/B=10$, $L/d=10$

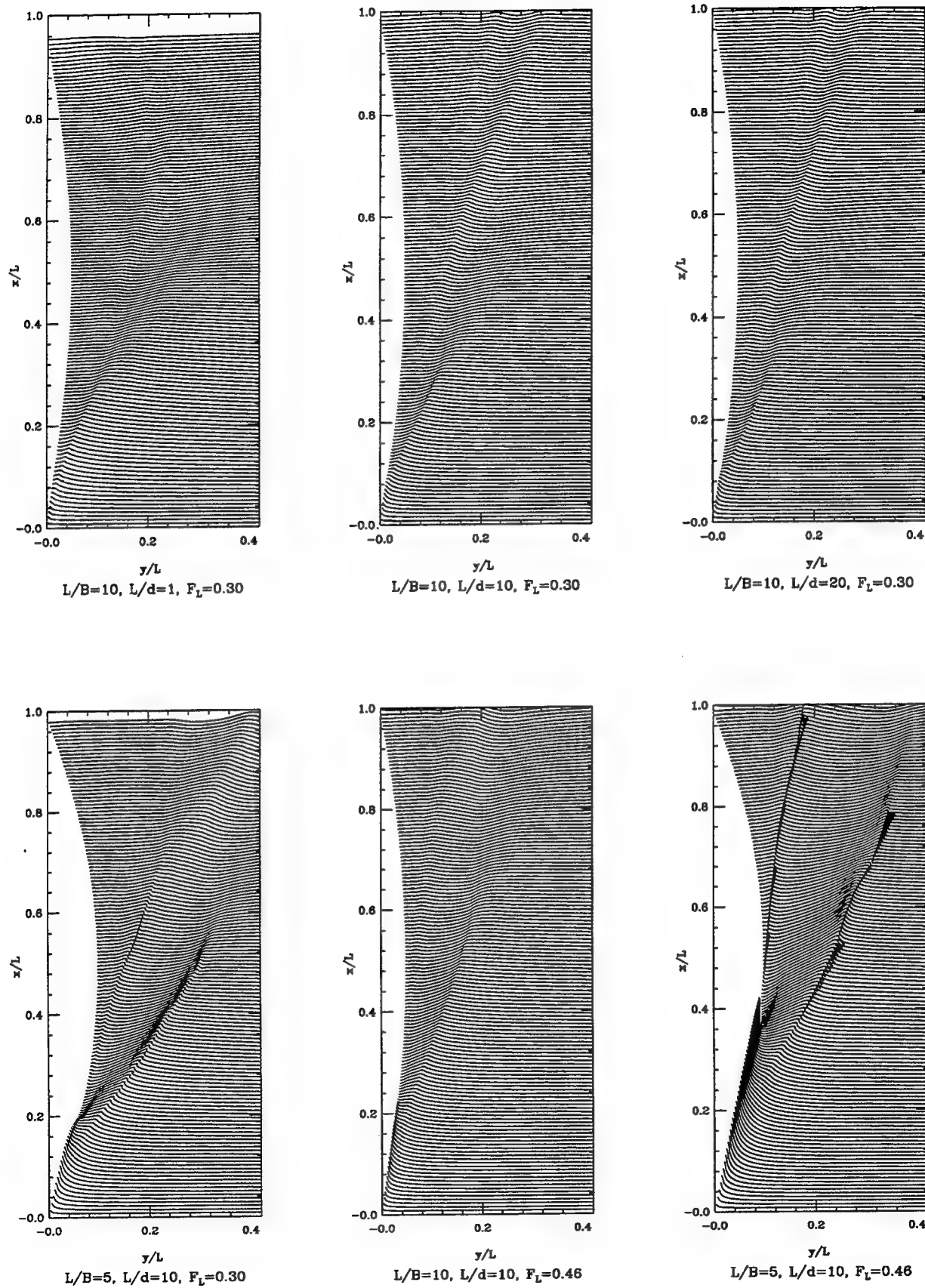


Figure 11: Wave Pattern of Wigley Hull at different L/d , L/B , F_L

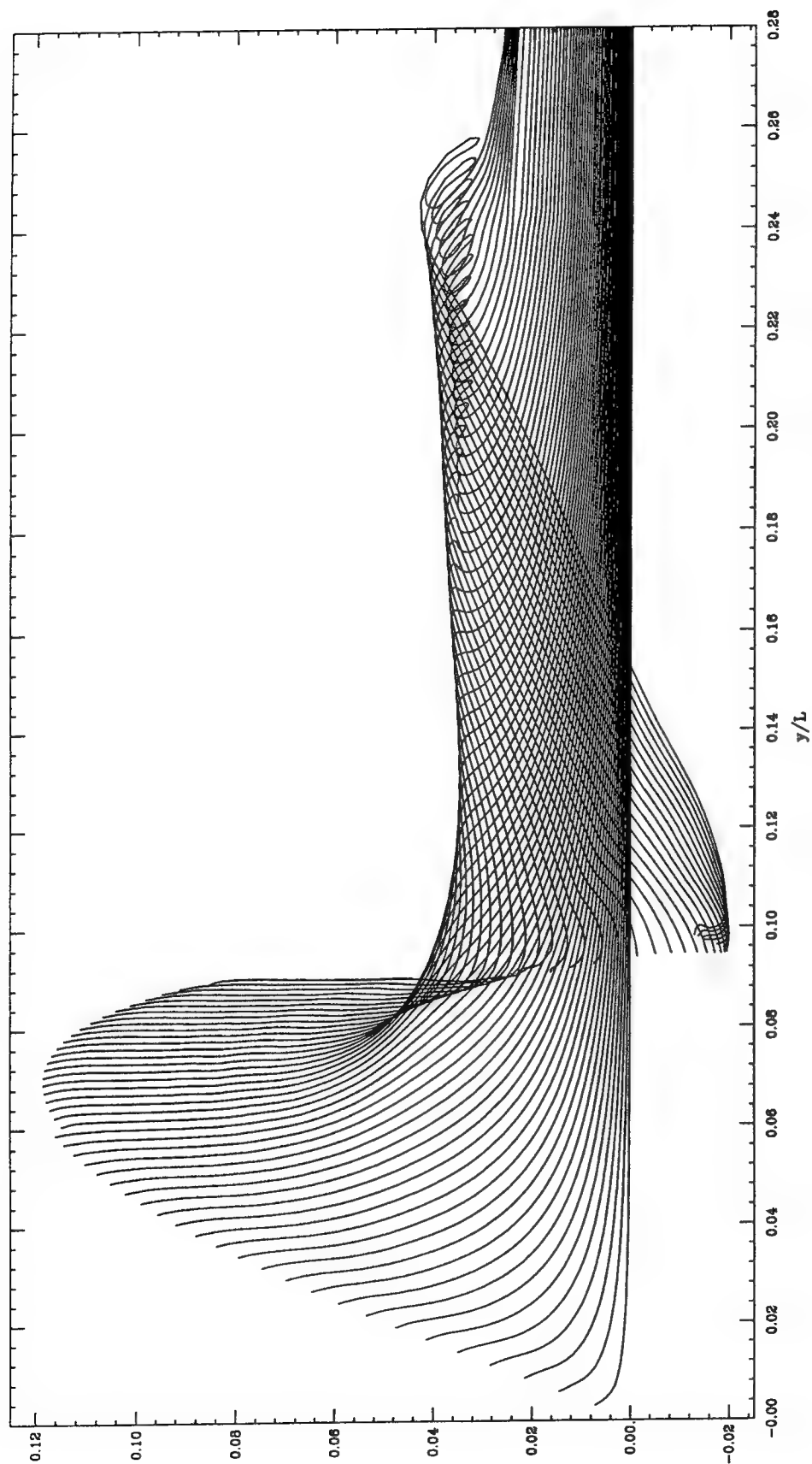


Figure 12: Breaking Bow Wave (A) and Jet Formation, Shown in Transverse Section, $x/L=0.0-0.493$

$B/L=0.2$, $D/L=0.1$, $F_L=0.46$

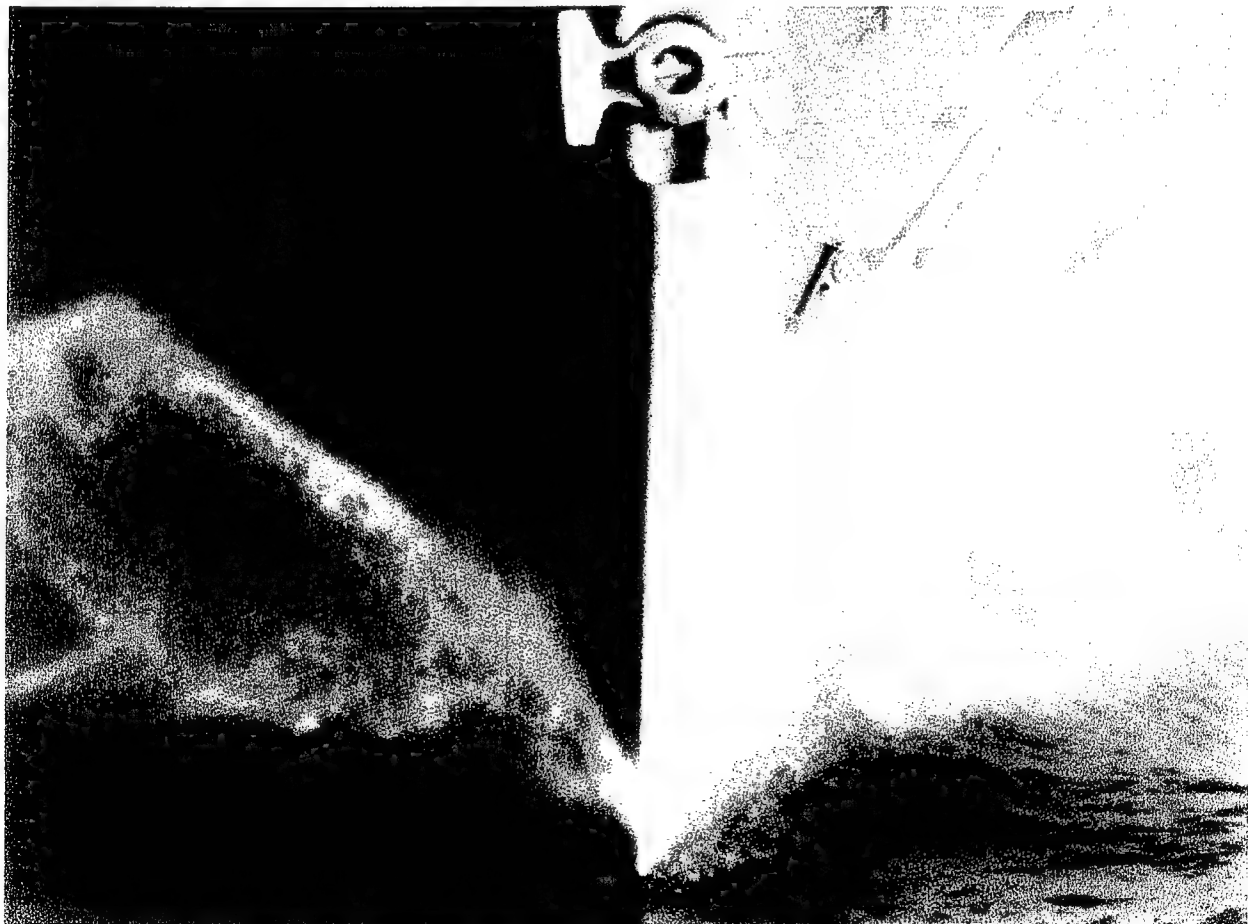
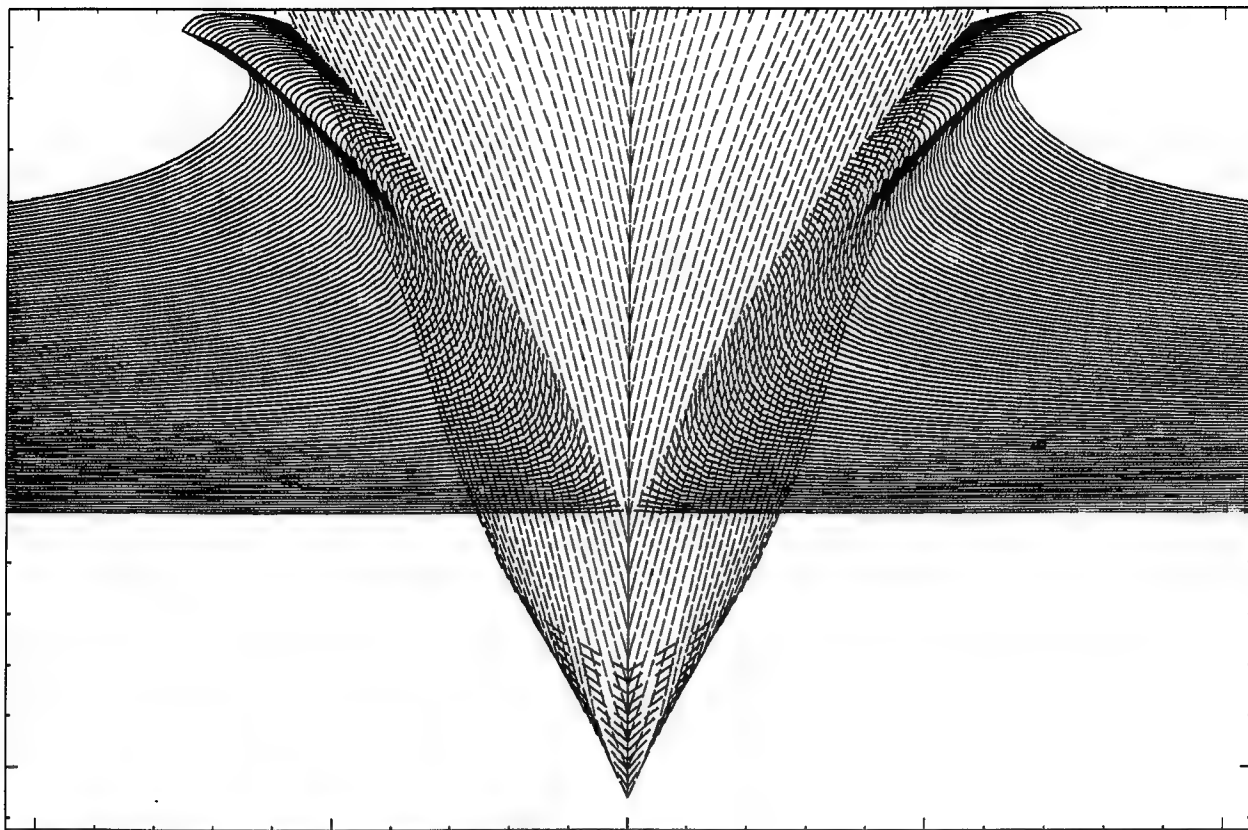
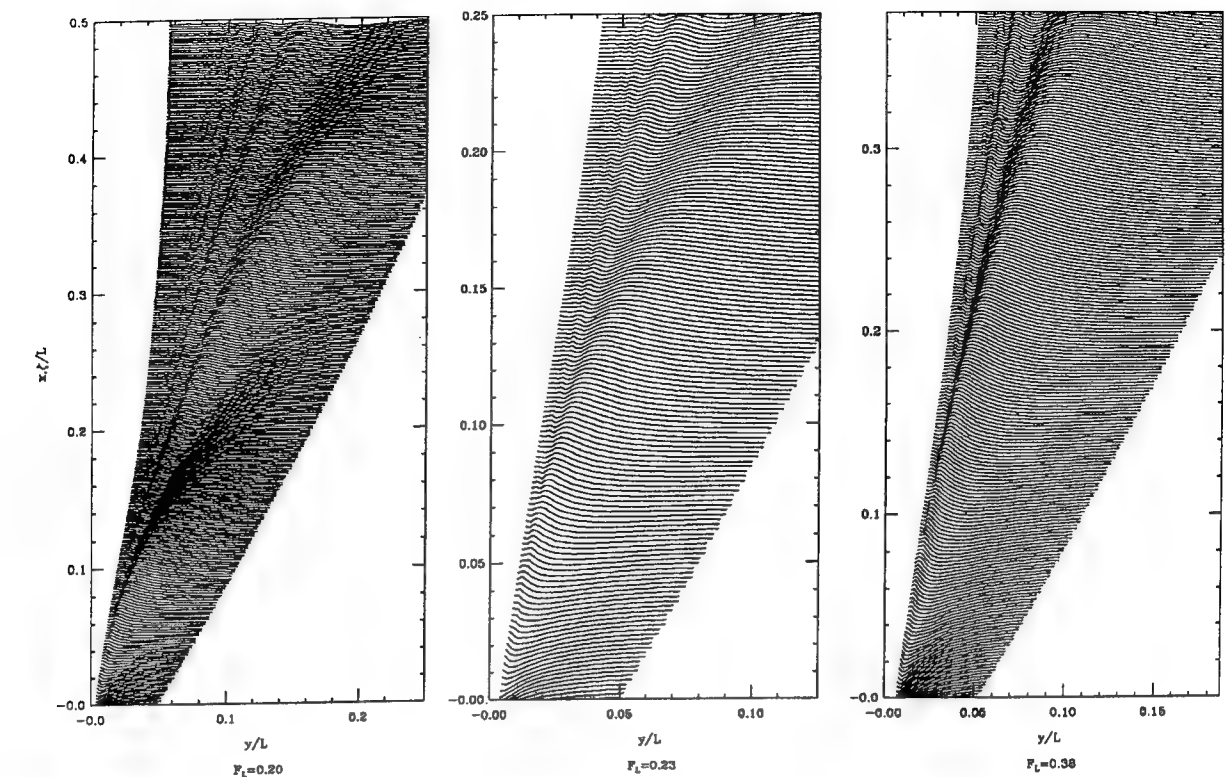


Figure 13: 2D+T Simulated Bow Wave by Frigate Hull, $F_L=0.5$ (top)
Photo (bottom), F_L Unknown



(Top) $B/L=0.11$, $d/L=0.072$

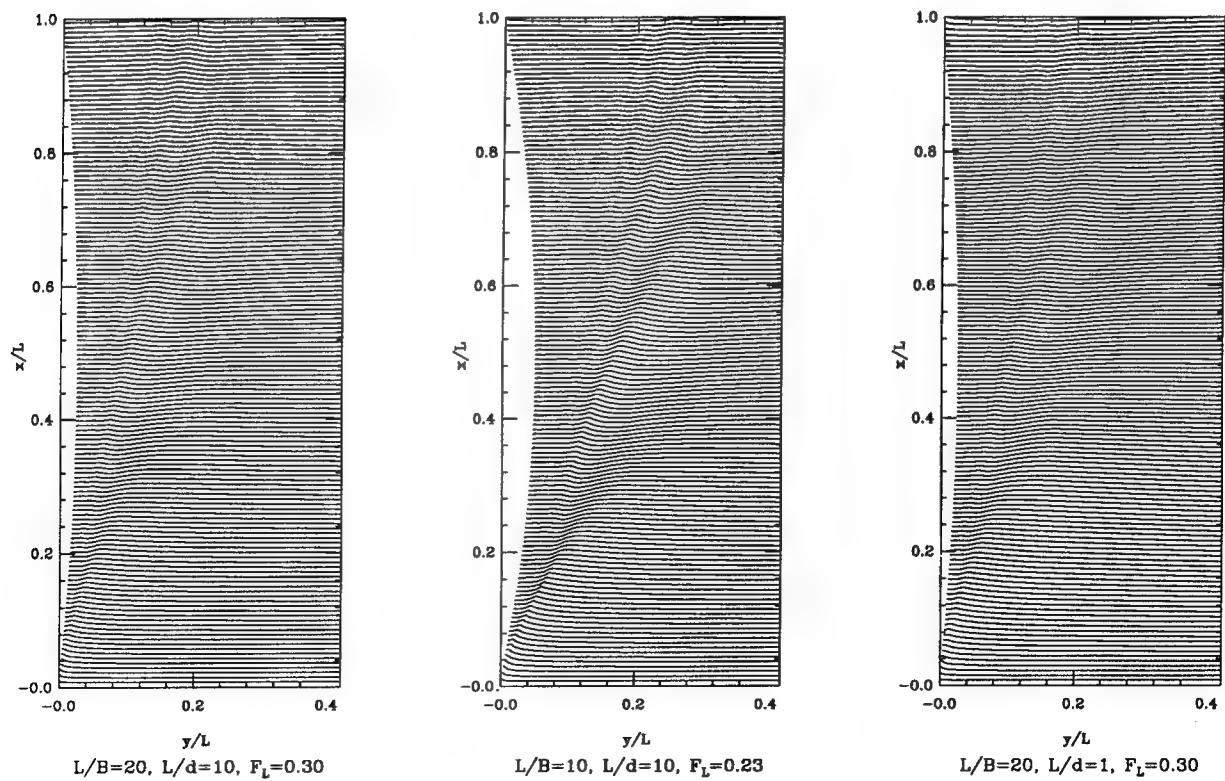


Figure 14: Comparison Between Calculated Bow Wave on Wigley Hulls
Linear (Michell) Distorted (top); Nonlinear 2D+T (bottom)

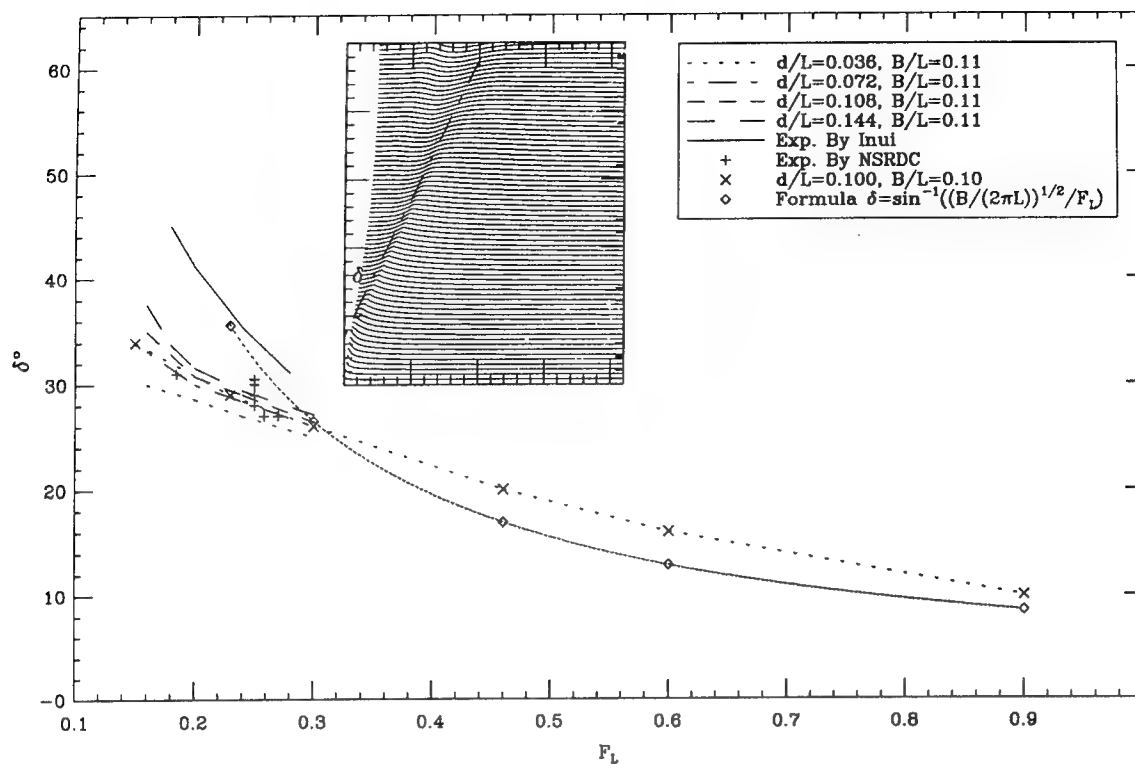


Figure 15: Inclination of Bow Wave (A) vs. F_L

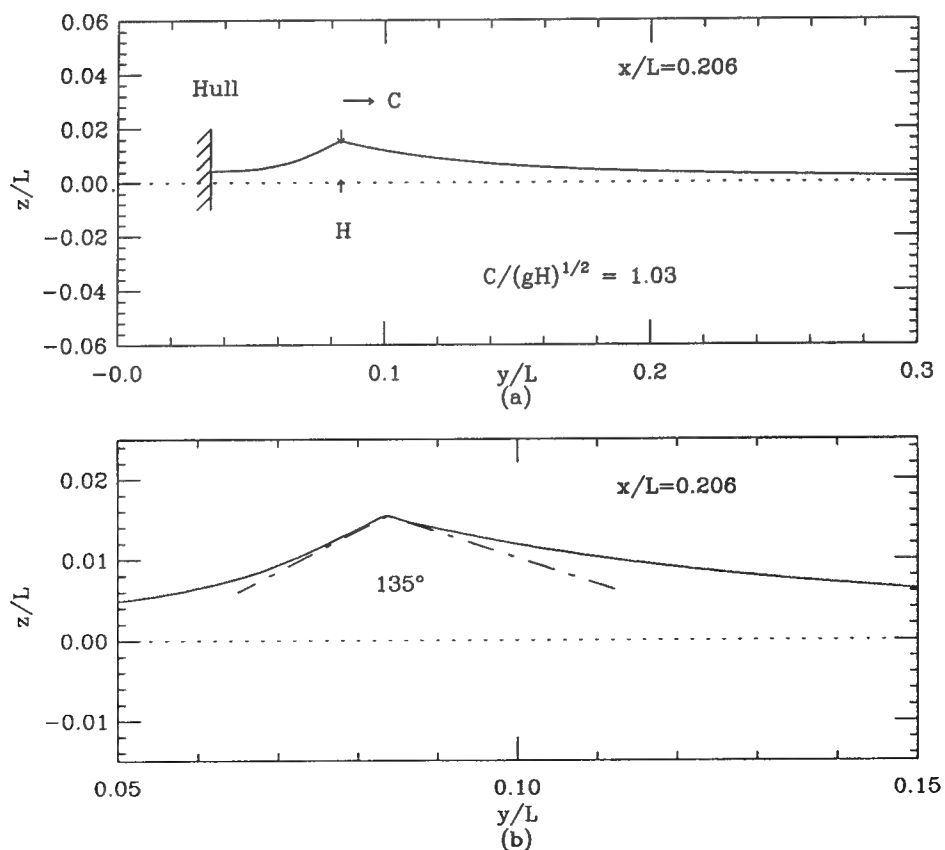


Figure 16: Bow Wave Crest Cut at $x/L=0.206$ for Parent Wigley Hull at $F_L=0.30$

A Method for the Optimization of Ship Hulls from a Resistance Point of View

C. Janson, L. Larsson (Chalmers University of Technology, Sweden)

Abstract

A method for optimizing ship hulls from a resistance point of view is presented. The SHIPFLOW program for computing the flow around ship hulls is linked to the OCTOPUS program for solving non-linear optimization problems. The resistance components including wave resistance from a potential-flow solution and viscous resistance from a boundary layer and a Navier-Stokes solution are included in the computation. In the optimization process a basic shape of the hull is given small disturbances and derivatives of the resistance and displacement with respect to the disturbances are computed. A linearized optimization problem can then be formulated and solved taking a displacement constraint into account. The optimized shape is used as a new basic shape and the procedure is iterated until convergence. Each iteration includes the generation of three computational models and a full resistance computation for the basic shape and every hull disturbance. The whole procedure is fully automatic and no user interference is needed during the optimization.

Experience from two examples shows that the optimization system works well from a computational point of view. The computed total resistance for the two cases was reduced by 11 and 9% respectively. However, experiments carried out for one of the examples did not confirm the improvements obtained in the computations. Three main reasons for the discrepancy between the computations and the experiments are discussed. The neglected viscous influence on the stern wave making seems to be the most important one.

Nomenclature

R_T	Total resistance
R_F	Friction resistance
R_{VP}	Viscous pressure resistance
R_W	Wave resistance
γ_j	Design variable, master variable
$\bar{\gamma}_j$	Upper bound for the design variable
$\underline{\gamma}_j$	Lower bound for the design variable
f_0	Objective function
f_i	Constraint function
\tilde{f}	Approximating function
\bar{f}_i	Bounds for the constraint
NC	Number of constraints
ND	Number of design variables
U_j	Upper moving asymptote
L_j	Lower moving asymptote
$L(\gamma, \lambda)$	Lagrange function
$\varphi(\lambda)$	Dual objective function
λ_i	Lagrange multiplier
(k)	Iteration number

1.0 Introduction

Resistance is one of the important areas that has to be taken into account in ship hull development. Prediction of ship resistance is in most cases based on results from experiments at model scale. If the resistance requirements are not fulfilled a modification of the hull shape is undertaken and another model test is carried out. This process forms a system for "manual optimization".

In recent years computational methods (CFD) have been introduced in the design process to predict the flow around the hull and in some cases also the resistance of the hull. Different design alternatives may be compared based on computed results and the best one is then selected for verification by model tests. In this way CFD methods may help to speed up the "manual optimization" process by reducing the number of "iterations" that are needed to find the final shape.

Another interesting possibility is to combine a CFD method and a mathematical optimization method together with a program for hull form variation. This system can then be used to find a hull form that is optimized with respect to properties computed by the CFD method, like the resistance, maximum wave height, velocity in the propeller plane, etc. One or more constraints, for instance displacement and hull main dimensions, must then be introduced to limit the modifications of the hull. This forms a system for "automatic optimization".

Many interesting works on hull form optimization from a hydrodynamic point of view have been presented through the years. Systems for "automatic optimization" as described above have been presented by Kim (1), Nowacki (2, 3), Papanikolaou et al. (4), Hsiung (5), Wyatt and Chang (6), Maisonneuve (7) and others. Different levels of approximation for the flow prediction, from thin ship theory for wave resistance and a simple formula like the ITTC-57 line for the viscous resistance to more advanced computational methods, both for the inviscid and the viscous flow, have been used.

Research in viscous and inviscid flow calculations has been carried out at SSPA Maritime Consulting and FLOWTECH International AB in collaboration with Chalmers University of Technology since about 1970. The computational methods developed in this research work, Xia (8), Kim (1), Larsson (9) and Broberg (10) are used in the present work together with an optimization method developed at the Royal Institute of Technology and at ALFGAM Optimization AB, Svanberg (11, 12) and Esping et al. (13, 14) to form a system for "automatic optimization" of ship hulls.

2.0 The Zonal approach

A zonal approach is used in SHIPFLOW to

compute the flow around the ship hull. The flow domain is divided into three zones, figure 1, and a computational method is developed for each zone. The first zone covers the entire hull and a part of its surrounding free-surface. A free-surface potential-flow method of Rankine-source type is used. The second zone is a thin layer at the hull surface and a boundary layer method of the momentum integral type is used. The momentum integral equations are solved along streamlines traced from the potential flow solution. Finally, the third zone includes the aft part of the hull and extends about half a ship length downstream of the hull. It also covers about half a ship length in the radial direction. A Navier-Stokes method of the RANS type using the $k-\epsilon$ model and a wall-law is used in zone three. The zones are computed in sequence and boundary conditions are generated for succeeding zones. The reason for the division of the flow field into zones is that the computational time may be reduced considerably compared to the global approach where the Navier-Stokes method is used in the entire computational domain.

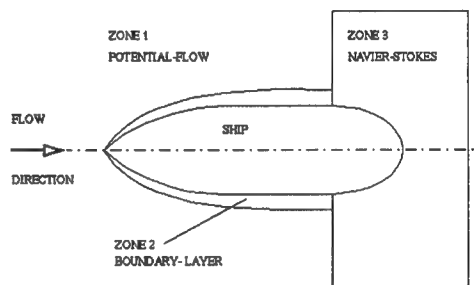


Fig. 1 The Zonal approach

2.1 The potential-flow method

Inviscid, irrotational flow is assumed and a velocity potential, whose gradient is equal to the local velocity may be defined. The potential is governed by the Laplace's equation which is an elliptic partial differential equation that requires boundary conditions on all boundaries of the computational domain. On the hull the flow in the hull surface normal direction must be zero and on the free-surface the flow must be tangent to the surface and the pressure must be constant. At infinity the disturbance due to the hull must vanish. One additional condition is also needed to prevent upstream waves. This condition is introduced together with the numerical method.

The potential-flow problem is non-linear and the free-surface boundary conditions have to be applied

on the wavy free-surface which is initially unknown. A linearization of the free-surface boundary conditions is therefore used and the conditions are applied to the undisturbed free-surface. To be able to make the linearization a known basic solution is required. A double-model solution as suggested by Dawson (15) is used as the basic solution in the present method. The exact non-linear problem can be solved as a series of linearized problems where the previous linear solution is used as the basic solution and the boundary conditions are applied on the wavy free-surface just obtained, Kim (1).

Quadrilateral panels are used to approximate the hull surface and part of the surrounding free-surface. The panels are of the Rankine-source type, Hess and Smith (16), and may be first order or higher order, Hess (17). The first order panels are flat having a constant source strength while the higher order panels are parabolic having a linear variation of the source strength. The source panels on the free-surface are in the present method positioned a small distance above the free-surface, a procedure that is known to improve the solution and to stabilize the non-linear computations, Xia (8), Raven (18) and Jensen et al. (19).

In their final form the free-surface boundary conditions contains second derivatives of the velocity potential. Two possibilities for computing the second derivatives are introduced in the present method. The first is to use an upstream four-point numerical operator as suggested by Dawson (15). The second is to use analytical formulas for the second derivatives as described by Jensen et al. (19) and Jensen (20). Upstream waves are automatically prevented when the upstream operator is used while a collocation point shift is introduced together with the analytical computation to fulfil this condition. Details of the potential-flow method is described in Kim (1), Janson (21), Larsson et al. (22) and (23).

2.2 The Boundary layer method

In a boundary layer the velocity changes from zero to approximately the ship speed across the boundary layer. If this is thin, the gradients in the hull surface normal direction dominate over the ones in the plane of the surface. It is thus possible to delete two of the stress derivatives in the Navier-Stokes equations. Since the velocity in the normal direction must be much smaller than the tangential velocities the equation for the normal velocity degenerates to the statement that the pressure is constant across the boundary layer. If the boundary layer is thin, it disturbs the potential flow very little, so the potential flow pressure distribution over the hull surface may be used for the pressure across the layer. The boundary layer equations are in the present method expressed in a curvi-linear orthogonal coordinate system. An integration of the equations in the normal direction gives the momentum integral equations. A further simplification of the equations is also introduced since the cross-flow in the boundary

layer is assumed to be small. The resulting ordinary differential equations are then solved using a Runge-Kutta technique along the potential flow streamlines traced on the hull surface.

Laminar and turbulent boundary layers can be computed in the present method. The computation of the former is started from a stagnation point, obtained from backwards streamline tracing, and is continued until transition occurs. After transition, initial conditions are generated for the turbulent boundary layer and the computation is continued along the streamlines. Alternatively the turbulent boundary layer computation may be started from initial values estimated from flat plate formulas. Details of the boundary layer method are described in Larsson (9).

Boundary layer methods are very accurate and efficient and can be used for the viscous flow over a large part of the hull as long as the boundary layer assumptions are valid. The thick viscous region close to the stern of a conventional hull cannot, however, be computed. But, the boundary layer solution can be used to generate the upstream boundary conditions for the Navier-Stokes method.

2.3 The Navier-Stokes method

The time averaged Navier-Stokes equations for incompressible flow are solved in zone three, and if all terms are included, the equations are elliptic. A predominant flow direction is often present for the flow around a ship hull and a somewhat simplified set of equations can be used, assuming that the stress derivative in this direction is small. The equations for the velocities then becomes parabolic and a marching technique can be used for the solution. The pressure calculation is, however, elliptic and the method can be referred to as partially parabolic. A curvi-linear non-orthogonal coordinate system is used and both the independent and the dependent variables are transformed to this system.

Transport equations are solved for the turbulent kinetic energy, k , and its rate of dissipation, ϵ . A wall law represents the velocity distribution close to the hull surface and the $k-\epsilon$ model can then be used for obtaining the turbulent viscosity in the entire flow domain.

Numerically the problem is solved using a finite-difference method. In the cross-plane a finite-analytic scheme is used while a second order upwind scheme is used in predominant direction. The pressure-velocity coupling is based on the SIMPLER algorithm.

Upstream, the boundary conditions are obtained from the boundary layer solution and from the potential flow solution outside this layer. The potential flow solution is used as boundary condition at the outer edge of the domain and at the downstream boundary

zero derivatives are specified for the dependent variables. Symmetry conditions are specified at the undisturbed free-surface level and at the centre plane. The theory for the Navier-Stokes method is described in detail in Broberg (10) and Larsson et al. (22) and (23).

2.4 Computation of resistance

There are three types of resistance components that can be computed in the present method, wave resistance, friction resistance and viscous pressure resistance. The potential-flow method may also include lift forces and induced drag.

Wave resistance is obtained from an integration of the potential flow pressure over the body surface. The pressure integration is for first order panels carried out as a summation over flat panels where the pressure and the normal direction are assumed to be constant over each panel. A more accurate integration is used if the computation is carried out for higher order panels. The pressure is then assumed to vary linearly over the panel and the normal direction is varying over the parabolic panel.

In case of a linear computation, where the body is panelized up to the undisturbed free-surface level, a resistance correction using the double-model resistance can be introduced. According to the d'Alemberts paradox the pressure integration over the double-model should be zero. This is however not true for a discretized body. A small resistance, positive or negative, is always obtained for the double-model. This double-model resistance should be small compared to the wave resistance if an accurate solution is to be obtained. A too high value of the double-model resistance indicates that the body is not well described by the chosen distribution of panels. The final wave resistance is then computed by subtracting the double-model resistance from the resistance obtained in the linear computation. It is thus assumed that the discretization error is the same in the free-surface and the double-model computations. The double-model correction can not be used for a non-linear computation since the body is panelized up to the wavy free-surface which excludes the possibility to compute a zero resistance case for comparison. A more accurate discretization of the body surface is therefore needed for non-linear computations.

Integration of the local skin friction coefficient over the hull surface is carried out to obtain the friction resistance. The local skin friction is computed as a part of the solution along the stream lines in the boundary layer method and from the wall shear stress of the wall law in the Navier-Stokes solution.

The potential-flow pressure over the stern part of the hull is changed due to viscous effects computed by the Navier-Stokes solution. An integration of the pressure including viscous effects gives the viscous pressure resistance. A form factor can also be com-

puted from the viscous pressure resistance and the friction resistance if the ITTC-57 line is used as reference.

3.0 The Optimization method

Optimization of a ship hull from a resistance point of view forms a non-linear optimization problem. The objective function (i.e. resistance) and the constraint (i.e. displacement) are non-linear functions of the design variables (hull modifications). The optimization problem may include multiple minima and a general optimization method cannot be expected to find a global minimum for this case. An optimization method, the Method of Moving Asymptotes, MMA, for solving non-linear optimization problems, Svanberg (11, 12), is implemented in the optimization program OCTOPUS, Esping et al. (13, 14), which is used in the present work. In MMA the solution is computed as a sequence of linearized sub-problems, where each sub-problem is obtained through a Taylor series expansion of the objective function and the constraints about the previous design point. The MMA method was originally developed for structural optimization problems but can also be applied to CFD problems as long as the objective functions, constraints and their gradients with respect to the design variable changes can be computed.

The non-linear optimization problem can be formulated as

$$\text{minimize: } f_0(\gamma) \quad (1)$$

$$\text{subject to: } f_i(\gamma) \leq \bar{f}_i \quad (2)$$

$$\underline{\gamma}_j \leq \gamma_j \leq \bar{\gamma}_j \quad i = 1, NC ; j = 1, ND \quad (3)$$

where γ is a vector of design variables.

An iterative approach for solving the non-linear optimization problem can be used if the function values and the gradients of the objective function and the constraints can be computed. The procedure is to select an initial design point (first iteration point) and compute the function values and the gradients. Then generate an explicit sub-problem that approximates the original problem. Find the optimal solution to the sub-problem with some suitable method and use the solution as the next iteration point. The iterations are continued until some convergence criterion is fulfilled.

The choice of approximating function is important for the success of the method and the approximating functions are preferably convex. The most obvious convex approximation is perhaps to use a first order Taylor expansion of the object function and the constraints.

minimize:

$$\tilde{f}_0^{(k)}(\gamma) = f_0(\gamma^{(k)}) + \sum_{j=1}^{ND} \left(\frac{\partial f_0}{\partial \gamma_j} \right)^{(k)} \cdot (\gamma_j - \gamma_j^{(k)}) \quad (4)$$

subject to:

$$\tilde{f}_i^{(k)}(\gamma) = f_i(\gamma^{(k)}) + \sum_{j=1}^{ND} \left(\frac{\partial f_i}{\partial \gamma_j} \right)^{(k)} \cdot (\gamma_j - \gamma_j^{(k)}) \leq \bar{f}_i \quad (5)$$

$$\underline{\gamma}_j \leq \gamma_j \leq \bar{\gamma}_j \quad i = 1, NC; j = 1, ND \quad (6)$$

This gives a linear programming problem which can be solved using the Simplex method. The convergence of the above method is, however, in some cases very slow.

In the MMA, both the objective function and the constraints are approximated by a first order Taylor expansion but the variables are in this case of the type

$$\frac{1}{(\gamma_j - L_j)} \text{ or } \frac{1}{(U_j - \gamma_j)}$$

where the first is used if the derivative of the object function or the constraints with respect to the design variable is negative and the second is used for a positive derivative. L_j and U_j are the lower and upper asymptotes for γ_j and γ_j will always be somewhere in between. L_j and U_j are adjusted in each iteration according to the behaviour of the solution. If the solution is oscillating in a design variable, the distance between L_j and U_j is diminished and if the change of the variable is monotonous a larger distance between L_j and U_j is allowed.

The original non-linear problem is reduced to a sequence of approximate sub-problems which can be formulated

minimize:

$$\tilde{f}_0^{(k)}(\gamma) = f_0(\gamma^{(k)}) \quad (7)$$

$$- \sum_{j=1}^{ND} \left(\frac{\partial f_0}{\partial \gamma_j} \right)^{(k)} (\gamma_j^{(k)} - L_j^{(k)})^2 \left[\frac{1}{(\gamma_j - L_j^{(k)})} - \frac{1}{(\gamma_j^{(k)} - L_j^{(k)})} \right]$$

or

$$+ \sum_{j=1}^{ND} \left(\frac{\partial f_0}{\partial \gamma_j} \right)^{(k)} (U_j^{(k)} - \gamma_j^{(k)})^2 \left[\frac{1}{(U_j^{(k)} - \gamma_j)} - \frac{1}{(U_j^{(k)} - \gamma_j^{(k)})} \right]$$

subject to:

$$\tilde{f}_i^{(k)}(\gamma) = f_i(\gamma^{(k)}) \quad (8)$$

$$- \sum_{j=1}^{ND} \left(\frac{\partial f_i}{\partial \gamma_j} \right)^{(k)} (\gamma_j^{(k)} - L_j^{(k)})^2 \left[\frac{1}{(\gamma_j - L_j^{(k)})} - \frac{1}{(\gamma_j^{(k)} - L_j^{(k)})} \right]$$

or

$$+ \sum_{j=1}^{ND} \left(\frac{\partial f_i}{\partial \gamma_j} \right)^{(k)} (U_j^{(k)} - \gamma_j^{(k)})^2 \left[\frac{1}{(U_j^{(k)} - \gamma_j)} - \frac{1}{(U_j^{(k)} - \gamma_j^{(k)})} \right] \leq \bar{f}_i$$

$$\underline{\gamma}_j \leq \gamma_j \leq \bar{\gamma}_j \quad i = 1, NC; j = 1, ND \quad (9)$$

where the first summation in equations (7) and (8) is used for the terms having a negative gradient and the second is used if the gradient is positive.

The constraints in the MMA approximation are convex and the objective function is strictly convex which gives the possibility to use dual methods to solve each sub-problem. In some sense, the dual problem is equivalent to the original sub-problem and is for the present formulation easy to solve numerically. The optimal solution of the original sub-problem can then be obtained from the solution of the dual problem. A Lagrangian function corresponding to the approximating sub-problem is the starting point for the dual formulation.

$$L(\gamma, \lambda) = \tilde{f}_0(\gamma) + \sum_{i=1}^{NC} \lambda_i (\tilde{f}_i(\gamma) - \bar{f}_i) \quad (10)$$

Where λ_i are Lagrangian multipliers which are required to be non-negative. The Lagrange function is then strictly convex and there is a unique $\gamma = \gamma(\lambda)$ which minimizes the Lagrange function. A dual objective function can be defined by minimizing the Lagrange function with respect to the design variables.

$$\varphi(\lambda) = \min_{\gamma} (L(\gamma, \lambda)) = L(\gamma(\lambda), \lambda) \quad (11)$$

The dual problem corresponding to the original minimizing sub-problem is then:

$$\text{maximize: } \varphi(\lambda) \quad (12)$$

$$\text{subject to: } \lambda \geq 0 \quad (13)$$

A solution to the dual problem can be computed using methods for unconstrained problems, for instance conjugate gradient or Newton methods. Once the optimal solution, λ^* , of the dual problem is found, the unique global optimum to the original sub-problem can be computed as $\gamma(\lambda^*)$. This correspondence

between the original and the dual problem holds because of the convexity of the constraints and the strict convexity of the objective function of the original approximating sub-problem.

4.0 A system for ship hull optimization

The SHIPFLOW code for computation of the flow around ship hulls and the program OCTOPUS for solving non-linear optimization problems are used to form a system for ship hull optimization, figure 2. Included in the system is also a geometry program ALADDIN. The optimization starts from an original shape defined by a set of offset-points on the hull surface. In the optimization procedure all or selected offset-points are attached to a design variable, figure 3, which represents the location of the point along a line, in the direction of which it is allowed to move (for instance the surface normal direction). The design variables may be either master or slave variables, the latter being determined as linear combinations of the former. Given the master and slave variable values the position of the offset-points on the surface is specified and so is the shape of the hull. Master and slave variables are attached to the offset-points in ALADDIN and a basic shape together with a number of variations are created. The variations are obtained through a small disturbance of the master variables, one at the time. SHIPFLOW then computes the resistance (objective function) for the basic shape and the derivative of the resistance with respect to the master variable variations. A computation of the displacement of the ship (constraint) together with the derivatives of the displacement with respect to the master variable variations is also performed. Enough information for creating and solving an approximate sub-problem of the optimization problem can then be formulated. The optimum of the sub-problem is computed in OCTOPUS and the new values of the design variables are computed and transferred to ALADDIN where a new basic shape together with variations are created. The process is iterated until the constraints are fulfilled and no further improvements are obtained within some convergence criteria.

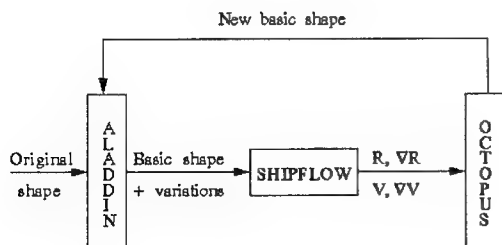


Fig. 2 The system for hull optimization

The coordinates of an offset-point, p , directly connected to a master variable, γ_j , are determined from

$$\begin{aligned} x_p &= x_{0p} + \alpha_x \cdot \gamma_j \\ y_p &= y_{0p} + \alpha_y \cdot \gamma_j \end{aligned} \quad (14)$$

$$z_p = z_{0p} + \alpha_z \cdot \gamma_j$$

where (x_{0p}, y_{0p}, z_{0p}) are the coordinates of the original position and $\alpha_x, \alpha_y, \alpha_z$ are linking factors between the master variable and the point.

Other offset-points, q , where a slave variable is assigned are computed in a similar way.

$$\begin{aligned} x_q &= x_{0q} + \sum_{j=1}^{ND} \beta_{xj} \cdot \gamma_j \\ y_q &= y_{0q} + \sum_{j=1}^{ND} \beta_{yj} \cdot \gamma_j \\ z_q &= z_{0q} + \sum_{j=1}^{ND} \beta_{zj} \cdot \gamma_j \end{aligned} \quad (15)$$

where (x_{0q}, y_{0q}, z_{0q}) are the coordinates of the original position and $\beta_{xj}, \beta_{yj}, \beta_{zj}$ are linking factors between the offset-point and each of the master variables.

Once the hull surface is defined, grids suitable for the potential flow calculation, the boundary layer calculation and the Navier-Stokes calculation may be generated using grid generators developed for each computational method, figure 4, 5 and 6.

In the present version of the optimization system the only possible objective function is the resistance.

$$R_T = R_F + R_{VP} + R_W \quad (16)$$

All or selected components of the resistance may be included in the total resistance depending on the number of zones that have been included in the flow computation. The only possible constraint is the displacement, V .

Gradients of the objective function and the constraint with respect to the master variable changes are obtained by numerical differentiation.

$$\frac{\partial R_T}{\partial \gamma_j} = \frac{R_T(\gamma_j + \delta \gamma_j) - R_T(\gamma_j)}{\delta \gamma_j} \quad (17)$$

$$\frac{\partial V}{\partial \gamma_j} = \frac{V(\gamma_j + \delta\gamma_j) - V(\gamma_j)}{\delta\gamma_j} \quad (18)$$

$j = 1, ND$

$\delta\gamma_j$ is the small disturbance of the master variables generated in ALADDIN before the flow computations in each iteration.

The iteration procedure is terminated when the following two criteria are fulfilled.

$$\frac{R_T^{(k)} - R_T^{(k-1)}}{R_T^{(k)}} \leq 0.0001 \quad (19)$$

$$\frac{V^{(k)}}{\underline{V}} \geq 1 - 0.01 \quad (20)$$

\underline{V} is the displacement of the original hull.

5.0 Optimization of the Series 60 hull

The optimization procedure was applied to the Series 60 $C_B=0.6$ hull at a Froude number of 0.316 and a Reynolds number of 5.0×10^6 . Sinkage and trim effects were not included. The hull was optimized with respect to the total resistance including wave resistance from a linear potential-flow solution and viscous resistance from boundary layer and Navier-Stokes solutions.

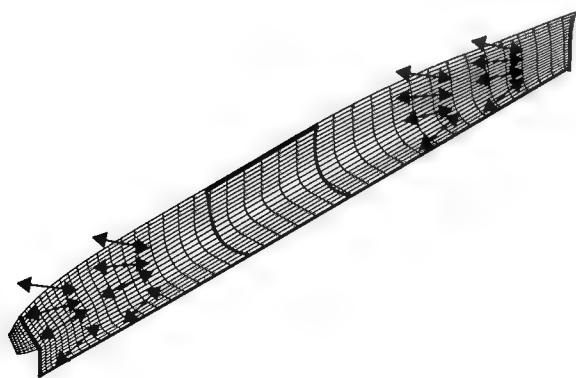


Fig. 3 Position of the master variables

A total of 16 master variables were used in the optimization model. The master variables were attached to four offset points at each of the stations $x/Lpp = 0.11, 0.22, 0.77$ and 0.90 as shown in figure 3.

Offset points located at the stem, stern and keel line were not allowed to move during the optimization. The midship section between $x/Lpp = 0.41$ and $x/Lpp = 0.6$ was also kept unchanged. Upper and lower limits for the master variable values were specified and the 16 attached offset points were allowed to move in the hull surface normal direction in the plane of the section. Slave variables, equation (15), were used to connect the neighbouring offset points to the master variables and the slave variable values varied linearly, both in the streamwise and girthwise directions, from a maximum value at the master variable in question to zero at the next master variable or fixed boundary.

Three computational models, one for each of the computational methods, were created for the basic shape and for each master variable change in each iteration which gives a total of 17 complete computations in each iteration. The computational model for the potential-flow solution, figure 4, included about 900 panels and a linear computation without sinkage and trim was performed. 10 potential-flow streamlines traced between 5% and 95% of the ship length, figure 5, were used for the boundary layer computation. A turbulent boundary layer was assumed at the starting point and the initial values were estimated from flat plate formulas. The computational model for the Navier-Stokes solution, figure 6, included 20000 points ($50 \times 20 \times 20$) and the mean value of the distance to the first point off the hull, y^+ , was about = 80. All Navier-Stokes solutions were started from a converged solution for the original hull (first basic shape). Each succeeding computation was then executed 15 more iterations. No user interference is needed during the optimization process.

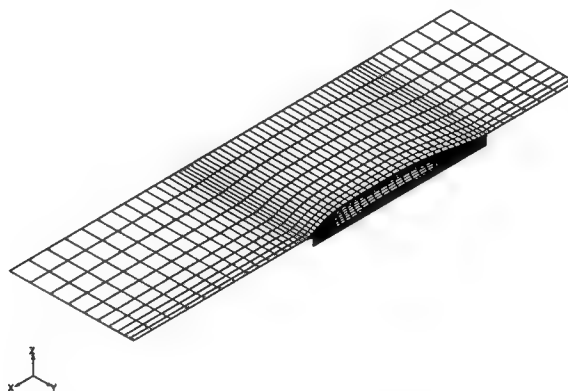


Fig. 4 Computational model for the potential-flow

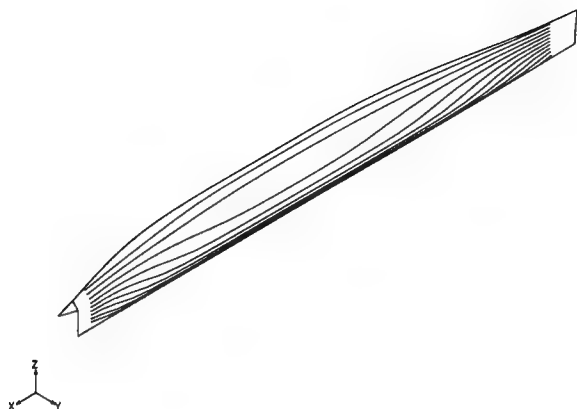


Fig. 5 Potential flow streamlines for boundary layer solution

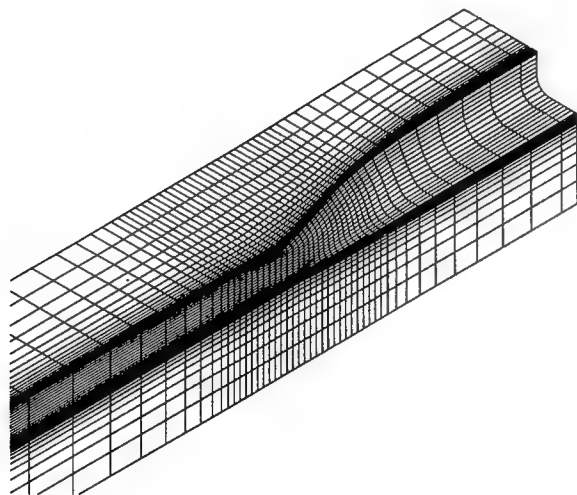


Fig. 6 Computational model for the Navier-Stokes solution

Two optimizations were carried out using different limitations, one larger and one smaller range, for the master variable changes. The constraint was in both cases that the displacement was not allowed to be smaller than for the original hull. The computed total resistance for the optimized hull was 11% less than for the original hull when the larger master variable range was used and 9% less for the smaller. Hull modifications outside the hull main dimensions were allowed for the larger range while the modifications were kept inside the main dimensions for the small range.

The original and optimized hulls for the large range are compared in figure 7 for the x/L_{pp} positions

0.1, 0.2 0.3 0.5 0.7 0.8 and 0.9. It is seen that the volume of the lower part of the fore body has increased dramatically and the fore body is now more bulb-shaped than the original one. The maximum draught is also increased at the fore body which indicates that the limits for the master variable changes close to the keel line are too wide, at least if the intention is to keep the hull main dimensions constant. The lines of the aft body are more U-shaped than the original ones and the volume close to the water line is decreased. Since the volume was constant during the optimization this means that volume was moved from the aft body close to the waterline to the lower part of the fore body and to the lower part of the aft body. The longitudinal position of the centre of buoyancy moved 1% forward and 0.15% of L_{pp} downwards.

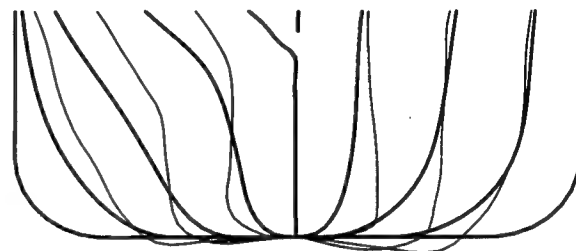


Fig. 7 Original and optimized hull, large range
Thick lines - original hull
Thin lines optimized hull

A comparison of the original and optimized hulls for the small range is shown in figure 8 for the same positions as in figure 7 and the two optimized shapes are compared in figure 9. As can be seen in the figures the aft body modifications are very similar for the smaller and the larger range. The volume in the fore body was positioned closer to the free-surface for the smaller range and the water line angle becomes larger.

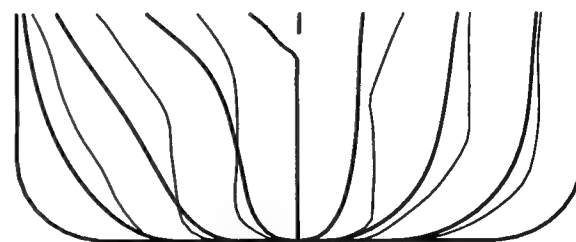


Fig. 8 Original and optimized hull, small range
Thick lines - original hull
Thin lines - optimized hull

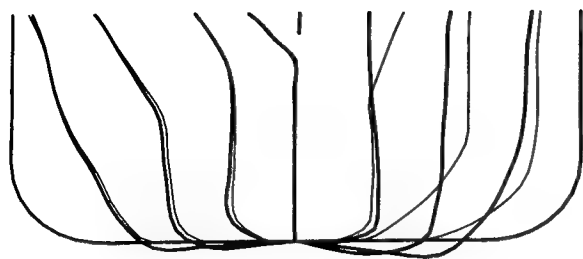


Fig. 9 Optimized hull
Thick lines - large range
Thin lines - small range

It is obvious that none of the two optimized hull forms are acceptable from a practical point of view but this can not be expected since the optimization system does not include any constraints on the hull modifications from a practical point of view or from a lines fairing point of view. The two optimizations also allowed for very large changes of the shape.

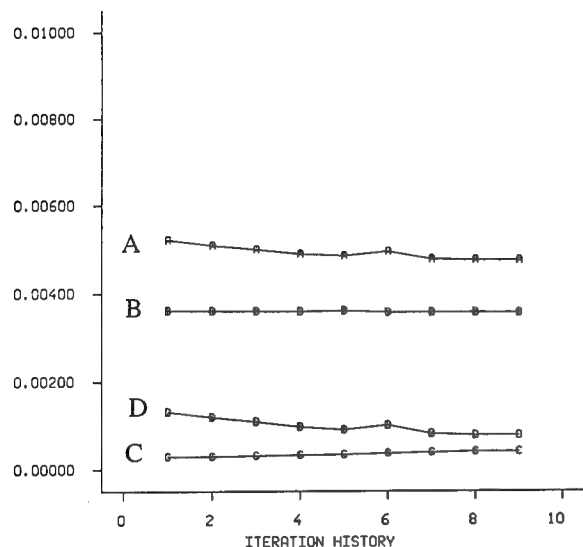


Fig. 10 Iteration history for the optimization
A - Total resistance
B - Friction resistance
C - Viscous pressure resistance
D - Wave resistance

The second case where the hull modifications were kept inside the main dimensions was selected for the discussion in the following sections. The iteration history of the resistance components, figure 10, shows that the main part of the reduction comes from the

wave resistance, while the friction resistance is almost constant and the viscous pressure resistance increases. The reduction of the wave resistance is much larger than the increase of the viscous pressure resistance. A total reduction of 9% is obtained in 9 iterations.

The wave profile at a longitudinal cut close to the hull side is compared for the original and the optimized hull in figure 11. The bow wave is slightly larger for the optimized hull, but the stern wave is reduced considerably which explains the lower wave resistance. This may be in accordance with the hull modifications where the volume was moved from the upper part of the aft body to the fore body. The hull modifications gave a more U-shaped aft body. This may result in a more pronounced bilge vortex that can explain the increase in the viscous pressure resistance.

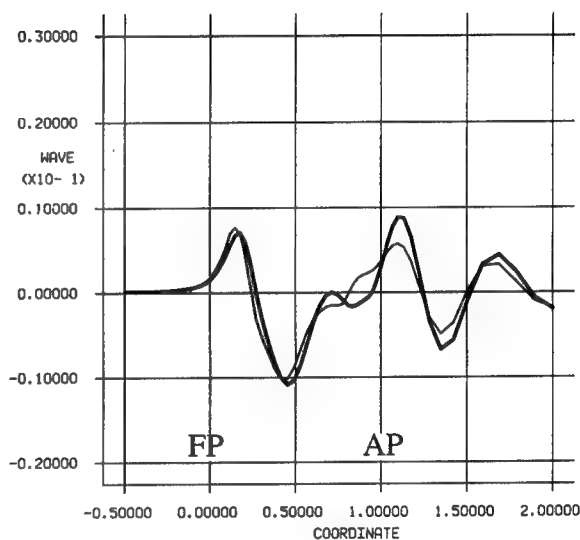


Fig. 11 Wave profile at $y/L_{pp} = 0.0755$
Thick line - original hull
Thin line - optimized hull

Both a finer and a coarser computational grid than in the optimization were used for the original and optimized hull to verify the result and it was found that the improvement was the same within 1% for all grids. It was therefore believed that the improvement came from the modification of the hull shape and not from the rearrangement of the computational grid during the optimization process.

6.0 Experiments

To finally verify the optimization a model test was carried out for both the original and the optimized hull. Resistance measurements for a model free condi-

tion and wave profile measurements for a fixed condition were carried out at SSPA Maritime Consulting. The optimized hull was introduced in the hull design program NAPA and the lines were slightly modified to smooth the hull, but great care was taken to keep the main features of the optimized hull. A final computation was thereafter performed using the coordinates from the faired lines. This additional computation was to verify that the main features of the optimized hull were not changed and that the total resistance reduction was the same as before the lines fairing. The slightly modified hull showed about 1% higher resistance. The length of the models was $L_{pp}=5.0$ m.

The resistance measurements for the model free condition, figure 12, did not verify the resistance reduction obtained in the computations. Based on the computations the increased resistance at low speeds was expected due to the higher viscous pressure resistance and the larger form factor for the optimized hull, but the residuary resistance was expected to be much lower at speeds close to the Froude number 0.316.

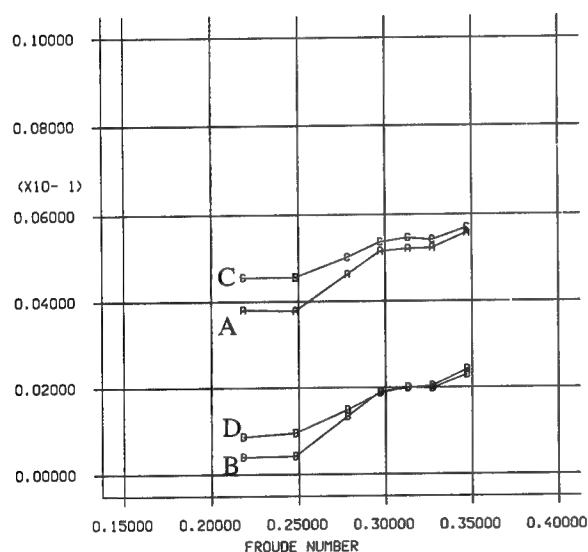


Fig. 12 Resistance measurements, model free condition.
A-Total resistance coefficient, original hull
B-Residuary resistance coefficient, original hull
C-Total resistance coefficient, optimized hull
D-Residuary resistance coefficient, optimized hull

Since the optimization worked well from a computational point of view, the question is now why the computations failed to find the same difference between the original and the optimized hull as the experiments. Were there flow phenomena missing in the computational model or was the grid resolution not good enough or was it a combination of both?

The potential-flow solution was first investigated. A linear computation without sinkage or trim

had been used in the optimization and the reduction of the wave resistance coefficient was 0.51×10^{-3} . Non-linear computations without sinkage and trim were now carried out and a reduction of 0.36×10^{-3} was obtained if the same grid distribution was used. Another non-linear computation was also carried out using a finer grid and the reduction was then 0.37×10^{-3} . It was therefore concluded that the absent non-linear effects can explain part of the discrepancy between computations and experiments. The grid refinement seems to be of minor importance.

In figures 13 and 14 a comparison of the computed and measured wave profiles is made close to the hull for the original and the optimized hull. The computed wave profiles agree well with the measurements but the bow wave amplitude is underpredicted. Both measurements and computations show a higher bow wave crest for the optimized hull and the irregular profile from the measurements indicates that wave breaking occurs for the optimized hull. The wave breaking, which cannot be captured in the potential flow model, was also observed in photos from the experiments. The reduction of the stern wave amplitude for the optimized hull is much more pronounced in the computations than in the measurements.

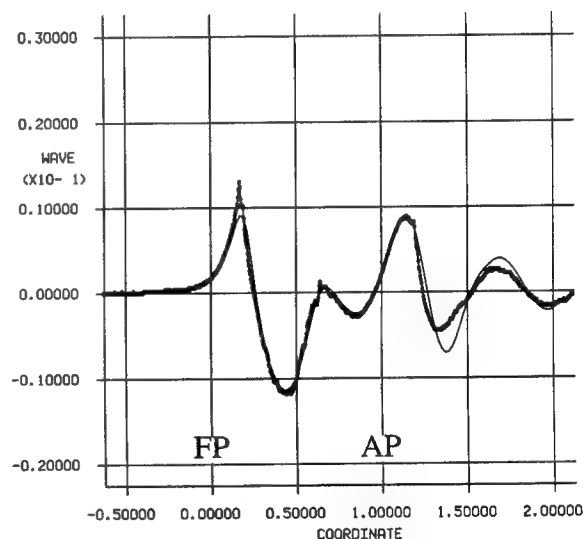


Fig. 13 Wave profile at $y/L_{pp} = 0.0755$, original hull
line with circles - experiments
line without circles - computations

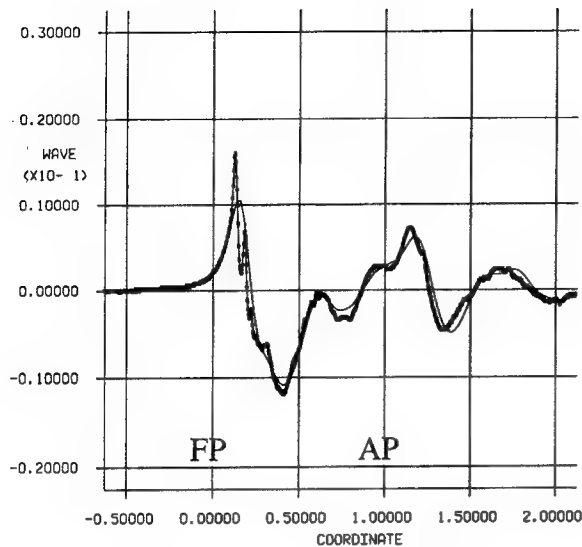


Fig. 14 Wave profile at $y/L_{pp} = 0.0755$, optimized hull
line with circles - experiments
line without circles - computations

Non-linear computations including sinkage and trim were also executed using the finer grid. The reduction of the wave resistance was in this case 0.44×10^{-3} which indicates that the optimized hull performs slightly better in model free condition than in model fixed compared to the original hull.

All potential-flow computations showed a large reduction of the stern wave for the optimized hull. The reduction was much smaller in the experiments and the grid refinement did not improve the prediction. One attempt was therefore made to investigate if the interaction between the viscous flow and the wave making at the stern is of importance. The displacement thickness obtained from the boundary layer solution was used to represent the effect of the viscosity on the potential flow. The shape of the original and the optimized hulls was modified by adding the displacement thickness. To make it possible to add the displacement thickness also at parts covered by the wave in the non-linear computations, a boundary layer computation was performed for a draught larger than the design draught. The potential flow computations were then repeated using the modified hull shapes and the finest grid. This procedure can not be considered very accurate since the boundary layer assumptions are not valid in the stern part of the hull and the boundary layer method used is of first order. The results may, however, give an indication if there is a significant influence of the viscous flow on the wave making.

There is also a question how to represent the modified hull downstream of the stern where only the

displacement thickness is present, Larsson and Chang (24). The hull was in the present computations closed downstream of the stern and three positions of the closure point were tested, 7.5%, 10% and 20% of L_{pp} downstream of AP. Only small differences were found for the three positions and 7.5% was selected for the final computations. A large reduction of the stern wave amplitude was obtained for both the original and optimized hull when the displacement thickness was added to the hull.

The wave resistance cannot be obtained from pressure integration over the hull surface when the displacement thickness is added since the modified surface does not represent the real shape of the hull. A longitudinal wave cut method described by Michelsen and Ubroi (25) and Lundgren and Åhman (26) was therefore used when the influence of the displacement thickness on the wave resistance was investigated. The difference between the original and the optimized hull was 0.52×10^{-3} without displacement thickness and 0.29×10^{-3} when the displacement thickness was included. It seems that the effect of including the displacement thickness is to reduce the influence of the hull modifications on the potential-flow solution. It was therefore concluded that in this case there is a significant influence between the viscous flow and the wave making at the stern but the magnitude of the influence cannot be determined from this investigation. The displacement effect was not included in the optimization and this is probably the main reason why a too large reduction of the stern wave was obtained.

The computation of the viscous forces was also investigated since the experiments showed an increase of the viscous forces by 7.7% for the optimized hull while the computations showed an increase of 2.3%. A grid refinement study was carried out and the finest grid including 75000 ($120 \times 25 \times 25$) points showed an increase of 3.5%. It was therefore concluded that only a small part of the difference can be referred to grid resolution. The form factor was in the experiments 0.07 for the original hull and 0.15 for the optimized hull while the computations for the finest grid showed 0.108 and 0.133 respectively. In general an overprediction of the form factor is obtained for slender hulls. The wakes for the original and optimized hull are plotted in figures 15 and 16. A more pronounced bilge vortex was obtained for the U-shaped aft body of the optimized hull. The strength of the vortex is probably underpredicted for both hulls which is a well known behaviour of the standard $k-\epsilon$ model. See the discussion at the workshops (27) and (28). The $k-\epsilon$ model together with the wall law may form a too "stiff" computational model for predicting the magnitude of the vortex changes between the hulls. This is a likely reason why the increase of the viscous forces was underpredicted.

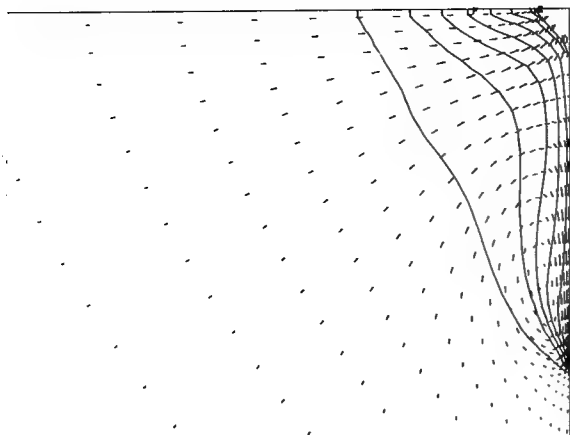


Fig. 15 Wake at AP, original hull
Isowakes for 0.5, 0.6, 0.7, 0.8 and 0.9

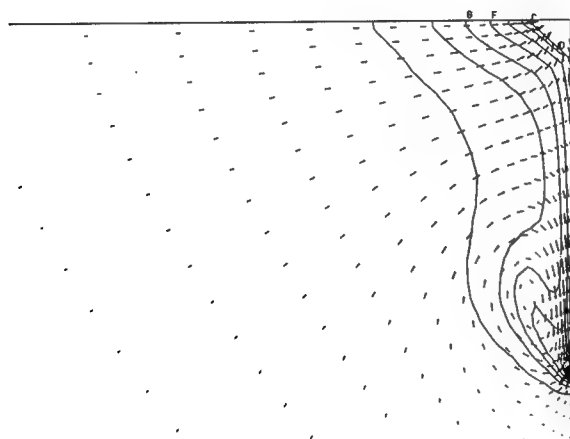


Fig. 16 Wake at AP, optimized hull
Isowakes for 0.5, 0.6, 0.7, 0.8 and 0.9

7.0 Conclusions

The optimization worked well from a computational point of view. Two optimizations were carried out for the Series 60 hull using different limits for the allowed hull modifications and the computed total resistance was reduced by 11 and 9% respectively.

The Method of Moving Asymptotes, MMA,

for optimization of non-linear problems performed well for the present application. When searching for an optimum MMA takes large steps in the right direction in the first iterations. This is interesting from an engineering point of view since only a few iterations are required to come close to the optimum. The convergence is, however, slower as the optimum is approached.

Experiments carried out for the original and one of the optimized hulls did not verify the resistance improvements obtained in the computations.

Three main reasons for the discrepancy between the computations and the experiments are found:

1. The neglected non-linear effects on the waves gave a too small increase of the bow wave system for the optimized hull.
2. A too large reduction of the stern wave was obtained for the optimized hull, probably due to the neglected viscous effects on wave making.
3. The increase of the viscous resistance was under predicted, partly due to grid resolution, but the main reason is probably that the $k-\epsilon$ model and the wall law give a computational model that is insensitive to hull modifications. This may influence the strength of the predicted bilge vortex.

For the three points above it may be noted that the computations predicted the right trends but the magnitude was wrong. The experiments showed a larger bow wave for the optimized hull. Linear computations of the waves, included in the optimization, showed a small increase of the bow wave and the increase was even more pronounced when the computations were repeated using non-linear free-surface boundary conditions. The stern wave was reduced in the experiments but the reduction was overpredicted in the computations. Both the experiments and the computations showed an increased viscous resistance but the increase was underpredicted.

In future work, parts of the optimization system must be improved. The most important improvement is a Navier-Stokes solver including the free-surface. Non-linear free-surface boundary conditions in the potential-flow solution may also improve the results. The routine for hull modifications must be improved to ensure hull forms of practical use.

Optimization from a wave resistance point of view must be restricted to fore body design until a Navier-Stokes method including the free-surface waves is introduced in the optimization system.

8.0 Acknowledgements

The authors would like to thank Dr. Keun-Jae Kim, who started the optimization work in the research group, for interesting discussions. Special thanks are also due to Dr. Björn Esping and Dr. Dan Holm at ALFGAM Optimization AB for the permission to use the OCTOPUS program and for their help when linking the SHIPFLOW and OCTOPUS programs. Thanks also to SSPA Maritime Consulting for carrying out the experiments and for manufacturing the optimized Series 60 model and to SVA, Potsdam, Germany, for lending us the original Series 60 model.

9.0 References

1. Kim, K.J., "Ship Flow Calculations and Resistance Minimisation," PhD Thesis, 1989, Department of Marine Hydrodynamics, Chalmers University of Technology, Gothenburg.
2. Nowacki, H., "Hull Form Variation and Evaluation," J. Kansai Society of Naval Architects, Japan, No 219, March 1993, pp. 173-184.
3. Nowacki, H., "Optimization Methods Applied to Viscous Drag Reduction," Proceedings of the Osaka International Colloquium on Ship Viscous Flow, Osaka, Japan, 1985.
4. Papanikolaou, A., Zaraphonitis, G. and Androulakis, M., "Preliminary Design of a High-Speed SWATH Passenger/Car Ferry," Marine Technology, Vol. 28, No. 3, 1991, pp. 129-141.
5. Hsiung, C.C., He, Y.J. and Cong L.Z., "Optimal Ship Forms for Minimum Total Resistance With the Consideration of Boundary Layer and Wake," 5th International Symposium on the Practical Design of Ships and Mobile Units, Newcastle upon Tyne, UK, Vol. 1, 1992, pp. 1.33-1.46.
6. Wyatt, D.C. and Chang, P.A., "Development and Assessment of a Total Resistance Optimized Bow for the AE-36," Marine Technology, Vol. 31, No. 2, April 1994, pp. 149-160.
7. Maisonneuve, J.J., "Optimization Tools for Ship Resistance and Seakeeping Problems," Proceedings of the Second International Conference on Fast Sea Transportation, Yokohama, Japan, Vol. 2, 1993, pp. 1465-1476.
8. Xia, F., "Numerical Calculation of Ship Flows, with Special Emphasis on the Free Surface Potential Flow," PhD Thesis, 1986, Department of Marine Hydrodynamics, Chalmers University of Technology, Gothenburg, Sweden.
9. Larsson, L., "Boundary Layers of Ships (Three-dimensional Effects)," PhD Thesis, 1975, Department of Applied Thermo and fluid Dynamics, Chalmers University of Technology, Gothenburg, Sweden.
10. Broberg, L., "Numerical Calculation of Ship Stern Flow," PhD Thesis, 1988, Department of Mechanics, Chalmers University of Technology, Gothenburg, Sweden.
11. Svanberg, K., "Convex Approximation Methods for Structural Optimization," COMETT-Seminar on Computer Aided Optimal Structural Design, Castle of Thurnau, Germany, May 18-22, 1992.
12. Svanberg, K., "Method of Moving Asymptotes - A New Method for Structural Optimization," International Journal for Numerical Methods in Engineering, Vol. 24, 1987, pp. 359-373.
13. "OASIS-ALADDIN User's Manual," Chapter 9, 1990, ALFGAM Optimizing AB, Stockholm, Sweden.
14. Esping, B., Clarin, P. and Romell, O., "OCTOPUS - A Tool for Distributed Optimization of Multi-Disciplinary Objectives", ALFGAM Optimizing AB, Stockholm, Sweden.
15. Dawson, C.W., "A Practical Computer Method for Solving Ship-Wave Problems," 2nd International Conference on Numerical Ship Hydrodynamics, Berkely, 1977, pp. 30-38.
16. Hess, J.L. and Smith, A.M.O., "Calculation of Non-lifting Potential Flow About Arbitrary Tree-Dimensional Bodies," Douglas Report No. E S 40622, 1962.
17. Hess, J.L., "A Higher Order Panel Method for Three-Dimensional Potential Flow," Douglas Report N62269-77-C0437, 1979.
18. Raven, H.C., "A Practical Nonlinear Method for Calculating Ship Wavemaking and Wave Resistance," 19th Symposium on Naval Hydrodynamics, Seoul, South Korea, 1992, pp. 349-364.
19. Jensen, G., Bertram, V. and Söding, H., "Ship Wave-resistance computations," 5th International Conference on Numerical Ship Hydrodynamics, Hiroshima, Japan, 1989, pp. 593-605.
20. Jensen, P.S., "On the Numerical Radiation Condition in the Steady-State Ship Wave Problem," Journal of Ship Research, Vol. 31, No. 1, 1987, pp. 11-28.
21. Janson, C.E., "A Method for the Prediction of Wave Resistance, Lift and Induced Drag," Lic. Eng. Thesis, 1993, Department of Naval Architecture and Ocean Engineering, Chalmers University of Technology, Gothenburg, Sweden.
22. Larsson, L., Broberg, L., Kim, K.J. and

Zhang, D.H., "New Viscous and Inviscid CFD Techniques for Ship Flows," 5th International Conference on Numerical Ship Hydrodynamics, Hiroshima, Japan, 1989.

23. Ohkusu, M., ed., Advances in Marine Hydrodynamics, Computational Mechanics Publications, Southampton, Boston, 1996, pp. 1-75.

24. Larsson, L., and Chang, M.S., "Numerical Viscous and Wave Resistance Calculations Including Interaction," 13th Symposium on Naval Hydrodynamics, Tokyo, Japan, 1980.

25. Michelsen, F.C. and Uberoi, S.B.S., "A Study of Wave Resistance Characteristics Through the Analysis of Wave Height and Slope Along a Longitudinal Track," Report No. Hy-15, 1971, Hydro og Aerodynamisk Laboratorium, Lyngby, Denmark.

26. Lundgren, H. and Åhman, M., "Experimentell och numerisk bestämning av vågmotstånd för ett tankfartyg (Dynetankern)," Report No. X-94/58, 1994, Department of Naval Architecture and Ocean Engineering, Chalmers University of Technology, Gothenburg, Sweden. (In Swedish).

27. Larsson, L., Patel, V.C. and Dyne, G., "Ship Viscous Flow," Proceedings of 1990 SSPA-CTH-IIHR Workshop, Flowtech International AB, Gothenburg, Sweden, Report No. 2, June 1991.

28. Proceedings of CFD Workshop Tokyo 1994, Tokyo, Japan, March 1994.

DISCUSSION

L.J. Doctors
University of New South Wales, Australia

The authors are to be congratulated on working on such a difficult problem—the optimization with respect to resistance based on nonlinear viscous computations. To their credit, the authors pointed out clearly that the optimization unfortunately generated a hull with greater resistance. This was due to the computed changes in resistance being incorrect, even though the computed changes of components of the total resistance possessed the correct sign.

My question is that one might be better advised to use a simpler method, such as the linear theory of Mitchell for the computation of the wave resistance. Although the results for the resistance might be less accurate, perhaps the trends might be more precisely predicted and hence this approach might be more suitable for an optimizer.

AUTHORS' REPLY

Thank you for your comment on using a simpler method for the computation of wave resistance. Due to the large computational effort included in the optimization it may be of interest to consider a simpler and faster method, as the linear theory of Mitchell, for the wave resistance. This, however, requires that viscous effects and nonlinear wave effects are of minor importance and that the derivatives of the wave resistance with respect to the shape modifications are close to the derivatives computed by more accurate methods.

In the paper, both fore body and aft body modifications were included and the total resistance was considered for the optimization. It turned out that not only the trend but also the magnitude of the change of each resistance component was of importance. This indicates that more accurate methods must be used for the predictions. In the optimization, the magnitude of the wave resistance change was not correctly predicted due to neglected displacement effects. This prediction can probably not be improved by changing from a Rankine source method to the linear theory of Mitchell.

DISCUSSION

H. Raven
Maritime Research Institute, The Netherlands,

Inspired by this interesting paper, I have a question on which I would like to hear your opinion. What will be the best way ahead in ship hull form design—automatic optimization or an expert system?

AUTHORS' REPLY

For a hull type where an expert system (data base) exists, this can be used to find a good initial design point. If further improvements are required, the automatic optimization system can be used as a tool for the designer in a local form optimization. If no data base is available for the hull type, an optimization may first be carried out for the global hull parameters as design variables. As a second step, a local form optimization can then be carried out. In both cases, the result of the automatic optimization is only one source of information among others for the designer when the decision for the final design is made.

One advantage of optimization together with CFD is that it gives information on the pressure and velocity distribution and the wave pattern around the hull—information that can be used to understand why one hull form performs better than the other.

DISCUSSION

H. Nowacki
Berlin Technical University, Germany

The authors are presenting interesting new evidence on the contrasting conclusions from CFD hull form optimization and from experiments. Qualitatively I find their results very plausible and noncontradictory.

- In potential flow analysis, whether by linear or nonlinear wave theory, it does appear promising to move displacement from a high region aft to a low region in the forebody. The optimization results are consistent with this.
- In viscous flow, the stern wave system is weaker than calculated for both the original and the optimized hull. The removal of

displacement there must be less effective than calculated. "Something that is not there cannot go away."

That much should be regarded as reassuring rather than disappointing.

Quantitatively it is more difficult to account for the differences. I agree that wave-viscous interaction effects may play a major role. Since trim and sinkage depend on viscous effects, this raises an open question. In the current study, trim and sinkage were not included in the optimization, but were later estimated apparently, as is customary, by pressure integration only in potential flow. How much did this sinkage and, in particular, trim differ from the measured results? If appreciably, as one might suspect in view of the viscous effects on the stern wave system, then this may be another cause for the observed discrepancies.

The displacement thickness approach does not seem to promise any hope. The displacement thickness is not defined to predict correct pressure distributions in way of the stern and it would be a miracle if it did.

In any case in optimization, I would tend to ensure realistic sinkage and trim as in a real fluid before proceeding to refine secondary flow and turbulence models.

Clearly, full Navier Stokes flow models with free surface hold much promise also for optimization. But before going to such extreme calculation effort, one should not neglect to examine approximate ways for indirectly, perhaps semi-empirically, allowing for viscous effects including trim and sinkage.

AUTHORS' REPLY

Thank you for pointing out the importance of sinkage and trim and the difference in sinkage and trim between potential flow and real fluid flow. For the 5-m models used in the measurements, the original hull showed a sinkage of 18.5 mm and a 7-mm trim on the bow while the computations showed a sinkage of 16 mm and a 6-mm trim on the stern. For the optimized hull, the measurements gave a sinkage of 15.5 mm and 7-mm trim on the bow while the computations gave a sinkage of 15 mm and 2-mm trim on the stern.

After preparation of the paper, additional resistance measurements were carried out for the model fixed

condition to exclude sinkage and trim effects as a possibility for the discrepancy between computations and measurements. For the Series 60, the measured difference in resistance between the original and the optimized hull was approximately the same with and without sinkage and trim.

DISCUSSION

A.D. Papanikolaou, G. Tzabiras
National Technical University of Athens,
Greece

The paper describes a fully automatic computer-aided method for optimization of ship hull forms from the resistance point of view. The method is based on the well-known code SHIPFLOW for the determination of the flow around the ship hull and the OCTOPUS code for the solution of the formulated nonlinear optimization problem. The application of the presented method to the optimization of a typical Series 60 hull form is satisfactory from the computational, but discouraging from the practical point of view when considering the validation of obtained theoretical-numerical results in comparison to model experimental data.

The discussors would like, at first, to commend the authors for the shown courage to present a "discouraging" case of application of their optimization system and not a straightforward one that could be easily produced, taking as reference a "bad" starting point. We should explore in the following the reasons for the shown discrepancies.

1. *Optimization Methodology.* The adopted methodology is briefly explained in chapter 4.0 and Fig. 2 of the paper. The method can be understood to address the last stage of hull form optimization (local form optimization), when adopting a multistage optimization strategy as, e.g., presented earlier in [4]. Therefore, we might first assume that the main dimensions and global characteristics of the hull form, to be optimized, are given and a refinement of the globally optimized hull is herein addressed. According to our experience, the geometric constraints set for the formulation of the optimization problem influence drastically the final result. Therefore, the proper formulation of these constraints seems to be the key for a

successful optimization procedure. Based on this, the following points are raised.

- How far can the “automation” of an optimization code go, what is the responsibility of the code user and the designer?
- The optimized hull forms, shown in Figs 7 and 9, suggest that the draft constraint has been implemented only at the ship’s centerplane. The depicted “tunnel” bow sections cannot be justified both from the physical and the practical point of view.
- The authors are optimizing the hull forms for the least total resistance. This is basically correct. However, it seems essential, before setting up the optimization procedure, to carefully consider the individual contributions of the viscous and wave components to the total resistance of the studied hull. In addition, with reference to propulsive aspects, the hull efficiency (wake and thrust deduction factors) of the stern should be taken into account, e.g., through specific geometric constraints. The rather U-shaped stern body suggests that possibly the studies will have not only increased viscous resistance, but possibly also inferior propulsive efficiency.

2. *Resistance Algorithms.* The authors show great courage to present the rather disappointing results of Fig 12, where the measured resistance of the original hull is below the corresponding one of the optimized hull. The above figure would greatly gain in clarity if the authors would add the computational results for the total resistance and its components for the original and the optimized hull. In any case, the conclusion is that the used resistance algorithms are partly problematic and the authors discuss several aspects for the shown discrepancies in their paper. Considering the complicated flow around a ship hull form, weaknesses in the employed resistance algorithms are to a certain degree acceptable. However, for a hull form optimization procedure, it is possibly of less importance the accurate prediction of the absolute value of the resistance and its components. Rathermore, it is the prediction of the relative value of resistance between hull alternatives that is essential. In the studies case, it seems that the theoretical predictions for the resistance of the optimized hull are more

“optimistic” than those for the original hull. This is the point that should be clarified, e.g., by checking the predictions for the individual resistance components step by step.

The authors discuss carefully many aspects and possible shortcomings of their potential (wave resistance) and viscous flow solution. The discussors agree with the authors that the shortcomings of the employed κ - ϵ model and the neglect of the influence of the free surface on the viscous calculations are the main points to be addressed in future work.

AUTHORS’ REPLY

Thank you for discussing several aspects on hull form optimization. As you point out, the intention of the present optimization was a local form optimization, but the changes allowed were probably too large to be considered as local variations.

The authors agree that it is necessary to include more aspects on hull performance in the optimization both in the objective function and as constraints. But an optimization system of this kind can only serve as one tool among others for the designer since many areas of hydrodynamic hull performance as well as practical considerations must be taken into account in the decision of the final design. Some of the considerations are probably difficult to include in an automatic optimization system.

Our experience is that the resistance algorithms work well for slender hulls like the Series 60. The problem in this case was that the physics of the flow around the stern was not well captured due to the neglected displacement effects in the wave prediction. The resistance algorithms may be more problematic for the full hull forms.

We agree that ranking is more important than absolute resistance values for numerical computations and optimization. But in cases where the total resistance is obtained as a summation of several resistance components also, the absolute value of the change of each component is important if the ranking is different for the components.

Hydrodynamic Optimization of Fast-Displacement Catamarans

A. Papanikolaou, P. Kaklis, C. Koskinas, D. Spanos
(National Technical University of Athens, Greece)

ABSTRACT

The paper addresses a systematic, computer-aided optimization procedure for the efficient hull form development of Fast Displacement Catamarans. The procedure is based on a methodology for the minimization of the calm water resistance, particularly the wave resistance, of slender, twin hull vessels of arbitrary shape, considering their seakeeping performance and various geometric parameters set by design or by other operational constraints. The presented hydrodynamic procedure is thought to be embedded within an overall optimization procedure with respect to specific economic criteria. Alternative mathematical models and computer algorithms for the wave resistance of arbitrarily shaped hull forms have been developed and applied herein, namely simplified approaches based on Michell's original source distribution concept, but accounting for the interaction of the demihulls and for any asymmetries of the slender/thin demihull forms through a doublet centerplane distribution, and alternatively a Neumann-Kelvin 3D panel source approach that is generally applicable to arbitrary hull forms. The developed theoretical-numerical methods have been applied systematically to the hull form development of a variety of Fast Displacement Catamarans and they are in general validated through model tests. Comparative results for the wave resistance and horsepower requirement of two SWATH ships and two Displacement Catamarans are presented and discussed, considering their overall hydrodynamic and efficiency performance.

1. INTRODUCTION

The past decade has witnessed a rapid growth of interest in the development of Fast (and Advanced) Marine Vehicles for various applications. Whereas, in the past, the design of fast marine vehicles appeared to be of interest only to navy authorities, the most recent developments seem to be

driven mainly by commercial applications. A state of the art in the field is outside the scope of the present paper, however the Proceedings of the FAST Marine Transportation Conferences (FAST'91, '93, '95) include several papers covering completely the subject.

The optimal hull form development of Fast Marine Vehicles is of particular interest, both from the hydrodynamic and design point of view, but also from the construction, operational and eventually economic point of view. The relatively high ship velocity requires increased effort as to the minimization of the ship's resistance, particularly the wave resistance, as well as to the seakeeping behaviour of ship under consideration. Stability proves to be a severe design constraint for fast ships in general, even in the intact case. Considering in addition the damage stability of fast ships after grounding or collision, it seems that certain advantages of the monohull concept against the multihulls, particularly the smaller wetted surface and structural weight for equal displacement, will have to be reconsidered in the future. Therefore, an increased interest into the design of Fast Multi-Hull Vessels can be expected in the future.

We consider herein so-called Fast Displacement Catamarans (FDCs), these are twin hull vessels operating at Froude numbers between approximately 0.4 and 0.8, thus ships practically operating at the end of the hollow *before* the "last hump" of the wave resistance coefficient and up to the stage of the begin of planing. This speed range is of major interest to hydrodynamicists, because of the rapid change and relative increase of the wave resistance coefficient, as compared to the other resistance components. In addition, the particular speed range fits within present design requirements in practice, when looking for medium to high-speed passenger/car ferries, fast shortsea cargo ships, cruising /patrol /surveillance /supply/ oceanographic vessels, and other ship types characterized by their appreciable speed and seaworthiness in moderate and

sometimes high seastates (see, [1] to [5] for examples). It is of particular interest to note, that depending on the specified service speed and payload capacity all designs mentioned above, except for the patrol vessel [4], have been developed assuming steel as main structural material, therefore avoiding the particular problems related to an aluminum alloy or synthetic material structure. The increased structural weight of a steel catamaran introduces additional requirements into the present hydrodynamic optimization problem.

The demihull form of the addressed twin hull vessels can be assumed, by common design sense, to be slender, thus changing slowly in the longitudinal direction, but else being of arbitrary shape. Thus we should consider herein symmetric or non-symmetric demihull sections, but in general arbitrarily shaped thin or slender hull forms, varying else arbitrarily in both the transverse and in the vertical direction. Therefore we address practically all thinkable displacement CATAMARAN hull forms, including SWATHs¹ and Hybrids².

The present paper is focusing on the calm water performance of Fast Displacement Catamarans and their hull form optimization with respect to least horsepower requirement, assuming the desired vessel's speed and displacement³ known and considering various geometric parameters set by design or by other operational constraints. The employed optimization procedure consists of two basic stages, namely, in the first phase a global procedure leading to the main dimensions and integral form and weight characteristics of the ship, whereas in the second phase a local form optimization is performed leading to the exact geometric characteristics and the final hull form of the vessel under consideration. The overall goal of the above optimization process is to generate, with the least possible computational and experimental effort, seakind catamaran hull forms with low weight and resistance characteristics. From the naval

architectural point of view these requirements are contradictory, because a seakind catamaran requires moderate stiffness (low to moderate metacentric height), thus small separation distance between the demihulls, what has the additional positive effect of low structural weight, whereas the low resistance (and especially, for fast catamarans, low wave resistance) requirement, that indirectly calls for reduced machinery and fuel weight, suggests a large separation distance for the demihulls, for avoiding the negative interference effects on resistance, that can easily triple the single demihull's resistance [6]. Therefore, a formal optimization procedure for fast catamarans should be looking for twin hull arrangements exhibiting the least possible separation distance for the demihulls, thus disposing reduced structural weight and moderate stiffness in roll direction, without compromising on the increase of the sum total of the demihulls' single resistance. Instead of, it is expected that through proper shaping of demihulls the interference resistance can be tuned to be, for the speed range of interest, small and even below zero. Because of the multiple parameters involved, it seems very difficult, if not impossible, considering reasonable effort, to address the problem of hydrodynamic optimization of fast displacement catamarans only by systematic model experiments. Therefore, a computer-aided hull form design procedure, as presented herein, seems essential for the concept and initial hull form development, that can be later on verified by a limited number of model tests.

The following paper is intended to explain the details of the above outlined theoretical/numerical methods, especially the essence of our thin, non-symmetric twin-hull wave resistance theory as well as our 3D panel source wave resistance method, including the related algorithms and the validation by model experiments. It should further show the impact of theoretical/numerical hydrodynamic methods on catamaran hull form design within a formal optimization procedure and finally to draw conclusions as to the methodology for the design of optimal Fast Displacement CATAMARAN hull forms.

The rest of the present paper is organized as following. Chapter 2 addresses briefly the overall design methodology and optimization procedure. Chapter 3 describes the essence of the employed hydrodynamic module within the formulated optimization procedure. Chapter 4 includes the presentation and discussion of theoretical results for

¹SWATH: Small Waterplane Area Twin Hull is synonym to SSC: Semi-Submerged Catamaran (MITSUI's Co. brand-name)

²Hybrids: herein understood as a mixture of a conventional displacement catamaran hull form with a SWATH: Medium Waterplane Area Twin Hulls (MWATHs), Fast Displacement Catamarans (FDCs, FBM Marine Ltd brand-name), etc.

³It is more correct to assume, instead of the displacement, the payload capacity given by the owner's requirements. However, an optimization with respect to the least horsepower requirement, as suggested herein, assuming the displacement and the speed of operation fixed, leads eventually for fast displacement catamarans to ship designs with maximum payload capacity.

the wave resistance and horsepower requirement for several Fast Displacement Catamaran hull forms, designed by the Ship Design Laboratory of NTUA, and their comparison with model experimental data. Finally, the attached Appendices refer to a more detailed outline of the employed wave resistance theories (simplified thin ship theory for nonsymmetric catamarans and strict Neumann-Kelvin 3D panel source approach).

2. DESIGN METHODOLOGY

Due to the innovative character of the design of Fast Displacement Catamarans, including SWATHs and Hybrids, it is essential to set-up a specific computer-aided design procedure, allowing the convenient and reliable repeat of the necessary steps following the design spiral. The overall design methodology and optimization procedure consists of several independent but interacting modules, namely (see Flowchart, Fig. 1, [7])

1. The *Conceptual Design Synthesis Program*, consisting of simplified algorithms and data bases of previous designs. It allows the generic design of a standardized ship, assuming the initial owner's requirements known. It might call, optionally, the hull geometry module (hull-form generator and shiplines fairing under shape and integral constraints [8]).

2. The technoeconomic *Parametric Economic Evaluation* module, that is employing the *Conceptual Design Synthesis Program* as a pre-processor (evaluation of shipbuilding cost, operational cost, Required Freight Rate RFR or Net Present Value NPV, [9]).

3. The *Hydrodynamic Optimization* module consisting of algorithms for the *Hydrodynamic Analysis* (evaluation of calm water resistance and of seakeeping, [10], [11], [12], [13], [14]) and for the formal *Hull Form Optimization* (global NLP optimization by the so-called Reduced Gradient Method [15] and local form optimization by LAGRANGE method, [9], [10]).

4. The *Preliminary Design Synthesis Program* consisting of various software packages for the handling of the hull geometry and preparation of common naval architectural drawings (ship lines and

general arrangements⁴), the powering, the seakeeping and the structural design (see [7] for details).

It is *Hydrodynamic Optimization* module, and especially the evaluation of wave resistance, that will be elaborated herein in more details.

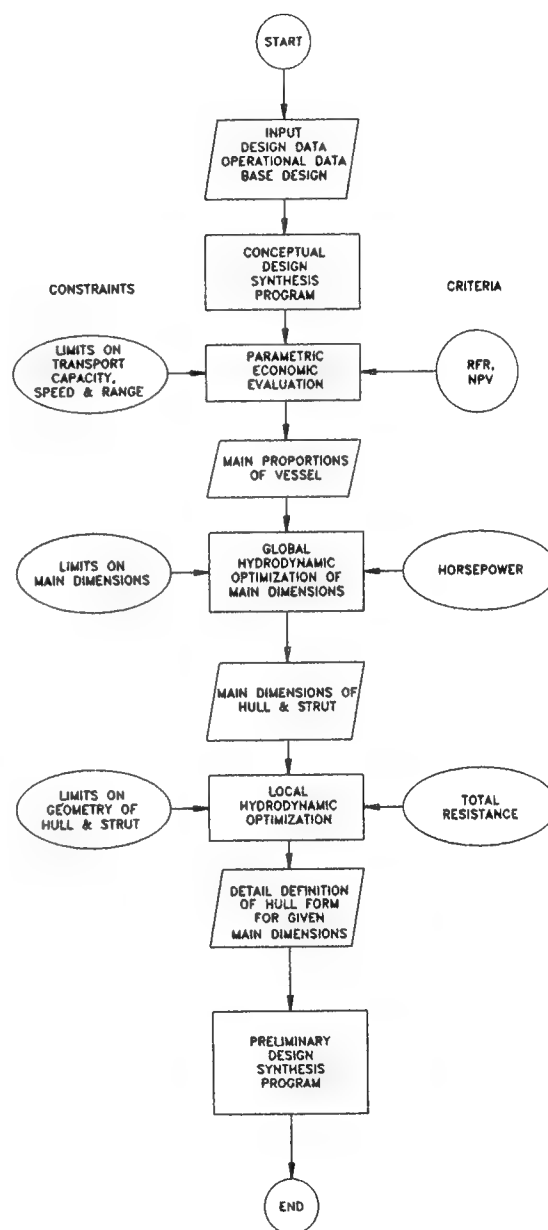


Fig. 1 Multi-stage optimization and global design procedure for Fast Displacement Catamarans

⁴AUTOCAD™, AUTOSHIP™

3. HYDRODYNAMIC MODULE

3.1 Twin Hull Wave Resistance

In the present paper, we restrict our attention to the address of efficient and reliable methods for the calculation of the wave resistance of fast displacement catamarans. In doing so we tacitly assume, that the frictional and the viscous-pressure part of resistance of slender hulls, as the demihulls of catamarans are, can be successfully approached by common semi-empirical methods (ITTC line with a form factor acc. to systematic experiments and semi-empirical formulas). Of course, the problem of catamaran stern flow separation at higher speeds, needs to be considered separately, in connection with the arrangement of an optimal propulsion system. In any case it can be assumed, due to the slenderness of the demihulls, that the uniformity of the propeller onset flow of fast displacement catamarans, and especially of those having SWATH-like stern sections, will eventually contribute to a relatively high propulsive efficiency⁵.

It is well established that the determination of the wave resistance of symmetric slender or thin twin hull vessels can be easily achieved by application of the classical theories of Michell-Havelock (monohulls) and Stretenskii-Eggers (monohull in a canal and twin-hulls) [16], [17]. They all lead to relatively simple formulas for the wave resistance, in terms of simple type centerline or centerplane Kelvin source distributions, the strength of which is derived immediately from the hull form characteristics of the studied vessel. These methods consider the effects of hull interaction on the catamaran wave resistance in an approximate way, namely by superposition of the individual demihull's far-field wave pattern and thereafter by employment of a modified KOCHIN function to calculate the catamaran's wave resistance. Eventually, there is a direct relation between the wave resistance and the ship's hull form, defined by the hull offsets. Extending this concept also to the frictional part of resistance, being directly proportional to the local Reynolds number and the hull surface area, it is possible to deduce a direct functional relationship between the sum total of the wave and frictional

resistance⁶ and the ship's hull form offsets, leading to the formulation of a systematic optimization procedure by Lagrange's multiplier method (see, Papanikolaou, A. and Androulakis, M., FAST'91, 1991, [10]). This method, that proves to be very efficient and fast, was applied successfully in the past to the design of several SWATHs and thin, but symmetric, Catamarans and the theoretical predictions have been validated, in most cases, successfully by model experiments.

Whereas the above procedure is limited to symmetric catamaran hull forms only, a fair portion of existing and under development displacement Catamarans have non-symmetric demihull forms for manifold practical reasons, including the hydrodynamic performance in calm water and in waves. The design of nonsymmetric catamaran hull forms has been addressed, until now, only by use of semiempirical methods and model experiments. We present herein an extension of the traditional wave resistance of Michell-Stretenskii for thin *non-symmetric* demihull forms. The proposed method extends Michell's original approach by including, in addition to the centerplane sources, a centerplane normal dipole distribution, the strength of which is related to the asymmetry of the demihull form. It can be determined numerically by solution of a properly formulated Hypersingular Integral Equation of first kind. Alternatively, the solution of the above integral equation can be approximated by an asymptotic expansion in terms of the local hull geometry characteristics (see details of the complete theory in Kaklis, P. and Papanikolaou, A., 1992, [11], Spanos, D., 1995 [13] and summary in Appendix A). This particular method, that is, at our knowledge, new in the international literature, has been applied systematically to a variety of standardized twin hull arrangements (non-symmetric demihull forms of WIGLEY or wallsided strut type). Therefrom, some important conclusions concerning the influence of the section asymmetry on the wave resistance, and especially on the hull interaction resistance, can be deduced. The implementation of this procedure into the overall optimization scheme, introduced before, will eventually lead to innovative demihull forms of least wave resistance, depending on the speed, displacement and separation distance of the

⁵Attention should be paid to the reduction of the propulsive efficiency at speeds, corresponding to extreme "humps" in the wave resistance curve, when the propeller is operating under a local wave "trough"

⁶it is essential to include in the formulation of local form optimization problem, by Lagrange's multipliers method, the frictional resistance, because of the "ill-conditioning" of the coefficient matrix, to be inverted for the problem solution (see, Salvesen, N., Von Kerczek, E. H., et al, Trans. SNAME, Vol. 93, pp. 325-346, 1985).

demihulls, specified by other design constraints. However, it remains to validate the obtained theoretical results for the nonsymmetric demihull forms by systematic model experiments.

For the validation of the above simplified methods, pertaining for thin demihull forms having a sufficiently large separation distance, and for accounting more general twin-hull arrangements, we employed a full 3D panel source method, that is based on a complete analytical-numerical solution to the well-known Neumann-Kelvin problem (see, Koskinas, C., 1995, [12]). This latter method, the computer algorithm of which has been recently completed at SDL-NTUA, is based on the evaluation of the 3D Green Function of the travelling source by use of Newman's methodology [18], as to the Double Integral term, whereas the Far Field disturbance term has been approached by the suggested method of Baar and Price [19], considering Bessho's expansions in Neumann series [20]. The developed 3D panel source approach has been validated successfully for a variety of hull forms, both monohulls and catamarans, as shown in the following example cases. A brief summary of the theory is given in Appendix B, but more details in [12].

Finally, the validation of the above presented theoretical-numerical methods has been established by systematic model experiments performed at the Marine Hydrodynamics Laboratory of NTUA and partly at the Towing Tank of VWS Berlin. The validation concerns a variety of standard Wigley twin-hull arrangements and several practical designs, developed at the Ship Design Laboratory of NTUA, namely here two high speed SWATHs and two medium to high speed displacement Catamarans.

3.2 Twin Hull Seakeeping

It is outside the scope of the present paper, to describe the theoretical methods used for the seakeeping analysis of the addressed Fast Displacement Catamarans. Details of the employed 3D, alternatively quasi 2D, panel source methods can be found in previous publications of the first of the authors ([14]). We restrict herein ourselves into the description of the general methodology for the design of Fast Displacement Catamarans with optimal seakeeping characteristics. The adopted methodology leads to specific design requirements that can be incorporated as constraints on the hull geometry or as qualitative criteria within the formal optimization

procedure for the ship's calm water performance, presented before.

The responses of a ship in a seaway are naturally determined by two basic aspects:

1. *The ship characteristics*: mainly the ship's mass, including the mass distribution, and her natural periods in heave, pitch and roll.
2. *The seaway characteristics*: the amplitude and period of the exciting waves and the resulting wave exciting forces and moments.

Given the speed of the ship, and indirectly her mass⁷, as well as the operational environment (wave characteristics), the methodology for reducing the ship responses, by design, consists in measures to tune the values of the ship's natural periods, to be outside the range of possible resonance with the exciting waves, and to reduce the amplitudes of the wave exciting forces, e.g. by proper hull form shaping and favourable weight distribution to the extent possible within the limits of design and operation of the vessel.

As to the tuning of the natural periods, it is well known that, besides the fine-tuning through motion damping devices (fins etc.), the only tool practically available to the designer is the variation of the waterplane area and, to a certain limited degree⁸, the variation of the ship's underwater hull form determining the "added" mass and moment values.

The slenderness and thinness of the demihulls of Fast Displacement Catamarans and the generally small waterplane area will contribute, in general terms, to a shift of the natural periods in heave, pitch and roll to relatively high values, therefore outside the range of resonance with short period waves, typical to many coastal areas⁹. In addition, assuming a high forward speed, the vessels will always tend to operate "undercritical", especially

⁷It is tacitly assumed, that, at the stage of evaluation of the seakeeping performance, the displacement of the ship is fixed through the initial design procedure (for given payload capacity and specific design arrangements, speed and range, an estimation of the weights for the structure, machinery, outfitting and consumables is possible).

⁸The underwater ship hull form, especially of a fast ship, is commonly determined by low resistance aspects.

⁹We assume that Fast Displacement Catamarans will be mainly operating in coastal areas with short period seas. A typical example is the Aegean Sea Archipelago with a typical year-round peak wave period of 5.0 sec.

in head seas, due to the effectively very small period of wave encounter. A typical representative of this type of ships, with excellent seakeeping characteristics especially in short seas, is the SWATH ship. However, Fast Displacement Catamaran hull forms and Hybrids, deviating from the original SWATH concept as to the smallness of the waterplane area and the underwater hull form, will naturally exhibit worse seakeeping behaviour, at the benefit of increased vertical plane stability. The main design tools for the tuning of the natural periods, to be positioned outside the range of the possible wave encounter periods, are:

- *For the roll natural period:* limitation of the transverse metacentric height GMT through the smallest possible¹⁰ separation distance of the demihulls and the positioning of heavy loads as high as possible. Maximization of the effective roll radius of gyration by proper mass distribution and shaping of the underwater hull form for increased added mass and moment coefficients. Both latter measures are very difficult to be implemented in practice, due to technical reasons or because of the contradiction to other requirements.

- *For the natural periods in heave and pitch:* a fine tuning is possible by limitation of the waterplane area to the extent possible. A concentration of the waterplane area around the center of flotation, leading to short and beamy waterlines, results to a relatively small longitudinal metacentric height GML and relatively high pitch eigenperiod, however at the expense of increased wave resistance, especially at higher Froude numbers. In any case, a large fast catamaran ship with appreciable mass and with small to medium waterplane area will contribute through her mass to reasonable values for the heave and pitch natural periods.

As to the second factor influencing the seakeeping behaviour of a ship, namely the magnitude of the exciting forces and moments, it is well established that ships with bulb-like cross sections will experience reduced wave exciting forces and moments, at least at the so-called "wave excitationless frequencies"¹¹. Again the SWATH type of ship is the best representative of the Fast Displacement Catamaran family fulfilling the above

criteria for a hull form with least possible wave excitation impact.

In evaluating the seakeeping behaviour of twin hull vessels alternative quasi 2D (strip or slender body theory approach) and more strict 3D panel methods can be employed. Due to the slenderness of the demihulls of Fast Displacement Catamarans, including SWATHs and Hybrids, the analysis of the seakeeping behaviour in head seas can be easily accomplished by either approach. However, the oblique and beam seas condition requires special care, due to strong interactions between the incident wave and the two demihulls as well as due to three-dimensional effects at the ends. These cases can be successfully approached by 3D panel method, accounting for the forward speed effects in the sense of a slender body theory [14]. For SWATH ships, additional attention should be paid to the following seas case, when at high forward speed, and the vertical plane instabilities due to the action of the so-called Munk moments. Also, the inclusion of the stabilizing fins and the estimation of the estimation of the viscous damping requires additional fine-tuning of the employed computer algorithms. However, these problems are considered solved in a satisfactory way by a variety of researchers, including related work at the Ship Design Laboratory of NTUA, therefore any details can be omitted herein for the sake of brevity.

4. DISCUSSION OF RESULTS

We concentrate our attention in the following to the assessment of the employed algorithms for the evaluation of wave resistance of Fast Displacement Catamarans with typical hull form characteristics, including SWATHs.

In Fig. 2¹² a comparison between theoretical predictions according to the suggested thin ship theory for symmetric demihulls [10], the presented strict 3D panel source theory and model experiments [21] for the wave resistance coefficient of a catamaran with WIGLEY demihulls ($L/B = 10.0$, $B/T = 1.6$, separation distance $s/L = 0.5$) is shown. The 3D calculation was based on a 2x160 panels/demihull model. The agreement of both theoretical methods to the experimental data is fully

¹⁰Limit set by the wave interaction resistance.

¹¹see, e.g., Matora, S., Koyama, T., Proc. 6th Symposium on Naval Hydrodynamics, 1996.

¹²In all following figures, results according to the presented thin ship theory for symmetric and nonsymmetric demihulls are indicated by "2D Calculation", whereas results of the employed 3D panel source method are indicated by "3D Calculation".

satisfactory, except at lower Froude numbers, below 0.35, for which the employed quasi 2D method, as expected for a Michell concept approach, delivers highly oscillatory results. In Fig. 3 a qualitative comparison between the simplified thin ship theory (lower part of figure) and the strict 3D panel method (upper part of figure) for the wave pattern of the lower hulls of a SWATH ship (lower hull length to diameter ratio $L/D = 13.2$, draft ratio $T/L = 0.12$, separation distance $s/L = 0.5$) at Froude 0.35 is depicted. The results of both methods are in excellent qualitative agreement, except in the region of the position of the demihulls (from -50 to 0), where some expected deviations exist, due to the simplified thin ship theory concept, that does not allow the inclusion of local interference effects.

In the following figures, the developed thin ship theory method for the wave resistance of twin hull vessels with symmetric or asymmetric demihulls has been applied systematically to a catamaran series with halved WIGLEY demihulls ($L/B = 10$, $B/T = 1.6$, constant displacement), placed alternatively with the wall-side inwards respectively outwards, and in various separation distances (see Fig. 4 for definitions, Fig. 5 for the wave resistance coefficient, $s/L = 0.4$). The wave interaction resistance was estimated and compared with the equivalent value of a catamaran with symmetric WIGLEY demihulls (Fig. 6) and the wave resistance coefficient of the symmetric demihull (Fig. 7). From the above figures it is concluded, that for Froude numbers up to 0.4 the wave interaction resistance changes rapidly and an inwards or outwards located asymmetry of the demihulls might deliver better resistance results, as compared to symmetric demihull arrangements. Considering the whole speed range of interest (Froude between 0.3 and 0.8), it seems that inwards flattened demihull arrangements are, from the wave resistance point of view, superior to the others, what is qualitatively supported by individual model experiments with asymmetric demihulls in the past.

From all the above, it can be concluded, that for twin hull arrangements with slender/thin symmetric or asymmetric demihulls at sufficient large separation distance the employed simplified thin ship theory is quite satisfactory, both for hull form design purposes, as well as for the prediction of various hydrodynamic phenomena related to the ship's wave system. However, it remains to validate the asymmetric demihull case by systematic model experiments, what we plan to do, in the next months, with Wigley demihulls at NTUA's Towing Tank.

In the following figures we present theoretical and experimental results for the horsepower requirement of four optimized Fast Displacement Catamaran hull forms, namely for two designed SWATH ships and two displacement catamarans with hybrid hull form features. In Figs 8 and 9 the theoretical predictions for the effective horsepower requirement of the 1.030 tons displacement SWATH Passenger car ferry design "Aegean Queen" and the 610 tons displacement SWATH Multipurpose Research Vessel SMURV are compared with data from model experiments, performed at the Ship Hydrodynamics Laboratory of NTUA. The particulars of the employed models in scale 1:17 ($L = 3.0\text{m}$) respectively 1:17.5 ($L = 2.0\text{m}$) can be found in [1] and [5]. The agreement between the employed simplified thin ship theory and the model experiments is good and fully satisfactory, not only for design purposes but also from the actual speed-power prediction point of view. The relative small deviations at higher Froude numbers are due to the observed stern flow separation and the related pressure-viscous resistance, that is not exactly accounted for at the used theoretical model. From the hull form optimization point of view, both vessels have been optimized for specific design and operational constraints, leading to geometrical global and local form limits. Therefore, the hull form of the "Aegean Queen", optimized for least total resistance at Froude 0.7 is "bottle-like", considering the fitting of the selected machinery in the rear part of the lower hulls (see Figs 10). On the other side the hull form of SMURV, optimized for a top speed of initially assumed 25.0 knots and a specific operational profile for the cruise and towing condition (15 knots respectively 4.5 knots), given the available machinery horsepower and the main dimensions (overall length, beam and max. draft), is characteristically "bone-like" and of relatively small slenderness ratio ($L/V^{1/3} = 5.3$). In Fig 11, the initially estimated horsepower requirement for alternative hull forms of SMURV, resulting from the global (hull form 0) and local form optimization with different geometrical constraints (hull form 1 and 2), is shown. From the hydrodynamic performance point of view both tested SWATH vessels exhibit the characteristic hump in the horsepower requirement at Froude 0.35, but they are expected to operate, according to their operational requirements, quite distant from this operational point.

In Figs 12 and 13 the corresponding results for two designed fast displacement catamarans are shown, namely the 450 tons displacement passenger

ferry "SIMICAT" and the 2180 tons displacement passenger/car ferry "GOUTCAT". The last one, a 80m LOA and 22m wide passenger/car ferry¹³, is built completely from steel, and is currently outfitted for completion in Piraeus-Greece. The model experiments, validating the present theoretical predictions for the horsepower requirement, were performed at the NTUA's Towing Tank (SIMICAT) respectively for GOUTCAT at the Versuchsanstalt f. Wasserbau & Schiffbau, VWS-Berlin. The agreement between the theoretical predictions of the employed simplified thin ship theory and especially the strict 3D source distribution method (number of panels $N = 2 \times 220$ /demihull) and the experimental data for SIMICAT is for design purposes very good. Both methods are underestimating the required horsepower requirement at higher speeds, apparently due to insufficient approach of the pressure-viscous resistance resulting from the significant stern flow separation at higher speeds. For the second tested hull (GOUTCAT), exhibiting strong interaction effects between the demihulls, that are quite close together ($s/L = 0.22$), the simplified thin ship theory method fails completely to predict correctly the resistance hump behaviour at Froude 0.35, whereas the 3D source panel method (herein number of used panels $N = 2 \times 180$ /demihull) overpredicts the experimental data, but follows very closely the character of the horsepower requirement curve. At higher speeds both theoretical methods deliver acceptable predictions. It is of interest to note, that the hull forms of both vessels, that resulted from a global and local optimization for a top speed, in both cases, of at least 19.0kn (Froude abt 0.50 respectively 0.40) are quite similar. Both hull forms are characterized by long but relatively narrow bow and stern bulbs (see Fig. 14, upper part, model of GOUTCAT tested at VWS Berlin, scale 1:16). However, due to the more strict requirement for the overall beam of GOUTCAT, to not exceed 22.0m¹⁴, leading to a demihull separation distance of merely 14.5m, the demihull interaction on the wave

resistance is herein very strong, especially at Froude numbers between 0.35 and 0.40. Finally, it should be noted, that at design speed of herein 20.0 knots, the wave interaction resistance for GOUTCAT is strongly negative and leads to a decrease of the doubled demihull resistance by 20%¹⁵. A view of the GOUTCAT model during the propulsion test at speed $v = 21$ knots is shown in the lower part of Fig. 14.

6. CONCLUSIONS

The paper addressed the main features of a methodology for the hydrodynamic optimization and systematic hull form development of fast displacement catamarans. The procedure is based on a methodology for the minimization of the calm water resistance, particularly the wave resistance, of slender, twin hull vessels of arbitrary shape, considering their seakeeping performance and various geometric parameters set by design or by other operational constraints. Alternative mathematical models and computer algorithms for the wave resistance of arbitrarily shaped hull forms have been developed and applied herein, namely simplified thin ship theory approaches based on Michell's original source distribution concept but accounting for asymmetries of the slender/thin demihull forms through a doublet distribution and alternatively a 3D panel source method, that is based on the 3D Green function approach and is generally applicable to arbitrary hull forms. The developed theoretical-numerical methods have been applied to the hull form development of a variety of Fast Displacement Catamarans. Comparative theoretical and experimental results for the wave resistance and horsepower requirement of two SWATH ships and two Displacement Catamarans were presented and discussed, considering their overall hydrodynamic and efficiency performance.

¹³The ferry "SUPERCAT-HAROULA"(NTUA code: GOUTCAT) is one of the largest steel catamaran ships ever built world-wide and the first one of this type and size built in Greece. With a transport capacity of 1.500 passengers (summer season) / 240 cars and an installed horsepower of 2×6.500 HP, she will have a service speed of abt 21.0 knots.

¹⁴The vessel's beam was fixed to the lowest possible limit by design requirements, namely the car-deck arrangements and the reduced structural weight. In addition, the small beam results to a relatively "small" GM value of between 8.20 and 11.05m, depending on the loading condition, and a reasonable eigenperiod for roll of abt 6.0 sec, what contributes greatly to an acceptable seakeeping behaviour for the designed vessel, as compared with other catamaran designs and related concepts.

¹⁵This value was at first theoretically predicted and later fully confirmed by the model experiments at VWS Berlin. The propulsive efficiency coefficient η_D , at design speed, is according to the model experiments approximately 75%.

ACKNOWLEDGEMENT

The reported work was partly supported by several past research projects of the Ship Design Laboratory of NTUA funded by the Greek Secr. General for Research and Technology and Alpha Marine Ltd (Mr. Nikos Daphnias). The authors like to thank Mr. E. Boulougouris, Dr.-Eng. cand., for his assistance in the 3D hull form development and the panel generation for the wave resistance calculations and the staff of VWS-Berlin (Dr.-Ing. B. Müller-Graf) for the excellent experimental work on the hydrodynamic performance of GOUTCAT. Finally, the substantial help of Dr.-Eng. G. Zaraphonitis and Dipl.-Eng. M. Androulakis in the development of some of herein employed software packages of SDL-NTUA is greatly acknowledged.

REFERENCES

1. Papanikolaou, A., Zaraphonitis, G., Androulakis, M., "Preliminary Design of a High-Speed SWATH Passenger Car Ferry", Journal Marine Technology, Vol. 28, 1991, pp. 129-141.
2. Papanikolaou, A., "SIMICAT: Hydrodynamic Analysis and Preliminary Design of a Fast Catamaran For the Greek Islands", SDL-NTUA Report, December 1994.
3. Papanikolaou, A., et al., "SMUCC: SWATH Multipurpose Container Carrier for Fast Shortsea Shipping", Proc. 3rd FAST'95 Conference, Travemünde, 1995, pp. 667-680.
4. Papanikolaou, A., Boulougouris, E., "Hydrodynamic Analysis and Preliminary Design of a SWATH Offshore Patrol Vessel for the Greek Navy", SDL-NTUA Report, March 1995.
5. Papanikolaou, A., Atlar, M., Khattab, O., "Hydrodynamic Analysis and Preliminary Design of a SWATH Multipurpose Research Vessel for the Mediterranean Sea", Proc. 2nd FAST'93 Conference, Yokohama, 1993.
6. Turner, H., Taplin, A., "The Resistance of Large Powered Catamarans", Trans. SNAME, Vol. 76, 1968, pp. 180-213.
7. Papanikolaou, A., "Computer - Aided Preliminary Design of a High-Speed SWATH Passenger Car Ferry", Proc. 4th IMSDC'91 Int. Conf., Kobe, 1991.
8. Pigounakis, K., Kaklis, P., Papanikolaou, A., "Ship-Hull Fairing under Shape and Integral Constraints", Proc. 7th IMAM Congress, Dubrovnik, 1995.
9. Papanikolaou, A., Nowacki, H., "Concept Design and Optimization of a SWATH Passenger/Car Ferry", Proc. IMAS-89 Int. Conf. on Applications of new Technology in Shipping, Athens, 1989.
10. Papanikolaou, A., Androulakis, M., "Hydrodynamic Optimization of High-Speed SWATH", Proc. 1st FAST'91 Conference, Trondheim, 1991.
11. Kaklis, P., Papanikolaou, A., "The Wave Resistance of a Catamaran with Non-Symmetric Thin Demihulls", Proc. 1st Nat. Congress on Comp. Mechanics, Athens, 1992.
12. Koskinas, C., "On the Solution of the Neumann-Kelvin Problem by a 3D Panel Source Method and Applications to Catamaran Hull Form Optimization", Dr.-Eng. Thesis, Progress Report, NTUA-SDL, Jan. 1995.
13. Spanos, D., "Study of the Wave Resistance of Slender Symmetric and Non-symmetric Catamaran Configurations", Diploma Eng. Thesis, Dep. of Naval Arch. & Marine Eng., NTUA, Athens, Feb. 1995.
14. Papanikolaou, A., Schellin, Th., "A three-dimensional panel method for motions and loads of ships with forward speed", Journal Schiffstechnik - Ship Tech. Research, Vol. 39, 1992.
15. Lasdon, L. S., Waren, A. D., "GRG2's User's Guide", Univ. of Texas at Austin, Dep. Of General Business Report, Austin, 1986.
16. Michell, J. H., "The wave resistance of a ship", Phil. Mag., Vol. 45, London, 1898, pp. 106-123.
17. Eggers, K., "Über Widerstandsverhältnisse von Zweikörperschiffen", Trans. STG, Vol. 49, 1955.
18. Newman, J. N., "Evaluation of the Wave Resistance Green Function: Part 1 - The Double Integral", Journal of Ship Research, Vol. 31, No. 2, June 1987, pp.79-90.
19. Baar, J. J. M., Price, W. G., "Evaluation of the Wavelike Disturbance in the Kelvin Wave Source Potential", Journal of Ship Research, Vol. 32, No. 1, March 1988, pp.44-53.
20. Bessho, M., "On the Fundamental Function in the Theory of the Wave-Making Resistance of Ships", Memoirs of the Defence Academy, Japan, Vol. IV, No. 2, pp. 99-199, 1964.
21. Insel, M., Molland, A. F., "An Investigation into the Resistance Components of High Speed Displacement Catamarans", Trans. RINA, Vol. 134, 1992.

Appendix A : The Wave Resistance of Arbitrarily Shaped Thin Catamarans

Consider the potential flow caused by a twin-hull floating body \mathcal{B} moving with constant forward speed U on the free surface of an ideal fluid of infinite depth and extent in a uniform gravitational field (g will indicate the acceleration due to gravity). The body $\mathcal{B} = \mathcal{B}_1 \cup \mathcal{B}_2$ (see Fig. 1) is assumed to be *thin*, i.e., the (common) length L of the two demihulls ($\mathcal{B}_1, \mathcal{B}_2$) is much greater than their (common) beam B . This geometrical assumption can be mathematically formulated by attributing the role of the *perturbation parameter* ϵ to the geometrical ratio B/L , that is,

$$B/L = \epsilon, \quad 0 < \epsilon \ll 1, \quad (1)$$

and correlating it asymptotically with the ratio T/L - T being the (common) draft of the two demihulls - and the Froude number $F_n = U/\sqrt{gL}$, which is the fundamental physical non-dimensional parameter of the flow under consideration. In the present work we assume

$$T/L = O(1), \quad F_n = O(1) \quad (2)$$

with respect to ϵ .

We shall restrict our attention to the flow field which is time invariant with respect to a Cartesian system of co-ordinates $O\tilde{x}_1\tilde{x}_2\tilde{x}_3$ fixed to the body $\mathcal{B}(\epsilon)$ with the $O\tilde{x}_3$ axis going vertically upwards, the $O\tilde{x}_1\tilde{x}_2$ plane lying on the calm fluid surface and the $O\tilde{x}_1$ axis pointing to the direction of the motion of the body. With respect to this system of reference, the fluid motion is characterized by the velocity potential $\tilde{\Phi}(\tilde{x})$, $\tilde{x} = (\tilde{x}_1, \tilde{x}_2, \tilde{x}_3) \in \tilde{\mathcal{D}}$, $\tilde{\mathcal{D}}$ being the region filled by the fluid and bounded by the free surface $\partial\tilde{\mathcal{D}}_F$, which is assumed to be a non-parametric surface with respect to the calm fluid surface $\tilde{x}_3 = 0$, namely $\tilde{x}_3 = \tilde{\eta}(\tilde{x}')$, $\tilde{x}' = (\tilde{x}_1, \tilde{x}_2)$. Since $\dim(\mathcal{B}(\epsilon)) = \dim(\mathcal{B}(0))$, the problem of determining $\tilde{\Phi}(\tilde{x})$ and $\tilde{\eta}(\tilde{x}')$ can be addressed by *regular perturbation theory*. Introducing

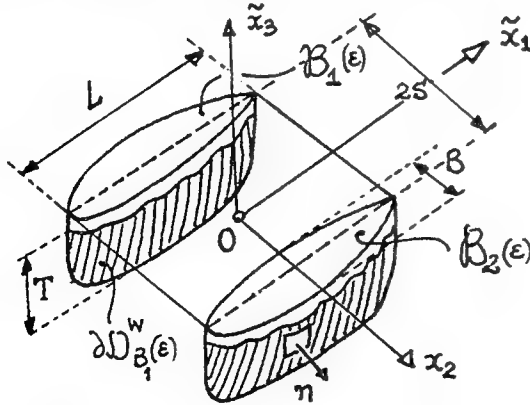


Figure 1: Co-ordinate system and geometry

the non-dimensional variables: $x_\ell = \tilde{x}_\ell/L$, $\ell = 1, 2, 3$, $\Phi(x) = \tilde{\Phi}(\tilde{x})/g^{1/2}L^{2/3}$ and $\eta(x') = \tilde{\eta}(\tilde{x}')/L$, and exploiting the fact that, for a thin hull with lengthwise slowly varying shape, the x_1 -component of its outer normal vector $\mathbf{n} = (n_1, n_2, n_3)$ is asymptotically small, namely $n_1 = O(\epsilon)$, we obtain after simple asymptotic reasoning the following result: the velocity potential $\Phi(x; \epsilon)$ and the free-surface elevation $\eta(x'; \epsilon)$ admit of the following asymptotic approximations :

$$\begin{aligned} \Phi(x; \epsilon) &= \Phi_0(x; \epsilon) + o(\Phi_0(x; \epsilon)), \\ \Phi_0(x; \epsilon) &= O(\epsilon), \quad x \in \mathcal{D}(0), \end{aligned} \quad (3)$$

$$\begin{aligned} \eta(x'; \epsilon) &= \eta_0(x'; \epsilon) + o(\eta_0(x'; \epsilon)), \\ \eta_0(x'; \epsilon) &= O(\epsilon), \quad x \in \partial\mathcal{D}_F(0), \end{aligned} \quad (4)$$

where

$$\eta_0(x'; \epsilon) = F_n \Phi_{0,1}(x; \epsilon), \quad x' \in \partial\mathcal{D}_F(0), \quad (5)$$

and $\Phi_0(x; \epsilon)$ satisfies the following boundary value problem :

$$\Phi_{0,11} + \Phi_{0,22} + \Phi_{0,33} = 0, \quad x \in \mathcal{D}(0), \quad (6)$$

$$\begin{aligned} \Phi_{0,2} &= -\epsilon F_n f_{(1 \text{ or } 2),1} \text{ as } x_2 \rightarrow (- \text{ or } +)s+, \\ \Phi_{0,2} &= +\epsilon F_n f_{(2 \text{ or } 1),1} \text{ as } x_2 \rightarrow (- \text{ or } +)s-, \\ &\quad x \in \partial\mathcal{D}_{B_i}^w(0), \end{aligned} \quad (7)$$

$$\mathcal{K}^{-1}\Phi_{0,11} + \Phi_{0,3} = 0, \quad x \in \partial\mathcal{D}_F(0), \quad \mathcal{K} = F_n^2, \quad (8)$$

$$\Phi_{0,\ell} \rightarrow 0, \quad \ell = 1, 2, 3, \quad x_3 \rightarrow -\infty, \quad (9)$$

and the so-called *radiation condition (R)*: the energy flux associated with the disturbance of the moving body is directed away towards $x_1 \rightarrow -\infty$.

In the above formulae, the subscript ℓ , after a comma, denotes partial differentiation with respect to the space variable x_ℓ , while $\mathcal{D}(0)$ denotes the open domain bounded by the calm fluid surface $x_3 = 0$ and the demihull centerplanes $\partial\mathcal{D}_{B_i}^w(0)$, $i = 1, 2$, to which degenerate the wetted surfaces $\partial\mathcal{D}_{B_i}^w(\epsilon)$, $i = 1, 2$, at the limit $\epsilon = 0$. $\partial\mathcal{D}_{B_i}^w(\epsilon)$ is represented as

$$\begin{aligned} x_2 &= -s + \epsilon f_1(x_1, x_3), \quad x_2 \geq -s, \\ x_2 &= -s - \epsilon f_2(x_1, x_3), \quad x_2 \leq -s, \quad (x_1, x_3) \in \Omega, \end{aligned} \quad (10)$$

with Ω being the projection of $\partial\mathcal{D}_{B_i}^w(0)$ onto the centerplane $x_2 = 0$, and analogously for $\partial\mathcal{D}_{B_2}^w(0)$. Finally, $\partial\mathcal{D}_F(0)$ denotes the open planar domain $\{x_3 = 0\} \setminus \bigcup_{i=1}^2 \partial\mathcal{D}_{B_i}^w(0; x_3 = 0)$, where $\partial\mathcal{D}_{B_i}^w(0; x_3 = 0)$ is the slit representing the degenerate waterline of $\partial\mathcal{D}_{B_i}^w(0)$, $i = 1, 2$.

Let $G(x; \xi)$, $x = (x_1, x_2, x_3)$, $\xi = (\xi_1, \xi_2, \xi_3)$, be the Green function, also referred to as *the Kelvin source*, associated with the Laplace field equation (6), the linearized free-surface condition (8), the "bottom" boundary condition (9) and the radiation condition (R). Furthermore, let the separation distance $2s$, between the axes of the two demihulls, be large enough so that local interference effects can be neglected. One may argue that this is the case if the geometrical rays, which represent the wave front of the Kelvin wave pattern and emanate from the bow of each demihull, do not intersect with the other demihull. Noting that each of these rays forms an angle of 19.28° degrees with the corresponding demihull axis, we conclude that, for

$$2s > \sin(19.28^\circ) \approx 0.33, \quad (11)$$

local interference effects can be neglected. It can then be proved, with the aid of potential theory, that the leading-order potential $\Phi_0(x_0; \epsilon)$ can be approximately decomposed as follows :

$$\Phi_0(x; \epsilon) \approx \Phi_{0,1}(x; \epsilon) + \Phi_{0,2}(x; \epsilon), \quad x \in \mathcal{D}(0), \quad (12)$$

where

$$\begin{aligned} \Phi_{0i}(x; \epsilon) = & \epsilon \frac{F_n}{4\pi} \int_{\partial \mathcal{D}_{B_i}^w(0)} G(x; \xi) (f_{1,1} + f_{2,1}) d\xi \\ & - \frac{(-1)^i}{4\pi} \int_{\partial \mathcal{D}_{B_i}^w(0)} \nu_i(\xi; \epsilon) \frac{\partial G(x; \xi)}{\partial \xi_2} d\xi, \\ & i = 1, 2. \end{aligned} \quad (13)$$

Here $\nu_1(x; \epsilon)$ is the solution of the following Fredholm integral equation of the first kind :

$$\begin{aligned} \epsilon F_n (f_{2,1} - f_{1,1}) = \\ \frac{1}{4\pi} \oint_{\partial \mathcal{D}_{B_1}^w(0)} \nu_1(\xi; \epsilon) \frac{\partial^2 G(x; \xi)}{\partial x_2 \partial \xi_2} d\xi, \\ x \in \partial \mathcal{D}_{B_1}^w(0), \end{aligned} \quad (14)$$

with the double-dash signifying the so-called principal value of the indicated integral according to Hadamard, and

$$\nu_2(x_1, s, x_3; \epsilon) = \nu_1(x_1, -s, x_3; \epsilon), \quad (x_1, x_3) \in \Omega. \quad (15)$$

It is worth-noticing that the kernel $K(x; \xi) = \partial^2 G(x; \xi) / \partial x_2 \partial \xi_2$ of (14) exhibits a non-integrable singularity of the form $|x - \xi|^{-3}$ and thus one can readily remark that the integral in the right-hand side of (14) can only exist as a principal-value integral. Furthermore, the singularity of $K(x; \xi)$ coincides with that of the kernel of the integral equation

which models the three-dimensional Neumann problem for the Laplace equation by using double-layer potentials; see, e.g., Hsiao (1990) [1]. Such equations form the so-called class of *hyper-singular Fredholm integral equations of the first kind*. Naturally, the question arises whether some other approach would yield a more tractable integral equation for $\nu_1(x)$, say, e.g., a Fredholm integral equation of the second type with weakly singular kernel. As already noted in [1], the answer is negative as a result of the fact that $\partial \mathcal{D}_{B_1}^w(0)$ is a flat surface.

An asymptotic approximation of the dipole distribution $\nu_1(x; \epsilon)$ can be easily obtained by assuming that the demihulls $B_i(\epsilon)$, $i = 1, 2$ are not only thin but also *a-bit-slender*, i.e.,

$$T/L = \epsilon_1, \quad \epsilon_1 = \epsilon^a, \quad 0 < a < 1. \quad (16)$$

Assume now that $\nu_1(\xi_1, \xi_3)$ is twice continuously differentiable in Ω and take its two-term Taylor expansion around the point (x_1, x_3) . Substituting this expansion into the right-hand side of (14) and taking into account the following expression for the Kelvin source :

$$G(x; \xi) = \frac{1}{|x - \xi|} + H_{reg}(x; \xi), \quad x_3, \xi_3 \in (-\infty, 0], \quad (17)$$

where $H_{reg}(x; \xi)$ is the so-called *regular part* of the Kelvin source, we arrive at an integro-differential equation for $\nu_1(x_1, x_3)$. After careful asymptotic analysis, one can show that the formula :

$$\begin{aligned} \nu_1^{approx}(x_1, x_3) = & \epsilon F_n (f_{2,1} - f_{1,1}) \\ & \left[\oint_{\partial \mathcal{D}_{B_1}^w(0)} \frac{\partial^2}{\partial x_2 \partial \xi_2} \left(\frac{1}{r(x; \xi)} \right) \right]^{-1}, \quad (x_1, x_3) \in \Omega, \end{aligned} \quad (18)$$

provides indeed an asymptotic approximation of the solution of this equation. Obviously, analogous results can be drawn for the dipole distribution $\nu_2(x_1, x_3)$; see (15). Since $\partial \mathcal{D}_{B_1}^w(0)$ is flat, the principal-value integral in (18) can be analytically evaluated over triangular subdomains of Ω .

Summarizing the hitherto obtained results we conclude: *the flow induced by the steady forward motion, at moderate Froude numbers (see the second estimate in (2)), of a catamaran with thin and a-bit-slender demihulls at sufficiently large separation distance (see (11)), can be modelled, to the leading order of approximation with respect to the small parameters ϵ and ϵ_1 , by two singularity distributions over the centerplane of each demihull, namely a Kelvin-source and a normal Kelvin-dipole distribution (see (12), (13) and (18)).*

These singularity distributions being known, the wave resistance of the catamaran can be easily calculated by appealing to the well known Kochin's formula; see Wehausen and Laitone (1960, §20) [2]. More analytically, the Kochin's function $H(k, \theta)$ takes in this case the following form :

$$H(k, \theta) = 2[P(k, \theta) + iQ(k, \theta)], \quad (19)$$

where

$$[P \text{ or } Q](k, \theta) = [P \text{ or } Q]_\sigma(k, \theta) - [P \text{ or } Q]_\nu(k, \theta), \quad (20)$$

and

$$[P \text{ or } Q]_\sigma(k, \theta) = \cos(k \sin \theta) \int \int_\Omega \exp^{k\xi_3} [\cos \text{ or } \sin](k\xi_1 \cos \theta) \sigma(\xi_1, \xi_3) d\xi_1 d\xi_3, \quad (21)$$

$$[P \text{ or } Q]_\nu(k, \theta) = k \sin(\theta) \sin(k \sin \theta) \int \int_\Omega \exp^{k\xi_3} [\cos \text{ or } \sin](k\xi_1 \cos \theta) \nu(\xi_1, \xi_3) d\xi_1 d\xi_3, \quad (22)$$

with $\sigma = \epsilon(f_{1,1} + f_{2,1})$ and $\nu(x_1, x_3) = \nu_1^{approx}$ (see (18)). After triangulating Ω and approximating $\sigma(x_1, x_3)$ by a piecewise linear and $\nu_1^{approx}(x_1, x_3)$ by a piecewise constant interpolant, over the constructed triangulation, the double integrals, appearing in the right-hand side of (21) – (22), are evaluated analytically.

Appendix B : The Wave Resistance of Arbitrarily Shaped Catamarans

In this appendix we describe a method for evaluating the wave resistance of a steadily moving catamaran with arbitrarily shaped demihulls. In this case, the perturbation potential $\varphi(P)$ can be represented as

$$\varphi(P) = \int \int_{\partial D_B^w} G(x; \xi) \sigma(\xi) d\xi + F_n^2 \int_C n_1 G(x; \xi) \sigma(\xi) d\ell, \quad (1)$$

where $\partial D_B^w = \partial D_{B_1}^w \cup \partial D_{B_2}^w$ denotes the wetted surface of the floating body and C denotes the intersection of ∂D_B^w with the undisturbed free surface $x_3 = 0$. Substituting (1) into the body boundary condition we arrive at the following Fredholm integral equation, of the second kind, for the unknown density $\sigma(x)$ of the Kelvin sources $G(x; \xi)$:

$$\begin{aligned} \frac{1}{2} \sigma(x) + \int \int_{\partial D_B^w} \frac{\partial G(x; \xi)}{\partial \mathbf{n}_x} \sigma(\xi) d\xi \\ F_n^2 \int_C n_1(\xi) \frac{\partial G(x; \xi)}{\partial \mathbf{n}_x} \sigma(\xi) d\ell = \\ F_n n_1(x), \quad x \in \partial D_B^w. \end{aligned} \quad (2)$$

The above equation is solved numerically by a panel discretization method, which approximates the wetted surface of the catamaran by a sufficiently dense mesh of planar panels (triangles or quadrilaterals). The density $\sigma(x)$ of the Kelvin-source distribution is assumed constant in each of these panels. Then, the discretization of (2) results into a system of linear equations, whose matrix M consists of the so-called *influence coefficients* M_{ij} .

The efficient and robust evaluation of the influence coefficients is directly connected with the efficient calculation of the Kelvin source $G(x; \xi)$ and its partial derivatives. It is well known that $G(x; \xi)$ can be written as the sum of three, qualitatively different, components. The first component represents the velocity potential of a Rankine source located at $x = \xi$. The second component represents the velocity potential of a local non-oscillatory disturbance, which is symmetric with respect to $x_1 - \xi_1$, while the third component contributes only to the downstream ($x_1 \rightarrow -\infty$) behaviour of $G(x; \xi)$, where it exhibits a strong oscillatory behaviour. The double integral of the second component is evaluated by a technique introduced by Newman (1987), whereas the oscillatory term is evaluated according to the method of Baar and Price (1988); see items [18] and [19] in the main reference list. Once the influence matrix has been obtained and the associated system is solved, we appeal to (1) for evaluating the velocity potential as well as any other field quantity of interest (velocities, pressure, wave profiles). In fine, the wave resistance, trim and sinkage of the catamaran are calculated by direct numerical integration of the pressure over the wetted surface of the floating body.

References

- [1] Hsiao, G.C., "Solution of Boundary Value Problems by Integral Equations of the First Kind – An Update", Center for the Mathematics of the Waves, TR-90-16, 1990, Dept. Mathematical Sciences, Univ. Delaware, Newark.
- [2] Wehausen, J.V., and Laitone, E.V., "Surface Waves", *Encyclopaedia of Physics*, Vol. 9, Springer Verlag, Berlin, 1960, pp.446-778.

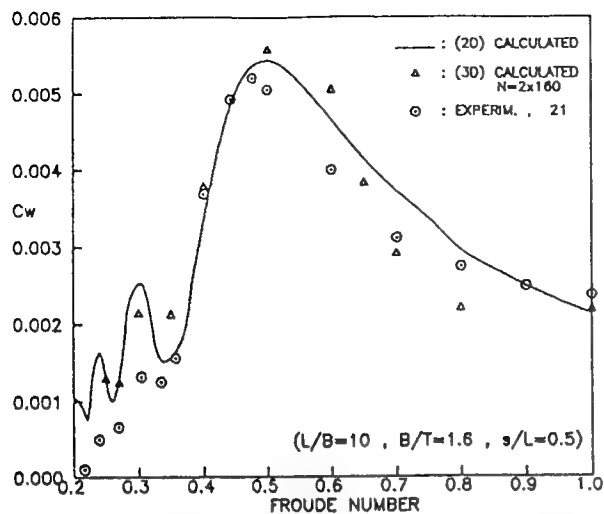


Fig. 2 Comparison of the wave resistance coefficient for a catamaran with Wigley demihulls

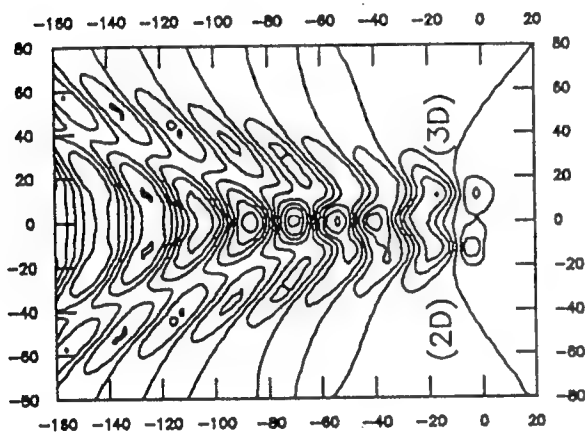


Fig. 3 Comparison of the wave pattern of the lower hulls of a SWATH ship

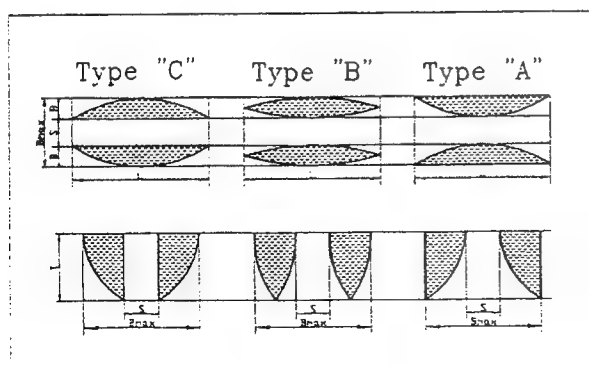


Fig. 4 Definition of equivalent symmetric and asymmetric WIGLEY twin-hulls

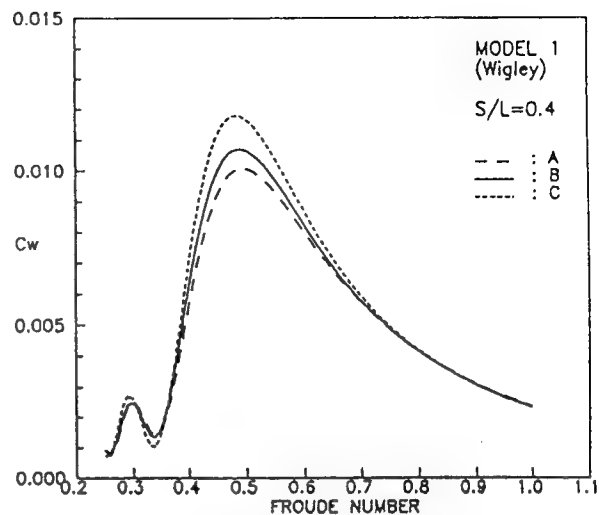


Fig. 5 Wave resistance coefficients of symmetric and asymmetric WIGLEY twin-hulls

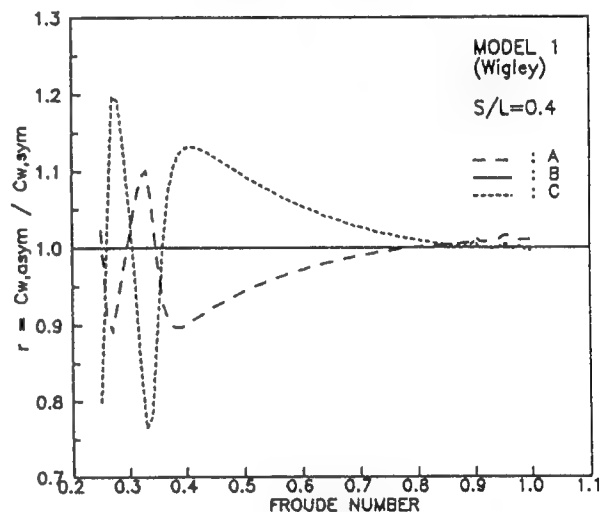


Fig. 6 Influence of asymmetry on the wave resistance of WIGLEY twin-hulls

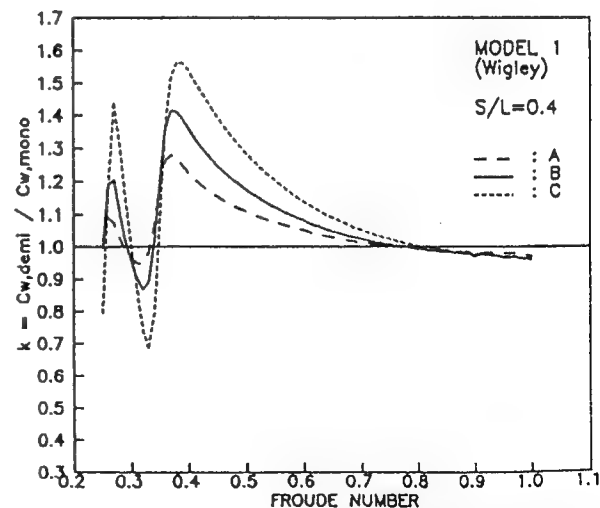


Fig. 7 Interaction wave resistance coefficient of symmetric and asymmetric WIGLEY twin-hulls

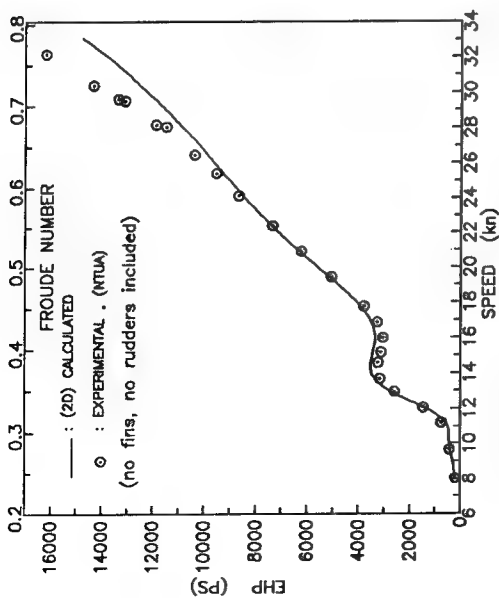


Fig. 8 Comparison between theoretical predictions and model experiments for the Effective Horse Power of *AEGEAN QUEEN*

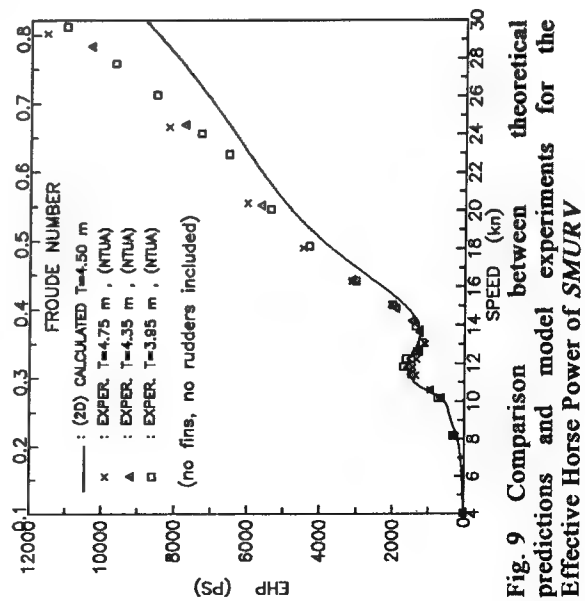


Fig. 9 Comparison between theoretical predictions and model experiments for the Effective Horse Power of *SMURV*



Fig. 10 3D rendering of high-speed SWATH passenger/car ferry *AEGEAN QUEEN*

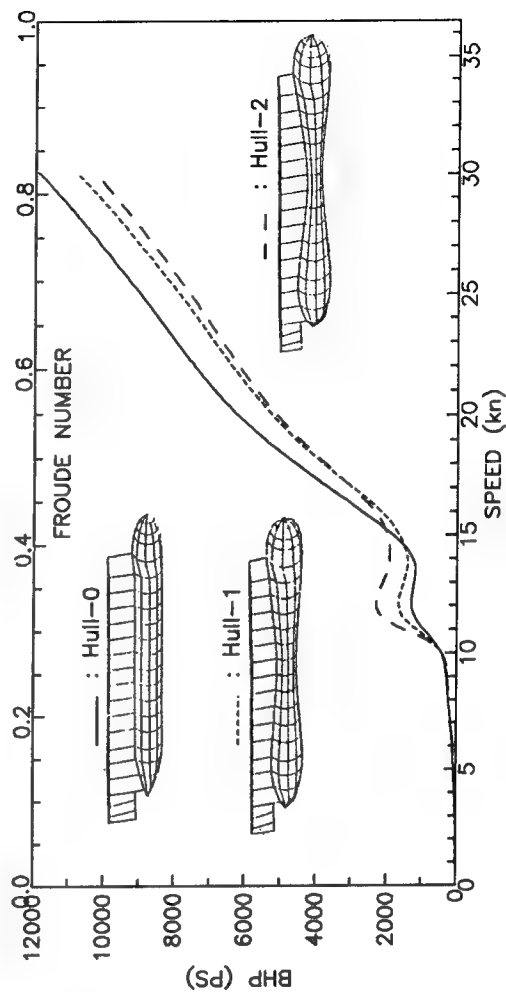


Fig. 11 Alternative *SMURV* Hull Forms optimized for $v=25$ kn

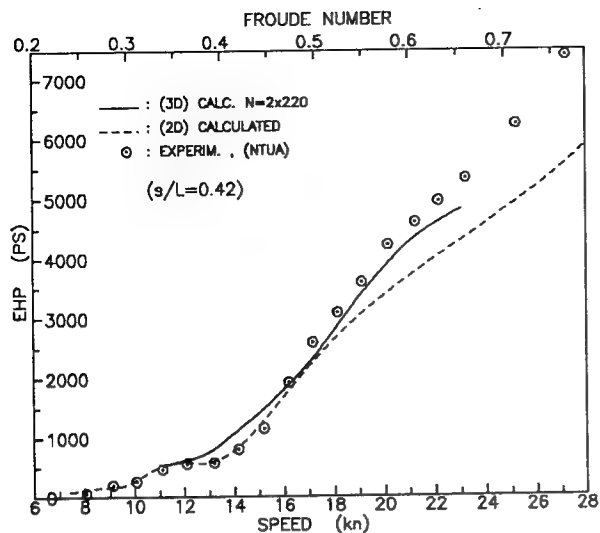


Fig. 12 Comparison between theoretical predictions and model experiments for the Effective Horse Power of *SIMICAT*

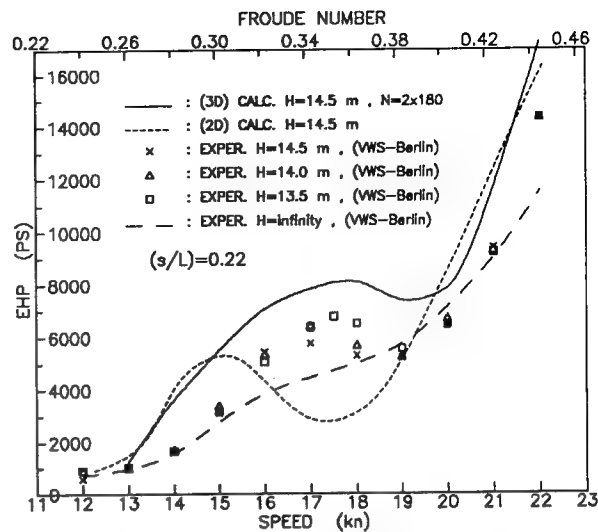


Fig. 13 Comparison between theoretical predictions and model experiments for the Effective Horse Power of *GOUTCAT*

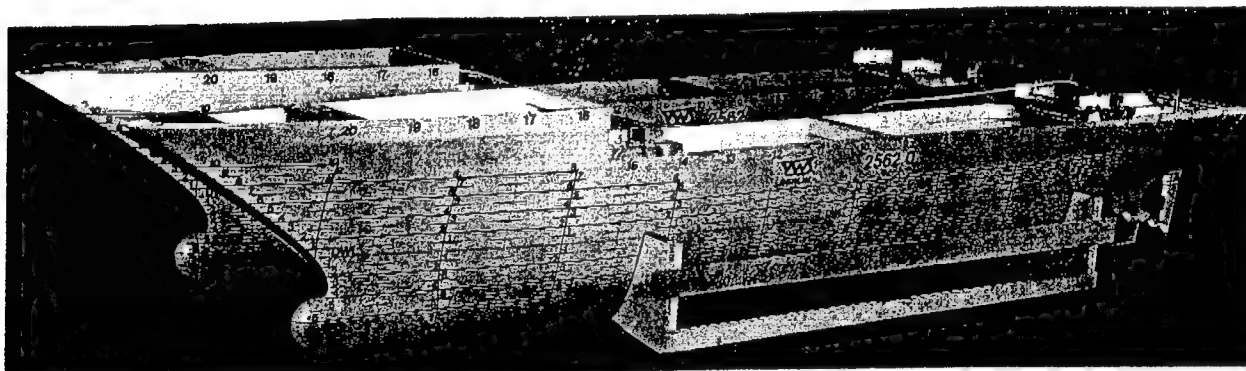
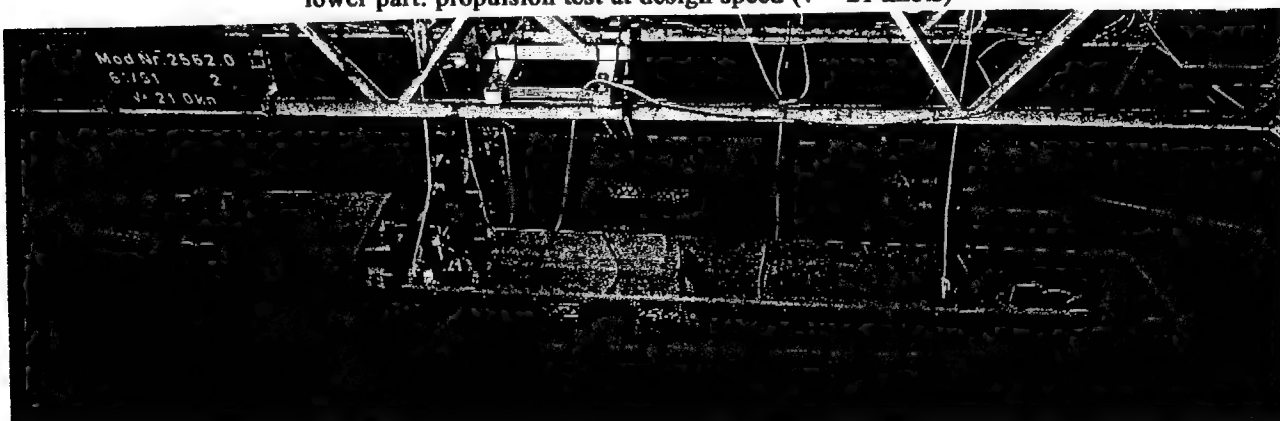


Fig. 14 View of *GOUTCAT* model tested at VWS Berlin
upper part: model in scale 1:16 (LOA = 4,928m)
lower part: propulsion test at design speed ($v = 21$ knots)



DISCUSSION

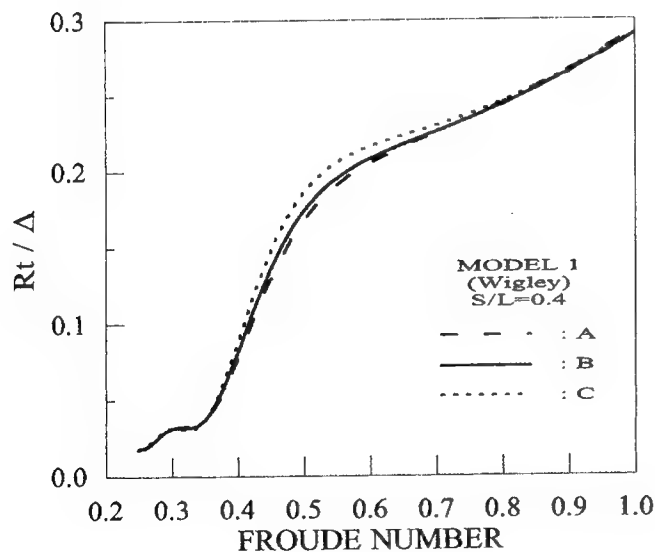
L.J. Doctors

University of New South Wales, Australia

Could the author kindly clarify the definition of the wave-resistance coefficient employed in Figure 5? Usually the wetted-surface area appears in the denominator of the definition of this coefficient. In that case, since the wetted area will be slightly less for Type B twin-hull than for Type A and Type C, the relative performance (in terms of resistance rather than resistance coefficient) will be altered to some degree.

AUTHORS' REPLY

In response to the question raised by Dr. Doctors, the authors would like to clarify that the depicted wave resistance coefficients are defined in the common way, namely with reference to the wetted surface area. Because of the slenderness of the studies hulls, the differences in the wetted area between Type B twin-hull and Type A or C, which all have the same displacement, are very small, therefore the results change very little. In any case, for the sake of completeness, we include below a graph of the ratio of total resistance divided by displacement indicating the relative performance of the three types of twin-hulls over the studies Froude range.



DISCUSSION

H. Nowacki
Berlin Technical University, Germany

My compliments to the authors for a valuable contribution to the hydrodynamic optimization of multihull ships. Their computational methods are showing encouraging agreement with experiments and hence are becoming a trustworthy tool for design studies. Such methods are almost indispensable for design, since it is evident that the multiparametric variety of multihull configurations and shapes cannot possibly be explored by experiment alone.

I should like to raise three design-related questions:

1. *On hull separation:* The paper alludes to the significance of hull separation on wave resistance interference, a well-known, often non-monotonic effect, but it does not give much practical evidence on it. Clearly a less than optimal separation may save hull weight. Does the authors' experience suggest that the resistance penalty for non-optimal separation may be of such magnitude that it would outweigh the weight savings?

2. *On asymmetric demihulls:* One would like to understand why the shape with flat inside should be more advantageous at high Froude numbers than the other two. Is it in part because the "effective" separation is increased when the hull mean line is curved outward? Or is perhaps a genuine camber effect creating favorable wave interference patterns that cannot be produced without curved mean lines? In short and in terms of an analogy, is the phenomenon mainly a "thickness/distance" effect or a "camber/curvature" effect? In any case, the results beg for an explanation.

3. *On SWATH vs. displacement catamarans:* In the Froude number range around 0.4, SWATH and FDC may be competitors. It would be of interest to see dimensionless comparisons of R_T/Δ versus Froude number for the four comparison designs. It is such a rare opportunity to be able to compare "optimized" catamarans and SWATH vessels.

Again, my appreciation for a very interesting paper.

AUTHORS' REPLY

The authors would like to thank Professor Nowacki for his very valuable, design-oriented questions. In response to the first raised question, namely on the often non-monotonic effect of hull separation on the wave resistance of displacement catamaran vessels, we would like to confirm that at intermediate Froude numbers (namely for Froude between about 0.3 and 0.45) the interference resistance depends strongly both on hull separation *and on the demihull displacement distribution* (including any asymmetry, see, e.g., Fig. 15 and Fig. 16).¹ At higher Froude numbers hull separation becomes less and less important. The resistance penalty for non-optimal separation can, in fact, outweigh weight savings, but a good designer should be looking for the optimal displacement distribution of the demihulls, assuming the hull separation as close as possible, what should automatically ensure least structural weight and acceptable seakeeping behavior (least possible GM value).

In response to the second question, we would like to note that at high Froude numbers (above 0.6) in fact all demihull forms (inward and outward flattened WIGLEY hulls and symmetric ones) tend to deliver similar results (see Fig. 5 and Fig. 16), but in accordance to the reply to the previous question, the general interaction phenomenon is a complex "thickness/distance" and "camber/curvature" effect that has to be studied carefully for the Froude number in question.

Finally, as to the last qualitative question, we prepared in response Fig. 17, showing that at Froude around 0.4, the two designed displacement catamarans are superior to the two SWATHs. This is not surprising since the catamarans have been purposely optimized for exactly this Froude range, namely around 0.4, whereas the SWATH *Aegean Queen* has an intended service at Froude number 0.7. Finally the SWATH *SMURV* (oceanographic vessel design) is herein not a real competitor to the others because of several design constraints that limited severely her geometry (see, however,

¹These figures show the experimental values for the total resistance coefficient that is more relevant to the vessel design. It should be noted that the wetted surface (and frictional resistance) of the asymmetric WIGLEY demihulls (type A and C) is higher than that of the "equivalent" symmetric demihull of equal displacement (type B).

Fig. 11, the results for the required horsepower of alternative *SMURV* hull forms when optimized without significant geometry constraints).

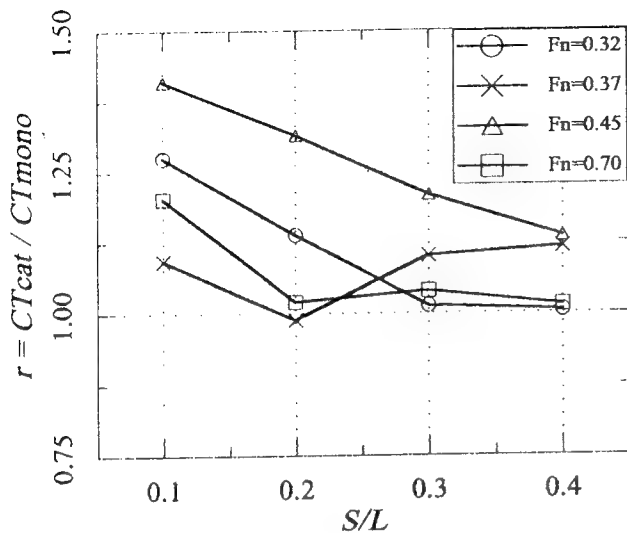


Fig. 15 Influence of separation distance on the total resistance coefficients of symmetric WIGLEY demihulls ($L/B=10$, $B/T=1.6$, exp. results [21])

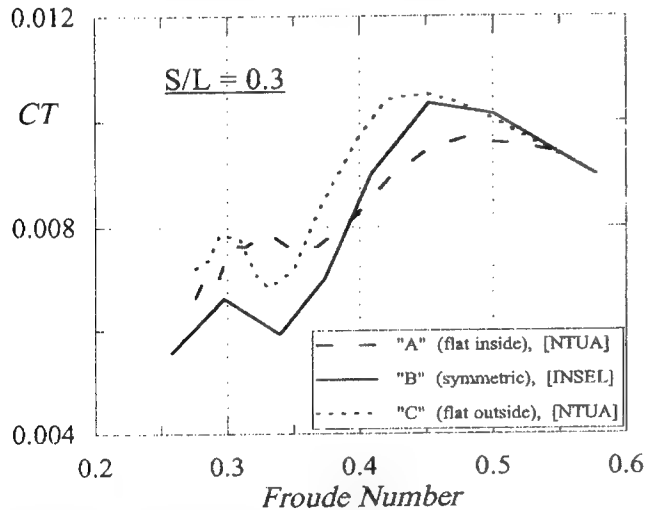


Fig. 16 Influence of asymmetry on the total resistance of WIGLEY demihulls ($L/B=10$, $B/T=1.6$, $s/L=0.3$, exp. results NTUA and [21])

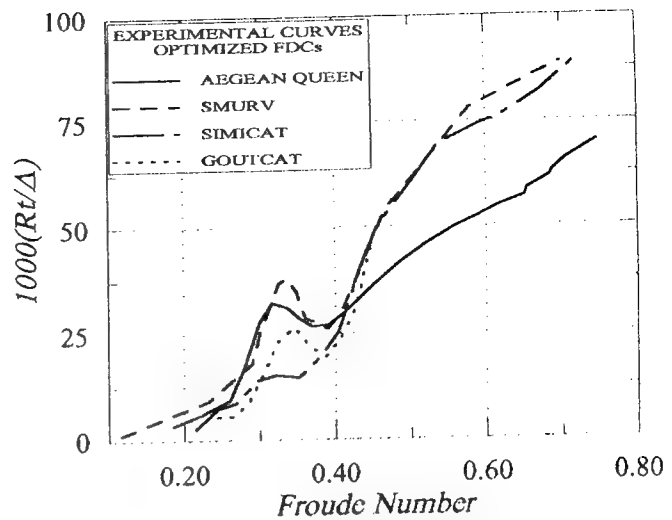


Fig. 17 Resistance/displacement ratio of optimized FDCs and SWATHs (exp. results NTUA and VWS Berlin)

On Ships at Supercritical Speeds

X.-N. Chen (University of Stuttgart, Germany),

S. Sharma (Mercator University, Germany)

ABSTRACT

This paper deals with the problem of a ship moving at supercritical speeds. Following the idea of shallow channel superconductivity (zero wave resistance) proposed in Chen & Sharma (1995), we continue to look for more nonlinear superconductive solutions within an improved theoretical model. We begin our study with an extended KP equation (eKP) that holds to same precision as the Boussinesq equations. First, we reduce the problem of a ship moving at supercritical speeds in horizontally unbounded shallow water to an "initial" value problem of the KdV equation. This reduction enables various analytical solutions, specially an N-soliton solution. Second, we construct an eKP solution of the interaction of solitons (or any wave packets) moving in different directions. Third, we derive a fore-and-aft asymmetric superconductive hullform from the 2-KdV-soliton and the solution of the interaction between itself and its reflection from the channel sidewall. Finally, we propose a heuristic method for improving the precision of the shallow-water wave models by comparing their dispersion relations with the exact one for finite depth. In the concluding remarks we point out possible practical applications of our theory.

NOMENCLATURE

Dimensional variables carry a superscript asterisk *, all others are nondimensional.

A^* typical wave amplitude

h^* water depth

$g^* = 9.80665 \text{ m/s}^2$ acceleration due to gravity

$k = k^* h^* / \sqrt{\varepsilon}$ circular wave number

$Oxyz$ coordinate system moving with the ship, x pointing forward, z upward.

$S(x) = S^*(x^*) / (\varepsilon h^{*2})$ submerged cross sectional area of ship at section x

$U = F_{nh} = U^* / \sqrt{g^* h^*}$ depth Froude number

U^* ship speed

w^* channel width

$(x, y) = \frac{\sqrt{\varepsilon}}{h^*} (x^*, y^*)$ horizontal coordinates

$\varepsilon = A^* / h^*$ smallness parameter for wave nonlinearity

$\varphi = \varphi^* / (h^* \sqrt{\varepsilon g^* h^*})$ depth-averaged potential

$\zeta = \zeta^* / (\varepsilon h^*)$ free surface elevation

INTRODUCTION

This paper deals with the problem of wave pattern and wave resistance of a slender ship moving steadily at supercritical speeds in shallow water. The critical speed is known to be $\sqrt{g^* h^*}$ and the depth Froude number U can be understood as the ratio of ship speed to critical speed. Supercritical ship speed means $U > 1$.

The depth Froude number plays an important role in shallow water ship hydrodynamics that is almost the same as that of the Mach number in aerodynamics (Tuck 1978), except that there is a dispersion effect in shallow water waves. It is well-known that there is a favorable supercritical speed range in which the absolute value of wave resistance is smaller than that in the transcritical speed range, e.g. Graff, Kracht & Weinblum (1964). Nevertheless, supercritical ships are not as common as supersonic airplanes. Most inland or coastal ships plying in shallow water operate well below the

critical speed. Only recently can one observe a worldwide interest in the commercial exploitation of supercritical speeds for ships, especially ferries.

It is probably less well-known that the favorable effect of wave interference between twin hulls of a catamaran in shallow water, which diminishes total wave resistance, is more significant in the supercritical speed range than in the subcritical speed range (and, of course, in deep water). This phenomenon has been reported earlier by Eggers (1955, Figs. 2 and 18) and Kirsch (1966, Figs. 2-9). It was recently rediscovered by Chen & Sharma (1994a, Fig. 5a) on the basis of a nonlinear theory and confirmed by model experiment. Even more exciting is the fact that when we tried to seek a fuller theoretical understanding of this interesting phenomenon, see Chen & Sharma (1995), we found that the wave resistance of a single-hull ship in a channel of suitable width can be made to vanish totally within the framework of a linear shallow-water wave approximation and, furthermore, also in a more accurate nonlinear theory, namely the standard KP equation. To put it simply in one sentence, the mechanism is that the bow wave after reflection from the channel sidewall hits the after-body and counteracts the stern wave so that the resultant wave in the ship wake disappears totally, if the hull geometry is adapted to ship speed and channel width according to certain rules. To our knowledge, this is a new type of ship and channel configuration marked by zero wave resistance. By analogy to electrical conductors, we have proposed the name "shallow channel superconductivity" for this phenomenon.

We would like to insert in the following three paragraphs a short review of shallow water wave theory as applied to ship hydrodynamics. The first relevant paper was by Tuck (1966) who developed a strictly linear technique of matched asymptotic expansions for a slender ship in shallow water. Lea & Feldman (1972) partly took account of nonlinearity and used an established transonic-flow numerical method for computing the transcritical motion of ships. Later on, Mei (1976) extended this work to include the dispersion effect in the near-critical speed range while still dealing with the steady problem. With due consideration to remarkable early towing tank experiment reports, e.g. Thews & Landweber (1935, 1936), Helm (1940), Kinoshita (1946), Graff (1962), and Graff, Kracht & Weinblum (1964), it may be stated that the recently revived interest in upstream solitons generated by a ship moving steadily at near-critical speeds stems from the experimental and numerical works by Huang et al. (1982) and Wu & Wu (1982). Since then various follow-up investigations have been done, e.g. Ertekin, Webster & Wehausen (1986) and Katsis & Akylas (1987) solved the 3-D free-surface pressure disturbance problem. Mei (1986), using matched

asymptotic expansions, derived an inhomogeneous Korteweg-de Vries (KdV) equation for a slender ship moving at near-critical speed in shallow water and theoretically demonstrated solitons propagating upstream. Mei & Choi (1987) further developed this theory to calculate hydrodynamic forces on the ship but only crude agreement with experiments was obtained because this theory cannot predict the two-dimensional waves around a real ship and in its wake. So Choi & Mei (1989) improved their theory by using a Kadomtsev-Petviashvili (KP) equation in the far field to take account of the 2-D effect. More numerical results were reported in Choi, Bai, Kim & Cho (1990) with another finite element method.

Chen & Sharma (1992) pursued this method further with the aim of practical application. The slender body theory in the near-field was refined by taking account of local wave elevation, longitudinal disturbance-flow velocity and ship squat. Moreover, it was extended to the more general case of asymmetric motion. The KP equation in the far field was solved numerically by an efficient finite difference method, namely, a fractional step algorithm with Crank-Nicolson-like schemes in each half step. Very good agreement with towing tank experiments was achieved in wave resistance, sinkage, and trim for several ship models. Furthermore, Chen & Sharma (1994a) derived a KP equation from the Boussinesq equations by keeping a higher-order nonlinearity in the lateral direction, thus making it valid for a wider speed range. More numerical results from this modified KP equation for a ship in a wider speed range were reported in Chen & Sharma (1994b) and compared with old model experiments of Graff et al. (1964) on a Taylor Standard Series hull as well as with new tests on a Series 60 hull. It was concluded that the method based on nonlinear shallow-water wave theory holds enough precision for the practical ship problem if higher-order effects in the near field are taken into account as indicated above.

Extension of the theory to the case of asymmetric ship motion also proved useful. The corresponding computer codes enabled us to treat a ship moving parallel to the channel axis off-center and/or at a drift angle. With vertical sidewalls this configuration is mathematically equivalent to a catamaran moving in a channel of twice the width. Numerical results were reported in Chen & Sharma (1994a). The calculated wave resistance, lateral force, yaw moment, sinkage and trim agreed very well with towing tank measurements on a Series 60 model hull both in off-center and in oblique motion, except for the lateral force and yaw moment in oblique motion at higher speeds. Especially the significant wave resistance reduction in the supercritical off-center case led us on to the discovery of superconductive ship-channel geometries marked by no trailing waves and

zero wave resistance, see Chen & Sharma (1995). More calculations for a projected catamaran passenger ferry were carried out by Jiang, Sharma & Chen (1995) with the same computer program and satisfactory agreement with measurements previously done by Heuser (1973) in the Duisburg Model Tank was obtained for a wide range of speed.

The idea of shallow channel superconductivity is not merely of academic interest but also of practical value. One of the authors (XNC) further exploited the asymmetric theory and invented a catamaran form with cambered hulls that theoretically has zero wave resistance. The hulls are so designed that no waves exist in the outside domain and in the wake of the catamaran for a certain depth Froude number larger than unity. This 100% wave-resistance elimination is possible in shallow water independent of channel width and sidewalls. As regards absolute speed, a depth Froude number $U=1.5$ in inland or coastal waters of 5-20 m depth corresponds to ship speeds ranging from 37.8 to 75.6 km/h, which are well within the range of present technical feasibility and economic interest. A German patent for this concept has been applied for. Details will be reported separately in the future.

Here, a few comments on the exciting topic of zero wave resistance are in order. Naval architects have always striven for ships with little waves. It would be a dream to build a ship without waves. Bow bulbs and submerged wings attached to ship hulls are good examples of devices conceived to achieve mutual cancellation of waves originating from different sources. In principle, ship waves can be even completely eliminated within linear theory. Several interesting theoretical proposals have been made recently by Tuck (1989), Tuck & Tulin (1992), and Tulin & Oshri (1994). The experimental investigation of Mori (1993) is also worth mentioning. But to our knowledge the idea of superconductive ships in shallow water has never been demonstrated or proposed before, even in the linear regime. Intuitively speaking, since wave dispersion is weaker in shallow water, the interference between waves becomes more effective than in deep water, specially in the supercritical range, where there are even nonlinear characteristic wave solutions. In this sense zero wave-resistance ships in shallow water are more feasible.

In this paper, we still concentrate on theoretical studies and develop a shallow water wave theory specially for ships symmetrically moving at supercritical speeds. First, we summarize the linear and nonlinear concepts of a superconductive channel already described in detail by Chen & Sharma (1995). The nonlinear solution was constructed from a two-soliton solution of a standard KP equation (Mei 1976). Then we report several new developments. The standard KP equation is believed

to be valid only in a near-critical speed range, so we begin our study here with an extended KP equation which holds for a wider speed range because higher-order transverse derivatives are taken into account. Although it lacks a useful property of the original KP equation, namely, an exact and explicit N-soliton solution, yet its single-soliton solution is still simple to find.

The main body of this paper comprises the following four steps: (i) For a ship in horizontally unbounded shallow water moving at supercritical speed, we reduce the ship wavemaking problem from the boundary value problem of the extended KP equation to an initial value problem of the KdV equation without loss of precision. The slowly varying transverse variable Y plays the same role as slowly varying time in the standard KdV equation. It is not surprising that for almost unidirectional free waves the stationary KP equation, or more generally the Boussinesq equations, can be reduced to a KdV equation. But it is rather astonishing that for arbitrary ship hulls the wave generation problem can be reduced to a KdV initial value problem, which can be solved so easily. (ii) The solution of interacting solitons moving in different directions is vital to the construction of superconductive ship hullforms. Fortunately, this interaction is weak in the sense of Miles (1977), which means that the interaction time is short. We show how to find an approximate solution. (iii) We construct a fore-and-aft symmetric superconductive hullform from the solution of two identical solitons in the same way as in the previous paper. Moreover, we construct a fore-and-aft asymmetric superconductive hullform from the N-soliton solution. (iv) Finally, we propose a heuristic method for improving the precision of various shallow-water wave models. Based on the fact that the wave pattern depends mostly on the dispersion relation, we compare the exact stationary dispersion relation in finite-depth water with the dispersion relations of various approximate shallow-water wave equations. As a consequence we introduce a speed-dependent coefficient into the equation and obtain a heuristic model whose dispersion relation is almost equal to the exact one. Hence, it is expected that this model will yield better results in applications to the ship wavemaking problem, specially in the superconductive mode.

RECAPITULATION OF PREVIOUS SOLUTIONS OF CHANNEL SUPER-CONDUCTIVITY

Originally, the idea was inspired by the numerical cum experimental result that the wave resistance at supercritical speeds is significantly reduced as the ship track is moved off the centerline

and brought closer to one of the channel sidewalls. For the Series 60, block 0.6 hull at depth Froude number 1.3 the reduction of wave resistance reaches 30% in both calculation and experiment (Chen & Sharma 1994a). The mechanism of this effect becomes clear as we directly see the calculated ship wave pattern. The bow wave (elevation) on the near-wall side is reflected by the channel sidewall and almost cancels the stern wave (depression) on the far-wall side. Naturally, one is tempted to try moving the far wall also close to the ship so that the opposite pair of bow and stern waves would also nearly cancel itself. It works. By numerical experiment we obtained 75% wave resistance reduction in an optimal narrow channel for the Series 60 hull (Chen & Sharma 1995).

Stimulated by this success we sought a fuller theoretical understanding of this intriguing phenomenon and discovered (Chen & Sharma 1995) that the wave resistance of a ship at supercritical speed in a channel can be made to vanish totally not only in linear shallow-water wave approximation (Tuck 1966) but also in a more accurate nonlinear theory (Mei 1976). In the linear analysis we showed that the wave resistance becomes zero for a suitable combination of body speed, water depth and channel width if the afterbody geometry is adapted to an arbitrary forebody according to a simple geometric rule. Further, we extended the idea by considering the standard stationary Kadomtsev-Petviashvili equation (stationary 2D KdV equation, Mei 1976). By exploiting its well-known two-soliton solution we still obtained a zero-wave-resistance ship, albeit with strong restrictions on body geometry. Here, we present a new graph to show this solution.

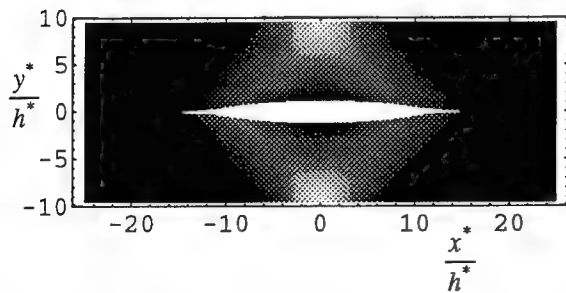


Fig. 1 The localized diamond-shaped wave pattern generated by a superconductive ship hull in the case of $U=1.5$, $A=0.1$ and $x_1=10$ (Chen & Sharma 1995).

REDUCTION TO KdV EQUATION

We begin our study with the mathematical model as formulated in Chen & Sharma (1994a, Eq. 19). Here only the symmetric and steady flow is considered,

$$(1-U^2)\varphi_{xx} + (1+\varepsilon U\varphi_x)\varphi_{yy} + \frac{\varepsilon U^2}{3}(\varphi_{xxx} + \varphi_{xyy}) + 3\varepsilon U\varphi_x\varphi_{xx} + 2\varepsilon U\varphi_y\varphi_{xy} = O(\varepsilon^2), \quad (1)$$

with the boundary condition at the ship location,

$$\left. \frac{\partial \varphi}{\partial y} \right|_{y=\pm 0} = \mp \frac{U}{2} \frac{dS(x)}{dx} + O(\varepsilon), \quad (2)$$

where ε is a smallness parameter that is defined as the ratio of typical wave amplitude to water depth. Eq. (1) is the stationary extended KP equation that holds for a wide speed range and is precise to the same order as the Boussinesq equations. If the higher order terms of the transverse derivatives are neglected, it becomes the standard KP equation (Mei 1976). In the boundary condition (2) the higher order terms are neglected for the sake of mathematical simplicity.

For supercritical speed $U > 1$ and $\sqrt{U^2 - 1} = O(1)$, we can apply a characteristic transformation for $y > 0$:

$$\xi = x + \sqrt{U^2 - 1}y, \quad Y = \varepsilon y / \sqrt{U^2 - 1}. \quad (3)$$

Then via

$$\frac{\partial}{\partial x} = \frac{\partial}{\partial \xi}, \quad \frac{\partial}{\partial y} = \sqrt{U^2 - 1} \frac{\partial}{\partial \xi} + \frac{\varepsilon}{\sqrt{U^2 - 1}} \frac{\partial}{\partial Y},$$

Equations (1) and (2) become

$$\varphi_{\xi Y} + \frac{3}{2}U^3\varphi_{\xi}\varphi_{\xi\xi} + \frac{U^4}{6}\varphi_{\xi\xi\xi\xi} = O(\varepsilon), \quad (4)$$

for $Y > 0$, and

$$\varphi_{\xi}(\xi, Y=0) = -\frac{U}{2\sqrt{U^2 - 1}} \frac{dS(x)}{dx} + O(\varepsilon). \quad (5)$$

It is clear that the problem is a standard initial-value problem of the KdV equation if we set $u = \varphi_{\xi}$. The variable Y plays exactly the same role as time in the original KdV equation. All solutions of the KdV equation are approximate solutions of the extended KP equation, specially the N-soliton solution.

This reduction is so wonderful that the problem can be solved even analytically for certain hullforms $S(x)$ by the well-known inverse scattering method and, in any case, numerically for arbitrary hullforms without any difficulty. Specially the forebody of a ship can emit either single or multiple oblique solitons, while the afterbody generates undulating

dispersive waves. We directly employ some examples given in Drazin & Johnson (1989) to explain these phenomena. Via a transformation

$$u = -\frac{U^3}{4} \varphi_\xi, \quad t = \frac{\sqrt{6}}{U^2} Y, \quad x = \frac{\sqrt{6}}{U^2} \xi,$$

Eq. (4) becomes the standard form of KdV (4.7) in Drazin & Johnson (1989). So now if the "initial condition" is taken as

$$\varphi_\xi(\xi, 0) = N(N+1) \frac{4}{U^3} \operatorname{sech}^2 \frac{\sqrt{6}}{U^2} (\xi - x_0),$$

i.e., the forebody is of the form:

$$\frac{dS(x)}{dx} = -8N(N+1) \frac{\sqrt{U^2-1}}{U^4} \operatorname{sech}^2 \frac{\sqrt{6}}{U^2} (x - x_0),$$

then from this initial single-peak wave packet N oblique solitons will evolve asymptotically as $Y \rightarrow \infty$. From (4.36) in Drazin & Johnson (1989) we have the detailed solution for $N=2$ as $x_0=0$:

$$\varphi_\xi(\xi, Y) = D(\xi, Y) \equiv \frac{48}{U^3} \times \frac{3 + 4 \cosh(2\xi - 8Y) \sqrt{6}/U^2 + \cosh(4\xi - 64Y) \sqrt{6}/U^2}{[3 \cosh(\xi - 28Y) \sqrt{6}/U^2 + \cosh(3\xi - 36Y) \sqrt{6}/U^2]^2}. \quad (6)$$

$D(\xi, Y)$ here means a double-soliton solution of the KdV equation. Its asymptotic wave form for $Y \rightarrow +\infty$ can be given as

$$\varphi_\xi(\xi, Y) \approx \frac{32}{U^3} \operatorname{sech}^2(\sqrt{6}/U^2) [2(\xi - 16Y) - \frac{1}{2} \log 3] + \frac{8}{U^3} \operatorname{sech}^2(\sqrt{6}/U^2) [2(\xi - 4Y) + \frac{1}{2} \log 3],$$

as $Y \rightarrow +\infty$. (6')

Mei (1976) found a forebody that generates a single oblique soliton. The method presented here will yield many forms that generate N solitons.

In the afterbody we have $dS(x)/dx > 0$, so $\varphi_\xi(\xi, 0) < 0$. Then the solution of the KdV equation (4) will develop without the emergence of a soliton. The initial wave packet will collapse and degenerate into a wave train which disperses into $\xi < 0$. As an example we can see Fig. 4.8 in Drazin & Johnson (1989, p.85). This is why we usually see dispersive undulating waves instead of a soliton in the wake.

We conclude that as a ship moves at supercritical speed in horizontally unbounded shallow

water its forebody can generate oblique solitary waves which extend to infinity along their characteristic lines while its afterbody generates an undulating wave train which disperses into $\xi < 0$.

APPROXIMATE SOLUTION OF WEAK INTERACTION OF SOLITONS

As is generally known, the KdV equation holds only for unidirectional waves. So the reduced KdV equation (4) is not valid for the interaction of waves in two different directions, specially for the reflection of a solitary wave by a channel sidewall. So we have to deal with such problems by means of the original Eq. (1). In the following, we develop a technique for constructing approximate solutions of arbitrary solitons moving in two different directions.

Since the interaction of solitons in two different directions is weak in the sense of Miles (1977), i.e., the interaction period is short, we can assume that the solution of (1) is of the form:

$$\varphi(x, y) = F(\xi + \varepsilon \sigma_1(\eta, Y), Y) + G(\eta + \varepsilon \sigma_2(\xi, Y), Y), \quad (7)$$

with

$$\xi = x + (U^2 - 1)^{1/2} y, \quad \eta = x - (U^2 - 1)^{1/2} y, \\ Y = \varepsilon y / \sqrt{U^2 - 1}, \quad (8)$$

where F and G are solitons propagating in different directions and $\varepsilon \sigma_1$, $\varepsilon \sigma_2$ are the phase functions. Substituting (7) into (1) and neglecting higher order terms, intermediate calculation

$$\begin{aligned} (1 - U^2) \varphi_{xx} + \varphi_{yy} &= 2\varepsilon F_{\xi Y} + 2\varepsilon G_{\eta Y} \\ -4\varepsilon(U^2 - 1) \left(F_{\xi\xi} \frac{\partial \sigma_1}{\partial \eta} + G_{\eta\eta} \frac{\partial \sigma_2}{\partial \xi} \right) &+ O(\varepsilon^2), \\ U \varphi_x \varphi_{yy} &= U(U^2 - 1)(F_\xi + G_\eta)(F_{\xi\xi} + G_{\eta\eta}) + O(\varepsilon) \\ &= U(U^2 - 1)(G_\eta F_{\xi\xi} + F_\xi G_{\eta\eta} + F_\xi F_{\xi\xi} + G_\eta G_{\eta\eta}), \\ 3U \varphi_x \varphi_{xx} &= 3U(F_\xi + G_\eta)(F_{\xi\xi} + G_{\eta\eta}) + O(\varepsilon) \\ &= 3U(G_\eta F_{\xi\xi} + F_\xi G_{\eta\eta} + F_\xi F_{\xi\xi} + G_\eta G_{\eta\eta}), \\ 2U \varphi_y \varphi_{xy} &= 2U(U^2 - 1)(F_\xi - G_\eta)(F_{\xi\xi} - G_{\eta\eta}) + O(\varepsilon) \\ &= 2U(U^2 - 1)(-G_\eta F_{\xi\xi} - F_\xi G_{\eta\eta} + F_\xi F_{\xi\xi} + G_\eta G_{\eta\eta}), \end{aligned}$$

yields, within the precision of the original equation,

$$\begin{aligned}
& 2F_{\xi Y} + 3U^3 F_{\xi} F_{\xi\xi} + \frac{U^4}{3} F_{\xi\xi\xi\xi} + \\
& 2G_{\eta Y} + 3U^3 G_{\eta} G_{\eta\eta} + \frac{U^4}{3} G_{\eta\eta\eta\eta} \\
& -4(U^2 - 1) \left(F_{\xi\xi} \frac{\partial \sigma_1}{\partial \eta} + G_{\eta\eta} \frac{\partial \sigma_2}{\partial \xi} \right) \\
& + U(4 - U^2)(G_{\eta} F_{\xi\xi} + F_{\xi} G_{\eta\eta}) = O(\varepsilon). \quad (9)
\end{aligned}$$

Since $F(\xi, Y)$ and $G(\eta, Y)$ are asymptotic soliton solutions, they satisfy the following KdV equations, respectively,

$$\begin{aligned}
2F_{\xi Y} + 3U^3 F_{\xi} F_{\xi\xi} + \frac{U^4}{3} F_{\xi\xi\xi\xi} &= 0, \\
2G_{\eta Y} + 3U^3 G_{\eta} G_{\eta\eta} + \frac{U^4}{3} G_{\eta\eta\eta\eta} &= 0.
\end{aligned}$$

If the small phase shifts $\varepsilon\sigma_1$, $\varepsilon\sigma_2$ are inserted into F and G as in Equation (7), they are still approximate solutions of the above KdV equations, respectively. If we now choose

$$\begin{aligned}
\sigma_1(\eta, Y) &= \frac{U(4 - U^2)}{4(U^2 - 1)} G(\eta, Y), \\
\sigma_2(\xi, Y) &= \frac{U(4 - U^2)}{4(U^2 - 1)} F(\xi, Y),
\end{aligned} \quad (10)$$

we have a complete approximate solution of (9) or (1) in the form (7).

σ_1 and σ_2 will change signs as U increases from $U < 2$ to $U > 2$. Specially at $U = 2$, $\sigma_1 = \sigma_2 = 0$, i.e., the solitons interact without phase shift. This is because the term $\varphi_y \varphi_{xy}$ produces a negative phase shift during soliton interaction that cancels the positive phase shift caused by the terms $\varphi_x \varphi_{xx}$ and $\varphi_x \varphi_{yy}$. To our knowledge, this is a new phenomenon in solitons. This may be due to the fact that one usually does not deal with the term $\varphi_y \varphi_{xy}$. We further note that F and G are not necessarily single soliton solutions, they can also be multiple solitons or even undulating dispersive wave solutions of the KdV equation.

We leave the task of solving for the N-soliton interaction to the next section and show here only the simplest example, namely, the two single-soliton interaction. The single-soliton solution of the KdV equations are:

$$F_{\xi}(\xi, Y) = A \operatorname{sech}^2 k_1(\xi - aY)$$

$$A = \frac{2a}{U^3}, \quad k_1 = \frac{\sqrt{6a}}{2U^2}$$

and

$$G_{\eta}(\eta, Y) = B \operatorname{sech}^2 k_2(\eta + bY),$$

$$B = \frac{2b}{U^3}, \quad k_2 = \frac{\sqrt{6b}}{2U^2}.$$

So the approximate solution becomes

$$\begin{aligned}
\varphi_x(x, y) &= F_{\xi}(\xi + \varepsilon\sigma_1(\eta, Y), Y) + G_{\eta}(\eta + \varepsilon\sigma_2(\xi, Y), Y) \\
&= A \operatorname{sech}^2 k_1(\xi - aY + \varepsilon\sigma_1) + \\
&\quad B \operatorname{sech}^2 k_2(\eta + bY + \varepsilon\sigma_2),
\end{aligned}$$

where

$$\begin{aligned}
\sigma_1(\eta, Y) &= \frac{U(4 - U^2)}{4(U^2 - 1)} G(\eta, Y), \\
\sigma_2(\xi, Y) &= \frac{U(4 - U^2)}{4(U^2 - 1)} F(\xi, Y).
\end{aligned}$$

This solution is equivalent to the solution of weak interactions obtained by Miles (1977). The corresponding fore-and-aft symmetric hullform can be derived from the boundary condition (2).

SUPERCONDUCTIVE SHIP HULLFORM DERIVED FROM THE N-SOLITON INTERACTION SOLUTION

Now we construct a superconductive hullform and its associated wave pattern in terms of an N-soliton solution. For simplicity we take $U = 2$, at which the phase shift is zero. Then according to (7)

$$\varphi_x(x, y) = F_x(x, y) + G_x(x, y) \quad \text{for } U = 2, \quad (11)$$

where for $y > 0$,

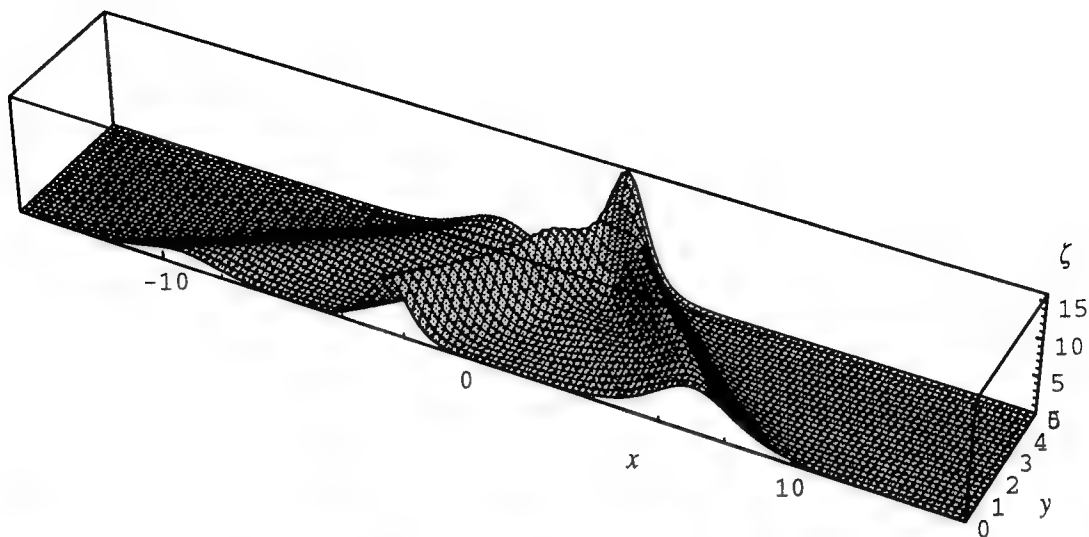
$$\begin{aligned}
F_x(x, y) &= D(x - x_1 + \sqrt{3}y, \varepsilon y / \sqrt{3}), \\
G_x(x, y) &= F_x(x, -y + w),
\end{aligned}$$

and $D(\xi, Y)$ was given in (6). The wave elevation to first order is

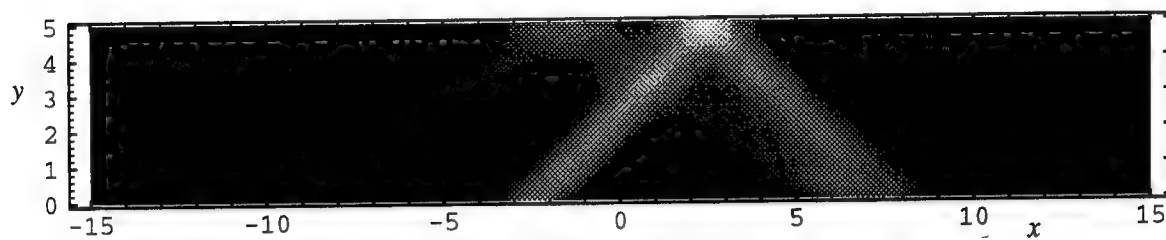
$$\zeta(x, y) = U\varphi_x(x, y). \quad (12)$$

We can easily check that the boundary condition on the sidewall is satisfied, i.e.,

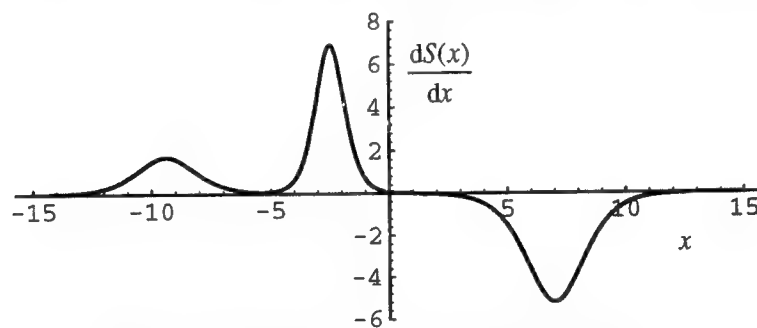
$$\left. \frac{\partial \varphi_x(x, y)}{\partial y} \right|_{y=w/2} = 0.$$



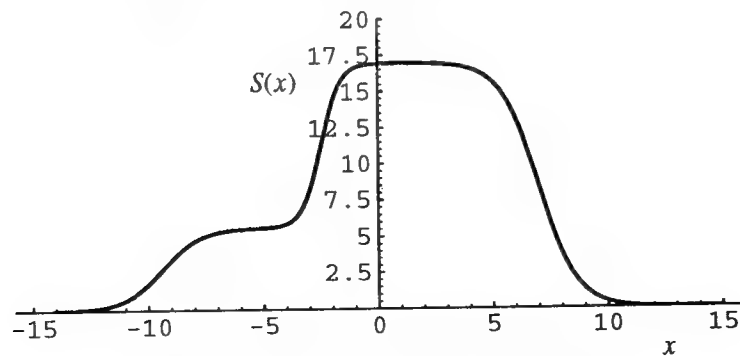
(a) 3-D plot of wave pattern, where only the half domain $y>0$ is presented.



(b) Density plot of the same wave pattern, where only the half domain $y>0$ is presented.



(c) The slope of the ship hull cross-sectional area curve.



(d) The ship hull cross-sectional area curve.

Fig. 2 The superconductive results of wave pattern and ship hullform as $\varepsilon = 0.08$, $x_1 = 7$ and $w = 10$.

According to the boundary condition (2), the hullform can be expressed approximately as,

$$\begin{aligned}\frac{dS(x)}{dx} &= -\frac{2}{U} \frac{\partial \phi}{\partial y} \Big|_{y=+0} \\ &\approx -\frac{2\sqrt{U^2-1}}{U} \operatorname{sgn}(x-1) \varphi_\xi \Big|_{y=+0} \\ &= -\frac{2\sqrt{U^2-1}}{U^2} \operatorname{sgn}(x-1) \zeta \Big|_{y=+0}. \quad (13)\end{aligned}$$

We select round parameter values $\varepsilon = 0.08$, $x_1 = 7$ and $w=10$ and display the results (12) and (13) in Fig. 2. The parameter values are so chosen that the phenomenon of interaction can be clearly observed. Consequently, the resulting ship length is very exaggerated. E.g., if we let $L=3x_1$ here, then $L^*/h^* = L/\sqrt{\varepsilon} = 74.2$ which is simply unrealistic. But it is not difficult to construct realistic hullforms by suitably selecting parameter values. In Fig. 2 (a, b) we see that the wave hump at the forebody evolves into two solitons along a characteristic direction and the evolution is continued after reflection by the sidewall along another direction. Thus two solitons reach the afterbody. For an afterbody determined by (13) no additional waves are generated and radiated out. The slope of the sectional area curve and the cross-sectional area itself are shown in Fig. 2 (c, d). The ship generates no waves in the wake; therefore, it does not experience any wave resistance.

Unlike Chen & Sharma (1995), the present hullform is obviously fore-and-aft asymmetric. The original problem has a built-in mathematical symmetry which implies that if $\phi(x, y)$ is a solution of (1) and (2) for $S(x)$, then $-\phi(-x, y)$ is a solution for $S(-x)$. It means that the ship is superconductive going both ways, i.e., forward or backward. The paradoxical equality of wave resistance in forward and backward motion seems to apply to ideal-fluid wavemaking in general.

HEURISTIC IMPROVEMENT OF THE PRECISION OF SHALLOW-WATER WAVE MODELS

There are various shallow-water wave models available for the ship wavemaking problem. One might naturally ask which one is better than others. It is difficult to answer this question intuitively. For example, one may believe that the Boussinesq equations would be better than the KP equation since the KP equation is obtained from the former by

neglecting higher order terms. But it is not really true according to our studies. The main deficiency of the shallow-water wave models in comparison to the exact finite-depth wave theory is the loss of higher order dispersion effect, which is not small in the off-critical cases. (On the other hand, higher order nonlinearities are also neglected; but this is permissible if the ship is really slender enough.) The wave pattern depends largely on the dispersion relation. Any deficiency will distort the wave pattern from its true form, which is crucial for superconductivity since it is required to predict the precise position where the reflected bow wave meets the afterbody. A reasonable method to determine which model is better in its linear part would be to compare the exact stationary dispersion relation in finite-depth water with the approximate dispersion relations of various linearized shallow-water wave equations. One can also heuristically introduce speed-dependent coefficients into the equation and obtain an even better model of which the dispersion relation is almost identical to the exact one.

Approximate and Exact Dispersion Relations

We study here two dispersion relations of stationary shallow-water wave models. One comes from the extended KP equation (1). This dispersion relation can be seen as Boussinesq's. The other comes from the standard KP equation, i.e., Eq.(1) without the term ϕ_{xxyy} . By setting the solution as a free-wave mode, i.e., $\phi \propto \exp(ik_x x + ik_y y)$, we can obtain dispersion relations from the linearized stationary equation (1) with and without the term ϕ_{xxyy} , respectively,

$$U^2 \cos^2 \theta = 1/[1 + \varepsilon k^2/3], \quad (14)$$

$$U^2 \cos^2 \theta = 1/[1 + (\varepsilon k^2/3) \cos^2 \theta]. \quad (15)$$

where k is the circular wave number, U is the depth Froude number and θ is the direction of wave propagation measured from the x -axis, i.e. $k_x = k \cos \theta$, $k_y = k \sin \theta$.

The exact stationary dispersion relation in finite-depth water is known to be

$$U^2 \cos^2 \theta = \frac{\tanh \sqrt{\varepsilon} k}{\sqrt{\varepsilon} k}. \quad (16)$$

The well-known Kelvin ship-wave pattern can be constructed from this dispersion relation by the method of stationary phase. The parameter ε just plays the role of a scale that has no sense in linear equations because if we transform the wave number

back to its dimensional form, i.e., $\sqrt{\varepsilon} k = k^* h^*$, ε is eliminated from (14-16). Equation (16) is now expanded as

$$U^2 \cos^2 \theta = 1/[1 + \varepsilon k^2/3 - \varepsilon^2 k^4/45 + 2\varepsilon^3 k^6/945 - \varepsilon^4 k^8/4725 + \dots].$$

We see that (14) and (15) are good approximations of (16) for small ε . Even if $\sqrt{\varepsilon} k = 1$ the error due to the remaining terms that stand in the lower line is only about 2%. But the wave number of elementary waves generated by a shiplike disturbance theoretically ranges from zero, or a certain positive value, up to infinity. The wave number is a function of U and varies with θ . When θ approaches its upper limit $\pi/2$, for so-called divergent waves, the wave number $\sqrt{\varepsilon} k = k^* h^*$ will be much larger than one. Thus the approximate dispersion relations (14) and (15) will not be so good at large θ . Although the high- θ waves contribute relatively little to wave resistance, the wave pattern itself would be somewhat distorted.

Comparison of Dispersion Relations

Figs. 3-6 show the numerical comparison. Surprisingly, we find that the KP dispersion relation is better than Boussinesq's in the subcritical range, as seen in Fig. 3 and 4 for $U=0.7$ and 1, respectively. This is in line with the fact that in the subcritical range our numerical ship wave patterns based on the KP equation, i.e., on Eq. (1) without the term φ_{xxyy} , look more realistic than those based on the extended KP equation (1).

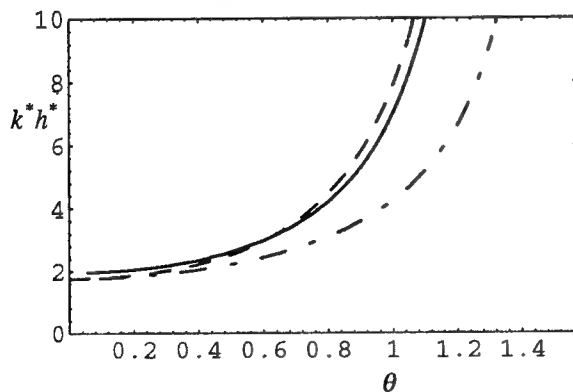


Fig. 3 Comparison of dispersion relations at $U=0.7$, where the exact one is represented by a solid line, KP's by a dashed line and Boussinesq's by a dot-dashed line.

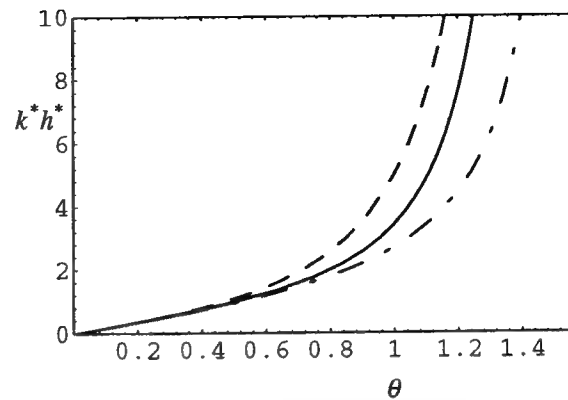


Fig. 4 Comparison of dispersion relations at $U=1$, where the exact one is represented by a solid line, KP's by a dashed line and Boussinesq's by a dot-dashed line.

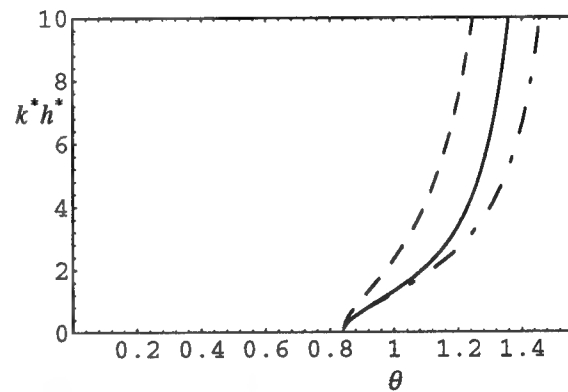


Fig. 5 Comparison of dispersion relations at $U=1.5$, where the exact one is represented by a solid line, KP's by a dashed line and Boussinesq's by a dot-dashed line.

Improvement of the extended KP equation

We introduce a coefficient to the term φ_{xxyy} in the following way,

$$2U\varphi_{xt} + (1 - U^2)\varphi_{xx} + (1 + \varepsilon U\varphi_x)\varphi_{yy} + \frac{\varepsilon U^2}{3}(\varphi_{xxxx} + \alpha(U)\varphi_{xxyy}) + 3\varepsilon U\varphi_x\varphi_{xx} + 2\varepsilon U\varphi_y\varphi_{xy} = O(\varepsilon^2). \quad (17)$$

This modification will yield a very good dispersion relation in the entire speed range compared with the exact one. The dispersion relation of the linear part of (17) is

$$U^2 \cos^2 \theta = 1/[1 + (\cos^2 \theta + \alpha \sin^2 \theta)\varepsilon k^2/3]. \quad (18)$$

We choose a smooth function for $\alpha(U)$

$$\alpha(U) = \begin{cases} 0.25U^2, & U \leq 1 \\ 0.8 - 0.55 \exp\{-\frac{11}{10}(U-1)\}, & U > 1 \end{cases}$$

as depicted in Fig. 6. This leads to the dispersion relation shown in Fig. 7.

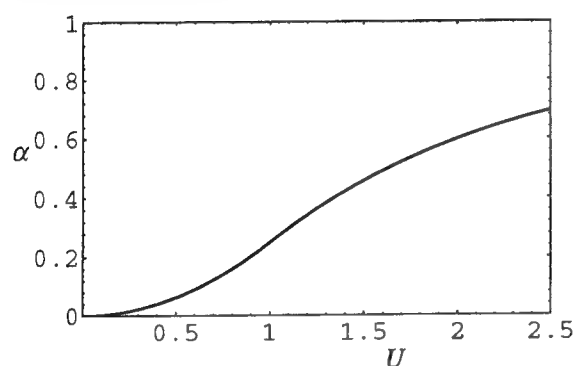


Fig. 6 The heuristically introduced coefficient $\alpha(U)$

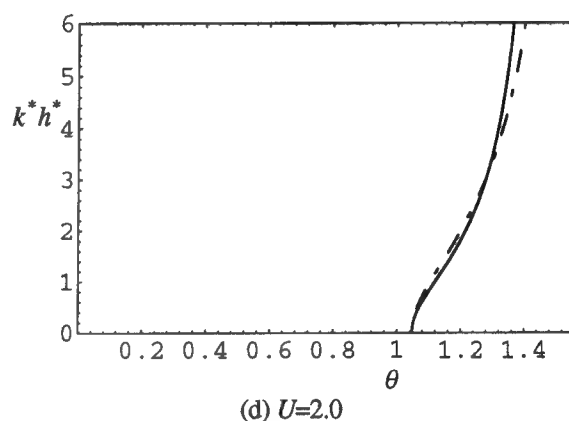
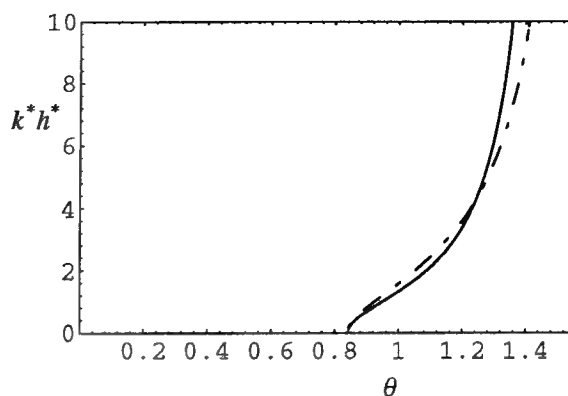
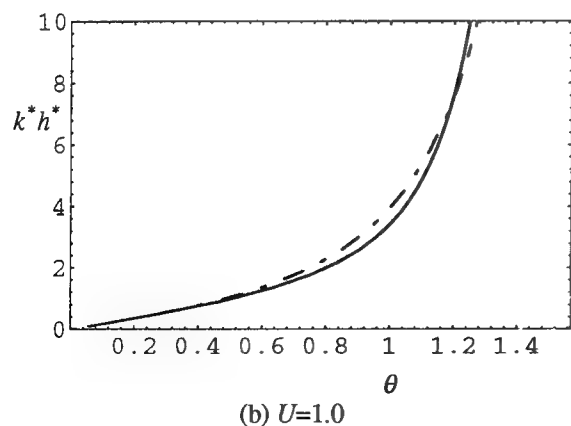
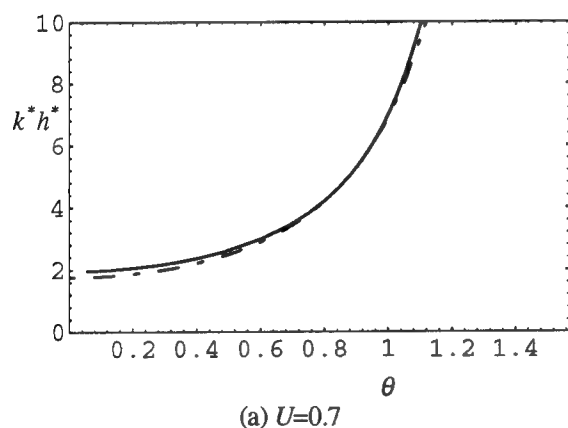


Fig. 7 The dispersion relation of the extended KP equation after introduction of a coefficient $\alpha(U)$ see (17), compared with the exact one, where the former is represented by dot-dashed lines and the latter by solid lines.

We believe that equation (17) will yield better results, specially less distorted wave patterns, than other shallow-water wave models. Certainly, one can also obtain superconductive solutions from it just by including the coefficient α appropriately.

CONCLUDING REMARKS

Although the superconductivity demonstrated here is only achieved for a monohull in a rather narrow channel, the idea can be further exploited to construct a more practical superconductive catamaran no longer dependent on sidewall reflection and channel width. A crucial feature is that although the catamaran as a whole is port-and-starboard symmetric, each individual hull has to be carefully cambered so that all waves are contained within the space between the two hulls. This requires our theory of asymmetric motion as presented at the last Symposium (Chen & Sharma 1994a). We hope to

undertake further efforts in this direction by analysis, computation and tank experiment.

ACKNOWLEDGMENT

One of the authors (X.-N. C.), who is being supported by a research grant of the German Federal Ministry of Research (BMBF Project SC7STU), thanks his supervisor Prof. Dr. K. Kirchgässner for his encouragement.

REFERENCES

- Chen, X.-N. and Sharma, S.D. 1992 "A slender ship moving at a near-critical speed in a shallow channel," Presented at a poster-session of the 18th International Congress of Theoretical and Applied Mechanics, Haifa, Israel and published in Journal of Fluid Mechanics, Vol. 291 (1995), pp. 263-285.
- Chen, X.-N. and Sharma, S.D. 1994a "Nonlinear theory of asymmetric motion of a slender ship in a shallow channel," Twentieth Symposium on Naval Hydrodynamics, Santa Barbara, CA, Preprints of Tuesday Sessions, pp.134-154.
- Chen, X.-N. and Sharma, S.D. 1994b "A slender ship moves in a shallow channel," International Conference on Hydrodynamics, Wuxi, China.
- Chen, X.-N. & Sharma, S.D. 1995 "Superconductivity of shallow channels for ships at supercritical speeds," Submitted to J. Fluid Mechanics.
- Choi, H.-S., Bai, J.-W. and Cho, I.-H. 1990 "Nonlinear free surface waves due to a ship moving near the critical speed in a shallow water," Proceedings of 18th Symposium on Naval Hydrodynamics, Ann Arbor, pp.173-189.
- Choi, H.S. and Mei, C.C. 1989 "Wave resistance and squat of a slender ship moving near the critical speed in restricted water," Proceedings of 5th International Conference on Numerical Ship Hydrodynamics, pp.439-454.
- Drazin, P.G. & Johnson, R.S. 1989 Solitons: an Introduction. Cambridge University Press.
- Eggers, K. 1955 "Über Widerstandsverhältnisse von Zweikörperschiffen," Jahrbuch der Schiffbautechnischen Gesellschaft, Vol. 49, pp. 516-537.
- Ertekin, R.C., Webster, W.C. and Wehausen, J.V. 1986 "Waves caused by a moving disturbance in a shallow channel of finite width," Journal of Fluid Mechanics, Vol. 169, pp. 275-292.
- Graff, W. 1962 "Untersuchungen über die Ausbildung des Wellenwiderstandes im Bereich der Stauwellengeschwindigkeit in flachem, seitlich beschränktem Fahrwasser," Schiffstechnik, Vol. 9, pp. 110-122.
- Graff, W., Kracht, A. and Weinblum, G. 1964 "Some extensions of D.W. Taylor's standard series," Transactions of Society of Naval Architects and Marine Engineers, Vol. 72, pp. 374-401.
- Helm, K. 1940 "Effect of canal depth and width on ship resistance (in German)," Hydrodynamische Probleme des Schiffsantriebs. Teil 2, Ed. G. Kempf, Verlag Oldenbourg, Munich and Berlin, pp.144-171.
- Heuser, H. 1973 "Systematic investigation of the resistance of twin-hull ships (in German)," Versuchsanstalt für Binnenschiffbau e.V Duisburg (VBD) Report, No. 661a.
- Huang, D.B., Sibul, O.J., Webster, W.C., Wehausen, J.V., Wu, D.-M. and Wu, T.Y. 1982 "Ships moving in the transcritical range," Proceedings of Conf. on Behaviour of Ships in Restricted Waters, Varna, Bulgaria, Vol.2, pp.26-10.
- Jiang, T., Sharma, S.D., and Chen, X.-N. 1995 "On the wavemaking, resistance and squat of a catamaran moving at high speeds in a shallow water channel," Proceedings of Third Int. Conf. on Fast Sea Transportation, Lübeck-Travenmünde, Germany, Vol.2, 1313-1325.
- Katsis, C., and Akylas, T.R. 1987 "On the excitation of long nonlinear water waves by a moving pressure distribution. Part 2. Three-dimensional effects," Journal of Fluid Mechanics, Vol. 177, pp. 49-65.
- Kinoshita, M. 1946 "On the restricted-water effect on ship resistance," Japan Society of Naval Architects, Vol.150, pp. 181-187.
- Kirsch, M. 1966 "Shallow water and channel effects on wave resistance," Journal of Ship Research, Vol. 10, pp.164-181.
- Lea, G.K., and Feldman, J.P. 1972 "Transcritical flow past slender ships," Proceedings of 9th

Symposium on Naval Hydrodynamics, pp.1527-1542.

Mei, C.C. 1976 "Flow around a thin body moving in shallow water," Journal of Fluid Mechanics, Vol. 77, pp. 737-752.

Mei, C.C. 1986 "Radiation of solitons by slender bodies advancing in a shallow channel," Journal of Fluid Mechanics, Vol. 162, pp. 53-67.

Mei, C.C. and Choi, H.S. 1987 "Forces on a slender ship advancing near the critical speed in a wide canal," Journal of Fluid Mechanics, Vol. 179, pp. 59-76.

Miles, J.W. 1977 "Obliquely interacting solitary waves," Journal of Fluid Mechanics, Vol. 79, pp.157-169.

Mori, K.-H. 1993 "Resistance and lifting force of a submerged body with a wing producing a downward lifting force," Proc. 8th Int. Workshop on Water Waves and Floating Bodies, St. John's, Newfoundland, Canada.

Thews, J.G. and Landweber, L. 1935 "The influence of shallow water on the resistance of a cruiser model," US Experimental Model Basin, Navy Yard, Washington, DC, Rep. no. 408

Thews, J.G. and Landweber, L. 1936 "A thirty-inch model of the SS Clariton in shallow water," US experimental Model Basin, Navy Yard, Washington, DC, Rep. no. 414.

Tuck, E.O. 1966 "Shallow water flows past slender bodies," Journal of Fluid Mechanics, Vol. 26, pp. 81-95.

Tuck, E.O. 1978 "Hydrodynamic problems of ships in restricted waters," Annual Review of Fluid Mechanics, Vol. 10, pp. 33-46.

Tuck, E.O. 1989 "A submerged body with zero wave resistance," Journal of Ship Research, Vol. 33, pp.81-83.

Tuck, E.O. & Tulin, M.P. 1992 "Submerged bodies that do not generate waves," Proc. 7th Int. Workshop on Water Waves and Floating Bodies, val de Reuil, France.

Tulin, M.P. & Oshri, O. 1994 "Free surface flows without waves; Applications to fast ships with low-wave resistance," Twentieth Symposium on Naval Hydrodynamics, Santa Barbara, CA, pp. 74-86.

Wu, De-Ming and Wu, T.Y. 1982 "Three-dimensional nonlinear long waves due to moving surface pressure," Proceedings of 14th Symposium on Naval Hydrodynamics, Ann Arbor, Mich., pp.103-129.

DISCUSSION

L.J. Doctors

University of New South Wales, Australia

In the verbal presentation of the research, you displayed a graph comparing the resistance of a monohull and a catamaran as a function of the speed. Assuming the displacement of the two vessels is the same (implying that the beam of the demihull is one half that of the monohull), then the resistance of the catamaran should asymptotically approach one half that of the monohull at high speeds. However, this feature does not appear on the graph. Could you please clarify this point?

AUTHORS' REPLY

It is true that if you compare a catamaran with an affine monohull of equal length, draft, and displacement, but necessarily, twice the beam, then as the hull separation tends to infinity, which is effectively the case for infinite depth Froude number, the wave resistance of the catamaran in linear theory asymptotically approaches one-half that of the monohull. However, following Heuser (1973), we compared the specific resistance of our catamaran with that of a monohull identical to one of the component hulls so that the displacement of the catamaran was twice that of the monohull. In this case, as the depth Froude number and, hence, the effective separation tends to infinity, the specific wave resistance of the catamaran should asymptotically equal exactly that of the monohull, even in nonlinear theory since the interference effects disappear. The same should apply, approximately, also to the specific viscous resistance. Our measurements as well as calculations, as shown, for example, in Fig. 7 of Jiang, Sharma, and Chen (1995) are compatible with this requirement. The practical implication is that the theoretical wave resistance reduction achieved for a finite design depth Froude number by exploiting the interference effect between the wave systems of the component hulls of a catamaran does not extend up to arbitrarily high depth Froude numbers.

The Influence of a Bottom Mud Layer on the Steady-State Hydrodynamics of Marine Vehicles

L. Doctors

(Australian Maritime Engineering Cooperative Research Center, Australia),
G. Zilman, T. Miloh (Tel-Aviv University, Israel)

Abstract

The work to be presented here is an extension of previous research into the influence of a uniform layer of silt or mud with a specified density and viscoelastic properties on the resistance of a marine vehicle undergoing rectilinear motion at a constant speed in water of finite and constant depth. The theory is therefore applicable to the wave-resistance and other hydrodynamic aspects of monohull and catamaran ferries in use on rivers as well as to landing craft in coastal regions. In these calculations, it is necessary to take into account both the finite width and the finite depth of the waterway.

In such physical situations, there are additional questions about the influence of a soft underlying layer of mud on the river bed, apart from the usual concerns regarding errors resulting from the use of a linearized inviscid theory. This theory had previously been applied to the following three cases: (a) an air-cushion vehicle (ACV) traveling over water with a muddy bed, (b) an ACV traveling over a muddy layer alone, and (c) a displacement vessel traveling over water with a muddy bed.

A principal feature of the analytic solution is that the wave resistance can be presented as the double integral over the longitudinal- and transverse-wavenumber domain. This result contrasts with the classic case of a purely inviscid flow in which the wave resistance can be expressed as

a single integral over the wavenumber space, because there is a unique relationship between the two abovementioned wavenumbers. In physical terms, this corresponds to the fact that the wave resistance can be connected by means of an energy argument to the downstream wave system, since no energy is dissipated by viscous means. One can no longer utilize this discussion when there is an underlying mud layer, because of the resulting viscous dissipation.

Although the integrand is rather poorly behaved, exhibiting the expected wave-like oscillations with respect to the two wavenumbers, one can perform the numerical integrations and predict some very interesting results, particularly when the water is relatively shallow. For example, the peak resistance, which traditionally occurs when the depth Froude number is unity, now occurs at some speed which is intermediate between the speeds corresponding to unit values of the depth Froude number based on the upper water layer alone and based on the total combined depth of mud and water. Indeed, the whole curve of wave resistance as a function of the speed is, in some general sense, an average between those two limiting extreme cases; however, one can only properly determine the precise influence of the mud layer by means of the detailed calculations required by the new theory, as described here.

In the current work, the theory has been extended to permit the computation of the hydro-

dynamic sinkage force and trimming moment on the vessel. Calculations have been completed for a standard Wigley hull. Once again, it is observed from the numerical results that the influence of the mud layer on these force components is such as to suggest that the equivalent overall water depth lies somewhere between that of the water layer alone and that of the total mud-water domain, depending on the physical properties of the mud.

1 Introduction

1.1 Previous Work

During the last few years, there has been a renewed effort to develop a better hydrodynamic understanding of marine vehicles in water of finite depth. Such cases of interest include coastal regions, harbors, rivers, lakes, and ocean inlets. A particular case of concern is the effect of the overlying mud layer in rivers on the hydrodynamics of fast moving craft (that is, at a depth Froude number greater than unity). Such an example is that of Australian river catamarans with a low keel clearance traveling in rivers and narrow channels with a movable muddy bed, with an average (length) Froude number of 0.65, and reported by Doctors, Renilson, Parker, and Hornsby [1].

The new physical feature of this problem, the subject of this paper, is the important effect of the underlying movable muddy sea bottom on the ship hydrodynamics. An example of recent work is that of Zilman and Miloh [2], which is applicable to slow ships (that is, moving in restricted water with a relatively low Froude number). They found that the compliance of the sea bottom has a profound effect on the hydrodynamic performance of such vessels when navigating in shallow water. In that work, the zero-Froude-number approximation was made; this resulted in the sea-surface being simplified and replaced by a rigid surface. Of course, the waves generated on the mud-water interface were modeled appropriately.

In the approximation used in that research, the mud was treated as a Newtonian viscous fluid. This approach had also been applied by Zilman, Miloh, and Kagan [3] to calculate the effect of mud viscosity on the added-mass and damping coefficients of two-dimensional ship cross sections under-

going periodic oscillations in the upper fluid layer.

This theoretical work on ship hydrodynamics in a two-layer environment was an outgrowth of earlier research in which the viscosity was ignored in both layers, but the effects of different densities were included. The results of such calculations were reported by Miloh, Tulin, and Zilman [4], where wave-drag calculations in a laterally unbounded domain were done.

More recently, the theory has been developed to the stage, where it is now analogous to the classical work of Michell [5] for a thin ship traveling in deep and inviscid water and that of Sretensky [6] for steady motion in a channel. That is to say, the traditional linearized free-surface conditions were used on both the sea surface and the mud-water interface by Zilman, Doctors, and Miloh [7]. The mud was modeled as a linear viscoelastic substance. The numerical test cases presented in that publication were applicable to an air-cushion vehicle (ACV) traveling over the sea with a muddy bottom, an ACV traveling over mud alone, and a ship traveling in a sea with a muddy bottom. The computations demonstrated interesting effects of the compliance of the mud with anticipated results in limiting cases, such as when the mud had either extremely low or high viscosity or stiffness.

One of the outcomes of the current research, naturally, is an ability to predict the sinkage and trim of a vessel. In reference, firstly, to purely inviscid hydrodynamics, we should acknowledge the pioneering theoretical work of Tuck [8], in which the shallow-water approximation was employed, and Tuck [9], where the influence of the finite-width of the channel was included in the analysis. Other work, of an experimental or empirical nature, was reported by Tuck [10], Dand and Ferguson [11], Barrass [12 and 13], Ferguson, Seren, and McGregor [14], and Ferguson [15].

Returning more to the subject of the current investigation, the significance of a silt-covered sea bed on the maneuvering characteristics of large vessels has been demonstrated by Sellmeijer and Oortmerssen [16] in a towing tank. Further work on this subject was reported by Vantorre [17], while a survey paper by d'Angremond, Deelen, and Vantorre [18] also described a number of experiments in which the mud properties, such as density, viscosity, and its rheology in general, were shown to be important.

1.2 Present Work

In the current work, we take the developmental work of Zilman, Doctors, and Miloh [7] one stage further, by computing all three of the components of generalized force on the vessel — that is, the wave resistance, sinkage force, and the bow-up moment.

In order to have an amenable model of these phenomena, we consider an upper layer of inviscid water on top of a second, and lower, layer of viscoelastic mud lying on a rigid horizontal bottom as shown in Figure 1(a). The fluid domain is also bounded by two vertical straight walls on each side, representing the walls of a channel or a towing tank. The two fluids are assumed to be immiscible and to be separated by the distinct mud-water interface. The vessel is immersed only in the upper layer and does not plough the interface.

As in the previous work discussed above, it is assumed that the sea-water mud behaves like a viscoelastic substance. To keep the analysis tractable, we will use here only a linear viscoelastic model, in which the shear stress is related to the rate of strain by a convolution-type integral, with the relaxation function serving as a kernel. The strong similarity between the gravitational waves generated by a moving ship and progressive surface sea waves allows us to use such a linear viscoelastic rheological model, previously suggested, for example, by Gade [19], Dalrymple and Liu [20], MacPherson [21], Hsiao and Shemdin [22], and Maa and Mehta [23].

Although, not used in the current work, the interested reader is referred to the studies of Foda, Hunt, and Chou [24], where nonlinear rheological aspects of the mud were considered.

2 Development of the Theory

2.1 Basic Hydrodynamic Equations

The coordinate system is shown in Figure 1(a). Here, an inertial reference frame is oriented so that the x axis is directed forward, the y axis is to port, and the z axis is measured vertically upward from the mud-water interface. The water has a density

ρ and a depth d . As usual, the water is assumed to be both inviscid and incompressible.

Hence, the flow in the water layer is irrotational, which implies that there exists a velocity potential ϕ which satisfies the Laplace equation:

$$\phi_{xx} + \phi_{yy} + \phi_{zz} = 0 \text{ for } 0 < z < d. \quad (1)$$

The mud has a thickness d' and is considered to be an incompressible viscoelastic medium. The general linearized equations of fluid motion in the mud layer for $-d' < z < 0$ are:

$$\rho' \frac{\partial \mathbf{U}}{\partial t} = -\nabla p' + \nabla \cdot \boldsymbol{\tau}, \quad (2)$$

$$\nabla \cdot \mathbf{U} = 0, \quad (3)$$

where \mathbf{U} denotes the three-component velocity vector, ρ' is the density of the mud, t is the time, p' is the total pressure and $\boldsymbol{\tau}$ is the stress tensor.

For a Newtonian fluid, the shear stress depends linearly on the rate-of-strain tensor:

$$\frac{d\boldsymbol{\epsilon}}{dt} = \frac{1}{2} [\nabla \mathbf{U} + (\nabla \mathbf{U})^T], \quad (4)$$

with the proportionality parameter being simply the dynamic viscosity.

2.2 Boundary Conditions

The usual linearized combined free-surface condition on the sea surface pertains to the problem under study here. It is

$$\phi_{tt} + g\phi_z = 0 \text{ for } z = d, \quad (5)$$

in which g is the acceleration due to gravity.

The linearized kinematic boundary condition on the mud-water interface requires only that there is continuity of the vertical component of velocity w , because the water is considered to be a perfect fluid. That is:

$$\zeta'_t = \phi_z \text{ for } z = 0. \quad (6)$$

The introduction of the unknown interface elevation ζ' requires an additional relationship in the form of a dynamic free-surface condition, the Bernoulli equation, whose linearized form is

$$\rho\phi_t + \rho g\zeta' + p' = 0 \text{ for } z = 0, \quad (7)$$

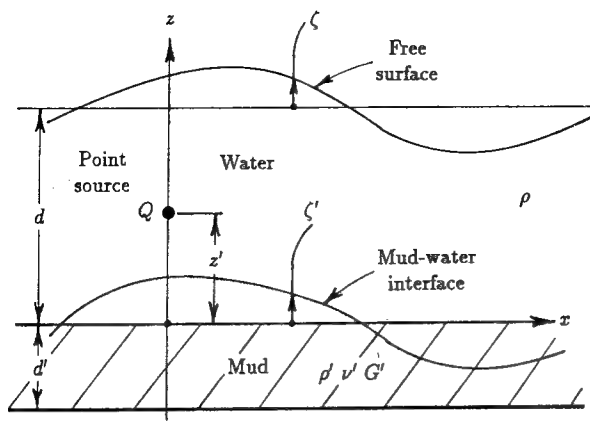


Figure 1: Problem Definition
(a) Coordinate System

where $p^I(x, y)$ is the pressure acting at the interface. Zero shear stress in the two horizontal directions on the interface between the mud and the water requires the pair of conditions:

$$\tau_{yz} = \tau_{xz} = 0 \text{ for } z = 0. \quad (8)$$

It may also be noted that the three velocity components must vanish on the bottom of the mud layer. That is:

$$U(u, v, w) = 0 \text{ for } z = -d'. \quad (9)$$

The assumption that the mud depth d' is small compared with a typical horizontal length scale (such as the interfacial wave length) suggests, in general, that both u and v and their derivatives with respect to x and y can be considered large with respect to w and its corresponding derivatives. It also follows that the pressure variation within the mud layer is essentially hydrostatic. That is, the shallow-water approximation can be used:

$$p'(x, y, z) = \rho'g(\zeta' - z) + p^I(x, y). \quad (10)$$

2.3 Solution for the Potential

The problem is now solved for the velocity potential ϕ for a point source of strength Q , located at the point (x', y', z') in the water above the mud-water interface, as shown in Figure 1(a), in a frame of reference moving *steadily* in the positive x direction, with a constant velocity U . Due to the linearity of the problem, it is convenient to utilize a

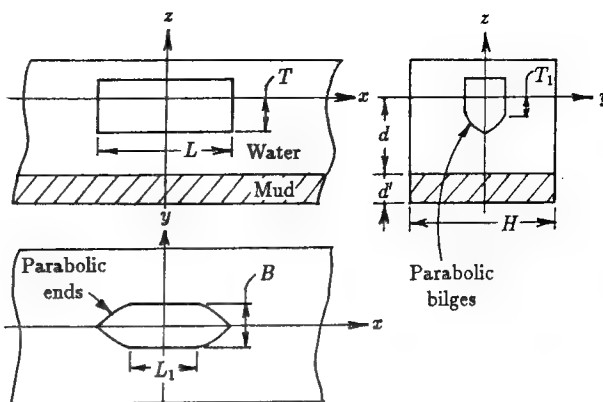


Figure 1: Problem Definition
(b) Modified Wigley Hull

double Fourier transform, as explained by Zilman, Doctors, and Miloh [7]. The result of this analysis is:

$$\phi = -\frac{Q}{4\pi r} - \frac{Q}{4\pi r'} + \varphi, \quad (11)$$

where we have defined

$$r = \sqrt{x^2 + y^2 + (z - z')^2}, \quad (12)$$

$$r' = \sqrt{x^2 + y^2 + (z + z')^2}, \quad (13)$$

and φ is regular and harmonic in the domain of interest (the upper inviscid fluid layer) and is given by the following set of formulas:

$$\varphi = \frac{1}{2\pi} \int_{-\infty}^{\infty} \int_{-\infty}^{\infty} \hat{\varphi}(k_x, k_y) \times \exp[i(k_x x + k_y y)] dk_x dk_y, \quad (14)$$

$$\hat{\varphi} = M_1 \cosh(kz) + M_2 \sinh(kz), \quad (15)$$

$$M_1 = -\frac{Q}{2\pi k \Delta} \{ E_1(gk + \omega^2) \cosh(kz') \times \exp(-kd) - E_2[gk \cosh(kd) - \omega^2 \sinh(kd)] \times \exp(-kz') \}, \quad (16)$$

$$M_2 = -\frac{Q}{2\pi k \Delta} \{ E_2(gk + \omega^2) \cosh(kz') \times \exp(-kd) + E_2[gk \sinh(kd) - \omega^2 \cosh(kd)] \times \exp(-kz') \}, \quad (17)$$

$$\Delta = E_1[gk \sinh(kd) - \omega^2 \cosh(kd)] + E_2[gk \cosh(kd) - \omega^2 \sinh(kd)], \quad (18)$$

$$E_1 = 1 - \epsilon g d' k^2 \delta / \omega^2, \quad (19)$$

$$E_2 = (1 - \epsilon) k d' \delta, \quad (20)$$

and

$$\delta \equiv 1 - \tanh(\gamma d')/(\gamma d'), \quad (21)$$

$$\gamma = \sqrt{-i\omega/\nu'_e}, \quad (22)$$

$$\epsilon = 1 - \rho/\rho', \quad (23)$$

$$\omega = Uk_x, \quad (24)$$

$$k^2 = k_x^2 + k_y^2. \quad (25)$$

The "effective" or complex kinematic viscosity ν'_e used in this analysis accounts for the viscoelastic nature of the mud; for the Kelvin-Voigt model employed in this work, we have

$$\nu'_e = \nu' + iJ/\omega,$$

and this is equivalent to evaluating the shear stress according to the formula:

$$\tau = G'e + \mu' \frac{de}{dt},$$

where e is the shear strain, the mud viscosity is $\mu' = \rho'\nu'$, $J = G'/\rho'$, and G' is the mud shear modulus.

2.4 Hydrodynamic Forces

The forces generated by the disturbance are defined as the relevant integrals of the normal stress over the surface area that characterizes the vehicle. For a displacement ship (that is, a body which is either partly or fully submerged), the required area is the area of the wetted surface.

The effect of the action of the vessel on the water can be reduced to the action of a source distribution with a density depending on the form of the vessel and the geometry of the channel. In the case of the classic thin ship, the source density has the interpretation of strength per unit area on the centerplane $y = 0$ of the vessel. If the local beam of the vessel is $b(x, z)$, the source density is given by Michell's form as

$$\sigma = -U \frac{\partial b}{\partial x}. \quad (26)$$

The wave resistance R_W , the sinkage force S_W , and the bow-up moment M_W (the three components of the generalized force) will be denoted symbolically by the notation R_W^* and are defined

in the usual way:

$$R_W^* = - \iint_{S_0} p \frac{\partial b}{\partial x} dx dz, \quad (27)$$

where S_0 is the centerplane area and p is the pressure on the surface of the hull, given by the linearized Bernoulli equation:

$$p = \rho U \phi_x, \quad (28)$$

in which the hydrostatic-pressure component is ignored. Finally, the generalized hull slope in Equation (27) is just

$$\frac{\partial b}{\partial x} = \begin{cases} \frac{\partial b}{\partial x} & \text{for wave resistance} \\ \frac{\partial b}{\partial z} & \text{for sinkage force} \\ z \frac{\partial b}{\partial x} - x \frac{\partial b}{\partial z} & \text{for bow-up moment} \end{cases} \quad (29)$$

We are now in a position to collect the above formulas in the traditional manner needed for a wave-resistance calculation. The generalized force is given by Equation (27), into which the pressure from Equation (28) and the gradients from Equation (29) are substituted. It is also necessary to utilize the potential for a point source in Equation (11) and its associated equations, together with the source strength in Equation (26). For this purpose, it is necessary to keep in mind that Equation (11) applies to a point source located directly above the origin, so that a simple translation of the frame of reference for the source is also required.

After the usual manipulations, one can obtain the following formula for the induced generalized forces on the vessel:

$$\begin{aligned} R_W^* = & \frac{\rho U^2}{4\pi} \iint_{S_0} \frac{\partial b}{\partial x} dx dz \iint_{S'_0} \frac{\partial b'}{\partial x'} dx' dz' \times \\ & \times \left\{ \frac{x - x'}{[(x - x')^2 + (z - z')^2]^{3/2}} + \right. \\ & \left. + \frac{x - x'}{[(x - x')^2 + (z + z' + 2d)^2]^{3/2}} \right\} - \\ & - \operatorname{Re} \left[\frac{i\rho U^2}{\pi^2} \int_0^\infty dk_x \int_0^\infty dk_y \frac{k_x}{k} \times \right. \\ & \times (D^{++} Q^{*+} \bar{Q}^{x+} + D^{+-} Q^{*+} \bar{Q}^{x-} + \\ & \left. + D^{-+} Q^{*-} \bar{Q}^{x+} + D^{--} Q^{*-} \bar{Q}^{x-}) \right], \quad (30) \end{aligned}$$

where the four coefficients are

$$\begin{aligned} D^{++} &= \frac{1}{4}(A_1 + A_3) \exp(2kd), \\ D^{+-} &= \frac{1}{4}(A_1 + 2A_2 + A_3 + 2A_4), \\ D^{-+} &= \frac{1}{4}(A_1 - A_3) = D^{+-}, \\ D^{--} &= \frac{1}{4}(A_1 + 2A_2 - A_3 - 2A_4) \times \\ &\quad \times \exp(-2kd), \end{aligned}$$

which are, in turn, given by the four formulas:

$$\begin{aligned} A_1 &= E_1(gk + \omega^2) \exp(-kd)/\Delta, \\ A_2 &= -E_2[gk \cosh(kd) - \omega^2 \sinh(kd)]/\Delta, \\ A_3 &= E_2(gk + \omega^2) \exp(-kd)/\Delta, \\ A_4 &= E_2[gk \sinh(kd) - \omega^2 \cosh(kd)]/\Delta. \end{aligned}$$

The wave functions in Equation (30) are given by

$$\begin{aligned} Q^{*\pm} &= Q_c^{*\pm} + iQ_s^{*\pm} \\ &= \iint_{S_0} \frac{\partial b(x, z)}{\partial *}\times \\ &\quad \times \exp(ik_x x \pm kz) dx dz. \end{aligned} \quad (31)$$

The prime ' in Equation (30) is used to denote variables in the source domain, while unprimed variables refer to those in the field domain.

The three major terms in this equation correspond to the three terms in Equation (11). The first two (source) terms do not contribute to the first component of the generalized force (the wave resistance) following d'Alembert's paradox. Additionally, the first two terms do not contribute to the third component (the bow-up moment) for a ship with fore-aft symmetry, such as the Wigley hull, to be considered later in the current work.

The fact that Equation (30) gives the forces in terms of a double integration over the wavenumber domain (k_x, k_y) is an indication that, in the physical problem, all such wave components contribute to these forces. This is in contrast to the classic inviscid case where one can use a far-field argument to demonstrate that only a one-dimensional spectrum of waves exists downstream.

In the limiting case of an infinitely deep upper layer (that is, $d \rightarrow \infty$), Equations (30) and (31) simplify to the classic result for a thin ship moving in deep water.

2.5 Influence of the Tank Walls

The influences of the tank walls can be incorporated by introducing "image" source distributions with a lateral spacing of the tank width H , which satisfy the tank-boundary condition, namely

$$v = 0 \text{ for } y = \pm H/2. \quad (32)$$

Thus, one must consider the infinite sum of functions of the type used in Equation (11). Regarding the third, or wave, term in Equation (30), the result can be simplified using the Poisson summation formula and this procedure has been followed by a number of researchers in similar circumstances.

The final result for the formula for the induced generalized forces on a vessel moving in a channel is

$$\begin{aligned} R_W^* &= \frac{\rho U^2}{4\pi} \sum_{i=-\infty}^{\infty} \iint_{S_0} \frac{\partial b}{\partial *} dx dz \iint_{S'_0} \frac{\partial b'}{\partial x'} dx' dz' \times \\ &\quad \times \left\{ \frac{x - x'}{[(x - x')^2 + y'^2 + (z - z')^2]^{3/2}} + \right. \\ &\quad \left. + \frac{x - x'}{[(x - x')^2 + y'^2 + (z + z' + 2d)^2]^{3/2}} \right\} - \\ &\quad - \operatorname{Re} \left[\frac{i\rho U^2}{\pi^2} \int_0^\infty dk_x \frac{2\pi}{H} \sum_{i=0}^\infty \epsilon_i \frac{k_x}{k} \times \right. \\ &\quad \times (D^{++} Q^{*+} \bar{Q}^{x+} + D^{+-} Q^{*+} \bar{Q}^{x-} + \\ &\quad \left. + D^{-+} Q^{*-} \bar{Q}^{x+} + D^{--} Q^{*-} \bar{Q}^{x-}) \right], \end{aligned} \quad (33)$$

in which

$$y' = iH, \quad (34)$$

$$\epsilon_i = \begin{cases} \frac{1}{2} & \text{for } i = 0 \\ 1 & \text{for } i \geq 1 \end{cases}, \quad (35)$$

$$k_y = 2\pi i/H. \quad (36)$$

The wavenumber index i has been omitted from all the variables in Equation (33), for the sake of brevity. It is observed that one can simply replace the integration with respect to the transverse wavenumber k_y in the third term by a summation, in which one effectively evaluates the integral by the trapezoidal formula with the abscissas provided by Equation (36).

2.6 Classic Case of a Rigid Bed

An important question is that relating to the behavior of Equations (11) to (25) in certain limiting cases. Thus, a careful examination of these formulas does indeed reveal that in the case of vanishing mud complex kinematic viscoelasticity ν'_e (together with the assumption of $\rho'/\rho = 1$), the classic case of inviscid wave resistance in water of depth $d + d'$ is recovered; the standard formula for the potential was published by Sretensky [6] and Lunde [25]. In a similar vein, if either the mud complex kinematic viscoelasticity ν'_e or the mud density ρ' approaches infinity, then the classic inviscid case corresponding to a water depth d is obtained, as expected. This behavior will also be demonstrated here by the computed results.

3 Results

3.1 Wave Functions

A hull, patterned after that proposed by Wigley [26], was used in the current work. The vessel is depicted in Figure 1(b) and its local beam $b(x, z)$ is defined in the following manner, for positive x :

$$b(x, z) = BF^{(x)}(x)F^{(z)}(z), \quad (37)$$

$$F^{(x)}(x) = 1 - H(x - a_1) \left[\frac{x - a_1}{a_2 - a_1} \right]^2, \quad (38)$$

$$F^{(z)}(z) = 1 - H(-z - c_1) \left[\frac{z + c_1}{c_2 - c_1} \right]^2, \quad (39)$$

in which $H(x)$ is the Heaviside step function and

$$a_1 = \frac{1}{2}L_1,$$

$$a_2 = \frac{1}{2}L,$$

$$c_1 = T_1,$$

$$c_2 = T,$$

and L is the length, B is the beam, and T is the draft. Finally, L_1 is the length of parallel middle body and T_1 is the depth of the wall-sides.

The wave functions for this vessel, defined by Equation (31), can be determined analytically,

as follows:

$$\begin{aligned} Q_c^{x\pm} &= 0, \\ Q_s^{x\pm} &= BI_1 J_1^\pm, \\ Q_c^{z\pm} &= BI_2 J_2^\pm, \\ Q_s^{z\pm} &= 0, \\ Q_c^{M\pm} &= 0, \\ Q_s^{M\pm} &= B(I_1 J_3^\pm - I_3 J_2^\pm), \end{aligned}$$

in which the new integrals are

$$I_1 = \frac{4}{\mathcal{A}_2 - \mathcal{A}_1} \left[\cos(\mathcal{A}_2) - \frac{\sin(\mathcal{A}_2) - \sin(\mathcal{A}_1)}{\mathcal{A}_2 - \mathcal{A}_1} \right],$$

$$I_2 = -I_1/k_x,$$

$$I_3 = \frac{4}{k_x^2(\mathcal{A}_2 - \mathcal{A}_1)^2} \left[(2\mathcal{A}_1 - 3\mathcal{A}_2) \cos(\mathcal{A}_2) + (3 + \mathcal{A}_1\mathcal{A}_2 - \mathcal{A}_2^2) \sin(\mathcal{A}_2) + \mathcal{A}_1 \cos(\mathcal{A}_1) - 3 \sin(\mathcal{A}_1) \right],$$

$$J_1^\pm = \pm \frac{1}{k} \left\{ 1 - \frac{2 \exp(\mp C_1)}{(C_2 - C_1)^2} + 2 \exp(\mp C_2) \times \left[\frac{1}{(C_2 - C_1)^2} \pm \frac{1}{C_2 - C_1} \right] \right\},$$

$$J_2^\pm = 1 \mp k J_1^\pm,$$

$$J_3^\pm = \frac{1}{k^2} \left[-1 + \frac{6 \pm 2C_1}{(C_2 - C_1)^2} \exp(\mp C_1) + \frac{2C_1 C_2 - 2C_2^2 \pm (4C_1 - 6C_2) - 6}{(C_2 - C_1)^2} \times \exp(\mp C_2) \right],$$

where

$$\mathcal{A}_1 = k_x a_1,$$

$$\mathcal{A}_2 = k_x a_2,$$

$$C_1 = k c_1,$$

$$C_2 = k c_2.$$

3.2 Numerical Details

The first term in Equation (33) was evaluated numerically in a straightforward manner. That is to say, the centerplane areas S_0 and S'_0 were divided into rectangular patches and the integrations computed using the midpoint rule. A typical choice of integration parameters was 204 patches in the

x and x' directions and 18 patches in the z and z' directions. Longitudinal symmetry was used to halve the actual computation. A conservative measure of the error in this calculation was obtained by comparing the result with that obtained using one-third the number of patches in the two centerplane directions, for which the midpoint rule could also be used without any further computation of the integrand. The abovementioned choice of parameters led to an integration error of less than one percent. It is also important to note that the numerical integration only has to be done once for any particular geometric configuration, since the numerical value of this term varies simply with the square of the speed of the ship U .

With regard to the image source distributions needed to model the influence of the tank walls, a typical selection was 65 images (that is, the original, central, vessel plus 32 on each side), for the case $H/L = 1$, which also led to an error of around one percent.

The second term in Equation (33) was calculated in conjunction with the first term, as implied by the algebraic grouping used there.

There is no doubt that these first two terms can be computed analytically for a Wigley-style hull, as an exploratory investigation confirmed. However, the resulting algebra would clearly be very error prone and the required effort quite excessive.

The double integral for the third term in Equation (33) was evaluated by means of the trapezoidal rule applied in the two directions of the (k_x, k_y) wavenumber domain. This approach had the advantage that it was both easy to program and that one could also obtain the result for laterally restricted water using the same method (just by selecting the appropriate spacing in the transverse-wavenumber direction k_y , given by Equation (36)).

One should be interested in four estimates of the errors in this numerical procedure. These are the two truncations errors, resulting from not carrying out the summations to infinity in Equation (33), and the two errors associated with using a finite step size.

The computer program was written to evaluate these four errors in a straightforward manner. Firstly, the generalized forces were computed

from user-supplied values of the two truncation points and the two step sizes. In addition, the program computed the forces four additional times, using (in turn) half the values of the truncation points or twice the step size, as the case may be. These additional calculations require negligible additional effort, since the integrands have already been determined.

The estimate of the error was then given by the relevant differences in these calculations. These estimates are, of course, quite conservative and a number of experiments was conducted to show that it is indeed safe to use them. It should be added that the "error" related to using different step sizes in the transverse wave number corresponds to the difference in generalized forces when running in channels of the relevant different widths; it can be used to estimate the restrictive influence of finite channel width.

Previous experience with oscillatory integrals with an infinite range of this nature has shown that it is difficult to improve on the procedure outlined here. Generally speaking, there was no difficulty in obtaining well converged results, except that the computer time became rather excessive and the specified errors in the generalized forces had to be relaxed to around one percent. Even so, very large numbers of points were often required. That is, truncation values of $k_x L = 20$ and $k_y L = 80$ were needed. These led to a requirement of up to 16×10^6 points in the k_x direction and 50 points in the k_y direction, for a tank-width-to-ship-length ratio H/L of 4.

3.3 Forces on a Vessel

The set of computed results to be presented here pertains to the Wigley hull form defined by Equations (37) to (39). The vessel has a beam-to-length ratio B/L of 0.1 and a draft-to-length ratio T/L of 0.0625. The water-depth-to-length ratio d/L was chosen to be 0.2 and the dimensionless mud-thickness d'/L was taken to be 0.1. A set of dimensionless tank widths H/L of 0.25, 0.5, 1, and 2 was considered in the calculations.

The usual three coefficients of the generalized force for a ship have been used in the plots.

That is:

$$C_W = R_W / \frac{1}{2} \rho U^2 S,$$

$$C_S = R_S / \frac{1}{2} \rho U^2 S,$$

$$C_M = R_M / \frac{1}{2} \rho U^2 SL,$$

where S is the wetted-surface area. For our selected vessel, the computed dimensionless wetted-surface area S/L^2 is 0.14879. For the abscissa, the inverse-square-Froude-number parameter:

$$A = 1/2F^2 = gL/2U^2,$$

was chosen. This has the advantage (over using the Froude number $F = U/\sqrt{gL}$ as the standard abscissa) of conveniently stretching the horizontal scale at low speeds, allowing one to study the oscillations in the wave-resistance curve more easily.

Computed data for five different types of mud were produced and the results for these cases appear in all of the figures. The properties for each of these muds appear in Table 1. In a qualitative sense, the muds range, in progression, from "loose" to "solid". Thus, Mud 1* has no viscosity at all. This case represents the classic inviscid situation. Results for this case were obtained from that theory with a dimensionless depth of 0.3. Mud 1 has a very low viscosity, causing it to behave almost like water; it was used to test the operation of the current computer program, by comparing the results with those from Mud 1*. Mud 2 possesses an intermediate viscosity. Mud 3 possesses both an intermediate viscosity and elasticity. Mud 4 is similar to Mud 3, but has twice the density. Next, Mud 5 has a very high viscosity, resulting in it behaving essentially like a solid. Finally, Mud 5* is the second limiting case. Solutions were obtained by using the classic theory with a dimensionless depth of 0.2.

The four parts of Figure 2 show the wave resistance in a channel whose dimensionless widths are 0.25, 0.5, 1, and 2, respectively. We first examine Figure 2(a) for the case of a dimensionless channel width of 0.25. The most striking feature of these results is the well-known jump in the resistance at the critical value of unity of the depth Froude number $F_d = U/\sqrt{gd}$, which is seen for the two limiting cases, namely Mud 1 and Mud 5. The first limiting case is that of a very low value of the dimensionless mud viscosity $\nu'/\sqrt{gL^3}$ of 10^{-5} . In this case, the mud behaves like (inviscid) water and

Mud	Density ρ'/ρ	Viscosity $\nu'/\sqrt{gL^3}$	Elasticity $G'/\rho gL$
1*	1	0	0
1	1	10^{-5}	0
2	1	10^{-2}	0
3	1	10^{-2}	10^{-2}
4	2	10^{-2}	10^{-2}
5	1	10^0	0
5*	1	∞	0

Table 1: The Five Types of Mud

the effective depth is $d + d'$, causing the discontinuity to occur at a speed parameter of $5/3$.

The matter of this discontinuity has been discussed many times in the literature, in particular, by Lunde [25]. The sudden loss of the transverse component of the wave system leads to a drop in the resistance, whose magnitude is given by

$$\Delta R_W = 3W^2/2\rho gHd^2, \quad (40)$$

in which W is the weight of the vessel.

The phenomenon of the drop in resistance is related to the energy carried by the transverse wave, which no longer exists as part of the spectrum of waves generated by the moving disturbance. This wave cannot, of course, travel faster than the critical speed. Experimental work confirms both the location (that is, the Froude number) and the magnitude (the value of the discontinuity in the resistance), provided the water is not too shallow and the ship is reasonably thin. Otherwise, the assumptions in the theory are violated and both viscous and nonlinear effects tend to limit the magnitude of the jump, as well as rounding its sharp (or sudden) characteristic.

Returning, now, to Figure 2(a), the results from a traditional wave-resistance program for Mud 1* (zero mud viscosity) are also provided and these appear as a dotted curve. Almost perfect agreement can be seen. One should not expect precise concurrence here for three reasons; firstly (as noted already) the current program cannot be run for the purely inviscid case; secondly, the current program requires an integration with respect to the longitudinal wavenumber (as noted in Equation (33)), which is not required in classic wave-resistance calculations; and thirdly, the fluid dynamics of the mud are modeled in the present research using the so-called "shallow-water" approx-

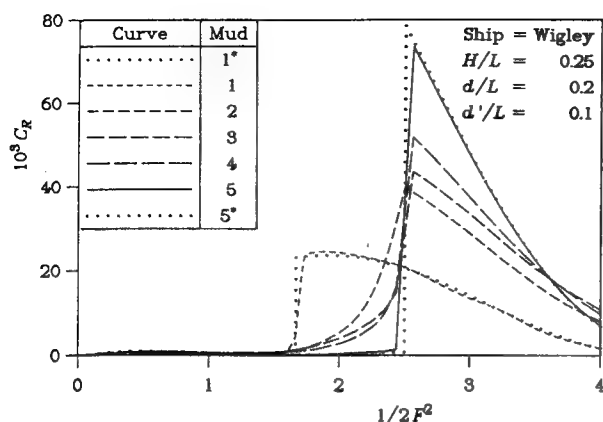


Figure 2: Wave Resistance
 (a) $H/L = 0.25$

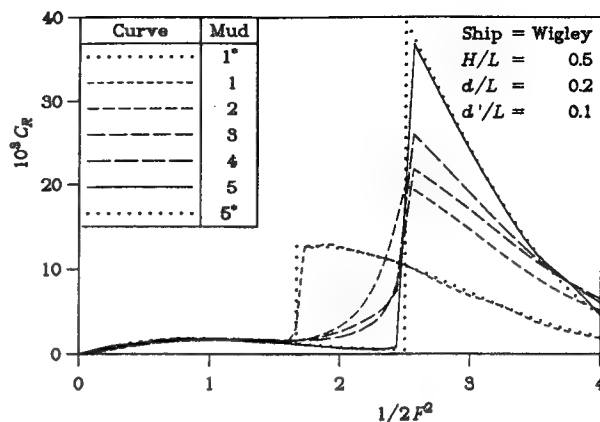


Figure 2: Wave Resistance
 (b) $H/L = 0.5$

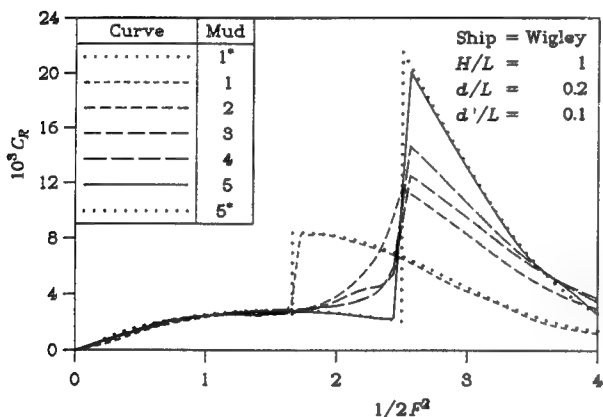


Figure 2: Wave Resistance
 (c) $H/L = 1$

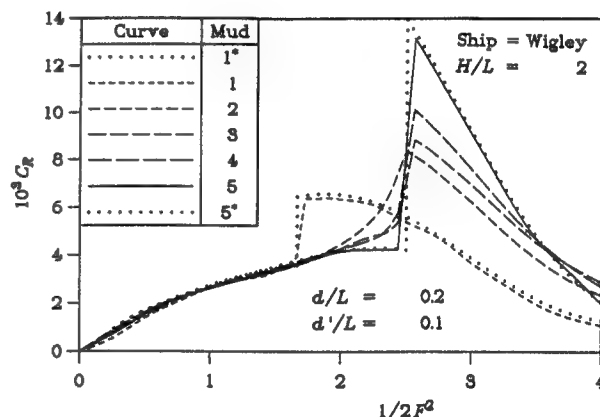


Figure 2: Wave Resistance
 (d) $H/L = 2$

imation, which is evidently quite accurate relative to the finite-depth theory, in this example.

Similarly, for a very high dimensionless viscosity of 10^0 , the case of Mud 5, one would expect the mud to behave as an immovable solid, thus providing us with the other limit of the classic inviscid case, namely Mud 5*, with a dimensionless depth of 0.2, whose critical speed occurs when the speed parameter equals 5/2. The numerical results correctly confirm this behavior.

Figure 2(a) shows other, intermediate, cases, as well. Thus, for Mud 2 with a dimensionless mud viscosity of 10^{-2} , a result somewhat midway between the abovementioned two extremes is observed. Furthermore, by *also including* mud

elasticity, as for Mud 3, with a dimensionless value $G'/\rho g L$ of 10^{-2} , the mud is seen to exhibit an even more solid behavior than when the viscosity alone is modeled. The next intermediate case, that of Mud 4, utilizes the same values of mud viscosity and shear modulus, *but also includes now* a higher dimensionless density ρ'/ρ , with a value of 2. This fourth case produces results approaching those of the previously noted instance of an almost solid mud layer, that of Mud 5.

Next, we discuss here the results for the wave resistance displayed in Figures 2(b), (c), and (d), corresponding respectively to dimensionless tank widths of 0.5, 1, and 2. The comments made regarding Figure 2(a) apply in these cases, too. The essential difference is that the behav-

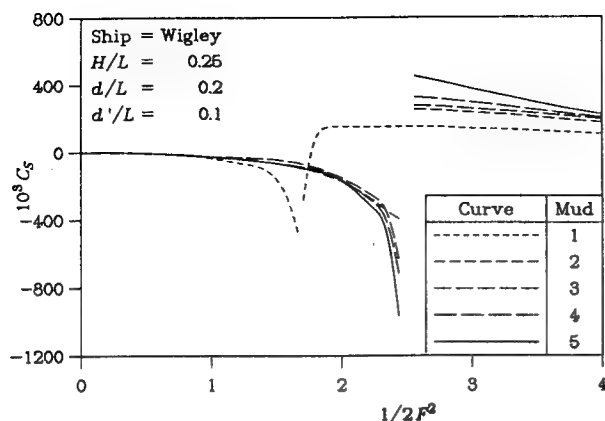


Figure 3: Sinkage Force
 (a) $H/L = 0.25$

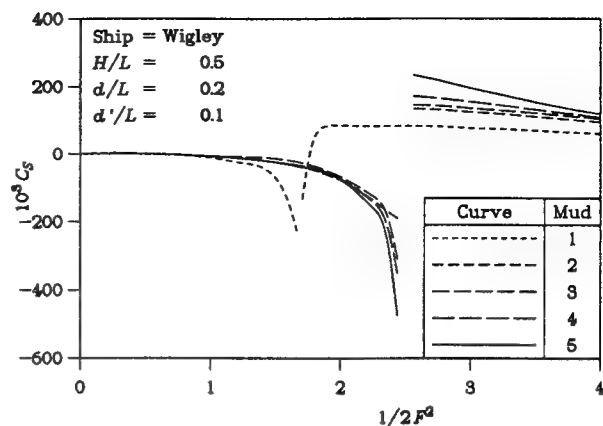


Figure 3: Sinkage Force
 (b) $H/L = 0.5$

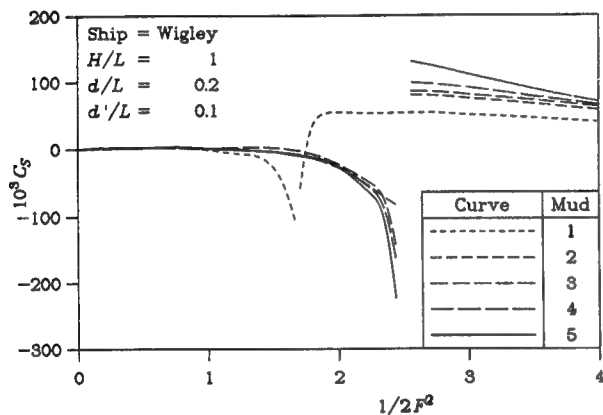


Figure 3: Sinkage Force
 (c) $H/L = 1$

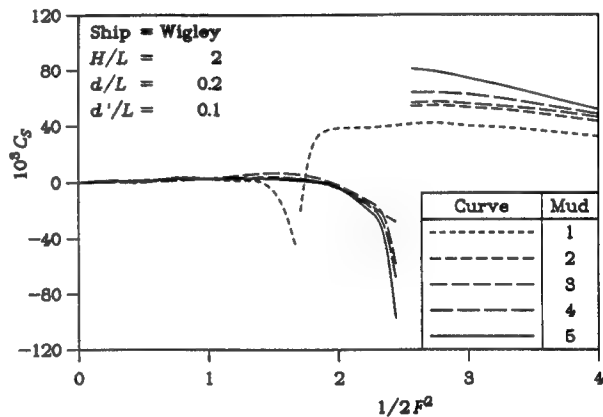


Figure 3: Sinkage Force
 (d) $H/L = 2$

ior of the curves is much more moderate, due to the greater tank widths under consideration. This point is epitomized by Equation (40), which states that the jump is inversely proportional to the channel width.

The four parts of Figure 3 show the sinkage force for the same four dimensionless tank widths. The general behavior is one in which the more solid mud yields results with more extreme behavior, particularly near the critical depth Froude number, as already discussed in the case of wave resistance.

Again, somewhat similar behavior can be seen in the four parts of Figure 4 for the bow-up moment, in the sense that the cases of a more solid mud generate curves with a stronger behavior.

3.4 Sinkage and Trim

It is straightforward to estimate the dependence of the sinkage s and bow-up trim t on the speed U of the vessel. Within the framework of linearized hydrostatics, which is consistent with the hydrodynamics employed here, the dimensionless sinkage and trim are given by the two formulas:

$$s/L = \frac{1}{2} C_S F^2 S / A_W, \quad (41)$$

$$t/L = \frac{1}{2} C_M F^2 S L^2 / I_W, \quad (42)$$

in which I_W is the longitudinal second moment of the waterplane area A_W . For this purpose, we have assumed that the longitudinal metacentric height \overline{GM}_L can be approximated by the longitudinal

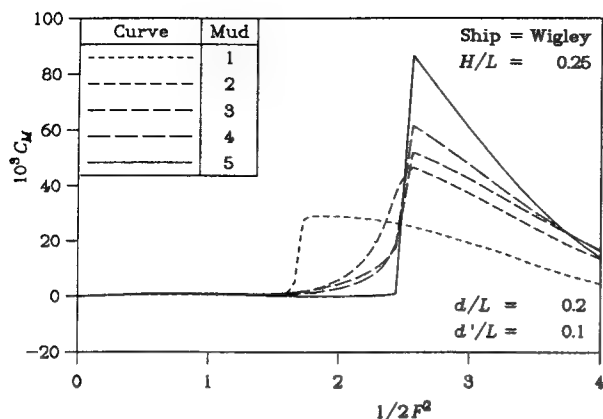


Figure 4: Bow-Up Moment
(a) $H/L = 0.25$

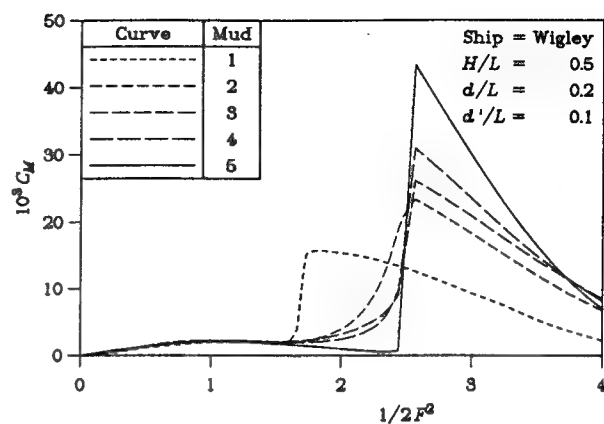


Figure 4: Bow-Up Moment
(b) $H/L = 0.5$

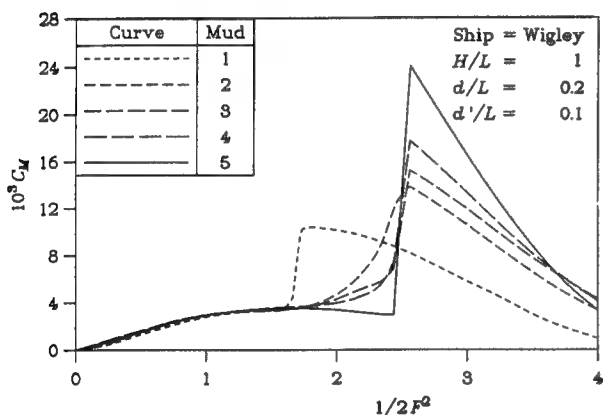


Figure 4: Bow-Up Moment
(c) $H/L = 1$

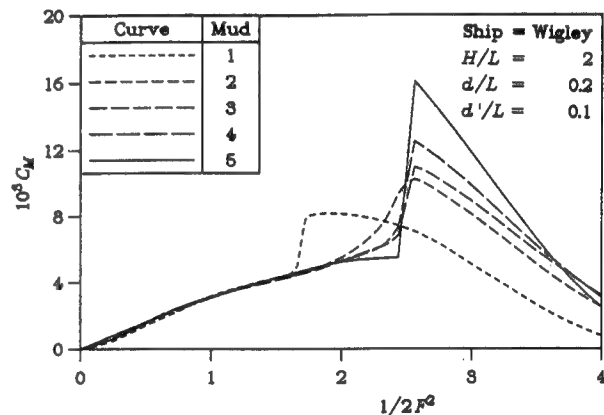


Figure 4: Bow-Up Moment
(d) $H/L = 2$

metacentric radius \overline{BM}_L . For a standard Wigley hull, these two formulas become:

$$\begin{aligned} s/L &= 1.116C_S F^2, \\ t/L &= 22.32C_M F^2. \end{aligned}$$

Figure 5 show the sinkage of the vessel in question for the four dimensionless tank widths under consideration. The curves for sinkage strongly resemble the previously discussed curves of sinkage force.

Finally, the bow-up trim is plotted in Figure 6. In the same way, the curves of bow-up trim are closely related to the curves of bow-up moment. So, one can see the discontinuities at the critical depth Froude number and also observe the

fact that the magnitudes of the discontinuities are greater when the mud is more solid and/or when the channel is narrower.

By way of comparison, it is instructive to consult the work of Tuck [8]. The current results for sinkage and bow-up trim bear a strong relationship to those of his calculations, particularly in regard to the singular behavior. However, exact conclusions cannot be drawn, because of the various additional simplifying assumptions made in his work—particularly that of infinite tank width. Furthermore, it is encouraging to note that the experimental data that he presented is even more in accordance with the results shown here. In his later paper, Tuck [9] did investigate the very strong effect of finite channel width, which is always to in-

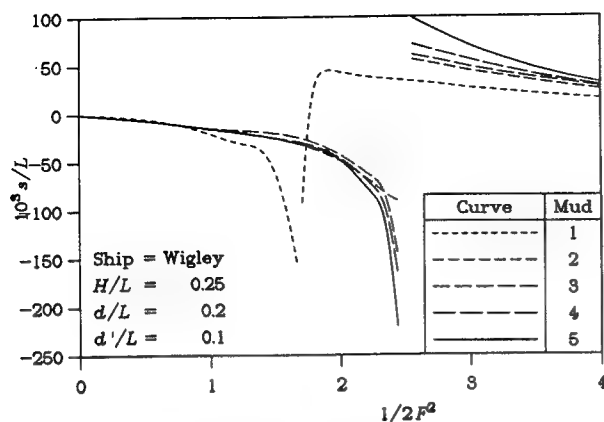


Figure 5: Sinkage
 (a) $H/L = 0.25$

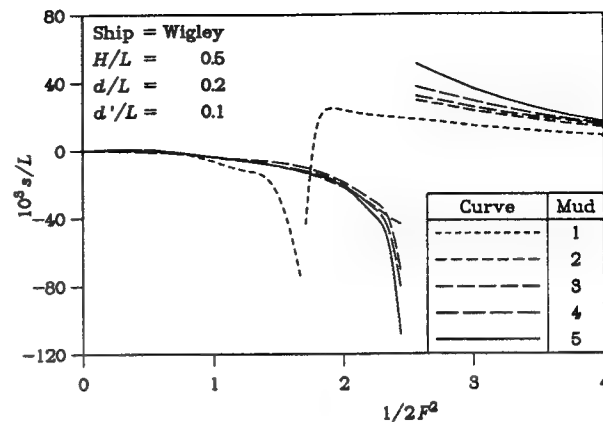


Figure 5: Sinkage
 (b) $H/L = 0.5$

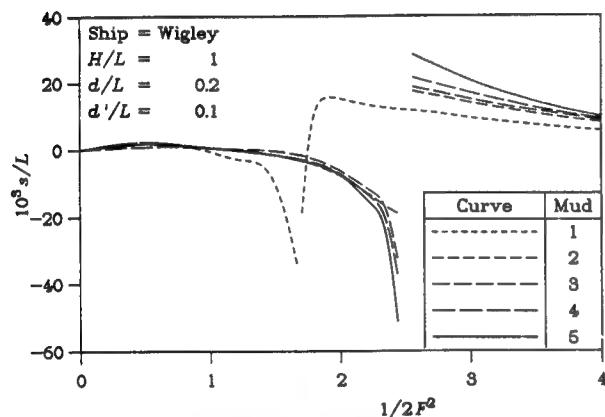


Figure 5: Sinkage
 (c) $H/L = 1$

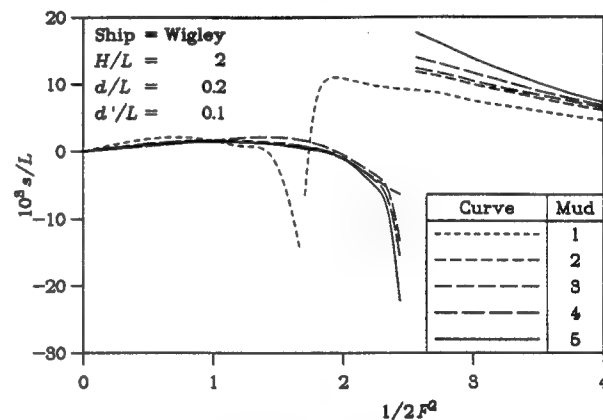


Figure 5: Sinkage
 (d) $H/L = 2$

crease the magnitude of the results, as confirmed by the present work.

4 Concluding Remarks

The analysis using the Kelvin-Voigt model implemented in this paper shows that the generalized forces due to a disturbance moving in the water layer above a dense mud layer depend strongly on the parameters of such a two-layer system. The most important feature of the curves for the forces is that the maximal values *are not always* a monotonic function of the mud density, mud viscosity, or elasticity.

The role of the mud viscosity is not obvious. On the one hand, the dissipation of the fluid energy in the lower viscous layer results in a decrease of the wave resistance. On the other hand, for a relatively large mud viscosity, such a dissipation can be negligibly small (the limiting case of infinitely large viscosity is a good illustration of this statement). Thus, roughly speaking, the resulting effect of the mud viscosity, at least in the vicinity of the maximal value of the wave drag, can be interpreted as an effective reduction in the total depth of the water.

It is almost universally true that the mud properties have a profound influence on the three components of the generalized force for subcritical speeds ($F_d < 1$). However, at least for the

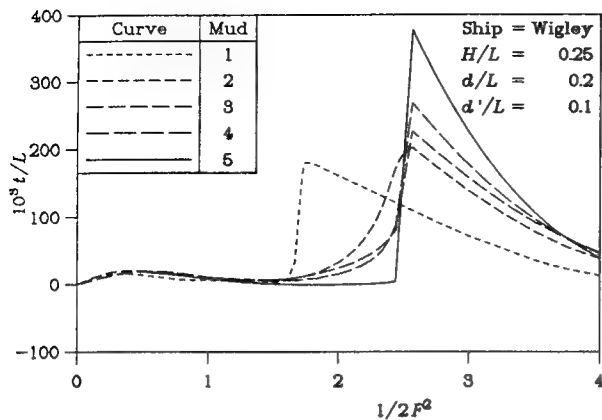


Figure 6: Bow-Up Trim
(a) $H/L = 0.25$

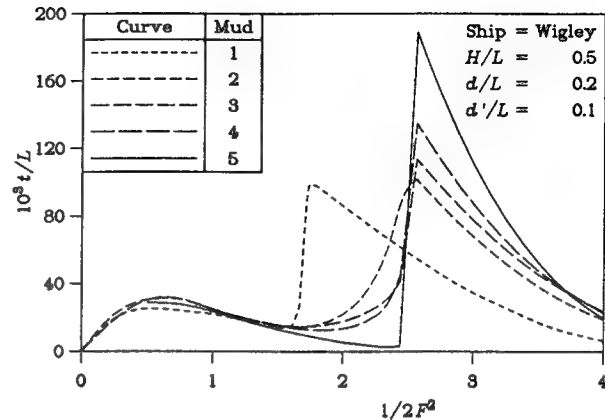


Figure 6: Bow-Up Trim
(b) $H/L = 0.5$

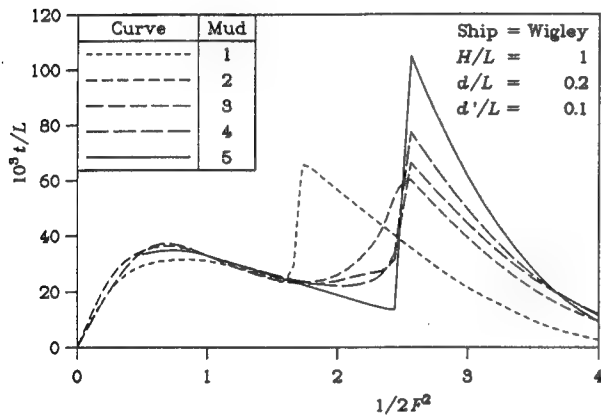


Figure 6: Bow-Up Trim
(c) $H/L = 1$

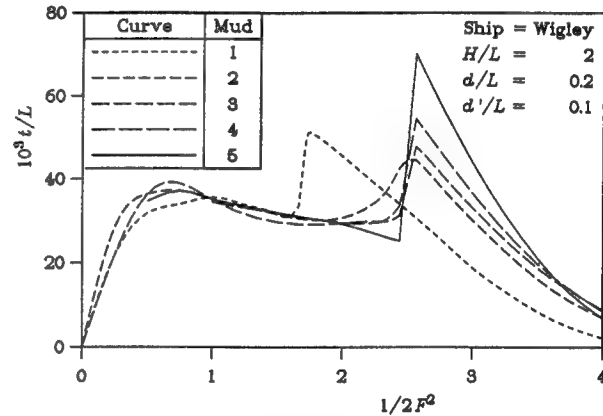


Figure 6: Bow-Up Trim
(d) $H/L = 2$

range of mud properties used in the present calculations, there is much less effect at supercritical speeds ($F_d > 1$), suggesting that the mud has less chance to respond to the hydrodynamic pressures at these higher speeds.

Certainly, for intermediate values of the mud properties, the general effects of the mud layer are to moderate any distinct features of the traditional linearized wave-resistance theory. One might therefore surmise that at least one explanation has been found for imperfect agreement between predictions and measurements of ship resistance in a river. Other reasons may, of course, include non-linear effects and wave breaking.

Future work in this area of research will

include the computation of the elevation of the interfacial wave so that the likelihood of grounding of the vessel can be estimated.

5 Acknowledgments

Prof. H. Söding of Hamburg University discussed many practical aspects of this problem with the authors. In addition, they would like to acknowledge the support of the Australian Maritime Engineering Cooperative Research Centre (AMECRC) (to which the first author is on partial secondment from The University of New South Wales) and Tel-Aviv University, as well as that of the Germany-Israel Foundation under Contract Number I-200-168.10.

6 References

- [1] DOCTORS, L.J., RENILSON, M.R., PARKER, G., AND HORNSBY, N.: "Waves and Wave Resistance of a High-Speed River Catamaran", *Proc. First International Conference on Fast Sea Transportation (FAST '91)*, Norwegian Institute of Technology, Trondheim, Norway, Vol. 1, pp 35-52 (June 1991)
- [2] ZILMAN, G. AND MILOH, T.: "Hydrodynamics of a Body Moving over a Mud Layer — Part 1: Wave Resistance", *J. Ship Research*, Vol. 39, No. 3, pp 194-201 (September 1995)
- [3] ZILMAN, G., MILOH, T., AND KAGAN, L.: "Hydrodynamics of a Body Moving over a Mud Layer", *Twentieth Symposium on Naval Hydrodynamics*, University of California, Santa Barbara, California, 17 pp (August 1994)
- [4] MILOH, T., TULIN, M.P., AND ZILMAN, G.: "Dead-Water Effects of a Ship Moving in Stratified Seas", *J. Offshore Mechanics and Arctic Engineering*, Trans. American Society of Mechanical Engineers, Vol. 115, No. 2, pp 105-110 (May 1993)
- [5] MICHELL, J.H.: "The Wave Resistance of a Ship", *Philosophical Magazine*, London, Series 5, Vol. 45, pp 106-123 (1898)
- [6] SRETENSKY, L.N.: "On the Wave-Making Resistance of a Ship Moving along in a Canal", *Philosophical Magazine*, Series 7, Supplement, Vol. 22, No. 150, pp 1005-1013 (November 1936)
- [7] ZILMAN, G., DOCTORS, L.J., AND MILOH, T.: "The Influence of a Bottom Mud Layer on the Resistance of Marine Vehicles", *Ship Technology Research: Schiffstechnik*, Vol. 43, No. 2, pp 51-61 (May 1996)
- [8] TUCK, E.O.: "Shallow-Water Flows past Slender Bodies", *J. Fluid Mechanics*, Vol. 26, Part 1, pp 81-95 (September 1966)
- [9] TUCK, E.O.: "Sinkage and Trim in Shallow Water of Finite Width", *Schiffstechnik*, Vol. 14, No. 73, pp 92-94 (1967)
- [10] TUCK, E.O.: "The Estimation of Squat", *Navigation*, J. Australian Institute of Navigation, Vol. 3, No. 3, pp 321-324 (December 1970)
- [11] DAND, I.W. AND FERGUSON, A.M.: "The Squat of Full Ships in Shallow Water", National Physical Laboratory, Ship Division, Report 175, 19 pp (December 1973)
- [12] BARRASS, C.B.: *Ship Squat*, Lorne & MacLean Marine Publishers, Luton, England, First Edition, 24+iv pp (October 1978)
- [13] BARRASS, C.B.: "The Phenomena of Ship Squat", *International Shipbuilding Progress*, Vol. 26, No. 294, pp 44-47 (February 1979)
- [14] FERGUSON, A.M., SEREN, D.B., AND MCGREGOR, R.C.: "The Prediction and Practical Measurement of Ship Squat in Shallow Water", *Proc. Conference on Marine Safety*, University of Glasgow, 19 pp (September 1983)
- [15] FERGUSON, A.M.: "An Extrapolation Method for Ship Resistance Based on the Variation of Sinkage and Trim with Froude Number", *Trans. Royal Institution of Naval Architects*, Vol. 126, pp 17-30, Discussion: 30-32 (December 1984)
- [16] SELMEIJER, R. AND VAN OORTMERSSEN, G.: "The Effect of Mud on Tanker Manoeuvres", *Trans. Royal Institution of Naval Architects*, Vol. 126, pp 105-120, Discussion: 120-124 (December 1984)
- [17] VANTORRE, M.: "Ship Behaviour and Control in Muddy Areas: State of the Art", *Proc. Conference on Manoeuvring and Control of Marine Craft (MCMC '94)*, pp 59-74 (September 1994)
- [18] D'ANGREMOND, K., DEELEN, C., AND VANTORRE, M.: "Nautical Depth Approach", Initial Report of the Joint Working Group 30, Permanent International Association of Navigation Congresses (PIANC), International Association of Ports and Harbours (IAPH), 17 pp (February 1994)
- [19] GADE, H.G.: "Effects of a Nonrigid, Impermeable Bottom on Plane Surface Waves in

Shallow Water", *J. Marine Research*, Vol. 16, No. 2, pp 61-82 (1958)

- [20] DALRYMPLE, R.A. AND LIU, P.L.-F.: "Waves over Soft Muds: A Two-Layer Fluid Model", *J. Physical Oceanography*, Vol. 8, No. 6, pp 1121-1131 (November 1978)
- [21] MACPHERSON, H.: "The Attenuation of Water Waves over a Non-Rigid Bed", *J. Fluid Mechanics*, Vol. 97, Part 4, pp 721-742 (April 1980)
- [22] HSIAO, S.V. AND SHEMDIN, O.H.: "Interaction of Ocean Waves with a Soft Bottom", *J. Physical Oceanography*, Vol. 10, No. 4, pp 605-610 (April 1980)
- [23] MAA, J.P.-Y. AND MEHTA, A.J.: "Soft Mud Response to Water Waves", *J. Waterway, Port, Coastal, and Ocean Engineering*,

Vol. 116, No. 5, pp 634-650 (September/October 1990)

- [24] FODA, M.A., HUNT, J.R., AND CHOU, H.-T.: "A Nonlinear Model for the Fluidization of Marine Mud by Waves", *J. Geophysical Research*, Vol. 98, No. C4, pp 7039-7047 (April 1993)
- [25] LUNDE, J.K.: "On the Linearized Theory of Wave Resistance for Displacement Ships in Steady and Accelerated Motion", *Trans. Society of Naval Architects and Marine Engineers*, Vol. 59, pp 25-76, Discussion: 76-85 (December 1951)
- [26] WIGLEY, W.C.S.: "A Comparison of Experiment and Calculated Wave-Profiles and Wave-Resistances for a Form Having Parabolic Waterlines", *Proc. Royal Society of London, Series A*, Vol. 144, No. 851, pp 144-159 + 4 plates (March 1934)

DISCUSSION

W.W. Schultz
University of Michigan, USA

Your potential flow upper layer ensures zero shear stress on the mud interface. How would you expect your conclusion to change if you added a boundary-layer at the interface to get the more realistic condition of high stresses?

AUTHORS' REPLY

We are grateful for Professor Schultz's discussion of our paper, as well as the other verbal discussion that took place after the presentation.

In summarizing our work, the mud layer is modeled as a viscoelastic substance and the flow is considered to be laminar. The concept of linearization of the problem, on the assumption of a small input disturbance, is quite realistic since the particle motions in both the mud and the water are small.

This smallness of motion implies that the boundary-layer effects at the mud-water interface would be unimportant. We therefore believe that the boundary layer in the water on top of the interface would not greatly affect the forces on the vessel - in the same way that the boundary layer in the bottom of a towing tank or a river (even in the case of relatively shallow water) is unlikely to have a significant influence on the predictions for the forces.

An interesting extension of this work would be to analyze a multilayer problem, so that the case of an indistinct interface could be studied. The principles are identical to those expounded in the paper, but the algebra and the corresponding computer program would be far more complicated.

A Hybrid Approach to Capture Free-Surface and Viscous Effects for a Ship in a Channel

V. Bertram (Institut für Schiffbau, Germany)

S. Ishikawa (Mitsubishi Heavy Industries, Japan)

Abstract

The flow about a Series-60 ($C_B = 0.6$) in a channel is computed by a new hybrid approach to capture most of the free-surface and viscous effects. First, a fully nonlinear wave resistance code computes the potential free-surface flow predicting the squat. Then the Reynolds-averaged Navier-Stokes equations are solved using the Baldwin-Lomax turbulence model. This step uses the squat predicted in the first step and the velocities at the lateral boundary of the RANSE domain, which spans only a small part of the channel width. The free-surface deformation is still neglected. An integrated propeller model interacts automatically with the RANSE computations. Results for flow details agree well with experiments for deep water and reproduce qualitatively all influences of the shallow water. Remaining differences are explained mainly by not capturing the free-surface deformation in the second step.

1. Introduction

Consider a ship moving steadily ahead in the center of a channel of constant depth and width at a subcritical depth Froude number $F_{nh} = U_0/\sqrt{gh} < 1$, where U_0 is the ship speed, $g = 9.81\text{m/s}^2$, and h the channel depth. The flow about the ship is steady except for turbulent fluctuations. It is considerably influenced by the shallow water. The influence of the channel walls is for usual channel geometries of secondary importance. Resistance and sinkage increase strongly near the critical depth Froude number, trim may change its sign. These global changes reflect changes in local flow details such as the wave pattern or the pressure distribution on the hull. The 20th ITTC [1] surveys measurements of global and local flow details for a Series-60 ($C_B = 0.6$) in a channel. A correct computational prediction of the pressures at channel bottom or the flow in the aft region of the

ship is difficult, because both viscous and free-surface effects play an important role.

Classical approaches following e.g. Sretensky [2] or Inui [3] focus on the prediction of wave resistance and wave pattern. They usually do not capture e.g. the influence of squat on the flow field and neglect all viscous effects. We refer to Lap [4] and Tuck [5] for a more comprehensive review of classical and semi-empirical approaches. More recently, Rankine singularity methods (RSM) have been applied to compute shallow-water flows about ships, using SHIPFLOW [6], [7], [8], REVA in Nantes [9], [10], panel codes of the IfS in Hamburg [11] to [17], and Yasukawa's code [18]. Delhommeau [10], Bertram, [15] to [18], and Yasukawa [18] include also side-wall effects for ships in channels. Bai [19] used a finite-element approach for simplified hull forms. The Duisburg Model Basin VBD [20] investigates various methods including an finite-volume Euler solver around a river cargo vessel in a channel. All these methods still neglect viscosity. Linear RSM ([13], [18]) and methods based on volume grids ([19], [20]) do not account for squat. Thus they improve hardly results compared to classical methods in most cases.

Cura uses a different approach calculating the flow for a Series-60 in a channel, [21], [22]. His RANSE (Reynolds-averaged Navier-Stokes equations) solver captures viscous effects but neglects free-surface effects, namely squat and trim. Cura predicts the pressure at the channel bottom quite accurately and discovers an error in published measurements, [1], [23], which "most probably explains previous differences between computations and [...] measurements". Remaining discrepancies are attributed to turbulence modelling, large grid cell distortion due to the wide, but shallow channel, and the neglect of free-surface effects.

We will present a combined numerical approach to capture most of these remaining effects. In a first step, a nonlinear Rankine source method will predict squat and trim for a ship in a channel. In a second step, a RANSE solver will use a grid for a ship fixed at the predicted squat and trim. The lateral extent of the grid will be considerably smaller than the actual channel. The velocities at the lateral boundary of the RANSE computational domain will be determined by the Rankine source code. However, the free-surface elevation will still be neglected assuming a flat undisturbed surface instead.

2. Computational Procedure

The flow is assumed to be symmetrical with respect to the hull center plane coinciding with the center plane of the channel. The problem is solved in two steps. In the first step, the inviscid free-surface flow in the channel is computed by a Rankine singularity method (RSM). Linear source panels are distributed above a finite section of the free surface. The panels are numerically evaluated by approximating them by a four-point source cluster, [24]. On the hull and the channel side wall, higher-order panels (parabolic in shape, linear in strength) are distributed. Mirror images of the sources at the channel bottom enforce that no water flows through the channel bottom. The nonlinear free-surface boundary condition is met in an iterative scheme that linearizes differences from arbitrary approximations of the potential and the wave elevation, Fig.1, [12]. The radiation and open-boundary conditions are enforced by shifting sources versus collocation points on the free surface. [25] gives more details on the method.

We describe now the automatic grid generation for the free-surface grid. The base 'wave length' is taken as $\lambda = \frac{2\pi}{g} U_0^2$. The upstream end of the grid is $1.5 \cdot \max(0.4L_{pp}, \lambda)$ before FP for shallow water. (For infinite water, the factor is 1.0 instead of 1.5). The downstream end of the grid is $\max(0.6L_{pp}, \lambda)$ behind AP. The outer boundary in transverse direction B_G is 0.35 of the grid length for unlimited flow, but taken at the channel wall ($0.8L$ in our case) for a ship in a channel. The intended number of panels per wave length is 10. The intended number of panels in transverse direction is $(B_G - \Delta x)/(1.5\Delta x) + 1$, where Δx is the grid spacing in longitudinal direction. However, if the intended number of free-surface panels plus the number of hull panels exceeds 2500, the grid spacing in x - and y -direction is increased by the same factor until this condition is met. The innermost row of panels uses square panels, the rest of the

panels is rectangular with a side-ratio ($\Delta y/\Delta x$) of approximately 1.5. The panels follow a 'grid waterline'. This is the upper rim of the discretized ship (1.5m above CWL in our case) which is modified towards the ends to enforce entrance angles of less than 31° . The channel wall grid follows the free-surface grid in longitudinal direction. In vertical direction the number of panels is the next integer to $(h - \Delta x)/(2\Delta x) + 1$, but at least two. The uppermost row uses square panels. The free-surface panels are desingularized by a distance of Δx .

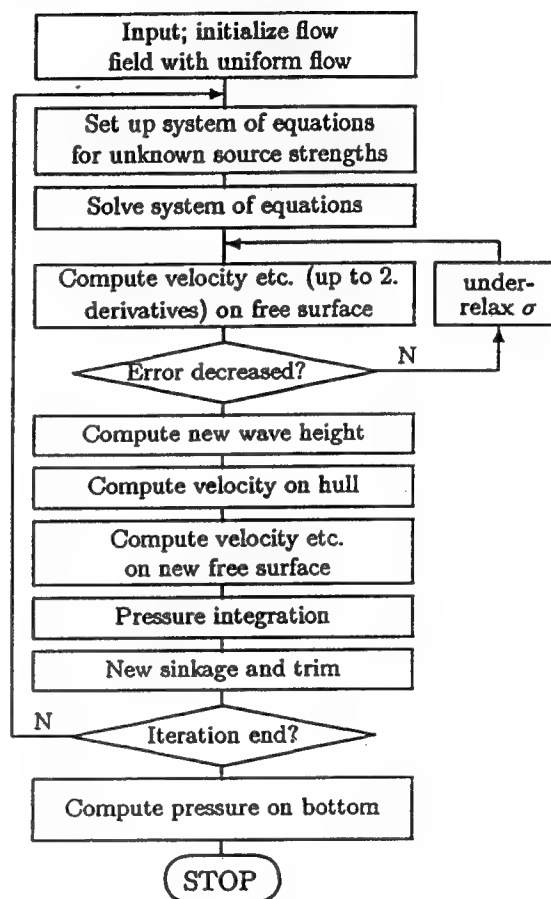


Fig.1: Flow chart of iterative solution

In a second step, the viscous flow around the ship is solved. The ship is assumed fixed at the squat calculated in the first step. The deformation of the water surface is neglected and the water surface substituted by a flat symmetry plane. The computational domain does not extend in lateral direction to the channel walls. Instead, the inviscid velocities of the first step are taken as boundary condition on the lateral boundary. The RANSE solver is based on Kodama's method, [26]. It solves the continuity equation including a pseudo-compressibility term and the three momentum equations for incompressible turbu-

lent flows. These equations are discretized in space by cell-centered finite volumes. The inviscid fluxes are evaluated by a third-order upwind scheme (MUSCL) with the flux difference-splitting method. The viscous fluxes are determined by central differences. The algebraic Baldwin-Lomax model accounts for turbulence, [27]. [29] gives more details on the method.

The propeller effect is considered by applying an equivalent body force in the right-hand side of the RANSE. Our RANSE solver with propeller effect is based on Hinatsu's method, [29]. This considers the body force in both thrust direction and rotative direction. The propeller force distribution is estimated by Yamazaki's [30] an infinite-blade propeller theory. The distribution obtained by this method depends on the propeller inflow and has to be determined by an iterative procedure:

- 1) Solve the RANSE for the ship without propeller
- 2) Calculate the wake distribution at the propeller plane
- 3) Define the required propeller thrust as ship resistance minus corrective towing force
- 4) Calculate the propeller force distribution using a propeller program with inflow and required thrust (as computed above) as input data
- 5) Solve the RANSE with equivalent body forces
- 6) If the resistance is equal to the required thrust, end the calculation. If not, calculate the new propeller inflow by subtracting the propeller induced velocity from the wake distribution at the propeller plane and go back to step 3)

This cycle is actually performed every 10 outer iterations of the RANSE computation. No problems with convergence were ever observed.

An H-O type grid is generated using Kodama's implicit geometrical method, [31]. An initial algebraically generated hull grid is modified so as to satisfy requirements of orthogonality, smoothness, clustering towards the ends, and minimum spacing. Grid lines are clustered towards bow and stern profiles in streamwise direction, and towards the hull in radial direction. Bow and stern profiles are followed by vertical grid lines avoiding the step curve approximation of Cura, [21], [22]. The horizontal lines are approximately orthogonal to the vertical grid lines, and also to both the bow and stern profiles.

3. Test Case: Series-60

The method was applied to a Series-60 ship ($C_B = 0.6$, $L = 6.096\text{m}$, $\lambda = 1.20$). Results are compared to experimental data of the Duisburg Model Basin VBD. The lateral wall of the towing tank lies $0.8L$ from the center plane. Experiments were performed for water depth-to-draft ratios $h/T = 3.2$, 2.0 , 1.5 , 1.2 . We computed the cases given in Table I, Fig.2. We denote the case $h/T = 3.2$ as 'deep' water, $h/T = 1.5$ as 'shallow' water.

Table I: Computed cases for Series-60

h/T	F_n	F_{nh}	R_n
3.2	0.15	0.363	$7.0 \cdot 10^6$
1.5	0.15	0.530	$7.0 \cdot 10^6$
3.2	0.16	0.387	$7.5 \cdot 10^6$
1.5	0.16	0.565	$7.5 \cdot 10^6$
3.2	0.18	0.436	$8.4 \cdot 10^6$
1.5	0.18	0.636	$8.4 \cdot 10^6$

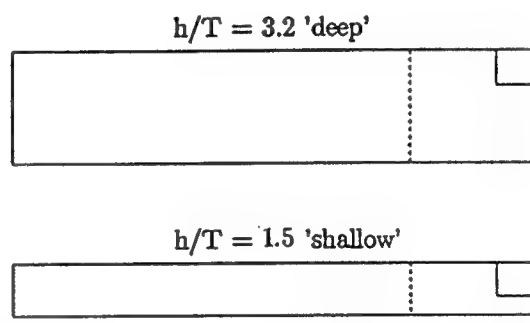


Fig.2: Computed cases for Series-60 at $F_n = 0.15$; dotted line RANSE grid boundary

503 elements discretized the hull up to a height of $0.23 T$ above the CWL, Fig.3. The free-surface grid extended $0.8L$ in lateral direction (to the channel wall), $0.6L$ ahead of FP and $0.5L$ behind AP. $96 \cdot 19 = 1824$ elements were used to discretize this area. This discretization resolves the wave pattern coarsely, but is deemed sufficient to capture effects relevant for squat and induced pressures. $96 \cdot 2 = 192$ elements were used to discretize the channel wall for $h/T = 1.5$, $96 \cdot 3 = 288$ elements for $h/T = 3.2$.

Figs.4 show the RANSE grid for $h/T = 1.5$. The grid extended $0.5L$ ahead of FP and L behind AP. The lateral extent was $0.2L$. $100 \cdot 24 \cdot 50 = 120000$ cells were used in total. The computations assumed a kinematic viscosity of $\nu = 1.01 \cdot 10^{-6} \text{m}^2/\text{s}$ and a water density of $\rho = 1000 \text{kg/m}^3$.

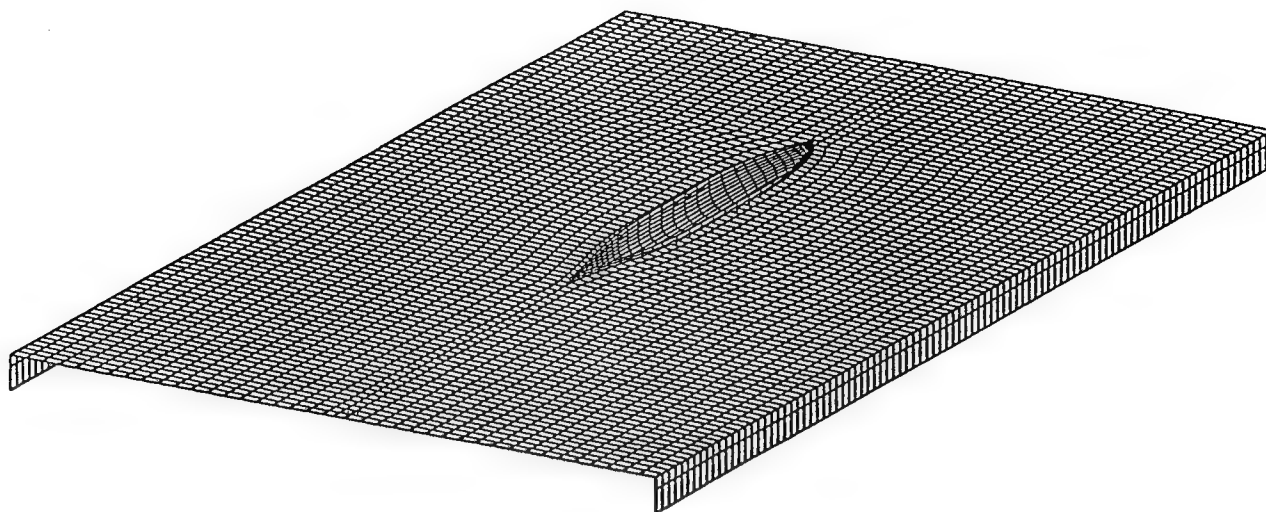


Fig.3: Grid for computations with Rankine Source Method (2519 elements)

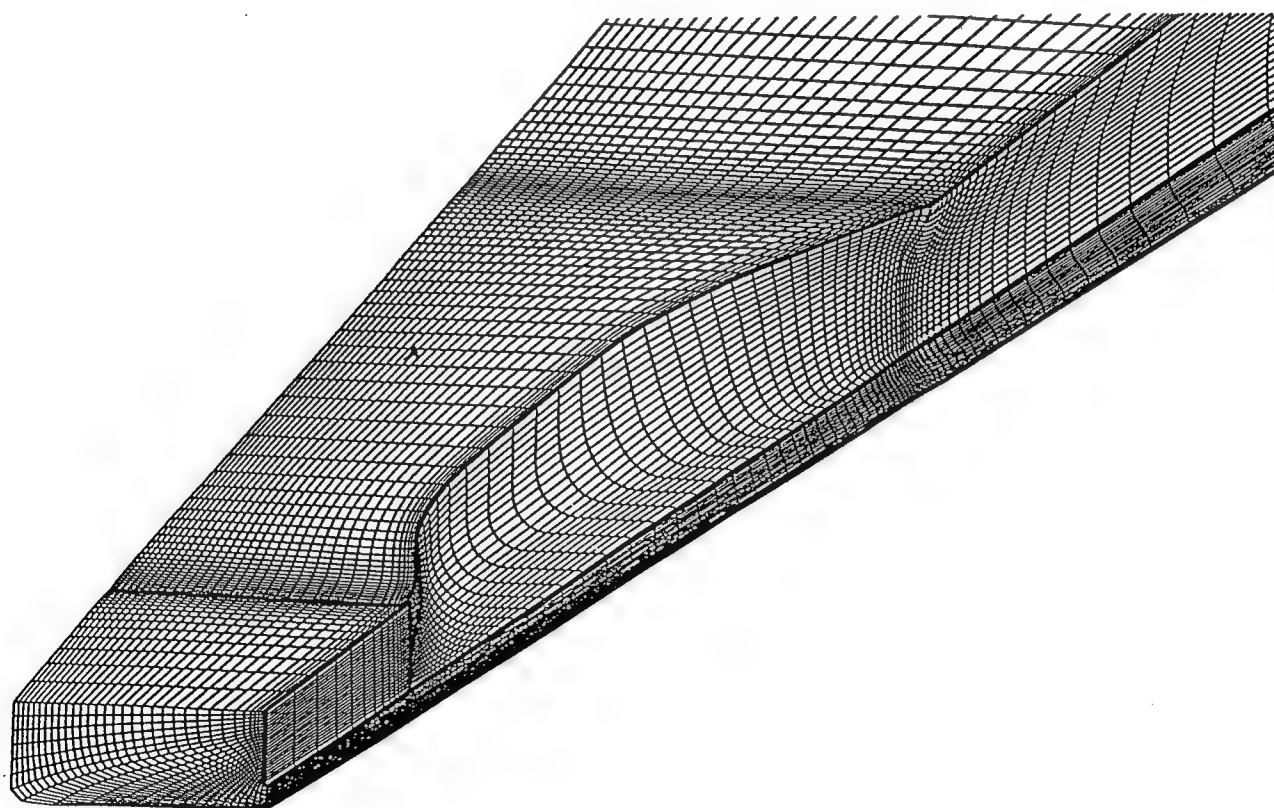


Fig.4a: RANSE grid covering near field (120000 cells)

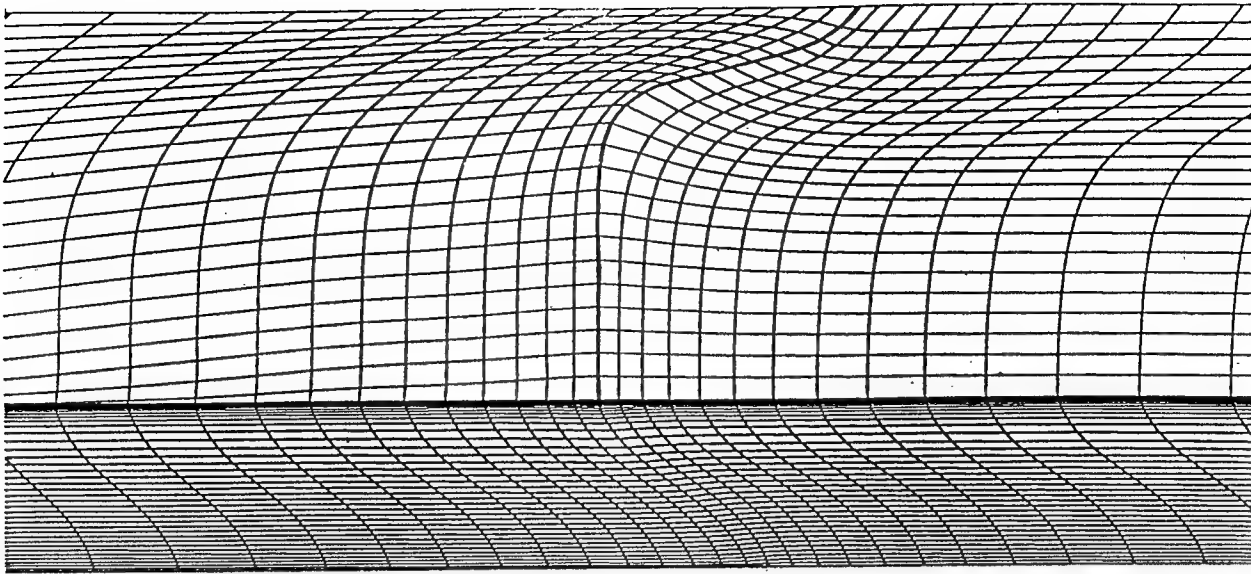


Fig.4b: Detail of RANSE grid at aftbody

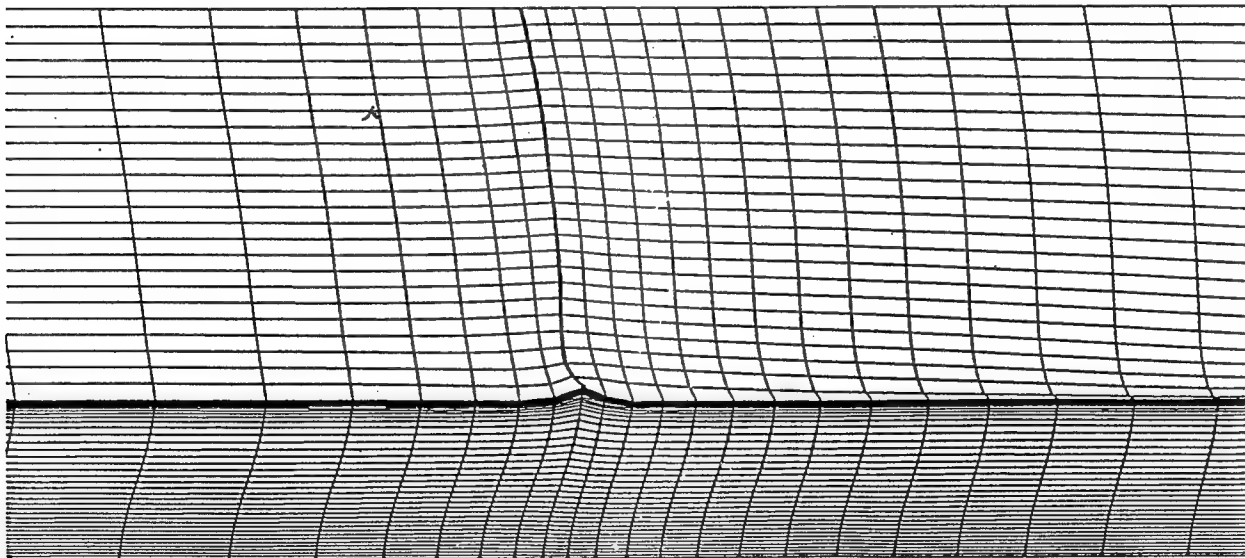


Fig.4c: Detail of RANSE grid at bow

4. Resistance test simulations

Local flow details of the first-step RSM computation like wave pattern, Fig.5, pressure on hull, and wave profile showed no irregularities. Free-surface grid variations gave almost exactly the same results.

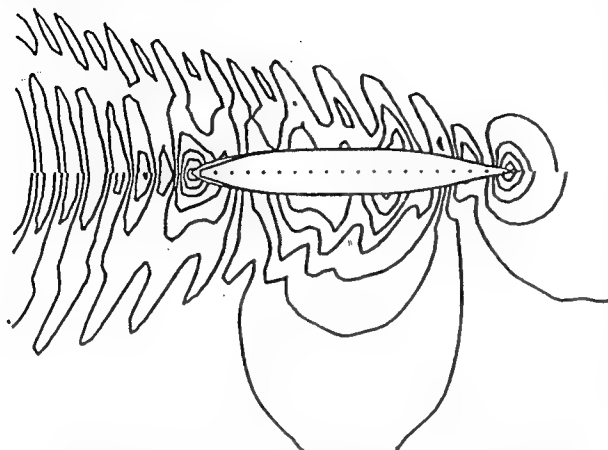


Fig.5: Wave pattern for $F_n = 0.15$ at $h/T = 3.2$ (top) and $h/T = 1.5$ (bottom)

Table II gives the computed and measured squat for $F_n = 0.15$. The computations capture the squat well. Measurements of various towing tanks, [1], show considerable scatter of measured squat for $h/T = 1.5$, ranging from $\Delta T/L = 0.00236$ to 0.00326 . Our computed result of 0.00269 lies well within this bandwidth. The difference of 7% between measured (VBD) and computed squat may be due to instationary flow effects in the experiments (VBD in personal communication), but neglect of the boundary layer may also contribute.

Table II: Sinkage and trim (positive for bow immersion) for Series 60 at $F_n = 0.15$

$F_n = 0.15$				
	experiment		RSM	
h/T	$\Delta T/L$	θ	$\Delta T/L$	θ
3.2	0.00118	0.00050	0.00120	0.00040
1.5	0.00285	0.00083	0.00269	0.00087
$F_n = 0.16$				
	experiment		RSM	
h/T	$\Delta T/L$	θ	$\Delta T/L$	θ
3.2	0.00139	0.00058	0.00135	0.00051
1.5	0.00348	0.00116	0.00326	0.00107

The pressure at the channel bottom is dominated by free-surface effects, namely the primary wave system with its long wave trough along the ship lengths. Towards the ends, the pressure at the channel bottom shows local maxima. The aft maximum

is less pronounced due to viscous effects. RANSE and RSM solution are blended with RSM solutions taken between $\pm 0.4L$, RANSE solution otherwise. The two solutions coincide in an intermediate region so that the blended solution is smooth. The pressure on the channel bottom is captured well for 'deep water', Fig.6. For 'shallow water', the tendency is captured well including a local maximum amidships, Fig.7. The difference between experiments and computations is 7%. For comparison, linear results of the RSM code (first iterative step) are also given. The hybrid CFD approach improves both the prediction of the pressure minimum (due to the consideration of squat and local wave trough) and the aft pressure maximum (due to capturing viscous effects). We attribute the remaining differences to the underpredicted squat which in turn might be due to a not fully stationary flow in experiments.

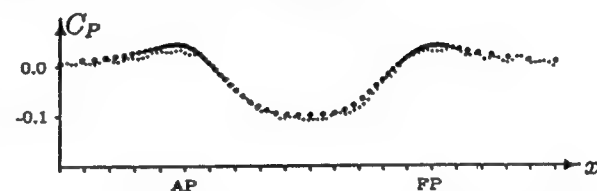


Fig.6: Pressure coefficient C_P along center line on channel bottom at $F_n = 0.15$; $h/T = 3.206$; experiments (·), hybrid CFD (•)

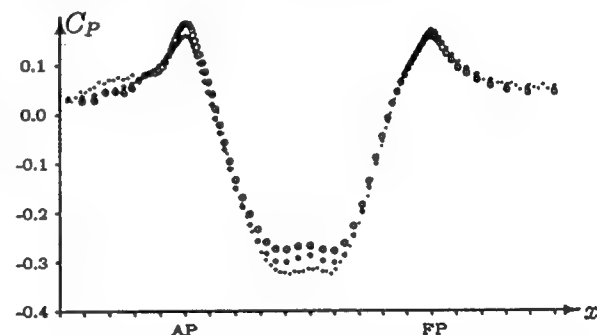


Fig.7: Pressure coefficient C_P along center line on channel bottom at $F_n = 0.15$; $h/T = 1.5$; experiments (·), hybrid CFD (•), linear RSM (o)

Fig.8 shows contour lines of the axial velocity for $F_n = 0.18$, $R_n = 8.4 \cdot 10^6$. Unfortunately only very few data were measured close to the hull. Subsequently, the inner contour lines of the experimental results cannot be very reliable. The original plots, [1], [23], do not reflect the quality of the measured data due to a poor plotting procedure. We therefore plotted our own curves based on the data supplied by VBD. In this way we wanted to exclude differences due to the employed plotting algorithms. Experiments and computations agree well for $h/T = 3.2$.

Shallow water strongly changes the experimental contour lines. They are inflated at the lower regime and get closer to the hull in the upper regime which makes their overall circumferential contour smoother. The computations capture this behaviour only qualitatively. The widening of the contour lines in the lower regime is overpredicted. Cura's [21], [22] RANSE computations show the same effect. Cura suspected as reason for his discrepancies: "The overprediction of widened contour lines in the lower regime is probably due to the neglected free-surface effects."

Especially the sinkage leads to higher blockage, thus to higher local velocities and contour lines closer to each other." However, our results indicate that including the sinkage does not remove the discrepancies. Cura's results agree better with experiments than ours. Maybe the strong wave trough over large part of the ship increases the blockage, but we are surprised that this still effects the flow so far aft. Turbulence modelling is a popular scapegoat. But for such a slender hull, it should not have such a large impact on the contour lines. Cura uses a different turbulence model and his results are quite similar to ours. This indicates that differences are rather due to the physical model (neglect of free surface deformation) or differences between computational methods and experiments as such. Computations including the free-surface deformation and further model tests, preferably from other towing tanks or with larger model scales, might give more insight into this phenomenon. With the data presently available, we cannot explain the differences between computations and experiments completely.

Fig.9a shows the computed pressure coefficient on 5 cross sections in the aftbody for $F_n = 0.16$, $R_n = 7.5 \cdot 10^6$. (No experimental data were available for $F_n = 0.15$). Shallow water induces strong low pressure over an extended region of the ship. The integral value of this effect is the increased squat. The three-dimensionality of the flow for deep water is shown by the curved pressure lines in the bilge region. Shallow water makes the flow rather two-dimensional. The pressures are nearly constant at each cross section. This agrees qualitatively well with all ITTC experiments, [1]. For deep water, experiments of VBD and our computations show differences in the order of $\Delta C_P = 0.02$. Various numerical tests produced only little differences in the computed results. We compared results for $F_n = 0.16$, $R_n = 3.2 \cdot 10^6$ with experiments of the University of Iowa, [32]. The different Reynolds number has virtually no effect on the computational results, Fig.9b. Our results agree well with the Iowa experiments. The differences between

the Iowa and VBD measurements, but also the differences between measurements on port and starboard for the VBD measurements alone, are an indication of the margin of uncertainty for the experimental results. Measuring pressure on the hull is difficult and no criticism of the experimenters is implied. We just want to point out that in the aftbody apparently the computations are already within the margin of uncertainty of available experiments.

For shallow water, only VBD measurements are available. Agreement is good for the two aftmost sections. For the third section ($x/L = 0.15$), the VBD measurements differ considerably between port and starboard. Computations agree well with measurements for one side. For the fourth and fifth section, the experimental pressures are noticeably lower than computed pressures. This is to be expected: Our viscous computations capture a numerically predicted squat, but not the deformation of the water surface. The strong wave trough for shallow water gives an additional blockage effect over the central part of the ship that leads to higher velocities and lower pressures. To capture this effect, the RANSE grid generator would have to incorporate the wave elevation predicted by the RSM code. At present, our grid generator does not have this capability.

Integrating the pressures and shear stresses gives the resistance coefficient (without wave resistance) based on $S_0 = L^2/5.83$. The RANSE computations integrated the pressure over the whole ship hull (including squat, excluding local wave deformation). The increase in resistance for shallow water is predicted correctly. However, the resistance is overestimated, Table III. The agreement is good for deep water, better than usually for fuller hulls, because the Series-60 is a slender hull with no flow separation in the aftbody. Subsequently the frictional resistance dominates and this is predicted relatively accurately by RANSE codes. We contribute the perfect agreement though to fortunate error cancellation. For shallow water, the overestimation in resistance is considerable. This is qualitatively expected. We neglect the deformation of the free surface in the viscous computation. This has two effects:

1. The actual wetted surface is smaller than the wetted surface in the computation.
2. The blockage effect is underpredicted. In reality the flow is faster, the boundary layer thinner.

A crude correction for the first effect is possible: We computed the actual wetted surface with the RSM

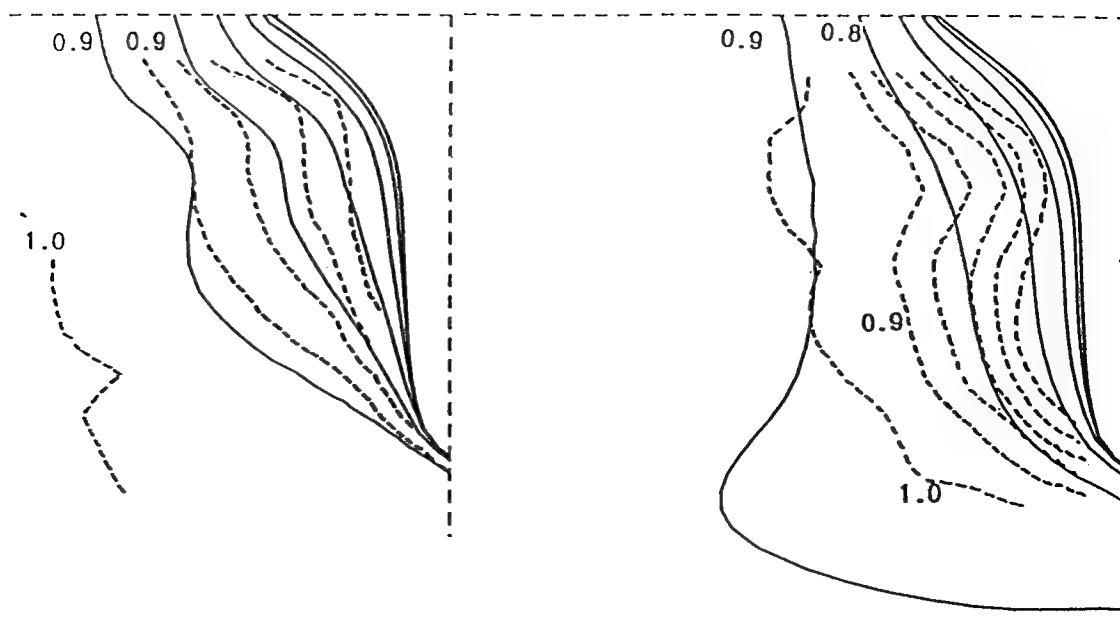


Fig.8: Contour lines of the axial velocity u/U_0 at $5\%L$ before AP, $F_n = 0.18$, $R_n = 8.4 \cdot 10^6$
 $h/T = 3.2$ (left) and $h/T = 1.5$ (right); - - - VBD, — CFD

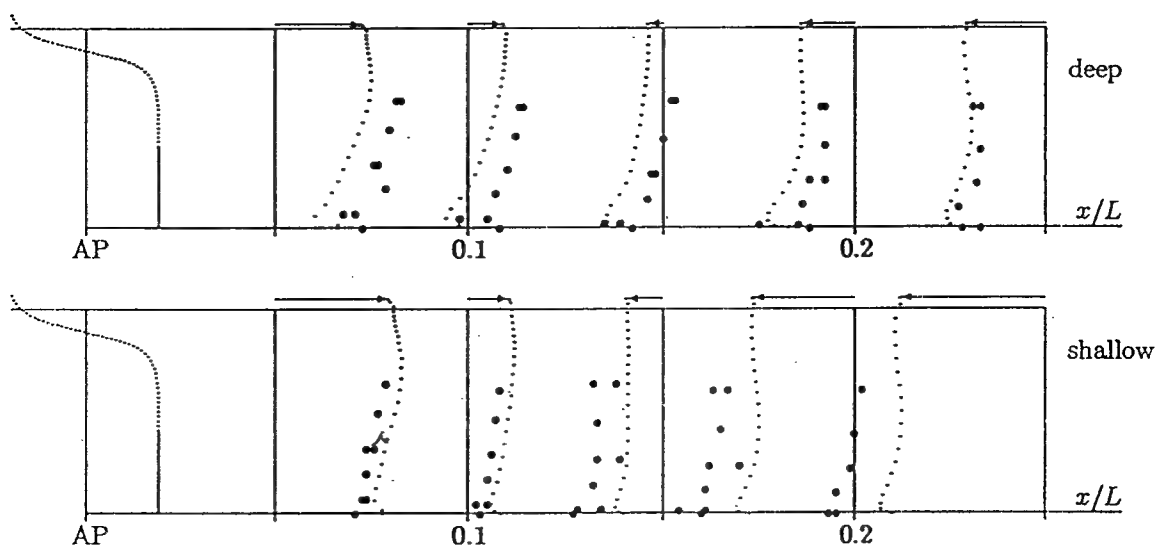


Fig.9a: Pressure distribution for resistance test, $F_n = 0.16$, $R_n = 7.5 \cdot 10^6$, • exp. VBD, • CFD

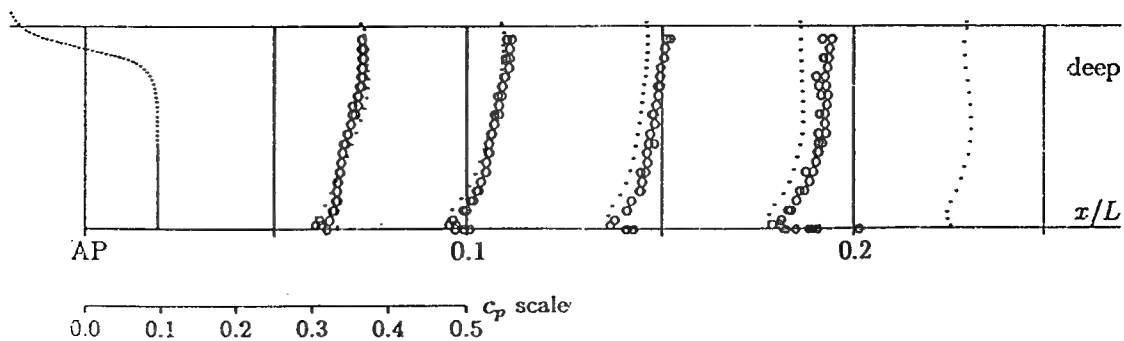


Fig.9b: Pressure distribution for resistance test, $F_n = 0.16$, $R_n = 3.2 \cdot 10^6$, o exp. Iowa, • CFD

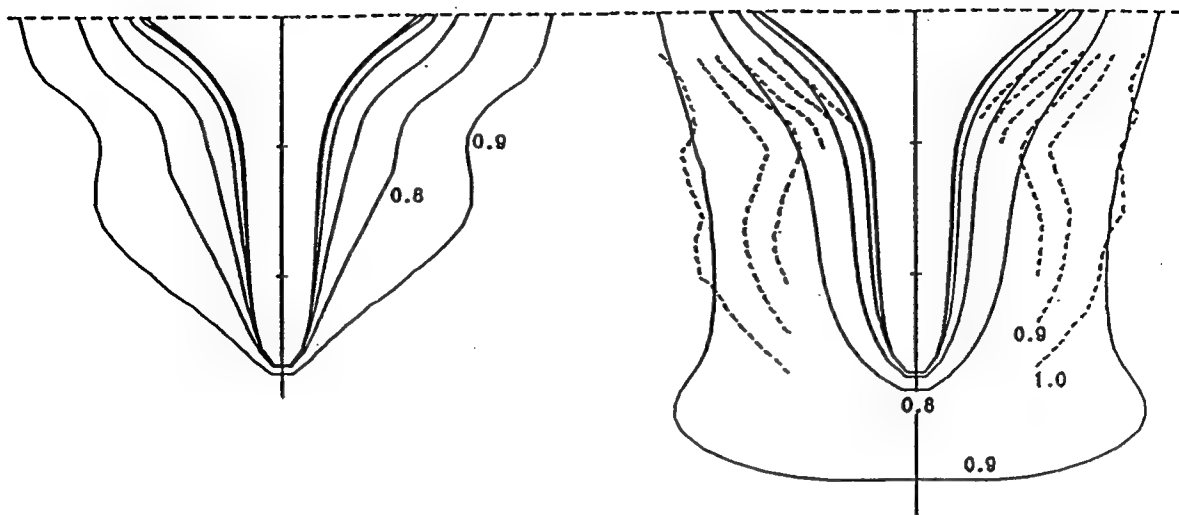


Fig.10: Contour lines of axial velocity u/U_0 at $5\%L$ before AP, $F_n = 0.18$, $R_n = 8.4 \cdot 10^6$, with prop. $h/T = 3.2$ (left) and $h/T = 1.5$ (right), ---- VBD, — CFD

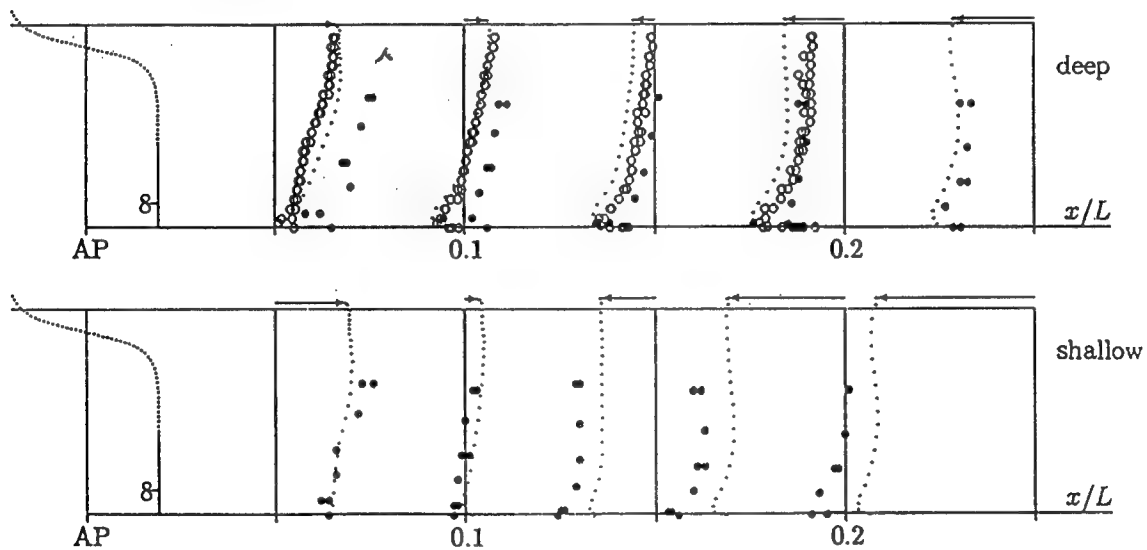


Fig.11: Pressure distribution for propulsion test, $F_n = 0.16$,
 • exp. VBD ($R_n = 7.5 \cdot 10^6$), ○ exp. Iowa ($R_n = 3.2 \cdot 10^6$), · CFD ($R_n = 7.5 \cdot 10^6$)

code. The ratio of the actual wetted surface to wetted surface assumed by the RANSE computation is 0.9945 for both water depths. So, this effect is not significant. Better quantitative agreement then requires a RANSE grid that follows the free surface deformation. This could be achieved either by a hybrid approach or by free-surface RANSE computations.

Table III: Computed (w/o wave resistance) and measured resistance coefficients

	F_n	R_n	$h/T = 3.2$	$h/T = 1.5$
CFD	0.15	$7 \cdot 10^6$	$3.86 \cdot 10^{-3}$	$5.79 \cdot 10^{-3}$
Exp	0.15	$7 \cdot 10^6$	$3.86 \cdot 10^{-3}$	$4.67 \cdot 10^{-3}$

The employed turbulence model might also contribute considerably to the error. The Baldwin-Lomax model inherently assumes that there is only one maximum in the flow profile for the product of wall distance and magnitude of vorticity at that point. This assumption already requires some care for deep water cases, as more than one local maximum may appear, e.g. [33]. For shallow water, a second maximum definitely will appear close to the channel bottom. We confirm Graf who investigated the two-dimensional flow around barges on shallow water, [34]. Maybe the Baldwin-Lomax turbulence model is generally unsuited for flows between two walls. In any case, we share the wide consensus that CFD methods are not yet accurate enough to predict resistance with practical accuracy.

5. Propulsion test simulations

The simulations for propulsion test required some assumptions, but as far as possible the conditions supplied by VBD were used. Table IV gives the propeller data used in the computations. The propulsion tests were performed for the ship self-propulsion point. A corrective towing force was applied based on ITTC-57 and $C_A = 0.0002$.

Fig.10 shows the contour lines of the axial velocity for $F_n = 0.18$, $R_n = 8.4 \cdot 10^6$. The qualitative effect of the propeller is captured as expected: The contour lines are getting closer to the hull compared to the resistance test, see Fig.8. At the considered station (5% before AP), the port/starboard asymmetric influence of the propeller is still very small. The quantitative agreement resp. disagreement between computed and measured contour lines is similar to the resistance test. Fig.11 shows the computed pressure coefficient on 5 cross sections in the aftbody for $F_n = 0.16$, $R_n = 7.5 \cdot 10^6$. As the different Reynolds number was proven to have no significant effect for the resistance test, we plotted Iowa

and VBD results this time in one figure. The starboard/port asymmetry of the pressure due to the propeller is at the considered stations negligibly small. So we plotted only the starboard computational results. The propeller accelerates the flow shifting the pressure generally to lower values. The computation not only reproduces this effect as expected, it also agrees well with experiments quantitatively. Only for the sections closer to amidships, the same differences as for the resistance test are apparent for the same reasons as discussed above.

Table IV: Propeller data ($\lambda = 1 : 20$)

propeller diameter	209.5mm
boss ratio	0.19
P/D	1.04
A_e/A_0	0.565
height over keel	160mm
position before AP	1% L
blades	4

Blade Geometry	
r [m]	chord length [m]
0.021348	0.05060
0.032328	0.05714
0.041114	0.06136
0.051346	0.06486
0.062326	0.06649
0.073306	0.06510
0.083538	0.05969
0.095983	0.04388
0.099066	0.03460
0.104750	0.0

Propeller open-water data		
J	K_T	K_Q
0.4	0.301	0.0481
0.5	0.263	0.0429
0.6	0.223	0.0373
1.09	0.0	

6. Conclusions

The hybrid approach computing first squat and potential flow field and then the viscous flow improves the quality of results and saves computational time for shallow water applications. A nonlinear potential flow code may be already sufficient for cases where only the pressure on the channel bottom is of interest. Discrepancies remain for the pressure on the hull in the middle section of the ship and the computed resistance. These discrepancies could be reduced by taking the free-surface deformation into account.

Acknowledgement

The research was performed during a stay of V. Bertram as a visiting scientist of MHI R&D Center in Nagasaki sponsored by the German Research Association (DFG). The authors are grateful for the assistance of VBD, namely Dipl.-Ing. A. Gronarz, for updated data on measurements. We thank H. Sato for his assistance for the RANSE computations.

References

1. ITTC (1993), "Report on cooperative experimental program in shallow water," 20th Int. Towing Tank Conf., Resistance and Flow Committee, San Francisco
2. Sretensky, L.N. (1937), "A theoretical investigation of wave resistance," Joukovsky Central Institute for Aero-Hydrodynamics Rep. 319 (in Russian)
3. Inui, T. (1954), "Wave-making resistance in shallow water sea and in restricted water with special reference to its discontinuities," J. Soc. Nav. Arch. of Japan 76, pp. 1-10.
4. Lap, A. (1972), "Ship resistance in shallow and restricted water," 13th Int. Towing Tank Conf., Appendix 5 to Report of Resistance Committee, Berlin/Hamburg
5. Tuck, E.O. (1978), "Hydrodynamic problems of ships in restricted water," Ann. Rev. Fluid Mech. 10, pp. 33-46.
6. Ni, S.Y. (1987), "Higher order panel method for potential flows with linear or nonlinear free surface boundary conditions," Ph.D. thesis, Chalmers Univ. of Technology, Sweden
7. Kim, K. and Choi, Y. (1993), "A numerical calculation of free surface potential flow field and of ship wave resistance in shallow water by fully nonlinear wave theory," 2nd Japan Korea Workshop, Osaka, pp. 111-120.
8. Kim, K., Choi, Y., Jansson, C., and Larsson, L. (1994), "Linear and nonlinear calculations of the free surface potential flow around ships in shallow water," 20th Symp. Naval Hydrodyn., Santa Barbara
9. Maissonneuve, J. and Delhommeau, G. (1991), "A computer tool for solving the wave resistance problem for conventional and unconventional ships," 3rd Int. Conf. CADMO, Key Biscaine
10. Delhommeau, G. (1993), "Wave resistance code REVA," 19th WEGEMT school on Num. Simulation of Hydrodyn., Nantes
11. Söding, H., Bertram, V., and Jensen, G. (1989), "Numerical computation of squat and trim of ships in shallow water," STG-Yearbook 83, Springer, pp. 42-48. (in German)
12. Jensen, G., Bertram, V., and Söding, H. (1989), "Ship wave-resistance computations," 5th Int. Conf. Num. Ship Hydrodyn., Hiroshima, pp. 593-606.
13. Kux, J. and Müller, E. (1992), "Shallow-water influence on ship flows demonstrated for a Series-60 ship, $C_B = 0.6$," STG-Yearbook 86, Springer, pp. 367-389. (in German)
14. Bertram, V. (1994), "Shallow water effects for SWATH ships," 9th Int. Workshop Water Waves and Floating Bodies, Kuju
15. Zibell, H.G. and Bertram, V. (1994), "Influence of the channel effect on resistance and flow field of a river cargo vessel," Binnenschiffahrt 49/17, pp. 34-38. (in German)
16. Bertram, V. and Jensen, G. (1992), "Side wall and shallow water influence on potential flow," 8th Int. Workshop Water Waves and Floating Bodies, Val de Reuil
17. Bertram, V. and Yasukawa, H. (1995), "Inviscid free-surface computations for a Series-60 in a channel," 4th Symp. Nonlinear and Free-Surface Flows, Hiroshima, pp. 13-16.
18. Yasukawa, H. (1989), "Calculation of the free surface flow around a ship in shallow water by Rankine source method," 5th Int. Conf. Num. Ship Hydrodyn., Hiroshima, pp. 643-655.
19. Bai, K.J. (1977), "A localized finite element method for steady three dimensional free surface flow problems," 2nd Int. Conf. Num. Ship Hydrodyn., Berkeley, pp. 78-87.
20. Pagel, W.; Rieck, K.; Grollius, W.; Gronarz, A. (1995), "Experimental and theoretical-numerical flow investigations for river cargo ships," VBD-Report 1366, Duisburg (in German)
21. Cura, A. (1994), "Influence of shallow water on the flow around a slender ship hull," 15th Duisburg Koll. Schiffstechnik/Meerestechnik, Univ. Duisburg, pp. 78-96. (in German)
22. Cura, A. (1995), "Influence of water depth on ship stern flows," Ship Techn. Res. 42/4, pp. 193-197.
23. Binek, H., Ter Jung, G., and Müller, E.

(1992), "Resistance and flow characteristics of ships with $C_B = 0.6$ on shallow water," VBD-Report 1320, Duisburg Model Basin, Duisburg, Germany (in German)

24. Bertram, V. (1990), "Fulfilling open-boundary and radiation condition in free-surface problems using Rankine sources," Ship Techn. Res. 37/2, pp. 47-52.

25. Hughes, M. and Bertram, V. (1995), "A higher-order panel method for steady 3-d free-surface flows," IfS-Report 558, Univ. Hamburg, Germany

26. Kodama, Y. (1992), "Computation of ship's resistance using a NS solver with global conservation - Flat plate and Series 60 ($C_B=0.6$) hull," J. Soc. Naval Arch. Japan 172, pp. 147-156.

27. Baldwin, B. and Lomax, H. (1978), "Thin layer approximation and algebraic model for separated turbulent flows prediction code," AIAA Paper 78-257

28. Ishikawa, S. (1994), "Application of CFD to estimation of ship's viscous resistance - A series of full hull forms," Trans. West-Japan Soc. of Naval Arch. 87, pp. 81-92.

29. Hinatsu, M.; Kodama, Y.; Fujisawa, J.; Ando, J. (1994), "Numerical simulation of flow around a ship hull including a propeller effect," Trans. West-Japan Soc. Naval Arch. 88, pp. 1-12. (in Japanese)

30. Yamazaki, R. (1966), "On the theory of screw propellers in non-uniform flows", Memoirs of the Faculty of Engineering, Kyushu Univ., Vol 25/2

31. Kodama, Y. (1991), "Grid generation around a practical ship hull form using the implicit geometrical method," J. Soc. of Naval Arch. Japan 169, pp. 27-38. (in Japanese)

32. Toda, Y., Stern, F., and Longo, J. (1991), "Mean-flow measurements in the boundary layer and wake and wave field of a series-60 $C_B = .6$ ship model for Froude numbers .16 and .316," IIHR Rep. 352, Univ. of Iowa

33. Bertram, V. (1994), "Numerical shiphydrodynamics in practice," IfS-Report 545, Univ. Hamburg, Germany (in German)

34. Graf, K. (1992), "Calculation of viscous flow around barge-like ship hulls," Ship Techn. Res. 39/3, pp. 107-117.

DISCUSSION

H. Kajitani

Kumamoto Institute of Technology, Japan

May I congratulate the authors on an impressive paper which describes a hybrid method to simulate the force and flow around a ship in a shallow channel? The blending of RANSE after RSM seems quite effective by the reason that we can consider how the inviscid and viscous flow characteristics are playing their own important roles on the flow. From this point of view, we should have expected if possible a more detailed and step-by-step explanation though we admit a new tendency toward quick, short, and symbolic way of the presentations.

The authors compare the wave patterns in the deep and shallow water cases. However, the wave angle spreading out from bow (or even from stern) seems to be unchanged between deep water and shallow water. This is, of course, due to the low Fn case. I have much interest in widening of the wave pattern at high Fn (or $Fn_h = 0.64$) in shallow water case how early or late it comes out.

In Table II, the measured and evaluated (RSM) sinkage and trim are compared which show a so well coincidence. But I'm afraid whether there is room to accept viscous effect. If you evaluate the sinkage force by RANSE, you might get a pronounced downwards local frictional force on the ship fore part, and less effect around the aft part, you may obtain a more closer evaluation. In this case, however, trim by bow moment is also increased. With regard to trim moment, shear stress on the ship bottom surface does not have its counter part, so trim by bow is mainly caused by this frictional force and the towing height has decisive effect both on measurement and evaluation. I would like to know the towing height applied both in experiment and evaluation.

Regarding pressure coefficient C_p along the centerline of the channel bottom (Fig. 7), the prediction by CFD seems to be a little less estimate. In advanced RANSE procedures, the trim and sinkage at the latest iteration are included in the next calculation. Even though the authors' RANSE free surface grid does not seem to follow or express the local depression of mean free surface around the midship region. This means a relaxed flow continuity around midship, which implies a less prediction of the velocities also a less evaluation of the C_p . These have a decisive effect

on the resistance evaluation (Table III). In this connection, it is hard to accept the overestimated resistance coefficient in shallow water case. The authors' second reason (2 under prediction of blockage effect...), if corrected by taking the effect of free surface depression into account, may work out a further resistance increment. So we need a more careful approach.

Propulsion test simulation is, I believe, a challenging problem which seems to be yet at the beginning stage. In this case, to check the dipping at AP (usually measured at this station) seems to be a good index whether the simulation is done well or not. I appreciate very much your comments about this including measured results.

AUTHORS' REPLY

The considered depth Froude number does not yet lead to a considerable widening of the wave contour angle. However, the method is capable of capturing this phenomenon as demonstrated previously for an inland water vessel at depth Froude number 0.9 [16].

The sinkage is not very strongly affected by either viscous effects or the towing force. However, the remarks of Prof. Kajitani concerning their influence on trim are qualitatively correct. The towing force may be incorporated in the RSM but no information for the experimental condition was available. So we did not include this option. Tentative initial computations for the deep-water case showed only small influence of changing the towing force between still-water line and propeller height. The effect on trim is expected to increase with shallow water. However, as far as pressures on the channel bottom are concerned, the main influence will be sinkage. As the computations are already within the margin of uncertainty of the experiments for sinkage and trim, we did not focus our efforts on a further improvement of the method in the ability to predict trim and sinkage.

We agree with Prof. Kajitani that we should focus instead on improving the resistance prediction which at present does not satisfy our expectations. Small differences of trim and sinkage affect the accuracy of the resistance prediction, especially for shallow water. So, in order to improve the resistance prediction to the required degree, we may need a free-surface RANSE solver with sinkage and trim effect. As the problem of insufficient resistance prediction is shared by many other colleagues, it appears that we will need

considerable more shared research worldwide before we see consistently accurate resistance predictions for real ship geometries, especially for the more complicated shallow-water hydrodynamics.

The propulsion test simulations predicted trim and sinkage using the RSM without propeller action, i.e., the same trim and sinkage as for the resistance test. Admittedly this is crude, but it is better than the usual practice of taking the zero-speed design floating condition. We do not have measured results in addition to the ones published with the kind permission of the Duisburg Towing Tank. We share Prof. Kajitani's wish for further details to validate our computational procedures and hope that maybe ITTC may provide in the future such data.

Shock Waves in Cloud Cavitation

C. Brennen, G. Reisman, Y.-C. Wang (California Institute of Technology, USA)

ABSTRACT

This paper describes experimental and computational investigations of the dynamics of clouds of cavitation bubbles. Recent studies have confirmed that the interactions between bubbles as they are manifest in the dynamics of bubble clouds lead to the generation of very large impulsive pressures which, in turn, cause substantial enhancement of the radiated noise and the material damage which results from this form of cavitation.

The experimental program focuses on cloud cavitation formed on the suction surface of a hydrofoil, both static and oscillating. Piezo-electric transducers mounted at a series of locations on the suction surface measured very large positive pressure pulses with amplitudes of the order of tens of atmospheres and with durations of the order of tenths of milliseconds. Two distinct types of pressure pulse were identified from high-speed films: "local pulses" which are registered by individual transducers and appear to be associated with the propagation of localized bubbly shocks and "global pulses" which result from larger scale, coherent collapses of bubble clouds. The experiments investigate the effects of reduced frequency, cavitation number and tunnel velocity on the magnitude of these pressure pulses.

The computational component continues the earlier work of Wang and Brennen (1, 2), which presented numerical solutions of the growth and collapse of a spherical cloud of bubbles. This confirmed the idea put forward by Mørch and his co-workers who speculated that collapse of the cloud involved the formation of a bubbly shock wave on the surface of the cloud and that inward propagation and geometric focussing of this shock would

lead to very large localized pressure pulses. Here we review how the radiated acoustic pulses depend on the governing parameters such as the bubble population density, the cavitation number and the ratio of the bubble size to the cloud size.

Understanding such bubbly flow and shock wave processes is important because these flow structures propagate the noise and produce the impulsive loads on nearby solid surfaces in a cavitating flow. How these shocks are formed and propagate in the much more complex cloud geometry associated with cavitating foils, propeller or pump blades is presently not clear. However, by combining the computational and experimental observations, we suggest some specific mechanisms which may be active in the dynamics and acoustics of these more complex flows.

1. NOMENCLATURE

A	Radius of the bubble cloud
A_0	Initial radius of the bubble cloud
c	Chord length of foil (m)
C_p	Pressure coefficient, $(p - p_0)/\frac{1}{2}\rho U^2$
C_{pmin}	Minimum pressure coefficient
D	Reference body size
f	Frequency (Hz)
I	Acoustic impulse ($Pa.s$)
k	Reduced frequency, $\omega c/2U$
p	Fluid pressure (Pa)
p_0	Upstream reference pressure (Pa)
p_a	Radiated acoustic pressure (Pa)
p_v	Vapor pressure
r	Dimensionless Eulerian radial coordinate
r_0	Dimensionless Lagrangian coordinate

R	Bubble radius
R_0	Initial radius of the bubble
t^*	Time (s)
t	Dimensionless time, Ut^*/R_0
t_p	Duration of low pressure perturbation
T	Period of foil oscillation (s)
U_∞	Reference velocity of the flow (m/s)
V_{bmax}	Maximum total volume of bubbles in the cloud
α	Void fraction of the bubbly mixture
α_0	Initial void fraction of bubbly mixture
β	Cloud interaction parameter, $\alpha_0(1 - \alpha_0)A_0^2/R_0^2$
η	Bubble population per unit liquid volume
ρ	Density of the liquid
σ	Cavitation number, $(p_0 - p_v)/\frac{1}{2}\rho U^2$
μ_e	Effective dynamic viscosity of the liquid
ω	Foil oscillation frequency (rad/s)
ω_n	Natural frequency of single bubbles

2. INTRODUCTION

In many cavitating flows of practical interest one observes the periodic formation and collapse of a "cloud" of bubbles. This temporal periodicity may occur naturally as a result of bubble-filled vortical structures or it may be the response to a periodic disturbance imposed on the flow. Common examples of imposed fluctuations are (a) the interaction between rotor and stator blades in a pump or turbine or (b) the interaction between a ship's propeller and the non-uniform wake created by the hull. Much recent interest has focused on the dynamics and acoustics of finite clouds of cavitation bubbles because of the very destructive effects which are observed to occur when such clouds form and collapse in a flow (see, for example, Knapp (3), Bark and van Berlekom (4), Soyama *et al.* (5)). Many authors such as Wade and Acosta (6), Bark and van Berlekom (4), Shen and Peterson (7, 8), Bark (9), Franc and Michel (10), Le *et al.* (11), Kubota *et al.* (12, 13), Hart *et al.* (14), McKenney *et al.* (15), Reisman *et al.* (16) and de Lange *et al.* (17) have studied the complicated flow patterns involved in the production and collapse of a cavitating cloud on a hydrofoil.

Analytical studies of the dynamics of cavitation clouds can be traced to the work of van Wijngaarden (18) who first attempted to model the behavior of a collapsing layer of bubbly fluid next to a solid wall. Later investigators explored numerical methods which incorporate the individual bubbles

(Chahine (19)) and continuum models which, for example, analyzed the behavior of shock waves in a bubbly liquid (Noordzij and van Wijngaarden (20), Kameda and Matsumoto (21)) and identified the natural frequencies of spherical cloud of bubbles (d'Agostino and Brennen (22))). Indeed the literature on the linearized dynamics of clouds of bubbles has grown rapidly (see, for example, Omta (23), d'Agostino *et al.* (24, 25), Prosperetti (26)). However, apart from some weakly non-linear analyses (27, 28, 29) only a few papers have addressed the highly non-linear processes involved during the collapse of a cloud of bubbles. Chahine and Duraiswami (30) have conducted numerical simulations using a number of discrete bubbles and demonstrated how the bubbles on the periphery of the cloud develop inwardly directed re-entrant jets. However, most clouds contain many thousands of bubbles and it therefore is advantageous to examine the non-linear behavior of continuum models.

Another perspective on the subject of collapsing clouds was that introduced by Mørch, Kedrinskii and Hanson (31, 32, 33). They speculated that the collapse of a cloud of bubbles involves the formation and inward propagation of a shock wave and that the geometric focusing of this shock at the center of cloud creates the enhancement of the noise and damage potential associated with cloud collapse. Recently Wang and Brennen (1, 2) have used the mixture models employed earlier by d'Agostino *et al.* (22, 24, 25) to study the non-linear growth and collapse of a spherical cloud of bubbles. A finite cloud of nuclei is subjected to a temporary decrease in the ambient pressure which causes the cloud to cavitate and then collapse. The calculations clearly confirm the view of cloud collapse put forward by Mørch and his co-workers. In the present paper, we present some further information from spherical cloud calculations.

How bubbly shocks are formed and propagate in the much more complex and non-spherical geometries associated with cavitating foils, propeller or pump blades is presently not very clear. The present experiments have allowed identification of some specific shock structures whose details remain to be resolved and modelled.

3. EXPERIMENTS

This section describes an experimental investigation of the large unsteady and impulsive pressures which are experienced on the suction surface of a

hydrofoil as a result of cloud cavitation. Both stationary and oscillating foils are studied. Earlier measurements of noise produced by cloud cavitation are characterized by pressure pulses of very short duration and large magnitude (4, 7, 8, 9, 11, 15, 16). Previous experiments in the present series have described measurements of the acoustic signature of the cavitating cloud and related that to the observations of the unsteady cavitation (15); we have also explored the dependence of the sound magnitude on the cavitation number, σ , reduced frequency, k , and total air content (16).

The present experiments used piezo-electric transducers to measure unsteady pressures at four locations along the chord of the foil and at two locations along the walls of the tunnel test section. These transducers measured very large positive pressure pulses with amplitudes of the order of tens of atmospheres and with durations of the order of tenths of milliseconds.

Two distinct types of pressure pulse were identified. "Local" pulses occurred at a single transducer location and were randomly distributed in position and time; several local impulses could be recorded by each transducer during an oscillation cycle. On the other hand, "global" impulses were registered by all the transducers almost simultaneously. Correlation of the transducer output with high speed movies of the cavitation revealed that they were produced by a large scale collapse of the bubble cloud. The location of the global impulses relative to the foil oscillation impulses was quite repeatable and produced substantial far-field noise. The high speed movies also showed that the local impulses were caused both by crescent-shaped regions of low void fraction and by small bubbly structures. These regions appear to be bounded by bubbly shock waves which are associated with the large pressure pulses.

The paper also quantifies the effect of reduced frequency, cavitation number and tunnel velocity on the strength of the pressure pulses by presenting the acoustic impulse for a range of flow conditions. The reduced frequency is an important parameter in the determination of the total impulse level and the local and global pulse distribution. Large impulses are present on the foil surface even at cavitation numbers which do not result in large levels of acoustic radiation or global impulse. The total impulse increases almost universally with increasing tunnel velocity.

4. PROCEDURE

The experiments were conducted in the Low Turbulence Water Tunnel (LTWT) at Caltech, a closed-circuit facility with test section dimensions of $30.5\text{cm} \times 30.5\text{cm} \times 2.5\text{m}$ (35). A modified NACA 0021 hydrofoil (thickness increased between the mid-chord and the trailing edge) with a rectangular planform, a chord of 15.2cm and a span of 17.5cm , was reflection-plane mounted in the floor of the test section as described in Hart *et al.* (14). A 750w DC motor is connected to the foil by a four-bar linkage such that it oscillates in pitch about an axis near the center of pressure, 0.38 of a chord from the leading edge. The mean angle of attack, the oscillation amplitude and frequency (up to 50Hz) are adjustable. An optical shaft encoder mounted to the DC motor provides a digital signal which was used to correlate the foil motion with the acoustic measurements and the high speed movies.

The unsteady pressures generated by the cavitation on the hydrofoil were measured by several transducers. A PCB model HS113A21 piezo-electric pressure transducer (bandwidth 100kHz , face diameter 3mm) was mounted flush with the floor of the test section, 5cm downstream of the trailing edge of the foil (this is later denoted by #F). Another HS113A21 transducer was mounted in the tunnel ceiling at approximately the same axial location. Four PCB model 105B02 pressure transducers (bandwidth 50kHz) were recess-mounted inside the foil at locations 26% span from the foil root and 30%, 50%, 70% and 90% chord from the leading edge (denoted respectively by #1 through #4). By driving a transmitting hydrophone with a voltage impulse, the resonant frequencies of the transducer cavities were determined to be about 35kHz . These values are in good agreement with the Helmholtz resonant frequency of 38kHz calculated for the recess. Great care was taken to avoid the presence of air bubbles in the cavities and the impulse response testing was able to confirm their absence by detecting any change in the cavity resonant frequency. All data taken by the foil transducers was digitally low pass filtered at 20kHz to avoid any effect of cavity resonance. The transmitting hydrophone was also used along with a second receiving hydrophone to confirm the manufacturer's calibration of the foil transducers. The output signals from all six transducers were low pass filtered at 45kHz (to avoid aliasing) and recorded digitally at a sampling rate of 100kHz .

A good measure of the magnitude of the collapse pulses contained in the transducer output is the

acoustic impulse, I (36, 37), defined as the area under the pulse or

$$I = \int_{t_1}^{t_2} p_a(t) dt \quad (1)$$

where t_1 and t_2 are obtained from a threshold crossing method to identify the beginning and end of the pulse. A threshold of 20 kPa was used for the floor and ceiling transducers while 200 kPa was used for the foil surface transducers.

High speed movies with a framing rate of 500 fps were taken to assist in the interpretation of the pressure transducer output. These movies were synchronized with the unsteady pressure measurements by triggering a timing light simultaneously with data acquisition commencement.

The data presented here were obtained from 40 samples at each operating condition where a single sample is defined by either one oscillation cycle or a 0.066 s time period in the case of the static foil experiments. The mean angle of attack was 5° , the oscillation amplitude was 5° . The foil was fixed at an angle of attack of 5° during the static foil experiments. Experiments were performed at cavitation numbers of 0.85, 0.95, and 1.05, at tunnel velocities of 7.5 m/s , 8 m/s and 8.5 m/s and at reduced frequencies of 0, 0.76, 1.00 and 1.22. The total air content was 9.3 ppm for the oscillating foil experiments and 8.2 ppm for the static foil experiments.

6. CAVITATION STRUCTURE

A typical set of output signals from the transducers is shown in figure 1 which represents a single foil oscillation cycle with the origin corresponding to the maximum angle of attack. The output signals are characterized by very large amplitude pressure pulses of very short duration. As exemplified by figure 1, the magnitudes of these pulses are of the order of tens of atmospheres with typical durations of the order of tenths of milliseconds. As previously described by Reisman *et al.* (16), the radiated acoustic pressure also contains pressure pulses which are illustrated by the bottom trace in figure 1. The magnitude of these pulses measured by the transducer in the tunnel floor is only on the order of one atmosphere. The closest approximation to the far field pressure is that measured by the transducer in the ceiling of the tunnel test section; this also contains impulses, but these pulses were of less than 10 kPa in amplitude. Although these

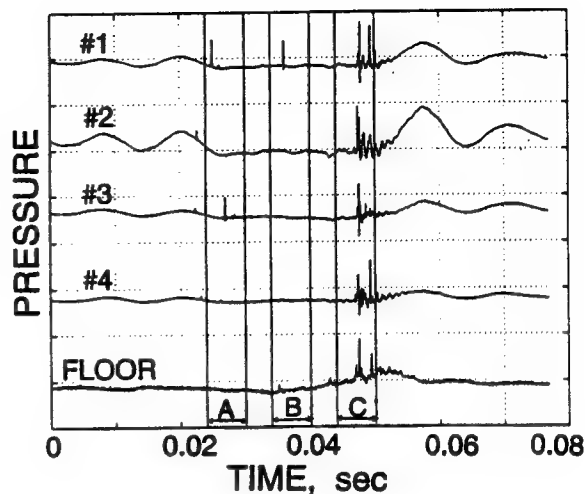


Figure 1: Typical transducer output during a single foil oscillation cycle. The top four traces are from the foil surface transducers and are numbered from the leading edge. The bottom signal is from the transducer mounted in the tunnel floor. The vertical axis scale is 1 MPa/div. for the foil surface transducers and 100 kPa/div. for the floor transducer. This typical data is for $\sigma = 0.95$, $k = 0.78$, $U = 8 \text{ m/s}$.

far field measurements are affected by both the directional dependence of the ceiling transducer and the tunnel test section acoustics, it is clear that there are order of magnitude differences in the amplitudes of the pulses measured on the foil, near the cavitating region and in the far field, respectively.

The low frequency variation present in the signal prior to the 0.025 s mark and after the 0.05 s mark was also observed at high cavitation numbers when the foil was fully wetted. This part of the signal is probably the result of stresses in the foil which are communicated through the transducer casings. This speculation is supported by the virtually instantaneous propagation of the low frequency disturbance and by the observation of similar signals even when the foil was oscillating in air.

Two different types of pressure pulses were identified and can be illustrated by figure 1. The pulses occurring before the 0.04 s mark are randomly distributed in time and space and are not repeated from cycle to cycle. We refer to these as *local* pulses. The pulses located between the 0.04 s and 0.05 s marks occur virtually simultaneously, are of

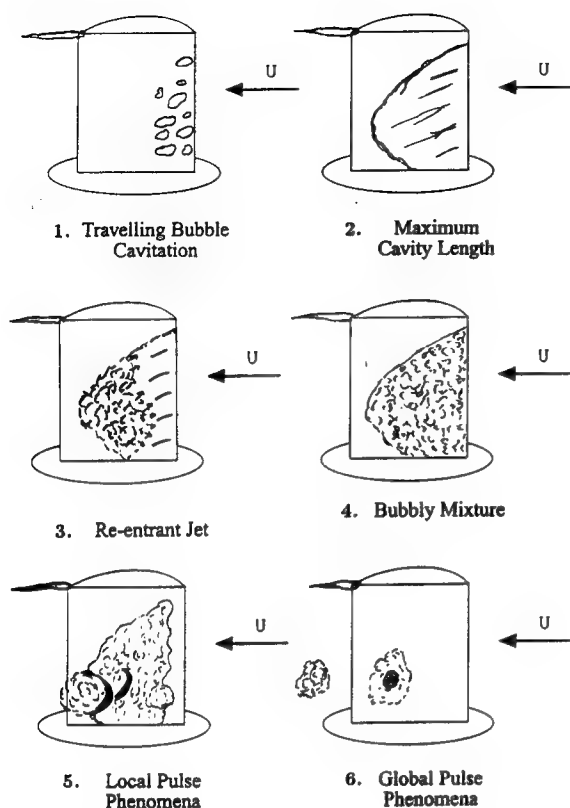


Figure 2: Cavitation structures observed during a single oscillation cycle. The angle of attack increases from sketch 1 to a maximum at sketch 2 and then decreases to a minimum at sketch 5.

higher amplitude and are repeated each cycle. We refer to these as *global* pulses; they produced substantial far-field noise and the location of the global impulses relative to the foil oscillation was quite repeatable.

The distinction between these two types of pressure pulse can be further elucidated by examining the high speed movies. These movies indicate that local pulses are caused by local disturbances in the cavitation structure while global pulses are generated by a larger scale cloud cavitation collapse.

The various stages of the cavitation observed during a single oscillation cycle are depicted in figure 2. Inception occurs in the tip vortex and is soon followed by travelling bubble cavitation in the area of C_{pmin} . As the angle of attack increases, the bubbles coalesce into a single attached cavitation sheet which attains its maximum length as the angle of attack reaches a maximum. At this point, a re-entrant liquid jet penetrates the attached cavity from the downstream edge and propagates toward

the leading edge of the foil. This re-entrant jet mechanism was first described by Knapp (3) and further explored in the work of Lush and Skipp (38), Kubota *et al.* (13), and de Lange *et al.* (17). The current observations, however, indicate that the process which occurs after the passage of the re-entrant jet is critical since the large pressure pulses are detected after the jet has reached the foil leading edge. The re-entrant jet breaks up the attached sheet cavity into a bubbly mixture which detaches from the foil surface and accelerates downstream. Local disturbances in the bubbly mixture are then observed and these structures have been correlated with the production of local pressure pulses, as explained in further detail below. Finally, the remains of the sheet cavity form a cloud of bubbles that undergo a coherent collapse as they are convected downstream. As shown later in this paper, this collapse results in only a slight change in the cloud radius but a large change in void fraction which propagates from the cloud perimeter to the cloud center.

Three specific intervals during the oscillation cycle are indicated in figure 1. Time interval *A* contains a local pulse in foil surface transducer #3. The cause of this pulse can be deduced from the high speed movie frames in figure 3. The downstream edge of the crescent shaped region of low void fraction indicated by the arrow passes over transducer #3 between the two frames. The existence of this type of transient flow structure is a common occurrence during the detachment of a cavitation cloud from a sheet cavity as noted by Shen and Peterson (7), Bark (9), and McKenney and Brennen (15). Examination of other high speed movies indicates the presence of a local pulse whenever the downstream edge of such a low void fraction structure passes over a transducer, and this observation is consistent with those of Shen and Peterson (7). The transducer located near the trailing edge is an exception to this rule, but the cavitating region might be separated from the foil surface at this location. The boundaries of these low void fraction regions are observed to move either in the upstream or downstream direction relative to the bubbly flow as the region expands. We emphasize that the crescent-shaped regions and their associated pressure pulse were observed with both the stationary and oscillating foil.

Time interval *B* and the corresponding movie frames of figure 4 contain a second kind of local pulse phenomena. The local pulse in the output from transducer #1 corresponds to the passage of



Figure 3: Crescent shaped flow structure of low void fraction. Consecutive high speed movie frames taken during time interval *A* of figure 1.

Figure 4: Local pulse generated by a small bubbly structure. Consecutive high speed movie frames taken during time interval *B* of figure 1.

the upstream boundary of a local cavitation cloud indicated by the arrow in figure 4. Other movie and pressure data also show the presence of a local pulse when the upstream edge of a small bubbly structure passes the transducer. These local structures are created when the sheet cavity detaches from the foil. As with the first type of local pulse, this second type is observed during a transition from a region of high void fraction to a region of low void fraction. The transitions which cause both types of local pulses are discrete and geometrically coherent.

Region *C* of figure 1 and the frames of figure 5 are representative of a global pulse. The cavitation cloud just upstream of the foil trailing edge undergoes a rapid and complete collapse between the two frames of figure 5. The collapse of this region radiates a pressure pulse which is detected

by all of the foil transducers and the transducer located in the tunnel floor. It should be noted that this cloud collapse is similar to that calculated by Wang and Brennen (1, 2) in that it does not involve large changes in the overall dimensions of the cloud; rather collapse involves large changes in the void fraction within the cloud.

A typical set of output signals from the transducers during the static foil experiments is shown in figure 6. The magnitude of the observed pulses is much lower than those measured while the foil was oscillating; they were typically only a few atmospheres in amplitude. There was a substantial reduction in the radiated noise, and only local events were observed. No global pulses were produced when the foil was stationary. The shedding of bubble clouds from the downstream edge of the attached cavity was not characterized by any par-



Figure 5: Global cloud collapse. Consecutive high speed movie frames taken during time interval *C* of figure 1.

ticular frequency; rather the clouds were detached in a continuous process.

7. IMPULSE MEASUREMENTS

The experimental results depicted in figures 7 through 11 illustrate the variation of the average acoustic impulses with reduced frequency, cavitation number and tunnel velocity for both the static and the oscillating foil. In each figure the calculated impulses are presented for both the global and local pressure pulses detected by the four foil mounted transducers and the transducer located in the tunnel test section floor. Each average acoustic impulse presented in the figures is based on data collected during 40 individual foil oscillation cycles.

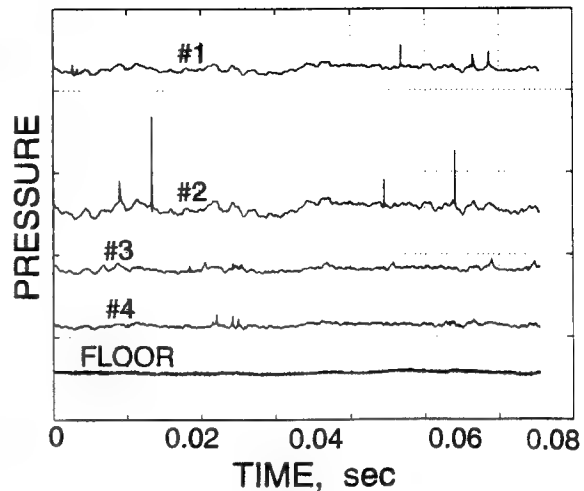


Figure 6: Typical transducer output during static foil experiments. The top four traces are from the transducers mounted on the foil and are numbered from the leading edge. The bottom signal is from the transducer mounted in the tunnel floor. The vertical axis scale is 500 *kPa*/div. for the foil surface transducers and 50 *kPa*/div. for the floor transducer. This typical data is for an angle of attack of 5°, $\sigma = 0.85$, $U = 8\text{ m/s}$.

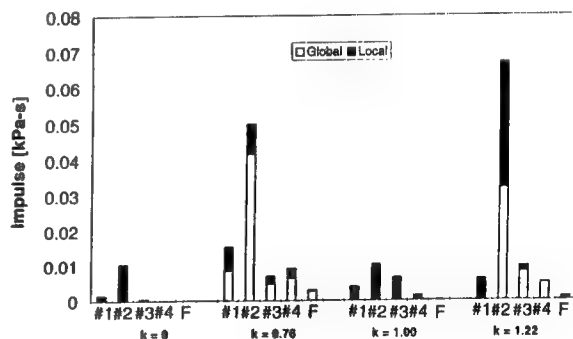


Figure 7: Effect of the reduced frequency, k , on the impulse, I . Data for $\sigma = 0.95$ and $U = 8\text{ m/s}$.

Figure 7 illustrates the variation in the magnitudes of the local and global impulses with reduced frequency at a constant cavitation number, σ , and tunnel velocity, U . Note that, with the exception of #2 at $k = 1.22$, the magnitudes of the local

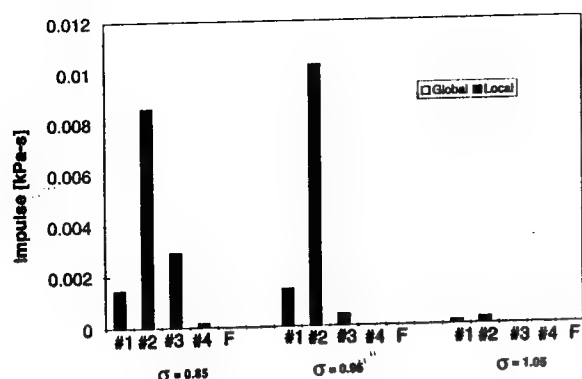


Figure 8: Effect of cavitation number, σ , on the impulse, I . Data for the static foil at an angle of attack of 5° and $U = 8\text{m/s}$.

impulses are quite independent of the reduced frequency and are therefore similar for the static and oscillating foils. On the other hand global impulses are virtually non-existent with the static foil under the conditions of figure 7. On the oscillating foil, there appears to be a broad range of reduced frequencies around unity in which the coherent collapses associated with global pulses are triggered. As seen in figure 7, there also appear to be specific frequencies like $k = 0.76$ and $k = 1.22$ which seem to produce the maximum global impulses. This general pattern of variation with reduced frequency is similar to that seen in the radiated noise by McKenney and Brennen (15) and Reisman *et al.* (16); note that the radiated noise measured by the floor transducer is only substantial when global pulses are present. We also note from figure 7 that the spatial distribution of the measured impulses is similar for all reduced frequencies; they tend to be larger at mid-chord where the sheet cavitation breaks up and collapses.

Figures 8 and 9 illustrate the variations in the impulses with the cavitation number, σ , for the static and oscillating foils, respectively. With the static foil the local impulses appear rather suddenly when σ is reduced below about 1.00. The largest impulses occur near transducer #2, close to the cavity closure region; however, as σ is decreased to 0.85 the values at #3 increase as the cavitation collapse extends to that location. Le *et al.* (1993) also noted that the largest pulses on their static foil occurred near cavity closure.

When the foil is oscillating, the global impulses produced are also very sensitive to changes in cavitation number with the largest global impulses

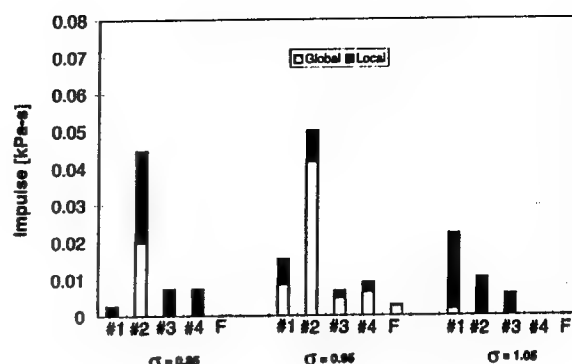


Figure 9: Effect of the cavitation number, σ , on the impulse, I . Data for the oscillating foil with $k = 0.76$ and $U = 8\text{m/s}$.

occurring in the middle of the cavitation number range. A similar effect was detected in the radiated impulses by McKenney and Brennen (15) and Reisman *et al.* (16), but the occurrence of cloud cavitation in the present experiments is more sensitive to changes in σ , perhaps due to the larger thickness of the present foil.

It is important to note that extremely large local pressure pulses occur at cavitation numbers which do not produce global shocks. An average local acoustic impulse in excess of $0.025\text{kPa}\cdot\text{s}$ is observed on #2 in figure 9 at $\sigma = 0.85$. This flow condition is characterized by sheet cavitation which extends well beyond the trailing edge of the foil and does not produce large radiated pressure pulses outside of the cavitating region.

Both with the static foil and with the oscillating foil (at high cavitation numbers), large local impulses occur on the foil surface without any substantial radiated impulse being registered by the floor transducer. This suggests that significant cloud cavitation damage could occur on a foil which is not exhibiting large acoustic radiation. Conversely, global pulses always produce substantial radiated noise which is registered by the floor transducer.

The effects of the magnitude of the tunnel velocity are illustrated in figures 10 and 11 for the static and oscillating foils, respectively (in the latter case, since the foil oscillation frequency was held constant at 12.7Hz , there is also a small variation in the reduced frequency as the tunnel velocity changes). With the static foil, the local impulses increase rapidly with increasing velocity as one would expect since cavitation noise normally scales with the velocity raised to some large power.

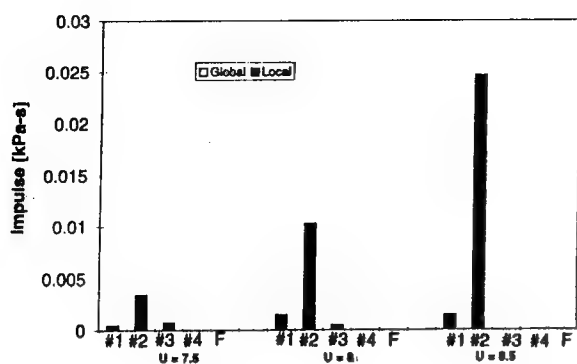


Figure 10: Effect of tunnel velocity, U , on the impulse, I . Data for a fixed angle of attack of 5° and $\sigma = 0.95$.

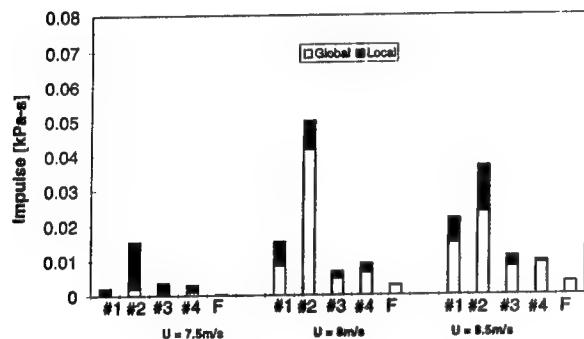


Figure 11: Effect of the tunnel velocity, U , on the impulse, I . Data for $\sigma = 0.95$ and $0.72 < k < 0.81$.

Note again the predominance of events near transducer #2. The imposition of oscillation changes this pattern. Note in figure 11, that the total impulse increases as the tunnel velocity is increased at constant σ . This occurs at every measuring location with the single exception of the value measured by the #2 transducer at $U = 8.5 \text{ m/s}$. The almost universal increase is primarily due to a growth in the global acoustic impulse. Unlike the behavior with the static foil, the local impulse magnitudes remain fairly constant as the tunnel velocity is changed.

8. GLOBAL PULSE PROPAGATION

By examining the time delays in the global pulse signals from the five transducers (four foil surface

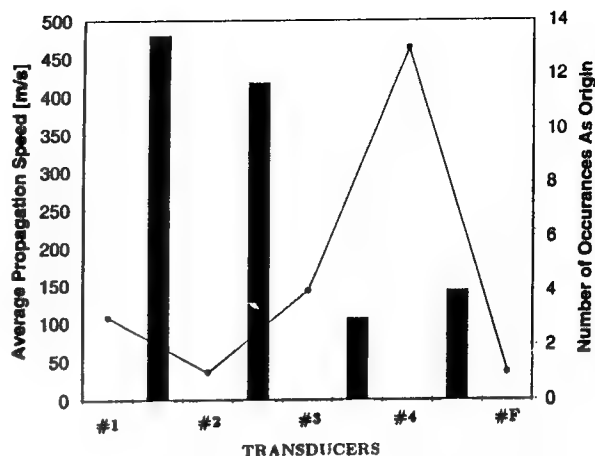


Figure 12: Speed of propagation and location of the origin of the global pressure pulses. Data for $\sigma = 0.95$, $k = 0.76$, $U = 8 \text{ m/s}$.

and the floor transducer) it was possible to extract some information on the location of the origin of the global pulses and on the speed of propagation of that pulse. This was accomplished by measuring the time intervals between peak occurrences in the transducer outputs for 41 events observed at one particular flow condition. The results of these calculations are shown in figure 12. The bar graphs represent the speeds of propagation between neighbouring transducers as calculated from the observed time intervals (the one on the right is the calculated speed between #4 and the floor transducer, #F). In all cases, the propagation speeds are a fraction of the sonic speed in either the pure liquid or pure vapor phase. The speeds calculated for the first two intervals are approximately 3.5 times as fast as those measured for the two downstream intervals. This difference is consistent with the void fraction distribution observed immediately after global cloud collapse. As shown in figure 2 and the photographs, the void fraction increases sharply downstream of the third foil transducer since the sheet cavitation remains have been carried away from the leading edge of the foil prior to the global cloud collapse.

The approximate origins of the global pulses were calculated by noting which transducer registered the earliest global pulse. The results of this tabulation are depicted by the line in figure 12. The global pulses most frequently originated near the fourth foil transducer; this is consistent with the high speed movie observations.

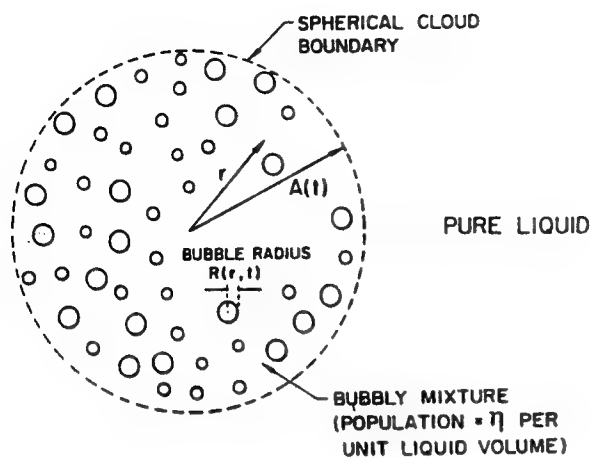


Figure 13: Schematic of a spherical bubble cloud.

9. THEORETICAL ANALYSES

We turn now to some results obtained by studying the dynamics and acoustics of cavitating clouds of bubbles. The investigations incorporate the interactive effects that the cavitating bubbles have on themselves and on the pressure and velocity of the liquid flow by coupling the conventional mass and momentum equations for the flow with the Rayleigh-Plesset equation for the bubble radius. The model is non-barotropic but homogeneous and neglects, for simplicity, the relative motion between the bubbles and the liquid. The basic equations are same as those used earlier by d'Agostino and Brennen (22, 24, 25) except that all the nonlinear terms are retained.

10. DYNAMICS OF A SPHERICAL CLOUD

We examine the dynamics of a spherical cloud of bubbles in an unbounded liquid which is at rest at infinity (figure 13). The pure liquid is assumed incompressible, with a density ρ_L . Since relative motion and the mass transfer between the two phases are neglected, it follows that if the population of bubbles per unit liquid volume, η , within the cloud, is uniform initially and if there is no coalescence or break-up then η is both constant and uniform within the cloud.

Some typical numerical results for the response of the spherical cloud are shown in figures 14 through and 18. These assume the properties typical of $R_0 = 100\mu\text{m}$ bubbles in a water flow at

20°C with a velocity of $U = 10\text{m/s}$. An effective liquid viscosity, μ_e , is employed in the Rayleigh-Plesset equation in order to model all the contributions to the bubble damping (39). The cloud is assumed to originate from a cloud of nuclei in equilibrium and to be convected through a simple sinusoidal pressure depression whose depth is given by C_{pmin} and whose duration is defined by t_p (consequently the length, D , of the low pressure region is given by $D = Ut_p$). Results were obtained for various cavitation numbers, σ , and initial void fractions, α_0 ; other important parameters are A_0/R_0 , D/R_0 , C_{pmin} , etc.

The characteristic cloud dynamics were found to be strongly dependent on the "cloud interaction" parameter, $\beta = \alpha_0(1 - \alpha_0)A_0^2/R_0^2$. When $\beta \gg 1$, that is at larger void fraction, bubble growth is severely restrained due to the strong bubble/bubble interaction effect. Under these circumstances the bubble growth rate within the cloud is quite uniform and all bubbles away from a near-surface region grow to about the same maximum size, as illustrated in figure 14.

Figure 14 presents typical bubble time histories for $\beta \gg 1$ at various Lagrangian locations within the cloud, from the surface, $r_0 = A_0$, to the cloud center, $r_0 = 0$. The shielding of the interior bubbles by the outer shell of bubbles is readily apparent in these results (see also 23, 25, 30). Note the formation and inward propagation of a shock wave whose typical structure is illustrated in figure 15. This structure which involves a series of rebounds and secondary collapses, is very similar to that of the gas/liquid shocks investigated by Noordij and van Wijngaarden (20) and Kameda and Matsumoto (21). The pressure pulse increases in amplitude as the shock propagates inwards and is focussed geometrically. Thus the pulse is large when the shock reaches the center of the cloud. The time history of the radius of the cloud is shown in figure 16. Note that, unlike single bubbles, the cloud radius, $A(t)$, only decreases to a size marginally smaller than its equilibrium size during the collapse process. On the other hand, when β is of order unity or less, the bubbles tend to behave as they would in an infinite fluid and, as illustrated in figure 17 (for which $\beta \approx 3$), the behaviour of the cloud is quite different under these circumstances. Then collapse occurs first at the cloud center and propagates out as an innocuous expansion wave. The resulting acoustic impulse is much smaller than when $\beta \gg 1$. Other parameters such as the ratio of initial bubble size to cloud size, R_0/A_0 , and the ratio

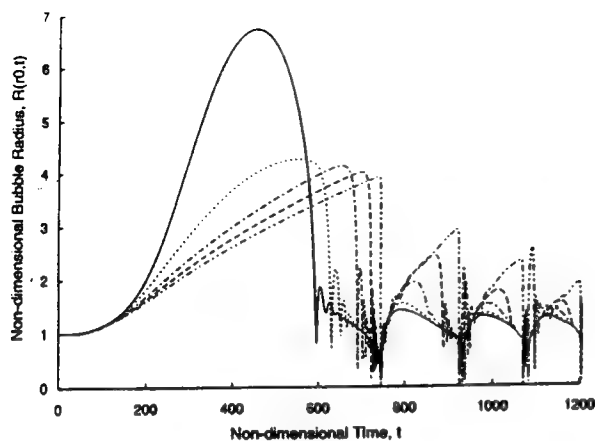


Figure 14: The time history of the dimensionless bubble size at five different positions in the cloud; $r_0 = 0$ (dash-dot-dot line), $r_0 = 0.5A_0$ (dashed line), $r_0 = 0.7A_0$ (dash-dot line), $r_0 = 0.9A_0$ (dotted line), and $r_0 = A_0$ (solid line). Parameters used are $\sigma = 0.45$, $C_{pmin} = -0.75$, $\alpha_0 = 3\%$, $A_0 = 100$, and $D/A_0 = 5$ (corresponds to $t_p = 500$).

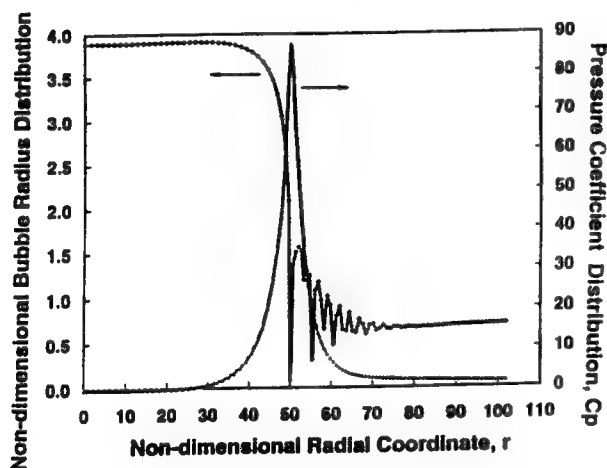


Figure 15: The bubble size distribution and pressure coefficient in the cloud as a function of the cloud radius at the dimensionless time, $t = 733.56$, for the case of figure 14.

of the initial cloud size to the dimension of the low pressure region, A_0/D , were exercised in order to explore the range of possible phenomena.

Wang and Brennen (1, 2) also examined the acoustic consequences of the shock wave. The normalized acoustic far-field noise, p_a , was calculated

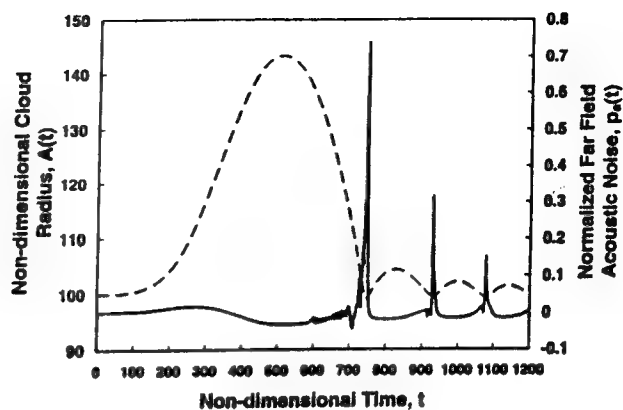


Figure 16: The time history of the dimensionless cloud radius, A/R_0 (dashed line), and the far field cloud acoustic noise (solid line) for the case of figure 14.

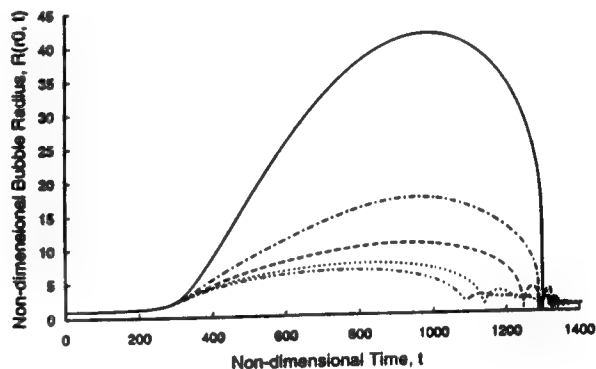


Figure 17: The time history of the dimensionless bubble size at five different positions in the cloud; $r_0 = 0$ (dash-dot-dot line), $r_0 = 0.3A_0$ (dotted line), $r_0 = 0.5A_0$ (dashed line), $r_0 = 0.7A_0$ (dash-dot line), and $r_0 = A_0$ (solid line). Parameters used are $\alpha_0 = 0.03\%$, $D/A_0 = 10$ or $t_p = 1000$. Other parameters as in figure 14.

from the volumetric acceleration of the cloud using

$$p_a(t) = \frac{2R_0}{D} \left[A^2(t) \frac{d^2 A(t)}{dt^2} + 2A(t) \left(\frac{dA(t)}{dt} \right)^2 \right] \quad (2)$$

where the normalizing length scale was chosen to be the length of the low pressure region, D . The first shock focus, which induces a large volumetric acceleration in the far-field cause a very large peak in the radiated acoustic noise as illustrated in figure

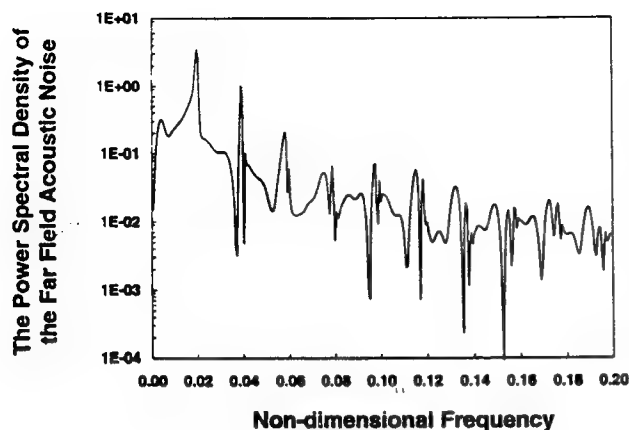


Figure 18: A non-dimensional power spectral density of the far field acoustic noise. In this case, the lowest cloud natural frequency of cloud is about 0.02. The natural frequency of a single bubble is 0.158.

16. The magnitudes of the subsequent peaks in each cloud collapse and rebound cycle may decay rapidly or slowly, depending on the collapse mode of the cloud. After several cycles, the cloud begins to oscillate at its natural frequency (22, 25).

A typical non-dimensional power spectral density of the acoustic noise is shown as a function of dimensionless frequency in figure 18. This spectrum exhibits the f^{-2} behavior for the frequency range below 0.25 (25kHz) which is typical of cavitation noise (see, for example, Arakeri and Shangu-manathan (40), Blake *et al.* (41)). Other cases exhibited a f^{-n} behavior with n in the range of $0.5 \rightarrow 2$. Some spectra also have large peaks at the natural frequency of the cloud and its higher harmonics. These are contributed by the regular oscillations of the cloud which can occur toward the end of the collapse and rebound process. In the case of figure 18, the first natural frequency of cloud is about 0.02 (2kHz) whereas the natural frequency of a single bubble in the cloud is 0.158 (15.8kHz).

The acoustic impulses (see equation (1)) from calculations using a wide variety of parameter choices (45 permutations) are found to be linearly correlated with the maximum total volume of the bubbles in the cloud normalized by the length of the low pressure perturbation, $V_{bmax}/(0.5D)^3$, as shown in figure 19. However, we should note that $V_{bmax}/(0.5D)^3$ decreases with increasing cavitation number and with increase in the initial void fraction, α_0 .

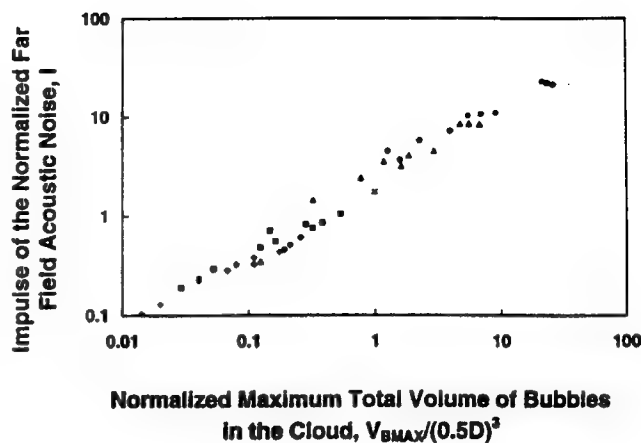


Figure 19: The impulse of the normalized far field acoustic noise correlated with the normalized maximum total volume of bubbles in the cloud at different ratios of the length scale of the low pressure perturbation to the initial radius of the cloud, D/A_0 , (31.25 = solid Δ , 15.625 = +, 10 = \diamond , 5 = solid \square , 3.125 = \times , 1 = \triangle , 0.5 = \bullet).

Thus it would appear that an understanding of the collapse shock dynamics and acoustics has important consequences and implications for the scaling of cloud cavitation noise and damage.

11. CAVITATION CLOUD COLLAPSE

Thus we have seen how a shock wave develops as part of the non-linear collapse of a spherical cloud of cavitation bubbles. The focusing of shock produces very high pressures at the center of the cloud and then causes rebound of the cloud. The volumetric acceleration induces a large pulse in the far-field noise. Moreover, there are further but weaker shocks which arrive at the center and thus produce a train of acoustic impulses which, eventually, lead to a regular oscillation of the cloud at the first cloud natural frequency. These results suggest that shock focusing may be one of the major mechanisms for the enhanced noise and damage potential associated with cloud cavitation.

The characteristic cloud dynamics are shown to be strongly dependent on the parameter $\beta = \alpha_0(1 - \alpha_0)A_0^2/R_0^2$ where α_0 is the initial void fraction, A_0 is the initial cloud radius and R_0 is the initial bubble radius. Two modes of collapse have been identified. At large values of this parameter, the collapse involves the formation of an inward propagating shock wave which initially forms

at the surface of the cloud. This shock dominates this first mode of collapse and strengthens rapidly due to geometric focusing and the coupling of the bubble dynamics with the flow. In this mode, a large pulse in the far-field noise is produced by the arrival of the shock at the cloud center. Moreover, there are further but weaker shocks which arrive at the center and thus produce a train of acoustic impulses which, eventually, leads into a regular oscillation of the cloud at the first cloud natural frequency.

A different mode of collapse occurs at low values of β . Then the shielding effects of the outer bubbles causes the bubbles in the core of the cloud to grow to a smaller maximum size and to collapse first. This creates an outward moving collapse front and a very different mode of collapse than occurs at high β . At intermediate values, we observe cases where collapse first occurs at an intermediate radius and collapse fronts then propagate both outward and inward from this location.

We have also correlated the far-field acoustic impulse produced in all these cases with the parameters of the problem. It was found that the impulse is strongly correlated with the maximum total volume of bubbles in the cloud. Moreover, this total volume decreases with increasing cavitation number and with increasing void fraction. It also varies with D/A_0 where D is the typical length of the low pressure perturbation.

12. DISCUSSION

This paper has examined the large positive pressure impulses which occur on the surface of a hydrofoil during cloud cavitation; both static and oscillating foils were investigated. The pulses were shown to have magnitudes on the order of tens of atmospheres with typical durations of the order of tenths of milliseconds. Pressure pulses of similar magnitude were observed by Le *et al.* (11), who measured pulse magnitudes of up to 7 MPa on a stationary foil at $\sigma = 0.81$, $U = 12\text{ m/s}$ and an angle of attack of 4.8° . Their experiments used flush-mounted transducers with face diameters of 1 mm and bandwidths over 300 kHz.

However, these pulse magnitudes are significantly greater than those measured by Shen and Peterson (7) who detected pulses with magnitudes comparable to the dynamic pressure, (up to 110 kPa). There are at least two explanations for this discrepancy. Both the amplitude of foil oscillation (up to 1.55°) and the mean angle of attack

(3.25°) were significantly less than those of the current experiments. Also, the transducers used by Shen and Peterson (7) had a bandwidth of only 2 kHz. The short duration impulses measured in our experiments have a broadband frequency content with substantial contributions above 2 kHz.

The radiated pulse magnitudes measured by Bark (9) and Bark and van Berlekom (4) were on the order of tens of kPa, but these were measured off the foil surface. These are similar to our far field measurements but are significantly smaller than the impulse amplitudes measured by the transducer mounted in our water tunnel floor. This reduction in amplitude may be attributed to the significantly lower velocities of the Bark and van Berlekom experiments which were performed at 5 m/s. It should be noted that our surface pressure measurements are several orders of magnitude lower than the massive impulses observed by Avellan and Farhat (34) which averaged 900 MPa in amplitude with extreme values as high as 2200 MPa.

High speed movies indicated the presence of a re-entrant jet which, as previously described by Knapp (3) and a number of recent investigators, penetrates the sheet cavity as the cavity reaches its maximum length. The jet then breaks the cavity into a bubbly mixture which detaches from the foil surface. In the present study, pressure pulses of either type were only detected after the passage of the re-entrant jet.

Furthermore, an examination of the movies led to the identification of two distinct types of pressure pulses. "Local" pulses, which are registered by a single transducer, are randomly distributed in time and space and are not repeated from cycle to cycle. Local pulses are caused at a given transducer location by the passage of either crescent-shaped regions of low void fraction or small bubbly structures. In either case, they are observed during a transition from a region of high void fraction to a region of low void fraction. The crescent-shaped regions are similar to the "depressions in the cavity surface" noted by Shen and Peterson (7) and the "deep inward buckling of the cavity interface" observed by Bark (9). The discrete boundaries of the crescent-shaped regions and the motion of these boundaries relative to the bubbly flow suggest that these boundaries are bubbly shock waves. The collapse of vapor bubbles within these waves could explain the large pressure impulses measured on the foil surface.

On the other hand, "global" pulses, which occur

almost simultaneously on all four transducers, are of higher amplitude, radiate substantial far field noise and are repeated at the same point of each oscillation cycle. Global pulses are caused by large scale cloud cavitation collapse and were not observed on the static foil.

By calculating the acoustic impulse, a quantitative measure of the effect of reduced frequency, k , cavitation number, σ , and tunnel velocity on the strength of the pressure pulses was obtained. The reduced frequency is an important parameter in the determination of the total impulse level and the local and global pulse distribution. The cavitation number has a significant effect on the global impulse strength, but large impulses are still present on the foil surface at values of σ where acoustic radiation is minimal and global pulses are rare or non-existent. The changes with tunnel velocity were significantly different for the stationary and oscillating foils. The local impulses on the stationary foil increased greatly with tunnel velocity and the global impulses on the oscillating foil did likewise. However, the local impulses on the oscillating foil did not change so dramatically with tunnel velocity. We also note that the spatial distribution of the impulse measurements, while highly influenced by the cavitation number, are virtually independent of the reduced frequency and tunnel velocity.

It seems clear that both the local and global surface pressure pulses could contribute to foil damage. Indeed, the very large magnitudes of these surface impacts could be responsible for the foil damage reported by Morgan (42), who observed trailing edges bent away from the suction surface and toward the pressure surface.

In order to shed some light on the experimental observations we have included results from calculations of the dynamics and acoustics of a spherical bubble cloud. These clearly confirm that shock wave formation is an integral part of the collapse of such a cloud provided the cloud interaction parameter, β , is of order one or greater. Fundamentally, this requires either the initial void fraction, α_0 , or the ratio of cloud size to bubble size, A_0/R_0 , be sufficiently large and this, in turn, is qualitatively in accord with the observation that cavitation must be quite extensive for the cloud phenomenon to be manifest. There is also a cautionary lesson to be drawn from the theoretical analysis. This concerns the scaling of cloud cavitation phenomena. Even if the nuclei have the same size, population and void fraction in the model and prototype, the cloud cavitation effects could be much larger in the prototype

due to the larger value of β .

Of course, most clouds are far from spherical. But, nevertheless the collapse of all or part of non-spherical clouds will produce points at which shock waves focus to produce large radiated pulses. However, it is not currently clear what three-dimensional forms the propagating shocks might take in the highly non-uniform bubbly environments which occur in real flows. The experimental observations do suggest that the bubbly region near the surface may act as a wave-guide for the propagation of the crescent-shaped shock structures associated with local impulses. But much clearly remains to be understood regarding these structures and their consequences.

ACKNOWLEDGEMENTS

We wish to thank John Van Deusen and Rodney Rojas for their help in fabricating the foil. The authors are also very grateful for the assistance provided by Amir Alagheband, Amy Herr, Don Kwak, Tricia Waniewski and Cecilia Lin. We are also deeply appreciative of the support of the Office of Naval Research who sponsored this research under grant number N00014-91-J-1295.

REFERENCES

1. Wang, Y.-C. and Brennen, C.E., "Shock wave development in the collapse of a cloud of bubbles," *ASME Cavitation and Multiphase Flow Forum*, 1994.
2. Wang, Y.-C. and Brennen, C.E., "The noise generated by the collapse of a cloud of cavitation bubbles," *ASME Symp. on Cavitation and Gas-Liquid Flows in Fluid Machinery and Devices*, 1995, FED-Vol. 226, pp. 17-29.
3. Knapp, R.T., "Recent investigation on the mechanics of cavitation and erosion damage," *Trans. ASME*, 1955, pp. 1045-1054.
4. Bark, G. and van Berlekom, W.B., "Experimental investigations of cavitation noise," *Proc. 12th ONR Symp. on Naval Hydrodynamics*, 1978, pp. 470-493.
5. Soyama, H., Kato, H. and Oba, R., "Cavitation observations of severely erosive vortex cavitation arising in a centrifugal pump," *Proc. Third I.Mech.E. Int. Conf. on Cavitation*, 1992, pp. 103-110.

6. Wade, R.B. and Acosta, A.J., "Experimental observations on the flow past a plano-convex hydrofoil," *ASME J. Basic Eng.*, 1966, Vol.88, pp. 273-283.
7. Shen, Y. and Peterson, F.B., "Unsteady cavitation on an oscillating hydrofoil," *Proc. 12th ONR Symp. on Naval Hydrodynamics*, 1978, pp. 362-384.
8. Shen, Y. and Peterson, F.B., "The influence of hydrofoil oscillation on boundary layer transition and cavitation noise," *Proc. 13th ONR Symp. on Naval Hydrodynamics*, 1980, pp. 221-241.
9. Bark, G., "Developments of distortions in sheet cavitation on hydrofoils," *Proc. ASME Int. Symp. on Jets and Cavities*, 1985, pp. 215-225.
10. Franc, J.P. and Michel, J.M., "Unsteady attached cavitation on an oscillating hydrofoil," *J. Fluid Mech.*, 1988, Vol. 193, pp. 171-189.
11. Le, Q., Franc, J.M. and Michel, J.M., "Partial cavities: global behaviour and mean pressure distribution," *ASME J. Fluids Eng.*, 1993, Vol. 115, pp. 243-248.
12. Kubota, A., Kato, H., Yamaguchi, H. and Maeda, M., "Unsteady structure measurement of cloud cavitation on a foil section using conditional sampling," *ASME J. Fluids Eng.*, 1989, Vol. 111, pp. 204-210.
13. Kubota, A., Kato, H. and Yamaguchi, H., "A new modelling of cavitating flows - a numerical study of unsteady cavitation on a hydrofoil section" *J. Fluid Mech.*, 1992, Vol. 240, pp. 59-96.
14. Hart, D.P., Brennen, C.E. and Acosta, A.J., "Observations of cavitation on a three dimensional oscillating hydrofoil," *ASME Cavitation and Multiphase Flow Forum*, 1990, FED-Vol. 98, pp. 49-52.
15. McKenney, E.A. and Brennen, C.E., "On the dynamics and acoustics of cloud cavitation on an oscillating hydrofoil," *Proc. ASME Symp. on Cavitation and Gas-Liquid Flows in Fluid Machinery and Devices*, 1994, FED-Vol. 190, pp. 195-202.
16. Reisman, G.E., McKenney, E.A. and Brennen, C.E., "Cloud cavitation on an oscillating hydrofoil," *Proc. 20th ONR Symp. on Naval Hydrodynamics*, 1994, pp. 78-89.
17. de Lange, D.F., de Bruin, G.J. and van Wijngaarden, L., "On the mechanism of cloud cavitation - experiment and modelling," *Proc. 2nd Int. Symp. on Cavitation*, 1994, pp. 45-49.
18. van Wijngaarden, L., "On the collective collapse of a large number of gas bubbles in water," *Proc. 11th Int. Conf. Appl. Mech.*, Springer-Verlag, Berlin, 1964, pp. 854-861.
19. Chahine, G.L. "Cloud cavitation theory," *Proc. 14th ONR Symp. on Naval Hydrodynamics*, 1982, p. 51.
20. Noordij, L. and van Wijngaarden, L., "Relaxation effects, caused by relative motion, on shock waves in gas-bubble/liquid mixtures," *J. Fluid Mech.*, 1974, Vol. 66, pp. 115-143.
21. Kameda, M. and Matsumoto, Y., "Structure of shock waves in a liquid containing gas bubbles," *Proc. IUTAM Symp. on Waves in Liquid/Gas and Liquid/Vapour Two-Phase Systems*, 1995, pp. 117-126.
22. d'Agostino, L. and Brennen, C.E., "On the acoustical dynamics of bubble clouds," *ASME Cavitation and Multiphase Flow Forum*, 1983, pp. 72-75.
23. Omta, R., "Oscillations of a cloud of bubbles of small and not so small amplitude," *J. Acoust. Soc. Am.*, 1987, Vol. 82, pp. 1018-1033.
24. d'Agostino, L. and Brennen, C.E., "Acoustical absorption and scattering cross-sections of spherical bubble clouds," *J. Acoust. Soc. of Amer.*, 1988, Vol. 84, No.6, pp. 2126-2134.
25. d'Agostino, L. and Brennen, C.E., "Linearized dynamics of spherical bubble clouds," *J. Fluid Mech.*, 1989, Vol. 199, pp. 155-176.
26. Prosperetti, A., "Bubble-related ambient noise in the ocean," *J. Acoust. Soc. Am.*, 1988, Vol. 84, pp. 1042-1054.
27. Kumar, S. and Brennen, C.E., "Non-linear effects in the dynamics of clouds of bubbles," *J. Acoust. Soc. Am.*, 1991, Vol. 89, pp. 707-714.

28. Kumar, S. and Brennen, C.E., "Harmonic cascading in bubble clouds," *Proc. Int. Symp. on Propulsors and Cavitation, Hamburg, 1992*, pp. 171-179.
29. Kumar, S. and Brennen, C.E., "Some non-linear interactive effects in bubbly cavitating clouds," *J. Fluid Mech.*, 1993, Vol. 253, pp. 565-591.
30. Chahine, G.L. and Duraiswami, R., "Dynamical interactions in a multibubble cloud," *ASME J. Fluids Eng.*, 1992, Vol. 114, pp. 680-686.
31. Mørch, K.A., "On the collapse of cavity cluster in flow cavitation," *Proc. First Int. Conf. on Cavitation and Inhomogenities in Underwater Acoustics, Springer Series in Electrophysics*, 1980, Vol. 4, pp. 95-100.
32. Mørch, K.A., "Cavity cluster dynamics and cavitation erosion," *Proc. ASME Cavitation and Polyphase Flow Forum*, 1981, pp. 1-10.
33. Hanson, I., Kedrinskii, V.K. and Mørch, K.A., "On the dynamics of cavity clusters," *J. Appl. Phys.*, 1981, Vol. 15, pp. 1725-1734.
34. Avellan, F. and Farhat, M., "Shock pressure generated by cavitation vortex collapse," *ASME Int. Symp. on Cavitation Noise and Erosion in Fluid Systems*, 1989, FED Vol.-88, pp. 199-125.
35. Gates, E. M., "The influence of freestream turbulence, freestream nuclei populations, and a drag-reducing polymer on cavitation inception on two axisymmetric bodies," *PhD thesis, Cal. Inst. of Tech.*, 1977.
36. Ceccio, S.L. and Brennen, C.E., "Observations of the dynamics and acoustics of travelling bubble cavitation," *J. Fluid Mech.*, 1991, Vol. 233, pp. 633-660.
37. Kuhn de Chizelle, Y., Ceccio, S.L. and Brennen, C.E., "Observations, scaling and modelling of travelling bubble cavitation," *J. Fluid Mech.*, 1995, Vol. 293, pp. 99-126.
38. Lush, P.A. and Skipp, S.R., "High speed cine observations of cavitating flow in a duct," *Int. J. Heat Fluid Flow*, 1986, Vol. 7, pp. 283-290.
39. Chapman, R.B. and Plesset, M.S., "Thermal effects in the free oscillation of gas bubbles," *ASME J. Basic Eng.*, 1971, Vol. 93, pp. 373-376.
40. Arakeri, V.H. and Shanmuganathan, V., "On the evidence for the effect of bubble interference on cavitation noise," *J. Fluid Mech.*, 1985, Vol. 159, pp. 131-150.
41. Blake, W. K., Wolpert, M. J. and Geib, F. E., "Cavitation noise and inception as influenced by boundary-layer development on a hydrofoil," *J. Fluid Mech.*, 1977, Vol. 80, pp. 617-640.
42. Morgan, W.B., personal communication, 1995.

Asymptotic Solution of the Flow Problem and Estimate of Delay of Cavitation Inception for a Hydrofoil with a Jet Flap

K. Rozhdestvensky, I. Belousov

(St. Petersburg State Marine Technical University, Russia)

ABSTRACT

In the present paper the method of matched asymptotic expansions is applied to treat the flow problem for a hydrofoil of arbitrary aspect ratio with a jet flap in the case of small magnitudes of the jet momentum coefficient. In the nearfield, i.e. in the vicinity of the trailing edge with a jet flap, the problem is reduced to a two-dimensional one. The relevant system of integro-differential equations, governing the local flow, is solved by means of Carleman inversion formulae and Mellin transforms. It is shown that for practical case of small jet momentum coefficients the farfield asymptotics of the local solution contains a square root singularity of hydrodynamic loading at the trailing edge, which is compatible with the "saddle-backed" character of the loading for a jet flapped wing observed in experiments. The matching principle not only prompts the increase of loading near the jet flapped trailing edge in inverse proportion to the square root of the distance from the edge, but also enables to express the strength of this singularity in terms of the jet deflection and momentum coefficient in corresponding cross sections of the wing spanwise. The outer description of the flow has been obtained through superposition of appropriate nonhomogeneous and homogeneous solutions of the integral equation of linear lifting surface theory. In case of the jet flap at the trailing edge the matching principle results in an additional condition, which plays the same role as a standard Kutta-Zhukovsky condition for a lifting surface without jet flap. Results are presented, illustrating dependence of the lift coefficient on the jet deflection angle and momentum coefficient, as well as upon the wing's

aspect ratio. In order to evaluate possibility of delay of cavitation inception minimum pressure diagrams are plotted with "edge branches" obtained from the local flow problem for the rounded edge and "bottom branches" - from linear theory with account of both lifting and thickness effects. Results are presented which show that for the same magnitude of the lift coefficient cavitation inception occurs later for the case of the lift induced by the jet flap as compared to the case of the incidence induced lift.

1. Introduction

The jet flap, formed by a high-speed jet of air or water injected from the trailing edge of the lifting surface, represents one of the effective devices of lift control accompanied by a drag reduction due to longitudinal component of the jet momentum, [1]. The possibility to increase lift by means of jet flap was demonstrated by Hager and Ruden (1938) in Germany. However, this demonstration did not evoke any interest until more extensive research work had been made at the National Gas Turbine Institute. Comprehensive survey of the evolution of this technical concept in historical retrospective can be found in [2]. Other aspects of application of the jet flap have been revealed and reported, concerning the possibility to delay cavitation inception for hydrofoils. As indicated in [3], application of the jet flap may become practical in development of high speed hydrofoil ships of large displacement of the order of 1,000 - 1,300 tonnes designed in the range of cruise speeds of 65 - 70 knots. The so called "law of square - cube" states that with increase of the ship's dimensions its weight increases in proportion

to the cube of its length, whereas for a given lift coefficient, the area of the lifting surfaces should be increased as a square of the ship's length. Therefore, to provide dynamic support of large hydrofoil ship one needs either to disproportionately increase the area of hydrofoils, or to increase the magnitude of the lift coefficient. The former measure results in heavy and "clumsy" hydrofoils whereas the latter measure normally requires an augmentation of the adjusted angle of attack and, consequently, leads to reduction of the speed range of noncavitating flow regime. Utilization of the jet flap, as follows from the article of Kaplan [3], allows to gain the same increment of lift as for the incidence induced lift case with diminution of the leading edge suction due to transition to the "saddle-backed" loading distribution. Kaplan and Goodman explored possibilities of utilization of jet flapped wings as anti-pitching devices, [4]. The same authors carried out experiments in water tunnel on symmetric hydrofoils with measurement of the lift and drag, estimation of required power and measurement of velocity distribution across the jet, [4]. In addition, Kaplan and Lehman conducted measurements of unsteady forces acting upon a wing due to unsteady variation of the jet deflection angle, in view of possible application to control surfaces of a submarine, [5].

One of the features of the flow problem for a lifting surface with a jet flap consists in a necessity to fulfil kinematic and dynamic boundary conditions upon the jet, the form of which is not known in advance. The important step in development of mathematical model of a jet flapped wing had been made by Spence in his research work [6], where the jet behind the wing was treated as a surface of tangential discontinuity, possessing a finite momentum and capable of withstanding pressure jump. In this and following publications [7], [8], [9] and [10]. Spence gave detailed analysis of the two-dimensional flow problem. Using linear theory, he replaced the wing and the jet by an equivalent vortex layer, distributed along the semi-infinite cut and subject to tangency condition on the foil as well as to kinematic and dynamic conditions upon the jet. The latter has been written as the requirement of proportionality of the pressure difference across the jet to its longitudinal curvature. The resulting mixed boundary problem had been solved by Spence, at first with use of Fourier expansions [6] and later on by means of the Mellin transform, [10]. Theoretical results of Spence are in fair agreement with experimental data up to sufficiently large magnitudes of the jet deflection angle of the order of 60° , which confirms the adequacy of the mathematical model of infinitely thin jet. Kuchemann [11] extended the approach of Spence to the case of the foil of small thickness and was able to calculate not

only the lift, but also pressure distributions on the upper and lower surfaces of the wing with jet flap. His calculated results confirmed that a typical loading distribution along the wing with a jet flap has a "saddle-backed" character with maxima both near the leading edge and the jet flap. The said loading distribution is essentially different from that for the foil without jet flap at an angle of attack. For the latter case there is only one peak of hydrodynamic loading near the leading edge. Comparing loading distributions for a wing with and without jet flap, one can easily conclude that for the same magnitude of the lift coefficient the maximum suction at the leading edge is lower for the jet flapped wing. With use of Fourier method Spence had calculated 9 terms of the series describing the strength of the vortex layer with a square root singularity at the leading edge and logarithmic singularity at the trailing edge. In a work [10] with use of the method of integral transforms an asymptotic expansion of the flow problem solution had been constructed for the case of small magnitude of the jet momentum coefficient. As a result the lift coefficient was found in the form

$$C_y = \frac{\partial C_y}{\partial \tau} \tau + \frac{\partial C_y}{\partial \alpha} \alpha$$

where

$$\frac{\partial C_y}{\partial \tau} = 4\sqrt{\pi\mu} \left\{ 1 - \frac{\mu}{2\pi} \ln \frac{\mu}{\beta} - \frac{\mu^2}{8\pi^2} \left[\left(\ln \frac{\mu}{\beta} \right)^2 + 4 \ln \frac{\mu}{\beta} - 4 \right] \right\},$$

$$\frac{\partial C_y}{\partial \alpha} = 2\pi \left[1 - \frac{\mu}{\beta} \left(1 + \frac{\mu}{\beta} \right) \ln \left(\frac{\mu}{\beta} - 1 \right) \right]$$

$$\beta = 4e^{\gamma_e}, \quad \mu = \frac{1}{4} C_j, \quad \gamma_e - \text{Euler constant}$$

To determine characteristics of a jet flapped wing Stratford [12] used an analogy between the wing with a jet flap and a wing with a mechanical flap. This approach resulted in an expression for the lift coefficient which for small values of the jet momentum coefficient was similar to that obtained by Spence in [6]. The work of Maskell and Spence [13] was the first where an attempt had been made to extend the approach of [6] to three-dimensional case. In [13] the flow problem for a wing of finite aspect ratio with a jet flap was formulated within linear theory of the lifting surface. Due to complexity of the problem the authors developed only approximate solution, based upon two-dimensional theory of Spence and assumption of uniform spanwise distribution of downwash which corresponds to elliptic loading along the span. As a matter of fact, the authors assumed that both local chord and momentum distribution along the span were elliptic for constant magnitudes of the incidence α and

jet deflection angle τ . Kerney [14] and Tokuda [15] considered the problem of the flow past a jet flapped wing of large aspect ratio by means of the method of matched asymptotic expansions. In Kerney's work the outer flow was modeled by a lifting line, and in the nearfield the problem was reduced to two-dimensional one, as treated by Spence. Matching of the farfield and nearfield descriptions of the flow gave the possibility to obtain closed expressions for coefficients of the lift, longitudinal moment and induced drag of the wing with a jet flap. Comparison with experimental data of Williams and Alexander, [16] for a flat wing of rectangular planform with no incidence and jet deflection angle $\tau = 31.3^\circ$ turned out to be quite good for a wing of aspect ratio $\lambda = 6.8$ and satisfactory for a wing of moderate aspect ratio $\lambda = 2.75$. It should be mentioned that, as pointed out by Tokuda [15], in Kerney's work no account had been taken of the fact that the lifting part¹ of the jet sheet, generally speaking, can extend into the outer flow region downstream of the trailing edge at distances of the order of $O(1)$. However, in our opinion, for small magnitude of the quantity $\tau\sqrt{C_j}$ the assumption, that the outer part of the trailing jet sheet can be treated as nonlifting one, should be valid. Tokuda [15] had made an attempt to introduce corrections, accounting for the influence of the lifting part of the jet sheet in the outer flowfield upon aerodynamics of the jet flapped wing. As follows from comparison of solutions of Kerney and Tokuda, the correction introduced by the latter author into the expression of the lift coefficient has the order of C_j/λ .

In the present paper there is considered a three-dimensional flow problem for a lifting surface of arbitrary planform and aspect ratio with a jet flap at the trailing edge. A linearized flow model is adopted in which for small incidences and jet deflection angles the system is supposed to produce small output of the same order. Such mathematical model, as shown through comparisons of existing experimental and theoretical data is valid for small angles of attack, but in surprisingly large range of the jet deflection angles. Such an "inequality" of parameters α and τ in what concerns correlation of calculated and measured results can be attributed to the fact that critical flow phenomena, such as separation from the leading edge, is much more sensitive to variation of the angle of attack than to variation of the jet deflection angle. The problem is solved by the method of matched asymptotic expansions [17], [18], [19], with a small parameter ε defined as $\varepsilon = C_{jo}/4$, where $C_{jo} = 2J_o/\rho U_o^2$, J_o the jet momentum in a root chord cross-section of the wing, ρ density of the fluid, U_o speed of the wing. Because in practical applications the jet momen-

tum coefficient C_j does not exceed 2, the parameter $\varepsilon \leq 1/2$. According to the technology of the method of matched asymptotic expansions the flow field is subdivided into an "outer" region (outside of the trailing edge flow region with a longitudinal dimension of the order of $O(\varepsilon)$) and the "inner" region (within the aforementioned local zone). Asymptotic dimension of the local (inner) region has been found by means of the least degeneracy principle as applied to the inner problem². In the inner region, in terms of stretched coordinate $\bar{x} = x/\varepsilon$, the problem is reduced to a system of integro-differential equations to be solved upon a semi-infinite axis with respect to a function of hydrodynamic loading γ^i and ordinates of the surface of the jet sheet. This system has been solved with use of Carleman inversion formulae and Mellin integral transformation. Although, the inner solution reveals logarithmic singularity at the point of jet injection, its outer asymptotics upon the wing contains a square root singularity of the loading. Simultaneously, it has been found that the slope of the jet sheet with respect to horizontal plane vanishes in downstream direction in inverse proportion to the square root of the distance from the trailing edge and becomes negligibly small at distances of the order of $O(1)$ and small magnitudes of the jet momentum coefficient. It can be concluded from the aforementioned that for the case of small jet momentum coefficient the outer solution should contain a square root singularity of loading at the trailing edge, and the outer part of the jet sheet, situated downstream from the trailing edge, is practically nonlifting and "almost" coincides with a free vortex sheet emanating from the wing's trailing edge. The conclusions obtained so far, enable to considerably simplify the problem. The outer solution is represented by a set of admissible solution of the integral equation of linear lifting surface theory. In particular, part of the solution due to the angle of attack is represented by Prandtl-Birnbaum double series with a square root singularity at the leading edge and square root zeros at the trailing edge and side edges. Representation of contribution of the jet flap into the loading differs due to the fact in compliance with the outer asymptotics of the local solution, there should be introduced in the outer solution a square root singularity at the trailing edge with the strength determined in terms of the jet deflection angle and momentum coeffi-

²Note, that as early 1956 in his investigation of the two-dimensional flow problem for the case of small jet momentum coefficient Spence had found such a coordinate transformation $\bar{x} = x/\Delta(C_j)$ (where $\Delta(C_j)$ is a stretching function) for which the integro-differential equation of the problem does not depend on the jet momentum coefficient. The stretching function derived in the above work turned out to be $\Delta(C_j) = C_j/4 = \varepsilon$.

¹That is the one with nonzero longitudinal curvature

cient at a given cross section by means of matching of the nearfield and farfield. Thickness of the wing is modeled in the outer region in the spirit of thin body theory by means of distributing upon an appropriate horizontal plane of a simple (sink-source) layer with the strength proportional the slope of thickness function in downstream direction. In order to evaluate the influence of the jet flap upon occurrence of cavitation the minimum pressure diagrams have been calculated and plotted with use of the approach proposed in [20] and [21]. The "edge" branches of these diagrams, corresponding to inception of cavitation at the leading edge, can be obtained directly from the local problem for a flow past a parabola, approximating a rounded leading edge. The "bottoms" of minimum pressure buckets, corresponding to cavitation occurrence in the mean part of the foil, can be determined from the outer solution. Note, that the method is readily extended to the case of a hydrofoil at finite submergences, if the corresponding outer solution accounts for the presence of the free surface. Similar approach can be applied to describe hydrodynamics of cascades and screw propellers with jet flaps.

2. Problem Formulation

Consider an irrotational flow of ideal incompressible fluid past a hydrofoil of small thickness and finite aspect ratio λ with a jet flap at the trailing edge. For the purpose of simplification, let us assume in what follows the wing has a rectangular planform and symmetric foil section³. In what follows all functions and quantities are rendered nondimensional with half of the root chord $c_o/2$ as a characteristic length and the speed of translatory motion U_o as a characteristic velocity. An attached Cartesian coordinate system x, y, z is used with axis x directed downstream, axis y directed upwards and z - axis forming the left-hand side coordinate system with x and y . The wing has an angle of attack α , and its thickness distribution is described by a function

$$y_t(x, z) = \pm \delta f_t(x, z), \quad x \in [-1, 1], \quad z \in [-\lambda, \lambda]. \quad (1)$$

The jet flap is activated by blowing the air from the trailing edge at an angle τ , the jet momentum coefficient being designated as C_j . Within the boundary problem formulation the velocity potential of the flow is governed by the three-dimensional Laplace equation and has to comply with kinematic boundary conditions of the flow tangency upon the upper and lower surfaces of the wing as well as

upon the surface of the jet flap which is not known in advance. Additionally there should be satisfied upon the jet sheet a dynamic condition, according to which the pressure jump across the jet is proportional to the jet momentum coefficient $C_j(z)$ and its longitudinal curvature at any cross section $z = \text{const}$. In linearized nondimensional form the said condition can be written down as

$$C_{p-}(x, z) - C_{p+}(x, z) = 2\gamma(x, z) = \frac{1}{2}C_j(z)\frac{\partial^2 y_j}{\partial x^2}, \quad x \geq 1, \quad |z| \leq \lambda, \quad (2)$$

where C_p is a the pressure coefficient, γ is the density of the equivalent vortex layer which replaces the jet sheet, $y_j(x, z)$ - ordinates of the jet sheet. With account of the aforementioned the integral equation of the linearized problem for the flow past a wing with a jet flap and zero incidence⁴ will take the form

$$\int_{-\lambda}^{\lambda} \int_{-1}^{\infty} \frac{\gamma(\xi, \zeta)}{(z - \zeta)^2} \left[1 + \frac{x - \xi}{\sqrt{(x - \xi)^2 + (z - \zeta)^2}} \right] d\xi d\zeta = 4\pi\beta(x, z) \quad (3)$$

with $\beta(x, z) = 0$ upon the wing $|x| \leq 1$, and $\beta(x, z) = y'_j(x, z)$ upon the jet sheet upon the jet sheet $x > 1$. Besides, in accordance with condition (2) the vortex density can be written as follows

$$\gamma(x, z) = \frac{1}{2}C_j(z)y''_{jxx}(x, z) = 2\varepsilon(z)y''_{jxx}(x, z), \quad (4)$$

and the condition of blowing at a given angle $\tau = \tau(z)$, which can vary spanwise, has the form

$$y'_j(1 + 0, z) = \tau(z) \quad (5)$$

3. Local Flow Problem in the Vicinity of the Trailing Edge with a Jet Flap

After introduction of stretching of local coordinates near the trailing edge

$$\bar{x} = \frac{x - 1}{\sigma(z)}, \quad \bar{y} = \frac{y}{\sigma(z)}, \quad \sigma(z) \rightarrow 0, \quad \text{when } \varepsilon \rightarrow 0. \quad (6)$$

the local flow problem becomes two-dimensional in the plane $z = \text{const}$ and the corresponding integral equation takes the form

$$\int_{-\infty}^{\infty} \frac{\gamma^t(\bar{\xi}, z)}{\bar{\xi} - \bar{x}} d\bar{\xi} = -2\pi\beta(\bar{x}, z),$$

³The proposed approach is valid for a wing of arbitrary planform and with arbitrary distribution of curvature within the frame of linear theory of lifting surface

⁴Due to the linearity of the flow problem the effects of the incidence and the jet flap can be studied separately, and their combined action can be estimated by means of superposition

$$\beta = 0 \quad \text{for } \bar{x} < 0,$$

$$\beta(\bar{x}, z) = \frac{d\bar{y}_j}{d\bar{x}}(\bar{x}, z) \quad \text{for } \bar{x} > 0, \quad (7)$$

where negative semi-axis corresponds to the wing, and positive semi-axis corresponds to the jet.

Applying the least degeneracy principle to the equation (7) with account of the formula (4) we can evaluate asymptotic dimension $\sigma = \sigma(z)$ of characteristic flow region near the jet-flapped trailing edge from the order equation

$$\varepsilon \frac{\sigma}{\sigma^2} \frac{d^2 \bar{y}_j}{d\bar{x}^2} = O\left(\frac{d\bar{y}_j}{d\bar{x}}\right) \quad (8)$$

wherefrom we can put $\sigma(z) = \varepsilon(z)$ and the equation (7) can be written in form of the following system

$$-\frac{1}{2\pi} \int_{-\infty}^0 \frac{\gamma^i(\bar{\xi}) d\bar{\xi}}{\bar{\xi} - \bar{x}} + \frac{1}{\pi} \int_0^{\infty} \frac{\bar{y}_j''(\bar{\xi}) d\bar{\xi}}{\bar{\xi} - \bar{x}} = 0, \quad \bar{x} < 0 \quad (9)$$

$$-\frac{1}{2\pi} \int_{-\infty}^0 \frac{\gamma^i(\bar{\xi}) d\bar{\xi}}{\bar{\xi} - \bar{x}} + \frac{1}{\pi} \int_0^{\infty} \frac{\bar{y}_j''(\bar{\xi}) d\bar{\xi}}{\bar{\xi} - \bar{x}} = \bar{y}_j'(\bar{x}), \quad \bar{x} > 0 \quad (10)$$

where differentiation in formulae (9) and (10) is performed with respect to stretched abscissa. Replacing $\bar{x} = -\bar{x}$ and defining $\gamma^i(\bar{\xi}) = \gamma^i(-\bar{\xi})$, we can reduce (9), (10) to the equation set

$$\frac{1}{2\pi} \int_0^{\infty} \frac{\gamma^i(\bar{\xi}) d\bar{\xi}}{\bar{\xi} - \bar{x}} + \frac{1}{\pi} \int_0^{\infty} \frac{\bar{y}_j''(\bar{\xi}) d\bar{\xi}}{\bar{\xi} + \bar{x}} = 0, \quad (11)$$

$$\frac{1}{2\pi} \int_0^{\infty} \frac{\gamma^i(\bar{\xi}) d\bar{\xi}}{\bar{\xi} + \bar{x}} + \frac{1}{\pi} \int_0^{\infty} \frac{\bar{y}_j''(\bar{\xi}) d\bar{\xi}}{\bar{\xi} - \bar{x}} = \bar{y}_j'(\bar{x}) \quad (12)$$

The equation of the form

$$-\frac{1}{\pi} \int_0^{\infty} \frac{\gamma^i(\bar{\xi}) d\bar{\xi}}{\bar{\xi} - \bar{x}} = h(\bar{x}) \quad (13)$$

can be reduced by means of change of variables to Carleman equation, solution of the latter being known. Therefore, the equation (13) can be written down as

$$\gamma^i(\bar{x}) = \frac{1}{\pi} \int_0^{\infty} \left(\frac{\bar{\xi}}{\bar{x}}\right)^{1/2} \frac{h(\bar{\xi}) d\bar{\xi}}{\bar{\xi} - \bar{x}} + \frac{C}{\bar{x}^{1/2}} \quad (14)$$

where C is a constant. Utilizing the following easily provable relationship,

$$\int_0^{\infty} \left(\frac{\bar{\xi}}{\bar{x}}\right)^{1/2} \frac{h(\bar{\xi}) d\bar{\xi}}{\bar{\xi} - \bar{x}} = \int_0^{\infty} \left(\frac{\bar{x}}{\bar{\xi}}\right)^{1/2} \frac{h(\bar{\xi}) d\bar{\xi}}{\bar{\xi} - \bar{x}} + \int_0^{\infty} \frac{\bar{\xi}^{-1/2} h(\bar{\xi}) d\bar{\xi}}{\bar{x}^{1/2}} \quad (15)$$

Substituting (15) into (14) we find

$$\gamma^i(\bar{x}) = \frac{1}{\pi} \int_0^{\infty} \left(\frac{\bar{x}}{\bar{\xi}}\right)^{1/2} \frac{h(\bar{\xi}) d\bar{\xi}}{\bar{\xi} - \bar{x}} + \frac{K}{\bar{x}^{1/2}},$$

$$K = \int_0^{\infty} \bar{\xi}^{-1/2} h(\bar{\xi}) d\bar{\xi} + C. \quad (16)$$

The equation (11) has the form (13). Then, using (16), we obtain

$$\gamma^i(\bar{x}) = \frac{2}{\pi^2} \int_0^{\infty} \left(\frac{\bar{x}}{\bar{\xi}}\right)^{1/2} \frac{1}{\bar{\xi} - \bar{x}} \int_0^{\infty} \frac{\bar{y}_j''(\bar{\eta}) d\bar{\eta}}{\bar{\eta} + \bar{\xi}} d\bar{\xi} + \frac{K}{\bar{x}^{1/2}}$$

With the help of the residue theory one can derive the following result

$$\int_0^{\infty} \frac{d\bar{\xi}}{\bar{\xi}^{1/2}(\bar{\xi} - \bar{x})(\bar{\eta} + \bar{\xi})} = -\frac{\pi}{\bar{\eta}^{1/2}(\bar{\eta} + \bar{x})} \quad (18)$$

Interchanging the order of integration in (17) we obtain with account of (18)

$$\gamma^i(\bar{x}) = -\frac{2}{\pi} \int_0^{\infty} \left(\frac{\bar{x}}{\bar{\xi}}\right)^{1/2} \frac{\bar{y}_j''(\bar{\eta})}{\bar{\eta} + \bar{x}} d\bar{\eta} + \frac{K}{\bar{x}^{1/2}} \quad (19)$$

To perform calculation of the first integral in formula (12) replace \bar{x} by $\bar{\xi}$ in (19) and accounting for the following result of the residue theory

$$\int_0^{\infty} \frac{\bar{\xi}^{1/2} d\bar{\xi}}{(\bar{\xi} + \bar{\eta})(\bar{\eta} + \bar{x})} = \pi \left[\frac{\bar{x}^{1/2}}{\bar{x} - \bar{\eta}} + \frac{\bar{\eta}^{1/2}}{\bar{\eta} - \bar{x}} \right]$$

$$\int_0^{\infty} \frac{d\bar{\xi}}{\bar{\xi}^{1/2}(\bar{\xi} + \bar{x})} = \frac{\pi}{\bar{x}^{1/2}} \quad (20)$$

we come to the following form of (12)

$$\frac{1}{\pi} \int_0^{\infty} \left(\frac{\bar{x}}{\bar{\eta}}\right)^{1/2} \frac{\bar{y}_j''(\bar{\eta})}{\bar{\eta} - \bar{x}} d\bar{\eta} + \frac{K}{2\bar{x}^{1/2}} = \bar{y}_j'(\bar{x}). \quad (21)$$

Due to the requirement that the magnitude of \bar{y}_j' must be finite for $\bar{x} \rightarrow 0$, we have to put $K = 0$. Designating $\omega(\bar{x}) = \bar{y}_j'(\bar{x})/\tau$ and $f(\bar{x}) = \gamma^i(\bar{x})/\tau$ we come to the following set of equations

$$f(\bar{x}) = -\frac{2}{\pi} \int_0^{\infty} \left(\frac{\bar{x}}{\bar{\xi}}\right)^{1/2} \frac{\omega'(\bar{\eta}) d\bar{\eta}}{\bar{\eta} + \bar{x}}, \quad (22)$$

$$\omega(\bar{x}) = \frac{1}{\pi} \int_0^{\infty} \left(\frac{\bar{x}}{\bar{\eta}}\right)^{1/2} \frac{\omega'(\bar{\eta}) d\bar{\eta}}{\bar{\eta} - \bar{x}}, \quad (23)$$

$$\omega(0) = 1 \quad (24)$$

$$\omega(\infty) = 0 \quad (25)$$

4. Solution of the Equation System Describing the Local Flow Problem

Solution of the equation (23) had been derived by Lighthill [22] in his investigation of the two-dimensional problem with use of Mellin integral transform

$$W(S) = \int_0^{\infty} \bar{x}^{S-1} \omega(\bar{x}) d\bar{x} \quad (26)$$

Then for a real C such that \bar{x}^{C-1} is integrable with respect to \bar{x} from 0 to ∞ it follows from inverse transform theorem

$$\omega(\bar{x}) = \frac{1}{2\pi i} \int_{C-i\infty}^{C+i\infty} \bar{x}^{-S} W(S) dS, \quad (27)$$

$$\omega'(\bar{x}) = \frac{1}{2\pi i} \int_{C-i\infty}^{C+i\infty} (-S) W(S) \bar{x}^{-S-1} dS \quad (28)$$

If the function $SW(S)$ is regular within the strip $C-1 < \text{Re} S < C$ then the integration path in (28) can be shifted to $\text{Re} S = C-1$. Then, replacing S by $S-1$, we obtain

$$\omega'(\bar{x}) = -\frac{1}{2\pi i} \int_{C-i\infty}^{C+i\infty} (S-1) W(S-1) \bar{x}^{-S} dS \quad (29)$$

Applying equation (29) together with (27) to formula (23), Lighthill derived the following equation for $W(S)$ and $|\text{Re} S| < 1/2$

$$W(S) - (S-1) \tan(\pi S) W(S-1) = 0 \quad (30)$$

Introducing the function $W_1(S)$ through a relationship

$$W(S) = \Gamma(S) W_1(S) \quad (31)$$

where $\Gamma(S)$ is the Euler Gamma function, and substituting (31) into (30) we come to the following equation for $W_1(S)$

$$W_1(S) - \tan(\pi S) W_1(S-1) = 0 \quad (32)$$

In order to comply with the condition $\omega(0) = 1$ we adopt $0 < C < 1/2$ and $W_1(0) = 1$. The corresponding solution of the equation (30) was found by Lighthill in the form

$$W_1(S) = W_1(-1/2 - S) = \prod_{n=1}^{\infty} \left[\frac{\left(1 - \frac{S}{n}\right) \left(1 + \frac{S}{n+1/2}\right)}{\left(1 + \frac{S}{n}\right) \left(1 - \frac{S}{n-1/2}\right)} \right]^n \quad (33)$$

Solution of the equation (32) can also be expressed by means of Alexeyevsky function

$$H(z+1) = (2\pi)^{0.5z} \exp[-0.5z(z+1) - 0.5\gamma z^2] \prod_{n=1}^{\infty} \left[\left(1 + \frac{z}{n}\right)^n \exp\left(-z + \frac{z^2}{2n}\right) \right] \quad (34)$$

satisfying the equation

$$H(1) = 1, \quad H(z+1) = \Gamma(z) H(z) \quad (35)$$

Making use of the latter definition

$$W_1(S) = \frac{1}{\sqrt{\pi}} \frac{H(1-S)H(3/2+S)}{H(1+S)H(1/2-S)} \quad (36)$$

With account of the result found by Bornes for representation of Alexeyevsky function Lighthill obtained the following formula

$$W_1(S) = (\cos \pi S)^{-1/2} \exp \left[\int_0^z \left(\frac{2\pi\xi}{\sin 2\pi\xi} \right) d\xi \right] \quad (37)$$

He also derived an expression for $W_1(S)$ for $|S| < 1/2$

$$W_1(S) = W_1(-1/2 - S) = 1 + S + \left(1 + \frac{\pi^2}{2}\right) \frac{S^2}{2!} + \left(1 + \frac{17\pi^2}{6}\right) \frac{S^3}{3!} + \dots \quad (38)$$

To obtain the function $\omega(\bar{x})$ we use the inverse Mellin transform (27). Then for $\bar{x} \leq 1$ $\omega(\bar{x})$ is equal to the sum of residues of the function

$$Q(S) = \bar{x}^{-S} \Gamma(S) W_1(S) \quad (39)$$

at its poles located to the left of the integration path, and for $\bar{x} > 1$ $\omega(\bar{x})$ is equal to minus sum of residues of the function $Q(S)$ at its right-hand side poles. It follows from (33) that $W_1(S)$ has the poles of the order n at points $S = -n, S = n - 1/2$, where $n = 1, 2, \dots$. Gamma function $\Gamma(S)$ is known to have the poles of the first order at points $S = 0, S = -n$. Thus, the function $\omega(\bar{x})$ will contain terms of the form of $\bar{x}^n \ln^m \bar{x}$ and $\bar{x}^{-n-1/2} \ln^p \bar{x}$, where $n, m, p = 0, 1, 2, \dots$ and $p, m \leq n$. Consider the first two terms of $\omega(\bar{x})$. The expansion of $\Gamma(S)$ in the vicinity of the point α

$$\Gamma(S + \alpha) = \Gamma(\alpha)(1 + \psi(\alpha)S) + O(S^2) \quad (40)$$

where $\psi(z)$ Gauss function which has the form

$$\psi(z) = \frac{\Gamma'(z)}{\Gamma(z)} = -\gamma_e + \int_0^1 \frac{1 - (-1)^{z-1}}{t} dt \quad (41)$$

where $\gamma_e \approx 0.577$ is the Euler constant. Joint consideration of (40) and (41) leads to

$$\Gamma(S+1) = 1 - \gamma_e S + O(S^2) \quad (42)$$

$$\Gamma(S+3/2) = \frac{\sqrt{\pi}}{2} [1 + (2 - \ln 4 - \gamma_e)S] + O(S^2) \quad (43)$$

Besides, it follows from the expansion (38)

$$W_1(S) = 1 + S + O(S^2),$$

$$W_1(S - 1/2) = 1 - S + O(S^2)$$

Then, using (30) and a functional equation for Gamma function $\Gamma(S+1) = S\Gamma(S)$, we obtain the following expression for $Q(S)$ near the poles

$$S = 0, \quad Q(S) = \frac{1 + (1 - \gamma_e - \ln \bar{x})S + O(S^2)}{S} \quad (44)$$

$$S = -1, \quad Q(S) = \frac{x[-1 + (\ln \bar{x} + \gamma_e - 2)(S + 1) + O[(S + 1)^2]]}{S + 1} \quad (45)$$

$$S = \frac{1}{2}, \quad Q(S) = \frac{\bar{x}^{-1/2}[1 + O(S - 1/2)]}{\sqrt{\pi}(S - 1/2)} \quad (46)$$

$$S = \frac{3}{2}, \quad Q(S) = \frac{\bar{x}^{-3/2}[1 + (1 - \gamma_e - \ln 4 - \ln \bar{x})(S - 3/2)]}{2\pi^{3/2}(S - 3/2)^2} \quad (47)$$

Then the function $\omega(\bar{x})$ can be written down as

$$\omega(\bar{x}) = 1 + \frac{\bar{x}}{\pi}(\ln \bar{x} + \gamma - 2) + O(\bar{x}^2) \quad \bar{x} < 1, \quad (48)$$

$$\omega(\bar{x}) = (\pi \bar{x})^{-1/2} +$$

$$\frac{1}{2}(\pi \bar{x})^{-3/2}(\ln 4 \bar{x} + \gamma_e - 1) + O(\bar{x}^{-5/2}) \quad \bar{x} > 1 \quad (49)$$

Function $\omega'(\bar{x})$ can be derived by means of differentiation of equations (47) and (48)

$$\omega'(\bar{x}) = \frac{1}{\pi} \ln \bar{x} + \frac{\gamma_e - 1}{\pi} + O(\bar{x}), \quad \bar{x} < 1 \quad (50)$$

$$\omega'(\bar{x}) = -\frac{1}{2}\pi^{-1/2}\bar{x}^{-3/2} - \frac{1}{4}\pi^{-3/2}\bar{x}^{-5/2}(3\ln 4\bar{x} + 3\gamma_e - 5) + O(\bar{x}^{-7/2}), \quad \bar{x} > 1 \quad (51)$$

Now, let us find $f(\bar{x})$. In this connection we shall use the same Mellin integral transform (26). Applying (26) to (23) we have

$$\int_{C-i\infty}^{C+i\infty} \bar{x}^{-S} F(S) dS = \frac{2}{\pi} \int_{C-i\infty}^{C+i\infty} (S-1)W(S-1) \int_0^\infty \left(\frac{\bar{x}}{\bar{\eta}}\right)^{1/2} \frac{\bar{\eta}^{-S} d\bar{\eta}}{\bar{\eta} + \bar{x}} dS \quad (52)$$

where

$$F(S) = \int_0^\infty \bar{x}^{S-1} f(\bar{x}) d\bar{x},$$

wherefrom

$$F(S) = \frac{2}{\pi}(S-1)W(S-1) \int_0^\infty \frac{z^{-1/2-S}}{1+z} dz \quad (53)$$

Performing integration in the right-hand side of the equation with the help of the residue theory and accounting for the formula (30), we derive from (53)

$$F(S) = 2 \frac{W(S)}{\sin \pi S} = 2 \frac{\Gamma(S)W_1(S)}{\sin \pi S} \quad (54)$$

The function $f(\bar{x})$ can be obtained in the same way as $\omega(\bar{x})$ with use of the inverse Mellin transform

$$f(\bar{x}) = \frac{1}{2\pi i} \int_{C-i\infty}^{C+i\infty} Q_1(S) dS, \quad Q_1(S) = \frac{2Q(S)}{\sin \pi S} \quad (55)$$

Analysing (55) it is easy to see that the order of the poles of the function $Q_1(S)$ at points $S = -n$ is equal to $n+2$, where $n = 0, 1, 2, \dots$. At points $S = n$, where $n = 1, 2, \dots$ the function $Q_1(S)$ has zeros of the order of $n-1$ for $n > 1$. Thus, $f(\bar{x})$ will contain terms of the form $\bar{x}^n \ln^m \bar{x}$ and $\bar{x}^{-n+1/2} \ln^p \bar{x}$, where $n, m, p = 0, 1, 2, \dots, p \leq m \leq n+1$.

Find the function $f(\bar{x})$ for large and small \bar{x} . Using the formulae (44)-(46) and (55) one can derive the following expansions of $Q_1(S)$ near the poles

$$S = 0, \quad Q_1(S) = \frac{2[1 + (1 - \gamma_e - \ln \bar{x})S]}{\pi S^2} \quad (56)$$

$$S = \frac{1}{2}, \quad Q_1(S) = -\frac{2\bar{x}^{-1/2}}{\sqrt{\pi}(S - 1/2)} \quad (57)$$

$$S = 3/2, \quad Q_1(S) = -\frac{\bar{x}^{-3/2}[1 + (1 - \gamma_e - \ln 4 - \ln \bar{x})(S - 3/2)]}{2\pi^{3/2}(S - 3/2)^2} \quad (58)$$

Then for small \bar{x} the function $f(\bar{x})$ will be approximately equal to the residue of $Q_1(S)$ for $S = 0$. For larger \bar{x} the function $f(\bar{x})$ will be approximately equal to the sum of residues of $Q_1(S)$ at points $S = 1/2$ and $S = 3/2$. Finally

$$f(\bar{x}) = -\frac{2}{\pi} \ln \bar{x} + \frac{2(1 - \gamma_e)}{\pi} + O(\bar{x}), \quad \bar{x} < 1 \quad (59)$$

$$f(\bar{x}) = 2(\pi \bar{x})^{-1/2} - (\pi \bar{x})^{-3/2}(\ln 4 \bar{x} + \gamma_e - 1) + O(\bar{x}^{-5/2}), \quad \bar{x} > 1 \quad (60)$$

It follows from (59) that for $\bar{x} \rightarrow 0$, ($x \rightarrow 1+0$) the hydrodynamic loading behaves as $\ln \bar{x}$ (or as $\ln |x - 1|$) which is in proper accordance to the results of the linear theory due to the jump of downwash. In order to be able to carry out the asymptotic matching of the local solution with the far field it is necessary to find the first term of expansion of $f(\bar{x})$ for $\bar{x} \rightarrow \infty$. It can be seen from observation of (60) that one-term outer expansion of the inner solution has the form

$$\gamma^{io}(x, z) = \frac{2\tau(z)\sqrt{\varepsilon(z)}}{\sqrt{\pi}\sqrt{1-x}} = \frac{2\tau_0\sqrt{\varepsilon_0}F_j(z)}{\sqrt{\pi}\sqrt{1-x}} \quad (61)$$

where $\tau_0\sqrt{\varepsilon_0}$ corresponds to magnitudes of the jet deflection angle and jet momentum coefficients at the root chord cross section,

$$F_j(z) = \tau(z)\sqrt{\varepsilon(z)}/\tau_0\sqrt{\varepsilon_0}$$

is a function characterizing distribution of the jet flap parameters spanwise. Simultaneously, consideration of asymptotics of longitudinal curvature ω' far from the place of blowing (see equation (51)) shows that for small magnitudes of the jet momentum coefficient C_j the pressure difference across the jet in the outer downstream region has the order of $O(\varepsilon_o \sqrt{\varepsilon_o})$. This means that for small C_j the contribution of the outer part of the jet sheet into the lifting capacity of the jet flapped wing can be neglected. Equation (61) prompts that the outer solution of the linear lifting surface theory, describing loading distribution upon the jet flapped wing, should have the order of $\tau_o \sqrt{C_{j_o}}$ and square root singularities not only at the leading (shock entry) but also at the trailing edge.

5. Outer Solution of the Leading Order

In the considered case of zero incidence and $\varepsilon_o \rightarrow 0$ in the outer limit the longitudinal dimension of the region of the jet evolution tends to zero, and the problem is reduced to solution of the homogeneous integral equation of the lifting surface theory

$$\int_{-\lambda}^{\lambda} \int_{-1}^1 \frac{\gamma^o(\xi, \zeta, \varepsilon_o)}{(z - \zeta)^2} \left[1 + \frac{x - \xi}{\sqrt{(x - \xi)^2 + (z - \zeta)^2}} \right] d\xi d\zeta = 0 \quad (62)$$

with additional condition of asymptotic matching with the inner description of the loading near the trailing edge. Represent the outer loading in form of an asymptotic expansion

$$\gamma^o(x, z, \varepsilon_o) = \delta_1(\varepsilon_o) \gamma_1^o(x, z) + \dots \quad (63)$$

where with account of the expression (61) the structure of the function $\gamma_1^o(x, z)$ is adopted in terms of angular variables $\theta = \arccos(-z/\lambda)$ and $\psi = \arccos(-x)$ with $x \in [-1, 1]$, $z \in [-\lambda, \lambda]$ in the form

$$\gamma_1^o(\psi, \theta) = \sum_{n=1}^{\infty} (a_{0n} \cot \frac{\theta}{2} + b_{0n} \tan \frac{\theta}{2} + \sum_{k=1}^{\infty} a_{kn} \sin k\psi) \sin n\theta \quad (64)$$

Matching of expressions (61) and (64) determines the scaling function $\delta_1(\varepsilon_o) = \tau_o \sqrt{\varepsilon_o}$ and supplies the aforementioned additional condition at the trailing edge⁵ in the form

$$\sum_{n=1}^{\infty} b_{0n} \sin n\theta = \sqrt{\frac{2}{\pi}} \mathcal{F}_j(\theta) \quad (65)$$

⁵This condition replaces conventional Kutta-Zhukovsky condition for a wing with a jet flap

or, with account of the orthogonality of the system $\{\sin n\theta\}$ upon the segment $\theta \in [0, \pi]$

$$b_{0n} = \frac{2\sqrt{2}}{\pi\sqrt{\pi}} \int_0^{\pi} \mathcal{F}_j(\theta) \sin n\theta d\theta \quad (66)$$

Corresponding contribution into a lift coefficient C_y can be found by means of the formula

$$C_y = \frac{\tau_o \sqrt{C_{j_o}}}{2\lambda} \int_{-\lambda}^{\lambda} \int_{-1}^1 \gamma_1^o(x, z) dx dz = \frac{\tau_o \sqrt{C_j}}{4} \int_0^{\pi} \int_0^{\pi} \gamma_1^o(\theta, \psi) \sin \theta \sin \psi d\theta d\psi \quad (67)$$

Correspondingly, the expression for the longitudinal moment coefficient with respect to the mid-chord of the order of $\tau_o \sqrt{\varepsilon_o}$ takes the form

$$m_z = \frac{\tau_o \sqrt{C_{j_o}}}{2\lambda} \int_{-\lambda}^{\lambda} \int_{-1}^1 \gamma_1^o(x, z) x dx dz = -\frac{\tau_o \sqrt{C_{j_o}}}{8} \int_0^{\pi} \int_0^{\pi} \gamma_1^o(\theta, \psi) \sin 2\theta \sin \psi d\theta d\psi \quad (68)$$

In a more general case of the jet flapped wing at an angle of attack α , designating the parameter $\tau_o \sqrt{\varepsilon_o} = q_j$, we can write the lift and moment coefficients in terms of hydrodynamic derivatives with respect to the incidence and characteristic similarity criteria of the jet flow q_j as

$$C_y = C_y^{\alpha} \alpha + C_y^{q_j} q_j, \quad m_z = m_z^{\alpha} \alpha + m_z^{q_j} q_j \quad (69)$$

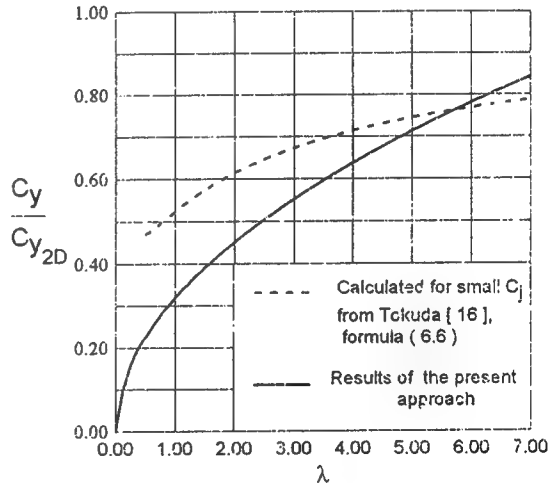


Fig.1 The ratio C_y/C_{y2D} versus aspect ratio for a rectangular wing with a jet flap. In Fig.1 there is

presented a dependence of the ratio C_y/C_{y2D} where C_y and C_{y2D} represent correspondingly lift coefficients of the wing of finite and infinite span) upon the aspect ratio λ of the rectangular wing. The

lift coefficient of the infinite-aspect-ratio wing was obtained by the approach of this paper and can be shown to be $C_y = C_{y2D} = 2\tau\sqrt{\pi C_j}$. This result coincides with the first term of the series solution by Spence, see Introduction of the present paper. For comparison in the same Figure some calculated results are plotted which are obtained from formulae of Tokuda [15] by putting $C_j \rightarrow 0$. Fig. 2 illustrates the lift coefficient of a rectangular jet flapped wing versus the angle of attack α for wing's aspect ratio $\lambda = 6.8$, jet deflection angle $\tau^0 = 31.3^\circ$ and the jet momentum coefficient $C_j = 0.42$. Calculated results are compared with experimental data of Williams and Alexander, [16] and theory of Tokuda.

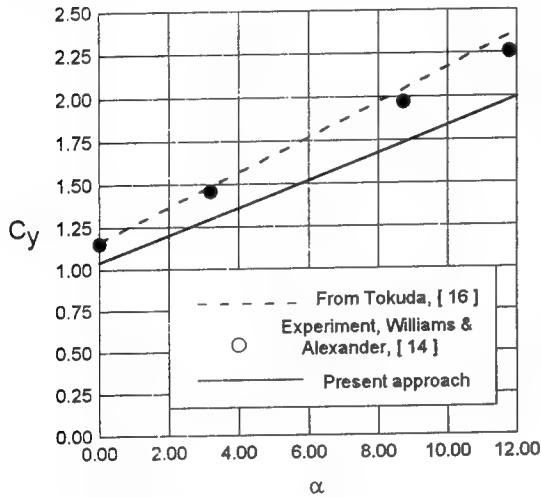


Fig. 2 The lift coefficient of a rectangular wing with a jet flap versus angle of attack, $\lambda = 6.8$, $\tau^0 = 31.3^\circ$, $C_j = 0.42$.

The above results have been obtained for the case of uniform distribution of the jet parameters span-wise.

6. Evaluation of the Possibility to Enlarge the Speed Range of Non-Cavitating Regime of the Flow Past a Hydrofoil of Finite Aspect Ratio by Means of the Jet Flap

Now, we shall pass over to discussion of the limiting cavitation diagrams, characterizing the regimes of cavitation inception in the middle part and at the leading edge of the hydrofoil. We shall use a simplified approach of determining the diagrams (of minimum pressures) advocated in [20], [21] and consisting in separate determination of the "edge" branches (from the local flow problem at the rounded leading edge) and the "bottom" branches (from the outer linearized flow field) of the diagram.

Let us derive the expression, describing the edge branch of the minimum pressure diagram. It can be shown that near a rounded leading edge the flow is close to that around a parabola in two-dimensions in the planes normal to the leading edge platform contour. At points of the surface of the wing near the rounded leading edge the velocity of the fluid can be found by means of the expression, [18].

$$v^i(X, z) = \sqrt{\frac{X}{X + \bar{\rho}_e}} \left[U_1(z) \pm \frac{U_2(z)}{\sqrt{X}} \right] \quad (70)$$

where $X = x + 1/\delta^2$, δ is a maximum relative thickness of the wing, $\bar{\rho} = \rho_e/\delta^2$, ρ_e - radius of curvature of the wing's leading edge. Functions $U_1(z)$ and $U_2(z)$ are determined by means of matching of the local solution with the outer description of the velocity upon the wing's surface. It can be shown, [20] that the maximum magnitude of the fluid velocity near the leading edge is achieved at the point with magnitude of stretched abscissa

$$X_m = \left(\frac{\bar{\rho}_e U_1}{2U_2} \right)^2 \quad (71)$$

Substitution of (71) into (70) gives the following expression for minimum magnitudes of the pressure coefficient at the leading edge

$$C_{p_{\min}}^i(z) = 1 - (v_{\max}^i)^2 = 1 - U_1^2 - \frac{2U_2^2(z)}{\bar{\rho}_e} \quad (72)$$

Let us determine $U_{1,2}(z)$ and the equation of the "bottom" of the minimum pressure diagrams. The flow velocity upon the wing's surface in its middle part is calculated with use of the outer linear solution in the form

$$v^o(x, z) = 1 + v_t^o(x, z) \mp \frac{\gamma^o(x, z)}{2} \quad (73)$$

where v_t^o is a velocity component due to thickness of the wing, and γ^o is a velocity component due to effects of "asymmetry" (angle of attack, curvature, jet flap, etc.). Accounting for the fact that the vortex component of the flow velocity, generally speaking, has a square root singularity at the leading edge, that is for $x \rightarrow -1$

$$\gamma^o(x, z) \rightarrow \frac{C_\gamma(z)}{\sqrt{1+x}} = \frac{\bar{\alpha} C_\gamma^\alpha(z) + \bar{q}_j C_\gamma^{qj}}{\sqrt{X}} \quad (74)$$

where $\bar{\alpha} = \alpha/\delta$, $\bar{q}_j = q_j/\delta = \tau_0 \sqrt{\epsilon_0}/\delta$ are assumed to be of the order of $O(1)$ ⁶. Now, it is not difficult to perform matching of expressions (71) and (74) and find $U_1(z)$ and $U_2(z)$ in the form

$$U_1(z) = 1 + v_t^o(-1, z), \quad U_2(z) = -\bar{\alpha} C_\gamma^\alpha(z) - \bar{q}_j C_\gamma^{qj}(z) \quad (75)$$

⁶This is quite practical assumption, implying that all perturbation parameters are of the order of thickness

Velocity component due to thickness is determined by means of thin body theory as

$$v_t^o(x, z) = -\frac{\delta}{2\pi} \int_{-\lambda}^{\lambda} \times \int_{-1}^1 \frac{\partial f_t(\xi, \zeta)}{\partial \xi} \frac{(x - \xi)}{[(x - \xi)^2 + (z - \zeta)^2]^{3/2}} d\xi d\zeta \quad (76)$$

In the case under consideration ($\alpha = 0$) the function $U_2(z)$ is easily found with account of (64) in the form

$$U_2^{qj}(\theta) = -\sqrt{2} \sum_{n=1}^{\infty} a_{0n} \sin n\theta \quad (77)$$

Minimum pressure in the middle part of the wing can be calculated as

$$C_{p\min}^o = 2[v_t^o(x_m, z) + \frac{1}{2}(\gamma^o)^{qj}(x_m, z)] \quad (78)$$

where x_m is the abscissa of minimum pressure. It is easy to write down a functional dependence of $C_{p\min}$ upon the lift coefficient of the wing with a jet flap. For the "edge" branch of the diagram we have

$$C_{p\min}^i(C_y) = 1 - U_1^2(z) - 2 \frac{C_y^2}{\bar{\rho}_{le}} \left(\frac{U_2^{qj}}{C_y^{qj}} \right)^2 \quad (80)$$

For the "bottom" branch of the diagram

$$C_{p\min}^o = 2 \left[v_t^o(x_m, z) + \frac{1}{2} C_y \frac{\gamma^{qj}(x_m, z)}{C_y^{qj}} \right] \quad (80)$$

As an example, consider the simplest case of a wing of infinite aspect ratio. In this case the present approach enables to obtain the following equation of the "edge branch" of the minimum pressure diagram in the case of symmetric foil with a jet flap.

$$C_{p\min} = -2\delta + \delta^2 - \frac{C_y^2}{4\pi^2 \delta^2 \bar{\rho}_{le}} \quad (81)$$

where, as earlier, δ is relative thickness of the foil, $\bar{\rho}_{le} = \rho_{le}/\delta^2$, ρ_{le} is radius of curvature of the leading edge. In the case of small jet momentum coefficients. C_j the lift coefficient is $C_y = C_{y2D} = 2\tau\sqrt{\pi C_j}$. For the purpose of comparison we can write corresponding expression for the case of the foil without jet flap at an angle of attack α

$$C_{p\min} = -2\delta + \delta^2 - \frac{C_y}{\pi^2 \delta^2 \bar{\rho}_{le}}, \quad (82)$$

where $C_y = C_{y2D} = 2\pi\alpha$. Comparing the formulae (81) and (82), we can see that for the same magnitude of the lift coefficient C_y the cavitation inception at the leading edge can be expected to occur later for the foil with a jet flap than for that without

the jet flap. The same conclusion can be deduced from comparison of the equations, describing "bottom" branches of the diagrams. These equations for the considered case of infinite-aspect-ratio wing have the form

$$C_{p\min} = C_{pt}(x_m) - \frac{C_y}{\pi} \frac{1}{\sqrt{1 - x_m^2}}, \quad (83)$$

$$C_{p\min} = C_{pt}(x_m) - \frac{C_y}{\pi} \sqrt{\frac{1 - x_m}{1 + x_m}}. \quad (84)$$

where $C_{pt}(x)$ is a thickness contribution to the pressure coefficient of the foil, x_m is the abscissa of the point of minimal pressure on the foil. Formulae (83) and (84) correspond respectively to the cases of the foil with and without jet flap. Figures 3 and 4 show plotted minimum pressure diagrams for a NACA four-digit wing sections NACA 008 and NACA 0012.

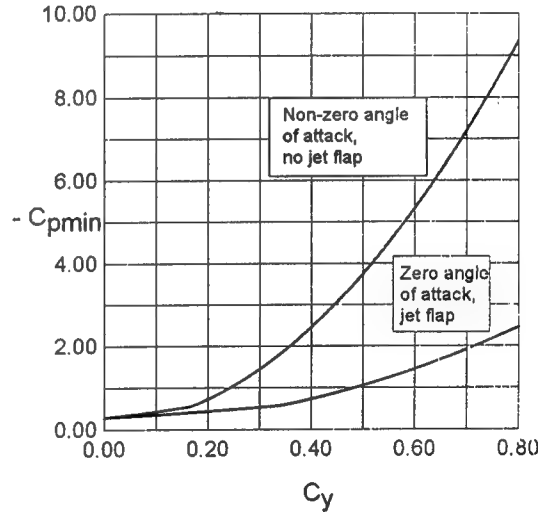


Fig. 3 Calculated minimum pressure diagrams for NACA 008 section for the case of the foil with and without jet flap.

These diagrams clearly indicate that use of jet flapped wings can be expected to result in delay of cavitation inception both in the middle part of the foil and near the leading edge.

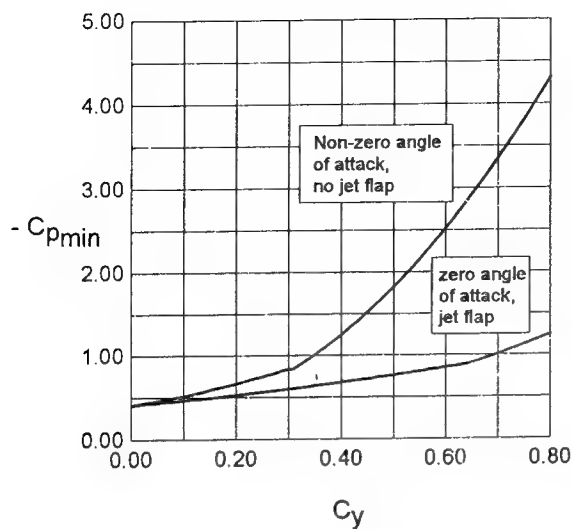


Fig. 4 Calculated minimum pressure diagrams for NACA 012 section for the case of the foil with and without jet flap.

The authors would like to thank Dr. G.M. Fridman for his valuable comments in connection with the present paper.

7. REFERENCES

1. Thwaites, B., "Incompressible Aerodynamics", Oxford at the Clarendon Press, 1960.
2. Davidson, I.M., *J. Roy. Aero. Soc.*, 60, pp. 25-41, 1956.
3. Kaplan, P., "An Integrated Propulsion-Lift-Control Design for Large High Speed Hydrofoil Craft", *Proceedings of the Second International Conference on Fast Sea Transportation*, Yokohama, Japan, 13 - 16 December 1993, pp. 501 - 512.
4. Kaplan, P. and Goodman, T.R., "Use of Jet-Flapped Hydrofoils as Ship Antipitching Fins", *Journal of Aircraft*, Vol. 4, No. 2 March - April, 1967.
5. Kaplan, P. and Lehman, A.F., "An Experimental and Analytical Study of Jet Flap Hydrodynamics for Application to Submarine Control Surfaces", *Oceanics Inc. Rpt No. 67 - 41*, November 1967.
6. Spence, D.A., "The Lift Coefficient of Thin, Jet-Flapped Wing", *Proc. Roy. Soc., Series A, Mathematical and Physical Sciences*, No. 1212, December 1956, Vol. A 238, 1956, pp. 46 - 68.
7. Spence, D.A., "Some Simple Results for Two-Dimensional Jet-Flapped Aerofoils", *The Aeronautical Quarterly*, November, 1958, pp. 46 - 58.
8. Spence, D.A., *Rep. Aero. Res. Coun.*, London, 20, 753, 1959.
9. Spence, D.A., "The Lift Coefficient of Thin Jet-Flapped Wing", *The Aeronautical Quarterly*, October, 1960, pp. 97 - 118.
10. Spence, D.A., "A Solution of the Integro-Differential Equation for the Slope of the Jet", *Proc. Roy. Soc., Ser. A, Mathematical and Physical Sciences*, No. 1304, April 1961, Vol. 261, pp. 97 - 118.
11. Kuchemann, D., "A Method for Calculating the Pressure Distribution of Jet Flapped Wings", *Gt. Britain Aero. Res. Council, Report & Memoranda 3036*, 1956.
12. Statford, B.S., "Early Thoughts on the Jet Flap", *The Aeronautical Quarterly*, Vol. VIII, Feb. 1956.
13. Maskell, E.C. and Spence, D.A., "A Theory of the Jet Flap in Three Dimensions", *Proc. Roy. Soc., London*, June 1959, Ser. A, 251, pp. 407 - 425.
14. Kerney, P.K., "An Asymptotic Theory of the High-Aspect-Ratio", Ph.D. Thesis, Graduate School of Engineering, Cornell University, 1967.
15. Tokuda, N., "An Asymptotic Theory of the Jet Flap in Three Dimensions", *J. Fluid Mech.*, 1971, vol. 46, part. 4, pp. 705 - 726.
16. Williams, J., Alexander, A.J., *Aeronautical Quarterly*, v. 9, 1957, pp. 395-406.
17. Rozhdestvensky, K.V., "Matched Expansions Method in Hydromechanics of Lifting Bodies", *Book of Abstracts, The Third International Congress on Industrial and Applied Mathematics*, Hamburg, 3 - 7 July, 1995, p. 144 (full text to appear in *Zeitschrift fur Angewandte Mathematik und Mechanik, ZAMM*)
18. Rozhdestvensky, K.V., *Method of Matched Asymptotics in Hydromechanics of Wings*, L., Sudostroenie, 1979, 208 p.
19. Van Dyke, M., "Perturbation Methods in Fluid Mechanics", *The Parabolic Press*, Stanford, 1975.
20. Rozhdestvensky, K.V., Mishkevich, V.G., "Application of the Method of Matched Asymptotic Expansions to the Determination of the Flow Past a Thin Foil in Unsteady Motion", *Sbornik Trudov po Proektirovaniyu Sudov*, No. 37, pp. 60 - 73 (in Russian)
21. Mishkevich, V.G., Rozhdestvensky, K.V., Bubentsov, V.P., "Unsteady Flows Near Leading Edges of Lifting Surfaces: Pressures, Flow Separation, Cavities", *Proc. Symposium "Bubble Noise and Cavitation Erosion in Fluid Systems"*, FED - Vol. 176, ASME 1993, pp. 9-19.

Examination of the Flow Near the Leading Edge and Closure of Stable Attached Cavitation

A. Leger, P.-W. Yu, K. Laberteaux, S. Ceccio (University of Michigan, USA)

Abstract: The flow near both the cavity detachment and closure region of attached cavitation is investigated. Cavity detachment from a ventilated sphere is examined, and the relationship between the location of cavity detachment and flow separation is related to the geometry of the cavity near detachment. The flow field near the closure of a natural partial cavity is investigated with Particle Imaging Velocimetry (PIV), and preliminary results are provided.

Introduction: The inception and dynamics of sheet cavitation is of considerable interest to designers of ship propellers. Sheet cavitation can cause a loss of performance, pressure pulsations, and cavitation erosion. Ideally, designers of these devices would have analytical tools which could be used to predict the occurrence of sheet cavitation, its potential for instability, and its potential for erosion. Today, however, the current design tools can only predict the general location of sheet cavitation inception, and this is usually done by examining the fully wetted potential flow around blade surfaces of the propeller.

Inception is predicted when the pressure on the lifting surfaces falls below the liquid vapor pressure (*e.g.* the $C_{P,MIN} = \sigma$ criteria). This method often cannot provide critical information about the detailed nature of the cavity sheet such as the topology of the sheet, the extent of the sheet, the erosiveness of the sheet, or its potential to become unstable and form cloud cavitation. In addition, models of attached cavitation often require *a priori* information about the cavitating flow.

Constraints which have been used in predicting inception include the location of cavity detachment and length of the cavity. Models of the closure region of the cavity must be used for the case of partial cavitation. These models often do not capture the detailed flows in that region.

In the present study, we are examining the flow fields near the inception and the closure of stable attached cavities, and our goal is to provide new insights into the physical processes of cavity formation and closure. Two parallel experimental research programs are described below. First, we are examining the process of cavity detachment on a bluff object. Second, we are examining the closure region of a closed partial cavity. The experimental techniques employed in each study are described, and current results are presented and discussed.

Experimental Methods: The experiments described here were conducted in the Cavitation and Multiphase Flow Laboratory at the University of Michigan Department of Mechanical Engineering and Applied Mechanics.

Measurements were made in the Blow Down Water Tunnel (BDWT), and a description of this facility is provided in Tassin *et al.* (1995). In brief, the BDWT consists of two 1.5 m^3 tanks connected via a contraction, a test section and a diffuser. Controlled application of pressure and vacuum to the two tanks are employed to produce the desired flow in the test section, which is 76.2 mm square and approximately

260 mm long. Between 10 and 20 seconds of steady flow can be produced with velocities in the range of 5 to 25 m/s (in the empty test section). The test section velocity is determined by measuring the pressure difference between the test section entrance and the pressure near the entrance of the contraction. This pressure difference was related to the test section velocity using LDV measurements of the average flow velocity in the center of the empty test section. The free and dissolved air content of the BDWT can be qualitatively controlled through deaeration and by allowing free gas bubbles to reach the free surfaces in the two tanks.

In the study of the detachment region of an attached cavity, results are presented here for the cavity flow over a 25.4 mm diameter brass sphere which was mounted on a sting within the BDWT test section. The surface of the sphere was either highly polished or roughened. The sting was plumbed to permit injection of air into the cavity, and a separate pressure tap was used to measure the difference between the cavity pressure and the static pressure of the flow upstream of the model. Five 203 μm diameter holes were placed in the sphere at an angular location of 22.5 degrees measured from the stagnation point, and fluorescein dye was injected

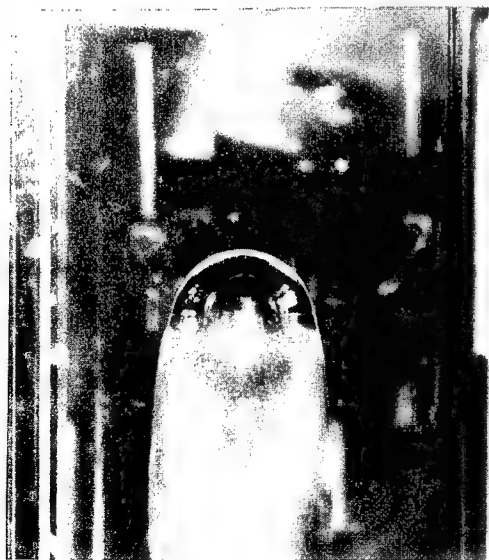


Figure 1: The 25.4 mm diameter sphere mounted on a sting in the BDWT test section. A ventilated cavity flow behind the sphere was created to study the region of cavity separation.

through these holes to permit visualization of the flow near the surface of the sphere. Flash photography and high speed video imaging were used to capture images of the dye streak as it flowed over the sphere. This setup is shown in Figure 1.

The flow streamlines near the surface of the sphere were recorded using particle tracers. The flow was illuminated with a continuous light sheet produced with an Argon-Ion laser, and silvered hollow glass spheres of nominally 10 μm diameter were added to the flow as tracers. Photographic images of the streamlines near the cavity were produced by time exposing the image of the flowing particles.

A wedge was used to produce a partial cavity in the study of the closure of partial cavitation. The wedge had an angle of 26.5 degrees and a step height of 19 mm, and was mounted to the wall of the test section. Partial cavities formed on the vertex of this wedge. An image of this setup is shown in Figure 2. Double pulsed Particle Imaging Velocimetry (PIV) was used to investigate the flow field in the closure region of the cavity. The details of the PIV experimental setup is provided in Tassin *et al.* (1995) and Yu (1995). Two frequency-doubled Nd-YAG lasers were used to produce a pulsed light sheet, and the flow was seeded with fluorescent latex particles with an average



Figure 2: A wedge mounted on the wall of the BDWT test section. A natural cavity separates from the vertex of the wedge.

diameter of $30\ \mu\text{m}$. The light sheet had an average thickness of $1\ \text{mm}$ and was positioned parallel to the mean flow direction with maximum intensity near the closure region of the cavity. Two cameras were placed on opposite sides of the sheet to record images of the light sheet. One camera recorded all the scattered light from the bubbles and particles within the sheet, and the second camera was equipped with a filter to block the scattered laser light while recording the fluorescent return of the particles. Thus, it was possible to detect only the motion of the particle tracers as they flowed in the bubbly region behind the cavity. The double pulsed images recorded on the photographs were digitized and processed to determine particle pairs.

Flow Field Near the Leading Edge of a Ventilated Cavity: Developed attached cavitation results from the detachment of the flow from either a smooth surface or at a discontinuity of the slope on the surface. It is often not clear where a cavity will separate from a smooth surface simply from examination of the fully wetted flow. Brennen (1969a and 1969b) examined the fully developed cavity flows over a sphere and cylinder, and Arakeri and Acosta (1973) and Arakeri (1975) studied flows over a variety of headforms. These studies revealed that the viscous flow near the surface strongly influences the inception and location of cavity detachment.

Arakeri (1975) studied the relationship between laminar boundary layer separation and cavity detachment. Cavities were shown to be preceded by laminar boundary layer separation in the non-cavitating flow, yet the location of the cavity detachment was not necessarily near the non-cavitating separation point. Figure 3 shows a schematic drawing of the cavity detachment for a nominally two dimensional cavity, as presented by Arakeri. The boundary layer is observed to separate upstream of the cavity detachment, and the cavity interface is observed to curve into the solid surface. Arakeri offered correlations to predict the location of boundary layer separation upstream of the cavity and the distance between the boundary layer separation and the cavity detachment, λ .

The position of boundary layer separation was found to be a weak function of Reynolds number and a strong function of cavitation number. λ was related to the Taylor-Saffman number, $\mu U_o / T$ (where μ is the dynamic viscosity of the fluid, T is the surface tension, and U_o is the freestream velocity), and to the momentum thickness of the non-cavitating boundary layer near the point of boundary layer separation.

Franc and Michel (1985) also significantly expanded the work of Arakeri with examination of the flow over a series of bodies, including hydrofoils. Franc and Michel also recognized the relationship between the presence of non-cavitating laminar boundary layer separation and the formation of attached cavitation, and they proposed a method to predict the location of cavity detachment on smooth surfaces. Their method recognizes that the presence of a cavity will alter the pressure distribution around the cavitating object, and this will modify the growth of the boundary layer upstream of the point of cavity detachment. It was shown that a cavity will detach if the modified boundary layer separates upstream of the cavity.

Franc and Michel point out the "cavity detachment paradox." A cavity must be preceded by laminar boundary layer separation. However, the cavity pressure may be the lowest pressure of the flow, and this would result in a favorable pressure gradient just upstream of the cavity. Thus, laminar separation would not be expected to occur. Need the region upstream of the cavity be in tension (or have pressure lower than the cavity pressure, in the case of a

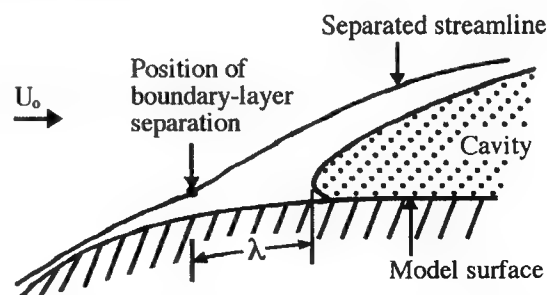


Figure 3: Schematic drawing of the cavity detachment region (after Arakeri, 1975).

ventilated cavity)? Moreover, the laminar separation streamline and the cavity free streamline enclose a region of fluid bounded by two stagnation points, and this would suggest that there is a fluid sink downstream of the cavity without a corresponding source. Thus, the flow may recirculate or be three-dimensional in the region upstream of cavity separation.

With these questions in mind, we have initiated our study of this flow by examining the detachment of a ventilated cavity flow behind a sphere. This is a well-characterized flow (both cavitating and non-cavitating), and we can use previous results for comparison and validation. First, we examined the non-cavitating flow around the sphere to determine whether blockage effects were significant and to determine the accuracy with which we can determine boundary layer separation with dye injection. Figure 4 presents the angle of flow separation measured from the front stagnation point as a function of Reynolds number, $Re = U_o D / \nu$, where D is the diameter of the sphere and ν is the liquid kinematic viscosity. Data from the present study is

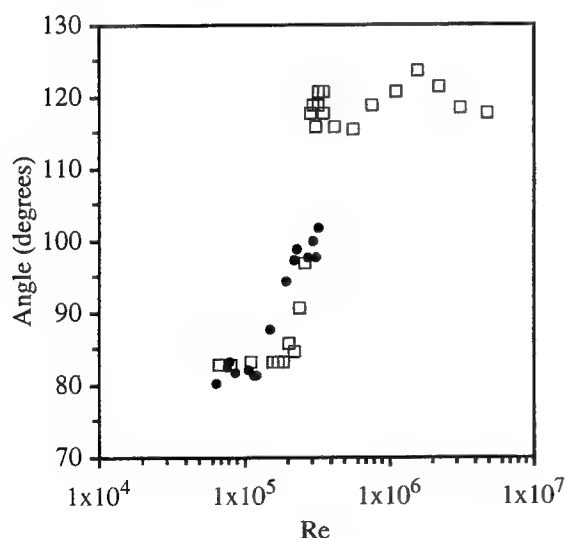


Figure 4: Angle of flow separation on the non-cavitating sphere for varying Reynolds number (\bullet). The angle is measured from the front stagnation point. The data of Achenbach (1975) is shown for comparison (\square).

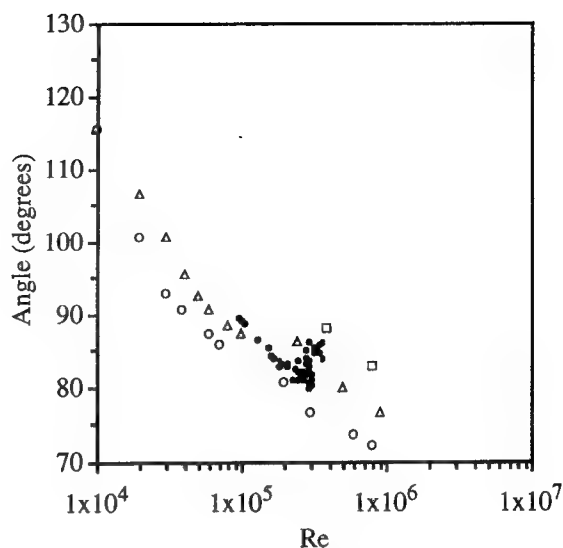


Figure 5: Angle of cavity detachment as a function of Reynolds number for $0.3 < \sigma < 0.5$ (\bullet). The data of Arakeri (1975) is presented for comparison for $\sigma = 0.1$ (\circ), $\sigma = 0.25$ (\square), and $\sigma = 0.5$ (Δ).

compared to that of Achenbach (1972), and the agreement is good.

The freestream pressure was reduced, and air was injected into the wake of the sphere forming a fully developed cavity. Figure 5 shows the angle of cavity detachment versus Reynolds number for a small range of cavitation numbers $\sigma_c = (P_o - P_c) / \frac{1}{2} \rho U_o^2$, where P_o is the freestream static pressure, P_c is the cavity pressure, and ρ is the fluid density. Data presented by Arakeri (1975) is also shown for cavitation on 6.35 and 12.7 mm diameter spheres, and the trends in the data are similar. The position of cavity detachment in these tests is upstream of the non-cavitating laminar separation point in the first set of tests, and this result also has been observed for developed cavity flows behind cylinders and hydrofoils (Arakeri and Acosta, 1973; Arakeri, 1975; and Franc and Michel, 1985).

Figure 6 presents a close-up side view of the cavity detachment region with associated dye visualization. The surface of the cavity forms a sharp curve as it detaches from the solid surface, and this implies a hydrophilic surface. Figure 7 shows a similar flow visualized with particle streaks, and the

separation streamline appears to intersect the cavity free streamline. Figure 8 is a close-up view of the detachment region, again employing particle streak visualization. These time exposed images reveal slowly moving particles recirculating in the separation region bounded by the cavity interface and the separation streamline.

The cavity has a finite thickness near the point of detachment which forms a forward facing step. The "step height", h , is a function of both the Reynolds number and the cavitation number, as shown in Figure 9. Interfacial tension between the liquid and cavity gas will result in a pressure difference across the interface in this region of steep curvature. The pressure jump across the cavity at the point of detachment, $P_D - P_C$, is approximated by $T / \frac{1}{2}h$. Here, $(P_D - P_C) / \frac{1}{2}\rho U_o^2 \approx 4T / h\rho U_o^2$ is roughly



Figure 6: A close-up side view of the cavity detachment region. $Re = 1.8 \times 10^5$ and $\sigma = 0.5$

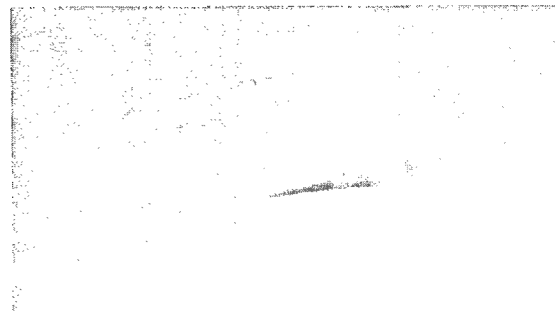


Figure 7: The flow near the cavity detachment region visualized by particle streaks. $Re = 1.2 \times 10^5$ and $\sigma = 0.2$

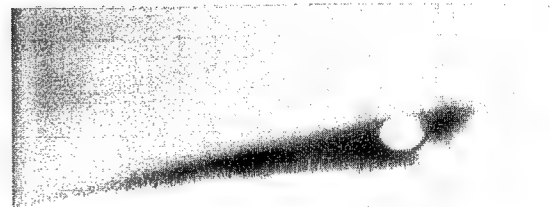
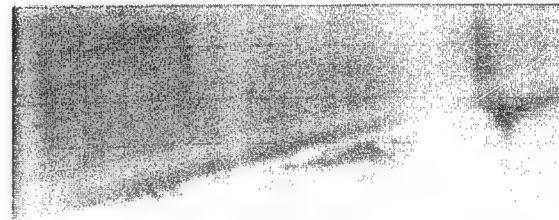


Figure 8: Close-up particle streak images of the recirculating region ahead of the cavity detachment. $Re = 1.1 \times 10^5$ and $\sigma = 0.1$

0.01, leading to only a small modification of the local cavitation number. Thus, it is expected that the gas/liquid interfacial tension will not play a significant role in the process of cavity detachment. However, the solid-liquid interfacial tension may play a more significant role.

In general, as the Reynolds number increases, h decreases. Also, as the cavitation number is reduced, h increases. Arakeri (1975) suggested that the momentum thickness of the boundary layer just upstream of cavity detachment strongly influences the region of cavity detachment. We do see that h is dependent on the Reynolds number, but the dependence is approximately linear, while the momentum thickness will vary as $Re^{1/2}$ for laminar boundary layers. The distance between boundary layer separation and cavity detachment, λ , can be related to the cavity thickness at cavity detachment. Figure 10 suggests such a relationship. A linear fit of the data reveals that $\lambda \approx 3h$.

The cavity thickness begins to increase for $Re > 2.6 \times 10^5$, and this is due to the increasing three-dimensionality of the flow near the point of cavity detachment. For $Re < 1 \times 10^5$, a smooth streamsurface

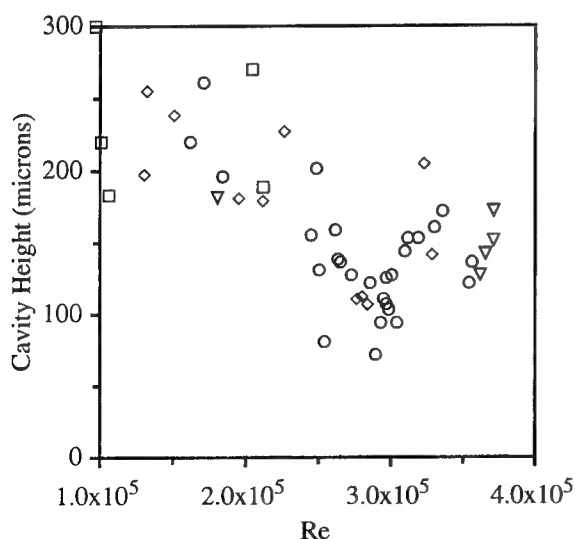


Figure 9: The cavity "step height", h , as a function of Reynolds number for varying cavitation numbers. $\sigma = 0.33-0.38$ (\square), $\sigma = 0.39-0.43$ (\diamond), $\sigma = 0.44 - 0.46$ (\circ), $\sigma = 0.47-0.52$ (∇).

separates from the sphere. But, as the Reynolds number increases, streamwise indentations begin to form near the point of cavity detachment. Figure 11 shows three images of the cavity with varying numbers of these features, which we will refer to as "divots". High speed video images show that a divot forms when a disturbance locally indents a region of the cavity interface, and this disturbance rapidly evolves into a single thin fluid-filled channel. A divot may persist for long periods of time, and it can remain stationary, oscillate, or travel in the circumferential direction. Some divots would merge together, and others would be destroyed by flow disturbances.

Increasing the Reynolds number increased the formation of these divots, but it appears that they do not form as the result of a periodic instability of the cavity interface. Brennen (1969b) examined these structures as they formed on the interface of spheres and cylinders in polymeric solutions, and it was found that a circumferential disturbance near the point of cavity detachment would grow in amplitude and frequency with increasing Reynolds number. In the present study, however, we did not observe this mechanism of divot formation. Instead,

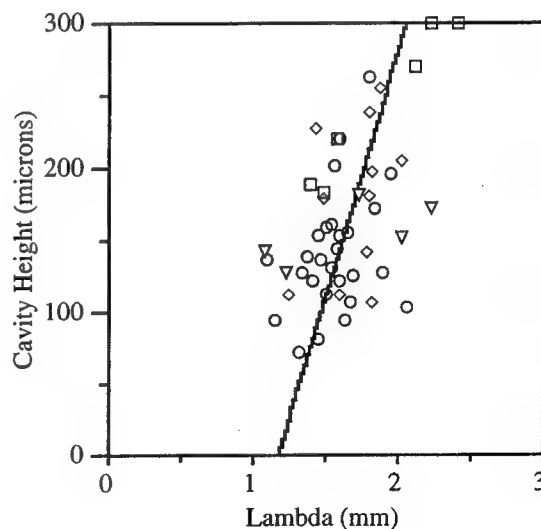


Figure 10: The cavity step height, h , as a function of separation distance, λ , for varying cavitation numbers. $\sigma = 0.33-0.38$ (\square), $\sigma = 0.39-0.43$ (\diamond), $\sigma = 0.44 - 0.46$ (\circ), $\sigma = 0.47-0.52$ (∇). The line represents a least-squares fit.

divots were formed at random locations on the sphere circumference, and, if the water in

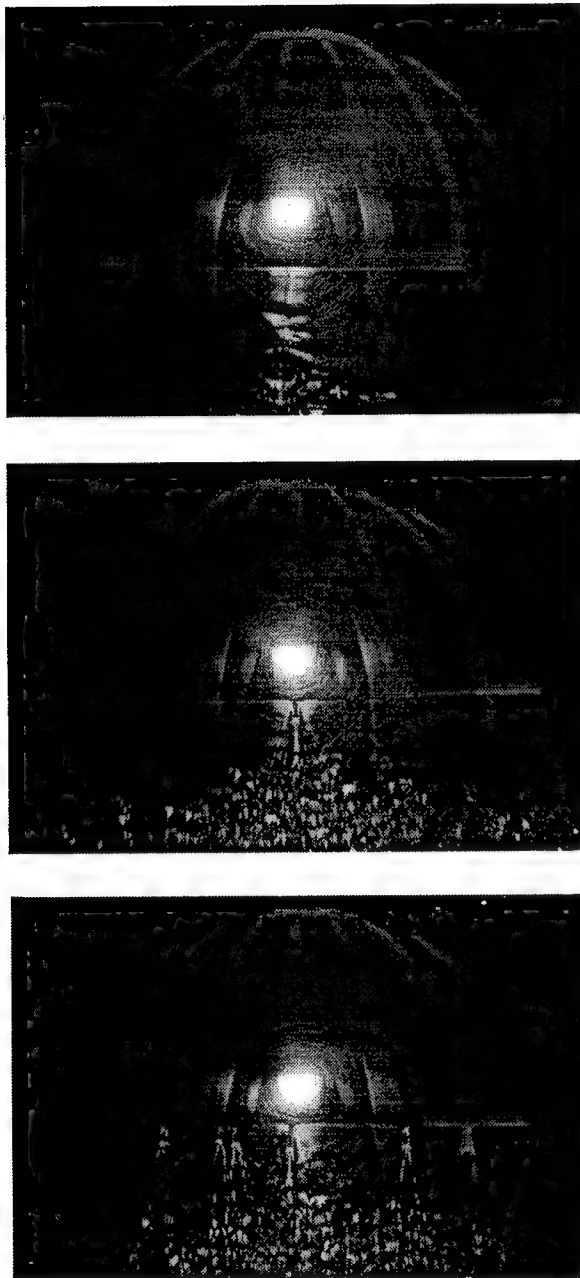


Figure 11: Three images of the cavity with varying number of divots. (a) $Re = 1.2 \times 10^5$ and $\sigma = 0.53$ (b) $Re = 1.9 \times 10^5$ and $\sigma = 0.44$ (c) $Re = 2.0 \times 10^5$ and $\sigma = 0.47$.

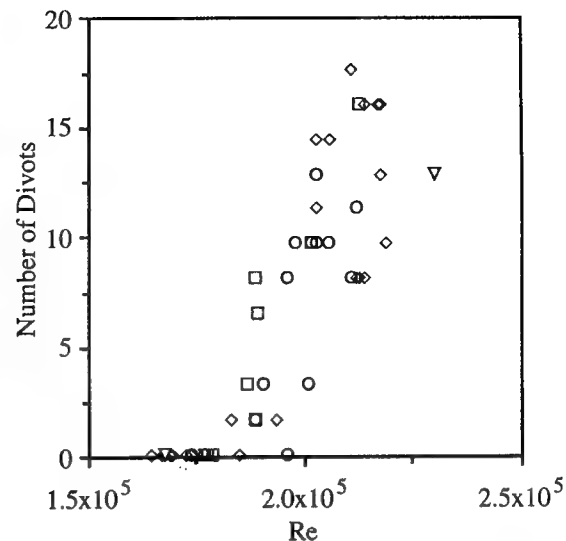


Figure 12: The average number of divots as a function of Reynolds number for varying cavitation numbers. The data represents flows in which re-entrant jets did not disturb the cavity detachment region. $\sigma = 0.33-0.38$ (\square), $\sigma = 0.39-0.43$ (\diamond), $\sigma = 0.44-0.46$ (\circ), $\sigma = 0.47-0.52$ (∇). The field of view covered 1/8th of the sphere circumference.

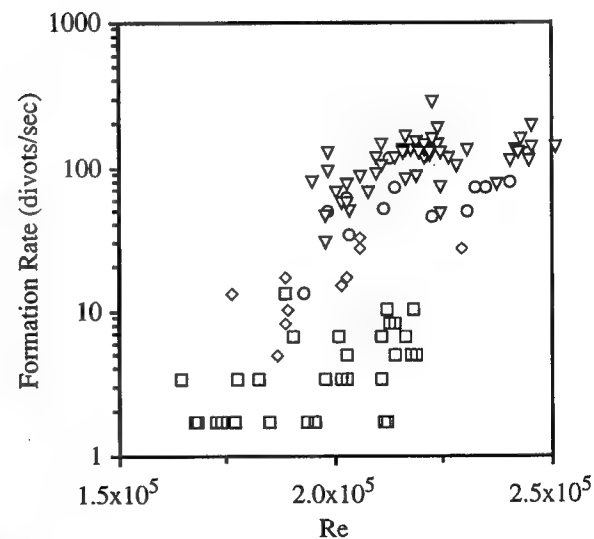


Figure 13: The rate of divot formation as a function of Reynolds number. Data is divided into four groups, ranging from flows with no re-entrant jet (\square) and with approximately 2 (\diamond), 6 (\circ) and >6 (∇) jets per second in the field of view which covered 1/8th of the sphere circumference.

the BDWT was allowed to settle for long time periods before an experiment, the number of divots created would be substantially reduced. The non-Newtonian nature of Brennen's flows may be responsible for the observed differences.

Divots were also created and destroyed by the action of a re-entrant flow which originated downstream of the cavity separation zone. Figure 12 presents the average number of divots as a function of Reynolds number for cavity flows where re-entrant jets were not observed to impinge on the cavity detachment region. Figure 13 shows the frequency of divot formation as a function of Reynolds number and the frequency of re-entrant jet formation. As the Reynolds number increases, the likelihood that a divot will form and persist increases.

A sphere was roughened to artificially trip the boundary layer upstream of cavity separation, and it was found that there was very little difference between the tripped and untripped flows, and this suggests that a strong favorable pressure gradient upstream of the cavity separation may lead to re-laminarization of the boundary layer.

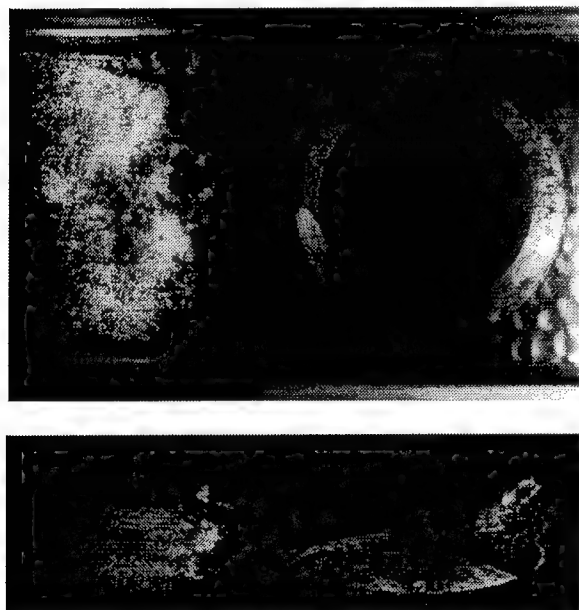
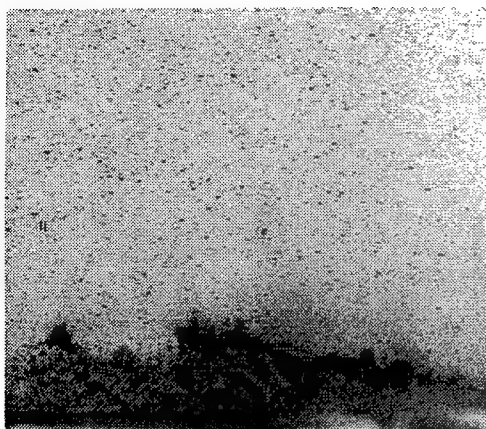


Figure 14: Plan and oblique view of a partial cavity which has formed at the vertex of the wedge. $U_o = 10 \text{ m/s}$, $\sigma = 1.2$, and the cavity length is approximately 50 cm.

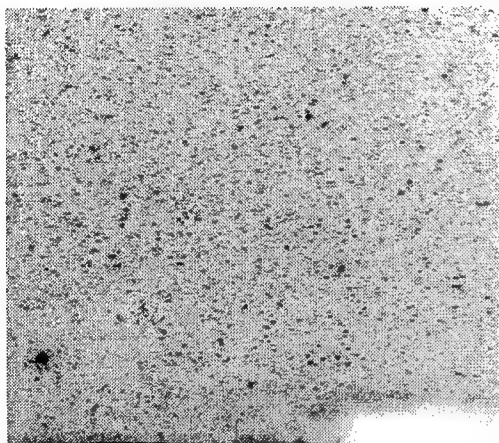
Flow Field in the Closure Region of a Stable Partial Cavity: The dynamics of partial cavitation has been examined by several investigators. The formation of cloud cavitation via the re-entrant jet is discussed by Knapp *et al.* (1970) and Furness and Hutton (1975). Recent experimental work has been conducted by Avellan *et al.* (1988), Kubota *et al.* (1989), Yamaguchi *et al.* (1990), and Le *et al.* (1993a and 1993b). In these studies, the details of the flow surrounding both steady and unsteady attached cavitation have been examined using a variety of experimental techniques. Avellan *et al.* (1988) and Kubota *et al.* (1989) employed LDV to determine the mean and phase averaged flow field around partial cavities, and Le *et al.* (1993a and 1993b) employed mean and dynamic pressure measurements. Detailed measurements near attached cavities are made difficult by the large range of flow scales, the presence of two phases, and the unsteadiness of the cavity surface and closure region.

We are currently examining the flow field near the closure region of partial cavities using Particle Imaging Velocimetry (PIV). A wedge is used to produce a partial cavity. By varying the angle of the wedge, it is possible to create both open and closed partial cavities. The images presented here are for closed cavities. A view of the cavitating wedge is shown in Figure 14, and Figures 15 and 16 present typical PIV images and the measured vector fields in a region close to the cavity closure. Shown in the figures are the filtered and unfiltered double-pulsed images and the vectors field reconstructed from the filtered images. These images are relatively lightly seeded, and particle tracking was used to identify individual velocity vectors of the flow. Comparison of the filtered and unfiltered images reveal the utility of fluorescent flow tracers. While bubbles may mask some of the particles, it is still possible to discern individual particle pairs quite close to the cavity closure.

Discussion: Our study of the detachment and closure region of attached cavitation is continuing; however, the results presented here reveal some new insights and will guide our studies.

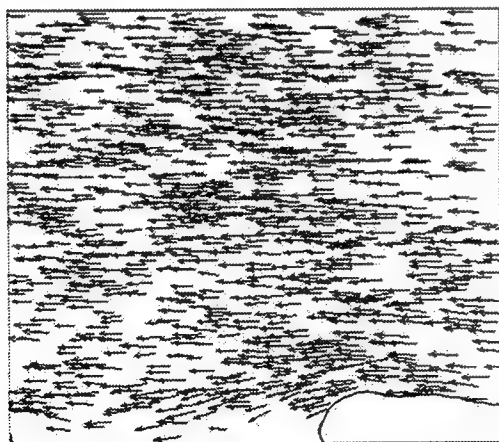


(a)



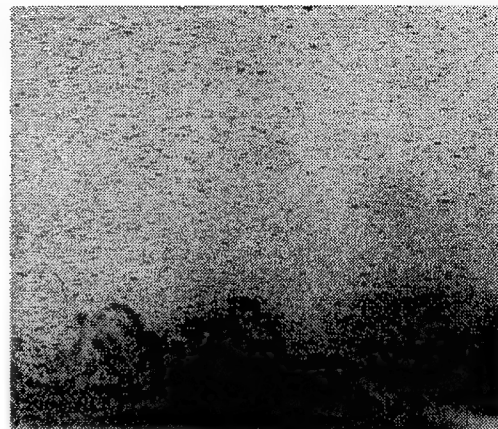
(b)

10 m/s 1.6 mm

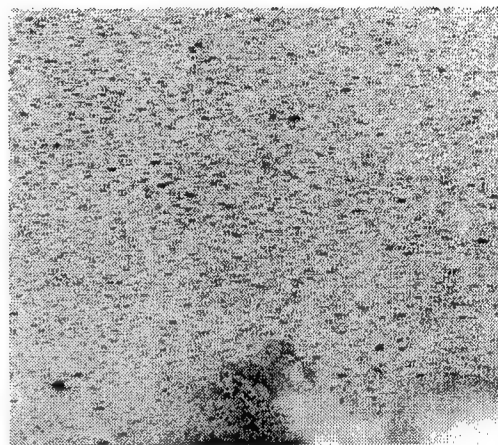


(c)

Figure 15: Three images of the closure region of a partial cavity- (a) unfiltered double-pulsed PIV image, (b) the filtered image, and (c) the velocity vectors recovered from the filtered image. Scales are shown.

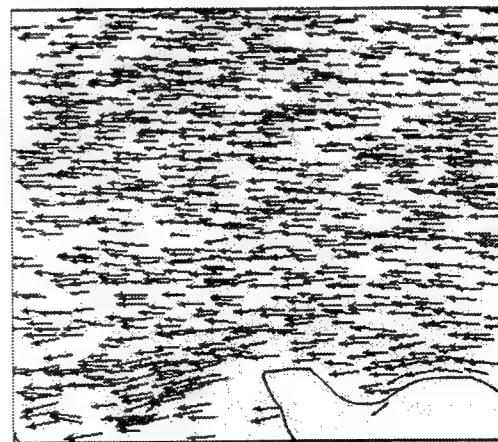


(a)



(b)

11 m/s 1.6 mm



(c)

Figure 16: Three images of the closure region of a partial cavity- (a) unfiltered double-pulsed PIV image, (b) the filtered image, and (c) the velocity vectors recovered from the filtered image. Scales are shown.

Detailed examination of the cavity detachment region has revealed that the local geometry of the cavity can be related to the position of boundary layer separation upstream of the cavity. The cavity forms a "forward facing step" with a step height which is 2 to 3 times larger than the boundary layer thickness. It is expected that such a geometry would lead to an upstream boundary layer separation. However, it is unclear how the location of flow separation is influenced by the local cavity geometry.

There is a recirculating region upstream of the cavity, and the flow in this region may be either two or three-dimensional. At higher Reynolds numbers, the interface develops small depressions or "divots." These divots are created and destroyed by disturbances in the flow such as freestream turbulence or the impingement of a re-entrant jet into the detachment region. As the Reynolds number increases, the overall number of divots also increases. These structures form when there is a local breakdown in the two-dimensional flow near the cavity detachment, resulting in a complex three-dimensional flow. It is unclear at present if a laminar separation is still present upstream of the cavity in these cases.

Lastly, we have developed techniques to examine the flow field in the closure region of a partial cavity. By employing fluorescent flow tracers, it is possible to detect Lagrangian flow tracers in the bubbly region just downstream of the cavity closure. We currently are employing particle tracking to analyze the PIV images, and we are striving to increase the density of vectors which can be measured. With PIV, we will be able to determine how the flow field closes behind the cavity and the momentum deficit in the cavity wake.

Acknowledgments: We would like to thank Prof. Joseph Katz for making available to us the fluorescent particles used in the PIV. This work is being supported under the Office of Naval Research contract number N00014-96-1-0076, Dr. E. P. Rood, technical monitor.

References:

- Achenbach, E. 1972. Experiments on the flow past spheres at very high Reynolds numbers. *J. Fluid. Mech.* **54**, pp. 565-575.
- Arakeri, V. H. 1975. Viscous effects on the position of cavitation separation from smooth bodies. *J. Fluid. Mech.* **68**, pp. 779-799.
- Arakeri, V.H. and Acosta, A.J. 1973. Viscous effects in the inception of cavitation on axisymmetric bodies. *Trans. ASME I: J. Fluids Eng.* **95**, pp. 519-527.
- Avellan, F.; Dupont, Ph.; and Rhyning, I. L. 1988. Generation mechanism and dynamics of cavitation vortex downstream of a fixed leading edge cavity, *Proc. 17th Symp. on Naval Hydrodyn.*, The Hague
- Brennen, C.E. 1969a. The dynamic balances of dissolved gas and heat in natural cavity flows. *J. Fluid. Mech.* **37**, pp. 115-127.
- Brennen, C.E. 1969b. A numerical solution of axisymmetric cavity flows. *J. Fluid. Mech.* **37**, pp. 671-688.
- Franc, J.P. and Michel, J.M. 1985. Attached cavitation and the boundary layer: experimental investigation and numerical treatment. *J. Fluid. Mech.* **154**, pp. 63-90.
- Furness, R. A. and Hutton, S. P. 1975. Experimental and technical studies of two-dimensional fixed-type cavities. *J. Fluids Eng.* **97**, pp 515-522.
- Knapp, R. T.; Daily, J. W.; and Hammit, F. G. 1970. *Cavitation*, McGraw-Hill.
- Kubota, A.; Kato, H.; Yamaguchi, H.; and Maeda, M. 1989. Unsteady structure measurement of cloud cavitation on a foil section using conditional sampling techniques. *J. Fluids Eng.*, **111**, pp 204-210.
- Le, Q.; Franc, J. P.; and Michel, J. M. 1993. Partial Cavities: Global Behavior and Mean Pressure Distribution, *J. Fluids Eng.*, **115**, pp 243-248.

Le, Q. , Franc, J. P., and Michel, J. M.
1993. Partial Cavities: Pressure Pulse
Distribution Around the Cavity *J. Fluids
Eng.*, **115**, pp 249-254.

Tassin, A. L.; Li, C.-Y; Ceccio, S. L.; and
Bernal, L. P. 1995. Velocity field
measurements of cavitating flows. *Exp. in
Fluids*, **20**, pp. 125-130.

Yu, P.-W. 1995. Experimental and
numerical investigation of cavitating flows.
Doctoral Thesis, University of Michigan

Numerical Investigation on the Turbulent and Vortical Flows Beneath the Free Surface Around Struts

U.-C. Jeong, Y. Doi, K.-H. Mori (Hiroshima University, Japan)

Abstract

Characteristics of turbulent and vortical flows around free surface piercing struts are numerically and experimentally investigated. Three dimensional Reynolds averaged Navier-Stokes and continuity equations are used for the numerical simulation. The LES method with the external disturbance is used to simulate the turbulent flow on the free surface. The governing equations are discretised by a finite different method in a body and free surface fitted curvilinear co-ordinate system. To investigate the curvature effect of the bow, four different struts having NACA0005, NACA0008, NACA0012, and NACA0024 sections are used.

The results show that vorticity production is required on the curved free surface to satisfy the no-shearing stress condition. The no-shearing stress condition is significantly important. The vorticity, whose strength is proportional to the free surface curvature, leads the generation of the vortical motions beneath the free surface in front of the bow. The bow with a larger curvature intensifies the concave curvature of the free surface and generates stronger vorticity than a smaller one. Above a certain velocity, the vortical motions become intensive and the free surface fluctuates with a high frequency around a bow. The proposed LES method can reveal the existence of the free surface turbulence which is observed in experiments prior to the overturning waves.

1 Introduction

Free surface flow around a surface piercing blunt bow is one of the most complicated phenomena in the field of ship hydrodynamics because of various non-linear characteristics. Many researchers have studied the bow breaking wave with the hope of understanding how it affects the resistance of a ship.

Baba[1] proposed wave breaking resistance as a new component of a ship resistance. He could provide quantitative evidence of a resistance component due to wave breaking around the bow through measuring head-loss by wake survey method. Taneda and Amamoto[2] explained the bow breaking wave as a vortex motion. They called it "necklace vortex" to distinguish from the horseshoe vortex which was mainly generated by the boundary layer flow around the body mounted on the plate. They also reported that this necklace vortex was strongly affected by the Froude number while the horseshoe vortex was affected by the Reynolds number.

Since then, many investigations have been made to clarify the mechanism of the bow wave breaking both experimentally and theoretically. However, the so-called bow breaking wave and necklace vortex are not so simple and the mechanism has not yet come to knowledge. Miyata et al.[3] and Groenbaugh and Yeung[4] showed an oscillatory motion of bow wave front which occurred when a certain critical speed was exceeded. However, it may be difficult to say that their findings are general characteristics of bow waves because they used two-dimensional floating bodies. Miyata et al.[3] also explained that overturning of waves generated a necklace vortex of which intensity depended on the strength of the overturning motion. Moreover, they reported that the vorticity generated by the breaking waves spread forward by the movement of wave front and backward by diffusive effect.

All the studies mentioned above is mainly concerned to the "broken" waves. However, to make clear the phenomena it may be necessary to study the early stage where the breaking is apt to occur. Honji[5] and Kayo and Takekuma[6] experimentally showed the existence of a vortical motion beneath the free surface around the bow at a very low Froude number even though no significant bow waves were generated. Patel et al.[7] explained the phenomenon

assuming the balance of a surface tension and a normal component of a viscous stress.

Mori[8] discussed the free surface flows before the wave breaking took place. He divided the flow into three stages; the development of the free surface shear layer, the formation of the necklace vortex and the production of unsteady turbulent free surface flow. It was called "sub-breaking waves" as a free surface turbulent flow in distinction from spilling or plunging breakers. He also deduced that the free surface curvature played a role to generate a vorticity on the curved free surface and the vorticity could be one of the sources of the necklace vortex. The theoretical background of the free surface shear layer was also given by Batchelor[9].

Mori and Shin[10] simulated the sub-breaking wave generated by two-dimensional submerged hydrofoil. They used experimental results to set the free surface boundary condition strictly. Mori and Lungu[11] simulated two-dimensional sub-breaking waves directly by imposing a disturbance for vertical velocity component while Coleman[12] used a disturbance of pressure on the free surface. The role of these disturbances might be a kind of a trigger for the transition to the turbulent flow and it might be assumed as a source that maintains the turbulence on the free surface.

Main objective of the present study is to make clear the characteristics of the flow at the early stage of bow wave breaking around surface piercing struts, especially the effect of the vorticity generated on the free surface on the vortical and turbulent flows beneath the free surface. To simplify the problem, the surface tension is excluded in the present investigations. Numerical investigations are made by solving the Reynolds averaged Navier-Stokes(NS) and continuity equations by finite difference method(FDM). Several computations are performed to investigate the effects of computational and physical parameters, for examples, grid dependency, the effects of the Reynolds and Froude numbers, free surface treatment and so on. To investigate the curvature effect of the bow, four different struts having NACA0005, NACA0008, NACA0012, and NACA0024 sections are used(called NS05, NS08, NS12 and NS24 respectively hereafter). The fluctuated free surface flows called sub-breaking waves are also studied by Large Eddy Simulation(LES). Some computed results are compared with the experimental results.

2 Observation of Bow Wave Patterns

An observation of bow wave patterns was performed for NS08, NS12 and NS24 models at the circulating water channel(CWC) of Hiroshima University. The length and draft of the models were 0.8m and 0.4m respectively. Experimental arrangement is shown in Fig.1. The wave patterns were photographed under the CWC. The striped-screen was fixed above the free surface to make the pictures clear. To remove a surface tension, a surfactant was used[13].

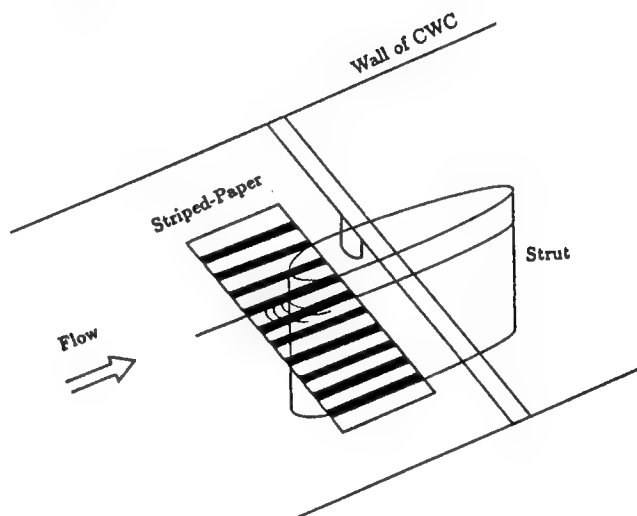


Fig.1 Experimental set-up.

Fig.2 shows a schematic view of the bow wave on the center plane. The "Zone-I" where the free surface has smooth concave curvature is the part ahead of the bow wave. Through a sharp change of the curvature, the flow enters "Zone-II" where the flow can not be stable any more. A border of these two zones is "wave front" where the curvature has a maximum[8].

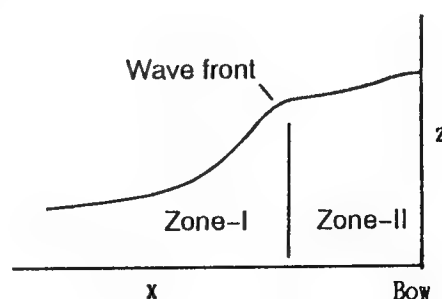


Fig.2 Schematic view of bow wave.

Fig.3 shows the bow wave pattern of NS12 at $Fn=0.15$. No clear waves are observed. However, at $Fn=0.20$ as shown in Fig.4, the wave front is observed surrounding the bow. Increasing the oncoming velocity($Fn=0.25$), the wave front appears clearly and the position moves away from the bow(Fig.5). At those Froude numbers, no significant features of turbulence appear on the free surface.



Fig.3 Picture of free surface flow of NS12, $Fn=0.15$, $Rn=2.3 \cdot 10^5$.

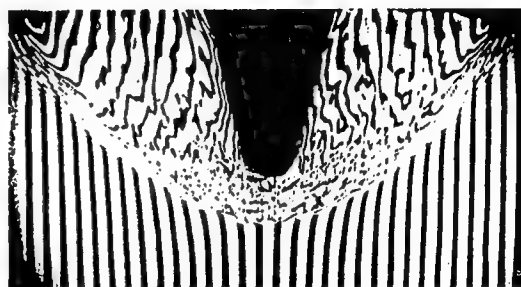


Fig.4 Same as Fig.3, $Fn=0.20$, $Rn=3.1 \cdot 10^5$.

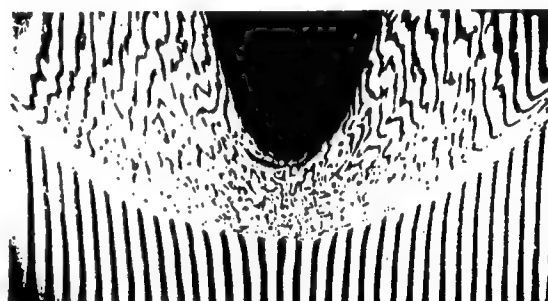


Fig.5 Same as Fig.3, $Fn=0.25$, $Rn=3.9 \cdot 10^5$.

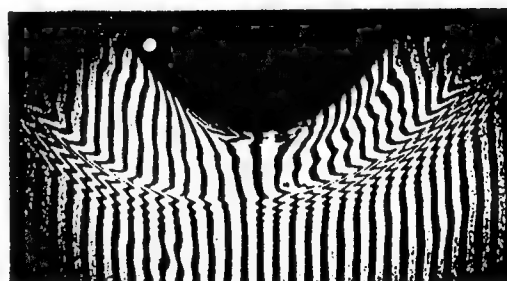
Fig.6 shows the bow wave patterns at $Fn=0.30$ for three models. The Reynolds number is $4.60 \cdot 10^5$. The free surface flows of NS08 and NS12 seem to be quite complicated and turbulent in "Zone-II" which can be called sub-breaking wave[8]. The wrinkles of NS08 and NS12 are more intensive than NS24 around the bow. The flow of NS24 looks still gentle. Here, a question may appear; why the intensity of the free surface wrinkles of NS08 is much stronger than that of NS24 although the bow of NS24 is much blunter?



(a) NS08



(b) NS12



(c) NS24

Fig.6 Pictures of free surface flows of NS08, NS12 and NS24, $Fn=0.30$, $Rn=4.6 \cdot 10^5$.

Similar experiments were carried out by Mori[8]. He used two models which were a circular cylinder and an elliptic strut. He showed that the elliptic strut generated more intensive wrinkle, which was a kind of free surface instability, than that generated by the circular cylinder at the same speed although the necklace vortex of the circular cylinder was more intensive than that of the elliptic strut. He explained that the reason might be the different free surface curvatures in front of the bows.

The detail discussions on the effect of bow curvature will be made by a numerical simulation in chapter 5.

3 Computational Method

3.1 Governing equations

Three dimensional incompressible Reynolds averaged Navier-Stokes and continuity equations are employed for the present numerical study. These governing equations are written as follows;

$$\begin{aligned} u_t + uu_x + vv_y + ww_z &= -\phi_x + \frac{1}{Rn} \nabla^2 u + R_x \\ v_t + uv_x + vv_y + ww_z &= -\phi_y + \frac{1}{Rn} \nabla^2 v + R_y \end{aligned} \quad (1)$$

$$\begin{aligned} w_t + uw_x + vw_y + ww_z &= -\phi_z + \frac{1}{Rn} \nabla^2 w + R_z \\ u_x + v_y + w_z &= 0 \end{aligned} \quad (2)$$

$$\phi = p + \frac{z}{Fn^2} - P_{at} + \frac{2}{3}k \quad (3)$$

where u , v and w are the velocity components in (x,y,z) -directions in the Cartesian co-ordinate system as shown in Fig.7; x in the uniform flow, y in the lateral and z in the vertical directions respectively. The origin is located at the leading edge of the strut on the undisturbed free surface. Subscripts represent partial differentiations with respect to the referred variables except R_x , R_y and R_z which are Reynolds stress components. Fn , Rn , ϕ , p , P_{at} and k are Froude number, Reynolds number, modified pressure, pressure, atmospheric pressure and turbulent energy respectively. All the variables are normalized by a uniform velocity(U_0) and the length of strut(L).

The Reynolds stress terms can be expressed as follows;

$$\begin{aligned} R_x &= \{\nu_t(u_x + u_x)\}_x + \{\nu_t(u_y + v_x)\}_y + \{\nu_t(u_z + w_x)\}_z \\ R_y &= \{\nu_t(u_y + v_x)\}_x + \{\nu_t(v_y + v_y)\}_y + \{\nu_t(v_z + w_y)\}_z \\ R_z &= \{\nu_t(u_z + w_x)\}_x + \{\nu_t(v_z + w_y)\}_y + \{\nu_t(w_z + w_z)\}_z \end{aligned} \quad (4)$$

The turbulence model for the flow with the free surface around ship like body is complicated and not well developed yet. The Baldwin-Lomax(BL) turbulence model[14] and its modification by Renze et al.[15] are widely used in CFD fields for the simplicity. However, Degani and Schiff[16] pointed out that the difficulty encountered in applying the BL model to bodies with crossflow separation was that of properly evaluating the eddy-viscosity in outer layer. Thus, they modified the BL model to calculate the eddy-viscosity in crossflow separation region. According to some numerical and experimental results, separated re-circulating flows exist on the free surface around shoulder part of the blunt body above a certain velocity[17,18]. Thus, in this study, the modified BL model(MBL) proposed by Degani and Schiff is used to simulate the turbulent flow around the body and it is assumed that the turbulent flow starts at $x=0.1$.

On the other hand, the SGS model[19] is introduced around bow to simulate the turbulent free surface flow at a high Froude number. This will be discussed in chapter 6.

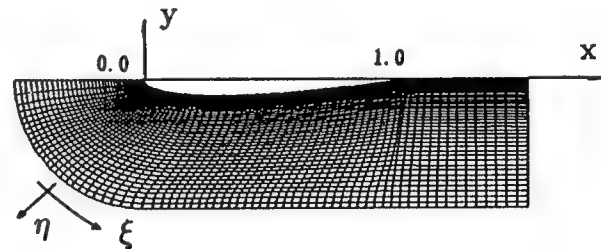


Fig.7 Co-ordinate systems and generated grid near body on horizontal plane(NS12).

3.2 Numerical algorithm

The basic concept of the solution algorithm is based on the MAC method. A finite difference method

is represented on a regular grid system. So all the variables are defined on the grid nodes. The first order difference form of the time derivatives in NS equations is used for an explicit advancement in time. The convective terms in NS equations are discretised by the third order upwind scheme (equation(5)). All the other spatial derivatives are discretised by the second order central difference scheme.

$$U = \frac{U_i}{12\Delta\xi} (u_{i-2} - 8u_{i-1} + 8u_{i+1} - u_{i+2}) + \alpha \frac{|U_i|}{4\Delta\xi} (u_{i-2} - 4u_{i-1} + 6u_i - 4u_{i+1} + u_{i+2}) \quad (5)$$

where $\alpha=1.0$ is used as a standard coefficient.

3.3 Grid generation

A numerical co-ordinate transformation is introduced into the body fitted co-ordinate system to simplify the computational domain and to facilitate the implementation of boundary conditions. C-H type grid is employed for the present computation. C-type grid is generated by using geometrical method[20] and the whole grid system is obtained by stacking them in the vertical direction algebraically. The grid topology near the body on a horizontal plane and the curvilinear co-ordinate system are shown in Fig.7. The ζ -axis of the body fitted co-ordinate system coincides with the z -axis. The grid lines are clustered near the body and the free surface to simulate properly the free surface and viscous interaction.

4 Boundary Conditions

4.1 Free surface conditions

The free surface location can be calculated to satisfy a kinematic condition which represents that the fluid particles of the free surface always remain on it. In the present study, the following Euler-type kinematic condition is used.

$$h_t + uh_x + vh_y - w = 0 \quad (6)$$

where $h(x, y, t)$ is the wave height and the subscripts represent partial differentiations with respect to the referred variables. The equation(6) is discretised by the first order forward scheme for the time integration and the third order upwind scheme for other terms.

On the other hand, the velocity and pressure can

be calculated by an equilibrium of stresses on the free surface as follows;

$$\sigma_{ij}n_j = \sigma_{ij}^*n_j \quad (7)$$

$$\sigma_{ij} = -p\delta_{ij} + \frac{1}{Rn} \left(\frac{\partial u_i}{\partial x_j} + \frac{\partial u_j}{\partial x_i} \right) - \overline{u'_i u'_j}$$

where σ_{ij} , σ_{ij}^* , n_j and δ_{ij} are fluid stress tensor, external stress tensor, unit outward normal vector to the free surface and Kronecker delta respectively in the Cartesian co-ordinate system.

Assuming no-shearing stress and excluding the surface tension, the equation(7) can be rewritten as follows;

$$\sigma_{ij}n_jn_i = P_{at} \quad (8)$$

$$\sigma_{ij}n_jt_i = 0 \quad (9)$$

where t_i is unit tangential vector to the free surface. Finally, the following equations can be used as a dynamic free surface boundary condition assuming that the normal component of the viscous and Reynolds stresses are negligibly small.

$$\phi = \frac{h}{Fn^2} \quad (10)$$

$$2u_xn_x + (u_y + v_x)n_y + (u_z + w_x)n_z = 0$$

$$(v_x + u_y)n_x + 2v_y n_y + (v_z + w_y)n_z = 0 \quad (11)$$

$$(w_x + u_z)n_x + (w_y + v_z)n_y + 2w_z n_z = 0$$

where, h , n_x , n_y and n_z are wave height and (x, y, z) -components of the unit outward vector normal to the free surface respectively. Solving equation(11), on the free surface the velocity components can be calculated.

The no-shearing stress condition leads a generation of vorticity on the free surface[9]. The axis of the vorticity is perpendicular to the streamwise direction and the strength of the vorticity is

$$\omega = 2k_s q_s \quad (12)$$

where, k_s and q_s are the curvature of streamline and streamwise velocity on the free surface respectively. Equation(12) means that the curvature of the free surface can generate the vorticity if the streamwise velocity is not zero.

A zero-gradient extrapolation for the velocity is commonly used on the free surface because of the simplicity. In the present study, the above two approaches are compared.

4.2 Other boundary conditions

On the body surface, no-slip condition is applied for the velocity and Neumann-type condition for the pressure. On the other hand, it is difficult to treat the intersection of the free surface and solid body strictly because the region is a kind of a singular region[21]. In the present study, no-slip condition is used for the velocity while the wave elevation on the body is linearly extrapolated using neighboring wave heights calculated by the kinematic free surface boundary condition. The pressure in this singular region is obtained by the dynamic free surface boundary condition directly.

In half-C type grid systems used in this study, there are two symmetry planes which are forward center plane and wake center plane. On the symmetry plane, the flow is assumed to be symmetric.

A uniform velocity and zero wave elevation are applied on the inflow boundary.

Sometimes, improper boundary conditions give some numerical troubles such as reflection or oscillation of waves on the outlet boundary. However, a simple zero-gradient extrapolation can be acceptable to investigate the flow near the body because the outer boundary or the grid arrangement around the far field region does not affect so much the flow near the body when the computational domain is large enough[22]. In the present numerical study, a simple zero-gradient extrapolation is used on the outlet boundary.

5 Numerical Simulations of Vortical Motions

5.1 Computational conditions

Several computations are performed for the four different struts as mentioned in chapter 1 which are NS05, NS08, NS12 and NS24 models. Computational conditions for the standard cases are listed in Table 1. These conditions are chosen through various test computations to investigate the effect of grid density, time increment and so on.

In the present computations, the flow is accelerated from a rest condition to the uniform velocity. The flow acceleration affects the bow wave formations; a sudden acceleration may lead strong oscillatory motion or overturning of wave around a bow. In order to avoid such a strong wave breaking, the flow is slowly accelerated up to nondimensional time $T=5.0$ in the present computations.

To validate the present computations, the computed wave profile is compared with the experimen-

tal one for NS12(Fig.8). The experiment was carried out at the circulating water channel of Hiroshima University. The length and draft of the strut are 0.15m and 0.50m respectively. Wave profiles on the body surface were measured by making use of an image processing system developed at Hiroshima University[23]. To remove the surface tension, a surfactant was also used[13]. The computed results give good agreement with the experimental one except near the wave trough. The reason of this difference may be that the flow around shoulder part of the blunt model is not steady including strong separated flow called shoulder wave breaking[17,18].

Table 1. Computational conditions for standard cases.

	Rn=5000	Rn=10 ⁵
Grid numbers		
- ξ -direction	91	110
- η -direction	45	60
- ζ -direction	20	20
Min. grid spacings		
- $\Delta\xi$	0.005	0.005
- $\Delta\eta$	0.002	0.0005
- $\Delta\zeta$	0.0015	0.0006
Time increment	0.001	0.00025
Computational domains	$-2.0 \leq x \leq 4.0$ $0.0 \leq y \leq 2.0$ $-1.0 \leq z \leq h_{max}$	

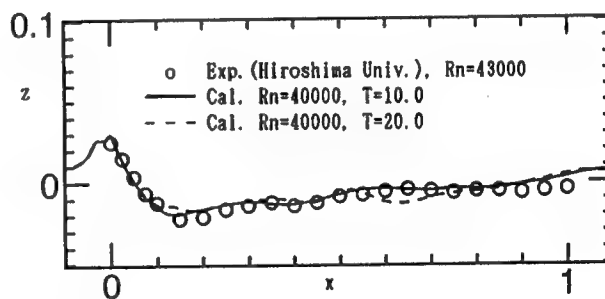


Fig.8 Comparison between computed and measured wave profiles on the body surface; NS12, $Fr=0.25$.

5.2 Vortical motions around bows

First, the effect of the dynamic free surface boundary condition is investigated. According to the equation(12), the vorticity can be generated to satisfy the no-shearing stress condition. However, the zero-

gradient extrapolation is often used because of the simplicity. Fig.9 shows the distributions of the computed velocity and vorticity on the center plane for two different treatments of the dynamic free surface boundary conditions for NS05 at $Fn=0.30$ and $Rn=5000$. In case of the zero-gradient extrapolation, the computed wave height at the bow is almost the same value as the position head at the stagnation point for inviscid fluid. On the other hand, the introduction of the no-shearing stress condition makes the counter-clockwise vorticity more intensive and the wave height decreases. This means that the energy accumulated around the wave crest is consumed by the generation of the vorticity.

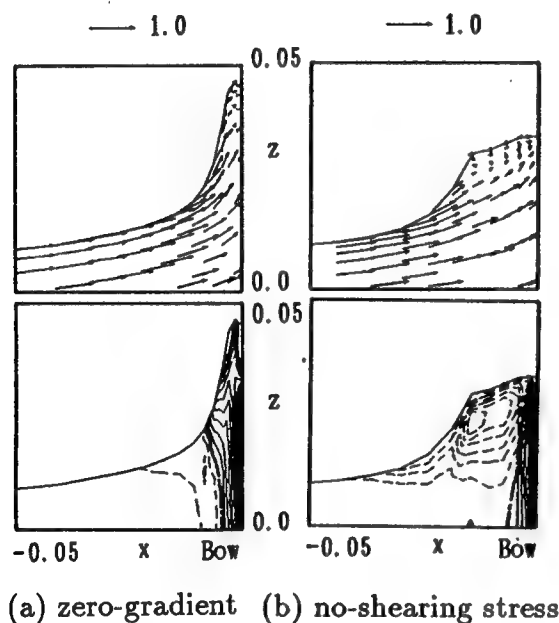


Fig.9 Computed velocity and vorticity(ω_y) distributions for two different treatment of dynamic free surface boundary condition; NS05, $Fn=0.30$, $Rn=5000$, $T=15.0$ (contour interval=10.0).

In case of a lower Froude number flow ($Fn=0.25$), however, there is no significant difference between the two results as shown in Fig.10.

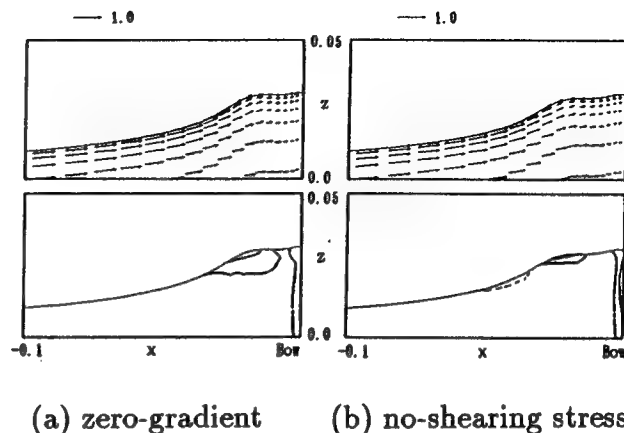


Fig.10 Same as Fig.9; NS12, $Fn=0.25$, $Rn=5000$, $T=15.0$ (contour interval=10.0).

From these results, it can be pointed out that the no-shearing stress condition on the free surface plays an important role to produce a vortical motion where the free surface curvature is large. The computations neglecting the no-shearing stress may lead misunderstanding of the phenomena. Thus, all the computations are performed taking into account the no-shearing stress condition hereafter.

Fig.11 compares the computed and experimented free surface flows between three models. The Reynolds numbers for the computation and experiment are 1.0×10^5 and 3.8×10^5 respectively. The wave front lines, which are defined in Fig.2, are clearly shown in both computed and experimented results except NS24. The computed distances between the leading edge ($x=0.0$) and the wave front on the center plane are about $0.03L$ ($x=-0.03$) and $0.04L$ ($x=-0.04$) for NS08 and NS12 respectively (L : length of the strut). It can be noted that the flow field around bow is almost steady both in the experimental and computed results when the Froude number is less than 0.25. The overall computed flow patterns are good agreement with the experimental results.

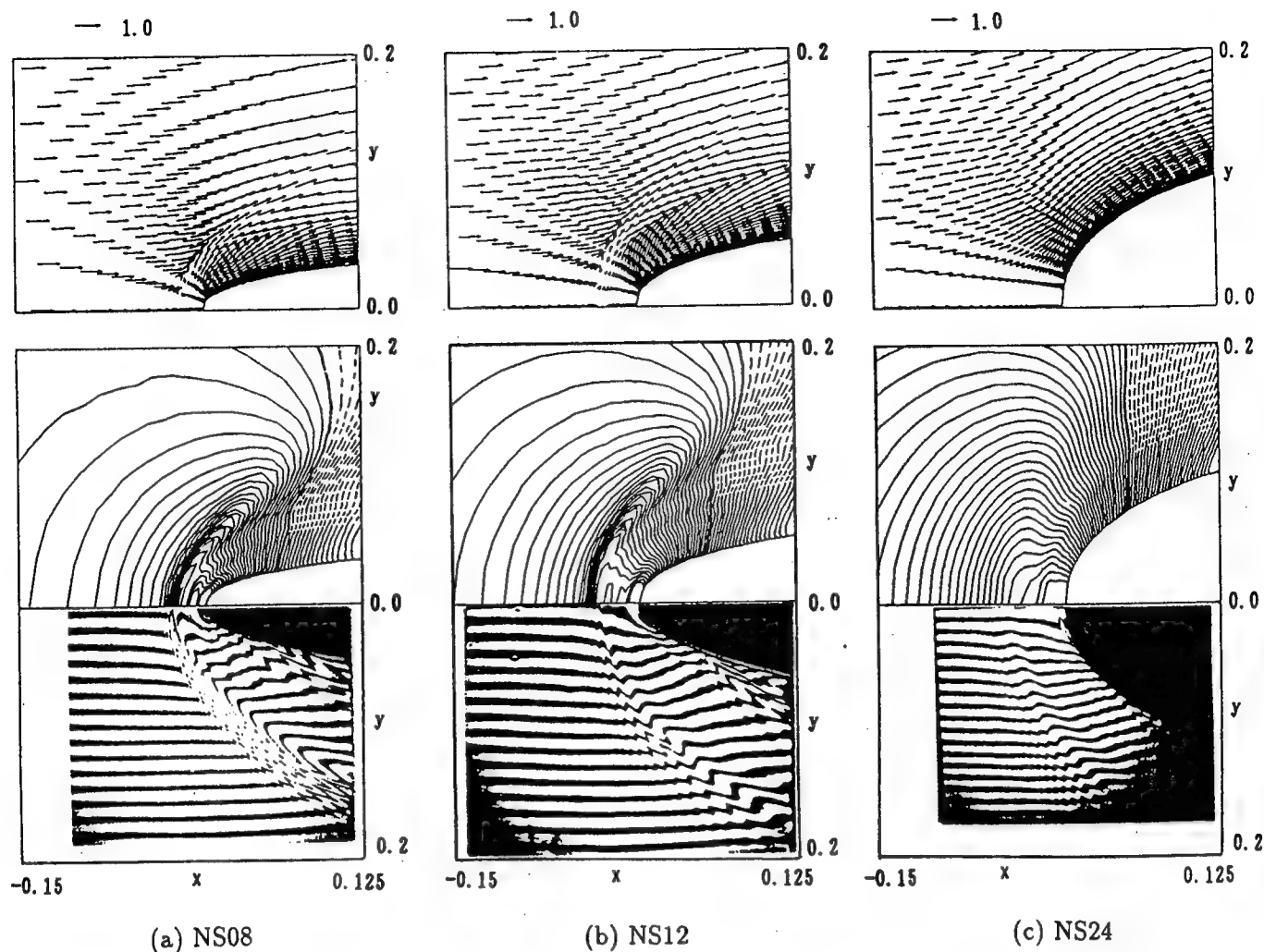


Fig.11 Comparison of computed and experimental free surface flows; NS08, NS12 and NS24, $Fn=0.25$, (upper; computed, $Rn=1.0 \cdot 10^5$, down; experimented, $Rn=3.9 \cdot 10^5$).

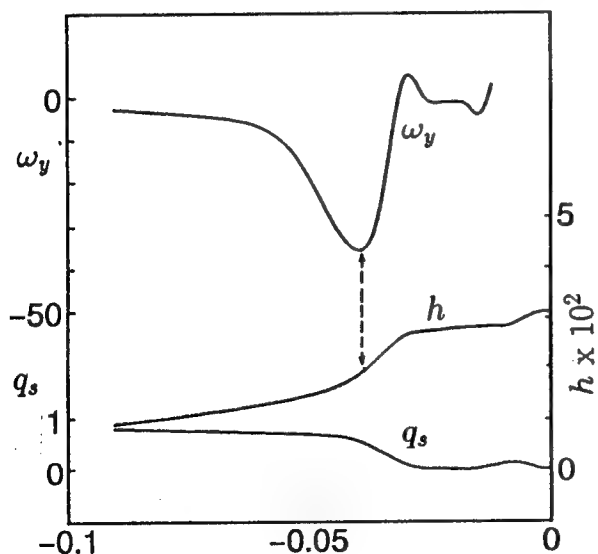


Fig.12 Relation between vorticity(ω_y), wave profile(h) and streamwise velocity(q_s) on the free surface on the center plane; NS12, $Fn=0.25$, $Rn=1.0 \cdot 10^5$.

The relation between the vorticity(ω_y), wave height(h) and the streamwise velocity(q_s) on the free surface is shown in Fig.12. The peak of the vorticity is located on the free surface having concave curvature as indicated by the dotted arrow. According to the no-shearing stress condition(equation(12)), the vorticity on the free surface can be expressed as a product of the free surface curvature and the streamwise velocity. Although the wave front has a larger curvature than that of the concave surface, the vorticity is smaller at the wave front because the streamwise velocity becomes smaller around there. This is the reason why the counter-clockwise vorticity occupies the region in front of the bow.

The comparison of the vorticity(ω_y) and velocity distributions for the three models is shown in Fig.13.

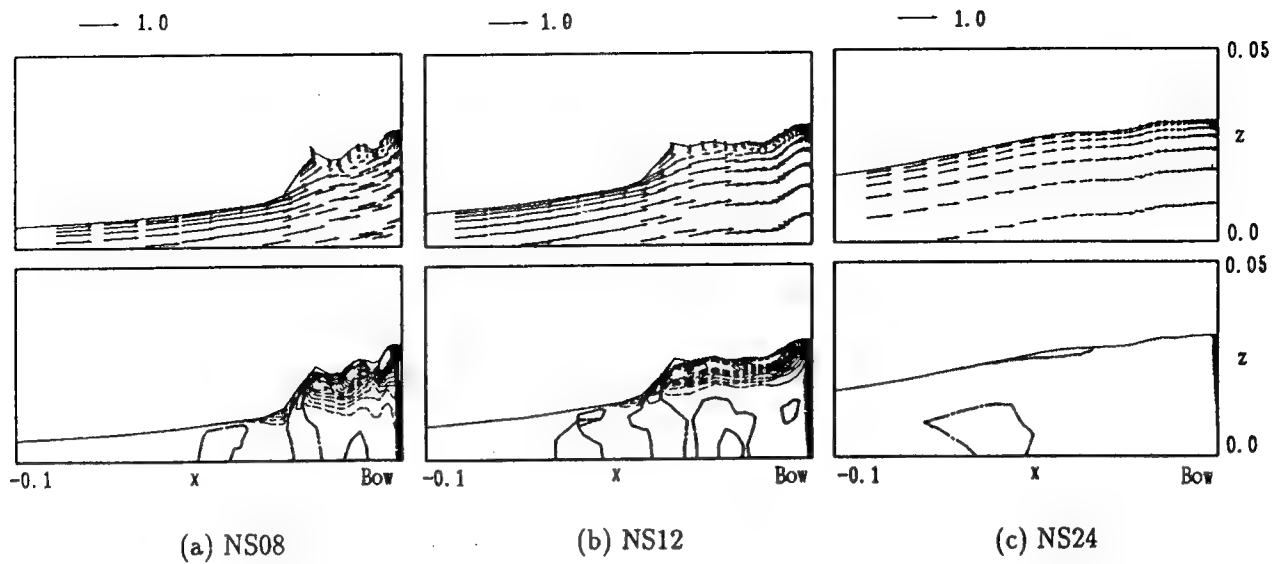


Fig.13 Computed velocity and vorticity(ω_y) distributions on the center plane in front of bows; NS08, NS12 and NS24, $Fn=0.25$, $Rn=1.0 \cdot 10^5$, $T=15.0$ (contour interval=10.0).

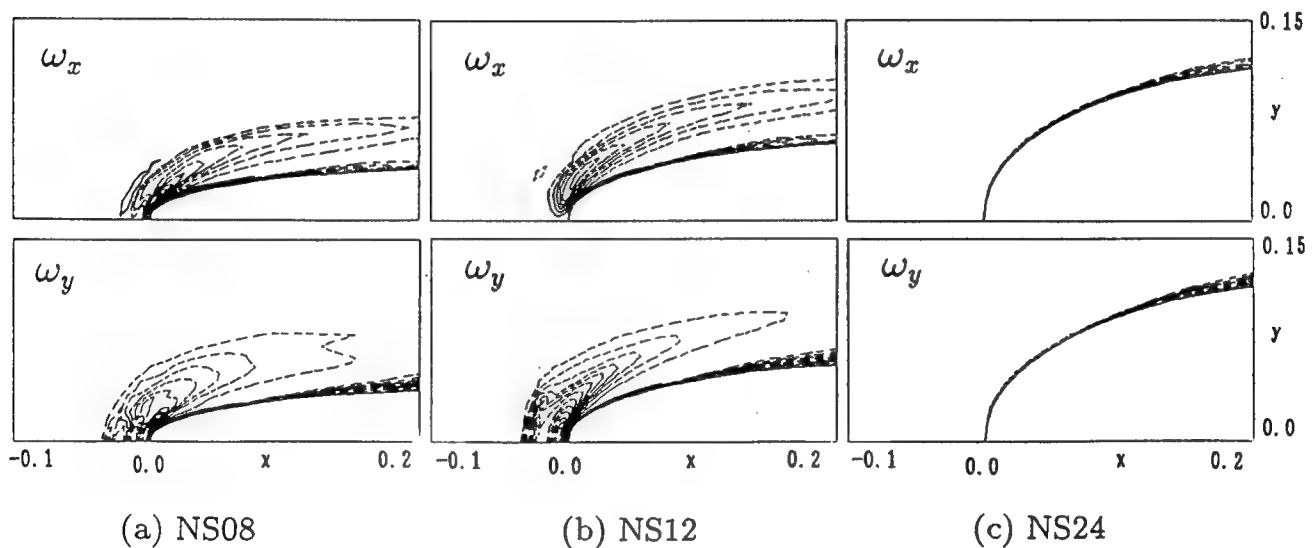


Fig.14 Computed vorticity(ω_x , ω_y) distributions beneath the free surface around bows; NS08, NS12 and NS24, $Fn=0.25$, $Rn=1.0 \cdot 10^5$, $T=15.0$ (contour interval=10.0).

The model with large curvature(NS08) generates the most intensive vorticity which is induced by the free surface curvature. The peaks of the vorticity are located beneath the free surface around the wave front for each models except NS24. In case of NS24, however, there are no such vortical motions because

the free surface is enough smooth. These results can give some explanations to the experimental findings as shown in Fig.6; the bow with a larger curvature(NS08) generates more intensive wrinkles than that with the smaller one(NS24).

Fig.14 shows the vorticity distributions on the

horizontal plane beneath the free surface around the bows at $Rn=10^5$ and $Fn=0.25$. The distance from the free surface is 0.003. The vorticity surrounding the bow, the so called "necklace vortex", is more intensive for NS12 than for NS08, although the strength of the vorticity in front of bow is not larger. These results show the same tendency with the results by Mori[8] as mentioned in chapter 2. However, in case of NS24, there are no such clear necklace vortex motions. The reason is that the free surface flow of NS24 is premature to generate the vortex motions at this Froude number.

From these results, It can be concluded that the bow shape has strong relation with the free surface curvature, especially concave shape, which is responsible for the vortical flows around the bow.

5.3 Grid dependency

Fig.15 shows the effect of grid density in the vertical direction around the free surface for NS12 at $Rn=10^5$ and $Fn=0.25$. The computations are performed for the three different minimum grid spacings ($\Delta\zeta$) of 0.0003, 0.0006 and 0.0012. The minimum grid spacing and the grid density in the normal direction to the body surface are kept almost same. In case of $\Delta\zeta=0.0012$, the vortical motions do not fully develop while they develop well for the other two cases and almost the same results are obtained.

It can be concluded that the grid density around the free surface is one of the important computational parameters; coarse grid can not detect the vortical flows beneath the free surface.

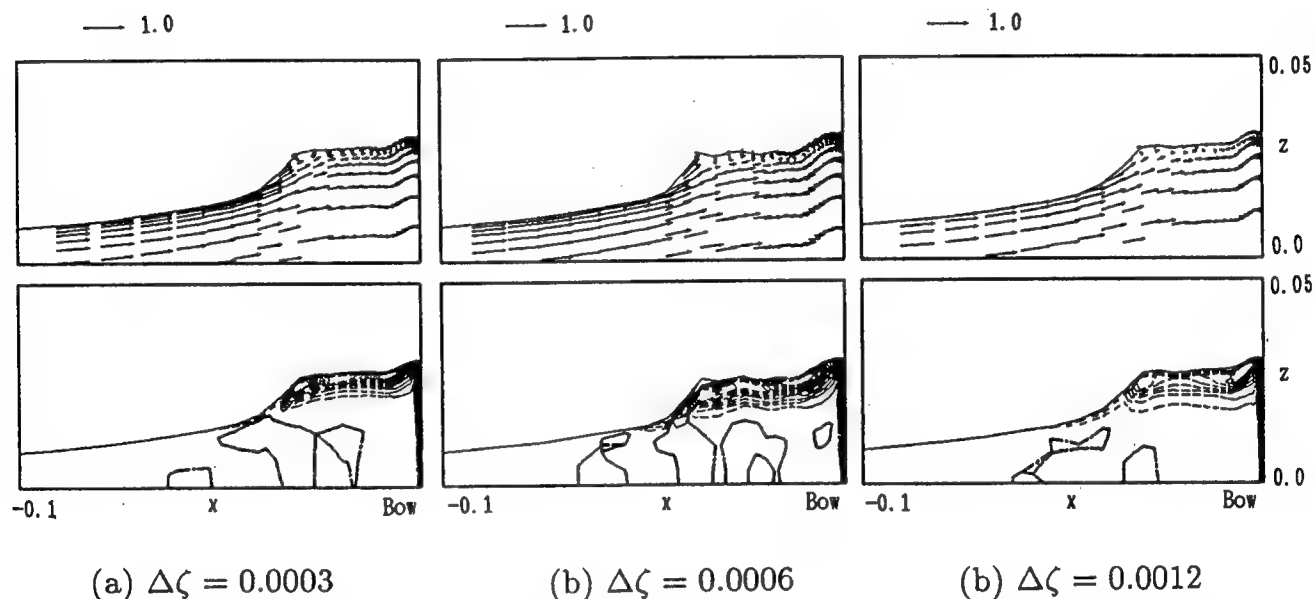


Fig.15 Grid dependency of the vortical flows on the center plane, NS12, $Fn=0.25$, $Rn=1.0 \cdot 10^5$, $T=15.0$ (contour interval=10.0).

6 Large Eddy Simulation of Sub-Breaking Waves

6.1 Computational conditions

One of the important characteristics of the sub-breaking waves is the intensive fluctuations of the free surface such as the turbulent flow in the boundary layer flow on a solid body[8]. The shear flow in the boundary layer developed on a body plays a role as a trigger for the transition to the turbulent flow and it may be assumed as a source that maintains the turbulence. Although the situation is a little different in case of the free surface flow, there exists boundary layer on the free surface which may induce the free surface turbulence.

As shown in Fig.6, the free surface flows of NS08 and NS12 are quite complicated. The situation can be assumed under the sub-breaking condition. In order to detect the sub-breaking waves, Large Eddy Simulation(LES) is performed for NS12 at $Fn=0.30$ and $Rn=10^5$. The basic equations for LES are given through a space averaging operation and they can be expressed in the same forms as equations(1)-(4).

The Sub-Grid Scale(SGS) turbulence model[19] is introduced for the simulation. So, in the computation at high Reynolds and high Froude numbers, two turbulence models are used together. One is the modified Baldwin-Lomax model(MBL) to simulate the flow in the boundary layer on the body and the other is the SGS model for the sub-breaking wave. The combination of these two models is sketched in Fig.16. The eddy-viscosity is smoothly changed in the streamwise direction through the intermediate region(INT) where the eddy-viscosity is calculated by the mean of SGS and MBL. To reduce an artificial viscosity, $\alpha=0.5$ is used in equation(5).

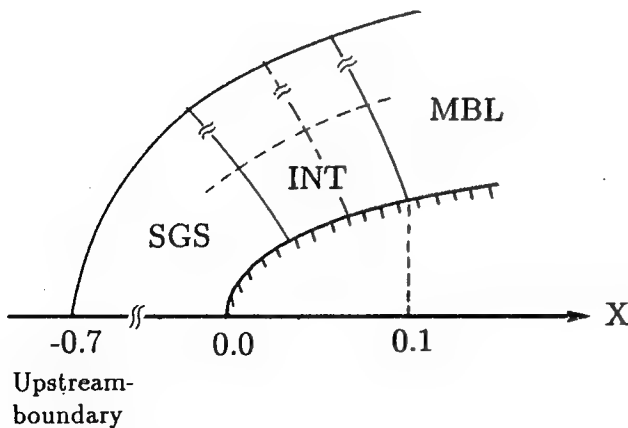


Fig.16 Combination of two different turbulent models.

In the present numerical study, the following numerical disturbance is introduced to generate the fluctuations on the free surface.

$$w' = \beta \cdot (0.5 \cdot u) \quad (13)$$

where β is a random constant ($-1.0 \leq \beta \leq 1.0$) and u is the calculated velocity of x -component. This disturbance is added in the region of SGS as indicated in Fig.16 only for two successive time steps after $T=4.0$.

Although a sufficient fine grid system and a small time increment are necessary to simulate the fluctuations directly with SGS turbulence model, it is hard to use satisfactory computational parameters because of a restriction of the memory size and the computing time. To avoid the difficulties, a smaller computational domain is used in the present sub-breaking computation. The computational domain and condition are tabulated in Table 2.

Table 2. Computational condition for Large Eddy Simulation of sub-breaking wave.

	$Rn=10^5, Fn=0.30$
Grid numbers	
- ξ -direction	72
- η -direction	60
- ζ -direction	20
Min. grid spacings	
- $\Delta\xi$	0.005
- $\Delta\eta$	0.0005
- $\Delta\zeta$	0.0006
Time increment	0.0001
Computational domains	$-0.7 \leq x \leq 1.5$ $0.0 \leq y \leq 0.7$ $-1.0 \leq z \leq h_{max}$

6.2 Results and discussions

Fig.17 shows the computed and observed flow patterns on the free surface around bow at $Fn=0.30$. The Reynolds numbers of the computation and experiment are 1.0×10^5 and 4.6×10^5 respectively. The distances between the wave front and the bow ($x=0.0$) are about $0.05L$ ($x=-0.05$) and almost the same for the both.

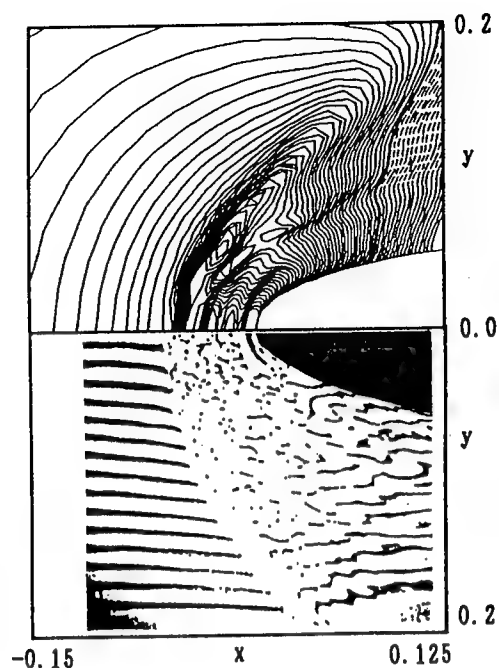


Fig.17 Comparison of computed and experimented free surface flows; NS12, $Fn=0.30$, (upper; computed, $Rn=1.0 \cdot 10^5$, down; experimented, $Rn=4.6 \cdot 10^5$).

The computed fluctuations in "Zone-II" are not so clear and small comparing with the experimental result. The reason may be that the grid system is still not so fine enough to simulate the wrinkles.

Fig.18 shows the computed velocity and vorticity(ω_y) distributions on the center plane at $T=10.0$. It must be noted that the flow around the bow is still fluctuating. Although there are slight reverse flows in the bow wave field, they are not followed by overturning wave. Several peaks of the free surface exist in the "Zone-II". The characteristics of the turbulence on the free surface are investigated at the six points around bow as shown in Fig.19.

Fig.20 shows the time histories of velocity components through $T=8.0-9.5$ at the six points. Although the initial disturbance is imposed all the domain around the bow including the point A, the fluctuations disappear at there. The velocity remains almost constant. The velocity fluctuates slightly at point B where the concave curvature of the free surface appears. The

fluctuations become intensive at point C which is just outside of the wave front and the free surface curvature is larger. It can be considered that the instability of the free surface starts there. At point D, the amplitude of the fluctuations of the velocity components becomes larger and the u-component is less than zero. This result indicates that the free surface flows at point D is turbulent and reverse flows exist there. The fluctuations become gradually weak at points E, and F. At point E, the u-component is still negative and it is a positive at point F. The reverse flow on the free surface disappears after the point E.

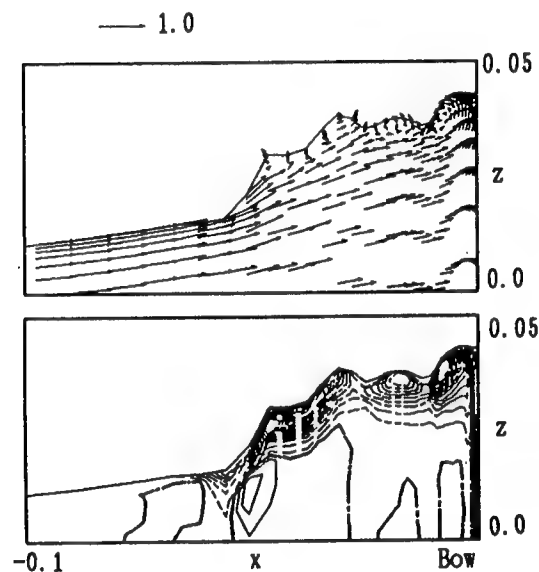


Fig.18 Computed velocity and vorticity(ω_y) distributions on the center plane in front of bows; NS12, $Fn=0.30$, $Rn=1.0 \cdot 10^5$, $T=10.0$ (contour interval=10.0).

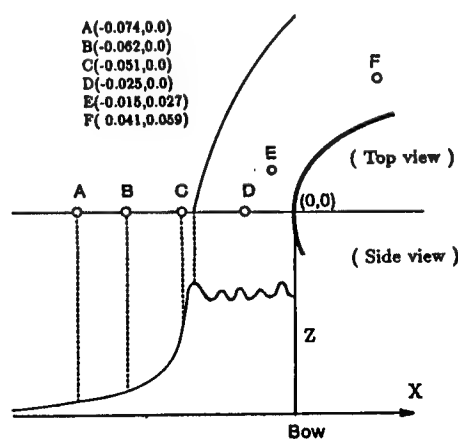


Fig.19 Schematic view of bow wave and the definition of six points for investigation of turbulent quantities.

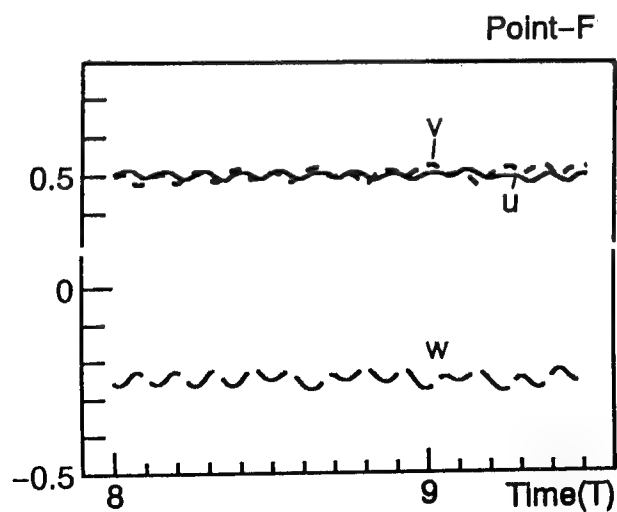
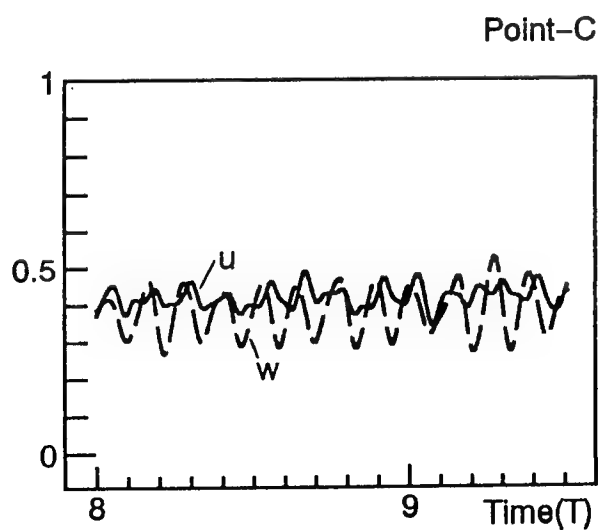
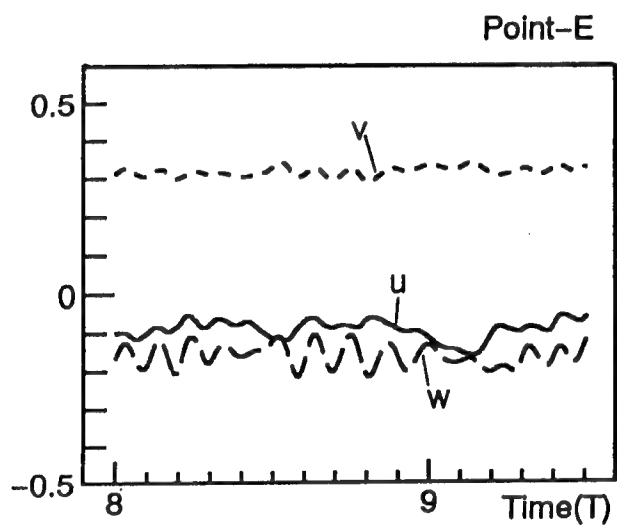
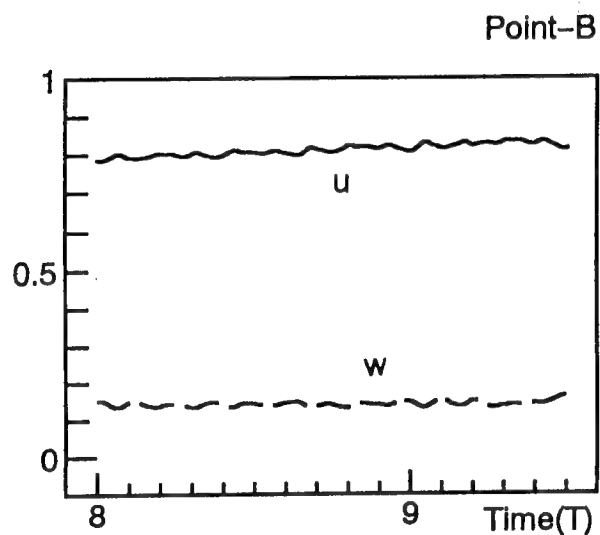
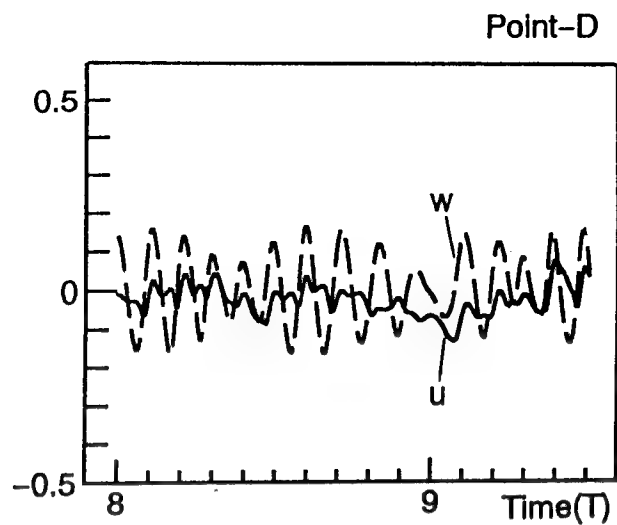
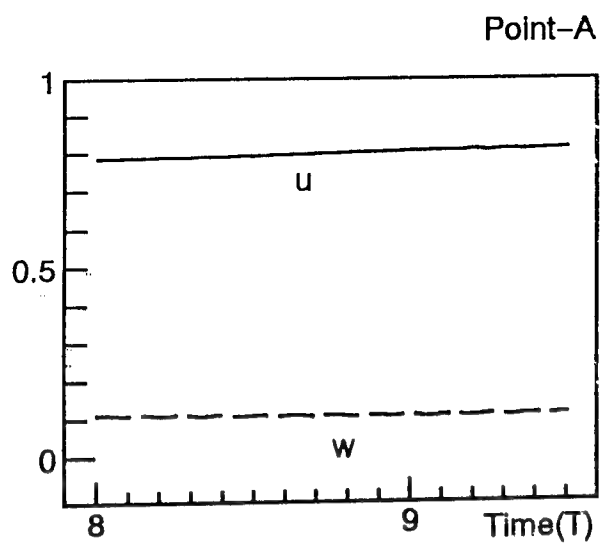


Fig.20 Computed time histories of velocity components at six points on the free surface; NS12, $Fn=0.30$, $Rn=1.0 \cdot 10^5$.

Fig.21 shows the distributions of time averaged velocity components in depthwise direction at points A and D. The velocity is averaged for 15000 time steps from $T=8.0$ to 9.5.

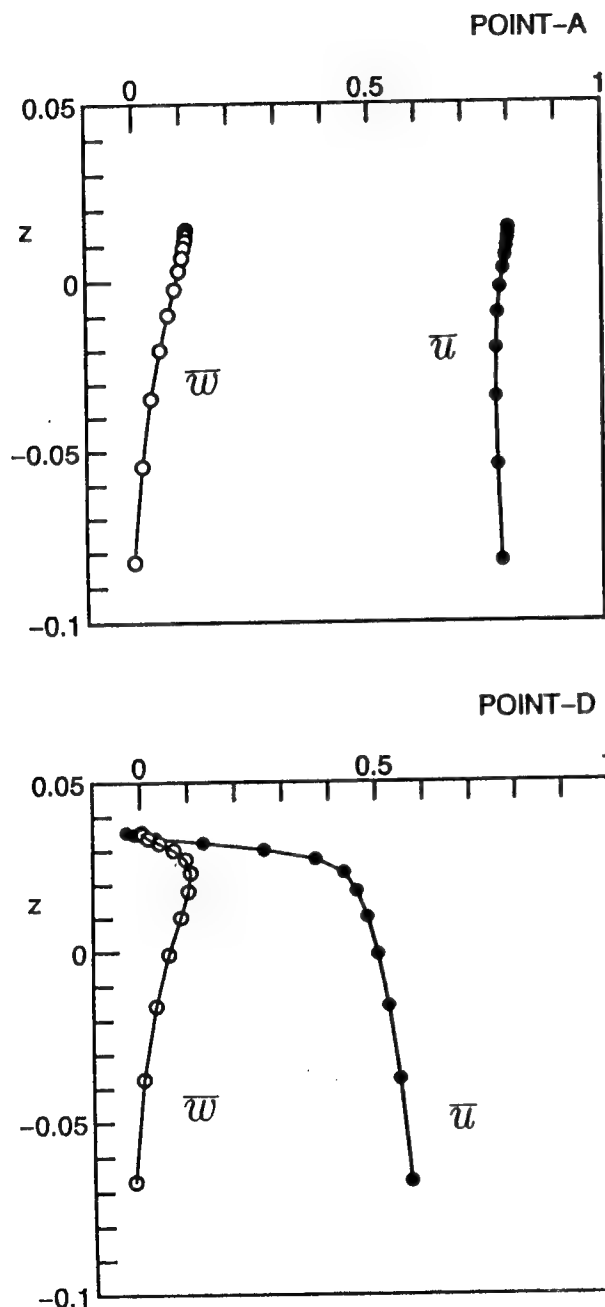


Fig.21 Computed mean velocity distributions at points A and D; $NS12$, $Fn=0.30$, $Rn=1.0 \cdot 10^5$.

At point D where the flow is fully turbulent the strong defect of the u -component exists close to the free surface while w -component has small defect. On the other hand, there is no such a velocity defect at point A where the free surface flow is laminar. These results are found in the experimental results by Mori[8] who measured the velocity components in front of a elliptic strut and a circular cylinder under the sub-breaking condition.

Fig.22 shows the computed Reynolds stress components at point D. The cross component ($\overline{u'w'}$) is almost zero on the free surface because the no-shearing stress condition is imposed on the free surface. On the other hand, other components become larger on the free surface. This is the same tendency with the experimental results by Mori[8].

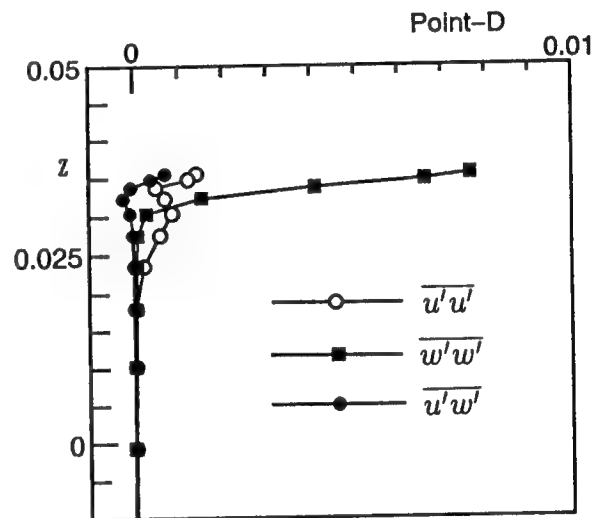


Fig.22 Computed Reynolds stress distributions at points D; $NS12$, $Fn=0.30$, $Rn=1.0 \cdot 10^5$.

Fig.23 shows the turbulent energy profiles in depthwise direction at points A and D. At point A, the turbulent energy is almost zero while, at point D, it is intensive on the free surface and it abruptly becomes weak at the depth of $0.02L$ from the free surface.

We can point out that the free surface turbulent flow referred to the sub-breaking wave generated without overturning waves. The numerical simulations neglecting the turbulence may lead a misunderstanding of the phenomena.

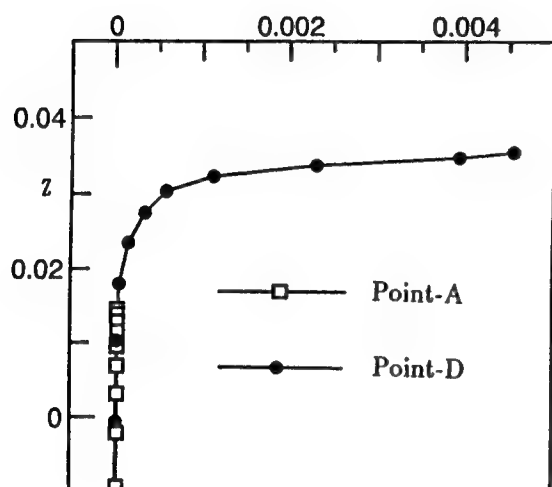


Fig.23 Computed turbulent energy distributions at points A and D; $NS12$, $Fn=0.90$, $Rn=1.0 \cdot 10^5$.

7 Concluding Remarks

Some characteristics of the turbulent and vortical flows around the free surface are numerically and experimentally investigated. Four different struts are used to investigate the curvature effect of the bow.

Findings through the present study are summarized as follow;

1) The no-shearing stress condition on the free surface is important to generate the vorticity beneath the free surface. And the vorticity induces vortical motions beneath the free surface when the free surface curvature is large.

2) The proposed LES method reveals the existence of the free surface turbulence called sub-breaking wave which is not followed by overturning waves.

3) The bow with a larger curvature intensifies the concave curvature of the free surface and generates a stronger vorticity than the bows with smaller curvature.

4) Grid density around the free surface is one of the important computational parameters; coarse grid can not detect the vortical flows beneath the free surface.

The authors express a lot of thanks to Dr. S. Ni-nomiya, research associate at Hiroshima University, for his kind support in experiments.

References

- [1] Baba, E.: *A New Component of Viscous Resistance of Ship*, *Journal of the Society of Naval Architects of Japan*, Vol.125, pp.23-34, 1969.
- [2] Taneda, S. and Amamoto, H.: *The Necklace Vortex of the Ship*, *Bulletin of Research Institute for Applied Mechanics*, Kyushu Univ., No.31, pp.17-28, 1969 (in Japanese).
- [3] Miyata, H., Kajitani, H., Shirai, M., Sato, T., Kuzumi, S. and Kanai, M.: *Numerical and Experimental Analysis of Nonlinear Bow and Stern Waves of a Two-Dimensional Body (4th Report)-Simulation of Breaking Waves and Experimental Analysis*, *Journal of the Society of Naval Architects of Japan*, Vol.157, pp.15-33, 1985.
- [4] Groesenbaugh, M. A. and Yeung, R. W.: *Non-linear Bow Flows-An Experimental and Theoretical Investigation*, *Proceedings of 17th Symposium on Naval Hydrodynamics*, Hague, Netherlands, pp.195-214, 1988.
- [5] Honji, H.: *The Necklace Vortex of the Ship*, *Bulletin of Research Institute for Applied Mechanics*, Kyushu Univ., No.43, pp.11-17, 1975 (in Japanese).
- [6] Kayo, Y. and Takekuma, K.: *On the Free Surface Shear Flow related to Bow Wave-Breaking of Full Ship Models*, *Journal of the Society of Naval Architects of Japan*, Vol.149, pp.11-20, 1981.
- [7] Patel, V. C., Landweber, L. and Tang, C. J.: *Free-Surface Boundary Layer and the Origin of Bow Vortices*, *2nd International Symposium on Ship Viscous Resistance*, Gotenburg, Sweden, pp.23:1-23:13, 1985.

- [8] Mori, K.: *Necklace Vortex and Bow Wave around Blunt Bodies*, Proceedings of 15th Symposium on Naval Hydrodynamics, Hamburg, Germany, pp.303-317, 1984.
- [9] Batchelor, G. K.: *An Introduction to Fluid Dynamics*, Cambridge University Press, pp.364-366, 1970.
- [10] Mori, K. and Shin, M. S.: *Sub-Breaking Wave: Its Characteristics, Appearing Condition and Numerical Simulation*, Proceedings of 16th Symposium on Naval Hydrodynamics, Hague, Netherlands, pp.499-511, 1988.
- [11] Mori, K. and Lungu, A.: *Sub-Breaking Wave and Its Numerical Simulation with Turbulent Characteristics*, Proceedings of 9th International Symposium on Ocean Waves and Floating Bodies, Kyushu, Japan, pp.143-146, 1994.
- [12] Coleman, R. M.: *Nonlinear Calculation of Breaking and Non-Breaking Waves Behind a Two-Dimensional Hydrofoil*, Proceedings of 16th Symposium on Naval Hydrodynamics, Berkeley, USA, pp.51-62, 1986.
- [13] Maruo, H. and Ikehata, H.: *Some Discussions on the Free Surface Flow around the Bow*, Proceedings of 16th Symposium on Naval Hydrodynamics, Berkeley, USA, pp.65-77, 1986.
- [14] Baldwin, B. S. and Lomax, H.: *Thin Layer Approximation and Algebraic Model for Separated Turbulent Flows*, AIAA Paper 78-257, 1978.
- [15] Renze, K. J., Buning, P. G. and Rajagopalan, R. G.: *A Comparative Study of Turbulence Models for Overset Grids*, AIAA Paper 92-0437, 1992.
- [16] Degani, D. and Schiff, L. B.: *Computation of Turbulent Supersonic Flows around Pointed Bodies Having Crossflow Separation*, Journal of Computational Physics, 66, pp.173-196, 1986.
- [17] Pogozelski, E., Katz, J., Huang, T.: *Flow Structure around a Surface-Piercing Blunt Body*, Proceedings of 20th Symposium on Naval Hydrodynamics, Santa Barbara, USA, pp.117A-117G, 1994.
- [18] Zhang, Z. J. and Stern, F.: *Wave-Induced Separation*, Forum on Advances in Numerical Modeling of Free Surface and Interface Fluid Dynamics, 1995 ASME IMECE, San Francisco, USA, 1995.
- [19] Deardorff, J. W.: *A Numerical Study of Three Dimensional Turbulent Channel-Flow at Large Reynolds Numbers*, Journal of Fluid Mechanics, 41, pp.453-480, 1970.
- [20] Kodama, Y.: *Three Dimensional Grid Generation around a Ship Hull Using the Geometrical Method*, Journal of the Society of Naval Architects of Japan, Vol.164, pp.1-8, 1998.
- [21] Farmer, J., Martinelli, L. and Jameson, A.: *Multigrid Solution of the Euler and Navier-Stokes Equations for a Series 60 $C_b=0.6$ Ship Hull for Froude Numbers 0.160, 0.220 and 0.316 (Program 1: Navier-Stokes Formulation)*, Proceedings of CFD WORKSHOP TOKYO 1994, Vol.1, pp.56-65, 1994.
- [22] Hinatsu, M.: *Numerical Simulation of Unsteady Viscous Nonlinear Waves Using Moving Grid System Fitted on a Free Surface*, Journal of the Kansai Society of Naval Architects of Japan, No.217, pp.1-11, 1992.
- [23] Ninomiya, S., Mori, K., Hosokawa, M.: *Measurements of Wave Height by Visualizing Air-Side Free-Surface and Illuminating the Wetted Surface of Hull through Water*, Journal of the Society of Naval Architects of Japan, Vol.174, pp.129-135, 1993 (in Japanese).

DISCUSSION

R.W. Yeung
University of California at Berkeley, USA

I would like to congratulate the authors for a very interesting paper on a subject area that complements and extends our work in the Seoul Symposium (Yeung and Ananthakrishnan [1]). Perhaps the authors are not aware of this work. In our paper, as well as a related publication (Ananthakrishnan and Yeung [2]), we have systematically investigated the effects of the free-surface boundary condition (free-slip, no slip, clean, or with surface contaminants) on the vortical structures below the free surface. Even though our works were two-dimensional, I feel what is stated in the present paper, in regard to the need to apply the zero-stress condition, has already been established in our earlier works. Our investigations and solutions covered a large range of scenarios.

As to qualitative features of the bow-flow results, the present authors' thick-body results (corresponding to NS24) are consistent with the limiting behavior of our (two-dimensional) blunt bow solution. However, the intensification of cross-stream vorticity due to an increase in waterline curvature (Fig. 9b and 13b) seems to suggest the presence of a (steady state) stagnation point on the free surface located between the clockwise and counter-clockwise vortices. Is this really physically plausible? If so, what would the topology of such a flow be like?

Another question that comes to mind concerns the accuracy of computations. In Fig. 15, the authors demonstrated that a grid density $\Delta\xi = .0003$ was needed to capture the surface and vortical details, while most of the computations utilize a grid spacing effectively almost 10 times larger (see Table 1). This fact, coupled with a grid aspect ratio (horizontal to vertical) of almost 10 can easily lead to inaccuracies. Perhaps the authors can comment on this difficulty, particularly in connection with the large artificial viscosity arising from a scheme like Eqn. (5).

My final remark concerns the LES and MBL modeling of the free surface. It appears to rather ad hoc as these models were established on the ground that the flow had no free boundaries. Given that the authors are convinced that the no-stress free-surface condition is an important one, it seems inconsistent to utilize such models. Perhaps it is not surprising that the mean values of computed

and measured velocities differ significantly in Figure 21.

REFERENCES

- [1] Yeung, R.W. and Ananthakrishnan, P. "Vortical flows with and without a surface-piercing body," *Proc. 19th Symp. Naval Hydrodyn.*, Seoul, Korea, 1992.
- [2] Ananthakrishnan, P. And Yeung, R.W. "Nonlinear interaction of a vortex pair with clean and surfactant-covered free surfaces," *Wave Motion*, **19**, pp. 343-365, 1994.

AUTHORS' COMMENTS

We would like to thank you for the remarks and comments.

The need to apply the zero-shear stress condition on the free surface was already discussed by Mori [8]. It was concluded the free-surface curvature was one of the sources for the shear flow and vortical motion beneath the free surface. So far as we understood, it was concluded that the free-surface vorticity generated by free-surface curvature was rather weak in the paper for Profs. Yeung and Ananthakrishnan.

The clockwise vorticity around the bow shown in Figs. 9b and 13b does not indicate a vortex but a shear flow on the body. The dominant vortical motion is counter-clockwise. As Prof. Yeung pointed out, there is a stagnation point on the free surface because a weak reverse flow is observed on the free surface.

The grid density high aspect ratio of the grid arrangement leads to inaccuracies when the flow is not parallel to the grid. In the present computation, the flow beneath the free surface is almost parallel to grid where the aspect ratio is high. The situation is the same as the flow simulation of the boundary layer developed on a solid surface.

LES was originally developed for the simulation of homogeneous turbulence. Successful implementation of LES for a turbulent flow with no free boundary such as a solid wall is achieved through a special modification of SGS modeling near wall. In the present simulation for a free-surface turbulence, Smagorinsky's closure is applied without a

modification. It is not inconsistent to utilize the model. Of course, it is important to develop some modification of the SGS and MBL models for free-surface turbulence.

Steep and Breaking Faraday Waves

L. Jiang, M. Perlin, W. Schultz (University of Michigan, USA)

Abstract

This paper examines the dynamics of steep to breaking standing waves on deep water generated by Faraday resonance. Physical experiments are compared with simulations by a two-dimensional spectral Cauchy-integral code. At larger forcing amplitude, we have observed experimentally a steep waveform with a double-peaked crest, while simulation of the same forcing condition results in a sharper crest (Jiang *et al.*, 1996). Increasing wave steepness leads first to a double-plunging breaker at the dimpled crest, then to more violent breaking in three recurrent modes (period tripling): sharp crest with breaking (A) \rightarrow dimple or flat crest with breaking (B) \rightarrow round crest without breaking (C). Nonlinear interaction between the fundamental mode and second temporal harmonic determines both the steep and breaking waveforms. Geometric features of the breaking wave are discussed, especially the extremely-large wave amplitude and sharp crest angle in mode A. Based on the periodicity of the flow, energy dissipation is directly estimated by integrating the support force as a function of the tank displacement. It is found that the breaking event increases the total dissipation in the system by about 100%. Large dissipation occurs during modes A and B due to spray, air entrainment and plunging.

Introduction

Synthetic Aperture Radar (SAR) images are often brighter near ocean features such as currents, shelves, and slicks that cause wave reflection. Since the backscattering of microwaves by the sea surface is sensitive to the curvature of surface features as well as Bragg periodicity, these strong SAR returns may be caused by higher surface curvature known to occur in standing waves that can be more peaked than their progressive wave counterparts. Therefore, accurate representation of steep and breaking standing waves, or more generally counterpropagating, periodic waves, is an essential feature required in the interpretation of SAR images. An even more complex phenomena: wave breaking, directly influences the specular and Bragg scattering. Since counterpropagating waves are very common in both open sea and coastal regions, their breaking mechanisms are crucial to wave modeling, e.g. (deep water and shoal-

ing) wave breaking criteria, and energy dissipation. To this end, the breaking standing wave and its energy dissipation serve as a good model to study.

In the absence of viscous dissipation, a solution has been obtained by Penney & Price (1952) for standing gravity waves on the free surface of deep water. Their solution describes a standing wave with a sinusoidal shape at modest amplitudes to one with a more peaked crest and flatter troughs (c.f. figure 1) at higher amplitudes. With further increase in wave steepness to 0.218, their analysis appears to reach a limiting waveform with a crest angle of 90° . Schwartz & Whitney (1981) determined that the maximum wave steepness H/λ is 0.197 by expansion and 0.208 by analytic continuation, less than 0.218. Here, H is the peak-to-peak wave height and λ is the wavelength. A numerical investigation by Schultz & Vanden-Broeck (1990) showed that the surface tension had to be included to obtain waves as steep as predicted by Penney & Price (1952) and that the 90° crest angle conjecture was flawed. With surface tension, the steepest waves had a crest sharper than 90° or had a bulbous protuberance.

The standing-wave form of Penney & Price has been observed experimentally (Taylor 1953) and numerically (Vanden-Broeck & Schwartz 1981). Nonetheless, the uniqueness of their solution is still undetermined. Their approach is only valid when resonance between different harmonics can be "avoided" (Tadjbakhsh & Keller 1960); symmetry in space and time is also a vital assumption in the success of a higher-order expansion by Schwartz & Whitney (1981). Recently, multiple forms of small-amplitude standing wave are discussed by Bryant & Stiasnie (1994) based on the Zakharov equation approach.

Taylor (1953) generated standing waves by simultaneously oscillating two hinged vertical paddles. Standing waves can also be excited by vertical oscillation through subharmonic resonance (Benjamin & Ursell 1954, Miles & Henderson 1990). Since the Faraday experiment ensures spatial periodicity by laterally fixed endwalls, this approach was adopted by Jiang *et al.* (1996) to study the Faraday resonance and nonlinear standing waveforms. According to the linear theory, the standing wave amplitude

$A_i(t)$ is governed by a Mathieu equation,

$$\frac{d^2 A_i}{dt^2} + (p - 2q \cos \omega_f t) A_i = 0 \quad (1)$$

where

$$p = \frac{4\omega_i^2}{\omega_f^2}, \quad q = 2fk_i \tanh(k_i h) \quad (2a, b)$$

and

$$\omega_i = [k_i(1 + \kappa \cdot k_i^2) \tanh(k_i h)]^{1/2} \quad (3)$$

Here, ω_f is the forcing frequency, f is the forcing amplitude. Subsequently, we use $1/k = \lambda/2\pi$ as the length scale and \sqrt{gk} as the time scale, where λ is the characteristic wave length and g is the gravitational acceleration. In equation (3), ω_i is the natural frequency for the i th spatial mode with wavenumber $k_i = i$ and dimensionless capillary number $\kappa = \sigma k^2 / \rho g$. The subharmonic resonance corresponds to $p \approx 1$, i.e. $\omega_f \approx 2\omega_i$. To excite the fundamental mode with one wavelength in the tank ($k = k_1 = 1$), the forcing frequency must satisfy $\omega_f \approx 2\omega_1 = 2\omega_N$. This forcing frequency eliminates the sloshing mode, thereby preserving the spatial symmetry about the tank centerline.

One notable result of Jiang *et al.* (1996) is that for larger wave steepness, unexpected flat and dimpled crests appear in the physical experiments while the numerical simulation presents a wave with much sharper crest. (The dimpled crest feature is seen in the numerics but for a different phase.) These intricate wave forms are not described by any standing-wave model. They are strongly asymmetric about the peak in time and only emerge at finite amplitudes.

The main theme of this paper is that the new standing wave leads eventually to breaking with period tripling in the physical experiments. Steep and breaking wave profiles are quantified by a non-intrusive optical system. At sufficiently large forcing amplitude, a steep wave with a dimpled crest generates two plungers breaking to each side of the tank centerline. Increasing the forcing amplitude further leads to period-tripling: breaking every two of three waves in a three-wave cycle. The dynamics of both steep and breaking standing waves are related to the interaction between the fundamental mode and its temporal second harmonic. To estimate the viscous dissipation and *dissipation due to breaking*, we present the first *direct* measurements based on the periodicity of the breaking events and accurate force measurements. Before presenting some preliminary results, we first describe briefly the method we use to measure wave dissipation.

Principle of wave dissipation measurement

For nonbreaking waves, experiments with a fixed forcing frequency and forcing amplitude can be divided into three stages: (1) initial state when the tank is oscillating but no wave growth is observed; (2) intermediate state when the wave amplitude grows to a maximum and then slowly decays to a finite amplitude; (3) the final periodic state when the limit-cycle amplitude of the Faraday wave remains constant. Using a load cell located between the shaker and the tank, we can measure the time history of

the support force during these three stages. The measured force is integrated with respect to the tank displacement to yield the work done by the shaker on the system. The wave dissipation can then be estimated as described below.

The total energy (work) input to the system is transformed into wave energy, wave dissipation and mechanical work. Here, mechanical work includes bearing dissipation, friction and other energy losses that are unrelated to the fluid motion in the tank. During stage 1, the wave surface remains horizontal so both wave energy and wave dissipation are negligible. The measured work per unit wave period represents mechanical work only. During stage 2, part of the work done by the shaker is converted into wave energy. The measured work in stage 3 should equal the mechanical work plus the wave dissipation as a periodic wave field exists. As both forcing frequency and amplitude are constant in the experiments, and the center of the water body is fixed relative to the oscillating tank, the mechanical work in stage 3 is the same as that determined in stage 1. The wave dissipation ΔE is then determined by $\Delta E = W_{total} - W_{mech}$.

Since this technique is based on the balance between energy input and energy dissipation, it only applies to periodic wave fields. *Breaking-wave dissipation* would be difficult to estimate because of the irreversible breaking process. Fortunately (also unexpectedly), the breaking waves in our experiments are periodic! At a forcing amplitude that first initiates breaking, double plungers appear (stage 4), but the waveform, once established, remains temporally and spatially periodic. At larger wave steepness (i.e. larger forcing), the dimpled waveform evolves into three different, but three-wave periodic breaking modes (stage 5): the most violent breaking mode, a sharp-crest wave with upward jet (A), occurs every three periods, followed repeatedly by a dimpled waveform with plunging breaking (B), and a round-crest mode (C). The energy dissipation during the three-wave periodic breaking is then estimated by calculating the average work every three periods in stage 5.

Numerical method

As in Jiang *et al.* (1996), we use the Cauchy integral method to simulate two-dimensional standing waves. In potential flow, the periodic free surface on the deep water can be conformally mapped to an approximate unit circle. The Lagrangian form of the kinematic and dynamic conditions are applied on the free surface:

$$\frac{D\xi}{Dt} = \frac{dw^*}{d\xi}, \quad (4)$$

$$\frac{D\phi}{Dt} = -y[1 - \omega_f^2 f \cos(\omega_f t)] + \frac{1}{2} \left| \frac{dw^*}{d\xi} \right|^2 - \kappa \frac{x_s y_{ss} - x_{ss} y_s}{(x_s x_s + y_s y_s)^{3/2}} - 2\gamma\phi. \quad (5)$$

Here, D/Dt represents the material derivative. The complex potential $w(\xi) = \phi + i\psi$ is solved on the free surface $\xi = x + iy$ and w^* is the complex conjugate of $w(\xi)$.

The subscripts represent the derivative of x and y with respect to s , a free-surface arclength parameter. To compute a Faraday wave, vertical oscillation is included as an effective acceleration. Measured damping coefficients γ are chosen to simulate physical experiments.

The principle-valued Cauchy integral equation

$$\oint_{\partial\Omega} \frac{w(\xi)}{\xi - \zeta_k} d\xi = i\alpha w(\zeta_k) \quad (6)$$

is discretized to solve for $w(\zeta_k)$ at the k th node, where α is the included angle. In the present scheme the integrand is expressed as a Cardinal function at the singularity and we evaluate the derivatives spectrally (Schultz *et al.* 1994). The algebraic equations are solved iteratively by GMRES (Saad & Schultz 1986) and a 4th-order modified Hamming predictor-corrector method is used for marching in time. All simulations presented use 64 nodes in the horizontal direction with an error tolerance of 10^{-10} for time marching and iterative matrix solving.

Numerical ("zigzag") instabilities occur for very steep waves. Then, we include an additional dissipation term $\gamma_1 \phi_{sss}$ in (5), where γ_1 is at most about 1% of γ . In the present application, it is more effective in suppressing the higher-mode numerical instability than other attempted filtering techniques.

Experimental apparatus

The inner dimensions of the rectangular glass tank are 600 mm long, 60 mm wide and 483 mm deep. The operational water depth is approximately 300 mm. With negligible lateral vibration (less than 3% of the vertical oscillation), this 10:1 tank aspect ratio ensures that the excited waves are two dimensional and symmetric in space ($\omega_N = 1.611$ Hz). The tank is fixed to a programmable shaker that is best suited to operate in low frequency range: 0.5 Hz to 5.0 Hz. The control system includes a Macintosh computer with National Instruments' LabVIEW software, data acquisition boards, and a transducer for the vertical displacements of the tank.

Wave measurements

Spatial surface profiles are obtained by a laser-sheet measurement technique (Perlin *et al.* 1993). Figure 2 shows the imaging system, including a 5 Watt Argon-Ion laser; attendant optics and a high-speed, 8 bit video system with intensified imager. We use a spherical lens to focus the laser and a cylindrical lens to expand the laser beam into a sheet. The laser sheet is introduced from above the water, parallel to the front glasswall. It illuminates the central plane of the tank with a thickness less than 1 mm at the still water level. Fluorescent dye (fluorescein) is added to the water to brighten the liquid such that there is a jump in light intensity at the free surface. In some experiments, due to the complex nature of the breaking wave, we also use silver-coated hollow spheres ($10\mu\text{m}$ diameter) as seeding particles to better illuminate the entire central plane.

We use a Kodak Ektapro CID intensified imager with controller to record the wave profile and use the Ektapro EM 1012 recorder for storage. The image is composed of 239 horizontal pixels by 192 vertical pixels. To capture the entire surface, we use a 50 mm camera lens on the intensified imager and the camera is located at 8 m from the tank. Its optical axis is oriented perpendicular to the laser sheet and at about a 15° angle with respect to the mean water surface (to remove any obstructing influence from the meniscus on the front glass wall). Using a precise target shows no significant image distortion in either direction. The average image resolution is 2.66 mm/pixel and the measurement error is about one pixel.

The images are recorded at 50 Hz through 250 Hz and transferred to computer via a standard GPIB interface. An edge-detection program identifies the wave profile from each image after a running-average smoothing is employed. The excellent repeatability of the profile measurements is demonstrated in Jiang *et al.* (1996).

To avoid surface contamination, the tank is scrubbed before and after each use with ethyl alcohol. Our treated water is de-ionized, carbon-adsorbed, and filtered to maintain a surface tension of 72 dyn/cm, close to that for pure water. The surface tension decreases to about 71 dyn/cm after the addition of fluorescein. By comparing with images taken by an 8 mm camera without dye present, we verified that the small change in surface tension does not cause a change in the wave profiles.

For the time history of surface elevation, we used a capacitance-type wave probe with an outside diameter of 1.6 mm positioned at the horizontal center of the tank. The measurement error is less than 1% of the wave height. The probe and feedback signals are low-pass filtered using two Krohn-Hite model 3342 analog filters with a cutoff frequency of 30 Hz. Then, the feedback signal is subtracted from the probe signal to obtain actual surface elevation.

Force and dissipation measurements

The dissipation measurement technique mentioned in the introduction is now fully discussed. The support force is measured by an OMEGA LCCA-100 load cell (strain gauge) placed between the platform and the tank. Its accuracy is: nonlinearity $< 0.03\%$ of full scale, hysteresis $< 0.02\%$ full scale, and non-repeatability $< 0.02\%$ full scale. The load cell has a maximum capacity of 445 N, sufficient for the 294 N water and tank. The tank is guided vertically by six rollers (two on the front, two on the sides and two on the rear) to reduce lateral displacement. A Tektronix PS503A provides the 15 V DC power supply for the load cell, while the dynamic force signal is amplified by a Tektronix AM502 differential amplifier with a DC offset for the static load. A 200 gain (maximum dynamic force = 27 lbs) is used to cover the range of forcing amplitude in our experiments.

The force signal is filtered by Krohn-Hite 3342 filters. There are higher harmonics evident in the 20 Hz to 25 Hz range that are attributed to the natural vibration mode

of the tank and shaker. These high-frequency components contribute to the total mechanical dissipation and should not be ignored. Therefore, the cut-off frequency of the low-pass (butterworth) filter is set at 100 Hz for both the force and displacement signals. The signals are then sampled at 300 Hz.

The instantaneous force is integrated with respect to tank displacement using Simpson's rule. The integrated work per wave cycle has a 7% standard deviation during stage 1 and a 2.5% standard deviation during stages 3 and 4. For the three-mode breaking wave, stage 5, the standard deviation for one wave period increases to more than 20% due to the unsteady nature of the breaking event. However, the deviation is reduced to less than 10% for the work per *three* wave periods, in agreement with the recurrence of the breaking events.

Steep standing waves

The experimental Faraday waves are similar to Penney & Price (1952) for moderate wave steepness, as in Figure 3(a). These waves are approximately symmetric in time, i.e. $\eta(x, t) = \eta(x, -t)$ where a crest occurs at $x = 0, t = 0$. (spatial symmetry is preserved in all nonbreaking waves.) However, the waveform changes for large wave steepness.

Steep Faraday waves are obtained by either increasing the forcing amplitude (Figure 3b) or decreasing the forcing frequency (Figure 4). In both situations, flat and dimpled crests appear in the forced standing waves when the wave steepness H/λ exceeds 0.15. The temporal symmetry is obviously broken for waves with the dimpled crest as shown in figure 5. The wave crest is more peaked in figure 5(a) when the central elevation is increasing. After achieving the maximum wave profile, the dimpled crest remains as the central wave elevation decreases (figure 5b).

These salient features, namely the dimpled crest and broken temporal symmetry, are intimately related to the interaction between the fundamental mode and its second harmonic in time (Jiang *et al.*, 1996). The phases of the first and second harmonic are defined as θ_1 and θ_2 , measured relative to the frequency $\omega_1 = \omega_f/2$. Amplitudes of the first two harmonics are a_1 and a_2 respectively. In the solution of Penney & Price (1952), the two harmonics are completely in phase ($\theta_2 - 2\theta_1 = 0$) and the second harmonic is small ($a_2/a_1 < 0.03$). Figure 6 presents the wave height (peak-to-peak elevation at the tank center), amplitude and phase of the first two harmonics from the wave-probe measurements. The dimpled crest corresponds to reduced wave height and increased second harmonic amplitude. More importantly, the phase difference $\theta_2 - 2\theta_1$ jumps when the dimpled crest first appears. For small forcing, the phase difference is still small, consistent with the observation of approximate temporal symmetry. However, increasing nonlinearity leads to a different phase between the first two harmonics, causing both temporal asymmetry and dimpled crest.

Jiang *et al.*, (1996) show the parametric space where

steep waves with flat or dimpled crest and breaking waves are observed. These waveforms exist over a wide range of frequency detuning and forcing amplitude. However, the numerical simulation reveals another steep wave form that does not resemble the waves with dimpled crest. Figure 7 shows the simulated Faraday wave with a forcing amplitude of 4.0 mm and forcing frequency of 3.22 Hz. It is strongly asymmetric in time and contains increased second harmonic. The phase difference between the first two harmonics is large, but has opposite sign compared with experiments. Therefore, the crest at the maximum position is sharply peaked, not dimpled.

The similarity and differences between numerics and physical experiments indicates that multiple forms of steep standing waves may exist. We can only speculate that under external forcing, the "resonance" or interaction is very sensitive to the damping mechanism and frequency detuning. Since we only simulate the dissipation with Rayleigh damping, it could affect the phase difference and eventually changing the standing wave form.

Breaking standing waves

Gentle breaking

In Taylor (1953), the tank aspect ratio was 2.17 and the extreme standing waves were three-dimensional. In our experiments with a tank aspect ratio of 10:1, the waves remain two-dimensional up to incipient breaking, corresponding to $H/\lambda \approx 0.216$. Figure 8 shows the limiting waveform with small breaking, where the forcing frequency and amplitude are 3.17 Hz, 4.04 mm. The maximum surface elevation is about 75 mm at either of the two protuberances at the dimpled crest, even though the surface elevation at the centerline only reaches 60 mm. Small ripples are generated around the two peaks in the dimpled crest. This is probably due to the high local curvature of the surface. Since the wave crest is more peaked when the central elevation is increasing, a spiller forms at the center when the crest changes from a peaked crest to a dimpled one (figure 8a,b). As the standing wave attains its maximum elevation at the tank centerline, two small plunging breakers forms to each side of the dimpled, but relatively flat crest. Shown in figure 8(c,d), these two plungers break outward from the centerline.

Three-mode breaking: spray and splash

The gentle breaking mode is unstable when the forcing amplitude is further increased. A series of images are taken at 50 Hz for a forcing amplitude and frequency of 4.6 mm and 3.20 Hz (figures 9-11). After several cycles of transition, period tripling follows. It first evolves into a distinct mode (A): the wave elevation reaches 140 mm, with a sharp crest angle - less than 45° (figure 9a). After reaching its maximum elevation at the centerline (0.20 s), the free surface elevation decreases, but the jet ejected at the crest lags behind, forming free water drops in a column. The jet then collides with the water surface, first forming a crater.

Then a rebounding jet and entrained air (bubbles). Significant acoustic energy is generated at this instant. The downward jet and the impinging process is shown in figure 9(b). The detected wave profiles show clearly a significant increase in the wave height and the sharp crest angle. Further evolution of mode A to a "rightward" or "leftward" breaker is discussed below.

This violent breaking mode A is followed by a wave form similar to that with a dimpled or flat crest (mode B), shown in figure 10. (Note that we have not separated the sets of images by the exact underlying wave period $T = 0.625$ s, nor have we presented an entire three-wave period sequence.) Splashes, remnants of the impinging process, are obvious in the first frame of figure 10(a). The rebounding jet at the tank center lasts more than a half wave period, from 0.44 s in figure 9(b) to 0.76 s in figure 10(a), creating turbulent motion at the wave crest. The stronger double plungers to each side of the crest (0.72 s) enhance dissipation in the entire wave field. Slight spatial asymmetry at the crest is observed in the detected wave profiles. Mode C (figure 11) follows mode B with a smooth wave profile similar to Penney & Price (1952). We call it the round-crest mode. No energetic breaking occurs in this stage. Mode A reappears with high wave elevation, spray and splash after mode C, forming a recurrent cycle with a three-wave period.

The same sequence of breaking occurs at the two ends of the tank with a phase difference of one and a half periods. The air-entrainment process then occurs twice in a three-wave period. However, the maximum elevation is not as high as that at the center of the tank (1.04 s in figure 10b,d); jets are only ejected occasionally when the crests are at the two ends; and the subsequent splash is less intense.

The wave profile is essentially two-dimensional in mode A, although it has a sharp crest. In figure 12, a perspective view of the wave is shown in a photograph taken from the upper-left corner of the oscillating tank. The photograph covers more than a half wavelength, with the sharp crest at the left side of the image (with strong light refraction). Except for some small perturbations, the standing wave is uniform along the tank-width direction.

Although the first sharp crest forms of an upward jet in mode A, it can also develop into a large plunger with its crest listing to one side. The appearance of an upward jet or plunger is random. Four frames of a "rightward" plunger are shown in figure 13. A "leftward" plunging breaker (figure 14) is captured with both seed particles and dye in the water (As a better view of the entire wave field is realized than with only fluorescent dye.) In mode B, the post-breaking double plunger slide down to each side of the dimpled crest in less than 0.1 s (figure 15), creating turbulence locally near the surface. The remnant air bubbles are also visible at the wave center. As shown in figure 11, mode C has the least breaking, and neither bubbles nor turbulent surface motions are observed in figure 16.

Recurrent breaking and second harmonic

Recurrent breaking in three distinct modes is exhibited at larger forcing amplitude and extreme wave steepness. Even though we cannot reproduce the recurrence in our numerical simulation, the breaking modes A and B are similar to the steep wave form in numerical and physical experiments respectively. Mode C with a round crest closely resembles the Penney & Price (1952) solution. As shown in the analysis of the dimpled waveform, when the second harmonic has relatively large amplitude, different phase angles between the second harmonic and the fundamental mode introduce different wave forms: a zero phase difference produces waveforms similar to that of Penney & Price (1952); a wave with a dimpled crest has a positive phase difference $\theta_2 - 2\theta_1$ between 90° and 180° ; a sharp-crested waveform has a negative phase angle $\theta_2 - 2\theta_1 \approx -40^\circ$ in the numerical experiments. Therefore, the three modes in the breaking events are strongly connected with the interaction between the first and second harmonics.

Here, we present the time series obtained by a wave probe to illustrate the connection between periodic breaking and the second harmonic. The wave elevation $y(t)$ at a fixed position can be expressed as

$$y(t) = a_1 \cos[\frac{1}{2}\omega_f t + \theta_1] + a_2 \cos[\omega_f t + \theta_2] + \dots$$

When period tripling occurs, the amplitudes $a_{1,2}$ and the phases $\theta_{1,2}$ are function of a longer time scale $3T$, where $T = 4\pi/\omega_f$ is the period of the first harmonic. From our data analysis, the frequencies of the first and second harmonics are indeed $\frac{1}{2}\omega_f$ and ω_f . Using complex demodulation (Bloomfield, 1976), we obtain the accurate modulation of amplitude $a_{1,2}$ for each harmonic and their phase difference $\theta_2 - 2\theta_1$. The phase difference is only allowed to be between 0° and 360° .

For the nonbreaking wave in figure 17, the demodulated first-harmonic amplitude reaches a steady value after 80 s. During wave growth, the second harmonic first grows, then decays to less than 1 mm, its phase angle is about 300° . As the first harmonic settles down to a steady amplitude, the second harmonic amplitude a_2 increases to above 5 mm and its phase angle jumps to 180° , corresponding to the appearance of a dimpled crest in the waveform. At the end of the record, the wave reaches steady state and the small oscillations in a_2 suggest instability. However, at this forcing amplitude, the dimpled crest observations persist for more than 10 minutes.

Figure 18 shows the transition from nonbreaking to three-mode breaking at 4.57 mm forcing. Due to the slight spatial asymmetry at the wave crest, the wave probe placed at the tank center does not always record the maximum wave elevation (140 mm in mode A). Before breaking, the phase angle exhibits the same trend as in figure 17. Once breaking occurs, there are small modulations in a_1 and a large modulation in both a_2 and their phase difference. An enlarged record is shown in figure 19 from 100 s to 120 s. The largest elevation corresponds to a maxima in a_1 , but not a_2 . The modulation of a_2 is locked to the modulation in a_1 . The modulation of phase difference $\theta_2 - 2\theta_1$ is

about 140° , corresponding to recurrent modes A to C. Interaction between the first and second harmonics explains the three distinct breaking modes, as shown in the strong modulation of phase angle and the phase lock between a_1 and a_2 .

Energy and dissipation in breaking standing waves

In this section, we are primarily concerned with the dissipation associated with the steep standing wave and *dissipation due to breaking*. In the current Faraday wave experiments, we only consider three control parameters: wavelength λ (limited by the tank configuration), forcing frequency ω_f and forcing amplitude f . Two other parameters, wave amplitude a and natural frequency ω_N can be determined by the above three parameters. Therefore, the dimensionless dissipation rate ϵ can be expressed as

$$\epsilon = \frac{4\pi^2 \Delta E}{\rho g b \lambda^3} = \epsilon \left(\frac{f}{\lambda}, \frac{\omega_f}{2\omega_N} \right) \quad (7)$$

where ΔE is the dimensional energy loss in a period and b is the tank width.

Figure 20 shows the surface elevation envelope and the power measured as work per wave period. Wave growth is accompanied by large oscillation in the total work expended by the shaker. The largest average work per period is in stage 5: three-mode breaking.

We also observe that the work per cycle is related to the dissipation mechanisms during the three-period breaking. Here, we estimate $\Delta E(t_0)$ in a one-wave-period window centered at t_0 . There is about a 6.4 Hz oscillation in $\Delta E(t)$ that is possibly due to the mechanical vibrations. To determine the modulation, a low-pass filter is applied to the (integrated) work with a cut-off frequency of 3 Hz. The measured work per wave period, shown in figure 21, has two peaks in each three-wave cycle. The first maximum ΔE does not correspond to the maximum elevation (mode A). Rather it occurs slightly less than one period later. The second peak in ΔE occurs one and a half periods later. As discussed above, the primary mechanisms of dissipation are the impinging jet and the ensuing air-entrainment that lags by a half period the maximum wave elevation. Following the energy loss in this process, there should be increased energy input, corresponding to the first peak in ΔE . Since the same dissipation process occurs exactly one and a half periods later (at the two ends of the tank), the second peak in ΔE is as expected.

Four different forcing frequencies: 3.18 Hz, 3.20 Hz, 3.22 Hz and 3.24 Hz are used in breaking-wave experiments. At each frequency, we increase the forcing amplitude and observe the limit-cycle wave amplitude until breaking occurs. Figure 22 summarizes the wave amplitude for these experiments. For nonbreaking waves, there is a relatively linear relationship between the excited wave amplitude and the forcing amplitude. When the amplitude increases to 60 mm, breaking occurs. Due to the difference

in the three breaking modes, the wave amplitude in an arbitrary mode has considerable scatter.

The total wave dissipation is presented in figure 23. For the 3.18 Hz and 3.20 Hz experiments, the dissipation rate ϵ slowly increases with forcing amplitude although at a lower rate than expected. Some dissipation data appears to decrease just below the forcing amplitude that causes breaking. The standard deviation in the data is about 20%-30%. For breaking waves that are excited with higher forcing amplitude, the dissipation rate jumps from an average value of 0.0052 ± 0.001 to 0.0114 ± 0.0015 , an increase of 100%. The same increase in energy dissipation is recorded in figure 23(b), with slightly more scatter. The dissipation rate increases from 0.004 ± 0.001 to 0.008 ± 0.001 for 3.22 Hz forcing, and increases from 0.0028 ± 0.001 to 0.0055 ± 0.0015 for 3.24 Hz forcing. Once breaking occurs, a further increase in the forcing amplitude does not cause an increase in the breaking-wave dissipation. Therefore for steep waves, the dissipation in one period is about 5% of the wave energy (based on the linear estimate $E = \frac{1}{4} \rho g b \lambda a^2$), and breaking increases the dissipation to 10% of the total energy.

The breaking-wave dissipation can be estimated by subtracting the averaged (viscous plus contact-line) dissipation for nonbreaking waves from the total dissipation. Shown in figure 24, the breaking-wave dissipation is largest for the lowest forcing frequency 3.18 Hz, and is decreasing for higher frequencies. We believe this frequency dependence is directly related to the effect of forcing frequency on the jet formation (spray) and the colliding intensity (splash). With higher forcing frequency, the sharp crest has less time to develop, thus less drops and air entrainment occurs. This frequency dependence therefore reinforces our claim that the primary dissipation mechanism is the air-entrainment and the jet reentry process.

Concluding Remarks

Here, we have observed previously unpredicted steep standing waves: flat and dimpled crests appear in the forced standing waves for larger wave steepness $H/\lambda \approx 0.15$. The maximum steepness for the new wave forms exceeds 0.21. The strong second harmonic and temporal asymmetry indicate internal resonance among the first and second temporal harmonics. The two-dimensional Faraday waves first break with two overturning plungers to each side of the crest.

Increasing the forcing amplitude or decreasing the forcing frequency causes the wave with dimpled crest to become unstable. It leads to period tripling with three breaking modes: mode A: sharp crest forms, the upward jet or the large plunger to each side impinges on the wave surface, creating bubbles and a strong rebounding jet; mode B: the waveform has a flat or dimpled crest, two outward plungers forms to each side of the crest; mode C: the crest is round and smooth, significant breaking is absent. The recurrence of mode A \rightarrow B \rightarrow C forms a three-period cy-

cle that occurs for all forcing frequencies with sufficient forcing amplitude. The strong modulation in the first two harmonics is investigated using complex demodulation of our wave-probe signal. More importantly, the large variation in phase angle demonstrates the interaction between the first two harmonics that directly causes the three distinct breaking modes.

We provide direct measurement of the energy dissipation due to viscous and contact-line effects and *breaking*. Instantaneous force measurements are integrated with respect to the tank displacement to provide the energy input to the system. The breaking wave increases the total wave dissipation by about 100%. Variations in the work per wave period is attributed to the strength of the different breakers: mode A provides the largest dissipation because of the reentrant jet and air entrainment. Strong frequency dependence is also shown in the dissipation rate.

We show that the sharp crest with an upward jet has a crest angle less than 45° , sometimes even less than 30° . Using our laser-sheet measuring system, we can examine local features of the wave crest with an average resolution of 0.4 mm/pixel. Magnification of the crest region shows its structure and the sharp angle in figure 25. Each frame is approximately 35 mm by 60 mm. These steep waveforms and breaking modes can cause drastically different radar returns due to the wedge-scattering mechanisms.

Acknowledgments

This research was supported by the Office of Naval Research partially under contract number N00014-93-1-0867 and partially under the University Research Initiative Ocean Surface Processes and Remote Sensing at the University of Michigan, contract number N00014-92-J-1650.

References

- BENJAMIN, T.B. & URSELL, F. 1954 The stability of the plane free surface of a liquid in vertical periodic motion. *Proc. R. Soc. Lond. A* **225**, 505–515.
- BLOOMFIELD, P. 1976 *Fourier Analysis of Time Series: An Introduction*. New York: Wiley, 118–149.
- BRYANT, P.J. & STIASSNIE, M. 1994 Different forms for nonlinear standing waves in deep water. *J. Fluid Mech.* **272**, 135–156.
- JIANG, L., TING, C., PERLIN, M. & SCHULTZ, W.W. 1996 Moderate and steep Faraday waves: instabilities, modulation and temporal asymmetries. submitted to *J. Fluid Mech.*
- MILES, J.W. & HENDERSON, D.M. 1990 Parametrically forced surface waves. *Ann. Rev. Fluid Mech.* **22**, 143–165.
- PENNEY, W.G. & PRICE, A.T. 1952 Finite periodic stationary gravity waves in a perfect liquid. *Phil. Trans. R. Soc. Lond. A* **244**, 254–284.
- PERLIN, M., LIN, H. & TING, C. 1993 On parasitic capillary waves generated by steep gravity waves: an exper-

imental investigation with spatial and temporal measurements. *J. Fluid Mech.* **255**, 597–620.

- SAAD, Y. & SCHULTZ, M.H. 1986 GMRES: a generalized minimal residual algorithm for solving nonsymmetric linear systems. *SIAM J. Sci. Stat. Comput.* **7**, 856–869.
- SCHULTZ, W.W., HUH, J. & GRIFFIN, O.M. 1994 Potential energy in steep and breaking waves. *J. Fluid Mech.* **278**, 201–228.
- SCHULTZ, W.W. & VANDEN-BROECK J.M. 1990 Computations of nonlinear standing waves. *Bull. Amer. Phys. Soc.* **35**, 2290.
- SCHWARTZ, L.W. & WHITNEY, A.K. 1981 A semi-analytic solution for nonlinear standing waves in deep water. *J. Fluid Mech.* **107**, 147–171.
- TADJBAKHSI, I. & KELLER, J.B. 1960 Standing surface waves of finite amplitude. *J. Fluid Mech.* **8**, 442–451.
- TAYLOR, G.I. 1953 An experimental study of standing waves. *Proc. R. Soc. Lond. A* **218**, 44–59.
- VANDEN-BROECK J.M. & SCHWARTZ, L.W. 1981 Numerical calculation of standing waves in water of arbitrary uniform depth. *Phys. Fluids* **24**, 812–815.

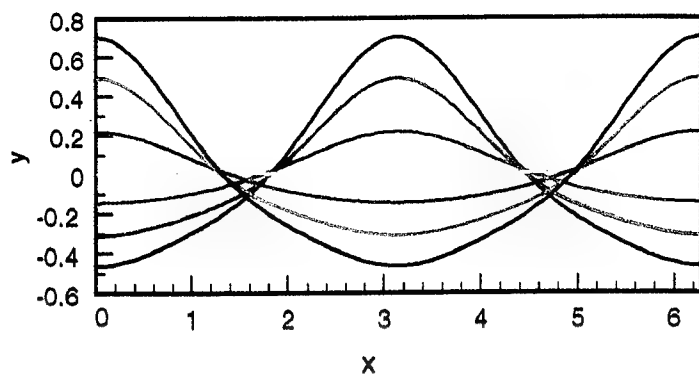


Figure 1. Standing wave profiles every $1/12$ period in a half period based on the third-order truncation of Penney & Price (1952). The length scales are chosen to make the primary wavenumber unity. Wave steepness, $H/\lambda = 0.186$. The vertical scale is twice as large as the horizontal scale.

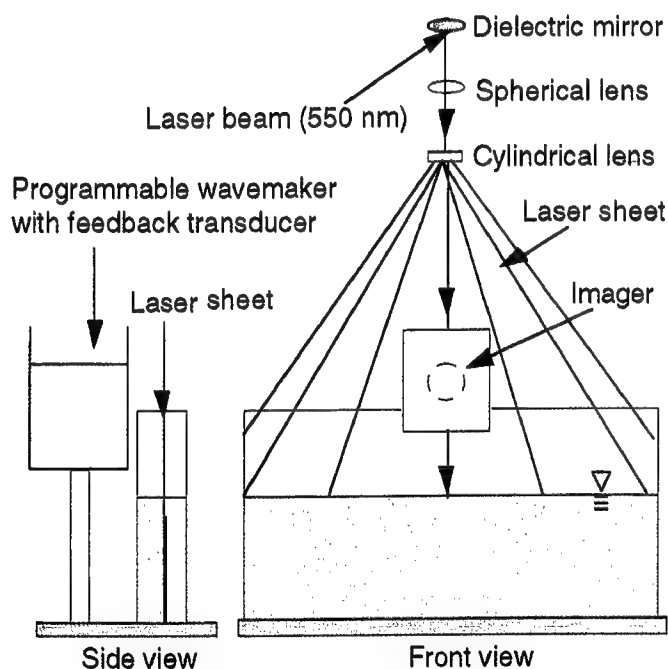


Figure 2. Experimental setup of the tank, lighting and imaging system. The spherical lens has a focal length of 1000 mm, the cylindrical lens has a focal length of 6.35 mm.

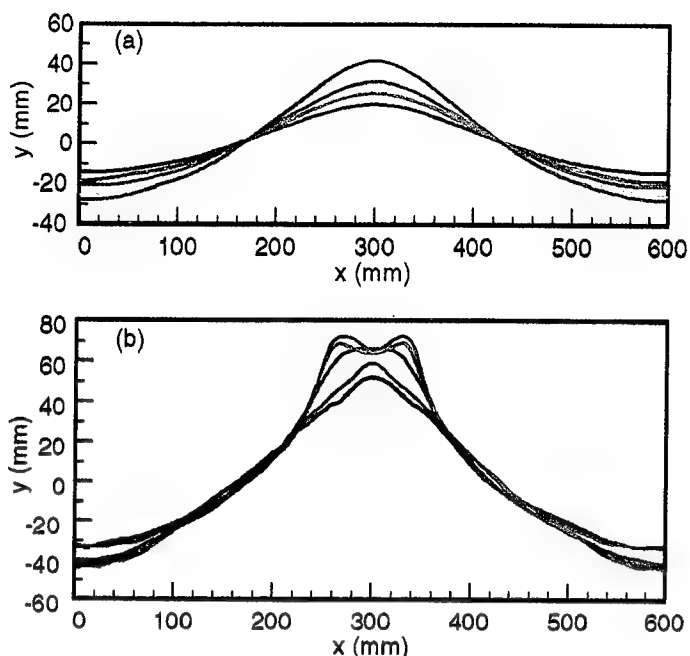


Figure 3. (a) Maximum wave profiles with crest at center for 3.32 Hz forcing in physical experiments. The five forcing amplitudes are 2.65 mm, 2.87 mm, 3.17 mm, 3.49 mm and 3.87 mm. (b) Forcing frequency is 3.20 Hz, forcing amplitudes are 1.61 mm, 1.92 mm, 3.17 mm, 3.49 mm and 3.88 mm. Wave amplitude increases with forcing amplitude. The vertical scale is twice as large as the horizontal scale.

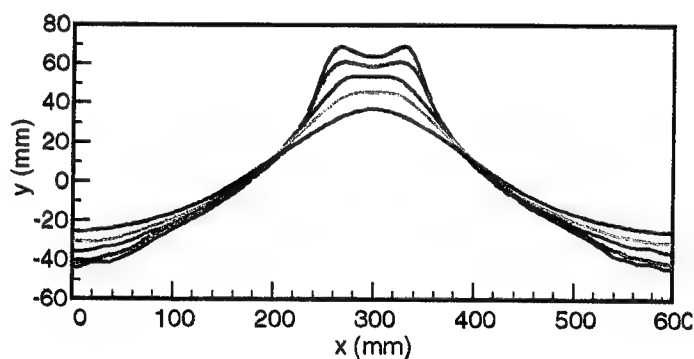


Figure 4. Maximum wave profiles from physical experiments, all at forcing amplitudes of 3.5 mm. Five forcing frequencies are 3.32 Hz, 3.29 Hz, 3.26 Hz, 3.23 Hz, and 3.20 Hz. Wave amplitude increases with decreasing forcing frequency. The vertical scale is twice as large as the horizontal scale.

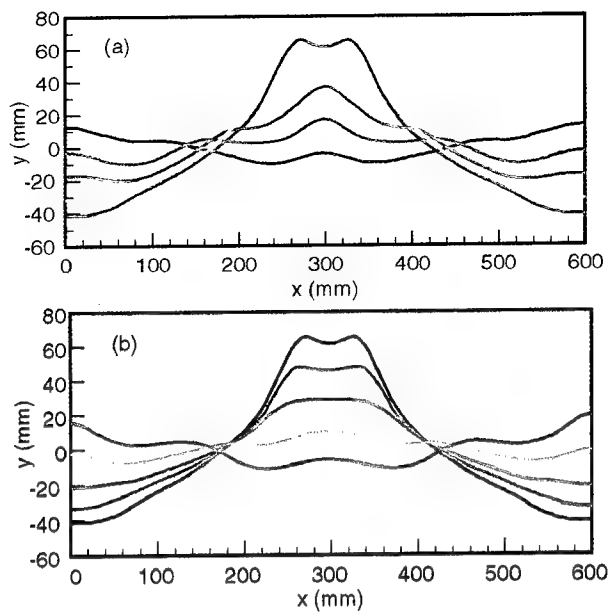


Figure 5. Experimental wave profiles with (a) increasing and (b) decreasing elevation at the centerline. Forcing frequency is 3.23 Hz, forcing amplitude is 3.85 mm. The time interval between each profile is about 0.04 s. The vertical scale is twice as large as the horizontal scale.

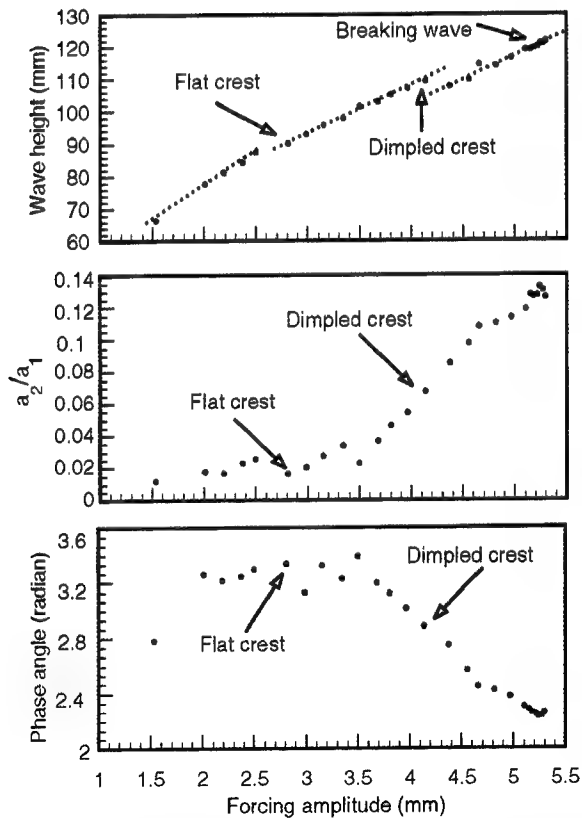


Figure 6. Wave height, the ratio of the second-harmonic amplitude to the first-harmonic amplitude, and the phase angle $\theta_2 - 2\theta_1$. Forcing frequency is 3.22 Hz.

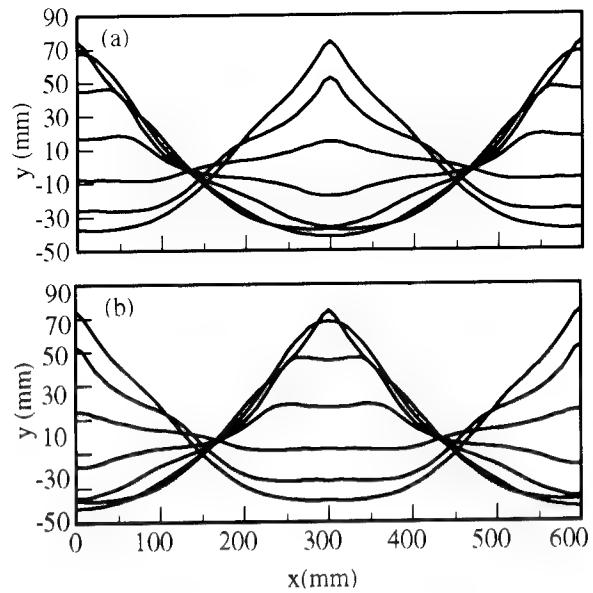


Figure 7. Numerical simulation of the forcing amplitude of 4.0 mm and forcing frequency 3.22 Hz. Surface tension is 72 dyn/cm. (a) Decreasing central elevation (b) Increasing central elevation. The wave profiles are graphed every 1/12 period. The vertical scale is twice as large as the horizontal scale.

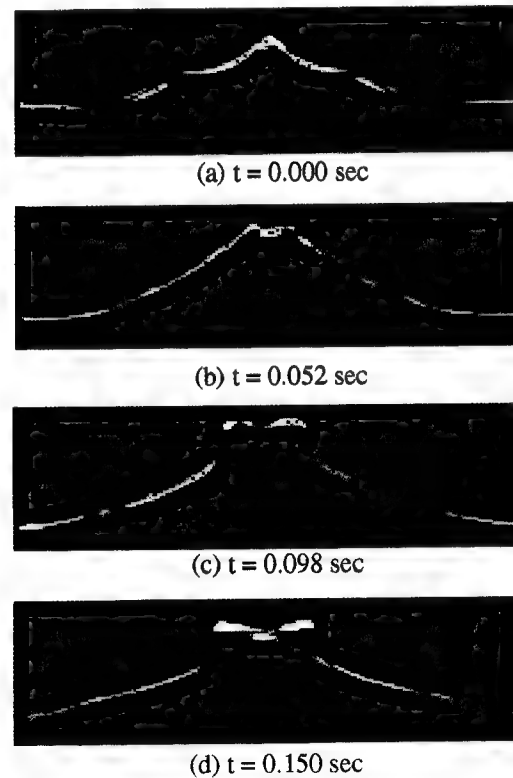


Figure 8. Small breaking at the dimpled crest. Forcing frequency is 3.17 Hz, forcing amplitude is 4.04 mm.

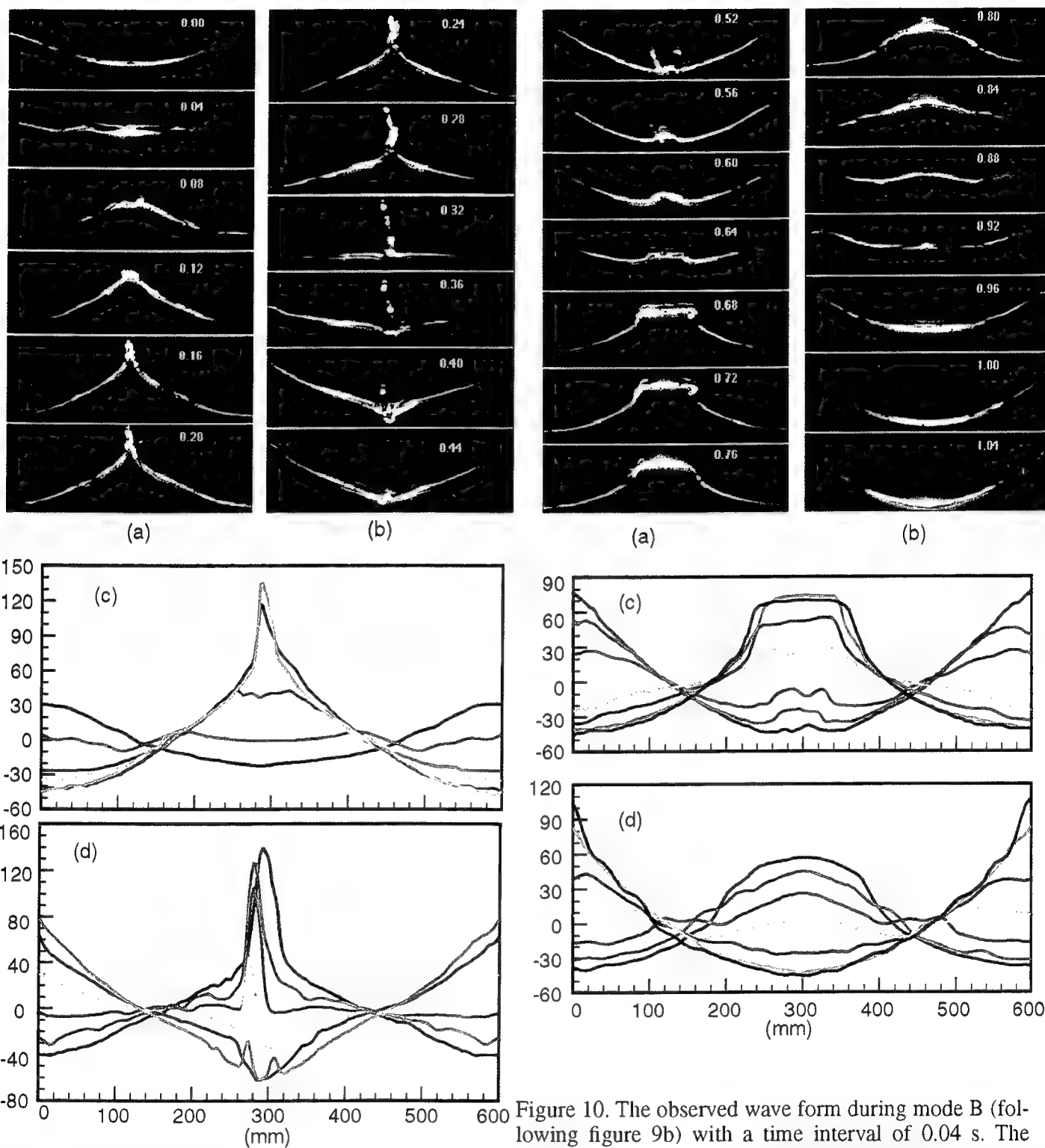
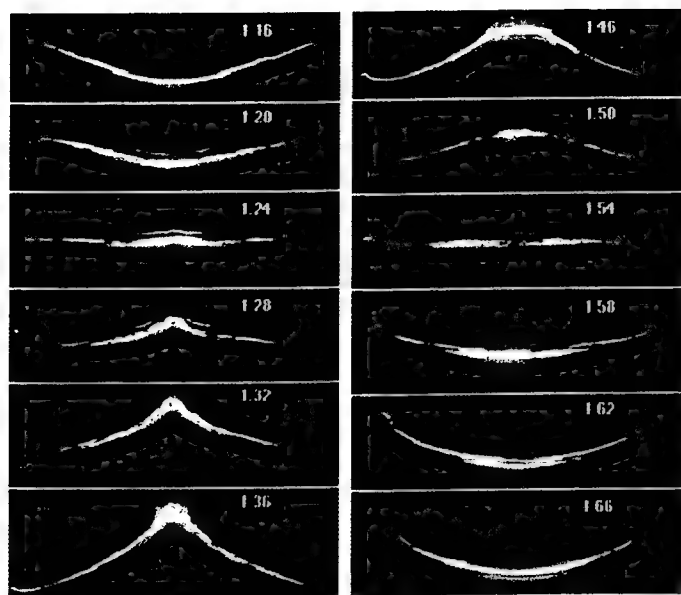


Figure 9. The observed wave form during mode A with a time interval of 0.04 s. Forcing amplitude is 4.6 mm, forcing frequency is 3.20 Hz. The detected wave profiles for column (a) and (b) are graphed in (c) and (d). In (c), (d), the vertical scale is 1.5 times the horizontal scale. The numbers shown in the images represent time in s.

Figure 10. The observed wave form during mode B (following figure 9b) with a time interval of 0.04 s. The numbers shown in the images represent time in s. Forcing parameters are the same as in figure 9. The detected wave profile is graphed in (c) and (d). In (c), (d), the vertical scale is 1.5 times the horizontal scale.



(a)

(b)

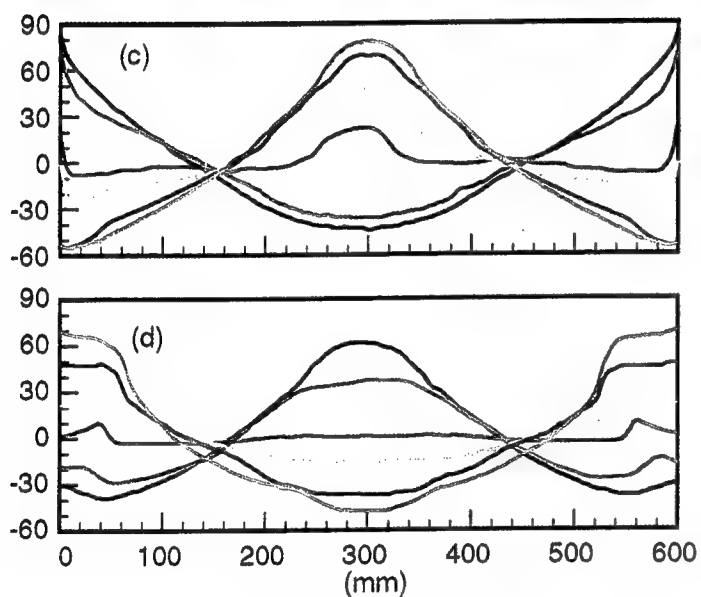


Figure 11. Mode C and detected wave profiles. Forcing parameters are the same as figure 9. In the detected wave profiles, the vertical scale is 1.5 times the horizontal scale.



Figure 12. A photograph of mode A with the sharp crest at the left of the image. Forcing parameters are the same as in figure 9.

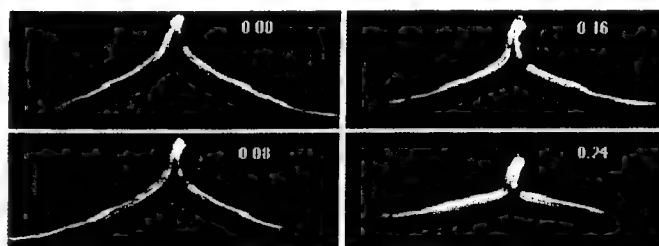


Figure 13. Breaking wave with "rightward" jet. The maximum wave profile is presented at $t=0.00$ s. Same forcing parameters are the same as in figure 9.

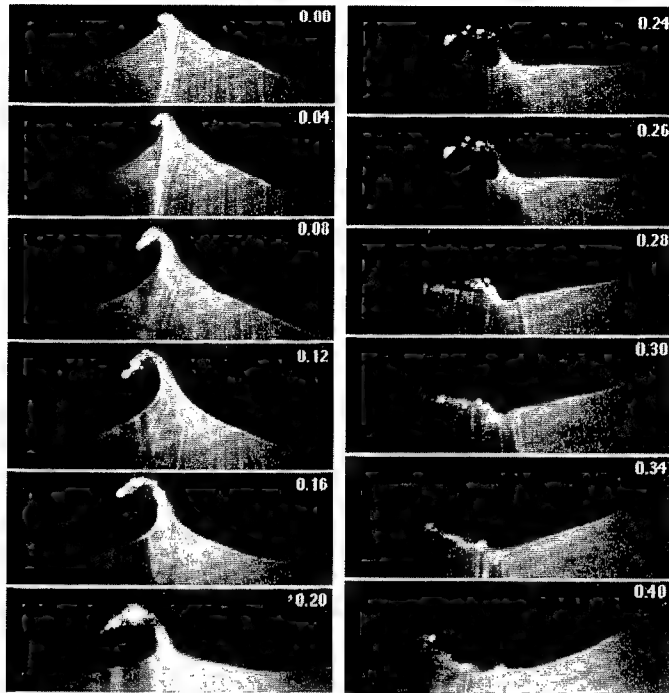


Figure 14. Mode A with "leftward" plunging breaker. The forcing amplitude is 4.6 mm, forcing frequency is 3.20 Hz. Note that the time intervals between frames are not the same.

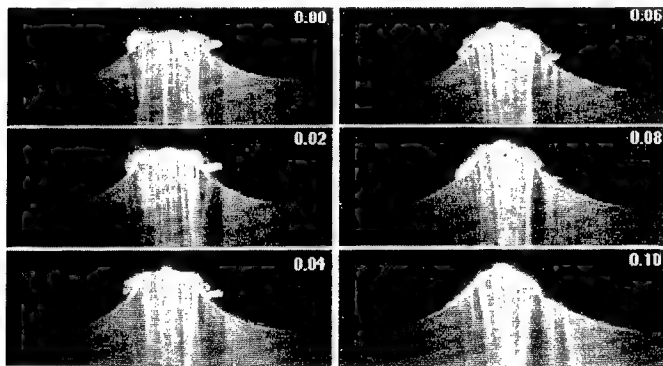


Figure 15. Double plunger to each side of the dimpled crest. Same forcing condition as in figure 14. The bulbous center at $t=0.04-0.08$ s is caused by the rebounding jet. The entrained air bubbles are clearly visible in the last four frames (under the crest).

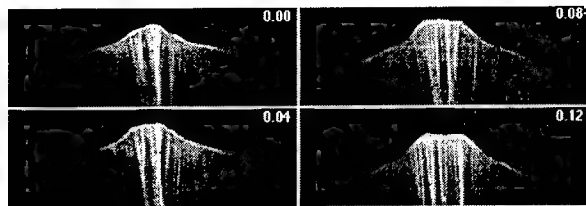


Figure 16. Mode C without breaking (same forcing condition), maximum elevation occurs at $t=0.04$ s.

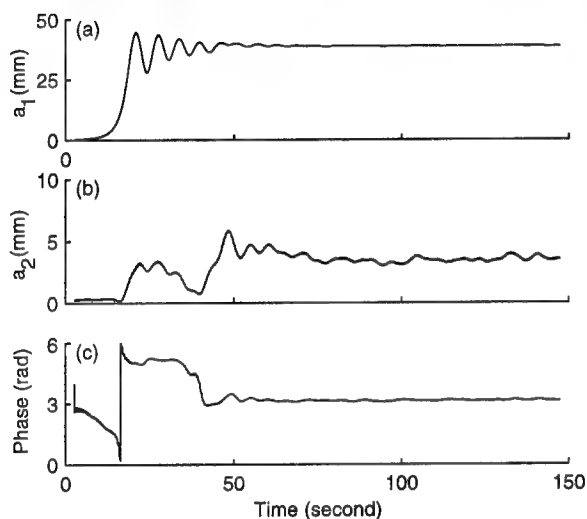


Figure 17. Complex demodulated wave probe signal at forcing frequency 3.20 Hz, forcing amplitude 4.15 mm. (a) Amplitude of the first harmonic (b) amplitude of the second harmonic (c) phase angle $\theta_2 - 2\theta_1$.

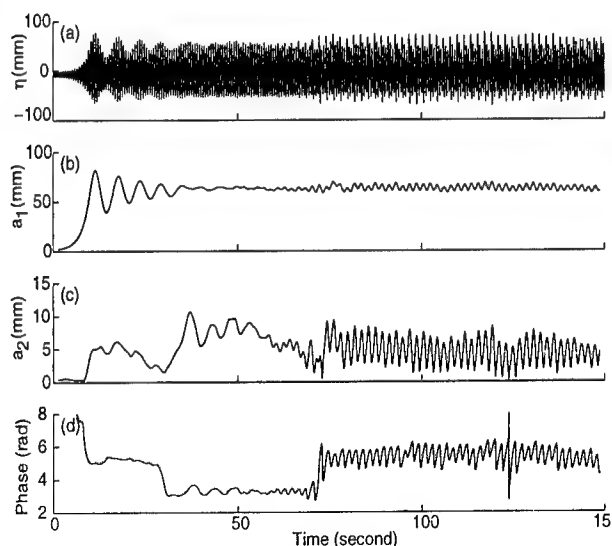


Figure 18. Complex demodulated wave probe signal at forcing frequency 3.20 Hz and forcing amplitude 4.57 mm. (a) Surface elevation (b) amplitude of the first harmonic (c) amplitude of the second harmonic (d) phase angle $\theta_2 - 2\theta_1$.

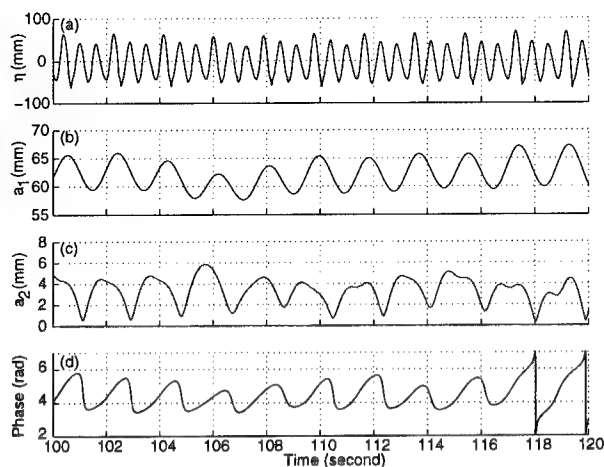


Figure 19. Same as previous figure.

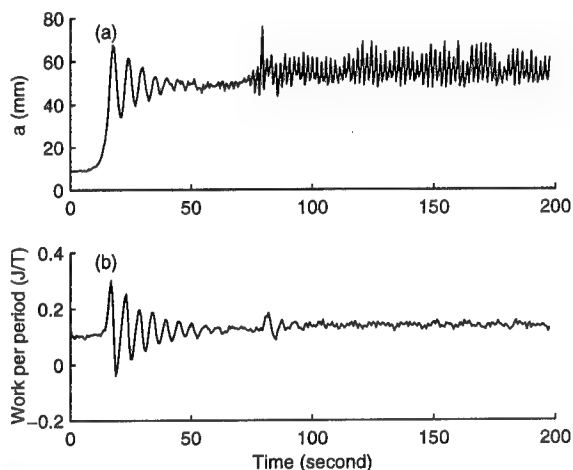


Figure 20. (a) Envelope of surface elevation and (b) work per wave period for forcing frequency 3.20 Hz and forcing amplitude 4.57 mm.

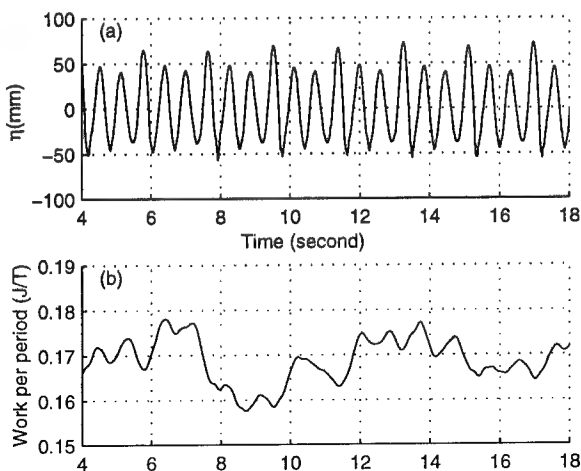


Figure 21. (a) Elevation at the centerline of the tank and (b) dimensional dissipation rate for forcing frequency 3.22 Hz, forcing amplitude 4.55 mm.

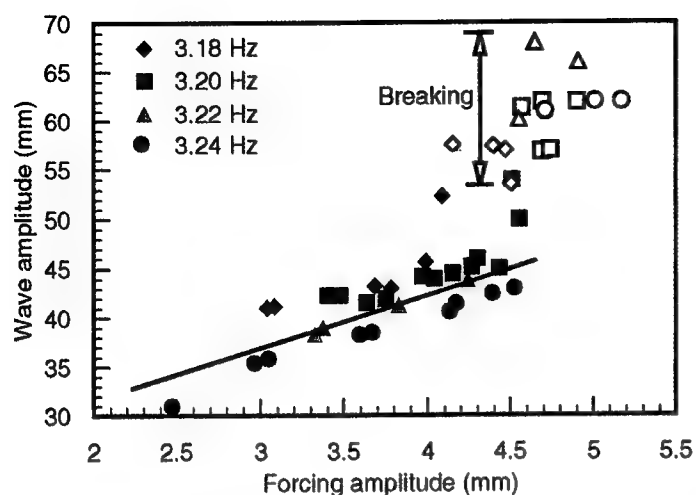


Figure 22. Amplitude of nonbreaking (solid symbols) and breaking (hollow symbols) waves for different forcing frequencies.

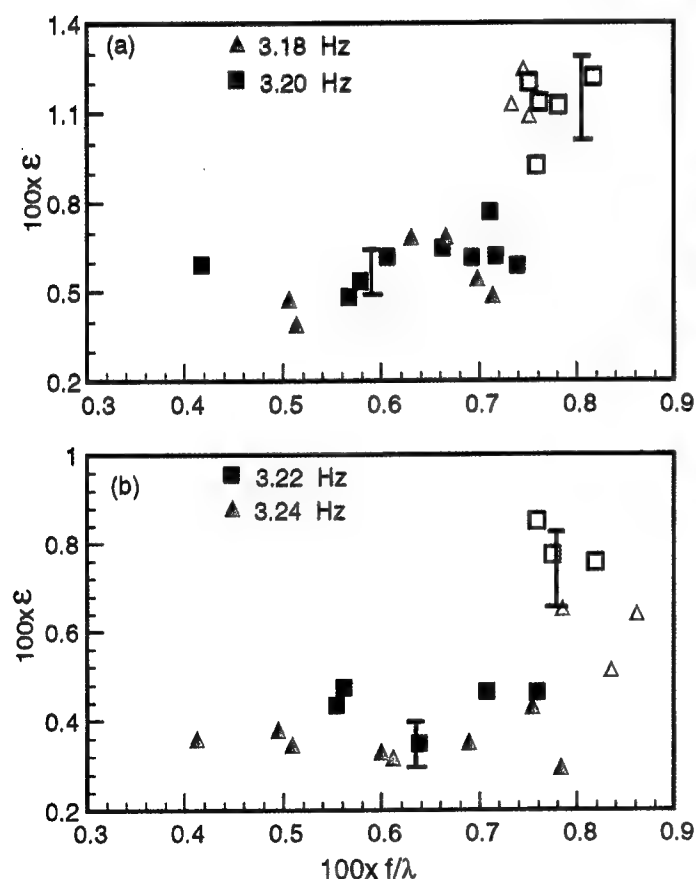


Figure 23. Dimensionless dissipation rate for nonbreaking (solid symbols) and breaking waves (hollow symbols). The lower and upper error bars reflect typical standard deviations for nonbreaking and breaking waves.

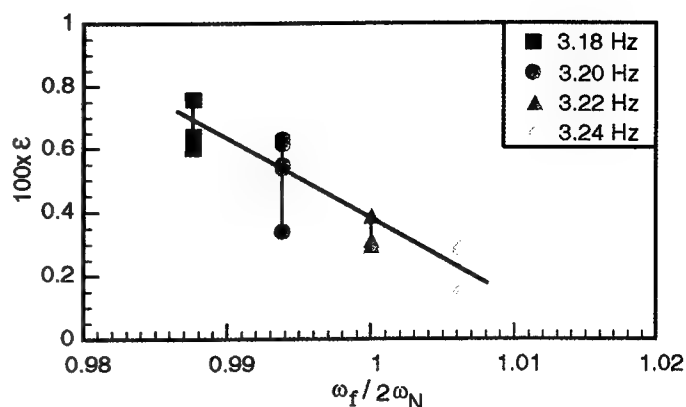
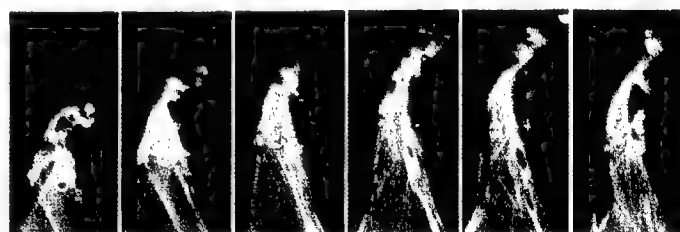


Figure 24. The breaking-wave dissipation vs. frequency detuning for four different forcing frequencies.



(a) Forcing frequency: 3.20 Hz



(b) Forcing frequency: 3.22 Hz

Figure 25. The crest structure at the maximum wave elevation of mode A. (a) Forcing amplitude is 4.57 mm. Time interval between each frames is 0.008 s. (b) Forcing amplitude is 4.6 mm. Time interval between frames is 0.016 s. The vertical scale is the same as the horizontal scale.

DISCUSSION

E. Palm

University of Oslo, Norway

It is an interesting and important topic which is discussed in this paper. In spite of this, the available, pertinent literature on the topic is very limited. The paper is of special value since it reports experimental as well as numerical results.

The main outcome of the numerical computations is displayed in Fig. 6, which shows the mean second-order forces acting on the submerged body as functions of $\omega^2 b/g_1$, for three different values of the pycnocline thickness, δ . As expected, it is found that for sufficiently long waves the pycnocline layer is of no importance if the body is situated from this layer. The figures suggest that the waves do not feel the pycnocline layer if $k\delta <$ about 0.5 (k incoming wave number), roughly speaking. It would be of interest to see also the data for other forms of the elliptic body, for example, a circular form or a flat plate.

The experimental and numerical results are compared in Figs. 7 and 8. It is surprising that in Figs. 7a and 7b a fair agreement is obtained for the horizontal force whereas the values for the vertical forces are more than 100% different. The authors believe it is due to nonlinear effects which obviously may be important. It is seen that for Figs. 7a and 7b the values of the second-order forces computed by the two-layer models are in reasonable agreement with those obtained from the three-layer model. This suggests that it would be of interest to apply a two-layer time-dependent nonlinear program to this problem to study the forces. Such programs exist.

AUTHORS' REPLY

NONE RECEIVED

The Forces Exerted by Internal Waves on a Restrained Body Submerged in a Stratified Fluid

N. Gavrilov, E. Ermanyuk, I. Sturova
(Lavrentyev Institute of Hydrodynamics, Russia)

ABSTRACT

This paper presents the results of experimental and theoretical studies of forces exerted by plane internal waves on the horizontal elliptic cylinder in the case of stratification simulating a pycnocline .

The experiments were performed in a test tank filled with two layers of miscible fluids. The upper layer was distilled water, the lower layer was a glycerine solution in water. The elliptic cylinder was positioned normally to the side walls of the test tank. In its cross-section the small axis was directed upwards and the ratio between axes was 2:1. The basin was equipped with both a wave maker and a wave breaker. The variable experimental parameters included: the amplitude and length of waves, the distance from the cylinder centre to the free surface, and the pycnocline thickness. The incident internal wave in experiments was represented by the first mode.

The linear 2-D problem of internal wave scattering on a restricted cylinder is considered theoretically. The fluid is assumed to be nonviscous, incompressible and composed of three layers (the upper and lower layers are homogeneous and the middle layer is linearly stratified), which provides an approximate model of the experimental conditions. The Boussinesq approximation is used. For the sharp pycnocline, the methods developed for surface waves are applied to study the forces acting on a body fully submerged in the fluid layer of constant density. The method of cou-

pled finite elements is most efficient for solving the present problem. For a body partially submerged in the middle layer, the problem is solved approximately. The comparison between theoretical and experimental data is presented.

1. INTRODUCTION

Exploration of the Ocean has stimulated the study of environmental factors acting on marine structures and deep-submersibles. A particular feature of real sea is the presence of vertical density gradient resulting from variation of temperature and salinity with depth. It is well-known that vertical density stratification allows internal waves to arise under the action of surface waves, tides, variation of atmospheric pressure, etc. (see, for example, Phillips [1], Miropolsky [2]). For submerged technical objects, short-period internal waves are of particular interest. These waves are typical for thermocline stratification .

In the case of a body located in homogeneous fluid layer, the action of internal waves is closely analogous to the action of surface waves but for the difference of characteristic time- and length-scales. The amplitude of internal waves may be as much as 5 – 10 times greater than the amplitude of surface waves. The frequency of short internal waves is less than the frequency of surface waves by 1.5 – 2 orders of magnitude. In the region of variable density, the dynamic interaction of body and waves is complicated by buoyancy-driven effects that have no direct analogy in the domain of surface waves.

Scattering of surface waves on restricted submerged bodies has been much studied theoretically and experimentally. In contrast, the investigation of internal wave scattering is not yet sufficiently advanced though the loads induced by internal waves on marine structures and submerged vehicles are quite essential as demonstrated by field and laboratory experiments (see, for example, Ermanyuk & Sturova [3], Razumeenko [4]).

In most cases, natural pycnocline structure is approximated as a two-layer fluid with a step change of density at the interface. However, a realistic smooth density variation gives rise to new physical effects that are beyond the domain of two-layer model.

The present paper deals with theoretical and experimental study of forces exerted by internal waves on horizontal elliptic cylinder in the case of stratification characterized by the presence of a finite region of high density gradient.

2. EXPERIMENTS

The experiments were carried out in a test tank ($4.5 \times 0.2 \times 0.6m$) filled with stratified two-layer fluid. The density of the upper layer (distilled water) was $\rho_1 = 0.999g/cm^3$, the density of the lower layer (glycerine - water solution) was $\rho_2 = 1.011g/cm^3$. The experimental installation is shown in Fig. 1. The waves were generated by heaving motion of a semi-cylinder 1. The test-tank was equipped with a wave-breaker 2. The elliptic cylinder 3 of 3cm minor axis and axis ratio 2 : 1 was mounted on the 2-component hydrodynamic scales 4 so that the gaps between the ends of the cylinder and the walls of the test tank did not exceed 0.1cm. The minimum natural frequency of scales was 2.4Hz. The maximum wave frequency throughout the experiments was 0.21Hz. The loads acting on the cylinder were transmitted to flexible elements 5 by the system of strings 6 and streamlined arms 7. The deformations of elements were measured by induction displacement sensors. As the maximum amplitude of wave loading in experiments did not exceed $1.1 \cdot 10^{-3}N$, the corresponding displacement

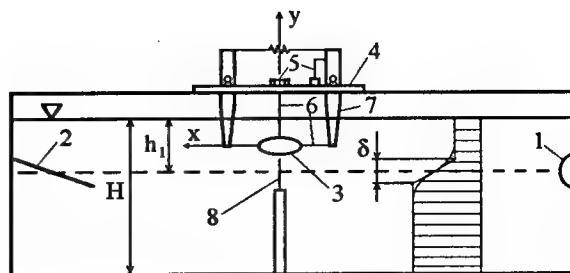


Fig. 1.

of the cylinder under the action of waves was less than $5 \cdot 10^{-3}mm$. A series of experiments was undertaken to study the influence of streamlined arms on the accuracy of force measurements. The corresponding error was found to be less than 0.5%.

In the reference frame with the origin taken at free surface (the y -axis points upwards), the measured density distribution closely matched the following relation:

$$\rho(y) = \rho_0 - \frac{\varepsilon \rho_1}{2} \tanh \frac{2(y + h_1)}{\delta}, \quad (1)$$

where $\rho_0 = (\rho_1 + \rho_2)/2$, $\varepsilon = (\rho_2 - \rho_1)/\rho_1$, h_1 is the depth of the upper layer, δ is the parameter characterizing the thickness of the region of large density gradient (pycnocline). The total depth of fluid was $H = 45cm$.

The parameters of wave motion were measured by resistive wave gauges 8 of length greater than the overall pycnocline thickness which is equal 3δ for the density distribution (1). The time-dependent output $w(t)$ of the wave gauges may be written as the integral of local conductivity variations over the length of probes. As the local conductivity is directly proportional to local density, the integral looks as follows:

$$w(t) = w_0 f(t) \int_{y_1}^{y_2} \eta(y) \frac{d\rho}{dy} dy, \quad (2)$$

where w_0 is dimensional constant, $\eta(y)$ is the distribution of local vertical displacements of fluid particles, y_1, y_2 are the ordinates of the ends of the probe, $f(t)$ is the harmonic function of time. The function $\eta(y)$ reaches its maximum η_m at

the middle of pycnocline for the first mode of internal waves. The function $d\rho/dy$ is appreciable only within the region of thickness δ . In this region $\eta(y) \approx \eta_m$ in the test range of wave frequency. Thus, to a high degree of accuracy the integral (2) is the measure of an average of local wave amplitudes over δ . The influence of other parameters on the output of the wave-gauges was taken into account by dynamic calibration; to do this, the response of the wave-gauges undergoing vertical oscillations of known amplitude and frequency was measured in the test range of δ . Analog outputs of wave and force measuring systems were converted to digital and analyzed by specialized computer.

Strictly speaking, the oscillations of the wave maker generate all the modes of wave motion. However, when the amplitude of the heave motion of the semi-cylinder used as the wave maker is small and its diameter is large compared to the pycnocline thickness, the high modes are weakly generated and quickly decay with distance. The test section was spaced at 1.8m from the wave maker. The visual examination of the wave pattern clearly indicated that the incident wave motion in experiments was represented by the first mode. To analyze the experimental data, the dispersion relation (see, Phillips [1]) was used:

$$\omega^2 = \varepsilon g k / [k\gamma + \coth kh_1 + \coth k(H - h_1)], \quad (3)$$

where k is the wave number, ω is the wave frequency, γ is the characteristic thickness of the pycnocline. The measurements showed that this dispersion relation agrees well with the experimental data under condition $\gamma = \delta$.

In the fluid system described, the forces exerted on the elliptic cylinder by internal waves of the first mode depend on the following non-dimensional parameters:

$$h_1/b, H/b, \bar{h} = h/b, \bar{\eta} = \eta/b, \bar{k} = kb, \beta = b\sqrt{\omega/\nu},$$

where b is the minor axis of elliptic cylinder, η is the amplitude of internal waves, h is the distance from the cylinder centre to the free surface, ν is the kinematic viscosity.

The value $H/b = 15$ was kept constant. Three typical locations of the cylinder were studied: $\bar{h} = 2$ (in the middle of the upper layer), $\bar{h} = 3.5$ (in the upper layer close to the interface), $\bar{h} = 5.4$ (in the lower layer close to the interface). For each location of the cylinder, parameter $\bar{\delta}$ varied in the range $0.4 < \bar{\delta} < 2.5$. The variation of $\bar{\delta}$ resulted from diffusion of glycerine.

For each set of parameters \bar{h} and $\bar{\delta}$ the loads on the cylinder were measured depending on the amplitude and the length of incident waves. These parameters varied in the ranges: $0.05 < \bar{\eta} < 0.4$; $0.2 < \bar{k} < 1.1$. The wave steepness ηk was less than 0.08.

The above-mentioned experimental conditions imply low values of Keulegan-Carpenter numbers. As it is shown by Sarpkaya [5], Chaplin [6], a variation of Stokes number β does not affect the wave loading under these conditions. Furthermore, in the present experiments parameter β varied in a narrow range from 20 to 30. The kinematic viscosities of upper and lower layers differed only by 10%.

The amplitudes of loads were normalized to the scale of inertial forces $\rho_0 S \dot{u}$ and $\rho_0 S \dot{v}$ so that

$$C_x = F_x / \rho_0 S \dot{u}, \quad C_y = F_y / \rho_0 S \dot{v}, \quad (4)$$

where \dot{u}, \dot{v} are the amplitudes of local horizontal and vertical accelerations of fluid particles calculated at $y = -h$, S is the cross-sectional area of elliptic cylinder, F_x and F_y are the amplitudes of horizontal and vertical loads acting on a cylinder of unit length.

The application of the first-order theory of Phillips [1] combined with dispersion relation (3) gives the following estimate of amplitudes of local accelerations:

$$\dot{u} = \frac{\eta \omega^2 \cosh kh}{\sinh kh_1}, \quad \dot{v} = \frac{\eta \omega^2 \sinh kh}{\sinh kh_1} \quad (5)$$

$$(-h_1 < y < 0),$$

$$\dot{u} = \frac{\eta \omega^2 \cosh k(H - h)}{\sinh k(H - h_1)}, \quad \dot{v} = \frac{\eta \omega^2 \sinh k(H - h)}{\sinh k(H - h_1)}$$

$$(-H < y < -h_1).$$

The normalization (4) provides a simple representation of experimental data for a body located in fluid layer of constant density in the case of dominant inertial forces (see, for example, Chaplin [6], Ermanyuk & Sturova [3]). In the region of density variation, the total wave induced loads depend on inertial, damping and buoyancy forces. However, to separate the components of total measured force, one should formulate a number of additional assumptions. Because of this, the normalization (4) is used for all the experimental data obtained. It should be kept in mind that relations (5) give overestimated values of local accelerations for fluid particles located in the pycnocline. In this case, these relations should be considered only as formal normalization parameters.

The experimental results for a cylinder located in the upper layer at $\bar{h} = 2$ are shown in Fig. 2 representing the dependencies of C_x and C_y on the non-dimensional wave number \bar{k} at different $\bar{\delta}$. Hereinafter, the sets of data *a*) and *b*) correspond to C_x and C_y , respectively. In this series, any action of buoyancy force is excluded. However, the presented data show essential dependence of the force coefficients on the pycnocline thickness $\bar{\delta}$.

The coefficients of inertial force for an elliptical cylinder of axis ratio 2 : 1 placed in oscillatory flow of nonviscous fluid are equal 1.5 and 3 for oscillations aligned with major and minor axis, respectively (see, Kochin et al.[7]). For sharp pycnocline ($\bar{\delta} = 0.5$), the coefficient C_x fairly well agrees with the above-mentioned theoretical estimate in a wide range of \bar{k} . It seems likely that the increase of C_x with $\bar{\delta}$ is associated with the effect kindred to flow contraction as the increase of pycnocline thickness decreases the upper layer of constant density. It should be noted that C_x did not depend on $\bar{\eta}$ under experimental conditions, to within the experimental error.

The coefficient of vertical force C_y shows complicated behavior depending on the test parameters. Generally, C_y decreases with \bar{k} and increases with $\bar{\delta}$ at low $\bar{\delta}$. However, at high $\bar{\delta}$ the

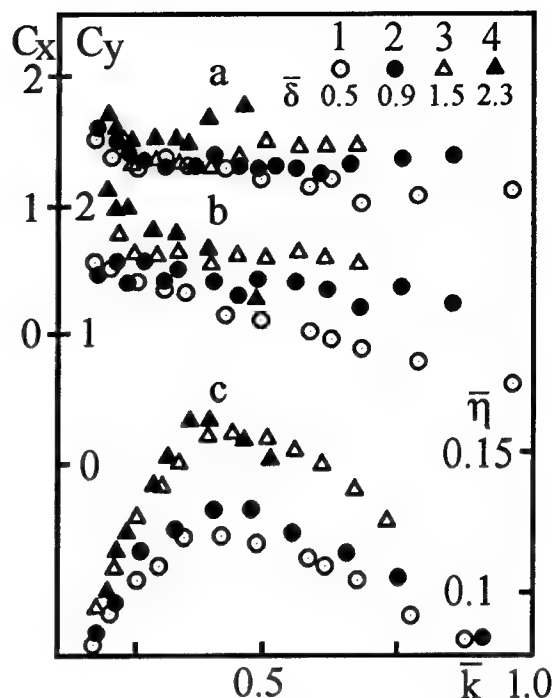


Fig. 2.

behaviour of C_y changes (points 4 shown in Fig. 2b). Moreover, at fixed \bar{k} and $\bar{\delta}$, C_y depends on $\bar{\eta}$. Because of this, the set of $C_y(\bar{k})$ dependencies is supplemented with the set of corresponding $\bar{\eta}$ versus \bar{k} data shown in Fig. 2c.

The dependence of C_y on wave amplitudes was studied at low $\bar{\delta}$. The range of amplitude variation was quite narrow. The upper limit was imposed by the onset of wave breaking. The specific limitations of the wave maker design imposed the lower limit of studied amplitudes. In the region covered by experiments, C_y decreases by 28% when the wave amplitude is doubled at constant \bar{k} and $\bar{\delta}$. This effect presumably corresponds to the non-linear reduction of inertial loads as reported by Chaplin [6].

The phase lags between the loads acting on the cylinder and oscillations of the pycnocline are $105^\circ \pm 1.5^\circ$ and $201^\circ \pm 2^\circ$ for horizontal and vertical force, respectively. The measurements have not revealed any clear dependence of these phase lags on the parameters of the problem.

For the cylinder located close to the pycno-

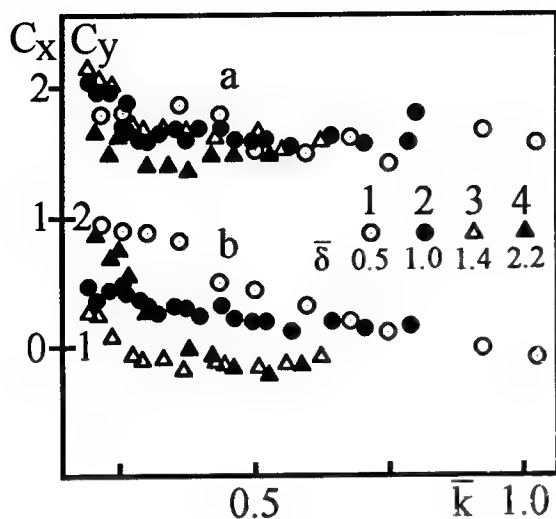


Fig. 3.

cline, the phase lags were not measured and the amplitude of waves was recorded at the distance of 12cm from the center of the cylinder.

As the cylinder approaches the pycnocline, the force coefficients C_x , C_y show increasingly stronger dependence on \bar{k} and $\bar{\delta}$. At the same time, the measurements have shown the linear increase of loading with $\bar{\eta}$. In other words, no amplitude dependence of C_x and C_y was observed, to within the experimental error. Presumably, the presence of density gradient in the vicinity of a body inhibits separation and reduces non-linear effects. For the cylinder located in the upper layer close to pycnocline at $\bar{h} = 3.5$, the results of measurements are presented in Fig. 3a,b. The comparison of Fig. 3a and Fig. 2a shows that the proximity of the interface increases C_x at low $\bar{\delta}$ compared to the case of cylinder located in the middle of the upper layer. However, at large $\bar{\delta}$ when the cylinder is completely surrounded by stratified fluid, C_x drops (points 4 in Fig. 3a).

The vertical wave loads decrease with the increase of $\bar{\delta}$. Razumeenko [4] showed that the buoyancy and inertial forces may partially cancel each other. Assuming that the density distribution is not distorted by waves and may be considered as linear in the vicinity of a body, one can show that the ratio of inertial and buoy-

ancy forces is governed by the parameter $\alpha = \omega^2/N^2(\bar{h})$, where $N(y) = \sqrt{-(g/\rho)d\rho/dy}$ is the buoyancy frequency or Brunt-Vaisala frequency. The parameter α has the physical sense of Froude number. Buoyancy force is major at $\alpha < 1$ while inertial loads dominate at $\alpha > 1$.

The case of the cylinder located in the lower layer close to the pycnocline at $\bar{h} = 5.4$ is illustrated in Fig. 4a,b. For all the wave numbers studied, the lower layer may be considered as infinitely deep ($k(H - h_1) > 3$). At low $\bar{\delta}$ ($\bar{\delta} = 0.4$), the vertical and horizontal loads exerted by waves in this case are lower compared to the case of the cylinder located right above the pycnocline ($\bar{\delta} = 0.5$) (see Figs. 3,4). The increase of loading is observed at $\bar{\delta} = 0.9$ when the upper portion of the cylinder is immersed in the pycnocline (points 2 in Fig. 4a,b). The further increase of $\bar{\delta}$ decreases the values of C_x and C_y markedly. However, complete cancellation of buoyancy and inertial forces was not observed though the parameter α varied in the range $0.1 < \alpha < \infty$. Apparently, the increase of $\bar{\delta}$ gives rise to additional diffraction loads.

The godographs of the summary force vector shown in Fig. 5 provide a vivid illustration to the change of the force pattern with the increase of $\bar{\delta}$. The godographs shown in Fig. 5 correspond to the case of the cylinder placed at $\bar{h} = 5.4$. The length of the summary force vector \bar{R} is normalized by the maximum amplitude of its horizontal component. At low $\bar{\delta}$, the godographs plotted at any \bar{k} closely approach elliptic curves. The curve 1 corresponds to the following parameters: $\bar{\delta} = 0.4, \bar{k} = 0.29$. At large $\bar{\delta}$ one can see an apparent direction along which the loading is maximal. The amplitude of forces acting normally to this direction is 5 - 6 times less. This effect is illustrated by the curve 2 obtained at $\bar{\delta} = 1.6, \bar{k} = 0.28$. The shape of curve 2 imply almost in phase oscillation of horizontal and vertical loads. For both the figures the arrows indicate the sequence of time.

It is interesting to note that the angle Θ between the horizontal direction and the direction

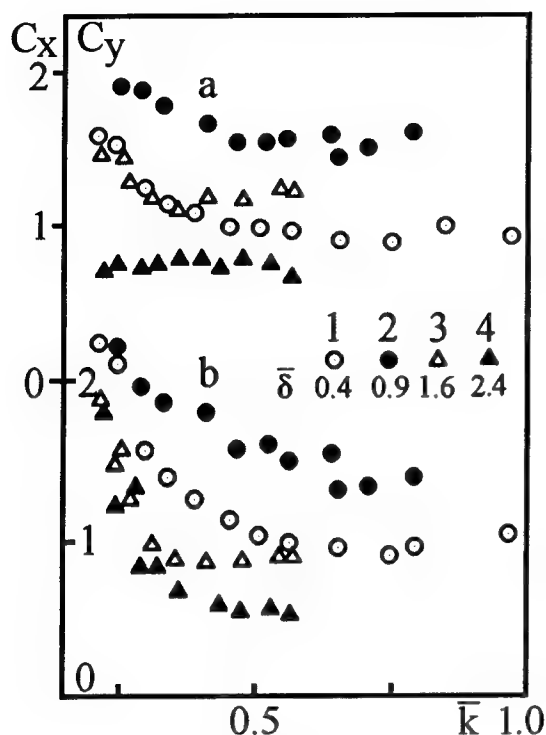


Fig. 4.

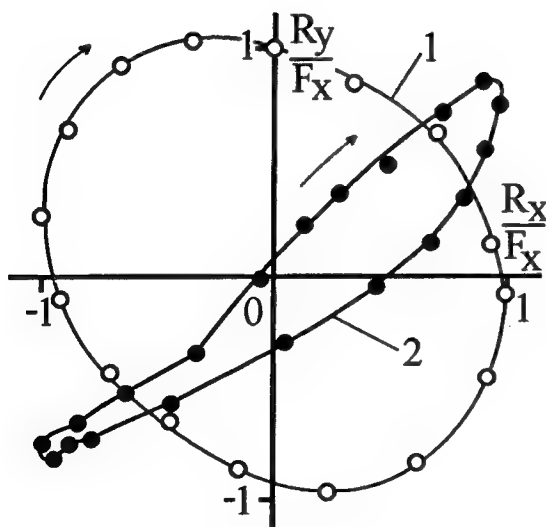


Fig. 5.

of maximum loading agrees with the relation $\Theta = \arcsin(\omega/N_m)$, where N_m is the maximum of the Brunt-Vaisala frequency $N(y)$. The sign of the angle depends on the direction of orbital motion of fluid particles so that the variants of a body placed above and below the interface give mirror image patterns.

The direction of rotation of the summary force vector coincides with the direction of orbital motion of fluid particles at any studied $\bar{\delta}$ as exemplified by curves 1,2 (see Fig. 5) recorded under conditions of inertia- and buoyancy dominated vertical loading, respectively.

3. THEORETICAL ANALYSIS

It is assumed that the inviscid incompressible fluid occupies the region $-\infty < x < \infty$, $-\infty < y < 0$ and there are three layers: homogeneous upper and lower ones and a linearly stratified middle one. Thus, density stratification in an undisturbed state $\rho(y)$ takes the form

$$\rho(y) = \begin{cases} \rho_1 & (H_1 < y < 0), \\ \rho_1[1 - \varepsilon(y + h_1)/\delta] & (-(H_1 + \delta) < y < -H_1), \\ \rho_2 & (-\infty < y < -(H_1 + \delta)), \end{cases}$$

where $H_1 = h_1 - \delta/2$ is the depth of upper layer. This three-layer fluid is the model of a smooth pycnocline and approximates the density distribution (1). Contrary to the experimental conditions, it is assumed that the depth of the lower layer is infinite.

The stable stratification of fluids, corresponding to an increasing density in the direction of the gravity force, allows the existence of internal waves. Small amplitude waves are described by the linear theory of internal waves presented in detail, for example, by Phillips [1], Miropolsky [2]. For a horizontally homogeneous fluid at rest there exists a countable number of free harmonic wave modes when a continuous density variation occurs only in a finite interval of depth. To each wave mode there corresponds a dispersion dependence of the wave frequency on the wave number.

We investigate the scattering of an internal wave of the first mode, incident on a solid horizontal elliptic cylinder. As the cylinder axis is

parallel to the front of the incident wave, the 2-D problem is considered. It is assumed that the upper layer is bounded by a rigid lid. This approximation allows to 'filter off' the surface waves without distorting significantly the internal ones. The disturbed oscillating motion of the fluid is assumed to be steady and the flow inside upper and lower layers is potential.

In the upper and lower homogeneous layers the total velocity potentials $\phi_{1,3}(x, y, t)$ satisfy the equations

$$\Delta\phi_1 = 0 \quad (-H_1 < y < 0),$$

$$\Delta\phi_3 = 0 \quad (-\infty < y < -(H_1 + \delta)),$$

where the subscripts 1 and 3 refer to the upper and lower layers, respectively.

The internal wave equations for the vertical velocity $v_2(x, y, t)$ in the middle layer are described within the Boussinesq approximation

$$\partial^2 \Delta v_2 / \partial t^2 + N^2 \partial^2 v_2 / \partial x^2 = 0$$

$$(-(H_1 + \delta) < y < -H_1),$$

where $N = \sqrt{2g_1/\delta}$ is constant, $g_1 = \varepsilon g / (2 + \varepsilon)$. The boundary conditions are the following

$$\partial\phi_1/\partial y = 0 \quad (y = 0),$$

$$\begin{aligned} \partial\phi_1/\partial y = v_2, \quad \partial^2\phi_1/\partial y^2 = \partial v_2/\partial y \\ (y = -H_1), \end{aligned}$$

$$\begin{aligned} \partial\phi_3/\partial y = v_2, \quad \partial^2\phi_3/\partial y^2 = \partial v_2/\partial y \\ (y = -(H_1 + \delta)), \end{aligned}$$

$$\partial\phi_3/\partial y \rightarrow 0 \quad (y \rightarrow -\infty).$$

From the theory of linear internal waves it follows that in such a fluid the existence of free internal waves is possible only with $\omega < N$. Let the wave incident from the right be an arbitrary internal mode with a vertical velocity

$$v(x, y, t) = \eta_0 \operatorname{Re}\{V(y) \exp[i(kx + \omega t)]\}. \quad (6)$$

The wave number k satisfies the dispersion relation

$$\tan \mu\delta = k\mu(1 + \tanh kH_1)/(\mu^2 \tanh kH_1 - k^2), \quad (7)$$

where $\mu = k\sqrt{N^2/\omega^2 - 1}$. There exists a countable number of values $k_j (k_1 < k_2 < \dots)$, satisfying the given dispersion relation. The eigenfunctions $V(y)$ of the wave modes are represented as

$$V(y) = \Lambda \begin{cases} \sinh ky & (-H_1 < y < 0), \\ k \cosh kH_1 \sin \mu(y + H_1)/\mu - \\ \sinh kH_1 \cos \mu(y + H_1) & \\ & (-(H_1 + \delta) < y < -H_1), \\ (\cosh kH_1 \cos \mu\delta - \\ \mu \sinh kH_1 \sin \mu\delta/k) \times \\ \exp[k(y + H_1 + \delta)] & \\ & (-\infty < y < -(H_1 + \delta)), \end{cases} \quad (8)$$

where

$$\begin{aligned} \Lambda = -i\omega\mu^2\delta/[k \cosh kH_1(1 - \cos \mu\delta) + \\ \mu \sinh kH_1 \sin \mu\delta]. \end{aligned}$$

It is supposed, that the incoming internal wave is represented only by the first mode with wave number k_1 . The feature of this mode is that its eigenfunction, determined in (8), has a constant sign over a depth of fluid. By analogy with Sect. 2 let us define the amplitude of this internal wave as the average value of the vertical displacements of fluid particles over the thickness of a stratified layer. The vertical displacement of fluid particle in internal wave $\eta(x, y, t)$ is determined from $\partial\eta/\partial t = v$. Similarly to (6) it is possible to express

$$\eta(x, y, t) = \eta_0 \operatorname{Re}\{E(y) \exp[i(kx + \omega t)]\},$$

where $E = -iV/\omega$. Normalizing multiplier Λ is introduced into (8) so that

$$\int_{-(H_1 + \delta)}^{-H_1} E(y) dy = \delta.$$

In this case η_0 is the dimensional value of internal wave amplitude.

When the cylinder is fully submerged in the upper or lower homogeneous layer, the solution of diffraction problem can be obtained numerically with the help of the coupled finite element method (CFEM). The velocity potential is represented by finite element method in a narrow

region surrounding a body and by the boundary integral equation in the outer region. This method is highly efficient and universal and can be used for complex-shaped bodies and for a system of bodies both in 2-D and 3-D flows. The examples of the solution of diffraction problem for two-layer fluid are given by Sturova [8]. To use CFEM, it is necessary to determine the Green function.

For a body located in the upper layer one should derive the Green function describing the field of a point source of pulsating strength which is placed at the fixed point (ξ, ζ) of the upper layer. In this case the Green function in the upper layer takes the form $G_1(x, y, \xi, \zeta)$:

$$G_1 = \ln(rr_1) + \frac{2N^2}{\omega^2} \text{pv} \int_0^\infty \frac{D(k, y, \zeta)}{T(k)} \times \cos k(x - \xi) dk - 2i\pi \frac{N^2}{\omega^2} \sum_{n=1}^\infty \frac{D(k_n, y, \zeta)}{T'(k_n)} \cos k_n(x - \xi), \quad (9)$$

where $r = [(x - \xi)^2 + (y - \zeta)^2]^{1/2}$,

$$r_1 = [(x - \xi)^2 + (y + \zeta)^2]^{1/2},$$

$$D(k, y, \zeta) = k \exp(-kH_1) \cosh k\zeta \cosh ky \times$$

$$\tan \mu\delta / \cosh kH_1,$$

$$T(k) = k\mu(1 + \tanh kH_1) -$$

$$\tan \mu\delta(\mu^2 \tanh kH_1 - k^2),$$

the symbol pv indicates the principal-value integration and the prime denotes differentiation with respect to k .

The Green function for the source in the lower layer was obtained previously by Sturova [9] and in the lower layer has the form

$$G_3 = \ln(rr_2) + 2\text{pv} \int_0^\infty \frac{C(k, y, \zeta)}{T(k)} \cos k(x - \xi) dk - 2i\pi \sum_{n=1}^\infty \frac{C(k_n, y, \zeta)}{T'(k_n)} \cos k_n(x - \xi), \quad (10)$$

where $r_3 = [(x - \xi)^2 + (y + \zeta + 2(H_1 + \delta))^2]^{1/2}$,

$$C(k, y, \zeta) = (k \tan \mu\delta + \mu \tanh kH_1) \times$$

$$\exp[k(y + \zeta + 2(H_1 + \delta))].$$

The expressions (9), (10) are somewhat simplified in the case of infinite thickness of the upper layer. Introducing the substitution $y_1 = y + H_1 + \delta/2$,

$\zeta_1 = \zeta + H_1 + \delta/2$ and assuming $H_1 \rightarrow \infty$, we shall obtain

$$G_{1,3} = \ln(r) + \frac{N^2}{\omega^2} \text{pv} \int_0^\infty \frac{\exp[k(\delta - |\zeta_1 + y_1|)]}{Z(k)} \times \tan \mu\delta \cos k(x - \xi) dk + \frac{2i\pi\omega^2}{\delta N^2} \sum_{n=1}^\infty \frac{\exp[k_n(\delta - |\zeta_1 + y_1|)]}{k_n} \cos k_n(x - \xi), \quad (11)$$

where $Z(k) = 2\mu + k(2 - N^2/\omega^2) \tan \mu\delta$.

In this case the explicit dependence of wave number on frequency may be derived from the dispersion relation (7)

$$k_n(\omega) = \frac{1}{\delta} \begin{cases} \frac{\omega}{\sqrt{N^2 - \omega^2}} [(n-1)\pi + \arctan(\frac{2\omega\sqrt{n^2 - \omega^2}}{N^2 - 2\omega^2})] & (\omega < N/\sqrt{2}), \\ \pi(n - 0.5) & (\omega = N/\sqrt{2}), \\ \frac{\omega}{\sqrt{N^2 - \omega^2}} [n\pi + \arctan(\frac{2\omega\sqrt{n^2 - \omega^2}}{N^2 - 2\omega^2})] & (\omega > N/\sqrt{2}). \end{cases}$$

The exciting forces on the body may be obtained by integration of pressure over the body surface. Omitting the hydrostatic term, the pressure $p(x, y, t)$ satisfies the relation

$$\partial^2 p / \partial x^2 = \rho_0 \partial^2 v / \partial t \partial y.$$

It is assumed that

$$p = \eta_0 \text{Re}[(P_0 + P)e^{i\omega t}],$$

where the pressure due to the incident wave $P_0(x, y)$ is equal to

$$P_0 = -\frac{i\omega\rho_0}{k} \frac{dV}{dy}$$

and the diffraction pressure $P(x, y)$ should be determined having regard to the boundary condition on a cylinder surface.

When the body is fully submerged in a layer of constant density, in which the flow is irrotational, the total velocity potential $\phi(x, y, t)$ can be written as

$$\phi = \eta_0 \text{Re}[(\Phi_0 + \Phi)e^{i\omega t}],$$

where the incident potential $\Phi_0(x, y)$ and the diffraction potential $\Phi(x, y)$ are

$$\Phi_0 = \frac{1}{k^2} \frac{dV}{dy}, \quad \Phi = \frac{iP}{\rho_0 \omega}.$$

For the potential flow the boundary condition at cylinder surface L has the form

$$\frac{\partial \Phi}{\partial n} = -\frac{\partial \Phi_0}{\partial n} \quad (x, y \in L),$$

where $\vec{n} = (n_x, n_y)$ is the inward normal to the cylinder surface. In addition, the scattered wave portion of the potential should satisfy the Sommerfeld radiation condition at infinity for outgoing waves.

The exciting forces F_x, F_y and the moment M are determined as

$$F_q = \eta_0 \int_L (P_0 + P) n_q ds \quad (q = 1, 2, 3),$$

where for the sake of convenience we introduce the notation $F_1 = F_x, F_2 = F_y, F_3 = M, n_1 = n_x, n_2 = n_y, n_3 = \vec{r} \times \vec{n}, \vec{r} = (x - x_0, y - y_0)$, x_0 and y_0 are the coordinates of the point about which the moment of exciting forces is determined.

In the considered problem it is of interest to investigate the influence of pycnocline thickness on the loads acting on the body entirely located in the upper or lower layer. Numerical results for exciting forces on elliptic cylinder submerged under the interface of two-layer fluid are presented by Sturova [8]. In this case the upper layer can be both infinite and bounded by a rigid lid or free surface. Here, we use only the results [8] for infinite two-layer fluid. In this fluid there is only one wave mode, for which $\omega^2 = g_1 k$. The numerical results of CFEM for horizontal force F_x , vertical force F_y and moment M of exciting forces relative to the axis of the cylinder are shown in Fig. 6. The cross-section of the cylinder represented the ellipse with a horizontal major axis and the aspect ratio 2:1, the distance from the cylinder axis to the middle of the stratified layer is equal to a minor axis of ellipse b , relative difference of density between layers is $\epsilon = 0.03$. Number of finite elements accounted by CFEM is equal 18.

In numerical realization, the main difference between two-layer fluid and smooth pycnocline is

that, in the latter case, the Green function has infinite number of simple poles in integral term and infinite number of items in a sum, what corresponds to the existence of countable number of free internal wave modes for pycnocline stratification. However, as the influence of high modes is very small, only finite number of modes was taken into account. This number increases with pycnocline thickness and can be more than 100.

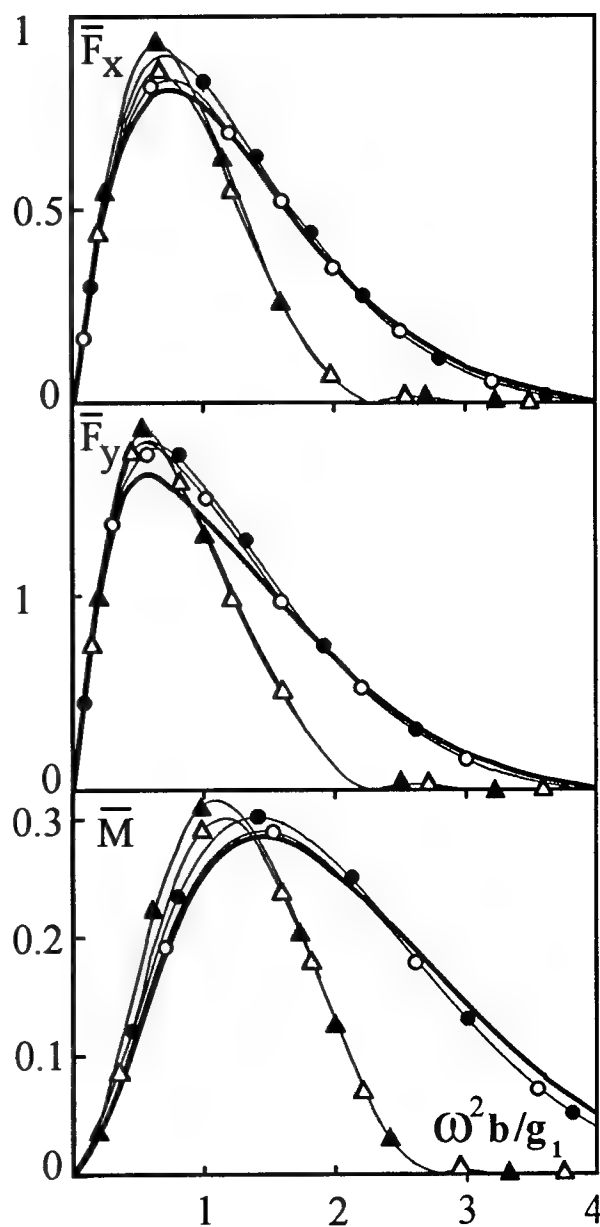


Fig. 6.

The following designations are used in Fig. 6

$$(\bar{F}_x, \bar{F}_y) = (|F_x|, |F_y|)/\rho_0 \eta_0 b g_1,$$

$$\bar{M} = |M|/\rho_0 \eta_0 b^2 g_1.$$

The solid lines show the results of Sturova [8] for two-layer fluid, the light and dark points correspond to the pycnocline thickness $\bar{\delta} = 0.05$, the light and dark triangles correspond to $\bar{\delta} = 0.5$. The light (dark) points and triangles represent the results for the body submerged in the upper (lower) layer.

It is evident, that the effect of pycnocline thickness is essential at $\omega^2 b/g_1 > 1$. At fixed wave frequency, the greater pycnocline thickness corresponds to shorter incident internal wave, with a consequent drop of diffraction loads.

In parallel with above-mentioned algorithm, the diffraction loads are determined approximately using the Green function

$$G = \ln r. \quad (12)$$

This Green function describes a field of point source in unbounded homogeneous fluid. This approximate solution for two-layer fluid (or its particular case of homogeneous fluid with free surface) closely approaches the fully consistent solution for a body located far away from the interface (see, Sturova [8]).

The comparison of theoretical and experimental results for exciting forces is shown in Fig. 7a-d. The experimental conditions are given in Table 1.

The elliptic cylinder was fully submerged in the upper layer well away from the pycnocline. Fig. 7a-c corresponds to the fixed depth of submergence and increasing thickness of pycnocline. The results for the body located close to the pycnocline are presented in Fig. 7d. The solid lines in Fig. 7 show the numerical results with the Green function (9), the dash lines show the approximate solutions with the Green function (12). The following designations are used

$$(\tilde{F}_x, \tilde{F}_y) = (|F_x|, |F_y|)/\rho_0 \eta_0 N^2 b^2.$$

The dark points (squares) represent the experimental values for \tilde{F}_x (\tilde{F}_y).

Table 1. Experimental conditions

Fig. No.		$h_1(\text{cm})$	$h(\text{cm})$	$\delta(\text{cm})$
Fig. 7	a	14	6.1	1.4
	b	14.3	6.1	2.7
	c	14.5	6.1	4.4
	d	13.9	10.8	1.5
Fig. 8	a	12.7	15	2.6
	b	15.2	10.8	6.6

There is a qualitative agreement between theory and experiment, in particular, the theory predicts well the position of maximal forces. For the horizontal force F_x , a good quantitative agreement is observed. The measured values of vertical force F_y are appreciably smaller than the theoretical results. This fact has not yet a coherent explanation. The reported comparisons of measured and calculated loads exerted by surface waves on a cylinder submerged in homogeneous fluid are restricted to the case of circular cylinder. In this case, the estimates of both components of wave-induced forces obtained within the framework of linear theory are in good agreement with the experimental values measured at low Keulegan-Carpenter numbers for the waves of small steepness (see, for example, Chaplin [6]). It seems likely that the non-uniform direction-dependent departure between the measured and calculated loads observed in the present study is conditioned by non-linear effects. The manifestations of flow separation are different depending on orientation of the elliptic cylinder in the flow.

The comparison of diffraction forces calculated by the exact and approximate algorithms shows that these solutions closely fit each other at large distances from sharp pycnocline; otherwise there exists an essential discrepancy.

The results obtained for the body partially submerged in pycnocline are shown in Fig. 8. The calculations are performed based on the approximate algorithm. In this case, the body experiences the action of periodic buoyancy force in addition to inertial loading. The buoyancy force

was derived from the parameters of the incident wave. The results of approximate solution are shown in Fig. 8 by solid lines, the experimental values are denoted analogously to Fig. 7. The experimental conditions are given in Table 1.

The agreement between the predicted and measured loads is better for the horizontal component as compared to the vertical component what is especially notable at high wave frequencies. In general, the results of this series of computations give better fit to the experimental data at low frequency (large length) of incident waves what is consistent with the physical assumptions used in the formulation of the approximate solution.

4. CONCLUSIONS

This study is among the first attempts to determine the diffraction loads induced by internal waves on restricted horizontal elliptic cylinder in the case of continuous pycnocline stratification. It is shown that the presence of a finite layer of variable density changes the character of wave loading compared to the case of two-layer fluid with a step change in density.

The comparison between the experimental data and the computations reveals that the vertical force is essentially overestimated by the linear theory. There are reasons to believe that this departure results from non-linear effects. The elliptic shape of cross-section implies different conditions for separation depending on orientation of the cylinder in the flow.

In future, it would be desirable to continue the investigation of internal wave scattering with the study on role of the shape of cylinder cross-section and refined account of effects conditioned by continuous stratification.

ACKNOWLEDGMENT

This work was made possible in part by Grant No. JHX 100 from International Science Foundation and Russian Government.

REFERENCES

1. Phillips, O.M., "The Dynamics of the Upper Ocean," 2nd ed. Cambridge Univ. Press, Cambridge e.a., 1977.
2. Miropolsky, Yu.Z., "Dynamics of Internal Gravity Waves in the Ocean," *Gidrometeoizdat*, Leningrad, 1981 (in Russian).
3. Ermanyuk, E. & Sturova, I., "Effects of Regular Waves on the Body Submerged in a Stratified Fluid," 20th Symposium on Naval Hydrodynamics, Santa Barbara, Calif., USA, Aug.1994, pp.232-246.
4. Razumeenko, Y.V., "Changeability of Hydro-physic Ocean Fields; Problems of Manoeuvrability of Submerged Objects in Real Ocean," *International Symposium on Ship Hydrodynamics*, St.-Petersburg, Russia, 1995, pp. 275-288 (in Russian).
5. Sarpkaya, T., "Forces on a Circular Cylinder in Viscous Oscillatory Flow at Low Keulegan-Carpenter Numbers," *Journal of Fluid Mechanics*, Vol. 165, Apr.1986, pp.61-77.
6. Chaplin, J.R., "Wave Forces on a Horizontal Cylinder Beneath Waves," *Journal of Fluid Mechanics*, Vol. 147, Oct.1984, pp. 449-464.
7. Kochin, N.E., Kibel, I.A., Rose N.V. "Theoretical Hydromechanics", *Fizmatgiz*, Moskva, P. 1, 1963 (in Russian).
8. Sturova, I.V., "Scattering of Surface and Internal Waves on Submerged Body," *Computational Technology*, Novosibirsk, Vol.2, No. 4, 1993, pp.30-45 (in Russian).
9. Sturova, I.V., "Effect of Anomalous Dispersion Dependences on Scattering and Generation to Internal Waves," *Journal of Applied Mechanics and Technical Physics*, Vol. 35, No. 3, Nov.1994, pp.366-372.

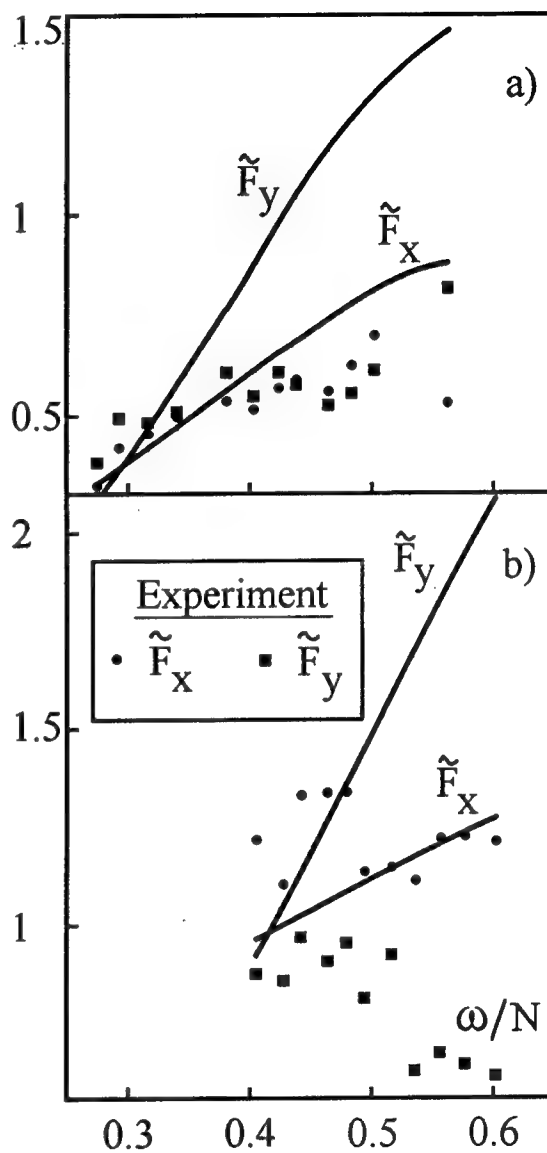
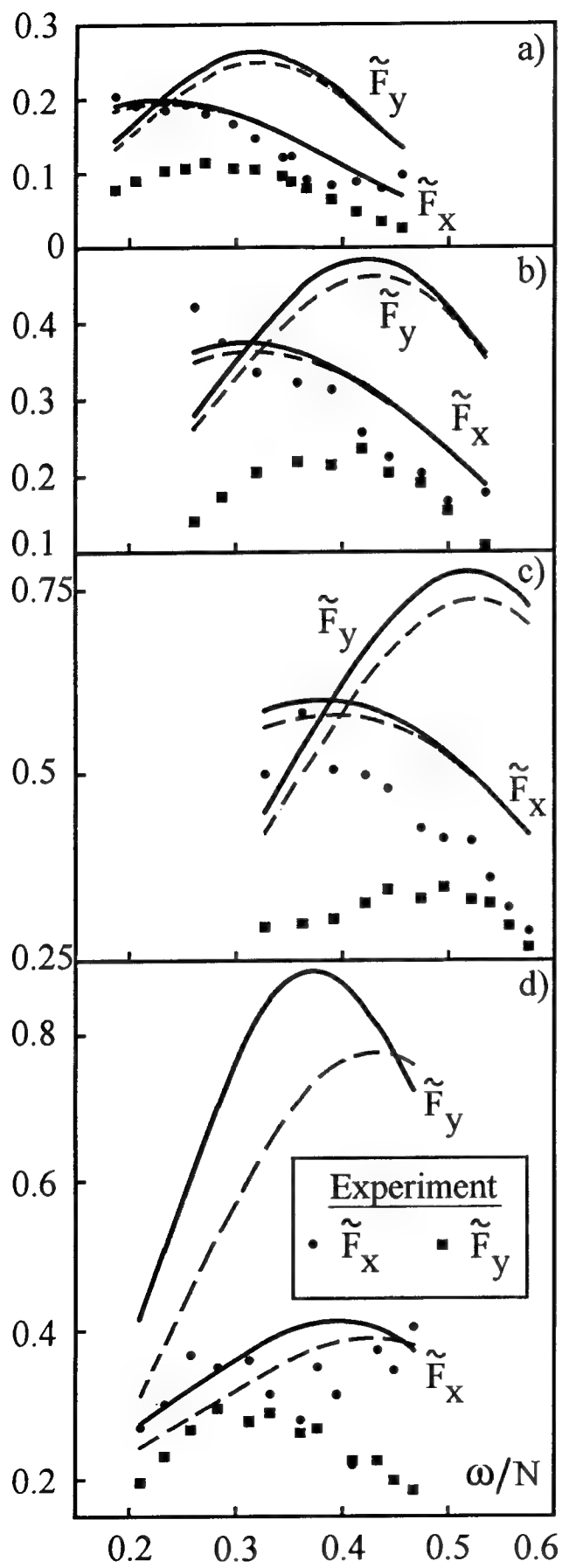


Fig. 8.

Influence of the Cavitation Nuclei on the Cavitation Bucket when Predicting the Full-Scale Behavior of a Marine Propeller

B. Gindroz (Bassin d'Essais des Carènes, France),

G. Bailo (MARISPENAV, Italy),

F. Matera, M. Elefante (MARISTAT SPMM, Italy)

ABSTRACT

The important role of nuclei on cavitation inception and cavitation development is now well known. Several recent studies, such as the large one suggested by the 20th ITTC and conducted in 1992 at the Grand Tunnel Hydrodynamique (GTH) of the Bassin d'Essais des Carènes, have allowed a precise correlation between cavitation inception for different types of cavitation on marine propellers and nuclei distributions (20th ITTC report) [33]. In a standard cavitation facility the nuclei distribution will depend on the hydrodynamic operating conditions, and can change during whole cavitation tests. Indeed, the "natural" nuclei spectrum of any cavitation facility depends on the history of the fluid through the different parts that constitute the facility. This means that this spectrum will depend on the hydrodynamic conditions, such as dissolved air content, pressure level and velocity, and the transit time through any part of the circuit, such as the main pump, vanes, resorber, etc. As a consequence, the "natural" spectra will be different in each cavitation facility. To quantify this effect, cavitation tests were conducted in the Italian Navy cavitation tunnel (CEIMM), on a frigate propeller. The inception cavitation characteristics of the model propeller (cavitation bucket) was determined, following the standard procedure of the CEIMM. In parallel, cavitation nuclei were measured for each operating condition. These measurements were conducted by the Bassin d'Essais des Carènes (French navy), using a Centerbody Venturi, similar to the one that equipped in standard the large French cavitation tunnel (GTH). In this paper, we describe the test procedure and the measurements. Then, the results

are analyzed, using the procedure suggested by Gindroz and Billet [1, 2, 3], which correlates nuclei distributions characteristics with cavitation inception data. This new approach is very interesting, as taking into account the nuclei characteristics leads to a unique cavitation inception bucket, independent of the hydrodynamic test conditions.

INTRODUCTION

Cavitation is one of the main limiting feature to the increase of hydrodynamic performances. Then, it is impossible to determine the performance of any hydraulic component without taking into account its cavitation behavior. Prediction of the cavitation performance of a propeller or a pump, a turbine, a vane, etc... is generally determined from model tests in cavitation facilities. The transposition from model results to full-scale characteristics is obtained by scaling laws and specific test procedures, established for some time by each organisation involved in hydrodynamic performances assessment. However, various problems remain unsolved, mainly due to the lack of knowledge of the local fluid mechanics and water quality. A significant illustration of this problem was given by Lindgren and Johnsson in 1966 [32], during the "standard" cavitation tests performed for the ITTC at several facilities. Then, many experiments were conducted that demonstrate the role of viscous effects [4, 5] and water quality [6, 7, 8] on cavitation.

Numerous research has been carried out to attempt to identify, understand, predict and control the physical mechanism leading to cavitation

inception. Rood [9], in his paper entitled "Mechanisms of Cavitation Inception", makes a precise review of research progress during the last twenty years. He underlines that the scaling laws to predict the full-scale cavitation behavior from the model tests, are based on empirical rules, defined on a correlation between measurements at model scale and observations of full-scale characteristics. The need to better understand the scale phenomena and to develop physical prediction laws has led to focus studies on real fluid characteristics. For an engineer, the purpose of any model scale test is the accurate prediction of the full-scale behavior.

Experimental observations have shown the persistence of microbubbles in a real fluid. These free microbubbles, called nuclei, have been found to be a major parameter in the cavitation inception process. According to the study of Billet [10] and Gindroz [11], natural waters such as rivers and oceans contain free microbubbles.

The influence of the nuclei on the cavitation behavior has been written in numerous publications [12 to 30]. To summarize all these studies, the role of free cavitation nuclei was found to be of major importance in the cavitation inception and developments processes. More particularly, we must be able to measure the nuclei content in a facility, when performing cavitation tests on a model.

Thus, in order to relate nuclei size distributions with inception cavitation in cavitation facilities, a test program was conducted in 1992 at the Grand Tunnel Hydrodynamique (GTH) of the Bassin d'Essais des Carènes. The GTH, which has a complete air control system including dissolved gas and nuclei (microbubbles) control, offered the opportunity to answer this question.

The tests were conducted on three 34 mm diameter propellers used by Kuiper [6], each of these propellers being characterized by a different cavitation type: bubble, sheet and vortex cavitation.

Four different nuclei distributions were generated (Figure 1) : strong degassed water (maximum tension, T4), low injection of medium size nuclei (medium tension-low content, T3), large injection of medium size nuclei (medium tension-high content, T2) and large injection of large nuclei (minimum tension, T1). By injecting medium size nuclei for a low content and a high content, we were able to examine the influence of the number of nuclei on the cavitation inception characteristic. During all the tests, the dissolved air content was kept constant.

The GTH on-line Cavitation Nuclei Counter (Centerbody Venturi) was used to measure both the water nuclei distribution and the liquid tension.

Figure 1 summarizes the influence of the nuclei characteristic distributions on the cavitation inception parameter, σ_i , referred to its value for the T4 nuclei distribution (maximum tension case). The

nuclei measurements are presented as a cumulative nuclei distribution, in Number of nuclei per ccm versus their critical pressure referred to the vapor pressure, $P_{cr} - P_v$ (Figure 1).

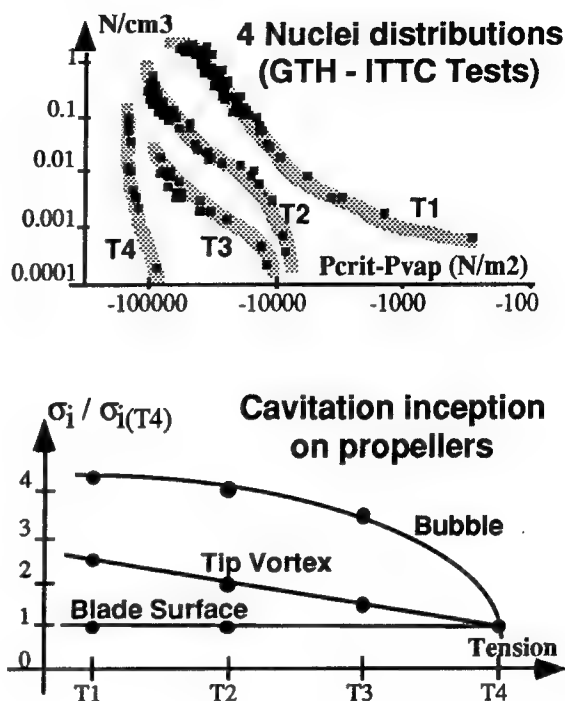
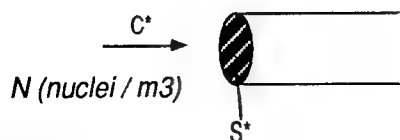


FIGURE 1 : NUCLEI INFLUENCE ON THE CAVITATION INCEPTION CHARACTERISTIC FOR SHIP PROPELLER

These tests at the GTH clearly demonstrate the direct influence of water quality on propeller cavitation inception (1, 2, 3). With a large increase in liquid tension, little change in cavitation inception was found for blade surface cavitation (sheet cavitation), but, in the case of both tip vortex cavitation and travelling bubble cavitation, the nuclei measurements from the GTH standard Centerbody Venturi correlated with many observed trends. Moreover, for the case of tip vortex cavitation inception, it appears that the measurement of both nuclei size (liquid tension) and nuclei number distribution (event rate) are necessary to correlate the data. Indeed, for the medium tension case, a strong influence on the inception of tip vortex cavitation can be observed from the two different nuclei concentrations (high and low).

The cavitation inception generally corresponds to an event rate of the order of magnitude of 1 event per second. When analyzing the cavitation inception results from the point of view of event rates Gindroz and Billet [3] show that the so-called "water tension" leading to cavitation inception

must be related to different nuclei concentrations, specific to each type of cavitation, mainly bubble and tip vortex cavitation for propellers. Thus, the tension T^* , corresponding to inception must be determined from the nuclei measurements. If S^* is the cross section of the cavitating flow, C^* is the absolute velocity of the flow through this section and $N = \mathcal{F}(P_v - P_{cr})$ is the number of activated nuclei per unit volume, the nuclei content leading to an event rate ξ can be defined as follows :



$$\xi(\text{events/s}) = N (\text{nb/m}^3) \cdot S^* (\text{m}^2) \cdot C^* (\text{m/s})$$

$$\Rightarrow N = \frac{\xi}{S^* \cdot C^*}$$

Then, considering that cavitation inception generally corresponds to an event rate of 1 per second, the corresponding number of activated nuclei N^* and the corresponding tension, T^* will be :

$$N^* = \frac{1}{S^* \cdot C^*}$$

$$\Rightarrow T^* = \mathcal{F}(N^*)$$

For the characteristic conditions of the GTH-ITTC 1992 tests [33], the nuclei content that must be activated to lead to cavitation inception was of the order of magnitude of 0.0001 N/ccm for the Bubble cavitation (B) and 0.01 N/ccm for the Tip vortex one (TV). Then, the corresponding inception tensions, T^* , were determined from each of the 4 nuclei distributions (Figure 2).

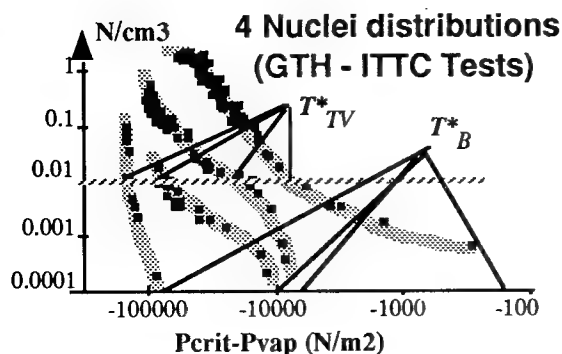


FIGURE 2 : NUCLEI DISTRIBUTIONS AND CORRESPONDING CHARACTERISTIC TENSIONS, T_B^* AND T_{TV}^*

Using these characteristic values, it was possible to precisely correlate the tension value T^* with the cavitation inception value, σ_i .

The relation between T^* and σ_i for both bubble and tip vortex cases are linear and the characteristic slope of the curves are equal to :

$$\text{Slope} = - \frac{1}{\frac{1}{2} \rho C_{ref}^2}$$

This means that the cavitation inception value, σ_i , directly depends on the normalized tension, T^* , based on the event rate analysis :

$$\sigma_i = \mathcal{F}(T^*) = \sigma_{i0} - T^*$$

$$\text{where } T^* = \text{Normalized "event rate" Tension} = \frac{T^*}{\frac{1}{2} \rho C_{ref}^2}$$

and σ_{i0} = σ_i value for zero tension ($T^* = 0$ N/m²)

Figure 3 represents this major result and leads to the conclusion that it is no longer possible to conduct meaningful cavitation tests without determining the complete nuclei distributions.

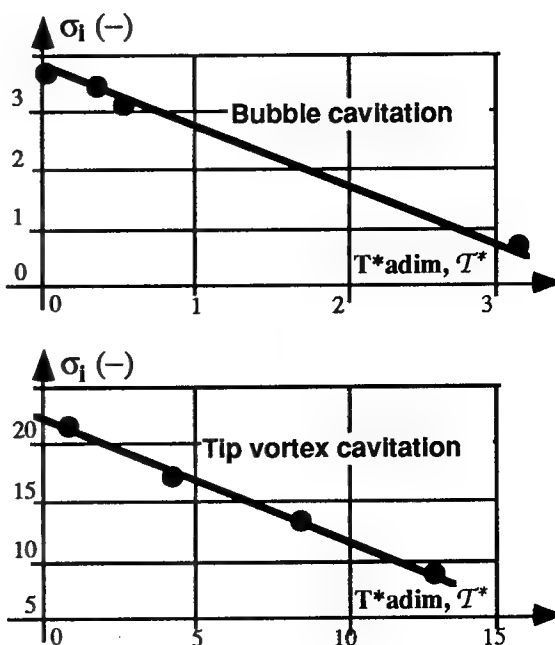


FIGURE 3 : INFLUENCE OF T_{adim}^* TENSION, T^* , ON CAVITATION INCEPTION

PURPOSE OF THE STUDY

The conclusion of the above study clearly shows the importance of understanding the role of nuclei distribution (liquid tension and nuclei number distribution) in the cavitation inception process. Minimizing the liquid tension and maximizing the number of nuclei (number distribution) is one method to reduce scale effects; however, in many facilities, this is not practical. Also, in some cases, this can alter the bubble dynamics and appearance of the cavitation, especially when the increase of nuclei number distribution is obtained by increasing the dissolved air content in the facility.

Rood in his review [9], underlines the fact that different facilities are characterized by different nuclei distributions, corresponding to the hydrodynamic configuration of each facility. The nuclei spectrum is affected by the whole nuclei time history through the facility. The use of a deaerator to remove air and a resorber to dissolve the small nuclei can change significantly the spectrum. As a consequence, the "natural" spectra will not only be different in each cavitation facility, but will also strongly depend on the facility operating conditions. This is not acceptable when determining a precise cavitation model bucket, that must be representative of the model characteristics.

Generally, scale effects between model and full-scale equipment are analyzed without taking into account any nuclei influence [38]. As a result, transposition laws established by hydrodynamic laboratories from theoretical analysis and many experimental results on both models and full-scale equipment, omit the major influence of the nuclei. This means that, for different nuclei distributions, the model results will be transposed exactly in the same way, without any water quality transposition parameter. Particularly, the four characteristic cavitation inception values corresponding to the four nuclei distribution generated during the GTH-ITTC tests (Figure 1), will be transposed with the exact same laws, as the transposition laws are mainly a function of the geometric scale, the Reynolds number and the surface roughness, but not of the free nuclei distribution :

$$J_{full-scale} / J_{model} = \mathcal{F}(\lambda, Re, K)$$

$$\sigma_{full-scale} / \sigma_{model} = \mathcal{F}(\lambda, Re, K)$$

The purpose of any model test is to try to predict the full-scale characteristic. It is then necessary to determine a precise cavitation bucket that corresponds to the model behavior, as its own

and unique characteristic. It has not to include the own facility and the water quality characteristics.

To quantify this effect, cavitation tests are conducted in the Italian Navy cavitation tunnel (CEIMM), on a frigate propeller. The inception cavitation characteristic of the model propeller (cavitation bucket) is determined visually, by the CEIMM staff, following their standard procedure. In parallel, cavitation nuclei are measured for each tunnel operating condition (each measured point). These nuclei measurements are conducted by the Bassin d'Essais des Carènes (French Navy), using a Centerbody Venturi [31, 34, 35], similar to the one that equipped in standard the large French cavitation tunnel (GTH), and that was used during the GTH-ITTC tests [1, 2, 3, 33].

The tests are carried out for two different dissolved O₂ contents, and their influence on the cavitation bucket is analyzed, using a similar approach that the one proposed by Gindroz and Billet [3] to correlate nuclei characteristics with cavitation inception data.

The main purpose of this study is to try to determine a unique characteristic cavitation bucket, which does not depend on the facility and its hydrodynamic operating conditions. The new bucket will correspond to a "zero tension" water quality, determined from the event rate analysis of Gindroz and Billet [3].

TEST FACILITIES AND INSTRUMENTATION

The tests are conducted in the CEIMM Cavitation Tunnel, designed in 1962 by Kempf & Remmers (Figure 4).

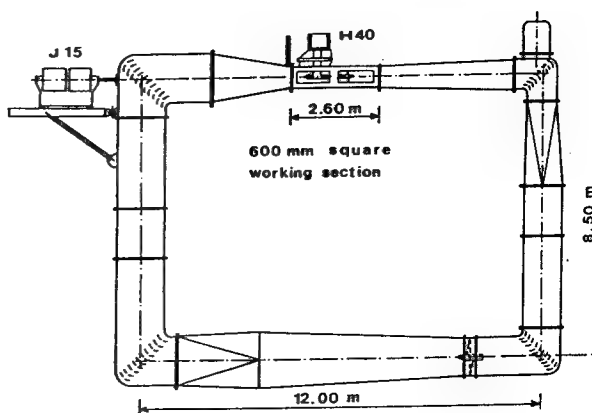


FIGURE 4 : CEIMM CAVITATION TUNNEL

It has the following technical characteristics:

- Length : 12 m
- Height : 8.5 m
- Stainless steel AISI 316
- Test section : 600mm x 600mm x 2.6 m
- Power : 213 kW, 4-blades axial flow impeller with Ward- Leonard
- Max. velocity : 12 m/s
- Max & Min abs pressure : 150 - 10 kPa
- Cavitation : $\sigma = 0.2$ and over

INSTRUMENTATION :

3 sets of propeller dynamometers,
3 & 5 components balances,
pressure transducers,
Laser Doppler,
Wake survey, hydrophones, etc...

PROPELLER SIZE RANGE :

Standard diameter : 250 mm
Maximum diameter : 300 mm

The tests are conducted on a 4-blades propeller, that equipped a LUPO Class frigate, characterized by a maximum velocity of 35 knots. The propeller model has a diameter of 274.1 mm and is installed in the CEIMM Tunnel test section with brackets on the main shaft inclined with $5^\circ 30'$ (Figure 5).

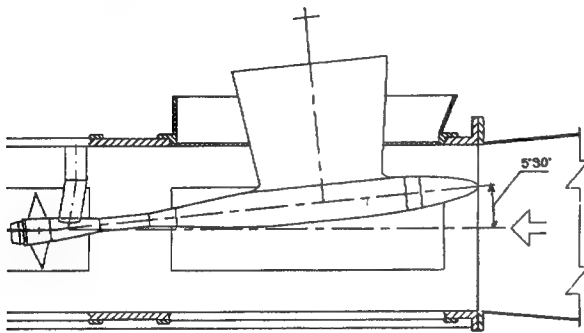


FIGURE 5 : PROPELLER TEST CONFIGURATION IN THE CEIMM CAVITATION TUNNEL

The cavitation nuclei distributions are measured by a fully calibrated Centerbody Venturi similar to the one that is used during standard cavitation tests on the GTH. The major advantage of the hydrodynamic technique of the Venturi is that the nuclei are determined using the same phenomenon that governs the cavitation development [11, 35, 36,37]. Thus, only the micro-bubbles (cavitation

nuclei) are counted, not the solid particles. This technique is particularly well-adapted to this kind of measurement.

MEASUREMENTS

The main purpose of this study is to determine how the nuclei distributions change with the tunnel operating conditions during model cavitation tests, and how they influence the global result, i. e. the whole cavitation bucket.

A cavitation bucket, σ_n versus J , is visually determined (Figure 6), within the following range of the advance ratio parameter, J :

$$0.93 J_N \leq J \leq 1.04 J_N$$

where J_N is the nominal advance value

$$J = \frac{V}{nD} \quad (-)$$

$$\sigma_n = \frac{(P_{ts} - P_v)}{\frac{1}{2} \rho (nD)^2} \quad (-)$$

V : Flow velocity (m/s)

n : Propeller rotational speed (rps)

D : Propeller diameter (m)

P_{ts} : Pressure in the test section (N/m²)

P_v : Vapor pressure (N/m²)

ρ : water density (kg/m³)

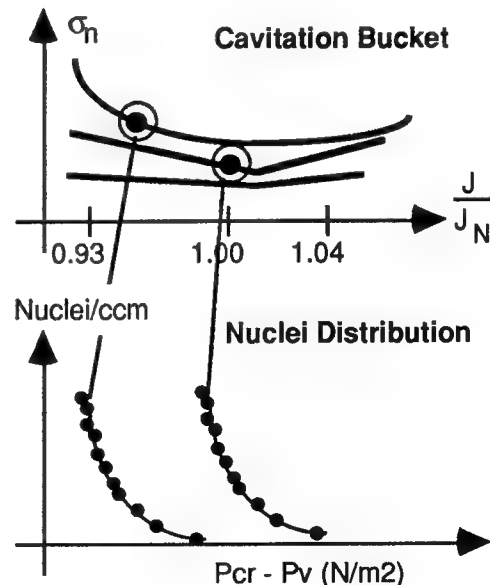


FIGURE 6 : CHARACTERISTIC MEASUREMENTS DURING THE CEIMM TESTS

Changing the J value, is obtained for a constant propeller rotational speed, n, by modifying the flow velocity, V. Thus, for the above defined range of J, the flow velocity varies within the following range :

$$8 \text{ m/s} \leq V \leq 8.9 \text{ m/s}$$

The "natural" nuclei spectrum of any cavitation facility depends on the history of the fluid through the different parts that constitute the facility. This means that this spectrum will depend on the hydrodynamic conditions, such as dissolved air content, pressure level and velocity, and the transit time through any part of the circuit, such as the main pump, vanes, resorber, etc. As a consequence, the "natural" spectra will change with the tunnel operating conditions. Thus, for each point of the bucket, a complete nuclei distribution is measured by the Centerbody Venturi (Figure 6). The results are presented as a cumulative nuclei distribution, in Number of nuclei per ccm versus their critical pressure referred to the vapor pressure, Pcr - Pv (Figure 6).

This complete sequence is measured for 2 different dissolved O₂ contents, respectively 3 ppm and 5 ppm, in order to analyze the influence of the dissolved air content on the nuclei "natural" distributions, and their consequence on the cavitation inception characteristics (Bucket). The dissolved O₂ content is directly measured with a Beckman equipment. In the CEIMM tunnel, it is possible to maintain constant the dissolved O₂ content, in a relatively wide range of values.

RESULTS

During the cavitation measurements, the pressure level in the test section (sigma value) and the dissolved O₂ content is found to strongly influence the nuclei distributions. However, due to the very good stability of the CEIMM tunnel and its deep resorber, the nuclei spectra are particularly well repetitive and stable for a given hydrodynamic condition. Figure 7 illustrates the direct influence of both parameters, i.e. pressure level in the test section and O₂ content. Within the narrow range of flow velocity ($8 \leq V \leq 8.9$ m/s), no sensible effect of this parameter was found.

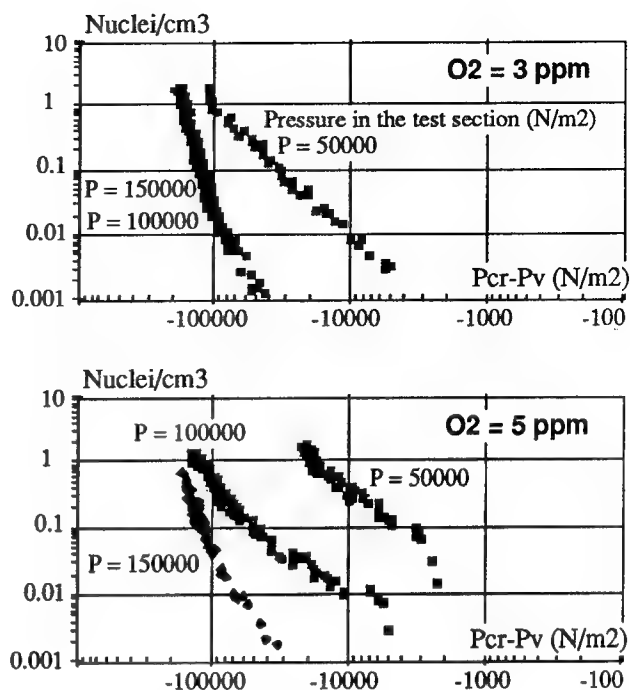


FIGURE 7 : INFLUENCE OF THE OPERATING CONDITIONS ON THE CHARACTERISTIC NUCLEI DISTRIBUTIONS, DURING THE CEIMM TESTS

The analysis of the above results shows a large influence of both the pressure value and the dissolved O₂ content on the nuclei characteristics. Thus, as the cavitation parameter, σ_n , is directly related to the absolute pressure level in the test section, this result means that the water tension, leading to cavitation inception, will change during the determination of a complete cavitation inception bucket, even if the dissolved O₂ content can be kept constant. To quantify this effect, figure 8 represents the evolution of the minimum normalized water tension, corresponding to the nuclei with the highest critical pressure, i.e. the "weakest nuclei" (the biggest ones), versus the cavitation parameter, σ_n . The tension is normalized by the same value than the cavitation parameter, σ_n :

$$T_{adim} = \frac{\text{Tension (N/m}^2\text{)}}{\frac{1}{2} \rho (nD)^2} = \mathcal{T} \quad (-)$$

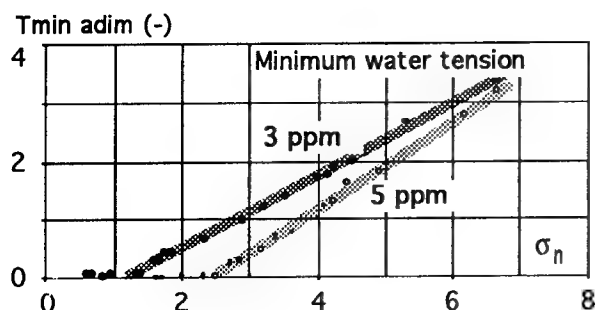


FIGURE 8 : INFLUENCE OF THE OPERATING CONDITIONS ON THE CHARACTERISTIC WATER TENSION, CORRESPONDING TO THE "WEAKEST" NUCLEI.

The evolution of the minimum tension versus the σ_n , can reasonably be represented by a linear curve, for both 3 ppm and 5 ppm dissolved O_2 contents. However, for σ_n value below 2.5, the tension is close to zero for the 5 ppm case, but remains relatively important for the 3 ppm case, for which the zero tension is reached only below $\sigma_n = 1$.

Under this modification of the nuclei characteristics, no wonder that the whole cavitation inception bucket will be influenced.

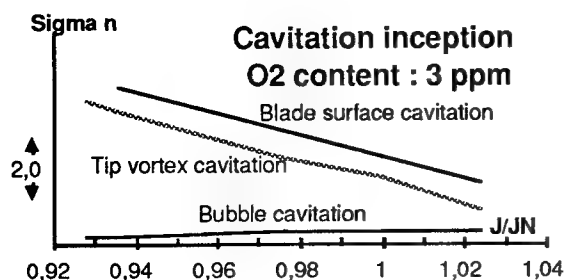


FIGURE 9 : CAVITATION INCEPTION BUCKET FOR 3 PPM O_2 CONTENT.

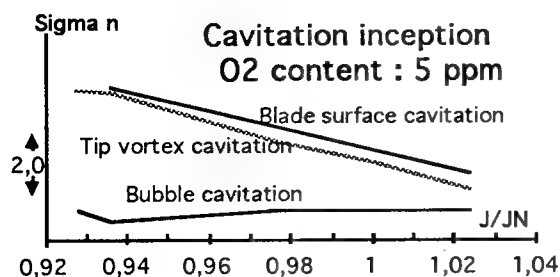


FIGURE 10 : CAVITATION INCEPTION BUCKET FOR 5 PPM O_2 CONTENT.

Figures 9 and 10 represent the global cavitation inception bucket, for blade surface cavitation, tip vortex and bubble cavitation, corresponding to a dissolved O_2 content of respectively 3 ppm and 5 ppm.

To better evaluate how the modification of nuclei characteristics through the change of O_2 content, influences the cavitation inception bucket, figure 11 represents both buckets on the same graph. The solid lines correspond to the 3 ppm case, while the dotted line to the 5 ppm case.

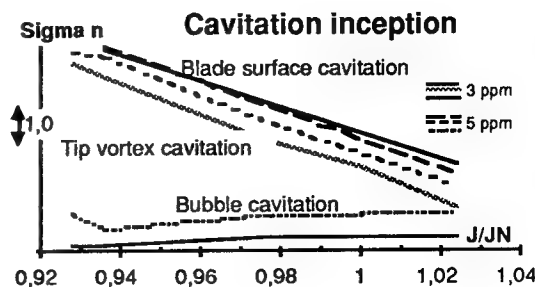


FIGURE 11 : CAVITATION INCEPTION BUCKETS FOR 3 AND 5 PPM O_2 CONTENTS.

A significant difference is observed between the two water conditions. Then, the practical question remains : which bucket is the correct one, leading to the accurate prediction of the full-scale cavitation behavior ? The answer can not be either the 3 ppm one or the other one. Indeed, when determining the "cavitation bucket" of a model propeller, how can we guarantee the model results when the nuclei distribution changes with the operating conditions (pressure, flow rate, dissolved air content) and when the nuclei distribution is not known ? Moreover, how can we transpose such a result to full-scale prediction, when the model free nuclei content changes with the operating conditions, which is not the case at sea, as the nuclei distributions will not directly depend on the advance velocity ?

Moreover, during a normal procedure, several problems can happen, as, for example, the increase of dissolved air content during the tests. In this case, if the tests are done quickly to ensure the dissolved gas content doesn't change significantly, the characteristic $\sigma_i - J$ inception curve will be one of those corresponding to a constant O_2 content (Figure 12, TV_A or TV_B). But, when the dissolved gas content changes during the cavitation bucket tests, results can be altered as shown in Figure 12. Depending where the tests start (either from point C or D, for example), the characteristic curves will be different. Indeed, if the tests start with a low

dissolved air content, the water will generally increase its air content with the time. Then, as the nuclei distributions change with the dissolved air content in the water (Figure 7), the cavitation behavior of the propeller will be influenced, and the characteristic inception curve will evolve along the TV_C or TV_D curve (Figure 12).

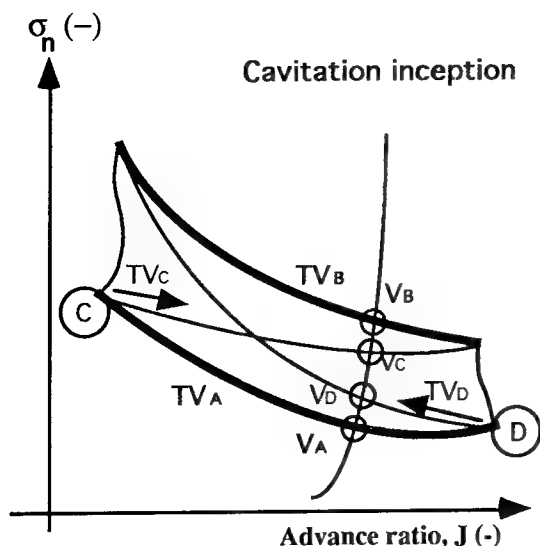


FIGURE 12 : INFLUENCE OF THE TESTS PROCEDURE ON THE CHARACTERISTIC CAVITATION INCEPTION CURVES

As a consequence, the prediction of the range of advance velocity free of cavitation depends on the procedure of the model tests. This is not acceptable when determining a precise cavitation model bucket that must be representative of its own cavitation characteristics. Then, as long as scale effects between model and full-scale equipment are analyzed without taking into account any nuclei influence, the four characteristic curves represented in figure 12 will be transposed with the exact same laws, which means that the corresponding uncertainty on the predicted full-scale advance velocity leading to cavitation inception can be as large as several knots.

Fortunately, the problem of O₂ content evolution during the tests doesn't appear in the CEIMM tunnel, as it is possible to reasonably maintain constant the dissolved gas content.

ANALYSIS

Following the same analysis than proposed by Gindroz and Billet [2, 3], to correlate nuclei distributions with cavitation inception data, there is an attempt to transpose the model cavitation bucket to

a model "zero tension" one, using the nuclei distribution characteristics. This means that this new cavitation inception bucket corresponds to a "weak water" with a zero tension, as defined in the introduction, and based on the events rate analysis. Applying this procedure to the CEIMM tests, must lead to the transposition of both 3 ppm and 5 ppm buckets to a single one, as schematically represented in figure 13.

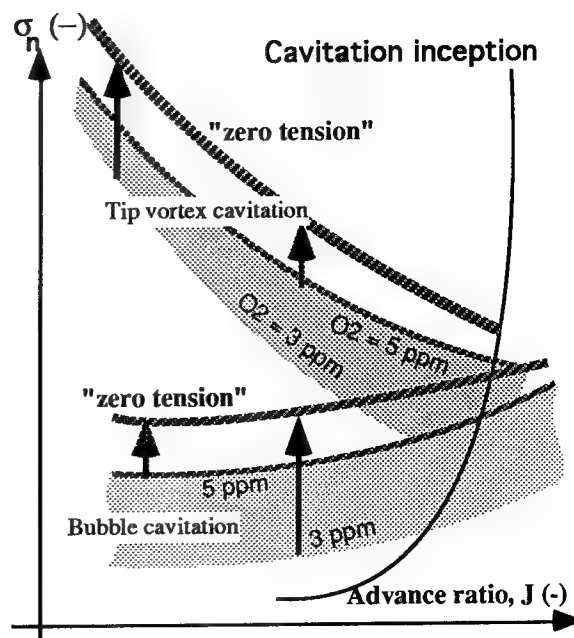


FIGURE 13 : "ZERO WATER TENSION" CHARACTERISTIC CAVITATION BUCKET

The transposition of the cavitation inception curves is made by adding the inception normalized tension, T^* , to the cavitation inception parameter, σ_{ni} :

$$\sigma_{ni}^{*0} = \sigma_{ni} + T^*$$

Where σ_{ni}^{*0} is the new transposed inception cavitation value, corresponding to a "zero tension" water.

For the application of the above described procedure, it is necessary to determine the tension, T^* , as a function of the nuclei content. Indeed, the tension leading to cavitation inception is based on an events rate analysis, which means that the number of activated nuclei corresponding to cavitation inception, will depend on the hydrodynamic conditions and the type of cavitation, as already

mentioned in the introduction [2, 3]. Thus, the evolution of the tension, T^* , with the cavitation parameter, σ_n , is determined for different nuclei contents, from the nuclei distributions measured during the CEIMM tests for each $\sigma_n - J$ point. Figures 14 et 15 represent the evolution of the normalized tension, T^* , for 4 different nuclei contents, resp. 0,001; 0,003; 0,005 and 0,01 Nucleus/ccm. Figures 14 and 15 correspond respectively to the 3 ppm and 5 ppm dissolved O_2 contents.

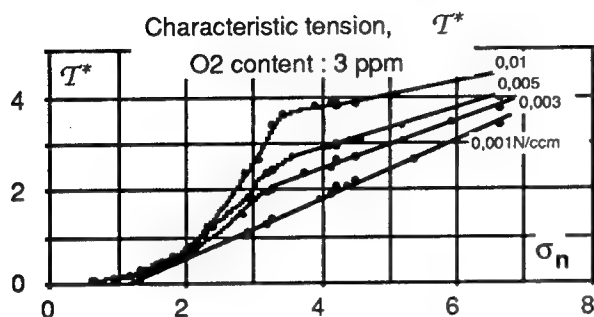


FIGURE 14 : EVOLUTION OF THE T^* NORMALIZED TENSION WITH THE σ_n PARAMETER, FOR DIFFERENT NUCLEI CONTENTS, AT 3 PPM OF DISSOLVED O_2

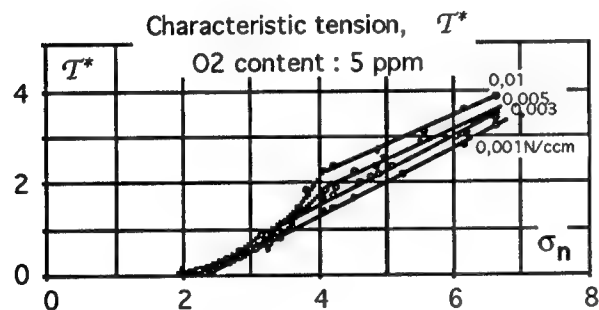


FIGURE 15 : EVOLUTION OF THE T^* NORMALIZED TENSION WITH THE σ_n PARAMETER, FOR DIFFERENT NUCLEI CONTENTS, AT 5 PPM OF DISSOLVED O_2

Large influence of the dissolved O_2 content can be observed. Indeed, within the range of σ_n values corresponding to cavitation inception, the normalized tension difference, ΔT^* , can be larger than 1,0 for the highest nuclei contents (0.005 and 0.01 N/ccm).

In order to determine the particular normalized tension, T^* , leading to cavitation inception, the corresponding number of activated nuclei (nuclei content), must be determined. This amount is specific to each type of cavitation. In this

study, we concentrate on tip vortex cavitation and bubble cavitation. Following the same analysis than used by Gindroz and Billet [2], the required nuclei content corresponding to tip vortex cavitation inception based on one event per second is of 0,003 N/ccm. The bubble cavitation only appears at the root of the blades. In this area, the absolute velocity and the cross section (see introduction) are not very important, which means that it is necessary to activate a rather large amount of nuclei. In our case, the corresponding nuclei content leading to bubble cavitation inception corresponds to about 0,05 N/ccm.

Then, from the above results, it is possible to determine the corresponding normalized tension, T^* (Figures 14 and 15). By adding the specific tension T^* to the measured cavitation inception parameter, σ_{ni} , we can reach the desired "zero tension" cavitation inception value, σ_{nio} . Figure 16 represents this final result.

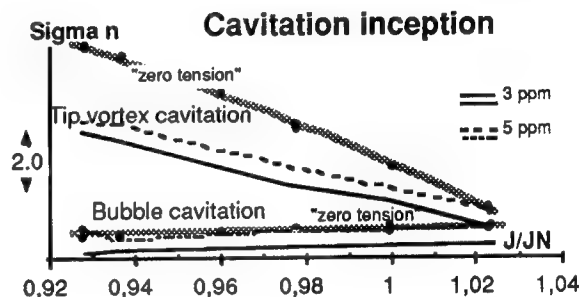


FIGURE 16 : "ZERO TENSION" CAVITATION INCEPTION BUCKET, MEASURED AT THE CEIMM TUNNEL

Interesting results are obtained here. Indeed, the two different cavitation inception curves corresponding to two different dissolved gas contents (3 ppm and 5 ppm in Figure 2), collapse on a single curve : the transposed "zero water tension" characteristics deduced from the nuclei measurements. This "new bucket", corresponding to the "zero water tension", is unique and does not depend on the hydrodynamic conditions.

SYNTHESIS AND PERSPECTIVE

In order to relate nuclei characteristics with the cavitation inception, a large study was conducted in 1992 at the Grand Tunnel Hydrodynamique (GTH) of the Bassin d'Essais des Carènes in cooperation with the ITTC cavitation committee [33]. The GTH, which has a complete air control system including dissolved gas and free nuclei (microbubbles) control,

offered the opportunity to answer this question. The main result of this study was the direct correlation between the cavitation inception and the water tension based on an events rate analysis. Indeed, as cavitation inception corresponds to a certain amount of events per second (generally of the order of magnitude of 1), it is necessary to activate a certain amount of nuclei in the flow. Thus, the tension T^* , corresponding to the minimum nuclei content leading to cavitation inception was defined from the measured nuclei distributions. Due to the GTH design, the nuclei distribution can be controlled and set as desired. This means that during the complete determination of a cavitation inception bucket, the nuclei distribution will stay constant. However, when conducting cavitation inception tests in a classical cavitation tunnel, we must be very careful to not only attribute the results to the propeller itself, but also to consider the influence of the free nuclei distribution that will change with the tunnel operating conditions. It is well known that comparing the results obtained with the same model in different facilities is almost impossible [32]. But we are convinced that a large part of the reason comes from the lack of knowledge about the nuclei characteristics and their evolution with the hydrodynamic conditions. In order to try to quantify this effect, this study was conducted at the CEIMM tunnel, in Roma, on a 4 blades frigate propeller. The results obtained confirm the strong influence of the tunnel hydrodynamic parameters on the nuclei distribution. Then, as the free nuclei mainly govern the whole cavitation inception process, no wonder that the global cavitation inception bucket is influenced.

Following the analysis from Gindroz and Billet [2, 3], who succeed in correlating the nuclei distribution and the cavitation inception characteristics, the results obtained at the CEIMM are transposed to a "zero tension" bucket. This transposition is made for 2 different O_2 contents, that lead to a large difference in the nuclei content. To ensure the upstream velocity field (wake field) doesn't change between the two different O_2 content conditions, the flow velocity was similar. Thus, if the reason why the cavitation buckets are different between the two conditions is mainly due to the free nuclei, the 2 transposed "zero tension" buckets must be similar. Then, the comparison made in figure 16 confirmed the direct influence of the free nuclei on the cavitation inception characteristics, which is shown in figure 16. This major result means that conducting cavitation inception tests in different facilities and/or for different water qualities, on the same model and ensuring the same upstream velocity field, can lead to the same global bucket only if the nuclei characteristics are taken into account. Then, the unique "zero tension" bucket could be defined as the own cavitation inception characteristic of the

model. In order to confirm this major result, similar tests will be conducted at the GTH, in the same configuration, for different nuclei distributions. Due to the specific design of the GTH, the nuclei distributions will be controlled, which means that it is possible to ensure no dependence of the tension with the σ_n value (Figure 17).

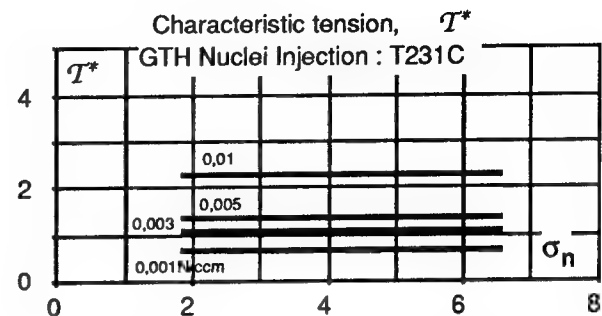


FIGURE 17 : EXAMPLE OF NUCLEI CHARACTERISTICS GENERATED AND CONTROLLED IN THE GTH.

From the generated nuclei distributions, the measured cavitation inception bucket will be transposed to its corresponding "zero tension" one. Cavitation inception buckets will be determined in the GTH on the same Italian frigate propeller for several nuclei characteristics, and transposed to their "zero tension" ones. Then, all these "zero tension" curves will be compared with the ones determined at the CEIMM tunnel. If the wake field is similar between both facilities, all these different characteristic "zero tension" curves must collapse to a unique one : The model cavitation inception characteristics.

Then, the prediction of the full-scale behavior could be made from this new "zero tension" model bucket, using the usual transposition laws, that do not take into account the nuclei characteristics. The so-determined full-scale bucket will then correspond to weak water without any tension. Then, finally, as a further perspective, the accurate evaluation of the full-scale risk of cavitation could be more precisely determined by taking into account the sea nuclei characteristics [39].

CONCLUSION

The present study shows the direct influence of the hydrodynamic operating conditions of a standard cavitation tunnel on the characteristic cavitation inception bucket of a propeller. Careful attention must be taken when conducting cavitation tests, as the final results can include important effects from the evolution of the nuclei with the tunnel

operating conditions and the water quality. However, due to the very good stability and repeatability of the CEIMM tunnel, it was possible to directly relate the nuclei distribution with the cavitation inception characteristics, and to transpose the results to an accurate unique "zero tension" bucket, that defines the own propeller behavior under the actual test configuration. This result is very important, but further studies will be conducted in order to confirm it and to examine its influence on the full-scale characteristic bucket.

Several vain attempts have been made for many years to try to compare similar tests carried out in different facilities, but this new approach looks promising.

ACKNOWLEDGEMENTS

The authors wish to acknowledge first the Italian Navy and the French Navy, who agreed in working together on this subject.

The authors wish to acknowledge all the colleagues from the CEIMM, and specially the staff of the cavitation tunnel, for their enthusiastic participation during the tests campaigns.

This work is supported financially by the Italian Navy and the DRET, that the authors wish to acknowledge more particularly.

REFERENCES

1. Gindroz, B., Billet, M.L., "Influence of the Nuclei on the Cavitation Inception for Different Types of Cavitation on Ship Propellers", Proceedings of the ASME WAM '93, December 1993, New Orleans, USA.
2. Gindroz, B., Billet, M.L., "Nuclei and Acoustic Cavitation Inception of Ship Propellers", Proceedings of the Second International Symposium on Cavitation, April 1994, Tokyo, Japan.
3. Gindroz, B., Billet, M.L., "Nuclei and Propellers Cavitation Inception", Proceedings of the ASME FED Symposium on Cavitation, June 1994, Lake Tahoe, USA.
4. Arakeri, V. H., Acosta A. J., "Viscous Effects in Inception of Cavitation on Axisymmetric Bodies", Journal of Fluid Engineering, Trans ASME, 1973, pp. 519-526.
5. Van der Meulen, J. H. J., "A Holographic Study of Cavitation on Axisymmetric Bodies and the Influence of Polymer Additives", Publication N°509, 1976, Netherlands Ship Model Basin, Wageningen, The Netherlands.
6. Kuiper, G., "Cavitation Inception on Ship Propellers Models", Ph. D. Dissertation, 1981, Wageningen, The Netherlands.
7. Gates, E. M., Billet, M. L., "Cavitation Nuclei and Inception", Proceedings of IAHR Symposium, 1980, Tokyo, Japan, pp 3-25.
8. Katz, J., "Cavitation Inception in Separated Flows", California Institute of Technology, 1981, Report N° Eng. 183-5.
9. Rood, E. P., "Review-Mechanisms of Cavitation Inception", Journal of Fluid Engineering, June 1991, vol. 113.
10. Billet, M. L., "Cavitation Nuclei Measurements-A Review", Proceedings of the Cavitation and Multiphase Flow Forum, 1985, ASME.
11. Gindroz, B., "Lois de similitude dans les essais de cavitation des turbines Francis", PhD. dissertation, 1991, Lausanne, Ecole Polytechnique Fédérale.
12. Henry, P., "Influence of the Amount of Bubble Nuclei on Cavitation Tests of a Francis Turbine", Proceedings of the ASME Symposium, Cavitation and Polyphase Flow Forum, 12-14 June, 1978, Fort Collins, pp. 23-28.
13. Avellan, F., Gindroz, B., Henry, P., Bachmann, P., Vulliod, G., Wegner, M., "Influence de la chute d'essai et de la nucléation sur les performances en cavitation des modèles de turbines Francis", Proceedings of the 13th I.A.H.R. Symp. on Progress in Technology, September 1986, Montréal, vol. 1, pp. 2-1, 2-15.
14. Billet, M. L., "The Importance and Measurement of Cavitation Nuclei", Advancements in Aerodynamics, Fluid Mechanics and Hydraulics, 1986, Minneapolis.
15. Billet, M. L., "Cavitation Nuclei Measurements", Proceedings of the International Symposium on Cavitation Inception, ASME WAM, 1984, New Orleans.
16. Kuiper, G., "Some Experiments With Distinguished Types of Cavitation on Ship Propellers", Proceedings of the International Symposium on Cavitation Inception, ASME WAM, 1979, New York.

17. Kuiper, G., "Some Experiments With Distinguished Types of Cavitation on Ship Propellers", Journal of Fluid Engineering, 1982, vol. 104.
18. Kuiper, G., "Reflections on Cavitation Inception," Proceedings of the Cavitation and Multiphase Flow Forum, ASME, 1985.
19. Gindroz, B., Avellan, F., Henry, P., "Similarity rules of cavitation tests : The case of the Francis turbine", Proceedings of the 14th I.A.H.R. Symp. on Progress within large and high-specific energy units, June 1988, Trondheim, vol. 2, Session L, pp 755-766.
20. Gindroz, B., Henry, P., Avellan, F., "Similarity of cavitation inception in Francis turbine", Proceedings of the 15h I.A.H.R. Symp., September, 1990, Belgrade, Yugoslavia.
21. Gindroz, B., Avellan, F., Henry, P., "Guide lines for performing cavitation tests", Proceedings of the 15h I.A.H.R. Symp., September, 1990, Belgrade, Yugoslavia.
22. Gowing, S., Shen, Y. T., "The Role of Microbubbles on Cavitation Inception on Head Forms", 1982, David Taylor Research Center Report.
23. Gowing, S., Shen, Y. T., "Cavitation Susceptibilities in Ocean Waters", 1987, David Taylor Research Center Report DTNSRDC-SHD-1241-01, Aug.
24. Brennen, C. E., Kuhn de Chizelle, Y., "Cavitation Nuclei Concentrations and Event Rates", Internal Report, CALTEC, Pasadena, CA, July 1992.
25. Shen, Y. T., Gowing, S., Pierce, R., "Cavitation Susceptibility Measurements by a Venturi", Proceedings of the International Symposium on Cavitation Inception, ASME WAM, 1984, New Orleans.
26. Shen, Y. T., Gowing, S., Eckstein, B., "Cavitation Susceptibility Measurements of Ocean, Lake and Laboratory Water", 1986, David Taylor Research Center Report No. 86/019.
27. Liu, Z., Brennen, C. E., "Cavitation Nuclei Measurements and Population Dynamics", Internal Report, California Institute of Technology (CALTEC), Pasadena, California, July 1992.
28. Tanger, H., Strechwall, H., Weitendorf, E.-A., Mills, L., "Recent Investigations of the Free Air Content and its Influence on Cavitation and Propeller-Exited Pressure Fluctuations", Proceedings of the ISPC, Hamburg, Germany, June 1992.
29. Keller, A. P., "Scale effects at beginning cavitation applied to submerged bodies", Proceedings of the ASME Int. Symp. on Cavitation Inception, 1984.
30. Meyer, R. S., Billet, M. L., Holl, J. W., "Free Stream Nuclei and Travelling-Bubble Cavitation", JFM, Vol. 114, December 1992.
31. Lavigne, S., Noe, Ph., "Venturi à ogive centrale", Rapport d'essais, R. 21.025, 1988.
32. Lindgren, H., Johnsson, C. A., "Cavitation Inception on Head Forms - ITTC Comparative Experiments", 1966, Pub. of the Swedish State Shipbuilding Exper. Tank N°58.
33. 20 ITTC, "Report of Cavitation Committee", 19-24 September 1993, San Francisco.
34. Lavigne, S., "Le Venturi analyseur de germes", Proceedings of the Journées DRET Cavitation, Arcueil 1991.
35. Gindroz, B., Billard, J.-Y., Lavigne, S., "Complete Study of a Well-improved Centerbody Venturi", Proceedings of the Second International Symposium on Cavitation, April 1994, Tokyo, Japan.
36. Gindroz, B., Briançon-Marjollet, L., "Experimental Comparison Between Different Techniques of cavitation Nuclei Measurements", Proceedings of the 2nd International Symposium on Propeller and Cavitation, September 1992, Hangzhou, China.
37. Gindroz, B., "Qualification of a Centerbody Cavitation Nuclei Counter Using Optical Techniques", Proceedings of the 16h I.A.H.R. Symp., September 1992, São Paulo, Brazil.
38. Gindroz, B., "Propeller Cavitation Characteristics : The practical Interest of Nuclei Measurements in Test Facilities and at Sea", Proceedings of the ASME FED Symposium on Cavitation, August 1995, Hilton Head Island, USA.
39. Gindroz, B., Billard, J.-Y., Geistdoerfer, P., "Cavitation Nuclei Measurements at Sea", Proceedings of the ASME WAM, November 1995, San Francisco CA, USA.
40. 19 ITTC, "Report of Cavitation Committee", 12-22 September 1990, Madrid, Spain.

Inception, Development, and Noise of a Tip Vortex Cavitation

L. Briançon-Marjollet, L. Merle (Bassin d'Essais des Carènes, France)

ABSTRACT

Experiments were conducted on a large hydrofoil, of elliptical planform and NACA 0020 cross section, to test the influence of the water quality on : the cavitation map, the diameter of the cavity within the tip vortex and the noise measurements. Water is characterised in term of oxygen and freestream bubbles content. We observe strong effects of the freestream nuclei content on the cavitation map and on time variation of the vapor core diameter. All results at cavitation inception can be correlated by introducing a corrective term calculated from the measured water quality. The growth of the diameter with time, as well as the hysteresis at the desinence cavitation, can be interpreted taking into account the non condensible gas diffusion. Acoustic data are presented in term of counts of acoustic peaks, or in term of peculiar frequencies associated to the vapor tube. These results are confronted with the visual data and modes of deformation of the vapor tube are given.

NOMENCLATURE

a	radius of the cavitating vortex core
c	maximum chord length
Cl	lift coefficient related to the surface of the foil
C_p	pressure coefficient at the vortex axis
D	cavitating core diameter
F	frequency
f	focal length
H	hysteresis
i	angle of attack of the foil
$K(x)$	experimental coefficient

N	aperture
P	pressure of the inlet flow at the middle of the test section
P_c	critical pressure of nuclei
P_s	susceptibility pressure of the fluid
P_v	vapour pressure of water
r	radius
Re	Reynolds number based on the maximum chord length
t	time
T	surface tension
V	free stream velocity
V_t	tangential velocity
x	abscissa
γ	Euler constant
Γ	circulation
ρ	volumic mass of liquid
σ	cavitation number
σ_0	cavitation number at the beginning of the developed cavity
∞	far from the vortex axis, in the perpendicular plan of the centerline vortex
PSD	Power Spectral Density
G.T.H.	Grand Tunnel Hydrodynamique
CSM	Cavitation Susceptibility Meter

1. INTRODUCTION

Even if the cavitation of tip vortex was studied for a long time by many authors, some aspects had to be clarified. The fact that this type of cavitation is closely link to propellers conduct to have a special attention on it. It's Reynolds number dependance was studied. However, some questions remain : what is the best way to perform and interprate model tests in

order to extrapolate the results to full scale ? In many papers, authors indicate that oxygen content acts on cavitation inception ([2], [3], [6], [9]) and on desinence cavitation[13]. We could ask if there is a best water quality for model tests. But the above mentioned studies do not permit to quantitatively correlate a parameter describing water quality and a cavitation number.

Many studies were conducted on different French tests facilities during the Action Concertée Cavitation. The aim was a better understanding of tip vortex roll-up and of associated cavitating phenomenon ([7], [8], [11]). Due to the fact that the water tunnel, the Grand Tunnel Hydrodynamique G.T.H., permits us to control the oxygen content independently from the freestream nuclei content, the Bassin d'Essais des Carènes was in charge of studying relation between oxygen content, freestream nuclei content and inception, development and desinence of cavitation [11].

The aim of this paper is first to recall the main results obtained during these tests. For the cavity within the tip vortex-roll up, a law was yet proposed as a function of the Reynolds number for a single water quality at the desinence cavitation [8]. We will see in this paper, how all the data for cavitation inception can be fitted on a single curve when taking into account freestream nuclei.

The diameter of the cavity within the vortex was also measured. This allowed to appreciate how the water quality affects the development of cavitation. Thus, the hysteresis at desinence can be explain by diffusion of non condensable gas as expected by Holl [13].

At the inception of the cavity, we observe bubbles growing in the center of the tip vortex for special water quality. These bubbles, captured by the vortex, could grow by diffusion of non condensable gas or could explode by vaporisation of liquid. We are particularly interested in the acoustic noise and, in the following, we will call cavitation inception, a phenomenon with two particularities : we can locate the tip vortex in the flow visually, and there is a raise of the acoustic noise.

For developed cavitation, specific frequencies were extracted in the spectrum signal. These frequencies are compared with the frequencies of modal deformations of the cavity.

2. EXPERIMENTAL SETUP

2.1 Flow parameters

Experiments were conducted in the G.T.H. [5], in the square test section of 1.14 m width, 1.14 m high and of 6 m long. The studies were made with an elliptical planform hydrofoil, the maximum chord is 475 mm and the half-span equals 753 mm (the aspect ratio is 3.8), the cross-section is a NACA 0020.

The tunnel permits us to control the inlet velocity between 2 m/s up to 20 m/s with an accuracy of 0.2 %. The pressure level varies between 2.10^4 Pa up to $4.5 \cdot 10^5$ Pa, with an accuracy of 0.5 %. The cavitation number σ is defined as :

$$\sigma = \frac{P - P_v}{0.5 \rho V^2} \quad (1)$$

with P, the total inlet pressure in the plane of the tip of the hydrofoil, P_v , the vapor pressure of water, ρ the volumic mass of water and V the inlet flow velocity. The precision of σ is 1 %.

The oxygen content is controlled between 25 % up to 160 % of saturation and is measured with an oxygen probe. The flow can be seeded with nuclei through injectors located upstream the tunnel nozzle. A Cavitation Susceptibility Meter based on a centerbody venturi (called VAG) measures the nuclei distribution in the fluid. Hence, the number of nuclei with a given critical pressure is known for each test configuration. Several nuclei injections patterns were tested. They are characterised by a specific susceptibility pressure, a concentration and a distribution in the test section. Hereafter, the higher P_s (lower tension) corresponds to the water with 'big' bubbles, then we have a medium P_s for 'small' bubbles and the water without injection have the lowest P_s (higher tension). For more details, see [3].

Cavitating data were collected with the two testing configurations of nuclei presented below.

2.2 First configuration

The hydrofoil is mounted vertically at the top of the test section (Figure 1). The angle of attack is changed

by hand with a precision of $\pm 0.1^\circ$. Measurements of the tangential and axial velocities in the subcavitating vortex were carried out at several positions along the axial distance with a LDV system, for different velocities and angles of attack [8].

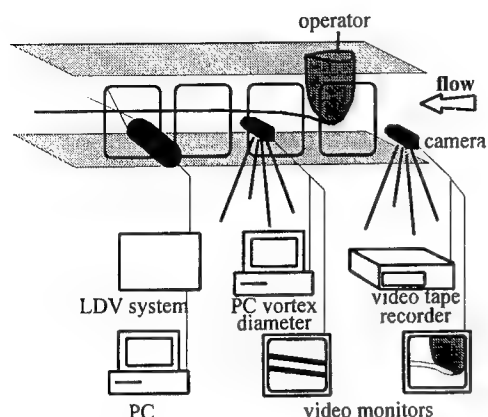


Fig. 1 : experimental facility, 1st configuration.
Location of apparatus is not represented.

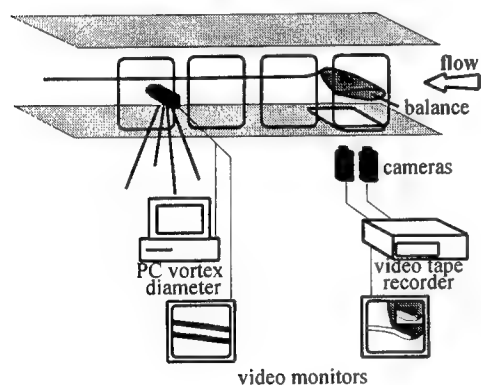


Fig. 2 : experimental facility, 2nd configuration.
Location of apparatus is not represented.

A map of the observed cavitation versus the angle of attack is drawn by looking at video records, for velocities between 5 m/s up to 15 m/s by step of 1 m/s. The water quality corresponds to a low oxygen content of 30 %, without nuclei injection. The pressure and the flow velocity are kept constant, whereas the angle of attack is slowly increased until

the inception and development of the cavity. Then, the angle of attack is decreased until desinence cavitation.

Further tests were performed at particular experimental points with different oxygen contents and nuclei injections. The diameter of the vapor tube is measured with a real time image analysis method. The sound radiated by the cavitation is analysed and recorded.

2.3 Second configuration

The hydrofoil is mounted horizontally on a side wall of the test section (Figure 2). The angle of attack is controlled by a balance with a precision of $\pm 0.01^\circ$. The influence of the water quality is largely studied in these experiments. Flows with oxygen content of 30 %, 56 % and 80 % are studied as well as flows with several nuclei injections with an oxygen content of 30 %. Again, a map of the observed cavitation as a function of the angle of attack is drawn by visualisation of video records for 3 velocities : 6 m/s, 10 m/s and 15 m/s. A more systematic investigation of the vapor tube diameter is carried out with the same image processing method as previously. The hydrodynamic coefficients are measured with the 6 components strain gauges balance. The acoustic signal is recorded and peaks are counted at the cavitation inception.

2.4 Set up for measuring the size of cavitating vortex

A special system was built using digital images from a video camera to measure the vortex size and to analyse the changes in size as a function of time and gas content. A video camera is focussed on the vortex core. The camera output is connected to a PC that records the image and calculates the mean diameter (Figure 3).

A black and white video camera with a $f=300$ mm focal length lens and $N=2.81$ aperture produces a magnification factor of 1/0.22. The video camera has a CCD sensor of 511×768 pixels, each pixel being $11\mu\text{m} \times 11\mu\text{m}$. The PC records a full frame of the image. The images are recorded every 30 seconds and they are analysed immediately afterwards. The grey level of the numerical image is set between 0 and 255.

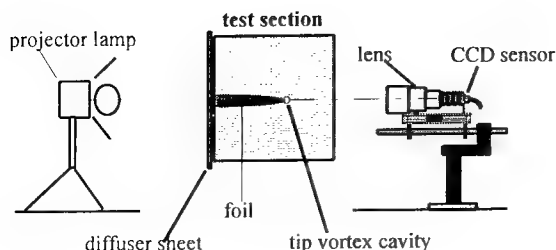


Fig. 3 : image recording system.

The lighting system is an halogen projector lamp with a diffuser sheet mounted at the back of the plexiglass window of the test section. The coaxial lighting makes a shadow view of the vortex on the recorded image so that the edge of the tip vortex core is very contrasted.

The vortex core has sufficient contrast such that its contour is directly obtained by converting the greyscale image into a binary image based on a threshold range. Then the diameter and the angle of the vortex are calculated (Figure 4).

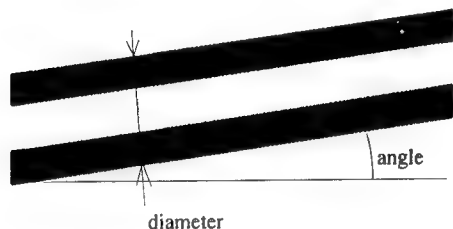


Fig. 4 : binary image of the vortex core.

The selected threshold level has little effect on the calculated diameter and the maximum diameter uncertainty is 0.2mm.

2.5 Acoustic apparatus

The sound radiated at cavitation inception and for developed cavitation is analysed in two ways, one for each configuration.

The most complete series of measurements are made in the first configuration (Figure 5). Three acoustic transducers are flush mounted on the walls of the water tunnel. One is below the hydrofoil and the two

others are on each side of the test section at 1.68 m of the wing tip. The acoustic signal may be analysed in real time or recorded by a numerical system (Enertec) and by digital system (DAT) for time/frequency post-treatment or statistical study.

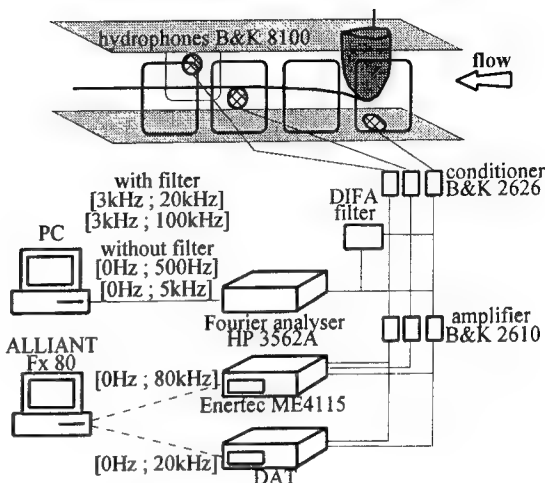


Fig. 5 : experimental facility, 1st configuration, acoustic apparatus.

The signal issued from the hydrophone below the tip is conditioned, high pass filtered and amplified. Then the signal is analysed in real time by generation of 4 PSDs of 8000 points on the bandwidths [0 Hz ; 500 Hz], [0 Hz ; 5 kHz], [3 kHz ; 20 kHz] and [3 kHz ; 100 kHz]. On each bandwidth, the Power Spectrum Density or PSD is the result of the mean of 20 analysed signal, except for [0 Hz ; 500 Hz] where only 10 were used.

The PSD on [0 Hz ; 100 kHz] is deduced from the previous spectral analysis. On each spectrum, the PSD values are averaged on 20 consecutive points which implies 400 points for the PSD. Then, we assemble the PSD values by taking the first spectrum and cutting the second spectrum on 500 Hz up to 5 kHz, the third on 5 kHz up to 20 kHz and the last on 20 kHz up to 100 kHz.

In the second test configuration, a count of noise peaks at the cavitation inception is made. A hydrophone B&K 8104 is flush mounted below the wing tip (Figure 6). A conditioner, a band pass filter [20 kHz ; 80 kHz] and a level discrimination are mounted in line before entering in the counter. This

acquisition needs a human intervention to have the best signal to noise ratio and to determine the level of the trigger according to the noise level of the test facility which have been measured during subcavitating phase. The peaks are identified and counted during 10 seconds. Moreover, 2 seconds of acoustic signal were recorded on a mascomp, for more information, with an acquisition frequency of 160 kHz.

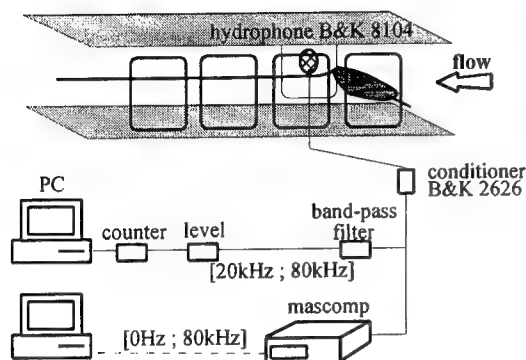


Fig. 6 : experimental facility, 2nd configuration, acoustic apparatus.

3. VISUAL DATA AND CORRELATION

3.1 Cavitation inception

The cavitation inception is first observed on video records, it might be a line of vapor at the center of the vortex, or several transient bubbles captured by the vortex.

As presented in [11], due to the unique fully gas content device of the G.T.H., for water without nuclei injection, the modification of the oxygen content do not affect cavitation inception, provided saturation condition are not reached. For oversaturated flow without injection, σ values at inception are similar to those obtained for low oxygen content and nuclei seeding. For this reason, results were only presented for 30 % of oxygen content without nuclei injection, and with two types of bubbles injection called 'small' and 'big'.

In Figure 7, the cavitation inception number is plotted as a function of the angle of attack for the three

different water qualities. 'Small' and 'big' nuclei seeding shift the results towards the small angle of attack. However, the shift is larger for the larger bubbles. Thus, the higher the susceptibility pressure, the easier water cavitates. This phenomenon has to be correlated with visual observations : without nuclei injection, the first cavitation occurrence is a vapor tube whereas, with nuclei seeding, nuclei are attracted in the center of the vortex where they grow, explode under the depression, and make the vortex visible.

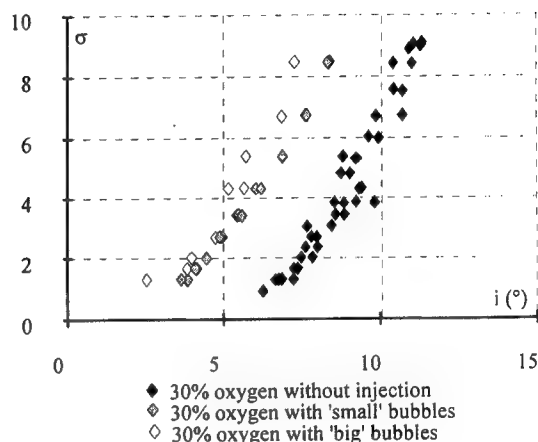


Fig. 7 : cavitation inception at $V=10$ m/s.

The minimum pressure coefficient, $C_p(x)$, in the center of the vortex at the abscissa x is given [8] by :

$$C_p(x) = -K(x) Cl^2 Re^{0.4} \quad (2)$$

where $K(x)$ is a coefficient determined experimentally, Cl the lift coefficient and Re the Reynolds number based on the maximum chord length. The lift coefficient is not dependant on the Reynolds number in our experiments, and the slope of the lift coefficient versus the angle of attack equals 0.0598° .

At inception, the minimum pressure within the vortex, P_{min} , can be assumed to be equal to P_v and :

$$\sigma = -C_p(x) \quad (3)$$

If the Reynolds number effects are correctly taken into account by this model, and if $P_{min} = P_v$ at inception, a single straight line for each water quality when plotting $\sigma/Re^{0.4}$ as a function of Cl^2 should be

obtained. As shown in Figure 8, a straight line fits the data for each water quality. Moreover, the slope increases with the ability of the liquid to cavitate (i.e. by changing the susceptibility pressure of the freestream nuclei).

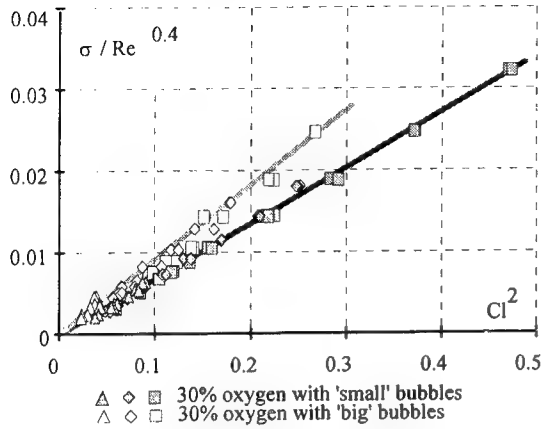


Fig. 8 : cavitation inception, triangle : $V = 15$ m/s, diamond : $V = 10$ m/s, square : $V = 6$ m/s.

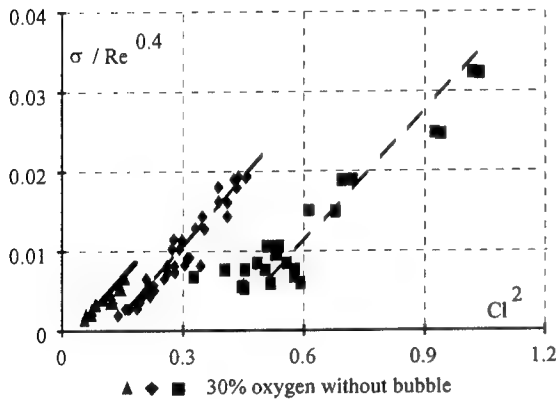


Fig. 9 : cavitation inception, triangle : $V = 15$ m/s, diamond : $V = 10$ m/s, square : $V = 6$ m/s.

For water with constant oxygen content and without injection, a strong velocity effect exists (Figure 9). Indeed, by decreasing the freestream velocity from 15 m/s to 6 m/s, for $\sigma/Re^{0.4} = 0.01$, the incidence angle at inception is increased by a factor of 2. For 6 m/s, we can notice a brake of the line for $Cl^2 < 0.6$; effectively, in these conditions, the flow is oversaturated and we observe a degassing phenomenon.

3.2 Correlation of the cavitation inception data

The objective is to obtain a correlation regardless of the water quality and the flow velocity. Using the centerbody venturi VAG, the water quality is characterised by a single parameter, the susceptibility pressure P_s , for a specific nuclei concentration (0.01 nuclei / cm^3). Figure 10 shows the fluid tension $P_v - P_s$ as a function of σ for the 'small' and the 'big' bubbles situations. The tension increases with σ for given nuclei injection, and is always significantly larger for the 'big' bubbles.

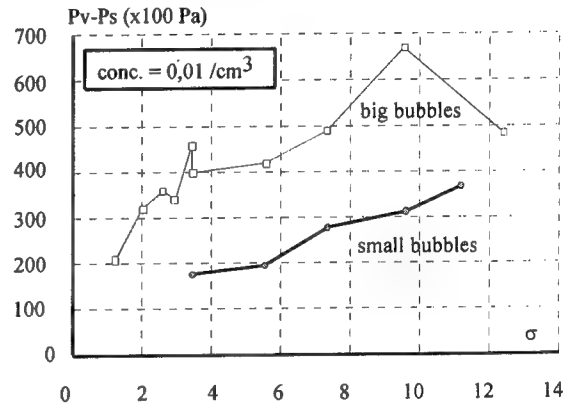


Fig. 10 : tension of the liquid versus σ for the nuclei injection used.

According to ([9], [11], [14]) it can be assumed that the cavitation inception occurs at P_s instead of P_v . Hence, the parameter related to the cavitating flow can be expressed by :

$$\sigma - \Delta\sigma = \frac{P - P_v}{0.5\rho V^2} - \frac{P_s - P_v}{0.5\rho V^2} \quad (4)$$

$$\sigma - \Delta\sigma = \frac{P - P_s}{0.5\rho V^2} \quad (5)$$

Using results similar to those presented in Figure 10, a new parameter $\sigma - \Delta\sigma$ is calculated. All the values are now well correlated in the non-dimensional representation (Figure 11), even those without nuclei injection. The main difficulty of this method is the evaluation of P_s . In this case, it is a statistical value, derived from a sample of several litres.

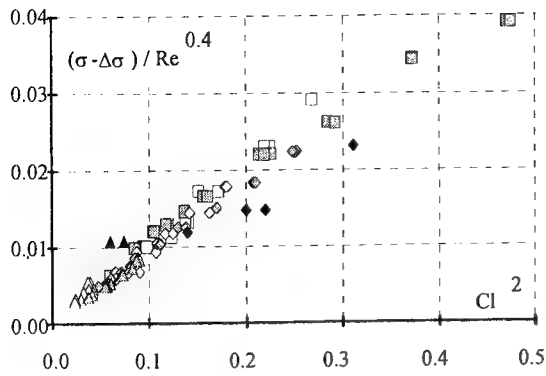


Fig. 11 : corrected cavitation parameter at inception versus square lift coefficient, convention for colours and symbols are as previously.

3.3 Developed cavitation

Here, the developed cavitation is characterised by time diameter measurements and estimation of the associated pressure variations.

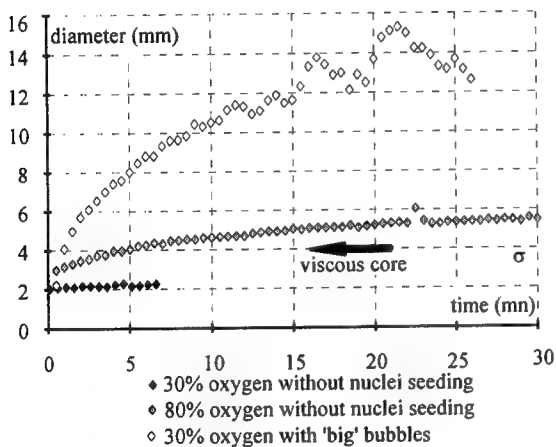


Fig. 12 : diameter of cavitating vortex as a function of time, $\sigma = 4.1$, $V = 10$ m/s, $i = 10^\circ$.

The time origin is chosen when the cavity is a developed vapor tube without collapse during time. The radius of the vapour tube at the beginning is smaller than the viscous core diameter of the tip vortex measured by LDV. The diameter varies between 1.5 mm to 15 mm (Figure 12). It increases with time in a way which is very dependent of the

water quality. The diameter can be nearly constant for the water with 30% oxygen content without nuclei injection, or increase by a factor 2 on 5 minutes for a water with 80% of oxygen content and no bubbles. For water with injected bubbles, the diameter is multiplied by 4 on the first 5 minutes.

The diameter varies with the flow parameters : the higher the pressure, the thinner the diameter, and the larger the angle of attack, the larger the diameter (Figure 13).

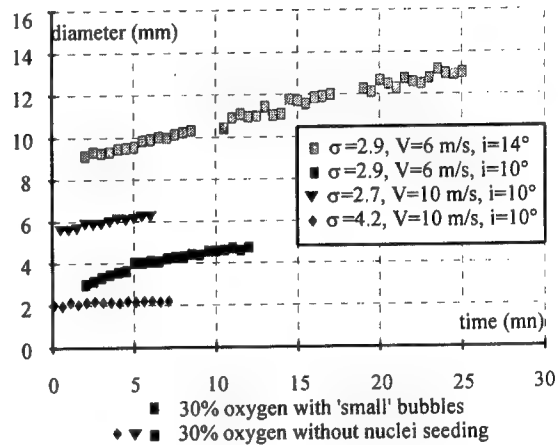


Fig. 13 : diameter of cavitating vortex versus time.

Assuming that the growth of the diameter of the vapour tube is due to the diffusion of non condensable gases, the pressure inside the cavity changes with time (from P_v to $P(t)$). One interesting problem is to estimate this pressure increase which would be responsible for the hysteresis at the desinence cavitation.

In non-cavitating conditions, the tangential velocity of a vortex roll-up, V_t , at the distance r from the center of the vortex, with Euler equations and with a circulation $\Gamma(x)$ is :

$$V_t = \frac{\Gamma}{2\pi r} \quad (6)$$

The depression between two points in the same plane in the flow, at positions r_1 and r_2 , in a steady axisymmetric potential flow, is :

$$P(r_2) - P(r_1) = -\rho \frac{\Gamma^2}{8\pi^2} \left(\frac{1}{r_2^2} - \frac{1}{r_1^2} \right) \quad (7)$$

Now, we apply equation (6) in cavitating conditions. We assume that the circulation is unchanged. At the beginning of the developed vapor tube without collapsus, the radius of the cavity is r_0 and the pressure of the cavity is P_v . Between two points, one taken far from the vortex, called ∞ , and another taken at the interface of the cavity, the depression is :

$$P_\infty - P_v = \rho \frac{\Gamma^2}{8\pi^2} \frac{1}{r_0^2} \quad (8)$$

with (1) :

$$\frac{1}{2} \rho V^2 \sigma_0 = \rho \frac{\Gamma^2}{8\pi^2} \frac{1}{r_0^2} \quad (9)$$

σ_0 is the cavitation number of the vapor tube at the beginning.

But the radius of the cavity grows with time. By assumption, this growth is linked to an increase of the pressure inside the vapor tube. At the time t , the cavity has a radius $r(t)$ and a pressure $P(t)$. Then, the depression between a point at the infinity and a point at the interface is :

$$P_\infty - P(t) = \rho \frac{\Gamma^2}{8\pi^2} \frac{1}{r(t)^2} \quad (10)$$

But :

$$P_\infty - P(t) = P_\infty - P_v - (P(t) - P_v) \quad (11)$$

We can define a parameter related to the hysteresis effect, called H , like :

$$H = \frac{P(t) - P_v}{\frac{1}{2} \rho V^2} \quad (12)$$

Then, by subtraction of (10) and (9), with (11) and (12) :

$$H = \sigma_0 \left(1 - \left(\frac{r_0}{r(t)} \right)^2 \right) \quad (13)$$

Figure 14 shows the variation of H as a function of time, corresponding to the diameters of Figure 12 for water with 30% and 80% of oxygen content. The magnitude of H increases asymptotically with time and depends on the oxygen content : higher oxygen content, higher hysteresis. The slope of the curve at the beginning is high, so, even for two minutes, $H > 1$.

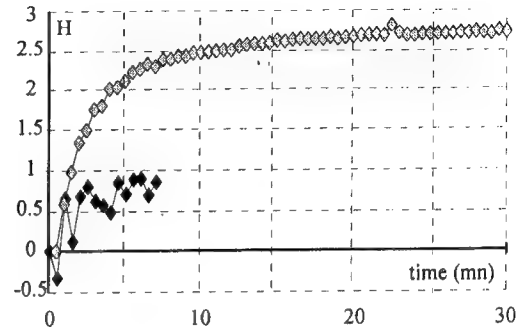


Fig. 14 : hysteresis effect during time, same symbols as Figure 12.

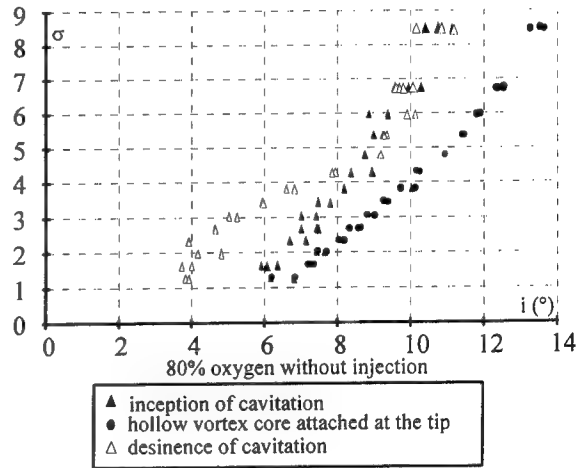


Fig. 15 : incipient, attached and desinent cavitation parameter versus angle of attack, $V = 10$ m/s.

Now, we will verify if this order of magnitude is acceptable. In Figure 15, observations of the inception and the desinence cavitation are reported as a function of the angle of attack. The tests were made at constant pressure and varying angle during time. Inception and desinence of cavitation are not at the same angle of attack, which is a consequence of the

hysteresis effect. We underline here that, for equations (6) through (12), we assume a constant circulation. In order to have a constant circulation, we have to provide cavitation tests at constant angle of attack. So, the variation of pressure inside the cavity would be given by the variation of the inlet pressure between the inception and the desinence of cavitation. In Figure 15, if we read the value at a constant angle of attack, for instance at 6° , H equals 2 which is the same order of value as in Figure 14. We notice that we could have directly the value of H if the cavitation tests are performed at constant angle of attack.

4. ACOUSTIC CHARACTERISTICS

In this part, the acoustic results are presented. We will first discuss about the non-cavitating PSD to characterise the noise of the test facility. Then we will see the influence of the cavity by superimposing the PSDs in non-cavitating and in cavitating conditions. The influence of different parameters like freestream velocity and angle of attack, are shown. The acoustic data are connected to the visual data for better understanding.

4.1 Global behaviour in subcavitating conditions

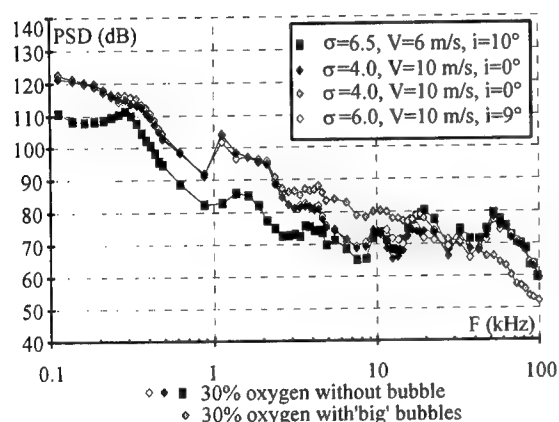


Fig. 16 : PSD in subcavitating conditions.

For a given water quality and a given inlet velocity, the acoustic level in subcavitating conditions is independent of the angle of attack and of the pressure level of the test section (Figure 16). The flow velocity affects essentially the bandwidth [100 Hz ; 10 kHz] for water without injection : the acoustic level decreases with velocity. At $V=10$ m/s, the nuclei

injection modifies the PSD on the bandwidth [1 kHz ; 100 kHz] : the slope is constant, 25 dB/decade, whereas, without injection, the decay of the PSD is of 40 dB on [1 kHz ; 10 kHz] and rather constant on [10 kHz ; 100 kHz]. A specific frequency of the test facility which is 1.25 kHz at $V = 10$ m/s, and 0.8 kHz at $V = 6$ m/s can be seen in Figure 16.

4.2 Cavitation inception

A criterion to detect the cavitation inception is the acoustic signal, and particularly the acoustic peaks radiated during the bubble growth when they cavitate. A systematic study was made for a flow with injected nuclei. The collected data are summarised by a count of acoustic peaks for each angle of attack near the angle of the cavitation inception.

Figure 17 shows the peaks during a 10 seconds period as a function of the incidence angle for three cavitation numbers. We obtain a gaussian curve which could be non symmetric. Three characteristic angles of attack can be defined : for the initiation at 1 peak/s, for the maximum count and for the disappearance at 1 peak/s. 1 peak/s corresponds roughly to the visual criterion for cavitation inception in tip vortex.

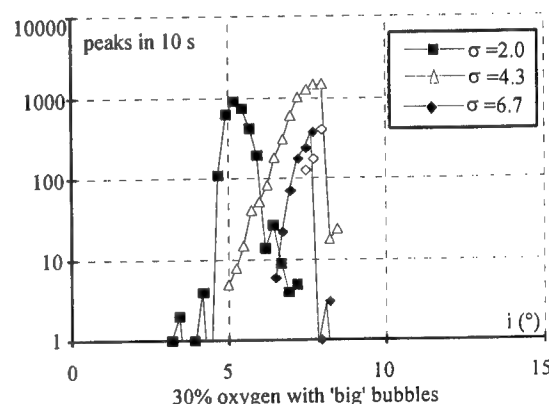


Fig. 17 : count of peaks, $V = 10$ m/s.

The acoustic results and the observed data are superimposed in Figure 18. The development of cavitation is added and corresponds to the visual criterion defined as a stable vapor tube attached at the tip of the hydrofoil. The best correlation is observed at 10 m/s : the visual inception corresponds to the first 1 peak/s and the maximum number of peaks is located for the development of cavitation (Figure 18).

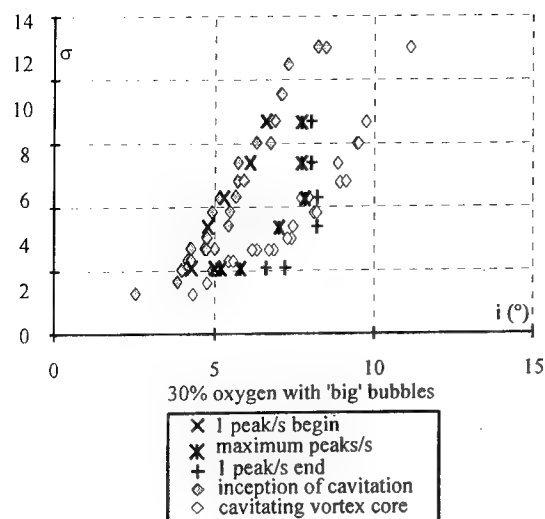


Fig. 18 : superimposed of visual and acoustic datas,
V = 10 m/s.

For $\sigma > 4.0$, the data at maximum peak/s and 1 peak/s are shifted compared to the visual data. It can be observed that, for these tests, the counts versus the angle of attack are non symmetric and do not extend for unknown reasons over 8° (Figure 17). There is perhaps a problem of level of signal to noise ratio, or the band-pass filter is not adequate for these points. Possibly a more detailed treatment and a best acquisition would give better results.

4.3 Developed cavitation

For water without injection, when cavitation occurs at $V=10$ m/s, the acoustic level on the bandwidth [500 Hz ; 50 kHz] is increased as compared to the subcavitating conditions (Figure 19).

The same phenomena is observed at $V = 6$ m/s on the bandwidth [500 Hz ; 20 kHz] (Figure 20). For water with 'big' bubbles, the bandwidth affected by the increase of the acoustic level is bigger : it begins at 500 Hz and covers the bandwidth until the end (Figure 21).

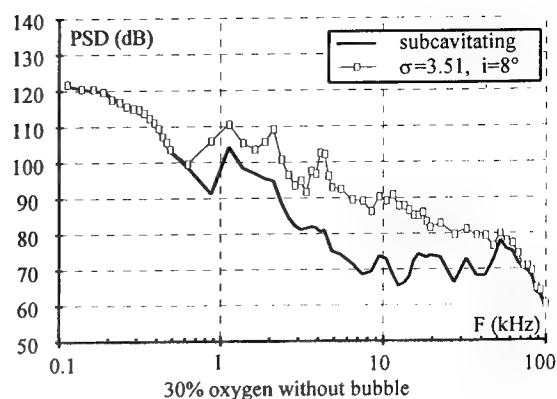


Fig. 19 : developed cavitation compared to no-cavitating point, V = 10 m/s.

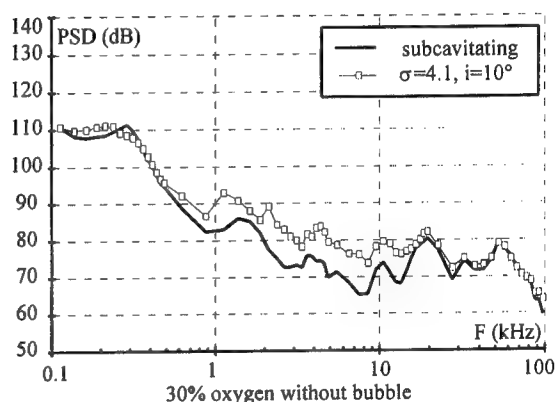


Fig. 20 : developed cavitation compared to no-cavitating point, V = 6 m/s.

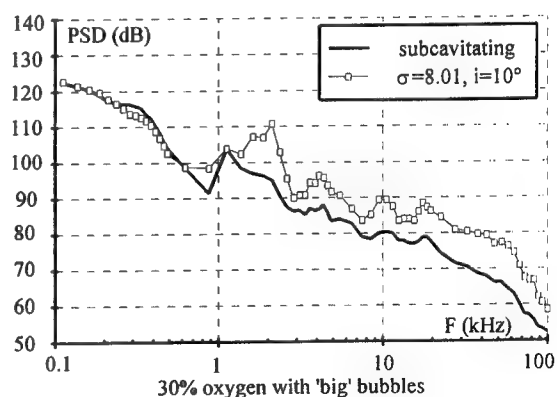


Fig. 21 : developed cavitation compared to no-cavitating point, V = 10 m/s.

4.4 Frequencies associated to the cavitating vortex core

By comparison of the PSD in subcavitating condition with the PSD in cavitating condition on the bandwidth [0 Hz ; 5 kHz], the frequencies, associated to the cavitating conditions were extracted. One or two frequencies are identified by this method for given conditions.

Previous authors, Higuchi et al. [12] and Maines and Arndt [16] for instance, speak about a "singing vortex". In this phenomenon, "a standing wave develops on the hollow vortex core which radiates significant noise at discrete tone". In their paper, Maines and Arndt correlate specific frequencies of the singing vortex extracted from acoustic records with the diameter of the cavity.

The possibility to undertake similar analysis on the PSD [0 Hz ; 5 kHz] was used. Results such as in Figure 22 were obtained. In this graph, marked lines represent the evolution of the difference between the PDS in non-cavitating and in cavitatin conditions. On each dotted curve, two peaks can be clearly seen : one near 500 Hz and the other near 1.5 kHz and there is no difference of the acoustic signal below 400 Hz. These frequencies vary with the angle of attack.

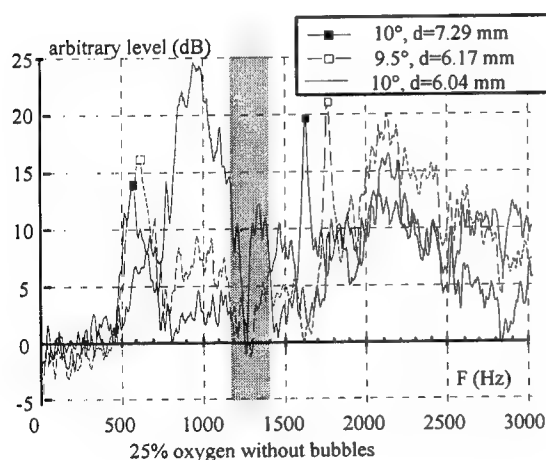


Fig. 22 : difference in PSD between non-cavitating and cavitating conditions, the grey region corresponds to the frequencies of the test facility

It can be noticed here a first difference with Maines and Arndt results : two frequencies were obtained for

an experimental condition whereas they obtain just one. See for example Figure 23 showing frequencies measured versus σ for two velocities (10 m/s and 11 m/s) and two angles of attack (8 deg. and 10 deg.). These measurements were made when the cavity within the tip vortex was attached to the tip of the profil or when the tip of the cavity within the tip vortex begins like a cone-shape in the fluid. Maines and Arndt limit their study to the case of the singing vortex which happens when the cavitating vortex core is attached.

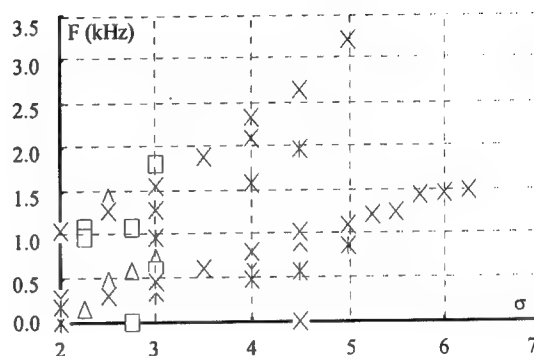


Fig. 23 : measured frequencies versus σ value, for two velocities and two angles of attack.

Similar results were observed for a variation of the inlet pressure at constant angle of attack : then the frequencies depend on the inlet pressure. At first order, it seems that frequencies are linked with the diameter of the cavitating vortex core. But, as seen in Figure 22, different informations can be noticed for similar flow conditions and for the same order of diameter : for the diameter $d = 6.17$ mm, we have two identified peaks which do not exist for the diameter $d = 6.04$ mm. This last observation can be related to the problems of reproducibility of the singing vortex encountered by Maines and Arndt.

With the continuous line which corresponds to a measurement made after 15 minutes under constant experimental parameters, a single important peak near 1 kHz appeared. A regular increase of the PSD on [500 Hz ; 5k Hz] with the diameter was observed. Unfortunately, the time of existence of the cavitating vortex tube was not systematically acquired during the acoustic measurements. After looking at videos, there is not a distinguishable phenomenon, except perhaps the stability of the tip of the cavity within the

tip vortex. The frequency of 25 Hz of the camera is perhaps not sufficient to analyse the phenomenon. However, the information of the diameter is not sufficient to deduce the frequencies emitted by the cavity.

4.4 Morozov's model

In the following, we use measured frequencies and associated measured diameter for several cavity within the tip vortex.

A Morozov's model [17] is used where the frequencies are linked to modal deformation of a vapor tube as a function of the mean diameter 'a'. For a cylindrical cavity within the tip vortex, at constant pressure P_v , the following formulae can be written :

For $m = 0$:

$$\ln\left(\frac{2}{\gamma}\right) - \ln\left(\frac{2\pi F}{c}\right) = \left(\frac{V_t}{2\pi F}\right)^2 \quad (14)$$

with γ is the Euler constant equated to 1.78, F is the frequency, c is the chord length and V_t is the tangential velocity.

For $m = 1$:

$$F_1 = \frac{V\sqrt{\sigma}}{\pi a} \quad (15)$$

where σ is the cavitation number.

For $m = 2$:

$$F_2 = \frac{V\sqrt{\sigma}}{2\pi a} \left(2 \pm \sqrt{2 + \frac{6T}{\rho a V^2 \sigma}} \right) \quad (16)$$

where T is the surface tension.

Each formula corresponds to a special deformation : when $m=0$, it is a variation of the diameter ; when $m=1$, it is a sinusoidal deformation of the centerline of the vortex, this phenomenon have to be related to wandering according to Fruman [8] ; when $m=2+$ or $2-$, it is an elliptic deformation of the diameter.

In Figure 24, we superimpose the Morozov's frequencies, calculated with the measured diameter, and the measured frequencies. Two possible modes are identified : $m=1$ and $m=2-$. It seems that an elliptic deformation and a wandering took place.

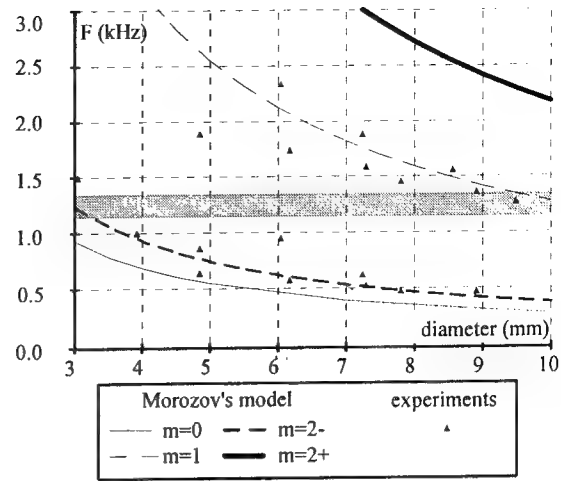


Fig. 24 : frequencies calculated and measured, the grey region corresponds to the frequencies of the test facility.

In order to enlarge this analysis for all the frequencies measurements, an estimation of the cavitating diameter D was made versus (σ , i and V). For this, as parameters do not vary on a large range, it is assumed that D can be written as :

$$D = a + b\sigma + ci + dV \quad (17)$$

Using size measurements available, parameters a, b, c, d , were identified. D was then calculated for all the test configurations for which peaks were observed and measured in the spectral analysis.

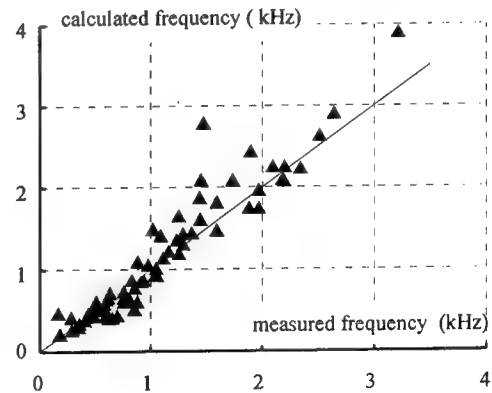


Fig. 25 : comparison between calculated and measured frequencies radiated by a developed cavitating vortex.

Figure 25 presents a comparison between frequencies measured in the spectra and frequencies calculated using (15), (16) and (17).

It must be noted that :

- a good correlation exists between measured and calculated frequencies.
- the mean error is of 16 %, but for 52 % of samples the maximum error is lower than 10 %, and for 77 % of samples the maximum error is lower than 20 %.

5. CONCLUSION

With an hydrofoil of large size, water quality effects on the cavitating vortex was studied. Water was characterised with free nuclei content and oxygen content.

In this experiment, all the data for cavitation inception can be correlated by introducing a cavitation parameter based on the measured susceptibility pressure of the water.

The growth of the cavity within the tip vortex can be explained by diffusive effects linked to the water quality. This leads to understand the hysteresis phenomenon at the desinence cavitation. In this analysis, the time must be introduced as an added parameter. Hence, the way the experiments are made is very important for the analysis of the results.

The analysis of the acoustic signal shows that the cavitating vortex radiates frequencies which could be linked to spatial deformation of the cavitating vortex core. In the tests described in this paper, the mode of deformation are $m=1$ (sinusoidal deformation) and $m=2$ (elliptic deformation of the diameter). An estimated value, within an error of 20 %, of the frequency radiated by the cavity within the tip vortex can be made.

ACKNOWLEDGEMENT

The authors wish to thank the Direction des Recherches et de la Technologie (D.R.E.T.), Ministère de la Défense, France, for his financial support.

REFERENCES

1. Abbott I.H., Von Doenhoff A.E., "Theory of wing sections", Dover publications, 1958
2. Arndt R.E.A., Arakeri V.H., Higuchi H., "Some observation of tip vortex cavitation", Journal of Fluid Mechanics, 1991, vol 229, pp 269-289
3. Arndt, R.E.A. and Keller, A.P., 1992, "Water Quality Effects on Cavitation Inception in a Trailing Vortex," ASME Jour. of Fluids Engineering, Vol. 114.
4. Billet, M.L. and Holl, W.J., 1979, "Scale Effects on Various Types of Limited Cavitation," Proc. Int. Symp. on Cavitation Inception, ASME Winter Annual Mtg., New York.
5. Briançon-Marjollet L, Fréchou D.; "Cavitation in Le Grand Tunnel Hydrodynamique", ISPC, China, sept 1992
6. Falcao de Campos J.A.C., George M.F., Mackay M.; "Experimental investigation of tip vortex cavitation for elliptical and rectangular wings", Cavitation and Multiphase Flow Forum, 1989, ASME FED-vol 79, pp 25-30
7. Fruman D.H., "Recent progress in the understanding and prediction of tip vortex cavitation", Second International Symposium on cavitation, Tokyo, Japan (1994). Proceedings H. Kato ed. pp 19 - 29
8. Fruman D.H., Dugué C., Pauchet A., Cerrutti, P., Briançon-Marjollet L., "Tip vortex roll-up and cavitation", 19th Symposium on Naval Hydrodynamics, august 1992, Seoul, Korea
9. Gindroz, B. and Billet, M. 1993, "Influence of the Nuclei on the Cavitation Inception for Different Types of Cavitation on Ship Propellers," Cavitation Inception, ASME FED Vol. 177.
10. Godefroy, V., 1994, "Imagerie Numérique Appliquée au Tourbillon Marginal Cavitant", Bassin d'Essais des Carenes, Rep't No. 4.2.97.3649.
11. Gowing S., Briançon-Marjollet L., Fréchou D., Godefroy V., "Dissolved gas and nuclei effects on tip vortex cavitation inception and cavitating core size", International Symposium on Cavitation, Cav'95, may 1995, Deauville, France
12. Higuchi H., Arndt R.E.A., Rogers M.F., "Characteristics of tip vortex noise", Journal of Fluids Engineering, december 1989
13. Holl J.W., "An effect of air content on the occurrence of cavitation". Journal of Basic engineering, 1960, pp 941-946.

14. Keller A.P., "Scale effects at beginning cavitation applied to submerged bodies". International symposium on cavitation inception 1984.

15. McCormick, "On vortex produced by a vortex trailing edge from a lifting surface", Journal of Basic Engineering, sept 1962, pp 369-379
Inception, ASME FED Vol. 177.

16. Maines B.H., Arndt R.E.A., "The case of the singing vortex", Cavitation and Multiphase Flow, ASME 1995, FED-vol. 21, pp69-74

17. Morozov V.P., " Theoretical analysis of the acoustic emission from cavitation line vortices" . Sov. Phys. Acoust., vol. 19, n° 5, 1974 pp 468-471.

DISCUSSION

D. Fruman
ENSTA/GPI, France

The authors have performed a very systematic investigation of tip vortex cavitation inception under various conditions of nuclei seeding. They propose a correction of the incipient cavitation number in order to collapse the data for two seeding conditions (small and large bubbles) in a now classical $\sigma_c/Re^{0.4}$ versus C_p^2 plot.

I have 2 types of questions

1. Why has the VAG method not been used to try to correlate also the data for the "no bubbles" situation? Have the measurements of (pc-pu) been conducted? How do the authors explain the very large velocity effects in Figure g?

2. It has been proposed, and used with good success, to obtain the "susceptibility" pressure directly from tip vortex tests (by plotting the difference between the free stream pressure for cavitation inception minus the vapor pressure as a function of the velocity to the power 2,4 for constant incidence angle). Why have the authors not performed these tests and why there is no comparison between theirs and previous methods?

AUTHORS' REPLY

NONE RECEIVED

Velocity and Turbulence in the Near-Field Region of Tip Vortices from Elliptical Wings: Its Impact on Cavitation

A. Pauchet (Ecole Nationale Supérieure de Techniques Avancées, France)

ABSTRACT

The tip vortex flow has been the subject of numerous experimental and numerical works, but the peculiarity of this very confine flow makes it one of the most difficult to describe by any measurement or computational means. This fact is obvious if we admit that the various problems that are engendered in aero and hydrodynamic are still partially solved and other literature continue to appear, presenting steps forward in advancing the understanding of the roll-up process at the vicinity of a wing. Most of the time, the subject of the research being the consequence of the vortical flow, drag increase, cavitation, wake perturbations, etc., some other secondary problems appearing within the context of these researches are not analysed. For example, the connection of the vortical flow and the axial flow that are coexisting, but also the turbulence that rests in the tip vortex core. The present work reviews the different papers dealing with the experimental description of the organisation of the tip vortex flow without any consideration of the main subject that has motivated the work. In order to keep this review to reasonable proportions, we confined ourselves to the literature presenting results on both axial and tangential velocities and the associated fluctuations in the near field of the wings. For a variety of flow conditions, foil planforms, cross sections, and locations of measurement along the vortex path, will found that the axial velocity in the vortex centre can be greater or smaller than the free stream velocity but this will not allow to conclude concerning the organisation of the axial flow with respect to the rotating flow. Using the data collected within the context of the Action Concertée Cavitation research program on tip vortex cavitation, some of these results are presented in a way so that some trends are set out.

For identical planforms foils the increase of Reynolds number seems to favoured the jet-like behaviour, but the increase of the axial velocity is not as high as it should be to balance the pressure drop governed by the rotating flow. The pressure loss corresponding to the difference between the maximum axial velocity that should occur due to the minimum pressure and the maximum axial velocity measured is for reasonable lift coefficients in order of magnitude, once the dynamic pressure and increases highly, up to six times the dynamic pressure as the lift coefficient increases. The same trend is noticed but not so markedly when the foil shape is sweep backward.

Concerning the fluctuations measured in the vortex core using various means (hot wire, holography, Laser Doppler Velocimetry, etc.) the literature often reports a high level of fluctuations in the vortex core on both components, attributed to the spatial modification of position of the vortex trajectory, or the velocity gradients encountered when passing through the vortex core. This particular problem is analysed concerning LDV measurements of axial and tangential velocity profiles measured close and far from an elliptical wing tip. It is shone that in the very near region to the foil tip where no fluctuation of position are measurable the axial fluctuations are important but they are decreasing for more distant positions downstream the tip for which the wandering is noticeable. The statistical analysis of the tangential instantaneous velocities for five positions of measurements performed as the measuring volume is crossing the vortex core very near the foil tip demonstrates that positive and negative velocities are both measured at the same time. The estimation of the standard deviation is then not well adapted in the case of histograms having two peaks and thus over estimates the maximum fluctuation level.

A simple and more appropriate method is applied by computing separately the deviations associated to the velocities of identical signs, in order to make a more realistic estimation of the standard deviation, inferior by a factor four to the classical computation. By this mean, the bias induced by the finite dimension of the measuring volume with respect to size of the vortex core is eliminated. In the case of superimposed fluctuation of positions, the method is not efficient but an other method is proposed.

In conclusion, the effect on the critical cavitation conditions of both the axial flow and the turbulence in the vortex core are found to be negligible.

NOMENCLATURE

a	tip vortex core radius
C_l	lift coefficient
c_{pmin}	minimum pressure coefficient on the vortex axis
c_{max}	maximum foil chord
k^*	non dimensional velocity fluctuations $((u'^2 + v'^2)/U_\infty^2)^{0.5}$
p_∞	static reference pressure
r^*	non dimensional distance to the vortex centre (r/c_{max})
U_∞	free stream velocity
U^*	non dimensional mean axial velocity (U/U_∞)
U_o^*	non dimensional mean axial velocity at the tip vortex centre (U_o/U_∞)
u^*	non dimensional instantaneous axial velocity (u/U_∞)
u'^*	non dimensional axial velocity fluctuation
V^*	non dimensional mean tangential velocity (V/U_∞)
v^*	non dimensional tangential instantaneous velocity (v/U_∞)
v'^*	non dimensional tangential velocity fluctuation
x^*	non dimensional distance to the wing tip in the free stream direction (x/c_{max})
δ	turbulent boundary layer thickness for a flat plate of length c_{max} and U_∞ without pressure gradient
ΔV^*	non dimensional maximum tangential velocity magnitude $(V_{max} - V_{min})/U_\infty$
δV^*	non dimensional difference between the maximum tangential velocity and the absolute value of the minimum tangential velocity $(V_{max} - V_{min})/U_\infty$
Γ_0	foil bound circulation at mid span
Γ^*	non dimensional local tip vortex intensity Γ/Γ_0
σ_d	desinent cavitation number

INTRODUCTION

Because of the possible interaction of the tip vortices of large aircrafts on following smaller planes, considerable attention has been given to the evolution of the tangential and axial velocities and the turbulence intensity in the far field region (more than 10 foil chords) (Spreiter and Sacks (1951), Staufenbiel and Vitting, (1990), Chow et al. (1991) Chigier and Cosiglia (1972), Orloff and Grant (1973), Baker and Saffman (1974), Cliffone and Orloff (1974), Singh and Uberoi (1976), McAlister and Takahashi (1991)). In this region, the roll-up of the vortices is fully achieved and the predominant effect is the diffusion of the tip vortex due to viscosity. Because tip vortex cavitation occurs at short distances from the wing tip, most recent works have been concerned on the very near region (less than a chord), Stinebring et al. (1991), Fruman et al. (1992a, 1992b, 1993, 1994, 1995a, b, c, 1996) and Pauchet et al. (1994, 1996), and the intermediate region (comprised between one and ten chords), Arndt and Keller (1991), Arndt et al (1991), Green and Acosta (1991).

In the very near region, the roll-up of the vortex is initiated and a rapid change of its local intensity (circulation) occurs. Moreover, it is in this same region that the boundary layer over the surface of the foil develops into the vortex viscous core. In this region the vortex is not axisymmetric as shown by flow visualization (Francis et Katz (1988), Chow et al. (1991), Pascal (1993), Liang et al. (1991)), Particle Image Velocimetry (PIV) (Green and Acosta (1991), Pogozelski et al. (1993), Shekarri et al. (1993)) and Laser Doppler Velocimetry measurements (Baker et al. (1974), Accardo et al. (1984), Higuchi et al. (1987), Stinebring et al. (1991), Arndt and Keller (1991), Fao de Campos (1989, 1992), Fruman, et al. (1992b)). Because of this lack of symmetry and uncompletion of the roll-up it is difficult to obtain, from a characteristic tangential velocity profile, informations on the tip vortex characteristics : vortex intensity and vortex core radius.

It should be pointed out that defining the vortex intensity in the near region is a subject of much debate. Indeed, let us assume that the velocity field is fully known in a plane normal to the vortex axis. The circulation of the velocity vector can be computed then over any closed path around the vortex. If the path encloses the whole wake of the wing, the tip vortex and a reasonable outboard surface, the circulation will be equal to the mid span bound circulation of the foil. If the path is now reduced in size, part of the circulation carried out by the wake will be ignored and the circulation around this path will decrease accordingly. If the viscous core region is reached by reducing the

dimension of the path, the circulation will be further reduced. In the limiting case of a very small close path around the vortex axis, the circulation will vanish. Because Stinebring et al. (1991) have determined, by conducting three component LDV surveys of the tip vortex issued from a trapezoidal wing in the very near region, that the contribution of the radial components was negligible in the outboard region of the wing along a line parallel to the span centred on the vortex axis, Fruman and co-workers have systematically measured the tangential velocities outboard of the wing and along a direction parallel to the span in tip vortices issued from elliptical wings for numerous positions comprised between the tip and one chord downstream and a variety of experimental conditions. These velocity profiles are characterized by an inner region where the velocities increase linearly as for a solid body rotation, an outer region where they decrease as for a potential vortex, and an intermediate region which assures a smooth transition between the previous ones. The viscous core radius is taken as the radial distance between the vortex axis and the position where the maximum tangential velocity occurs. The local intensity of the vortex is estimated by determining the asymptotic value of the angular momentum per unit mass, product of the local tangential velocity and its distance to the vortex axis, far from the vortex axis. Even if the absolute value of the vortex intensity so estimated is not the intrinsic one, it gives, if the procedure is systematically applied, a very good idea of the roll-up process along the vortex path.

Using such a procedure, the effects of the wing Reynolds number, the cross section, the tripping of the laminar to turbulent boundary layer transition, the water and polymer solution mass flow ejection, the background turbulence, etc., on tip vortex roll-up in the very near region have been investigated for foils having an elliptical distribution of the chord along the span. It has been possible to show that at the tip of the wing the vortex intensity has already a finite value which, for the same flow conditions, increases when the foil tip moves from an upstream to a downstream position (Fruman et al. 1995a). The local circulation increases with increasing lift coefficient and distance to the foil tip, and reaches, for large enough distances, the mid-span bound circulation of the foil. The vortex core radius is, at the tip of the foil, of about half of the thickness of the turbulent boundary layer, computed as for a flat plate of length equal to the maximum chord, decreases to a minimum at a distance comprised between one and two tenths of the maximum chord and then steadily increases because of diffusion. The evolution of the local vortex intensity and core radius remains nearly the

same even if the flow conditions are modified by changing the foil cross section, by tripping the laminar to turbulent boundary layer transition or by increasing the background turbulence. A considerable amount of information was also obtained on the fluctuations of the tangential velocities and detailed analysis of the effect of the finite dimension of the measuring volume and vortex wandering were conducted by Fruman et al. (1994) and Fruman and Billard (1996). Measurements of the velocity fluctuations have also demonstrated quite conclusively that they result from the contribution of vortex wandering and "true" turbulence. If due account is taken of the wandering effect (Orloff and Grant (1973), Baker et al. (1974), Green and Acosta (1991), Green (1991), Fruman et al. (1994)), the "true" turbulence is seen to increase considerably, as compared to the background values, in the inner, solid body rotation, region.

The interpretation of the measurements of the axial velocity profiles is not straightforward. Data available show that both a jet-like (Chigier and Corsiglia (1972), Orloff and Grant (1973), Accardo et al. (1984), Staufenbiel and Vitting, (1990), McAlister and Takahashi (1991) Arndt and Keller (1991), Chow et al. (1991), Green and Acosta (1991), Fruman et al. (1992a,)) or a wake-like (Orloff and Grant (1973), Baker et al. (1974), Accardo et al. (1984), Staufenbiel and Vitting, (1990), McAlister and Takahashi (1991), Stinebring et al. (1991), Green and Acosta (1991), Fruman et al. (1992a, 1993)) behaviour can be present depending on a multitude of parameters : foil planform and tip geometry, incidence angle (lift coefficient), Reynolds number, surface roughness, etc. Because the pressure in the vortex core decreases as a result of the rotation, the axial velocity on the vortex axis has to increase to satisfy Bernoulli's equation without head losses and a jet-like behaviour should therefore result. The wake-like behaviour near the tip can be interpreted schematically by considering that the vortex core consist essentially of liquid which has transited within the boundary layer and thus has velocities much reduced as compared to the free stream velocity.

Using the tangential velocities measured outboard of the wing along a direction parallel to the span and the simplified radial momentum equation, assuming that the radial velocity component can be neglected, Stinebring et al. (1991) have estimated the pressure coefficient at a position where cavitation first occur. Comparison with the desinent cavitation number (with sign changed) was very favorable. Fruman et al. (1992a, 1992b), Pauchet et al. (1993) have extended this procedure and shown that the minimum pressure on

the vortex axis occurs at a distance of the tip of the order of one tenth of the maximum chord for elliptical planform foils. The minimum pressure coefficient (with sign changed) compares remarkable well with the desinent cavitation numbers for a variety of foil planform, cross section and Reynolds numbers. This satisfactory agreement seems to indicate that the peculiarities of the axial velocity profiles in the core region as well as the turbulent velocity fluctuations do not participate in the equilibrium conditions of the nuclei captured by the vortex and, therefore, in the onset of cavitation. The purpose of this paper is to revisit these questions and to shed some light of the reasons leading to both jet- and wake-like behaviour of the axial velocities but also to find some explanation to the high level of turbulence that prevails in the vortex core.

BASIC EQUATIONS

Following Batchelor (1964) let us write Bernoulli's equation along a stream line leading to the axis of the tip vortex,

$$p_{\infty} + \frac{1}{2}\rho U_{\infty}^2 = p_{r=0} + \frac{1}{2}\rho U_{r=0}^2 + \Delta p \quad [1]$$

where p_{∞} and U_{∞} are the pressure and the velocity of the free stream flow, ρ is the liquid density, $U_{r=0}$ is the velocity of the vortex axis and Δp is the head loss by viscosity along the streamline. Assuming that the radial velocities do not contribute to the radial equilibrium, we can write,

$$\frac{dp}{dr} = \rho \frac{V^2}{r} \quad [2]$$

where V is the tangential component of the velocity and r is the distance to the vortex axis. Integration of equation [2] and substitution in to equation [1] gives,

$$\left(\frac{U_{(r=0)}}{U_{\infty}}\right)^2 = 1 + 2 \left[\int \left(\frac{V}{U_{\infty}}\right)^2 \frac{dr}{r} - \frac{\Delta p}{r U_{\infty}^2} \right] \quad [3]$$

$U_{(r=0)}$ is the axial velocity on the vortex axis since the radial and tangential components vanish. A jet- and a wake-like behaviour of the axial velocity corresponds respectively to a positive or negative value of the term between brackets. The pressure drop associated with the dissipation due to viscosity must thus exceed the gain brought by setting the fluid in rotation in order to achieve a wake-like effect. If expression [3] is computed for the

position downstream of the tip where the minimum pressure coefficient occurs, $x=x_{min}$, we have, taking into account that it has been rather conclusively demonstrated that,

$$\sigma_d = -Cp_{min} \quad [4]$$

where Cp_{min} is the minimum of the pressure coefficient on the axis of the vortex,

$$\frac{2\Delta p}{\rho V_{\infty}^2} = 1 + \sigma_d - \left(\frac{V_{a(r=0, x=x_{min})}}{V_{\infty}} \right)^2 = \Delta p^* \quad [5]$$

Since σ_d can be expressed (Billet and Holl (1979)) as a function of the lift coefficient, C_l and the wing Reynolds number, Re , by,

$$\sigma_d = k Re^{0.4} C_l^2 \quad [6]$$

the expression giving the pressure loss is,

$$\frac{2\Delta p}{\rho V_{\infty}^2} = 1 + k Re^{0.4} C_l^2 - \left(\frac{U_{(r=0, x=x_{min})}}{U_{\infty}} \right)^2 \quad [7]$$

where k is a constant whose value depends on the planform and the cross section of the foil, Fruman et al. (1992b), Pauchet et al. (1993).

If the planform and the cross section of the foil are kept constant, the term between brackets will be only a function of Re and C_l . Our next objective is to try to determine, using the very large data base acquired during the Action Concertée Cavitation (ACC) program (Fruman (1995)), the trend followed by the non dimensional axial velocity at the vortex centreline.

EXPERIMENTAL

Experiments were performed in the ENSTA Cavitation Tunnel (ECT), the Ecole Navale Cavitation Tunnel (ENCT) and the Grand Tunnel Hydrodynamique (GTH) of the Bassin d'Essais des Carènes. They essentially consisted in determining the cavitation conditions and tangential and axial velocity profiles along the path of tip vortices issued from wings of elliptical planform and NACA 16020 and 0020 cross sections. Table 1 gives a summary of the height, H , and width, W , of each test section, the semi-span, s , and maximum chord, c_{max} , of each of the foils tested, the range of Reynolds numbers relative to the maximum chord, Re , reached in the tests sections and the length of the measuring volume of the LDV arrangement, L_{mv} , employed for measuring the velocities, non dimensionalized by the thickness, δ , of the

boundary layer which will develop over a flat plate, of length c_{max} , without pressure gradient in the fully turbulent regime.

Table 1 : Dimensions of the tests sections and of the foils, range of Reynolds numbers and non dimensional length of the measuring volume of the LDV arrangement.

	HxW (mm ²)	S x c _{max} (mm ²)	Re (x10 ⁻⁶)	L _{mv} /δ
ECT	80 x 150	60 x 40	0.1 - 0.5	1.6
ENCT	192 x 192	120 x 80	0.5 - 1.2	2.8
GTH	1114 x 1114	713 x 475	2.5 - 8.0	1.7

Let be x the direction of the free stream velocity, y the direction of the wing span, z the direction normal to the xy plane and select the tip of the wing as the origin of x and the centre of the vortex as the origin of y and z . Velocities in the x (axial, U) and z (tangential, V) directions were measured in the ECT and the ENCT along the y axis while in the GTH x and y (tangential) components were measured along the z axis. Dantec LDV systems were operated in the back scattering mode in the ECT and ENCT and in the forward scattering mode in the GTH.

Prior to measuring the velocity profiles, the centre of the vortex at each axial position was determined as described by Fruman et al. (1992b), by : letting the measuring volume coincide with the bubbles within the vortex core at cavitation inception conditions ; displacing the measuring volume in the outboard direction (ECT and ENCT tunnels) or in the suction side direction (in the GTH tunnels) up to reaching a maximum tangential velocity ; measuring over a short distance on either side of this position the z component (ECT and ENCT) or the y component (GTH) and determining the position of the largest "tangential" component. At this position, the y and z axis are supposed to cross the centre of the vortex and the whole velocity profiles are then measured.

In the ECT and ENCT the measuring directions of the LDV are made to coincide with the x and z directions. In the GTH they are rotated 45° with respect to the x and y directions. This later arrangements allows to reduce the statistical bias between the two velocity components.

RESULTS AND DISCUSSION

Velocities

It is by now well substantiated (Fruman et al (1992a and b, 1993, 1995)) that : a) the tangential velocity profiles can be described, whatever the generating conditions, by three zones, the viscous region ($0 < r < 0.8a$) where V is increasing with the distance from the centre proportionally to the angular velocity, $\omega = \Gamma/2\pi$, a potential region ($2a < r < \infty$) where V is decreasing as the inverse of the radius, and a transition zone between these two regions, b) the maximum tangential velocity is reached at a distance a from the vortex centre corresponding to around 50 percent of the boundary layer thickness computed as for a flat plate of length equal to the maximum chord, c) the roll-up process is already initiated at the foil tip and the local vortex intensity is a fraction of the mid span bound circulation, d) the maximum tangential velocity reaches an absolute maximum along the vortex path at about one tenth of the maximum chord from the tip, corresponding to the position where the local vortex core radius is a minimum.

A large amount of information available on axial velocity distribution in tip vortices show that both a jet or a wake behaviour can exist depending on a multitude of parameters : foil planform and tip geometry, incidence angle (lift coefficient), Reynolds number, surface roughness, etc. This can be clearly seen in Figure 1, where the non dimensional axial velocity on the vortex axis at varied stations along the vortex path within a distance of up to ten chords from the tip, given by the references listed in Table 2, has been plotted as a function of the Reynolds number, comprised between 0.15 to 4.75×10^6 . Some general trends can be described : i) the extreme values (excess or deficit) of the axial velocity are reached at the centre of the viscous core, ii) for a given incidence angle and free stream velocity, when an excess (or a deficit) is present in the core, its maximum (minimum) occurs very close to the foil tip, iii) downstream the tip, the velocity excess (deficit) decreases gradually, iv) when the incidence is increased, it tends to accentuate the jet-like (wake-like) behaviour at a given position down from the tip.

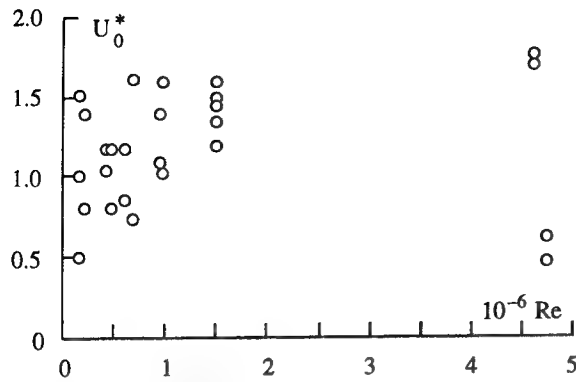


Figure 1 : Maximum axial velocity, non dimensionalized with the free stream velocity, as a function of the Reynolds numbers, sources listed in Table 2.

Table 2 : Extreme values of the reduced axial velocity measured in the tip vortex for distances less than ten chords from the tip of various foil planforms and cross sections for Reynolds numbers comprised between 0.15 to 4.75×10^6 .

	U_0^*	Re ($\times 10^{-6}$)	x^*	Incid. Angle	Cross. Sect/Planf.
Singh (1976)	1,52	0,15	0,80	-	NACA ₆₄ 618
	1,00	0,15	2,40	-	Rectangular
	0,50	0,15	5,00	-	
Green (1991)	1,62	0,68	2,00	10°	NACA 66 209
	0,74	0,68	10,00	10°	Rectangular
Green et al. (1991)	1,17	0,41	2,00		NACA 66 209
	1,04	0,41	0,96		-
	0,96	0,41	15,00		
Stinebring et al. (1991)	0,47	4,75	0,07	-	-
	0,63	4,75	0,67	-	Trapezoidal
Chow et al. (1991)	1,77	4,60	0,74	10°	NACA 0012
	1,69	4,60	1,42	10°	Rectangular
Chigier et al. (1972)	1,40	0,95	close	12°	NACA 0015
	1,10	0,95	far	12°	Rectangular
Arndt et al. (1991)	1,60	0,97	2,35	12°	NACA 66 415
	1,03	0,97	2,35	4°	Elliptical
Staufenbiel et al (1990)	1,40	0,15	0,20	13°	CLARK Y
	0,80	4,00	0,20	13°	Rectangular
Orloff et al. (1993)	0,85	0,60	2,00	8°	NACA 0015
	1,18	0,60	2,00	12°	Rectangular
MacAlister et al. (1991)	1,60	1,50	0,10		NACA 0015
	1,35	1,50	1,00		Rectangular
	1,20	1,50	4,00		
	1,50	1,50	0,10		
	1,45	1,50	0,10		
	1,20	1,50	0,10		
Accardo et al. (1984)	1,17	0,48	0,09	10°	NACA 0014
	0,80	0,48	0,70	10°	Rectangular

Recently, very systematic investigations of the axial and tangential velocity evolution with distance to the tip have been conducted for elliptical chord distributions along the span. Particular attention has been given to the very near region comprised within one chord from the tip. For an elliptical planform foil of cross section NACA 16020 at 10° incidence and equal lift coefficient, Figures 2 shows the non dimensional axial velocity at the vortex axis as a function of the distance to the tip. For the three Reynolds numbers tested, a jet behaviour occurs and it is amplified when the Reynolds number increases. The maximum of the axial velocity seems to move downstream from the tip when the Reynolds number increases, but remains in all cases confined to a distance of less than 20 percent of the maximum chord. After reaching the maximum, the jet effect decays all the more so that the Reynolds number is smaller. This behaviour can be paralleled with that of the maximum tangential velocity as shown in Figure 3 for the same flow conditions. Indeed, a maximum occurs at a distance of about ten percent of the maximum chord whatever the Reynolds numbers and decays downstream.

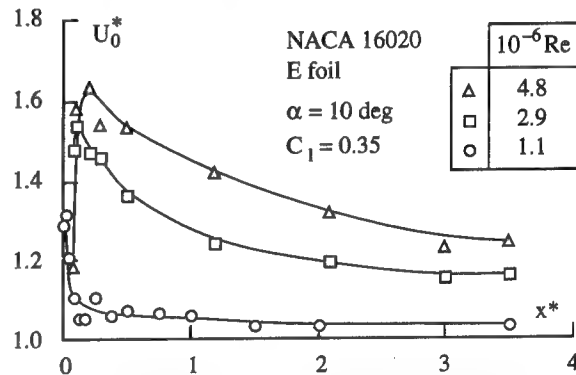


Figure 2 : Non dimensional maximum axial velocity as a function of the non dimensional distance to the foil tip.

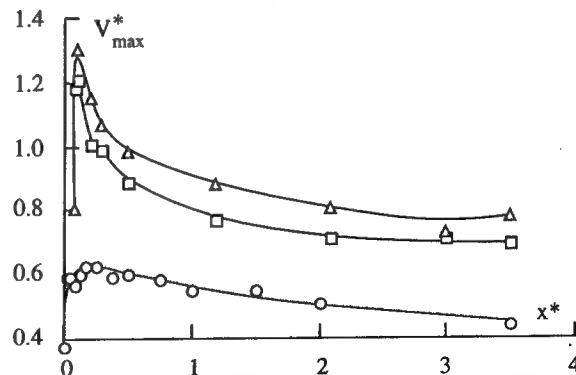


Figure 3 : Non dimensional maximum tangential velocity as a function of the non dimensional distance to the foil tip (same conditions as in Figure 2).

The effect of modifying the foil planform, but keeping the same spanwise elliptical chord distribution, on axial velocities is illustrated in Figure 4 (Fruman et al. (1993, 1995)) for an equal incidence angle, position downstream and Reynolds number. For a Straight Leading Edge (SLE) planform, there is a clear indication of a jet behaviour. When the tip of the wing is moved downstream and the planform becomes Elliptical (E), the jet behaviour is practically eliminated. With a Strait Trailing Edge (STE), the farthest downstream position of the tip, a strong wake-like behaviour develops. The jet and wake behaviour can be somehow correlated with the size of the viscous core as shown in Figure 5 where the radial distribution of the tangential velocity has been plotted. It is clear that the downstream displacement of the tip induces an increase of the viscous core size, a modification of the angular velocity in the viscous core and a modification of the local tip vortex intensity. The augmentation of the viscous core radius and reduction of the angular velocity can only be related to the process of roll-up initiation along the leading edge of the foil and the wrapping of the boundary layer. In the STE foil case, a larger amount of low momentum fluid participates in the core formation and, because of the short distance between the measuring station and the tip, neither the outside, nearly unperturbed, axial flow nor the axial pressure gradient are capable of achieving the acceleration of the core stream. It seems very much clear that momentum transfer by shear between the retarded or accelerated core flow and the outside flow is very much reduced in this rotating flow configuration if compared to what it can be expected in a usual jet or wake shear layer.

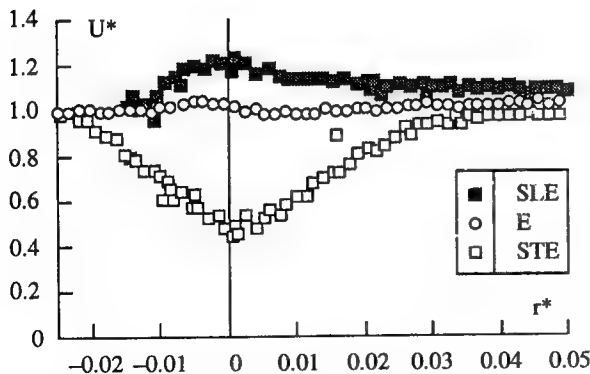


Figure 4 : Radial distribution of the axial velocity measured at $x^*=0.12$ and a Reynolds number of 1.1×10^6 for foil having three different planforms.

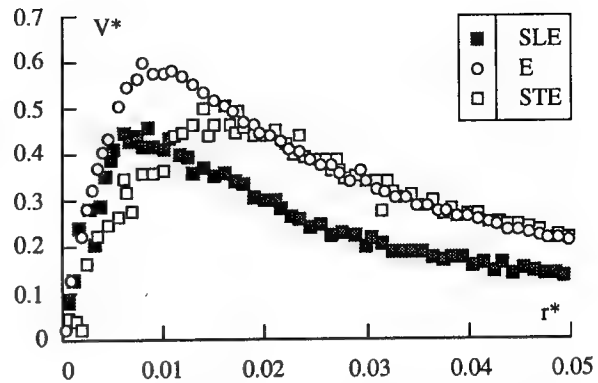


Figure 5 : Radial distribution of the axial velocity measured at $x^*=0.12$ and a Reynolds number of 1.1×10^6 for foil having three different planforms.

It has to be recalled here that the measurements of the axial and tangential velocities conducted in the GTH, in a direction normal to the plane defined by the free stream velocity and the foil span, shows very clearly the three dimensional character of the flow in the near region. The difference between the absolute values of the maximum and minimum of the tangential velocity, δV , have been plotted in Figure 6 for three flow situations and the same Reynolds number. It shows clearly that the three dimensionality is confined to a distance of about one chord downstream the tip (the near region) and that it is independent of the foil and incidence (lift coefficient). In this region, a good estimate of the azimuthal gradient of the tangential velocity can be obtained by dividing δV^* by the viscous core radius and π . The order of magnitude of this velocity gradient is, taking a core radius of 2.5 mm, of 1300 reciprocal seconds at the first measuring station and at least one order of magnitude less one chord from the tip. By continuity, this velocity gradient has to be compensated by the axial gradient of the axial velocity and the radial gradient of the radial velocity. Figure 7 shows, for the flow conditions of Figure 6, the non dimensional axial velocity on the vortex axis as a function of the distance to the tip. The axial gradient, evaluated between the tip and the station where the maximum occurs, is at the most only one tenth of the value estimated above in the very vicinity of the tip (130 s^{-1}). Therefore, the contribution of the radial gradient of the radial component should be preponderant in this region, as Stinebring et al. (1991) have shown and the evolution of the axial velocity do not respond to the need of satisfying the continuity equation.

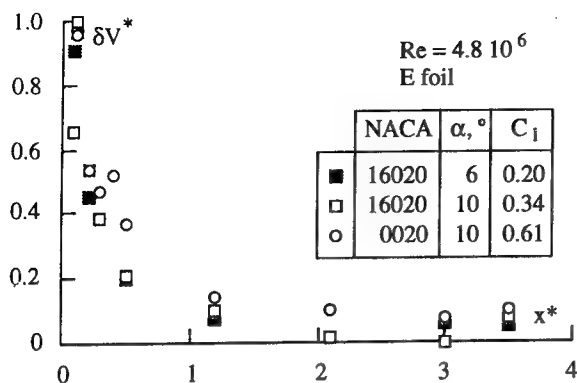


Figure 6 : Non dimensional difference between the two extreme values of tangential velocity profile as a function of the non dimensional distance to the foil tip.

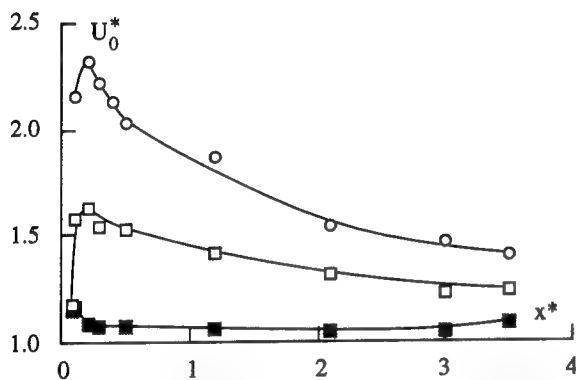


Figure 7 : Non dimensional maximum axial velocity as a function of the non dimensional distance to the foil tip.

The non dimensional pressure loss computed using expression [7] has been plotted in Figure 8 as a function of the Reynolds number ranging from 0.5 to 5×10^6 . In spite of the limited data available, it seems that the pressure loss either remains nearly constant or decreases slightly when the Reynolds number increases. Also, it increases when the lift coefficient increases whatever the cross section of the elliptical foil and the manipulation undergone by the boundary layer, Figure 9. The pressure is less than the unperturbed dynamic pressure for the lowest lift coefficients and increases to more than six times the dynamic pressure for the largest lift coefficients. The latter can be related to the breakdown of the vortex occurring at the highest values of the incidence angle (>12 deg). In these flow conditions, a peculiar radial distribution of the axial velocity was observed, Figure 10. As shown, a kind of annular jet-like region surrounds a central region where the velocities drop rather sharply and reach a minimum. This central region corresponds to a wake behaviour. The axial velocity profile modification can be correlated with observations

made during tip vortex cavitation and showing, Figure 11, that a continuous vapour tube extends from the tip to a distance corresponding to the position of the minimum pressure ($x^*=0.2$), thereafter the vortex is only feed by tiny bubbles escaping from the rear of the tube. Finally, the effect of modifying the planform of the foil, keeping constant the chord distribution, is illustrated in Table 3 for the NACA 16020 cross section and two incidence angles. When the tip is moved downstream, going from the SLE to the STE position, the non dimensional pressure loss increases in agreement with the already mentioned change of the axial velocity behaviour (see Figure 4). It is interesting to see that the non dimensional pressure loss can be as low as 0.2 in the case of the SLE and 6° incidence. The pressure loss can therefore be related to the viscous dissipation over the foil surface during vortex initiation along the foil leading edge.

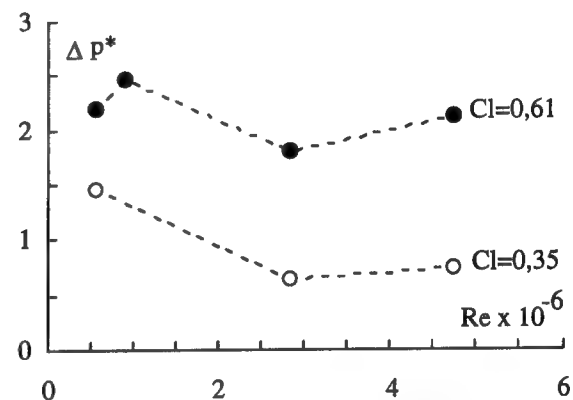


Figure 8 : Evolution of the pressure loss non dimensionalized by the dynamic pressure based on the upstream velocity as a function of the Reynolds number for the NACA 16020 E foil at 6 and 10 deg incidence.

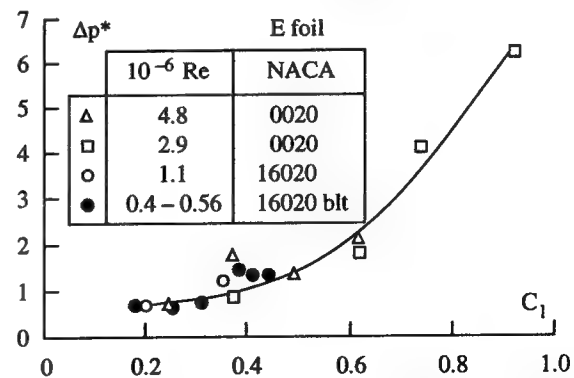


Figure 9 : Evolution of the pressure loss non dimensionalized by the dynamic pressure based on the upstream velocity as a function of the lift coefficient.

Table 3 : Pressure loss non dimensionalized by the dynamic pressure based on the upstream velocity for three different foils at 6 and 10 deg incidence

		10 deg $Re=1.1 \times 10^6$	6 deg $Re=1.2 \times 10^6$
ΔP^*	SLE	1.1	0.2
	E	1.5	1.0
	STE	2.3	1.6

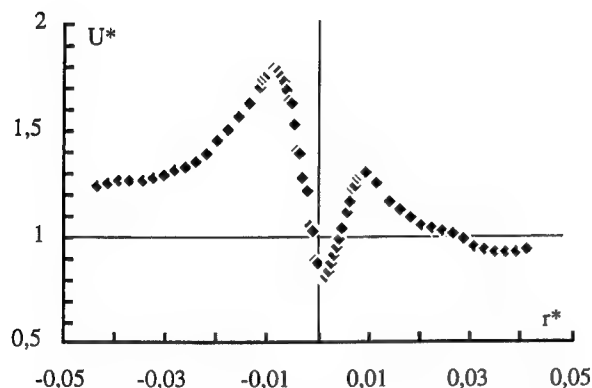


Figure 10 : Radial distribution of the axial velocity measured at $x^*=0.3$ from the NACA 0020 E foil tip at 15 deg incidence and 6 m/s (GTH).



Figure 11 : Tip vortex cavitation developing at the NACA 0020 foil extremity at 17.7 deg for $\sigma=16.4$ and $Re=3 \times 10^6$ (GTH).

Velocity fluctuations

Numerous measurements have demonstrated that velocity fluctuations increase considerably, as compared to the background levels, in the viscous core of the vortex. Fluctuations as high as 60 percent and 55 percent for the tangential and axial components respectively on the vortex axis have been reported (Fruman et al. (1992b)). These fluctuations decay radially quite rapidly and reach the background level at a distance corresponding to the theoretical limit of the region where viscous effects predominates; i.e. twice the viscous core radius.

Figures 12a and b, show the maximum of the axial and tangential fluctuations as a function of the distance to the tip for the NACA 16020 elliptical foil at 10° incidence and three Reynolds numbers, 1.1, 2.8 and 4.8×10^6 . The maximum of the axial fluctuations vary little with distance and increase with increasing Reynolds numbers Figure 12a. This upward trend is directly proportional to the Reynolds number, the ratio $u^*/Re \times 10^{-6}$ is varying between 0.1 and 0.15 for distance larger than $x^*=0.1$. The maximum value occurs near the foil tip ($0.1 < x^* < 0.2$) and slowly decreases to reach an asymptotic value behind $x^*=2.0$.

The evolution of the maximum tangential velocity fluctuations along the vortex path do not seems to be modified by the Reynolds number augmentation Figure 12b. The absolute maximum tangential velocity fluctuation occurs very near the tip of the foil at $x^* < 0.2$, corresponding to the position of maximum axial velocity peak, it's also the position where the difference between the minimum and the maximum tangential velocity reaches an extremum and also, where the minimum pressure coefficient occurs, Fruman et al. (1992b). Then following downstream the vortex centre line, the maximum tangential fluctuations markedly decreases down to $x^*=1$ and then reaches a constant value equal to 0.4.

Figure 13a and b, shows the dependence of the maximum axial and tangential fluctuations with the distance to the tip of the NACA 16020 elliptical foil for three different values of the lift coefficient at equal Reynolds number, 4.8×10^6 . In the very near region to the tip $x^* < 0.3$, the maximum axial fluctuation is increasing with increasing lift coefficient Figure 13a, downstream this trend is not so clear. The rise of the maximum tangential velocity fluctuations is controlled by the lift coefficient increase Figure 13b, in each condition the extreme value occurs in the proximity of the foil tip and then v^* slowly fall with downstream distance.

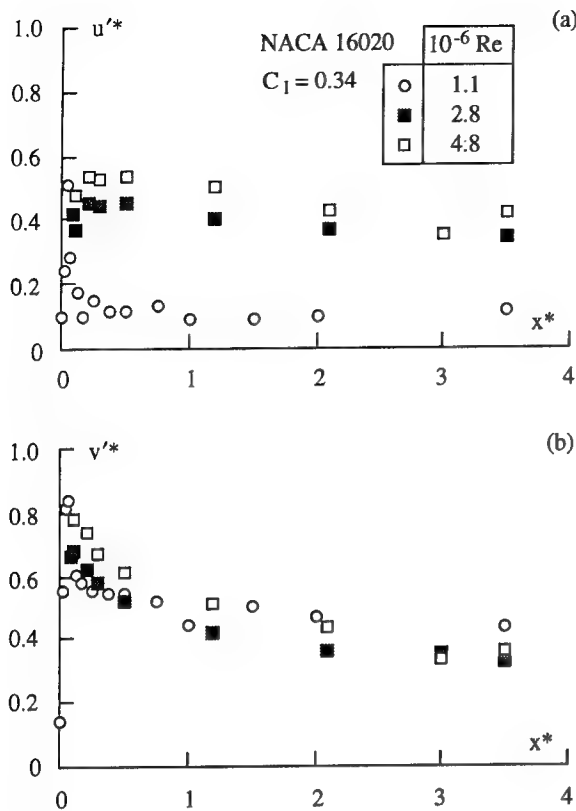


Figure 12 : Fluctuations associated to the axial (a) and tangential (b) velocities as a function of the non dimensionalized distance from the NACA 16020 Elliptical foil at 10 deg incidence.

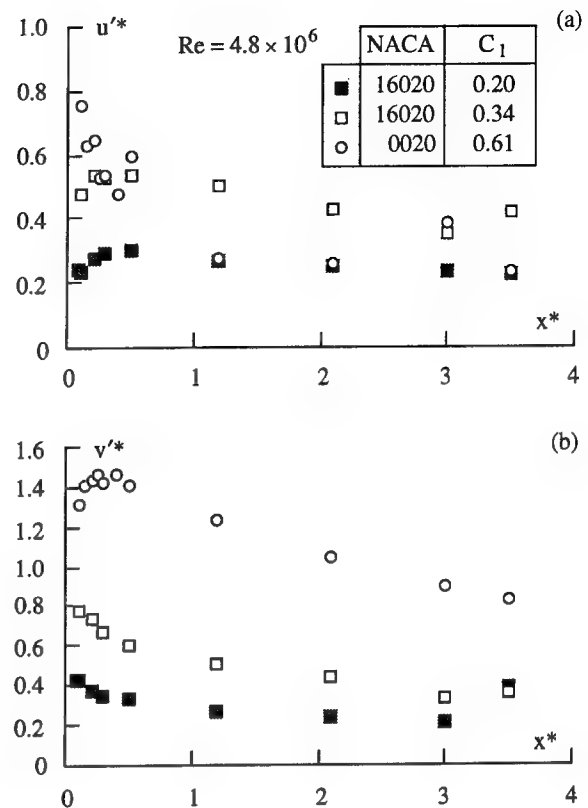


Figure 13 : Fluctuations associated to the axial (a) and tangential (b) velocities as a function of the non dimensionalized distance from Elliptical foils for three different lift coefficient.

Figure 14 shows the evolution of both the maximum tangential and axial velocity fluctuations with the vortex angular velocity measured at $x^*=0.2$ for the elliptical foils having a NACA 0020 at 4, 6, 8, 10 deg for $Re=4.8 \times 10^6$ and a NACA 16020 cross section at 6, 10 deg for $Re=4.8 \times 10^6$ and 10 deg for $Re=2.8 \times 10^6$. The tangential velocity fluctuations are in both cases much greater than the axial ones, in accordance with the results presented in the previous Figures 12 and 13 a,b. The fluctuations associated with the two components vary linearly with the angular velocity, the slope of the tangential velocity being slightly greater than the axial one. In the case of an elliptical planform, Pauchet et al. (1996) have conducted experiments to analyze the effect of the turbulence on the TVC and they have found that the trajectory of the vortex emitted from of an elliptical foil is very stable in the near region of the tip ($x^*<0.2$) even when the upstream turbulence is homogeneously increased from 1.5 percent to 3.5 percent. We can then consider that the major part of

the tangential velocity fluctuations increase shown in the Figure 14 can be directly related to the increase of the tangential velocity gradient encountered when the measuring volume coincides with the vortex centre, without any contribution of the vortex wandering, Fruman et al. (1994). In order to reinforce this fact, the mean velocity fluctuation k^* divided by the maximum amplitude ΔV^* has been plotted as a function of the distance x^* in Figure 15 for various incidence angles, two different cross sections, and Reynolds numbers comprised between 2.74×10^6 and 5.70×10^6 . Close to the foil tip the mean value is 0.6, with a scattering of ± 8 percent and decreases downstream to reach a value of 0.45 with a scattering of ± 20 percent. It must be reminded that far downstream the vortex wandering can not be neglected Fruman et al. (1994), Pauchet et al. (1996), and must be accounted for the scatter increase of the measured velocities.

In order to have a better idea of how the tangential velocity gradient contributes in the estimated fluctuations when the measuring volume is close to

the vortex centre, we have analysed the statistical distribution of the data for both components. Figures 16a and b are respectively showing the mean axial and tangential velocity profiles measured at $x^*=0.2$ from the tip of the NACA 0020 elliptical foil at 10 deg incidence and a Reynolds number of 5.7×10^6 . Associated to five positions of measurements within the vortex core, the non dimensionalized instantaneous velocity distributions for a sample of 600 measurements are shown. Figure 16a, a nearly gaussian distributions is observed regardless of the position. The central position of each of the five distribution is exactly corresponding to the maximum mean axial velocity $U_o^*=2.3$. The deviation is giving a good estimate of the maximum fluctuation $u^*=0.58$. For the five positions the tangential instantaneous velocities are distributed around two values of opposite signs which describes an histogram with two nearly gaussiens Figure 16b. The gap between the two peaks is greater than the difference between the maximum and the minimum mean values (ΔV^*) of the tangential velocity profile. Depending on the position of the measuring volume with respect to the vortex centre, the area under the left peak is decreasing as the area of the second peak is increasing. This reveals two important facts : i) when the measuring volume is crossing the vortex centre, both positive and negative tangential velocities are measured; the calculation of the standard deviation is absurd for the present statistical distribution, being not gaussian, $v^*=1.40$, ii) the instantaneous tangential velocities can reach values as large as 1.5 time the maximum (or minimum) mean value.

In order to make a more realistic estimation of the fluctuations, it is possible to separate the computation of the standard deviation for each histogram peak. This is obtained by first the separation of the negative and the positive instantaneous velocities and secondly by the separate calculation of the mean and the deviation associated of the two samples corresponding to the negative and the positive velocities. The mean tangential velocity profile is then not modified by the summation of each separate mean values, negative and positive. If the same operation is applied to the deviations corresponding to each sample, the maximum fluctuations is decreased by a factor of 4, Figure 17. This treatment is cutting down the maximum deviation by approximately the difference between the two extreme mean values of the tangential velocity profile, $v^*(\text{corrected})=0.28$. By this method, in the case of LDV measurements in a vortical flow spatially stable (without wandering), the bias due to the finite dimension of the measuring volume on the standard deviation can be eliminated.

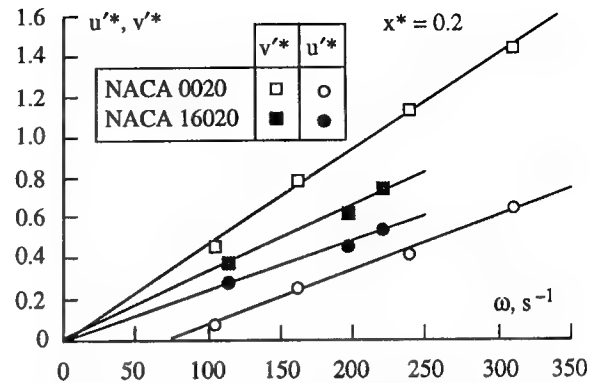


Figure 14 : Axial and tangential velocity fluctuations as a function of the vortex angular velocity.

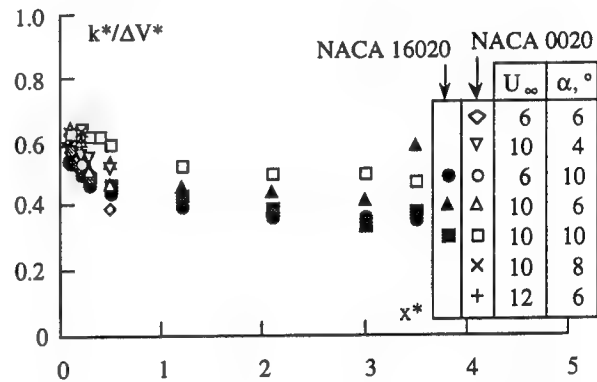


Figure 15 : Evolution of the mean velocity fluctuation k^* divided by the maximum amplitude Δv^* as a function of the distance x^* .

The next step will be to applied the same procedure to a case where the errors due to the measuring volume dimension and the spatial fluctuations of the vortex centre are superimposed. This particular condition can be achieved when moving downstream along the vortex path for the same flow conditions as previously. At $x^*=3.5$, the amplitude of the vortex wandering was estimated to be 5 mm Fruman *et al.* (1992) by positioning the LDV measuring volume on the two extreme locations taken by the vapour tube for conditions just below the critical cavitation conditions. This amplitude is closely the same as the vortex core extension "a" as well as the same order of magnitude of the measuring volume length (4.7 mm). Figures 18a and b are respectively showing the mean axial and tangential velocity profiles measured at $x^*=3.5$, with the non dimensionalized instantaneous velocity distributions to five positions in the vortex core.

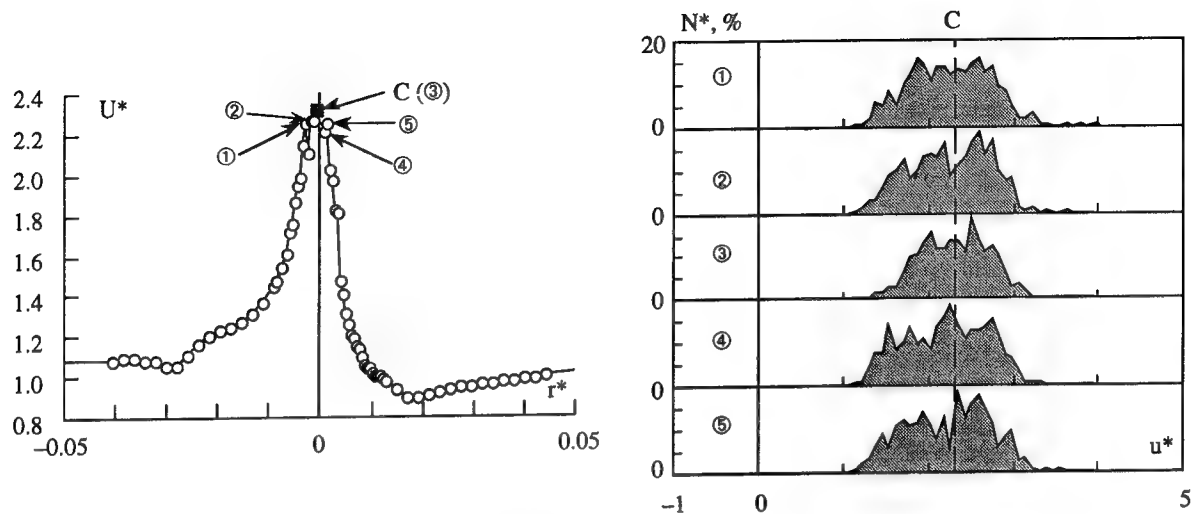


Figure 16 a : Radial distribution of the mean axial velocity measured at $x^*=0.2$ from the tip of the NACA 0020 elliptical foil at 10 deg incidence and a Reynolds number of 5.7×10^6 . The non dimensionalized instantaneous velocity distributions (sample of 600 measurements) associated to five positions of measurement in the vortex core are described.

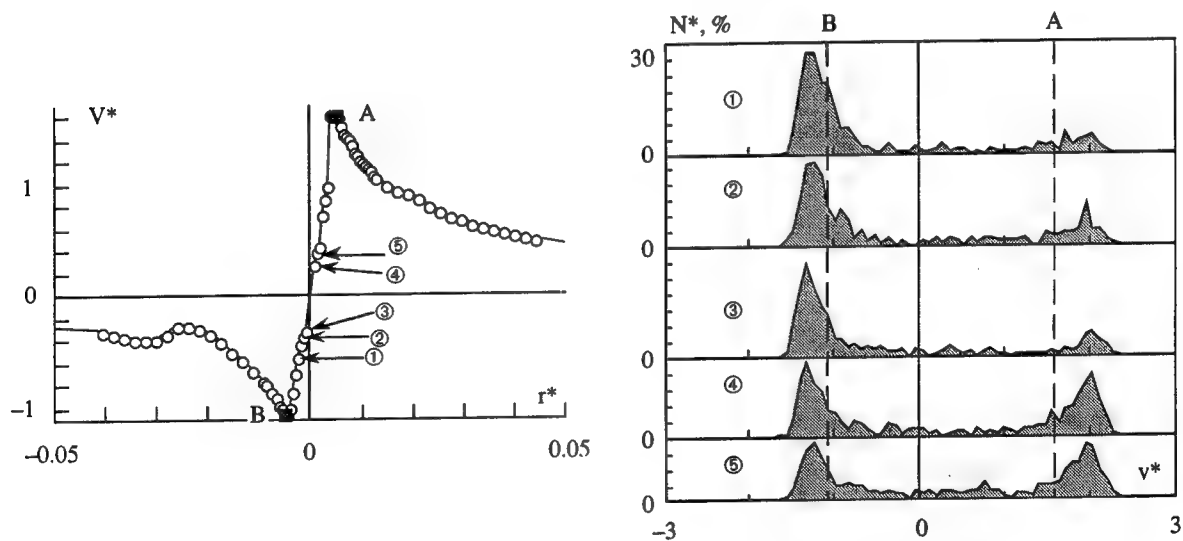


Figure 16 b : Radial distribution of the mean tangential velocity measured at $x^*=0.2$ from the tip of the NACA 0020 elliptical foil at 10 deg incidence and a Reynolds number of 5.7×10^6 . The non dimensionalized instantaneous velocity distributions (sample of 600 measurements) associated to five positions of measurement in the vortex core are described.

The sampling being unchanged, probably not sufficient for these conditions, the scattering noticed on both components in the region corresponding to the core extension clearly indicates the effect induced by the modification of the position of the vortex trajectory during the measurement process. Surprisingly enough, the instantaneous axial velocity distribution is restricted around the maximum mean value that leads to a much smaller velocity fluctuation level ($u^*=0.25$) compared to the relatively scattered distribution measured to the position close to the foil tip where the wandering is negligible. The double peak histogram is still present in the instantaneous tangential velocity distributions Figures 18b. The two peaks are at equal distance from the zero velocity as a result of the symmetry of tangential velocity profile and closer as the angular velocity is decreasing. The position of each peak is still "outside" the two extreme mean values of the tangential velocity profile indicating that at the position corresponding to a mean velocity close to zero, the instantaneous velocities are much greater or smaller than respectively the maximum and the minimum mean tangential velocity. An important scatter of the tangential velocity distributions is observed between the two main peaks. This particular characteristic can be attributed to the fluctuation induced by the "wandering". But in spite of that, the classical estimation of the deviation (applying the standard computation of the deviation to the total sample without any corrections) is entirely governed by the velocity amplitude corresponding to the distance between the two peaks of the statistical distribution because the scattering that appears between the two peaks due to the spatial fluctuations has in fact a very low influence on the variance computation. This fact has been confirmed by Pauchet et al. (1996). In the previous case, when the tangential velocity profile is measured close to the foil tip where no wandering is measurable, the simple statistical treatment applied is efficient enough in first order to filter out the bias induced by the

dimension of the measuring volume with respect to the velocity gradient encountered. But this procedure do not seams appropriated to be directly applied to the statistical distribution shown Figure 18b. It appears difficult to find a perfect double peak histogram in the statistical distributions shown Figure 18b, n°1 and 5 for examples, compared to the ones in Figure 16b. Then, an other statistical procedure must be found to separate the bias induced by the wandering and the dimension of the measuring volume. One solution can be obtained by applying a Pearson law, derived from the Gaussian law. It will allow to distinguish the wandering effect on the statistical distribution from the pure geometrical bias by qualifying the dissymmetry on each side of the distribution. This method is actually in its development phase and will be presented later.

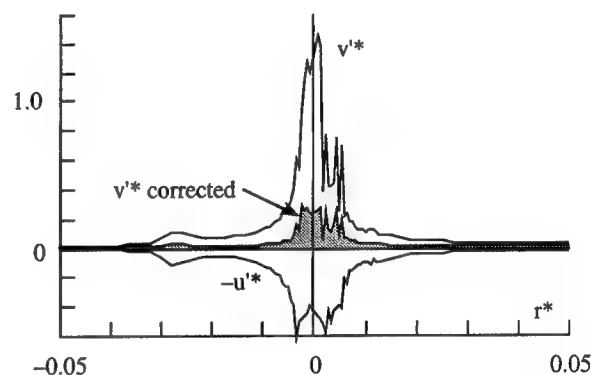


Figure 17 : Radial distribution of the tangential velocity fluctuations corrected and non corrected, and the opposite value of the axial velocity fluctuations measured at $x^*=0.2$ from the tip of the NACA 0020 elliptical foil at 10 deg incidence and a Reynolds number of 5.7×10^6 .

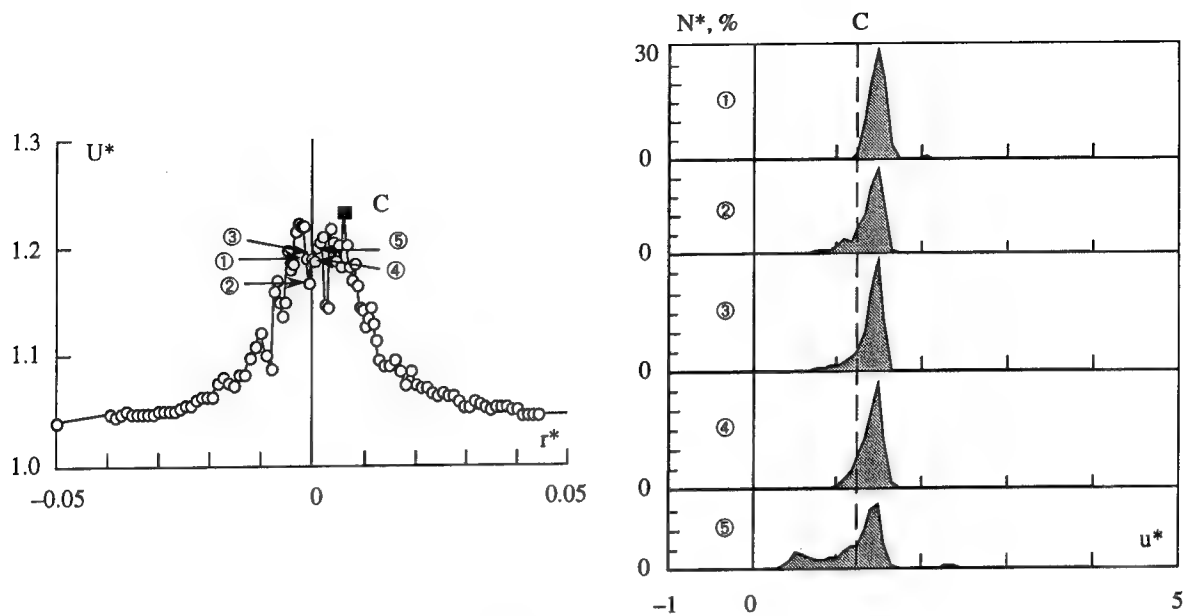


Figure 18 a : Radial distribution of the mean axial velocity measured at $x^*=3.5$ from the tip of the NACA 0020 elliptical foil at 10 deg incidence and a Reynolds number of 5.7×10^6 . The non dimensionalized instantaneous velocity distributions (sample of 600 measurements) associated to five positions of measurement in the vortex core are described.

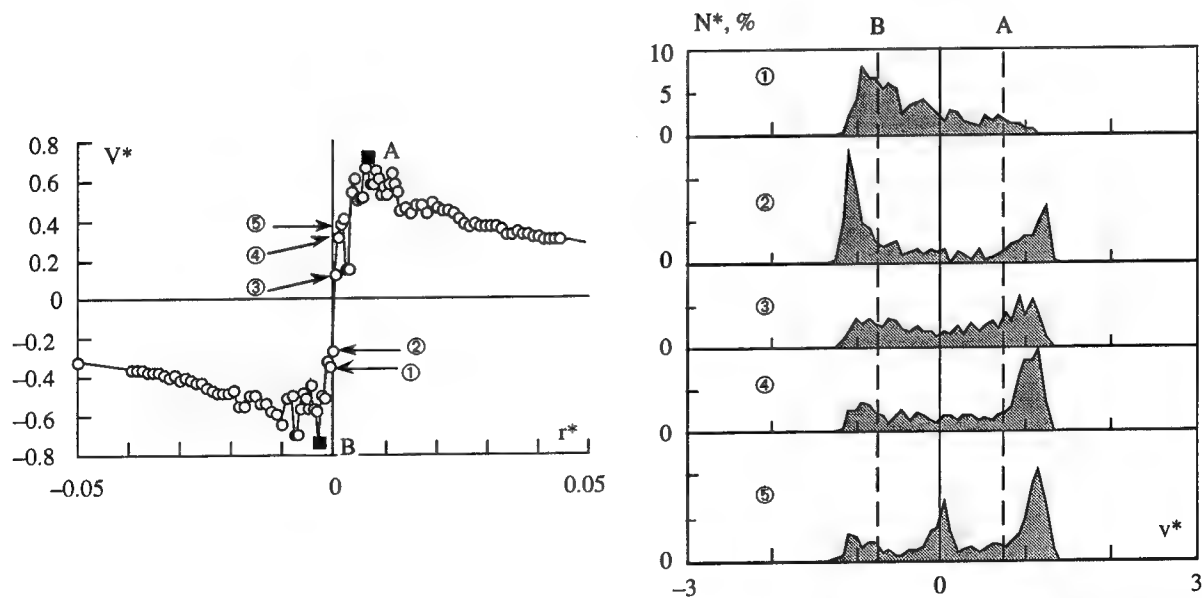


Figure 18 b : Radial distribution of the mean tangential velocity measured at $x^*=0.2$ from the tip of the NACA 0020 elliptical foil at 10 deg incidence and a Reynolds number of 5.7×10^6 . The non dimensionalized instantaneous velocity distributions (sample of 600 measurements) associated to five positions of measurement in the vortex core are described.

CONCLUSION

The three dimensionality of the tip vortex flow is confined to a distance of about one chord downstream the tip and in that region, the azimuthal gradient of the tangential velocity is not compensated by the axial gradient of the axial velocity. Therefore, the contribution of the radial gradient of the radial component should be preponderant in this region. It seems very much clear that momentum transfer by shear between the retarded or accelerated core flow and the outside flow is very much reduced in this rotating flow configuration if compared to what it can be expected in a usual jet or wake shear layer. The increase of Reynolds number seems to favoured the jet-like behaviour, but the increase of the axial velocity is not as high as it should be to balance the pressure drop governed by the rotating flow. The pressure loss corresponding to the difference between the maximum axial velocity that should occur due to the minimum pressure and the maximum axial velocity measured is for reasonable lift coefficients in order of magnitude, once the dynamic pressure. The pressure loss increases up to six times the dynamic pressure as the lift coefficient increases. For identical flow conditions, the pressure loss is very low in the case of the SLE foil and increases moderately when the foil shape is sweep backward.

The statistical analysis conducted on LDV data obtained for positions of measurements crossing the vortex centre demonstrates that the maximum velocity fluctuation estimated is completely determined by the velocity gradient encountered when passing through the vortex core and the wandering has, in that case, a very poor effect on the fluctuations measured. Concerning the axial velocity fluctuations, it appears that near the foil tip, the jet present in the core is very turbulent, far downstream the maximum axial velocity has decreased as well as the fluctuations. The wandering do not seems to significantly influence the axial fluctuations measured.

A method is applied to correct the standard deviation value associated to the tangential velocity. The configuration of the flow field into the vortex core induces the measurements of both positive and negative instantaneous velocities at the same time. Thus the distribution of the velocity is not gaussian as it would be normally found but distributed according a double peak histogram. Without fluctuations of the vortex position, the instantaneous velocity distribution is concentrated on two gaussian peaks, each one corresponding to positive and negative velocities, respectively larger than the maximum mean tangential velocity and smaller than the minimum mean tangential velocity.

This statistical phenomenon is induced by a measuring volume dimension in the same order of magnitude of the vortex core dimension. The consequence is an important over estimation of the tangential fluctuations based on the classical estimation of the standard deviation during the measurements performed inside the solid body rotation core region. In that case the axial fluctuations are less important than the tangential ones as shone in Figure 19. If an appropriate statistical method is applied the tangential fluctuations are drastically reduced and finally are found to be 50 percent lower than the axial fluctuations Figure 19. It is therefore obvious that the fluctuations in the vortex close to its initiation but already detached from the foil surface is not isotropic. The tangential fluctuations are in order of magnitude close to the boundary layer fluctuations (20 percent) that develops over the foil tip while the axial ones are at an extremely high level, the highest being located precisely where minimum value of the pressure coefficient along the vortex axis occurs but also where the tip vortex cavitation is initiated. Consequently we must admit that these highly turbulent properties of the axial flow do not modifies the minimum pressure coefficient. There are still some objections that can be suggest. First, the bias due to the axial velocity gradient is not corrected at all and may be also an important parameter to a certain over estimation of the axial fluctuations especially where the jet behaviour is the most important, some work still needs to be done on the subject, but we can imagine that the corrections brought will go in the same way as the reduction of fluctuations found for the tangential component. Secondly the bias induced on both the axial and tangential mean velocity profiles are not corrected in spite of the fact that they might be important, in particular for the tangential velocity profiles. In spite of all these uncertainties, the essential point is in fact that even if these errors have been left unresolved because of time, they can be qualified as systematic errors. Thus, if we admit that these errors are determined by the ratio shone in the Table 1, the length of the measuring volume of the LDV arrangement, L_{mv} , non dimensionalized by the thickness, δ , of the boundary layer which will develop over a flat plate, of length c_{max} , without pressure gradient in the fully turbulent regime. This crucial point fully confirms the validity of all the results and the analysis conducted within the context of the ACC research program because of its systematic approach adopted by all the members of the ACC, for the description of the tip vortex velocity field. Our knowledge of the tip vortex flow organisation very close to the foil extremity has progressed, in spite of the fact that the absolute values of the flow field is not perfectly described.

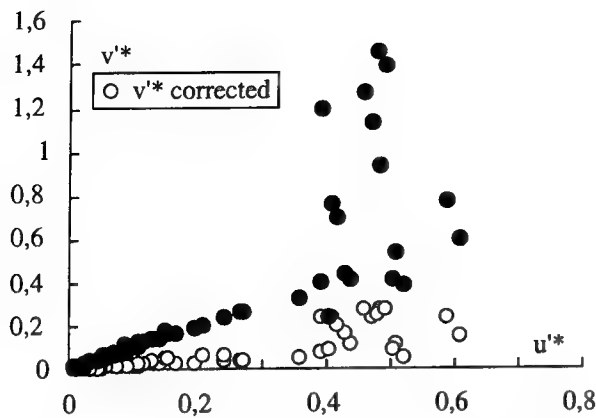


Figure 19 : Radial distribution of the tangential velocity fluctuations corrected and non corrected as a function of the axial velocity fluctuations measured at $x^*=0.2$ from the tip of the NACA 0020 elliptical foil at 10 deg incidence and a Reynolds number of 5.7×10^6 .

ACKNOWLEDGEMENTS

This work has been sponsored by the Direction des Recherches, Etudes et Techniques (DRET) of the Ministry of Défense, France, and is part of the Action Concertée Cavitation program. I wish to acknowledge Dr. D.H. Fruman for reviewing the manuscript and helpful discussion.

REFERENCES

- Accardo, L., Cenedese, A., Cioffi, F., (1984). "Experimental analysis of tip vortex by Laser Doppler anemometry". Symposium on application of Laser Anemometry in Fluid Mechanics - II, Lisbon, Portugal.
- Arndt, R.E.A., Arakeri, V.H., Higuchi, H., (1991), "Some observations of tip-vortex cavitation". *J. Fluid Mech.*, vol 229, pp 269-289.
- Arndt, R.E.A., Keller, A.P., (1991). "Water quality effects on cavitation inception in a trailing vortex." Cavitation '91, ASME FED 116, pp 1-8 and (1992). *Journal of Fluids Engineering*, 114, pp. 430-438.
- Bacheleor G. K. (1964). "Axial flow in trailing line vortices". *J Fluid Mech*, vol 20, pp 645-658.
- Baker, G.R., Barker, S.J., Bofah, K.K., Saffman, P. G., (1974). "Laser anemometer measurements of trailing vortices in water". *J. of Fluid Mech.*, Vol 65, part 2, pp. 325-336.
- Billet, M.L., Holl, J.W., (1979), "Scale effects on various types of limited cavitation". ASME International Symposium on cavitation inception, NY, USA.
- Cliffone, D.L., Orloff, K.L., (1974). "Axial flow flow measurements in trailing vortices". *AIAA Journal*, Vol. 12, No. 8, p. 1154.
- Chigier and Cosiglia (1972). "Tip vortices - velocity distributions". *AIAA Journal* paper No 72-41.
- Chow J. S., Zigliac G. G., Bradshaw P. (1991). "Initial roll-up of a wing tip vortex". Federal Aviation Administration International Wake Vortex Symposium, Washington DC, october.
- Falcao de Campos, J. A. C., George, M.F., Mackay, M., (1989). "Experimental investigation of tip vortices". Cavitation and Multiphase Flow Forum, ASME FED 79, pp. 25-30.
- Falcao de Campos, J. A. C., (1992). "Laser Doppler Velocity measurements on tip vortices in non cavitating and cavitating conditions". Cavitation and Multiphase Flow Forum, ASME FED 135.
- Francis, T.B., Katz, J., (1988). "Observation on the development of a vortex on a rectangular hydrofoil". ASME Fluids Engineering, Vol. 110, pp. 208-215.
- Fruman, D.H., Dugué, C. and Cerrutti, P., (1992a). Enroulement et cavitation de tourbillon marginal. *Revue Scientifique et Technique de la Défense*, pp. 133-141.
- Fruman, D.H., Dugué, C., Pauchet, A., Cerrutti, P., Briançon-Marjollet, L., (1992b). "Tip vortex roll-up and cavitation". Nineteenth Symposium on Naval Hydrodynamics, August 24-28, Seoul..
- Fruman, D.H., Cerrutti, P., Pichon, T., Dupont, P., (1993). "Effect of hydrofoil planform on tip vortex roll-up and cavitation". 4th International Symposium on Cavitation Inception, New Orleans, ASME FED-Vol. 177, pp. 113-124 and (1995a), transaction of the ASME FED-Vol 177, pp. 162-169, and *Journal of fluids engineering* 117, March.
- Fruman D.H., Castro, F., Pauchet, A., Pichon, T., (1994). "On tip vortex turbulence, wandering and cavitation occurrence." Second International Symposium on Cavitation, Tokyo, Japan, Proceedings, H. Kato ed., pp. 151-157.
- Fruman, D.H., Cerrutti, P., Pichon, T. and Dupont, P., (1995a), "Effect of hydrofoil planform on tip vortex roll-up and cavitation". *Journal of*

- Fluids Engineering, 117, pp. 113-124, March.
- Fruman, D.H., Pichon, T., Cerrutti, P., (1995b), "Effect of drag-reducing polymer solution ejection on tip vortex cavitation". Journal of marine science and technology, Tokyo, Japan.
- Fruman D.H., (1995c). The "Action Concertée Cavitation" research program and accomplishments. International symposium on cavitation, Deauville, France.
- Fruman D.H., Billard, J.Y., (1996). "The tip vortex : effect of drag reducing agent on confined turbulence". ASME Fluids Engineering Division Summer Meeting, San Diego, California, USA.
- Green, S.I., (1991). "Correlating single phase flow measurements with observations of trailing vortex cavitation". Journal of Fluids Engineering, 113, pp. 125-129.
- Green, S.I. and Acosta, A.J., (1991). "Unsteady flow in trailing vortices". J. Fluid Mechanics, 227, PP. 107-134.
- Higushi, H., Quadrelli, J.C., Farell C., (1987). Vortex roll-up from a elliptic wing. AIAA Journal, Vol. 25, No. 12, pp. 1537-1542.
- Liang, X., Ramaprian B. R. (1991). "Visualisation of the Wing-Tip Vortex in Temporal and Spatial Pressure gradients". Journal of Fluids Engineering, Vol. 113, pp. 511-515.
- McAlister K. W., Takahashi R. K. (1991). "NACA 0015 wing pressure and trailing vortex measurements". NASA Technical Paper 3151, AVSCOM Technical Report 91-A-003.
- Orloff K. L. and Grant G. R. (1973). "The application of scanning laser doppler velocimeter to trailing vortex definition and alleviation". AIAA Journal, paper No. 73-680.
- Pascal, Ph., (1993). "Etude experimentale de l'évolution d'un écoulement tourbillonnaire". Rech. Aérosp., n° 1993-6, Novembre - Décembre, p. 27-44.
- Pauchet, A., Briançon Marjollet L., Fruman, D.H., (1993). "Recent results on the effect of cross section on hydrafoil tip vortex cavitation occurrence at high Reynolds numbers". Cavitation and Multiphase Flow Forum, ASME-Vol. 153, pp. 81-86, Washington D.C., June.
- Pauchet, A., Briançon Marjollet L., Gowing, S., Cerrutti, P, Pichon, T., (1994). "Effect of foil size and shape on tip vortex cavitation occurrence". Second International Symposium on Cavitation, Tokyo, H. Kato ed. pp 133-139.
- Pauchet, A., Viot, X., Fruman, D.H.F., (1996). "Effect of turbulence on Tip Vortex Cavitation". ASME Fluids Engineering Division Summer Meeting, San Diego, California, USA.
- Pogozelski, E. M., Shekariz, A., Katz, J. and Huang, T.T., (1993). "Three dimensional near field behaviour of a tip vortex developing on an elliptic foil". 31st Aerospace Sciences Meeting and Exhibit, Reno, NV, January.
- Shekariz, A., Fu, T.C., Katz, J. and Huang, T.T., (1993). "Near field behavior of a tip vortex". AIAA Journal, 31, 1, pp. 112-118.
- Singh, P. I., Uberoi M. S., (1976). "Experiment on vortex stability". The Physics of Fluids, Vol. 19, No. 12, December.
- Spreiter J.R., Sacks, A.H., (1951), "The rolling up of the trailing vortex sheet and its effect on the downwash behind wings". Journal of the aeronautical sciences 18, pp. 21-32 et 72.
- Staufenbiel R., Vitting T., (1990). Formation of vortices and vortex wake alleviation by tip vortices. ICAS-90-3.2.2.
- Stinebring, D.R., Farrell, K. J., Billet, M. L., (1991), "The structure of three-dimensional tip vortex at high Reynolds numbers". Journal of fluids engineering, September, Vol 113 pp. 496-503.

Calculations of Pressure Fluctuations on the Ship Hull Induced by Intermittently Cavitating Propellers

Y.-Z. Kehr, C.-Y. Hsin, Y.-C. Sun (National Taiwan Ocean University, Taiwan)

Abstract

The object of this work is to develop a numerical method to calculate the hull surface forces induced by cavitating propellers. In this paper, a method based on the numerical model developed by Breslin, is presented. In this method, the effective wake is calculated by the method developed by Huang and Groves, and later modified by Wilson, Van Houten and Kerwin. MIT-PUF-3A is then used to analyze the unsteady flow around propellers in the effective wake, and to compute the propeller induced potentials on the hull surface. A potential based higher order panel method is used to calculate the flow around the ship hull including the propeller influences. In this higher order panel method, a second order panel geometry is used, and a second order normal dipole is distributed on each panel. An internal Dirichlet boundary condition is imposed at each panel that the total potential on the body inner surface is set to be zero. The pressure fluctuations on the hull surface can then be calculated from solutions of the dipole strength by applying Bernoulli's equation. In this paper, the pressure fluctuations generated by propellers on a flat plate and on a ship hull are presented, and the computational results are compared with experimental data.

1 Introduction

When propellers work in the wake of hulls, the nonuniform inflow results in both the unbalanced bearing forces and pressure fluctuations on the hull surface. The latter one is especially serious when the propeller is cavitating. In this paper, a method of predicting the pressure fluctuations on hull surface by a cavitating propeller is presented.

The problems caused by propeller induced pressure fluctuations on hull surface brought naval architects' attentions in 1970's. At that time, loadings on propellers have been dramatically increased due to the demands of higher speed commercial ships. Some serious structure failures due to vibrations were occurred on these high speed ships, and it was found that most of these vibrations were caused by propellers generated exciting forces. Since then, the topics of reducing propeller generated vibrations have been investigated and studied by various institutes and researchers. Recently, NTOU (National Taiwan Ocean University) has begun a series of studies to understand propeller generated vibrations. These researches include better designs of the stern hull forms which may reduce the nonuniformity in the wake, designs of highly skewed propellers which can help to reduce propeller generated vibrating forces, development of new sections for reducing cavitations, establishment of skills of measuring pressure fluctuations on hull surfaces, and development of a numerical prediction model for propeller generated pressure fluctuations. This prediction model which has been developed for the past two years is described in this paper.

The present method is based on the numerical model developed by Breslin, etc. [2], however, the ship hull is completely simulated by a higher order panel method. In the present work, the effective wake is first calculated by a method developed by Huang and Groves [5], and later modified by Wilson, Van Houten and Kerwin [16],[2]. MIT-PUF-3A is then used to analyze the unsteady flow around propellers in the effective wake, and to compute the propeller induced potentials on the hull surface. Finally, a potential based higher order panel method is used to calculate the flow around

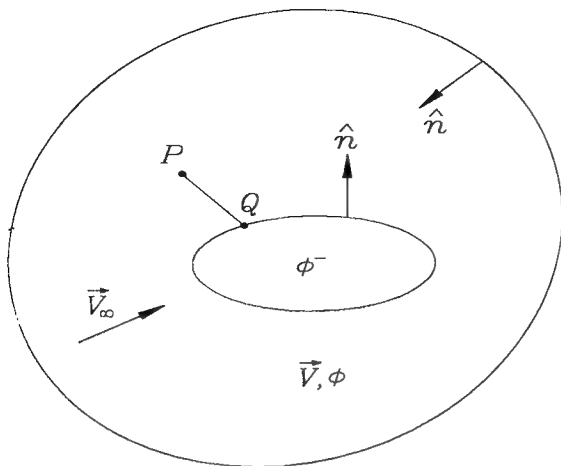


Figure 1: Internal and external flow domain defined in the equation (2)

the ship hull including the propeller influences. In this panel method, a quadratic dipole distribution is distributed over each panel on the body surface, and an internal Dirichlet boundary condition is imposed at the control point of each panel. The pressure fluctuations on the hull surface can then be calculated from solutions of the dipole strength by applying Bernoulli's equation.

2 Representation of the Ship Hull

In order to calculate the propeller generated pressure fluctuations, we need first to develop a numerical method to represent the ship hulls. In the present work, the free surface effect is approximated by a positive or negative hull image. Therefore, it is equivalent to solving the flow around submerged bodies. Hess and Smith [4] first developed a velocity based panel method to calculate the flow around a submerged body. In their method, the source singularities are distributed over the body surface, and the Neumann boundary condition is imposed for solutions. In the present work, the flow around a ship hull is analyzed by a higher order, potential based panel method. A dipole sheet is distributed on the surface of hull, and an internal Dirichlet boundary condition is imposed.

2.1 Governing Equation

Assuming the flow around the body is incompressible, inviscid, and irrotational, namely,

potential flow, then the governing equation of this flow is the Laplace's equation:

$$\nabla^2 \phi = 0 \quad (1)$$

where ϕ is the velocity potential.

If we let ϕ to be the external flow velocity potential, and ϕ^- to be the internal flow velocity potential (Figure 1), then from Lamb [13], and Kervin, etc.[10], we have the following equation:

$$\begin{aligned} \phi(P) = & \iint_S [\phi(Q) - \phi^-(Q)] \frac{\partial}{\partial n_Q} \left[\frac{1}{4\pi R(P;Q)} \right] dS \\ & - \iint_S \left[\frac{\partial \phi(Q)}{\partial n_Q} - \frac{\partial \phi^-(Q)}{\partial n_Q} \right] \frac{1}{4\pi R(P;Q)} dS \end{aligned} \quad (2)$$

where P is a field point in the flow field, Q is a point on the body surface, and R is the distance between P and Q . In equation (2), we can interpret the term $[\phi(Q) - \phi^-(Q)]$ as a dipole strength, and the term $\left[\frac{\partial \phi(Q)}{\partial n} - \frac{\partial \phi^-(Q)}{\partial n} \right]$ as a source strength. Most of panel methods used in the fluid dynamics area are based on equations derived from equation (2) with a proper boundary condition imposed [6].

2.2 Boundary Condition

When solving the problems of non-lifting bodies, velocity based panel methods are commonly used. That is, a source sheet is distributed on the body surface, and the Neumann boundary condition is imposed.

$$\frac{\partial \phi}{\partial n} = -\nabla \phi_\infty \cdot \hat{n} = -V_\infty \cdot \hat{n} \quad (3)$$

If we define the total potential as the sum of the inflow potential, ϕ_∞ , and the perturbation potential, ϕ , then, we can rewrite equation (3) as follows:

$$\frac{\partial \phi_\infty}{\partial n} + \frac{\partial \phi}{\partial n} = \frac{\partial \Phi}{\partial n} = \vec{V} \cdot \hat{n} = 0 \quad (4)$$

where \vec{V} is the total velocity.

However, for the convenience of calculating the pressure fluctuations on the hull surface, a potential based panel method which a dipole sheet distributed on the body surface is preferred [2]. As we know, the normal velocity is continuous through a dipole sheet, therefore,

$$\frac{\partial \phi}{\partial n} = \frac{\partial \phi^-}{\partial n} \quad (5)$$

We can let the velocity potential at the inner surface to be $-\phi_\infty$, and the total inner potential thus becomes to be zero. This is the internal Dirichlet boundary condition we are going to use. From the above statements, equation (2) can be rewritten as:

$$\phi(P) = \iint_S (\phi(Q) + \phi_\infty) \frac{\partial}{\partial n_Q} \left[\frac{1}{4\pi R(P; Q)} \right] dS \quad (6)$$

where $\phi + \phi_\infty = \Phi$ is the total potential, and it can also be interpreted as the dipole strength, μ . Equation (6) is therefore the dipole only formulation derived from equation (2).

If a point P is on the external surface, then equation (6) becomes:

$$\phi(P) = \frac{\mu(P)}{2} + \iint_S \mu(Q) \frac{\partial}{\partial n_Q} \left(\frac{1}{4\pi R} \right) dS \quad (7)$$

Similarly, we will get the following equation if P is on the inner surface:

$$\phi^-(P) = -\frac{\mu(P)}{2} + \iint_S \mu(Q) \frac{\partial}{\partial n_Q} \left(\frac{1}{4\pi R} \right) dS \quad (8)$$

If we apply the internal Dirichlet boundary condition (*total internal potential to be zero*), then it becomes,

$$\phi_\infty - \frac{\mu(P)}{2} + \iint_S \mu(Q) \frac{\partial}{\partial n_Q} \left(\frac{1}{4\pi R} \right) dS = 0 \quad (9)$$

The dipole strength, μ , can be solved from equation (9). The velocities and pressure distribution thus can be obtained by taking the gradients of velocity potentials.

2.3 Higher Order Panel Method

In the present work, a higher order panel method based on Johnson [8],[7] is used. In this method, both the panel geometry and the dipole strength are of the second order. The panel geometry is approximated by a quadratic surface, and can be described by

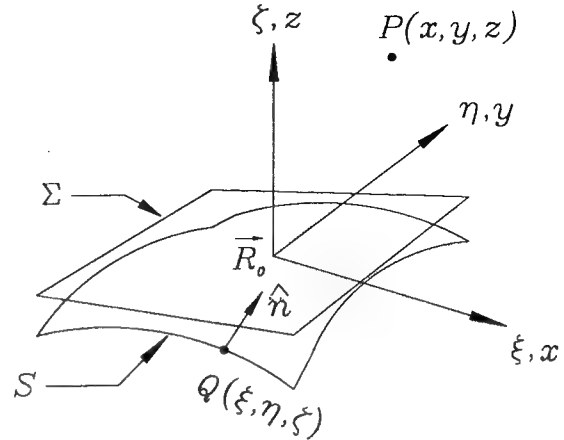


Figure 2: The coordinate system of the panel geometry used in the present method.

$$\zeta(\xi, \eta) = a\xi^2 + b\eta^2 \quad (10)$$

after several coordinate transformations. Please refer to Johnson [8] [3] for the detailed descriptions of modeling panel geometries. Figure 2 shows the local coordinate system of a panel. The second order dipole strength thus can be described in terms of the local coordinate system (ξ, η) :

$$\begin{aligned} \mu(\xi, \eta) = & \mu_0 + \mu_\xi \xi + \mu_\eta \eta + \frac{1}{2} \mu_{\xi\xi} \xi^2 + \mu_{\xi\eta} \xi \eta \\ & + \frac{1}{2} \mu_{\eta\eta} \eta^2 \end{aligned} \quad (11)$$

where coefficients $\mu_0, \mu_\xi, \mu_\eta, \mu_{\xi\xi}, \mu_{\xi\eta}, \mu_{\eta\eta}$ are determined from dipole strength at control points of neighboring panels through a fitting process. In the present method, 9 panels (8 neighboring panels and the self panel) are used for this fitting process by the least squares method. By introducing this quadratic dipole strength into the governing equation, and calculating the induced potentials, a linear system is finally obtained for the solutions of the dipole strength at the control point of each panel. The dipole strength coefficients can then be calculated, thus the dipole strength distribution can be obtained from equation (11) (see Appendix).

2.4 Numerical Solutions

The velocity potentials on the surface of a sphere in a uniform flow (Figure 3) are calculated by this potential based higher order panel method, and the results are compared with both the exact

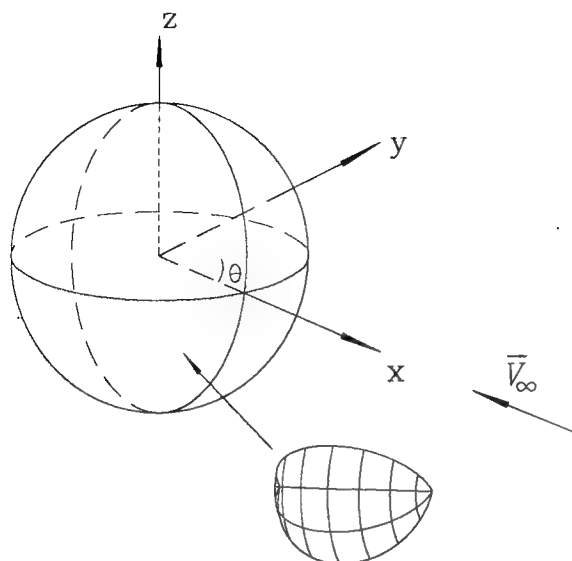


Figure 3: A sphere with its discretized geometry

solutions and numerical solutions from a velocity based panel method.

Since the solutions of a sphere are symmetrical, only one fourth of the sphere geometry is discretized and used for the calculations. Figure 4 shows the relative computational errors in percentage of a sphere with 18 panels/quadrant (6 panels in the θ direction, and 3 panels in the z direction). It shows that the results are satisfactory, and even the maximum error is less than 1%. The relative error is defined as the difference between the computational result and the exact solution. However, if we use a velocity based panel method with a linear source distribution on each panel, then 40 panels (8 panels in the θ direction, and 5 panels in the z direction) are needed to obtain the same accuracy (Figure 5). Figure 5 shows the comparison of the results from a constant source panel method, a linear source panel method and the present method. It shows that the present method gives the most accurate results, and the computational time of the present method is about the same as the linear source panel method by the same given number of panels. In this potential based panel method, velocities can be calculated by taking the gradients of the solved potentials (dipole strength). Figure 6 shows the calculated velocity distributions on the sphere surface by different panel methods compared to the exact solutions. In this figure, velocity distribution is directly calculated from the induced velocities for the source (velocity based) panel method. However, the velocity distribution is calculated from potentials by a finite

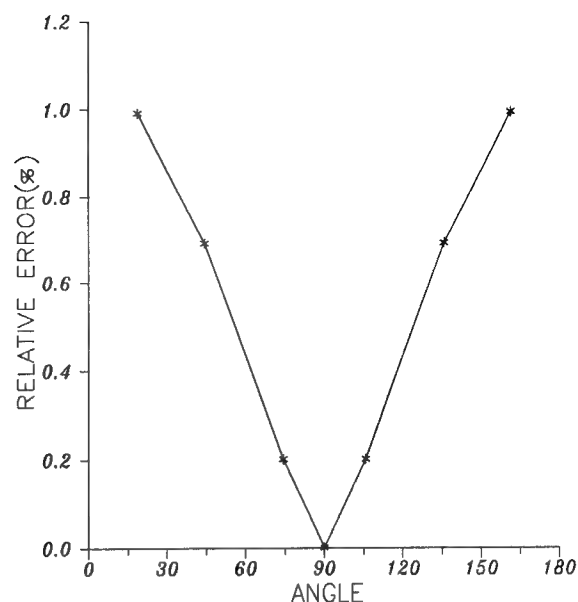


Figure 4: Relative errors of the total potentials of a sphere in the uniform flow calculated by the present higher order panel method, and totally 18 panels are used at each quadrant.

difference method for the dipole (potential based) panel method.

This panel method is also used to calculate *Series 60* ship hulls ($C_B = 0.6$ and $C_B = 0.82$) to make further comparisons between the potential based and velocity based panel methods. Results show that both methods generate very similar results [3].

3 Solutions of the Intermittently Cavitating Propellers

In the present method, MIT-PUF-3A is used to calculate potentials on the hull surface induced by intermittently cavitating propellers. We have discussed how ship hulls are modeled by a higher order panel method in the last section, and we will briefly introduce how PUF-3A simulates propeller effects.

3.1 Calculation of the Effective Wake

When we calculate the flow field around propellers, a ship model wake measured in the towing tank is usually used to be the inflow. This velocity distribution is purely generated by the ship hull without the consideration of propellers, and this is so

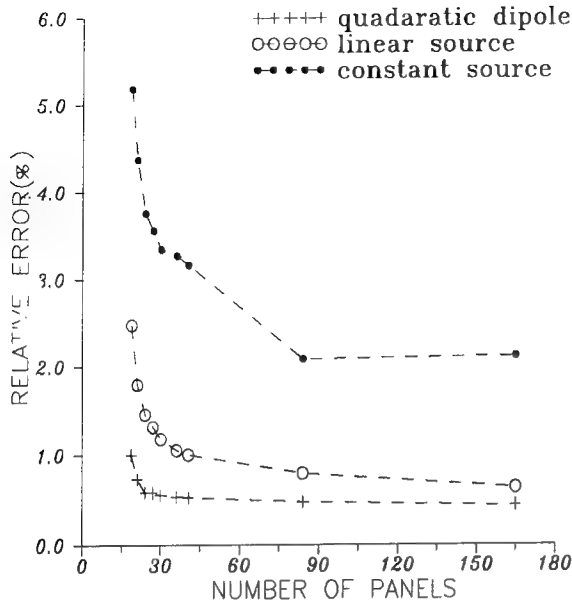


Figure 5: The maximum errors of the total potentials of a sphere in the uniform flow calculated by different panel methods for different numbers of panels.

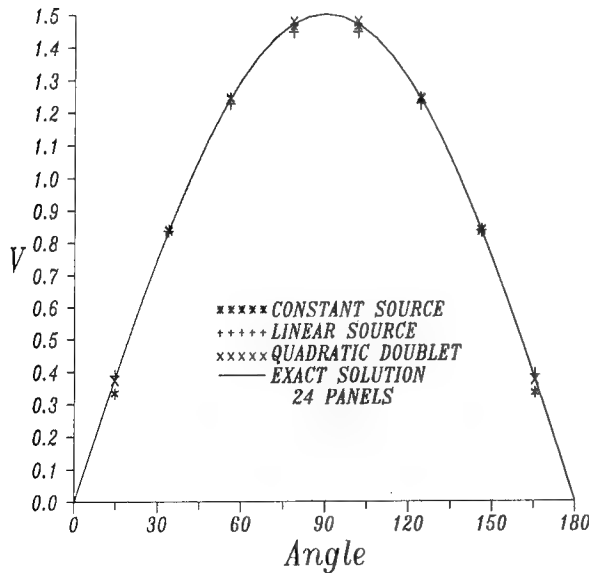


Figure 6: Velocity distribution calculated by different panel methods compared to the exact solutions.

called "nominal wake". However, the interaction between a propeller and a ship hull will change the wake distribution, and the modified wake distribution is called the "effective wake". In order to calculate the pressure fluctuations generated by propellers in the wake of hulls accurately, we need first to calculate the "effective wake". Numerical solutions of Navier-Stokes equations can certainly provide a relatively accurate effective wake distribution. However, in the present method, a simple approach used by PUF-3A is adopted. This approach is based on the model established by Huang and Groves [5], and later modified by Wilson, Van Houten and Kerwin [16],[2].

Huang and Groves' model is used to calculate the effective wake of bodies of revolution in an incompressible, irrotational flow field. It assumes that the axial velocity gradient is small compared to the radial velocity gradient as in a boundary layer, and that the energy in a stream tube is constant. In order to apply this model to the non-axisymmetric flow, such as a ship hull wake, Wilson, Van Houten and Kerwin made the following assumptions [16],[2]:

- "The circumferential gradient in the nominal wake is due to radial vortex lines convecting downstream with the mean velocity field",
- "The radial vortex lines change only in length and move inward as the flow contracts. Their circumferential points remain steady".

Therefore, one can find the following relationship from the vorticity equation:

$$\frac{\omega_{r_{eff}}}{\omega_{r_{nom}}} = \frac{\frac{1}{r_{eff}} \frac{\partial U_e}{\partial \theta}}{\frac{1}{r_{nom}} \frac{\partial U_x}{\partial \theta}} = \frac{\Delta r_{eff}}{\Delta r_{nom}} \quad (12)$$

where $\omega_{r_{eff}}$ and $\omega_{r_{nom}}$ are the radial vorticities of the effective wake and nominal wake, U_e and U_x are the axial effective velocity and axial nominal wake velocity, Δr_{eff} and Δr_{nom} are the length of a vortex filament in the effective wake and nominal wake. Therefore, the Fourier coefficients of the velocities can be obtained.

Figure 7 and Figure 8 show the nominal wake measured in the towing tank and the effective wake calculated by PUF-3A of an 1100 TEU container ship built by CSBC (China Ship Building Corporation). Figure 7 shows circumferential distributions of the nominal wake and the effective wake at 0.7 propeller radius. Figure 8 shows radial distributions of the average nominal wake and the average effective wake. The calculated model mean effective wake of this case is 0.298, and it is very

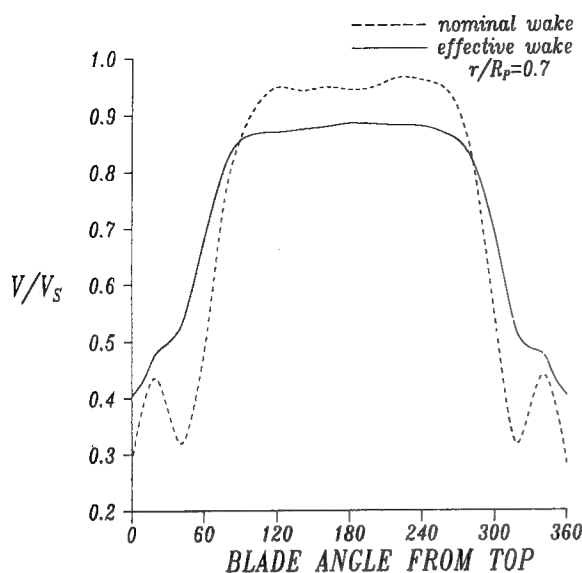


Figure 7: Circumferential distributions of the nominal wake and the effective wake of the CSBC 1100 TEU container ship at 0.7 propeller radius.

close to the value from a model propulsion test, 0.308.

3.2 Numerical Solutions of Propellers

Once the effective wake has been calculated, it can be input as the inflow of propellers. PUF-3A, a vortex lattice method based on the lifting surface theory, is used to solve propeller unsteady flow problems. The "unsteady flow" here actually means the propeller inflow varies spatially, such as the circumferentially nonuniform flow in the hull wake. However, it is equivalent to unsteady flow problems for propeller sections moving in this circumferentially varying inflow. Therefore, we can treat each angular position that propeller rotates to as a time step. An efficient time march scheme is adopted by PUF-3A to solve the unsteady flow problems in the time domain. PUF-3A also includes the calculations of cavitation extensions, and field point induced potentials. The detailed theory and schemes behind PUF-3A are described in [11],[12],[9],[2], and we will not repeat here.

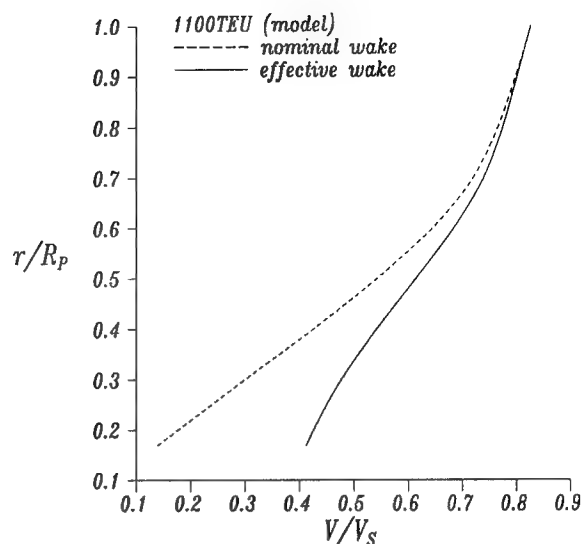


Figure 8: Radial distributions of the average nominal wake and the average effective wake of the CSBC 1100TEU container ship.

4 Propeller Generated Pressure Fluctuations

The calculations of the propeller generated pressure fluctuations include the considerations of the ship hull, propellers and the water surface (free surface). As described in the last two sections, the solutions of the ship hull problems can be obtained by a panel method. On the other hand, propellers in the wake of hulls can be calculated by a lifting surface vortex lattice method. Once we include the free surface effect, the propeller induced potentials on the hull surface can be computed by coupling these methods. The induced pressure fluctuations then can be obtained by applying the Bernoulli's equation.

In the present method, the free surface effect is approximated by the hull images. For the low frequency free surface, the free surface boundary condition is approached by the zero frequency free surface condition (rigid surface boundary condition). That is, the normal derivative of the perturbation velocity potential should be zero on the free surface.

$$\frac{\partial \phi}{\partial n} = 0 \quad (13)$$

In order to satisfy this boundary condition, a positive hull image to the water plane is used, and the influence of the propeller on the hull sur-

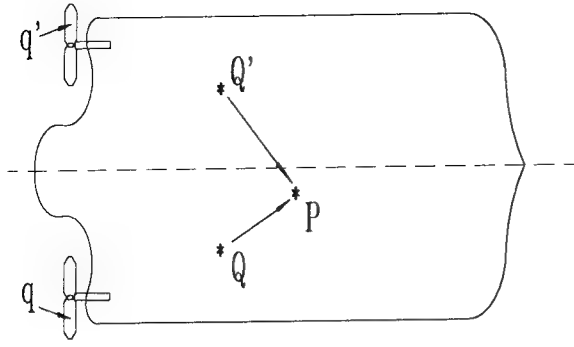


Figure 9: Depiction of the double hull with a propeller and its image

face should include the positive image of that propeller. The "positive image" means that the dipole strength at each panel on the "image hull" surface is the *same* as its corresponding panel on the "real hull" surface. Therefore, the solutions of the ship hull problems include the hull, the hull image, a propeller, and the propeller image. On the other words, for each panel on the hull surface, the total induced potentials include these from the hull, from the image hull, from the propeller, and from the image propeller.

Therefore, if we define the propeller induced potentials as ϕ_{pr} , then the solutions of the dipole strength on the hull surface panels can be obtained by solving the following equation:

$$0 = \frac{1}{4\pi} \iint_S \mu(Q) \frac{\partial}{\partial n_Q} \left(\frac{1}{R(P, Q)} + \frac{1}{R(P, Q')} \right) dS + \phi_\infty + \phi_{pr}(P, q) + \phi_{pr}(P, q') \quad (14)$$

where P represents a field point on the hull surface, and Q, Q' represent points on the hull surface and on the image hull surface, q and q' represent points on the propeller and on its image as shown in Figure 9.

For the high frequency free surface, the perturbation velocity potential should be zero on the free surface.

$$\phi = 0 \quad (15)$$

In order to satisfy this boundary condition, a negative hull image to the water plane is used, and the influence of the propeller on the hull surface should include the negative image of that propeller. The "negative image" means that the dipole strength at each panel on the "image hull" surface has the

same magnitude as its corresponding panel on the "real hull" surface but with a different sign.

Therefore, the solutions of the dipole strength on the hull surface can be obtained by solving the following equation:

$$0 = \frac{1}{4\pi} \iint_S \mu(Q) \frac{\partial}{\partial n_Q} \left(\frac{1}{R(P, Q)} - \frac{1}{R(P, Q')} \right) dS + \phi_\infty + \phi_{pr}(P, q) - \phi_{pr}(P, q') \quad (16)$$

The potential solution is a function of position and time, therefore, it can be expressed as a Fourier series:

$$\Phi(P, t) = \mu(P, t) = C_0(P) + \sum_{k=1}^{N_H} C_k(P) \cos(k\omega t - \epsilon_k) \quad (17)$$

where P again represents a point on the hull surface, C_k is the Fourier coefficient, N_H is the total number of Fourier series terms, and ω is the rotational speed of a propeller.

The pressure distribution on the hull surface thus can be calculated by using the Bernoulli's equation:

$$p_\infty + \frac{1}{2} \rho U_\infty^2 = p(t) + \frac{1}{2} \rho U(t)^2 + \rho \frac{\partial \Phi(t)}{\partial t} \quad (18)$$

The $\frac{\partial \Phi}{\partial t}$ term can be directly calculated from equation (17):

$$\frac{\partial \Phi}{\partial t} = - \sum_{k=1}^{N_H} k\omega C_k \sin(k\omega t - \epsilon_k) \quad (19)$$

and the total velocities can be calculated by making the gradients of potentials. Therefore, we can obtain the time varying pressure distribution on the hull surface. Again, this time varying pressure distribution can be represented as a Fourier series:

$$p(P, t) = F_0(P) + \sum_{k=1}^{N_H} F_k \cos(k\omega t - \epsilon_k) \quad (20)$$

where F_k is the k^{th} Fourier coefficient. A commonly used nondimensional parameter K_p is then defined as

$$K_p = \frac{F_k}{\rho n^2 D^2} \quad (21)$$

Table 1: Geometric parameters of propeller 1242

r/R	P/D	c/D	f_0/C	t_0/D
0.29	0.9469	0.1780	0.0253	0.0528
0.40	1.0530	0.2460	0.0253	0.0383
0.50	1.1498	0.3089	0.0266	0.0314
0.60	1.1690	0.3717	0.0225	0.0247
0.70	1.1150	0.4346	0.0153	0.0186
0.80	1.0192	0.4386	0.0095	0.0132
0.90	0.8961	0.2868	0.0058	0.0085
0.95	0.8172	0.1745	0.0021	0.0061
1.00	0.7281	0.0277	0.0001	0.0017

(There are no rake and no skew for this propeller)

5 Computational Results

In this section, we will show computational results from the present method.

5.1 Pressure Fluctuations on a Flat Plate Generated by Propellers

The calculations of propellers generated pressure fluctuations on a flat plate are similar to those of propellers generated pressure fluctuations on ship hulls. However, because the geometry is flat, the potentials at each panel induced by the plate itself will only come from the self panel. It can also be shown that the dipole strength on the flat plate equals to twice of the propeller induced potential plus the inflow potential, $2(\phi_{pr} + \phi_\infty)$. Therefore, the flat plate case can be used to check the calculations of cavitating propellers and pressure fluctuations.

In 1973, Weitendorf [15] published a series of experimental data of the pressure fluctuations on a flat plate measured in a cavitation tunnel. We will compare the computational results by the present method with these experimental data. The propeller we select is the propeller 1242, and it is a 5-blade propeller with geometric parameters shown in Table 1. We will show the calculated pressure fluctuations, K_P , on the plate (at $a/R = 0.352$) generated by this propeller in a nonuniform flow, and more computational results can be seen in [14]. Figure 10 shows the depiction of the propeller and the flat plate, and the wake data can be obtained from [15]. Figure 11 to Figure 14 show the comparisons between computational results and experimental data of propeller 1242 in a nonuniform inflow at different tunnel pressures. One can find

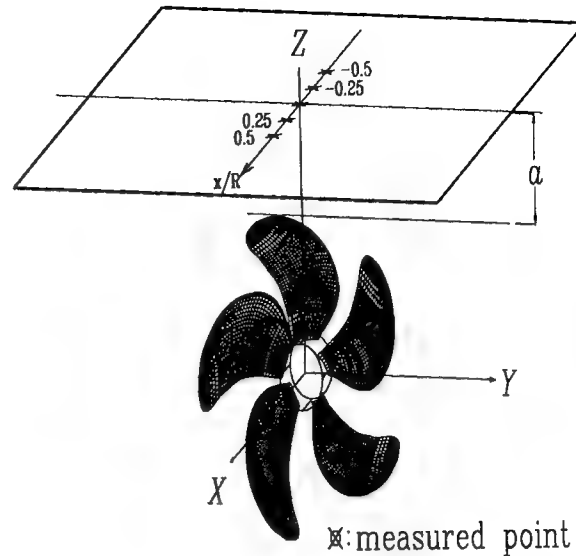


Figure 10: Depiction of the relative positions of the propeller and the flat plate.

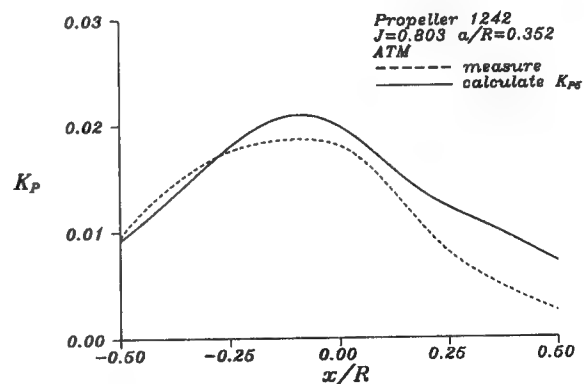


Figure 11: Comparison between the computational K_P and the experimental values for propeller 1242 in a nonuniform inflow. The tunnel pressure is at the atmospheric pressure.

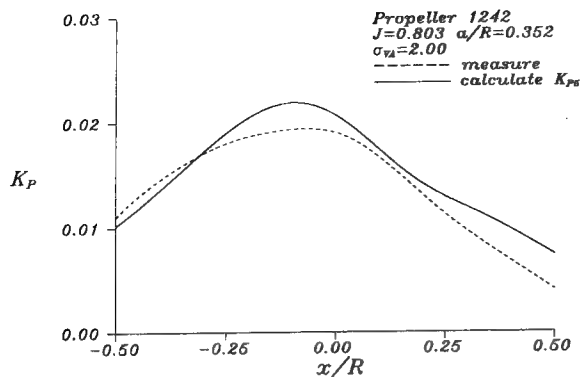


Figure 12: Comparison between the computational K_P and the experimental values for propeller 1242 in a nonuniform inflow. The tunnel pressure is at the cavitation number $\sigma_{VA} = 2.0$.

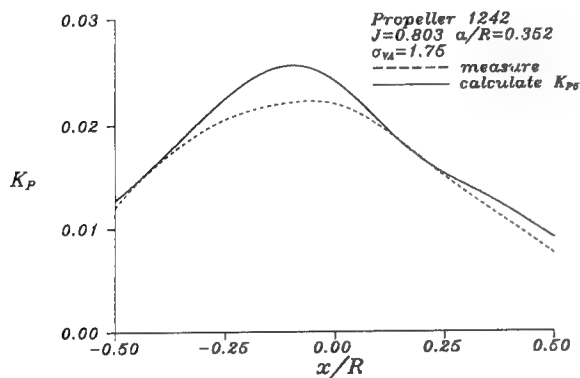


Figure 13: Comparison between the computational K_P and the experimental values for propeller 1242 in a nonuniform inflow. The tunnel pressure is at the cavitation number $\sigma_{VA} = 1.75$.

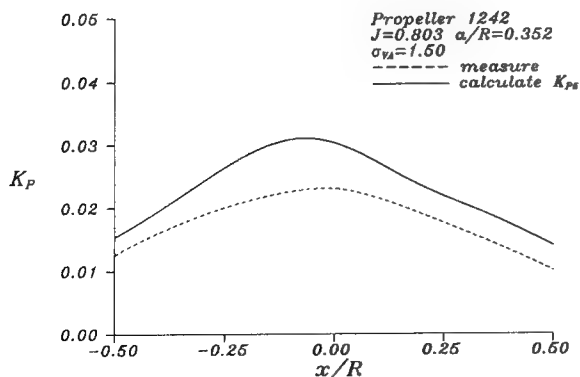


Figure 14: Comparison between the computational K_P and the experimental values for propeller 1242 in a nonuniform inflow. The tunnel pressure is at the cavitation number $\sigma_{VA} = 1.5$.

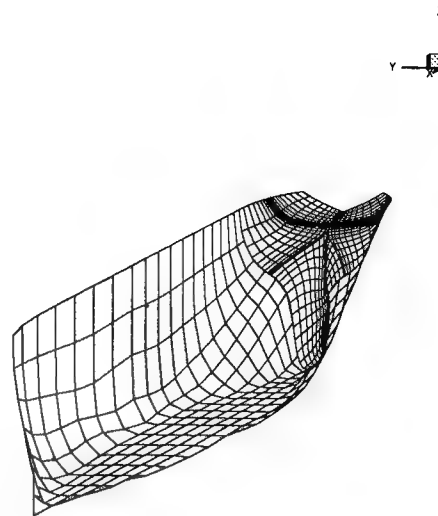


Figure 15: Discretized geometry of the ship hull used for the calculations. 900 panels are distributed on the hull surface.

that the difference between the computational K_P and the experimental value increases as the cavitation number decreases. This may be caused by the linear approximation of the cavity thickness in PUF-3A.

5.2 Pressure Fluctuations on a Ship Hull Generated by Propellers

We then compute the pressure fluctuations on a ship hull generated by a cavitating propeller. The computational case we use here is the same case presented in Breslin, etc. [2]. The dimensions of this RO/RO ship model are listed in [2], and the propeller is designed at a speed of 22 knots and RPM of 126. In Breslin etc.'s paper, only lines of the stern part are provided. Therefore, a fake front part of the hull form is made, and is faired with the stern part. Figure 15 shows the panelized geometry of this ship hull with 900 panels. Figure 16 shows the nominal wake, and Figure 17 shows the calculated effective wake, and the model mean effective wake coefficient we calculate is 0.35. It is larger than the full-scale mean effective wake coefficient, 0.29 [2], and this is reasonable since the model mean effective wake should be greater than the full-scale mean effective wake. The propeller calculations show that the mean value of K_T is 0.179, and it is very close to the experimental K_T , 0.182. The advance ratio, J_A , is 0.580, and it is the same as the one obtained from the experiment. Figures 18

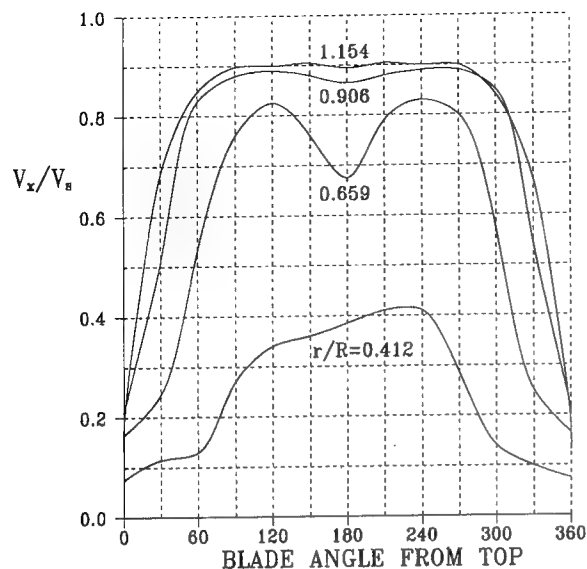


Figure 16: Nominal wake of the model test

and 19 show the computed cavitation extensions and cavitation volumes. The computed cavitation extensions near zero degree and before seem to be larger than those of the model test. However, we are not able to make the comparisons of the cavitation volumes since the measured data are not available. We know that PUF-3A assumes the cavitation occurs when the pressure on the propeller surface is less than the vapor pressure, and this assumption is more similar to the full-scale phenomenon. Also, Blake, Kerwin, etc. [1] point out that the scale effect of the sheet cavitation of a conventional model propeller geometry (as presented in this paper) shows delayed inception due to bubble dynamics. Therefore, the computational results are reasonable since cavitation extensions on a full-scale propeller should be larger than those measured by the model test for conventional propeller geometries.

Figure 20 shows the contour plot of K_P at the blade frequency for zero-frequency free surface (rigid surface), and Figure 21 shows the contour plot of K_P at the blade frequency for high-frequency free surface. It can be seen that the calculated pressure fluctuations at the high frequency free surface condition are lower than those at the rigid surface condition, especially for regions near the free surface. Table 2 then shows the calculated K_P and measured K_P [2]. The computational results at Gage 3 are apparently larger than the measured values for both the blade frequency and twice blade frequency. However, the computational results may be reasonable due to the following rea-

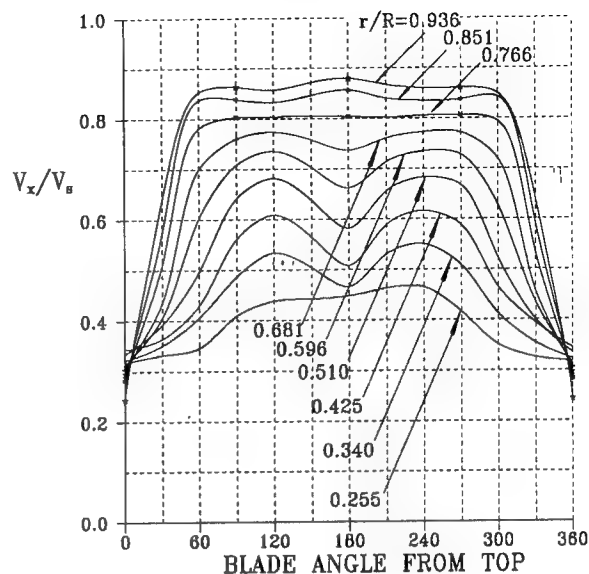


Figure 17: Effective wake calculated by PUF-3A.

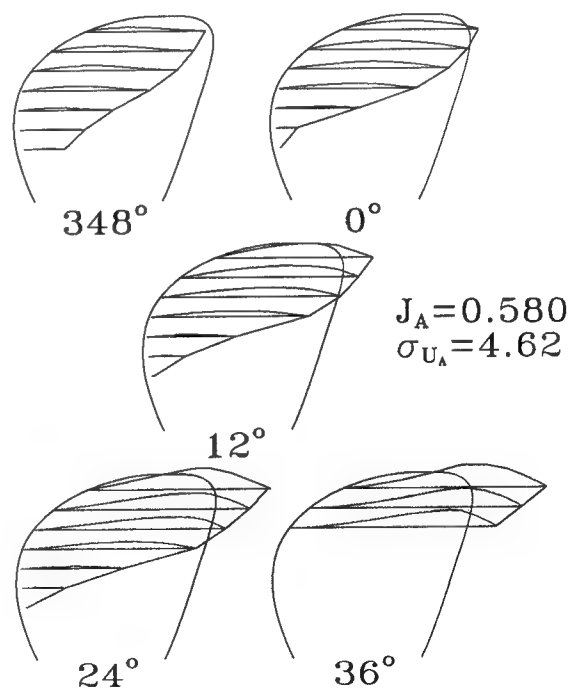


Figure 18: Computed cavitation extensions at 5 different representative angular positions

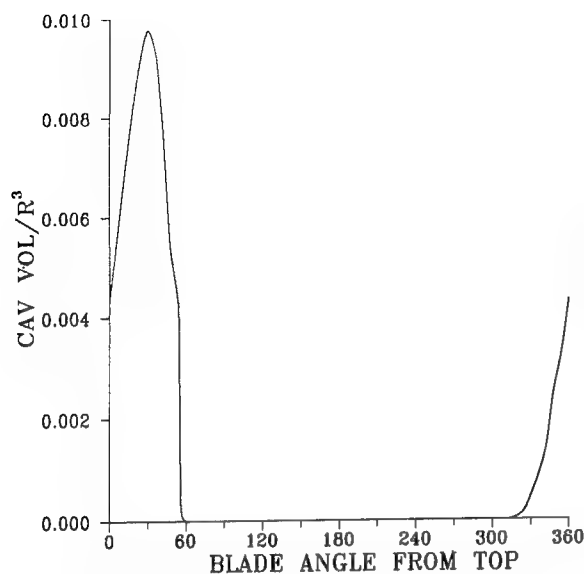


Figure 19: Calculated cavitation volumes.

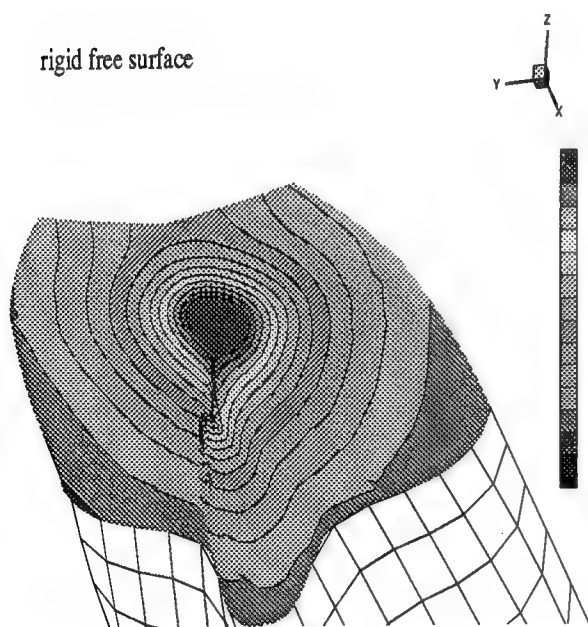


Figure 20: Contour plot of the blade frequency K_P at the zero-frequency free surface (rigid surface) condition. Only the pressure fluctuations near the stern are shown here.

high-freq. free surface

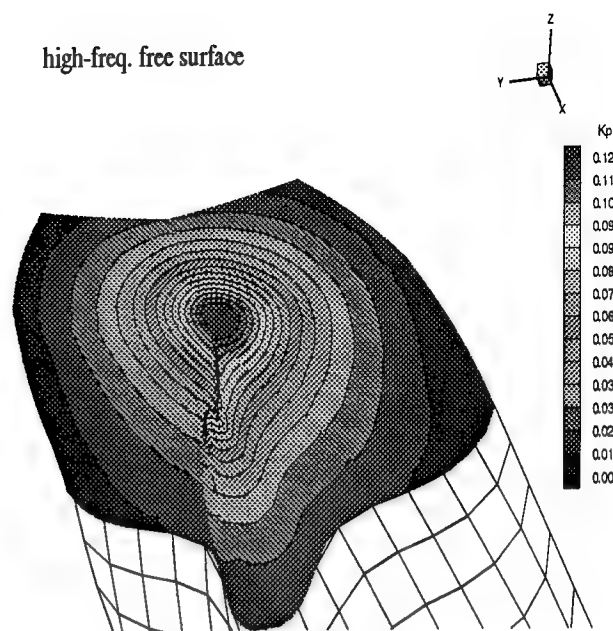


Figure 21: Contour plot of blade frequency K_P at the high-frequency free surface condition. Only the pressure fluctuations near the stern are shown here.

sons: First, the pressure fluctuation at Gage 3 was measured by a hydrophone, and this hydrophone was placed outside the hull surface (Figure 8 of [2]). Therefore, we can expect that the ratio of K_P at the measured point to the point just above it and on the hull surface, where K_P is calculated, should be between 0.5 and 1.0. Form Table 2, we can see that the ratios are 0.650 and 0.585 for high-frequency free surface and rigid surface respectively, and both are within the range of 0.5 and 1.0. Secondly, the calculated results of pressure fluctuations generated by propellers in a model wake should be larger than those in a full-scale wake because the high wake zone of the model wake is wider than that of the full-scale wake. The location of this high wake zone is at the 12 o'clock direction of the propeller, therefore, the influence will be only on Gage 3, not on Gage 4 and Gage 5 whose locations are further away from the high wake zone. Our computational results agree with this statement when referring to Figure 9 in [2] and Figure 17 in [1]. For results at Gage 4 and Gage 5, the comparisons between the calculated values and the measured values are closer. The differences between the rigid surface results and the high-frequency free surface results are larger than those of Gage 3, and it is because that the free surface effect is strong at these two points. The computational results of twice blade

Table 2: Comparison of measured and computational $2K_P$ for the blade frequency and twice blade frequency under two water surface conditions.

$\frac{2F_k}{\rho n^2 D^2}$						
G	Meas.	Calculated Amplitudes		Ratio Meas'd/Calc'd		Ratio Free Rigid
		Free	Rigid	Free	Rigid	
Blade Frequency						
3	0.165	0.254	0.282	0.650	0.585	0.901
4	0.105	0.082	0.117	1.280	0.897	0.701
5	0.069	0.054	0.090	1.278	0.767	0.600
Twice Blade Frequency						
3	0.065	0.128	0.146	0.508	0.445	0.877
4	0.024	0.040	0.054	0.600	0.445	0.741
5	0.016	0.020	0.038	0.800	0.421	0.526

("G" is the gage number)

frequency K_P are all larger than the measured values, and this is because the calculated cavitation extensions are larger than those of model tests.

6 Conclusions

In this paper, the flow field around a ship hull and its propeller is solved by coupling a higher order potential based panel method and a lifting surface vortex lattice method. The advantages of this method are: First, potentials on the ship hull surface can be directly calculated, and the computational time is less than a velocity based panel method since only one scalar term (potential) rather than three components of velocities needed to be computed. Secondly, the propeller induced potentials can be directly added to potentials on the ship hull surface. Thirdly, the $\frac{\partial \Phi}{\partial t}$ term in the Bernoulli's equation can be easily calculated by differentiating the solved potentials in time. Finally, this higher order panel method has been proved to be more accurate than a low order panel method at the same given computational time.

The unsteady flow around a propeller is analyzed by MIT-PUF-3A. By investigating the computational results, it is found that the cavitation extensions calculated by PUF-3A are overestimated for conventional model propeller geometries when comparing to the model test results. This may be due to the cavity model in PUF-3A is corresponding to the full-scale.

The computational results have been compared with the experimental data. For pressure

fluctuations on a flat plate generated by propellers in a nonuniform inflow, the computational results agree well with the experimental data for cavitation numbers higher than 1.5. For cavitation numbers lower than 1.5, the pressure fluctuations have been overestimated. For pressure fluctuations on a ship hull, the differences between the computed and measured values are relatively large at the point above the propeller. However, the differences can be explained, and the reasons are described in the paper. The comparisons between computed and measured values at other points are good.

For future works, the pressure fluctuations at the actual measured point of Gage 3 (outside the shil hull) should be calculated to confirm our inferences. The effective wake should be calculated by a more accurate method such as solving the Navier-Stokes equations. Finally, the computed hydrodynamic results should be incorporated with structure and vibration calculations.

Acknowledgment

This work was supported by the National Science Council, Taipei, and the project number is NSC-85-2611-E-019-018. Additional support was provided by China Ship Building Corporation, Keelung, under project CSBC-RD-0372. The authors would like to thank Mr. Y.-H Lee at NTOU, Mr. J.-T. Chen and Mr.S.-K. Chou at USDDC for their assistances in generating hull panels.

References

- [1] William K. Blake, Justin E. Kerwin, K. Meyne, E. Weiendorf, and J. Frisch. Design of apl c-10 propeller with full-scale measurements and observations under service conditions. In *Transactions, SNAME*, 1990.
- [2] J.P. Breslin, R.J. Van Houten, J.E. Kerwin, and C-A Johnsson. Theoretical and experimental propeller-induced hull pressures arising from intermittent blade cavitation, loading, and thickness. *Trans. SNAME*, 90, 1982.
- [3] H.-F. Chen. *The application of higher order doublet panel method on computation of ship potential flow field (in Chinese)*. Master's thesis, Department of Mechanical and Marine Engineering, National Taiwan Ocean University, June 1995.

- [4] J. L. Hess and A. M. O. Smith. Calculation of nonlifting potential flow about arbitrary three dimensional bodies. *Journal of Ship Research*, vol 8(no 2), September 1964.
- [5] T.T. Huang and Groves N.C. Effective wake : theory and experiment. In *13th Symposium on Naval Hydrodynamics*, Tokyo, October 1980.
- [6] B. Hunt. The mathematical basis and numerical principles of the boundary integral method for incompressible potential flow over 3-d aerodynamic configurations. In *Numerical Methods in Applied Fluid Dynamics*, pages pp 49-135, Academic Press, 1980.
- [7] F.T. Johnson. *A General Panel Method for the Analysis and Design of Arbitrary Configurations in Incompressible Flows*. Technical Report CR-3079, NASA, 1980.
- [8] F.T. Johnson, F.E. Ehlers, and P.E. Rubbert. A higher order panel method for general analysis and design applications in subsonic flow. In *Proceedings of fifth International Conference on Numerical Methods in Fluid Dynamics*, Springer Verlag, 1976.
- [9] J. E. Kerwin and D. S. Greeley. *Numerical Method for the Calculation of Field Point Potential Due to a Cavitating Propeller: MIT-PUF3FPP Program Documentation and Listings*. Technical Report 83-11, MIT, Department of Ocean Engineering, June 1983.
- [10] J.E. Kerwin, S.A. Kinnas, J-T Lee, and W-Z Shih. A surface panel method for the hydrodynamic analysis of ducted propellers. *Trans. SNAME*, 95, 1987.
- [11] J.E. Kerwin and C-S Lee. Prediction of steady and unsteady marine propeller performance by numerical lifting-surface theory. *Trans. SNAME*, vol 86, 1978.
- [12] S.A. Kinnas. *A Numerical Method for the Analysis of Cavitating Propellers in a Nonuniform Flow, MIT-PUF-3 Program Documentation*. Technical Report 83-7, MIT, Department of Ocean Engineering, June 1983.
- [13] Sir Horace Lamb. *Hydrodynamics*. Cambridge University Press, sixth edition, 1932.
- [14] Y.-C. Sun. *Calculations of the exciting forces at a flat plate induced by an intermittently cavitating propeller (in Chinese)*. Master's thesis, Department of Naval Architecture, National Taiwan Ocean University, June 1995.
- [15] E.A. Weitendorf. Experimentelle untersuchungen der durch kavitierende propeller erzeugten druckschwankungen. *SCHIFF UND HAFEN*, Jahrgang 25. Heft 11, November 1973.
- [16] H. B. Wilson and R. J. Van Houten. *A Program for Interpolation, Smoothing, Fourier Analysis, and Effective Wake Estimation of Propeller Inflow Fields: MIT-WKPROC Program Documentation and Listings*. Technical Report 83-8, MIT, Department of Ocean Engineering, June 1983.

Appendix

Solutions of the Quadratic Dipole Strength Coefficients

As described in equation (11), the quadratic dipole strength distribution on the body surface, $\lambda(\xi, \eta, \zeta)$, can be expressed in terms of the local coordinate system, (ξ, η) , on the projection plane Σ (Figure 2):

$$\begin{aligned}\lambda(\xi, \eta, \zeta) &= \mu(\xi, \eta) \\ &= \mu_0 + \mu_\xi \xi + \mu_\eta \eta + \frac{1}{2} \mu_{\xi\xi} \xi^2 + \mu_{\xi\eta} \xi \eta \\ &\quad + \frac{1}{2} \mu_{\eta\eta} \eta^2\end{aligned}\quad (22)$$

The coefficients $\mu_0, \mu_\xi, \mu_\eta, \mu_{\xi\xi}, \mu_{\xi\eta}, \mu_{\eta\eta}$ are determined from dipole strength at control points of neighboring nine panels (8 neighboring panels and the self panel) through a fitting process. If we now define λ_k as the dipole strength on the control point of the k^{th} neighboring panel, then we can expressed the dipole strength of these 9 panels as follows:

$$\begin{aligned}\lambda_k(\xi_k, \eta_k, \zeta_k) &= \left[1, \xi_k, \eta_k, \frac{1}{2} \xi_k^2, \xi_k \eta_k, \frac{1}{2} \eta_k^2 \right] \begin{Bmatrix} \mu_0 \\ \mu_\xi \\ \mu_\eta \\ \mu_{\xi\xi} \\ \mu_{\xi\eta} \\ \mu_{\eta\eta} \end{Bmatrix} \\ &= \bar{V}_k^T \bar{\mu}_k\end{aligned}\quad (23)$$

where $k = 1, 2, \dots, 9$. By the least squares, we have the array $[\bar{\mu}]$:

$$[\bar{\mu}] = \left[\sum_{k=1}^{N_D} w_k \bar{V}_k \bar{V}_k^T \right]^{-1} \sum_{k=1}^{N_D} w_k \lambda_k \bar{V}_k^T \quad (24)$$

Equation (24) shows that the dipole strength at each panel is determined by neighboring N_D panels ($N_D = 9$ here). By substituting the above equations into the governing equation (equation (9)), we can obtain the induced potentials at a point P by the panel that Q is located. Assuming the point Q is at panel j , and the field point P is at panel i , then the induced potential at P by panel j , φ_{ij} , can be expressed as follows:

$$\begin{aligned} \varphi_{ij} = & \mu(x, y)I(1, 1) + \mu_x(x, y)I(2, 1) \\ & + \mu_y(x, y)I(1, 2) + \frac{1}{2}\mu_{xx}(x, y)I(3, 1) \\ & + \mu_{xy}(x, y)I(2, 2) + \frac{1}{2}\mu_{yy}(x, y)I(1, 3) \end{aligned} \quad (25)$$

where,

$$\begin{cases} \mu(x, y) = \mu_0 + \mu_\xi x + \mu_\eta y \\ \quad \quad \quad + \frac{1}{2}\mu_{\xi\xi}x^2 + \mu_{\xi\eta}xy + \frac{1}{2}\mu_{\eta\eta}y^2 \\ \mu_x(x, y) = \mu_\xi + \mu_{\xi\xi}x + \mu_{\xi\eta}y \\ \mu_y(x, y) = \mu_\eta + \mu_{\xi\eta}x + \mu_{\eta\eta}y \\ \mu_{xx}(x, y) = \mu_{\xi\xi} \\ \mu_{xy}(x, y) = \mu_{\xi\eta} \\ \mu_{yy}(x, y) = \mu_{\eta\eta} \end{cases} \quad (26)$$

and

$$\begin{aligned} I(M, N) = & \frac{1}{4\pi} \{ hH(M, N, 3) + a[H(M+2, N, 3) \\ & + 3h^2H(M+2, N, 5) + 6xh^2H(M+1, N, 5)] \\ & + b[H(M, N+2, 3) + 3h^2H(M, N+2, 5) \\ & + 6yh^2H(M, N+1, 5)] + c[-H(M, N, 3) \\ & + 3h^2H(M, N, 5)] \} \end{aligned}$$

$$H(M, N, K) = \iint_{\Sigma} \frac{(\xi - x)^{M-1}(\eta - y)^{N-1}}{(\sqrt{(\xi - x)^2 + (\eta - y)^2 + h^2})^K} d\xi d\eta$$

where $c = ax^2 + by^2 - z_0$, and a and b are defined in equation (10). The I and H integrals are defined in Johnson [7].

The internal Dirichlet boundary condition specifies the total internal potential to be zero, and

the induced potential at a point i on the inner surface by panel j , φ_{ij}^- , can be obtained from equations (25), (26),

$$\varphi_{i,j}^- = [I] \begin{Bmatrix} \mu_0 \\ \mu_\xi \\ \mu_\eta \\ \mu_{\xi\xi} \\ \mu_{\xi\eta} \\ \mu_{\eta\eta} \end{Bmatrix} \quad (27)$$

where

$$[I] = \begin{bmatrix} I(1, 1) \\ xI(1, 1) + I(2, 1) \\ yI(1, 1) + I(1, 2) \\ \frac{1}{2}x^2I(1, 1) + xI(2, 1) + \frac{1}{2}I(3, 1) \\ xyI(1, 1) + yI(2, 1) + xI(1, 2) + I(2, 2) \\ \frac{1}{2}y^2I(1, 1) + yI(1, 2) + \frac{1}{2}I(1, 3) \end{bmatrix}^T \quad (28)$$

Notice that the dipole coefficient array can be related to the dipole strength from equation (23):

$$\begin{Bmatrix} \mu_0 \\ \mu_\xi \\ \mu_\eta \\ \mu_{\xi\xi} \\ \mu_{\xi\eta} \\ \mu_{\eta\eta} \end{Bmatrix}_j = [\bar{B}]_j \{ \lambda_k \}_j \quad (29)$$

where $\{ \lambda_k \}_j$ stands for the dipole strength array of N_D neighboring panels to panel j , and

$$\begin{aligned} \bar{B} &= \bar{B}_1^{-1} \bar{B}_2 \\ \bar{B}_1 &= \sum_{k=1}^{N_D} w_k \bar{V}_k \bar{V}_k^T \\ \bar{B}_2 &= \sum_{k=1}^{N_D} w_k \bar{V}_k^T \end{aligned}$$

The discretized governing equation with the boundary condition thus becomes

$$\sum_{j=1}^{N_P} \varphi_{ij} = -(\phi_\infty)_i, \quad i = 1, 2, \dots, N_P \quad (30)$$

where N_P is total number of panels. ϕ_∞ can be obtained by the product of the inflow velocity and the position vector of the panel control point.

$$(\phi_\infty)_i = \vec{V}_\infty \cdot \vec{R}_i \quad (31)$$

Substituting equations (27) and (29) into equation (30), then we have

$$\sum_{j=1}^{N_P} [I]_j [\bar{B}]_j \{\lambda_k\}_j = -(\phi_\infty)_i, i = 1, 2, \dots, N_P \quad (32)$$

After transferring the local panel indices to the global panel indices of λ and rearranging coefficients, we can get the following matrix form:

$$[A_{ij}] \begin{Bmatrix} \lambda_1 \\ \vdots \\ \lambda_{N_P} \end{Bmatrix} = - \begin{Bmatrix} (\phi_\infty)_1 \\ \vdots \\ (\phi_\infty)_{N_P} \end{Bmatrix} \quad (33)$$

Solutions of this matrix will be the dipole strength at the control point of each panel. Therefore, the dipole strength coefficients can be obtained from equation (29), and the dipole strength distribution at each panel can be calculated by equation (23).

DISCUSSION

C.-A. Johnsson
SSPA Maritime Consulting AB, Sweden

I could make several comments to this interesting paper, but I have to limit myself to a short discussion of different boundary conditions.

The authors claim that the hydrophone does not have the same "mirror" effect as the flushmounted transducers. Comparative tests made at SSPA on a flat plate indicated, however, no significant differences between the transducers in this respect and therefore we used a hydrophone in one of the positions in order to increase the frequency range.

In connection with the investigation reports in the authors' Ref. [2], it was argued that the plywood roof with water above and below is more or less nonreflecting and thus does not correspond to the rigid surface case. This discussion is summarized in [D2] in which Prof. Breslin concludes that the appropriate conditions are the mean value between the free surface and rigid cases. In this particular case, the difference between the two cases is however much smaller than the differences between the calculations in the authors' paper and those from their Ref. [2], which is evident from Fig. D1. The latter are most likely due to differences in the peripheral volume variations obtained by the two calculations, which are not that large. Thus, Fig. D1 gives an indication of the degree of accuracy that can be expected from calculations of this kind.

The influence of the height and shape of the stern wave is not considered in the calculations.

An indication about this influence is obtained by Fig. D2 which is based on measurements on the class of ships considered in the paper. It is evident from this figure that the Froude number is even more important than the draught. Having these results in mind, we at SSPA decided to concentrate on empirical methods for estimating the influence of the free surface rather than on theoretical methods. The first results of these efforts were published in [D2].

REFERENCES

- D1. Breslin, J.P. and Andersen, P. "Hydrodynamics of Ship Propellers," Cambridge Ocean Technology Series 3, Cambridge 1994.
- D2. Johnsson, C.-A. "Simple Methods for First Estimate of Propeller Induced Pressure Fluctuations and Vibration," *PRADS 83*, Tokyo and Seoul 1983.

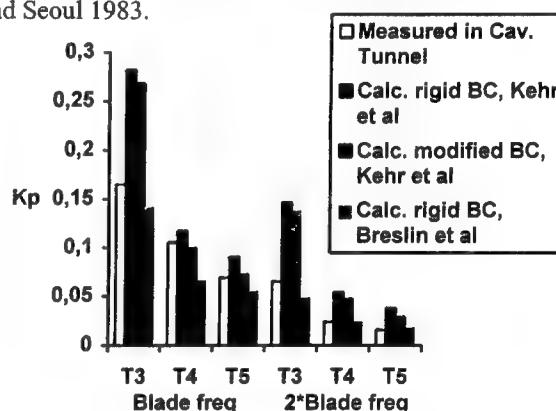


Figure D1: SSPA RO-RO ship model. Calculated and measured pressure fluctuations at three transducer positions in the stern

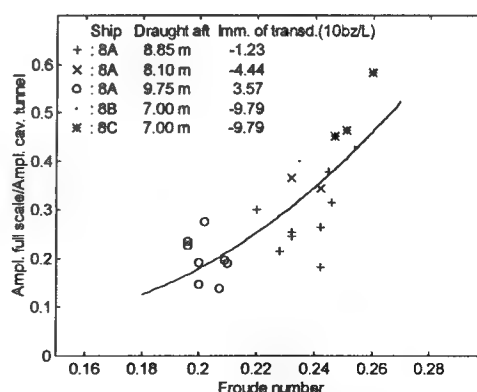


Figure D2: Comparison of pressure fluctuations in model and full scale. Blade frequency

AUTHORS' REPLY

The authors would first like to thank Mr. Johnsson for his valuable comments. Mr. Johnsson did point out some key points in this paper. Mr. Johnsson may be right about the effect of the hydrophone position. The authors will continue to investigate if the hydrophone extruded outside the ship having any influence on the pressure fluctuations.

Regarding the difference between the computations results presented in the paper and carried out by Breslin and Andersen [D1], the authors have carefully investigated the results and conclude that this difference can be explained.

First, we know that the ship effective mean wake is 0.29, and the model nominal mean wake is 0.436. The model effective mean wake calculated is 0.35 by the present paper, and 0.254 by [2]. Therefore, the result calculated by the present paper is more reasonable since the model effective mean wake should be higher than the ship effective mean wake. When authors use the effective wake distribution calculated by [2], the magnitudes of pressure fluctuations calculated decrease as expected. However, they are still higher than those calculated by [2] (as in Figure 1). This is apparently because the ship hull is modeled differently by two methods. Anyhow, we have to point out that the computations of the effective wake distributions in the present paper are rough due to the simplicity of the model.

Because the pressure fluctuations measured in SSPA cavitation tunnel were clearly smaller than those of the full scale, SSPA took the average of the max 5% as the measured values to have a better correlation with the full scale. This however may

suggest that the experimental data are too low. On the other hand, as described in the paper, the computational results are supposed to be larger since it is according to the model effective wake distribution instead of the full scale effective wake distribution. This is also supported by the investigation of Blake et al. [1], in which they found that the surface forces calculated or measured by the model wake distribution were larger than those at the full-scale condition. The experimental results in HYKAT by Friesch, et. Al., [R1] (Fig. 15) also showed the same tendency.

The figure Mr. Johnsson presented about the influence of the height and shape of the stern wave is very interesting. The authors will include a free-surface calculation to consider these effects in the future.

REFERENCE

[R1] J. Friesch, C. Johannsen, and H.G. Payer. Correlation studies on propeller cavitation making use of a large cavitation tunnel. *Trans. SNAME*, 100:pp. 65-92, 1992.

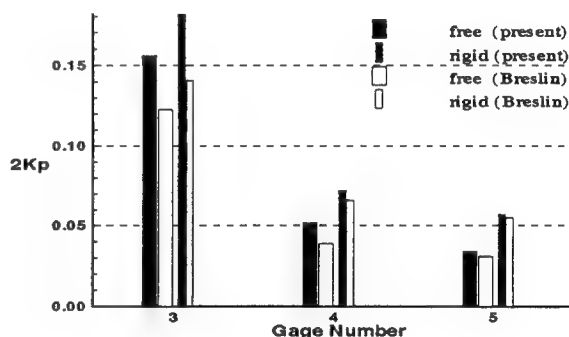


Figure 1: Calculated pressure fluctuations by the present method and by Breslin et al. at the blade frequency. Both methods use the same effective wake distribution.

Hydroacoustic Considerations in Marine Propulsor Design

M. Sevik (David Taylor Model Basin, USA)

ABSTRACT

Hydroacoustics is based on firm theoretical foundations which overlap with those of aeroacoustics. Hydroacoustics is characterized by low Mach numbers, a high impedance relative to air, and important fluid loading effects on submerged structures. Fluid flow fields affecting marine propulsors are unsteady and give rise to time-dependent pressures which excite internal and adjacent external structures into vibrations. In the absence of cavitation, dipole sources on stationary and rotating blade rows of ship propulsors are the dominant contributors to the acoustic far field. When located in an elastic enclosure, the near-field of dipoles close to the blade tips excite the structure which adds additional energy to the sound field. The combined levels and directivity patterns are different from those of an open propeller in free-field. At this time, the complex flow fields and the response of structures cannot be reliably predicted by numerical techniques. Large, quiet, high speed water tunnels have been equipped with acoustic arrays in order to provide a preliminary assessment of the performance of alternative propulsor designs.

HISTORICAL REMINDERS

The study of flow-induced noise was stimulated in the early fifties when airliners powered by jet engines entered the commercial market. A fundamental paper which explained the physics of sound generation by turbulence was published by Lighthill⁽¹⁾ in 1952. In the same time-frame, pioneering work by Powell⁽²⁾, Ffowcs Williams⁽³⁾ and Curle⁽⁴⁾ provided insights which paved the way for future progress.

At a symposium dedicated to hydrodynamics, it is appropriate to recall that the wave equation is derived from the familiar equations of momentum and continuity. Since sound is a very weak disturbance to a fluid at rest, viscosity can be ignored and motions can be restricted to vanishingly small values. The fluctuations of density ρ and pressure p vary little about their mean values. Away from the turbulence, both satisfy the homogeneous wave equation

$$\partial^2 \rho / \partial t^2 - c^2 \nabla^2 \rho = 0 \quad (1)$$

If fluid or momentum is created in a region, a function $Q(\mathbf{x}, t)$ representing the acoustic source density is added to the right hand side. If an external force F_i acts on the fluid, $Q(\mathbf{x}, t)$ has the form of a divergence $\partial F_i / \partial x_i$. For turbulence, $Q(\mathbf{x}, t)$ is a double divergence and the inhomogeneous wave equation has the form

$$\partial^2 \rho / \partial t^2 - c^2 \nabla^2 \rho = \partial^2 T_{ij} / \partial x_i \partial x_j \quad (2)$$

Solutions of these basic equations which satisfy various boundary conditions have provided the major tools of noise control.

SOUND RADIATION FROM WATERBORNE VEHICLES

The sound radiated by waterborne vehicles which are propelled at moderate to high speeds involves complex interactions between fluid dynamics and structural acoustics. Cavitation is avoided by the designers whenever radiated noise requirements are imposed and will not be considered in this paper. The remaining problem of radiated noise control involves flow fields that are spatially and temporally random. All structures within such flows are compliant and respond dynamically to time-dependent pressures. The sound field is therefore caused by vibrations and by fluctuating pressures on various surfaces. Mathematically, the acoustic density fluctuations at \mathbf{x} in the fluid due to a normal velocity v and a pressure p at a point \mathbf{y} on the surface S have been expressed by Ffowcs Williams⁽⁵⁾ in the form:

$$\rho = (1/4\pi c^2 x) \frac{\partial}{\partial t} \int_S n_i \{ \rho_0 v_i + (x_i/x)(p/c) \} (y, t - |\mathbf{x} - \mathbf{y}| c^{-1}) dy \quad (3)$$

In most marine applications, the flow velocity is much smaller than the speed of sound. Typical Mach numbers are on the order of 10^{-2} . Under these conditions length scales of flow or boundary fluctuations are usually compact on an acoustic wavelength scale and retarded time changes are negligible. Dimensional analysis yields simple expressions for the density fluctuations. For example, the first term under the integral sign is due to small amplitude motions of the surface S . If this motion is induced by a flow of velocity U and length scales L , the frequencies will be of the order U/L and

$$\rho^2 \sim \rho_0^2 U^4 L^2 \{ c^4 x^2 \}^{-1} \quad (4)$$

The second term under the integral sign is due to pressure fluctuations which may be caused by flow or structural vibrations. Dimensional analysis yields:

$$\rho^2 \sim \rho_0^2 U^6 L^2 \{c^6 x^2\}^{-1} \quad (5)$$

This dependence on the sixth power of the flow is characteristic of dipoles on a compact scale. However, even at the low Mach numbers prevailing in underwater acoustics, sources are not always compact and consequently a different speed dependence will apply.

Generally, the flow is not affected by structural vibrations since the amplitudes are much smaller than the characteristic length scales of the fluid. An exception is the well-known phenomenon of propeller "singing" where blade vibrations tend to increase the coherence of a periodically shed vortex wake which, in turn, feeds more energy into the structure.

At moderate to high speeds, the propulsor is the most important contributor to a vehicle's radiated noise. The major sources are due to the following effects:

a) The response of rotating blade rows to flow disturbances caused by upstream hydrofoils, such as stator vanes, control surfaces and other fixed appendages. The radiation consists of tonals at blade passage frequencies whose amplitudes are randomly modulated, as shown in Fig. (1).

b) The response of stationary or rotating blade rows to ingested turbulence which may be generated

on the hull of the vehicle.

c) The response of rotating blade rows to self-generated flow distortions, as shown in Fig. (2) and of stators located downstream.

d) The scattering of boundary layer turbulence from trailing edges.

e) Radiation from structures which are coupled to the propulsor through hydrodynamic, acoustic and structural paths.

An authoritative treatise covering these topics is provided by Blake⁽⁶⁾ in "Mechanics of Flow-Induced Sound and Vibration".

SOME CASE HISTORIES

In the mid-sixties, the fluctuating thrust of open propellers subjected to a turbulent inflow was of interest. A study of this problem was reported by Sevik⁽⁷⁾ at the Seventh Symposium on Naval Hydrodynamics. Experiments were performed in the Water Tunnel at the Applied Research Laboratory of the Pennsylvania State University. Its test section has a diameter of 1.22 m and a length of 4.27 m. The advantage of this facility is that relatively large propellers can be tested at high Reynolds numbers. Fig. (3) shows the installation of a ten bladed propeller in the test section. It had a diameter of 20.3 cm and its chord length was 2.54 cm. The fluctuating thrust was measured with a high impedance dynamometer which had a linear response over the frequency range of interest.

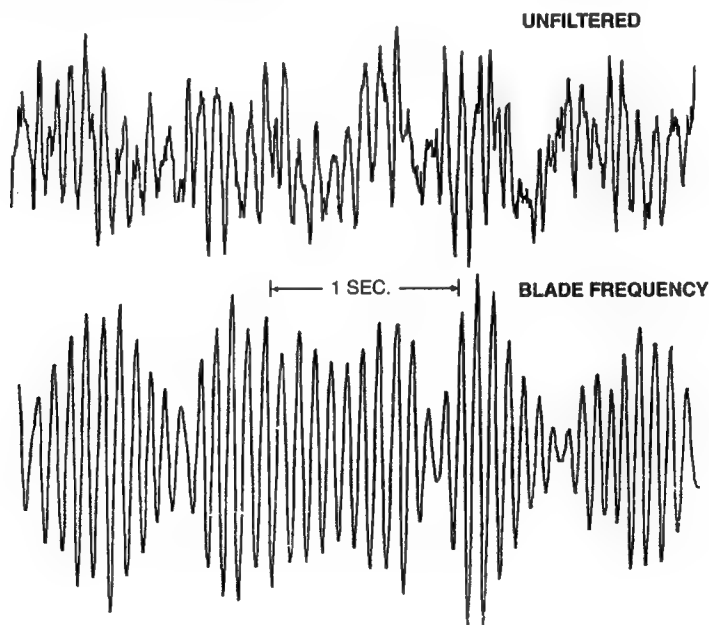


FIG. 1 ACOUSTIC LEVELS AT BLADE RATE FREQUENCY (FROM STRASBERG)

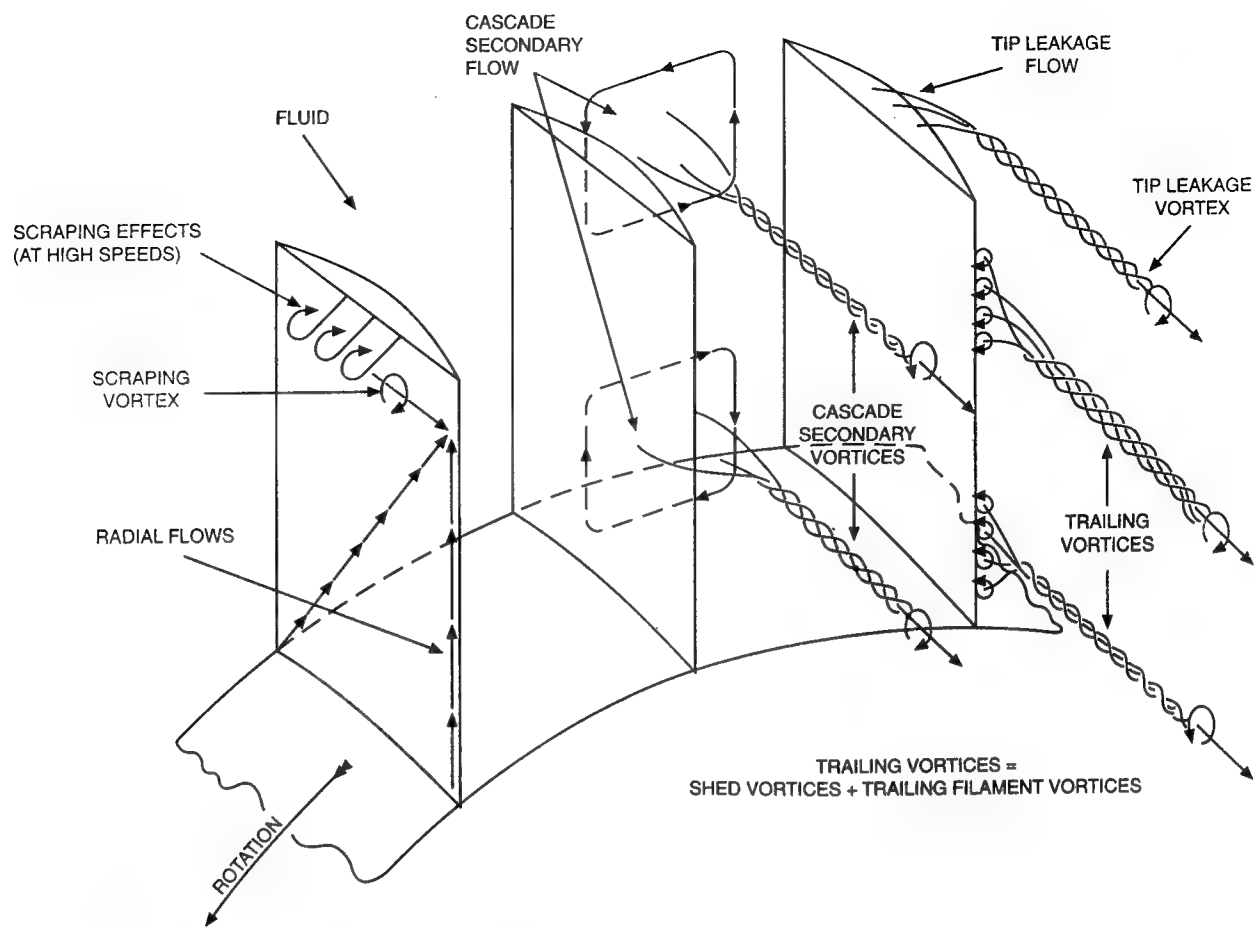


FIG. 2 FLOW FIELD IN A ROTATING BLADE ROW (FROM LAKSHMINARAYANA AND HORLOCK)

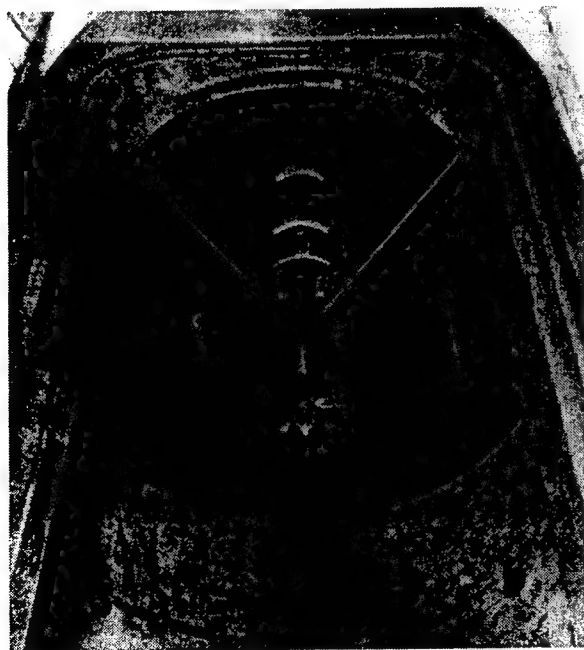


FIG. 3 FREE-STREAM PROPELLER AND BALANCE HOUSING MOUNTED IN THE WATER TUNNEL TEST SECTION

In order to simplify the interpretation of the data, an attempt was made to generate the simplest form of turbulence possible. For this purpose, two grids were installed sequentially upstream of the propeller, as shown in Fig. (4). The mesh sizes were 10.2 and 15.2 cms, respectively. The results of the experiment are shown in Figs. (5) and (6). The principal features of the data are as follows:

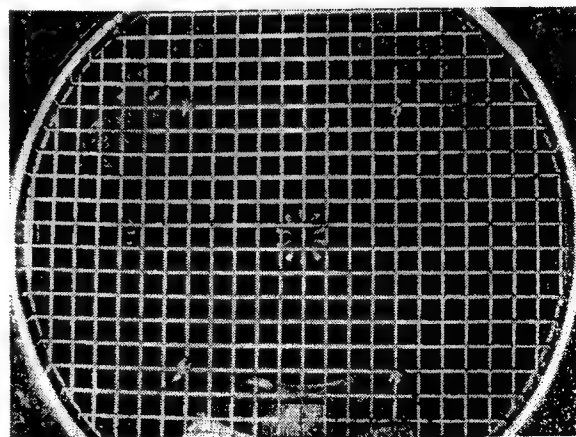


FIG. 4 PROPELLER AS SEEN THROUGH A 4-INCH GRID UPSTREAM OF THE PROPELLER

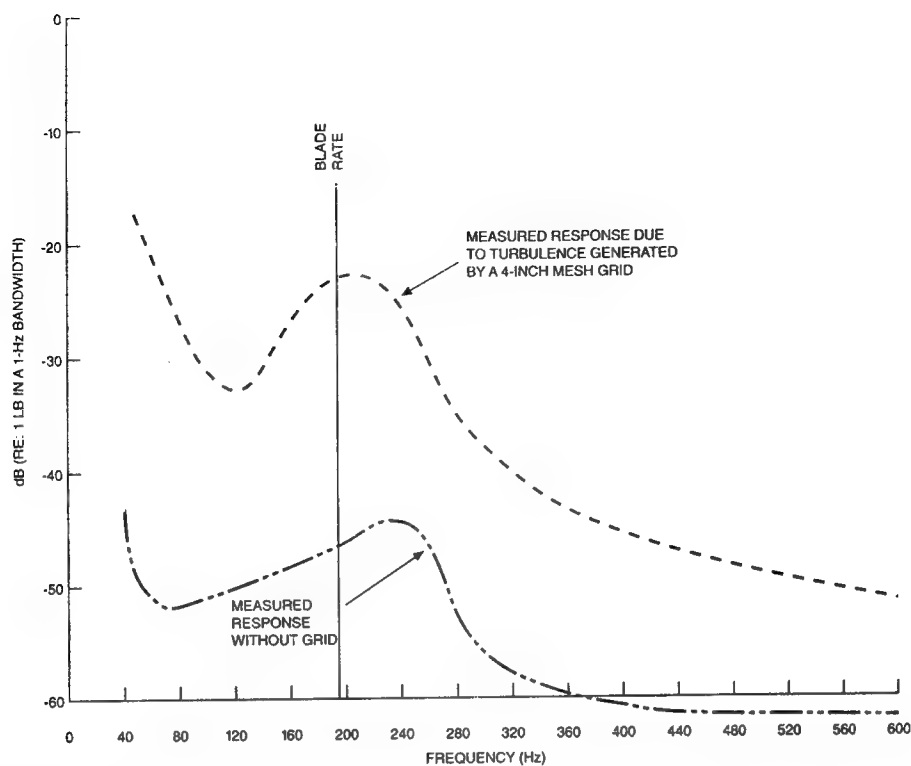


FIG. 5 POWER SPECTRAL DENSITY OF THE RESPONSE OF A TEN-BLADED, 8-INCH-DIAMETER PROPELLER TO TURBULENCE DISTANCE BETWEEN THE GRID AND THE PROPELLER = 20 M = 80 INCHES; MEASURED WATER-TUNNEL TURBULENCE LEVEL WITHOUT THE GRID $U = 0.0011U$; TURBULENCE LEVEL AT THE PROPELLER DUE TO THE GRID $U = 0.03U$; TUNNEL VELOCITY $U = 15.4$ FT/SEC; PROPELLER ADVANCE RATIO $J = 1.22$)

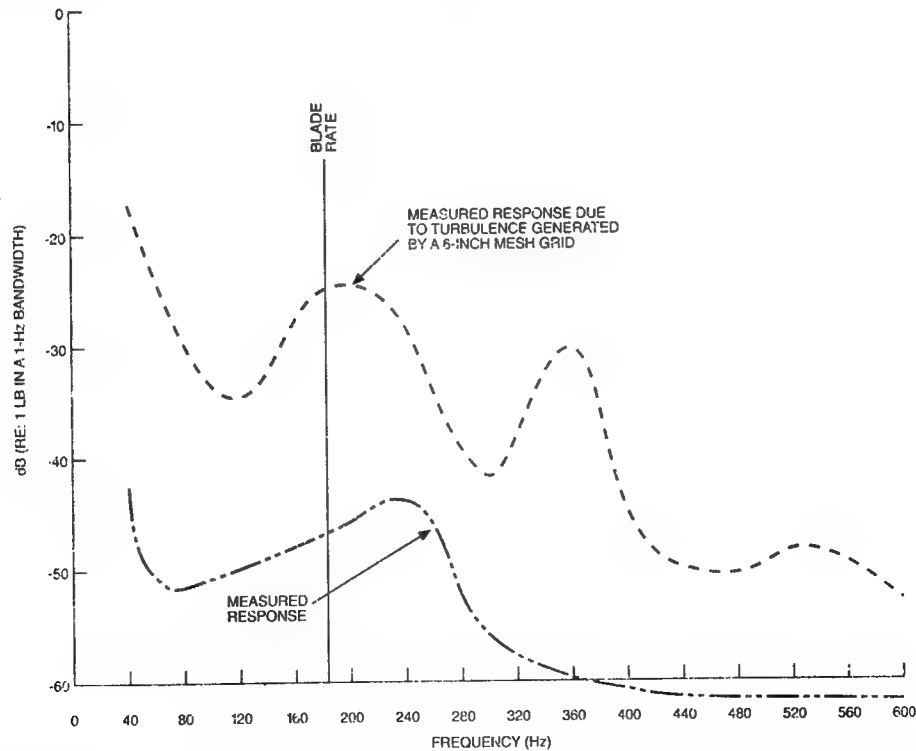


FIG. 6 POWER SPECTRAL DENSITY OF THE RESPONSE OF A TEN-BLADED, 8-INCH-DIAMETER PROPELLER TO TURBULENCE DISTANCE BETWEEN THE GRID AND THE PROPELLER = 20 M = 120 INCHES; MEASURED WATER-TUNNEL TURBULENCE LEVEL WITHOUT THE GRID $U = 0.0011U$; TURBULENCE LEVEL AT THE PROPELLER DUE TO THE GRID $U = 0.03U$; TUNNEL VELOCITY $U = 15.1$ FT/SEC; PROPELLER ADVANCE RATIO $J = 1.22$)

a) "humps" of energy are superimposed on a broadband spectrum;

b) the humps peak at a frequency slightly higher than the blade rate frequency.

An understanding of these observations has been provided in recent papers by Jiang et al⁽⁸⁾, by Martinez⁽⁹⁾ as well as, earlier, by Blake. Basically, the propeller acts as a spatial filter: at any instant of time, it responds preferentially to all circumferential wavelengths of the turbulence that are integral numbers of the blade spacing. Most analytic formulations are therefore based on a wavenumber decomposition of the turbulence. Using this approach, Martinez successfully explained the major features of the experimental results. Jiang et al chose a "correlation" approach and used the classical equations for the longitudinal and lateral velocity correlations for homogeneous and isotropic

turbulence. The longitudinal correlation function is expressed as an exponential

$$f(r) = e^{-r(\tau)/\Lambda} \quad (6)$$

where Λ is the integral scale of the turbulence.

$r(\tau)$ accounts for the free stream velocity V , for the rotational speed of the propeller Ω and for the distance between points α and β located on the propeller. It is of the form:

$$r(\tau)^2 = (V\tau)^2 + r_\alpha^2 + r_\beta^2 + 2r_\alpha r_\beta \cos(\theta_\alpha - \theta_\beta + \Omega\tau) \quad (7)$$

The results of this analysis are plotted in Figs. (7) and (8). As before, the theory predicts the major features of the measured data. The theories of Jiang and Martinez are general and apply to all correlation lengths and frequencies. The directivity of the sound field corresponds to that of a compact dipole.

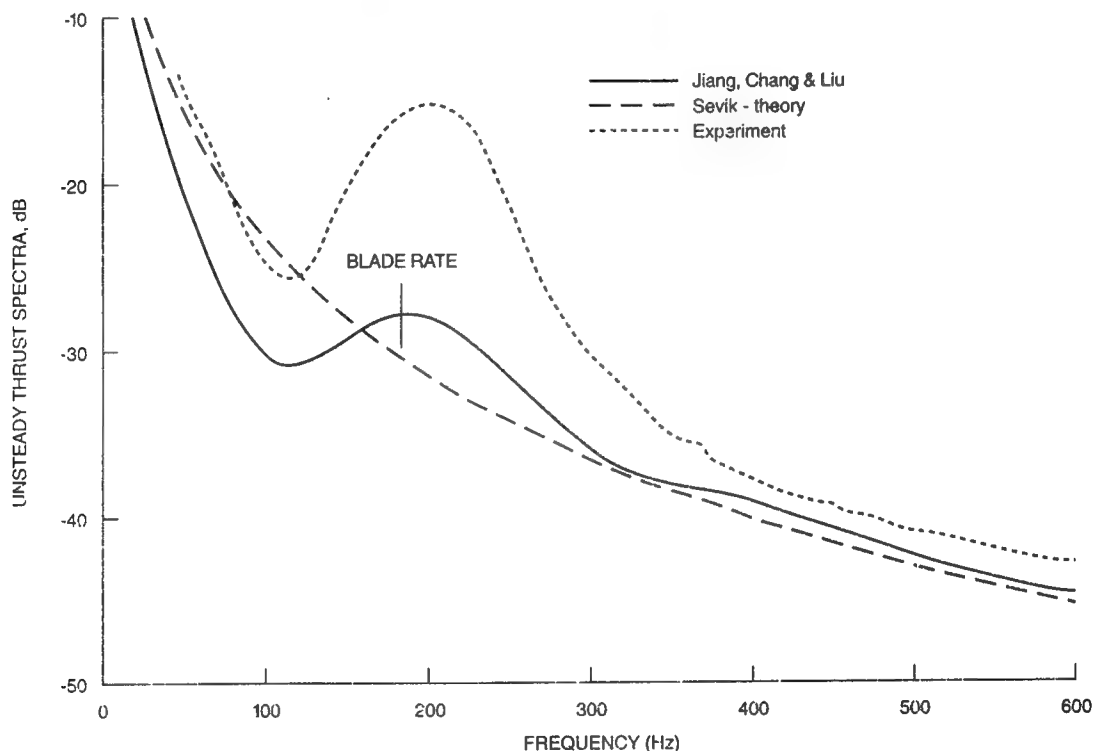


FIG. 7 COMPARISON OF THEORY AND EXPERIMENT (FROM REF. 8)

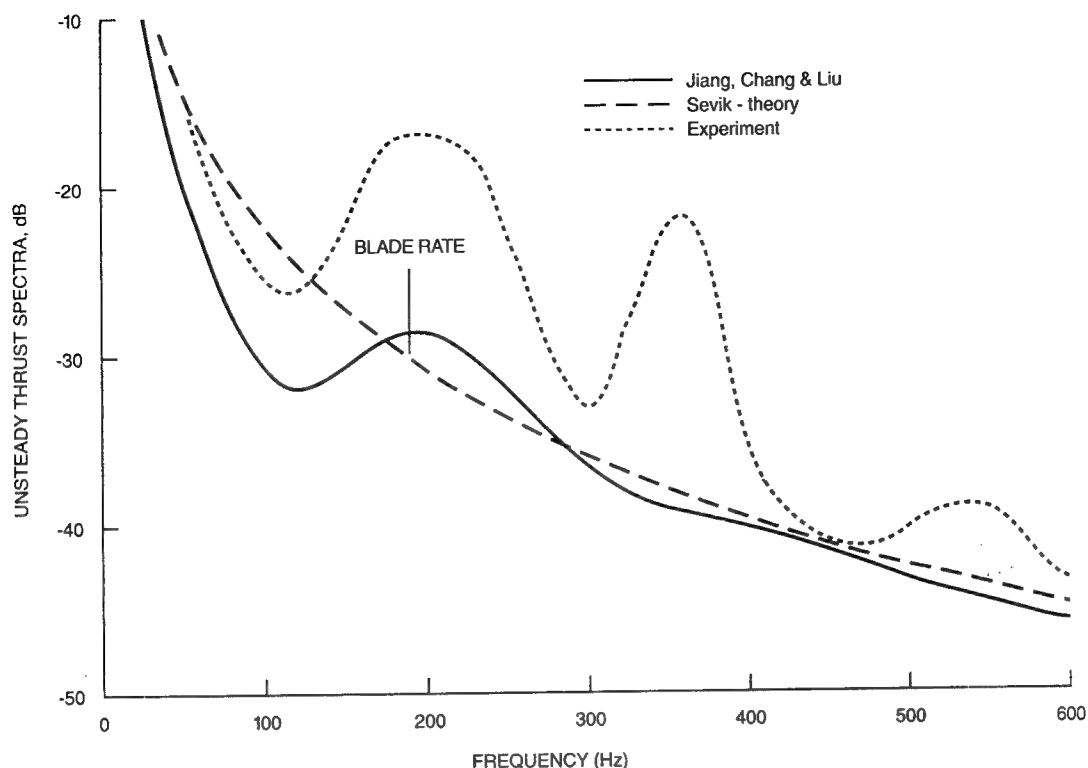


FIG. 8 COMPARISON OF THEORY AND EXPERIMENT (FROM REF. 8)

For clarity, the major design parameters which affect the response of a rotor will be given for small and large correlation lengths of the turbulence. Equations for the mean square value of the unsteady thrust are given by Blake. From these, the mean square value of the density fluctuations depends upon the following parameters:

$$\rho^2 \sim (U/c)^6 (u/U)^2 [S(\omega b/U)]^2 F[\Lambda m B/R]^2 / \{A_s (2\pi\omega/B \Omega)\}^2 \quad (8)$$

where U = the resultant velocity at the tip of the blades, B = the number of blades, S denotes an unsteady hydrodynamic response function (b = chord/2), A_s = the spatial filtering function of the propeller.

For large correlation lengths, the function $\{A_s\}^2 = B^2$ for $f/n_s = mB$, where f = frequency and n_s is the shaft rotation velocity $\Omega/2\pi$. The corresponding bandwidth is $\Delta f = n_s$.

Small correlation lengths occur when the axial scale 2Λ is much smaller than the blade spacing projected in the axial direction. In this case $\{A_s\}^2 = 1$ and each blade responds to the flow independently of the others. Fig. (9) extracted from Blake, illustrates

the spectra of the fluctuating thrust for small and large correlation lengths.

Clearly, the propulsor designer will prefer an inflow containing low levels of turbulence and small correlation lengths. Subject to additional requirements such as propulsive efficiency and cavitation, he will select a low blade tip speed and a hydrofoil geometry which is non-responsive to upstream flow fluctuations. Normally, these conditions are difficult to meet.

In some turbomachinery applications, rotors may be located within an elastic enclosure of finite length. The nearfield of the sources at the tips of the blades apply unsteady pressures on the enclosure which is set into vibrations and radiates sound. A recent paper by Kim⁽¹⁰⁾ illustrates this effect for cases of dipole sources at the tips.

The problem considered is shown in Fig. (10). A free-flooded cylindrical shell is excited by a radial force. The governing equation whose simultaneous solution is required are given in Fig. (11). As a specific illustration, Kim analyzed a steel shell submerged in water. For each axial mode m , the

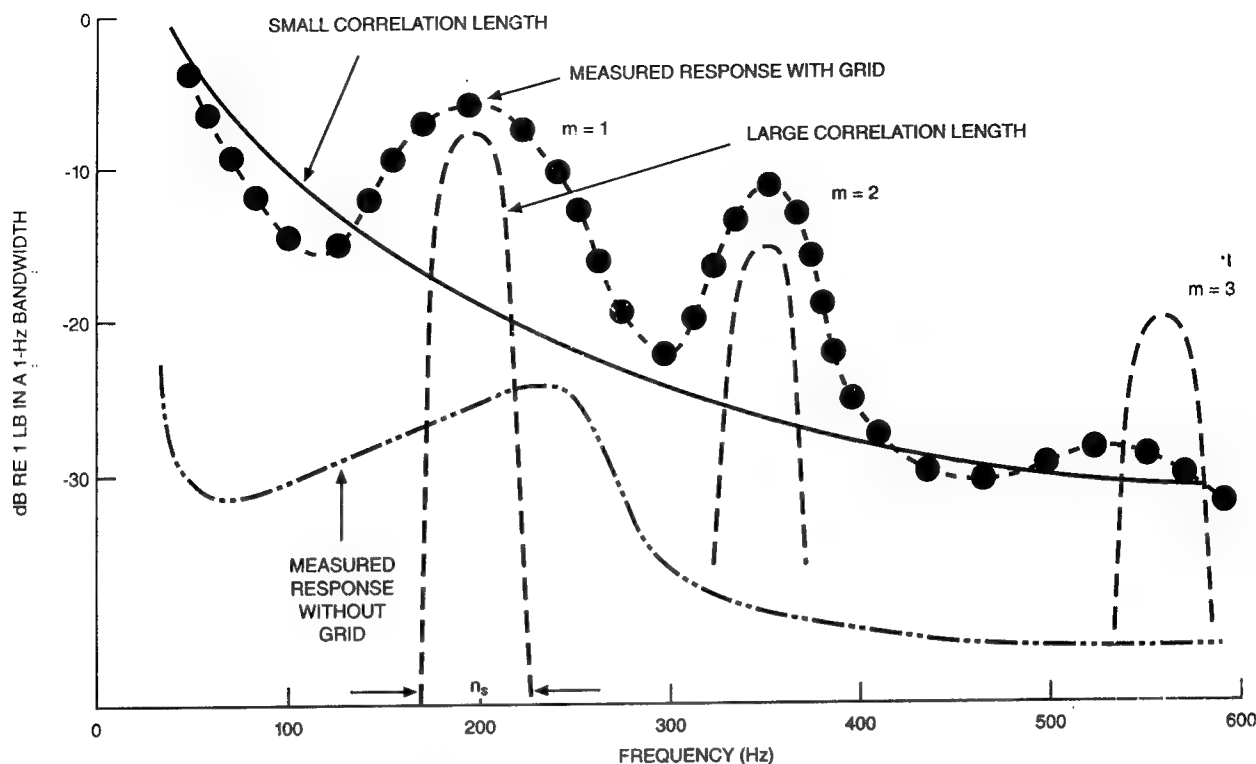


FIG. 9 SPECTRUM ($\Delta f = 1$ Hz BAND) OF UNSTEADY THRUST ON A 10-BLADED ROTOR DOWN-STREAM OF A 6-IN. GRID WIRE SCREEN FOR WHICH THE MEASURED $\Delta\theta = 0.5R_T$, $R_T = 4$ IN., $n_s = 19$ REV/MIN. (ADAPTED FROM SEVIK [146].) (FROM REF. 6)

response of the cylinder for various circumferential N modes are calculated. Resonances appear as "beads" in Figs. (12) to (15). These figures show the amplitudes of forced acceleration of the shell (in color) as a function of both circumferential mode order and frequency. The farfield acoustic pressure for the same shell whose length to diameter ratio is equal to one is shown in Fig. (16). The nearfield patterns for this shell in Fig. (17) indicate intense regions of radiation near the point of application of the radial force as well

as at the ends of the cylinder where flexural waves are scattered and launch acoustic energy into the farfield. This effect is also evident in Fig. (18) for a somewhat larger shell ($L/a = 3$). In this case, however, the contribution from the region of the drive point is relatively more pronounced. Kim's example demonstrates that the sound field generated by a blade row encased in an elastic shell has a complex directivity pattern, quite different from that of a dipole.

A FINITE SHELL RADIATION GEOMETRY

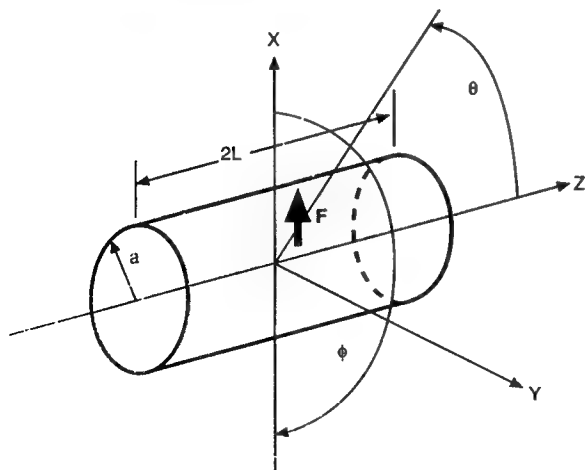


FIG. 10 FREE-FLOODED SHELL EXCITED BY A POINT FORCE (FROM KIM)

GOVERNING EQUATIONS

• Helmholtz Equation

$$(\nabla^2 + k^2) p(\vec{x}) = 0 \quad (\vec{x} \text{ in } V)$$

• Shell Equations

$$[D] \begin{Bmatrix} u(\vec{x}) \\ v(\vec{x}) \\ w(\vec{x}) \end{Bmatrix} = \begin{Bmatrix} 0 \\ 0 \\ P_s \end{Bmatrix} \quad (\vec{x} \text{ in Shell})$$

• Shell - Fluid Interaction

$$\frac{\partial p(\vec{x})}{\partial \vec{n}} = -\rho \vec{w}(\vec{x}) \quad (\vec{x} \text{ on Surface})$$

FIG. 11 EQUATIONS USED BY KIM TO SOLVE PROBLEM IN FIG. 10 (REF. 10)

FREQUENCIES OF MAX. RESPONSE
($m=1$, $L/a=1$, in water)

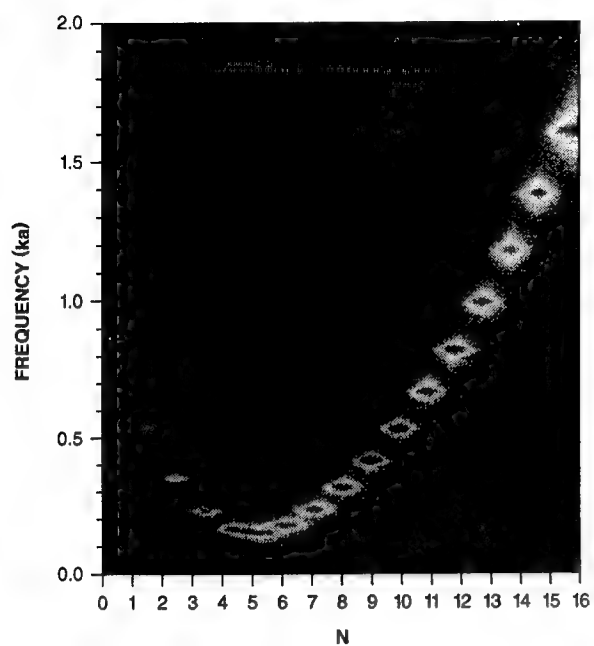


FIG. 12 (FROM KIM) REF. 10

FREQUENCIES OF MAX. RESPONSE
($m=3$, $L/a=1$, in water)

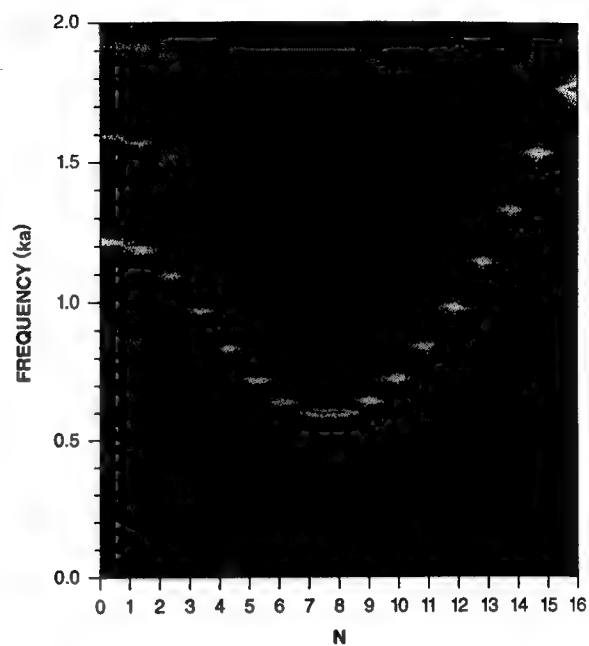


FIG. 14 (FROM KIM) REF. 10

FREQUENCIES OF MAX. RESPONSE
($m=2$, $L/a=1$, in water)

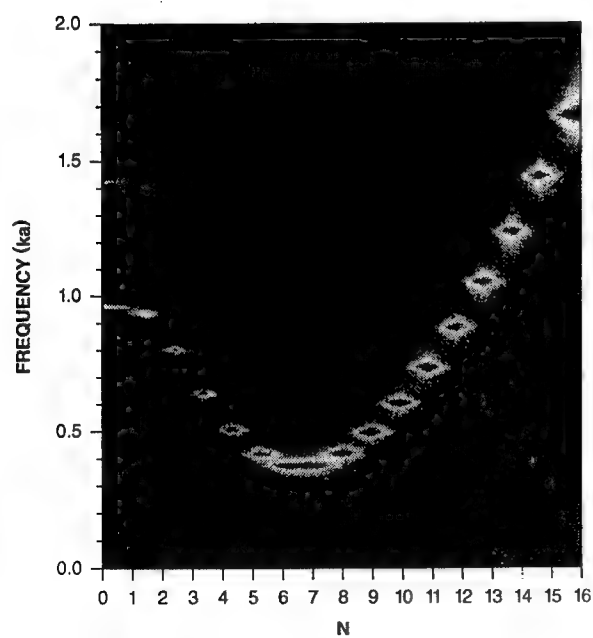


FIG. 13 (FROM KIM) REF. 10

FREQUENCIES OF MAX. RESPONSE
($m=4$, $L/a=1$, in water)

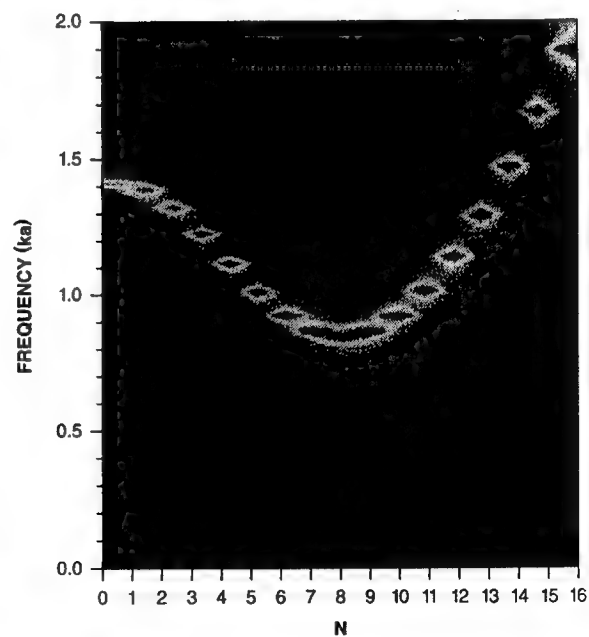


FIG. 15 (FROM KIM) REF. 10

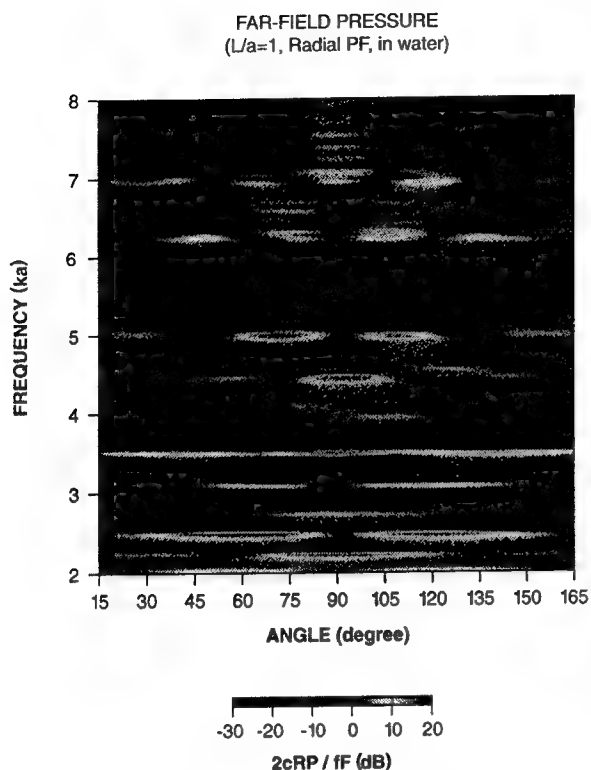


FIG. 16 WHERE P IS THE PRESSURE AT DISTANCE R (FROM KIM) REF. 10

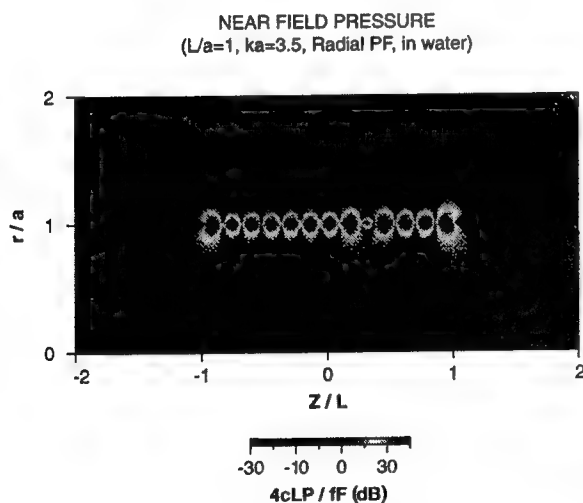


FIG. 17 (FROM KIM) REF. 10

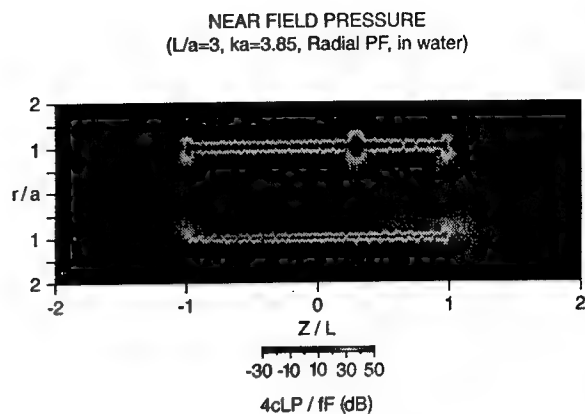


FIG. 18 (FROM KIM) REF. 10

A method for noise mitigation has been suggested by Howe⁽¹¹⁾. He considered the effects of a pressure-release coating of finite extent installed on an elastic plate located adjacent to hydroacoustic dipole sources. He predicted the influence of the coating on the sound radiated by the dipoles and on the vibrations of the plate.

His analysis involves longitudinal dipoles oriented parallel to the plate, as they would be on the tips of an enclosed blade. The effect of the pressure-release material is to produce equal and opposite images which reduce the efficiency of radiation to quadrupole sources.

Fig. (19) illustrates the model analyzed. For a steel plate of thickness h in water, the radiated sound level and the plate response are plotted as a function of the applied to the coincidence frequency. For values of $d/h < 5$, Fig. (20) illustrates the excess sound scattered by the edge of the coating due to its proximity to the dipole and its ability to extract energy from its nearfield. However, when the coating extends approximately 10-plate thicknesses beyond the location of the dipole, very significant reductions in radiated sound power can be achieved, except at frequencies near coincidence.

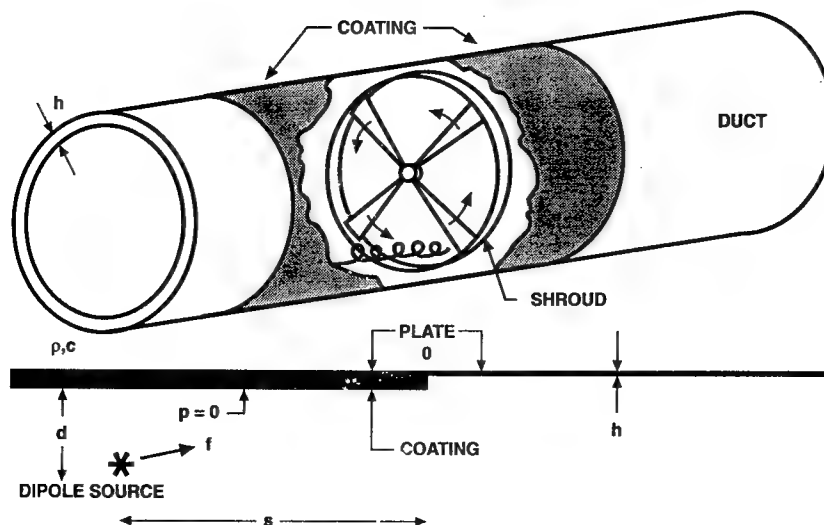


FIG. 19 BLADE-VORTEX INTERACTIONS IN A DUCT CONSIDERED BY HOWE (FROM REF. 11)

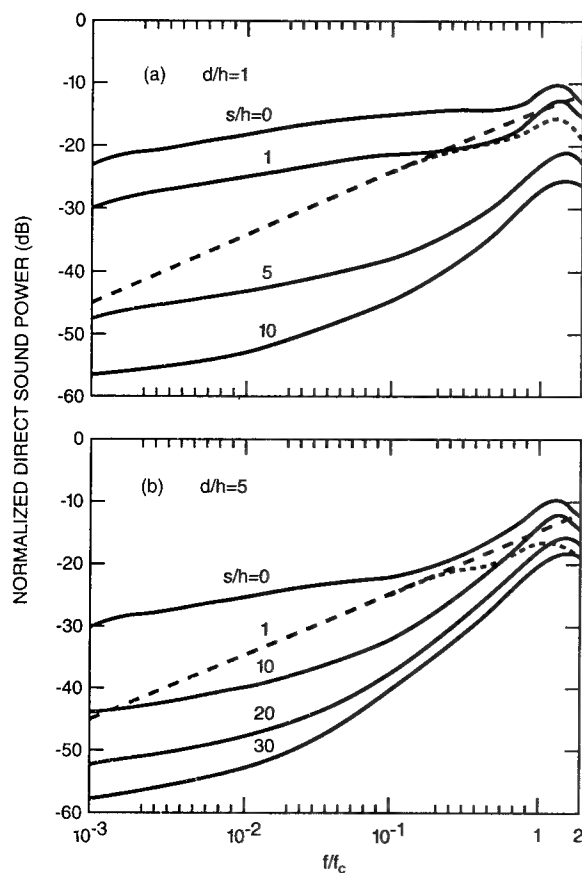


FIG. 20 SOUND POWER FOR A STEEL PLATE AS A FUNCTION OF APPLIED TO COINCIDENCE FREQUENCY FOR:

- (—) COATED PLATE
- (---) UNCOATED PLATE
- (- - -) NO PLATE

(NOTE: $\frac{2\pi f_c h}{c} \approx 0.952$)

(FROM REF. 11)

HYDROACOUSTIC TEST FACILITIES

In spite of considerable progress, current numerical techniques are not able to predict reliably the complex flow fields and time-dependent interactions which occur on the blades and nearby structures of modern propulsors. Hydroacoustic test facilities - specifically large, quiet, high speed water tunnels - are essential tools for assessing the hydrodynamic and hydroacoustic performance of alternative designs.

The two principal facilities in the United States are the Large Cavitation Channel (LCC) of the Naval Surface Warfare Center, located in Memphis, Tennessee, and the 48-inch Water Tunnel of the Applied Research Laboratory (ARL), at the Pennsylvania State University, in State College, Pennsylvania. These facilities contain complementary and mutually supportive capabilities.

Fig. (21) shows the installation of two sets of acoustic sensors in the LCC, one in an anechoically treated trough under the test section and a second located in the main diffuser section. This arrangement allows a model to be acoustically scanned along its beam aspect and also measured at stern aspect with the acoustic lens. Details of the nested arrays are shown in Figs. (22) and (23). The general design features of the acoustic lens are provided in Fig. (24). Table (I) lists the frequencies and beam widths of the various acoustic sensors. Under non-cavitating conditions, useful data can be acquired up to 80kHz, depending on the characteristics of the test object. The omniphones give an early warning of incipient cavitation. The measured self noise levels of the nested arrays as a function of tunnel speed are given in Fig. (25).

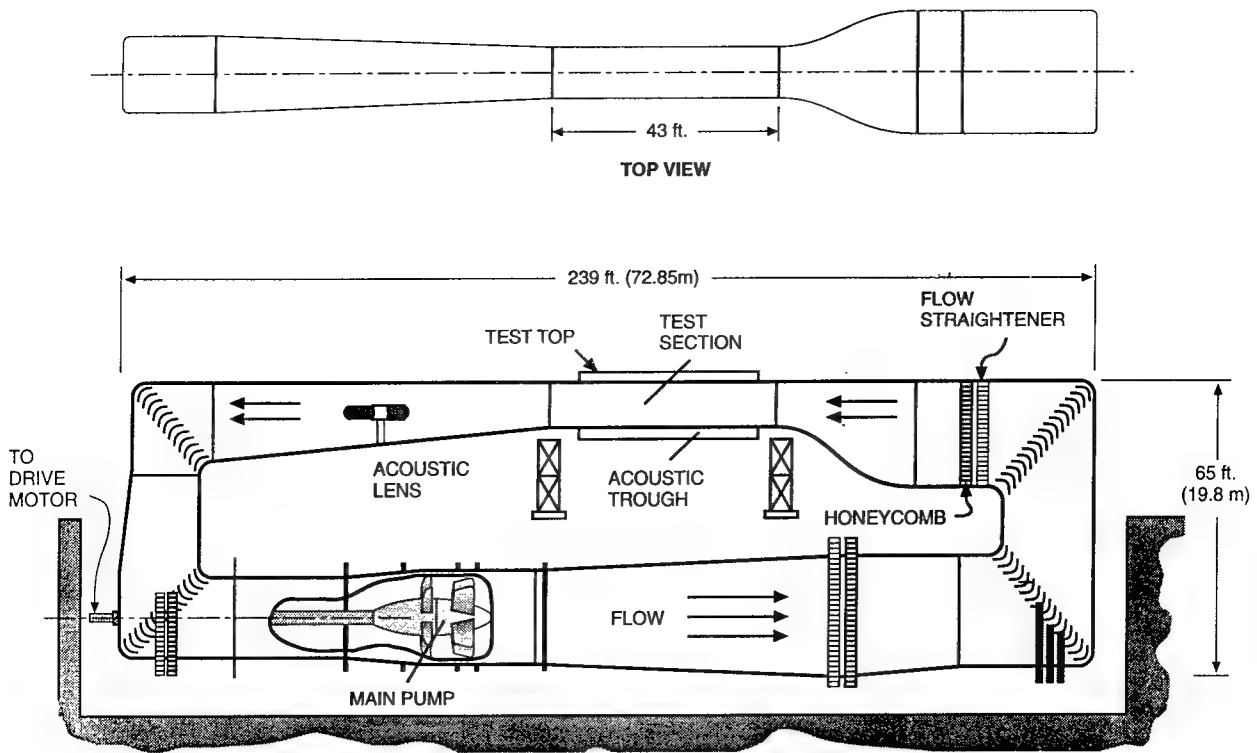


FIG. 21 LARGE CAVITATION CHANNEL (LCC)

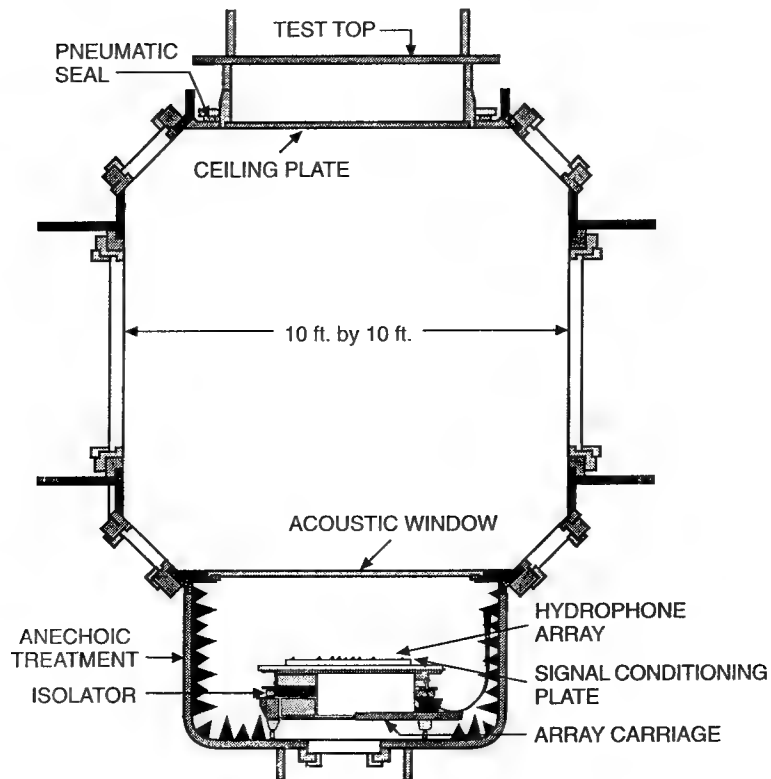
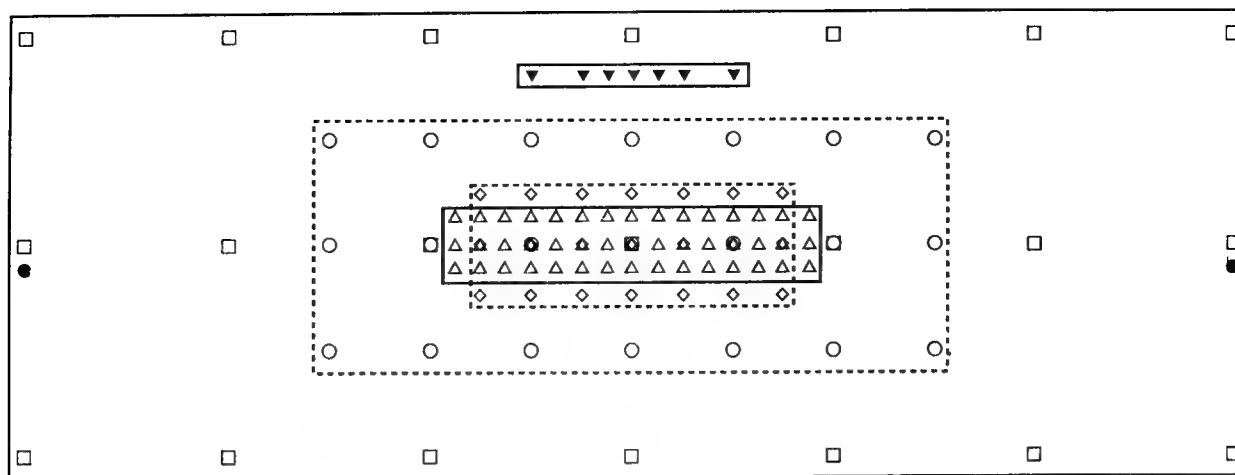


FIG. 22 LARGE CAVITATION CHANNEL (LCC)



95 ELEMENT PLANAR ARRAY

- | | |
|-----------------|-------------------------------|
| △ 1X-SUBARRAY | ◇ 2X-SUBARRAY |
| ○ 4X-SUBARRAY | □ 8X-SUBARRAY |
| ▼ HF LINE ARRAY | ● OMNIDIRECTIONAL HYDROPHONES |

FIG. 23 LCC ELEMENT ARRAY LOCATIONS

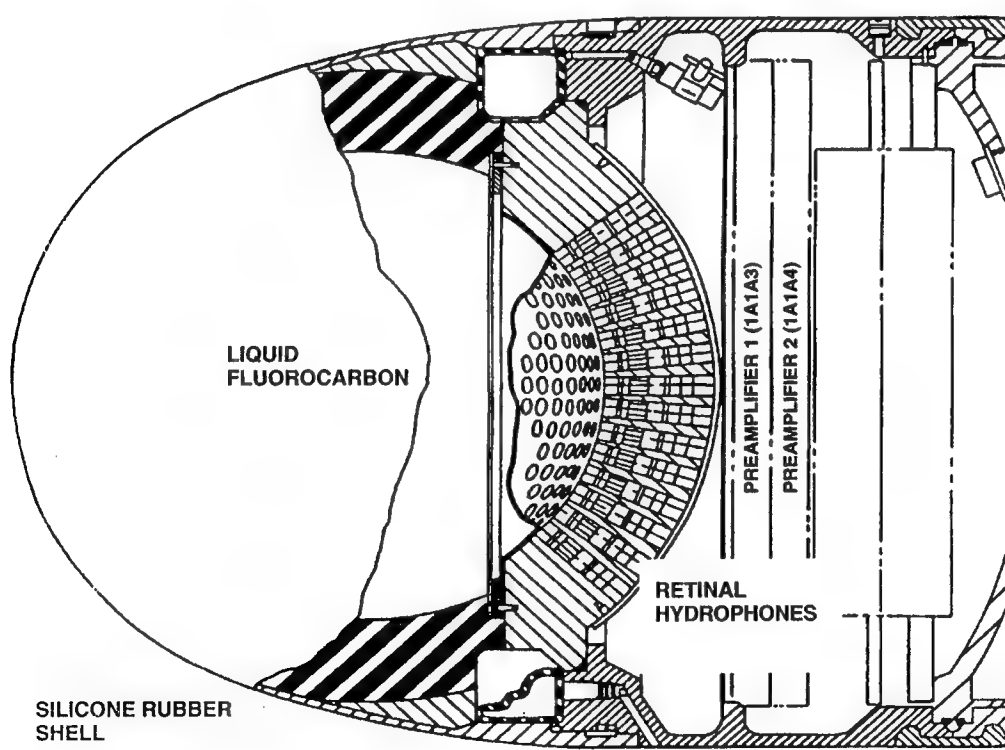


FIG. 24 LCC ACOUSTIC LENS

TABLE I: LCC ACOUSTIC SENSORS

SubArray	Design Frequency (kHz)	Frequency Range (kHz)	Subarray Configuration	Element Spacing (cm)	3 dB 2θ-Beamwidth (deg)
LF-Array					
1X	20.0	0.2 – 16	45 (3 X 15)	3.75	8° – 16 kHz
2X	10.0	0.2 – 8	21 (3 X 7)	7.5	18° – 8 kHz
4X	5.0	0.2 – 4	21 (3 X 7)	15	18° – 4 kHz
8X	2.5	0.2 – 2	21 (3 X 7)	30	18° – 2 kHz
HF-Array					
1X	20.0	8 – 40	5 (1 X 5)	3.8	21° – 20 kHz
2X	10.0	8 – 20	5 (1 X 5)	7.6	21° – 10 kHz
HF Lens Beam	—	4 – 100	—	6 deg.	4° – 80 kHz
Omniphones					
Trough	Omni	0.2 – 125	—	—	120° – 125 kHz
Fillet	Omni	5 – 100	—	—	60° – 200 kHz

The models suitable for installation in the LCC range from full-scale to less than a tenth scale. Although satisfactorily high Reynolds numbers are achievable even on the smaller models, full-scale geometrical details are difficult to reproduce. The ingenious device in the 48-inch water tunnel of the ARL provides a means to acquire vibration data at larger scales. Its concept is evident from Fig. (26).

Although acoustic radiation cannot be measured directly, a relationship can be established between the vibration levels on the blades of a rotor, for instance, and the resulting radiated power. A large reverberant tank at ARL provides the required transfer function from vibration to sound. Examples of the type of instrumentation generally used are provided in Figs. (27) and (28).

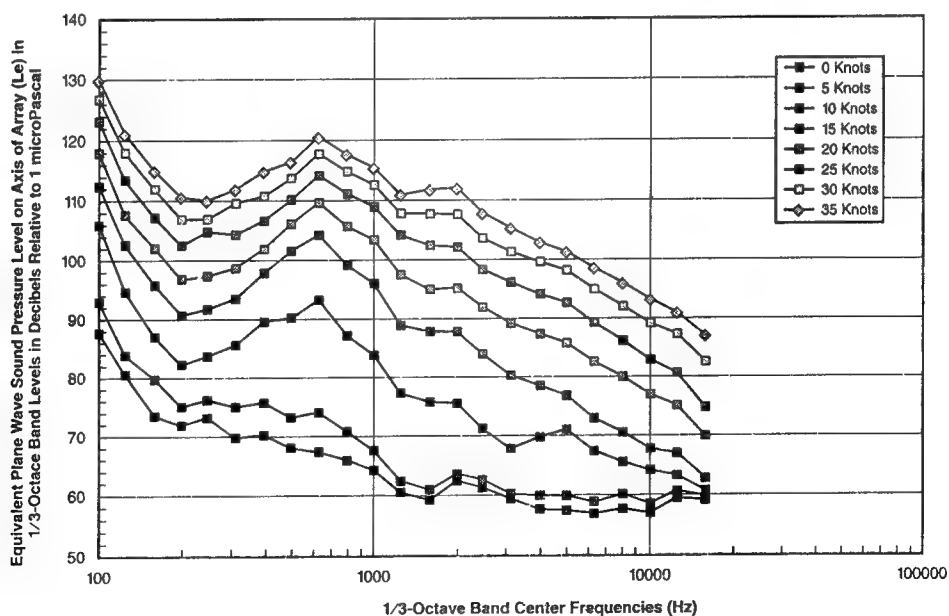


FIG. 25 MEASURED COMPOSITE ARRAY SELF-NOISE (L_e) VERSUS SPEED FOR AN EMPTY TUNNEL

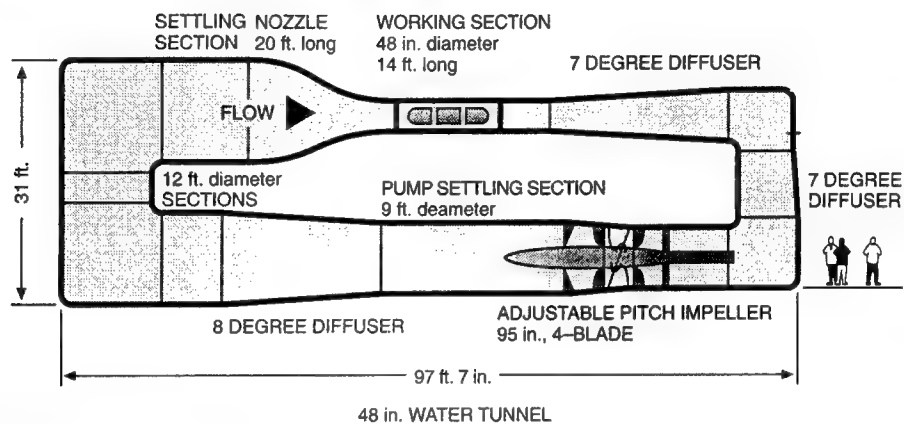
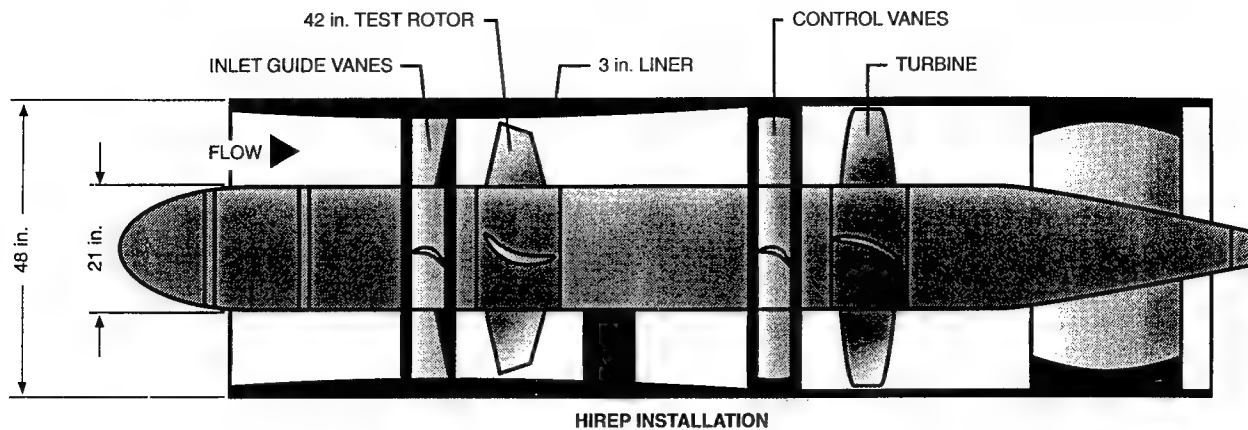


FIG. 26 ARL PENN STATE 48-INCH DIAMETER WATER TUNNEL AND HIGH REYNOLDS NUMBER PUMP INSTALLATION



FIG. 27 INSTALLATION OF TRANSDUCERS ON BLADE

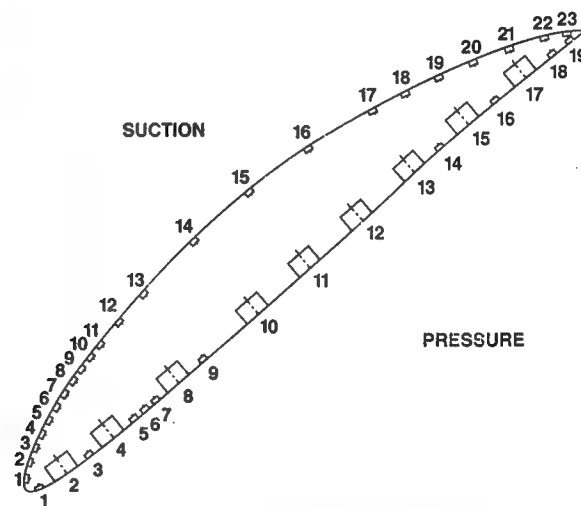


FIG. 28 SCHEMATIC OF PRESSURE TRANSDUCER AND ACCELEROMETER INSTALLATION

IN CONCLUSION

As in the past, today's propulsor designers still rely heavily on a combination of numerical and experimental inputs in order to meet powering, cavitation and acoustic requirements. Some time in

the future it is reasonable to expect that supercomputers and physically correct descriptions of the flow and of structural responses will be capable of predicting all required performance parameters with confidence. A program aimed at achieving this objective would be a very ambitious and costly

undertaking. However, it would have a major payoff in saving design time, and the very high cost of experimental hardware and facilities. It would also provide "agility" to the ship design process, as rapid means for assessing the merits and limitations of various options will be at hand.

REFERENCES

1. Lighthill, M.J., "On Sound Generated Aerodynamically, I, General Theory." *Proc. R. Soc., London, Ser. A* 211, 564-587 (1952).
2. Powell, A., "Theory of Vortex Sound." *J. Acoust. Soc. Am.* 36, 177-195 (1964).
3. Ffowcs Williams, J.E., "Sound Radiation from Turbulent Boundary Layers Formed on Compliant Surfaces." *J. Fluid Mech.* 22, 347-358 (1965).
4. Curle, N., "The Influence of Solid Boundaries upon Aerodynamic Sound." *Proc. R. Soc. London, Ser. A* 231, 505-514 (1955).
5. Ffowcs Williams, J.E., "Modern Methods in Analytical Acoustics, Chapter 11". Springer Verlag, (1994).
6. Blake, W.K., "Mechanics of Flow-Induced Sound and Vibration". Academic Press, (1986).
7. Sevik, M., "The Response of Propulsors to Turbulence". *Seventh Symposium on Naval Hydrodynamics*. Office of Naval Research, DR.-148, 293-313 (1968).
8. Jiang, C.W., Chang, M.S., Liu, Y.N., "The Effect of Turbulence Ingestion on Propeller Broadband Thrust." *David Taylor Model Basin, Report Number DTRC/SHD-1355-02*, (1991).
9. Martinez, R., "Asymptotic Theory of Broadband Rotor Thrust; Parts I and II". Cambridge Acoustical Associates, Inc. (1995).
10. Kim, S.K., "Radiation of Sound by a Point-Excited Free-Flooded Cylindrical Shell of Finite Length". *David Taylor Model Basin*, (1995).
11. Howe, M.S., "Production of Structural and Acoustic Waves by Dipole Sources Adjacent to an Elastic Plate with a Pressure-Release Coating". *J. Acoust. Soc. Am.* 91 (3), (1992)

Prediction of Unsteady Performance of Marine Propellers with Cavitation Using Surface-Panel Method

Y.-G. Kim (Samsung Heavy Industries Co., Ltd., Korea),

C.-S. Lee (Chungnam National University, Korea)

Abstract

This paper describes a low order potential-based panel method formulated for the prediction of the unsteady performance of a cavitating marine propeller that operates behind a ship. The method employs normal dipoles and sources distributed on the blade, hub and wake surfaces to represent the potential flow around the cavitating propeller.

The kinematic boundary condition on the wetted portion of the boundary surface is satisfied by requiring that the normal component of the total velocity should vanish on the boundary surface. By applying Bernoulli's equation, the dynamic boundary condition on the cavity surface is replaced by a kinematic condition; that is, the velocity potential on the cavity surface is expressed in terms of the velocity potential and the perturbation velocity both at the cavity detachment point and other geometric quantities. Sources are introduced to represent the presence of the cavity on the cavitating portion of the body. It is expected that the sources will serve as a normal flux generator, which may be integrated in the streamwise direction to form the cavity shape, in a similar manner as in the thickness problem of the thin wing theory.

The blade and cavity surfaces are discretized into a set of quadrilateral panel elements and the strengths of sources and dipoles are assumed constant at each panel. Applying this approximation to the boundary conditions leads to a set of simultaneous equations. The unsteady problem is treated in discretized time domain by rotating the propeller with constant angular spacing.

In order to reduce computing time and to ensure the convergence, the cavity surface is collapsed

to the real blade surface or to the mean wake surface. The linearization in cavity thickness is shown not to deteriorate the accuracy compared to the nonlinear theory.

Systematic numerical tests show that the present numerical method is fast and stable, and is applicable to the 2- or 3-dimensional geometry of arbitrary shape. In order to demonstrate a practical aspect of the present method, sample computations are carried out first for the case of a propeller equipped to a 6300 TEU container ship which has been cavitation-tested behind a full-size model ship, and then for the case of a model propeller operating in screen-generating wake. Comparisons between the predictions and experiments at cavitation tunnels show promising correlation.

1 Introduction

Cavity is known as a major source of noise aboard a ship and fluctuating pressures on the stern hull surface. An ability to predict the behavior of the cavity on propeller blades is therefore in need to design a more comfortable and vibration-free vessel.

When the cavity is absent, the traditional lifting surface method has been applied with success in predicting the global performance of the steady and unsteady performance of marine propellers. See, for example, Kerwin and Lee[1]. The lifting surface approach was then extended to solve the cavitating propeller problem by Lee[2]. The linearized lifting surface theory however shows an unreasonable singular behavior at the leading edge, where the cavity begins. It is therefore expected that the linear theory overpredicts the cavity extent and also the cavity volume, which will consequently lead to overprediction

of the cavity induced pressure impulses on the hull.

Efforts to improve the prediction of the flow around the leading edge followed, among which the work of Kinnas[3] should be noted. He applied the method of Lighthill's correction to the streamwise velocity component obtained in linear theory and was successful in reducing the cavity volume from the original work of Lee[4]. The linear cavity theory is however found later to give a wrong trend by Uhlman[5] and also by Lee et al[6], who show in their nonlinear theory that the predicted cavity extent decreases when the thickness of the blade increases, contrary to the trend in linear theory. The need to treat the finite blade thickness effect is evident.

Recently a surface panel method based on Morino's[7] formulation has been applied successfully to the propeller problem with an improvement on the leading edge solution. Application to the cavitating flow problem is a natural extension. The method was first applied to a two-dimensional hydrofoil problem by Lee[4], Lee et al[6] and also by Kinnas and Fine [8]. They solved the exact nonlinear steady problem, in either partially or super-cavitating steady flow condition.

Kim et al[9] then extended the method for the solution of the 3-D steady and unsteady cavitating hydrofoil problem, where the cavity surface was linearized on the suction side of the blade. By avoiding the linearization in blade thickness as in the lifting surface theory they could maintain the resolution of the flow prediction, especially in the area of the blade leading edge, and hence the cavity behavior could be predicted without losing accuracy.

The unsteady flow problem around a marine propeller was solved subsequently by Fine[10] and Kim[11]. In the present paper we present the potential-based formulation of Kim[11] to solve the steady or unsteady cavitating propeller flow.

The same formulation is applicable to 2- and 3-dimensional cavity flow problems. To verify the numerical procedure, we first show that the method is applicable to the analysis of the 2-dimensional unsteady hydrofoil in either heave or gust mode for both the partially and super-cavitating flow conditions. We then show the same method is applicable to the 3-dimensional hydrofoil with rectangular planform. Finally we predict the cavity behavior around the blades of two marine propeller operating either in screen-generated wake or in wake generated behind a ship model. Our predictions compares fairly well with the cavitation patterns observed at cavitation tunnels.

2 Statement of Boundary-Value Problem

2.1 Basic assumptions

Let's consider a cavitating propeller operating in a nonuniform ship wake with a constant rotational speed n at a constant advance speed V_s . Boundaries such as the rudder and free-surface in contact with the atmosphere are ignored, and the presence of the hull is recognized only by the effective wake, which is assumed to be known. We assume the viscous effect on the blades and the trailing vortex sheets is confined within the infinitesimally thin boundary layer. The cavity is assumed to be a constant pressure surface which grows on the suction side of the blades. We assume that the cavity is a thin sheet cavity and the detachment point of the sheet cavity is known. The ship wake is nonuniform and is assumed undeformable under the influence of the propeller action, and the propeller is operating in an inviscid, incompressible and irrotational fluid field.

2.2 Coordinate systems

A Cartesian coordinate is chosen as shown in Figure 1; the x -axis coincides with the shaft centerline, defined positive downstream, the positive y -axis points upward, and the z -axis completes a right hand coordinate system. The cylindrical coordinate system is defined for convenience; r being the radius and θ the angle from the positive y -axis positive counterclockwise when looking downstream.

2.3 Governing equation and boundary conditions

The perturbation velocity \vec{v} may be expressed by the perturbation velocity potential ϕ as $\vec{v} = \nabla\phi$. Then conservation of the mass applied to the potential flow gives the Laplace equation as a governing equation in the fluid region, that is,

$$\nabla^2\phi = 0 \quad (1)$$

Motion of the flow satisfying the Laplace equation (1) can be uniquely defined by imposing the following boundary conditions on the boundary surfaces.

1. Quiescence condition at infinity upstream:

$$\nabla\phi \rightarrow \vec{0} \quad (2)$$

2. Kinematic boundary condition(KBC) on the wetted surface S_B^{WET} :

$$\hat{n} \cdot \vec{V} = \hat{n} \cdot \vec{U}_r + \frac{\partial \phi}{\partial n} = 0 \quad (3)$$

where \vec{V} is the total velocity, \hat{n} the unit vector normal to the blade surface, defined positive when pointing into the fluid region. $\vec{U}_r(r, \theta)$ is the oncoming flow at a point \vec{x} which may be expressed in terms of the effective velocity $\vec{U}_A(r, \theta)$ and the rotational velocity $\vec{\Omega}$ as follows:

$$\vec{U}_r(r, \theta) = \vec{U}_A(r, \theta) - \vec{\Omega} \times \vec{x}$$

3. Kutta condition at the trailing edge(T.E.):

$$|\vec{V}_{T.E.}| < \infty \quad (4)$$

4. Kinematic boundary condition(KBC) on the wake surface S^W :

$$\Delta \frac{\partial \phi}{\partial n} = (\hat{n} \cdot \nabla \phi)^+ - (\hat{n} \cdot \nabla \phi)^- = 0 \quad (5)$$

where + and - denote the upper and lower surfaces of the wake, respectively.

5. Dynamic boundary condition(DBC) on the wake surface S^W :

$$\Delta p = p^+ - p^- = 0 \quad (6)$$

The conditions above are sufficient to describe the fluid motion when the cavity is absent. When the cavity appears, we need additional conditions to be imposed on the cavity surface.

6. Kinematic boundary condition(KBC) on the cavity surface S^C :

$$\frac{DF}{Dt} = 0 \quad (7)$$

where $F(x, y, z, t)$ is the equation for the cavity surface.

7. Dynamic boundary condition(DBC) on the cavity surface S^C :

$$p = p_v \quad (8)$$

where p_v is the vapor pressure inside the cavity.

8. Cavity closure condition:

$$T^c(\vec{x}_{cte}) = 0 \quad (9)$$

where $T^c(\vec{x})$ represents the cavity thickness function and \vec{x}_{cte} denotes the cavity trailing end position.

3 Integral Equations

From the Green's theorem, we may derive an expression for the potential in the flow field by distributing the normal dipoles and sources on the body and wake surfaces to deal with the cavity flow problem. The sources on the cavitating portion of boundary surfaces will serve as a normal flux generator, which may be integrated in the streamwise direction to form the cavity shape, in a similar manner as in the thickness problem of the thin wing theory. For brevity, we will not derive the integral equations, but will adopt the final forms only from Kim et al[9].

3.1 Linearization of cavity location

In the nonlinear theory of Lee et al[6], the exact location of the cavity surface is computed iteratively. At each step they relocated the cavity surface where the unknown singularity is distributed and recomputed the induction integrals. Although this procedure could produce the exact solution in the 2-dimensional steady flow, it is obviously impractical for the analysis of the 3-dimensional unsteady cavity flow, due to lack of the robustness of the procedure and unaffordable increase of computing time.

In the present work, the cavity surface is collapsed onto the solid blade surface if the cavity is above the blade surface and onto the mean wake surface if the cavity extends beyond the trailing edge of the blade. The linearization in thickness is not only justified theoretically under the assumption of the thin cavity thickness but also welcomed due to the drastic reduction of the computing time and storage requirements. It is also shown by Kim et al[9] that the linearization does not deteriorate the resolution significantly compared with the nonlinear solution, if a true girth length is considered when evaluating the potential along the cavity surface. Figure 2 shows that the evaluation with the true girth length along the cavity surface(labeled 'Present Method') compares very well with the nonlinear solution, whereas the evaluation with the girth length of the blade surface(labeled 'Simply L. M') overpredicts the cavity extent and volume for the case of the partially cavitating flow. This effect is insignificant for the supercavitating flow as shown in Figure 3. This will be illustrated further later.

3.2 Fully wetted flow or partially cavitating flow

The perturbation velocity potential is expressed as follows:

$$\begin{aligned}\phi(\vec{p}) = & \int_{S^{WET} \cup S^C} \{-\phi(\vec{q})\} \frac{\partial}{\partial n_q} G(\vec{p}; \vec{q}) dS \\ & + \int_{S^{WET} \cup S^C} \left\{ \frac{\partial \phi(\vec{q})}{\partial n_q} \right\} G(\vec{p}; \vec{q}) dS \\ & + \int_{S^W} \{-\Delta \phi_w\} \frac{\partial}{\partial n_q} G(\vec{p}; \vec{q}) dS \quad (10)\end{aligned}$$

where $G(\vec{p}; \vec{q})$ is the Green's function, and \vec{p} , \vec{q} the control and singularity points, respectively. S^B , S^C and S^W represent the body, cavity and wake surfaces, respectively.

3.3 Supercavitating flow

The perturbation velocity potential is expressed as follows:

$$\begin{aligned}\phi(\vec{p}) = & \int_{S^B} \{-\phi(\vec{q})\} \frac{\partial}{\partial n_q} G(\vec{p}; \vec{q}) dS \\ & + \int_{S^B} \left\{ \frac{\partial \phi(\vec{q})}{\partial n_q} \right\} G(\vec{p}; \vec{q}) dS \\ & + \int_{S^{CB}} \{-\phi(\vec{q})\} \frac{\partial}{\partial n_q} G(\vec{p}; \vec{q}) dS \\ & + \int_{S^{CB}} \left\{ \frac{\partial \phi(\vec{q})}{\partial n_q} \right\} G(\vec{p}; \vec{q}) dS \\ & + \int_{S^{CW}} \frac{\partial(\phi^+ - \phi^-)}{\partial n} G(\vec{p}; \vec{q}) dS \\ & + \int_{S^W} (-\Delta \phi)_w \frac{\partial G(\vec{p}; \vec{q})}{\partial n_q} dS \quad (11)\end{aligned}$$

where S^{WET} denotes the wetted surface, and S^{CB} and S^{CW} denote the supercavitating portion projected upon the blade surface and wake sheet, respectively. The superscripts + and - denote both sides of the cavity extending beyond the trailing edge with the positive sign for the surface connecting the suction side of the blade.

Due to the characteristics of singularities, the governing equation (1) and the quiescence condition (2) will automatically be satisfied.

We know the strength of the sources distributed on the wetted portion of blades from (3) and that of normal dipoles on the cavity from (8) (as will be described later), and hence (10) and (11) become integral equations for the unknown strengths of the sources on the cavity surface and the normal dipoles on the wetted surface.

4 Numerical Implementation

4.1 Discretization of propeller blades and wake

For numerical computation, the propeller and cavity surfaces are replaced by a set of non-planar quadrilateral panels as shown in Figure 4. The flow near the leading edge and tip of the blades varies more rapidly than any other region around the blade, and hence the surface panel size should be smaller in this region. We adopted a so-called cosine spacing in the chordwise direction and a half-cosine spacing in the radial direction, as is evidenced in Figure 4.

Modeling of the shed vortex wake is very important in accurately predicting the performance. We adopted the Greeley and Kerwin's nonlinear wake model which is derived from the LDV measurement at the cavitation tunnel. Figure 5 shows the wake panels trailing a single blade. Details for discretization of the blade and shed wake may be found in Kim [11].

4.2 Numerical procedure

After discretization, we assume the singularity strength be constant on each panel, and then the integral equations (10) and (11) can be replaced into a set of simultaneous equations with unknown strengths of the potential or the normal derivative of the potential. With a proper use of the cavity KBC (7) and the closure condition (9), we may also determine the cavity shape and the cavity volume.

For the unsteady behavior, we solve the boundary-value problem iteratively by advancing the propeller by a discrete angular spacing in time domain as in Lee[2]. The cavity extent is a part of the solution, which has to be known in advance to distribute appropriate singularities on the panel surfaces. We therefore have to resort to another iterative procedure for search of the cavity extent; that is, one in the chordwise direction and the other in the spanwise direction. As is proved in Lee[2], this space-domain iteration is found very efficient and shows very fast convergence characteristics.

Besides the Green functions, the only significant difference between 2-dimensional and 3-dimensional problems in the present numerical procedure is the interaction between the chordwise strips. Once adopted the spanwise iterative procedure we may confine the analysis onto the only one chordwise strip with the influence of the other strips assumed known or updated through iteration. In the subsequent sections, we will restrict the formulation along

a particular chordwise strip without mentioning the influence of the other strip and also that of the other blades. The hub is present in all sample computations, but will not be included in the formulation for brevity.

4.3 Unsteady DBC on cavity surface, S^C

If we apply Bernoulli's equation to the cavity surface S^C , we have

$$p_\infty + \frac{\rho}{2} U_r^2 = \rho \frac{\partial \phi}{\partial t} + p + \frac{\rho}{2} V^2 + \rho g Y_s \quad (12)$$

where $U_r = |\vec{U}_r|$, $V = |\vec{V}|$, and Y_s denotes the vertical coordinate in ship-fixed coordinate system, g the gravitational acceleration.

We define the cavitation numbers σ_n and σ as follows:

$$\sigma_n = \frac{p_\infty - p_v}{1/2 \rho n^2 D^2} \quad \sigma \equiv \frac{p_\infty - p_v}{1/2 \rho V_s^2} = \frac{\sigma_n}{J_s^2} \quad (13)$$

where J_s denotes the advance coefficient based on the ship speed.

Since the DBC has to be satisfied along the cavity surface, we have

$$\sigma = \left(\frac{V}{V_s}\right)^2 - \left(\frac{U_r}{V_s}\right)^2 + \frac{2gR Y_s}{V_s^2 R} + \frac{2}{V_s^2} \frac{\partial \phi}{\partial t} = \text{constant} \quad (14)$$

where R denotes the propeller tip radius.

Let us define the Froude number as follows:

$$F_n \equiv \frac{n^2 D}{g} \quad (15)$$

Then (14) may be expressed as follows:

$$\sigma = \left(\frac{V}{V_s}\right)^2 - \left(\frac{U_r}{V_s}\right)^2 + \frac{1}{F_n J_s^2} \frac{Y_s}{R} + \frac{2\pi}{J_s} \frac{\partial \phi}{\partial \theta} \frac{\phi}{RV_s} \quad (16)$$

If we apply (16) on an arbitrary point with index j and the cavity detachment point (cdp) at the blade leading edge, we obtain the following: (For convenience, all physical variables are to be nondimensionalized; that is, the speed by V_s , the length by R and the velocity potential by RV_s . We will use the same symbols after nondimensionalization.)

$$V_{cdp}^2 + \frac{Y_{cdp}}{F_n J_s^2} + \frac{2\pi}{J_s} \frac{\partial \phi_{cdp}}{\partial \theta} = V_c^2 + \frac{Y_c}{F_n J_s^2} + \frac{2\pi}{J_s} \frac{\partial \phi_c}{\partial \theta} \quad (17)$$

where the subscript c denotes a point on the cavity surface.

Keeping in mind the iteration scheme, (17) may be rearranged as follows:

$$V_c = V_{cdp} + \left\{ \frac{Y_{cdp} - Y_c}{F_n J_s^2} + \frac{2\pi}{J_s} \frac{\partial(\phi_{cdp} - \phi_c)}{\partial \theta} \right\} / (V_{cdp}^* + V_c^*) \quad (18)$$

where the superscript $*$ denotes that the corresponding variable is assumed known from the previous time step or updated through iteration.

Noticing that the perturbation tangential speed v_c on S^C is always larger than the tangential speed of oncoming flow, we may express the perturbation speed on S^C as follows:

$$\begin{aligned} v_c &= -(\vec{U}_r \cdot \hat{t})_c + V_{cdp} + \left\{ \frac{Y_{cdp} - Y_c}{F_n J_s^2} + \frac{2\pi}{J_s} \frac{\partial(\phi_{cdp} - \phi_c)}{\partial \theta} \right\} / (V_{cdp}^* + V_c^*) \\ &\equiv -(\vec{U}_r \cdot \hat{t})_c + V_{cdp} + b_c^* \end{aligned} \quad (19)$$

where \hat{t} denotes the unit tangential vector along the chordwise direction.

4.4 Discretization of DBC on cavity surface, S^C

Using (19) derived from the dynamic boundary condition on the cavity surface, we may express the velocity potential on the cavity as follows:

$$\begin{aligned} \phi &= \phi_{cdp} + \int_0^{l_g} v_c dl \\ &= \phi_{cdp} - \int_0^{l_g} (\vec{U}_r \cdot \hat{t}) dl + V_{cdp} \int_0^{l_g} dl \\ &\quad + \int_0^{l_g} b_c^* dl \end{aligned} \quad (20)$$

where l_g denotes the girth length along the cavity surface from the cavity detachment point to the point where the potential is calculated.

The perturbation potential at the j -th control point on the chordwise strip may now be expressed in discretized form as follows:

$$\begin{aligned} \phi_j &\simeq \phi_{N_{cdp}} + \sum_{m=N_{cdp}+1}^j v_m l_m \\ &= \phi_{N_{cdp}} + \sum_{m=N_{cdp}+1}^j \{-\vec{U}_r \cdot \hat{t}_m + V_{N_{cdp}} + b_m^*\} l_m \end{aligned} \quad (21)$$

where N_{cdp} denotes the panel index of the cavity detachment point. In (21), note that the dummy index m are defined around the blade section beginning from 1 at the lower surface of the trailing edge leading to N^P at the upper surface of the trailing edge.

The speed at the cavity detachment point $V_{N_{cdp}}$ is the only unknown quantity within the braces in (21), since all the other quantities are already known or may be evaluated from the previous time step. The perturbation potential on the cavity surface may now be recast as follows:

$$\phi_j = \phi_{N_{cdp}} + g_v V_{N_{cdp}} + g_u \quad (22)$$

where

$$\begin{aligned} g_u &= \sum_{m=N_{cdp}+1}^j \{-\vec{U}_r \cdot \hat{t}_m + b_m^*\} l_m \\ g_v &= \sum_{m=N_{cdp}+1}^j l_m \end{aligned} \quad (23)$$

4.5 Influence of dipoles and sources on cavity surface, S^C

We assume that the strengths of potential and its normal derivative are constant on each panel, and thus in all subsequent analysis, the induction integrals are to be separated out and be evaluated analytically.

The potential induced by dipoles on S^C may be expressed, using (22), as follows:

$$\begin{aligned} & \int_{S^C} \phi \frac{\partial G}{\partial n} dS \\ & \simeq \int_{S^C} (\phi_{N_{cdp}} + g_v \cdot V_{N_{cdp}} + g_u) \frac{\partial G}{\partial n} dS \\ & = \phi_{N_{cdp}} \int_{S^C} \frac{\partial G}{\partial n} dS + V_{N_{cdp}} \int_{S^C} g_v \frac{\partial G}{\partial n} dS \\ & \quad + \int_{S^C} g_u \frac{\partial G}{\partial n} dS \end{aligned} \quad (24)$$

Note that there are only two unknowns, $V_{N_{cdp}}$ and $\phi_{N_{cdp}}$, in the above equation.

The potential induced by the sources, $\partial\phi/\partial n$, on the cavity surface, S^C , may also be discretized as:

$$\int_{S^C} \frac{\partial\phi}{\partial n} G dS \simeq \sum_{j_c=1}^{N^C} \left(\frac{\partial\phi}{\partial n} \right)_{j_c} \int_{S_{j_c}^C} G dS \quad (25)$$

where N^C denotes the number of cavity source panels in the chordwise strip in question and $S_{j_c}^C$ the quadrilateral element where the integration will be performed.

4.6 Numerical Kutta condition

Kutta condition (4) should be implemented appropriately depending upon the formulation. In the present study, we follow the form derived by Kim[11] as follows:

$$\{\Delta\phi\}_{T.E.} = \phi_{N^P} - \phi_1 + H \quad (26)$$

where the function H is defined as a function of the geometrical quantities at the trailing edge and the potential variation at the panel adjacent the trailing edge. We observe that the first two terms in (26) are the terms found in the Morino's numerical Kutta condition[7]. Kim[11] showed that the last term H is negligible near the mid-radius but becomes significant in the blade tip region.

4.7 Influence of shed dipoles on trailing wake, S^W

The strength and the position of the trailing dipoles in wake should be determined in principle by satisfying the kinematic and dynamic boundary conditions on the wake surface. In linear theory, the trailing vortices shed downstream with the speed of the oncoming uniform flow, while keeping the strength obtained when leaving the trailing edge of the blade. The strength of the dipole at time t , in θ^W may be expressed by the potential jump at the trailing edge as follows:

$$\Delta\phi(\theta^W, t) = \Delta\phi_{T.E.} \left(t - \frac{\theta^W - \theta_{T.E.}}{\Omega} \right) \quad (27)$$

From (27) the potential induced by the shed dipole is expressed as follows:

$$\begin{aligned} & \int_{S^W} \Delta\phi(\theta^W, t) \frac{\partial G}{\partial n} dS \\ & = \int_{S^W} \Delta\phi_{T.E.} \left(t - \frac{\theta^W - \theta_{T.E.}}{\Omega} \right) \frac{\partial G}{\partial n} dS \end{aligned} \quad (28)$$

Equation (28) may be discretized as follows:

$$\begin{aligned} & \sum_{j=1}^{N^W} \Delta\phi_{T.E.} \left(t - \frac{\theta^W - \theta_{T.E.}}{\Omega} \right) \int_{S_j^W} \frac{\partial G}{\partial n} dS \\ & = \sum_{j=1}^{N^W} \Delta\phi_{T.E.}^{(\tau-j+1)} \int_{S_j^W} \frac{\partial G}{\partial n} dS \end{aligned} \quad (29)$$

where τ and j denote the present time step and the dipole index located in shed wake, respectively.

4.8 Discretization of integral equation for partially cavitating flow

Applying (10) to the i -th control point either on S_B^{WET} or on S^C , we obtain the following equation, that is,

$$\begin{aligned} & \phi_i(p) \\ & + \sum_{j=1}^{N^{WET}} \phi_j \int_{S_j^{WET}} \frac{\partial G}{\partial n} dS + \sum_{j_c=1}^{N^C} \phi_{j_c} \int_{S_{j_c}^C} \frac{\partial G}{\partial n} dS \\ & - \sum_{j=1}^{N^{WET}} \left(\frac{\partial \phi}{\partial n} \right)_j \int_{S_j^{WET}} G dS - \sum_{j_c=1}^{N^C} \left(\frac{\partial \phi}{\partial n} \right)_{j_c} \int_{S_{j_c}^C} G dS \\ & + \sum_{j_w=1}^{N^W} (\Delta \phi_W)_{j_w} \int_{S_{j_w}^W} \frac{\partial G}{\partial n} dS = 0 \end{aligned} \quad (30)$$

where N^{WET} and N^W denote the number of cavity panels on the wetted portion of the blade and that in the wake, respectively.

The normal flux $\partial \phi / \partial n$ is known on the wetted portion of the blade S_B^{WET} by the kinematic boundary condition (3), while it remains to be unknown on the cavitating portion S^C , and hence (30) may be rearranged as:

$$\begin{aligned} & \phi_i(p) \\ & + \sum_{j=1}^{N^{WET}} \phi_j \int_{S_j^{WET}} \frac{\partial G}{\partial n} dS + \sum_{j_c=1}^{N^C} \phi_{j_c} \int_{S_{j_c}^C} \frac{\partial G}{\partial n} dS \\ & - \sum_{j_c=1}^{N^C} \left(\frac{\partial \phi}{\partial n} \right)_{j_c} \int_{S_{j_c}^C} G dS \\ & + \{ \Delta \phi_W \}_{T.E.} \int_{S_{j_w=1}^W} \frac{\partial G}{\partial n} dS \\ & = \sum_{j=1}^{N^{WET}} \left(\frac{\partial \phi}{\partial n} \right)_j \int_{S_j^{WET}} G dS \\ & - \sum_{j_w=2}^{N^W} (\Delta \phi_W)_{j_w} \int_{S_{j_w}^W} \frac{\partial G}{\partial n} dS \end{aligned} \quad (31)$$

As observed in (24), the potential on S^C or the second term in (31) may be replaced by terms containing $\phi_{N_{cdp}}$, $V_{N_{cdp}}$ and other known quantities. Applying at the same time the numerical Kutta condition (26) and also rearranging all known terms in the right hand side, we obtain for the i -th control point the final form for the partially cavitating flow as follows:

$$\sum_{j=1}^{N^{WET}} \phi_j \beta_{ij} + \phi_{N_{cdp}} \sum_{j_c=1}^{N^C} \beta_{ij_c} + (\phi_{N^P} - \phi_1) \beta_{i(j_w=1)}$$

$$\begin{aligned} & - \sum_{j_c=1}^{N^C} q_{j_c}^{CB} \alpha_{ij_c} + V_{N_{cdp}} \sum_{j_c=1}^{N^C} g_{ij_c} \beta_{ij_c} \\ & = - \sum_{j=1}^{N^{WET}} (\vec{V}_{N_{cdp}} \cdot \hat{n}) \alpha_{ij} - \sum_{j_w=2}^{N^W} \{ \Delta \phi^W \} \beta_{ij_w} \\ & - \sum_{j_c=1}^{N^C} g_{ij_c} \beta_{ij_c} - H \beta_{i(j_w=1)} \end{aligned} \quad (32)$$

where

$$\begin{aligned} \beta_{ij} &= \int_{S_j^{WET, C, W}} \frac{\partial}{\partial n} G(\vec{p}_i; \vec{q}_j) dS \\ \alpha_{ij} &= \int_{S_j^{WET, C, W}} G(\vec{p}_i; \vec{q}_j) dS \\ q_{j_c}^{CB} &= \frac{\partial \phi}{\partial n} \end{aligned} \quad (33)$$

The influence functions above have to be evaluated on the appropriate quadrilateral elemental areas as indicated by the superscripts. Note that for the self-induced potential of the dipole $\beta_{ii} = 0.5$. We introduce a new symbol q^{CB} to represent the cavity source above the blade surface.

4.9 Discretization of integral equation for supercavitating flow

Applying (11) to the i -th control point on S^C , we obtain the following equation for the supercavitating flow, that is,

$$\begin{aligned} & \phi_i(p) \\ & + \sum_{j=1}^{N^{WET}} \phi_j \int_{S_j^{WET}} \frac{\partial G}{\partial n} dS + \sum_{j_c=1}^{N^{CB}} \phi_{j_c} \int_{S_{j_c}^{CB}} \frac{\partial G}{\partial n} dS \\ & - \sum_{j=1}^{N^{WET}} \left(\frac{\partial \phi}{\partial n} \right)_j \int_{S_j^{WET}} G dS - \sum_{j_c=1}^{N^{CB}} q_{j_c}^{CB} \int_{S_{j_c}^{CB}} G dS \\ & - \sum_{j_c=1}^{N^{CW}} q_{j_c}^{CW} \int_{S_{j_c}^{CW}} G dS \\ & + \sum_{j_w=1}^{N^W} (\Delta \phi_W)_{j_w} \int_{S_{j_w}^W} \frac{\partial G}{\partial n} dS = 0 \end{aligned} \quad (34)$$

where N^{CB} and N^{CW} are the number of panels on S^{CB} and S^{CW} , respectively, giving $N^C = N^{CB} + N^{CW}$, and the cavity sources in the wake is represented as:

$$q_{j_w}^{CW} = \left\{ \frac{\partial(\phi^+ - \phi^-)}{\partial n} \right\}_{j_w} \quad (35)$$

Rearranging (34) we obtain

$$\begin{aligned}
& \phi_i(p) \\
& + \sum_{j=1}^{N^{WET}} \phi_j \int_{S_j^{WET}} \frac{\partial G}{\partial n} dS + \sum_{j_c=1}^{N^{CB}} \phi_{j_c} \int_{S_{j_c}^{CB}} \frac{\partial G}{\partial n} dS \\
& - \sum_{j_c=1}^{N^{CB}} q_{j_c}^{CB} \int_{S_{j_c}^{CB}} G dS \\
& - \sum_{j_c=1}^{N^{CW}} q_{j_c}^{CW} \int_{S_{j_c}^{CW}} G dS + (\Delta\phi)_{T.E.} \int_{S_{(j_w=1)}^W} \frac{\partial G}{\partial n} dS \\
& = \sum_{j=1}^{N^{WET}} \left(\frac{\partial \phi}{\partial n} \right)_j \int_{S_j^{WET}} G dS \\
& - \sum_{j_w=2}^{N^W} (\Delta\phi_W)_{j_w} \int_{S_{j_w}^W} \frac{\partial G}{\partial n} dS
\end{aligned} \tag{36}$$

The equation (36) takes a different form depending upon the position of the control point as give below. Again we apply the relation (22) to express the potential on the cavity surface.

When the control point falls on S_B^{WET} or S^{CB} , (36) becomes as follows:

$$\begin{aligned}
& (\beta_{i1} - \beta_{i(j_w=1)})\phi_1 + \sum_{j=2}^{N_{cdp}-1} \beta_{ij}\phi_j \\
& + (\beta_{iN_{cdp}} + \sum_{j_c=1}^{N^{CB}} \beta_{ij_c} + \beta_{i(j_w=1)})\phi_{N_{cdp}} \\
& + V_{N_{cdp}}(g_{N^P}^v \beta_{i(j_w=1)} + \sum_{j_c=1}^{N^{CB}} g_{j_c}^v \beta_{ij_c}) \\
& - \sum_{j_c=1}^{N^{CB}+N^{CW}} \alpha_{ij_c} q_{j_c}^C \\
& = \sum_{j=1}^{N^{WET}} \alpha_{ij} \left(\frac{\partial \phi}{\partial n} \right)_j - \sum_{j_w=2}^{N^W} \beta_{ij_w} (\Delta\phi_W)_{j_w} \\
& - \beta_{i(j_w=1)} g_{N^P}^u - \sum_{j_c=1}^{N^{CB}} \beta_{ij_c} g_{j_c}^u
\end{aligned} \tag{37}$$

For the Kutta condition in supercavitating flow, we use the relation (26) without H term. For the potential on the upper surface of the trailing edge, we used from (22) the relation $\phi_{N^P} = \phi_{N_{cdp}} + g_{N^P}^v V_{N_{cdp}} + g_{N^P}^u$.

When the i_c -th control point falls on S^{CW} , recalling that the potential at the control point on the cavity is $\phi_{i_c}^+ = \phi_{N_{cdp}} + g_{i_c}^v V_{N_{cdp}} + g_{i_c}^u$ from (22), we

obtain the following:

$$\begin{aligned}
& (\beta_{i1} - \beta_{i(j_w=1)})\phi_1 + \sum_{j=2}^{N^{WET}-1} \beta_{ij}\phi_j \\
& + (1 + \beta_{iN^{WET}} + \sum_{j_c=1}^{N^{CB}} \beta_{ij_c} + \beta_{i(j_w=1)})\phi_{N_{cdp}} \\
& + V_{N_{cdp}}(g_{i_c}^v + g_{N^P}^v \beta_{i(j_w=1)} + \sum_{j_c=1}^{N^{CB}} g_{j_c}^v \beta_{ij_c}) \\
& - \sum_{j_c=1}^{N^{CB}+N^{CW}} \alpha_{ij_c} q_{j_c}^C \\
& = \sum_{j=1}^{N^{WET}} \alpha_{ij} \left(\frac{\partial \phi}{\partial n} \right)_j - \sum_{j_w=2}^{N^W} \beta_{ij_w} (\Delta\phi_W)_{j_w} \\
& - g_{i_c}^u - \beta_{i(j_w=1)} g_{N^P}^u - \sum_{j_c=1}^{N^{CB}} \beta_{ij_c} g_{j_c}^u
\end{aligned} \tag{38}$$

4.10 Cavity closure condition and representation of cavity shape

The cavity closure condition (9) assumes that the thickness of the cavity along its boundary surface outline should vanish. To derive a relation between the cavity shape and the source strengths on the cavity, we take time derivative to the cavity surface function $F = \eta - h(s, t) = 0$ along the surface and linearize on the cavity surface to obtain (neglecting the spanwise derivative)

$$\begin{aligned}
\frac{DF}{Dt} &= \left(\frac{\partial}{\partial t} + \vec{V} \cdot \nabla \right) (\eta - h(s, t)) \\
&= -\frac{\partial h}{\partial t} + v_\eta - U_r \frac{\partial h}{\partial s} = 0
\end{aligned} \tag{39}$$

In the present linearized problem, the real cavity surface is collapsed upon the upper surface of the blade. We will satisfy the dynamic boundary condition only on the cavitated portion of the blade to determine the strength of the normal flux $\partial\phi/\partial n$. This term may be considered an error in kinematic boundary condition on linearized cavity surface and be related to cavity thickness as follows:

$$\vec{U}_r \cdot \hat{n} + \frac{\partial \phi}{\partial n} \simeq v_\eta = \frac{\partial h}{\partial t} + U_r \frac{\partial h}{\partial s} \tag{40}$$

The cavity thickness, $T^c(s, t)$ may be defined as the difference of the upper and lower surfaces of the cavity $h^+(s, t)$ and $h^-(s, t)$. In the present partially cavitating flow, the lower surface coincides with the blade surface. Equation (40) is a one-dimensional wave equation and has to be solved in time and space.

Since we assume the unsteadiness is small in the present study, we drop without proof the time derivative term to simplify our numerical procedure.

As in thin wing theory, the cavity thickness function is then expressed as an integral of the normal flux obtained in (40)

$$T^c(s, t) = \frac{1}{U_r} \int_{cdp}^s \left(\frac{\partial \phi}{\partial n} + \vec{U}_r \cdot \hat{n} \right) ds \quad (41)$$

The cavity closure condition requires that the thickness at the cavity trailing end(cte) be zero, that is, $T^c(s_{cte}, t) = 0$, and hence we have

$$0 = \int_{cdp}^{cte} \left(\frac{\partial \phi}{\partial n} + \vec{U}_r \cdot \hat{n} \right) ds \quad (42)$$

We may discretize the above equation and rearrange to obtain, recalling (33) and (35),

$$\sum_{j_c=1}^{N^C} (q^C)_{j_c} \Delta s_{j_c} = - \sum_{j_c=1}^{N^C} (\vec{U}_r \cdot \hat{n})_{j_c} \Delta s_{j_c} \quad (43)$$

4.11 Formation of simultaneous equations and solution procedure

For the partially cavitating flow, by applying (32) to the control points on both S_B^{WET} and S^C , together with the closure condition equation (43), we obtain $N^P + 1$ linear simultaneous equations for the total of $N^P + 1$ unknowns (which consists of N^{WET} ϕ_j 's, N^C $\frac{\partial \phi}{\partial n}$'s and the speed at the leading edge $V_{N_{cdp}}$) and hence we can uniquely determine the unknowns. The same statement may be made for the supercavitating case. The total number of unknowns, $N^{WET} + N^C + 1$, may be matched by the same number of equations derived from KBC and DBC, along with a closure condition.

Since the cavity extent is not known a priori, we assume the cavity extent at each time step and compute the cavitation number, σ_{com} , corresponding to $V_{N_{cdp}}$. We then check whether the specified cavitation number, σ in (13), falls between the two consecutive computed cavitation numbers. By observing that the cavity length is inversely proportional to the cavity number, we interpolate the cavity extent and also all other physical quantities for the specified cavitation number.

Once the values of the flux $\partial \phi / \partial n$ is known, the cavity shape is computed using (41), and constructed on the upper surface of the blade.

5 Results and Discussions

5.1 2-D cavitating hydrofoil in gust

The present formulation was already applied successfully to the steady 2-dimensional cavity flow by Lee et al[6]. As a next unsteady example, we select a foil advancing in heave mode with the reduced frequency $k = \omega c / 2U = 0.5$, and the cavitation number based on the oncoming mean free stream speed, U , $\sigma = 1.2$. The reduced frequency, $k = 0.5$, is a representative of a typical container ship propeller. The foil has a symmetric NACA profile with 6% thickness, and is positioned at an angle of attack $\alpha = 4$ deg. The foil surface is discretized with $N^P = 60$, and the time domain is discretized to have the number of steps per wave length, $N_\lambda = 40$. Figures 6, 7 and 8 show the lift coefficient, the cavity volume and the cavity pattern variation as a function of time. In Figure 8 the vertical scale is exaggerated arbitrarily to facilitate the observation. See Kim and Lee[12] for details.

5.2 3-D rectangular hydrofoil

3-D Convergence test: A systematic convergence test is carried out with a rectangular hydrofoil of aspect ratio, $A.R. = 5.0$, located in a uniform stream at $\alpha = 5.0$ deg., with $\sigma = 1.2$. The hydrofoil has an NACA0006 section at the midspan, tapering elliptically to zero at the tip of hydrofoil. Figure 9 shows the convergence of the cavity extent for the partially cavitating case. We observe that, increasing the number of panels, the cavity extent converges to smaller values. A similar behavior is observed for the supercavitating flow[9]. We observe that for both cases the cavity shape at the midspan of the hydrofoil is similar to the solutions in the corresponding 2-D problem. For both cases the number of chordwise panel $N^P = 40$ and the number of spanwise panel $M^P = 20$ are recommended to assure the convergence. We may conclude that the present numerical scheme produces reasonable results for both the partially and supercavitating 3-D hydrofoils in steady motion. The cavity thickness distribution for the partially cavitating case is shown in Figure 10. The lift and drag coefficients converges faster than the cavity shape. See Kim et al[9] for details.

3-D hydrofoil in heave: For the same rectangular hydrofoil in heave, the unsteady partially cavitating behavior is predicted for the conditions of $\sigma = 1.2$, $k = 0.5$, $\alpha = 5$ deg and the heaving amplitude $A_h/c = 0.01$. See Kim[11] for details.

5.3 Cavity prediction in steady propeller flow

To check the prediction of the steady cavity flow, we selected DTRC Propeller 4381 for which cavity extent observations by Boswell[13] and Lee[2] are available. Figure 11 shows the cavity extent predicted by the present method and that predicted by Lee[2] together with observations by Boswell[13] and Lee for the propeller operating in uniform flow with the cavitation number $\sigma_n = 1.92$ at $J_A = 0.7$. We observe that the correlation with Boswell's observation is reasonably good from the hub up to $r/R = 0.8$, while the difference grows nearing the tip. We believe that the solution at or near the tip strip is not reliable yet and hence the solution inboard from the tip strip may be deteriorated.

5.4 Unsteady cavitation on propeller in ship wake

To investigate the validity of the present formulation in unsteady ship wake flow, we selected a 6300 TEU container ship propeller (HSVA Model 2395) whose geometrical particulars may be found in Figure 12. Figure 13 shows the nominal velocity contour measured at the towing tank of HSVA(Hamburg Ship Model Basin). Unfortunately the wake pattern at the HYKAT(HSVA large cavitation tunnel) is not measured. We use the model nominal wake for our computation.

The time history of the cavitating pattern, computed with $\Delta\theta_p = 6$ deg. intervals, is shown at selected angular positions in Figure 14 for the container ship propeller with the cavitation number $\sigma_n = 1.7144$, the Froude number $F_n = 2.4868$ and the advance coefficient $J_A = 0.7013$. Experimental observations of the cavity extent at HYKAT are shown in Figure 15.

We observe that the predicted cavity extent is slightly larger than that observed. It should however be noted that the speed at the cavitation tunnel is about three times faster than that at the towing tank, and hence the boundary layer near the stern at HYKAT is considered thinner than the corresponding value at the towing tank. To find out the source of discrepancy between the tunnel result and the present prediction, further study is necessary with the wake measured directly at the cavitation tunnel.

For the same case, Figure 16 shows the cavity volume variation for the first five revolutions of the propeller. We observe that the cavity volume variation in each cycle converges to an asymptote very rapidly. This cavity volume variation will be the most

important information in judging the cavity influence upon the fluctuating pressures on an adjacent hull surface.

In Figure 17, the axial thrust variation under the cavitating condition is compared with the corresponding variation under the noncavitating condition. We observe that the loading on a cavitating propeller slightly increases due to the additional camber effect of the cavity.

To check the influence of the angular step, we repeated the same computing but this time by doubling the angular step $\Delta\theta_p = 12$ deg, and compared with that obtained with 6 deg spacing, as shown in Figure 18. The two results are almost identical except the supercavity portion near the tip. This is caused by the longer panel size(doubled in chordwise direction). Although all the sample computations are made with finer angular step, 6 degree spacing is a good alternative in estimating the cavitation behavior at the initial design stage, since it reduces the CPU time by a factor of two.

5.5 Unsteady cavitation on propeller in screen-generated wake

Further computations are carried out with another propeller for which the wire-mesh generated wake data is available. The geometrical particulars of the Propeller KP325 may be found in Figure 19. Figure 20 shows the nominal velocity contour simulated at the KRISO cavitation tunnel for a 4400TEU container carrier.

The time history of the cavitating pattern is shown at selected angular positions in Figure 21 with the cavitation number $\sigma_n = 2.04$, the Froude number $F_n = 2.072$ and the advance coefficient $J_A = 0.7642$. Experimental observations of the cavity extent at the KRISO cavitation tunnel are shown in Figure 22.

We observe that the correlation is very good, especially the close resemblance at the blade angle of 320 degrees when the cavity just starts. In general the predicted cavity extent is slightly larger than that observed. We expect that the correlation might be improved further once the effective velocity distribution is taken into consideration in the propeller-cavity analysis procedure.

6 Conclusions

A low order potential-based panel method is developed to treat the partial- or super-cavitating propellers operating in ship-generated wake.

The method is systematically validated through a series of tests varying the geometry from the simple 2-D profile to 3-D rectangular foil and propeller and also covering the steady and unsteady cavitation phenomena. The numerical formulation and procedure is evidenced robust and stable.

The cavity behavior predicted for the propeller operating behind a model ship and that operating in screen-generated wake shows good correlations with experiments.

The CPU for a typical six-bladed propeller is about 4 hours on the CRAY YMP2(16 GFLOPS) supercomputer for 5 rotations of propeller. This is the only drawback of the current procedure, which may still be considered to be a strong and reliable candidate to substitute the model experiments in saving the cost and time.

References

- [1] Kerwin, J. E. & Lee, C.-S., "Prediction of steady and unsteady marine propeller performance by numerical lifting surface theory," *Trans. SNAME*, Vol. 86, 1978, pp. 218-258
- [2] Lee, C.-S., "Prediction of steady and unsteady performance of marine propellers with or without cavitation by numerical lifting surface theory," Ph.D. Thesis, M.I.T., Cambridge, Mass., 1979.
- [3] Kinnas, S.A., "Leading edge correction to the linear theory of partially cavitating hydrofoils," *J. of Ship Research*, Vol. 35, No. 1, March 1991, pp. 15-27.
- [4] Lee, C.-S., "A potential-based panel method for the analysis of a 2-dimensional partially cavitating hydrofoil," *J. of Soc. of Naval Arch. of Korea(SNAK)*, Vol. 26, No. 4, 1989, pp. 27-34.
- [5] Uhlman, J. S., "The surface singularity method applied to partially cavitating hydrofoils," *J. of Ship Research*, Vol. 31, No. 2, June 1987, pp. 107-124.
- [6] Lee, C.-S., Kim, Y.-G. & Lee, J.-T., "A potential-based panel method for the analysis of a two-dimensional super- or partially cavitating hydrofoil," *J. of Ship Research*, Vol. 36, No. 2, June 1992, pp. 168-181
- [7] Morino, L. and Kuo, C.-C., "Subsonic potential aerodynamic for complex configurations: a general theory," *AIAA Journal*, Vol. 12, No. 2, 1974, pp. 191-197.
- [8] Kinnas, S. A. & Fine, N. E., "Nonlinear analysis of the flow around partially or supercavitating hydrofoils by a potential based panel method," *IABEM-90 Symposium of the International Association for Boundary Element Methods*, Springer-Verlag, Rome, Italy, 1990, pp. 289-300.
- [9] Kim, Y.-G., Lee, C.-S. and Suh, J.-C., "Surface panel method for prediction of flow around a 3-D steady or unsteady cavitating hydrofoil," *Cavitation '94, The Second International Symposium on Cavitation*, Tokyo, Japan, 1994, pp. 113-120.
- [10] Fine, N. E., "Nonlinear analysis of cavitating propellers in nonuniform flow," Ph.D. Thesis, M.I.T., Cambridge, Mass., 1992.
- [11] Kim, Y.-G., "Prediction of unsteady performance of marine propellers with cavitation using surface panel method," Ph.D. Thesis, Chungnam National University, Taejeon, Korea, 1995.
- [12] Kim, Y.-G. and Lee, C.-S., "Prediction of unsteady cavity behavior around a 2-D hydrofoil in heave or gust," *The second Japan-Korea Joint Workshop on Ship and Marine Hydrodynamics*, Osaka, Japan, June 28 - 30, 1993, pp.299-308.
- [13] Boswell, R.J., "Design, cavitation performance, and open-water performance of a series of research skewed propellers," *DTNSRDC Report 3339*, March 1971.

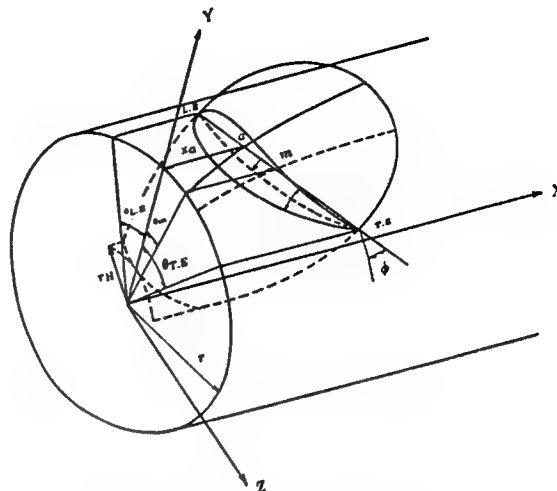


Figure 1: Coordinate system

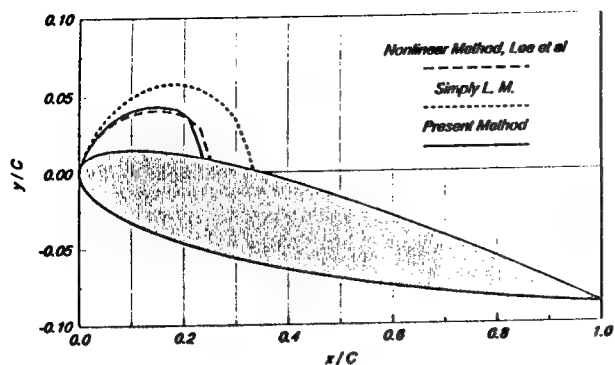


Figure 2: Comparison of cavity shapes predicted by linear and nonlinear theories for partial cavity

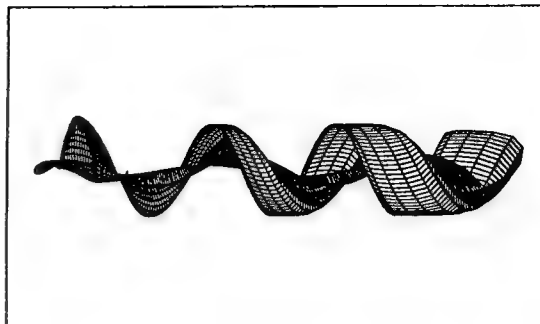


Figure 5: Nonlinear wake geometry

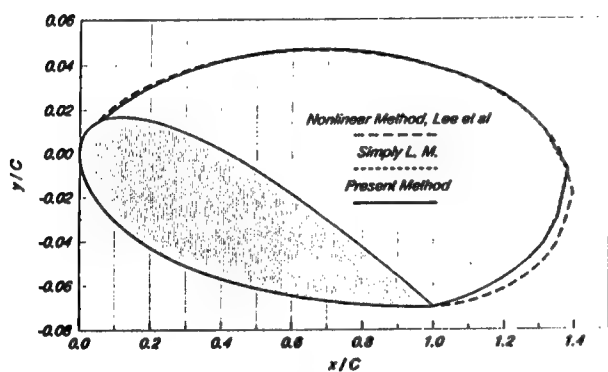


Figure 3: Comparison of cavity shapes predicted by linear and nonlinear theories for super-cavity

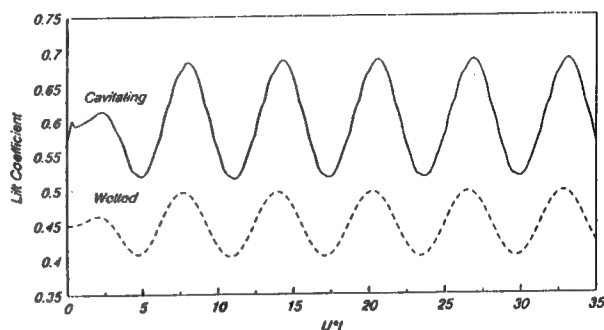


Figure 6: Lift coefficient variation with time for a partially cavitating hydrofoil in heave

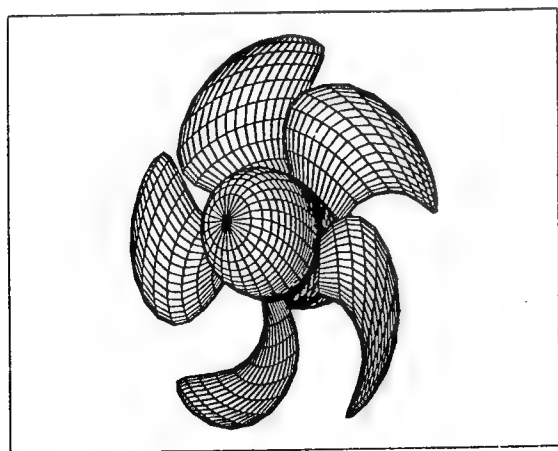


Figure 4: Quadrilateral representation of a propeller blade

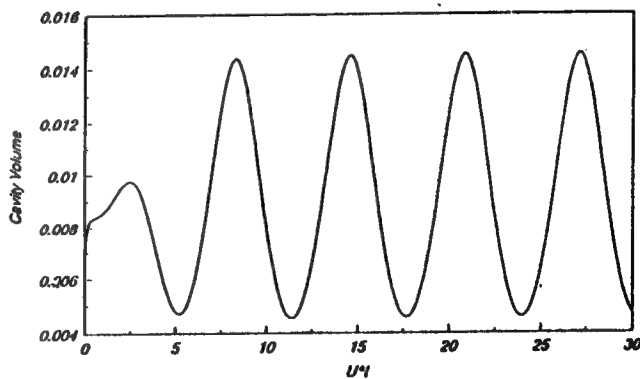


Figure 7: Cavity volume variation with time for a partially cavitating hydrofoil in heave

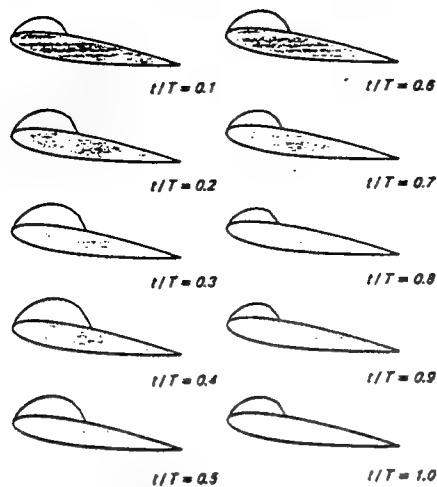


Figure 8: Cavity shape variation with time for a partially cavitating hydrofoil in heave; T = Period of heaving motion

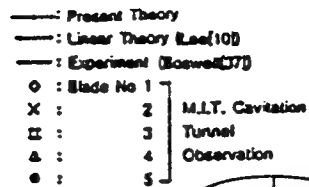


Figure 11: Comparison of cavity extent between predictions and observations for DTRC Propeller 4381 at $J_A = 0.7$ with $\sigma_n = 1.92$

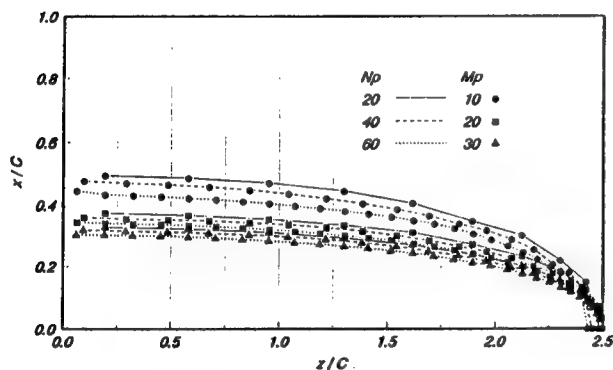


Figure 9: Convergence characteristics of cavity extent with the number of panels distributed on a rectangular hydrofoil

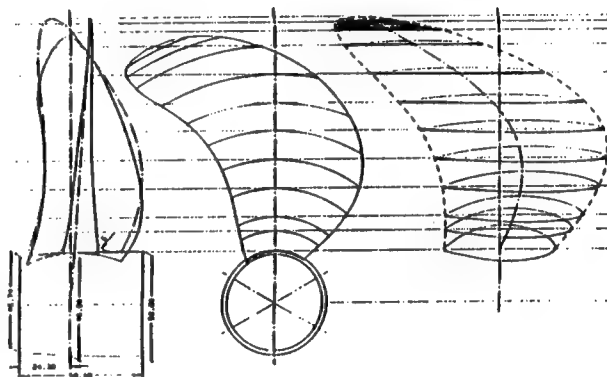


Figure 12: Drawing of 6300 TEU Propeller

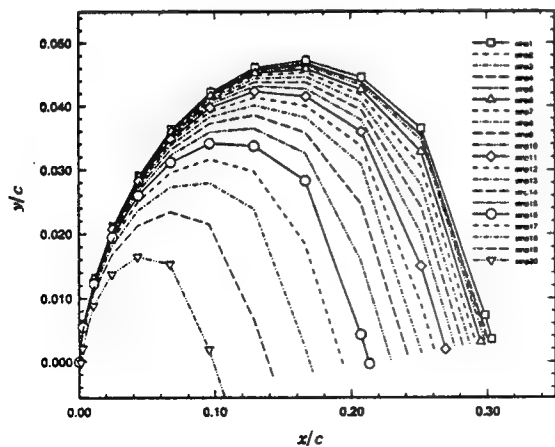


Figure 10: Cavity shape for a partially cavitating rectangular hydrofoil

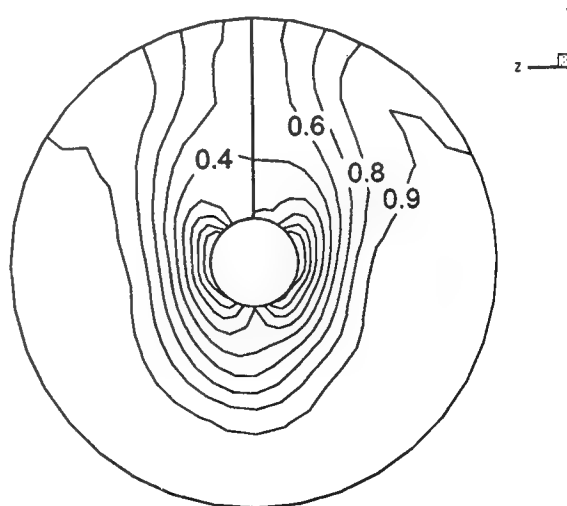


Figure 13: Iso-axial velocity (V_A/V_s) contours of the wake measured at HSVA towing tank

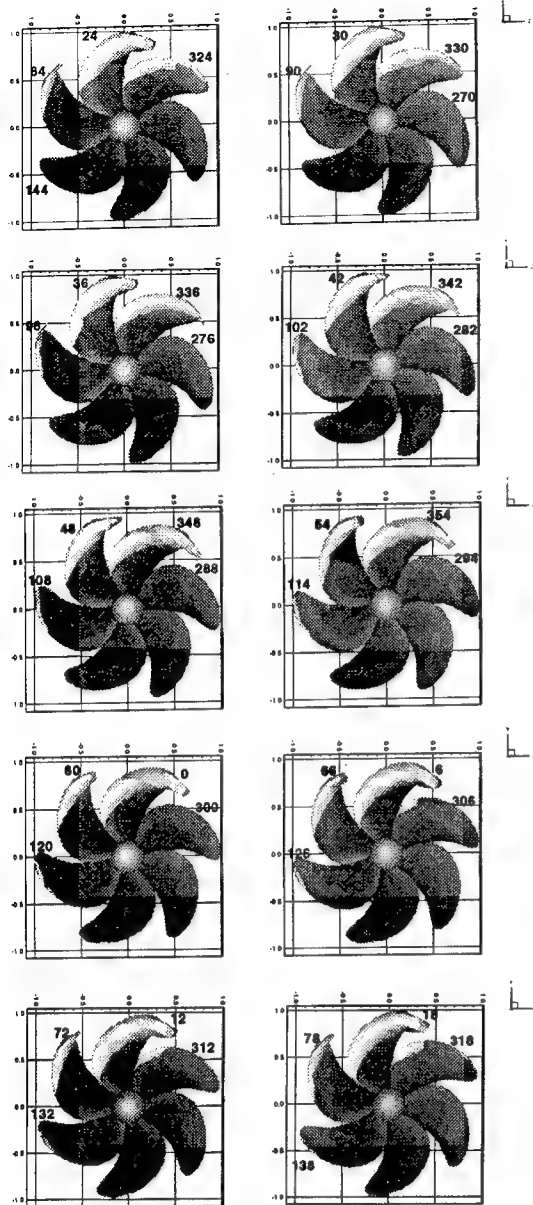


Figure 14: Predicted cavity pattern for HSVA Propeller at $J_A = 0.7013$ with $\sigma_n = 1.7144$ and $F_n = 2.4868$

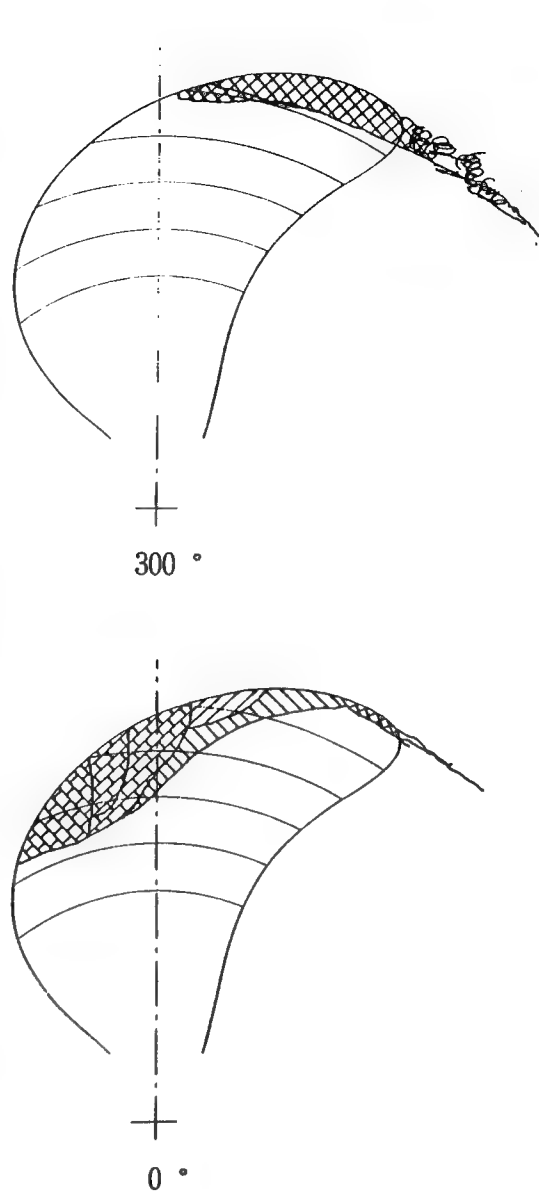


Figure 15: Sketch of the cavitation pattern on HSVA Propeller (Full-load condition)

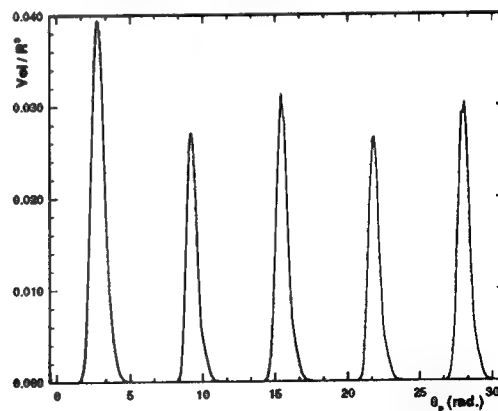


Figure 16: Cavity volume on the key blade versus blade angle for HSVA Propeller

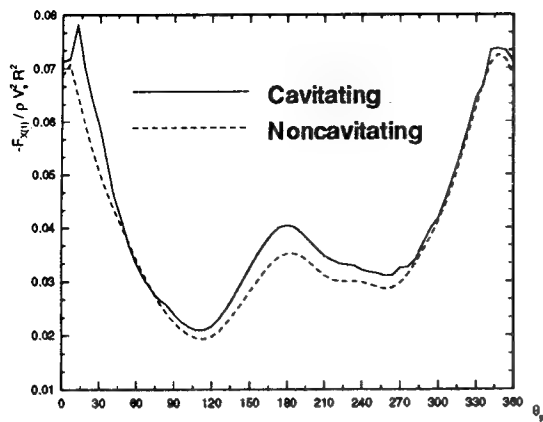


Figure 17: Thrust on the key blade versus blade angle for HSVA Propeller

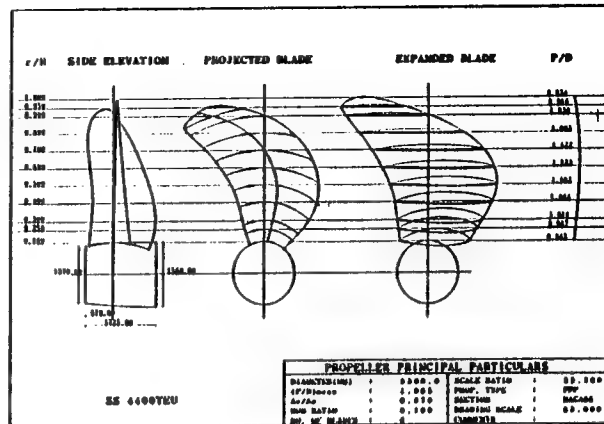


Figure 19: Drawing of KP325 Propeller

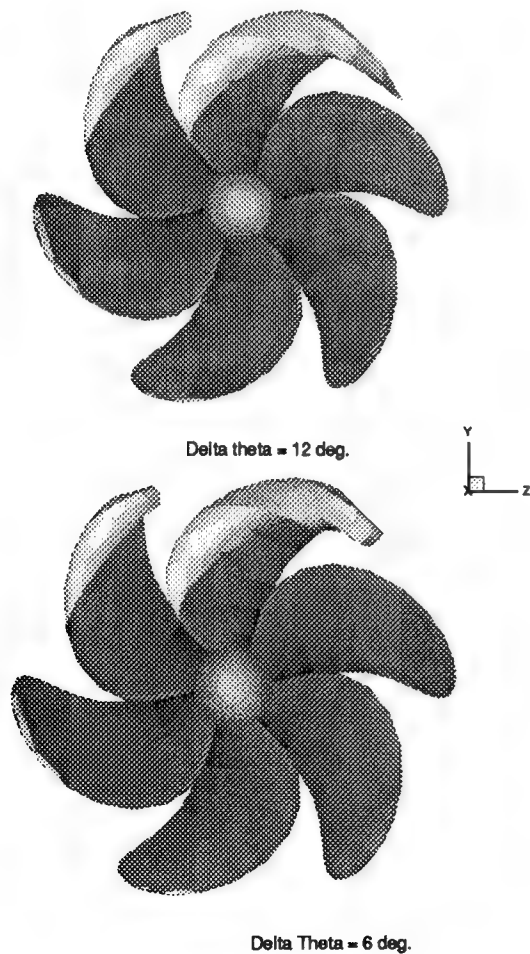


Figure 18: Comparison of cavity extents predicted with $\Delta\theta_p = 12$ deg(top) and 6 deg(bottom)

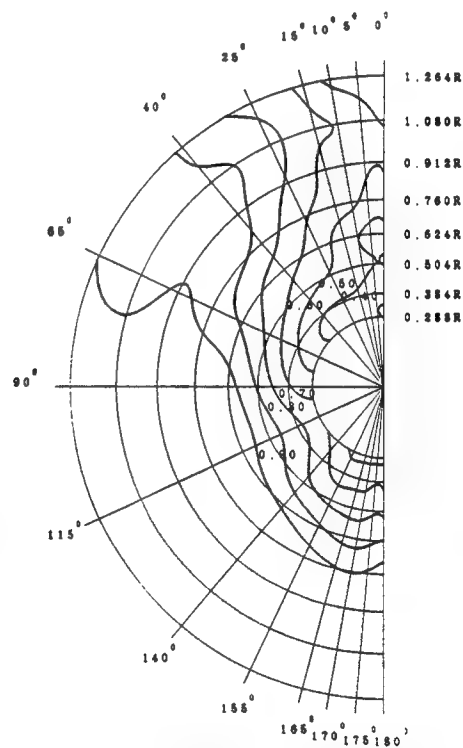


Figure 20: Iso-axial velocity (V_A/V_s) contours of the wake simulated at KRISO cavitation tunnel

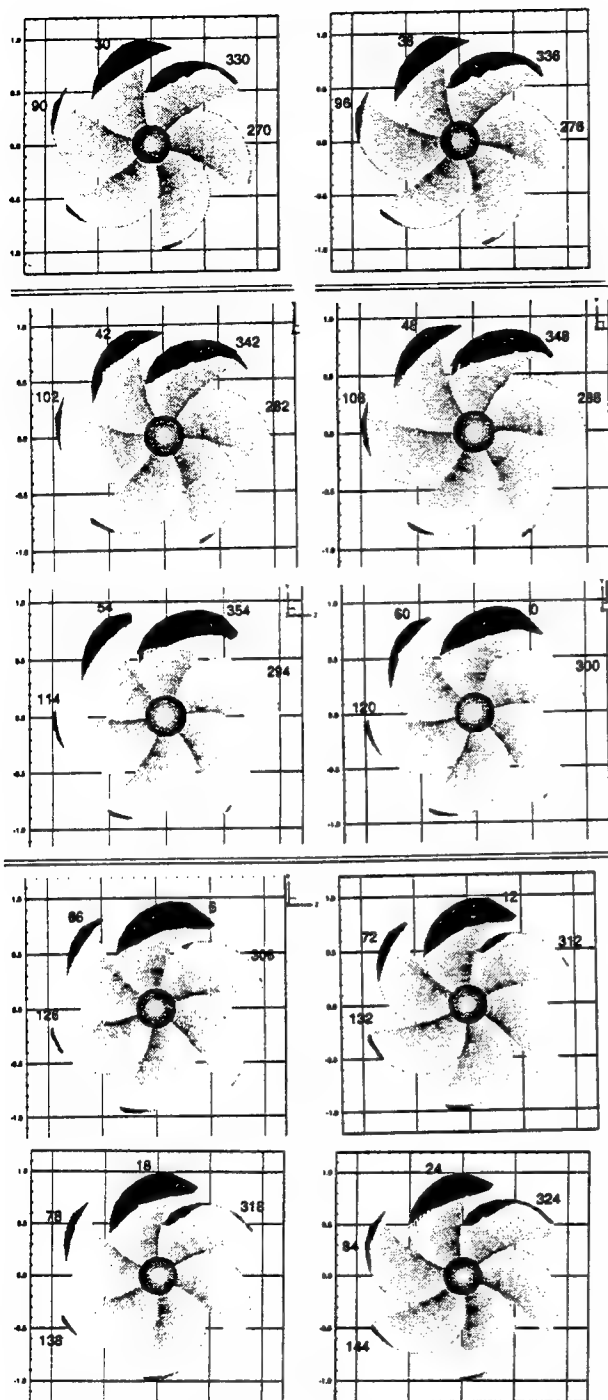


Figure 21: Predicted cavity pattern for KP325 Propeller at $J_A = 0.7642$ with $\sigma_n = 2.040$ and $F_n = 2.072$

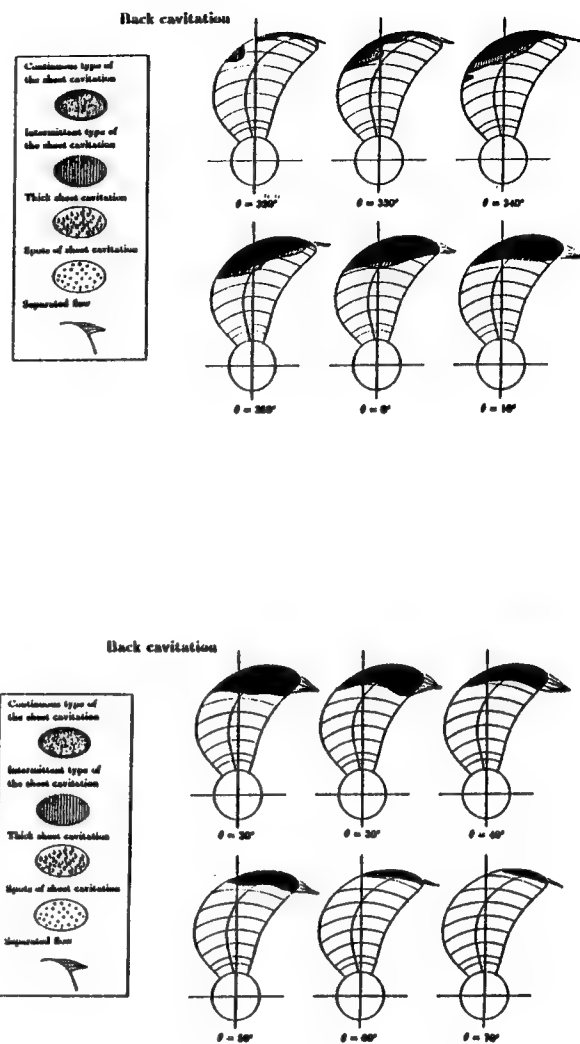


Figure 22: Sketch of the cavitation pattern on KP325 Propeller (Full-load condition)

DISCUSSION

S.A. Kinnas

University of Texas at Austin, USA

The authors should be commended for their efforts to implement a panel method for the prediction of unsteady propeller cavitation. A very similar method was presented at the 19th CNR Symposium on Naval Hydrodynamics (1992) by Kinnas and Fine. It would be interesting to hear the author's comments on the following issues:

(a) How do they determine the cavity detachment point?

(b) How do they plan to improve the slow convergence of the predicted cavity platform (see Fig. 9)? In the work mentioned above we found that we had to develop a special treatment of the panel at which the cavity ends (the so-called "split-panel") in order to improve the convergence.

(c) From Figures 4 and 18 it appears that they have only used 10 panels in the spanwise direction. Has this been found to be sufficient for predicting the cavity shapes on the propeller, especially since they show that their predicted cavity shapes converge slowly with number of panels?

It would be nice to include in their reply a convergence study with number of panels for one of the propellers for which they compare their results with measurements.

AUTHORS' REPLY

NONE RECEIVED

A Comparative Study of Conventional and Tip-Fin Propeller Performance

P. Anderson (Technical University of Denmark, Denmark)

ABSTRACT

During more than a decade several attempts have been made to obtain higher propeller efficiencies by radically modifying the geometry in the tip region of the blade. In the tip-fin propeller a tip fin or winglet is attached to the blade tip and integrated into the blade in such a way that the blade tip is softly curved towards the suction side.

Whereas the developments previously have been concentrated mainly on increasing the efficiency of the propeller, the emphasis of current efforts has been on both high efficiency as well as good cavitation properties. This has resulted in a design with a combination of skew and tip fin. To evaluate the design, open-water, self-propulsion and cavitation model tests have been carried out. The tests are done for the conventional propeller originally designed for the ship and for a tip-fin propeller designed for the same ship under the same operating conditions.

The results of the model tests show higher open-water efficiency of the tip-fin propeller as well as higher over-all propulsive efficiency. Depending on the method used in the full-scale extrapolation this corresponds to a reduction in propulsive power of 3.7 to 4.7 per cent. Both propellers suffer from slight suction side sheet cavitation in the inhomogeneous wake field behind the ship. The tip-fin propeller suffered a little more from cavitation than the conventional propeller which gave rise to maximum, measured, first-order pressure pulses of 1.3 to 1.4 times those of the conventional propeller.

INTRODUCTION

The idea of obtaining higher efficiencies of ship propellers by modifying the tip of the blades, which

lead to the present design, was originally initiated by a paper by Prandtl and Betz [1]. In 1924 they conducted a series of wind tunnel tests with aircraft wings fitted with elliptical end plates and found considerably improved lift-drag ratios at higher loadings. About 50 years later, in the mid seventies, NASA took up the idea of wing tip modifications and developed aerodynamically shaped fins called winglets that were fitted to the wing tips [2]. Many modern airliners now feature such winglets. During the adoption of the concept of winglets to propellers it soon became apparent that a rational criterion would be necessary if a successful design should be achieved. The reason is that adding blade area in the tip region gives larger frictional drag, which must be more than annulled by the otherwise beneficial effects of the tip modifications. A theoretical procedure was established by which it was possible to carry out calculations for optimum propellers with winglets or tip fins [3]. It was found that the winglet should be integrated in the blade by a curved transition area ending in the tip fin. Moreover, the tip fin should point towards the suction side of the blade. These basic guidelines characterize the tip-fin propeller and have been retained in later work.

Other concepts of blade-tip modification use pressure-and-suction-side pointing bladelets [4], [5] or end plates towards the suction side [6]. The latter is based on a design using a "Cascades Theory" and several successful full-scale applications are claimed. Optimally designed propellers with two-sided shifted end plates on the blades have been developed by highly sophisticated lifting-surface theory [7] and increases in efficiency are confirmed by model tests [8].

For tip-fin propellers designed according to the guidelines outlined above, experimental verification of predicted improvements in efficiency was reported in [9]. Although the propellers of the small series tested were designed for open water conditions, experiments with a propeller in behind condition and cavitation experiments gave promising results in form of predicted power savings of 5 to 6 per cent for a 225 m, 22 knot container ship.

The examination reported in the present paper was conducted to see, whether the promises would be fulfilled for a tip-fin propeller designed for a given ship. The idea was to make a complete tip-fin propeller design computation and model tests consisting of resistance, open-water, self-propulsion and cavitation tests and compare and analyse those results with similar results for the conventional propeller, designed for the same ship. Although such model tests with the conventional propeller had been conducted earlier, all tests were repeated to exclude as many errors and inaccuracies as possible. This comparative study with analyses of results will be presented in the following sections after an outline of the tip-fin propeller design method which is given next.

DESIGN METHOD

In the first publications on tip-fin propellers in which the present author was involved [3], [9], a simple criterion was used to find the optimum distribution of loading over the span of the blade and tip fin. Since then improvements have been implemented and now a numerical method is used based on a variational approach. It is essentially the same procedure as that published by Kerwin and his colleagues [10] but modified to suit the special geometry. It will be outlined below.

The mid-chord line is given and is described in a cylindrical coordinate system by its coordinates $(x(s), r(s), \theta(s))$, all functions of the arc length s , cf. Figure 1. The velocity in a point on this line is

$$\begin{aligned} U_a &= V_a + u_a \\ U_r &= V_r + u_r \\ U_t &= \omega r - u_t \end{aligned} \quad (1)$$

where V_a and V_r are the axial and radial components of the circumferentially constant but radially varying wake velocity, ωr is the tangential component due to rotation and u_a , u_r and u_t are the velocity components induced by the propeller.

If all bound circulation over the blade were concentrated in the mid-chord line and had the

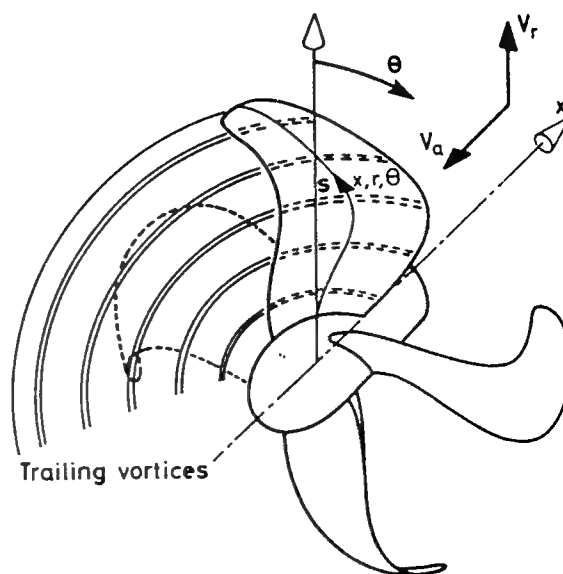


Figure 1 Geometry of propeller with lattice of free, trailing vortices.

strength $\Gamma(s)$ the thrust and torque without friction could be written as

$$T = \rho Z \int_{s_{\min}}^{s_{\max}} \Gamma(s) \left(\frac{\partial r}{\partial s} (\omega r - u_t) - r \frac{\partial \theta}{\partial s} (V_r + u_r) \right) ds \quad (2)$$

$$Q = \rho Z \int_{s_{\min}}^{s_{\max}} \Gamma(s) r \left(\frac{\partial r}{\partial s} (V_a + u_a) - \frac{\partial x}{\partial s} (V_r + u_r) \right) ds$$

where Z is the number of blades. Note that if $\theta \equiv 0$, $x \equiv 0$, then $s = r$, $\partial r / \partial s = 1$ and (2) would be the force expressions used in normal lifting-line theory.

To proceed as in [10] the mid-chord line is subdivided into segments as indicated in Figure 1. The integrations in (2) then become sums and, moreover, the induced velocities are given as

$$u_{a,r,t}(i) = \sum_{j=1}^N \Gamma_j u_{a,r,t}(i,j) \quad (3)$$

where $u_a(i)$ is the axial velocity induced in the mid-chord line segment no. i . This gives the following expressions for the thrust and torque

$$T = \rho Z \sum_{i=1}^N \Gamma_i \left\{ \frac{\partial r_i}{\partial s} \left(\omega r_i - \sum_{j=1}^N \Gamma_j u_r(i, j) \right) - r_i \frac{\partial \theta_i}{\partial s} \left(V_r(r_i) + \sum_{j=1}^N \Gamma_j u_r(i, j) \right) \right\} \Delta s_i \quad (4)$$

$$Q = \rho Z \sum_{i=1}^N \Gamma_i r_i \left\{ \frac{\partial r_i}{\partial s} \left(V_a(r_i) + \sum_{j=1}^N \Gamma_j u_a(i, j) \right) - \frac{\partial x_i}{\partial s} \left(V_r(r_i) + \sum_{j=1}^N \Gamma_j u_r(i, j) \right) \right\} \Delta s_i$$

As shown by Kerwin et al. [ibid.] a variational approach is then used to establish a system of linear equations in Γ_i (and the Lagrange multiplier) which will lead to the optimum propeller with minimum torque for required thrust. An iterative scheme is adapted using values of previous loops in computing the frictional components of thrust and torque and in aligning the trailing vortices behind the propeller.

Because the velocities are computed on the curved mid-chord line, the influence coefficients $u_{a,r,i}(i, j)$ are computed with free and bound vortices distributed over the blade in a fashion similar to the one used in the vortex-lattice method. The trailers are aligned on helical lines. The integrations are carried out directly.

The optimization is carried out for a given geometry of the mid-chord line, and the general idea is to do several calculations with systematically varied geometries. The output of each optimization is a preliminary blade geometry which can be evaluated not only with respect to efficiency, but also taking other criteria, such as security against cavitation etc. into account. Once the, in its total sense, optimum preliminary propeller has been found, the preliminary blade geometry and the loading is given as input to a lifting-surface computer program which upon the specified chordwise distribution of loading traces the blade geometry of the final propeller.

COMPARATIVE PROPELLER DESIGN

To secure the most realistic comparison between a tip-fin and a conventional propeller from a shipowner's or a shipyard's point of view the design was carried out for an actual ship. Results were available of open-water, self-propulsion and cavitation tests with the model of the propeller originally designed for the ship. Main particulars of the ship are given in Table 1.

Table 1 Main particulars of ship and design data

Ship type: container, single screw	
L_{pp}	124.55 m
B	20.80 m
T	7.50 m
V	14255.7 m ³
Speed	9.03 m/s (17.55 knots)
Thrust deduction fraction	0.136
Mean wake fraction	0.267
Thrust	706.7 kN
Resistance allowance	9 per cent

In addition to ship and propeller models being available they were selected for the comparative study out of consideration for the propeller loading, which was moderate ($C_{Th} = 1.545$), a wake field which was typical for a ship of that size and displacement and a combination of thrust loading coefficient and advance ratio which was favourable for both the conventional and tip-fin propeller.

Drawing and main particulars of the conventional or reference propeller are shown in Figure 2. The propeller was designed for the ship by the Danish Maritime Institute, DMI. In the design the highest possible efficiency was emphasized, but in the same time a certain amount of tip unloading was applied to limit the extent of possible noise and vibration. The propeller was designed to absorb a given power at a given rate of revolutions, producing as high a thrust as possible. The expected corresponding ship speed was found from the model test results. In this case it corresponds to an allowance or increase in resistance of 9 per cent.

The tip-fin propeller was designed to have the same number of blades, the same diameter and the same expanded-area ratio as the comparative propeller. It was also designed to operate in the same wake field and to produce the same thrust at minimum power. This design for given thrust is in contrast to the reference propeller which was designed for given power absorption. This means that the tip-fin propeller may operate at a rate of revolutions different from that of the conventional propeller for a given ship speed. The reason for this selection of constant parameters is that the diameter is considered as the more restrictive variable than the rate of revolutions, since the diameter should generally be selected as large as is physically

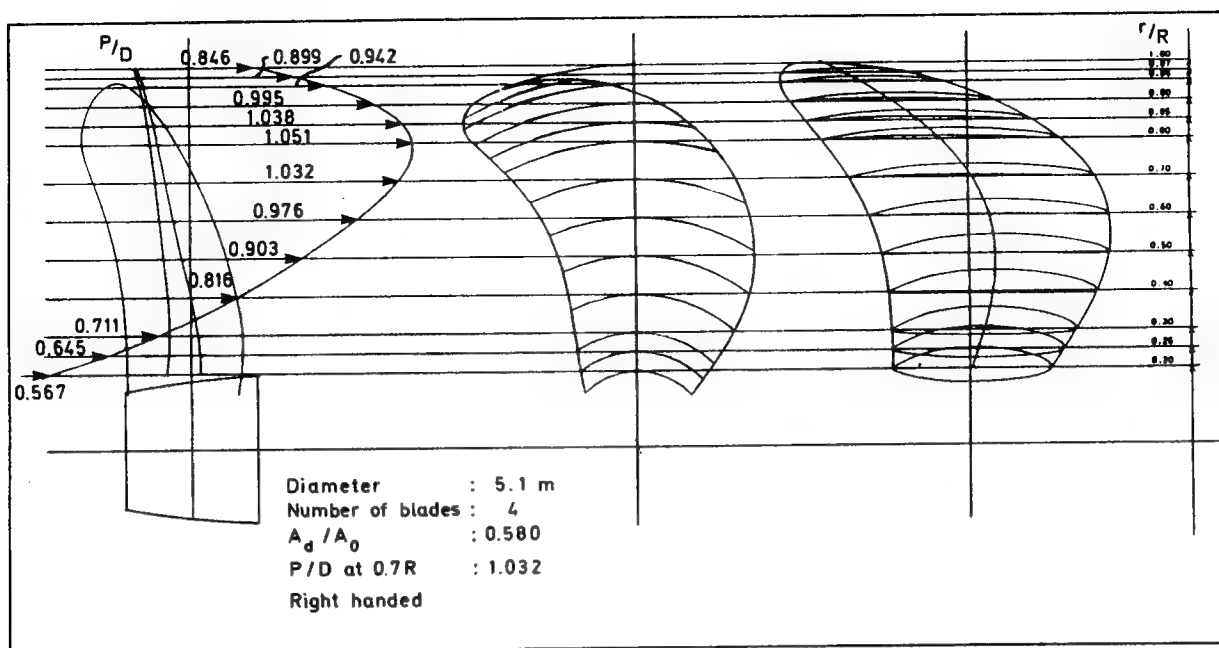


Figure 2 Conventional (reference) propeller.

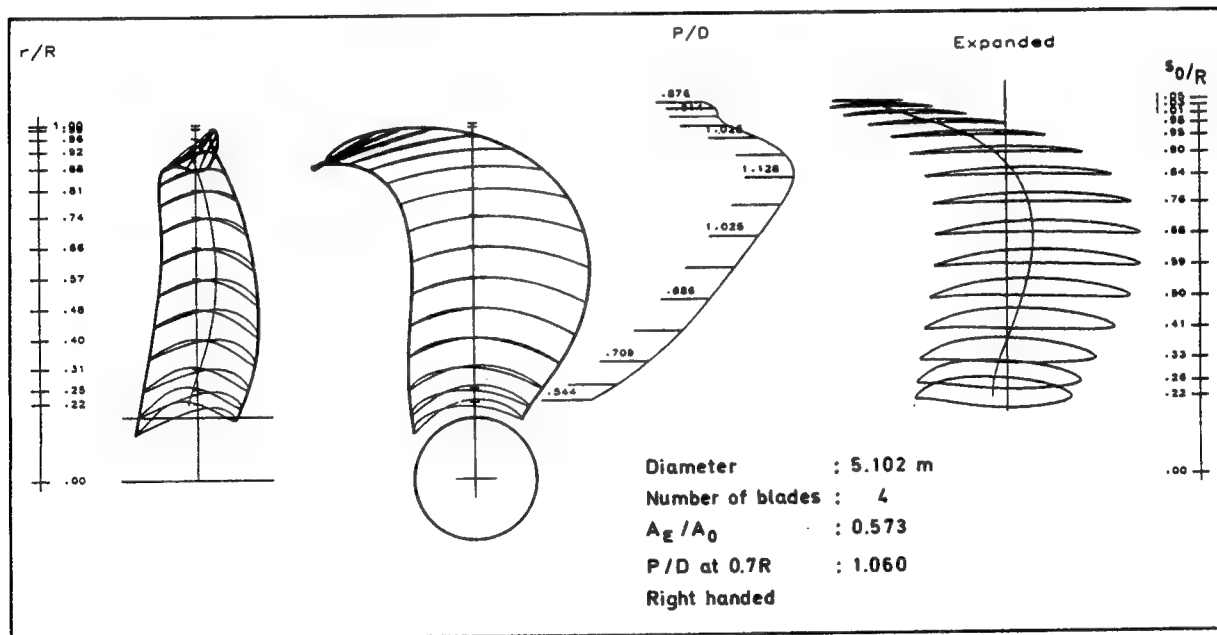


Figure 3 Tip-fin propeller.

possible. But the rate of revolutions can always be adjusted (within limits) when the optimum operation point of the engine is selected. Although it was expected that the effective wake field, the thrust deduc-

tion fraction and the relative rotative efficiency would be slightly different due to the modified radial distribution of loading of the tip-fin propeller, the same values as for the conventional design were used.

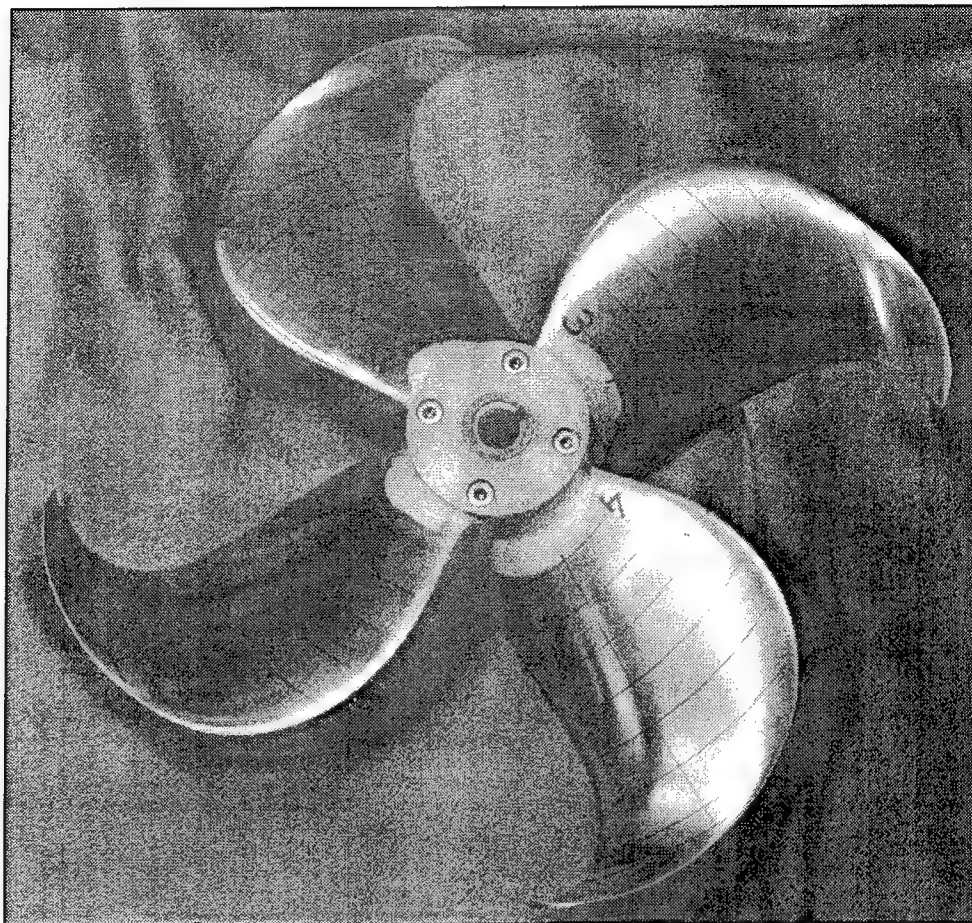


Figure 4 Tip-fin propeller model.

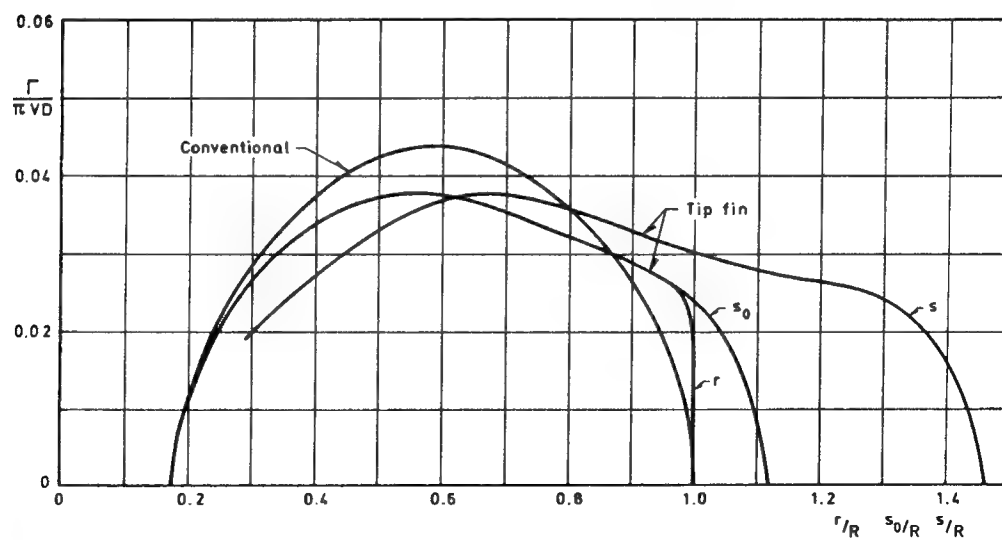


Figure 5 Spanwise distribution of loading in form of chordwise integrated circulation for conventional propeller and tip-fin propeller as function of radius, length of mid-chord-line arc-length s and s_0 . s_0 is the arc-length of the mid-chord line which would arise if skew was removed.

Distribution of thickness was also kept the same as for the conventional propeller with adjustments to accommodate the modified tip. When comparing Figures 3, tip-fin propeller, and 2, conventional propeller it can be seen that the distribution of skew in the inner part of the blade as well as the total skew are approximately the same for the two models, while the distribution of rake is different. The tip geometry was designed on the basis of earlier model experiments as well as experience with a vast number of theoretical design studies carried out using the procedure outlined in the previous section. This gave information on the shape of the tip, i.e. the rounding from blade to fin and the length of the fin. It is the general experience that the fin should be perpendicular to the helix surface of the otherwise conventional part of the blade. In the present case, this was adopted in the outermost part of the blade, but the curved transition region as well as the fin itself was given skew to minimize pressure pulses on the ship hull. Once the geometry of the mid-chord line, the area and the thickness distribution have been established the optimum distribution of spanwise load is obtained by the previously described procedure. Before transferring these data to the vortex-lattice program that carries out the final tracing of the blade surface a slight unloading of the tip was made relative to the optimum load distributions.

The spanwise distribution of blade loading is shown in Figure 5. It can be seen that the tip-fin propeller has a much higher loading in the tip, for given position of r . Despite that, because of the skew the tip loading goes gradually to zero as it must.

OPEN-WATER TESTS

Manufacturing of the tip-fin propeller model was subcontracted to MARINTEK who laboriously made a high-precision bronze model. A photograph of this model is shown in Figure 4. The diameter of this model was 237.5 mm, the same as for the conventional propeller model.

Results of open-water tests are shown in Figure 6. The tests were carried out with a standard set-up. The Reynolds numbers obtained were in the range $5.0\text{--}5.6 \cdot 10^5$ based on chord length at $0.7 R$ and the figure shows model test results with no scaling included. Propeller efficiencies as function of thrust loading are shown in Figure 7. Results at the design thrust loading are summarized in Table 2.

From Figure 6 it can be seen that the tip-fin propeller has higher efficiency over a practical range of advance ratios around the design ratio 0.64. The higher efficiency is maintained over a practical range of propeller loadings. At design loading the increase in efficiency is 0.020 (3.2 per cent relative), cf. Table 2.

This table also shows estimates of the contributions due to friction in model and full scale and estimates of thrust and torque coefficients and efficiency in full scale. They are based on simple calculations using the well-known drag coefficient

$$C_D = \frac{0.075}{(\log_{10} Rn_c - 2)^2} \quad (5)$$

for the propeller sections. The efficiency of the full scale tip-fin propeller is 0.025 better than the conventional propeller (3.8 per cent relative). This increase is due to the fact that the tip-fin propeller has relatively more area at the outer sections of the blade where the velocities are higher.

Table 2 Open-water model test results and full scale extrapolation.

	Tip-fin	Conventional
C_{Th}	1.545	1.545
Model, D= 237.5 mm		
J	0.641	0.634
K_T	0.249	0.244
K_Q	0.0405	0.0403
η_0	0.628	0.608
$dK_{T \text{ friction}}$	- 0.00442	- 0.00436
$dK_{Q \text{ friction}}$	0.00432	0.00361
R_c	$5.2 \cdot 10^5$	$5.2 \cdot 10^5$
Full scale, D = 5.100 m		
J	0.643	0.636
K_T	0.250	0.245
K_Q	0.0380	0.0383
η_0	0.673	0.648
$dK_{T \text{ friction}}$	-0.00199	- 0.00194
$dK_{Q \text{ friction}}$	0.00197	0.00161
R_c	$3.2 \cdot 10^7$	$2.9 \cdot 10^7$

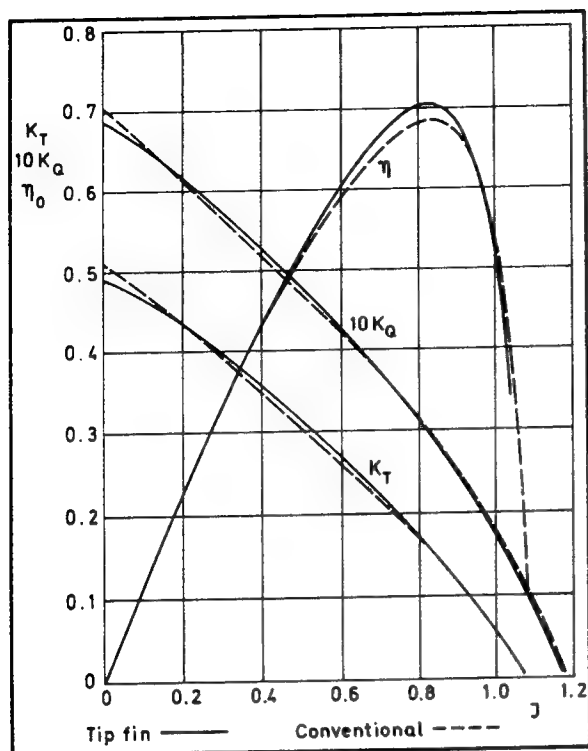


Figure 6 Open-water characteristics for tip-fin and conventional propeller models. Uncorrected model test results $R_e = 5.0 - 5.6 \cdot 10^5$.

SELF-PROPULSION TESTS

Results of the self-propulsion tests in form of a power prognosis is shown in Figure 8. The prognosis includes an extrapolation from model to full scale according to the standard procedure adopted by DMI. In this procedure the resistance of the model is extrapolated to full scale using form factor, allowance coefficient etc.. The rest of the extrapolation uses model test results throughout, except for the wake coefficient which is reduced by 0.044. Results of this prediction at design speed 9.03 m/s are shown in Table 3. Note that this procedure does not allow for differences in propeller characteristics due to friction. The table also shows results extrapolated to ship scale where the wake fraction was extrapolated by use of the ITTC-78 procedure [11]. Instead of using the frictional correction on the propeller as suggested by ITTC-78, the computed correction outlined in the previous paragraph, cf. Table 2, is used. Finally, a combination of methods is used where the DMI-scaling procedure is used for the wake fraction but the frictional correction of the propeller characteristics is as before.

From the table it can be seen that the total efficiency with the tip-fin propeller is 0.026 (3.7 per cent relative) higher than with the conventional propeller, when the DMI extrapolation is used. With the ITTC-method it is 0.029 (3.8 per cent relative) higher and with the DMI-ITTC procedure 0.037 (4.7 per cent relative) higher. The predicted power savings will equal the relative increases in efficiency.

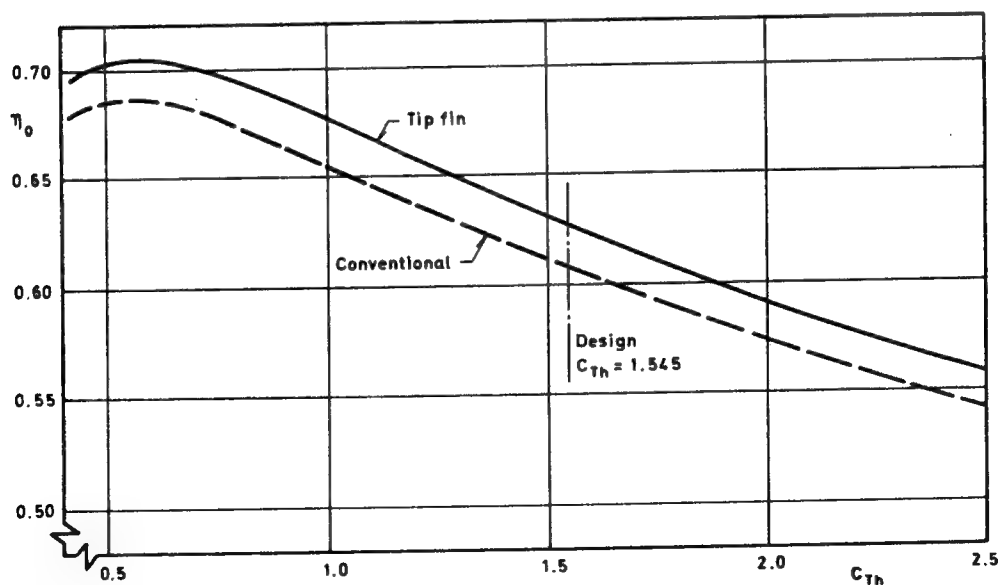


Figure 7 Efficiency as function of thrust loading, based on uncorrected test result of open-water model tests.

Table 3. Propulsion coefficients, power and rate of revolutions obtained by model experiments and three different extrapolations and by theoretical predictions.

V = 9.03 m/s	DMI extrapolation		ITTC-78 extrapolation		DMI-ITTC extrapolation		Design*	
	Tip-fin	Conv.	Tip-fin	Conv.	Tip-fin	Conv.	Tip-fin	Conv.
w	0.299	0.274	0.270	0.260	0.299	0.274	0.263	0.263
t	0.155	0.158	0.155	0.158	0.155	0.158	-	-
η_R	1.000	1.018	1.000	1.018	1.000	1.018	1.000	1.000
η_H	1.205	1.160	1.158	1.137	1.205	1.160	-	-
η_0	0.625	0.615	0.684	0.659	0.671	0.653	-	-
η_D	0.753	0.727	0.792	0.763	0.809	0.772	-	-
$\frac{\eta_{D \text{ tip fin}}}{\eta_{D \text{ conventional}}}$	1.037	1	1.038	1	1.047	1	-	-
P_D [kW]	6724	6975	6405	6649	6270	6567	6845*	7256*
n [1/s]	1.950	1.990	1.975	2.010	1.946	1.994	1.974	2.008
C_{Th}	1.583	1.485	1.461	1.424	1.583	1.485	1.545*	1.545*

*Design includes an increase in resistance (allowance) of 9 per cent.

It is interesting to note that with the tip-fin propeller the thrust deduction is only slightly reduced. This is relative to that of the reference propeller. But the inflow speed as integrated by the propeller is 1 - 3 per cent higher, whereas the relative rotative efficiency is lower. These changes must be due to the modified radial distribution of blade loading for the tip-fin propeller, which is designed with higher loadings in the tip region, cf. Figure 5. The differences in wake fraction and thrust deduction coefficients result in hull efficiencies that are higher for the tip-fin propeller. But the product of hull efficiency and relative rotative efficiency is almost the same for the two propellers when using the ITTC-method. The other methods give a 2 per cent higher value for this product for the tip-fin propeller. One may therefore conclude that on the basis of the DMI and DMI-ITTC extrapolations the increase in overall efficiency with the tip-fin propeller can be explained as due to both differences in η_H and η_R in combination with a higher propeller efficiency (open water) and that the two contributions to the increase ($\eta_H \cdot \eta_R$ and η_0) are of the same order of magnitude. But by the ITTC extrapolation the difference in overall efficiency is entirely due to the increase in open water efficiency of the tip-fin propeller.

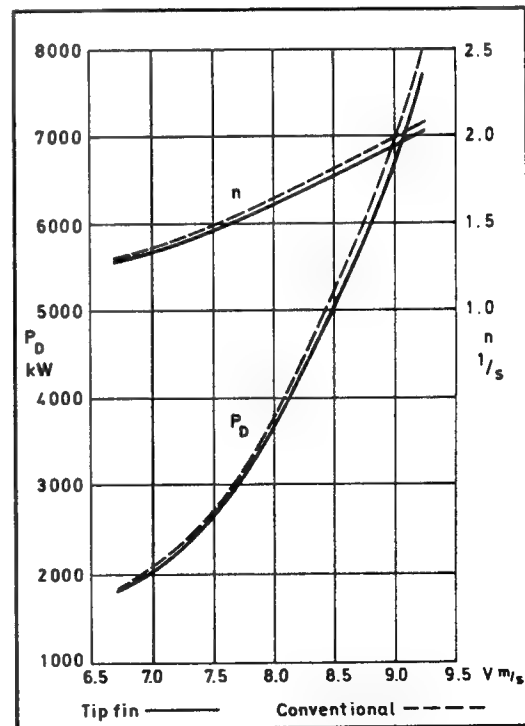


Figure 8 Power and rate of revolutions as function of ship speed. Prognosis on basis of model-test results by DMI-procedure.

According to all three procedures the tip-fin propeller operates at a slightly higher thrust loading (2 - 6 per cent) but in all cases with higher open water efficiency.

When comparing the model test results with those computed in the design process it should be noted that the designs were made with an allowance and hence an increase in resistance (and in thrust) of 9 per cent.

CAVITATION TESTS

The cavitation tests were carried out in a conventional circulating-water cavitation test facility. The transverse dimensions of the test section are 0.8×0.8 m and the length 1.45 m. It accommodates a dummy afterbody model which, together with suitably adjusted screens, creates the assumed full scale wake field. The tunnel can be evacuated to 95 per cent vacuum.

The wake field created for the cavitation tests was based on a survey of the wake field made in the towing tank. This wake was then transformed to estimated full scale wake and established behind the dummy model in the cavitation tunnel. The axial flow field is shown in Figure 9. It corresponds to the assumed full scale wake field for the ship in full load service conditions.

Results of cavitation tests in form of cavitation inception diagrams are shown in Figure 10. The tests were conducted in the non-uniform wake behind the dummy model. Because of the nature of the wake field, sheet cavitation will inevitably exist in conditions close to the two test conditions. The cavitation inception diagrams show iso-lines of different levels of extent of suction side cavitation, rather than actual inception of the suction side cavitation.

The propellers were tested at two conditions which are outlined in Table 4. The conditions at 100 and 90 per cent engine power apply to the conventional propeller and the parameters of the tests were so adjusted that the tip-fin and conventional propellers would give the same thrust. This means that the ship would sail at the same velocity for a given condition. If the power had applied to the tip-fin propeller it would have given the ship a higher speed than the conventional propeller.

Photographs of the cavitating propellers in Conditions 1 are shown as Figure 11. The conditions are also indicated in Figure 10. During the tests both propellers suffered from sheet cavitation on the suction side around the 12 o'clock positions of the blades. This was expected from the nature of the wake field. Neither pressure side nor bubble cavitation were observed in any condition, nor did thrust breakdown occur. For the tip-fin propeller in Condition 1 (service), the cavitation started at blade position -20°

and vanished at 60° (blade position 0° corresponding to 12 o'clock). The largest extent was from slightly less than $0.8R$ and outwards, leaving, however, the outermost part of the blade, i.e. the tip fin itself free of cavitation. It is interesting to note that a similar behaviour, i.e. cavitation over the curved transition area between blade and tip fin, was observed in the earlier model tests with the tip-fin propeller designed for open water [9]. Note that the tip-fin propeller exhibited very little, if any, tip vortex cavitation. The conventional propeller suffered from slightly less suction side sheet cavitation (Condition 1), starting at 10° and vanishing at 60° . At its maximum it extended over the entire suction side of the tip region down to appr. $0.85 R$. It had a pronounced tip vortex.

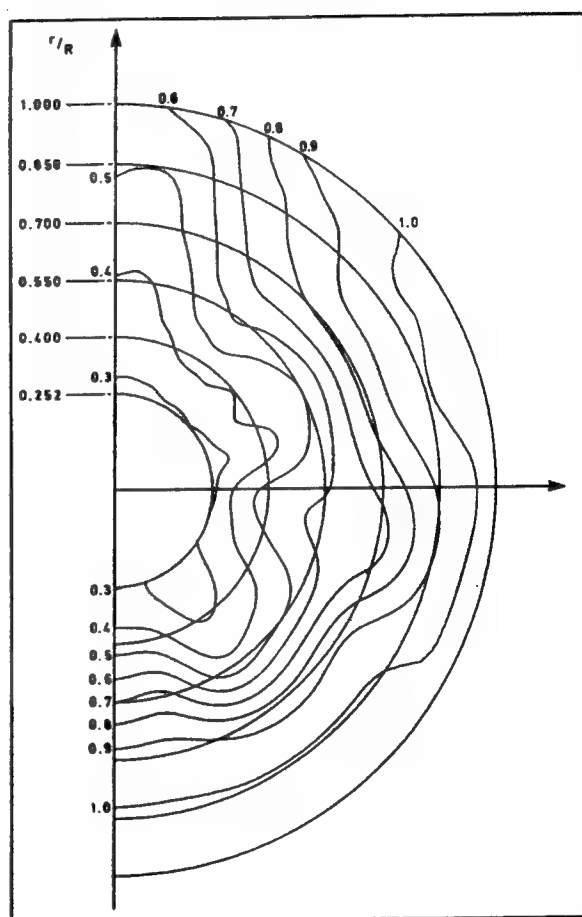


Figure 9 Iso-curves of axial wake behind dummy model, full scale as modelled in cavitation tunnel.

In Condition 2 (trial) a similar behaviour was observed, but at a reduced level of cavitation extent. The tip-fin propeller suffered from more cavitation than the reference propeller but had no cavitating tip vortex.

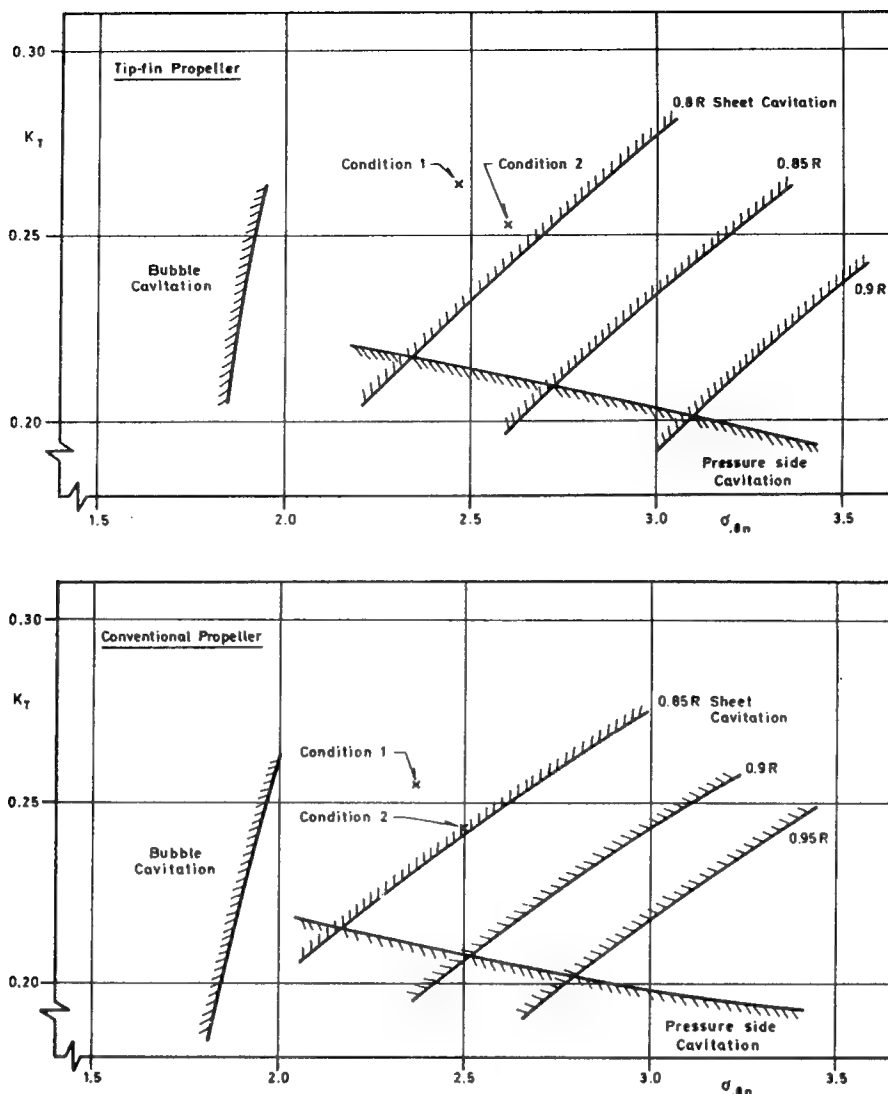


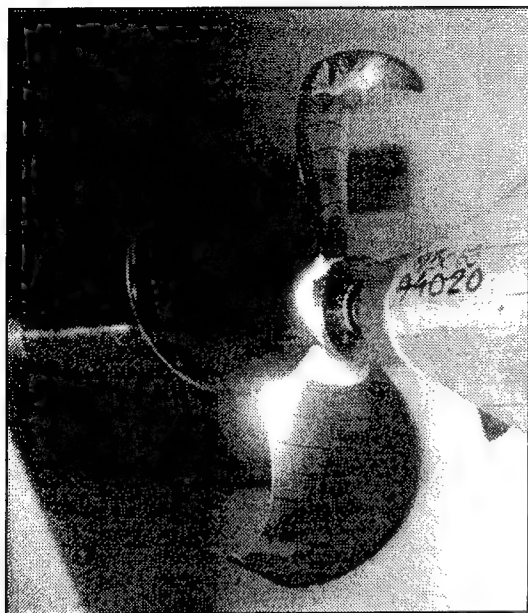
Figure 10 Cavitation inception diagrams: (upper) tip-fin propeller, (lower) reference propeller

Table 4 Conditions for cavitation tests with 237.5 mm diameter propeller models at rate of revolution appr. 25 1/s.

	Condition 1		Condition 2	
	Tip fin	Conventional	Tip fin	Conventional
V [m/s]	9.04	8.99	9.09	9.09
P _D [kW]	7818	8062	6987	7256
n [1/s]	2.03	2.07	1.97	2.01
J _A	0.615	0.619	0.635	0.644
K _T	0.264	0.255	0.252	0.243
σ _{0.8}	0.368	0.354	0.386	0.371
σ _{0.8n}	2.466	2.371	2.597	2.499

Condition 1: Service condition: Design draught 7.5 m, trial resistance + 15 per cent service allowance, 100 per cent engine power with conventional propeller. Wake distribution as in Figure 9.

Condition 2: Trial condition: Design draught 7.5 m, trial resistance, 90 per cent engine power with conventional propeller. Wake distribution as in Figure 9.

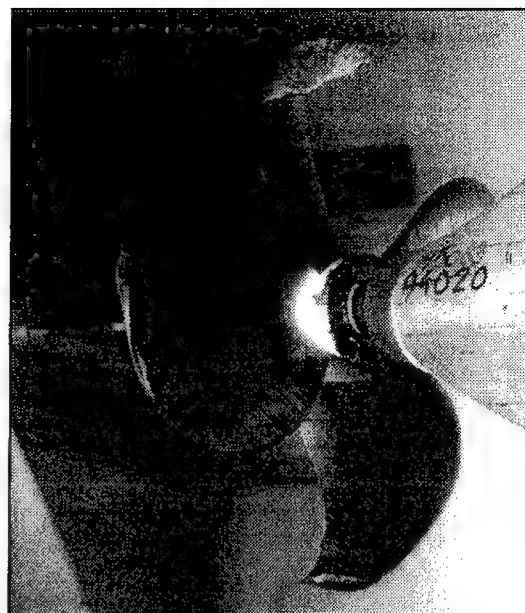


a. Tip-fin propeller
Blade position 0°

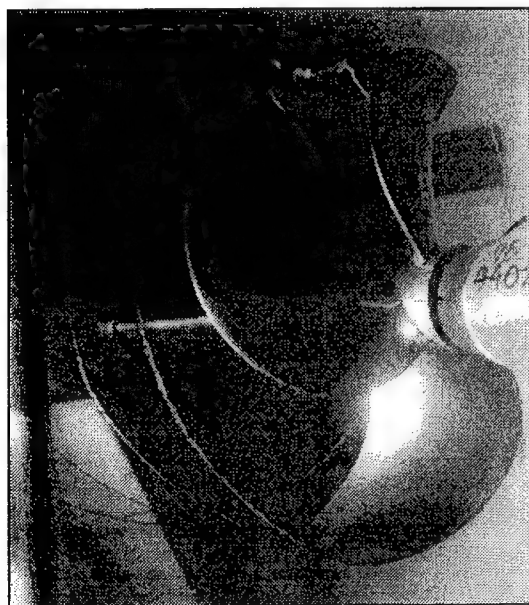
$$\sigma_{0.8n} = 2.47$$

$$K_T = 0.264$$

$$J = 0.615$$



b. Tip-fin propeller
Blade position 20°



c. Conventional propeller
Blade position 0°

$$\sigma_{0.8n} = 2.37$$

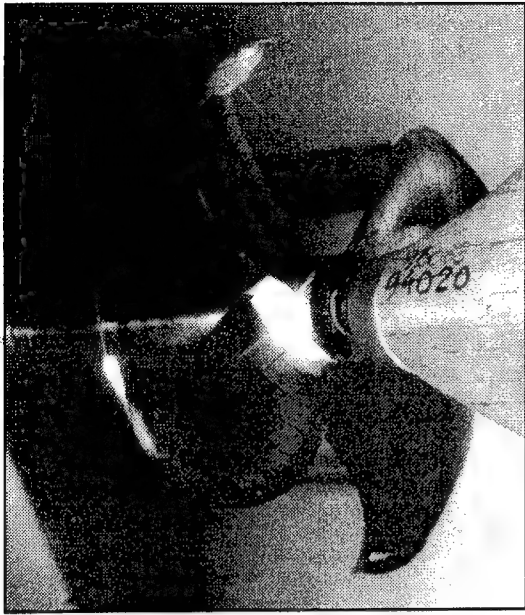
$$K_T = 0.255$$

$$J = 0.619$$



f. Conventional propeller
Blade position 20°

Figure 11 Cavitating tip-fin and reference propellers.



c. Tip-fin propeller
Blade position 40°

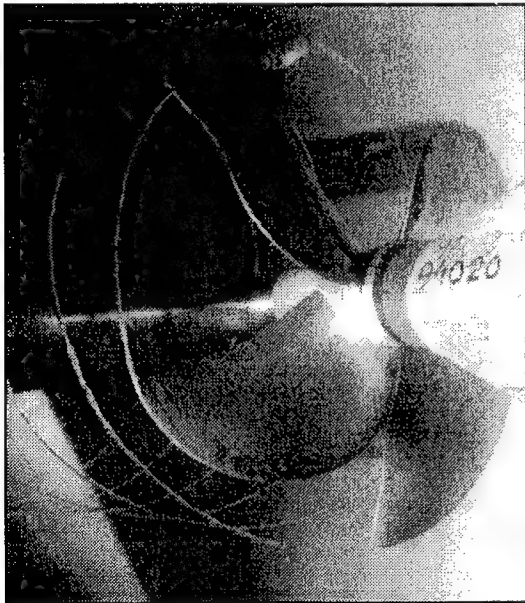
$$\sigma_{0.8n} = 2.47$$

$$K_T = 0.264$$

$$J = 0.615$$



d. Tip-fin propeller
Blade position 60°



g. Conventional propeller
Blade position 40°

$$\sigma_{0.8n} = 2.37$$

$$K_T = 0.255$$

$$J = 0.619$$



h. Conventional propeller
Blade position 60°

Figure 11 Cavitating tip-fin and reference propellers.

Table 5 Measured pressure levels i kPa for tip-fin and conventional propeller, scaled to ship scale. Maximum values underlined.

Order of blade frequency	Tip-fin					
	Condition 1			Condition 2		
	Port	Centre	Starboard	Port	Centre	Starboard
1	6.90	<u>7.74</u>	7.67	4.40	<u>5.20</u>	4.98
2	1.00	<u>1.70</u>	1.28	0.72	<u>1.31</u>	1.01
3	0.00	0.00	0.00	0.22	0.41	0.61
Order of blade frequency	Conventional					
	Condition 1			Condition 2		
	Port	Centre	Starboard	Port	Centre	Starboard
1	4.90	4.74	<u>5.93</u>	2.37	2.95	<u>3.68</u>
2	1.00	<u>1.46</u>	1.06	0.87	<u>1.29</u>	1.03
3	0.00	0.00	0.00	0.00	0.00	0.00
Order of blade frequency	Ratio: Tip-fin/Conventional					
	Condition 1			Condition 2		
	Port	Centre	Starboard	Port	Centre	Starboard
1	1.41	1.63	1.29	1.86	1.76	1.35
2	1.00	1.16	1.21	0.82	1.02	0.98
3	-	-	-	-	-	-
Order of blade frequency	Ratio, maxima: Tip-fin/Conventional					
	Condition 1			Condition 2		
	Ratio, maxima	Hydrophones		Ratio, maxima	Hydrophones	
1	1.31	centre/starboard		1.41	centre/starboard	
2	1.16	centre/centre		1.02	centre/centre	

During the cavitation tests measurements of pressure pulses were made in three positions above the propeller. The hydrophones were placed in the same longitudinal position 0.43 m (full scale) forward of the reference line of the conventional propeller which corresponds to a further 0.43 m forward of the reference line of the tip-fin propeller. The hydrophones were positioned symmetrically with the centre hydrophone 3.471 m above the propeller axis and the two others 0.814 m to port and starboard, 4.029 m above the plane of propeller axis. The difference in positions of

the two propeller reference lines was chosen to obtain the same axial position of the tip regions of the two propellers. It was maintained through all the experiments. Figure 12 shows the tip-fin propeller behind the dummy model and the hydrophones.

Results of pressure level measurements are shown in Table 5. As expected from the observations of cavitation extent the tip-fin propeller gives the largest pressure levels for the same condition, and the service condition has the largest pressure levels for both tip-fin and reference propeller. This applies to the first-

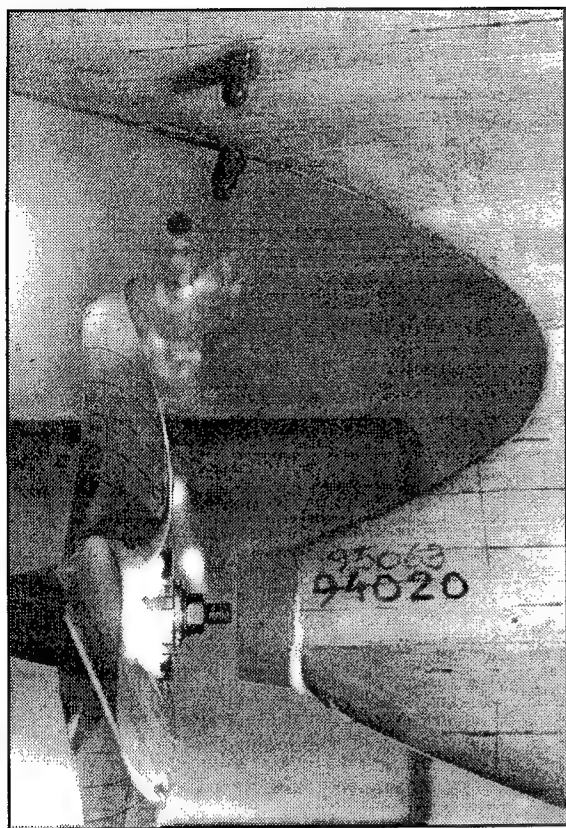


Figure 12 Tip-fin propeller behind dummy model with hydrophones.

order pressure pulses which for given hydrophones for the tip-fin propeller were in the order of magnitude of 1.3 to 1.9 times those of the reference propeller. The second-order pressure pulses were of the same order of magnitude for the two propellers, and no or only vanishingly small third-order components were measured. Higher-order components were not found. This indicates that the cavitation formation is stable.

Although only three gauges can hardly be said to be representative for the distribution of pressure over the hull, it is interesting to note that for the first-order pulses the maximum occurs at the center hydrophone for the tip-fin propeller but for the starboard hydrophone for the reference propeller. This is of course in accordance with the history of the cavity growth and collapse as can be seen in Figure 11. But when comparing the maximum values the tip-fin propeller gives pulses 1.31 (Condition 1) and 1.41 (Condition 2) times those of the reference propeller.

As a reason for the larger extent of cavitation and greater pressure-pulse levels for the tip-fin propeller one may offer the simple explanation that the propeller has more load in the tip region, cf. Figure 5, and is hence more susceptible to cavitation due to variation

in inflow. Furthermore, during the design process the sectional loading over the tip fin was slightly reduced relative to the optimum prediction. This reduction might have increased the loading in the curved transition region. It may be conjectured that a higher tip loading may be possible without cavitation, thus reducing the loading and cavitation in the transition region. Finally, there may easily be interaction effects between the curved blade sections which has not yet been taken into account in the design procedure.

CONCLUSION

A tip-fin propeller was designed for the same 125 m, 17.5 knot, small container ship and the same condition as the conventional propeller actually fitted to the ship. The performances of both propellers were analysed by open-water, self-propulsion and cavitation tests. From these results it can be concluded that the method used in designing the tip-fin propeller is able to provide a design with satisfactory accuracy as far as thrust and rate of revolutions are concerned. Furthermore, the predicted increase in efficiency was confirmed by the model tests. Depending on the method used in extrapolation to full scale, a reduction in power of 3.7 to 4.7 per cent was found. The tip-fin propeller had higher open-water efficiency than the conventional propeller over a practical range of advance ratios and thrust loading coefficients. In the self-propulsion tests minor differences in thrust deduction and wake fraction coefficients and in relative rotative efficiencies were found for the two propellers.

In the inhomogeneous wake field both propellers suffered from suction side cavitation around 12 o'clock blade position. Slightly more cavitation was found for the tip-fin propeller. This appeared over the curved transition region from blade to tip fin, whereas the tip fin itself was free of cavitation. In contrast to the conventional propeller no cavitating tip vortex was observed for the tip-fin propeller. As a consequence of the difference in cavitation performance higher pressure pulses on the ship hull were found for the tip-fin propeller. Maximum, measured, first-order pulses were of the order of 1.3 to 1.4 times those of the conventional propeller.

ACKNOWLEDGEMENT

The author is grateful to Mr. J.J. Kappel, who invented the concept of the integrated tip-fin propeller, for this constant and enthusiastic co-operation and support. Invaluable help with the final details of the tip-fin propeller surface was provided by Mr. J.A. Clayton, STONE MANGANESE MARINE Ltd.. The project was carried out in co-operation with the Danish Maritime Institute, who made the model tests.

REFERENCES

1. Prandtl, L. and Betz, A. "Der induzierte Widerstand von Flügeln mit Endscheiben", *Ergebnisse der Aerodynamischen Versuchsanstalt zu Göttingen, III. Lieferung*. Verlag R. Oldenburg, München und Berlin, 1927.
2. Whitcomb, R. "A Design Approach and Selected Wind-Tunnel Results at High Subsonic Speeds for Wing-Tip Mounted Winglets", NASA Langley Research Center, Technical Note, NASA, 1976.
3. Andersen, S. Vogt and Andersen, P. "Hydrodynamic Design of Propellers with Unconventional Geometry", Trans. of The Royal Institution of Naval Architects, Vol. 129, 1987, pp. 201-221.
4. Itoh, S., Tagori, T., Ishii, N. & Ide, T.: "Study of the Propeller with Small Blades on the Blade Tips (1st Report)", Journal of the Society of Naval Architects of Japan, Vol. 159, June 1986, pp. 82-89.
5. Itoh, S. "Study of the Propeller with Small Blades on the Blade Tips (2nd Report)", Journal of the Society of Naval Architects of Japan, Vol. 161, June 1987, pp 82-91.
6. Gómez, G.P. and Gonzáles-Adalid, J. "Tip Loaded Propellers (CLT). Justification of their Advantages over Conventional Propellers Using the Momentum Theory", International Ship-building Progress, Vol. 42, No. 429, April 1995, pp. 5-60.
7. de Jong, K. "On the Optimization and the Design of Ship Screw Propellers with and without End Plates", Thesis, University of Groningen, Department of Mathematics, November 1991.
8. de Jong, K., Sparenberg, J., Falcão de Campos, J. and van Gent, W. "Model Testing of an Optimally Designed Propeller With Two-Sided Shifted End Plates on the Blades", Proceedings of Nineteenth Symposium on Naval Hydrodynamics, National Academy Press, Washington, D.C. 1994, pp. 461-475.
9. Andersen, P. and Schwanecke, H. "Design and Model tests of Tip Fin Propellers", Trans. of The Royal Institution of Naval Architects, Part B, Vol. 134, 1992, pp. 315-328.
10. Kerwin, J.E., Coney, W.B and Hsin, C.-Y. "Optimum Circulation Distributions for Single- and Multi-Component Propulsors". Proceedings of Twenty-First American Towing Tank Conference (ATTC) National Academy Press, Washington D.C., 1986, pp. 53-62.
11. ITTC-78. "Report of the Performance Committee", Proceedings of the 15th International Towing Tank Conference, Netherlands Ship Model Basin, Wageningen, 1978, pp. 359-404.

DISCUSSION

L.J. Doctors

University of New South Wales, Australia

Figure 7 is interesting in that neither the conventional nor the tip-fin propeller appears to be operating at its optimum efficiency. In fact, the plot shows a design efficiency of 61% or 63% compared to an optimum value of 68% or 71%. Is this simply a problem of there not being sufficient space behind the vessel for a (larger) optimally sized propeller?

AUTHORS' REPLY

The discussor correctly points out the remarkable fact that despite optimization neither the tip-fin nor the conventional propeller operate at their highest efficiencies. They are obtained at thrust loading coefficient $C_{Th} = 0.57$ (Figure 7) and advance ratio $J = 0.83$, appr. (Figure 6), whereas the propellers were designed for $C_{Th} = 1.545$ and $J = 0.64$ (appr.).

This is typical for propeller designs. The propeller is optimized with a constraint, in this case on thrust loading coefficient, resulting in an optimum geometry and advance ratio. A decrease in thrust loading coefficient relative to the design value for the given propeller is obtained by increasing the advance ratio. The blade sections will then experience less inflow angle and lift, and also less induced drag. This will give higher efficiency of the entire propeller. For a sufficiently high-advance ratio, the thrust produced by the lift of the blade sections will be annulled by the negative thrust from the frictional drag of the sections. That will also give zero efficiency. In between this and the design advance ratio, the propeller will have a maximum efficiency.

In the present case, the thrust loading coefficient $C_{Th} = 0.57$, where the maximum efficiencies are obtained, would correspond to a propeller diameter of 8.4 m which is not practicable. Even if it were, these propellers would not be optimal since they were designed for a different thrust loading, and an optimization for that much lower thrust loading would give propellers of even higher efficiencies.

A New Way of Simulating Whale Tail Propulsion

J. van Manen (Whale Tail Development, The Netherlands),

T. van Terwisga (Maritime Research Institute, The Netherlands)

1. INTRODUCTION

Up to the Seventies of the Twentieth Century, the conventional screw propeller has shown a supremacy among the modes of ship propulsion. During the last decades some hesitation has appeared in the domination of this screw propeller by the development of "special purpose" ship types. Especially the development of wide, shallow-draft ship types causes restrictions in the maintenance of optimal efficiencies of the screw propeller.

Today, advanced ships demand a well-balanced compromise between the main requirements for a ship propeller, such as: high efficiency, minimum danger of cavitation, noise and erosion, minimum propeller excited vibratory forces, good stopping abilities and manoeuvrability, minimum vulnerability and low initial and maintenance costs.

During the last decades the non-conventional propulsion devices have shown to be competitive to the screw propeller. Especially the ducted propellers, the contra-rotating propellers and the waterjet propulsors have shown remarkable positive results. In the last years, the growing interest into fish, whale and dolphin propulsion is remarkable.

In 1963 for the first time systematic tests have been carried out with a group of vertical axis, "cycloidal" propellers, having an eccentricity of " e " > 1 , referred to as "trochoidal" propellers. The blade motion of the "trochoidal" propeller is quite reminiscent of the movement of a fish (Fig. 1). These vertical axis propellers belonged to an unknown

area of ship propulsion. The test results showed promising high efficiencies at high speeds and light propeller loading.

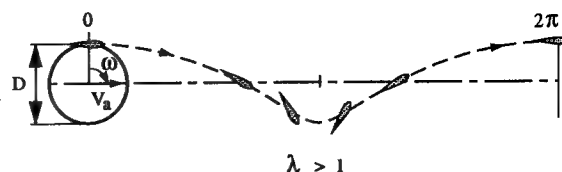


Fig. 1 Trochoidal blade trajectory.

At that time there was not sufficient interest for this extremely high speed area for ships. Nowadays the interest for ship propulsion for wide, shallow draft ship types is growing. The efficiencies of the screw propeller for these ship forms are by far not optimal, caused by the restrictions of the screw diameter and the propeller rotation rate. In fact for these ships only a wide, shallow draft rectangle is available for ship propulsion.

The break-through idea, thirty years after the first systematic tests with the vertical axis "trochoidal" propellers is the development of these propellers with a horizontal axis. The "trochoidal" propeller with a horizontal axis is mounted in the hull's afterbody over a large part of its width. The propeller is further characterized by a relatively large span of the blades, which are clenched on both ends of the blades. These end connections

enforce a specified blade angle as a function of blade orbit position. Intermediate supports distributed over the span are applied where necessary to ensure sufficient stiffness of the blades (see Fig. 2).

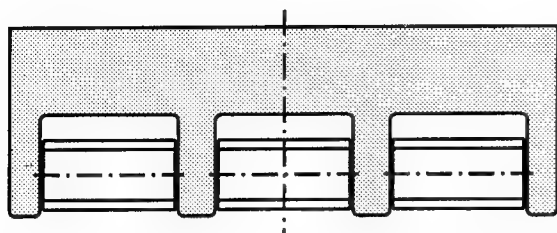


Fig. 2 Stern view of an aftbody with Whale Tail Wheel propulsion.

The allowable large area of the propeller and the almost two-dimensional flow about the blades give it an unequalled high performance potential for the requirements of many ship types. The large area of the propeller is expressed in a low thrust loading per unit envelope area. This allows the required change in momentum of the flow to be obtained by a relatively small acceleration of fluid. A corresponding high ideal efficiency is obtained. The trochoidal propeller with a horizontal axis, 'Whale Tail Wheel' in the following, is a combination of the tail propulsion of a living creature and the wheel, invented by mankind.

The choice of the dimensions of the Whale Tail Wheel can lead to a minimum thrust loading per unit envelope area and consequently to the optimum of the maximal efficiency curve of the trochoidal propeller with a horizontal axis. A shape of afterbody adapted to the two-dimensional character of the lightly loaded Whale Tail Wheel will realise promising conditions for the control of cavitation and vibration risks.

2. HISTORY

A summary of the historic review by Brockett (1) is presented here:

'Different configurations of the cycloidal propulsor were independently developed by Kirsten (2), (3) and Schneider (4) during or prior to the 1920's. The blade angle control of Kirsten is fixed by gears and has experienced only limited development. The more complex but controllable blade angle orientation using linkages proposed by

Schneider has received considerable development.

There are two traditional regions of pitch control. One for low-pitch propellers (associated with orbit circumferential velocities $\omega D/2$ greater than the advance speed V_0), and one for high-pitch propellers (associated with circumferential velocities less than the advance speed). Low speed manoeuvring requirements have led to extensive development of the low pitch configuration (Schneider (4)). Such propellers have top speeds usually less than 20 knots. High pitch propellers have hydrodynamic efficiency values greater than for low pitch propellers and permit high speed operation. These latter propellers have to date however, received most attention at only research level (e.g. van Manen (5)).

A survey of cycloidal propulsion has been given by Henry (6). He presents a history and a description of some kinematics of the motion of a cycloidal propeller, as well as a critical review of early attempts to model the flow field. Some of his suggestions for improved modelling have yet to be implemented. Improvements in performance were addressed by Sparenberg (7), (8) and James (9), who attempt to define blade angle control specifications for improved efficiency based on two-dimensional flow models.

Systematic series data are presented by Nakonechny (10), (11), Van Manen (5), Ficken (12) (who includes Nakonechny's data in his faired curves), Bjarne (13) (see also Kallstrom and Loid (14)), and Bose and Lai (15). The most extensive of these series are those of Van Manen and Ficken. The main variable in these investigations is pitch control, but several blade shapes are also evaluated. Van Manen includes evaluation of the blade angle motions derived by Sparenberg (7), which did produce improvements in efficiency over his conventional cycloidal blade angle variations.

Van Manen's experiments (with low pitch propellers) produced generally lower efficiency values than expected, which has been partially explained by Ruys (16) as a viscous effect. Van Manen's data for high-pitch propellers had quite respectable efficiency values ($\eta_0 \approx 0.7$). (Brockett (1)).

3. WORKING PRINCIPLE

Propulsion fundamentals

The general principle underlying the thrust production of any propeller is strongly summarized in the conservation law of momentum. A conse-

quence of this physical law is, that an action force is required to accelerate a certain amount of fluid. This action force is exerted on the fluid by an actuator. The actuator often consists of a conventional propeller. But it may also consist of a paddle wheel or a cycloidal propeller with either a vertical shaft (e.g. Voith Schneider propeller) or a horizontal shaft (Whale Tail Wheel).

In an ideal non-viscous flow, the acceleration of the flow through the actuator, not only creates a reaction force of the flow on the actuator (thrust), but also causes an energy loss. This energy loss is manifest through the kinetic energy in the wake of the propulsor. The energy loss is the difference between the added kinetic energy to the wake, and the work done by the propulsor. It is conveniently accounted for in the so-called ideal efficiency η_i , which is plotted as a function of the so-called thrust loading coefficient C_T in Fig. 3. This thrust loading coefficient is a measure of the thrust production per unit propulsor area and is given by:

$$C_T = \frac{T}{\frac{1}{2} \rho V_0^2 A_0} \quad (1)$$

where T = delivered thrust
 ρ = specific mass of fluid
 V_0 = speed of advance of propulsor
 A_0 = propulsor envelope area.

Fig. 3 also shows the open water efficiencies of some actual Wageningen B-series propellers. From a comparison of the ideal efficiency and the open water efficiencies of the propellers, the importance of the ideal efficiency becomes evident. The maximum propeller open water efficiency appears to be roughly some 70% of the ideal efficiency over the plotted range of thrust loading coefficients.

It can be observed from Fig. 3 that the ideal efficiency decreases with increasing thrust loading. So in order to attain the highest propulsive efficiency, one would like to design at the lowest possible thrust loading. When considering the optimal propulsor for a given ship at given speed, the thrust is a fixed requirement. The only way to decrease the thrust loading then, is to increase the propulsor area.

The propulsor area of a propeller is usually dictated by the draft of the hull (a propeller protruding below the baseline is often not allowed), and the allowable geometry of the local hull form. It is noted here that not only a certain propeller tip

clearance to the hull is required, but also a sufficiently withdrawn hull form ahead of the propeller. Sufficient space between aftbody and propeller is required to decrease the drag increment due to the propeller action, and to provide the propeller with an acceptable inflow field.

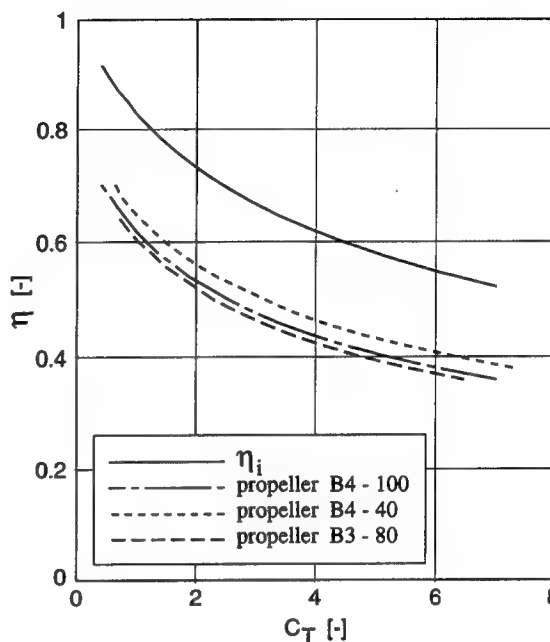


Fig. 3 Ideal efficiency and propeller open water efficiencies as a function of thrust loading coefficient C_T .

It is largely the above principle, expressed in the η_i - C_T relation, that holds promise for a non-precedented high efficiency of the Whale Tail Wheel, at yet acceptable cavitation erosion and vibration problems.

Working principle cycloidal propellers

'The cycloidal propulsor is a thrusting device with an axis of rotation that is approximately perpendicular to the direction of travel. A number of lifting blades (typically 4 to 7) equally spaced at a fixed orbit diameter D , rotate about this axis. Each blade is further controlled in its orbit such that a component of force in a desired direction is obtained. It is thus a special case of a controllable pitch propeller.' (Brockett (1)).

A sketch of the cross section of a cycloidal propulsor, including reference frames and nomenclature for orientation of the blades along an orbit path, is shown in Fig. 4.

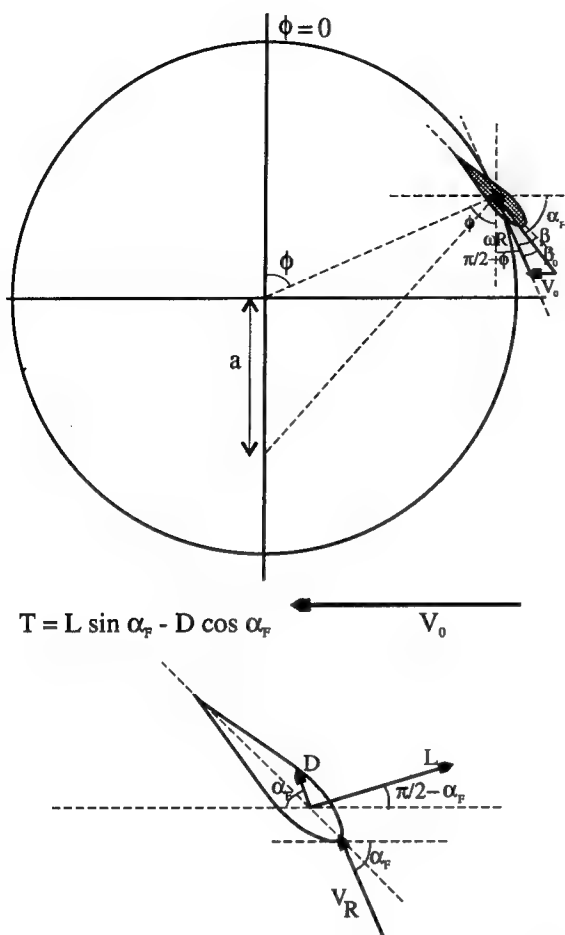


Fig. 4 Sketch of a cross section of a cycloidal propeller, including reference frames and nomenclature.

Drift or drag forces occur whenever a body is moving through a fluid and act by definition in the direction of the inflow. Examples of its application are for example the paddle of a canoe or the paddle wheel of the Mississippi Steamers.

The Whale Tail Wheel seeks to combine the benefits of both the paddle wheel and the propeller. The paddle wheel often shows a favourable efficiency because it allows for a large propulsor area and therefore a low propulsor loading. A major drawback of this propulsor is however that only a small part of the blade orbit can be used for thrust production, because of the force generation principle of drift.

This setback is avoided when thrust is generated through the principle of lift generation for blades that can be optimally oriented along their entire orbit of 360 deg. The principle of lift generation for thrust furthermore also keeps the advan-

tage that lift is a more effective agency for force production than drift, giving promise to higher thrust production at lower rotation rates with smaller propulsors.

4. RELEVANT PARAMETERS

Important parameters that govern the efficiency of a conventional propeller are its diameter D , its pitch-diameter ratio P/D and its blade-area ratio A_E/A_0 . The effect of these three parameters will be discussed in the order of diminishing importance on efficiency.

The effect of the propeller diameter is reflected in the thrust loading coefficient C_T , which effect is already discussed in the preceding section.

The pitch diameter ratio is an equivalent for the average blade angle of attack with the incident flow. It determines the propeller rotation rate for a given thrust requirement. For each thrust loading coefficient, a pitch-diameter ratio can be distinguished that provides an optimal efficiency. It can be found from e.g. the $Bp-\delta$ diagram, that this optimal pitch-diameter ratio increases with decreasing thrust loading. Or in other words, the optimal non-dimensional propeller rotation rate (reciprocal value of the propeller advance coefficient; $1/J$) decreases with decreasing thrust loading.

A certain minimal blade-area ratio is required to give the required strength to the propeller blade for the lower thrust loadings, or to yield acceptable cavitation characteristics for the higher thrust loadings. Increasing the blade-area ratio always has an adverse effect on propeller efficiency (when compared on a base of equal thickness/chord ratio of the blade profile).

In analogy with the above prime parameters governing the propeller performance, corresponding parameters can be defined for the Whale Tail Wheel.

Wheel dimensions

Equivalent to the propeller disk area or propeller diameter is the Whale Tail Wheel envelope area A_0 , that is projected in the plane oriented at right angles with the propulsor heading. Because of the geometry of the cycloidal propeller, this area is not only determined by the orbit diameter of the blades, but also by the span of the blades. The larger this projected area, the lower the thrust loading coefficient and consequently the higher the ideal efficiency η_I .

Pitch or eccentricity

Equivalent to the propeller pitch-diameter ratio is the blade angle of attack along its orbit. This angle of attack is determined by the geometric blade pitch angle β and the hydrodynamic pitch angle β_0 , without effect of induced velocities (see Fig. 4).

Perhaps the most common representation of the blade angle $\beta(\phi)$, is that of pure cycloidal motion. In such a motion, the normal to the blade nose-tail at the pivot point passes through a fixed point in space, called the pitch point. The distance between this pitch point and the orbit centre is called the eccentricity a (Fig. 4). The geometrical blade angle for this motion is obtained from:

$$\beta(\phi, e) = \text{atan} \frac{e \sin \phi}{1 + e \cos \phi} \quad (2)$$

where e = eccentricity, expressed as a fraction of the orbit radius; $e = a/R$.

Analogous to a conventional propeller, the pitch can be introduced as the traversed path in the translation direction for one complete revolution at slip zero ($\beta - \beta_0 = 0$). For a pure cycloidal motion, the non-dimensional pitch is obtained from the following relation:

$$\frac{P}{\pi D} = e = \sin \beta_{\max} \quad (3)$$

Fig. 5 shows the blade angle β for a number of blade motion distributions for the same maximum blade angle value. The alternative distributions aim at either a higher propeller efficiency or at a simplified mechanical construction.

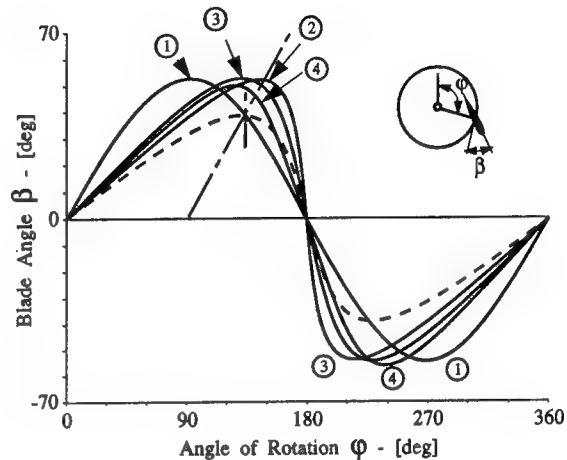
The working point of the propeller is characterized by the velocity ratio λ , which is defined as:

$$\lambda = \frac{V_0}{\pi n D} \quad (4)$$

where V_0 = propeller speed of advance
 n = propeller rotation rate
 D = propeller diameter.

Two distinct type of blade trajectories can be distinguished, as depicted in Fig. 6. For values of $\lambda < 1$, we speak of an epicycloidal blade path trajectory. For values of $\lambda > 1$, we speak of a trochoidal blade path trajectory. It is interesting to

observe that the blade trajectory of a conventional paddle wheel is necessarily of the epicycloidal type, should a positive thrust be generated. A similar restriction in blade trajectory type holds for the cycloidal propeller with pitch ratios $e < 1$. For pitch ratios $e > 1$, both types of blade trajectories can be used for a positive thrust production.



(1) Sinusoidal blade motion:

$$\beta(\phi) = 53.13^\circ \sin \phi$$

(2) Cycloidal blade motion:

$$\beta(\phi) = \text{atan} \left[\frac{0.8 \sin \phi}{1 + 0.8 \cos \phi} \right]$$

(3) Amplified cycloidal blade motion

$$\beta(\phi) = 1.387 \text{atan} \left[\frac{0.62 \sin \phi}{1 + 0.62 \cos \phi} \right]$$

(4) Compensated amplified cycloidal blade motion

$$\beta(\phi) = \sum_{n=1}^{13} b_n \sin n\phi + a_0 + \sum_{n=1}^{13} a_n \cos n\phi$$

Fig. 5 Various blade angle distributions (from Brockett (1)).

The most common pitch control for existing cycloidal propellers, is that with a pitch ratio $e < 1$, which will be referred to as low pitch. An upper limit of these low pitch values occurs near $e = 0.8$, to restrict the accelerations experienced by the blade near $\phi = \pi$ (Mueller (17)). To obtain pitch values greater than $e = 1$, special mechanical constructions are needed.

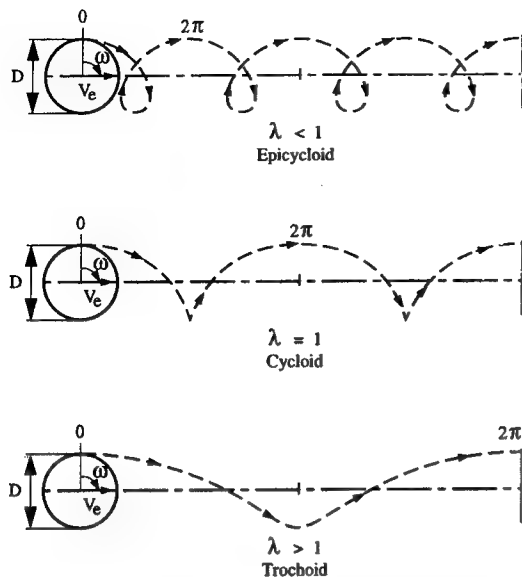


Fig. 6 Various types of trajectories described by the blades of cycloidal propellers (Van Manen (5)).

It is interesting to note at this point, that for lightly loaded cycloidal propellers (low C_T value) with limited blade span, the optimum pitch ratio values e appear to be in excess of 1 (Fig. 7, Van Manen (5)).

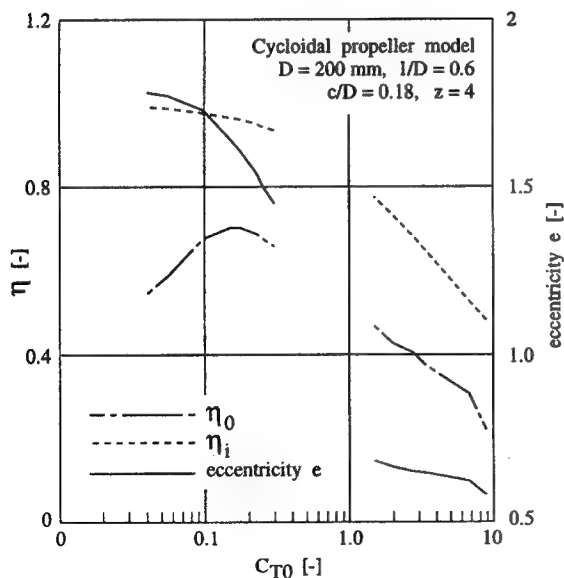


Fig. 7 Optimum efficiency and eccentricity obtained from experiments on a cycloidal propeller (derived from Van Manen (5)).

Blade area ratio

Equivalent to the propeller blade area ratio A_B/A_0 is for example the ratio of total lateral blade area A_L to propeller envelope area A_0 :

$$\frac{A_L}{A_0} = \frac{z\bar{l}\bar{c}}{D} \quad (5)$$

where z = number of blades
 l = length or span of blade
 \bar{c} = mean chord length of blade
 D = propeller diameter.

Similar to conventional propellers, this blade area ratio is preferably kept as small as possible to minimize frictional losses. It is anticipated that strength requirements govern this minimal blade area ratio. Cavitation is expected to be a less dominating factor for the Whale Tail Wheel than it is for a conventional propeller. This expectation is based on the lower thrust loading, causing lower inflow velocities to the blades and the anticipated smaller variations in blade angle of attack for the Whale Tail Wheel. Only in the lower part of the blade orbit, a high rate of change in angle of attack is experienced.

Blade angle rate

An important parameter with respect to cavitation is the blade angle velocity distribution along the blade orbit. This parameter plays an important role with respect to the distribution of the free vortices, induced by the time derivative of the bound vortex (circulation) of the rotating blades. It is expected that the highest blade pitch rate (occurring in the lower part of the blade orbit) determines the point of inception and the character of developed cavitation, induced by these free vortices.

5. ASSESSMENT OF PERFORMANCE POTENTIAL

Computational model CYCLOPS

Based on a computational model for performance analysis of cycloidal propellers by Brockett (1), a simplified model was implemented in the QUAESTOR knowledge base, designated CYCLOPS. A description of the knowledge system QUAESTOR is given by Van Hees (18).

As can be inferred from Fig. 4, the thrust and torque are simply obtained from the profile lift and drag. The profile's lift is computed from the

following relation:

$$L = \frac{1}{2} \rho V_R^2 c l C_L \alpha_{kin} \quad (6)$$

where

$$\bar{V}_R = (V_0 + \Delta U_a) \bar{i} + \omega R \bar{e}_\theta \quad (7)$$

and V_0 = inflow velocity in propeller
 ω = propeller rotation rate
 R = radius of blade orbit
 ΔU_a = local increase in axial velocity due to thrust production.

The local increase in axial velocity is obtained from momentum considerations on an actuator disk, and reads:

$$\frac{\Delta U_a}{V_0} = \frac{\sqrt{1 + \Delta C_{T0}} - 1}{2} \quad (8)$$

The lift coefficient is computed from:

$$C_L = 2\pi \left(1 - \frac{t}{c}\right) \quad (9)$$

where t/c = blade thickness ratio.

The drag is computed from

$$D = \frac{1}{2} \rho V_R^2 c l C_D \quad (10)$$

where

$$C_D = 2C_F \left(1 + \frac{t}{c} + 100 \left(\frac{t}{c}\right)^4\right) (1 + C_L^2) \quad (11)$$

The simplifications relative to the computational model by Brockett comprise the neglect of 3D effects in the flow about a foil. The Aspect Ratio of the foils of the Whale Tail Wheel are considered to have an infinitely large value. This simplification is justified by the fact that the Whale Tail Wheel can be extended over a major part of the width of the ship, allowing for large aspect ratios of the blades. The propeller blades are furthermore clenched in between two end-plates, causing a theoretical increase in effective aspect ratio towards infinity.

Another simplification is the addition of a constant and uniform induced velocity in x-direction over the total propulsor area, whereas Brockett uses an axially induced velocity that varies over the blade's orbit.

Throughout the computation, all time derivatives have been neglected, as is the case in the model of Brockett. It is to be noted however, that especially near positions in the blade orbit, where the blade angle of attack rapidly changes, these time derivatives may have a non-negligible effect on especially torque. This would decrease the efficiency.

It is yet believed that this simple model provides a realistic indication of the upper limit of attainable efficiencies at the required thrust coefficient. Brockett concludes on his computational model the following: 'The simple procedure for flow modelling described herein has been able to correctly predict the trends and levels of performance in powering and cavitation for cycloidal propulsors. In general, there is greater accuracy in the load predictions for high-pitch (eccentricity $e > 1$) than for low-pitch operation, since the interaction between the blades is reduced at high-pitch operation (as it is for the conventional propeller) and the predictions appear to be more accurate for symmetrical blade sections than for cambered profiles.' (Brockett (1)).

The Whale Tail Wheel that has been evaluated for this study has blade profiles without camber (symmetrical profiles) and has the pivot point located at half chord length. To provide sufficient stiffness to the blades, a tentative number of 3 additional support disks were considered as part of the propulsor. The additional torque for these support disks has been included in the results.

Selected blade angle path

Two blade angle paths were considered during this study. First a blade angle path was computed with Sparenberg's criterion for optimal efficiency. This criterion comes down to the constraint for constant circulation about the blade section. If this criterion is met, no free vortices are shed and consequently no additional kinetic energy is lost. This criterion cannot be used however in the top and bottom position of the blade orbit ($\phi = 0$ and π respectively). This will be explained with the Figs. 8 and 9.

Fig. 8 shows the geometrical blade angle β over the blade orbit for three types of blade motion. The path indicated 'Sparenberg' shows a non-zero pitch angle at the top position ($\phi = 0$), due to the

constant circulation constraint. This causes a significant negative thrust contribution around the top position however, as is illustrated in Fig. 9. In this figure, the instantaneous thrust and torque values along the blade orbit are plotted for a Sparenberg type blade motion.

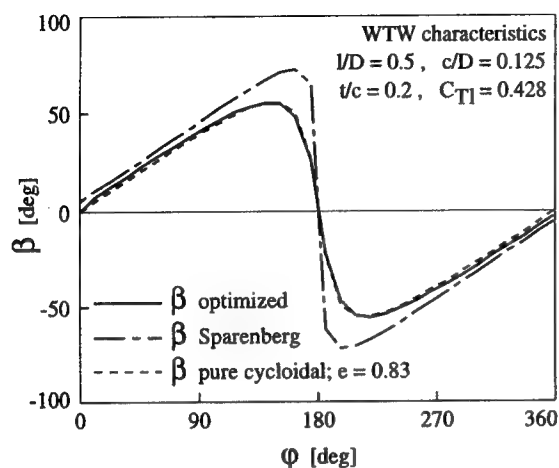


Fig. 8 Various blade angle paths for test case.

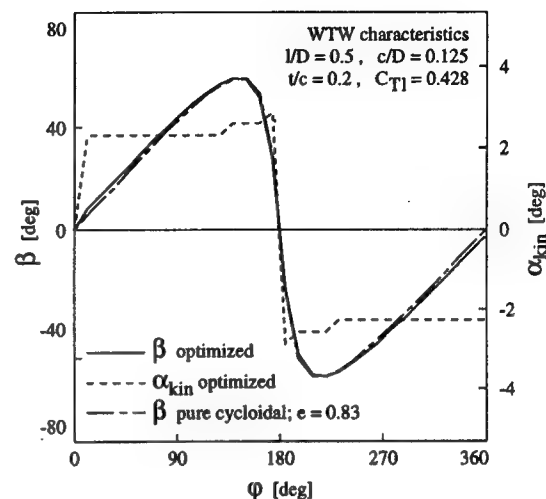


Fig. 10 Optimized blade angle path and angle of attack for test case.

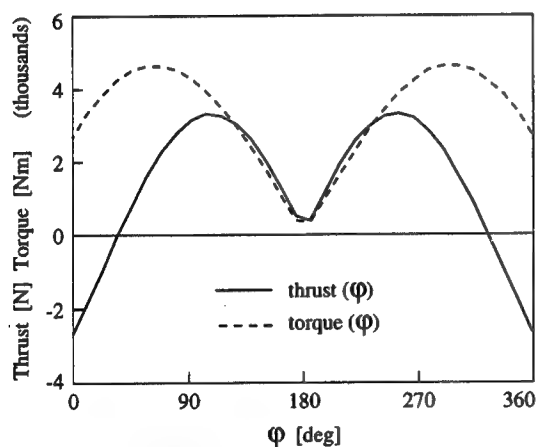


Fig. 9 Instantaneous thrust and torque for one blade during a complete revolution at constant blade circulation.

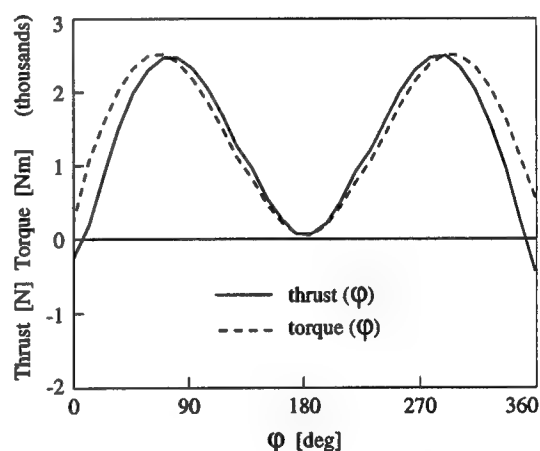


Fig. 11 Instantaneous thrust and torque for one blade during a complete revolution at optimized blade angle path.

In the bottom position, the blade angle has to quickly change sign, in order to allow the blade to maintain a positive thrust contribution in the upward part of its orbit. This implies a discontinuity in the blade's circulation.

The resulting blade angle path and angle of attack are plotted in Fig. 10. Also plotted in this figure is the blade angle path of a pure cycloidal blade motion of similar pitch value ($e = 0.83$). A good correspondence occurs between these two types of blade motion.

An almost constant optimum blade angle of attack of approx. 2.4 deg resulted from the blade angle optimization. This optimum angle will increase however for increasing aspect ratio of the blades. For the presented test case, an aspect ratio of 4 was applied. It is expected however that the trend in the angle of attack with blade position remains unaltered, and therefore the blade angle of attack was set at a constant 4 deg over the major part of the blade orbit. Adaptations to this constant angle of attack were only necessary in both the top and bottom position of the orbit.

The effect of the optimized blade angle or kinematic angle of attack (α_{kin}) on instantaneous thrust and torque is plotted in Fig. 11. Comparison of this figure with Fig. 9 shows a clear difference in instantaneous efficiency (thrust/torque ratio) in the upper part of the orbit.

It is to be noted that, due to the addition of 3-D effects in the results of the latter figure, the trends in thrust and torque are comparable, but not so their absolute values however.

Analysis of Whale Tail Wheel applications

To obtain a realistic indication of the performance of a Whale Tail Wheel behind a vessel, it is not sufficient to only consider the maximum propeller efficiency attainable. One should also take the thrust requirement and allowable size of the propeller into account.

To this end, four vessel types were selected; a coaster, a short sea ferry, a high speed catamaran and an inland waterway vessel. For each vessel, the main dimensions of a representative design for that type of vessel are listed in Table 1. The total resistance for a representative design speed was then computed.

Table 1
Characteristics of selected cases

Designation		Coaster	Short Sea Ferry	Catamaran	Inland Waterway Vessel
Geometric characteristics					
L_{pp}	- length between perpendiculars [m]	85.3	118.5	35.5	80.0
B	- moulded breadth [m]	13.5	21	11.5	11.4
T	- design draft [m]	5.15	5.8	1.25	3.0
$DISV$	- displacement volume [m]	4970	9000	77.1	2470
C_B	- block coefficient [-]	0.838	0.624	0.755	0.90
Powering characteristics					
<i>Whale Tail Wheel</i>					
V_D	- design speed [kn]	12.0	20.0	30.0	8.1
R_T	- total resistance [kN]	175	635	129	100
D	- propeller diameter [m]	2.0	2.0	0.8	1.5
l/B	- non-dimensional span of propeller blades [-]	0.8	0.8	0.6	0.8
c/D	- non-dimensional chord length of propeller blades [-]	0.18	0.18	0.18	0.18
z	- number of blades [-]	6	6	6	6
C_T	- propulsor loading coefficient [-]	0.19	0.16	0.09	0.39
η_0	- open water efficiency [-]	0.81	0.83	0.84	0.74
P_D	- delivered power [kW]	1476	8560	2467	681
n	- propeller rotation rate [RPM]	46	67	161	63
λ	- propeller velocity ratio [-]	1.14	1.29	2.01	0.74
<i>Conventional propeller</i>					
N	- number of propellers	1	2	2	1
D	- propeller diameter [m]	2.60	4.00	0.90	2.25
η_0	- open water efficiency [-]	0.51	0.63	0.68	0.47

The dimensions of the Whale Tail Wheel were roughly selected as to house a large but yet feasible propeller. To this end, the width of the Wheel was set at 80% for the monohulls and 60% for the catamaran. The wheel diameter was then selected so as to not exceed either 65% of the hull's draft or an absolute value of 2.0 m.

Whale Tail Wheel dimensions and computed performance results are listed in Table 1. The results have been computed on the assumption of a 10% increase in thrust due to the propulsor action and a 12% wake fraction.

Representative open water efficiencies for conventional propeller propulsion are listed for reference purposes. These efficiencies lie in the range from 0.45 to 0.70, the higher values for the lighter propeller loading coefficients.

Fig. 12 shows the open water efficiency of the Whale Tail Wheel in relation to the open water efficiencies of a number of B-series propellers and the waterjet system, as a function of thrust loading coefficient C_T . It is clearly seen that the Whale Tail Wheel is a lightly loaded propeller in the selected applications, allowing for a high propulsive efficiency.

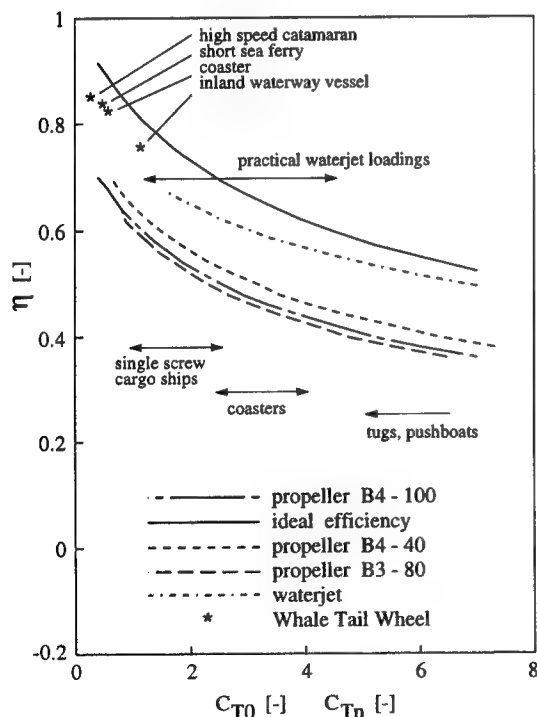


Fig. 12 Comparison of open water efficiencies of the Whale Tail Wheel, propeller and waterjet.

The open water efficiency is roughly some 10% points higher than for the propeller at the same loading coefficient. This advantage should at least partly be attributed to the lack of 3D flow effects on the foils of the Whale Tail Wheel.

It should however be noted that a comparison at equal thrust loading coefficient is interesting from the point of view of hydrodynamics, but that it is not a relevant comparison for realistic designs. This is caused by the difference in allowable propulsor dimensions. The Whale Tail Wheel allows for a much bigger envelope area A_0 than the conventional propeller. And thus, the thrust coefficient of a Whale Tail Wheel is relatively lower, leading to a more favourable efficiency.

To obtain an indication of the validity of the simplified computational model, computed open water efficiencies are compared with ideal efficiencies and measured efficiencies on a low aspect ratio cycloidal propeller (blade aspect ratios of 3.3 and 5.0). These efficiencies are plotted as a function of thrust loading coefficient in Fig. 13. After incorporation of the physical mechanisms that have been neglected in the present study, the Whale Tail Wheel open water efficiencies are expected to come out in between the plotted Whale Tail Wheel values and the experimental cycloidal propeller values.

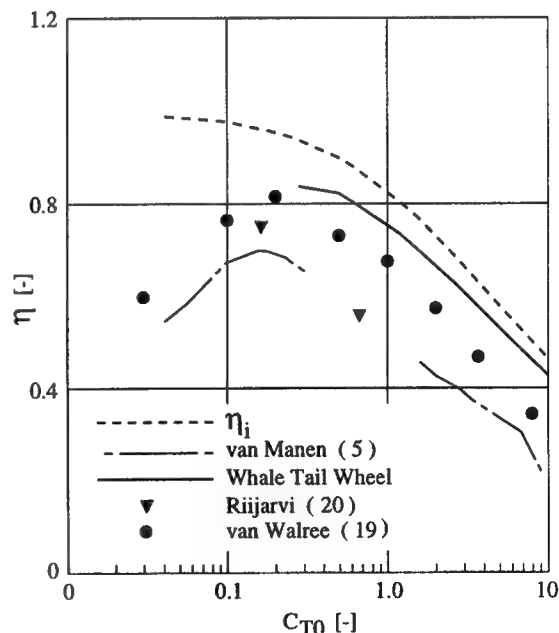


Fig. 13 Comparison of computed Whale Tail Wheel efficiencies with ideal and measured (5) open water efficiencies.

Recent data by Van Walree (19), obtained from an improved prediction model are also added. These computations were made for a cycloidal propeller with blades showing an aspect ratio of approximately 6.

6. FINAL REMARKS

Conclusions

The present pilot study was partly based on the computer program CYCLOPS, which aims at predicting the powering characteristics of a Whale Tail Wheel. The program is based on 2D flow considerations, incorporating a rough induced flow correction based on actuator disk considerations. A few physical mechanisms have not been included yet, such as the effect of the shedding of free vortices, which is likely to occur at particularly the lower part of the blade orbit.

The present study shows that the Whale Tail Wheel has a great potential for high propulsive efficiencies for a wide variety of vessels. Preliminary estimates of the open water efficiency of the propulsor when applied to four selected vessel types show values around 80%. It is anticipated that in the computation of these efficiencies and appropriate thrust and torque values, the most important physical mechanisms are included. A number of mechanisms has deliberately not been included in this pilot study however, which are likely to cause a slightly lower efficiency in reality. The predicted values here can therefore be regarded as an upper limit of the attainable efficiency. It should be noted that transmission losses are not included in the given efficiency figures.

The relatively high efficiency is obtained for mainly two reasons:

1. The propulsor is extremely lightly loaded due to the fact that it can be extended over a major part of the width of the vessel. This increases the ideal efficiency of the propulsor and consequently the actual open water efficiency.
2. The aspect ratio of each blade approaches infinity, causing the lift/drag ratio of each blade to be much higher than in the finite lift/drag ratio propulsors such as the conventional cycloidal propeller (e.g. Voith Schneider) and the conventional screw propeller.

Due to the lightly loaded propulsor, relatively low rotation rates occur (around 60 RPM for the selected cases).

Furthermore, the blades are expected to

remain cavitation free for the greater part of their orbit. Cavitation may occur in the lower part of the blade orbit, where a high blade pitch rate occurs. The very low thrust coefficient of the Whale Tail Wheel, combined with the control of blade angle rate by an adjustable eccentricity of the blades along their orbit allow for a control of cavitation inception and developed cavitation phenomena at the cost of only small efficiency reductions.

Prospects

Improvement of performance prediction

A first improvement that is readily implemented is an improved model for the induced velocities. This model should correctly account for the induced velocities of the upstream blades on the downstream blades. This is done by implementing the Vortex Lattice Method (VLM). This method also allows for 3D effects about free tips of the blades (19) and can consequently be used for any cycloidal propulsor.

Another improvement is the incorporation of the effect of time derivatives in the hydrodynamic blade loading. This effect is incorporated through the so-called Theodorsen function, including effects of periodically shed vortices for pitch and heave motions.

As a third improvement, an empirical model for the steady lift-drag characteristics of a 2D profile for the complete range of possible angles of attack (0 to π) is implemented.

Despite the incorporation of the VLM, allowing for 3D induced velocities, the modelling of the effect of the endplates on the circulation distribution over the blades remains uncertain. As long as no reliable information for this model is available, the geometry of the blades is treated as 2-Dimensional. More certainty on the effect of the endplates will be obtained from model experiments.

Application in ship designs

The surprising aspects of the Whale Tail Wheel with the "wide and restricted draft" propulsion area are:

- The extremely high hydrodynamic efficiency as a consequence of the realized light thrust loading.
- The dependence of the hydrodynamic efficiency of the propeller span and as such its important effect on the choice of the ships beam, draft and length.
- The possibility to optimize this dependence of the ship dimensions and the Whale Tail Wheel

for both deep and shallow water.

- The possibility to optimize short sea vessels by integration of sea- and inland waterway transport and the elimination of cargo handling in the mainport on their way to subterminals. This elimination may lead to a substantial operational reduction of the cargo-handling costs.
- The extremely light propeller loading of the Whale Tail Wheel (eccentricity > 1) leads to a simplification of the ship's afterbody (largely 2-dimensional), to a more homogeneous wake field and consequently to favourable circumstances to avoid the risk of cavitation related phenomena like noise and vibrations.

REFERENCES

1. Brockett, T., "Hydrodynamic Analysis of Cycloidal Propulsors", SNAME Propellers/Shafting '91 Symposium, Virginia Beach, Sept. 17-18, 1991.
2. Kirsten, F.K., "A New Type of Propeller", S.A.E. Journal, Vol. XXII, Jan. 1928, pp. 77-80.
3. Kirsten, F.K., "The Cycloidal Propeller in Marine Application", University of WA, Aeronautical Laboratory, Report 322.
4. Schneider, E., "Cycloidal Propulsion Wing" (in German), Werft-Reederei-Hafen, June 1933, pp. 161-169.
5. Manen, J.D. van, "Results of Systematic Tests with Vertical Axis Propellers", International Shipbuilding Progress, Vol. 13, Dec. 1966, pp. 382-398.
6. Henry, C.J., "A Survey of Cycloidal Propulsion", Davidson Laboratory, Report No. 728, Dec. 1959.
7. Sparenberg, J.A., "On the Efficiency of a Vertical Axis Propeller", Proceedings of Third Symposium on Naval Hydrodynamics (High Performance Ships) ONR ACR-65, 1960, pp. 45-60.
8. Sparenberg, J.A. and Graaf, R. de, "On the Optimum One-Bladed Cycloidal Propeller", Journal Eng. Math., Vol. 3, 1969, pp. 1-20.
9. James, E.C., "A Small Perturbation Theory for Cycloidal Propellers", PhD Thesis CIT, Pasadena, 1971.
10. Nakonechny, B.V., "Experimental Performance of a Six Bladed Vertical Axis Propeller", DTMB Report 1446, Jan. 1961.
11. Nakonechny, B.V., "Design of a 9 inch Cycloidal Propeller Model Unit and Some Experimental Results", NSRDC Report 3150, 1975.
12. Ficken, N.L., "Conditions for the Maximum Efficiency Operation of Cycloidal Propellers", SNAME Chesapeake Section Paper, April 1966.
13. Bjarne, E., "Comparison of a Cycloidal Propeller with Azimuth Thrusters with Regard to Efficiency, Cavitation and Noise", Proceedings of International Conference on Propulsion for Small Craft, RINA, Nov. 1982.
14. Kallstrom, C.G. and Loid, H.P., "Hydrodynamic Investigations of a Mine Hunter Project", Proceedings of RINA International Symposium on Mine Warfare Vessels and Systems, Paper No. 6, June 1984.
15. Bose, N. and Lai, P.S.K., "Experimental Performance of a Trochoidal Propeller with High-Aspect Ratio Blades", Marine Technology, Vol. 26, No. 3, July 1989.
16. Ruys, A.W., "A Comparison of Some Published Results of Tests on Vertical Axis Propellers", International Shipbuilding Progress, Vol. 13, Dec. 1966.
17. Mueller, H., "Recent Developments in the Design and Application of the Vertical-Axis Propeller", Trans. SNAME, Vol. 63, 1955.
18. Hees, M.Th. van, "QUAESTOR: A Knowledge Based System for Computations in Preliminary Ship Design", PRADS'92 Symposium, Newcastle upon Tyne, May 1992.
19. Walree, F. van, "An Improved Mathematical Model for Whale Tail Wheel Analysis", MARIN Report 13505-1-SE, April 1996.
20. Riijärvi, T., Li, J., Veitch, B.J. and Bose, N., "Experimental Performance and Comparison of Performance Prediction Methods for a Trochoidal Propeller Model", International Shipbuilding Progress, 41, No. 426, 1994.

NOMENCLATURE

- | | |
|---------------|--|
| a | - eccentricity; distance from pitch point to orbit centre (Fig. 4) |
| A_0 | - propulsor envelope area; $A_0 = \frac{1}{4}\pi D^2$ for propellers, $A_0 = D^2$ for the Whale Tail Wheel |
| A_E | - expanded blade area of propellers |
| A_L | - total lateral blade area; $A_L = zlc$ |
| c | - chord length of blade |
| C_D | - drag coefficient |
| C_F | - frictional drag coefficient of flat plate |
| C_L | - lift coefficient |
| C_T, C_{T0} | - thrust loading coefficient;
$C_T = T/(\frac{1}{2}\rho V_0^2 A_0)$ |

C_{Ti}	- thrust loading coefficient; $C_{Ti} = T/(\frac{1}{2}\rho V_0^2 zcl)$	T	- total thrust by propulsor
C_{Tn}	- thrust loading coefficient based on waterjet nozzle area A_n	t	- maximum thickness of profile
D	- diameter of blade circle	V_a	- speed of advance
D	- hydrodynamic drag	V_R	- resultant velocity kinematic
e	- non-dimensional eccentricity; $e = a/R$	V_0	- free stream velocity
\bar{e}_ϕ	- unit normal vector along blade orbit	z	- number of blades
i	- unit normal vector in direction of head- ing	α_F	- kinematic angle of inflow relative to (horizontal) x-axis
K_{Fy}	- transverse force coefficient; $K_{Fy} = F_y/(\rho D^4 n^2)$	β	- geometric pitch angle
K_Q	- torque coefficient; $K_Q = Q/(\rho D^5 n^2)$	β_0	- hydrodynamic pitch angle without effect of induced velocities
K_T	- thrust coefficient; $K_T = T/(\rho D^4 n^2)$	ΔU_a	- local increase in axial velocity due to thrust production
J	- advance ratio; J (or Λ) = $V_0/(nD)$	η_0	- open water efficiency
L	- hydrodynamic lift	λ	- velocity ratio; $\lambda = V_0/(\omega R)$
l	- span of blade	ρ	- mass density of water
n	- propulsor rotation rate	ϕ	- blade orbit angular position
R	- radius of blade circle	ω	- angular rotation rate [rad/s]

All quantities in SI-units

Effects of Tip-Clearance Flows

Y.-T. Lee,¹ J. Feng,² C. Merkle,² M. Tse¹

(¹David Taylor Model Basin, ²Pennsylvania State University, USA)

ABSTRACT

Tip-leakage flows for a linear compressor cascade and a one-stage shrouded pump rotor are discussed in this paper. A numerical method solving the Reynolds averaged Navier Stokes equations is used to explore various detail features of the tip-leakage flows. Calculation results for the cascade provide an assessment for predicting flow past a non-rotating blade passage with zero and 2% chord clearances. On the other hand, the pump rotor configuration provides a swirling passage flow with the complication of a trailing-edge separation vortex mixed with the tip-clearance and passage vortices and produces a very complex three-dimensional flow in the rotor wake. The physical aspects of the tip-clearance flows are discussed including suction-side reloading and pressure-side unloading due to a tip clearance and formation and transportation of the tip-leakage vortex. Detailed velocity comparisons in the blade passage and the tip gap region are shown to indicate the difficulty of predicting tip-leakage flow. The pressure at the core of the tip vortex is also examined to evaluate the strength of the tip-leakage vortex.

NOMENCLATURE

c	chord
C_p	pressure coefficient
L.E.	leading edge
E,F,G	defined in Eq. (2)
E_v, F_v, G_v	viscous terms
H	source term
p	static pressure
Q	defined in Eq. (2)
s	pitch
S	shear stress tensor

t	pseudo-time
T.E.	trailing edge
TLF	tip-leakage flow
TLV	tip-leakage vortex
u	velocity in x-direction
v	velocity in y-direction
w	velocity in z-direction
U	contravariant velocity in Eq. (3)
UREF	reference velocity
V	contravariant velocity in Eq. (3)
V_x	axial velocity
V_t	tangential velocity
W	contravariant velocity in Eq. (3)
x, y, z	physical coordinates
β	cascade inflow or outflow angle; artificial compressibility coefficient
Γ	defined in Eq. (2)
ν_t	viscosity
τ	shear stress or tip gap size
ω_b	blade rotational speed
ξ, η, ζ	transformed coordinates

INTRODUCTION

Tip-leakage flow (TLF) past ducted or shrouded blade tips occurs in many turbomachinery applications including axial-flow machines, centrifugal impellers and ducted propulsors. Similarly, tip leakage occurs in the gap between stators and a rotating hub. Because of the relative movement between the blade tip and the adjacent wall, the gap flows in rotating machinery applications are typically driven by a combination of the pressure difference between the pressure and suction sides of the blade and the viscous forces arising from the relative motion between the adjacent surfaces. Depending on the parameters and

the geometries involved, either of these may be the primary driver in a given application. When the gap is large and the blade loading is high, the tip-gap flows are generally dominated by pressure effects, while very narrow gaps or low blade loading lead to gap flows that are more dependent on the relative movement between the blade tip and the casing. In general, however, inertial forces in this narrow gap region are sufficient to generate a tip-leakage vortex (TLV) on the suction side of the blade that not only produces substantial losses, but may also initiate blade surface cavitation [1]. Over the life span of a turbomachine, the machine efficiency and operating margin deteriorate due to the increase in tip gap spacing.

The engineering importance of tip gap flows, and the complexity of the physics they contain, has stimulated numerous previous studies of these phenomena. Recent studies of tip-leakage flow have involved various turbomachinery configurations, including linear cascades, compressors, turbines and pumps. Experimental studies of tip-gap flows in cascades have been reported by Kang and Hirsch [2,3], while Lakshminarayana et al. [4], Inoue et al. [5,6], Suder and Celestina [7], and Foley and Ivey [8], have conducted measurements in compressors. Tip-gap flows in turbines have been studied experimentally by Chan et al. [9], Yamamoto et al. [10], and DeCecco et al. [11] while pump flow experiments have been reported by Graham [12] and Zierke et al. [13, 14].

In addition to these experimental investigations, many analytical studies and numerical simulations of tip-gap flows have also been reported. Because our emphasis in the present paper is computational in nature we emphasize the latter here. Previous computational studies have included the simulations reported by Hah [15], Dawes [16], Crook [17], Adamczyk et al. [18], Copenhagen et al. [19], and Kang and Hirsch [20]. Of the numerous analytical studies, we here cite only the work of Chen et al. [21] who have developed a similarity scaling for the crossflow in the clearance region and a generalized description of the tip-leakage vortex based on inviscid-flow modeling. A comparison of our tip-leakage vortex trajectories with the model of Chen et al. [21] is presented later.

Although the experimental investigations and numerical simulations cited above have revealed many features of tip-leakage flows, many unsettled issues still remain. In general, the results to date have shown that several characteristic features tend to dominate the tip gap region in most cases. These

include: (i) the formation, transport and trajectory of the tip-leakage vortex; (ii) the interaction of the tip-leakage flow with vortices generated by other mechanisms; and (iii) the size of the tip clearance and the blade loading. Despite these similarities, the detailed characteristics of the tip-leakage flow vary from one type of machine to another. For example, the relative motion between the blade tip and the shroud acts in an opposite direction in compressors and turbines. In compressor rotors, the relative movement between the blade tip and the casing or shroud tends to enhance tip leakage by dragging fluid through the gap region in the same direction as the pressure drop. By contrast, the relative motion in turbine rotors is in the opposite direction and tends to negate the effects of pressure drop. In fact, observations in turbines have been reported in which the tip gaps were so small that the leakage flow was reduced to zero by the relative movement [9].

The present study investigates the physical processes involved in the generation and transport of the tip-leakage vortex by means of numerical solutions of the three-dimensional Navier-Stokes equations. Results are presented for both a stationary cascade and a high Reynolds number axial rotor. The cascade geometry and operating conditions are chosen to match the low-speed compressor cascade experiments of Kang and Hirsch [2,3] who have provided a detailed map of the passage and tip-leakage flow at three different tip clearance conditions. The axial-flow rotor computations are chosen to match the conditions tested by Zierke et al. [13,14] who have furnished a reasonably complete outline of the wake of a pump rotor in the rotating frame including information on the transport of the tip-leakage vortex. The passage flow for this rotor has been investigated numerically by [22, 23, 24]. Dreyer and Zierke [23] quantitatively compared their predicted tip flow with the measured data at the design tip gap size. The cascade experiments were obtained with a stationary wall so that the gap flows are driven by pressure drop alone, while the pump rotor experiment involves the effects (in the relative frame) of a moving shroud. Thus, these two cases not only provide us with detailed experimental data against which we can check our computations, but they also represent an interesting comparison of the effects of the moving wall. Our emphasis therefore is on comparing the details of the tip gap flow in a cascade with a stationary wall with those in a rotating pump stage where there is relative motion between the blade and the casing.

In the following sections, we first present the numerical method along with the numerical gridding techniques with particular emphasis on the tip-clearance region. Then a brief summary of the experimental data used for comparison is given. The formation and the transport of the tip-leakage vortex for both cases are then examined in detail in the results section. In particular, we present numerical solutions for two tip gap clearances for both the cascade and the pump rotor.

NUMERICAL METHOD

Computational solutions of the Reynolds-averaged Navier Stokes equations were performed to explore the features of tip-leakage flow. The numerical flow solver used is designed to solve either compressible or incompressible flows. For the present incompressible applications, an artificial compressibility term is added to the continuity equation to facilitate convergence. A brief discussion of this numerical approach is given next.

Governing Equations and Turbulence Closure

The incompressible Reynolds-averaged Navier Stokes equations are formulated as

$$\Gamma \frac{\partial Q}{\partial t} + \frac{\partial}{\partial \xi} (E - E_v) + \frac{\partial}{\partial \eta} (F - F_v) + \frac{\partial}{\partial \zeta} (G - G_v) = H \quad (1)$$

where

$$Q = \begin{bmatrix} \rho \\ u \\ v \\ w \end{bmatrix}; E = \begin{bmatrix} U \\ uU + \xi_x p \\ vU + \xi_y p \\ wU + \xi_z p \end{bmatrix}; F = \begin{bmatrix} V \\ uV + \eta_x p \\ vV + \eta_y p \\ wV + \eta_z p \end{bmatrix}; G = \begin{bmatrix} W \\ uW + \zeta_x p \\ vW + \zeta_y p \\ wW + \zeta_z p \end{bmatrix}; \Gamma = \begin{bmatrix} \frac{1}{\beta} & 0 & 0 & 0 \\ \frac{1}{\beta} & 1 & 0 & 0 \\ \frac{1}{\beta} & 0 & 1 & 0 \\ \frac{1}{\beta} & 0 & 0 & 1 \end{bmatrix} \quad (2)$$

and

$$\begin{aligned} U &= \xi_x u + \xi_y v + \xi_z w & E_v &= v_t S \cdot (\xi_x, \xi_y, \xi_z)^T \\ V &= \eta_x u + \eta_y v + \eta_z w & F_v &= v_t S \cdot (\eta_x, \eta_y, \eta_z)^T \\ W &= \zeta_x u + \zeta_y v + \zeta_z w & G_v &= v_t S \cdot (\zeta_x, \zeta_y, \zeta_z)^T \end{aligned} \quad (3)$$

with

$$S = \begin{bmatrix} 0 & 0 & 0 \\ \tau_{xx} & \tau_{xy} & \tau_{xz} \\ \tau_{yx} & \tau_{yy} & \tau_{yz} \\ \tau_{zx} & \tau_{zy} & \tau_{zz} \end{bmatrix}; H = \begin{bmatrix} 0 \\ 0 \\ \omega_b^2 y + 2\omega_b w \\ \omega_b^2 z - 2\omega_b v \end{bmatrix} \quad (4)$$

The inclusion of the time-derivative in the continuity equation changes the Navier Stokes equations from a

partially elliptical system in time to a hyperbolic system. Thus a time marching scheme to update the primitive variables (p,u,v,w) is feasible. For steady state flows, the time derivative terms in the equations approach zero as the solution converges so that the converged solution satisfies the steady-state incompressible Navier Stokes equations.

The coefficient v_t in Eq. (3) represents the effective viscosity which includes contributions from both the molecular viscosity and the turbulent viscosity. A standard two-equation k- ϵ turbulence model [25] was used to provide the turbulent viscosity closure in Eq. (3) for the computations presented in this paper. To facilitate resolution near the walls, a wall-function approach was used to enforce wall boundary conditions. In this wall-function procedure, the tangential velocity on the wall is determined by applying its normal derivative at the half grid point from the wall to satisfy the law of the wall. This finite wall velocity scheme was validated over a range of grid resolutions near the wall prior to conducting the present computations to verify its appropriateness.

Numerical Procedure

The combined Reynolds-averaged Navier Stokes equation and the two equation turbulence model in Eq. (1) were jointly solved by means of a four-stage Runge-Kutta time marching approach [26]. In the formulation, both viscous and inviscid spatial derivatives are computed by means of second-order central difference representations. Fourth-order artificial dissipation is applied to prevent odd-even splitting in the numerical solution. A local time step size is defined in conjunction with the artificial compressibility coefficient to obtain an optimal convergence rate. In regions of primarily inviscid flow, the convergence rate is controlled by the convective terms, and β in Eq. (2) is chosen to minimize the disparity among the system eigenvalues. In viscous-dominated regions where the convergence is mostly subject to the rate of viscous diffusion, the time step size is determined by viscous terms. β is then chosen such that an optimal time step size is still achievable for that part of the convective terms whose eigenvalue corresponds to the downstream-running acoustic characteristic.

A multi-block structure is employed to model blade passages with tip clearance. As shown in Fig. 1, the layout of the grid for both the cascade and the pump rotor consists of five H-type blocks. They include the inlet block (from the inlet to the

blade leading edge), the blade passage block (from the blade leading edge to the blade trailing edge and from the hub to the blade tip), two blade tip blocks between the blade tip and the casing, and the exit block from the blade trailing edge to the exit. Grid lines are continuous across block interfaces.

There are three types of boundary conditions associated with these grid structures: inlet and exit boundaries, periodic boundaries between adjacent blade passages, and non-slip wall boundaries including rotating and nonrotating blade surfaces and the stationary casing. For the present applications, Method of Characteristics (MOC) procedures are used to derive the number of inlet and exit boundary conditions [26]. This follows the hyperbolic equation concept that information that propagates into the flow field must be specified at the boundary while information that propagates across the boundary from the interior of the domain is dictated by the governing equations. These boundary conditions are then enforced by specifying the velocity components at inlet boundaries and extrapolating the static pressure from conditions on the inside. At outflow boundaries, the static pressure is calculated from local radial equilibrium and the velocity is extrapolated.

On solid surfaces, the non-slip condition supplemented by the normal momentum condition is used to determine the flow quantities. In the rotational frame, this leads to zero velocity on the blade and hub surfaces and a specified tangential velocity on the counter-rotating casing surface. Periodic boundary points are treated in a manner analogous to that used for field points.

NUMERICAL RESULTS

Description of Geometries Studied

As noted above, two geometries are used to study tip-leakage flow. The first is a stationary linear compressor cascade studied experimentally by Kang and Hirsch [2,3]. The second is a one-stage stator-rotor pump measured by Zierke et al. [13,14]. For the cascade case, the wall is stationary, and the tip-leakage flow is totally pressure driven. For the rotor case, the tip-leakage flow is also facilitated by the relative motion at the blade tip. The results show that the tip-leakage flow of the cascade case presents stronger mixing phenomena including tip leading edge separation, a larger tip-leakage vortex and more pronounced blade suction-side reloading.

The blades used in the linear cascade tests of Kang and Hirsch [2,3] have a modified NACA 65-1810 cross section with a rounded trailing edge. As shown in Fig 2, the blade has a chord of 200 mm and a solidity of 1.1. The stagger angle is 10 degrees and the blade aspect ratio is unity. At the design condition, the inflow angle is 29.3 degrees and the flow deflection angle is about 40 degrees. The inflow is turbulent and has a Reynolds number of 3×10^5 based on the average inlet velocity and the blade chord length. The cascade flow was measured at tip-gap clearances of 0%, 1% and 2% of the chord. Predictions of both the 0% and 2% cases are presented in this paper.

The axial-flow pump consists of a 13-blade inlet guide vane (IGV) followed by a 7-blade backward swept rotor. This stator-rotor configuration is referred to as the HIREP rotor [13,14]. The separation between the IGV blade row and the rotor blade row at the outer casing is approximately 1.3 IGV chord lengths. The pump has a constant hub diameter of 0.533 m and a constant casing diameter of 1.067 m. The IGV blades have a constant spanwise chord of 0.175 m. The chord length of the rotor blades decreases from 0.285 m at the hub to 0.266 m at the tip. The corresponding solidity values are 1.19 at the hub and 0.56 at the tip. The tip section of the rotor blade has a thickness-to-chord ratio of 10.1%. The nominal rotor tip clearance is 0.330 mm, which corresponds to 0.64 % of the pump casing radius. The pump operates at an inlet velocity of 10.7 m/s and an inlet pressure of 3.04 kg/cm². The rotational speed and tip speed are 260 RPM and 14.5 m/s, respectively, while the flow coefficient 1.36. The tested Reynolds number based on the chord of the IGV blade is 2.3×10^6 . The details of the measurement hardware and results are given in Zierke et al. [13, 14].

Tip-Gap Flow in the Cascade

Calculations of the cascade geometry were made for two blade tip clearances, zero and 2% chord (and span), at an inflow angle corresponding to the design condition. For the tip clearance calculation, the blade height was decreased by 2%, thereby reducing the blade aspect ratio to 0.98. In both cases, the embedded H-type grid described above was used. As shown in Fig. 1a, the embedded grid provides a good representation of both the blade leading and trailing edge regions while also providing a smooth grid change from the blade tip to the tip-clearance region. The grid has 95 nodes in the axial direction, 51 nodes from blade to blade, and

41 nodes from hub to tip. For the case of 2% tip gap, the grid is heavily stretched near the blade tip and there are ten grid points in the spanwise direction between the blade tip and the endwall. Twelve grid points are placed inside the gap in the blade-to-blade direction. Such a grid resolution appears to satisfy the minimum accuracy requirement needed to capture most features of the tip-leakage flow [20].

In Fig. 3, the blade surface pressure distributions for both the zero and 2% tip gap cases are presented at three span locations, 50%, 85% and 98.5%. The predicted pressure distributions for the zero tip clearance case which are shown in Fig. 3a agree well with the experimental data. The flow, which is approximately symmetric about the mid-span, separates near the mid-chord at the endwall. This separation region grows rapidly until it covers about 25% of the span at the trailing edge.

For the 2% tip gap case, the predicted pressures at mid-span (49%) and 83.3% span shown in Fig. 3b again agree quite well with the measured values. At the 96.5% span, the experimental measurements show a local minimum in the suction side pressure distribution at about the 40% chord location. This minimum is evidence that a strong tip-leakage vortex exists. The impact of the reloading characteristics of this vortex are indicated by the fact that the minimum pressure peak at 96.5% span is even lower than that at 49% span. Similarly, the computational pressure distribution shows a minimum in the suction side pressure distribution at 96.5% span that is also lower than that at 49% span indicating that the prediction clearly captures the qualitative features of the leakage vortex. Quantitative comparison of the experimental and computational results, however, shows that both the location and the magnitude of the suction side reloading is somewhat different from the experimental measurements. Similar suction-side reloading is also seen by the experimental investigations of Graham [12] and Foley et al. [6] and suggests that the tip gap may not always lead to blade tip unloading, as has been widely assumed.

The tip reloading noted in Fig. 3b is governed by the details of the transport of the tip-leakage vortex as is demonstrated in more detail in Fig. 4. Because of the relatively high blade loading in the cascade, the tip vortex starts to separate relatively close to the blade leading edge as shown in Fig. 4a. After separating from the tip at about 30% chord, the vortex core is washed away from the suction side of the blade in the lateral direction and is also pushed down towards the hub as it is

convected downstream. The overall trajectory of the vortex is shown in Fig. 4b.

An indication of the variation in the local strength of the vortex can be deduced from measurements of the static pressure at the vortex center. Representative results of this nature are shown in Fig. 4c for both the experiment and the computations. The pressure measurements in Fig. 4c indicate that the vortex strength is a maximum where it first separates from the blade tip. As it is convected away from the blade and in the downstream (chord-wise) direction, it begins to weaken and disperse although it continues to grow in size. Figure 4c shows comparisons between the calculated pressure along the vortex core and the measurements [2,3]. The two vortex trajectories are similar in shape and magnitude, although the predictions are somewhat displaced from the experimental results.

The tip-leakage flow can also be evaluated from the flow pattern on the endwall in the vicinity of the tip as shown in Fig. 5. The comparison between the calculated endwall streamlines in Fig. 5a and the experimental paint traces in Fig. 5b indicates that the experimental suction-side separation line in the blade wake region is closer to the suction side than in the computational prediction. The predicted pressure contours on the tip endwall are shown in Fig. 5c. The high pressure-gradient region on the suction side of the blade matches with the suction-side separation line shown in Fig. 5a. A comparison of these two figures also clearly shows that the tip-leakage vortex leaves the blade tip section at the minimum pressure location.

Figure 6 presents a more detailed comparison of the predicted and measured velocity components. This comparison shows two velocity components in the blade-to-blade plane at three axial sections, 11%, 55% and 99% chord. In particular, the axial velocity component, u , and the blade-to-blade velocity component, w , are compared. At each of the three sections results for two spanwise locations, mid-span ($y=0.48$) and near tip ($y=0.96$), are presented. The mid-span predictions agree well with the measurements at all three locations. For the near-tip section, the agreement is good at 11% chord (Fig. 6a), where the tip-leakage vortex is not yet formed. At mid-chord (Fig. 6b), where the tip-leakage vortex is well established, its influence is clearly reflected in the two velocity components. The axial velocity dips strongly and the lateral velocity accelerates dramatically because of the presence of the tip-leakage vortex on the suction side. The computation slightly overpredicts the dip

while it underpredicts the tangential peak. This difference implies a small disagreement in the vortex location and/or the vortex core orientation between the computation and the experiment. This disagreement is augmented somewhat at the trailing-edge section further downstream (see Fig. 6c). Here, the computational solutions predicts the magnitude of the tangential velocity peak reasonably well, but its location is too close to the suction side. Meanwhile, the peak in the axial velocity is much too large in the predictions.

The downstream remnants of the gap flow on the cascade wake are shown Fig. 7. Here we show the contours of the absolute cross sectional velocity in the blade-to-blade and hub-to-tip plane for both the predictions and the measurements. These results are presented at an axial section that is 25% chord downstream of the blade trailing edge. Figure 7a presents the predicted cross-sectional velocity contours, while Fig. 7b shows the corresponding experimental results. It is important to note that Fig. 7b presents only the upper half (mid-span to casing) of the flow passage, while Fig. 7a shows the full passage (hub to casing). The local concentration of velocity contours on the suction side of the blade near the tip in both figures represents the tip-leakage vortex. The passage vortex (PV) occupies the center region of the cross section and is labeled in both Fig. 7a and 7b. The horseshoe vortex generated at the leading-edge of the blade exists only in the immediate vicinity of the leading edge and then quickly disperses and merges with the passage vortex. Consequently it can no longer be distinguished in the wake, and so is not visible in these contour plots.

As a last comparison in the wake, Fig. 7c shows the axial and blade-to-blade velocity components on hub-to-tip lines passing through the center of the tip-leakage vortex and the center of the passage vortex as determined from Figs. 7a and 7b. The axial velocity on the line passing through the passage vortex shows only the characteristics of a normal boundary layer: the velocity decreases monotonically from the mean passage to both the casing and the hub. The experimental and computational comparisons for both the u and w velocity components on this line are seen to be in quite good agreement. The velocity components on the line passing through the tip-leakage vortex, however, show considerably different behavior. The tip leakage vortex causes the axial velocity to dip to a minimum considerably before reaching the casing wall. The blade-to-blade velocity component, however, shows a very complicated shape with,

particularly, a strong peak near the casing wall because of the residual strength of the tip leakage vortex. For these much more sensitive profiles, the comparisons between the measurements and the computations are again qualitatively similar, but quantitatively quite different. The computation clearly overpredicts the tip-leakage vortex velocity, but its general features are reasonably well captured.

In summary, the comparisons between the predictions and the measurements for the cascade case show that the pressure distributions with and without tip clearance effects agree quite well with the measured values. In general, however, pressure levels are less sensitive and easier to predict than the cross-plane velocities. The comparisons of the more sensitive flow quantities such as the tip-leakage vortex core velocity and pressure are qualitatively accurate, but there is some difficulty in predicting the exact location and strength of the tip-leakage vortex. Overall, the comparisons suggest that the flow features are captured reasonably although there remains room for improvement.

Tip-Gap Flow In the HIREP Rotor

As compared to a stationary blade, a rotating pump stage facilitates the gap flow because the blade rotates in the opposite direction to the gap flow, and hence, the casing tends to pump the flow in the tip region and to enhance the gap flow effects. Obviously, the degree of such rotational effects depends on the tip gap height, the RPM, the blade loading and the blade thickness. As noted above, the computations were carried out for the HIREP rotor for which detailed experimental measurements have been carried out by Zierke et al [13,14].

An H-type multi-block embedded grid structure similar to that shown in Fig. 1b is used to describe the rotor blade geometry. Two grid sizes are used for the present investigation: a coarse grid of $79 \times 53 \times 47$ nodes in the axial, blade-to-blade and spanwise directions respectively, and a fine grid of $105 \times 108 \times 87$ nodes. Like the linear cascade, the coarse grid maintains 12×10 grid points inside the gap. The fine grid has 24×12 grid points inside the gap and approximately doubles the grid everywhere else on each axial, cross-sectional plane. Because the coarse grid is approximately similar in grid resolution to the cascade grid, we first present solutions on the coarse grid and compare them with experiment. After that, the fine grid solutions are used to ascertain the accuracy of the coarse grid solution. Unless specifically mentioned, the computational solutions were presented for the

coarse grid. Again the blade leading and trailing edges are adequately represented with both grids.

Three different tip clearance cases were computed. They are 0.64%, 1.17% and 3.22% of the outer casing radius respectively. For all three gap sizes, the number of grid nodes inside the tip gaps remained the same. For all computations presented in this paper, the rotor inflow was determined from the circumferentially averaged stator exit flow solution. The profiles of the velocity components obtained from this averaging process are shown in Fig. 8. This simple mixed-out approach was proven to be adequate in handling the present stage flow in a steady manner [22, 24].

The design tip clearance for the HIREP rotor is 0.64% of the outer casing radius. The predicted tip-leakage flow for this design condition is shown in Fig. 9. Because of the interaction of the tip-leakage vortex and the trailing-edge vortex, the tip vortex travels further tangentially as it is convected downstream as compared to the tip-leakage vortex in the cascade computations.

Figure 10 shows a comparison between an experimental visualization of the interaction between the tip vortex and the trailing-edge vortex and the corresponding predictions. This visualization photograph was obtained by reducing the tunnel pressure to the point that cavitation appeared at the core of both vortices. Based on the sizes of the cavitating vortices, the tip-leakage vortex seems to have a larger strength than the trailing-edge vortex. The two vortices pass one another at different radii and do not intersect. The present photo shows only the last 30% of the blade chord. Both Inoue and Kuroumaru [4] and Zierke et al. [13] located the onset of the tip-leakage vortex roll-up as the point of minimum pressure on the suction surface.

The predicted results indicate that the tip-leakage vortex passes over the tip section from the pressure side to the suction side at about 15% of the chord as shown in Fig. 11a at the design clearance. This location is in good agreement with that observed by Zierke et al. [13] for the onset of vortex roll-up on the suction side. Also shown in Fig. 11a is the predicted vortex path by Chen et al. [21]. Figure 11b shows the spanwise location of the tip-leakage vortex downstream of the trailing edge. In this figure, the origin of the abscissa, $x/c_{TP} = 0$, corresponds to the trailing edge of the rotor. For both the predictions and the measurements, the path of the tip-leakage vortex moves radially inward by approximately 1% of the casing radius in the near wake and then levels off at an essentially constant radius from the near wake to the far wake. The

sudden change in radial location may relate to the development of the blade passage boundary layer to the free-shear wake flow. Considering the difficulty in locating the exact location of the vortex core, the trajectory of the tip-leakage vortex in both the blade-to-blade and the spanwise directions compares favorably with the experimental data. The calculation also correctly predicts the relative size and the crossover location of both vortices.

A comparison of the effect of tip gap height on the pressure distribution in the rotor is shown in Fig. 12 for each of the three tip gap sizes mentioned above. The results on Fig. 12 are presented for three radial blade locations: 1%, 3% and 5% of the casing radius away from the blade tip. The only available measurement is performed at a radial location of 95% of the casing radius at the design condition (0.64% tip gap). As can be seen in Fig. 12a, when the tip gap is small (0.64%), the pressure distribution shows little gap unloading like that seen in the cascade even close to the tip gap, however, as the gap spacing increases, the unloading develops. At the largest gap (3.22%), the tip unloading toward the outer radius becomes significant as indicated by the reduction of the enclosed area between the pressure and suction side pressure distributions as can be seen on Fig. 12c. Comparing against the cascade case, the reloading on the suction side appears to be weaker and does not appear until much further downstream, indicating a much weaker tip leakage vortex. However, the suction-side reloading starts around 1% tip gap as indicated in Fig. 12b.

In Fig. 13, the pressure distributions at three radii from hub to tip are presented together with corresponding experimental measurements at the design clearance, 0.64%. For brevity, the 1.17% case is omitted in this figure. The computations and the experiments are in excellent agreement, except near the blade trailing edge where a small difference exists. Also note that the unloading occurs at 90% span for the larger gap case.

Figure 14 shows the comparison of the wake velocity at 16.1% casing radius (or 32.4% tip chord) downstream of the tip trailing edge. Although the test data is only for the small gap, the comparison between the experiment and the calculation is made for both gap sizes. Two radial sections are selected for comparisons, i.e. $r = 0.786$ (mid-span) and 0.971 (near tip) respectively. Although the calculation overpredicts the thickness of the shear layer, the fine grid solution captures the blade wake more precisely as shown for the mid-span comparison. For the tip velocity comparison, the blade wake becomes much smaller in both size

and magnitude, and the TLV dominates the variation of the velocity distribution. The prediction at the design gap clearly captures the vortex activity but underpredicts the strength of the TLV. The difference is also related to the deviation in predicting the location of the TLV as shown in Fig. 11a where the axial distance for this wake comparing section is 0.324. For the larger gap, the blade wake at the tip shown in Fig. 14 disappears and the TLV covers the whole passage from the suction side to the pressure side. Figure 11 indicates that this TLV leaves the suction side around 60% tip chord, and moves closer to the suction side and to the casing wall than the smaller gap TLV. However, the sharp drop-off seen for the small gap solution in Fig. 11b exists also for the large gap solution, but with a milder slope.

CONCLUSIONS

Numerical solutions obtained by solving the Reynolds-averaged Navier Stokes equations, with a two-equation $k-\epsilon$ turbulence model and a wall-function model, were compared with the measured tip-leakage flows for a compressor cascade and a one-stage pump rotor. The grid topology used in the tip gap region is an embedded grid approach, which ensures the precise representation of the blade tip geometry and the smooth grid variation from the blade region to the tip clearance region. The tip-clearance sizes studied in this paper are 0% and 2% chord for the cascade, and 0.64%, 1.77% and 3.22% casing radius for the pump rotor. The tip-leakage flow for the pump rotor is not well-structured as the cascade, but many flow characteristics are similar. In addition, the radial-moving trailing-edge vortex further complicate the rotor tip-leakage flow near the tip trailing edge. Although the present cascade calculation was performed for a full turbulent flow simulation, the transition model should be examined in order to evaluate the Reynolds number effect on these calculations. The present calculation captures almost all the features of the tip-leakage flow and the transport of the tip-leakage vortex for both the cascade and the rotor. Some specific conclusions are as follows.

1. Both the cascade and the rotor show suction-side reloading and pressure-side unloading when the tip clearance size exceeds a certain size. For the pump rotor, this happens when the tip clearance is about 1% of the casing radius. This

suction-side reloading is a by-product of the transport of the tip-leakage vortex.

2. The tip-leakage vortex leaves the suction side from 15% to 60% chord depending on the gap size and the rotor speed. This location matches with the location of the minimum pressure on the casing endwall. A sharp large drop in spanwise direction when the vortex leaves the suction side, another smaller drop happens when the vortex leaves the blade passage and into the wake.

3. The velocity distributions associated with the passage vortex and the tip-leakage vortex are quite different. The former is a regular boundary-layer type and the latter has several peaks due to stronger effect from the tip-leakage vortex.

4. The present coarse grid resolution is adequate for the passage flow calculation, particularly the blade loading prediction. Fine grid provides better prediction for the viscous blade wake. For the tip-clearance region, however, the 10 or 12 spanwise grids and 12 or 24 blade-to-blade grids may not be enough in capturing the vortex generation and transportation precisely.

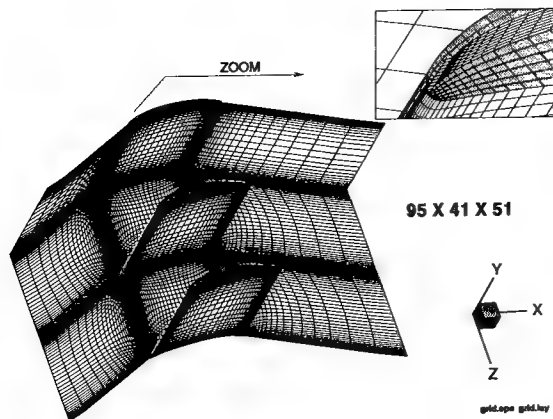
ACKNOWLEDGMENTS

The two experimental data sets were provided by Drs. S. Kang and C. Hirsch of the Vrije Universiteit Brussel and by Messrs. W. C. Zierke, P. D. Taylor and W. A. Straka of Pennsylvania State University. This work was funded under the Applied Hydrodynamics Program and the Block Program for Hydrodynamics and Hydroacoustics of Internal Flow. The program monitor at the Office of Naval Research is Dr. P. Purtell. The computing time was provided by the DOD High Performance Computational Program.

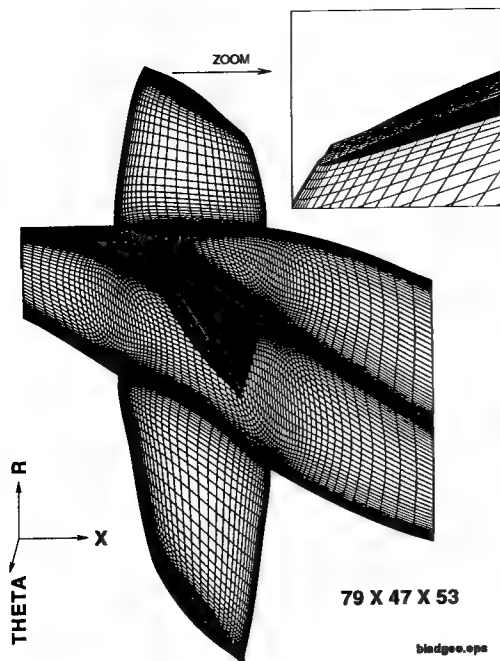
REFERENCES

1. Farrell, K. J., and Billet, M. L., "A Correlation of Leakage Vortex Cavitation in Axial-Flow Pumps," *ASME Journal of Fluid Engineering*, Vol. 116, No. 3, 1994, pp. 551-557.
2. Kang, S., and Hirsch, C., "Experimental Study on the Three Dimensional Flow within a Compressor Cascade with Tip Clearance: Part II - The Tip Leakage Vortex," *ASME Journal of Turbomachinery*, Vol. 115, 1989, pp. 444-452.

3. Kang, S., and Hirsch, C., "Tip Leakage Flow in a Linear Compressor Cascade," ASME Paper GT-93-303, 1993.
4. Lakshminarayana, B., Sitaram, N., and Zhang, J., "End-Wall and Profile Losses in a Low-Speed Axial Flow Compressor Rotor," ASME Journal of Engineering for Gas Turbines and Power, Vol. 108, 1986, pp. 22-31.
5. Inoue, M., Kuroumaru, M., and Fukuhara, M., "Behavior of Tip Leakage Flow Behind an Axial Compressor Rotor," ASME Journal of Engineering for Gas Turbines and Power, Vol. 108, 1986, pp. 7-14.
6. Inoue, M. and Kuroumaru, M., "Structure of Tip Clearance Flow in an Isolated Axial Compressor Rotor," ASME Journal of Turbomachinery, Vol. 111, 1989, pp. 250-256.
7. Suder, K. L., and Celestina, M. L., "Experimental and Computational Investigation of the Tip Clearance Flow in a Transonic Axial Compressor Rotor," ASME Paper 94-GT-365, 1994.
8. Foley, A. C., and Ivey, P. C., "Measurement of Tip-Clearance Flow in a Multi-Stage, Axial Flow Compressor," ASME Paper 94-GT-431, 1994.
9. Chan, J. K. K., Yaras, M. I., and Sjolander, S. A., "Interaction Between Inlet Boundary Layer, Tip-Leakage and Secondary Flows in a Low-Speed Turbine Cascade," ASME Paper 94-GT-250, 1994.
10. Yamamoto, A., Matsunuma, T., Ikeuchi, K., and Outa, E., "Unsteady Endwall/Tip-Clearance Flows and Losses due to Turbine Rotor-Stator Interaction," ASME Paper 94-GT-461, 1994.
11. De Cecco, S., Yaras, M. I., and Sjolander, S. A., "Measurements of the Tip-Leakage Flow in A Turbine Cascade with Large Clearances," ASME Paper 95-GT-77, 1995.
12. Graham, J. A. H., "Investigation of a Tip Clearance Cascade in a Water Analogy Rig," ASME Journal of Engineering for Gas Turbines and Power, Vol. 108, 1986, pp. 38-46.
13. Zierke, W. C., Farrell, K. J., and Straka, W. A., "Measurement of the Tip Clearance Flow for a High Reynolds Number Axial-Flow Rotor: Part 1 - Flow Visualization," ASME Paper 94-GT-453, 1994.
14. Zierke, W. C., Farrell, K. J., and Straka, W. A., "Measurement of the Tip Clearance Flow for a High Reynolds Number Axial-Flow Rotor: Part 2 - Detailed Flow Measurements," ASME Paper 94-GT-454, 1994.
15. Hah, C., "A Numerical Modeling of Endwall and Tip-Clearance Flow of an Isolated Compressor Rotor," ASME Journal of Engineering for Gas Turbine and Power, Vol. 108, 1986, pp. 17-21.
16. Dawes, W. N., "A Numerical Analysis of the Three-Dimensional Viscous Flow in a Transonic Compressor Rotor and Comparison with Experiment," ASME Journal of Turbomachinery, Vol. 109, 1987, pp. 83-90.
17. Crook, A. J., "Numerical Investigation of Endwall/Casing Treatment Flow Phenomena," M.S. Thesis, Department of Aeronautics and Astronautics, Massachusetts Institute of Technology, 1989.
18. Adamczyk, J. J., Celestina, M. L., Beach, T. A., and Bartnett, M., "Simulation of Three-Dimensional Viscous Flow Within a Multi-Stage Turbine," ASME Journal of Turbomachinery, Vol. 112, 1990, pp. 370-376.
19. Copenhaver, W. W., Mayhew, E. R., and Hah, C., "The Effect of Tip Clearance on a Swept Transonic Compressor Rotor," ASME Paper 94-GT-363, 1994.
20. Kang, S., and Hirsch, C., "Numerical Simulation of 3D Viscous Flow in a Linear Compressor Cascade with Tip Clearance," ASME Paper 94-GT-364, 1994.
21. Chen, G. T., Greitzer, E. M., Tan, C. S., Marble, F. E., "Similarity Analysis of Compressor Tip Clearance Flow Structure," ASME Journal of Turbomachinery, Vol. 113, 1991, pp. 260-271.
22. Yang, C. I., "A Simulation of Viscous Incompressible Flow Through a Multiple-Blade-Row Turbomachinery with a High-Resolution Upwind Finite Differencing Scheme," ASME FED Vol. 227, Numerical Simulations in Turbomachinery, 1995.
23. Dreyer, J. J., and Zierke, W. C., "Solution of the Average-Passage Equation for the Incompressible Flow Through Multiple-Blade_row Turbomachinery," Report No. TR 94-05, The Pennsylvania State University/Applied Research Laboratory, 1994.
24. Lee, Y. T., Hah, C., and Loellbach, J., "Flow Analyses in a Single-Stage Propulsion Pump," ASME Journal of Turbomachinery, Vol. 118, 1996.
25. Chien, K. Y., "Predictions of Channel and Boundary-Layer Flows with a Low-Reynolds-Number Turbulence Model," AIAA Journal, Vol. 20, No. 1, 1982, pp. 33-38.
26. Merkle, C. L. and Tsai, Y-L. P., "Application of Runge-Kutta Schemes to Incompressible Flows," AIAA Paper 86-0553, AIAA 24th Aerospace Sciences Meeting, Reno, NV, Jan. 1986.



(1a) Compressor cascade



(1b) Pump rotor

Fig.1 Surface computational grids

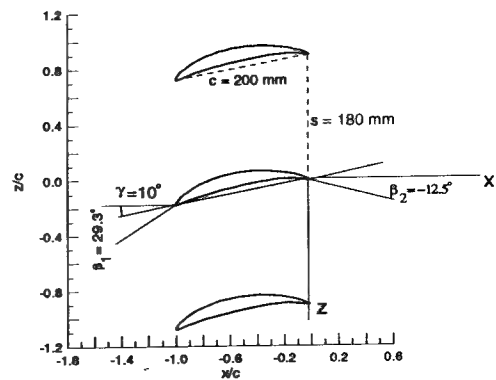
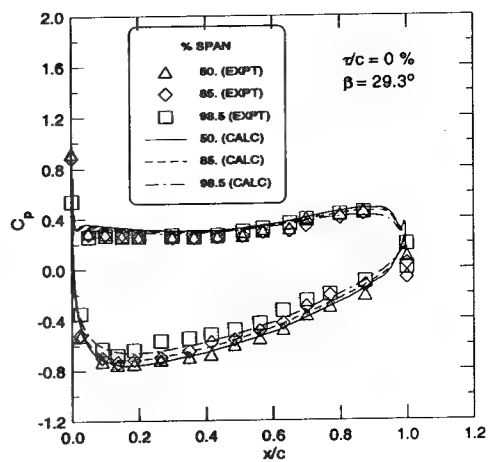
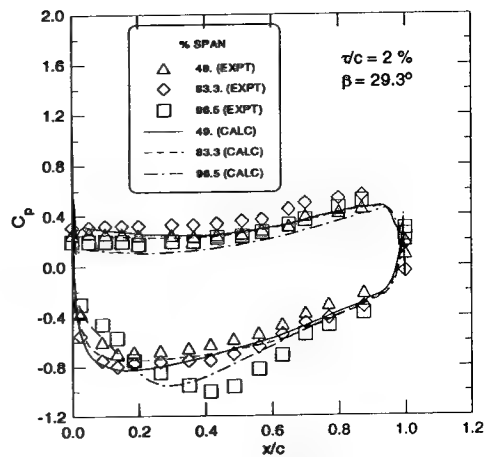


Fig. 2 Cascade parameters

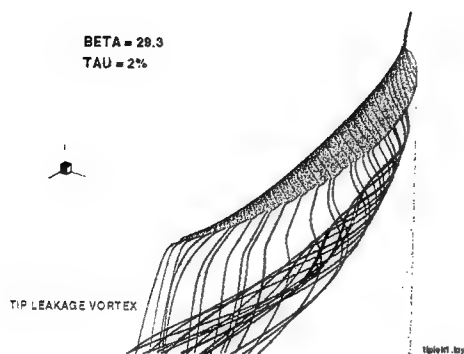


(3a) Zero clearance

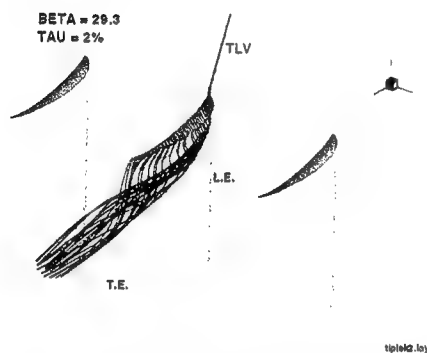


(3b) 2% clearance

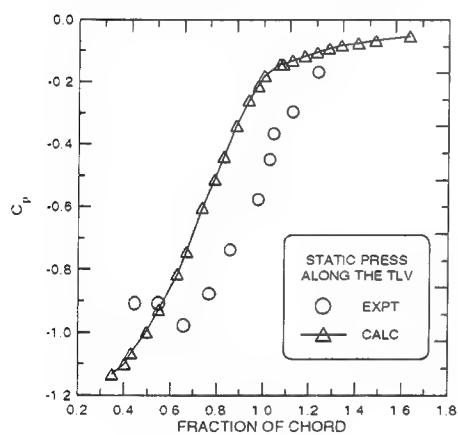
Fig. 3 Pressure distributions on blade surface



(4a) Separation on blade tip

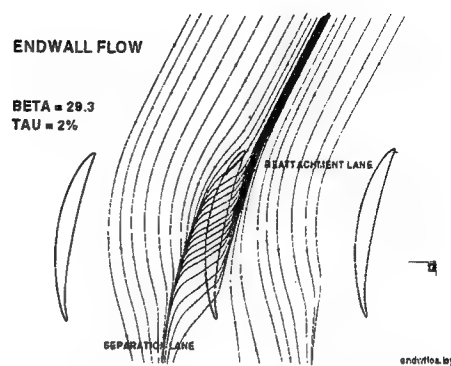


(4b) Tip-leakage vortex on suction side



(4c) Pressure at vortex core

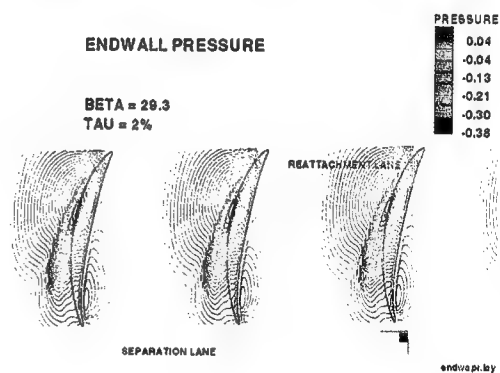
Fig. 4 Features of cascade tip-leakage vortex



(5a) Streamline traces

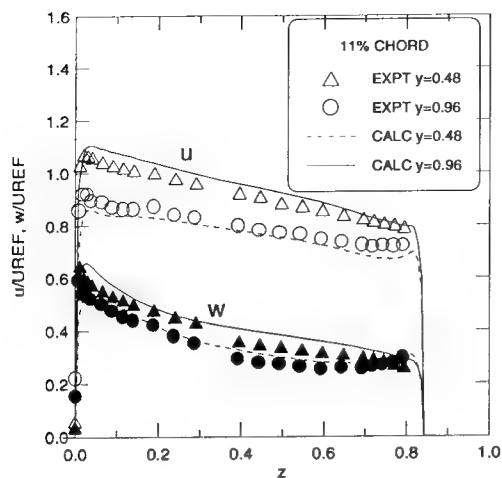


(5b) Flow visualization

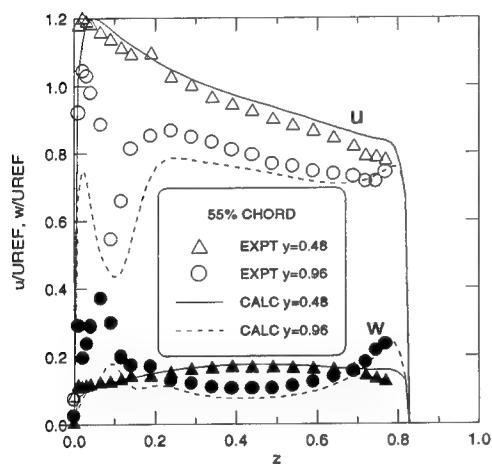


(5c) Pressure contours

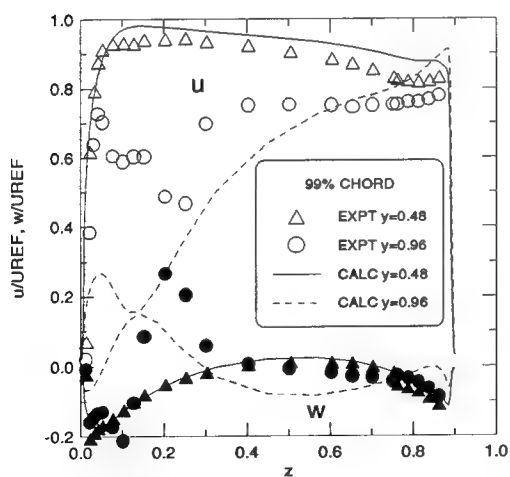
Fig. 5 Flow pattern on tip endwall



(6a) 11% chord

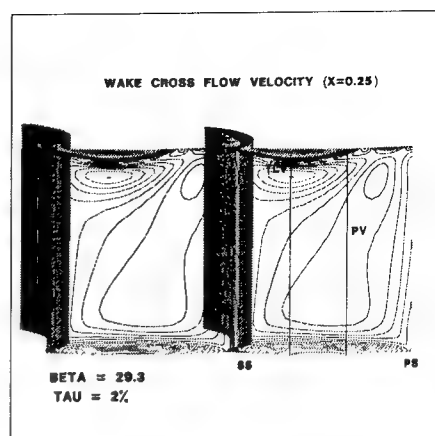


(6b) 55% chord

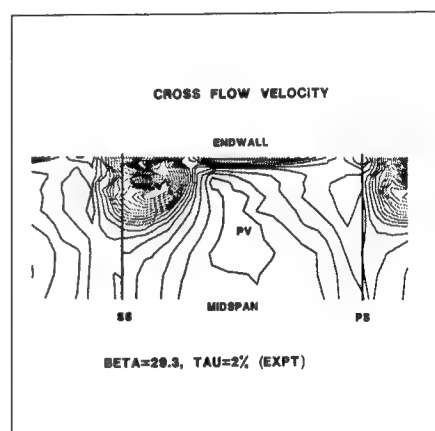


(6c) 99% chord

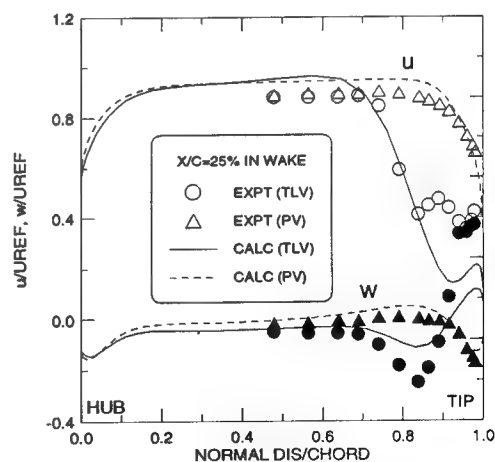
Fig. 6 Velocity comparisons along blade passage



(7a) Predicted velocity contours



(7b) Measured velocity contours



(7c) Velocity comparisons

Fig. 7 Comparison in blade wake at $x=0.25$

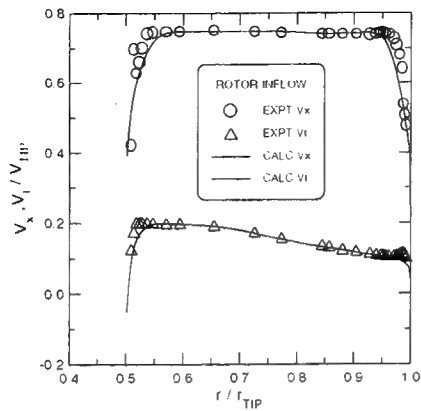
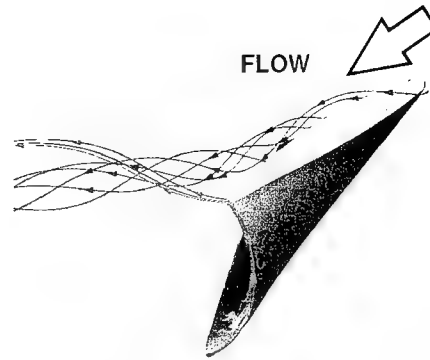


Fig. 8 Inflow velocity for pump rotor



(10b) Prediction
Fig. 10 Vortices near blade tip trailing edge

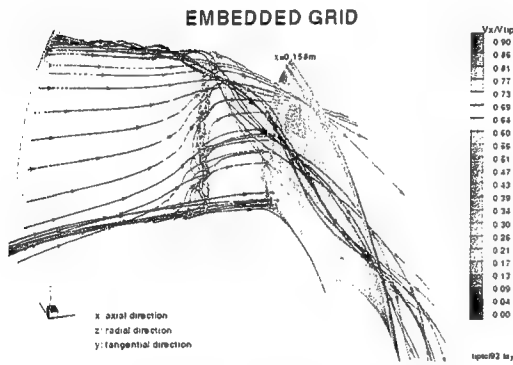
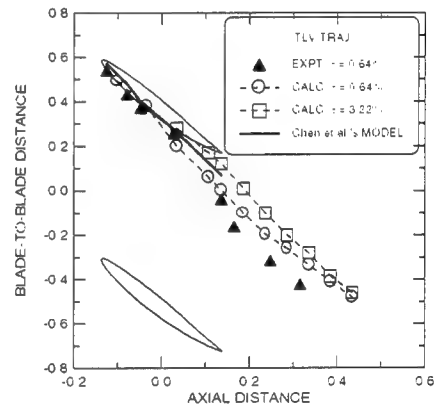
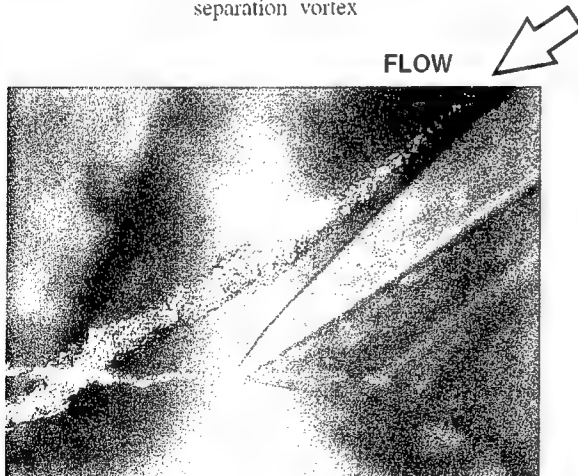


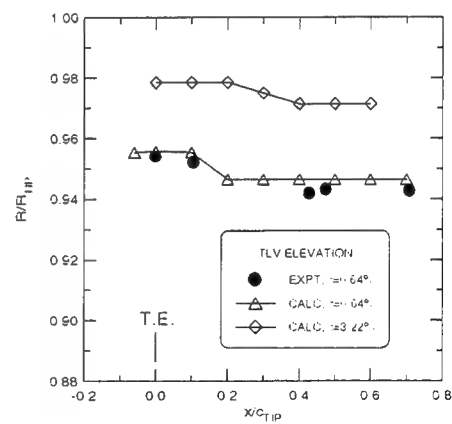
Fig. 9 Predicted tip-leakage flow and trailing-edge separation vortex



(11a) Blade-to-blade direction



(10a) Flow visualization



(11b) Spanwise direction
Fig. 11 Trajectory of tip-leakage vortex

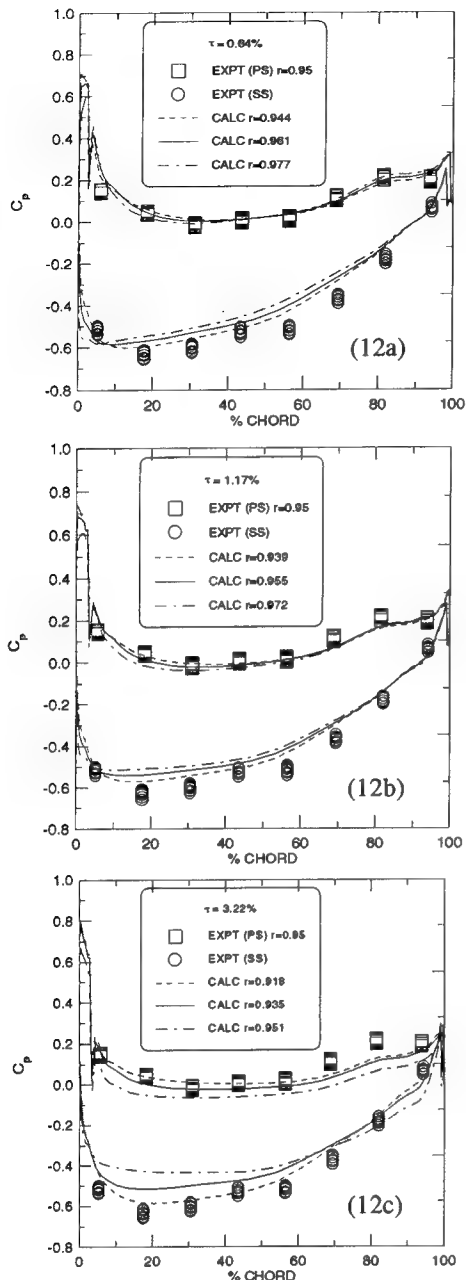


Fig. 12 Blade pressure distributions for three clearances

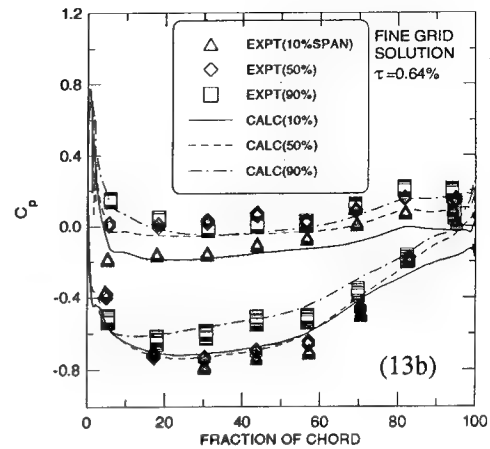
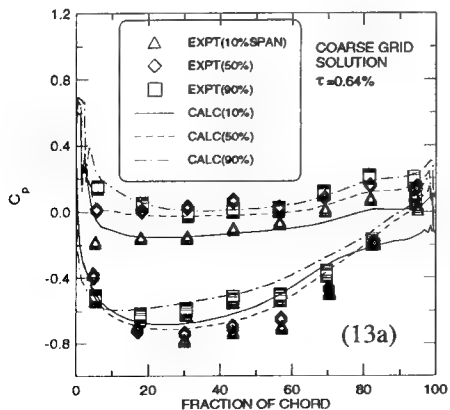
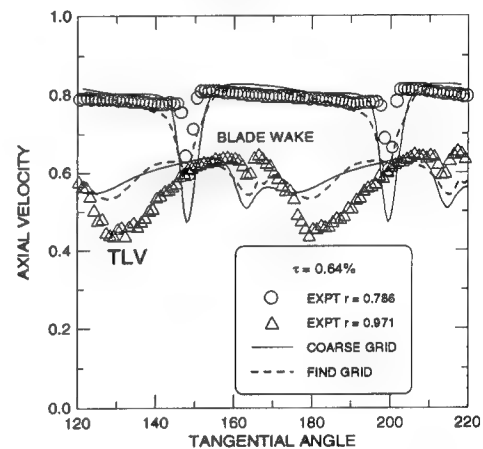
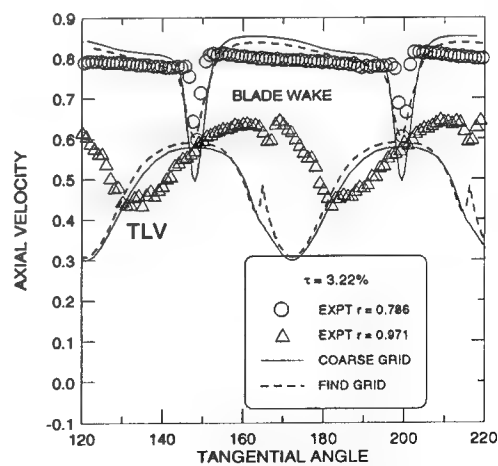


Fig. 13 Blade surface pressure in the spanwise direction



(14a) 0.64% tip clearance



(14b) 3.22% tip clearance

Fig. 14 Axial-velocity comparisons at mid-span and near tip

Experiments in the Swirling Wake of a Self-Propelled Axisymmetric Body

A. Sirviente, V. Patel (University of Iowa, USA)

Abstract

Measurements were made in the zero-momentum wake of an axisymmetric body propelled by a swirling jet issuing symmetrically from the tail. This study follows that of Hyun and Patel (1), who made measurements in the wake of the same body propelled by a marine propeller. Here, the jet conditions were adjusted to reproduce the overall effects of the propeller. Use of the same wind tunnel and similar instrumentation enabled a comparative study of the momentumless wake in the two cases.

Triple-sensor hot-wire anemometry was employed to measure the three mean velocity components and the six Reynolds stresses. The total and static pressure distributions were also measured with pitot probes, giving a complete set of data. This paper describes the experiments and a preliminary analysis of the data to elucidate the evolution of the wake. The momentumless wake of the jet-propelled body provides insights into the near-field mixing of the body boundary layer with the swirling jet, and their evolution toward a single flow.

Introduction

Swirl and longitudinal vorticity are basic characteristics of all three-dimensional turbulent shear flows. The wake of a body driven by a propeller or a jet, with appendages and controls in operation, is easily among the most complex of shear flows. A propeller introduces unsteadiness, high levels of turbulence, and tip and hub vortices, adding to the general complexity of the flow. The measurements of Hyun and Patel (1) indicate that, at a distance of the order of two propeller diameters downstream, the individual vortical structures are smeared and the flow is essentially a steady rotationally-symmetric shear layer with swirl but no net flux of axial momentum. The present experiment was designed to study the initial development of such a momentumless wake with swirl. The primary effects of a propeller,

namely the addition of axial and circumferential momenta to the fluid, are reproduced here by means of a swirling jet issuing symmetrically from the tail of the body. The resulting flow is, of course, simpler in comparison to the propeller wake, but retains considerable complexity when compared to canonical turbulent shear flows such as boundary layers, jets and wakes.

The flow in the near wake of the jet-propelled body, in reality, depicts the mixing between the body boundary layer and an axisymmetric swirling jet. Sufficiently far downstream, there emerges a single shear flow, the momentumless axisymmetric wake with swirl, which is known to admit similarity solutions under certain simplifying assumptions. This, therefore, is also a study in the evolution of a single flow from the merger of two well documented shear flows. The experiment described below is the final experiment in a series conducted to study the development of the individual component flows and their combination, see Sirviente (2).

Design of Experiments

A new model of the axisymmetric body referred to in earlier studies as the "Iowa Body" was constructed with the tail truncated at a diameter of 3.96 cm to accommodate a swirling jet of diameter $D = 3.9$ cm issuing from the base, as shown in Figure 1. The jet diameter is smaller than the diameter, $D_p = 10.16$ cm, of the propeller used by Hyun and Patel (1). The modified body has a length (L) of 143.45 cm and a maximum radius (R) of 6.95 cm.

The boundary layer on the body was tripped by a 1.2-mm diameter wire, located at a distance of 9.5 cm from the nose. The thickness of the boundary layer at the tail, δ , was then 4.38 cm, i.e., $\delta/D = 1.12$. Air was supplied through a 1.24 cm diameter pipe along the body axis, entering the body at the nose, to provide axial momentum to the jet. Air was also introduced separately through a 3.0 cm diameter

pipe concentric with the first pipe to impart tangential momentum to the flow. The tangential flow was injected into the axial stream at a distance 39 cm upstream from the jet exit through four 1.0 cm x 0.5 cm tangential slots. This method of swirl generation is simple, has no moving parts, and provides independent control of axial and tangential momenta.

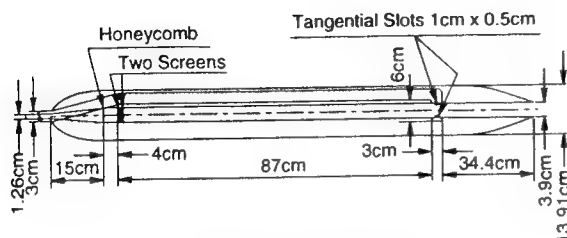


Figure 1. Modified Iowa Body

The experiments were conducted in the 1.07-m octagonal, open test-section, return-circuit wind tunnel of the Iowa Institute of Hydraulic Research. Figure 2 shows the wind tunnel and model arrangement along with the coordinate system used to report the data. The uniformity of mean velocity and turbulence intensity in the tunnel was investigated by Hyun (3), who reported a mean-flow uniformity better than 0.25% and a turbulence intensity of 0.5% in the test section. The freestream velocity U_0 was set at 16.5 m/s, resulting in a Reynolds number based on body length ($Re = U_0 L / \nu$) of 1.58×10^6 , where ν is the kinematic viscosity of air. The jet velocity was adjusted to realize the self-propelled condition, i.e., such that the axial momentum of the jet was just equal to the momentum loss due to the body drag. This condition was achieved with a maximum axial velocity at the jet exit equal to twice the freestream velocity, i.e., $U_j = 2U_0$. The tangential momentum was adjusted such that it matched that of the propeller employed by Hyun and Patel (1). The maximum tangential velocity at jet exit was then $W_{mj} = 0.95U_0$. These operating conditions translate into a swirl number,

$$S = \frac{2M_{\theta x}^j}{M_x^j D} \quad (1)$$

based on jet radius ($D/2$), of 0.34, where M_x^j and $M_{\theta x}^j$ are, respectively, the axial fluxes of axial and tangential momenta of the swirling jet.

As shown in Figure 1, the model was mounted with a part of it extending into the tunnel contraction to maximize the axial length over which the wake could be studied. This enabled

measurements in the axial direction up $x/D = 19.531$, or $x/L = 0.531$, where x is measured from the jet exit. It will be seen later that this distance was just sufficient to establish the asymptotic state of the wake. In the radial direction, measurements were made up to $r/R = 4.5$ to recover the freestream conditions.

As this flow is, in principle, steady and rotationally symmetric, its description requires measurements along a single radial line at each axial position. However, measurements were taken across the (vertical) diameter to monitor flow symmetry. The measurements were made with a triple-sensor hot-wire probe and a five-hole Pitot probe. The latter was used to determine the mean flow direction so that proper yaw and pitch angles for the hot-wire probe could be selected. It also provided redundant data for the mean-velocity components. The probes were traversed in the vertical direction by a simple computer-controlled mechanism. Detailed description of the experimental equipment, instrumentation, and measurement procedures can be found in Sirviente (2), along with an analysis of the uncertainty in the data. There it is shown that the uncertainties of the mean velocity components measured with the hot-wire were less than $0.02U_0$ and those in flow directionality were 1.5 degrees. Uncertainties of the axial Reynolds stress, \overline{uu} , and the shear stress, \overline{uv} , were estimated to be 10%, while those of the remaining stresses were 20%. Measurements with the five-hole Pitot probe had uncertainties of $0.02U_0$ in velocity magnitude and ± 1.5 degrees in flow direction. The software used to control the experiments, and acquire and process the data, is described by Walter (4).

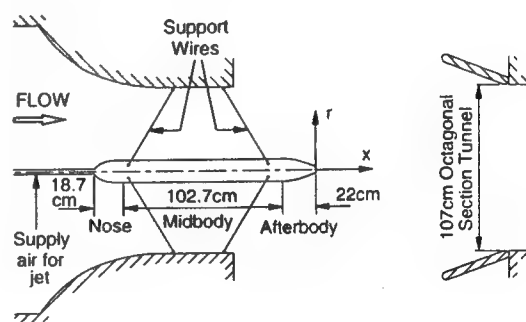


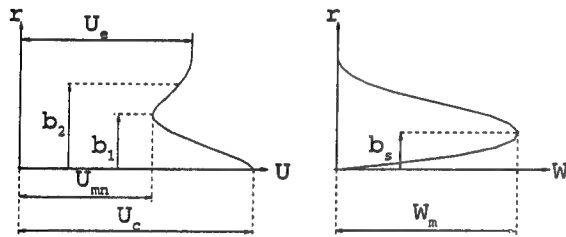
Figure 2. Wind Tunnel and Model Arrangement

Results

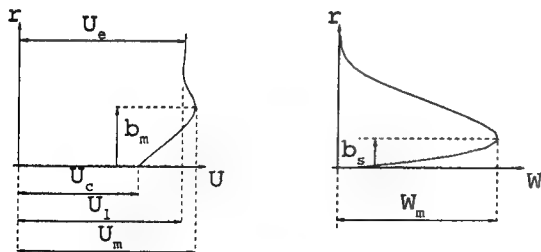
In the following, the data are presented in cylindrical polar coordinates (x, r, θ) where x is measured along the body axis from the base (jet exit). The mean and fluctuating velocity components in these directions are (U, V, W) and (u, v, w),

respectively. The freestream velocity U_0 and either the body radius R or the jet diameter D are used to nondimensionalize the data.

Figure 3 shows sketches of typical profiles of the axial (U) and tangential or swirl (W) components of mean velocity for the jet- and popeller-driven flows. It is clear that these flows are characterized by multiple velocity and length scales, unlike simple wakes and jets. In the jet-driven flow three velocities, namely, centerline (U_c), minimum (U_{mn}) and edge (U_e), are required to describe the axial component, and at least two radii, one (b_1) where the local velocity is U_{mn} , and the other (b_2) where it is $(U_e - U_{mn})/2$ are required to describe the axial component. In the near wake, yet another velocity scale, the maximum velocity (U_m), different from U_c (and not shown in Figure 3a) can be distinguished. The maximum swirl velocity (W_m) and the radius where it occurs (b_s) are needed to describe the tangential velocity distribution. To all of these, may be added the velocity and length scales associated with distributions of the Reynolds stresses. To facilitate comparisons with the data of Hyun, Figure 3b shows similar sketches of the profiles of circumferentially-averaged velocity components in the wake of a propeller. Recall that the propeller diameter was $D_p = 10.16$ cm. In this case, yet another velocity, at the edge of the propeller slipstream (U_l), is needed along with the radius (b_m) where the velocity is maximum (U_m).



(a) Swirling-Jet-driven Flow

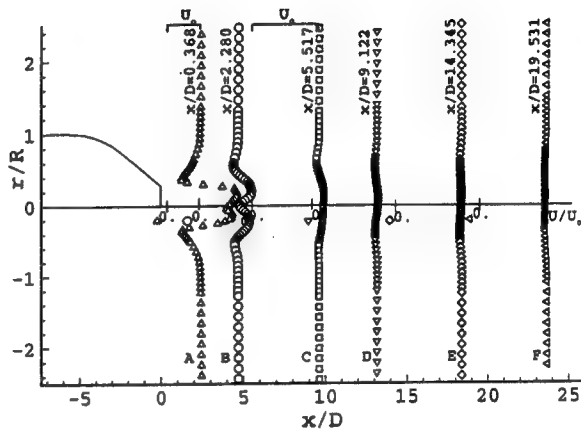


(b) Propeller-driven Flow

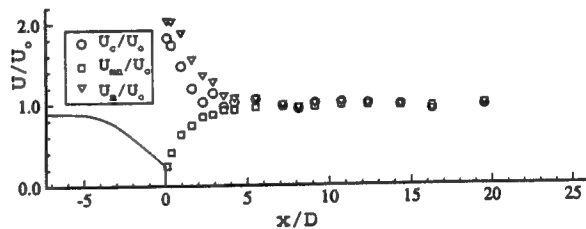
Figure 3. Typical Axial (U) and Tangential (W) Velocity Profiles

Streamwise Development

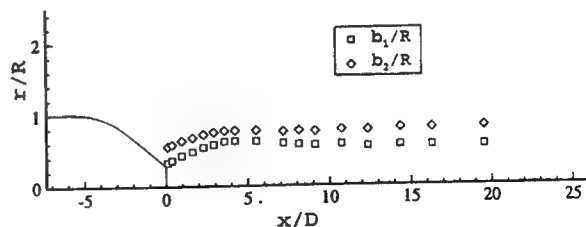
Figure 4a shows the mean velocity profiles at six representative streamwise stations, labeled A through F, from close to the jet exit at $x/D = 0.368$ to the last station at $x/D = 19.531$. The velocity and length scales described above are shown in Figures 4b and 4c, respectively, for all measurement stations. As the measurements indicated little difference between the velocity (U_e) at the edge of the wake and the constant freestream-velocity (U_0), except at the



(a) Velocity Profiles



(b) Velocity Scales

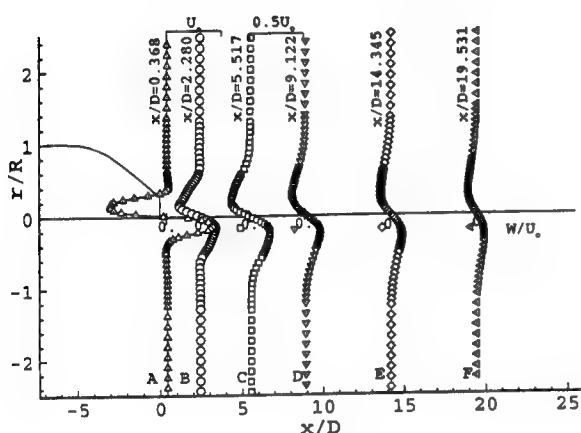


(c) Length Scales

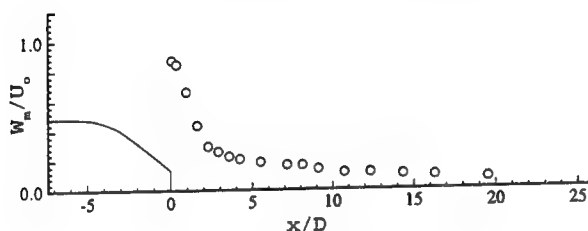
Figure 4. Streamwise Development of Axial Velocity Field

first few stations, U_e is not shown in Figure 4b. The profiles of the swirl (W) velocity and the scales associated with it are plotted in a similar format in Figure 5.

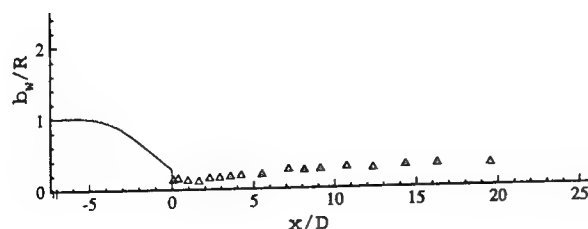
The symmetry of the data is evident from the velocity profiles (Figures 4a and 5a). Also seen from there is the very rapid mixing between the boundary layer and the jet in the axial velocity, and a somewhat slower decay of swirl. The axial velocity profile shows a peculiar hump in the central part of the wake, with a maximum velocity different from the centerline velocity. This is a characteristic of jets with moderate to strong swirl number and is produced by the centrifugal forces that are dominant in this



(a) Tangential Velocity Profiles



(b) Velocity Scale



(c) Length Scale

Figure 5. Overview of the Mean Tangential Velocity

region. This feature of the near-field flow is also evident from Figure 4b, where U_m and U_c are plotted, and the turbulence data presented later. By $x/D = 5$, and well before station C, the velocity maximum occurs at the centerline, the through in the axial velocity profile disappears, and the profile is as sketched in Figure 3a.

From Figure 4b it is seen that, within a distance of about $x/D = 4$, the axial velocity along the wake centerline decreases rapidly from $2U_0$ at jet exit to very close to $1.1U_0$ where it becomes coincident with the maximum velocity, and the minimum velocity increases from zero at the jet exit to $0.9U_0$. Thus, the usual small-defect assumption made in classical similarity theory of wakes is met quite early in the development of this flow. However, Figure 5b shows that it takes a distance of almost $15D$ for the maximum swirl velocity to decay from its value of $0.95U_0$ at the jet exit to $0.1U_0$.

Following an initial increase and a decrease, the length scale b_2 , where the axial velocity is $(U_e - U_{mn})/2$, slowly increases after a streamwise distance of about $x/D = 10$. On the other hand, there is an initially rapid increase in the scale b_1 from $D/2$ at the jet exit, to follow a similar trend to that of b_2 afterwards. From Figure 5c it is seen that the distance b_s , where the swirl velocity is maximum, increases from about $D/4$ and follows a trend similar to b_1 , but remains smaller than b_1 throughout. In other words, the location of maximum swirl velocity is much closer to the centerline than the minimum axial velocity, indicating a rather remarkable coherence of the swirl and its slow diffusion in the radial direction. It should be pointed out, however, that as the flow progresses downstream, all of these length scales are difficult to determine precisely from the data because the velocity variations across the wake become quite small.

Momentum Balance

The integral form of the axial-momentum equation under the usual thin-layer (boundary layer) assumptions of nearly parallel mean streamlines may be written:

$$\int_{-\infty}^{\infty} \left(1 - \frac{U}{U_0}\right) \frac{U}{U_0} \frac{r}{R} d\left(\frac{r}{R}\right) - \int_{-\infty}^{\infty} \frac{\overline{uu}}{U_0^2} \frac{r}{R} d\left(\frac{r}{R}\right) - \frac{1}{2} \int_{-\infty}^{\infty} \frac{p}{\rho U_0^2} \frac{r}{R} d\left(\frac{r}{R}\right) = 0 \quad (2)$$

where the three terms represent the contributions from the mean velocity, turbulence and pressure, respectively. These terms were evaluated from the data and the results are plotted in Figure 6. In the wake of a self-propelled body, their sum is zero because there is no net force in the axial direction.

The maximum deviation of the sum of the three terms in Figure 6 was no more than 0.01 (i.e., 1% of $\rho\pi U_0^2 R^2$). In fact, preliminary experiments were conducted in which these terms were measured at several locations and the jet conditions were adjusted to obtain the self-propelled (momentumless) state. Therefore, Figure 6 may be regarded also as a confirmation of the experimental procedures.

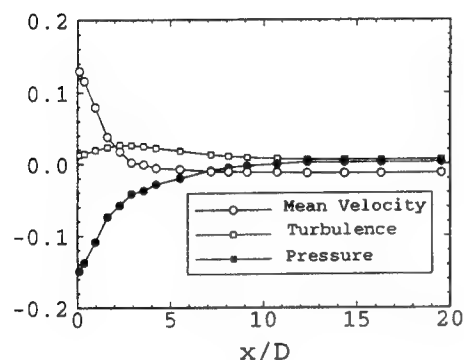


Figure 6. Axial Momentum Balance

Figure 6 shows that the contribution of pressure to the momentum equation is significant until about $x/D = 13$. The negative pressure contribution is associated with increasing pressure in the axial direction, and is compensated by decreasing convection of momentum by the mean flow. The contribution from the turbulence term is also quite significant in the near field, reaching a peak around $x/D = 2.5$.

The integral form of the tangential momentum equation under the same assumptions can be written:

$$\int_{-\infty}^{\infty} \frac{UW}{U_0^2} \left(\frac{r}{R} \right)^2 d\left(\frac{r}{R} \right) = M_{\theta x} \quad (3)$$

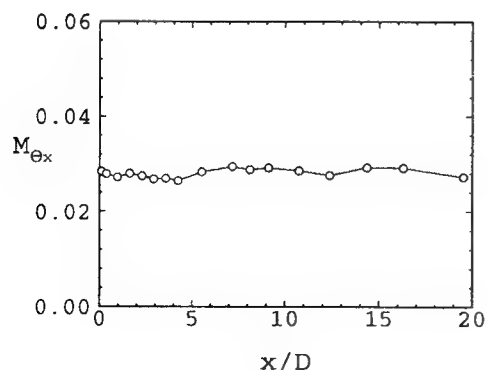


Figure 7. Flux of Tangential Momentum

As shown in Figure 7, this term remains constant at 0.028 ± 0.002 along the wake. This momentum flux corresponds to that introduced by the propeller in Hyun and Patel's experiments. The difference in the numerical values of $M_{\theta x}$ and the propeller torque coefficient (0.01614) lies in the different definitions of the two quantities. The constancy of $M_{\theta x}$ is an indication that the axial symmetry of the mean flow is preserved.

On the basis of the mean-flow results presented in Figures 4-6, the wake of the jet-propelled body may be subdivided into at least three regions: (1) the near field, $x/D < 3$, in which there is rapid decrease in axial and swirl velocities due to the intense shear and mixing between the fluid from the near-wall region of the body boundary layer and the outer layers of the jet; (2) an intermediate region, $3 < x/D < 13$, where the pressure induced by the swirl continues to affect the momentum balance and the mixing between the boundary layer and the jet gradually encompasses the entire flow; and (3) the developed wake, $x/D > 13$, say, where the mixing is complete, the pressure returns to its ambient value, the boundary layer and the jet lose their identity, and there results a single shear flow, that has the same status as other canonical free shear layers. This is, to be sure, a simplified picture, which makes no reference to the turbulence properties or structure.

Approach to Similarity of the Mean Flow

The existence of different velocity and length scales, and their different behaviors in the near and intermediate regions, are of course the most obvious characteristics of interacting shear layers. On the other hand, classical similarity theory applied to free shear layers is based on the assumption that multiple scales, if present, are in some constant proportion, i.e., each flow is described by just one velocity scale and one length scale. Clearly, it is of interest to inquire at what downstream distance does a momentumless swirling wake achieves such similarity conditions, if at all, or alternatively, whether the developed-wake region, $x/D > 13$, satisfies the requirements of similarity theory.

Similarity solutions for two-dimensional and axisymmetric momentumless wakes have been known for some time, and Tennekes and Lumley (5) indicate that in the momentumless wake of an axisymmetric body (without swirl), the velocity scale decreases in proportion to $x^{-4/5}$ and the length scale increases as $x^{1/5}$. Ferry and Piquet (6) analyzed axisymmetric momentumless wakes, without and with swirl, and concluded that the powers just quoted are appropriate only for weak swirl, in which terms related to swirl in the axial-momentum equation are neglected. For weak swirl, the swirl velocity decays as $x^{-3/5}$. For the case with strong swirl, they showed

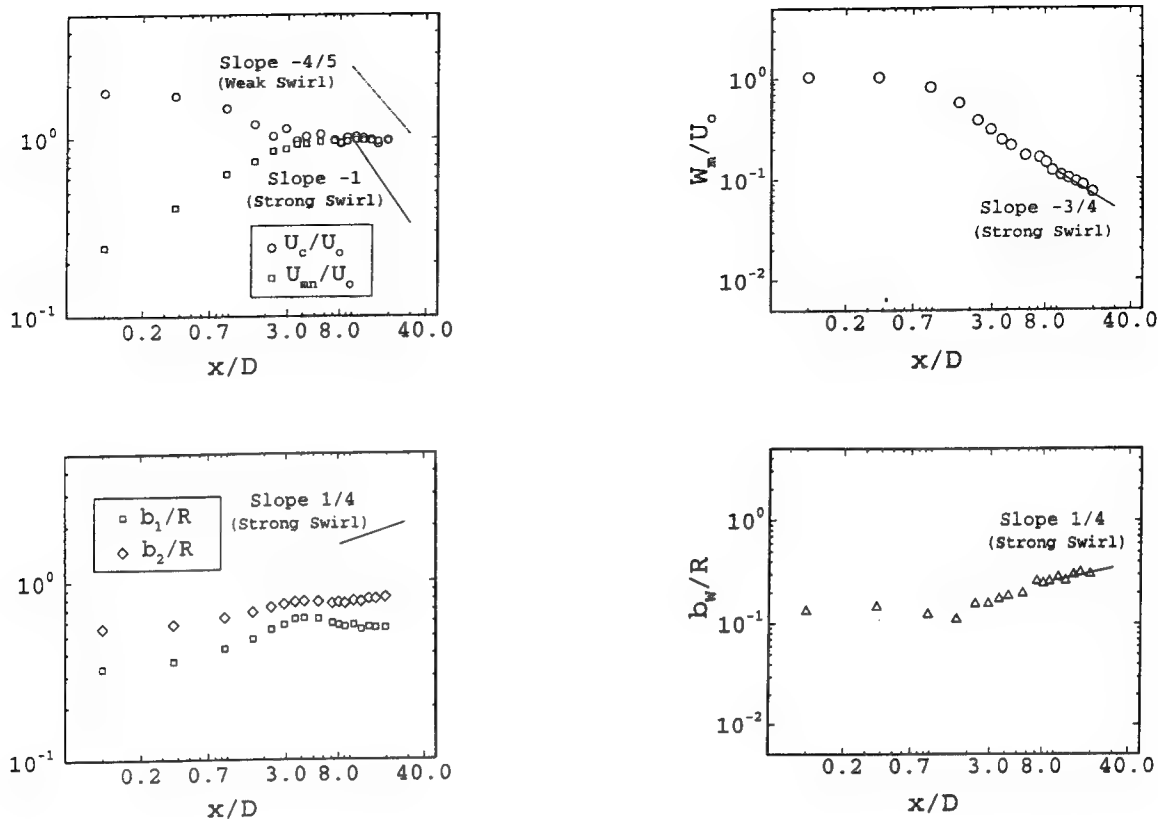


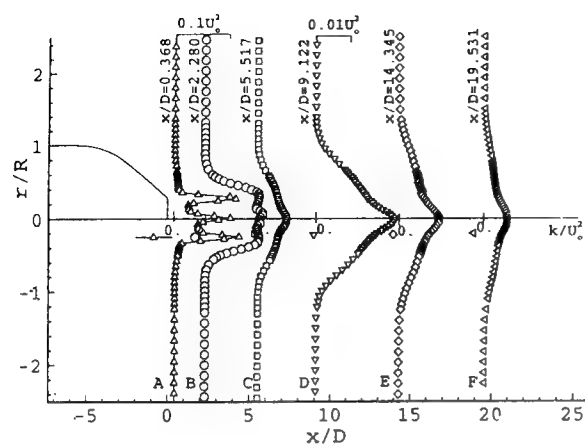
Figure 8. Log Plot of Mean Flow Velocity and Length Scales

that the axial velocity scale decays as x^{-1} , the swirl velocity as $x^{-3/4}$, and the length scale grows as $x^{1/4}$. While a complete review of the theory is beyond the scope of this paper, it is of interest to plot the various velocity and length scales of Figures 4 and 5 to observe their approach to the predicted power laws. This is done in Figure 8.

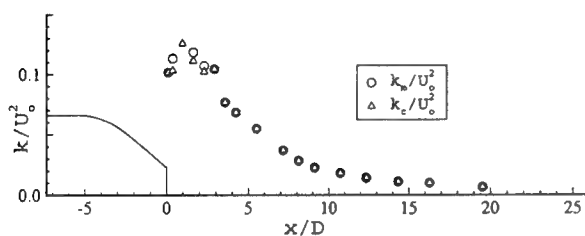
The two characteristic axial velocities, U_c and U_{mn} , do not follow either the $-4/5$ or the -1 power law, and instead approach the freestream velocity U_0 rather early in the streamwise development. The corresponding length scales, b_1 and b_2 , also do not grow with the expected $1/4$ power. They appear to grow at a much slower rate. In spite of this, the velocity and length scales of the tangential (swirl) velocity show behaviors that are consistent with similarity theory for strong swirl at $x/D > 10$, approximately. The different rates of growth and decay of the axial and tangential flows are quite surprising and would suggest that the mixing between the boundary layer and the jet is incomplete.

Streamwise Development of Turbulence

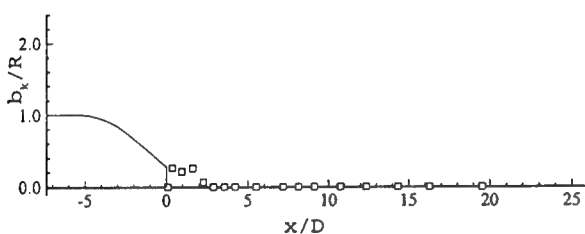
All six $(\overline{uu}, \overline{vv}, \overline{ww}, \overline{uv}, \overline{uw}, \overline{vw})$ Reynolds stresses were measured in the experiments. For the purpose of the present paper we shall consider only the sum of the three normal stresses, i.e., the turbulent kinetic energy, $k = 1/2(\overline{uu} + \overline{vv} + \overline{ww})$, and two of the three shear stresses. The normal stresses at all stations were in the order: $\overline{ww} > \overline{vv} > \overline{uu}$, with the anisotropy persisting to the last station. Although none of the three shear stresses is zero in this flow, we shall consider only \overline{uv} and \overline{vw} , because they comprise important terms in the axial and tangential (swirl) momentum equations, respectively. The three chosen turbulence quantities are shown in Figures 9, 10 and 11 in the same format as the mean-velocity components in Figures 4 and 5. However, in the present case, changes in plotting scales were demanded by the very large changes in these quantities as the flow evolves downstream.



(a) Turbulence Kinetic Energy Profiles



(b) Turbulence Kinetic Energy Intensity Scale

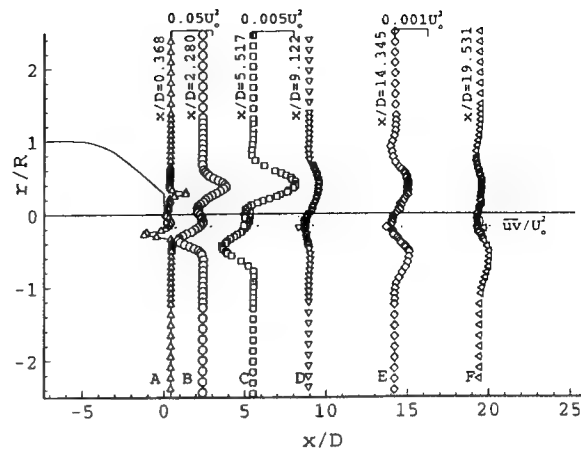


(c) Turbulence Kinetic Energy Length Scale

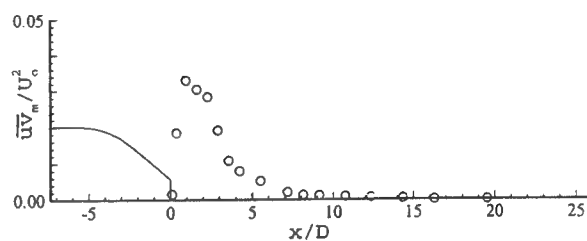
Figure 9. Overview of Turbulence Kinetic Energy

Each figure also shows appropriate intensity and length scales that describe the profile shape. The scales are of interest in the discussion of the approach to similarity conditions.

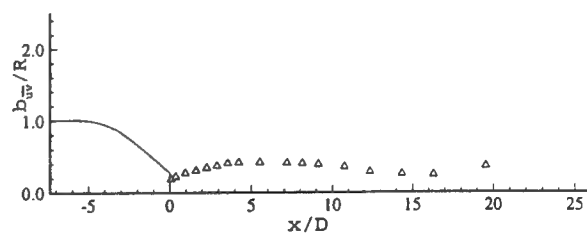
The profiles in Figures 9a-11a show certain common features which are discussed first. At the first two stations (A and B), which lie in the previously defined near field, $x/D < 3$, all turbulence profiles show the coexistence of two shear layers, one associated with the large gradient of the swirl velocity at the center, and the other with the mixing between the jet and the boundary layer. Both produce peaks in the turbulence kinetic energy and shear stresses. The



(a) \overline{uv}/U_o^2 Profiles



(b) \overline{uv} Intensity Scale

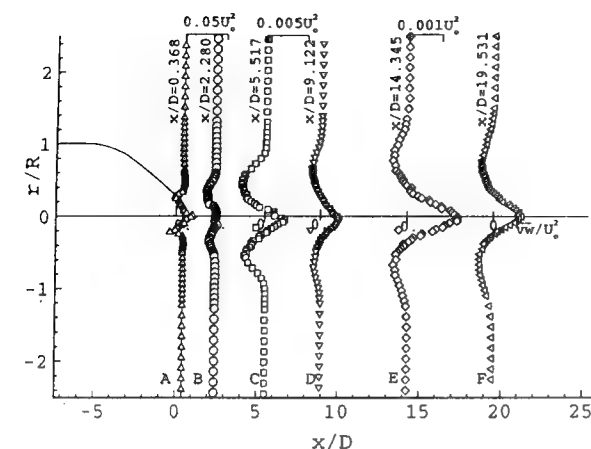


(c) \overline{uv} Length Scale

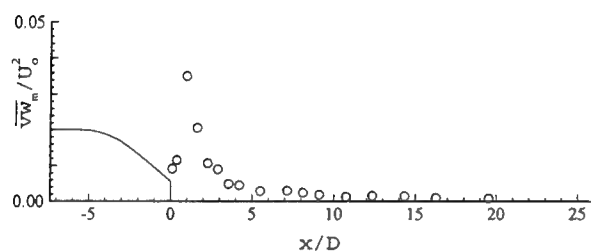
Figure 10. Overview of the \overline{uv}/U_o^2 Shear Stress

centerline peaks in k and \overline{vw} are associated with the swirl velocity, which is zero at the center and reaches a maximum before the interface between the jet and the body boundary layer. In fact, these peaks persist at all downstream stations, another indication of the slower decay of swirl noted earlier (Figure 5).

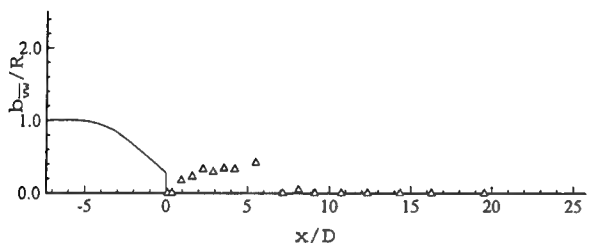
The turbulence profiles at the next two stations (C and D) indicate that mixing between the boundary layer and the jet gradually penetrates to the flow centerline. Recall that this was judged to be a feature of the intermediate wake, $3 < x/D < 13$. The magnitudes of the turbulence quantities have decreased such that an enlarged scale is needed to show the profile shape. It is also very significant that the



(a) \overline{vw}/U_0^2 Profiles



(b) \overline{vw} Intensity Scale



(c) \overline{vw} Length Scale

Figure 11. Overview of the \overline{vw}/U_0^2 Shear Stress

shear stresses have practically vanished, being smaller than the estimated uncertainty limits of the data, although there remains significant levels of turbulent kinetic energy.

At the last two stations (E and F), lying in what was termed the developed-wake region on the basis of the mean flow, $x/D > 13$, the magnitudes have further decreased such that yet another scale change is needed. Now the shapes of the shear-stress profiles have changed but the data themselves are no longer meaningful in the light of their uncertainties. For all practical purposes, the shear stresses

transporting axial and tangential momentum are now negligible, and the turbulent kinetic energy slowly decays. It was found by Ridjanovic (7) and Wang (8) that an axisymmetric momentumless wake without swirl becomes shear-free beyond a certain distance, and consequently the flow in that region could be considered as that produced by a point source of turbulence. The flow at the last two measurement stations could be considered as nearly homogenous but anisotropic with nearly uniform mean velocity. This then is the region where the rate of turbulence production is small, and there is a balance between convection, diffusion and dissipation.

The intensity and length scales plotted on Figures 9b,c-11b,c convey the foregoing observations in an integral sense. Thus, for example, Figure 9b shows the three stages in the decay of k , while 9c shows that the maximum value of k occurs at the wake centerline after the initial region. Similarly, Figure 10b shows the vanishing of the uv shear stress within the intermediate zone, while Figure 11b shows a slower collapse of the vw shear stress, as expected from the slower decay of swirl.

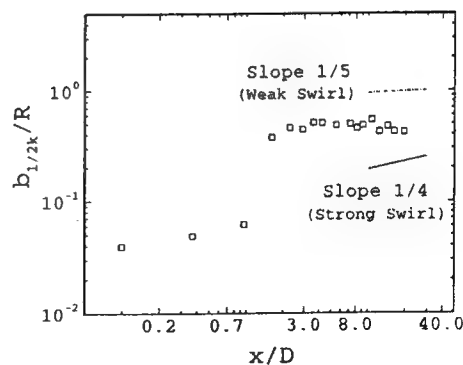
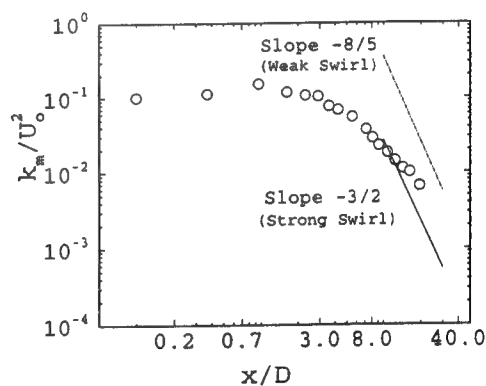


Figure 12. Turbulent Kinetic Energy Intensity and Length Scales

As pointed out by Ridjanovic (7) and Naudascher (9), length scales based on profiles of the turbulence quantities are better suited to define the overall length scale of the flow in the developed region because, as already implied, in that region the differences in mean velocity become small. Therefore, the scales presented in Figures 9b,c-11b,c are better suited for the study of the approach to similarity than those based on the mean velocity profiles (Figure 8).

Following Ferry and Piquet (6), similarity theory, under the assumption of weak swirl, predicts $k \sim x^{-8/5}$, $\overline{uv} \sim x^{-8/5}$, and $\overline{vw} \sim x^{-7/5}$ and all the length scales $b \sim x^{1/5}$. The results for strong swirl are: $k \sim x^{-3/2}$, $\overline{uv} \sim x^{-7/4}$, $\overline{vw} \sim x^{-3/2}$ and $b \sim x^{1/4}$. The maximum values of k , \overline{uv} and \overline{vw} are plotted in logarithmic scales in Figures 12-14. All figures also show the power laws for weak and strong swirl. It can be seen that the intensity scales of the three turbulence quantities closely follow the power laws, initially with the powers corresponding to strong swirl and then showing a tendency toward weak swirl behavior. The latter is not complete, however, by the last measurement station.

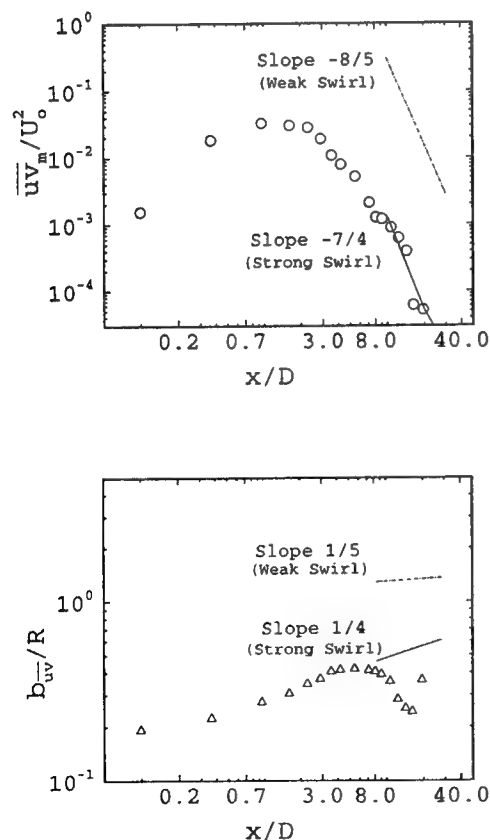


Figure 13. \overline{uv}/U_o^2 Intensity and Length Scales

As the maximum values of k and \overline{vw} occur at the centerline, the most appropriate length scales for these quantities are the radii, $b_{1/2}$ say, where they are one-half their respective maxima. For \overline{uv} , however, the location of the maximum suffices. The length scales so defined are also shown in Figures 12-14. It is seen that the data show a mixed behavior, with only the length scale of the \overline{vw} stress indicating the 1/4-power growth predicted with the strong swirl assumption. The scale of k shows a behavior closer to that expected for weak swirl, while that of \overline{uv} shows a decay. The latter feature is not entirely due to the low levels of stress and a deterioration in the accuracy of the data, however. It is an indication of the fact that this is not yet a single shear layer, i.e., the wake turbulence is not fully developed.

The approach to similarity of the mean flow and turbulence in the far wake also could be investigated by nondimensionalization of the velocity and the turbulence profiles using appropriate scales. Limitations of space preclude considerations of these aspects in the present paper. Reference should be made to Sirviente (2) for a more detailed discussion of this topic.

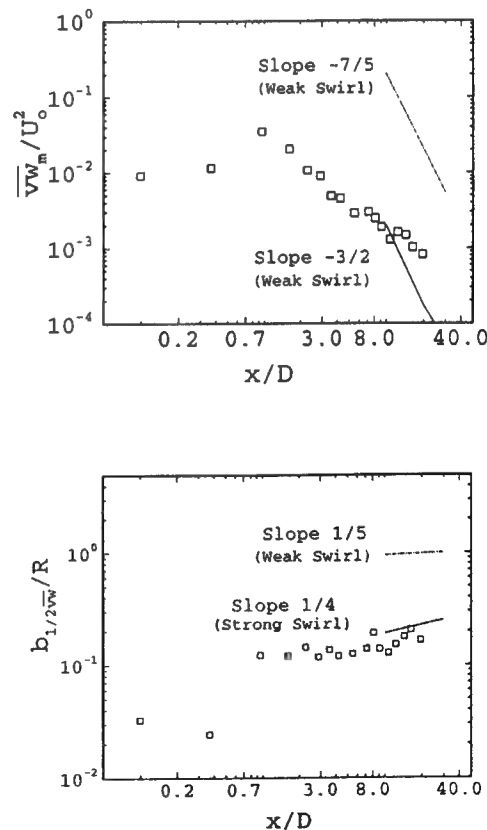


Figure 14. \overline{vw}/U_o^2 Intensity and Length Scales

Propeller-driven Flow versus Swirling-jet-driven Flow

The most obvious difference between these two flows is the periodicity of the flow behind a propeller. The experiments of Hyun and Patel (1), Petersson et al. (10) and Faure (11) show that the wakes of the individual propeller blades are practically mixed with the ambient flow within a distance of approximately two propeller diameters. The wakes of propeller-driven and jet-driven bodies continue to evolve somewhat differently further downstream. On the other hand, similarity analysis suggests that the two flows must eventually have the same properties. In view of this, it is of interest to investigate the nature of the two wakes at some large distance downstream of the origin.

The present data are compared with the measurements of Hyun and Patel (1). Figure 15 shows a comparison of the streamwise variations of the centerline and maximum axial velocities in the two cases, the axial distance being normalized by the jet (D) or propeller (D_p) diameter. The maximum

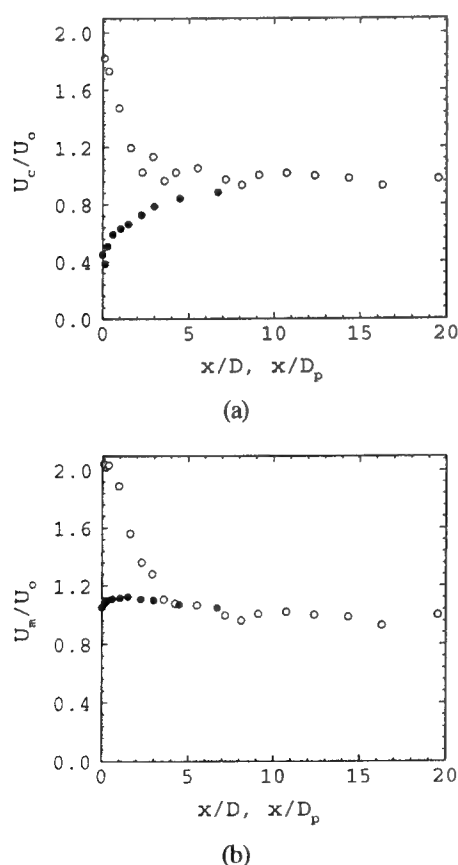


Figure 15. Comparisons of U_c and U_m . Swirling-Jet-driven Flow (Open Symbols), Propeller-driven Flow (Filled Symbols).

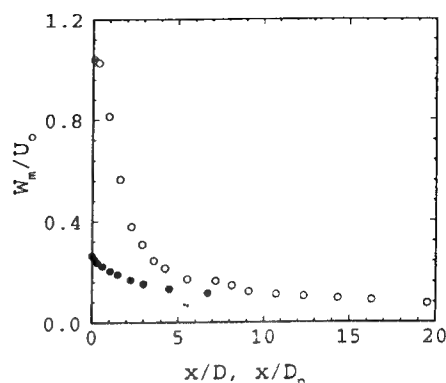


Figure 16. Comparisons of W_m . Swirling-Jet-driven Flow (Open Symbols), Propeller-driven Flow (Filled Symbols).

swirl velocities are compared in Figure 16 in a similar format. These results should be interpreted with reference to Figure 3, which shows the velocity profiles in the near field. Immediately downstream of a propeller the maximum axial velocity occurs some distance away from the centerline (around $r/R_p = 0.7$ in Hyun and Patel (1), 0.5 in Petersson et al. (10), and 0.4 in Faure (11)), depending on the propeller characteristics. Figure 15a shows that the centerline velocity decreases with downstream distance in the jet-driven flow while it increases in the propeller-driven flow, but they become nearly the same at about 7 jet or propeller diameters. This is also the case for the maximum axial and tangential velocities. It is therefore interesting to take a closer look at the details of the two flows at this distance.

Figure 17 shows the axial and tangential velocity profiles at the last measurement station of Hyun and Patel (1) and a comparable location in the present experiment. Here the radial distance is

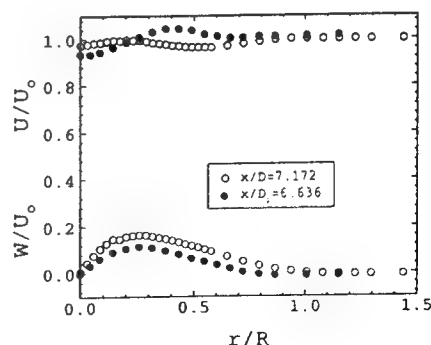


Figure 17. Mean Velocity Profiles. Swirling-Jet-driven Flow (Open Symbols), Propeller-driven Flow (Filled Symbols).

normalized by the body radius, R , which is the same in both cases. The difference in the axial velocity profile is clearly seen. In the jet-driven flow, the axial velocity is maximum at the centerline, reaches a minimum value below the freestream and then recovers to the freestream. In the propeller-driven flow, the centerline velocity is lower than the freestream while the maximum occurs some distance away from the centerline. Similarity theory requires that, sufficiently far downstream, the two profiles should assume the same shape, that of the jet-driven flow. The data of Hyun and Patel (1) do not extend to

such distances but the recent measurements of Faure (11), which were continued to $x/D_p = 50$, show this behavior at and beyond $x/D_p = 17.5$. Figure 17 also shows that the swirl velocity distributions in the two cases are quite similar.

The profiles of the six Reynolds stresses are compared in Figure 18. Clearly, the normal stresses in the jet-driven case are almost three times larger than those behind a propeller. The magnitudes of the shear stresses are small in both cases, and the differences in their profiles are consistent with the differences in the mean velocity shapes.

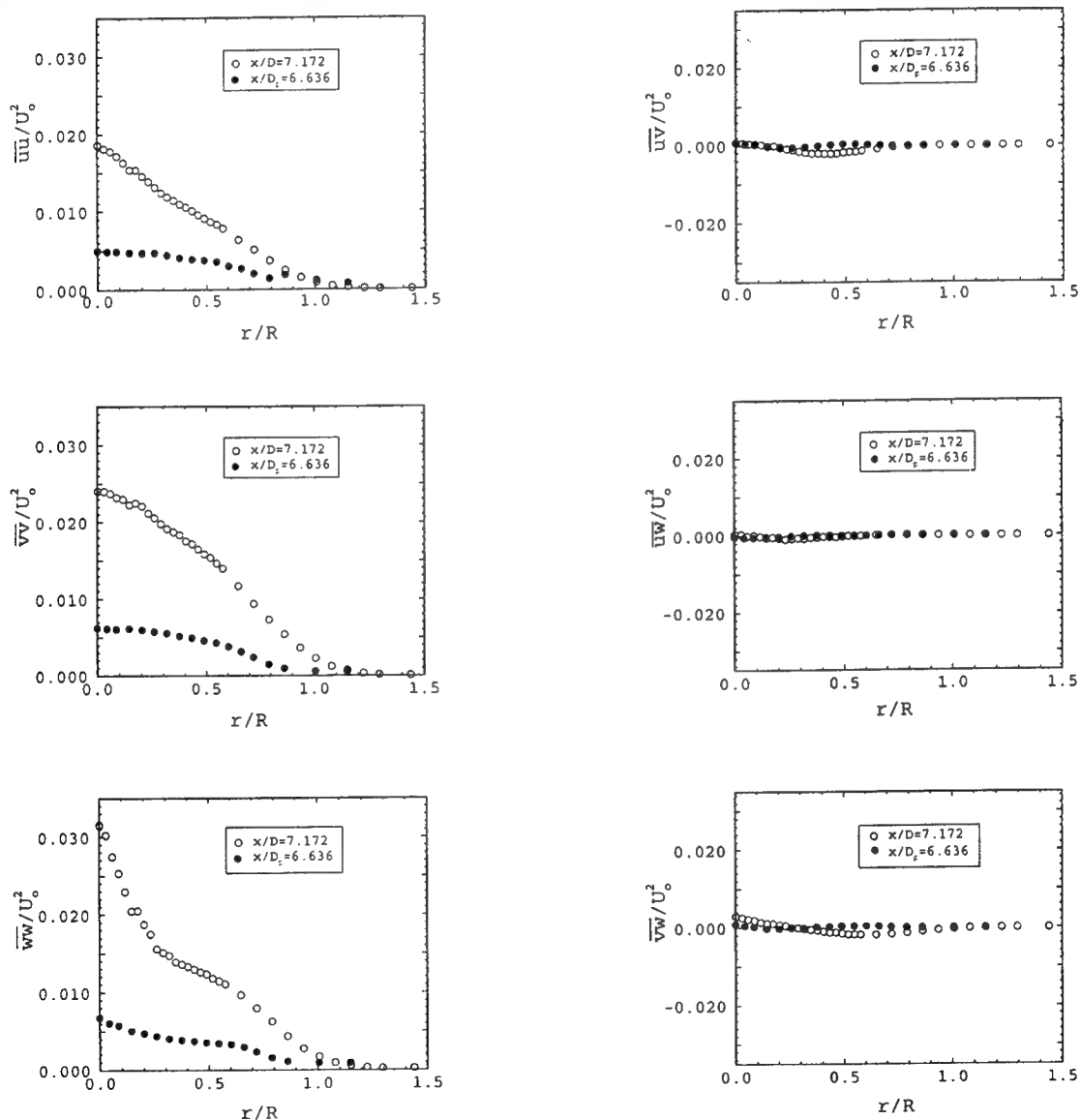


Figure 18. Reynolds Stress Profiles. Swirling-Jet-driven Flow (Open Symbols), Propeller-driven Flow (Filled Symbols).

Conclusions

This paper reports detailed mean-flow and turbulence measurements in the momentumless wake of an axisymmetric body propelled by a swirling jet. The data elucidate the process of mixing between the boundary layer of the body and the jet and the evolution of the momentumless wake. It is found that the wake evolves in at least three stages. The first of these is the near-wake, extending to about 3 jet diameters, where the flow from the near-wall region of the boundary layer mixes with the jet periphery to produce an intense shear layer, distinct from the swirl-induced shear layer that is present at the jet center. There is rapid decay of the mean shear and turbulence in this region. In the second, intermediate region, extending to about 13 jet diameters, the mixing penetrates to the wake centerline, the individual shear layers are assimilated, the pressure field induced by the stern geometry and the swirling jet decays, and the mean shear and the Reynolds shear stresses become negligible by the end of this region. In the third region, called the developed-wake, the flow acquires the characteristics of a single shear layer, with very low levels of mean shear and shear stresses, implying negligible production of new turbulence, and decay of the normal stresses produced upstream.

Analysis of the data in the format of classical similarity theory reveals that the axial and swirling flows develop at quite different rates, as do the corresponding turbulence characteristics. Not all properties of the flow conform with the power-laws predicted by similarity theory. The decay of the swirl initially follows the trends predicted for high swirl and gradually moves towards those expected for weak swirl. However, not all flow properties show asymptotic behaviors, and therefore, it is concluded that a considerably larger streamwise distance is needed for the wake to achieve complete similarity. Further analysis of the data is needed to establish this limit.

The present flow was compared with that of Hyun and Patel (1) to reveal similarities and differences between momentumless wakes of jet- and propeller-driven bodies. Although the near-fields of the two flows are grossly different, as expected, there is strong similarity between the two after a distance of about 7 jet and propeller diameters. Hyun and Patel had shown that the periodicity of the flow associated with the wakes of the individual propeller blades died out beyond a distance of about 2 propeller diameters. The present data reveal that the identity of the jet and the body boundary layer is preserved up to at least 3 jet diameters. Further mixing is needed in both cases for the flow to acquire the characteristics of a single free shear layer. Similarity theory indicates that the two flows must evolve into a single unique

state. Neither the experiments of Hyun and Patel nor the present extend into this range, but the comparisons presented here suggest that the two flows acquire considerable resemblance, justifying the intent of the present study to reproduce some elements of propeller wakes in a simpler environment.

Finally, it is important to point out that the present data, along with the data from complementary experiments in wakes and jets without swirl (see Sirviente (2)), comprise a rather comprehensive and unique set documenting the mixing of shear layers with diverse velocity and length scales, and their evolution toward a single shear layer. Consequently, these data are likely to prove of great value in the development and validation of models for nonequilibrium turbulent flows.

This research was partially supported by the Office of Naval Research, Grant N00014-91-J-1204, monitored by Dr. L.P. Purtell.

References

1. Hyun, B.S. and Patel, V.C., "Measurements in the Flow around a Marine Propeller at the Stern of an Axisymmetric Body. Part 1: Circumferentially-Averaged Flow," Experiments in Fluids, Vol. 11, pp. 33-44. "Part 2: Phase-Averaged Flow," Experiments in Fluids, Vol. 11, 1991, pp. 105-117.
2. Sirviente, A.I., "Wake of an Axisymmetric Body Propelled by a Jet with and without Swirl," Ph.D. Thesis, 1996, Mechanical Engineering, The University of Iowa, Iowa City.
3. Hyun, B.S., "Measurements in the Flow around a Marine Propeller at the Stern of an Axisymmetric Body," Ph.D. Thesis, 1990, Mechanical Engineering, The University of Iowa, Iowa City.
4. Walter, J.A., "Measurements in Near Wake of a Surface Mounted Semi Ellipsoidal Obstacle," Ph.D. Thesis, 1996, Mechanical Engineering, The University of Iowa, Iowa City.
5. Tennekes, H. and Lumley, J.L., "A First Course in Turbulence," M.I.T. Press, Cambridge. (1972).
6. Ferry, M. and Piquet, J., "Sillage Visqueux Lointain D'un Corps Sous-Marin Autopropulsé," Rapport D'étude Sirehna 86/14/R, 1987.
7. Ridjanovic, M., "Wake with Zero Change of Momentum Flux," Ph.D. Thesis, 1963, Mechanics and Hydraulics, The University of Iowa, Iowa City.
8. Wang, H., "Flow Behind a Point Source of Turbulence," Ph.D. Thesis, 1965, Mechanics and Hydraulics, The University of Iowa, Iowa City.

9. Naudascher, E., "Flow in the Wake of Self-Propelled Bodies and Related Sources of Turbulence," Journal of Fluid Mechanics, Vol. 22, 1965, pp. 625-656.

10. Petersson, P., Larson, M. and Jönsson, L., "Measurements of the Velocity Field Downstream an Impeller," to appear in Journal of Fluids Engineering, 1996.

11. Faure, T., "Étude Expérimentale du Sillage Turbulent d'un Corps à Symétrie de Révolution Autopropulsé par Hélice," 1995, Docteur Thesis, École Centrale de Lyon, France.

Hydrodynamic Forces on a Surface-Piercing Plate in Steady Maneuvering Motion

Z.-J. Zou (Wuhan Transportation University, China)

ABSTRACT

This paper describes a three dimensional numerical method for calculating the hydrodynamic forces acting on a surface-piercing vertical plate of small aspect ratio in steady maneuvering motion. Under the potential flow assumption and using a nonlinear vortex model, the disturbance velocity potential is represented by a Rankine source distribution on the free surface and a Rankine-type vortex distribution on the plate and on the vortex sheet in the wake. The vortex and source strengths are determined by satisfying the boundary conditions on the plate and on the free surface, whereas the Kutta condition at the trailing edge and the radiation condition at large distance from the plate are satisfied explicitly.

The proposed method is applied to flat plates of $T/L=0.1$ and 0.2 in oblique motion and turning motion up to moderate and large drift angle and yaw rate. Numerical results are compared with available experimental results which shows satisfying agreements.

NOMENCLATURE

$$C_Y = Y / \left(\frac{1}{2} \rho V_0^2 T L \right), \text{ lateral-force coefficient}$$

$$C_N = N / \left(\frac{1}{2} \rho V_0^2 T L^2 \right), \text{ yaw-moment coefficient}$$

$$F_n = u / \sqrt{gL}, \text{ Froude number}$$

$$g \text{ gravitational acceleration}$$

$$L \text{ length of the plate}$$

$$N \text{ yaw moment}$$

$$N_F \text{ number of panels on the free surface}$$

$$N_L \text{ number of panels on the plate in longitudinal direction}$$

$$N_Z \text{ number of panels on the plate in vertical direction}$$

$$N_P = N_L \times N_Z, \text{ number of panels on the plate}$$

$$p \text{ pressure in the fluid}$$

$$r \text{ yaw rate of the plate}$$

$$r' = rL/u, \text{ nondimensional yaw rate}$$

$$T \text{ draft of the plate}$$

$$\vec{V}_0 \text{ translation velocity of the plate at the undisturbed free surface}$$

$$V_0 = |\vec{V}_0|$$

$$u = V_0 \cos \beta, \text{ forward speed of the plate}$$

$$v = -V_0 \sin \beta, \text{ sway speed of the plate}$$

$$v' = -\tan \beta, \text{ nondimensional sway speed}$$

$$\vec{V}_s = (u - ry, v + rx, 0), \text{ velocity of the plate in maneuvering motion}$$

$$\vec{W} = (\nabla \Phi - \vec{V}_s), \text{ relative velocity in double-body flow}$$

$$Y \text{ lateral force}$$

$$\beta \text{ drift angle}$$

$$\beta_L = -\tan^{-1}[(v + rx)/(u - ry)], \text{ local drift angle}$$

$$\gamma \text{ vortex strength}$$

$$\gamma_0 \text{ vortex strength in double-body flow}$$

$$\gamma_1 \text{ vortex strength due to free-surface effects}$$

$$\zeta \text{ free-surface elevation}$$

$$\lambda_e = 2T/L, \text{ effective aspect ratio}$$

ρ	fluid density
σ	source strength
ϕ	disturbance velocity potential
Φ	disturbance velocity potential in double-body flow
φ	disturbance velocity potential due to free-surface effects

1. INTRODUCTION

For theoretical prediction of the hydrodynamic forces acting on a maneuvering ship, the ship's hull may be considered to be a lifting body of very small aspect ratio. Although a free surface is present, it may be replaced by a rigid horizontal plane in the range of low speeds. In such a case, the effective aspect ratio of the hull is twice its draft-to-length ratio, and the flow is equivalent to the so-called double-body flow to which various theoretical methods developed in aerodynamics may be applied directly. On the other hand, for ships at higher speeds, the free-surface displacement may have a significant influence on the hydrodynamic forces, thus the free-surface effects must be included in the theoretical analysis.

Since the maneuvering behavior of a ship is mainly determined by its lateral underwater profile, a vertical flat plate with the same draft and length may be a useful model for calculating the hydrodynamic forces acting on the ship. For a surface-piercing plate in maneuvering motion, a successful numerical method was proposed by Chapman (1), (2) under the slender-body assumption. Since the flow separation along the lower edge is neglected in this method, its applicability is confined to small lateral motions, and although the aspect ratio is assumed to be small, better agreements between numerical and experimental results were obtained for plates of larger aspect ratios.

Another important fact is that the wake influence is fully neglected in the slender-body theory. As we known, the aspect ratio is an important measure of the

effects of three dimensionality and the trailing wake is an inevitable consequence of these effects. In the case of very large aspect ratio, the flow around a vertical plate may be viewed as two dimensional in the horizontal plane, whereas in the limiting case of zero aspect ratio the flow is essentially two dimensional cross flow in the lateral plane. On the other hand, for a plate with small but finite aspect ratio, three dimensional flow effects may be important, and the influence of trailing wake must be taken into account.

For a yawed surface-piercing flat plate, Maniar et al. (3) proposed a three-dimensional panel method using Kelvin singularities. In correspondence with the conventional linear lifting-surface theory, the normal dipole distribution on the plate and in the wake downstream of the trailing edge is put on the plane of the plate. Thus this method, just as Chapman's method, is only applicable to a plate of moderate or larger aspect ratio at small drift angle.

Recently, for a surface-piercing plate in steady turning motion, Landrini and Campana (4) presented a three dimensional numerical method using Rankine singularities. The Neumann-Kelvin boundary-value problem was solved by coupling a standard panel method on the free surface with a vortex lattice procedure on the body and wake surface, where corresponding to the nonlinear lifting-surface theory a nonlinear wake modeling was used.

In the present paper, a three-dimensional Rankine panel method for free-surface flow around a vertical plate of small aspect ratio in steady oblique motion and/or turning motion is presented. The flow is assumed to separate from the trailing edge and the lower edge. The wake is modeled by a nonlinear vortex sheet. The boundary condition on the free surface is linearized with respect to the double-body flow. To solve the linearized boundary-value problem, a source distribution on the free surface and a vortex distribution on the plate and in the wake are used, whereas the singularity strengths are determined by satisfying the corresponding boundary conditions.

Calculations were performed for rectangular flat plates of draft-to-length ratio 0.1 and 0.2. Numerical results were presented and compared with other theoretical, numerical and experimental results where available.

2. MATHEMATICAL FORMULATION

We consider a vertical rectangular plate in steady maneuvering motion at the plane of the undisturbed free surface. The geometric aspect ratio, the draft-to-length ratio T/L , is assumed to be small.

We adopt a right-handed Cartesian coordinate system $o-xyz$ which is fixed with respect to the moving plate, see Fig. 1. The translation velocity of the plate in the horizontal plane is \vec{V}_0 , and the yaw rate about the vertical axis is r . The velocity components in the longitudinal and lateral directions are $u = V_0 \cos \beta$ and $v = -V_0 \sin \beta$, respectively, where β is the drift angle and $V_0 = |\vec{V}_0|$.

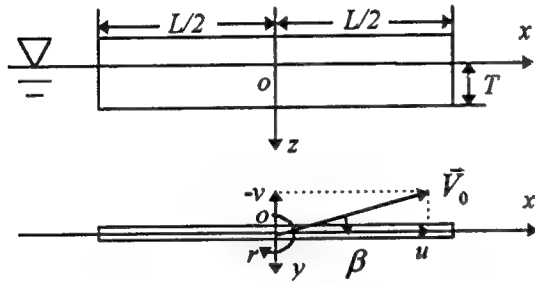


Fig.1 Coordinate system

The fluid is assumed to be inviscid and incompressible. The flow is assumed to be irrotational except in the wake which is to be modeled by a trailing vortex sheet. The disturbance velocity of the fluid can be expressed by the gradient of a velocity potential ϕ which satisfies the Laplace equation

$$\nabla^2 \phi = 0 \quad (1)$$

in the fluid domain and some boundary conditions.

On the plate which is located on the plane

$y = 0$, the boundary condition is given by

$$\phi_y = v + rx. \quad (2)$$

On the free surface $z = \zeta(x, y)$ the velocity potential should satisfy a kinematic boundary condition and a dynamic boundary condition:

$$(\nabla \phi - \vec{V}_s) \cdot \nabla \zeta - \phi_z = 0, \quad (3)$$

$$\zeta = \frac{1}{g} \left(-\vec{V}_s \cdot \nabla \phi + \frac{1}{2} \nabla \phi \cdot \nabla \phi \right) \quad (4)$$

where ζ is the free-surface elevation, g is the gravitational acceleration and

$$\vec{V}_s = (u - ry, v + rx, 0).$$

Together with the boundary conditions on the free surface, a radiation condition must be imposed to ensure that there are no waves radiated upstream.

Moreover, the disturbance created by the motion of the plate should decay to zero at infinity:

$$\lim_{R \rightarrow \infty} \nabla \phi = (0, 0, 0), \quad (5)$$

where $R = \sqrt{x^2 + y^2 + z^2}$.

The kinematic and dynamic boundary conditions (3) and (4) are combined to give a single boundary condition on the free surface:

$$(\nabla \phi - \vec{V}_s) \cdot \nabla \left(-\vec{V}_s \cdot \nabla \phi + \frac{1}{2} \nabla \phi \cdot \nabla \phi \right) - g \phi_z = 0. \quad (6)$$

This boundary condition is nonlinear and should be imposed on the exact free surface $z = \zeta$ which is not known in advance. To solve the boundary-value problem for the velocity potential ϕ , we decompose ϕ into a velocity potential for the double-body flow, Φ , and another one due to the free-surface effects, φ .

Assuming that $|\nabla\varphi| \ll |\nabla\Phi|$ on the undisturbed free surface $z = 0$, we linearize the boundary conditions on the free surface about the double-body flow at $z = 0$ in correspondence with Dawson's method (5).

Since $\Phi_z = 0$ and $\Phi_{xz} = \Phi_{yz} = 0$ on $z = 0$, it follows from (4) that

$$\zeta = \frac{\vec{W} \cdot \nabla\varphi - \vec{V}_s \cdot \nabla\Phi + \frac{1}{2} \nabla\Phi \cdot \nabla\Phi}{g}, \quad \text{on } z = 0, \quad (7)$$

where $\vec{W} = \nabla\Phi - \vec{V}_s$.

Similarly, since $\Phi_{xz} = \Phi_{yz} = \Phi_{yz} = 0$ on $z = 0$, we obtain from (6)

$$\begin{aligned} & \vec{W} \cdot \nabla(\vec{W} \cdot \nabla\varphi) - g\varphi_z \\ & + \left[\nabla \left(-\vec{V}_s \cdot \nabla\Phi + \frac{1}{2} \nabla\Phi \cdot \nabla\Phi \right) - \Phi_{zz} \vec{W} \right] \cdot \nabla\varphi \\ & = -\vec{W} \cdot \nabla \left(-\vec{V}_s \cdot \nabla\Phi + \frac{1}{2} \nabla\Phi \cdot \nabla\Phi \right) \\ & + \Phi_{zz} \left(-\vec{V}_s \cdot \nabla\Phi + \frac{1}{2} \nabla\Phi \cdot \nabla\Phi \right), \quad \text{on } z = 0. \quad (8) \end{aligned}$$

Correspondingly, the boundary condition (2) on the plate can be rewritten as

$$\varphi_y = -[\Phi_y - (v + rx)]. \quad (9)$$

Once the double-body flow is known, the linearized boundary-value problem for the velocity potential φ can be solved by distributing singularity elements with unknown strengths over the boundary surfaces. Considering a surface-piercing plate of zero thickness, we represent the flow around the plate by a Rankine source distribution on the free surface surrounding the plate and a Rankine-type vortex distribution on the plate and in the wake.

Corresponding to the vortex distribution, a Kutta condition should be imposed at the trailing edge (T.E.) to determine the circulation. This condition can be satisfied by requiring that the vortex strength along the trailing edge is zero, i.e.

$$\gamma_{T.E.} = 0.$$

Moreover, a dynamic boundary condition should be imposed on the trailing vortex sheet which states that there is no pressure difference across the vortex sheet in the wake. In principle, an iterative procedure is required to satisfy this condition, since the location of the trailing vortex sheet is not known in advance. However, for practical applications in engineering problem it is usually sufficient to assume the shape and location of the trailing vortex sheet in advance.

For a plate of small aspect ratio the flow may separate from the lower edge along the length even if the drift angle or yaw rate is small. Therefore, a nonlinear trailing vortex model is required. In the present paper, we use a nonlinear vortex model which is an extension of Bollay's nonlinear theory (6). It is assumed that the trailing vortices separate from the plate at the trailing edge and lower edge at some angle to the plane of the plate and extend to infinity downstream in some prescribed manner. The vertical plate is divided horizontally into lifting strips. On each lifting strip the vortex strength changes only in the longitudinal direction, whereas from one lifting strip to another the vortex strength changes its value in the vertical direction. For a plate of extremely small aspect ratio, one lifting strip is sufficient, and the proposed vortex model is consistent with Bollay's model. On the other hand, for a plate at extremely small drift angle or yaw rate the trailing vortices may be put on the plane of the plate, then the vortex model corresponds to the conventional linear lifting-surface theory.

With the shape and location of the trailing vortex sheet assumed in advance, the source and vortex

strengths can be determined by satisfying the boundary conditions on the free surface and on the plate. Then we can calculate the free-surface elevation by (7) and the hydrodynamic forces on the plate by integrating the fluid pressure over the plate.

In the body-fixed coordinate system the dynamic pressure in the fluid relative to the atmospheric pressure is given by

$$p = \rho \left(\vec{V}_s \cdot \nabla \phi - \frac{1}{2} \nabla \phi \cdot \nabla \phi \right),$$

where ρ is the fluid density.

Since on the plate $y = 0$ and

$$\phi_x^+ = -\phi_x^-, \phi_y^+ = \phi_y^-, \phi_z^+ = -\phi_z^-,$$

where the superscripts $+$ and $-$ denote the right and left sides of the plate, $y = +0$ and $y = -0$, respectively, the jump of dynamic pressure across the plate is

$$p^+ - p^- = \rho u (\phi_x^+ - \phi_x^-),$$

or with the relation $\phi_x^+ - \phi_x^- = -\gamma$, where γ is the bound vortex strength, the vertical component of the vortex strength vector,

$$p^+ - p^- = -\rho u \gamma. \quad (10)$$

Corresponding to the decomposition of ϕ , γ can be divided into a part in the double-body flow and a part due to the free-surface effects:

$$\gamma = \gamma_0 + \gamma_1,$$

where,

$$\gamma_0 = -(\Phi_x^+ - \Phi_x^-) \text{ and } \gamma_1 = -(\phi_x^+ - \phi_x^-).$$

Consequently, the lateral force and yaw moment acting on the plate are given by

$$Y = \rho u \int_0^T \int_{-\frac{L}{2}}^{\frac{L}{2}} (\gamma_0 + \gamma_1) dx dz, \quad (11)$$

$$N = \rho u \int_0^T \int_{-\frac{L}{2}}^{\frac{L}{2}} (\gamma_0 + \gamma_1) x dx dz \quad (12)$$

which can be expressed in nondimensional form as

$$C_Y = \frac{Y}{\frac{1}{2} \rho V_0^2 TL} \text{ and } C_N = \frac{N}{\frac{1}{2} \rho V_0^2 TL^2}.$$

3. NUMERICAL SOLUTION

A three-dimensional panel method is applied to solve the potential flow problem. In order to construct the numerical solution, the boundary surfaces and the singularity distributions are discretized.

The plate is discretized into panels. On each of the panels, a collocation point is selected to satisfy the boundary condition on the plate. Correspondingly, the vortex distribution on the plate and on the trailing vortex sheet is discretized and replaced by concentrated vortex elements. As conventional, the vortex strength vector is decomposed into a vertical component (bound vortex) and a horizontal component (free vortex). For steady flow considered here, it follows from the dynamic boundary condition on the trailing vortex sheet that the vertical component of the vortex strength vector is zero in the wake.

On the plate, the longitudinal and vertical locations of the line vortices and the collocation points are determined in a similar way as by the well-known quasi-continuous method (QCM), Lan (7). Assuming that on the plate there are N_L panels and N_z panels in the longitudinal and vertical directions respectively, then for $i=1,2,\dots, N_L$, and $j=1,2,\dots, N_z$ the locations of the line vortices are given by

$$x_{vi} = \frac{L}{2} \cos \left[(i-3/4) \frac{\pi}{N_L} \right],$$

$$z_{vj} = \frac{T}{2} \left\{ 1 - \cos \left[j \frac{\pi}{N_z} \right] \right\},$$

and the locations of the collocation points by

$$x_{ci} = \frac{L}{2} \cos \left[(i-1/4) \frac{\pi}{N_L} \right],$$

$$z_{cj} = \frac{T}{2} \left\{ 1 - \cos \left[(j-1/2) \frac{\pi}{N_Z} \right] \right\}.$$

The line vortices separate from the plate at the trailing and lower edges and extend to infinity downstream, thus form a discrete vortex system with $N_P = N_L \times N_Z$ unknown vortex strengths γ_k , $k=1,2,\dots,N_P$.

Neglecting the free-surface effects, the vortex strengths γ_{ok} corresponding to the double-body flow can be determined by satisfying the boundary condition on the plate, $\Phi_y = v + rx$, at the collocation points $(x_{ci}, 0, z_{cj})$.

For the free-surface flow, besides the discretization of the plate and the vortex distribution the undisturbed free surface is discretized into quadrilateral panels whose length is approximately constant. On each of these panels, a source distribution with constant strength is covered, and the "middle point" is selected as collocation point at which the boundary condition on the free surface is satisfied. Assuming that there are N_F panels on the free surface, the source strength σ_j ($j=1,2,\dots,N_F$) and the vortex strength γ_{1k} ($k=1,2,\dots,N_P$) are determined simultaneously by satisfying the boundary conditions (8) and (9) at the collocation points on the free surface and on the plate. On the other hand, the radiation condition is satisfied explicitly by the numerical technique of "staggered grids", see e.g. Jensen et al. (8), where the source panels on the undisturbed free surface are shifted backwards by one panel length relative to the corresponding free surface panels.

4. NUMERICAL RESULTS

The proposed numerical method was applied to

flat plates of $T/L=0.1$ and 0.2 in oblique motion and in turning motion.

For a plate in oblique motion the local drift angle is constant and equal to the drift angle of the plate. Similarly to Bollay's vortex model we assume that the free vortices are straight line vortices which separate from the trailing edge and lower edge at an angle equal to half of the drift angle and extend to infinity downstream.

In order to verify the proposed method, calculations were first performed for a plate of $T/L=0.1$ in oblique motion in double-body flow. The corresponding effective aspect ratio is $\lambda_e=0.2$.

Fig.2 shows the numerical results obtained by the present method together with experimental results by Flachsbarth, see (6), and theoretical results. The numerical results are obtained with $N_L \times N_Z = 20 \times 10$ panels on the plate. The "theoretical" results are obtained by the following formula, see e.g. Thieme (9):

$$C_Y = \frac{\pi}{2} \lambda_e \beta + \frac{\pi}{4} \lambda_e r' + (2 + 1.64 \sqrt{\lambda_e}) \beta^2, \quad (13)$$

$$C_N = \frac{\pi}{4} \lambda_e \beta - \frac{\pi}{16} \lambda_e r' - \frac{1}{16} r'^2, \quad (14)$$

where $r' = r L/u$ is the nondimensional yaw rate, and $r'=0$ in the present case.

As shown in Fig.2, the present results agree quite well with both the experimental and theoretical results. The nonlinear dependence of the lateral force on the drift angle is predicted very well by the present method.

The proposed method was then applied to surface-piercing plates. Fig.3 shows the numerical results for a plate of $T/L=0.1$ in oblique motion at $F_n=0.30$. The free-surface grid reaches about $0.25L$ upstream and $1.5L$ downstream of the plate, and $1.0L$ laterally. The panel length is about $0.05L$ which corresponds to approximately 12 panels per wave length. In Fig.3 numerical results obtained for the

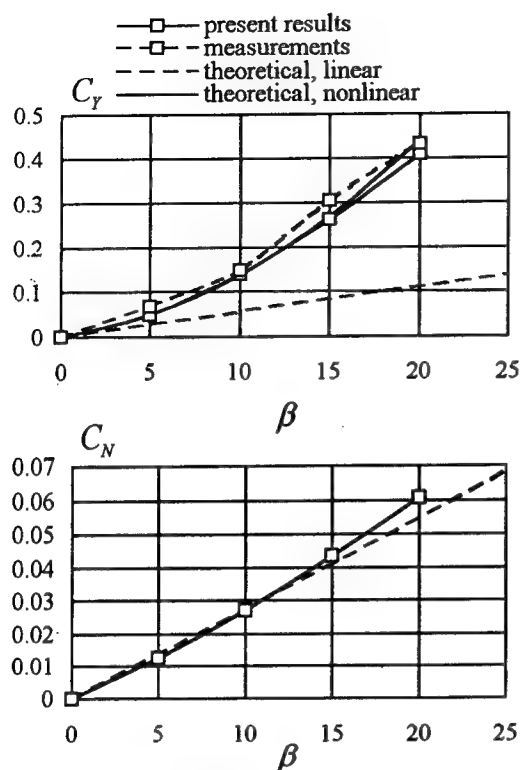


Fig. 2 Lateral-force and yaw-moment coefficients for a plate of $\lambda_s = 0.2$ in oblique motion in double-body flow

plate in double-body flow are also shown for comparison. It can be seen that in this case the free-surface effects on the hydrodynamic forces can be neglected.

Fig. 4 shows the calculated hydrodynamic coefficients versus nondimensional sway speed $v' = -\tan \beta$ for a plate of $T/L = 0.2$ in double-body flow and in free-surface flow at $F_n = 0.32$. The discretization of the plate and the free surface is the same as in the case of the plate of $T/L = 0.1$. In Fig. 4, the numerical results are compared with measurements by van den Brug et al. (10). Regarding the yaw-moment, the agreement of the numerical results with measurements is quite satisfactory. On the other hand, although the nonlinear dependence of the lateral force on drift angle is predicted by the present method, quantitatively, there is a discrepancy between

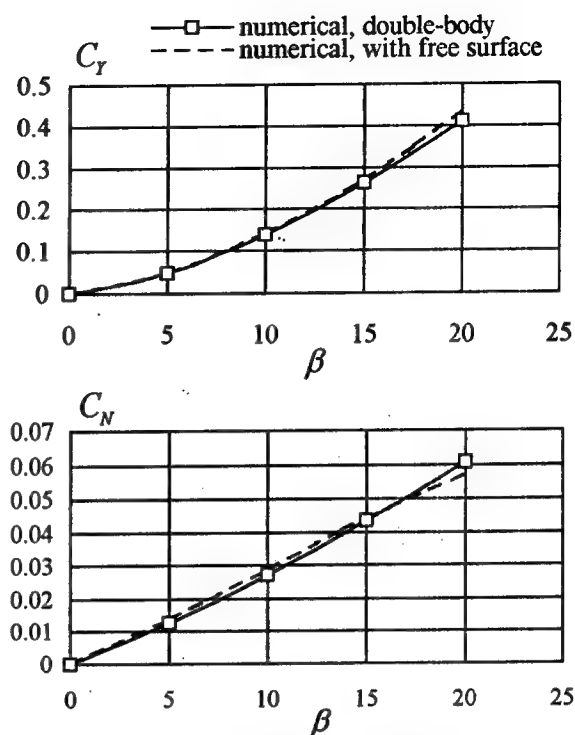


Fig. 3 Lateral-force and yaw-moment coefficients for a plate of $T/L = 0.1$ in oblique motion at $F_n = 0.30$

the numerical results and measurements, especially at large drift angle. In addition, comparison between the numerical results obtained for double-body flow and free-surface flow shows that also in this case the free-surface effects are not significant.

For a plate in steady turning motion, the local drift angle at point (x, y, z) is given by

$$\beta_L = -\tan^{-1} \left(\frac{v + rx}{u - ry} \right).$$

We assume that the free vortices leave the plate at the trailing and lower edges at an angle equal to half of the local drift angle and travel downstream along curved routes. The free vortices are discretized into straight vortex segments, the length of which is approximately equal to the length of free-surface

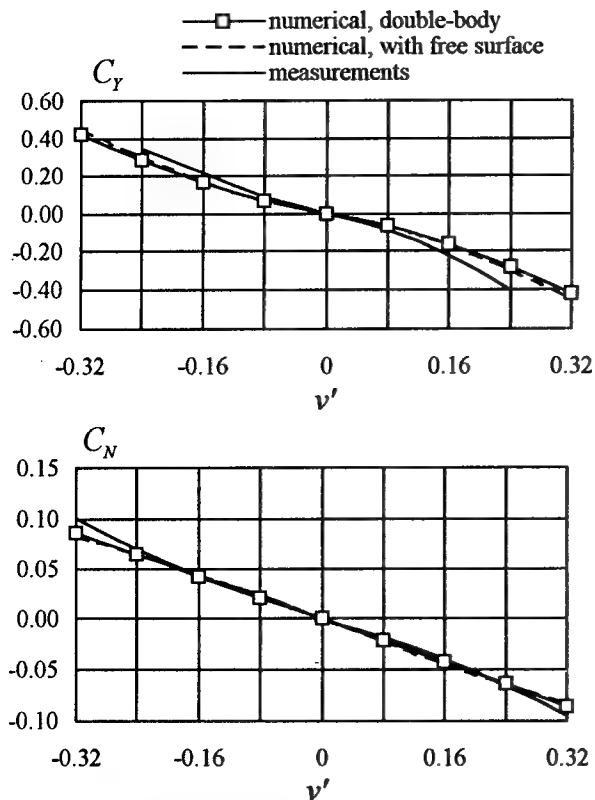


Fig.4 Comparison of the lateral-force and yaw-moment coefficients for a plate of $T/L=0.2$ in oblique motion at $F_n=0.32$

panels. Starting from the trailing edge or the lower edge, the free vortices in their discrete form go backwards at an angle equal to $\frac{1}{2}\beta_L$. At large distance from the plate, the free vortices are replaced by straight line vortices which extend to infinity downstream.

Calculations were performed for surface-piercing plates of $T/L=0.1$ and 0.2 in steady turning motion at $F_n=0.3$ and 0.32 , respectively.

The sizes of the free surface grid and free surface panels are approximately equal to those used for the plate in oblique motion, whereas the discretization of the plate is exactly the same.

In Fig.5 the calculated lateral-force and yaw-moment coefficients versus nondimensional yaw rate

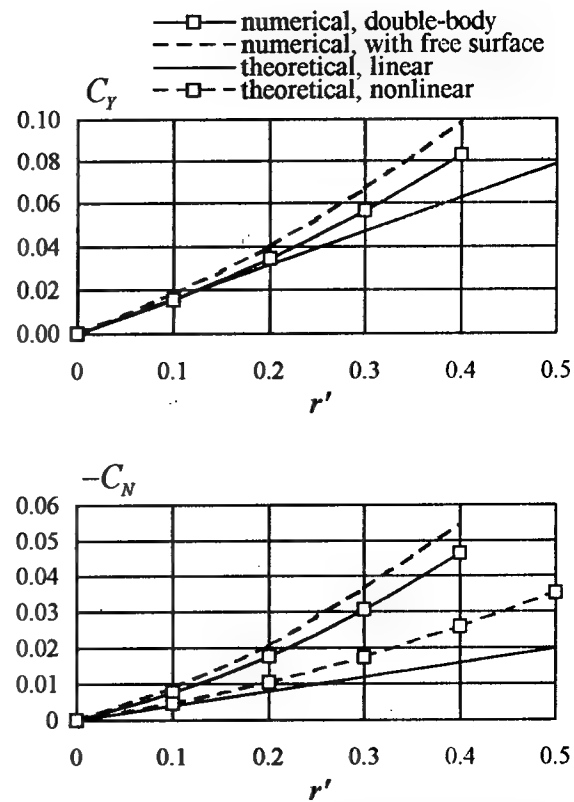


Fig.5 Lateral-force and yaw-moment coefficients for a plate of $T/L=0.1$ in turning motion at $F_n=0.30$

r' is shown together with theoretical results obtained by (13) and (14) for the plate of $T/L=0.1$ at $F_n=0.30$. In contrast to the theoretical prediction, the present results show a strong nonlinear dependence of the hydrodynamic force and moment on the yaw rate, especially for the yaw-moment. Moreover, comparison between the numerical results obtained for the plate in double-body flow and in free-surface flow indicates that the free-surface effects tend to increase the hydrodynamic force and moment, especially at large yaw rate, and thus should not be ignored in these cases.

Fig.6 shows the calculated lateral-force and yaw-moment coefficients for the plate of $T/L=0.2$ in turning motion at $F_n=0.32$ in double-body flow and in free-surface flow. It can be seen that the free-

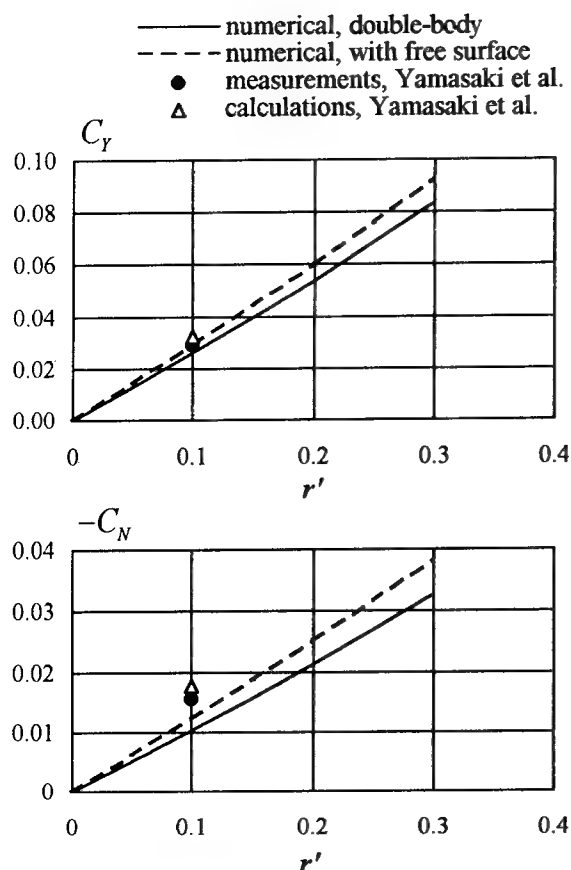


Fig.6 Comparison of the lateral-force and yaw-moment coefficients for a plate of $T/L=0.2$ in turning motion at $F_n=0.32$

surface effects are remarkable in this case. In Fig.6 the measurements and numerical results by Yamasaki et al. (11) are also plotted for comparison, where the numerical results are obtained by an approach similar to Chapman's method. The lateral force calculated by the present method is in very good agreement with the measurement, whereas the yaw moment is underestimated by the present method in comparison with the measurement.

5. CONCLUSIONS

A three-dimensional panel method using Rankine singularities and a nonlinear vortex model is developed for calculating the hydrodynamic forces acting on a vertical surface-piercing plate of small aspect ratio in steady oblique motion and turning

motion. The numerical results are compared with other theoretical, numerical and experimental results which are available. It is shown that the present method can predict very well the free-surface effects on the hydrodynamic forces and the nonlinear dependence of the hydrodynamic forces on the drift angle and yaw rate.

For applications in ship maneuvering problem, the proposed method is to be extended to bodies including the effect of thickness.

ACKNOWLEDGEMENTS

The computations were performed at the Computer Center of Hamburg University during the author's stay in Hamburg. The author is grateful to Prof. Soeding for valuable discussions.

REFERENCES

1. Chapman, R.B., "Free-Surface Effects for Yawed Surface-Piercing Plates", *Journal of Ship Research*, Vol.20, No.3, 1976, pp.125-136.
2. Chapman, R.B., "Prediction of Free-Surface Effects on Ship Manoeuvring", *Proceedings of the 11th Symposium on Naval Hydrodynamics*, London, England, 1976, pp.533-543.
3. Maniar, H., Newman, J.N., and Xu, H., "Free-Surface Effects on a Yawed Surface-Piercing Plate", *Proceedings of the 18th Symposium on Naval Hydrodynamics*, Ann Arbor, USA, 1990, pp.273-282.
4. Landrini, M., and Campana, E., "Wave and Forces about a Turning Flat Plate", *Proceedings of the 10th International Workshop on Water Waves and Floating Bodies*, Oxford, UK., 1995, pp.141-144.
5. Dawson, C.W., "A Practical Computer Method for Solving Ship-Wave Problems", *Proceedings of the 2nd International Conference on Numerical Ship Hydrodynamics*, Berkeley, USA, 1977, pp.30-38.

6. Bollay, W., "A Non-linear Wing Theory and its Application to Rectangular Wings of Small Aspect Ratio", Z. angew. Math. Mech., Bd. 19, No.1, 1939, pp.21-35.
7. Lan, C.E., "A Quasi-Vortex-Lattice Method in Thin Wing Theory", Journal of Aircraft, Vol.11, No.9, 1974, pp.518-527.
8. Jensen, G., Soeding, H., and Mi, Z.-X., "Rankine Source Methods for Numerical Solutions of the Steady Wave Resistance Problem", Proceedings of the 16th Symposium on Naval Hydrodynamics, Berkeley, USA, 1986, pp.575-581.
9. Thieme, H., "Ueber Stroemungstechnische Grundlagen zur Bestimmung von Steuereigenschaften", Schiff und Hafen, H.9, 1954, pp.510-518
10. Van den Brug, J.B., Beukelman, W., and Prins, G.J., "Hydrodynamic Forces on a Surface Piercing Flat Plate", Report Nr.325, 1971, Shipbuilding Laboratory, Delft University of Technology.
11. Yamasaki, K., Fujino, M., and Kawamura, T., "Hydrodynamic Forces Acting on the Three Dimensional Body Advancing on the Free Surface", Journal of the Society of Naval Architects of Japan, Vol.154, 1983, pp.305-313.

DISCUSSION

E.F. Campana
INSEAN, Italy

As a general comment, the present results by Dr. Zou seem to confirm the main conclusions of the paper by Dr. Landrini and myself which was presented at the Workshop on Water Waves and Floating Bodies (10th WWFBB) held in Oxford last year. There and in a subsequent paper [1] we showed some results concerning the steady drift and turning motion of a surface-piercing flat plate described by a linearized free-surface problem according to the Dawson procedure. In particular, by adopting a simplified but still nonlinear wake model, the relevant role of the keel vortex in determining the force coefficients was there emphasized.

I have a few specific comments on the paper included in the proceedings:

- Concerning both trailing edge and tip vortices, we had used an iterative solution to adjust the direction of the trailing vortices with the "local" velocity. Have you already tried to follow that procedure? If not, in what sense is the model you considered nonlinear?
- Dealing with the double body linearization, we experienced very sharp gradients of the second derivatives of the double body solution near the intersection between the leading edge of the plate and the undisturbed water plane. Although not adopting a low-pass filter, as suggested by Nakos and Sclavounos [2], we obtain satisfactory values for the convergence. What is your experience on that problem?
- In the computation, we have found it useful to neglect the influence of the (perturbation) trailing vortex nearest to the free surface. This is because that vortex may generate a jerky behavior of the solution, being too close to the free surface collocation points. How do you handle this problem?
- In our computations, increasing discrepancies between experiments and numerics were observed in the higher Froude range (see, for example, figure 9 in [3]). Could you please comment on this?

REFERENCES

[1] M. Landrini, E.F. Campana, "Steady Waves and Forces About a Yawing Flat Plate," *Journal of Ship Research*, 1996. In press.

[2] D.E. Nakos, P.D. Sclavounos, "Kelvin Wakes and Wave Resistance of Cruiser and Transom-Ships, *Journal of Ship Research*, Vol. 38, No. 1, pp. 9-29, 1994.

[3] A. DiMascio, M. Landrini, E.F. Campana, "On the Modeling of the Flow past a Free-Surface Piercing Flat Plate," *21st Symposium on Naval Hydrodynamics*, Trondheim, Norway, this volume.

AUTHOR'S REPLY

- The vortex model used in the present work is an extension of Bolley's model which is nonlinear in the sense that the trailing vortices leave the plate at some angle to the plane of the plate and thus form a vortex sheet which does not lie in that plane. As the numerical results indicated, this vortex model is efficient to predict the nonlinear dependence of the hydrodynamic forces on drift angle and yaw rate.
- For the linearized boundary condition on the free surface, derivatives of the double-body velocity potential up to the second order need to be calculated. In my calculation, for each drift angle or yaw rate only one free-surface grid is used. The inmost collocation points on the free surface lie at a small distance away from the intersection of the plate and the undisturbed free surface. I did not investigate the details of the flow near the leading edge.
- The vortex distribution on the plate is discretized by a quasi-continuous method, resulting in a system of horseshoe vortices. The uppermost horseshoe vortices are between the inmost collocation points on both sides of the free surface and are included in the calculation.
- In a potential-flow method for lifting problem, a Kutta condition is imposed at the trailing edge to fix the value of lift force which is ultimately due to viscosity. For a surface-piercing plate, the experimentally observed jump in the free-surface elevation across the wake just behind the trailing edge above some critical Froude number is contrary to the Kutta condition of pressure continuity. There, it cannot be expected that the potential-flow method would predict correctly the lift force at range of higher Froude number.

Advances in Panel Methods

H. Söding (Institut für Schiffbau, Germany)

Abstract

In spite of improving computers, a number of inviscid CFD problems still suffer from excessive storage and/or computing time requirements. Examples are detailed pressure distributions on propellers in a wake field, ship wave effects for low Froude numbers, ship encounters in a channel, 3D seakeeping problems and instationary flows which are not time-harmonic. Three measures to reduce the computer requirements for such problems are demonstrated: the multigrid method, panel clustering, and a new higher-order panel method. Further, the 'patch' method is presented which allows more accurate resistance computations without increasing time or unknowns.

1. Introduction

Computational fluid dynamics (CFD) supports to an increasing extent model tests. An important field are "wave-resistance" computations, which use almost exclusively Rankine panel methods to analyse local flow details, to optimise local hull shapes (especially the bulbous bow) and to align of shaft brackets etc. [1], [2]. However, the resistance is not predicted with sufficient accuracy, and reliability to substitute model experiments. Ordinary higher-order panels increase accuracy for simple test cases (spheroids, Wigley hulls, etc.), but failed only recently to show consistent improvements for real ships in an investigation at our institute, [3]. For slow ships (tankers, inland water vessels), due to time and storage limitations the free-surface grids are chosen often too coarse to resolve the short waves.

Panel methods gain in importance for manoeuvring calculations, [4], [5]. Due to the usually low speeds involved and the asymmetry of the flow, problems with a sufficiently fine and extended dis-

cretisation are even more severe. Two-ship encounter simulations are generally not tackled using Rankine panel methods due to the large number of unknowns required. Seakeeping computations using Rankine panels for bodies with forward speed were reviewed this year by [6]. Here generally the covered free-surface area is larger than in wave-resistance computations, and the grid spacing should be finer to cover a wide band-width of wave lengths that may appear in one computation.

In summary, various hydrodynamical computations of practical relevance would benefit from techniques that allow to use more panels without increasing storage and CPU time requirements. Multigrid and cluster techniques can serve this purpose. For a fixed discretisation, the accuracy can be significantly improved by the 'patch' method. Also a new higher-order panel technique with numerical integration appears promising. Advantages will be demonstrated here for steady double-body flows and one example of a free-surface flow, but all techniques are suitable for steady and unsteady flows with and without a free-surface.

2. Patch Method

The aim of the patch method [7] is to increase the accuracy of pressure forces and velocity *averages* over a patch on a body surface compared to the usual first-order panel methods, without introducing a finer discretisation or the complexity of higher-order panel methods. For a given discretisation, the computing time of the panel method and the patch method are about the same, and so are the program complexity and the accuracy of velocities at single points.

Consider an arbitrary body in an infinite ideal fluid (double-body flow). The boundary condi-

tion on the hull (body surface) is that no water flows through the hull. The usual approach in boundary element methods discretises the hull into a number of elements (panels). The boundary condition is then exactly enforced at one point, the collocation point, located approximately at the panel center.

In the 'patch' method, on the other hand, the total flow through each surface element (patch), and not just at its center, is made to vanish. Using sources distributed over plane or curved panels would lead to complicated integrations; therefore in the patch method simple point sources are used. They are located within the body near to the patch centres. The distance between patch centre and source point may be chosen as the minimum of the following lengths:

- Square root of patch area;
- 1/3 of the local body breadth;
- 1/2 the radius of longitudinal curvature;
- 1/2 the radius of transverse curvature.

The results are not sensitive to this distance; in many applications simply 1/10 of the patch length is used.

In the panel method, velocity and pressure can be determined on the hull directly only at the panel centres; at other points, interpolation has to be used. Pressure forces are, typically, determined by multiplying the pressure at the panel centre with the panel area. The patch method aims just to improve this force formula. In the patch method, potential and velocity are determined at the patch corners instead of at the patch centre, i.e. at a reasonable distance from all point sources. The potential at the patch corners allows a better approximation of the *average* velocity within the patch than the value at the panel centre, and combining the potential and the velocity at the patch corners allows to determine an accurate *average* of the pressure within the patch.

For a body in uniform flow to negative x direction, the potential is

$$\phi = -Ux + \sum_{i=1}^n \sigma_i G_i. \quad (1)$$

U is the speed of the uniform flow, σ the source strength, G the potential of a Rankine point source:

$$G = \ln r \quad \text{in 2D, and} \quad G = -1/r \quad \text{in 3D,} \quad (2)$$

where $r = |\vec{x} - \vec{s}|$ is the distance between field point \vec{x} and source point \vec{s} .

Let M_i be the outflow through a patch induced by a point source of unit strength. Then the zero-flow condition for a patch is

$$-UAn_x + \sum_i \sigma_i M_i = 0. \quad (3)$$

Here \vec{n} is the outward normal on the hull, index x (and later z) designates the respective component of \vec{n} , and An_x is the projection of the patch area on a plane $x = \text{constant}$ (with appropriate sign); for the 2d case of Fig. 1: $An_x = y_A - y_B$.

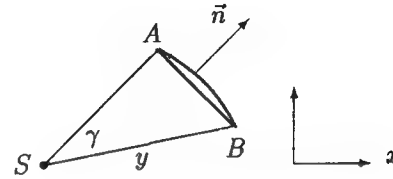


Fig. 1: Patch (from A to B) and source point S

2.1 2-d Formulation

The outflow due to the unit source potential $\ln r$ into all directions is 2π . The outflow M due to the unit source in \vec{s} passing through the patch in Fig. 1 is thus equal to the angle γ under which the patch is seen from \vec{s} — both for a straight and a curved patch. If \vec{A} and \vec{B} are the vectors from S to A and B respectively, γ is easily determined from the vector and scalar products of \vec{A} and \vec{B} :

$$M = \gamma = \arctan \frac{[\vec{B} \times \vec{A}]_z}{\vec{B} \cdot \vec{A}}. \quad (4)$$

From the value of the potential ϕ at the end points A and B , the average modulus \bar{v} of the velocity \vec{v} is found as $|\phi_A - \phi_B|/l$, where l is the length of the patch. The direction of \vec{v} is parallel to the contour. The velocity \vec{v} at the end points, designated here as \vec{x} , is found as $\nabla G = (\vec{x} - \vec{s})/r^2$.

The pressure force on a straight patch is

$$\vec{f} = \vec{n} \int p \, dl = \vec{n} \frac{\rho}{2} \left(U^2 \cdot l - \int v^2 \, dl \right) \quad (5)$$

where v , the modulus of \vec{v} , is not constant. To evaluate this expression, v is approximated by the second-order polynomial giving the known values v_A , v_B and \bar{v} :

$$v = v_A + (6\bar{v} - 4v_A - 2v_B)t + 3(v_A + v_B - 2\bar{v})t^2 \quad (6)$$

t is the tangential coordinate directed from A to B . From this expression follows the integral in (5):

$$\int v^2 \, dl = l \bar{v}^2 = l \cdot \left((\bar{v})^2 + \frac{2(v_A - \bar{v})^2 + 2(v_B - \bar{v})^2 - (v_A - \bar{v})(v_B - \bar{v})}{15} \right). \quad (7)$$

As a test case, a symmetric profile with circular nose, parabolic run and a sharp tail, with thickness-chord ratio of 2, was investigated at zero angle of attack. The resistance, which should be zero due to d'Alembert's paradox, is used to indicate the error. (A test body should not be symmetric in x to avoid cancellation of the discretisation error.) The panel method used for comparison applied straight elements of constant source strength, a collocation scheme and constant pressure over each element.

Table I: Relative resistance (= error) for a foil-shaped profile; comparison of patch method (PTM) with first-order panel method (OPM)

elem. no.	12	24	48	96	192
PTM	17%	13%	5%	1.4%	0.5%
OPM	100%	47%	22%	10%	5%

The patch method proved to be about 5 times more accurate than the panel method, Table I. In other words, only 1/4 of the number of elements of the ordinary panel method sufficed for the patch method to obtain the same force accuracy.

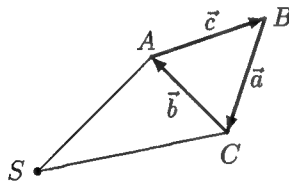


Fig. 2: Source point S and patch ABC

2.2 3-d Formulation

The outflow due to the unit source potential $-1/r$ into all space directions is 4π . The outflow due to the unit source in S passing through the triangular patch in Fig. 2 is thus equal to the space angle γ under which the patch ABC is seen from S . Quadrilateral patches are handled by combining two triangles. For straight patch sides, the rules of spherical geometry give γ as the sum of the angles between each pair of planes SAB , SBC and SCA , minus π :

$$\alpha = \beta_{SAB,SBC} + \beta_{SBC,SCA} + \beta_{SCA,SAB} - \pi \quad (8)$$

where e.g.

$$\beta_{SAB,SBC} = \arctan \frac{-(\vec{A} \times \vec{B}) \times (\vec{B} \times \vec{C}) \cdot \vec{B}}{(\vec{A} \times \vec{B}) \cdot (\vec{B} \times \vec{C}) |\vec{B}|}$$

Here \vec{A} , \vec{B} , \vec{C} are the vectors pointing from the source point S to the panel corners A, B, C . Note that a curvature of the patch does not influence the result if the panel edges remain straight. If curved patch sides are approximated by straight lines, the error made in one patch occurs at the neighbouring patch with opposite sign.

γ maybe approximated by A^*/d^2 if the distance d between patch center and source point exceeds a given limit. A^* is the patch area projected on a plane normal to the direction from the source to the patch center:

$$\vec{d} = \frac{1}{3}(\vec{A} + \vec{B} + \vec{C}) \quad (9)$$

$$A^* = \frac{1}{2}(\vec{a} \times \vec{b}) \cdot \frac{\vec{d}}{d} \quad (10)$$

With known source strengths σ_i , one can determine the potential ϕ and its derivatives $\nabla\phi$ at all patch corners. From the ϕ values at the corners A, B, C , the average velocity within the triangle is found as

$$\vec{v} = \overline{\nabla\phi} = \frac{\phi_A - \phi_C}{\vec{n}_{AB}^2} \vec{n}_{AB} + \frac{\phi_B - \phi_A}{\vec{n}_{AC}^2} \vec{n}_{AC} \quad (11)$$

with

$$\vec{n}_{AB} = \vec{b} - \frac{\vec{c} \cdot \vec{b}}{\vec{c}^2} \vec{c} \quad \text{and} \quad \vec{n}_{AC} = \vec{c} - \frac{\vec{b} \cdot \vec{c}}{\vec{b}^2} \vec{b}. \quad (12)$$

With known \vec{v} and corner velocities \vec{v}_A , \vec{v}_B , \vec{v}_C , the pressure force on the triangle can be determined from (5) where l is now the patch area. (7) has the following 3-d equivalent:

$$\int \vec{v}^2 dl = \quad (13)$$

$$l \cdot \left((\vec{v})^2 + \frac{(\vec{v}_A - \vec{v})^2 + (\vec{v}_B - \vec{v})^2 + (\vec{v}_C - \vec{v})^2}{30} - \frac{(\vec{v}_A - \vec{v})(\vec{v}_B - \vec{v}) + (\vec{v}_B - \vec{v})(\vec{v}_C - \vec{v}) + (\vec{v}_C - \vec{v})(\vec{v}_A - \vec{v})}{90} \right)$$

2.3 Test Cases

Test cases concerned a sphere and two ships. The HSVA tanker, used often as a test for RANSE flow codes, has a 'parabolical' bow shape and a much finer afterbody, thus showing the strong asymmetry in x direction which makes it well-suited to compare the numerically computed resistance in double-body

flow conditions with the correct value of 0. For comparison, Jensen's "sphere method" [12] and a first-order Hess&Smith panel method were applied (Table II). The patch method was more accurate by one order of magnitude for the same discretisation (corresponding roughly to same CPU time and storage requirements for the 3 methods).

Table II. Numerical resistance coefficient $-2F_x/\rho U^2 S$ by different methods

method	no. of panels/patches	1000 · resistance coefficient
Patch	421	-0.16
Sphere	421	+1.54
Patch	780	+0.03
Sphere	780	+0.20
Hess&Smith	1788	+0.20

Table III shows a comparison of the force on 1/8 of a full sphere in uniform flow. For radius 1 and speed 1, the exact force components on the positive octant are $f_x = -\pi/64 = 0.04909$ and $f_y = f_z = 11\pi/128 = 0.26998$. Here the patch method was compared by Hughes and Bertram [3] with an ordinary higher-order panel method OHM (parabolic in shape, linear in source strength). The patch method is roughly of same accuracy (but much faster) for the longitudinal force, but 3 times more inaccurate for the transverse force. Results of the patch method in Table III refer to a mesh of equilateral triangles; it was found, however, that combining two such triangles to a quadrilateral produced nearly the same error with about half the number of patches.

Table III: Error in force on 1/8 sphere

patch method PTM		
elements	F_x error	F_y error
16	0.006	0.050
64	0.001	0.012
256	0.00005	0.0025
higher-order panel OHM		
elements	F_x error	F_y error
15	0.006	0.017
66	0.002	0.004
231	0.0007	0.0013

Fig. 3 shows the wave resistance coefficient for the Series 60 - $C_B = 0.6$ hull as a function of Froude number, computed by a non-linear Rankine source / patch method. For the hull boundary condition up to the deformed water surface and for the force integration, the patch method was used,

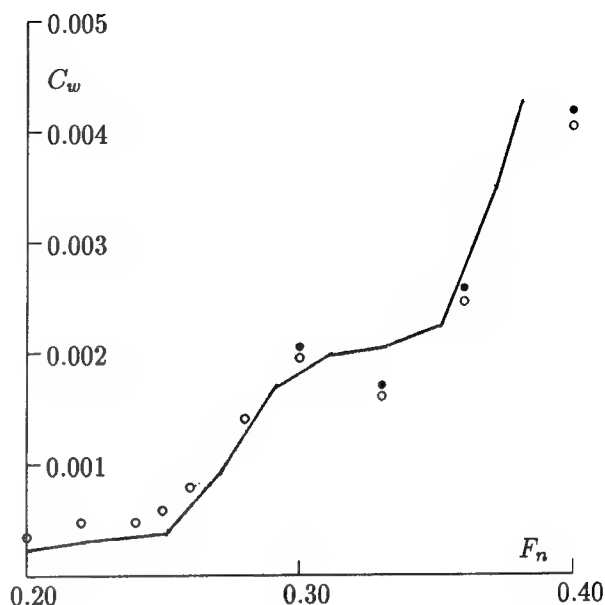


Fig. 3. Wave resistance coefficient of Series 60 ($C_B = 0.6$) model according to experiments ([13], line) and patch method (o). Symbols • include interaction with viscous resistance.

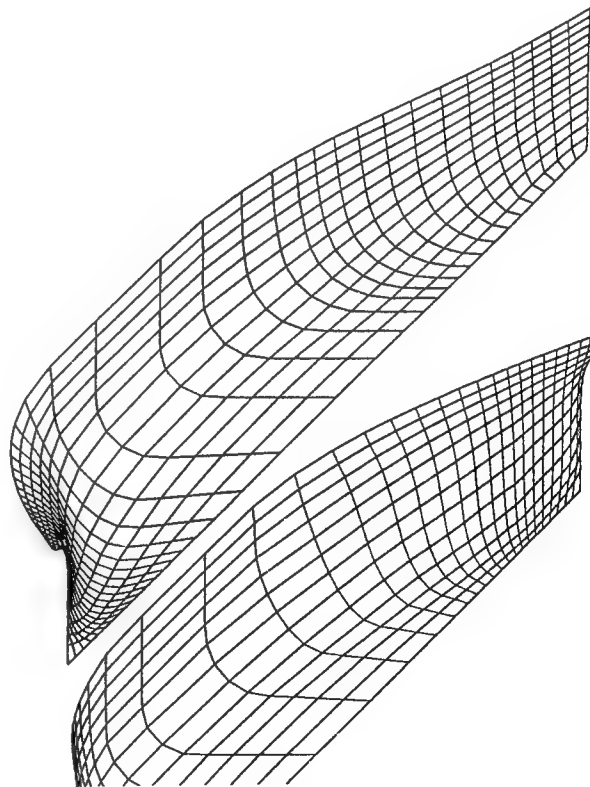


Fig. 4. Patch arrangement on Series 60 hull

whereas the free surface condition was satisfied, as in earlier methods, by point collocation and point sources above the water surface shifted backwards relative to the collocation points. Symbols \bullet include a rough approximation of the interaction between wave and viscous resistance: the difference between \bullet and \circ corresponds to the change of viscous resistance with F_n estimated to be proportional to the change of wetted surface and to the mean squared non-viscous velocity at the hull surface.

To test the accuracy of the patch method, the hull discretisation shown in Fig. 4 with $37 \cdot 13$ patches was modified to have twice the number of patches, either in transverse or in longitudinal direction. The results of the wave resistance were practically the same for all three meshes.

3. Cluster and Multigrid Method

3.1 Clustering

In the following only the boundary condition on the body (no flow through the hull) is considered; but clustering and the multigrid technique are even well applicable also for free-surface flow problems.

The discretisation of the hull boundary condition yields a system of linear equations for the unknown source strengths σ_i in (1):

$$K\sigma = g \quad (14)$$

K is the coefficient matrix, σ the vector of source strengths, and g the vector of the inhomogeneous parts. An element k_{ij} of K can be interpreted as flow through a patch i per time induced by a source of unit strength at point ξ_j . The elements of g give the negative flow per time through the patches induced by the uniform flow. Eq. (14) enforces that the superposition of all source flows and the parallel flow add up to zero flow through all patches.

Clustering aims to reduce the computer time and storage requirements for generating the matrix K , and it simplifies the application of the multigrid method (next chapter); however, clustering and multigrid can be applied also separately. The cluster/multigrid technique is combined here with the patch method, but it could be applied also to ordinary panel methods.

Here, a cluster is a set of 4 by 4 patches of the normal (fine) grid. The 16 patches of each cluster are generated to have similar size and shape, and the surface covered by a cluster should be smooth; if it is not, the cluster should be made smaller.

The scalar equations in (14) referring to a

line of four patches in a cluster are added and subtracted to the following four combined equations:

- 1: + + + +
- 2: + - + -
- 3: + + - -
- 4: + - - +

If the combined equations are satisfied, so are the original ones. The absolute values of coefficients of the combined equations 2, 3, and especially 4 decrease stronger with distance from the main diagonal in K than those of the original equations and of combination 1.

Correspondingly also the four rows of patches within a cluster are combined to the following 16 combinations of 16 equations:

- 1: + + + + + + + + + + + + + + + +
- 2: + - + - + - + - + - + - + - + - +
- 3: + + - - + + - - + + - - + + - - + +
- 4: + - - + + - - + - + - + - - + + -
- 5: + + + + - - - - + + + + - - - -
- 6: + - + - - + - + + - + - - + - + -
- 7: + + - - - - + + - - + + - - - - + +
- 8: + - - + - + + - + - - + - + + - +
- 9: + + + + + + + + - - - - - - - -
- 10: + - + - + - + - - + - + - + - + -
- 11: + + - - + + - - - - + + - - + +
- 12: + - - + + - - + - + - - + + - + +
- 13: + + + + - - - - - - - - + + + +
- 14: + - + - - + - + - + - + + - + - +
- 15: + + - - - - + + - - + + - - + + - -
- 16: + - - + - + + - - + + - - + - - +

As the cluster consists of patches of approximately equal size and orientation, for a distant source the influence functions of all combinations will nearly cancel (due to the positive and negative contributions) with the exception of the first combination which adds all influence functions. The purpose of combining the influence of elements within a cluster is, that for large distances between source and patch (resp. collocation point and panel in a conventional panel method) the combined influence functions are so small that they can be neglected. This saves storage space, time for solving the system of equations and - if one can determine a priori which combinations will be neglected - time for computing the influence functions, because only the combined influence functions for all elements of a cluster or for 2 by 2 patch blocks need to be computed.

The mixed influence functions (containing positive and negative contributions) decay even more rapidly with distance as also sources within a source cluster of 16 sources are combined by adding and subtracting their influence. Contrary to patch clusters, however, experience has shown that it is not sufficiently accurate to use just one single point source to represent a whole source cluster even for large distances. Thus, forming source clusters reduces storage requirements, but not time to compute the coefficient matrix.

The matrix K is subdivided into blocks of $16 \cdot 16 = 256$ elements. Each block represents the influence of one source cluster on one patch cluster. A block element represents initially the influence function of a source of unit strength on one patch; if 4 or 16 patches are combined to save computation time, each patch of the group is assumed to have $1/4$ resp. $1/16$ of the computed total influence. Then the block elements are 'mixed' according to the above combinations. A direct superposition of each of the 256 elements of a 'mixed' block by adding and subtracting all elements of the original block would require $2 \cdot 256^2$ arithmetical operations per block. Mixing can be accelerated by combining, stepwise, at first two adjacent elements, then more removed elements. An example of 4 elements may illustrate the process: Original coefficients (o indicates that a neighbour coefficient does not contribute):

+ o o o o + o o o + o o o +

Neighbours added/subtracted:

+ + o o + - o o o o + + o o + -

Neighbours once removed added/subtracted:

+ + + + + - + - + + - - + - - +

For 256 elements, this process requires only $2 \cdot 256 \cdot 8$ operations. After 'mixing', each of the 256 block elements represents the combined influence of 16 sources/sinks on the \pm combination of 16 patches.

Five types of blocks are distinguished according to their arrangement of non-zero elements, Fig. 5. The threshold for setting an element to zero was taken such that the error in neglecting *all* zero elements contributes less than $10^{-4}U$ to the final velocity. The definition of block types was based on trial computations to achieve favourable storage and CPU time conditions; however, a higher number of block types may be worthwhile to further reduce the storage requirements. Each block of matrix K is stored without the zero elements in one storage area. The full matrices of type 1 appear mostly along the main diagonal, whereas the sparse blocks of higher block type are located farther away from the main diagonal, where large distances between patch and source

```

x x x x x x x x x x x x x x
x x x x x x x x x x x x x x
x x x x x x x x x x x x x x
x x x x x x x x x x x x x x
x x x x x x x x x x x x x x
x x x x x x x x x x x x x x
x x x x x x x x x x x x x x
x x x x x x x x x x x x x x
x x x x x x x x x x x x x x
x x x x x x x x x x x x x x
x x x x x x x x x x x x x x
x x x x x x x x x x x x x x
x x x x x x x x x x x x x x
x x x x x x x x x x x x x x
x x x x x x x x x x x x x x
x x x x x x x x x x x x x x
x x x x x x x x x x x x x x
x x x x x x x x x x x x x x
x x x x x x x x x x x x x x
x x x x x x x x x x x x x x

```

Type 1

```

x x x x x x x . x x x x x . x .
x x x . x . . . x . x . . . .
x x x x x . x . x x x x x . x .
x . x . . . . . x . x . . . .
x x x . x . . . x . x . . . .
x . . . . . . . . . . . . . .
x . x . . . . . x . x . . . .
. . . . . . . . . . . . . . .
x x x x x . x . x x x x x . x .
x . x . . . . . x . x . . . .
x x x x x . x . x x x . x . . .
x . x . . . . . x . . . . . .
x . x . . . . . x . x . . . .
. . . . . . . . . . . . . . .
x . x . . . . . x . . . . . .
. . . . . . . . . . . . . . .

```

Type 2

```

x x x x x . x . x x x . x . . .
x . x . . . . . x . . . . . .
x x x . x . . . x . x . . . .
x . . . . . . . . . . . . . .
x . x . . . . . x . . . . . .
. . . . . . . . . . . . . . .
x . . . . . . . . . . . . . .
. . . . . . . . . . . . . . .
x x x . x . . . x . x . . . .
x . . . . . . . . . . . . . .
x . x . . . . . x . x . . . .
. . . . . . . . . . . . . . .
x . . . . . . . . . . . . . .
. . . . . . . . . . . . . . .
. . . . . . . . . . . . . . .

```

Type 3

group are represented.

3.2 Multigrid Method

The multigrid method is frequently used for solving differential equations of viscous fluid flow, but it works even better for potential flow problems, i.e. for solving integral equations. The principles of both applications are elaborated in [8]. For panel methods the multigrid technique reduces the time needed to solve the system of linear equations (14) to a negligible fraction of the total computing time.

First, the rows in K and g are multiplied by factors such that the elements of K on the main diagonal are all 1. Then a multigrid solution can be determined as follows: Starting from $\sigma = \vec{0}$, a Jacobi iteration step improves σ by smoothing the error in the system of equations on the normal (finest) grid:

$$\bar{\sigma}_l = g_l + (I - K)_l \sigma_l^i \quad (15)$$

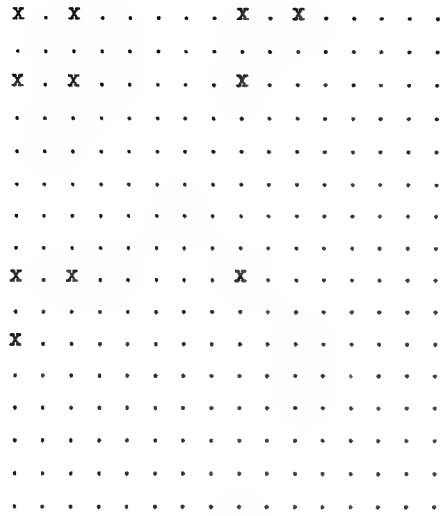
Index l indicates the grid level: $l = 3$ denotes the finest grid in the investigated 3-grid method, $l = 1$ the coarsest grid. Superscripts i denote the iteration step. I is the unit matrix, $\bar{\sigma}$ the improved vector of unknown source strengths.

A straight-forward Jacobi iteration of (15) would take $\bar{\sigma}_l$ as next iterative solution σ_l^{i+1} . The multigrid method improves convergence by setting

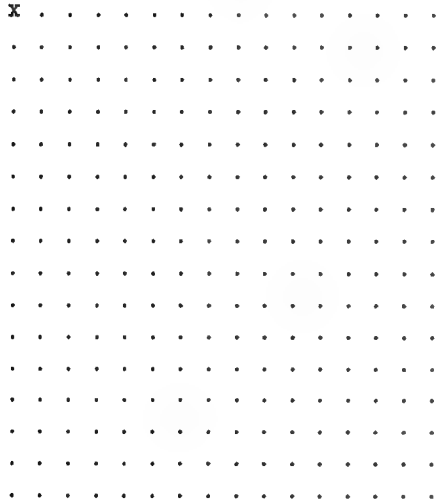
$$\sigma_l^{i+1} = \bar{\sigma}_l - p K_{l-1}^{-1} r \underbrace{(K_l \bar{\sigma}_l - g_l)}_{\mathcal{R}_l}. \quad (16)$$

The vector of residuals \mathcal{R}_l gives the error of all equations. This residual is restricted to a shorter vector, here to 1/4 of the original number of elements, by the restriction operator r explained later. K_{l-1} is, correspondingly, a restricted coefficient matrix with 1/4 of the original columns and rows. Multiplication of the residuals with the inverse matrix K_{l-1}^{-1} yields the necessary corrections to enforce the equations exactly. Because we perform the corrections on a coarser grid, we have to transform them to the original, fine grid by applying the prolongation operator p (see later). The prolonged corrections added to the approximation $\bar{\sigma}$ yield the next approximation σ_l^{i+1} . This is again used in (15) and improved by (16) until the residual is decreased by 5 to 6 orders of magnitude.

To determine $K_2^{-1} r \mathcal{R}_3$ requires to solve a system of linear equations having 1/4 of the original number of unknowns. This system is also solved by applying the multigrid equations (15) and (16), now with $l = 2$. There remains a system of 1/16 of the original number of unknowns, which is effectively solved by Gauss' algorithm.



Type 4



Type 5

Fig. 5: Arrangement of non-zero elements (x) in five block types

Combined with our clustering technique, the restriction and prolongation operators become extremely simple: For $l = 3$, in each block of 16 vector components the restriction operator eliminates 12 components, keeping only the 1st, 3rd, 9th and 11th. That means: In (16) only the flow through $2 \cdot 2$ patch groups is considered, not the flow through single patches. The solution $K_2^{-1} r R_3$ gives corrections of the source combinations 1, 3, 9, and 11, i.e. corrections of the combined source strength for groups of $2 \cdot 2$ sources. To this end, K_2 is produced from K_3 by keeping in each block of $16 \cdot 16$ elements only those in rows and columns no. 1, 3, 9 and 11. For prolongation, the additional elements, i.e. the corrections of the differences between single source strengths within a block of $2 \cdot 2$ sources, are simply set to zero; these differences are effectively corrected by the Jakobi step (15).

For $l = 2$, the restriction operator keeps only the first element of each block of 4 elements, i.e. the combined flux through a $4 \cdot 4$ panel group, and the prolongation operator adds 4 zero elements in each group of 4 components. Matrix K_1 contains the 1st, 5th ... row and column of K_2 .

3.3 Test Case

As a test case, the double-body flow around a Wigley hull with 1600 patches (100 clusters) on one ship side was computed. This number of elements is more than necessary for this flow; it is used here only to demonstrate the effect of multigrid and clustering for the typical, larger panel numbers in practical applications. A full coefficient matrix would have required $1600^2 = 2.56 \cdot 10^6$ coefficients. Clustering reduced this to $0.35 \cdot 10^6$ (14%) coefficients. The additional storage space is negligible: For each of the 10000 storage blocks, block type and starting address in the coefficient array have to be stored.

On a 12 Mflop computer, the computing time was 73s for determining the coefficient matrix, 2.5s for solving and 33s for determining end results (velocities, pressures, forces). It was necessary to use double precision of the real variables; otherwise the multigrid method did not converge to sufficiently small residuals. A comparison with a coarser discretisation of the Wigley hull involving only 30 clusters (480 patches) showed that the storage requirement was $\sim n^{1.25}$, the total computing time $\sim n^{1.78}$. Only for systems with more than about 800 elements, the multigrid and clustering approach saved CPU time. However, storage savings are attained already for considerably smaller systems of equations.

4. New Higher-Order Panel Method

The purpose of higher-order panels is to increase the accuracy for a given number of unknowns, and to determine spatial derivatives of flow velocities which – for decreasing grid spacing – converge to the correct values. The latter is necessary for sea-keeping calculations with forward speed that linearise around the steady flow potential around the body [9]. The usual higher-order panels following the original work of Hess [10] can compute the necessary velocity derivatives, but they failed to improve accuracy for real ship geometries in [3]. Furthermore they involve quite complicated formulas especially for higher derivatives of the potential.

The new higher-order panel method presented here varies the approach of Kouh and Ho [11]. Both methods are based on a modification of the integrals which give the influence of a source (in my method: and dipole) distribution on the body surface, such that the integrand is non-singular even if the field point is on the body surface, too. This allows to substitute the complicated analytical integration of the singular integrand by a simple numerical scheme.

Differently from [11] and from eq. (1), the 'direct' method is used here. It applies a distribution of sources and dipoles on the body surface and solves directly for the potential at many points on the body surface. Comparisons seemed to indicate that for non-lifting flows (without circulation and without a Kutta condition) both the direct and the indirect method are about even well suited, whereas for lifting flows the direct method is superior in accuracy to the indirect method, which – for lifting flows – uses also sources and line vortices (corresponding to dipole panels).

The well-known equation for the direct (source-dipole) panel method is

$$\begin{aligned} \frac{1}{2}\phi(\vec{x}_0) - \int_{S_b} \phi(\vec{x}) \vec{n}(\vec{x}) \nabla_{\vec{x}} G(\vec{x}, \vec{x}_0) dS(\vec{x}) \\ = - \int_{S_b} U n_x(\vec{x}) G(\vec{x}, \vec{x}_0) dS(\vec{x}) \end{aligned} \quad (17)$$

with the Green function

$$G = -1/(4\pi|\vec{x} - \vec{x}_0|), \quad (18)$$

ϕ = disturbance potential, \vec{n} = unit normal vector on the closed surface S_b , U = ship speed and \vec{x}_0 = a field point on S_b . The integrals in (17) are desingularised (without moving the singularities into the interior of

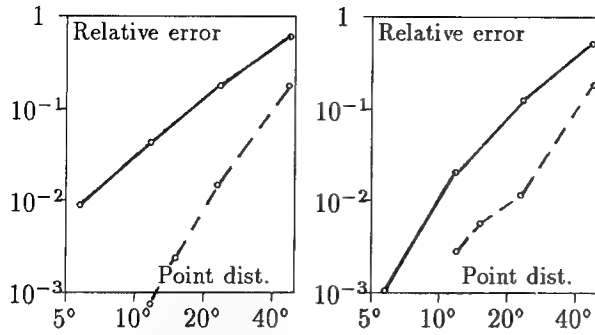


Fig. 6. Relative error of transverse (left) and longitudinal (right) pressure force on 1/8 of a sphere for patch (continuous) and higher-order method (broken line)

the body) in the following equivalent equation:

$$\begin{aligned} \phi(\vec{x}_0) - \int_{S_b} [\phi(\vec{x}) - \phi(\vec{x}_0)] \vec{n}(\vec{x}) \nabla_x G(\vec{x}, \vec{x}_0) dS(\vec{x}) \\ = - \int_{S_b} \left(Un_x(\vec{x}) - \frac{Un_x(\vec{x}_0)\delta(\vec{x})}{\delta(\vec{x}_0)} \right) G(\vec{x}, \vec{x}_0) dS(\vec{x}) \\ - \frac{Un_x(\vec{x}_0)}{\delta(\vec{x}_0)} \phi_0 \end{aligned} \quad (19)$$

ϕ_0 is the constant potential generated by the source distribution δ in the space surrounded by S_b , i.e. inside the body. δ is the 'eigen potential' following from the homogeneous integral equation

$$\frac{1}{2} \delta(\vec{x}_0) + \int_{S_b} \delta(\vec{x}) \vec{n}(\vec{x}_0) \nabla_{x_0} G(\vec{x}, \vec{x}_0) dS(\vec{x}) = 0 \quad (20)$$

Eq. (20) has a solution δ which has non-zero values everywhere on S_b . Eq. (20) is also desingularised:

$$\int_{S_b} [\delta(\vec{x}) \vec{n}(\vec{x}_0) + \delta(\vec{x}_0) \vec{n}(\vec{x})] \nabla_x G(\vec{x}, \vec{x}_0) dS(\vec{x}) = 0 \quad (21)$$

The nonsingular integrals in (21) and (19) are evaluated by Simpson's rule using 9-knot panels (8 on the circumference, one in the center), to obtain a system of linear algebraic equations for the potential at each knot. Numerical interpolation and differentiation over the panels gives velocities, velocity derivatives, and pressures on S_b .

For a sphere in uniform flow, Fig. 6 compares relative errors of the pressure force on 1/8 sphere between the higher-order and the patch method. For both methods, the mesh consisted of quadrilaterals bounded by meridians and latitude circles with uniform angular spacing, poles being at the stagnation points. (Results for the patch method given

in Fig. 6 differ somewhat from Table III because there a mesh of nearly uniform, equilateral triangles was used.) The higher-order method is, roughly, 10 times more accurate than the patch method which is again much more accurate than an ordinary first-order panel method. For more complicated bodies, however, the difference is expected to be much smaller. Both the maximum error in ϕ (not shown) and the pressure force (Fig. 6) converge with errors $\sim h^{3.5}$ to h^4 , where h is the grid spacing.

References

1. Bertram, V., "Numerische Schiffshydrodynamik in der Praxis", rep. 545, 1994, Inst. für Schiffbau, Hamburg Univ., Germany
2. Bertram, V.; Jensen, G., "Recent applications of computational fluid dynamics", *Ship Techn. Res.* 41/3, 1994, pp. 131-134
3. Hughes, M.; Bertram, V., "A higher-order panel method for 3-d free surface flows", rep. 558, 1995, Inst. für Schiffbau, Hamburg Univ., Germany
4. Zou, Z.; Söding, H., "A panel method for lifting potential flows around a yawed ship in shallow water", 20th Symp. on Ship Hydrodyn., 1994, Santa Barbara
5. Zou, Z., "Calculation of the three-dimensional free-surface flow about a yawed ship in shallow water", *Ship Techn. Res.* 42/1, 1995, pp. 45-52
6. Bertram, V.; Yasukawa, H., "Rankine source methods for seakeeping problems", Proc. Schiffbautechn. Gesellschaft, Springer, Berlin, Heidelberg, New York, Tokyo, 1996
7. Söding, H., "A method for accurate force calculations in potential flow", *Ship Techn. Res.* 40/3, 1993, pp. 176-186
8. Hackbusch, W., *Multi-grid methods and applications*, Springer, Berlin, Heidelberg, New York, Tokyo, 1980
9. Bertram, V., "Ship motions by a Rankine source method", *Ship Techn. Res.* 37/4, 1990, pp. 143-152
10. Hess, J.L., "A higher order panel method for three-dimensional potential flow", NADV-Report, MDC J8519, 1979
11. Kouh, J.S.; Ho, C.H., "A high order panel method based on source distribution and Gaussian quadrature", *Ship Techn. Res.* 43/1, 1996, pp. 38-47

12. Jensen, G.; Söding, H., "Ship wave-resistance computations", Notes on Num. Fluid Mech. Vol. 25: "Finite approximations in fluid mechanics", Springer, Berlin, Heidelberg, New York, Tokyo, 1989

13. Kajitani, H., "A wandering in some resistance components and flow", Ship Techn. Res. 34/3, 1987, pp. 105-131

DISCUSSION

W.W. Schultz
University of Michigan, USA

The patch method results are impressive. Is this improvement due primarily to moving the singularity distribution within the body or is the matching of the outflow through the patch also required? Specifically since (3) appears to ensure $\Sigma \sigma_i = 0$ inside the closed body, is the extra effort in evaluating the trigonometric functions worth it?

Does the higher-order method you present make the patch method obsolete? Why would you still use the patch method?

AUTHOR'S REPLY

The improvement in the patch method is not due to moving the singularities into the body, but due to "averaging" both the boundary condition and the results (e.g., the pressure) over each patch. Moving the singularity into the body would be helpful, but is possible only if the body surface is sufficiently smooth and if the body breadth is sufficient; these conditions are not satisfied at typical ships' ends. The extra effort for computing trigonometric functions appears only in comparison with a point-source-point-collocation method, which does not work well for typical ships; compared to a usual first-order panel method the numerical effort per panel/patch is about the same.

The higher-order method is more accurate for smooth bodies, but somewhat more complex to program. Comparisons for less smooth bodies like ships with sharp ends have not yet been made. Extension to free-surface flows may further change the rating.

Effect of Ship Motion on DD-963 Ship Airwake Simulated by Multizone Navier-Stokes Solution

T. Tai (David Taylor Model Basin, USA)

Abstract

The airwake about a DD-963 ship configuration is simulated by using a multi-zone, thin-layer Navier-Stokes method. The ship's superstructure is modelled by two blocked structures, followed by a flight deck and a lower missile deck. The ship motion is represented by change of ship attitude in a steady state flow environment. Two ship attitudes are considered: (1) the ship at two-degree pitch, and (2) the ship at one-degree pitch and five-degree roll. The freestream has a wind speed of 15.44 m/s (30 knots) at a direction of 30 degrees. The flow is fully turbulent with a Reynolds number of 177 million based on ship length. In general, the flow is largely separated behind the superstructure. The ship pitched bow down yields an airwake thinner than that of a ship at even keel traveling at the same speed. The ship with pitch or roll has larger local reversed flow regions characterized by backward-facing-step type flow.

Introduction

It is well known that the interface of aircraft/helicopter and ship poses problems in operability and survivability for naval aviation. Current aircraft/helicopter operations aboard the ship are characterized by restrictions due to weather and the need to often alter the ship's course into the wind to establish necessary wind-over-the-deck conditions for a successful landing. The interface environment becomes more complicated by the presence of massive, turbulent airwake from the ship's superstructure. The technical issues here involves aspects concerning both the air vehicle and the ship. For aircraft, the lift characteristics become very sensitive to the surrounding environment due to relatively low freestream velocity and use of high

lift devices. In case of the rotorcraft, the controllability in the final approach and landing is greatly influenced by the ship airwake.

The ship airwake is defined as an arbitrary volume of air, namely an air burble, surrounding the ship. The effect of airwake on the aircraft/ship interface operation is determined by the airflow disturbances caused by the ship that are perceptible to the pilot, and the final approach and landing patterns required for shipboard operation. Alleviation of the airwake effect would improve operability of the aircraft in a seabase interface environment [1-7].

The complexity of the problem requires use of the Navier-Stokes type method to reveal correct flow features. Advances in numerical algorithm schemes along with increased computer speed and capacity have made the computational fluid dynamics (CFD) feasible to provide answers to complex aerodynamic problems. Although physical modeling of unsteady, vortex dominated flows over complex geometry remains prohibitive, reasonably accurate simulated results based on steady-state solutions have been obtained during the past decade. Tai and Carico [8] applied three-dimensional, implicit finite-volume type Reynolds-averaged Navier-Stokes (RANS) scheme to consider the airwake problem behind a simplified DD-963 ship configuration. Computed viscous flow results have demonstrated good correlation with measurements. Later, Tai [9] simulated the airwake flowfield about a LPD ship with rather complex surface geometry representation and obtained reasonably useful steady-state flow results.

The present effort is an extension of previous work on the DD-963 ship airwake [8] to include the effect of ship motion. The ship motion is represented by change of ship attitude in a steady-state flow solution. The same multi-zone, RANS scheme used in Ref. 8 is employed with enhanced grid in the simulation.

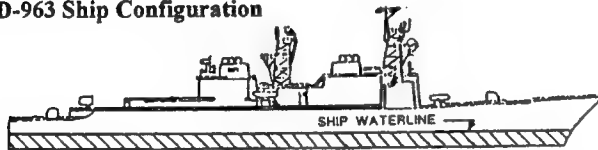
Simulation Method

The simulation method, or the computational method employed includes two main elements: 1) the grid generation and 2) the flow solving. The description of the method therefore will be centered around these two topics, which are of equal importance.

Grid Generation and Grid Topology

A structured, curvilinear, body-conforming grid is generated. First, a surface grid is constructed from the designer's blueprint. The forward and midship superstructures are represented by two numerical blocked structures, followed by a flight deck, and a lower missile deck. The numerical model for the surface grid is derived by using the Tai simplification scheme called the area-volume rule for representing the surface components of a ship [10], see Fig. 1. Computationally, the model consists of a

DD-963 Ship Configuration



Present Computational Model



Fig. 1 - DD-963 ship configuration.



Fig. 2 - Ship model with 2-degree pitch (bow down)

series of rectangular volume blocks in tandem. The ship model is then pitched and/or rolled with respect to the base plane that coincides with the water surface. Pitch was performed about the center of gravity and roll about the ship centerline through the center of gravity. Figure 2 shows the ship attitude (forward portion only) when it pitches two degrees into the water (bow down).

The NASA Ames 3DGRAPE code [11] is used for basic grid generations. A cylindrical grid topology is adopted for its capability to treat a body with a sharp nose. The topology is basically an H-O mixed type, with H-type in the longitudinal plane, and O-type in the crossflow plane. The outer cylindrical surface is set at 2.5 ship lengths from the ship centerline. The most forward plane is set at 1.0 ship length from the bow of the ship, and 3.0 ship lengths for the wake. Assuming symmetry about the centerplane, only half of the ship needs to be modeled in constructing the surface grid. The half model is then unfolded to whole ship in generating the volume grid. This size has been employed in other configurations and proved to be adequate.

An overall coarse grid is generated first by 3DGRAPE using a multi-block procedure. The radial distances are then clustered near the surface and stretched in the outer region for shear layer development. The complete grid has a total of 99x59x57 points with 57 points in the radial direction. This number is larger than those for aircraft because of very low speed freestream involved in the present work. Previous study [12] indicates that when using a compressible flow code at low Mach numbers, an increased mesh density is needed. The details of the grid generation and advantage of the grid topology adapted were discussed in Ref. 8. The grid resolution was enhanced by increasing the number of normal points from previous 51 points to 57 points in the present extension.

Flow Solver

The NASA Langley thin-layer Navier-Stokes code, namely the CFL3D code [13] with multi-zone capability, is used as the basic flow solver. Appropriate modifications to the code for applying specific boundary conditions are implemented. The code is based on a finite volume algorithm with a spatially factored diagonalized, implicit scheme for discretizing the three-dimensional, Reynolds-

averaged Navier-Stokes equations. The upwind-biased differencing technique is used for the inviscid terms and central differencing for all viscous terms. The method is globally second-order accurate and well suited for patched grids in a multizone domain. Details are given by Thomas et al [13].

The code is upgraded with a variety of turbulence models, including the basic Baldwin and Lomax algebraic model [14], the one-equation models [15,16], along with the standard two-equation models, among others. These turbulence models have been carefully examined and evaluated by Rumsey and Vatsa [17]. In the present work, the Baldwin and Lomax model with a Degani-Schiff type modifications [18] is used. The modification determines proper length scales for separated flows.

Boundary Conditions

The boundary conditions for the Navier-Stokes flow solver are: 1) atmospheric boundary layer flow at upstream, 2) atmospheric pressure recovery at downstream, 3) characteristic form of inflow-outflow condition at the cylindrical outer boundary, and 4) viscous nonslip flow at the surface of the ship. The atmospheric boundary layer is approximated by a power-law profile:

$$V/V_\infty = (z/h)^n \quad (1)$$

where h is reference height and n varies from 0.10 to 0.14 [19]. The h is set to be the height of flight deck above the water surface, $h = 0.061$ ship length, and n is set to its mean value of 0.12.

At downstream, instead of imposing the usual freestream recovery, the static atmospheric pressure condition is satisfied along with velocity components being extrapolated from the interior. The use of characteristic form of inflow-outflow boundary condition at the cylindrical outer boundary is known to improve convergence of solution at low speed.

The water surface is assumed to be flat and waveless at which the flow properties in the airwake remain unmixed with the water. The assumption makes the water surface neither viscous nor inviscid. Thus, a reflective boundary is applied. The application in fact is a post-priori after some other attempts of treating the water boundary failed. It turns out to be a good approximation after all except that the vertical velocity component must vanish at the water surface.

Wind Direction Coordinates

It is useful to define the wind direction coordinate system used in the present work. The wind direction is measured with respect to the ship's centerline. With reference to the sketch shown in Fig. 3, the 0-degree indicates a head wind coming over the bow, 90-degree coming over the starboard beam, 180-degree a tail wind coming over the stern, and 270-degree coming over the port beam.

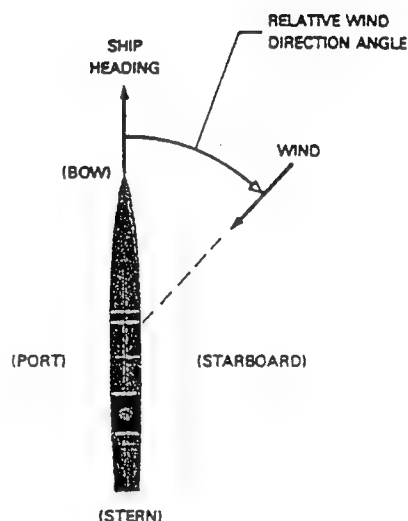


Fig. 3 - Wind direction coordinate system.

Results and Discussion

Numerical results of the flow over a DD-963 ship configuration subject to an atmospheric wind speed of 15.44 m/s (30 knots) and a wind direction of 30 degrees are obtained. The flow condition yields a Reynolds number of 177 million based on the ship length for the full-scale ship. If the ship's beam is used for the Reynolds number basis, the above Reynolds number would have to be reduced approximately by a factor of 10. Whichever the way the Reynolds number is calculated, the flow falls into the turbulent flow range.

All the computations were performed on the Cray facilities at both NASA Ames Research Center and the DoD High Performance Computing facility at the Naval Ocean Center. Converged results were obtained in about 6,000 to 7,000 iterations (time

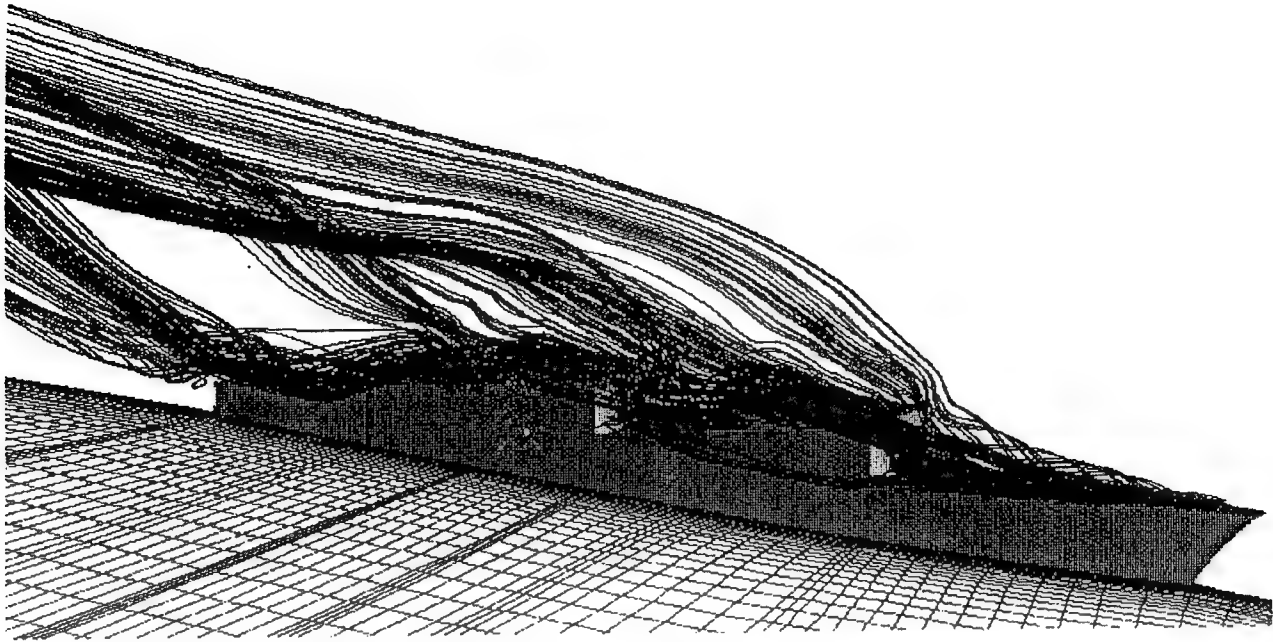


Fig. 4 - Particle trace over DD-963 ship at even keel at 15.44 m/s (30 knots) and wind angle of 30 degrees from starboard. Perspective view.

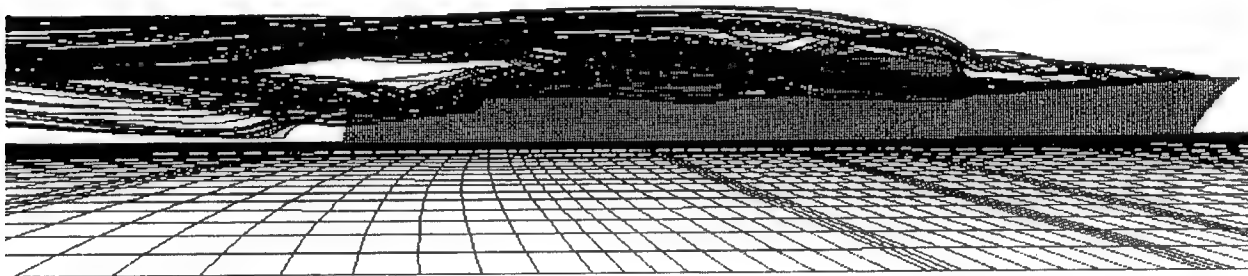


Fig. 5 - Particle trace over DD-963 ship at even keel at 15.44 m/s (30 knots) and wind angle of 30 degrees from starboard. Profile view.

steps) requiring approximately five hours of Cray C-90 CPU time. The large number of iterations is due to the very low freestream Mach number used in the compressible flow solver. The resulting CPU time is reasonable and affordable in today's environment of computer resources.

Particle Trace

Different views of particle trace of the streamlines emanating from various stations on the ship surface are shown in Figs. 4 through 9 for three ship

attitudes considered, namely ship at even keel, ship at 2-degree pitch bow down, and ship at 1-degree pitch and 5-degree roll. These figures all indicate that the flow is mostly separated, with free vortices originated from virtually all sections. There are two types of separation: one due to viscosity and the other due to sharp corners of the volume blocks representing the superstructure. The former is closely influenced by the types of flow involved which is Reynolds number dependent. The latter is purely an inviscid phenomenon, independent of the Reynolds number. Both types of separation create

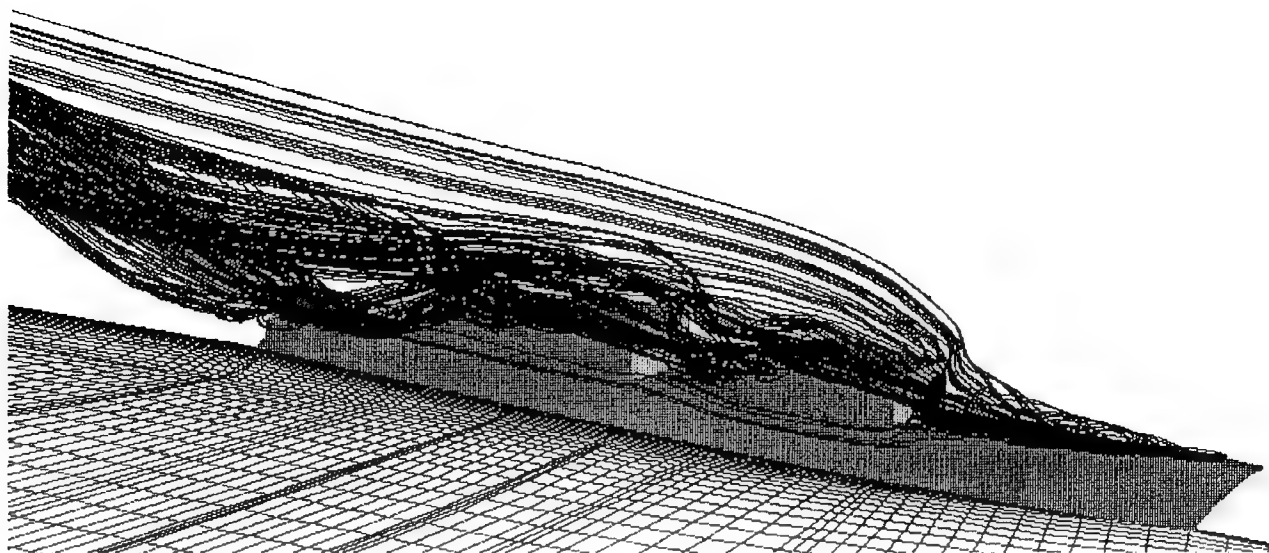


Fig. 6 - Particle trace over DD-963 ship with 2-degree pitch at 15.44 m/s (30 knots) and wind angle of 30 degrees from starboard. Perspective view.

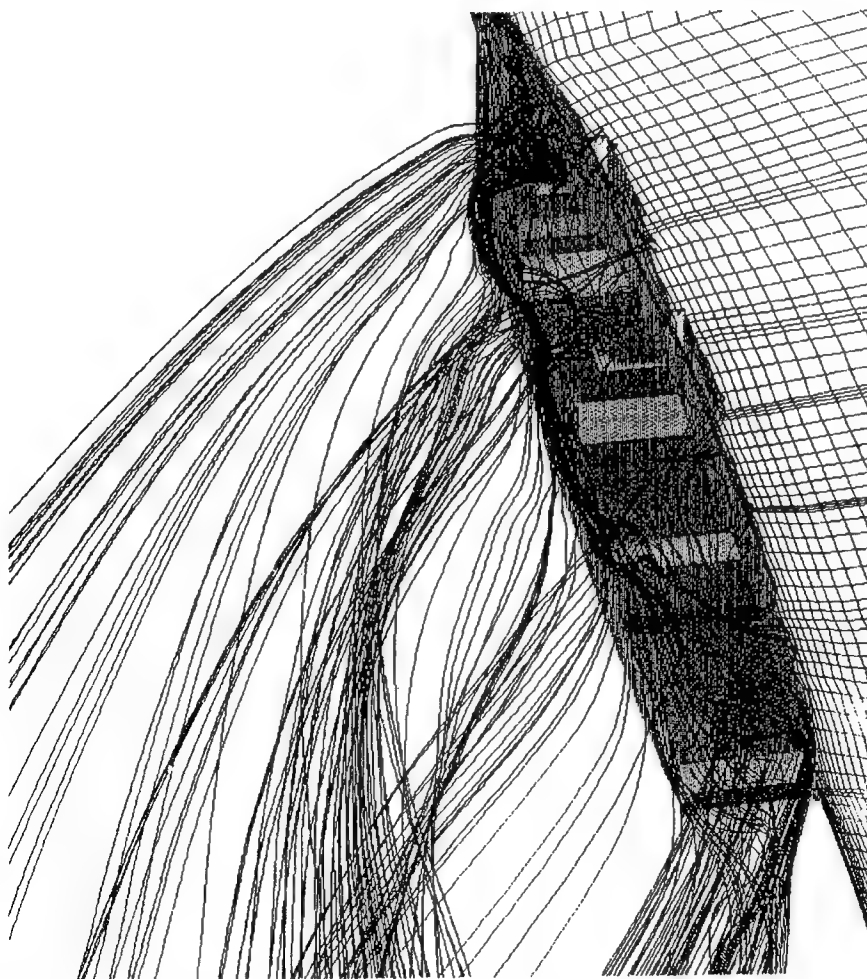


Fig. 7 - Particle trace over DD-963 ship with 2-degree pitch at 15.44 m/s (30 knots) and wind angle of 30 degrees from starboard. Astern view.

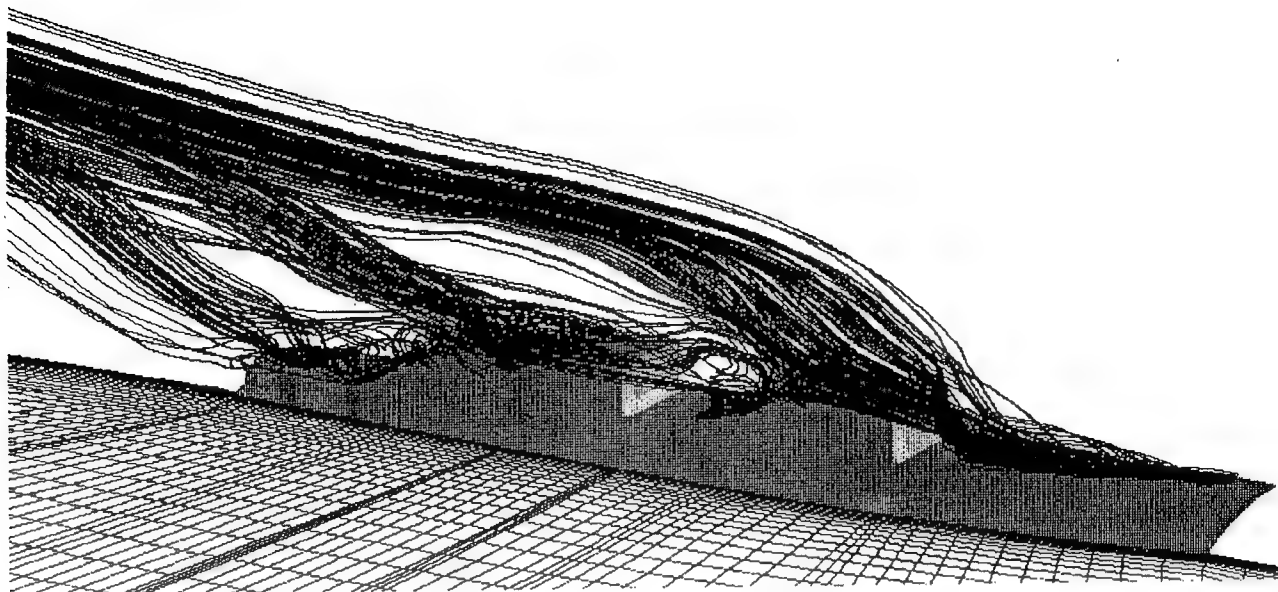


Fig. 8 - Particle trace over DD-963 ship with 1-degree pitch and 5-degree roll at 15.44 m/s (30 knots) and wind angle of 30 degrees from starboard. Perspective view.

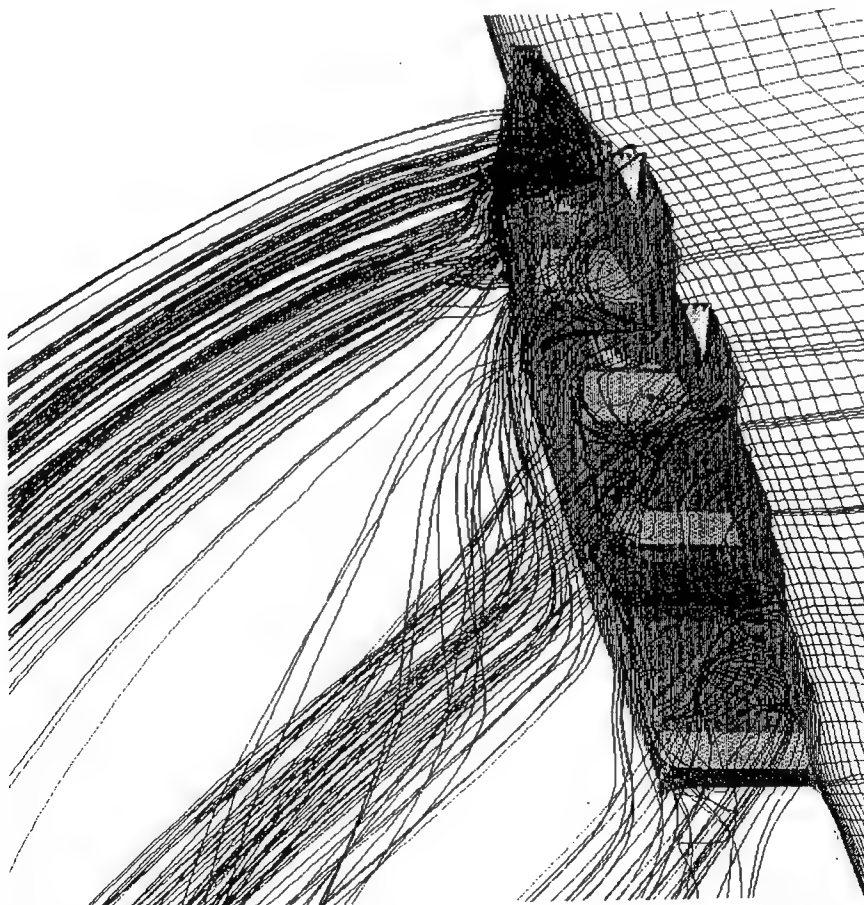


Fig. 9 - Particle trace over DD-963 ship with 1-degree pitch and 5-degree roll at 15.44 m/s (30 knots) and wind angle of 30 degrees from starboard. Astern view.

free vortices as evidenced by streamlines rolling up forward and aft of the superstructure, on the flight deck, and aft of the stern. Figure 4 shows the perspective view of the particle trace and Fig. 5 gives the profile view of the same airwake over the ship at even keel. The profile view helps indicate the actual height of the air burble (airwake) that might be misled by the perspective view. Of course the height, as well as the overall size, of the air burble grows as the flow proceeds downstream. The height can be twice as much as shown here in about three ship lengths away.

The size and shape of the air burble is directly affected by the aforementioned flow mechanisms. By comparing Figs. 4, 6, and 8, it appears that the bow-down pitch of the ship makes instantaneous streamlines from all the region suppressed somewhat; the greater the pitch, the more the suppression. As a result, the ship pitched at two degrees (Fig. 6) has an air burble thinner than that without pitch (Fig. 4), and the thickness of the burble from the ship with 1-degree pitch yields an airwake size somewhere in between. Furthermore, since the 1-degree pitch attitude also includes a 5-degree roll, the instantaneous streamlines at the same time tend to hold down in the transverse direction, see Fig. 8.

Figures 7 and 9 show the astern view of the particle trace of the ship attitudes at 2-degree pitch bow down and 1-degree pitch with 5-degree roll, respectively. Very complex flow patterns over the flight and missile decks are observed. Over the flight deck, except about one-third of the deck in the stern right corner where the flow is exposed to the freestream without influence of the hangar, much of the flow curves inboard and then upwards before proceeding aft. Free vortices are formed from viscous-vortex interactions which are characterized by massive flow separation. The inward flow from the port side might be caused in part by the crossflow reversal to be discussed later. The phenomena was also observed in wind tunnel measurements [5] as well as in the previous results [8] for the case of the ship at even keel.

Velocity Distribution

Figures 10 and 11 depict the contour of the velocity magnitude at the ship's center plane for cases of ship at even-keel attitude and pitched at two degrees bow down. In general, the velocity exhibits

large deficiencies in the regions resembling the backward facing step, such as the mid-ship section aft of the forward superstructure, the flight deck aft of the hangar, the missile deck aft of the flight deck, and finally, the wake region aft of the stern. The flow in these region in fact can be characterized by that of a backward-facing step: massive flow separation involving reversed flow accompanied by circulation. In addition, there are two forward facing steps where the flow may have approached local stagnation. Outside the viscous region, the velocity recovers to the undisturbed stream at a height about half of the ship length.

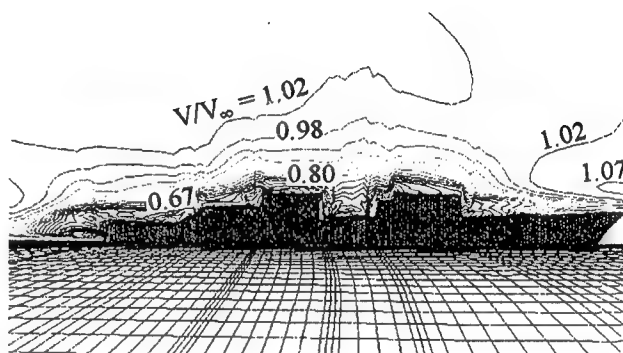


Fig. 10 - Contour of resultant velocity along the center plane. Ship at even keel..

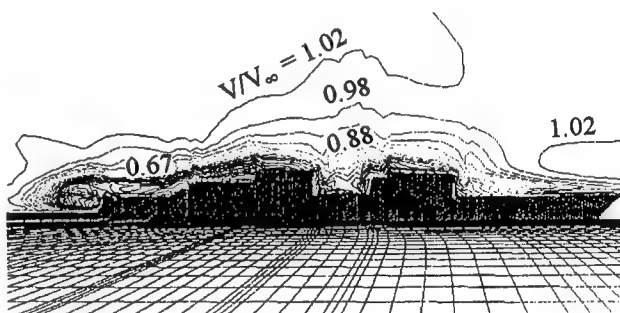


Fig. 11 - Contour of resultant velocity along the center plane. Ship at 2-degree pitch bow down.

The effect of pitching is noted by increased local reversed flow regions for the pitched ship as compared to the ship without pitch. Also, values of local velocities in the separated flow regions generally are slightly lower in the pitched ship case.

The transverse velocity components for the three ship attitudes at a cross section passing through the bulls eye (the center of helicopter landing zone) are shown in Figs. 12, 13, and 14, for cases of the even-keel ship, the ship with a two-degree bow-down pitch, and that with one-degree pitch and 5-degree roll, respectively. The negative values imply velocities follow the projected wind in the transverse direction, i.e., from starboard to port. The shear layer grows from the windward side (starboard side) to the leeward side (port side). Strictly speaking, however, the shear layer grows in both longitudinal and transverse directions, starting from the ship's bow. The sectional distributions help identify the crossflow reversal being significant as indicated by the positive values. These reversed crossflows are responsible for the inward instantaneous streamlines depicted in the particle trace.

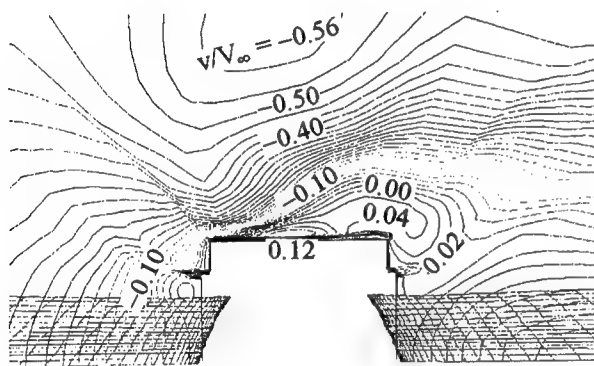


Fig. 12 - Contour of transverse velocity over flight deck. Ship at even keel.

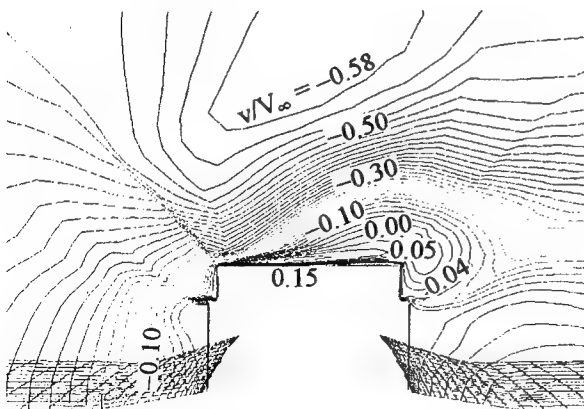


Fig. 13 - Contour of transverse velocity over flight deck. Ship at 2-degree pitch bow down.

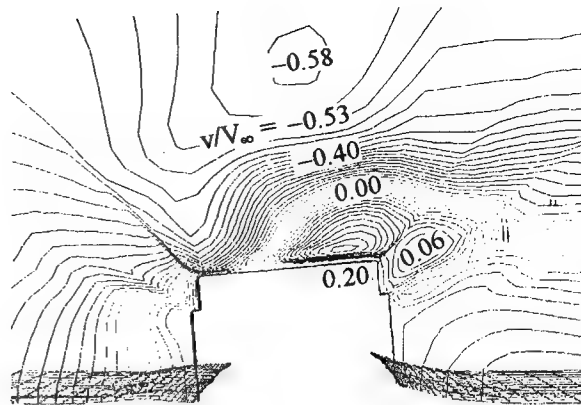


Fig. 14 - Contour of transverse velocity over flight deck. Ship at 1-deg pitch and 5-deg roll.

The pitch of the ship seems to have imposed little influence on the transverse velocity distribution as evidenced by remarkable similarity of the two contours, see Figs. 12 and 13. However, the distribution is significantly altered by the rolling of the ship, see Fig. 14. The crossflow reversal is postponed but further extended to the port side. Since the wind has a direction of 30 degrees from the starboard, the port side in fact serves as a backward-facing step for the transverse component flow. Geometrically, the rolling of the ship raises the height of the port side and therefore increases the size of the local separation region. It is noted that in Figs. 13 and 14 the water surface adjacent to the ship was inclined slightly in order to blend the water surface naturally with the ship hull.

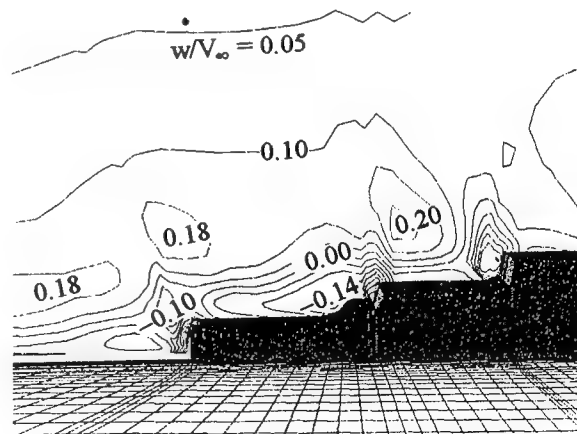


Fig. 15. - Contour of vertical velocity over flight and missile decks, Ship at even keel.

Figure 15 and 16 show the vertical velocity contours over the flight and missile decks for the ship at even keel and the ship pitched at two degrees bow down, respectively. Upward velocities are marked positive. The variation of vertical velocity, especially in the downward direction, is considerably larger in case of the pitched ship than that for the ship at even keel. The trend is consistent with the size of the local separated flow region observed in Figs. 10 and 11.

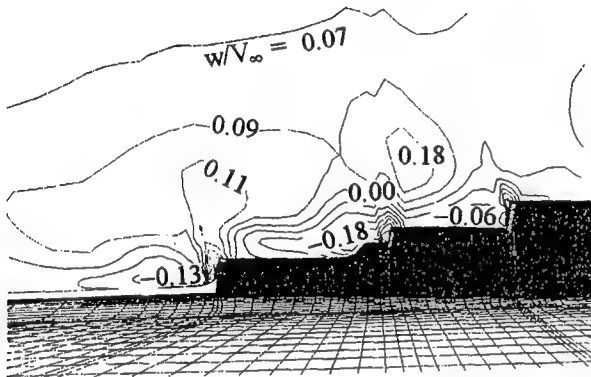


Fig. 16 - Contour of vertical velocity over flight and missile decks, Ship at 2-deg pitch.

Mean Velocities along Flight Path

To evaluate the effect of ship pitch and roll on the helicopter landing operation, the mean velocities along the flight path directly aft the ship stern are examined. Having a 2.5-degree inclination with respect to the flight deck, the flight path starts more than one ship length away from the flight deck and ends at 5.91 meters (15 feet) above the bulls eye (center of flight deck), see Fig. 17. The longitudinal, transverse, and vertical components of mean velocities along the flight path are shown in Figs. 18, 19 and 20, respectively, from data with and without ship motion. The velocities are normalized by the freestream value and the distance is normalized by ship length.



Fig. 17 - Geometry of the flight path having an inclination of 2.5 degrees

In general, the velocity decreases over the flight and missile decks because of the backward-facing-step type wake flow, as discussed previously. The magnitude of the longitudinal velocity is reduced by 50% at a point 5.91 meters above the bulls eye for ship at even keel. For a ship subject to pitch and/or roll, further drop in velocity is observed, see Fig. 18. All three conditions yield an abrupt reduction in velocity right above the stern. This trend holds also for the transverse components if one considers their absolute values, ignoring the negative sign in Fig. 19 which is merely an indication of direction. The effect of ship pitch and roll becomes noticeable about one ship length away from the bulls eye, and is significant about half of ship length away, and turns very severe within the ship's stern.

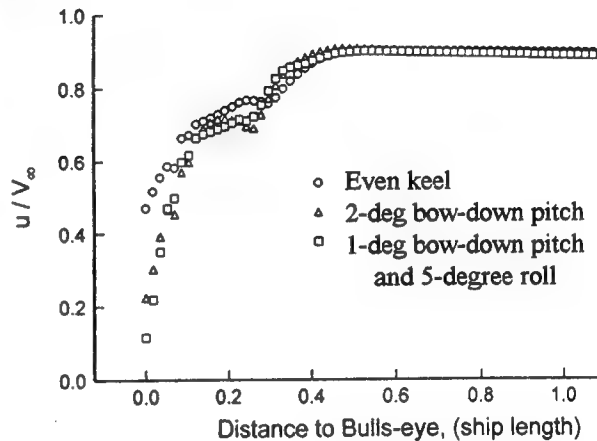


Fig. 18 - Longitudinal velocities along flight path

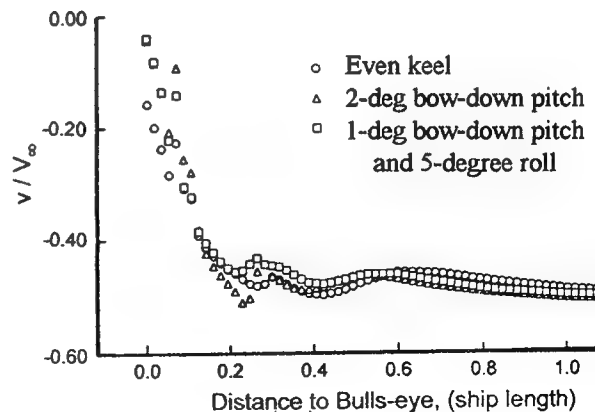


Fig. 19 - Transverse velocities along flight path

For the vertical velocities, the variations are more drastic as shown in Fig. 20. The magnitude of the vertical component varies as much as 10% of the freestream value in both upward and downward direction. For ship at even keel, however, only positive w components are seen for this flight path. The effect of ship motion becomes noticeable about one ship length away from the bulls eye, and intensifies as it approaches the stern. The upward w component reaches its maximum above the stern, and then decrease continuously over the missile deck where it changes direction again. Above the flight deck, the viscous/vortex interaction becomes so intensive that no consistent trend can be found for this fluctuating velocity component.

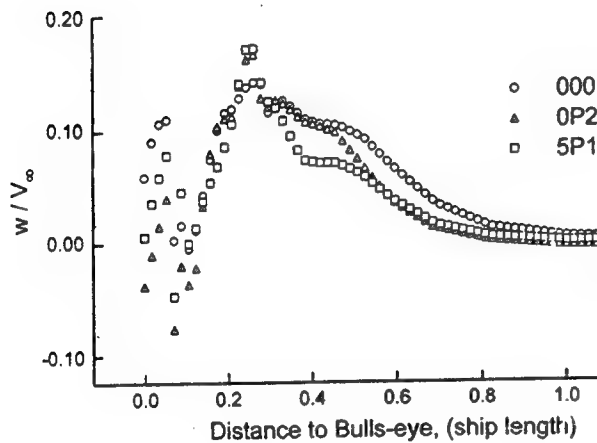


Fig. 20 - Vertical velocities along flight path

Concluding Remarks

The airwake of a DD-963 ship configuration subject to atmospheric wind of 15.44 m/s (30 knots) at wind angle of 30 degrees is simulated by using a multi-zone, thin-layer Navier-Stokes method. The effect of ship motion is implemented by simulating the steady-state flowfield over the basic ship configuration that has pitched and/or rolled with respect to the water surface.

The resulting flow contains regions of massive flow separation along with free vortices. Major flow features including viscous-vortex interactions are captured. Some concluding remarks may be drawn:

1) The ship pitched bow down yields an air burble (airwake) thinner than that of a ship at even keel traveling at the same speed. Similarly, the ship

rolled towards starboard results in a thinner air burble in the transverse direction.

2) The flow behind the superstructure or the hangar has characteristics of a backward-facing step with massive flow separation involving reversed flow accompanied by circulation. The pitched ship has larger local reversed flow regions than those of a ship at even keel.

3) The transverse velocity distribution seems to be little influenced by the pitch angle of the ship, but much affected by ship roll angle. On the other hand, the vertical velocities are significantly influenced by both pitch and roll angles.

Acknowledgment

The present work was supported by the Naval Air Warfare Center, Aircraft Division. The NASA Ames Research Center and DoD High Performance Computing facility provided the Cray CPU time.

References

1. Garnett, T.S. Jr., "Investigation to Study the Aerodynamic Ship Wake Turbulence Generated by a DD963 Destroyer," Report No. NADC-77214-30, Boeing Vertol Company, Philadelphia, PA, Oct 1979.
2. Healey, J.V., "The Prospects for Simulating the Helicopter/Ship Interface," *Naval Engineers Journal*, Vol. 99, No. 2, 1987. pp.45-63.
3. Carico, D., Reddy, W., DiMarzio, C., "Ship Airwake Measurement and Modeling Options for Rotorcraft Applications," AGARD Symposium on Aircraft Ship Operations, Paper 100, Seville, Spain, May 1991.
4. Blanc, T.V. and Larson, R.E., "Superstructure Flow Distortion Corrections for Wind Speed and Direction Measurements Made from NIMITZ Class (CVN68-CVN73) Ships," NRL Report 9215, Naval Research Laboratory, Washington, DC, Oct 1989.
5. Healey, J.V., "The Airwake of a DD-963 Class Destroyer," *Naval Engineers Journal*, Vol. 101, No. 2, 1989. pp. 36-42.
6. Healey, J.V., "A Data Base for Flight in the Wake of a Ship," AIAA Paper 92-0295, Jan 1992.
7. Healey, J.V., "Wind Tunnel Datatape on DD-963 Class Destroyer," Naval Post-Graduate School, Monterey, CA, 1990.
8. Tai, T.C. and Carico, D., "Simulation of DD-963 Ship Airwake by Navier-Stokes Method," AIAA Paper 93-3002, July 1993. Also *Journal of Aircraft*, Vol. 32, No. 6, 1995. pp. 1399-1401.

9. Tai, T.C., "Simulation of LPD Ship Airwake by Navier-Stokes Method," Proceedings of the Sixth Asian Congress of Fluid Mechanics, Vol. II, May 1995, Singapore
10. Tai, T.C., "A Single Structured Grid for Complex Ship Geometry," in Numerical Grid Generation in Computational Fluid Dynamics and Related Fields, Edited by N.P. Weatherill, Pineridge Press Limited, Swansea, U.K. 1994.
11. Sorenson, R.L., "The 3DGRAPE Book: Theory, Users' Manual, Examples," NASA Technical Memorandum 102224, July 1989.
12. Volpe, G., "On the Use and Accuracy of Compressible Flow Codes at Low Mach Numbers," AIAA Paper 91-1662, presented at AIAA 22nd Fluid Dynamics, Plasma Dynamics & Lasers Conference, Honolulu, HI, June 1991.
13. Thomas, J.L., Krist, S.T., and Anderson, W.K., "Navier-Stokes Computations of Vortical Flows over Low-Aspect-Ratio Wings," AIAA Journal, Vol. 28, No. 2, 1990. pp. 205-212.
14. Baldwin, B.S., and Lomax, H., "Thin-Layer Approximation and Algebraic Model for Separated Turbulent Flows," AIAA Paper 78-0257, Jan 1978.
15. Baldwin, B. and Barth, T., "A One-Equation Turbulent Transport Model for High Reynolds Number Wall-Bounded Flows," NASA TM-102847, 1990.
16. Spalart, P., and Allmaras, S., "A One-Equation Turbulence Model for Aerodynamic Flows," AIAA Paper 92-0439, Jan 1992.
17. Rumsey, C.L., and Vatsa, V.N., "A comparison of the Predictive Capabilities of Several Turbulence Models Using Upwind and Central-Difference Computer Codes," AIAA Paper 93-0192, Reno, NV, Jan 1993.
18. Degani, D., and Schiff, L.B., "Computation of Supersonic Viscous Flows Around Pointed Bodies at Large Incidence," AIAA Paper 83-0034, 1983.
19. Plate, E.J., Engineering Meteorology, Elsevier Scientific Publishing Co., Amsterdam, 1982, pp. 527-569.

Large-Eddy Simulation of Decaying Free-Surface Turbulence with Dynamic Mixed Subgrid-Scale Models

M. Salvetti (Università di Pisa, Italy),

Y. Zang, R. Street (Stanford University, USA),

S. Banerjee (University of California at Santa Barbara, USA)

Abstract

This paper describes the large eddy simulation of the decaying turbulence in an open channel, using the dynamic two-parameter model of Salvetti and Banerjee [Phys. of Fluids, 7, 1995] and the finite volume Navier-Stokes equations solver of Zang, Street and Koseff [J. Comp. Phys., 114, 1994]. A direct numerical simulation of this flow conducted by Pan and Banerjee [Phys. of Fluids, 7, 1995] showed that near the free surface turbulence has a quasi-two-dimensional behavior. Moreover, the quasi-two-dimensional region increases in thickness with the decay time, although the structure remains three dimensional in the central regions of the flow. The objective of this work is to study the behavior of the subgrid-scale model in the neighborhood of the free surface, and, in particular, to demonstrate the ability of the two-parameter model to handle the anisotropic nature of the flow.

1 Introduction

Many environmental flows, e.g., interactions between the atmosphere and the ocean or the persistent signature of vessel wakes, are strongly influenced by free-surface turbulence. Due to difficulties in measurement and simulation, the amount of information presently available on the structure of turbulence near the interfaces is far from exhaustive. Direct numerical simulation (DNS) is restricted to low Reynolds number flows and simple geometries, because of the need to resolve all the spatial scales of turbulence. On the other hand, large eddy simulation (LES), in which only the large scale motion is computed and the subgrid scales are modeled, provides an effective tool for tackling this type of flow. The critical point in LES is to accurately capture the

effects of the unresolved subgrid-scale (SGS) motion.

The dynamic model (DSM) proposed by Germano *et al.* (1) has been successfully applied in several LES computations. In the DSM the base model is the Smagorinsky eddy-viscosity model, widely used in earlier LES, in which the coefficient is computed using the information from the smallest resolved scales. In spite of its many desirable features, the DSM has still some aspects to be improved, related to the use of the Smagorinsky model. The most serious problem in LES computations with the DSM is the presence of large fluctuations of the model coefficient, arising when it is computed locally, which often lead to numerical instability.

Zang *et al.* (2) proposed a dynamic mixed model (DMM) using an extension (the modified Leonard term) of the Bardina scale-similarity model, together with the dynamic model with a Smagorinsky kernel. Salvetti and Banerjee (3) improved upon that model and employed two dynamic coefficients in constructing their dynamic two-parameter model (DTM). They showed that dynamic coefficients could be computed for each element of the model, i.e., for the modified Leonard term and for the Smagorinsky term. The dynamic two-parameter model was evaluated through the use of a priori tests. The dynamic-mixed model was tested by using it in the LES of a recirculating, lid-driven flow in a cavity (2). The results showed that these models combine the essential features of energy dissipation and energy backscatter, needed for modeling SGS effects.

The main objective of this work is to investigate the behavior of these SGS models in the large eddy simulation of free-surface turbulent flows. To this end, we simulate the decaying free-surface turbulence in an open channel. Starting from the statistically steady state computed in the direct simulation of Pan and Banerjee (4), we simulate a case where the no-slip boundary condition on the bot-

tom solid wall is changed to a free-slip condition. By this changing of boundary conditions, the mechanism of turbulence generation is eliminated and the flow begins to decay. This problem is of interest to understand how the free-surface turbulence evolves far from the region of turbulence generation, e.g., in the wake of a vessel. The direct simulation by Pap and Banerjee showed that, near the free surface, the structure of turbulence is quasi two-dimensional, with the quasi-two-dimensional-region increasing in thickness in the decaying process. Thus, this test case is particularly severe for SGS models, which have a three-dimensional structure. The point at issue in this work is whether large eddy simulation, using SGS dynamic mixed models and, in particular, the dynamic two-parameter model, may reproduce the nearly two-dimensional nature of the turbulence near the free surface.

2 Mathematical formulation and numerical method

We now briefly summarize the mathematical formulation of the dynamic-mixed models used in the present simulations. More details can be found in (2) and (3).

For the incompressible and constant density flow considered here, the basic governing equations are the grid-filtered Navier-Stokes and continuity equations (omitted here for sake of brevity), in which the effect of the unresolved subgrid scales is represented by the SGS stress tensor:

$$\tau_{ij} = \overline{u_i u_j} - \overline{u_i} \overline{u_j} \quad (1)$$

The overbar denotes a grid-filtered variable.

In the dynamic two-parameter model, the SGS stress tensor is modeled as follows (3):

$$\tau_{ij} - \frac{\delta_{ij}}{3} \tau_{kk} = -2C \overline{\Delta}^2 |\overline{S}| \overline{S}_{ij} + K (L_{ij}^m - \frac{\delta_{ij}}{3} L_{kk}^m) \quad (2)$$

where: $\overline{S}_{ij} = \frac{1}{2}(\frac{\partial \overline{u_i}}{\partial x_j} + \frac{\partial \overline{u_j}}{\partial x_i})$ is the resolved strain rate tensor, $|\overline{S}| = (2\overline{S}_{ij}\overline{S}_{ij})^{1/2}$, and $L_{ij}^m = \overline{\overline{u_i} \overline{u_j}} - \overline{u_i} \overline{u_j}$ is the "modified Leonard stress" (5). It represents the resolved part of the SGS stress. The grid

filter width ($\overline{\Delta}$) is defined as:

$$\overline{\Delta}^3 = \overline{\Delta}_1 \overline{\Delta}_2 \overline{\Delta}_3$$

where $\overline{\Delta}_i$ is the grid spacing in i direction. The two unknown coefficients C and K in (2) are computed dynamically in the way described below.

Following the procedure of Germano *et al.* (1), a test-filter, denoted by a hat, is applied to the governing equations; the sub-test scale stress tensor is then obtained:

$$T_{ij} = \widehat{\overline{u_i u_j}} - \widehat{\overline{u_i}} \widehat{\overline{u_j}} \quad (3)$$

It is modeled in the same manner as the SGS stress tensor:

$$T_{ij} - \frac{\delta_{ij}}{3} T_{kk} = -2C \widehat{\Delta}^2 |\widehat{S}| \widehat{S}_{ij} + K (L_{ij}^t - \frac{\delta_{ij}}{3} L_{kk}^t) \quad (4)$$

where: $\widehat{S}_{ij} = \frac{1}{2}(\frac{\partial \widehat{\overline{u_i}}}{\partial x_j} + \frac{\partial \widehat{\overline{u_j}}}{\partial x_i})$, $|\widehat{S}| = (2\widehat{S}_{ij}\widehat{S}_{ij})^{1/2}$ and $L_{ij}^t = \widehat{\overline{\overline{u_i} \overline{u_j}}} - \widehat{\overline{u_i}} \widehat{\overline{u_j}}$ is the modified Leonard term for the test-scale filter (2) (3). The width of the test filter ($\widehat{\Delta}$) is assumed to be larger than that of the grid filter. The ratio between the width of the test and grid filters is denoted by α ($=2$ here as in most applications in the literature).

Using the Germano identity (1) and equations (2) and (4), we obtain:

$$\mathcal{L}_{ij} - \frac{\delta_{ij}}{3} \mathcal{L}_{kk} = -2C \overline{\Delta}^2 M_{ij} + K (H_{ij} - \frac{\delta_{ij}}{3} H_{kk}) \quad (5)$$

where: $\mathcal{L}_{ij} = \widehat{\overline{\overline{u_i} \overline{u_j}}} - \widehat{\overline{u_i}} \widehat{\overline{u_j}}$, $M_{ij} = \alpha^2 |\widehat{S}| \widehat{S}_{ij} - |\overline{S}| \overline{S}_{ij}$ and $H_{ij} = \widehat{\overline{\overline{u_i} \overline{u_j}}} - \widehat{\overline{u_i}} \widehat{\overline{u_j}}$. Using a least square approach as suggested by Lilly (6), the unknown coefficients are evaluated by setting $\partial Q / \partial C = 0$ and $\partial Q / \partial K = 0$, where Q is the square of the error in (5).

The expression of the SGS stress tensor in the DMM is given by Eq. (2) in which K is set equal to unity (2). Following the same dynamic procedure as previously, the model parameter C can be obtained by setting $\partial Q / \partial C = 0$, Q being the square of the error in (5) with $K = 1$.

For reference, the dynamic subgrid-scale model (DSM) of Germano et al. (1) is obtained by setting $K = 0$ above and the model parameter C can be computed by setting $\partial Q/\partial C = 0$, Q being the square of the error in (5) with $K = 0$.

For our computations, the governing equations are transformed into a general curvilinear coordinate system and discretized on a non-staggered grid using a Finite-Volume approach. A fractional step method is employed and the pressure Poisson equation is solved with a multigrid method. Time marching is semi-implicit with the formal accuracy being second order in both space and time. The details of the numerical method can be found in (7) and (8).

3 Results and discussion

The simulation starts from the statistically steady pressure-driven flow between a no-slip wall and a rigid free-slip surface computed in Ref. (4). The streamwise direction is denoted by x_1 , the spanwise direction by x_2 , and the normal direction by x_3 . The velocity components in these directions are given by u_1, u_2 and u_3 . All quantities are nondimensionalized with the channel half-depth h and the effective shear velocity u_e , defined as (4):

$$u_e = \sqrt{\frac{h}{\rho} \left| \frac{dP}{dx_1} \right|}, \quad (6)$$

where $\left| \frac{dP}{dx_1} \right|$ is the magnitude of the mean pressure gradient which drives the flow and ρ is the fluid density. Thus, the effective Reynolds number, equal to 60.4, is defined as:

$$Re = \frac{u_e h}{\nu}, \quad (7)$$

where ν is the kinematic viscosity. A nondimensional time is also defined as: $\bar{t} = \frac{t u_e}{h}$. In the following, for simplicity, t denotes the nondimensional time. Periodical conditions are applied in the streamwise and spanwise directions. The dimensions of the computational box are $L_1 = 4\pi$, $L_2 = 2\pi$ and $L_3 = 2$, in the streamwise, spanwise and normal directions, respectively.

In the direct numerical simulation of Pan and Banerjee, 64 Fourier modes were used in the

streamwise and spanwise directions and 65 Chebyshev modes in the wall-normal direction. The details of the direct simulation can be found in Ref. (4). For our computations, a grid of $32 \times 32 \times 32$ points was used. The grid is non-uniform in the normal direction to cluster the points near the wall and the free-surface, but is uniform in the streamwise and spanwise directions.

At the beginning of the simulation the no-slip boundary condition on the bottom wall is changed to a free-slip boundary condition and at the same time the pressure gradient which drives the flow is turned off. This change of boundary conditions eliminates turbulence generation and the flow begins to decay.

Large-eddy simulations have been carried out with the DSM, DMM and DTM. The results showed that both the DMM and the DTM are able to reproduce the features of the decay process observed in the DNS and that they have similar mechanisms of interaction between subgrid and resolved scales. Nevertheless, the addition of the second model coefficient in the DTM improved the agreement with the direct simulation. Therefore, we will present the results of a comparison of the DTM and DMM in (9). Here, we present the results obtained with the DSM and compare these to the DTM results, in order to show the significant differences in the modelling of the interactions between subgrid and resolved scales and their effects on the decay process.

3.1 The decay process

The time evolution of the plane averaged streamwise velocity, obtained respectively with DSM and DTM, is shown in Figs. 1a and 1b (here the wall is at $x_3=0$ and the free surface at $x_3=2$). Once the bottom boundary condition is changed to free slip ($t=0$), the velocity profile decays and tends to become essentially uniform, as found also in Ref. (4). A slight delay is observed in the time evolution of the profiles obtained with the DTM compared to those shown in Fig. 6a of Ref. (4), but the trend is the same, and, within 6 nondimensional time units, the velocity profile is nearly flat. The delay is more noticeable with the DSM.

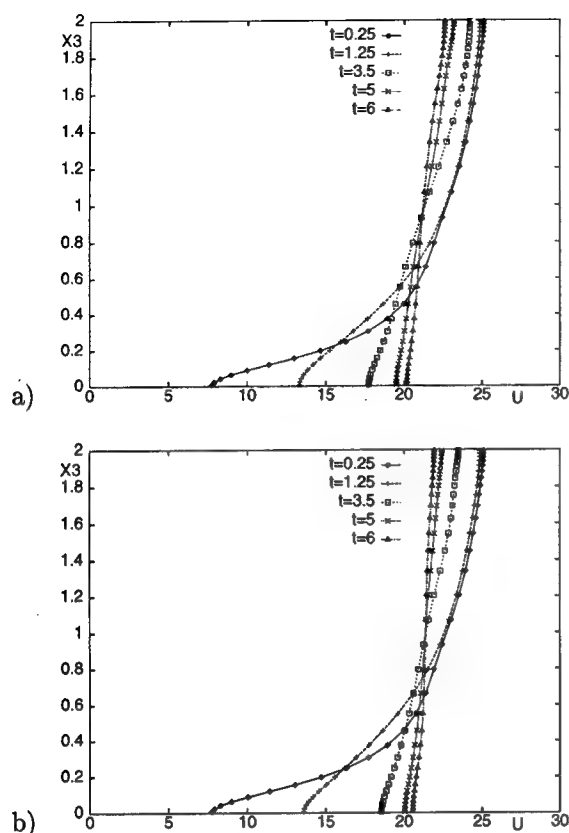


Figure 1: Time evolution of the plane-averaged streamwise velocity. a) DSM b) DTM

In Fig. 2a the r.m.s. of the three velocity components at the initial statistically-steady state are plotted with respect to the depth of the channel. The fluctuating velocity component in the i direction is defined as: $u'_i = u_i - \langle u_i \rangle$, where $\langle u_i \rangle$ is the average on the homogeneous horizontal planes. A high peak in the r.m.s of streamwise velocity is observed near the wall, and is related to the quasi-streamwise structures typical of this region (4).

The r.m.s. values obtained with the DSM and the DTM are shown in Figs. 2b and 2c, which correspond to $t=3.5$ and $t=7$. As expected, since the mechanisms of turbulence generation are turned off by the change in boundary conditions at the wall, the r.m.s. values of all the velocity components decrease during the decay process. Moreover, the r.m.s. distribution of the streamwise and spanwise components

tends to become uniform along the channel depth.

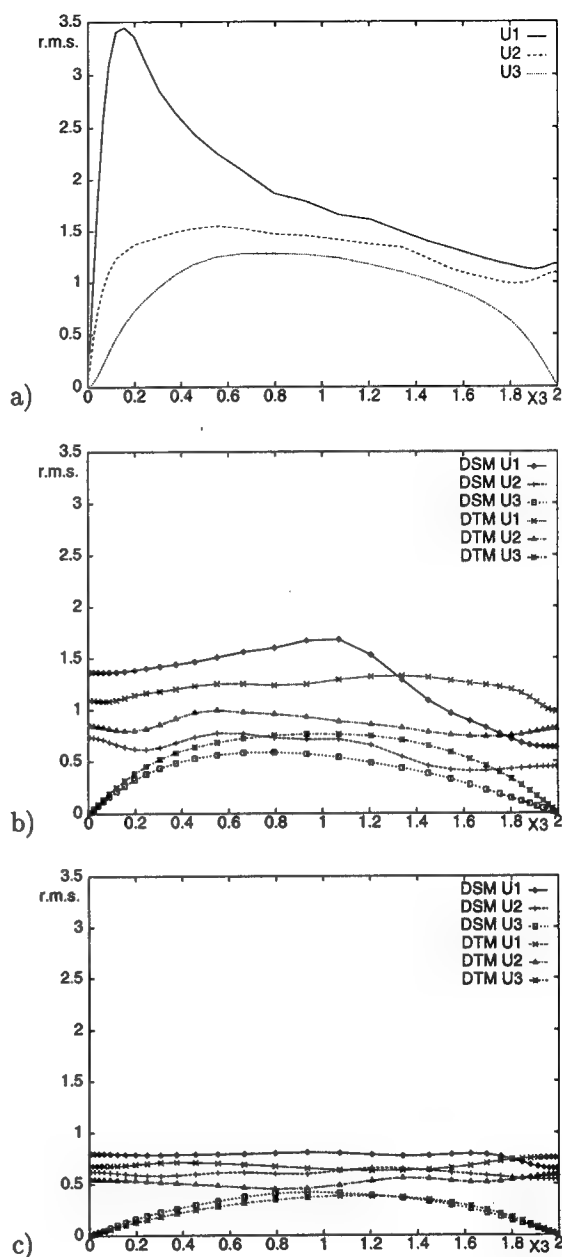


Figure 2: R.m.s. of the velocity components. a) $t=0$ b) $t=3.5$ c) $t=7$.

For the DSM a noticeable variation of the r.m.s of

u_1 along the channel depth is still present at $t=3.5$, indicating a delay in the decay process, as already observed from Fig. 1a. Also, at $t=3.5$ the r.m.s. of all the velocity components obtained with the DSM in the region near the free surface are noticeably lower than those obtained with the DTM. This is still true at $t=7$, but the differences are less important. Thus the DSM seems to be considerably more dissipative near the free surface than the DTM, especially in the first phase of the decay process.

The signature of the large structures found in the DNS at the same nondimensional time (Figure 7d of Ref. (4)) are present in the flow obtained with the DTM. Some vortices and small scales are missing in Fig. 4, but this is caused by the filtered velocity field of the large eddy simulation and it is consistent with the analysis of filtering effects in Fig. 17 of Ref. (4). The instantaneous streamlines obtained at the same nondimensional time with the DSM (Fig. 5) are completely different, indicating again that the SGS modelling noticeably affects the decay process.

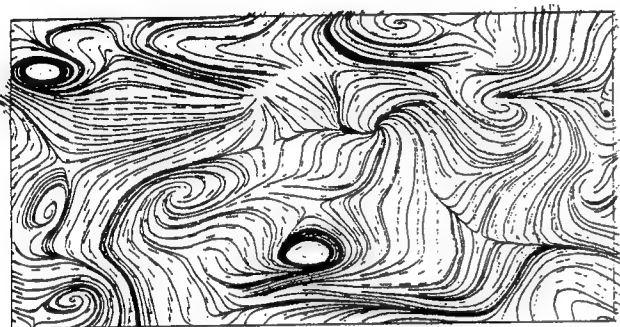


Figure 3: Streamlines at $t=0.25$. DTM

In Fig. 3 the instantaneous streamlines of the fluctuating velocity field obtained with the DTM are shown at the beginning of the simulation ($t=0.25$). The typical structures of fully developed free surface turbulence, identified in Ref. (4), can be observed: upwellings, corresponding to the zones where streamlines fan out, attached vortices, mostly at the edges of upwellings, and downdrafts, corresponding to the stagnation lines (in the right lower part, for example). At this early stage of the simulation, the instantaneous streamlines obtained with the DSM are almost identical than those obtained with the DTM in Fig. 3, because the differences in the SGS models have not yet had enough time to manifest themselves. As observed in Ref. (4), since turbulence generation is suppressed, the upwellings and downdrafts become less pronounced with increasing time, as shown for instance by the instantaneous streamlines obtained by DTM at $t=7.17$ in Fig. 4.

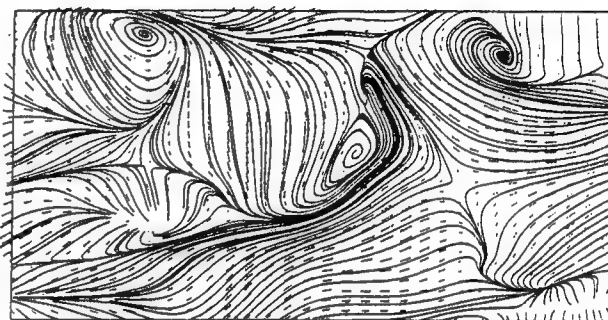


Figure 4: Streamlines at $t=7.17$. DTM

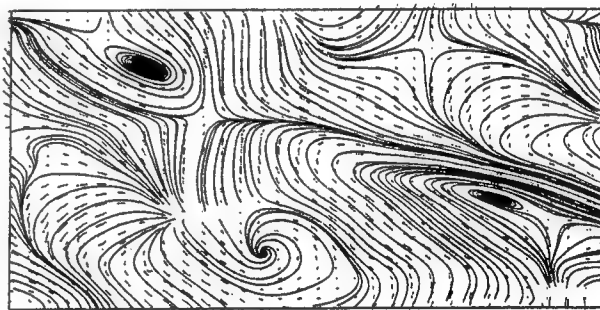


Figure 5: Streamlines at $t=7.17$. DSM

Figs. 6a and 6b show the evolution during the decay process of the one-dimensional, streamwise and spanwise energy spectra for the surface-parallel

velocity components at the free surface obtained with the DTM. Good agreement is obtained with the DNS (Fig. 10 of Ref. (4)) and, in particular, the reverse cascade of energy from high to low wave numbers observed at the free surface in the DNS seems to be properly taken into account in the large eddy simulation with the DTM. Indeed, as in Ref. (4), the spectra change primarily by steepening at large wave numbers from the initial slope of $k^{-3.5}$ to $k^{-9.5}$ and $k^{-5.5}$ for spanwise and streamwise spectra, while low wave numbers decay much more slowly. As pointed out also by Pan and Banerjee, this behavior is typical of decaying two-dimensional turbulence.

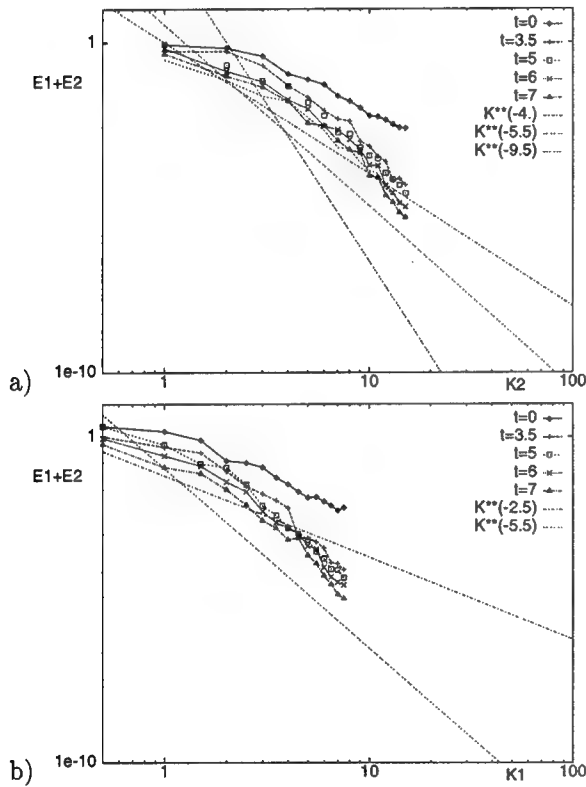


Figure 6: Time evolution of one-dimensional energy spectra $E_1 + E_2$ of the surface-parallel velocity components obtained with the DTM: a) spanwise; b) streamwise.

Pan and Banerjee also found that at $t=3.5$ the high wave-number spectra at various depths from

the free surface become identical and that at low wave numbers the $k^{-5/3}$ region propagates downwards during the decay, i.e., the quasi-two-dimensional region thickens.

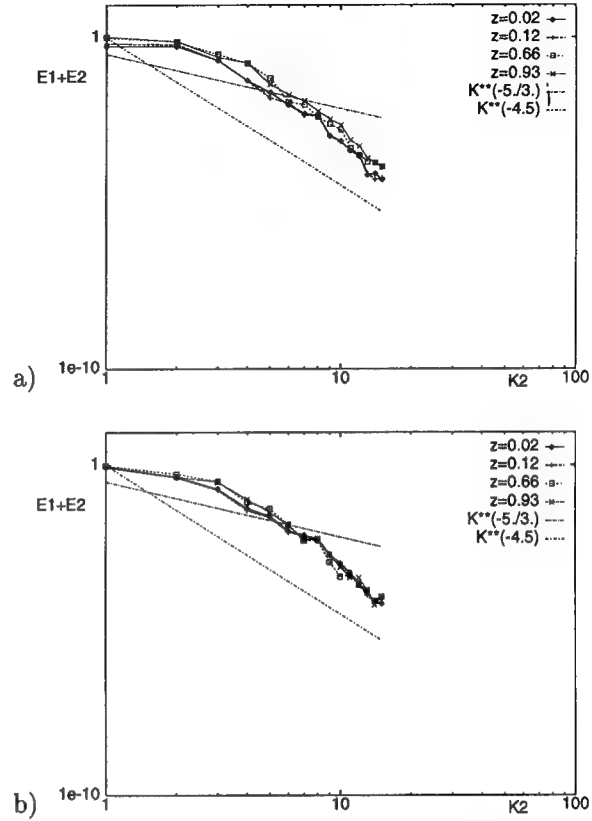


Figure 7: Spanwise one-dimensional energy spectra $E_1 + E_2$ of the surface-parallel velocity components obtained with the DTM on different horizontal planes, with z measured down from the free surface: a) $t=3.5$; b) $t=4$.

In Figs. 7a and 7b, the spanwise one-dimensional energy spectra of the surface-parallel velocity components obtained with the DTM on different horizontal planes are shown, at $t=3.5$ and $t=4$. The distance from the free surface is denoted by z . At $t=3.5$ differences can be observed in the high wave numbers portion of the spectra on the different planes, but they have disappeared at $t=4$. Moreover, at

$t=4$ a slope of $k^{-5/3}$ is found in the low wave number part of the spectra, also on the planes near the center of the channel. As concerns direction-related aspects of the energy spectra, Fig. 8 shows the spanwise one-dimensional energy spectra of the surface-normal velocity component, obtained with the DTM on different horizontal planes at $t=4$. As in the DNS, the spectra for the surface-normal velocity undergo little change in slope compared to the steady state (Fig. 12a in Ref. (4)), except for decay. Thus, even with a slight delay, already pointed out in the analysis of Fig. 1b, the large eddy simulation with the DTM reproduces the spectral features of the decay process observed in the DNS in Ref. (4).

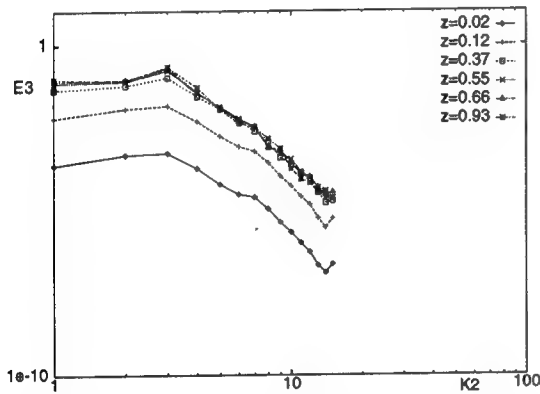


Figure 8: Spanwise one-dimensional energy spectra E_3 of the surface-normal velocity at $t=4$.

In Figs. 9a and 9b the time evolution of the one-dimensional energy spectra of the surface-parallel velocity components obtained with the DSM is shown. Some discrepancies from the DNS can be observed in the decay of the energy spectra. First, the high wave-numbers portion of the streamwise spectrum, with increasing time, takes a slope of $k^{-9.5}$ instead of $k^{-5.5}$. Moreover, for both spanwise and streamwise spectra, a rapid decrease of energy for all the wave-numbers is observed in the first phase of the decay process at $t = 3.5$ and the slope of the high wave-numbers portion steepens to $k^{-9.5}$ (see Fig. 10a). Between $t=3.5$ and $t=5$ (Fig. 10b) the energy contained in all the wave numbers increases again and the shape of the spectrum does not change.

Finally, as time increases, high wave numbers continue to decay faster than low wave numbers and the slope of the intermediate portion of spectrum changes. On the contrary, in the DNS and in the large eddy simulation with the DTM a progressive decay and change in slope of the energy spectra is observed.

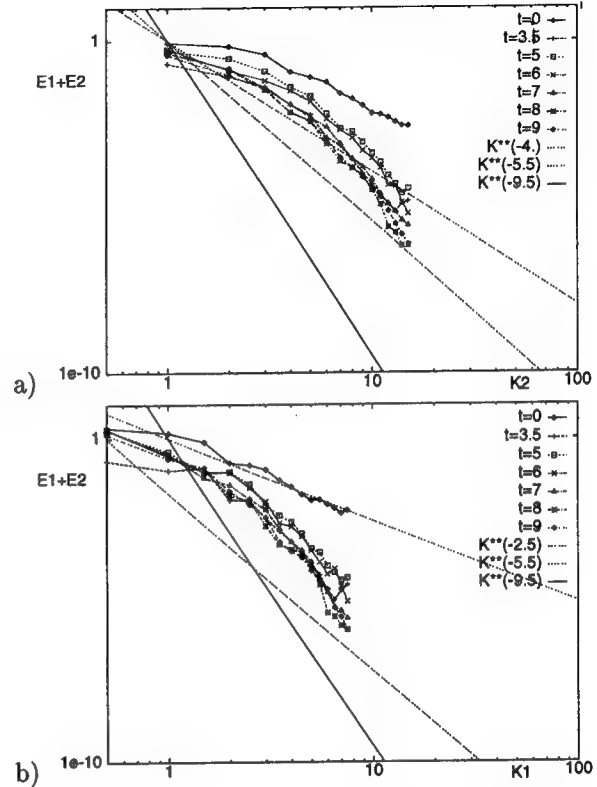


Figure 9: Time evolution of one-dimensional energy spectra of the surface-parallel velocity components obtained with the DSM: a) spanwise; b) streamwise.

Moreover, the spanwise energy spectra in Fig. 11, obtained with the DSM at $t=10$ on different normal planes, show that even very late in the simulation the high wave-numbers portion is different on different planes and that, on planes close to the center of the channel, the low wave-numbers portion does not take the $k^{-5/3}$ slope.

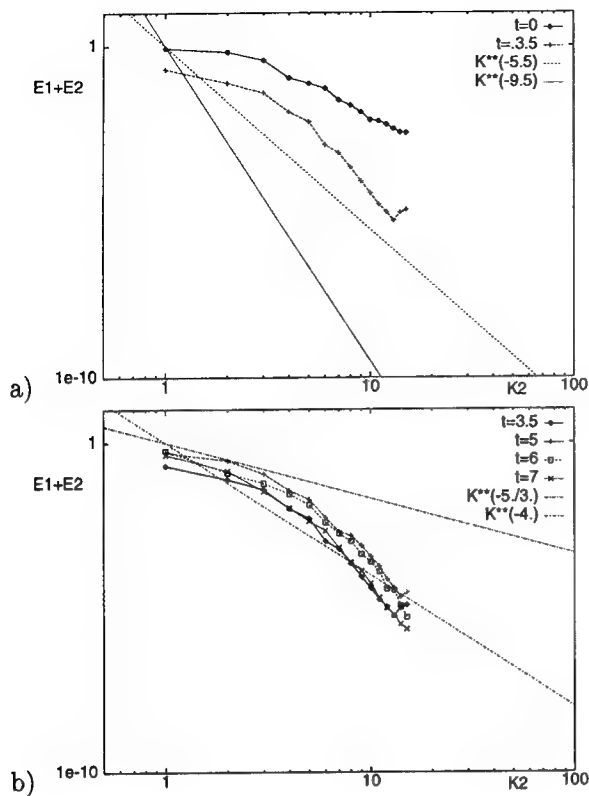


Figure 10: Time evolution of spanwise energy spectrum of the surface-parallel velocity components obtained with the DSM: a) $t=0-3.5$; b) $t=3.5-7$.

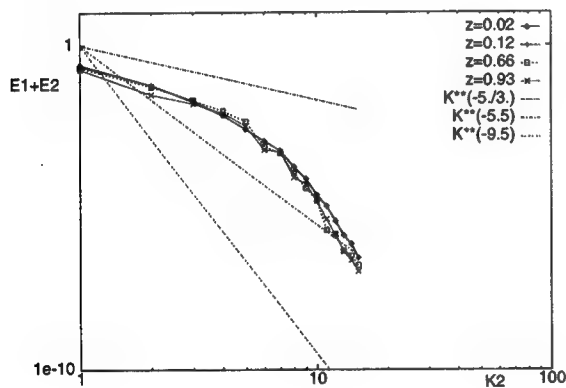


Figure 11: Spanwise one-dimensional energy spectra of the surface-parallel velocity components obtained with the DSM on different horizontal planes at $t=10$.

In order to investigate the effects of grid refinement on the decay process, the same large eddy simulation has been carried out on a finer grid of $64 \times 64 \times 64$ points with the DTM. As in the previous case, the grid is non uniform in normal direction and the points are clustered near the wall and the free surface. Incidentally, even if the number of computational points is equal to the number of modes used in the direct numerical simulation in Ref. (4), the resolution obtained with a second-order accurate Finite-Volume simulation is much lower than that of a Fourier-Chebyshev spectral method, especially in the normal direction near the wall and the free surface.

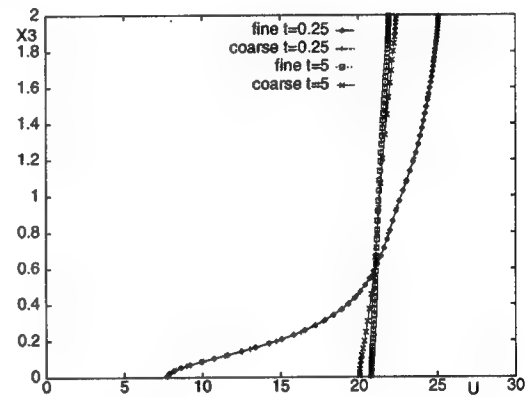


Figure 12: Effects of grid refinement on the time evolution of mean streamwise velocity. DTM.

At the beginning of the simulation ($t=0.25$) the profile of mean streamwise velocity is the same as that obtained previously on the coarser grid (Fig. 12) and then a slight delay is observed with respect to the DNS. Afterwards, the time evolution of the mean velocity profile obtained with the finer grid is faster and closer to the DNS (see for example $t=5$ in Fig. 12). An acceleration of the decay process is confirmed by the r.m.s. of the three velocity components on horizontal planes, plotted in Fig. 13 for $t=5$: for all the components, the r.m.s. obtained with the finer grid is noticeably lower than that with the coarser grid. This acceleration is also confirmed by the comparison of the one-dimensional energy spectra of the surface-parallel velocity components obtained with the two different grids (Fig. 14a and 14b) at $t=5$.

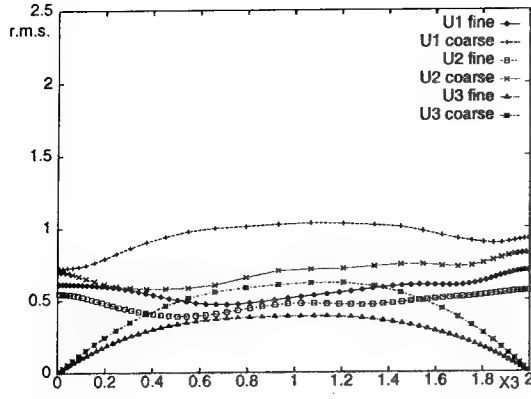


Fig 13: Effects of grid refinement on the r.m.s of the velocity components at $t=5$. DTM

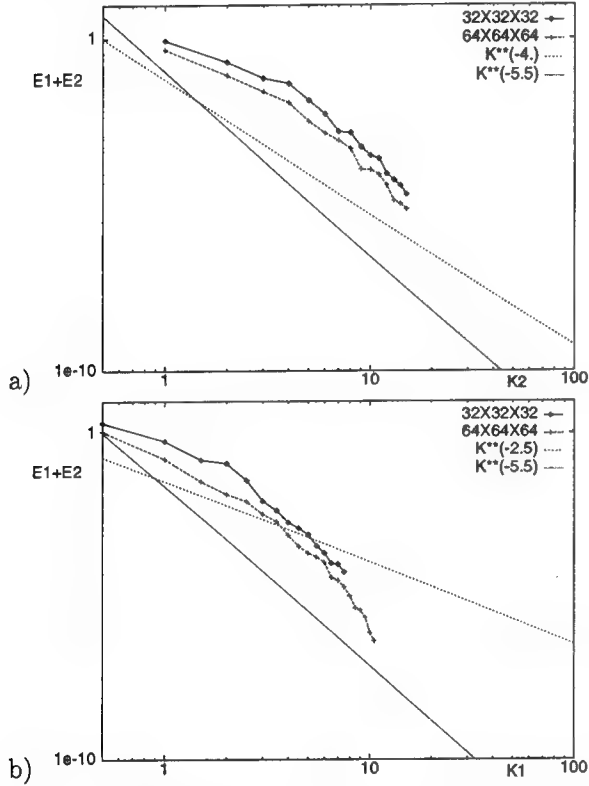


Fig 14: One-dimensional energy spectra of the surface-parallel velocity components obtained with the DTM on two different grids at $t=5$: a) spanwise; b) streamwise.

Indeed, the energy contained both at low and high wave numbers in the streamwise and spanwise spec-

tra is less with the finer grid than with the coarser grid. Nevertheless, the shape of the spectra is practically the same and, hence, the basic mechanisms of the decay process are not affected by the grid resolution.

3.2 Subgrid scale energy transfer and model parameters

In the previous Section we pointed out that the SGS modelling strongly affects the basic features of the decay process at the free surface. In order to investigate more in detail the behavior of the subgrid model during the decay process, we examine now the energy transfer between resolved and subgrid scales, obtained in the simulations with the DSM and the DTM. The energy transfer between resolved and subgrid scales is represented by the "subgrid-scale dissipation", $\varepsilon_{sgs} = \tau_{ij} \bar{S}_{ij}$. If this quantity is negative, the subgrid scales remove energy from the resolved ones, which is called forward scatter; if it is positive, they release energy to the resolved scales, which is called backscatter. The backward and forward scatter components of ε_{sgs} , respectively denoted by ε_+ and ε_- , are defined as (10) (4):

$$\varepsilon_+ = \frac{1}{2}(\varepsilon_{sgs} + |\varepsilon_{sgs}|), \quad \varepsilon_- = \frac{1}{2}(\varepsilon_{sgs} - |\varepsilon_{sgs}|) \quad (8)$$

Both the SGS backward and forward scatter are normalized by the volume averaged absolute value of the viscous dissipation defined as:

$$\varepsilon_v = |-(2/Re)\bar{S}_{ij}\bar{S}_{ij}| \quad (9)$$

In Fig. 15a the distribution along the channel depth of plane-averaged SGS backward and forward scatter, obtained with the DTM, is shown. At the beginning of the computation, both the backward and forward scatter peak in the near "wall" region, at approximately $z=0.2$, since this region is still characterized by strong Reynolds shear stress. This result is consistent with the analysis of subgrid-scale energy transfer carried out in Ref. (10) using the DNS data of a turbulent channel flow. However, even at the very beginning of the computation a noticeable amount of backscatter is present at the "wall", because of the new free-slip boundary conditions. As the time increases, the peak of forward scatter disappears and the distribution tends to become uniform

along the channel depth. In a first phase of the decay process ($t=3.5$) a larger amount of forward scatter is found everywhere, except in the former peak region; in a second phase, the forward scatter decreases everywhere, except near the free surface. During the whole decay process, a large amount of backscatter is present at the free surface and near the "wall": the ratio between backward and forward scatter is noticeably higher there than in the center of the channel. This result seems to confirm that the DTM properly takes into account the reverse cascade of energy from small to large scales at the free surface, as observed also previously from the energy spectra.

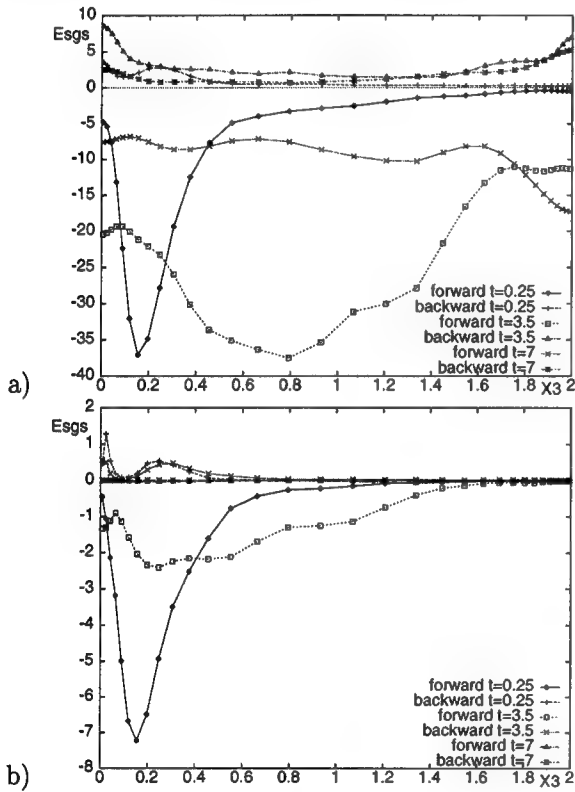


Figure 15: Time evolution of plane-averaged forward and back scatter. a) DTM b) DSM

In Fig. 15b the distribution along the channel depth of plane-averaged SGS backward and forward scatter, obtained with the DSM, is plotted. At the beginning of the simulation the distribution is

qualitatively similar to that obtained with the DTM, but the amount of both backward and forward scatter is significantly smaller: for instance, the peak of forward scatter is approximately five times lower than that obtained with the DTM. Later on, the peak in the wall region disappears, as for the DTM, but in this case both backward and forward scatter decrease noticeably everywhere during the whole decay process. At the free surface the SGS energy transfer is very low during all the simulation: in particular the reverse energy transfer, which is a basic feature of freely decaying two-dimensional turbulence, is negligible compared to the volume averaged viscous dissipation.

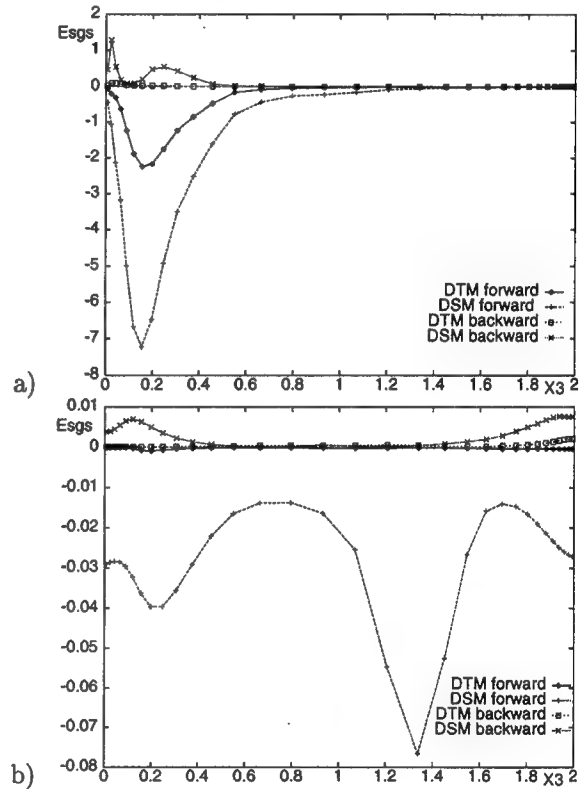


Figure 16: Plane-averaged forward and back scatter obtained with DSM and the Smagorinsky part of the DTM. a) $t=0.25$ b) $t=7$.

Significantly, the SGS backward and forward scatter obtained with the DTM are mainly due to the

model component which is proportional to the modified Leonard tensor. This is evident from Figs. 16a and 16b, in which the backward and forward scatter due to the Smagorinsky part of the DTM are compared to those obtained with the DSM at $t=0.25$ and $t=7$. Both backward and forward scatter given by the Smagorinsky part of the DTM (except in a region near the wall at the beginning of the simulation) are negligible compared to those obtained with the DSM, which in turn are much lower than those given by all the terms in the DTM. This result is confirmed by the comparison of the Smagorinsky part coefficient in the DTM and the model parameter in the DSM during the decay process.

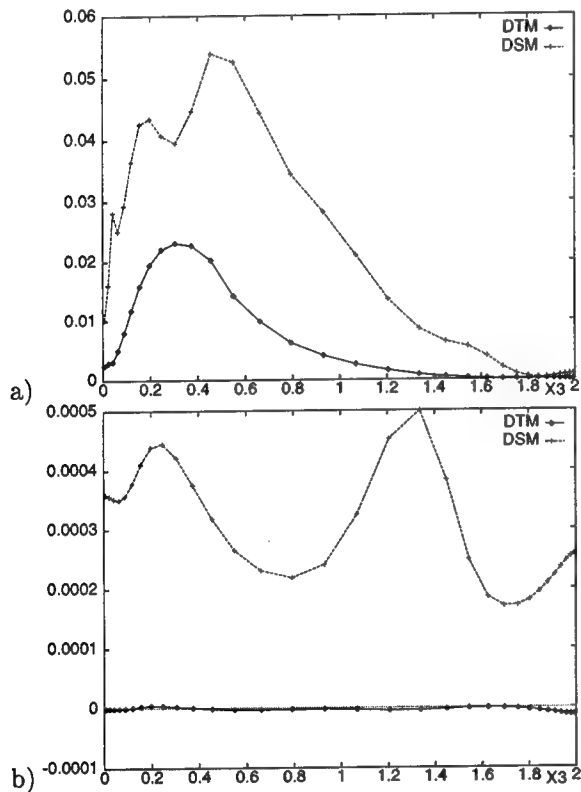


Figure 17: Plane-averaged ν_t/ν obtained with DSM and DTM. a) $t=0.25$ b) $t=7$.

In Figs. 17a and 17b the plane-averaged values of ν_t/ν obtained with the DSM and the DTM are compared at the same previous nondimensional times; ν_t

is the eddy viscosity, defined as:

$$\nu_t = C\bar{\Delta}^2|\bar{S}| \quad (10)$$

The eddy viscosity given by the Smagorinsky part in the DTM is always much lower than that obtained with the DSM, and tends to vanish faster, with increasing time during the decay. This result is not surprising, since, as pointed out in Ref. (3), in the DTM less burden is put on the coefficient related to the Smagorinsky part, and it is consistent with the results of the *a priori* tests in Ref. (3).

The plane-averaged value of the second parameter in the DTM (Fig. 18), at the beginning of the simulation, shows a peak at the "wall", probably related to the change in boundary conditions, then decreases to reach a value of approximately 1.2, almost uniform along the rest of the depth. During the decay, the value of K is almost constant along the whole channel depth and decreases slightly with increasing time.

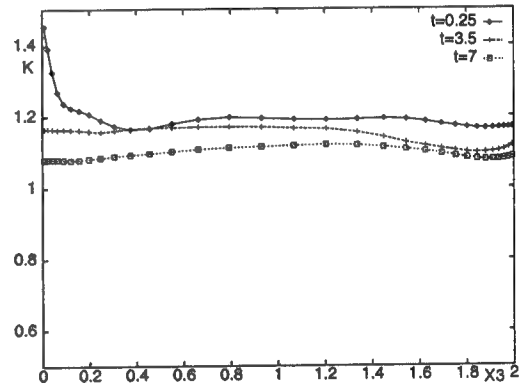


Figure 18: Time evolution of the plane-averaged K parameter in the DTM.

In order to analyse the behavior of the model parameters more locally at the free surface, the values of ν_t/ν obtained with the DSM and the DTM at the free surface for $t=0.25$ are shown in Figs. 19a and 19b, respectively. The eddy viscosity for the DSM shows large peaks, both positive and negative, about two order of magnitude larger than the plane-averaged value. Incidentally, the model coefficient C , computed by the dynamic procedure described in

Section 2, is averaged locally in space within the test-filtering volume with a stencil of three grid points in each direction. As expected on the basis of the results in Ref. (3), these peaks disappear in the DTM. This behavior is clearly a desirable feature in LES computations to avoid numerical instabilities. The second parameter in the DTM also varies on horizontal planes (Fig. 20) but as a small percentage of its averaged value, without exhibiting large isolated peaks.

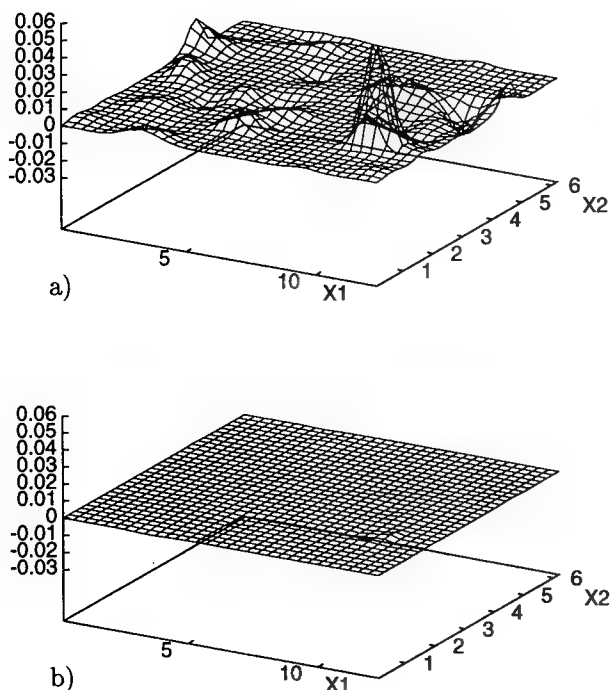


Figure 19: ν_t/ν at the free surface obtained with DSM and DTM at $t=0.25$. a) DSM (Plane-averaged value: $8.6 \cdot 10^{-4}$) b) DTM (Plane-averaged value: $1.3 \cdot 10^{-5}$).

The isocontours of the SGS energy transfer (normalized by the volume-averaged absolute value of the viscous dissipation) given at the free surface by the Leonard part of the DTM are plotted in Fig. 21 for $t=0.25$. As previously pointed out, the Smagorin-

sky part in the DTM gives a negligible contribution to the SGS energy transfer at the free surface: thus, the isocontours in Fig. 21 practically represent the whole SGS energy transfer obtained with the DTM. The regions of high forward energy transfer correspond to the stagnation streamlines and to the outskirts of the vortices, where high shear stress is present (see Fig. 3). Strong backward energy transfer occurs mostly in the regions with upwelling. The same qualitative behavior of the SGS energy transfer was observed at the free-surface by Pan and Banerjee in Ref. (4), by filtering their DNS data with a cutoff filter in the wave-number space. Thus, the DTM, and, in particular the part related to the modified Leonard tensor, captures the basic mechanisms of SGS energy transfer at the free surface.

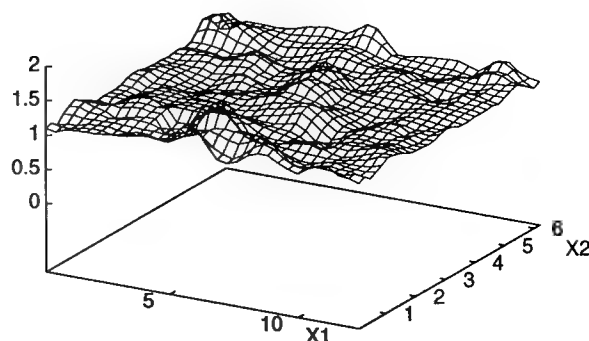


Figure 20: K parameter in the DTM at the free surface for $t=0.25$. Plane-averaged value: 1.17.

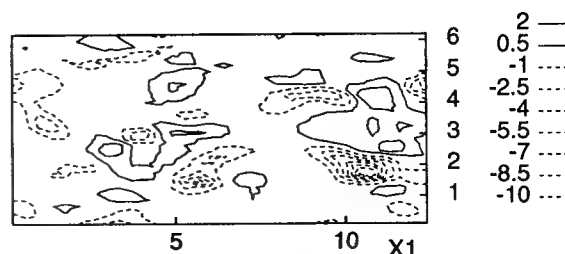


Figure 21: Iso-contours of the SGS energy transfer due to the Leonard part of the DTM at the free surface. $t=0.25$.

The same isocontours obtained with the DSM are shown in Fig. 22. First, as previously noted for the analysis of plane-averaged values, noticeably less SGS energy transfer (both forward and backward) occurs with the DSM than with the DTM. Moreover, it is clear that the zones of non-negligible backward and forward scatter correspond to the peaks (negative and positive) of the model parameter, observed in Fig. 19a. In particular, most of the forward transfer corresponds to the stagnation streamline in the right lower part (see Fig. 3), where ν_t/ν assumes the highest positive peak. Only a region of very low backscatter is observed in the right upper part of the domain, where an upwelling occurs. Thus, even if the dynamic procedure of determination of the model parameter seems to be effective in some way, since high peaks of C correspond to regions where physical phenomena (downdraft or upwelling) actually occur, the DSM seems to be generally inadequate to account for the energy transfer between unresolved and resolved scales at the free surface.

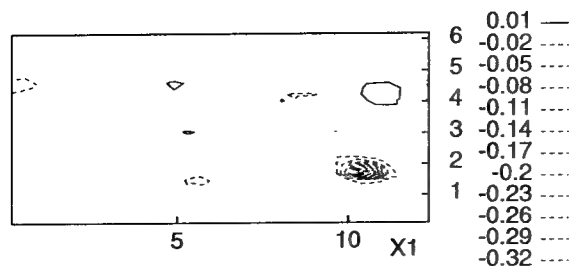


Figure 22: Iso-contours of the SGS energy transfer obtained at the free surface by the DSM. $t=0.25$.

4 Conclusions

The large eddy simulation of free-surface decaying turbulence with the dynamic two-parameter model compares very favorably with the direct numerical simulation. In particular, the reverse cascade of energy from small scales to large scales at the free surface, which is a feature of freely decaying two-

dimensional turbulence, is properly taken into account by the DTM. Moreover, as in the DNS, the two-dimensional region thickens during the decay. A slight delay in the decay process is observed in the large eddy simulation, with respect to the DNS, but it is reduced by increasing the grid resolution near the free surfaces. Nevertheless, the basic mechanisms of the decay process are not affected by grid resolution.

Using the dynamic subgrid model (DSM), a large eddy simulation was carried out for the same flow geometry and boundary and initial conditions as for the DTM. Significant discrepancies were observed between the DSM and the DNS simulations during the decay process at the free surface.

The analysis of the SGS energy transfer shows that the DTM, and, in particular, the part related to the modified Leonard tensor, captures the basic mechanisms of interscale energy transfer, observed at the free surface by filtering the DNS data. Conversely, the DSM seems to be generally inadequate to account for the energy transfer between resolved and unresolved scales at the free surface: in particular, very low backscatter is observed there during the whole simulation.

As expected, the magnitude of the dynamically computed eddy viscosity in the DTM is significantly reduced compared with that in the DSM; the contribution of the Smagorinsky part to SGS energy transfer in the DTM becomes negligible with increasing decay time. Moreover, the large isolated peaks observed in local values of the eddy viscosity in the DSM almost disappear for the DTM.

References

1. Germano M., Piomelli U., Moin P., Cabot W.H., "A dynamic subgrid-scale eddy-viscosity model", *Phys. Fluids A*, Vol. 3, No. 7, 1991, pp. 1760-1765.
2. Zang Y., Street R.L., Koseff J.R., "A dynamic mixed subgrid-scale model and its application to turbulent recirculating flows", *Phys. Fluids A*, Vol. 5, No. 12, Dec. 1993, pp. 3186-3196.
3. Salvetti M.V., Banerjee S., "A Priori Tests of a New Dynamic Subgrid-Scale

Model for Finite-Difference Large-Eddy Simulations", Phys. Fluids, Vol. 7, No. 11, Nov. 1995, pp. 2831-2847.

4. Pan Y., Banerjee S., "A numerical study of free-surface turbulence in channel flow", Phys. Fluids, vol. 7, No. 7, July 1995, pp. 1649-1664.

5. Germano M., "A proposal for a redefinition of the turbulent stresses in the filtered Navier-Stokes equations", Phys. Fluids 29, 1986, pp. 2323.

6. Lilly D.K., "A proposed modification of the Germano subgrid scale closure method", Phys. Fluids A, vol. 4, No. 3, March 1992, pp. 633-635.

7. Zang Y., Street R.L., Koseff J.R., "A non-staggered grid, fractional step method for time-dependent incompressible Navier-Stokes equations in general curvilinear coordinate systems", J. Comput. Phys., vol. 114, n. 1, 1994, pp. 18-33.

8. Zang Y., Street R.L., "A composite multigrid method for calculating unsteady incompressible flows in geometrically complex domains", Int. Journal for Num. Meth. in Fluids, vol. 20, 1995, pp. 341-361.

9. Salvetti M.V., Zang Y., Banerjee S., Street R.L., "A two-parameter, dynamic-mixed subgrid-scale model applied to a turbulent recirculating incompressible flow", to be submitted to Phys. of Fluids.

10. Piomelli U., Cabot W.H., Moin P., Lee S., "Subgrid-scale backscatter in turbulent and transitional flows", Phys. Fluids A 3, Vol. 3, No. 7, July 1991, pp. 1766-1771.

DISCUSSION

M. Sreedhar and F. Stern
University of Iowa, USA

The authors should be congratulated for such an interesting paper. The dynamic two-parameter model (DTM) seems to have overcome many of the drawbacks of the original Smagorinsky (DSM) subgrid scale model. We have the following questions and comments.

(1) Usually, in the quasi-two dimensional free surface turbulent field, the energy of the surface-parallel velocity components tends to increase while the surface normal velocity component decays. The one dimensional energy spectrum (Fig. 7 in the paper) which shows the energy contents of the surface parallel velocity components obtained with the DTM model at different horizontal components planes does not seem to indicate this feature. Is it due to the decaying nature of the turbulent field? Any comments on this?

(2) The figures and discussion on the time evolution of plane-averaged forward and back scatter are very interesting. The superiority of the DTM model is very clearly demonstrated. Inclusion of the results of forward and back scatter computed from the DNS data (after proper filtering) in a few of the figures would be very welcome.

AUTHORS' REPLY

(1) This behavior is actually due to the decaying nature of the flow. Indeed, since the mechanisms generating turbulence are eliminated, the normal velocity component is generally lower than in the turbulent open channel and hence, the damping of this component at the free surface is less important. As a consequence, the increase in the surface normal components at the free surface becomes negligible; this can be seen, for example, from the r.m.s. of these components in Fig. 2 that tend to become straight along the channel depth.

(2) We agree with this excellent suggestion, and we have been developing more quantitative comparisons for this flow. In Salvetti and Banerjee (Phys. Fluids, vol. 7, n. 11, Nov 1995) quantitative comparisons were made between DNS, DMM, and DTM behaviors.

DISCUSSION

E. Novikov
University of California, San Diego, USA

In this paper the decaying turbulence is considered in an open horizontally periodic flow with free-slip top and bottom conditions. Large eddy simulation (LES) is described for dynamic models with Smagorinsky term and with a combination of Smagorinsky and Bardina terms. A quantitative comparison is made between results, obtained with these models. Some qualitative comparison of LES results with direct numerical simulation (DNS) is also mentioned. The value of this work will be greatly increased if the comparison between LES models and DNS will be made quantitative.

AUTHORS' REPLY

As we noted in response to the second point by Sreedhar and Stern, we are continuing work on this flow and will add more quantitative comparisons in future publications. The quality of the DMM and DTM SGS models has, however, been directly compared to DNS results via a priori tests in Salvetti and Banerjee (Phys. Fluids, vol. 7, n. 11, Nov. 1995) as we note above.

Fully Nonlinear Hydrodynamic Calculations for Ship Design on Parallel Computing Platforms

G. Cowles, L. Martinelli (Princeton University, USA)

1 Introduction

The prediction of the total drag experienced by an advancing ship is a complicated problem which requires a thorough understanding of the hydrodynamic forces acting on the ship hull, the physical processes from which these forces arise and their mutual interaction. The advent of powerful computers - exhibiting both fast processing speed and large storage capabilities - has now made possible computational solutions of the full set of mathematical equations which describe the coupled wave structure and viscous boundary layer interaction. Notable previous computational approaches in this area include: the finite difference, velocity-pressure coupling approach of Hino [3]; the finite volume, velocity-pressure coupling approach of Miyata *et. al.* [4]; and the interactive approach of Tahara *et. al.* [5] which combines the finite analytic approach of Chen *et. al.* [6] and the "SPLASH" panel method of Rosen *et. al.* [7]. These methods all represent major advances in the computational solution of the coupled wave structure and viscous boundary layer interaction problem as it applies to ship hulls in general. However, they are all computationally intensive, requiring significant amounts of CPU time.

The motivation behind the present work follows directly from the shortcomings of the CFD techniques currently available for ship analysis and design. A method which is robust and accurate for realistic hull shapes will greatly enhance hull design capabilities - from the naval architect designing frigates and destroyers, to the sailing yacht designer optimizing the performance of an America's Cup hull. This task demands that techniques for incorporating the fully nonlinear free surface boundary condition be included in the CFD analysis.

The ability to model the fully nonlinear ship wave problem, in a robust and accurate fashion, is in and of itself still not sufficient for effective design practice. Thus, despite the advances that have been made, CFD is still not being exploited as effectively as one would like in the design process. This is partly due to the long set-up and high costs, both human and computational of complex flow simulations, and improvements are still needed. In particular, the fidelity of modelling of high Reynolds number viscous flows continues to be limited by computational costs. Consequently accurate and cost effective simulation of viscous flow at Reynolds numbers associated with full scale ships, remains a challenge. Several routes are available toward the reduction of computational costs, including the reduction of mesh requirements by the use of higher order schemes, improved convergence to a steady state by sophisticated acceleration methods, and the exploitation of massively parallel computers.

This paper presents recent advances in our work to accomplish these goals. The basic flow solver methodology follows directly from the cell-vertex formulation outlined in our previous work [8, 9]. This approach has proven to be accurate, through use of an efficient moving grid technique which permits application of the fully nonlinear free surface boundary condition, and which in turn permits simulation of the interaction between wavemaking and the viscous boundary layer. A cell-center formulation is also developed and used in the present work because it facilitates the implementation on parallel architectures using the method of domain decomposition.

The establishment of an efficient baseline steady state flow solver is extremely important because it provides the platform from which several powerful ship analysis tools can be launched. In particular, it enables the implementation of

automatic design techniques based on control theory [10] as well as the extension of a time accurate multigrid driven, implicit scheme [11] for the analysis of "seakeeping", and maneuvering.

2 Mathematical Models

For a viscous incompressible fluid moving under the influence of gravity, the differential form of the continuity equation and the Reynolds Averaged Navier-Stokes equations (RANS) in a Cartesian coordinate system can be cast, using tensor notation, in the form,

$$\frac{\partial \bar{U}_i}{\partial x_i} = 0.$$

$$\rho \left(\frac{\partial \bar{U}_i}{\partial t} + \bar{U}_j \frac{\partial \bar{U}_i}{\partial x_j} \right) = -\frac{\partial \bar{P}}{\partial x_i} + \frac{\partial}{\partial x_j} \left(\mu \frac{\partial \bar{U}_i}{\partial x_j} - \rho \bar{u}_i \bar{u}_j \right) + \bar{F}_i$$

Here, \bar{U}_i is the mean velocity components in the x_i direction, \bar{P} , the mean pressure, and \bar{F}_i the gravity force acting in the i -th direction, and $\bar{u}_i \bar{u}_j$ is the Reynolds stress which requires an additional model for closure. For implementation in a computer code, it is more convenient to use a dimensionless form of the equation which is obtained by dividing all lengths by the ship (body) length L and all velocity by the free stream velocity U_∞ . Moreover, one can define a new variable Ψ as the sum of the mean static pressure P minus the hydrostatic component $-x_k Fr^{-2}$. Thus the dimensionless form of the RANS becomes:

$$\left(\frac{\partial \bar{U}_i}{\partial t} + \bar{U}_j \frac{\partial \bar{U}_i}{\partial x_j} \right) = -\frac{\partial \Psi}{\partial x_i} + \frac{1}{Re} \frac{\partial}{\partial x_j} \left(\frac{\partial \bar{U}_i}{\partial x_j} - \bar{u}_i \bar{u}_j^* \right)$$

where $Fr = \frac{U_\infty}{\sqrt{gL}}$ is the Froude number and the Reynolds number Re is defined by $Re = \frac{U_\infty L}{\nu}$ where ν is the kinematic viscosity, and $\bar{u}_i \bar{u}_j^*$ is a dimensionless form of the Reynolds stress.

Figure 1 shows the reference frame and ship location used in this work. A right-handed coordinate system $Oxyz$, with the origin fixed at the intersection of the bow and the mean free surface is established. The z direction is positive upwards, y is positive towards the starboard side and x is positive in the aft direction. The free stream velocity vector is parallel to the x axis and points in the same direction. The ship hull pierces the uniform flow and is held fixed in place, i.e. the ship is not allowed to sink (translate in z direction) or trim (rotate in $x-z$ plane).

It is well known that the closure of the Reynolds averaged system of equation requires a model for the Reynolds stress. There are several alternatives of increasing complexity. Generally speaking, when the flow remains attached to the body, a simple turbulence model based on the Boussinesq hypothesis and the mixing length concept yields predictions which are in good agreement with experimental evidence. For this

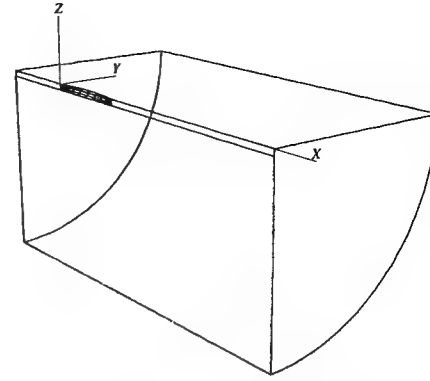


Figure 1: Reference Frame and Ship Location

reason a Baldwin and Lomax turbulence model has been initially implemented and tested [14]. On the other hand, more sophisticated models based on the solution of additional differential equations for the component of the Reynolds stress may be required. Notice that when the Reynolds stress vanishes, the form of the equation is identical to that of the Navier Stokes equations. Also, the inviscid form of the Euler equations is recovered in the limit of high Reynolds numbers. Thus, a hierarchy of mathematical model can be easily implemented on a single computer code, allowing study of the controlling mechanisms of the flow. For example, it has been shown in reference [18] that realistic prediction of the wave pattern about an advancing ship can be obtained by using the Euler equations as the mathematical model of the bulk flow, provided that a non-linear evolution of the free surface is accounted for. This is not surprising, since the typical Reynolds number of an advancing vessel is of the order of 10^8 .

Free Surface Boundary Conditions

When the effects of surface tension and viscosity are neglected, the boundary condition on the free surface consists of two equations. The first, the dynamic condition, states that the pressure acting on the free surface is constant. The second, the kinematic condition, states that the free surface is a material surface: once a fluid particle is on the free surface, it forever remains on the surface. The dynamic and kinematic boundary conditions may be expressed as

$$p = \text{constant}$$

$$\frac{d\beta}{dt} = w = \beta_t + u\beta_x + v\beta_y \quad (1)$$

where $z = \beta(x, y, t)$ is the free surface location.

Hull and Farfield Boundary Conditions

The remaining boundaries consist of the ship hull, the meridian, or symmetry plane, and the far field of the computational

domain. In the viscous formulation, a no-slip condition is enforced on the ship hull. For the inviscid case, flow tangency is preserved. On the symmetry plane (that portion of the (x,z) plane excluding the ship hull) derivatives in the y direction as well as the v component of velocity are set to zero. The upstream plane has $u=U_o$, $v=0$, $w=0$ and $\psi=0$ ($p=-zFr^{-2}$). Similar conditions hold on the outer boundary plane which is assumed far enough away from the hull such that no disturbances are felt. A radiation condition should be imposed on the outflow domain to allow the wave disturbance to pass out of the computational domain. Although fairly sophisticated formulations may be devised to represent the radiation condition, simple extrapolations proved to be sufficient in this work.

For calculations in the limit of zero Froude number (double-hull model) the (x,y) plane is also treated as a symmetry plane.

3 Numerical Solution

The formulation of the numerical solution procedure is based on a finite volume method (FVM) for the bulk flow variables (u, v, w and ψ), coupled to a finite difference method for the free surface evolution variables (β and ψ).

Bulk Flow Solution

The finite volume solution for the bulk flow follows the same procedures that are well documented in references [8, 9]. The governing set of differential flow equations are expressed in the standard form for artificial compressibility [15] as outlined by Rizzi and Eriksson [16]. In particular, letting \mathbf{w} be the vector of dependent variables:

$$\mathbf{w}_t + (\mathbf{f} - \mathbf{f}_v)_x + (\mathbf{g} - \mathbf{g}_v)_y + (\mathbf{h} - \mathbf{h}_v)_z = 0 \quad (2)$$

Here $\mathbf{f}, \mathbf{g}, \mathbf{h}$ and $\mathbf{f}_v, \mathbf{g}_v, \mathbf{h}_v$ represent, respectively, the inviscid and viscous fluxes.

Following the general procedures used in the finite volume formulation, the governing differential equations are integrated over an arbitrary volume V . Application of the divergence theorem on the convective and viscous flux term integrals yields

$$\frac{\partial}{\partial t} \int_V \mathbf{w} dV + \int_{\partial V} (\mathbf{f} dS_x + \mathbf{g} dS_y + \mathbf{h} dS_z) = \int_{\partial V} (\mathbf{f}_v dS_x + \mathbf{g}_v dS_y + \mathbf{h}_v dS_z) \quad (3)$$

where S_x, S_y and S_z are the projections of the area ∂V in the x, y and z directions, respectively. In the present approach the computational domain is divided into hexahedral cells. Two discretization schemes are considered in the present work. They differ primarily in that in the first, the flow variables are stored at the grid points (cell-vertex) while in the second they are stored in the interior of the cell (cell-center). While the details of the computation of the fluxes

are different for the two approaches, both cell-center and cell-vertex schemes yield the following system of ordinary differential equations [13]

$$\frac{d}{dt} (V_{ijk} \mathbf{w}) + C_{ijk} - V_{ijk} = 0$$

where C_{ijk} and V_{ijk} are the discretized evaluations of the convective and viscous flux surface integrals appearing in equation 3 and V_{ijk} is the volume of the computational cell. In practice, the discretization scheme reduces to a second order accurate, nondissipative central difference approximation to the bulk flow equations on sufficiently smooth grids. A central difference scheme permits odd-even decoupling at adjacent nodes which may lead to oscillatory solutions. To prevent this "unphysical" phenomena from occurring, a dissipation term is added to the system of equations such that the system now becomes

$$\frac{d}{dt} (V_{ijk} \mathbf{w}) + [C_{ijk}(\mathbf{w}) - V_{ijk}(\mathbf{w}) - D_{ijk}(\mathbf{w})] = 0. \quad (4)$$

For the present problem a fourth derivative background dissipation term is added. The dissipative term is constructed in such a manner that the conservation form of the system of equations is preserved. The dissipation term is third order in truncation terms so as not to detract from the second order accuracy of the flux discretization.

Discretization of the Viscous Terms

The discretization of the viscous terms of the Navier Stokes equations requires an approximation to the velocity derivatives $\frac{\partial u_i}{\partial x_j}$ in order to calculate the stress tensor. In order to evaluate the derivatives one may apply the Gauss formula to a control volume V with the boundary S .

$$\int_V \frac{\partial u_i}{\partial x_j} dv = \int_S u_i n_j ds$$

where n_j is the outward normal. For a hexahedral cell this gives

$$\frac{\partial \hat{u}_i}{\partial x_j} = \frac{1}{\text{vol}} \sum_{\text{faces}} \hat{u}_i n_j s \quad (5)$$

where \hat{u}_i is an estimate of the average of u_i over the face. Alternatively, assuming a local transformation to computational coordinates ξ_j , one may apply the chain rule

$$\frac{\partial u}{\partial x} = \left[\frac{\partial u}{\partial \xi} \right] \left[\frac{\partial \xi}{\partial x} \right] = \frac{\partial u}{\partial \xi} \left[\frac{\partial x}{\partial \xi} \right]^{-1} \quad (6)$$

Here the transformation derivatives $\frac{\partial x_i}{\partial \xi_j}$ can be evaluated by the same finite difference formulas as the velocity derivatives $\frac{\partial u_i}{\partial \xi_j}$. In this case $\frac{\partial u}{\partial \xi}$ is exact if u is a linearly varying function.

For a cell-centered discretization (figure 2a) $\frac{\partial u}{\partial \xi}$ is needed at each face. The simplest procedure is to evaluate $\frac{\partial u}{\partial \xi}$ in each cell, and to average $\frac{\partial u}{\partial \xi}$ between the two cells on either side of a face. The resulting discretization does not have a compact stencil, and supports undamped oscillatory modes. In a one dimensional calculation, for example, $\frac{\partial^2 u}{\partial x^2}$ would be discretized as $\frac{u_{i+2} - 2u_i + u_{i-2}}{4\Delta x^2}$ [17]. In order to produce a compact stencil $\frac{\partial u}{\partial x}$ may be estimated from a control volume centered on each face, using formulas (5) or (6). This is computationally expensive because the number of faces is much larger than the number of cells. In a hexahedral mesh with a large number of vertices the number of faces approaches three times the number of cells.

This motivates the introduction of dual meshes for the evaluation of the velocity derivatives and the flux balance as sketched in figure 2. The figure

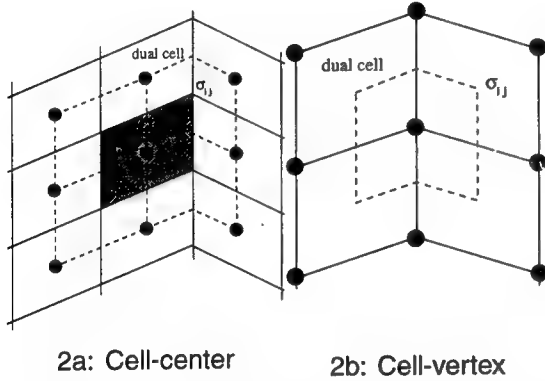


Figure 2: Viscous discretizations for cell-centered and cell-vertex algorithms.

shows both cell-centered and cell-vertex schemes. The dual mesh connects cell centers of the primary mesh. If there is a kink in the primary mesh, the dual cells should be formed by assembling contiguous fractions of the neighboring primary cells. On smooth meshes comparable results are obtained by either of these formulations [23, 24, 25]. If the mesh has a kink, the cell-vertex scheme has the advantage that the derivatives $\frac{\partial u_i}{\partial x_j}$ are calculated in the interior of a regular cell, with no loss of accuracy.

Multigrid time-stepping

Equation 4 is integrated in time to steady state using an explicit multistage scheme. For each bulk flow time step, the grid, and thus V_{ijk} , is independent of time. Hence equation 4 can be written as

$$\frac{d\mathbf{w}_{ijk}}{dt} + R_{ijk}(\mathbf{w}) = 0 \quad (7)$$

where the residual is defined as

$$R_{ijk}(\mathbf{w}) = C_{ijk}(\mathbf{w}) - V_{ijk}(\mathbf{w}) - D_{ijk}(\mathbf{w})$$

and the cell volume V_{ijk} is absorbed into the residual for clarity.

The full approximation multigrid scheme of this work uses a sequence of independently generated coarser meshes by eliminating alternate points in each coordinate direction. In order to give a precise description of the multigrid scheme, subscripts may be used to indicate the grid. Several transfer operations need to be defined. First the solution vector on grid k must be initialized as

$$\mathbf{w}_k^{(0)} = T_{k,k-1} \mathbf{w}_{k-1},$$

where w_{k-1} is the current value on grid $k-1$, and $T_{k,k-1}$ is a transfer operator. Next it is necessary to transfer a residual forcing function such that the solution grid k is driven by the residuals calculated on grid $k-1$. This can be accomplished by setting

$$P_k = Q_{k,k-1} R_{k-1}(\mathbf{w}_{k-1}) - R_k[\mathbf{w}_k^{(0)}],$$

where $Q_{k,k-1}$ is another transfer operator. Then $R_k(\mathbf{w}_k)$ is replaced by $R_k(\mathbf{w}_k) + P_k$ in the time-stepping scheme. Thus, the multistage scheme is reformulated as

$$\begin{aligned} \mathbf{w}_k^{(1)} &= \mathbf{w}_k^{(0)} - \alpha_1 \Delta t_k [R_k^{(0)} + P_k] \\ &\vdots \\ \mathbf{w}_k^{(q+1)} &= \mathbf{w}_k^{(0)} - \alpha_{q+1} \Delta t_k [R_k^{(q)} + P_k]. \end{aligned}$$

The result $\mathbf{w}_k^{(m)}$ then provides the initial data for grid $k+1$. Finally, the accumulated correction on grid k has to be transferred back to grid $k-1$ with the aid of an interpolation operator $I_{k-1,k}$. Clearly the definition of $T_{k,k-1}, Q_{k,k-1}, I_{k-1,k}$ depends on whether a cell-vertex or a cell-center formulation is selected. A detailed account can be found in reference [22].

With properly optimized coefficients, multistage time-stepping schemes can be very efficient drivers of the multigrid process. In this work we use a five stage scheme with three evaluation of dissipation [17] to drive a W -cycle of the type illustrated in Figure 3.

In a three-dimensional case the number of cells is reduced by a factor of eight on each coarser grid. On examination of the figure, it can therefore be seen that the work measured in units corresponding to a step on the fine grid is of the order of

$$1 + 2/8 + 4/64 + \dots < 4/3,$$

and consequently the very large effective time step of the complete cycle costs only slightly more than a single time step in the fine grid.

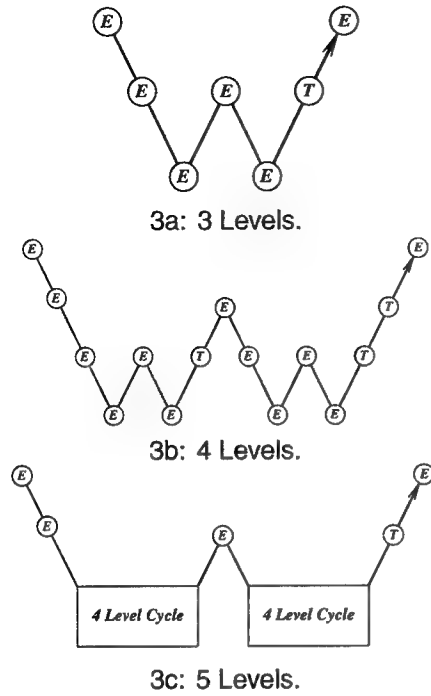


Figure 3: Multigrid W -cycle for managing the grid calculation. E , evaluate the change in the flow for one step; T , transfer the data without updating the solution.

Free Surface Solution

Both a kinematic and dynamic boundary condition must be imposed at the free surface which require the adaption of the grid to conform to the computed surface wave. Equation 1 can be cast in a form more amenable to numerical computations by introducing a curvilinear coordinate system that transforms the curved free surface $\beta(x, y)$ into computational coordinates $\beta(\xi, \eta)$. This results in the following transformed kinematic condition

$$\beta_{t^*} + \tilde{u}\beta_{\xi} + \tilde{v}\beta_{\eta} = w \quad (8)$$

where \tilde{u} and \tilde{v} are contravariant velocity components given by

$$\tilde{u} = u\xi_x + v\xi_y = (uy_{\eta} - vx_{\eta}) J^{-1}$$

$$\tilde{v} = u\eta_x + v\eta_y = (vx_{\xi} - uy_{\xi}) J^{-1}$$

and $J = x_{\xi}y_{\eta} - x_{\eta}y_{\xi}$ is the Jacobian.

Equation 8 is essentially a linear hyperbolic equation, which in our original method was discretized by central differences augmented by high order diffusion [8, 9]. Such a scheme can be obtained by introducing anti-diffusive terms in a standard first order formula. In particular, it is well known that for a one-dimensional scalar equation model, central difference approximation of the derivative may be corrected by adding

a third order dissipative flux:

$$d_{j+\frac{1}{2}} = \alpha_{j+\frac{1}{2}} \left\{ \Delta\beta_{j+\frac{1}{2}} - \frac{1}{2} (\Delta\beta_{j+\frac{1}{2}} + \Delta\beta_{j-\frac{1}{2}}) \right\} \quad (9)$$

where $\alpha_{j+\frac{1}{2}} = \frac{1}{2} |\tilde{u}_{j+\frac{1}{2}}|$ at the cell interface. This is equivalent to the scheme which we have used until now to discretize the free surface, and which has proven to be effective for simple hulls. However, on more complex configurations of interest, such as combatant vessels and yachts, the physical wave at the bow tends to break. This phenomenon cannot be fully accounted for in the present mathematical model. In order to avoid the overturning of the wave and continue the calculations lower order dissipation must be introduced locally and in a controlled manner. This can be accomplished by borrowing from the theory of non-oscillatory schemes constructed using the Local Extremum Diminishing (LED) principle [19, 20]. Since the breaking of a wave is generally characterized by a change in sign of the velocity across the crest, it appears that limiting the antidiffusion purely from the upstream side may be more suitable to stabilize the calculations and avoid the overturning of the waves [21]. By adding the anti-diffusive correction purely from the upstream side one may derive a family of UpStream Limited Positive (USLIP) schemes:

$$\begin{aligned} d_{j+\frac{1}{2}} &= \alpha_{j+\frac{1}{2}} \left\{ \Delta\beta_{j+\frac{1}{2}} - L(\Delta\beta_{j+\frac{1}{2}}, \Delta\beta_{j-\frac{1}{2}}) \right\} \\ &\text{if } \tilde{u}_{j+\frac{1}{2}} > 0 \\ d_{j+\frac{1}{2}} &= \alpha_{j+\frac{1}{2}} \left\{ \Delta\beta_{j+\frac{1}{2}} - L(\Delta\beta_{j+\frac{1}{2}}, \Delta\beta_{j+\frac{3}{2}}) \right\} \\ &\text{if } \tilde{u}_{j+\frac{1}{2}} < 0 \end{aligned}$$

Where $L(p, q)$ is a limited average of p and q with the following properties:

P1. $L(p, q) = L(q, p)$

P2. $L(\alpha p, \alpha q) = \alpha L(p, q)$

P3. $L(p, p) = p$

P4. $L(p, q) = 0$ if p and q have opposite signs.

A simple limiter (α -mean) which limits the arithmetic mean by some multiple of the smaller of $|p|$ or $|q|$, has been used with success. It may be cast in the following form:

$$L(p, q) = S(p, q) \min \left(\frac{|p+q|}{2}, \alpha|p|, \alpha|q| \right).$$

It is well known that schemes which strictly satisfy the LED principle fall back to first order accuracy at extrema even when they realize higher order accuracy elsewhere. This

Properties P1–P3 are natural properties of an average, whereas P4 is needed for the construction of an LED scheme.

difficulty can be circumvented by relaxing the LED requirement. Therefore the concept of essentially local extremum diminishing (ELED) schemes is introduced as an alternative approach. These are schemes for which, in the limit as the mesh width $\Delta x \rightarrow 0$, maxima are non-increasing and minima are non-decreasing. In order to prevent the limiter from being active at smooth extrema it is convenient to set

$$L(p, q) = \frac{1}{2} D(p, q) (p + q)$$

where $D(p, q)$ is a factor designed to reduce the arithmetic average, and become zero if u and v have opposite signs. Thus, for an ELED scheme we take

$$D(p, q) = 1 - R(p, q) \quad (10)$$

where

$$R(p, q) = \left| \frac{p - q}{\max(|p| + |q|, \epsilon \Delta x^r)} \right|^s \quad (11)$$

and $\epsilon > 0$, r is a positive power, and s is a positive integer. Then $D(p, q) = 0$ if p and q have opposite signs. Also if $s=1$, $L(p, q)$ reduces to minmod, while if $s=2$, $L(p, q)$ is equivalent to Van Leer's limiter. By increasing s one can generate a sequence of limited averages which approach a limit defined by the arithmetic mean truncated to zero when p and q have opposite signs. These smooth limiters are known to have a benign effect on the convergence to a steady state of compressible flows. Figures 5a and 5b compare waterline profiles on a combatant vessel using ELED and LED methods in the free surface dissipation. One can see that, when compared with the experimental data, the ELED (solid line) profile is more accurate. Figures 5c and 5d show overhead free surface contours for the same geometry. The ELED scheme gives better resolution of the far field waves in solution of both the Euler and RANS equations.

Integration and Coupling with The Bulk Flow

The free surface kinematic equation may be expressed as

$$\frac{d\beta_{ij}}{dt^*} + Q_{ij}(\beta) = 0$$

where $Q_{ij}(\beta)$ consists of the collection of velocity and spatial gradient terms which result from the discretization of equation 8.

Once the free surface update is accomplished the pressure is adjusted on the free surface such that

$$\psi^{(n+1)} = \beta^{(n+1)} F_T^{-2}.$$

The free surface and the bulk flow solutions are coupled by first computing the bulk flow at each time step, and then using the bulk flow velocities to calculate the movement of

the free surface. After the free surface is updated, its new values are used as a boundary condition for the pressure on the bulk flow for the next time step. The entire iterative process, in which both the bulk flow and the free surface are updated at each time step, is repeated until some measure of convergence is attained: usually steady state wave profile and wave resistance coefficient.

Since the free surface is a material surface, the flow must be tangent to it in the final steady state. During the iterations, however, the flow is allowed to *leak* through the surface as the solution evolves towards the steady state. This leakage, in effect, drives the evolution equation. Suppose that at some stage, the vertical velocity component w is positive (cf. equation 1 or 8). Provided that the other terms are small, this will force β^{n+1} to be greater than β^n . When the time step is complete, ψ is adjusted such that $\psi^{n+1} > \psi^n$. Since the free surface has moved farther away from the original undisturbed upstream elevation and the pressure correspondingly increased, the velocity component w (or better still $\mathbf{q} \cdot \mathbf{n}$ where $\mathbf{n} = \frac{\nabla F}{|\nabla F|}$ and $F = z - \beta(x, y)$) will then be reduced. This results in a smaller $\Delta\beta$ for the next time step. The same is true for negative vertical velocity, in which case there is mass leakage into the system rather than out. Only when steady state has been reached is the mass flux through the surface zero and tangency enforced. In fact, the residual flux leakage could be used in addition to drag components and pressure residuals as a measure of convergence to the steady state.

This method of updating the free surface works well for the Euler equations since tangency along the hull can be easily enforced. However, for the Navier-Stokes equations the no-slip boundary condition is inconsistent with the free surface boundary condition at the hull/waterline intersection. To circumvent this difficulty the computed elevation for the second row of grid points away from the hull is extrapolated to the hull. Since the minimum spacing normal to the hull is small, the error due to this should be correspondingly small, comparable with other discretization errors. The treatment of this intersection for the Navier-Stokes calculations, should be the subject of future research to find the most accurate possible procedure.

4 Parallelization Strategy

The objective of a fast flow solver for design and analysis motivates parallel implementation. The method of domain decomposition is utilized for this work. The grid is divided into sections which are sent to separate processors for solution. This method is very compatible with the cell-center flux discretization. In the cell-vertex scheme, processors corresponding to adjoining sections of the mesh must update coincidental locations on the common face. Thus both single processor and parallel versions of the code have been developed using the cell-center formulation. Figure 6 displays

validation of the parallel, cell-center version by comparison with the previously developed, single processor, cell-vertex code. Figure 7 displays comparison between a single processor cell-center code and experimental data. Figures 8 and 9 show overhead wave profiles around the Model 5415 hull [26] for speeds of 15 and 20 knots respectively. These were computed using the cell-center discretization and the limited free surface dissipation described in section 3. Figure 14 displays pressure contours on the bulbous bow of the 5415 using this method. The parallelization strategy has been developed and extensively tested thus far using a single block implementation. Due to topological constraints, more complicated geometries cannot be treated with a single block structured mesh. As an example, the racing yacht pictured in figure 15 has multiple appendages which result in skewness and lowered efficiency of a single block grid. Transom sterns and inclusion of propellers cause similar difficulties. To circumvent these problems, a multiblock version of the code is currently being developed.

Single Block Parallel Implementation

The initial three-dimensional meshes for the hull calculations are generated using the GRIDGEN [27].

The computer code is parallelized using a domain decomposition model, a SPMD (Single Program Multiple Data) strategy, and the MPI (Message Passing Interface) Library for message passing. The choice of message passing library was determined by the requirement that the resulting code be portable to different parallel computing platforms as well as to homogeneous and heterogeneous networks of workstations [29].

Communication between subdomains is performed through halo cells surrounding each subdomain boundary. Since both the convective and the dissipative fluxes are calculated at the cell faces (boundaries of the control volumes), all six neighboring cells are necessary, thus requiring the existence of a single level halo for each processor in the parallel calculation. The dissipative fluxes are composed of third order differences of the flow quantities. Thus, at the boundary faces of each cell in the domain, the presence of the twelve neighboring cells (two adjacent to each face) is required. For each cell within a processor, Figure 4 shows which neighboring cells are required for the calculation of convective and dissipative fluxes. For each processor, some of these cells will lie directly next to an interprocessor boundary, in which case, the values of the flow variables residing in a different processor will be necessary to calculate the convective and dissipative fluxes.

In the finest mesh of the multigrid sequence, a two-level halo was sufficient to calculate the convective and dissipative fluxes for all cells contained in each processor. In the coarser levels of the multigrid sequence, a single level halo suffices since a simplified model of the artificial dissipation terms is

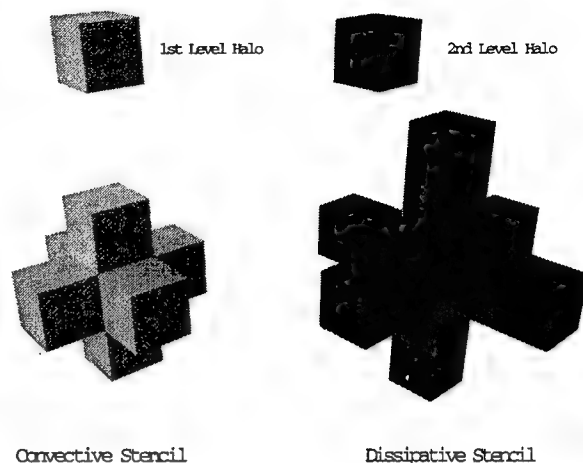


Figure 4: Convective and Dissipative Discretization Stencils.

used.

Similar constructs are required for the free surface solution. A double halo of free surface locations is passed across interprocessor boundaries.

The communication routines used are all of the asynchronous (or non-blocking) type. In the current implementation of the program, each processor must send and receive messages to and from at most 6 neighboring processors (left and right neighbors in each of the three coordinate directions). The communication is scheduled such that at every instant in time pairs of processors are sending/receiving to/from one another in order to minimize contention in the communication schedule.

For a given number of subdomains in a calculation, there are several ways to partition the complete mesh according to the scheme explained above. Depending on the choice of partitions, the bounding surface area of each subdomain will vary, reaching a minimum when the sizes in each of the three coordinate directions are equal. Figure 10 shows an H-O grid around a combatant ship divided into 8 subdomains corresponding to 8 processors. Currently the partition of the global mesh is an input to the code, but work is in progress to determine, in a pre-processing step, the optimal block distribution in order to minimize the communication requirements. Efficiency of the parallelization is a function of many factors, including numerical discretization, system of equations, choice of hardware/software, number of processors, and size of the mesh. The granularity, or ratio of bytes a processor passes to work it performs, helps quantify several of these aspects. The lower the granularity, the higher the efficiency. Switching to a more complex set of equations, for example, a RANS set, increases the amount of processor effort with only a small effect on the total message passes. Granularity decreases. Cutting a given mesh into more pieces (processors), or equivalently, using a coarser mesh, increases the ratio of

interprocessor faces to interior cells which is directly proportional to the granularity, and efficiency decays. Figure 11 displays parallel performance for the Euler equations, evaluated on an IBM SP2, a distributed memory machine, and confirms the good scalability of our algorithm. The effects of increasing the number of processors and increasing the size of the mesh are both apparent. Results of parallel RANS solvers under development in our laboratory for aeronautical applications confirm the theoretical efficiency increase that will be obtained when viscous fluxes are switched on.

Multiblock Parallel Implementation

The essential algorithm (convective and dissipative flux calculation, multigrid, viscous terms, etc.) is exactly the same as the one applied to the single block case. The only difference resides in the fact that an additional outer loop over all the blocks in the domain is added [28]. The parallelization strategy, however, is quite different. Similarly to the single block code, the multiblock is parallelized using a domain decomposition model, a SPMD strategy, and the MPI Library for message passing. Since the sizes of the blocks can be quite small, sometimes further partitioning severely limits the number of multigrid levels that can be used in the flows. For this reason, it was decided to allocate complete blocks to each processor.

The underlying assumption is that there always will be more blocks than processors available. If this is the case, every processor in the domain would be responsible for the computations inside one or more blocks. In the case in which there are more processors than blocks available, the blocks can be adequately partitioned during a pre-processing step in order to at least have as many blocks as processors. This approach has the advantage that the number of multigrid levels that can be used in the parallel implementation of the code is always the same as in the serial version. Moreover, the number of processors in the calculation can now be any integer number, since no restrictions are imposed by the partitioning in all coordinate directions used by the single block program.

The only drawback of this approach is the loss of the exact load balancing that one has in the single block implementation. All blocks in the calculation can have different sizes, and consequently, it is very likely that different processors will be assigned a different total number of cells in the calculation. This, in turn, will imply that some of the processors will be waiting until the processor with the largest number of cells has completed its work and parallel performance will suffer. The approach that we have followed to solve the load balancing problem is to assign to each processor, in a pre-processing step, a certain number of blocks such that the total number of cells is as close as possible to the exact share for perfect load balancing.

One must note that load balancing based on the total number of cells in each processor is only an approximation to the

optimal solution of the problem. Other variables such as the number of blocks, the size of each block, and the size of the buffers to be communicated play an important role in proper load balancing, and are the subject of current study. The implementation is fully scalable. Figure 12 shows an H-O grid around the Model 5415 hull divided into 20 blocks. Figure 13 shows speedups obtained on the 5415 for the zero Froude number condition. The shapes in the curves results from an interplay of forces. Increased cache hits push the curve to a superlinear (better than ideal) region. The wiggles are a result of deviations in the load balance from unity, or equal work (number cells) in each processor. Since the blocks are not all equal in size, the constraint that blocks are not shared among processors causes the taper as the number of processors approaches the number of blocks in the grid.

Conclusion

By utilizing a cell-center formulation suitable for parallel computing, flow solutions about complex geometries on the order of a half hour for a grid size up to one million mesh points have been achieved on 16 processors of an IBM SP2. Such efficiency makes our methodology suitable for routine calculations in the early stages of ship design. Also, an extension to the computation of unsteady flows has been made feasible by the speedup. Underwater control surfaces and transom sterns warrant the necessity of multiblock meshes. Preliminary testing of a multiblock version displays the scalability and efficiency of the method.

Acknowledgment

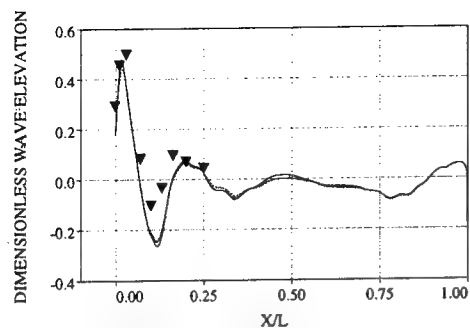
Our work has benefited greatly from the support of the Office of Naval Research through Grant N00014-93-I-0079, under the supervision of Dr. E.P. Rood. The selection, and implementation of the parallelization strategy presented here is the fruit of extensive collaborations with other students of the Princeton University CFD Laboratory. In particular we wish to acknowledge the contribution of Juan J. Alonso, and Andrey Belov.

REFERENCES

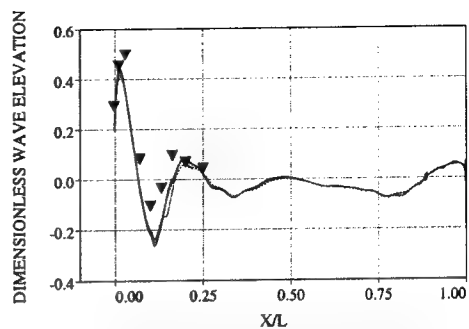
- [1] Toda, Y., Stern, F., and Longo, J., "Mean-Flow Measurements in the Boundary Layer and Wake and Wave Field of a Series 60 $C_B=0.6$ Ship Model-Part1: Froude Numbers 0.16 and 0.316," *Journal of Ship Research*, v. 36, n. 4, pp. 360-377, 1992.
- [2] Longo, J., Stern, F., and Toda, Y., "Mean-Flow Measurements in the Boundary Layer and Wake and Wave Field of a Series 60 $C_B=0.6$ Ship Model-Part2: Effects on Near-Field Wave Patterns and Comparisons with Inviscid Theory," *Journal of Ship Research*, v. 37, n. 1, pp. 16-24, 1993.
- [3] Hino, T., "Computation of Free Surface Flow Around an Advancing Ship by the Navier-Stokes Equations," *Proceedings*,

Fifth International Conference on Numerical Ship Hydrodynamics, pp. 103-117, 1989.

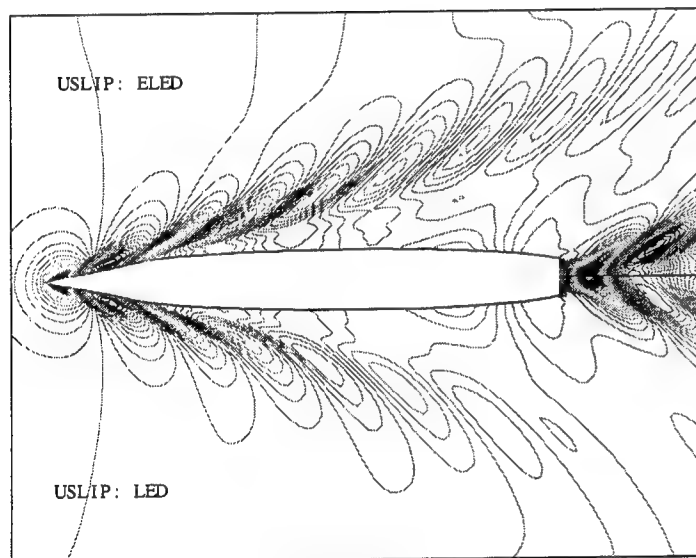
- [4] Miyata, H., Zhu, M., and Wantanabe, O., "Numerical Study on a Viscous Flow with Free-Surface Waves About a Ship in Steady Straight Course by a Finite-Volume Method," *Journal of Ship Research*, v. 36, n. 4, pp. 332-345, 1992.
- [5] Tahara, Y., Stern, F., and Rosen, B., "An Interactive Approach for Calculating Ship Boundary Layers and Wakes for Nonzero Froude Number," *Journal of Computational Physics*, v. 98, pp. 33-53, 1992.
- [6] Chen, H.C., Patel, V.C., and Ju, S., "Solution of Reynolds-Averaged Navier-Stokes Equations for Three-Dimensional Incompressible Flows," *Journal of Computational Physics*, v. 88, pp. 305-336, 1990.
- [7] Rosen, B.S., Laiosa, J.P., Davis, W.H., and Stavetski, D., "SPLASH Free-Surface Flow Code Methodology for Hydrodynamic Design and Analysis of IACC Yachts," *The Eleventh Chesapeake Sailing Yacht Symposium*, Annapolis, MD, 1993.
- [8] Farmer, J.R., Martinelli, L., and Jameson, A., "A Fast Multigrid Method for Solving the Nonlinear Ship Wave Problem with a Free Surface," *Proceedings, Sixth International Conference on Numerical Ship Hydrodynamics*, pp. 155-172, 1993.
- [9] Farmer, J.R., Martinelli, L., and Jameson, A., "A Fast Multigrid Method for Solving Incompressible Hydrodynamic Problems with Free Surfaces," *AIAA Journal*, v. 32, no. 6, pp. 1175-1182, 1994.
- [10] Jameson, A., "Optimum Aerodynamic Design Using CFD and Control Theory," *Proceedings, 12th Computational Fluid Dynamics Conference, San Diego, California, 1995*
- [11] Belov, A., Martinelli, L., Jameson, A., "A New Implicit Algorithm with Multigrid for Unsteady Incompressible Flow Calculations," *AIAA Paper 95-0049*, June 1995
- [12] Farmer, J.R., Martinelli, L., and Jameson, A., "Multigrid Solutions of the Euler and Navier-Stokes Equations for a Series 60 $C_b=0.6$ Ship Hull For Froude Numbers 0.160, 0.220 and 0.316," *Proceedings, CFD Workshop Tokyo 1994*, Tokyo, Japan, March 1994.
- [13] Jameson, A., "A Vertex Based Multigrid Algorithm For Three Dimensional Compressible Flow Calculations," *ASME Symposium on Numerical Methods for Compressible Flows*, Anaheim, December 1986.
- [14] Baldwin, B.S., and Lomax, H., "Thin Layer Approximation and Algebraic Model for Separated Turbulent Flows," *AIAA Paper 78-257, AIAA 16th Aerospace Sciences Meeting*, Reno, NV, January 1978.
- [15] Chorin, A., "A Numerical Method for Solving Incompressible Viscous Flow Problems," *Journal of Computational Physics*, v. 2, pp. 12-26, 1967.
- [16] Rizzi, A., and Eriksson, L., "Computation of Inviscid Incompressible Flow with Rotation," *Journal of Fluid Mechanics*, v. 153, pp. 275-312, 1985.
- [17] Martinelli, L., "Calculations of Viscous Flows with a Multigrid Method," Ph.D. Thesis, MAE 1754-T, Princeton University, 1987.
- [18] Farmer, J., "A Finite Volume Multigrid Solution to the Three Dimensional Nonlinear Ship Wave Problem," Ph.D. Thesis, MAE 1949-T, Princeton University, January 1993.
- [19] A. Jameson, "Analysis and design of numerical schemes for gas dynamics 1, artificial diffusion, upwind biasing, limiters and their effect on multigrid convergence," *Int. J. of Comp. Fluid Dyn.*, To Appear.
- [20] A. Jameson, "Analysis and design of numerical schemes for gas dynamics 2, artificial diffusion and discrete shock structure," *Int. J. of Comp. Fluid Dyn.*, To Appear.
- [21] J. Farmer, L. Martinelli, A. Jameson, and G. Cowles, "Fully-nonlinear CFD techniques for ship performance analysis and design," *AIAA paper 95-1690*, AIAA 12th Computational Fluid Dynamics Conference, San Diego, CA, June 1995.
- [22] A. Jameson, "Multigrid algorithms for compressible flow calculations," In *Second European Conference on Multigrid Methods*, Cologne, October 1985. Princeton University Report MAE 1743.
- [23] L. Martinelli and A. Jameson, "Validation of a multigrid method for the Reynolds averaged equations," *AIAA paper 88-0414*, 1988.
- [24] L. Martinelli, A. Jameson, and E. Malfa, "Numerical simulation of three-dimensional vortex flows over delta wing configurations," In M. Napolitano and F. Sabbetta, editors, *Proc. 13th International Conference on Numerical Methods in Fluid Dynamics*, pages 534-538, Rome, Italy, July 1992. Springer Verlag, 1993.
- [25] F. Liu and A. Jameson, "Multigrid Navier-Stokes calculations for three-dimensional cascades," *AIAA paper 92-0190*, AIAA 30th Aerospace Sciences Meeting, Reno, Nevada, January 1992.
- [26] T. Ratcliffe W. Lindenmuth, "Kelvin Wake Measurements Obtained on Five Surface Ship Models," *DTRC Report DTNSRDC 89/038*
- [27] J. Steinbrenner J. Chawner, "User's Manual for Gridgen,"
- [28] J. Reuther, A. Jameson, J. Farmer, L. Martinelli, and D. Saunders, "Aerodynamic Shape Optimization of Complex Aircraft Configurations via an Adjoint Formulation," *AIAA Paper 96-0094, AIAA 34th Aerospace Sciences Meeting*, Reno, NV, January 1996.
- [29] J. Alonso, and A. Jameson "Automatic Aerodynamic Optimization on Distributed Memory Architectures," *AIAA paper 96-0409, AIAA 34th Aerospace Sciences Meeting*, Reno, NV, January 1996.



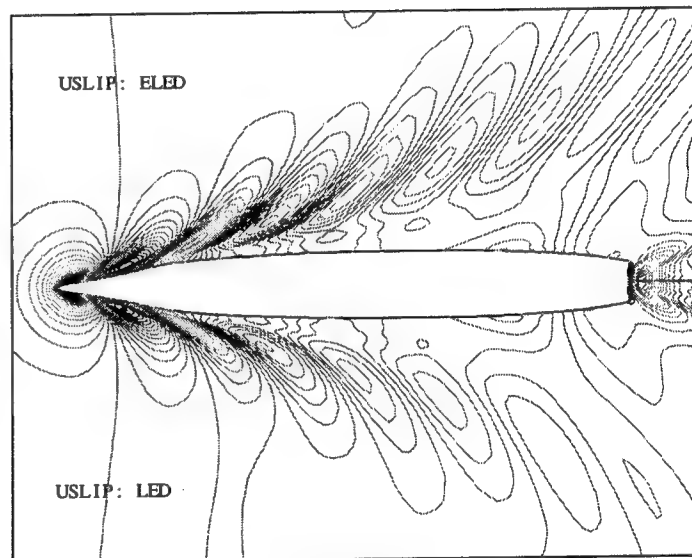
5a: Computed – Measured Waterlines
Euler Equations – $289 \times 49 \times 65$.



5b: Computed – Measured Waterlines
RANS Equations – $289 \times 49 \times 65$.



5c: Computed wave elevation – Euler Equations
 $289 \times 49 \times 65$.



5d: Computed wave elevation – RANS Equations –
 $289 \times 49 \times 65$.

Figure 5: Comparison of computed wave elevations using the Euler (left) and RANS (right) equations.

Comparison of Discretizations: Series 60 $Fr=.316$

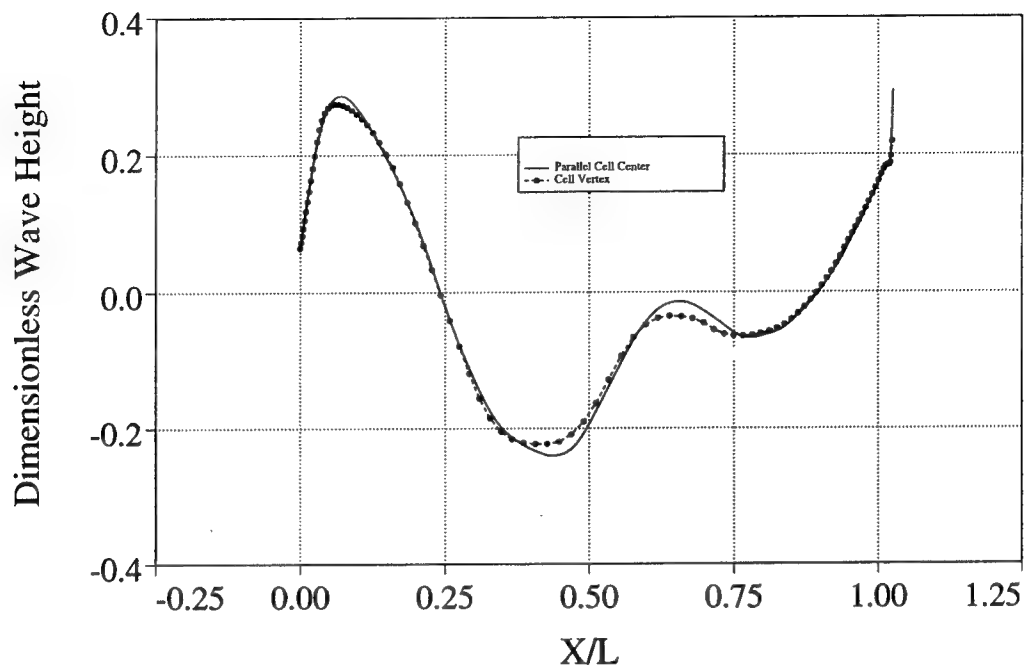


Figure 6:

Comparison with Experiment: Series 60 $Fr = .316$

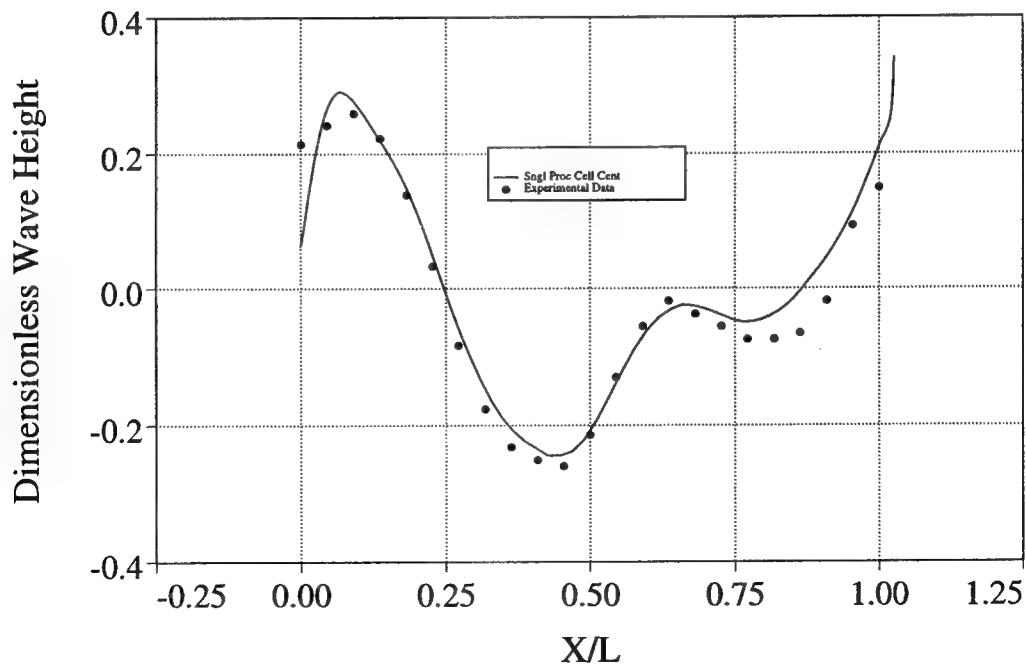


Figure 7:



Figure 8: Free Surface Contours: 5415 Fr = .2067

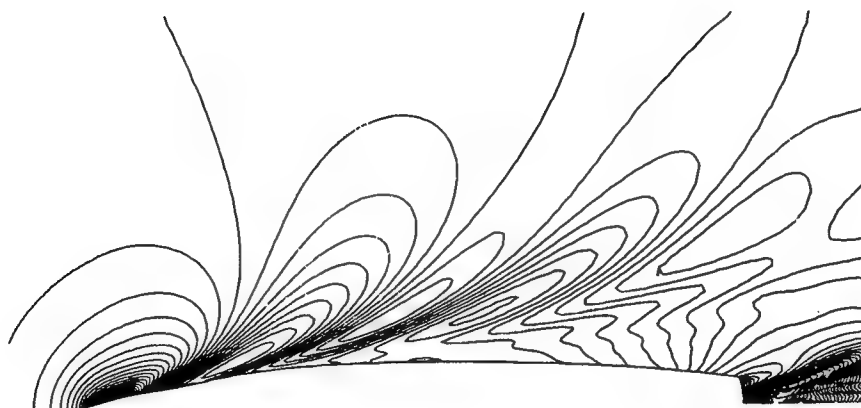


Figure 9: Free Surface Contours: 5415 Fr = .2760

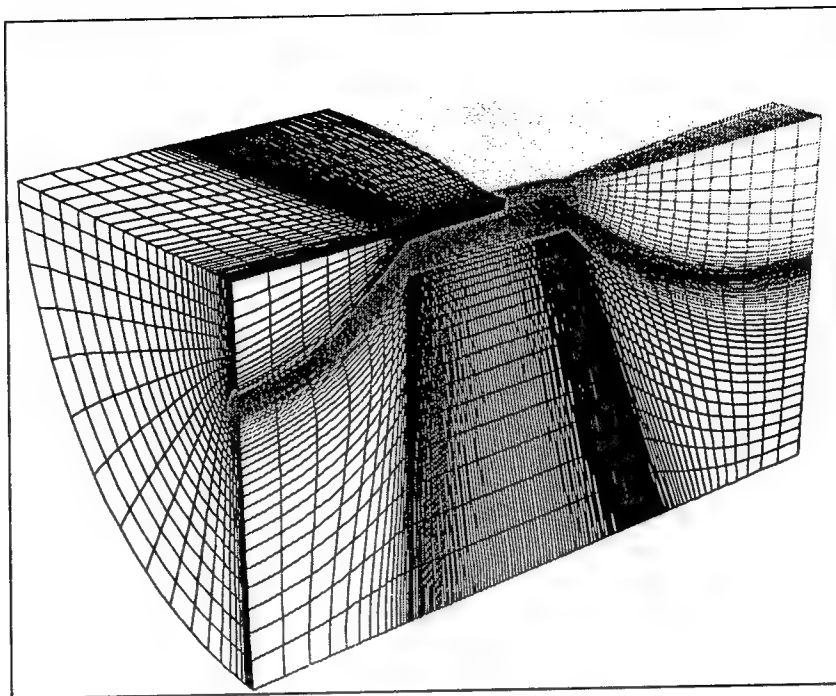


Figure 10: Domain Decomposition

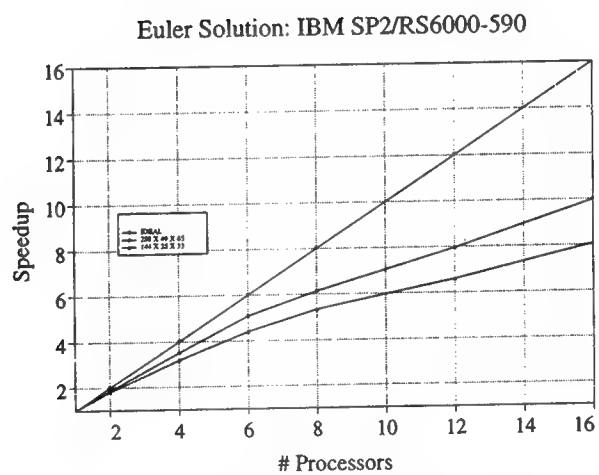


Figure 11: Parallel Speedup: Single Block H-O

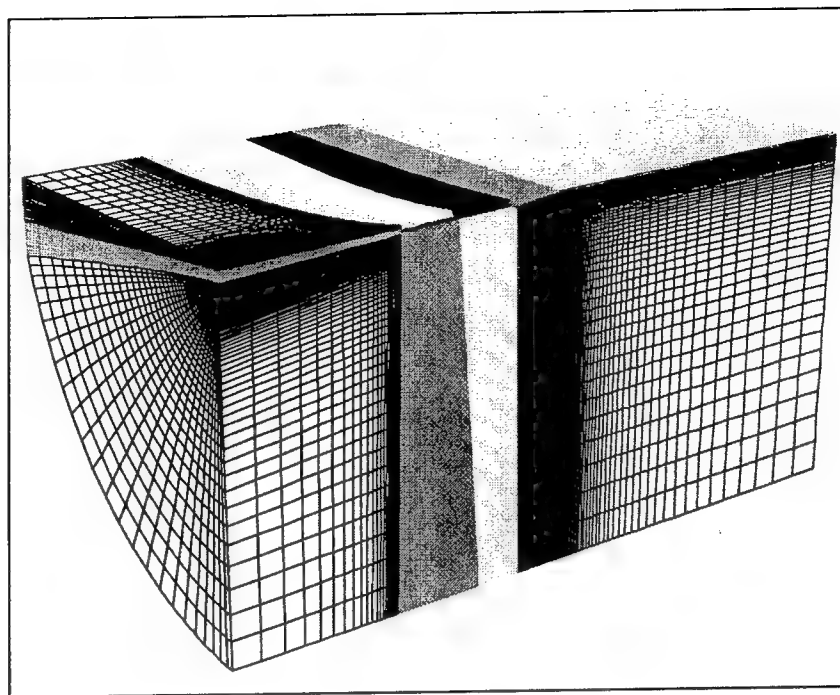


Figure 12: Model 5415 MESH: 20 BLOCKS

Parallel Speedup: 20 Blocks (IBM SP2/RS6000)

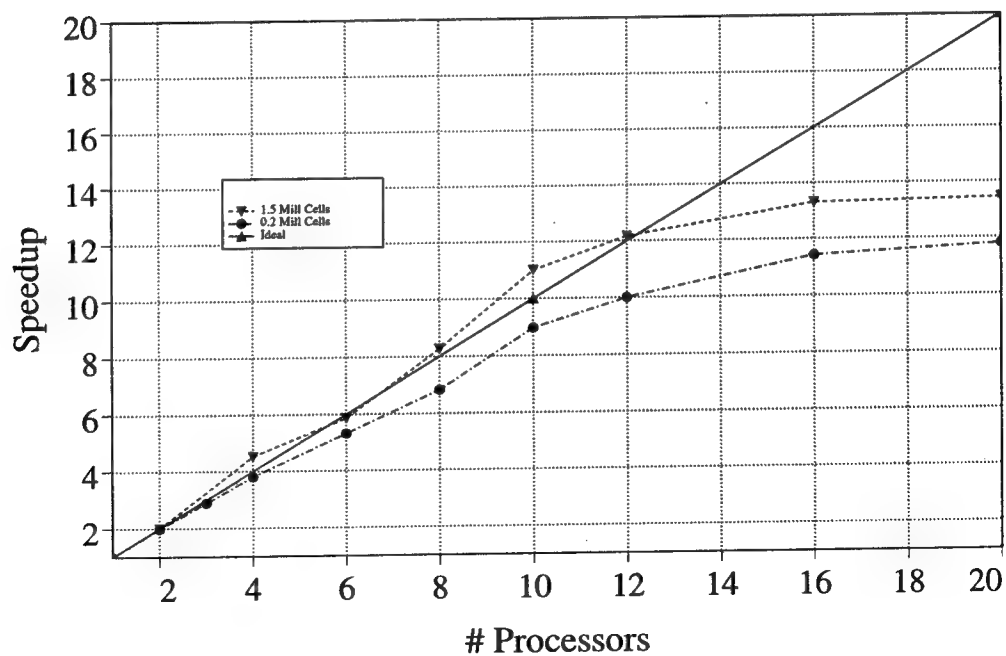


Figure 13: Parallel Speedup: Multiblock H-O

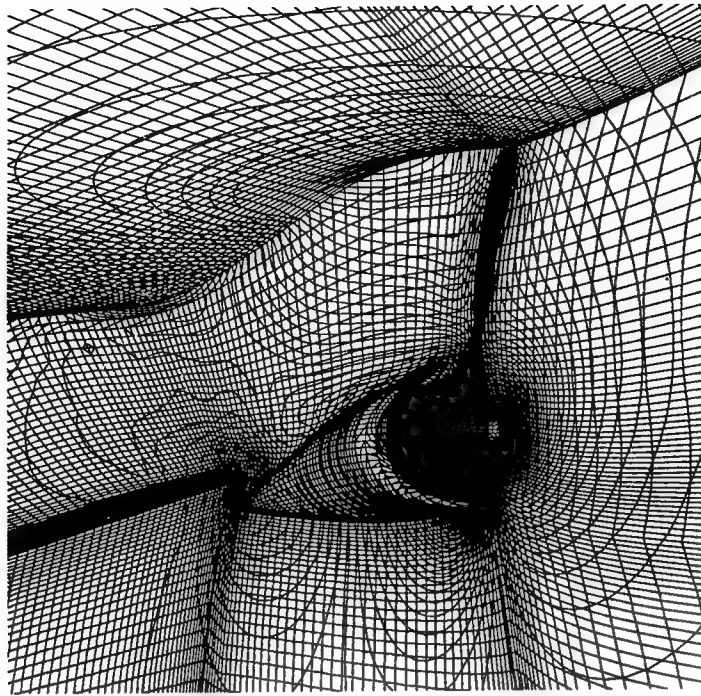


Figure 14: Pressure Contours on Sonar Dome

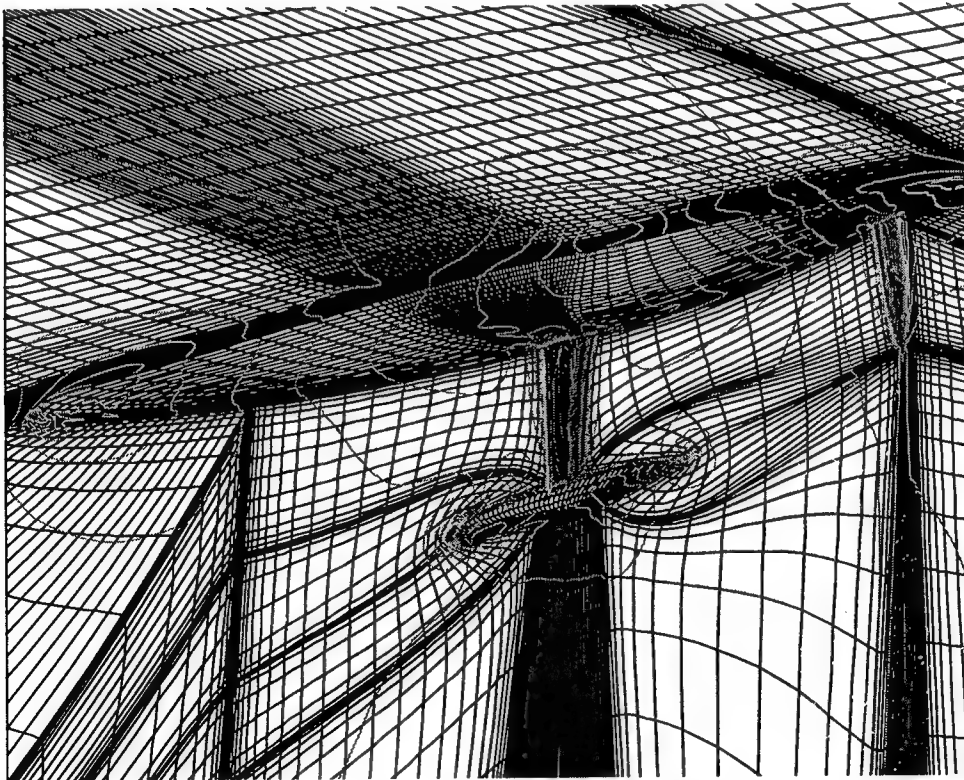


Figure 15: Single Block Mesh: IACC Yacht Hull

Validation of Incompressible Flow Computation of Forces and Moments on Axisymmetric Bodies Undergoing Constant Radius Turning

C.-H. Sung, T.-C. Fu, M. Griffin, T. Huang (David Taylor Model Basin, USA)

ABSTRACT

A numerical approach based on multiblock, multigrid, local refinement and preconditioning methods has been developed to solve the incompressible Reynolds-averaged Navier-Stokes (RANS) equations. Three-dimensional flow computations for axisymmetric bodies at angles of attack and yaw with and without steady turn are presented. In solving engineering problems, a numerical solution is considered "converged" after 4 to 5 orders of magnitude drop in the root-mean-square residual of the pressure and is considered grid-independent if all of the computed flow variables change less than 1% after the grid space has been reduced by at least a 50% increase in the grid cells in all three directions. Computations on four grids: $24 \times 8 \times 12$, $48 \times 24 \times 32$, $96 \times 48 \times 64$ and $144 \times 48 \times 72$ were performed to study the behavior of convergence and grid sensitivity. It is concluded that the solution with the $144 \times 48 \times 72$ grid for bodies at incidence is both converged and grid independent. The convergence rate is fast and is on the order of 1.5×10^{-5} cpu second per grid point per multigrid cycle based on a computation on a grid with 0.5 million grid cells on a single Cray C90 processor. The accuracy in the prediction of the forces and moments at various incidence angles is as good as the experimental accuracy ($\pm 5\%$). To achieve this level of accuracy, it is essential to use a $k-\omega$ turbulence model and to modify the standard Baldwin-Lomax turbulence model for the effects of the thick boundary layer near the stern and the cross-flow separation near the leeward side as the angle of attack increases. Both modifications are described. The converged solutions with the $96 \times 64 \times 48$ grid for body undergoing steady turns at various angles of attack and yaw may still be grid dependent. However, the computed forces and moments are within $\pm 20\%$ of the measured results and the trends of the computed results are in agreement with the data. The unique features of separated flow fields associated with turning bodies at combined angles of attack and yaw

are illustrated. The present work has made a significant advance towards the accurate prediction of the forces and moments acting on axisymmetric bodies at various angles of attack and yaw with and without steady turns, which is an essential step towards the accurate hydrodynamic prediction on realistic maneuvering vehicles for practical design purposes.

INTRODUCTION

Recent advances in Computational Fluid Dynamics (CFD) based on the numerical solutions of the Reynolds-Averaged Navier-Stokes (RANS) equations have demonstrated the capability to simulate complex turbulent flows of practical interest. Two major requirements for practical engineering applications are computational speed and accuracy. In particular, the computational accuracy must meet the accuracy required by the designers in order for a computer code to be really useful. One of the most challenging problems today in CFD is the prediction of the forces and moments acting on a realistic body at high Reynolds numbers on the order of 10^6 to 10^9 with computational accuracy within $\pm 5\%$ of the measured data. To meet the stringent requirements of speed and accuracy, sophisticated numerical techniques must be implemented. The purpose of this paper is to demonstrate that the speed and accuracy requirements can be met in the prediction of the forces and moments acting on the bodies of revolution at a Reynolds number on the order of 10^7 and at a wide range of incident angles. The accuracy of forces and moments predictions for a turning axisymmetric body at various angles attack and yaw achieved is about $\pm 20\%$. This achievement is a key step towards the realization of using a computer code as a practical design tool for maneuvering marine vehicles.

The computer code used in this paper is called IFLOW and has been developed by the authors over

the past few years (References 1-5). IFLOW incorporates most of the recently developed numerical techniques, including multiblock, multigrid, local refinement, preconditioning, and adaptive artificial dissipation model. The code is designed for general-purpose applications. It can be used for arbitrary 2D and 3D complex geometries and it can also be used to solve both steady and unsteady problems. At present, only the $k-\omega$ and the modified Baldwin-Lomax turbulence model are actively being used. These two simple models are quite adequate for attached turbulent boundary layer flows. Modifications of Baldwin-Lomax model are necessary because of some unique flow characteristics often encountered in ship hydrodynamic applications. These include the so-called thick boundary layers near ship sterns and the cross-flow separations typically occurring on maneuvering vehicles. In this paper, the numerical schemes implemented will be described and the modifications necessary to overcome the difficulties mentioned above will be presented. Practical definitions of a converged solution, a grid-independent solution and two measures of errors are given. The computed results on the 4 grids are then analyzed based on the definitions given.

NUMERICAL METHOD

The three-dimensional, incompressible, Reynolds-averaged Navier-Stokes equation is solved using the artificial compressibility approach first proposed by Chorin⁶ and subsequently generalized and improved by Turkel.⁷⁻⁸ This approach has been successfully used by Chang and Kwak⁹ and many others. The origin of the body coordinate system is fixed at the center of gravity of the vehicle as shown in Fig. 1. The x_b -axis is along the longitudinal axis of the vehicle with the positive x_b pointing forward, y_b in lateral direction with the y_b positive pointing to the starboard, and z_b in normal direction with the positive z_b pointing downward. Fig. 2 shows the velocity and angle of inclination of an axisymmetric body undergoing steady right turn. The turning radius is denoted by R_{turn} and the body with a total length L is rotating around a center point C with an angular velocity Ω in the positive z direction (pointing downward). The velocity components $[u, v, w]$ and angular velocity components $[p, q, r]$ relative to the body fixed axes $[x_b, y_b, z_b]$. The coordinate system attached to the rotating center C is $[x, y, z]$. The angles of attack and drift α and β are related to the velocity components by $\sin \beta = -v/U$ and $\tan \alpha = +w/u$, where $U^2 = u^2 + v^2 + w^2$. For a constant radius steady turn we have $x = x_b$, $z = z_b$, $y = y_b - R_{\text{turn}}$, when $\alpha = \beta = 0$. In hydrodynamics the orientation of a body in space is usually described in terms of angles of yaw (ψ), then of pitch (θ), and finally of roll (ϕ) and has the following relationship:

$$\begin{bmatrix} p \\ q \\ r \end{bmatrix} = \begin{bmatrix} \dot{\phi} - \dot{\psi} \sin \theta \\ \dot{\psi} \cos \theta \sin \phi + \dot{\theta} \cos \phi \\ \dot{\psi} \cos \theta \cos \phi + \dot{\theta} \sin \phi \end{bmatrix}; \quad \begin{bmatrix} u \\ v \\ w \end{bmatrix} = \begin{bmatrix} U \cos \alpha \cos \beta \\ -U \sin \beta \\ U \sin \alpha \cos \beta \end{bmatrix}$$

When the axisymmetric body executes a constant radius steady turn, the heading angular velocity is equal to the angular velocity of turn ($\dot{\psi} = \Omega$), and the angles of pitch and roll ($\phi = 0$) are constant. Then:

$$\begin{bmatrix} p \\ q \\ r \end{bmatrix} = \begin{bmatrix} -\dot{\psi} \sin \theta \\ \dot{\psi} \cos \theta \sin \phi \\ \dot{\psi} \cos \theta \cos \phi \end{bmatrix}; \quad \begin{bmatrix} u \\ v \\ w \end{bmatrix} = \begin{bmatrix} U \cos \alpha \cos \beta \\ -U \sin \beta \\ U \sin \alpha \cos \beta \end{bmatrix} = \begin{bmatrix} U \cos \theta \cos \psi \\ -U \sin \psi \\ U \sin \theta \cos \psi \end{bmatrix}$$

Let $\tau_{c.f.}$ be the local resultant cross flow angle positive clockwise (looking forward) with respect to the body coordinate y_b (positive starboard). Then:

$$\tau_{c.f.} = \tan^{-1} \left(\frac{-w + qx_b}{-v - rx_b} \right) = \tan^{-1} \left(\frac{-\Omega R_{\text{turn}} \sin \theta \cos \psi}{\Omega R_{\text{turn}} \sin \psi - x_b \dot{\psi} \cos \theta} \right)$$

In this case $\alpha = \theta$ and $\beta = \psi$. The nondimensional turning angular velocity $\dot{\psi}^* = \dot{\psi}/(U/L) = \Omega/(U/L) = L/R_{\text{turn}} = \tau^*$ for small angles of pitch and yaw, where R_{turn} is the turning radius and L is the body length.

The formulation of IFLOW developed at the David Taylor Model Basin is based on the following conservative formulation

$$P_0^{-1} q_t + F_x + G_y + H_z = S \quad (1)$$

where the subscripts indicate partial differentiations with respect to time t , and the three Cartesian coordinates x, y , and z . The preconditioned matrix P_0 in the conservative form and the column vectors of the dependent variable q and fluxes F, G, H and the source term S are defined as

$$P_0^{-1} = \begin{bmatrix} (1+\gamma)\beta^{-2} & \gamma\beta^{-2}u & \gamma\beta^{-2}v & \gamma\beta^{-2}w \\ (1+\alpha+\gamma)\beta^{-2}u & 1+\gamma\beta^{-2}u^2 & \gamma\beta^{-2}uv & \gamma\beta^{-2}uw \\ (1+\alpha+\gamma)\beta^{-2}v & \gamma\beta^{-2}vu & 1+\gamma\beta^{-2}v^2 & \gamma\beta^{-2}vw \\ (1+\alpha+\gamma)\beta^{-2}w & \gamma\beta^{-2}wu & \gamma\beta^{-2}wv & 1+\gamma\beta^{-2}w^2 \end{bmatrix},$$

$$q = \begin{bmatrix} p^* = \frac{p}{\rho} \\ u \\ v \\ w \end{bmatrix}, \quad F = \begin{bmatrix} u \\ u^2 + p^* - \tau_{xx} \\ uv - \tau_{xy} \\ uw - \tau_{xz} \end{bmatrix}, \quad G = \begin{bmatrix} v \\ uv - \tau_{yx} \\ v^2 + p^* - \tau_{yy} \\ vw - \tau_{yz} \end{bmatrix}$$

$$H = \begin{bmatrix} w \\ uw - \tau_{zx} \\ vw - \tau_{zy} \\ w^2 + p^* - \tau_{zz} \end{bmatrix}, \quad \text{and} \quad S = \begin{bmatrix} 0 \\ \Omega(\Omega x + 2v) \\ \Omega(\Omega y - 2u) \\ 0 \end{bmatrix} \quad (2)$$

where p is the pressure, ρ is the constant density, u , v and w are the three Cartesian velocity components. The Reynolds stresses are defined as

$$\tau_{ij} = R_L^{-1} \nu \left\{ \frac{\partial u_i}{\partial x_j} + \frac{\partial u_j}{\partial x_i} \right\}, \quad i, j = 1, 2, 3 \quad (3)$$

where $\mathbf{u} = (u, v, w)$, $\mathbf{x} = (x, y, z)$, ν is the sum of the kinematic and eddy viscosities, and R_L is the Reynolds number based on the body length. The variables are nondimensionalized in the conventional manner.

The three parameters α , β^{-2} , and γ are the preconditioning parameters to be determined for fast convergence. The spatial discretization is based on the cell-centered central difference finite-volume formulation in the semi-discrete form. An explicit one-step, five-stage Runge-Kutta time-stepping scheme is used. In this scheme the artificial dissipation term is evaluated only at the first, third and fifth stage with an appropriate weighting at each stage to increase the stability limit. Specifically, the parabolic stability limit along the real axis has been raised to 9 which has some advantage in stability when solving the Navier-Stokes equations. The techniques used to accelerate the rate of convergence are particularly emphasized. They include preconditioning, bulk viscous damping, local time-stepping, implicit residual smoothing, adaptive artificial dissipation and multigrid.^{1,2}

Multiblock Multigrid Local Refinement Technique

The multigrid method developed by Jameson¹⁰ to accelerate the convergence of a system of hyperbolic equations has been adopted. By the cyclic use of a sequence of fine to coarse grids, the multigrid technique is very effective in damping the solution modes with long wave lengths which are primarily responsible for slow convergence. V-, W-, and F-cycle multigrid techniques have been implemented. Boundary conditions are updated at each Runge-Kutta stage at every grid level in the fine-to-coarse path, but they are not updated in the coarse-to-fine path. This practice is mainly to avoid introducing boundary condition interpolation errors to finer grids. For ease of coding the grid cell number in each coordinate direction for a coarse grid is half of that used in the next finer grid.

A new numerical technique based on multiblock, multigrid and local refinement methods has been implemented in IFLOW. In this approach, the computational grid is generated in the following manner: A very fine grid with a sufficiently large number of grid cells to achieve the desired resolution including the near wall region is first generated. In

complex geometry, a multiblock structure may be used. The purpose of the multiblock structure is designed mainly to make the grid generation of complex geometries easier and smoother. The grid is then locally refined by patches of finer meshes in the regions where flow variation is relatively rapid. Thus, the final grid will have a hierarchical structure with different mesh levels, blocks and zones. The grid spacing of the fine grid is kept at one half of the next coarser grid spacing as in the standard multigrid. The solution procedure is the following: First, a global solution is obtained by a standard multigrid method on a global grid with the multiblock structure. The resolution of the global solution is then successively improved by a local refinement technique which is also based on the multigrid method for fast convergence. The coupling of multigrid and local refinement is the main difference between the present method and the conventional local refinement methods. Numerical instability and lack of flux conservation may occur in the coarse/fine grid interface. The possibility of these numerical difficulties is believed to be greatly minimized by using the present local refinement method for the following reason. In the present method, the finer mesh is embedded entirely in the next coarser mesh while in the conventional methods, the fine and coarse meshes are connected only by the coarse/fine grid interface. Clearly the communication between the fine and coarse mesh is much better in the present method. The communication is further enhanced by the use of the multigrid technique. Despite all the arguments, it has been found that although it is easy to maintain continuity of the mean flow variables such as the pressure and the mean velocity across the coarse/fine interface, the continuity across the interface is much harder to achieve with the shear stress near the wall. This is an area which requires further research.

Preconditioning Technique

Preconditioning is a method used to reduce the condition number of the iterative methods in linear algebra. This concept used to accelerate the rate of convergence was applied by Chorin⁶ to obtain the steady-state solution of the incompressible flow problems. Chorin introduced an artificial time derivative of the pressure to the continuity equation with a multiplicative variable β which has the physical meaning of the speed of sound. Since the speed of sound in incompressible flow is much faster than the fluid velocity, the system of the governing equations is very stiff with a large condition number. Consequently, the rate of convergence of the numerical solution will be very slow. However, if only the steady-state solution is of interest and the accuracy during the transient state is not of concern then the value of β can be kept on the

same order of magnitude as the fluid velocity during the transient state. In this manner, the condition number is small and the rate of convergence will be significantly improved. This is the so called artificial compressibility method and is a primitive form of preconditioning. Rewriting the system of equations in conservative form (1) in nonconservative form

$$P^{-1}q_t + Aq_x + Bq_y + Cq_z = 0 \quad (4)$$

where $q = (p, u, v, w)^T$. The preconditioning matrix P^{-1} in nonconservative form is different from P_0^{-1} in conservative formulation and is given by

$$P^{-1} = \begin{bmatrix} (1+\gamma)\beta^{-2} & \gamma\beta^{-2}u & \gamma\beta^{-2}v & \gamma\beta^{-2}w \\ \alpha\beta^{-2}u & 1 & 0 & 0 \\ \alpha\beta^{-2}v & 0 & 1 & 0 \\ \alpha\beta^{-2}w & 0 & 0 & 1 \end{bmatrix} \quad (5)$$

Appropriate choice of the three preconditioning parameters α , β , and γ can improve convergence and stability. It can also improve the accuracy in the sense that a smaller amount of artificial dissipation can be used. Therefore, a smaller numerical diffusion is introduced in the solution. The original Chorin preconditioning is obtained by setting $\alpha=0$ and $\gamma=0$. The condition gives a symmetric precondition and ensures that the system of partial differential equations (4) is well-posed. Recent numerical experimentation indicates that an optimal choice of the preconditional parameters is

$$\alpha = 1, \gamma = 0 \text{ and } \beta^{-2} = \max(|u|^2, \varepsilon_\beta), \varepsilon_\beta = 0.7 \quad (6)$$

This can be understood by an observation that the four eigenvalues of the characteristic matrix have the same magnitude (implying a condition number of 1).

To maintain numerical stability, a proper amount of artificial dissipation must be added to the right hand side of (4)

$$q_t + PAq_x + PBq_y + PCq_z = [PA]q_{xxx} + [PB]q_{yyy} + [PC]q_{zzz} \quad (7)$$

Thus for conservation formulation:

$$P_0^{-1}q_t + F_x + G_y + H_z = (P_0^{-1}[PA]q_{xxx})_x + (P_0^{-1}[PB]q_{yyy})_y + (P_0^{-1}[PC]q_{zzz})_z \quad (8)$$

The present formulation shown in (8) for the incompressible flow with preconditioning parameters

given in (6) is equivalent to the highly accurate matrix dissipation technique demonstrated by Swanson and Turkel¹¹ and Turkel and Vatsa¹² for the compressible flow.

Boundary Conditions

The boundary conditions used on the solid wall of a rotating body are that the three velocity components and the normal pressure gradient are set equal to zero:

$$u=v=w=0, \text{ and}$$

$$\hat{n} \cdot \nabla [p - \frac{1}{2}\Omega^2(x^2 + y^2)] = 0, \quad (9)$$

The far field inflow boundary conditions relative to the rotating system are based on the prescribed values for the three velocity components and pressure:

$$[u, v, w, p] = [\Omega y, -\Omega x, 0, p_0], \quad (10)$$

The far field outflow boundary conditions are based on a zero-gradient for the three velocity perturbation components and a non-reflecting condition for the pressure:

$$[u, v, w] = [\Omega y + u', -\Omega x + v', w'], \quad (11)$$

$$\hat{n} \cdot \nabla [u', v', w'] = 0, p: \text{nonreflecting}$$

The non-reflecting boundary condition used here evolved from the technique developed in Hedstrom¹³, and Rudy and Strikewerda¹⁴ and is particularly important for computation when a relatively small computational domain is used as in the present computation. This condition is obtained by setting the time derivative of the characteristic variable corresponding to the wave coming into the computational domain as described by Sung.¹⁵

Turbulence Model

The standard $k-\omega$ turbulence model¹⁶ and Baldwin-Lomax turbulence model¹⁷ with modifications are used in this paper. The standard two-equation $k-\omega$ model developed by Wilcox¹⁶ is used in this paper,

$$\frac{\partial K}{\partial t} + \bar{u}_i \frac{\partial K}{\partial x_i} = \tau_{ij} \frac{\partial \bar{u}_i}{\partial x_j} - \beta^* K \omega + \frac{\partial}{\partial x_i} [(v + \sigma^* v_T) \frac{\partial K}{\partial x_i}]$$

$$\frac{\partial \omega}{\partial t} + \bar{u}_i \frac{\partial \omega}{\partial x_i} = \alpha \frac{\omega}{K} \tau_{ij} \frac{\partial \bar{u}_i}{\partial x_j} - \beta \omega^2 + \frac{\partial}{\partial x_i} [(v + \sigma v_T) \frac{\partial \omega}{\partial x_i}] \quad (12)$$

$$\text{Where } v_T = \gamma^* \frac{k}{\omega}, \gamma^* = 1, \sigma = \sigma^* = 0.5, \beta^* = \frac{9}{100}, \beta = \frac{3}{40}$$

Near the wall: @ $y \approx 0$; $\tau_{12} = -\overline{u_1' u_2'} = \nu_T \frac{\partial u}{\partial y}$

$$u = \frac{u_\tau}{\kappa} \ln\left[\frac{u_\tau y}{\nu}\right]; K = \frac{u_\tau^2}{\sqrt{\beta^*}}; \omega = \frac{u_\tau}{(\sqrt{\beta^*} \kappa y)};$$

$$\frac{\tau}{K} = \sqrt{\beta^*} = \frac{3}{10} \text{ (data); } \alpha = \frac{\beta}{\beta^*} - \frac{\sigma \kappa^2}{\sqrt{\beta^*}} \approx \frac{5}{9}$$

The model can be extended to treat flow transition and surface roughness (Wilcox¹⁶).

The Baldwin-Lomax formulation of the eddy viscosity without using the boundary layer displacement thickness is easier to implement than the equivalent model of Cebeci and Smith.¹⁸ Crucial to the model is the maximum value F_{\max} of the F -function defined as $F(y) = y|\omega|[1 - e^{-y/A^*}]$ and y_{\max} of the corresponding value of y where F_{\max} occurs. Modification of them and the correct way to locate them constitute the main changes to the standard Baldwin-Lomax turbulence model.

Two major modifications are made to overcome the difficulties arising from (1) the so-called thick boundary layer unique in ship hydrodynamic application occurring near the ship stern and (2) the cross-flow separation in a maneuvering vehicle. Both difficulties result in excessive eddy viscosity causing the mean velocity to be overpredicted and the flow separation to be delayed or suppressed.

Two corrections are needed to overcome the difficulty in the thick boundary layer. The experimental data of Huang, et al.^{19,20,21} indicate that the mixing length computed by a standard eddy viscosity model is approximately twice as large compared to the mixing length derived from the experimental data near the stern where the body cross sectional area is rapidly diminishing. A correction on the outer eddy viscosity near the stern has been proposed by Huang.^{19,20,21} The other correction is an attempt to account for the effect of the adverse pressure gradient which also occurs near the stern and has been discussed in Refs. 3 and 4. In the symmetric wake of a single axisymmetric body or a two-dimensional foil, the modified eddy viscosity of Renze, Buning, and Rajagopalan²² is considered.

The second modification to account for the cross-flow separation is the most crucial to accurate prediction of the forces and moments. As the incidence angle increases, the cross-flow separation eventually results in vortex roll-up which then departs from the body. As a result, another local maximum of the F -function occurs near center of the departing concentrated vorticity in addition to the local maximum near the center of the attached wall shear layer. Since the distance to the wall of the departing

vortex can be several orders of magnitude larger than that of the wall shear layer, the predicted eddy viscosity may be several orders of magnitude too large and flow separation is likely to be delayed or suppressed. The problem of multiple peaks just described has been reported by Degani and Schiff²³ and they have also proposed a method to locate the correct peak in the wall shear layer, or the so-called first peak. The modification of the Baldwin-Lomax model made by them has been implemented in IFLOW. The search for the first peak has been found to be notoriously difficult and unreliable. This difficulty has been overcome by using a method where a range is first defined and then a maximum is searched for just inside the range.

RESULTS AND DISCUSSION

Solution Convergence and Grid-Independent Solution

Validation of computed results with measured data must be performed with care. This is because both computation and experiment have their own errors and, in addition, there are many factors which can affect the computed result but can not be precisely defined. In general, code validation can be meaningful only if the numerical solution can be shown to have converged and is also grid independent. It is possible to drive the convergence to machine zero but it will not be necessary nor practical to make such a demand for real engineering problems. It is our experience after many comparisons between computations and experiments that a numerical solution can be considered as converged after 4 to 5 orders of magnitude drop in the root-mean-square residual of the pressure. It is even harder to give a meaningful definition of grid independence for practical engineering problems. Nevertheless, a numerical solution will be called grid independent if the pressure, mean velocity components, the shear stress, and the force and moment do not change more than 1% after the grid space has been reduced by at least a 50% increase in grid cells in all three directions.

Solution Convergence

The optimal preconditioning described by (6) has been implemented in IFLOW. The overall quality of the optimal preconditioning technique is illustrated in Figs. 3 through 5. The residual is defined as the RMS difference between the nondimensional pressures at the current and previous multigrid cycles. Fig. 3 shows that the residuals drop to machine zero in about 2000 iterations for a 24x8x12 grid and in about 4000 iterations for a 48x24x32 grid of a SUBOFF axisymmetric body at angles of attack of 0 and 16 degrees. Fig. 4 illustrates the rates of convergence for a 144x48x72 grid at various angles of attack. The reduction of residuals by 4 or 5 orders of magnitude can be

achieved very quickly for all angles of attack. The residual continues to drop for zero angle of attack but not for higher angles of attack. This probably implies that the grid quality must be refined for higher angles of attack in order to further improve the convergence rate. Fig. 5 demonstrates the rates of convergence for the flow on DTMB body1 executing steady starboard turn. Both 0° and 8° yaw angles with a constant turning radius of $R_{turn}=1.54L$ are included in Fig. 5. A $48 \times 32 \times 24$ grid and a $96 \times 48 \times 32$ grid are used. The reduction of residuals by 4 orders of magnitude can also be achieved within 100 iterations for turning computations. During the course of computation it was noted that grid cells with large aspect ratios and rapid variation of two adjacent grid spacings tend to reduce the rate of convergence. In order to improve the rate of convergence the values of y_1^+ , the aspect ratios of grid cells, and the variation of adjacent grid spacings must be carefully controlled and must also be adapted to the flow field characteristics. Flow adapted grid distributions to improve the rate of convergence is an area for further research. It is important to note that the present computational speed of 1.5×10^{-5} cpu second per grid cell per multigrid cycle in a single Cray C90 processor has been achieved for all angles of attack with the one-half million grid cells.

Grid-Independent Solution

To identify a grid independent solution, computations on 4 grids: ((axial) x (circumferential) x (normal)) = $24 \times 8 \times 12$, $48 \times 24 \times 32$, $96 \times 48 \times 64$ and $144 \times 48 \times 72$ were performed. The outflow boundary is located 2.5 body lengths downstream of the tail of the body and the outer boundary is about 0.68 body lengths. The grid distributions in the axial and circumferential directions were selected with finer grids concentrated in rapidly changing flow regions such as the nose, tail and near the leeward side where the flow separates. The distribution in the direction normal to the wall is made so that the boundary layer characteristics on the hull can be resolved. This requires that the maximum value of y_1^+ be limited to less than 7 and the average value of y_1^+ not to exceed 5. Comparison of the results from the $96 \times 32 \times 48$ and $144 \times 48 \times 72$ grids shows that the computed pressure, the mean velocity, force and moment differ by less than 1% and the shear stress differs by less than 2%. Thus the computed solutions based on a $96 \times 32 \times 48$ grid and a $144 \times 48 \times 72$ grid satisfy the definition of a grid-independent solution for an axisymmetric body at incidence. Because of limited experience in computing a turning axisymmetric body, we are not sure that a $96 \times 48 \times 32$ grid presented in this paper had achieved the grid-independent solution. The present computed force and moment coefficients are within the $\pm 20\%$ of

the unpublished measured data. The computed results have revealed many unique flow features associated with a turning axisymmetric body, especially at combined yaw and pitch.

Error Analysis

Two measures of error will be used. One is the root-mean-square (RMS) value of the difference between the reference and the solution to be compared denoted as v^f and v^c respectively. The second measure is the distance weighted average angle error. They are defined respectively as

RMS Error,

$$\epsilon_{rms} = \frac{[\sum_{i=1}^N (v_i^f - v_i^c)^2 / N]^{1/2}}{[(\sum_{i=1}^N (v_i^f)^2 / N) (\sum_{i=1}^N (v_i^c)^2 / N)]^{1/4}} \quad (12)$$

Distance Weighted Average Angle Error,

$$\epsilon_1 = \frac{\sum_{i=1}^N D_i \alpha_i}{\sum_{i=1}^N D_i} \quad (13)$$

where $D_i = \sqrt{(v_i^f)^2 + (v_i^c)^2}$, and

$$\alpha_i = \cos^{-1} \left\{ \frac{|v_i^f + v_i^c|}{\sqrt{2[(v_i^f)^2 + (v_i^c)^2]}} \right\}$$

where N is the total number of data values used in the comparison. These definitions can also be applied to experimental data. Applying these error measures to the computed results shown in Fig. 6 gives the following error estimates.

Computed Force and Moment on Axisymmetric Bodies at Incidence

The comparison of the computed ($144 \times 48 \times 72$ and $96 \times 32 \times 48$ grids) and the measured values of the axial force X, normal force Z, and the pitching moment M for the SUBOFF ($L/D=8.6$) body is shown in Fig. 6 and for Body 1 ($L/D=11.0$), Albacore ($L/D=7.3$), and DTMB Model 4156 ($L/D=6.0$) in Fig. 7. These models cover the range of typical underwater vehicle geometry. The experiments were conducted in the Deep Water Basin of the David Taylor Model Basin by Roddy.²⁴ The measurements of the Albacore body were made by Dempsey²⁵ in the same model basin. The unpublished data for Body 1 and Model 4156 were also obtained by Dempsey using the same measuring apparatus in the same facility. The measurement uncertainties of the data are estimated to be 5% for the normal force and pitch moment and 15% for the axial force. It is important to note that both the RMS errors of the computed axial and normal forces and the pitching moment for all the axisymmetric bodies at incidence shown in Figs. 6 and 7 are all within 5% from the faired

measured data when either the standard $k-\omega$ or the modified Baldwin-Lomax turbulence model is used with either the $96 \times 32 \times 48$ or $144 \times 48 \times 72$ grid. The standard Baldwin-Lomax turbulence model underpredicts the magnitudes of the normal force and overpredicts the magnitudes of the pitching moment. The present work has made a significant advance towards the accurate prediction of the forces and moments on the axisymmetric bodies at incidence. This achievement is an essential step towards the prediction of the forces and moments on maneuvering vehicles.

Computed Force, Moment, and Flow Field on Axisymmetric Bodies Undergoing Steady Turns

Using the nomenclature shown in Figs. 1 and 2, the nondimensional forces $[X', Y', Z']$ and moments $[K', M', N']$ coefficients are the linear forces $[X, Y, Z]$ along the body axes divided by $\rho U^2 L^3/2$ and moments $[K, M, N]$ about the body axes by $\rho U^2 L^3/2$. The nondimensional turning radius is denoted by $r' = L/R_{turn} = \Omega/(U/L)$, where $U = \Omega R_{turn}$. The unpublished DTMB data of Bedel, et al., obtained in the DTMB Rotating Arm Facility with an uncertainty of $\pm 20\%$ are used to compare the computed force and moment coefficients. This type of comparison can only be used to guide the development computational capability for maneuvering applications and may not be used for rigorous code validation.

When the axisymmetric body executing a constant radius right turns at a zero angle of attack and yaw, the body is subjected to a negative side force ($-Y$) due to centrifugal force and a negative yawing moment ($-N$), and they are in the plane of motion. The computed and measured unbalance "in-plane" side force and yawing moment coefficients, Y' and N' , are shown in Fig. 8 for the DTMB body 1 at various turning radii. The amplitude of both $-Y'$ and N' increase with decreasing turning radius, R_{turn} , or increasing nondimensional yaw rate $r' = L/R_{turn}$. The computed values agree with the measured data to within $\pm 20\%$.

The effect of yaw angle on the "in-plane" axial force (drag= $-X$), side force and yawing moment coefficients are shown in Fig. 9 for the nondimensional turning radius of $r' = 0.65$ at zero angle of attack. As expected the drag coefficient increases with increasing yawing angle during a turn. The negative values of side force and yawing moment coefficients, $-Y'$ and $-N'$, decrease with increasing yawing angle. It is interesting to note that the zero yawing moment is at yaw angle equal to about 10 degrees. Again the computed values agree with the measured data to within $\pm 20\%$.

Fig. 10 shows the computed and measured vertical force and pitch moment coefficients, Z' and M' , which is out of the plane of motion. It is important to note that the "out-of plane" pitching

moment coefficient increases with increasing pitch angle for the body at zero yaw angle; this is a destabilizing condition. The "out-of-plane" pitch moment coefficient, however, decreases with increasing pitch angle for body at 12° yaw angle; this becomes a stabilizing condition. The combination of yaw and pitch angles during a turn can produce drastic different stability conditions for a body undergoing a steady turn.

The separated flow fields associated a turning body at combined angles of attack and yaw are very complex. Fig. 11 shows the computed vorticity field of a starboard turning body at pitch angle equal to -4° . Recall that $\tau_{c.f.}$ is the local resultant cross flow angle positive clockwise (looking forward) with respect to y_b .

$$\tau_{c.f.} = \tan^{-1}\left(\frac{-w + q x_b}{-v - r x_b}\right) = \tan^{-1}\left(\frac{-\Omega R_{turn} \sin \theta \cos \psi}{\Omega R_{turn} \sin \psi - x_b \dot{\psi} \cos \theta}\right)$$

When $\theta = \psi = 0$, then $\tau_{c.f.}$ is zero. Upstream of the center of gravity (C.G.) x_b is positive, the resultant cross flow points to port. The dotted cross flow vector shown in Fig. 11 indicates the cross flow at the body nose ($x_b = \bar{x}_{C.G.} - \bar{x}$ and $\bar{x} = 0$ is at the body nose and points to the stern). The resultant cross flow points to starboard for negative x_b (solid cross flow vector shown in Fig. 11). The resultant cross flow is in the plane of motion and changes direction at C. G.. The separated flow field is symmetrical with respect to the y_b axis shown in Fig 11a. When the body with a pitch angle of -8° is executing a port turn as shown in Fig. 11b, the resultant cross-flow angle is no longer in the plane of motion and changes direction along the body. The separated flow is no longer symmetrical with respect to the y_b axis. The variation of cross-flow angle along the body axis shown in Fig. 11b is caused by the combined negative pitch angle of -8° and the nondimensional turn rate of $r' = 0.65$. Under these conditions the cross-

flow angle for a left turning body is $\tau_{c.f.} = \tan^{-1}[0.2162/(x_b/L)]$. The computed vorticity field of a starboard turning body at a combination of yaw and pitch angles equal to 12° and -8° is shown in Fig 11c. The variation of cross-flow caused by combination of yaw and pitch angles and turning rate of $r' = 0.65$ are shown in Fig. 11c. The solid and dotted vectors indicate the directions of the local cross flow and reference cross flow at the body nose. As indicated in Fig. 10, the cross flow variation along the body axis has a profound influence on the "out-of-plane" forces and moments. It is the first time that this type of complex flow has satisfactorily been predicted by a Reynolds-Averaged Navier-Stokes (RANS) calculation and the computed forces and moments are within the measurement uncertainties.

CONCLUSIONS

An incompressible Reynolds-averaged Navier-Stokes computational procedure has been presented. Numerous computations were carried out on axisymmetric bodies at various angles of attack and yaw, with and without a steady turn to investigate the effects of grid sensitivity and turbulence model on the computed flows and the forces and moments acting on the body. We consider that a numerical solution is "converged" after 4 to 5 orders of magnitude drop in the root-mean-square residual of the pressure. We define that a solution is grid-independent when all the computed flow variables change less than 1% after the grid space has been reduced by at least a 50% increase in grid cells in all three directions.

The standard $k-\omega$ and modified Baldwin-Lomax turbulence models are used in this paper. Two simple modifications of the standard Baldwin-Lomax turbulence model were made: one for the ship stern flows where the boundary layer is thick and the other for the flows with cross-flow separations. The accuracy in the prediction of the forces and moments at various incidence angles using the two turbulence models with a $144 \times 48 \times 72$ grid is as good as the experimental accuracy (within $\pm 5\%$ of the measured data).

The converged solutions with the $96 \times 48 \times 64$ grid for a body undergoing steady turns at various angles of attack and yaw may still be grid dependent. However, the computed forces and moments for a body undergoing steady turns at various angles of attack and yaw agree with the measured results to within $\pm 20\%$ and the trends of the computed results are in agreement with the data. The unique features of separated flow fields associated with turning bodies at combined angles of attack and yaw were illustrated.

The present work has made a significant advance towards the accurate prediction of the forces and moments acting on axisymmetric bodies at various angles of attack and yaw with and without steady turns. This advance is an essential step towards the accurate prediction of the forces and moments on realistic maneuvering vehicles for practical design purposes.

It has been observed that when the average values of y_1^+ of the first grid cell center from the wall is smaller than 5, both the RMS and average angle error between all the measured forces and moments are within the measurement uncertainties. Present computations indicate that multiblock (for complex geometry), multigrid (for fast solution) and local refinement (for efficient use of grid cells) techniques implemented in the computer code called

IFLOW is fast. A typical computation based on one half million grid cells requires 300 multigrid cycles using 37 cpu minutes of a single Cray C90 processor to reduce the pressure residual by 5 to 6 orders of magnitude. This implies a speed of approximately 1.5×10^{-5} cpu seconds per grid point per multigrid cycle in a single Cray C90 processor.

ACKNOWLEDGMENT

This work was supported by the Office of Naval Research under the Fluid Dynamics Programs, element 61153N. We are grateful for the technical support of the ONR scientific officers, Dr. L. P. Purtell and Mr. James A. Fein. The authors appreciate the contributions of our long time friends, Mr. W. E. Smith and Dr. M. Martin for their tutor and introduction to the prediction techniques and flow physics associated with vehicle maneuvers. The concept of asymmetric flow separation from an axisymmetric body caused by combined rotation, pitch, and yaw was first developed by Dr. M. Martin (1991) and then refined by Drs. M. Martin and M. S. Chang (1994). The authors thank our colleagues, Mr. R. M. Curphey and Dr. M. S. Chang, for their technical discussions during the course of this work.

REFERENCES

1. Sung, C.-H., and Griffin, M. J., "Improvement in Incompressible Turbulent Horseshoe Vortex Junction Flow Calculations," AIAA Paper 91-0022, AIAA 29th Aerospace Sciences Meeting, Reno, Nevada, January 7-10, 1991.
2. Sung, C.-H., Griffin, M. J., and Coleman, R. M., "Numerical Evaluation of Vortex Flow Control Devices," AIAA paper 91-1825, AIAA 22nd Fluid Dynamics, Plasma Dynamics & Laser Conference, Honolulu, Hawaii, June 24-26, 1991.
3. Tsai, J. F., Sung, C. H., Griffin, M. J., and Huang, T. T., "Effects of Grid Resolution on Axisymmetric Stern Flows Computed by an Incompressible Viscous Flow Solver," paper presented at the ASME Summer Fluids Engineering Conference, FED-Vol. 158, pp 99-108, June 20-24, 1993.
4. Sung, C.-H., Tsai, J. F., Huang, T. T., and Smith, W. E., "Effects Of Turbulence Models on Axisymmetric Stern Flows Computed by An Incompressible Viscous Flow Solver," paper presented at the 6th International Conference on Numerical Ship Hydrodynamics, Iowa City, Iowa, August 2-5, 1993.
5. Sung, C.-H., Griffin, M. J., Huang, T. T., and Fu, T. C., "A Multiblock Multigrid Local Refinement Method for the Prediction of Double-Model Viscous Ship Flows," paper presented at an

International Workshop for Improvement of Hull Form Designs, Tokyo, Japan, March 22-24, 1994.

6. Chorin, A. J., "A Numerical Method for Solving Incompressible Viscous Flow Problems," J. Comp. Phys., vol. 2, pp. 12-26, 1967.

7. Turkel, E., "Preconditioned Methods for Solving Incompressible and Low Speed Compressible Equations," NASA ICASE Report 86-14, 1986.

8. Turkel, E., "A Review of Preconditioning Methods for Fluid Dynamics," Applied Numerical Mathematics, 12, pp. 257-284, 1993.

9. Chang, J. L. C., and Kwak, D., "On the Method of Pseudo Compressibility for Numerically Solving Incompressible Flows," AIAA Paper-0252, 1984.

10. Jameson, A., "Multigrid Algorithms for Compressible Flow Calculation," in Multigrid Methods II, Lecture Notes in Mathematics series, no. 1228, Hackbusch, W., and Trottenberg, U. Eds., Springer-Verlag, New York, 1986.

11. Swanson, R. C. and Turkel, E., "Aspects of a High-Resolution Scheme for the Navier-Stokes Equations," AIAA-93-3372-CP, AIAA 11th Computational Fluid Dynamics Conference, Orlando, FL, July 6-9, 1993.

12. Turkel, E., and Varsa, V. N., "Effect of Artificial Viscosity on Three Dimensional Flow Solutions," AIAA 90-1444, AIAA 21st Fluid Dynamics, Plasma Dynamics and Lasers Conference, Seattle, WA, June 18-20, 1990.

13. Jameson, A., "Multigrid Algorithms for Compressible Flow Calculation," in Multigrid Methods II, Lecture Notes in Mathematics series, no. 1228, Hackbusch, W., and Trottenberg, U. Eds., Springer-Verlag, New York, 1986.

14. Hedstrom, G. W., "Nonreflecting Boundary Conditions for Nonlinear Hyperbolic System," J. Computational Physics, vol. 30, pp 222-237, 1979.

15. Rudy, D. H., and Strikwerda, J. C., "Boundary Conditions for Subsonic Compressible Navier-Stokes Equations," Computers and Fluids, vol.9, pp 327-338, 1981.

16. Sung, C.-H., "An Explicit Method for 3D Incompressible Turbulent Flows," Report DTNSRDC/SHD-1244-01, July, 1987.

17. Wilcox David C., Turbulence Modeling for CFD, DCW Industries, Inc., La Canada, CA 1993.

18. Baldwin, B. S., and Lomax, H., "Thin Layer Approximation and Algebraic Model for Separated Turbulent Flows," AIAA 78-257, AIAA 16th Aerospace Sciences Meeting, Huntsville, Alabama, January 16-18, 1978.

19. Cebeci, T. and Smith, A. M. O., Analysis of Turbulent Boundary Layers, Academic, New York, 1974.

20. Huang, T. T., Santelli, N., Belt, G., "Stern Boundary-Layer Flow on Axisymmetric Bodies,"

Paper presented at the 12th Symposium on Naval Hydrodynamics, Wash. D. C., June 5-9, 1978, National Academy of Sciences Wash. D. C., pp 127-157, 1978.

21. Huang, T. T., Groves, N.C., and Belt, G. S., "Boundary Layer Flow on an Axisymmetric Body with an Inflected Stern," DTNSRDC Report 80/064, 1980.

22. Huang, T. T., Liu, H.-L., Groves, N. C., Forlini, T. J., Blanton, J. N., and Gowing, S., "Measurements of Flows Over an Axisymmetric Body with Various Appendages (DARPA SUBOFF Experiments)" Paper presented at the 19th Symposium on Naval Hydrodynamics, Seoul, Korea,

23. Renze, K. J., Buning, P. G., and Rajagopalan, R. G., "A Comparative Study of Turbulence Models for Overset Grids, paper 92-0437, AIAA 30th Aerospace Sciences Meeting, Reno, Nevada, Jan. 6-9, 1992.

24. Degani, D., and Schiff, L. B., "Computation of Turbulent Supersonic Flows around Pointed Bodies Having Crossflow Separation," J. Comp. Phys., Vol. 66, pp 173-196, 1986.

25. Munk, Max M., "Aerodynamics of Airships," Division Q, Volume VI, in Aerodynamics Theory, W. F. Durand, Editor-in-Chief, Dover Publications, Inc., New York, 1963.

26. Roddy, R. F., "Investigation of the Stability and Control Characteristics of Several Configurations of the DARPA SUBOFF Model (DTRC Model 5470) from Captive-Model Experiments," David Taylor Research Center Report DTRC/SHD-1298-08, September, 1990.

27. Dempsey, E., "Static Stability Characteristics of a Systematic Series of Stern Control Surfaces on a Body of Revolution," David Taylor Naval Ship Research and Development Center Report 77-0085, Aug. 1977.

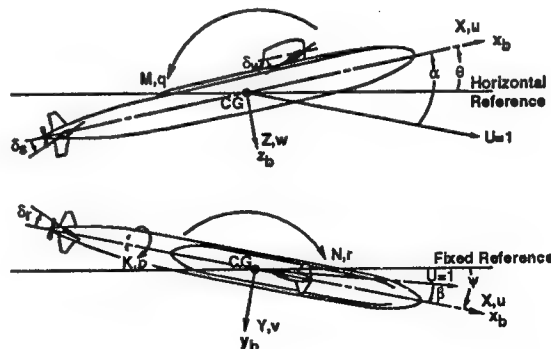


Fig. 1. Sketch showing positive directions of axes, angles, velocities, forces, and moments.

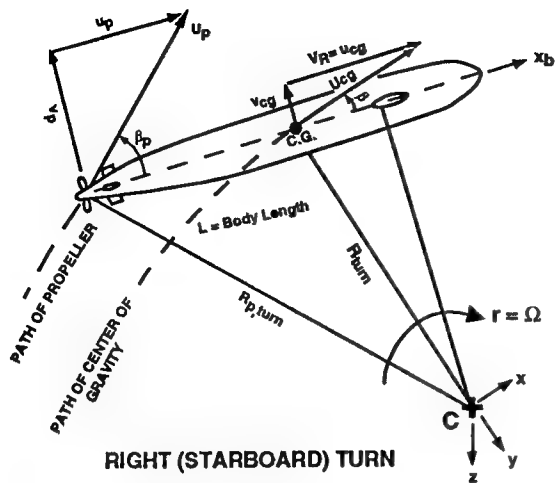


Fig. 2. Velocity and angle of inclination of a body undergoing a steady turn.

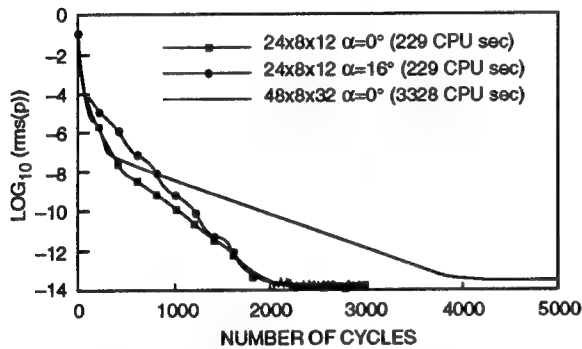


Fig. 3. Demonstration of pressure residual convergence to machine 0, SUBOFF bare hull $R_L = 1.2 \times 10^7$.

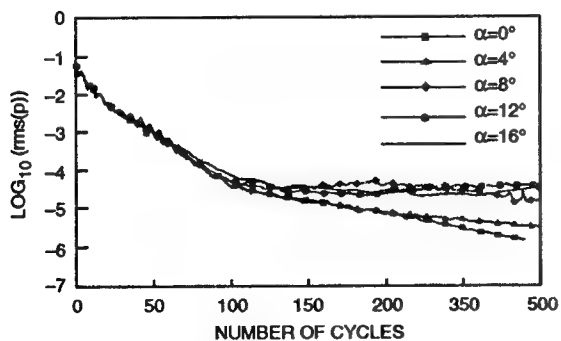


Fig. 4. Demonstration of pressure residual convergence of 144x48x72 grid for various angles of attack. (2230 Cray C90 CPU seconds, $R_L = 1.2 \times 10^7$).

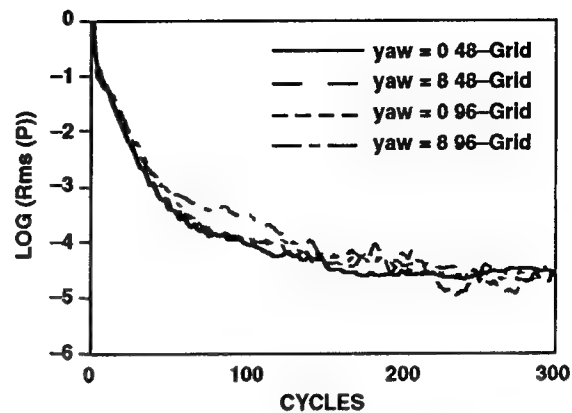


Fig. 5. Demonstration of pressure residual convergence of 96x64x48 and 48x48x32 grids for constant radius turning with yaw angles of 0° and 8°. ($R_L = 1.4 \times 10^7$).

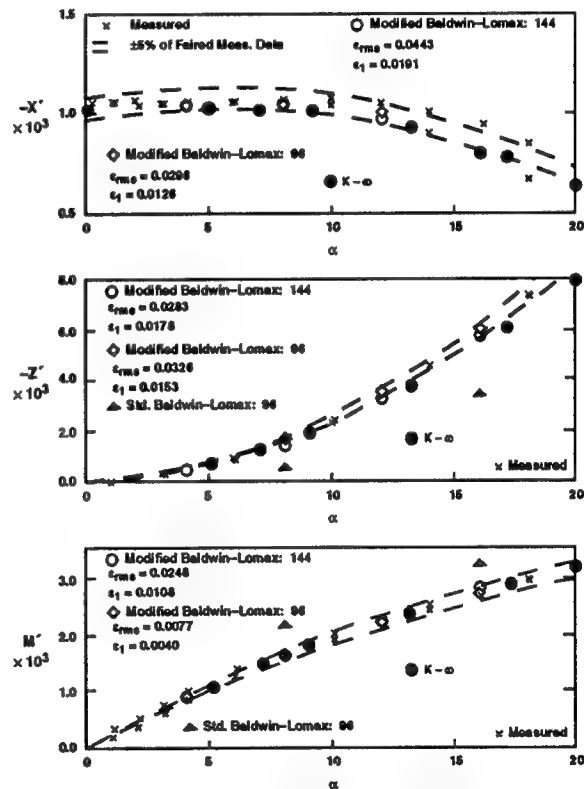


Fig. 6. Comparison of measured and computed non-dimensional axial force X' , normal force Z' , and pitching moment M' on the SUBOFF axisymmetric body at incidence. (Grid size: 144x48x72 and 96x32x48, $R_L = 1.2 \times 10^7$)

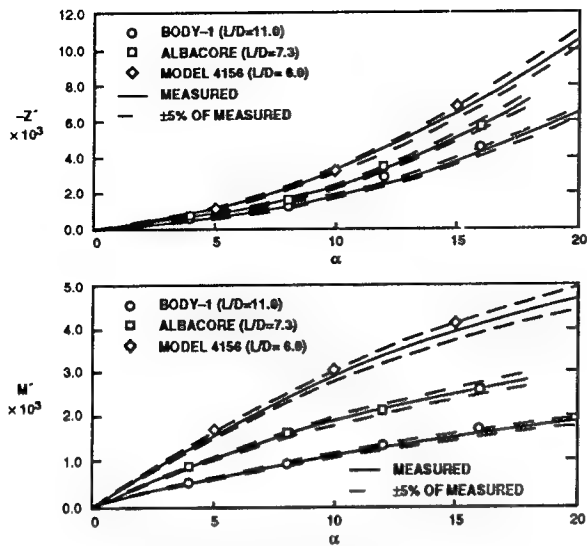


Fig. 7. Comparison of measured and computed non-dimensional normal force Z' , and pitching moment M' on Body 1, Albacore and DTMB Model 4156 axisymmetric bodies at incidence. (Grid Size: $144 \times 48 \times 72$, $R_L = 1.2 \times 10^7$)

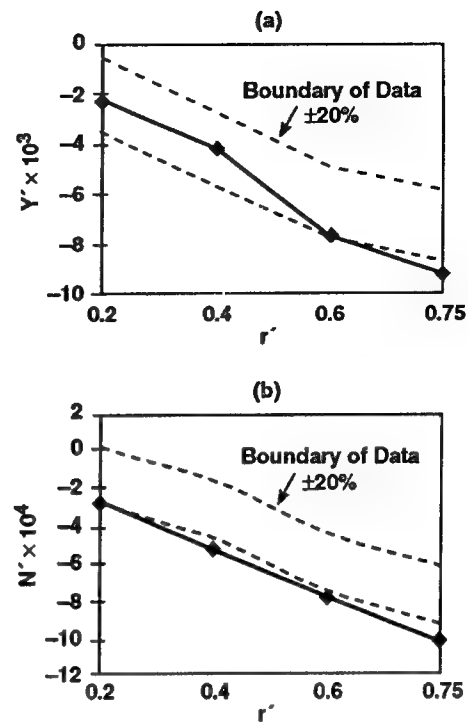


Fig. 8. Effect of nondimensional turning radius, $r' = (L/R_{turn})$ on the computed coefficients of (a) side force (Y') and (b) yawing moment (N') of DTMB Body 1, at zero yaw and pitch angle.

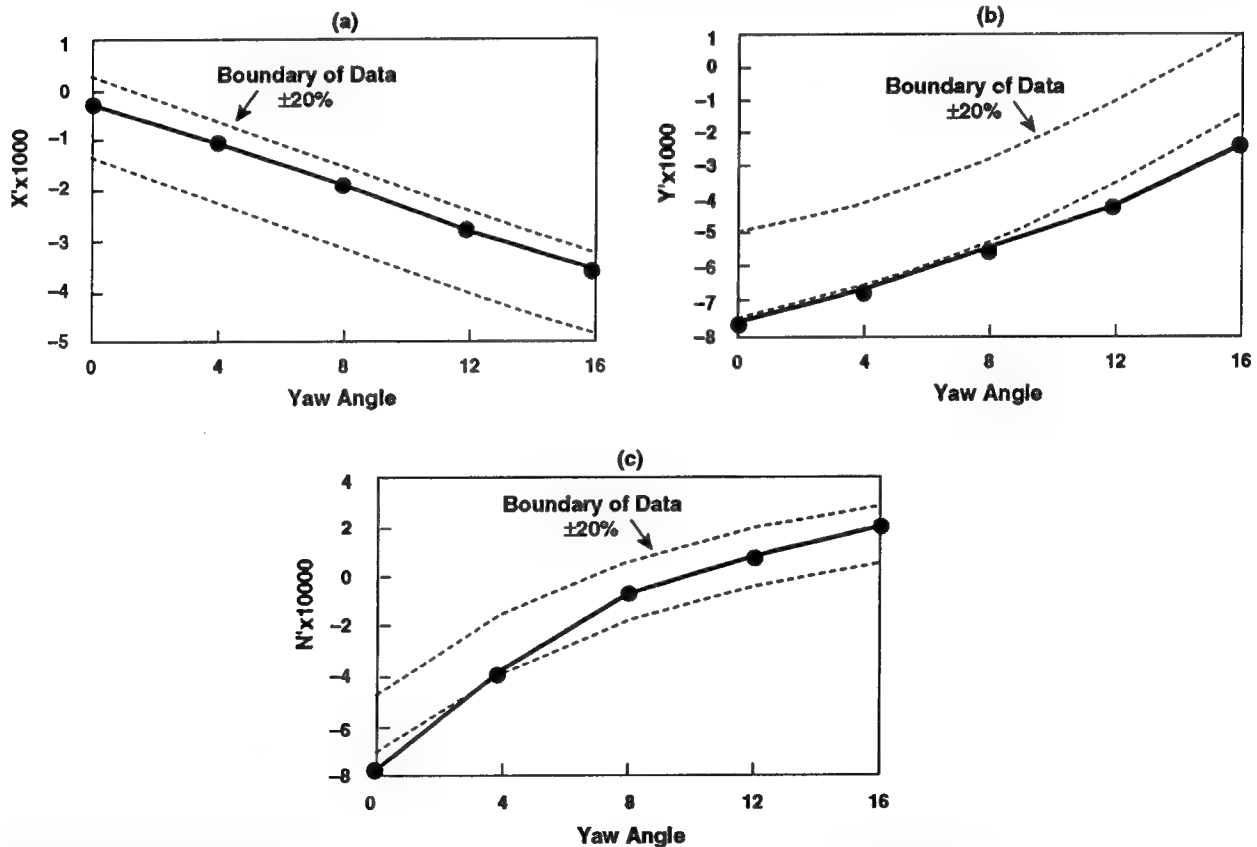


Fig. 9. Effect of yaw angle on the computed coefficient of (a) axial force (X'), (b) side force (Y'), and (c) yawing moment (N'), for DTMB Body 1 undergoing a constant radius turn of $r' = (L/R_{turn}) = 0.65$.

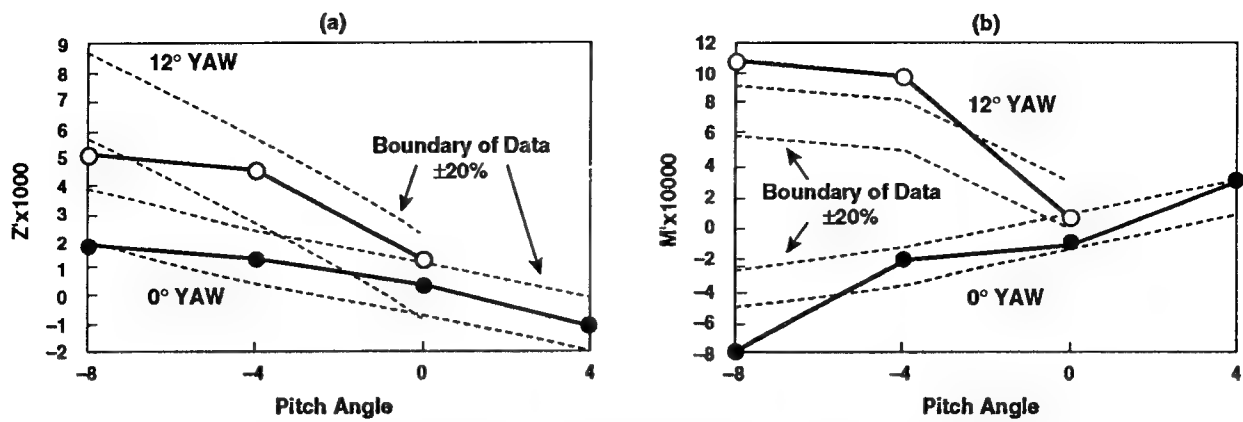


Fig. 10. Effect of pitch angle on the computed coefficient of (a) normal force (Z') and (b) pitching moment (M'), for DTMB Body 1 undergoing a constant radius turn of $r' = (L/R_{turn}) = 0.65$.

a) yaw = 0° , pitch = 0° .

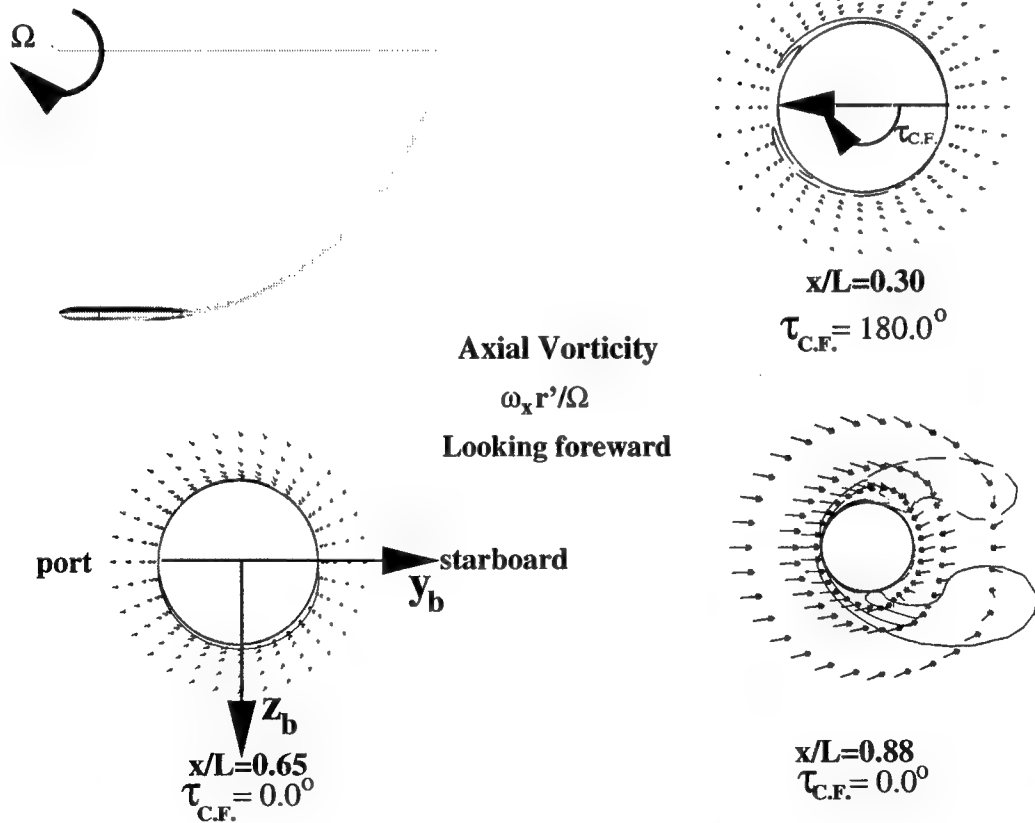


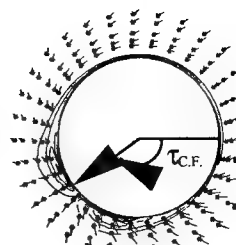
Figure 11; Computed cross flows and vorticities on a turning axisymmetric body at $Re = 1.4 \times 10^7$ and $r' \sim 0.65$. Dashed contours denote negative vorticity. The magnitude of the outermost contours is 7 and the increment between contours is 15.

b) yaw = 0° , pitch = -8° .

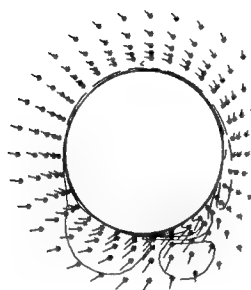


Axial Vorticity

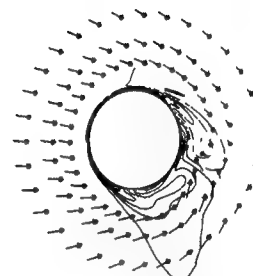
$$\omega_x r' / \Omega$$



$x/L=0.30$
 $\tau_{C.F.}=144.8^\circ$



$x/L=0.65$
 $\tau_{C.F.}=49.0^\circ$

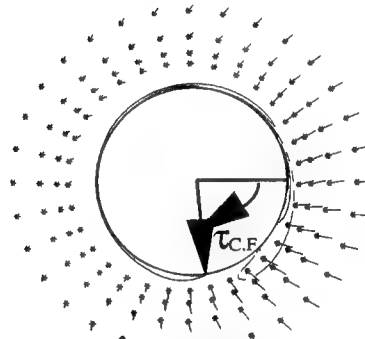


$x/L=0.88$
 $\tau_{C.F.}=27.4^\circ$

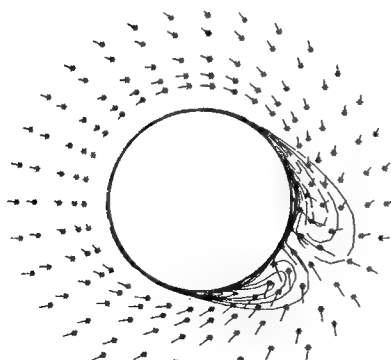
c) yaw = 12° , pitch = -8° .



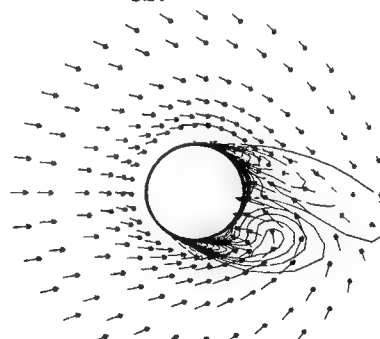
Looking forward



$x/L=0.30$
 $\tau_{C.F.}=85.5^\circ$



$x/L=0.65$
 $\tau_{C.F.}=22.5^\circ$



$x/L=0.88$
 $\tau_{C.F.}=16.0^\circ$

Figure 11: Computed cross flows and vorticities on a turning axisymmetric body at $Re=1.4 \times 10^7$ and $r' \sim 0.65$. Dashed contours denote negative vorticity. The magnitude of the outermost contours is 7 and the increment between contours is 15 (continued).

The Validation of CFD Predictions of Nominal Wake for the SUBOFF Fully Appended Geometry

P. Bull (Defence Research Agency, United Kingdom)

Introduction

Good propulsor design requires knowledge of the flow entering the region just upstream of a propulsor. For both submarine and surface ships, it is desirable that the hull provides as uniform a nominal wake as possible in this region. In this context, the wake can be defined to be the fluid velocity distribution. Detailed knowledge of the velocity distribution will result in the propulsor designer being able to produce an efficient and effective propulsion system.

Whilst the fluid velocity distribution can be measured by using a scale model in a towing tank or wind tunnel, there are difficulties in applying results obtained at model scale to the full scale hull. Furthermore, experiments of this type require many detailed measurements to be taken in the region of interest. These can be both costly and time consuming.

An alternative approach is to use Computational Fluid Dynamics (CFD) to predict the fluid velocity distribution by solving the fundamental equations of motion using numerical methods. An advantage of this approach is that it has the potential to remove the difficulties associated with the traditional methods, since predictions can be made at both model and full scale. The fundamental equations for fluid flow, which describe the conservation of fluid mass and momentum, are the equation of continuity and the Navier-Stokes equations. In practice, it is impossible to solve these equations directly since the fastest supercomputer with the largest memory available falls short of the required performance by many orders of

magnitude. However, if the fundamental equations are averaged over a period of time, the computer requirements for the resolution of the flow features are eased enormously. These time-averaged equations are known as the Reynolds-Averaged Navier Stokes Equations (RANS) equations. The time-averaging process introduces new variables into the equations that are known as the Reynolds stresses. Turbulence models are introduced which require assumptions to be made on the relationships between the Reynolds stresses and the mean flow parameters. The numerical methods used to solve these equations and the turbulence models introduce errors into the prediction of the flow parameters.

Therefore, both experiments and CFD computations have degrees of uncertainty with the accuracy of the predictions of the flow parameters for full scale flows. This gives rise to the need for validation of both the measurements and computations for the prediction of such flows, in order to quantify the uncertainty levels. This can be achieved by comparison between high quality experiments, where the uncertainty is carefully evaluated and quoted, and computations, where a systematic approach is used to quantify the uncertainty in the various stages of the numerical methods [1].

One such high quality experiment data set is the DARPA SUBOFF [2,3,4] set of measurements which provide a comprehensive set of data for a number of different geometry configurations. This paper describes a comprehensive validation exercise which has been carried out at the Defence Research Agency (DRA) at Haslar for one of the SUBOFF configurations. This configuration was chosen as

representative of the other configurations at zero angle of attack.

The SUBOFF experiments

The SUBOFF experiments were funded by DARPA and conducted at the David Taylor Model Basin during 1988 and 1989. A number of submarine configurations, ranging from an axisymmetric body to a fully appended submarine were constructed in order to provide flow measurements for CFD validation. Each of the models was placed in the Anechoic Flow Facility (AFF) wind tunnel. The dimensions of the wind tunnel and layout of the model are shown in figure 1. The flow was measured at a Reynolds number of 1.2×10^7 . This paper considers the flow past configuration AFF-1-, the axisymmetric body of revolution and configuration AFF-8-, the fully appended geometry at zero angle of attack.

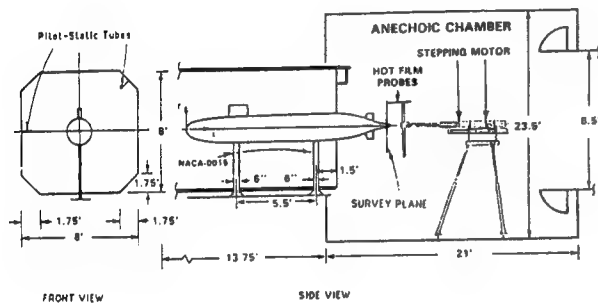


Figure 1
The wind tunnel

For each configuration, pressure taps on the hull surface connected to rotary pressure scanners provided measurements for surface pressure. The wall shear stress was also measured at the location of selected pressure taps. A traversing mechanism was used to position hot film probes in order to measure mean and fluctuating components of the velocity. The uncertainty of the measurements, with 95% confidence, was 2.5% of U_∞ for the mean flow components and 0.2% for the Reynolds stresses, where U_∞ is the free stream inlet velocity. The uncertainty of the absolute values of the pressure and wall shear stress was within ± 0.015 and ± 0.0002 of their measured values respectively. A complete description of the measurement system and their uncertainty is given in reference 1.

For the axisymmetric naked hull case, AFF-1-, measurements were taken at non-dimensionalised positions of $x/L = 0.875, 0.904, 0.927, 0.956$ and at the propulsor plane $x/L = 0.978$ where x is the position along the hull and L is the total length of the hull. For the fully appended case, AFF-8-, measurements were taken at positions $x/L = 0.978, 1.040, 1.096$ and 1.200 . For the AFF-8- case, the flow was measured at two degree intervals for radii between $r/R_{\max} = 0.25$ and 2.00 where r is the distance of the probe from the axis of the hull and R_{\max} is the maximum radius of the hull. The quantities obtained at each location of these wake surveys were

$$\frac{u}{U_\infty}, \frac{v_r}{U_\infty}, \frac{v_\theta}{U_\infty}, \frac{u'}{U_\infty}, \frac{v'}{U_\infty}, \frac{w'}{U_\infty}, \frac{-u'v'}{U_\infty^2}, \frac{-u'w'}{U_\infty^2}$$

and the static pressure. The non-dimensional quantities C_p and C_τ are then defined by

$$C_p = (p - p_\infty) / \frac{1}{2} \rho U_\infty^2$$

$$C_\tau = \tau_w / \frac{1}{2} \rho U_\infty^2$$

where u = mean axial velocity component
 v_r = mean radial velocity component
 v_θ = mean tangential velocity component
 u', v', w' = fluctuating components
 p = static pressure
 p_∞ = free stream static pressure
 ρ = fluid density
 and τ_w = wall shear stress

Grid generation

In order to perform a validation exercise of this type, it is necessary to have a fast, efficient grid generation system which is capable of producing high quality grids with sufficient grid density to resolve the flow features. The system chosen was the SAUNA [5,6] system produced for the DRA by the Aircraft Research Association Ltd. The system uses the elliptic multiblock method to generate grids around fully appended geometries. This system is currently being developed to generate hybrid structured and unstructured grids with hexahedral, pyramidal, prismatic and tetrahedral cells. The SAUNA system takes separate geometry component definitions and combines them together into the required configuration, calculating intersections, as required.

For the SUBOFF configurations, the geometry of the hull, sail and aft appendages were analytically defined, although the aft appendage fin tips were modified to have elliptical caps.

A background grid topology is used to form the basis of a grid and individual topologies, associated with each geometry component, are automatically embedded with this. A local topology is applied in each of the two parametric directions of a geometry component. For aerofoil-like components, such as a sail or an aft appendage, these directions are equivalent to the chord and the span. Three different topologies, H,C and O can be combined to give a choice of 6 topologies for appendage and 3 for hulls. Illustrations of the topologies chosen around a sail are shown in the figure 2. The full volume topology is created automatically.

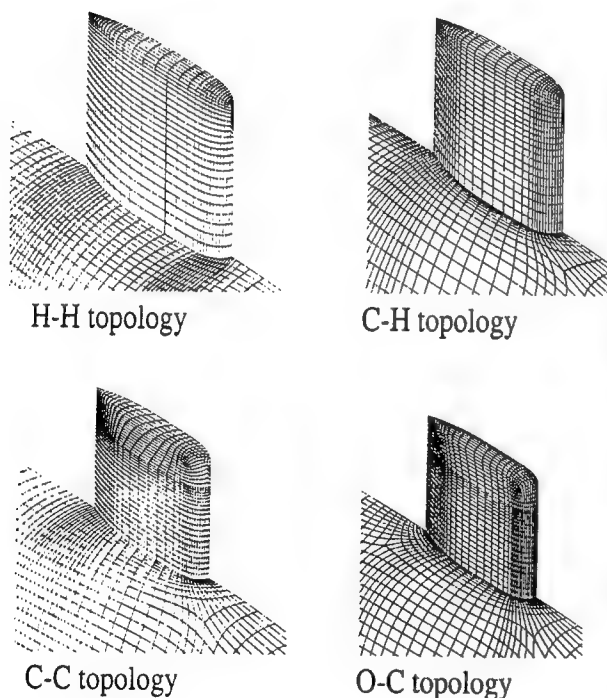


Figure 2
Types of topology around the sail

Surface grids are generated for each geometry component and for the bounding surfaces of the domain, using the appropriate block faces from the full volume topology. These grids are generated as solutions of a two dimensional set of partial

differential equations. For geometry components, the surface grids are generated in parametric co-ordinates. Internal grid control surfaces are also generated which extend from certain components. These are used to control grid quality. Initial surface grid distributions are automatically defined by the SAUNA system around key contours of the components. The volume grid is formed in two stages. Initially a coarse grid is generated as a solution of a three-dimensional set of elliptic partial differential equations. This grid is refined algebraically with the blocks abutting the geometry in order to provide cells of aspect ratio suitable for capturing the viscous boundary layer around the geometry. The algebraic refinement is propagated into additional adjoining blocks to satisfy continuity of cell distribution. This provides extra refinement to help capture viscous wakes when C and H topologies are used. An example of the type of grid produced by SAUNA for the SUBOFF AFF-8-configuration using an O-O topology around the hull and C-C topology around the appendages is shown in figure 3.

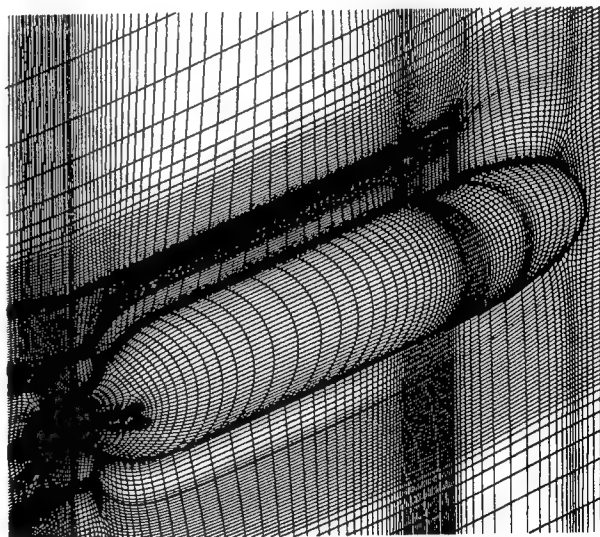


Figure 3
Typical SUBOFF grid

A number of grids were generated with cell numbers ranging from 250,000 cells to 1,000,000 cells and for four topologies, H-H, C-H, C-C and O-O around the appendages. Additional grids were also generated using a preliminary version of the hybrid system with prismatic cells surrounding the geometry and tetrahedral cells elsewhere. The same domain size was used for all grids. In addition, care was taken to

ensure that the first cell spacing, which controls the accuracy and applicability of a wall function approach, was consistent for all the grids. This cell spacing was chosen to give an approximate value of 50 for the non-dimension parameter y^+ , along the length of the hull and appendages.

Table 1 defines a grid identifier for each of these grids and outlines the number of cells and topology for each.

Table 1
Grid Properties

| Grid Identifier | Hull Topology | Appendage Topology | Number of Geometry Cells | Number of Fluid Cells |
|-----------------|---------------|--------------------|--------------------------|-----------------------|
| Grid A | O-O | N/A | 72 | 2,496 |
| Grid B | O-O | N/A | 120 | 4,096 |
| Grid C | O-O | N/A | 176 | 5,472 |
| Grid D | Unstr | N/A | 7,458 | 309,162 |
| Grid E | O-O | H-H | 5,568 | 271,104 |
| Grid F | O-O | H-H | 7,745 | 526,720 |
| Grid G | O-O | H-H | 18,496 | 1,042,048 |
| Grid H | O-O | C-H | 6,032 | 271,448 |
| Grid I | O-O | C-H | 7,168 | 476,928 |
| Grid J | O-O | C-H | 17,616 | 1,023,232 |
| Grid K | O-O | C-C | 10,048 | 511,744 |
| Grid L | O-O | C-C | 19,792 | 1,032,192 |
| Grid M | O-O | O-O | 11,792 | 476,096 |
| Grid N | O-O | O-O | 22,224 | 997,376 |
| Grid O | Unstr | Unstr | 14,434 | 432,180 |
| Grid P | Unstr | Unstr | 32,208 | 1,243,689 |

Brief description of flow solution algorithms

Several distinct types of flow solution algorithms are potentially applicable to the prediction of the nominal wake. These algorithms use different methods for discretising the RANS equations which fall into three broad categories: finite difference, finite volume and finite element. Each method has different advantages, depending on the complexity and nature of the application. In addition, a number of different turbulence models can be used to estimate the Reynolds stresses with varying degree of sophistication and accuracy. Some of the important turbulence models are given below:

- Zero equation Baldwin-Lomax
- Two equation $k-\epsilon$
- Renormalisation Group two equation $k-\epsilon$
- Differential Reynolds Stress transport model

The differences in discretisation approaches, in numerical techniques used to segregate and linearise the equations; in turbulence models and in boundary condition and wall functions lead to many distinct CFD algorithms. These algorithms govern the behaviour of individual RANS flow codes when applied to the prediction of nominal wakes.

The RANS flow codes used in this validation exercise are outlined briefly below:

CFDS-FLOW3D [7] is a multi-block structured, control volume based finite difference flow code. The governing equations are discretised, based on a curvilinear grid to enable computations on complex and irregular geometries. Interpolation is accomplished via a wide range of different advection schemes. CFDS-FLOW3D offers a choice of $k-\epsilon$, RNG $k-\epsilon$ and the Reynolds Stress turbulence models which can be used in conjunction with standard near-wall modelling methods.

FLUENT/UNS [8] is an unstructured control volume flow code which is based on solution adaptive, fully unstructured grids with cell centred discretisation schemes. A pressure based segregated solution scheme is used for the velocity-pressure coupling and algebraic multigrid methods are used to accelerate convergence. A first or second order upwind scheme is used for convection terms and a second order reconstruction scheme is used for diffusion terms. FLUENT/UNS offers a choice of $k-\epsilon$ or the RNG $k-\epsilon$ turbulence models which can be used in conjunction with two different near wall modelling methods.

FIDAP [9] is an unstructured finite element flow code based on the iterative solution of the discretised equations using the Petrov-Galerkin method. The equations are solved in a segregated form, using pressure correction to ensure mass conservation. FIDAP offers a choice of $k-\epsilon$ or extended $k-\epsilon$ with different models for the eddy viscosity and near-wall modelling based on a Reichart wall element.

Although this list of flow codes is not exhaustive, the flow solution methods were chosen to be representative of the types commercially available. Each of these flow codes is a general purpose fluid dynamics package which can be used for a wide range of problems. This paper is only concerned with their application to high Reynolds' number flows around the SUBOFF geometry.

Measures for validation

For any validation exercise of this type, it is important to decide on suitable measures for comparing the computed flow results with the measured data.

Comparison between the axial variation of the non-dimensional static pressure coefficient C_p and the skin friction coefficient C_f is appropriate for the naked hull configuration AFF-1-. Boundary layer profiles of the axial velocity component and turbulent kinetic energy at stations along the hull are also compared.

It is more difficult to define suitable measures of the accuracy of the flow computations for the fully appended configuration AFF-8- due to the three-dimensional nature of the flow features. For this paper the following measures were used:

- Contours of the Taylor wake fraction in the propulsor plane.
- Wake survey of flow parameters at various radii in the propulsor plane
- The averaged circumferential Taylor wake fraction at various radii in the propulsor plane.
- Harmonics of the Taylor wake fraction.

The Taylor wake fraction and the averaged Taylor wake fraction are defined as

$$W(r, \theta) = u(r, \theta) / U_\infty$$

and

$$W_1(r) = \frac{1}{2\pi U_\infty} \int_0^{2\pi} u(r, \theta) d\theta$$

respectively, where

$u(r, \theta)$ = axial velocity component in the propulsor plane

r = radial distance from the axis

and θ = circumferential angle

The angle θ is measured from $\theta = 0$ at the upper symmetry plane and $\theta = \pi$ at the lower symmetry plane.

The wake harmonics are defined to be the amplitude coefficients, $A_n(r)$ of the Fourier series representation of the Taylor wake fraction as given by:

$$W(r, \theta) = W_1(r) + \sum_{n=1}^{\infty} A_n(r) \cos(n\theta - \phi_n(r))$$

where

$$A_n(r) = \sqrt{a_n^2(r) + b_n^2(r)}$$

$$a_n(r) = \frac{1}{\pi} \int_0^{2\pi} u(r, \theta) \cos(n\theta) d\theta$$

$$b_n(r) = \frac{1}{\pi} \int_0^{2\pi} u(r, \theta) \sin(n\theta) d\theta$$

$$\cos(\phi_n(r)) = \frac{a_n(r)}{A_n(r)},$$

$$\sin(\phi_n(r)) = \frac{b_n(r)}{A_n(r)}$$

This definition gives $W_1(r)$ as the zeroth order harmonic of the Taylor wake fraction.

Results for the AFF-1- Configuration

Preliminary computations for the AFF-1- configuration were made using the flow code FIDAP. These computations were used to investigate the sensitivity of such flows to changes in the initial and input parameters. The chosen parameters were checked using FLUENT/UNS to ensure that consistent results could be obtained using a different flow solution algorithm.

Computations using the FLUENT/UNS flow code were performed for grids A, B and C using $k-\epsilon$ and RNG $k-\epsilon$ turbulence models. Figure 4 shows comparison between the measured data and the computations, for the pressure and skin friction coefficients respectively, for each of these models. The measured data are given as symbols and the

predictions for each grid are given by solid, dashed and dotted lines for grids A, B and C respectively.

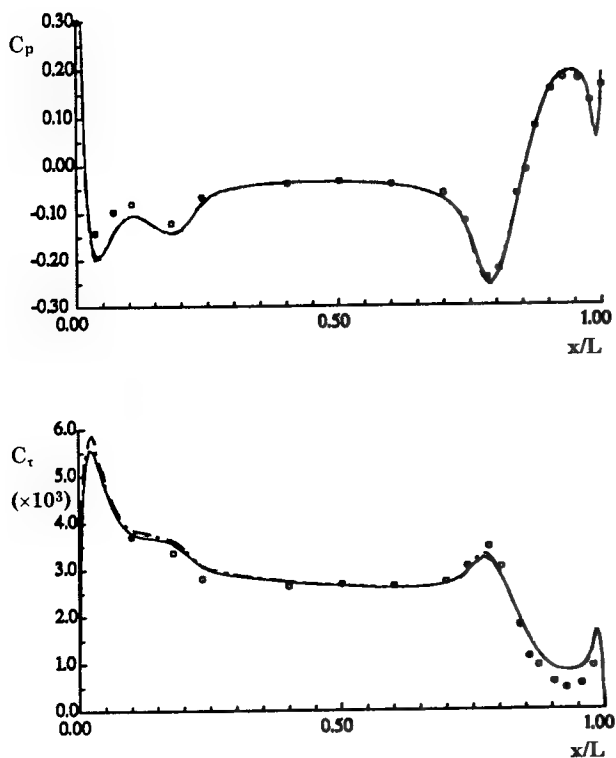


Figure 4
Pressure and skin coefficients for the AFF-1-configuration

Comparisons of the boundary layer profiles at the axial stations $x/L = 0.875, 0.904, 0.956$ and 0.978 are shown in figure 5. The measured data are given as symbols and the predicted data for grid A, B and C using solid, dashed and dotted lines respectively.

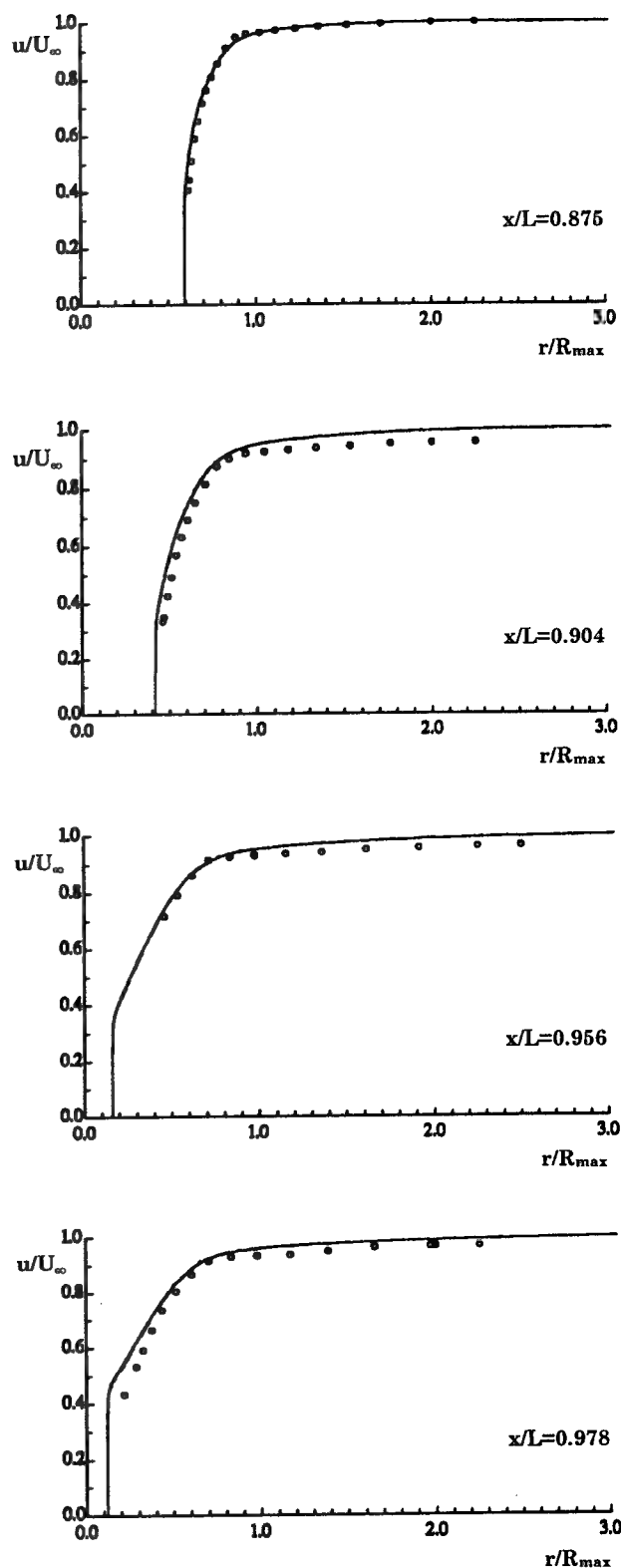


Figure 5
Axial velocity profiles for the AFF-1- configuration

A later computation, using the hybrid unstructured grid E, was also carried out for the AFF-1-configuration. The pressure coefficient for this prediction and the equivalent prediction for grid B are shown in figure 6 with boundary layer profiles in figure 7.

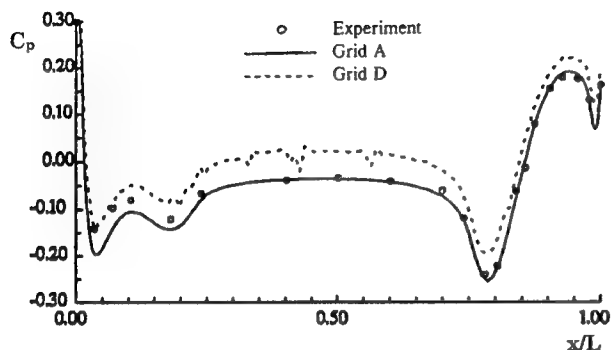


Figure 6
Pressure coefficient for structured and unstructured grids

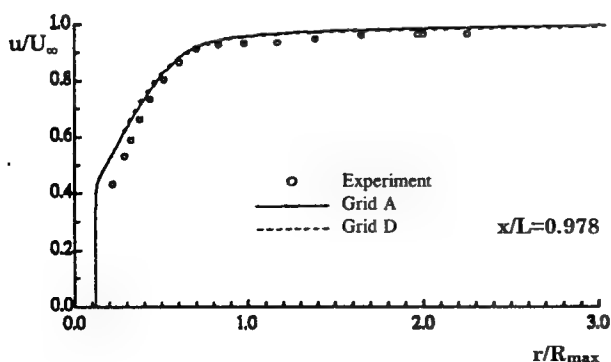
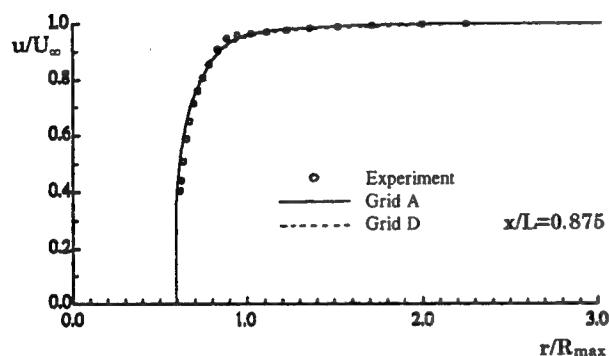


Figure 7
Boundary layer profiles for structured and unstructured grids

Results for the AFF-8- Configuration

Computations were made for the AFF-8-configuration for the grids described above using the flow codes FLUENT/UNS, FIDAP and CFDS-FLOW3D. Care was taken to ensure that the same inlet and initial conditions were used for each computation by using non-dimensional parameters. The initial and inlet conditions were defined as:

$$\begin{aligned} U_{\infty} &= 1.0 \\ L &= 12.926 \\ \rho &= 1.0 \\ \mu &= 1.191 \times 10^{-6} \\ k &= 1.332 \times 10^{-4} \\ \varepsilon &= 4.47 \times 10^{-5} \end{aligned}$$

These parameters give a Reynolds number of

$$Re = 1.2 \times 10^7$$

where

$$Re = \frac{\rho L U_{\infty}}{\mu}$$

The chosen parameters for the turbulence were based on the sensitivity study carried out using FIDAP for the AFF-1- configuration. The turbulent dissipation rate, ε , was chosen by prescribing the ratio of molecular to turbulent viscosity. The value chosen for this ratio was

$$\frac{\mu_T}{\mu} = 30.$$

where

$$\mu_T = \rho C_{\mu} \frac{k^2}{\varepsilon}$$

Initial computations were made with grids E,F and H,I; the H-H and C-H topology grids with 250,000 and 500,000 cells respectively. Contour plots of the Taylor wake fraction, W , in the plane of the propulsor at $x/L = 0.978$ are shown in figures 8 to 14, for the measured experiment values and for each of the flow codes. All the contours are plotted to the same scale and range from a minimum value of 0.4 to a maximum of 0.9 with an increment of 0.05. The predictions for the grids E and H are shown on the left with grids F and I on the right of each figure.

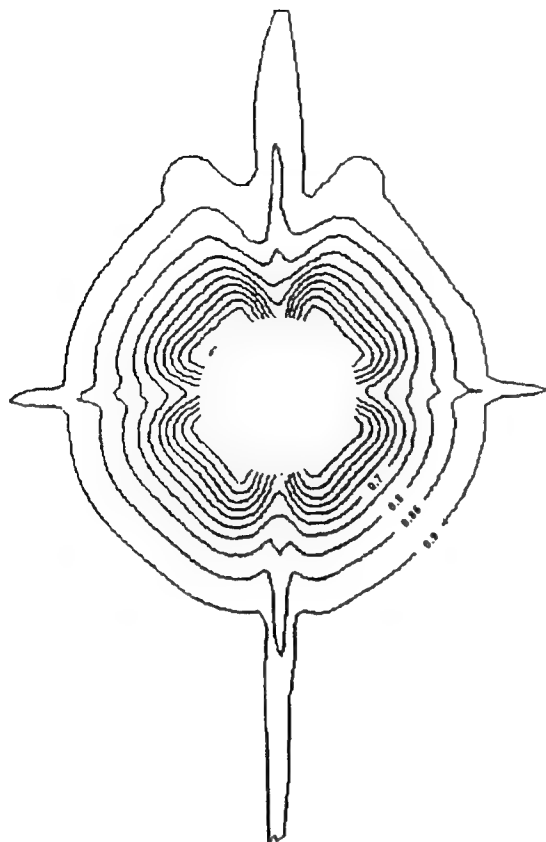


Figure 8
Taylor wake contours for measured experiment data

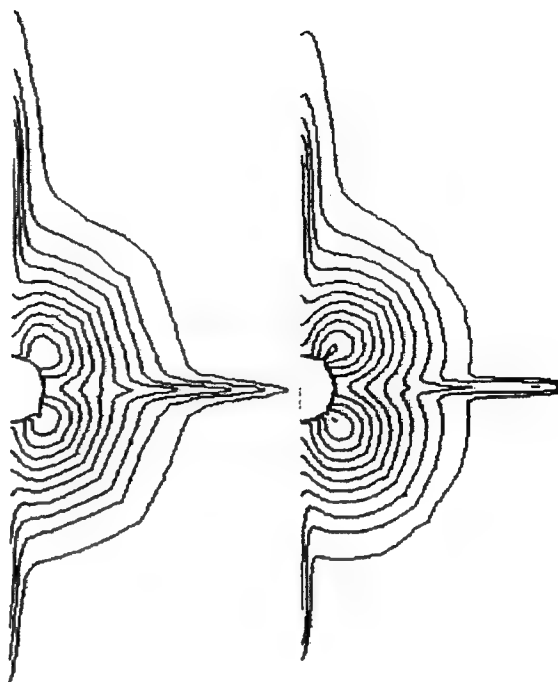


Figure 10
Taylor wake contours for FLUENT/UNS
H-H topology grids

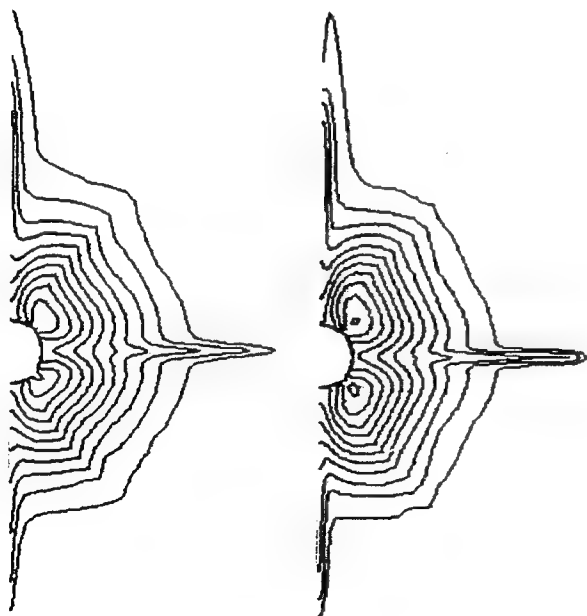


Figure 9
Taylor wake contours for FLUENT/UNS
C-H topology grids

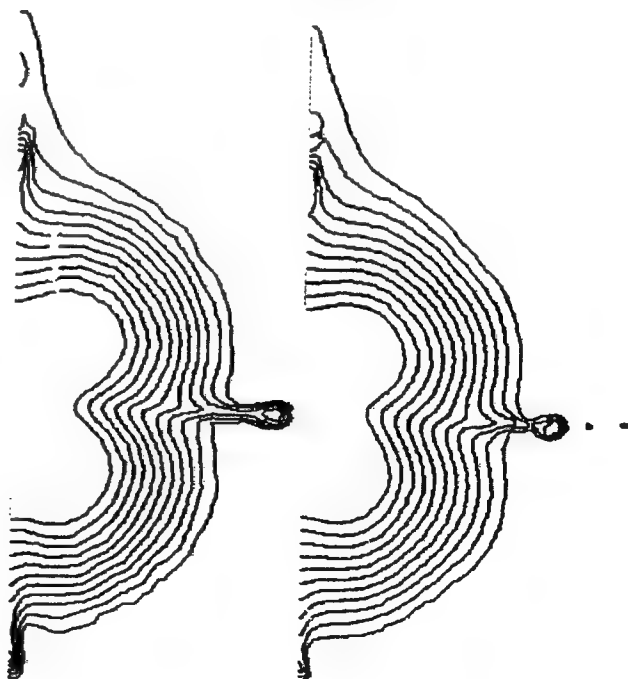


Figure 11
Taylor wake contours for FIDAP
C-H topology grids

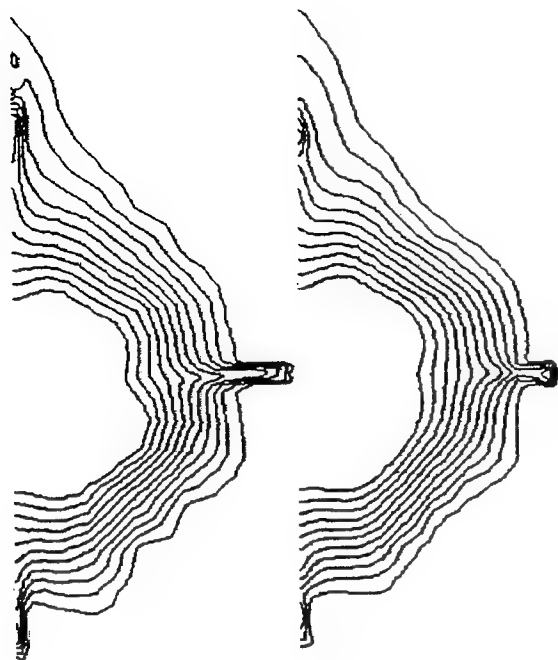


Figure 12
Taylor wake contours for FIDAP
H-H topology grids

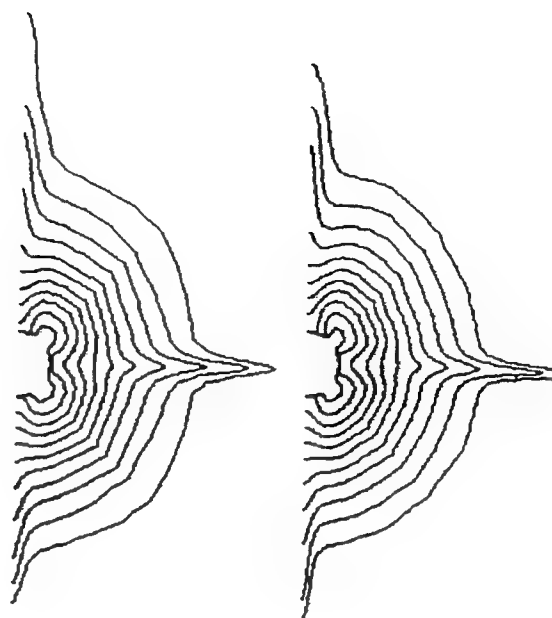


Figure 14
Taylor wake contours for FLOW3D
H-H topology grids

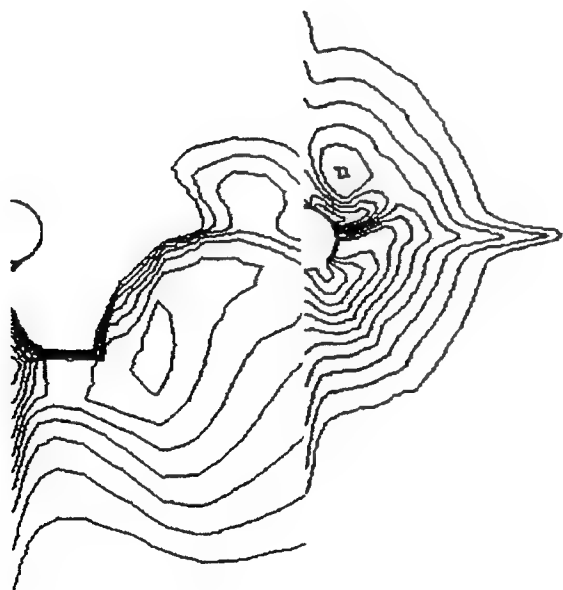


Figure 13
Taylor wake contours for FLOW3D
C-H topology grids

It is clear that the predictions obtained by FLOW3D failed to converge for the C-H topology grids. This was due to grid singularities in the C-H topology grids due to the embedding of C grids around the leading edges of the appendages in SAUNA. This causes degenerate cells to be generated above the fin tips. These degenerate cells were not present in the H-H topology grids.

It is also evident that the development of the hull boundary layer was unstable in the predictions obtained by FIDAP. This was because the hull surface grid density was insufficient for the Reichard wall function model implemented in FIDAP.

Comparison between the predicted and experiment velocity components and turbulent kinetic energy are given in figures 15 and 16 for the FLUENT/UNS computations. The figures show the variation of the flow parameters u, v, w and k at a radius of $r/R_{\max} = 0.25$. Data are plotted at 2° from the upper centreline of the hull, in the plane of the propulsor at $x/L = 0.978$. The computational predictions were linearly interpolated from values at cell vertices to the locations of the measured data. The predictions are shown as dotted lines and the measured experiment values as a solid line.

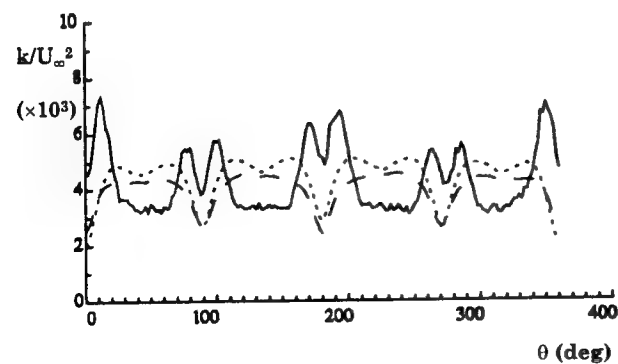
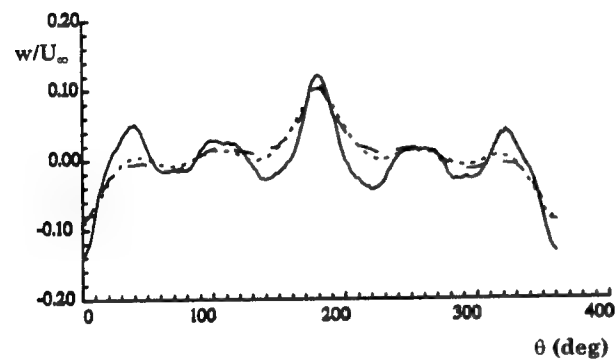
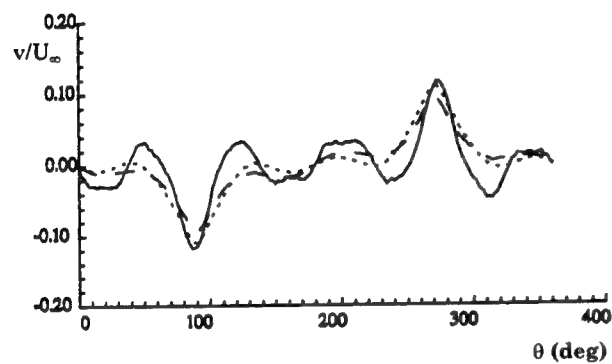
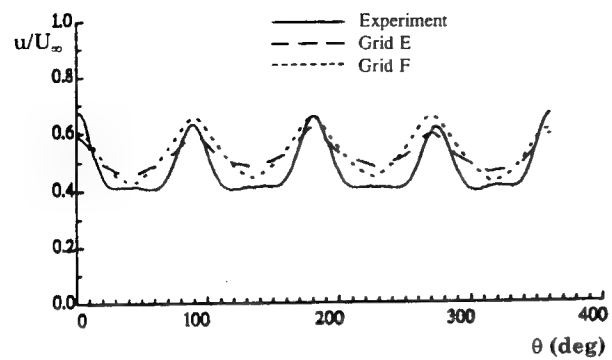


Figure 15
Wake survey for grids E and F

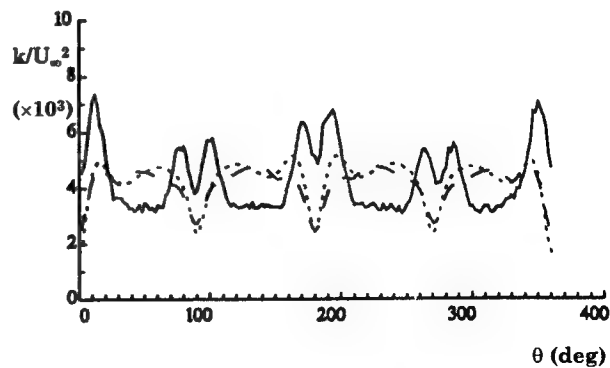
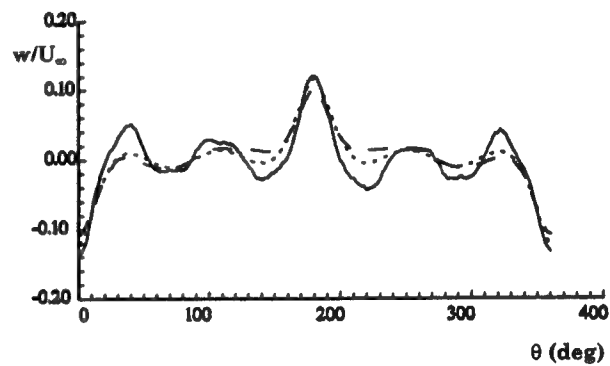
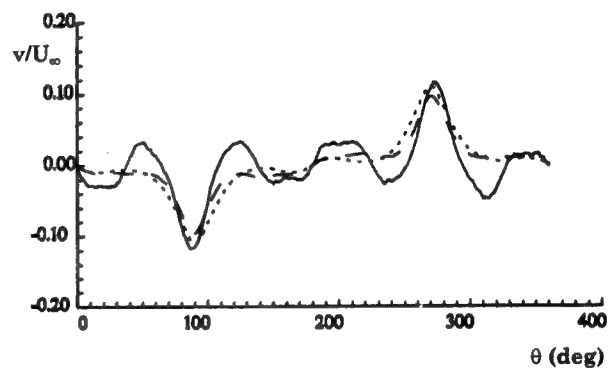
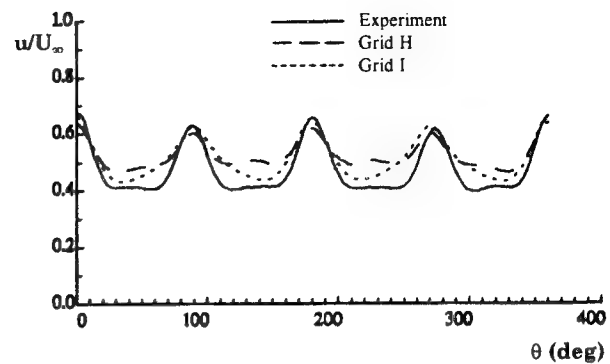


Figure 16
Wake survey for grids H and I

The averaged circumferential Taylor wake fractions, W_1 , in the plane of the propulsor, are given in Table 2 for these computations. The table gives values of W_1 for each flow computation for a number of radii, namely $r/R_{max} = 0.25, 0.35$ and 0.45 . The values of W_1 , derived from the measured experiment data, are 0.474, 0.597 and 0.746 for each of the respective radii.

Table 2
Averaged circumferential Taylor wake fractions for each flow code

| r/R_{max} | Grid | FLUENT | FIDAP | FLOW3D |
|-------------|------|--------|-------|--------|
| 0.25 | E | 0.519 | 0.241 | 0.517 |
| | F | 0.528 | 0.229 | 0.519 |
| | H | 0.523 | 0.288 | 1.747 |
| | I | 0.512 | 0.304 | 0.617 |
| 0.35 | E | 0.634 | 0.311 | 0.637 |
| | F | 0.631 | 0.296 | 0.640 |
| | H | 0.635 | 0.344 | 1.407 |
| | I | 0.619 | 0.367 | 0.657 |
| 0.45 | E | 0.743 | 0.409 | 0.738 |
| | F | 0.740 | 0.398 | 0.740 |
| | H | 0.742 | 0.422 | 1.089 |
| | I | 0.736 | 0.451 | 0.735 |

The FLUENT/UNS results indicated that further computations with alternative topologies and higher grid resolutions could lead to more accurate predictions of the flow parameters.

Further computations were carried out using FLUENT/UNS for grid G and for grids J to P, the H-H, C-H, C-C and O-O topology grids with 500,000 cells or 1,000,000 cells and the unstructured grids. All of these computations were carried out with identical initial parameters for the inlet conditions and boundary conditions. The same number of iterations were used for every computation; namely 250 iterations, which gave, on average, a reduction of residuals by four orders of magnitude. It was observed that the residuals for earlier FLUENT/UNS predictions for grids F and I had been reduced by only three orders of magnitude. Therefore the computations for grids F and I were repeated.

Contours of the Taylor wake fraction for these predictions are given in figures 17 to 21. These figures show the predicted nominal wake for each of the structured grid topologies and for the unstructured hybrid grids. The smaller grids are shown on the left and the larger grids on the right. Comparison between these prediction and the measured data can be made by comparing these figures with figure 8.

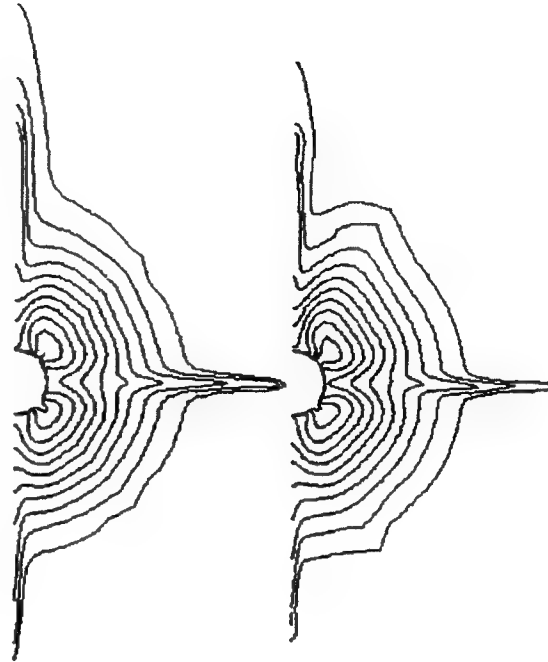


Figure 17
Taylor wake contours for H-H topology grids

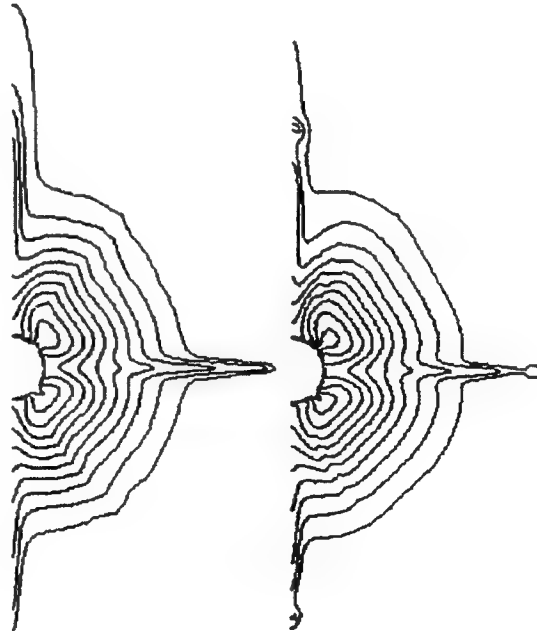


Figure 18
Taylor wake contours for C-H topology grids

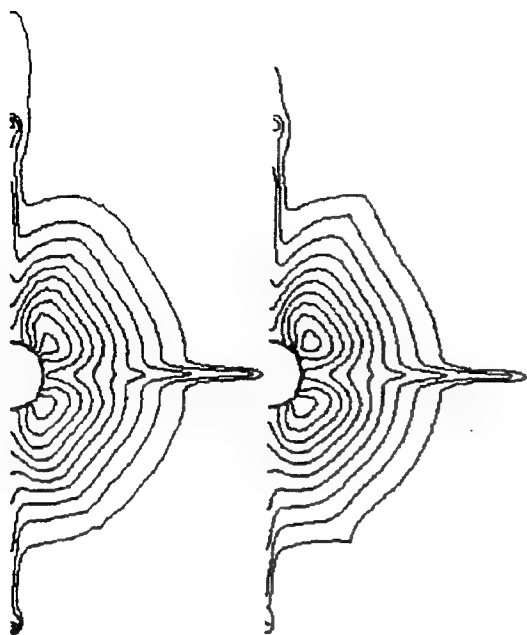


Figure 19
Taylor wake contours for C-C topology grids



Figure 21
Taylor wake contours for unstructured grids

The averaged circumferential Taylor wake fractions W_1 are shown in Table 3 for each of the grids. These indicate that there is little variation in the predictions for changes in the topology or for increases in grid resolution.

Table 3
Averaged circumferential Taylor wake fractions for each grid

| r/R_{max} | Resolution | H-H | C-H | C-C | O-O | Unstr |
|-------------|------------|-------|-------|-------|-------|-------|
| 0.25 | 500,000 | 0.522 | 0.527 | 0.536 | 0.539 | 0.573 |
| | 1,000,000 | 0.533 | 0.540 | 0.538 | 0.541 | 0.595 |
| 0.35 | 500,000 | 0.634 | 0.638 | 0.645 | 0.646 | 0.685 |
| | 1,000,000 | 0.646 | 0.654 | 0.649 | 0.649 | 0.743 |
| 0.45 | 500,000 | 0.743 | 0.744 | 0.750 | 0.745 | 0.779 |
| | 1,000,000 | 0.751 | 0.760 | 0.752 | 0.752 | 0.817 |

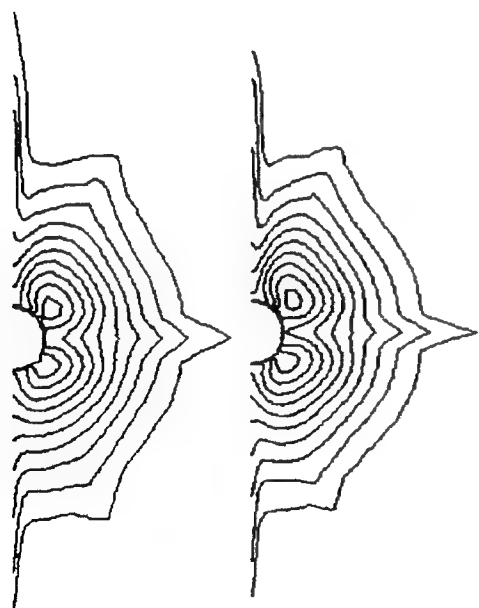


Figure 20
Taylor wake contours for O-O topology grids

Comparisons of the wake surveys for the predicted and measured velocity components and the turbulent kinetic energy for each of the C-H topology grids are shown in figure 22. This figure indicates the dependency of the predictions on the grid resolution. Comparison between the predicted and measured data for each of the topologies are shown in figures 23 and 24 which indicate the dependency of the predictions on the grid topology.

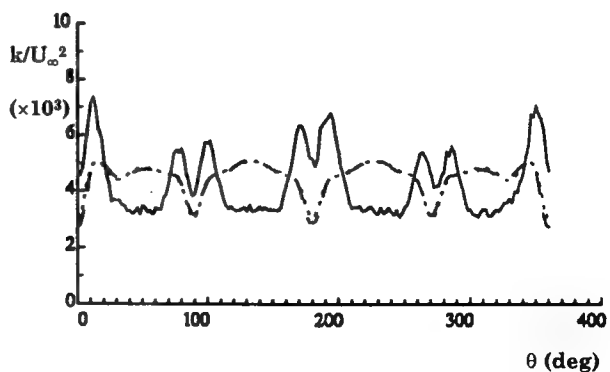
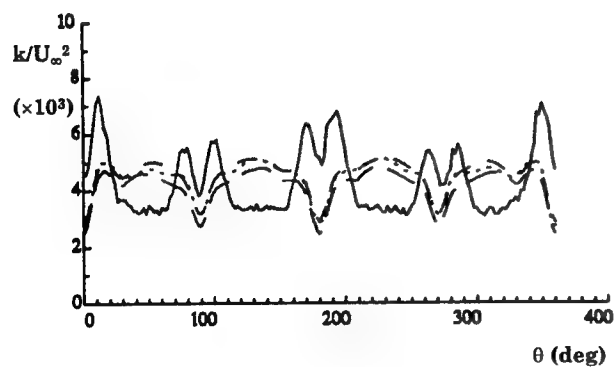
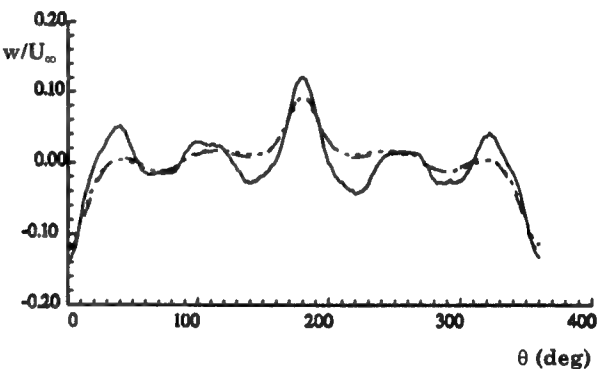
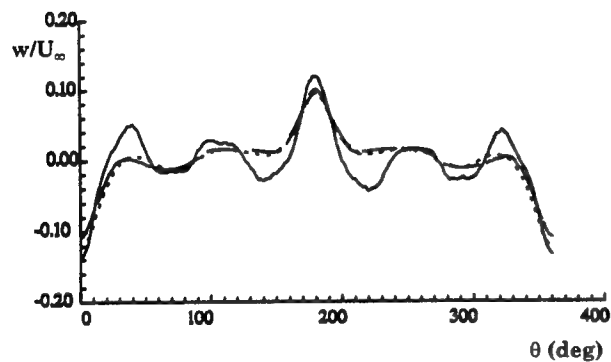
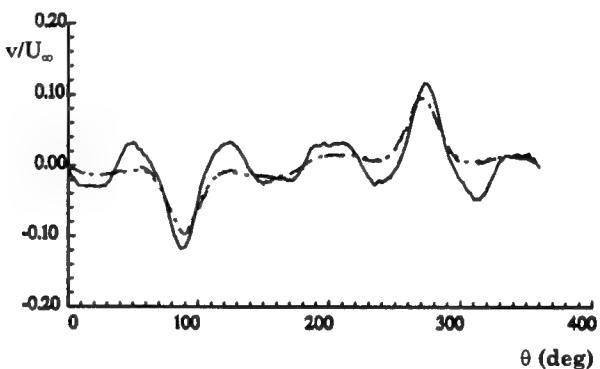
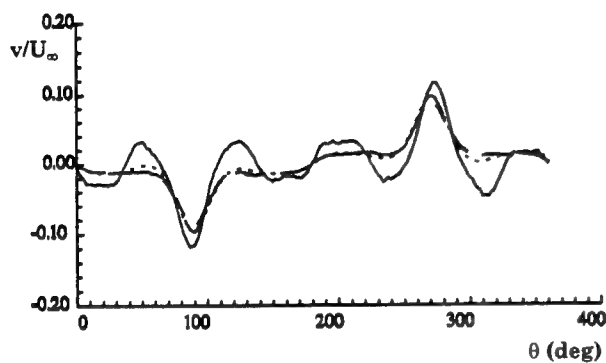
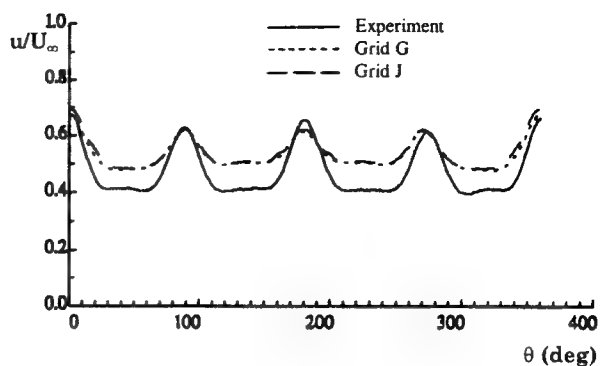
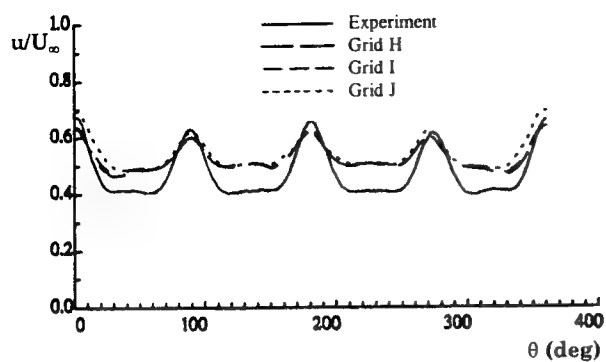


Figure 22
Wake survey comparison between
grids H, I and J

Figure 23
Wake survey comparison between
grids G and J

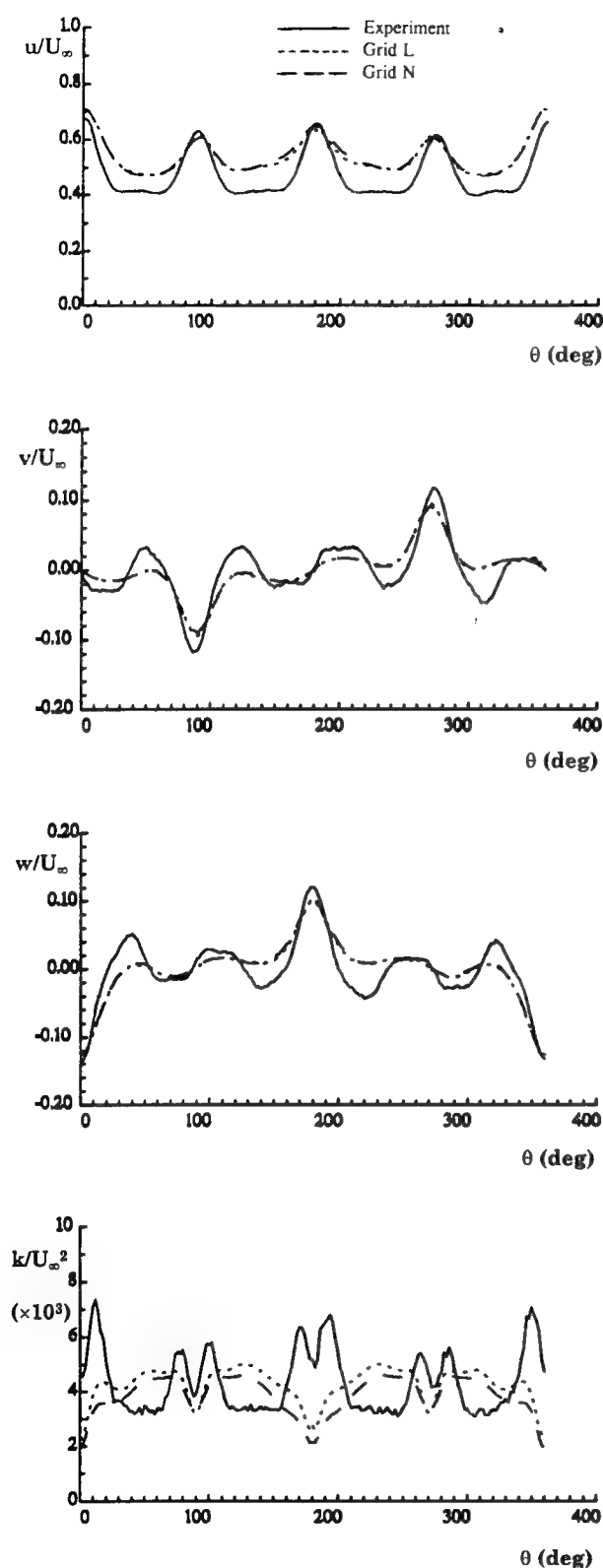


Figure 24
Wake survey comparison between
grids L and N

In addition to the study on grid topology and resolution using FLUENT/UNS, a further study was carried out using CFDS-FLOW3D on variations in the discretisation schemes and turbulence models. Since FLOW3D failed to converge for the C-H topology grids, grid F was used for this study. Six computations were carried out using the $k-\epsilon$, RNG $k-\epsilon$ and the differential Reynolds Stress turbulence models for first order 'hybrid' and third order 'curvature corrected quadratic upwind' discretisation schemes. The third order scheme is guaranteed to preserve the positivity of the turbulence parameters, unlike a standard quadratic upwind scheme.

Taylor wake contours for each of the turbulence models and for each discretisation scheme are given in figures 25 to 27. The 'hybrid' first order discretisation scheme is shown on the left and the 'curvature corrected' third order scheme on the right.

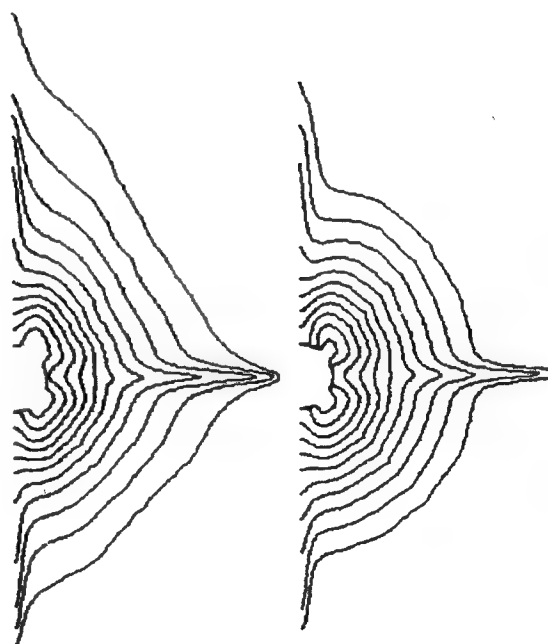


Figure 25
Taylor wake contours for $k-\epsilon$ turbulence model

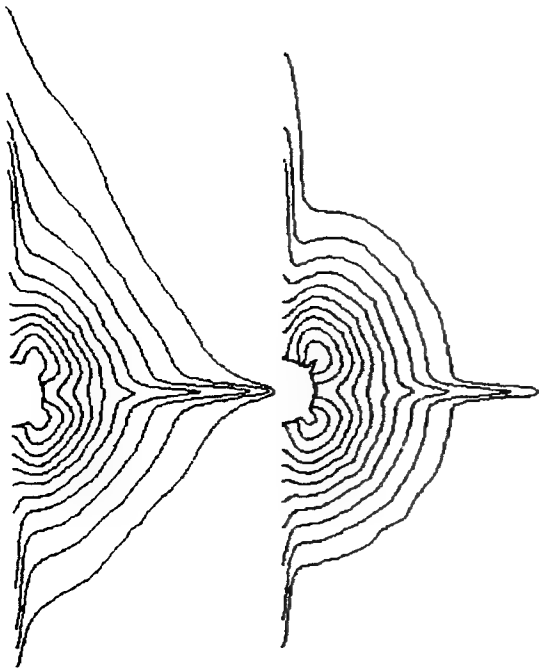


Figure 26
Taylor wake contours for RNG k- ϵ turbulence model

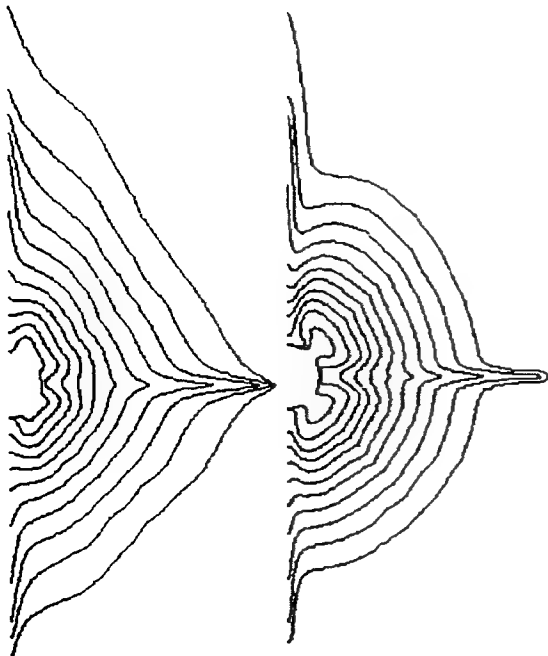


Figure 27
Taylor wake contours for Reynolds Stress model

Figure 28 shows the wake survey data for each of the third order predictions

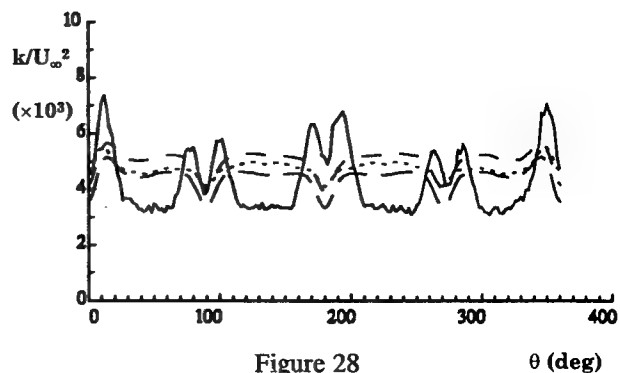
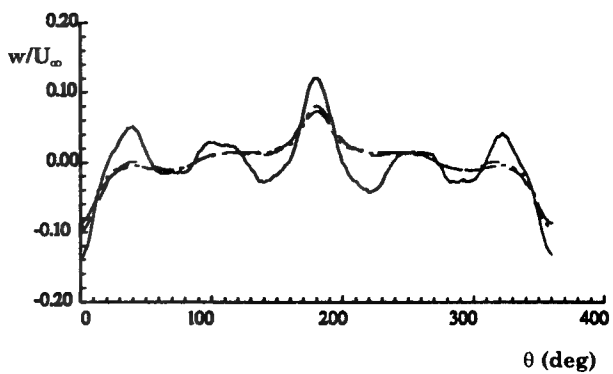
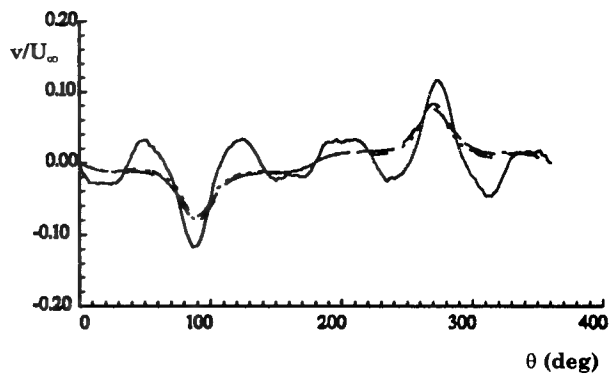
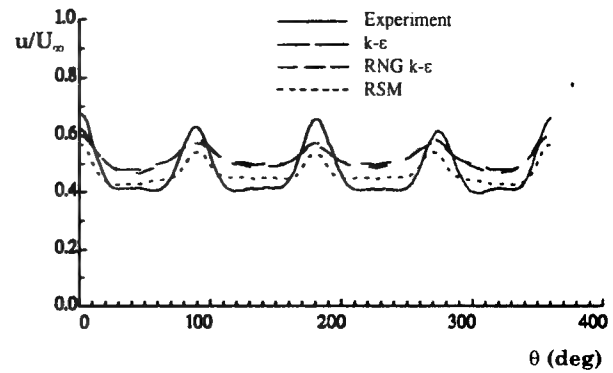


Figure 28
Wake survey data for third order scheme

Finally, it is useful to compare the amplitude coefficients of the harmonics of the wake survey data. These amplitude coefficients provide useful information when designing the propulsion system.

Comparison between the coefficients derived from the measured data and the predictions are given below in table 4.

Table 4
Amplitude coefficient of the wake harmonics (x1000)

| Harmonic Number | 1 | 2 | 3 | 4 | 5 | 6 | 7 | 8 | 9 | 10 | 11 | 12 | 13 | 14 | 15 | 16 |
|-----------------|------|-------|-------|--------|-------|------|------|-------|------|------|------|-------|------|------|------|------|
| Experiment | 4.28 | 12.58 | 6.51 | 102.36 | 10.74 | 5.66 | 8.63 | 50.00 | 9.48 | 4.48 | 2.61 | 10.72 | 2.10 | 0.58 | 0.80 | 1.65 |
| H-H grid | 2.11 | 8.85 | 10.70 | 63.09 | 12.73 | 3.40 | 1.23 | 26.86 | 2.45 | 0.21 | 0.17 | 6.21 | 0.67 | 0.01 | 0.21 | 2.03 |
| C-H grid | 7.17 | 16.00 | 14.27 | 66.18 | 12.32 | 4.18 | 1.73 | 26.63 | 1.56 | 1.10 | 0.10 | 5.61 | 0.16 | 0.12 | 0.32 | 2.64 |
| C-O grid | 6.32 | 30.45 | 16.00 | 71.50 | 12.12 | 2.73 | 1.59 | 26.12 | 1.08 | 1.15 | 0.05 | 5.58 | 0.28 | 0.57 | 0.37 | 1.03 |
| O-O grid | 0.03 | 34.90 | 13.06 | 74.88 | 13.57 | 2.37 | 2.75 | 21.87 | 1.96 | 0.52 | 0.44 | 4.52 | 0.24 | 0.61 | 0.07 | 1.09 |
| k-ε | 0.40 | 2.44 | 7.22 | 39.41 | 7.42 | 5.93 | 2.80 | 14.25 | 1.18 | 1.89 | 0.38 | 4.18 | 0.27 | 0.19 | 0.17 | 0.25 |
| RNG k-ε | 1.31 | 1.32 | 9.13 | 51.65 | 8.38 | 5.51 | 2.79 | 15.41 | 1.52 | 1.49 | 0.67 | 4.87 | 0.49 | 0.32 | 0.25 | 0.12 |
| DSM | 2.50 | 1.38 | 7.61 | 42.60 | 7.01 | 4.84 | 3.60 | 24.87 | 1.52 | 1.66 | 0.50 | 12.06 | 0.08 | 0.07 | 0.04 | 2.28 |

Conclusions

The capability of the CFD approach to the prediction of nominal wake has been quantified by comparison with high quality experiment data. In the region of the propulsor, the predictions are qualitatively correct in that the flow features are captured. The predictions have an overall error of around 5% of the reference velocity in the fluid velocity distribution. This compares with an error of 2.5% associated with the measured data. The predictions also fail to capture adequately the harmonics of the measured velocity distribution.

However, the predictions obtained appear to be independent of grid resolution and topology for a given flow solution algorithm. Changing from the isotropic two-equation turbulence models to the anisotropic Reynold Stress model requires further evaluation.

The author wishes to acknowledge the invaluable help and assistance in the preparation of these predictions and this paper by the Computational Hydrodynamics Team at DRA Haslar.

References

1. Report of the 20th ITTC Resistance and Flow Committee. Proceedings of the 20th ITTC. Volume 1. San Francisco, California, September 1993.
2. Huang TT, Liu H-L, Groves NC, Forlini TJ, Blanton JN and Gowing S. "Measurements of Flows Over an Axisymmetric Body with Various Appendages (DARPA SUBOFF Experiments)."

Proceedings of the 19th Symposium on Naval Hydrodynamics. Seoul, Korea. August 1992.

3. Groves NC, Huang TT, Chang MS. "Geometrical Characteristics of DARPA SUBOFF Hulls (DTRC Models Nos. 5470 and 5471)". DTRC/SHD-1298-01 March 1989. David Taylor Research Center, Bethesda, Maryland 20084-5000
4. Lin CW, Smith GD, Fisher SC. "Numerical Flow Simulations on the DARPA SUBOFF Configurations". DTRC/SHD-1298-09 July 1990. David Taylor Research Center, Bethesda, Maryland 20084-5000
5. Shaw JA, Georgala JM, May NE, Pocock MF. "Application of Three-Dimensional Hybrid Structured /Unstructured Grids to Land, Sea and Air Vehicles". Proceedings of Numerical Grid Generation in Computational Fluid Dynamics and Related Fields. Swansea, UK. 1994, pp 687-695
6. Patis CCP, Bull PW. "The Generation of Viscous Grids for Hydrodynamic Vehicles". Mississippi State University, Starkville, April 1996.
7. "CFDS-FLOW3D Users' Guide". CFDS. Building 8.19, Harwell Laboratory, Oxfordshire, OX11 0RA. United Kingdom
8. "FLUENT/UNS Users' Guide". Fluent Inc., Centerra Resource Park, 10 Cavendish Court, Lebanon. USA. NH 03766
9. "FIDAP 7.5 Users' Guide" FDI Inc., 500 Davis Street, Suite 600, Evanston, USA. Illinois 60201.

Twenty-First Symposium on
NAVAL HYDRODYNAMICS

Appendix—List of Participants

AUSTRALIA

Lawrence J. Doctors
University of New South Wales

AUSTRIA

Gerhard Strasser
Vienna Model Basin

CANADA

Sander M. Calisal
University of British Columbia

Jerry Huang
Technical University of Nova Scotia

David C. Murdey
National Research Council, Canada

CHINA

Ching-Yeh Hsin
National Taiwan Ocean University

Young-Zher Kehr
National Taiwan Ocean University

Yung-Ching Sun
National Taiwan Ocean University

Zao-Jian Zou
Wuhan Transportation University

DENMARK

Poul Andersen
Technical University of Denmark

Harry Bingham
International Research Centre for
Computational Hydrodynamics

Antoine Garapon
International Research Centre for
Computational Hydrodynamics

Per Madsen
International Research Centre for
Computational Hydrodynamics

Stefan Mayer
International Research Centre for
Computational Hydrodynamics

Zhaohui Wang
Technical University of Denmark

Jinzhu Xia
Technical University of Denmark

FINLAND

Tom Sundell
VIT Manufacturing Technology

FRANCE

Bertrand Alessandrini
Ecole Centrale de Nantes

Alain Cariou
Institut de Recherches de la Construction Navale

Xial-Bo Chen
Bureau Veritas, DTO

Stephane Cordier
Bassin D'Essais des Carènes

Jean-Claude Dern
Ministere de la Défense (DCN/STSN)

Franck Desit
French Defense Ministry (DRET)

F.-X. Dumez
Bassin D'Essais des Carènes

Pierre Ferrant
SIREHNA

Bernard Gindroz
Bassin d'Essais des Carènes

Lucie Merle
Bassin d'Essais des Carènes

Michel Visonneau
Ecole Centrale de Nantes

GERMANY

Khaled Ben Nasr
Technical University Hamburg

Xue-Nong Chen
University of Stuttgart

Som D. Sharma
Mercator University

Heinrich Söding
Institut für Schiffbau

GREECE

Apostolos Papanikolaou
National Technical University of Athens

ITALY

Andrea Di Mascio
Istituto Nazionale per Studi ed Esperienze di
Architettura Navale

Maurizio Landrini
Istituto Nazionale per Studi ed Esperienze di
Architettura Navale

Roberto Penna
Istituto Nazionale per Studi ed Esperienze di
Architettura Navale

Maria Vittoria Salvetti
Università di Pisa

Frederica Valdinazzi
Cetena

JAPAN

Jun Ando
Kyushu University

Yasuaki Doi
Hiroshima University

Takao Inui
University of Tokyo

Satoru Ishikawa
Mitsubishi Heavy Industries, Ltd.

Un-Cheul Jeong
Hiroshima University

Hideaki Miyata
University of Tokyo

Makoto Ohkusu
Kyushu University

KOREA

Kyung-Nam Chung
Hyundai Heavy Industries Co., Ltd.

Keun Jae Kim
Daewoo Heavy Industries Ltd.

Young-Gi Kim
Samsung Heavy Industries Co., Ltd.

Chang-Sup Lee
Chungnam National University

Choung Mook Lee
Pohang Institute of Science and Technology

I.-G. Oh
Samsung Heavy Industries Co., Ltd.

THE NETHERLANDS

Leon J.M. Adegeest
Delft University of Technology

Martin Hoekstra
Maritime Research Institute

Rene Huijsmans
Maritime Research Institute

M.W.C. Oosterveld
Maritime Research Institute

Hoyte C. Raven
Maritime Research Institute

Lisette M. Sierevogel
Delft University of Technology

Carlo Van der Stoep
IHC Gusto Engineering

J. Dick van Manen
Whale Tail Development

Tom J.C. van Terwisga
Maritime Research Institute

NORWAY

Jan V. Aarsnes
Marine Technology Centre

Arne Braathen
Det Norske Veritas

Odd Magnus Faltinsen
Norwegian University of Science and
Technology

Dariusz Fathi
Marine Technology Centre

Arne Fredheim
Norwegian University of Science and
Technology

John Grue
University of Oslo

Guttorm Grytoyr
Norwegian University of Science and
Technology

Kjell Herfjord
Norsk Hydro

Ole Andreas Hermundstad
Marine Technology Centre

Jan Roger Hoff
Marine Technology Centre

Kjell Olav Holden
Marine Technology Centre

Morten Huseby
University of Oslo

Jorgen Jorde
Norwegian Naval Material Command

Morten Kjeldsen
Norwegian University of Science and
Technology

Gudmond Kleiven
Norsk Hydro

Geir Loland
Marine Technology Centre

Knut J. Minsaas
Marine Technology Centre

Jens Olav Nygaard
University of Oslo

Ole David Okland
Norwegian University of Science and
Technology

Bjornar Pettersen
Norwegian University of Science and
Technology

Emil Spjotvoll
Norwegian University of Science and
Technology

Carl Trygve Stansberg
Marine Technology Centre

Sverre Steen
Marine Technology Centre

Rune Tonnesen
Norwegian University of Science and
Technology

Karsten Trulsen
University of Bergen

Tore Ulstein
Marine Technology Centre

Torgeir Vada
Det Norske Veritas

Ming-Kang Wu
Marine Technology Centre

Rong Zhao
Marine Technology Centre

POLAND

Jan Szantyr
Institute of Fluid Flow Machinery

PORTUGAL

Luis Eça
Instituto Superior Técnico

SINGAPORE

Eng Kwee Png
Ministry of Defense

Kiang Heng Ti
Defence Science Organization

Qian Xi Wang
Gateway Technology Services

SPAIN

Jose A. Alaez
Pardo Model Basin

SWEDEN

Jacob Ancker
Kockums AB

Per Croner
Kamewa Marine Laboratory

Karl Garne
Royal Institute of Technology (KTH)

Carl-Erik Janson
Chalmers University of Technology

Lars Larsson
Chalmers University of Technology

Per Lindell
SSPA Maritime Consulting AB

Olle Rutgersson
Royal Institute of Technology (KTH)

UNITED KINGDOM

Richard Arkell
Imperial College of Science, Technology and
Medicine

Peter W. Bearman
Imperial College of Science, Technology and
Medicine

Peter William Bull
Defence Research Agency

J. Michael Graham
Imperial College of Science, Technology and
Medicine

Michael Stanier
Defence Research Agency

Stephen James Peter Watson
Defence Research Agency

G.-X. Wu
University College London

UNITED STATES

Robert F. Beck
University of Michigan, College of Engineering

Christopher E. Brennen
California Institute of Technology

Susan Brown
Massachusetts Institute of Technology

Steven L. Ceccio
University of Michigan

David Coakley
David Taylor Model Basin

Geoffrey Cowles
Princeton University

Dana Dabiri
California Institute of Technology

Donald Danmeier
Massachusetts Institute of Technology

Douglas G. Dommermuth
Science Applications International Corp.

Craig E. Dorman
Office of Naval Research, Europe

James H. Duncan
University of Maryland

Allen Engle
Naval Sea Systems Command

Gerard M. Faeth
University of Michigan

Thomas Farstad
Massachusetts Institute of Technology

Jinzhang Feng
Pennsylvania State University

Thomas T. Huang
David Taylor Model Basin

Chen-Wen Jiang
David Taylor Model Basin

Stephen Jordan
Naval Undersea Warfare Center

Joseph Katz
Johns Hopkins University

F. Thomas Korsmeyer
Massachusetts Institute of Technology

David Kring
Massachusetts Institute of Technology

Chang-Ho Lee
Massachusetts Institute of Technology

Yu-Tai Lee
David Taylor Model Basin

Woei-Min Lin
Science Applications International Corp.

Joe Longo
University of Iowa

Michael S. Longuet-Higgins
University of California at San Diego

Peter Majumdar
Office of Naval Research, Europe

Hiren Maniar
Massachusetts Institute of Technology

Luigi Martinelli
Princeton University

Jerome Milgram
Massachusetts Institute of Technology

William B. Morgan
David Taylor Model Basin

David Newman
Brown University

J. Nicholas Newman
Massachusetts Institute of Technology

Francis Noblesse
David Taylor Model Basin

Eric G. Paterson
University of Iowa

Marc Perlin
University of Michigan

L. Patrick Purtell
Office of Naval Research

Edwin P. Rood
Office of Naval Research

Kurt Roth
David Taylor Model Basin

Fred Saalfeld
Office of Naval Research

Nils Salvesen
Science Applications International Corp.

Turgut Sarpkaya
Naval Postgraduate School

William W. Schultz
University of Michigan

Paul D. Slavounos
Massachusetts Institute of Technology

Stephen Scorpio
University of Michigan

Maurice Sevik
David Taylor Model Basin

Yung Sup Shin
American Bureau of Shipping

Roger Simpson
Virginia Polytechnic Institute and State
University

Ana I. Sirviente
University of Iowa

Frederick Stern
University of Iowa

Thomas Swain
Office of Naval Research

Tsze C. Tai
David Taylor Model Basin

Armin W. Troesch
University of Michigan

Marshall P. Tulin
University of California at Santa Barbara

David L. Whitfield
Mississippi State University

Ronald W. Yeung
University of California at Berkeley

Xuemei Zhu
Massachusetts Institute of Technology

PLEASE CHECK THE APPROPRIATE BLOCK BELOW:

-AO # M97-12-6356

☒ 1 copies are being forwarded. Indicate whether Statement A, B, C, D, E, F, or X applies.

☒ DISTRIBUTION STATEMENT A: Per Dixie Gordon
APPROVED FOR PUBLIC RELEASE: DISTRIBUTION IS UNLIMITED

☐ DISTRIBUTION STATEMENT B:
DISTRIBUTION AUTHORIZED TO U.S. GOVERNMENT AGENCIES ONLY; (Indicate Reason and Date). OTHER REQUESTS FOR THIS DOCUMENT SHALL BE REFERRED TO (Indicate Controlling DoD Office).

☐ DISTRIBUTION STATEMENT C:
DISTRIBUTION AUTHORIZED TO U.S. GOVERNMENT AGENCIES AND THEIR CONTRACTORS; (Indicate Reason and Date). OTHER REQUESTS FOR THIS DOCUMENT SHALL BE REFERRED TO (Indicate Controlling DoD Office).

☐ DISTRIBUTION STATEMENT D:
DISTRIBUTION AUTHORIZED TO DoD AND U.S. DoD CONTRACTORS ONLY; (Indicate Reason and Date). OTHER REQUESTS SHALL BE REFERRED TO (Indicate Controlling DoD Office).

☐ DISTRIBUTION STATEMENT E:
DISTRIBUTION AUTHORIZED TO DoD COMPONENTS ONLY; (Indicate Reason and Date). OTHER REQUESTS SHALL BE REFERRED TO (Indicate Controlling DoD Office).

☐ DISTRIBUTION STATEMENT F:
FURTHER DISSEMINATION ONLY AS DIRECTED BY (Indicate Controlling DoD Office and Date) or HIGHER DoD AUTHORITY.

☐ DISTRIBUTION STATEMENT X:
DISTRIBUTION AUTHORIZED TO U.S. GOVERNMENT AGENCIES AND PRIVATE INDIVIDUALS OR ENTERPRISES ELIGIBLE TO OBTAIN EXPORT-CONTROLLED TECHNICAL DATA IN ACCORDANCE WITH DoD DIRECTIVE 5230.25, WITHHOLDING OF UNCLASSIFIED TECHNICAL DATA FROM PUBLIC DISCLOSURE, 6 Nov 1984 (Indicate date of determination). CONTROLLING DoD OFFICE IS (Indicate Controlling DoD Office).

☐ This document was previously forwarded to DTIC on _____ (date) and the AD number is _____.

☐ In accordance with provisions of DoD instructions, the document requested is not supplied because:

☐ It will be published at a later date. (Enter approximate date, if known).

☐ Other. (Give Reason)

DoD Directive 5230.24, "Distribution Statements on Technical Documents," 18 Mar 87, contains seven distribution statements, as described briefly above. Technical Documents must be assigned distribution statements. 21st Symposium

Sgt Mawley for

Dixie Gordon
Authorized Signature/Date

DIXIE GORDON
Print or Type Name

(202) 334-3523
Telephone Number

19970924 050